Jiujun Zhang

Editor

PEM Fuel Cell Electrocatalysts and Catalyst Layers

Fundamentals and Applications

Springer

PEM Fuel Cell Electrocatalysts and Catalyst Layers

Jiujun Zhang
Editor

PEM Fuel Cell Electrocatalysts and Catalyst Layers

Fundamentals and Applications

Jiujun Zhang, PhD
Institute for Fuel Cell Innovation (IFCI)
National Research Council Canada (NRC)
4250 Wesbrook Mall
Vancouver, BC, V6T 1W5
Canada

Preface

In today's world, the demand for clean and sustainable energy sources has become a strong driving force in continuing economic development, and thus as well in the improvement of human living conditions. Proton exchange membrane (PEM) fuel cells, as clean energy-converting devices, have drawn a great deal of attention in recent years due to their high efficiency, high energy density, and low or zero emissions. PEM fuel cells have several important application areas, including transportation, stationary and portable power, and micro-power. From the 1960s to the present, great progress has been made in the research and development of PEM fuel cells, in terms of stack power density increases and cost reduction. Nonetheless, two major technical gaps hindering commercialization have been identified: high cost and low reliability/durability. Fuel cell catalysts, such as platinum (Pt)-based catalysts and their associated catalyst layers, are the major factors in these challenges. Although a great deal of effort has been put into the exploration of cost-effective, active, and stable fuel cell catalysts, we have not yet had any real breakthroughs. Therefore, exploring new catalysts, improving catalyst activity and stability/durability, and reducing catalyst cost are currently the major tasks in fuel cell technology and commercialization.

In a PEM fuel cell, both the anodic hydrogen (or liquid fuel) oxidation reaction (HOR) and the cathodic oxygen reduction reaction (ORR) take place within the respective catalyst layers. Electrocatalysts and their corresponding catalyst layers thus play critical roles in fuel cell performance. In our present state of technology, the most practical catalysts in PEM fuel cells are highly dispersed Pt-based nanoparticles. However, Pt-based catalysts have several drawbacks, such as high cost, sensitivity to contaminants, no tolerance for methanol oxidation (in a direct methanol fuel cell, DMFC, application), fewer completed four-electron reduction reactions, and Pt dissolution. In the search for alternative low-cost non-Pt catalysts, researchers have looked at several others, including supported platinum group metal (PGM) types such as Pd-, Ru-, and Ir-based catalysts, bimetallic alloy catalysts, transition metal macrocycles, and transition metal chalcogenides. However, these approaches are as yet in the research stage, as the catalyst activities and stabilities are still too low to be practical in comparison with Pt-based catalysts. Another approach is to reduce Pt loading in a catalyst or catalyst layer

using alloying and carbon supports. However, due to rapid increases in the cost of platinum, all efforts to reduce Pt loading have thus far been offset by rising prices. Non-noble metal catalysts would therefore appear to be a possible solution for the sustainable commercialization of PEM fuel cells.

Another significant challenge is gaining a fundamental understanding of fuel cell catalyst structures and their corresponding catalytic reaction mechanisms. Current approaches rely largely on trial and error. To design new, breakthrough catalysts, we need a well-defined theoretical approach. Theoretical studies will provide a platform not only for understanding catalyst performance but also for exploring the structure-activity relationship at the electron/molecular level, and ultimately for rationally designing new catalysts.

To accelerate breakthroughs in the research and development of PEM fuel cells and their sustainable commercialization, a comprehensive and in-depth book that focuses on both fundamental and application aspects of PEM fuel cell electrocatalysts and catalyst layers is definitely needed, to build upon the several important books that have previously been published in the area of electrocatalysts.

This book contains comprehensive information on PEM fuel cell eletrocatalysts and catalyst layers, with a particular focus on: (1) the fundamentals of electrochemical catalysis within PEM fuel cells, including both H_2/O_2 (air) and liquid-fuels/O_2 (air) fuel cells; (2) electrocatalyst/catalyst layer synthesis, characterization, and activity validation and modelling; and (3) the integration of electrocatalysts/catalyst layers into fuel cells, and their performance validation, including catalyst layer structure functioning and optimization, catalyst degradation and diagnosis, and strategies to mitigate failure modes.

The contributors to the volume are fuel cell scientists and engineers with excellent academic records as well as strong industrial fuel cell expertise. This book contains the latest research and development in PEM fuel cell catalysis, and indicates important new directions for fuel cell commercialization. Readers will find numerous figures, photographs, and data tables, as well as comprehensive reference materials for each chapter. We hope that this book will be used by industry researchers, by scientists and engineers working in the areas of energy, electrochemistry science/technology, fuel cells, and electrocatalysis, and by post-secondary students. We have endeavoured to make easily accessible the latest information on fuel cell catalysis fundamentals and applications.

Each chapter is relatively independent of the others, a structure which we hope will help readers quickly find topics of interest without necessarily having to read through the whole book. Unavoidably, however, there is some overlap, reflecting the interconnectedness of the research and development in this dynamic field.

I would like to acknowledge with deep appreciation all my colleagues at the Institute for Fuel Cell Innovation, National Research Council of Canada (NRC-IFCI). Financial support for this book's editing and indexing from NRC-IFCI is also gratefully acknowledged. Special thanks go to Dr. Hui Li, Ms. Lei Zhang, Dr. Chaojie Song, Dr. Zheng Shi, Dr. Hansan Liu, Dr. Kunchan Lee, Dr. Jianlu Zhang, Mr. Ryan Baker, Dr. Xiao-Zi Yuan, Dr. Rob Hui, Dr. Dave Ghosh, Ms. Maja Veljkovic, Ms. Eva Sharpe, Dr. David P. Wilkinson, Dr. Simon (Zhong-Sheng) Liu, Dr. Haijiang Wang, Dr. Jun Shen, Dr. Radenka Maric, and Dr. Steve Holdcroft at NRC-IFCI for their strong support, encouragement, and suggestions. I

also wish to thank Dr. Dania Sheldon for her effective editing and indexing services. Finally, my special appreciation goes to my wife, my son, and my daughter for their understanding and support of my work.

If technical errors exist in this book, I and all of the authors would deeply appreciate the readers' constructive comments for correction and further improvement.

Jiujun Zhang
Institute for Fuel Cell Innovation,
National Research Council of Canada
Vancouver, BC, Canada
May 2008

Contents

9 Catalyst Synthesis Techniques 447

Christina Bock, Helga Halvorsen and Barry MacDougall

10 Physical Characterization of Electrocatalysts.. 487

Shijun Liao, Baitao Li and Yingwei Li

1

PEM Fuel Cell Fundamentals

Xiao-Zi Yuan and Haijiang Wang

1.1 Overview

1.1.1 Introduction

A fuel cell is an electrochemical device that continuously and directly converts the chemical energy of externally supplied fuel and oxidant to electrical energy. Fuel cells are customarily classified according to the electrolyte employed. The five most common technologies are polymer electrolyte membrane fuel cells (PEM fuel cells or PEMFCs), alkaline fuel cells (AFCs), phosphoric acid fuel cells (PAFCs), molten carbonate fuel cells (MCFCs) and solid oxide fuel cells (SOFCs). However, the popularity of PEMFCs, a relatively new type of fuel cell, is rapidly outpacing that of the others.

Unlike most other types of fuel cells, PEMFCs use a quasi-solid electrolyte, which is based on a polymer backbone with side-chains possessing acid-based groups. The numerous advantages of this family of electrolytes make the PEM fuel cell particularly attractive for smaller-scale terrestrial applications such as transportation, home-based distributed power, and portable power applications. The distinguishing features of PEMFCs include relatively low-temperature (under 90 °C) operation, high power density, a compact system, and ease in handling liquid fuel.

1.1.1.1 A Brief History of PEM Fuel Cells

Invention of the Fuel Cell—1839
The idea of the gaseous fuel cell can be traced back to Sir William Grove, a Welsh judge, inventor, and physicist, who is recognized as "the father of the fuel cell." A reproduction of his drawing of a fuel cell, from 1838, can be seen in Figure 1.1. In 1839 Grove found that electrolysis (using electricity to split water into hydrogen and oxygen) could be performed in reverse with the right catalyst, producing electricity. In 1842, Grove developed a stack of 50 fuel cells, which he called a "gaseous voltaic battery". However, for almost a century after Grove's discovery

the fuel cell did not make any practical progress, remaining only a scientific curiosity.
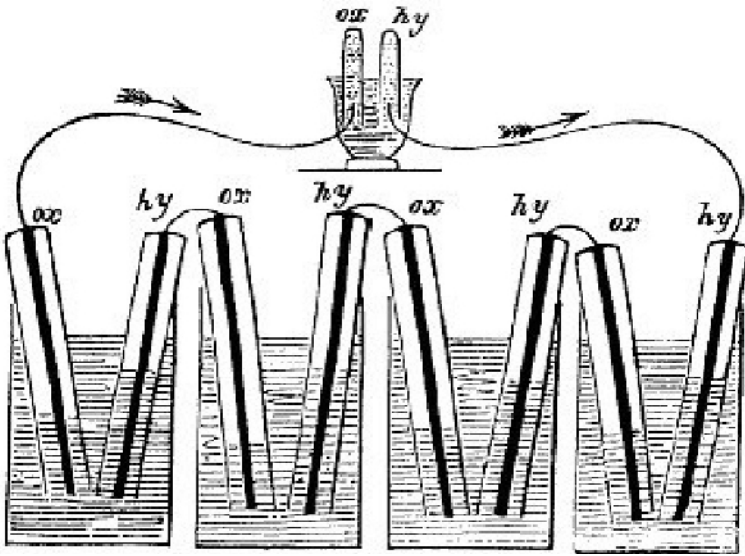
Figure 1.1. The first fuel cell. (Originally printed in Grove, W. R. (1838). On a new voltaic combination. Philosophical Magazine and Journal of Science 13, 430.)

In 1937, Francis T. Bacon, an Englishman, started to work on practical fuel cells. By the end of the 1950s [1] he had developed a 40-cell stack capable of 5 kW. The stack was able to power a welding machine, circular saw, and forklift.

PEM Fuel Cell Development—1960s
The PEM fuel cell was invented at General Electric (GE) in the early 1960s, through the work of Thomas Grubb and Leonard Niedrach. Initially, sulfonated polystyrene membranes were used as the solid electrolytes, but these were soon replaced by Nafion® membranes in 1966. The Nafion membrane has proved to be superior in performance and durability, and it is still the most popular membrane in use today.

Gemini Space Program—1950–1970
PEM fuel cell technology served as part of NASA's Gemini Program (Figure 1.2), the main objective of which was to test equipment and procedures for Apollo. GE's PEM fuel cells were selected, but the earliest model PB2 cell repeatedly encountered technical difficulties, including internal cell contamination and leakage of oxygen through the membrane. Gemini I through IV flew with batteries instead. Due to PB2's malfunctions and poor performance, a new model, P3, was designed. The first mission to utilize PEMFCs was Gemini V. However, they were replaced by alkaline fuel cells in the Apollo program and in the space shuttle. This delayed the development of PEM fuel cells for a decade [2, 3].
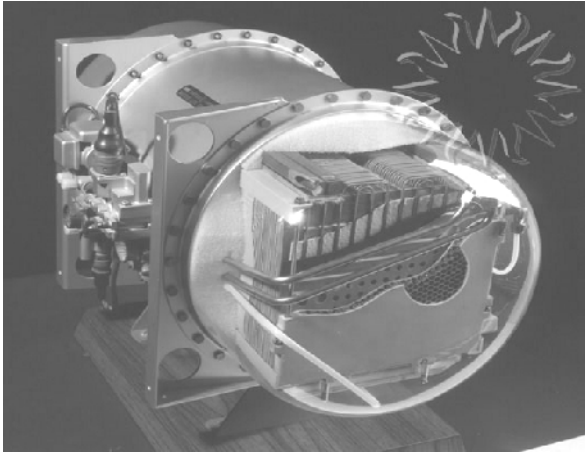
Figure 1.2. Gemini space mission used fuel cells. (Image courtesy of NASA.)

Ballard Breakthrough—1980–2000
Due to their high cost, fuel cell systems were limited to space missions and other special applications. It was not until the late 1980s and early 1990s, when research by Ballard Power Systems (founded in 1979) resulted in a resurgence in interest in PEMFCs and the development of fuel cells, that fuel cells became a real option for wider applications. In 1983, Ballard began developing PEM fuel cells. Proof-of-concept fuel cells followed, and sub-scale and full-scale prototype systems (Figure 1.3) were developed to demonstrate the technology. Their milestones in the 1990s are as follows:

Mk900 (2000)	Mk800 (1997)	Mk700 (1995)	Mk500 (1993)	Mk300 (1991)
80 kW	50 kW	25 kW	10 kW	5 kW

| (a) | (b) | (c) |
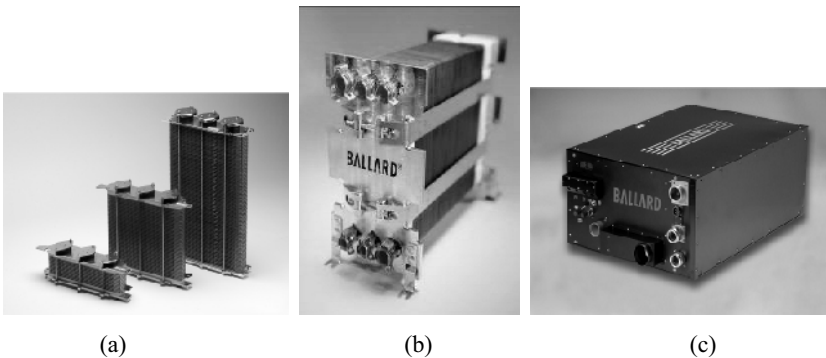
Figure 1.3. Fuel cells produced by Ballard Power Systems. (a) Mark1020 ACS™, (b) Mark1030™ V3, (c) Heavy-Duty Fuel Cell Module (HD6). (Images courtesy of Ballard Power Systems.)

Figure 1.4. A map of the Hydrogen Highway in British Columbia, Canada. (Image courtesy of BC Hydrogen Highway™.)

PEM Fuel Cells Today

Since interest in PEM fuel cell research and development has intensified, more and more universities and institutes all over the world are becoming involved. So far several key innovations, such as low platinum catalyst loading, novel membranes, and new bipolar plates, make the application of PEMFC systems more or less realistic. Demonstration activities in every corner of the world are overwhelming. Figure 1.4 shows an example of a hydrogen and fuel cell demonstration project, the Hydrogen Highway in British Columbia, Canada. British Columbia's Hydrogen Highway is actually both a demonstration program and a market development program; it features an evolving network of hydrogen and fuel cell technologies, including vehicle fuelling infrastructure. The project leaders and participants come from British Columbia's hydrogen and fuel cell industries, government, industry associations, and academic institutions. Fully implemented in time for the 2010 Olympic and Paralympic Winter Games, the program will operate a fleet of 20 buses in Victoria and Whistler.

After the Canadian government announced funding for the world's first hydrogen highway, California's Governor Schwarzenegger committed to the building of a California Hydrogen Highway Network on a similar timescale, by signing an executive order creating a public/private partnership.

1.1.1.2 Principles of PEM Fuel Cells

The conversion of chemical energy to electrical energy in a PEM fuel cell occurs through a direct electrochemical reaction. It takes place silently without combustion. The key part of a PEM fuel cell, which is known as a membrane electrode assembly (MEA), consists of a polymer electrolyte in contact with an anode and a cathode on either side. To function, the membrane must conduct hydrogen ions (protons) and separate either gas to pass to the other side of the cell. A schematic representation of a PEM fuel cell is shown in Figure 1.5.
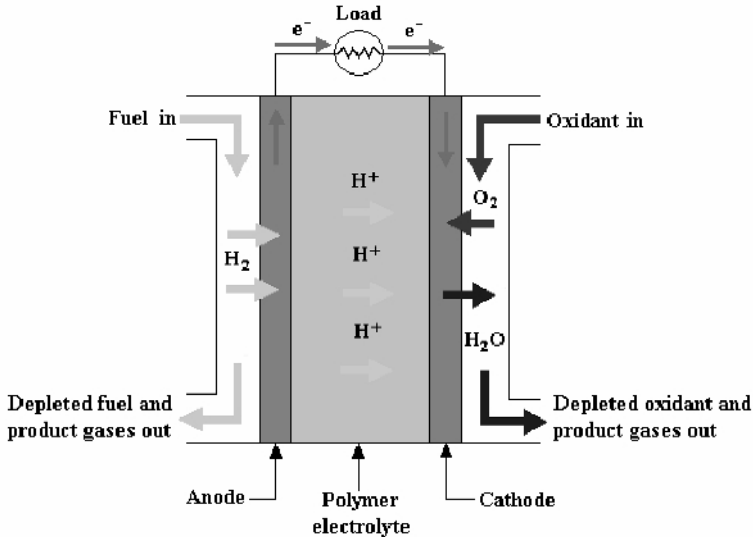
Figure 1.5. Diagram of PEM fuel cell principle

Unlike in a conventional battery, the fuel and oxidant are supplied to the device from external sources. The device can thus be operated until the fuel (or oxidant) supply is exhausted. As seen in Figure 1.5, on one side of the cell, hydrogen is delivered through the flow field channel of the anode plate to the anode. On the other side of the cell, oxygen from the air is delivered through the channeled plate to the cathode. At the anode, hydrogen is decomposed into positively charged protons and negatively charged electrons. Positively charged protons pass through the polymer electrolyte membrane (PEM) to the cathode, whereas the negatively charged electrons travel along an external circuit to the cathode, creating an electrical current. At the cathode, the electrons recombine with the protons, and together with the oxygen molecules, form pure water as the only reaction by-product, which flows out of the cell.

The splitting of the hydrogen molecule is relatively easy using a platinum catalyst. However, the splitting of the stronger oxygen molecule is more difficult, which causes significant activation loss. So far platinum is still the best option for the oxygen reduction reaction (ORR). Another significant source of performance loss is the resistance of the membrane to proton flow, which is minimized by making it as thin as possible (around 50 μm). Nevertheless, the PEM fuel cell is a

system whose successful operation with a high power output depends on all the sub-systems; its performance depends on components such as flow field design, catalyst, and membrane, and also on parameters such as temperature and humidity.

1.1.1.3 Single Cell, Stack, and System

Single Cell
A single PEM fuel cell includes only one anode and one cathode; therefore, the operating voltage of a single cell is less than 1 V. When it is operated under a given current, the voltage is even less. An acceptable performance for a state-of-the-art single cell is at least 1 A/cm^2 at a voltage of 0.6 V. Here are two examples of single cell designs.

An in-house fabricated single cell designed by the National Research Council of Canada Institute for Fuel Cell Innovation (NRC-IFCI) is shown in Figure 1.6. The single cell components include the bladder plate, piston, plastic plate, anode current collector, anode plate, gaskets, cathode plate, cathode current collector, and another plastic plate and bladder plate. The graphite plate/current collector are isolated from the aluminum end plate by a plastic plate, which also serves as a gas manifold. Gaskets are used to seal the MEA. A variable pressure bladder, controlled with nitrogen gas, is used to compress and seal the cell assembly. Cell heating is accomplished by two pairs of heat tape pieces. The inner 60 W heat tape, which is glued onto the copper current collector plates, allows the cell to operate at temperatures up to 120 °C.
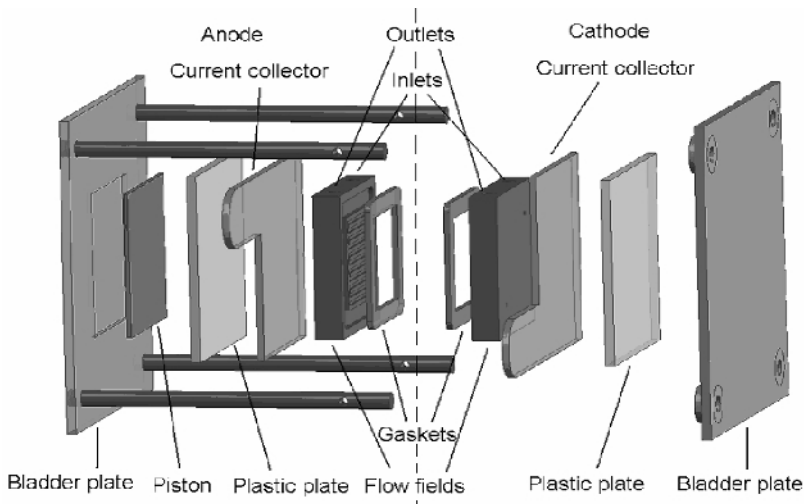
Figure 1.6. A single PEM fuel cell with an active area of 4.4 cm^2 designed by NRC-IFCI. (Reproduced by permission of ECS—The Electrochemical Society, from Tang Y, Zhang J, Song C, Liu H, Zhang J, Wang H, et al. Temperature-dependent performance and *in situ* AC impedance of high-temperature PEM fuel cells using the Nafion-112 membrane.)

Figure 1.7 shows the assembly diagram of a diagnostic modeling PEM fuel cell also designed by NRC-IFCI. The active area of this single cell is 192 cm^2. A

straight channel configuration is chosen for the cathode plate to simplify the modeling process, ease the integration of sensors, and result in a relatively small pressure drop. Two-path serpentine channels are used for the anode plate, with the coolant channels in the back covering the entire active area. Two additional plates are used in the assembly of the single cell. One is the end plate, which seals the coolant channels on the anode plate. It is a blank plate, void of any distribution channels or seal grooves, marked only by holes for the reactant gases, coolant, and alignment pin. The other is the coolant plate, which cools the cathode plate and consists of a hole for the alignment pin, a seal groove, and coolant channels. At one end of the distribution plates, the manifold has ports for the hose fittings to connect to the distribution channels in the various plates. The relatively soft insulating material is able to electrically isolate the fuel cell. Between the plates and the insulators are the current collectors, which have a high electrical conductivity. The main components of the compression hardware are the alignment plate, tie rods, tie rod screws, bushings, and compression plate and bladder. The compression plate and bladder provide the compression force. It is a pneumatic system allowing accurate control of the compressive force, which ensures proper sealing and guarantees that the MEA is in contact with the reacting gases. A picture of the assembled diagnostic single cell is shown in Figure 1.8.
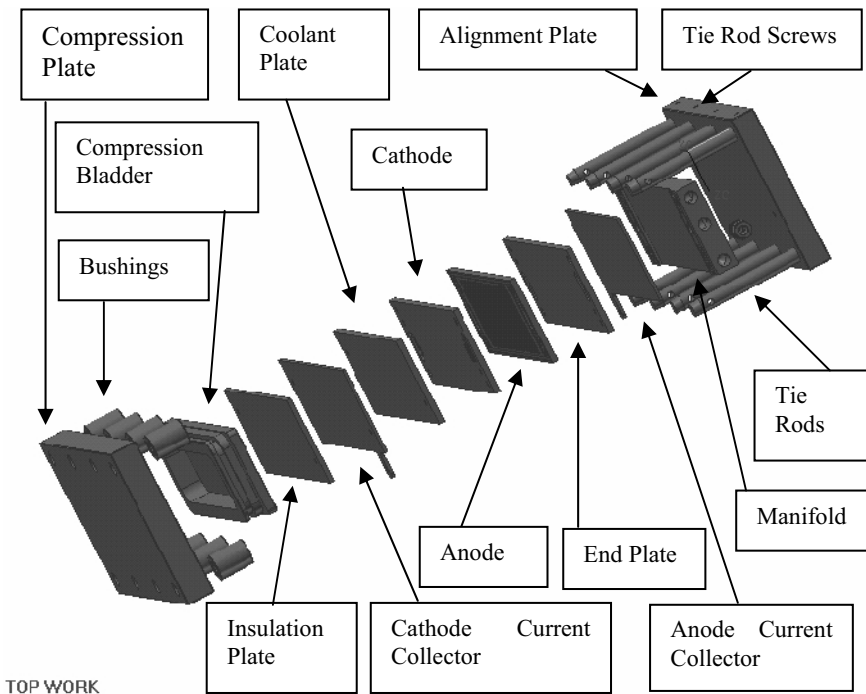
Figure 1.7. Assembly diagram of a diagnostic modeling PEM fuel cell with an active area of 192 cm^2, designed by NRC-IFCI [6]

Figure 1.8. Assembled diagnostic modeling cell [6]

Stack

Single cells produce less than 1 V of electricity, which is far from enough to power a vehicle. In order to produce a useful voltage, multiple cells must be assembled into a fuel cell stack. This can be achieved in a parallel and/or a series mode to supply feed gas to the stacks. In a parallel gas supply fuel cell stack, all cells are fed in parallel from a common hydrogen/air inlet. In the serial configuration the gas from the outlet of the first cell is fed to the inlet of the second cell and so on until the last cell, which helps prevent non-uniform gas distribution. To avoid a large pressure drop this arrangement can be used only for stacks with a small number of fuel cells [7].

A discussion of the distribution of the reactant gases must address the flow field design. The essential requirement for flow field design is uniform distribution of the reactant gases over the respective active electrode surface. A non-uniform distribution will result in a non-uniform current density distribution leading to lower catalyst utilization, lower energy efficiency, and, last but not least, a reduced cell life. Usually, flow fields are designed around their maximum power operating point with the goals of maximizing performance and minimizing pressure drop between the inlet and outlet of the flow field. Nevertheless, when designing a flow field, several considerations must be taken into account, including flow rate, water management, thermal management, and pressure drop.

For a typical planar PEMFC design, feeding channels are often designed with one of three basic flow field structures: serpentine, parallel, or interdigitated [8]. Due to the length of the channels, serpentine flow fields have large pressure losses between the inlet and the outlet. The straight parallel design exhibits lower pressure differences; however, inhomogeneous reactant gas distribution can easily

occur. The interdigitated flow field, which consists of dead-ended inlet and outlet channels, forces the reactant gas to flow through the electrode in order to exit, and helps solving the cathode-flooding problem.

In most commercial fuel cell stacks, the separator plates are designed to be bipolar, with one side of the plate being the anode of one cell and the other side being the cathode of the adjacent cell. The series electrical connection between cells is made through the electrically conducting separator plate. The potential power generated by a series-connected fuel cell stack depends on the number and size of the individual fuel cells that comprise the stack and the surface area of the PEM.

A typical PEM fuel cell stack is shown in Figure 1.9. Individual cells are electrically connected with interconnects. The interconnect becomes a separator plate, which provides an electrical series connection between adjacent cells and a gas barrier that separates the fuel and oxidant of adjacent cells.
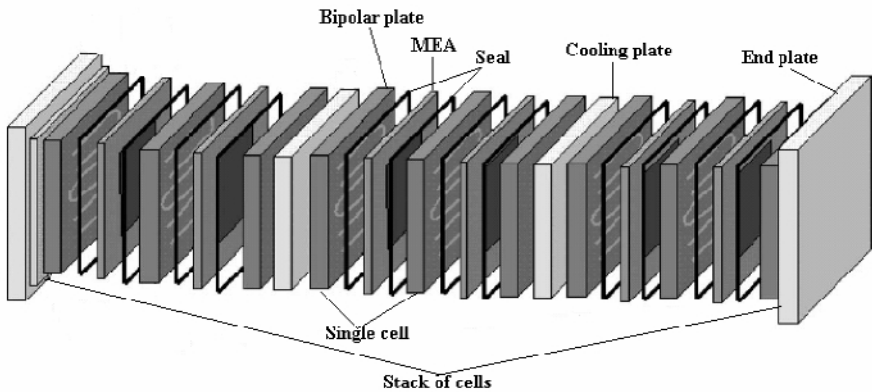
Figure 1.9. PEM fuel cell stack. (Reprinted and modified from [9]. Journal of Power Sources, 114(1), Mehta Viral and Cooper Joyce Smith, Review and analysis of PEM fuel cell design and manufacturing, 70–79, ©2003, with permission from Elsevier.)

System
In addition to the stack, practical fuel cells such as those in fuel cell vehicles (FCVs) require several other sub-systems and components to work as a system. Generally speaking, most fuel cell systems contain the following:

- Hydrogen reformer or hydrogen purification: When a fuel other than hydrogen are used, it must be reformed to form a hydrogen-rich anode feed mixture. Even if hydrogen gas is used, it can contain impurities, which can cause deactivation of the catalysts. The impurities are removed through a process of purification.
- Air supply: This includes air compressors or blowers as well as air filters.
- Water management: Inlet gases normally must be humidified, and water is a reaction product.
- Thermal management: All fuel cell systems require careful management of the fuel cell stack temperature [10].

The specific arrangement of the fuel cell systems varies, depending on the fuel cell type, the fuel choice, and the application. An example of a fuel cell system with direct hydrogen gas feeding is depicted in Figure 1.10(a).

Methanol and some other liquid fuels can be fed to a PEM fuel cell directly without being reformed, thus forming a direct methanol fuel cell (DMFC), direct ethanol fuel cell (DEFC), direct formic acid fuel cell (DFAFC), and so on.
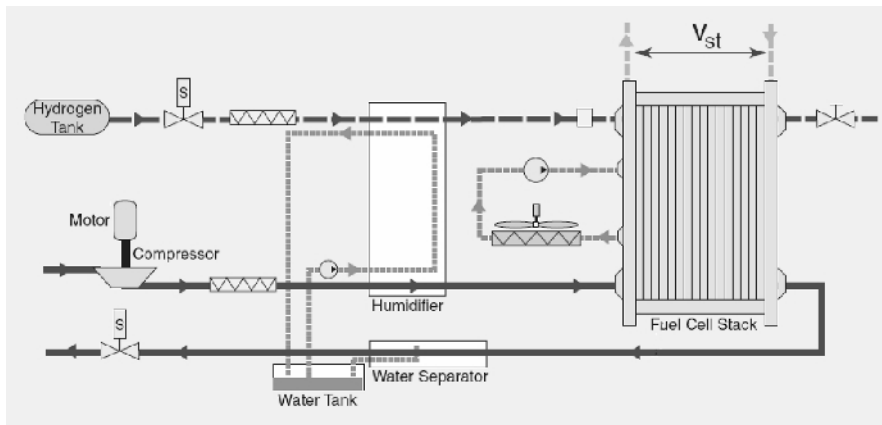
Figure 1.10(a). Block diagram of a PEM fuel cell system [11]. (Pukrushpan JT, Stefanopoulou AG, Peng H. IEEE Control Systems Magazine, Control of fuel cell breathing. ©2004 IEEE. Reprinted with permission.)
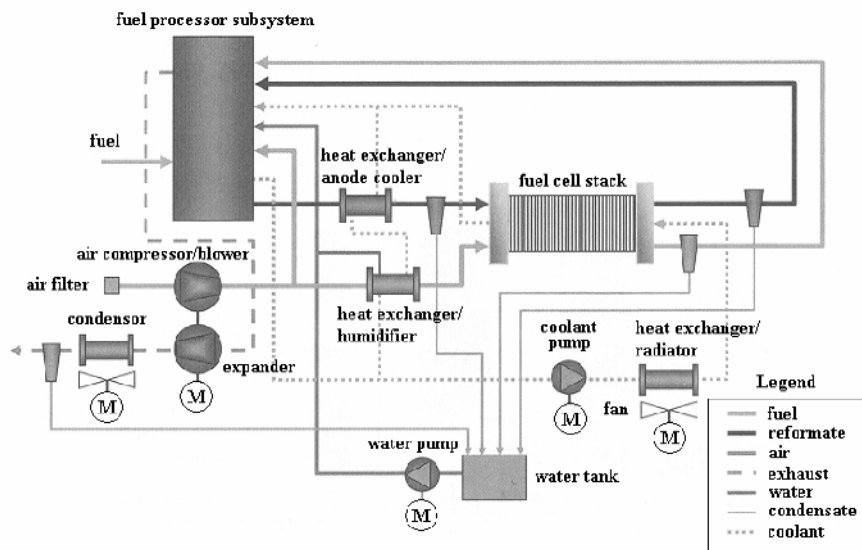
Figure 1.10(b). A complete fuel cell system integrated with a fuel processor [1]. (Reprinted from Barbir F. PEM fuel cells: theory and practice. New York: Elsevier Academic Press, ©2005, with permission from Elsevier.)

Typical systems utilize on-board reformation, processing the gasoline, methanol, or other carbon-based fuel into hydrogen-rich gas. A complete fuel cell system integrated with a fuel processor is shown in Figure 1.10(b). The system contains the four sub-systems explained above. Currently, complete systems such as this are available in the market. The most well-known manufacturers of PEM systems include Ballard Power Systems, UTC Power (also known as UTC Fuel Cells), PEMEAS USA, E-TEK Inc., DuPont, 3M, Johnson Matthey, WL Gore, Hydrogenics, and Plug Power [3].

1.1.2. Main Cell Components and Materials

1.1.2.1 Membrane

The main function of the membrane in PEM fuel cells is to transport protons from the anode to the cathode; membrane polymers have sulfonic groups, which facilitate the transport of protons. The other functions include keeping the fuel and oxidant separated, which prevents mixing of the two gases and withstanding harsh conditions, including active catalysts, high temperatures or temperature fluctuations, strong oxidants, and reactive radicals. Thus, the ideal polymer must have excellent proton conductivity, chemical and thermal stability, strength, flexibility, low gas permeability, low water drag, low cost, and good availability [12].

Different types of membranes have been tested for use in PEM fuel cells. The membranes are usually polymers modified to include ions, such as sulfonic groups. These hydrophilic ionic moieties are the key for allowing proton transport across the membrane. The favored polymer structure has changed to improve membrane lifetime and slow down membrane degradation [13].

The very early membranes, fabricated by Grubb and Niedrach of GE, were phenol-formaldehyde sulfonic acids produced by the condensation of phenolsulfonic acid and formaldehyde. Unfortunately, they hydrolyzed easily and were extremely weak. These were followed by membranes with a partially sulfonated polystyrene backbone. Their performance was also unsatisfactory, achieving a lifetime of only 200 hours at 60 °C. The first membranes to have sufficient physical strength were "D" membranes, manufactured by American Machine Foundry. They were fabricated by grafting styrene-divinylbenzene into a fluorocarbon matrix, followed by sulfonation. "D" membranes achieved life spans of 500 hours at 60 °C and were utilized in the fuel cells as auxiliary power sources for seven Gemini space missions [14].

Degradation of the "D" membranes was linked to the reactivity of the alpha C-H bond in the polymer. A series of membranes that did not contain this bond were then synthesized. $\alpha,\beta,\beta-$trifluorostyrene sulfonic acid was determined to have chemical and thermal stability, but poor physical properties (Figure 1.11(a) [15]). This was somewhat improved by using a triethyl phosphate plasticizer to combine polyvinylidine fluoride with the trifluorostyrene sulfonic acid polymer, reaching a lifetime of up to 5000 hours at 80 °C. This lifetime was doubled by a fluorocarbon matrix grafted with trifluorostyrene, and then further improved by a membrane composed of trifluorostyrene and substituted trifluorostyrene copolymers [16, 17]. The latter membrane (Figure 1.11(b)), developed by Ballard Power Systems,

achieved a performance time of more than 15,000 hours (for the BAM3G series) [14, 18].

(a)   (b)

(c)   (d)

(e)

(f)

Figure 1.11. Types of PEMs: (a) Monomer units of α,β,β-trifluorostyrene sulfonic acid (b) BAM3G (c) Nafion (d) Dow membrane (e) polysulfone (f) polyetherketone [24]. (Reprinted from International Journal of Hydrogen Energy, 31, Colliera A, Wang H, Yuan XZ, Zhang J, Wilkinson DP. Degradation of polymer electrolyte membranes, 1838–54, ©2006 with permission from Elsevier.)

One of the most widely used membranes today is Nafion, a polymer created by the DuPont company. Nafion (Figure 1.11(c) [13]) has an aliphatic perfluorinated backbone with ether-linked side chains ending in sulfonate cation exchange sites [14, 19]. It is a copolymer of tetrafluoroethylene and sulfonyl fluoride vinyl ether [20] and has a semi-crystalline structure [21]. This structure, which resembles Teflon, gives Nafion long-term stability in oxidative or reductive conditions [12]. In the dry state it has reverse micelle morphology, in which the ionic clusters are

dispersed in a continuous tetrafluoroethylene phase. When the membrane absorbs water, the ionic domains swell and form proton-conducting channels above a critical water content. The conductivity increases with the water content up to a point. As the water content increases further, the concentration of protons is diminished and the conductivity is decreased. Nafion 120 was reported to reach 60,000 hours of operation (43 °C–82 °C) [14].

The Dow Chemical Company manufactured a similar membrane (Figure 1.12(d) [13]) with shorter side chains, which was shown to attain a power density more than double that of Nafion. However Nafion remains the most popular membrane due to lower cost and ease of fabrication [22]. Nafion is still quite expensive, and the industry is striving to find a more affordable substitute to allow commercialization.

Several other types of polymers, such as polyetherketones, polyimide, and polyethersulfone (Figures 1.11(e) and 1.11(f)) are also being studied [18, 23].

Generally, it is the lifetime of the PEM that determines the life of the PEMFC. Thinner membranes, although they increase performance efficiency and proton conductivity, have lower physical strength and higher gas permeability, allowing more gas crossover, which accelerates degradation. According to H_2/air PEMFC testing, Nafion 112 has reached a maximum lifetime of just over 10,000 hours [14]. The technology for solid polymeric electrolytic membranes calls for the thinnest film that is electrochemically stable. At present, polymeric solid state fuel cell membranes, thinner than 50 microns, seldom work mechanically during fuel cell operation. When approaching the thin film limits, interfacial effects become significant to structure dynamics and consequently, the stability of the membranes [25].

1.1.2.2 Electrodes

Platinum has been considered to be the best catalyst for both the anode and the cathode though there is a large difference between the ORR and the hydrogen oxidation reaction (HOR) using the same catalyst. A great deal of effort has been made by many researchers toward developing appropriate catalyst materials, especially for the ORR, and platinum is so far still the best option. Therefore, in many PEMFCs, the anode and the cathodes use an identical catalyst: platinum.

Usually, the platinum catalyst is formed into small particles on a surface of somewhat larger particles that act as a supporter, known as carbon powder. A widely used carbon-based powder is Vulcan XC72® (by Cobalt). This way the platinum is highly divided and spread out, so that a very high proportion of the surface area will be in contact with the reactant, resulting in a great reduction of the catalyst loading with an increase in power. In the early days of PEM fuel cell development, the catalyst was used at the rate of 28 mg/cm^2 of platinum. In recent years the usage has been reduced to around 0.2 mg/cm^2 with an increase in power. The basic raw-material cost of the platinum in a 1 kW PEMFC at such loadings would be about $10—a small portion of the total cost [26].

Basically, there are two methods to form the MEA of a PEM fuel cell. One alternative is using appropriate techniques to add the carbon-supported catalyst to a porous and conductive material, such as carbon cloth or carbon paper, called a gas diffusion layer (GDL). Normally, polytetrafluoroethylene (PTFE) and Nafion

solution are added. PTFE, which is hydrophobic, can expel the product water to the surface where it can evaporate. Nafion can help attach the catalyst layer to the membrane, and it also helps increase the ionic conductivity of the catalyst layer. Then the catalyst-surfaced GDL is hot-pressed together with the pre-treated membrane, which has catalyst on each side. This fairly standard procedure for fabricating an MEA is described in many papers. For example, Lee et al. [27], cleaned the electrolyte membrane by immersing it first in boiling 3% hydrogen peroxide in water for 1 hour, and then in boiling sulfuric acid for the same amount of time, to ensure as full protonation of the sulfonate group as possible. The membrane was rinsed in boiling deionised water for 1 hour to remove any remaining acid. The electrodes were then put onto the electrolyte membrane and the assembly was hot pressed at 140 °C at high pressure for 3 minutes to complete the process.
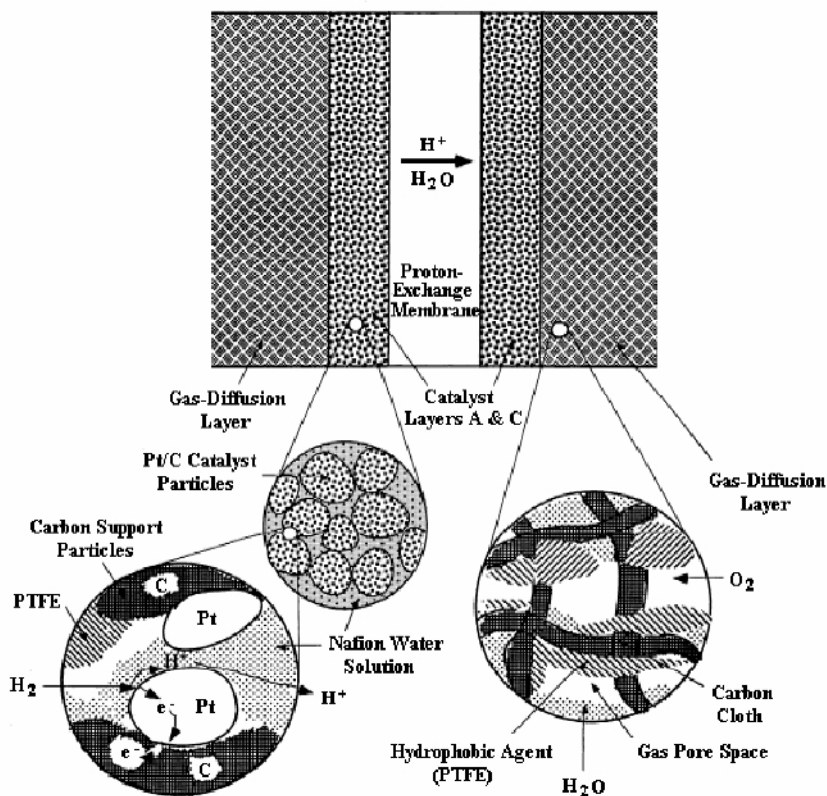
Figure 1.12. Diagram of a typical MEA structure [31]. (Reprinted from Catalysis Today, 67(1–3), Thampan Tony, Malhotra Sanjiv, Zhang Jingxin and Datta Ravindra, PEM fuel cell as a membrane reactor, 15–32, ©2001, with permission from Elsevier.)

Another method is to build the electrode directly onto the membrane. In this method, the catalyst mixed with hydrophobic PTFE is directly manufactured onto

the membrane using various techniques such as rolling methods [28], spraying [29], or an adapted printing process [30]. However, the literature seldom gives details about the method used. Once the catalyst is fixed to the membrane, a GDL is then applied when assembling the cell.

The MEAs manufactured by both of the above methods have similar sandwich-like structures. As depicted in Figure 1.12, the outer layers of the sandwich are GDLs. The membrane is in the middle, with catalysts between the GDL and membrane. The anode, the negative side of the fuel cell, conducts the electrons freed from the hydrogen oxidation so that they can be used in an external circuit. The cathode, the positive side of the fuel cell, conducts the electrons back from the external circuit to the catalyst, where they can recombine with the hydrogen ions and oxygen to form water. The PEM—a specially treated material—conducts only positively charged ions and blocks the electrons, which is crucial to PEM fuel cell technology.

The thickness of the membrane in an MEA varies with the type of membrane. The thickness of the catalyst layer depends upon how much platinum is used in each electrode. For catalyst layers containing about 0.15 mg Pt/cm^2, the thickness of the catalyst layer is close to 10 μm. The thickness of an MEA depends on the thickness of the membrane, catalysts, and GDL. The MEA, with a total thickness of about 200 μm, can generate more than 0.5 A/cm^2 at a voltage of 0.7 V when encased in well-chosen key materials—membrane, backing layers, bipolar plates, catalysts, and other components, such as flow fields, and current collectors [32].

1.1.2.3 Gas Diffusion Layer

GDLs are critical components in PEMFCs. The GDLs (or the backing layers), together with the flow fields and current collectors, are designed to achieve high performance from the operation of the PEM fuel cell. But the GDLs may or may not be an integral part of the MEA [26].

The main function of the GDL is to diffuse the gas. The porous nature of the backing material facilitates the effective diffusion of each reactant gas to the catalyst on the MEA. The GDL is also an electrical connection between the carbon-supported catalyst and the bipolar plate or other current collectors. In addition, the GDL also helps in managing water in the fuel cell as it carries the product water away from the electrolyte surface [32].

The GDL is usually made of a carbon-based porous substrate, such as carbon paper or carbon cloth, with a thickness of about 0.2 to 0.5 mm and a dual-layer structure. A schematic of the GDL between the flow field and the catalyst layer is presented in Figure 1.13. The first layer of the GDL, in contact with the flow field and the inlet gas in the flow channels, is a macro-porous carbon substrate, serving as a current collector, a physical support for the catalyst layer, and an elastic component of the MEA. The elastic component is necessary for the fuel cell to handle the compression needed to establish an intimate contact. The second layer of the GDL, in contact with the catalyst layer, is a thinner microporous layer consisting of carbon black powder and some hydrophobic agent, which provides proper surface pore size and hydrophobicity to avoid flooding and to enhance intimate electronic contact at its interface with the catalyst layer [33].
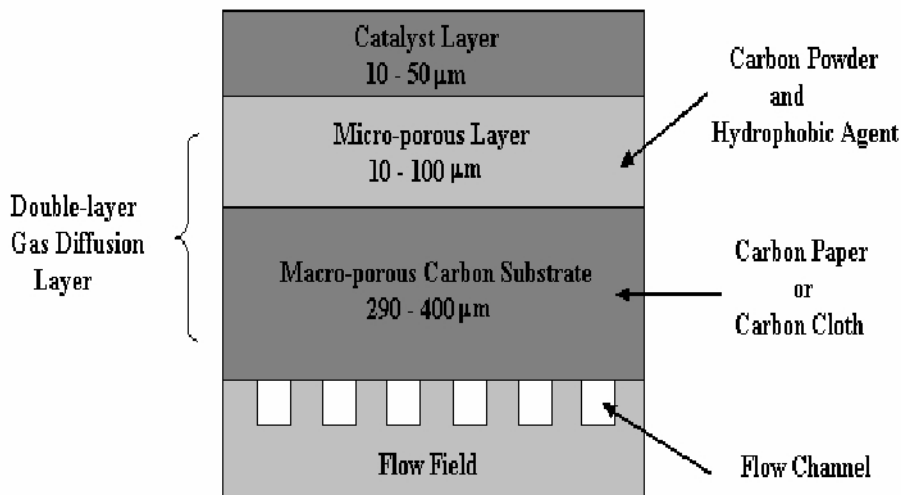
Figure 1.13. Schematic of a double-layer GDL [33]. (Reproduced by permission of ECS—The Electrochemical Society, from Williams MV, Begg E, Bonville L, Kunz HR, Fenton JM. Characterization of gas diffusion layers for PEMFC.)

An ideal GDL is required to effectively transport the gas reactants to the catalyst layers, have low electronic resistance, have a surface that enhances good electronic contact, and have proper hydrophobicity for each application. In particular, for the highest power output when the fuel cell is operated at a relatively high current density, a higher flux of gas feed is needed, which requires the ideal GDL to effectively transport reactant gases to the catalyst surfaces at a high rate [33].

1.1.2.4 Bipolar Plates
Among the components of the fuel cell stack, the bipolar plate is considered to be one of the most costly and problematic. In addition to meeting cost constraints, bipolar plates must possess a host of other properties. The search for suitable, low-cost bipolar plate materials is a key concern in PEMFC stack development [34].

The bipolar plate is a multi-functional component. Its primary function is to supply reactant gases to the gas diffusion electrodes (GDEs) via flow channels. The effectiveness of the reactant transport depends partially on the art of the flow-field design [35], so an alternative name for the bipolar plate is the flow-field plate. Bipolar plates must provide electrical connections between the individual cells. They have to remove the water produced at the cathode effectively [36]. Bipolar plates must also be relatively impermeable to gases, sufficiently strong to withstand stack assembly, and easily mass-produced. For transport applications, low weight and low volume are essential [37]. As bipolar plates operate in constant contact with the acidic water (pH $\approx$ 5) that is generated under the operating conditions of the stack, high chemical stability and corrosion resistance are required. Not only can oxides formed during corrosion migrate and poison the catalyst but they can also increase the electrical resistivity of the plates, and

therefore result in reduced fuel cell performance. In addition, the bipolar plate material must be able to resist a temperature of 80°C or more, high humidity, and an electrical potential [38]. To summarize, the PEMFC bipolar plate technical design criteria or major constraints are as follows:

1. Low cost (< $2/plate)
2. Ease of gas flow
3. High electric conductivity (> 100 Scm^{-1})
4. Low impermeability to gases
5. High manufacturability
6. Reasonable strength
7. Low weight
8. Low volume
9. High chemical stability and corrosion resistance (< 16 μAcm^{-2})
10. Low thermal resistance

Potential bipolar plate materials should meet all of these requirements and, in the long run, should be inexpensive and readily available for the purpose of mass production [39].

Generally speaking, graphite is an excellent material for fuel cell bipolar plates, but both the material cost and the processing cost are very high for large-scale production. Although graphite plates are not considered to be the most effective material for PEM fuel cell applications, they are preferred for space applications due to their superior corrosion resistance without coating when compared to metal plates. Now more attention is being paid to composites and metals. It has been concluded that the most promising for fuel cell commercialization are the graphite polymer composites and metallic materials with coatings. Carbon polymer composites and sheet metal are potentially low-cost materials and are especially suitable for mass production because flow fields can be molded directly into carbon polymer composites, and thin sheet metal can be stamped to plates in an established mass production process. Nevertheless, there is still a great deal of work needed to obtain satisfactory bipolar plate materials. Not only should an optimal bipolar plate meet the property requirements above, but its fabrication process should also be easy fabrication and inexpensive. The art of the flow-field design of bipolar plates is another important feature for the performance of the fuel cells. The fate of potential materials will ultimately determined by all these factors [34].

1.1.3 PEM Fuel Cell Operation

1.1.3.1 Operation Conditions
The principle of how a PEM fuel cell generates electricity is straightforward. However, the cell power output depends on material properties, cell design and structure, and operation conditions, such as the gas flow, pressure regulation, heat, and water management. High performance of a PEM fuel cell requires maintaining optimal temperature, membrane hydration, and partial pressure of the reactants

across the membrane to avoid any degradation of performance. These critical operation parameters must be controlled over a wide range of current [11].

Operating Pressure

A PEM fuel cell can be operated at ambient pressure or at a higher pressure. A fuel cell usually obtains better performance when the pressure is increased. But note that to increase the operating pressure, extra compression power is needed. From the system point of view, the net gain of pressurized operation is questionable when compression power is taken into account. In addition, the issue of pressurization is related to the issue of water management [1].

Very often, the reactant gas is fed from a pressurized tank to the fuel cell at the inlet. The pressure, known as the backpressure, is controlled by a pressure regulator installed at the outlet. This backpressure regulator keeps the desired pressure at the fuel cell outlet, while the inlet pressure is sometimes not even recorded. However, the inlet pressure, which is always higher than the outlet pressure as there is a pressure drop between the inlet and outlet along the flow channels, is sometimes the pressure that matters. For example, there are two types of air supply systems for the cathode inlet [1].

Air blowing: In an air-blowing system, air is supplied to the cathode by a mechanical device, a compressor or a blower. The compressor or the blower must be able to deliver the air at the required flow rate and desired pressure. The backpressure regulator may still be installed to control the backpressure either at ambient pressure or at a higher pressure.

Air breathing: Conventional air-blowing PEM fuel cell systems are limited for portable applications because they need power-consuming auxiliary devices, such as pumps, valves, fans, and humidifiers. Thus, air-breathing PEM fuel cells have been developed to overcome these limitations. In an air-breathing system, air is supplied to the cathode by diffusion and natural convection from the surroundings without humidification, so that the entire system is simplified. Nevertheless, there are obstacles for the air-breathing system despite the advantages of its system design. For example, the cell performance of an air-breathing cell is not as good as that of an air-blowing cell due to the poor transportation of air to the cathode, and there is no convective flow for the cathode to help manage the water balance in the system, which is crucial to the PEM fuel cell system [40].

Operating Temperature

The cell temperature is another operating parameter that plays an important role in the cell operation. Generally speaking, a higher operating temperature results in higher cell potential or performance. However, for each fuel cell design there is an optimal operating temperature. Better performance will be obtained when the cell is operated at the optimal temperature, but a PEM fuel cell does not have to be heated up to this temperature in order to become operational 1. From the system point of view, the operating temperature of a practical fuel cell should be selected, as with the operating pressure, by taking into account not only the cell performance, but also the system requirements, such as the parasitic power requirements of the heat management sub-system.

The fuel cell reaction is exothermal; therefore it generates heat as a by-product. To maintain the desired temperature, heat must be removed from the system. Some heat dissipates from the outer surface of the fuel cell and the rest must be taken away with a cooling system. The cooling medium may be air, water, or a special coolant. The inner design of the fuel cell must allow the coolant to pass through, for example, a coolant plate or coolant channel on the back of the anode or cathode plate. Small fuel cells need a heater to reach the operating temperature because so much heat is being taken away from the outer surface [1]. The heat balance within a fuel cell can be written as

$$Q_{gen} + Q_{react,in} = Q_{dis} + Q_{react,out} + Q_{cool} \tag{1.1}$$

where Q_{gen}, $Q_{react,in}$, Q_{dis}, $Q_{react,out}$, and Q_{cool} refer to the heat generated in the fuel cell, the heat brought into the cell with reactant gases, the heat dissipation from the cell surface to the surroundings, the heat taken away by the reactant gases leaving the cell, and the heat carried away by the coolant, respectively.

In addition, the temperature inside a fuel cell may not be uniform. It may vary from the inlet to the outlet, from the inside to the outside, or from the cathode to the anode. Very often the measured fuel cell temperature could be the surface temperature, the temperature of the air leaving the cell, or the temperature of the coolant leaving the cell.

Reactant Flow Rate
The reactant flow rate at the inlet of a fuel cell must be equal to or higher than the consuming rate of the reactant in the cell. A reactant-starved condition is detrimental to the fuel cell performance, since starvation can lead to cell reversal, which is often recognized by a negative cell potential. In this case, a hydrogen-starved anode is forced to oxidize water to generate oxygen and an oxygen-starved cathode is forced to reduce protons to hydrogen. Then, the presence of oxygen in the hydrogen electrode and hydrogen in the oxygen electrode can result in local hot spots on the membrane, leading to membrane degradation and failure of the fuel cell [7]. The solution is to ensure adequate gas flow to all the cells by using high stoichiometric gas flow rates (λ_{air} and λ_{H_2}) and proper flow-field designs to prevent one cell or a group of cells from receiving most of the gas flow while other cells become reactant starved during operation.

The usage of the cathode and anode reactants can be calculated based on Faraday's law. For each mole of oxygen, four electrons are transferred; therefore,

$$O_2 \text{ usage} = \frac{I}{4F} \, mol/s \tag{1.2}$$

$$\text{Air usage} = \frac{I}{4F} \times \frac{1}{0.21} \, mol/s \tag{1.3}$$

For each mole of hydrogen, two electrons are transferred,

$$H_2 \text{ usage} = \frac{I}{2F} \, mol \, / \, s \tag{1.4}$$

For a stack with n cells, the reactant usages become

$$\text{Air usage} = \frac{I}{4F} \times \frac{n}{0.21} \, mol \, / \, s \tag{1.5}$$

$$H_2 \text{ usage} = \frac{In}{2F} \, mol \, / \, s \tag{1.6}$$

Adding the cathode and anode excess gas ratio, λ_{air} and λ_{H_2}, the two equations can be written as

$$\text{Air usage} = \frac{I}{4F} \times \frac{n}{0.21} \times \lambda_{Air} \, mol \, / \, s \tag{1.7}$$

$$H_2 \text{ usage} = \frac{In}{2F} \times \lambda_{H_2} \, mol \, / \, s \tag{1.8}$$

As most fuel cell test stations are controlled by regulating the flow rate at standard liter per minute (slpm), the above two equations are then transferred with a unit of slpm by using the ideal gas law. The results are as follows:

$$\text{Air usage} \approx 0.0166 n I \lambda_{air} \, \text{slpm} \tag{1.9}$$

$$H_2 \text{ usage} \approx 0.0070 n I \lambda_{H_2} \, \text{slpm} \tag{1.10}$$

Reactant consumption using other units is listed in Table 1.1.

Table 1.1. Reactant consumption (under the condition of per Ampere, per cell, 25 °C, and ambient atmosphere)

Unit	Oxygen consumption	Air consumption	Hydrogen consumption	Water generation
$mol \, s^{-1}$	2.59×10^{-6}	1.23×10^{-5}	5.18×10^{-6}	5.18×10^{-6}
$g \, s^{-1}$	8.29×10^{-5}	3.94×10^{-4}	1.04×10^{-5}	9.33×10^{-5}
$cm^3 s^{-1}$	0.063	0.302	0.126	9.33×10^{-5}
slpm	0.0038	0.0181	0.0076	N/A
$sm^3 h^{-1}$	2.28×10^{-4}	1.08×10^{-3}	4.56×10^{-4}	N/A

Reactant Humidity

Water balance and management are an important concern in PEM fuel cell system control. Dynamic water balance and management have become one of the major technical challenges for PEM fuel cell design and operation because they have a direct influence on the performance and lifetime of PEM fuel cell systems.

Generally speaking, reactant gases with inlet relative humidity (RH) equal to or less than 100% are needed during the cell operation. The supply of reactant humidity is necessary and important because the membrane (e.g., Nafion) requires full hydration in order to maintain good performance and lifetime. It is widely recognized that membrane hydration can be achieved by supplying fully humidified reactant gas streams to both the anode and the cathode.

The conductivity of the membrane in a PEMFC is directly related to its water content, which depends on (1) the water carried by the humidified reactant gases; (2) the water generated at the cathode as a result of electrochemical reaction; (3) the electroosmotic drag—that is, the water carried by the protons from the anode to the cathode; and (4) the water back diffusion from the cathode to the anode. Therefore, it is obvious that water management is a complex issue.

Water management is very delicate for fuel cell users to control. Too much or too little water can degrade both the performance and therefore the lifetime of PEM fuel cells. If the membrane is too dry, it results in a direct decrease of membrane conductivity. If water is not removed adequately from the cell, especially at the cathode, liquid water flooding occurs, which leads to PEM fuel cell performance that is unpredictable, unreliable, and unrepeatable under identical operating conditions. Therefore, maintaining a perfect water balance during dynamic operation processes is crucial to fuel cell performance and lifetime [41].

It should be pointed out that in addition to the reactant humidity control, the flow channel layout, channel dimensions, and specifications of other cell components also influence water removal and the performance of the cell, which indicates that proper design of the flow fields and other components may help achieve better water balance and management in PEM fuel cells.

1.1.3.2 Failure Modes and Accelerated Testing [42]

Fuel cell commercialization has been delayed again and again due to technical barriers such as on-board storage, infrastructure for the hydrogen fuel and the fuel cell system and its durability. Durability, which is always defined as the maximum lifetime of a fuel cell system with no more than 10% loss in efficiency at the end of life, is one of the most stringent requirements for PEM fuel cells to be accepted as a viable product. The requirements for fuel cell lifetime vary significantly for different products. The fuel cell industry has set standards including: a lifetime durability of more than 40,000 hours and 8,000 hours of uninterrupted service at over 80% power for stationary applications. For buses and cars, more than 20,000 and 6,000 operating hours are required, respectively [43, 44].

Various studies have focused on the degradation mechanisms of either the fuel cell system or its components under steady or accelerated operational conditions. The major failure modes of different components of PEM fuel cells are listed in Table 1.2.

Table 1.2. Major failure modes of different components in PEM fuel cells

Component	Failure modes	Causes
Membrane	Mechanical degradation	Mechanical stress due to non-uniform press pressure; inadequate humidification or penetration of the catalyst particles; fluoride loss
	Thermal degradation	Thermal stress; drying of membrane
	Chemical/electrochemical degradation	Trace metal contamination (foreign cations, such as Ca^{2+}, Fe^{3+}, Cu^{2+}, Na^+, K^+, and Mg^{2+}); radical attack (e.g., peroxy and hydroperoxy)
Catalyst/Catalyst layer	Loss of activation;	Sintering or dealloying of electrocatalyst;
	Conductivity loss;	Corrosion of electrocatalyst support;
	Decrease in mass transport rate of reactants;	Mechanical stress;
	Loss of reformate tolerance;	Contamination;
	Decrease in control of water management	Change in hydrophobicity of materials due to Nafion or PTFE dissolution
GDL	Decrease in mass transport;	Degradation of backing material;
	Conductivity loss;	Mechanical stress (e.g., freeze/thaw cycle);
	Decrease in control of water management	Corrosion; Change in hydrophobicity of materials
Bipolar plates	Conductivity loss;	Corrosion; Oxidation;
	Fracture/deformation	Mechanical stress
Sealing gasket	Mechanical failure	Corrosion; mechanical stress

Traditional lifetime data analysis in engineering involves analyzing times-to-failure data obtained under normal operating conditions in order to quantify the life characteristics of the product, system, or component. For fuel cells, the times-to-failure data are always very difficult to obtain due to the prolonged test periods necessary and high costs. To reduce the experimental time, different strategies to accelerate PEM fuel cell and component degradation have been suggested. Generally accelerated test methods for PEM fuel cell lifetime analysis are summarized in Table 1.3.

Table 1.3. General accelerated test methods in PEM fuel cell lifetime analysis

Component	Methods
Fuel cell/stack	Open circuit voltage (OCV); dynamic load cycling; thermal cycling; reduced/variable humidity; fuel or oxidant contaminates; fuel or oxidant starvation
Membrane	OCV at reduced humidity for chemical stability; RH cycling for mechanical degradation
Catalyst/catalyst layer	Potential cycles; acid washing; elevated temperature; fuel or oxidant contaminates
GDL	Chemical oxidation in H_2O_2; elevated potential; low humidity
Bipolar plates	Press-stress; acid treatment; potential cycling; temperature cycling
Sealing gasket	Temperature; acid treatment; deformation/press-stress

As a commercial product, the failure or reliability information of the fuel cell under typical operation conditions should be included. Basically, the durability of the fuel cell is not defined by a single lifetime test. Lifetimes at variable stresses are always statistical distributions. The detailed scheme of a typical statistical accelerated lifetime model is illustrated in Figure 1.14 [45, 46].

The process starts by collecting data from quantitative accelerated life tests followed by selecting an appropriate life distribution. Three different lifetime distributions, the 1-parameter exponential, the 2-parameter Weibull, and the lognormal distributions, are commonly used in accelerated life test analysis. Among them, the 1-parameter exponential is most commonly employed due to its simplicity. Then, the lifetime characteristic of the distribution at each stress level is estimated using the probability plotting method; this is followed by the selection of a life-stress relationship according to variables. The Arrhenius model is often utilized when the acceleration variable or stress is thermal, whereas the Eyring model and the inverse power law model are suitable for temperature-humidity stresses and non-thermal accelerated stresses, respectively. Finally, the real lifetime of the component or fuel cell under normal conditions can be predicted by extrapolation.
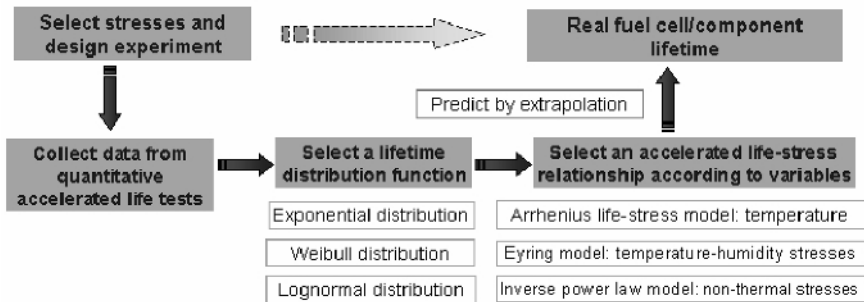
Figure 1.14. Principle of statistical accelerated lifetime testing model [42]

Based on the statistical model, Hicks [47] successfully predicted 3M MEA lifetimes under normal conditions (70 °C cell and 100% RH) from accelerated testing conditions. Weibull data distribution and the Arrhenius temperature model were employed. The statistical analysis and MEA lifetime prediction shown in Figure 1.15(a) were obtained. The load cycle with a near-open circuit voltage (OCV) setting was used in the accelerated tests, as shown in Figure 1.15(b).
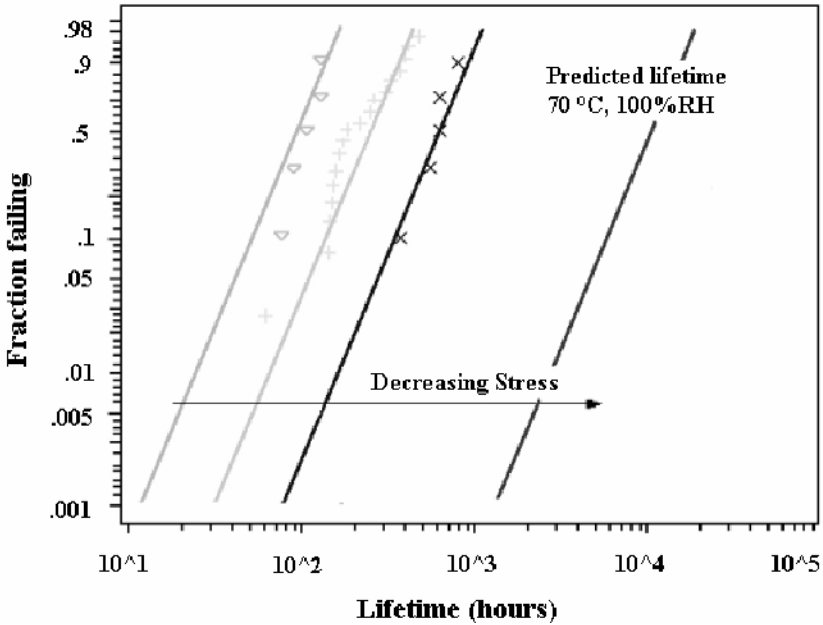
Figure 1.15(a). Statistical analysis of accelerated test data with MEA lifetime prediction done by 3M (Symbols—data points; lines—model fits) [47]. (Reprinted with permission from Hicks M. Membrane and catalyst durability under accelerated testing. In: Conference proceedings of fuel cell durability: stationary, automotive, portable. ©2005 Knowledge Press.)
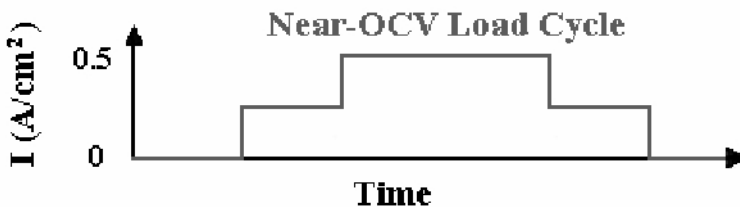
Figure 1.15(b). Near-OCV load cycle profile used in 3M accelerated testing [47]. (Reprinted with permission from Hicks M. Membrane and catalyst durability under accelerated testing. In: Conference proceedings of fuel cell durability: stationary, automotive, portable. ©2005 Knowledge Press.)

1.1.4 PEM Fuel Cell Applications

Since PEM fuel cells can generate power from a fraction of a watt to hundreds of kilowatts, they can be used in almost any application, from stationary power to vehicles of all sizes down to mobile phones. The application areas of PEM fuel cells with a variety of power levels are listed in Table 1.4.

Table 1.4. Application areas of PEM fuel cells with a variety of power level

Level of power	Applications
> 1 MW	Local distributed power station
100 kW–1 MW	Large transportation vehicles, such as naval ships, submarines, and buses; small portable power station; small stationary power station
10 kW–100 kW	Transportation vehicles such as cars and mid-size buses; backup power for mid-size communication station; small power station
1 kW–10 kW	Transportation vehicles such as motorcycles, utility vehicles, cars, yachts; various portable power devices used for field working, underwater platform; backup power; uninterruptible power, residential power system
100 W–1 kW	Simple riding devices such as bicycles, scooters, and wheelchairs; backpack power; power for exhibition or demo; UPS for small services, terminals, and computers
10 W–100 W	Portable power such as for emergency working power supply and military equipment; battery replacements; lighting; signal light power
< 10 W	Small portable power device; cell phone

Aside from military and space flight use, the less specialized fuel cell applications can be categorized into four main groups: transportation, stationary power, backup power, and portable power. PEM fuel cells are ideal for all these applications due to the availability of various power levels. Applications for transportation, such as automobiles, buses, utility vehicles, scooters, and bicycles have already been widely demonstrated. Applications for stationary power can be at the level of an individual home, a building, or a community, offering tremendous flexibility in power supply. Also, fuel cells are attractive as backup power generators compared with internal combustion engine generators (due to noise, fuel, reliability, and maintenance considerations) or batteries (due to weight, lifetime, and maintenance considerations). And small fuel cells as portable power generators offer several advantages over conventional batteries [1].

1.1.4.1 Transportation
The development of PEM fuel cell technology and the demonstration of its application to transportation vehicles have grown rapidly in the last 15 years. In 1993, Ballard demonstrated the first PEM fuel cell-powered bus. Then, following the announcement of the first fuel cell stack with a power density of 1 kW/l, a

Ballard phase 2 bus powered by a 200 kW unit was demonstrated. Later, demonstrations and testing of buses and cars powered by PEM fuel cells were like a rising wind and scudding clouds. Car producers have played an important role in these demonstrations. As air quality regulations grow steadily stricter, car manufacturers like Ford and Volkswagen are spending billions annually on the development of PEM fuel cell stacks for hybrid and electric cars [48].

Aside from buses and cars, there are many other types of transportation vehicles being demonstrated. Some transportation applications are shown in Figure 1.16.
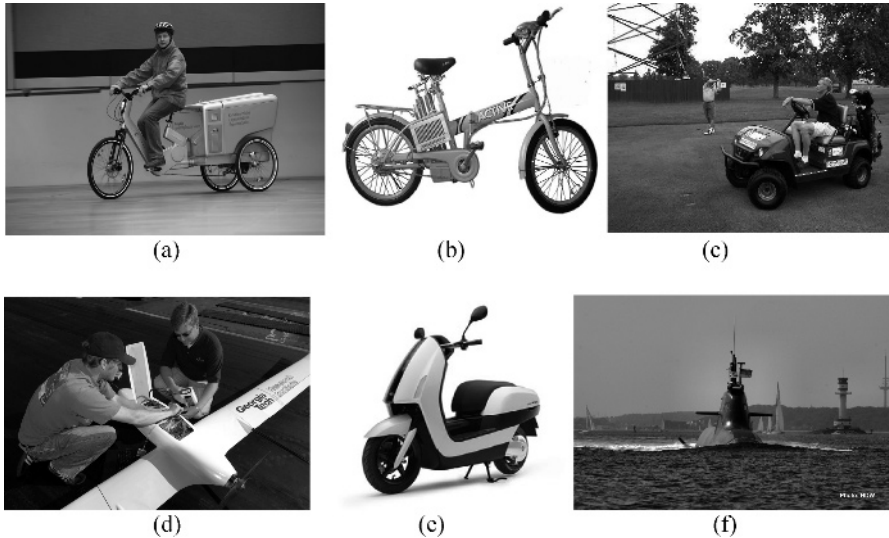
Figure 1.16. Some transportation applications of PEM fuel cells: (a) three-wheeled cargobike (image courtesy of Masterflex); (b) fuel cell bicycle (image courtesy of Pearl Hydrogen); (c) golf cart (image courtesy of Ohio State University); (d) PEMFC hydrogen aircraft (image courtesy of Georgia Institute of Technology); (e) Yamaha FC-AQEL scooter (image courtesy of Yamaha); (f) U212 submarine (image courtesy Howaldtswerke-Deutsche Werft GmbH).

An FCV can be powered directly using pure hydrogen as a fuel. Gaseous hydrogen is generally stored in high-pressure tanks so that it provides enough fuel to power the vehicle with a suitable driving range. Some hydrogen FCVs are powered by one electric motor. Others use a separate electric motor for each wheel, which together produce enough power to propel FCVs at speeds comparable to those of conventional vehicles.

Some FCVs employ a battery to store electricity produced from the fuel cell stack. The stored electricity can be used to help power the electric motor or other electrical devices. Some FCVs are designed to use a liquid fuel such as gasoline or methanol, which is stored in a conventional, non-pressurized tank. FCVs using these fuels need a reformer—a fuel processor that breaks the fuel down into hydrogen for the fuel cell, carbon dioxide, and water. Although this process

generates carbon dioxide, it produces much less than the amount generated by gasoline-powered vehicles [49].

1.1.4.2 Stationary Power

With the development of PEM fuel cell systems for transportation applications, the performance targets and cost objectives set by the car manufacturers define an attractive and competitive fuel cell system for stationary applications. Since the mid-1980s, PEM development has included stationary power applications, such as the GPU and Ballard 250 kW plant at Crane Naval Air Station in Indiana (1991); a 5 kW PEM unit powering a home in Albany, New York; and 6 PEM Alpha units tested by Bonneville Power Administration (2000).

Stationary power generation applications include not only large-scale utility plants but also smaller scale systems, such as those for distributed electricity and for heat generation in buildings and individual homes. The PEM fuel cell units for mobile applications in the range of 2 to 10 kW can be adapted to smaller stationary systems, which had been considered impractical with units in this capacity range. Battelle Memorial Institutes (USA) is identifying the most likely markets and the economic impacts of the stationary PEM fuel cells in the range of 1 to 250 kW in the United States by the year 2015. One likely scenario is that in 2015 PEM fuel cells will be limited to commercial and industrial customers in the range of 50 to 200kW with a market size of less than US$ 5 billion a year [50].

Figure 1.17 presents some examples of stationary power generators; Figure 1.17(a) shows small-scale systems and Figures 1.17(b) to 1.17(e) show large-scale utility plants.

<table>
<tr><td>(i)</td><td>(ii)</td></tr>
</table>
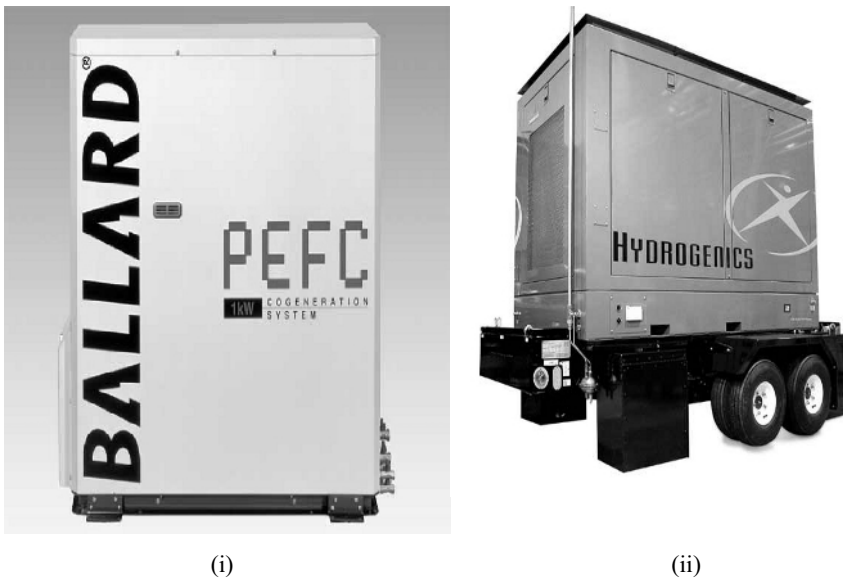
Figure 1.17(a). Small stationary fuel cells: (i) Ballard 1 kW PEM, (ii) Hydrogenics mobile 25 kW fuelcell. (Images courtesy of Ballard Power Systems (i) and Hydrogenics (ii).)

Figure 1.17(b). Ballard 250 kW power generator. (Image courtesy of Ballard Power Systems.)

Figure 1.17(c). UTC Fuel Cells PC25 6 × 200 kW. (Image courtesy of UTC Power Corporation.)

Figure 1.17(d). FuelCell Energy DFC3000™ 2 MW power generator. (Image courtesy of FuelCell Energy.)
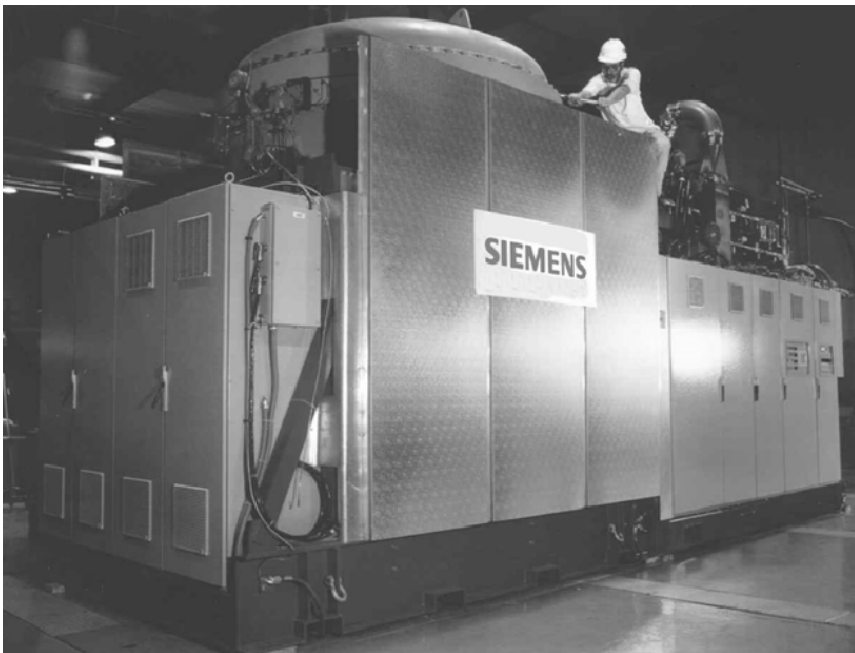
Figure 1.17(e). Siemens 220 kW power generator. (Image courtesy of Siemens.)

1.1.4.3 Backup Power

A backup power device provides an instantaneous, uninterruptible power source. The term UPS (uninterruptible power supply) is often used to refer to backup power. But it may also stand for systems that supply AC power, or systems that supply power for no more than 30 to 60 minutes. A more general definition of backup power covers all types of power outputs and all backup times. Typical applications for backup power include telecommunication systems, information technology and computer systems, manufacturing processes, security systems, utility substations, and railway applications.

Availability and reliability are two of the major concerns for backup power sources. The realization that the power generation system might be vulnerable to interruptions increased the need for backup power sources significantly. For many years, valve-regulated lead-acid battery systems and engine-generator sets have been the dominant sources for backup power. Ultra capacitors, flywheels, and new battery technologies later have joined the group of power providers. Most recently, backup power equipped with fuel cells has been employed by designing the systems to meet the requirements for backup power.

Normally, backup power will use hydrogen as fuel instead of reformate because one of the most important system requirements for backup power is to start instantly upon a power outage. In addition, backup power units are required to operate only intermittently, meaning that a short system lifetime is needed. The operational lifetime requirement for a fuel cell backup power is less than 2,000 hours. This duty cycle is more achievable with today's fuel cell technology than are those needed for FCVs and stationary power. Thus, backup power may become the first commercialized application of PEM fuel cells.

1.1.4.4 Small Portable Power

The convergence of voice, data, and multimedia is driving an endless demand for more power in cell phones, laptop computers, and other portable devices. PEMFCs or DMFCs may someday replace the batteries that power these portable electronic devices. PEM fuel cells have several advantages over batteries. The major drawbacks of batteries for these applications are limited capacity and slow recharging, whereas a fuel cell system can achieve higher power and energy capacity. In addition, battery performance deteriorates when the charge level drops, whereas fuel cells operate at a constant level as long as fuel is supplied.

During the past years, portable versions of fuel cells have emerged. The most promising miniature fuel cell is the DMFC, which is inexpensive and convenient, has a reasonable electrochemical performance, and does not require pressurized hydrogen gas.

In 2000, a portable fuel cell prototype produced 0.24 W and 0.9 V. A fuel cell stack made up of eight of these modules can power a cell phone. Toshiba developed a prototype fuel cell for a laptop, as shown in Figure 1.18, but as they describe the technology is in its infancy. The micro fuel cell on the left is able to provide 300 mW of continuous power with 99.5% pure methanol stored in a 10 mL tank. The picture on the right illustrates the refueling cartridge and refueling process.
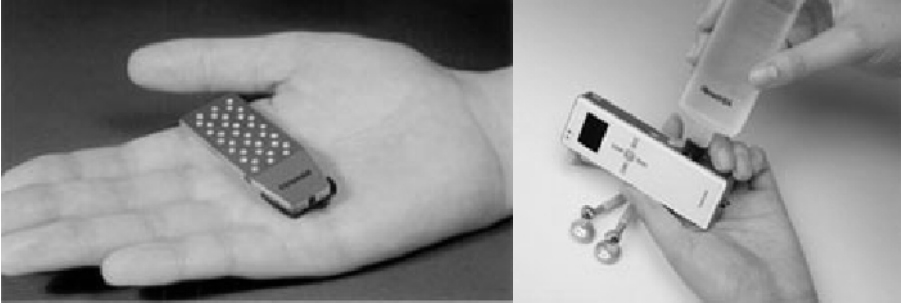
Figure 1.18. Toshiba fuel cell with refueling cartridge [51]. (Images courtesy of Toshiba of Canada Limited.)

1.2 Thermodynamics

1.2.1 Basic Reactions

A PEM fuel cell consists of an electrolyte sandwiched between two electrodes. At the surfaces of the two electrodes, two electrochemical reactions take place. At the anode, over which hydrogen gas passes, occurs the HOR. At the cathode, over which oxygen or air passes, occurs the ORR. The two electrode reactions are as follows:

Anode Reaction:

$$H_2 \rightarrow 2H^+ + 2e^- \tag{1.11}$$

corresponding to an anode potential $E_a^0 = 0.00V$ (under standard conditions) versus SHE.

Cathode Reaction:

$$1/2O_2 + 2H^+ + 2e^- \rightarrow H_2O \tag{1.12}$$

corresponding to a cathode potential $E_c^0 = 1.229V$ (under standard conditions) versus SHE. Therefore, the overall reaction of the fuel cell is

$$H_2 + 1/2O_2 \rightarrow H_2O \tag{1.13}$$

with the equilibrium standard electromotive force calculated to be 1.229 V.

1.2.1.1 Oxygen Reduction Reaction
The ORR is well recognized as sluggish. The slow kinetics constitutes one of the major voltage losses due to a high reduction overpotential in the performance of a

PEMFC, and is one of the most limiting factors in the energy conversion efficiency of the state-of-the-art PEMFC [52]. Thus, investigation of the ORR remains a major focus of PEMFC research [53–56].

Generally speaking, the ORR process on Pt catalysts includes several individual reactions, as shown in Figure 1.19. Two general processes are the most examined, with each process containing a few discrete steps. One is the production of water through a four-electron pathway, and the other is production of hydrogen peroxide through a two-electron pathway. The desired route for a successful ORR catalyst would reduce oxygen molecules to water through the four-electron pathway. Incomplete reduction of oxygen to hydrogen peroxide not only leads to low energy conversion efficiency, but also produces reactive intermediate that can further convert to harmful free radical species.
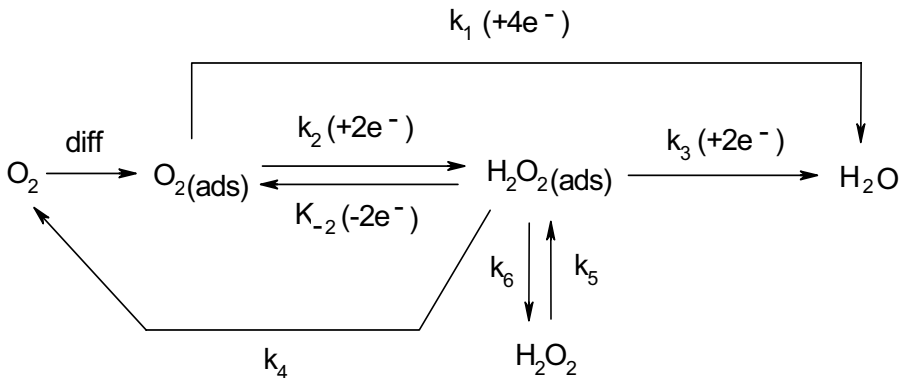
Figure 1.19. Oxygen reduction mechanism on noble catalysts [52]. (Reprinted from Journal of Power Sources, 152(2), Wang Bin, Recent development of non-platinum catalysts for oxygen reduction reaction, 1–15, ©2005, with permission from Elsevier.)

Table 1.5. ORR catalysts

Noble metals		Non-noble metal electrodes	Organometallic complexes
Bulk noble metals	**Nanoparticulate noble metals**		
Pt	Titanium dioxide nanoparticles on gold (Au/TiO$_2$) [60]	Copper [65]	Transition metal complexes with porphyrin ligands [71–73]
Ru [57]		Ni [66]	
Cu/Ru [58]	Palladium nanoparticles on gold [62]	TiO$_2$ on Ti [67]	
Au [59, 60]		Vanadium oxides [68]	Transition metal complexes with non-porphyrin ligands [74–78]
Pd /Co [61]	Palladium nanoparticles on carbon nanotubes [63]	WC+Ta [69]	
	Silver nanoparticles on carbon [64]	Lanthanum manganite [70]	

Minimizing the kinetic voltage loss resulting from the slow ORR on Pt catalysts has been studied over the past decades. As Pt is scarcely available even at a high price, alternative materials are highly sought after for fuel cell applications. To date, noble metal electrodes, non-noble metal electrodes, and organometallic complexes have been developed and studied to catalyze the ORR for PEMFCs, as listed in Table 1.5.

1.2.1.2 Hydrogen Oxidation Reaction

At the anode, hydrogen is stripped of its electrons and becomes protons and electrons. For electrochemical reactions, even if a simple one electron reaction is not that simple and is always with a reaction mechanism involving several steps. The overall reaction rate depends on the slowest elementary reaction, which is called the rate determining step. The steps of H_2 oxidation on Pt electrode include the following:

$$H_2 + Pt \rightarrow Pt\text{-}H_2 \tag{1.14}$$

$$Pt\text{-}H_2 \rightarrow Pt\text{-}H_{ads} \tag{1.15}$$

$$Pt\text{-}H_{ads} \rightarrow Pt + H^+ + e^- \tag{1.16}$$

Platinum (Pt)-based catalysts are widely used as the anodic electrode material for hydrogen oxidation. The HOR on Pt catalysts has a lower oxidation overpotential and a higher kinetic rate. The apparent exchange current density of the HOR has been calculated to be $i^0_{anode} = 0.1 A cm^{-2}$, which is extremely high compared with that of ORR ($i^0_{cathode} = 6 \mu A cm^{-2}$), according to the charge transfer resistances of the cathode and anode obtained from electrochemical impedance spectroscopy (EIS) measurements done by Wagner et al. [79]. This proves the extreme fast reaction kinetics of HOR. Table 1.6 presents the exchange current densities of the hydrogen evolution reaction at different electrode materials in aqueous 1 M H_2SO_4 solution at ambient temperature [80].

Unfortunately, for many practical applications, the presence of a trace level (parts per million (ppm)) of carbon monoxide (CO) in the hydrogen-rich gas mixture produced by the reforming of other fuels is inevitable. CO can strongly adsorb on the Pt catalyst in the anode. The adsorbed CO, even mere traces (10 ppm), blocks the catalytically active area, thereby significantly decreasing its reactivity and causing so-called "CO poisoning." Due to this, an excellent anode catalyst in PEM fuel cells has to show not only high catalytic activity toward hydrogen oxidation, but also enhanced activity in the presence of CO. The search for CO-tolerant catalysts has been a challenging task in the successful development of more efficient PEMFC systems [81].

Electrocatalysts based on Pt and oxophilic elements, such as ruthenium (Ru), tin (Sn), molybdenum (Mo), and tungsten (W), have shown significant improvement in CO tolerance compared to pure Pt. Two mechanisms have been proposed for explaining the enhanced CO tolerance of these materials, a bifunctional mechanism, through which the poisoning effect is reduced by the

occurrence of a surface reaction between Pt-adsorbed CO and oxygenated species produced at oxophilic neighbor sites, and an electronic effect, which is associated with an energy shift of the Pt electronic states caused by the second element and results in a weakening of the Pt-CO interactions [81].

Table 1.6. Exchange current densities of the hydrogen evolution reaction at different electrode materials in aqueous 1 M H_2SO_4 solution at ambient temperature [80]. (Reprinted from Wendt H, Spinacé EV, Oliveira Neto A, Linardi M. Electrocatalysis and electrocatalysts for low temperature fuel cells: fundamentals, state of the art, research and development. Quím Nova 2005;28:1066–75. With permission from Sociadade Brasileira de Química.)

Metal	i^0 / Acm^{-2}
Palladium, Pd	1.0×10^{-3}
Platinum, Pt	8.0×10^{-4}
Rhodium, Rh	2.5×10^{-4}
Iridium, Ir	2.0×10^{-4}
Nickel, Ni	7.0×10^{-6}
Gold, Au	4.0×10^{-6}
Tungsten, W	1.3×10^{-6}
Niobium, Nb	1.5×10^{-7}
Titanium, Ti	7.0×10^{-8}
Cadmium, Cd	1.5×10^{-11}
Manganese, Mn	1.3×10^{-11}
Thallium, Tl	1.0×10^{-11}
Lead, Pb	1.0×10^{-12}
Mercury, Hg	0.5×10^{-13}

PtRu, the current choice for HOR catalysts, exhibits excellent CO tolerance, which could be ascribed to a decrease in CO binding energy on Pt due to electronic substrate effects and to the oxidation of chemisorbed carbon monoxide being catalyzed at low potentials by the activation of H_2O [82]. Ternary Pt-based catalysts have also been investigated in which a third oxophilic component such as Sn, Ir, Rh, Os, Mo, W, WO_3, or Re is added to promote CO oxidation at lower potentials [83].

1.2.1.3 Methanol/Ethanol/Formic Acid Oxidation
In recent years, interest in the development of direct liquid fuel cell (DLFC) has increased considerably due to its advantages: easy handling and storing of the liquid fuel, no need for reforming, and favorable power capability for the use portable electronics powered by miniature fuel cells. Most investigators are

exploring DMFCs [84, 85] for this purpose, while some are focused on DEFCs and DFAFCs [86–90].

Besides methanol, ethanol, and formic acid, other liquid chemicals have also been investigated as fuels for different DLFCs, such as 2-propanol, dimethyl ether, ethylene glycol, dimethoxymethane, trimethoxymethane, tetramethyl orthocarbonate, and hydrazine [91].

Simple organic compounds, such as methanol, ethanol, and formic acid, have several advantages with regard to their use as fuels. They are easy to store and handle. They possess a high energy density in the order of 1 kWh/kg, and they can be readily generated from biomass. Last but not least, due to their simple structures they should have the simplest and most straightforward reaction mechanisms of all the possible organic fuels [92]. Although more complex organic fuels are of academic interest, they probably are more expensive and have more complicated reaction mechanisms due to the fact that a molecule possesses several carbon atoms.

Strategies for the development of novel catalytic materials and the design of highly active catalysts for DLFC applications largely depend on a detailed understanding of the reaction mechanism and, in particular, of the rate-limiting step(s) during the electrooxidation under continuous reaction conditions. The most commonly used technique in the electrochemical studies of fuel cell reaction mechanisms has been voltammetry, chronoamperometry (chronopotentiometry), *in situ* spectroscopic techniques, e.g., electrochemically modulated infrared spectroscopy (EMIRS) and infrared reflection-absorption spectroscopy (IRRAS), differential electrochemical mass spectroscopy (DEMS) and ex-situ techniques, e.g., X-ray photoelectron spectroscopy (XPS) [92].

Methanol Oxidation

The oxidation of methanol has been thoroughly studied for many years and the mechanism is now well established. The overall oxidation reaction involves six electrons and one water molecule,

$$CH_3OH + H_2O \rightarrow CO_2 + 6H_{aq}^+ + 6e^- \tag{1.17}$$

corresponding to an anode potential $E_a^0 = 0.016 V$ (under standard conditions) versus SHE, resulting in the equilibrium standard electromotive force of 1.213 V for a DMFC. The overall reaction of the cell is

$$CH_3OH + 1.5O_2 \rightarrow CO_2 + 2H_2O \tag{1.18}$$

As Pt is the best anode for hydrogen oxidation, numerous studies deal with the direct oxidation of methanol on Pt in acid media, as well as in alkaline media [93]. It is reported that the dissociative adsorption of methanol on Pt-based catalysts occurs via the formation of irreversibly adsorbed CO species (a reaction intermediate), either linearly bonded or bridge bonded to the Pt surface [94]; the CO species acts as a poison to the catalytic surface, rapidly lowering its activity.

The coverage degree by linearly bonded CO can reach 90% on a pure Pt electrode, so that most of the active sites are blocked.

Since the oxidation of methanol to CO includes six electrons, the reaction process must involve several steps with several products or intermediates. The results from mass spectral measurements, high performance liquid chromatography (HPLC), and gas chromatography (GC) absorbance have showed that H&O, HCOOH, HCOOCH, and CO_z were all produced during the oxidation of methanol on Pt in acid solutions. These species were formed initially but eventually became CO [92]. In addition, some other adsorbed species such as $(CHO)_{ads}$ or $(COOH)_{ads}$ were identified by infrared reflectance spectroscopy or Fourier transform infrared reflectance spectroscopy. The detailed reaction mechanism of methanol oxidation on a Pt electrode is shown in Figure 1.20 [94].
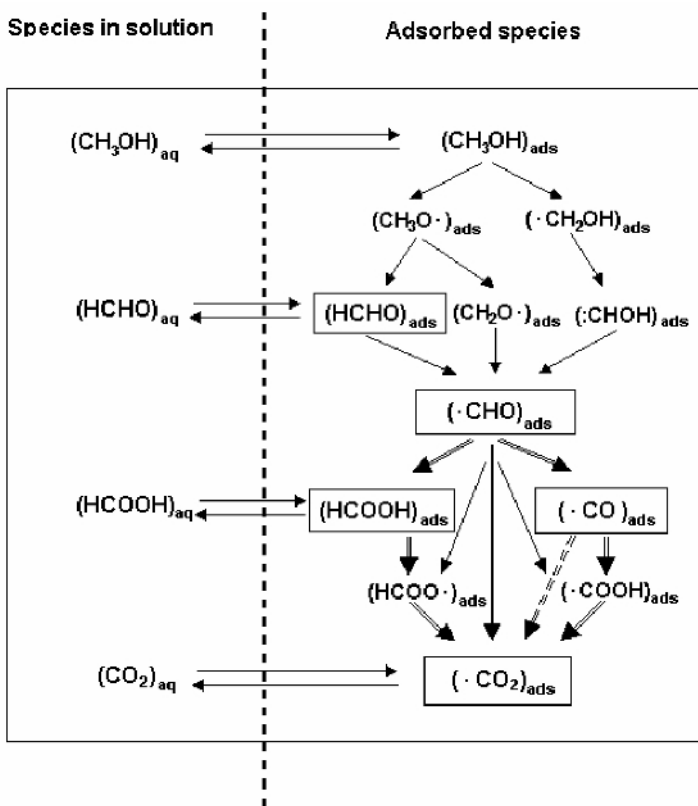
Figure 1.20. Detailed reaction mechanism of methanol oxidation on a Pt electrode [94]. (Reprinted from Journal of Power Sources, 105(2), Lamy C, Lima A, LeRhun V, Delime F, Coutanceau C, Léger J-M, Recent advances in the development of direct alcohol fuel cells (DAFC), 283–96, ©2002, with permission from Elsevier.)

In this mechanism, the adsorbed species $(CHO)_{ads}$ plays a key role. Therefore, the strategy to develop efficient electrocatalysts is to favor this adsorbed species and to avoid the subsequent formation of adsorbed CO, either to prevent its

formation by blocking neighbouring Pt sites, to oxidize it at lower potentials, or to remove it [94].

To overcome CO deactivation, alloys of Pt with more oxophilic elements have been investigated as methanol electrooxidation catalysts. PtRu bifunctional catalysts are presently the most active for methanol oxidation. It is believed that Ru serves the role of removing CO_{ads} as CO_2 [93]:

$$Ru-OH + Pt-CO \rightarrow Ru + Pt + CO_2 + H^+ + e^- \tag{1.19}$$
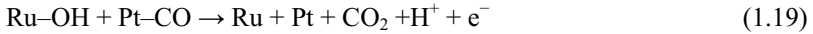
Its role is thought to be a combination of two effects: (1) a bifunctional mechanism in which a partially oxidized Ru surface supplies the oxygenated species necessary for complete oxidation to CO_2 of the methanol adsorption residue, and (2) the ligand effect, in which the presence of Ru atoms close to Pt changes the electronic structure of Pt, allowing the weakening of the Pt–CO bond [95].

Studies of the temperature dependence of methanol oxidation indicate apparent activation energies of 41 to 56 kJ/mol [96] and 55 kJ/mol [97], which suggests that the methanol adsorption is rate determining because these values are comparable to the adsorption energies [96].

Ethanol Oxidation
Since ethanol is the major renewable bio-fuel and is less toxic than other alcohols, it is a promising alternative liquid fuel for directly fuelled DLFC systems. A schematic of a DEFC is shown in Figure 1.21.
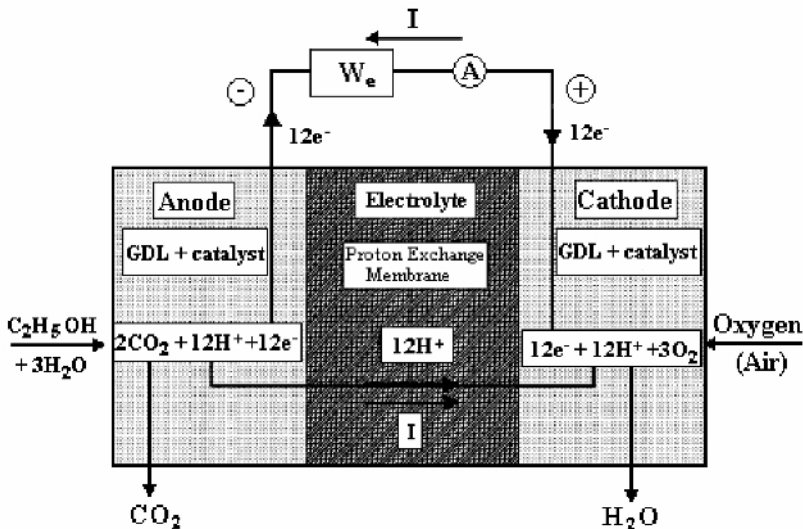
Figure 1.21. Schematic of a DEFC 95. (Reprinted from Journal of Power Sources, 105(2), Lamy Claude, Lima Alexandre, LeRhun Véronique, Delime Fabien, Coutanceau Christophe and Léger Jean-Michel, Recent advances in the development of direct alcohol fuel cells (DAFC), 283–96, ©2002, with permission from Elsevier.)

The electrode reactions of a DEFC are expressed as follows [98]:

Anode reaction:

$$CH_3CH_2OH + 3H_2O \rightarrow 2CO_2 + 12H^+ + 12e^- \qquad (1.20)$$
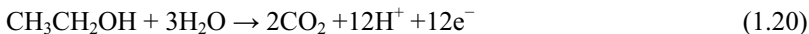
corresponding to an anode potential $E_a^0 = 0.084V$ versus SHE as calculated from thermodynamic data [94].

Cathode reaction:

$$3O_2 + 12H^+ + 12e^- \rightarrow 6H_2O \qquad (1.21)$$

corresponding to a cathode potential $E_c^0 = 1.229V$ versus SHE.

Overall reaction:

$$CH_3CH_2OH + 3O_2 \rightarrow 2CO_2 + 3H_2O \qquad (1.22)$$

Therefore, the equilibrium standard electromotive force can be calculated to be 1.145 V.

As the complete electrooxidation of ethanol in an acid medium yields two molecules of CO_2 and 12 electrons per ethanol molecule and involves the cleavage of the C–C bond, which requires rather high activation energy, the anodic ethanol electrooxidation on Pt is very sluggish, especially at low temperatures [99]. Despite significant efforts and numerous studies, the mechanism of the ethanol electrooxidation reaction still remains unclear; some studies are even contradictory. Nevertheless, electrooxidation of ethanol often does not proceed to completion, yielding adsorbed intermediates such as acetaldehyde [100, 101]:

$$CH_3CH_2OH \rightarrow CH_3CHO + 2H^+ + 2e^- \qquad (1.23)$$
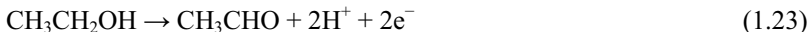
Much of the effort on the electrooxidation of ethanol has been devoted mainly to identifying the adsorbed intermediates on the electrode and elucidating the reaction mechanism by means of various techniques, as differential electrochemical mass spectrometry, *in situ* Fourier transform infrared spectroscopy, and electrochemical thermal desorption mass spectrometry. The established major products include CO_2, acetaldehyde, and acetic acid, and it has been reported that methane and ethane have also been detected. Surface-adsorbed CO is still identified as the leading intermediate in ethanol electrooxidation, as it is in the methanol electrooxidation. Other surface intermediates include various C_1 and C_2 compounds such as ethoxy and acetyl [102]. There is general agreement that ethanol electrooxidation proceeds via a complex multi-step mechanism, which involves a number of adsorbed intermediates and also leads to different by-products for incomplete ethanol oxidation, as shown in Figure 1.22.
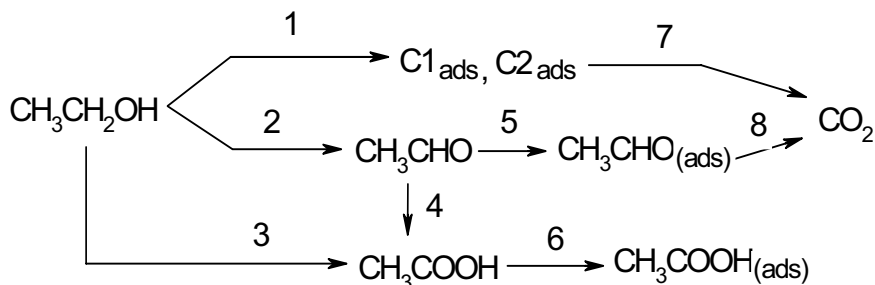
Figure 1.22. A probable reaction pathway for the electrooxidation of ethanol [103]. (Reproduced by permission of ECS—The Electrochemical Society, from Oliveira Neto A, Giz MJ, Perez J, Ticianelli EA, Gonzalez ER. The electrooxidation of ethanol on Pt-Ru and Pt-Mo particles supported on high-surface-area carbon.)

Total oxidation:

$$CH_3CH_2OH \rightarrow CH_3CH_2OHad \rightarrow C_1ad, C_2ad \rightarrow CO_2 \qquad (1.24)$$

Partial oxidation:

$$CH_3CH_2OH \rightarrow CH_3CH_2OHad \rightarrow CH_3CHO \rightarrow CH_3COOH\ 105 \qquad (1.25)$$
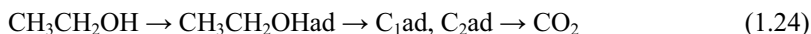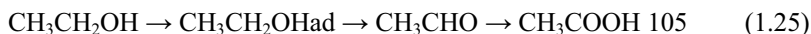
CO_2 is the most common product. Other products and by-products such as acetaldehyde and acetic acid will inevitably decrease the fuel efficiency. The electrooxidative removal of CO-like intermediates and the cleavage of the C–C bond are the two main obstacles and rate determining steps. It is clear that ethanol electrooxidation involves more intermediates and products than that of methanol, and thus more active electrocatalysts are needed to promote ethanol electrooxidation at lower temperatures [102]. Although there are some similarities in the oxidation of low molecular weight alcohols on Pt (e.g., CO is produced as intermediate), the best catalyst is not the same for all situations. Contrary to what was found for the oxidation of methanol, the more effective catalyst for the oxidation of ethanol is not necessarily a Pt-Ru alloy [104].

The presence of both poisoning species and intermediate reaction products requires the development of new electrocatalysts able to break the C-C bond and to oxidize adsorbed CO at low temperatures [94]. Numerous studies have been carried out to develop more active electrocatalysts for ethanol electrooxidation. Besides Pt, other metals such as gold, rhodium, and palladium have been investigated as anode catalysts for ethanol electrooxidation and show certain activities [105]. On gold in an acid medium, the oxidation reaction leads mainly to the formation of acetaldehyde [94]. The oxidation of ethanol on rhodium proceeds mainly through the formation of acetic acid and CO.

Rousseau et al. [106] and Song et al. [107] investigated Pt-based catalysts for ethanol electrooxidation. Zhou et al. [102, 105] studied bi- and tri-metallic Pt-based catalysts with the addition of Ru, Pd, Sn and H. Wang et al. [108] developed ethanol electrooxidation catalysts on carbon-supported Pt, PtRu and Pt_3Sn. Colmati

et al. [104] also studied carbon-supported PtSn electrocatalysts. CuNi alloy-supported electrocatalysts has been investigated by Gupta et al. [93, 109]. Lux and Cairns [100, 101] developed lanthanide-platinum intermetallic compounds for ethanol oxidation.

Formic Acid Oxidation
As formic acid is nontoxic and has two orders of magnitude less crossover through a Nafion membrane than methanol [110], DFAFCs have been attracting increasing attention [88].

   The electrooxidation of formic acid itself has been intensively investigated. The overall oxidation reaction of formic acid is

$$HCOOH \rightarrow CO_2 + 2H^+ + 2e- \tag{1.26}$$

corresponding to an anode potential $E_a^0 = -0.171V$ (under standard conditions) versus SHE. Therefore, the equilibrium standard electromotive force of the overall cell reaction,

$$HCOOH + 1/2\ O_2 \rightarrow CO_2 + H_2O \tag{1.27}$$

is calculated to be 1.400 V for a DFAFC [91].

   In most cases, formic acid oxidation has been studied at Pt or modified Pt surfaces [111, 112]. Pt-Pd [113] and Pt-Ru [114] have also been studied. A variety of other catalyst investigations have been carried out, including palladium (Pd-C [115], Pd-P [116], Pd-M, where M is a base transition metal (M = Ti, Zr, Hf, V, Nb, Ta, Cr, Mo, W, or Au)), rhodium, iridium, and gold [117].

   The oxidation of formic acid is not straightforward, although there is general agreement concerning the mechanism of formic acid electrooxidation on a Pt surface. The reaction is thought to branch into two pathways. In the first, formic acid is oxidized directly and relatively rapidly to CO_2 via a weakly bound reactive intermediate [113, 114, 118]:

$$HCOOH + Pt \rightarrow X \rightarrow CO_2 + 2H^+ + 2e^- \tag{1.28}$$
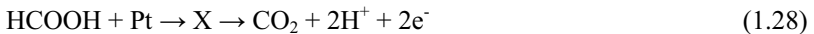
   In the second pathway, formic acid is indirectly oxidized to CO_2 relatively slowly through a strongly bound, poisoning CO intermediate:

$$HCOOH + Pt \rightarrow Pt\text{-}CO + H_2O \tag{1.29}$$

$$Pt + H_2O \rightarrow Pt\text{-}OH + H^+ + e^- \tag{1.30}$$

$$Pt\text{-}CO + Pt\text{-}OH \rightarrow 2Pt + CO_2 + 2H^+ + 2e^- \tag{1.31}$$
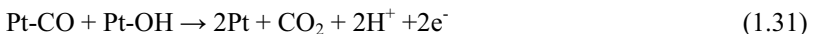
   The poisoning CO intermediate limits the activity of pure Pt toward formic acid oxidation by blocking the reaction sites. It is reported that Pt/Ru can activate water on the Ru atoms to create the added reaction pathway [114].

$$Ru + H_2O \rightarrow Ru\text{-}OH + H^+ + e^- \qquad (1.32)$$

$$Pt\text{-}CO + Ru\text{-}OH \rightarrow Pt + Ru + CO_2 + H^+ + e^- \qquad (1.33)$$
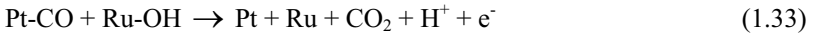
Since Ru forms surface hydroxides readily at lower potentials (0.3 V) than Pt (0.6 V), Reaction 1.33 occurs more swiftly than Reaction 1.31, which provides a faster pathway for CO oxidation and improves activity toward oxidation of formic acid [114].

1.2.2 Heat of Reaction

1.2.2.1 Enthalpy of Reaction
For a hydrogen fuel cell, the overall reaction (Equation 1.13) is the same as the reaction of hydrogen combustion, which is an exothermic process.

$$H_2 + 1/2O_2 \rightarrow H_2O + Heat \qquad (1.34)$$

The heat or enthalpy of a chemical reaction is the difference between the heats of formation of products and reactants. For the above equation, the heat or enthalpy is

$$\Delta H = (h_f)_{H_2O} - (h_f)_{H_2} - 1/2(h_f)_{O_2} \qquad (1.35)$$

The heat of formation of liquid water is –286 kJ/mol at 25 °C and heat of formation of elements is by definition equal to zero. Therefore,

$$\Delta H = -286kJ / mol - 0 - 0 = -286kJ / mol \qquad (1.36)$$

The negative sign of the enthalpy means that this is an exothermic reaction. The fuel cell reaction can now be written as

$$H_2 + 1/2O_2 \rightarrow H_2O(l) + 286 \text{ kJ/mol} \qquad (1.37)$$

This equation is valid at 25 °C only, meaning that both the reactant gases and the product water are at 25 °C. At 25 °C and atmospheric pressure water is in liquid form [1].

The enthalpy of the hydrogen combustion reaction is also called the hydrogen's heating value. The value 286 kJ/mol is known as hydrogen's higher heating value (HHV), which means that 1 mol of hydrogen is fully combusted with ½ mol of oxygen and cooled down to 25 °C. If hydrogen is combusted with sufficient excess oxygen and cooled down to 25 °C, the value will become 242 kJ/mol, which is known as hydrogen's lower heating value (LHV) [1].

1.2.2.2 Gibbs Free Energy

The change in Gibbs free energy (ΔG_f) of a reaction is the difference between the Gibbs free energy of the product and the Gibbs free energy of the reactants. For the hydrogen/oxygen fuel cell reaction (Equation 1.13), the change in Gibbs free energy is

$$\Delta G_f = G_{f,products} - G_{f,reactants} = G_{f,H_2O} - G_{f,H_2} - G_{f,O_2} \qquad (1.38)$$

The change in Gibbs free energy varies with both temperature and pressure,

$$\Delta G_f = \Delta G_f^0 - RT \ln\left[\frac{p_{H_2} p_{O_2}^{1/2}}{p_{H_2O}}\right] \qquad (1.39)$$

where ΔG_f^0 is the change in Gibbs free energy at standard pressure, which varies with the temperature T of the fuel cell, in Kelvin. p_{H_2}, p_{O_2}, and p_{H_2O} are the partial pressure of the hydrogen, oxygen, and vapor, respectively. R is the universal gas constant (8.314 $J/(kg \cdot K)$). The fact that the value of ΔG_f^0 is negative means that the energy is released from the reaction [119].

1.2.2.3 Reversible Fuel Cell Potential

If the fuel cell is reversible, which means that all the Gibbs free energy would be converted to electrical energy, the voltage of the fuel cell is related to the change of Gibbs free energy of the reaction by the following equation,

$$\Delta G_f = -nFE \qquad (1.40)$$

where F is Faraday constant (96485 coulombs) and E is the voltage of the fuel cell. The number n in the equation is the number of electrons. In the case of a hydrogen fuel cell, for each mole of hydrogen two moles of electrons pass around the external circuit ($n = 2$). So the physical meaning of $2FE$ is the electrical work (charge × voltage). E is called the reversible fuel cell potential, also known as the thermodynamic potential.

1.2.3 Effect of Operation Conditions on Reversible Fuel Cell Potential

1.2.3.1 Temperature Dependence of the Reversible Fuel Cell Potential

The reversible voltage of the fuel cell, also known as Nernst voltage, can be expressed using the Nernst equation,

$$E = \frac{-\Delta G_f}{2F} = \frac{-\Delta G_f^0}{2F} + \frac{RT}{2F} \ln\left[\frac{p_{H_2} p_{O_2}^{1/2}}{p_{H_2O}}\right] \qquad (1.41)$$

At standard state (25 °C and 1 atm), the value of the term $\dfrac{-\Delta G_f^0}{2F}$ is

$$E = \frac{-\Delta G_f^0}{2F} = \frac{237{,}200\,J\,/\,mol}{2 \times 96485\,As\,/\,mol} = 1.229\ V \tag{1.42}$$

Therefore, the reversible (theoretical) hydrogen/oxygen fuel cell potential is 1.229 V at standard state (25 °C and 1 atm). This value varies with temperature,

$$\frac{-\Delta G_f^0}{2F} = 1.229 + (T - T^0)\left(\frac{\Delta S^0}{2F}\right) \tag{1.43}$$

where T^0 is the standard-state temperature, which is 298.15 K, and ΔS^0 is the entropy change. The entropy change of a given reaction is approximately constant and can be set to the standard value, as follows [119]:

$$\frac{-\Delta G_f^0}{2F} = 1.229 - 0.85 \times 10^{-3}(T - 298.15) \tag{1.44}$$

The calculated change in the Gibbs free energy of the fuel cell reaction, ΔG_f^0, and the reversible fuel cell voltage (reversible OCV) at standard pressure are given in Table 1.7. The reversible fuel cell potential at different temperatures and standard pressure is also depicted in Figure 1.23.

Table 1.7. Change in Gibbs free energy, reversible cell voltage, and efficiency limit (HHV basis) of hydrogen fuel cell reaction at different temperatures [26]. (From Larminie J, Dicks A. Fuel cell systems explained. ©2003 John Wiley & Sons Limited. Reproduced with permission.)

Form of Water Product	Temperature (°C)	ΔG_f^0 (kJ/mol)	Reversible cell voltage (V)	Theoretical Efficiency (%)
Liquid	25	−237.2	1.23	83
Liquid	80	−228.2	1.18	80
Gas	100	−225.2	1.17	79
Gas	200	−220.4	1.14	77
Gas	400	−210.3	1.09	74
Gas	600	−199.6	1.04	70
Gas	800	−188.6	0.98	66
Gas	1000	−177.4	0.92	62
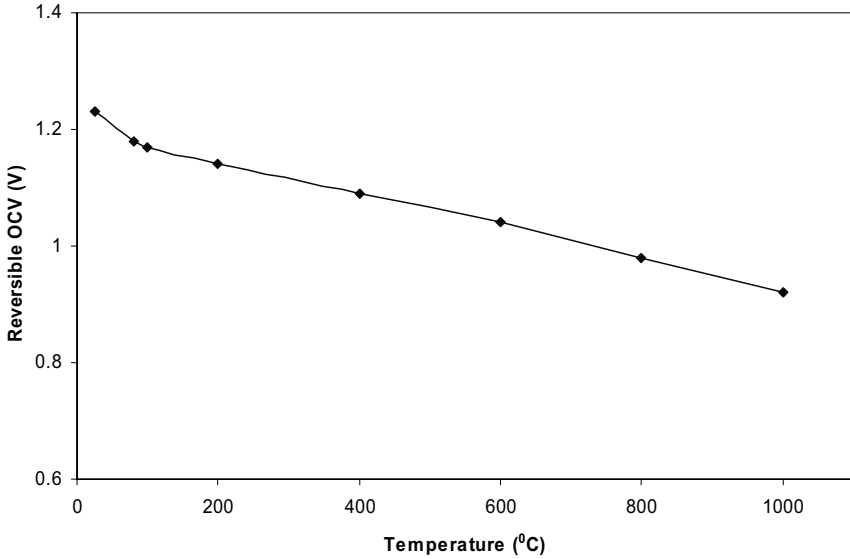
Figure 1.23. Reversible OCV at different temperatures and standard pressure

1.2.3.2 Pressure Dependence of the Reversible Fuel Cell Potential
The reversible cell potential or Nernst voltage of a hydrogen fuel cell is yielded according to Equation 1.41 and 1.44,

$$E_{Nernst} = 1.229 - 0.85 \times 10^{-3}(T - 298.15) + 4.3085 \times 10^{-5}T[\ln(p_{H_2}) + 1/2\ln(p_{O_2})]$$
(1.45)

where T is expressed in Kelvin, and p_{H_2}, and p_{O_2} are expressed in atm. It can be seen in Equation 1.45 that both the temperature and the pressure will affect the reversible cell potential [119].

1.2.4 Open Circuit Voltage

1.2.4.1 Theoretical OCV
As described in Section 1.2.3.2, the reversible cell potential or Nernst voltage of a hydrogen fuel cell can be expressed as Equation 1.45. This value is what we call the theoretical OCV, and it is affected by both the temperature and the pressure.

A theoretical fuel cell OCV, E_{Theor}^{OCV}, can be written as

$$E_{Theor}^{OCV} = E_c^r - E_a^r$$
(1.46)

where E_c^r and E_a^r can be expressed in the Nernst form shown in Equation 1.47 and 1.48, respectively:

For cathode reaction: $O_2 + 4H^+ + 4e^- \leftrightarrow 2H_2O$

$$E_c^r = E_c^0 + \frac{RT}{4F}\ln(P_{O_2}[H^+]^4) \tag{1.47}$$

For anode reaction: $H_2 \leftrightarrow 2H^+ + 2e^-$

$$E_a^r = E_a^0 + \frac{RT}{2F}\ln(\frac{[H^+]^2}{P_{H_2}}) \tag{1.48}$$

In Equations 1.47 and 1.48, E_c^o and E_a^o are the standard cathode and anode potentials, respectively. E_c^o is a temperature-dependent constant (= 1.229–0.00085 × (T–298.15) [120]). E_a^o is zero at any temperature. P_{O_2} and P_{H_2} are the partial pressures (atm) of O_2 and H_2, respectively, and $[H^+]$ is the molar concentration of protons (mol/L). A theoretical OCV can be calculated by deriving Equations 1.47 and 1.48 to yield Equation 1.49, which can be further derived to yield Equation 1.45:

$$E_{theor}^{OCV} = 1.229 - 0.00085(T - 298.15) + \frac{RT}{4F}\ln[P_{O_2}(P_{H_2})^2] \tag{1.49}$$

$$= 1.229 - 0.85\times10^{-3}(T - 298.15) + 4.3085\times10^{-5}T[\ln(p_{H_2}) + 1/2\ln(p_{O_2})]$$

The theoretical OCV has the same value as the reversible cell potential. However, even when no current is drawn from a fuel cell, there is irreversible voltage loss, which means that the actual values of the OCV are always lower than the theoretically expected values. To date, a quantitative explanation for such OCV behavior has not been clear in the literature. One explanation attributes this behavior to H_2 crossover and/or internal current, as described in the fuel cell book written by Larminie and Dicks [26]. A mixed potential [121–124] has also been widely used to interpret the lower OCV. The combined effects of fuel crossover, internal short, and parasitic oxidation reactions occurring at the cathode are the source of the difference between the measured open circuit cell voltage and the theoretical cell potential. Therefore, the actual OCV is expressed as

$$E_{OCV} = E_{theor}^{OCV} - E_{cross} - E_{mix} \tag{1.50}$$

1.2.4.2 Mixed Potential

In general, the mixed potential is composed of both the cathodic O_2/H_2O reaction potential

$$O_2 + 4H^+ + 4e^- \leftrightarrow 2H_2O \ (E_c^o = 1.229 \text{ V vs. SHE}) \tag{1.51}$$
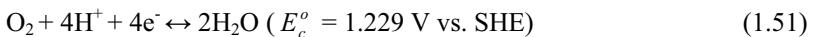
and the Pt/PtO anodic reaction potential

$$Pt + H_2O \leftrightarrow PtO + 2H^+ + 2e^- \qquad (E^o_{Pt/PtO} = 0.88 \text{ V vs. SHE}) \qquad (1.52)$$
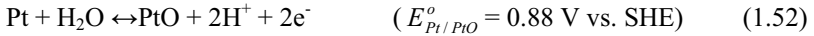
The local electrochemical reaction on the Pt surface creates a Pt-O surface coverage of 30%, and the remaining 70% remains as pure Pt. At steady-state mixed potential, a complete layer of Pt-O can never be achieved in order to keep the reaction of Pt to Pt-O continued due to the diffusion of Pt-O into the bulk metal. The reported mixed cathode potential is around 1.06 V (vs. SHE) at standard conditions (25 °C, 1 atm) with an O_2 partial pressure dependence of 15 mV atm^{-1} [124, 125].

1.2.4.3 Fuel Crossover
Another OCV loss is caused by the crossover of fuel through the electrolyte. Ideally the electrolyte allows the transport of only ions. In reality, however, some fuel permeates across the membrane from the anode to the cathode. In addition, some direct transfer of electrons across the membranes can occur and cause electronic short. A fuel loss due to crossover leads to a current loss. The current loss associated with an electrical short is generally small (ca. few milli-amperes) relative to the typical operating current of a fuel cell, and therefore is not a significant source of current inefficiency. However, these effects have a significant effect on the OCV of the cell. This is particularly true of a low-temperature cell, in which activation losses are considerable [126].

Fuel that has crossed over can react with O_2 to produce a corresponding cathodic current density in the same order of magnitude, resulting in a depression of the cathode potential. It is believed that the H_2 that has crossed over can form a local half-cell electrochemical reaction on the cathode, such as $H_2 \leftrightarrow 2H^+ + 2e^-$, resulting in a mixed cathode potential, in a way similar to that of the half-cell reaction ($Pt + H_2O \leftrightarrow PtO + 2H^+ + 2e^-$).

H_2 Crossover
For a hydrogen fuel cell, H_2 crossover can be measured by linear sweep voltammetry or chronocoulometry. The linear sweep voltammetry procedure is similar to the cyclic voltammetry (CV) technique, with the principal difference being the irreversible scan. Humidified H_2 and N_2 are supplied to the anode and cathode sides of the fuel cell, respectively. The scan potential ranges from 0 to 0.8 V, with higher voltages being avoided to prevent Pt oxidation [127]. The experimental procedure involves controlling the potential of the fuel cell cathode (working electrode) and monitoring any electrochemical activity that occurs in the form of a current. Since N_2 gas is the only substance introduced into the cathode side, any current generated in the given potential range is attributed solely to the electrochemical oxidation of H_2 gas that crosses over from the anode side through the membrane. The crossover current typically increases with the scan potential and rapidly reaches a limiting value when the potential grows to around 300 mV [128]. At this value all crossover H_2 is instantaneously oxidized due to the high overpotential applied. Based on the limiting current, one can, ultimately, calculate

the flux of H_2 gas using Faraday's law. Using this diagnostic method, Song et al. [129] determined the hydrogen crossover rate through a Nafion 112 membrane at elevated temperatures up to 120 °C. A sample of a linear sweep voltammogram for different types of MEAs is presented in Figure 1.24 [127].
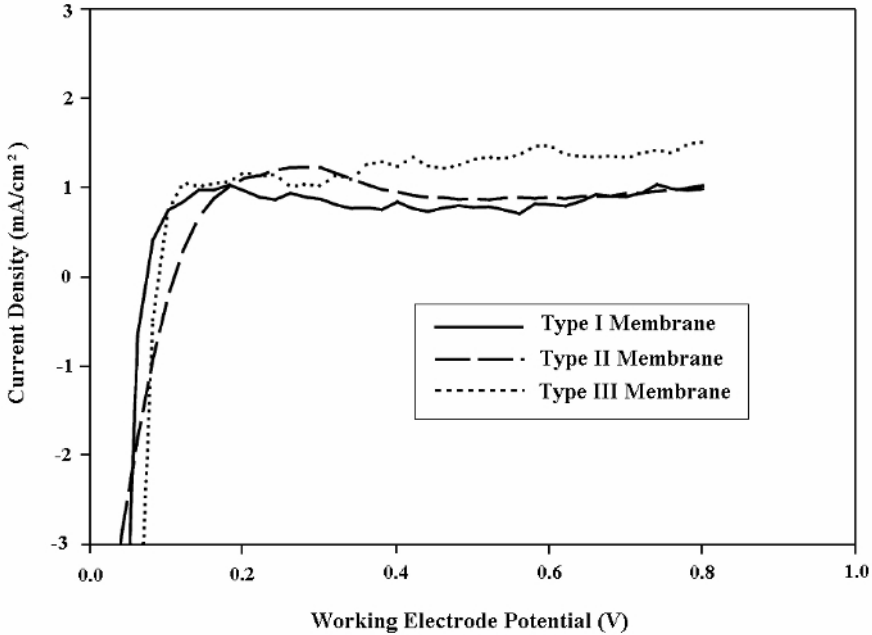
Figure 1.24. Sample of a linear sweep voltammogram on MEAs containing Nafion/PTA membranes of Types I–III (25% PTA loading). Scan rate 4 mV/s; room temperature; ambient pressure operation; 200 cm^3 H_2 on anode; 200 cm^3 N_2 on cathode [127]. (Reprinted from Journal of Membrane Science, 232, Ramani V, Kunz HR, Fenton JM, Investigation of Nafion®/HPA composite membranes for high temperature/low relative humidity PEMFC operation, 31–44 ©2004 with permission from Elsevier.)

Another method for measuring H_2 crossover through the membrane is chronocoulometry [130, 131]. The fuel cell is operated with hydrogen at the anode and nitrogen at the cathode. A certain potential, such as 0.5 V, is applied to the cathode side of the cell, which serves as the working electrode, instead of a potential scan. Hydrogen crossing over the membrane from the reverse electrode is oxidized completely at this potential. The electrical charge passing through this electrode is recorded as a function of time. By measuring the coulombs evolved by the oxidation, the H_2 crossover rate can be calculated as a mass transfer limited current.

Methanol Crossover
Fuel crossover occurs to some degree in all low-temperature fuel cells, particularly in DMFCs. For a DMFC, methanol crossover not only results in additional fuel consumption, but also reduces the cell voltage by the effect of mixed potential, and

the potential of the oxygen cathode is strongly influenced by the crossover of methanol through the membrane.

The most conventional method to determine methanol crossover in a DMFC is to monitor the CO_2 content in the cathode exhaust gas flux by using an optical infrared sensor, by gas chromatographic analysis, or by mass spectrometry [132]. However, these measurements are based on the assumptions that the crossed over methanol at the cathode is completely oxidized and that there is no CO_2 permeation from the anode to the cathode. In reality, in particular for operation at high current density, a large amount of CO_2 permeates from the anode to the cathode in the DMFC. So far, no reliable method is available to measure the methanol crossover through the membrane from the anode to the cathode at the operating status.

Nevertheless, efforts have been made to determine the CO_2 crossover. One method is to determine the CO_2 flux using half-cell measurements. At the anode, CO_2 is produced and passes together with methanol through the membrane to the cathode. At the cathode, nitrogen gas is flushed. The CO_2 flux through the membrane is determined because methanol is not oxidized at the cathode. Another method utilizes methanol-tolerant catalysts at the cathode in order not to oxidize the permeating methanol. The amount of CO_2 permeated to the cathode can be calculated from the missing CO_2 fraction in the anode exhaust by using a method of gravimetric determination of $BaCO_3$ [133].

1.2.5 Fuel Cell Efficiency

1.2.5.1 Carnot Efficiency

The efficiency of any energy conversion device is defined as the ratio between useful energy output and energy input. The efficiency limit for heat engines, such as steam and gas turbines, is known as the Carnot limit. If the maximum temperature of the heat engine is T_1, and the heated fluid is released at temperature T_2, which is never likely to be smaller than room temperature (about 290 K), then the Carnot limit of the efficiency can be calculated by

$$\text{Carnot limit} = \frac{T_1 - T_2}{T_1},$$
(1.53)

where both the temperatures are in Kelvin. For a steam turbine operating at 400 °C (673 K) with water exhausted through a condenser at 50 °C (323 K), the Carnot efficiency limit is

$$\frac{673 - 323}{673} = 52\%$$
(1.54)

Basically, there must be some heat energy, proportional to the lower temperature T_2 that is always thrown away or wasted. Thus, the practical efficiency is always lower than the efficiency limit.

1.2.5.2 Theoretical Fuel Cell Efficiency

For a fuel cell, the useful energy output is the electrical energy produced, and energy input is the enthalpy of hydrogen. Assuming that all of the Gibbs free energy can be converted into electrical energy, the maximum possible (theoretical) efficiency of a fuel cell at 25 °C by using the hydrogen HHV is

$$\eta = \frac{\Delta G_f^0}{\Delta H^0} = \frac{237.1 kJ / mol}{286 kJ / mol} = 83\% \tag{1.55}$$

If both ΔG and ΔH are divided by nF, the fuel cell efficiency may be expressed as a ratio of two potentials:

$$\eta = \frac{\Delta G_f^0}{\Delta H^0} = \frac{\dfrac{-\Delta G_f^0}{nF}}{\dfrac{-\Delta H^0}{nF}} = \frac{1.23}{1.48} = 83\% \ \ (25°C, 1 \text{ atm}) \tag{1.56}$$

where 1.23 V is the theoretical cell potential, and 1.48 is the potential corresponding to hydrogen's HHV, or the thermoneutral potential.

The theoretical efficiency is sometimes also known as the thermodynamic efficiency or the maximum efficiency limit. The theoretical efficiency at different temperatures and standard pressure is shown in Figure 1.25. The data are also given in Table 1.7. It is clear that there is a connection between the reversible OCV of a cell and its theoretical efficiency (or maximum efficiency) based on the above equation.
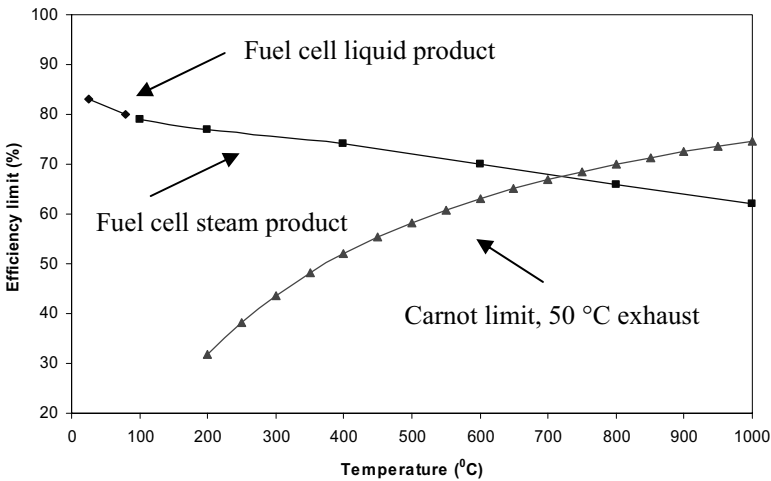
Figure 1.25. Theoretical H_2 fuel cell efficiency at standard pressure based on HHV [26]. (From Larminie J, Dicks A. Fuel cell systems explained. ©2003 John Wiley & Sons Limited. Reproduced with permission.)

1.2.5.3 Energy Conversion Efficiency for Fuel Cells

The actual efficiency of the cell is defined as the actual voltage divided by the thermoneutral potential, that is,

$$\text{Cell efficiency} = \frac{V_{cell}}{1.48} \times 100\% \text{ (based on HHV)} \tag{1.57}$$

If using the LHV, then

$$\text{Cell efficiency} = \frac{V_{cell}}{1.23} \times 100\% \tag{1.58}$$

In practice, a fuel cell is normally operated under conditions such that not all the fuel that is fed to the cell is consumed. Some fuel has to pass through unreacted. Therefore, there is another parameter that needs to be taken into account to calculate the cell efficiency, the fuel utilization coefficient, which is defined as

$$\mu_f = \frac{\text{mass of fuel reacted in cell}}{\text{mass of fuel input to cell}} \tag{1.59}$$

Thus, the fuel cell efficiency is expressed as [26]:

$$\text{Cell efficiency} = \mu_f \frac{V_{cell}}{1.48} \times 100\% \text{ (HHV)} \tag{1.60}$$

and

$$\text{Cell efficiency} = \mu_f \frac{V_{cell}}{1.23} \times 100\% \text{ (LHV)} \tag{1.61}$$

1.2.6 Summary

A comparison of the reactions, cell potentials, energy densities, theoretical efficiency, and other selected properties for PEM fuel cells with different fuels is summarized in Table 1.8.

Fuels		Reactions	$-\Delta G_f^0$ (kJ mol^{-1})	Theoretical potential, E^0(V)	$-\Delta H^0$ (kJ mol^{-1})	Theoretical energy efficiency (%)
Hydrogen	Anode:	$H_2 \rightarrow 2H^+ + 2e^-$	0	0.000		
	Cathode:	$2H^+ + 2e^- + (1/2)O_2 \rightarrow H_2O_{(l)}$		1.229		
	Overall:	$H_2 + (1/2)O_2 \rightarrow H_2O$	237.1	1.229	285.8	0.830
Methanol	Anode:	$CH_3OH_{(l)} + H_2O \rightarrow CO_2 + 6H^+ + 6e^-$	9.3	0.016		
	Cathode:	$6H^+ + 6e^- + (3/2)O_2 \rightarrow 3H_2O_{(l)}$		1.229		
	Overall:	$HCOOH_{(l)} + (1/2)O_2 \rightarrow CO_2 + H_2O_{(l)}$	270	1.400	254.3	0.967
Ethanol	Anode:	$C_2H_5OH_{(l)} + 3H_2O \rightarrow 2CO_2 + 12H^+ + 12e^-$	97.3	0.084		
	Cathode:	$12H^+ + 12e^- + 3O_2 \rightarrow 6H_2O_{(l)}$		1.229		
	Overall:	$C_2H_5OH_{(l)} + 3O_2 \rightarrow 2CO_2 + 3H_2O_{(l)}$	1325	1.145	1367	0.969
Formic acid	Anode:	$HCOOH_{(l)} \rightarrow CO_2 + 2H^+ + 2e^-$	−33	−0.171		
	Cathode:	$2H^+ + 2e^- + (1/2)O_2 \rightarrow H_2O_{(l)}$		1.229		
	Overall:	$HCOOH_{(l)} + (1/2)O_2 \rightarrow CO_2 + H_2O_{(l)}$	270	1.400	254.3	1.062
2-Propanol	Anode:	$C_3H_7OH_{(l)} + 5H_2O \rightarrow 3CO_2 + 18H^+ + 18e^-$	186.3	0.107		
	Cathode:	$18H^+ + 18e^- + (9/2)O_2 \rightarrow 9H_2O_{(l)}$		1.229		
	Overall:	$C_3H_7OH_{(l)} + (9/2)O_2 \rightarrow 3CO_2 + 4H_2O_{(l)}$	1948	1.122	2005.6	0.971

Table 1.8. Comparison of selected properties for PEM fuel cells with different fuels under standard condition (25°C, 1 atm) [91]. (Reprinted from Journal of Power Sources, 154(1), Qian W, Wilkinson DP, Shen J, Wang H, Zhang J, Architecture for portable direct liquid fuel cells, 202–13, ©2006, with permission from Elsevier.)

Fuels		Reactions	$-\Delta G_f^0$ (kJ mol^{-1})	Theoretical potential, E^0 (V)	$-\Delta H^0$ (kJ mol^{-1})	Theoretical energy efficiency (%)
Hydrazine	Anode:	$N_2H_{4\,(l)} \rightarrow N_2 + 4H^+ + 4e^-$	−149.2	−0.386		
	Cathode:	$4H^+ + 4e^- + O_2 \rightarrow 2H_2O_{(l)}$		1.229		
	Overall:	$N_2H_{4\,(l)} + O_2 \rightarrow N_2 + 2H_2O_{(l)}$	623.4	1.615	622.2	1.002
Dimethyl ether	Anode:	$(CH_3)_2O_{(g)} + 3H_2O \rightarrow 2CO_2 + 12H^+ + 12e^-$	35.4	0.031		
	Cathode:	$12H^+ + 12e^- + 3O_2 \rightarrow 6H_2O_{(l)}$		1.229		
	Overall:	$(CH_3)_2O_{(g)} + 3O_2 \rightarrow 2CO_2 + 3H_2O_{(l)}$	1387.2	1.198	1460.3	0.950
Ethylene glycol	Anode:	$C_2H_6O_{2\,(l)} + 2H_2O \rightarrow 2CO_2 + 10H^+ + 10e^-$	8.78	0.009		
	Cathode:	$10H^+ + 10e^- + 5/2O_2 \rightarrow 5H_2O_{(l)}$		1.229		
	Overall:	$C_2H_6O_{2\,(l)} + 5/2O_2 \rightarrow 2CO_2 + 3H_2O_{(l)}$	1176.7	1.220	1189.5	0.990
Dimethoxymethane	Anode:	$(CH_3O)_2CH_{2\,(l)} + 4H_2O \rightarrow 3CO_2 + 16H^+ + 16e^-$	2.18	0.002		
	Cathode:	$16H^+ + 16e^- + 4O_2 \rightarrow 8H_2O_{(l)}$		1.229		
	Overall:	$(CH_3O)_2CH_{2\,(l)} + 4O_2 \rightarrow 3CO_2 + 4H_2O_{(l)}$	1894.6	1.227	1937.5	0.978

Table 1.8. (continued)

1.3 Reaction Kinetics

1.3.1 Electrode Reactions

A fuel cell is an electrochemical energy converter. Its operation is based on the following electrochemical reactions occurring simultaneously on the anode and the cathode [1]:

Anode Reaction:

$$H_2 \rightarrow 2H^+ + 2e^- \qquad (1.62)$$

At the anode, hydrogen is stripped of its electrons and become protons and electrons.

Cathode Reaction:

$$1/2 O_2 + 2H^+ + 2e^- \rightarrow H_2O \qquad (1.63)$$
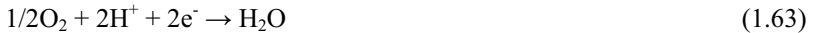
At the cathode, oxygen is oxidized, meaning that it takes the electrons and forms water. As described in Section 1.2, the HOR on Pt catalysts has a lower oxidation overpotential and a higher kinetic rate, whereas the ORR is sluggish, involving sequential and parallel steps.

1.3.2 Reaction Rate

More commonly, we use the following reaction to represent the anode and cathode reactions above.

$$O_x + ne- \rightarrow R_d \qquad (1.64)$$

where Ox stands for the oxidized form of the reactant and Rd stands for the reduced form of the reactant. The rate of an electrochemical reaction proceeding on the electrode surface is the speed at which the electrons are released or consumed.

1.3.2.1 Current Density and Exchange Current Density

Since electrode reactions are heterogeneous, their reaction rates are usually described in units of mol s^{-1} per unit area. In Equation 1.64, both elementary reactions are active at all times, and the rate of the forward process v_f (mol s^{-1} cm^{-2}) is

$$v_f = k_f C_{Ox} \qquad (1.65)$$

whereas the rate of the reverse reaction is

$$v_b = k_b C_{Rd} \tag{1.66}$$

The rate constants, k_f and k_b, have dimensions of s^{-1}, and one can easily show that they are the reciprocals of the mean lifetimes of O_x and R_d, respectively. C_{Ox}, and C_{Rd} are the surface concentrations of the reacting species with a unit of mol/cm^2. The net conversion rate of O_x to Rd is

$$v_{net} = k_f C_{Ox} - k_b C_{Rd} \tag{1.67}$$

The rate of an electrochemical reaction is determined by an activation energy barrier that the charge must overcome to move from electrolyte to a solid electrode or vice versa, and is described using the electrical current. Very often, we use current density (the current per unit area of the surface). The current density, i, is related to the charge transferred, the consumption of reactant, and the surface area by Faraday's law.

$$i = nFv \tag{1.68}$$

where F is Faraday's constant (96485 C/mol), and the physical meaning of nF is the charge transferred. v is the reactant consumed with a unit of mols^{-1} cm^{-2}.

The reaction rate, current density, is easy to measure. But note that this current density is a net current density, which is the difference between the forward and reverse current densities on the electrode. Generally, for a reaction in Equation 1.64, the net current density can be expressed as

$$i = nF(k_f C_{Ox} - k_b C_{Rd}) \tag{1.69}$$

where k_f is the forward reaction rate constant (s^{-1}), C_{Ox} is the surface concentration of the reacting species (mol cm^{-2}), k_b is the reverse reaction rate constant (s^{-1}), and C_{Rd} is the surface concentration of the reacting species (mol cm^{-2}).

At equilibrium, the net current is equal to zero. However, this does not mean that both the forward reaction and the backward reaction stop. Actually, both reactions proceed in opposite directions but with the same speed. The rate at which they proceed at equilibrium is called the exchange current density, i_0 [1].

$$i_0 = nFk_f C_{Ox} = nFk_b C_{Rd} \tag{1.70}$$

The value of the exchange current density depends on the inherent speed of the electrode reaction: a slow reaction (with a small exchange current density) will require a larger overpotential for a given current density than a fast reaction (with a large exchange current density).

1.3.2.2 Arrhenius Equation and Transition State Theory
The Arrhenius equation shows the dependence of the rate constant of chemical reactions on the temperature and activation energy. Its form is

$$k = A \exp(-\frac{E_a}{RT}) \tag{1.71}$$

where E_a is the activation energy, which has units of energy. A is known generally as the pre-exponential factor or frequency factor [134].

According to transition state theory, the rate constant for an electrochemical reaction is a function of the Gibbs free energy [1].

$$k = \frac{k_B T}{h} \exp(\frac{-\Delta G}{RT}) \tag{1.72}$$

where k_B is Boltzmann's constant and h is Planck's constant.

The Gibbs free energy for electrochemical reactions is considered to consist of both chemical and electrical terms. Therefore, for reduction reaction

$$\Delta G = \Delta G_{ch} + \alpha_{Rd} nFE \tag{1.73}$$

and for oxidation reaction

$$\Delta G = \Delta G_{ch} - \alpha_{Ox} nFE \tag{1.74}$$

where ΔG_{ch} is the chemical component of the Gibbs free energy, α is the transfer coefficient, F is Faraday's constant, and E is the potential. The value of α is theoretically between 0 and 1, and most typically for the reactions on a metallic surface it is around 0.5. The relationship of α_{Rd} and α_{Ox} is as follows:

$$\alpha_{Rd} + \alpha_{Ox} = 1 \tag{1.75}$$

Thus, the forward reduction and backward oxidation reaction rate constant can be expressed as

$$k_f = k_{0,f} \exp[\frac{-\alpha_{Rd} nFE}{RT}] \tag{1.76}$$

$$k_b = k_{0,b} \exp[\frac{\alpha_{Ox} nFE}{RT}] \tag{1.77}$$

where $k_{0,f}$ and $k_{0,b}$ are the standard rate constants for the forward reaction and backward reaction, respectively; that is, they are the rate constants when the electrodes are at thermodynamic standard potentials.

1.3.2.3 Butler-Volmer Equation

By introducing Equations 1.75, 1.76, and 1.77 into Equation 1.69, the net current density is obtained:

$$i = nF[k_{0,f}C_{Ox} \exp(\frac{-\alpha_{Rd}nFE}{RT}) - k_{0,b}C_{Rd} \exp(\frac{(1-\alpha_{Rd})nFE}{RT})] \qquad (1.78)$$

At equilibrium, we have

$$i_0 = nFk_{0,f}C_{Ox}^b \exp(\frac{-\alpha_{Rd}nFE_{eq}}{RT}) = nFk_{0,b}C_{Rd}^b \exp(\frac{(1-\alpha_{Rd})nFE_{eq}}{RT}) \qquad (1.79)$$

where E_{eq} is the reversible or equilibrium potential, and C_{Ox}^b and C_{Rd}^b are the bulk concentration of the reacting species (mol/cm^2). As described in Section 1.2, the reversible or equilibrium potential at the fuel cell anode and cathode at 25 °C and atmospheric pressure are 0 and 1.229 V, respectively. For simplicity, we define α as α_{Rd}.

According to Equation 1.78 and 1.79, we have

$$i = i_0[\frac{C_{Ox}}{C_{Ox}^b} \exp(\frac{-\alpha nF(E-E_{eq})}{RT}) - \frac{C_{Rd}}{C_{Rd}^b} \exp(\frac{(1-\alpha)nF(E-E_{eq})}{RT})] \qquad (1.80)$$

Then Equation 1.80 can be simplified as

$$i = i_0[\frac{C_{Ox}}{C_{Ox}^b} \exp(\frac{-\alpha nF\eta}{RT}) - \frac{C_{Rd}}{C_{Rd}^b} \exp(\frac{(1-\alpha)nF\eta}{RT})] \qquad (1.81)$$

where η is the overpotential (for the anode reaction $\eta_a = E_a - E_{eq} > 0$; for the cathode reaction $\eta_c = E_c - E_{eq} < 0$). Assuming $C_{Ox} = C_{Ox}^b$, and $C_{Rd} = C_{Rd}^b$,

$$i = i_0[\exp(\frac{-\alpha nF\eta}{RT}) - \exp(\frac{(1-\alpha)nF\eta}{RT})] \qquad (1.82)$$

Equation 1.82 is known as the Butler-Volmer equation, describing the current-potential relationship.

Applying the Butler-Volmer equation to a fuel cell anode and cathode reaction, the anodic and cathodic kinetic current densities can be expressed as Equations 1.83 and 1.84, respectively, and it is obvious that we have $i_c = -i_a$, where the

cathode current density is defined as positive and anode current density is defined as negative, when the fuel cell is under load.

$$i_a = i_{0,H_2}[\exp(\frac{-\alpha_H n_{\alpha,H} F \eta_a}{RT}) - \exp(\frac{(1-\alpha_H)n_{\alpha,H} F \eta_a}{RT})]$$ (1.83)

$$i_c = i_{0,O_2}[\exp(\frac{-\alpha_O n_{\alpha,O} F \eta_c}{RT}) - \exp(\frac{(1-\alpha_O)n_{\alpha,O} F \eta_c}{RT})]$$ (1.84)

where

i_c	=	the cathodic current density
i_α	=	the anodic current density
i_{0,O_2}	=	the apparent exchange current density for cathodic O_2 reduction
i_{0,H_2}	=	the apparent exchange current density for the anodic H_2 oxidation reaction
R	=	the universal gas constant ($8.314\ J/mol \cdot K$)
T	=	the temperature (K).
F	=	Faraday constant (96485 C/mol)
$n_{\alpha,O}$	=	the electron transfer number in the rate determining step for cathodic O_2 reduction
$n_{\alpha,H}$	=	the electron transfer number in the rate determining step for anodic H_2 oxidation reaction
α_O	=	the transfer coefficient in the rate determining step for cathodic O_2 reduction ($\alpha_O = \alpha_{O,Rd}$)
α_H	=	the transfer coefficient in the rate determining step for anodic H_2 oxidation ($\alpha_H = \alpha_{H,Rd}$)

The value of $n_{\alpha,H}$ is 1.0, which has been widely reported in the literature [135–137]. For the value of $n_{\alpha,O}$, the literature presents two Tafel slopes for the oxygen reduction polarization curve [138–141]. The first case, where the slope is approximately 60 mV/decade at 25 °C, corresponds to a $n_{\alpha,O}$ value of 2.0 for $\alpha_o \approx$ 0.5 in the low current density range (the higher cathode potential range where the electrode surface is partially covered by PtO). For the second case, the Tafel slope in the higher current density range is around 120 mV/decade with a $n_{\alpha,O}$ value of 1.0, corresponding to a low cathode potential range where the electrode surface is pure Pt.

α_O and α_H in Equations 1.83 and 1.84 are the electron transfer coefficients for cathodic O_2 reduction and anodic H_2 oxidation, respectively. On a Pt electrode, α_O is a temperature-dependent parameter as reported in the literature [142–145], and can be expressed as

$$\alpha_O = \alpha_O^0 T \tag{1.85}$$

where $\alpha_{O-Pt/PtO}^0 = 0.00168$ K^{-1} in the temperature range of 20 °C to 250 °C. However, α_H for H$_2$ oxidation on a Pt electrode seems to be independent of temperature and a value of 0.5 is widely reported in the literature [146–148].

1.3.2.4 Linear Polarization

At a small overpotential, that is, $\left|\dfrac{nF\eta}{RT}\right| \ll 1$, the Butler-Volmer equation can be simplified as

$$i = i_0[1 - \frac{\alpha nF\eta}{RT} - (1 + (1-\alpha)\frac{nF\eta}{RT})] \tag{1.86}$$

That is,

$$i = -i_0 \frac{nF\eta}{RT} \tag{1.87}$$

Therefore, we have

$$R_{ct} = -\eta / i = \frac{RT}{nFi_0} \tag{1.88}$$

where R_{ct} is the charge transfer resistance, which refers to the barrier across which the electrons passes from the electrode surface to the adsorbed species or from the adsorbed species to the electrode. The resistance is related to the electrode potential, or more precisely, to the overpotential. R_{ct} is a very important kinetic parameter, describing the speed of the electrode reaction. R_{ct} can be obtained by AC impedance method.

Again, the electron number refers only to the electrons involved in the rate determining step. For a multi-electron, multi-step reaction, n does not equal the total electrons involved in the whole reaction. For example, the ORR involves a total of 4 electrons. However, the apparent electron number changes with the Tafel slope. At the low current density range (low overpotential), a Tafel slope of 60 mV/dec has been observed, indicating that the apparent electron number in the rate determining step is 2.

1.3.2.5 Tafel Equation – Simplified Activation Kinetics

At high overpotential, one term in the Butler-Volmer equation can be ignored and the equation can be simplified. For the forward reaction,

$$i = i_0 \exp(\frac{-\alpha nF\eta}{RT})$$ (1.89)

For the backward reaction,

$$i = -i_0 \exp(\frac{(1-\alpha)nF\eta}{RT})$$ (1.90)

Rearrangement of the two equations gives the forward reaction as

$$\eta = \frac{RT}{\alpha nF} \ln i_0 - \frac{RT}{\alpha nF} \ln i$$ (1.91)

$$\eta = \frac{2.303RT}{\alpha nF} \log i_0 - \frac{2.303RT}{\alpha nF} \log i$$ (1.92)

Assuming

$$a = \frac{2.303RT}{\alpha nF} \log i_0$$ (1.93)

$$b = -\frac{2.303RT}{\alpha nF}$$ (1.94)

then Equation 1.92 is simplified as

$$\eta = a + b \log i$$ (1.95)

At 25 °C, $a = \frac{0.059}{\alpha n} \log i_0$, and $b = -\frac{0.059}{\alpha n}$. Equation 1.95 is the well-known
Tafel equation, which tells us that in a certain current density range, overpotenital
is linearly dependant on the logarithm of current density. The exchange current
density can be obtained from the intercept at the current density axis. The slope of
the line is called the Tafel slope. The higher the Tafel slope, the slower the reaction
kinetics.

For the backward reaction,

$$\eta = -\frac{RT}{(1-\alpha)nF} \ln i_0 + \frac{RT}{(1-\alpha)nF} \ln(-i)$$ (1.96)

$$\eta = -\frac{2.303RT}{(1-\alpha)nF} \log i_0 + \frac{2.303RT}{(1-\alpha)nF} \log(-i)$$ (1.97)

Assuming

$$a = -\frac{2.303RT}{(1-\alpha)nF}\log i_0 \tag{1.98}$$

$$b = \frac{2.303RT}{(1-\alpha)nF} \tag{1.99}$$

then for the backward reaction we also have

$$\eta = a + b\log(-i) \tag{1.100}$$

The values of $-\dfrac{2.303RT}{\alpha nF}$ and $\dfrac{2.303RT}{(1-\alpha)nF}$ are the Tafel slopes for the forward and backward reactions, respectively.

Now we can apply the Tafel equation to fuel cell electrode reactions. As the overpotential at the anode is positive ($\eta_a > 0$), the first term in Equation 1.83 is negligible. Equation 1.83 can be simplified as

$$i_a = -i_{0,H_2}\exp(\frac{(1-\alpha_H)n_{\alpha,H}F\eta_a}{RT}) \tag{1.101}$$

Similarly, as the overpotential at the cathode is negative ($\eta_c < 0$), Equation 1.84 can be simplified as

$$i_c = i_{0,O_2}\exp(\frac{-\alpha_O n_{\alpha,O}F\eta_c}{RT}) \tag{1.102}$$

Their Tafel forms are therefore written as follows:

$$\eta_a = -\frac{2.303RT}{(1-\alpha_H)n_{\alpha,H}F}\log i_{0,H_2} + \frac{2.303RT}{(1-\alpha_H)n_{\alpha,H}F}\log(-i_a) \tag{1.103}$$

$$\eta_c = \frac{2.303RT}{\alpha_O n_{\alpha,O}F}\log i_{0,O_2} - \frac{2.303RT}{\alpha_O n_{\alpha,O}F}\log i_c \tag{1.104]}$$

1.3.3 Mass Transfer

Transport processes are involved when a current is passed through a fuel cell. Ions and neutral species that participate in the electrochemical reactions at the anode or cathode have to be transported to the respective electrode surfaces. In Section 1.3.2, we introduced the charge transfer kinetics-controlled electrode reactions in

which the rates of mass transfer processes are very rapid compared to those of all associated chemical reactions. The Tafel characteristic is representative of an irreversible electrode reaction in which the exchange current density is very small. Another case is the mass transfer-controlled reactions in which the rates of all associated chemical reactions are very rapid compared to those of the mass transfer processes.

1.3.3.1 Fast-Speed Electrode Reaction
Rearrangement of Equation 1.81 gives

$$\frac{i}{i_0} = \frac{C_{Ox}}{C_{Ox}^b} \exp(\frac{-\alpha nF\eta}{RT}) - \frac{C_{Rd}}{C_{Rd}^b} \exp(\frac{(1-\alpha)nF\eta}{RT}) \qquad (1.105)$$

When the exchange current density is very large compared with the electrode reaction current density, that is, $i_0 \gg i$, the left side of Equation 1.105 is approximately equal to zero. Then Equation 1.105 can be written as

$$\frac{C_{Ox}}{C_{Rd}} = \frac{C_{Ox}^b}{C_{Rd}^b} \exp(\frac{nF(E - E_{eq})}{RT}) \qquad (1.106)$$

Based on the Nernst equation,

$$E_{eq} = E_{eq}^0 + \frac{RT}{nF} \ln \frac{C_{Ox}^b}{C_{Rd}^b} \qquad (1.107)$$

That is,

$$\frac{C_{Ox}^b}{C_{Rd}^b} = \exp[\frac{nF(E_{eq} - E_{eq}^0)}{RT}] \qquad (1.108)$$

We obtain

$$E = E_{eq}^0 + \frac{RT}{nF} \ln \frac{C_{Ox}}{C_{Rd}} \qquad (1.109)$$

Equation 1.109 has the same form as the Nernst equation. It indicates that the surface concentrations of species involved in the Faradaic process are related to the electrode potential by an equation of the Nernst form when the exchange current density is very large. Such electrode reactions are often called reversible or Nernstian, because the principal species obey thermodynamic relationships at the electrode surface.

1.3.3.2 Modes of Mass Transfer

For a reversible electrode reaction, the electrode potential is related to the surface concentrations of species by the Nernst equation. The net rate of the electrode reaction, v_{net}, is then governed completely by the rate at which the electroactive species is brought to the surface by mass transfer, v_{mt}. Hence,

$$v_{net} = v_{mt} = \frac{i}{nF} \tag{1.110}$$

There are three modes of mass transfer, which plays an important role in electrochemical dynamics.

1. Migration: movement of a charged body under the influence of an electric field (a gradient of electrical potential).
2. Diffusion:. movement of a species under the influence of a gradient of chemical potential (i.e., a concentration gradient).
3. Convection: stirring or hydrodynamic transport. Generally fluid flow occurs because of natural convection (convection caused by density gradients) and forced convection, and may be characterized by stagnant regions, laminar flow, and turbulent flow.

Mass transfer to an electrode is governed by the Nernst-Planck equation, written for one-dimensional mass transfer along the *x*-axis as

$$J_i = -D_i \nabla C_i - \frac{Z_i F}{RT} D_i C_i \nabla \phi + C_i v \tag{1.111}$$

where J_i is the flux of species i (mols^{-1} cm^{-2}) at distance *x* from the surface, D_i is the diffusion coefficient (cm^{2}s), ∇ is a vector operator, C_i is the concentration, ϕ is the electrical potential, Z_i is the charge number, v is the velocity of the solution, and F is the Faraday constant. The three terms on the right-hand side represent the contributions of diffusion, migration, and convection, respectively, to the flux. A rigorous solution is generally not very easy when all three forms of mass transfer are in effect; hence electrochemical systems are frequently designed so that one or more of the contributions to mass transfer are negligible. For example, the migrational component can be reduced to negligible levels by the addition of an inert electrolyte (a supporting electrolyte) at a concentration much larger than that of the electroactive species. Convection can be avoided by preventing stirring and vibrations in the electrochemical cell.

1.3.3.3 Semi-Empirical Treatment of Steady-State Mass Transfer

For the cathode reaction of a reversible electrode reaction (Reaction 1.64), without considering migration and convection, the electrode reaction rate equals the diffusion rate of O$_x$ at the electrode surface:

$$v_{mt} = -D_{Ox}(\frac{\partial C_{Ox}(x)}{\partial x})_{x=0} \tag{1.112}$$

Under the condition of steady-state diffusion, we assume that the diffusion distance is δ. Equation 1.112 turns out to be

$$v_{mt} = D_{Ox} \frac{C_{Ox}^b - C_{Ox}}{\delta} \tag{1.113}$$

where C_{Ox} is the surface concentration of O_x. Then we have,

$$\frac{i}{nF} = D_{Ox} \frac{C_{Ox}^b - C_{Ox}}{\delta} \tag{1.114}$$

Obviously, if $C_{Ox} = 0$ or $C_{Ox} \ll C_{Ox}^b$,

$$\frac{i_l^f}{nF} = \frac{D_{Ox} C_{Ox}^b}{\delta} \tag{1.115}$$

where i_l^f is the forward limiting current density. Equation 1.114 can be transformed to

$$i = \frac{nFD_{Ox}}{\delta} C_{Ox}^b (1 - \frac{C_{Ox}}{C_{Ox}^b}) \tag{1.116}$$

Then,

$$\frac{C_{Ox}}{C_{Ox}^b} = 1 - \frac{i}{i_l^f} \tag{1.117}$$

Similarly,

$$\frac{C_{Rd}}{C_{Rd}^b} = 1 - \frac{i}{i_l^b} \tag{1.118}$$

where i_l^b is the backward limiting current density.

1.3.3.4 Effect of Mass Transfer on Voltage-Current Relationship
Substitution of the expressions in Equations 1.117 and 1.118 into 1.81 yields

$$i = i_0[(1 - \frac{i}{i_l^f})\exp(\frac{-\alpha nF\eta}{RT}) - (1 - \frac{i}{i_l^b})\exp(\frac{(1-\alpha)nF\eta}{RT})] \qquad (1.119)$$

Equation 1.119 is the $i - \eta$ relationship including the effect of mass transfer.

When the overpotential is very small, that is, $\left|\frac{nF\eta}{RT}\right| << 1$,

$$\exp(\frac{-\alpha nF\eta}{RT}) \approx 1 - \frac{\alpha nF\eta}{RT} \qquad (1.120)$$

$$\exp(\frac{(1-\alpha)nF\eta}{RT}) \approx 1 + \frac{(1-\alpha)nF\eta}{RT} \qquad (1.121)$$

These two expressions combine with Equation 1.119 to yield

$$i = i_0[(1 - \frac{i}{i_l^f})(1 - \frac{\alpha nF\eta}{RT}) - (1 - \frac{i}{i_l^b})(1 + \frac{(1-\alpha)nF\eta}{RT})] \qquad (1.122)$$

When the overpotential is very small, we also have $i/i_l^f << 1$, and $i/i_l^b << 1$. Then $\frac{i}{i_l^f}(\frac{\alpha nF\eta}{RT})$ and $\frac{i}{i_l^b}(\frac{(1-\alpha)nF\eta}{RT})$ are negligible and Equation 1.122 becomes

$$\frac{i}{i_0} = -\frac{i}{i_l^f} + \frac{i}{i_l^b} - \frac{nF\eta}{RT} \qquad (1.123)$$

or

$$\eta = -i(\frac{RT}{nFi_0} + \frac{RT}{nFi_l^f} - \frac{RT}{nFi_l^b}) \qquad (1.124)$$

Previously we defined $\frac{RT}{nFi_0}$ as the charge transfer resistance (see Equation 1.88). Similarly, $\frac{RT}{nFi_l^f}$ and $\frac{RT}{nFi_l^b}$ have the same unit as $\frac{RT}{nFi_0}$. So they are defined as the mass transfer resistance, $R_{mt,c}$ and $R_{mt,a}$, respectively; that is,

$$R_{mt,f} = \frac{RT}{nFi_l^f} \qquad (1.125)$$

$$R_{mt,b} = -\frac{RT}{nFi_l^b} \qquad (1.126)$$

Therefore, Equation 1.124 can be written as

$$\eta = -i(R_{ct} + R_{mt,f} + R_{mt,b}) \qquad (1.127)$$

Obviously, when i_0 is very large, we have

$$R_{ct} \ll R_{mt,f} + R_{mt,b} \qquad (1.128)$$

and when i_0 is very small, we have

$$R_{ct} \gg R_{mt,f} + R_{mt,b} \qquad (1.129)$$

Note that the equations derived in this section apply when the overpotential is small. Therefore, Equations 1.128 and 1.129 indicate that near the equilibrium electrode potential, the overpotential is controlled by the mass transfer when i_0 is very large. On the contrary, near the equilibrium electrode potential, the overpotential is controlled by the charge transfer when i_0 is very small.

1.3.4 Multiple Kinetics

1.3.4.1 Electrode Kinetic and Mass Transfer for Fuel Cell Reactions

For the reaction occurring inside a porous three-dimensional catalyst layer, a thin-film flooded agglomerate model has been developed [149, 150] to describe the potential-current behavior as a function of reaction kinetics and reactant diffusion. For simplicity, if the kinetic parameters, such as the exchange current density and diffusion limiting current density, can be defined as apparent parameters, the corresponding Butler-Volmer and mass diffusion relationships can be obtained [134]. For an H_2/air (O_2) fuel cell, considering both the electrode kinetic and the mass transfer, the $i - \eta$ relationships of the fuel cell electrode reactions within the catalyst layer can be expressed as Equations 1.130 and 1.131, respectively, based on Equation 1.122. The $i - \eta$ relationship of the catalyzed cathode reaction within the catalyst layer is

$$i_c = i_{0,O_2} [(1 - \frac{i_c}{i_{l,O}^f}) \exp(\frac{-\alpha_O n_{\alpha,O} F \eta_c}{RT}) - (1 - \frac{i_c}{i_{l,O}^b}) \exp(\frac{(1 - \alpha_O) n_{\alpha,O} F \eta_c}{RT})]$$

$$(1.130)$$

and the corresponding $i - \eta$ relationship of the anode reaction is

$$i_a = i_{0,H_2}[(1-\frac{i_a}{i_{l,H}^f})\exp(\frac{-\alpha_H n_{\alpha,H} F\eta_a}{RT}) - (1-\frac{i_a}{i_{l,H}^b})\exp(\frac{(1-\alpha_H)n_{\alpha,H} F\eta_a}{RT})]$$

$$(1.131)$$

where R is the gas constant (8.314 Jmol^{-1}K^{-1}) and T is the temperature (K). i_c and i_a are the cathode and anode current densities, respectively. i_{0,O_2} and i_{0,H_2} are the apparent exchange current densities for cathodic O_2 reduction and anodic H_2 oxidation reactions, respectively. $i_{l,O}^f$ and $i_{l,O}^b$ are the apparent diffusion limiting current densities for the cathodic forward and reverse reactions, respectively, and $i_{l,H}^f$ and $i_{l,H}^b$ are the corresponding apparent diffusion limiting current densities for anode reactions. It is assumed that these six apparent current densities are all a function of the morphology and structure of the three-dimensional catalyst layer matrix [151]. η_c and η_a in Equations 1.130 and 1.131 are the cathodic and anodic overpotentials, respectively. η_c can be expressed as $E_c - E_c^{eq}$, and η_a can be expressed as $E_a - E_a^{eq}$, where E_c^{eq} and E_a^{eq} are the thermodynamic electrode potentials (or reversible electrode potentials) for cathodic O_2 reduction and anodic H_2 oxidation, respectively. $n_{\alpha O}$ and $n_{\alpha H}$ in Equations 1.130 and 1.131 are the electron transfer numbers in the rate determining steps for the cathodic O_2 reduction and anodic H_2 oxidation reactions, respectively.

1.3.4.2 Low Current Density

In the low current density range, the contribution of mass transfer polarization is negligible and the electrode charge transfer and membrane resistance polarization are significant. In this case, Equations 1.130 and 1.131 can be simplified into Equations 1.132 and 1.133, respectively.

$$i_c = i_{0,O_2}[\exp(\frac{-\alpha_O n_{\alpha,O} F\eta_c}{RT}) - \exp(\frac{(1-\alpha_O)n_{\alpha,O} F\eta_c}{RT})]$$

$$(1.132)$$

$$i_a = i_{0,H_2}[\exp(\frac{-\alpha_H n_{\alpha,H} F\eta_a}{RT}) - \exp(\frac{(1-\alpha_H)n_{\alpha,H} F\eta_a}{RT})]$$

$$(1.133)$$

From the AC impedance spectra, the exchange current density of the ORR can be calculated from the charge transfer resistance. In the low current density range (< 0.4 A/cm^2, the Pt catalyst surface will be covered partially by a PtO layer with surface coverage of approximately 0.3 [125, 152, 153], the numerical relationship between η_c and i_c can thus be obtained.

1.3.4.3 High Current Density

In the high current density range (> 0.4 A/cm^2, the catalyst surface will be covered with pure Pt [154, 155]), the diffusion-related terms in Equations 1.130 and 1.131 must be considered. As a result, at high overpotentials (both η_c and η_a are large),

the second terms will be insignificant compared to the first terms, suggesting that the second terms are negligible. Therefore, Equations 1.130 and 1.131 can be simplified as Equations 1.134 and 1.135, respectively:

$$i_c = i_{0,O_2}[(1 - \frac{i_c}{i_{l,O}^f})\exp(\frac{-\alpha_O n_{\alpha,O} F\eta_c}{RT})]$$
(1.134)

$$i_a = -i_{0,H_2}(1 - \frac{i_a}{i_{l,H}^b})\exp(\frac{(1 - \alpha_H)n_{\alpha,H} F\eta_a}{RT})$$
(1.135)

1.3.5 Polarization Curve and Voltage Losses

1.3.5.1 Polarization
When the fuel cell operates, the actual voltage of the cell is less than the value of the OCV. Cell voltage is the actual voltage of the fuel cell and the current density, i, is the cell current, I, per cell active area, A.

$$i = \frac{I}{A}$$
(1.136)

The cell current is equal to the stack current because the stack is formed by connecting the individual cells in series.
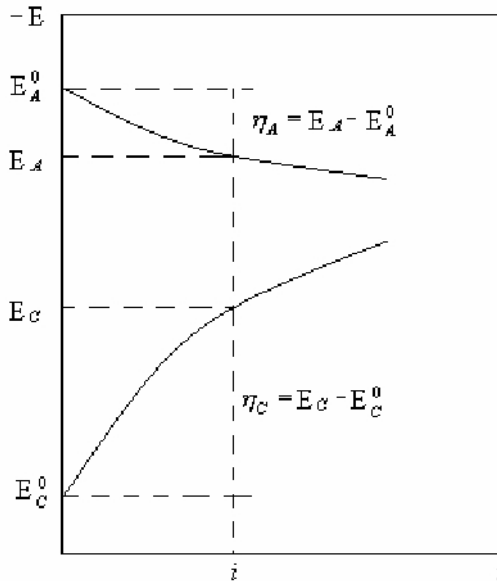
Figure 1.26. A schematic plot of electrode polarization and voltage drop

Once the fuel cell circuit is connected, there is a current flow, which causes the electrode to be polarized. This means that the anode electrode potential will move to a more positive value, and the cathode electrode potential will move to a more negative value, resulting in a decrease in the cell voltage, which is known as the voltage loss. The principle is shown in Figure 1.26.

1.3.5.2 Polarization Curve
A plot of cell potential against current density under a set of constant operating conditions, known as a polarization curve, is the standard electrochemical technique for characterizing the performance of fuel cells (both single cells and stacks) [156]. It yields information on the performance losses in the cell or stack under operating conditions. A steady-state polarization curve can be obtained by recording the current as a function of cell potential or recording the cell potential as the cell current changes. A non-steady-state polarization curve can be obtained using a rapid current sweep [157]. By measuring polarization curves, certain parameters such as the effects of the composition, flow rate, temperature, and RH of the reactant gases on cell performance can be characterized and compared systematically. A sample polarization curve is shown in Figure 1.27. Very often, polarization curves are converted to power density versus current density plots by multiplying the potential by the current density at each point of the curve, also seen in Figure 1.27.
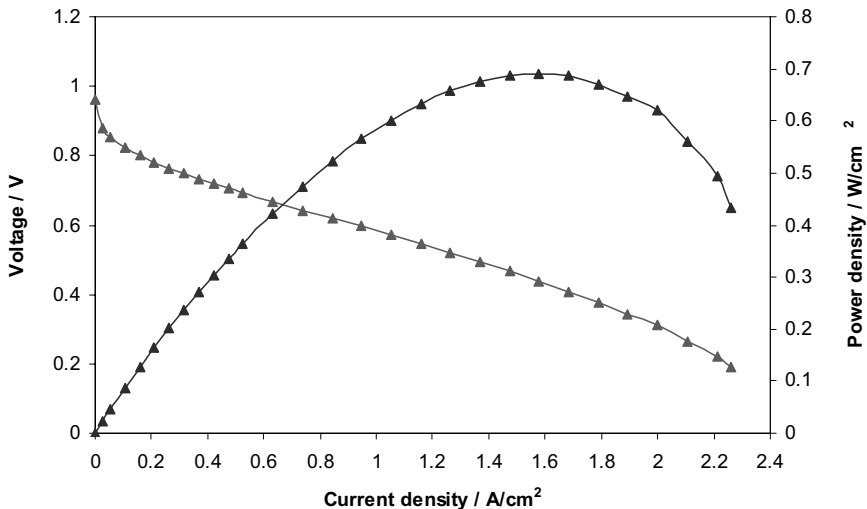
Figure 1.27. A sample fuel cell polarization curve obtained from the diagnostic modeling PEM fuel cell with an active area of 192 cm^2, designed by NRC-IFCI

Polarization curves provide information on the performance of the cell or stack as a whole. While they are useful indicators of overall performance under specific operating conditions, they fail to produce much information about the performance of individual components within the cell. They cannot be obtained during normal operation of a fuel cell and take significant time. In addition, they fail to

differentiate different mechanisms; for example, flooding and drying inside a fuel cell cannot be distinguished in a single polarization curve. They are also incapable of resolving time-dependent processes occurring in the fuel cell and the stack. For the latter purpose, current interrupt, EIS measurements, and other electrochemical approaches are preferred. These techniques will be introduced in the following sections.

1.3.5.3 Voltage Loss

The fuel cell voltage losses are classified into three categories: the activation loss (activation polarization), the ohmic loss (ohmic polarization), and the concentration loss (concentration polarization). Plots of voltage drops caused by each of the losses are shown in Figure 1.28. At low current densities (the region of activation polarization), the cell potential drops sharply and the majority of these losses are due to the sluggish kinetics of the ORR [1]. At intermediate current densities (the region of ohmic polarization), the voltage loss caused by ohmic resistance becomes significant and results mainly from resistance to the flow of ions in the electrolyte and resistance to the flow of electrons through the electrode [158]. In this region, the cell potential decreases nearly linearly with current density, while the activation overpotential reaches a relatively constant value [1]. At high current densities (the region of concentration polarization), mass transport effects dominate due to the transport limit of the reactant gas through the pore structure of the GDLs and electrocatalyst layers, and cell performance drops drastically [159].
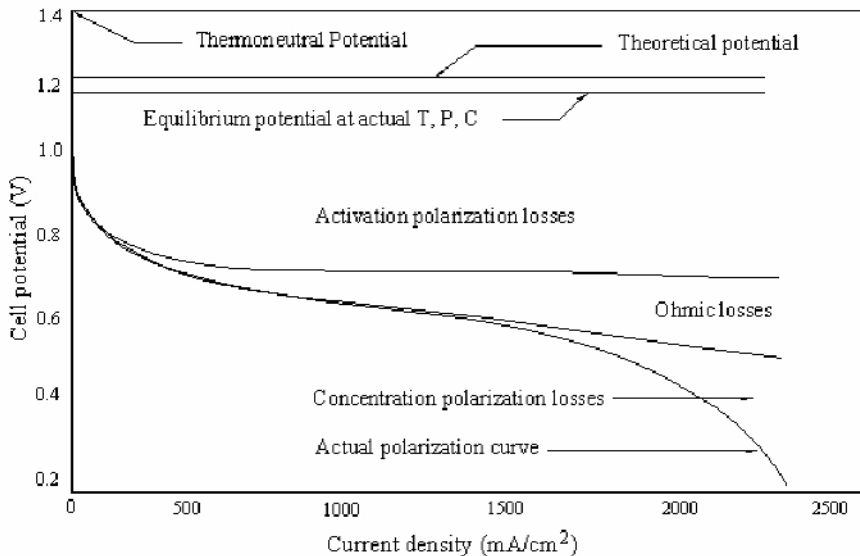
Figure 1.28. Schematic of an ideal polarization curve with the corresponding regions and overpotentials [1]. (Reprinted from Barbir F. PEM fuel cells: theory and practice. New York: Elsevier Academic Press, ©2005, with permission from Elsevier.)

The output voltage of a single cell, E_{cell}, can be defined as follows:

$$E_{cell} = E_{OCV} - \Delta E_{act} - \Delta E_{ohmic} - \Delta E_{con} \tag{1.137}$$

where E_{cell} is the voltage for a certain operating condition, E_{OCV} represents the fuel cell OCV, ΔE_{act} is the voltage drop associated with the activation of the anode and of the cathode, ΔE_{ohmic} is the ohmic voltage drop associated with the conduction of protons and electrons, and ΔE_{con} is the voltage drop resulting from the decrease in the concentration of oxygen and hydrogen. Each of these losses is discussed separately in the following sections.

Activation Loss
Activation overvoltage or activation loss is caused by activation polarization, which arises from the need to move electrons and to break and form chemical bonds in both the anode and the cathode.

$$\Delta E_{act} = |\eta_a| + |\eta_c| \tag{1.138}$$

In low- and medium-temperature fuel cells, activation overvoltage is the most important irreversibility and cause of voltage drop. The relation between activation overvoltage and current density is described by the Tafel equation, e.g.,

$$\eta_c = a + b \log i \tag{1.139}$$

Therefore, based on Equations 1.103 and 1.104, the activation loss can be expressed as

$$\Delta V_{act} = [-\frac{2.303RT}{(1-\alpha_H)n_{\alpha,H}F} \log i_{0,H_2} + \frac{2.303RT}{(1-\alpha_H)n_{\alpha,H}F} \log i]$$
$$+ [-\frac{2.303RT}{\alpha_O n_{\alpha,O}F} \log i_{0,O_2} + \frac{2.303RT}{\alpha_O n_{\alpha,O}F} \log i] \tag{1.140}$$

This is simplified as

$$\Delta V_{act} = A_c \ln(\frac{i}{i_{0,O_2}}) + A_a \ln(\frac{i}{i_{0,H_2}}) \tag{1.141}$$

where $A_c = \dfrac{RT}{\alpha_O n_{\alpha,O}F}$ and $A_a = \dfrac{RT}{(1-\alpha_H)n_{\alpha,H}F}$.

As the reaction of hydrogen oxidation at the anode is much faster than that of oxygen reduction at the cathode the voltage drop due to the activation loss is

dominated by the cathode reaction, and activation overvoltage occurs mainly at the cathode.

Then, Equation 1.140 is simplified as

$$\Delta V_{act} = -\frac{2.303RT}{\alpha_O n_{\alpha,O} F} \log i_{0,O_2} + \frac{2.303RT}{\alpha_O n_{\alpha,O} F} \log i \tag{1.142}$$

or

$$\Delta V_{act} = A_c \ln(\frac{i}{i_{0,O_2}}) \tag{1.143}$$

Activation overvoltage at both electrodes is important in cells using fuels other than hydrogen, such as methanol. At higher temperatures and pressures the activation overvoltage becomes less important.

Mass Transport or Concentration Loss
Concentration polarization will cause concentration loss or concentration overvoltage, which arises from the drop in concentration of the reactants as they are consumed in the reaction. This concentration loss can cause rapid voltage drop at high current density. As the concentration loss or voltage drop is composed of concentration polarization on the anode and the cathode, the total concentration loss is expressed as

$$\Delta E_{con} = \Delta E_{con,c} + \Delta E_{con,a} \tag{1.144}$$

According to the Nernst equation, we have

$$\Delta E = \frac{RT}{nF} \ln(\frac{C_{Ox}^b}{C_{Ox}}) \tag{1.145}$$

By combining Equations 1.145, 1.114, and 1.115, a relationship for voltage loss due to concentration polarization is obtained:

$$\Delta E_{con,c} = \frac{RT}{nF} \ln(\frac{i_{l,c}}{i_{l,c} - i}) \tag{1.146}$$

Similarly, we have

$$\Delta E_{con,a} = \frac{RT}{nF} \ln(\frac{i_{l,a}}{i_{l,a} - i}) \tag{1.147}$$

Therefore, the total concentration loss is written as

$$\Delta E_{con} = \frac{RT}{nF}\ln(\frac{i_{l,c}}{i_{l,c}-i}) + \frac{RT}{nF}\ln(\frac{i_{l,a}}{i_{l,a}-i}) \qquad (1.148)$$

Ohmic Loss

Ohmic loss is the simplest voltage loss to understand. Ohmic loss or ohmic overvoltage is caused by ohmic polarization, which arises from the resistance of the polymer membrane to the transfer of ions and the resistance of the electrode and the collector plate to the transfer of electrons.

The voltage drop related to the ohmic polarization is described by Ohm's law,

$$\Delta E_{ohm} = iR_{ohm} \qquad (1.149)$$

where R_{ohm} (Ωcm^2) is the internal electrical resistance, which includes ionic, electronic, and contact resistances. In most fuel cells, electronic resistance is almost negligible, even when graphite or graphite/polymer composites are used as current collectors, and the resistance is caused primarily by the electrolyte (ionic), though the contact resistances can also be important. Generally, it is possible to distinquish this particular voltage loss from other voltage losses through tecniques like AC impedance and current interruption.

Summary

There is another voltage loss, which is caused by fuel crossover and internal currents. Basically, fuel crossover and internal currents have very marked effects on the OCV, E_{OCV}. For more information on this voltage loss, please see Section 1.2.4.

To summarize, the cell potential is equal to the open circuit potential reduced by the potential loss or voltage drop [1]:

$$E_{cell} = E_{OCV} - E_{loss} \qquad (1.150)$$

where the voltage drop is composed of activation and concentration polarization losses on both the anode and the cathode and of ohmic losses,

$$E_{loss} = (\Delta E_{act} + \Delta E_{con})_a + (\Delta E_{act} + \Delta E_{con})_c + \Delta E_{Ohmic} \qquad (1.151)$$

and the actual OCV is expressed as

$$E_{OCV} = E_{theor}^{OCV} - E_{cross} - E_{mix} \qquad (1.152)$$

A theoretical OCV can be obtained as described in Section 1.2.4.1:

$$E_{theor}^{OCV} = 1.229 - 0.000846(T - 298.15) + \frac{RT}{4F}\ln[P_{O_2}(P_{H_2})^2] \qquad (1.153)$$

1.3.5.4 Empirical Equations for the Polarization Curves

So far, numerous modeling studies have been carried out to elucidate the electrochemical behavior of PEM fuel cells, and for this purpose, many empirical equations have been introduced to mimic the polarization curves. Srinivasan et al. [160, 161] developed the following equation to describe the relation between the cell voltage, *E,* and current density, *i,* in the low and intermediate current density ranges, where the electrochemical reaction is controlled by the activation and ohmic losses:

$$E = E_0 - b\log(i) - Ri \tag{1.154}$$

where $E_0 = E_r + b\log i_0$ and the two subsequent terms describe the different loss mechanisms. E_r is the reversible potential of the cell, and i_0 and b are the exchange current density and the Tafel slope for oxygen reduction, respectively. The second term in Equation 1.154 is predominant at low current densities and describes the activation overpotential. In the third term, *R* represents the resistance that causes a linear variation of the cell potential with the current density, which is predominant in the intermediate current density region.

Kim et al. [162] modified Equation 1.154 by introducing an additional term in order to fit the cell voltage against current density behavior over the whole current density range:

$$E = E_0 - b\log(i) - Ri - m\exp(ni) \tag{1.155}$$

where *m* and *n* are the parameters related to mass transport limitation. Bevers et al. [163] found in their one-dimensional model that *m* correlates to the electrolyte conductivity and *n* to the porosity of the GDL. In the high current density region the last term becomes predominant, and is used to match the losses due to the mass transport limitations.

Lee et al. [164] took into account the influence of pressure parameters on the concentration polarization in PEM fuel cell stack models,

$$E = E_0 - b\log(i) - Ri - m\exp(ni) - a\log(\frac{P}{P_{O_2}}) \tag{1.156}$$

where *P* is the total pressure, P_{O_2} is the partial pressure of oxygen, and *a* is an empirical equation constant.

Squadrito et al. [165] developed a logarithmic equation based on a mechanistic analysis in order to find an expression for the concentration polarization, which was then modified to fit a set of experimental data:

$$E = E_0 - b\log(i) - Ri + \alpha i^k \ln(1 - \beta i) \tag{1.157}$$

where the term αi^k accounts for the pre-logarithmic terms attributed to the different contributions and acts as an "amplification term," expressed in potential units; k is a dimensionless number; β is a the inverse of the limiting current density; and α is the transfer coefficient. Squadrito et al. further claimed that Equation 1.157 is able to predict a more accurate behavior at high current densities since k influences primarily the point at which there is departure from the linear behavior, and α determines the shape of the curve at high current densities.

The non-linear contributions to the cell potential drop at high current densities result from interface phenomena occurring in the cathode reactive region. Pisani et al. [166] developed a semi-empirical equation, based on the integral of the oxygen concentration over the reactive region,

$$E = E_0 - b\ln(i) - Ri + a\ln\left(1 - \frac{i}{i_l}S^{-\mu(1-i/i_l)}\right) \tag{1.158}$$

where S is a flooding parameter, μ is an empirical constant, and i_l is the limiting current density.

More complex empirical equations based on Equation 1.155 have also been developed. For example, Amphlett et al. [167] presented empirical equations and terms that relate activation losses, internal resistance, and all temperature dependencies through fitting parameters. Sena et al. [168] analyzed the catalyst layer and considered it as a thin-film flooded agglomerate; thus, the GDE is assumed to be formed by an assembly of flooded zones (catalytic zones) and empty zones (no catalyst present). The final equation relates the oxygen diffusion effects in the GDE:

$$E = E_0 - b\log(i) - Ri + b\log\left(1 - \frac{i}{i_L^{O_2}}\right) \tag{1.159}$$

where $i_L^{O_2}$ is the limiting current density due to a limiting oxygen diffusion effect.

1.3.5.5 Distinguishing the Voltage Losses

Current Interruption
In general, the current interruption method is used to measure the ohmic losses in a PEM fuel cell. The principle of the technique is that the ohmic losses vanish much faster than the electrochemical overpotentials when the current is interrupted, as shown in Figure 1.29. It is shown that the ohmic losses disappear almost immediately and the electrochemical (or activation) overpotentials decline to the OCV at a considerably slower rate. Therefore, rapid acquisition of the voltage transient data is of vital importance to adequate separation of the ohmic and activation losses.
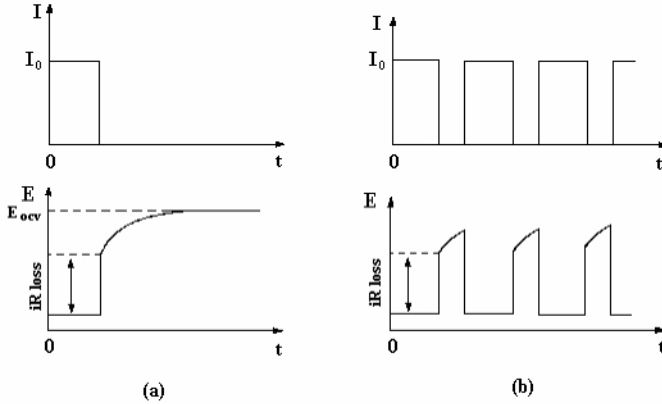
Figure 1.29. An ideal voltage transient in a fuel cell after current interruption, (a) single interruption technique, (b) periodic interruption technique

The crucial issue in measuring *in situ* ohmic losses is to separate the above two processes [169]. Many attempts using this method have been made to determine the ohmic resistances in single cells or individual cells of a PEM fuel cell stack. For example, Mennola et al. [170] have employed this method to determine the ohmic resistances in individual cells of a PEM fuel cell stack. Figure 1.30 shows one of their results. It was achieved by producing voltage transients and monitoring them with a digital oscilloscope connected in parallel with the individual cell. Their results show good agreement between the ohmic losses in the entire stack and the sum of the ohmic losses in each individual cell
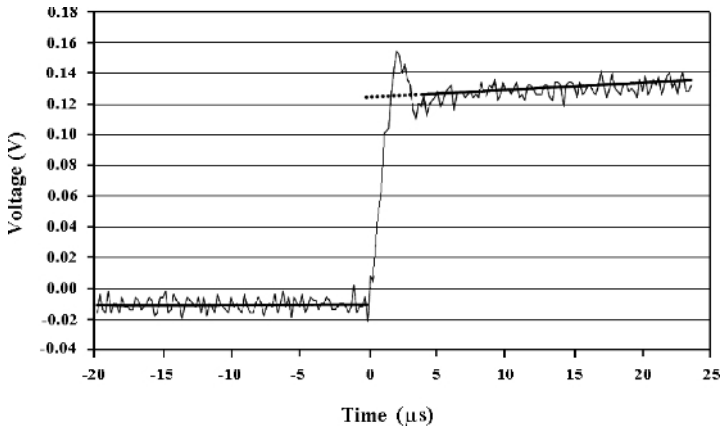
Figure 1.30. Voltage transient (thin line) and fitted average voltage (bold line) for the whole stack. Extrapolation is indicated with a dotted line. Air supply: free convection; i = 200 mA cm^{-2} 171. (Reprinted from Journal of Power Sources, 112(1), Mennola Tuomas, Mikkola Mikko, Noponen Matti, Hottinen Tero and Lund Peter, Measurement of ohmic voltage losses in individual cells of a PEMFC stack, 261–72, ©2002, with permission from Elsevier.)

Compared to other methods, the current interrupt method has the advantage of relatively straightforward data analysis. However, one of the weaknesses of this method is that the information obtained for a single cell or stack is limited. Another issue with this method is the difficulty in determining the exact point at which the voltage jumps instantaneously; thus, a fast oscilloscope should be used to record the voltage changes.

AC Impedance

AC impedance, also known as EIS, applies a small AC voltage or current perturbation/signal to the cell and the amplitude and phase of the resulting signal are measured as a function of frequency. This may be repeated through a wide range of frequencies. Basically, impedance is a measure of the ability of a system to impede the flow of electrical current; thus, EIS is a powerful technique that can resolve various sources of polarization loss in a short time and has been widely applied to PEM fuel cells.

Impedance spectra are conventionally plotted in both Bode and Nyquist form. In a Bode plot, the amplitude and phase of the impedance are plotted as a function of frequency, while in a Nyquist plot the imaginary part of the impedance is plotted against the real part at each frequency. Figure 1.31 shows the typical EIS spectra in Nyquist form with two arcs, where the frequency increases from the right to the left. The simple form of the equivalent circuit for the spectra in Figure 1.31 is depicted in Figure 1.32. The high-frequency intercept is related to the ohmic resistance of the stack, R_Ω, which can be directly compared with the data obtained from current interrupt measurements. The high-frequency arc reflects the combination of the double-layer capacitance in the catalyst layer and the effective charge transfer resistance. The low-frequency arc corresponds to the impedance due to mass transport limitations. The reason for replacing C, the double layer capacitor, by the constant phase element (CPE) results from the fact that the capacitance due to the double-layer charging is distributed along the length of the pores in the porous electrode.
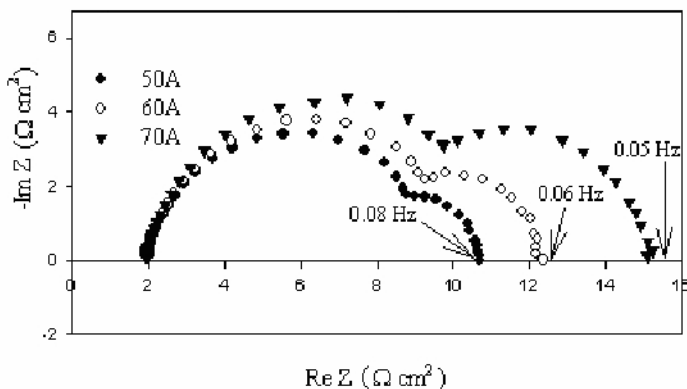
Figure 1.31. Typical impedance spectra of a PEM fuel cell. The spectra were obtained at 30 °C using a Ballard Mark V six-cell stack with an active area of 280 cm^2.
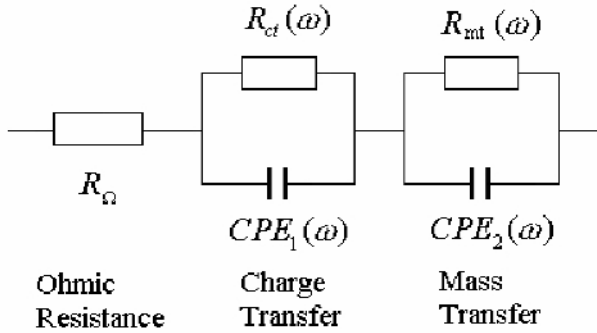
Figure 1.32. Simple equivalent circuit for the spectra in Figure 1.31

The impedance can be measured using various instruments and techniques, ranging from a simple oscilloscope display to a fast Fourier transform analyzer. The most common instrument used is a frequency response analyzer (FRA), such as a Solartron FRA. The AC impedance or FRA is a four-terminal measurement. Figure 1.33 shows a typical electronic connection for an AC impedance measurement between the Solartron 1260 FRA, TDI loadbank (RBL 488 series 100–60–400), and fuel cell.
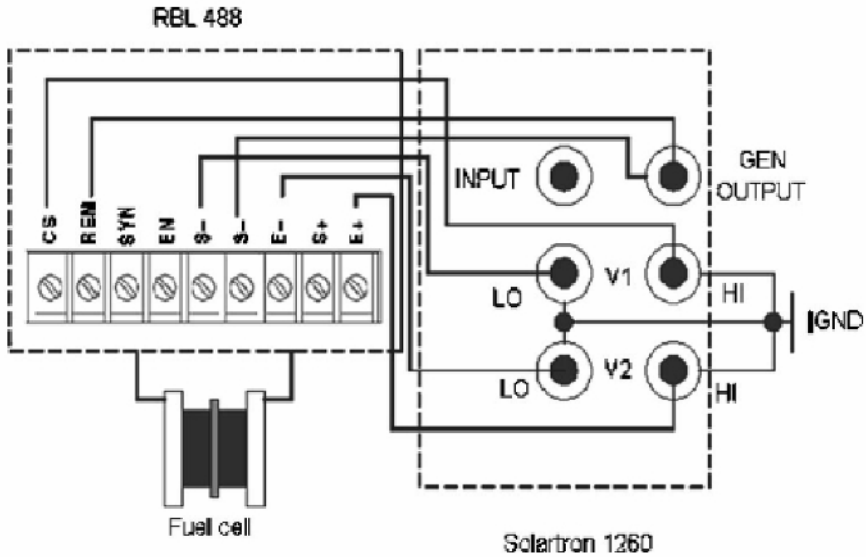
Figure 1.33. Typical electronic connections of AC impedance measurement of a PEM fuel cell [5]. (Reproduced by permission of ECS—The Electrochemical Society, from Tang Y, Zhang J, Song C, Liu H, Zhang J, Wang H, et al. Temperature-dependent performance and *in situ* AC impedance of high-temperature PEM fuel cells using the Nafion-112 membrane.)

The Solartron 1260 FRA can perform flexible signal processing. The TDI loadbank is a single channel loadbank that can be controlled with signals via an external program. When a controlling DC, AC, DC/AC combination, or FRA-generated waveform is connected into the REM and S- ports located on the rear panel of the loadbank, the loadbank will transfer the signal into the fuel cell load level. The values of all signals are referred to as S-. In Tang et al.'s [40] impedance experiments, the differential input with a floating ground was chosen to reduce noise and harmonic signals from externally wired circuits. An oscilloscope was connected to the fuel cell current collectors to monitor the noise level. The results showed that this electronic connection can effectively reduce noise. During the measurements, the FRA port, GEN OUTPUT, gave a software-command signal to the loadbank through the REM and S- ports. The cell voltage response went to FRA V1 and V2 for analysis. The obtained impedance information was sent to a computer for data display and more sophisticated data analysis performed by the powerful software Z-plot.

However, there are still unresolved issues regarding the explanation of the impedance spectra. For example, it is difficult to distinguish the individual contributions from the anode and cathode sides, although it is generally considered that the rapid kinetics and mass transport of the HOR result in a negligible impedance contribution from the anode catalyst layer. In addition, the interpretation of the low-frequency feature can be very sophisticated.

1.3.6 Measures to Improve Cell Performance [26]

1.3.6.1 Reducing the Activation Overvoltage
As described in the previous sections, the exchange current density, i_0, is a crucial factor in reducing the activation overvoltage. Therefore, the most important step for improving the fuel cell performance is to increase the value of i_0, especially at the cathode. The increase of i_0 can be achieved in several ways summarized, as follows:

- Raising the cell temperature. For a low-temperature cell, i0 at the cathode will be about 0.1 mAcm−2, whereas for a typical 800 °C cell, it will be about 10 mAcm−2, a 100-fold improvement.
- Using more effective catalysts.
- Increasing the roughness of the electrodes. This increases the real surface area of the electrodes, leading to an increase in i_0.
- Increasing reactant concentration. This is achieved by greater occupation of reactants on the catalyst sites.
- Increasing the pressure. This is also achieved by increasing catalyst site occupancies.

1.3.6.2 Reducing the Concentration Overvoltage
Reducing the concentration overvoltage can be achieved by enhancing mass transfer through the following ways:

- Increasing reactant concentration by, for example, using pure O_2 instead of air.

- Increasing the gas flow rate or pressure to enhance mass transfer.
- Designing the flow field to help mass transfer through the channels.
- Optimizing the GDL porosity and improving GDL structure.

1.3.6.3 Reducing the Ohmic Overvoltage

There are three main ways of reducing the internal resistance of the cell:

- The use of electrodes with the highest possible conductivity.
- Good design and use of appropriate materials for the bipolar plates or cell interconnects.
- Making the electrolyte as thin as possible. However, this is often difficult because the electrolyte needs to be thick enough to support the electrodes, or it needs to be wide enough to allow a circulating flow of electrolyte.

References

1. Barbir F. PEM fuel cells: theory and practice. New York: Elsevier Academic Press, 2005.
2. Smithsonian Institute [homepage on the Internet]. Washington, DC: National Museum of American History; c1990–2008 [updated 2004]. PEM fuel cells. Available from: http://americanhistory.si.edu/fuelcells/pem/pemmain.htm.
3. Wikipedia [updated 18 April 2008]. Proton exchange membrane fuel cells. Available from: http://en.wikipedia.org/wiki/Proton_exchange_membrane_fuel_cell.
4. Ballard Power Systems [homepage on the Internet]. Burnaby, Canada: Ballard Power Systems; c2008 [updated 2008]. Company history. Available from: http://www.ballard.com/About_Ballard/Corporate_Information/Company_History.htm
5. Tang Y, Zhang J, Song C, Liu H, Zhang J, Wang H, et al. Temperature-dependent performance and in situ AC impedance of high-temperature PEM fuel cells using the Nafion-112 membrane. J Electrochem Soc 2006;153(11): A2036–43.
6. Martin J, Blanco M, Pazos-Knoop S, Gu E, Wang H, Vanderhoek T, et al. (National Research Council of Canada Institute for Fuel Cell Innovation). Controlled Technical Report. Vancouver (BC) Canada: NRC-IFCI; 2005. Report No.: IFCI-PEMFC-CTR-015.
7. Nguyen TV, Knobbe MW. A liquid water management strategy for PEM fuel cell stacks. J Power Sources 2003;114:70–79.
8. Wilkinson D, Vanderleeden O. Handbook of Fuel Cells: Fundamentals, Technology and Applications Vol. 3. In: Vielstich W, Lamm A, Gasteriger HA, editors. Chicester, England: John Wiley and Sons, 2003; 315–36.
9. Mehta V, Cooper JS. Review and analysis of PEM fuel cell design and manufacturing. J Power Sources 2003;114:32–53.
10. EG&G Technical Services, Ltd. Fuel cell handbook. Morgantown, West Virginia: U.S. Department of Energy, 2004.
11. Pukrushpan JT, Stefanopoulou AG, Peng H. Control of fuel cell breathing. IEEE Control Systems Magazine 2004;24:30–46.
12. Panchenko A. Polymer electrolyte membrane degradation and oxygen reduction in fuel cells: an EPR and DFT investigation. Doctoral thesis, Institute für Phzsikalische Chemie der Universität, Stuttgart, 2004. Available from: http://elib.uni-stuttgart.de/opus/volltexte/2004/2088/pdf/Panchenko.pdf.

13. Kadirov MK, Bosnjakovic A, Schlick S. Membrane-derived fluorinated radicals detected by electron spin resonance in UV-irradiated Nafion and Dow ionomers: effect of counterions and H_2O_2. J Phys Chem B 2005;109:7664–766.
14. LaConti AB, Hamdan M, McDonald RC. Mechanisms of chemical degradation. In. Handbook of fuel cells: fundamentals, technology, and applications, vol. 3. Vielstich W, Lamm A, Gasteiger H, editors. Chicester, England: John Wiley and Sons; 2003;647–62.
15. Hodgdon RB Jr, Enos JF, Aiken EJ. Sulfonated polymers of $\alpha, \beta, \beta-$ trifluorostyrene, with applications to structures and cell. US Patent 3 341 366 1967.
16. Hodgdon RB Jr, Enos JF, Aiken EJ. Process of sulfonating poly-alpha, beta, beta-trifluorostyrene. US Patent 3 442 825 1969.
17. D'Agostino VF, Lee JY, Cook EH. Trifluorostyrene sulfonic acid membranes. US Patent 4 012 303 1977.
18. Yu J, Yi B, Xing D, Liu F, Shao Z, Fu Y, Zhang H. Degradation mechanism of polystyrene sulfonic acid membrane and application of its composite membranes in fuel cells. Phys Chem Chem Phys 2003;5:611–5.
19. Feldheim DL, Lawson DR, Martin CR. Influence of the sulfonate counteraction on the thermal stability of Nafion perfluorosulfonate membranes. J Polym Sci Part B: Polym Phys 1993;31:953–7.
20. Patil YP, Seery TAP, Shaw MT, Parnas RS. In-situ water sensing in a Nafion membrane by fluorescence spectroscopy. Ind Eng Chem Res 2005;44:6141–7.
21. Huang C, Tan KS, Lin J, Tan KL. XRD and XPS analysis of the degradation of the polymer electrolyte in H_2–O_2 fuel cell. Chem Phys Lett 2003;371:80–5.
22. Hinds G. Performance and durability of PEM fuel cells: a review. Teddington, UK: National Physical Laboratory; 2004. NPL Report No.: DEPC-MPE 002.
23. Bauer B, Jones DJ, Rozière J, Tchicaya L, Alberti G, Casciola M, et al. Electrochemical characterization of sulfonated polyetherketone membranes. J New Mat Electrochem Systems 2000;3:93–8.
24. Colliera A, Wang H, Yuan XZ, Zhang J, Wilkinson DP. Degradation of polymer electrolyte membranes. Intern J Hydrogen Energy 2006;31:1838–54.
25. Perahia, D. Structure and dynamics of thin ionomer films: a key to a stable fuel cell membrane. American Physical Society Meeting; 2000 March 20–24; Minneapolis, MN. Available from: http://flux.aps.org/meetings/YR00/MAR00/abs/S4010.html.
26. Larminie J, Dicks A. Fuel cell systems explained. Chicester, England: John Wiley and Sons, 2003.
27. Lee JH, Lalk TR. Modeling fuel cell stack systems. J Power Sources 1998;73:229–41.
28. Bever D, Wagner N, VonBradke M. Innovative production procedure for low cost PEFC electrodes and electrode/membrane structures. Intern J Hydrogen Energy 1998;23:57–63.
29. Giorgi L, Antolini E, Pozio A, Passalacqua E. Infuence of the PTFE content in the diffusion layer of low-Pt loading electrodes for polymer electrolyte fuel cells. Electrochim Acta 1998;43:3675–80.
30. Ralph TR, Hards GA, Keating JE, Campbell SA, Wilkinson DP, Davis H, et al. Low-cost electrodes for proton exchange membrane fuel cells. J Electrochem Sci 1997;144:3845–57.
31. Itescu, J. Polymer electrolyte fuel cells: the gas diffusion layer [monograph on the Internet]. Princeton Institute for the Science and Technology of Materials. Princeton, NJ: Princeton University; 2004. Available from: http://www.princeton.edu/~pccm/outreach/REU2004/REU-2004-Presentations/JOHANNAH%20ITESCU.pdf.
32. US Department of Energy [homepage on the Internet]. Parts of a fuel cell. Washington, DC: US Department of Energy; c2008 [last updated 2007 Jan 31]. Hydrogen, fuel cells

and infrastructure technologies program. Available from: http://www.eere.energy.gov/hydrogenandfuelcells/fuelcells/fc_parts.html.

33. Williams MV, Begg E, Bonville L, Kunz HR, Fenton JM. Characterization of gas diffusion layers for PEMFC. J Electrochem Soc 2004;151:A1173–80.

34. Yuan XZ, Wang HJ, Zhang JJ, Wilkinson D. Bipolar plates for PEM fuel cells – from materials to processing. J New Mat Electrochem Syst 2005;8:257–67.

35. Cooper JS. Design analysis of PEMFC bipolar plates considering stack manufacturing and environment impact. J Power Sources 2004;129:152–69.

36. Davies DP, Adcock PL, Turpin M, Rowen SJ. Stainless steel as a bipolar plate material for solid polymer fuel cells. J Power Sources 2000;86:237–42.

37. Busick D, Wilson M. Development of composite materials for PEFC bipolar plates. Mat Res Soc Symp Proc 2000;575:247–51.

38. Heinzel A, Mahlendorf F, Niemzig O, Kreuz C. Injection moulded low cost bipolar plates for PEM fuel cells. J Power Sources 2004;131:35–40.

39. Borup RL, Vanderborgh NE. Design and testing criteria for bipolar plate materials for PEM fuel cell applications. Mat Res Soc Symp Proc 1995;393:151–5.

40. Jung UH, Jeong SU, Park KT, Lee HM, Chun K et al. Improvement of water management in air-breathing and air-blowing PEMFC at low temperature using hydrophilic silica nanoparticles. Intern J Hydrogen Energ. In press, 2007.

41. Li X, Sabir I, Park J. A flow channel design procedure for PEM fuel cells with effective water removal. J Power Sources 2007;163:933–42.

42. Wu J, Yuan XZ, Wang H, Blanco M, Martin J, Wilkinson DP, et al. Durability of PEM fuel cells. Presented at: Hydrogen and Fuel Cells 2007 International Conference and Trade Show; 2007 Apr 29–May 3; Vancouver, Canada.

43. Healy J, Hayden C, Xie T, Olson K, Waldo R, Brundage M, et al. Aspects of the chemical degradation of PFSA ionomers used in PEM fuel cells. Fuel Cells 2005;5:302–8.

44. Knights SD, Colbow KM, St-Pierre J, Wilkinson DP. Aging mechanisms and lifetime of PEFC and DMFC. J Power Sources 2004;127:127–34.

45. Meeker WQ, Escobar LA. Statistical methods for reliability data. New York: John Wiley and Sons, 1998.

46. Nelson W. Accelerated testing: statistical models, test plans, and data analyses. New York: John Wiley and Sons, 1990.

47. Hicks M. Membrane and catalyst durability under accelerated testing. In: Conference Proceedings of Fuel Cell Durability: Stationary, Automotive, Portable; 2005 Dec 8–9; Washington, DC. Brookline, MA: Knowledge Press; 2005.

48. Bonneville Power Administration [homepage on the Internet]. Portland, OR: Bonneville Power Administration; c2008 [updated 2004 Apr 19]. PEM fuel cells. Available from: http://www.bpa.gov/energy/n/tech/fuel_cell/pem_fuel_cells.cfm.

49. Fueleconomy.gov [homepage on the Internet]. Washington, DC: US Environmental Protection Agency; c2008 [updated 2008 Apr 18]. How they work: fuel cell systems. Available from: http://www.fueleconomy.gov/feg/fcv_components.shtml#.

50. Millett S, Mahadevan K. Commercialization scenarios of polymer electrolyte membrane fuel cell applications for stationary power generation in the United States by the year 2015. J Power Sources 2005;150:187–91.

51. BatteryUniversity.com [homepage on the Internet]. Richmond, Canada: Cadex Electronics Inc.; c2008 [updated 2006 Nov]. The miniature fuel cell. Available from: http://www.batteryuniversity.com/parttwo-52A.htm.

52. Wang B. Recent development of non-platinum catalysts for oxygen reduction reaction. J Power Sources 2005;152:1–15.

53. Neyerlin KC, Gu W, Jorne J, Gasteiger HA. Determination of catalyst unique parameters for the oxygen reduction reaction in a PEMFC. J Electrochem Soc 2006;153:A1955–63.
54. Ilevbare GO, Scully JR. Oxygen reduction reaction kinetics on chromate conversion coated Al-Cu, Al-Cu-Mg, and Al-Cu-Mn-Fe intermetallic compounds. J Electrochem Soc 2001;148:B196–207.
55. Neyerlin KC, Gasteiger HA, Mittelsteadt CK, Jorne J, Gu W. Effect of relative humidity on oxygen reduction kinetics in a PEMFC. J Electrochem Soc 2005;152:A1073–108.
56. Xu, Song Y, Kunz HR, Fenton JM. . Electrochem Soc 2005;152(9):A1828–36.
57. Prakash J, Joachin H. Electrocatalytic activity of ruthenium for oxygen reduction in alkaline solution. Electrochim Acta 2000;45:2289–96.
58. Otero R, Calleja F, García-Suárez VM, Hinarejos JJ, de la Figuera J, Ferrer J, et al. Tailoring surface electronic states via strain to control adsorption: O/Cu/Ru(0 0 0 1). Surf Sci 2004;550:65–72.
59. Xu Y, Mavrikakis M. Adsorption and dissociation of O_2 on gold surfaces: effect of steps and strain. J Phys Chem B 2003;107:9298–307.
60. Stiehl JD, Kim TS, McClure SM, Mullins CB. Evidence for molecularly chemisorbed oxygen on TiO_2 supported gold nanoclusters and Au(111). J Am Chem Soc 2004;126:1606–7.
61. Fernández JL, Walsh DA, Bard AJ. Thermodynamic guidelines for the design of bimetallic catalysts for oxygen electroreduction and rapid screening by scanning electrochemical microscopy. M–Co (M:Pd, Ag, Au). J Am Chem Soc 2005;127:357–365
62. Shen Y, Bi L, Liu B, Dong S. Simple preparation method of Pd nanoparticles on an Au electrode and its catalysis for dioxygen reduction. New J Chem 2003;27:938–41.
63. Lin Y, Cui X, Ye X. Electrocatalytic reactivity for oxygen reduction of palladium-modified carbon nanotubes synthesized in supercritical fluid. Electrochem Commun 2005;7:267–274
64. Demarconnay L, Coutanceau C, Léger JM. Electroreduction of dioxygen (ORR) in alkaline medium on Ag/C and Pt/C nanostructured catalysts: effect of the presence of methanol. Electrochim Acta 2004;49:4513–21.
65. Ohno S, Yagyuu K, Nakatsuji K, Komori F. Dissociation preference of oxygen molecules on an inhomogeneously strained Cu(0 0 1) surface. Surf Sci 2004;554:183–92.
66. Lescop B, Jay J-Ph, Fanjoux G. Reduction of oxygen pre-treated Ni(111) by H_2 exposure: UPS and MIES studies compared with Monte Carlo simulations. Surf Sci 2004;548:83–94.
67. Mentus SV. Oxygen reduction on anodically formed titanium dioxide. Electrochim Acta 2004;50:27–32.
68. Limoges BR, Stanis RJ, Turner JA, Herring AM. Electrocatalyst materials for fuel cells based on the polyoxometalates $[PMo_{(12-n)}VnO_{40}]^{(3+n)-}$ (n = 0–3). Electrochim Acta 2005;50:1169–79.
69. Lee K, Ishihara A, Mitsushima S, Kamiya N, Ota K. Stability and electrocatalytic activity for oxygen reduction in WC + Ta catalyst. Electrochim Acta 2004;49:3479–85.
70. Hayashi M, Uemura H, Shimanoe K, Miura N, Yamazoe N. Reverse micelle assisted dispersion of lanthanum manganite on carbon support for oxygen reduction cathode. J Electrochem Soc 2004;151:A158–63.
71. Yoshimoto S, Inukai J, Tada A, Abe T, Morimoto T, Osuka A, et al. Adlayer structure of and electrochemical O_2 reduction on cobalt porphine-modified and cobalt octaethylporphyrinmodified Au(1 1 1) in $HClO_4$. J Phys Chem B 2004;108:1948–54.

72. Chang CJ, Loh ZH, Shi C, Anson FC, Nocera DG. Targeted proton delivery in the catalyzed reduction of oxygen to water by bimetallic Pacman porphyrins. J Am Chem Soc 2004;126:10013–20.

73. Shen Y, Liu J, Jiang J, Liu B, Dong S. Fabrication of a metallopoyphyrin-polyoxometalate hybrid film by a layer-by-layer method and its catalysis for hydrogen evolution and dioxygen reduction. J Phys Chem B 2003;107:9744–8.

74. Araki K, Dovidauskas S, Winnischofer H, Alexiou ADP, Toma HE. A new highly efficient tetra-electronic catalyst based on a cobalt porphyrin bound to four 3-oxo-ruthenium acetate clusters. J Electroanal Chem 2001;498:152–60.

75. Yoshimoto S, Tada A, Suto K, Itaya K. Adlayer structures and electrocatalytic activity for O_2 of metallophthalocyanines on Au(1 1 1): in situ scanning tunnelling microscopy study. J Phys Chem B 2003;107:5836–43.

76. Zhang CX, Liang HC, Kim E, Shearer J, Helton ME, Kim E, et al. Tuning copper-dioxygen reactivity and exogenous substrate oxidations via alterations in ligand electronics. J Am Chem Soc 2003;125:634–5.

77. Kieber-Emmons MT, Schenker R, Yap GPA, Brunold TC, Riordan CG. Spectroscopic elucidation of a peroxo $Ni_2(\mu\text{-}O_2)$ intermediate derived from a nickel(I) complex and dioxygen. Angew Chem Int Ed 2004;43:6716–18.

78. Aboelella NW, Lewis EA, Reynolds AM, Brennessel WW, Cramer CJ, Tolman WB. Snapshots of dioxygen activation by copper: the structure of a 2002;1:1 Cu/O_2 adduct and its use in syntheses of asymmetric bis(-oxo) complexes. J Am Chem Soc 124: 10660–1.

79. Wagner N, Schnurnberger W, Mueller B, Lang M. Electrochemical impedance spectra of solid-oxide fuel cells and polymer membrane fuel cells. Electrochim Acta 1998;43:3785–93.

80. Wendt H, Spinacé EV, Oliveira Neto A, Linardi M. Electrocatalysis and electrocatalysts for low temperature fuel cells: fundamentals, state of the art, research and development. Quím Nova 2005;28:1066–75.

81. Santiago EI, Batista MS, Assaf EM, Ticianelli EA. Mechanism of CO tolerance on molybdenum-based electrocatalysts for PEMFC. J Electrochem Soc 2004; 151: A944–9.

82. Papageorgopoulos DC, de Heer MP, Keijzer M, Pieterse JAZ, de Bruijn FA. Nonalloyed carbon-supported PtRu catalysts for PEMFC applications. J Electrochem Soc 2004; 151: A763–8.

83. Lu G, Cooper JS, McGinn PJ. SECM characterization of Pt–Ru–WC and Pt–Ru–Co ternary thin film combinatorial libraries as anode electrocatalysts for PEMFC. J Power Sources 2006; 161: 106–14.

84. Blum A, Duvdevani T, Philosoph M, Rudoy N, Peled E. Water-neutral micro direct-methanol fuel cell (DMFC) for portable applications. J Power Sources 2003; 117: 22–5.

85. Chang H, Kim JR, Cho JH, Kim HK, Choi KH. Materials and processes for small fuel cells. Solid State Ionics 2002; 148: 601–6.

86. Rice C., Ha S, Masel RI, Waszczuk P, Wieckowski A, Barnard T. Direct formic acid fuel cells. J Power Sources 2002; 111: 83–9.

87. Rice C, Ha S, Masel RI, Wieckowski A. Catalysts for direct formic acid fuel cells. J Power Sources 2003; 115: 229–35.

88. Ha S, Adams B, Masel RI. A miniature air breathing direct formic acid fuel cells. J Power Sources 2004; 128: 119–24.

89. Zhu Y, Ha S, Masel RI. High power density direct formic acid fuel cells. J Power Sources 2004; 130: 8–14.

90. Ha S, Larsen R, Zhu Y, Masel RI. Direct formic acid fuel cells with 600Acm^{-2} at 0.4V and 22 °C. Fuel Cells 2004; 4: 337–43.

91. Qian W, Wilkinson DP, Shen J, Wang H, Zhang J. Architecture for portable direct liquid fuel cells. J Power Sources 2006; 154: 202–13.
92. Parsons TV. The oxidation of small organic molecules: A survey of recent fuel cell related research. J Electroanal Chem 1988; 257: 9–45.
93. Gupta SS, Datta J. Electrode kinetics of ethanol oxidation on novel CuNi alloy supported catalysts synthesized from PTFE suspension. J Power Sources 2005; 145: 124–32.
94. Lamy C, Lima A, LeRhun V, Delime F, Coutanceau C, Léger JM. Recent advances in the development of direct alcohol fuel cells (DAFC). J Power Sources 2002; 105: 283–96.
95. Vigier F, Coutanceau C, Hahn F, Belgsir EM, Lamy C. On the mechanism of ethanol electro-oxidation on Pt and PtSn catalysts: electrochemical and in situ IR reflectance spectroscopy studies. J Electroanal Chem 2004; 563: 81–9.
96. Raicheva SN, Christov MV, Sokolova EI. Effect of the temperature on the electrochemical behaviour of aliphatic alcohols. Electrochim Acta 1981; 26: 1669–76.
97. Ota K, Nakagawa Y, Takahashi M. Reaction products of anodic oxidation of methanol in sulfuric acid solution. J Electroanal Chem 1984; 179: 179–86.
98. Andreadis G, Song S, Tsiakaras P. Direct ethanol fuel cell anode simulation model. J Power Sources 2006; 157: 657–65.
99. Wang ZB, Yin GP, Zhang J, Sun YC, Shi PF. Investigation of ethanol electrooxidation on a Pt–Ru–Ni/C catalyst for a direct ethanol fuel cell. J Power Sources 2006; 160: 37–43.
100. Lux KW, Cairns EJ. Lanthanide-platinum intermetallic compounds as anode electrocatalysts for direct ethanol PEM fuel cells. J Electrochem Soc 2006; 153: A1139–47.
101. Lux KW, Cairns EJ. Lanthanide-platinum intermetallic compounds as anode electrocatalysts for direct ethanol PEM fuel cells. J Electrochem Soc 2006; 153: A1132–38.
102. Zhou WJ, Li WZ, Song SQ, Zhou ZH, Jiang LH, Sun GQ, et al. Bi- and tri-metallic Pt-based anode catalysts for direct ethanol fuel cells. J Power Sources 2004; 131: 217–23.
103. Oliveira Neto A, Giz MJ, Perez J, Ticianelli EA, Gonzalez ER. The electro-oxidation of ethanol on Pt-Ru and Pt-Mo particles supported on high-surface-area carbon. J Electrochem Soc 2002; 149: A272–9.
104. Colmati F, Antolini E, Gonalez ER. Ethanol oxidation on carbon supported Pt-Sn electrocatalysts prepared by reduction with formic acid. J Electrochem Soc 2007; 154: B39–47.
105. Zhou WJ, Song SQ, Li WZ, Sun GQ, Xin Q, Kontou S, et al. Pt-based anode catalysts for direct ethanol fuel cells. Solid State Ionics 2004; 175: 797–803.
106. Rousseau S, Coutanceau C, Lamy C, Léger JM. Direct ethanol fuel cell (DEFC): Electrical performances and reaction products distribution under operating conditions with different platinum-based anodes. J Power Sources 2006; 158: 18–24.
107. Song SQ, Zhou WJ, Zhou ZH, Jiang LH, Sun GQ, Q. Xin, et al. Direct ethanol PEM fuel cells: The case of platinum based anodes. Intern J Hydrogen Energy 2005; 30: 995–1001.
108. Wang H, Jusys Z, Behm RJ. Ethanol electro-oxidation on carbon-supported Pt, PtRu and Pt$_3$Sn catalysts: A quantitative DEMS study. J Power Sources 2006; 154: 351–9.
109. Gupta SS, Mahapatra SS, Datta J. A potential anode material for the direct alcohol fuel cell. J Power Sources 2004; 131: 169–74.
110. Rhee YW, Ha S, Rice C, Masel RI. Crossover of formic acid through Nafion® membranes. J Power Sources 2003; 117:35–8.

111. Lee J, Christoph J, Strasser P, Eiswirth M, Ertl G. Spatio-temporal interfacial potential patterns during the electrocatalyzed oxidation of formic acid on Bi-modified Pt. J Chem Phys 2001; 115: 1485–92.
112. Becerik İ, Kadirgan F. Electr-oxidation of formic acid on highly dispersed platinum and perchlorate doped polypyrrole electrodes. J Electrochem Soc 2001; 148: D49–54.
113. Zhao M, Rice C, Masel RI, Waszczuk P, Wieckowski A. Kinetic study of electro-oxidation of formic acid on spontaneously-deposited Pt/Pd nanoparticles. J Electrochem Soc 2004; 151: A131–6.
114. Larsen R, Masel RI. Kinetic study of CO tolerance during electeo-oxidation of formic acid on spontaneously deposited Pt/Pd and Pt/Ru nanoparticles. Electrochem Solid-State Lett 2004; 7: A148–50.
115. Zhang L, Lu T, Bao J, Tang Y, Li C. Preparation method of an ultrafine carbon supported Pd catalyst as an anodic catalyst in a direct formic acid fuel cell. Electrochem Commun 2006; 8: 1625–7.
116. Zhang L, Tang Y, Bao J, Lu T, Li C. A carbon-supported Pd-P catalyst as the anodic catalyst in a direct formic acid fuel cell. J Power Sources 2006; 162: 177–9.
117. Larsen R, Zakzeski J, Masel RI. Unexpected activity of palladium on vanadia catalysts for formic acid electro-oxidation. Electrochem Solid-State Lett 2005; 8: A291–3.
118. Weber M, Wang JT, Wasmus S, Savinell RF. Formic acid oxidation in a polymer electrolyte fuel cell. J Electrochem Soc 1996; 143: L158–60.
119. Pukrushpan JT, Stefanopoulou AG, Peng H. Control of Fuel Cell Power Systems: Principles, Modeling, Analysis, and Feedback Design. London Berlin Heidelberg New York Hong Kong Milan Paris Tokyo: Springer, 2004; 31–56.
120. Amphett JC, Baumert RM, Peppley RF, Roberge PR, Harris TJ. Performance modeling of the Ballard Mark IV solid polymer electrolyte fuel cell. J Electrochem Soc 1995; 142: 9–15.
121. Wroblowa H, Rao MLB, Damijanovic A, Bockris JO'M. Adsorption and kinetics at platinum electrodes in the presence of oxygen at zero net current. J Electroanal Chem 1967; 15: 139–50.
122. Bockris JO'M, Srinivasan S. Fuel Cells: Their Electrochemistry. New York: McGraw-Hill, 1969.
123. Appleby AJ. Oxygen reduction on oxide-free platinum in 85% orthophosphoric acid: temperature and impurity dependence. J Electrochem Soc 1970; 117: 328–35.
124. Hoare JP. Rest potentials in the platinum-oxygen-acid system. J Electrochem Soc 1962; 109: 858–65.
125. Thacker R, Hoare JP. Sorption of oxygen from solution by noble metals: I. Bright platinum. J Electroanal Chem 1971; 30:1–14.
126. Cooper KR, Ramani V, Fenton JM, Kunz HR. Experimental Methods and Data Analyses for Polymer Electrolyte Fuel Cells, Edition 1.2. Scribner, 2005.
127. Ramani V, Kunz HR, Fenton JM. Investigation of Nafion®/HPA composite membranes for high temperature/low relative humidity PEMFC operation. J Membr Sci 2004; 232: 31–44.
128. Ramani V, Kunz HR, Fenton JM. Stabilized composite membranes and membrane electrode assemblies for elevated temperature/low relative humidity PEFC operation. J Power Sources 2005; 152: 182–8.
129. Song Y, Fenton JM, Kunz HR, Bonville LJ, Williams MV. High-performance PEMFCs at elevated temperatures using Nafion 112 membranes. J Electrochem Soc 2005; 152: A539–44.
130. Cleghorn S, Kolde J, Liu W. Handbook of Fuel Cells: Fundamentals, Technology and Applications (Vol. 3). In: Vielstich W, Gasteiger HA, Lamm A, editors. Chicester: John Wiley & Sons, 2003; 566–75.

131. Yu J, Matsuura T, Yoshikawa Y, Islam MN, Hori M. In situ analysis of performance degradation of a PEMFC under nonsaturated humidification. Electrochem Solid-State Lett 2005; 8: A156–8.
132. Paganin VA, Sitta E, Iwasita T, Vielstich W. Methanol crossover effect on the cathode potential of a direct PEM fuel cell. J Appl Electrochem 2005; 35: 1239–43.
133. Jiang R, Chu D. Comparative Studies of Methanol Crossover and Cell Performance for a DMFC. J Electrochem Soc 2004; 151: A69–76.
134. Bard AJ, Faulkner LR. Electrochemical Methods: Fundamentals and applications (2nd edition). New York: John Wiley and Sons, 2001.
135. Vogel W, Lundquist J, Ross P, Stonehart P. Reaction pathways and poisons—II: The rate controlling step for electrochemical oxidation of hydrogen on Pt in acid and poisoning of the reaction by CO. Electrochim Acta 1975; 20: 79–93.
136. Jiang J, Kucernak A. Investigations of fuel cell reactions at the composite microelectrodesolid polymer electrolyte interface. I. Hydrogen oxidation at the nanostructured PtNafion$^{\circledR}$ membrane interface. J Electroanal Chem 2004; 567: 123–37.
137. Markovic NM, Grgur BN, Ross PN. Temperature-Dependent Hydrogen Electrochemistry on Platinum Low-Index Single-Crystal Surfaces in Acid Solutions. J Phys Chem B 1997; 101: 5405–13.
138. Parthasarathy A, Srinivasan S, Appleby AJ. Temperature dependence of the electrode kinetics of oxygen reduction at the platinum/Nafion interface-a microelectrode investigation. J Electrochem Soc 1992; 139: 2530–7.
139. Appleby AJ, Baker BS. Oxygen reduction on platinum in trifluoromethane sulfuric acid. J Electrochem Soc 1978; 125: 404–6.
140. Damjanovic A, Genshaw MA. Dependence of the kinetics of O_2 dissolution at Pt on the conditions for adsorption of reaction intermediates. Electrochim Acta 1970; 15: 1281–3.
141. Damjanovic A, Brusic V. Electrode kinetics of oxygen reduction on oxide-free platinum electrodes. Electrochim Acta 1967; 12: 615–28.
142. Appleby AJ. Evolution and reduction of oxygen on oxidized platinum in 85% orthophosphoric acid. J Electroanal Chem 1970; 24: 97–117.
143. Yeager E. Electrocatalysts for O_2 reduction. Electrochim Acta 1984; 29: 1527–37.
144. Clouser SJ, Huang JC, Yeager E. Temperature dependence of the Tafel slope for oxygen reduction on platinum in concentrated phosphoric acid. J Appl Electrochem 1993; 23: 597–605.
145. Damjanovic A. Temperature dependence of symmetry factors and the significance of experimental activation energies. J Electroanal Chem 1993; 355: 57–7.
146. Mello RMQ, Ticianelli EA. Kinetic study of the hydrogen oxidation reaction on platinum and Nafion $^{\circledR}$ covered platinum electrodes. Electrochim Acta 1997; 42: 1031–9.
147. Bockris JO'M, Gochev A. Temperature dependence of the symmetry factor in electrode kinetics. J Electroanal Chem 1986; 214: 655–74.
148. Ulstrup J. Temperature dependence of the transfer coefficient in electron and atom group transfer processes. Electrochim Acta 1984; 29: 1377–80.
149. Giner J, Hunter C. The mechanism of operation of the Teflon-bonded gas diffusion electrode: a mathematical model. J Electrochem Soc 1969; 116: 1124–30.
150. Springer TE, Raistrick ID. Electrical impedance of a pore wall for the flooded-agglomerate model of porous gas-diffusion electrodes. J Electrochem Soc 1989; 136: 1594–603.
151. Zhang J, Wang H, Wilkinson DP, Song D, Shen J, Liu Z. Model for the contamination of fuel cell anode catalyst in the presence of fuel stream impurities. J Power Sources 2005; 147: 58–71.

152. Nagerl K, Dietz H. Elektrochemisches verhalten anodisch hergestellter oxidschichten auf platin. Electrochim Acta 1961; 4: 1–11.
153. Dietz H, Göhr H. Über den elektrochemischen aufbau und abbau von sauerstoff- und wasserstoff-belegungen auf platin in wässriger lösung. Electrochim Acta 1963; 8: 343–59.
154. Damjanovic A, Bockris JO'M. The rate constants for oxygen dissolution on bare and oxide-covered platinum. Electrochim Acta 1966; 11: 376–7.
155. Sawyer DT, Day RJ. Kinetics for oxygen reduction at platinum, palladium and silver electrodes. Electrochim Acta 1963; 8: 589–94.
156. Li X. Principle of Fuel Cells. New York: Taylor and Francis, 2006.
157. Lim CY, Haas HR. A diagnostic method for an electrochemical fuel cell and fuel cell components. WO patent 2006029254, 2006.
158. Hirschenhofer JH, Stauffer DB, Engleman RR, Klett MG. Fuel Cell Handbook (4th edition). Reading PA: Parsons Corporation for U.S. Dept. of Energy, Office of Fossil Energy, Federal Energy Technology Center, 1998.
159. Ju H, Wang CY. Experimental validation of a PEM fuel cell model by current distribution data. J Electrochem Soc 2004; 151: A1954–60.
160. Srinivasan S, Ticianelli EA, Derouin CR, Redondo A. Advances in solid polymer electrolyte fuel cell technology with low platinum loading electrodes. J Power Sources 1988; 22: 359–75.
161. Srinivasan S, Velew OA, Parthasarathy A, Manko DJ, Appleby AJ. High energy efficiency and high power density proton exchange membrane fuel cells – electrode kinetics and mass transport. J Power Sources 1991; 36: 299–320.
162. Kim J, Lee SM, Srinivasan S. Modeling of proton exchange membrane fuel cell performance with an empirical equation. J Electrochem Soc 1995; 142: 2670–4.
163. Bevers D, Wohr M, Yasuda K, Oguro K. Simulation of a polymer electrolyte fuel cell electrode. J Appl Electrochem 1997; 27: 1254–64.
164. Lee JH, Lalk TR, Appleby AJ. Modeling electrochemical performance in large scale proton exchange membrane fuel cell stacks. J Power Sources 1998; 70: 258–68.
165. Squadrito G, Maggio G, Passalacqua E, Lufrano F, Patti A. An empirical equation for polymer electrolyte fuel cell (PEFC) behaviour. J Appl Electrochem 1999; 29: 1449–55.
166. Pisani L, Murgia G, Valentini M, D'Agurnno B. A new semi-empirical approach to performance curves of polymer electrolyte fuel cells. J Power Sources 2002; 108: 192–203.
167. Amphlett JC, Baumert RM, Mann RF, Peppley BA, Roberge PR, Harris TJ. Performance modeling of the Ballard Mark IV solid polymer electrolyte fuel cell. J Electrochem Soc 1995; 142: 1–8.
168. Sena DR, Ticianelli EA, Paganin VA, Gonzalez ER. Effect of water transport in a PEFC at low temperatures operating with dry hydrogen. J Electroanal Chem 1999; 477: 164–70.
169. Büchi FN, Marek A, Scherrer GG. In situ membrane resistance measurements in polymer electrolyte fuel cells by fast auxiliary current pulses. J Electrochem Soc 1995; 142: 1895–901.
170. Mennola T, Mikkola M, Noponen M. Measurement of ohmic voltage losses in individual cells of a PEMFC stack. J Power Sources 2002; 112: 261–72.

2

Electrocatalytic Oxygen Reduction Reaction

Chaojie Song and Jiujun Zhang

2.1 Introduction

Oxygen (O_2) is the most abundant element in the Earth's crust. The oxygen reduction reaction (ORR) is also the most important reaction in life processes such as biological respiration, and in energy converting systems such as fuel cells. ORR in aqueous solutions occurs mainly by two pathways: the direct 4-electron reduction pathway from O_2 to H_2O, and the 2-electron reduction pathway from O_2 to hydrogen peroxide (H_2O_2). In non-aqueous aprotic solvents and/or in alkaline solutions, the 1-electron reduction pathway from O_2 to superoxide (O_2^-) can also occur.

In proton exchange membrane (PEM) fuel cells, including direct methanol fuel cells (DMFCs), ORR is the reaction occurring at the cathode. Normally, the ORR kinetics is very slow. In order to speed up the ORR kinetics to reach a practical usable level in a fuel cell, a cathode ORR catalyst is needed. At the current stage in technology, platinum (Pt)-based materials are the most practical catalysts. Because these Pt-based catalysts are too expensive for making commercially viable fuel cells, extensive research over the past several decades has focused on developing alternative catalysts, including non-noble metal catalysts [1]. These electrocatalysts include noble metals and alloys, carbon materials, quinone and derivatives, transition metal macrocyclic compounds, transition metal chalcogenides, and transition metal carbides. In this chapter, we focus on the O_2 reduction reaction, including the reaction kinetics and mechanisms catalyzed by these various catalysts.

To assist readers, we first provide an overview of the following background information: the major electrochemical O_2 reduction reaction processes, simple ORR kinetics, and conventional techniques for electrochemical measurements.

2.1.1 Electrochemical O_2 Reduction Reactions [2, 3]

Table 2.1 lists several typical ORR processes with their corresponding thermodynamic electrode potentials at standard conditions. The mechanism of the electrochemical O_2 reduction reaction is quite complicated and involves many

intermediates, primarily depending on the natures of the electrode material, catalyst, and electrolyte. The mechanism catalyzed by different catalysts is discussed in detail later in this chapter.

Table 2.1. Thermodynamic electrode potentials of electrochemical O_2 reductions [2, 3]

Electrolyte	ORR reactions	Thermodynamic electrode potential at standard conditions, V
Acidic aqueous solution	$O_2 + 4H^+ + 4e^- \rightarrow H_2O$	1.229
	$O_2 + 2H^+ + 2e^- \rightarrow H_2O_2$	0.70
	$H_2O_2 + 2H^+ + 2e^- \rightarrow 2H_2O$	1.76
Alkaline aqueous solution	$O_2 + H_2O + 4e^- \rightarrow 4OH^-$	0.401
	$O_2 + H_2O + 2e^- \rightarrow HO_2^- + OH^-$	–0.065
	$HO_2^- + H_2O + 2e^- \rightarrow 3OH^-$	0.867
Non-aqueous aprotic solvents	$O_2 + e^- \rightarrow O_2^-$	a
	$O_2^- + e^- \rightarrow O_2^{2-}$	b

a, b: The thermodynamic potentials for the 1-electron reduction reaction to form a superoxide, and its further reduction to O_2^{2-}, are not listed in Table 2.1 because their values are strongly dependent on the solvent used.

In Table 2.1, the reduction pathways such as the 1-, 2-, and 4-electron reduction pathways have unique significance, depending on the applications. In fuel cell processes, the 4-electron direct pathway is highly preferred. The 2-electron reduction pathway is used in industry for H_2O_2 production. The 1-electron reduction pathway is of importance in the exploration of the ORR mechanism.

2.1.2 Kinetics of the O_2 Reduction Reaction

It is desirable to have the O_2 reduction reaction occurring at potentials as close as possible to the reversible electrode potential (thermodynamic electrode potential) with a satisfactory reaction rate. The current-overpotential is given in Equation 2.1 [3]:

$$I_c = i_{O_2}^o (e^{\frac{n_{aO}\alpha_O F\eta_c}{RT}} - e^{-\frac{n_{aO}(1-\alpha_O)F\eta_c}{RT}})\tag{2.1}$$

where I_c is the oxygen reduction reaction current density, $i_{O_2}^o$ is the exchange current density, n_{aO} is the number of electrons transferred in the rate determining step, α_o is the transfer coefficient, η_c is the overpotential of ORR, F is the Faraday constant, R is the gas constant, and T is the temperature in Kelvin. To obtain high

current at low overpotential, the exchange current density $i_{O_2}^o$ should be large, and/or $\dfrac{RT}{\alpha_o n_{ao} F}$ should be small.

2.1.2.1 Tafel Slope

If the overpotential is large, the backward reaction is negligible and Equation 2.1 can be simplified as

$$I_c = i_{O_2}^0 e^{\frac{n_{ao} \alpha_o F \eta_c}{RT}} \tag{2.2}$$

The plot of $\eta_c \sim \log(I_c)$ gives a linear relationship, and the slope is $\dfrac{2.303RT}{\alpha_o n_{ao} F}$.

This slope is called the Tafel slope. Since all other parameters in the Tafel slope are known, the parameters determining the Tafel slope are actually α_O and $n_{\alpha O}$. The higher the Tafel slope, the faster the overpotential increases with the current density. Thus, for an electrochemical reaction to obtain a high current at low overpotential, the reaction should exhibit a low Tafel slope or a large $\alpha_O n_{\alpha O}$. For ORR, usually two Tafel slopes are obtained, 60 mV/dec and 120 mV/dec, respectively, depending on the electrode materials used and on the potential range. Details for individual materials are given in later sections of this chapter. The electron transfer coefficient is a key factor determining the Tafel slope. For ORR, the transfer coefficient is dependent on temperature. On a Pt electrode, the transfer coefficient of ORR increases linearly with temperature in the range of 20–250 °C, following Equation 2.3 [4, 5]:

$$\alpha_O = \alpha_O^0 T \tag{2.3}$$

where α_O is the electron transfer coefficient of ORR, α_O^0 equals 0.001678, and T is temperature in Kelvin. Relative humidity (RH) has also been found to affect the transfer coefficient [6]. Our recent study showed that in PEMFCs, at 120 °C the RH dependence of transfer coefficient change for ORR follows Equation 2.4:

$$\alpha_O = (0.001552RH_c + 0.000139)T \tag{2.4}$$

where RH_c is the relative humidity of the cathode compartment.

2.1.2.2 Exchange Current Density

Exchange current density is an important kinetic parameter representing the electrochemical reaction rate at equilibrium. For an electrochemical reaction,

$$O + ne^- \leftrightarrow R \tag{2.5}$$

both forward and backward reactions can occur. At equilibrium, the net current density of the reaction is zero. The current density of the forward reaction equals that of the backward reaction [3]. This current density is called exchange current density. The magnitude of the exchange current density determines how rapidly the electrochemical reaction can occur.

The exchange current density of an electrochemical reaction depends on the reaction and on the electrode surface on which the electrochemical reaction occurs. For example, on a Pt electrode, the exchange current density of hydrogen oxidation is several orders larger than that of ORR. The O_2 reduction reaction shows a higher exchange current density on a Pt electrode than on an Au electrode. Therefore, electrode materials or catalysts have a strong effect on ORR kinetics. Different materials can give different exchange current densities. Table 2.2 lists the ORR exchange current densities on various electrode materials.

Table 2.2. ORR exchange current densities on various electrode materials

Electrode material /catalyst	ORR exchange current density, $A.cm^{-2}$	Electron transfer co-efficiency	Electron transfer num. in rate determining step	Measurement conditions	Ref.
Pt	2.8×10^{-7}	0.48	-	At Pt/Nafion interface at 30 °C	7
PtO/Pt	1.7×10^{-10}	0.46	-	At Pt/Nafion interface at 30 °C	7
FePc	1.3×10^{-7}	-	-	In pH 1.3 solution	61
PtFe/C	2.15×10^{-7}	0.55	1	In 0.5 M H_2SO_4 at 60 °C	47
PtW$_2$C/C	4.7×10^{-7}	0.45	2	In 0.5 M H_2SO_4 at 25 °C	75
	5.0×10^{-5}	0.47	1		
Ru$_x$Se$_y$	2.22×10^{-8}	0.52	1	In 0.5 M H_2SO_4 at 25 °C	67
Ru$_x$Fe$_y$Se$_z$	4.47×10^{-8}	0.51	1	In 0.5 M H_2SO_4 at 25 °C	68

The exchange current density is related to the true electrode area and to the reactant concentration (or partial pressure, for a gas), especially for ORR on the Pt electrode in fuel cells. The true electroactive area of Pt is significantly different from its geometric area, and the partial pressure of O_2 is not 1 atm. Thus, the intrinsic exchange current density should be used, which is shown in Equation 2.6 [4]:

$$i_{O_2}^{o-apparent} = (EPSA)_c \, i_{O_2}^{o} \, (\frac{P_{O_2}}{P_{O_2}^{o}})^{\alpha_O}$$ (2.6)

where $i_{O_2}^{0-apparent}$ is the apparent exchange current density; $(EPSA)_c$ is the electroactive Pt surface area of the cathode catalyst; $i_{O_2}^{0}$ is the intrinsic exchange current density; $P_{O_2}^{0}$ is the standard O_2 partial pressure; P_{O_2} is the actual O_2 pressure; and α_O is the transfer coefficient of ORR. Since the apparent exchange current density does not reflect the true situation of ORR, hereafter all reference to exchange current density will be to the intrinsic exchange current density.

The exchange current density is also temperature dependent. The relationship between exchange current density and temperature follows the Arrhenius equation,

$$i_{O_2}^{0} = I_{O_2}^{0} e^{-(E_a/RT)}$$ (2.7)

where $I_{O_2}^{0}$ is the exchange current density at T = infinite, E_a is the activation energy, and R, T have their usual significance. Studies on the temperature dependence of ORR on Pt electrodes have been investigated both in half-cells and in fuel cells. Parthasarathy et al. [7] investigated the temperature dependence of ORR kinetics at the Pt/Nafion interface, and Wakabayashi et al. [8] studied the temperature dependence of ORR kinetics at a Pt electrode in an acidic solution. Recently, we studied ORR kinetics in a wide temperature range (from 23 °C–120 °C) in PEMFCs [4]. A wide range of ORR activation energy has been reported: from 21 to 83 kJ/mol for both Tafel regions, depending on the catalyst and method used. We reported values of 28.3 kJ/mol on a PtO/Pt surface and of 57.3 kJ/mol on a pure Pt surface, measured in a fuel cell environment [4].

2.1.3 Techniques Used in Electrocatalytic O_2 Reduction Reactions

The most frequently used techniques for ORR catalysis studies are steady-state polarization, cyclic voltammetry, rotating disk electrode (RDE), and rotating ring-disk electrode (RRDE).

2.1.3.1 Steady-state Polarization
Polarization means that the potential of the electrode surface shifts away from its equilibrium value, leading to an electrochemical reaction. In general, for an elementary electrochemical reaction, $O + e^- \leftrightarrow R$, the polarization follows the Butler-Volmer equation [3]:

$$i = i^0 (e^{\frac{\beta F \eta_c}{RT}} - e^{-\frac{(1-\beta)F \eta_c}{RT}})$$ (2.8)

where i^0 is the exchange current density, η_c is the overpotential for the reduction of reactant O, and β is the symmetry factor. In the reaction, only part of the overpotential activates the forward reaction, and the symmetry factor represents the fraction of the overpotential affecting the forward reaction. All other parameters have their usual significance.

Most of the electrochemical reactions, however, are not elementary, especially for multiple electron transfer reactions. Even a 1-electron transfer reaction may involve several other steps. The whole reaction consists of multiple elementary reactions, including electron transfer steps and chemical steps. Each elementary reaction has a reaction rate. Each elementary step involving electron transfer gives a Butler-Volmer equation, and each chemical step gives a reaction rate equation. The whole reaction rate or electrochemical current is determined by the slowest step. Other steps also contribute to the whole reaction rate, depending on their reaction rates. Deduction of the whole reaction rate is complicated. In some cases, a chemical step is the rate determining step (rds). For example, in a carbon catalyzed ORR, adsorbed superoxide migration might be the rds (see Section 2.2, below). To simplify, for an electrochemical reaction involving multiple electron transfer, the rate determining step is considered a pseudo-elementary step with an electron transfer number of n. For ORR, n might be 1 or 2, depending on the catalysts used and the potential range. This pseudo-elementary step gives a current-overpotential relationship, as shown in Equation 2.9:

$$i = i^0 (e^{\frac{\alpha n F \eta_c}{RT}} - e^{-\frac{(1-\alpha) n F \eta_c}{RT}}) \tag{2.9}$$

where n is the electron transfer number in the pseudo-elementary rate determining step, and α is the transfer coefficient representing the fraction of overpotential that activates the forward direction of the pseudo-elementary rate determining step. The exchange current density and Tafel slope have already been explained in Section 2.1.2.

A steady-state polarization curve describes the relationship between the electrode potential and the current density, which is recorded by either holding the electrode potential and recording the stable current response, or holding the current density and recording the stable potential response. The criteria to evaluate a polarization curve depend on its application. In fuel cells, for both ORR and fuel cell performance, high current density is expected at lower overpotential (ORR) or at higher cell voltage (fuel cell), which gives maximum power density. Figure 2.1 shows the steady-state polarization curves of a PEMFC at 23 °C and 80 °C [4]. At any current density, cell voltage obtained at 80 °C is higher than that at 23 °C, indicating the fuel cell shows better performance at 80 °C than at 23 °C. Fitting the polarization curves or plotting the overpotential vs. log (I) gives the Tafel slope and the exchange current density. We fitted the polarization curves of PEMFCs at low current density range (< 0.4 A/cm^2) and at high current density range (> 0.4 A/cm^2), which resulted in two exchange current densities. For example, at 80 °C, on a PtO/Pt surface (< 0.4 A/cm^2), an exchange current density of 6.25×10^{-6} A/cm^2

was obtained for ORR, and on a Pt surface (> 0.4 A/cm^2), an exchange current density of 5.26×10^{-6} A/cm^2 was obtained [4].
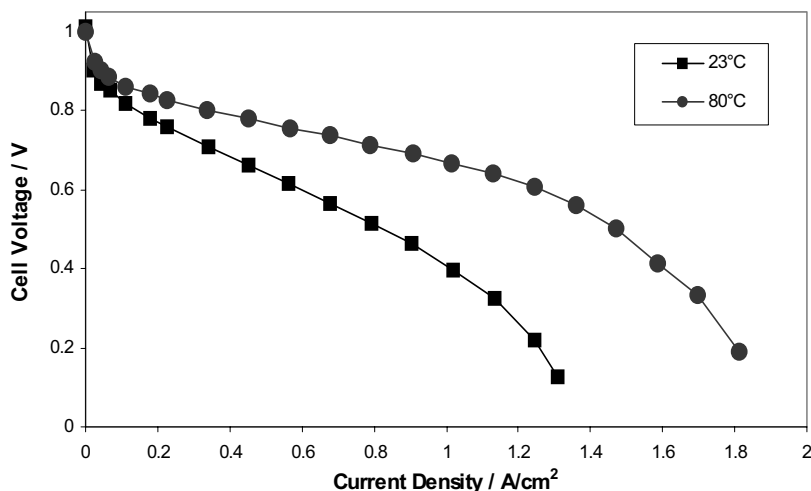
Figure 2.1. Polarization curves obtained at 23 °C and 80 °C with a backpressure of 30 psig. MEA active area: 4.4 cm^{-2}. H$_2$/Air gases with 100% relative humidity, adapted from [4]. (Reprinted from Electrochimica Acta, 52(7), Song C, Tang Y, Zhang J, Zhang J, Wang H, Shen J, et al., PEM fuel cell reaction kinetics in the temperature range of 23–120 °C, 2552–61. ©2007, with permission from Elsevier.)

2.1.3.2 Cyclic Voltammetry

Cyclic voltammetry is the most useful technique in electrochemistry. It can quickly provide qualitative information about catalysts and electrochemical reactions, such as the electrochemical response of catalysts and the catalytic activity of the catalysts with respect to some electrochemical reactions. The principles of this technique have been discussed in detail in other chapters. Here, we simply look at the application of the technique in ORR catalyzed by surface adsorbed catalysts.

Figure 2.2 shows the cyclic voltammogram of an FePcCl$_{16}$ adsorbed graphite electrode in 0.1 M H$_2$SO$_4$ solution. In the potential range of 1.15 V to –0.15 V, four waves (from high to low potential) – attributed to the redox pairs of Fe(IV)/Fe(III), Fe(III)/Fe(II), Fe(II)/Fe(I), and the macrocyclic ring redox pair, respectively – can be observed [9, 10].

The peak currents of the wave of Fe(III)/Fe(II) increase linearly with the potential scan rate, which is a typical feature of the reaction of an electrode surface adsorbed redox couple. From the slope, the electron number can be calculated according to the following equation [3, 9]:

$$I_p = \frac{n_{Fe^{III}P_cCl_{16}}{}^2 F^2}{4RT} A \nu \Gamma_{Fe^{III}P_cCl_{16}} \tag{2.10}$$

where $n_{Fe^{III}P_cCl_{16}}$ is the electron transfer number involved in the electrochemical reaction of $Fe^{III}P_cCl_{16}$, A is the electrode area, ν is the potential scan rate, and $\Gamma_{Fe^{III}P_cCl_{16}}$ is the surface concentration of the adsorbed species. From the slope of I_p vs. ν, the surface concentration of FeP_cCl_{16} can be calculated.
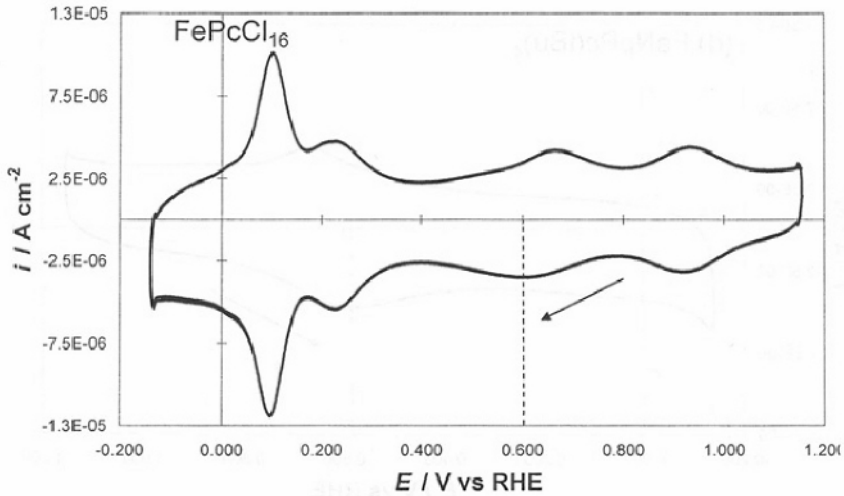
Figure 2.2. Cyclic voltammogram of $FePcCl_{16}$ adsorbed on a graphite electrode at 20 °C. Supporting electrolyte: 0.1 M H_2SO_4. Potential scan rate: 100 mV.s^{-1} [9]. (Reprinted from Electrochimica Acta (forthcoming), Baker R, Wilkinson DP, Zhang J. Electrocatalytic activity and stability of substituted iron phthalocyanines towards oxygen reduction evaluated at different temperatures. ©2008, with permission from Elsevier.)

The redox peak potential change that occurs with pH change sheds light on the electrochemical reaction mechanism of the surface adsorbed species. For a reaction involving either a proton or OH⁻, e.g.,

$$O + mH^+ + ne^- \leftrightarrow R$$
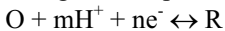
the change in the formal potential (the average of the anodic potential and cathodic potential) vs. pH follows Equation 2.11:

$$E^f = E^0 - 2.303\frac{mRT}{nF}pH \tag{2.11}$$

where E^f is the formal potential, E^0 is the Nernst potential, and the other terms have their usual significance [3, 10, 11].

In the case of FeP_cCl_{16}, as shown in Figure 2.2, the peak potential of Fe(III)/Fe(II) as marked by the dotted line changes linearly with pH, and a slope of 56 mV.pH^{-1} can be observed in the pH range of 0 to 14, which is reasonably close to a value of 58 mV.pH^{-1} (20 °C), a theoretically expected value for a reversible reaction involving one electron and one proton [9, 10].

The onset potential and peak current demonstrate the catalytic activity of a catalyst. For example, CoHFPC has strong electrocatalytic activity towards oxygen reduction. Figure 2.3 compares the cyclic voltammograms of a bare graphite electrode (a) and a CoHFPC-coated graphite electrode in air-saturated 0.1 M Na_2SO_4 solution (b). Both electrodes catalyze the O_2 reduction reaction, and the onset potential of ORR on the CoHFPC-coated electrode is 100–200 mV earlier than that of the bare graphite electrode [12].
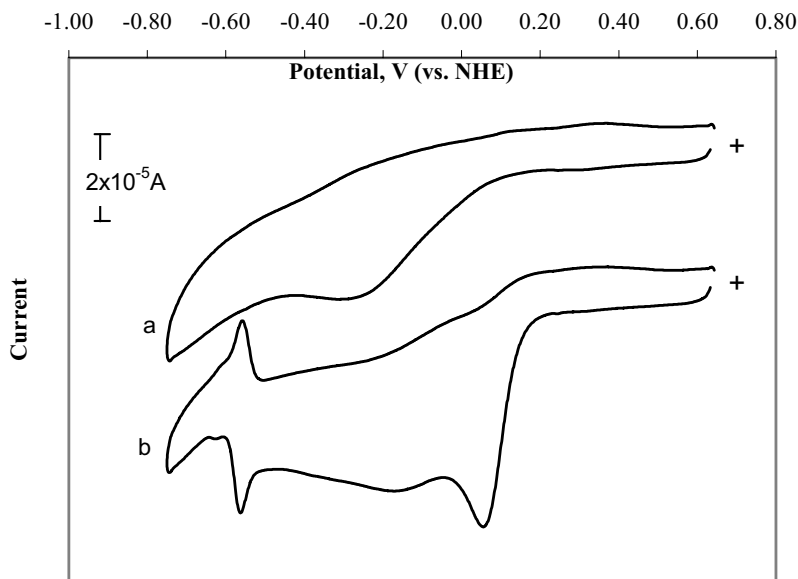
Figure 2.3. Cyclic voltammograms of (a) bare graphite electrode and (b) CoHFPC adsorbed graphite electrode, in air-saturated 0.1 M Na_2SO_4 buffered at pH 6. Potential scan rate: 100 $mV.s^{-1}$ [12]. (From Song C, Zhang L, Zhang J, Wilkinson DP, Baker R. Temperature dependence of oxygen reduction catalyzed by cobalt fluorophthalocyanine adsorbed on a graphite electrode. Fuel Cells 2007;7:9–15. ©2007 Wiley-VCH Verlag GmbH & Co. KGaA. Reproduced with permission.)

2.1.3.3 Rotating Disk Electrode
Equations used for RDEs are as follows [3]:

$$\frac{1}{I} = \frac{1}{I_k} + \frac{1}{I_{lev}}$$

(2.12)

(the Koutecky-Levich equation) where I is the disk current density, I_k is the kinetic current density, and I_{lev} is the Levich current density. I_k can be expressed as Equation 2.13:

$$I_k = nFAK_{O_2}C_{O_2}\Gamma_{catalyst}$$

(2.13)

where n is the overall electron transfer number, A is the electrode area, C_{O_2} is the concentration of dissolved O_2, and $\Gamma_{catalyst}$ is the surface concentration of the catalyst, or the catalyst loading. I_{lev} can be expressed as Equation 2.14:

$$I_{lev} = 0.201 nFAC_{O_2} D_{O_2}^{\frac{2}{3}} v^{-\frac{1}{6}} \omega^{\frac{1}{2}} \tag{2.14}$$

where D_{O_2} is the diffusion coefficient of O_2, v is the kinematic viscosity of the electrolyte solution, and ω is the rotation rate represented by rpm.

An example of RDE application in ORR is shown in Figures 2.4 and 2.5. Figure 2.4 shows the RDE results obtained with a 5,10,15,20-Tetrakis (pentafluorophenyl)-21H,23H-porphine iron (III) (abbreviated as $Fe^{III}TPFPP$) coated graphite electrode in air-saturated 0.1 M H_2SO_4 solution. Figure 2.5 shows the Koutecky-Levich plot using results obtained from Figure 2.4. The slope of the Koutecky-Levich plot is the same as that of a 4-electron ORR theoretical line, meaning that the $Fe^{III}TPFPP$ can catalyze a 4-electron oxygen reduction reaction. The $Fe^{III}TPFPP$-catalyzed ORR reaction constant was calculated to be 3.8×10^8 $mol^{-1}.cm^3.s^{-1}$ [11].
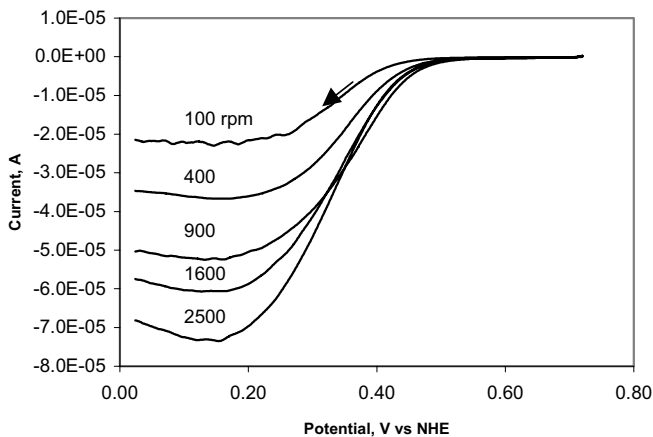
Figure 2.4. Current-potential curves for $Fe^{III}TPFPP$ adsorbed on a rotating graphite disk electrode with different rotating rates, as marked on each trace, recorded in a 0.5 M H_2SO_4 air-saturated solution at 55 °C [11]. (Reproduced by permission of ECS—The Electrochemical Society, from Zhang L, Song C, Zhang J, Wang H, Wilkinson DP. Temperature and pH dependent oxygen reduction catalyzed by iron fluoro-porphyrin adsorbed on a graphite electrode.)

For RDE data analysis, three non-electrochemical kinetic parameters, such as the diffusion coefficient of O_2, the kinematic viscosity of the electrolyte solution, and the solubility of O_2 must be known accurately. These parameters are all temperature dependent. Their values are also slightly dependent on the electrolyte used. Table 2.3 lists these parameters at various conditions.
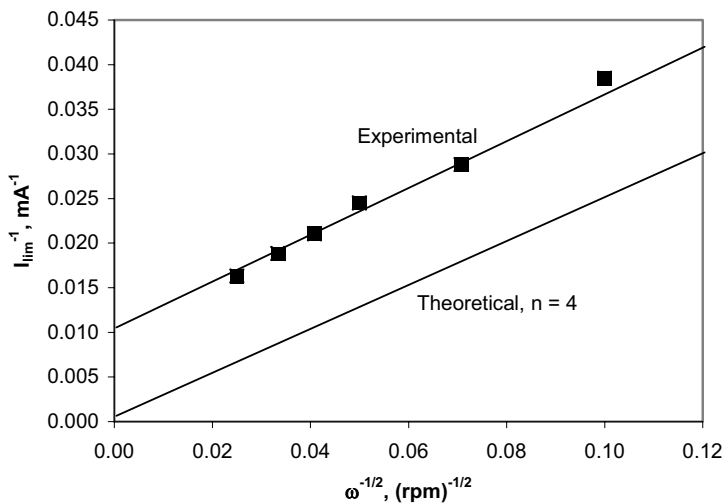
Figure 2.5. Koutecky-Levich plot using data from Figure 2.4. The theoretical line is calculated according to Levich theory for a 4-electron O_2 reduction process [11]. (Reproduced by permission of ECS—The Electrochemical Society, from Zhang L, Song C, Zhang J, Wang H, Wilkinson DP. Temperature and pH dependent oxygen reduction catalyzed by iron fluoro-porphyrin adsorbed on a graphite electrode.)

Table 2.3. Non-electrochemical kinetic parameters for RDE data analysis

Experiment conditions (T, P, electrolyte)	Diffusion coefficient of O_2, $cm^2.s^{-1}$	Kinematic viscosity of the electrolyte solution, $cm^2.s^{-1}$	Solubility of O_2, $mol.cm^{-3}$	Ref.
0.1 M $HClO_4$, 20°C, 1 atm O_2	1.67×10^{-5}	-	1.38×10^{-6}	8
0.5 M H_2SO_4, 25°C, 1 atm O_2	1.4×10^{-5}	0.010	1.1×10^{-6}	68
0.1 M KOH, 25°C, 1 atm O_2	1.9×10^{-5}	-	1.2×10^{-6}	7
1 M NaOH, 25°C, 1 atm O_2	1.65×10^{-5}	0.011	8.4×10^{-7}	15
0.1 M TBAP quinoline, 25°C, 1 atm O_2	1.71×10^{-5}	0.033	1.49×10^{-6}	92

2.1.3.4 Rotating Ring-disk Electrode (RRDE)

In the RRDE method, the O_2 reduction reaction occurring on the disk electrode produces intermediates, which can be detected on the ring and are used to deduce the ORR mechanism. An example is using RRDE to study the O_2 reduction reaction catalyzed by Pt/C catalysts with different particle sizes. On the disk, 2-

electron and 4-electron ORR can occur, and on the ring electrode, H_2O_2 is further oxidized to H_2O [13].
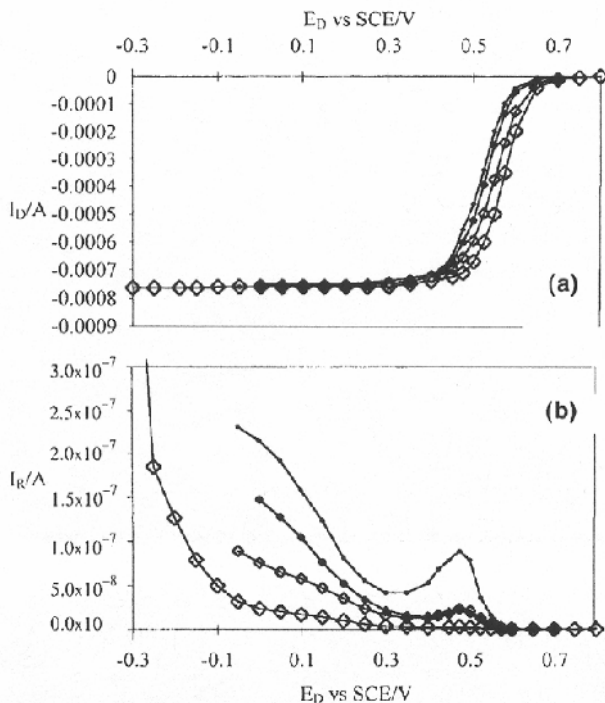
Figure 2.6. Oxygen reduction current (a) on a disk electrode for active layers with different Pt mass ratios Pt/(Pt+C) and H_2O_2 oxidation curves, (b) on the ring electrode (1 mV s^{-1}; 0.1 M H_2SO_4; 293 K; L$\approx$ 3 μm; Nafion/caron volume ratio = 1; 10% Pt/(Pt+C): (◊) d- 2.5 nm, S_{Pt} = 7.6 cm^2; 20%: (◊)d = 3.4 nm, S_{Pt} = 13.9 cm^2; 30%: (◊)d = 4.1 nm, S_{Pt} = 19.4 cm^2; 40%: (◊)d = 5.1 nm, S_{Pt} = 24.3 cm^2) [13]. (With kind permission from Springer Science+Business Media: Journal of Applied Electrochemistry, RRDE study of oxygen reduction on Pt nanoparticles inside Nafion®: H_2O_2 production in PEMFC cathode conditions, 30, 2004, 839–844, O. Antoine, Figure 1, ©2004 Springer.)

The 2-electron reduction current (I_{2e^-}) is given by

$$I_{2e^-} = I_R / N \tag{2.15}$$

where I_{2e^-} is the 2-electron ORR on the disk electrode and N is the collecting coefficient number. The ORR current (I_D) on disk electrode can be expressed as Equation 2.16:

$$I_D = I_{2e^-} + I_{4e^-} \tag{2.16}$$

where I_{4e^-} is the 4-electron ORR current. The following equation is used to obtain the average electron number (n_{e^-}) involved in ORR:

$$\frac{I_D}{n_{e^-}} = \frac{I_{4e^-}}{4} + \frac{I_{2e^-}}{2} \tag{2.17}$$

By rearranging Equation 2.17, we get Equation 2.18, which is used to calculate n_{e^-}:

$$n_{e^-} = \frac{4I_D}{I_D + I_R / N} \tag{2.18}$$

Figure 2.6 shows the ring-disk currents of ORR on different Pt/C catalyst with different particle sizes. Figure 2.7 shows the average electron transfer numbers calculated based on Equation 2.18. The numbers are close to 4 for all catalysts investigated, indicating a weak platinum particle size effect on H_2O_2 production. Larger particle size shows a higher proportion of H_2O_2.
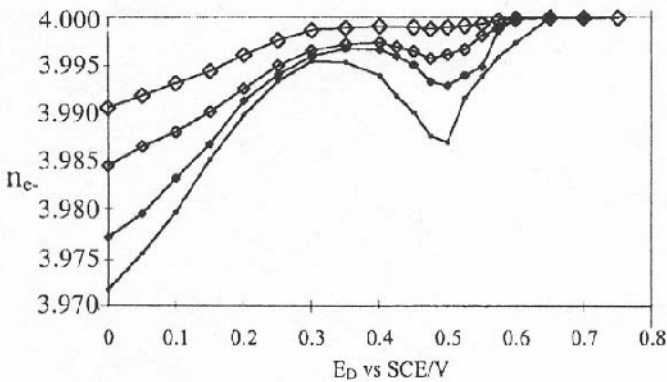
Figure 2.7. Average number of exchanged electrons during oxygen reduction on the disk active layer. Data obtained based on Figure 2.6 [13]. (10% Pt/(Pt+C): ($\Diamond$) d = 2.5 nm, S_{Pt} = 7.6 cm^2; 20%: ($\Diamond$)d = 3.4 nm, S_{Pt} = 13.9 cm^2; 30%: ($\Diamond$)d = 4.1 nm, S_{Pt} = 19.4 cm^2; 40%: ($\Diamond$)d = 5.1 nm, S_{Pt} = 24.3 cm^2). (With kind permission from Springer Science+Business Media: Journal of Applied Electrochemistry, RRDE study of oxygen reduction on Pt nanoparticles inside Nafion®: H_2O_2 production in PEMFC cathode conditions, 30, 2004, 839–844, O. Antoine, Figure 2, ©2004 Springer.)

2.2 Oxygen Reduction on Graphite and Carbon

It seems that all carbon materials have some electrocatalytic activity towards ORR in alkaline solutions [2]. The materials that have been studied include graphite,

glassy carbon, active carbon, and carbon nanotubes [2, 14–22]. Depending on the type of carbon, the catalytic ORR activity and mechanism vary widely. For example, glassy carbon and pyrolytic graphite normally catalyze a 2-electron transfer oxygen reduction, producing H_2O_2. On an oxidized glassy carbon electrode [14] and oxidized graphite electrodes [15], the H_2O_2 can be further reduced to water at more negative potentials. On carbon nanotubes [16], the O_2 reduction product is H_2O_2 or a mixture of H_2O_2 and OH^-, depending on the preparation method and potential of the carbon nanotube-modified electrode.

2.2.1 Oxygen Reduction Reaction Mechanisms

2.2.1.1 ORR on Graphite and Glassy Carbon
Two mechanisms have been proposed for carbon-catalyzed ORR. On a glassy carbon electrode, the following reaction mechanism has been proposed [2]:

$$O_2 \rightarrow O_{2(ads)} \tag{2.19}$$

$$O_{2(ads)} + e^- \rightarrow [O_{2(ads)}]^- \tag{2.20}$$

$$[O_{2(ads)}]^- \rightarrow O_{2(ads)}^{\,-} \tag{2.21}$$

$$O_{2(ads)}^{\,-} + H_2O \rightarrow HO_{2(ads)} + OH^- \tag{2.22}$$

$$HO_{2(ads)} + e^- \rightarrow HO_2^{\,-}{}_{(ads)} \tag{2.23}$$

$$HO_2^{\,-}{}_{(ads)} \rightarrow HO_2^{\,-} \tag{2.24}$$
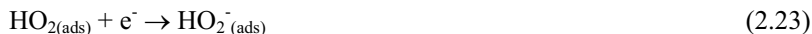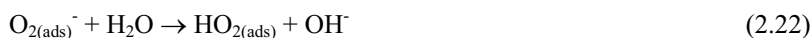
The subscripts "ads" indicate the corresponding species are adsorbed on the electrode surface. The reactant and product in Reaction 2.21 are two different forms of the superoxide ion on the carbon surface. The left one is a relatively inert form adsorbed on an inert graphite site, and the right one is the same species, but migrating to an active site according to Reaction 2.21. It was confirmed that Reaction 2.21 was the rate determining step. However, Taylor et al. [14, 17] found that the rate determining step was dependent on pH. At pH > 10, Reaction 2.21 was the rate determining step, and at pH < 10, Reaction 2.20 was the rate determining step.

On pyrolytic graphite electrodes, the first reaction was also proposed as Reaction 2.19, followed by:

$$O_{2(ads)} + e^- \rightarrow O_2^{\,-}{}_{(ads)} \tag{2.25}$$

$$2O_2^{\,-}{}_{(ads)} + H_2O \rightarrow O_2 + HO_2^{\,-} + OH^- \tag{2.26}$$

and the rate determining step was believed to be Reaction 2.25.
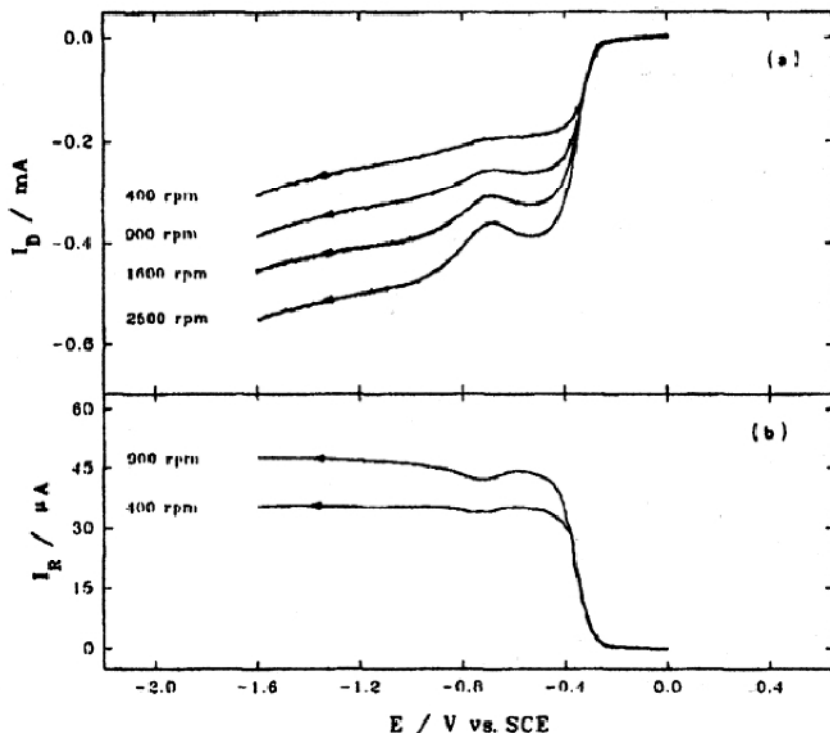
Figure 2.8. (a) Current-potential curves for O_2-saturated 1.0 M NaOH solution at a polished glassy carbon disk electrode, T = 298 K. Potential scan rate: 5 mV/s; (b) response at a Pt ring held at 0.0 V vs. SCE during the potential scan at the disk. Rotation rates are given on the figure [21]. (Reprinted from Journal of Electroanalytical Chemistry, 382(1–2), Baez Victor B. and Pletcher Derek, Preparation and characterization of carbon/titanium dioxide surfaces—the reduction of oxygen, 59–64, ©1995, with permission from Elsevier.)

For ORR current-potential curves recorded on either a graphite or a glassy carbon electrode surface, two waves were observed, both of which were attributed to the 2-electron transfer reduction of O_2, producing H_2O_2. Figure 2.8 shows the RRDE results for O_2 reduction on a glassy carbon electrode. On the disk electrode, the first steep wave appears at the formal potential ($E_{1/2}$) of –0.34 V vs. SCE and the second one at $E_{1/2}$ = –0.78 V. The oxidation current at the ring shows that both waves correspond to H_2O_2 production. This 2-electron reduction occurs at two different potential ranges, suggesting that there are two kinds of ORR active sites on glassy carbon. In a further experiment with 1 M NaOH solution containing 5 mM H_2O_2, no reduction wave was observed. This result confirmed that H_2O_2 could not be further reduced on a glassy carbon electrode [21].

The ORR activity of a graphite electrode is dependent on graphite planes. The activity on an edge plane is higher than that on a basal plane, as shown in Figure 2.9 [22]. This reflects the difference in electrocatalytic activity of these two orientations. This catalytic activity difference is mainly due to there being more functional groups on an edge plane than on a basal plane.
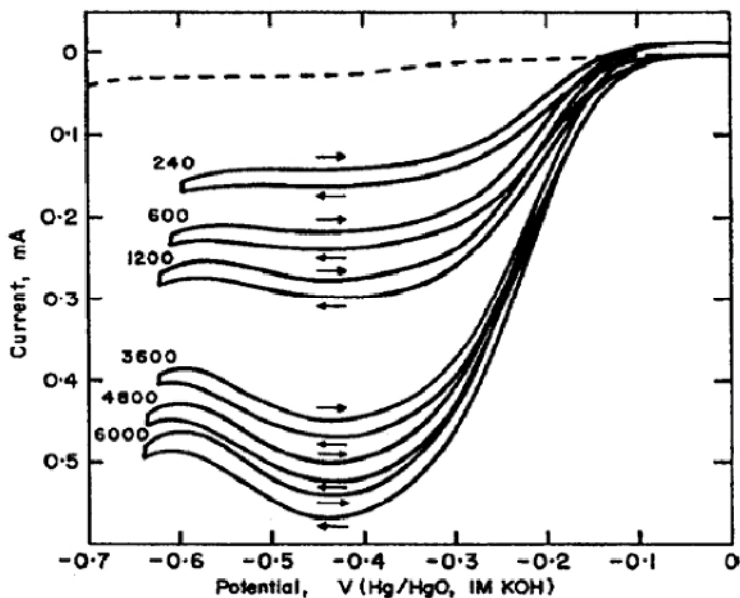
Figure 2.9. Current-potential curves for O_2-saturated 1 M KOH solution on high pressure annealed pyrolytic graphite: — edge plane, --- basal plane [22]. (Reprinted from Electrochimica Acta, 15(6), Morcos I. and Yeager E., Kinetic studies of the oxygen— peroxide couple on pyrolytic graphite, 953–75, ©1970, with permission from Elsevier.)

2.2.1.2. ORR on Carbon Nanotubes

Carbon nanotubes are a new kind of material with extensive applications. Recently, oxygen reduction reaction catalyzed by carbon nanotubes has been investigated by several groups [16, 20], which found that the catalyzed ORR was dependent on the preparation method for the carbon nanotube films. Zhang et al. [16] prepared multiwalled carbon nanotube (MWCNT) films by a dihexadecyl hydrogen phosphate (DHP) method on a glassy carbon electrode and found that the films could catalyze O_2 reduction by two 2-electron processes, producing OH⁻. At a potential range of –0.4 – –0.8 V vs. Ag/AgCl, the first reduction current plateau on the RDE curve was observed, and was attributed to a 2-electron process producing H_2O_2. At potentials more negative than –0.9 V, a second plateau appeared, which was attributed to the further reduction of H_2O_2, producing OH⁻ (see curve 1' in Figure 2.10). Jurmann et al. [20] prepared similar films using the same method on a highly oriented pyrolytic graphite electrode, and reported that the first 2-electron process could be observed at the potential range of –0.4 – –0.6 V vs. SCE, while the second plateau was not clearly discerned. A mixture process of 2- and 4-electron reduction could be observed at more negative potentials. Jurmann et al. [20] also found that on MWCNT films prepared by the poly(diallyldimethylammonium chloride) method, the electron transfer number of ORR was in the range of 3 – 3.5 at the potential range of –0.4 – –1.2 V. Figure 2.10 shows the results, together with those obtained on a bare glassy carbon electrode for comparison. It can be seen that on a glassy carbon electrode, the ring

current increases as disk current increases in the potential range of –0.4 to –1.2 V. However, on an MWCNT-modified electrode, the ring current decreases as the disk current increases in the similar potential range, indicating less H_2O_2 is produced.
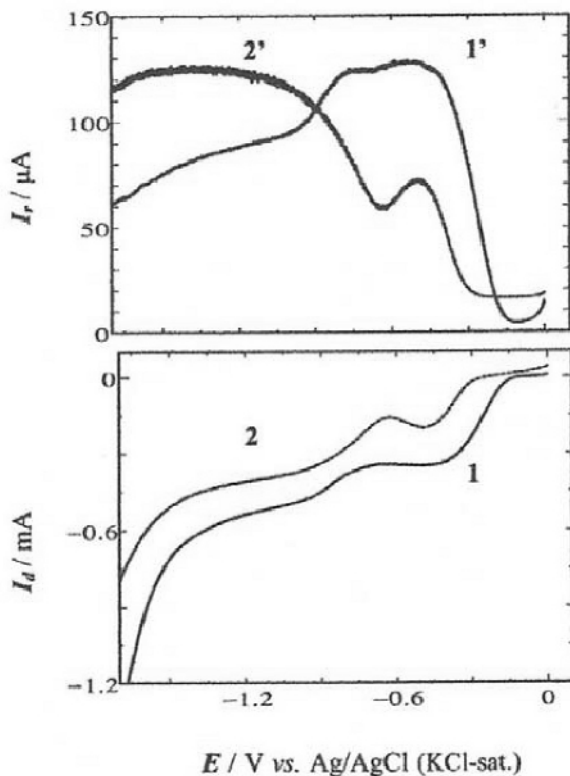
Figure 2.10. RRDE voltammograms for O_2 reduction at the PDDA/MWCNTs/GC (curve 1) and bare GC (curve 2) disk electrodes in O_2-saturated 0.10 M KOH solution. Curves 1' and 2' represent the current for the oxidation of HO_2^- produced at the corresponding disk electrodes. Potential scan rate: 10 mV/s; electrode rotating rate: 400 rpm. The Pt ring electrode was polarized at +0.50 V for the oxidation of HO_2^- [16]. (Reprinted with permission from Langmuir 2004;20;8781–5. Copyright 2004 American Chemical Society.)

2.2.1.3. ORR on Heteroatom Doped Carbons
Doping carbon with heteroatoms such as nitrogen can change the carbon's properties. For example, nitrogen (N)-doped carbon shows high oxidation resistance capability and higher catalytic activity toward ORR. Maldonado and Stevenson [23] found that N-doped carbon fiber showed improved catalytic activity by shifting the ORR potential up by 70 mV (Figure 2.11), and the electron transfer number of ORR catalyzed by N-doped carbon fiber was close to 4. They discussed that N-doped carbon can not only catalyze O_2 reduction reaction but also catalyze H_2O_2 decomposition [23].
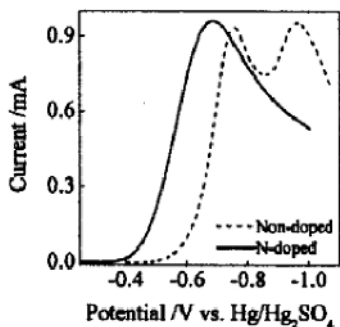
Figure 2.11. Background subtracted voltammetric responses of a nondoped CNF electrode (dashed line) and an N-doped CNF electrode (solid line) immersed in an O_2-saturated 1 M KNO_3 solution. Scan rate = 0.1 V s^{-1} [23]. (Reprinted with permission from J Phys Chem B 2005;109.10:4707–16. Copyright 2005 American Chemical Society.)

The active sites in N-doped carbon are carbon atoms adjacent to the N atom. Using a cluster model, Sidik et al. [24] did theoretical calculations and found that carbon radical sites adjacent to the substitutional N showed strong bonding ability to adsorbed OOH, favoring the production of H_2O_2 [24], which improves its catalytic activity.

2.2.1.4 ORR on Pre-treated Carbon Surface

Pre-treatment of carbon materials can significantly improve their catalytic activity towards ORR and change their electrochemical behavior. A variety of treatment methods have been used, including polishing the electrode, radio frequency plasma treatment, heating at low pressures, *in situ* laser irradiation, vacuum heat treatment, chemical oxidation, and electrochemical oxidation [25–28].

It is not clearly understood why pre-treatment of carbon surfaces improves their catalytic activity. Pre-treatment does create more surface functional groups, and exposes fresh carbon edges, microparticles, and defects [25–27]. Jia et al. [28] found that pre-treatment of carbon supports and Pt-loaded carbon supports resulted in ionic resistance decrease, indicating that surface functional groups such as carboxylic acid were generated. Pre-treatment also might increase the surface area of carbon by generating porous surface films [29]. Sullivan et al. [29] found that surface oxidation of glassy carbon at 1.95 V vs. SCE leads to the formation of porous carbon film, and that the film thickness increased linearly with oxidation time. Overall, pre-treatment of carbon can change its surface state. The surface groups or changed surface state facilitate ORR by acting as an electron transfer mediator or by increasing adsorption sites for O_2^- species, which enhances the kinetics of ORR.

Figure 2.12 shows the current-potential curves of an unoxidized glassy carbon electrode that had then been oxidized at 2 V vs. RHE in 0.5 M H_2SO_4 at different times. Increasing the oxidization time resulted in decreased ORR onset potential and increased ORR reduction current.

Pretreated carbon also affects the activity of other catalysts supported on it. For example, pretreatment of a carbon support followed by deposition of Pt on it and

treatment of carbon-supported Pt also resulted in significant increases in the ORR catalytic activity of Pt. Jia et al. [28] reported that an untreated catalyst (Pt deposited on untreated carbon supports) gave a kinetic current of 0.3±0.1 mA at 0.6 V vs. SCE, while Pt deposited on pretreated carbon showed a kinetic current of 1.6±0.7 mA, and posttreated carbon-supported Pt catalyst (refluxing carbon-supported Pt catalyst in nitric acid) could give a kinetic current of 7.7±1.7 mA.
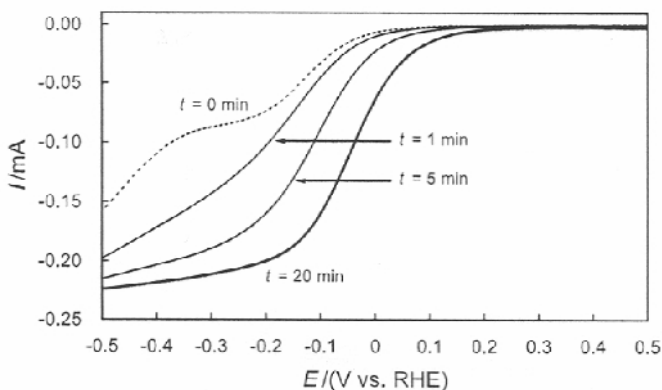
Figure 2.12. Hydrodynamic voltammograms for O_2 reduction at a bare glassy carbon RDE in O_2-saturated 0.5 M H_2SO_4. Glassy carbon surface oxidation time: 0 min (dashed line); 1 min (thin line); 5 min (thick line); 20 min (very thick line). Scan rate: 10 mV/s; rotation speed: 2000 rpm [27]. (Reprinted from Journal of Electroanalytical Chemistry, 527(1–2), Maruyama J, Abe I, Cathodic oxygen reduction at the interface between Nafion® and electrochemically oxidized glassy carbon surfaces, 65–70, ©2002, with permission from Elsevier.)

2.2.2 Kinetics of the ORR on Carbon Materials

On a glassy carbon electrode, the Tafel slope was observed to be 60 mV/dec in alkaline solutions, and at pH < 10, the Tafel slope was 120 mV/dec. These values are in accordance with the proposed mechanisms. In the case of 120 mV/dec, the first electron transfer is the rate determining step. In the case of 60 mV/dec, the current-potential relationship observed from the multiple-electron transfer process of ORR on carbon electrodes was expressed as Equation 2.27, given by Taylor and Humffray [14, 17]:

$$i = i_0 \{ \exp[\frac{n-\gamma}{\nu} - r\beta) \frac{F\eta}{RT}] - \exp[-(\frac{\gamma}{\nu} + r\beta) \frac{F\eta}{RT}] \} \tag{2.27}$$

where η is the overpotential, γ is the number of electrons transferred before the rate determining step (rds), n is the number of electrons involved in the overall reaction, β is the symmetry factor of the rds, r is the number of electrons transferred in the rds if the rds involves charge transfer (if no electron transfer is involved in the rds, $r = 0$), and ν is the stoichiometric number of the reaction.

The stoichiometric number ν was evaluated from the current-potential measurements in the region of low overpotential, according to the following relation:

$$\left(\frac{\partial \eta}{\partial i}\right)_{i \to 0} = \frac{\nu RT}{nFi_0} \tag{2.28}$$

On carbon materials, ν usually equals 1. Using Allen and Hickling's graphical treatment, Taylor and Humffray found that the Tafel slope is $2.303 \dfrac{RT}{\left(\frac{\gamma}{\nu} + r\beta\right)F}$ and that its numerical value is 60 mV/dec. This indicates that $\gamma = 1$ and $r = 0$, meaning that the migration step is the rds.

2.2.3 Catalytic Sites on Carbon Materials

The catalytic ORR activity of carbon materials is generally attributed to the quinone groups [2]. Yeager [2] cited Garten and Weiss's mechanism for O_2 reduction on carbon surfaces, as shown in Figure 2.13. A similar mechanism was also proposed for a carbon nanotube surface, as in Figure 2.14 [16]. Although this mechanism has not been confirmed, electrodes modified with a variety of quinone compounds have shown great catalytic activity towards 2-electron oxygen reduction reaction for H_2O_2 production (see Section 2.3).
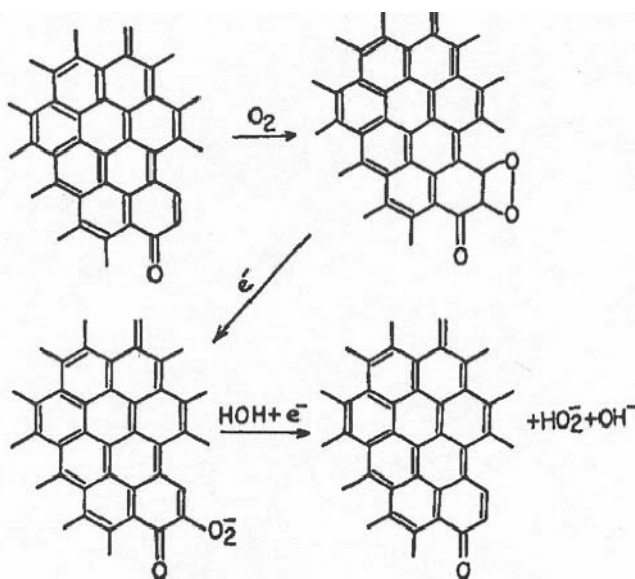
Figure 2.13. Garten and Weiss's mechanism for reduction on carbon surface [2]. (Reprinted from Journal of Molecular Catalysis, 38(1–2), Yeager Ernest, Dioxygen electrocatalysis: mechanisms in relation to catalyst structure, 5–25, ©1986, with permission from Elsevier.)
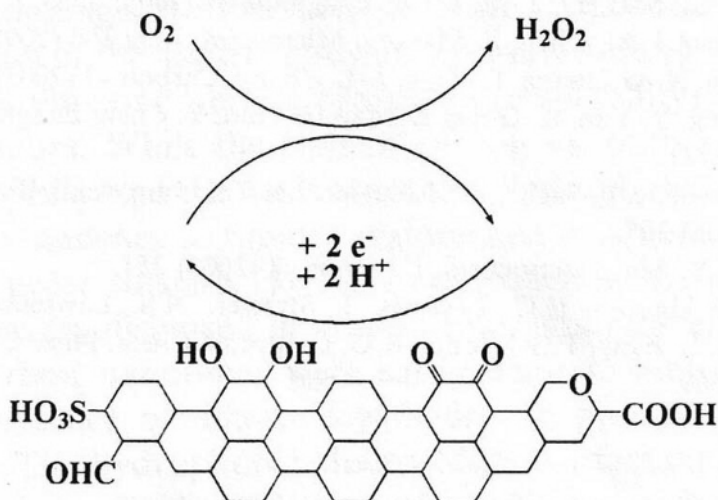
Figure 2.14. Mechanism of O_2 reduction on carbon nanotube surface [20]. (Reprinted from Journal of Electroanalytical Chemistry, 597(2), Jürmann Gea and Tammeveski Kaido, Electroreduction of oxygen on multi-walled carbon nanotubes modified highly oriented pyrolytic graphite electrodes in alkaline solution, 119–26, ©2006, with permission from Elsevier.)

2.3 Oxygen Reduction Catalyzed by Quinone and Derivatives

As discussed above, the surface quinone group on a carbon electrode can catalyze a 2-electron O_2 reduction reaction, producing H_2O_2. This ORR process has attracted significant attention in terms of fundamental understanding and applications [30–41].

2.3.1 AO Process for O_2 Reduction to Produce H_2O_2

H_2O_2, a product of the 2-electron transfer reduction of O_2, has wide industrial applications, including pulp and paper, textiles, chemical synthesis, as well as environmental protection such as waste-water treatment. The most commonly used industrial production procedure is the anthraquinone process, or "AO process". The chemical reaction involved in the process is expressed in Figure 2.15.

The catalyst used in this process is Raney Ni, or Pd/Al_2O_3. Anthraquinone dissolved in a solvent mixture was hydrogenated by the catalyst, then oxidized with air. By this method, H_2O_2 can be produced and the starting material, anthraquinone, recovered [31]. In the process, anthraquinone degradation is a problem and results in decreased efficiency. Researchers are therefore trying to replace the chemical reduction step of anthraquinone with electrochemical reduction [30, 32, 33].
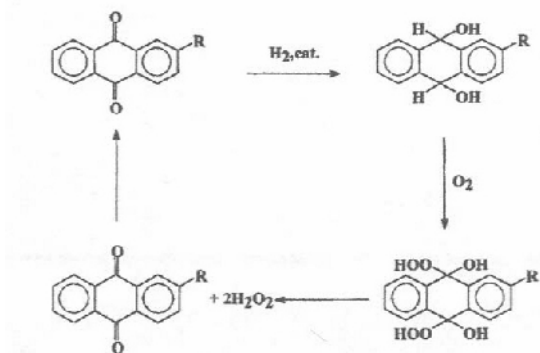
Figure 2.15. The anthraquinone process (AO process) to produce H_2O_2 [30]. (With kind permission from Springer Science+Business Media: Journal of Applied Electrochemistry, Electrochemical reduction of 2-ethyl-9,10-anthraquinone (EAQ) and mediated formation of hydrogen peroxide in a two-phase medium Part I: Electrochemical behaviour of EAQ on a vitreous carbon rotating disc electrode (RDE) in the two-phase medium, 29, 2004, 11–16, A. Huissoud, Scheme 1, ©Springer.)

2.3.2 ORR Mechanism Electrochemically Catalyzed by Quinone

The O_2 reduction of O_2 catalyzed by the quinone group is proposed to proceed by the following electrochemical-chemical (EC) process [30, 37]:

$$Q + e^- \rightarrow Q^{\bullet-} \tag{2.29}$$

$$Q^{\bullet-} + O_2 \rightarrow O_2^{\bullet-} + Q \tag{2.30}$$

$$O_2^{\bullet-} + H_2O + e^- \rightarrow HO_2^- \tag{2.31}$$

or

$$2O_2^{\bullet-} + H_2O \rightarrow HO_2^- + O_2 + OH^- \tag{2.32}$$

where Q represents the quinone group. Reaction 2.30 was considered to be the rate determining step. Quinones with different substituted groups, such as ethyl group modified anthraquinones, were also investigated in order to improve the catalytic activity and stability [38].

2.4 Oxygen Reduction on Metal Catalysts

2.4.1 ORR Mechanism on Pt

Oxygen reduction reaction on a Pt electrode has been the most extensively studied mechanism. This catalytic ORR is a multi-electron process with a number of

elementary steps, involving different reaction intermediates. The simplified version of the mechanism is shown in Figure 2.16; the only two products are H_2O_2 and H_2O. RRDE measurements show that on a Pt surface, O_2 reduction is a major 4-electron transfer process from O_2 to H_2O in both acid and alkaline aqueous electrolytes if adsorbed impurities are absent [42]. At this point, the mechanism of ORR on Pt is still not well understood.
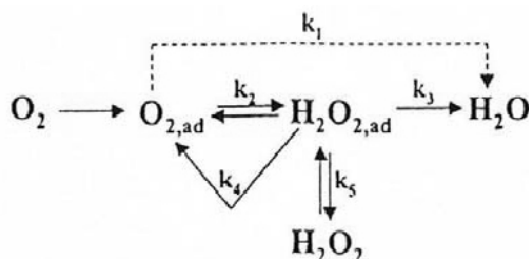
Figure 2.16. The oxygen reduction reaction mechanism on Pt [42]. (Reprinted from Surface Science Reports, 45(4–6), Markovi N. M. and Ross P. N., Surface science studies of model fuel cell electrocatalysts, 117–229, ©2002, with permission from Elsevier.)

The mechanism shown in Figure 2.16 indicates that O_2 can be reduced either directly to water (direct 4-electron reduction) electrochemically with the rate constant k_1, or to adsorbed hydrogen peroxide ($H_2O_{2,ad}$) with the rate constant k_2 ("series" 2-electron reduction). $H_2O_{2,ad}$ can be further reduced to water with the rate constant k_3, chemically decomposed on the electrode surface (k_4), and/or desorbed into the electrolyte solution (k_5). Some experimental results suggest that a series pathway via an $(H_2O_2)_{ad}$ intermediate is the most possible pathway. For example, only a very small amount of H_2O_2 could be observed during ORR, and the electron transfer number is close to 4. This series ORR mechanism suggests a special case of $k_1 = 0$.

The ORR mechanism on Pt has also been investigated by theoretical calculation based on the electronic structure, using density functional theory [43–45]. The dissociative mechanism and the associative mechanism are proposed for a low current density range and a high current density range, respectively [43, 44]:

(1) Dissociative Mechanism:

$$1/2 O_2 + * \rightarrow O* \tag{2.33}$$

$$O* + H^+ + e \rightarrow OH* \tag{2.34}$$

$$OH* + H^+ + e \rightarrow H_2O + * \tag{2.35}$$

where * denotes a site on the Pt surface. In this mechanism, no H_2O_2 is produced. On a Pt surface, O_2 adsorption breaks the O-O bond and forms adsorbed atomic O, which further gains two electrons in the two consecutive steps, forming water.

Since there is no adsorbed O_2 on the Pt surface, H_2O_2 cannot be formed. This mechanism can be considered a detailed form of the direct 4-electron pathway.

(2) Associative Mechanism:

$$O_2 + * \rightarrow O_2* \tag{2.36}$$

$$O_2* + H^+ + e \rightarrow HO_2* \tag{2.37}$$

$$HO_2* + H^+ + e \rightarrow H_2O + O* \tag{2.38}$$

$$O* + H^+ + e \rightarrow OH* \tag{2.39}$$

$$OH* + H^+ + e \rightarrow H_2O + * \tag{2.40}$$

This mechanism also does not involve H_2O_2. Since adsorbed O_2 is present, the O-O bond may not be broken in the following steps, resulting in the formation of H_2O_2. The H_2O_2 could either be further reduced to H_2O or be a final product. Therefore, this mechanism might be an alternative expression of that in Figure 2.16.

2.4.2 Mixed Pt Surface and Rest Potential on Pt

The thermodynamic potential of ORR (1.23 V vs. NHE at standard conditions) is so high that no electrode materials can remain pure. At 1.23 V, electrode materials undergo oxidation, which changes their surface properties.

On Pt and at high potential, the following reaction occurs:

$$Pt + 1/2O_2 \rightarrow PtO \qquad E^0 = 0.88 \text{ V} \tag{2.41}$$
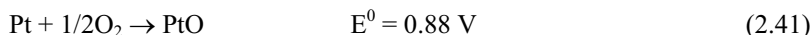
Thus, in the presence of O_2, the Pt surface is a mixture of Pt and PtO. Therefore, a steady-state open circuit potential (OCP) of 1.23 V is rarely observed, due to the formation of PtO. Rather, the steady-state rest potential of a Pt electrode in O_2 saturate 1 M H_2SO_4 is 1.06 V, a mixed value of the thermodynamic potential of O_2/H_2O and of Pt/PtO, because two reactions occur: Pt oxidation and O_2 reduction [46].

For Pt oxidation, the oxidation current-overpotential relationship is given by

$$I_{Pt/PtO} = i^o_{Pt/PtO}(e^{\frac{n_{a,Pt/PtO}\alpha_{a,Pt/PtO}F\eta_{Pt/PtO}}{RT}} - e^{-\frac{n_{a,Pt/PtO}(1-\alpha_{a,Pt/PtO})F\eta_{Pt/PtO}}{RT}}) \tag{2.42}$$

where $I_{Pt/PtO}$ is the Pt oxidation current, $i^o_{Pt/PtO}$ is the exchange current density of Pt oxidation, $n_{a,Pt/PtO}$ is the apparent electron transfer number in the electrochemical reaction, $\alpha_{a,Pt/PtO}$ is the electron transfer coefficient, and

$\eta_{a,Pt/PtO} = E^{rest} - 0.88$ is the overpotential (E^{rest} is the steady-state rest potential of the system).

Assuming the overpotential is small, this equation can be approximated as follows:

$$I_{Pt/PtO} = i^o_{Pt/PtO} \frac{n_{\alpha,Pt/PtO}F}{RT}(E^{rest} - 0.88) \tag{2.43}$$

For the O_2 reduction reaction on Pt, a similar equation can be written as:

$$I_{O_2/H_2O} = i^o_{O_2/H_2O} \frac{n_{\alpha,O_2/H_2O}F}{RT}(1.23 - E^{rest}) \tag{2.44}$$

where I_{O_2/H_2O} is the O_2 reduction current, $i^o_{O_2/H_2O}$ is the exchange current density of O_2 reduction, $n_{\alpha,O_2/H_2O}$ is the apparent electron transfer number in the electrochemical reaction, $\alpha_{a,O_2/H_2O}$ is the electron transfer coefficient, and $E^{rest} - 0.88$ is the overpotential.

Since no net current is flowing from the system or given to the system, $I_{Pt/PtO} = I_{O_2/H_2O}$. Thus,

$$n_{\alpha,Pt/PtO}i^o_{Pt/PtO}(E^{rest} - 0.88) = n_{\alpha,O_2/H_2O}i^0_{O_2/H_2O}(1.23 - E^{rest}) \tag{2.45}$$

Assuming the exchange current density and apparent electron transfer number for Pt oxidation and O_2 reduction are the same, the value of E^{rest} can be obtained through Equation 2.45, and is 1.06 V. However, the value of this rest potential can be changed by altering the extent to which PtO covers the electrode surface.

2.4.3 ORR Kinetics on Pt

The electrode potential can play a significant role in changing the Pt surface structure in the presence of O_2, due to the mixed potential discussed above. At higher potentials (> 0.8 V), the electrode surface is a mixture of Pt and PtO, while at lower potentials, the Pt surface is pure Pt. Thus, the kinetics of O_2 reduction on Pt is not expected to be the same in different potential ranges. Figure 2.17 shows the two Tafel slopes observed for ORR on a Pt electrode surface [8]. At a low current density range (high potential), a Tafel slope of 60 mV/dec was obtained. At a high current density range (low potential), a value of 120 mV/dec was observed. The difference in Tafel slope indicates that the mechanism on a Pt/PtO surface is different from that on a pure Pt surface. On a Pt/PtO surface, the rate determining step is a pseudo 2-electron procedure, which gives a Tafel slope of 60 mV/dec. However, on a pure Pt surface, the first electron transfer is the rate determining step, resulting in a Tafel slope of 120 mV/dec.
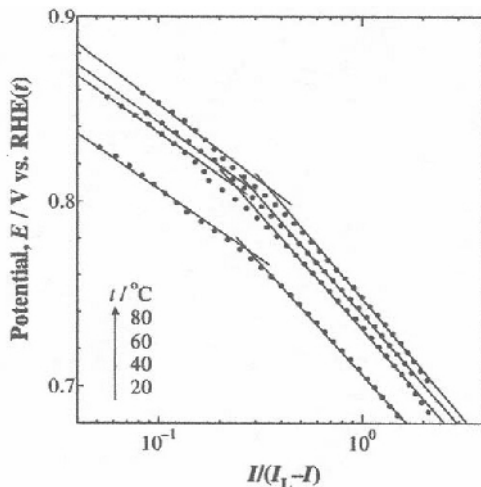
Figure 2.17. Tafel plots for oxygen reduction reaction at a Pt working electrode [8]. (Reprinted from Journal of Electroanalytical Chemistry, 574(2), Wakabayashi Noriaki, Takeichi Masayuki, Itagaki Masayuki, Uchida Hiroyuki and Watanabe Masahiro, Temperature-dependence of oxygen reduction activity at a platinum electrode in an acidic electrolyte solution investigated with a channel flow double electrode, 339–46, ©2005, with permission from Elsevier.)

Using a DFT model, Norskov et al. [44] calculated the dissociative mechanism and gave a Tafel slope of 60 mV/dec. Unfortunately, the literature does not devote enough attention to the associative mechanism.

The ORR exchange current density on a Pt electrode can be obtained by extrapolating the potential-log(I) plot along the Tafel line to the thermodynamic potential. Two Tafel slopes give two exchange current densities, one at a low current density (high potential), and the other in a high current density range (low potential). The values of the ORR exchange current densities on Pt vary widely in the literature, depending primarily on the morphology of the Pt catalyst. This can also be seen in Table 2.2. For example, Parthasarathy et al. [7] reported that the values on a Pt wire/Nafion membrane interface at 80 °C are 1.8×10^{-8} A/cm^2 at high potential range (low current density, with Tafel slope of 60 mV/dec) and 1.4×10^{-6} A/cm^2 at low potential range (high current density, with a Tafel slope of 120 mV/dec). Our recent study on the kinetics of ORR in PEM fuel cells showed that at 80 °C, the exchange current density is 6.25×10^{-6} at high potential range (low current density) and 3.87×10^{-4} A/cm^2 at low potential range (high current density), respectively [4]. For the catalyst, we used Pt nanoparticles supported on Vulcan carbon.

2.4.4 ORR on Pt Alloys

The catalytic activity of Pt towards ORR strongly depends on its O_2 adsorption energy, the dissociation energy of the O-O bond, and the binding energy of OH on the Pt surface. The electronic structure of the Pt catalyst (Pt d-band vacancy) and

the Pt-Pt interatomic distance (geometric effect) can strongly affect these energies [47]. Theoretical calculations on O_2 and OH binding energy on several metals have predicted that Pt should have the highest catalytic activity among other metals with the ORR activity of Pt > Pd > Ir > Rh, which is in agreement with the experimental results. Regarding the Pt alloy catalysts, calculations have also predicted that PtM (M=Fe, Co, Ni, etc.) alloys should have higher catalytic activity than pure Pt, which has again been proven by experiments [44].

The activity enhancement that occurs when Pt is alloyed with other metals is explainable by the change in electronic structure (the increased Pt d-band vacancy) and in geometric effect (Pt-Pt interatomic distance). Alloying causes a lattice contraction, leading to a more favorable Pt-Pt distance for the dissociative adsorption of O_2. The d-band vacancy can be increased after alloying, producing a strong metal-O_2 interaction then weakening the O-O bonds. Figure 2.18 shows the Tafel plots of Pt and PtFe alloys for the O_2 reduction reaction. The Tafel slopes for the two catalysts are the same. However, the exchange current density of oxygen reduction on PtFe is higher than on Pt. In the Tafel region of 120 mV/dec, the exchange current density for a Pt catalyst is 1.63×10^{-8} A/cm^2, while that for PtFe catalysts is 2.15×10^{-7} A/cm^2, indicating a nine-fold increase [47].
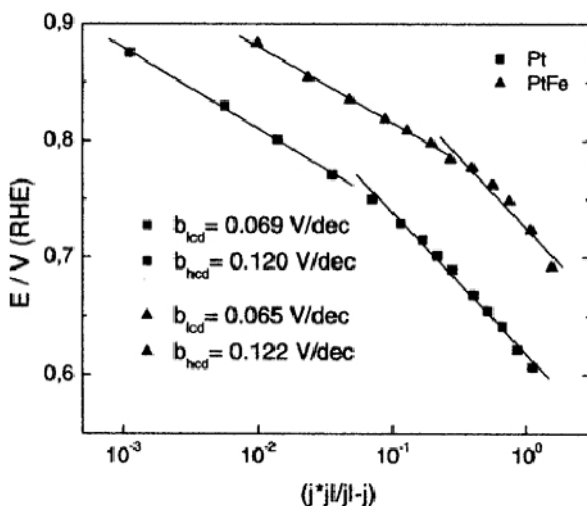
Figure 2.18. Tafel plots for ORR in 0.5 M H_2SO_4 on different catalysts; b_{lcd}: Tafel slope at low current density; b_{hcd}: Tafel slope at high current density [47]. (With kind permission from Springer Science+Business Media: Journal of Applied Electrochemistry, Electrocatalytic behaviour for oxygen reduction reaction of small nanostructured crystalline bimetallic Pt–M supported catalysts, 36, 2006, 1143–1149, A. Stassi, Figure 9, ©Springer.)

Stamenkovic et al. [48] recently found that on Pt$_3$Ni, the O_2 reduction reaction is 90 times faster than on pure Pt. Unfortunately, dissolution of the transition metal alloyed in the PtM catalysts is a major drawback because these transition metals are electrochemically soluble at a potential range between 0.3 to 1 V vs. NHE in low pH media [47]. More effort is needed to solve this problem.

2.4.5 Catalytic ORR on Other Metals

Oxygen reduction reaction on other metal surfaces such as Au, Ir, Rh, etc. has also been extensively investigated [46]. However, these metals show lower catalytic activity towards ORR than Pt; in addition, they are not electrochemically stable (and therefore are more easily oxidized than Pt).
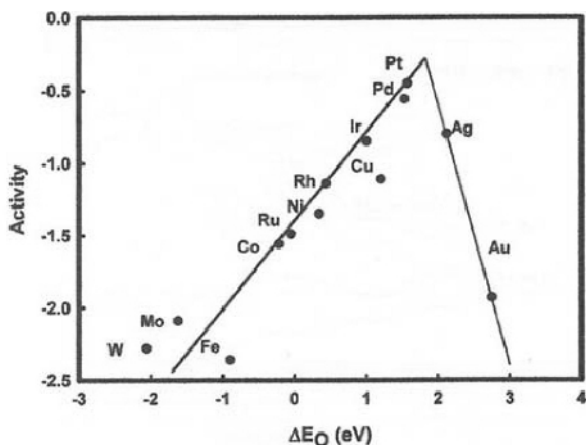
Figure 2.19. Trends in oxygen reduction activity plotted as a function of the oxygen binding energy [44]. (Reprinted with permission from J Phys Chem B 2004;108:17886–92. Copyright 2004 American Chemical Society.)
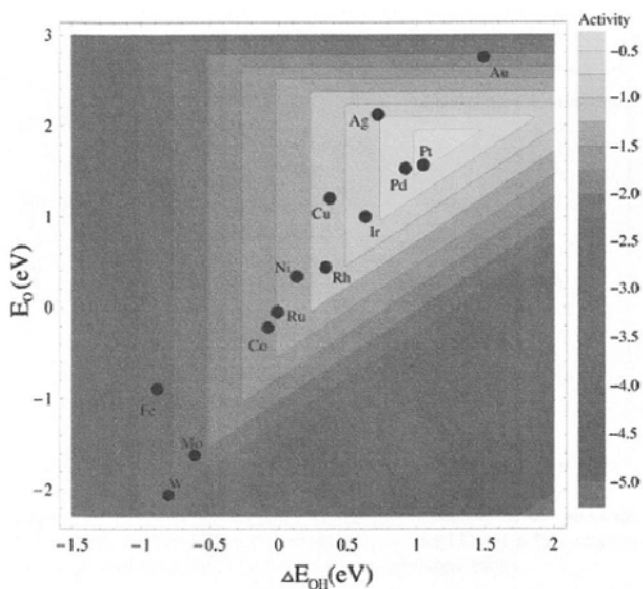
Figure 2.20. Trends in oxygen reduction activity plotted as a function of both the O and the OH binding energy [44]. (Reprinted with permission from J Phys Chem B 2004;108:17886–92. Copyright 2004 American Chemical Society.)

Figure 2.19 shows the trend in oxygen reduction activity as a function of the oxygen binding energy, and Figure 2.20 shows the trend as a function of both the O and the OH binding energy. Both figures show that Pt is the most active ORR catalyst.

2.5 ORR on Macrocyclic Transition Metal Complexes

2.5.1 ORR Mechanisms Catalyzed by Transition Metal Macrocyclic Complexes

Transition metal macrocyclic complexes can catalyze the O_2 reduction reaction through a 2-electron or 4-electron transfer pathway to produce either H_2O_2 or H_2O. Sometimes, they can also catalyze ORR through a mixed pathway of 2- and 4-electron transfer reduction. In rare cases, transition metal macrocyclic complexes can also catalyze a 1-electron O_2 reduction, producing superoxide ions.

The catalytic reaction mechanism is proposed to be a modified "redox catalysis" procedure [1, 49]. In the first step, the adduct between oxygen and the metal ion center of the macrocyclic compound is formed, followed by an intra-adduct electron transfer from the metal ion to the oxygen. The addition of protons from the electrolyte, together with the electron transfer, then produces H_2O_2. The H_2O_2 is either the final product or can be further reduced to produce water, depending on the individual transition metal macrocyclic compounds used. The mechanism can be summarized as follows:

$$[LMe^{II}] + O_2 \leftrightarrow [LMe^{\delta+}\ldots\ldots O_2^{\delta-}] \tag{2.46}$$

$$[LMe^{\delta+}\ldots\ldots O_2^{\delta-}] + H^+ \rightarrow [LMe^{III}\ldots\ldots O_2H]^+ \tag{2.47}$$

$$[LMe^{III}\ldots\ldots O_2H]^+ + H^+ + 2e^- \rightarrow [LMe^{II}] + H_2O_2 \tag{2.48}$$

$$H_2O_2 + 2e^- + 2H^+ \rightarrow 2H_2O \tag{2.49}$$

$$H_2O_2 \rightarrow H_2O + 1/2O_2 \tag{2.50}$$
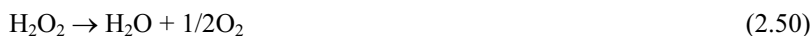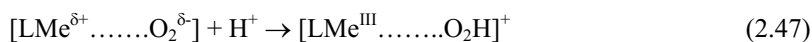
where L represents the ligand and Me is the metal center.

2.5.2 Transition Metal Macrocycles as ORR Catalysts

2.5.2.1 Metal Centers and the Ligand Effect on ORR Activity
The catalytic activity of transition metal macrocyclic compounds towards ORR strongly depends on the individual transition metal center and the macrocyclic ligand, as well as the size of the π electron system. Compounds studied previously include a variety of metal centers and ligands. The transition metals used in macrocyclic catalysts include Fe, Co, Ni, and Cu, and the macrocyclic ligands include chelating atoms N_4, N_2O_2, N_2S_2, O_4, and S_4. The conjugate π electron

compounds usually include metal phthalocyanine and porphyrin, as well as their derivatives [1, 49].

The activity of these compounds changes with respect to the central metal ions in the following order: Fe>Co>Ni>Cu. For a metal center, the chelating atoms of the macrocyclic ring can also change the ORR activity. For example, the active sequence of Fe complexes is as follows: $N_4>N_2O_2>N_2S_2>O_4\approx S_4$ (inactive); for Co centers: $N_2O_2>N_4>N_2S_2>O_4\approx S_4$; for Cu centers: $N_4>O_4>N_2O_2>N_2S_1>S_4$ (inactive); and for Ni centers: $O_4>N_2O_2>N_2S_2>N_4$. With respect to these active sequences, recent research has mainly focused on Fe and Co centers, and for macrocyclic rings, on the N_4 system. In this section, the discussion will focus on the Fe-N_4 and Co-N_4 systems.

2.5.2.2 M-N₄ ORR Catalysts

M-N_4 complexes can strongly and irreversibly adsorb on a graphite electrode surface to form a monolayer or multilayers of ORR catalysts. This adsorption can create a well-defined electrode surface, then provide a theoretical treatable situation for fundamental understanding of the catalyst activity and mechanism [50–52].

For Fe-based N_4 catalysts (Fe-N_4), the ORR normally takes a 4-electron transfer pathway to produce H_2O, as reported by Zagal et al. [50]. Shi et al. [51] found that oxygen reduction catalyzed by Fe tetrakis(4-N-methylpyridyl) porphyrin produced a mixture of H_2O and H_2O_2. With respect to the ligand effect, Shigehara et al. [52] found that ligands had a strong effect on the ORR activity catalyzed by Fe porphyrins; both Fe meso-tetraphenylporphine (FeTPP) and Fe protoporphyrin IX (FePPIX) can catalyze a 4-electron oxygen reduction, while Fe meso-tetra(3-pyridyl)porphine (FeTPyP) only catalyzes a 2-electron oxygen reduction [51, 52]. Nonetheless, in most cases, Fe-N_4 can catalyze 4-electron oxygen reduction and the product is water.

In general, mononuclear Co-N_4 complexes can only catalyze 2-electron O_2 reduction reaction. Zagal et al. [50] studied Co and Fe tetrasulfonate phthalocyanines and found that the Co complex only catalyzed a 2-electron oxygen reduction process. However, bi-nuclear Co-N_4 complexes or Co-N_4 dimers have some different behaviors from those of mononuclear Co-N_4 complexes. They can catalyze not only 2-electron but also 4-electron O_2 reduction reactions. A planar bi-cobalt complex such as $(Co_2TAPH)^{4+}$, as shown in Figure 2.21, catalyzes a 4-electron reduction of O_2 in alkaline solutions. This catalytic activity was found to be due to the interaction between O_2 and the Co metal centers. This interaction can effectively weaken the O-O bond, rendering it easily broken. Furthermore, face-to-face di-Co-N_4 complexes also favor a 4-electron transfer pathway, depending on the Co-Co distance in the molecules (Figure 2.22). When the Co-Co distance is around 4 Å, the O-O bridge between the Co-Co centers can be formed as shown in Figure 2.23, resulting in a 4-electron transfer of ORR. If the Co-Co distance is larger or smaller, only the 2-electron transfer pathway to peroxide is favored. This can be explained by the formation of a cis- or trans-configuration (Figure 2.23). The cis-configuration favors the 4-electron ORR to H_2O, while the trans- does not [53].
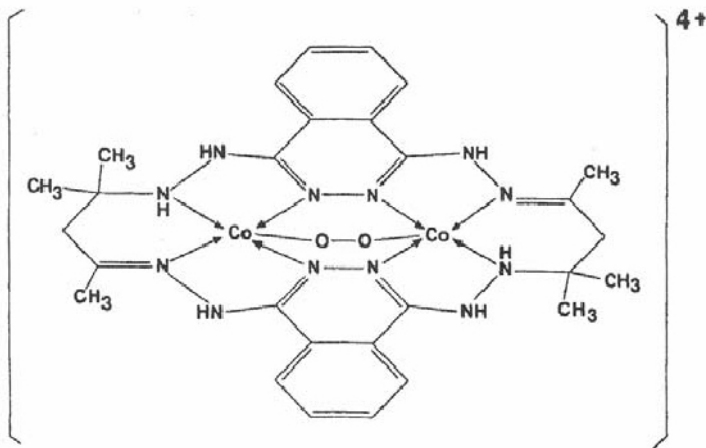
Figure 2.21. Dimetal complex $(Co_2TAPH)^{4+}(NO_3)_4$. (TAPH = 6,7,8,9,12,19, 20,21,22,25-decahydro-8,8,10,21,21,23,-hexamethyl-5,26:13,18-bis(azo)-dibez(1,2,6,7,12,13,17,18)oxa-azacyclodocosine) [2]. (Reprinted from Journal of Molecular Catalysis, 38(1–2), Yeager Ernest, Dioxygen electrocatalysis: mechanisms in relation to catalyst structure, 5–25, ©1986, with permission from Elsevier.)
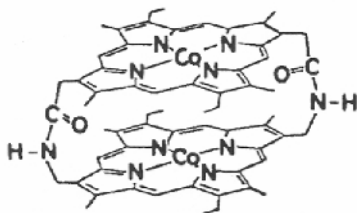
Figure 2.22. Face-to-face Co-Co 4-porphyrin [2]. (Reprinted from Journal of Molecular Catalysis, 38(1–2), Yeager Ernest, Dioxygen electrocatalysis: mechanisms in relation to catalyst structure, 5–25, ©1986, with permission from Elsevier.)
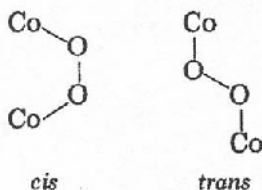
Figure 2.23. Cis- and trans-Co-O-O-Co facial configuration [2]. (Reprinted from Journal of Molecular Catalysis, 38(1–2), Yeager Ernest, Dioxygen electrocatalysis: mechanisms in relation to catalyst structure, 5–25, ©1986, with permission from Elsevier.)

Recently, Kadish et al. [54] synthesized three series of Co corroles (shown in Figure 2.24) and investigated their catalytic activity toward the O_2 reduction reaction [54]. The mixed valent Co(II)/Co(III) complexes, $(PCY)Co_2$, and the

biscorrole complexes, $(BCY)Co_2$, both contain two Co(III) ions in their air-stable forms. It was found that all of these complexes could catalyze the direct 4-electron pathway for O_2 reduction to H_2O in aqueous acidic electrolyte. The most efficient catalysis process was observed when the complex had an anthracene spacer. This catalyzed 4-electron transfer pathway was further confirmed by RRDE measurement. Only a relatively small amount of hydrogen peroxide was detected at the ring electrode in the vicinity of $E_{1/2}$: 0.47 V vs. SCE for $(PCA)Co_2$ and 0.39 V for $(BCA)Co_2$, respectively. The cobalt(III) monocorrole $(Me_4Ph_5Cor)Co$ could also catalyze ORR at $E_{1/2} = 0.38$ V, with the final products being an approximate 50% mixture of H_2O_2 and H_2O.
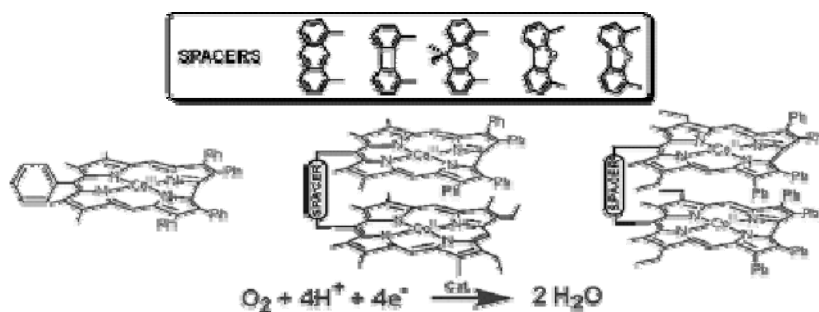
Figure 2.24. Co-corrole compounds for O_2 reduction reaction [54]. (Reprinted with permission from J Am Chem Soc 2005;127:5625–31. Copyright 2005 American Chemical Society.)

Theoretical approaches have in addition predicted that the substituents on the macrocyclic rings can also affect ORR catalytic activity. Co-phthalocyanine complexes with electron donating substituents should show improved ORR catalytic activity because the substituents can increase the binding energy between O_2 and the metal center(s) [55]. Calculation indicates that the catalytic activity of the transition metal macrocyclic complexes is due to the partial electron transition between the filled d_{xz}, d_{yz}, and empty d_{z^2} orbitals of the transition metals, and the anti-bonding π orbitals of O_2. Based on molecular orbital theory, Alt et al. [56] explained that in the interaction between O_2 and a transition metal, electron transition occurs first from oxygen into the empty d_{z^2} orbital, forming a σ bond, lowering the anti-bonding π orbitals and raising the energy of the d_{xz} and d_{yz} orbitals of the transition metals, thus allowing the electron transition from these filled orbitals to the anti-bonding π orbital, and resulting in enhanced interaction. The order of catalytic ORR activity for both the tetramethoxyphenylporphyrin (TMPP) and the dihydrodibenzotetraazaannulene (DHDBTAA) systems is: Co>Fe>Ni≈Cu. This order can be well explained in terms of molecular orbital theory [49, 56].

2.5.2.3 Heat-treated Transition Metal Macrocyclic Complexes
Normally, transition metal macrocyclic complexes do not have long-term stability in concentrated acidic or alkaline solutions. It has been found that thermal

treatment of these compounds after they have been adsorbed on high-surface-area carbon support particles in the temperature range of 450–900 °C not only increases their stability, but also improves their catalytic activity [1, 2, 57]. The thermal treatment was performed in an inert atmosphere, where pyrolysis of the compounds would occur. Thermal treatment temperature can affect the stability and catalytic activity of the M-N$_4$ compounds, and usually high temperature (> 800 °C) is necessary to obtain stable catalysts.

Although heat treatment can destroy the macrocyclic ring, the N$_4$ ring structure in porphyrin and similar macrocycles is still retained. Heat treatment can also be performed by heat-treating the macrocycles adsorbed on carbon substrates, followed by the addition of transition metal salts. The pyrolyzed macrocycles on carbon supports provide coordination sites, including N$_4$, to bind transition metals such as Fe and Co, forming M-N$_4$ coordination complexes. However, it was also found that the ORR catalytic activity loss of these heat-treated M-N$_4$ catalysts in long-term operation was due to the loss of the transition metal from the pyrolyzed macrocycle surface.

Thermal treatment might lead to phase change in the transition metal macrocyclic complexes. Using XRD measurements, Baranton [58] found that received iron phthalocyanine was under α phase and that after being heat-treated at 450 °C it was under β phase.

It is worth noting that as yet, the enhancement mechanisms of activity and stability after heat treatment of these M-N$_4$ catalysts are not fully understood. It is necessary to ascertain whether the metal is part of the active catalytic site, and also to identify the nature of the catalytic site.

2.5.3 ORR Kinetics Catalyzed by Transition Metal Macrocyclic Complexes

Tafel slopes of ORR catalyzed by M-N$_4$ complexes have different values, depending on the individual catalyst used. Zagal et al. [50, 59] reported that Co(II) tetrasulfonatephthalocyanine (CoTSP) could catalyze a 2-electron O$_2$ reduction reaction, producing H$_2$O$_2$ in both acid and alkaline solutions, with Tafel slope values of 120, 135, and 155 mV/dec, respectively. Collman et al. [60] reported a Tafel slope of 65 mV/dec on dicobalt porphyrin dimers in acid solution. For Fe-N$_4$ catalysts, Zagal et al. [50] reported two Tafel slopes of FeTSP catalyzed oxygen reduction reaction, which were dependent on pH. At low overpotential, a Tafel slope of 65 mV/dec was obtained at pH 4.4, which decreased to 29 mV/dec when pH was increased to 13.9. At high overpotential, a Tafel slope of 120 mV/dec was observed at pH 4.4, which changed slightly to 130 mV/dec at pH 13.8. These two Tafel slopes are the same as those reported by Baranton et al. [58] for α-FePc-catalyzed ORR in acid solution. However, for β-FePc, only one Tafel slope (63 mV/dec) was obtained, indicating that the ORR mechanism was different.

The exchange current density of ORR catalyzed by M-N$_4$ complexes is seldom reported. Zagal et al. [59] found that in acid solution, ORR catalyzed by Co(II)TSP had an exchange current density of 10^{-11} A/cm^2 for O$_2$/H$_2$O reaction, while in alkaline solution, the value became 10^{-7} A/cm^2. Note that in both solutions, Co(II)TSP could only catalyze a 2-electron O$_2$ reduction reaction. In the early stage of M-N$_4$-catalyzed ORR research, Savy et al. [61] studied ORR catalyzed by

porphyrin complexes with Fe, Co, Ni, and Cu metal centers, and they reported the exchange current densities of ORR catalyzed by each. For example, FePc showed exchange current densities of 1.3×10^{-7} A/cm^2 at pH 1.3 and 1.5×10^{-8} A/cm^2 at pH 6.7.

2.6 ORR Catalyzed by Other Catalysts

2.6.1 ORR Catalyzed by Transition Metal Chalcogenides

2.6.1.1 Chalcogenides and Oxygen Reduction Reaction Products

Transition metal chalcogenides are a group of materials that show catalytic activity towards ORR. The materials are classified into two types, based on the structure, the Chevrel phase-type compounds such as $Mo_4Ru_2Se_8$, and amorphous phase compounds such as Ru_xS_y [1]. Figure 2.25 shows the structure of $Mo_4Ru_2Se_8$, where the octahedral transition metal core acts as an electron reservoir [62].
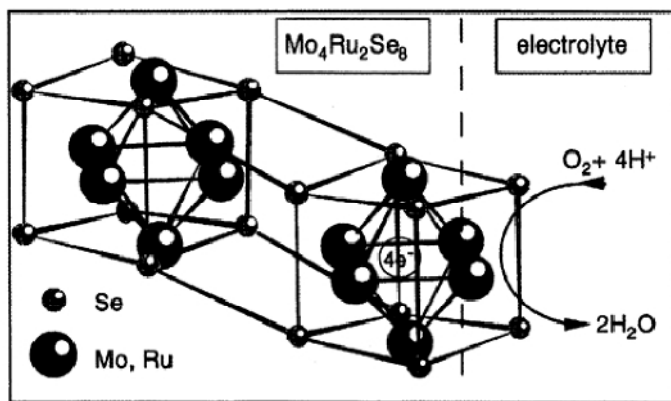
Figure 2.25. Structure of $Mo_4Ru_2Se_8$ and interaction of O_2 at the Chevrel phase clusters-electrolyte interface [62]. (Reprinted from J Phys IV, Alonso-Vante N, Fieber-Erdmann M, Rossner H, Holub-Krappe E, Giorgetti Ch, Tadjeddine A, et al. The catalytic center of transition metal chalcogenides vis-à-vis the oxygen reduction reaction: an *in situ* electrochemical EXAFS study, 7:887–9. ©1997 with permission of EDP Sciences.)

Chalcogenides can catalyze either 2-electron or 4-electron O_2 reduction, depending on the catalysts used. For example, $Mo_4Ru_2Se_8$, $Ru_{1.92}Mo_{0.08}SeO_4$, $Ru_xS_y(CO)_n$, Ru_xSe_y, etc. catalyze 4-electron transfer [62–68], while W-Co-Se catalyzes a 2-electron O_2 reduction reaction [69].

2.6.1.2 Chalcogenide-catalyzed ORR Mechanism

The origin of the ORR catalytic activity of a chalcogenide is strongly associated with its semiconducting property. It is believed that the catalytic activity occurs through the interaction of O_2 with the transition metal d-states originating from the mixed metal cluster. Figure 2.26 shows the schematic of the energy and molecular

statuses of the semiconducting cluster at the interface, under charge transfer conditions.
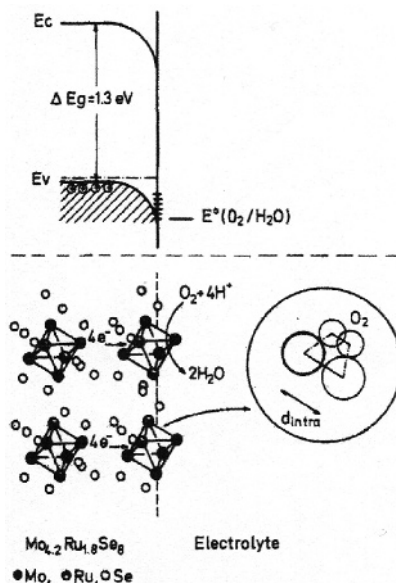
Figure 2.26. Schematic energy and molecular representation of the semiconducting $Mo_{4.2}Ru_{1.8}Se_8$ cluster and the redox couple (O_2/H_2O) at the interface, under charge transfer conditions. The insert shows a supposed interaction of the molecular bridge type at two adjacent transition metal atoms [63]. (Reprinted with permission from J Am Chem Soc 1987;109:3251–7. Copyright 1987 American Chemical Society.)

In this $Mo_{4.2}Ru_{1.8}Se_8$ compound, the energy gap between the valence and the conductance band is 1.3 eV, which is a characteristic of the compound as a degenerated p-type semiconductor. The O_2 reduction reaction will start when the Fermi level of the electrode is 0.35 V above the O_2/H_2O redox potential. It is most possible that O_2 interacts with a transition metal atom of a cluster through a bridge-type bonding to two adjacent metal atoms in the same cluster. The electron transfer between the cluster and the O_2 could result in a metal distance increase, which possibly facilitates the breaking of the O-O bond and an upward shift of the electronic level due to the loss of electrons. The cluster volume can increase by 15% when it loses its electrons. Refilling of the cluster with electrons is expected because the Fermi level is above the edge of the valence band [63].

The ORR mechanism catalyzed by a chalcogenide is different from that catalyzed by Pt or other catalysts. Although the mechanism is still not clear, most possibly it is not a stepwise subsequent electron process involving an intermediate. Rather, it may involve a synergistic multielectron transfer, or a self-organized electron transfer. The electrons are not transferred independently, but rather are dependent on each other. An initiating electron transfer event could produce a "positive friction" loop, trigging subsequent loops. If the feedback can be adjusted adequately, the electrons will transfer in a cooperative way without producing

intermediates [70, 71]. This feedback is possibly reflected in the distance change between the metal atoms.

2.6.1.3 Kinetics of ORR Catalyzed by Chalcogenides

The catalytic activity of a chalcogenide towards ORR can reach a level of 30–40% of the Pt catalyst activity. The Tafel slope varies from 100 mV/dec up to 167 mV/dec, depending on the materials used and the preparation method. Duron et al. [66] reported two Tafel slopes for ORR on a $Ru_xS_y(CO)_n$ cluster: 124 mV/dec at low overpotential and 254 mV/dec at high overpotential. Susac et al. [72] reported a Tafel slope of 167 mV/dec on Co-Se catalyst. There seems to be no reported data in the literature about the exchange current density of ORR catalyzed by chalcogenides.

2.6.2 ORR Catalyzed by Transition Metal Carbide

Transition metal carbide, in particular tungsten carbide, is another type of non-noble catalyst showing activity towards the oxygen reduction reaction. However, the main catalytic activity of carbide is not in the oxygen reduction reaction, but rather in other reactions such as H_2 oxidation. Mazza et al. [73] reported that WC, TaC, TiC, and TiN showed catalytic activity towards ORR in acid solutions. However, these materials are not stable in alkaline solution. For example, even in acid solutions, WC did not show long-term stability in the presence of O_2 [73]. Lee et al. [74] found that the addition of Ta to WC could significantly improve its catalytic activity and stability.

Although pure WC has no significant ORR catalytic activity, the addition of it to Pt could lead to an improvement [75, 76]. Figure 2.27 shows the linear sweep curves of ORR on W_2C, Pt/C, and W_2C-Pt/C catalysts. The best activity can be observed with a W_2C-Pt/C catalyst.
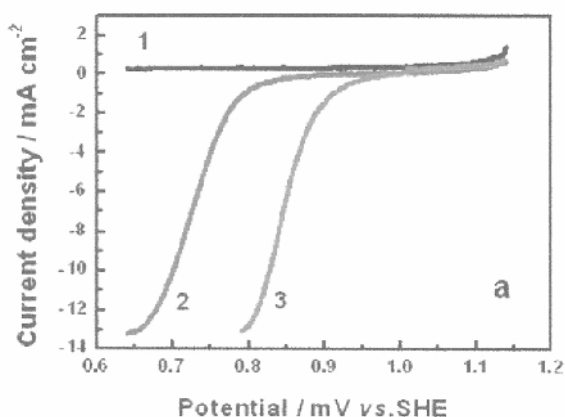
Figure 2.27. Linear sweep curves of oxygen reduction on different catalysts in O_2-saturated 0.5 M H_2SO_4 solution at 25 °C: curve 1, 80 µg W_2C; curve 2, 80 µg Pt/C; curve 3, 40 µg Pt+80 µg W_2C; scan rate: 2 mV/s [75]. (Reprinted with permission from J Phys Chem B 2005;109:22705–9. Copyright 2005 American Chemical Society.)

The mechanism of the ORR activity enhancement induced by adding W_2C to Pt is not yet clear. Experimental results show that most possibly this is due to the synergistic effect between tungsten carbide nanoparticles and Pt at the interface.

There seems to be no report about the Tafel slope of WC-catalyzed ORR. The Tafel slope of W_2C-Pt/C-catalyzed ORR is similar to that of Pt/C: 66 mV/dec at low overpotential and 126 mV/dec at high overpotential. The presence of W_2C can significantly decrease ORR overpotential, as shown in Figure 2.28.
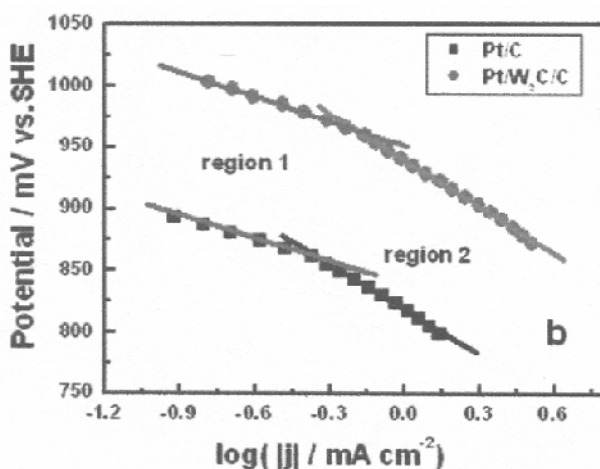
Figure 2.28. Tafel slopes for oxygen reduction reaction on Pt/C and Pt-W_2C/C electrocatalysts [75]. (Reprinted with permission from J Phys Chem B 2005;109:22705–9. Copyright 2005 American Chemical Society.)

The exchange current density of ORR on W_2C-Pt/C could also be increased. For example, Pt/C gave two exchange current densities: 5.25×10^{-10} A/cm^2 at low overpotential and 3.16×10^{-7} A/cm^2 at high overpotential. While on W_2C-Pt/C, the values were found to be 4.7×10^{-7} A/cm^2 at low overpotential and 5.01×10^{-5} A/cm^2 at high overpotential, showing a two- to three-order increase compared to pure Pt/C catalyst [75].

2.7 Superoxide Ion

2.7.1 Production of Superoxide Ion by Other Methods

Superoxide ion is an important intermediate in the fundamental understanding of the ORR mechanism. This species has significant implications in chemistry and biology. Superoxide ion was initially produced from radiolysis. In a solution containing a large excess of sodium formate saturated with O_2, the radiolytic electron flux could reduce O_2 to produce O_2^- [77,78]:

$$O_2 + e^-_{(aq)} \rightarrow O_2^- \tag{2.51}$$

$$HCOO^- + HO\bullet \rightarrow \bullet COO^- + H_2O \tag{2.52}$$

$$O_2 + \bullet COO^- \rightarrow O_2^- + CO_2 \tag{2.53}$$

$$O_2 + H\bullet \rightarrow HOO\bullet \rightarrow H_3O^+ + O_2^- \tag{2.54}$$

Superoxide ion could be also produced by an electrochemical method in aprotic organic solvents [79–83], in ionic liquid systems (room temperature) [84–87], on organic-compound-coated electrode surfaces [88], and on Co-macrocyclic-complex-coated electrodes [89, 90]. The electrochemical response of superoxide ion is reversible in aprotic organic solvents such as DMSO, and in ionic liquid systems.

2.7.2 Properties of Superoxide Ion

The thermodynamic reduction potential for the O_2/O_2^- pair has been determined using redox mediator dyes and spectrophotometry [77, 78]. The reaction is expressed as: $O_2(g, 1 \text{ atm}) + e^- \leftrightarrow O_2^-$, and its corresponding standard electrode potential is $(E^0)_{pH,5-14} = -0.33$ V vs. NHE or -0.16 V for O_2 at unit activity. The redox potential of the O_2/O_2^- is dependent on the solvent and the electrode materials. Table 2.4 summarizes the redox potentials of O_2/O_2^-, concentration and the diffusion coefficient of O_2 in different solvents. The formal potential was taken as the average of the anodic peak and the cathodic peak potentials from CV at a scan rate of 0.1 V/s.

Table 2.4. Redox potentials for O_2/O_2^- in different solvents (1 atm O_2) [78–86]

Solvent	C_{O_2} (mM)	$D_{O_2} \times 10^5$ (cm^2 s^{-1})	$E^{0'}$ (V) vs. NHE
H_2O	1.0	2.1	–0.16
DMSO	2.1	2.1	–0.54
DMF	4.8	5.0	–0.62
Py	4.9	5.7	–0.62
MeCN	8.1	7.2	–0.63
Quinoline	1.5	1.8	–0.63
EMIBF$_4$	1.1	1.7	–0.61
PMIBF$_4$	1.0	1.3	–0.58
BMIBF$_4$	1.1	1.2	–0.62
[bmim]HFP	3.6	0.22	–0.64
Hydrocarbons	~10	-	-
Fluorocarbons	~25	-	-

Table 2.5. The formal potentials at different electrode materials [78]

Solvent	Formal potentials at electrodes (V) vs. NHE			
	C	**Pt**	**Au**	**Hg**
DMSO	−0.54	−0.78	−0.55	-
DMF	−0.62	−0.62	−0.64	-
Py	−0.64	−0.65	−0.63	
MeCN	−0.63	−0.65	−0.65	−0.63

The formal potential change with solvent is due to the salvation energy of O_2^- in different solvents. The value becomes more positive with increasing salvation energy. Thus, the salvation energy of O_2^- in these aprotic solvents follows the sequence:

$$H_2O >> DMSO > PBIBF_4 > EMIBF_4 > DMF \sim Py \sim BMIBF_4 > MeCN > [bmim]HFP.$$

2.7.3 Stability of Superoxide Ion

Superoxide ion is not stable in the presence of water and protonic species, which results in the disproportionation of the superoxide ions and leads to the production of H_2O_2 [78, 79, 84], according to Equation 2.55:

$$2O_2^- + 2H_2O \leftrightarrow H_2O_2 + O_2 + 2OH^- \qquad K = 10^9 \text{ M atm} \qquad (2.55)$$

2.7.4 Superoxide Production by Electrocatalysis

In aqueous systems, superoxide ion was only observed on electrodes modified in alkaline solutions by surfactant (triphenylphosphine oxide) [91], organic groups (methyl phenyl) [88], or metal macrocyclic compounds [88, 89, 92]. The surfactant and organic groups can cover the electrode surface, preventing water from reaching the electrode surface and stabilizing the produced O_2^-. The reversibility of the O_2/O_2^- electrochemical response depends on the alkalinity [88, 90]. In less alkaline solutions, the redox behavior becomes less reversible, due to the kinetics of the reaction.

Superoxide ion production by electrocatalysis was observed on Fe(III) phthalocyanine, Co(II)$_2$-disalophen, and Co(II)HFPC-modified Hg or carbon electrodes. However, on Fe(III)phthalocyanine-modified Hg electrode surfaces, further scanning the potential to more negative values resulted in further reduction of O_2^-, forming H_2O_2 and OH^- [92]. On Co(II)$_2$-DSP and Co(II)HFPC modified electrodes [89, 90], stable superoxide ion could be produced in alkaline solutions. The catalytic mechanism has been proposed as follows:
For Co(II)$_2$-DSP:

$$Co(II)_2\text{-DSP} + 2O_2 \leftrightarrow Co(III)_2\text{-DSP} \bullet 2O_2^- \qquad (2.56)$$

$$Co(III)_2\text{-}DSP\bullet 2O_2^- + 2e^- \rightarrow Co(II)_2\text{-}DSP + 2O_2^- \tag{2.57}$$

For Co(II)HFPC:

$$[HO\text{-}Co(II)HFPC]^- + O_2 \leftrightarrow [Co(III)HFPC\text{-}O_2^-] + OH^- \tag{2.58}$$

$$[Co(III)HFPC\text{-}O_2^-] + OH^- + e^- \rightarrow [HO\text{-}Co(II)HFPC]^- + O_2^- \tag{2.59}$$
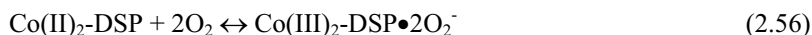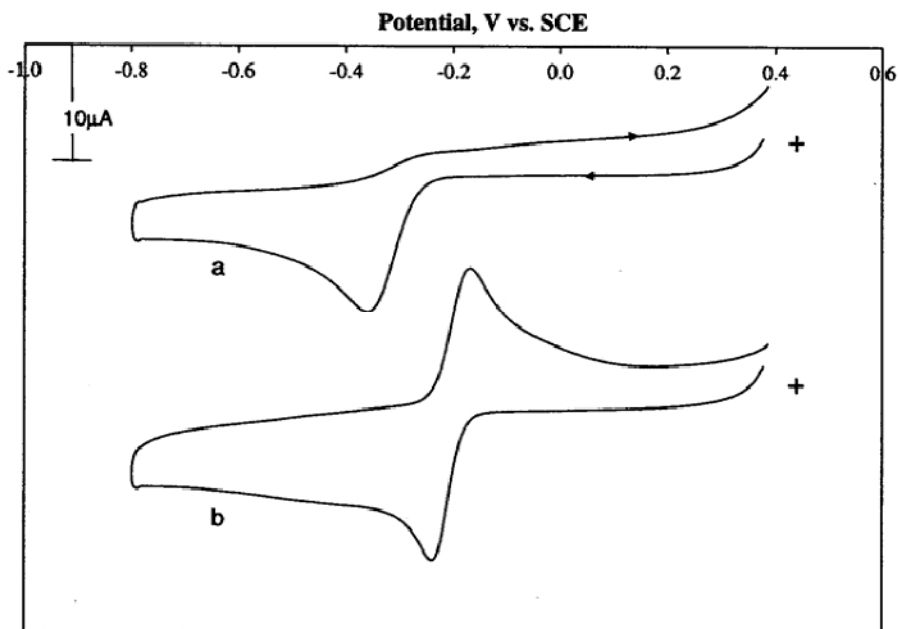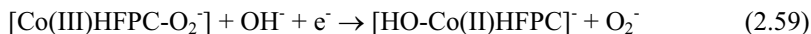
Figure 2.29. (a) Cyclic voltammograms of a bare graphite electrode and (b) a $Co^{II}HFPC$ adsorbed graphite electrode in an air-saturated 1 M NaOH solution. Scan rate: 50 mV/s [90]. (Reprinted from Journal of Electroanalytical Chemistry, 587(2), Song C, Zhang L, Zhang J, Reversible one-electron electro-reduction of O_2 to produce a stable superoxide catalyzed by adsorbed Co(II) hexadecafluoro-phthalocyanine in aqueous alkaline solution, 293–8, ©2006, with permission from Elsevier.)

The formal potential of the O_2/O_2^- redox couple is very close to the redox potential of the catalyst. For both $Co(III)_2$-DSP and Co(II)HFPC systems, the formal potential of O_2/O_2^- is ~0.0 V vs. NHE, normalizing the air pressure to O_2 pressure. This value is close to that reported in [78] for the initial reversible 1-electron transfer process of O_2 in aqueous solution at inert electrodes:

$$O_2 + e^- \leftrightarrow O_2^- \qquad (E_{1/2})_{pH12}, \ 0.0 \text{ V vs. NHE} \tag{2.60}$$
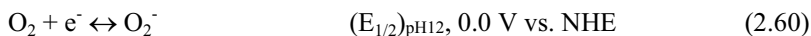
2.8 Conclusions

The catalytic mechanism of ORR and its kinetic parameters, including Tafel slopes and exchange current densities, can be obtained from techniques such as cyclic voltammetry, steady-state polarization, rotating disk electrode, and rotating ring-disk electrode. Catalysts used for ORR include carbon materials, quinone and derivatives, noble metal and noble metal alloy materials, transition metal macrocyclic compounds, chalcogenide materials, as well as transition metal carbide. Electrocatalytic ORR has been investigated in a wide range of electrolytes, ranging from acid to basic solutions, and in a wide range of solvent systems, including aqueous, non-aqueous aprotic, and room temperature ionic liquid systems.

Electrocatalytic ORR carries out in three pathways: the 1-electron transfer pathway, producing superoxide ion; the 2-electron transfer pathway, producing hydrogen peroxide; and the 4-electron transfer pathway, producing water. In a non-aqueous aprotic solvent system, a room-temperature ionic liquid system, and on specific transition-metal, macrocyclic-compounds-coated graphite electrodes in alkaline solutions, 1-electron reduction can be observed. Carbon materials, quinone and derivatives, mono-nuclear cobalt macrocyclic compounds, and some chalcogenides can only catalyze 2-electron ORR. Noble metal, noble metal alloy materials, iron-macrocyclic complexes, di-nuclear cobalt macrocyclic complexes, some chalcogenides, and transition-metal carbide-promoted Pt catalysts can catalyze 4-electron reduction.

The Tafel slope of the electrocatalytic ORR is usually 60 mV/dec or 120 mV/dec, or both 60 and 120 mV/dec, depending on the overpotential range. On carbon materials, a Tafel slope of either 60 or 120 mV/dec was observed depending on the pH of the electrolyte and on the carbon materials. On noble metal and noble metal alloys, two Tafel slopes were observed at different overpotential regions. At low overpotential (low current density), a Tafel slope of 60 mV/dec was obtained, while at high overpotential (high current density), a Tafel slope of 120 mV/dec was observed. On chalcogenide catalysts, Tafel slopes of larger than 120 mV/dec were reported. On other materials, Tafel slopes have rarely been studied.

The exchange current density of electrocatalytic ORR is mainly reported on Pt and Pt alloy catalysts. Because there are two Tafel regions, two exchange current densities can be obtained. At low overpotential, the exchange current density is around 10^{-10} A/cm^2, and at high overpotential, the exchange current density is around 10^{-6} A/cm^2. The values of exchange current density vary depending on the catalyst as well as the research method. On other catalysts, the exchange current density of ORR has seldom been reported.

References

1. Zhang L, Zhang J, Wilkinson DP, Wang H. Progress in preparation of non-noble electrocatalysts for PEM fuel cell reactions. J Power Sources 2006;156.2:171–82.

2. Yeager E. Dioxygen electrocatalysis: mechanism in relation to catalyst structure. J Mol Catal 1986;38:5–25.
3. Bard AJ, Faulkner LR. Electrochemical methods: fundamentals and applications. New York: Wiley, 1980.
4. Song C, Tang Y, Zhang J, Zhang J, Wang H, Shen J, et al., PEM fuel cell reaction kinetics in the temperature range of 23–120 °C. Electrochim Acta 2007;52:2552–61.
5. Damjanovic A. Temperature dependence of symmetry factors and the significance of the experimental activation energies. J Electroanal Chem 1993;355:57–77.
6. Zhang J, Tang Y, Song C, Xia Z, Wang H, Zhang J, et al. Effect of relative humidity on PEM fuel cell performance at elevated temperature. Forthcoming 2008.
7. Parthasarathy A, Srinivasan S, Appleby AJ, Martin CR. Temperature dependence of the electrode kinetics of oxygen reduction at the platinum/Nafion interface – a microelectrode investigation. J Electrochem Soc 192;139:2530–7.
8. Wkabayashi N, Takeichi M, Itagaki M, Uchida H, Watanabe M. Temperature dependence of oxygen reduction activity at a platinum electrode in an acidic electrolyte solution investigated with a channel flow double electrode. J Electroanal Chem 2005;574:339–46.
9. Baker R, Wilkinson DP, Zhang J. Electrocatalytic activity and stability of substituted iron phthalocyanines towards oxygen reduction evaluated at different temperatures. Electrochim Acta. Forthcoming 2008.
10. Lever ABP. The phthalocyaninds-molecules of enduring value: a two-dimensional analysis of redox potentials. J Porphyrins Phthalocyanines 1999;3:488–99.
11. Zhang L, Song C, Zhang J, Wang H, Wilkinson DP. Temperature and pH dependent oxygen reduction catalyzed by iron fluoro-porphyrin adsorbed on a graphite electrode. J Electrochem Soc 2005;152:A2421–6.
12. Song C, Zhang L, Zhang J, Wilkinson DP, Baker R. Temperature dependence of oxygen reduction catalyzed by cobalt fluorophthalocyanine adsorbed on a graphite electrode. Fuel Cells 2007;7:9–15.
13. Antoine O, Durand R. RRDE study of oxygen reduction on Pt nanoparticles inside Nafion: H_2O_2 production in PEMFC cathode conditions. J Appl Electrochem 2000;30:839–844.
14. Taylor RJ, Humffray AA. Electrochemical studies on glassy carbon electrodes II. Oxygen reduction in solutions of high pH (pH>10). J Electroanal Chem 1975;64:63–84.
15. Paliteiro C, Hamnett A, Goodenough JB. The electroreduction of oxygen on pyrolytic graphite. J Electroanal Chem 1987;233:147–59.
16. Zhang M, Yan Y, Gong K, Mao L, Guo Z, Chen Y. Electrostatic layer by layer assembled carbon nanotube mutilayer film and its catalytic activity for oxygen reduction reaction. Langmuir 2004;20;8781–5.
17. Taylor RJ, Humffray AA. Electrochemical studies on glassy carbon electrodes II. Oxygen reduction in solutions of low pH (pH<10). J Electroanal Chem 1975;64:85–94.
18. Davis M, Clark M, Yeager E, Hovorka F. Oxygen electrode. J Electrochem Soc 1959;106:56.
19. Appel M, Appleby AJ. A ring disk electrode study of the reduction of oxygen on active carbon in alkaline solution. Electrochim Acta 1978;23:1243–6.
20. Jurmann G, Tammeveski K. Electroreduction of oxygen on multi-walled carbon nanotube modified highly oriented pyrolytic graphite electrodes in alkaline solution. J Electroanal Chem 2006;597:119–26.
21. Baez VB, Pletcher D. Preparation and characterization of carbon/titanium dioxide surfaces – the reduction of oxygen. J Electroanal Chem 1995;382:59–64.
22. Morcos I, Yeager E. Kinetic studies of the oxygen-peroxide couple on pyrolytic graphite Electrochim Acta 1970;15:953–75.

23. Maldonado S, Stevenson KJ. Influence of nitrogen doping on oxygen reduction electrocatalysis at carbon nanofiber electrodes. J Phys Chem B 2005;109.10:4707–16.
24. Sidik RA, Anderson AB, Subramanian NP, Kumaraguru SP, Popov BN. O_2 reduction on graphite and nitrogen doped graphite: experiment and theory. J Phys Chem B 2006;110:1787–93.
25. Hu I, Karweik DH, Kuwana T. Activation and deactivation of glassy carbon electrodes. J Electroanal Chem 1985;188:59–72.
26. Sljukic B, Banks CE, Compton RG. An overview of the electrochemical reduction of oxygen at carbon based modified electrodes. J Iranian Chem Soc 2005;2:1–25.
27. Maruyama J, Abe I. Cathodic oxygen reduction at the interface between Nafion and electrochemically oxidized glassy carbon surfaces. J Electroanal Chem 2002;527:65–70.
28. Jia N, Martin RB, Qi Z, Lefebvre MC, Pickup PG. Modification of carbon supported catalysts to improve performance in gas diffusion electrodes. Electrochim Acta 2001;46:2863–9.
29. Sullivan MG, Kotz R, Haas O. Thick active layers of electrochemically modified glassy carbon, electrochemical impedance studies. J Electrochem Soc 2000;147:308–17.
30. Huissoud A, Tissot P. Electrochemical reduction of 2-ethyl-9,10-anthraquinone (EAQ) and mediated formation of hydrogen peroxide in a two-phase medium. J Appl Electrochem 1999;29:11–25.
31. Chen Q. Toward cleaner production of hydrogen peroxide in China. J Cleaner Production 2006;14:708–12.
32. Huissoud A, Tissot P. Electrochemical reduction of 2-ethyl-9,10-anthraquinone on reticulated vitreous carbon and mediated formation of hydrogen peroxide. J Appl Electrochem 1998;28:653–7.
33. Gyenge EL, Coloman CW. Electrosynthesis of hydrogen peroxide in acidic solutions by mediated oxygen reduction in a three-phase (aqueous/organic/gaseous) system. J Appl Electrochem 2003;33:655–63, 665–74.
34. Tammeveski K, Kontturi K, Nichols RJ, Potter RJ, Schiffrin DJ. Surface redox catalysis for O_2 reduction on quinone modified glassy electrodes. J Electroanal Chem 2001;515:101–12.
35. Sarapuu A, Helstein K, Schiffrin DJ, Tammeveski K. Kinetics of oxygen reduction on quinone modified HOPG and BDD electrodes in alkaline solution. Electrochem Solid-State Lett 2005;8:E30–3.
36. Mirkhalaf F, Tammeveski K, Schiffrin DJ. Substituent effects on the electrocatalytic reduction of oxygen on quinone modified glassy carbon electrodes. Phys Chem Chem Phys 2004;6:1321–7.
37. Vaik K, Sarapuu A, Tammeveski K, Mirkhalaf F, Schiffrin DJ. Oxygen reduction on phenanthrenequinone-modified glassy carbon electrodes in 0.1 M KOH. J Electroanal Chem 2004;564:159–66.
38. Sarapuu A, Vaik K, Schiffrin DJ, Tammeveski K. Electrochemical reduction of oxygen on anthraquinone modified glassy carbon electrodes in alkaline solution. J Electroanal Chem 2003;541:23–9.
39. Keita B, Nadjo L. Catalytic synthesis of hydrogen peroxide: an attractive electrochemical and photoelectrochemical route to the reduction of oxygen. J Electroanal Chem 1983;145:431–7.
40. Salimi A, Eshghi H, Sharghi H, Golabi SM, Shamsipur M. Electrocatalytic reduction of dioxygen at the surface of glassy carbon electrodes modified by some anthraquinone substituted podands. Electroanalysis 1999;11:114–9.

41. Wilson T, Zhang J, Oloman CC, Wayner DDM. Anthraquinone-2-carboxylic-allyl ester as a new electrocatalyst for dioxygen reduction to produce H_2O_2. Int J Electrochem Sci 2006;1:99–109.

42. Markovic NM, Ross PN. Surface science studies of model fuel cell electrocatalysts. Surf Sci Rep 2002;45:117–229.

43. Zhdanov VP, Kasemo B. Kinetics of electrochemical O_2 reduction on Pt. Electrochem Commun 2006;8:1132–6.

44. Norskov JK, Rossmeisl J, Logadotir A, Lindqvist L, Kitchin JR, Bligaard T, et al. Origin of the overpotential for oxygen reduction at a fuel cell cathode. J Phys Chem B 2004;108:17886–92.

45. Shi Z, Zhang J, Liu Z, Wang H, Wilkinson DP. Current status of ab initio quantum chemistry study for oxygen electroreduction on fuel cell catalysts Electrochim Acta 2006;51:1905–16.

46. Hoare JP. The electrochemistry of oxygen. New York: Wiley, 1968.

47. Stassi A, D'Urso C, Baglio V, Di Blasi A, Antonucci V, Arico AS, et al. Electrocatalytic behaviour for oxygen reduction reaction of small nanostructured crystalline bimetallic Pt-M supported catalysts. J Appl Electrochem 2006;36:1143–9.

48. Stamenkovic VR, Mun BS, Wang G, Ross PN, Lucas CA, Markovic NM. Improved oxygen reduction activity on $Pt_3Ni(111)$ via increased surface site activity. Science 2007;315:493–7.

49. Jahnke H, Schonborn M, Zimmermann G. Organic dyestuffs as catalysts for fuel cells. Top Cur Chem 1976;61:133–81.

50. Zagal J, Bindra P, Yeager E. A mechanistic study of O_2 reduction on water soluble phthalocyanines adsorbed on graphite electrodes. J Electrochem Soc 1980;127:1506–17.

51. Shi C, Anson FC. Catalytic pathways for the electroreduction of O_2 by iron terakis(4-N-methylpyridyl)porphyrin or iron tetraphenylporphyrin adsorbed on edge plane pyrolytic graphite electrodes. Inorg Chem 1990;4298–305.

52. Shigehara K, Anson FC. Electrocatalytic activity of three iron porphyries in the reductions of dioxygen and hydrogen peroxide at graphite electrodes. J Phys Chem 1982;86:2776–83.

53. Liu H, Weaver M, Wang C, Chang C. Dependence of electrocatalysis for dioxygen reduction by adsorbed cofacial dicobalt porphyrins upon catalyst structure. J Electroanal Chem 1983;145:439–47.

54. Kadish KM, Fremond L, Ou Z, Shao J, Shi C, Anson FC, et al. Cobalt(III) corroles as electrocatalysts for the reduction of dioxygen: reactivity of a monocorrole, biscorrole, and porphyrin-corrole dyads. J Am Chem Soc 2005;127:5625–31.

55. Shi Z, Zhang J. Density functional theory study of transitional metal macrocyclic complexes' dioxygen-binding abilities and their catalytic activities toward oxygen reduction reaction. J Phys Chem C 2007;111:7084–90.

56. Alt H, Binder H, Sandstede G. Mechanism of electrocatalytic oxygen reduction on metal chelates. J Catal 1973;28:8–19.

57. Bezerra CWB, Zhang L, Lee K, Liu H, Marques ALB, Marques EP, et al. A review of Fe-N/C and Co-N/C catalysts for the oxygen reduction reaction. Electrochim Acta. Submitted 2008.

58. Baranton S, Coutanceau C, Garnier E, Leger J-M. How does α-FePc catalyst dispersed onto high specific surface carbon support work toward oxygen reduction reaction (orr)? J Electroanal Chem 2006;590:100–10.

59. Zagal J, Sen RK, Yeager E. Oxygen reduction by Co(II) tetrasulfonatephthalocyanine irreversibly adsorbed on a stress annealed pyrolytic graphite electrode surface. J Electroanal Chem 1977;83:207–13.

60. Collman JP, Marrocco M, Denisevich P. Potent catalysis of the electroreduction of oxygen to water by dicobalt porphyrin dimers adsorbed on graphite electrode. J Electroanal Chem 1979;101:117–22.

61. Savy M, Andro P, Bernard C, Magner G. Studies of oxygen reduction on the monomeres and polymeres-i. Principles, fundamentals, and choice of the central ion. Electrochim Acta 1973;18:191–7.

62. Alonso-Vante N, Fieber-Erdmann M, Rossner H, Holub-Krappe E, Giorgetti Ch, Tadjeddine A, et al. The catalytic center of transition metal chalcogenides vis-à-vis the oxygen reduction reaction: an in situ electrochemical EXAFS study. J Phys IV France 1997;7:887–9.

63. Alonso-Vante N, Jaegermann W, Tributsch H, Honle W, Yvon K. Electrocatalysis of oxygen reduction by chalcogenides containing mixed transition metal clusters. J Am Chem Soc 1987;109:3251–7.

64. Alonso-Vante N, Tributsch H. Energy conversion catalysis using semiconducting transition metal cluster compounds. Nature 1986;323:431–2.

65. Schmidt TJ, Paulus UA, Gasteiger HA, Alonso-Vante N, Behm RJ. Oxygen reduction on $Ru_{1.92}Mo_{0.08}SeO_4$, Ru/Carbon, and Pt/Carbon in pure and methanol-containing electrolytes. J Electrochem Soc 2000;147:2620–4.

66. Duron S, Rivera-Noriega R, Leyva MA, Nkeng P, Poillerat G, Solorza-Feria O. Oxygen reduction on a $Ru_xS_y(CO)n$ cluster electrocatalyst in 0.5 M H_2SO_4. J Solid State Electrochem 2000;4:70–4.

67. Gonzalez-Huerrta RG, Chavez-Carvayar JA, Solorza-Feria O. Electrocatalysis of oxygen reduction on carbon supported Ru-based catalysts in a polymer electrolyte fuel cell. J Power Sources 2006;153:11–17.

68. Gochi-Ponce Y, Alonso-Nunez G, Alonso-Vante N. Synthesis and electrochemical characterization of a novel chalcogenide electrocatalyst with an enhanced tolerance to methanol in the oxygen reduction reaction. Electrochem Commun 2006;8:1487–91.

69. Lee K, Zhang L, Zhang J. Ternary non-noble metal chalcogenide (W-Co-Se) as electrocatalyst for oxygen reduction reaction. Electrochem Commun 2007;9:1704–8.

70. Pohlmann L, Tributsch H. Self-organized electron transfer. Electrochim Acta 1997;42:2737–48.

71. Tributsch H, Pohlmann L. Electron transfer: classical approaches and new frontiers. Science 1998;279:1891–5.

72. Susac D, Sode A, Zhu L, Wong P, Teo M, Bizzotto D, et al. A methodology for investigating new nonprecious metal catalysts for PEM fuel cells. J Phys Chem B 2006;110:10762–70.

73. Mazza F, Trassatti S. Tungsten, titanium, and tantalum carbides and titanium nitrides as electrodes in redox system. J Electrochem Soc 1963;110:847–9.

74. Lee K, Ishihara A, Mitsushima S, Kamiya N, Ota K. Stability and electrocatalytic activity for oxygen reduction in WC-Ta catalyst. Electrochim Acta 2004;49:3479–85.

75. Meng H, Shen P. Tungsten carbide nanocrystal promoted Pt/C electrocatalysts for oxygen reduction. J Phys Chem B 2005;109:22705–9.

76. Nie M, Shen P, Wu M, Wei Z, Meng H. A study of oxygen reduction on improved Pt-WC/C electrocatalysts. J Power Sources 2006;162:173–6.

77. Gordon S, Hart EJ, Matheson MS, Rabani J, Thomas JK. Reaction constants of the hydrated electron. J Am Chem Soc 1963;85:1375–7.

78. Sawyer DT, Sobkowiak A, Roberts Jr. JL. Electrochemistry for chemists. New York:Wiley, 1995; 358–402.

79. Maricle DL, Hodgson WG. Reduction of oxygen to superoxide anion in aprotic solvents. Anal Chem 1965;37:1562–5.

80. Peover ME, White BS. Electrolytic reduction of oxygen in aprotic solvents: the superoxide ion. Electrochim Acta 1966;11:1061–7.

81. Vsudevan D, Wendt H. Electroreduction of oxygen in aprotic media. J Electroanal Chem 1995;392:69–74.
82. Saha MS, Ohsaka T. Electrode kinetics of the O_2/O_2-redox couple at Hg electrode in the presence of PVC in aprotic media. Electrochim Acta 2005;50:4746–51.
83. Wu J, Che Y, Okeyoshi T, Okajima T, Matsumoto F, Tokuda K, et al. Hydrodynamic chronocoulometric determination of diffusion coefficients and concentrations of dioxygen in media containing quinoline, isopuinoline, and methyquinolines. Anal Chem 1999;71:4056–60.
84. AlNashef IM, Leonard ML, Kittle MC, Matthews MA, Weidner JW. Electrochemical generation of superoxide in room temperature ionic liquids. Electrochem Solid-State Lett 2001;4:D16–18.
85. AlNashef IM, Leonard ML, Matthews MA, Weidner JW. Superoxide electrochemistry in an ionic liquid. Ind Eng Chem Res 2002;41:4475–8.
86. Zhang D, Okajima T, Matsumoto F, Ohsaka T. Electrochemical reduction of dioxygen in 1-n-alkyl-3-methylimidazolium tetrafluoroborate room temperature ionic liquids. J Electrochem Soc 2004;151:D31–7.
87. Katayama Y, Onodera H, Yamagata M, Miura T. Electrochemical reduction of oxygen in some hydrophobic room temperature molten salt systems. J Electrochem Soc 2004;151:A59–63.
88. Yang H, McCreery RL. Elucidation of the mechanism of dioxygen reduction on metal free carbon electrodes. J Electrochem Soc 2000;147:3420–8.
89. Choi Y, Chjo K, Park S. Oxygen reduction at Co(II)2-disalophen modified carbon electrodes. J Electrochem Soc 1995;142:4107–12.
90. Song C, Zhang L, Zhang J. Reversible one-electron electro-reduction of O_2 to produce a stable superoxide catalyzed by adsorbed Co(II) hexadecafluoro-phthalocyanine in aqueous alkaline solution. J Electroanal Chem 2006;587:293–8.
91. Chevalet J, Rouelle F. Electrogeneration and some properties of the superoxide ion in aqueous solutions. J Electroanal Chem Interf Electrochem 1972;39:201–16.
92. Beyer W, von Sturm F. Polarographic reduction of oxygen in presence of phthalocyanine complex. Angew Chem 1972;84:154–5.

3

Electrocatalytic H$_2$ Oxidation Reaction

Hui Li, Kunchan Lee and Jiujun Zhang

3.1 Introduction

Hydrogen (H$_2$), an important material and product in chemical industries, has been investigated as a new clean energy source for many decades [1–3]. With the rapid development of proton exchange membrane (PEM) fuel cell technology, in which H$_2$ is used as a fuel, the chemical energy stored in this H$_2$ can be electrochemically converted to electric energy with zero emissions and high efficiency. The dream of a hydrogen economy era therefore seems closer to reality. Beginning in the 1990s, the advantages of PEM fuel cells, including zero/low emissions, high energy efficiency, and high power density, have attracted world-wide research and development in several important application areas, including automotive engines, stationary power generation stations, and portable power devices [4]. With successful demonstrations of fuel cell technology, in particular in automotive applications, commercialization of this technology has become a strong driving force for further development in the critical areas of cost reduction and durability. The major cost of a PEM fuel cell is the platinum (Pt)-based catalysts. At our current technological stage, these Pt-based catalysts for both the cathodic O$_2$ reduction reaction (ORR) and the anodic H$_2$ oxidation reaction (HOR) are the most practical catalysts in terms of catalytic activity and lifetime stability. Therefore, research and development to improve catalytic activity and stability has shot to the fore in recent years. Although both theoretical and experimental approaches have resulted in great progress in fuel cell catalysis [2, 3, 5, 6], continuous effort is necessary to develop breakthrough fuel cell catalysts that are cost-effective and highly durable for commercial use.

With respect to fuel cell catalysis, most research has been focused on cathode ORR catalysts development, because the ORR kinetics are much slower than the anodic HOR kinetics; in other words, the fuel cell voltage drop polarized by load is due mainly to the cathode ORR overpotential [7, 8]. However, in some cases the overpotential of the anodic HOR can also contribute a non-negligible portion of the overall fuel cell voltage drop [8]. Therefore, the catalytic HOR on the fuel cell anode catalyst is also worth examining.

On the other hand, aside from its importance in fuel cell applications, hydrogen electrooxidation catalysis is also a model system for the fundamental understanding of electrochemical kinetics, electrocatalysis, and electrochemical surface science, which have been studied for over a century [3, 5]. Indeed, the hydrogen evolution/oxidation reaction (HER/HOR) is the simplest and most widely studied electrochemical process. Almost all the basic laws of electrode kinetics and the concepts of electrocatalysis were developed and verified by the examination of these two reactions.

This chapter summarizes the kinetics and mechanisms of the electrocatalyzed HOR on different electrode materials, including platinum group metals, carbides, and transition metals. Advances in CO-tolerant electrocatalysts for the HOR in fuel cells are also briefly introduced. Despite its wide range of topics, the main purpose of this chapter is to provide a fundamental understanding of the electrocatalysis of the HOR, the most important reaction other than the ORR in the PEM H_2 fuel cell.

3.2 Electrooxidation of Hydrogen [5, 6, 9, 10]

3.2.1 Mechanism of the Hydrogen Oxidation Reaction

The overall reactions of anodic hydrogen oxidation in acidic and alkaline mediums can be expressed as Equations 3.1 and 3.2, respectively:

$$\tfrac{1}{2}\,H_2 \rightarrow H^+ + e^- \tag{3.1}$$

$$\tfrac{1}{2}\,H_2 + OH^- \rightarrow H_2O + e^- \tag{3.2}$$
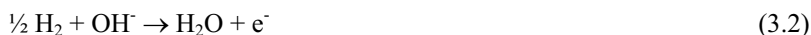
The hydrogen oxidation reaction may occur by the following three sequential steps:

1) Adsorption step: the hydrogen molecule diffuses from the electrolyte to the electrode, then adsorbs on the electrode surface to form surface species ($H_{2,ad}$):

$$H_2 \rightarrow H_{2,solv} \rightarrow H_{2,ad} \tag{3.3}$$

2) Hydration/ionisation step: the adsorbed hydrogen forms adsorbed H atoms (H_{ad}) through process (a) or (b):
   (a) Tafel-Volmer route

$$H_{2,ad} \rightarrow 2H_{ad} \text{ (Tafel reaction)} \tag{3.4}$$

and

$$H_{ad} \rightarrow H^+ + e^- \qquad \text{(Volmer reaction in acidic medium)} \tag{3.5}$$

or

$$H_{ad} + OH^- \rightarrow H_2O + e^- \quad \text{(Volmer reaction in alkaline medium).} \quad (3.6)$$

(b) Heyrovsky-Volmer route:

$$H_{2,ad} \rightarrow H_{ad}.H^+ + e^- \rightarrow H_{ad} + H^+ + e^- \qquad\qquad (3.7)$$
(Heyrovsky reaction in acidic medium)

or

$$H_{2,ad} + OH^- \rightarrow H_{ad}.H_2O + e- \rightarrow H_{ad} + H_2O + e^- \qquad (3.8)$$
(Heyrovsky reaction in alkaline medium)

and

$$H_{ad} \rightarrow H^+ + e^- \qquad\qquad \text{(Volmer reaction in acidic medium)} \quad (3.9)$$

$$H_{ad} + OH^- \rightarrow H_2O + e^- \quad \text{(Volmer reaction in alkaline medium)} \quad (3.10)$$
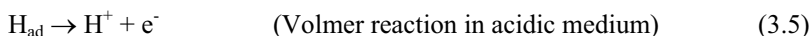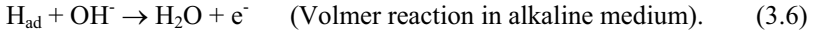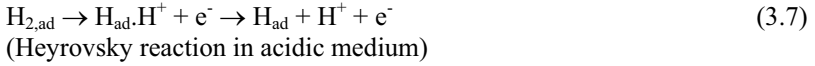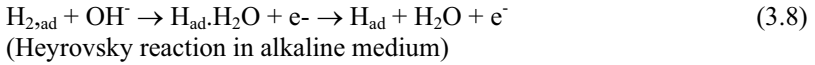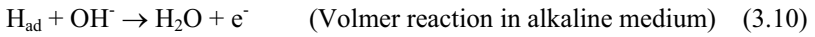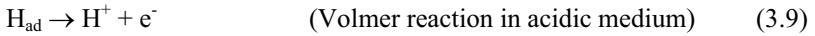
3) Desorption step: the products, such as H$^+$ and H$_2$O, are desorbed and then transported into the electrolyte.

In each step of the above routes, the overall reaction rate can be controlled by a step which is sufficiently slow compared with the others. This is the rate determining step (rds). The rate determining steps have been identified for several mechanisms:

(a-1) The slow Volmer-rapid Tafel mechanism (the slow-discharge mechanism):

$$H_2 \rightarrow 2H_{ad}, H_{ad} \rightarrow H^+ + e^- \text{(rds)} \qquad\qquad (3.11)$$

(a-2) The rapid Volmer-slow Tafel mechanism (the slow combination or the catalytic mechanism):

$$H_2 \rightarrow 2H_{ad} \text{ (rds)}, H_{ad} \rightarrow H^+ + e^- \qquad\qquad (3.12)$$

$$H_{ad} + OH^- \rightarrow H_2O + e^- \qquad\qquad (3.13)$$

(b-1) The slow Volmer-rapid Heyrovsky mechanism:

$$H_{2,ad} \rightarrow H_{ad}.H^+ + e^- \rightarrow H_{ad} + H^+ + e^- \text{ (rds)} \qquad (3.14)$$

and

$$H_{2,ad} + OH^- \rightarrow H_{ad}.H_2O + e^- \rightarrow H_{ad} + H_2O + e^- \text{ (rds)} \qquad (3.15)$$
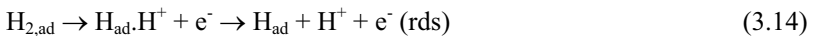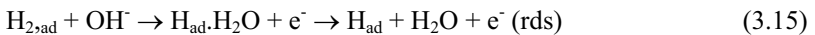
(b-2) The rapid Volmer-slow Heyrovsky mechanism:

$$H_{2,ad} \text{ (rds)} \rightarrow H_{ad}.H^+ + e^- \rightarrow H_{ad} + H^+ + e^- \tag{3.16}$$

and

$$H_{2,ad} + OH^- \text{ (rds)} \rightarrow H_{ad}.H_2O + e^- \rightarrow H_{ad} + H_2O + e^- \tag{3.17}$$
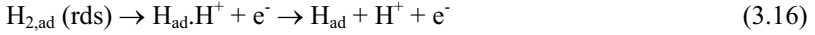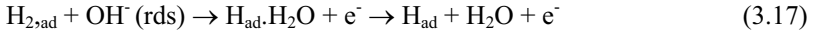
In the past, the majority of the basic laws and concepts in electrode kinetics were developed and verified by Tafel [11], Volmer [12], and Frumkin [13] using the hydrogen electrode. Two important reaction mechanisms are well recognized and experimentally validated. The first is the Volmer-Tafel mechanism, shown in Equations 3.11–3.13. The other, which is more important for the hydrogen electrode, is the Hyrovsky-Volmer mechanism, expressed in Equations 3.14–3.17.

3.2.2 Thermodynamic Considerations for the Hydrogen Electrode Reaction

The conventional thermodynamic relations for the hydrogen electrode reaction in Equation 3.1 are the following:

$$E_H = -\frac{\Delta G}{F} \text{ with}$$

$$\Delta G = \frac{1}{2}\mu_{H_2} - \mu_{H^+} = \left(\frac{1}{2}\mu_{H_2}^o - \mu_{H^+}^o\right) + RT \ln \frac{P_{H_2}^{1/2}}{a_{H^+}} \tag{3.18}$$

$$E_H = E_H^o - \frac{RT}{F} \ln \left(\frac{P_{H_2}^{1/2}}{a_{H^+}}\right) \tag{3.19}$$

where ΔG is the Gibbs free energy, μ_{H_2} and μ_{H^+} are the chemical potentials for H_2 and H^+, a_{H^+} is the activity of the proton, F is the Faraday constant, and a_{H^+} has a practical significance through the conventional definition of pH. E_H^o is defined as the standard hydrogen electrode potential with $E_H^o = 0$ V at standard conditions [14].

3.2.3 The Kinetics of the Hydrogen Oxidation Reaction [9, 10]

1) Volmer Expression
For the hydrogen oxidation reaction in Equations 3.1 and 3.2 in acidic and alkaline media, respectively, the Volmer expression deals with the pure charge-transfer process ($H_{ad} \leftrightarrow H^+ + e^-$). The total (or net) current density for this two-directional charge-transfer process, $i = i_f - i_b$, could be expressed as follows:

$$i = k_f c_H \exp(\frac{\alpha FE}{RT}) - k_b c_{H^+} \exp(-\frac{(1-\alpha)FE}{RT}) \tag{3.20}$$

where i is the net current density; i_f and i_b are the current densities in the forward and backward (or anodic and cathodic) directions, respectively; k_f and k_b are the corresponding rate constants; c_H and c_{H^+} are the surface concentrations of adsorbed atomic hydrogen and protons, respectively; α is the charge-transfer coefficient; R is the gas constant; T is the temperature; and E is the electrode potential. For the hydrogen oxidation (forward direction)/reduction reaction (backward direction) in acid solution, the charge-transfer reaction, i.e., Volmer expression, could be written alternatively as Equation 3.21:

$$i_V = k_f[H]\exp(\frac{\alpha_V FE}{RT}) - k_b[H^+]\exp(-\frac{(1-\alpha_V)FE}{RT}) \tag{3.21}$$

where α_V is the charge-transfer coefficient of the Volmer reaction. This equation is the basic relation given by Volmer and was later generalized to all charge-transfer reactions. [H] is the surface concentration of atomic hydrogen and is proportional to the degree of surface coverage of adsorbed hydrogen atom (θ). Assuming that the adsorption of hydrogen atoms on the electrode surface follows a Langmuir isotherm, and that the reactions occur on a homogeneous surface, a Langmuir model can be used to describe the surface behavior of H for small or large coverage areas. Equation 3.21 could be modified as Equation 3.22 if [H] can be expressed as surface coverage (θ). Note that the backward (or cathodic) reaction ($H^+ + e^- \rightarrow H_{ad}$) occurs in the Volmer reaction only at the part of the surface which is not covered by adsorbed hydrogen atoms. This part equals $1-\theta$.

$$i_V = k_f \theta \exp(\frac{\alpha_V FE}{RT}) - k_b[H^+](1-\theta)\exp(-\frac{(1-\alpha_V)FE}{RT}) \tag{3.22}$$

According to the reaction expressed in Equation 3.6 in an alkaline solution, the current-potential relationships can be expressed as Equations 3.23 and 3.24, respectively:

$$i_V = k_f[H][OH^-]\exp(\frac{\alpha_V FE}{RT}) - k_b[H_2O]\exp(-\frac{(1-\alpha_V)FE}{RT}) \tag{3.23}$$

$$i_V = k_f \theta[OH^-]\exp(\frac{\alpha_V FE}{RT}) - k_b[H_2O](1-\theta)\exp(-\frac{(1-\alpha_V FE}{RT}) \tag{3.24}$$

where the transfer coefficient α_V in an alkaline medium may have a different value from that in an acidic medium.

If the redox reaction equilibrium can be established, the partial forward current density will equal the partial backward current density. Equations 3.21 and 3.22 could also be expressed in terms of the exchange current density, i_0, as in Equations 3.25 and 3.26, respectively. These $i_{0,V}$ are the values at the equilibrium potential (E_{eq}) where the net current is zero:

$$i_{0,V} = k_f[H]\exp(\frac{\alpha_V FE_{eq}}{RT}) = k_b[H^+]\exp(-\frac{(1-\alpha_V)FE_{eq}}{RT}) \tag{3.25}$$

$$i_{0,V} = k_f\theta\exp(\frac{\alpha_V FE_{eq}}{RT}) = k_b(1-\theta)[H^+]\exp(-\frac{(1-\alpha_V)FE_{eq}}{RT}) \tag{3.26}$$

When taking into consideration the overpotential ($\eta = E{-}E_{eq}$), which designates the hydrogen overpotential, Equations 3.21–3.24 may be rewritten as 3.27:

$$i_V = i_{0,V}[\frac{\theta}{\theta_0}\exp(\frac{\alpha_V F\eta}{RT}) - \frac{1-\theta}{1-\theta_0}\exp(-\frac{(1-\alpha_V)F\eta}{RT})] \tag{3.27}$$

where θ_0 is the surface coverage of atomic hydrogen at the equilibrium electrode potential. It is obvious that when $\theta = \theta_0$, Equation 3.27 can be simplified as 3.28:

$$i = i_{0,V}[\exp(\frac{\alpha_V F\eta}{RT}) - \exp(-\frac{(1-\alpha_V)F\eta}{RT})] \tag{3.28}$$

Note that in general, the value of θ is current-density dependent.

2) Tafel Expression
In Equation 3.4 for the HOR/HER, if the Tafel reaction is a pure chemical reaction, the dissociation of the hydrogen molecule to form surface adsorbed atomic hydrogen will be the rate determining step. Therefore, the rate constant in the reaction should not depend upon the electrode potential. If all reactions that occur before and after the Tafel reaction are fast, the slow Tafel reaction (or rate determining step) can lead to a pure reaction overpotential, η_r , which can be expressed as Equation 3.29:

$$\eta_r = \frac{\nu RT}{mnF}\ln\left(1-\frac{i_T}{i_r}\right) \tag{3.29}$$

where i_T and i_r are the net Tafel current density and limiting reaction current density, respectively, m is the reaction order, ν represents the sign of overpotential (if ν is positive, the rate determining reaction will occur in the

direction of oxidation; if negative, the rate determining reaction will be in the reduction direction). In the case of the anodic (or forward) reaction, the order of the hydrogen atom (m) is 2, as given by Tafel. At large anodic overpotential, i.e., $|i_T| \gg i_r$, the Tafel relation for the hydrogen overpotential can be expressed:

$$\eta = -\frac{RT}{2F}\ln i_r + \frac{RT}{2F}\ln|i_T| \tag{3.30}$$

This equation deals with the anodic direction of the reaction (the dissociation of H₂), therefore, $v = -1$. For the cathodic reaction direction, where $v = 1$, the Tafel equation can be expressed as Equation 3.31 at large cathodic overpotential:

$$\eta = \frac{RT}{2F}\ln i_r - \frac{RT}{2F}\ln|i_T| \tag{3.31}$$

In the case of the anodic reaction, the limiting anodic current density, $i_{r,a}$, should be approximately equal to the dissociation rate of molecular hydrogen into the adsorbed atoms. In the cathodic reaction, the limiting cathodic current density, $i_{r,c}$, should be the rate of hydrogen recombination on the electrode surface. Note that the limiting cathodic current density will appear when the current-dependent degree of coverage (θ) reaches its maximum value, i.e., $\theta = 1$.

If the net Tafel reaction rate, i_T, for either H$_{ad}$ recombination or H₂ dissociation can be expressed as Equation 3.32:

$$i_T = -F\frac{d[H]}{dt} = -Q_H\frac{d\theta}{dt} = k_b(1-\theta)^2 - k_f\theta^2 \tag{3.32}$$

the equilibrium can be described by the Langmuir adsorption isotherms, where Q_H (C·cm^{-2}) is the amount of charge for the formation of a monatomic layer of hydrogen per cm². At equilibrium, the net current density is equal to zero, that is, $i = 0$ for Equation 3.22 or 3.24, and the electrode potential will be expressed as Equation 3.33:

$$E = E_{0,V} + \frac{RT}{F}\ln[H^+] - \frac{RT}{F}\ln\frac{\theta}{1-\theta} \tag{3.33}$$

Therefore, the overpotential is:

$$\eta_r = -\frac{RT}{F}\ln\left[\frac{\theta}{\theta_0}\frac{1-\theta_0}{1-\theta}\right] \tag{3.34}$$

where θ_0 is the equilibrium degree of coverage.

If the reaction equilibrium is established, the partial anodic reaction current density should be equal to the partial cathodic reaction current density; then, the Tafel exchange current density can be written as Equation 3.35:

$$i_{0,T} = i_r = k_f\left(1-\theta_0\right)^2 = k_b \cdot \theta_0^{\ 2} \tag{3.35}$$

From Equation 3.35, the relationship between the current density for the Tafel reaction and the overpotential can be rewritten as a function of the degree of coverage:

$$i_T = i_{o,T}\left(\left(\frac{1-\theta}{1-\theta_0}\right)^2 - \left(\frac{\theta}{\theta_0}\right)^2\right) \tag{3.36}$$

(3) Heyrovsky Expression

The Heyrovsky reaction in Equations 3.7 and 3.8 is a pure charge-transfer reaction. The reaction rate in the cathodic reaction direction is proportional to the degree of surface coverage of atomic hydrogen (θ), and the concentration of H^+ (acid solution) or H_2O (alkaline solution). On the other hand, the anodic partial reaction is proportional to the concentration of molecular hydrogen $[H_2]$ and the free surface $(1-\theta)$. Based on the current-overpotential equation for the charge-transfer reaction, the Heyrovsky current density (i_H) expression can be written as Equations 3.37 and 3.38 for acid and alkaline solutions, respectively:

$$i_H = k_f[H_2](1-\theta)\exp\left(\frac{\alpha_H FE}{RT}\right) - k_b[H^+]\theta\exp\left(-\frac{(1-\alpha_H)FE}{RT}\right) \quad \text{(acid)} \tag{3.37}$$

$$i_H = k_f[H_2][OH^-](1-\theta)\exp\left(\frac{\alpha_H FE}{RT}\right) - k_b[H_2O]\theta\exp\left(-\frac{(1-\alpha_H)FE}{RT}\right)$$
$$\text{(alkaline)} \tag{3.38}$$

where α_H is the transfer coefficient of the Heyrovsky reaction.

When the reaction is at equilibrium ($i = 0$), the Heyrovsky exchange current density (i_H) for the Heyrovsky reaction is:

$$i_{0,H} = k_f(1-\theta)\exp\frac{\alpha_H FE_{eq}}{RT} = k_b\theta[H^+]\exp\left(\frac{-(1-\theta)FE_{eq}}{RT}\right) \tag{3.39}$$

If $\theta = \theta_0$, the Heyrovsky current-overpotential relationship can be expressed as Equation 3.40:

$$i_H = i_{0,H} \left[\exp\left(\frac{\alpha_H F \eta}{RT} \right) - \exp\left(-\frac{(1-\alpha_H)F\eta}{RT} \right) \right] \qquad (3.40)$$

If the degree of coverage is dependent on the reaction current, the current density then becomes:

$$i_H = i_{0,H} \left[\frac{1-\theta}{1-\theta_0} \exp\left(\frac{\alpha_H F \eta}{RT} \right) - \frac{\theta}{\theta_0} \exp\left(-\frac{(1-\alpha_H)F\eta}{RT} \right) \right] \qquad (3.41)$$

where the Heyrovsky exchange current density for the reaction in acid solution could be different from that in alkaline solution. Furthermore, the charge-transfer coefficient value of the Heyrovsky reaction may also differ from the value of the Volmer reaction.

3.2.4 Hydrogen Adsorption Behavior

The adsorption of hydrogen on metal electrodes such as platinum has been studied extensively in electrochemical systems over the last several decades [15–18]. The mechanism for the hydrogen oxidation reaction on a platinum electrode in an acid electrolyte is usually assumed to proceed by the initial adsorption of molecular hydrogen. This initial adsorption step involves either slow dissociation of H$_2$ molecules into atoms (Tafel reaction) or the ion-atom recombination step (Heyrovsky reaction). This is followed by the fast charge-transfer step, including both Tafel-Volmer reaction and Heyrovsky-Volmer reaction sequences. If we assume that kinetic parameters, such as the Tafel slopes and the reaction activation energies, are the same for the HOR and the HER at low overpotentials, the mechanism for the HER would be the same as that for the HOR, i.e., the first fast charge-transfer step is followed by either the Tafel-Volmer sequence or the Heyrovsky-Volmer sequence. It is important to note that the adsorbed hydrogen (H$_{ad}$) on the metal electrode is the reactive intermediate in both the HOR and the HER. Therefore, the kinetics of the hydrogen reaction is largely affected by the interaction between H$_{ad}$ and platinum surface atoms. This interaction can be described by the adsorption energy of H$_{ad}$ and its surface coverage. Such hydrogen coverage and adsorption energy will definitely affect the activity of the electrode. The reaction pathways of the HER/HOR in alkaline solution are similar to those in acid solution, except that hydrogen is discharged from H$_2$O rather than from hydronium ions (H$_3$O$^+$).

The difference between hydrogen adsorption from the electrolyte and from the gas phase is important for understanding the elementary reaction steps involved in the processes of hydrogen adsorption on metallic catalyst surfaces. In general, hydrogen electroadsorption (or electrosorption) can be accomplished from either acidic or basic aqueous solutions. In fuel cell research, it is especially necessary to understand the adsorption of hydrogen from the electrolyte environment on metallic catalysts. Markovic et al. [18] and Jerkiewicz et al. [19] well demonstrated the characteristics of hydrogen adsorption on Pt single crystals. Their approaches

focused on the thermodynamic aspect, by calculating the Gibbs free energy, entropy, and enthalpy of hydrogen adsorption, then comparing hydrogen electroadsorption from the electrolyte and from the gas phase on Ru and Pt single crystals, respectively. Markovic et al. [18] distinguished the different possible states of adsorbed hydrogen. They employed thermodynamic notations and defined the strongly adsorbed states as underpotentially deposited hydrogen, H_{upd}, and the weakly adsorbed states as the reactive intermediate, H_{ad} (i.e., overpotentially deposited hydrogen, H_{opd}). It is well-recognized that the H_{upd} is strongly dependent on the crystallographic orientation of the Pt surface [20]. However, it is still not clear whether this H_{upd} is the reactive intermediate, H_{ad}, of the HER and the HOR. It has been reported that H_{ad} is a weakly adsorbed state of hydrogen that becomes populated only at potentials close to the Nernst potential [21, 22]. These researchers proposed that the weakly adsorbed state of H_{ad} on Pt single crystals could couple to the strongly adsorbed state of the H_{upd}, so that there would be an indirect effect of the H_{upd} on the kinetics with an attendant crystallographic sensitivity. They suggested that H_{upd} therefore might play an important role in the kinetics of the HER and the HOR in aqueous electrolyte solutions. The two major effects of H_{upd} on H_{ad} can be summarized as follows: (1) H_{upd} adatoms block the adsorption of the active intermediate H_{ad}, i.e., they compete with each other for the same site, and/or (2) H_{upd} adatoms affect the adsorption energy of H_{ad} on the bare Pt sites that are neighboured by the H_{upd}.

The research on hydrogen underpotential deposition (UPD) at electrodes has identified the Gibbs energy of H-binding on the surface (ΔG_{MeH}) and the half-bond energy of H_2 ($\Delta G_{\frac{1}{2}H_2}$). It has been found that $\Delta G_{MeH} < \Delta G_{\frac{1}{2}H_2}$, so that the UPD equilibria at various θ were established at potentials more positive than that of the HER equilibrium ($H^+ + Me + e^- \Leftrightarrow \frac{1}{2} H_2$, where Me refers to the metal reaction site). The UPD of H can be expressed as Equation 3.42 [4]:

$$H_3O^+ + Me + e^- \text{ (in Me)} \Leftrightarrow MeH_{ad} + H_2O \qquad (3.42)$$

At a potential of E, the proton concentration of C_{H+}, and a surface H coverage of θ, the fraction of surface vacant site can be expressed as $1-\theta$. The simplest electrochemical thermodynamic relation can be expressed as a function of the electrode potential:

$$\theta /(1-\theta) = K_H c_{H^+} \exp(-\frac{EF}{RT}) \qquad (3.43)$$

where K_H is the reaction constant. Alternatively, Equation 3.43 can be rewritten as a Nernst form:

$$E(\theta) = \frac{RT}{F}\ln(K_H c_{H^+}) - \frac{RT}{F}\ln(\theta /(1-\theta)) \qquad (3.44)$$

The existence of underpotentially deposited hydrogen on metal electrodes was confirmed by an electrochemical technique called cyclic voltammetry. Surface waves on the cyclic voltammogram curves were used to identify both qualitatively and quantitatively the formation and ionization of deposited hydrogen through the Volmer reaction (H$_{upd}$ $\leftrightarrow$ H$^+$+e$^-$). These surface waves are called the hydrogen waves. The most extensive studies of hydrogen adsorption and desorption are carried out on the electrode surface of Pt metal groups. For example, several research groups [23–26] have recently investigated the nature of adsorbed hydrogen on Pt (hkl) in both acidic and alkaline electrolytes. In this section, we briefly introduce the electrochemical behavior of adsorbed hydrogen on polycrystalline noble metal catalysts, including Pt, Ir, Rh, and Pd, which are known to show the underpotential deposition of hydrogen at potentials more positive than the thermodynamic reversible potential of hydrogen, E = 0 V vs. NHE. These metals have high catalytic activity towards the HER/HOR, and are the most frequently used electrocatalysts for PEM fuel cells.

Figure 3.1 shows the behavior of hydrogen adsorption/desorption on various noble metal electrodes. The hydrogen wave usually appears in the potential region between 0 and 0.4 V. The potential range is more positive than the reversible hydrogen electrode potential (0.00 V at standard conditions). Therefore, this hydrogen adsorption/desorption is called "underpotential deposition of hydrogen". These hydrogen waves show almost symmetrical anodic (ionization) and cathodic (deposition) features, particularly on a platinum surface, indicating a very rapid rate of the Volmer reaction [23–26].

As shown in Figure 3.1(a), the hydrogen waves on the cyclic voltammogram correspond to the monolayer of adsorbed hydrogen on the platinum surface [23, 27, 28]. The charge associated with a monolayer of adsorbed hydrogen (Q$_{aH}$) on a smooth Pt electrode surface has been commonly adopted as 210 μC·cm^{-2}. This standard value was justified by the predominance of the Pt(100) plane [29] or by the equal distribution of the three low-index planes [30]. The calculated monolayer charge is 208 μC·cm^{-2} for the (100) plane, 241 μC·cm^{-2} for the (111) plane, and 147 or 296 μC·cm^{-2} for the (110) plane, depending in the last case on whether the surface atoms are defined [27, 31]. Therefore, with this standard charge value, the real surface area of platinum could be calculated based on the charges under the areas of the hydrogen adsorption/desorption wave, using this monolayer charge as the standard.

Iridium (Ir) (Figure 3.1(b)) shows very similar hydrogen adsorption peaks to those of Pt. The two peaks observable in the cyclic voltammogram for Ir are attributed to two types of adsorbed hydrogen, one having a higher adsorption energy than the other. This behavior is the same as that of Pt. However, the hydrogen oxidation region on the Ir electrode overlaps with that of Ir oxide formation [25]. The charge of the monolayer hydrogen adsorption on an Ir surface is very similar to that of other metals, which is 220 μC·cm^{-2} based on the (100) plane [28, 32].
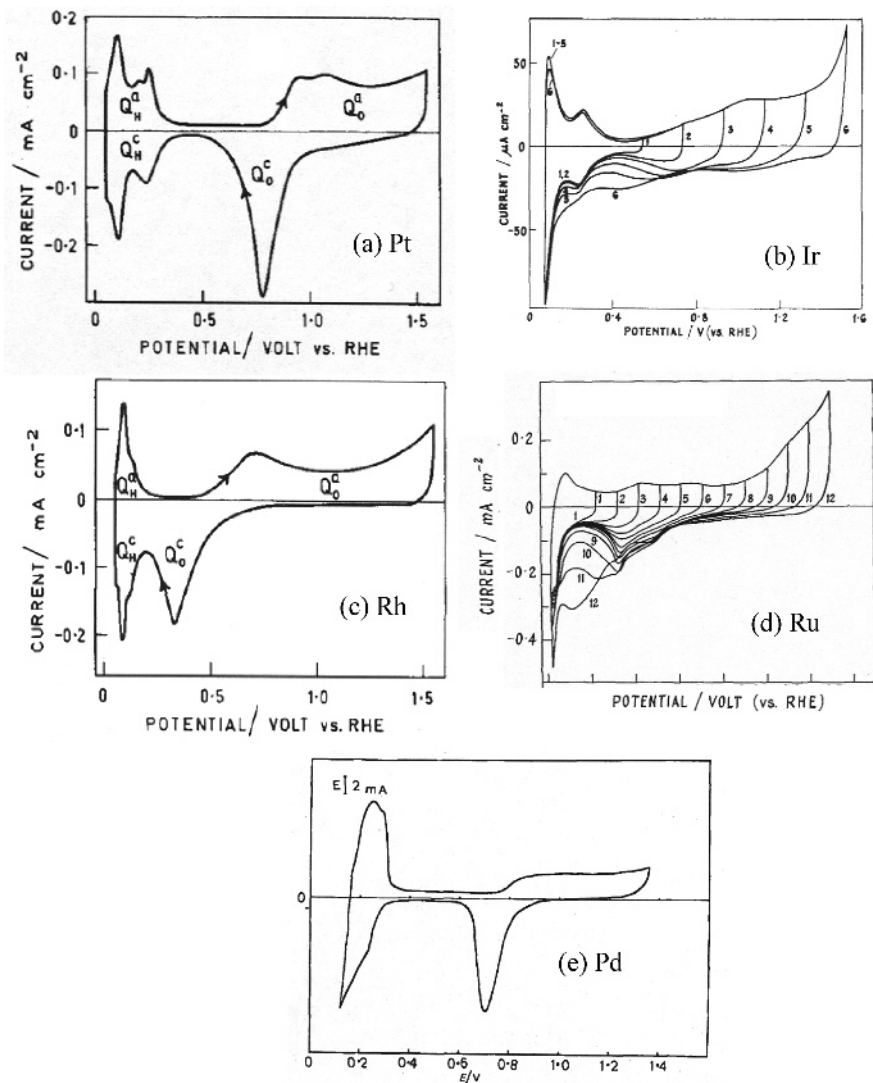
Figure 3.1. Electrochemical behaviors of various noble metal electrodes in sulfuric acid [23–26]. (Graphs (a) & (c) reprinted from Journal of Electroanalytical Chemistry, 35, Rand DAJ, Woods R, A study of the dissolution of platinum, palladium, rhodium and gold electrodes in 1 M sulphuric acid by cyclic voltammetry, 209–18, ©1972; (b) reprinted from J Electroanal Chem, 55(3), Rand DAJ, Woods R, Cyclic voltammetric studies on iridium electrodes in sulphuric acid solutions: nature of oxygen layer and metal dissolution, 375–81, ©1974; (d) reprinted from J Electroanal Chem, 89(1), Michell D, Rand DAJ, Woods R, A study of ruthenium electrodes by cyclic voltammetry and X-ray emission spectroscopy, 11–27, ©1978; (e) reprinted from J Electroanal Chem, 39(2), Capon A, Parsons R, The effect of strong acid on the reactions of hydrogen and oxygen on the noble metals. A study using cyclic voltammetry and a new teflon electrode holder, 275–86, ©1972, all with permission from Elsevier.)

Rhodium (Rh) (Figure 3.1(c)) in acidic media shows similar behavior to Pt, in terms of the surface processes of hydrogen ionization/deposition. However, hydrogen is less strongly bonded to the Rh than to the Pt [33]. Woods et al. [34] suggested that the charge of adsorbed hydrogen on the Rh(100) plane should be 221 µC·cm^{-2}. Peuckert [35] reported that the average of the charges on the (111), (100), and (110) planes of fcc Rh for the monolayer of absorbed hydrogen could be 221 µC·cm^{-2}.

Although the hydrogen adsorption/desorption behavior on Pt, Rh, and Ir electrodes is well-known, the behavior of hydrogen on an Ru electrode (Figure 3.1 (d)) is not well-characterized because there are no suitable potential regions on an Ru surface for H deposition [36]. Several factors prevent the observation of H adsorption/desorption: (a) the overlap between regions of H deposition and Ru oxide reduction or between regions of H ionization and Ru oxide formation, (b) significant absorption/penetration of H into the Ru [37], and (c) re-oxidation of evolved H$_2$. In particular, the hydrogen deposition processes that might normally be observed in the cathodic sweep are obscured by the slow reduction of surface Ru oxide. However, it could be possible to estimate the real surface area of an Ru electrode from the hydrogen adsorption charge, in the same way as with Pt [35]. For this purpose, a standard value of 251 µC·cm^{-2} for a Ru surface has been used [24].

Palladium (Figure 3.1(e)), with the same outer electronic configuration as Pt, displays similar electrochemical properties to a platinum electrode. Additionally, their catalytic activities for the HER and the HOR are also very similar [38, 39]. Two mechanisms have been proposed for hydrogen adsorption onto palladium [40–45]: indirect and direct adsorption. Chevillot et al. [46] studied the electrochemical behavior of hydrogen adsorption on a Pd black surface, and distinguished two superficially adsorbed forms of hydrogen species. However, the behavior of both adsorption and desorption of hydrogen on Pd is still not completely understood. Because hydrogen penetrates the palladium bulk, it seems we cannot accurately determine the real surface area from the charge of adsorbed hydrogen on a palladium surface with a hydrogen monolayer.

3.2.5 The Kinetic Parameters of the Hydrogen Oxidation Reaction

The Tafel equation $\eta = b \times \exp(i/i_o)$ describes the relationship between overpotential and current density. Two parameters, i.e., exchange current density i_o and Tafel slope b, are the most important kinetic parameters to measure the electrochemical activity of an electrode material. Exchange current density i_o is analogous to the rate constant used in chemical kinetics, and a high value of i_o often translates into a fast electrochemical reaction. On the other hand, a smaller Tafel slope is desirable from the kinetic point of view to obtain a smaller overpotential. As for any electrochemical reaction, the Tafel slope b is a function of temperature in the form of $b = \dfrac{RT}{\alpha \, n_\alpha F}$, where n_α is the electron transfer number and α is the electron transfer coefficient. For the HOR, n_α is widely reported as 2.0 and α is reported to be independent of temperature, with a well-recognized value of 0.5; this contrasts

with α for O_2 reduction, which is a temperature-dependent parameter [8]. Table 3.1 provides the exchange current density and Tafel slope of the HOR in acidic solutions on various metals that are currently and potentially useful for PEM fuel cell applications.

Table 3.1. Kinetic parameters for the HOR in acidic solutions on various metals [14]. (Reprinted with permission from Appleby AJ, Kita H, Chemla M, Bronoel G. Hydrogen. In: Encyclopedia of the electrochemistry of the elements IXa. Bard AJ, editor. New York: Marcel Dekker: 1973.)

Substrate	Solution	Temp. °C	i_0, A cm^{-2}	b, mV	Form
Pt	0.5 M H$_2$SO$_4$	25	2.57×10^{-3}	25	Small sphere
Rh	1 M H$_2$SO$_4$	29	1.58×10^{-3}	118	Wire
Ru	1 M H$_2$SO$_4$	25	4.47×10^{-5}	117	Electrodeposition
Re	0.145 M HCl	25	7.24×10^{-6}	29.2	Wire
Ir	1 M H$_2$SO$_4$	25	1.62×10^{-3}	122	-
Pd	0.1 M HCl	26	1.58×10^{-3}	110	Wire
Ni	1 M H$_2$SO$_4$	24	6.31×10^{-6}	95	Plate
Co	1 M H$_2$SO$_4$	25	1.38×10^{-5}	109	Electrodeposition
Au	1 M H$_2$SO$_4$	20	4.37×10^{-6}	116	Wire
Sn	1 M H$_2$SO$_4$	25	2.00×10^{-8}	115	-
W	5 M HCl	25	1.00×10^{-5}	110	Wire

It must be noted that those kinetic parameters depend not only on the measurement conditions, such as temperature, but also on the structures of the catalyst. Table 3.2 lists the exchange current density of the HOR as a function of temperature on the PtRu/C anode in a real PEM fuel cell, measured and simulated by Song et al. [8] and Zhang et al. [47].

Table 3.2. Measured and simulated i_0 of the HOR in a PEM fuel cell [8, 47]. (Data reprinted from Electrochimica Acta, 52.7, Song C, et al., PEM fuel cell reaction kinetics in the temperature range of 23–120 °C, 2552–61 and from Journal of Power Sources, 172.1, Zhang J, et al., Polybenzimidazole-membrane-based PEM fuel cell in the temperature range of 120–200 °C, 163–71, both ©2007, with permission from Elsevier.)

Temp. °C	23[a]	40[a]	60[a]	80[a]	100[a]	120[b]	140[b]	160[b]	180[b]	200[b]
i_0 10^{-3} A cm^{-2}	1.73	4.06	7.21	12.3	32.5	10.2	21.8	35.1	68.2	116.0

[a] Fuel cell operated at 3.0 atm (absolute) and 100% relative humidity; [b] Fuel cell operated at ambient pressure and 0% relative humidity.

3.3 Electrocatalysis of Hydrogen Oxidation

The electrocatalysis of the HOR is one of the important areas in fuel cell applications. In general, electrocatalysis can be considered a specific type of heterogeneous catalysis whereby reactants and products adsorb onto the catalyst surface during the reaction process. The reactants, activated by interaction with the catalyst surface, are rapidly and selectively converted to adsorbed products. Then, the adsorbed products leave the catalyst surface in a desorption step, freeing the surface for the next cycle of the reaction to continue. Since the catalyzed electrochemical reaction occurs at the catalyzed electrode/electrolyte interface, the intrinsic kinetic rate of an electrochemical reaction (measured by the exchange current density) strongly depends on the potential difference between the catalyst surface and the electrolyte, as well as on the kind of catalyst and its surface morphology. For electrode reactions, the exchange current density can vary from about 10^{-3} A·cm^{-2} at a platinum electrode to 10^{-12} A·cm^{-2} at a mercury electrode for the anode reaction (HOR), and from 10^{-10} A·cm^{-2} at a platinum electrode to 10^{-8} A·cm^{-2} at a copper electrode for the cathode reaction (ORR) [48]. Under normal conditions, the HOR on Pt is approximately 5 to 7 magnitudes more rapid than the ORR, and has one of the fastest known specific rate constants in aqueous solutions [49].

Studies on HOR electrocatalysis have built up a foundation for all modern electrocatalysis. Since the pioneering work of the 1960s, when the dependence of hydrogen adsorption upon the crystallographic orientation of the platinum surface was discovered, the study of the relationship between electrochemical activity and surface structure has been the main theme of electrochemical research [50]. In this section, we first introduce the electrocatalysis of the HOR on Pt and Pt-alloy electrodes, with detailed discussion of the structure-sensitivity of hydrogen adsorption on well-defined Pt surfaces. Then we discuss two types of non-noble catalysts for the HOR: carbides and Raney nickels.

3.3.1 Platinum and Platinum Group Metals (Pt, Ru, Pd, Ir, Os, and Rh)

Since adsorption and desorption of reactants on a catalyst surface can directly affect its catalytic ability, a "Volcano curve" is often plotted to correlate the exchange current density of the HOR with the enthalpy of H adsorption. If the enthalpy is too small, a slow adsorption kinetic will result and limit the rate of the overall reaction; if the enthalpy is too high, the desorption of H becomes difficult. Hence, this H desorption step will become a rate determining step within the overall reaction. Therefore, an intermediate value in the enthalpy of H adsorption on a catalyst is required in order for it to be an active catalyst. As shown in Figure 3.2, Pt and Pt-group metals all have intermediate values of H adsorption and display high catalytic activities [5]. Platinum-group metals, including Pt, Ru, Pd, Ir, Os, and Rh, have long been known as catalysts for both the ORR and the HOR [51]. On platinum-group metal surfaces, the chemisorption of hydrogen can easily remove the adsorbed oxygen with the formation of water at room temperature, which does not normally occur on other transition metals because they bind oxygen

too strongly [52]. Another characteristic of platinum-group metals is their ability to dissociate H_2 in the presence of H_2O.
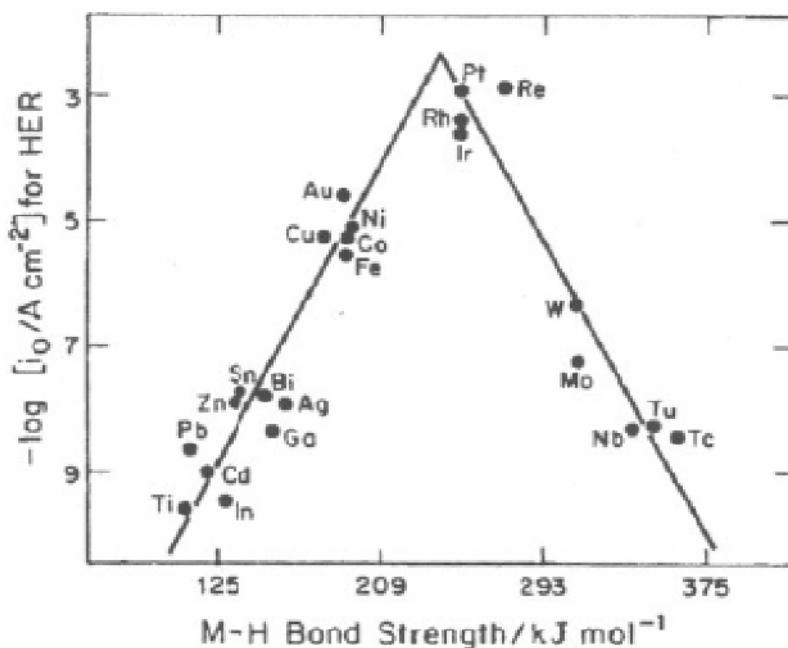
Figure 3.2. Volcano plot for electrocatalysis of the hydrogen reaction, in terms of ($logi_0$) as a function of the enthalpy of hydrogen adsorption on various catalysts [5]

3.3.1.1 Pt (hkl)

Among the platinum-group metals that are the most electrocatalytically active electrode materials for the HOR, platinum exhibits the highest exchange current density [53]. The major effort in HOR electrocatalysis has been focused on understanding rate dependency on the atomic-scale morphology of a platinum single-crystal surface. Almost all the early kinetic studies of the HER/HOR were carried out on either polycrystalline platinum electrodes [9] or platinum single crystals [54] that had poorly defined surface structures. In the early studies, the kinetics of the HER/HOR on Pt (hkl) was reported to be insensitive to the surface crystallography. Only recently, catalysis studies on well-defined Pt single-crystal electrodes clearly demonstrated that the HER/HOR kinetics on Pt (hkl) vary with a crystal face that has "structure sensitivity" [2, 55]. This sensitivity is mainly caused by the structure-sensitive adsorption of hydrogen and electrolyte anions. It has been recognized that the Pt plane is the most active surface for the HOR [53].

A well-defined and clean Pt (hkl) single-crystal electrode can be prepared either by techniques such as sputtering and annealing in ultrahigh vacuum (UHV) [56, 57] or by annealing the single crystal in a hydrogen-air flame [58–60]. The atomic scale structures and surface chemistry of well-defined pure Pt surfaces can be interrelated with the adsorption/desorption of reactive species (hydrogen),

intermediate species, as well as "spectator" species in terms of the HOR catalytic kinetics. Within the limited framework of this chapter, we do not intended to review the full spectrum of the structure and surface chemistry of Pt (hkl) and Pt bimetallic alloy surfaces. A number of reviews should be consulted for further information on this topic [53].
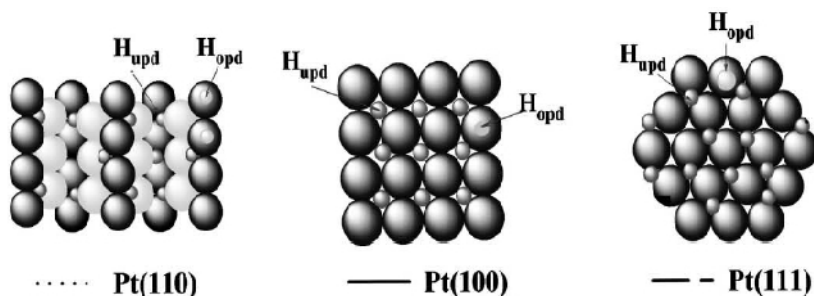
Figure 3.3. Ideal models for the adsorption of H$_{upd}$ and H$_{opd}$ on Pt (hkl) surfaces [53]. (Reprinted from Surface Science Reports, 45(4–6), Markovic N. M. and Ross P. N., Surface science studies of model fuel cell electrocatalysts, 117, ©2002, with permission from Elsevier.)

As discussed above, the mechanism for the HOR on a platinum electrode in acid electrolyte proceeds through two pathways, Tafel-Volmer and Heyrovsky-Volmer, both of which involve the adsorption of molecular hydrogen (H$_{ad}$), followed by a fast charge-transfer step:

$$Pt + H_2 \rightarrow 2Pt–H_{ad} \text{ (rate determining step, Tafel)} \qquad (3.43)$$

$$Pt + H_2 \rightarrow H^+ + Pt–H_{ad} + e^- \text{ (rate determining step, Heyrosky)} \qquad (3.44)$$

$$Pt–H_{ad} \rightarrow Pt + H^+ + e^- \text{ (fast charge-transfer, Volmer)} \qquad (3.45)$$
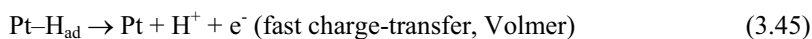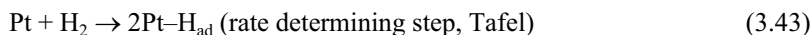
With respect to these mechanisms, it has been established that H$_{ad}$ is the reactive intermediate in the HOR, and therefore the kinetics of the HOR is mainly determined by the interaction between H$_{ad}$ and the Pt surface atoms [21, 53]. As discussed above, there are two different possible states of adsorbed hydrogen. One is the H$_{upd}$ (the underpotentially deposited hydrogen), which is the "strongly" adsorbed state formed on the surface at potentials more positive than the Nernst potential, and the other is the H$_{opd}$ (the overpotentially deposited hydrogen), which is the "weakly" adsorbed state formed close to or negative with respect to the Nernst potential [18, 22]. Markavié et al. [50] conducted comprehensive laboratory studies in an effort to understand the structural sensitivity of the HOR/HER kinetics and the mechanism catalyzed by Pt (hkl) surfaces in aqueous electrolyte. They proposed that H$_{opd}$ and H$_{upd}$ are the reactive intermediate and the spectator in the HOR, respectively. H$_{upd}$ can indirectly affect the state of H$_{opd}$, thus changing the HOR kinetics on Pt (hkl) through two modes: (1) H$_{upd}$ may block the

adsorption of H_{opd} on active Pt sites, i.e., H_{upd} competes for the same site, and (2) H_{upd} may alter the adsorption energy of H_{opd} on the bare Pt sites neighboured by H_{upd}. Depending on the surface structure of the well-defined Pt, i.e., (110), (100), or (111), the influence of the H_{upd} state on the HOR kinetics is different, resulting in different mechanisms. Figure 3.3 shows the structural model for both H_{upd} and H_{opd} on the Pt(111)-(1×2), Pt(100)-(1×1), and Pt(111)-(1×1) surfaces, and Table 3.3 lists the kinetic parameters for the HER and the HOR on Pt (hkl) in 0.05 M H_2SO_4 at different temperatures.

Table 3.3. Kinetic parameters for the HER and the HOR on Pt (hkl) in 0.05 M H_2SO_4 at different temperatures [50]

Pt (hkl)	$\partial E/\partial \log i$ (mV dec^{-1})	i_o (mA cm^{-2})			Activation energy (kJ mol^{-1})	Mechanism (rds)
		274 K	303 K	333 K		
Pt(110)	2.3RT/2F	0.65	0.98	1.35	9.5	Tafel-Volmer
Pt(100)	low CD: 2.3RT/3F high CD: 2×2.3RT/F	0.36	0.60	0.76	12	Heyrovsky-Volmer
Pt(111)	≈ 2.3RT/F	0.21	0.45	0.83	18	Heyrovsky or Tafel-Volmer

3.3.1.2 Pt Alloy and CO-tolerant Catalysts

Although the HOR has a fast kinetics on pure Pt catalyst surfaces, a serious poisoning problem arises when the PEM fuel cell is supplied with impure hydrogen containing carbon monoxide. In this case, CO is adsorbed strongly and irreversibly at the active sites on a pure Pt surface, mostly through bridge-bonding. This not only affects the reactivity of the accessible electrode surface by blocking H_2 adsorption but also lowers the reactivity of the remaining uncovered sites through dipole interactions and electron capture. Another disadvantage of pure platinum as a catalyst for the HOR is its high price and the possibility of depleting these mineral reserves if fuel cells were to be widely used [61]. Therefore, intensive research efforts in the last few decades have been focused on developing electrocatalysts by alloying Pt with other metals to increase the CO tolerance (defined as the maximum level of CO up to which the kinetics of the HOR are largely unperturbed) and reducing the use of Pt. Generally, alloying Pt with a second element can enhance the catalytic ability of the primary element, Pt, through one or more of the following effects: (1) bifunctional effects, whereby the second component provides one of the necessary reactants; (2) ligand (electronic) effects, in which the second component (promoter) alters the electronic properties of the catalytically active metal to affect the adsorption/desorption of the reactants/intermediates/poisons; and (3) ensemble (morphological) effects, in which the dilution of the active component, Pt, with the catalytically inert metal changes the distribution of the active sites, thereby opening different reaction

pathways [2]. The bifunctional model was first introduced into electrocatalysis by Watanabe and Motoo [62] for the oxidation of bulk CO_2/CO on a Pt surface modified by electrodeposited Ru. In the development of electrocatalysts for the HOR, the most commonly used strategy is to modify a Pt electrode by depositing atoms of elements such as Ru [63], Sn [64], Rh [65], Mo, Ni [66], etc. on its surface to form a binary alloy. Some of the alloy catalysts can free the Pt surface by catalyzing the oxidation of CO at potentials much lower than those observed for Pt (bifunctional effects). A typical example is a Pt-Ru alloy catalyst with a 1:1 atomic ratio [67, 68]. Some other alloy catalysts, such as Pt-Ni and Pt-Fe, can also lower the adsorption of CO at the electrode surface by modifying the electronic structure (i.e., the ligand effect, which is illustrated in Figure 3.4) and thus suppressing CO coverage through alloying Pt with the second metal [69]. In the case of the ensemble effect, some alloys can modify the nature of the CO adsorption by introducing a steric, as observed with Pd-Ag alloys [70]. Efforts have also been made to improve the CO tolerance of Pt-Ru catalysts by adding a third component into the binary metal catalyst, such as W [70], WO_2 [70, 71], Sn [70], Os, Pd [72], Co, Ir, Mn, Cr [73], Au, Ag, Rh, or W_2C [74] to make a ternary alloy. These third components help in CO oxidation (bifunctional effects) and/or reduce CO adsorption on Pt.
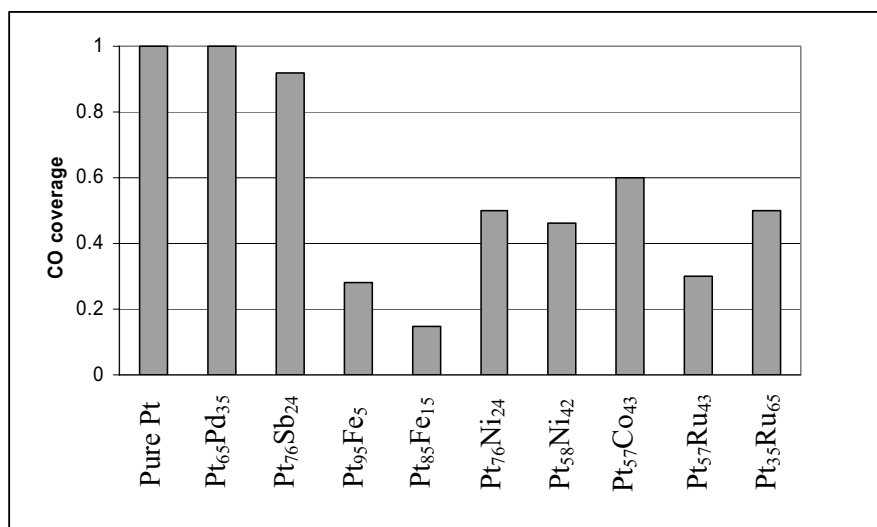
Figure 3.4. CO coverage on various surfaces of alloy electrodes, under steady H_2 oxidation conditions at 20 mV vs. RHE in 0.1 M $HClO_4$ saturated with 100 ppm CO/H_2 at room temperature [69]. (Reproduced by permission of ECS—The Electrochemical Society, from Holleck GL, Pasquarello DM, Clauson SL. Carbon monoxide tolerant anodes for proton exchange membrane fuel cells.)

Despite significant achievements in alloying Pt with other metal(s) to form active and CO-tolerant catalysts, there remain some unsolved problems for the applicability of these alloy catalysts to real fuel cell systems. One of the major

barriers is the physical-chemical instability of the modified catalyst surfaces. With respect to this, a new research approach is to develop catalysts with an ordered Pt-based intermetallic phase in order to fabricate alloy catalysts; this approach seems to hold great promise for applications in real electrochemical systems [61, 75]. These intermetallic materials offer the possibility of controlling the electron density pattern and the disposition of active sites over the surface, by varying the composition of the elements present in the intermetallic phase. In this way, the adsorption of H_2 at the catalyst surface can be modulated. In addition, these metal materials provide great physical-chemical stability for real applications. For example, Innocente et al. [61] experimentally investigated the HOR kinetics and mechanisms catalyzed by Pt-ordered intermetallic materials in acid medium, using the RDE method [61]. In their report, PtSb and PtSn, which contain 50% less Pt than a pure Pt electrode, exhibited markedly improved kinetic current densities and exchange current densities compared with Pt under the same conditions. However, more research is needed to validate the experimental results obtained with ordered intermetallic phases within a real fuel cell operating environment.

3.3.1.3 Supported Pt Catalysts

Since catalyst performance for the HOR is strongly dependent on the total active surface area, supported catalysts have been developed to maximize the catalyst surface area. Compared to bulk Pt catalysts, supported catalysts show higher activity and stability due to fine dispersion, high utilization, and stable nanoscale metallic particles.

At present, carbon black materials are the most commonly used carbon supports for PEM fuel cell catalysts. Supported catalysts have several advantages over unsupported catalysts [76]: (1) they have relatively higher stability than unsupported catalysts in terms of agglomeration under fuel cell operating conditions; (2) the porosity of carbon black assures gas diffusion to the active sites; (3) the good electric conductivity of the carbon support allows electron transfer from catalytic sites to the conductive carbon electrodes and then to the external circuit; and (4) the small dimensions of catalyst particles (nanoscale) dispersed on a carbon support can maximize the contact area between catalyst and reagents. There are many types of carbon blacks, which are usually manufactured by pyrolyzing hydrocarbons. Different carbon blacks show different physical and chemical properties. These properties have strong effects on the properties of the supported metal catalysts, such as metal particle size, morphology, size distribution, alloyed degree, stability, and dispersion, and on the preparation procedures as well. Therefore, in order to optimize the performance of the catalyst, a suitable carbon black support has to be down-selected, taking into consideration properties such as specific area, porosity, morphology, surface functional groups, electronic conductivity, corrosion resistance, etc.

Nanostructured carbon such as carbon nanotubes (CNTs) [76, 77–79] is another type of carbon support. CNTs are a promising kind of material for catalyst support in fuel cell catalysis applications, due to their unique electrical and structural properties. The reported studies have shown that CNTs are superior to carbon blacks as catalyst supports for PEM fuel cells [80]. Matsumoto et al. [81] reported that a CNT-supported Pt catalyst with 12 wt% Pt loading could give a 10% higher

fuel cell voltage and twice the power density of a carbon-black-supported catalyst with 29% Pt loading [81]. However, CNT supports currently face some challenges for fuel cell application in terms of large-scale production and cost-effectiveness, due to the harsh conditions required for their synthesis and the low production yields.
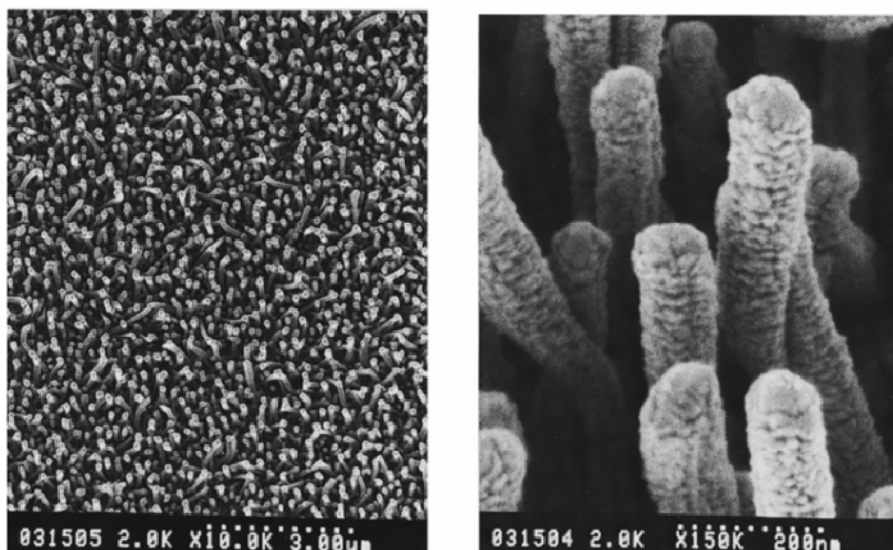
Figure 3.5. SEM pictures of Pt-coated nanostructured whiskers. Left: the plane view at 10,000 magnification; right: 45° angle view at 150,000 magnification [82]. (Reprinted with permission from Stahl JB, Debe MK, Coleman PL. Enhanced bioadsorption characteristics of a uniquely nanostructured thin film. J Vac Sci Techno A 1996;14(3):1761–5. ©1996 American Vacuum Society.)

Another example of novel catalyst support is the ultra-thin nanostructured (NS) film system. This support system consists of a uniquely structured thin film composed of highly oriented, densely packed crystalline organic whiskers. On these whiskers, the catalyst particles are deposited by vacuum coating methods (Figure 3.5) [82]. Due to the well-defined and highly controllable nature of the oriented thin film, the process for making a catalyst supported on this thin film intrinsically results in extremely high degrees of catalyst uniformity. However, this uniformity may not be obtainable for the heterogeneous surface of a conventional carbon black support [83]. In addition, the long-term stability of this system can be an issue.

Recently, carbon aerogels and carbon cryogel have attracted a great deal of attention as new mesoporous supports of electrocatalysts for the HOR in PEM fuel cells, due to their advanced characteristics such as a tortuous open-cell structure, ultrafine particle and pore size, and high specific surface area [84–86]. Their unique microstructure originates from their wet-chemical preparation by the solution sol-gel method and their subsequent solvent removal via supercritical- or freeze-drying. Despite their superior properties as catalyst supports, their very

costly preparation procedure limits large-scale commercialization. Babic et al. [87] investigated the effect of the specific surface area of a carbon support on the catalytic properties of Pt/C electrodes, using both carbon cryogel and commercial Vulcan XC72. In their report, Pt/C catalyst prepared by the carbon cryogel material has a lower mean particle size (2.6 nm) and a narrower particle size distribution than that prepared by the Vulcan XC72 support. In addition, larger electrochemical surface area and higher Pt utilization were also reported with catalysts prepared by carbon cryogel.

3.3.2 Carbides

Extensive research efforts have attempted to identify cheaper substitutes for the Pt-based catalysts in PEM fuel cell applications [88]. In 1973, Levy et al. [52] found that carbides of Groups IV-VI elements showed catalytic properties similar to those of Pt-group metals. Among those, tungsten carbide has been the most extensively studied as an electrocatalyst for the HOR in PEM fuel cells because of its Pt-like catalytic behavior, its stability in acid solutions at anodic potentials, and its resistance to CO poisoning [89, 90]. It was reported that the Pt-like catalytic properties of tungsten carbides are due to a change in the electron distribution of tungsten by the addition of carbon [91]. In particular, carbon could reduce the high reactivity of tungsten towards oxygen by adding its valence electrons to tungsten, which helps the latter to remove adsorbed oxygen with hydrogen [52]. However, the electrocatalytic activity of tungsten carbide and its immunity to CO are highly sensitive to the synthesis technique [91, 92]. The preparation of tungsten carbide involves synthesis of the oxide precursors, followed by their reduction in flowing hydrogen, carburization with different carbiding gases, and then passivation treatment [52, 93]. Hara et al. [88] studied the electrocatalytic activity of tungsten carbides (WC) with different crystalline phases. They reported that α-WC with a hexagonal lattice is the most favorable catalyst candidate for the HOR among the WCs with various types of crystalline phases. The introduction of a small amount of Pt onto the α-WC could lead to a specific activity much greater than that of the commercially available Pt catalyst. The enhanced HOR activity of a Pt-WC catalyst is considered to be a result of the better utilization of Pt and the synergistic effect between Pt and α-WC.

3.3.3 Raney Nickel

Transition metal alloys, notably Raney nickel, have also been investigated extensively as catalysts because of their interesting electronic and chemical properties [94]. Raney nickel is a solid catalyst, composed of fine grains of a nickel-aluminum alloy, and has been used in many industrial processes. Its application in the fuel cell field has been focused on alkaline fuel cells (AFC) rather than PEM fuel cells, due to potential corrosion in PEM operation media. Raney nickel's unique catalytic activity for the HOR as a non-noble catalyst makes it worth inclusion in this chapter.

Raney nickel consists of a nickel lattice with a large number of defects, formed during its production by dissolution of aluminum from aluminum-nickel alloys in

concentrated sodium hydroxide [95]. The porous structure left behind after this aluminum dissolution has a large surface area, which yields high catalytic activity. The residual aluminum content, depending upon the conditions of dissolution, varies between 3 to 25% of the original content [96]. The number of H atoms bonded per Ni atom in freshly prepared Raney nickel has been measured as a function of pre-treatment. The results reported in the literature run from 0.12 to 2.0. Normally, the HOR proceeds in a potential range of 0 to 0.15 V in alkaline electrolyte. If the potential is too high, oxidation of nickel occurs, resulting in inactivation of the catalyst [96]. The exchange current density for the HOR was estimated by Sturm et al. [96] to be about 1×10^{-5} Acm^{-2}, referring to the real surface area.

The Raney nickel catalyst can usually be stabilized by 2 to 4 wt% titanium and additionally activated by a small percentage of molybdenum [95] or platinum [97]. Although Raney nickel has excellent hydrogen adsorption ability and relatively large surface area, some disadvantages have also been reported, such as high electrolyte diffusion resistance due to low pore volume and small pore size [98, 99], and insufficient conductivity [97]. One type of mitigation is to support Raney nickel on carbon blacks, which will decrease its electrolyte diffusion resistance and increase its electrical conductivity [97].

Great efforts have been made to modify Raney nickel-based electrocatalysts to improve the performance of the fuel cell. Jenseit et al. [100] and Al-Saleh et al. [101] reported that impregnating Raney nickel with copper yielded a higher exchange current density and a lower activation energy. Tomido et al. [102] demonstrated that spongy Raney nickel prepared by spraying molten aluminum on nickel spongy plate provided good thermal and electrical conductivity, as well as good mechanical strength. The Kiros group [103] showed that doping Raney nickel with Cr, La, Ti, Cu, and Fe could have positive effects on the activity and stability of the catalysts. Linnekoski et al. [97] reported that mechanically alloying Raney nickel and carbon using a ball mill with the addition of 2 wt% Pt remarkably improved the performance of the fuel cell.

3.3.4 Typical Example Analysis – PtRu Alloy as a CO-tolerant Catalyst for the HOR

A CO level in the hydrogen stream as low as 5 ppm can cause significant degradation of Pt activity toward the HOR. Developing CO-tolerant catalysts for the fuel cell HOR is necessary if the fuel cell uses a reformate gas as fuel feed. PtRu alloys have been the most promising catalysts for the HOR in alleviating the CO poisoning problem. This section introduces the PtRu electrocatalysis mechanism of CO tolerance, which is mostly based on work by Gasteiger et al. [104, 105] and Watanabe [69, 106].

The oxidation reaction of adsorbed CO on most metal surfaces, including Pt and Ru, takes place by reacting with oxygen-containing species OH_{ad} through a Langmuir-Hinshelwood (L-H)-type reaction to form CO_2 [2, 107]:

$$CO_{ad} + OH_{ad} \rightarrow CO_2 + H^+ + e^- \tag{3.46}$$

where OH_{ad} results from oxidative water decomposition in acid solution or from OH^- discharge in alkaline solution.

It is well known that a Pt surface has a very high affinity towards CO adsorption through strong and irreversible bridge-bonding [108], and that CO oxidation on a Pt electrode does not commence before ≈ 0.6 V (vs. SHE) [107]. Therefore, the HOR on a Pt electrode in the presence of CO is suppressed until the electrode potential reaches a value at which CO can be oxidized [105]. For a PtRu catalyst, the adsorption of CO on a Ru surface is as simple as on a Pt surface, forming a strongly adsorbed saturated monolayer. However, the Ru-induced nucleation of OH_{ad} starts at relatively low electrode potentials, resulting in a reduced overpotential for CO oxidation (≈ 0.25 V) [105].

Despite its superior activity toward CO oxidation, Ru is a poor catalyst for the HOR, several orders of magnitude less active (≈ 0.003 A cm^{-2}) as compared with pure Pt (≥ 0.3 A cm^{-2}) [105]. Due to the extremely high activity of pure Pt for the HOR, a PtRu alloy surface with Ru atomic ratio $\geq 50\%$ can still sustain the HOR at a practical current density level (≈ 500 mA cm^{-2}). It is believed that the activity enhancement of PtRu compared with pure Pt in the presence of CO is due to the bifunctional mechanism, wherein the lower electrode potential for OH_{ad} (and thus a reduced overpotential for CO oxidation on Ru) would reduce the steady-state coverage of CO and provide free surface sites for the HOR.
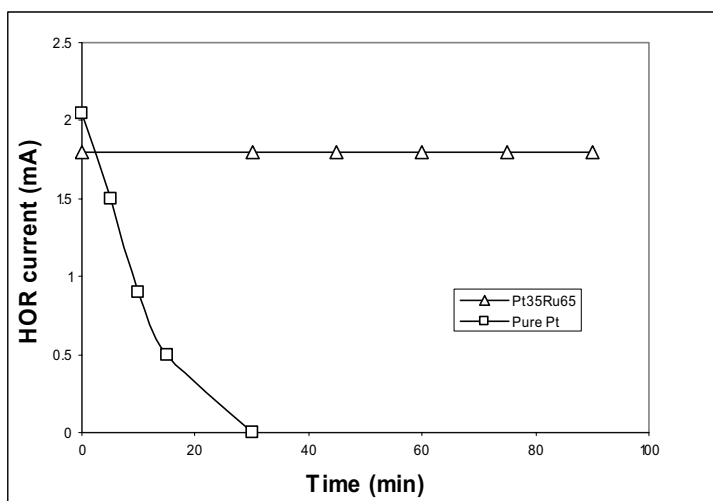
Figure 3.6. Hydrogen oxidation current on rotating disk electrode at 20 mV in 0.1 M HClO$_4$ saturated with 100 ppm CO/H$_2$ at room temperature [69]. (Reproduced by permission of ECS—The Electrochemical Society, from Holleck GL, Pasquarello DM, Clauson SL. Carbon monoxide tolerant anodes for proton exchange membrane fuel cells.)

Watanabe et al. [106] prepared a Pt$_{35}$Ru$_{65}$ alloy on a glass disk plate by sputtering Pt and Ru elements simultaneously, and tested the CO tolerance for the HOR using a rotating disk electrode in 0.1 M HClO$_4$ saturated with 100 ppm CO/H$_2$. For comparison, a pure Pt electrode was also tested under the same

conditions to assess the kinetic currents for the HOR as a function of CO poisoning time [69, 106]. Their experimental results, shown in Figure 3.6, indicate that PtRu exhibited no degradation in the current over a prolonged time period, while the current on pure Pt declined completely within 30 minutes [69, 106].

3.4 Conclusions

This chapter has focused on the fundamental aspects of the catalyzed hydrogen oxidation reaction (HOR), which occurs at the anode side of PEM fuel cells. The kinetics and mechanisms of the HOR have been introduced, with detailed discussion of hydrogen surface adsorption and reaction. The HOR proceeds through either the Volmer-Tafel sequence or the Volmer-Heyrovsky sequence, depending on the nature of the electrode and the electrolyte, and its pathway directly relates to its kinetic parameters. The electrocatalysis of the HOR was discussed in detail with respect to various electrocatalysts, including well-defined Pt, Pt alloys, carbides, and Raney nickel. A typical Volcano curve was introduced as the means of determining the effectiveness of a particular HOR catalyst. Finally, the chapter has ended with an example of a state-of-the-art electrocatalyst for the HOR, i.e., the PtRu catalyst. It is hoped that readers will come away with a fundamental understanding of the kinetics, mechanisms, and electrocatalysis of the HOR.

References

1. Conway BE, Bockris JOM. Electrolytic hydrogen evolution kinetics and its relation to the electronic and adsorptive properties of the metal. J Chem Phys 1957;26:532–41.
2. Markovic NM. Chapter 26. In: Handbook of fuel cells: fundamentals, technology and applications. Vielstich W, Lamm A, Gasteiger H, editors. New York: John Wiley & Sons, 2003.
3. Wendt H. Chapter 2. In: Electrochemical hydrogen technologies: electrochemical production and combustion of hydrogen. Wendt H, editor. New York: Elsevier, 1990.
4. Li H, Tang Y, Wang Z, Shi Z, Wu S, Song D, et al. A review of water flooding issues in the proton exchange membrane fuel cell. J Power Sources 2008;178(1):103–17.
5. Conway BE. Chapter 9. In: Interfacial electrochemistry: theory, experiment, and applications. Wieckowski A, editor. New York: Marcel Dekker, 1999.
6. Envo M. In: Comprehensive treatise of electrochemistry, Vol.7. Horsman P, Conway B, Yaeger E. New York: Plenum Press, 1983.
7. Antolini E. Formation of carbon-supported PtM alloys for low temperature fuel cells: a review. Mater Chem Phys 2003;78(3):563–73.
8. Song C, Tang Y, Zhang JL, Zhang J. PEM fuel cell reaction kinetics in the temperature range of 23–120 °C. Electrochim Acta 2007;52(7):2552–61.
9. Breiter MW. In: Handbook of fuel cells: fundamentals: technology and applications. Vol. 2. New York: John Wiley & Sons, 2003.
10. Vetter KJ. Electrochemical kinetics – theoretical and experimental aspect. New York: Academic Press, 1967.
11. Tafel J. Polarization cathodic hydrogen development. Z Physik Chem 1905;50:641–712.

12. Erdey-Gruz T, Volmer M. The theory of hydrogen overvoltage. Z Physik Chem 1930;A150:203–13.

13. Frumkin A. Theory of hydrogen overvoltage. Z Physik Chem 1932;A160:116–8; Hydrogen overvoltage and structure of the double layer. Z Physik Chem 1933;A164:121–3.

14. Appleby AJ, Kita H, Chemla M, Bronoel G. Hydrogen. In: Encyclopedia of the electrochemistry of the elements IXa. Bard AJ, editor. New York: Marcel Dekker: 1973.

15. Ludwig F, Sen RK, Yeager E. Mechanism of hydrogen liberation and ionization on platinum in acid solution. Élektrokhimiya 1977;13:847–54.

16. Conway BE, Bai L. Determination of adsorption of OPD H species in the cathodic hydrogen evolution reaction at Pt in relation to electrocatalysis. J Electroanal Chem 1986;198(1):149–75.

17. Bai L, Harrington DA, Conway BE. Behavior of overpotential–deposited species in Faradaic reactions–II. AC Impedance measurements on H_2 evolution kinetics at activated and unactivated Pt cathodes. Electrochim Acta 1987;32(12):1713–31.

18. Markovic NM, Grgur BN, Ross PN. Temperature-dependent hydrogen electrochemistry on platinum low-index single-crystal surfaces in acid solutions. J Phys Chem B 1997;101(27):5405–13.

19. Jerkiewicz G, Zolfaghari A. Comparison of hydrogen electroadsorption from the electrolyte with hydrogen adsorption from the gas phase. J Electrochem Soc 1996;143(4):1240–8.

20. Kita H, Ye S, Gao Y. Mass transfer effect in hydrogen evolution reaction on Pt single-crystal electrodes in acid solution. J Electroanal Chem 1992;334(1–2):351–7.

21. Protopopoff E, Marcus P. Effect of chemisorbed sulfur on the hydrogen adsorption and evolution on metal single-crystal surface. J Chim Phys 1991;88:1423–52.

22. Markovic NM, Sarraf TS, Gasteiger HA, Ross PN. Hydrogen electrochemistry on platinum low-index single-crystal surfaces in alkaline solution. J Chem Faraday Trans 1996;92:3719.

23. Rand DAJ, Woods R. A study of the dissolution of platinum, palladium, rhodium and gold electrodes in 1 M sulphuric acid by cyclic voltammetry. J Electroanal Chem 1972;35:209–18.

24. Michell D, Rand DAJ, Woods R. A study of ruthenium electrodes by cyclic voltammetry and X-ray emission spectroscopy. J Electroanal Chem 1978;89(1):11–27.

25. Capon A, Parsons R. The effect of strong acid on the reactions of hydrogen and oxygen on the noble metals. A study using cyclic voltammetry and a new teflon electrode holder. J Electroanal Chem 1972;39(2):275–86.

26. Rand DAJ, Woods R. Cyclic voltammetric studies on iridium electrodes in sulphuric acid solutions: Nature of oxygen layer and metal dissolution. J Electroanal Chem 1974;55(3):375–81.

27. Biegler T, Rand DAJ, Woods R. Limiting oxygen coverage on platinized platinum; Relevance to determination of real platinum area by hydrogen adsorption. J Electroanal Chem 1971;29(2):269–77.

28. Woods R. Hydrogen adsorption on platinum, iridium and rhodium electrodes at reduced temperatures and the determination of real surface area. J Electroanal Chem 1974;49(2):217–26.

29. Brummer SB. The use of large anodic galvanostatic transients to evaluate the maximum adsorption on platinum from formic acid solutions. J Phys Chem 1965;69(2):562–71.

30. Gilman S, Bard AJ, editors. Electroanalytical chemistry vol 2. London: Arnold, 1967.

31. Nicholas JF. An atlas of models of crystal surface. New York: Gordon and Breach, 1965.

32. Podlovchenko BI, Kolyadko EA. Effect of the nature of platinum group metals on the formation and properties of adatom silver coatings. J Electroanal Chem 1987;224(1–2):225–35.

33. Vukovic M. Electrochemical investigation of an electrodeposited rhodium electrode in acid solutions. J Electroanal Chem 1988;242(1–2):97–105.

34. Rand DAJ, Woods R. The nature of adsorbed oxygen on rhodium, palladium and gold electrodes. J Electroanal Chem 1971;31(1):29–38.

35. Peuckert M. A comparison of thermally and electrochemically prepared oxidation adlayers on rhodium: Chemical nature and thermal stability. Surf Sci 1984;141(2–3):500–14.

36. Hadzi-Jordanov S, Angerstein-Kozlowska H, Vukovic M, Conway BE. The state of electrodeposited hydrogen at ruthenium electrodes. J Phys Chem 1977;81(24):2271–9.

37. Tuseeva EK, Skundin AM, Bagotskii VS. Sorption of hydrogen by compact ruthenium. Electrokhimiya 1973;9:1541–1545.

38. Pletcher D. A first course in electrode processes. The Electrochemical Consultancy Ltd.. Romesy. UK.. 1991:119.

39. Hu C-C, Wen T-C. Voltammetric investigation of hydrogen sorption/desorption at/within oxide-derived Pd electrodes in NaOH and H$_2$SO$_4$. J Electrochem Soc 1994;141(11):2996–3001.

40. Bockris JOM, McBreen J, Nanis L. The hydrogen evolution kinetics and hydrogen entry into a-iron. J Electrochem Soc 1965;112(10):1025–1031.

41. Lasia A, Gregoire D. General model of electrochemical hydrogen absorption into metals. J Electrochem Soc 1995;142(10):3393–3399.

42. Frumkin AN. Advances in electrochemistry and electrochemical engineering. vol 3. Interscience. New York 1963.

43. Zheng G, Popov BN, White RE. Hydrogen-atom direct-entry mechanism into metal membranes. J Electrochem Soc 1995;142(1):154–156.

44. Lim C, Pyun S-I. Impedance analysis of hydrogen absorption reaction on Pd membrane electrode in 0.1 M LiOH solution under permeable boundary conditions. Electrochim Acta 1994;39(3):363–373.

45. Lasia A. On the mechanism of the hydrogen absorption reaction. J Electroanal Chem 2006;593(1–2):159–166.

46. Chevillot J-P, Farcy J, Hinnen C, Rousseau A. Electrochemical study of hydrogen interaction with palladium and platinum. J Electroanal Chem 1975;64(1):39–62.

47. Zhang J, Tang Y, Song C. Polybenzimidazole-membrane-based PEM fuel cell in the temperature range of 120–200 °C. J Power Sources 2007;172(1):163–171.

48. Li X. Principles of fuel cells. Ch. 3. Taylor & Francis. New York. 2006.

49. Parthasarathy A, Martin CR, Srinivasan S. Investigations of the O$_2$ reduction reaction at the platinum Nafion interface using a solid-state electrochemical cell. J Electrochem Soc 1991;138(4):916–921.

50. Marković NM, Ross P Jr. Electrocatalysis at well-defined surfaces: kinetics of oxygen reduction and hydrogen oxidation/evolution on Pt(hkl) electrodes. In: Interfacial electrochemistry: theory, experiment and applications. Wieckowski A, editor. New York: Marcel Dekker, 1999: 821–42.

51. Piccolo L, Piednoir A, Bertolini J-C. Absorption and oxidation of hydrogen at Pd and Pd-Au (1 1 1) surfaces. Surf Sci 2006;600(18):4211–5.

52. Levy RB. Platinum-like behavior of tungsten carbide in surface catalysis. Science 1973;181:547–9.

53. Markovic NM, Ross PN. Surface science studies of model fuel cell electrocatalysts. Surf Sci Rep 2002;45(4–6):117.

54. Schuldiner S, Rosen M, Flinn DR. Comparative activity of (111), (100), (110), and polycrystalline platinum electrodes in H_2-saturated 1M H_2SO_4 under potentiostatic control. J Electrochem Soc 1970;117(10):1251–9.

55. Markovic NM, Ross PN. Surface science studies of model fuel cell electrocatalysts*. Surf Sci Rep 2002;45(4–6):121.

56. Ross JPN. The effect of anions on hydrogen chemisorption and oxide formation on Pt in aqueous acids. J Electroanal Chem 1977;76(1):139–45.

57. Yamamoto K, Kolb DM, Kötz R, Lehmpfuhl G. Hydrogen adsorption and oxide formation on platinum single crystal electrodes. J Electroanal Chem 1979;96(2):233–9.

58. Clavilier J, Faure R, Guinet G, Durand R. Preparation of monocrystalline Pt microelectrodes and electrochemical study of the plane surfaces cut in the direction of the {111} and {110} planes. J Electroanal Chem 1979;107(1):205–9.

59. Markovic N, Hanson M, McDougall G, Yeager E. The effects of anions on hydrogen electrosorption on platinum single-crystal electrodes. J Electroanal Chem 1986;214(1–2):555–66.

60. Wasberg M, Palaikis L, Wallen S, Kamrath M, Wieckowski A. LEED/Auger verification of the in situ method of preparation of Pt (111) single crystal electrodes. J Electroanal Chem 1988;256(1):51–63.

61. Innocente AF, Angelo ACD. Electrocatalysis of oxidation of hydrogen on platinum ordered intermetallic phases: Kinetic and mechanistic studies. J Power Sources 2006;162(1):151–159.

62. Watanabe M, Motoo S. Electrocatalysis by ad-atoms: Part III. Enhancement of the oxidation of carbon monoxide on platinum by ruthenium ad-atoms. J Electroanal Chem 1975;60(3):275–283.

63. Janssen MMP, Moolhuysen J. Binary systems of platinum and a second metal as oxidation catalysts for methanol fuel cells. Electrochim Acta 1976;21(11):869–78.

64. Andrew MR, McNicol BD, Short RT, Drury JS. Electrolytes for methanol-air fuel cells. I. The performance of methanol electro-oxidation catalysts in sulphuric acid and phosphoric acid electrolytes. J Appl Electrochem 1977;7(2):153.

65. Ross PN, Kinoshita K, Scarpellino AJ, Stonehart P. Electrocatalysis on binary alloys: I. Oxidation of molecular hydrogen on supported Pt-Rh alloys. J Electroanal Chem 1975;59(2):177–89.

66. Grgur BN, Zhuang G, Markovic NM, Ross PN. Electrooxidation of H_2/CO mixtures on a well-characterized $Pt_{75}Mo_{25}$ alloy surface. J Phys Chem B 1997;101(20):3910–3.

67. Schmidt TJ, Jusys Z, Gasteiger HA, Behm RJ, Endruschat U, Boennemann H. On the CO tolerance of novel colloidal PdAu/carbon electrocatalysts. J Electroanal Chem 2001;501(1–2):132–40.

68. Wise H. Role of surface composition in co adsorption on Pd–Ag catalysts. J Catal 1976;43(1–3):373–5.

69. Holleck GL, Pasquarello DM, Clauson SL. Carbon monoxide tolerant anodes for proton exchange membrane fuel cells. Electrochem Soc Proceedings 1999;98(27):150–162.

70. Gotz M, Wendt H. Binary and ternary anode catalyst formulations including the elements W, Sn and Mo for PEMFCs operated on methanol or reformate gas. Electrochim Acta 1998;43(24):3637–44.

71. Chen KY, Shen PK, Tseung ACC. Anodic oxidation of impure H_2 on Teflon-bonded Pt-Ru/WO_3/C electrodes. J Electrochem Soc 1995;142(10):L185-L187.

72. He C, Kunz HR, Fenton JM. Evaluation of platinum-based catalysts for methanol electro-oxidation in phosphoric acid electrolyte. J Electrochem Soc 1997;144(3):970–979.

73. Holleck GL, Pasquariello DM, Clauson SL. Proton conducting membrane fuel cells II. Electrochem Soc Proceedings 1999;98(27):162–76.

74. Venkataraman R, Kunz HR, Fenton JM. Development of new CO tolerant ternary anode catalysts for proton exchange membrane fuel cells. J Electrochem Soc 2003;150(3):A278-A284.

75. Tada T. Handbook of fuel cells: fundamentals: technology and applications. 2003. 3(38).

76. Rodriguez NM, Chamber A, Baker RT. Catalytic engineering of carbon nanostructures. Langmuir 1995;11:3862–6.

77. Costamagna P, Srinivasan S. Quantum jumps in the PEMFC science and technology from the 1960s to the year 2000: Part I. Fundamental scientific aspects. J Power Sources 2001;102(1–2):242–252.

78. Liu H, Song C, Zhang L, Zhang J, Wang H, Wilkinson DP. A review of anode catalysis in the direct methanol fuel cell. J Power Sources 2006;155(2):95–110.

79. Liu Z, Lin X, Lee JY, Zhang WS, Han M, Gan LM. Preparation and characterization of Pt-based electrocatalysts on multiwalled carmon nanotubes for PEM fuel cells. Langmuir 2002;18(10):4054–4060.

80. Wang C, Waje M, Wang X, Tang JM, Haddon RC, Yan Y. Proton exchange membrane fuel cells with carbon nanotube based electrodes. Nano Lett 2004;4:345–348.

81. Matsumoto T, Komatsu T, Arai K, Yamazaki T, Kijima M, Shimizu H, et al. Reduction of Pt usage in fuel cell electrocatalysts with carbon nanotube electrodes. Chem Comm 2004;840–841.

82. Stahl JB, Debe MK, Coleman PL. Enhanced bioadsorption characteristics of a uniquely nanostructured thin film. J Vac Sci Techno A 1996;14(3):1761–1765.

83. Debe MK. Handbook of fuel cells: fundamentals: technology and applications. Vol. 3. Ch. 45. John & Sons. New York. 2003.

84. Ye S, Vijh AK. Non-noble metal-carbonized aerogel composites as electrocatalysts for the oxygen reduction reaction. Electrochem Comm 2003;5(3):272–275.

85. Yang K, Yiacoumi S, Tsouris C. Electrosorption capacitance of nanostructured carbon aerogel obtained by cyclic voltammetry. J Electroanal Chem 2003;540:159–67.

86. Ye S, Vijh AK, Dao LH. Fractal dimension of platinum particles dispersed in highly porous carbonized polyacrylonitrile microcellular foam. J Electrochem Soc 1997;144(5):1734–1738.

87. Babic BM, Vracar Lj M, Radmilovic V, Krstajic NV. Carbon cryogel as support of platinum nano-sized electrocatalyst for the hydrogen oxidation reaction. Electrochim Acta 2006;51(18):3820–6.

88. Hara Y, Minami N, Itagaki H. Synthesis and characterization of high-surface area tungsten carbides and application to electrocatalytic hydrogen oxidation. Appl Catal A 2007;323:86–93.

89. Ganesan R, Lee JS. Tungsten carbide microspheres as a noble-metal-economic electrocatalyst for methanol oxidation. Angew Chem Int Ed 2005;44:6557–60.

90. Barnett CJ, Burstein GT, Kucernak AR, Williams KR. Electrocatalytic activity of some carburised nickel, tungsten and molybdenum compounds. Electrochim Acta 1997;42(15):2381–8.

91. McIntyre DR, Burstein GT, Vossen A. Effect of carbon monoxide on the electrooxidation of hydrogen by tungsten carbide. J Power Sources 2002;107(1):67–73.

92. Fleischmann R, Bohm H. Wasserstoffoxidation an verschiedenen wolframcarbidmaterilien. Electrochim Acta 1977;22(10):1123–8.

93. Bronoel G, Museux E, Leclercq G, Leclercq L, Tassin N. Study of hydrogen oxidation on carbides. Electrochim Acta 1991;36(10):1543–7.

94. Stancheva M, Manev S, Lazarov D. Oxidation of hydrogen on the catalyst surfaces obtained from amorphous Ni-Cu-P alloys. React Kinet Catal Lett 1997;61:103.

95. Briter MW. Chapter VII. Electrochemical processes in fuel cells. New York: Springer-Verlag, 1969.

96. Sturm FV, Richter G. Untersuchung des wasserstoffaustausches an Raney-Nickel mit hilfe einer magnet-elektrode. Electrochim Acta 1965;10(12):1169–83.

97. Linnekoski JA, Juha A, Krause, AO, Keskinen J, Lamminen J, Anttila T. Processing of Raney-nickel catalysts for alkaline fuel cell applications. J Fuel Cell Sci Technol 2007;4(1):45–8.

98. Shim J-P, Park Y-S, Lee H-K, Lee J-S. Hydrogen oxidation characteristics of Raney nickel electrodes with carbon black in an alkaline fuel cell. J Power Sources 1998;74(1):151–4.

99. Kenjo T. Chromium-doped Raney nickel catalyst for hydrogen electrodes in alkaline fuel cells. J Electrochem Soc 1985;132(2):383–6.

100. Jenseit W, Khalil A, Wendt H. Material properties and processing in the production of fuel cell components: I. Hydrogen anodes from Raney nickel for lightweight alkaline fuel cells. J Appl Electrochem 1990;20(6):893.

101. Al-Saleh MA, Gultekin S, Al-Zakri AS, Khan AA. Steady state performance of copper impregnated Ni/PTFE gas diffusion electrode in alkaline fuel cell. Intern J Hydrogen Energy 1996;21(8):657–61.

102. Tomida T, Okamura K, Ashida T, Nakaboyashi I. Relation between the conditions of preparation and the polarization characteristics of spongy Raney nickel electrodes used as anodes for fuel cells. J Electrochem Soc 1992;139(4):981–4.

103. Kiros Y, Majari M, Nissinen TA. Effect and characterization of dopants to Raney nickel for hydrogen oxidation. J Alloys Compd 2003;360(1–2):279–85.

104. Gasteiger HA, Markovic NM, Ross PN. H_2 and CO electrooxidation on well-characterized Pt, Ru, and Pt-Ru. 2. Rotating disk electrode studies of CO/H_2 mixtures at 62 °C. J Phys Chem 1995;99(45):16757–67.

105. Gasteiger HA, Markovic NM, Ross PN. H_2 and CO electrooxidation on well-characterized Pt, Ru, and Pt-Ru. 1. Rotating disk electrode studies of the pure gases including temperature effects. J Phys Chem 1995;99(20):8290–301.

106. Watanabe M, Igarashi H, Fujino T. Design of CO tolerant anode catalysts for PEM fuel cell. Electrochemistry 1999;67:1194–6.

107. Gasteiger HA, Markovic N, Ross PN Jr, Cairns EJ. Carbon monoxide electrooxidation on well-characterized platinum-ruthenium alloys. J Phys Chem 1994;98(2):617–25.

108. Watanabe M. Chapter 28. Handbook of fuel cells: fundamentals: technology and applications. Vol. 2. New York: John Wiley & Sons, 2003.

4

Electrocatalytic Oxidation of Methanol, Ethanol and Formic Acid

Előd Gyenge

4.1 Introduction

4.1.1 Historical Overview: 1960–1990

Detailed investigations of CH_3OH, C_2H_5OH, and $HCOOH$ electrooxidation started about five decades ago, with the advent of modern potentiodynamic techniques, driven initially by the goal of elucidating some of the most interesting and challenging electrode kinetic problems. Many pioneering studies that withstood the test of time and the continuous sophistication of surface electrochemistry techniques were published in the 1960s by Petry, Bagotzky, Daniel-Bek, Breiter, and others [1–14]. Important results were obtained, such as: (i) phenomenological interpretation of anodic polarization curves (e.g., determination of Tafel parameters for CH_3OH oxidation on Pt [3], C_2H_5OH oxidation in alkaline media on Ni and Pd/C [4], $HCOOH$ oxidation on Pd [6] and Pt/C [7]); (ii) discovery of the co-catalytic effect of Ru with respect to Pt for CH_3OH oxidation [1, 8]; (iii) investigation of the potential dependent adsorption of CH_3OH and $HCOOH$ on Pt and the associated parallel (or dual) pathway mechanism [9–12]; and (iv) mathematical modeling of flooded porous electrode behavior [13, 14].

The possibility of power generation utilizing CH_3OH, C_2H_5OH, and $HCOOH$ as anodic fuels coupled with an O_2 or air gas diffusion cathodes (i.e., what is now commonly referred to as *direct* fuel cells, Figure 4.1) was recognized early on. Initially, ionic conductivity on the anode side was provided by liquid electrolytes (e.g., concentrated H_2SO_4, H_3PO_4, or KOH). The patent literature from the 1960s is very rich in ideas that are still of interest today. Sandstede et al. described ternary and quaternary Pt alloys with elements such as Ir, Os, Mo, Ru, and Re supported on Au grid, as anodic catalysts for both methanol and formic acid direct fuel cells [15]. Furthermore, the use of Ti electrodes (mesh or compacted powder) with 0.1 to 10 wt% Pt coating was proposed as a direct methanol fuel cell anode in acid media [16]. In the case of the direct ethanol fuel cells, electrodes composed of Pt alloyed with Mo, V, Cu, W, Mn, or Ce supported on porous graphite were investigated as anodes in 30 vol% C_2H_5OH and 30 wt% H_2SO_4 solution. Promising

results were reported for the Pt-Mo formulation (0.72 V at 40 mA cm^{-2}, 328 K) in an undivided fuel cell design, where the C_2H_5OH-H_2SO_4 solution was suspended in a silica gel-filter paper pulp slurry and the cathode was PbO_2 [17]. Binder et al. employed a W/C (1:1 weight ratio) anode for the direct formic acid fuel cell in 3 N H_2SO_4, thus searching for ways to eliminate the use of precious metal catalysts [18].

Anode: $C_xH_yO_z + (2x-z)H_2O \rightarrow xCO_2 + (4x+y-2z)H^+ + (4x+y-2z)e^-$

Cathode: $(x+y/4-z/2)O_2 + (4x+y-2z)H^+ + (4x+y-2z)e^- \rightarrow (2x+y/2-z)H_2O$

Fuel cell reaction: $C_xH_yO_z + (x+y/4-z/2)O_2 \rightarrow xCO_2 + (y/2)H_2O$
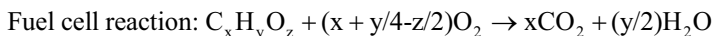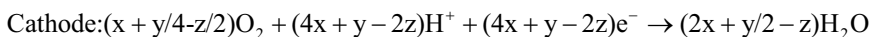
Table 4.1. Direct fuel cell standard potentials at 298 K

Fuel		E^0_{cell} (at 298 K) / V
$x=1$; $y=4$; $z=1$	CH_3OH	1.19
$x=1$; $y=2$; $z=2$	HCOOH	1.43
$x=2$; $y=6$; $z=1$	C_2H_5OH	1.14

In the 1970s and 1980s the major trend was to study the electrooxidation reaction mechanisms and elucidate the surface adsorbed species acting as intermediates and/or catalytic poisons. This was facilitated by progress in experimental apparatus (e.g., development of methods for electrode potential-dependent analysis of surface and bulk intermediates and reaction products) and introduction of new techniques for easy preparation of clean single crystal electrodes (i.e., the Clavilier method [19]).

Thus, the structural sensitivity of CH_3OH electrooxidation was demonstrated using Pt single crystal electrodes. It was first shown by Bagotzky et al. that Pt crystal faces with denser atomic packing yielded higher methanol oxidation rates, although the adsorption isotherms were identical. Therefore, electronic effects rather than active center-based surface structures were invoked to explain the observed results [20]. In the early 1980s Clavilier and co-workers refined these concepts using more precise experimental methods and showed that Pt(110) is the most active plane but also very sensitive to poisoning by CO_{ad} (both linearly and bridge bonded). Pt(111) on the other hand is less affected by poisoning, whilst Pt(100) is blocked by adsorbed intermediates over a wide potential range but could be cleaned at high anode potentials [21, 22].

Extensive studies were carried out in the same time period regarding the structural sensitivity of HCOOH electrooxidation. The rate of formic acid oxidation was highest on Pt(111), and up to four-fold current enhancement was reported for a 60% (111) oriented surface compared to a polycrystal [23–25]. Interestingly, in contrast to the methanol case, Pt(111) exposed to formic acid was less poisoned by CO_{ad} [26]. Weaver and collaborators compared the structural sensitivity of CH_3OH, C_2H_5OH, and HCOOH electrooxidation on single crystal Pt using real-time FTIR coupled with quasi-steady state voltammetry [27]. This study

underlined the effectiveness of Pt(111) for all three fuels, characterized by low CO_{ad} surface coverage. On the other hand, CO_{ad} surface coverage of 0.7 and higher was detected for HCOOH oxidation on either Pt(110) or Pt(100). Ethanol was predominantly oxidized to acetic acid on Pt(111) by a $4e^-$ mechanism with some contribution by the $12e^-$ oxidation to CO_2. On Pt(100) and Pt(110) the $2e^-$ oxidation to acetaldehyde was observed, especially at low overpotentials [27].

Furthermore, Conway and co-workers discovered an interesting activation effect for the electrochemical oxidation of HCOOH. Trace amounts of acetonitrile (e.g., 5×10^{-4} M CH_3CN) and Hg (electrodeposited from 3×10^{-6} M Hg_2SO_4) enhanced up to six times the HCOOH oxidation peak current density on Pt (occurring at around 0.6 V vs. SHE) [28]. This was attributed to a third-body effect caused by CH_3CN and Hg adsorption at potentials below 0.35 V vs. SHE. A similar activation effect was identified in the case of adsorbed sulfur [29, 30] and iodide [31]. For CH_3OH on Pt, however, the presence of acetonitrile inhibited the reaction, since the number and arrangement of active sites required for electrooxidation are different [28].

Considerable effort was directed toward finding efficient co-catalysts or promoters that, together with Pt, could enhance the rate of anodic oxidation of methanol and formic acid. The oxidation of ethanol received comparatively less attention in the 1970s and 1980s, most likely due to the more complex electrode kinetics and catalysis imposed by the C-C bond.

A seminal contribution to understanding the mechanism of HCOOH electrooxidation on Pt and Pt-Pd alloys was carried out by Capon and Parsons. They analyzed the experimental data on the basis of the dual-pathway mechanism involving both CO_{ad} and another more reactive intermediate [32, 33]. Research in the area of non-Pt catalysts was less extensive, and arguably the only practical alternative put forward in that period was Pd, in the case of HCOOH [34]. Interesting results were published on the electrocatalysis of formic acid oxidation using Pt modified with various adatoms, obtained by underpotential deposition. Adatoms such as Pb, Bi, and Sn were found to be effective in enhancing the electrocatalytic activity for both smooth and porous Pt electrodes [35–38]. For the latter electrode type, using Pt/Sn_{ad} Minevski and Adzic reported good long-term performance, up to 100 h in a 1 M HCOOH – 1 M $HClO_4$ solution. The superficial current density for HCOOH oxidation at 0.5 V vs. SHE was approximately three times higher after 100 h of operation for porous Pt/Sn_{ad} compared to commercial Pt [36]. The proposed mechanism was based on the role of Sn in preventing HCOOH oxidation inhibition by either H_{ad} or other adsorbed intermediates [34, 38].

Regarding ethanol oxidation on Pt, unfortunately the adatom third-body effect operative for formic acid was found to be ineffective, e.g., Bi_{ad}, Te_{ad}, and Se_{ad} had no benefcal effect [39]. Wiilsau and Hietbaum elucidated by isotope labelling some of the elementary steps involved in ethanol electrooxidation [40]. According to this study, the first step seems to be the oxidative H removal from the α-C atom, leading to CH_3CHO. The formation of a strongly adsorbed intermediate was also detected, which could be oxidized only at potentials above 0.7 V vs. RHE [40]. Vielstich and co-workers identified the products of C_2H_5OH oxidation on Pt, showing the formation of CO_{ad} and COH_{ad} on the surface, whilst CO_2 and CH_3CHO were detected in bulk, underlining the complexity of the reaction [41].

Isotope labelling techniques were also used in the 1970s by Wieckowski and co-workers for studies of methanol and formic acid adsorption on Pt electrodes [42–44]. Some of the findings were as follows: i) an inverse kinetic isotope effect was found for HCOOH adsorption on Pt in D_2SO_4 vs. H_2SO_4 that led to the suggestion of reductive HCOOH adsorption in the presence of hydronium ions, therefore contradicting the very popular Capon and Parsons mechanism based on dual pathways [32]; ii) the reductive adsorption of HCOOH was proposed to take place either with H_{ad} (in the hydrogen region of the potential domain) or by direct electron transfer (in the double-layer region), both options leading to a $C(OH)_2H_{ad}$ intermediate; and iii) for CH_3OH adsorption no measurable isotope exchange was observed between hydrogen from methyl groups and deuterium in solution. Some of these results were not thoroughly substantiated by further experimental studies.

Regarding methanol oxidation, important results were obtained in the the co-catalytic effect of certain elements such as Ru (e.g., the bifunctional mechanism), Sn, Ir, and Os [45]. Watanabe and Motoo demonstrated unequivocally the bifunctional effect of Ru adatoms on the mechanism of CH_3OH oxidation, enhancing the catalytic activity compared to pure Pt and favoring the $6e^-$ oxidation route [46]. Based on the Langmuir-Hinshelwood rate determining step between two adsorbed species, the role of Ru relates to the dissociative chemisorption of H_2O forming OH_{ad}, which oxidizes the CH_3OH oxidation products adsorbed on Pt (e.g., CO_{ad}). Janssen and Moolhuysen investigated twenty-five Pt-based binary catalysts classified according to their adsorption behavior toward OH_{ad}. PtTi was proposed to have comparable performance to PtRu and Pt Sn [47].

From the fuel cell application point of view, it is important to highlight from the 1970s–1980s the contributions of the Oxford (Goodenough and Hamnett) and Shell groups (McNicol and Short), aimed at improving carbon-supported Pt (or Pt-alloy) catalyst dispersion and activity. These researchers carried out systematic studies related to the catalyst/carbon support interaction and its impact on catalyst particle size, electrochemically active surface area, catalyst load, and long-term stability and activity under operating conditions. It was conclusively demonstrated that carbon-supported Pt nanoparticles behave differently compared to bulk polycrystalline Pt, therefore, making difficult the "translation" of some fundamental electrochemical research to porous electrode designs relevant to practical application. Goodenough, Hamnett, and co-workers examined these issues in the 1980s and showed that supported Pt particles poison more slowly than bulk Pt, with possibly different surface-adsorbed CH_3OH oxidation products being involved in conjunction with different Pt oxide coverage ([48], literature therein).

McNicol and co-workers found that activation in air at 573 K of carbon fiber paper acting as catalyst support, followed by galvanostatic anodic treatment at 2 mA cm^{-2} for 90 min in 1% v/v HNO_3 improved the mass specific activity toward CH_3OH oxidation of the supported Pt catalyst (prepared by ion-exchange using $Pt(NH_3)_4(OH)_2$) [49]. It was proposed that the activity enhancement was due to both increased Pt dispersion on the oxidized carbon surface and changes in the electronic interaction between Pt and the support, as indicated by lowering of the Pt oxide reduction potential in the case of the treated carbon support surface.

Manoharan et al. applied a different type of gas activation (CO_2 atmosphere at 1213 K for 1 h) to carbon particles (Vulcan XC72) and observed that the activity

and stability of Pt/C catalyst toward both CH_3OH oxidation and O_2 reduction was greatly enhanced. It was speculated that the origin of catalyst stability was the removal by the activation process of the weak surface sites that would be ineffective anchors of Pt over longer periods of time [50].

Inspired by H_2-O_2 fuel cell design, a major advancement in direct liquid fuel cell technologies has been the introduction of the proton exchange membrane (PEM or polymer electrolyte membrane, such as Nafion®) acting as ionic conductor in both the bulk and catalyst layers. The thin PEM (about 50 to 200 μm thickness, depending on type) opened up the possibility of a compact design while eliminating the need for bulk liquid electrolyte (e.g., 1–3 M H_2SO_4), facilitating the potential for commercialization and heralding what could be called the "modern" era of direct fuel cells.

Ledjeff et al. in 1990 were the first to present methanol polarization data using catalyst coated membrane (CCM) (i.e., unsupported Pt, PtRu, and PtRuSn on Nafion® 117) [51]. Employing a load of 5 mg cm^{-2}, the highest current density was obtained with PtRuSn (Figure 4.1). Unfortunately, the catalyst composition was not detailed.
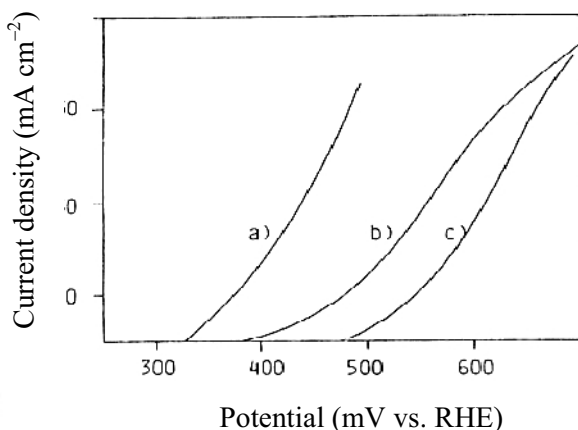
Figure 4.1. The first published methanol oxidation voltammograms using catalyst coated membranes (Nafion® 117) reported by Ledjeff et al. in 1990 [51]; 298K. 1 M aqueous methanol. a) PtRuSn, b) PtRu, c) Pt. Load of 5 mg cm^{-2}. (Reprinted with permission from Ledjeff K, Ahn J, Zylka D, Heinzel A. Ion exchange membranes as electrolyte for electrochemical energy conversion. Ber Bunsenges Phys Chem 1990;94:1005–8. ©1990 German Chemical Society.)

Work at the Jet Propulsion Laboratory (California Institute of Technology) and University of South California, Los Angeles, demonstrated for the first time the power output capability of a DMFC equipped with PEM [52]. From this work, Figure 4.2(a) shows the improved polarization performance of the PtRu/C anode with Nafion® 117 electrolyte compared to 0.5 M H_2SO_4, whilst Figure 4.2(b) exemplifies the fuel cell performance with the catalyst coated membrane.

a)

b)
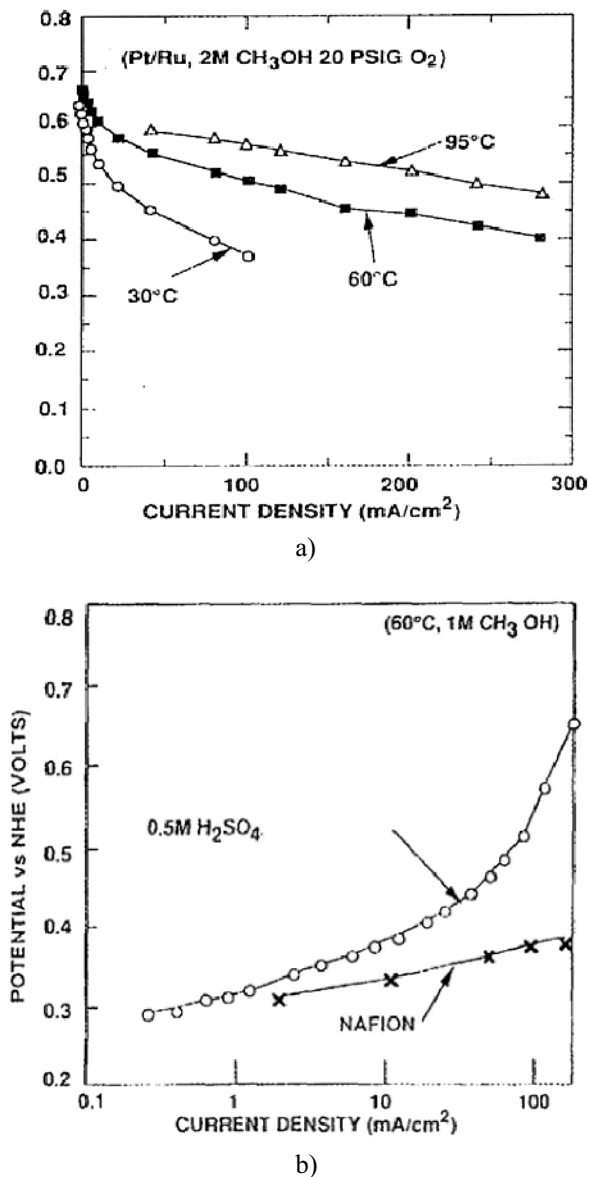
Figure 4.2. DMFC polarization behavior using aqueous methanol and solid polymer electrolyte (SPE: Nafion® 117) [52]. a) Anode half-cell polarization comparison between SPE and 0.5 M H_2SO_4, PtRu/C 0.5 mg cm^{-2}, b) fuel cell polarization curve using 2 M CH_3OH in water: effect of temperature. PtRu/C coated Nafion® 117 membrane. Note: the anode and cathode catalyst loads in the case of fuel cell experiments were not specified in [52]. (Reproduced from Journal of Power Sources, 47(3), Surampudi S, Narayanan SR, Vamos E, Frank H, Halpert G, LaConti A, Kosek J, Surya Prakash GK, and Olah GA, Advances in direct oxidation methanol fuel cells, 377–85, 1994, with permission from Elsevier.)

Furthermore, Olah and co-workers introduced the term "methanol economy", proposing methanol as the key chemical raw material and energy carrier of the future, with production shifting increasingly toward alternative sources such as biomass and atmospheric CO_2 instead of syn-gas derived from methane and/or coal [53]. Furthermore, methanol is the raw material for formic acid synthesis by the carbonylation route, leading to methyl formate ($HCOOCH_3$), which is hydrolyzed while formic acid is separated by a combination of extraction and distillation steps [54]:

$$CH_3OH + CO \xrightarrow[\substack{353K;4.5MPa)}]{\substack{CH_3ONa(2.5\%w;}} HCOOCH_3 \xrightarrow{+H_2O} HCOOH + CH_3OH. \quad (4.1)$$

In recent years ethanol is receiving a great deal of attention as well, due to its production from agricultural resources and, potentially, from biomass (cellulosic ethanol). Therefore, all three fuels could be major players in the alternative energy sector.

4.1.2 Objectives

The previous section highlighted the efforts in the area of catalysis carried out up to 1990. The aim was to show how different research ideas in this field originated and evolved in order to better understand the more recent developments and chart some possible future trends. Since 1990 there has been an explosion of research and development activity for all three types of fuel cells, amidst concerns regarding the use of fossil fuels from the perspectives of both climate change and non-renewable resource depletion.

The present review attempts to bridge the often-encountered gap between fundamental electrocatalysis/surface science studies and fuel cell development. Obvious evidence for the existence of this gap is the limited commercial success thus far of direct fuel cells compared to other power sources such as nickel-metal hydride or lithium batteries. The focus will be on the synergies between surface electrochemistry, kinetics, and electrode engineering aimed at improving the anode catalyst mass specific activity and fuel utilization. The total (anode plus cathode) Pt load target of ≤ 0.2 g kW^{-1} at cell voltages ≥ 0.65 V, as suggested by Gasteiger et al. for the economic viability of the H_2-O_2 fuel cell in the automotive field [55], is extremely difficult to achieve in the case of direct liquid fuel cells, with state of the art technology today at about 10–80 g kW^{-1} (at 333 K, depending on fuel type and operating conditions). However, the relative cost of building the hydrogen delivery and fuelling infrastructure compared to a liquid fuelling network must be also factored in. These topics are beyond the objective of the present review. Nevertheless, breakthroughs in both electrocatalysis and electrochemical engineering are required to advance the direct liquid fuel cell technologies. The most likely short- to midterm application of the three direct fuel cells under consideration here is in the area of micro- and portable electronics [56].

4.2 Reaction Pathways, Catalyst Selection, and Performance: Example Analysis

Understanding from a fundamental research point of view which catalysts are effective and what is the link between the catalyst physico-chemical properties, preferred reaction pathways, and overall activity in operating fuel cells is of outmost significance and could eventually guide the rational design of novel non-precious metal catalysts.

4.2.1 Methanol Electrooxidation

4.2.1.1 Pt and Pt-M Binary Catalysts with M other than Ru: M = Mo, Os, Sn, Ni, and Macrocyle Complexes
The electrooxidation of CH_3OH (Equation 4.2) on Pt is best described by a multi-pathway mechanism, which originated in the work of Breiter as parallel (or dual) pathways [12, 57, 58]. Figure 4.3 depicts the multi-pathway scheme. Accordingly, one route leads to CO_{ad} and ultimately to CO_2 at high potentials, while the other one passes through adsorbed intermediates, which are more reactive than CO_{ad} and can generate soluble products (HCOOH, HCHO) as well as $CO_{2(g)}$.

$$CH_3OH + H_2O \Leftrightarrow CO_2 + 6H^+ + 6e^-; E^0_{298} = 0.04 \text{ V vs. SHE.} \qquad (4.2)$$
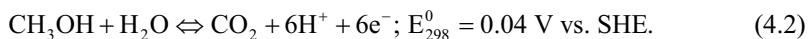
The intermediates and reaction products depend synergistically on a number of factors such as electrode potential, catalyst crystallographic features, elemental surface composition, methanol concentration, temperature, supporting electrolyte (e.g., $HClO_4$ vs. H_2SO_4), and reaction time.

Partial experimental verification of the reaction scheme shown by Figure 4.3 has been obtained on both single crystal and polycrystalline Pt electrodes. On Pt(111) at 0.6 V_{RHE} and 0.1 M CH_3OH – 0.1 M $HClO_4$, Stuve et al. showed by both experiments and mathematical modeling that the rate of CO_2 production from CO_{ad} was lower at all times compared to its formation by a parallel route based on a reactive intermediate with a stoichiometry of H:C:O = 1:1:1 (i.e., either HCO or COH) [59]. It must be noted that a similar intermediate was proposed early on by Bagotzky and Vasi'lev [3]. Hence, these studies confirmed the existence of a parallel non-CO route.

Iwasita and coworkers measured the products of anodic oxidation on Pt(111) at 0.6 V vs. RHE after 15 min electrolysis at 293 K using both 1 M CH_3OH – 0.1 M $HClO_4$ and 1 M CH_3OH – 0.5 M H_2SO_4 [60]. The approximate molar ratios of the products CO_2:HCHO:HCOOH were 9:6:1 in $HClO_4$ and 0.4:6:1 in H_2SO_4, respectively. Two main conclusions can be drawn: (i) high amounts of formaldehyde were detected, and (ii) the presence of $SO_4^{2-}{}_{ad}$ inhibited the pathways leading to CO_2 formation and overall lowered the methanol oxidation faradaic efficiency.

The adsorbed formate intermediate ($HCOO_{ad}$) has been detected on polycrystalline Pt in 0.1 M $HClO_4$ only at potentials higher than 0.5 V vs. RHE [61]. Therefore, it is likely that oxide formation on the Pt surface plays a role in the

generation of this intermediate. Furthermore, both linear and bridge bonded CO_{ad} ((Pt—CO and $(Pt)_2CO$, respectively) were clearly identified over a wide potential range starting from 0.05 V and up to 1 V vs. RHE [61, 62]. The linearly bonded CO_{ad} was in a much higher proportion, especially at potentials between 0.05 and 0.7 V. Only at potentials exceeding 1 V could the surface be considered clean of CO_{ad}, whilst the $HCOO_{ad}$ surface coverage peaked at 1 V and vanished only at about 1.3 V [61].

Baltruschat et al. introduced mass transport related considerations in the analysis of product distribution. In a flow-through cell equipped with polycrystalline Pt electrode it was found that the average current efficiency for CO_2 evolution (calculated over a potential range between 0.45 and 1.50 V vs. RHE) decreased with an increase of CH_3OH concentration (e.g., from 46% at 10^{-3} M methanol to 30% at 0.1 M methanol concentration) [63]. Moreover, the CO_2 current efficiency also decreased slightly with the increase of methanol solution flow rate (e.g., in 0.1 M $CH_3OH - 0.5$ M H_2SO_4 from 30% at 1.1 µl s^{-1} to 28% at 5 µl s^{-1}). Thus, the local concentrations and residence times of the reactive (weakly adsorbed) intermediates such as $HCOOH_{ad} \Leftrightarrow HCOOH_{bullk}$ and $HCHO_{ad} \Leftrightarrow HCHO_{bulk}$ play a role in determining the overall product distribution. The longer these intermediates can stay close to the electrode surface the higher the current efficiency for CO_2 production, since in that case pathways going through non-CO_{ad} can also contribute to complete methanol oxidation. Additionally, the formation of methylformate ($HCOOCH_3$) has also been detected at 0.6 V in experiments with higher methanol concentrations, such as 0.1 M [63].
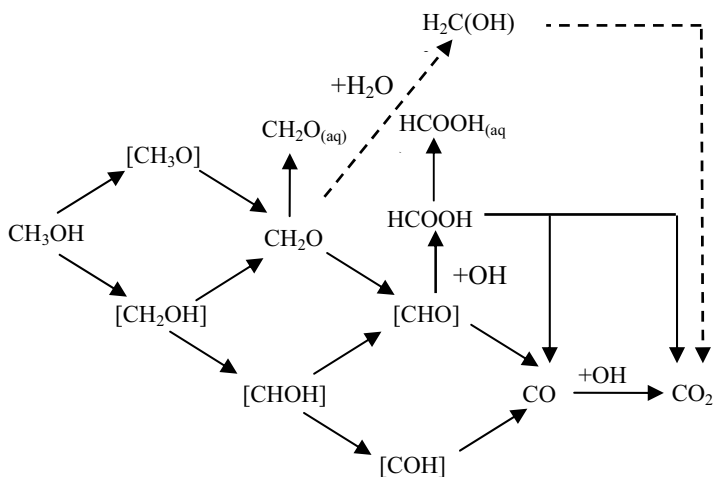
Figure 4.3. Multi-pathway scheme for methanol oxidation with the participation of OH_{ad}

In a related study but using supported Pt electrode (Pt 40 wt%/Vulcan XC72) Blatruschat et al. found that the average current efficiency for CO_2 was 90% in 0.1 M CH_3OH – 0.5 M H_2SO_4 [64]. Since the porous electrode thickness of 20–30 μm matched the Nernst diffusion layer thickness, the probability is high for the reactive dissolved intermediates to readsorb on the surface and to be subsequently oxidized, forming CO_2.

Analyzing Figure 4.3, a number of important questions emerge: i) what makes a good CH_3OH dissociative chemisorption/dehydrogenation catalyst, ii) what are the relative stabilities of the intermediates formed in the stepwise oxidative dehydrogenation, and iii) could elements other than Pt accomplish this important step in the overall scheme of methanol electrooxidation?
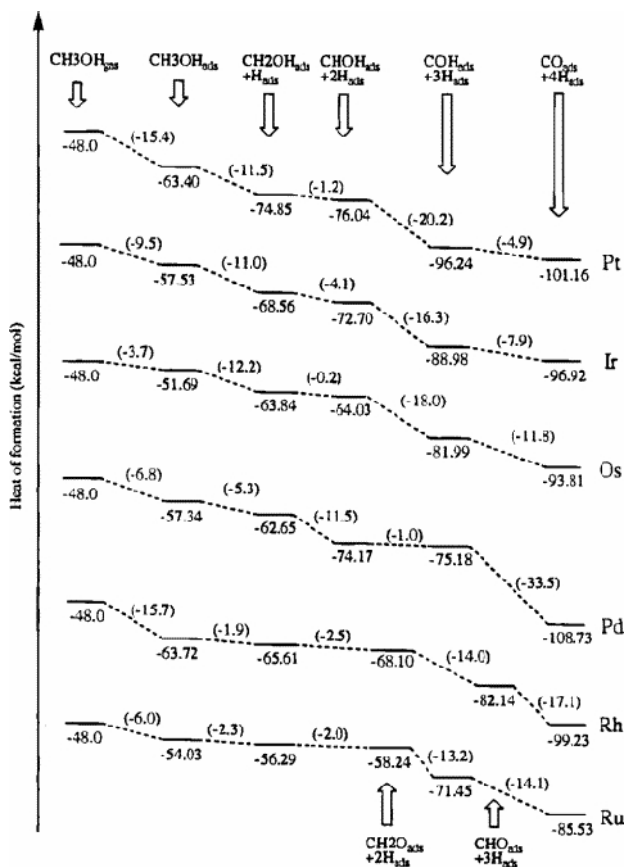
Figure 4.4. CH_3OH stepwise dehydrogenation pathway and corresponding heats of formation on Pt, Ir, Os, Pd, Rh, and Ru [65]. (Reproduced with permission from J Am Chem Soc 1999;121:10928–41. Copyright 1999 American Chemical Society.)

Kua and Goddard carried out a comprehensive theoretical study employing nonlocal density functional theory comparing 2nd- and 3rd-row group VIII transition metal elements for CH_3OH dehydrogenation ability based on binding energies and

heats of formation [65]. Figure 4.4 compares the CH_3OH dehydrogenation pathways for Pt, Ir, Os, Pd, Rh, and Ru, whilst Figure 4.5 shows the various isomers and binding sites on a Pt_8 cluster.
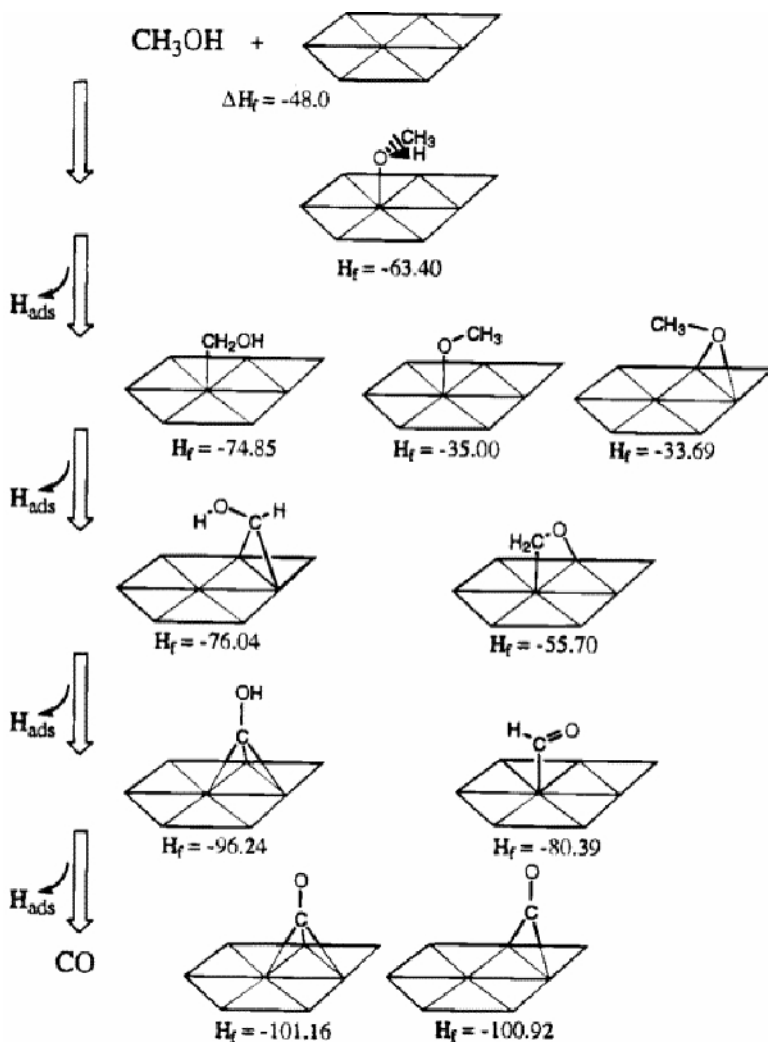
Figure 4.5. Possible surface binding options for CH_3OH dehydrogenation intermediates on Pt_8 cluster [65]. H_f – heat of formation (kcal mol^{-1}). (Reproduced with permission from J Am Chem Soc 1999;121:10928–41. Copyright 1999 American Chemical Society.)

On all the metals under consideration the CH_3OH dehydrogenation to CO_{ad} is exothermic, but on Pt this reaction is the most facile, specifically in the latter stages involving the removal of the third hydrogen atom from the carbon, i.e., $CHOH_{ad} \Rightarrow COH_{ad} + H_{ad}$ (Figure 4.4). On the other hand, the CH_3OH chemisorption/dehydrogenation is least favorable on Ru, especially for breaking

the first two C-H bonds, only about 2 kcal mol^{-1} being released with the formation of CH_2OH_{ad} and $CHOH_{ad}$, respectively, from CH_3OH_{ad}/Ru.

However, one has to take into account the effect of temperature when discussing the dissociative dehydrogenation of methanol, which is missing from the theoretical analysis of Kua and Goddard. There is evidence that at high temperatures (333 K or above) methanol dehydrogenation can take place on Ru sites as well [66].

Another interesting aspect of the diagram for Pt shown by Figure 4.4 is the relative closeness on the energy diagram of COH_{ad} and CO_{ad} (only –4.9 kcal mol^{-1} difference), hence, augmenting the possibility that COH_{ad} could participate as a reactive intermediate as discussed earlier (see Figure 4.3).

Figure 4.5 shows the adsorption modes of the dehydrogenation intermediates. There are a number of important points to be made: (i) Kua and Goddard proposed that CH_3OH_{ad} binds to the surface using the electron pairs of oxygen, (ii) starting with CH_2OH_{ad} the preferred binding is via the C atom, (iii) two CO_{ad} modes were envisaged, the three-site "cap" and the two-site "bridge" modes (Figure 4.5). However, the energy difference between the two is very small. This work does not explicitly mention the existence of a linearly bonded CO_{ad} [65].

Furthermore, the existence of other more reactive intermediates, namely adsorbed formate isomers (e.g., $COOH_{ad}$) was also put forward [65].

The stepwise dehydrogenation of CH_3OH on Pt and oxidation to CO_2 through the CO_{ad} route can be summarized based on the theoretical model of Kua and Goddard (see also Figures 4.3–4.5) as follows:

$$CH_3OH_{ad} + Pt \rightarrow Pt - CH_2OH + H^+ + e^- \tag{4.3}$$

$$Pt - CH_2OH + Pt \rightarrow Pt_2 - CHOH + H^+ + e^- \tag{4.4}$$

$$Pt_2 - CHOH + Pt \rightarrow Pt_3 - COH + H^+ + e^- \tag{4.5}$$

$$Pt_3 - COH \rightarrow Pt_{(3-y)} - CO + yPt + H^+ + e^- \tag{4.6}$$
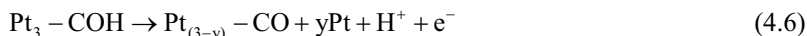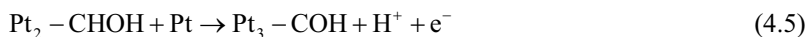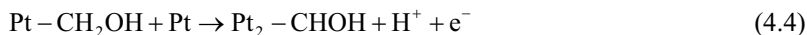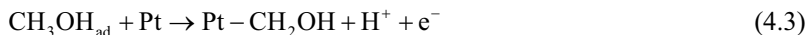
with $y = 0,...,2$ depending on the CO_{ad} binding: y = 0 (cap) [65], y = 1 (bridge) and y = 2 (linear).

As shown by Figure 4.3, in addition to CH_3OH dehydrogenation, the role of H_2O chemisorption and OH_{ad} formation are crucial for efficient methanol oxidation. Thus,

$$H_2O_{ad} + Pt \rightarrow Pt - OH + H^+ + e^- \tag{4.7}$$

$$Pt_{(3-y)} - CO + Pt - OH \rightarrow (4-y)Pt + CO_2 + H^+. \tag{4.8}$$
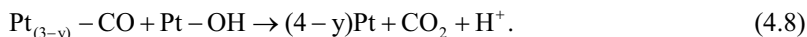
The complexity of the surface reaction network described is very well reflected by the experimentally measured potential oscillations around 0.64 V vs. SHE for the galvanostatic oxidation of methanol (Figure 4.6) [67]. The oscillations were attributed to the formation (at the potential maximum) and depletion (at the potential minimum) of OH_{ad}. The topic of OH_{ad} has received a great deal of attention in the literature. It has been very well known experimentally for a long time that the formation of OH_{ad} on Pt starts only at high potentials, i.e., $E > 0.55$ V vs. RHE [68] (depending on crystallographic features) whilst on surface defects the onset of OH_{ad} formation could be lower. Burke and co-workers argued that active surface metal atoms could undergo oxidation at lower potentials (e.g., 0.4 V vs. RHE) and those active surface atoms could generate hydroxy or oxy species by bonding to H_2O molecules [69]. These authors put forward methods to create active surface states on Pt and Au electrodes such as thermal (e.g., 1178 K for 20 s in Ar) or galvanostatic cathodic (e.g., 300 A m^{-2} for 21–39 h in 1 M H_2SO_4) pretreatments. While this work has not been fully validated yet, nevertheless it draws attention to the importance of high-energy surface states and advocates their role in electrocatalysis.
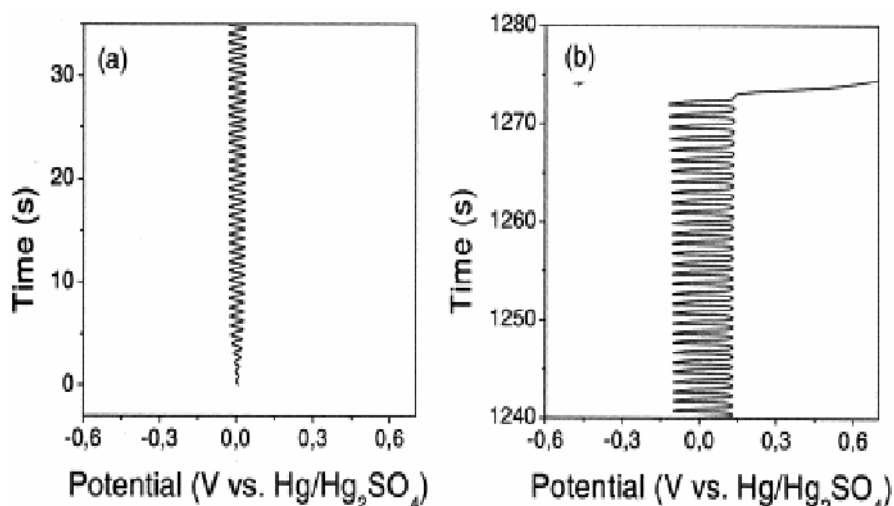
Figure 4.6. Pt electrode potential oscillations around 0.64 V vs. SHE (i.e., 0 V vs. Hg/Hg$_2$SO$_4$) in the presence of methanol measured under galvanostatic conditions. Electrolyte: 0.03 M CH$_3$OH – 0.1 M HClO$_4$ [67]. (Reproduced from Electrochimica Acta, 47(13–14), Lee J, Eickes C, Eiswirth M, Ertl G, Electrochemical oscillations in the methanol oxidation on Pt, 2297–301, 2002, with permission from Elsevier.)

To activate H_2O_{ad} (Equation 4.9) the alloying of Pt has been practiced, as mentioned in Section 4.1.

$$H_2O_{ad} + M \rightarrow M - OH + H^+ + e^- \qquad (4.9)$$

Anderson et al. calculated H_2O binding energies with respect to substitutional atoms in a Pt alloy cluster (Figure 4.7) [70]. Elements to the left of Pt in the periodic Table (i.e., Groups 3–9) bind H_2O more strongly than Pt, with the exception of Rh and Ir. Alloying elements to the right, Groups 11–16, bind H_2O more weakly than Pt with no exception (Figure 4.7). The strongest binding energy (about 2.5 eV) was obtained for Ru, followed by Cr, Mo and W.

Alloying Atom

a)

Position in Periodic Table

b)
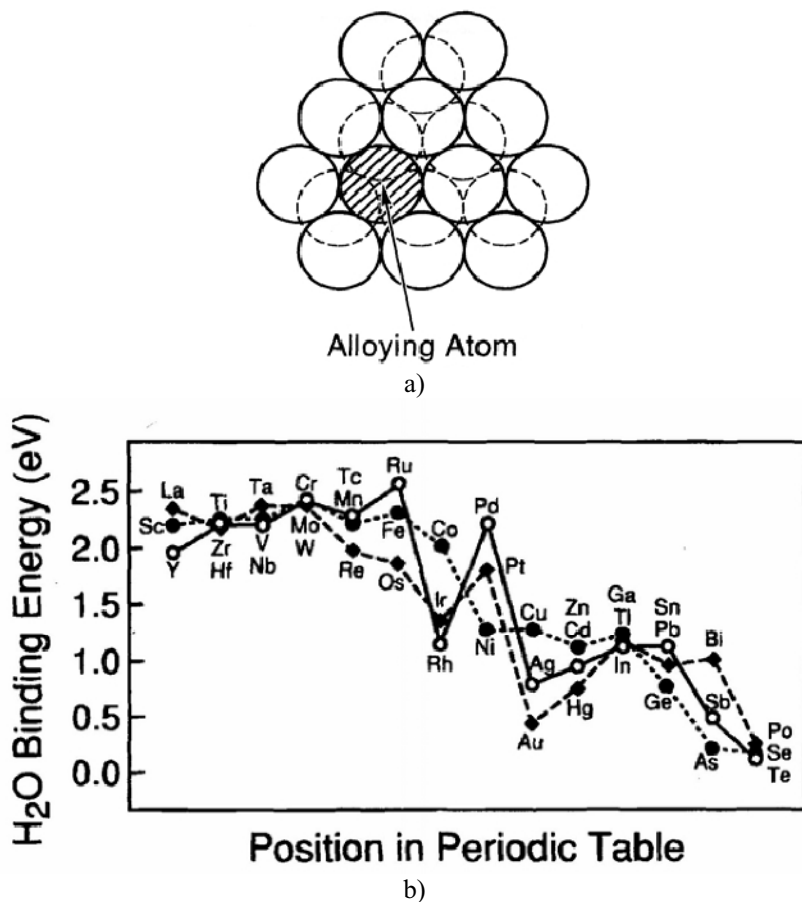
Figure 4.7. a) Cluster model of Pt-alloy used for calculation of the H_2O binding energy, b) calculated H_2O binding energies over substitutional alloying atoms as a function of their position in the periodic table [70]. (Reproduced by permission of ECS—The Electrochemical Society, from Anderson A, Grantscharova E, Seong S. Systematic theoretical study of alloys of platinum for enhanced methanol fuel cell performance.)

Following H_2O_{ad} the second step is the breaking of the OH bond and release of H (Figure 4.8(a)). First principle theoretical calculations predicted that alloying elements such as Ti, Cr, Fe, Mo, Pd and Zr have lower activation energies for bond breaking in H_2O_{ad} compared to Ru (Figure 4.8(b)) [70]. Thus, theoretically they could be suitable as Pt co-catalysts toward CH_3OH electrooxidation in a similar

manner to Ru. Furthermore, Kua and Goddard argued that Os combines both capabilities required of the bifunctional mechanism, namely methanol dehydrogenation and water activation [65].

(a)

(b)
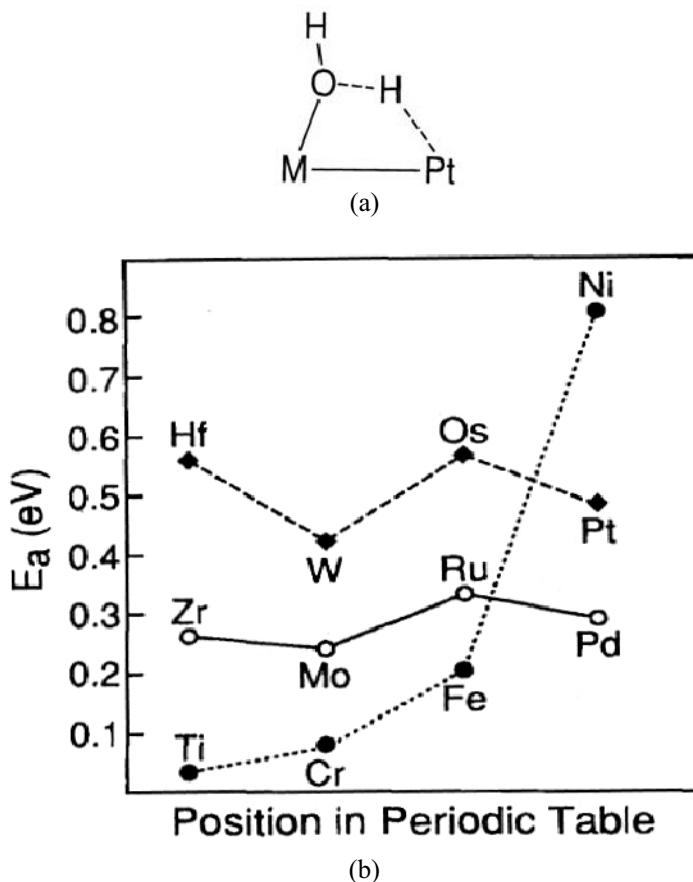
Figure 4.8. (a) A model of H_2O_{ad} on a Pt-M alloy, (b) activation energies for OH bond dissociation in H_2O_{ad} [70]. (Reproduced by permission of ECS—The Electrochemical Society, from Anderson A, Grantscharova E, Seong S. Systematic theoretical study of alloys of platinum for enhanced methanol fuel cell performance.)

These theoretical studies, rooted in the bifunctional model, invite the question how do binary catalyst formulations Pt-M (with M other than Ru, such as Os, Mo, Sn, Ni, W) compare experimentally with Pt and PtRu (the benchmark bimetallic catalyst since the mid 1960s)? The case of Os is especially intriguing based on the promising theoretical calculations. However, Os alone and Os-V, Os-Mo, and Os-Sn supported on Vulcan XC72 were electrocatalytically inactive toward CH_3OH oxidation as shown by cyclic voltammetry [71]. PtOs bimetallic (atomic ratio 3:1) catalysts, on the other hand, prepared by a carbonyl route and supported on Vulcan XC72 gave higher current densities for methanol oxidation than both E-TEK PtRu

(1:1) and Pt in cyclic voltammetry and chronoamperometry (up to 1 h reaction time). It was proposed that metallic Os is the active form in electrocatalysis, while OsO_2 formation must be avoided since it inhibits the adsorption of methanol, thereby decreasing the oxidation rate [72]. Following on the same idea, it was suggested that for efficient catalysis the highest surface Os content in a bimetallic PtOs catalyst is 20 at% since at higher Os levels coverage of Pt by an Os oxide occurs, which is detrimental for performance [73].

Mukerjee and Urian compared the activity of PtMo/C (3:1 atomic ratio) with PtRu/C (1:1 atomic ratio) and Pt/C under conditions relevant for DMFCs. During anodic polarization in 1 M CH_3OH at 363 K, using Nafion 117 and 4 mg cm^{-2} catalyst load, the electrode potential at 100 mA cm^{-2} was about 170 mV more positive for PtMo compared to PtRu. Moreover, PtMo performed slightly worse than pure Pt as well [74]. The effect of Mo as an alloying element with respect to CH_3OH oxidation was in sharp contrast with its beneficial role for enhancing the CO tolerance of Pt from a reformate feed. This indicates yet again the major difference between CO and CH_3OH electrooxidation catalysis.

Using XANES (X-ray absorption near-edge structure) the oxidation of Mo was observed at E ≥ 0 V vs. RHE generating Mo(V), most likely a Mo oxo-hydroxide. The latter species was considered responsible for CO oxidation from reformate feed; however, it was inactive in the case of methanol oxidation [74]. Consequently, the real experimental situation for PtMo is more complex than what the bifunctional mechanism would suggest.

A weak electronic interaction between Pt and Mo was detected in the XANES spectra of PtMo/C. This is indicated by an increase of the 5d orbital vacancy of Pt from 0.312 per Pt atom (for pure Pt) to about 0.337 with 70 at% of Mo in PtMo alloy (Figure 4.9) [75]. The different behavior of Ru is noteworthy in this respect. Up to 30 at% Ru the d-band vacancy of Pt was fairly constant, followed by an exponential rise for higher Ru content (Figure 4.9), suggesting strong electronic interaction.

In addition to Mo co-catalyst, PtSn formulations have received considerable attention. The co-catalytic activity of Sn for the enhancement of CO oxidation has been well documented and the optimum catalyst composition was found to be Pt:Sn = 3:1 (atomic ratio) [76–78]. Ross and co-workers proposed the following mechanism for Sn promotion in the framework of Langmuir-Hinshelwood kinetics, also implicating surface SnO_2 in H_2O dissociation [76]:

$$Pt + CO \rightarrow Pt–CO_{ad} \tag{4.10}$$

$$Sn + H_2O \rightarrow Sn–OH_{ad} + H^+ + e- \tag{4.11}$$

$$SnO_2 + H_2O \rightarrow SnO_2–OH_{ad} + H^+ + e- \tag{4.12}$$

$$Pt–CO_{ad} + Sn–OH_{ad} \rightarrow CO_2 + H^+ + e- \tag{4.13}$$

$$Pt–CO_{ad} + SnO_2–OH_{ad} \rightarrow CO_2 + H^+ + e- \tag{4.14}$$
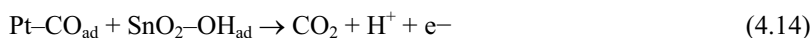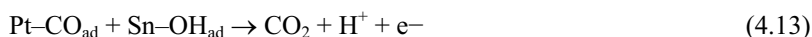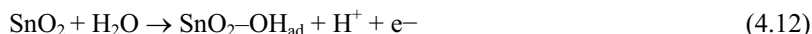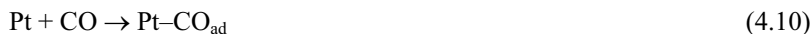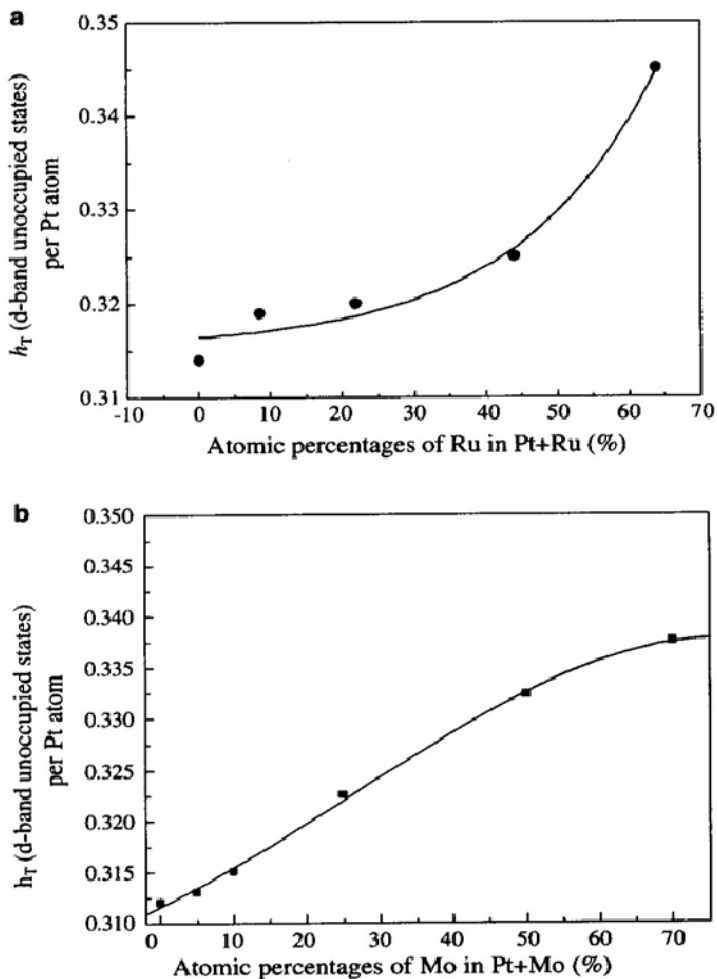
Figure 4.9. Effect of Ru and Mo on the 5d electron energy band vacancy of Pt. a) Ru, b) Mo [75]. (Reprinted from Chemical Physics Letters, 412(4–6), Mylswamy S, Wang CY, Liu RS, Lee J-F, Tang M-J, Lee J-J, Weng BJ, Anode catalysts for enhanced methanol oxidation: an *in situ* XANES study of PtRu/C and PtMo/C catalysts, 444–8, 2005, with permission from Elsevier.)

Regarding the co-catalytic role of Sn for methanol oxidation, on the other hand, the experimental evidence is less conclusive compared to the case of CO oxidation. Colmati et al. prepared PtSn/C catalyst formulations (9:1 and 3:1 atomic ratio) using formic acid reduction and compared the activity with commercial (E-TEK Inc.) Pt/C and PtSn (3:1)/C, including DMFC fuel cell experiments [79]. Unfortunately, no comparison with PtRu was presented. Employing 0.4 mg cm^{-2} anode catalyst load and 3 atm O$_2$ pressure, the maximum fuel cell power output at 343 K was obtained with PtSn (3:1) produced by the formic acid method, 400 mW

cm^{-2} vs. 360 mW cm^{-2} for pure Pt, respectively [79]. Thus, there has been a slight improvement due to Sn. However, further studies are required to establish the longer-term stability of the PtSn anode during DMFC operation. Leaching of Sn could be detrimental for the ionic conductance of the PEM.

It is interesting to note the difference in performance between commercial and in-house (i.e., formic acid produced) 3:1 PtSn formulations, the latter exhibiting a superior performance, whilst the commercial Sn-containing catalyst was worse than pure Pt/C. The authors stressed the importance of the degree of alloying and the need to balance the positive and negative aspects of Sn presence related to CO_{ad} and CH_3OH adsorption/dehydrogenation, respectively [79].

In a preliminary chronoamperometry experiment Neto et al. observed higher Pt mass specific activities (A g^{-1}_{Pt}) for CH_3OH oxidation at 0.5 V vs. RHE on PtSn(1:1)/C compared to either PtRu or PtRuSn formulations. All catalysts were produced by the ethylene glycol reduction method [80].

In contrast to the above-discussed results, Gotz and Wendt found that Sn brought about a decrease of catalytic activity compared even to the pure Pt. Utilizing 0.4 mg cm^{-2} anode catalyst load and operating the DMFC at 378 K the order of activity was PtRu > PtW > PtMo > Pt > PtSn [81]. Gotz and Wendt synthesized the catalysts by the colloidal Bonneman method [82–84] that leads to a very high degree of alloying. Therefore, it is possible that the catalyst synthesis method had an impact on performance by affecting the microstructural features. This hypothesis is further supported by the study of Liu et al. reporting increased peak power outputs compared to Pt for PtSn/C prepared by a microwave assisted polyol method and a Pt:Sn (atomic ratio) between 1:1 and 4:1 (Figure 4.10) [85]. XPS analysis showed the existence of a high proportion of SnO_2 on the surface. A direct comparison with PtRu/C is missing from this study as well.

It must be noted however, with 4 mg cm^{-2} loading of PtRu (1:1)/C the peak power density of a DMFC at 333 K is typically in the range of 87–100 mW cm^{-2} [86], which is substantially better compared to PtSn/C at 353 K (Figure 4.10), notwithstanding some differences in other operating conditions. Hence, a thorough comparison of PtSn/C and PtRu/C is called for.

Regarding other binary catalyst formulations, Gotz and Wendt presented very interesting results with PtNi and PtCo, PtRh, PtMn macro-cycles complexes, all supported on Vulcan XC72 [87]. PtNi prepared by the colloidal Bonneman method was compared with Pt/C having macrocycle complexes such as Co-phthalocyanine (CoPC), Ni-phthalocyanine-tetrasulfonic acid (NiPCTSA), Rh-tetrasulfonated tetraphenylporphyrin (RhTPP-S), and Mn-phthalocyanine-chloride (MnPC-Cl) adsorbed in a ¼ molar ratio of macrocycle to Pt. The macrocycle complexes showed catalytic activity only after temperature activation, i.e., pyrolysis for 1 h at 973 K in N_2 atmosphere. This is expected based on the similar and well-documented behavior of macrocycles toward oxygen electroreduction. Figure 4.11 shows the polarization curves at 368 K for a DMFC equipped with 0.4 mg_{Pt} cm^{-2} loads of the various binary catalysts. The best result was obtained with Pt-NiPCTSA and PtNi, whilst the Rh and Mn composite catalysts performed worse than Pt/C. The activity of PtNiPCTSA was comparable to the commercial PtRu (from E-TEK Inc. [87]). A remarkable finding of this study was the long-term

performance, over 400 h without notable degradation ($\pm$ 5%). Therefore, this line of research warrants further investigation.

a

b
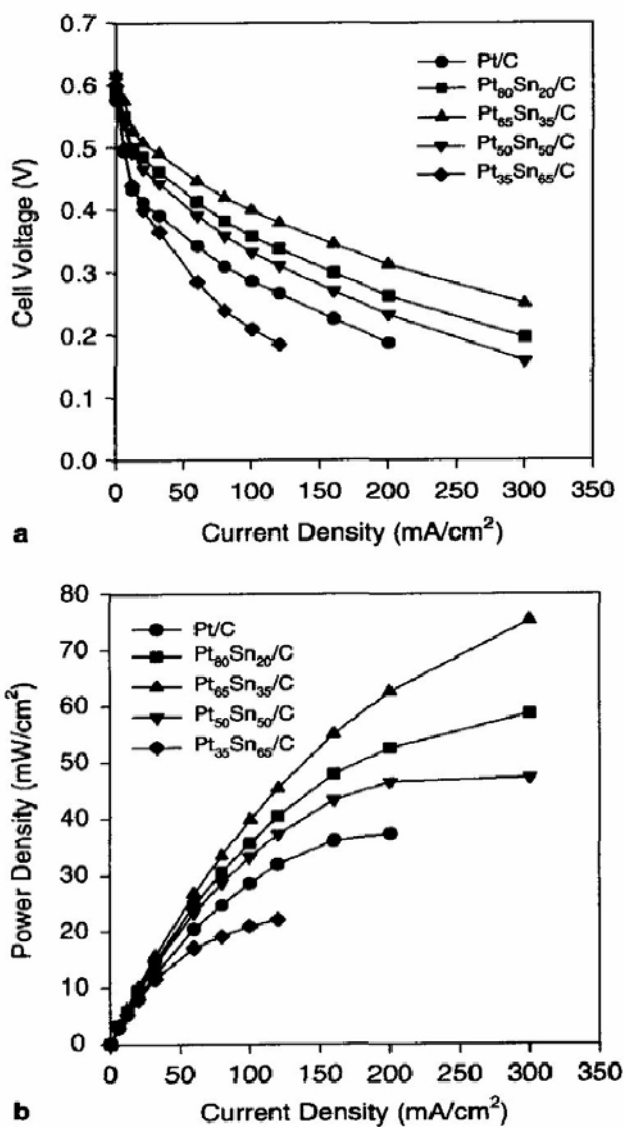
Figure 4.10. DMFC polarization curves using PtSn anode catalysts produced by a microwave-assisted polyol method. Anode catalyst load: 4 mg cm^{-2}, 2 M CH$_3$OH with 2 ml min^{-1}, cathode: Pt/C 3 mg cm^{-2}, O$_2$ pressure not specified in the original source, O$_2$ flow rate 500 cm^3 min^{-1}; 353 K [85]. (Reproduced from Electrochemistry Communications, 8(1), Liu Z, Guo B, Hong L, Lim TH, Microwave heated polyol synthesis of carbon-supported PtSn nanoparticles for methanol electrooxidation, 83–90, 2006, with permission from Elsevier.)
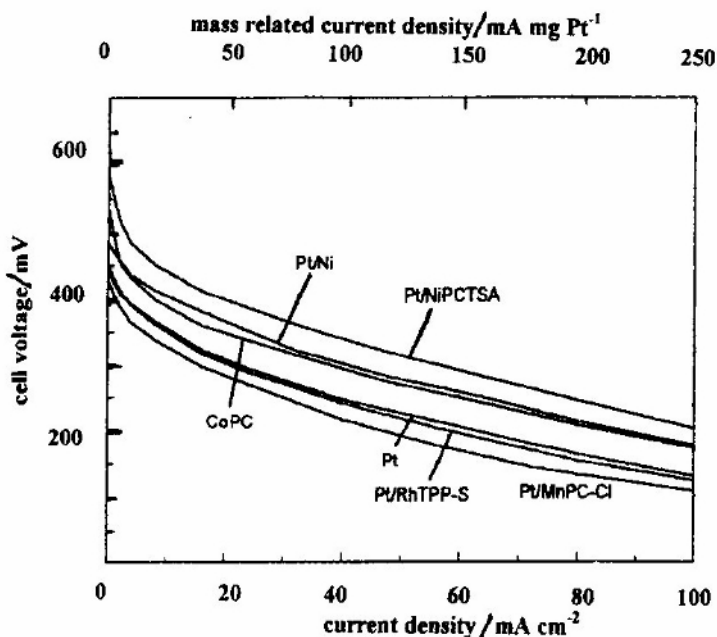
Figure 4.11. The effect of various binary anode catalyst formulations on DMFC polarization: PtNi and Pt/macrocycles (Ni, Co, Mn, and Rh). Anode: Pt load 0.4 mg cm^{-2}, 1 M CH$_3$OH, 1 ml min^{-1}; cathode operated with dry O$_2$ at atmospheric pressure; 368 K [87]. (With kind permission from Springer Science+Business Media: Journal of Applied Electrochemistry, Composite electrocatalysts for anodic methanol and methanol-reformate oxidation, 31, 2001, 811–17, Goetz M, Wendt H, figure 4.)

Bett et al. investigated metal phthalocyanines (Fe, Co, Ni, and Sn) as Pt co-catalysts for methanol oxidation [88]. These authors reported an approximately 100 mV lower anode potential compared to Pt/C for Pt/Sn-phthalocyanine at 333 K; however, the anode potential was 30 mV more positive compared to PtRu/C. In this study the macrocycles were not heat activated.

Okada et al. investigated the binary system Pt-Co(MPQH) (where MPQH: mono-8-quinolyl-o-phenylenediamine) [89]. The catalysts were heat treated in Ar atmosphere for 2 h. The optimum heat treatment temperature was 873 K. The mass specific catalytic activity of the binary catalysts supported on carbon was 5 A g$_{Pt}$$^{-1}$ compared to 40–60 A g$_{Pt}$$^{-1}$ for PtRu. It was also shown that the nature and structure of the ligand coordinating the Co had an effect on performance. Co(NH$_3$)$_6$Cl$_3$ did not exert any catalytic effect when combined with Pt, while porphyrin based complexes of Co heat treated at 1073 K yielded approximately 20 to 30 mV lower overpotentials compared to catalyst formulations using Co(MPQH).

The mechanism of the macrocycle co-catalytic effect was related to H$_2$O dissociation activation [88]. The interaction between H$_2$O and Co(III)-octaethylporphyrin (Co(OEP)) adsorbed on a graphite electrode with respect to CO oxidation to CO$_2$ was discussed by Shi and Anson [90]. They found no evidence of

CO oxidation in non-aqueous solvents such as CH_2Cl_2, whilst in aqueous electrolytes (e.g., 1 M $HClO_4$) a large CO oxidation wave was observed (Figure 4.12). The proposed mechanism (Equations 4.15–4.18) invokes both CO chemisorption (coordination) on the Co(III) macrocycle and the activation of H_2O dissociation [90]. The rate determining step is the conversion of coordinated CO by nucleophilic H_2O attack (Equation 4.17). Consequently, some Co macrocycle complexes might offer the possibility of non-precious metal bifunctional catalysts. Further studies are required in this area combining fundamental investigations with fuel cell experiments.

$$Co^{II}(OEP)_{ad} - e^- \rightarrow Co^{III}(OEP)_{ad}^+ \tag{4.15}$$

$$Co^{III}(OEP)_{ad}^+ + CO \Leftrightarrow (OC)Co^{III}(OEP)_{ad}^+ \tag{4.16}$$

$$(OC)Co^{III}(OEP)_{ad}^+ + H_2O \Leftrightarrow ((HO)(O)C)Co^{III}(OEP)_{ad} + H^+ \tag{4.17}$$

$$((HO)(O)C)Co^{III}(OEP)_{ad} - 2\ e^- \rightarrow CO_2 + Co^{III}(OEP)_{ad}^+ + H^+ \tag{4.18}$$
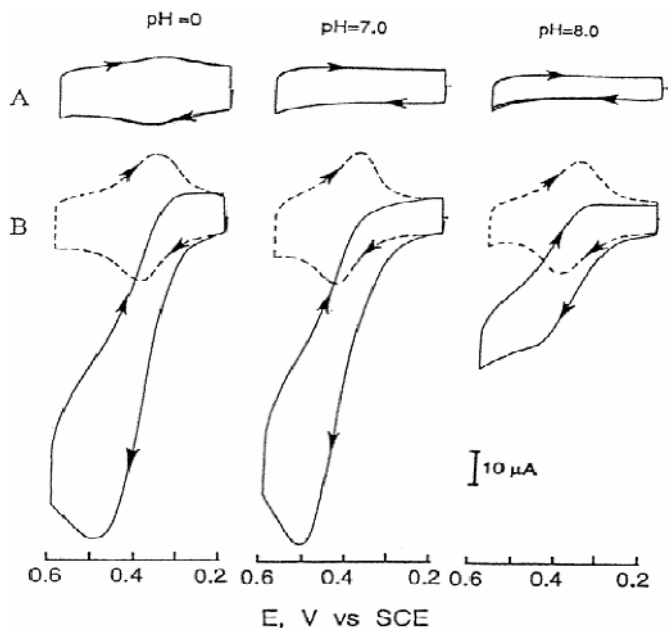
Figure 4.12. Catalysis of CO electrooxidation in aqueous electrolytes by Co(OEP) adsorbed on graphite electrode. A: bare graphite (with and without CO: two curves virtually superimposed). B: Co(II)(OEP) adsorbed on graphite (~8×10^{-10} mole cm^{-2}). Dashed curve: Ar purge, solid curve: CO saturated solution; electrolyte: 1 M $HClO_4$ or 1 M $NaClO_4$ + 10 mM Britton-Robinson buffer; scan rate 50 mV s^{-1}; 295 K [90]. (Reproduced with permission from Inorg Chem 2001;40:5829–33. Copyright 2001 American Chemical Society.)

4.2.1.2 The Case of PtRu: Catalyst Preparation and the Optimum Pt:Ru Atomic Ratio

The previous sections indicated that at present PtRu remains the most effective binary catalyst for methanol oxidation. A significant amount of work has been carried out and various theoretical and experimental techniques have been brought to bear in order to reveal the details of the Pt-Ru catalytic/co-catalytic effect. For DMFC performance enhancement, which is the prevalent point of view adopted in this review, the situation is further complicated since in addition to intrinsic kinetic effects, the anode performance depends in a synergistic and often poorly understood manner on the PtRu catalyst preparation method, PtRu atomic ratio, surface morphology (e.g., roughness), presence and type of support, operating anode potential range, methanol concentration, and temperature.

The effect of Ru on the long-term anode performance was very well illustrated by, among others, Wieckwoski and co-workers employing potentiostatic oxidation at 0.3 V vs. RHE of chemisorbed CH_3OH as a function of Ru packing density (Figure 4.13) [91].
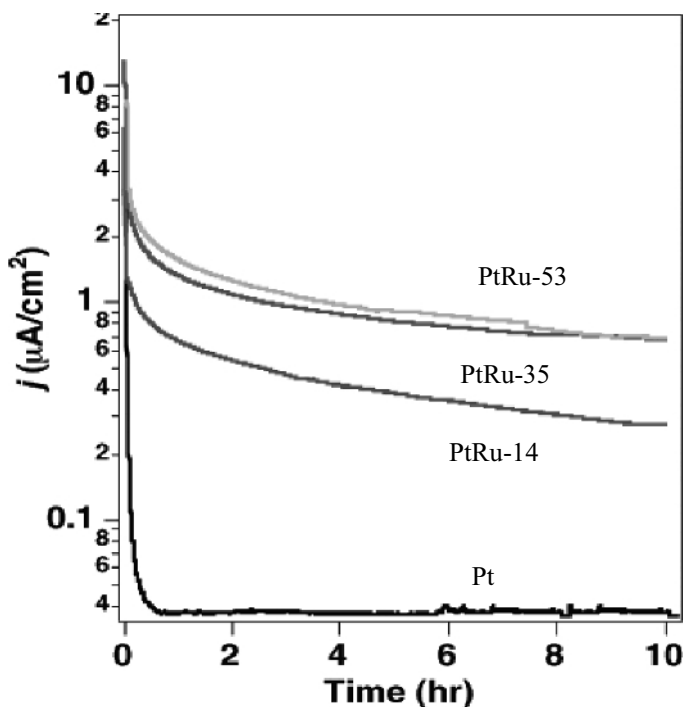
Figure 4.13. Effect of Ru packing density on the potentiostatic oxidation of chemisorbed CH_3OH at 0.3 V vs. RHE in 0.5 M H_2SO_4. Legend: Packing density (ratio between nr. of surface Ru atoms per Pt surface atoms) in %: 14, 35 and 53 [91]. (Reproduced with permission from J Am Chem Soc 2002;124:468–73. Copyright 2002 American Chemical Society.)

After 10 h of operation the presence of Ru islands on Pt increased the oxidation current density approximately 20-fold in the case of PtRu-53, followed closely by PtRu-35. Combining cyclic voltammetry with surface NMR two CO_{ad} populations were identified: CO_{ad} close to (or possibly on) Ru sites undergoing fast thermally activated diffusion and CO_{ad} on Pt characterized by slow diffusion [91]. These two types of CO_{ad} are responsible for two separate peaks in CO stripping voltammetry, at low (~0.3 V) and high (above 0.4 V) potentials, respectively. Ru decreases the activation barrier for CO_{ad} surface diffusion by reducing electron back-donation.

Another consequence of the changes in Pt electronic structure caused by the presence of Ru (i.e., creation of electron deficiency on Pt by decreasing the Fermi level density of states and reducing the Pt-Pt distance) is the increased rate of dissociative methanol adsorption [92]. Thus, in addition to H_2O activation (according to the bifunctional mechanism [93]) Ru plays a significant role with respect also to methanol chemisorption and surface diffusion of CO_{ad}.

Furthermore, an interesting aspect of the Ru effect relates to the effect of temperature and the optimum Pt:Ru ratio. Gasteiger et al. showed that dissociative methanol adsorption can occur on Ru sites as well, but it is a temperature-activated process [94]. Therefore, at low temperatures (e.g., 298 K) a higher Pt:Ru atomic ratio (above 1:1) is required to facilitate the dissociative adsorption and dehydrogenation of methanol preferentially on Pt, whilst at high temperatures (e.g., 333 K and above) a surface richer in Ru is beneficial (e.g., 1:1 at. ratio) since Ru becomes active for chemisorption and the rate determining step switches to the reaction between CO_{ad} and OH_{ad} [94].

Employing PtRu/C catalysts, Dickinson et al. confirmed at 298 K the higher activity of the catalyst formulation richer in Pt (i.e., Pt:Ru at. ratio 3:2 vs. 1:1) over the entire range of anode potential from about 0.3 to 0.8 V vs. RHE [95]. However, at higher temperatures (318 K and 338 K) there was an interaction effect between thermal activation and anode potential. At both 318 and 338 K there was virtually no significant difference between the two compositions at potentials below 0.5 V vs. RHE. Only at E > 0.5 V did the formulation richer in Ru (1:1 atomic ratio) better performance at higher temperatures.

The role of temperature and anode potential affecting the optimum Pt:Ru ratio has also been explored by Lamy and co-workers [96]. They investigated a wide catalyst composition range, including Pt:Ru atomic ratios of 1:1; 2.33:1, and 4:1, respectively. The Arrhenius plot shown in Figure 4.14 obtained at 0.5 V vs. RHE indicates that between 293 K and 318 K the Pt:Ru atomic ratio of 2.33:1 (and 4:1) gave the highest mass specific activity for methanol oxidation. However, for the temperature range 318 K and 383 K a catalyst richer in Ru was recommended, with a Pt:Ru atomic ratio of 1:1 [96]. A similar conclusion was reached also by Bock et al. [97].
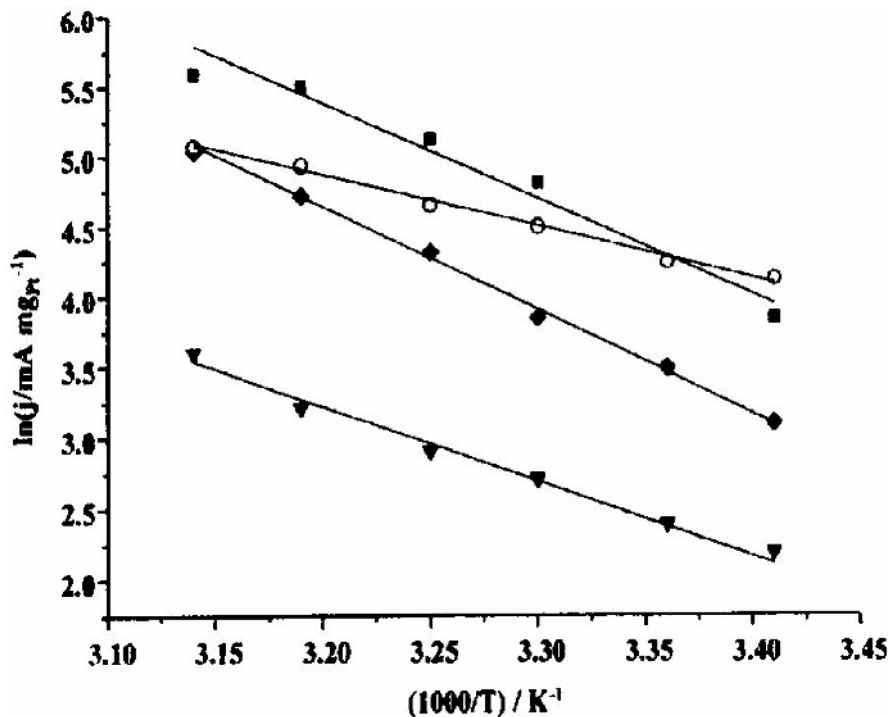
Figure 4.14. Arrhenius plot for methanol electrooxidation at 0.5 V vs. RHE using colloidal PtRu catalyst supported on Vulcan XC72. Electrolyte: 1 M CH_3OH – 0.5 M H_2SO_4. Scan rate: 1 mV s^{-1}. Pt:Ru atomic ratios: ■ 2.33:1, ♦1:1, ○ 4:1 and ▼ Pt/C [96]. (With kind permission from Springer Science+Business Media: Journal of Applied Electrochemistry, Electrooxidation of methanol at platinum-ruthenium catalysts prepared from colloidal precursors: atomic composition and temperature effects, 33, 2003, 419–49, Dubau L, Coutanceau C, Garnier E, Leger J-M, Lamy C, figure 11.)

The catalyst preparation has a significant effect on performance. The best method to prepare the anode catalyst is still very much a matter of debate in the literature. A number of studies by Wieckowski and co-workers suggest that for the same elemental composition, Pt nanoparticles decorated with Ru nanoparticles or islands (called also Ru adlayer) are electrocatalytically more active toward methanol oxidation compared to a homogeneous PtRu alloy [49, 97–99]. Figure 4.15 shows that Pt decorated with spontaneously deposited Ru [100] gave up to two times higher oxidation current density as compared with a commercial PtRu alloy of similar Ru packing density (defined as the ratio between Ru and Pt surface atoms). The spontaneous deposition of Ru was carried out for 1 h from a 1 mM $RuCl_3$ – 0.1 M $HClO_4$ solution followed by electrochemical reduction at 0.3 V vs. SHE of the adsorbed Ru precursor (probably $RuO(H_2O)_4$). STM images of the Pt surface decorated with Ru are presented in Figure 4.16.

In a slightly different variant of the technique, Ru was directly electrodeposited on top of Pt at a constant potential of 0.3 V vs. SHE [101]. The resulting catalyst,

especially the Pt(111) surface decorated with Ru, possessed enhanced electrocatalytic activity [101].

In order to control the surface Ru content, Cao and Bergens developed a Ru deposition method using an organometallic precursor $Ru_4(\mu\text{-}H)_4(CO)_{12}$ which self-poisons the deposition process via its CO group when a specific surface coverage has been formed on Pt [102]. These authors prepared catalysts with a Ru packing density of 0.10 and obtained good DMFC performance, 0.43 V at 100 mA cm^{-2} and 363 K. Unfortunately, no comparison was made with commercial PtRu.
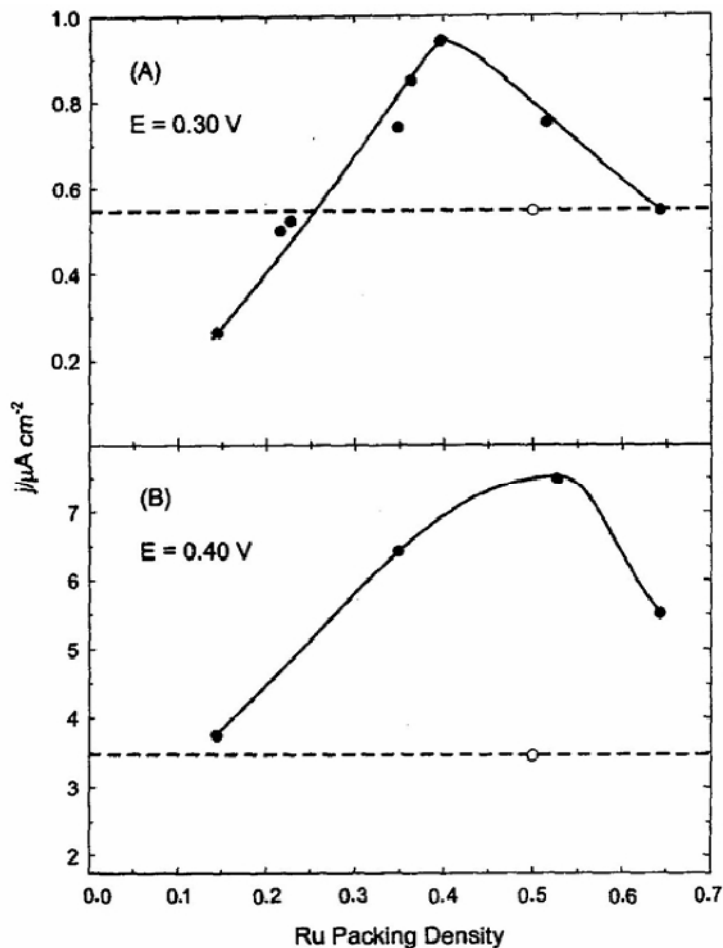
Figure 4.15. Comparison between Pt decorated with Ru (●) and a commercial Johnson Matthey PtRu alloy catalyst (○). Methanol oxidation current density measured after 20 h in 0.5 M CH$_3$OH – 0.5 M H$_2$SO$_4$; 293 K. Potential referred vs. SHE. [98]. (Reprinted from Journal of Catalysis, 203, Waszczuk P, Solla-Gullon J, Kim H-S, Tong YY, Montiel V, Aldaz A, et al., Methanol electrooxidation on platinum/ruthenium nanoparticle catalysts, 1–6, Copyright 2001, with permission from Elsevier.)
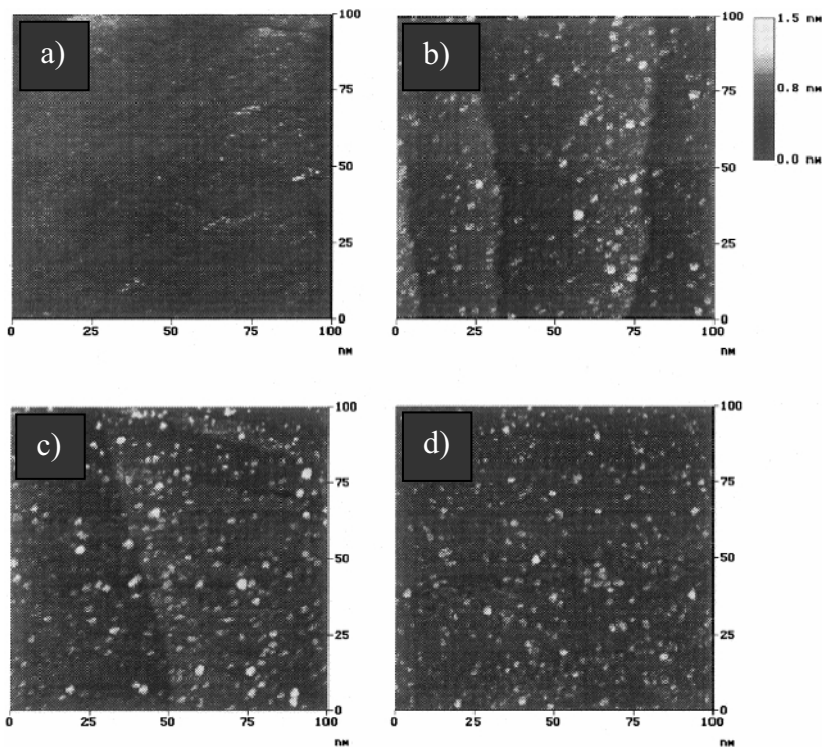
Figure 4.16. STM images of Ru-decorated Pt(111) prepared by spontaneous deposition according to the method of Chrzanowski and Wieckowski [100]. Deposition times: a) 10 s, b) 20 s, c) 40 s, and d) 90 s [99]. (Reproduced from Journal of Electroanalytical Chemistry, 500(1–2), Crown A, Moraes IR, Wieckowski A, Examination of Pt(111)/Ru and Pt(111)/Os surfaces: STM imaging and methanol oxidation activity, 333–43, 2001, with permission from Elsevier.)

Interestingly, in the debate over whether PtRu alloys or heterogeneous PtRu structures are more effective catalysts, Bock et al. reached a different conclusion than Wieckowski et al. by examining both non-homogeneous PtRu (Ru adlayer on Pt) and homogeneous (alloyed PtRu and PtRuO$_2$) catalysts [103]. Bock et al. showed that the alloyed catalysts gave significantly higher methanol oxidation current densities over the potential range between 0.2 and 0.65 V vs. RHE. At E < 0.4 V vs. RHE, the best performer was the PtRuO$_2$ alloy obtained by ball-milling Pt and RuO$_2$ [103]. These results seemingly contradict the previously discussed studies that showed enhanced activity for the non-homogeneous, Ru adlayer/Pt catalyst formulations. However, it is important to note that the catalyst synthesis and post-treatment activation procedures were different in the work of Bock et al. Consequently, not only does the fact of whether the catalyst is alloyed or not play a role but the entire sequence of steps employed for catalyst layer preparation will affect – in a poorly understood manner – the morphology, microstructure, electrochemically active surface area, catalyst utilization efficiency, and ultimately, the experimentally measured electrocatalytic activity.

Further evidence for this proposition is given by the work of Iwasita et al. examining two Ru adatom formation techniques on Pt(111) and comparing the performance with a PtRu alloy formed by H_2 reduction [104]. The Ru adlayer preparation techniques were: (i) spontaneous adsorption of $RuCl_3$ on Pt and (ii) evaporation of Ru onto Pt(111). While the first one is apparently similar to the technique used by Wieckowski and co-workers [98, 100], there were a number of significant differences that must be emphasized and that might have affected the results. Iwasita et al. used a freshly prepared solution of $RuCl_3$ and short adsorption times (between 10 s and 10 min) repeated several times with water rinse between, while Wieckowski et al. used aged (e.g., for 1 week) acidic $RuCl_3$ solution in $HClO_4$ with long adsorption times (1 h). Furthermore, the latter authors subjected the catalyst to electrochemical activation post-treatment by constant potential reduction at 0.3 V vs. SHE.

Iwasita et al. found that the alloy (PtRu atomic ratio of 5.66:1) gave more than four times higher oxidation current density at 0.5 V vs. RHE in 0.5 M CH_3OH – 0.1 M $HClO_4$ compared to the Pt(111)/Ru_{ad} formed by spontaneous adsorption (Figure 4.17) [104].

Highly active PtRu nano-alloys supported on Vulcan XC72 were also produced by colloidal methods, including the co-reduction of Pt(acac)$_2$ and Ru(acac)$_2$ (where acac = acetylacetonate) with 1,2-hexadecanediol in octyl ether with oleylamine and oleic acid surfactants controlling the particle growth [105]. The average particle size was 2.4 nm $\pm$ 0.5 nm and the Pt:Ru atomic ratio was 1:1. The mass activity of the PtRu nano-alloy at 0.45 V vs. SHE was 32.9 mA mg^{-1} compared to 11.7 mA mg^{-1} for the commercial E-TEK Inc. catalyst [105].
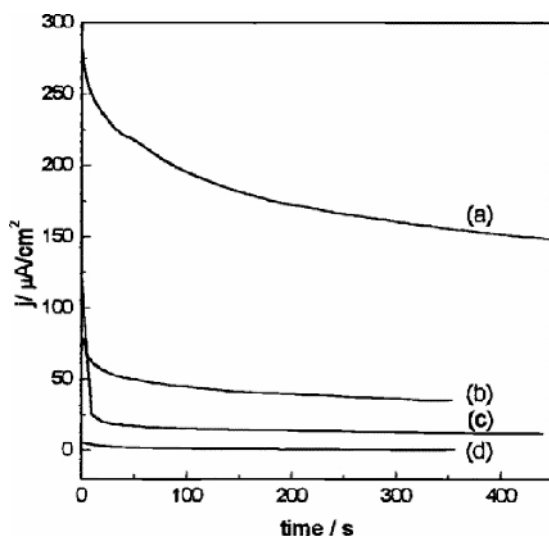
Figure 4.17. Chronoamperometry of different PtRu electrodes at 0.5 V vs. RHE in 0.5 M CH_3OH – 0.1 M $HClO_4$; 298 K. a) PtRu alloy (5.66:1 at. ratio; produced by H_2 reduction), b) Pt(111)/Ru_{ad} spontaneous adsorption, c) Pt(111)/Ru by evaporation, d) clean Pt(111) [104]. (Reprinted with permission from Langmuir 2000;16:522–9. Copyright 2006 American Chemical Society.)

The catalyst preparation method affects also the surface morphology, which in turn has an impact on the electrochemical performance. Hoster et al. demonstrated that rough PtRu surfaces formed by electrodeposition, with a large number of defects (steps, kinks, etc.) are much more resistant to poisoning compared to smooth PtRu surfaces of the same composition [106]. Another example of catalyst preparation methodology affecting the surface properties has been provided by Gonzalez and co-workers. Using the formic acid (FAM) reduction method catalysts with PtRu atomic ratios of 3:1, 5.25:1 and 11.5:1 were prepared [107]. Interestingly, the formic acid reduction technique produced catalysts with very well defined Pt(111) peaks in the XRD diagram compared to the commercial PtRu/C (E-Tek Inc.) (Figure 4.18(a)). It has been recognized that Pt(111) is a very active crystal face in methanol electrooxidation (Section 4.1.1), hence, the catalysts produced by FAM gave higher methanol oxidation current densities at 0.5 V vs. RHE, especially the formulations with 3:1 and 5.25:1 Pt:Ru atomic ratios (Figure 4.18(b)) [107]. Moreover, it is important to note that the CH_3OH concentration effect was most pronounced up to about 1 M. Higher concentrations did not increase significantly the oxidation current.

The complexity of the Ru surface with respect to its oxidation state adds another degree of difficulty in the optimization of the anode catalyst formulation for DMFC. Rolison and co-workers argued that Ru surface oxo-hydroxide formation (RuO_xH_y) is essential for good catalytic activity toward methanol oxidation since it offers a proton conducting network linking the catalytic sites [108, 109]. This conclusion was reached by comparing as-received commercial PtRu blacks (E-TEK Inc.) with samples where the commercial catalyst was subjected to reductive pretreatment either by H_2 or electrolysis. In typical PEM fuel cell catalyst layers the proton conductivity is provided by Nafion. The proton conductivity of RuO_xH_y is in the range of approximately $1–10$ mS cm^{-1} [108], comparable at the low end with Nafion. Using a combination of physical methods of analysis (XRD, EDX, lattice imaging etc.) Rolison and co-workers showed that the low activity catalyst obtained by H_2 reduction, is a single-phase *fcc* PtRu alloy, while the highly active as-received catalyst is mixed phase and it has a core-shell structure with a Ru-hydrous oxide rich shell [110]. The hydrous content was estimated at about 2.4 wt% by thermogravimetric analysis.

The importance of Ru-oxides were also considered by Frelink and co-workers attributing mainly a catalytic role to Ru-oxide (Equation 4.19) since by ellipsometry the disappearance of the Ru oxide film was observed in the presence of methanol [111, 112]. The same observation was made with regard to Sn as a co-catalyst. Furthermore, based on EDX analysis it was proposed that the oxide formation on PtRu leads to $(PtRu)O_x(HSO_4)$ with x ~2 and y ~4, and the optimum Ru surface coverage for methanol oxidation activity is 15% [112].

$$RuO + Pt - CO \rightarrow CO_2 \qquad\qquad (4.19)$$
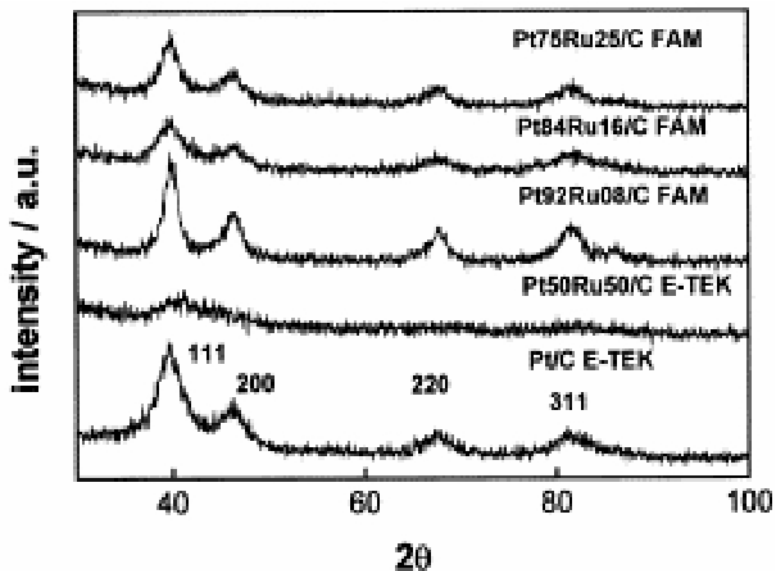
a)
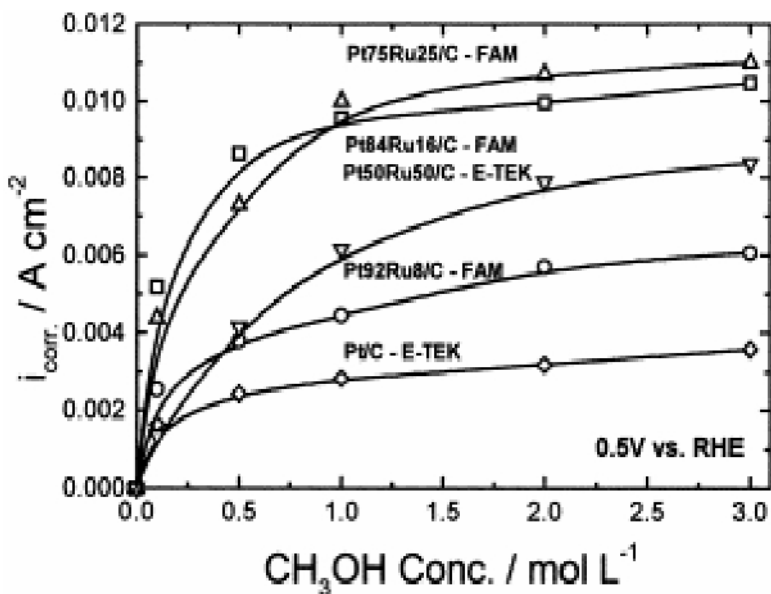
b)

Figure 4.18. a) Comparative XRD patterns of PtRu/C obtained by the formic acid reduction method (FAM) and a commercially available E-Tek Inc. catalyst sample, b) Methanol oxidation current (at 0.5 V vs. RHE, after 30 min, 293 K) as a function of methanol concentration [107]. (Reprinted from Electrochimica Acta, 47(22–23), Lizcano-Valbuena WH, Paganin VA, Gonzalez ER, Methanol electrooxidation on gas diffusion electrodes prepared with Pt-Ru/C catalysts, 3715–22, 2002, with permission from Elsevier.)
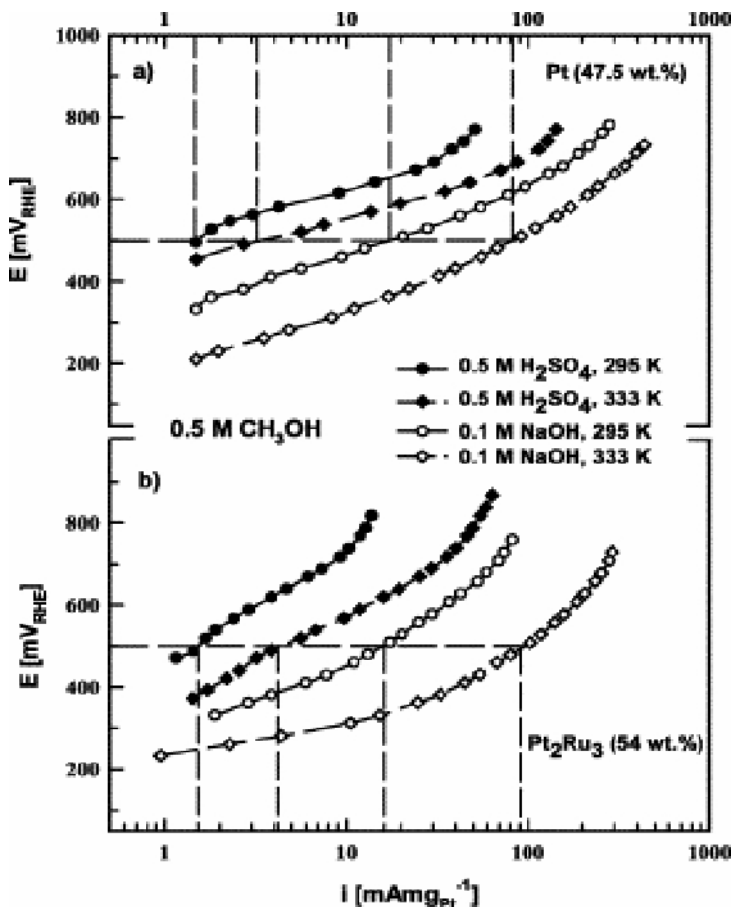
Figure 4.19. Electrooxidation of methanol in 0.1 M NaOH and 0.5 M H_2SO_4 as a function of temperature and catalyst composition: a) Pt/C and b) PtRu/C [115]. (Reprinted from Electrochimica Acta, 47(22–23), Tripkovi AV, et al., Methanol electrooxidation on supported Pt and PtRu catalysts in acid and alkaline solutions, 3707–14, ©2002, with permission from Elsevier.)

In a comprehensive study on the role of Ru oxides, PtRu catalysts were synthesized by a modified Adams-Shriner method using various temperatures between 673 K and 873 K [113]. The composition and particle size (1:1 atomic ratio and 2–4 nm, respectively), were virtually independent of the synthesis temperature. However, the crystalline RuO_2 content increased with temperature, at 873 K all the Ru was present as RuO_2 [113]. The lowest overpotential for methanol oxidation was measured for the catalyst synthesized at an intermediate temperature (743 K), which also exhibited the highest capacitive behavior in cyclic voltammetry indicative of double layer charging due to the hydrous Ru oxide phase. Therefore, the presence of mixed phases including PtRu alloy and Ru hydrous oxide were found to be beneficial for good catalytic activity toward methanol oxidation [113].

Thus far this review has focused on methanol oxidation kinetics under acidic conditions due to compatibility with the most commonly employed practical cell setup using Nafion polymer electrolyte membrane. However, it is important to note briefly the pH effect on the methanol oxidation kinetics. Moreover, in some cases the anion effect is superimposed for example when comparing the oxidation kinetics in H_2SO_4 and NaOH. A comprehensive study of methanol oxidation on Pt polycrystalline electrodes in alkaline media has been recently published by Cohen et al. emphasizing particularly the determination of the activation energy [114].

Tripkovic et al. presented a comparison of the mass-specific steady-state current densities for methanol oxidation in 0.5 M H_2SO_4 and 0.1 M NaOH, respectively, as a function of temperature (Figure 4.19) [115]. On both Pt and Pt_2Ru_3 the methanol oxidation kinetics was much faster in alkaline media. The mass specific current density at a constant potential (e.g., 0.5 V vs. RHE) was typically over one order of magnitude higher for 0.1 M NaOH compared to 0.5 M H_2SO_4. Furthermore, in alkaline media there was virtually no difference in the activities of Pt and Pt_2Ru_3 catalysts.

Electrooxidation of methanol in alkaline media could facilitate the introduction of non-precious metal catalysts based on Ni (Section 4.2.4). However, the practical application of the alkaline media for DMFCs is limited mainly by two factors: (i) the ionic conductivity of the polymer electrolyte membrane and (ii) possible carbonation of the electrolyte, which could lead to plugging of the mesopores in the gas diffusion electrode.

4.2.1.3 Ternary and Quaternary Catalyst Formulations: $PtRuM_1/C$ and $PtRuM_1M_2/C$

Recognizing the paramount significance of the Ru presence, research was also directed toward further improving the catalytic activity using ternary and quaternary formulations. There has been an interest in adding metal oxides (WO_x, MoO_x and VO_x) as co-catalysts. In preliminary studies it was found that metal oxides such as WO_x, MoO_x and VO_x lower the methanol oxidation overpotential compared to Pt and PtRu possibly by the involvement of surface redox couples acting as oxidation mediators such as W^{6+}/W^{4+} or W^{6+}/W^{5+}, V^{5+}/V^{4+} and Mo^{6+}/Mo^{4+} [116, 117]. Detailed investigations in this area, combining electrochemical and surface analysis experiments, were carried out by Roth et al. [118], Yang et al. [119] and Jusys et al. [120]. Employing the Bonneman colloidal method for catalyst preparation, crystalline $PtRuWO_x$ (Pt:Ru:W at. ratio = 1:1:1.5) nanoparticles of 1–2 nm diameter were synthesized and homogeneously dispersed on carbon particles of micrometer size (Figure 4.20) [118]. The DMFC polarization curves corresponding to Pt loading of 0.4 mg cm^{-2} showed up to about 100 mV higher cell voltage for $PtRuWO_x$ compared to commercial PtRu at 368 K (Figure 4.21).

The performance enhancement for methanol oxidation of ternary, oxide containing, formulations has been also demonstrated by Yang et al. using a different $PtRuWO_x$ preparation methodology, based on borohydride reduction [119]. Furthermore, it was confirmed that W is present in either the (+6) or (+5) oxidation states and x ~2.5–3. No electronic effect induced by the oxide on PtRu

was observed, supporting therefore the surface redox mediation as the primary mechanism for catalytic activity enhancement.
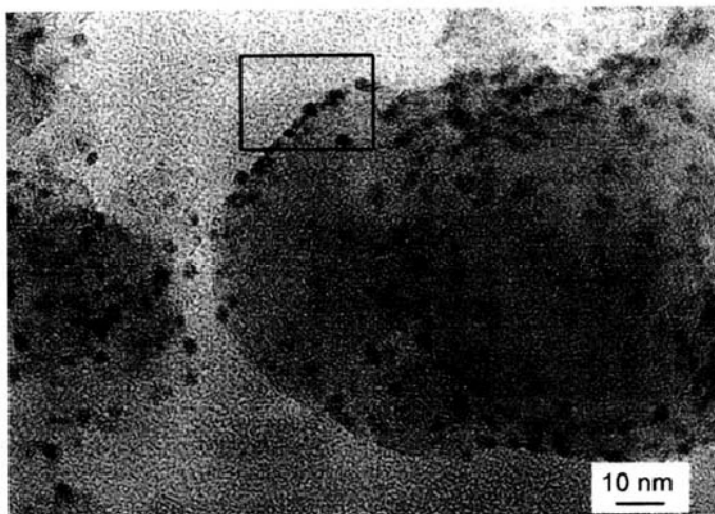
a)
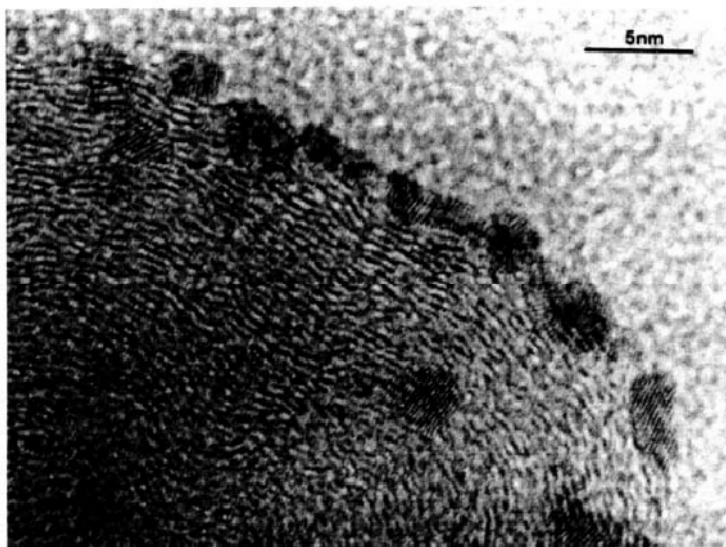
b)

Figure 4.20. PtRuWO$_x$/C (1:1:1.5) catalyst microstructure a) TEM; b) HRTEM [118]. (With kind permission from Springer Science+Business Media: Journal of Applied Electrochemistry, Synthesis and characterization of carbon-supported PtRuWO$_x$ catalysts by spectroscopic and diffraction methods, 31, 2001, 793–8, Roth C, Goetz M, Fuess H, figures 1 and 2.)
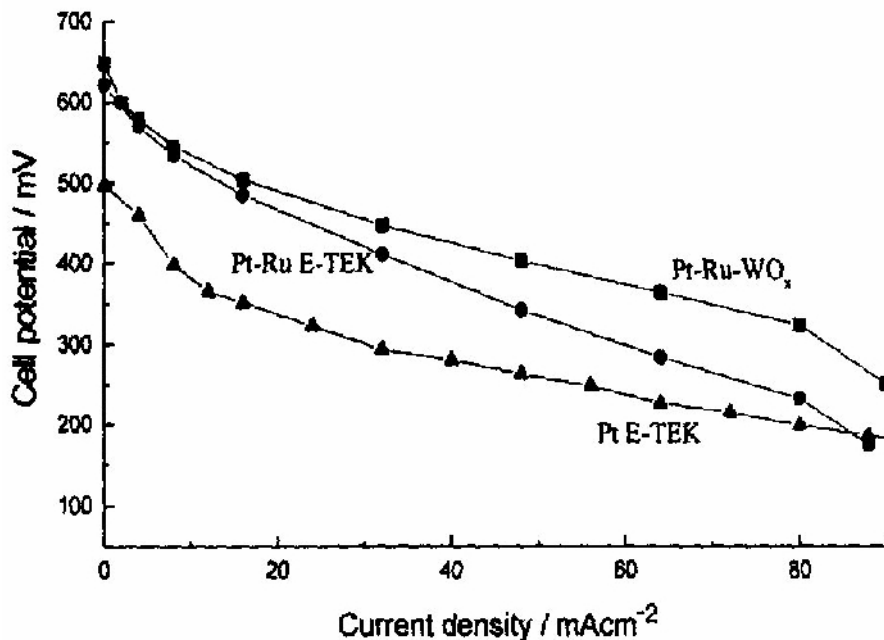
Figure 4.21. DMFC polarization comparison between various supported anode catalysts: PtRuWO$_x$/C, PtRu/C (E-Tek Inc.) and Pt/C (E-Tek Inc.). 368 K. Pt load 0.4 mg cm^{-2}. 1 M CH$_3$OH. [118]. (With kind permission from Springer Science+Business Media: Journal of Applied Electrochemistry, Synthesis and characterization of carbon-supported PtRuWO$_x$ catalysts by spectroscopic and diffraction methods, 31, 2001, 793–8, Roth C, Goetz M, Fuess H, figure 7.)

Somewhat different conclusion has been reached by Jusys et al. based on experiments involving unsupported PtRuMO$_x$ with M = W, Mo and V [120]. The ternary catalysts with atomic compositions of Pt:Ru:M = 7.7:5.6:1, were synthesized by the Adams method which involved melt fusion at 773 K followed by H$_2$ reduction. Note that the third metal component (M) was in significantly lower proportion compared to the previously discussed studies. The intrinsic catalytic activity was expressed as the methanol oxidation current normalized to the electrochemically active surface area estimated by CO adsorption and stripping [120]. Potentiostatic polarization after 30 minutes indicated the following order of activities: PtRuVO$_x$ > PtRuMO$_x$ > PtRu > PtRuWO$_x$ = PtRu (commercial E-Tek Inc.). Thus, in this study VO$_x$ was the most beneficial ternary component, whilst WO$_x$ provided virtually no improvement compared to commercial PtRu. More extensive studies involving longer-term fuel cell experiments coupled with surface analysis are required to further asses, the role of metal oxides of W, Mo and V acting as ternary co-catalysts.

Carbon particle supported (typically Vulcan XC72) non-oxide ternary combinations of PtRu with elements such as W, Mo, Sn were also investigated by a number of authors. Again the catalyst preparation technique in conjunction with the elemental composition had a big impact on the catalytic activity. Gotz and

Wendt reported lower activity compared to commercial PtRu (E-Tek Inc.) for ternary catalyst formulations in the following order: PtRuW (–40 mV) > PtRuMo (–60 mV) > PtRuSn (–100 mV). In paranthesis the magnitude of cell voltage loss compared to the commercial PtRu is given at 40 mA cm^{-2} and 368 K. These catalysts were prepared by the colloidal Bonneman method followed by impregnation on the support [81]. It is important to note however, that with respect to a binary PtRu catalyst prepared under identical in-house conditions, the ternary formulations with the exception of the one with Sn, gave higher activities.

The poor activity for methanol oxidation of PtRuSn was also reported for the catalyst obtained by ethylene glycol reduction [80]. Contradictory results were presented regarding the effect of Mo. The addition of Mo to PtRu with 1:1:0.5 and 1:1:1 PtRuMo atomic ratios, coupled with thermal treatment at 673 K in H$_2$ atmosphere, improved the methanol oxidation current density in linear voltammetry experiments, e.g., at 0.5 V vs. RHE the mass activity for PtRuMo (1:1:1) at 293 K was 1 A g$_{Pt}^{-1}$ [121]. However, longer-term DMFC experiments were not presented. Many of these studies lack fundamental insights into the observed electrocatalytic effects

Gurau et al. published a comprehensive study of binary, ternary and quaternary catalysts for methanol oxidation consisting of Pt, Ru, Ir and Os [122]. The theoretical foundation for this work has been the metal–carbon and metal–oxygen bond strength. Pt and Ir are forming strong bonds with carbon, while Ru and Os are both oxophilic. Furthermore, it was found that the best catalysts are those that maximize the content of Ru, Os and Ir in the *fcc* Pt phase based on solubility limits. XPS spectra showed that the catalyst surfaces were enriched with Ru, Os and Ir present either as oxide or hydrous oxide species [122].

Figure 4.22 compares the mass-normalized current as a function of anode potential and methanol concentration for selected quaternary catalyst formulations and a binary PtRu (1:1). The novel formulation with an atomic ratio of: Pt:Ru:Os:Ir = 2.35:1.45:1:0.2 increased more than 10 times the catalyst mass-normalized current compared to the industry standard Pt:Ru (1:1). In spite of promising results, to the knowledge of the present author there has been no industrial follow up on the PtRuIrOs quaternary catalyst formulation.

The co-catalytic role of Ir has been recognized by others as well, hence, PtRuIr [123] and PtRuIrSn [124] catalysts were also considered. Employing vacuum vapor deposition of organometallic precursors Pt(acac)$_2$, Ru(acac)$_3$ and Ir(acac)$_3$ or Ir(acac)$_2$ (acac, acetylacetonate) applied in two steps (i.e., first PtRu deposition followed by Ir), PtRuIr nanoparticles of approximately 2.5 nm diameter were deposited on Vulcan XC72 [123]. Ru and Ir were alloyed into the Pt *fcc* structure. The electrocatalytic activity was assessed by voltammetry and chronoamperometry using a low catalyst load of 0.075 mg cm^{-2}. The catalyst with an atomic composition of Pt:Ru:Ir 1.8:1:0.05 gave over twelve times higher methanol oxidation current (at 0.6 V vs. SHE) compared to the commercial PtRu [123]. The quaternary catalyst containing Sn, namely PtRuIrSn (3:3:3:1 at. ratio) showed also improved activity compared to the commercial catalyst in linear voltammetry [124].
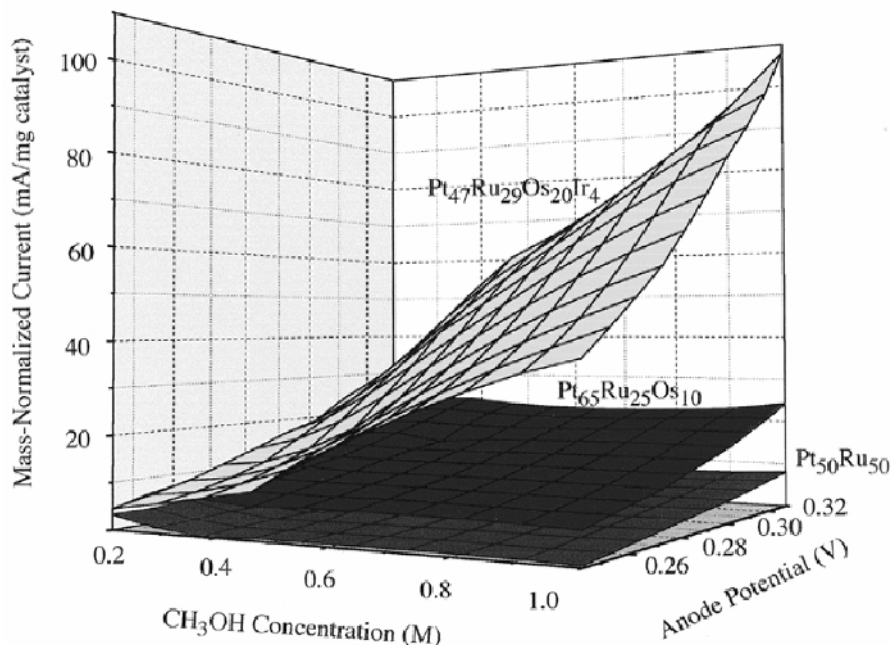
Figure 4.22. Mass-normalized anode current vs. methanol concentration and anode potential for selected quaternary catalyst compositions. 333 K [122]. Anode conditions: methanol solution flow rate 12.5 mL min^{-1}, 0 psig, 60 °C. Cathode conditions are the following: 400 sccm dry air, 0 psig. The electrolyte is Nafion 117. Potential V vs. RHE. (Reproduced with permission from J Phys Chem B 1998;102:9997–10003. Copyright 1998 American Chemical Society.)

An interesting quaternary catalyst, namely PtRuRhNi was proposed by Park et al. [125]. Rh has been considered early on for CH_3OH oxidation as a co-catalyst with Pt in binary PtRh formulations, with maximum acitivity (compared to pure Pt) observed at low Rh loadings of ~10 at% [126]. In the quaternary composition prepared by the borohydride reduction method, low Rh and Ni content was employed corresponding to Pt:Ru:Rh:Ni = 10:8:1:1 atomic ratios [125]. In DMFC experiments using 5 mg cm^{-2} anode catalyst load a maximum power output at 343 K of 180 mW cm^{-2} was achieved with PtRuRhNi compared to 160 mW cm^{-2} obtained with PtRu. Moreover, the quaternary catalyst showed very good stability over an extended operation time of 20 h [126].

4.2.1.4 Combinatorial Catalyst Screening
There are many opportunities to be explored in the area of binary, ternary and quaternary anode catalyst formulations for methanol oxidation. Most of the studies to date, with the exception of the work by Gurau et al. on PtRuIrOs [122], explored a rather limited number of catalyst compositions, typically less than five. In order to search and discover the optimum formulation and composition, fast and efficient electrocatalyst screening techniques are required that are able to provide electrochemical performance evaluations under conditions directly applicable to

fuel cells. The challenge for screening technologies is to assure high fidelity between the conditions and electrode designs suitable for fast detection in half-cell experiments and those required for fuel cell operation. Furthermore, another challenge is the inefficacy of recording simultaneously quasi steady-state state polarization curves from arrays composed of tens to several hundreds of electrodes each with different catalyst formulations.

Combinatorial electrochemistry techniques that have been applied to catalyst screening for methanol oxidation are based on automated multi-electrode arrays and optical detection. Reddington et al. published a seminal paper in this area implementing optical fluorescent detection of the electrocatalytic activity by measuring the proton concentration generated during methanol oxidation using an acid-base indicator connected to an array composed of 645 electrodes [127]. The fluorescent indicator in acid media was quinine. This system was investigated for both ternary (PtRhOs) and quaternary (PtRuOsIr) catalyst compositions. The best performing compositions, namely Pt:Rh:Os = 4.8:1.9:1 (atomic ratio) and Pt:Ru:Ir:Os = 4.4:4.1:1:0.5 (atomic ratio), were identified as brightly fluorescing spots among the array of catalyst compositions supported on Toray carbon paper and employed as working electrodes.

In order to increase the sensitivity of fluorescence imaging, the effect of catalyst loading and time on the intensity was studied using Pt and PtSn [128]. The best measurements were obtained with 0.25 µmol cm^{-2} catalyst load on Toray carbon paper, whilst the long-term catalyst performance could be visualized as a decrease in the brightness of the fluorescence spots in time, monitored by a CCD camera.

Fluorescence imaging in an electrolyte composed of 100 µM quinine, 6 M methanol and pH 7, detected using UV light at 254 nm, was employed to screen 275 different compositions of PtRu, PtMo, PtW and ternary PtRuMoW [129]. The most active compositions that were identified were PtRu (atomic ratios 1:1 and 4.5:1) and PtRuMoW (18.5:5:1:0.5 and 19.25:4.25:1:0.5). Methanol anodic polarization experiments at 298 K showed that the ternary formulations gave up to about 150 mV lower anode potentials compared to the binary PtRu. These findings were not yet validated by fuel cell experiments.

An interesting variant for optical detection of local proton concentration was developed by Brace et al. [130]. An electrochromic counter electrode is utilized with WO_3-coated conducting glass functioning as H^+-insertion electrode. The protons generated at the methanol oxidation catalyst migrate to the counter electrode and cause by intercalation a color change from colorless to blue in the WO_3-coated counter electrode (Figure 4.23). This method was used to study the effect of Pt-black catalyst loading deposited on vitreous carbon with respect to methanol oxidation.

A different approach for combinatorial screening was proposed by Jiang and Chu [131]. Employing a movable electrolyte probe, electrolyte solutions of various compositions of interest are placed on the array of working electrodes with one common counter electrode, which is an air electrode. Thus, full cell measurements were made in an arrangement approximating the direct methanol fuel cell. The method was used to investigate the effect of anode catalyst loading and methanol concentration.

Recently an electrochemical robotic system was developed, resembling the automatic titration devices, for high throughput electroanalysis and electrosynthesis. It uses standard microtitration plates as reaction vessels and miniaturized three-electrode arrangements that are accurately placed by an automated motion system in each and every reaction vessel [132]. A variety of electrochemical techniques (such as chronoamperometry and cyclic voltammetry) can be carried out in parallel. A typical miniaturized three-electrode system consisted of a Pt disk working electrode (10–250 μm diameter), Pt wire counter electrode and Ag/AgCl, 3 M KCl reference electrode. While the applicability is more suited for electrosynthesis and electroanalysis, the potential for electrocatalyst screening could be envisioned where the working disk electrodes are custom made such that to cover different compositions of interest for methanol oxidation.
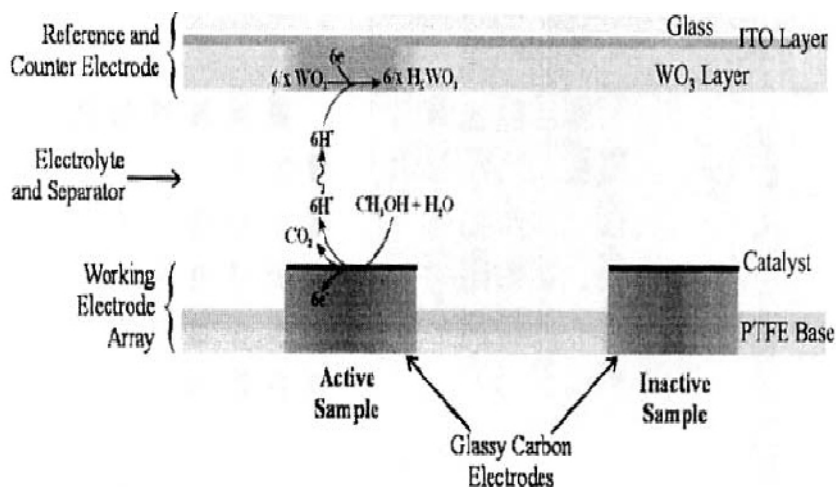
Figure 4.23. Electrochromic detection of anodically generated protons at the WO_3-coated counter electrode [130]. (Brace KM, Hayden BE, Russell AE, Owen JR: A parallel optical screen for the rapid combinatorial electrochromic analysis of electrochemical materials. Advanced Materials. 2006. 18. 3253–7. Copyright Wiley-VCH Verlag GmbH & Co. KGaA. Reproduced with permission.)

4.2.2 Formic Acid Electrooxidation

As a framework for discussion of formic acid oxidation on various electrodes, it is helpful to consider the reaction scheme based on four pathways (Figure 4.24): i) two faradaic steps and ii) two heterogeneous non-faradaic decompositions, dehydration and dehydrogenation, respectively. Complex interactions among various variables such electrocatalyst composition, potential, temperature and electrolyte composition (such as pH and the presence of certain anions and additives) will influence the relative rates of the four pathways, the overall electrooxidation rate and the long-term catalytic activity. Many details about the scheme shown by Figure 4.24 are unknown at present, especially regarding

interdependencies and inter-conversions among the four pathways and the exact nature of the intermediates [F_I, F_{II}, H_I and H_{II}] as a function of electrode material, potential and temperature.
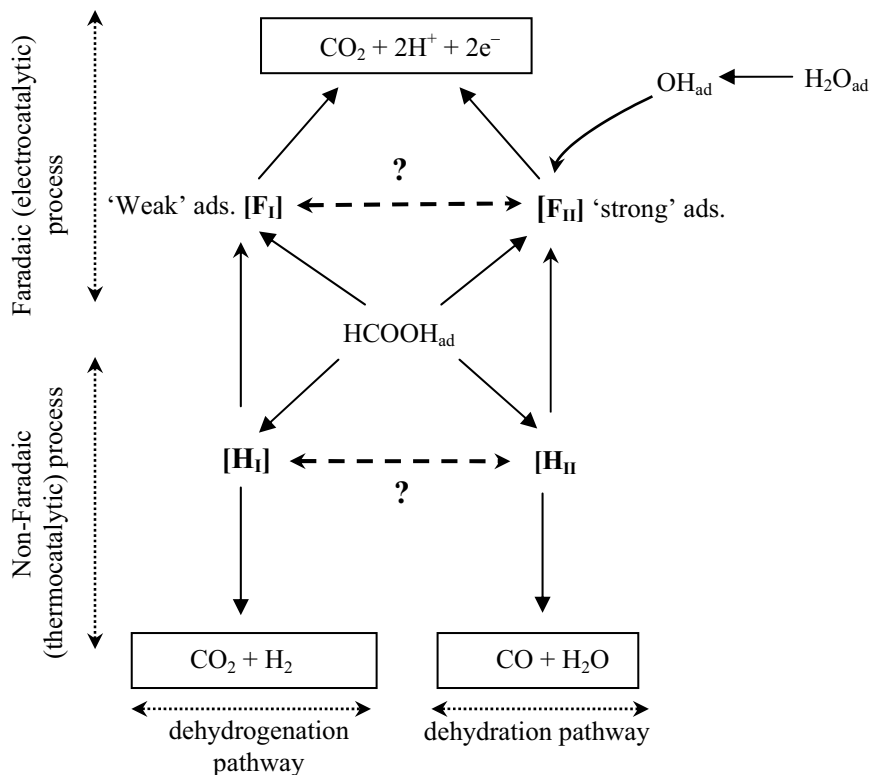
Figure 4.24. Schematic diagram of formic acid electrooxidation and non-faradaic decomposition

It must be emphasized that the symbols [F_I, F_{II}, H_I and H_{II}] do not necessarily imply one intermediate each, since there could be a number of surface adsorbed species present for every step. Moreover, it is likely that some of the intermediates in the faradaic and non-faradaic routes are similar, such as [F_I] could have the same molecular formulae as [H_I] or [F_{II}] and [H_{II}] could be identical.

Regarding the faradaic section of the scheme (Figure 4.24), the conventional thinking based on the dual pathway mechanism (e.g., Capon and Parsons [133]), is that there are two parallel routes, one via weakly adsorbed (reactive) intermediates [F_I] obtained on the dehydrogenation section, while the other one goes through strongly adsorbed surface poisons [F_{II}] related to the dehydration of formic acid. The nature of these intermediates were not always conclusively determined and they will be discussed in the following sections as a function of electrode material and experimental conditions. Generally, [F_{II}] could be CO_{ad} or COH_{ad} (or its isomers) whilst candidates for [F_I] are species such as $HCOO_{ad}$ (or its isomers). The case of adsorbed hydrogen H_{ad} is interesting since it could be either weakly or

strongly adsorbed (i.e., either $[F_I]$ or $[F_{II}]$) depending on the catalyst (e.g., Pt vs. Pd). More details are provided in the upcoming sections

Furthermore, surface reactions and interconversions between the various adsorbed species formed in the diverse pathways could be envisaged [32, 36] such as:

$$2H_{ad} + COOH_{ad} \rightarrow COH_{ad} + H_2O \qquad (4.20)$$

Analyzing Figure 4.24 a number of intriguing questions emerge: (i) is the faradaic dual pathway mechanism completely parallel or under certain conditions (e.g., catalyst or co-catalyst, potential, temperature) an interconversion between the 'labile' and 'strongly' adsorbed intermediates, $[F_I]$ and $[F_{II}]$ respectively, can occur (as exemplified by Equation 4.20)? (ii) what is the contributions of the non-faradaic, thermocatalytic, pathway during formic acid electrooxidation on various electrocatalysts (e.g., $[H_{II}] = [F_{II}] = CO_{ad}$)?, (iii) what catalyst compositions favor the pathway of least kinetic resistance to oxidation (i.e., via the intermediate $[F_I]$)?, (iv) what is the role of H_{ad} and under what conditions OH_{ad} plays a role in the overall reaction scheme?

4.2.2.1 Pt and Related Binary Catalysts PtM (M = Ru, Pb, Co, Bi, Sb, $PW_{12}O_{40}{}^{3-}$, Macrocyle and Sn)

The fundamentals of formic acid electrooxidation on Pt have been intensely investigated. Behm and co-workers carried out authoritative studies as a function of temperature (between 298 K and 353 K) combining electrochemical techniques with IR spectroscopy [134, 135]. Two adsorbates were detected on Pt under all reaction conditions: CO_{ad} (both linearly and multifold bonded $CO_{ad,L}$ and $CO_{ad,M}$, respectively) and $HCOO_{ad}$ (bridge bonded). Thus, based on the scheme given in Figure 4.24, $HCOO_{ad}$ is either $[F_I]$ or $[H_I]$, while CO_{ad} is either $[F_{II}]$ or $[H_{II}]$. Temperature had a significant impact on the surface coverages of the two types of adsorbed species: the surface coverage of CO_{ad} increased whilst the coverage by $HCOO_{ad}$ decreased with an increase of temperature [134]. Hence, temperature favored the dehydration of formic acid and the consumption of the weakly adsorbed (reactive) formate intermediate.

Chronoamperometry curves corroborated by surface IR spectra revealed the temperature and potential dependent behavior of the adsorbed species. For a large potential step from 0.05 V to 0.75 V vs. RHE, it was found that independent of temperature the characteristic IR signal intensity of $CO_{ad,L}$, reflecting its surface coverage, disappeared within 45 s, whilst the $CO_{ad,M}$ signal intensity decreased at slower rate (e.g., 2 min). This shows differences in oxidation rates for the two types of surface-bonded CO_{ad}, with the former reacting faster. At the same time the $HCOO_{ad}$ IR signal intensity increased rapidly after the potential step has been applied reaching a maximum at 20 s indicating the contributions of the non-CO route [134].

The dynamic changes occurring on the surface in terms of adsorbed intermediates as a function of electrode potential and temperature, inherently lead to the possibility of complex oscillatory phenomena occurring during formic acid

oxidation. This topic has received considerable attention [136–142]. Figure 4.26 exemplifies the oscillatory phenomena occurring during galvanostatic oxidation of HCOOH at 0.15 mA cm^{-2} on a polycrystalline Pt electrode [136]. It shows the oscillation of the electrode potential in conjunction with corresponding changes in the output frequency of a quartz crystal resonator Δf, and its surface energy $\Delta \gamma^s$. The latter parameter was calculated based on measurements using electrochemical Koesters laser interferometry [136].

The oscillation started after an induction period of about 1500 s due to the accumulation of CO_{ad} on the electrode. The valleys in the potential oscillations are accompanied by peaks of the surface mass of the electrode as indicated by a decrease of the resonant output frequency (Figure 4.25). This can be interpreted as the formation of surface oxide species at about 0.6 V vs. SSCE (SSCE = Ag/AgCl, KClstd.) reacting with the chemisorbed poison (with some contributions possibly by adsorbed water) thereby, causing a sharp drop of the anode potential ('cleaning' the surface). Moreover, Samjeske and Osawa stressed the importance of $HCOO_{ad}$ in the oscillation phenomena, suggesting that at high formate surface coverage its decomposition rate to CO_2 (the rate determining step according to these authors) is lowered while CO_{ad} acts also as a suppressor of the formate decomposition [137–139].
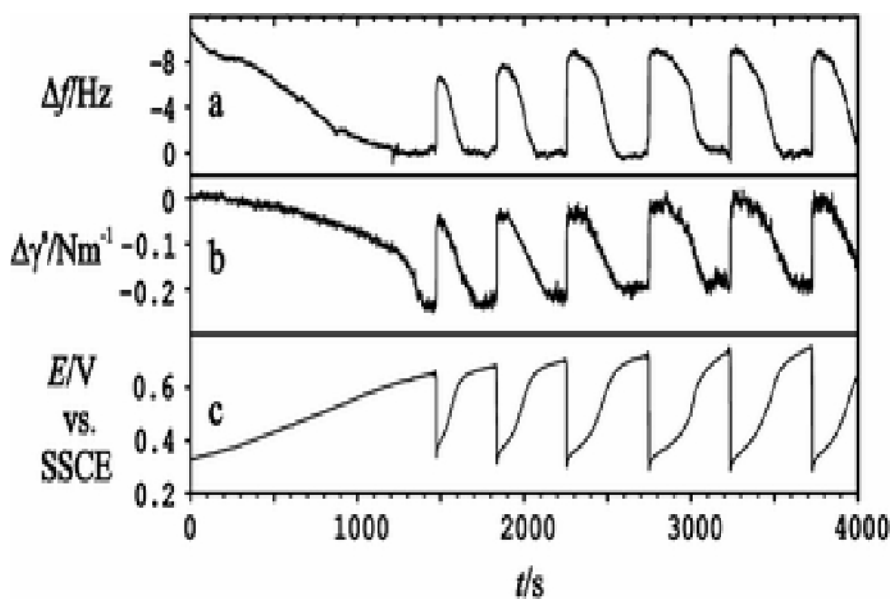
Figure 4.25. Oscillatory phenomena during galvanostatic oxidation of HCOOH on Pt at 0.15 mA cm^{-2} in 0.9 M HCOOH – 0.5 M H$_2$SO$_4$ [136]. a) Pt electrode mass (indicated as frequency change Δf in quartz crystal microbalance measurements), b) Pt surface energy $\Delta \gamma^s$ and c) electrode potential (With kind permission from Springer Science+Business Media: Journal of Solid State Electrochemistry, Simultaneous oscillations of surface energy, superficial mass and electrode potential in the course of galvanostatic oxidation of formic acid, 9, 2005, 347–53, Lang GG, Seo M, Heusler KE, figure 4.)
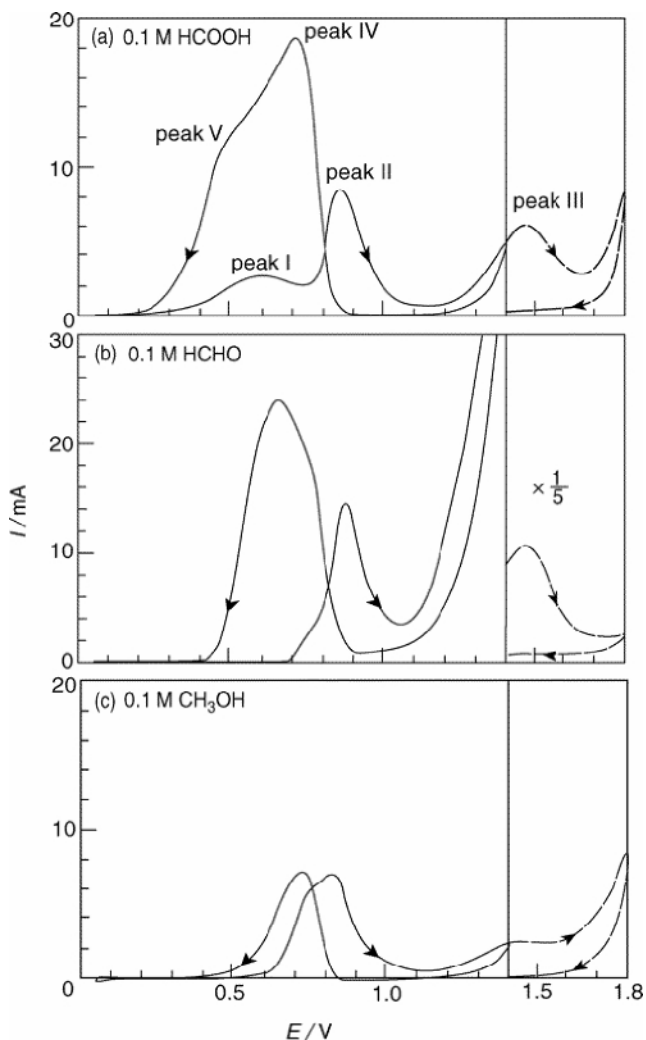
Figure 4.26. Typical cyclic voltammogram of HCOOH on Pt compared to HCHO and CH$_3$OH. 0.5 M H$_2$SO$_4$, 315 K, 100 mV s^{-1} [143]. Electrode potential vs. SHE. (Reproduced with permission from Phys Chem B, 2005;109:15659–66. Copyright 2005 American Chemical Society.)

A typical HCOOH cyclic voltammogram on Pt is given by Figure 4.26(a). Five waves were identified and they can be assigned as follows according to Okamoto et al. [143]:

Wave I:

$$\text{rising portion: HCOOH}_{ad} \rightarrow \text{HCOO}_{ad} + \text{H}^+ + \text{e}^- \tag{4.21}$$

$$\text{HCOO}_{ad} \rightarrow \text{CO}_2 + \text{H}^+ + \text{e}^- \tag{4.22}$$
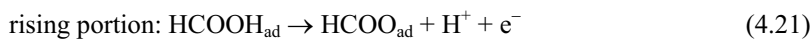
Peak I has been attributed to the accumulation of CO_{ad} formed by the non-faradaic heterogeneous reaction (see also Figure 4.24 and [H_{II}]):

$$HCOOH_{ad} \rightarrow CO_{ad} + H_2O \tag{4.23}$$

Wave II:

$$CO_{ad} + H_2O_{ad} \rightarrow CO_2 + 2\ H^+ + 2e^- \tag{4.24}$$

Also in this region the oxidation of H_2O with surface oxide and hydroxide formation occurs simultaneously:

$$H_2O_{ad} \rightarrow OH_{ad} + H^+ + e^- \tag{4.25}$$

$$H_2O_{ad} \rightarrow O_{ad} + 2H^+ + 2e^- \tag{4.26}$$

$$OH_{ad} \rightarrow O_{ad} + H^+ + e^- \tag{4.27}$$

Wave III: is probably due to reactions (4.21) and (4.22) on the oxidized surface.
Wave IV (on the reverse scan) is due to formic acid oxidation (Reaction 4.21 and 4.22) on clean and possibly re-activated surface.
Wave V (on the reverse scan) could be due to a combination of processes such as surface rearrangement, decrease of the rate of formic acid direct oxidation and increase of the heterogeneous non-faradaic reaction rate (4.23) [143].

Mathematical modeling is useful to interpret the polarization curves and to obtain relevant kinetic parameters. Lovic et al. published a kinetic study of HCOOH oxidation using supported high-surface area Pt/C (Tanaka Precious Metal Group) [144]. Therefore, this work has immediate relevancy to fuel cell application. The authors proposed a rate determining expression based on the oxidation of HCOOH according to reactions (4.21) and (4.22), where the adsorption of HCOOH was expressed by the Frumkin isotherm considering that $\theta_{HCOOH} \sim 0.5$. Hence, the formic acid surface coverage is expressed by:

$$\exp\left(\frac{r\theta_{HCOOH}}{RT}\right) = K_0 C_{HCOOH} \tag{4.28}$$

where C_{HCOOH} is the formic acid concentration, K_0 is the equilibrium constant of adsorption and r is the Frumkin interaction parameter (typically 20–60 kJ mol^{-1}).

Thus, following the arguments made by Lovic et al [144] and taking into account the surface coverages of both $HCOOH_{ad}$ and CO_{ad}, the current density is expressed as:

$$i = Fk_a \left(1 - \theta_{CO}\right) \theta_{HCOOH} \exp\left(\frac{\alpha_a FE}{RT}\right) \tag{4.29}$$

where k_a is the anodic heterogeneous rate constant for Equation 4.21 and α_a is the anodic transfer coefficient.

Furthermore, k_a is also a function of θ_{HCOOH} since according to the Frumkin model not only the Gibbs free energy of adsorption (influencing the equilibrium constant of adsorption), but also the free energy of activation (influencing the rate constant), is dependent on $r\theta_{HCOOH}$ (for a general discussion of these aspects see [145]). Thus, k_a is given by:

$$k_a = k_{a,0} \exp\left(\frac{\alpha_a r\theta_{HCOOH}}{RT} \right),$$ (4.30)

According to Equation 4.30 high repulsion among adsorbates expressed by $r\theta_{HCOOH} \gg 0$ lowers the activation energy in the anodic direction and favors the surface oxidation of HCOOH$_{ad}$. Conversely if $r < 0$, there is attraction among the adsorbed molecules and the surface reaction rate is lowered. In other words conditions that make HCOOH$_{ad}$ less 'sticky' to the surface enhance the oxidation rate. An alternative interpretation of parameter r could be based on surface inhomogenities

Substituting Equation 4.30 into Equation 4.29 one obtains:

$$i = Fk_{a,0} \left(1 - \theta_{CO}\right)\theta_{HCOOH} \exp\left(\frac{\alpha_a r\theta_{HCOOH}}{RT} \right)\exp\left(\frac{\alpha_a FE}{RT} \right)$$ (4.31)

Expressing the HCOOH surface coverage dependent exponential term using Equation 4.28 the oxidation current density is given by:

$$i = k\left(1 - \theta_{CO}\right)\theta_{HCOOH} C_{HCOOH}^{\alpha_a} \exp\left(\frac{\alpha_a FE}{RT} \right)$$ (4.32)

where all the constants were incorporated in k.

Equation 4.32 shows that the oxidation current depends on the anode surface coverage by HCOOH and CO, θ_{HCOOH} and θ_{CO}, respectively, and it relates therefore, to the oscillatory phenomena discussed earlier. Experimentally, Lovic et al. determined a Tafel slope of 150 mV dec^{-1} on Pt/C in both H$_2$SO$_4$ and HClO$_4$ up to an anode potential of 200 mV vs. SCE (i.e., 440 mV vs. SHE), with further increase (almost doubling) at higher potentials [144]. It was shown that various θ_{CO} values could simulate to some extent the measured experimental current densities [144]. Furthermore, the porous nature of the electrode with mass transfer and ionic conductivity related limitations effects also the apparent Tafel slope, inducing what is referred to as multiple Tafel slope behavior [146].

Considering $\alpha_a = 0.5$ Equation 4.32 predicts a reaction order of 0.5, which was confirmed experimentally for HCOOH concentrations below 0.5 M [144]. At higher concentrations the surface coverage saturation by CO$_{ad}$ limits the oxidation rate.

In order to improve the performance of the Pt various modifications were proposed, including adatoms (see also Section 4.1.1) and binary alloys. The case of PtPd will be discussed in the next section after a presentation of the Pd effect.

Gasteiger and co-workers examined PtRu alloys [147, 148]. The role of Ru was attributed to the formic acid dehydration pathways with subsequent oxidative activation of water and removal of CO_{ad} (see Figure 4.24). The proposed optimum alloy composition was a 1:1 atomic ratio. The oxidation of HCOOH on PtRu is highly sensitive to temperature: the rate increases significantly at 333 K as compared to 295 K [149]. A Ru layer eletrodeposited onto Pt was also found to be effective in catalyzing the oxidation of HCOOH (Figure 4.27) [150]. At peak 4 in Figure 4.27, current density increased almost four times for the Ru/Pt bilayer electrodeposited onto a Pt electrode.
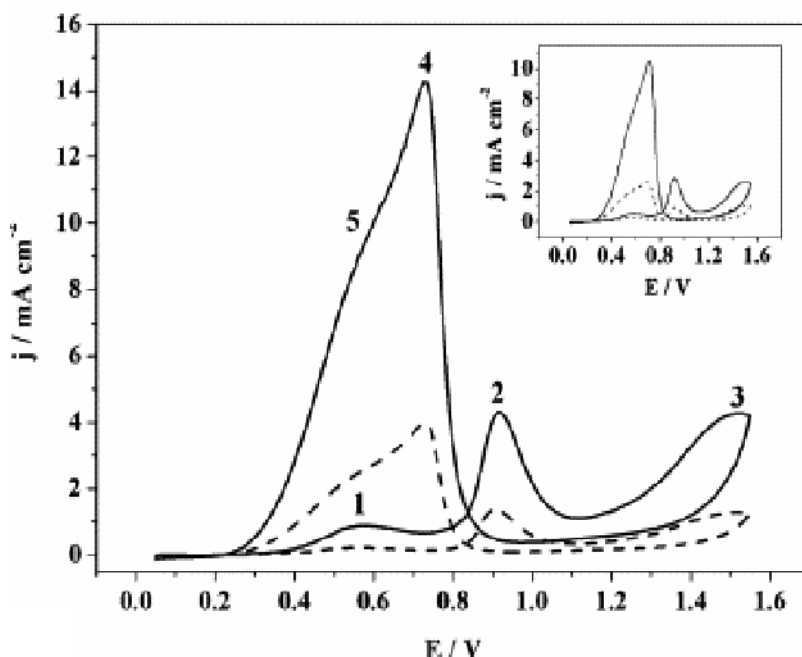
Figure 4.27. The effect of Ru/Pt layer electrodeposited over Pt on the HCOOH cyclic voltammogram. Solid line: Ru/Pt deposited onto Pt; dashed line: polycrystalline Pt. Electrolyte: 1 M HCOOH – 0.1 M $HClO_4$ and 1 M HCOOH–0.1 M H_2SO_4 (inset figure). 298 K. Scan rate 20 mV s^{-1}. Electrode potential expressed vs. RHE [150]. (Reprinted from Journal of Power Sources, 163(2), Lemos SG, Oliveira RTS, Santos MC, Nascente PAP, Bulhões LOS, Pereira EC, Electrocatalysis of methanol, ethanol and formic acid using a Ru/Pt metallic bilayer, 695–701, 2007, with permission from Elsevier.)

Pb alloyed with Pt also enhanced the HCOOH oxidation rate [151–153]. Intermetallic PtPb nanoparticles (diameter ~20–32 nm) synthesized in THF and diglyme from organometallic precursors showed mass-specific activities toward HCOOH oxidation up to almost ten times higher compared to commercial PtRu (Figure 4.28) [152]. Fuel cell experiments are awaited to further validate the

practical applicability of PtPb nanoparticles. The beneficial effect of Pb has been attributed to favoring the weakly adsorbed reactive intermediate route as opposed to the CO_{ad} pathway. Moreover, in the PtPb alloy the Pt-Pt bond length was increased from 2.77 Å to 4.24 Å; therefore, the bridge-mode adsorption of CO was hampered, facilitating the removal of CO_{ad} [151].
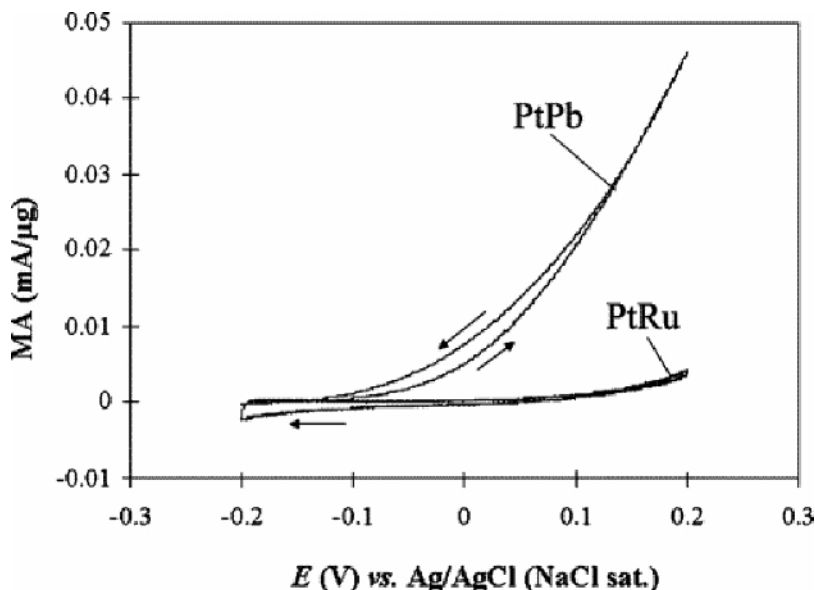
Figure 4.28. Mass specific activity with respect to HCOOH oxidation for PtPb nanoparticles (prepared from organometallic precursors in diglyme) compared to commercial PtRu/C. 0. 5 M HCOOH – 0.1 M H_2SO_4, 10 mV s^{-1}; 298 K [152]. (Reproduced with permission from Chem Mater 2006;18:5591–6. Copyright 2006 American Chemical Society.)

PtCo bimetallic nanoparticles supported on highly oriented pyrolitic graphite showed good activity toward HCOOH oxidation compared to pure Pt, particularly in the composition range Pt:Co between 1:1.1 and 1:3.5 (atomic ratio) [154].

Bismuth as an adatom or alloying element with Pt has been proposed as an extremely active co-catalyst for HCOOH oxidation on Pt. The unusual activity of Bi has been attributed to a combination of geometric (third-body) and electronic effects [155–157]. However, the role of Bi is quite complex and in some cases contradictory results were obtained. Tripkovic et al. clearly showed the activity of PtBi is dependent on the redox behavior of Bi and on its surface arrangement [158]. Oxidized Bi^{3+} species such as Bi_2O_3 and BiO(OH) were identified by XPS on the surface at both open circuit and anodic potentials. Furthermore, the possibility of Bi leaching was proposed, with subsequent underpotential deposition of the resulting Bi^{3+} on the surface forming *in-situ* an adlayer, which could also contribute to the enhanced catalytic activity, as shown by a shift of the HCOOH oxidation onset potential by –0.25 V compared to pure Pt [158].

Schmidt et al. carried out detailed potentiodynamic investigations on this topic using Pt(111) with spontaneously adsorbed Bi [159]. It was found that after about

20 min of potentiostatic operation at 0.65 V vs. RHE and 303 K the catalytic effect of Bi on Pt(111) disappeared. Two opposite effects of Bi were proposed: i) increased formation of OH_{ad} on Pt sites situated next to Bi enhancing the catalytic activity and ii) the inhibiting effect of Bi layer on the Pt catalytic activity [159].

Complex spatio-temporal oscillatory patterns of the HCOOH oxidation rate on Pt were observed in the presence of $\sim 10^{-6}$ M Bi^{3+} in the solution (i.e., in effect a Bi underpotential deposited layer on the Pt surface) [160]. The instabilities are exemplified in the cyclic voltammogram shown by Figure 4.29. It was concluded that there is a continuous oscillatory deactivation-reactivation of the surface with major impact from surface defects, as well.
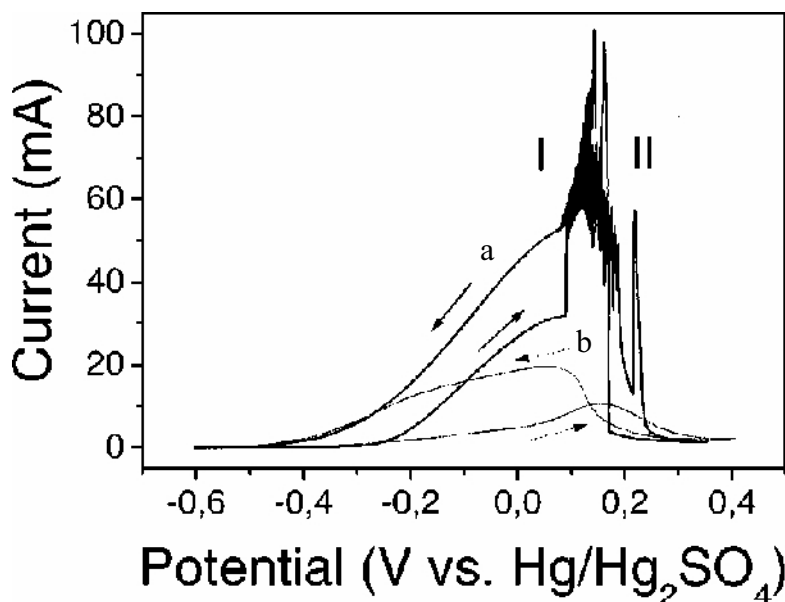
Figure 4.29. Cyclic voltammetry of HCOOH oxidation on Pt, a) in the presence of 10^{-6} M Bi^{3+} and b) in its absence. 0.5 M H_2SO_4 – 1 M HCOOH. Scan rate 10 mV s^{-1} [160]. (Reprinted with permission from Lee J, Christoph J, Strasser P, Eiswirth M, Ertl G. Spatio-temporal interfacial potential patterns during electrocatalyzed oxidation of formic acid on Bi-modified Pt. J Chem Phys 2001;115:1485–92. Copyright 2001 American Institute of Physics.)

The co-catalytic role of Sb is somewhat similar to that of Bi. The redox behavior of Sb in conjunction with H_{ad} on Sb determines the electrocatalytic activity in a Pt structure-sensitive fashion [161, 162]. Sb modification had a beneficial effect on the HCOOH electrooxidation activation energies on Pt(111) and Pt(331), while exercising an inhibitory role on Pt(100), Pt(110), and Pt(320) [161]. But the same group presented cyclic voltammetry data showing increased HCOOH oxidation currents on Sb-modified Pt(110) and Pt(320) [162]. The effect of Sb_{ad} was very dependent on its surface coverage and there was an interaction

effect between Sb_{ad} surface coverage and the Pt crystal face. It is clear more investigations and longer-term studies are needed with respect to the effect of Sb.

Petry and co-workers published a study on the effect of oxotungstate adlayers on the electrocatalytic activity of Pt toward HCOOH oxidation [163]. In the presence of 1 mM $Na_3PW_{12}O_{40}$ in 0.5 M H_2SO_4 – 0.1 M HCOOH, at E < 0.55 V vs. RHE the oxidation current on a Pt electrode was higher by about 2.5–3 times. The direction of scanning also had an effect on the relative behavior with respect to phosphotungstate, since conditions had to be created on the surface for its effective adsorption [163].
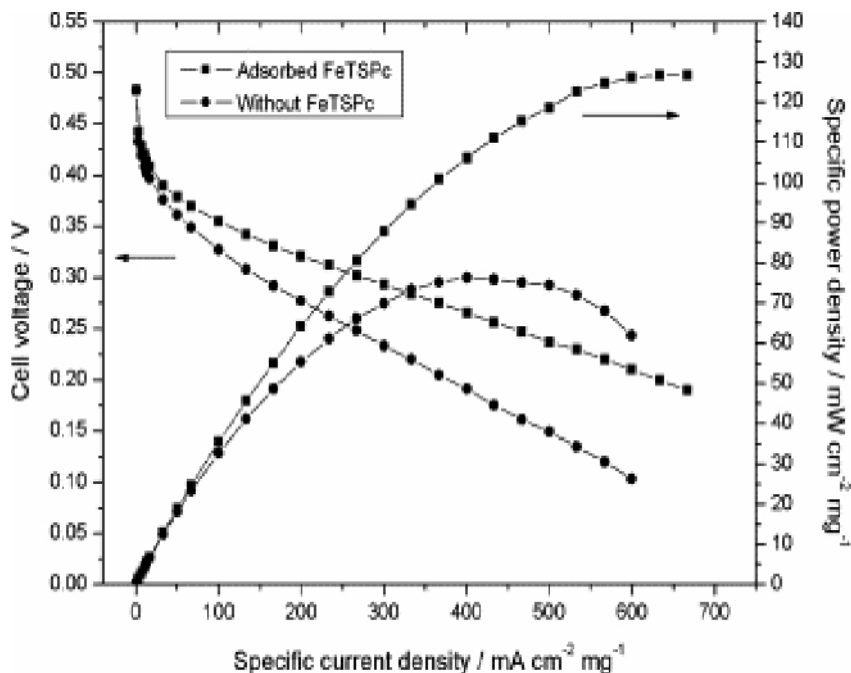
Figure 4.30. Effect of Pt-FeTSPc$_{ad}$ anode catalyst in a direct formic acid fuel cell; 333 K, atmospheric pressure, 6 M HCOOH. Anode: Pt loading 0.5 mg cm^{-2}, fuel flow rate 1.0 ml min^{-1}. Cathode: Pt loading 1.5 mg cm^{-2}, 100 cm^3 min^{-1} of dry O_2 at STP [164]. (Reproduced from Electrochemistry Communications, 9(7), Zhou X, Xing W, Liu C, Lu T, Platinum-macrocycle co-catalyst for electrooxidation of formic acid, 469–73, 2007, with permission from Elsevier.)

Using the Pt/macrocycle (Fe-tetrasulfophthalocyanine, FeTSPc) catalytic system Zhou et al. obtained an approximately two times higher peak current density for HCOOH oxidation with Pt-FeTSCPc$_{ad}$ as compared to bare Pt electrode [164]. Moreover, these authors presented direct formic acid fuel cell results proving the power output increased over virtually the entire operating range for the macrocycle-adsorbed Pt electrode (Figure 4.30) [164]. In the fuel cell setup the adsorption of FeTSPc on the Pt anode was achieved by pumping 4 μg ml^{-1} FeTSPc for 2 h in the anode chamber of the fuel cell followed by thorough washing with

0.5 M H_2SO_4 and H_2O. The peak power density increased with the macrocycle catalyst from about 80 mW cm^{-2} mg^{-1}_{Pt} to 130 mW cm^{-2} mg^{-1}_{Pt}. The role of the macrocycle was related to both intrinsic kinetics (since the apparent oxidation activation energy was lowered) and geometric influence (i.e., steric hindrance of CO adsorption) [164]. These very promising results definitely warrant further investigations of macrocycle co-catalysts.

Recent results with PtSn/C obtained by the Tekion Inc. group demonstrated stable operation over extended periods of time at various temperatures [165], confirming previous results in this area by Adzic and co-workers [36]. Figure 4.31 exemplifies the half-cell performance of Pt/Sn at 100 mA cm^{-2}. Furthermore, it shows that for the same metal and ionomer load in the catalyst layer (3 mg cm^{-2} and 0.75 mg cm^{-2} Nafion, respectively) and an identical atomic ratio of Pt:Sn = 4:1, the catalyst with 25 wt% metal dispersion on the support gave about 25 mV lower anode potential [165]. Thus, in this case it is likely that the interface between PtSn/Nafion/carbon support controlled the overall anode performance, affecting the catalyst utilization. These aspects are further detailed in Section 4.3 of this chapter.
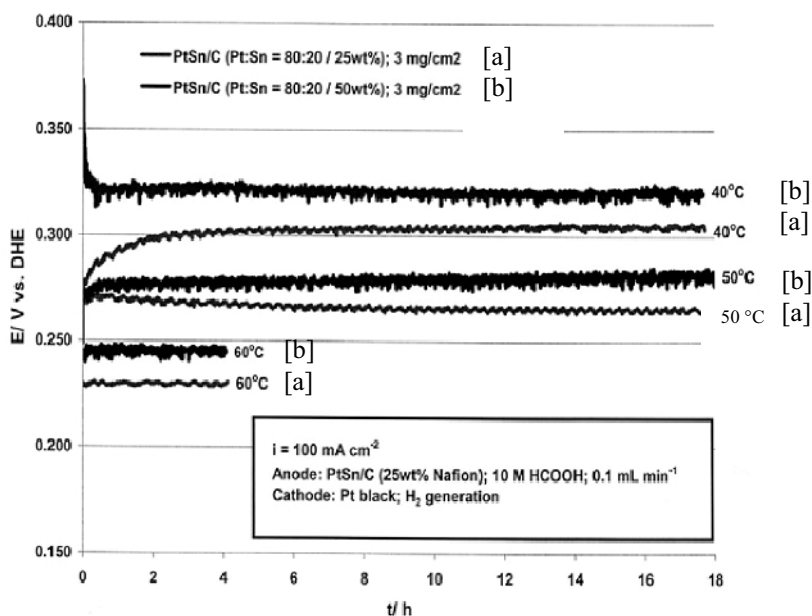
Figure 4.31. Long-term performance of PtSn/C as a function of temperature and catalyst dispersion. Pt:Sn at. ratio 4:1, catalyst load 3 mg cm^{-2}, 10 M HCOOH, 0.1 ml min^{-1} [165]. (Reproduced with permission of the authors.)

Regarding the intrinsic kinetic effect of Sn, Xia investigated $PtSn_{ad}$ (obtained by underpotential deposition) employing on-line mass spectroscopy in conjunction with electrochemical techniques [166]. The maximum electrocatalytic activity in 0.01 M HCOOH – 0.1 M $HClO_4$ was observed for a Sn_{ad} surface coverage of ~0.70

independent of the potential in the range of 0.2–0.4 V vs. RHE. Quasi-steady state polarization curves revealed up to two orders of magnitude higher HCOOH oxidation current density at 0.4 V vs. RHE for PtSn$_{ad}$ (θ_{Sn} ~0.7) compared to pure Pt. The Sn adlayer was stable up to 0.65 V vs. RHE. The mechanism proposed by Xia for the effect of Sn seems the most comprehensive to date and is composed of two main parts, depending on the anode potential [166]: i) at E < 0.2 V vs. RHE the role of Sn is mainly an electronic effect modifying the HCOOH adsorption on the Pt sites and also influencing the distribution of the water molecules at the interface; ii) at E > 0.2 V vs. RHE, Sn$_{ad}$ is oxidized to Sn$^{2+}_{ad}$ and the involvement of corresponding hydroxide species in terms of the bifunctional mechanism was invoked as follows [166]:

$$Sn^{2+}_{ad} + H_2O \rightarrow [Sn(OH)]^+_{ad} + H^+ \qquad (4.33)$$

$$CO_{ad} + [Sn(OH)]^+_{ad} \rightarrow Sn^{2+}_{ad} + CO_2 + H^+ + 2e^- \qquad (4.34)$$

$$COH_{ad} + [Sn(OH)]^+_{ad} \rightarrow Sn^{2+}_{ad} + CO_2 + 2H^+ + 2e^- \qquad (4.35)$$
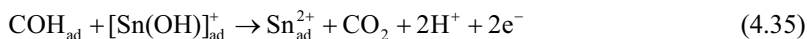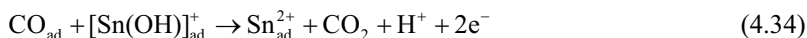
4.2.2.2 Pd and Related Binary Catalysts

The electrocatalysis of HCOOH oxidation on Pd constitutes a special case and represents an exception when compared to CH$_3$OH and C$_2$H$_5$OH. Some of the early work on this topic has been presented in Section 4.1. The cyclic voltammogram of Pd(111) in 0.1 M H$_2$SO$_4$ is shown by Figure 4.32 [167]. Key features are: i) pronounced underpotentially deposited hydrogen peaks (adsorption/desorption) around −0.05 V vs. SCE, ii) ordered SO$_4^{2-}$ adlayer formation at +0.1 V vs. SCE, and iii) Pd surface oxidation at 0.8 V vs. SCE and reduction of the surface oxides at 0.4 V on the cathodic scan, generating irreversible surface defects [167].

However, the surface properties of the single-crystal Pd electrode are different compared to polycrystalline or pseudomorphic Pd monolayers. This is well illustrated by the hydrogen desorption peak potential and oxidation current on Pd monolayers (Pd$_{ML}$) deposited on various substrates (Figure 4.33(a)) [167a]. There are large variations among the Pd-monolayers, and also in comparison to Pd(111), with respect to hydrogen adsorption strength. The more negative the hydrogen oxidation potential the weaker the hydrogen adsorption on Pd.

Thus, based on Figure 4.33(a), in the case of Pd$_{ML}$/Re there was virtually no H$_{ad}$, whilst at the other extreme strong H$_{ad}$ occurred on Pd$_{ML}$/Au(111) [167a]. This has been correlated with the d-band center energy level shift according to the Norskov et al. model [168]. The change in the d-band center energy was due to the different lattice parameter of the overlayer vs. bulk substrate (geometric effect) and/or electronic interaction between the two phases, surface and bulk (ligand effect). The dilatation of the Pd monolayer caused by the underlying bulk metal substrate, as in the case of Pd$_{ML}$/Au(111), leads to strong hydrogen adsorption; conversely, a compression of the Pd monolayer, as in Pd$_{ML}$/Re and Pd$_{ML}$/Ru, generated weak H$_{ad}$ on the surface [167a].
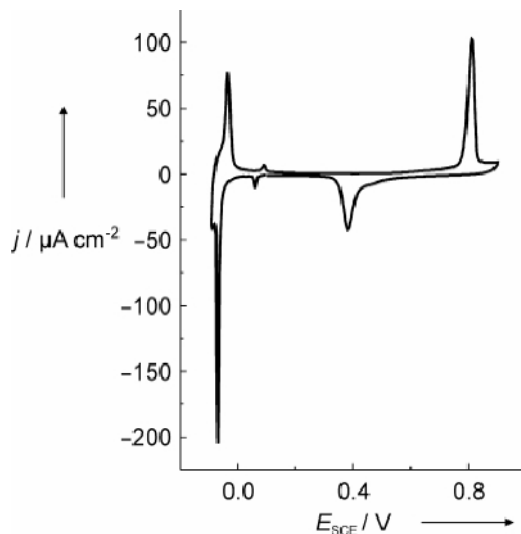
Figure 4.32. First scan cyclic voltammogram of Pd(111) in 0.1 M H$_2$SO$_4$ starting at 0.1 V$_{SCE}$ and scanned in the negative direction first. Scan rate 10 mV s^{-1}, 298 K [167a]. (Reprinted with permission from Kibler LA, El-Aziz AM, Hoyer R, Kolb DM. Tuning reaction rates by lateral strain in a palladium monolayer. Angew Chem Int Ed 2005;44:2080–4. ©2005 German Chemical Society.)

All these surface structural changes of Pd will impact its electrocatalytic activity toward HCOOH oxidation. According to Figure 4.33(b), compression of Pd$_{ML}$ (i.e., lowering the *d*-band center energy level) is favorable for reducing the onset potential for HCOOH oxidation. In other words, the weaker the H$_{ad}$ on Pd the lower the HCOOH oxidation onset potential. This result also supports the idea that very strong H$_{ad}$ could play an inhibitory role during HCOOH oxidation. However, there is a compromise since the HCOOH oxidation current is also lowered when H$_{ad}$ is weak (Figure 4.33). Presumably, a weak hydrogen adsorption implies weak formic acid adsorption and low surface coverage. The best results were obtained for Pd$_{ML}$/Pt(111) and Pd$_{ML}$/PtRu(111), where the oxidation onset potential was lowered whilst the oxidation current increased compared to bulk Pd(111) [167a].

Related studies on Pd$_{ML}$/Pt(111) by Arenz et al. demonstrated conclusively the reaction mechanism differences between Pd and Pt [167b and c]. In the context of Figure 4.24 the HCOOH electrooxidation on Pd occurs exclusively through the dehydrogenation pathway, leading to CO$_2$ formation via the weakly adsorbed intermediates [F$_I$]. On Pt, however, depending on the potential, both dehydrogenation and dehydration pathways can occur. The latter prevails at low potentials (< 0.45 V), leading to CO$_{ad}$ ([F$_{II}$]), which is further oxidized to CO$_2$ by OH$_{ad}$. At high potentials where the dehydrogenation pathway and/or the oxidative CO$_{ad}$ removal are favored, the presence of OH$_{ad}$ poisons the electrode surface, according to Arenz et al. [167b and c].

Furthermore, the importance of competitive adsorption among species such as HCOOH$_{ad}$, H$_{ad}$ and SO$_4{}^{2-}{}_{ad}$ must be emphasized. It has been recognized that H$_{ad}$ behaves as a poisoning species over the entire electrode potential range [167c].
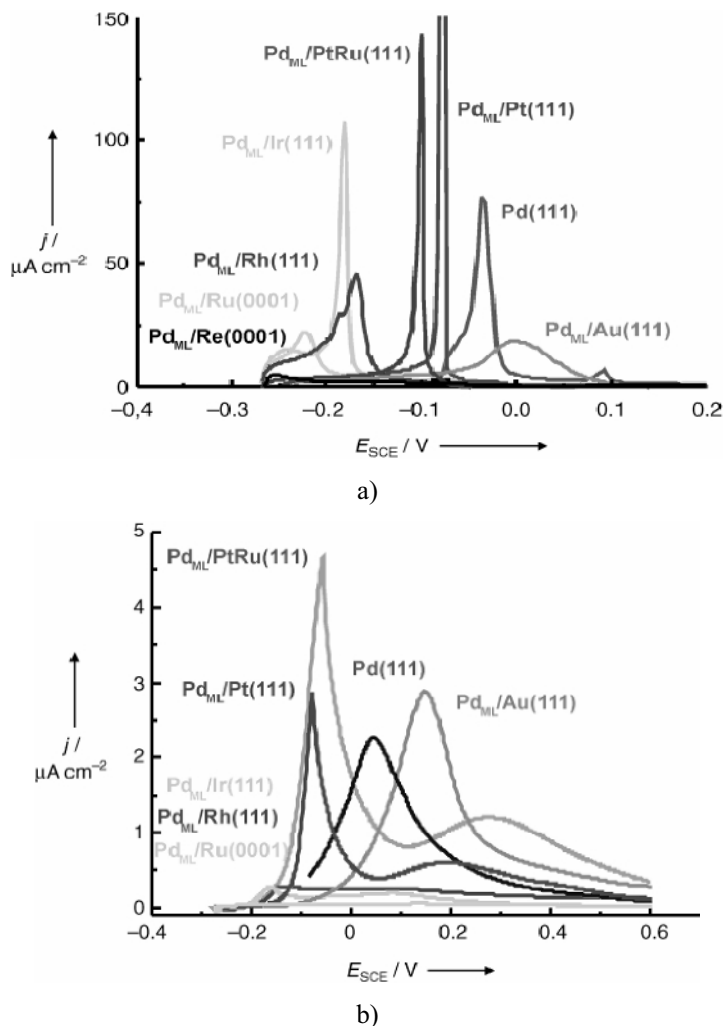
Figure 4.33. a) Anodic polarization curve corresponding to H_{ad} desorption on Pd(111) and Pd monolayers (Pd_{ML}) deposited on various substrates. 0.1 M H_2SO_4. Scan rate 10 mV s^{-1} [167a]. b) Anodic polarization curves for HCOOH on Pd(111) and Pd monolayers (Pd_{ML}) deposited on various substrates. 0.2 M HCOOH–0.1 M H_2SO_4. Scan rate 20 mV s^{-1} [167a]. (Reprinted with permission from Kibler LA, El-Aziz AM, Hoyer R, Kolb DM. Tuning reaction rates by lateral strain in a palladium monolayer. Angew Chem Int Ed 2005;44:2080–4. ©2005 German Chemical Society.)

The role of Pd surface layers was also investigated by Waszczuk et al., showing good catalytic activity for spontaneously deposited Pd (from 5 mM Pd(NO$_3$)$_2$ – 0.1 M H$_2$SO$_4$ for 5 min) on high surface area Pt and PtRu, respectively. After 8 h of operation at 0.27 V vs. RHE in 0.1 M HCOOH – 0.1 M H$_2$SO$_4$ the current measured with Pd/Pt was about two orders of magnitude higher compared to pure Pt [169].

Differential electrochemical mass spectrometry was used by Vidal-Iglesias et al. to study the HCOOH oxidation on Pd submonolayers deposited on Pt(100) and Pt(111) [170]. It was found that the adsorption of SO_4^{2-} inhibits HCOOH oxidation. Competitive adsorption between hydrogen and sulfate was responsible for the voltammetric peak at 0.26 V vs. RHE on Pd, while at 0.3 V vs. RHE, H_{ad} was completely displaced by the adsorbed sulfate. At E > 0.3 V the SO_4^{2-} adsorption was stronger, further diminishing the HCOOH oxidation current on the Pd modified electrodes [170]. The deposition mechanism and surface analysis of Pd on Pt(111) was published by Ball et al. [171].

In addition to Pd surface layers, carbon-supported PdPt catalysts with various degrees of alloy formation were investigated for HCOOH electrooxidation. The catalyst preparation technique typically had a significant effect on the activity. Li and Hsing prepared Pt_xPd_{1-x} (x = 0–1) nanocatalysts supported on Vulcan XC72 using surfactant stabilization to control particle growth [172]. The average particle size and surface area were 2.2–2.9 nm and 64.5–80.5 m^2 g^{-1}, respectively, whilst a commercial PtPd/C (1:1 atomic ratio, E-TEK Inc.) had larger particle sizes of about 4.5 nm and a smaller area of 46.7 m^2 g^{-1}. Due to these morphological differences, the surfactant stabilized PtPd/C catalyst (1:1 at. ratio) gave almost four times higher mass-specific HCOOH oxidation current densities at 0.5 V vs. RHE compared to the commercial catalyst [172].
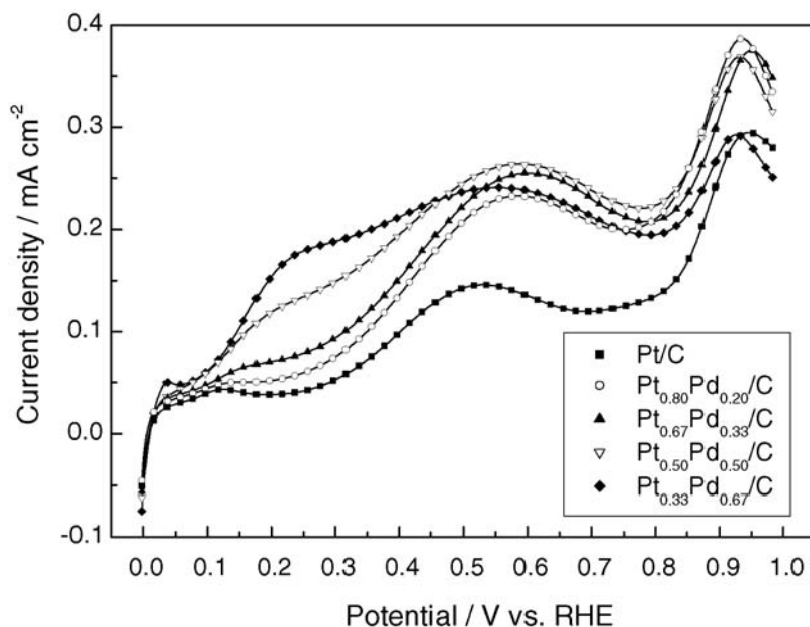
Figure 4.34. Formic acid oxidation on Pt_xPd_{1-x}/C nanocatalysts prepared by a surfactant stabilized method using methanol as the reducing agent. 293 K, 50 mV s^{-1}, 0.25 M HCOOH – 0.25 M $HClO_4$ [172]. (Reproduced from Electrochimica Acta, 51(17), Li X, Hsing I-M, Electrooxidation of formic acid on carbon supported Pt_xPd_{1-x} (x = 0–1) nanocatalysts, 3477–83, 2006, with permission from Elsevier.)

Regarding the optimum Pd/Pt atomic ratio, the same authors reported that in the practical potential domain for direct formic acid fuel cells and at 293 K, the catalyst with a 2:1 Pd:Pt atomic ratio gave the highest HCOOH oxidation superficial current densities (Figure 4.34) [172]. However, in a direct comparison of PdPt (2:1)/C and pure Pd/C by cyclic voltammetry the oxidation current on the anodic scan was over five times higher on the pure Pd/C catalyst.

The superior activity of Pd/C compared to Pt/C, both produced by the microwave assisted polyol method, was also demonstrated in direct formic acid fuel cells [173]. With Pd/C as the anode catalyst the maximum power output at 298 K was 120 mW cm^{-2} while Pt/C yielded only 65 mW cm^{-2}. The catalyst load was 8 mg cm^{-2} in both cases and the formic acid concentration in the fuel cell 3 M.

An interesting discussion has emerged in the literature regarding the long-term stability of Pd catalysts in direct formic acid fuel cells. There is evidence of catalytic activity loss over time of pure Pd as opposed to Pt and PdPt alloys. The chronopotentiometry data shown by Figure 4.35, obtained at 100 mA cm^{-2} in 10 M HCOOH and 293 K [174], indicates that although Pd is more active compared to Pt and PtPd by operating at 0.2–0.25 V more positive potentials, the anode potential on Pd gradually shifts toward higher values, exceeding the Pt-based catalysts after 6 hrs. This was partly attributed to Pd catalyst deactivation over time [174]. Hence, either Pd catalyst regeneration must be performed or a new formulation must be implemented that stabilizes the Pd while maintaining its activity.
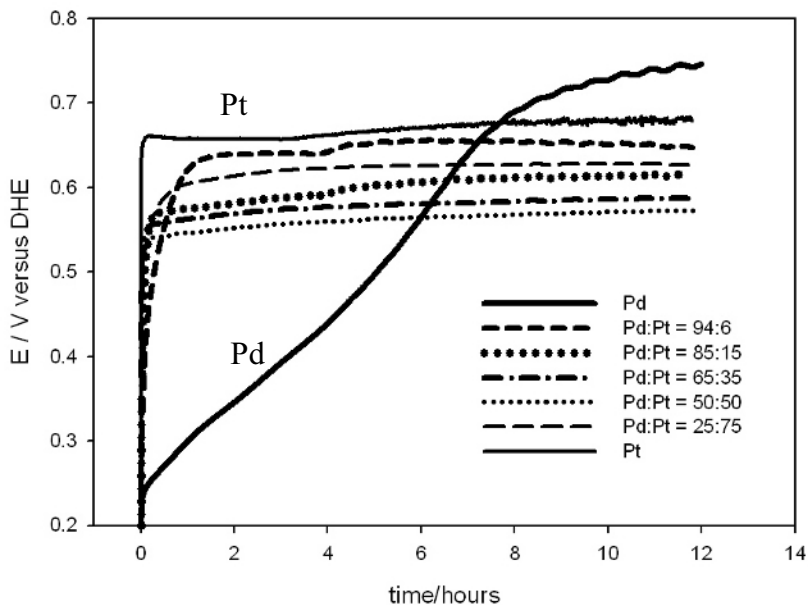
Figure 4.35. Chronopotentiometry of formic acid oxidation on Pd, PdPt (prepared by the polyol method), and Pt. 10 M HCOOH – 0.1 M H$_2$SO$_4$, 293 K, 100 mA cm^{-2}. Catalyst load 6 mg cm^{-2}. The Pd:Pt atomic ratios are listed [174]. (Reproduced by permission of ECS—The Electrochemical Society, from Blair S, Lycke D, Iordache C. Palladium-platinum alloy anode catalysts for direct formic acid fuels.)

Based on Figure 4.35, the major role of Pt was to stabilize Pd at the expense, unfortunately, of the catalytic activity. The best performance was obtained with a 1:1 Pd:Pt atomic ratio [174]. The long-term poisoning mechanism of Pd has not been discussed. The elucidation of the role of hydrogen adsorption and absorption into the bulk Pd electrode, in conjunction with CO_{ad} and/or oxidation of the Pd surface, could represent venues to be explored in order to shed light on the deactivation mechanism.

The Pd nanoparticle size has a strong influence on the electrocatalytic activity and stability with respect to formic acid oxidation. Liu et al. compared two Pd/C (20 wt% Pd) catalysts with different particle sizes [175]. Both catalysts were prepared by $NaBH_4$ reduction in alkaline media. However, in one case the $PdCl_2$ precursor was mixed with H_3BO_3 and NH_4F before creating the suspension with the Vulcan XC72 support and adding the $NaBH_4$ solution. This technique yielded Pd nanoparticles of 3.2 nm diameter whilst the same reduction technique but without the H_3BO_3 and NH_4F additives gave much larger particles (15.5 nm) [175]. These differences obviously impacted the electrocatalytic activity; the smaller nanoparticles and correspondingly higher specific surface area catalyst gave HCOOH oxidation current densities about an order of magnitude higher at 0.1 V vs. RHE in 0.5 M HCOOH – 0.5 M H_2SO_4 after 1000 s of operation. Furthermore, the rate of activity decay in time was slower for the smaller Pd nanoparticles.

In another approach to improve the long-term activity of Pd catalysts, a Pd-P composite formulation was proposed [176]. The P was incorporated into the catalyst by employing the same $NaBH_4$ reduction method as described above (i.e., with H_3BO_3 and NH_4F present) but NaH_2PO_2 was also added to the solution. The Pd:P atomic ratio was 1:0.09. Chronoamperometric curves at 0.1 V vs. RHE over 100 min showed improved activity and stability for the P-modified catalyst compared to pure Pd [176].

An alternative method to recover the activity of the Pd anode catalyst was proposed by Masel and co-workers, based on applying an anode potential spike of 1.2 V for a few seconds [177]. They also showed that Pd deactivation worsens with increasing HCOOH concentration, e.g., at 293 K in 10 M HCOOH the current density loss at a constant cell voltage of 0.53 V was about 28.5 mA cm^{-2} h^{-1}, while in 15 M HCOOH it doubled to 57 mA cm^{-2} h^{-1}. The Pd load in this study was 8 mg cm^{-2} [177].

Moreover, there is some indication in the literature that the purity of formic acid might play a role in affecting the order of stability among Pd, Pt, and PdPt. The long-term activity of Pd improved with enhanced formic acid purification [176]. This effect has not yet been thoroughly validated.

Another observation, which might relate to either electrocatalysis or other aspects of the catalyst layer (e.g., porosity), was the enhancement of the direct formic acid fuel cell performance following methanol conditioning under load [178]. Conditioning was performed by passing 1 ml min^{-1} CH_3OH through the anode compartment at 343 K under polarization, with cell voltages between 0.4 and 0.1 V. The anode catalyst was a Pd surface layer deposited on 4 mg cm^{-2} Pt. Following thorough flushing with deionized water, when the cell was switched to the 9 M HCOOH feed the maximum power density surprisingly increased from 33 to 119 mW cm^{-2} at 333 K [178]. The exact cause of this effect has not been

established yet. Some changes in the catalyst due to methanol conditioning were observed by the CO stripping voltammetry peak broadening, indicating possible modifications in the surface crystallography. Also, the hypothesis of pore structure alignment in the catalyst layer as a result of Nafion ionomer exposure to methanol under load was put forward [178].

4.2.3 Ethanol Electrooxidation

Increasing the number of carbon atoms in the fuel molecule inherently increases the number of electrooxidation steps and the potential reaction pathways [179]. Figure 4.36 summarizes the network of reactions for ethanol electrooxidation, generating products such as CH_3CHO, CH_3COOH, and CO_2.
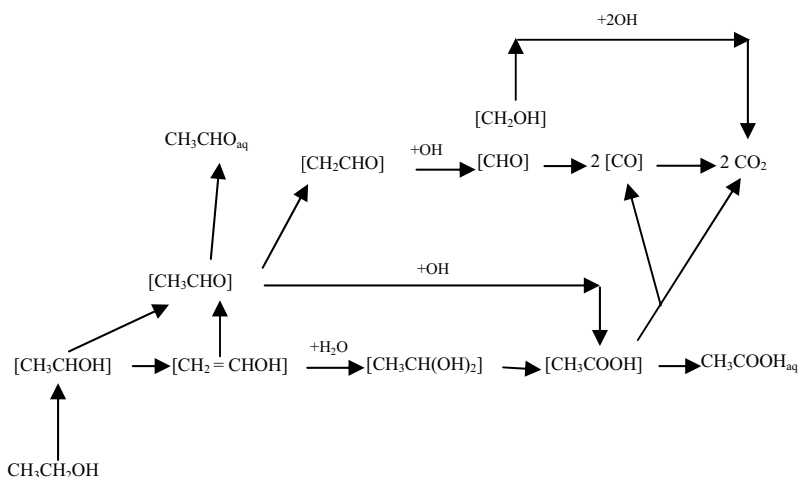
Figure 4.36. Multi-pathway reaction model for ethanol electrooxidation

Recently, Wang et al. published a comprehensive investigation of ethanol oxidation, with detection of both surface adsorbed and bulk species and determination of respective current efficiencies [180]. They compared three catalysts, Pt/C, PtRu (1:1 at. ratio)/C, and PtSn (3:1 at. ratio)/C, all prepared by the ethylene glycol method. On all three catalysts, for the investigated potentials (between 0.4 and 0.7 V vs. RHE) after 15 min of reaction time in 0.1 M ethanol – 0.5 M H_2SO_4, the highest yield was obtained for CH_3CHO (between 47 and 70%), followed by CH_3COOH (between 29 and 41%), and lastly, small amounts of CO_2 were detected (yield between 0.3 and 1.1%) [180]. Generally, on all three electrodes the yield of acetic acid increased with increasing electrode potential, at the expense of acetaldehyde formation. The strongest electrode potential dependence was observed in the case of PtRu/C, where at 0.4 V the yield of CH_3CHO was about 59% and at 0.7 V vs. RHE it dropped to 47%.

Using *in situ* spectroscopy the same authors revealed the roles of Sn and Ru as alloying elements. The rate of dissociative ethanol adsorption was lower on the

alloy catalysts compared to pure Pt but the advantage of the alloying element consisted in the higher oxidation rate of the intermediates, therefore lowering the steady-sate CO_{ad} surface coverage (especially the linearly bonded type $CO_{ad,L}$) [180]. By FTIR measurements CH_3CHO_{ad} and CH_3COOH_{ad} could not be distinguished, according to Wang et al., but C=O species were identified on the surface [180].
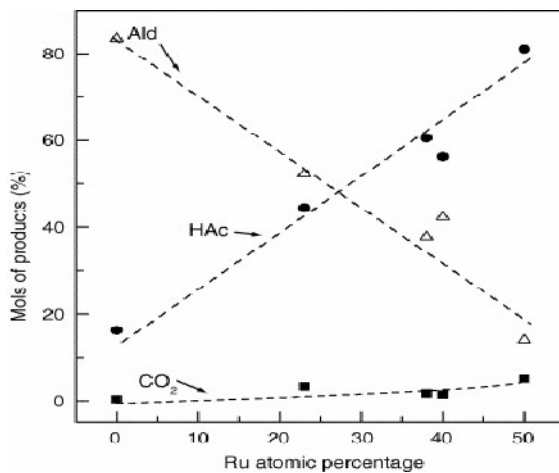
(a)
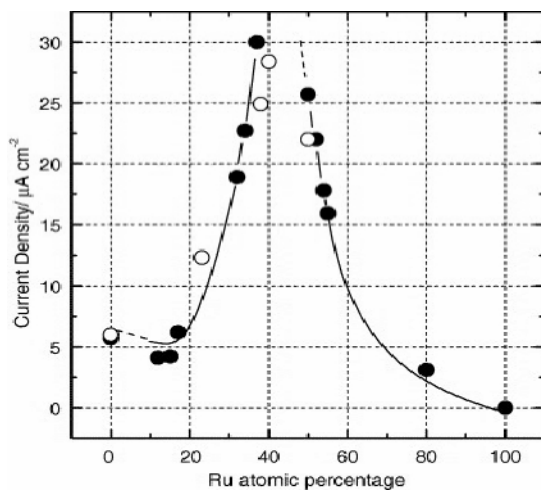
(b)

Figure 4.37. Effect of Ru content on ethanol electrooxidation: (a) product distribution after 3 min of polarization at 0.5 V vs. RHE, (b) oxidation current density after 30 min of polarization at 0.5 V vs. RHE. 1 M C_2H_5OH – 0.5 M H_2SO_4; 298 K [182]. (Reproduced from Journal of Electroanalytical Chemistry, 585(1), Camara GA, de Lima RB, Iwasita T, The influence of PtRu atomic composition on the yields of ethanol oxidation: a study by *in situ* FTIR spectroscopy, 128–31, 2005, with permission from Elsevier.)

On the same issue of product distribution, Iwasita and co-workers noted the ethanol concentration dependence [181–182]. At ethanol concentrations below 0.05 M the yield of acetaldehyde on Pt at 0.5 V vs. RHE was virtually zero. Only for ethanol concentrations higher than 0.15 M did the yield of acetaldehyde exceed that of acetic acid [181].

In the case of Pt alloys such as PtRu, the elemental composition of the catalyst has a pronounced effect on the product distribution [182]. Figure 4.37(a) shows that the CH_3COOH yield increases with Ru content. The highest ethanol oxidation current density (at 0.5 V vs. RHE) was measured for the 40 at% Ru catalyst, with acetic acid as the majority product (Figure 4.37(b)).

Following up on half-cell experiments, it is of great interest to characterize the products obtained in direct ethanol fuel cells. Rousseau et al. investigated direct ethanol fuel cells employing Pt, PtSn (9:1 at. ratio), and PtSnRu (8.6:1:0.4) anode electrocatalysts supported on Vulcan XC72 prepared by the Bonnemann colloidal method (3 mg cm^{-2} Pt content) [183].
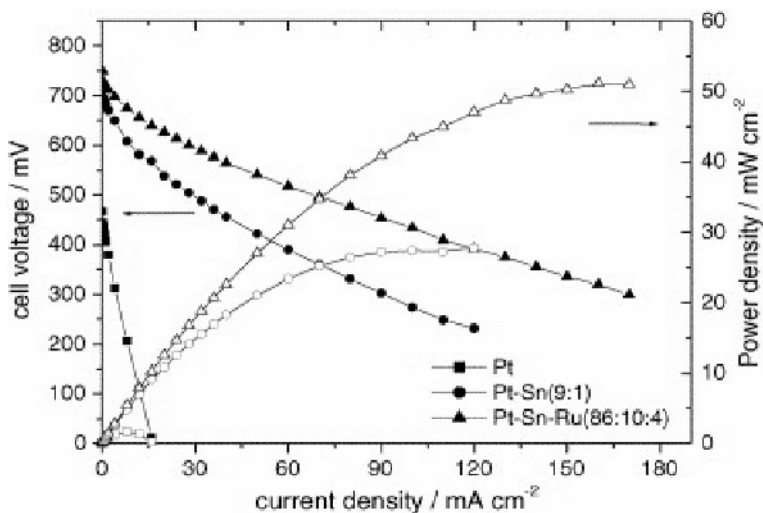
Figure 4.38. Direct ethanol fuel cell polarization curves at 353 K. Ethanol concentration 2 M, Nafion 117, O_2 pressure 3 bar [183]. (Reproduced from Journal of Power Sources, 158(1), Rousseau S, Coutanceau C, Lamy C, Léger J-M, Direct ethanol fuel cell (DEFC): electrical performances and reaction products distribution under operating conditions with different platinum-based anodes, 18–24, 2006, with permission from Elsevier.)

Figure 4.38 shows the maximum power output (52 mW cm^{-2} at 353 K) was obtained with the ternary formulation, compared to only 27 mW cm^{-2} with the binary catalyst. The product distribution is given in Table 4.2 [183]. Adding Sn to the catalyst formulations favored the formation of CH_3COOH, and lowered the amounts of CO_2 and CH_3CHO. Furthermore, the CO_2 content was also much higher (between 10–20%) than those reported based on half-cell experiments [180]. Therefore, these findings at the fuel cell level contradict the half-cell results of Wang et al. discussed previously [180]. Differences in catalyst loading,

temperature, ethanol concentration, electrolyte composition (i.e., H_2SO_4 or $HClO_4$ in half-cell studies and aqueous ethanol in fuel cells), and operating time might be partially responsible for the discrepancies between the fuel cell and half-cell product analysis.

Table 4.2. Product distribution (chemical yields) after 4 h operation of the direct ethanol fuel cell (Figure 4.38) at 0.3 V for Pt/C and 0.5 V for PtSn/C and PtSnRu/C [183]. (Reproduced from Journal of Power Sources, 158(1), Rousseau S, Coutanceau C, Lamy C, Léger J-M, Direct ethanol fuel cell (DEFC): Electrical performances and reaction products distribution under operating conditions with different platinum-based anodes, 18–24, 2006, with permission from Elsevier.)

Catalyst	CH_3COOH (%)	CH_3CHO (%)	CO_2 (%)
Pt/C	32.5	47.5	20.0
PtSn (9:1)/C	76.9	15.4	7.7
PtSnRu (8.6:1:0.4)/C	75.0	15.2	9.8

The beneficial role of Sn as an alloying element with regard to ethanol oxidation has been extensively discussed in the literature [80, 180, 183–195]. There seem to be two schools of thought: one attributes the Sn effect to the enhanced oxidation of ethanol without breaking the C–C bond, producing mainly acetaldehyde and acetic acid [184], while the second approach proposes that Sn also affects the CO_2 generation rate, not via the CO route but by enhancing the oxidation rate of CH_3CHO to CO_2 [179, 186].

There is now fairly conclusive evidence that PtSn performs better than PtRu, PtPd, PtRe, and PtW in direct ethanol fuel cell experiments, especially at temperatures equal to and above 343 K [185–186, 188–192]. Furthermore, the long-term stability of PtSn (9:1 at. ratio) was promising, as the cell voltage was virtually constant around 0.45 V for 240 min at 32 mA cm^{-2} and 353 K [183].

The mass specific activities of the catalysts for ethanol electrooxidation are unfortunately quite low, between about 5 mW mg^{-1} at 323 K and 9–11.5 mW mg^{-1} at 353 K based on peak power outputs [183–184, 186]. Zhou et al. reported somewhat higher mass specific activities, reaching 23 mW mg^{-1} at 333 K [188b]. Utilizing extended reaction zone anodes could also improve the mass specific activity (see also Section 4.3) [190].

There is some debate regarding the optimum Pt:Sn atomic ratio. The interaction effects between catalyst preparation method, temperature, ethanol concentration, and electrode potential will affect the performance of various formulations. The typical investigated range was between Pt:Sn 9:1 and 1:1 (atomic ratio). Zhou et al. noted the temperature dependence of the optimum Pt:Sn ratio: 1.5:1 at 333 K and 2:1 at 363 K, respectively [188b]. At elevated temperatures (between 363 K and 403 K) the performance of PtSn-based catalysts improved considerably. Jiang et al. reported an unusually high mass-specific peak power output of 53 mW mg^{-1} for PtSn (3:1 at. ratio) at 363 K [193], while Colmati et al., at the same temperature and catalyst composition, reported only 18–20 mW mg^{-1} [186, 194]. However, the catalysts were prepared by different techniques.

The role of Sn oxides at high temperatures was invoked and PtSnO and PtSnInO catalysts produced by the polyol method were found to be effective for ethanol oxidation [192, 193]. Other ternary formulations that showed promise are PtSnRu [183, 196] (Figure 4.38) and PtSnNi (1.25:1:0.4) [187]. For DEFC operated at 383 K a ternary formulation composed of PtSnRu/C (1:1:0.3 at. ratio) improved the peak power output compared to PtSn/C (1:1) from 27 mW cm^{-2} to 32 mW cm^{-2} using 1 mg cm^{-2} catalyst load, 1 M ethanol and 3 atm O_2 pressure [196].

There have been a few attempts to replace Pt as the basis for ethanol oxidation electrocatalysis. The ethanol oxidation on Au in both 0.1 M $HClO_4$ and 0.1 M NaOH was sluggish and the product analysis after 60 h showed acetaldehyde as the majority product [197]. Pd, on the other hand, was found to be a more promising catalyst candidate. Zheng et al. investigated Pd nanoparticles (3–6 nm diameter) supported on carbon black (C), activated carbon fiber (ACF), and multiwalled carbon nanotubes (MWCNT) [198]. The ethanol oxidation experiments were carried out in alkaline media (1 M KOH). The cyclic voltammogram (Figure 4.39) shows that Pd/MWCNT provided the highest oxidation current densities. However, the comparison is incomplete since Pt was supported only on carbon black. Thus, the effect of MWCNT cannot be established.
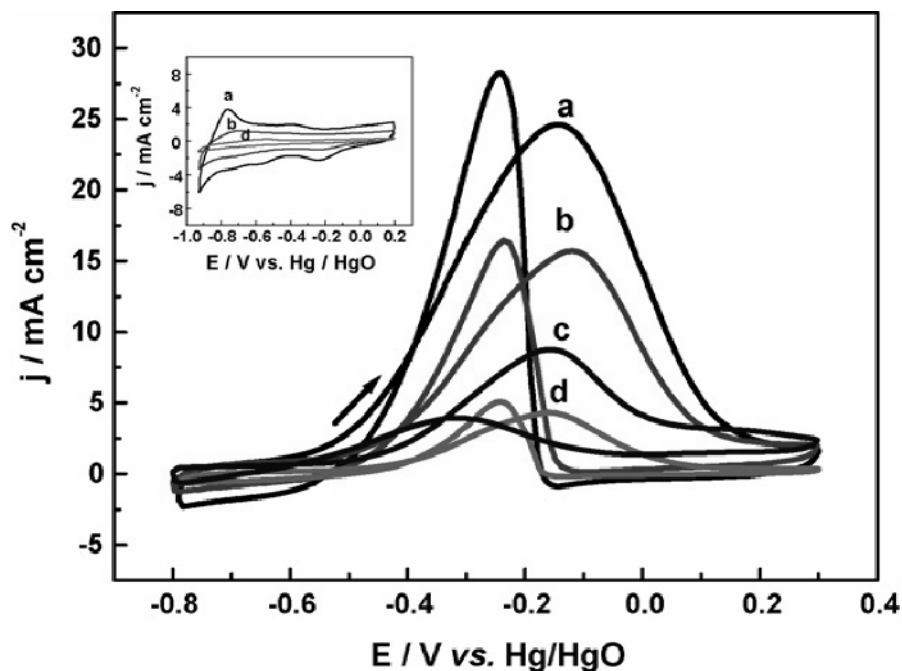
Figure 4.39. Cyclic voltammogram of ethanol oxidation in alkaline media on Pd and Pt catalysts. 1 M ethanol – 1 M KOH, sweep rate 50 mV s^{-1}, 293 K. [198]. E [Hg/HgO, a(OH–) = 1] = 0.098 V vs. SHE. a) Pd/MWCNT, b) Pd/C, c) Pt/C, and d) Pd/ACF. (Reproduced from Journal of Power Sources, 163(1), Zheng HT, Li Y, Chen S, Shen PK, Effect of support on the activity of Pd electrocatalyst for ethanol oxidation, 371–5, 2006, with permission from Elsevier.)

Nevertheless, under identical conditions Pd/C also gave better results than Pt/C [198] (Figure 4.39). Interestingly, chronopotentiometry revealed strong anode potential oscillatory behavior on Pt/C, while the Pd/MWCNT system was stable over the entire 250 min duration of the experiment [198]. Furthermore, TiO_2 nanotubes could also serve as Pd catalyst supports for ethanol oxidation in alkaline media [199].

In alkaline media, Ni-based supports were also explored in conjunction with PtRu and PtRuMo electrocatalysts [200–202]. Pt:Ru compositions between 1.1:1 and 2.1:1 atomic ratio supported on Ni were found to yield the lowest faradaic resistances for the oxidation of 1 M ethanol in 1 M NaOH, determined by electrochemical impedance spectroscopy [200]. It was speculated that the role of Ni support extends beyond purely mechanical passive interaction with the catalyst, and Ni could contribute to the electrocatalytic activity by its surface and electronic properties as an oxophilic element. Further studies are required in this area.

Gupta and Datta developed CuNi alloys (70:30) as substrates for fabricating the anode compartment of direct ethanol fuel cells [201–202]. Surfactant assisted (i.e., 2 wt% PTFE) galvanostatic electrodeposition at 15 mA cm^{-2} was employed to deposit PtRu and PtMo on the substrate [201]. The activity of PtMo/CuNi was superior only over short time periods (below 200 s) compared to PtRu/CuNi. The reaction products were not analyzed and alkaline direct ethanol fuel cell experiments were thus far not presented using these catalysts.

4.2.4 Non-precious Metal Catalysts for Methanol, Formic Acid, and Ethanol Oxidation

Replacing Pt and other precious metals in the electrocatalyst formulations would represent a major advancement toward commercialization of fuel cells and could assure the sustainability of industrial-scale production for a variety of applications. At present, the state-of-the-art total Pt load (anode plus cathode) in direct fuel cells is typically around 4 mg cm^{-2} (or higher) and the maximum power output varies widely in the range of 10 to 150 mW cm^{-2} at 333 K (the lowest values are typically for ethanol fuel cells). Reducing either partially or completely the need for Pt and other precious metals poses a fundamental challenge in electrocatalysis, where breakthroughs of practical significance are very difficult to achieve. Essentially, two schools of thought have emerged. One is centered on organometallic macrocycle complexes and the other one proposes carbides (e.g., tungsten carbides) as replacements for Pt and other precious-metal-based electrocatalyst formulations for direct fuel cell anodes.

The role of organometallic complexes as co-catalysts with Pt for methanol electrooxidation was mentioned earlier. Can they also act alone and replace Pt completely? For the anodic oxidation of methanol, ethanol, and formic acid, studies looking at CO oxidation by various porphyrin complexes with Ir, Rh, and Co in aqueous electrolytes (both acid and alkaline) are relevant [90, 203, 204]. The mechanism proposed by Shi and Anson for the activity Co-octaethylporphyrin considers the oxidation of Co(II) to Co(III) in conjunction with coordination of CO to the Co(III) centres, followed by nucleophilic H_2O attack leading to catalytic oxidation forming CO_2 (see Equations 4.15–4.18) [90].

There have been no follow up studies on the activity of Co-octaethylporphyrin for electrooxidation of methanol, ethanol, or formic acid. Mukherjee et al. investigated pyrolized Co and Fe tetraphenylporphyrins and reported that the macrocycle N_4 centre together with the metal and metal oxide nanocrystallites played a role in electrocatalysis [205].

In alkaline media Ni macrocyle complexes showed some degree of activity toward the electrooxidation of alcohols. Trevin et al. synthesized electropolymerized Ni macrocycle films on vitreous carbon and indium tin oxide electrodes [206]. For the poly NiSalen film (Salen = bis(salicylidine) ethylenediamine), obtained by successive cycling between 0 and 1 V vs. SSCE in a solution composed of 0.1 M NaOH and 2 mM Ni-Salen, Figure 4.40 indicates that there was a correlation between the ethanol concentration, Ni surface concentration (Γ_{Ni}), and catalytic ethanol oxidation current. In order to achieve high catalytic oxidation currents, the ethanol to Γ_{Ni} ratio had to be less than about 0.5×10^6 cm^2 L^{-1} [206]. Thus, low ethanol concentration in combination with high Ni-Salen loading could assure efficient oxidation. The explored ethanol concentrations were below 2.5 mM, hence, micro-direct fuel cell applications might be feasible based on the available information. The methanol and ethanol oxidation onset potentials in 0.1 M NaOH were about 0.45–0.5 V vs. SSCE.
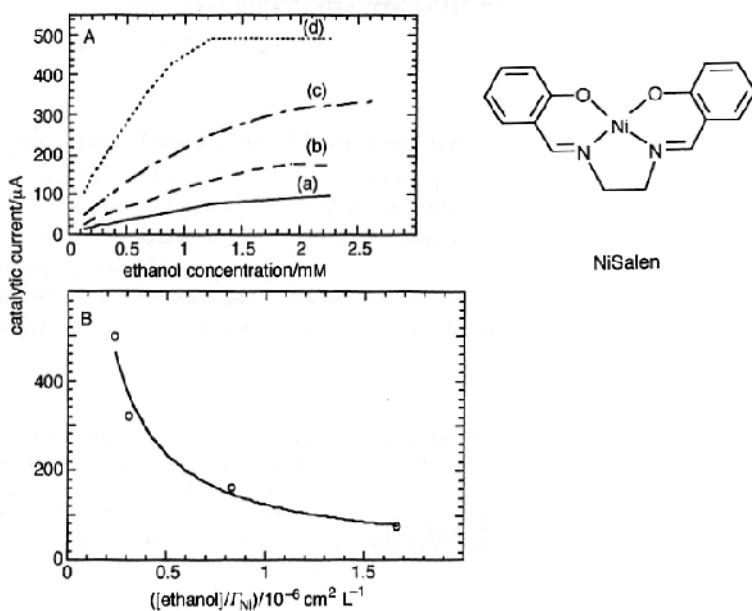
Figure 4.40. Ethanol oxidation currents (at 0.65 V vs. SSCE) on poly-NiSalen films deposited on vitreous carbon. The effect of ethanol concentration and NiSalen surface coverage Γ_{Ni} (mol cm^{-2}): a) 0.9×10^{-9}; b) 1.8×10^{-9}; c) 4.75×10^{-9}; d) 6.2×10^{-9}. 0.1 M NaOH, 293 K [206]. (Trevin S, Bedioui F, Villegas MGG, Charreton-Bied C. Electropolymerized nickel macrocycle complex-based films: design and electrocatalytic application. J Mater Chem 1997;7:923–8. Reproduced by permission of The Royal Society of Chemistry.)

Ciszevski and Milczarek reported roughly similar oxidation onset potentials for methanol and ethanol in 0.1 M NaOH using Ni(II) tetrakis(3-methoxy-4-hydroxyphenyl) porphyrin film (poly-NiTMHPP). However, they explored catalytic oxidations up to 0.5 M methanol concentration [207]. Since the alcohol electrooxidation occurs at potentials more positive than the redox potential of Ni(III)/Ni(II) (i.e., Ni(III) is the electrocatalytically active form), a direction to improve the performance would be to find macrocycles that negatively shift the Ni(III)/Ni(II) potential. Another variant would be to develop mixed macrocycle catalysts by incorporating elements that promote OH_{ad} formation, since on Ni polymer films the methanol oxidation was strongly dependent on the OH^- concentration [207].
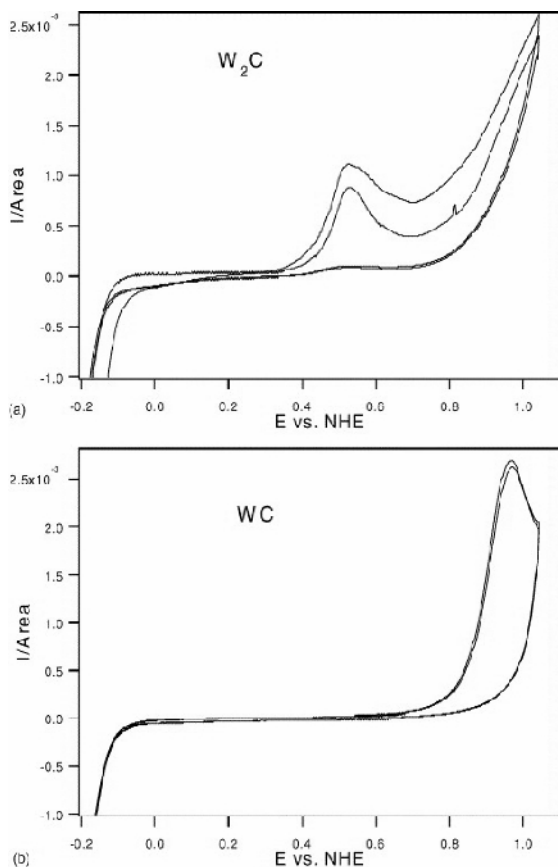
Figure 4.41. Cyclic voltammogram of W_2C and WC films supported on carbon paper in 0.5 M H_2SO_4 saturated with N_2 [210]. (Reproduced from Catalysis Today, 99(3–4), Zellner MB, Chen JG, Surface science and electrochemical studies of WC and W_2C PVD films as potential electrocatalysts, 299–307, 2005, with permission from Elsevier.)

The other approach for the development of more economical non-noble metal electrocatalysts focuses on carbides, particularly tungsten carbides (WC and W_2C).

The interest in these compounds stems from the idea that they posses Pt-like electronic behavior in catalytic reactions, which theoretically could make them attractive candidates as catalysts for direct liquid fuel cells [208, 209]. One of the first issues to be considered, however, is the stability of these materials under anodic conditions. Zellner and Chen recorded the cyclic voltammograms of WC and W_2C deposited on carbon paper in 0.5 M H_2SO_4 (Figure 4.41) [210]. WC was stable up to 0.6 V vs. SHE while W_2C was susceptible to oxidation forming W_xO_y starting from about 0 V and giving a peak at 0.5 V vs. SHE.

Furthermore, surface studies on WC have shown the possibility of methanol and water adsorption, both essential to methanol electrooxidation catalysis [210–212]. It must be noted, however, that these studies were not conducted under electrode polarization conditions but in ultra high vacuum chamber. Electrochemical polarization experiments in which methanol was present were not given.

Arguably the most detailed electrochemical studies on tungsten and double carbides (e.g., with Mo) were performed by Kawamura et al. [213–215]. Tungsten carbide (WC) itself showed weak activity toward CH_3OH electrooxidation (Figure 4.42). However, the carburization period, addition of Mo as a co-element in the carbide, and oxidative pre-treatment in O_2 and boiling water followed by alkaline treatment of the carbide samples all contributed to yield an up to ten-fold increase in the mass specific activity for methanol oxidation at 0.5 V vs. RHE (Figure 4.43) [213–215]. The role of the oxidative and alkaline treatments was to remove surface carbon formed during the preparation method and to create oxide sites that were active in electrocatalysis. Methanol oxidation polarization curves as a function of temperature with $(W_{0.8}Mo_{0.2})C$ are shown in Figure 4.44. It is important to note that the mixed $W_{0.8}Mo_{0.2}C$ catalyst did not deactivate and experiments were carried out at high (up to 8 M) methanol concentration.
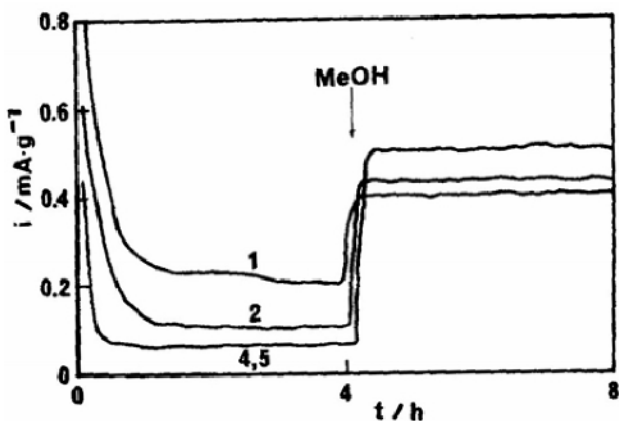
Figure 4.42. Chronoamperometry curves of CH_3OH oxidation on WC. Arrow indicates addition of methanol, numbers represent the number of runs. Conditions: 323 K, 0.5 V_{RHE}, 1 M H_2SO_4, 4 M CH_3OH [213]. (Reproduced by permission of ECS—The Electrochemical Society, from Kawamura G, Okamoto H, Ishikawa A, Kudo T. Tungsten molybdenum carbide for electrocatalytic oxidation of methanol.)
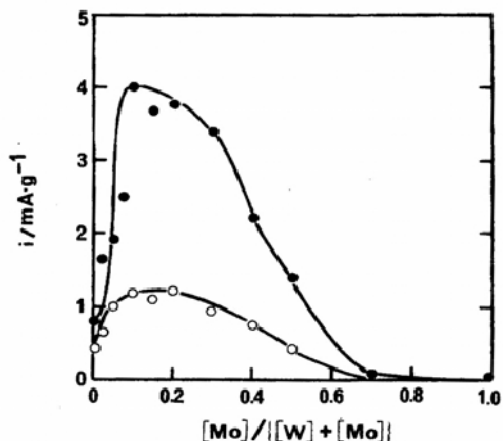
Figure 4.43. Effect of Mo content (atomic percentage) on the methanol oxidation activity of (W,Mo)C. Legend: ● catalyst subjected to alkaline treatment, ○ catalyst without alkaline treatment. Conditions: 323 K, 0.5 V_{RHE}, 1 M H_2SO_4, 4 M CH_3OH [213]. (Reproduced by permission of ECS—The Electrochemical Society, from Kawamura G, Okamoto H, Ishikawa A, Kudo T. Tungsten molybdenum carbide for electrocatalytic oxidation of methanol.)
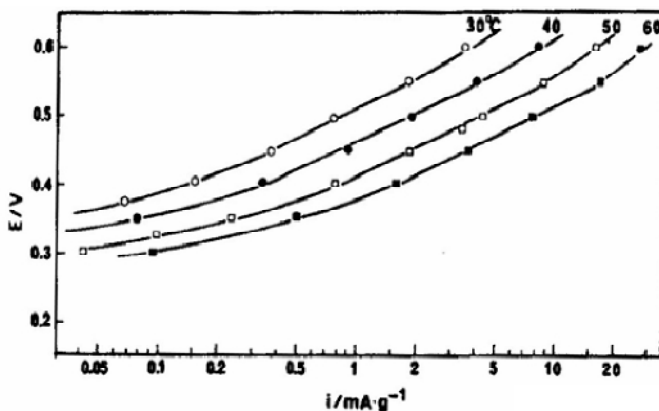
Figure 4.44. Anodic polarization curves of CH_3OH on $W_{0.8}Mo_{0.2}C$ catalyst as a function of temperature. Catalyst load: 0.2 g cm^{-2}, 4 M CH_3OH and 1 M H_2SO_4 [213]. (Reproduced by permission of ECS—The Electrochemical Society, from Kawamura G, Okamoto H, Ishikawa A, Kudo T. Tungsten molybdenum carbide for electrocatalytic oxidation of methanol.)

Since the 1987 papers by Kawamura et al., it is surprising that the promising results with double carbides, (W, Mo)C, were not followed up in later studies. Recently, Li et al. developed a preparation method for WC-carbon nanotube composites [216]. This new material, with WC nanoparticles (200 nm diameter) well-dispersed on the outside of carbon nanotubes, should be tested for methanol oxidation.

In the context of a microbial fuel cell, WC was investigated as anodic catalyst for the oxidation of hydrogen, formate, ethanol, and lactate formed as fermentation products at pH 5, 293 K, and atmospheric pressure [217]. The WC anode was found to be inactive toward ethanol oxidation. Figure 4.45 shows the cyclic voltammogram of formate and lactate on WC deposited on graphite foil electrode. In both cases enhanced oxidation starts at around 100 mV vs. SSCE, indicating significant surface overpotential. Nevertheless, there is promise for the use of inexpensive WC (or in modified variants with other elements) as electrocatalyst for formate (or formic acid) based fuel cells targeting micro-scale applications.
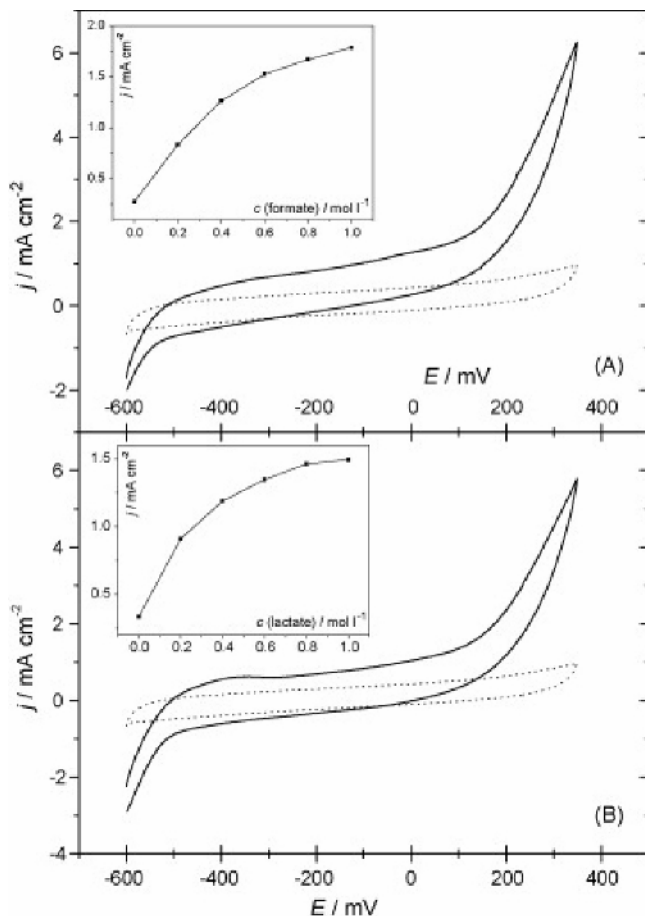
Figure 4.45. Cyclic voltammogram of 1 M formate (A) and lactate (B) on WC/graphite foil electrode at pH 5 in 0.1 M KCl at 293 K. Catalyst load: 20 mg cm^{-2}. The electrode potential is given vs. Ag/AgCl (SSCE.) Inset figures show the current density measured at 0.2 V vs. SSCE as a function of anolyte concentration [217]. Dashed curve = blank electrolyte, solid curve = electrolyte with formate (A) or lactate (B). (Reproduced from Applied Catalysis B: Environmental, 74(3–4), Rosenbaum M, Zhao F, Quaas M, Wulff H, Schröder U, Scholz F, Evaluation of catalytic properties of tungsten carbide for the anode of microbial fuel cells, 261–9, 2007, with permission from Elsevier.)

4.3 Advances in Anode Catalyst Layer Engineering: Example Analysis

The electrode performance in any electrochemical system depends on the complex interaction between intrinsic kinetics and various transport processes involving reactants, products, and the electrolyte. In the particular case of direct fuel cells, the catalyst support (when employed), the hydrophobic-hydrophilic properties of the diffusion substrate, the ionomer load in the catalyst layer, and the electrode design, including the current collector, all have a great impact on the power output. The goal in the present section is to give an overview of the experimental advances in the area of catalyst layer engineering and anode structures.

4.3.1 Engineering of the Catalyst Surface and Morphology

In addition to improvements in the intrinsic electrocatalytic activity, research has been carried out to modify ("design", possibly) the catalyst surface in order to enhance the catalyst utilization efficiency and ultimately the fuel oxidation superficial current density. The latter can be expressed in terms of catalyst layer physico-chemical properties as [218]:

$$i = \gamma_c \cdot a_v \int_0^\tau i_x dx = \gamma_c \cdot a_m \cdot \frac{m_c}{\tau} \int_0^\tau i_x dx \qquad (4.36)$$

where a_v is the volume specific total catalyst surface area (m^2_{total} m^{-3}_{geom}), a_m is the total catalyst surface area per unit weight (referred to as the mass specific surface area (m^2_{total} g^{-1})), i_x is the local current density (A m^{-2}_{eff}), m_c is the catalyst load (g m^{-2}_{geom}), γ_c is the catalyst utilization efficiency reflecting the effective area participating in the electrochemical reaction (m^2_{eff} m^{-2}_{total}), and τ is the electroactive reaction zone (or catalyst layer) thickness (m_{geom}). Note that τ may or may not be equal to the physical thickness of the catalyst layer, depending on the reactant penetration depth [146] and the availability of the ionic conductor network linking the catalytic sites.

The local current density i_x is expressed by various electrode polarization scenarios, such as intrinsic kinetic control, or mixed control involving intrinsic electrode kinetics together with reactant mass transfer and/or ionic conductivity effects, leading to multiple apparent Tafel slopes [146].

Thus, in terms of Equation 4.36, modifying a_m, γ_c, and τ could significantly increase the superficial current density i for a given catalyts load m_c and electrode polarization condition (i.e., overpotential).

Regrading the catalyst particle geometry, while nanoparticles are commonly described by the cubo-octahedral model [219], recently Tian et al. developed an electrochemical method for the surface "design" of tetrahexahedral Pt nanocrystals (Figure 4.46) [220]. A square wave potential function (between –0.20 V vs. SCE and +1.20 V vs. SCE with a frequency of 10 Hz) was applied to electrodeposited Pt

nanospheres (of 750 nm diameter, supported on glassy carbon) to induce surface reshaping and preferential crystal face formation [220–222].
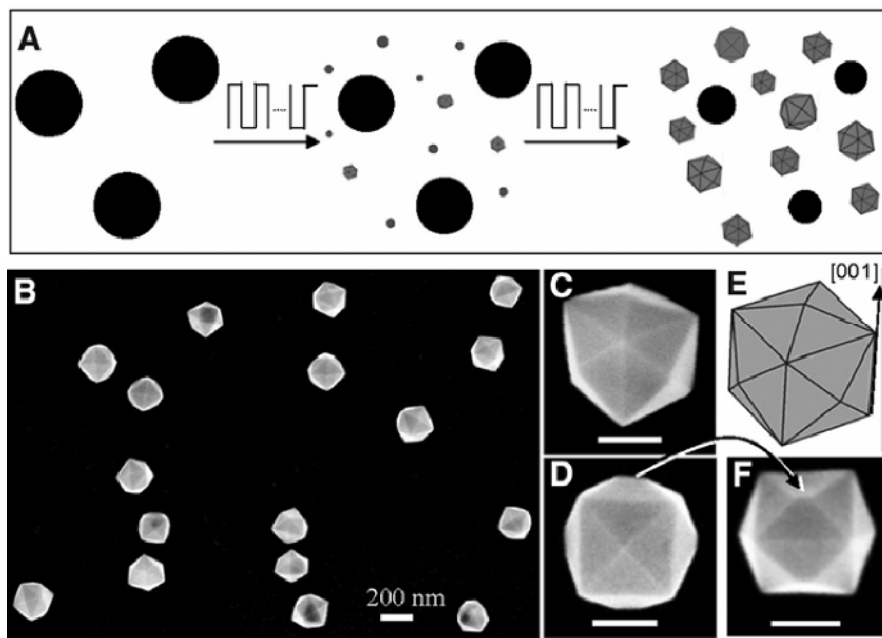
Figure 4.46. (A) Schematic of the tetrahexahedral Pt surface geometry formation by applying square-wave voltammetry. (B), (C), (D), and (F) are low- and high-magnification SEM images, and (E) is a conceptual model of the tetrahexahedral Pt [220]. (Reproduced with permission from Tian N, Zhou Z-Y, Sun S-G, Ding Y, Wang ZL. Synthesis of tetrahexahedral platinum nanocrystals with high-index facets and high electrooxidation activity. Science 2007;316:732–5.)

A preliminary investigation of the electrocatalytic activity showed that Pt tetrahexahedral particles exhibited enhanced activities on a surface area basis toward both HCOOH and C_2H_5OH electrooxidation when compared to either Pt nanospheres or commercial Pt/C (E-TEK Inc.) catalyst [220]. Figure 4.47 shows chronoamperometry curves recorded in the case of formic acid and ethanol, respectively. However, since the particle sizes were fairly large (in the order of ~80 nm) the mass specific activity of the tetrahexahedral catalyst was not satisfactory and further research must be performed to reduce the particle size. Unfortunately, the paper by Tian et al. omitted to report the catalys load [220].

Gonzalez and co-workers provided other evidence for the catalyst morphology effect on direct fuel cell polarization behavior [223]. Their objective was to compare Pt-Ru catalysts of the same particle size but with different morphology, imparted by the various preparation methods based on formic acid reduction. For a narrow particle size range distribution (3.8–4.8 nm diameter) the catalysts with more homogeneous Ru deposits on the surface gave higher power outputs for the DMFC [223].
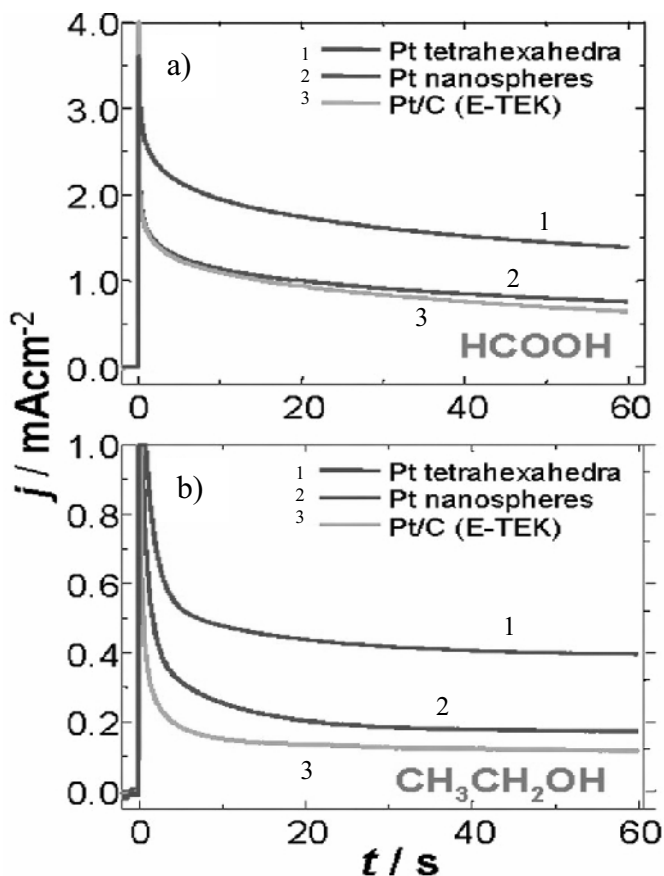
Figure 4.47. Effect of Pt surface reshaping by square wave voltammetry on the electrocatalytic activity toward formic acid and ethanol oxidation. a) Formic acid oxidation at 0.25 V vs. SCE in 0.25 M HCOOH – 0.5 M H_2SO_4. b) Ethanol oxidation at 0.3 V vs. SCE in 0.1 M EtOH – 0.1 M $HClO_4$; 295 K [220]. (Reproduced with permission from Tian N, Zhou Z-Y, Sun S-G, Ding Y, Wang ZL. Synthesis of tetrahexahedral platinum nanocrystals with high-index facets and high electro-oxidation activity. Science 2007;316:732–5.)

The structural sensitivity of electrode reactions such as oxygen reduction and oxidation of organic molecules is well known. This is brought about by the particle size dependence of various physico-chemical factors such as heats of adsorption, Fermi level density of states, electron binding energies in the catalyst, and selective surface segregation in the case of multi-component catalysts [224–229].

Weaver et al. published an authoritative study comparing the particle-size dependence of the rates of methanol, formic acid, and formaldehyde electrooxidations on Pt/C catalysts with diameters between approximately 2–8 nm [230]. Using cyclic voltammetry and two different concentrations of species (10 mM and 0.1 M) it was found that the HCOOH and CH_3OH oxidation rates had opposite trends with respect to particle size. In the case of HCOOH the effective oxidation current densities increased with a decrease of Pt particle size, in the

order: I (2 nm) > I (8.8 nm) ≥ I (flat polycrystalline electrode). For CH_3OH, on the other hand, the opposite was true, namely, the effective oxidation current densities increased with an increase of particle size: I (flat polycrystalline electrode) > I (8.8 nm) > I (2.2 nm) [230]. It must be noted that the current densities were expressed in terms of the effective Pt surface area, therefore the changes in catalyst particle size reflected intrinsic electrode kinetic differences.

Weaver and co-workers explained the particle size effect in terms of an ensemble effect related to surface morphology [230]. For Pt nanoparticles of diameter ≤ 4 nm it was experimentally determined [231] that the fraction of flat terrace sites diminished considerably as compared to edge sites. Therefore, the probability of ensemble of active site formation situated on the terraces and needed for methanol dehydrogenation (especially for the removal of the first three hydrogen atoms) is lower for particles with diameters below 4 nm. It was estimated that the 2.5 nm diameter particle has an approximately five times lower availability of adjacent Pt atoms compared to the 8.8 nm diameter particle [230]. In the case of formic acid oxidation, on the other hand, it was proposed that Pt ensembles are not required for catalysis. Interestingly, the CO_{ad} surface coverage decreased with particle size for both CH_3OH and HCOOH.

The group of Wieckowski and Masel confirmed for the case of unsupported Pd nanoparticles that the smaller the particle size the higher the electrocatalytic activity toward HCOOH oxidation [232]. They investigated particles of 9 to 40 nm diameter subjected to cyclic voltammetry and chronoamperometry. Based on XPS results it was reasoned that the smaller the particle, the greater the shift of the *d*-electron band center, resulting in a decrease in the heat of adsorption of the formate intermediate, hence facilitating the oxidation reaction [232].

Regarding ethanol oxidation, studies of thermochemical oxidative ethanol dehydrogenation at 303 K revealed structure sensitivity for Pt particle sizes lower than 2 nm. The turnover frequency decreased by a factor of two when the particle size decreased from 2 nm to 1.5 nm [233]. In the case of electrocatalytic ethanol oxidation the experimental evidence is less clear. However, due to the nature of the reaction, involving potentially C–C bond dissociation, structure sensitivity is expected to occur. More studies are required, aimed at clarifying the structure sensitivity of ethanol electrooxidation.

Indirect evidence could be inferred from the study by Colmenares et al. comparing Pt/C, PtRu/C, and PtSn(3:1)/C commercial electrocatalysts of 3–4 nm diameter with catalysts of identical composition but prepared by a polyol method yielding smaller particle sizes, between 2–3 nm [234]. The intrinsic electrocatalytic activity for ethanol oxidation, evaluated from Tafel plots, was generally superior for the larger (i.e., commercial E-TEK Inc.) catalyst particle sizes. This was tentatively attributed to the lower degree of alloying in the case of small nanoparticles produced by the polyol method [234], which is in line with the established particle size sensitivity of alloy segregation [227]. Moreover, the less alloyed polyol-type catalysts produced a higher fraction of acetic acid as oxidation product, while for the larger catalyst particle sizes acetaldehyde was the major product. Whether other particle-size-related factors contributed as well to the electrocatalytic differences between the commercial and polyol-produced catalysts was not discussed in this work.

On large ~0.8 μm diameter PtSn particles ethanol was oxidized mainly to acetic acid [235]. Structure sensitivity of ethanol and acetaldehyde electrooxidation was also implied in experiments using Au nanoparticles where the electrocatalytic activity per real surface area increased with an increase in particle diameter [236].

In addition to nanoparticles, other precious metal catalyst structures have been investigated such as mesoporous nanostructured layers. In a series of publications Attard, Elliott, Bartlett, and co-workers described the formation of mesoporous Pt and PtRu films by lyotropic liquid crystalline phase templated electroless or electrochemical (faradaic) deposition [237–243]. Using non-ionic surfactants (e.g., polyethylene glycols such as $C_{12}EO_8$, $C_{16}EO_8$, and $C_{18}EO_{10}$) at concentrations above 30 wt% in order to assure the formation of a homogeneous liquid crystalline phase, the surfactant molecular aggregates in the bulk electrolyte could serve as templates for nanostructured deposition of metal ions from the interstitial spaces.

a)   b)

c)   d)
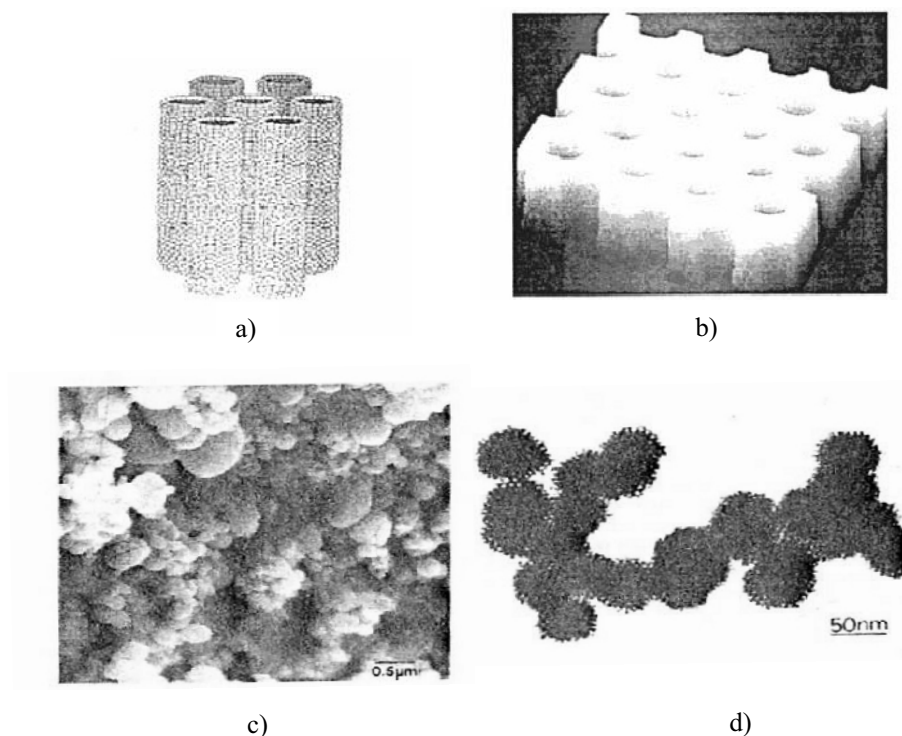
Figure 4.48. Liquid crystal templated catalyst synthesis: a) Conceptual representation of non-ionic surfactant aggregation forming a hexagonal liquid crystalline phase, b) expected nanostructured catalyst layer formed by either electroless or electrochemical deposition after removal of the template, c) SEM image of the Pt catalyst layer obtained in practice, and d) microstructure of the Pt catalyst layer (TEM image) [240, 242]. (Images (a) and (b) reprinted with permission from Chem Mater 1999;11:3602–9. Copyright 1999 American Chemical Society. Images (c) and (d) reprinted with permission from Attard GS, Göltner CG, Cirker JM, Henke S, Templer RH. Liquid-crystal templates for nanostructured metals. Angew Chem Int Ed Engl 1997;36:1315–7. ©1997 German Chemical Society.)

Figure 4.48(a) and (b) show an idealized schematic of the hexagonal 3D template and the expected nanoporous catalyst film on a solid support [242]. Following the deposition process, the templating surfactant can be removed by successive washing steps and possibly heat treatment. For the reduction of the metal ions a variety of techniques were used, such as electroless deposition using hydrazine, sodium borohydride, formaldehyde, Fe, or hydrogenation under pressure, and potentiostatic electrodeposition of Pt between +0.1 V vs. SCE and −0.4 V vs. SCE. Figure 4.48(c) and (d) present the resulting Pt catalyst macro- (Figure 4.48(c)) and microstructures (Figure 4.48(d)) using hydrazine as the reducing agent [240]. Catalyst particles of 90–500 nm in diameter were formed, with the hexagonal porous nanostructure having a ~3 nm pore diameter.

The pore diameter and consequently the specific surface area of the catalyst film can be controlled by the selection of the surfactant (i.e., shorter or longer chains) and the use of swelling additives (e.g., heptane). For instance, for the electrodeposition of Pt from H_2PtCl_6 the pore diameters of the films were ~1.8 nm using $C_{12}EO_8$, ~2.5 nm for $C_{16}EO_8$, and ~4 nm with $C_{16}EO_8$, n-heptane (1:1 molar ratio) added as a swelling agent [242].

Yamauchi et al. developed a modified version of liquid crystalline templation where liquid crystallinity appears progressively during ethanol solvent evaporation. This technique was used for the templated potentiostatic electrodeposition at −0.144 V vs. SCE of 50–800 nm PtRu particles with internal mesochannels [244].

Jiang and Kucernak explored the potential for electrocatalysis of liquid crystal templated mesoporous Pt and PtRu nanostructures (supported typically on Au) with respect to the electrooxidation of CO, CH_3OH [245–247], and HCOOH [248]. The mesoporous Pt film showed enhanced tolerance toward CO poisoning at potentials below 0.5 V vs. RHE compared to a commercial Johnson Matthey catalyst. In half-cell experiments a mass specific activity on Pt of 20 A g^{-1} was reported in 1 M CH_3OH and 0.5 M H_2SO_4 at 0.55 V vs. RHE and 338 K [245, 246]. Three factors related to catalyst morphology were proposed in order to explain the enhanced catalytic activity of the mesoporous Pt: a) improved H_2O activation, b) higher proportion of crystallographic faces that favor methanol electrooxidation, and c) acceleration of the parallel (non-CO) pathway [245].

By employing mesoporous PtRu prepared by liquid crystal templated reduction, the mass specific activity more than doubled compared to pure Pt [247]. The highest mass-specific activities (about 43 A g^{-1} at 0.38 V vs. RHE and 333 K) were obtained at CH_3OH concentrations between 1 and 2 M (Figure 4.49). Further increase of the methanol concentration was detrimental for the electrode kinetics (as discussed earlier).

In the case of HCOOH electrooxidation, the Pt mesoporous film with pore diameters between 1.8–2.5 nm and specific surface area of 60 m^2 g^{-1} showed promising electrocatalytic activity, with a maximum mass specific activity of 8.6 A g^{-1} obtained for 1 M HCOOH (at 0.38 V_{RHE} and 333 K) [248]. It must be noted that the liquid crystal templated mesoporous Pt films prepared by Jiang and Kucernak were not investigated in direct CH_3OH or HCOOH fuel cells. The reason might be that the mesoporous films were supported on flat Au substrates, which are not suitable as fuel cell electrodes. Bauer et al. developed a technique for non-ionic surfactant-assisted electrodeposition of PtRu on graphite fiber matrix acting as a

three-dimensional electrode and investigated its applicability as a novel anode in direct methanol fuel cells [86, 249, 250]. This work is more extensively reviewed in Section 4.3.2.4.
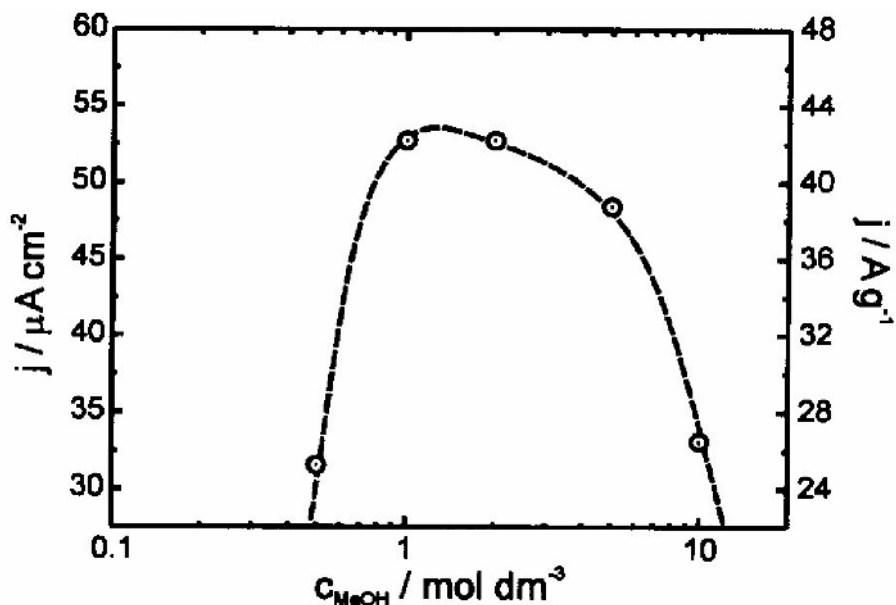
Figure 4.49. Electrocatalytic activity of mesoporous PtRu as a function of CH_3OH concentration. Catalyst film prepared by liquid crystal (surfactant $C_{16}EO_8$) templated reduction using Zn. Electrode potential: 0.38 Vvs. RHE, 333 K. Data taken after 900 s of polarization [247]. (Reproduced from Journal of Electroanalytical Chemistry, 543(2), Jiang J, Kucernak A, Electrooxidation of small organic molecules on mesoporous precious metal catalysts: II: CO and methanol on platinum–ruthenium alloy, 187–99, 2003, with permission from Elsevier.)

4.3.2 The Catalytic Interface: Catalyst/Support/Ionomer Interaction

In addition to studies focusing exclusively on the catalyst surface, the catalyst support (when employed) can play a major role in enhacing the activity/selectivity via morphologic, electronic, and physico-chemical effects. These factors have been extensively explored in the case of thermochemical heterogeneous reactions where a variety of compounds and structures have been successfully used on an industrial scale as catalyst supports (e.g., oxides, sulfides, meso- and microporous materials (molecular sieves), polymers, carbons [251–256]). In electrocatalysis, on the other hand, the practical choice of support in gas diffusion electrodes has been largely limited thus far to carbon black particles. The high electronic conductivity requirement, combined with electrochemical stability and cost effectivness, imposes serious restrictions on the type of materials that could be employed as supports in electrocatalysis.

4.3.2.1 Carbon Particle Supported and Unsupported Catalyst Layers for Direct Fuel Cell Anodes

An important question to be addressed is whether carbon particle supported or unsupported catalysts are preferable for direct methanol, ethanol, and formic acid fuel cell anodes. Note that "unsupported catalyst" here refers to the case when the precious metal catalyst particles are applied directly onto the membrane without the presence of carbon particles (i.e., unsupported catalyst coated membrane).

A major reason for using carbon particle support is to increase the catalyst dispersion and the electrochemically active specific surface area, which is a function of the three-phase interfacial structure composed of catalyst/ionomer/support. Furthermore, based on the pore size distribution and the hydrophobic-hydrophilic balance of the carbon surface, the support can influence the two-phase transport of species to and from the catalytically active sites.

Additionally, from an economic point of view, since the precious metal catalyst load on the anode is high in direct fuel cells (typically $\geq$ 1 mg cm^{-2}), catalyst recovery and recycling will be of utmost importance for the commercial viability of these power sources. In this context, research from Degussa AG has shown that the procedure of precious metal catalyst recovery is generally made easier by the use of carbon support, since it can be burnt off followed by efficient metal recovery from the ashes [252].

A number of reviews have been published on the properties of various carbons and their application in electrochemical systems, including fuel cell catalyst supports [257–261]. Therefore, more general aspects related to carbon properties will not be discussed here. The objective of the present section is to focus exclusively on the carbon particle support-catalyst interaction for direct fuel cell anodes.

Takasu et al. compared seven different carbon black supports for PtRu and evaluated their impact on methanol electrooxidation [262]. The supports ranged in BET surface area from 29 m^2 g^{-1} (carbon black type Mitsubishi 3030B) to 233 m^2 g^{-1} (Vulcan XC72R) and 802 m^2 g^{-1} (Ketjen EC), respectively. It was found that the PtRu (1:1 atomic ratio) catalyst surface area generally increased with the surface area of the support for the same catalyst preparation method, e.g., supports of ~200 m^2 g^{-1} gave PtRu areas (determined by CO_{ad} stripping voltammetry) of 45–57 m^2 g^{-1}, while the area of PtRu supported on Ketjen EC was ~70 m^2 g^{-1} [262]. Thus, it has been confirmed that the specific surface area of the support affects the PtRu catalyst particle size and surface distribution. The intrinsic catalytic activity toward CH_3OH electrooxidation (expressed as the anodic current per real PtRu surface area, A m$^{-2}_{PtRu}$, measured at 0.5 V vs. RHE) showed a maximum for supports of ~200 m^2 g^{-1} (i.e., Vulcan XC72). The optimum catalyst diameter for methanol oxidation was about 4 nm (Figure 4.50).

Interestingly, the degree of PtRu alloying was also a function of the specific area and type of the support. Namely, the smaller the PtRu particles (formed on the supports with large areas), the lower the extent of alloying [262].
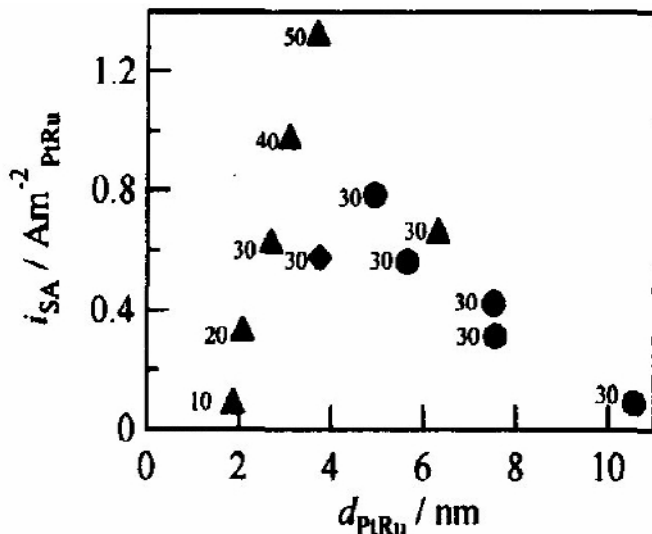
Figure 4.50. Dependence of the specific activity for methanol oxidation on the mean PtRu (1:1 atomic ratio) particle size supported on various carbon powders. ▲ Vulcan XC72, ● Mitsubishi, ◆ Ketjen EC. The numbers next to each symbol indicate the catalyst mass loading in g_{PtRu} m^{-2}_{carbon}. 333 K, 0.5 V vs. RHE, 1 M CH_3OH – 0.5 M H_2SO_4 [262]. (Reproduced from Electrochimica Acta, 48(25–26), Takasu Y, Kawaguchi T, Sugimoto W, Murakami Y, Effects of the surface area of carbon support on the characteristics of highly-dispersed Pt-Ru particles as catalysts for methanol oxidation, 3861–8, 2003, with permission from Elsevier.)

In addition to the effect of support on the catalyst dispersion, the interaction with the ionomer (Nafion®) is crucial for the electrochemical performance of the catalyst layer in the fuel cell. Catalyst nanoparticles that are isolated from the ionomer network are electrochemically inactive. Furthermore, the distribution of the ionomer will affect the ohmic resistance and the mass transport of the reactants and/or products in the catalyst layer. Hence, the interface between the catalyst/support/ionomer will influence the overall polarization behavior of the anode.

Mastragostino et al. investigated composites of Nafion and carbon black supports from the point of view of specific capacitance, electric resistance, and accessible surface area (calculated as the Nafion-covered fraction of the total support BET surface area) [263]. The carbon-to-Nafion weight ratio was 13.3:1 (i.e., 2:1 weight ratio of carbon-to-Nafion 5 wt% soln.). In this work carbon supports were selected with BET specific surface areas between 254 m^2 g^{-1} (Vulcan XC72) and 2130 m^2 g^{-1} (PICAFLOW HP-120). For a given Nafion loading, the accessible specific surface area was only 3 to 50% of the total BET surface area of the support. Interestingly, two supports of comparable BET surface area, Vulcan XC72 (254 m^2 g^{-1}) and Timrex HSAG300M-291 (313 m^2 g^{-1}), gave very different Nafion accessible specific surface area ratios, 15 and 50%, respectively [263].

Thus, not only the carbon surface area but also the carbon surface physico-chemical properties affecting the adhesional wetting and agglomeration of Nafion micelles (diameter > 40 nm) on the porous carbon surface will determine the distribution of the ionomer. The composites with the lowest Nafion accessible specific surface areas gave the highest electric resistances. Therefore, the ohmic drop across the catalyst layer is implicitly a strong function of surface properties. More studies are required to investigate the relationship between carbon surface properties and Nafion adhesional wetting.

In order to evaluate the impact of the Nafion ionomer separately (i.e., without carbon support) on the activity of PtRu toward CH_3OH electrooxidation, Chu et al. carried out an ingenious combinatorial study employing a wide range of Pt-Ru-Nafion ratios [264]. It was found that the methanol oxidation onset potential and the CO_{ad} desorption potential were a function of the Nafion load. The presence of ~36 wt% Nafion (the rest being PtRu of 1:1 atomic ratio) was essential in order to lower the CH_3OH oxidation onset potential by about 90 mV [264]. The same 36:64 weight ratio of Nafion content to PtRu catalyst was validated as the best-performing in direct methanol fuel cell experiments at 383 K.

However, the study by Arico et al. contradicts this finding, showing that at 363 K the unsupported PtRu catalyst with 33 wt% Nafion gave much worse performance compared to a 15 wt% Nafion load. The operating current density of the direct methanol fuel cell at 0.5 V cell voltage was 40 mA cm^{-2} for 33 wt% Nafion and 140 mA cm^{-2} for 15 wt% Nafion, respectively [265]. The carbon black supported PtRu catalyst, on the other hand, performed better when loaded with 33 wt% Nafion. Thus, there seemed to be a difference between the required Nafion load for supported and unsupported PtRu catalysts. In the case of supported catalysts a higher Nafion load was preferable. Furthermore, in the same study [265], direct comparison of the power output between supported and unsupported catalysts of the same load of 2 mg cm^{-2} revealed that at temperatures of 363 K and 403 K the unsupported catalysts gave higher peak power outputs, e.g., 262 mW cm^{-2} (unsupported) vs. 200 mW cm^{-2} (supported), both with optimized Nafion content. It was argued that the better performance of the unsupported catalysts was due to a more homogeneous catalyst and Nafion distribution in the catalyst layer, facilitating the mass transport of the reacting species.

On the same topic of DMFC performance with supported vs. unsupported catalysts Smotkin and co-workers concluded that at 363 K the supported PtRu (1:1) catalyst with a load of 0.46 mg cm^{-2} performed as well as an unsupported PtRu (1:1) with over four times higher load, i.e., 2 mg cm^{-2} [266]. It is likely that these differences between various studies are related not only to the intrinsic activity of the respective anode catalys layers but also to the manufacturing procedures such as catalyst layer preparation and application techniques, MEA hot pressing conditions (temperature, pressure and time), presence or absence of other binders (such as PTFE) and fuel cell compression. All these MEA manufacturing variables can affect, in a poorly understood manner at present, the structure, morphology and composition of the catalyst layer in the operating fuel cell. Therefore, in fuel cell experiments it is difficult to isolate the truly physico-chemical effect of the support on the catalytic activity.

In another study, Arico et al. also presented a comprehensive physico-chemical investigation of the catalyst/support/Nafion interface using a combination of techniques such as XPS, XRD, SEM-EDAX, and TEM [267]. A very important finding was the identification of large inverted Nafion micelles (200 nm diameter) in contact with the carbon support (primary carbon particle diameter of 30 nm). Thus, the homogeneous distribution of the large Nafion micelles and formation of a continuous interconnected ionomer network throughout the pores of the carbon agglomerates and linking up with the catalyst particles was to a large extent impeded [267]. Using a solvent with either a high dielectric constant or high ionic strength to dissolve the Nafion before applying it to the catalyst layer formulation might reduce the size of inverted micelles, thereby helping to assure a better ionomer distribution throughout the catalyst layer. The colloidal and surface properties of Nafion necessitate more detailed investigations.

Recently, Uchida et al. carried out 3D imaging of the catalyst layer using electron tomography [268]. To differentiate between Nafion and epoxy resin, the Nafion was prepared with Ag^+ instead of H^+, giving a bright image in TEM. In order to improve the Nafion penetration in the pores of the carbon support, an autoclave treatment was applied involving heating at 473 K in a N_2 atmosphere. This treatment reduced the size of the inverted Nafion micelles and enhanced the penetration throughout the catalyst layer, forming a better dispersed ionomer network, as shown in Figure 4.51 [268].
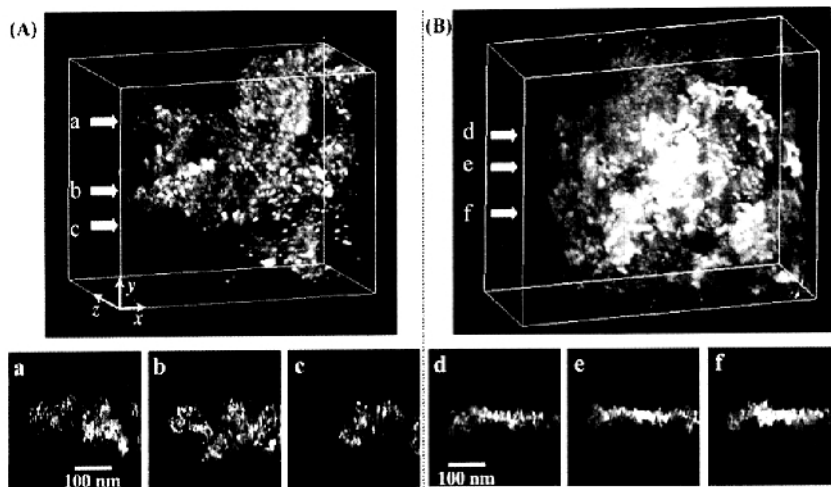
Figure 4.51. 3D reconstructed images of Ag^+ exchanged Nafion in contact with Pt/C. (A) with autoclave treatment, (B) without autoclave treatment [268]. (Reproduced with permission from J Phys Chem B 2006;110:13319–21. Copyright 2006 American Chemical Society.)

A number of studies looked at the intrinsic electronic interaction between the carbon support and the precious metal catalyst in order to determine the potential influence on methanol electrooxidation [269, 270]. There seems to be a consensus

in the literature that electronic interaction takes place between the carbon support and Pt. The binding energy for the 4f Pt energy level was found to be higher for small Pt particles and clusters (~71.6 eV) compared to the bulk metal (i.e., 71.1 eV); furthermore, an additional change has been observed as a function of the Pt/carbon support weight ratio. The 4f binding energy of Pt/C was typically lower compared to Pt black particles; values in the range of 71.3–71.4 eV were measured by XPS [269].

Thus, the presence of the carbon support somewhat weakens the 4f electron binding in Pt as compared to the unsupported nanocatalyst, making it more susceptible for interaction with adsorbed organic molecules. Interestingly, temperature was found to impact the electronic interaction between Pt and C support [270]. Increasing the heat treatment temperature of carbon-supported Pt nanoparticles caused an increase in the 4f binding energy, from 71.3 eV (without heating) to 72.2 eV (heating at 673 K for 4 h) [270]. This positive shift of the binding energy due to electron donation from Pt to C brought about a substantial decrease in electrocatalytic activity toward CH_3OH oxidation, as indicated by cyclic voltammetry [270]. Furthermore, XPS studies consistently showed the presence, in addition to Pt^0, of higher oxidation states (Pt^{2+} and Pt^{4+}) on the nanoparticle surface in a proportion of typically less than 30%.

In the context of direct liquid fuel cell anodes, virtually no attention has been devoted to the issue of carbon support degradation. While the anode potential is not expected to play a major role since under normal fuel cell operating conditions it is low compared to the range in which carbon oxidation can occur (i.e., ≥ 1.2 V vs. SHE), the presence of an organic solvent (CH_3OH, C_2H_5OH, and $HCOOH$) in conjunction with temperature could generate, over time, degradation of the carbon support catalyzed by Pt nanoparticles. Stevens and Dahn have shown that Pt nanoparticles catalyze the combustion of the carbon support at temperatures between 398 and 468 K [271], which is further aggravated by high levels of humidity [272].

4.3.2.2 Nanostructured Carbon Supports

Since the discovery of carbon nanotubes in the early 1990s [273] there has been emerging interest in their applicability as catalyst supports for low-temperature PEMFCs. Recently, Lee et al. reviewed the area of Pt electrocatalyst preparation techniques using carbon nanotubes and nanofibers as supports [274]. Here, the emphasis will be on the impact of novel nanostructured carbon supports (ordered mesoporous materials, nanotubes, and nanofibers) on the electrocatalytic activity with respect to direct fuel cell anodes.

Kim et al. synthesized mesoporous carbon xerogels by sol-gel polymerization of resorcinol and formaldehyde using colloidal silica particles of 12 nm diameter as templates [275]. The main pore size range of the resulting carbon xerogels was between about 30–40 nm, and the BET surface areas varied as a function of the preparation pH between 321 m^2 g^{-1} (at pH 1.5) and 654 m^2 g^{-1} (at pH 9). The PtRu nanoparticles synthesized and deposited on the support had diameters between 2.2 and 2.8 nm (the larger the support surface area, the smaller the catalyst particle size).

Figure 4.52 shows the DMFC performance as a function of mesoporous xerogel (NC) carbon support for PtRu in comparison with an activated carbon (AC) [275]. The fuel cells with the NC anode support performed better than those with the AC support, in spite of the larger specific surface area of the latter (i.e., 901 m^2 g^{-1}). Thus, the high degree of microporosity of the activated carbon support was less useful for catalyst dispersion as compared to the mesoporous xerogel.
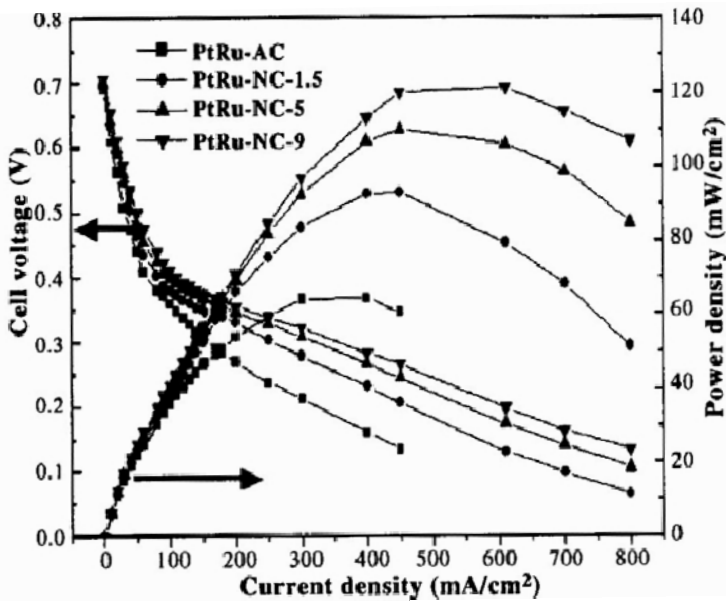
Figure 4.52. DMFC performance as a function of PtRu anode catalyst support. NC = mesoporous carbon xerogel support. The number indicates the preparation pH. AC = activated carbon. Anode PtRu 3 mg cm^{-2}. Cathode Pt 4 mg cm^{-2}. Temperature 348 K. Methanol flow rate 1 ml min^{-1}, dry oxygen flow rate 500 ml min^{-1} [275]. (Reproduced from Journal of Power Sources, 145(2), Kim P, Kim H, Joo JB, Kim W, 2005, with permission from Elsevier.)

Using a similar methodology of silica-templation, Chai et al. produced ordered porous carbon supports with a wide range of pore sizes between 10 and 100 nm [276]. Figure 4.53 shows SEM images of the various meso- and macroporous monolithic carbon supports prepared by silica templating. The highest catalytic activity was obtained for the support in which the pore size distribution peaked at 25 nm diameter with a BET area of 845 m^2 g^{-1}. Employing 3 mg cm^{-2} PtRu (1:1 at. ratio) supported on the novel mesoporous carbon, the peak power density of DMFC was 170 mW cm^{-2} at 600 mA cm^{-2} and 343 K, whilst under similar conditions the commercial PtRu catalyst (E-TEK Inc.) yielded 115 mW cm^{-2} at 450 mA cm^{-2} [276]. Pore interconnectivity, structural integrity and specific surface area were the main factors that determined the performance of the catalyst supports.
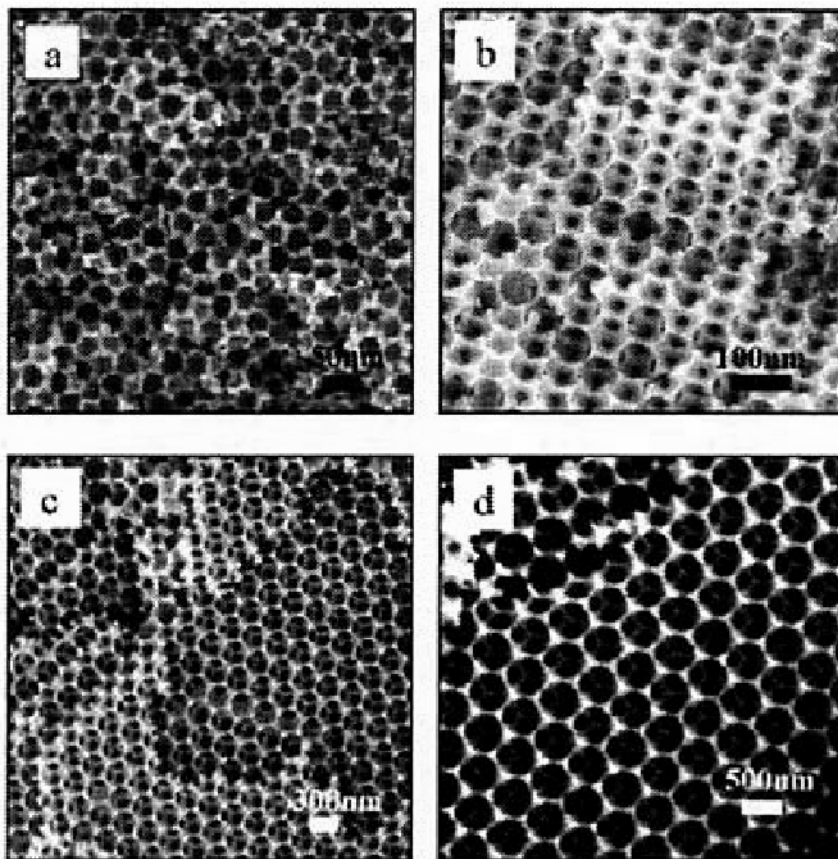
Figure 4.53. SEM images of meso- and macroporous carbon supports prepared by silica templating. Pore diameters: a) 25 nm, b) 68 nm, c) 245 nm, and d) 512 nm [276]. (Reprinted with permission from J Phys Chem B 2004;108:7074–9. Copyright 2004 American Chemical Society.)

In a different approach to catalyst support, monolithic 3D matrices were prepared with multiwalled carbon nanotube (MWCNT) contents between 66 and 89 wt% (Figure 4.54) [277]. The employed technique consisted of dispersing various amounts of MWCNT in chitosan, followed by freezing in liquid N_2. The resulting 3D structure was characterized by high electronic conductivity, namely 2.5 S cm^{-1} for 89 wt% MWCNT content (the rest being chitosan). Therefore, it could function as a novel 3D anode substrate replacing the gas diffusion electrode. Pt nanoparticles of ~5 nm diameter were deposited onto the MWCNT matrix with 10 wt% Pt load. Preliminary tests of the electrocatalytic activity showed mass-specific anodic currents for methanol oxidation up to 250 mA mg$^{-1}_{Pt}$ at 0.76 V vs. SCE [277]. Interestingly, it was proposed that the support also contributes to the catalytic function by providing the OH groups necessary for removal of CO_{ad}.
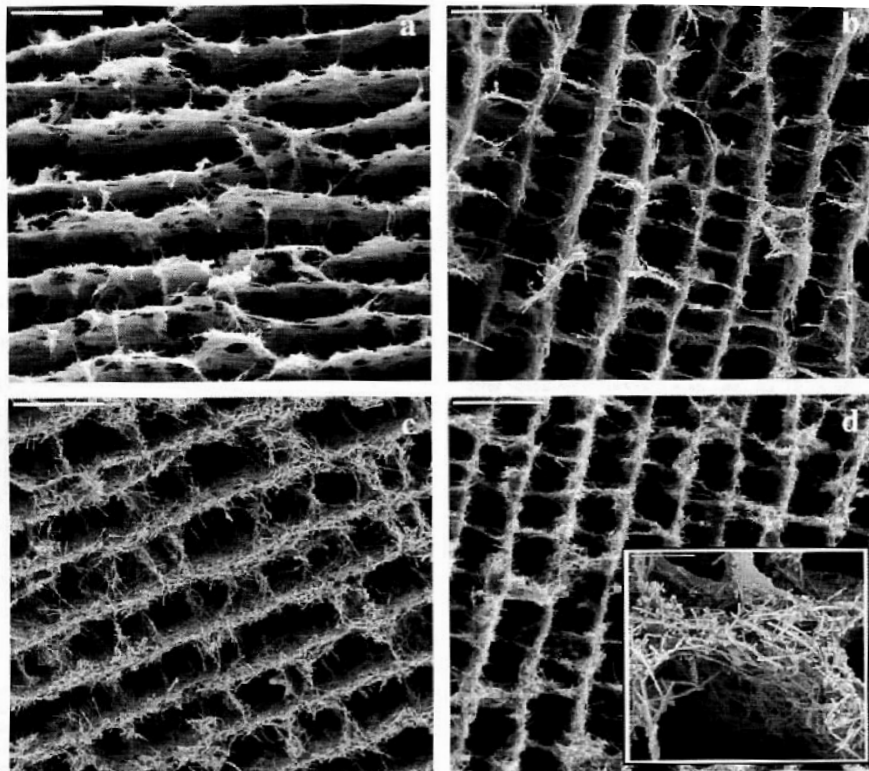
Figure 4.54. SEM images of the MWCNT 3D matrices with different MWCNT contents (the rest is chitosan). a) 66 wt%, b) 80 wt%, c) 85 wt%, and d) 89 wt% [277]. (Reprinted with permission from J Phys Chem C 2007;111:5557–60. Copyright 2007 American Chemical Society.)

The possibility of using carbon nanocoils (CNC) as PtRu catalyst supports for the DMFC was successfully explored by Hyeon et al. [278]. The carbon nanocoils were 5–10 nm thick, forming agglomerates of ~100 nm diameter. Comparative voltammetry experiments of methanol oxidation carried out with PtRu supported on CNC and Vulcan XC72 (1:1 at. ratio, 60 wt% metal, 2.3 nm particle diameter) revealed significantly higher anodic currents for the catalyst supported on CNC, (e.g., 80 A g^{-1} at 0.4 V_{SHE}) in conjunction with lower methanol oxidation onset potential (Figure 4.55). The enhanced activity was attributed not only to the surface area effect but also to the higher crystallinity of the CNC, increasing thereby the support electronic conductivity (compared to the amorphous Vulcan XC72) and possibly affecting the catalyst-support electronic interaction [278]. DMFC experiments with PtRu (2 mg cm^{-2}) supported on CNC revealed peak power densities of 90 mW cm^{-2} at 303 K, and 230 mW cm^{-2} at 333 K, respectively. Furthermore, the CNC showed excellent stability in an operating DMFC for up to 100 h.
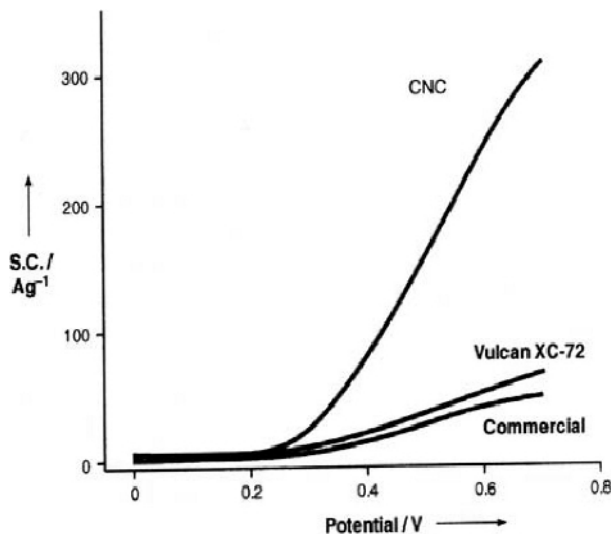
Figure 4.55. Comparative methanol oxidation voltammogram (V vs. SHE) using PtRu (1:1) supported on carbon nanocoil (CNC), Vulcan XC72, and commercial supported catalyst [278]; 298 K. (Hyeon T, Han S, Sung Y-E, Park K-W, Kim Y-W, High-performance direct methanol fuel cell electrodes using solid phase synthesized carbon nanocoils, Angewandte Chemie International Edition, 2003;42:4352–6. ©2003 Wiley-VCH Verlag GmbH & Co. KGaA. Reproduced with permission.)

Graphitic nanofibers with herringbone structure (for description and preparation method see [279]) were also employed as supports for PtRu (1:1) [280]. The total metal content was 42 wt% and the catalyst particle size was 6 nm. DMFC polarization experiments showed an approximately 50% improvement in superficial current density at constant cell voltage for the supported vs. unsupported catalyst over the entire polarization curve [280].

In spite of promising results using a variety of carbon nanostructures, challenges still remain with respect to manufacturing the novel supports, and their incorporation into the fuel cell electrode design. Dodelet and co-workers developed a method for 3D multiwalled carbon nanotube (MWCNT) network growth directly on carbon fiber paper [281] (Figure 4.56). Pt nanoparticles (~3–4 nm diameter) were deposited onto the MWCNT/carbon paper composite. The anchoring and dispersion of Pt precursors on the carbon nanotubes required surface functionalization, which was accomplished by treatment with a silane derivative [282]. The electroactive area of the Pt-MWCNT/carbon paper electrode was surprisingly lower than that for a commercial Pt gas diffusion electrode of similar loading (0.4 mg Pt cm^{-2}), 60 m^2 g^{-1} vs. 100 m^2 g^{-1}, respectively [282]. This raises the possibility of substantial Pt deposition onto the carbon paper instead of the MWNT and/or Pt nanoparticle agglomeration due to sponatenous electroless deposition.

Dodelet and co-workers did not employ the Pt-MWCNT/carbon paper as a direct liquid fuel cell anode. However, oxygen electroreduction experiments

showed that despite the lower active area, the novel electrode performed better compared to the commercial gas diffusion design in liquid electrolyte (e.g., H_2SO_4 pH 1), where the 3D property of the MWCNT/carbon paper electrode (thickness ~170–200 μm) is fully utilized, generating an extended reaction zone.
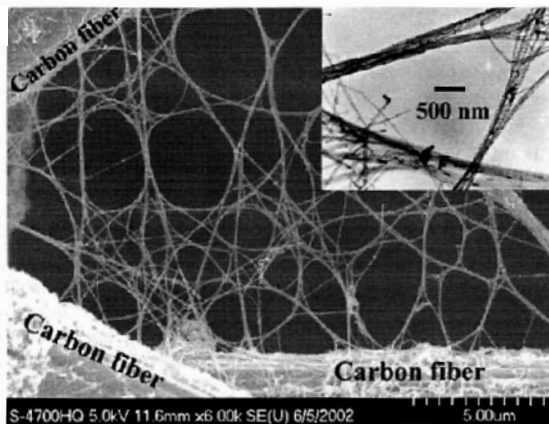
Figure 4.56. SEM image of carbon MWCNTs grown onto carbon fiber paper. Inset shows the high magnification of the MCWNT bundles [281]. (Reproduced from Chemical Physics Letters, 394(4–6), Sun X, Li R, Stansfield B, Dodelet JP, Désilets S, 3D carbon nanotube network based on a hierarchical structure grown on carbon paper backing, 266–79, 2004, with permission from Elsevier.)

Further experimental evidence of enhanced catalyst utilization dispersed on carbon nanotube supports has been provided by Wu et al. [283]. These authors measured higher double-layer capacitance in 0.5 M H_2SO_4 for both single and multiwalled carbon nanotubes compared to Vulcan XC72 (Figure 4.57(a)). This indicates higher concentration of surface functional groups for the nanotubes, thereby facilitating enhanced Pt catalyst dispersion and liquid electrolyte penetration. As a result of these effects, the methanol oxidation current density in 0.5 M H_2SO_4 at 0.45 V_{SCE} was almost three times higher on Pt/MWCNT compared to Pt/Vulcan XC72.

Following up on the possible catalyst support effect, Prabhuram et al. carried out a comparative DMFC investigation of PtRu deposited on carbon MWNT and Vulcan XC72, respectively [284]. In both cases the supported PtRu catalyst was applied onto the gas diffusion layer (carbon cloth). For the same anode catalyst load (2.1 mg cm^{-2}), composition (Pt:Ru 1:1 atomic ratio), and particle size (~2.7–2.8 nm), the multiwalled carbon nanotube-supported anode yielded 35% higher DMFC peak power output versus the one using Vulcan XC72. Deactivation experiments, however, conducted by chronoamperometry carried out over 3000 seconds showed a higher degradation rate for Pt/MWCNT, which was attributed to the preferential poisoning of Pt(110) formed in higher proportion on the multiwalled nanotube support [284]. Thus, it can be inferred that this study revealed mainly differences in the crystallographic features of PtRu supported on either MWNT or Vulcan XC72 affecting the performance.
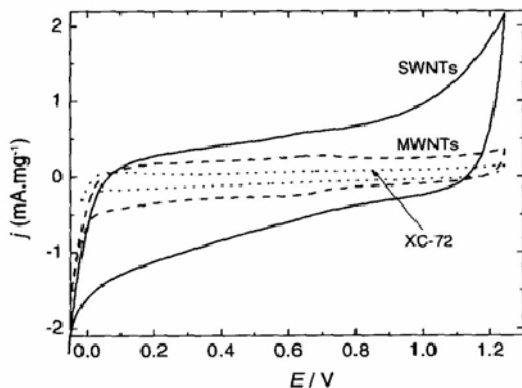
a)
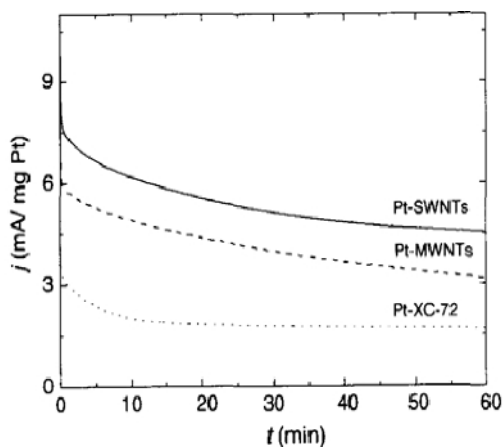
b)

Figure 4.57. a) Cyclic voltammograms of various carbon supports in 0.5 M H_2SO_4 at 20 mV s^{-1}: SWNT, MWNT (MWCNT), and Vulcan XC72. b) Methanol oxidation current density as a function of time at 0.45 V vs. SCE. Pt load 0.1 mg cm^{-2}, 296 K [283]. (Reproduced from Electrochemistry Communications, 7(12), Wu G, Chen Y-S, Xu B-Q, Remarkable support effect of SWNTs in Pt catalyst for methanol electrooxidation, 1237–43, 2005, with permission from Elsevier.)

A few studies also showed the importance of nanotube oxidative pretreatment (e.g., in 2.6 M HNO_3 at 130 $^{\circ}$C for 30 h) for the attachment of Pt particles to the surface via surface functional groups such as –COOH, –COH, and –C=O [285, 286].

For ethanol oxidation, Zheng et al. investigated the effect of multiwalled carbon nanotubes, carbon black, and activated carbon fiber (ACF) supports on the catalytic activity of Pd in alkaline media [287]. It was found that the support had a significant influence on performance, with the Pd/MWNT system giving the lowest faradaic resistance as determined by electrochemical impedance spectroscopy. It

was argued that the support influences the ethanol electrooxidation reaction mechanism on Pd and minimizes poison formation. With the MWNT support, a stable anode potential response was observed by chronopotentiometry at 1 mA cm^{-2} for over 250 minutes, indicating diminished electrode poisoning compared to both carbon black and activated carbon fiber [287].

4.3.2.3 Inorganic Supports: Oxides, Carbides, and Sulfides

The interaction of inorganic supports with Pt and other metal catalysts relevant to direct liquid fuel cells has started to receive attention. For methanol oxidation in alkaline media, vanadium oxide (VO$_x$) nanotubes were investigated as support for Pd catalysts [288]. A major practical advantage of using VO$_x$ as opposed to carbon nanotubes is its easy synthesis by a hydrothermal process. This involves formation of a suspension composed of V$_2$O$_5$ and long-chain amines (e.g., C$_n$H$_{2n+1}$NH$_2$, n = 4–22) in ethanol-water mixture, followed by thermal treatment at 180 $^\circ$C [289–291]. Figure 4.58 shows a TEM image of typical VO$_x$ nanotubes, revealing their multiwalled structure. The nanotube lengths were between 0.5–15 μm, with inner diameters of 5–50 nm and outer diameters of 15–100 nm [290]. The nanotube structure (e.g., wall thickness, inner diameter) can be controlled by the type of amine used in its synthesis. Furthermore, the choice of amine could affect the stability of the resulting VO$_x$-NT in a manner that is not fully understood at present [291].
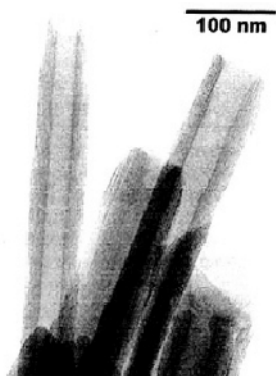
Figure 4.58. TEM image of multiwall VO$_x$-nanotubes formed with n-C$_{22}$H$_{45}$NH$_2$ [290]. (Muhr H-J, Krumeich F, Schonholzer UP, Bieri F, Niederberger M, Gauckler LJ, et al., Vanadium oxide nanotubes – a new flexible vanadate nanophase, Advanced Materials 2000;12:231–4. ©2000 Wiley-VCH Verlag GmbH & Co. KGaA. Reproduced with permission.)

For electrochemical and surface analytical investigations, the VO$_x$-NTs were attached to pyrolitic graphite electrodes with the help of chitosan acting as binder. In addition to morphological features, VO$_x$-NTs are very interesting supports due to their intrinsic electrochemical (redox) activity involving the V^{5+}/V^{4+} and V^{4+}/V^{3+} redox couples in conjunction with H$_2$O adsorption on the oxide surface [291]. Generally, the interaction of oxide surfaces with H$_2$O leads to changes in surface

acid/base behavior, double layer capacitance, and potential as a function of pH (Equations 4.37–4.39) [292]. Such modifications of the oxide surface chemistry could profoundly affect the catalyst-support interaction.

$$M\!-\!O + H_2O \Rightarrow M \diagdown \begin{matrix} OH \\ OH \end{matrix} \tag{4.37}$$

$$M \diagdown \begin{matrix} OH \\ OH \end{matrix} + H^+ \Rightarrow M \diagdown \begin{matrix} OH_2^+ \\ OH \end{matrix} \tag{4.38}$$

$$M \diagdown \begin{matrix} OH \\ OH \end{matrix} + OH^- \Rightarrow M \diagdown \begin{matrix} O^- \\ OH \end{matrix} \tag{4.39}$$
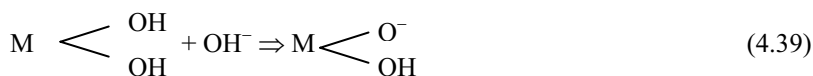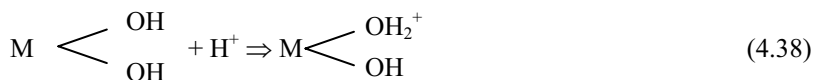
Regarding the activity of Pd/VO$_x$-NT for methanol oxidation in 0.1 M NaOH, preliminary cyclic voltammetry experiments showed oxidation peaks at fairly negative potentials (0.07 V vs. SCE and –0.23 V on the anodic and cathodic scans, respectively), which, coupled with very good long-term stability of over 400 cycles at a rate of 100 mV s^{-1}, show promise for fuel cell applications [288].

MoO$_x$ prepared by electrooxidation of layered MoSe$_2$ was investigated by Bolivar et al. as novel support for Pt [293]. Nanoparticles of Pt were electrodeposited onto the support by potential cycling between –0.25 and 1.1 V vs. SCE for 1 h using a 1 mM K$_2$PtCl$_6$ solution in 0.5 M H$_2$SO$_4$. It was found by voltammetry studies that although the Mo-based support did not increase the methanol oxidation current density on Pt, it contributed to prolonging the Pt catalytic activity. This was attributed to surface OH$_{ad}$ formation on the Mo sites contributing to the oxidation of CO$_{ad}$, thereby minimizing catalyst poisoning.

The effect of oxides present on carbon black (Vulcan XC72R) support was also investigated in relation to ethanol electrooxidation on both Pt and Pd in 1 M KOH [294]. CeO$_2$-C and NiO-C supports were prepared, followed by Pt and Pd nanoparticle synthesis and *in-situ* deposition on the support using the borohydride reduction method. Interestingly, while the crystalline lattices were the same irrespective of the support type, the catalyst nanoparticle size decreased for both Pt and Pd as a function of support, in the order C > C-CeO$_2$ > C-NiO. The Pd-based catalysts typically were more active toward ethanol electrooxidation in alkaline media, but a very important finding was that the presence of NiO considerably enhanced the activity of Pd, e.g., the peak current density for ethanol electrooxidation increased five times compared to the pure Pd case [294]. The optimum NiO content was 0.05 mg cm^{-2}. Furthermore, TiO$_2$-containing supports (carbonized TiO$_2$ nanotubes) were effective as well for the promotion of Pd catalytic activity [295].

Oxide promotion of Pt catalytic activity toward ethanol oxidation was also demonstrated using SnO$_2$ nanoparticles (~3 nm diameter, synthesized by the ethyleneglycol method) [296] and RuO$_2$ [297]. Figure 4.59 shows that the DEFC peak power output increased eight times with SnO$_2$ promotion of Pt. The mechanism of SnO$_2$ promotion was not investigated.

Additionally, Ni and CuNi supports were also explored for ethanol oxidation in alkaline media using PtRu and PtMo catalysts [201, 298]. EDX analysis showed that Ni was mostly present in metallic state, with some contribution from an oxide layer. The ethanol oxidation current density increased linearly on a logarithmic scale with the NaOH concentration (10^{-2} M to 2 M) for both PtRu and PtMo supported on CuNi (70:30 wt%) [201]. Unfortunately, no direct comparison was performed with carbon-supported catalysts. Thus, the contribution of the support to the observed electrocatalytic effect could not be assessed. PtMo had a higher initial activity; however, after about 200 minutes its activity dropped below that of PtRu. Anodes with PtRu atomic ratios between 1.1:1 and 2.1:1 supported on Ni gave the lowest Tafel slopes for ethanol oxidation [298].
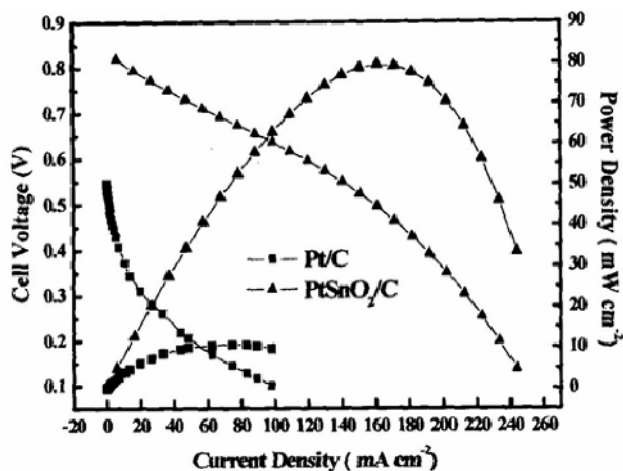
Figure 4.59. Effect of SnO_2 nanoparticle promotion on Pt activity toward ethanol electrooxidation in a DEFC; 363 K; 1 M ethanol; flow rate 1 mL min^{-1}. Anode: PtSnO$_2$/C 1.5 mg of Pt cm^{-2}, SnO$_2$ load not specified in the original source. Cathode: Pt/C, 1 mg cm^{-2}, O$_2$ pressure 0.2 MPa(abs). O$_2$ flow rate not specified in the original source [296]. (Reprinted with permission from J Phys Chem B 2005;109:8774–8. Copyright 2005 American Chemical Society.)

The promotion of formic acid electrooxidation on Pt and Pd by SbO_2, SnO_2, IrO_2, ZrO_2, CeO_2, TiO_2, and their combinations has been recently investigated [299]. The oxides were employed as composite supports together with carbon black (Vulcan XC72R). Figure 4.60 shows the oxide effect on the HCOOH oxidation voltammograms expressed in terms of catalyst mass-specific activity. In the case of Pd catalyst, CeO_2 and ZrO_2 were the only ones that enhanced the HCOOH oxidation mass-specific activity, while on Pt the highest activity was obtained with the Sb_2O_5–SnO_2 mixture, followed by CeO_2. It was proposed that the oxide support provides local oxygen species assisting the oxidation of the surface poison on the catalyst surface. In the case of CeO_2 the existence of labile surface oxygen, high oxygen defect mobility, and the facile Ce(IV)/Ce(III) redox shuttle might all contribute to the promotion of HCOOH oxidation. These effects are

particularly intensified on ceria nanoparticle (e.g., ~6 nm diameter) surfaces and were extensively discussed in relation to CO oxidation catalyzed by CeO_2 [300].
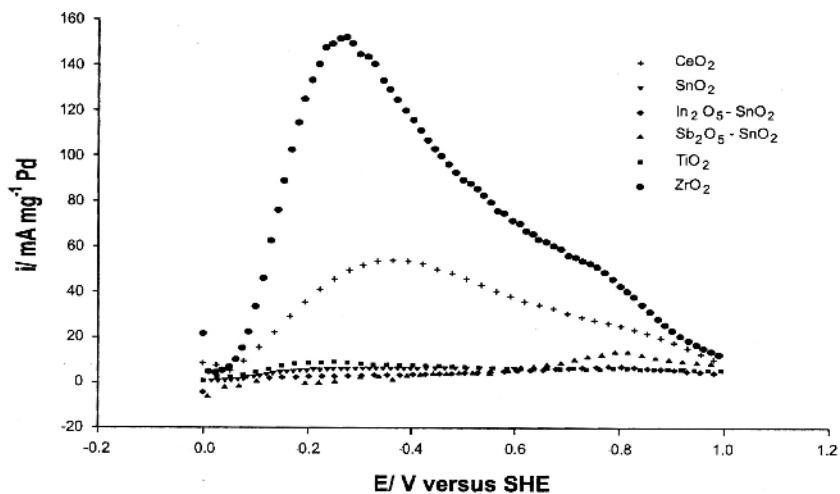
(a)
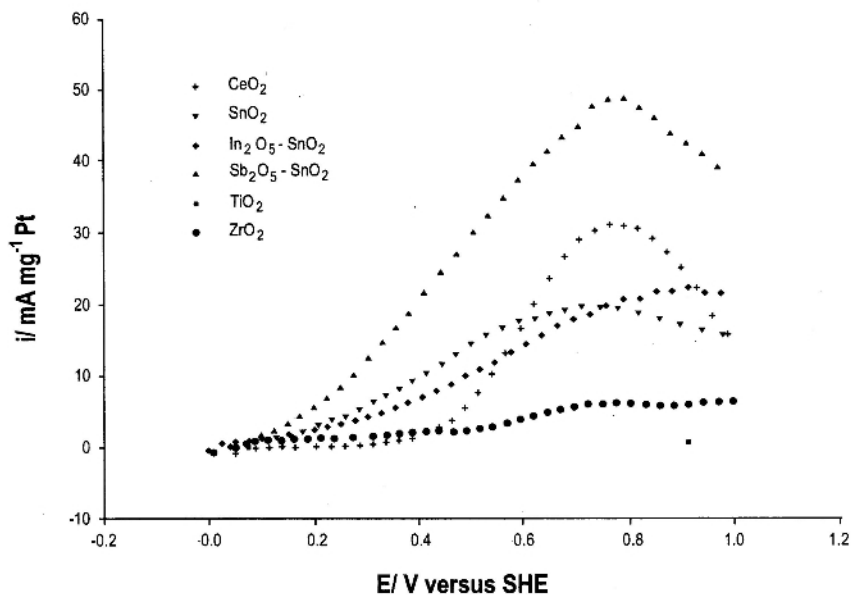
(b)

Figure 4.60. The effect of metal oxide–carbon black (Vulcan XC72R) composite (85:15 wt%) support on HCOOH oxidation. (a) Pd catalyst and (b) Pt catalyst. 1 M HCOOH – 1 M H_2SO_4, 5 mV s^{-1}, 298 K [299].

Chen et al. employed a mesoporous silica framework (hexagonal SBA-15 molecular sieve, average pore diameter 26 nm, BET surface area 910 m^2 g^{-1}) as Pt support for methanol oxidation [301]. The catalyst was synthesized by impregnation of K_2PtCl_6 onto the SBA-15 followed by application of the suspension on a glassy carbon (GC) substrate and electroreduction of Pt(IV) by potential cycling between 0.1 and –0.25 V vs. SHE. Using CO purged in 0.1 M H_2SO_4, the onset potential for CO_{ad} oxidation was remarkably 0.4 V lower than that on unsupported polycrystalline Pt. Two reasons were put forward: i) the presence of Si-OH in the meso-size channels of SBA-15 contributing to the oxidation of CO_{ad} and ii) efficient diffusion of CO_2 away from the catalytic sites. The latter is an advantage for mesoporous molecular sieves compared to the microporous zeolites. For methanol oxidation, the onset potential on Pt-SBA15/GC was more positive by 0.20 V compared to Pt/Au, indicating clearly that the interaction between the molecular sieve and Pt facilitates the electrooxidation reaction [301]. These promising preliminary results of the Pt-mesoporous system must be followed up with thorough investigations by electrochemical/surface science techniques and fuel cell tests.

In order to address the protonic conductivity of the catalyst layer in conjunction with the support effect, hydrous ruthenium oxide was evaluated as support for Pt [302]. $RuO_2 \bullet xH_2O$ is a mixed electronic-protonic conductor, the latter being generated by the water adsorbed in the grain boundary regions.
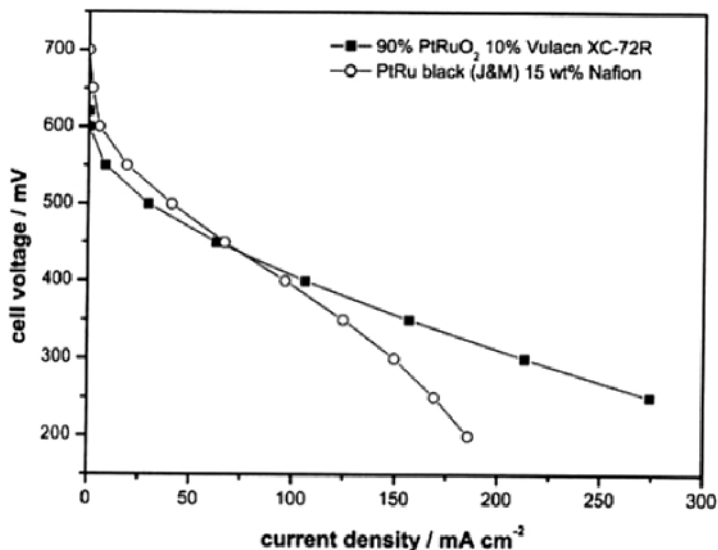
Figure 4.61. Polarization curve for a direct methanol fuel cell, comparing Pt/$RuO_2 \bullet xH_2O$/Vulcan XC72R (-■-) and unsupported PtRu black (-o-). Anode catalyst load: 2.3 mg cm^{-2}. Cathode: 4 mg cm^{-2} Pt black. Membrane: Nafion NE-105. 323 K. 1 M methanol at 6 ml min^{-1} and air at 500 ml min^{-1} (STP) [302]. (Scheiba F, Scholz M, Cao L, Schafranek R, Roth C, Cremers C, et al.: On the suitability of hydrous ruthenium oxide supports to enhance intrinsic proton conductivity in DMFC anodes, Fuel Cells 2006;6:439–46. Copyright Wiley-VCH Verlag GmbH & Co. KGaA. Reproduced with permission.)

Comparison of Pt/RuO$_2$•xH$_2$O on Vulcan XC72R (9:1 weight ratio) with unsupported PtRu black containing 15 wt% Nafion in a direct methanol fuel cell (Figure 4.61) revealed that in the kinetic region there was a 30 to 50 mV loss in the anode potential with the Ru-based support [302]. In the ohmic region, on the other hand, the trend reversed and the RuO$_2$•xH$_2$O supported system performed better due to a combination of enhanced ionic conductivity and methanol utilization efficiency.

4.3.2.4 Extended Reaction Zone Catalyst Supports: Synergy between Electrocatalysis and Electrode Engineering

The catalytic (supported or unsupported) interface in the vast majority of direct liquid fuel cell studies is realized in practice either as a catalyst coated membrane (CCM) or catalyst coated diffusion layer (CCDL). Both configurations in essence are part of the electrode design category, which is referred to as a gas diffusion electrode, characterized by a macroporous gas diffusion and distribution zone (thickness ~100–300 μm) and a mainly mesoporous, thin reaction layer (thickness ~5–50 μm). The various layers are typically hot pressed, forming the gas diffusion electrode-membrane assembly. Extensive experimental and mathematical modeling research has been performed on the gas diffusion electrode-membrane assembly, especially with respect to the H$_2$-O$_2$ fuel cell. It has been established that the catalyst utilization efficiency (defined as the electrochemically available surface area vs. total catalyst surface area measured by BET) in a typical gas diffusion electrode is only between 10–50%, hence, the fuel utilization efficiency can be low in such electrodes. Furthermore, the low fuel utilization efficiency contributes to an increased crossover rate through the membrane, which deteriorates the cathode performance.

In order to improve the methanol utilization efficiency in DMFC, Wilkinson et al. patented the multilayer anode concept, where a number of CCDLs are stacked together to provide an enhanced reaction zone volume [303]. They reported that for the same total anode catalyst load, the distribution of the carbon-supported PtRu catalyst onto three separate diffusion layers (carbon fiber sheets, 300 μm total thickness) enhanced the methanol utilization efficiency by 33% compared to a single CCDL at a constant current density of 200 mA cm^{-2} and 388 K.

A variant of the enhanced reaction zone concept is to utilize as catalyst support various porous three-dimensional electrodes with thickness between 200 to 2,000 μm. Thus, the electric contact resistance between the individual layers is eliminated. The three-dimensional matrix (such as various graphite felts, reticulated vitreous carbon, metal mesh, felt, and foam) supporting uniformly dispersed electrocatalysts (nanoparticles or thin mesoporous coating) could assure an extended reaction zone for fuel (methanol, ethanol, and formic acid) electrooxidation, providing an ionic conductor network is established to link the catalytically active sites and the proton exchange membrane. The patent by Wilkinson et al. also suggests such electrode configurations (e.g., carbon foam, expended metal and reticulated metal) but experimental results were not provided [303].
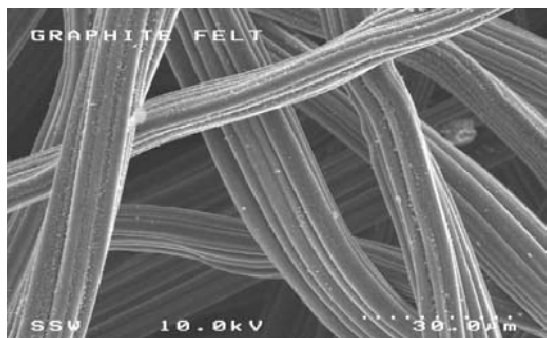
(a)
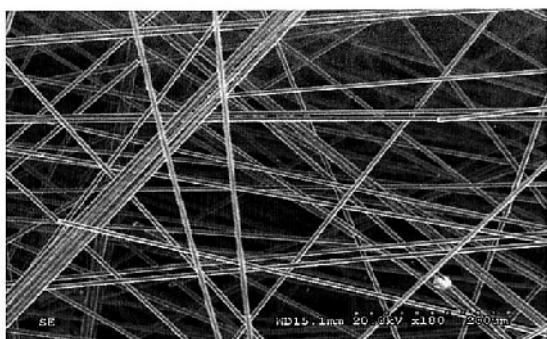
(b)
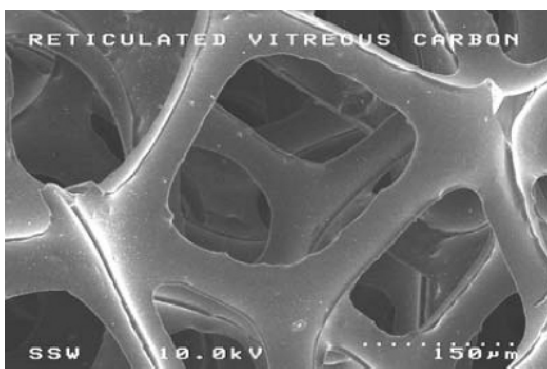
(c)

Figure 4.62. Examples of three-dimensional supports for extended reaction zone anodes in direct liquid fuel cells. (a) unpressed graphite felt UGF, (b) pressed graphite felt GF, (c) reticulated vitreous carbon RVC [250, 305]. (Reprinted from Electrochimica Acta, 51(25), Bauer A, Gyenge EL, Oloman CW, Electrodeposition of Pt–Ru nanoparticles on fibrous carbon substrates in the presence of nonionic surfactant: Application for methanol oxidation, 5356–64, 2006, with permission from Elsevier; and reproduced by permission of ECS—The Electrochemical Society, Gyenge EL, Oloman CW. The surfactant-promoted electroreduction of oxygen to hydrogen peroxide.)

The role played by the three-dimensional support is intricate, affecting in addition to intrinsic catalyst-support interactions the electrode mass transfer characteristics. By exploiting the support surface properties impacting the wetting behavior and the macroporous structure, the three-dimensional support could improve the multiphase (S/L/G) mass transfer in direct fuel cell anodes compared to gas diffusion electrodes. In the latter case, based on the Laplace equation expressing the equilibrium gas bubble pressure, the meso- and micropores of the catalyst layer constrict the bubble growth and detachment from the surface. Hence, the gaseous CO_2 disengagement from the catalyst layer is impeded, lowering the effective electrolyte conductivity, disturbing the current distribution, and increasing the concentration overpotential of the reactant situated in the liquid phase. The larger macropores (diameter > 50 nm) of the three-dimensional support (a few examples are shown in Figure 4.62) are more conducive to bubble growth, coalescence, and detachment processes. Furthermore, the local gas evolution can enhance the reactant mass transfer to the surface, thereby lowering the concentration overpotential.

A major challenge regarding the three-dimensional support is the synthesis and uniform dispersion of catalysts on the surface and through the thickness of the support matrix. Electrodeposition techniques using various colloidal media were successfully developed for the preparation of PtRu, PtRuMo, and PtSn nanoparticles and nanostructures on graphite felts, reticulated vitreous carbon, and Ti mesh with thicknesses ranging from ~200 μm to 3,000 μm [86, 190, 218, 249–250]. The colloidal media, consisting of either surfactant agglomerates (micelles, liquid crystals) or reverse microemulsion, had a major impact on various aspects of the deposition process, such as i) the co-deposition rates of alloying elements, ii) the catalyst morphology, and iii) the catalyst penetration throughout the matrix thickness.

Without the colloid present (i.e., electrodeposition from pure aqueous media), a Pt-rich catalyst was formed, typically only on the outer surface of the three-dimensional support, without significant penetration into the matrix. For co-deposition throughout the thickness of the support of binary and ternary catalyst formulations, with atomic compositions relevant to fuel cell application, the presence of the colloidal system was essential. The mechanism of action for the surfactant or water-in-oil microemulsion is believed to be related to selective blocking of the surface, creating a high-Pt electrocrystallization overpotential, thereby lowering the Pt electrodeposition rate relative to the alloying elements (e.g., Ru, Mo, or Sn).

Figure 4.63 compares the effect of the novel extended reaction zone supports on the electrocatalytic activity of PtRu for methanol electrooxidation. The catalyst characteristics are presented in Table 4.3. The catalyst surface morphology on all three supports could be characterized as predominantly mesoporous coating composed of nanoparticle agglomerates (Figure 4.64).
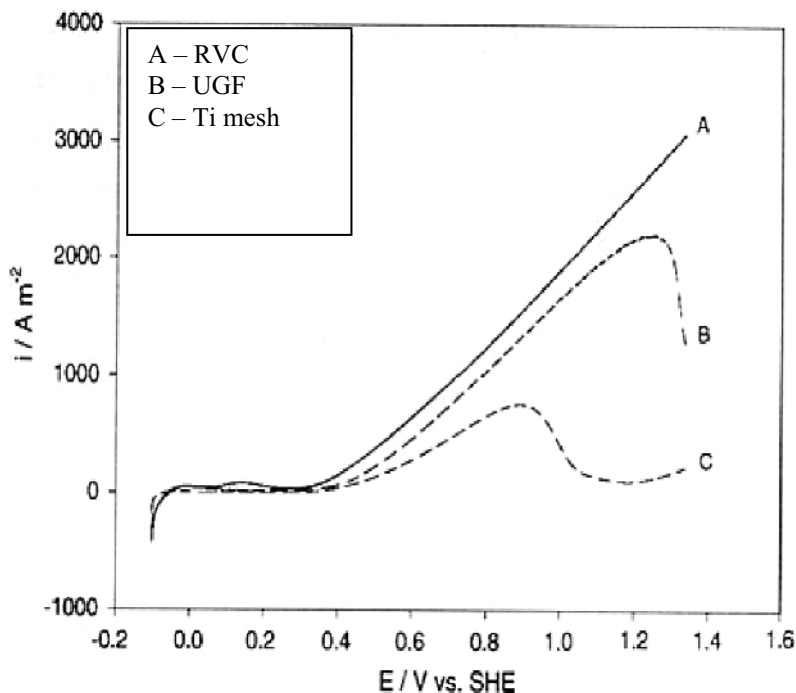
Figure 4.63. Comparison of methanol electrooxidation superficial current density for PtRu supported on RVC, UGF, and Ti mesh. 1 M CH_3OH – 0.5 M H_2SO_4, 298 K, scan rate 5 mV s^{-1} [218]. (With kind permission from Springer Science+Business Media: Journal of Applied Electrochemistry, Direct methanol fuel cells with reticulated vitreous carbon, uncompressed graphite felt and Ti mesh anodes, 38, 2008, 51–62, Cheng T, Gyenge E, figure 7.)

Table 4.3. Effect of three-dimensional support on the PtRu catalyst characteristics produced by galvanostatic electrodeposition from a colloidal media containing 25 vol% Triton X-100/isopropanol (1:4 v/v ratio) and 75 vol% aqueous phase (with 2.5×10^{-4} M H_2PtCl_6 and $(NH_4)_2RuCl_6$ each). Deposition current density 20 A m^{-2}, 120 min, 341 K [218]. RVC = reticulated vitreous carbon, UGF = graphite felt (uncompressed). (With kind permission from Springer Science+Business Media: Journal of Applied Electrochemistry, Direct methanol fuel cells with reticulated vitreous carbon, uncompressed graphite felt and Ti mesh anodes, 38, 2008, 51–62, Cheng T, Gyenge E, table 3.)

Support	Catalyst load (mg cm$^{-2}_{geom}$)	Pt:Ru atomic ratio	Catalyst surface area per geometric area of the support (m^2 m$^{-2}_{geom}$)*
RVC	1.20	3.6:1	144
UGF	0.98	4.0:1	352.8
Ti mesh	0.28	4.5:1	89.6

* Determined by anodic stripping of the underpotential deposited Cu monolayer
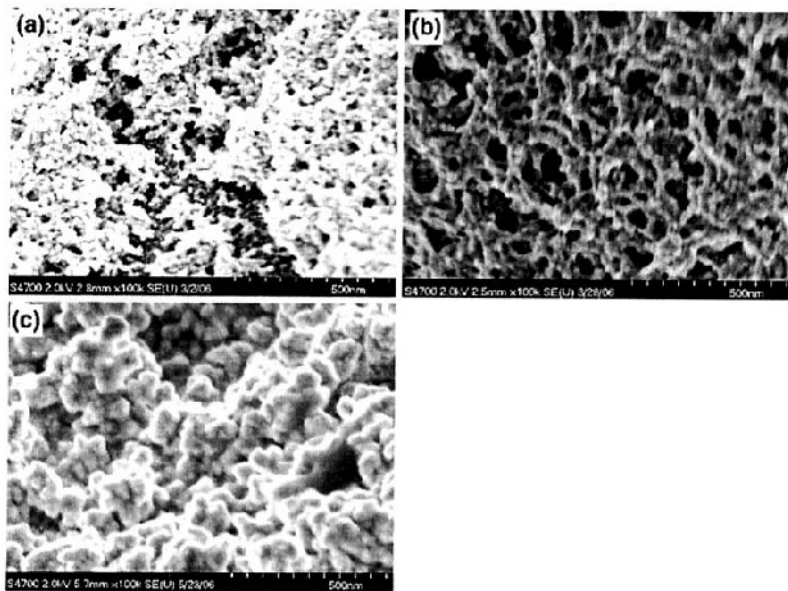
Figure 4.64. Mesoporous PtRu catalyst layer supported on a) RVC, b) UGF, and c) Ti mesh. Galvanostatic electrodeposition using micellar media based on Triton X-100. 20 A m^{-2}, 341 K [218]. (With kind permission from Springer Science+Business Media: Journal of Applied Electrochemistry, Direct methanol fuel cells with reticulated vitreous carbon, uncompressed graphite felt and Ti mesh anodes, 38, 2008, 51–62, Cheng T, Gyenge E, figure 7.)

The methanol electrooxidation superficial current densities using the PtRu catalysts presented in Table 4.3 were strongly influenced by the type of three-dimensional support (Figure 4.63). Based exclusively on a surface area effect, the highest catalytic activity was expected for graphite felt. However, both the lowest onset potential and the highest current density for methanol oxidation were obtained on RVC-supported PtRu. These results point to catalyst-support interaction effects. Further studies, coupling experimental work with mathematical modeling, are required to understand the fundamental differences in performance for various extended reaction zone anodes. It is proposed that the support morphology influences the crystallographic features of the electrodeposited PtRu and also, possible differences in catalyst-support electronic interaction among the three supports might contribute to the observed polarization behavior.

The novel anode structures have been employed in direct methanol [86, 218, 249, 305–307], ethanol [190], and formic acid fuel cell [308, 309] investigations. A general conclusion emerging from most of these studies is the enhancement of anode catalyst layer utilization efficiency by the extended reaction zone (or three-dimensional) support. This is manifested, for instance, by consistently higher peak power output based on the anode catalyst mass compared to convential gas diffusion type designs. Figure 4.65 exemplifies the performance of pressed graphite felt with PtRu and PtRuMo, at temperatures between 333 and 353 K [86]. Table 4.4 presents the corresponding anode catalyst characteristics.

a)

b)
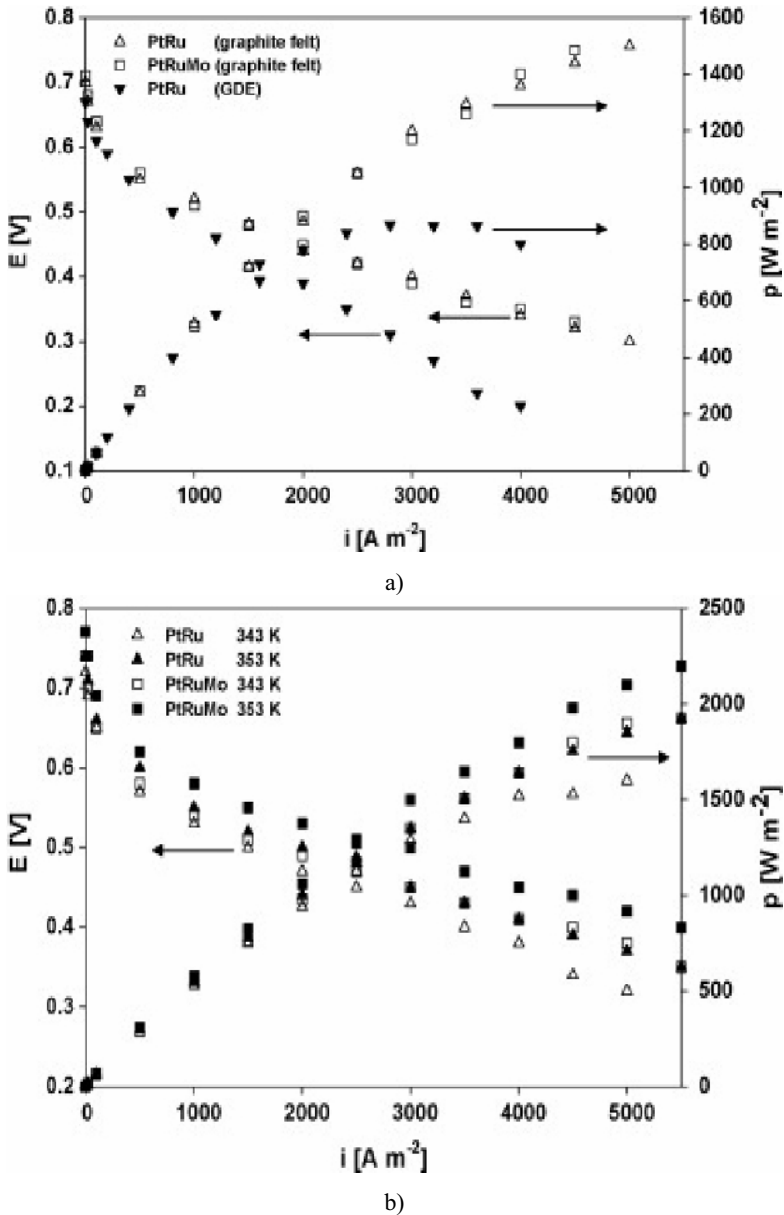
Figure 4.65. Performance comparison of DMFC equipped with extended reaction zone anode composed of pressed graphite felt with PtRu and PtRuMo, obtained by electrodeposition from a colloidal solution [86, 250]. a) 333 K, b) 343, and 353 K. Anode catalyst characteristics are given in Table 4.4. Anolyte: 1 M CH_3OH – 0.5 M H_2SO_4, 5 mL min^{-1}, ambient pressure. Cathode: 4 mg cm^{-2} Pt black, O_2 flow rate 500 ml min^{-1} at 2 atm (abs). [86]. (Reprinted from Journal of Power Sources, 167(2), Bauer A, Gyenge EL, Oloman CW, Direct methanol fuel cell with extended reaction zone anode: PtRu and PtRuMo supported on graphite felt, 281–7, 2007, with permission from Elsevier.)

Table 4.4. PtRu catalyst characteristics for DMFC experiments (Figure 4.65). PtRu and PtRuMo on pressed graphite felt, produced by galvanostatic electrodeposition from a colloidal media containing 40 wt% Triton X-100 and 60 wt% aqueous phase. Deposition current density 60 A m^{-2}, 2×90 min, 333 K [86]. (Reprinted from Journal of Power Sources, 167(2), Bauer A, Gyenge EL, Oloman CW, Direct methanol fuel cell with extended reaction zone anode: PtRu and PtRuMo supported on graphite felt, 281–7, 2007, with permission from Elsevier.)

Properties	PtRu on pressed graphite felt	PtRuMo on pressed graphite felt	PtRu unsupported* (CCM)
Pt:Ru:(Mo) atomic ratio	1.4:1	1:1:0.3	1:1
Total catalyst load (mg cm^{-2})	4.3	5.2	4.0
Effective Pt surface area** (m^2 m^{-2}$_{geom}$)	712	254	NA

* Commercial product from Lynntech Inc.
** Determined by anodic stripping of underpotential deposited Cu monolayer.

Figure 4.65(a) indicates that the three-dimensional support caused a 38% increase in the peak power density at 333 K compared to the catalyst coated membrane (CCM), while at current densities below 2000 A m^{-2}, in the electrode kinetic zone, the performances were similar. Since at the peak power output conditions, both ionic and reactant mass transfer effects impact the anode polarization behavior, it is proposed that in the case of pressed graphite felt support the enhanced utilization of the catalyst is related to the latter effects rather than the intrinsic kinetics.

Regarding the catalyst formulation, in contrast to 333 K, at both 343 and 353 K PtRuMo had a higher activity than PtRu (Figure 4.65(b)). Thus, a strong positive interaction effect between temperature and Mo presence in the catalyst was detected [86]. However, Mo surface segregation and oxidation was observed, compromising the longer-term catalytic activity [86].

Similarly, for direct ethanol fuel cell anodes, higher PtSn mass specific activities and utilization efficiencies were reported on uncompressed graphite felt compared to conventional gas diffusion anodes (catalyst coated membrane variant) [190]. These investigations point toward the possibility of reducing the precious metal anode catalyst load by exploiting the support-catalyst interaction. Future studies using carbon-based extended reaction zone anodes must focus on quantitative assessment of the liquid and gaseous mass transfer and the fuel crossover flux. Regarding the latter, it is of interest to evaluate whether dispersing the catalyst load throughout a larger reaction volume brings about a decrease in crossover rate, or whether the CCM design providing a more compact barrier at the membrane surface is more effective in this respect.

In addition to carbon and graphite-based extended reaction zone supports, Ti mesh has been fairly extensively investigated for direct methanol fuel cells in both acid and alkaline conditions, and also for formic acid cells [218, 305–307, 309–313]. Compared to three-dimensional carbons, Ti mesh has the advantage of a

mechanically strong yet flexible metallic structure with physical properties such as electronic conductivity and porosity, independent of compression in the fuel cell. Furthermore, the higher effective electronic conductivity renders Ti mesh a better current collector. The major drawbacks, however, are high cost and the spontaneous formation on the Ti surface of an oxide film that must be removed (for example, by immersion in either boiling 35 wt% HCl [307] or 10 wt% oxalic acid at 80 $^\circ$C [306]) prior to the application of any catalyst deposition procedure.

The performance in a DMFC of a Ti mesh anode support coated with mesoporous PtRu produced by electrodeposition (Figure 4.64 and Table 4.3) was very promising in terms of anode catalyst mass-specific peak power output and current density; namely, 50 W g^{-1} at 200 A g^{-1} was obtained [218]. However, due to the large pore sizes of the mesh coupled with a very low catalysy loading (0.28 mg cm^{-2}, Table 4.3), the methanol crossover was severe for this anode structure, as reflected by the low open-circuit cell voltage (e.g., 0.54 V at 333 K) [218]. This conclusion is also supported by the methanol concentration dependence of the Ti mesh anode performance, reported by Lim et al. [312]. In a direct comparison with a conventional gas diffusion electrode employing identical PtRu load and composition, the Ti mesh anode support gave higher power output only at 0.5 M methanol concentration, whereas at 1 and 2 M methanol the GDE was better [312].

In an alkaline (1 M NaOH) DMFC, on the other hand, where crossover to the cathode is alleviated, the Ti mesh-supported Pt outperformed the GDE in 1 M methanol over the entire investigated range of superficial current densities (up to 70 mA cm^{-2}) [311]. Thus, in the development and performance analysis of novel extended reaction zone supports, one must take into account the multitude of complex interactions involving support morphology, physico-chemical properties, electronic effects affecting the intrinsic electrocatalytic activity, and various mass transfer processes.

In the case of a direct formic acid fuel cell equipped with Ti mesh anode support, Chetty and Scott carried out a comprehensive comparative investigation of Pd and PtSn catalysts prepared by either thermal or electrochemical deposition [309]. Generally, PtSn/Ti mesh performed better than Pd/Ti mesh; the maximum power output for each at 333 K using 1 M HCOOH was about 20 mW cm^{-2} and 37 mW cm^{-2}, respectively. It is noteworthy that according to this study the Ti mesh-supported PtSn gave about three times higher peak power density than the GDE with commercial carbon supported PtSn [309]. Furthermore, the performance of the three-dimensional anode improved with formic acid concentration up to 7 M, and excellent catalyst stability was observed during 72 h of continuous operation.

4.3.2.5 Electronically Conductive Polymer Supports

A different approach to improve the catalyst-support interactions in direct fuel cells is based on electronically conductive polymer supports. Multiple functions could be envisaged for the polymer supports, such as enhancement of the catalyst nanoparticle dispersion, superior physico-chemical stability compared to carbon, potentially beneficial electronic interaction with the catalyst, and surface properties conducive to the transport and adsorption of reactive species.

In the context of direct fuel cell anodes, polyaniline (PAni) was the first investigated polymer support due to its straightforward synthesis by

electropolymerization of aniline [314]. Hable and Wrighton carried out among the first comprehensive studies of CH_3OH and C_2H_5OH electrooxidation on PtRu/PAni and PtSn/PAni [315]. The catalyst particles (diameter 300–500 nm and load of 0.25–1 mg cm^{-2}) were incorporated in the polymer matrix by potential cycling deposition on PAni-GC. Electrocatalytic acitivity toward alcohol electrooxidation was detected only in the region of electronic conductivity for PAni, i.e., at potentials higher than ~0 V vs. SCE when PAni is in the emeraldine state. Otherwise, the resisitivity of the polymer film impedes the electrochemical response. PtSn was the most active toward ethanol oxidation, whilst for methanol oxidation PtRu and PtSn gave identical responses. The accumulation of intermediate species such as acetaldehyde and formaldehyde in the PAni matrix unfortunately compromised the long-term electronic conductivity of PAni and decreased the performance [315].

In a different study, a direct comparison of Pt electrodeposited directly on carbon versus Pt electrodeposited on PAni-modified carbon revealed that the latter gave consistently higher methanol oxidation current densities at 0.5 V vs. SCE [316, 317a]. The role of PAni morphology was also explored, showing that the granular form of the polymer, produced by electropolymerization in H_2SO_4 or HNO_3, is preferred since for the same amount of Pt catalyst it gave up to about six times higher methanol oxidation superficial current density compared to fibrous PAni obtained in HBF_4 or $HClO_4$ [317a]. These results were attributed to surface area and associated catalyst dispersion effects. However, other researchers reported that fibrous PAni (diameter 70–100 nm) produced by a pulse galvanostatic method is a better support compared to the granular morphology, which is obtained by conventional galvanostatic electropolymerization [317b].

Bagotzky et al. investigated the true catalytic effect of Pt/PAni by evaluating the particle size and the total catalyst surface area, and normalizing accordingly the methanol oxidation current (referred to as specific or intrinsic electrocatalytic activity) [318]. The constant potential (0.05 V vs. RHE) electrodeposition of Pt on PAni on a rotating disk electrode setup at various deposition times produced a wide range of particle sizes (between 2 to 850 nm) and specific surface areas. For example, at a load of 750 μg cm^{-2} a fairly continuous Pt film formed on the PAni surface, composed of large, ~150–850 nm diameter agglomerates. The corresponding specific surface area (determined by underpotential hydrogen adsorption/desorption) was only about 10 m^2 g^{-1} [318]. Conversely, for lower loads (below 60 μg cm^{-2}) almost monodisperse particles of 2–5 nm diameter were produced with specific surface area up to 24 m^2 g^{-1}.

Figure 4.66 shows the methanol oxidation current density per total catalyst area as a function of Pt load for Pt/PAni. A number of interesting observations can be made. At low Pt load the intrinsic electrocatalytic activity was virtually independent of potential as a result of slow methanol adsorption (chemisorption) on the small catalyst particles embedded in the polymer film [318]. However, at higher loadings (60 to 750 μg cm^{-2}) two regions can be identified: i) for 0.55 V_{RHE} < E < 0.66 V_{RHE} the polarization corresponds to the Tafel behavior (Tafel slope of 90–100 mV dec^{-1}), and ii) at E > 0.66 V vs. RHE adsorption becomes the rate controlling step. Furthermore, the Pt/PAni specific electrocatalytic activity for methanol oxidation was consistently higher than that of Pt/Pt (platinized Pt

produced under similar conditions but without PAni), indicating a true catalytic effect. At ~750 µg cm^{-2} the current density approached that of smooth Pt.
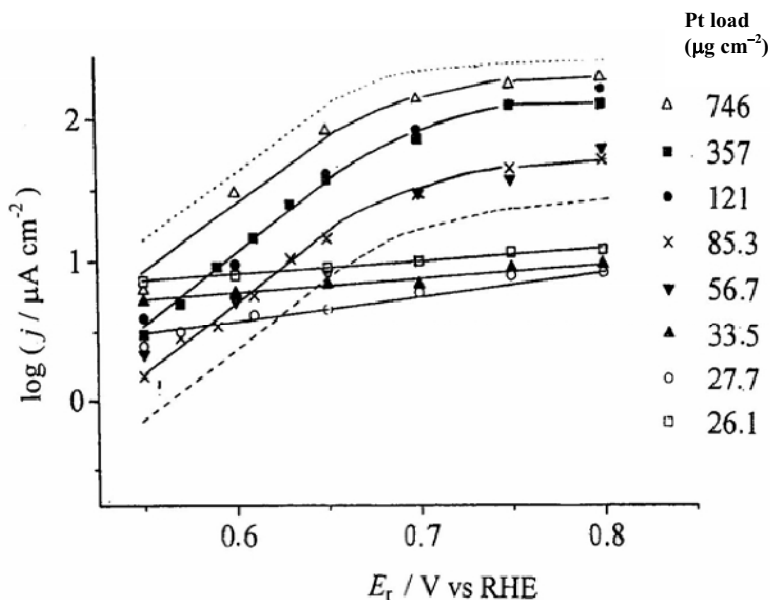
Figure 4.66. Intrinsic electrocatalytic activity of Pt/PAni as a function of Pt load (symbols: µg cm^{-2}) [318]. Dotted line: smooth Pt; dashed line: Pt/Pt. 1 M CH$_3$OH – 0.5 M H$_2$SO$_4$. (Reproduced from Journal of Electroanalytical Chemistry, 509(2), Mikhaylova AA, Molodkina EB, Khazova OA, Bagotzky VS, Electrocatalytic and adsorption properties of platinum microparticles electrodeposited into polyaniline films, 119–27, 2001, with permission from Elsevier.)

It must be emphasized that similar results were obtained with Pt dispersed in a Nafion$^{®}$ film [318], suggesting that Pt nanoparticles electrodeposited into polymeric matrices are more active than Pt/Pt.

Moreover, the intrinsic activity of uncatalyzed PAni toward methanol oxidation must also be considered. Surprisingly, it was reported that PAni itself deposited on a Pt substrate enhanced by 50% to 320% the methanol oxidation peak current density vs. pure Pt at methanol concentrations between 2 to 10 M in 0.5 M H$_2$SO$_4$ [319]. However, at methanol concentrations below 1 M, PAni was inactive toward methanol oxidation. Other researchers contradicted this finding and reported the inactivity of PAni toward methanol oxidation [320, 321]. More research is required in this area since thus far no explanation has been offered for the peculiar activity of PAni toward methanol oxidation at high concentrations [319].

Lima et al. presented IR spectroscopic evidence for the enhanced CO$_{ad}$ oxidation on PtRuMo/PAni (film thickness 0.5 µm). The corresponding oxidation potential was 150 mV and 500 mV lower than on PtRu/PAni and Pt/PAni, respectively [320]. No information was provided regarding the potential role of the polymer.
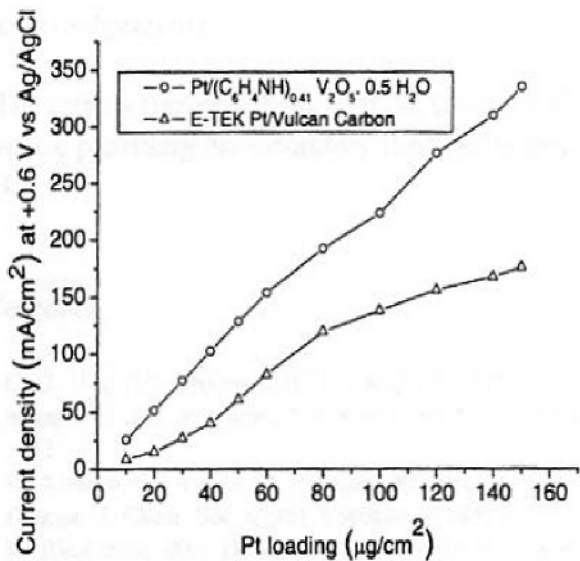
(a)
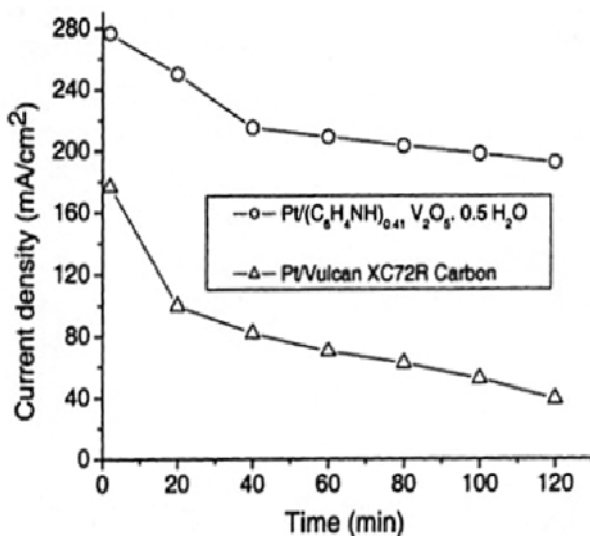
(b)

Figure 4.67. The effect of catalyst support, PAni-V_2O_5, and Vulcan on the superficial current density (i.e., per geometric electrode area) for methanol oxidation on Pt. 1 M CH_3OH – 1 M H_2SO_4 [322]. (a) comparison as a function of Pt load, (b) time profile at a constant Pt load of 120 µg cm^{-2}. (Reprinted from Journal of Power Sources, 141(1), Rajesh B, Thampi KR, Bonard J-M, Mathieu HJ, Xanthopoulos N, Viswanathan B, Electronically conducting hybrid material as high performance catalyst support for electrocatalytic application, 35–8, 2005, with permission from Elsevier.)

Other studies confirmed as well the catalytic activity of Pt/PAni composites for the oxidation of small organic molecules relevant to fuel cells. Rajesh et al. prepared an interesting catalyst layer composed of Pt/PAni-V_2O_5 whereby the polymer was produced by homogeneous polymerization [322]. V_2O_5 acted as both redox catalyst for polymerization, forming V^{4+}, and as the host for the intercalation of PAni in its layered structure. The stoichiometry of the composite support was $(C_6H_4NH)_{0.41}V_2O_5 \cdot 0.5H_2O$.

In a direct comparison with Pt supported on Vulcan, the novel composite support induced a significant increase in methanol oxidation superficial current density for the identical amount of Pt catalyst (Figure 4.67(a)). Furthermore, the long-term catalytic activity of Pt was improved with the PAni-V_2O_5 composite support (Figure 4.67(b)).

The incorporation of H_xMoO_3 as co-catalyts with Pt in the PAni support matrix prepared by electrodeposition was investigated for methanol, formic acid, and formaldehyde oxidation [323]. In addition to surface area enhancement-related increase in the oxidation current densities for the three C1 molecules, both Pt/PAni and Pt-H_xMoO_3/PAni revealed true catalytic effects as well, according to Wu et al. [323]. Figure 4.68 illustrates the case of formic acid oxidation. Compared to Pt/Pt, the polyaniline support brought about an increase of both peak currents on the forward scans, at 0.3 and 0.6 V vs. SCE, followed by a pronounced expansion of the oxidation wave on the return scan. The presence of H_xMoO_3 in the catalyst formulation increased the formic acid electrooxidation rate, especially in the low potential region of the forward scan, between 0 and 0.5 V vs. SCE (Figure 4.68), whereas on the return sweep the oxidation wave was close to the Pt/PAni case.
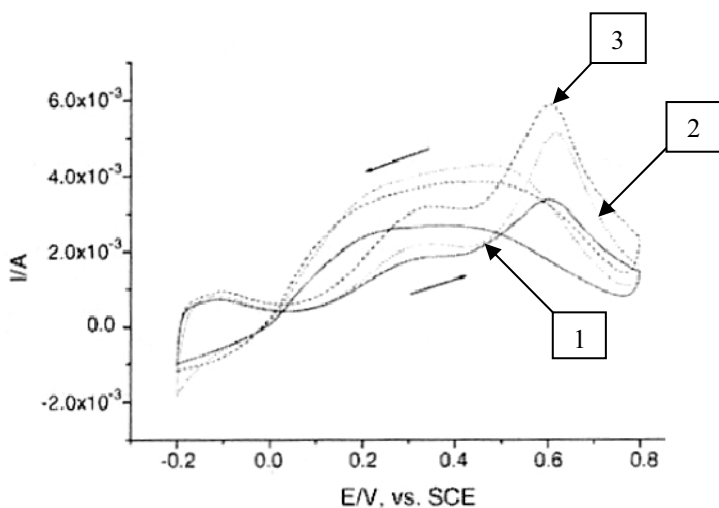
Figure 4.68. The effect of PAni support and H_xMoO_3 co-catalyst on formic acid oxidation on Pt. 1) Pt/Pt, 2) Pt/PAni, and 3) Pt-H_xMoO_3/PAni. 0.1 M HCOOH – 0.5 M H_2SO_4, 100 mV s^{-1} [323]. (Reprinted from Journal of Power Sources, 145(2), Wu YM, Li WS, Lu J, Du JH, Lu DS, Fu JM, Electrocatalytic oxidation of small organic molecules on polyaniline-Pt-H_xMoO_3, 286–91, 2005, with permission from Elsevier.)

The method of catalyst preparation (especially in the case of alloys) and the catalyst interaction with the polymer support matrix play important roles in determining the resultant electrocatalytic effect. The catalyst/support couple PtSn/PAni (0.5 μm thickness) with PtSn synthesized by electroreduction at 0.1 V vs. RHE was found to be an effective catalytic system for formic acid oxidation, lowering the anode potential by over 100 mV compared to pure Pt/PAni and PtRu/PAni [324]. Moreover, the oxidation of formic acid on PtSn/PAni commences at low potentials, in the hydrogen adsorption region, around 0.1–0.2 V vs. RHE.

Doping the PAni support with polystyrene sulfonic acid (PSS) has recently been shown to be an effective method for further improvement of the catalytic activity of Pt toward methanol oxidation [325]. The $-SO_3H$ sites in the polymer assist in the uniform dispersion of the catalyst precursor Pt^{4+} throughout the network, bringing about an even distribution of the resulting Pt sites. Furthermore, the sulfonate groups form a proton-conducting network, which is also essential for catalytic activity. Another PAni composite support type that attracted attention is one obtained by electropolymerization of aniline in the presence of single-wall carbon nanotubes (SWNT) forming a PAni-SWNT composite film [326]. The PAni-SWNT support of about 60 nm thickness provided an extended electrochemically effective specific surface area and higher support electronic conductivity for the electrodeposited Pt catalysts. These effects, combined, imparted a more than three-fold enhancement of the methanol oxidation superficial current density (Figure 4.69).

In addition to PAni, a number of other electronically conductive polymers have been investigated as catalyst supports, especially in relation to methanol electrooxidation. Pickup and co-workers introduced the PEDOT support (i.e., poly(3,4-ethylenedioxythiophene) [327]. Composites of PEDOT with either poly(styrene-4-sulfonate) (PSS) or polyvinylsulfate (PVS) possess both electronic and ionic conductivity. Methanol oxidation voltammograms on PtRu showed that both PEDOT-PSS and PEDOT-PVS supports were less effective compared to carbon [327]. However, as shown recently by Juttner and co-workers, the performance of the PEDOT supported catalytic system can be substantially enhanced by electrochemical oxidative treatment of the polymer support [328]. The oxidative activation treatment consisted of successive potential cycles up to 1.5 V vs. RHE. The irreversible oxidation of PEDOT changed the polymer morphology, increasing its porosity, which in turn improved the methanol permeation flux and access of the Pt active sites. The electrochemical activation doubled the maximum power output of a Pt/PEDOT catalyst system in a DMFC [328]. Similar catalytic activation was observed after long-term storage (e.g., 6 months) of Pt/PEDOT. The latter method was more effective than the oxidative treatment.

The PEDOT-PSS composite support was employed in conjunction with Pt, PtSn, and PtPb for ethanol electrooxidation catalysis, showing the expected beneficial effect of Sn [329]. No comparison was provided with conventional carbon-supported or unsupported catalyst layers; therefore, the effectivness of the support cannot be judiciously analyzed.
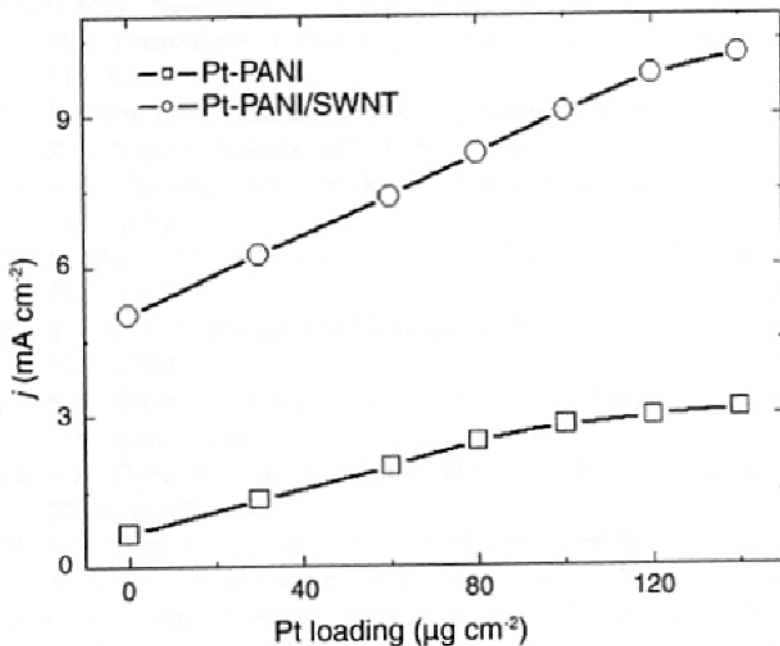
Figure 4.69. Methanol oxidation superficial current density at 0.65 V_{RHE} as a function of Pt load supported on PAni and PAni-SWNT, respectively. Data obtained from cyclic voltammogram in 0.5 M CH_3OH – 0.5 M H_2SO_4; 298 K [326]. (Reprinted from Journal of Power Sources, 155(2), Wu G, Li L, Li J-H, Xu B-Q, Methanol electrooxidation on Pt particles dispersed into PANI/SWNT composite films, 118–27, 2006, with permission from Elsevier.)

Polypyrrole (PPY) based supports have also received considerable attention as direct liquid fuel cells anode catalysts. Rajesh et al. reported a method to produce by alumina membrane template-assisted electropolymerization PPY nanotubes of 200 nm outer diameter deposited on carbon cloth [330]. Subsequently, Pt was galvanostatically electrodeposited inside the PPY nanotubes, and it was shown by voltammetry that the nanotube morphology of the PPY support induces up to three times higher methanol oxidation current densities compared to untemplated PPY; the latter was less effective since dense Pt crystallite agglomerates formed on its surface, with lower electrochemically available surface area. The same templated synthesis method was applied to produce poly-3-methylthiophene (PMT) with nanocone morphology [331]. Figure 4.70 reveals that the carefully controlled nanocone support morphology obtained by templating was crucial for the enhancement of the catalytic acitivity toward methanol oxidation. The Pt loading was kept constant at 80 μg cm^{-2}. Without the templating procedure, interestingly the PMT support gave worse activity than the carbon support (see GC/20% Pt/C from E-TEK Inc., Figure 4.70). Thus, the special morphology of the support was key in order to assure high utilization of the Pt catalyst.
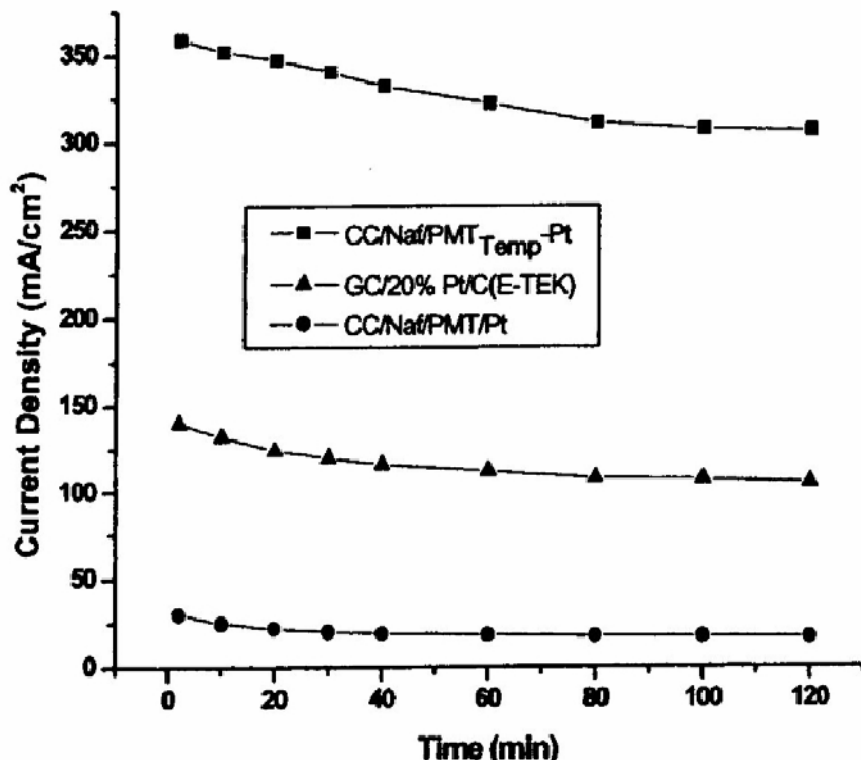
Figure 4.70. Effect of PMT electronically conductive polymer support on the methanol oxidation current density at a constant Pt load of 80 μg cm^{-2}. 1 M CH$_3$OH – 1 M H$_2$SO$_4$; 0.6 V$_{SSCE}$, 298 K [331]. Legend: CC/Naf/PMT$_{Temp}$-Pt: Nafion coated carbon cloth with PMT support produced by templating (i.e., nanocone morphology); CC/Naf/PMT-Pt: same as before but without templation; GC/20%Pt/C: commercial (E-TEK Inc.) supported catalyst. (Reprinted from Journal of Power Sources, 133(2), Rajesh B, Thampi KR, Bonard J-M, McEvoy AJ, Xanthopoulos N, Mathieu HJ, Viswanathan B, Pt particles supported on conducting polymeric nanocones as electro-catalysts for methanol oxidation, 155–61, 2004, with permission from Elsevier.)

In situ polymerization of pyrrole in the presence of multiwalled carbon nanotubes (MWCNT) yielded PPY-MWCNT composite support for Pt and PtPd nanoparticles of 2 to 5 nm [332]. The resulting catalytic system was evaluated for activity toward formic acid electrooxidation. The presence of Pd in the catalyst formulation shifted the HCOOH oxidation onset potential to more negative values, with oxidation commencing around 0.2 V vs. SCE. It was proposed that Pd favors the direct oxidation pathway of formic acid, and therefore it is less susceptible to CO poisoning [332]. Similar support architecture was also employed for Pt and PtRu catalysis of methanol oxidation [333]. Kulesza et al. showed that PtRu can also be incorporated into a poly-N-methylpyrrole (PMPy) matrix in the form of spatially dispersed Pt and Ru(III,IV)-oxo sites [334]. The latter species were introduced during the electropolymerization stage, when the positive charge of the

polymer is balanced by the dopant anionic species, Ru(III,IV) oxide/cyanoruthenate. Pt sites were formed by electroreduction of H_2PtCl_6 (0.012 M in 0.5 M H_2SO_4) with potential cycling in the range of 0.8 to –0.3 V vs. RHE.

Bensebaa et al. employed ethylene glycol reduction in a microwave oven (at 436 K) in order to synthesize PtRu nanoparticles and to incorporate *in-situ* the catalyst nanoparticles in a polymer matrix of polypyrrole-di(2-ethylhexyl) sulfosuccinate (PPyDEHS). Figure 4.71 shows the excellent dispersion of the nanoparticles on the polymer support [335]. Morover, the polymer also served as a colloid stabilizer during nanoparticle synthesis. Preliminary methanol oxidation polarization curves showed fairly good activity for such catalytic systems, giving a Pt mass specific current density of 20 A g^{-1} at 0.4 V vs. SCE. Further studies are required to test the long-term stability and feasibility of the PtRu/PPyDEHS system for DMFC anodes.
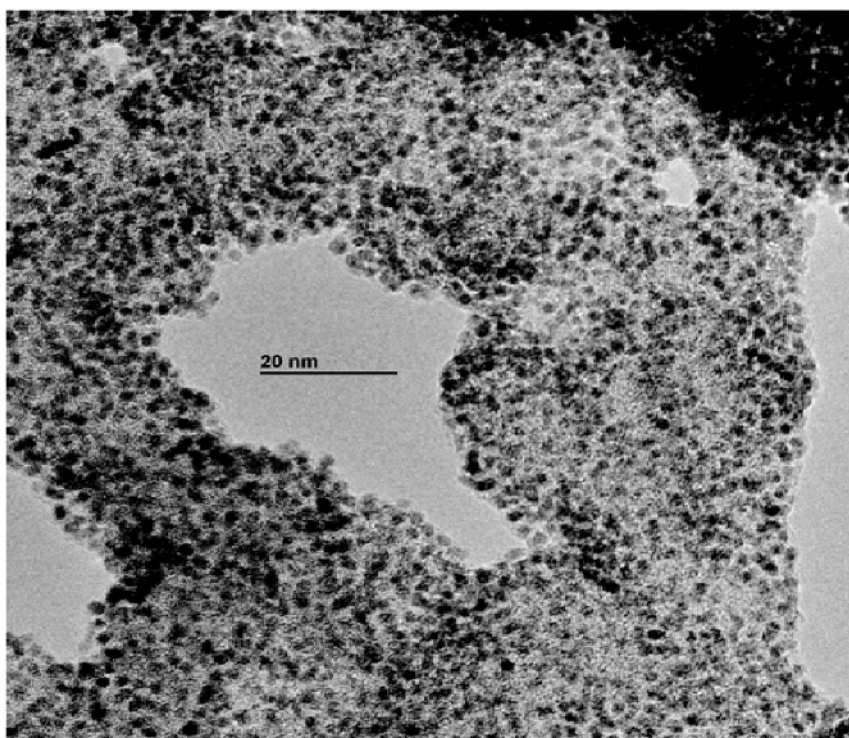
Figure 4.71. TEM of PtRu nanoparticles incorporated in the conducting polymer PPyDEHS (see text) [335]. (Reprinted with permission from J Phys Chem B 2005;109:15339–44. Copyright 2005 American Chemical Society.)

In the case of polypyrrole, Juttner and co-workers compared three different preparation techniques: I) Pt potentiostatically deposited onto pre-synthesized PPY film (0.5 μm thickness preferred); II) Pt deposited onto the PPY film simultaneously with film formation by electropolymerization; and III) the same

simultaneous deposition procedure was applied but the Pt/PPY sample was also subjected to post-deposition electrochemical treatment in order to remove the chloride ions from the precursor Pt salt [336]. The sizes of the Pt crystallites for all three deposition procedures were rather large, in the range of 0.1–0.4 μm depending on the load. Interestingly, at 298 K samples II) and III) showed no electrocatalytic acitivity toward methanol oxidation, even when the film thickness was reduced to 0.1 μm. Only sample (I) (obtained by deposition onto pre-synthesized PPY) had activity. Furthermore, the more negative the Pt deposition potential the higher the methanol oxidation current density for Pt/PPY(I). An important finding of this work was the enhanced stability of the Pt supported on PPY(I) compared to GC [336]. After only ~10–20 minutes of oxidation, the former catalytic system gave higher methanol oxidation current densities than Pt/GC at 0.5 V vs. RHE, in 1 M CH_3OH – 0.5 M H_2SO_4. Since the Pt particles obtained on GC were larger than those obtained on PPY(I) (1–2 μm diameter compared to 0.4 μm) the observed long-term enhancement effect was explained based on the higher electrochemically active surface area and possibly more subtle support-catalyst electronic interaction effects.

Poly-3-methylthiophene (P3MT) was produced by electropolymerization on graphite and utilized as a Pt and PtPb catalyst support for formic acid oxidation [337]. In chronoamperometry experiments, after 300 s at a constant potential of 0.8 V vs. SCE the Pt catalyst supported on P3MT/graphite gave up to an order of magnitude higher HCOOH oxidation current density compared to the bare graphite support. Further improvement of the HCOOH oxidation was reported when small amounts of Pb were incorporated onto the Pt/P3MT/graphite [337]. The co-catalytic effect of Pb produced up to an approximately three-fold increase in HCOOH oxidation current density. The promising fundamental studies using P3MT support must be followed up by fuel cell experiments, in which a number of interacting effects between electrode kinetics, mass transfer, and electronic conductivity will play an important role.

4.4 Conclusions

The present chapter has presented a comprehensive review of electrode kinetic and catalytic aspects associated with methanol, ethanol, and formic acid oxidation. The prevalent point of view in selecting and organizing the vast amount of information in this area was that of practical applicability in order to advance the technology of direct fuel cells. Emphasis was placed on the "catalytic system", starting with catalyst preparation methods and focusing on the interaction of catalyst/support/ionomer/chemical species. The development of catalytic systems was followed, from fundamental electrochemical and surface science studies to fuel cell experiments (whenever experimental data was available). Advances in both fundamental electrocatalysis and electrochemical engineering hold promise for the development of high-performance and cost-effective direct liquid fuel cells.

References

1. Petry OA. Activity of electrolytically deposited platinum and ruthenium on the electrooxidation of methanol. Dokl Akad Nauk SSSR 1965;160:871–4.
2. Lal H, Petry OA, Podlovchenko BI. Adsorption of intermediate reaction products in the electro-oxidation of MeOH in an acid solution. Elektrokhimiya 1965;1:316–20.
3. Bagotsky VS, Vasil'ev YuB. Mechanism of electrooxidation of methanol on the platinum electrode. Electrochim Acta 1967;12:1323–43.
4. Vitvitskaya GV, Daniel-Bek VS. Electrooxidation of ethanol in basic media at low values of anodic polarization. Zh Prikl Khim 1965;38:1043–8.
5. a) Raicheva SN, Kalcheva SV, Khristiv MV, Sokolova EI. Mechanism of the electrooxidation of ethyl alcohol and acetaldehyde on a smooth platinum electrode. I. Contribution of the chemical and electrochemical reactions to the overall anodic process. J Electroanal Chem 1974;55:213–22. b) Korchinskii, GA. Electrooxidation of ethanol with the superimposing of an alternating current on a direct current. Elektrokhimiya 1969;5:733–5. c) Podlovchenko, BI, Gladysheva, TD, Stenin, VF, Levina, VI. Mechanism of ethanol electro-oxidation on a platinum electrode. Electrokhimiya. 1973;9:1680–3.
6. Polyak AG, Vasil'ev YuB, Bagotsky VS, Smirnova RM. Electrochemical oxidation of formic acid on palladium. Elektrokhimiya 1967;3:1076–9.
7. Glazatova TN, Daniel-Bek VS. Electrooxidation of formic acid in acid medium in the range of small anodic polarizations. Elektrokhimiya 1966;2:1042–6.
8. Entina VS, Petry OA. Methanol electro-oxidation on platinum+ruthenium and ruthenium electrodes at various temperatures. Elektrokhimiya 1968;4:678–81.
9. Breiter MW. Anodic oxidation of methanol on platinum. III Adsorption kinetics in acidic solutions. J Electrochem Soc 1963;110:449–52.
10. Breiter MW. Oxidation mechanism of formic acid on platinum at low potentials in acidic solutions. J Electrochem Soc 1964;111:1298–199.
11. Breiter MW. The nature of formic acid adsorption at platinum electrodes in perchloric acid solution. Electrochim Acta 1965;10:503–8.
12. Breiter MW. Role of adsorbed species for the anodic methanol oxidation on platinum in acidic electrolytes. Disc Faraday Soc 1968;45:79–86.
13. Vol'fkovich YuM, Gurevich IE, Bagotsky VS. Functioning of a liquid porous electrode as illustrated by the electrooxidation of methanol. I. Polarization characteristics and a comparison of schemes. Elektrokhimiya 1969;5:111–14.
14. Vol'fkovich YuM, Gurevich IE, Bagotsky VS. Functioning of a liquid porous electrode as illustrated by the electrooxidation of methanol. II. Mixed types of operation for a porous electrode as studied by comparing characteristics. Elektrokhimiya 1969;5:128–31.
15. Sandstede G, Binder H, Koehling A. Electrodes, especially for the anodic oxidation of methanol. France patent 1481338. 1967.
16. Hauel A, Hill J, Reilly W. Fuel cell with titanium containing electrode. United States patent 3437525. 1969.
17. Waters RF, Cook HD. Electrodes having an intimate mixture of platinum and second metal. United States patent 3468721. 1969.
18. Binder H, Koehling A, Kuhn W, Sandstede G. Acid-proof tungsten carbide electrodes for fuel cells. Germany patent 1903521. 1970.
19. Clavilier J, Faure R, Guinet G, Durand R. Preparation of monocrystalline platinum microelectrodes and electrochemical study of the plane surface cut in the direction of the {111} and {110} planes. J Electroanal Chem 1980;107:205–9.
20. a) Bagotsky VS, Vasil'ev YuB, Pyshnogaeva II. Role of structural factors in electrocatalysis. I. Smooth platinum electrodes. Electrochim Acta 1971;16:2141–67. b)

Pyshnogaeva II, Vasil'ev YuB, Bagotsky VS. Adsorption and electrooxidation of methanol on different faces of a platinum single crystal. Elektrokhimiya 1970;6:433–6.

21. Clavilier J, Lamy C, Leger J-M. Electrocatalytic oxidation of methanol on single crystal platinum electrodes. Comparison with polycrystalline platinum. J Electroanal Chem 1981;125:249–54.

22. Lamy C, Leger J-M, Clavilier J, Parsons R. Structural effects in electrocatalysis. A comparative study of the oxidation of carbon monoxide, formic acid and methanol on single crystal platinum electrodes. J Electroanal Chem 1983;150:71–7.

23. Motoo S, Furuya N. Electrochemistry of platinum single crystal surfaces. Part II. Structural effects on formic acid oxidation and poison formation on platinum (111), (110) and (100). J Electroanal Chem 1985;184:303–16.

24. Adzic RR, Tripkovic AV, Vesovic VB. Structural effects in electrocatalysis: oxidation of formic acid and hydrogen adsorption on single-crystal stepped surfaces. J Electroanal Chem 1986;204:329–41.

25. Palaikis L, Wieckowski A. A catalytic study of formic acid oxidation on preferentially oriented platinum electrodes. Cat Lett 1989;3:143–58.

26. Sun SG, Clavilier J, Bewick A. The mechanism of electrocatalytic oxidation of formic acid on platinum (100) and (111) in sulfuric acid. An EMIRS study. J Electroanal Chem 1988;240:147–59.

27. Chang SC, Leung LWH, Weaver MJ. Metal crystallinity effects in electrocatalysis as probed by real-time FTIR spectroscopy: electrooxidation of formic acid, methanol, and ethanol on ordered low-index platinum surfaces. J Phys Chem 1990;94:6013–21.

28. Angerstein-Kozlowska H, MacDougall B, Conway BE. Origin of activation effects of acetonitrile and mercury in electrocatalytic oxidation of formic acid. J Electrochem Soc 1973;120:756.

29. Binder H, Koehling A, Sandstede G. Acceleration of the electrochemical oxidation of formic acid by sulfur and selenium adsorbed on platinum catalysts. Nature 1967;214:268–9.

30. Jayaram R, Contractor AQ, Lal H. Formic acid oxidation at platinized platinum electrodes. Part IV Effect of preadsorbed sulfur and related studies. J Electroanal Chem 1978;87:225–37.

31. Jayaram R, Lal HJ. Formic acid oxidation at platinized platinum electrodes. Part III The effect of preadsorbed iodide layer. J Electroanal Chem 1977;79,121–8.

32. Capon A, Parsons R. The oxidation of formic acid at noble metal electrodes: Part III Intermediates and mechanism on platinum electrodes. J Electroanal Chem 1973;45:205–31.

33. Capon A, Parsons R. The oxidation of formic acid at noble metal electrodes. Part 4: Platinum+palladium alloys. J Electroanal Chem 1975;65:285–305.

34. Solis V, Iwasita T, Pavese A, Vielstich W. Investigation of formic acid oxidation on palladium by on-line mass spectrometry. J Electroanal Chem 1988;255:155–62.

35. Pletcher D, Solis V. A further investigation of the catalysis by lead ad-atoms of formic acid oxidation at a platinum anode. J Electroanal Chem 1982;131:309–23.

36. Minevski LV, Adzic RR. Oxidation of formic acid at a high surface area supported platinum modified by foreign metal adatoms. J Appl Electrochem 1988;18:240–4.

37. Watanabe M, Horiuchi M, Motoo S. Electrocatalysis by ad-atoms: Part XXIII. Design of platinum ad-electrodes for formic acid fuel cells with ad-atoms of the IVth and the Vth groups. J Electroanal Chem 1988;250:117–25.

38. Shabrang M, Mizota H, Bruckenstein S. Adatom coverage dependences and specificity effects on the rate of formic acid electro-oxidation at polycrystalline platinum. J Electrochem Soc 1984;131:306–14.

39. Shibata M, Furuya N, Watanabe M. Electrocatalysis by ad-atoms. Part XXV: Electrocatalytic effects on the elementary steps in ethanol oxidation by non-oxygen-adsorbing ad-atoms. J Electroanal Chem 1989;267:163–70.

40. Willsau J, Heitbaum J. Elementary steps of ethanol oxidation on Pt in sulfuric acid as evidenced by isotope labeling. J Electroanal Chem 1985;194:27–35.

41. Bittins-Cattaneo B, Wilhelm S, Cattaneo E, Buschmann HW, Vielstich W. fdce4Intermediates and products of ethanol oxidation on platinum in acid solution. Ber Bunsen-Ges 1988;92:1210–18.

42. Wieckowski A. Kinetic isotope effects between light and heavy water in HCOOH and CH_3OH adsorption and oxidation on Pt. J Electroanal Chem 1977;78:229–41.

43. Wieckowski A, Sobkowski J. Comparative study of adsorption and oxidation of formic acid and methanol on platinized electrodes in acidic solution. J Electroanal Chem 1975; 63:365–77.

44. Wieckowski A, Sobkowski J. Adsorption of methanol on Pt. J Electroanal Chem 1976; 73:317–25.

45. Parsons R, VanderNoot T. The oxidation of small organic molecules: A survey of recent fuel cell related research. J Electroanal Chem 1988;257:9–45.

46. Watanabe M, Motoo S. Electrocatalysis by ad-atoms. Part II Enhancement of the oxidation of methanol on platinum by ruthenium ad-atoms. J Electroanal Chem 1975;60:267–73.

47. Janssen MMP, Moolhuysen J. Binary systems of platinum and a second metal as oxidation catalysts for methanol fuel cells. Electrochim Acta 1976;21:869–78.

48. Hamnett A, Weeks SA, Kennedy BJ, Troughton G, Christensen PA. Long-term poisoning of methanol anodes. Ber Bunsenges Phys Chem 1990;94:1014–20.

49. Lowde DR, Williams JO, Atwood PA, Bird RJ, McNicol BD, Short RT. Characterization of electrooxidation catalysts prepared by ion-exchange of platinum salts with surface oxide groups on carbon. J Chem Soc Faraday Trans 1 1979;75:2312–24.

50. Manoharan R, Goodenough JB, Hamnett A. High-performance carbon electrodes for acid methanol-air fuel cells. J Appl Electrochem 1987;21:413–18.

51. Ledjeff K, Ahn J, Zylka D, Heinzel A. Ion exchange membranes as electrolyte for electrochemical energy conversion. Ber Bunsenges Phys Chem 1990;94:1005–8.

52. Surampudi S, Narayanan SR, Vamos E, Frank H, Halpert G, Laconti A, et al. Advances in direct oxidation methanol fuel cells. J Power Sources 1994;47:377–85.

53. Olah GA, Goeppert A, Surya Prakash GK. Beyond oil and gas: the methanol economy. Weinheim:Wiley-VCH Verlag GmbH, 2006.

54. Drury DJ. Formic acid. In: Kirk-Othmer Encyclopedia of Chemical Technology. New York:John Wiley and Sons, 2007.

55. Gasteiger HA, Kocha SS, Sompalli B, Wagner FT. Activity benchmarks and requirements for Pt, Pt-alloy and non-Pt oxygen reduction catalysts for PEMFC. Appl Cat B 2005;56:9–35.

56. Gottesfeld S. Comparative evaluation of direct methanol fuel cells portable power sources: state of the art and projections. In: Small fuel cells for portable applications, 5th edition. Salem, MA:William Andrew, 2004;173–95.

57. Iwasita T. Electrocatalysis of methanol oxidation. Electrochim Acta 2002;47:3663–74.

58. Cao D, Lu G-Q, Wieckowski A, Wasileski SA, Neurock M. Mechanism of methanol decomposition on platinum: a combined experimental and ab initio approach. J Phys Chem B 2005;109:11622–33.

59. Sriramulu S, Jarvi TD, Stuve EM. Reaction mechanism and dynamics of methanol electrooxidation on platinum(111). J Electroanal Chem 1999;467:132–42.

60. Batista EA, Malpass GRP, Motheo AJ, Iwasita T. New insight into the pathways of methanol oxidation. Electrochem Commun 2003;5:843–6.

61. Chen YX, Miki A, Ye S, Sakai H, Osawa M. Formate, an active intermediate for direct oxidation of methanol on Pt electrode. J Am Chem Soc 2003;125:3680–1.

62. Zhu Y, Uchida H, Yajima T, Watanabe M. Attenuated total reflection: Fourier transform infrared study of methanol oxidation on sputtered Pt film electrode. Langmuir 2001;17:146–54.

63. Wang H, Löffler T, Baltruschat H. Formation of intermediates during methanol oxidation: a quantitative DEMS study. J Appl Electrochem 2001;31:759–65.

64. Wang H, Wingender C, Baltruschat H, Lopez M, Reetz MT. Methanol oxidation on Pt, PtRu and colloidal Pt electrocatalysts: a DEMS study of product formation. J Electroanal Chem 2001;509:163–9.

65. Kua J, Goddard WA III. Oxidation of methanol on 2nd and 3rd row group VIII transition metals (Pt, Ir, Os, Pd, Rh and Ru): application to direct methanol fuel cells. J Am Chem Soc 1999;121:10928–41.

66. Dickinson AJ, Carrette LPL, Collins JA, Friedrich KA, Stimming U. Performance of methanol oxidation catalysts with varying Pt:Ru ratio as function of temperature. J Appl Electrochem 2004;34:975–80.

67. Lee J, Eickes C, Eiswirth M, Ertl G. Electrochemical oscillations in the methanol oxidation on Pt. Electrochim Acta 2002;47:2297–301.

68. Climent V, Gomez R, Orts JM, Feliu JM. Thermodynamic analysis of the temperature dependence of PH adsorption on Pt(111) and Pt(100) electrodes in acidic media in the absence of specific anion adsorption. J Phys Chem B 2006;110:11344–51.

69. Burke LD, Horgan MA, Hurley LM, Nagle LC, O'Mullane AP. Superactivation of metal electrode surfaces and its relevance to CO_{ads} oxidation at fuel cell anodes. J Appl Electrochem 2001;31:729–38.

70. Anderson A, Grantscharova E, Seong S. Systematic theoretical study of alloys of platinum for enhanced methanol fuel cell performance. J Electrochem Soc 1996;143:2075–82.

71. Atwan M, Northwood D, Gyenge EL. Evaluation of colloidal Os and Os-alloys (Os-Sn, Os-Mo and Os-V) for electrocatalysis of methanol and borohydride oxidation. Int J Hydrogen Energy 2005;30:1323–31.

72. Huang J, Yang H, Huang Q, Tang Y, Lu T, Akins DL. Methanol oxidation on carbon-supported Pt-Os bimetallic nanoparticle electrocatalysts. J Electrochem Soc 2004;151:A1810–15.

73. Gokagac G, Kennedy BJ. Carbon supported Pt+Os catalysts for methanol oxidation. Z Naturforsch 2002;193–201.

74. Mukerjee S, Urian RC. Bifunctionality in Pt alloy nanocluster electrocatalyst for enhanced methanol oxidation and CO tolerance in PEM fuel cells: electrochemical and in situ synchotron spectroscopy. Electrochim Acta 2002;47:3219–31.

75. Mylswamy S, Wang CY, Liu RS, Lee J-F, Tang M-J, Lee J-J, et al. Anode catalysts for enhanced methanol oxidation: an in situ XANES study of PtRu/C and PtMo/C catalysts. Chem Phys Lett 2005;412:444–8.

76. Arenz M, Stamenkovic V, Blizanac BB, Mayrhofer KJ, Markovic NM, Ross PN Jr. Carbon-supported Pt–Sn electrocatalysts for the anodic oxidation of H_2, CO, and H_2/CO mixtures. Part II: The structure–activity relationship. J Catal 2005;232:402–10.

77. Radmilovic V, Richardson TJ, Chen SJ, Ross PN Jr. Carbon-supported Pt–Sn electrocatalysts for the anodic oxidation of H_2, CO, and H_2/CO mixtures Part I. Microstructural characterization. J Catal 2005;232:199–209.

78. Dupont C, Jugnet Y, Loffreda D. Theoretical evidence of PtSn alloy efficiency for CO oxidation. J Am Chem Soc 2006;128:9129–36.

79. Colmati F, Antolini E, Gonzalez ER. Pt-Sn/C electrocatalysts for methanol oxidation synthesized by reduction with formic acid. Electrochim Acta 2005;50:5496–503.

80. Neto AO, Dias RR, Tusi MM, Linardi M, Spinacé EV. Electro-oxidation of methanol and ethanol using PtRu/C, PtSn/C and PtSnRu/C electrocatalysts prepared by an alcohol-reduction process. J Power Sources 2007;166:87–91.

81. Gotz M, Wendt H. Binary and ternary anode catalyst formulations including elements W, Sn and Mo for PEMFCs operated on methanol and reformate gas. Electrochim Acta 1998;43:3637–44.

82. Bonneman H, Brijoux W, Brinkmann R, Dinjus E, Jouβen T, Korall B. Formation of colloidal transition metals in organic phases and their application in catalysis. Angew Chem Int Ed Engl 1991;30:1312–14.

83. Bonneman H, Britz P, Vogel W. Structure and chemical composition of a surfactant-stabilized Pt_3Sn alloy colloid. Langmuir 1998;14:6654–7.

84. Bonneman H, Richards RM. Nanoscopic metal particles-synthetic methods and potential applications. Eur J Inorg Chem 2001;2455–80.

85. Liu Z, Guo B, Hong L, Lim TH. Microwave heated polyol synthesis of carbon supported PtSn nanoparticles for methanol electrooxidation. Electrochem Commun 2006;8:83–90.

86. Bauer A, Gyenge EL, Oloman CW. Direct methanol fuel cell with extended reaction zone anode: PtRu and PtRuMo supported on graphite felt. J Power Sources 2007;167:281–7.

87. Goetz M, Wendt H. Composite electrocatalysts for anodic methanol and methanol-reformate oxidation. J Appl Electrochem 2001;31:811–17.

88. Bett JS, Kunz HR, Aldykiewicz Jr AJ, Fenton JM, Bailey WF, McGrath DV. Platinum-macrocycle co-catalysts for the electrochemical oxidation of methanol. Electrochim Acta 1998;43:3645–55.

89. Okada T, Suzuki Y, Hirose T, Ozawa T. Novel system of electro-catalyst for methanol oxidation based on platinum and organic metal complexes. Electrochim Acta 2004;49:385–95.

90. Shi C, Anson F. Catalysis of the electro-oxidation of carbon monoxide by cobalt octaethylporphyrin. Inorg Chem 2001;40:5829–33.

91. Tong YY, Kim HS, Babu PK, Waszczuk P, Wieckowski A, Oldfield E. An NMR investigation of CO tolerance in a Pt/Ru fuel cell catalyst. J Am Chem Soc 2002;124:468–73.

92. Waszczuk P, Wieckowski A, Zelenay P, Gottesfled S, Coutanceau C, Leger J-M, et al. Adsorption of CO poison on fuel cell nanoparticle electrodes from methanol solutions: a radioactive labeling study. J Electroanal Chem 2001;511:55–64.

93. Gasteiger H, Markovic N, Ross PN Jr, Cairns EJ. Methanol electrooxidation on well-characterized Pt-Ru alloys. J Phys Chem 1993;97:12020–9.

94. Gasteiger HA, Markovic N, Ross PN Jr, Cairns EJ. Temperature-dependent methanol electro-oxidation on well-characterized Pt-Ru alloys. J Electrochem Soc 1994;141:1795–1803.

95. Dickinson AJ, Carrette LPL, Collins JA, Friedrich KA, Stimming U. Performance of methanol oxidation catalysts with varying Pt:Ru ratio as a function of temperature. J Appl Electrochem 2004;34:975–80.

96. Dubau L, Coutanceau C, Garnier E, Leger J-M, Lamy C. Electrooxidation of methanol at platinum-ruthenium catalysts prepared from colloidal precursors: atomic composition and temperature effects. J Appl Electrochem 2003;33:419–49.

97. Bock C, MacDougall B, LePage Y. Dependence of CH_3OH oxidation activity for a wide range of PtRu alloys. J Electrochem Soc 2004;151:A1269–78.

98. Waszczuk P, Solla-Gullon J, Kim H-S, Tong YY, Montiel V, Aldaz A, et al. Methanol electrooxidation on platinum/ruthenium nanoparticle catalysts. J Catal 2001;203:1–6.

99. Crown A, Moraes IR, Wieckowski A. Examination of Pt(111)/Ru and Pt(111)/Os surfaces: STM imaging and methanol oxidation activity. J Electroanal Chem 2001;500:333–43.

100. Chrzanowski W, Wieckowski A. Ultrathin films of ruthenium on low index platinum single crystal surfaces: an electrochemical study. Langmuir 1997;13:5974–8.

101. Chrzanowski W, Wieckowski A. Surface structure effects in platinum/ruthenium methanol oxidation electrocatalysis. Langmuir 1998;14:1967–70.

102. Cao D, Bergens SH. An organometallic deposition of ruthenium adatoms on platinum that self poisons at a specific surface composition. A direct methanol fuel cell using platinum-ruthenium adatom anode catalyst. J Electroanal Chem 2002;533:91–100.

103. Bock C, Blakely M-A, MacDougall B. Characteristics of adsorbed CO and CH₃OH oxidation reactions for complex Pt/Ru catalyst systems. Electrochim Acta 2005;50:2401–14.

104. Iwasita T, Hoster H, John-Anacker A, Lin WF, Vielstich W. Methanol oxidation on PtRu electrodes. Influence of surface structure and Pt-Ru atom distribution. Langmuir 2000;16:522–9.

105. Lee YH, Lee G, Shim JH, Hwang S, Kwak J, Lee K, et al. Monodisperse PtRu nanoalloy on carbon as a high-performance DMFC catalyst. Chem Mater 2006;18:4209–11.

106. Hoster H, Iwasita T, Baumgartner H, Vielstich W. Current-time behavior of smooth and porous PtRu surfaces for methanol oxidation. J Electrochem Soc 2001;148:A496–501.

107. Lizcano-Valbuean WH, Paganin VA, Gonzalez ER. Methanol electro-oxidation on gas diffusion electrodes prepared with PtRu/C catalysts. Electrochim Acta 2002;47:3715–22.

108. Long JW, Stroud RM, Swider-Lyons KE, Rolison DR. How to make electrocatalysts more active for direct methanol oxidation-avoid PtRu bimetallic alloy. J Phys Chem B 2000;104:9772–6.

109. Rolison DR, Hagans PL, Swider KE, Long JW. Role of hydrous ruthenium oxide in Pt-Ru direct methanol fuel cell anode electrocatalysts: the importance of mixed electron/proton conductivity. Langmuir 1999;15:774–9.

110. Stroud RM, Long JW, Swider-Lyons KE, Rolison DR. Transmission electron microscopy studies of the nanoscale structure and chemistry of Pt₅₀Ru₅₀ electrocatalysts. Microsc Microanal 2002;8:50–7.

111. Frelink T, Visscher W, van Veen JAR. On the role of Ru and Sn as promoters of methanol electro-oxidation over Pt. Surf Science 1995;335:353–60.

112. Frelink T, Visscher W, van Veen JAR. Measurement of the Ru surface content of electrocodeposited PtRu electrodes with the electrochemical quartz crystal microbalance: implications for methanol and CO electrooxidation. Langmuir 1996;12:3702–8.

113. Lach K, Jorissen L, Friedrich KA, Garche J. The function of ruthenium oxides in Pt-Ru catalysts for methanol electro-oxidation at low temperatures. J Solid State Electrochem 2003;7:619–25.

114. Cohen JL, Volpe DJ, Abruna HD. Electrochemical determination of activation energies for methanol oxidation on polycrystalline platinum in acidic and alkaline electrolytes. Physical Chemistry Chemical Physics 2007;9:49–77.

115. Tripkovic AV, Popovic KD, Grgur BN, Blizanac B, Ross PN, Markovic NM. Methanol electrooxidation on supported Pt and PtRu catalysts in acid and alkaline solutions. Electrochim Acta 2002;47:3707–14.

116. Lasch K, Jorissen L, Garche J. The effect of metal oxides as co-catalysts for the electro-oxidation of methanol on platinum-ruthenium. J Power Sources 1999;64:225–30.

117. Shukla AK, Ravikumar MK, Arico AS, Candiano G, Antonucci V, Giordano N, et al. Methanol electro-oxidation on carbon-supported Pt-WO$_{3-x}$ electrodes in sulphuric acid electrolyte. J Appl Electrochem 1995;25:528–32.

118. Roth C, Goetz M, Fuess H. Synthesis and characterization of carbon-supported PtRuWO$_x$ catalysts by spectroscopic and diffraction methods. J Appl Electrochem 2001;31:793–8.

119. Yang LX, Bock C, MacDougall B, Park J. The role of WO$_x$ ad-component to Pt and PtRu catalysts in the electrochemical CH$_3$OH oxidation reaction. J Appl Electrochem 2004;34:427–35.

120. Jusys Z, Schmidt TJ, Dubau L, Lasch K, Jorissen L, Garche J, et al. Activity of PtRuMeO$_x$ (Me = W, Mo or V) catalysts towards methanol oxidation and their characterization. J Power Sources 2002;105:297–304.

121. Neto OA, Franco EG, Arico E, Linardi M, Gonzalez ER. Electro-oxidation of methanol and ethanol on PtRu/C and PtRuMo/C electrocatalysts prepared by Bonnemann's method. J Eur Ceram Soc 2003;23:2987–92.

122. Gurau B, Viswanathan R, Liu R, Lafrenz TJ, Ley K, Smotkin E, et al. Structural and electrochemical characterization of binary, ternary and quaternary platinum alloy catalysts for methanol electro-oxidation. J Phys Chem B 1998;102:9997–10003.

123. Sivakumar P, Tricoli V. PtRuIr nanoparticles prepared by vapor deposition as a very efficient anode catalyst for methanol fuel cells. Electrochem Solid-State Lett 2006;9:A167–70.

124. Neburchilov V, Wang H, Zhang J. Low Pt content Pt-Ru-Ir-Sn quaternary catalysts for anodic methanol oxidation in DMFC. Electrochem Commun 2007;9:1788–92.

125. Park KW, Choi JH, Lee SA, Pak C, Chang H, Sung YE. PtRuRhNi nanoparticle electrocatalyst for methanol electrooxidation in direct methanol fuel cell. J Catal 2004;224:236–42.

126. Podlovchenko BI, Aliua L. Effect of the deposition potential on the properties of mixed Pt-Rh electrolytic deposits. Elektrokhimiya 1972;8:460–4.

127. Reddington E, Sapienza A, Gurau B, Viswanathan R, Sarangapani S, Smotking ES, et al. Combinatorial electrochemistry: a highly parallel, optical screening method for discovery of better electrocatalysts. Science 1998;280:1735–7.

128. Gruber K, Kronberger H, Fafilek G, Nauer G, Besenhard J-O. Optical measurements of platinum based electrocatalysts for the electrooxidation of methanol. Fuel Cells 2003;3:3–7.

129. Choi WC, Kim DJ, Woo SI. Quaternary Pt-based electrocatalyst for methanol oxidation by combinatorial electrochemistry. Catalysis Today 2002;74:235–40.

130. Brace KM, Hayden BE, Russell AE, Owen JR. A parallel optical screen for the rapid combinatorial electrochromic analysis of electrochemical materials. Adv Mat 2006;18:3253–7.

131. Jiang R, Chu D. A combinatorial approach toward electrochemical analysis. J Electroanal Chem 2002;527:137–42.

132. Erichsen T, Reiter S, Ryabova V, Bonsen EM, Schumann W. Combinatorial microelectrochemistry: development and evaluation of an electrochemical robotic system. Rev Sci Instr 2005;76(6):062204–062204–11.

133. Capon A, Parsons R. The oxidation of formic acid at noble metal electrodes. I. Review of previous work. J Electroanal Chem 1973;44:1–7.

134. Chen YX, Ye S, Heinen M, Jusys Z, Osawa M, Behm RJ. Application of in-situ attenuated total reflection-Fourier transformed infrared spectroscopy for the understanding of complex reaction mechanism and kinetics: formic acid oxidation on a Pt film electrode at elevated temperatures. J Phys Chem B 2006;110:9534–44.

135. Chen YX, Ye S, Heinen M, Jusys Z, Behm RJ. Kinetics and mechanism of the electrooxidation of formic acid – spectroelectrochemical studies in a flow cell. Angew Chem Int Ed 2006;45:981–5.
136. Lang GG, Seo M, Heusler KE. Simultaneous oscillations of surface energy, superficial mass and electrode potential in the course of galvanostatic oxidation of formic acid. J Solid State Electrochem 2005;9:347–53.
137. Samjeske G, Osawa M. Current oscillations during formic acid oxidation on a Pt electrode: insight into the mechanism by time-resolved IR spectroscopy. Angew Chem Int Ed 2005;44:5694–8.
138. Samjeske G, Miki A, Ye S, Yamakata A, Mukouyama Y, Okamoto H, et al. Potential oscillations in galvanostatic electrooxidation of formic acid on platinum: a time-resolved surface-enhanced infrared study. J Phys Chem B 2005;109:23509–16.
139. Samjeske G, Miki A, Ye S, Osawa M. Mechanistic study of electrocatalytic oxidation of formic acid at platinum in acidic solution by time-resolved surface-enhanced infrared spectroscopy. J Phys Chem B 2006;110:16559–66.
140. Okamoto H. Mechanistic studies of the potential oscillation and induction period in the oxidation of formic acid on platinum. Electrochim Acta 1992;37:37–42.
141. Markovic N, Ross PN Jr. Oscillatory behavior in the electrochemical oxidation of formic acid on platinum (100). J Phys Chem 1993;97:9771–8.
142. Inzelt Gy, Kertesz V. Experimental evidence for the periodical changes of the amount of chemisorbed species accompanying oscillations produced in the course of galvanostatic oxidation of formic acid on platinum. Electrochim Acta 1993;38:2385–6.
143. Okamoto H, Kon W, Mukouyama Y. Five current peaks in voltammograms for oxidations of formic acid, formaldehyde and methanol on Pt. J Phys Chem B, 2005;109:15659–66.
144. Lovic JD, Tripkovic AV, Gojkovic SL, Popovic KD, Tripkovic DV, Olszevski P, et al. Kinetic study of formic acid oxidation on carbon-supported platinum electrocatalyst. J Electroanal Chem 2005;581:294–302.
145. Gileadi E. Electrode kinetics for chemists, chemical engineers and materials scientists. New York:Wiley-VCH, 1993;266–73.
146. Gyenge EL. Dimensionless numbers and correlating equations for the analysis of the membrane-gas diffusion electrode assembly in polymer electrolyte fuel cells. J Power Sources 2005;152:105–21.
147. Gasteiger H, Markovic N, Ross PN Jr, Cairns EJ. Electro-oxidation of small organic molecules on well-characterized Pt-Ru alloys. Electrochim Acta 1994;39:1825–32.
148. Markovic NM, Gasteiger HA, Ross PN Jr. Electro-oxidation mechanism of methanol and formic acid on Pt-Ru alloy surfaces. Electrochim Acta 1995;40:91–8.
149. Tripkovic AV, Popovic KDJ, Lovic JD, Markovic NM, Ramilovic V. Formic acid oxidation on Pt/Ru nanoparticles: temperature effects. Materials Science Forum 2005;494:223–8.
150. Lemos GS, Oliveira RTS, Santos MC, Nascente PAP, Bulhoes LOS, Perreira EC. Electrocatalysis of methanol, ethanol and formic acid using a Ru/Pt metallic bilayer. J Power Sources 2007;163:695–701.
151. Zhang LJ, Wang ZY, Xia DG. Bimetallic PtPb for formic acid electro-oxidation. J Alloys and Comp 2006;426:268–71.
152. Alden LR, Han DK, Matsumoto F, Abruna HD, DiSalvo F. Intermetallic PtPb nanoparticles prepared by sodium naphthalide reduction of metal-organic precursors: electrocatalytic oxidation of formic acid. Chem Mater 2006;18:5591–6.
153. Alden LR, Roychowdrhury C, Matsumoto F, Han DK, Zeldovich VB, Abruna H, et al. Synthesis, characterization and electrocatalytic activity of PtPb nanoparticles prepared by two synthetic approaches. Langmuir 2006;22:10465–71.

154. Chi N, Chan K-Y, Philips DL. Electrocatalytic oxidation of formic acid by Pt/Co nanoparticles. Cat Lett 2001;71:21–6.

155. Casado-Rivera E, Gal Z, Angelo ACD, Lind C, DiSalvo FJ, Abruna HD. Electrocatalytic oxidation of formic acid at an ordered intermetallic PtBi surface. Chem Phys Chem 2003;4:193–9.

156. Volpe D, Casad-Rivera E, Alden L, Lind C, Downie C, Vazquez-Alvarez T, et al. Surface treatment effect on the electrocatalytic activity and characterization of intermetallic phases. J Electrochem Soc 2004;151:A971–7.

157. Volpe D, Casad-Rivera E, Alden L, Lind C, Downie C, Vazquez-Alvarez T, et al. Electrocatalytic activity of ordered intermetallic phases for fuel cell applications. J Am Chem Soc 2004;126:4043–9.

158. Tripkovic AV, Popovic KDJ, Stevanovic RM, Socha R, Kowal A. Activity of a PtBi alloy in the electrochemical oxidation of formic acid. Electrochem Commun 2006;8:1492–8.

159. Schmidt TJ, Behm RJ, Grgur BN, Markovic NM, Ross PN Jr. Formic acid oxidation on pure and bismuth-modified Pt(111): temperature effects. Langmuir 2000;16:8159–66.

160. Lee J, Christoph J, Strasser P, Eiswirth M, Ertl G. Spatio-temporal interfacial potential patterns during electrocatalyzed oxidation of formic acid on Bi-modified Pt. J Chem Phys 2001;115:1485–92.

161. Yang Y-Y, Sun S-G. Effects of Sb adatoms on kinetics of electrocatalytic oxidation of HCOOH at Sb-modified Pt(100), Pt(111), Pt(110), Pt(320), and Pt(331) surfaces: an energetic modeling and quantitative analysis. J Phys Chem B 2002;106:12499–507.

162. Yang Y-Y, Sun S-G, Gu Y-J, Zhou Z-Y, Zhen C-H. Surface modification and electrocatalytic properties of Pt(100), Pt(110), Pt(320) and Pt(331) electrodes with Sb towards HCOOH oxidation. Electrochim Acta 2001;46:4339–48.

163. Tze W, Borzenko MI, Tsirlina GA, Petry OA. Electrooxidation of organic substances on platinum modified with oxotungstate adlayers. Russ J Electrochem 2002;38:1380–5.

164. Zhou X, Xing W, Liu C, Lu T. Platinum-macrocycle co-catalyst for electro-oxidation of formic acid. ElectrochemComm 2007;9:1469–73.

165. Iordache C, Lycke D, Huff S. Tekion Inc. Burnaby BC, Canada. Unpublished data, 2007.

166. Xia XH. New insights into the influence of upd Sn on the oxidation of formic acid on platinum in acidic solution. Electrochim Acta 1999;45:1057–66.

167. a) Kibler LA, El-Aziz AM, Hoyer R, Kolb DM. Tuning reaction rates by lateral strain in a palladium monolayer. Angew Chem Int Ed 2005;44:2080–4. b) Arenz M, Stamenkovic V, Ross PN, Markovic NM. Surface (electro-)chemistry on Pt(111) modified by a pseudomorphic Pd monolayer. Surf Science 2004;573:57–66. c) Arenz M, Stamenkovic V, Schmidt TJ, Wandelt K, Ross PN, Markovic NM. The electro-oxidation of formic acid on Pt-Pd single crystal bimetallic surfaces. Phys Chem Chem Phys 2003;5:4242–51.

168. Ruban A, Hammer B, Stoltze P, Skriver HL, Norskov JK. Surface electronic structure and reactivity of transition and noble metals. J Mol Cat A 1997;115:421–9.

169. Waszczuk P, Barnard TM, Rice C, Masel RI, Wieckoeski A. A nanoparticle catalyst with superior activity for electrooxidation of formic acid. Electrochem Comm 2002;4:599–603.

170. Vidal-Iglesias FJ, Solla-Gullon J, Herrero E, Aldaz A, Feliu JM. Formic acid oxidation on Pd-modified Pt(100) and Pt(111) electrodes: a DEMS study. J Appl Electrochem 2006;36:1207–14.

171. Ball MJ, Lucas CA, Markovic NM, Stamenkovic V, Ross PN Jr. From sub-monolayer to multi-layer: an in situ X-ray diffraction study of the growth of Pd films on Pt(111). Surf Sci 2002;518:201–9.
172. Li X, Hsing M-I. Electrooxidation of formic acid on carbon supported Pt_xPd_{1-x} (x = 0–1) nanocatalysts. Electrochim Acta 2006;51:3477–83.
173. Zhang L, Lu T, Bao J, Tang Y, Li C. Preparation method of an ultrafine carbon supported Pd catalyst as an anodic catalyst in a direct formic acid fuel cell. Electrochem Comm 2006;8:1625–7.
174. Blair S, Lycke D, Iordache C. Palladium-platinum alloy anode catalysts for direct formic acid fuels. ECS Trans 2006;3:1325–32.
175. Liu Z, Hong L, Tham MP, Lim TH, Jiang H. Nanostructured Pt/C and Pd/C catalysts for direct formic acid fuel cells. J Power Sources 2006;161:831–5.
176. Zhang L, Tang Y, Bao J, Lu T, Li C. A carbon-supported Pd-P catalyst as the anodic catalyst in a direct formic acid fuel cell. J Power Sources 2006;162:177–9.
177. Zhu Y, Khan Z, Masel RI. The behavior of palladium catalysts in direct formic acid fuel cells. J Power Sources 2005;139:15–20.
178. Ha S, Rice CA, Masel RI, Wieckowski A. Methanol conditioning for improved performance of formic acid fuel cells. J Power Sources 2002;112:655–9.
179. Léger J-M, Rousseau S, Coutanceau C, Hahn F, Lamy C. How do bimetallic electrocatalysts work for reactions involved in fuel cells? Example of ethanol oxidation and comparison to methanol. Electrochim Acta 2005;50:5118–25.
180. Wang Q, Sun GQ, Jiang LH, Xin Q, Sun SG, Jiang YX, et al. Adsorption and oxidation of ethanol on colloid-based Pt/C, PtRu/C and Pt₃Sn/C catalysts: in situ FTIR spectroscopy and on-line DEMS studies. Phys Chem Chem Phys 2007;9:2686–96.
181. Camara GA, Iwasita T. Parallel pathways of ethanol oxidation: The effect of ethanol concentration. J Electroanal Chem 2005;578:315–21.
182. Camara GA, de Lima RB, Iwasita T. The influence of PtRu atomic composition on the yields of ethanol oxidation: a study by in situ FTIR spectroscopy. J Electroanal Chem 2005;585:128–31.
183. Rousseau S, Coutanceau C, Lamy C, Léger J-M. Direct ethanol fuel cell (DEFC): electrical performances and reaction products distribution under operating conditions with different platinum-based anodes. J Power Sources 2006;158:18–24.
184. Lamy C, Rousseau S, Belgsir EM, Coutanceau C, Léger J-M. Recent progress in the direct ethanol fuel cell: development of new platinum-tin electrocatalysts. Electrochim Acta 2004;49:3901–8.
185. Vigier F, Coutanceau C, Perrard A, Belgsir EM, Lamy C. Development of anode catalysts for direct ethanol fuel cell. J Appl Electrochem 2004;34:439–46.
186. Colmati F, Antolini E, Gonzalez ER. Effect of temperature on the mechanism of ethanol oxidation on carbon supported Pt, PtRu and Pt₃Sn electrocatalysts. J Power Sources 2006;157:98–103.
187. Spinacé EV, Linardi M, Neto AO. Co-catalytic effect of nickel in the electro-oxidation of ethanol on binary Pt-Sn electrocatalysts. Electrochem Comm 2005;7:365–9.
188. a) Zhou W, Zhou Z, Song S, Li W, Sun G, Tsiakaras P, et al. Pt based anode catalysts for direct ethanol fuel cells. App Cat B: Env 2003;46:273–85. b) Zhou WJ, Song SQ, Li WZ, Zhou ZH, Sun GQ, Xin Q, et al. Direct ethanol fuel cells based on PtSn anodes: the effect of Sn content on the fuel cell performance. J Power Sources 2005;140:50–8.
189. Sine G, Foti G, Comninellis Ch. Boron-doped diamond (BDD)-supported Pt/Sn nanoparticles synthesized in microemulsion systems as electrocatalysts of ethanol oxidation. J Electroanal Chem 2006;595:115–24.

190. Lycke DR, Gyenge EL. Electrochemically assisted organosol method for Pt-Sn nanoparticle synthesis and in situ deposition on graphite felt support: extended reaction zone anodes for direct ethanol fuel cells. Electrochim Acta 2007;52:4287–98.

191. Delime F, Léger J-M, Lamy C. Enhancement of the electrooxidation of ethanol on a Pt-PEM electrode modified by tin. Part I: Half cell study. J Appl Electrochem 1999;29:1249–54.

192. Mann J, Yao N, Bocarsly AB. Characterization and analysis of new catalysts for direct ethanol fuel cell. Langmuir 2006;22:10432–6.

193. Jiang L, Sun G, Sun S, Liu J, Tang S, Li H, et al. Structure and chemical composition of supported Pt-Sn electrocatalysts for ethanol oxidation. Electrochim Acta 2005;50:5384–9.

194. Colmati F, Antolini E, Gonzalez ER. Ethanol oxidation on a carbon-supported $Pt_{75}Sn_{25}$ electrocatalyst prepared by reduction with formic acid: Effect of thermal treatment. App Cat B: Env 2007;73:106–15.

195. Colmati F, Antolini E, Gonzalez ER. Ethanol oxidation on a carbon-supported PtSn electrocatalyst prepared by reduction with formic acid. J Electrochem Soc 2007;154:B39–47.

196. Antolini E, Colmati F, Gonzalez ER. Effect of Ru addition on the structural characteristics and the electrochemical activity for ethanol oxidation of carbon supported Pt-Sn alloy catalysts. Electrochem Comm 2007;9:398–404.

197. Tremiliosi-Filho G, Gonzalez ER, Motheo AJ, Belgsir EM, Léger J-M, Lamy C. Electro-oxidation of ethanol on gold: analysis of the reaction products and mechanism. J Electroanal Chem 1998;444:31–9.

198. Zheng HT, Li Y, Chen S, Shen PK. Effect of support on the activity of Pd electroxatalyst for ethanol oxidation. J Power Sources 2006;163:371–5.

199. Hu F, Ding F, Song S, Shen PK. Pd electrocatalyst supported on carbonized TiO_2 nanotube for ethanol oxidation. J Power Sources 2006;163:415–9.

200. Bagchi J, Bhattacharya K. The effect of composition of Ni-supported Pt-Ru binary anode catalysts on ethanol oxidation for fuel cells. J Power Sources 2007;163:661–70.

201. Gupta SS, Datta J. Electrode kinetics of ethanol oxidation on novel CuNi alloy supported catalysts synthesized from PTFE suspension. J Power Sources 2005;145:124–32.

202. Gupta SS, Mahapatra SS, Datta J. A potential anode material for direct alcohol fuel cell. J Power Sources 2004;131:169–74.

203. van Baar JF, van Veen JAR, de Wit N. Selective electro-oxidation of carbon monoxide with carbon-supported Rh and Ir-porphyrins at low potentials in acid electrolyte. Electrochim Acta 1982;27:57–9.

204. van Baar JF, van Veeb JAR, van der Ejik JM, Peters Th.J, de Wit N. Electrochemical oxidation of carbon monoxide with carbon-supported groups VIII metal chelates: mechanistic aspects. Electrochim Acta 1982;27:1315–9.

205. Mukherjee S, Zyla R, Atanassov P. Non-platinum macrocycle electrocatalysts based on pyrolzed transition metal macrocycles. AIChE – Ann Meet Arch 2002;2436–43.

206. Trevin S, Bedioui F, Villegas MGG, Charreton-Bied C. Electropolymerized nickel macrocycle complex-based films: design and electrocatalytic application. J Mater Chem 1997;7:923–8.

207. Ciszewski A, Milczarek G. Electrocatalytic oxidation of alcohols on glassy carbon electrodes electrochemically modified by conductive polymeric nickel(II) tetrakis(3-methoxy-4-hydroxyphenyl)porphyrin film. J Electroanal Chem 1996;413:137–42.

208. Levy R, Boudart M. Platinum-like behavior of tungsten carbide in surface catalysis. Science 1973;181:547–9.

209. Hwu HH, Chen JG. Potential application of tungsten carbides as electrocatalysts: 4. Reactions of methanol, water and carbon monoxide over carbide-modified W(110). J Phys Chem B 2003;107:2029–39.
210. Zellner MB, Chen JG. Surface science and electrochemical studies of WC and W_2C PVD films as potential electrocatalysts. Cat Today 2005;99:299–307.
211. Hwu HH, Chen JG, Kourtakis K, Lavin JG. Potential application of tungsten carbides as electrocatalysts. 1. Decomposition of methanol over carbide-modified W(111). J Phys Chem B 2001;105:10037–44.
212. Hwu HH, Polizzotti BD, Chen JG. Potential application of tungsten carbides as electrocatalysts: 2. Coadsorption of CO and H_2O on carbide-modified W(111). J Phys Chem B 2001;105:10045–53.
213. Kawamura G, Okamoto H, Ishikawa A, Kudo T. Tungsten molybdenum carbide for electrocatalytic oxidation of methanol. J Electrochem Soc 1987;134:1653–8.
214. Okamoto H, Kawamura G, Ishikawa A, Kudo T. Characterization of oxygen in tungsten carbide catalysts and its role in electrocatalytic activity for methanol oxidation. J Electrochem Soc 1987;134:1645–9.
215. Okamoto H, Kawamura G, Ishikawa A, Kudo T. Activation of tungsten molybdenum carbide (W,Mo)C methanol anodic oxidation catalysts using alkaline solution. J Electrochem Soc 1987;134:1649–53.
216. Li G, Ma C, Tang J, Sheng J. Preparation and electrocatalytic property of WC/carbon nanotube composite. Electrochim Acta 2007;52:2018–23.
217. Rosenbaum M, Zhao F, Quaas M, Wulff H, Schröder U, Scholz F. Evaluation of catalytic properties of tungsten carbide for the anode of microbial fuel cells. Appl Cat B: Env 2007;74:261–9.
218. Cheng T, Gyenge E. Direct methanol fuel cells with reticulated vitreous carbon, uncompressed graphite felt and Ti mesh anodes. J Appl Electrochem 2008;38:51–62.
219. Kinoshita K. Electrochemical oxygen technology. New York:John Wiley & Sons 1992; 43–51.
220. Tian N, Zhou Z-Y, Sun S-G, Ding Y, Wang ZL. Synthesis of tetrahexahedral platinum nanocrystals with high-index facets and high electro-oxidation activity. Science 2007;316:732–5.
221. Egli WA, Visintin A, Triaca WE, Arvia AJ. The development of faceting and roughening at platinum polyfaceted single-crystal electrodes in a chloroplatinic acid solution. Appl Surf Sci 1993;68:583–93.
222. Visintin A, Canullo JC, Triaca WE, Arvia AJ. Changes in real surface area, crystallographic orientation and morphology of platinum electrodes caused by periodic potential treatments: phenomenological approach. J Electroanal Chem 1988;239:67–89.
223. Lizcano-Valbuena WH, Paganin VA, Leite CAP, Galembeck F, Gonzalez ER. Catalysts for DMFC: relation between morphology and electrochemical performance. Electrochim Acta 2003;48:3869–78.
224. Grunes J, Zhu J, Somorjai GA. Catalysis and nanoscience. In: Nanotechnology in catalysis, Vol 1. Zhou B, Hermans S, Somorjai G, editors. London: Springer, 2004;1–15.
225. van Bokhoven JA, Miller JT. d Electron density and reactivity of the d band as a function of particle size in supported gold catalysts. J Phys Chem C 2007;111:9245–9.
226. Guerin S, Hayden BE, Pletcher D, Rendell ME, Suchsland J-P, Williams LJ. Combinatorial approach to the study of particle size effects in electrocatalysis: synthesis of supported gold nanoparticles. J Com Chem 2006;8:791–8.
227. Gizjeman OLJ. Surface segregation in small supported particles. Appl Surf Sci 1993;64:9–20.

228. Stara I, Matolin V. The influence of particle size on CO adsorption on Pd/alumina model catalysts. Surf Sci 1994;313:99–106.
229. Schalow T, Brandt B, Starr DE, Laurin M, Shaikhutdinov SK, Schauermann S, et al. Particle size dependent adsorption and reaction kinetics on reduced and partially oxidized Pd nanoparticles. Phys Chem Chem Phys 2007;9:1347–61.
230. Park S, Xie Y, Weaver MJ. Electrocatalytic pathways on carbon-supported platinum nanoparticles: comparison of particle size-dependent rates of methanol, formic acid and formaldehyde electrooxidation. Langmuir 2002;18:5792–8.
231. Park S, Wasileski SA, Weaver MJ. Electrochemical infrared characterization of carbon supported platinum nanoparticles. J Phys Chem B 2001;105:9719–25.
232. Zhou WP, Lewera A, Larsen R, Masel RI, Bagus PS, Wieckowski A. Size effects in electronic and catalytic properties of unsupported palladium nanoparticles in electrooxidation of formic acid. J Phys Chem B 2006;110:13393–8.
233. van den Tillaart JAA, Kuster BFM, Marin GB. Platinum particle size effect on the oxidative dehydrogenation of aqueous ethanol. Cat Lett 1996;36:31–6.
234. Colmenares L, Wang H, Jusys Z, Jiang L, Yan S, Sun GQ, et al. Ethanol oxidation on novel, carbon supported Pt alloy catalysts-Model studies under defined diffusion conditions. Electrochim Acta 2006;52:221–33.
235. Gonzalez MJ, Hable CT, Wrighton MS. Electrocatalytic oxidation of small carbohydrate fuels at Pt-Sn modified electrodes. J Phys Chem B 1998;102:9881–90.
236. Tateishi N, Hishimura K, Yahikozawa K, Nakagawa M, Yamada M, Takasu Y. Electrocatalytic properties of ultrafine gold particles towards oxidation of acetaldehyde and ethanol. J Electroanal Chem 1993;352:243–52.
237. Attard GS, Edgar M, Göltner CG. Inorganic nanostructures from lyotropic liquid crystal phases. Acta Mater 1998;46:751–8.
238. Attard GS, Bartlett PN, Coleman NRB, Elliott JM, Owen JR, Wang JH. Mesoporous platinum films from lyotropic liquid crystalline phases. Science 1997;278:838–40.
239. Elliott JM, Birkin PR, Bartlett PN, Attard GS. Platinum microelectrodes with unique high surface areas. Langmuir 1999;15:7411–5.
240. Attard GS, Göltner CG, Cirker JM, Henke S, Templer RH. Liquid-crystal templates for nanostructured metals. Angew Chem Int Ed Engl 1997;36:1315–7.
241. Attard GS, Leclerc SAA, Maniguet S, Russell AE, Nandhakumar I, Bartlett PN. Mesoporous Pt/Ru alloy from the hexagonal lyotropic liquid crystalline phase of a nonionic surfactant. Chem Mater 2001;13:1444–6.
242. Elliott JM, Attard GS, Bartlett PN, Coleman NRB, Merckel DAS, Owen JR. Nanostructured platinum (H_I-ePt) films: effects of electrodeposition conditions on film properties. Chem Mater 1999;11:3602–9.
243. Nandhakumar I, Elliott JM, Attard GS. Electrodeposition of nanostructured mesoporous selenium films (H_I-eSe). Chem Mater 2001;13:3840–2.
244. Yamauchi Y, Ohsuna T, Kuroda K. Synthesis and structural characterization of a highly ordered mesoporous Pt-Ru alloy via 'evaporation-mediated templating'. Chem Mater 2007;19:1335–42.
245. Kucernak A, Jiang J. Mesoporous platinum as a catalyst for oxygen reduction and methanol electrooxidation. Chem Eng J 2003;93:81–90.
246. Jiang J, Kucernak A. Electrooxidation of small organic molecules on mesoporous precious metal catalysts I: CO and methanol on platinum. J Electroanal Chem 2002;533:153–65.
247. Jiang J, Kucernak A. Electrooxidation of small organic molecules on mesoporous precious metal catalysts II: CO and methanol on platinum-ruthenium alloy. J Electroanal Chem 2003;543:187–99.
248. Jiang J, Kucernak A. Nanostructured platinum as an electrocatalyst for the electrooxidation of formic acid. J Electroanal Chem 2002;520:64–70.

249. Bauer A, Gyenge EL, Oloman CW. Direct methanol fuel cell with extended reaction zone anode. ECS Trans 2006;3:1271–7.
250. Bauer A, Gyenge EL, Oloman CW. Electrodeposition of Pt-Ru nanoparticles on fibrous carbon substrates in the presence of nonionic surfactant: application for methanol oxidation. Electrochim Acta 2006;51:5356–64.
251. Kung HH, Ko EI. Preparation of oxide catalysts and catalyst supports: a review of recent advances. Chem Eng J 1996;64:203–14.
252. Auer E, Freund A, Pietsch J, Tacke T. Carbons as supports for industrial precious metal catalysts. Appl Cat A: General 1998;173:259–71.
253. Stiles AB. The alkaline earth salts as catalyst supports and stabilizers. Cat Today 1992;14:269–76.
254. Breysse M, Portefaix JL, Vrinat M. Support effects on hydrotreating catalysts. Cat Today 1991;10:489–505.
255. Schmitt JL. Carbon molecular sieves as selective catalyst supports – 10 years later. Carbon 1991;29:743–5.
256. Delmond B. Dynamic processes in active phase-support interactions. J Molec Cat 1990;59:179–206.
257. Kinoshita K. Carbon: electrochemical and physicochemical properties. New York:John Wiley & Sons, 1988.
258. Fialkov AS. Carbon application in chemical power sources. Russ J Electrochem 2000;36:345–66.
259. Dicks AL. The role of carbon in fuel cells. J Power Sources 2006;156:128–41.
260. Wisler M. Graphite and carbon powders for electrochemical applications. J Power Sources 2006;156:142–50.
261. Liu H, Song C, Zhang L, Zhang J, Wang H, Wilkinson DP. A review of anode catalysis in direct methanol fuel cell. J Power Sources 2006;155:95–110.
262. Takasu Y, Kawaguchi T, Sugimoto Y, Murakami Y. Effects of the surface area of carbon support on the characteristics of highly-dispersed Pt-Ru particles as catalysts for methanol oxidation. Electrochim Acta 2003;48:3861–8.
263. Mastragostino M, Missiroli A, Soavi F. Carbon supports for electrodeposited Pt-Ru catalysts for DMFCs. J Electrochem Soc 2004;151:A1919–24.
264. Chu Y-H, Shul YG, Choi WC, Woo SI, Han H-S. Evaluation of the Nafion effect on the activity of Pt-Ru electrocatalysts for the electro-oxidation of methanol. J Power Sources 2003;118:334–41.
265. Arico AS, Shukla AK, El-Khatib KM, Creti P, Antonucci V. Effect of carbon-supported and unsupported Pt-Ru anodes on the performance of solid-polymer-electrolyte direct methanol fuel cells. J Appl Electrochem 1999;29:671–6.
266. Liu L, Pu C, Viswanthan R, Fan Q, Liu R, Smotkin ES. Carbon supported and unsupported Pt-Ru anodes for liquid feed direct methanol fuel cells. Electrochim Acta 1998;43:3657–63.
267. Arico AS, Creti P, Antonucci PL, Cho J, Kim H, Antonucci V. Optimization of operating parameters of a direct methanol fuel cell and physico-chemical investigation of catalyst-electrolyte interface. Electrochim Acta 1998;43:3719–29.
268. Uchida H, Song JM, Suzuki S, Nakazawa E, Baba N, Watanabe M. Electron tomography of Nafion ionomer coated on Pt/C black in high utilization electrode for PEFCs. J Phys Chem B 2006;110:13319–21.
269. Hall SC, Subramanian V, Teeter G, Rambabu B. Influence of metal-support interaction in Pt/C on CO and methanol oxidation reactions. Solid State Ionics 2004;175:809–13.
270. Sen F, Gokagac G. Different sized platinum nanoparticles supported on carbon: an XPS study on these methanol oxidation catalysts. J Phys Chem C 2007;111:5715–20.
271. Stevens DA, Dahn JR. Thermal degradation of the support in carbon-supported platinum electrocatalysts for PEM fuel cells. Carbon 2005;43:179–88.

272. Stevens DA, Hicks MT, Haugen GM, Dahn JR. Ex situ and in situ stability studies of PEMFC catalysts: effect of carbon type and humidification on degradation of carbon. J Electrochem Soc 2005;152:A2309–15.

273. Harris PJ. Carbon nanotubes and related structures. Cambridge:Cambridge University Press, 1999.

274. Lee K, Zhang J, Wang H, Wilkinson DP. Progress in the synthesis of carbon nanotube- and nanofiber-supported Pt electrocatalysts for PEM fuel cell catalysis. J Appl Electrochem 2006;36:507–22.

275. Kim P, Kim H, Joo BJ, Kim W, Song IK, Yi J. Preparation and application of nanoporous carbon templated by silica particle for use as a catalyst support for direct methanol fuel cell. J Power Source 2005;145:139–46.

276. Chai GS, Yoon SB, Yu J-S, Choi J-H, Sung Y-E. Ordered porous carbons with tunable pore sizes as catalyst supports in direct methanol fuel cell. J Phys Chem B 2004;108:7074–9.

277. Gutierrez MC, Hortiguela MJ, Amarilla JM, Jomenez R, Ferrer ML, del Monte F. Macroporous 3D architecture of self-assembled MWCNT surface decorated with Pt nanoparticles as anodes for a direct methanol fuel cell. J Phys Chem C 2007;111:5557–60.

278. Hyeon T, Han S, Sung Y-E, Park K-W, Kim Y-W. High-performance direct methanol fuel cell electrodes using solid phase synthesized carbon nanocoils. Angew Chem Int Ed 2003;42:4352–6.

279. Anderson PE, Rodriguez NM. Growth of graphite nanofibers from the decomposition of CO/H_2 over silica-supported iron-nickel particles. J Mater Res 1999;14:2912–21.

280. Steirgewalt ES, Deluga GA, Cliffel DE, Lukehart CM. A Pt-Ru/graphitic nanofiber nanocomposite exhibiting high relative performance as a direct methanol fuel cell anode catalyst. J Phys Chem B 2001;105:8097–101.

281. Sun X, Li R, Stansfield B, Dodelet JP, Desilets S. 3D Carbon nanotube network based on a hierarchical structure grown on carbon paper backing. Chem Phys Lett 2004;394:266–79.

282. Villers D, Sun SH, Serventi AM, Dodelet JP, Desilets S. Characterization of Pt nanoparticles deposited onto carbon nanotubes grown on carbon paper and evaluation of this electrode for the reduction of oxygen. J Phys Chem B 2006;110:25916–25.

283. Wu G, Chen Y-S, Xu B-Q. Remarkable support effect of SWNTs in Pt catalyst for methanol electrooxidation. Electrochem Comm 2005;7:1237–43.

284. Prabhuram J, Zhao TS, Tang ZK, Chen R, Liang ZX. Multiwalled carbon nanotube supported PtRu for the anode of direct methanol fuel cells. J Phys Chem B 2006;110:5245–52.

285. Lordi V, Yao N, Wei J. Method for supporting platinum on single-walled carbon nanotubes for a selective hydrogenation catalyst. Chem Mater 2001;13:733–7.

286. Huang J-E, Guo D-J, Yao Y-G, Li H-L. High dispersion and electrocatalytic properties of platinum nanoparticles on surface-oxidized single-walled carbon nanotubes. J Electroanal Chem 2005;577:93–7.

287. Zheng HT, Li Y, Chen S, Shen PK. Effect of support on the activity of Pd electrocatalyst for ethanol oxidation. J Power Sources 2006;163:371–5.

288. Zhang K-F, Guo D-J, Liu X, Li J, Li H-L, Su Z-X. Vanadium oxide nanotubes as the support of Pd catalysts for methanol oxidation in alkaline solution. J Power Sources 2006;162:1077–81.

289. Niederberger M, Muhr H-J, Krumeich F, Bieri F, Gunther D, Nesper R. Low-cost synthesis of vanadium oxide nanotubes via two novel non-alkoxide routes. Chem Mater 2000;12:1995–2000.

290. Muhr H-J, Krumeich F, Schonholzer UP, Bieri F, Niederberger M, Gauckler LJ, et al. Vanadium oxide nanotubes – a new flexible vanadate nanophase. Adv Mater 2000;12:231–4.
291. Liu A, Ichihara M, Honma I, Zhou H. Vanadium-oxide nanotubes: synthesis and template-related electrochemical properties. Electrochem Comm 2007;9:1766–71.
292. Ardizzone S, Trasatti S. Interfacial properties of oxides with technological impact in electrochemistry. Adv Colloid Interface Sci 1996;64:173–251.
293. Bolivar H, Izquierdo S, Tremont R, Cabrera CR. Methanol oxidation at Pt/MoO$_x$/MoSe$_2$ thin film electrodes prepared with exfoliated MoSe$_2$. J Appl Electrochem 2003;33:1191–8.
294. Xu C, Shen PK, Liu Y. Ethanol electrooxidation on Pt/C and Pd/C catalysts promoted with oxide. J Power Sources 2007;164:527–31.
295. Hu F, Ding F, Song S, Shen PK. Pd electrocatalyst supported on carbonized TiO$_2$ nanotube for ethanol oxidation. J Power Sources 2006;163:415–9.
296. Jiang L, Sun G, Zhou Z, Sun S, Wang Q, Yan S, et al. Size-controllable synthesis of monodispersed SnO$_2$ nanoparticles and application in electrocatalysts. J Phys Chem B 2005;109:8774–8.
297. Suffredini HB, Tricoli V, Vatistas N, Avaca LA. Electro-oxidation of methanol and ethanol using a Pt-RuO$_2$/C composite prepared by the sol-gel technique and supported on boron-doped diamond. J Power Sources 2006;158:124–8.
298. Bagchi J, Bhattacharya SK. The effect of composition of Ni-supported Pt-Ru binary anode catalysts on ethanol oxidation for fuel cells. J Power Sources 2007;163:661–70.
299. Iordache C, Lycke D, Blair S. Catalysts including metal oxides for organic fuel cells. Tekion Inc. Burnaby BC, Canada. United States patent WO/2008/00620. 2008 Jan 17.
300. Sayle TXT, Parker SC, Sayle DC. Oxidising CO to CO$_2$ using ceria nanoparticles. Phys Chem Chem Phys 2005;7:2936–41.
301. Chen ZF, Jiang YX, Wang Y, Xu JM, Jin LY, Sun SG. Electrocatalytic oxidation of carbon monoxide and methanol at Pt nanoparticles confined in SBA-15: voltammetric and in situ infrared spectroscopic studies. J Solid State Electrochem 2005;9:363–70.
302. Scheiba F, Scholz M, Cao L, Schafranek R, Roth C, Cremers C, et al. On the suitability of hydrous ruthenium oxide supports to enhance intrinsic proton conductivity in DMFC anodes. Fuel Cells 2006;6:439–46.
303. Wilkinson DP, Johnson MC, Colbow KM, Campbell SA. Method and apparatus for reducing reactant crossover in a liquid feed electrochemical fuel cell. United States patent 5874182. 1999 Feb 23.
304. Gyenge EL, Oloman CW. The surfactant-promoted electroreduction of oxygen to hydrogen peroxide. J Electrochem Soc 2005;152:D42–53.
305. Shao Z-G, Lin W-F, Zhu F, Christensen PA, Li M, Zhang H. Novel electrode structure for DMFC operated with liquid methanol. Electrochem Comm 2006;8:5–8.
306. Shao Z-G, Zhu F, Lin W-F, Christensen PA, Zhang H. PtRu/Ti anodes with varying Pt:Ru ratio prepared by electrodeposition for the direct methanol fuel cell. Phys Chem Chem Phys 2006;8:2720–6.
307. Allen RG, Lim C, Yang LX, Scott K, Roy S. Novel anode structure for the direct methanol fuel cell. J Power Sources 2005;143:142–9.
308. Cheng T, Gyenge EL. Manuscript in preparation, 2008.
309. Chetty R, Sott K. Characterization of thermally deposited platinum and palladium catalysts for direct formic acid fuel cells. J New Mat Electrochem Systems 2007;10:135–42.
310. Yang LX, Allen RG, Scott K, Christinsen P, Roy S. A study of Pt-RuO$_2$ catalysts thermally formed on titanium mesh for methanol oxidation. Electrochim Acta 2004;5:1217–23.

311. Yu EH, Scott K. Direct methanol alkaline fuel cell with catalyzed metal mesh anodes. Electrochem Comm 2004;6:361–5.
312. Lim CK, Scott K, Allen RG, Roy S. Direct methanol fuel cells using thermally catalyzed Ti mesh. J Appl Electrochem 2004;34:929–33.
313. Yang LX, Allen RG, Scott K, Christinsen P, Roy S. A comparative study of PtRu and PtRuSn thermally formed on Ti support for methanol electrooxidation. J Power Sources 2004;137:257–63.
314. Diaz AF, Logan JA. Electroactive polyaniline films. J Electroanal Chem 1980;111:111–4.
315. Hable CT, Wrighton MS. Electrocatalytic oxidation of methanol and ethanol: a comparison of platinum-tin and platinum-ruthenium catalyst particles in a conducting polyaniline matrix. Langmuir 1993;9:3284–90.
316. Niu L, Li Q, Wei F, Wu S, Liu P, Cao X. Electrocatalytic behaviour of Pt-modified polyaniline electrode for methanol oxidation: effect of Pt deposition modes. J Electroanal Chem 2005;578:331–7.
317. a) Kitani A, Akasahi T, Sugimoto K, Ito S. Electrocatalytic oxidation of methanol on platinum modified polyaniline electrodes. Syn Met 2001;121:1301–2. b) Zhou HH, Jiao SQ, Chen JH, Wei WZ, Kyuang YF. Effects of conductive polyaniline (PANI) preparation and platinum electrodeposition on electroactivity of methanol oxidation. J Appl Electrochem 2004;34:455–9.
318. Mikhaylova AA, Molodkina EB, Khazova OA, Bagotzky VS. Electrocatalytic and adsorption properties of platinum microparticles electrodeposited into polyaniline films. J Electroanal Chem 2001;509:119–27.
319. Prasad KR, Munichandraiah N. Electrooxidation of methanol on polyaniline without dispersed catalyst particles. J Power Sources 2002;103:300–4.
320. Lima A, Hahn F, Leger J-M. Oxidation of methanol on Pt, Pt-Ru and Pt-Ru-Mo electrocatalysts dispersed in polyaniline: an in situ infrared reflectance spectroscopy study. Russ J Electrochem 2004;43:326–36.
321. a) Laborde H, Leger J-M, Lamy C. Electrocatalytic oxidation of methanol and C1 molecules on highly dispersed electrodes. Part I: Platinum in polyaniline. J Appl Electrochem 1994;24:219–26. b) Laborde H, Leger J-M, Lamy C. Electrocatalytic oxidation of methanol and C1 molecules on highly dispersed electrodes. Part II: platinum-ruthenium in polyaniline. J Appl Electrochem 1994;24:1019–27.
322. Rajesh B, Thampi RK, Bonard J-M, Mathieu HJ, Xanthopoulos N, Viswanathan B. Electronically conducting hybrid material as high performance catalyst support for electrocatalytic application. J Power Sources 2005;141:35–8.
323. Wu YM, Li WS, Lu J, Du JH, Lu DS, Fu JM. Electrocatalytic oxidation of small organic molecules on polyaniline-Pt-H_xMoO_3. J Power Sources 2005;145:286–91.
324. Napporn WT, Laborde H, Leger J-M, Lamy C. Electro-oxidation of C1 molecules at Pt-based catalysts highly dispersed into a polymer matrix: effect of the method of preparation. J Electroanal Chem 1996;404:153–9.
325. Huang L-M, Tang W-R, Wen T-C. Spatially electrodeposited platinum in polyaniline doped with poly(styrene sulfonic acid) for methanol oxidation. J Power Sources 2007;164:519–26.
326. Wu G, Li L, Li J-H, Xu B-Q. Methanol electrooxidation on Pt particles dispersed into PANI/SWNT composite films. J Power Sources 2006;155:118–27.
327. Lefebvre MC, Qi Z, Pickup PG. Electronically conducting proton exchange polymers as catalyst supports for proton exchange membrane fuel cells. J Electrochem Soc 1999;146:2054–8.
328. Drillet J-F, Dittmeyer R, Juttner K. Activity and long-term stability of PEDOT as Pt catalyst support for the DMFC anode. J Appl Electrochem 2007;37:1219–26.

329. Biallozor S, Kupniewska A, Jasulaitene V. Electro-oxidation of methanol and ethanol on poly(3,4-ethylenedioxythiophene) with dispersed Pt, Pt+Sn and Pt+Pb particles. Fuel Cells 2003;3:8–14.

330. Rajesh B, Thampi RK, Bonard J-M, Mathieu HJ, Xanthopoulos N, Viswanathan B. Conducting polymeric nanotubes as high performance methanol oxidation catalyst support. Chem Comm 2003;16:2022–3.

331. Rajesh B, Thampi RK, Bonard J-M, McEvoy AJ, Xanthopoulos N, Mathieu HJ. Pt particles supported on conducting polymeric nanocones as electro-catalysts for methanol oxidation. J Power Sources 2004;133:155–61.

332. Selvaraj V, Alagar M, Kumar SK. Synthesis and characterization of metal nanoparticles-decorated PPY-CNT composite and their electrocatalytic oxidation of formic acid and formaldehyde for fuel cell applications. Appl Cat B: Environ 2007;75:129–38.

333. Selvaraj V, Alagar M. Pt and PtRu nanoparticles decorated polypyrrole/multiwalled carbon nanotubes and their catalytic activity towards methanol oxidation. Electrochem Comm 2007;9:1145–53.

334. Kulesza PJ, Matczak M, Wolkiewicz A, Grzybowska B, Galkowski M, Malik MA, et al. Electrocatalytic properties of conducting polymer based composite film containing dispersed platinum microparticles towards oxidation of methanol. Electrochim Acta 1999;44:2131–7.

335. Bensebaa F, Farah AA, Wang D, Bock C, Du X, Kung J, et al. Microwave synthesis of polymer-embedded Pt-Ru catalyst for direct methanol fuel cell. J Phys Chem B 2005;109:15339–44.

336. Bouzek K, Mangold K-M, Juttner K. Electrocatalytic activity of platinum modified polypyrrole films for the methanol oxidation reaction. J Appl Electrochem 2001;31:501–7.

337. Ocon P, Herrasti P, Rojas S. Galbanostatic and pulse potential synthesis of poly-3-methylthiophene. Polymer as catalytic support. Polymer 2001;42:2439–48.

5

Application of First Principles Methods in the Study of Fuel Cell Air-Cathode Electrocatalysis

Zheng Shi

5.1 Introduction

First principles modeling has enjoyed widespread use in many traditional areas of chemistry (e.g., organic, inorganic) for decades and its success has made it an indispensable tool in these areas. Use of first principles modeling in electrochemistry, however, is a recent story. This delay has largely been due to complex interface problems. Nevertheless, with recent advances in computer technology and electronic structure calculation algorithms, quantum chemistry calculation is rapidly becoming a necessary tool in the field of electrochemistry. Several publications and reviews on quantum chemistry methodologies in electrochemistry and surface reaction are available [1–8]. To understand electron transfer at a metal-solution interface, it is essential to have microscopic information about the equilibrium and nonequilibrium structure of the solvent, the specific adsorption of ions, and the state of reactants and products near the charged surface of a metal. However, despite tremendous developments in the modern experimental *in situ* method, experimentally probing the interface process is still a challenge. Therefore, theoretical modeling can play an important role, as it complements experimental measurements and offers the possibility of providing a detailed description of the interface process at the atomistic and molecular levels.

In recent years, the number of publications on the application of the first principles methods in the area of fuel cell electrocatalysis has grown significantly. Electrocatalyst material is one of the major obstacles for fuel cell technology. The widely used catalyst, Pt, suffers from several drawbacks, namely slow kinetics, low efficiency, high cost, and limited abundance in the earth's crust. Development of new catalyst materials with low cost, high performance, and durability is the goal.

This chapter concentrates on the first principles studies of fuel cell air-cathode electrocatalysts, i.e., oxygen reduction reaction (ORR) electrocatalysis. Recent progress in theoretical methodologies will be introduced and the current status of first principles studies of the ORR will be reviewed. The chapter is organized as follow: first, the background theory and the oxygen reduction reaction will be introduced, and then theoretical applications in the study of the ORR will be

reviewed in four sections, according to theoretical approach. In each section, the computational method is presented with examples, the research findings from theoretical studies are discussed, and the capabilities of the present quantum chemistry methods are illustrated.

5.2. Background

5.2.1 Theoretical Methods

In this section, the density functional theory (DFT) method is reviewed. Other methods applied in the study of electrochemistry, such as the *ab initio* (or first principle) molecular dynamics method (AIMD), the wave-function-based method, the Monte Carlo method, and the semi-empirical method are reviewed elsewhere [3, 9–13].

Density functional theory has been the method of choice for large systems, especially solid-state surfaces. This is largely due to its computational efficiency and accuracy. Density functional theory is based on the Hohenberg-Kohn theorems [14], according to which the electron density determines the ground-state wave function and all other electronic properties of the system. Furthermore, a variational principle exists for the density: the correct density is the one that produces the minimum energy. Because the electron density is a function of the three-dimensional coordinates, regardless of the number of electrons in the system, the density functional approach could significantly reduce computational demand.

To obtain the electron density, Kohn-Sham introduced a fictitious reference system of non-interacting particles. The electron density of this fictitious state can be obtained exactly by solving a set of one-electron Schrödinger equations (Kohn-Sham orbital [15], Equation 5.1):

$$\left\{ -\frac{1}{2}\nabla^2 + v_{ext}(\mathbf{r}) + v_H(\mathbf{r}) + v_{xc}(\mathbf{r}) \right\} \Psi_i(\mathbf{r}) = \varepsilon_i \Psi_i(\mathbf{r}) \tag{5.1}$$

where external potential

$$v_{ext}(\mathbf{r}) = -\sum_a \frac{Z_a}{|\mathbf{r} - \mathbf{R}_a|}$$

Hartree potential

$$v_H = \int \frac{\rho(\mathbf{r}')}{|\mathbf{r} - \mathbf{r}'|} d^3\mathbf{r}'$$

and $v_{xc}(\mathbf{r})$ is the exchange-correlation potential.

In principle, if the true exchange-correlation term is known, one can get the exact electron density. However, in reality, the exchange-correlation term is

unknown and there is no systematic way of deriving it. In practice, an approximate functional is proposed. There are several types of approximate functionals, such as Local Density Approximation (LDA) and Generalized Gradient Approximation (GGA) [16]. Examples of GGA exchange-correlation functionals include LYP [17], PW91 [18, 19], P86 [20], BPW91 [18, 19, 21], BLYP [16, 17], PBE [22], and B3LYP [17, 21]. The quality of the functional employed directly affects the quality of the DFT calculation. In general, as the exchange-correlation functional contains both exchange and Coulomb correlation terms, the DFT provides better quality than the single determinant Hartree-Fock (HF) method, which does not have a Coulomb correlation term.

In addition to the choice of functionals, one must make a number of other selections in order to perform a study effectively. These include the surface model, basis set, and effective potentials. There are two generally employed surface models, namely, the cluster and the slab [3, 9]. The cluster model represents the surface using a limited number of atoms (10–50), to reduce the cost of the computation. These calculations are computationally convenient and are widely used to investigate surface reactions' transition states and analyze the chemisorption bond. Most importantly, solvent effects can be incorporated into the cluster model. However, the electronic structure of clusters can be quite different from the corresponding structure of the semi-infinite surface. Another issue with the cluster method is that it does not work well for charged surfaces: excess charges accumulate on the surface and even in a larger cluster, most of the atoms are on the surface, so that the charge distribution differs considerably from that on a semi-infinite system. Furthermore, an increase in cluster size does not resolve the convergence problem. The slab method, on the other hand, describes the surface as a slab with a periodic structure. The size of the surface unit cell determines the computational effort. Three or four slabs usually are needed to obtain an effective model. It is now generally agreed upon that slab calculations give more reliable binding energetics. The problem with the slab method is that periodicity limits it to a fairly high adsorbate coverage.

Depending on the surface model, there are two classes of basis sets, the localized and the plane wave. For the cluster model, localized basis sets are generally employed. These basis sets are atomic functions with their origins at the centers of cluster atoms. In the slab model, delocalized plane waves are usually applied. To further reduce the computational cost, effective potential can be employed. In a localized basis set, inner electrons are frozen and only the valence s, p, and d electrons are included in the calculation. In the slab model, pseudopotentials are applied.

5.2.2 Oxygen Reduction Reaction

Numerous reviews of the oxygen reduction reaction and its mechanisms have been published. The most recent ones include Adzic [23], Gatteerell and MacDougall [24], and Ross Jr. [25]. The ORR is a multi-electron reaction, which may include a number of elementary steps and involve different reaction intermediates and pathways. Figure 5.1 illustrates the possible reaction pathways.
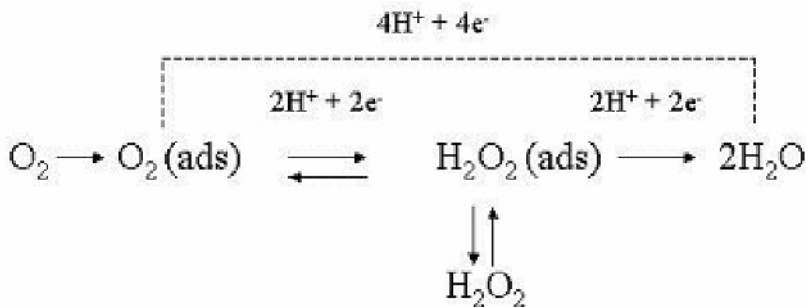
Figure 5.1. Oxygen reduction reaction pathways

Adzic [23] summarized the following possibilities:

1. a "direct" four-electron reduction to H_2O (in acid media) or to OH^- (in alkaline media);
2. a two-electron pathway involving reduction to hydrogen peroxide;
3. a "series" pathway with two- and four-electron reduction;
4. a "parallel" pathway that is a combination of 1), 2) and 3);
5. an "interactive" pathway in which the diffusion of species from a "series" path into a "direct" path is possible.
6. The following are the standard potentials for direct four-electron, two-electron, and one-electron reactions involved in the ORR [1]:

$$O_2 + 4H^+ + 4e- \rightarrow 2H_2O \qquad 1.23 \text{ V} \qquad\qquad (5.2)$$

$$O_2 + 2H^+ + 2e- \rightarrow H_2O_2 \qquad 0.68 \text{ V} \qquad\qquad (5.3)$$

$$H_2O_2 + 2H^+ + 2e- \rightarrow 2H_2O \qquad 1.77 \text{ V} \qquad\qquad (5.4)$$

$$O_2 + H^+ + e^- \rightarrow HO_2 \qquad -0.13 \text{ V} \qquad\qquad (5.5)$$
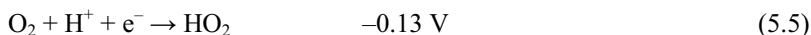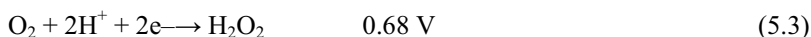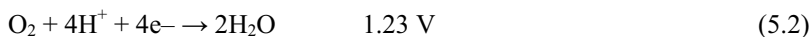
A four-electron oxygen reduction yields water, while a two-electron reduction produces hydroxide, which not only reduces the efficiency but also poisons the catalysis and cell because of its high oxidizability.

Three types of ORR catalyst are presently used: transition metals and alloys; non-noble metals and metal oxides; and transition-metal macrocyclic complexes. For transition metal catalysts, two-electron reduction is reported for less active metals such as Au and Hg. For the most active catalyst, Pt, four-electron reduction is generally believed to occur, although its pathways and mechanisms are still elusive. For the ORR on Pt, two Tafel regions have been observed in both acid and alkaline solutions. At low current densities, a Tafel slope of –60 mV/dec was noted and at high current densities, a slope of –120 mV/dec [26]. The difference in Tafel slopes is attributed to partial coverage of the Pt surface by intermediates, especially by O. It is reported that at a potential > 0.8 V (NHE), Pt coverage by O could reach

about 30% [27]. Thus, the adsorbed intermediates and coverage on Pt affect the ORR kinetics dramatically. There are two different views on the first electron transfer step. Damjanovic and Brusic [28] proposed that proton transfer occurs simultaneously with charge transfer and is the rate determining step. Yeager et al. [29] proposed that the first step involves dissociative chemisorption of the O_2 molecule, which occurs simultaneously with charge transfer; the rate determining step appears to be the addition of the first electron to the adsorbed O_2. Experimentally, there is no simple adequate spectroscopic method for identifying adsorbed intermediates so it is difficult to determine the nature and coverage of adsorbed reaction intermediates and, hence, the reaction mechanism [23].

5.3 Surface Adsorption

The difficulty in the reduction of oxygen to water originates from the multiple bonding nature of the oxygen molecule, which makes the bond very strong. The mechanism of catalysis is to facilitate the dissociation of the O–O bond. The catalyst's ability to interact with oxygen and the degree of this interaction are crucial for its catalytic activity toward oxygen reduction. Catalysts that bind oxygen too weakly or too strongly are poor candidates. The ideal catalyst possesses an optimum binding energy that maximizes catalytic activity. This concept is referred to as Sabatier's principle [30].

Three types of interactions between transition metals and oxygen are generally accepted. These are the side-on, end-on, and bridge types (Figure 5.2).
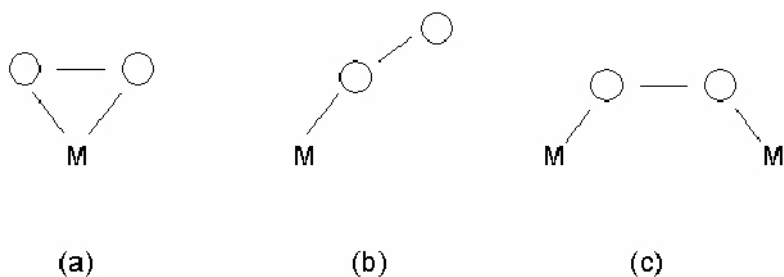
Figure 5.2. Oxygen adsorption models: (a) the Griffiths model, (b) the Pauling model, (c) the Yeager model

Studies have revealed that the type of interaction between catalyst and oxygen dictates the oxygen reduction reaction pathway and end products. The direct four-electron pathway requires dissociation of oxygen prior to the transfer of the first electron [25]. Research has demonstrated that both side-on and bridge interactions weaken the O–O bond to such an extent that a break is inevitable. Therefore, four-electron reduction will follow and the final product will be water. On the other hand, catalysts that cannot effectively stretch the O–O bond will only end up with the two-electron reduction product H_2O_2, which makes the catalyst unstable and degrades the fuel cell system [31].

The catalyst's ORR activity is also affected by its bond strength with ORR intermediates. The ORR involves the following possible intermediates: OH, OOH, O, and H_2O_2. If the interactions are too strong, surface blockage results. The OH radical is one of the most important intermediates in the ORR and is formed in large amounts during the processes of oxygen reduction and water oxidation. OH adsorption is generally held to be responsible for blocking oxygen adsorption sites.

In this section, we introduce computational methods employed in surface adsorption studies. Examples of theoretical studies of the adsorption of molecular oxygen and ORR intermediates on transition metals and alloys will be provided. Insights and findings from theoretical modeling will also be discussed.

5.3.1 Computational Methods

Both cluster and slab methods are employed to investigate interactions between the surface and adsorbates [9, 10, 32]. Usually, the solvent is ignored. These methods work best if a strong chemisorption bond is formed so that the other interactions are secondary. The adsorption energy is calculated using Equation 5.6:

$$E = E_{(adsorbate)} + E_{(substrate)} - E_{(adsorbedsystem)} \tag{5.6}$$

For adsorption on metal, Hammer and Nørskov [33] have proposed a model that can predict the adsorption bond strength based on the electronic properties of the metal. According to this model (Equation 5.7), three surface properties contribute to the ability of the surface to make and break adsorbate bonds: (1) the energy center ε_d of the d-bands, defined as the centroid of the d-type density of states in an atomic sphere centered at a surface atom, (2) the degree of filling f of the d-bands (number of d electrons), and (3) the coupling matrix element V between the adsorbate states and the metal d-states:

$$E_{d-hyb} = -2(1-f) \frac{V^2}{|\varepsilon_d - \varepsilon_a|} + 2(1+f)\alpha V^2 \tag{5.7}$$

where $E_{d\text{-}hyb}$ is the energy gained from hybridization of the adsorbate orbital with the metal d-band, ε_a is the adsorbate orbital energy (renormalized by the metal sp-bands), and α is a constant that is independent of the metal and depends weakly on the identity of the adsorbate.

The interaction between the adsorbate states and the metal d states is an important part of the interaction energy, and this is attributed to the narrowness of the d-band and its sensitivity to the environment. In addition to the electronic property that affects the d-band center, so does the geometric arrangement of the surface metal atoms [34]. When the structure of the surface changes, for example by the introduction of a step, the d-band center will alter due to a change in the number of metal neighbours, the metal coordination number. The general rule is that the lower the coordination number, the smaller the local bandwidth and the higher the ε_d. This is the origin of the reactivity difference due to the surface structure.

5.3.2 Adsorption on Transition Metals

5.3.2.1 Oxygen Adsorption
Experiments at the platinum-UHV interface have shown that oxygen adsorbs both dissociatively and molecularly on the (111) surface. Adsorbed molecular oxygen is found at 150K; at higher temperatures, dissociation takes place [35]. On a Pt(111) surface, near-edge X-ray absorption fine structure spectroscopy (NEXAFS) [36] revealed a superoxo species (O_2^-). Electron energy loss spectroscopy (EELS) [37] showed the existence of two different O-O stretching frequencies. The EELS results were first interpreted in terms of a nonmagnetic peroxo species (O_2^{2-}); a superoxo species was postulated on the basis of the NEXAFS result. The peroxo species is often referred to as a precursor state for dissociation. Dissociation on Pt(111) proceeds by sequential population of superoxo and peroxo precursor states. Atomic oxygen is the energetically most stable configuration of oxygen on a Pt surface.

Computational studies of oxygen adsorption on Pt(111) were reported by Eichler and Hafner [38] with the GGA-PW91 functional and a slab model. The study reported two distinct but energetically almost degenerate chemisorbed molecular precursor state types for O_2 on Pt(111) at distances of 1.8 –1.9 Å. The first type was a superoxo-like (O_2^-) paramagnetic precursor formed at the bridge site (t-b-t) with the molecule parallel to the surface (see t-b-t site in Figure 5.3):
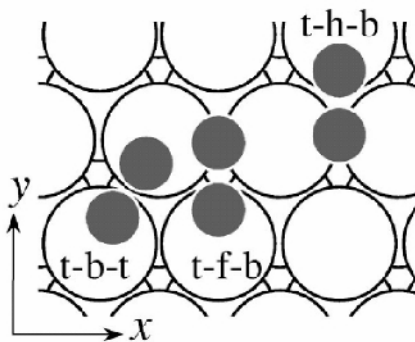
Figure 5.3. A top view of the adsorption sites for O_2 precursors on transition metal (111) surface. (Reprinted with permission from Ye Xu and Manos Mavrikakis, J Chem Phys 116 (2002) 10846. ©2002 American Institute of Physics.)

The O-O bond length was 1.39Å and the O-O stretching frequency was 850 cm^{-1}. The calculated adsorption energy was 0.72eV. The second type was a peroxo-like (O_2^{2-}) nonmagnetic precursor formed in the three-fold hollow, with the atom slightly canted in a top-hollow-bridge geometry (t-f-b and t-h-b sites in Figure 5.3). The O-O bond length was 1.43Å for t-f-b (1.42Å for t-h-b), the O-O stretching frequency was 690 cm^{-1} (710 cm^{-1} for t-h-b), and the adsorption energy was 0.68eV (0.58 eV for t-h-b).

Šljivančanin and Hammer [39] reported oxygen dissociation at close-packed Pt terraces (Pt(111)), Pt steps (Pt(211)), and Ag-covered Pt steps. With a slab model and GGA-RPBE functional, their investigation illustrated that the most favorable dissociation pathway at the terraces (Pt(111)) is a t-f-b one. The dissociation energy barrier with respect to the molecular precursor states is 0.6eV. The O-O bond length in the transition state (TS) is 2.4Å. An alternative pathway is from t-b-t with a dissociation barrier of 0.9eV. On stepped Pt (Pt(211)), the chemisorption energy increased dramatically from 0.1eV at terraces to 0.9eV at steps. Dissociation of the O_2 proceeded via elongation of the molecules. The O-O distance at the TS is 3.0Å. The TS potential energy with respect to the gas phase O_2 is 0.0eV compared with 0.5eV at Pt(111). The study also investigated the influence of pre-adsorbed oxygen atoms and molecules on O_2 dissociation on a Pt(111) surface. They observed no evidence of dissociation enhancement from pre-adsorbed oxygen. The study reported that at smaller distances, the O_2 felt strong repulsion from pre-adsorbed species. Furthermore, the authors analysed the results of different Pt surfaces with a *d*-band model. For Pt(111), the surface atoms were nine-fold coordinated. For Pt(211), the step edge Pt atoms were seven-fold coordinated. The differences in the coordination caused variations in the local Pt *d*-band widths. The changes in the local electronic structure influenced the strength of the interaction between the surface atoms and the adsorbates. Their study showed that the calculated molecular potential energies for the precursor and transition states were well correlated to the positions of the *d*-band centers of the relevant Pt atoms, as illustrated in Figure 5.4. Thus, *d*-band centers could be employed to estimate the dissociation energy barrier.
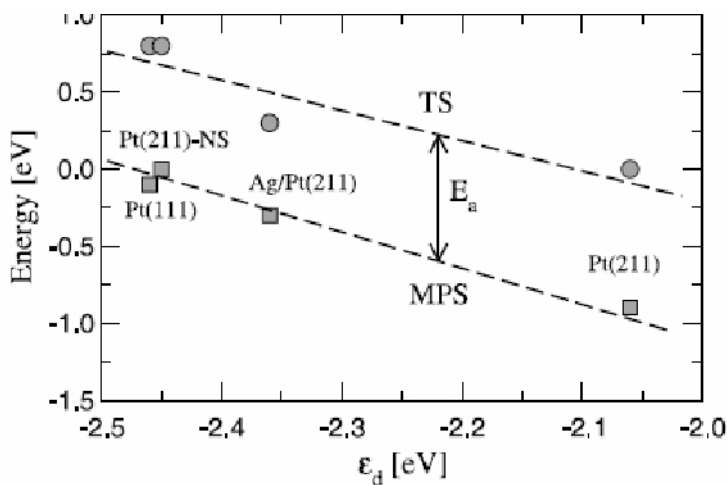
Figure 5.4. The MPS potential energies (squares) and approximate TS energies (circles) as functions of the d-electron centers. Only similar O_2 configurations (t-b-t) are compared [39]. (Reproduced from Surface Science, 515(1), Sljivancanin Z, Hammer B. Oxygen dissociation at close-packed Pt terraces, Pt steps, and ag-covered Pt steps studied with density functional theory, 235–44, 2002, with permission from Elsevier.)

Studies of oxygen adsorption on other transition metals have been reported [40–43]. Table 5.1 summarizes the calculated molecular oxygen adsorption properties.

Table 5.1. Calculated molecular oxygen adsorption properties on different transition metals[a]

Adsorption site	Surface	E(eV)[b]	Z(Å)[c]	D(Å)[d]	$\mu(\mu_B)$[e]	Ref.
t-f-b	Ir(111)	1.17	1.75	1.48	0	[40]
	Ni(111)	1.65	1.62	1.47	0.22	[41]
	Pd(111)	1.01	1.75	1.39	0	[41]
	Pt(111)	0.68	1.78	1.43	0	[41]
	Cu(111)	0.56	1.55	1.48	0	[40]
t-h-b	Ir(111)	1.18	1.74	1.50	0	[40]
	Ni(111)	1.67	1.62	1.46	0.22	[41]
	Pd(111)	0.92	1.79	1.41	0	[41]
	Pt(111)	0.58	1.81	1.42	0	[41]
	Cu(111)	0.52	1.65	1.44	0	[40]
t-b-t	Ir(111)	1.27	1.90	1.43	0	[40]
	Ni(111)	1.41	1.77	1.42	0.44	[41]
	Pd(111)	0.89	1.91	1.36	0.3	[41]
	Pt(111)	0.72	1.92	1.39	0.4	[41]
	Cu(111)	0.45	1.88	1.35	0.99	[40]
	Au(211)	0.15	2.07	1.29	1.2	[42]

[a] Based on the DFT slab method with the GGA-PW91 functional. [b] E(eV) adsorption energy. [c] Z distance to the surface. [d] D distance between oxygen atoms. [e] Magnetic moment.

5.3.2.2 Field Dependence Adsorption

Investigation of the electric field effect on oxygen adsorption has been reported in the literature. With a cluster model, Panchenko et al. [44] showed that lowering the field (making it more negative) attracts the molecule to the Pt surface, lengthens the O–O adsorbate bond, and increases the charge transfer from the Pt to the anti-bonding orbital of the oxygen molecule. The effect of homogeneous electric fields on the adsorption energies of atomic and molecular oxygen, and the dissociation activation energy of molecular oxygen on Pt(111), were reported by Hyman and Medlin [45]. In their study both cluster and slab models were employed. For cluster calculation, a finite cluster with 3 to 22 atoms was used with the Amsterdam Density Functional (ADF). The Pt–Pt distance was fixed at the experimental bulk distance of 2.772Å. Calculations were performed with the GGA-BP86 or GGA-PW91 functional. The effect of a homogeneous electronic field was

modelled with fields of ± 0.5 and ± 1.0 V/Å applied perpendicularly to the surface. For slab calculations, a (2×2) Pt(111) surface unit cell with four substrate layers was employed. Both frozen substrate calculations and relaxed substrate calculations (with the bottom two layers frozen) were executed. In agreement with previous studies, they found that the adsorption of both atomic and molecular oxygen on Pt(111) is stabilized by negative electric fields and destabilized by positive electric fields, and that this is mainly due to the (de)stabilization of the static dipole moment. The more accurate slab calculation results illustrated that the adsorption energies of atomic and molecular oxygen on Pt(111) are only slightly affected by the imposition of large electric fields. A modest shift in the oxygen dissociation barrier of approximately 0.1eV is predicted for the application of a positive electric field of 0.5 V/Å. The authors suggested that the thermodynamics of O_2 adsorption and dissociation are not substantially affected by the presence of an electric field, but that the kinetics may be altered, and the destabilization of adsorbate dipoles may play a certain role in controlling the mechanism of O_2 reduction at fuel cell cathodes.

5.3.2.3 ORR Intermediate Adsorption

Investigation of the properties of intermediate OH, OOH, H_2O_2 adsorption on (111), (100), and (110) Pt surfaces have been conducted by Panchenko et al. [44]. Two geometrical models were used to study adsorption: slab geometry and cluster geometry. The former was studied using the VASP program, the latter using Gaussian 98. For slab calculations, the surfaces were modeled as four-layer slabs having four atoms in each layer, separated by five layers of vacuum with an equilibrium lattice constant of 2.82Å, as found from the VASP calculation. The study showed that atomic oxygen adsorbed most strongly on the (110) bridge site (adsorption energy 4.47eV) and the least strongly on the hollow (100) site, whereas OH adsorbs most strongly on Pt(100), with an adsorption energy of 2.74eV at the bridge site, and most weakly on a Pt(111) surface. The study implied that the strong adsorption of OH on Pt(100) may explain why this particular surface shows the lowest activity for the ORR in alkaline and perchloric acid media. They found that on a (111) surface, OOH has an adsorption energy of 1.07eV and an O-O distance of 1.45Å. On (100) and (110) surfaces the radical was found to be unstable and dissociated into OH_{ads} and O_{ads}. Their calculations illustrated that H_2O_2 was not stable on all three low-index Pt surfaces and dissociated into two hydroxyls or a water molecule and atomic oxygen.

Adsorption and decomposition of OOH and H_2O_2 on a Pt cluster were investigated by Wang and Balbuena [46]. Both thermodynamics and kinetics indicated that OOH readily decomposed into O and OH before a second electron transfer took place. The authors suggested that a favorable pathway for the second electron transfer should occur on the coadsorbed O and OH species. Based on these findings, the study proposed that O_2 reduction on a Pt surface may proceed via a parallel pathway: the direct four-electron (with no H_2O_2 generation) and the series (with generation of H_2O_2) occurring simultaneously, with the direct as the dominant pathway.

Study of intermediates and reaction paths for the ORR on another transition metal, gold, has been conducted as well [43]. In this theoretical investigation,

adsorption energies and geometry specifications of various intermediates (O_2, OOH, O, OH, H_2O_2) on Au(100) and Au(111) surfaces were examined. The results indicate that the oxygen adsorption energies on either of the surfaces are very small. The relative stability of the other intermediates also suggests that on either of the surfaces it is thermodynamically favorable to dissociate the O-O bond of either of O_2, OOH, or H_2O_2. Thus, the relative stability of the intermediates cannot fully describe the observed experimental data of the structure selectivity of Au(100) and Au(111) electrodes in alkaline solution. The study suggested that the activation energies of elementary steps, including the role of water, have to be considered in order to comprehend the mechanism. The study also showed that since the oxygen molecule can be easily converted to OOH, hydroperoxyl is one of the most important intermediates on the surface and its stability determines the final outcome of the reduction process.

5.3.3 Adsorption on Bimetallic Alloys

Platinum-based bimetallics (Pt-M, M=Ti, Cr, V, Mn, Fe, Co, Ni, Cu, etc.) have been shown to exhibit enhanced activity toward the ORR. Several rationales have been proposed [47, 48] including: enhanced chemisorption of intermediates; a lattice change of Pt that results in the shortening of Pt-Pt inter-atomic distances by alloying; the formation of skin Pt which has increased d-electron vacancy of the thin Pt surface layer, caused by the underlying alloy; and a redox-type process involving the first-row transition alloying element and the anchor effect of alloy metals on a carbon carrier. Theoretical studies have been conducted in an effort to understand the enhanced activity of the bimetallic alloys.

The effect of an alloy on the *d*-band center is examined by Ruban et al. [49]. They reported the *d*-band trends for 110 combinations of metals, based on the DFT method. The study revealed that the shift of the *d*-band depended on the difference in the size of the metals, and moving a layer of one kind of metal atoms to another substrate had the important effect of modifying the electron density or the "size" of the atom. This in turn changed the center of the *d*-bands. When a "small" metal atom is moved into the lattice of a "larger" one, the neighbours are further away and the *d*-band width at the atom becomes smaller than at the surface of the elemental metal. This causes an up-shift in the *d*-band center in order to maintain the same *d*-band filling locally. Based on this model, for a given adsorbate, the *d*-band center controls the activity of the metal. To modify the activity of the metal, one can alter its surroundings. One possibility is to deposit it as an overlayer or alloy it into the surface layer of another metal.

Investigation of the relationship between alloys' electronic structure, their oxygen binding ability, and their ORR catalytic activity have been reported by several groups [50–59]. Xu et al. [51] carried out self-consistent periodic density functional theory calculations (GGA-PW91) to study the adsorption of atomic oxygen and molecular oxygen, as well as the dissociation of O_2 on the (111) facets of ordered Pt_3Co and Pt_3Fe alloys and on monolayer Pt skins covering these two alloys. The paper explicitly investigated the strain effect by a 2% compression (corresponding to the lattice constant in Pt_3Co and Pt_3Fe) of the equilibrium lattice of Pt(111). The study revealed that there is a linear relationship between atomic

oxygen binding energy and the oxygen dissociation barrier on the transition metals and alloys (Figure 5.5). The more strongly a material binds atomic oxygen, the more effective it will be in dissociating molecular oxygen. So, instead of conducting a complicated and expensive transition-state study, a more affordable atomic binding study can be used to screen for and design better oxygen reduction catalysts.
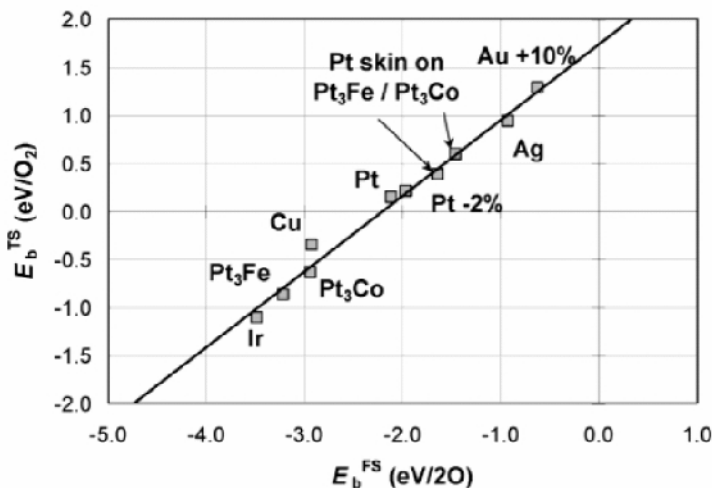
Figure 5.5. Binding energies of the transition states of O_2 dissociation (E_b^{TS}) vs. binding energies of the atomic final states with respect to gas-phase O_2 (E_b^{FS}) on the (111) facets of several fcc transition metals and alloys. (Reprinted with permission from Ye Xu, Andrei V. Ruban and Manos Mavrikakis, J Am Chem Soc 126 (2004) 4717. ©2004 American Chemical Society.)

Through DFT calculations, the authors reported that Co atoms on the Pt_3Co surface allowed O_2 to dissociate more easily than on Pt(111). The lowest activation energy on Pt_3Co was 0.24 eV/O_2 compared with 0.77e V/O_2 on pure Pt, and the oxygen bound to Pt_3Co more strongly (0.92 eV/O_2 and 4.29 eV/O) than it did to Pt (0.62e V/O_2 and 3.88e V/O). They observed that the Pt skin on top of Pt_3Co(111) was the least reactive surface in their study, in terms of oxygen binding energy (0.34 eV/O_2 and 3.50e V/O). Similar results were found for Pt_3Fe(111). The 2% compressed Pt surface was more reactive than the Pt skin but less reactive than the Pt in equilibrium geometry. The paper attributed the reduced reactivity of compressed Pt to the lowering of the *d*-band center from the Fermi level, and rationalized that although the Pt skin has lower oxygen dissociation activity than Pt, it is more reactive for the ORR because it is less poisoned by O, and hence facilitates the formation of O-containing intermediates in the ORR.

In line with this thinking is another study by Stamenkovic et al. [55], which examined the O adsorption ability and ORR activity of Pt_3M (M = Fe, Co, Ni, Ti) systems. According to their model, Pt binds oxygen a little too strongly, and finding a better electrocatalyst for the ORR amounts to finding a surface that binds oxygen more weakly than Pt does, by about 0.2 eV. Their calculated oxygen

adsorption figures of Pt$_3$Ms are all weaker than pure Pt and the predicted ORR activities are compatible with the experimental measurements.

Zhang et al. [53] reported their study on the electrocatalytic activity of a platinum monolayer supported on Au(111), Rh(111), Pd(111), Ru(0001), and Ir(111). The authors proposed that for the ORR, an electrocatalyst's activity is associated with its ability to break the O-O bond and to form the O-H bond. A surface with a higher-lying center of the d-band (ε_d) can bind adsorbates more strongly and thus catalyzes the dissociation of adsorbates more efficiently, whereas a surface with a low-lying ε_d will bind the adsorbates more weakly and thereby facilitate the formation of bonds amongst them. The paper reasoned that the most active platinum monolayer should have an ε_d with an intermediate value. The study reported the activation energies (E_a) for O$_2$ dissociation and the O hydrogenation reaction. Their results illustrated that the E_a for O$_2$ dissociation is the smallest on Pt$_{ML}$/Au(111) and the largest on Pt$_{ML}$/Ir(111), while the E_a for the hydrogenation of O had the largest barrier on Pt$_{ML}$/Au(111) and the smallest one on Pt$_{ML}$/Ir(111) (Figure 5.6). The activation energies on Pt(111) lay close to the crossing of the two E_a trend lines. The paper suggested that the ideal catalyst should have E_a values lying at the crossing of the two E_a trend lines. They discovered that the only platinum monolayer that fell in the vicinity of the crossing was Pt$_{ML}$/Pd(111) which, according to their experiment, had an activity comparable to that of Pt(111).
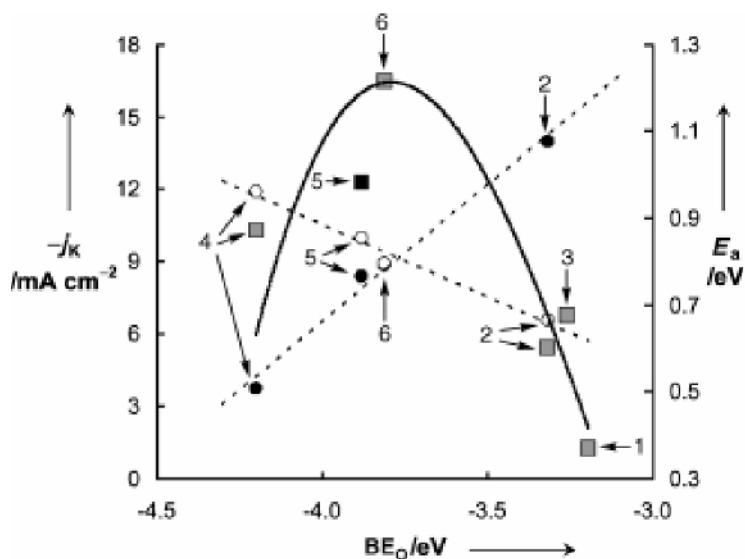
Figure 5.6. Kinetic currents (j_k; square symbols) at 0.8 V for O$_2$ reduction on the platinum monolayer in a 0.1 M HClO$_4$ solution, and the activation energies for O$_2$ dissociation (filled circles) and for OH formation (open circles) on Pt$_{ML}$/Au(111), Pt(111), Pt$_{ML}$/Pd(111), and Pt$_{ML}$/Ir(111), as functions of the calculated binding energy of atomic oxygen (BE$_o$). Labels: 1. Pt$_{ML}$/Ru(0001), 2. Pt$_{ML}$/Ir(111), 3. Pt$_{ML}$/Rh(111), 4. Pt$_{ML}$/Au(111), 5. Pt(111), 6. Pt$_{ML}$/Pd(111). (Reprinted with permission from Junliang Zhang, Miomir B. Vukmirovic, Ye Xu, Manos Mavrikakis, and Radoslav R. Adzic, Ang Chem Int Ed 44 (2005) 2132. ©2005 Wiley-VCH Verlag GmbH & Co.)

Correlation between the calculated *d*-band center of Pd in palladium alloys and ORR activity was reported by Shao et al. [56]. The study elucidated a linear relationship between the O binding energies and the *d*-band position of the Pd atom on M surfaces (M = Ru, Ir, Rh, Pt, Au) (Figure 5.7(a)). The authors discussed the ORR activities of these systems based on the argument that a good ORR electrocatalyst exhibits a moderate interaction with the adsorbates; thus, Pd/Ru(0001), Pd/Ir(111), and Pd/Rh(111) are not expected to be very active because of their slow kinetics in breaking O-O bonds, whereas Pt/Au(111), with an ε_d close to the Fermi level, bonds strongly with O, hindering subsequent reaction steps and slowing the kinetics of oxygen reduction. Pd/Pt(111), with an ε_d lying in the middle and therefore forming a moderate bond with the adsorbates, may be a good catalyst for the ORR. The plot of experimentally obtained half-wave potentials vs. the calculated *d*-band center confirms theoretical predictions (Figure 5.7(b)) that a catalyst with a moderate ε_d value has good ORR activity.
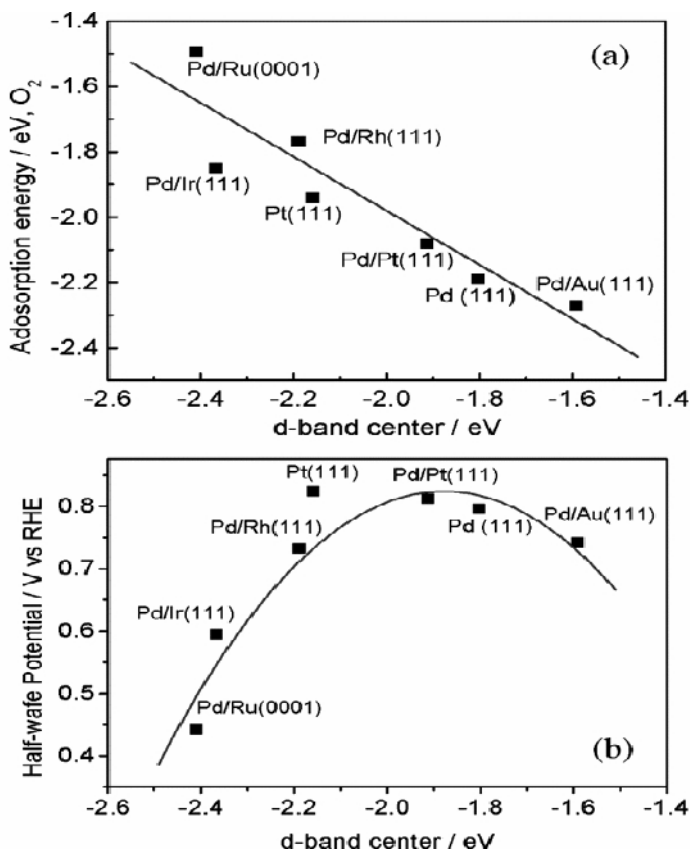
Figure 5.7. Calculated O_2 adsorption energies on Pd monolayers on various substrates (a) and half-wave potentials for the ORR on Pd monolayers on different substrates in a 0.1 M $HClO_4$ solution (b), both as a function of the calculated Pd *d*-band center (relative to the Fermi level). The Pt(111) data are included for comparison [56]. (Reprinted with permission from Langmuir 2006 Dec 5;22(25):10409–15. ©2006 American Chemical Society.)

Another Pd alloy study [58] was reported by Suo et al. In this study, a linear relationship was observed between the adsorption energy of $O_{(ads)}$ and the lattice strain ratio described by the ratio of the lattice constant of Pd. The authors suggested that the lattice-strain effect resulted in weakened M-O bonding and increased activity for the ORR, and proposed that this relationship could serve as a guideline for the design of Pd alloys. The authors also pointed out that alloying Pd with elements of smaller atomic size would improve the ORR activity of Pd-based catalysts and it is possible to find Pd-based alloys that are more active than Pt, by reducing adsorption energy through lattice contraction.

Study of oxygen adsorption on pseudomorphic PtRu overlayers [60] revealed that the properties of the PtRu overlayer systems are not intermediate between those of the two constituents. Rather, they bind adsorbates less strongly than the two elementary metals. The same observation was made in a Pd-alloy study [58].

A comparison study of the electronic structure properties of bulk Pt and bulk Pt_3Cr, and the surface properties of a monolayer Pt skin on a three-layer Pt_3Cr alloy slab with Pt(111) modeled by a four-layer slab, was reported by Rogues and Anderson [61]. The study illustrated that the bulk lattice constant decreased from 3.99 Å (Pt) to 3.94 Å (Pt_3Cr) and there was electron transfer from chromium to platinum atoms. The study also revealed that the most stable adsorption sites for OH and H_2O at 1/4 ML coverage are one-fold atop. Subsurface Cr atoms in the alloy reduced the adsorption energies of both OH and H_2O on the Pt skin surface relative to Pt(111), but the reduction for OH was greater (0.13 vs. 0.02 eV for OH and H_2O respectively). Based on an empirical model, the change in onset reversible potential due to alloying for the reaction

$$(\text{catalyst})\text{-OH} + H^+(aq) + e^- \leftrightarrow (\text{catalyst})\text{-OH}_2$$
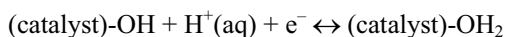
was calculated using the following equation:

$$
\begin{aligned}
\Delta U^0 &= U^0(alloy) - U^0(Pt) \\
&= \left[E_{ads}(OH)_{Pt} - E_{ads}(OH)_{alloy} - E_{ads}(H_2O)_{Pt} + E_{ads}(H_2O)_{Alloy} \right] / nF
\end{aligned}
\tag{5.8}
$$

A positive shift of 0.11 V on the Pt skin relative to the Pt(111) surface was predicted. The experiment showed a positive shift of 0.04 to 0.05 V. The study supports the hypothesis that there is a direct connection between the onset reversible potential for OH_{ads} formation and the overpotential for O_2 reduction on Pt fuel cell cathodes, and that alloying Cr with Pt reduces the overpotential. This approach was employed in their investigation of a Pt_3Co system as well [62, 63], and a positive shift of $\Delta U^0 = 0.08 V$ was calculated for the Pt skin on $Pt_3Co(111)$. The positive shift correlates with the experimental observation of a positive shift in the onset potential for formation of OH_{ads} on the alloy, relative to the Pt catalyst, at around 0.8 V and suggests that the improvement with the Pt_3Co alloy can be attributed to this positive onset potential shift, which thereby allows O_2 to adsorb at higher potentials and reduces the overpotential for O_2 reduction. Subsequent experimental study [59] confirmed that fractional coverage by OH_{ads} is reduced on a Pt_3Fe skin and Pt skeleton surface, compared with pure Pt. The Tafel slope and

the activation energies are almost identical for the ORR on pure Pt, Pt$_3$Fe skeleton, and Pt$_3$Fe skin. The reaction mechanism – a "series 4e$^-$ reduction" – is the same. The activity of the ORR increases in the order Pt < Pt-skeleton < Pt-skin. The experimentally measured d-band center demonstrated that the average energy of the d states is different and downshifted on Pt electronically modified by subsurface Fe, which means that the fractional coverage by OH$_{ads}$ is reduced on these surfaces compared with pure Pt.

In another experimental and theoretical investigation consisting of a monolayer of Pt or mixed monolayer of Pt and another later transition metal (Au, Pd, Ir, Ru, Rh, Re, or Os) deposited on a Pd(111) single crystal or on carbon-supported Pd nanoparticles [54, 64], superior activity was observed for several of these catalysts and was attributed to low OH coverage on Pt, caused by the lateral repulsion between the OH adsorbed on Pt and the OH or O adsorbed on neighbouring late transition metal atoms (other than Pt). The study illustrated a correlation between measured kinetic current density and DFT-calculated effective repulsion energy between two OH$_{ads}$ or an O$_{ads}$ (Figure 5.8).
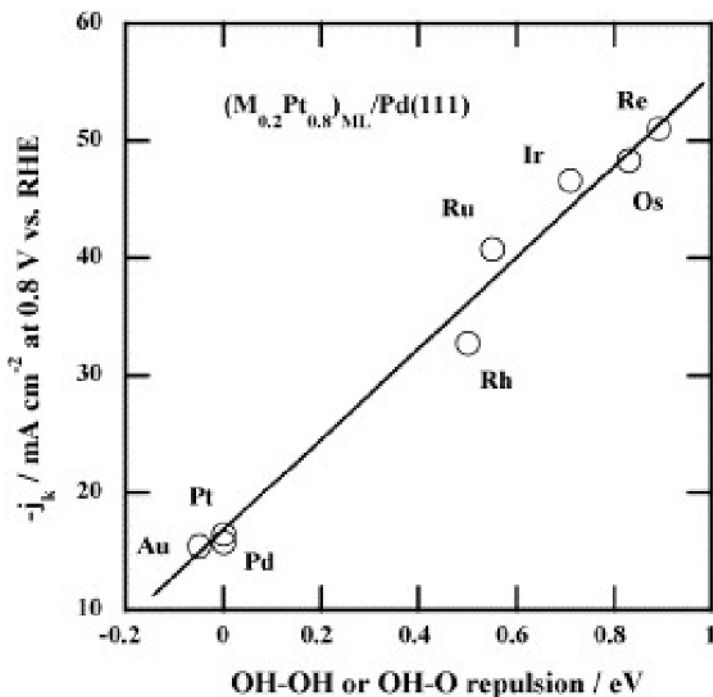
Figure 5.8. Kinetic current densities at 0.80 V as a function of the calculated interaction energy between two OHs, or OH and O in a 2×2 unit cell, relative to the corresponding interaction on Pt$_{ML}$/Pd(1 1 1) for several mixed monolayers at a Pt/M ratio of 80/20. Positive (negative) energies indicate more (less) repulsive interaction between adsorbed OHs, respectively, compared to Pt$_{ML}$/Pd(1 1 1) [64]. (Reprinted from Electrochimica Acta, 52(6), Vukmirovic MB, Zhang J, Sasaki K, Nilekar AU, Uribe F, Mavrikakis M, et al. Platinum monolayer electrocatalysts for oxygen reduction, 2257–63, ©2007 with permission from Elsevier.)

Hyman and Medlin also examined intermediates' adsorption on model Pt(111)-alloy surfaces [65]. Their study illustrated that the primary mechanism of OH destabilization on a Pt/Pt₃M surface is due to compressive strain, which also destabilizes adsorption of all of the intermediates. This is consistent with the study on Pd alloy [58]. Whereas shifts in binding energy due to strain correlate well for all of the intermediates examined, shifts in O adsorption energy resulting from ligand contributions were found not to correlate with the other intermediates. The authors also pointed out that the adsorption energy of oxygenate intermediates does not depend solely on the *d*-band center of the surface, but is also dependent on the electron density near the Fermi level.

In an attempt to develop a rapid screening tool for catalyst selection, Greeley and Nørskov [66] proposed a general scheme for the estimation of oxygen binding energies on binary transition metal surface alloys. The scheme incorporates the effects of chemical composition, strain, and ligands through a single parameter, the surface *d*-band center. For the large majority of alloys investigated, the scheme could reproduce the full DFT calculations quite well, indicating that the surface *d*-band center is a parameter of considerable descriptive power for the analysis of adsorption on surface alloys. The authors pointed out that the simple scheme failed for some systems, thus indicating that other parameters, such as the shape of the *d*-band, together with changes in the role of s and p electrons, can be important in certain cases.

The effect of carbon support upon the catalysts (Pt/C and Pt₃Fe/C) was reported by Wei et al. [67]. In this investigation, the DFT method was applied with the B3LYP functional. A cluster model consisting of carbon atoms and Pt or Fe on the three major surfaces, (100), (110), and (111), of Pt and Pt₃Fe was used to simulate the carbon supported Pt catalysts. The authors found that the Pt₃Fe/C alloy catalyst had a lower total energy compared with Pt/C. The adhesion force between the Pt₃Fe alloy catalyst and the C was stronger than that seen between the Pt catalyst and the C substrate. The enhanced catalysis effect of Pt₃Fe was confirmed by an increase in the HOMO energy of the carbon-based catalyst that enhanced the electron donating ability of the catalyst, and by the weakening of O-O bond strength. So carbon, together with the second metal, participated in the modification of Pt catalytic properties.

In summary, the *d*-band center, which is sensitive to the electronic and geometric properties of its neighbours, is a very descriptive parameter in the study of metal and alloy adsorbates interactions. The *d*-band center has been successfully employed to correlate catalyst activity with various properties and guide the fine-tuning of catalysts. However, as pointed out by Greeley, Nørskov, Hyman, and Medlin [66, 65], other parameters, such as the shape of the *d*-band, s and p electrons, and the electron density near the Fermi level, can be important in certain cases. The different activities demonstrated by different catalyst surfaces originated primarily from the difference in adsorption strengths toward O₂ and ORR intermediates. Weak adsorption with OH is associated with better ORR activity. The enhanced activity of alloys can be attributed to accelerated O₂ dissociation, or less intermediate blocking, or reduced overpotential. These fundamental concepts offer the possibility of designing better ORR electrocatalysis.

5.4 Activation Energy

The activation energy for the elementary electron transfer step is a key to understanding the electrocatalyzed reaction mechanism. Experimentally measured activation energy usually corresponds to the activation energy of the rate determining step. For a multi-electron transfer reaction, identifying the rate determining step is a challenge. Even for the one-electron transfer hydrogen evolution reaction (HER), a consensus has not been reached on the predominant reaction mechanism [68]. Computation modelling is a viable tool, offering quantitative description of elementary steps that are inaccessible for experiments. Several theoretical models to account for electron transfer process have been developed since the initial work by Gurney [69–76] (see [2, 77, 78] and the references therein). Bockris and Abdu [79] reported the first theoretical prediction of activation energy for the first step of the ORR, based on Gurney's model. Anderson and Albu [80, 81] introduced another approach, called local reaction center electron transfer theory, to evaluate the potential dependence of redox activation energy. In this model, the formation of an electronic equilibrium between the transition state complex and the electrode at each potential U is assumed and a pre-exponential factor is not treated. In this section, we will present their approach to evaluate potential dependence activation energy and show examples of their studies.

5.4.1 Computational Method

In Anderson and Albu's approach, the electrode is modeled by a donor D, with an ionization potential (IP) for a reduction reaction or an electron acceptor A, with an electron affinity (EA) for an oxidation reaction. Suppose that D (or A) is able to exchange an electron with a reaction center R, which has an electron affinity EA(R) dependent on its structure. Due to thermal fluctuations, R will pass through structures for which its electron affinity matches the electron chemical potential of the donor. For these structures, it is assumed that electron transfer takes place by radiationless tunnelling,

$$D + R' \rightarrow D^+ + R'^- \tag{5.9}$$

where R' stands for the reactant in this activated structure. Following electron transfer, the reaction can continue to form the reduction product.

The electron chemical potential of the electrode is the negative of the thermodynamic work function, φ

$$\mu = -\varphi \tag{5.10}$$

The energy of R is dependent on structure, as is its electron affinity, which is determined by the energy difference between the energy of R and the energy of R^- with the same structure. The calculations in the study proceeded by identifying structures where EA(R') = μ(D) and searching for the one having the lowest

energy. For ORR systems, this structure also corresponds to the transition state, because of the bond order changes accompanying the electron transfer. The transition state energy minus the reactant energy yields the activation energy that is predicted by this approach. Since such transition states are at the intersection of two energy surfaces, they are not characterized by saddle points with negative second derivatives, as is the case for transition states over a fixed electronic state energy surface. Because the donor is isolated from the reduction center, it need not be explicitly present in the energy computation and no explicit donor is used in the present work. An automated program was developed that increased the efficiency, capability, and accuracy of the method [82].

5.4.2 Example Calculations

Anderson and Albu reported potential dependent activation energies for the following four elementary steps:

$$O_2(g) + H^+(aq) + e^- (U) \rightarrow HO_2\bullet(aq) \tag{5.11}$$

$$HO_2\bullet(aq) + H^+(aq) + e^- (U) \rightarrow H_2O_2(aq) \tag{5.12}$$

$$H_2O_2(aq) + H^+(aq) + e^- (U) \rightarrow HO\bullet(g) + H_2O(aq) \tag{5.13}$$

$$HO\bullet(g) + H^+(aq) + e^- (U) \rightarrow H_2O(aq) \tag{5.14}$$
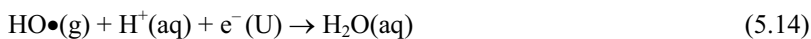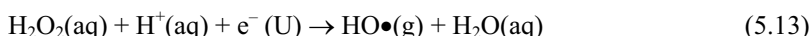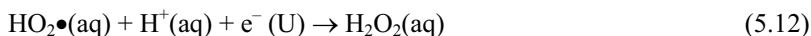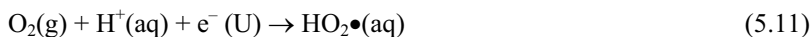
The MP2/6–31G** method is employed. The solvated proton was modeled with three water molecules $(H_3O^+(H_2O)_2)$. Using three bond lengths as varying parameters (see Figure 5.9) and keeping the rest at initial optimized reactant complex geometry, the authors explored the potential energy surface of each of the elementary reactions and calculated their corresponding EAs.
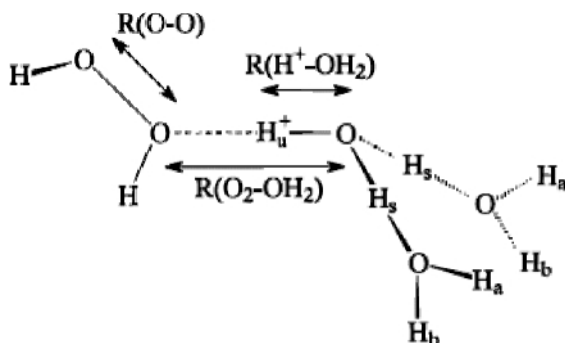
Figure 5.9. Structure of the reaction complex and definition of variables optimized. The hydrogen peroxide molecule is shown as an example. (Reprinted with permission from Alfred B. Anderson and Titus V. Albu, J. Am. Chem. Soc. 121 (1999) 11855. ©1999 American Chemical Society.)

The transition state was identified as the one with the lowest energy in the system that had electron affinity equal to (4.6 eV (the hydrogen reference electrode) + the potential of the electrode). For example, for the elementary Reaction 5.11, the transition state structure at potential 0.727 V is located by identify the minimum potential energy structure of the $(OO...H^+...e–)$ system, which has an EA = 4.6 + 0.727 = 5.327 eV. This identified transition state structure has an O-O bond length of 1.2576 and an H^+-O bond length of 1.09 Å. The activation energy at this electrode potential is the energy difference between this identified structure and the reactant system, which is 0.924 eV for this reaction. Similarly, the transition state structures for Reactions 5.12, 5.13, and 5.14 were identified at an electrode potential of 0.727 eV, and the activation energies for these steps were 0.226, 1.514, and 0.002 eV, respectively.

In this study, the activation energies corresponding to electrode potentials of 0–2 V (standard hydrogen electrode) were investigated. The results indicated that H_2O_2 reduction (Reaction 5.13) had the highest activation energy. These results were consistent with experimental observation of H_2O_2 generation over weakly interacting electrodes such as mercury and gold. The study also revealed that the activation energies increased as the electrode potential increased. The activation energies for the four steps are, in order: third step (Equation 5.13) > first step (Equation 5.11) > second step (Equation 5.12) > fourth step (Equation 5.14). Based on these numbers, the authors proposed that an efficient four-electron reduction catalyst must activate the first and third reduction steps without deactivating the other two steps. An electrode surface that stretches the HO-OH bond will increase its electron affinity and catalyze the reaction. Surfaces that stabilize the adsorbed reduction products through strong bonding are likely to lengthen the O-O bond and increase its electron affinity, and hence reactivity.

In a subsequent paper [77], Anderson et al. reported the effect of platinum on oxygen reduction using a similar MP2 method. A single platinum atom was used for coordinating with O_2, $HO_2\bullet$, H_2O_2 and $HO\bullet$:

$$Pt\text{-}O_2 + H^+(aq) + e^- (U) \rightarrow Pt\text{-}OOH \qquad (5.15)$$

$$Pt\text{-}OOH + H^+(aq) + e^- (U) \rightarrow Pt\text{-}(OHOH) \qquad (5.16)$$

$$Pt\text{-}OHOH + H^+(aq) + e^- (U) \rightarrow Pt\text{-}OH + H_2O \qquad (5.17)$$

$$Pt\text{-}OH + H^+(aq) + e^- (U) \rightarrow Pt\text{-}OH_2 \qquad (5.18)$$

With this simple model, the study found that binding the Pt atom to the one-electron reduction reactants O_2, $HO_2\bullet$, and H_2O_2 stretched O-O bonds. The effect was largest in the order $H_2O_2 > O_2 > HO_2\bullet$. The Pt atom had a significant effect on the most difficult reduction step, the reduction of HOOH to $HO\bullet + H_2O$ (Equation 5.17). The activation energy for this step was reduced by about 1 eV over the 0 – 2 V potential range. The activation energy for the first electron transfer (Equation 5.15) was reduced substantially as well, and the activation energy for the second step, OOH reduction to H_2O_2 (Equation 5.16), was decreased. However, the

bonding of OH to Pt increased the activation energy of the fourth step: OH reduction to H_2O (Equation 5.18) (see Figure 5.10):
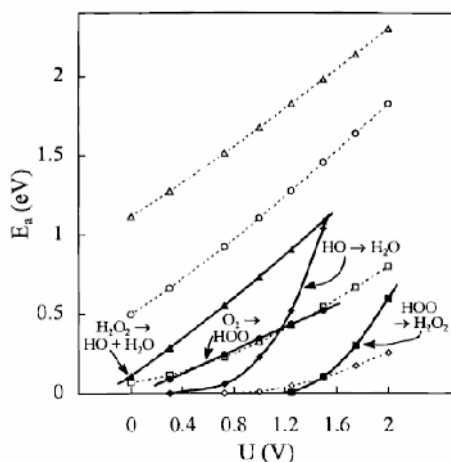
Figure 5.10. Activation energy for the four steps of oxygen reduction to water as a function of electrode potential, U. Heavy lines connect points with species undergoing reduction bonded to a platinum atom. Dotted lines connect points with no bonding to the platinum. The same key applies to both sets of curves. (Reproduced by permission of ECS—The Electrochemical Society from Anderson AB, Albu TV, Catalytic effect of platinum on oxygen reduction.)

At 1.25 V potential, with oxygen binding to a one-fold site in an end-on configuration, the calculated activation energy for the first-electron transfer step was 0.43 eV compared, with the experimental result of 0.44 eV for clean platinum in weak acid at 1.23 V.

The same team [83] further studied oxygen reduction when oxygen bonded to Pt dual sites. Using the B3LYP functional, a platinum dimer, Pt_2, with the bulk distance of 2.775 Å was used to provide one- and two-fold bonding sites for coordinating O_2, HOO•, HO•, and O•.

The study observed that the O_2 adsorption energy for one-fold end-on was 0.43 eV and for two-fold was 0.94 eV. Two-fold bonded oxygen was more stable than one-fold. The dissociation energy for two-fold bonded O_2 was 0.74 eV, while the activation barrier for the first reduction step to OOH was less than 0.60 eV at 1.23 V electrode potential. In other words, the first electron transfer has a smaller barrier than that of O_2 dissociation. Furthermore, the dissociation barrier for the first electron transfer product OOH was much smaller, 0.06 eV. So, the authors concluded that O_2 did not dissociate before the first reduction step, and OOH easily dissociated once formed after the first electron transfer step. The paper also demonstrated that the electronic field of the proton increased the electron affinity of the reactant complex and therefore facilitated the reaction. Thus, they proposed that for oxygen reduction on Pt in acid, proton transfer would be involved in the rate determining step because of the ability of its electric field to enhance the electron attracting capability of the surface-coordinated O_2. The authors concluded

that the first electron transfer was the rate determining step. Their calculated activation energy for this step was 0.60 eV at 1.23 V potential, which is close to the experimental value of 0.44 eV.

The theoretical predicted activation energies were compared in a later paper with experimental data for platinum alloys [84]. Overall agreement between the theoretical prediction and the measured current density was observed, which suggested that (i) the first electron-reduction step, forming OOH_{ads}, is the rate-limiting step, and (ii) the active catalyst sites for the various catalyst systems are similar and the presence of alloying atoms adjacent to the active site does not dramatically affect the activation energy.

Other methods for calculating the activation energies of the ORR have been reported in the literature. Based on the linear Bronsted-Evans-Polanyi relationship, Nørskov et al. [85] proposed a method to estimate the least activation energy by calculating the stability of the reaction intermediate. With this simple model, the study reported a Tafel slope of 60 mV at 300 K (71 mV at 357 K). The value was consistent with experimental results.

Wang and Balbuena [86] performed an AIMD study of the first electron transfer step $O_2 + H^+(H_2O)_3$ /Pt(111) at 350 K. For the initial configuration, the oxygen was placed parallel to the Pt(111) surface at a distance of 3.5Å, while the hydrated proton $(H^+(H_2O)_3)$ was 2.55 Å farther away from the O_2. With this model, they discovered that the proton transfer took place first, then end-on chemisorption was observed, which induced the electron transfer from the slab. Finally, the H-O-O-Ptn dissociated into H-O and O without a clear barrier.

To account for the electronic field, the authors modeled the $O_2 + H^+(H_2O)_3 + e^-$/Pt(111) system. The study observed that at first the proton transfer intermediate was formed rapidly, similar to results reported by Jinnouchi et al. [87], then end-on chemisorption and electron transfer proceeded. The formation of the end-on chemisorption precursor H-O-O-Pt had an energy barrier of about 0.4 eV. They suggested that the mechanism for the first electron transfer involved: 1) proton transfer; 2) electron transfer; 3) dissociation and hydroxyl adsorption (Figure 5.11):
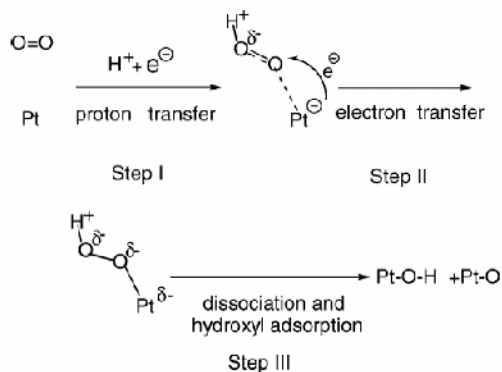
Figure 5.11. Proposed mechanism for the first electron transfer of the ORR. (Reprinted with permission from Yixuan Wang and Perla B. Balbuena, J. Phys. Chem B. 108 (2004) 4376. ©2004 American Chemical Society.)

Hyman and Medlin [88] reported an activation barrier for O_2 protonation and OOH dissociation. Using an H_5O_2+ cluster to simulate the acid solution, the study showed that O_2 protonation has a more stable precursor and lower activation barrier (0.07 eV) than O_2 dissociation (0.22 eV). Comparison of the two pathways suggested that O_2 protonation preceded dissociation in the oxygen reduction reaction.

In summary, theoretical predicted activation energies are in line with experimental numbers. Activation energy studies suggest that with Pt as the catalyst, proton transfer precedes O_2 dissociation and is involved in the rate determining step of the oxygen reduction reaction. Without catalysts, the third-electron transfer step has the largest activation energy, followed by the first-electron transfer step. An efficient ORR catalyst should activate the first- and third-electron transfer steps.

5.5 Thermodynamic Properties: Reversible Potential and Reaction Energy

In discussions of electrochemical reactions, redox potentials and reversible potentials are essential information. In this section, example applications of reversible potentials and reaction thermodynamics in the study of the ORR mechanism are provided and information pertinent the ORR reaction mechanism is discussed.

5.5.1 Reversible Potential

Reversible potential shift in the formation of OH from H_2O in acid solution was reported by Roques and Anderson [62]. They presented a model that can calculate the shift of reversible potential between two unlike catalyst compositions, using the relationship between the Gibbs free energy for a reduction reaction and the reversible potential. For the $OH_{(ads)}$ formation reaction

$$OH + H^+ + e^-(U^0) \leftrightarrow H_2O \qquad (5.19)$$

the reversible potential can be calculated as

$$U^0 = -\Delta G^0 / nF \qquad (5.20)$$

where ΔG^0 is the free Gibbs energy change of Reaction 5.19, n is the number of electrons involved in the reaction, and F is the Faraday constant.

In their model, the Gibbs energy change is replaced by the reaction energy, E_r plus a constant c, representing the missing terms $P\Delta V$ and $T\Delta S$, to give the working formula:

$$U^0 = -(E_r / nF) - 4.6V + c \qquad (5.21)$$

The value of –4.6 V in Equation 5.21 relates the energy of an electron at 0 V on the electrochemical scale to its –4.6 eV value on the physical (vacuum) scale (with a standard hydrogen electrode). The value of the constant c was found by fitting known redox reactions involving H_xO_y species in acid solution. For OH reduction on a catalyst surface, Equation 5.19 takes the form:

$$\text{(catalyst)-OH} + H^+ + e^-(U^0) \leftrightarrow \text{(catalyst)-OH}_2 \qquad (5.22)$$

The change in reaction between Equation 5.22 and 5.19 with a Pt slab as catalyst is

$$\Delta E_r = [E(OH) + E(Pt_{slab}) - E(Pt_{slab} - OH)] - [E(H_2O) + E(Pt_{slab}) - E(Pt_{slab} - H_2O)]$$
$$= E_{ads}(OH)_{Pt} - E_{ads}(H_2O)_{Pt} \qquad (5.23)$$

where $E_{ads}(OH)_{Pt}$ and $E_{ads}(H_2O)_{Pt}$ are the respective adsorption energies of OH and H_2O on the Pt slab. Assuming the constant c is unchanged, the reversible potential for Equation 5.22 is:

$$U^0(\text{Equation 5.22}) = U^0(\text{Equation 5.19}) - \Delta E_r / nF$$
$$= U^0(\text{Equation 5.19}) + [E_{ads}(H_2O_{Pt} - E_{ads}(OH)_{Pt}]/nF \qquad (5.24)$$

With Equation 5.24, we can calculate a useful approximation of the reversible potential on a specific catalyst surface using the adsorption energies of each species involved in the reaction, if we know the reversible potential of a redox reaction in aqueous solution, or we can calculate the shift of the onset reversible potential between two unlike catalyst surface compositions if the absolute reversible potential in aqueous phase for a specific redox reaction is not known. For example, the change in onset reversible potential due to a Pt surface and an alloy will be

$$\Delta U^0 = U^0(alloy) - U^0(Pt)$$
$$= [E_{ads}(OH)_{Pt} - E_{ads}(OH)_{Alloy} - E_{ads}(H_2O)_{Pt} + E_{ads}(H_2O)_{Alloy}]/nF \quad (5.25)$$

With this model, the paper investigated the cobalt concentration effect in $Pt_{1-x}Co_x$ on the reversible potential for Reaction 5.19. The paper reported that OH_{ads} formation depended significantly on the sub-surface composition, and alloying platinum with cobalt led to an increasingly positive shift of the reversible potential for forming OH_{ads}. Since there is a direct connection between the decrease of the overpotential for O_2 reduction and the positive shift of the onset reversible potential for forming OH_{ads}, the study suggested that alloying more Co with Pt would enhance the reduction in overpotential. However, beyond 75% cobalt concentration in the $Pt_{1-x}Co_x$ catalysts, the effect of alloying is essentially unchanged.

5.5.2 Reaction Thermodynamics

Nørskov et al. [85, 89] proposed a method for estimating the thermochemistry of electrochemical reactions by calculating the stability of the reaction intermediate.

According to this model, the free energy change of an electrochemical reaction can be calculated as follows:

1) Simplify the electrochemical reaction by relating the chemical potential for $(H^+ + e^-)$ to that of $1/2\ H_2$ in the gas phase. At standard conditions (U = 0, pH = 0, p = 1 bar, T = 298 K), the free energy change for the reaction $*AH \rightarrow A + H^+ + e^-$ can be calculated as the free energy change for $*AH \rightarrow A + 1/2H_2$, where $*$ stands for an active site.

2) The free energy change is calculated by $\Delta G_0 = \Delta E + \Delta ZPE + T\Delta S$. The reaction energy ΔE and ΔZPE are obtained from DFT calculation. $T\Delta S$ is obtained from standard tables for gas phase molecules.

3) The effect of the electrode potential is accounted for by $-eU$, where U is the electrode potential relative to the standard hydrogen electrode, $\Delta G_U = -eU$.

4) The pH correction to the free energy is evaluated by the concentration dependence of the entropy:

$$\Delta G_{pH}(pH) = -kT \times \ln[H^+] = kT \times \ln 10 \times pH \tag{5.26}$$

where k is Boltzmann's constant and T is temperature.

The total reaction free energy is given by

$$\Delta G(U, pH, p_{H_2} = 1bar, T) = \Delta G_0 + \Delta G_U + \Delta G_{pH} \tag{5.27}$$

The effect of a local electric field can be evaluated by adding the term ΔG_{field} to Equation 5.27. This term accounts for the change in reaction energy caused by the electric field and is obtained by varying the external electric field in the density functional theory calculations.

With this method, the authors investigated the ORR through two possible mechanisms: an "associative" mechanism

$$O_2^* + 4H^+ + 4e^- \rightarrow OOH^* + 3H^+ + 3e^- \tag{5.28}$$

$$OOH^* + 3H^+ + 3e^- \rightarrow H_2O + O^* + 2H^+ + 2e^- \tag{5.29}$$

and a dissociative mechanism,

$$O_2^* + 4H^+ + 4e^- \rightarrow 2O^* + 4H^+ + 4e^- \tag{5.30}$$

$$2O^* + 4H^+ + 4e^- \rightarrow OH^* + O^* + 3H^+ + 3e^- \tag{5.31}$$

$$OH^* + O^* + 3H^+ + 3e^- \rightarrow H_2O + O^* + 2H^+ + 2e^- \tag{5.32}$$
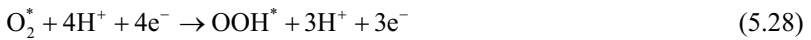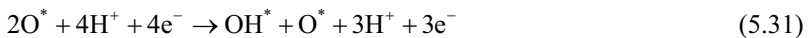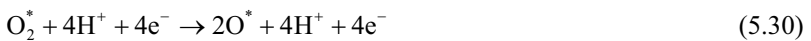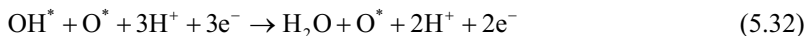
The study showed that at a high potential region, two effects of the electric field are notable: O_2^{TS} is destabilized by about 0.1 eV and OH is stabilized by the same amount. The first effect shifts the mechanism to the associative pathway, since the barrier for O_2 dissociation will increase as an effect of the electric field. Thus, at a potential around 0.9 V, the associative mechanism determines the top of the volcano. The second effect, the stabilization of OH at positive potentials, makes OH on the surface the most stable intermediate (see Figure 5.12). Therefore, the authors argued that the coverage effect of OH should be included in a kinetic model, but not that of O. Nevertheless, due to the correlation between the binding energies of O, OH, and OOH, it should be possible to construct the volcano plot using the adsorption energy of any of these adsorbates. Figure 5.13 demonstrates the trend in the oxygen reduction activity as a function of oxygen binding energy for U = 0.0, 0.75, and 1.23 V. The authors concluded that the overall activity trend did not change significantly when electric field effects were taken into account. However, for accurate predictions at oxygen reduction potentials close to the volcano top, local electric field effects may be important.
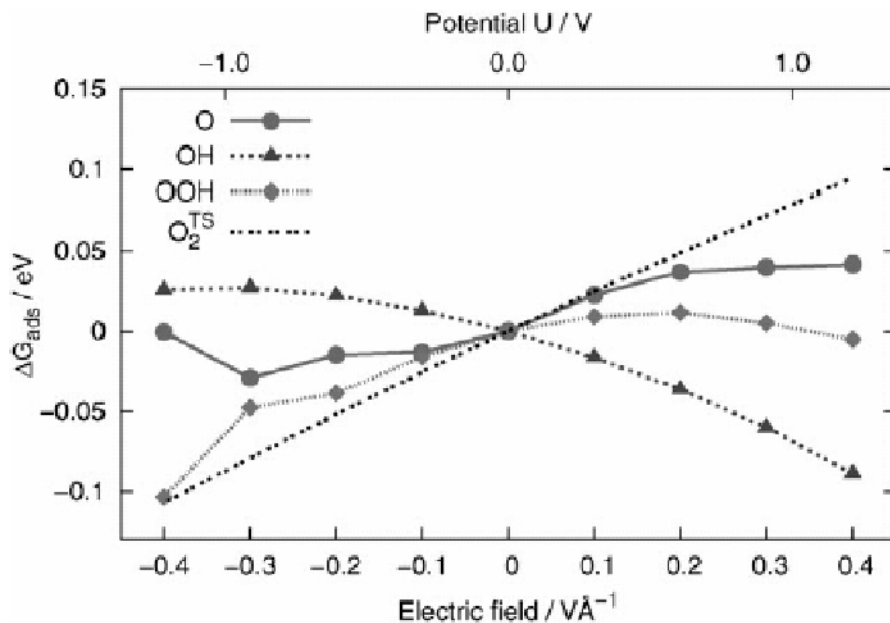
Figure 5.12. The change in adsorption energy for O, OH, and OOH as a function of the electric field strength [89]. (Karlberg GS, Rossmeisl J, Norskov JK. Estimations of electric field effects on the oxygen reduction reaction based on the density functional theory. Phys Chem Chem Phys 2007;9(37):5158–61. Reproduced by permission of The Royal Society of Chemistry.)
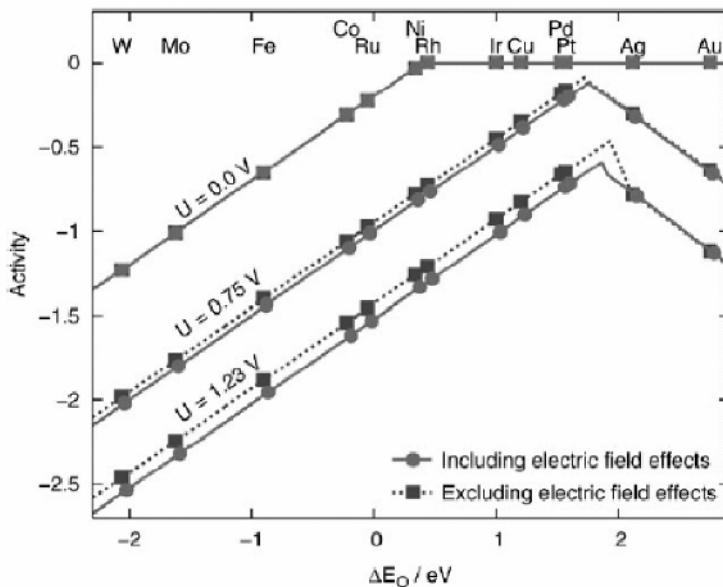
Figure 5.13. Trends in the oxygen reduction activity as a function of the oxygen binding energy for $U = 0.0$, 0.75, and 1.23 V, including and excluding local electric field effects [89]. (Karlberg GS, Rossmeisl J, Norskov JK. Estimations of electric field effects on the oxygen reduction reaction based on the density functional theory. Phys Chem Chem Phys 2007;9(37):5158–61. Reproduced by permission of The Royal Society of Chemistry.)

A reaction thermodynamics study of a group of chemical and electrochemical reactions was conducted by Gu and Balbuena [90] to determine the relative stability of Pt atoms and other transition metal atoms (Ir, Pd, Rh, Ni, and Co) toward the dissolution reactions in an acidic environment. The study demonstrated that thermodynamically favorable dissolution reactions are electrochemical, and involve adsorbed oxygenated compounds that are intermediate species of the ORR. Iridium is found to be the most stable among the various pure metals, in comparison with Pt. Alloys of Pt – M (M = Ir, Pd, Ru, Co) cause a decrease in Pt stability against dissolution, while Pt-Ni alloy does not affect Pt stability. Comparing the relative stabilities to a given dissolution reaction of Pt and another metal species in the same alloy cathode catalyst, Ir and Co are found to be more stable than Pt in PtIr and PtCo.

The same group also reported thermodynamic analysis of the reactivity of Pt_xPd_y alloy clusters [91]. The analysis was performed on the basis of the thermodynamics of two reactions: the first consists of the first electron and proton transfer to O_2 in the presence of the metal, yielding adsorbed hydroperoxyl radical OOH; the second reaction is a combination of the last three electron and proton transfers to adsorbed O and OH species, yielding water. It is demonstrated that as the concentration of Pd increases, the change of Gibbs free energy for the first electron transfer step becomes increasingly favorable. This is due largely to increased binding energies for OOH. To favor the second reaction, the adsorption strength of O and OH should be intermediate so that O and OH can be further

reduced to water. It was found that Pt_3Pd_7 favored the two reactions. Based on this thermodynamic analysis, the authors concluded that Pt_3Pd_7 clusters should act as better catalysts for the ORR.

In summary, simplified procedures have been developed to calculate the thermodynamic properties of electrochemical reactions. These procedures are useful in providing trends in relative activity. One direction for improving Pt's catalytic activity is to positively shift the onset reversible potential for OH_{ads} formation from H_2O, through alloying. Electric field effects the ORR pathways and at a high potential (V = 0.9 V), the associative pathway dominates. An electric field, however, does not have a significant influence on the ORR activity trend.

5.6 Study of Non-noble Catalysts

Development of non-precious metal oxygen reduction catalysts is crucial for the commercialization of fuel cell technology, due to the limited abundance and high cost of Pt. For decades, research on non-precious metal ORR catalysis was limited mainly to transition metal macrocyclic complexes and chalcogenides. Major drawbacks of these systems are low activity and, especially, instability. Heat treatment of transition metal macrocyclic complexes improves their stability. However, under fuel cell operating conditions, the stability is still far from satisfactory. Improving both the stability and the activity of non-precious metal ORR catalysts are major challenges. In this section, theoretical studies of non-noble ORR electrocatalysis are presented. These examples employ properties evaluation introduced in previous sections, and provide information regarding ORR mechanisms.

Oxygen electroreduction on Fe(II) and Fe(III) coordinated to N_4 chelates $(Fe(NH_2)_2(NH_3)_2)$ were studied by Anderson et al. [92] using the DFT method. In this study, reversible potentials for the following steps were evaluated:

$$L_4Fe\text{-}OH_2 + O_2 + H^+(aq) + e^-(U) \leftrightarrow L_4Fe\text{-}OOH + H_2O \qquad (5.33)$$

$$U^o = 0.91 \ (0.01) \ V$$

$$L_4Fe\text{-}OOH + H^+(aq) + e^-(U) \leftrightarrow L_4Fe\text{-}(OHOH) \qquad (5.34)$$

$$U^o = 0.96 \ (1.83) \ V$$

$$L_4Fe\text{-}OOH + H^+(aq) + e^-(U) \leftrightarrow L_4Fe\text{-}O + H_2O \qquad (5.35)$$

$$U^o = 0.44 \ (1.24) \ V$$

$$L_4Fe\text{-}O + H^+(aq) + e^-(U) \leftrightarrow L_4Fe\text{-}OH \qquad (5.36)$$

$$U^o = 2.96 \ (2.26) \ V$$

$$L_4Fe\text{-}(OHOH) + H^+(aq) + e^-(U) \leftrightarrow L_4Fe\text{-}OH + H_2O \qquad (5.37)$$

$$U^o = 2.43\ (1.67)\ V$$

$$L_4Fe\text{-}OH + H^+(aq) + e^-(U) \leftrightarrow L_4Fe\text{-}OH_2 \qquad (5.38)$$
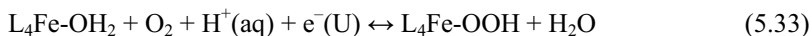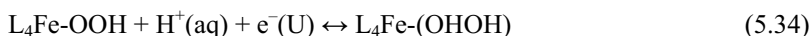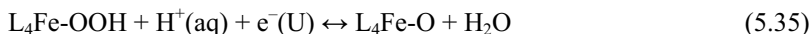
$$U^o = 0.64\ (1.44)\ V$$

The values in brackets are for Fe(III), while those without brackets are for Fe(II).

The study discovered that the binding energy with O_2 was 0.12 eV for Fe(II) and 0.06 eV for Fe(III), while the binding energy with H_2O was 0.10 eV for Fe(II) and 0.53 eV for Fe(III). So, O_2 was able to displace H_2O from Fe(II) but not from Fe(III). Compared with Fe(III), Fe(II) formed a strong bond with OOH and a weak bond with H_2O. The combination of the two resulted in a total 0.90 eV higher reversible potential for Fe(II) (Equation 5.33). Thus, Fe(II) was favored over Fe(III) in the first electron transfer step and Fe(II) was the active site for four-electron reduction of oxygen by iron.

The paper further revealed that the reduction on Fe(II) of OH, formed from water oxidation, had a reversible potential of 0.64 V for Fe(II) (Equation 5.38), which was about the same as that calculated for 1-fold bond Pt (0.61 V at the B3LYP level). The paper suggested that the Fe-OH formation contributed to the observed overpotential on iron macrocycles in the same way that it did for the platinum electrode. In comparison with Pt, the paper concluded, the important difference was the hydrogen bond interaction between (OHOH) bonded to Fe(II) and a nitrogen lone-pair orbital in the N_4 chelate. This interaction prevented hydrogen peroxide from leaving as a two-electron reduction product and provided a path for reduction to water.

Theoretical modeling of a Co_9S_8 system is reported by Sidik et al. [93]. In this study, three surfaces of Co_9S_8 were evaluated for their possible catalytic activity toward the ORR. The adsorption energies of reactants, reaction intermediates, and products in both O_2 reduction and water oxidation in acid were calculated. The results indicated that the sulfur-rich (002) surface has the right properties for two-electron ORR. The H_2O and O_2 adsorption energies are very close to those on Pt, and the OH adsorption bond is weaker than that on Pt. The end-on adsorption orientation for O_2 on the isolated Co sites on this surface is more stable. This should lead to peroxide formation, and it precludes four-electron reduction to water. Thus, a (002) surface is a proposed candidate for the observed peroxide generation on Co_9S_8.

Based on the adsorption bond strengths of the reactants, intermediates, and products for water oxidation and O_2 reduction, the study implied that the partially OH-covered (202) surface of Co_9S_8 should be active toward O_2 reduction and water does not block active sites on this surface. It also showed O bonding to S, a non-metallic surface site. The study suggested that experimental characterization of the surfaces of Co_9S_8 oxygen cathodes would be worthwhile.
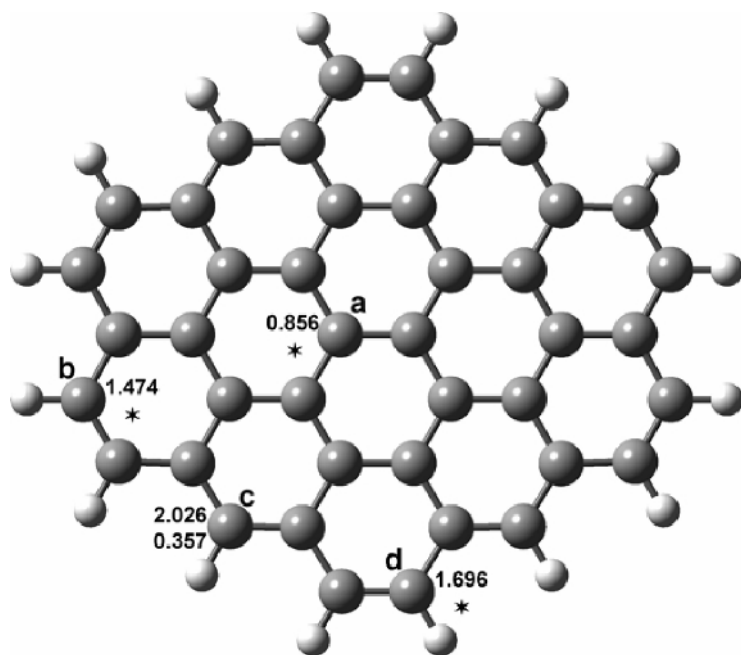
Figure 5.14. The H (first number) and OOH (second number) radical adsorption bond strengths (eV) on the pure graphite sheet, $C_{42}H_{16}$. The * indicates that the calculations for that site did not converge [94]. (Reprinted with permission from J Phys Chem B 2006;110(4):1787–93. Copyright 2006 American Chemical Society.)

Theoretical and experimental study of oxygen reduction to peroxide on graphite and nitrogen-doped graphite was reported by Sidik et al. [94] The paper reported an oxygen reduction onset potential for nitrided Ketjenblack at 0.5 V (SHE) and for untreated carbon at 0.2 V. Adsorption energies for H, OOH, and H_2O_2 on the radical sheet cluster $C_{41}NH_{16}$ and on $C_{42}H_{16}$ were calculated, and reversible potentials for the oxidation of H and O_2 reduction intermediates were evaluated. For undoped graphite, based on OOH adsorption energy, a reversible potential of 0.311 V is predicted for the formation of OOH on site c (see Figure 5.14) and this is attributed to the cause of the observed current onset potential on Ketjenblack.

For graphite nitride, using the site with OOH bond strength of 0.891 eV (the site adjacent to N in Figure 5.15), reversible potentials of 0.845 and 0.545 V were predicted for the first and second electron-transfer steps. The second potential matched the observed current onset potential for H_2O_2 generation on nitrogenated Ketjenblack. The results showed that carbon radical sites which formed adjacent to substitutional N in graphite are active for O_2 electroreduction to H_2O_2 in acid electrolyte, and this may explain the catalytic effect observed for nitrided carbon. The weak catalytic effect of untreated carbon can be attributed to the weaker bonding of the OOH_{ads} reaction intermediate to H-atom-terminated graphite edge sites. Substitutional N atoms that are far from the graphite sheet edges will be more active, and those that are close to the edges will be less active.
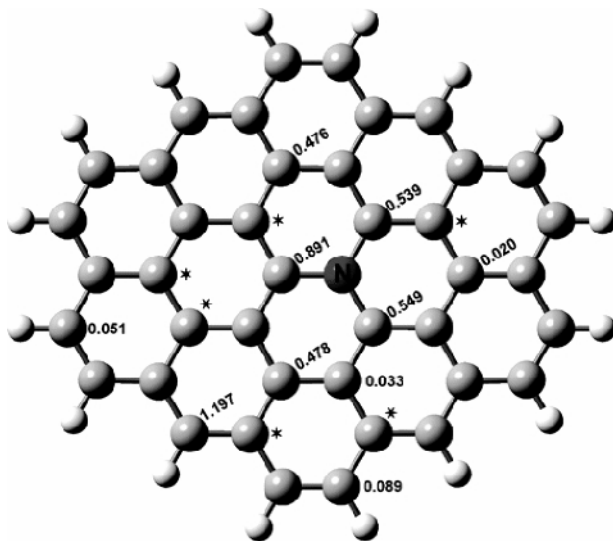
Figure 5.15. OOH adsorption bond strengths (eV) to $C_{41}NH_{16}$ as a function of position. The * indicates that the calculations for that site did not converge [94]. (Reprinted with permission from J Phys Chem B 2006;110(4):1787–93. Copyright 2006 American Chemical Society.)
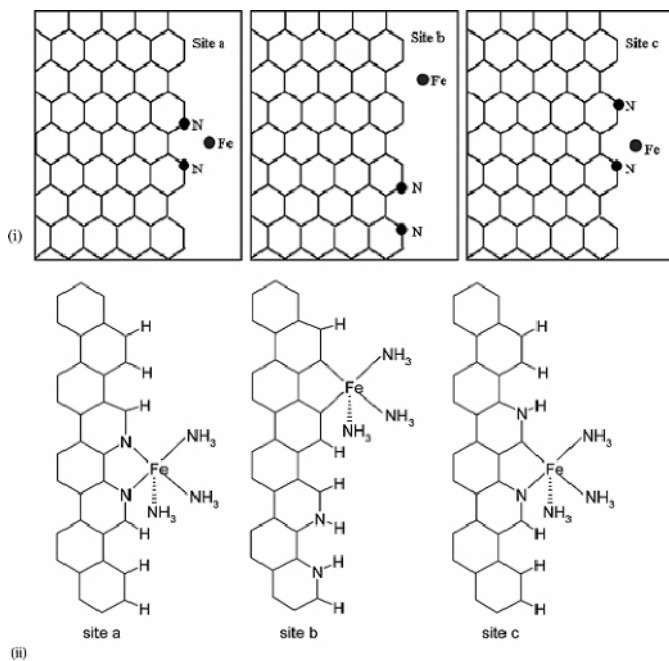
Figure 5.16. Positions of Fe atoms on the edge of nitrogenated graphene: (i) Fe bond sites a, b, c; (ii) models of nitrided graphene edge being passivated by hydrogen atoms and bonded with Fe. Here Fe is coordinated with three NH_3 ligands [95]. (Reprinted with permission from J Phys Chem B 2006;110(9):4179–85. Copyright 2006 American Chemical Society.)

The active-site structure of the heat-treated $Fe-N_4$ system is an unresolved issue. Jain et al. [95] carried out a DFT study to elucidate the structure of Fe-based electrocatalysts. In this study, lowest energy configurations for the incorporation of nitrogen in bulk on a graphene sheet as well as on the edge were determined. It was found that substitution of nitrogen in bulk on a graphene sheet is endothermic. On the edge, however, the results depend on the presence/absence of hydrogen. While in the absence of hydrogen the substitution is exothermic, in the presence of hydrogen the substitution is endothermic. It is concluded that the majority of added nitrogen atoms on a graphene sheet are likely to reside at the edges rather than the interior sites of the graphene. Energies of various configurations for the incorporation of iron on the edge of the nitrided graphene sheet were also examined. Energetically, when there is no hydrogen passivation on the graphene edge, iron prefers to bond with nitrogen and a carbon atom. When the nitrided graphene edge is passivated by hydrogen, iron prefers to bond with two nitrogen atoms (Figure 5.16[i], site a).

An active site theoretical study for cobalt-graphite-nitride systems was reported by Vayner and Anderson [96]. In this study, the adsorption energies of ORR intermediates and products were calculated. The linear Gibbs free energy relationship was employed to calculate the reversible potential for each of the electron transfer steps. The calculations illustrated that a bare graphite edge with one N atom is inactive (Figure 5.16(a)) toward the two- and four-electron reduction of oxygen. This is based on the calculation result that at potentials greater than 0.3 V, N is not hydrogenated and is not active for O_2 reduction because OOH bonds too weakly, while at potentials lower than 0.3 V, for which N is hydrogenated and becomes a radical center, the NH edge is not active for O_2 reduction because OOH bonds too strongly, resulting in a high overpotential for its reduction to H_2O_2 on this site. Whether other configurations of substituting N atoms, such as two or more on adjacent edge sites, are active for oxygen reduction is not explored in this paper. Over a Co site bridging two N atoms substituting for CH on an edge (Figure 5.17 b, c, d, e), the onset formation potential for OOH_{ads} is about 0.4 V for Co^0, 0.8 V for Co^{II} in the form of $Co(OH)_2$, 0.7 V for Co^{II} in the form of $H_2O-Co(OH)_2$, and 0.7 V for Co^{III} as $Co(OH)_3$. Later electron transfer steps have higher predicted reversible potentials. Thus, two forms of attached Co^{II} and attached Co^{III} are predicted to have oxygen reducing capability. For the $H_2O-Co(OH)_2$ site, the H_2O_{2ads} bonds more strongly than H_2O, which implies that H_2O_2 can remain at the site for further reduction into water. For the Co^{III} site, H_2O_{2ads} bonds more weakly than H_2O, which is consistent with Co^{III} sites providing a route for hydrogen peroxide generation, and H_2O may poison the site. A water molecule bonds to each of the Co centers but most weakly in the case of $H_2O-Co(OH)_2$, which suggests this cobalt center is least likely to be poisoned by a strongly held water molecule. The catalyst is not expected to be stable, as the cobalt complexes are weakly bonded to the graphite edge N atoms with binding energy in the range 0.9 to 1.5 eV (1.28 eV for Co^0, 0.84 eV for Co^I, 1.02 eV for Co^{II}, 1.47 eV for $Co^{II}OH_2$, and 1.17 eV for Co^{III}).
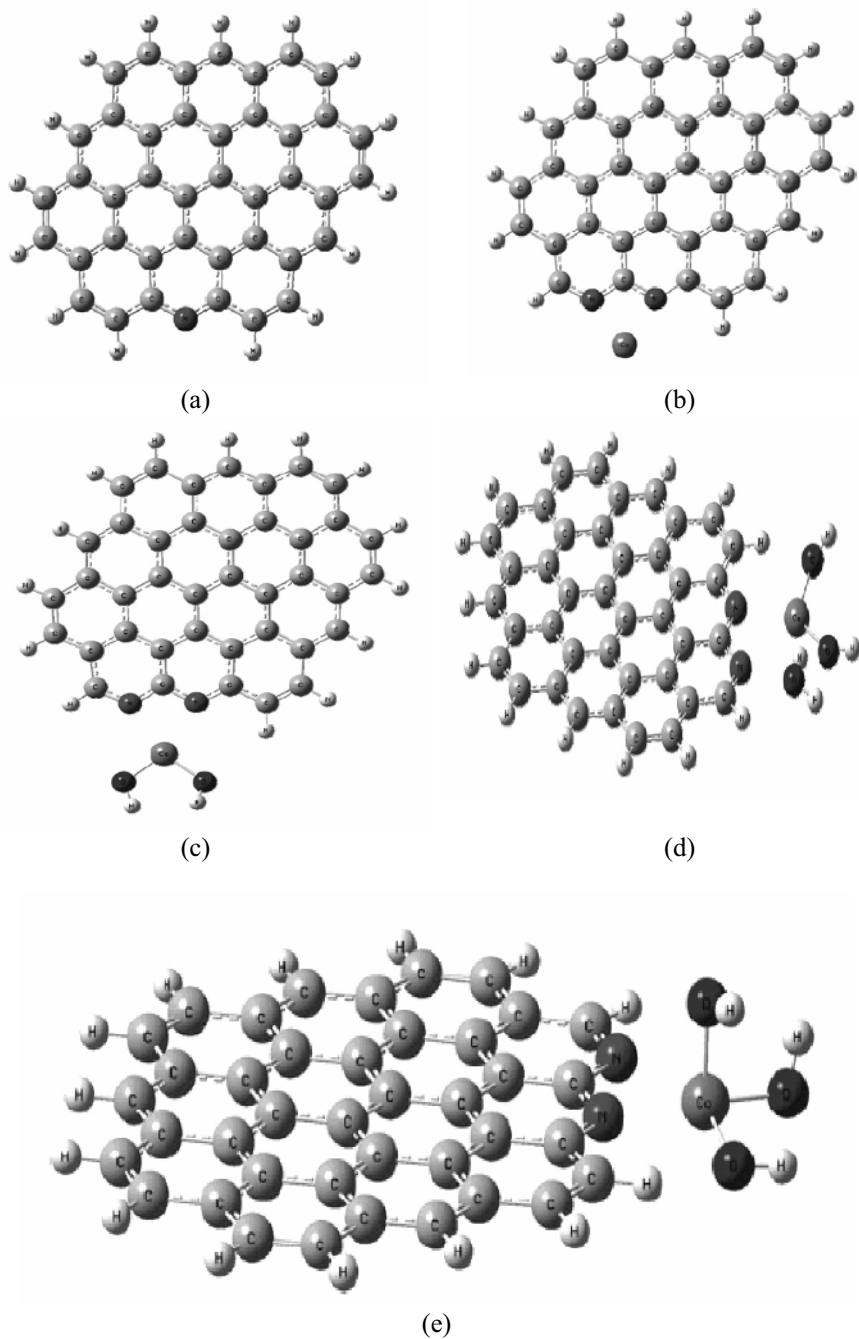
Figure 5.17. Structures of cobalt-graphite-nitride systems [96]. (Reprinted with permission from J Phys Chem C 2007;111(26):9330–6. Copyright 2007 American Chemical Society.)

DFT studies of iron-porphyrin and (imidazole) iron-porphyrin were reported by Tsuda et al. [97]. Investigation of cobalt- and iron-substituted phthalocyanine and porphyrin systems was conducted by Shi and Zhang [98]. In this study, the dioxygen binding mode, energy, charge, and ionization potential (IP) of these catalysts were investigated. The effects of the central metal, ligand, and substituents on the catalyst's dioxygen binding ability and catalytic activity were discussed. The general activity trend observed for phthalocyanines and porphyrins was rationalized with the calculated properties. The study indicated that calculated cobalt systems can form stable end-on dioxygen adducts while side-on adsorptions were not stable. These findings explained the observed two-electron ORR mechanism of these systems. The study also discussed the electronic structure difference between these systems and hence their ORR activity.

The general activity trend observed for phthalocyanines and porphyrins is rationalized with the calculated properties. It has been illustrated that the catalyst's oxygen reduction activity is related to its ionization potential and dioxygen binding ability. This is consistent with Radin and Beck's redox mechanism, i.e., the rate determining step is $M(III) + e^- \rightarrow M(II)$. In terms of ionization potential, for porphyrin derivatives, the central metal affects its ionization potential greatly; in other words, the electron can be considered extracted from an orbital which has major contributions from the central metal d orbital. Thus, cobalt porphyrin derivatives usually have higher IP values than the corresponding iron porphyrin derivatives. For phthalocyanine systems, the central metal has no significant effect on IP because the electron is extracted from an orbital, which is mainly a ring orbital. Therefore, the difference in ionization potential between cobalt and iron phthalocyanine systems is usually small (< 0.13 eV) for the reported systems. Cobalt porphyrin derivatives have high ionization potentials that make them better catalysts than the corresponding iron derivatives, whereas for phthalocyanine systems, iron derivatives have large ionization potential and better dioxygen binding ability, which make them good catalysts.

Theoretical modeling of oxygen reduction by cobalt hydroxide and oxyhydroxide was reported by Wass et al. [99]. The reduction reaction was initiated by adding an electron with O_2 present at the Co(II) site. This produces a superoxide ligand, which upon protonation is able to undergo further reduction to HO_2^- as Co(III) is formed at the site. Adding a second electron leads to detachment of HO_2^- as Co(II) is restored (Figure 5.18).

Four-electron reduction of O_2 over multiple Cu(I) centers was tested through theoretical study [100] (see Figure 5.19). In this study, Cu and Cu+ centers, with and without N-bearing ligands and ending with one, two and three H_2N-Cu-imidazole Cu^I centers, were investigated. Through calculation of bond strength and reverse potential, the study demonstrated that the reduction potential for OH bonded to the model is higher than that calculated for Pt; H_2O bonds weakly to the Cu(I) centers and does not poison them. And, loosely coordinated Cu(I) centers present opportunities for four-electron oxygen reduction at low overpotential.
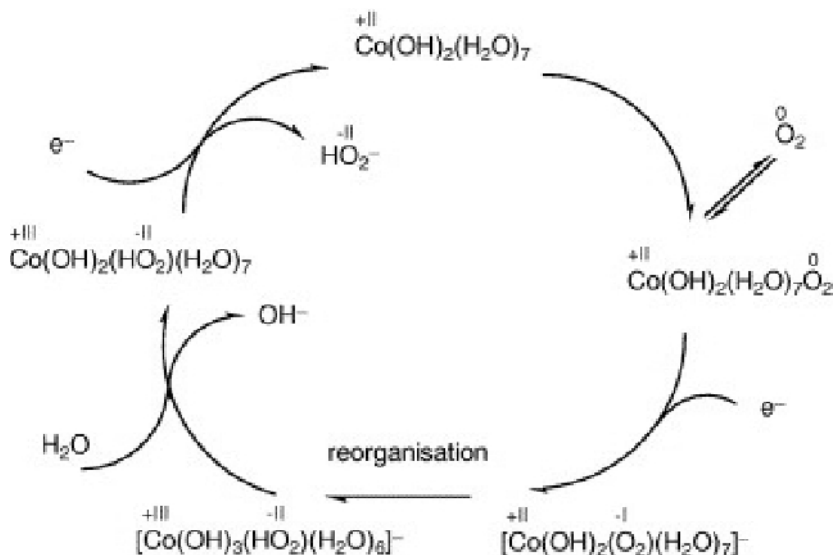
Figure 5.18. Proposed redox cycle for the electrocatalytic reduction of oxygen to hydrogen peroxide on Co(II) hydroxide [99]. (Reprinted from Journal of Electroanalytical Chemistry, 599(2), Wass Tobias Johnsson JR, Panas I, Asbjornsson J, Ahlberg E. Quantum chemical modelling of oxygen reduction on cobalt hydroxide and oxyhydroxide, 295–312, ©2007 with permission from Elsevier.)
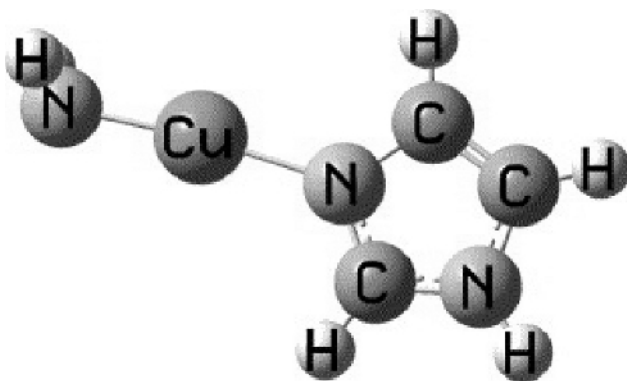
Figure 5.19. Structure of the H_2N–Cu–imidazole model for the Cu^I sites in laccases [100]. (Reprinted from Journal of Electroanalytical Chemistry, 607(1–2), Vayner E, Schweiger H, Anderson AB. Four-electron reduction of O_2 over multiple CUI centers: quantum theory, 90–100, ©2007 with permission from Elsevier.)

In summary, for non-Pt catalysts, elucidating the active site structure is a challenge. Theoretical modeling has supplied valuable structural information, facilitating our basic understanding of active site structures. Theoretical modeling is a viable tool in screening potential catalysts and in the novel design of new catalysts.

5.7 Summary

The application of first principles methods to the study of electrocatalysis in fuel cells has gained significant momentum in recent years. Browse any issue of a journal with theoretical electrochemistry content and you will notice a few theoretical study articles. Theoretical modeling in electrochemistry has certainly reached the stage at which it "can begin to complement experimental methods, and provide insight into the atomic scale features that control the chemistry at the aqueous/metal interface" [101].

Among the computational approaches, study of adsorption abilities (reactant, intermediate, and product) is the most widely employed approach in understanding catalyst activity and the design of electrocatalysts. The interaction between catalyst and reaction species governs the reaction, and adsorption energy is relatively easier to compute than reaction energy and activation energy, especially the latter, which is computationally expensive.

Theoretical procedures have provided quantitative predictions about elementary processes and offered invaluable insights for our basic understanding of the oxygen reduction reaction mechanism, especially our understanding of catalyst active site structures, elementary reaction kinetics, thermodynamics, and energetics. These fundamental advances have been employed to fine-tune catalyst activity and design new catalysts. Efforts have been made to correlate catalyst structures with catalyst activity. These structural properties include adsorption energy, activation energy, *d*-band center, and ionization energy. The identification of structural properties that are responsible for catalyst activity is crucial for the rational design of catalysts and the further development of virtual high throughput catalyst screening, which has recently been successfully employed in HER catalyst screening [102]. Theoretical studies of catalyst stability, another very important issue in catalyst design, are emerging as well. Study of the effect of catalyst support is limited and more research in this direction is needed. Theoretical computation has demonstrated a unique capability in providing a basic understanding of the reaction mechanism. No doubt, the endeavors of theoretical modeling combined with experimental study will accelerate the development of new catalysts.

References

1. Bockris JOM, Khan SUM. Phenomenological electrode kinetics. In: Surface electrochemistry: a molecular level approach. New York: Plenum Press, 1993; 211–406.
2. Nazmutdinov RR. Quantum-chemical description of charge transfer processes at the metal/solution interface: yesterday, today, and tomorrow. Russian Journal of Electrochemistry 2002;8(2):111–22.
3. Koper MTM. Ab initio quantum-chemical calculations in electrochemistry. In: Vayenas CG, Conway BE, White RE, editors. Modern aspects of electrochemistry, No. 36. New York: Springer, 2003; 51–130.
4. Schmickler W. Recent progress in theoretical electrochemistry. Annu Report Prog Chem Sect C 1999;95:117–61.

5.   Khan SUM. Quantum-mechanical formalisms of electron transfer reactions at electrode-electrolyte interfaces. In: Murphy OJ, Srinivasan S, Conway BE, editors. Electrochemistry in Transition. New York: Plenum; 1992.

6.   Anderson AB. Quantum chemical modeling of electrocatalytic reactions, including potential dependence: beginning stages. In: Wieckowski A, editor. Interfacial electrochemistry: theory, experiments, and applications. New York: Marcel Dekker, 1999; 83–96.

7.   Koper MTM. Combining experiment and theory for understanding electrocatalysis. J Electroanal Chem 2005;574(2):375–86.

8.   Nazmutdinov RR, Shapnik MS. Contemporary quantum chemical modelling of electrified interfaces. Electrochim Acta 1996;41(14):2253–65.

9.   Groß A. Theoretical surface science: a microscopic perspective. Berlin: Springer; 2003.

10. Whitten JL, Yang H. Theory of chemisorption and reactions on metal surface. Surf Sci Rep 1996;24:55–124.

11. Car R, Parrinello M. Unified approach for molecular dynamics and density-functional theory. Phys Rev Lett 1985;55(22):2471–4.

12. Groß A. Reactions at surface studied by ab initio dynamics calculations. Surf Sci Rep 1998;32:291–340.

13. Tse JS. Ab initio molecular dynamics with density functional theory. Ann Rev Phys Chem 2002;53(1):249–90.

14. Hohenberg P, Kohn W. Inhomogeneous electron gas. Phys Rev 1964;136:B864.

15. Kohn W, Sham L. Self-consistent equations including exchange and correlation effects. Phys Rev 1965;140:A1133.

16. Becke AD. Density-functional exchange-energy approximation with correct asymptotic behavior. Phys Rev A 1988;38:3098.

17. Lee C, Yang W, Parr R. Development of the Colle-Salvetti correlation-energy formula into a functional of the electron density. Phys Rev B 1988;37:785.

18. Perdew JP, Chevary JA, Vosko SH, Jackson KA, Pederson MR, Singh DJ, et al. Atoms, molecules, solids, and surfaces: applications of the generalized gradient approximation for exchange and correlation. Phys Rev B 1992;46:6671.

19. Perdew JP, Wang Y. Accurate and simple analytic representation of the electron-gas correlation energy. Phys Rev B 1992;45:13244.

20. Perdew JP. Density-functional approximation for the correlation energy of the inhomogeneous electron gas. Phys Rev B 1986;33:8822.

21. Becke AD. Density-functional thermochemistry. III. The role of exact exchange. Journal of Chemical Physics 1993;98:5648.

22. Perdew JP, Burke K, Ernzerhof M. Generalized gradient approximation made simple. Phys Rev Lett 1996;77(18):3865.

23. Adzic R. Recent advances in the kinetics of oxygen reduction. In: Lipkowski J, Ross PN, editors. Electrocatalysis. New York: Wiley-VCH, 1998; 197–242.

24. Gattrell M, MacDougall B. Reaction mechanism of the O_2 reduction/evolution reaction. In: Vielstich W, Gasteiger HA, Lamm A, editors. Handbook of fuel cells – fundamentals, technology and applications; volume 2: electrocatalysis. John Wiley & Sons, 2003; 443–63.

25. Ross PN Jr. Oxygen reduction reaction on smooth single crystal electrodes. In: Vielstich W, Gasteiger HA, Lamm A, editors. Handbook of fuel cells – fundamentals, technology and applications, volume 2: electrocatalysis. John Wiley & Sons, 2003; 465–80.

26. Sepa DB, Vojnovic MV, Damjanovic A. Reaction intermediates as a controlling factor in the kinetics and mechanism of oxygen reduction at platinum electrodes. Electrochim Acta 1981;26(6):781–93.

27. Zhang J, Tang Y, Song C, Zhang J, Wang H. Pem fuel cell open circuit voltage (OCV) in the temperature range of 23 °C to 120 °C. J Power Sources 2006;163(1):532–7.

28. Damjanovic A, Brusic V. Electrode kinetics of oxygen reduction on oxide-free platinum electrodes. Electrochim Acta 1967;12(6):615–28.

29. Yeager E, Razaq M, Gervasio D, Razaq A, Tryk D, Scheerson D, et al., editors. Proceedings of the workshop on structural effects in electrocatalysis and oxygen electrochemistry. Vol.92. New Jersey: The Electrochemical Society; 1992.

30. Sabatier P. Hydrogenation and dehydrogenation by catalysis. Ber Dtsch Chem Ges 1911;44:1984–2001.

31. Yeager E. Dioxygen electrocatalysis: mechanisms in relation to catalyst structure. J Mol Catal 1986;38(1–2):5–25.

32. Groß A. Reactions at surfaces studied by ab initio dynamics calculations. Surf Sci Rep 1998;32:291–340.

33. Hammer B, Nørskov JK. Theoretical surface science and catalysis–calculations and concepts. Advances in Catalysis 2000; 45:71–129.

34. Mavrikakis M, Nørskov JK. Catalysis from first principles. AIChE Symposium Series. New York: American Institute of Chemical Engineers; 2001.

35. Luntz AC, Grimblot J, Fowler DE. Sequential precursors in dissociative chemisorption: O_2 on Pt(111). Phys Rev B 1989;39(17):12903.

36. Outka DA, Stöhr J, Jark W, Stevens P, Solomon J, Madix RJ. Orientation and bond length of molecular oxygen on Ag(110) and Pt(111): a near-edge X-ray-absorption fine-structure study. Phys Rev B 1987;35(8):4119.

37. Steininger H, Lehwald S, Ibach H. Adsorption of oxygen on Pt(111). Surf Sci 1982;123(1):1–17.

38. Eichler A, Hafner J. Molecular precursors in the dissociative adsorption of O_2 on Pt(111). Phys Rev Lett 1997;79(22):4481.

39. Sljivancanin Z, Hammer B. Oxygen dissociation at close-packed Pt terraces, Pt steps, and Ag-covered Pt steps studied with density functional theory. Surf Sci 2002;515(1):235–44.

40. Xu Y, Mavrikakis M. Adsorption and dissociation of O_2 on Ir(111). J Chem Phys 2002;116(24):10846–53.

41. Eichler A, Mittendorfer F, Hafner J. Precursor-mediated adsorption of oxygen on the (111) surfaces of platinum-group metals. Phys Rev B 2000;62(7):4744.

42. Xu Y, Mavrikakis M. Adsorption and dissociation of O_2 on gold surfaces: effect of steps and strain. J Phys Chem B 2003;107(35):9298–307.

43. Vassilev P, Koper MTM. Electrochemical reduction of oxygen on gold surfaces: a density functional theory study of intermediates and reaction paths. J Phys Chem C 2007;111(6):2607–13.

44. Panchenko A, Koper MTM, Shubina TE, Mitchell SJ, Roduner E. Ab initio calculations of intermediates of oxygen reduction on low-index platinum surfaces. J Electrochem Soc 2004;151(12):A2016–27.

45. Hyman MP, Medlin JW. Theoretical study of the adsorption and dissociation of oxygen on Pt(111) in the presence of homogeneous electric fields. J Phys Chem B 2005;109(13):6304–10.

46. Wang Y, Balbuena PB. Potential energy surface profile of the oxygen reduction reaction on a Pt cluster: adsorption and decomposition of OOH and H_2O_2. J Chem Theory Comput 2005;1(5):935–43.

47. Toda T, Igarashi H, Uchida H, Watanabe M. Enhancement of the electroreduction of oxygen on Pt alloys with Fe, Ni, and Co. J Electrochem Soc 1999;146(10):3750–6.

48. Ruban AV, Skriver HL, Nørskov JK. Surface segregation energies in transition-metal alloys. Phys Rev B 1999;59(24):15990.

49. Ruban A, Hammer B, Stoltze P, Skriver HL, Nørskov JK. Surface electronic structure and reactivity of transition and noble metals. J Mol Catal A: Chemical 1997;115(3):421–9.

50. Kitchin JR, Nørskov JK, Barteau MA, Chen JG. Modification of the surface electronic and chemical properties of Pt(111) by subsurface 3d transition metals. J Chem Phys 2004;120(21):10240–6.

51. Xu Y, Ruban AV, Mavrikakis M. Adsorption and dissociation of O_2 on Pt-Co and Pt-Fe alloys. J Am Chem Soc 2004;126:4717–25.

52. Balbuena PB, Altomare D, Agapito L, Seminario JM. Theoretical analysis of oxygen adsorption on Pt-based clusters alloyed with Co, Ni, or Cr embedded in a Pt matrix. J Phys Chem B 2003;107(49):13671–80.

53. Zhang J, Vukmirovic MB, Xu Y, Mavrikakis M, Adzic RR. Controlling the catalytic activity of platinum-monolayer electrocatalysts for oxygen reduction with different substrates. Angew Chem Int Ed 2005;44(14):2132–5.

54. Zhang J, Vukmirovic MB, Sasaki K, Nilekar AU, Mavrikakis M, Adzic RR. Mixed-metal Pt monolayer electrocatalysts for enhanced oxygen reduction kinetics. J Am Chem Soc 2005;127(36):12480–1.

55. Stamenkovic V, Mun BS, Mayrhofer KJJ, Ross PN Jr, Markovic NM, Rossmeisl J, et al. Changing the activity of electrocatalysts for oxygen reduction by tuning the surface electronic structure. Angew Chem Int Ed 2006;45(18):2897–901.

56. Shao MH, Huang T, Liu P, Zhang J, Sasaki K, Vukmirovic MB, et al. Palladium monolayer and palladium alloy electrocatalysts for oxygen reduction. Langmuir 2006;22(25):10409–15.

57. Li H, Sun G, Li N, Sun S, Su D, Xin Q. Design and preparation of highly active Pt-Pd/C catalyst for the oxygen reduction reaction. J Phys Chem C 2007;111(15):5605–17.

58. Suo Y, Zhuang L, Lu J. First-principles considerations in the design of Pd-alloy catalysts for oxygen reduction. Angew Chem Int Ed 2007;46(16):2862–4.

59. Stamenkovic VR, Mun BS, Arenz M, Mayrhofer KJJ, Lucas CA, Wang G, et al. Trends in electrocatalysis on extended and nanoscale Pt-bimetallic alloy surfaces. Nat Mater 2007 ;6(3):241–7.

60. Lischka M, Mosch C, Groß A. Tuning catalytic properties of bimetallic surfaces: oxygen adsorption on pseudomorphic Pt/Ru overlayers. Electrochim Acta 2007;52(6):2219–28.

61. Roques J, Anderson AB. Electrode potential-dependent stages in OH_{ads} formation on the Pt_3Cr alloy (111) surface. J Electrochem Soc 2004;151(11):E340–7.

62. Roques J, Anderson AB. Cobalt concentration effect in $Pt_{1-x}Co_x$ on the reversible potential for forming OH_{ads} from H_2O_{ads} in acid solution. Surf Sci 2005;581(2–3):105–17.

63. Roques J, Anderson AB, Murthi VS, Mukerjee S. Potential shift for OH(ads) formation on the Pt skin on $Pt_3Co(111)$ electrodes in acid. J Electrochem Soc 2005;152(6):E193–E199.

64. Vukmirovic MB, Zhang J, Sasaki K, Nilekar AU, Uribe F, Mavrikakis M, et al. Platinum monolayer electrocatalysts for oxygen reduction. Electrochim Acta 2007;52(6):2257–63.

65. Hyman MP, Medlin JW. Effects of electronic structure modifications on the adsorption of oxygen reduction reaction intermediates on model Pt(111)-alloy surfaces. J Phys Chem C 2007;111(45):17052–60.

66. Greeley J, Nørskov JK. A general scheme for the estimation of oxygen binding energies on binary transition metal surface alloys. Surf Sci 2005;592(1–3):104–11.

67. Wei ZD, Yin F, Li LL, Wei XW, Liu XA. Study of Pt/C and Pt-Fe/C catalysts for oxygen reduction in the light of quantum chemistry. J Electroanal Chem 2003;541:185–91.

68. Skulason E, Karlberg GS, Rossmeisl J, Bligaard T, Greeley J, Jonsson H, et al. Density functional theory calculations for the hydrogen evolution reaction in an electrochemical double layer on the Pt(111) electrode. Phys Chem Chem Phys 2007;9(25):3241–50.

69. Gurney RW. The quantum mechanics of electrolysis. Proc Roy Soc 1931;A:137–54.

70. Marcus RA. Electron transfer reactions in chemistry theory and experiment. J Electroanal Chem 1997;438(1–2):251–9.

71. Koper MTM, Voth GA. A theory for adiabatic bond breaking electron transfer reactions at metal electrodes. Chem Phys Lett 1998;282(1):100–6.

72. Ignaczak A, Schmickler W. Theoretical study of a non-adiabatic dissociative electron transfer reaction. J Electroanal Chem 2003;554–5:201–9.

73. Hammes-Schiffer S, Iordanova N. Theoretical studies of proton-coupled electron transfer reactions. Biochim Biophys Acta, Bioenerg 2004;1655:29–36.

74. Cukier RI. Theory and simulation of proton-coupled electron transfer, hydrogen-atom transfer, and proton translocation in proteins. Biochim Biophys Acta, Bioenerg 2004;1655:37–44.

75. Anderson PW. Localized magnetic states in metals. Phys Rev 1961;124(1):41.

76. Newns DM. Self-consistent model of hydrogen chemisorption. Phys Rev 1969;178(3):1123.

77. Anderson AB, Albu TV. Catalytic effect of platinum on oxygen reduction an ab initio model including electrode potential dependence. J Electrochem Soc 2000;147(11):4229–38.

78. Taylor CD, Kelly RG, Neurock M. A first-principles analysis of the chemisorption of hydroxide on copper under electrochemical conditions: a probe of the electronic interactions that control chemisorption at the electrochemical interface. J Electroanal Chem 2007;607(1–2):167–74.

79. Bockris JO, Abdu R. A theoretical study of the electrochemical reduction of oxygen. J Electroanal Chem 1998;448(2):189–204.

80. Anderson AB, Albu TV. Ab initio approach to calculating activation energies as functions of electrode potential trial application to four-electron reduction of oxygen. Electrochem Comm 1999;1(6):203–6.

81. Anderson AB, Albu TV. Ab initio determination of reversible potentials and activation energies for outer-sphere oxygen reduction to water and the reverse oxidation reaction. J Am Chem Soc 1999;121(50):11855–63.

82. Anderson AB, Cai Y, Sidik RA, Kang DB. Advancements in the local reaction center electron transfer theory and the transition state structure in the first step of oxygen reduction over platinum. J Electroanal Chem 2005;580(1):17–22.

83. Sidik RA, Anderson AB. Density functional theory study of O_2 electroreduction when bonded to a Pt dual site. J Electroanal Chem 2002;528(1–2):69–76.

84. Anderson AB, Roques J, Mukerjee S, Murthi VS, Markovic NM, Stamenkovic V. Activation energies for oxygen reduction on platinum alloys: theory and experiment. J Phys Chem B 2005;109(3):1198–203.

85. Nørskov JK, Rossmeisl J, Logadottir A, Lindqvist L, Kitchin JR, Bligaard T, et al. Origin of the overpotential for oxygen reduction at a fuel-cell cathode. J Phys Chem B 2004;108(46):17886–92.

86. Wang Y, Balbuena PB. Roles of proton and electric field in the electroreduction of O_2 on Pt(111) surfaces: results of an ab-initio molecular dynamics study. J Phys Chem B 2004;108(14):4376–84.

87. Jinnouchi R. New insight into microscale transport phenomena in PEFC by quantum md. Nanoscale and Microscale Thermophysical Engineering 2003;7(1):15–31.

88. Hyman MP, Medlin JW. Mechanistic study of the electrochemical oxygen reduction reaction on Pt(111) using density functional theory. J Phys Chem B 2006;110(31):15338–44.

89. Karlberg GS, Rossmeisl J, Norskov JK. Estimations of electric field effects on the oxygen reduction reaction based on the density functional theory. Phys Chem Chem Phys 2007;9(37):5158–61.

90. Gu Z, Balbuena PB. Dissolution of oxygen reduction electrocatalysts in an acidic environment: density functional theory study. J Phys Chem A 2006;110(32):9783–7.

91. Calvo SR, Balbuena PB. Density functional theory analysis of reactivity of Pt_xPd_y alloy clusters. Surf Sci 2007;601(1):165–71.

92. Anderson AB, Sidik RA. Oxygen electroreduction on Fe^{ii} and Fe^{iii} coordinated to N_4 chelates. Reversible potentials for the intermediate steps from quantum theory. J Phys Chem B 2004;108(16):5031–5.

93. Sidik RA, Anderson AB. Co_9S_8 as a catalyst for electroreduction of O_2: quantum chemistry predictions. J Phys Chem B 2006;110(2):936–41.

94. Sidik RA, Anderson AB, Subramanian NP, Kumaraguru SP, Popov BN. O_2 reduction on graphite and nitrogen-doped graphite: experiment and theory. J Phys Chem B 2006;110(4):1787–93.

95. Jain M, Chou S, Siedle A. In search for structure of active site in iron-based oxygen reduction electrocatalysts. J Phys Chem B 2006;110(9):4179–85.

96. Vayner E, Anderson AB. Theoretical predictions concerning oxygen reduction on nitrided graphite edges and a cobalt center bonded to them. J Phys Chem C 2007;111(26):9330–6.

97. Tsuda M, Diño WA, Nakanishi H, Kasai H. Hemoglobin components as cathode electrode catalyst in polymer electrolyte fuel cells. e-Journal of Surface Science and Nanotechnology 2004;2:226–9.

98. Shi Z, Zhang J. Density functional theory study of transitional metal macrocyclic complexes' dioxygen-binding abilities and their catalytic activities toward oxygen reduction reaction. J Phys Chem C 2007;111(19):7084–90.

99. Wass Tobias Johnsson JR, Panas I, Asbjornsson J, Ahlberg E. Quantum chemical modelling of oxygen reduction on cobalt hydroxide and oxyhydroxide. J Electroanal Chem 2007;599(2):295–312.

100. Vayner E, Schweiger H, Anderson AB. Four-electron reduction of O_2 over multiple CUI centers: quantum theory. J Electroanal Chem 2007;607(1–2):90–100.

101. Taylor CD, Wasileski SA, Filhol JS, Neurock M. First principles reaction modeling of the electrochemical interface: consideration and calculation of a tunable surface potential from atomic and electronic structure. Phys Rev B (Condensed Matter and Materials Physics) 2006;73(16):165402–16.

102. Greeley J, Jaramillo TF, Bonde J, Chorkendorff I, Nørskov JK. Computational high-throughput screening of electrocatalytic materials for hydrogen evolution. Nat Mater 2006;5(11):909–13.

6

Catalyst Contamination in PEM Fuel Cells

Hui Li, Chaojie Song, Jianlu Zhang and Jiujun Zhang

6.1 Introduction

The effects of impurities on fuel cells, often referred to as fuel cell contamination, is one of the most important issues in fuel cell operation and applications. Contamination is closely associated with proton exchange membrane fuel cell (PEMFC) durability and stability, both of which are important factors in the development and commercialization of PEMFC technology. Studies have identified that the membrane electrode assembly (MEA), the heart of the PEMFC, is the fuel cell component most affected by contamination. Impurities in the air and fuel streams damage the MEA by affecting both the anode and cathode catalyst layers (CLs), the gas diffusion layers (GDLs), as well as the proton exchange membrane (PEM), causing MEA performance degradation or even fuel cell failure. In general, PEMFC contamination effects can be categorized into three major types: (1) kinetic losses caused by the poisoning of both anode and cathode catalyst sites or a decrease in the catalyst activity; (2) ohmic losses due to an increase in the resistance of membrane and ionomer, caused by alteration of the proton transportation path; and (3) mass transfer losses due to changes in structure and in the ratio between the hydrophobicity and hydrophilicity of CLs, GDLs, and the PEM. Among those effects, the most significant is the kinetic effect of the anode and cathode electrocatalysts. This chapter presents PEMFC contamination with a focus on the anode and cathode catalyst layers. Catalyst contamination mechanisms, experimental results, modeling, as well as mitigation strategies are also covered in detail. For further information, such as contamination effects on other parts of PEMFCs, the reader is referred to a recent review paper [1].

6.2 Anode Catalyst Layer Contamination

The dominant type of PEMFC is the hydrogen/oxygen fuel cell, in which the anode is fed by hydrogen and the cathode is fed by oxygen or air. In this section, we will focus our attention on anode catalyst contamination caused by impurities in the hydrogen stream.

Due to the high cost and the difficulties associated with hydrogen production, infrastructure, as well as onboard storage, it is not practical to run PEM fuel cells with pure hydrogen for either mobile or stationary applications. Therefore, alternative carbon-based fuels such as natural gas, methanol, gasoline, and diesel, are attractive and practical options to produce hydrogen onboard as a direct fuel for PEMFCs through reformation processes [2–4]. These reformation processes produce a hydrogen-rich reformate gas comprising some 40–75% hydrogen, 15–25% CO_2, and 1–2% CO [2–7]. In practice, although the CO is always removed through a series of clean-up processes including the water-gas shift reaction, selective oxidation, or a membrane reactor, a trace amount of CO is often present, which can have an unacceptable negative effect on the performance of a PEMFC. In addition to CO_x (CO_2 and CO), hydrogen produced by the reformation process also contains impurities such as sulfur compounds, including H_2S and sulfur organics.

The inevitable existence of hydrogen fuel impurities is a severe hindrance upon PEMFC performance, prompting intense research activities into the investigation of anode contamination. In fact, the research on contamination of anode catalysts has been more active than that on the contamination of cathode catalysts due to the catastrophic poisoning of the platinum anode by CO at a level of even 50 ppm, or more severely by H_2S at a level of just 20 ppb. In particular, CO poisoning has been and still is one of the most extensively studied PEMFC research topics, due to the high incidence of H_2 production through the reformation processes; more than 130 publications on this subject have been issued since the 1980s.

CO strongly adsorbs on the Pt catalyst surface, competing for the available active Pt sites of hydrogen adsorption and electrooxidation. Experimental tests with PEMFCs indicate that more than 10 ppm CO in the fuel stream can cause a significant cell performance loss, especially during low-temperature operation, i.e., < 100 °C. Several strategies have been developed to mitigate CO poisoning, such as using CO-tolerant PtRu alloy catalyst, introducing a small amount of oxidant (for example, air or oxygen) into the fuel stream, and operating the PEMFC at elevated temperatures (> 120 °C) [1]. Because of the huge influence and prevalence of CO poisoning, a separate chapter in this book is assigned specifically to the effect of CO on PEMFC catalysts. Therefore, we exclude CO contamination from this chapter and only discuss anode contamination caused by impurities other than CO, namely CO_2 and H_2S.

6.2.1 Impacts of Carbon Dioxide

CO_2, as a by-product in the production of hydrogen-rich reformate gas, exists at a concentration level of more than 25% in the produced gas [8]. Experimental results suggest that CO_2 has significant poisoning effects on fuel cell performance, especially at higher current densities. As shown in Figure 6.1, for a PEMFC catalyzed by pure Pt at the anode, with a load of 0.35 mg Pt cm^{-2} and with 20% CO_2 content in the fuel stream, a performance loss of about 47% can be observed at 0.6 A cm^{-2} [8]. This CO_2 poisoning effect is due to the *in situ* production of CO from CO_2 on the platinum surface through either the reverse water-gas shift reaction (Equation 6.1) or the electrochemical reduction of CO_2 (Equation 6.2).

The subsequent adsorption of produced CO on the active platinum sites could block the reaction sites for hydrogen oxidation, causing a performance drop. According to thermodynamic calculations [9], in a common reformate gas that contains about 25% CO_2 approximately 20–100 ppm CO in equilibrium concentrations can be produced simply from the reversed water-gas shift reaction. Even at a low CO_2 level of 1%, enough CO can be produced to poison more than 50% of the Pt surface sites at normal PEMFC operating conditions, resulting in significant cell voltage losses [10, 11]. As seen in Reaction 6.1, since CO_2 can react with the pre-adsorbed hydrogen, any factor that affects the pre-adsorption of hydrogen could influence the reaction between CO_2 and hydrogen, thus affecting the CO_2 poisoning. For example, CO_2 poisoning is sensitive to the nature of the anode catalyst materials [12], the operational temperature of the PEMFC, as well as the water content in the fuel stream [9]. In addition, the presence of both CO and CO_2 has a synergetic poisoning effect on cell performance. For instance, for a PEMFC catalyzed with a PtRu anode catalyst (1 mg cm^{-2}) at 80 °C, 100 ppm CO in the fuel stream could cause a cell performance loss of about 200 mV at a current density of 170 mA cm^{-2} as compared with a pure hydrogen fuel stream. When 25% CO_2 was added into this 100 ppm CO-containing fuel, a further performance drop of about 200 mV was observed at the same current density [13].

$$CO_2 + 2Pt - H_{ads} \rightarrow Pt - CO_{ads} + H_2O + Pt \qquad (6.1)$$
(reverse water-gas shift reaction)

$$2Pt + CO_2 + H^+ + e^- \rightarrow Pt - CO_{ads} + Pt - OH_{ads} \qquad (6.2)$$
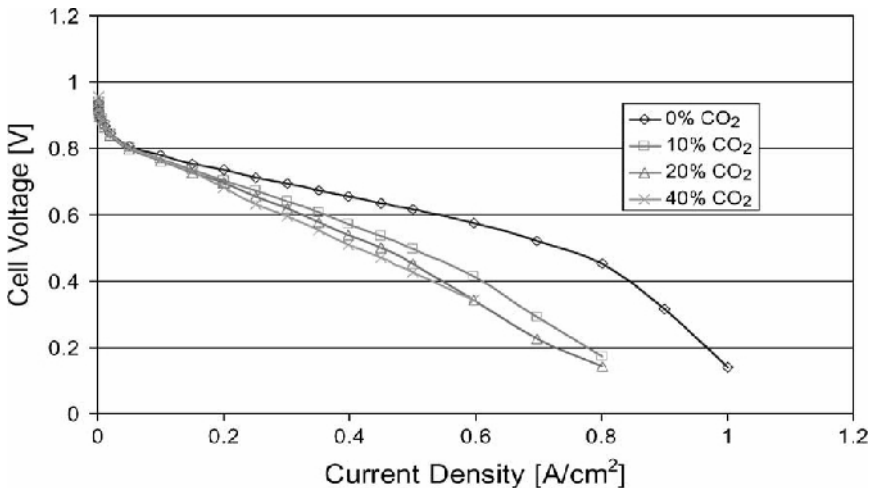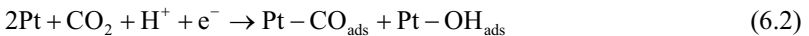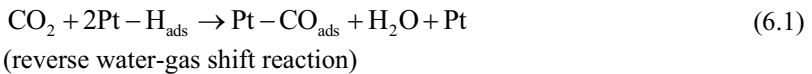
Figure 6.1. Effect of CO_2 concentration on PEM fuel cell performance. Catalyst loadings for both anode and cathode are 0.35 mg Pt cm^{-2}; Nafion 105 membrane; fuel cell temperature $T_{cell} = 60$ °C and pressure $P = 1.5$ bar [9]. (Reprinted from Journal of Power Sources, 110(1), de Bruijn F. A., Papageorgopoulos D. C., Sitters E. F. and Janssen G. J. M., The influence of carbon dioxide on PEM fuel cell anodes, 117–24, ©2002, with permission from Elsevier.)

6.2.2 Impacts of Hydrogen Sulfide (H₂S)

Hydrogen sulfide, as a fuel impurity, causes much greater PEMFC anode degradation than CO, mainly through the poisoning of the catalyst. For example, as shown in Figure 6.2, at 0.6 A cm^{-2} and 60 °C, 30 ppm H₂S causes a cell voltage drop of about 130 mV (equivalent to 19%) within one hour of operation, compared with a cell voltage drop of about 30 mV (equivalent to 4.5%) caused by 30 ppm of CO. When the H₂S concentration is increased from 30 ppm to 50 ppm, the cell voltage drop within one hour can be increased to 310 mV. Obviously, H₂S poisoning is a strong function of concentration and exposure time [14].
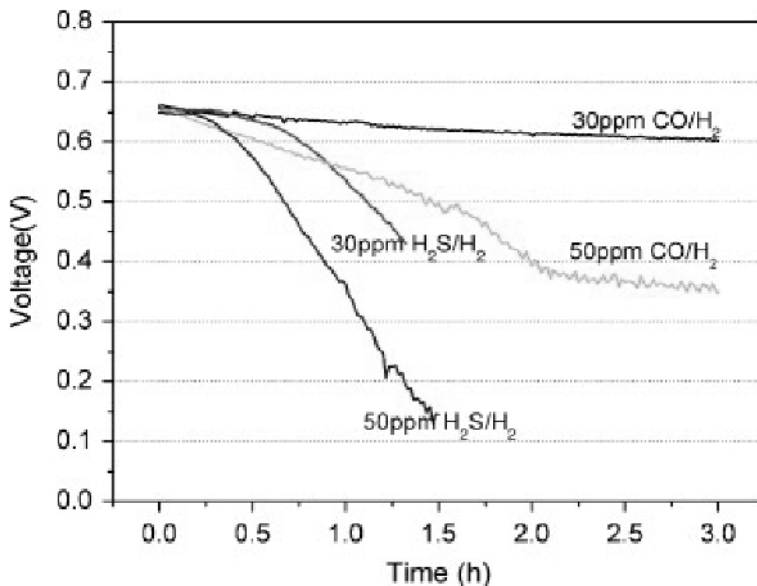
Figure 6.2. Comparison of the effects of CO and H₂S on PEMFC performance. Both anode and cathode catalyst loadings: 0.4 mg cm^{-2} Pt/C; Nafion 212 membrane; cell temperature: 60 °C; current density: 0.6 A cm^{-2} [14]. (Reprinted from International Journal of Hydrogen Energy, 32, Shi W, Yi B, Hou M, Shao Z, The effect of H₂S and CO mixtures on PEMFC performance, 4412–17, ©2007 with permission from Elsevier.)

Similar to CO, H₂S also strongly adsorbs on the Pt catalyst, competing for the active sites with hydrogen adsorption and hydrogen oxidation. In aqueous solutions containing H₂S, the adsorption of H₂S, HS⁻, and H⁺ occur through the following reactions [15, 16]:

$$Pt + H_2S \rightarrow Pt - H_2S_{ads} \tag{6.3}$$

$$Pt + HS^- \rightarrow Pt - HS^-_{ads} \tag{6.4}$$

$$Pt + H^+ \rightarrow Pt^+ - H_{ads} \tag{6.5}$$
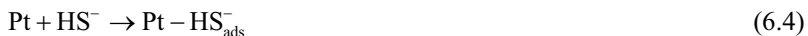
where Pt^+ represents an equivalent charge on the Pt surface. Reactions 6.4 and 6.5 result in an electrochemical potential, which may cause the following dissociative adsorption:

$$2Pt + H_2S \rightarrow Pt-SH_{ads} + Pt-H_{ads} \qquad (6.6)$$
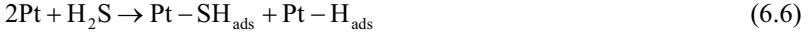
The dissociative potentials of H_2S on Pt are about 0.4 V at 90 °C, 0.5 V at 60 °C, and 0.6 V at 30 °C [17]. Following the dissociative adsorptions, oxidation of the adsorbed SH and H_2S occurs to form platinum sulfide [16]:

$$Pt-SH_n \rightarrow Pt-S + nH^+ + ne^- \quad (n = 1 \text{ or } 2) \qquad (6.7)$$
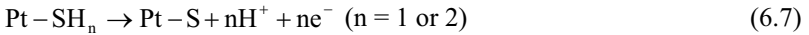
The adsorption rate, coverage, and stability of H_2S species are strongly affected by temperature [18]. It is known that the adsorbed H_2S and SH are highly unstable on Pt, while the adsorbed S and H are the most stable intermediates on Pt [19]. The formation of the sulfide film on the platinum surface not only causes poisoning of the catalyst surface but also makes it impossible for the fuel cell to recover from contamination [17, 20, 21].
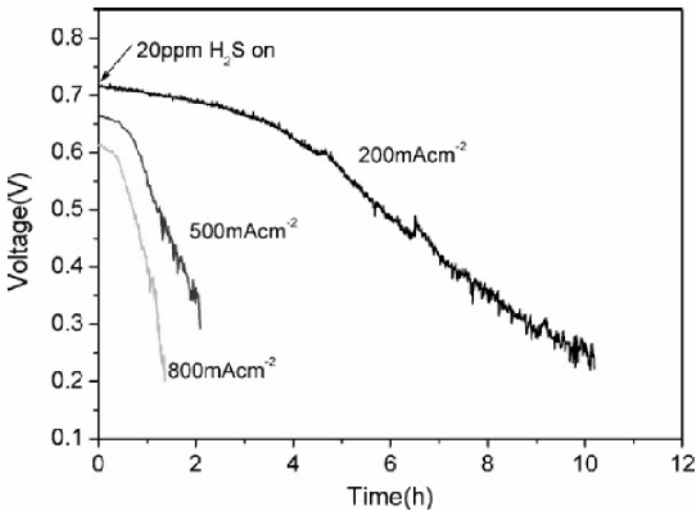
Figure 6.3. Effect of current density on performance degradation during exposure to 20 ppm H_2S in the H_2 stream. Anode catalyst loading: 0.3 mg cm^{-2} Pt/C; cathode catalyst loading: 0.5 mg cm^{-2} Pt/C; Nafion 212 membrane; cell temperature: 70 °C [17]. (Reprinted from Journal of Power Sources, 164(1), Shi Weiyu, Yi Baolian, Hou Ming, Jing Fenning, Yu Hongmei and Ming Pingwen, The influence of hydrogen sulfide on proton exchange membrane fuel cell anodes, 272–7, ©2007, with permission from Elsevier.)

Studies show that the severity of the H_2S poisoning depends not only on the concentration of H_2S, as mentioned above, but also on current density and cell temperature. However, the H_2S poisoning does not seem to be noticeably affected

by anode humidification [17]. Figure 6.3 shows the effect of current density on cell performance. After exposing the anode to 20 ppm H_2S for 1 hour, the cell performance decreases by 2% at 200 mA cm^{-2} as compared to 17% at 500 mA cm^{-2} and 35% at 800 mA cm^{-2}. Figure 6.4 shows the effect of temperature on cell performance with 10 ppm and 20 ppm H_2S present in the fuel stream, respectively. After the anode is exposed to 10 ppm H_2S for 3 hours, the cell performance degrades by 45% at 35 °C, 32% at 60 °C, but by only 25% at 90 °C, indicating that the H_2S poisoning rate decreases with increasing temperature.

(a)

(b)
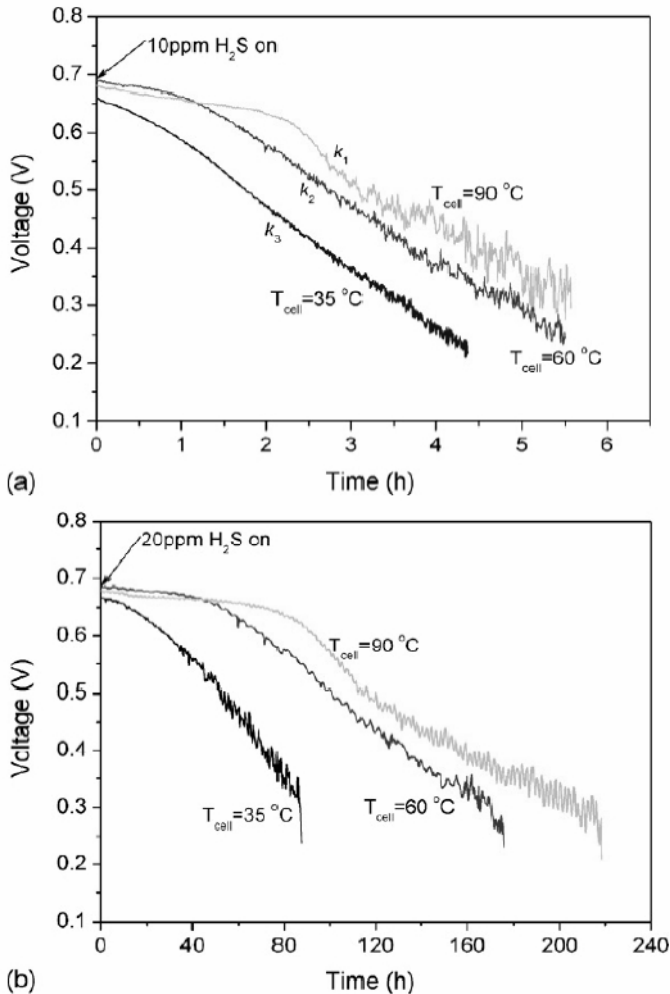
Figure 6.4. Effect of temperature on cell performance deterioration during exposure to (a) 10 ppm and (b) 20 ppm H_2S/H_2 at 0.5 A cm^{-2} [17]. (Reprinted from Journal of Power Sources, 164(1), Shi Weiyu, Yi Baolian, Hou Ming, Jing Fenning, Yu Hongmei and Ming Pingwen, The influence of hydrogen sulfide on proton exchange membrane fuel cell anodes, 272–7, ©2007, with permission from Elsevier.)

6.2.3 Impacts of Ammonium (NH₃)

Ammonium (NH_3) is present in the hydrogen-rich fuel stream, either due to the use of NH_3 as the hydrogen carrier [22], or because the reforming process involves homogeneous pre-combustion with air [23], or because the fuel itself contains nitrogen-containing species [24]. NH_3 in the fuel stream of a PEMFC, even at the level of a few ppm, can cause significant cell performance loss [25]. It has been identified that the presence of NH_3 in a PEMFC system can degrade cell performance mainly by increasing membrane conductivity through the NH_3 reacting with protons in both the bulk membrane and the ionomer in the catalyst layer [25, 26]:

$$NH_3 (gas) \rightarrow NH_3 (membrane) \tag{6.8}$$

$$NH_3 (membrane) + H^+ \rightarrow NH_4^+ \tag{6.9}$$

The effect of NH_3 on the hydrogen oxidation reaction (HOR) has not been fully identified. Uribe et al. [25] reported that NH_3 did not adsorb significantly on Pt surface sites, thus not affecting the HOR. But Halseid et al. [27] observed that the presence of NH_3 shifted the potentials of the hydrogen adsorption process on a Pt surface in aqueous solutions. Clearly, more work is required to understand the effect of NH_3 on the HOR.

6.2.4 Modeling of the Contamination of the PEMFC Anode Catalyst

Modeling of fuel cell contamination serves as an important tool in fundamentally understanding contamination mechanisms, predicting performance degradation and durability, and developing mitigation strategies. Due to the dominance of CO poisoning in PEMFC contamination, most of the reported modelling studies have focused on CO, and mainly on the steady-state CO poisoning effect [28–30]. A general and complete kinetic model for the contamination of the PEMFC anode catalyst has been developed by Zhang et al. [31], and can be used for all impurities present in the fuel streams. In this model, the following reactions are used to describe the surface and electrochemical processes at the anode for a general contaminant, P:

$$Pt + H_2 \underset{k_{1b}}{\overset{k_{1f}}{\Longleftrightarrow}} Pt - H_2 \tag{6.10}$$

$$Pt - H_2 + Pt \underset{k_{2b}}{\overset{k_{2f}}{\Longleftrightarrow}} 2Pt - H \tag{6.11}$$

$$Pt - H \underset{k_{3b} = \exp(-(1-\alpha_3)n_3 F\eta_a/RT)}{\overset{k_{3f} = \exp(\alpha_3 n_3 F\eta_a/RT)}{\Longleftrightarrow}} Pt - P + H^+ + e^- \tag{6.12}$$
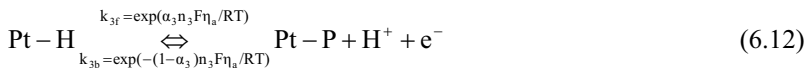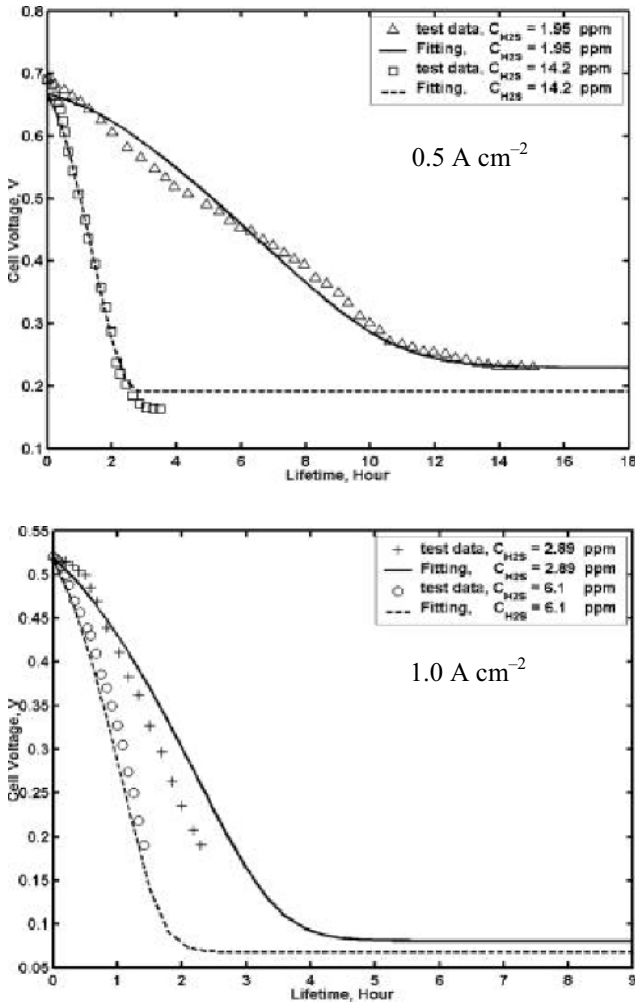
Figure 6.5. Modelled data and experimental results. Top: current density = 0.5 A cm^{-2}; bottom: current density = 1.0 A cm^{-2} [33]. (Reproduced by permission of ECS—The Electrochemical Society, from Shi Z, Song DT, Zhang JJ, Liu ZS, Knights S, Vohra R, et al. Transient analysis of hydrogen sulfide contamination on the performance of a PEM fuel cell.)

$$P + Pt \underset{k_{4b}}{\overset{k_{4f}}{\Longleftrightarrow}} Pt - P \tag{6.13}$$

$$P + Pt - H \underset{k_{5b} = \exp(-(1-\alpha_5)n_5 F\eta_a/RT)}{\overset{k_{5f} = \exp(\alpha_5 n_5 F\eta_a/RT)}{\Longleftrightarrow}} Pt - P + H^+ + e^- \tag{6.14}$$

$$P + Pt - H_2 \underset{k_{6b}}{\overset{k_{6f}}{\Longleftrightarrow}} Pt - P + H_2 \tag{6.15}$$

$$Pt - P + mH_2O \underset{k_{7b}=\exp(-(1-\alpha_7)n_7 F\eta_a/RT)}{\overset{k_{7f}=\exp(\alpha_7 n_7 F\eta_a/RT)}{\Longleftrightarrow}} Pt - P' + qH^+ + qe^- \qquad (6.14)$$

$$Pt - P + mH_2O \underset{k_{8b}=\exp(-(1-\alpha_8)n_8 F\eta_a/RT)}{\overset{k_{8f}=\exp(\alpha_8 n_8 F\eta_a/RT)}{\Longleftrightarrow}} Pt + P' + qH^+ + qe^- \qquad (6.16)$$
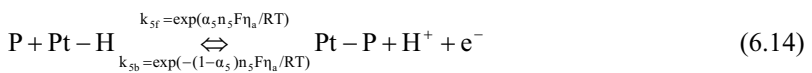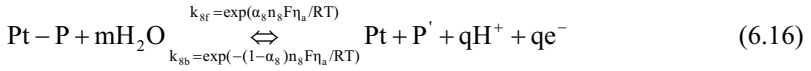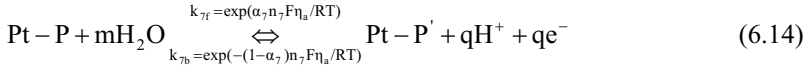
where P' is the product of the electrochemical oxidation of impurity P, $\alpha_{3,5,7,8}$ are the electron transfer coefficients for individual electrochemical half-cell reactions, and η_a is the anode overpotential. Reactions 6.10–6.12 are the mechanism for hydrogen oxidation, in which the slow dissociative chemical adsorption of adsorbed H_2 has been considered the rate determining step for H_2 oxidation [28, 32]; Reactions 6.13–6.15 are the surface adsorption and surface electrochemical reactions of the impurity P; Reaction 6.15 or 6.16 is the oxidation of adsorbed contaminant on the Pt surface, resulting in a product that could be either a surface adsorbed species (Pt-P') or a soluble species (P'). In the case that P is not electrochemically active, Reactions 6.15 and 6.16 would be removed from the proposed mechanism. From these proposed reaction mechanisms, the fuel cell current density expression as a function of anode and cathode is derived, and several characteristics, such as performance loss, contamination transient time constant, and recovery are introduced to the model, which enables it to predict performance degradation and recoverability.

Based on the above general model, Shi et al. [33] has proposed a transient kinetic model to describe the contamination of the PEM anode catalyst layer by H_2S present in the fuel feed stream. Figure 6.5 shows the model-predicted cell voltages in comparison with experimental results. It can be seen that their model provides an excellent fit with the experimental results.

6.2.5 Mitigation of Anode Contamination

Mitigation of anode contamination has so far mainly focused on CO, and mitigation strategies for other contaminants were not reported. For CO mitigation, four strategies have been developed: CO-tolerant catalysts, Pt alloy catalysts, air/oxygen bleeding, high operation temperature, and pre-treatment of the reformate, among which, the pre-treatment of the reformate or the fuel is the most feasible way to mitigate other contaminants such as NH_3 and H_2S. Further studies on this issue are needed.

6.3 Cathode Catalyst Layer Contamination

The slow kinetics of the cathode oxygen reduction reaction (ORR) plays the key role in limiting PEMFC performance when pristine hydrogen is used as the fuel. Therefore, improving the catalytic activity for the ORR has drawn most of the research attention in catalysis studies. Cathode contamination has attracted less attention compared with anode contamination, and only a limited number of papers have been published. Pollutants in air include NO_x (NO_2 and NO), SO_x (SO_2 and

SO_3), NH_3, O_3, and some volatile organic species (VOCs) such as toluene. The major sources of these contaminants are vehicle exhaust, industrial emissions, and agricultural activities. In special cases such as military applications, battlefield contaminants released from either chemical warfare or normal warfare, or both, should also be considered. These contaminants include Sarin, sulfur mustard, cyanogen chloride, hydrogen cyanide, and so on, which could cause significant irreversible performance drops. Since NO_x and SO_x are the main air pollutants, in this section we will mainly discuss NO_x and SO_x contamination. Contamination caused by other pollutants will also be touched upon.

6.3.1 SO_x Contamination

Sulfur oxides, in particular SO_2, are common air contaminants resulting from fossil fuel combustion and other human activities. They can be found in high concentrations in urban areas with heavy traffic, areas with agricultural activities, or close to some chemical plants. When the air stream of the fuel cell contains acidic impurities such as SO_x, the pH inside the MEA is decreased, resulting in free acids in the MEA and causing potential shifts. SO_x can also adsorb on the Pt surface, competing with oxygen adsorption and leading to performance degradation. This section will focus on contamination by SO_x (mainly from SO_2) at the cathode side of PEMFCs.

6.3.1.1 The Effect of SO_x on Fuel Cell Performance
A trace of SO_2 can cause a significant degradation in PEM fuel cell performance. As shown in Figure 6.6 [34], after the PEM fuel cell was exposed to 1 ppm SO_2/air for 100 hours at 70 °C at a current density of 0.5 A/cm^2, 35% degradation in cell performance was observed, with a cell voltage decrease from 0.68 V to 0.44 V.
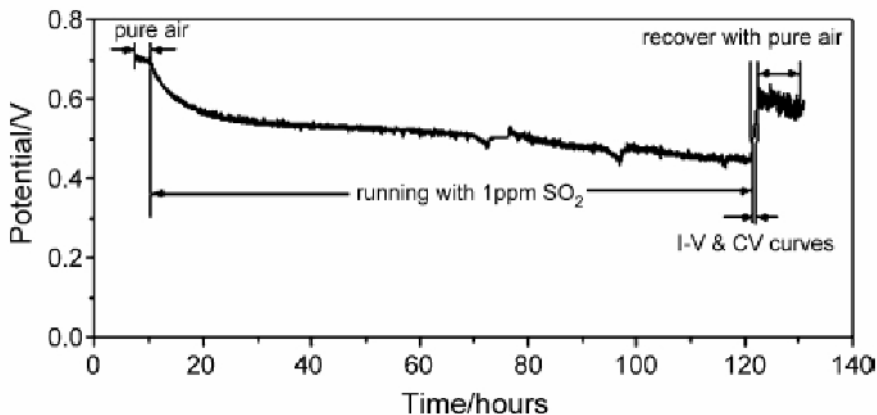
Figure 6.6. Constant-current discharging curve of the PEMFC during running with 1 ppm SO_2/air for 100 hours at 70 °C. Current density: 0.5 A cm^{-2} [34]. (Reprinted from Journal of Power Sources, 166(1), Jing Fenning, Hou Ming, Shi Weiyu, Fu Jie, Yu Hongmei, Ming Pingwen and Yi Baolian, The effect of ambient contamination on PEMFC performance, 172–6, ©2007, with permission from Elsevier.)

The fuel cell performance degradation appears to be a function of SO_2 concentration in the air stream. A 78% cell performance decrease was observed for air containing 5 ppm SO_2, while a 53% decrease was observed for air containing 2.5 ppm SO_2 at the same applied dosage [35]. There was no detrimental effect on cell performance with 500 ppb SO_2 in the air stream [36]. The poisoning effect of SO_2 on fuel cell performance also depends on the operating cell voltage. The lower the cell operating voltage, the greater is the effect of the poisoning [37]. The fuel cell operating temperature, pressure, and relative humidity might also have an impact upon the poisoning effect of SO_2. However, to date there is no published work investigating these issues.

6.3.1.2 The Mechanism of SO_2 Contamination

The SO_x (mainly SO_2) in the air stream can cause degradation in fuel cell performance by poisoning the catalyst sites, changing MEA properties such as hydrophilicity/hydrophobicity, and then affecting water management. The major effect is believed to be poisoning of the catalyst sites, thereby decreasing catalytic activities.

Table 6.1. Pt/VC mass activities at 0.9 V as a function of $\theta_{S,i}$ (sulfur coverage) [41]. (Reproduced by permission of ECS—The Electrochemical Society, from Garsany Y, Baturina OA, Swider-Lyons KE. Impact of sulfur dioxide on the oxygen reduction reaction at Pt/Vulcan carbon electrocatalysts.)

Sulfur coverage ($\theta_{S,i}$)	Mass activity (A/mg$_{Pt}$)	% Mass activity	Overpotential /V ($j = 1.5$ ma/cm^2)
0	0.16	100	0.92
0.012	0.11	69	0.90
0.14	8.01×10^{-3}	5	0.81
0.37	1.71×10^{-4}	0.11	0.69
1	8.76×10^{-4}	0.56	0.54

Cycle voltammetry (CV) studies [34, 35] revealed that there were some sulfur species on the surface of the Pt catalyst during the SO_2 poisoning process. The SO_2 adsorbed on the Pt surface was reduced electrochemically to sulfur through the formation of an SO intermediate, as shown in Reactions 6.17 and 6.18 [35, 38]. The end products of SO_2 adsorption on a Pt electrode are linearly and bridge adsorbed sulfur [39].

$$Pt + SO_2 + 2H^+ + 2e^- \rightarrow Pt - SO + H_2O \qquad (6.17)$$

$$Pt - SO + 2H^+ + 2e^- \rightarrow Pt - S + H_2O \qquad (6.18)$$

Studies [40, 41] also indicated that SO_2 poisoning had a great effect on the kinetics for the ORR, and would change the ORR mechanism when the sulfur coverage reached a certain level. The reaction pathway of the ORR was changed from a 4-electron to a 2-electron process on the Pt/Vulcan carbon catalyst as well as the Pt_3Co/Vulcan carbon catalyst when the sulfur coverage levels on the Pt surfaces reached levels of 37% [41] and 96% [40], respectively. Table 6.1 shows that when the sulfur surface coverage on the Pt surface was 1.2% and 14%, 31% and 95% losses of Pt mass activity were obtained, respectively.

6.3.1.3 Recoverability of Fuel Cell Performance After SO_x Contamination

The fuel cell performance could be partially recovered after SO_2 poisoning if the cell voltage was set at open circuit voltage (OCV) [37, 42]. Operating a fuel cell with pure air [34] and CV scanning [34, 35] after the contamination source was cut off were also proven to be two ways of partially recovering performance. Performance recovery can be attributed to the electrochemical oxidation of adsorbed SO_2 at high potential. Mangun and Debarr [43] suggested that due to the presence of delocalized electrons at the edge sites of carbons where oxygen can chemisorb, the absorbed SO_2 can react with the oxygen to form SO_3, which then reacts with water to form H_2SO_4. Therefore, the reactions of adsorbed SO_2 on the Pt/C electrocatalyst surface can be described by Reactions 6.19 and 6.20 [34, 43]:

$$2Pt-SO_2+O_2+4e^- \rightarrow 2Pt-SO_3 \tag{6.19}$$

$$2Pt-SO_3+2H_2O \rightarrow H_2SO_4+Pt \tag{6.20}$$

Based on the assumption that one atom of sulfur gets bound onto the surface atom of Pt, Loucka [44] suggested that the adsorbed sulfur could be oxidized by 6 electrons to SO_3 or SO_4^{2-}, according to Reaction 6.21 or 6.22:

$$Pt-S_{ads}+3H_2O \rightarrow SO_3+6H^++6e^-+Pt \tag{6.21}$$

$$Pt-S_{ads}+4H_2O \rightarrow SO_4^{2-}+4H^++2e^-+Pt \tag{6.22}$$
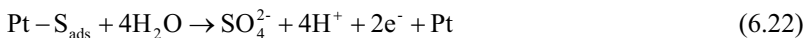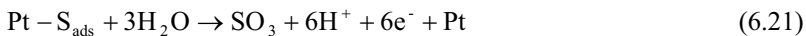
However, complete performance recovery would not occur because the absorbed sulfur species could not be completely desorbed by either pure air operation or CV scanning. The remaining species could still occupy the active sites of the Pt electrocatalyst.

6.3.1.4 Mitigation of SO_x Contamination

Since fuel cell performance cannot be totally recovered after SO_x poisoning, it is critical to prevent the cathode from SO_x contamination in the air stream. Unfortunately, to date few studies have addressed the mitigation of SO_x contamination at the cathode side. Two methods deal with air contamination of fuel cells: increasing catalyst tolerance to impurities [45] and/or filtering contaminants from the air [46–48]. A Pt-Fe phosphate catalyst (Pt-FePO) was

recently developed [45] that has strong tolerance to air impurities (such as CO and SO_2). However, because a variety of contaminants exist in the air, developing new catalysts seems to be difficult, time consuming, and possibly expensive. Therefore, the more effective and easier method for preventing fuel cells from contamination seems to be the adsorptive filtration of contaminants from the air. However, optimization of the filter design requires a methodology incorporating air properties, fuel cell attributes, and design options. On the other hand, due to the low concentration of SO_x in the air (< 0.1 ppm), designing and fabricating such air filters is extremely challenging. Although the incorporation of a filter into a fuel cell system will increase the burden of the system due to the air pressure drop across the filter, filtering is still the most feasible way to remove SO_x from air. An example is shown in Section 6.3.2.4.

6.3.2 NO_x Contamination

NO_x is one of the main air pollutants, emitted mainly from internal combustion engine vehicles. The NO_x concentration in air fluctuates, especially in an urban environment. During rush hour traffic, the NO_x concentration is much higher than at other times of the day. The concentration change may result in confusion during fuel cell evaluation when comparing data obtained at different sites or different times on the same day.

6.3.2.1 The Effect of NO_x on Fuel Cell Performance
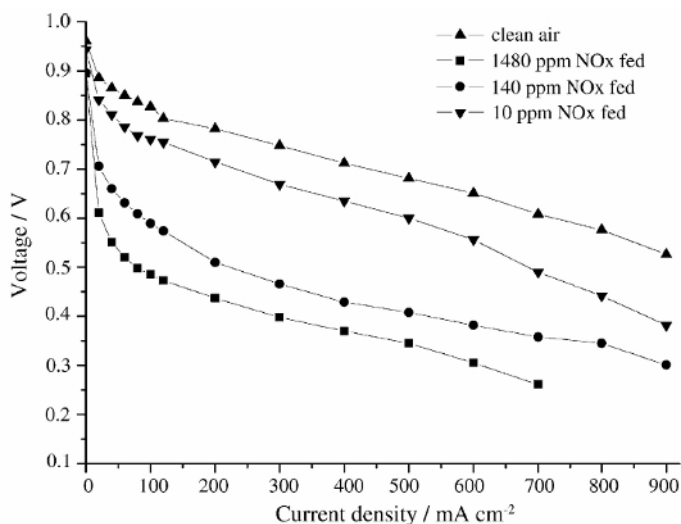
Figure 6.7. Polarization curves for different concentrations of NO_x. Cell temperature: 60°C, H_2/air (1.2/3.3); relative humidity: H_2 95% and air 0%; backpressure: 1.5 atm [49]. (Reprinted from Electrochimica Acta, 51(19), Yang Daijun, Ma Jianxin, Xu Lin, Wu Minzhong and Wang Haijiang, The effect of nitrogen oxides in air on the performance of proton exchange membrane fuel cell, 4039–44, ©2006, with permission from Elsevier.)

Small amounts of NO_x can cause fuel cell performance drops. Knights et al. [21] found that a NO_x concentration of even 115 ppb could cause a cell performance drop of more than 25 mV at 0.175 A/cm^2. They also found that as NO_x concentration increased, cell voltage drop also increased accordingly [21]. Mohtadi et al. [35] found that the performance decay was increased as NO_x concentration was increased from 2.5 to 5 ppm, and Yang et al. [49] reported that when NO_x concentration was increased from 10 to 1480 ppm, the performance dropped significantly, as shown in Figure 6.7.

The relationship between the voltage drop and NO_x concentration is somewhat complicated. Knight et al. [21] found that the voltage dropped linearly as the NO_x concentration was increased from 0.016 to 0.115 ppm. However, in the concentration range of 2.5 and 5 ppm, and 10 to 1480 ppm, a linear relationship was not observed. One possible reason is that this relationship is dependent on the NO_x concentration range. To obtain a clear understanding, further research is needed.

Although the PEMFC contamination caused by NO_x was reported for a wide range of NO_x concentrations (from 16 ppb to 1480 ppm) [21, 34, 35, 49, 50], it is difficult to draw a general conclusion about NO_x contamination because the results in the literature were obtained under different conditions.

6.3.2.2 Recoverability of Fuel Cell Performance after NO_x Contamination
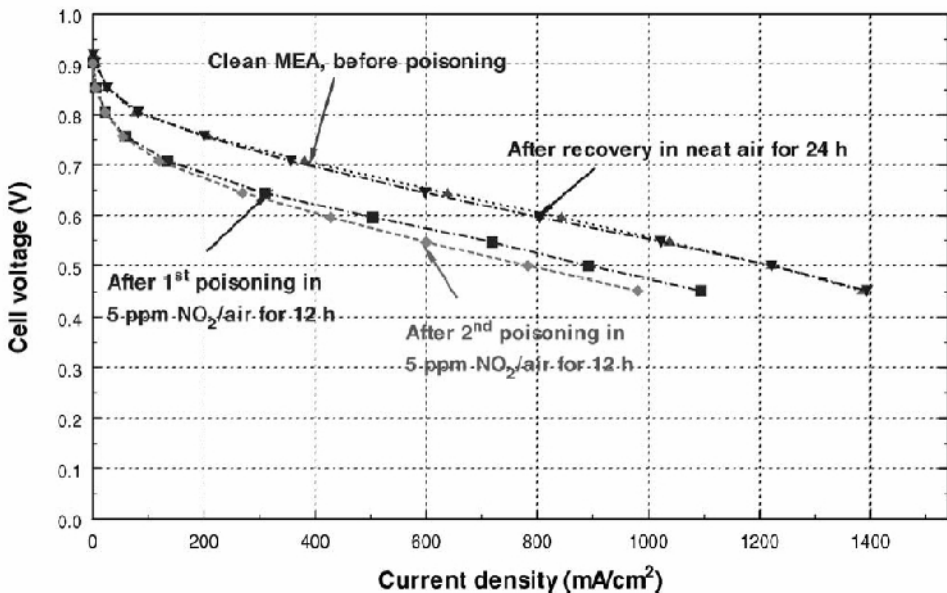
Figure 6.8. Polarization curve showing the effects of NO_2. Cell temperature: 70 °C, Stoich: 1.2/2, ambient pressure, RH 100% for both air and fuel side [35]. (Reprinted from Journal of Power Sources, 138(1–2), Mohtadi R, Lee W-K, Van Zee JW, Assessing durability of cathodes exposed to common air impurities, 216–25, ©2004, with permission from Elsevier.)

In the literature, it is generally agreed that NO_x contamination is recoverable. When the contaminant source was shut off and pure air was turned on for a certain period of time, e.g., 24 hours, fuel cell performance could be totally recovered. Figure 6.8 shows the polarization curves of a PEMFC before NO_x contamination, after contamination, and after recovery. However, if the PEMFCs were exposed to NO_x continuously for a long period of time (e.g., 500 hours), performance could not be fully recovered [50]. This recoverability reduces the concern about the NO_x contamination effect on PEMFC performance.

6.3.2.3. The Mechanism of NO_x Contamination Recovery

There are mainly two proposed mechanisms for NO_x contamination recovery: NO_x reduction and NO_x oxidation. Mohtadi et al. [35] proposed a NO_x reduction mechanism [35]:

$$O_2(g) + 8H^+ + 7e^- \rightarrow NH_4^+ + 2H_2O \qquad E^0 = +0.897 \text{ V vs. RHE} \qquad (6.23)$$

Jing et al. [34] proposed a NO_x oxidation mechanism:

$$O_2 + H_2O \rightarrow NO_3^- + 2H^+ + e^- \qquad E^0 = +0.80 \text{ V vs. RHE} \qquad (6.24)$$

They formed a hypothesis that the NO could be oxidized to NO_2 on the Pt surface, and then NO_2 could react with H_2O and O_2, forming nitric acid [49].

Due to the limited published studies of NO_x contamination, it is difficult to determine which mechanism is more possible. However, the mechanism of NO_x adsorption on the Pt surface described in the literature should be useful for increasing our understanding. As mentioned above, NO_x mainly contains NO_2 and NO. At low coverage (a < 0.03 monolayer) NO adsorbs on the Pt surface irreversibly, while at high coverage it could adsorb reversibly, and could decompose into N_2 and O_2 as well. NO_2 adsorption on the Pt surface is partly irreversible, and the adsorbed NO_2 can be easily decomposed to NO and O [51]. On the other hand, NO oxidation on the Pt electrode is more difficult compared to NO reduction. Vooys et al. [52] found that even if the electrode was held at 1.4 V vs. RHE for 15 minutes, NO oxidation was still not completed, and that NO was reduced easily at a potential < 0.7 V, which is in the operational potential region of the PEMFC cathode [52]. Oxidation of NO_2 was even observed at a more positive potential. Broder et al. [53] found that NO_2 oxidation on the Pt electrode occurred at 1.10 V and 2.24 V vs. ferrocene (1.5 V and 2.64 V vs. RHE, respectively) [53]. In a PEMFC under normal operating conditions, this high cathode potential is not feasible. Based on these results, we believe that the reduction mechanism (Reaction 6.23) is the most feasible, and the reversibility of NO_x contamination is possibly due to the reversible adsorption of both NO_2 and NO at high coverage. At low coverage, the presence of excess air after the contaminant is shut off can effectively remove the irreversibly adsorbed NO_x over a period of time, e.g., 24 hours or longer.

6.3.2.4. Mitigation of NO_x Contamination

Although NO_x contamination is recoverable, temporary NO_x contamination can also result in fuel cell performance degradation, affecting its application. For example, in the case of mining vehicles, certain amounts of NO_x exist in the mining environment, and long-term exposure to NO_x might result in PEMFC failure, as well as more or less permanent degradation of the PEMFC. Thus, strategies to mitigate NO_x contamination are required.

The best strategy is to filter it from the air. Development of effective adsorbents to remove NO_x and other air contaminants such as SO_x is the most feasible way. Ma et al. [48] investigated the use of activated carbon adsorbent for cathode air filtration, and found that the adsorbent is effective in avoiding NO_x and SO_x contamination. Figure 6.9 shows the results with and without air filtration [48].
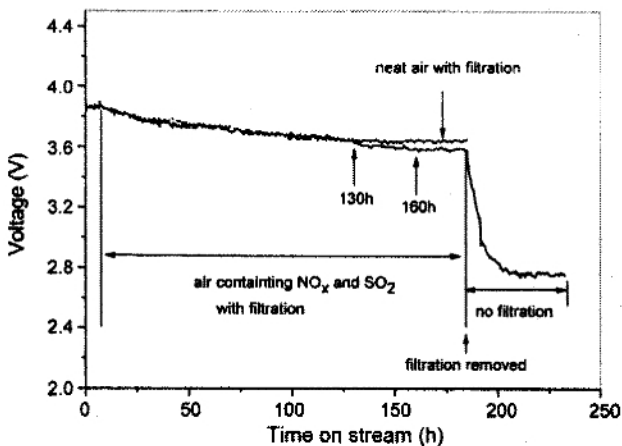
Figure 6.9. Polarization curves with and without NO_x, SO_2 filtration (air pressure: 1.5 atm, air flow rate: 30 L/min, 0.28 A/cm^2) [48]. (Reprinted from Journal of Power Sources, 175(1), Ma Xiaowei, Yang Daijun, Zhou Wei, Zhang Cunman, Pan Xiangmin, Xu Lin, Wu Minzhong and Ma Jianxin, Evaluation of activated carbon adsorbent for fuel cell cathode air filtration, 383–9, ©2008, with permission from Elsevier.)

6.3.3 NH$_3$ and H$_2$S Contamination

Although NH$_3$ and H$_2$S are usually present in the PEMFC fuel, contaminating the anode, they are also present in air. The mechanism of NH$_3$ contamination at the cathode is not clear. Since NH$_3$ is stable at the cathode potential region, electrochemical oxidation of NH$_3$, producing species that could poison the catalytic sites, is unlikely. However, Halseid et al. [27] also listed this issue as one possible contamination effect. As discussed above, the NH$_3$ could react in a major way with the protons in the ionomer, reducing proton conductivity in the catalyst layer [27, 54]. The gradient in the double layer might also be influenced by the formation of NH_4^+ in the catalyst layer, which affects the symmetry factor for oxygen adsorption [27, 55].

The presence of H_2S in the air at the cathode side severely degrades fuel cell performance. Mohtadi et al. [35] found that in the presence of 200 ppm, at a cell voltage of 0.68 V, the current density decreased sharply from around 500 mA/cm^2 to less than 150 mA/cm^2 in under 10 hours. After 60 hours of neat air flushing, the current density was only recovered to 170 mA/cm^2, indicating that H_2S poisoning is almost un-recoverable [35].

Similar to the mechanism at the anode, the mechanism of the H_2S poisoning effect is assigned to strong sulfur adsorption on Pt, blocking oxygen adsorption sites:

$$H_2S + Pt \rightarrow Pt\text{-}S + H_2 \qquad\qquad (6.25)$$

6.3.4. Volatile Organic Compounds (VOCs) Contamination

In an environment of PEMFC residential applications as backup power supplies, some volatile organic compounds (VOCs), including benzene and toluene, exist due to decorative materials. For military applications, the VOCs are different. In battlefields, chemical warfare can release significant amount of VOCs such as Sarin, HCN, and so on [36]. These VOCs could result in disastrous degradation of PEMFC performance.

The effect of benzene contamination on cell performance is dependent on the operating current density. When a fuel cell was fed with air containing 50 ppm benzene over a period of 30 minutes, at 50 mA/cm^2, a 5% reduction of power output was observed in comparison with pure air. At 200 mA/cm^2, the output reduction was more than 38%. These performance drops were not fully recovered after the benzene was shut off and the fuel cell was purged with pure air over a period of 10 minutes [36].

Toluene contamination in air could affect fuel cell performance, mainly resulting in performance degradation in the kinetic region (low current densities). This contamination also results in easy flooding at the cathode side, possibly changing the hydrophilicity of the cathode catalyst layer. The mechanism of toluene contamination is not clear [56].

Fuel cell cathode contamination caused by chemical warfare gases is disastrous. With 1780 ppm HCN in air, the power output of a PEMFC was only 13% of the original value, and the degraded performance was only partly recoverable. After 30 minutes of purging with neat air, the output recovered to 45% of the original value [36].

Contamination with Sarin and sulfur mustard is even more disastrous as compared with HCN. For a PEMFC fed with air containing 15 ppm sulfur mustard, the power output was only 13% of the original value. This degradation is totally unrecoverable. The same is true for Sarin. Air contaminated with 170 ppm Sarin resulted in a 70% performance degradation, and no recovery was observed when the cell was purged with pure air [36].

The mechanism of chemical warfare gas contamination is not clear. So far, no report on a mechanism study has been found. Most possibly, these gases are permanently adsorbed on the Pt surface, blocking oxygen adsorption.

Mitigation of VOCs in PEMFC contamination has been seldom studied. For benzene and toluene, an air filter such as activated carbon could be usable. For chemical warfare gases, special apparatus should be used.

6.3.5 Ozone Contamination

Ozone is a strong oxidant that is present in air at a very low concentration. Unlike with other contaminants, ozone contamination in oxygen leads to cell performance improvement. Bussayajarn et al. [57] found that a PEMFC fed with a mixture of ozone and oxygen at the cathode side showed significantly improved performance at low current densities, and that at high current densities, no improvement was observed [57]. Ozone introduction in air could eliminate the VOCs in air. The high oxidizing ability of ozone may in fact destroy the VOCs. Both aspects of ozone in air lead to improvement in PEMFC performance.

6.3.6 The Contamination Effects of Multi-contaminants
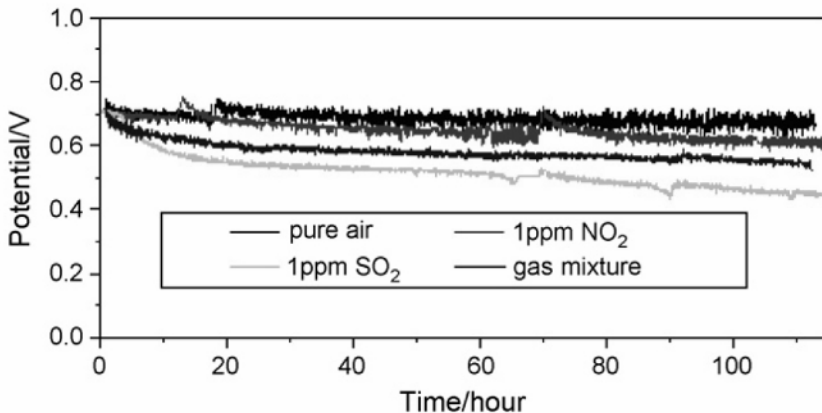
Figure 6.10. The constant current discharging curve of the PEMFC during running with different cathode gas for 100 hours. Current density: 500 mA/cm^2; cell temperature: 70 °C; RH: anode 65 °C, and cathode 68 °C dew points, ambient pressure [34]. (Reprinted from Journal of Power Sources, 166(1), Jing F, Hou M, Shi W, Fu J, Yu H, Ming P, et al., The effect of ambient contamination on PEMFC performance, 172–6, ©2007, with permission from Elsevier.)

In real applications, compressed air contains multiple pollutants, including NO_x, SO_x, H_2S, VOCs, and so forth. Here we present one example to demonstrate the effect of mixed NO_x and SO_x on fuel cell performance. Figure 6.10 shows the voltage change with time when a fuel cell was fed with air containing different or no contaminants. The performance obtained with these gases is in the sequence of pure air > air containing 1 ppm NO_2 > air containing mixed pollutants (1 ppm NO_2 + 1 ppm SO_2) > air containing 1 ppm SO_2. The effect of the mixed contaminants seemed not to be the sum of the effects of the individual contaminants. Rather, it was less than the more severe contaminant (SO_2) but larger than the less severe

contaminant (NO_2). This phenomenon was explained by the competitive adsorption of NO_2 and SO_2 on the Pt surface, which results in less contribution to performance degradation from SO_2 with mixed contaminants than from air containing only SO_2 [34].
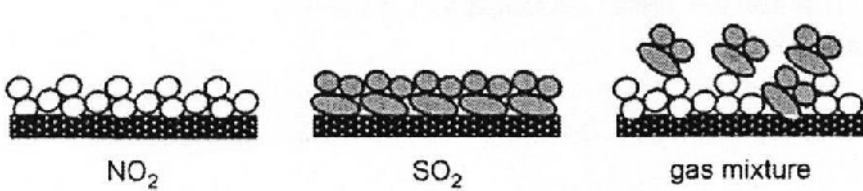
Figure 6.11. Schematic of air contaminants adsorbing on the catalyst layer [34]. (Reprinted from Journal of Power Sources, 166(1), Jing F, Hou M, Shi W, Fu J, Yu H, Ming P, et al., The effect of ambient contamination on PEMFC performance, 172–6, ©2007, with permission from Elsevier.)

6.3.7 Modeling of PEMFC Cathode Catalyst Contamination

As discussed above, currently the modeling work on PEMFC contamination is mainly focused on the anode side. The only work on cathode catalyst modeling was published by Knight et al. [21], who presented an equation to fit the fuel cell performance caused by NO_2 and SO_2 contamination at the cathode, as shown in Equation 6.26 [21]:

$$E_c = E_0 - (b_1 + K_{cK}C)\log(I) + K_{cK}C\log(I)\exp(-K_3 t) - R_0 I \qquad (6.26)$$

Obviously, E_c is the cell voltage, E_0 is the theoretical cell voltage, I is the current density, b_1 is the Tafel slope, C is the contaminant concentration, and R_0 is the membrane resistance. However, the physical meaning of the other parameters was not given. Most possibly, these are kinetic parameters related to NO_2 and SO_2 adsorption on the Pt surface.

6.4 Additive Effects of Anode and Cathode Contamination

The additive effect of multiple contaminants on fuel cell performance is found when the air contains a mixture of NO_2 and SO_2, and the H_2 fuel contains H_2S. Figure 6.12 shows the performance of a PEMFC fed with air containing each individual pollutant, and with the mixture. The effect of the mixed contaminants is the sum of their individual effects [21]. Recovery from the mixed contaminants was not reported, and more work is needed to gain a clear understanding.
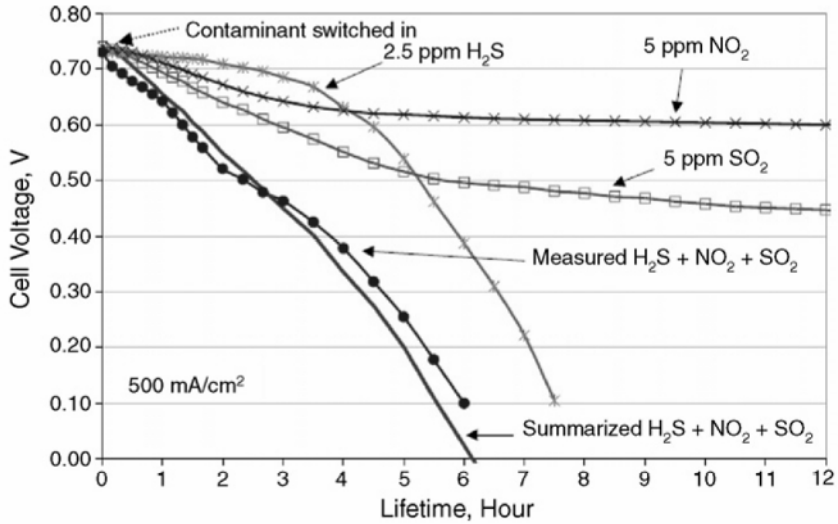
Figure 6.12. Additive effects of contaminants, 2.5 ppm H_2S in fuel, 5 ppm SO_2 and 5 ppm NO_2 in air, 500 mA/cm^2. Cell temperature: 55 °C, Stoich: H_2 1.25/O_2 2.0, RH: 100% [21]. (Reprinted with permission of the authors.)

6.5 Summary

PEMFC performance can be affected by contaminants in the fuel and air feed streams through catalyst poisoning processes. Performance degradation is dependent on the type of contaminants. At the anode catalyst layer, common contaminants other than CO are CO_2, H_2S, and NH_3. The effect of CO_2 contamination on the anode catalyst layer is similar to that of CO. CO_2 is reduced to CO, which strongly adsorbs to Pt, blocking H_2 adsorption. The effect of H_2S contamination is due to the formation of strongly adsorbed sulfur on the Pt surface, which permanently poisons the catalyst surface. High current density or low temperature operation of PEMFCs is more severely affected by H_2S contamination than low current density or high temperature operation. The effect of NH_3 contamination on the anode catalyst layer is due to its reaction with the bulk electrolyte membrane and the ionomer in the catalyst layer, reducing proton conductivity. However, NH_3 seems not to poison the catalysts. Modeling of anode contamination based on the reaction kinetics provides an excellent fit to the experimental results.

At the cathode catalyst layer, the common contaminants include SO_x, NO_x, H_2S, NH_3, VOCs, and ozone. A trace amount of SO_x in air can cause a significant performance decrease. Increases in SO_x concentration accelerate the degradation. This degradation is due to the adsorbed sulfur on the Pt surface produced from SO_x reduction, which not only poisons the catalyst but also changes the ORR mechanism. The fuel cell performance is only partly recovered after SO_x contamination. NO_x contamination of the cathode catalyst is also concentration-

dependent. Higher NO_x concentration leads to more severe PEMFC performance degradation. The mechanism of NO_x contamination is most possibly due to NO_x reduction on the Pt surface, which competes with oxygen adsorption. PEMFC performance can be fully recovered in most cases after the NO_x contaminants are eliminated. NH_3 and H_2S contamination of the cathode catalyst layer is similar to that of the anode catalyst layer. Civilian VOCs contamination of the cathode catalyst layer is not severe and is somewhat recoverable. However, battlefield contaminants such as chemical warfare gases are disastrous to PEMFCs, resulting in permanent performance degradation. The presence of ozone in air improves PEMFC performance. It is believed that adding a filter to the air is an effective way to mitigate cathode contamination.

The presence of contaminants in both fuel and air results in an additive contamination effect: PEMFC performance degradation is the sum of the cathode and the anode degradation.

References

1. Cheng X, Shi Z, Glass N, Zhang L, Zhang J, Song D, et al. A review of PEM hydrogen fuel cell contamination: impacts, mechanisms, and mitigation. J Power Sources 2007;165:739–56.
2. Mughal A, Li X. Experimental diagnostics of PEM fuel cells. Int J Environ Stud 2006;63:377–89.
3. Larminie J, Dicks A. Proton exchange membrane fuel cells. In: Fuel cell systems explained. 2nd ed. London: John Wiley & Sons, 2003; 67–120.
4. Li X. Chapter 7. Principles of fuel cells. New York: Taylor & Francis Group, 2006.
5. Dicks AL. Hydrogen generation from natural gas for the fuel cell systems of tomorrow. J Power Sources 1996;61:113–24.
6. Hohlein B, Boe M, Bogild-Hansen J, Brockerhoff P, Colsman G, Emonts B, et al. Hydrogen from methanol for fuel cells in mobile systems: development of a compact reformer. J Power Sources 1996;61:143–7.
7. Schmidt VM, Brockerhoff P, Hohlein B, Menzer R, Stimming U. Utilization of methanol for polymer electrolyte fuel cells in mobile systems. J Power Sources 1994;49:299–313.
8. Rajalakshmi N, Jayanth TT, Dhathathreyan KS. Effect of carbon dioxide and ammonia on polymer electrolyte membrane fuel cell stack performance. Fuel Cells 2003;3:177–80.
9. de Bruijn FA, Papageorgopoulos DC, Sitters EF, Janssen GJM. The influence of carbon dioxide on PEM fuel cell anodes. J Power Sources 2002;110:117–24.
10. Janssen GJM. Modelling study of CO_2 poisoning on PEMFC anodes. J Power Sources 2004;136:45–54.
11. Gu T, Lee WK, Zee JWV. Quantifying the 'reverse water gas shift' reaction inside a PEM fuel cell. Appl Catal B: Environ 2005;56:43–9.
12. Papageorgopoulos DC, de Bruijn FA. Examining a potential fuel cell poison: A voltammetry study of the influence of carbon dioxide on the hydrogen oxidation capability of carbon-supported Pt and PtRu anodes. J Electrochem Soc 2002;142:A140–5.
13. Divisek J, Oetjen HF, Peinecke V, Schmidt VM, Stimming U. Components for PEM fuel cell systems using hydrogen and CO containing fuels. Electrochim Acta 1998;43:3811–15.

14. Shi W, Yi B, Hou M, Shao Z. The effect of H_2S and CO mixtures on PEMFC performance. Intern J Hydrogen Energy 2007;32:4412–17.
15. Mathieu MV, Primet M. Sulfurization and regeneration of platinum. Appl Catal 1984;9:361–70.
16. Ramasubramanian N. Anodic behavior of platinum electrodes in sulfide solutions, the formation of platinum sulfide. J Electroanal Chem 1975;64:21–37.
17. Shi W, Yi B, Hou M, Jing F, Yu H, Ming P. The influence of hydrogen sulfide on proton exchange membrane fuel cell anodes. J Power Sources 2007;164:272–7.
18. Mohtadi R, Lee W-K, Van Zee JW. The effect of temperature on the adsorption rate of hydrogen sulfide on Pt anodes in a PEMFC. Applied Catalysis B: Environmental 2005;56:37–42.
19. Michaelides A, Hu P. Hydrogenation of S to H_2S on Pt(111): A first-principles study. J Chem Phys 2001;115:8570–4.
20. Mohtadi R, Lee W-K, Cowan S, Van Zee JW, Murthy M. Effect of hydrogen sulfide on the performance of a PEMFC. Electrochem Solid State Lett 2003;6:A272–4.
21. Knights S, Jia N, Chuy C, Zhang J. Fuel cell reactant supply: effects of reactant contaminants. Fuel cell seminar 2005: fuel cell progress, challenges and markets; 2005 Nov 14–18; Palm Springs, California; Burnaby, BC: Ballard Power Systems; 2005: 121–5.
22. Chellappa AS, Fischer CM, Thomson WJ. Ammonia decomposition kinetics over Ni-Pt/Al_2O_3 for PEM fuel cell applications. Appl Catal A, Gen 2002;227:231–40.
23. Arthur D. Little Inc. Cost analysis of fuel cell system for transportation: baseline system cost estimate. Cambridge, MA: 2000 Mar. Ref. No.: 49739. SFAA No.: DE-SCO2–98EE50526. Sponsored by the US Department of Energy. Available from: http://www.eere.energy.gov/afdc/pdfs/baseline_cost_model.pdf.
24. Borup R, Inbody M, Tafoya J, Semelsberger T, Perry L. Durability studies: gasoline/reformate durability. 2002 National Laboratory R&D Meeting, DOE Fuel Cells for Transportation Program. Los Alamos, NM: Los Alamos National Laboratory Fuel Cell Program. 2002. Available from: http://www.eere.energy.gov/ hydrogenandfuelcells/pdfs/nn0123ba.pdf.
25. Uribe FA, Gottesfeld S.TA, Zawodzinski. Effect of ammonia as fuel impurity on proton exchange membrane fuel cell performance. J Electrochem Society 2002;149:A293–6.
26. Soto HJ, Lee WK, Van Zee JW, Murthy M. Effect of transient ammonia concentrations on PEMFC performance. Electrochem Solid-State Lett- 2003;6:A133–7.
27. Halseid R, Vie PJS, Tunold R. Effect of ammonia on the performance of polymer electrolyte membrane fuel cells. J Power Sources 2006;154:343–50.
28. Vogel W, Lundquist J, Ross P, Stonehart P. Reaction pathways and poisons—II: The rate controlling step for electrochemical oxidation of hydrogen on Pt in acid and poisoning of the reaction by CO. Electrochim Acta 1975;20:79–93.
29. Springer TE, Rockward T, Zawodzinski TA, Gottesfeld S. Model for polymer electrolyte fuel cell operation on reformate feed: effects of CO, H_2 dilution, and high fuel utilization. J Electrochem Soc 2001;148:A11–23.
30. Chan SH, Goh SK, Jiang SP. A mathematical model of polymer electrolyte fuel cell with anode CO kinetics. Electrochim Acta 2003;48:1905–19.
31. Zhang JJ, Wang HJ, Wilkinson DP, Song DT, Shen J, Liu ZS. Model for the contamination of fuel cell anode catalyst in the presence of fuel stream impurities. J Power Sources 2005;164:58–71.
32. Stonehart P, Kohlmayr G. Effect of poisons on kinetic parameters for platinum electrocatalyst sites. Electrochim Acta 1972;17:369–82.

33. Shi Z, Song DT, Zhang JJ, Liu ZS, Knights S, Vohra R, et al. Transient analysis of hydrogen sulfide contamination on the performance of a PEM fuel cell. J Electrochem Society 2007;154:B609–15.

34. Jing F, Hou M, Shi W, Fu J, Yu H, Ming P, et al. The effect of ambient contamination on PEMFC performance. J Power Sources 2007;166:172–6.

35. Mohtadi R, Lee W, Van Zee JW. Assessing durability of cathodes exposed to common air impurities. J Power Sources 2004;138:216–25.

36. Moore JM, Adcock PL, Lakeman JB, Mepsted GO. The effects of battlefield contaminants on PEMFC performance. J Power Sources 2000;85:254–60.

37. Garzon F, Brosha E, Pivovar B, Rockward T, Uribe F, Urdampolleta I, et al. Effect of fuel and air impurities on PEM fuel cell performance. DOE hydrogen program–FY 2006 annual progress report: 905–9.

38. Contractor AQ, Lal H. The nature of species adsorbed on platinum from SO_2 solutions. J Electroanal Chem 1978;93:99–107.

39. Contractor AQ, Lal H. Two forms of chemisorbed sulfur on platinum and related studies. J Electroanal Chem 1979;96:175–81.

40. Garsany Y, Baturina O, Swider-Lyons KE. Impact of SO_2 on the kinetics of Pt_3Co/Vulcan carbon electrocatalysts for oxygen reduction. ECS Trans 2007;11:863–75.

41. Garsany Y, Baturina OA, Swider-Lyons KE. Impact of sulfur dioxide on the oxygen reduction reaction at Pt/Vulcan carbon electrocatalysts. J Electrochem Soc 2007;154:B670–5.

42. Brosha E, Garzon F, Pivovar B, Rockward T, Springer T, Uribe F, et al. Effect of fuel and air impurities on PEM fuel cell performance. In: 2006 Annual DOE Fuel Cell Program Review. Arlington, Virginia, May 16–19, 2006.

43. Mangun CL, DeBarr JA, Economy J. Adsorption of sulfur dioxide on ammonia-treated activated carbon fibers. Carbon 2001;39:1689–96.

44. Loucka T. Adsorption and oxidation of sulphur and of sulphur dioxide at the platinum electrode. J Electroanal Chem 1971;31:319–32.

45. Bouwman P, Teliska ME, Lyons K. Increased poisoning tolerance of Pt-FePO oxygen reduction catalysts. In: Proton conducting membrane fuel cells IV. Van Zee et al., editors. Electrochemical Society Proceedings 2004.

46. Kennedy DM, Cahela DR, Zhu W, Westrom KC, Nelms RM, Tatarchuk BJ. Fuel cell cathode air filters: Methodologies for design and optimization. J Power Sources 2007;168:391–9.

47. Betournay MC, Bonnell G, Edwardson E, Paktunc D, Kaufman A, Lomma AT. The effects of mine conditions on the performance of a PEM fuel cell. J Power Sources 2004;134:80–87.

48. Ma X, Yang D, Zhou W, Zhang C, Pan X, Xu L, et al. Evaluation of activated carbon adsorbent for fuel cell cathode air filtration. J Power Sources 2008;175:383–9.

49. Yang D, Ma J, Xu L, Wu M, Wang H. The effect of nitrogen oxides in air on the performance of proton exchange membrane fuel cell. Electrochim Acta 2006;51:4039–44.

50. Uribe F, Smith W, Wilson M, Valerio J, Rockward T, Garzon F, et al. Electrodes for polymer electrolyte membrane operation on hydrogen/air and reformate/air. FY 2003 Report. Los Alamos, NM: Los Alamos National Laboratory. Available from: http://www1.eere.energy.gov/hydrogenandfuelcells/pdfs/ive12_uribe.pdf.

51. Wickham DT, Banse BA, Koel BE. The adsorption of nitric oxide and nitrogen dioxide on polycrystalline platinum. Surf Sci 1989;223:82–100.

52. de Vooys ACA, Beltramo GL, van Riet B, van Veen JAR, Koper MTM. Mechanisms of electrochemical reduction and oxidation of nitric oxide. Electrochim Acta 2004;49:1307–14.

53. Broder TL, Silvester DS, Aldous L, Hardacre C, Compton RG. Electrochemical oxidation of nitrite and the oxidation and reduction of NO_2 in the room temperature ionic liquid [C_2mim][NTf_2]. J Phys Chem B 2007;111:7778–85.
54. Szymanski ST, Gruver GA, Katz M, Kunz HR. The effect of ammonia on hydrogen-air phosphoric acid fuel cell performance. J Electrochem Soc 1980;127:1440–4.
55. Halseid R, Bystron T, Tunold R. Oxygen reduction on platinum in aqueous sulphuric acid in the presence of ammonium . Electrochim Acta 2006;51:2737–42.
56. Li H, Zhang JL, Fatih K, Wang Z, Tang Y, Shi Z, et al. PEM fuel cell contamination: testing and diagnosis of toluene-induced cathode degradation. J Power Sources, forthcoming.
57. Bussayajarn N, Therdthianwong S, Therdthianwong A. Improvement of cathodic reaction of proton exchange membrane fuel cell by ozone. Int J Hydrogen Energy 2007;32:392–9.

7

PEM Fuel Cell Catalyst Layers and MEAs

Pei Kang Shen

7.1 Fundamentals of Catalyst Layers

Proton exchange membrane fuel cells (PEMFCs) have attracted intensive attention as a result of their applicability to transportation systems and portable electronic products [1]. The important challenges in PEMFC research arise in the catalyst layers (CLs) because these are complex and heterogeneous. The catalyst layers need to be designed so as to generate high rates of the desired reactions and minimize the amount of catalyst necessary for reaching the required levels of power output. To meet the goal, the following requirements need to be considered: (1) large three-phase interface in the CL, (2) efficient transport of protons, (3) easy transport of reactant and product gases and removal of condensed water, and (4) continuous electronic current passage between the reaction sites and the current collector. A CL with a thickness around several micrometers is a critical component of a PEMFC and requires more elaborate treatment [2]. The CL is in direct contact with the membrane and the gas diffusion layer (GDL), as shown in Figure 7.1. It is also referred to as the active layer [3]. Gottesfeld and Zawodzinski provided a good overview of the CL structure and functions [4]. The overall CL performance depends on all these critical factors and is therefore essential to identify the electrode structures and operation conditions. In this section, the functions and the technical impacts of the CLs will be described.
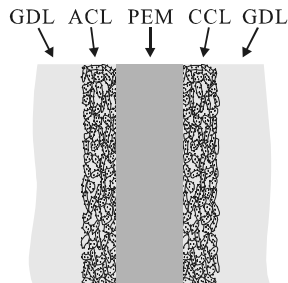
Figure 7.1. Schematic diagram of a catalyst layer structure. GDL – gas diffusion layer; ACL – anode catalyst layer; CCL – cathode catalyst layer; PEM – proton exchange membrane.

7.1.1 Components and Structure

The catalyst ink usually includes catalyst, carbon powder, binder, and solvent. Sometimes, other additives are added to improve the dispersion of the components and stabilize the catalyst ink. The catalyst either covers the surface of the GDL or directly coats the surface of the membrane (catalyst coated membrane, CCM). The CL usually consists of: (1) an ionic conductor such as perfluorosulfonate acid (PFSA) ionomer to provide a passage for protons to be transported in or out, (2) metal catalysts supported on a conducting matrix like carbon, to provide a means for electron conduction, and (3) a water-repelling agent such as polytetrafluoroethylene (PTFE) to provide sufficient porosity for the gaseous reactants to be transferred to catalyzed sites [5, 6]. Every individual factor must be optimized to provide the best overall performance of a CL.

Conventional CL uses either PTFE or PFSA ionomer as a binder [7-9]. The hydrophobicity or hydrophilicity of the CL is determined by the amount of the binder added. Zheng and Shi reported a dual-bonded CL structure [10]. They fabricated a dual-bonded CL by combining one PFSA ionomer-bonded CL and one PTFE-bonded CL to alleviate inherent problems of conventional CLs caused by different properties of binder materials. This novel structure uses PTFE-bonded CL to enhance mass-transport of the gaseous reactants and ionomer-bonded CL to increase the proton conductivity. Zheng and Shi showed that the catalyst utilization increased by using this dual-bonded CL. As the electrochemical reaction occurs at the three-phase interface of the CL, it is necessary to investigate the hydrophobicity and/or hydrophilicity properties of CLs, which have a large impact on the water transport and even on the performance of the PEMFC. Yu et al. used environmental scanning electron microscopy (ESEM) to measure the hydrophilicity and hydrophobicity in the CL microstructure [11]. Useful information has been gained to assist in understanding CLs from catalyst coated membranes.

Wei et al. used a random cluster model to simulate the CL of PEMFC [12]. The factors influencing catalyst utilization were thoroughly discussed. In the case of high catalyst utilization, numerical results showed that there is a threshold for the ratio of Pt/C catalyst loading to PFSA ionomer. Beyond this threshold, the catalyst utilization may drop dramatically. Generally, there is high catalyst utilization around the ratio of 1. Results also showed that the lower the PTFE loading in the CL, the higher the catalyst utilization will be. However, the Pt/C catalyst with higher Pt content can tolerate relatively higher PTFE loading than that with a lower Pt content.

7.1.2 Functions and Reactions

The basic function of a CL is to provide a place for electrochemical reactions. The main processes occurring in a CL include mass transport of the reactants, interfacial reactions of the reactants at the electrochemically active sites, proton transport in the electrolyte phase, and electron conduction in the electronic phase. The hydrogen oxidation reaction (HOR) takes place in the anode CL and the oxygen reduction reaction (ORR) occurs in the cathode CL. Both anodic and

cathodic reactions require active catalyst sites to break the molecular bond in the diatomic gaseous reactant molecules, due to the low-temperature environment of a PEMFC. HOR has a relatively lower overpotential and a higher reaction rate than ORR, which leaves ORR as a source of large voltage loss in PEMFC.

The CL should keep the phase equilibrium with other PEM materials [13]. The CLs applied onto both sides of the PEM are highly interconnected with the membrane by their content of proton-conducting PFSA ionomer. The typical MEA structures show strains of PFSA ionomer running through the CLs, connecting catalyst particles to the membrane on the ionic conductor level. These strains form an ionic connection to the membrane not only for mobile protons, but also for all species which can enter the pores within these materials. In the normal case, the phase equilibrium at the interface between the CLs and the PEM material is always assumed to be established.

In both anode and cathode, the CL is the location of the half-cell reaction in a PEM fuel cell [3]. The CL is applied either to the membrane or to the GDL. In either case, the objective is to place the catalyst particles within close proximity of the membrane. The first generation of PEMFC used PTFE-bound Pt black catalysts that exhibited excellent long-term performance, but at a prohibitively high cost. These conventional CLs generally featured expensive platinum loadings of 4 mg cm^{-2}. Pt loadings as low as 0.014 mg cm^{-2} have recently been reported, using novel sputtering methods [14, 15]. Consequently, the cost of the catalyst is no longer the major barrier to the commercialization of PEMFCs. In addition to catalyst loading, there are a number of CL properties that have to be carefully optimized to achieve high utilization of the catalyst material: reactant diffusivity, ionic and electrical conductivity, and the level of hydrophobicity all have to be carefully balanced.

The design of the cathode CL receives more attention, since the ORR kinetics is slower compared to that of the anode HOR [10, 16, 17]. The influence of catalyst gradients on active layer performance has been demonstrated by Antoine et al. and confirmed by using active layer models [17]. The catalyst utilization efficiency largely depends on diffusion and ionic ohmic drop limitations. Thus, for a non-porous active layer, diffusion is a rate-limiting step with regard to ohmic drop, and the best performance is obtained for catalyst particles located close to the GDL. On the other hand, for a porous active layer, ionic ohmic drop becomes a rate-limiting step and performance is improved when the catalyst particles are located close to the proton exchange membrane side. These results show that the optimal catalyst utilization is obtained with a thin porous active layer and a preferential location of Pt nanoparticles close to the proton exchange membrane side. In the CL, the transport of reactants, protons, and electrons, i.e., the formation of three-phase interface, can be illustrated in Figure 7.2 [18].

The reactions in the CL depend on the fuel used. For an H_2/O_2 (or air) fuel cell, the reaction in the anode CL is hydrogen oxidation, and the reaction in the cathode CL is oxygen reduction:

Anode: $2H_2 \rightarrow 4H^+ + 4e^-$ $E^o = 0.00$ V   (7.1)

Cathode: $O_2 + 4H^+ + 4e^- \rightarrow 2H_2O$ $E^o = 1.23$ V   (7.2)

Overall: $2H_2 + O_2 \rightarrow 2H_2O$ $E_{cell} = 1.23$ V   (7.3)
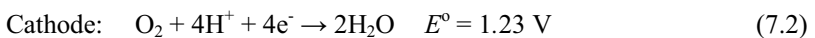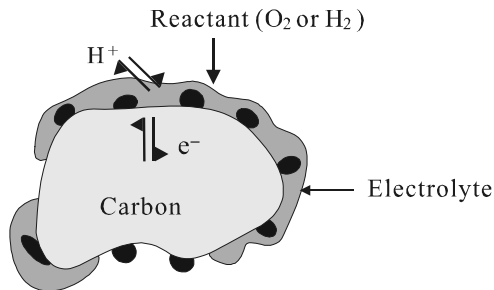
Figure 7.2. Three-phase interface formed in catalyst layer.

In the case of the direct alcohol fuel cells (DAFCs), e.g., direct methanol fuel cell (DMFC), the anode of a liquid-feed DMFC is supplied with a diluted methanol aqueous solution, while the cathode is fed with air or pure oxygen, which can be either forced by an external blower or driven by natural convection [19, 20]. Due to the combined effect of both convection and diffusion, the methanol and the oxygen reach the anode and cathode CLs, respectively, where they undergo the overall electrochemical reactions:

$$\text{Anode:} \quad CH_3OH + H_2O \rightarrow 6H^+ + CO_2 + 6e^- \quad E^o = 0.02 \text{ V} \quad (7.4)$$

$$\text{Cathode:} \quad O_2 + 4H^+ + 4e^- \rightarrow 2H_2O \quad\quad\quad E^o = 1.23 \text{ V} \quad (7.5)$$

$$\text{Overall:} \quad 2CH_3OH + 3O_2 \rightarrow 4H_2O + 2CO_2 \quad E_{cell} = 1.21 \text{ V} \quad (7.6)$$
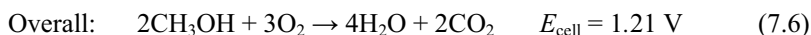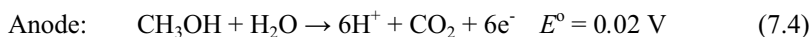
Due to methanol crossover, Reaction 7.4 accounts for methanol oxidation at both the anode and the cathode, while Reaction 7.5 accounts for oxygen reduction at the cathode. The protons generated at the anode by Reaction 7.4 diffuse across the proton exchange membrane, while the electrons pass as current through the external circuit to reach the cathode, where oxygen is reduced by the protons and the electrons to form water, according to Reaction 7.5. Figure 7.3 shows the difference at the anode between H_2/O_2 (or air) fuel cell and DMFC.
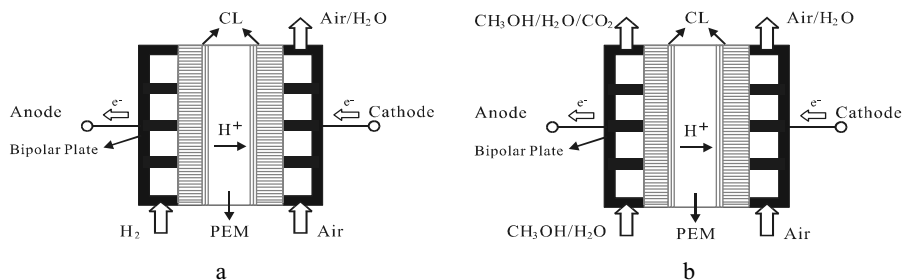
Figure 7.3. Comparison of the electrochemical processes in ACLs between (a) H_2/O_2 (or air) fuel cell and (b) DMFC.

7.1.3 Factors Affecting the Performance of CLs

Analyzing the factors affecting the performance of CL is complex. In this section, we only describe the primary factors affecting the performance of the CLs.

1) *Polarization during operation.* Fuel cells convert chemical energy directly into electrical energy. In the ideal case, the change in Gibbs free energy, ΔG, of the reaction is available as useful electric energy at the temperature of the conversion. At standard conditions of 25 °C (298 °K) and 1 atmosphere, the thermal energy (ΔH) in the hydrogen/oxygen reaction is 285.8 kJ mole^{-1}, and the free energy available for useful work is 237.1 kJ mole^{-1}. Thus, the thermal efficiency of an ideal fuel cell operating reversibly on pure hydrogen and oxygen at standard conditions is:

$$\eta_{ideal} = \frac{237.1}{258.8} = 0.83 \qquad (7.7)$$

The efficiency of an actual fuel cell is often expressed in terms of the ratio of the operating cell voltage to the ideal cell voltage. The actual cell voltage is less than the ideal cell voltage because of losses associated with cell polarization and ohmic losses. The thermal efficiency of a hydrogen/oxygen fuel cell can then be written in terms of the actual cell voltage:

$$\eta = \frac{0.83 V_{actual}}{E_{ideal}} \qquad (7.8)$$

The actual cell voltage is decreased from its ideal potential because of several types of polarization losses, including activation polarization, ohmic polarization, and concentration polarization. Figure 7.4 schematically shows the polarization characteristics for a H_2/O_2 fuel cell and a DMFC in use. The output potential for a single fuel cell is usually lower than that of the theoretical voltage (E^o) even at open circuit state (the theoretical voltage for a single H_2/O_2 PEMFC is 1.23 V as mentioned above). The output voltage for an actual single is

$$E = E_{ocv} - E_{iR} - E_{ae} - E_{ce} = E^o - E_l - E_a - E_M - E_{diff} \qquad (7.9)$$

where E_{ocv} is the open circuit voltage for a single fuel cell, E_{iR} is the ohmic overpotential, E_{ae} is the anodic overpotential and E_{ce} is the cathodic overpotential. Alternatively, the output voltage can be represented as the difference between theoretical voltage (E^o) and all polarizations, where E_l is the loss in voltage due to leaks across the membrane for a liquid fuel cell. The presently used proton exchange membrane is methanol-permeable; therefore, the value could be over 200 mV for a single liquid methanol fuel cell. It can be seen from Figure 7.4(b) that the anodic polarization for a DMFC is more serious than that of the PEMFC. E_a is the activation overpotential due to slow electrode reactions at both anode and cathode. Activation losses are caused by sluggish electrode kinetics. In reality, activation losses are the result of complex surface electrochemical reaction steps, each of

which has its own reaction rate and activation energy. Usually, the rate parameters and activation energy of one or more rate-limiting reaction steps control the voltage drop caused by activation losses on a particular electrode under specific conditions. In any case, the activation overpotential for a PEMFC is almost entirely due to the slow kinetics in the cathode [21]. Although the ohmic losses are usually induced by resistance to the flow of ions in the membrane and resistance to the flow of electrons through the electrode, only the resistance of the membrane is taken into account, since it dominates the total ohmic losses. Here, E_M represents the ohmic losses due to resistance in the membrane. It has been recognized that reducing the resistance within the CL is a big challenge in improving cell performance. E_{diff} is the mass transport-related overpotential due to mass diffusion limitations. A concentration gradient is formed during cell operation. At low current densities and high bulk reactant concentrations, mass-transport losses are not significant, but under practical conditions (high current densities, low fuel and air concentrations), they often contribute significantly to loss in cell potential. It is extremely important to minimize the polarization by optimizing the CL design. For a given cell design, it is possible to improve the cell performance by modifying the operating conditions.
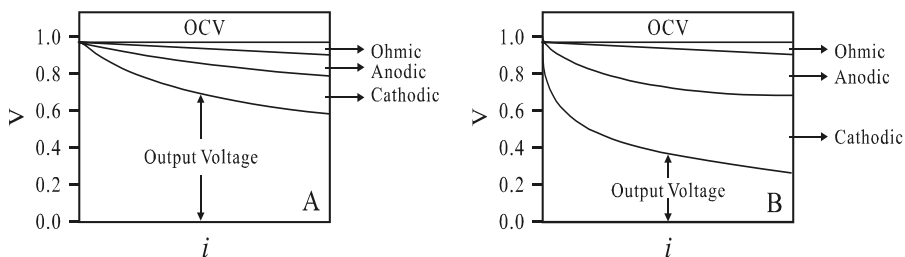
Figure 7.4. Actual fuel cell voltage/current characteristic of (a) PEMFC and (b) DMFC. OCV – open circuit voltage; Ohmic – ohmic overpotential; Anodic – anodic overpotential; and Cathodic – cathodic overpotential.

2) *Binder type and content in CL*. PTFE and ionic conducting polymers like PFSA ionomer are commonly used as binders in CLs. The content of binders in the CL affects simultaneously the gas permeability, the catalytic activity, and the ionic conductivity [22]. Hence, optimizing binder content in the CL is necessary for better performance. The resistance of the CL could be reduced at the optimized binder content, increasing the utilization of the catalysts.

The amount of polyelectrolyte binder used in CLs is not as large as that in membranes [18]; however, the amount is important because it is closely related to CL performance, catalyst utilization, and MEA durability [23, 24]. In current PEMFCs, PFSA ionomers are employed in the CL as binders and in the proton conducting electrolyte to extend the formation of the electrochemical three-phase interface [3]. The latter is important for obtaining desirable catalyst utilization and, thus, high performance of MEA. Since the reactant must be transported through the proton conducting electrolyte before it arrives at the reaction sites to carry out reactions, the binder in the CL must be reactant-permeable to avoid reactant mass transport limitations [25]. The reactant-permeable property of the binder is

completely different from the polymer electrolyte used in membranes, which requires much less or no reactant permeability [26, 27].

Song et al. found that the optimal amount of ionomer in the CL is approximately 0.8 mg cm^{-2} when Pt loadings are kept at 0.4 mg cm^{-2} [28]. These values are rationalized in terms of the catalyst active area and the transport of the involved species for the electrode reaction. Previous studies looking at the influence of PFSA content on cell performance revealed that the optimal amount of the PFSA ionomer is about 0.8 mg cm^{-2} in the case of the carbon-supported Pt catalyst [5, 29, 30]. But the optimal amount should depend on the Pt catalyst loadings in the CL [31]. Investigations of CLs with alternative ionomers, and their application in MEAs, have recently been reported [25, 32, 33].

Binder durability directly affects cell durability. Attention should be particularly paid to the cathode CL, since H_2O_2 is unavoidably formed during ORR, even on the Pt catalyst. The three-phase boundaries in CL where the catalyst are covered by the binder are the places for ORR and form more or less H_2O_2. In other words, the concentration of H_2O_2 is higher in the CL. The binder in the CL is more likely to suffer damage from this strongly oxidative H_2O_2. The Fenton's reagent test, i.e., putting the membrane in H_2O_2/Fe^{2+} solution to test its chemical stability, is widely used for stability evaluation [34, 35]. Nafion membrane shows a desirably high chemical stability in a Fenton's reagent test and under actual PEMFC working conditions. However, a new analysis technique is expected to be established for evaluating the chemical stability of the binder in CL, since the concentration of H_2O_2 in CL is relatively high and the CL may be damaged with the degradation of the binder.

3) *Supports for catalysts.* The carbon-supported Pt catalyst is normally used in current PEMFC CLs. The carbon support enables uniform dispersion of Pt nanoparticles, in addition to providing electronic continuity. Moreover, it somewhat retards the sintering or agglomeration of Pt nanoparticles [36]. Carbon as a support has good chemical and electrochemical stability. However, carbon will be oxidized or corroded at potentials near the open circuit voltage (OCV) of a single fuel cell (0.9–1.0 V). The higher the potential, the higher the oxidation rate. The presence of Pt could accelerate the carbon corrosion rate [37], particularly at places where Pt particles reside. This would weaken the attachment of Pt particles to the carbon support, and eventually lead to the detachment of Pt particles from that support. In addition, the loss of carbon due to corrosion could decrease the electronic continuity of the CL, so the isolated Pt particles would not be able to participate in the electrochemical reactions.

Tang et al. proposed a reaction model for an unprotected fuel cell. They found that the cathode chamber and anode chamber still have air and hydrogen, respectively, after the cell is shut down, resulting in a higher OCV. If the anode exhaust port is not closed after shut-down, air will gradually diffuse into the anode side, creating an air/hydrogen boundary. The boundary moves to the other end of the flow channel and thus, the cell will bear a high OCV. Both water electrolysis and carbon oxidation could happen in the cathode at significant rates, according to Equations 7.10, 7.11, and 7.12:

$$2H_2O \rightarrow O_2 + 4H^+ + 4e^- \qquad (7.10)$$

$$C + 2H_2O \rightarrow CO_2 + 4H^+ + 4e^- \quad\quad\quad (7.11)$$

$$C + O_2 \rightarrow CO_2 \quad\quad\quad (7.12)$$
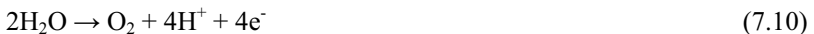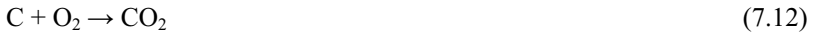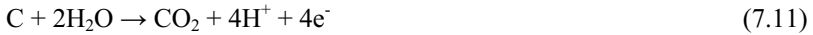
The surface of the Pt particles could also be oxidized, according to Equations 7.13 and 7.14:

$$Pt + xH_2O \rightarrow PtO_x + 2xH^+ + 2xe^- \quad\quad\quad (7.13)$$

$$Pt + xO_2 \rightarrow PtO_{2x} \quad\quad\quad (7.14)$$
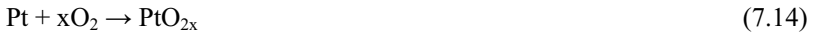
Reactions 7.10–7.14 will stop when the hydrogen is completely consumed and the anode is eventually filled with air. However, when hydrogen is fed to the anode during the restart of the fuel cell, a new air/fuel boundary forms, causing the cathode in the region that faces the anode air section to corrode as described in Reactions 7.10–7.14.

Stevens and Dahn showed that the platinum particles were able to catalyze the degradation of the carbon support at moderate temperatures [37]. The amount of carbon that was lost after extended oven exposure at a constant temperature was shown to depend on both temperature and Pt loading. A simple first-order kinetic model described the results. Cai et al. found that carbon oxidation in the presence of Pt follows two pathways: an oxygen pathway that leads to mass loss due to formation of gaseous products, and a water pathway that results in mass gains, especially for high BET area supports [38]. These processes may be assisted by the formation of highly reactive OH and OOH radicals. Pt/C catalysts decompose quantitatively in air to Pt at 400 °C, compared to > 700 °C for Vulcan XC72 carbon alone [39]. At higher Pt catalyst levels, lower onsets of thermal decomposition temperatures are observed. Pt also catalyzes the decomposition of binder in CLs. The thermal decomposition temperature of Nafion is lowered by about 150 °C to 300 °C in the presence of 46 wt% Pt/C. Although Pt lowers the Nafion decomposition temperature, the temperature is still well above PEM fuel cell operation levels. The low-temperature kinetic data for carbon support oxidation may be used to estimate carbon mass loss for a PEM fuel cell at a typical operating temperature, and for automotive application at 80 °C. For a cell using a 46 wt% Pt/C catalyst, about 10 wt% loss of carbon support is predicted after 1 year of continuous operation. This percent mass loss may be a lower limit, as more rapid oxidation occurs at the cathode under electrochemical conditions [40, 41]. Using on-line mass spectrometry, Roen et al. detected increased CO_2 emission at cathodes with higher Pt loadings [41]. Samms et al. investigated the thermal stability of a CL consisting of 20 wt% Pt black and 80 wt% of Nafion by TGA-MS. They found that Pt lowers the decomposition temperature of Nafion by 40 °C [42].

The durability of the catalysts and their supports has been investigated in real or simulated low-temperature PEMFC condition [18, 39, 45]. It has been found that the electrochemical active surface area of the electrodes will be decreased during PEMFC running [45, 46]. The decrease in the electrochemical active surface area contributes to the main performance degradation of PEMFC [47]. Pt or Pt-alloy

nanoparticles that are deposited on carbon black can agglomerate through diffusion on carbon surface, to form larger particles during PEMFC operation or under the accelerated aging test [43]. Pt will also dissolve in an acidic environment [45]. When carbon corrodes, some Pt or its alloy particles will peel from the electrode. Carbon corrosion will increase the electrode resistance by decreasing electric contact with the current collector. Graphitization of carbon support produces a material that is highly resistant to oxidation and carbon corrosion, perhaps resulting in highly durable catalysts [48]. However, metal deposition on such graphitized supports is more difficult.

Some researchers have observed enhanced electrocatalytic activity and durability on nitrogen-doped [59, 50] or boron-doped [51] carbon-supported electrocatalysts for potential application in PEMFC. It is believed that the nitrogen-doping effect is due to the electron-donating nature of nitrogen, which improves the ability of graphite to donate electrons to O_2 in the cathode CL and makes the reaction of oxygen to water occur more easily. Shen's group investigated the carbides and oxides that supported Pt [54] or non-Pt catalysts [57] for both oxygen reduction and alcohol oxidation. Figure 7.5(a) shows the performance of oxygen reduction on a Pt-WC/C catalyst. There is a 100 mV improvement, even at lower Pt loadings, compared to the conventional Pt/C catalyst [52]. The Ag-WC/C catalyst shows activity comparative to the Pt/C catalyst [55]. Figure 7.5(b) shows typical performance of the Pd-NiO/C catalyst for ethanol oxidation. The onset potential shifts to the more negative side over 200 mV than does that of the Pt/C catalyst [56]. Investigations on non-platinum catalysts have made advances recently [58, 59], but the durability of these catalysts under high temperature needs further study.
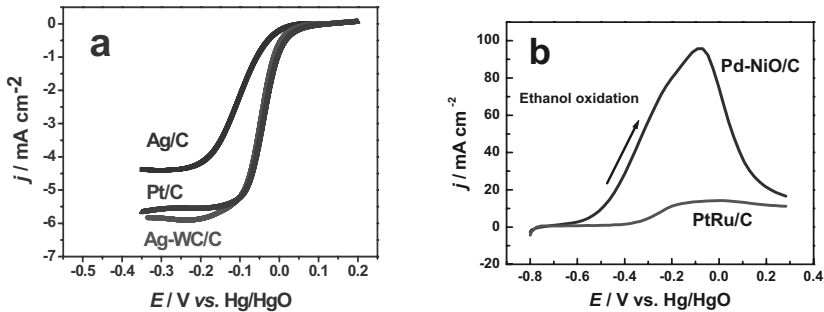
Figure 7.5. (a) ORR on different catalysts in O_2 saturated 1 mol dm^{-3} KOH solution, and (b) ethanol oxidation on Pd-NiO/C catalyst in 1.0 mol dm^{-3} ethanol/1.0 mol dm^{-3} KOH [55, 56]. (Graph (a) reprinted from Electrochemistry Commununications, 8, Meng H, Shen PK. Novel Pt-free catalyst for oxygen electroreduction, 588–94, ©2006 with permission from Elsevier. Graph (b) reprinted from Electrochemistry Commununications, 8, Alcohol oxidation on nanocrytalline oxide Pd/C promoted electrocatalyst, 184–8, ©2006 with permission from Elsevier.)

4) *Catalyst durability.* Pt is the key to fuel cells because of its unusually high catalytic activity. Unfortunately, Pt is expensive and has limited availability. The cost of the PEMFC is too high for practical applications. One of the strategies to

reduce the cost is to increase the utilization of Pt catalyst or use non-Pt catalyst in CL. Zeng et al., aiming to maximize the electrochemical surface area and, consequently, the specific activity of fuel cell reactions, proposed a catalyst preparation method to increase Pt utilization [60]. Pt/C electrocatalysts were obtained by first depositing Pt nanoparticles on colloidal silica and then adsorbing them with the carbon support. It was found that the silica-modified catalyst is three times as active as a catalyst prepared without silica for methanol oxidation.

Stamenkovic et al. demonstrated that the $Pt_3Ni(111)$ surface is 10-fold more active for the ORR than the corresponding Pt(111) surface, and 90-fold more active than the Pt/C catalysts for PEMFC [61]. The $Pt_3Ni(111)$ surface has an unusual electronic structure (*d*-band center position) and arrangement of surface atoms in the near-surface region. Under operating conditions relevant to fuel cells, its near-surface layer exhibits a highly structured compositional oscillation in the outermost and third layers, which are Pt-rich, and in the second atomic layer, which is Ni-rich. The weak interaction between the Pt surface atoms and nonreactive oxygenated species increases the number of active sites for O_2 adsorption.

A continuing problem in vehicle applications of PEMFC is the degradation of the CL due to sintering of Pt, corrosion of carbon support, and so on. Increasing the CL durability should stablize the catalyst. It has been recognized that damage is caused by cell reversal during PEMFC operation with fuel starvation [62]. The loss of platinum surface area through sintering or recrystallization has also been observed during reversal experiments. Zhang et al. recently reported that Pt oxygen-reduction fuel-cell electrocatalysts can be stabilized against dissolution under potential cycling regimes, by modifying Pt nanoparticles with Au clusters [63]. This behavior was observed under the oxidizing conditions of the ORR and potential cycling between 0.6 and 1.1 volts in over 30,000 cycles. There were insignificant changes in the activity and surface area of the Au-modified Pt over the course of cycling, in contrast to sizable losses observed with the pure Pt catalyst under the same conditions. *In situ* X-ray absorption near-edge spectroscopy and voltammetry data suggest that the Au clusters confer stability by raising the Pt oxidation potential. Pt nanocatalysts supported on multi-walled carbon nanotubes showed a higher durability and catalytic activity than was supported on Vulcan XC72 carbon black [43, 64]. Alloying Pt with other metals can improve not only the catalytic activity but also the durability [64, 65], due to so-called "anchor effects" [44, 65].

Transient study showed that the porosity of the CL affects the cell performance [66]. When CL porosity $\varepsilon_{cl} < 0.1$, the liquid water effect is obvious, but when $\varepsilon_{cl} > 0.1$, the liquid water effect is not very apparent. An optimum value appears between $\varepsilon_{cl} = 0.06$ and $\varepsilon_{cl} = 0.1$. Pai et al. found that the CL performance was enhanced by using clay for dispersion in the anode CL [67]. Yoon et al. studied the effect of pore structure in the cathode CL on PEMFC performance [68].

5) *Operating conditions.* As common sense would suggest, operating conditions such as the temperature, pressure, and humidity of the reactant gases directly affect CL performance. An increase in the operating temperature leads to an increase in the diffusion rate to reduce the mass transport resistance, and the ohmic-ion conductivity of the binder in the CL also increases. The most important

factor affecting the performance of the PEMFC is the mass transport limitation, including the transport of reactant and oxidant gases to active sites on the CL, the transport of the proton from the anode side to the cathode side through the membrane, and the transport of produced water from the cathode side to the anode side by the back-diffusion mechanism. Operation at higher pressure and elevated temperature with humidified reactant gases is favored for a fuel cell [69]. Similarly, mass transport can be improved by increasing the operating pressure. It has been observed that the pressurized cathode side has a better effect on cell performance than does the pressurized anode side. This phenomenon could be explained by water transport across the membrane from the cathode side to the anode side by the back-diffusion mechanism, which enhances the hydration level of the membrane.

6) *Preparation method.* The preparation method affects the formation of the electron transfer channels (catalyst), gas diffusion channels (pores), proton transport channels (electrolyte), water transport channels (hydrophilic electrolyte), and most importantly, the three-phase interface in the CLs.

Traditionally, the CL is applied to the GDL by various methods, including spraying, painting, rolling, and screen printing, as well as others [1]. Screen printing is one of the most popular methods used for the fabrication of CLs, either in the membrane or in the electrode of the PEMFC [70]. In the direct printing or screen printing process, the catalyst ink was applied to the membrane in Na^+ form or TBA (tetrabutylammonium) form to stabilize the CL, enhancing the physical strength of the membrane. A series of parameters affecting the CL microstructure in PEMFC electrodes have been studied by Fernandez et al. [71], who have shown that the deposition of the CL in the gas diffusion support depends not only on the ink deposition method but also on the characteristics of the solvent used to disperse both the catalyst and the PFSA ionomer. A novel method based on the electrospray technique has been developed by Benítez et al. [72] and is characterized by different techniques, which showed both morphological and structural improvements that contribute to better catalyst utilization in comparison with conventional methods. Xu et al. [73] recently reduced the Nafion content in the CL by incorporating the sulfonic acid group in the carbon-supported catalyst particles, thereby decreasing the resistivity, and the performance was found to be higher than with the unsulfonated counterpart. Giorgi et al. [74] reported preparation methods based on the electrochemical and sputter deposition of low-loading Pt nanoparticles on gas diffusion electrodes. The PEMFC electrodes prepared by this method showed improved performance and catalyst utilization versus commercial chemical deposited Pt. Rajalakshmi and Dhathathreyan developed a new process for the fabrication of CL by combining the screen printing and decal processes in order to increase interfacial contact between the membrane and the catalyst layer [1]. Kim and Popov developed a pulse electrodeposition technique for preparation of CLs, which ensures that most of the Pt is in close contact with the membrane [75]. Using this method, it is possible to increase the Pt/C ratio up to 75 wt% near the surface of the electrode, resulting in a 5 μm-thick CL. Another method of CL fabrication is by electrophoretic deposition (EPD), as reported by Morikawa et al. [76], in which a suspension consisting of ethanol, carbon powders with Pt catalyst, and PFSA ionomer is used to obtain a stable dispersed solution. The thickness of

the prepared CL is controlled by the EPD duration or the concentration of the suspension. The 3D CLs were also prepared by the ink-jet printing method [77].

A catalyst-applied-to-membrane method (catalyst coated membrane, CCM) was invented by Wilson and Gottesfeld in 1992 [6, 78]. The CCMs have unique advantages that will be described in detail in Section 7.2.

7.1.4 Catalyst Layers for Liquid Fuel Cells

PEMFCs can be design to be fed with liquid fuels; this method could lead to a very simple system with a fuel that has a relatively high energy density and is a liquid under ambient conditions.

The liquid fuel cells described here correspond in particular to direct alcohol fuel cells (DAFCs), and the most intensively interesting types include direct methanol fuel cells (DMFCs) and direct ethanol fuel cells (DEFCs). DAFCs have been considered a favorable option in terms of fuel usage and feed strategies [79]. Compared to hydrogen-fed fuel cells, DAFCs use liquid and renewable alcohol fuels, which are easily stored and transported, and simplify the fuel cell system. The voltage output of the cell is lower for DAFCs, typically ranging from 0.25 to 0.4 V. This low cell voltage is recognized mainly due to the high anode overpotential caused by absorption of the partial decomposition products of alcohol (e.g., CO) and the high cathode overpotential, caused by poisoning of the cathode catalyst by cross-over alcohol and its reaction intermediates.

The mechanism of methanol oxidation on the Pt surface has been investigated extensively for decades. According to a well-described mechanism [80], methanol oxidation is a dehydronation process involving the formation of the CO-like intermediates. These intermediates adsorb on the surface of Pt to reduce the catalytic activity. The Pt-Ru alloy has been found to be the most active anti-poisoning anode catalyst for DAFCs. The enhanced activity of the Pt–Ru catalyst for methanol oxidation has been attributed to a bi-functional mechanism [81]. This bi-functional mechanism involves the adsorption of oxygen-containing species on Ru atoms at lower potentials, thereby promoting the oxidation of CO to CO_2, which can be summarized as follows [82]:

$$Pt + CH_3OH \rightarrow Pt\text{-}CO_{ads} + 4H^+ + 4e^- \tag{7.15}$$

$$Ru + H_2O \rightarrow Ru(OH)_{ads} + H^+ + e^- \tag{7.16}$$

$$Pt\text{-}CO_{ads} + Ru(OH)_{ads} \rightarrow CO_2 + Pt + Ru + H^+ + e^- \tag{7.17}$$
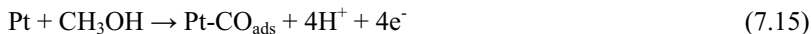
The catalytic activity of the Pt–Ru catalyst is strongly dependent on the composition, structure, morphology, particle size and alloying degree.

The contact between the metal nanoparticles and Nafion micelles in the CL of a DMFC is affected by carbon-support-particle pore size and distribution [79]. Rao et al. investigated the effect of carbon porosity on the specific activity of the Pt–Ru/C catalyst for methanol oxidation [83]. They found that a higher content of small pores (< 20 nm) containing metal particles, where the Nafion ionomer could not easily enter, resulted in poor contact between the metal nanoparticles and

Nafion micelles and there was, therefore, a lower level of methanol oxidation activity. The cathode CL in DMFCs has been optimized through a balance of ionomer and porosity distributions, both playing important roles in affecting proton conduction and oxygen transport through a thick CL of DMFC [84]. CLs in the form of CCM have higher cell open circuit voltages (OCVs) and higher limiting current density, while catalyzed-diffusion-media (CDM) CLs display better performance in the moderate current density region. The CL with a composite structure, consisting of both CCM and CDM, shows better performance in both kinetic and mass-transport limitation regions, due to a suitable ionomer distribution across the CL.

Scott et al. pointed out that carbon dioxide gas will be generated in the anode structure at a position dependent upon local conditions of pressure, temperature, carbon dioxide solubility and bubble nucleation [85]. Due to the moderate solubility of carbon dioxide in the aqueous methanol solution, bubble generation will occur away from the thin anode catalyst surface. In practice, the methanol solution is recycled to the cell from a reservoir and thus will contain a significant amount of dissolved carbon dioxide. Thus, it is likely, and is assumed here, that gas bubbles will be formed in the diffusion layer and flow counter-current to the mass transport of liquid.

The structural design of the CL for liquid-feed fuel cells is important. Several models for liquid-feed DMFCs were proposed [19, 86–88]. The porosities of both anode CL and cathode CL affect the cell performance. The concentration polarization is easier to form in normal density CL, due to the liquid sealing effect in liquid fuel cells. Therefore, the design of the CL structure is particularly important. Chen et al. designed a CL by loading catalyst nanoparticles on a well-defined macroporous carbon matrix [89]. The carbonization and further Pt-Co alloy deposition on the macroporous and mesoporous bimodal pore structured conducting matrix resulted in a higher activity towards the electrooxidation of ethanol in alkaline solution. Liang and Zhao reported a new DMFC anode structure consisting of Pt nanowires that are electrochemically deposited onto a partial layer of a Nafion membrane. The Pt-nanowire network formed in such a Pt-Nafion integrated electrode not only provides the electron conducting pathways but also functions as the catalyst for the methanol oxidation reaction [90]. Pt-nanowire array catalysts were used for ethanol electrooxidation by Wang et al [91]. The micrometer-sized pores and channels in Pt-nanowire array catalysts act as structural units. They make liquid fuel diffuse into and products diffuse out of the CL much more easily [91].

7.1.5 Catalyst Layers for Anion Exchange Membrane Fuel Cells

Using an anion exchange membrane instead of a liquid caustic alkali electrolyte in an alkaline fuel cell allows avoids problems of leakage, carbonation, precipitation of carbonate salts, and gas electrode flooding, increasing the volumetric energy density. It appears that the anion exchange membrane fuel cells (AEMFCs) have the potential to succeed in portable applications [92, 93].

A schematic diagram of the AEMFC is shown in Figure 7.6. Hydrogen and alcohols could be used as fuels. One of the differences between the acidic direct

methanol fuel cell and alkaline direct methanol fuel cell is that in the acidic condition, water is the product of oxygen reduction on the cathode, while in alkaline conditions, OH⁻ diffuses through the membrane and forms water on the anode. The reverse electroosmotic drag reduces the crossover of alcohol from fuel side to air side.
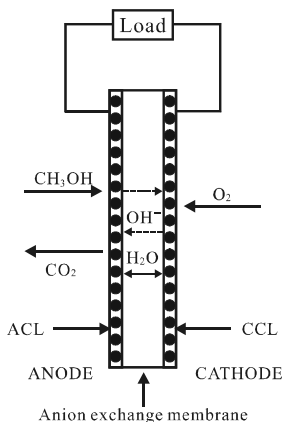
Figure 7.6. Schematic diagram of an anion exchange membrane fuel cell

The reactions are as follows:

Anode: $CH_3OH + 6OH^- \rightarrow 5H_2O + CO_2 + 6e^-$ $E^o = -0.81$ V   (7.18)

Cathode: $3/2O_2 + 3H_2O + 6e^- \rightarrow 6OH^-$ $E^o = 0.40$ V   (7.19)

Overall: $CH_3OH + 3/2O_2 \rightarrow 2H_2O + CO_2$ $E^o = 1.21$ V   (7.20)
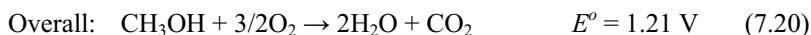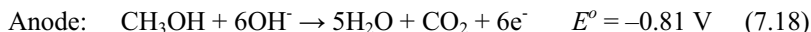
where E^o represents the standard potential of an electrochemical reaction. The open potential for a single DMAFC should close this value if polarization is negligible.

Yu and Scott prepared membrane assembly electrodes (MEAs) with Pt loadings in both anode and cathode CLs of about 2 mg cm^{-2} for a direct methanol alkaline fuel cell using an anion exchange membrane. They found that the cell performance increased dramatically with an MEA that did not include the GDL on the anode, because of lower reactant mass transfer resistance [94]. They also used platinized Ti mesh as the anode and current collector in the AEMFC. The cathode was a standard gas diffusion electrode with a Pt loading of approximately 2 mg cm^{-2}, which consisted of a backing layer (carbon paper), a GDL and a CL. The novel anode showed higher catalytic activity than the conventional Pt/C electrode, and gave stable fuel cell performance [95].

Shen's group focused on the studies of the Pt-free catalysts preparation and the effect of the CL structure on fuel cell performance. They developed oxide-promoted Pd catalysts prepared by a novel intermittent microwave heating technique [56, 96, 97]. All the oxide-Pd catalysts on carbon showed higher catalytic activities than those of Pt/C or Pt-Ru/C catalysts. The Pd-NiO/C catalyst

showed the best performance for ethanol oxidation. The catalytic currents of the oxides-promoted Pd catalysts for ethanol oxidation begin to rise much more sharply at more negative potentials, which will directly improve the fuel cell efficiency.

The understanding of the kinetic limitations of the oxygen reduction reaction (ORR) on different catalysts is a problem of outstanding interest in fuel cell research. Carbon-supported platinum catalysts still serve as the most widely used electrocatalysts in the air electrodes of low-temperature PEMFCs [98]. Ineffective electrode structures increase the voltage losses even further. However, cheaper non-Pt catalysts can be used in AEMFCs. The investigation of the ORR on Ag [99], Au [100], nanoparticle Au [101], Pd [102,103] and Ru [104] metals in alkaline media was reported. Some oxides catalysts were found to be active towards ORR. The most popularly studied are manganese oxides (MnO_x). These, including Mn_2O_3, Mn_3O_4, Mn_5O_8 and MnOOH, show catalytic activity for the disproportionation reaction of HO_2^- to O_2 and OH^-, and thus, the O_2 reduction in the air electrode was considered to include an initial two-electron reduction of O_2 to HO_2^-, followed by a disproportionation reaction catalyzed by MnO_x [105]. Recent work in Shen's group showed that the performance for ORR is significantly improved by co-deposition of tungsten carbides nanocrystals and Ag (Ag-WC/C). The performance of Ag-WC/C composite catalysts for ORR is equivalent to that of the best Pt catalyst [55].

7.2 Principles of Membrane Electrode Assembly (MEA)

The MEA is the heart of PEMFCs, where the electrochemical reactions take place to generate electrical power. The primary components of an MEA are an ion conducting electrolyte (membrane), a cathode CL, and an anode CL, plus a GDL attached to each CL, as shown schematically in Figure 7.7. These three are sandwich structured and are often referred to as the membrane electrode assembly (MEA).
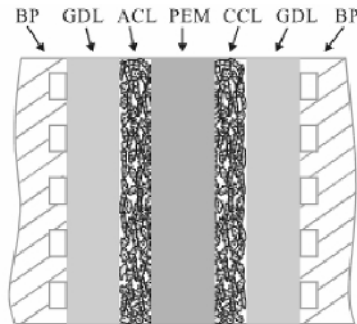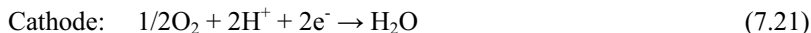

Figure 7.7. Schematic diagram of an MEA structure. BP – bipolar plate; GDL – gas diffusion layer; ACL – anode catalyst layer; CCL – cathode catalyst layer; PEM – proton exchange membrane.

Analogous cathode and anode reactions in the MEA for a H_2/O_2 fuel cell are:

Cathode: $1/2 O_2 + 2H^+ + 2e^- \rightarrow H_2O$ (7.21)

Anode: $H_2 \rightarrow 2 H^+ + 2e^-$ (7.22)

The flow of ionic charge through the electrolyte must be balanced by the flow of electronic charge through an outside circuit, and it is this balance that produces electrical power.

7.2.1 Classification of MEA Materials

As mentioned above, there are three main components in an MEA, including membrane, CL and GDL.

1) *Membrane*. Perfluorosulfonic acid (PFSA) is the most commonly used membrane material [4]. PFSA membranes are relatively strong and stable in both oxidative and reductive environments, since the structure of PFSA is based on a PTFE backbone. The conductivity of a well-humidified PFSA membrane can be as high as $0.2 S\ cm^{-2}$. As is well known, fuel cell operation at elevated temperatures can increase the rates of reaction, reduce problems related to catalyst poisoning, reduce the use of expensive catalysts, and minimize problems due to electrode flooding. Unfortunately, a PFSA membrane must be kept hydrated to retain its proton conductivity. Moreover, a PFSA membrane is alcohol permeable if it is used in DAFCs. Because of the disadvantages of PFSA membranes, many alternatives have been proposed [106]. Five categories of membranes are classified: (1) perfluorinated, (2) partially fluorinated, (3) non-fluorinated, (4) non-fluorinated composite, and (5) others.

2) *Catalyst layer*. In intimate contact with the membrane and the backing layer is the CL. This CL, integral with its binder, forms the electrode. Although we know that the reaction of oxygen and hydrogen to form water is a thermodynamically spontaneous reaction, the reaction rate is extremely slow at normal conditions. That is why the catalysts should be used to accelerate the reactions.

The type of catalyst used in PEMFCs depends on the type of fuel used. Pt/C is a frequently used catalyst for both anode and cathode in an H_2/O_2(air) PEMFC. It has been found that oxygen reduction on a $Pt_3Ni(111)$ surface is 10-fold more active for the ORR than the corresponding Pt(111) surface, and 90-fold more active than the current state-of-the-art Pt/C catalysts [61]. Zhang et al. reported that Pt catalysts can be stabilized against dissolution under potential cycling regimes by modifying Pt nanoparticles with Au clusters [63]. However, tolerance to CO is an important issue for catalysts used in DAFCs. It has been proven that PEMFC performance drops with a CO concentration of only several ppm. This is due to the strong chemisorption force of CO onto Pt catalyst [107]. Catalyst alloying is one of the methods to solve the CO problem. Mehta and Cooper summarized 26 anode catalysts in their review paper [108]. It is well known that Pt-Ru/C is the most accepted CO-tolerant catalyst for DAFCs [82].

Non-Pt catalysts are extremely interesting, due to limited Pt sources and high cost. Pd-based [57,1011], Ag-based [55] and WC promoted [57] cathode catalysts

are recently reported. It is found that the Pd-Ti, Pd-Fe, Pd-Au and Pd-Co-Au catalysts show better performance than that of pure Pd catalyst. Suo et al. suggested that the key to improving Pd-based catalysts for ORR is alloying Pd with elements of smaller atomic size to form a "Pd-shell/alloy-core" structure so as to take advantage of the lattice-strain effect and to prevent the disadvantageous surface-ligand effect [111]. Shen's group prepared Ag on tungsten carbide catalysts for ORR [55]. These Pt-free catalysts showed high activities similar to those of Pt-based catalysts. The novel catalysts demonstrate unique selectivity towards the ORR in the presence of methanol, ethanol, isopropanol and glycerol. The Pd-Au supported on the WC catalyst showed a more than 70 mV reduction on the overpotential for ORR compared to that of Pt/C catalyst, indicating a synergistic effect [57].

3) *Gas diffusion layer (GDL)*. The polymer membrane is sandwiched between two sheets of porous backing media, which are referred to as gas diffusion layers (or current collectors). The GDLs are usually made of a porous carbon paper or carbon cloth, typically 1000 μm thick. The GDL acts as a gas diffuser, provides mechanical support and an electrical pathway for electrons, and transfers water away from the electrodes. The porous structure allows the gas to spread out as it diffuses so that the gas will be in contact with the entire surface area of the catalyzed membrane. The GDL is typically water-proofed to ensure the rapid gas diffusion necessary for good fuel cell performance.

7.2.2 Methods for MEA Fabrication

There are different coating processes for the generation of CLs in MEAs. The traditional mode is that the CL is applied to the GDL, followed by membrane addition [1]. The other mode is that the CL is directly applied to the membrane (catalyst coated membrane, CCM) followed by GDL addition [6, 78]. Figure 7.8 shows the configuration of MEAs for two preparation modes.

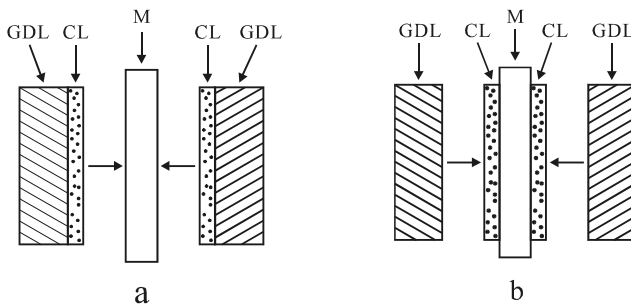
Figure 7.8. The configuration of MEAs for (a) the CL on GDL mode and (b) the CL on membrane mode. GDL – gas diffusion layer; CL – catalyst layer; M – membrane.

There are several methods for creating the CL on a GDL or membrane. For mode one, five methods are summarized here.

Spreading: The spreading method spreads PTFE-containing catalyst ink on a carbon matrix and then heat treats it.

Spraying [112]: In this method, the catalyst ink is repeatedly sprayed on a sheet of carbon paper. Between each spraying, the carbon matrix is heated to evaporate the solvent, in order to prevent the components from re-dissolving in the next spraying.

Catalyst powder deposition [113]: Bevers et al. described this method, in which all the powder components are mixed in a fast running knife mill and then are applied onto the carbon matrix.

Ionomer impregnation [4]: In this method, the catalyst and PFSA suspension in alcohol and water are premixed before the CL is deposited. The GDL/catalyst assembly is formed by applying the catalyst ink onto the carbon matrix.

Electrodeposition [4, 114]: In this method, the metal catalyst is deposited at conducting sites on a carbon matrix.

Mode two had five methods, outlined here:

Impregnation reduction [115]: The membrane is pre-exchanged to the Na^+ form. One side of the membrane is faced to an aqueous Pt salt-containing solution for impregnation and the other side of the membrane is in contact with aqueous $NaBH_4$ reductant. The Pt precursor on the other side is reduced to metal Pt by diffusing the reductant through the membrane. Pt loadings in the order of mg Pt cm^{-2} can be deposited.

Catalyst decal transfer [6, 78]: In the catalyst decaling method, the catalyst ink is cast onto a PTFE blank for transfer to the membrane by hot pressing. A thin CL is left on the membrane when the PTFE blank is peeled away. Finally, the catalyzed membrane is re-hydrated and ion-exchanged to the H^+ form by immersing it in hot dilute H_2SO_4 solution.

Evaporative deposition [115]: Low Pt loadings CLs can be prepared by this method. The difference with the impregnation reduction method is that after the Pt precursor is evaporatively deposited onto a membrane, the entire membrane is immersed in a reductive solution rather than only one side contacting the solution. Catalyst loadings of ≤ 0.1 mg Pt cm^{-2} can be prepared.

Dry spraying [116]: In this method, the components are mixed in a knife mill. The mixture is then atomized and sprayed in a nitrogen steam through a slit nozzle and onto the membrane. A CL with a thickness as little as 5 μm can be prepared by this method.

Painting [4, 79, 80]: In the painting method, the catalyst ink is painted directly onto a dry membrane in the Na^+ form. Caution should be taken to avoid distortion and cracking during drying.

Wee and co-workers recently reviewed the fabrication methods for low-Pt-loading electrocatalysts in PEMFCs. Various methods reported since 2000 for reducing the Pt loadings and increasing the Pt utilization of electrocatalysts in PEMFCs were summarized and compared [117].

7.2.3 Technical Considerations

Tremendous progress has been made in CL technology in recent years. However, there is still room for further improvement in the area of technical considerations, as this section describes.

(1) *How to maximize the three-phase interface of the CL*. It is well known that the performance of a CL depends on its electrochemically active surface area. Optimizing the ratios of the components, the structure, the thickness and the hydrophobicity or hydrophilicity is necessary.

(2) *How to stabilize the metal particles on the support*. The metal particles on supports, like carbon powder or carbon nanotubes, undergo agglomeration or detach from the support. This is because the nanoparticles are active and mobile—and thus have a tendency to agglomerate together—and there are no chemical bonds between the particles and the support. It is necessary to structure the support in such a way that allows the metal particles to anchor tightly on the surface of the support.

(3) *How to reduce the degradation of the components in a CL*. As described above, the catalyst particles, binder and carbon support degrade during the operation due to chemical and electrochemical corrosion. Graphitization is one way to increase the stability and conductivity of the support. Another possible way is to make uniform defects on the outer walls of the carbon nanotubes to anchor the metal particles. Part of the metal particle embeds into the etched pore on the surface, and these embedded particles can increase the contact area and consequently increase the stability.

(4) *How to accelerate the activation of the CL*. Technically, there is a key step in making a fuel cell stack work. This step is the activation of the MEA. In fact, this process dredges the CL to reach its maximum activity. Activation of the MEA usually takes a long time, depending on the CL structure and the method used. Understanding this process well is important for optimizing the CL structure and activation method.

7.2.4 MEA for Anion Exchange Membrane Fuel Cells

It is still a problem to make MEAs for AEMFCs. The main obstacle is the lack of a binder which matches the anion exchange membrane. Varcoe et al. prepared catalyst layers on carbon cloth, for both anode and cathode, by using PTFE as the binder. They found that it is difficult to laminate the catalyst layer to a poly(ethylene-co-tetrafluoroethylene) membrane by hot press [118]. The electrodes and membrane are therefore simply assembled into the fuel cell fixture, non-laminated.

Matsuoka et al. used a 240 μm-thick ammonium-type anion exchange membrane (AHA) to prepare an MEA [119]. The AHA membrane is composed of tetraalkyl ammonium groups as fixed cation groups bonded to a polyolefin backbone chain. The Cl-form membrane was changed to an OH-form before use. Commercial quarternalized poly(4-vinylpyridine) (MW ca. 102,000) was used as the CL binder. The results showed that the alkaline direct alcohol fuel cells using silver as a cathode catalyst gave good performance, comparable to those using a platinum catalyst with mol dm^{-3} ethylene glycol. Park et al. prepared anion-exchange membranes by mixing an amine agent of trimethylamine (TMA) as a monoamine and various diamines, such as *N,N,N',N'*-tetramethylmethanediamine (TMMDA), *N,N,N',N'*-tetramethylethylenediamine (TMEDA), and so on. They used 5 wt% chloromethylated polysulfone (CMPsf) in DMAc as the ionomer

binder to prepare MEA [120]. The H_2/air AEMFC performance of the MEA with 0.5 mg cm^{-2} Pt/C at the anode and the cathode, respectively, was comparable to the performance of one with 0.5 mg cm^{-2} Pt/C at the anode and 2.0 mg cm^{-2} Ag/C at the cathode to reach the 20 mW cm^{-2} of the peak power density.

7.3 Conclusions

As electrochemical reaction sites, CLs play an extremely important role in the performance of fuel cell stacks. A CL mainly consists of catalyst, support and binder. The CL is usually coated on the surface of the GDL. Another method has the CL directly applied to the membrane (catalyst coated membrane, CCM). The selection of the components, the proper ratios of those components, the structure of the formed CL and the formation method of the CL are critical factors in the performance of a fuel cell. The stability of the fuel cell performance is directly related to the stabilities of the catalyst, binder and support in the CL. Degradation of catalytic activity would be due to the agglomeration of the catalyst particles and their detachment from the support, the degradation of the binder, and the oxidation and corrosion of the support, particularly at the cathode. Further improvement in CL performance is possible. The basic technical considerations include how to maximize the three-phase interface of the CL, how to stabilize the metal particles on the support, and how to reduce the degradation of the components in the CL.

The membrane electrode assembly is a sandwich structure, consisting of membrane, catalyst layer and gas diffusion layer. The flow of ionic charge through the membrane is balanced by the flow of electronic charge through an outside circuit. Mass transfer and heat and water management in an MEA are recognized as important for maintaining better steady-state performance of a PEMFC.

References

1. Rajalakshmi N, Dhathathreyan KS. Catalyst layer in PEMFC electrodes: fabrication, characterization and analysis. Chem Eng J 2007;129:31–40.
2. Wang CY. Fundamental models for fuel cell engineering. Chem Rev 2004;104:4727–66.
3. Litster S, McLean G. PEM fuel cell electrodes. J Power Sources 2004;130:61–76.
4. Gottesfeld S, Zawodzinski TA. Polymer electrolyte fuel cells. In: Alkire RC, Kolb DM, editors. Advances in electrochemical science and engineering. New York: Wiley-VCH; 1997. 5:195–301.
5. Ticianelli EA, Derouin CR, Redondo A, Srinivasan S. Methods to advance technology of proton exchange membrane fuel cells. J Electrochem Soc 1988;135:2209–14.
6. Wilson MS, Gottesfeld S. High performance catalyzed membranes of ultra-low Pt loadings for polymer electrolyte fuel cells. J Electrochem Soc 1992;139:L28–30.
7. Passalacqua E, Lufrano F, Squadrito G, Pattia A, Giorgi L. Influence of the structure in low-Pt loading electrodes for polymer electrolyte fuel cells. Electrochim Acta 1998;43:3665–73.
8. Yoon YG, Yang TH, Park GG, Lee WY, Kim CS. A multi-layer structured cathode for the PEMFC. J Power Sources 2003;118:189–92.

9.   Passalacqua E, Lufrano F, Squadrito G, Patti A, Giorgi L. Nafion content in the catalyst layer of polymer electrolyte fuel cells: effects on structure and performance. Electrochim Acta 2001;46:799–805.
10. Zhang XW, Shi PF. Dual-bonded catalyst layer structure cathode for PEMFC. Electrochem Commun 2006;8:1229–34.
11. Yu HM, Ziegler C, Oszcipok M, Zobel M, Hebling C. Hydrophilicity and hydrophobicity study of catalyst layers in proton exchange membrane fuel cells. Electrochim Acta 2006;51:1199–1207.
12. Wei ZD, Ran HB, Liu XA, Liu Y, Sun CX, Chan SH, Shen PK. Numerical analysis of Pt utilization in PEMFC catalyst layer using random cluster model. Electrochim Acta 2006;51:3091–96.
13. Schultz T, Sundmacher K. Mass, charge and energy transport phenomena in a polymer electrolyte membrane (PEM) used in a direct methanol fuel cell (DMFC): modelling and experimental validation of fluxes. J Membrane Sci 2006;276:272–85.
14. Cha SY, Lee WM. Performance of proton exchange membrane fuel cell electrodes prepared by direct decomposition of ultrathin platinum on the membrane surface. J Electrochem Soc 1999;146:4055–60.
15. O'Hayre R, Lee SJ, Cha SW, Prinz FB. A sharp peak in the performance of sputtered platinum fuel cells at ultra-low platinum loading. J Power Sources 2002;109:483–93.
16. Passos RR, Paganin VA, Ticianelli EA. Studies of the performance of PEM fuel cell cathodes with the catalyst layer directly applied on Nafion membranes. Electrochim Acta 2006;51:5239–45.
17. Antoine O, Bultel Y, Ozil P, Durand R. Catalyst gradient for cathode active layer of proton exchange membrane fuel cell. Electrochim Acta 2000;45:4493–4500.
18. Shao YY, Yin GP, Wang ZB, Gao YZ. Proton exchange membrane fuel cell from low temperature to high temperature: material challenges. J Power Sources 2007;167:235–42.
19. Vera M. A single-phase model for liquid-feed DMFCs with non-Tafel kinetics. J Power Sources 2007;171:763–77.
20. Sundmacher K, Schultz T, Zhou S, Scott K, Ginkel M, Gilles ED. Dynamics of the direct methanol fuel cell (DMFC): experiments and model-based analysis. Chem Eng Sci 2001;56:333–41.
21. Haile SM. Fuel cell materials and components. Acta Materialia 2003;51:5981–6000.
22. Sasikumar G, Ihm JW, Ryu H. Dependence of optimum Nafion content in catalyst layer on platinum loading. J Power Sources 2004;132:11–17.
23. Yang Y, Holdcroft S. Synthetic strategies for controlling the morphology of proton conducting polymer membranes. Fuel Cells 2005;5:171–86.
24. Hickner MA, Pivovar BS. The chemical and structural nature of proton exchange membrane fuel cell properties, Fuel Cells 2005;5:213–29.
25. Kraemer SV, Puchner M, Jannasch P, Lundblad A, Lindbergh G. Gas diffusion electrodes and membrane electrode assemblies based on a sulfonated polysulfone for high-temperature PEMFC. J Electrochem Soc 2006;153:A2077–84.
26. Hickner MA, Ghassemi H, Kim YS, Einsla BR, McGrath JE. Alternative polymer systems for proton exchange membranes (PEMs). Chem Rev 2004;104:4587–612.
27. Li QF, He RH, Jensen JO, Bjerrum NJ. Approaches and recent development of polymer electrolyte membranes for fuel cells operating above 100 °C. Chem Mater 2003;15:4896–915.
28. Song JM, Cha SY, Lee WM. Optimal composition of polymer electrolyte fuel cell electrodes determined by the AC impedance method. J Power Sources 2001;94:78–84.
29. Poltarzewski Z, Staiti P, Alderucci V, Wieczorek W, Giordano N. Nafion distribution in gas diffusion electrodes for solid-polymer-electrolyte-fuel-cell applications. J Electrochem Soc 1992;139:761–65.

30. Paik W, Springer TE, Srinivasan S. Kinetics of fuel cell reactions at the platinum/solid polymer electrolyte interface. J Electrochem Soc 1989;136:644–49.
31. Paganin VA, Ticianelli EA, Gonzalez ER. Development and electrochemical studies of gas diffusion electrodes for polymer electrolyte fuel cells. J Appl Electrochem 1996;26:297–304.
32. Easton EB, Astill TD, Holdcroft S. Properties of gas diffusion electrodes containing sulfonated poly(ether ether ketone). J Electrochem Soc 2005;152:A752–8.
33. Kim YS, Sumner MJ, Harrison WL, Riffle JS, McGrath JE, Pivovar BS. Direct methanol fuel cell performance of disulfonated poly(arylene ether benzonitrile) copolymers. J Electrochem Soc 2004;151:A2150–6.
34. Roziere J, Jones DJ. Non-fluorinated polymer materials for proton exchange membrane fuel cells. Ann Rev Mater Res 2003;33:503–55.
35. Tang HL, Pan M, Wang F, Shen PK, Jiang SP. Highly durable proton exchange membranes for low temperature fuel cells. J Phys Chem B 2007;111:8684–90.
36. Tang H, Qi ZG, Ramani M, Elter JF. PEM fuel cell cathode carbon corrosion due to the formation of air/fuel boundary at the anode. J Power Sources 2006;158:1306–12.
37. Stevens A, Dahn JR. Thermal degradation of the support in carbon-supported platinum electrocatalysts for PEM fuel cells. Carbon 2005;43:179–88.
38. Cai M, Ruthkosky MS, Merzougui , Swathirajan S, Balogh MP, Oh SH. Investigation of thermal and electrochemical degradation of fuel cell catalysts. J Power Sources 2006;160:977–86.
39. Baturina OA, Aubuchon SR, Wynne KJ. Thermal stability in air of Pt/C catalysts and PEM fuel cell catalyst layers. Chem Mater 2006;18:1498–1504.
40. Kangasniemi KH, Condit DA, Jarvi TD. Characterization of Vulcan electrochemically oxidized under simulated PEM fuel cell conditions. J Electrochem Soc 2004;151:E125–32.
41. Roen LM, Paik CH, Jarvi TD. Electrocatalytic corrosion of carbon support in PEMFC cathodes. Electrochem Solid-State Lett 2004;7:A19–22.
42. Samms SR, Wasmus S, Savinell RF. Thermal stability of Nafion® in simulated fuel cell environments. J Electrochem Soc 1996;143:1498–1504.
43. Liu YH, Yi BL, Shao ZG, Xing DM, Zhang HM, Carbon nanotubes reinforced Nafion composite membrane for fuel cell applications. Electrochem Solid-State Lett 2006;9:A356–9.
44. Colón-Mercado HR, Kim H, Popov BN, Durability study of Pt_3Ni_1 catalysts as cathode in PEM fuel cells. Electrochem Commun 2004;6:795–9.
45. Yasuda K, Taniguchi A, Akita T, Ioroi T, Siroma Z. Platinum dissolution and deposition in the polymer electrolyte membrane of a PEM fuel cell as studied by potential cycling. Phys Chem Chem Phy. 2006;8:746–52.
46. Teranishi K, Kawata K, Tsushima S, Hirai S. Degradation mechanism of PEMFC under open circuit operation. Electrochem. Solid-State Lett. 2006;9:A475–7.
47. Knights SD, Colbow KM, St-Pierre J, Wilkinson DP. Aging mechanisms and lifetime of PEFC and DMFC. J Power Sources 2004;127:127–34.
48. Maeda M, Hagiwara A, Sotouchi H, Sato H, Zhao X, Morikawa S, et al. The effect of the graphitization degree of carbon material on corrosion rate. Electrochemistry 1999;67:155–9.
49. Matter PH, Zhang L, Ozkan US. The role of nanostructure in nitrogen-containing carbon catalysts for the oxygen reduction reaction. J Catal 2006;239:83–96.
50. Maldonado S, Stevenson KJ. Influence of nitrogen doping on oxygen reduction electrocatalysis at carbon nanofiber electrodes. J Phys Chem B 2005;109:4707–16.
51. Acharya CK, Turner CH. Stabilization of platinum clusters by substitutional boron dopants in carbon supports. J Phys Chem B 2006;110:17706–10.

52. Meng H, Shen PK. Tungsten carbides nanocrystals promoted Pt/C electrocatalysts for oxygen reduction. J Phys Chem B, 2005;109:22705–9.
53. Meng H, Shen PK. The beneficial effect of the addition of tungsten carbides to Pt catalysts on the oxygen electroreduction. Chem Commun 2005;4408–10.
54. Xu CW, Shen PK. Novel Pt/CeO$_2$/C catalysts for electrooxidation of alcohols in alkaline media. Chem Commun 2004;2238–9.
55. Meng H, Shen PK. Novel Pt-free catalyst for oxygen electroreduction. Electrochem Commun 2006;8:588–94.
56. Shen PK, Xu CW. Alcohol oxidation on nanocrytalline oxide Pd/C promoted electrocatalyst. Electrochem Commun 2006;8:184–8.
57. Nie M, Shen PK, Wei ZD. Nanocrystalline tungsten carbide supported Au-Pd electrocatalyst for oxygen reduction. J Power Sources 2007;167:69–73.
58. Zhang L, Zhang JJ, Wilkinson DP, Wang HJ. Progress in preparation of non-noble electrocatalysts for PEM fuel cell reactions. J Power Sources 2006;156:171–82.
59. Bashyam R, Zelenay P. A class of non-precious metal composite catalysts for fuel cells. Nature 2006;443:63–6.
60. Zeng J, Lee JY, Chen J, Shen PK, Song SQ. Increased metal utilization in carbon-supported Pt catalysts by adsorption of preformed Pt nanoparticles on colloidal silica, Fuel Cells. 2007;4:285–90.
61. Stamenkovic VR, Fowler B, Mun BS, Wang GF, Ross PN, Lucas CA, et al. Improved oxygen reduction activity on Pt$_3$Ni(111) via increased surface site availability. Science 2007;315:493–7.
62. Taniguchi A, Akit T, Yasuda K, Miyazaki Y. Analysis of electrocatalyst degradation in PEMFC caused by cell reversal during fuel starvation. J Power Sources 2004;130:42–9.
63. Zhang J, Sasaki K, Sutter E, Adzic RR. Stabilization of platinum oxygen-reduction electrocatalysts using gold clusters. Science 2007;315:220–2.
64. Wang X, Li WZ, Chen ZW, Waje M, Yan YS. Durability investigation of carbon nanotube as catalyst support for proton exchange membrane fuel cell. J Power Sources 2006;158:154–9.
65. Wei ZD, Guo HT, Tang ZY. Heat treatment of carbon-based powders carrying platinum alloy catalysts for oxygen reduction: influence on corrosion resistance and particle size. J Power Sources 1996;62:233–6.
66. Chang SM, Chu HS. Transient behavior of a PEMFC. J Power Sources 2006;161:1161–8.
67. Pai YH, Ke JH, Chou CC, Lin JJ, Zen JM, Shieu FS. Clay as a dispersion agent in anode catalyst layer for PEMFC. J Power Sources 2006;163:398–402.
68. Yoon YG, Park GG, Yang TH, Han JN, Lee WY, Kim CS. Effect of pore structure of catalyst layer in a PEMFC on its performance. Inter J Hydrogen Energy 2003;28:657–62.
69. Amirinejad M, Rowshanzamir S, Eikani MH. Effects of operating parameters on performance of a proton exchange membrane fuel cell. J Power Sources 2006;161:872–5.
70. Ihm JW, Ryu H, Bae JS, Choo WK, High performance of electrode with low platinum loading prepared by simplified direct screen printing process in fuel cells. J Mater Sci 2004;39:4647–9.
71. Fernández R, Ferreira-Aparicio P, Daza L. PEMFC electrode preparation: influence of the solvent composition and evaporation rate on the catalytic layer microstructure. J Power Sources 2005;151:18–24.
72. Benítez R, Chaparro AM, Daza L. Electrochemical characterisation of Pt/C suspensions for the reduction of oxygen. J Power Sources 2005;151:2–10.

73. Xu Z, Qi Z, Kaufman A. Superior catalysts for proton exchange membrane fuel cells sulfonation of carbon-supported catalysts using sulfate salts. Electrochem Solid-State Lett 2005;8:A313–5.

74. Giorgi L, Pilloni L, Giorgi R, Serra E, Alvisi M, Galtieri G, et al. Electrodeposition and sputter deposition of platinum nanoparticles on gas diffusion electrodes. In: Proceedings of the 3rd European PEFC forum; 2005; Lucerne: Fuel Cell Forum 2005 (PEFC); 2005. 124.

75. Kim H, Popov BN. Development of novel method for preparation of PEMFC electrodes. Electrochem Solid-State Lett 2004;A71–4.

76. Morikawa H, Tsuihiji N, Mitsui T, Kanamura K. Preparation of membrane electrode assembly for fuel cell by using electrophoretic deposition process. J Electrochem Soc 2004;151:A1733–7.

77. Taylor AD, Kim EY, Humes VP, Kizuka J, Thompson LT. Ink jet printing of carbon supported platinum 3-D catalyst layers for use in fuel cells. J Power Sources 2007;171:101–6.

78. Wilson M, Gottesfeld S. Thin film catalyst layers for polymer electrolyte fuel cell electrodes. J Appl Electrochem 1992;22:1–7.

79. Liu HS, Song CJ, Zhang L, Zhang JJ, Wang HJ, Wilkinson DP. A review of anode catalysis in the direct methanol fuel cell. J Power Sources 2006;155:95–110.

80. Lamy C, Leger JM, Srinivasan S. Direct methanol fuel cells: from a twentieth century electrochemist's dream to a twenty-first century emerging technology. In: Bockris JO'M, Conway BE, White RE, editors. Modern aspects of electrochemistry. New York: Kluwer Academic Pub; 2001. 34:53–118.

81. Watanabe M, Motoo S. Electrocatalysis by ad-atoms: part II. Enhancement of the oxidation of methanol on platinum by ruthenium ad-atoms. J Electroanal Chem 1975;60:267–73.

82. Frelink T, Visscher W, Van Veen JAR. On the role of Ru and Sn as promotors of methanol electro-oxidation over Pt. Surf Sci 1995;335:353–60.

83. Rao V, Simonov PA, Savinova ER, Plaksin GV, Cherepanova S, Kryukova G, et al. The influence of carbon support porosity on the activity of PtRu/Sibunit anode catalysts for methanol oxidation. J Power Sources 2005;145:178–87.

84. Liu FQ, Wang CY. Optimization of cathode catalyst layer for direct methanol fuel cells Part I. Experimental investigation. Electrochim Acta 2006;52:1417–25.

85. Scott K, Argyropoulos P, Sundmacher K. A model for the liquid feed direct methanol fuel cell. J Electroanal Chem 1999;477:97–110.

86. Argyropoulos P, Scott K, Taama WM. Modelling pressure distribution and anode/cathode streams vapour–liquid equilibrium composition in liquid feed direct methanol fuel cells. Chem Eng J 2000;78:29–41.

87. Yang WW, Zhao TS. A two-dimensional, two-phase mass transport model for liquid-feed DMFCs. Electrochim Acta 2007;52:6125–40.

88. Ge JB, Liu HT. A three-dimensional two-phase flow model for a liquid-fed direct methanol fuel cell. J Power Sources 2007;163:907–15.

89. Chen SX, Zhang X, Shen PK. Macroporous conducting matrix: fabrication and application as electrocatalyst support. Electrochem Commun 2006;8:713–19.

90. Liang ZX, Zhao TS. New DMFC anode structure consisting of platinum nanowires deposited into a Nafion membrane. J Phys Chem C 2007;111:8128–34.

91. Wang H, Xu CW, Cheng FL, Jiang SP. Pd nanowire arrays as electrocatalysts for ethanol electrooxidation. Electrochem Commun 2007;9:1212–16.

92. Varcoe, J R, Slade RCT. Prospects for alkaline anion-exchange membranes in low temperature fuel cells. Fuel Cells 2005;2:187–200.

93. Shen PK, Xu CW, Meng H, Zeng R. Anion exchange membrane fuel cells. In: Zhang XW, editor. Advances in fuel cells. Kerala, India: Research Signpost; 2005.149–79.

94. Yu EH, Scott K. Development of direct methanol alkaline fuel cells using anion exchange membranes. J Power Sources 2004;137:248–56.
95. Yu EH, Scott K. Direct methanol alkaline fuel cell with catalysed metal mesh anodes. Electrochem Commun 2004;6:361–65.
96. Hu FP, Ding FW, Song SQ, Shen PK. Pd electrocatalyst supported on carbonized TiO_2 nanotube for ethanol oxidation. J Power Sources 2006;163:415–19.
97. Xu CW, Shen PK, Liu YL. Ethanol electrooxidation on Pt/C and Pd/C catalysts promoted with oxide. J Power Sources 2007;164:527–31.
98. Paulus UA, Wokaun A, Scherer GG, Schmidt TJ, Stamenkovic V, Radmilovic V, et al. Oxygen reduction on carbon-supported Pt-Ni and Pt-Co alloy catalysts. J Phys Chem B 2002;106:4181–91.
99. Wagner N, Schulze M, Gülzow E. Long-term investigations of silver cathodes for alkaline fuel cells. J Power Sources 2004;127:264–72.
100. Blizanac BB, Lucas CA, Gallagher ME, Arenz M, Ross PN, Marković NM. Anion adsorption, CO oxidation, and oxygen reduction reaction on a Au(100) surface: the pH effect. J Phys Chem B 2004;108:625–34.
101. Zhang Y, Suryanarayanan V, Nakazawa I, Yoshihara S, Shirakashi T. Electrochemical behavior of Au nanoparticle deposited on as-grown and O-terminated diamond electrodes for oxygen reduction in alkaline solution. Electrochim Acta 2004;49:5235–40.
102. Chang CC, Wen TC, Tien HJ. Kinetics of oxygen reduction at oxide-derived Pd electrodes in alkaline solution. Electrochim Acta 1997;42:557–65.
103. Arenz M, Schmidt TJ, Wandelt K, Ross PN, Marković NM. The oxygen reduction reaction on thin palladium films supported on a Pt(111) electrode. J Phys Chem B 2003;107:9813–19.
104. Prakash J, Joachin H. Electrocatalytic activity of ruthenium for oxygen reduction in alkaline solution. Electrochim Acta 2000;45:2289–96.
105. Maoa L, Zhang D, Sotomura T, Nakatsu K, Koshiba N, Ohsaka T. Mechanistic study of the reduction of oxygen in air electrode with manganese oxides as electrocatalysts. Electrochim Acta 2003;48:1015–21.
106. Rikukawa M, Sanui K. Proton conducting polymer electrolyte membranes based on hydrocarbon polymers. Prog Polym Sci 2000;25:1463–1502.
107. Iwasw M, Kawatsu S. Optimized CO tolerant electrocatalysts for polymer electrolyte fuel cells. In: Gottesfeld S, Halpert G, Landgrebe A, editors. Proceedings of the first international symposium on proton conducting membrane fuel cells; Pennington, NJ: The Electrochemical Society; 1995. 1:12–18.
108. Mehta V, Cooper JS. Review and analysis of PEM fuel cell design and manufacturing. J Power Sources 2003;114:32–53.
109. Fernández JL, Raghuveer V, Manthiram A, Bard AJ. Pd-Ti and Pd-Co-Au electrocatalysts as a replacement for platinum for oxygen reduction in proton exchange membrane fuel cells. J Am Chem Soc 2005;127:13100–1.
110. Shao MH, Sasaki K, Adzic RR. Pd-Fe nanoparticles as electrocatalysts for oxygen reduction. J Am Chem Soc 2006;128:3526–7.
111. Suo YG, Zhuang L, Lu JT. First-principles considerations in the design of Pd-alloy catalysts for oxygen reduction. Angew Chem Int Ed 2007;46:2862–4.
112. Kumar GS, Raja M, Parthasarathy S. High performance electrodes with very low platinum loading for polymer electrolyte fuel cells. Electrochim Acta 1995;40:280.
113. Bevers D, Wagner N, Bradke M. Innovative production procedure for low cost PEFC electrodes and electrode membrane structures. Int J Hydrogen Energy 1998;23:57–63.
114. Taylor E, Abdreson E, Vilambi N. Preparation of high platinum utilization gas diffusion electrode for proton exchange membrane fuel cells. J Electrochem Soc 1992;139:L45–6.

115. Fedkiw P, Her W. An impregnation reduction method to prepare electrodes on Nafion SPE. J Electrochem Soc 1989;136:899–900.
116. Gulzow E, Schulze M, Wagner N, Kaz T, Reissner R, Steinhilber G, et AL. Dry layer preparation and characterization of polymer electrolyte fuel cell components. J Power Sources 2000;86:352–62.
117. Wee JH, Lee KY, Kim SH. Fabrication methods for low-Pt-loading electrocatalysts in proton exchange membrane fuel cell systems. J Power Sources 2007;165:667.
118. Varcoe JR, Slade RCT. An electron-beam-grafted ETFE alkaline anion-exchange membrane in metal-cation-free solid-state alkaline fuel cells. Electrochem Commun 2006;8:839–43.
119. Matsuoka K, Iriyama Y, Abe T, Matsuoka M, Ogumi Z. Alkaline direct alcohol fuel cells using an anion exchange membrane. J Power Sources 2005;150:27–31.
120. Park JS, Park SH, Yim SD, Yoon YG, Lee WY, Kim CS. Performance of solid alkaline fuel cells employing anion-exchange membranes. J Power Sources 2008;178:626.

8

Catalyst Layer Modeling: Structure, Properties and Performance

Michael H. Eikerling, Kourosh Malek and Qianpu Wang

8.1 Introduction

Polymer Electrolyte Fuel Cells (PEFCs) are promising electrochemical devices for the direct conversion of chemical energy of a fuel into electrical work [1–5]. Enormous research programs worldwide explore PEFCs as power sources that could replace internal combustion engines in vehicles and provide power to portable and stationary applications. Typically PEFCs operate below ~80 °C. Anodic oxidation of H_2 produces protons that migrate through the polymer electrolyte membrane (PEM) to the cathode, where reduction of O_2 produces water. Meanwhile, electrons, produced at the anode, perform work in external electrical appliances or engines. Unrivalled thermodynamic efficiencies, high energy densities, and ideal compatibility with hydrogen distinguish PEFCs as a primary solution to the global energy challenge.

In spite of the abundance of promising demonstrations of vehicles and devices powered by PEFCs, success at the commercial stage is far from being guaranteed. New generations of fuel cells have to surpass established energy conversion technologies in power density, operational flexibility, stability, and cost. To give an idea of the magnitude of this challenge: currently used PEFC stacks in prototype cars are about 100 times more expensive than conventional combustion engines (~\$30/kW), albeit distinctly inferior in durability [5].

Ten years ago it was a common view among stakeholders in industry and academia that requisite progress could be achieved with engineering-type optimization, relying on existing materials. Nowadays, it is widely recognized, that progress in PEFC technology hinges on breakthroughs – not incremental changes! – in design, fabrication and implementation of innovative materials. Specific targets for improvement involve (i) increasing kinetic rates of electrocatalytic processes at electrodes, (ii) minimizing parasitic voltage losses due to transport of protons and electrons in conduction media and of reactants and water in porous diffusion media, (iii) providing uniform distributions of reaction rates, (iv) balancing water and heat fluxes, and (v) improving the long-term stability of materials. In operational PEFCs all components have to cooperate well in order to

optimize the complex interplay of transport and reaction. This optimization involves more than 50 parameters [6].

The toughest competitions between random composite morphology and complex coupled processes unfold in the catalyst layers (CLs), the cathode catalyst layer (CCL) in particular [7]. All species and all processes that occur in the cell also occur in the catalyst layers: electrochemical reaction, diffusion of hydrogen or hydrocarbon-based fuels (anode) and oxygen (cathode), migration and diffusion of protons, migration of electrons, water transport by diffusion, permeation, electroosmotic drag, as well as vaporization/condensation of water. Electrical current is generated/consumed at nanoparticles of Pt, which are randomly dispersed on a high-surface carbon matrix [8]. During fabrication, the colloidal solution of carbon/Pt and ionomer self-organizes into a phase-segregated composite with interpenetrating percolating phases for the transport of electrons, protons, and gases [7]. As explored in [7], the process of microstructure formation depends on the type of the supported catalyst (carbon, Pt), the type and amount of ionomer added, the type of dispersion medium used during ink preparation, and the fabrication conditions (temperature, pressure).

Electrochemical reactions occur only at those Pt particles where the three phases meet. Major constraints of this design are: (1) statistical limitations of the Pt utilization due to the random three-phase morphology and (2) highly non-uniform reaction rate distributions that arise when the thickness of the layer ($L_{CL} \sim 10$ μm) is large compared to the so-called "reaction penetration depth" δ_{CL} that is determined by the interplay of transport and reaction. These conditions lead to underutilization of Pt and irreversible voltage losses, with those due to oxygen reduction in the CCL (~400 mV) diminishing cell efficiency by 30–40%. An increase by a factor 10 in the surface area of Pt reduces these losses by 60–120 mV. Pt is, however, an expensive and limited resource. For a 60 kW fuel cell vehicle, the current cost of Pt is over $2400 [5]. A simple estimate shows that replacing combustion engines in all existing vehicles by fuel cell drive systems at no penalty in power would by far exhaust all known reserves of Pt. It is thus evident that drastic improvements in power density, durability, and cost would be impossible without a breakthrough in the concept of CLs.

Outline. In this chapter we will provide a detailed overview of recent efforts in theory, molecular modeling, and performance modeling of CLs in modern PEM fuel cells. Our major focus will be on state-of-the-art CLs with porous carbonaceous substrates and random composite morphology. We will evaluate the pertinent design and compare it with recent advanced design strategies. In Section 8.2, we will provide a general discussion of structure and processes in catalyst layers and how they transpire in the evaluation of performance. Section 8.3 reviews the state of the art in theory and modeling. In Section 8.4, we will discuss aspects related to self-organization phenomena in catalyst layer inks during fabrication, controlled by fundamental interactions between the various components. These phenomena determine the evolution of effective properties for transport and electrocatalytic activity. Thereafter, we will present catalyst layer models in Section 8.5 that involve parameters related to structure, processes, and operating

conditions and describe the concepts that have been developed to relate these ingredients to performance.

From the insights presented we will draw conclusions about potential improvements of catalyst effectiveness, voltage efficiency, water handling capabilities, and stability through optimized operating conditions and through radically new structural design. In this chapter we will not include the modeling of the electrochemical impedance response of porous electrodes or catalyst layers. Recent comprehensive coverage on this important topic can be found in the literature [3, 9].

8.2 Understanding Structure and Operation of Catalyst Layers

8.2.1 Challenges for the Structural Design

Overall, FC design can be thought of as an optimization problem in a space of several tens of parameters; the optimization targets include power density, energy density, voltage efficiency, cost, and lifetime. The detailed requirements depend on the envisaged application. The large number of parameters opens up a broad field for fundamental physics and chemistry, experimental research, materials science, and engineering [1–2, 6]. Theory and modeling form the solid bedrock to guide these efforts.

For the catalyst layers, the foremost objective is to obtain the highest reactivity or transfer current density with respect to the desired electrochemical reactions with a minimum amount of the catalyst (DOE target for 2010: 0.29 g Pt per kW). This requires a huge electrocatalytically active surface area, small kinetic barriers to bulk transport and interfacial transfer of protons, electrons and reactant gases, and proper handling of product water and waste heat.

No homogeneous phase could fulfill the conflicting needs for high electrochemical activity and high rates of transport of involved species simultaneously. CLs in general demand composite morphologies of several interpenetrating phases. A solid substrate is needed for electron conduction. In current CLs this corresponds to the carbon phase. A water phase in the void spaces of the solid substrate could act as a medium for diffusion and permeation of protons, water and reactants. Such fully-flooded two-phase CLs could work well when they are made extremely thin, not exceeding thicknesses of $L_{CL} \simeq 100 - 200 \text{ nm}$, so that rates of diffusion of reactant molecules and protons in liquid water are sufficient for providing uniform reaction rate distributions over the entire thickness of the layer.

Gas diffusion is a much more effective mechanism of reactant supply and water removal. Yet, CLs with sufficient gas porosity, usually in the range $X_P \sim 30\% - 60\%$, have to be made much thicker, $L_{CL} \sim 10 \text{ μm} - 20 \text{ μm}$. At such thicknesses, proton diffusion in liquid water is not sufficient for providing uniform reaction conditions. Porous gas diffusion electrodes are therefore impregnated with proton-conducting ionomer, usually Nafion [1–2, 4]. Resulting CLs are random composite media of carbon/Pt, ionomer, and a complex pore space.

The two major improvements in the catalyst layer design have been the incorporation of Pt or Pt group metal nanoparticles with sizes in the range of 2–5 nm and the impregnation or colloidal mixing of the high surface area carbon support with ionomer. The former step provides a significantly enhanced electrocatalytically active surface area. The latter step ensures uniform access of protons to active Pt surface throughout the complete layer. As first demonstrated by Ian D. Raistrick at Los Alamos National Laboratory (LANL), these steps enabled a dramatic reduction of catalyst loading [10]. This preparation technique, later refined at LANL [11], evolved into the standard method of catalyst layer and MEA fabrication. It has been employed and continuously improved by laboratories worldwide. Nowadays, ionomer completely replaces the PTFE that had formed a major component as a binder and hydrophobizing agent in early fabrication methods. By these measures catalyst loadings have been reduced from about 4–10 mg Pt/cm^2 (in the 1980s) to about 0.4 mg Pt/cm^2 today.

How can we depict the process of catalyst layer formation? Self-organization of ionomer and carbon/Pt in colloidal ink solution leads to the formation of phase-segregated agglomerated morphologies. Agglomerates (with radii $R_a \sim 30\ \mathrm{nm} - 100\ \mathrm{nm}$) consist of primary particles of carbon (with sizes in the range of $5\ \mathrm{nm} - 10\ \mathrm{nm}$) onto which Pt nanoparticles are deposited. It was found in [7] that ionomer molecules do not penetrate into the Pt/carbon clusters. Instead they form a separate proton-conducting film of thickness ~10 nm that is attached to the surface of agglomerates. Notice that penetration of Nafion into the agglomerates depends on fabrication technique, Nafion concentration, type of carbon, and the kinetics of the agglomeration process.

The typical agglomerated structure provides a bimodal, bi-functional Pore Size Distribution (PSD), with primary pores between Pt/C particles inside of agglomerates (with pore radii $r_\mu \simeq 1 - 10\ \mathrm{nm}$) and secondary pores between agglomerates ($r_M \simeq 1 - 10\ \mathrm{nm}$). There is a competition between secondary pores and ionomer domains to occupy the voids between agglomerates.

Coarse-Grained Molecular Dynamics (CGMD) studies of self-organization phenomena in catalyst layer inks during fabrication have recently confirmed this structural picture [7]. We will describe these calculations and the insights into structural formation and correlations in detail in Section 8.4. Agglomeration and the dual porosity network, occurring spontaneously in the formation process, are essential for operation, as we will discuss in detail in Section 8.5. The notion of agglomerates is, moreover, consistent with the majority of experimental data [12].

8.2.2 Porous Electrode Theory: Historical Perspective

The importance of structural effects in gas diffusion electrodes was realized long before the development of the current generation of CLs for PEFCs. The basic theory of gas diffusion electrodes, including the interplay of reactant transport through porous networks and electrochemical processes at highly dispersed electrode|electrolyte interfaces, dates back to the 1940s and '50s [13, 14]. Later work realized the importance of surface area and utilization of electrocatalysts in porous electrodes [15]. A series of seminal contributions by R. De Levie opened

the way to the exploration of the electrochemical impedance response for the characterization of porous electrodes [16–18]. The transmission line approach of De Levie constituted the seed for the study of interfacial phenomena in fractal electrodes [19–24].

Major contributions to the development of the macrokinetic or macrohomogeneous theory of porous electrodes were made by Yu. A. Chizmadzhev and Yu. G. Chirkov [25–27]. In these works the importance of the interplay of oxygen diffusion and interfacial kinetics had already been realized. For oxygen reduction electrodes, a large electrocatalytically active surface area per unit volume, S_{el}, has to compensate for the smallness of the intrinsic activity per unit real surface area, i.e., of j^{0*}, of any known electrocatalyst. The characteristic pore dimension, r_p, should be small in order to guarantee a large S_{el}, which scales roughly as $S_{el} \sim 1/r_p$. On the other hand, high rates of the electrochemical reaction should spread over the entire thickness of the electrode, L_{el}, requiring high rates of transport of reactants and products via diffusion paths. In the limit of fast reactant diffusion, the internal electrode surface would be utilized uniformly for current conversion, i.e., resulting in the following proportionalities of the Faradaic current density $j \propto j^{0*} S_{el} L_{el}$. This proportionality is only valid at low thickness, $L_{el} \ll \delta_{el}$, where δ_{el} is the so-called "reaction penetration depth". We will elaborate on this property below. The necessity to optimize the pore space in view of gaseous transport and electrochemical reaction was already well comprehended at that time [25].

The importance of microstructural optimization of hydrophobic gas diffusion electrodes was emphasized in an article by Tantram and Tseung from 1969 [28]. These authors considered porous electrodes that consisted of mixtures of finely dispersed Pt black particles, bonded by polytetrafluoroethylene (PTFE). Hydrophobic and hydrophilic parts formed interconnected networks of porous PTFE and porous catalyst aggregates. These authors recognized the importance of agglomeration and dual hydrophobic/-philic porosity. The functional distinction of hydrophobic mesopores and hydrophilic micropores led to the development of the flooded agglomerate model by Giner and Hunter, who explored the effects of intrinsic catalyst activity, internal porosity, and real catalyst surface area on electrochemical performance of Teflon-bonded electrodes [29]. Their original model considers the electrode as a bunch of parallel flooded cylinders that consist of a homogeneous mixture of catalyst and liquid electrolyte. Elongated, sample-spanning void spaces between the cylinders provide the pathways for gaseous diffusion.

Similar agglomerate approaches were adopted by Iczkowski and Cutlip [30] and by Björnbom [31]. Those works already identified the doubling of the apparent Tafel slope as a universal signature of the interplay of mass transport limitations and interfacial electrochemical kinetics. Flooded agglomerate models have been employed since then to analyze sources of irreversible voltage losses, optimum electrode thickness, and effectiveness of catalyst utilization. Moreover, it was

suggested that electrodes with continuous distributions of catalyst and electrolyte cannot give rise to diffusion-limited current densities.

Simple pore models, [32] thin film models, [33] macrohomogeneous models, and refined variants of agglomerate models are still being applied and further developed for the present generation of ionomer-bound composite catalyst layers in PEFCs [34–38]. Effectiveness factor approaches have been elaborated as quantitative tools to compare active layers [39]. Moreover, macrohomogeneous electrode models have been integrated into simulation approaches for complete PEFCs [40]. Notably, in spite of the widely recognized importance of microstructural effects in CLs, many earlier approaches in fuel cell modeling at the cell and stack levels, e.g., those employing computational fluid dynamics, were treating CLs as infinitesimally thin interfaces without structural resolution, whose only physical property explicitly considered is the rate of current conversion or exchange current density. This could lead to wrongful or misleading conclusions about the causes of the main detrimental effects in PEFC performance. Nowadays, pertinent CFD models of fuel cells, implemented in FLUENT and CFD Ace+, account for structural details and two-phase flow phenomena in catalyst layers [41].

A model for composition effects in ionomer-bound catalyst layers of PEFCs was developed by Tom Springer and colleagues at LANL [42, 43]. Springer's one-dimensional macrohomogeneous model accounts for irreversible voltage losses due to gas transport, ionic conductivity, and interfacial kinetics at the Pt/ionomer interface. It represents a first significant attempt to relate these losses to operating conditions and effective parameters of transport and reaction in PEFCs. A fit between model and experimental data allowed quantifying voltage losses caused by kinetic processes and transport of oxygen and protons.

Since then, other groups have adopted similar models. Assets of this approach are versatile: (i) it relates global performance of CCLs to immeasurable local distributions of reactants, electrode potential and reaction rates; (ii) it defines a penetration depth of the active zone; and (iii) it suggests an optimum range of current density and catalyst layer thickness with minimal performance losses and highest utilization of the catalyst.

Combination of the macrohomogeneous approach for porous electrodes with a statistical description of effective properties of random composite media, employing concepts of percolation theory [44–46], significantly enhanced capabilities of catalyst layer models with respect to systematic evaluation of performance and optimization of thickness, composition, and porous structure [3, 47–48]. The resulting structure-based model correlates the performance of the CCL with the volumetric amounts of Pt, C, ionomer, and pores. The basis for the percolation approach is that a catalyst particle can take part in reactions only if it is connected to three percolating clusters of carbon/Pt, ionomer phase, and pore space. It has been employed to determine optimum compositions of CCLs with respect to maximum voltage efficiency and maximum catalyst utilization [47]. The general outline of this structure-based modeling framework is depicted in Figure 8.1. We will provide a detailed discussion in Section 8.5.
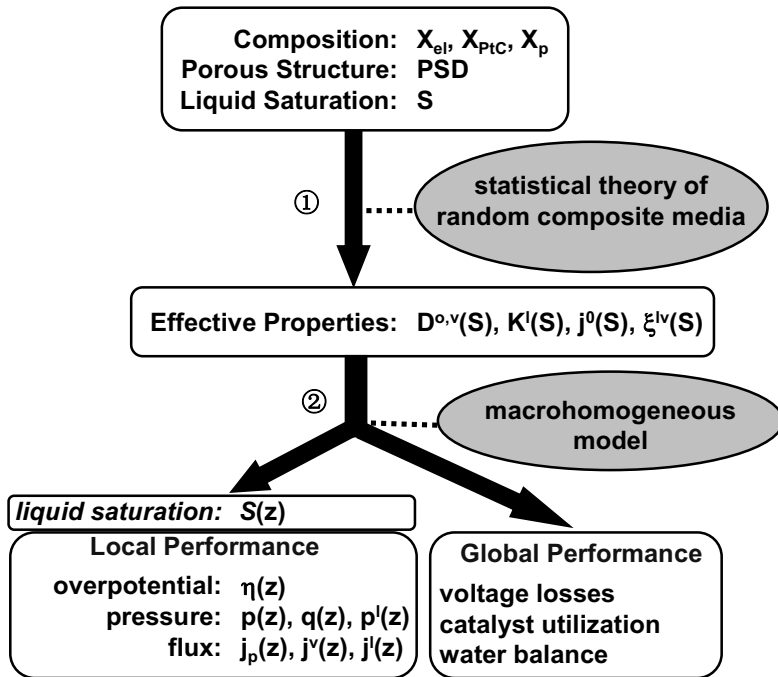
Figure 8.1. Outline of the general framework for structure-based modeling of catalyst layer operation in polymer electrolyte fuel cells [51]. (Reprinted from Electrochimica Acta 53.13, Liu J, Eikerling M. Model of cathode catalyst layers for polymer electrolyte fuel cells: The role of porous structure and water accumulation, 4435–46, ©2008, with permission from Elsevier.)

8.2.3 Misapprehensions and Controversial Issues

In spite of the long history of porous electrode theory and the recent successes of structure-based models of thin-film, ionomer-bound CLs in PEFCs, tenacious misapprehensions and controversial issues persist. To begin with, it is not clear which type of interfaces, viz. Pt|gas, Pt|liquid water and Pt|ionomer, is most abundant and makes the major contribution to the electrocatalytically active surface area. Pt|vapor interfaces are disconnected from the proton-supplying network; they thus have to be deemed inactive. Water in CCLs is, therefore, primarily produced in liquid form. Nevertheless, modeling approaches often include a misleading assumption that water is produced in vapor form and that the issue of water management is to prevent condensation [49].

   The relative contributions to electrocatalytic conversion due to Pt|ionomer and Pt|water interfaces depends on phase segregation, porous morphology, and wetting properties of pores. A larger fraction of hydrophilic micropores will increase the contribution of Pt|water interfaces relative to that of Pt|ionomer interfaces [50, 51].

   The nature of electrocatalytically active catalyst surfaces is related to the vital but largely unsettled issue of agglomeration of carbon/Pt and spontaneous phase segregation between primary particles of carbon/Pt and ionomer molecules. This

motivates recent studies on self-organization phenomena in catalyst layer inks. Agglomerates are in general difficult to identify and characterize. The majority of data supporting the existence of agglomerates are based on TEM micrographs and porosimetry [12, 52–53]. Controversy evolves around size and composition of agglomerates. The structure and distribution of ionomer and interactions between ionomer and carbon/Pt are of key importance in this context. Commonly encountered views are to consider (i) uniform mixtures of ionomer and carbon/Pt particles in agglomerates, (ii) a thin uniform film of ionomer surrounding agglomerates of C/Pt or, (iii) random uncorrelated percolating phases of C/Pt and ionomer. As for the first possibility, simply on the basis of size considerations it seems impossible that ionomer fibrils could penetrate into nm-sized pores of carbon/Pt agglomerates and form an embedded proton conducting phase therein. The ionomer phase itself depends on internal nm-size pores in order to attain adequate proton mobilities. In spite of this size paradox many approaches in agglomerate modeling employ the so-called Thiele modulus [54, 55], which demands uniform penetration of agglomerate pores by an intrinsically proton-conductive medium. The other two options, i.e., assuming a thin ionomer film uniformly coating agglomerates or independent percolating phases, depend on type and strength of adhesive forces between carbon and ionomer. Next, the role of the bimodal porous morphology and water accumulation in pores has only recently moved into the focus of modeling studies. In general, a large fraction of small hydrophilic pores inside of agglomerates with sizes in the range of $1\,nm\ -10\,nm$ is advantageous in view of providing a large surface area for the deposition of the catalyst. These pores should be flooded with liquid water. For this purpose, it is beneficial if they are hydrophilic. On the other hand, larger secondary pores between agglomerates are vital for the gaseous transport of reactants. These pores should be hydrophobic. As emphasized in [50, 51], understanding the interplay between composition, porous structure, wetting properties, and operating conditions is crucial for determining distribution, fluxes, and transformation of water in cathode catalyst layers. Possible macroscopic manifestations of these phenomena are limiting current behavior and the occurrence of bistability in current-voltage relations of CCLs. These non-linear phenomena play an important role in the selection of operating conditions, and for systematic improvement of the structural design of CCLs.

8.2.4 Effectiveness of Catalyst Utilization

Numerous publications in fuel cell research dwell on the key issues that are related to Pt utilization in PEFCs. A brief survey of representative studies that focus on Pt utilization and effectiveness factors can be found in [56]. In the past, ambiguous definitions of catalyst utilization have been exploited and rather contradictory values have been reported. This could lead to a wrongful assessment as to how much the performance of fuel cells could be improved by advanced structural design of catalyst layers. As a matter of fact, the accurate distinction and determination of catalyst utilization and effectiveness factors has a major impact on defining priorities in catalyst layer research.

Pt utilization is a materials property. It is defined as the ratio of the electrocatalytically active surface area, which is accessible to electrons and protons, to the total surface area of Pt,

$$u_{Pt} = \frac{S_{ESA}}{S_{tot}} \tag{8.1}$$

Pt utilization has been considered under different conditions, viz. in the catalyst powder and in the membrane electrode assembly (MEA) of an operational fuel cell. The electrocatalytically active surface area in the catalyst powder, $S_{Pt,ESA}$, can be estimated from the charge under the H-adsorption or CO-stripping waves measured by thin-film rotating disk electrode (TF-RDE) voltammetry in H_2SO_4 solution [57–59]. The total surface area, S_{tot}, can be calculated from the mean particle size determined by XRD experiments [57, 58] or from HR-TEM images [59], based on the assumption that the particles are spheres with surface area $4\pi r_{Pt}^2$. For powders of carbon-supported Pt nanoparticles values of u_{Pt} were reported to be 109% by Easton and Pickup [57], 125% by Shan and Pickup [58], and 100% by Schmidt et al. [59]. The fact that the estimated utilization is greater than 100% is usually attributed to contributions from background currents (e.g., including that for H_2 evolution) to the measured charge.

The purpose of studying Pt utilization in the catalyst powder is to evaluate the electronic connectivity of carbon/Pt and maximum ionic accessibility of Pt nanoparticles. 100% of Pt utilization means that all of the Pt nanoparticles are connected to the electronic conduction network and the entire Pt surface is accessible for protons. Close to 100% Pt utilization in the powder immersed in liquid electrolyte is possible, since only a negligible fraction of the Pt surface is covered by carbon particles. If Pt nanoparticles were supported by a polymer material such as poly(3,4-ethylenedioxythiophene)/poly(styrene-4-sulfonate), Pt utilization was reported to be only 43–62%, which is due to poor electronic contact of Pt nanoparticles with the polymer support and blocking of the Pt surface with the polymer [58].

The Pt utilization in the catalyst layer of an operational MEA can be estimated from the charge under the H-adsorption waves in cyclic voltammetry (CV) using driven-cell mode [59]. For example, to determine the accessible Pt surface area of a cathode, the cathode compartment of a single cell is purged with humidified nitrogen, serving as the working electrode, while the anode compartment is purged with humidified hydrogen, serving as both counter and reference electrode. In some studies, S_{tot} was calculated from the mean particle size, and Pt utilization in the cathode was reported to be 34% by Dhathathreyan et al. [60], 45% by Cheng et al. [61], 52% by Sasikumar et al. [62], and 55–76% by Li and Pickup [63]. As mentioned above, S_{tot} could also be obtained by the TF-RDE method, and Pt utilization in the cathode was reported to be 86–87% [59], and 90% by Gasteiger et al. [64]. Compared with Pt utilization in the catalyst powder, the reduced Pt utilization in the catalyst layer of a fully functional MEA originates from two effects. Some Pt nanoparticles may be encapsulated by ionomer and, therefore, lose

electronic contact during the fabrication process. The other effect is that a fraction of the Pt particles are neither covered by ionomer electrolyte nor wetted by liquid water, implying that they are disconnected from the proton-supplying network.

The foregoing discussion reveals large uncertainties in determining Pt utilization in experiment. The total charge transferred upon hydrogen adsorption may involve non-wetted inactive catalyst surface area or include the catalytically inert substrate surface due to spillover effects [65]. Usually, the surface area obtained from hydrogen adsorption and CO-stripping methods could be different from the active area in an operating fuel cell. Moreover, the values u_{Pt} provided do not account for non-uniform reaction rate distributions, which arise at finite rates of reactant transport and consumption under stationary fuel cell operation.

The universal physical parameter for evaluating successful design of CLs is the exchange current density per unit apparent surface area of the electrode, j^0. It is the key property to relate complex structures and processes in CLs to catalyst utilization, distributions of reaction rates, irreversible voltage losses, and non-linear phenomena in current-voltage response curves. j^0 represents the capability of a CL to convert chemical flux of reactants into electronic current. The following expression suggested in [50] elucidates challenges at multiple scales that the design of CLs is facing,

$$j^0 = 2 \cdot 10^3 \left[m_{Pt} \right] j^{0*} \Gamma_{stat}, \quad \text{with } \Gamma_{stat} = \varepsilon^{S/V} \Gamma_a g(S_r) \frac{f\left(X_{PtC}, X_{el}\right)}{X_{PtC}} \tag{8.2}$$

In order to minimize parasitic voltage losses in the cell, j^0 should be maximal. Catalyst loading, $\left[m_{Pt} \right]$ (in units $\mathrm{mg\,cm^{-2}}$), should be minimal in order to minimize costs. All remaining factors in Equation 8.2 should, thus, be maximal. The factor $2 \cdot 10^3$ is the ideal Pt surface area per real electrode surface area for spreading a Pt loading of $1\,\mathrm{mg\,cm^{-2}}$ as a monoatomic layer; this value is a theoretical baseline for total active surface area at the atomistic scale. The specific exchange current density, j^{0*}, normalized to the unit surface area of the electrocatalyst, is the target of fundamental studies in electrocatalysis [8, 66–67]. It is known from numerous experimental studies that size, surface morphology, electronic structure of catalyst nanoparticles as well as the properties of the substrate determine the electrochemical activity, i.e., j^{0*}. Predictive relations between particle size and activity are, however, difficult to establish, since the size of particles also affects electronic and geometric properties at their surface.

The factors in Γ_{stat} in Equation 8.2 account for statistical limitations of catalyst utilization on a hierarchy of scales. At the nanoscale, $\varepsilon^{S/V}$ is the surface-to-volume atom ratio of Pt nanoparticles, which scales roughly as $1/r_{Pt}$. Particles with diameters $< 3\,\mathrm{nm}$ give $\varepsilon^{S/V} > 50\%$. Since only surface atoms could be potentially active, this has a direct impact on catalyst utilization. Additional structural effects

at the single particle level include the presence of active and inactive sites on the catalyst surface [68]. At the mesoscopic scale, the effectiveness factor of catalyst utilization of agglomerates, Γ_a, is mainly an electrostatic phenomenon [69]. The factor $g(S_r)$, where S_r is the liquid water saturation, is the wetted fraction of pore surface area in the CL, accounting for the fact that only water-wetted Pt can be reached by protons and, therefore, be active. The last factor $\dfrac{f(X_{PtC}, X_{el})}{X_{PtC}}$ represents the statistical fraction of Pt particles at or near the triple phase boundary of solid carbon/Pt phase (volume fraction X_{PtC}), ionomer phase (X_{el}), and pore space ($X_P = 1 - X_{PtC} - X_{el}$) [3, 47–48]. Overall, maximizing the ratio $j^0/[m_{Pt}]$ is a major objective in fuel cell research. This task represents a joint challenge for electrocatalysis and for understanding statistical inhomogeneity in random composite media with hierarchical structure.

At this point, it is important to realize that the ultimate optimization target of electrode design is not Pt utilization, which is a static statistical property of a catalyst layer, but more importantly the effectiveness factor, which includes as well the effects of non-uniform reaction rate distributions due to mass transport phenomena at finite current densities in the operating fuel cell. In simple 1D electrode theory, the interplay of j^0 with transport parameters of reactants, protons, and electrons determines the "reaction penetration depth" δ_{CL} [3]. The criterion for uniform reaction rate distributions is that the reaction penetration depth is comparable to or larger than the thickness of the CL, $\delta_{CL} > L_{CL}$.

8.2.5 Evaluating the Performance of CLs

In general, the performance of PEFCs can be rated based on the dependence of the fuel cell working voltage on current density, i.e., $E(j_0)$. The deviations of $E(j_0)$ from the equilibrium or open circuit voltage, E^{eq}, can be interpreted as a fingerprint of various sources of irreversible voltage losses. This interpretation is, however, highly nontrivial and often controversial.

The voltage efficiency is

$$\varepsilon_V = \frac{E(j_0)}{E^{eq}}. \tag{8.3}$$

The total efficiency of a PEFC, ε_{cell}, is given by the product

$$\varepsilon_{cell} = \varepsilon_{th} \cdot \varepsilon_V \tag{8.4}$$

with the thermodynamic efficiency,

$$\varepsilon_{th} = \frac{\Delta G}{\Delta H} = \frac{-n_t F E^{eq}}{-n_t F E^{eq} + T \Delta S} \qquad (8.5)$$

where ΔS is the entropy change of the reacting system and E^{eq} is the reversible cell voltage, given by the Nernst equation,

$$E^{eq} = -\frac{\Delta G}{n_t F} = E^{eq,c} - E^{eq,a} = E^0 + \frac{RT}{2F} \ln \left(\frac{[H_2][O_2]^{1/2}}{[H_2O]} \right) \qquad (8.6)$$

At stack and system levels, additional factors due to non-optimal reactant consumption have to be taken into account in evaluating the overall energy efficiency.

If we only focus on the operation of membrane electrode assemblies (MEAs), E mainly includes irreversible voltage losses due to proton conduction in the polymer electrolyte membrane (PEM) and voltage losses due to transport and electrocatalytic activation of ORR in CCLs,

$$E(j_0) = E^{eq} - R_{PEM} j_0 - \eta_{CCL}(j_0) \qquad (8.7)$$

where R_{PEM} is the Ohmic membrane resistance [70]. Non-uniform distribution of water in PEMs due to improper water balance can lead to non-linear effects in the membrane resistance. Under extreme conditions, PEM dehydration on the anode side can give rise to a limiting current density in $E(j_0)$. In general, R_{PEM} should be considered as a function of j_0 [3]. The term $\eta_{CCL}(j_0) = \eta(z = 0) = \eta_0$ accounts for irreversible voltage losses in the CCL. Equation 8.7 neglects other parasitic losses, e.g., those due to kinetic hindrances and poisoning in the anode catalyst layer or due to flooding and reactant starvation in flow fields.

The problem is that experimentally determined $E(j_0)$ relations are usually relatively featureless and their interpretation is, thus, ambiguous. They can be reproduced with certain ingredients, involving mass transport limitations in any of the fuel cell components and activation barriers of kinetic processes in the electrodes, which do not necessarily reflect true physical phenomena in CCLs. $E(j_0)$ curves thus do not provide unique relations between microscopic structural characteristics, physico-chemical processes and performance in CCLs. This can lead to misconceptions, e.g., in the understanding of the causes of limiting current behavior or of bistability phenomena, often observed in fuel cell operation. Additional diagnostic tools are needed in order to unravel the complex interplay between structure, processes, and performance. Compared to the steady-state polarization experiment, electrochemical impedance spectroscopy (EIS) is more useful for the study of mass-transport limitations in a PEMFC. In an EIS experiment, a cell is perturbed from its steady-state operating conditions by superimposition of a small sinusoidal signal in the form of either cell potential or

operating current over a wide range of frequency. An impedance plot allows resolving processes occurring in the cell with different time constants, including double layer charging, charge transfer, ion conduction, mass transport, adsorption, and desorption. Simple analogues (e.g., in the form of equivalent circuits) or physical models are usually needed to deconvolute these processes in impedance spectra and extract physical parameters of transport processes and interfacial kinetics. Because the dominating processes in PEFCs often change with the change of steady-state operating conditions, a better understanding of the transport limitations in cells can be obtained from a series of EIS experiments carried out at different steady-state current densities. Moreover, transient techniques like current interrupt measurements can be used to extract time constants and corresponding rate constants of kinetic processes in operating fuel cells.

A 1D model for the physical evaluation of effects of structure and distributed processes on stationary catalyst layer performance requires a minimum of two phenomenological parameters, the exchange current density j^0 and the reaction penetration depth δ_{CL}. Each of them is a complicated but unique function of structure and operating conditions. Neglecting further complicating traits, for instance, issues related to the liquid water balance, these two parameters uniquely define the relation between j^0 and $\alpha_C \eta_0$, where α_C is the transfer coefficient of the electrode reaction on the cathode side. Thereby, voltage efficiency, energy density, power density, and effectiveness of catalyst utilization at given current density and catalyst loading can be calculated.

As discussed above, j^0 is a static materials property. It is the product of the specific electrocatalytic activity of the catalyst surface times statistical factors that arise at all scales due to the random morphology and distribution of the catalyst in the composite CL, as considered in Equation 8.2. The reaction penetration depth δ_{CL} is a steady state property, which is mainly determined by the nonlinear coupling between transport of oxygen and protons and exchange current density. Together, both parameters, j^0 and δ_{CL}, determine the overall effectiveness of catalyst utilization.

For illustration purposes we consider here a simple scenario of this interplay. We evaluate the effectiveness factor at a fixed cell voltage and thus at a fixed CL voltage loss, η_0. We can express the corresponding current density as a two-variable function $j_0 = f\left(j^0, \delta_{CL} \right)$, where δ_{CL} is a function of η_0. This relation can be used to determine the effectiveness factor, Γ_{CL}, of the catalyst layer. In the case of severely limited oxygen diffusion, we have the following relations for local oxygen partial pressure and current density:

$$p(z) = \exp\left[-\frac{L_{CL}}{\delta_{CL}}\left(1 - \frac{z}{L_{CL}}\right)\right],$$

$$j(z) = I\frac{L_{CL}}{\delta_{CL}}\left\{1 - \exp\left[-\frac{L_{CL}}{\delta_{CL}}\left(1 - \frac{z}{L_{CL}}\right)\right]\right\} \qquad (8.8)$$

$$\frac{\delta_{CL}}{L_{CL}} = \sqrt{\frac{j^0}{I}}\exp\left(-\frac{\eta_0}{2b}\right)$$

where $z = 0$ is the PEM|CCL boundary and $z = L_{CL}$ is the CCL|GDL boundary. In Equation 8.8, $p = P_{O_2}/\overline{P}_{O_2}$ is the non-dimensional oxygen partial pressure, where $\overline{P}_{O_2}$ is the O_2 partial pressure at the CCL|GDL interface, $b = \dfrac{RT}{\alpha_c n_t F}$ is the Tafel-parameter, and $I = \dfrac{4F\overline{P}_{O_2}D^o}{RTL_{CL}}$ is a characteristic current density of diffusive flux through the layer (with unit A cm^{-2}).

For a fixed η_0, the overall effectiveness of Pt utilization can be defined by

$$\Gamma_{CL} = \Gamma_{stat} \cdot \Gamma_\delta = \frac{j^0}{2\cdot10^3\left[m_{Pt}\right]j^{0*}}\frac{j_0}{j_0^{id}} \qquad (8.9)$$

where the first quotient on the right hand side, Γ_{stat}, corresponds to statistical factors in Equation 8.2 and the second quotient, Γ_δ, gives the ratio of the actual current density, including transport limitations, relative to the ideal current density that would be obtained if reaction rates were distributed in an ideal uniform way without any transport limitations. Using Equations 8.8 and 8.9 it can be easily demonstrated that

$$\Gamma_{CL} = \Gamma_{stat} \cdot \frac{\delta_{CL}}{L_{CL}}\left\{1 - \exp\left(-\frac{L_{CL}}{\delta_{CL}}\right)\right\} \qquad (8.10)$$

In general, Equation 8.10 highlights the importance of adjusting thickness and effective properties of transport and reaction in such a way that $\delta_{CL} \sim L_{CL}$. If we replace δ_{CL} by η_0, using Equation 8.8, we obtain the explicit dependence of the effectiveness factor on the catalyst layer voltage loss:

$$\Gamma_{CL} = \Gamma_{stat} \cdot \sqrt{\frac{j^0}{I}}\exp\left(-\frac{\eta_0}{2b}\right)\left\{1 - \exp\left[-\sqrt{\frac{j^0}{I}}\exp\left(-\frac{\eta_0}{2b}\right)\right]\right\} \qquad (8.11)$$

Equations 8.8 to 8.10 provide a simple means for evaluating various catalyst layer designs. This can be applied for $\delta_{CL} < L_{CL}$ but it becomes inaccurate for $\delta_{CL} \simeq L_{CL}$. The crude framework for evaluating catalyst layer performance that was described in this section could be refined by including additional transport limitations, water accumulation, and higher dimensional effects.

8.3 State of the Art in Theory and Modeling: Multiple Scales

The objective of catalyst layer modeling is to establish relations between fabrication procedures and conditions, structure, effective properties of transport and reaction, and performance. The foregoing sections illustrated that structure and function of catalyst layers evolve over a wide range of scales, from microsopic processes at supported catalyst nanoparticles to the operation in a fuel cell at the macroscopic device level. The modeling of structure and operation of CLs is, therefore, a multiscale problem. The challenges for theory and modeling of catalyst layer operation are markedly reduced if we realize that the main structural effects occur at well-separated scales, viz. at catalyst nanoparticles ($r_{Pt} \sim 2\ nm$), at agglomerates of carbon/Pt ($R_a \sim 100\ nm$), and at the macroscopic device level ($L_{CL} \sim 10\ \mu m$) of an operating fuel cell, at which CLs can be considered as effective homogeneous media. Separate approaches in theory and modeling can thus be considered at these different scales, as illustrated in Figure 8.2.
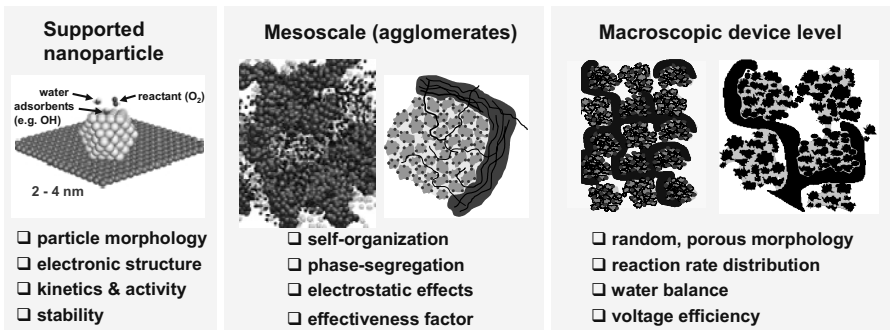

Supported nanoparticle	Mesoscale (agglomerates)	Macroscopic device level
❑ particle morphology ❑ electronic structure ❑ kinetics & activity ❑ stability	❑ self-organization ❑ phase-segregation ❑ electrostatic effects ❑ effectiveness factor	❑ random, porous morphology ❑ reaction rate distribution ❑ water balance ❑ voltage efficiency

Figure 8.2. Illustration of structures and phenomena at multiple scales that control the performance of catalyst layers in PEFCs. Left: Pt nanoparticle on carbonaceous substrate (~ 3 nm); middle: phase-segregation and agglomerate formation at mesoscale (~ 50 nm); right: the catalyst layer as a complex composite medium at the macroscopic scale (~ 10 μm).

At the nanoparticle level, the specific exchange current density, j^{0*}, in Equation 8.2 is sensitive to size, surface morphology, and the surface electronic structure of Pt nanoparticles as well as to the properties of the substrate [8, 71–75]. A better understanding of the relationships between particle size and activity, including those effects, is critical in view of the design of highly performing catalyst systems [68, 76–78]. Obviously, a reduction in particle size improves the

surface-to-volume ratio of catalyst atoms. Yet, the relation between particle size and activity is highly non-trivial, since the size of the particles also affects electronic and geometric properties at their surface [79]. A complex interplay of elementary surface processes, including molecular adsorption, surface diffusion, charge transfer, recombination, and desorption, determines observable rates of relevant reactions, i.e., reduction of oxygen and oxidation of hydrogen, methanol, or carbon monoxide [68, 74–75, 79].

Studies of stable conformations of supported nanoparticles as well as of the elementary processes on their surface demand density functional theory calculations as well as kinetic modeling of reactivities based on Monte-Carlo simulations or Mean Field approximations [68, 80]. Due to the complex nature of structural effects in electrocatalysis only a very few theoretical studies have been successful in establishing systematic trends in structure vs. reactivity relations. The most successful exception is the d-band model of Hammer and Norskov [81–83]. It manages to relate trends in chemisorption energies for various adsorbates on transition metal surface to the position of the d-band center, the first moment of the density of states from the Fermi-level. Systematic DFT calculations and experiments on series of polycrystalline alloy films of the type Pt_3M (M = Ni, Co, Fe, and Ti) have confirmed predicted correlations between the position of the d-band center, oxygen chemisorption energies, and electrode activities for the oxygen reduction reaction [84]. This success of the d-band model has fostered efforts in devising DFT-based high throughput combinatorial screening schemes for identifying highly active electrocatalyst materials [85].

Usually, insights gained from DFT calculations are not straightforwardly applicable to materials design. In electrocatalysis, direct DFT calculations have been applied predominantly for studying elementary surface processes on catalyst systems with well-defined periodic slab geometries that mimic single-crystalline surface structures. Technical catalyst systems that use supported nanoparticles represent special challenges, due to effects of quantum confinement, irregular surface structures with a large portion of low-coordination atoms, and the widely unexplored role of the substrate [86, 87]. Supported catalyst nanoparticles are relatively large systems, consisting of several 100s of atoms and exhibiting disordered surface structures. Moreover, substrate effects have to be accounted for. Recent efforts employing DFT calculations focused explicitly on morphologies and electrocatalytic properties of small metal nanoclusters [88, 89]. *Ab initio* calculations in [90] have explored the strongly modified chemical properties of Pd nanoclusters supported on Au(111). They help in evaluating the electronic structure effects exerted by the substrate and the consequences of the low coordination of the cluster atoms on the energetics and kinetics of binding small atomic or molecular species, e.g., OH_{ad}, CO_{ad}, H_{ad}

At the mesoscopic scale, interactions between molecular components control the self-organization phenomena between molecular components that lead to random phase-segregation during fabrication of CLs [7]. Mesoscale simulations can describe the morphology of heterogeneous materials and rationalize their effective properties beyond length- and time-scale limitations of atomistic simulations. A recently introduced computational method allows evaluation of the key factors during fabrication of CLs. These simulations rationalize structural

factors such as pore sizes, internal porosity, and wetting properties of the internal/external surfaces of agglomerates. They help elucidate whether or not ionomer is able to penetrate into primary pores inside agglomerates [91]. Moreover, dispersion media with distinct dielectric properties can be evaluated in view of capabilities for controlling sizes of carbon/Pt agglomerates, ionomer domains, and the resulting pore network topology. The relative contributions to the total electrocatalytically active surface area of wetted Pt at the walls of water-filled pores inside agglomerates, at the surfaces of agglomerates or at interfaces with wetted ionomer, can be rationalized. These insights are highly valuable for the structural design of catalyst layers with optimized performance and stability.

In a porous catalyst layer, as a random heterogeneous nanoporous medium, macroscopic properties such as diffusion and reaction rates are usually defined as averages of the corresponding microscopic quantities [92]. These averages must be taken over representative elementary volume elements (REVs) which are large compared to microscopic structural elements (pores, particles) and phase domains, but at the same small compared to the system size. At every point in a porous medium one uses the smallest such volume to fulfill requirements of transport equations such as Fick's laws of diffusion and to treat the usual macroscopic variations of diffusivity, reaction rate, conductivity, connectivity, etc. Complex morphologies of the emerging media can be related to relevant effective properties that characterize transport and reaction, using concepts from the theory of random heterogeneous media [93].

Finally, conditions for stationary operation at the macroscopic device level can be defined and balanced equations for involved species, i.e., electrons, protons, reactant gases and water, can be established on the basis of fundamental conservation laws. The general ingredients of a macrohomogeneous model of catalyst layer operation are source terms for electrochemical current conversion, using, e.g., the Butler-Volmer equation or first principles of transition state theory, and for the transformation of water at interfaces (vaporization, condensation), and terms that account for the transport of species, i.e., the migration of electrons/protons in conduction media, diffusion of dissolved oxygen and protons in water-filled pores, and diffusion of oxygen and vapor in the gas-filled phase.

The two-step strategy in physical modeling of catalyst layer operation is depicted in Figure 8.1 In the first step, it relates structure to physical properties of the layer considered as an effective medium. In the second step it relates these effective properties to performance. The overall relations between structure and performance can be complicated by the formation of liquid water, which affects effective properties and performance. Solution of such a model provides full relations between structure, properties, and performance, which in turn allow predicting architectures of materials and operating conditions that optimize fuel cell operation.

8.4 Structure Formation of Catalyst Layers and Effective Properties

In this section, we discuss theoretical and computational studies that provide insights into structural correlations and dynamical behavior of species in CLs. Structural complexity is an inherent trait of CLs. Advanced fabrication aims to improve Pt utilization by enhancing the interfacial area of Pt with water in pores and with Nafion ionomer [12, 94–95]. A practical way to achieve this is by mixing ionomer with dispersed Pt/C catalysts in the ink suspension prior to deposition to form a CL. The solubility of the ionomer depends upon the choice of a dispersion medium. This influences the microstructure and pore size distribution of the CL [95]. Self-organization of ionomer and carbon/Pt in the colloidal ink leads to the formation of phase-segregated agglomerated morphologies.

Independent computational strategies are generally needed in order to simulate the structure-related properties of CLs at different length- and time-scales. For instance, the structure of the ionomer-phase in CLs cannot be straightforwardly inferred from that in membrane simulations, as there are distinct forces and correlations between Nafion, water, and carbon/Pt particles in CLs.

This section presents a review of atomistic simulations and of a recently introduced meso-scale computational method to evaluate key factors affecting the morphology of CLs. Most of the effort in molecular dynamics simulations for PEFCs has concentrated on dynamic motion of proton and water through the hydrated membrane [96–104]. Little attempt has been made to employ MD techniques for elucidating the structure and transport of CLs, particularly in three-phase systems of carbon/Pt, ionomer, and gas phase. In the following subsections, we discuss various MD simulations to study the transport and dynamic behavior of CLs in terms of water and proton diffusivity, Pt-supported electrocatalyst, and microstructure formation.

8.4.1 Molecular Dynamics Simulations

In classical molecular dynamics (MD) simulations, the system is treated as a set of N interacting particles [105]. The atoms are presented by spherical nuclei that attract and repel each other. Their electronic structure is not considered explicitly. After assigning point charges to each particle, the forces acting on the particles are derived from a combination of bonding, non-bonding, and electrostatic potentials. The motions of the atoms are calculated using the laws of classical mechanics. Before starting a simulation, a model system is built consisting of all chemical components in a simulation box. Just like any real experiment, this system needs to be carefully prepared. It should be a realistic representation of the system that is to be studied. The result of a molecular dynamics simulation is a trajectory in time of positions and velocities of all N particles in the system. If simulated with an appropriate time step and for a sufficiently long time, thermodynamic properties, spatial and temporal correlation functions, and transport properties can be reliably calculated. The meaningful time of trajectory needed depends on the length-scale of the system under study and the time-scale needed for calculation of physical

parameters. Nowadays, computationally feasible time trajectories in atomistic MD simulations extend from a few nanoseconds (ns) up to hundreds of nanoseconds.

The time trajectory of an MD system is obtained from solving a system of second order differential equations that follow from Newton's second law,

$$m_i \frac{d^2 \vec{r}_i}{dt^2} = \sum_j \vec{F}_{ij} + \sum \vec{F}_k \qquad i = 1...N \tag{8.12}$$

Here i denotes the considered particle, with m_i and r_i the mass and the position vector of this particle, respectively. The forces $\vec{F}_{ij}$ represent two-body interactions between atom i and atom j. Forces $\vec{F}_k$ due to the action of external fields, e.g., electric fields, are added as extra terms. After determining these forces as functions of atomic and molecular degrees of freedom, the equations of motion can be integrated. The combination of forces in the model, including van der Waals interactions and electrostatic interactions, is called the force field. The choice of the force field is the key to accurate results that appropriately reproduce the true physical phenomena in the system. The forces acting on the nuclei are derived from the gradients of the potential energy function,

$$\vec{F}_i = -\vec{\nabla}_{r_i} V \tag{8.13}$$

The force fields can be split up into two contributions due to non-bonded interactions between all nuclei and bonded interactions between nuclei that are part of the same molecule. The non-bonded interactions consist of the following terms: electrostatic interactions, van der Waals interactions, and polarization effects. Polarization effects are the result of varying electron densities; they cannot be described explicitly using force field methods, which invariably ignore electron dynamics. It is common practice to include them implicitly in the van der Waals interactions. This leaves two terms for the non-bonded interactions. The first term corresponds to Coulomb interactions

$$V = \sum_{ij} \frac{q_i q_j}{4\pi \varepsilon_0 r_{ij}} \tag{8.14}$$

between two charged spheres at a distance r_{ij} from each other. In this equation q_i represents the charge of particle i and ε_0 is the dielectric permittivity of vacuum. Particles can be assigned partial charges or integer values in the case of ions. The second type of non-bonded interactions corresponds to dispersion or van der Waals forces. These are the interactions between atoms that arise from (quantum) fluctuations of the electronic charge densities. Both these interactions are represented in a second term for non-bonded interactions, for which the use of the Lennard-Jones potential has become a standard procedure in MD simulations,

$$V = 4\varepsilon \left[\left(\frac{\sigma}{r} \right)^{12} - \left(\frac{\sigma}{r} \right)^{6} \right] \qquad (8.15)$$

In the equation above ε represents the depth of the potential at the minimum ($r_{min} = 2^{1/6}\sigma$) and σ is the point at which $V = 0$.

For atoms that are part of molecules the bonded interactions also have to be calculated. These interactions can be one of the following: bond stretching (2-body), bond angle (3-body), and dihedral angle (4-body) interactions. The first two interactions can be described using a harmonic potential. The same mechanism can also be used to describe the motion of a vibrating spring or a pendulum. The dihedral interaction cannot be described using a harmonic potential; rather, a periodic function is used because of the rotational symmetry. Together with the bonded interactions, the dihedrals confer flexibility to the molecular structure. They play an important role in simulations of hydrated Nafion ionomer [99–107].

8.4.2 Atomistic MD Simulations of CL

The Pt/Carbon composite of a typical CL is fabricated by a "colloidal crystal templating technique" [106]. Besides carbon black (Vulcan or Ketjen black by Tanaka), synthetic porous carbon particles have recently been used to improve surface area and electrochemical activities. In a standard fabrication process, platinum particles are deposited by reducing H_2PtCl_6 agents on the carbon surface [107]. Carbon particles are dispersed in a tetrahydrofuran solution of H_2PtCl_6 by an ultrasonic treatment, while formic acid is added as the reducing agent. Filtering the solution collects the dispersed Pt/carbon particles.

In MD simulations, the molecular adsorption concept is used to interpret the Pt-C interactions during the fabrication processes. The Pt complexes are mostly attached to the hydrophilic sites on carbon particles, viz. carbonyl or hydroxyl groups [108]. The adsorption is based on both physical and chemical adsorption. Carbon particle preparations, impregnation, and reduction are three main steps of the catalyst preparation. The point of zero charge (PZC) determines the pH range at which the impregnation step should be carried out. The PZC is an important parameter in catalyst preparation.

Several studies have focused on extensive MD simulations of Pt nanoparticles adsorbed on carbon in the presence or absence of ionomers [109–113]. Lamas and Balbuena performed classical molecular dynamics simulations on a simple model for the interface between graphite-supported Pt nanoparticles and hydrated Nafion [113]. In MD studies of CLs, the equilibrium shape and structure of Pt clusters are usually simulated using the embedded atom method (EAM). Semi-empirical potentials such as the many-body Sutton-Chen potential (SC) [114] are popular choices for the close-packed metal clusters. Such potential models include the effect of the local electron density to account for many-body terms. The SC potential for Pt-Pt and Pt-C interactions provides a reasonable description of the properties of small Pt clusters. The potential energy in the SC potential is expressed by

$$U = \varepsilon_{pp} \sum_{1}^{N} \left[\frac{1}{2} \sum_{j \neq i}^{N} \left(\frac{\sigma_{pp}}{r_{ij}} \right)^{n} - c\sqrt{\rho_i} \right], \text{ with } \rho_i = \sum_{j \neq i}^{N} \left(\frac{\sigma_{pp}}{r_{ij}} \right)^{m} \tag{8.16}$$

where for Pt-Pt interaction $\varepsilon_{pp} = 0.019833 eV$, $\sigma_{pp} = 3.92$ Å, n = 10, m = 8, and c = 34.408. The first term is a pair-wise repulsive potential and the second one represents the metallic bonding energy associated with the local electron density. The weak interaction between a Pt cluster and a graphite substrate is defined by 6–12 LJ interactions with $\varepsilon_{Pt-C} = 0.022 eV$ and $\sigma_{Pt-C} = 2.905$ Å in Equation 8.15. In order to obtain reasonable results, the size of Pt clusters should be sufficiently large. The LJ parameters for Pt-Pt interactions are obtained by fitting the LJ equation to the SC potential with the values of $\varepsilon_{Pt-Pt} = 2336 K$ and $\sigma_{Pt-Pt} = 2.41$ Å. These simulations based on adapted LJ interactions from the SC potential allow one to account for platinum cluster-cluster interactions as well. Nafion is represented by oligomer models interacting through the Dreiding force field [97, 115], which is represented by a series of bonded, angular, dihedral, and non-bonded (LJ and electrostatic) interactions. A two-site model and Single-Point-Charge (SPC) models are used for oxygen and water, respectively [116]. Figure 8.3 shows a simulation set-up used in [112], which contains three Pt_{256} clusters (each of ~1.6 nm in diameter) deposited over a position-restrained graphite substrate, modeled by an AB arrangement of two graphite sheets. Molecular dynamics simulations have been used to examine the properties of Pt nanoparticles supported by graphite [116, 117]. Diffusion of platinum nanoparticles on graphite has been investigated, and high diffusion coefficients, on the order of 10^{-5} cm^2/s, have been predicted [117].
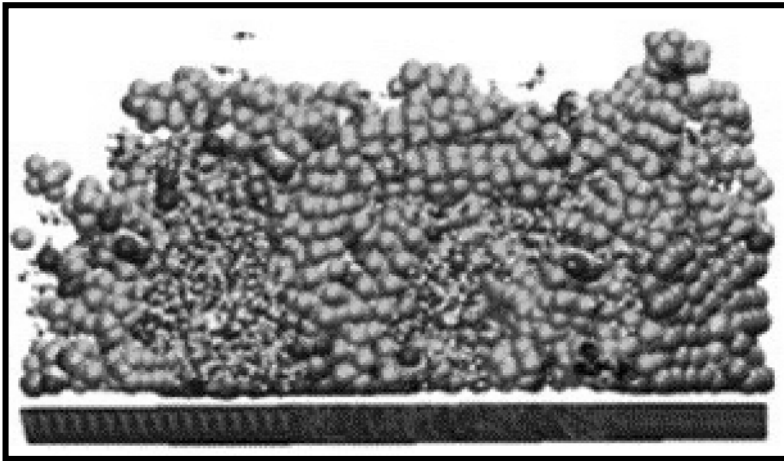

Figure 8.3. Side view of the MD simulation system used in [112] at the maximum Nafion content. The graphite layer is represented by the two parallel planes shown at bottom. (Reprinted from Electrochimica Acta, 51.26, Lamas EJ, Balbuena PB. Molecular dynamics studies of a model polymer–catalyst–carbon interface, 5904–11, ©2006, with permission from Elsevier.)
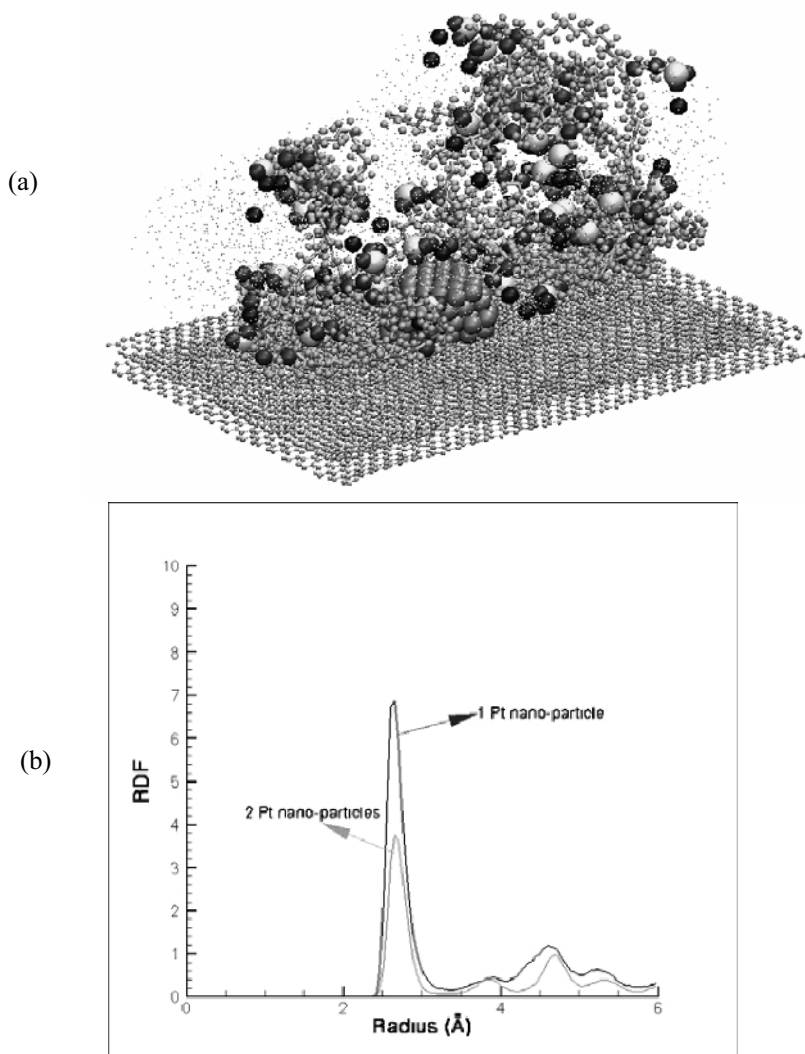
(a)

(b)

Figure 8.4. (a) Initial configuration of a small Pt nanocluster deposited on a static graphite substrate in the presence of Nafion backbones, sidechains, water, and hydronium ions. (b) Pt-Pt radial distribution function for one-cluster systems compared to that of a two-cluster simulation set-up. (Reprinted from Cheng CH, Malek K, Djilali N. Investigation of Pt cluster size effects on the nano-scale structure of PEMFC catalyst layers, internal report, 2007, NRC-IFCI).

More importantly, the MD results show that it is possible to alter the morphology and mobility of metal nanoparticles by changing their support. When deposited on carbon nanotubes, platinum particles diffuse at a slower rate than on graphite, which decreases sintering and should lead to increased long-term performance in catalytic applications [117]. Figure 8.4(a) shows a simulation set up in which the two graphite sheets are parallel to each other and are perpendicular to

the z-axis. Normal periodic boundary conditions are maintained in the x and y directions. This simulation system consists of multiple Pt clusters on the model graphite surface, Nafion, water, and hydronium ions. Several simulations were carried out to test the relative stability of various cluster morphologies for different sizes. Figure 8.4(b) shows the radial distribution function (RDF) of Pt atoms for using one and two Pt clusters on a graphite surface. In these simulations, Pt-Pt interactions are represented by the SC potential. Although the RDFs share the same qualitative behavior, the three peaks corresponding to the different layers of Pt clusters are much more enhanced in the one-cluster system due to the particular packing in this case.

The MD simulations in [113] and [114] showed how the dynamic properties of water in the vicinity of the catalyst surface change as a function of Nafion contents. Observed water structures ranged from the ones similar to those in the bulk membrane region to somewhat disconnected set of clusters. Water dynamics varies according to the contribution from different mechanisms as a function of the water content (or Nafion content). One diffusional mechanism emerges at low water contents and is due to strong electrostatic interactions between water molecules and polar head groups at sidechains. The other mechanism corresponds to hydraulic flux of bulk-like water relative to the porous membrane matrix, which is observed at high water contents, when the MEA is flooded.

8.4.3 Meso-scale Model of CL Microstructure Formation

Despite recent progress in developing multiscale modeling approaches [117], enormous challenges remain in bridging between atomistic simulations of realistic structures and continuum models that describe the operation of functional materials for PEFC applications. While full multiscale methods will not be available in the near future, meso-scale simulation techniques can close the gap between atomistic simulations and macroscopic properties of the system. Such simulations provide vital insight into self-organization phenomena and adhesion properties that have to be considered in the fabrication and operation of CL materials for PEFCs [118].

To improve the structure-dynamics relationships of CLs, the effects of applicable solvents, particle sizes of primary carbon powders, wetting properties of carbon materials, and composition of the catalyst layer ink should be explored. These factors determine the complex interactions between Pt/carbon particles, ionomer molecules, and solvent molecules and, therefore, control the catalyst layer formation process. Mixing the ionomer with dispersed Pt/C catalysts in the ink suspension prior to deposition will increase the interfacial area between ionomer and Pt/C nanoparticles. The choice of a dispersion medium determines whether ionomer is to be found in the solubilized, colloidal, or precipitated forms.

A significant number of meso-scale computational approaches have been employed to understand the phase-segregated morphology and transport properties of water-swollen Nafion membranes. Coarse-grained molecular simulation (CG-MS) techniques can describe the system at the micro-to-meso level, while still being able to capture the morphology at long time and length scales [119–123]. Because of computational limitations, full atomistic models are not able to probe the random morphology of these systems. As demonstrated by these simulations

and applications to other random composite media, meso-scale models are computationally feasible to capture their morphology. Several approaches have been used, such as cellular automata and coarse-grained meso-dynamics based on self-consistent mean field theory [120, 121].

For mesoscale simulations of catalyst layer formation, we consider three main types of spherical beads: polar, nonpolar, and charged beads [124]. Clusters including a total of four water molecules or three water molecules plus a hydronium ion are represented by polar beads of radius 0.43 nm. The configuration of an unfolded Nafion chain is shown in Figure 8.5. A sidechain unit in Nafion ionomer has a molecular volume of 0.306 nm^3, which is comparable to the molecular volume of a four-monomeric unit of polytetrafluoroethylene (PTFE) (0.325 nm^3) [120]. Therefore, each four monomeric unit (-[-CF2-CF2-CF2-CF2-CF2-CF2-CF2-CF2-]-) (represented by an apolar bead) and each sidechain (represented by a charged bead) are coarse-grained as beads of volume 0.315 nm^3 (r = 0.43 nm). The hydrophobic Nafion backbone is replaced by a coarse-grained chain of apolar beads, as illustrated in Figure 8.5.
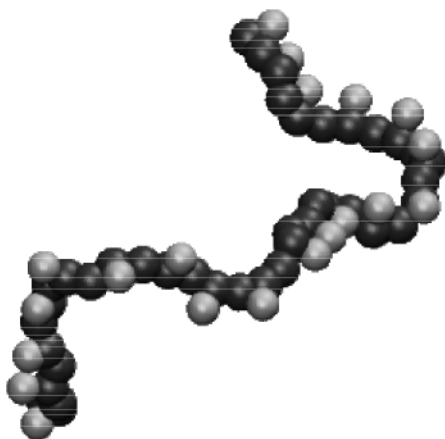
Figure 8.5. (a) Sketch of the coarse-grained model of Nafion used in simulations of self-organization phenomena in catalyst layers of PEFCs. Nafion polymer is represented by 20-unit oligomers of length ~30 nm.The spheres show the coarse-grained beads corresponding to the hydrophobic backbone (black) or hydrophilic sidechains (gray) [7]. (Reprinted with permission from J Phys Chem C, 2007, 111, 13627–34. Copyright 2007 American Chemical Society.)

Carbonaceous particles can be coarse-grained in various ways, building upon a new technique called multi-scale coarse graining (MS-CG) [125–127]. In this method, the CG potential parameters are systematically obtained from atomistic-level interactions [127]. Using this technique, a model was built for semispherical carbon particles based on CG nonpolar sites in the C60 system.

The interactions between non-bonded beads are modeled by the Lennard-Jones (LJ) potential. In this potential, the effective bead diameter is $r_{ij} = 0.43$ nm for sidechain, backbone, and water beads. The strength of interactions is limited to five possible values ranging from weak (1.8 kJ mol^{-1}) to strong (5 kJ mol^{-1}) [125]. The

electrostatic interactions between charged beads are described by the Coulombic interaction with relative dielectric constant ε_r. The effect of solvent is incorporated by changing ε_r as well as by varying the degree of dissociation of Nafion sidechains. Interactions between chemically bonded beads (in Nafion chains, for example) are modeled by harmonic potentials for bond length and bond angle, where the force constants are $K_{bond} = 1250$ kJ mol^{-1}nm^{-2} and $K_{angle} = 25$ kJ mol^{-1}, respectively. The size of the simulation box can vary from $50 \times 50 \times 50$ nm^3 to $500 \times 500 \times 500$ nm^3.

Snapshots of the final microstructure were analyzed in terms of density map profiles, radial distribution functions (RDFs), pore size distributions, and pore shapes. Figure 8.6 shows a snapshot of the carbon-Nafion-water-solvent (CNWS) blend. The interaction parameters of the carbon particles are selected to mimic the properties of Vulcan-type C/Pt particles. They are hydrophobic, with a repulsive interaction with water and Nafion sidechains, and semi-attractive interactions with other carbon particles as well as with Nafion backbones.

(a)   (b)
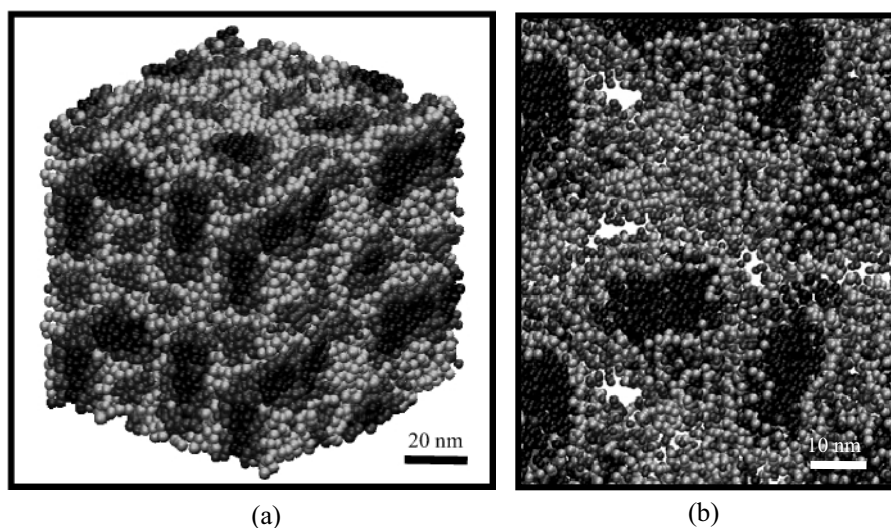
Figure 8.6. Final equilibrium structure of a catalyst blend composed of carbon, Nafion, water, hydronium ions, and implicit solvent. Carbon particles are in black; hydrophilic domains (water, hydronium ions, and sidechains) are shown in dark grey; hydrophobic polymer domains (backbone aggregates) are in light grey. (b) Magnification of part of the blend in (a) [7]. (Figure 8.6(a) reprinted with permission from J Phys Chem C, 2007, 111, 13627–34. Copyright 2007 American Chemical Society.)

Structural analysis based on site-site RDFs is shown in Figure 8.7. The RDFs reveal general features of phase segregation, shown in microstructure formation in Figure 8.6. There is a strong correlation between carbon particles. As expected, hydrated protons (H) and water (W) behave similarly. The correlation between hydrophilic species (H and W) and ionomer (N) is significantly stronger than that between those species and carbon (C). The autocorrelation functions g_{SS} and g_{HH} exhibit a similar structure as g_{WW}. This indicates a strong clustering of sidechains

and hydronium ions due to the aggregation and folding of polymer backbones. The primary S-S and H-H peaks are, however, suppressed compared to the primary peak in g_{WW} due to electrostatic repulsion between these charged beads. g_{BB} and g_{CC} exhibit upturns towards smaller r, superimposed on the primary bead-bead correlations, which correspond to the characteristic dimensions of carbon particles (~5 nm diameter) and backbone clusters (~2–3 nm).
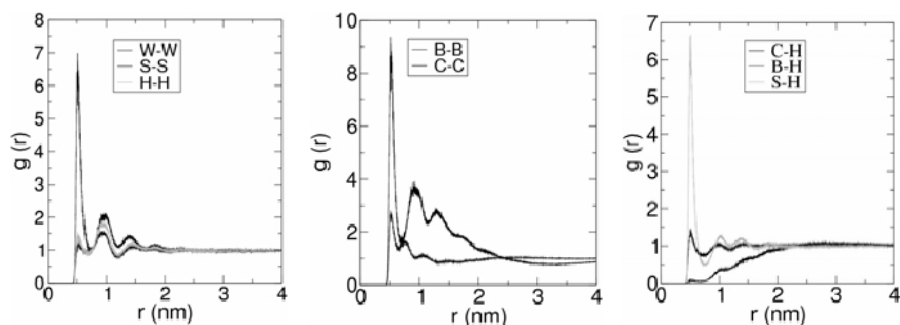

Figure 8.7. Selected structural correlation functions (or site-site radial distribution functions) between distinct components of self-organized CL inks (C: carbon particles, B: ionomer backbones, S: ionomer sidechains, W: water molecules, H: hydronium ions) [7]. (Reprinted with permission from J Phys Chem C, 2007, 111, 13627–34. Copyright 2007 American Chemical Society.)

Overall, the correlation functions discussed above provide valuable structural information at the nanometer scale that allows refining the picture of the phase-segregated catalyst layer morphology. Analysis of RDFs reveals a strong correlation between carbon particles and polymer backbones (g_{CB}) [7]. The correlation between hydrophilic species and ionomer is significantly stronger than that between those species and carbon particles. Ionomer backbones form clusters or fibers that are attached to the surface of carbon particles. Sidechains are buried inside of hydrophilic domains with a weak contact to carbon domains. Water and hydronium ions tend to maximize their separation from the carbon while trying to stay in the vicinity of the sidechains. Structural conformations demonstrate that sidechains, hydronium ions, and water molecules form interconnected clusters inside of ionomer domains. A key finding is that ionomer molecules do not penetrate into the carbon agglomerates. Sidechain A layer of ionomer of ~10 nm thickness with well-packed morphology around Pt/C clusters was evident in the presence of polar solvents. Notice that the compactness of carbon agglomerates is affected by the polarity of solvent.

The effect of the solvent dielectric constant on structural correlations was also examined in [7]. These simulations showed that polar solvents ($\varepsilon_r = 20, 80$) behave similarly, while the effect of the apolar solvent ($\varepsilon_r = 2$) is markedly different. Low ε_r implies stronger correlations between C and hydrophobic polymer backbones, exhibiting a stronger tendency to phase-segregate into hydrophobic and hydrophilic domains. The magnitude of short-range interactions and the carbon agglomerate size steadily decreases by increasing ε_r. Therefore, the carbon

agglomerates become more separated as the pore size between agglomerates increases. The peak positions for long-distance correlations are shifted to large distances for the apolar solvent. A low dielectric solvent causes the formation of a separate clustered phase of carbon particles confined between thick fibrous aggregates of ionomer. In the presence of apolar solvent, the structural organization into separate hydrophilic and hydrophobic domains spans higher distances compared to polar solvents.

This coarse-grained molecular dynamics model helped consolidate the main features of microstructure formation in CLs of PEFCs. These showed that the final microstructure depends on carbon particle choices and ionomer-carbon interactions. While ionomer sidechains are buried inside hydrophilic domains with a weak contact to carbon domains, the ionomer backbones are attached to the surface of carbon agglomerates. The evolving structural characteristics of the catalyst layers (CL) are particularly important for further analysis of transport of protons, electrons, reactant molecules (O_2) and water as well as the distribution of electrocatalytic activity at Pt/water interfaces. In principle, such meso-scale simulation studies allow relating of these properties to the selection of solvent, carbon (particle sizes and wettability), catalyst loading, and level of membrane hydration in the catalyst layer. There is still a lack of explicit experimental data with which these results could be compared. Versatile experimental techniques have to be employed to study particle-particle interactions, structural characteristics of phases and interfaces, and phase correlations of carbon, ionomer, and water in pores.

8.4.4 Structure-related Effective Properties of CL

The theory of random heterogeneous materials provides information to explore the relations between microstructure and the required effective properties of transport and reaction in CLs [128]. Continuum models, to some extent, can account for the effects of porosity. However, more realistic network models of random heterogeneous media are generally preferred. The pore space morphology affects the gaseous transport to the active Pt sites. Hence, together with the effect of network *topology*, and in particular pore interconnectivity, the effect of pore heterogeneity (e.g., roughness in nanoscale pores) should be accounted for as well. Parameterizations of effective transport properties such as diffusion coefficients of gases, proton conductivity, and liquid permeability are described based on percolation in the interpenetrating networks of electron-conducting, proton-conducting, and porous phases.

For materials with random morphologies, the effect of microscopic composition, i.e., of size, shape, and random distribution of phase domains and of their connectedness, on its macroscopic properties is the topic addressed by percolation theory [129, 130]. Here, we briefly describe the basic concepts of this theory and outline their application to determine the morphology and effective properties of random composite materials. We refer the interested reader to Stauffer and Aharony [46] and Sahimi [129] for detailed discussion of percolation theory and its applications.

Percolation phenomena deal with the effect of clustering and connectivity of microscopic elements in a disordered medium [129]. Percolation theory represents a random composite material as a network or lattice structure of two or more distinct types of microscopic elements or phase domains, the so-called percolation sites. These elements represent mutually exclusive physical properties, e.g., electrically conducting vs. isolating phase domains, pore space vs. solid matrix, atoms with spin up vs. spin down states. Here, we will refer to "black" and "white" elements for definiteness. The network onto which "black" and "white" elements of the composite medium are distributed could be continuous (continuum percolation) or discrete (discrete or lattice percolation); it could be a disordered or regular network. With a probability p a randomly chosen percolation site will be occupied by a "white" element. With the complementary probability $(1-p)$ the element occupying the site will be "black", see Figure 8.8.

(a)   (b)
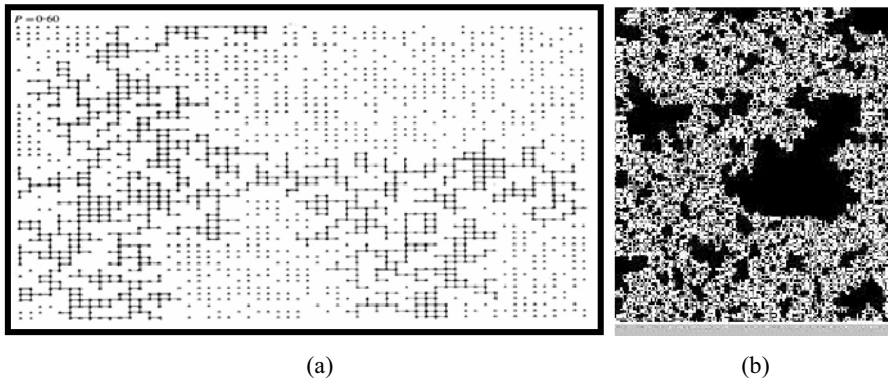
Figure 8.8. (a) Formation of a sample-spanning bond-percolation cluster on a square lattice at the percolation threshold (p = 0.6). (b) Cluster of conductive zones in a conductor-insulator mixture formed above the percolation threshold [46, 155]. (Image (a) reprinted with permission from Stauffer D, Aharony A. Introduction to percolation theory, London: Taylor & Francis, 1994; (b) reproduced from Chem Phys Lett, 375(5–6), Malek K. Dynamic Monte-Carlo simulation of electrochemical switching of a conducting polymer film, 235–44, 2002, with permission from Elsevier.)

Percolation theory deals with the size and distribution of connected "black" and "white" domains and the effects on macroscopic observable properties, e.g., electric conductivity of a random composite or diffusion coefficient of a porous rock. A percolation cluster is defined by a set of connected sites of one color (e.g., "white") surrounded by sites of the complementary color (i.e., "black"). If p is sufficiently small, the size of any connected cluster is likely to be small compared to the size of the sample. There will be no continuously connected path between the opposite faces of the sample. On the other hand, the network should be entirely connected if p is close to 1. Therefore at some well-defined intermediate value, the so called "*percolation threshold*", p_c there is a transition in the topological structure of the percolation network from disconnected to macroscopically

connected. In an infinite lattice the *site percolation threshold* is the smallest occupation probability p of sites, at which an infinite cluster of sites (vertices) emerges.

In the metal/isolator composite, p_c is the threshold above which the composite will be conducting. In the vicinity of the percolation threshold, for $p \geq p_c$, the effective conductivity of the composite is determined by a critical law

$$g_e(p) \propto (p - p_c)^\mu \Theta(p - p_c) \tag{8.17}$$

where $\Theta(x)$ is the Heaviside step function.

The behavior of the effective diffusivity $D_e(p)$ near p_c is given by

$$D_e(p) \sim \frac{g_e(p)}{P(p)} \sim (p - p_c)^{\mu - \beta} \tag{8.18}$$

where $P(p) \sim (p - p_c)^\beta$ is the percolation probability. A diffusing species can move on all macroscopically connected clusters of the conductive phase. Above p_c, however, only the largest cluster, the so-called "*sample-spanning cluster*", significantly contributes to transport. Other physical properties like correlation lengths and percolation probabilities follow similar potential laws in the vicinity of p_c, however with different critical exponents. Values of the critical exponent μ in Equation 8.17 in 2D and 3D are known from computer simulations [45]. In 2D it is $\mu \approx 1.3$ and in 3D it is $\mu \approx 2.0$. While critical exponents are universal, i.e., they are independent of the topology of the network and only depend on the dimensionality, values of percolation thresholds depend strongly on the lattice topology and the type of the percolation problem considered. For lattice percolation, two types of problems are distinguished. For the hitherto described site percolation problems, clusters are formed by "white" or "black" sites of the lattice. For bond percolation, the same statistical concept is applied to the connections or bonds between lattice sites: with probability p a randomly chosen bond will be occupied by a "white" element and otherwise, i.e., with the complementary probability $(1 - p)$, the bond will remain "black".

Percolation thresholds for several lattice types are listed in Table 8.1. In 1D it is trivially, $p_c = 1$. In 2D, values for p_c are known exactly for specific lattice types. In 3D values of p_c can only be found with the help of computer simulations. Percolation theory has been successfully applied to such diverse phenomena as hopping conductivity in semiconductors [130], gelation in polymer melts [131], permeability of porous rocks [129, 130], spreading of epidemics [132], and spreading of wildfires [133]. In PEFC research, percolation theory has been employed for establishing relations between water uptake of polymer electrolyte membranes and their proton conductivities [98]. Moreover, percolation concepts

play an important role in theoretical efforts to unravel structure vs. function relations of porous composite catalyst layers [47–48, 50].

Table 8.1. Critical fraction of lattice points (percolation threshold) that must be filled to create a continuously connected path of nearest neighbours from one side to another. Values are taken from Stauffer and Aharony [46].

Dim.	Lattice type	Site percolation	Bond percolation
2	square	≈ 0.59	0.5 (exact)
2	triangular lattice	0.5 (exact)	$2\sin(\pi/18)$ (exact)
2	honeycomb lattice	≈ 0.7	$1 - 2\sin(\pi/18)$ (exact)
3	simple cubic	≈ 0.31	≈ 0.25
3	bcc	≈ 0.25	≈ 0.18
3	fcc	≈ 0.20	≈ 0.12
3	diamond	≈ 0.43	≈ 0.39

Continuum percolation theory can be used to describe the effective properties of CLs, expressed through the volume fractions of components. For instance, the proton conductivity is given by

$$\sigma_{el} = \sigma_0 \frac{(X_{el} - X_c)^2}{(1 - X_c)^2} \Theta(X_{el} - X_c) \tag{8.19}$$

where σ_0 is the bulk electrolyte conductivity and X_c is the percolation threshold in the random network of secondary pores. Previous parameterization gave reasonable results with percolation threshold $X_c \approx 0.12$ [46]. Other effective properties of CLs depend decisively on the water distribution in the pore space. Transport of oxygen (superscript "o") and vapor (superscript "v") is given by Knudsen diffusivity with percolation-type dependence, with the same percolation threshold X_c

$$D^{o,v}(S_r) = D_0^{o,v} \frac{(X_P - X_\mu - X_c)^{2.4}}{(1 - X_c)^2 (X_P - X_c)^{0.4}} \left\{ \left[\frac{(1 - S_r)X_P - X_c}{X_P - X_\mu - X_c} \right]^{2.4} \Theta\left(S_r - \frac{X_\mu}{X_P} \right) + \Theta\left(\frac{X_\mu}{X_P} - S_r \right) \right\} + D^{res} \tag{8.20}$$

with $D_0^{o,v} = \sqrt{\dfrac{2RT}{\pi M^{o,v}}} \dfrac{4}{3} r_{crit}$, where r_{crit} is a critical pore radius (bottleneck pores),

e.g., obtained from critical path analysis [134] and $M^{o,v}$ is the molar mass of the diffusing gas molecules [47–48, 50]. It is assumed that gas diffusion occurs only through air-filled pores. The main mechanism of diffusion contributing to

$D^{o,v}(S_r)$ in Equation 8.20 is due to percolation in gas pores. Above a critical liquid water saturation $S^{crit} = 1 - X_c/X_p$, only a residual diffusion due to transport of dissolved species remains finite, accounted for by D^{res}.

The relation between liquid permeability and porous structure is given by

$$K^1(S_r) = \frac{\delta}{24\tau^2}\left\{ r_{el}^2 \varepsilon_{el} X_{el} + r_\mu^2 \left[S_r X_p \Theta\left(\frac{X_\mu}{X_p} - S_r\right) + X_\mu \Theta\left(S_r - \frac{X_\mu}{X_p}\right) \right] \right.$$
$$\left. + \tau^2 r_M^2 \frac{\left[S_r X_p - X_\mu - X_c\right]^2}{\left(1 - X_c\right)^2} \Theta\left(S_r - \frac{X_\mu}{X_p}\right) \Theta\left(S_r X_p - X_\mu - X_c\right) \right\} \quad (8.21)$$

This expression entails three different contributions due to water-filled pores in the ionomer (radius r_{el}, corresponding water volume portion ε_{el}), micropores (radius r_μ) and mesopores (radius r_M). δ is a constrictivity factor and τ is a tortuosity factor [135].

Such relations show how the random composite morphology can steer effective transport properties of CLs on the basis of percolation theory. Notice that the bimodality of the pore network in a CL (primary and secondary pores) plays a key role in balancing different catalyst layer functions. A large porosity due to primary pores is beneficial for the exchange current density, since it guarantees that a large fraction of catalyst sites inside agglomerates could be reached by protons. Moreover, increasing the fraction of primary pores could results in a larger liquid/vapor interfacial area and thus, higher rates of evaporation, as we will see below. Secondary pores on the other hand largely contribute to the gas diffusivity in the layer.

It is infeasible, if not impossible, to make exact predictions for the effective properties of composite materials with the simple models of morphology presented above. Both continuum and discrete models have been applied to provide the effective properties of random heterogeneous materials. As described above, continuum models represent the classical approach to describing and analyzing transport processes in materials of complex and irregular morphology. Thus, the effective properties of materials are defined as averages of the corresponding microscopic quantities. The shortcoming of discrete models such as random network models, Bethe lattice models, etc. compared to continuum modes is the demand for large computational effort to represent a realistic model to describe the material and simulate its effective properties. It is of course a challenging problem to generate a realization of a heterogeneous material for which limited microstructure information is available.

8.5 Performance Modeling and Optimization Studies

8.5.1 General Framework of Performance Modeling

A fuel cell electrode can be seen as a highly dispersed interface between Pt nanoparticles and electrolyte (ionomer or water). Random composition, phase-segregated morphology, pore size distribution, and wetting properties of pores determine the complex spatial distributions of (i) potentials, (ii) concentrations of reactants and water, and (iii) local rates of electrocatalytic processes that evolve under operation. A subtle electrode theory has to establish the links between these distributions in order to determine catalyst utilization, voltage efficiency (or power density), and water handling capability.

Our presentation in this section focuses on steady-state phenomena during catalyst operation. In the main part, we discuss 1D modeling approaches of species transport and reaction in the through-plane direction under isothermal conditions. The phase-segregated, agglomerated structure that is formed via self-organization during MEA fabrication is assumed to be fixed. This treatment ignores degradation phenomena. Moreover, fluxes and conversion rates of species are constant.

For the purpose of physical modeling of catalyst layer operation, it is expedient to consider the layer essentially as a two-scale system (cf. Figure 8.2). At the mesoscopic scale, operation is determined by the properties of agglomerates of carbon and Pt, which are partially coated by a film of ionomer. Primary pores in agglomerates should be maximally wetted in order to provide a large active Pt surface area. At the macroscopic scale, gaseous diffusion of oxygen is vital in order to ensure uniform utilization of catalyst throughout the complete layer. This requires a percolating network of gas-filled secondary pores between agglomerates. These pores should be hydrophobic. The volume fractions of primary and secondary pores are X_μ and X_M, respectively, with $X_P = X_\mu + X_M$. Agglomeration and bimodal PSDs are vital in view of the conflicting structural requirements for transport and reaction. Structural control during fabrication should thus focus not only on composition but also on effects of agglomeration, porous morphology, and wetting properties of pores.

The steps involved in modeling performance and water balance in CCLs are indicated in Figure 8.2 [50, 51]. At the materials level, it requires constitutive relations between random composition, dual porous morphology, liquid water accumulation, and effective physico-chemical properties, including proton conductivity, gas diffusivities, liquid permeabilities, electrochemical source term, and vaporization source term. The set of relationships between structure and physico-chemical properties has been discussed in [3, 47, 50–51]. Since the liquid water saturation $S(z)$ is a spatially varying function at $j_0 > 0$, these physico-chemical properties become spatially varying functions in an operating cell. This demands a self-consistent solution for non-linearly coupled properties and performance.

Accounting for the peculiar role of water in physical models of CCL operation requires knowledge of the following two aspects in theory and experiment.

Local equilibrium of water in CCLs. How does the local water content in CCLs depend on materials morphology and operating conditions? By which mechanisms does it attain local equilibrium? The approach pursued in [50, 51] proposes that capillary forces at the liquid-gas interfaces in pores equilibrate the local water content in CCLs. This approach neglects surface film formation or droplet formation in pores of CLs. *Ex situ* diagnostics, probing porous structures and water sorption characteristics, are needed to relate equilibrated water distributions to structure and conditions in CCLs.

Processes involving water transport and transformation. What are the relevant mechanisms and transport coefficients of water fluxes (diffusion, convection, hydraulic permeation, electroosmotic drag)? What are relevant mechanisms and rates of phase changes (between liquid water, water vapor, surface water, water in membrane)? These mechanisms and relevant parameters are amenable to evaluation by *ex situ* diagnostics. The statistical theory of random composite media [136–138] and percolation theory [44–46] provides various tools for assessing effective parameters of transport and interfacial processes, as discussed in Section 8.4.

On the cathode side of a PEFC under normal operating conditions, one is concerned about excessive amounts of liquid water and flooding of gaseous supply channels due to a net electroosmotic flux through the PEM and the production of water. Under these conditions, it is reasonable to assume full hydration of the ionomer phase in the CCL. Proton conductivity of the layer is, thus, considered constant. Due to the assumption of capillary equilibrium in pores, pore-filling is controlled by the Young-Laplace equation, which relates capillary pressure, p^c, and capillary radius, r^c, to local gas pressure, p^g, and liquid pressure, p^l,

$$p^c = \frac{2\sigma \cos(\theta)}{r^c} = p^g - p^l \tag{8.22}$$

where σ is the surface tension of water and θ is the wetting angle in pores. The wetting angle is a complex structural function that is difficult to measure and control in experiment and fabrication. We assume that small primary pores inside agglomerates are hydrophilic and consider operating regimes (p^g, p^l), for which these pores are filled completely with water. The relevant value of θ to be used in calculations is, thus, the wetting angle for secondary pores, in which the front of liquid water advances under normal operating conditions. Wettability of secondary pores is, therefore, vital for controlling the water formation in CCLs. Assuming that these pores are hydrophilic, the liquid water saturation is given by an integral expression containing the differential pore size distribution $dX_p(r)/dr$

$$S_r = \frac{1}{X_p} \int_0^{r_c} dr' \frac{dX_p(r')}{dr'}. \tag{8.23}$$

Pores with radius $r' \leq r_c$ are filled with liquid water and pores with $r' > r_c$ are filled with gas. In an operating fuel cell, S_r depends, therefore, on details of the PSD, wetting angles, and local pressures (p^g, p^l). These local conditions are coupled to stationary fluxes of species and rates of current generation and net evaporation via the set of flux and conservation equations that we will present below [50].

Bimodal log - normal pore size distribution
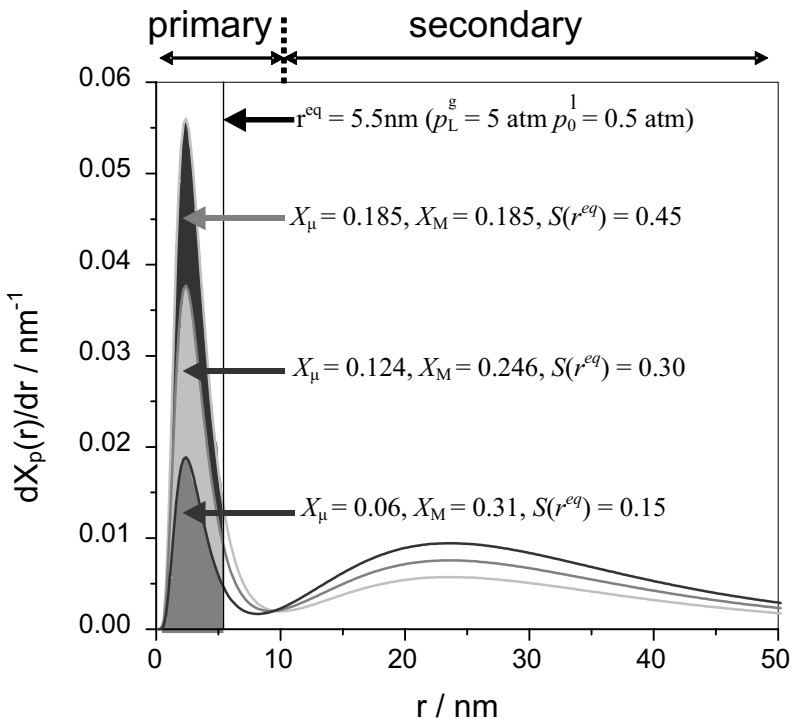
Figure 8.9. Bimodal pore size distributions with varying portions of primary and secondary pores, obtained with Equation 8.24. Shaded areas represent the liquid water saturation at given operating conditions [50]. (Reproduced by permission of ECS – The Electrochemical Society, from Eikerling M. Water management in cathode catalyst layers of PEM fuel cells.)

The present structure-based model employs a bimodal log-normal pore size distribution (PSD), defined as

$$
\frac{dX_P(r)}{dr} = \frac{1 - X_{PtC} - X_{el}}{\sqrt{\pi}\left[\ln s_\mu + \chi_M \ln s_M\right]} \frac{1}{r} \times
$$
$$
\left\{ \exp\left[-\left(\frac{\ln(r/r_\mu)}{\ln s_\mu}\right)^2\right] + \chi_M \exp\left[-\left(\frac{\ln(r/r_M)}{\ln s_M}\right)^2\right] \right\}
$$

(8.24)

Here, r_μ, r_M determine the positions of the two peaks and s_μ, s_M their widths. The parameter χ_M controls the relative contributions of primary and secondary pores. The distribution in Equation 8.24 is normalized to the total porosity X_P. Porosities due to primary and secondary pores are given by

$$
X_\mu = \int_0^{r_{cut}} dr' \frac{dX_P(r')}{dr'} \text{ and } X_M = \int_{r_{cut}}^\infty dr' \frac{dX_P(r')}{dr'}
$$

(8.25)

where r_{cut} ($r_\mu < r_{cut} < r_M$) separates the two domains.

A PSD of the form given in Equation 8.24 can capture the main characteristics of the random phase-segregated, agglomerated morphology. Experimental data [139–141] have also suggested such log-normal pore size distributions in the mesoporous region. Typical pore size distributions obtained with this parameterization are depicted in Figure 8.9.

8.5.2 Transport and Reaction in Catalyst Layers

The main fluxes in catalyst layers and boundary conditions are illustrated in Figure 8.10. Processes inside the layer are related by mass conservation laws for involved species, expressed in the form of continuity equations. The general form of the continuity equation is

$$
\frac{\partial \rho(\vec{r},t)}{\partial t} + \nabla \cdot \vec{j}(\vec{r},t) = Q(\vec{r},t)
$$

(8.26)

where $\rho(\vec{r},t)$ is the density field of the considered species, $Q(\vec{r},t)$ is a source/sink density, and $\vec{j}(\vec{r},t)$ is a flux density. For steady state operation, we have $\partial \rho(\vec{r},t)/\partial t = 0$.
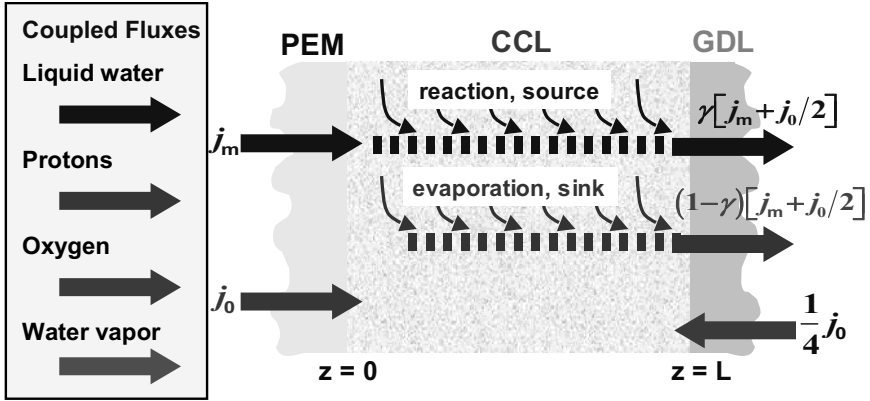
Figure 8.10. Illustration of the coupled fluxes of species in operational CCLs [50]. (Reproduced by permission of ECS – The Electrochemical Society, from Eikerling M. Water management in cathode catalyst layers of PEM fuel cells.)

Continuity equations including all species and processes are discussed in [50]. A number of simplifications lead to the following set of equations

$$\frac{d\eta(z)}{dz} = -\frac{j_p(z)}{\sigma_{el}} \tag{8.27}$$

$$\frac{dj_p(z)}{dz} = -Q^{ec}(z) \tag{8.28}$$

$$\frac{dP_{O_2}(z)}{dz} = \frac{(j_0 - j_p(z))}{4 fD^o(S(z))} \tag{8.29}$$

$$\frac{dj^v(z)}{dz} = Q^{lv}(z) \tag{8.30}$$

$$\frac{dq(z)}{dz} = -\frac{j^v(z)}{fD^v(S(z))} \tag{8.31}$$

$$\frac{dp^l(z)}{dz} = \frac{1}{B_0 fK^l(S(z))}\left[\left(n+\tfrac{1}{2}\right)\left(j_p(z) - j_0\right) + j^v(z) + nj_0 - j_m\right] \tag{8.32}$$

$$\frac{dj^l(z)}{dz} = \frac{1}{2}Q^{ec}(z) - Q^{lv}(z) \tag{8.33}$$

where $f = \dfrac{F}{RT}$, $B_0 = \dfrac{RT}{V_m \mu^l}$. Equation 8.32 includes terms accounting for water transport due to electroosmotic drag with drag coefficient n. The solution of Equations 8.27 to 8.33 provides the local partial pressure of oxygen, $P_{O_2}(z)$, and water vapor, $q(z)$, the liquid water pressure, $p^l(z)$, the local electrode potential, $\eta(z)$, as well as the flux densities of protons, $j_p(z)$, liquid water, $j^l(z)$, and water vapor, $j^v(z)$.

The electrochemical source term, $Q^{ec}(z)$, accounts for the effectiveness factor of Pt utilization due to random composition and processes in agglomerates. The value of this term is obtained by averaging the current generated inside agglomerates over the volume of a representative elementary volume element (REV). It is here that the macrohomogeneous model is linked with the agglomerate model,

$$Q^{ec}(z) = \frac{f(X_{PtC}, X_{el})}{X_{PtC}} g(S_r) \frac{3(X_{PtC} + X_\mu)}{R_a^{\,3}} \int_0^{R_a} i_F^z(r) r^2 \mathrm{d}r \qquad (8.34)$$

where r is the radial coordinate inside agglomerates. The volumetric Faradaic current density, $i_F^z(r)$, is determined by the concentrations of dissolved oxygen and protons and by the electrostatic potential inside the agglomerate, as we will discuss below. Dissolution of oxygen into water-filled pores is implicitly accounted for by incorporating a Henry's law factor, H_{O_2}, in $i_F^z(r)$.

The oxygen partial pressure is related to the oxygen concentration via the ideal gas law, $P_{O_2}(z) = RTc_{O_2}(z)$. The cathodic overpotential is the (positive) difference

$$\eta = E^{eq} - E \;,\; \text{with } E = \phi_{PtC} - \phi_{el} \qquad (8.35)$$

where E^{eq} is the equilibrium cathode potential, defined via the Nernst equation. Employing the usual assumption of a high electronic conductivity of the Pt/C phase (> 10 S cm^{-1}), this phase can be considered equipotential, i.e., $\phi_{PtC} = \text{const.}$, for a given fuel cell current density, j_0. Using this condition, the total overvoltage incurred by the cathode is given by the local value of the overpotential at $z = 0$,

$$\eta_0 = \eta(z = 0) \qquad (8.36)$$

Moreover, $\eta(z) = \phi_{el}(z) - \phi_{C/Pt}$ replaces the local electrolyte potential $\phi_{el}(z)$ in Equation 8.27.

The source term of water vapor due to net evaporation is

$$Q^{lv}(z) = \frac{e_0 \kappa^e}{L} \xi^{lv}(S_r) \{ q_r^s(T) - q(z) \}$$

(8.37)

where κ^e denotes the intrinsic rate constant of evaporation and $q_r^s(z)$ is the saturated vapor pressure in pores at the capillary radius $r^c(z)$, given by the Kelvin equation

$$q_r^s(z) = q^{s,\infty} \exp\left(-\frac{2\sigma \cos(\theta) V_m}{RTr_c(z)} \right), \quad q^{s,\infty} = q^0 \exp\left(-\frac{E_a}{k_B T} \right)$$

(8.38)

with saturation pressure $q^{s,\infty}(T)$ for a planar vapor|liquid interface, surface tension σ, molar volume of liquid water V_m, wetting angle θ, molar gas constant R. A typical value of the activation energy of evaporation is $E_a \approx 0.44$ eV (corresponding roughly to the strength of two hydrogen bonds).

In addition to the conservation laws, a locally valid condition of mechanical equilibrium is needed. Here it is assumed that local pore filling is controlled by capillary equilibrium corresponding to the Laplace equation,

$$p^c(z) = \frac{2\sigma \cos(\theta)}{r_c(z)} = p^g(z) - p^l(z) = P_{O_2}(z) + q(z) + p^r - p^l(z)$$

(8.39)

This relates the local distributions of liquid and gas pressures to the local capillary radius, r_c, which further determines the local liquid water saturation, $S(z) = S_r$, via Equation 8.23. Thereby, all transport coefficients can be obtained and a closed system of equations is provided. Due to complex relations $p^c \rightarrow r_c \rightarrow S_r$ and $S_r \rightarrow D^{o,v,r}(S(z)), K^l(S(z)), i^0(S(z)), \xi^{lv}(S(z))$ the system of equations is highly non-linear. Obtaining self-consistent solutions warrants, in general, numerical procedures.

8.5.3 Spherical Agglomerates

Subsequently, we will discuss effective rates of current conversion at the agglomerate level. Most commonly it is assumed that agglomerates in CCLs either comprise a homogeneous mixture of carbon/catalyst particles and perfluorosulfonated ionomer (PFSI) or that they consist of aggregated carbon/catalyst particles and water-filled pores which are coated on the external surface by a film of ionomer. These types of agglomerates represent the two limiting structures in terms of ionomer distribution at the mesoscopic scale, and both of them may exist simultaneously.

Different mathematical models are used to describe the transport processes and the electrochemical reactions happening inside the different types of agglomerates. For ionomer-filled agglomerates, effectiveness factors are obtained from the well-known Thiele modulus [54]. For water-filled agglomerates, a valid approach is based on Poisson and Nernst-Planck equations [142, 143]. We will focus on this case. As discussed, simple size considerations for primary pores in carbon/Pt aggregates and ionomer phase domains as well as coarse-grained MD simulations (Section 8.4) support the idea of having ionomer-free aggregates. Single strands of ionomer could penetrate into primary pores, but it is unlikely that they could impart noticeable proton conductivity to agglomerates. Several questions remain to be addressed, e.g., whether ionomer domains adhere to agglomerate surfaces with their hydrophobic or hydrophilic parts or whether the coating ionomer film is partial (weak adhesion) or complete. The latter question is vital in view of the role of percolation effects for catalyst utilization and the observation of limiting current density behavior in $E(j_0)$ relations.
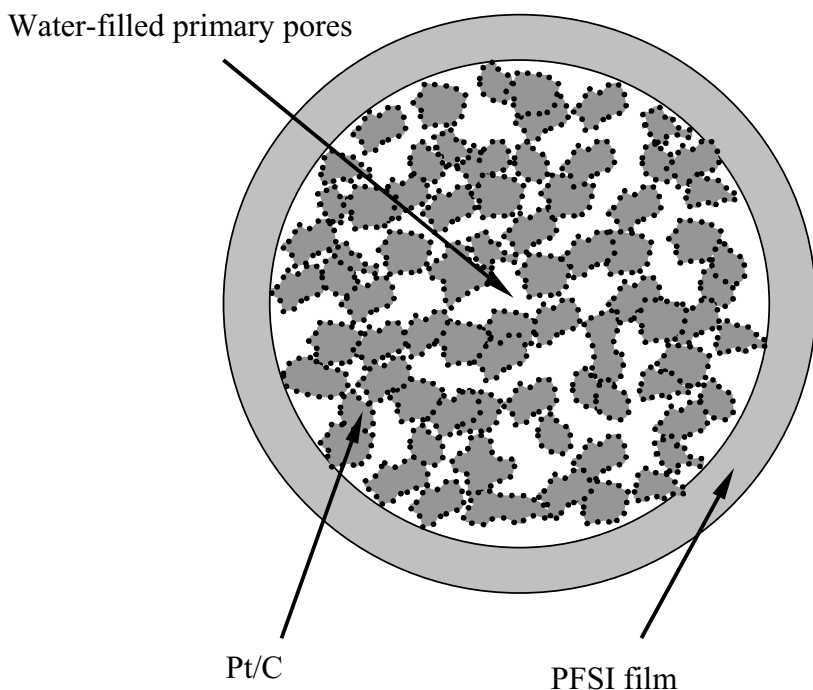
Figure 8.11. Model of spherical agglomerate of carbon/Pt with ionomer-coating of uniform film thickness [69]. (Reprinted from Journal of Electroanalytical Chemistry, 573(1), Wang Q, Eikerling M, Song D, Liu Z. Structure and performance of different types of agglomerates in cathode catalyst layers of PEM fuel cells, 61–9, ©2004, with permission from Elsevier.)

The simplified model system of agglomerate performance, considered in detail in [69], is depicted in Figure 8.11. This model is currently undergoing extensive

revisions. The basic version that we discuss here has, nevertheless, provided vital insights into catalyst effectiveness at the mesoscopic scale. The agglomerate is spherical with radius R_a. It consists of a Pt/C matrix, with primary pores completely wetted by liquid water. As a simplification, we assume a uniform ionomer coating on the agglomerate surface. Proton and oxygen concentrations (c_{H^+}, c_{O_2}) and electric potential in pore water (electrolyte) (ϕ_{el}) inside of agglomerates are functions of the radial agglomerate coordinate r. Uniform boundary conditions apply at $r = R_a$. Since the Pt/C phase is assumed to be equipotential, we can consider variations in overpotential, $\eta_a(r)$, instead of $\phi_{el}(r)$. The functions $c_{H^+}(r)$, $c_{O_2}(r)$ and $\eta_a(r)$ determine the Faradaic current density (in [A cm^{-3}]), given by the Tafel equation,

$$i_F(r) = i_a^0 \left(\frac{c_{O_2}(r)}{c_{O_2}^{ref}} \right)^{\gamma_{O_2}} \left(\frac{c_{H^+}(r)}{c_{H^+}^{ref}} \right)^{\gamma_{H^+}} \exp \left(\frac{\alpha_c F}{RT} \eta_a(r) \right) \tag{8.40}$$

The reference proton concentration $c_{H^+}^{ref}$ on the surface of the agglomerate is determined by the type of ionomer, in particular its ion-exchange capacity, and the volume portion of ionomer with which the catalyst layer is impregnated. For an orientation, a typical value is $c_{H^+}^{ref} \approx 0.5$ mol l^{-1}. The value of the reference oxygen concentration $c_{O_2}^{ref}$ in Equation 8.40 has to be consistent with the concentration used in defining the equilibrium electrode potential.

Equation 8.2 can be used to determine the exchange current density (per unit volume) at the agglomerate level, i_a^0. The factor $f(X_{PtC}, X_{el})/X_{PtC}$, which accounts for macroscopic percolation effects in the three-phase composite, has to be omitted. Moreover, assuming complete flooding of primary pores, i.e., $g(S_r) \equiv 1$, we obtain

$$i_a^0 = \frac{2 \cdot 10^3 \left[m_{Pt} \right] \varepsilon^{S/V}}{\left(X_{PtC} + X_\mu \right)} \frac{j^{0*}}{L} \tag{8.41}$$

The factor $\left(X_{PtC} + X_\mu \right)$ in the denominator is a correction for the volume occupied by agglomerates relative to the total volume of an REV. According to Parthasarathy et al. [144], at high current density the 1-electron transfer step $O_2 + H^+ + e^- \rightarrow \left(O_2 H \right)_{ad}$ is rate determining. Therefore, the reaction orders γ_{O_2} and γ_{H^+} are taken as unity.

The steady-state flux of hydrated protons in the agglomerate is due to diffusion and migration in the internal electric field. It is dictated by the Nernst-Planck

equation, with a sink term i_F due to electrochemical reactions at the dispersed Pt|water interfaces in agglomerates,

$$-FD_{H^+}^{eff} \frac{1}{r^2} \frac{d}{dr} \left[r^2 \left(\frac{dc_{H^+}}{dr} + \frac{F}{RT} c_{H^+} \frac{d\eta_a}{dr} \right) \right] = -i_F \tag{8.42}$$

We use the Bruggemann formula to relate the effective diffusion coefficient of protons in micropores, $D_{H^+}^{eff}$, to the relative volume portion of micropores in agglomerates and the proton diffusion coefficient in water,

$$D_{H^+}^{eff} = D_{H^+}^{w} \left(\frac{X_\mu}{X_{PtC} + X_\mu} \right)^{3/2}. \tag{8.43}$$

The variation in local electrostatic potential is obtained from the Poisson equation,

$$-\varepsilon_r \varepsilon_0 \frac{1}{r^2} \frac{d}{dr} \left(r^2 \frac{d\eta_a}{dr} \right) = -Fc_{H^+}, \tag{8.44}$$

where ε_r is the relative dielectric permittivity of water in pores and ε_0 is the dielectric constant. Oxygen diffusion is given by Fick's law

$$-FD_{O_2-W}^{eff} \frac{1}{r^2} \frac{d}{dr} \left(r^2 \frac{dc_{O_2}}{dr} \right) = -\frac{i_F}{4} \tag{8.45}$$

where the effective oxygen diffusion coefficient is related by Bruggemann's relation

$$D_{O_2-W}^{eff} = D_{O_2}^{w} \left(\frac{X_\mu}{X_{PtC} + X_\mu} \right)^{3/2} \tag{8.46}$$

to agglomerate composition and the bulk diffusion coefficient of oxygen in liquid water, $D_{O_2}^{w}$.

Equations 8.44 and 8.45 form the basis of the Poisson-Nernst-Planck (PNP) theory, which is widely used in the context of ion transport through biological membranes [145–147]. In dimensionless form the equations are

$$-\frac{1}{\rho^2} \frac{d}{d\rho} \left[\rho^2 \left(\frac{dC_p}{d\rho} + C_p \frac{d\Phi}{d\rho} \right) \right] = -K_1 C_o C_p \exp(\alpha_c \Phi) \tag{8.47}$$

$$\frac{1}{\rho^2}\frac{d}{d\rho}\left(\rho^2\frac{d\Phi}{d\rho}\right) = -K_2 C_{\mathrm{p}} \tag{8.48}$$

$$-\frac{1}{\rho^2}\frac{d}{d\rho}\left(\rho^2\frac{dC_{\mathrm{o}}}{d\rho}\right) = -\delta K_1 C_{\mathrm{o}} C_{\mathrm{p}} \exp\left(\alpha_{\mathrm{c}}\Phi\right) \tag{8.49}$$

where $\rho = r/R_{\mathrm{a}}$, $C_{\mathrm{o}} = c_{\mathrm{O}_2}/c_{\mathrm{O}_2}^{\mathrm{ref}}$, $C_{\mathrm{p}} = c_{\mathrm{H}^+}/c_{\mathrm{H}^+}^{\mathrm{ref}}$, $\Phi = \dfrac{F}{RT}\eta_{\mathrm{a}}$ and

$K_1 = \dfrac{i_{\mathrm{a}}^0}{Fc_{\mathrm{H}^+}^{\mathrm{ref}}D_{\mathrm{H}^+}^{\mathrm{eff}}}R_{\mathrm{a}}^2$, $\delta = \dfrac{D_{\mathrm{H}^+}^{\mathrm{eff}}c_{\mathrm{H}^+}^{\mathrm{ref}}}{4D_{\mathrm{O}_2-W}^{\mathrm{eff}}c_{\mathrm{O}_2}^{\mathrm{ref}}}$, $K_2 = \dfrac{R_{\mathrm{a}}^2}{\lambda_{\mathrm{D}}^2}$ with   the   Debye-length

$\lambda_{\mathrm{D}} = \left(\dfrac{\varepsilon_{\mathrm{r}}\varepsilon_0 RT}{F^2 c_{\mathrm{H}^+}^{\mathrm{ref}}}\right)^{1/2}$.   Spherical   symmetry   imposes   the   boundary   conditions

$\left.\dfrac{d\Phi}{d\rho}\right|_{\rho=0} = 0$, $\left.\dfrac{dC_{\mathrm{o}}}{d\rho}\right|_{\rho=0} = 0$, $\left.\dfrac{dC_{\mathrm{p}}}{d\rho}\right|_{\rho=0} = 0$. The effectiveness factor of water-filled agglomerates is defined as the ratio of the overall electrocatalytic turnover rate to the total rate that would be obtained if reactions were distributed uniformly

$$\Gamma_{\mathrm{a}}\left(R_{\mathrm{a}},\Phi_1,C_{\mathrm{o},1},C_{\mathrm{p},1}\right) = \frac{3\int_0^1 \rho^2 \mathrm{d}\rho\, C_{\mathrm{o}}(\rho) C_{\mathrm{p}}(\rho)\exp\left(\alpha_{\mathrm{c}}\Phi(\rho)\right)}{C_{\mathrm{o},1}\exp\left(\alpha\Phi_1\right)} \tag{8.50}$$

This property can be used to rationalize the effects of boundary values $\Phi(\rho=1)=\Phi_1$, $C_{\mathrm{o}}(\rho=1)=C_{\mathrm{o},1}$, $C_{\mathrm{p}}(\rho=1)=C_{\mathrm{p},1}\equiv 1$, and agglomerate structure on current conversion [69].

 The results showed that the effectiveness factor of agglomerates, Γ_{a} , is mainly affected by electrostatic effects, which are determined by the non-linear distribution of proton concentration and the radial variation of the electrostatic potential, $\eta_{\mathrm{a}}(r)$. Figure 8.12(a) shows the radial function $c_{\mathrm{H}^+}(r)$ for various agglomerate radii. It decreases from the agglomerate surface towards the center over a characteristic length corresponding to λ_{D} . In Figure 8.12 (b), $\eta_{\mathrm{a}}(r)$ increases in the same direction. In the corresponding Faradaic current density, shown in Figure 8.12 (b),

$$i_{\mathrm{F}}(r) \propto c_{\mathrm{H}^+}(r)\exp\left[\frac{\alpha_{\mathrm{c}}F}{RT}\eta_{\mathrm{a}}(r)\right] \tag{8.51}$$

the two effects partially counterbalance each other. A smaller radius of agglomerates corresponds to more uniform $i_{\mathrm{F}}(r)$ and, thus, to more effective

utilization of catalyst. As apparent from Equation 8.51, the cathodic transfer coefficient α_c steers this interplay.
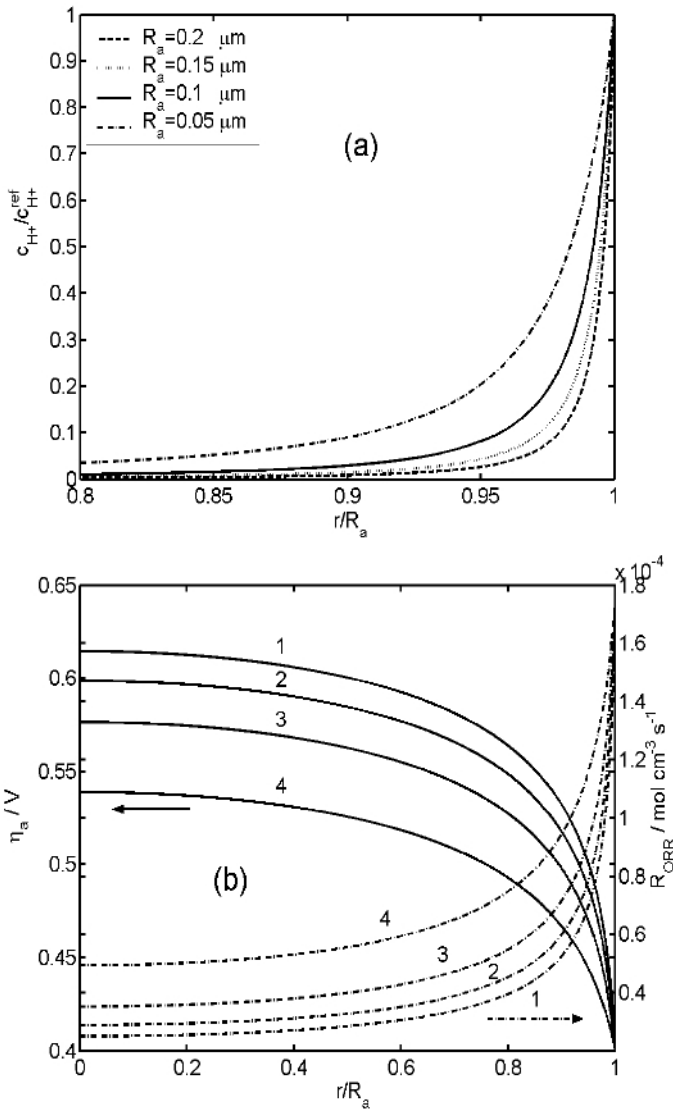
Figure 8.12. Radial distributions of (a) proton concentration (c_{H^+}) and (b) electrical potential (η_a) and electrochemical reaction rates (R_{ORR}) for various radii of agglomerates ($R_a = 0.2, 0.15, 0.1, 0.05\,\mu m$) [69]. (Reprinted from Journal of Electroanalytical Chemistry, 573(1), Wang Q, Eikerling M, Song D, Liu Z. Structure and performance of different types of agglomerates in cathode catalyst layers of PEM fuel cells, 61–9, ©2004, with permission from Elsevier.)

For negligible oxygen diffusion limitations, an integral expression for the effectiveness factor of ideal spherical agglomerates was found,

$$\Gamma_a = 3 \int_0^1 \rho^2 d\rho \; \exp\left[-(1-\alpha_c)\tilde{\Phi}(\rho)\right], \; \tilde{\Phi}(\rho) = \Phi(\rho) - \Phi_1 \tag{8.52}$$

The potential distribution, $\tilde{\Phi}(\rho)$, is obtained from the solution of the Poisson-Boltzmann-like expression

$$\frac{1}{\rho^2} \frac{d}{d\rho}\left(\rho^2 \frac{d\tilde{\Phi}}{d\rho}\right) = -K_2 \exp\left(-\tilde{\Phi}\right) \tag{8.53}$$
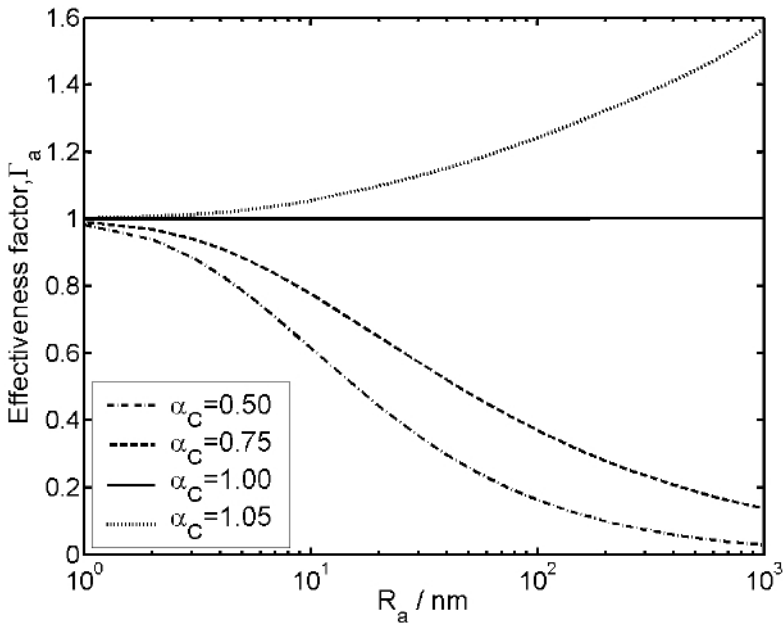
Figure 8.13. Effectiveness factors as function of agglomerate radius R_a for distinct values of the cathode transfer coefficient, α_c [69]. (Reprinted from Journal of Electroanalytical Chemistry, 573(1), Wang Q, Eikerling M, Song D, Liu Z. Structure and performance of different types of agglomerates in cathode catalyst layers of PEM fuel cells, 61–9, ©2004, with permission from Elsevier.)

As can be seen from Equations 8.52 and 8.53, Γ_a depends solely on α_c and $K_2 \propto R_a^2$. For $\alpha_c = 1$, the approximate analytical solution predicts $\Gamma_a \equiv 1$, i.e., ideal catalyst utilization at the agglomerate level. Equation 8.52 links catalyst utilization in agglomerates and fundamental electrode kinetics, represented by α_c, at a rather rudimentary level. Figure 8.13 comprises the effects of α_c and R_a on

Γ_a. The effectiveness factor increases with increasing α_c. It will be $\Gamma_a \equiv 1$ at $\alpha_c = 1$ and larger than 1 for $\alpha_c > 1$. Γ_a decreases with increasing R_a for $\alpha_c < 1$.

How important are effects at the agglomerate level for the overall performance of a CCL? This depends on the relation between the two major length scales R_a and L_{CL}. For the most general case in conventional CCLs agglomerates will be small compared to the electrode thickness, $R_a << L_{CL}$, but their effects on catalyst effectiveness and voltage efficiency have to be accounted for. In this case, the fully coupled system of equations at agglomerate and CCL levels has to be solved self-consistently in order to calculate reaction rate distributions in CCLs. The limit $R_a \rightarrow L_{CL}$ corresponds to ionomer-free two-phase CCLs, which will be considered in Section 8.6. In the opposite limit, $R_a <<< L_{CL}$, agglomerate effects are negligible and the pure macrohomogeneous approach could be used. In this case, only Equations 8.27 to 8.33 are relevant and $Q^{ec}(z)$ in Equation 8.33 is given by

$$Q^{ec}(z) = 2 \cdot 10^3 \left[m_{Pt} \right] j^{0*} \varepsilon^{S/V} \frac{f(X_{PtC}, X_{el})}{X_{PtC}} g(S_r) \frac{H_{O_2}}{RT c_{O_2}^{ref}} P_{O_2}(z) \exp\left[\frac{\alpha_c F}{RT} \eta(z) \right] \quad (8.54)$$

We will discuss the main results of the macrohomogeneous model first.

8.5.4 Main Results of the Macrohomogeneous Approach

In the past, studies of the macrohomogeneous model have explored the effects of thickness and composition on performance and catalyst utilization. At the outset, it should be noted that these works neglected the effects of liquid water accumulation in pores on performance. The specific effects due to the complex coupling between porous morphology, liquid water formation, oxygen transport, and reaction rate distributions will be discussed in Section 8.5.5. The results presented in this section are only valid at sufficiently small current densities, for which liquid water accumulation in secondary pores is not critical.

The relevant solutions of the macrohomogeneous model for the case of negligible agglomerate effects have been discussed in detail in [3, 43, 47]. Analytical relations for reaction rate distributions and relations between fuel cell current density and overvoltage losses in the CCL were obtained for limiting cases of fast oxygen diffusion and fast proton transport [43, 47]. In [148] double layer charging was included in the model. With this extension, the complex impedance response of the layer could be calculated. The model of impedance amplifies the diagnostic capabilities of the model, e.g., providing the proton conductance of the CCL from the linear branch of impedance spectra (in Cole-Cole representation) in the high frequency limit.

Three different regimes of current density exist in electrode polarization curves: (1) a kinetic regime at small current densities, $j_0 \ll I$, which exhibits a simple

Tafel dependence $\eta_0 \approx b \ln\left(j_0/j^0\right)$ with $b = \dfrac{RT}{\alpha_c F}$; (2) an intermediate regime for $j_0 \sim I$ with prevailing double Tafel-slope characteristic

$$\eta_0 \approx 2b \ln\left(\frac{j_0}{I}\right), \text{ with } \quad I = \frac{4F\bar{P}_{O_2} D^o}{RTL_{CL}} \; , \qquad\qquad (8.55)$$

where $\bar{P}_{O_2} = P_{O_2}\left(z = L_{CL}\right)$ is the oxygen partial pressure at the CCL|GDL interface; and (3) an oxygen depletion regime for $j_0 \gg I$, in which all oxygen is consumed in a sublayer of thickness $\delta_{CL} \ll L_{CL}$. For a given composition, the thickness and the target current density of fuel cell operation should be adjusted in order to operate the catalyst layer in the intermediate regime, since it represents the best compromise between transport losses and kinetic losses. Although reaction rates distributions exhibit a pronounced non-uniformity in this regime, all parts of the layer are used for reactions. There are, thus, no inactive parts. As long as the CCL is operated in the intermediate regime, overvoltage losses are almost independent of the thickness. In [3] these findings were displayed in the form of a phase diagram.

The existence of a maximum thickness beyond which the performance degrades is due to the concerted impact of oxygen and proton transport limitations. Considered separately, each of these limitations would only suffice to define a minimum thickness, below which performance worsens due to insufficient electroactive surface. The thickness of the effective layer in which current density is predominantly generated is given by the reaction penetration depth:

$$\delta_{CL} = \frac{I}{j_0} L_{CL} \qquad\qquad (8.56)$$

In the oxygen depletion regime, $j_0 \gg I$, only a thin sublayer with thickness $\delta_{CL} \ll L_{CL}$, adjacent to the GDL, is active. The remaining sublayer with thickness $\left(L - \delta_{CL}\right) \approx L_{CL}$, adjacent the PEM side, is not used for reactions, due to starvation in oxygen. This highly non-uniform reaction rate distribution implies underutilization of catalyst. The inactive part causes overpotential losses due to proton transport in the embedded ionomer phase, which could cause limiting current behavior, if the proton conductivity is poor. In summary, $\delta_{CL} \sim L_{CL}$ should be warranted. This corresponds to operation of the CCL in the intermediate regime, which ensures a good balance of high performance (i.e., minimal overpotential losses) and effective catalyst utilization.
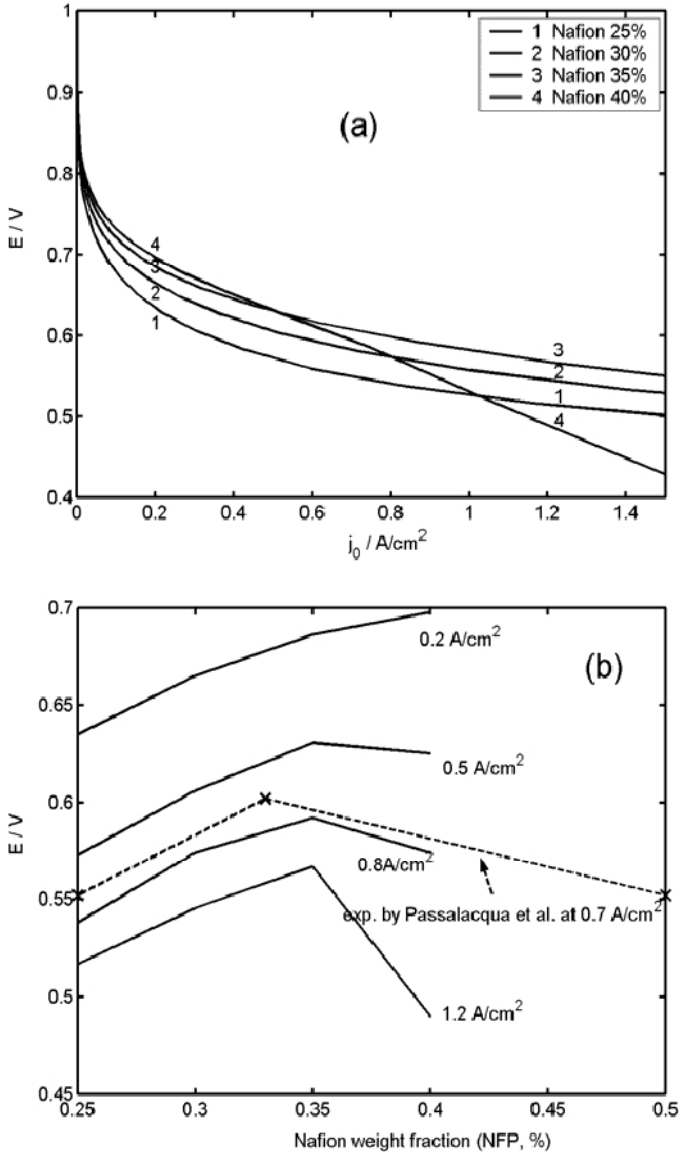
Figure 8.14. (a) Effect of the Nafion weight fraction, Y_{el}, in cathode catalyst layers with uniform composition on the performance of the fuel cell, shown in the form of $E(j_0)$ relations. (b) Variation of cell potential as a function of Nafion weight fraction Y_{el} for different operating current densities j_0. Experimental data taken from [151] are shown for comparison. The experimental data have been corrected for the membrane contribution, displaying only the contribution of the cathode catalyst layer to E [149]. (Reproduced by permission of ECS – The Electrochemical Society, from Wang Q, Eikerling M, Song D, Liu S, Navessin T, Xie Z, et al. Functionally graded cathode catalyst layers for polymer electrolyte fuel cell.)

The macrohomogeneous model was exploited in optimization studies of the catalyst layer composition, using the relations specified in Section 8.4. The theory of composition-dependent performance reproduces very well experimental findings [12, 53, 149–151]. The dependence of $E(j_0)$ on mass fraction of ionomer Y_{el} for a cathode catalyst layer with uniform composition is illustrated in Figure 8.14(a) [149]. The optimum value of Y_{el} that gives the highest voltage efficiency depends on the current density range. At intermediate current densities, $0.5 \text{ A cm}^{-2} \leq j_0 \leq 1.2 \text{ A cm}^{-2}$, the best performance is obtained with $Y_{el} \simeq 35 \text{ wt\%}$. Increasing Y_{el} to values $> 35 \text{ wt\%}$ in this range, leads to reduced $E(j_0)$ because of its deleterious impact on oxygen diffusion. Further increase in Y_{el} enhances $E(j_0)$ only at low current densities, i.e., $j_0 \leq 0.5 \text{ A cm}^{-2}$, for which oxygen diffusion is not rate limiting. In this range, larger values of Y_{el} lead to a reduction of ohmic losses. At various current densities in the range $j_0 > 0.5 \text{ A cm}^{-2}$ the cell potential is shown in Figure 8.14(b) as a function of Y_{el} in comparison with experimental data by Passalacqua et al. [151]. The effect of Nafion weight fraction on performance predicted by the model is consistent with the experimental trends.

The model was also used to explore novel design ideas. It was predicted and confirmed in experiment that functionally graded layers result in improved voltage efficiency compared to standard CCLs with uniform composition [53, 150]. In this design, the catalyst layer is fabricated as a sublayer structure with gradually varying composition. Compared with the layer of uniform composition with $Y_{el} = 35 \text{ wt\%}$, corresponding to the optimum in Figure 8.14, a simple three-sublayer structure with 30 wt% Nafion content in the sublayer towards the GDL side, 35 wt% Nafion content in the middle sublayer, and 40% wt Nafion content in the sublayer towards the membrane side improves $E(j_0)$ by about 5%. Another advantage of this design is the reduced Ohmic resistance at the PEM|CCL interface due to the improved contact area between electrolyte phases at higher Nafion loading on the CCL side. In the interface between GDL and CCL, lower Nafion loading will decrease the probability of blockage of pores by Nafion and, thereby, facilitate water removal via the GDL.

8.5.5 Water Management in CCLs

The effects of the porous structure and liquid water accumulation on steady-state performance were explored in [50, 51], employing the structural picture and the corresponding framework model of catalyst layer operation, as discussed in Section 8.5.2.

The equations were solved with the following boundary conditions:
(i) At the CCL|GDL boundary ($z = L_{CL}$), the electrode potential is fixed, $\eta(z = L) = \eta^L$; this determines the working point of the fuel cell, i.e., the proton

flux at the PEM|CCL boundary ($z = 0$), $j_0 = j_p(z = 0)$. It also fixes the value of the oxygen flux at the CCL|GDL boundary.

(ii) The oxygen partial pressure at $z = L_{CL}$ is $\bar{P}_{O_2}$. In [50], $\bar{P}_{O_2}$ was considered as an externally controlled parameter. Instead, in [51], the oxygen partial pressure at the interface between GDL and flow field (FF) was assumed to be controlled and diffusive gas transport in the GDL was taken into account, using Fick's law,

$$\bar{P}_{O_2} = P_{O_2}(GDL \,|\, FF) - \frac{j_0 \cdot L_{GDL}}{4\, f D_{GDL}^{o}} \tag{8.57}$$

where D_{GDL}^{o} is the oxygen diffusion coefficient and L_{GDL} the thickness of the GDL. This allowed the identification of distinct signatures in $E(j_0)$ response curves due to due to limited oxygen transport in either the CCL or the GDL.

(iii) The proton flux is completely consumed in the CCL and, therefore, $j_p(z = L_{CL}) = 0$.

(iv) Since the PEM is assumed to be gas-tight, we have $j^v(z = 0) = 0$.

(v) A value of the liquid pressure at the PEM|CCL boundary is assumed, i.e., $p^l(z = 0) = p^{l0}$.

(vi) The liquid flux at the PEM|CCL boundary is $j^l(z = 0) = j_m$.

(vii) At the CCL|GDL boundary, the liquid flux is $j^l(z = L) = \gamma(j_m + j_0/2)$. The parameter γ, thus represents the portion of water that leaves the CCL towards the GDL side in liquid form. The remaining portion, i.e., $j^v(z = L) = (1 - \gamma)(j_m + j_0/2)$, will be in vapor form. Complete liquid-to-vapor conversion corresponds to $\gamma = 0$.

In principle, a full MEA model would be needed to obtain values of the parameters p_0^l, j_m, and γ from solutions of the complete set of balance equations. Since here we focus on the CCL model only, these values cannot be determined self-consistently. They have to be considered as controlled parameters. In order to reduce the number of undetermined parameters, we impose a condition on γ: for any given operating conditions we assume the maximum conversion of liquid water into water vapor, i.e., γ should be minimal. As discussed in [50], this condition defines a critical current density of fuel cell operation, below which the CCL could completely vaporize liquid water. This critical current density represents the liquid-to-vapor conversion capability of a CCL. The condition of minimal γ implies optimum vapor removal out of the MEA through the GDL and FF. Such conditions are realistic for operation of the PEFC with dry reactant on the cathode side. Moreover, the GDL should possess high gas diffusivity.

In [50], the continuous psd was replaced by a bimodal δ-distribution

$$\frac{dX_p(r)}{dr} = X_\mu \delta(r - r_\mu) + X_M \delta(r - r_M).\tag{8.58}$$

This assumption permits a full analytical solution and readily reveals major principles of water handling and performance in CCLs. At the same time, it still captures essential physical processes, critical phenomena, operation conditions, and major structural features such as typical pore sizes (r_μ, r_M) and distinct contributions to porosity from primary and secondary pores (X_μ, X_M).

In terms of liquid water saturation and water management in the CCL, the bimodal δ-distribution leads to a three-state model. The three states that any REV could attain are the dry state ($S_r \approx 0$, water-free system), the ideally wetted state ($S_r = X_\mu/X_p$, primary pores are completely water-filled while secondary pores are water-free), and the fully saturated state ($S_r = 1$). In the ideally wetted state, catalyst utilization and exchange current density are high ($g \approx 0.8 - 0.9$). The surface area for evaporation, ξ^{lv}, is large as well. Moreover, diffusion coefficients will still be high, since secondary pores remain water-free. In the fully saturated state major parts of the layer are deactivated due to the blocking of oxygen diffusion pathways by liquid water.

An expression for the characteristic current density, below which complete liquid-to-vapor conversion is possible, was obtained,

$$j_{crit}^{lv} = \frac{2q_2^s fD_2^v}{\lambda_v} \tanh\left(\frac{L}{\lambda_v}\right) - 2j_m, \ \lambda_v = \left(\frac{fD_2^v L}{e_0 \kappa^e \xi_2^{lv}}\right)^{1/2}\tag{8.59}$$

where q_2^s, D_2^v, ξ_2^{lv} represent saturated vapor pressure, vapor diffusion coefficient, and liquid|vapor interfacial area in the ideally wetted state.

Moreover, the cathode catalyst layer fulfils an important function in regulating opposite hydraulic fluxes towards PEM and GDL sides. The results also strongly suggest the CCL as a critical fuel cell component in view of excessive flooding that could give rise to critical effects in $E(j_0)$-relations. Under certain conditions ($j_{crit}^{fl} > j_{crit}^{lv}$), critical liquid water formation arises first in the interior of the layer, close to the CCL|GDL interface and not at the PEM|CCL boundary.

The model revealed sensitive dependencies of CCL operation on porous structure, thickness, wetting angle, total gas pressure on cathode side, and net liquid water flux from the membrane. With rather favorable parameters (10 μm thickness, 5 atm cathodic gas pressure, 89° wetting angle), the critical current density of CCL flooding is found in the range $2 - 3$ A cm^{-2}. For increased thickness, smaller gas pressure, or slightly reduced wetting angles of secondary pores, CCLs could be flooded at current densities well below 1 A cm^{-2}. The contact angle is an important parameter in this context, highly influential but difficult to control in fabrication [146, 152].

Solutions of the physical model of CCL operation for general continuous pore size distributions were recently presented in [51]. With this extension the full coupling between composite porous morphology, liquid water accumulation, transport of reactants and products, and electrochemical conversion rate in the oxygen reduction reaction could be explored (cf. Figure 8.15). Continuous PSDs allow the relating of global performance effects to local distributions of water, fluxes and concentrations of reactants, and reaction rates in the layer. It was found that a CCL alone cannot give rise to limiting current behavior in current-voltage response curves. The explanation is simple and intuitive: in the fully saturated state, the layer retains a residual oxygen diffusivity through liquid-water filled pores $D_{fl}^{o} = 2.0 \cdot 10^{-6}\,\mathrm{cm^2 s^{-1}}$; the main effect of excessive water accumulation will be a corresponding drastic decrease in the reaction penetration depth δ_{CL} to values in the range of $100\,\mathrm{nm} \ll L_{CL}$; the overvoltage of the CCL will increase accordingly so that the smaller fraction of active Pt atoms in the active part can maintain the fixed total current density; the voltage increase is related logarithmically to the factor by which the reaction penetration depth decreases, following the dependence imposed by the Butler-Volmer equation.
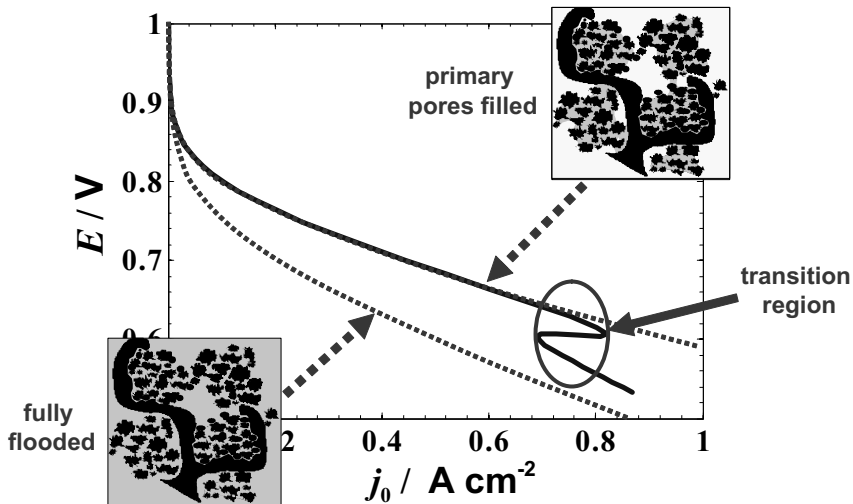
Figure 8.15. Plot of cell potential vs. fuel cell current density, $E(j_0)$, indicating the effect of liquid water accumulation in the CCL on performance (solid line). The interplay of liquid water accumulation in pores and impeded oxygen transport causes the transition from the ideally wetted state to the fully saturated state (dotted lines), as indicated [51]. (Reprinted from Electrochimica Acta, 53.13, Liu J, Eikerling M. Model of cathode catalyst layers for polymer electrolyte fuel cells: The role of porous structure and water accumulation, 4435–46, ©2008, with permission from Elsevier.)

Upon increasing the current density generated by the fuel cell, a transition between two principal states of operation occurs, as illustrated in Figure 8.15. The ideally wetted state at low current densities exhibits levels of liquid water

saturation well below the critical value for pore blocking, corresponding to relatively uniform distributions of reactants and reaction rates and thus effective utilization of the catalyst. In the fully saturated state, liquid water saturation exceeds the critical value in parts of the layer. These parts could sustain only low residual gas diffusivity. Corresponding reactant and reaction rate distributions will be highly non-uniform. The main part of the CCL will be inactive. The transition between the two states of operation can occur monotonously or it could involve bistability, as a signature of nonlinear coupling between liquid water accumulation, gaseous transport, and electrochemical conversion rate. Bistability means that two stable steady-state solutions of the continuity equations coexist in the transition region.
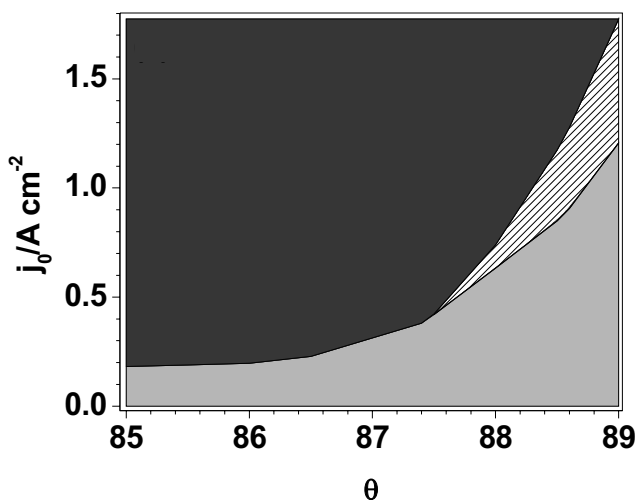
Figure 8.16. The stability diagram of the cathode catalyst layer, displaying the effect of the wetting angle on the state of operation over a relevant range of operating current densities [51]. The different regions correspond to ideally wetted state (light gray), bistability region (shaded), and fully saturated state (dark). (Reprinted from Electrochimica Acta, 53(13), Liu J, Eikerling M. Model of cathode catalyst layers for polymer electrolyte fuel cells: The role of porous structure and water accumulation, 4435–46, ©2008, with permission from Elsevier.)

The critical current density of the transition from ideally wetted state to transition region or fully saturated state is the major optimization target of CCLs in view of their water handling capabilities. A larger critical current density allows the extracting of higher voltage efficiency and power density from PEFCs. Critical current densities depend on structural parameters and operating conditions. Stability diagrams have been introduced for assessing the effects of these parameters on CCL performance. The stability diagram in Figure 8.16 displays the effect of the wetting angle on fuel cell operation, distinguishing between ideally wetted state (light gray), bistability region (shaded), and fully saturated state (dark gray). The task of water management in CCLs is to push back capillary equilibrium to small enough pores so that liquid water formation cannot block gaseous

transport in secondary pores. Beneficial conditions in view of this objective are high total porosity, large volume fraction of secondary pores, a wetting angle that closely approaches 90°, a high total gas pressure, and high temperature of operation.

8.6 Comparison and Evaluation of Catalyst Layer Designs

The key metrics for the evaluation of successful designs of catalyst layers are the effectiveness factor of catalyst utilization, voltage efficiency, and water handling capability in operational PEFCs. Of course, the evaluation can be performed on the basis of empirical data collected with standard experimental characterization tools that have been established over recent decades in countless research institutes worldwide. A purely empirical approach cannot, however, rationalize the complex relations between random composite morphologies, physico-chemical properties of transport and electrochemical kinetics, distribution of reactants and water, and performance. Moreover, it fails in accurately predicting what the reserves for catalyst layer improvement are and how they could be harnessed, viz. by catalyst design at the nanoscale, optimization of the substrate in view of porous morphology and wetting properties, optimization of thickness, and composition of the complete layer. As a consequence, many controversial issues related to catalyst layer characterization and operation persist today.

As described in this chapter, the physical theory and molecular modeling of catalyst layers provide various tools for relating the global performance metrics to local distributions of physical parameters and to structural details of the complex composite media at the hierarchy of scales from nanoscale to macroscale. The subsisting challenges and recent advances in the major areas of theoretical catalyst layer research include: (i) structure and reactivity of catalyst nanoparticles, (ii) self-organization phenomena in catalyst layers at the mesoscopic scale, (iii) effectiveness of current conversion in agglomerates of carbon/Pt, and (iv) interplay of porous structure, liquid water formation, and performance at the macroscopic scale.

In this section we will apply tools in physical theory and molecular modeling to compare various designs of catalyst layers. The major design parameter, the effectiveness of catalyst utilization, is most difficult to evaluate for conventional CLs with 3-phase composite morphology, due to the interplay of statistical factors and processes at 3 major scales. Partial wetting of pores further complicates this interplay, as discussed in Section 8.5.5. Well-defined approaches can be defined at separate scales; however, the reconciliation of agglomerate model and percolation model, as suggested at a rudimentary level in Equation 8.2, is not trivial. This will require further refinement in future works. Fully flooded, ultrathin CLs essentially eliminate one phase, viz. the ionomer phase, and one structural level, viz. effects of percolation and partial wetting at the macroscopic scale. This simplifies the evaluation of the statistical factors in relation to composition and of the reaction penetration depth in relation to thickness.

8.6.1 Conventional Catalyst Layers

At the macroscopic scale, catalyst utilization is severely limited by the statistical constraints imposed by the 3-phase random composite structure. Only catalyst particles that are simultaneously accessible to electrons, protons, and oxygen could be electrochemically active. These requirements are included in the factors $f\left(X_{\mathrm{PtC}}, X_{\mathrm{el}}\right)/X_{\mathrm{PtC}}$ and $g\left(S_{\mathrm{r}}\right)$ in Equation 8.2. It was suggested in [3, 6, 47, 50] that due to these factors alone the upper limit of catalyst utilization lies in the range of ~20%.

At the mesoscopic scale, the effectiveness factor Γ_{a} of agglomerates is a strong function of agglomerate radius and cathodic transfer coefficient, as discussed in Section 8.5.2. At values $\alpha_{\mathrm{c}} < 0.9$ and $R_{\mathrm{a}} > 50\,\mathrm{nm}$, Γ_{a} could be markedly smaller than 1. Moreover, factors at the nanoparticle level in Equation 8.2 further reduce catalyst utilization, viz. the atomistic surface-to-volume ratio of catalyst atoms, $\varepsilon^{\mathrm{S/V}}$, and the fraction of active catalyst sites. What's more, the remaining fraction of electrochemically active sites could be used ineffectively. Vast parts of the catalyst layer could be inactive due to the starvation in oxygen for $\delta_{\mathrm{CL}} \ll L_{\mathrm{CL}}$, i.e., when the thickness and current density of the fuel cell do not conform well to each other.

A calculation of the overall effectiveness of catalyst utilization in conventional CCLs has been recently performed in [56], including all of the aforementioned detrimental factors. This estimate suggests that less than 10% of the catalyst is effectively utilized for reactions. Ineffectiveness of catalyst utilization is a major downside of random 3-phase composite layers.

8.6.2 Ultra-thin Two-phase Catalyst Layers

The alternative is to fabricate CCLs as ultrathin two-phase composites ($L_{CL} \sim 100\,\mathrm{nm} - 200\,\mathrm{nm}$), in which electroactive Pt could form the electronically conducting phase, or Pt nanoparticles could be supported on a conductive substrate. The remaining volume should be filled with liquid water, as the sole medium for proton and reactant transport. The ultra-thin two-phase catalyst layer was explored by using the Poisson-Nernst-Planck (PNP) equations as employed for water-filled spherical agglomerates [69, 118]. The equations in Section 8.5.2 can be rewritten for the 1D planar situation

$$-\frac{\mathrm{d}}{\mathrm{d}\zeta}\left(\frac{\mathrm{d}C_{\mathrm{p}}}{\mathrm{d}\zeta} + C_{\mathrm{p}}\frac{\mathrm{d}\Phi}{\mathrm{d}\zeta}\right) = -K_{1}C_{\mathrm{O}}C_{\mathrm{p}}\exp\left(\alpha_{\mathrm{c}}\Phi\right) \tag{8.60}$$

$$\frac{\mathrm{d}^{2}\Phi}{\mathrm{d}\zeta^{2}} = -K_{2}C_{\mathrm{p}} \tag{8.61}$$

$$-\frac{d^2 C_O}{d\zeta^2} = -\delta K_1 C_O C_p \exp(\alpha_c \Phi) \tag{8.62}$$

where $\zeta = z / L_{CL}$, $\quad C_O = c_{O_2} / c_{O_2}^{ref}$, $\quad C_p = c_{H^+} / c_{H^+}^{ref}$, $\quad \Phi = \dfrac{F}{RT}\eta$,

$K_1 = \dfrac{S^{eff} j^0}{F c_{H^+}^{ref} D_{H^+}^{eff}} L_{CL}^2$, $\quad \delta = \dfrac{D_{H^+}^{eff} c_{H^+}^{ref}}{4 D_{O_2-W}^{eff} c_{O_2}^{ref}}$, $\quad K_2 = \dfrac{L_{CL}^2}{\lambda_D^2}$ with the Debye-length

$\lambda_D = \left(\dfrac{\varepsilon \varepsilon_0 RT}{F^2 c_{H^+}^{ref}} \right)^{1/2}$. In the current density range of 10^{-3} A cm^{-2} to 10^{-1} A cm^{-2},

oxygen concentration will be uniform. Moreover, the reaction term can be neglected in the Poisson-Nernst-Planck equation. Therefore, an analytical solution in implicit form could be found [118]. The profiles of $\Phi(\rho)$ and $C_p(\rho)$ are determined by

$$\frac{d^2\Phi}{d\zeta^2} = -K_2 \exp(-\Phi)\exp(\Phi_1) \tag{8.63}$$

and

$$C_p = \exp\left[-(\Phi - \Phi_1)\right] \tag{8.64}$$

The solution gives

$$\Phi = \Phi_1 + 2\ln\left\{\cos\left[\sqrt{\frac{K_2}{2}}\exp\left(\frac{\Phi_1-\Phi_0}{2}\right)\zeta\right]\cos^{-1}\left[\sqrt{\frac{K_2}{2}}\exp\left(\frac{\Phi_1-\Phi_0}{2}\right)\right]\right\} \tag{8.65}$$

where Φ_0 and Φ_1 are the dimensionless electrolyte potential at $\zeta = 0$ and $\zeta = 1$, which are related by

$$\Phi_0 = \Phi_1 - 2\ln\left\{\cos\left[\sqrt{\frac{K_2}{2}}\exp\left(\frac{\Phi_1 - \Phi_0}{2}\right)\right]\right\} \tag{8.66}$$

The effectiveness factor is

$$\Gamma_{uc} = \int_0^1 d\zeta \cos^{2(1-\alpha_c)}\left[\sqrt{\frac{K_2}{2}}\exp\left(\frac{\Phi_1-\Phi_0}{2}\right)\right]\cos^{-2(1-\alpha_c)}\left[\sqrt{\frac{K_2}{2}}\exp\left(\frac{\Phi_1-\Phi_0}{2}\right)\zeta\right] \tag{8.67}$$

A modified Tafel law can be written for the current-voltage performance

$$j_0 = LS^{\mathrm{eff}}\, j^0 \Gamma_{\mathrm{uc}}\, \frac{c_{\mathrm{O}}^0}{c_{\mathrm{O}}^{\mathrm{ref}}}\, \frac{c_{\mathrm{p}}^{\mathrm{L}}}{c_{\mathrm{p}}^{\mathrm{ref}}}\, \exp\!\left(\frac{\alpha F \eta_{\mathrm{L}}}{RT}\right) \tag{8.68}$$

Γ_{uc} accounts for the deviations from the generic Tafel characteristics. It can be seen from Equation 8.67 that for $\alpha_c \approx 1$, catalyst utilization becomes uniform, $\Gamma_{\mathrm{uc}} \approx 1$ and the unmodified Tafel law is retained. This implies that the total intrinsic surface area of Pt, S^{eff}, could be utilized in the ultrathin CCLs if complete wetting of the Pt surface is assumed. This is in contrast to conventional CCLs, in which S^{eff} is reduced by a factor ~1/5 relative to the total intrinsic surface area of Pt due to the three-phase composite structure and incomplete wetting of pores.
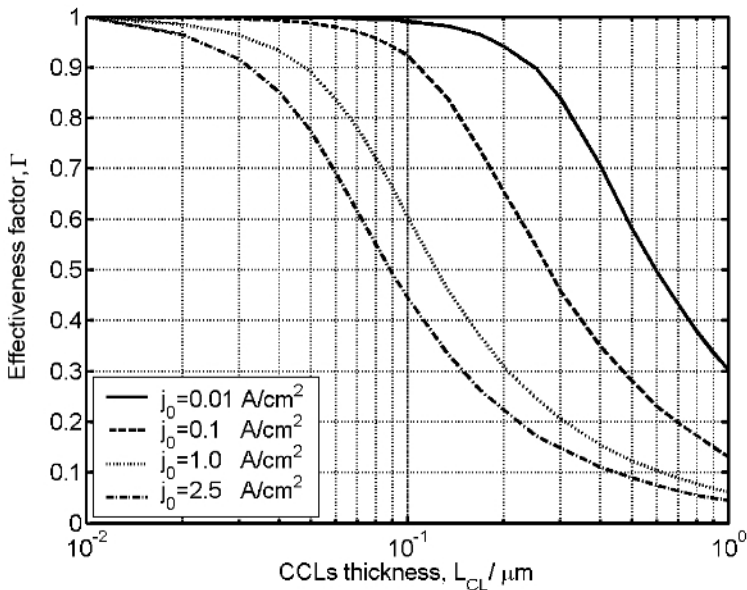
Figure 8.17. Effectiveness factor of ultrathin two-phase catalyst layers as a function of thickness, L_{CL}, at different current densities. (Reproduced by permission of ECS – The Electrochemical Society, from Wang Q, Eikerling M, Song D, Liu S. Modeling of ultrathin two-phase catalyst layers in PEFCs.)

The results show that L_{CL} and α_c are the two major factors for the performance of ultrathin CCLs with two-phase composite structure. The solution of Equations 8.60 to 8.62, including for finite oxygen transport, is shown in Figure 8.17. This shows the effect of L_{CL} on Γ_{uc} for $\alpha_c = 1$ at different j_0. As expected, Γ_{uc} exhibits a pronounced decrease with the increase of L_{CL} at all current densities. At

$j_0 = 1.0$ A cm^{-2}, Γ_{uc} decreases from $> 80\%$ to $\sim 20\%$, for L_{CL} increasing from 60 nm to 300 nm. Figure 8.17 displays the proper thickness of the CCL, if the fuel cell is to be operated at a certain current density with a specified effectiveness factor.

As an example of how to use the insights conveyed in this chapter we provide an explicit comparison of overall effectiveness of Pt utilization (by atom number or catalyst weight) for conventional 3-phase composite and ultrathin CCLs, in Table 8.2. For conventional catalyst layers, the main detrimental factors arise at the nanoparticle scale ($\varepsilon^{S/V}$) and at the macroscopic scale due to triple-phase boundary requirements. For the nanostructured ultrathin CCLs it is assumed that a sputter-deposited continuous Pt layer is needed to provide electronic conductivity. It was suggested in [153] on the basis of cyclic voltammetry measurements that the irregular surface morphology of such catalysts corresponds to grain sizes of ~ 10 nm with $\varepsilon^{S/V} = 0.15$.

Table 8.2. Comparison of conventional three-phase composite and ultrathin CCLs in terms of effectiveness factors.

	Conventional 3-phase CCL	Ultrathin CCL
Current density, j_0	1.0 A cm^{-2}	1.0 A cm^{-2}
O$_2$ partial press at $z = L_{CL}$, p_L	1.0 atm	1.0 atm
Thickness, L_{CL}	10 µm	200 nm
Transfer coefficient, α_c	1.0	1.0
Pt particle/grain size, r_{Pt}	1.5 nm	5 nm
S-to-V atom ratio, $\varepsilon^{S/V}$	$\simeq 0.4$	$\simeq 0.15$
Agglomerate radius, R_a	50 nm	NA
Effectiveness at mesoscale	$\Gamma_a \simeq 1$	$\Gamma_{uc} \simeq 0.6$
Fraction of wetted surface area in pores, $g(S_r)$	$\simeq 0.8$	$\simeq 1.0$
Fraction of Pt at 3-phase boundary, $f(X_{PtC}, X_{el})/X_{PtC}$	$\simeq 0.28$	NA
O$_2$ diffusion coefficient	$2 \cdot 10^{-4}$ cm^2 s^{-1}	$2 \cdot 10^{-6}$ cm^2 s^{-1}
Reaction penetration depth, δ_{CL}	$\delta_{CL} \simeq 3 \cdot L_{CL}$	NA
Overall effectiveness of Pt utilization (by atom number)	0.09	0.09

The rough estimates in Table 8.2, which distinguish factors due to statistical inhomogeneities and non-uniformities of reaction rate distributions at scales from nano- to macroscale, indicate that the two kinds of CCL exhibit similar effectiveness factors of Pt utilization. All in all, any of the factors is fraught with a certain error – thus overall, the estimation would be somewhat speculative. On the other hand, the message is clear. The effectiveness of catalyst utilization in currently fabricated CCL, viz. three-phase composite gas-diffusion CCLs and ultrathin nanostructured CCLs, is most likely < 10% and not close to 100%, as suggested recently by Neyerlin et al. [154]. This assessment demonstrates the prospects for raising the ratio (current conversion rate)/(Pt loading) by a significant factor through structural design of catalyst layers.

8.7 Summary and Outlook

In this chapter, we have provided an overview of the theoretical understanding of CCL operation at a hierarchy of scales. The long-term objective, facilitated by this systematic understanding, will be to develop nanostructured architectures for catalyst layers with high activity, low catalyst loading, and high stability.

Basically, a fuel cell electrode can be seen as a highly dispersed interface between Pt and electrolyte (ionomer or water). Due to the random composition, complex spatial distributions of electrode potential, reaction rates, and concentrations of reactants and water evolve under PEFC operation. A subtle electrode theory has to establish the links between these distributions.

The modeling of structure and operation of CLs is a multiscale problem. The challenges for the theory and modeling of catalyst layer operation are, however, markedly reduced if we realize that the main structural effects occur at well-separated scales, viz. at catalyst nanoparticles (a few nm), at agglomerates of carbon/Pt (~ 100 nm), and at the macroscopic device level.

Any development in fuel cell catalysts and catalyst layer materials relies on understanding self-organization phenomena during structure formation, electrokinetics of the ORR and HOR at highly dispersed catalyst surfaces, transport phenomena in porous composite media, integration between CLs and other components in the fuel cell. in particular with respect to water management, and degradation phenomena in view of the CL stability. To identify most active electrocatalyst materials and appropriate substrates, combined computational and theoretical methods (DFT, OF-DFT, kinetic Monte Carlo simulations, MD simulations) are needed to overcome the size and time-scale limitations of conventional DFT techniques. Simulations of physical properties of realistic Pt/C nanoparticle systems could provide interaction parameters needed in models of self-organization phenomena (agglomeration and phase segregation). Theoretical models of electrokinetic mechanisms, on the other hand, are needed to establish trends between catalyst structure and oxygen reduction kinetics.

Atomistic and coarse-grained MD simulations of self-organization in catalyst layers suggest that the resulting structures are inherently unstable. Applicable solvents with different dielectric constants correspond to different stable conformations in terms of agglomerate sizes, sizes of ionomer domains, pore space

morphology, and connectivity of phase domains. The replacement of low-dielectric solvents used during fabrication of catalyst layers by water as the working liquid in the operating fuel cell will thus destabilize the initially formed structures, causing a drift towards a new stable conformation. Complementarily, statistical computational and continuum approaches towards modeling of the CL at the pore-network level provide guidelines to correlate fabrication processes to microstructure and effective properties. Dynamic simulations of structural changes during formation processes lend themselves equally well to the study of mechanisms underlying structural degradation.

In spite of the complexity of catalyst layers, the presented theoretical tools contribute to the fundamental understanding of structure-function relations and they provide guidelines for upgraded diagnostics and optimized design. Parasitic voltage losses that are caused by reduced activity of the catalyst, impaired mass transport, and insufficient water management could be identified and minimized.

The best strategy to approach the optimization of catalyst layers would be a concerted experimental-theoretical effort. Since the theory inevitably has to invoke quite a number of simplifying assumptions, often of uncontrollable nature, offering a pure theoretically driven optimization would be irresponsible. *Ex situ* diagnostics is needed to characterize structural details and explore their relations to effective properties. The availability of such experimental data defines the level of detail of structure-property relationships that the theory could employ. *In situ* experimental studies, exploring the performance and comparing it with the theoretical predictions, provide the essential benchmark for optimization. The theory, corroborated by these systematic experimental procedures, could then be used to (i) identify salient features of good or bad catalyst layer performance, (ii) explain causes of catalyst layer failure, (iii) identify the needs of new material designs, and (iv) suggest catalyst particle sizes, porous structure, wetting properties, thickness, composition, operating conditions, etc. for attaining the highest fuel cell efficiencies and power densities. Examples of how to employ instructive theoretical tools in this process, leading from understanding to new design, have been provided throughout this chapter.

Naturally, the success of this strategy depends decisively on the ability to fabricate catalyst layers in a reproducible and stable way. Moreover, processes in catalyst layers are coupled strongly and nonlinearly to the operation of other components in the fuel cell. As emphasized in [47], fuel cells have to be designed as a whole, not as a collection of stand-alone parts. A full optimization has to account for these cooperative phenomena.

References

1. Vielstich W, Lamm A, Gasteiger H, editors. Handbook of fuel cells: fundamentals, technology, applications. Weinheim: VCH-Wiley, 2003.
2. Eikerling M, Kornyshev AA, Kucernak AR. Water in polymer electrolyte fuel cells: friend or foe? Phys Today 2006;59:38–44.
3. Eikerling M, Kornyshev AA, Kulikovsky AA. Physical modeling of fuel cells and their components. In: Bard AJ, Stratmann M, Macdonald D, Schmuki P, editors.

Encyclopedia of electrochemistry, volume 5, electrochemical engineering. Weinheim: VCH-Wiley, 2007: 447–543.

4. Gottesfeld S, Zawodzinski TA. Polymer electrolyte fuel cells. In: Advances in electrochemical science and engineering, volume 5. Alkire RC, Gerischer H, Kolb DM, Tobias CW. Weinheim: Wiley-VCH, Weinheim, 1997: 195–301.

5. Carlson EJ. DOE hydrogen program annual merit review, May 16–19, 2006. Available from http://hydrogendoedev.nrel.gov/annual_review06_proceedings.html.

6. Eikerling M, Kornyshev AA, Kulikovsky AA. Can theory help to improve fuel cells? Fuel Cell Review 2005;1:15–25.

7. Malek K, Eikerling M, Wang Q, Navessin T, Liu Z. Self-organization in catalyst layers of polymer electrolyte fuel cells. J Phys Chem C 2007;111:13627–34.

8. Wieckowski A, Savinova ER, Vayenas CG. Catalysis and electrocatalysis at nanoparticle surfaces. New York: Marcel Dekker, 2003.

9. Lasia A. Applications of the electrochemical impedance spectroscopy to hydrogen adsorption, evolution and absorption into metals. In: Modern aspects of electrochemistry, volume 35. Conway BE, White RE, editors. New York: Kluwer/Plenum, 2002: 1–49.

10. Raistrick ID. In: Van Zee JW, White RE, Kinoshita K, Burney HS, editors. Diaphragms, separators, and ion exchange membranes. Pennington, NY: The Electrochemical Society Proceedings Series, 1986: 156.

11. Wilson MS, Gottesfeld S. High performance catalyzed membranes of ultra-low Pt loadings for polymer electrolyte fuel cells. J Electrochem Soc 1992;139(2):L28–30.

12. Uchida M, Aoyama Y, Eda E, Ohta A. New preparation method for polymer-electrolyte fuel cells. J Electrochem Soc 1995;142(2):463–8.

13. Frumkin AN. Zh Fiz Khim 1949;23:1477.

14. Ksenzhek OS, Stender VV, Dokl A. NSSSR 1956;107:280.

15. Mund K, Sturm FV. Degree of utilization and specific effective surface area of electrocatalysts in porous electrodes. Electrochim Acta 1975;20:463–7.

16. De Levie R. On porous electrodes in electrolyte solutions: I. Capacitance effects. Electrochim Acta 1963;8(10):751–80.

17. De Levie R. Electrochemical response of porous and rough electrodes. In: Advances in electrochemistry and electrochemical engineering, volume 6. New York: Wiley Interscience, 1967: 329–97.

18. Raistrick ID. Impedance studies of porous electrodes. Electrochim Acta 1990;35(10):1579–86.

19. Sapoval B, Chazalviel J-N, Peyriere J. Electrical response of fractal and porous interfaces. Phys Rev A 1988;38:5867–87.

20. Wang JC. Impedance of a fractal electrolyte–electrode interface. Electrochim Acta 1988;33, 707–11.

21. Sapoval B. Fractal electrodes and constant phase angle response: exact examples and counter examples. Solid State Ionics 1987;23(4):253–9.

22. Kaplan T, Gray LJ, Liu SH. Self-affine fractal model for a metal-electrolyte interface. Phys Rev B 1987;35:5379–81.

23. Halsey TC. Stability of a flat interface in electrodeposition without mixing. Phys Rev A 1987;35:3512–14.

24. Pajkossy T, Nyikos L. Scaling-law analysis to describe the impedance behavior of fractal electrodes. Phys Rev B 1990;42:709–19.

25. Chizmadzhev YA, Markin VS, Tarasevich MR, Chirkov YG. The macrokinetics of processes in porous media. J Electrochem Soc 119;10:292C.

26. Chizmadzhev YA, Chirkov YG. In: Horsman P, Conway BE, Yeager E, editors. Comprehensive treatise of electrochemistry, volume 6. London: Plenum Press, 1983: 356.

27. Chizmadzhev YA, Chirkov YG. In: Kazarinov VE, editor. The kinetics of complex electrochemical reactions. Moscow: Nauka, 1988: 340.

28. Tantram ADS, Tseung ACC. Structure and performance of hydrophobic gas electrodes. Nature 1969;221:167–8.

29. Giner J, Hunter C. The mechanism of operation of the Teflon-bonded gas diffusion electrode: a mathematical model. J Electrochem Soc 1969;116(8):1124–30.

30. Iczkowski RP, Cutlip MB. Voltage losses in fuel cell cathodes. J Electrochem Soc 1980;127(7):1433–40.

31. Björnbom P. Modelling of a double-layered PTFE-bonded oxygen electrode. Electrochim Acta 1987;32(1):115–9.

32. Srinivasan S, Hurwitz HD, Bockris JMO. Fundamental equations of electrochemical kinetics at porous gas-diffusion electrodes. J Chem Phys 1967;46(8):3108–22.

33. Srinivasan D, Hurwitz HD. Theory of a thin film model of porous gas-diffusion electrodes. Electrochim Acta 1967;12(5):495–512.

34. Glaoguen F, Durand R. Simulations of PEFC cathodes: an effectiveness factor approach. J Appl Electrochem 1997;27:1029–35.

35. Sun W, Peppley BA, Karan K. An improved two-dimensional agglomerate cathode model to study the influence of catalyst layer structural parameters. Electrochim Acta 2005;50.16:3359–74.

36. Karan K. Assessment of transport-limited catalyst utilization for engineering of ultra-low Pt loading polymer electrolyte fuel cell anode. Electrochem Comm 2007;9(4):747–53.

37. Jaouen F, Lindbergh G, Sundholm G. Investigation of mass-transport limitations in the solid polymer fuel cell cathode. J Electrochem Soc 2002;149(4):A437–47.

38. Kulikovsk AAy. Performance of catalyst layers of polymer electrolyte fuel cells: exact solutions. Electrochem Comm 2002;4(4):318–23.

39. Stonehart P, Ross P. The use of porous electrodes to obtain kinetic rate constants for rapid reactions and adsorption isotherms of poisons. Electrochim Acta 1976;21(6):441–5.

40. Bernardi DM, Verbrugge MV. A mathematical model of the solid-polymer-electrolyte fuel cell. J Electrochem Soc 1992;139(9):2477–91.

41. You L, Liu H. A two-phase flow and transport model for PEM fuel cells. J Power Sources 2006;155(2):219–30.

42. Springer TE, Gottesfeld S. Fuel cells. In: White RE, Verbrugge MW, Stockel JF, Appleby AJ, editors. Proceedings of the symposium on modeling of batteries and fuel cells. The Electrochemical Society 1991:PV 91–10:197.

43. Springer TE, Wilson MS, Gottesfeld S. Modeling and experimental diagnostics in polymer electrolyte fuel cells. J Electrochem Soc 1993;140(12):3513–26.

44. Broadbent SR, Hammersley JM. Percolation processes. I. Crystals and mazes. Proc Camb Phil Soc 1957;53;629–41.

45. Isichenko MB. Percolation, statistical topography, and transport in random media. Rev Mod Phys 1992;64(4):961–1043.

46. Stauffer D, Aharony A. Introduction to percolation theory. London: Taylor & Francis, 1994.

47. Eikerling M, Kornyshev AA, Ioselevich AS. How good are the electrodes we use in PEFC? (Understanding structure vs. performance of membrane-electrode assemblies). Fuel Cells 2004;4(3):131–40.

48. Eikerling M, Kornyshev AA. Modelling the performance of the cathode catalyst layer of polymer electrolyte fuel cells. J Electroanal Chem 1998;453:89–106.

49. Nam JH, Kaviany M. Effective diffusivity and water-saturation distribution in single- and two-layer PEMFC diffusion medium. Int J Heat Mass Transfer 2003;46.24:4595–611.

50. Eikerling M. Water management in cathode catalyst layers of PEM fuel cells. J Electrochem Soc 2006;153(3):E58–70.

51. Liu J, Eikerling M. Model of cathode catalyst layers for polymer electrolyte fuel cells: the role of porous structure and water accumulation. Electrochim Acta 2008;53.13:4435–46.

52. Xie J, Wood DL III, More KL, Atanassov P, Borup RL. Microstructural changes of membrane electrode assemblies during PEFC durability testing at high humidity conditions. J Electrochem Soc 2005;152(5):A1011–20.

53. Xie Z, Navessin T, Shi K, Chow R, Wang Q, Song D, et al. Functionally graded cathode catalyst layers for polymer electrolyte fuel cells. J Electrochem Soc 2005;152(6):1171–9.

54. Thiele EW. Ind Eng Chem 1939;31:916–20.

55. Perry ML, Newman J, Cairns EJ. Mass transport in gas-diffusion electrodes: a diagnostic tool for fuel-cell cathodes. J Electrochem Soc, 1998;145(1):5–15.

56. Xia Z, Wang Q, Eikerling M, Liu Z. Effectiveness factor of Pt utilization in cathode catalyst layer of polymer electrolyte fuel cells. Can J Chem. In press.

57. Easton EB, Pickup PG. An electrochemical impedance spectroscopy study of fuel cell electrodes. Electrochim Acta 2005;50.12:2469–74.

58. Shan J, Pickup PG. Characterization of polymer supported catalysts by cyclic voltammetry and rotating disk voltammetry. Electrochim Acta 2000;46(1):119–25.

59. Schmidt TJ, Gasteiger HA, Stäb GD, Urban PM, Kolb DM, Behm RJ. Characterization of high-surface-area electrocatalysts using a rotating disk electrode configuration. J Electrochem Soc 1998;145(7):2354–8.

60. Dhathathreyan KS, Sridhar P, Sasikumar G, Ghosh KK, Velayutham G, Rajalakshmi N, et al. Development of polymer electrolyte membrane fuel cell stack. Int J Hydrogen Energy 1999;24.11:1107–15.

61. Cheng X, Yi B, Han M, Zhang J, Qiao Y, Yu J. Investigation of platinum utilization and morphology in catalyst layer of polymer electrolyte fuel cells. J Power Sources 1999;79(1):75–81.

62. Sasikumar G, Ihm JW, Ryu H. Dependence of optimum Nafion content in catalyst layer on platinum loading. J Power Sources 2004;132(1):11–17.

63. Li G, Pickup PG. Ionic conductivity of PEMFC electrodes. J Electrochem Soc 2003;150.11:C745–52.

64. Gasteiger HA, Panels JE, Yan SG. Dependence of PEM fuel cell performance on catalyst loading. J Power Sources 2004;127(1):162–71.

65. Zhdanov VP, Kasemo B. Kinetics of rapid reactions on nanometer catalyst particles. Physical Review B 1997;55(7):4105–8.

66. Stamenkovic VR, Mun BS, Arenz M, Mayrhofer KJ, Lucas CA, Wang GF, et al. Trends in electrocatalysis on extended and nanoscale Pt-bimetallic alloy surfaces. Nature Mat 2007;6(3):241–7.

67. Stamenkovic VR, Fowler B, Mun BS, Wang G, Ross PN, Lucas CA, et al. Improved oxygen reduction activity on $Pt_3Ni(111)$ via increased surface site availability. Science 2007;315.5811:493–7.

68. Andreaus B, Maillard F, Kocylo J, Savinova E, Eikerling M. Kinetic modeling of CO_{ad} monolayer oxidation on carbon-supported platinum nanoparticles. J Phys Chem B 2006;110.42:21028–40.

69. Wang Q, Eikerling M, Song D, Liu Z. Structure and performance of different types of agglomerates in cathode catalyst layers of PEM fuel cells. J Electroanal Chem 2004;573(1):61–9.

70. Eikerling M, Kharkats YI, Kornyshev AA, Volfkovich YM. Phenomenological theory of electro-osmotic effect and water management in polymer electrolyte proton-conducting membranes. J Electrochem Soc 1998;145(8):2684–99.

71. Lucas CA, Markovic NM. Structure relationships in electrochemical reactions. In: Bard AJ, Stratmann M, Calvo EJ, editors. Encyclopedia of electrochemistry, volume 2. Interfacial kinetics and mass transport. Weinheim: Wiley-VCH, 2003.

72. Housmans THM, Wonders AH, Koper MTM. Structure sensitivity of methanol electrooxidation pathways on platinum: an on-line electrochemical mass spectrometry study. J Phys Chem B 2006;110(20):10021–31.

73. Boudart M. Catalysis by supported metals. Adv Catal 1969;20;153–66.

74. Eikerling M, Meier J, Stimming U. Hydrogen evolution at a single supported nanoparticle: a kinetic model. Z Phys Chem 2003;217(4):395–414.

75. Maillard F, Eikerling M, Cherstiouk OV, Schreier S, Savinova E, Stimming U. Size effects on reactivity of Pt nanoparticles in CO monolayer oxidation: The role of surface mobility. Faraday Discuss 2004;125:357–77.

76. Cherstiouk OV, Simonov PA, Savinova ER. Model approach to evaluate particle size effects in electrocatalysis: preparation and properties of Pt nanoparticles supported on GC and HOPG. Electrochim Acta 2003;48.25:3851–60.

77. Maillard F, Schreier S, Heinzlik M, Savinova ER, Weinkauf S, Stimming U. Influence of particle agglomeration on the catalytic activity of carbon-supported Pt nanoparticles in CO monolayer oxidation. Phys Chem Chem Phys 2005;7(2):385–93.

78. Maillard F, Savinova ER, Stimming U. CO monolayer oxidation on Pt nanoparticles: further insights into the particle size effects. J Electroanal Chem 2006;599(2):221–32.

79. Hansen LB, Stoltze P, Nørskov JK, Clausen BS, Niemann W. Is there a contraction of the interatomic distance in small metal particles? Phys Rev Lett 1990;64.26:3155–8.

80. Andreaus B, Eikerling M. Active site model for CO adlayer electro-oxidation on nanoparticle catalysts. J Electroanal Chem 2007;607:121–32.

81. Norskov JK, Christensen CH. Toward efficient hydrogen production at surfaces. Science 2006;312.5778:1322–3.

82. Hammer B, Nørskov JK. Theoretical surface science and catalysis – calculations and concepts. Advances in Catalysis 2000;45:71–129.

83. Hammer B, Nørskov JK. Why gold is the noblest of all the metals. Nature 1995;376:238–40.

84. Stamenkovic VR, Mun BS, Mayrhofer KJJ, Ross PN, Markovic NM, Rossmeisl J, et al. Changing the activity of electrocatalysts for oxygen reduction by tuning the surface electronic structure. Angew Chem Int Ed 2006;45.18:2815–983.

85. Greeley J, Jaramillo TF, Bonde J, Chorkendorff I, Norskov JK. Computational high-throughput screening of electrocatalytic materials for hydrogen evolution. Nature Mat 2006;5:909–13.

86. Gross A. Reactivity of bimetallic systems studied from first principles. Topics in Catalysis 2006;37(1):29–39.

87. Kolb DM, Engelmann GE, Ziegler JC. On the unusual electrochemical stability of nanofabricated copper clusters. Angew Chemie Int Ed 2000;39(6):1123–5.

88. Xiao L, Wang L. Structures of platinum clusters: planar or spherical? J Phys Chem A 2004;108.41:8605–14.

89. Song C, Ge Q, Wang L. DFT studies of Pt/Au bimetallic clusters and their interactions with the CO molecule. J Phys Chem B 2005;109.47:22341–50.

90. Roudgar A, Gross A. Local reactivity of supported metal clusters: Pd_n on Au(1 1 1). Surf Sci 2004;559(2):L180–6.

91. Fernandez R, Ferriera-Aparicio P, Daza L. PEMFC electrode preparation: influence of the solvent composition and evaporation rate on the catalytic layer microstructure. J Power Sources 2005;151:18–24.

92. Sahimi M, Gavalas GR, Tsotsis TT. Statistical and continuum models of fluid-solid reactions in porous media. Chem Eng Sci 1990;45(6):1443–502.

93. Torquato S. Random hetergeneous materials. New York: Springer-Verlag, 2002.

94. Uchida M, Aoyama Y, Eda E, Ohta A. Investigation of the microstructure in the catalyst layer and effects of both perfluorosulfonate ionomer and PTFE-loaded carbon on the catalyst layer of polymer electrolyte fuel cells. J Electrochem Soc 1995;142.12:4143–9.

95. Uchida M, Fuuoka Y, Sugawara Y, Eda N, Ohta A. Effects of microstructure of carbon support in the catalyst layer on the performance of polymer-electrolyte fuel cells. J Electrochem Soc 1996;143(7):2245–52.

96. Vishnyakov A, Neimark AV. Molecular dynamics simulation of microstructure and molecular mobilities in swollen Nafion membranes. J Phys Chem B 2001;105(39):9586–94.

97. Jang SS, Molinero V, Cagin T, Goddard WA III. Nanophase-segregation and transport in Nafion 117 from molecular dynamics simulations: effect of monomeric sequence. J Phys Chem B 2004;108.10:3149–57.

98. Eikerling M, Kornyshev AA, Stimming U. Electrophysical properties of polymer electrolyte membranes: a random network model. J Phys ChemB 1997;101.50:10807–20.

99. Vishnyakov A, Neimark AV. Molecular simulation study of Nafion membrane solvation in water and methanol J Phys Chem B 2000;104.18:4471–8.

100. Spohr E, Commer P, Kornyshev AA. Enhancing proton mobility in polymer electrolyte membranes: lessons from molecular dynamics simulations. J Phys Chem B 2002;106.41:10560–9.

101. Cui S, Liu J, Selvan ME, Keffer DJ, Edwards BJ, Steele WV. A molecular dynamics study of a Nafion polyelectrolyte membrane and the aqueous phase structure for proton transport. J Phys Chem B 2007;111(9):2208–18.

102. Devanathan R, Venkatnathan A, Dupuis M. Atomistic simulation of Nafion membrane. 2. Dynamics of water molecules and hydronium ions. J Phys Chem B 2007;111.45:13006–13.

103. Devanathan R, Venkatnathan A, Dupuis M. Atomistic simulation of Nafion membrane: I. Effect of hydration on membrane nanostructure. J Phys Chem B 2007;111.28:8069–79.

104. Devanathan R, Venkatnathan A, Dupuis M. Atomistic simulations of hydrated Nafion and temperature effects on hydronium ion mobility. J Phys Chem B 2007;111.25:7234–44.

105. Allen MP, Tildesley DJ. Computer simulation of liquids. New York: Oxford University Press, 1989.

106. Moriguchi I, Nakahara F, Furukawa H, Yamada H, Kudo T. Colloidal crystal-templated porous carbon as a high performance electrical double-layer capacitor material. Electrochem Solid-State Lett 2004;7(8):A221–3.

107. Yamada H, Nakamura H, Nakahara F, Moriguchi I, Kudo T. Electrochemical study of high electrochemical double layer capacitance of ordered porous carbons with both meso/macropores and micropores. J Phys Chem C 2007;111(1):227–33.

108. Hao X, Spieker WA, Regalbuto JR. A further simplification of the revised physical adsorption (RPA) model. J Coll Interface Sci 2003;267:259–64.

109. Lamas EJ, Balbuena PB. Adsorbate. Effects on structure and shape of supported nanoclusters: a molecular dynamics study. J Phys Chem B 2003;107:11682–9.

110. Huang SP, Balbuena PB. Platinum nanoclusters on graphite substrates: a molecular dynamics study. Molecular Phys 2002;100.13:2165–74.

111. Chen J, Chan - KY. Size-dependent mobility of platinum cluster on a graphite surface. Molecular Simulation 2005;31:527–33.

112. Lamas EJ, Balbuena PB. Molecular dynamics studies of a model polymer–catalyst–carbon interface. Electrochim Acta 2006;51.26:5904–11.

113. Balbuena PB, Lamas EJ, Wang Y. Molecular modeling studies of polymer electrolytes for power sources. Electrochim Acta 2005;50.19:3788–95.
114. Sutton AP, Chen J. Long-range Finnis-Sinclair potentials. Philos Mag Lett 1990;61(3):139–46.
115. Goddard W III, Merinov B, van Duin A, Jacob T, Blanco M, Molinero V, et al. Multi-paradigm multi-scale simulations for fuel cell catalysts and membranes. Molecular Simulation 2006;32(3–4):251.
116. Reid RC, Prausnitz JM, BE. Poling in the properties of gases and liquids. Boston: McGraw Hill, 1987.
117. Morrow BH, Striolo A. Morphology and diffusion mechanism of platinum nanoparticles on carbon nanotube bundles. J Phys Chem C 2007;111:17905–13.
118. Wang Q, Eikerling M, Song D, Liu S. Modeling of ultrathin two-phase catalyst layers in PEFCs. J Electrochem Soc 2007;154(6):F95–101.
119. Wescott JT, Qi Y, Subramanian L, Capehart TW. Mesoscale simulation of morphology in hydrated perfluorosulfonic acid membranes. J Chem Phys 2006;124.13:134702–14.
120. Galperin DY, Khokhlov AR. Mesoscopic morphology of proton-conducting polyelectrolyte membranes of Nafion® type: a self-consistent mean field simulation. Macromol Theory Simul 2006;15(2):137–46.
121. Groot RD, Warren PB. Dissipative particle dynamics: bridging the gap between atomistic and mesoscopic simulation. J Chem Phys 1997;107.11:4423–35.
122. Mologin DA, Khalatur PG, Kholhlov AR. Structural organization of water-containing Nafion: a cellular-automaton-based simulation. Macromol Theory Simul 2002;11(5):587–606.
123. Khalatur PG, Talitskikh SK, Khokhlov AR. Structural organization of water-containing Nafion: the integral equation theory. Macromol Theory Simul 2002;11(5):566–86.
124. Marrink SJ, de Vries AH, Mark AE. The MARTINI force field: coarse grained model for biomolecular simulations. J Phys Chem B 2007;111:7812–24.
125. Izvekov S, Violi A. A coarse-grained molecular dynamics study of carbon nanoparticle aggregation. J Chem Theory Comput 2006 ;2(3):504–12.
126. Izvekov S, Violi A. A multiscale coarse-graining method for biomolecular systems. J Phys Chem B 2005;109:2469–73.
127. Izvekov S, Violi A, Voth GA. Systematic coarse-graining of nanoparticle interactions in molecular dynamics simulation. J Phys Chem B 2005;109:17019–24.
128. Sahimi M. Heterogeneous materials, Part I and Part II. Heidelberg: Springer, 2003.
129. Sahimi M. Flow phenomena in rocks: from continuum models to fractals, percolation, cellular automata, and simulated annealing. Rev Mod Phys 1993;65(4):1393–1534
130. Shklovskii BI, Efros AL. Electronic properties of doped semiconductors. New York: Springer, 1982.
131. De Gennes PG. Scaling concepts in Polymer physics. Ithaca: Cornell University, 1979.
132. Grassberger P. On the critical behavior of the general epidemic process and dynamical percolation. Math Biosci 1983;63(2):157–72.
133. MacKay G, Jan N. Forest fires as critical phenomena. J Phys 1984;A17.14:L757–60.
134. Ambegaokar VN, Halperin BI, Langer JS. Hopping conductivity in disordered systems. Phys Rev B, 1971;4(8):2612–20.
135. Dullien FAL. Porous media. New York: Academic Press, 1979.
136. Kirkpatrick S. Percolation and conduction. Rev Mod Phys 1973;45(4):574–88.
137. Torquato S. Random heterogeneous materials. Springer: New York, 2002.
138. Milton GW. The theory of composites. New York: Cambridge University Press, 2002.
139. Alcaniz-Monge J, Linares-Solano A, Rand B. Water adsorption on activated carbons: study of water adsorption in micro- and mesopores. J Phys Chem B 2001;105:7998–8006.

140. Lundblad A. Materials characterization of thin film electrodes for PEFC survey of methods and an example. J New Mat Electrochem Sys 2004;7(1):21–8.

141. Ihonen J, Jaouen F, Lindbergh G, Lundblad A, Sundholm G. Investigation of mass-transport limitations in the solid polymer fuel cell cathode II. Experimental. J Electrochem Soc 2002;149(4):A448–54.

142. Samson E, Marchand J, Robert JL, Bournazel JP. Modelling ion diffusion mechanisms in porous media. Int J Numer Meth Eng 1999;46(12):2043–60.

143. Moya AA, Horno J. Application of the network simulation method to ionic transport in ion-exchange membranes including diffuse double-layer effects. J Phys Chem B 1999;103(49):10791–9.

144. Parthasarathy A, Srinivasan S, Appleby AJ, Martin CR. Temperature dependence of the electrode kinetics of oxygen reduction at the platinum/Nafion® interface–a microelectrode investigation. J Electrochem Soc 1992;139(9):2530–7.

145. Eisenberg RS. From structure to function in open ionic channels. J Membrane Biol 1999;171(1):1–24.

146. Alfredo AE, Cárdenas RD, Kurnikova MG. Three-dimensional Poisson-Nernst-Planck theory studies: influence of membrane electrostatics on Gramicidin A channel conductance. Biophys J 2000;79(1):80–93.

147. Corry B, Kuyucak S, -Chun SHg. Dielectric self-energy in Poisson-Boltzmann and Poisson-Nernst-Planck models of ion channels. Biophys J 2003;84(6):3594–606.

148. Eikerling M, Kornyshev AA. Electrochemical impedance of the cathode catalyst layer of polymer electrolyte fuel cells. J Electroanal Chem 1999;475(2):107–23.

149. Wang Q, Eikerling M, Song D, Liu S, Navessin T, Xie Z, et al. Functionally graded cathode catalyst layers for polymer electrolyte fuel cell. J Electrochem Soc 2004;151(7):A950–7.

150. Lee SJ, Mukerjee S, McBreen J, Rho YW, Kho YT, Lee TH. Effects of Nafion impregnation on performances of PEMFC electrodes. Electrochim Acta 1998;43.24:3693–701.

151. Passalacqua E, Lufrano F, Squadrito G, Patti A, Giorgi L. Nafion content in the catalyst layer of polymer electrolyte fuel cells: effects on structure and performance. Electrochim Acta 2001;46(6):799–805.

152. Studebaker ML, Snow CW. The influence of ultimate composition upon the wettability of carbon blacks. J Phys Chem 1955;59:973–6.

153. Debe MK. Novel catalysts, catalysts support and catalysts coated membrane methods. Chapter 45. In: Vielstich W, Lamm A, Gasteiger H, editors. Handbook of fuel cells: fundamentals, technology, applications. Weinheim: VCH-Wiley, 2003: 576–89.

154. Neyerlin KC, Gasteiger HA, Mittelsteadt CK, Jorne J, Gu W. Effect of relative humidity on oxygen reduction kinetics in a PEMFC. J Electrochem Soc 2005;152(6):A1073–80.

155. Malek K. Dynamic Monte-Carlo simulation of electrochemical switching of a conducting polymer film. Chem Phys Lett 2002;375(5-6):477-83.

9

Catalyst Synthesis Techniques

Christina Bock, Helga Halvorsen and Barry MacDougall

9.1 Introduction

This chapter deals with aspects of the synthesis of fuel cell catalysts. Practical catalysts for low-temperature fuel cells are typically in the nano-size range and are frequently formed or deposited on high-surface-area supports. Pt is the most commonly used catalyst for both cathode and anode in proton exchange membrane fuel cells (PEMFCs). In the case of the cathode, combined catalyst systems such as Pt nanoparticles supported on Au or Pt alloy catalysts, as well as Pt-skin catalysts formed in combination with the iron group metals have also attracted attention. Much work has been carried out on the development of "non-noble" metal (Pt-free) catalysts, the synthesis of which will be discussed in Section 9.5. In the case of the anode, bi-metallic catalysts are typically employed unless the fuel is neat H_2. Pt-Ru is the state-of-the-art catalyst for both methanol and reformate fuel cells. For the latter, other anode catalysts such as Pt/MoO_x and Pt/Sn are also considered promising.

In this chapter we present an overview of methods used to synthesize fuel cell catalysts, with a focus on catalysts for PEMFCs and direct methanol fuel cells (DMFCs). Examples for the synthesis of catalysts for other low-temperature fuel cells, such as formic acid, are not included in this chapter. The synthesis of both Pt-based and Pt-free catalysts is discussed, and dedicated sections describe methods that allow control of catalyst size and composition. First, general catalyst synthesis methods are introduced. Subsequently, the reader is introduced to particle size and "structure" control of fuel cell catalysts.

9.2 Catalysis Synthesis Methods

The purpose of this sub-section is to present to the reader with a general overview of the most common synthetic methods for fabricating Pt-based catalysts. Although no single method is superior to the others, depending on the end application of the catalyst and the instrumentation available, one method may be advantageous over

another. Therefore, the reader is advised to consider the intrinsic advantages and disadvantages of each method when selecting which to use.

9.2.1 Low-temperature Chemical Precipitation

Platinum and platinum-based nanocatalysts can be made by chemical precipitation at low temperatures. The use of this synthesis method dates back several decades [1]. Its advantage is preparation under "mild" conditions, i.e., at low temperatures. Supported and unsupported catalysts can be made, and the process is in principle simple, involving the addition of a reducing agent to a platinum-salt solution. Bi-metallic catalysts can be made by the co-precipitation of a solution of two metal precursor salts, e.g., Pt- and Ru-salts. Ideally, the precursor salt is reduced to the metallic state and precipitates out of solution, forming unsupported catalysts that can be filtered and washed. Single and bi-metallic Pt and Ru catalysts of 3 to 12 m^2g^{-1} surface area were made by reducing and co-reducing aqueous solutions of H_2PtCl_6 and $RuCl_3$ using sodium borohydride and hydrazine hydrate [1]. Sodium borohydride seems to be the preferable reducing agent. The final products are PtRu alloy powders, which are frequently reduced at 300 °C in H_2. However, it has been shown more recently that H_2 treatment at such high temperatures is not essential for PtRu alloy formation and complete reduction [2].

An attractive low-temperature route is to use carbonyl precursors that decompose at low temperatures and avoid chloride contamination [3, 4]. Many studies use the synthesis methods reported by Chini and Adams for monometallic carbonyls and heterometallic carbonyls [5, 6]. The metal-carbonyl can be formed by bubbling CO through a solution of, e.g., platinic acid (H_2PtCl_6), which has been reported to result in the formation of a $Pt(CO)_2$ precipitate that can be washed, filtered, and dried [4]. To form supported catalysts, carbon black is added prior to the reduction of the metal-carbonyls. Unsupported particles grow more rapidly than supported particles; typically they are at least twice the size of supported particles [7]. Despite this limitation, platinum electrocatalysts as small as 3 nm have been fabricated with $[Pt_3(CO)_6]_{\sim 10}^{2-}$ as the platinum source and hydrogen as the reducing agent. Platinum alloys can be made by first fabricating the bimetallic carbonyl via:

$$[Pt_3(CO)_6]_{\sim 10}^{2-} + M_yX_n \rightarrow [Pt_xM_y(CO)_z]_{\sim 10}^{2-} \qquad (9.1)$$
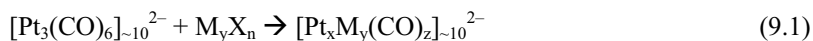
where M = Sn, Ni, Cr, Co, and X = Cl$^-$ followed by hydrogen reduction. As an example, Pt-Sn particles (of atomic ratio 3:1) with an average size of 2.4 ± 1 nm have been made by this method [7]. Supported, bi-metallic Pt-Ru catalysts have also been made by dissolving Pt and Ru-carbonyl precursors in o-Xylene [4]. Vulcan XC72 was added and the mixture was refluxed at 143 °C for 24 h to form the carbon-supported, nanosized Pt-Ru catalysts.

9.2.2 Colloidal

The colloidal method of generating nanocatalysts is similar to the chemical catalyst precipitation method. However, it involves the added benefit of a capping agent

that allows for size control of the catalysts and prevents agglomeration of the catalyst particles. Any molecule that adsorbs onto the catalyst has the potential to act as a capping agent. The experimental procedure is as simple as combining the metal source, a reducing agent, and a capping agent together and mixing. Bi-metallic and other colloidal catalysts can be prepared by co-reduction. If dihydrogen gas is the reducing agent, it is typically bubbled through the solution. To synthesize supported catalysts a carbon support is added to the mixture before or after the formation of the catalyst particles. If a fast reducing agent is used the reactions can be completed within less than 30 minutes [8]. Conversely, slow reducing agents, like dihydrogen gas at room temperature, require longer reaction times and are generally allowed to react overnight or for at least 12 h.

Initial reports for the synthesis of bi-metallic, nanosized PtRu catalysts involved a number of steps. A well-known synthesis of bi-metallic carbon-supported Pt/Ru catalysts of high surface area (ca. 80 m^2g^{-1} Pt + Ru) is the Watanabe method [9]. They first formed colloidal "PtO$_2$" from platinic acid (H$_2$PtCl$_6$) with the reduction of NaHSO$_3$ and oxidative decomposition with H$_2$O$_2$ at a fixed pH of 5, according to the following, possible reaction scheme [10]:

$$H_2PtCl_6 + 3NaHSO_3 + 2H_2O \rightarrow H_3Pt(SO_3)_2OH + Na_2SO_4 + NaCl + 5HCl$$

(9.2)

$$H_3Pt(SO_3)_2OH + 3H_2O_2 \rightarrow PtO_2 + 3H_2O + 2H_2SO_4 \tag{9.3}$$
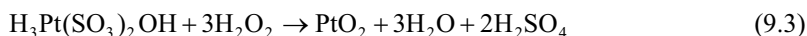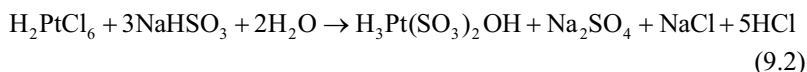
Subsequently, RuCl$_3$ was added and the formation of a brown-colored colloid "RuO$_2$" was suggested to have taken place as follows:

$$RuCl_3 + 3/2H_2O_2 \rightarrow RuO_2 + 3HCl + 1/2O_2 \tag{9.4}$$
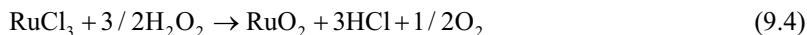
Carbon black was added to the solution and H$_2$ was bubbled through it for complete reduction and formation of the carbon-supported PtRu alloys. PtRu alloy formation was proposed to have taken place, as TEM images of the formed nanosized particles indicated a face centered cubic structure (fcc) rather than hexagonally closed packed (hcp) structure typical for metallic Ru.

The colloidal synthesis method has also been successfully tailored to allow for particle size and composition control, as well as shape control for Pt-based nanoparticles. Control of these factors will be discussed in Section 9.3.

9.2.3 Sol-gel

The sol-gel technique begins with the formation of a liquid solution of suspended particles (a sol) that is aged and dried to form a semi-solid suspension of particles in a liquid (a gel), which is finally calcified, resulting in a mesoporous solid or powder. There are four distinct steps to the sol-gel technique [8]: (1) formation of the gel; (2) aging to allow fine-tuning of the gel properties; (3) drying to remove the solvent from the gel; and (4) calcination to permanently change the physical and chemical properties of the solid. The aging and calcination steps allow for fine

control of the pore size distribution and volume by controlling experimental parameters like time, temperature, heating rate, and pore liquid composition.

Metallic nanocatalysts can be incorporated into the mesoporous structure by a variety of methods. Prefabricated nanoparticles can be incorporated into mesoporous solids by adding the particles into the sol-gel mixture or, if the particles are formed by microemulsions (see Section 9.2.5), the microemulsion can be incorporated into the preformed mesoporous structure. Alternatively, metal salts can be added during gel formation or after the mesoporous structure has formed [12]. An example of the former is the synthesis of WO_x and WO_x/Pt films that were made by synthesizing $W(OC_2H_5)_6$ and H_2PtCl_6 sol-gel solutions, followed by aging and calcination [13]. A significant drawback associated with this method is that the catalytic nanoparticles may be buried within the structure rather than near the pores. If the particles are not located near the pores they will not be accessible to reactants and therefore will not be efficient catalysts.

Adding nanocatalysts after the mesoporous structure has formed, i.e., after calcination, ensures that the particles form in the pores, provided that the particle size/pore ratio is suitable. Particle formation and deposition can be accomplished by impregnating the structure with the metal ions, followed by a reduction step (see Section 9.2.4) [13]. The impregnation technique allows for controlled particle growth, as the pore size limits particle growth. Impregnation can be facilitated by functionalizing the mesoporous structure with organic groups that anchor metal compounds and/or interact with the surface of the growing nanoparticles. For example, a gel containing acidic functionality on its backbone was required to facilitate the doping of an organic gel with $Pt(NH_3)_4Cl_2$ [14]. Functionalizing pores with cationic surfactants allows for ion exchange – i.e., the metal cations can replace the cationic surfactants [13]. Since monovalent surfactant cations are replaced with multivalent metal cations, entropy drives this efficient ion exchange. Once the ion exchange is completed the metal cations are reduced to form nanocatalysts. Chemical vapor deposition (see Section 9.2.8) is another method for adding nanocatalysts to prefabricated mesoporous structures [13]. This method should be restricted to thin films or particles (i.e., not to monolithic samples) to prevent uneven distribution of the metal compounds within the material.

9.2.4 Impregnation

Due to the ease of preparation, impregnation is one of the most commonly used techniques to fabricate catalysts. High-surface-area carbon black can be impregnated with catalyst precursors by mixing the two in an aqueous solution [15]. Other methods of impregnating a substrate involve depositing an aliquot of solution containing the catalyst precursor onto a substrate and allowing it to air dry [16]. Following the impregnation step, a reduction step is required to reduce the catalyst precursor to its metallic state. As reduction occurs after the impregnation step, the nature of the support plays a crucial role in controlling particle size [17]. Common liquid phase reducing agents are $Na_2S_2O_3$, $NaBH_4$, $Na_4S_2O_5$, N_2H_4, and formic acid. H_2 is the predominant gas phase reducing agent.

The most common platinum precursors used for impregnation are chloride salts; however, it has been argued that the metal chloride salts might lead to

chloride poisoning, which could affect the catalytic activity of the particles [18]. To avoid chlorine poisoning, metal sulfite salts, metal carbonyl complexes, and metal nitrate salts have been used instead [17]. Metal carbonyl complexes are particularly attractive as precursors since they can easily be made by direct oxidation of the metal chloride salt with carbon monoxide. Additionally, an external reducing agent is not required, as nanoparticles can then be formed by thermal decomposition of the metal carbonyl complexes impregnated onto carbon supports [4, 19]. When forming PtRu alloys, care must be taken during the decomposition process since Ru carbonyl decomposition is more favorable than Pt carbonyl decomposition, resulting in Ru-rich products [17]. Using a single-source precursor, a single compound that contains both metals, can overcome this problem.

Experimental factors, such as reduction temperature, can significantly influence the morphology of the catalyst. For example, $(\eta\text{-}C_2H_4)(Cl)Pt(\mu Cl)_2Ru(Cl)(\eta^3,\eta^3\text{-}C_{10}H_{16})$ reduced under hydrogen or argon at 400 °C gave 2.5 ± 1 nm particles, while reduction temperatures of 650 °C gave 5 ± 3 nm particles [20]. The impregnation technique is a comparatively green method to synthesize catalysts; reduction reactions occur either at low or room temperatures, minimizing energy consumption, and organic solvents are avoided by using aqueous media. Drawbacks of the impregnation technique are related to using liquid solutions as the processing medium. In solution, particles can easily agglomerate. Furthermore, the high surface tension of liquid solutions can cause fragile supports, such as aerogels, to collapse [21].

9.2.5 Microemulsions

The use of microemulsions or reversed micelles to synthesize nanosized particles has been explored for almost twenty years [22, 23]. Microemulsion techniques have been used for the synthesis of semiconductor, metal, and alloy nanocrystals. Much work has been done on producing Cu and Ag nanocrystals [22, 24–26]. More recent work has also been devoted to the synthesis of Pt and PtRu nanoparticles for the use of potential fuel cell catalysts and their electrochemical characterization [27, 28]. At high water concentrations an emulsion consists of small oil droplets surrounded by surfactants in a continuous water phase, and vice versa, at high oil concentrations an emulsion consists of small water droplets surrounded by surfactants in a continuous oil phase. Since most metal precursors are inorganic salts they are soluble in water, not in oil. Therefore, emulsions with high oil concentrations and low water concentrations are used almost exclusively. Reverse micelles are water-in-oil droplets stabilized by a surfactant. A very commonly used surfactant is sodium 2 bis (2-ethylhexyl)sulfosuccinate (Na(AOT)). A schematic of a reversed micelle using a Na^+-ion (AOT) surfactant is shown in Figure 9.1. Alkylthiols (C_nSH), -amines (C_nNH_2), and -isocyanides are examples of other stabilizers that have also been used to make microemulsions. The droplets are displaced randomly in solution and are subject to Brownian motion. They exchange their water content and re-form into distinct micelles. The size of the water-in-oil droplets likely increases with increasing water content. The

droplet size, i.e., resulting particle size, can also be influenced by the chain length of the stabilizer.
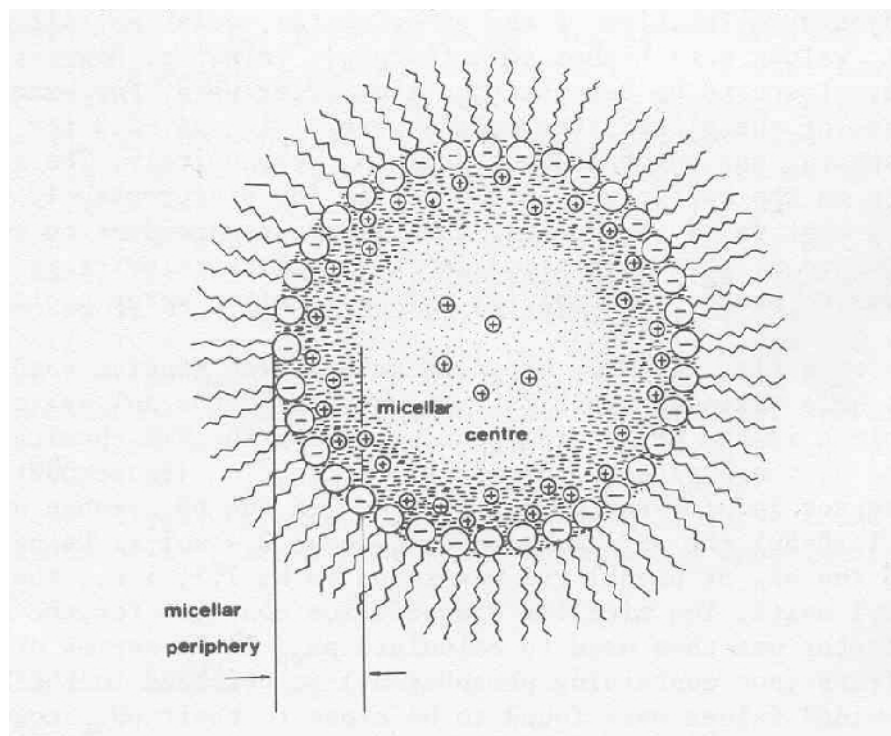
Figure 9.1. Schematic of a reversed micelle formed using Na^+-AOT as surfactant ion. (Reprinted with permission from O.A. El Seoud, Acidities and basicity in reversed micellar systems, in Reverse Micelles. Biological and Technological Relevance of Amphiphilic Structures in Apolar Media, edited by P.L. Luisi and B.E. Straub, Plenum Press, New York and London, 1984, figure on p.86.)

In order to obtain the catalyst nanoparticles, the metal salt is reduced by adding a reducing agent into the microemulsion system. Another approach is to mix the microemulsion system that contains a reducing agent with a microemulsion system that contains the metal salt [17, 29]. Once the nanocatalysts are formed they can be deposited onto a support, which is done by adding a solvent like tetrahydrofuran (THF) in conjunction with the support powder to the microemulsion [29]. The solvent destabilizes the microemulsion by competing with the surfactant to adsorb onto the particles, and in the destabilized system the particles will adsorb onto the support. However, Pt and PtRu catalysts formed using the microemulsion technique have also been directly deposited onto carbon blacks such as Vulcan XC72 by simply mixing and stirring the emulsion with the support, i.e., without the need of an emulsion-breaking solvent [27, 28]. After deposition, residual surfactant molecules are typically removed by heat treatment [17]. Emulsion systems are very sensitive to temperature and therefore the oil and surfactant must be carefully

selected [29]. Unfortunately, catalyst fabrication by microemulsion is costly since expensive surfactants and oils are needed. Furthermore, both the surfactants and the oils can have a negative environmental impact.

Size control with microemulsions appears more complicated than preliminary research indicated. Originally, the water droplets containing dissolved metal salts stabilized by a surfactant were often described as a "micro-reactor" or "nano-cage" [30]. Since the reduction is confined within the nanoscaled microemulsion it was originally believed that catalyst size is exclusively controlled by the size of the water droplets in the microemulsion [17]. However, it has been found that particle size is a more complicated phenomenon involving the nature of the reducing agent as well as the size of the water droplets in the microemulsion [29]. Small particles are formed by fast nucleation caused by a fast or efficient reducing agent [29]. Hydrazine is an example of a fast reducing agent, while dihydrogen gas is a relatively slow reducing agent.

The size of the water droplet is influenced by the ratio of water to surfactant and the surfactant concentration (at fixed water/oil ratios). As the ratio of water to surfactant increases, the size of the water droplet increases and consequently, the catalyst size also increases. However, a maximum particle size is reached and further increasing the water-to-surfactant ratio has no effect on catalyst size [27, 28, 31]. For example, in a microemulsion system of water/n-heptane with the surfactant sodium dioctyl sulfosuccinate the Pt-Ru particle size increases from 2.4 ± 0.1 to 3.2 ± 0.1 nm when the ratio of water to sodium dioctyl sulfosuccinate increases from 4 to 8 [28]. However, increasing the water-to-dioctyl-sulfosuccinate ratio to 10 does not result in any further increase in catalyst size [28]. Droplet size can also be controlled by varying the surfactant concentration while keeping the concentrations of water and oil constant. For example, increasing the surfactant concentration, with constant water and oil concentrations, increases the number of droplets. As a result, droplet size decreases, resulting in fewer metal ions per droplet and a consequently decreased particle size.

Droplet size, however, does not directly or absolutely control particle size. For example, it was estimated that there are five $PtCl_6^{2-}$ ions in each water droplet in the microemulsion system of water in hexane, stabilized by the surfactant pentaethyleneglycol dodecylether [29, 32]. However, TEM analysis indicated that the platinum catalyst formed had an average diameter of 3.5 nm, which corresponds to 100–1500 metal atoms (depending on the shape of the particle). This example illustrates that the final particle is not formed inside the droplet. It is likely that the formation of catalysts via the microemulsion process proceeds by two steps: (1) nucleation of the metal catalyst inside the droplet, followed by (2) aggregation of multiple nuclei via collision and coalescence of droplets to form the final nanocatalysts [29].

9.2.6 Electrochemical

Electrochemical deposition has been used to deposit Pt and Pt-based nanoparticles on a wide variety of substrates, including glassy carbon [33], highly ordered pyrolytic graphite (HOPG) [34, 35], carbon black inside Nafion [36], carbon nanotubes [37], and PAN-based carbon fibers [38]. A number of papers also

discuss the preparation of Ru nanoparticles onto Pt single crystals, mainly Pt(111). These were made as model catalyst systems for methanol and CO oxidation [39, 40]. Electrochemical deposition occurs at the interface of an electronically conductive substrate and an electrolyte solution containing the salt of the metal to be deposited. There are five stages to electrochemical deposition of metals [41, 42]: (1) transport of metal ions in solution to the electrode surface, (2) electron transfer, (3) formation of metal ad-atoms via adsorption, (4) nucleation and growth, two- or three-dimensional, of metal particles, and (5) growth of the three-dimensional bulk metal phase. If the growth process is stopped after the fourth step, then nanosized catalysts are produced. If, however, the particles are allowed to grow, then the end result is the formation of metal films.

Deposition occurs by supplying the substrate, called the working electrode, with a sufficient potential to reduce the metal salt to its zero valent state:

$$M^{z+} + ze^- \rightarrow M^0 \tag{9.5}$$

The substrate is therefore immersed in a metal salt solution, usually containing a supporting electrolyte to decrease the resistivity of the solution. The cathode, where the oxidation reaction occurs, and a reference electrode, used for potential control, are also immersed in the solution. If the binding energy of the metal ad-atom to the substrate is lower than the binding energy of the metal ad-atom to itself then 3D growth of the nuclei occurs. Conversely, if the binding energy of the metal ad-atom to the substrate is higher than the binding energy of the metal ad-atom to itself then 2D growth of the nuclei occurs. 2D and 3D growth can also be controlled by utilizing underpotential deposition (UPD) and overpotential deposition (OPD), respectively; UPD refers to deposition initiated at a potential more positive than the reversible potential of the M/M^{z+} metal ion electrode, while OPD occurs at a potential more negative than the reversible potential [33]. Electrodeposition also has the potential to deposit nanosized catalysts without the use of stabilizers, as discussed in Section 9.3.3.

9.2.7 Spray Pyrolysis

The experimental procedure of spray pyrolysis is simple. First, an aqueous solution containing the metal precursor is atomized into a carrier gas that is passed through a furnace. Second, the atomized precursor solution deposits onto a substrate, where it reacts and forms the final product [43]. The process has many advantages compared to other metal-forming techniques [44]: (1) it is very easy to dope films or form alloys in any proportion by manipulating the spray solution; (2) neither high-purity targets and substrates nor vacuum set-ups are required; (3) deposition rates and therefore film thickness can easily be controlled by controlling the spray parameters; (4) moderate operation temperatures (100–500 °C) allow for deposition on temperature-sensitive substrates and ensure that the overall process is less energy intensive; (5) the technique has relatively limited environmental impact since aqueous precursor solutions can be used; and (6) the process is scalable, with production rates as high as 1.1 kg/h [45].

Ultrasonic nebulizers [44] can be used to form micrometer- and submicrometer-sized droplets. Droplets formed by ultrasonic waves have very small sizes and size distributions. To deposit the droplets onto a substrate the aerosol is transported to the heated substrate, where the solvent vaporizes. A heterogeneous reaction occurs that leads to the formation of thin solid films. The spray jet can be scanned continuously to coat a large area. To form nanoparticles the aerosol is pyrolyzed. To improve the deposition efficiency, the ratio of atoms effectively deposited to those supplied, a corona discharge is used to control the transport of aerosol droplets towards the substrate [44]. Electrostatic spray pyrolysis is another method used to control the transportation of the atomized precursor solution from the atomizer to the substrate. It is accomplished by applying a positive voltage, up to 12.5 kV, to the spray nozzle, forming a positively charged spray. Electrostatic forces guide the spray to the hot substrate where pyrolysis takes place.

Although spray pyrolysis is usually used to form thin films of metals it can also be used to form nanoparticles. Pt-Ru/C catalysts have been formed by spray pyrolysis using H_2PtCl_6 and $RuCl_3$ as the precursors, dissolved in an aqueous solution containing carbon black and various molecular lengths of polyethylene glycol (PEG). Once atomized, the droplets of precursor solution in the carrier gas were passed through a quartz tube that was heated to 180 °C by a tube furnace. The solvent evaporation and precursor decomposition resulted in nanoparticles forming on the carbon black. Interestingly, PEG plays an integral role in particle stability against agglomeration. If the PEG chain is too short (PEG with average molecular weight 200 g mol^{-1} PEG200) the Pt-Ru particles agglomerate. If the PEG chain is too long, e.g., PEG1000, the PEG molecules aggregate and do not protect the particles from agglomeration. However, at intermediate PEG length, PEG600, the precursors mix well with the polymer and agglomeration is prevented.

9.2.8 Vapor Deposition

9.2.8.1 Chemical Vapor Deposition (CVD)

CVD is an ideal method for forming thin metal films. Furthermore, film growth can potentially be controlled mono-layer by mono-layer using atomic layer deposition, a specific type of CVD. A typical CVD process [46] begins by vaporizing the precursor, an inorganic compound containing the desired metal(s). The substrate is placed in a reaction chamber into which the vaporized precursor, mixed with a carrier gas and any other gaseous reactants, is introduced. The precursors diffuse or are carried to and adsorb onto the substrate surface where they decompose thermally, forming the metallic film. The precursor is designed to ensure that any reaction by-products are gaseous and desorb into the gas phase. Metal alloys can be fabricated by CVD when a heterometallic precursor is used. Heterometallic (single-source) precursors typically have ligands which contain a second metal atom connected to the central metal atom. Using a single-source precursor (that remains coordinated in the vapor phase) allows for precise control of the ratio of the two metals. [CpRu(η^5-C$_5$H$_3$CH$_2$NMe$_2$)Pt(hfac)] (see Figure 9.2) is an example of a single-source precursor that has been used to make Pt/Ru and Pt/RuO$_2$ films to be tested for fuel cell catalysts [48]. The Pt/Ru stoichiometry of

this single source precursor is 1:1. This structure has been specifically synthesized, as it has sufficient volatility and good stability at low temperatures.
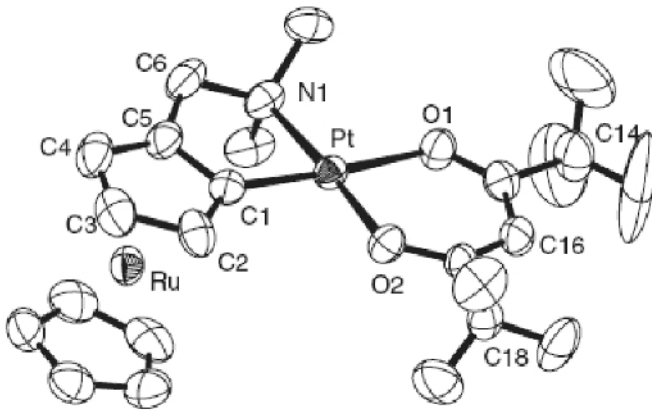
Figure 9.2. Drawing of a single source precursor for CVD [47]. (Reprinted with permission from Huang SF, Chi Y, Bock C, MacDougall B, Carty A. Preparation of the Ru-Pt alloyed thin-films by chemical vapor deposition using single source precursor. Chem Vap Dep 2003;3:9; Figure 1.)

CVD is typically used to form thin films but it can also be used to make nanoparticles. Pt-Ru particles 2 nm in diameter have been formed by vapor deposition using commercially available single metal precursors, namely platinum(II)-acetylacetonate and ruthenium(III)-acetylacetonate [48]. The precursors were adsorbed onto carbon black by sublimation and subsequently decomposed at 320 °C in H_2 or N_2. While particle size was virtually independent of sublimation temperature, the Pt:Ru ratio decreased as sublimation temperature increased from 170 to 240 °C. A maximal Pt:Ru ratio, equaling the Pt:Ru ratio of the precursor salts, was reached at 220 °C. The composition is affected by the sublimation temperature, as the vapor pressures of the two precursors are influenced by the sublimation temperature. This example illustrates how the vapor pressure of the precursors can act as a limitation upon CVD alloy formation [21]. CVD is also limited by processing temperature and mass-transfer kinetics [21]. One final disadvantage of CVD to note is that precursors can be highly toxic and therefore difficult to work with [49].

9.2.8.2 Physical Vapor Deposition (PVD)
Mechanical methods, such as cathodic sputtering, and thermal methods, like evaporation, are grouped together under the term physical vapor deposition [50]. All PVD experiments have four essential components: (1) they occur in vacuum, they have (2) a source to supply the material, called a target, (3) a substrate on which the film is deposited, and (4) an energy supply to transport the material from the source to the substrate. The types of PVD vary in how energy is imparted to the particles and how the energized particles are transported to the substrate.

Evaporation PVD occurs by heating the material to be deposited. Under vacuum a molecular beam of the catalyst material is formed thermally. In a molecular beam, atoms and molecules move in a well-defined direction without colliding [51]. When the system is oil-free and the substrate is atomically clean before deposition, molecular beam epitaxial (MBE) deposition is possible. Depositing alloys is difficult with evaporation PVD, since the vapor pressures of the various elements may be different and therefore the deposited film becomes richer in the less volatile species [51].

Cathodic sputtering occurs by generating a plasma between the substrate and a target, the target being made of the material to be deposited. The target acts as the cathode, emitting atoms to the substrate, which acts as the anode. Nickel coatings were developed as the anode for protonic ceramic fuel cells (PCFCs) based on $BaCe_{0.9}Y_{0.1}O_3$ as the electrolyte [51]. By utilizing a pulsed cathodic sputtering technique, the microstructure and adhesion of the thin film anode to the ceramic electrolyte were optimized, leading to higher-quality anodes and therefore longer stack life of the fuel cell. The main disadvantage associated with cathodic sputtering is low deposition rates.[52] Sputter deposition has been frequently applied to make Pt based catalysts. Systems with multiple targets consisting of different metals have been used to prepare and screen a large range of binary, ternary and quaternary catalysts of broad composition range.

9.2.9 High-energy Ball Milling

High-energy ball-milling is a mechanical alloying process and a method of grinding and mixing materials in the absence or presence of a liquid. The milling is done in a rotating cylinder or conical mill using balls or pebbles; typically, a powdered catalyst is prepared. Ball-milling is an interesting technique that has the potential to extend the solubility limit of one element into the other, alloy difficult elements, make alloys of defined grain size down to the nanometer range, and synthesize new crystalline and quasi-crystalline phases. Ball-milling has been used to prepare CO-tolerant fuel cell catalysts [53–55]. Catalyst precursors can be prepared by milling together, e.g., Pt and Ru metal powders, a dispersing agent, and often a process control agent. It is also possible to at least partially reduce metal-oxide precursors when milling in a reducing (H_2-containing) atmosphere. Typical fuel cell catalysts that have been prepared by ball-milling are unsupported Pt and PtRu alloy powders. BET catalyst surface areas in the range of 10 to 40 m^2g^{-1} of catalyst have been made using ball-milling [55]. After ball-milling, the powdered samples contain "impurities", namely the dispersing and process controlling agent, and typically also parts of the mill equipment (i.e., from the vials, balls, and pebbles). Tungsten carbide (WC) balls and vials are often used in ball-mill equipment to make fuel cell catalysts. Aluminum is a typical dispersing agent. Attempts have been made to leach the Al after milling in 1 M NaOH solutions. However, PtAl alloys may be formed that potentially have a beneficial catalytic effect. Typical process control agents (PCAs) used in ball-milling are organic compounds such as stearic acid, hexane, oxalic acid, and polyvinyl pyridine. The PCAs act as surface active agents, interfering with the solid by lowering the surface tension. Organic PCAs typically decompose during ball-

milling and are incorporated into the catalyst as carbides and oxides. Hence, inorganic PCAs have been tested [55]. Denis et al. [56] found the most promising PCAs to be NaF and MgH_2; the last has the dual function of acting as a PCA as well as a dispersing agent [55]. MgH_2 partially decomposes during milling, releasing H_2, and perhaps forms metallic Mg that may be incorporated into the catalyst lattice.

9.3 Particle Size and Shape Control

A major breakthrough in PEMFC technology was achieved decades ago when the concept of supported catalysts was introduced. This allowed for the better distribution and hence better utilization of expensive noble metal catalysts. Pt was supported on carbon black, as shown in the example of a commercially available catalyst in Figure 9.3 [56]. A substantial gain in supporting the noble metal catalysts is, of course, the increase in the ratio of surface atoms to bulk atoms. However, as early work showed, a smaller catalyst size does not yield a higher activity [57–59]. In fact, the activity for many reactions shows a maximum at a particular particle size. A number of possible explanations have been put forward to explain the particle size effect [57–59]. One of them discusses the importance of crystal phases for catalytic reactions, as shown in Figure 9.4 [59]. Hence, the synthesis of catalysts of particular sizes and shapes has attracted a significant amount of interest for fundamental studies as well as practical applications. Achievements in these areas are discussed in this section.
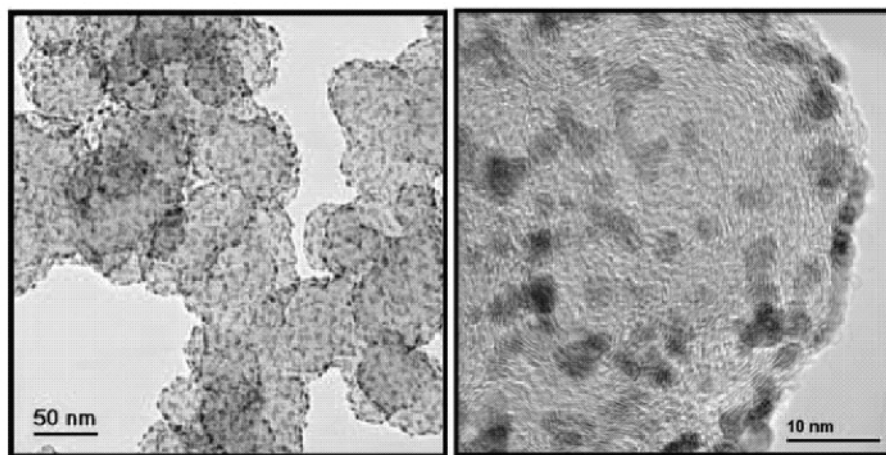
Figure 9.3. TEM images of 40 wt% Pt catalyst supported on carbon (Pt/C) [56]. (Reproduced by permission of ECS—The Electrochemical Society, from He C, Desai S, Brown G, Bollepalli S.)
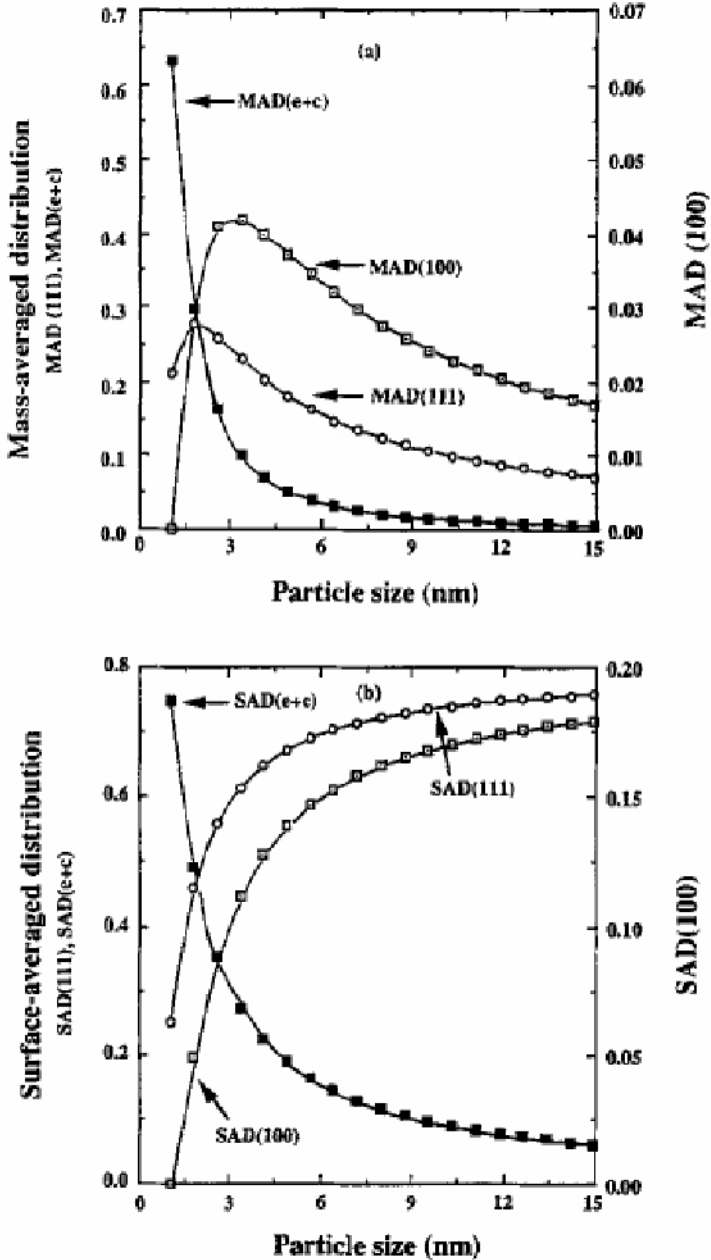
Figure 9.4. Calculated mass averaged distribution (MAD, Figure 9.4(a)) and calculated surface-averaged distribution (SAD, Figure 9.4(b)) for edge (e) and corner (c) sites, and 100 and 111 crystal planes for cubo-octahedral Pt as a function of the particle size [59]. (Reproduced by permission of ECS—The Electrochemical Society, from Kinoshita K, Particle size effects for oxygen reduction on highly dispersed platinum in acid electrolytes.)

9.3.1 Mechanism for Size Control Using Colloidal Synthesis Methods

Chemical methods, specifically colloidal synthesis methods, are discussed in this section because of their simplicity for preparing catalysts on a large scale. Furthermore, colloidal synthesis methods offer the benefit of forming nanosized catalysts of controlled size and composition in a simple manner. Stabilizers can be selected so as to provide minimal blockage of the catalyst surface, as discussed below. It should be noted that the substrate, used for subsequent deposition of the prepared colloids, may affect the final catalyst particle size. However, this seems to be dependent on the synthesis method used, as well as the catalyst composition and catalyst loading on the substrate. For example, it has been found that Pt/Ru colloids could be deposited onto carbon blacks without loss of catalyst surface area per weight of catalyst, up to high weight percentages [60]. However, using the same synthesis method, the final particle size of mono-metallic Pt particles showed a dependence on the weight percentage of catalyst per weight of carbon [61].

9.3.1.1 Pt-sols Made Using Organic Stabilizers

Being able to synthesize fuel cell catalysts in the 1 to 5 nm range, i.e., the size range of interest in practical fuel cell catalysis, in a controlled manner is very important. In the case of the reduction of O_2 (ORR), Pt particles in the 3.5 to 4 nm size range are believed to be the most active catalysts, while for bi-metallic Pt/Ru catalysts the optimal size range appears to be in the range of 2.5 nm. Colloidal methods provide an excellent method to control particle size via multiple factors, such as the concentration of the metal precursor salts, the stabilizing agent, and the synthesis temperature. In many cases, the prepared colloids can be deposited onto a suitable substrate. Preferably, the stabilizer molecule is removed after deposition, as otherwise fuel access to the catalyst surface is hindered. This is of particular concern when large stabilizer molecules are used. The synthesis of Pt and other noble metal colloids has been explored for many years. A wide range of methods to prepare Au-sols was published in 1951 by Turkevich et al. [62] (where references to earlier metal sol preparation can also be found). Pt-sols have, for example, been prepared in aqueous solutions using citrate as a reducing agent and stabilizer [63]. The stabilizer adsorbs on the surface of the Pt nuclei and prevents them from agglomerating. Many factors influence the resulting particle size and size distribution, such as the rate of Pt reduction and the rate at which the stabilizer interacts with the Pt atoms. The Pt reduction rate depends on the temperature and the Pt-precursor as well as the concentration and strength of the reducing agent. The resulting particle size depends on the relative concentrations of nuclei and citrate, adsorption strength, and steric hindrance to avoid further growth. Stable, mono-metallic Pt particles in the size range of 1.6 to 3 nm have been prepared in a reproducible manner by reducing H_2PtCl_6 using citrate. Other sizes of Pt-sol have been prepared by changing the reaction temperature, and the concentrations of the Pt precursor salt and sodium citrate. An important factor in stabilizing the metal colloids is the pH of the solution. For example, the pK_a for step 3 of citric acid is 6.4 [64]. The anionic form, citrate, is the effective stabilizer; hence, the pH of the synthesis solution needs to be kept sufficiently high to ensure that the anionic form is present.

9.3.1.2 Modified Polyol Methods

The principle of colloidal synthesis has been widely applied to a number of metals, stabilizers, and reducing agents. The synthesis of high surface area catalysts in ethylene glycol, referred to as the polyol method, has been widely applied. The ethylene glycol method has been used to make Pt and Pt/Ru black catalysts, and Pt and Pt/Ru catalysts on carbon black [65–67]. Wang et al. used the polyol method to prepare mono-metallic Pt and Ru colloids [66]. They suggested that the size of the Pt and Ru colloids can be controlled by the addition of H_2O to the synthesis solution. The polyol method is very attractive as it provides a straightforward, "inexpensive" catalyst synthesis method of low toxicity. In the polyol method ethylene glycol acts as solvent and reducing agent. Ethylene glycol (A) can be oxidized via two pathways [67]:

$$(9.6)$$

and

$$(9.7)$$
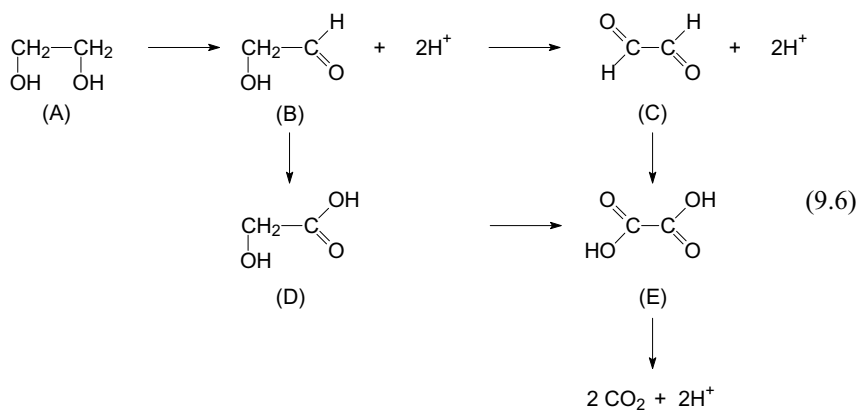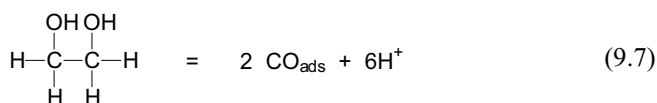
It has been shown that both reactions take place for the synthesis of Pt/Ru colloids. It has also been shown that a large amount of glycolic acid (D) is formed and this is believed to act as a stabilizer for the Pt/Ru colloids. Depending on the solution pH, this molecule is present either as the anion, glycolate, or as glycolic acid. Similar to the synthesis of Pt-sols from H_2PtCl_6 using citrate as reducing agent and stabilizer, the Pt-Ru particle size can be adjusted by adjusting the synthesis solution pH. This is shown in Figure 9.5 for the example of Pt/Ru colloids that were deposited on Vulcan XC72. The synthesis solution pH was adjusted by adding different amounts of NaOH. Other advantages of this method are that the stabilizer molecule can be removed at low temperatures (< 160 °C) without changing the properties of the Pt/Ru catalysts (the importance of this is further discussed in Section 9.4.1.1), and that high-loading catalysts can be prepared without loss of surface area per mass of catalyst [60].
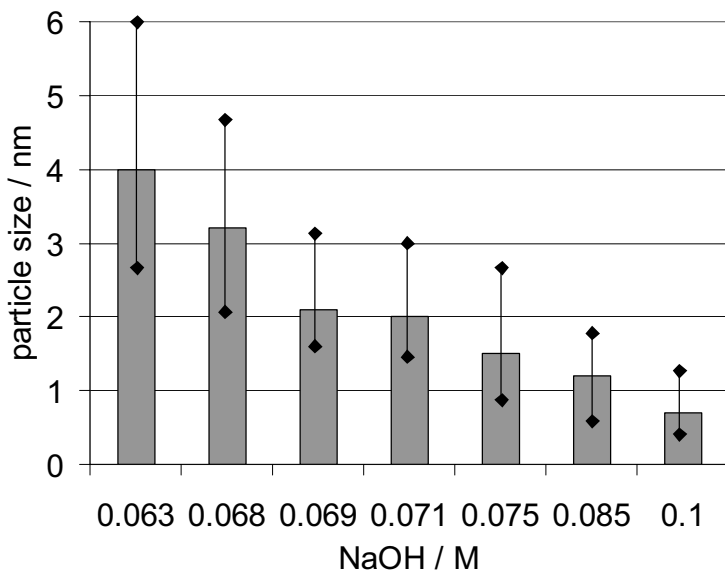
Figure 9.5. Control of Pt-Ru/C particle size via the synthesis solution pH using a modified polyol method [67]. (Reprinted with permission from J. Am. Chem. Soc., 2004, 126 (25), 8028, Figure 2. Copyright 2004 American Chemical Society.)

9.3.1.3 The Boennemann Synthesis Method

Much work has been carried out using the Boennemann synthesis method for the preparation of fuel cell catalysts [68]. In this synthesis, mono- and bi-metallic colloidal catalysts are formed by starting with the corresponding metal precursor salts that are then dissolved in tetrahydrofuran (THF), according to Equation 9.8. Tetraoctylammoniumtriethylhydroborate, $N(Oct)_4[BEt_3H]$, is utilized as reducing agent and stabilizer at the same time [67]:

$$PtCl_2 + 2N(Oct)_4[BEt_3H] \xrightarrow{\text{THF/Argon}} Pt\left[N(Oct)_4Cl\right]_2 + 2BEt_3 + H_2 \quad (9.8)$$
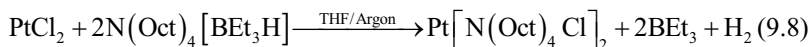
A number of fuel cell catalysts have been synthesized in this manner, such as Pt colloids, Pt/Sn colloids, and Pt/Ru colloids of different Pt to Ru ratios. A drawback of the Boennemann synthesis method is that oxidative removal of the stabilizer molecule requires temperatures higher than 300 °C [69]. High-temperature treatment of Pt-based catalysts should be avoided as changes in the structure, namely preferential surface segregation of Pt or RuO_2, typically take place (this is further discussed in Section 9.4.1). To the best of our knowledge the Boennemann method has not been used to make catalysts of the same composition but different sizes.

9.3.1.4 Other Methods

More recently, a method utilizing different amounts of a large stabilizer has been reported to make Pt and Pt/Ru catalysts of controlled size [70]. The catalysts were

formed from metal-acetylacetonate precursors reduced by polyalcohols. Oleylamine was used as the stabilizer and the resulting particle size was controlled in the size range of 3.5 to 6.5 nm Pt/Ru, utilizing different amounts of the stabilizer. The work discussed the removal of the stabilizer by a repeated washing and dispersing of the colloids in tetramethylammoniumhydroxide (TMAOH). The colloids were reported to be electrostatically stabilized in the TMAOH solution.

9.3.2 Size Control Using Electrochemical Methods

Formation of fuel cell catalysts using electrochemical methods may not be as attractive for the preparation of large-scale catalysts as, for example, chemical methods. However, electrochemical methods provide advantages over other synthesis methods that make them interesting methods for the preparation of "model" catalysts. Electrochemical deposition offers the advantages that (1) stabilizers and/or capping agents, which should be avoided since residues of stabilizers likely influence the catalytic activity of the nanoparticles, are not required and (2) the particle size can be controlled by varying the length and the amplitude of the potential pulse. The nuclei density can be increased by electrodepositing at a large overpotential [35]. However, increasing the overpotential may result in other reactions occurring in addition to the metal reduction, i.e., hydrogen adsorption and evolution [52]. If metal reduction is not the only process occurring then it is not possible to extract valuable information, such as the type of nucleation or the amount of platinum deposited, from current-time transients.

Platinum nanocatalysts have been electrochemically deposited onto highly ordered pyrolytic graphite (HOPG) from an aqueous H_2PtCl_6 solution containing HCl as the supporting electrolyte. The catalyst size was varied by varying the time the deposition potential was applied: 10 ms deposition time generated particles 2.5 ± 0.9 nm in height and 100 ms deposition time generated particles 7.2 ± 3.2 nm in height [34]. The large increase in size distribution indicates that the nucleation is progressive, i.e., the number of nuclei increases with deposition time. Ideally the deposition process occurs in an instantaneous fashion, that is, the number of nuclei is constant and equal to that at time t = 0 of the deposition process. Assuming that all the nuclei grow at the same rate, instantaneous nucleation results in mono-sized particles and is therefore preferable in fabricating nanocatalysts of a specific size. It has been shown that increasing the deposition overpotential or increasing the electrolyte conductivity (using chloride, sulfate, and perchlorate anions) causes a shift from progressive to instantaneous nucleation [35].

9.3.3 Assistance of Templates and Template Preparation

9.3.3.1 Preparation of Mesoporous Catalyst Films
Preparation and control of the size and structure of fuel cell catalysts in the nano-size range using templates synthesis methods has attracted some attention. The best known synthesis method is probably the deposition of metal films from lyotropic liquid crystalline mixtures developed to by Phil Bartlett's group [71–73]. They have used the method to deposit films of Pt, Pt/Ru alloys, and other metals,

consisting of regular arrays of cylindrical pores at the nanometre scale. The Pt films prepared showed a similar area as Pt blacks, i.e., in the 20 m^2g^{-1} range [71]. In this method, the metal is electrodeposited from a solution that contains a non-ionic surfactant such as octaethyleneglycol monohexadecyl ether or octaethyleneglycol monododecyl ether and a metal deposition salt, e.g., H_2PtCl_6. The resulting film structure is influenced by the chain length of the surfactant as well as the deposition conditions such as the potential and electrode size [72]. In the case of Pt, the electrodeposition is complicated. Two reduction reactions can take place, as follows:

$$PtCl_6^{2-} + 2e^- \rightarrow PtCl_4^{2-} + 2Cl^- \qquad E°: 0.726 \text{ V vs. NHE} \qquad (9.9)$$

$$PtCl_4^{2-} + 2e^- \rightarrow Pt + 4Cl^- \qquad E°: 0.758 \text{ V vs. NHE} \qquad (9.10)$$

Furthermore, the Pt^{2+} in the $PtCl_4^{2-}$ compound is not stable and dissociates into Pt and Pt^{4+}; i.e., a competitive reaction with Equation 9.10 may take place. Depending on the electrode size, Pt films of different roughness factors (surface areas) are formed. It has been suggested this is due to different diffusion rates of Pt^{2+} away from the electrode surface. The roughness and order of the resulting films is also influenced by the deposition potential, particularly when other processes such as H_2 evolution also take place. Rougher and less ordered films are obtained in the latter case.
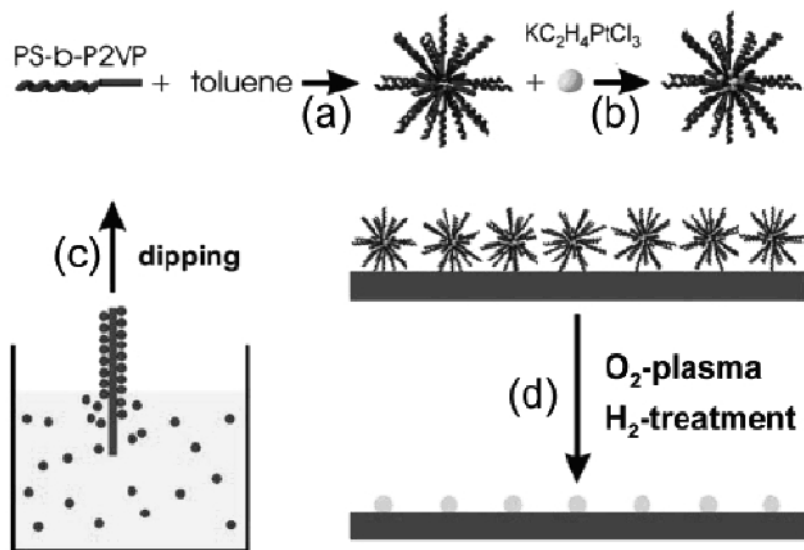
Figure 9.6. Schematic description of the preparation procedure of the model electrodes by deposition and postprocessing of Pt-salt micelles. (a) Preparation of the inverse micelles, (b) Pt salt loading, (c) deposition on the glassy carbon substrate by dip coating, and (d) removal of the polymer stabilizer shell and reduction of the Pt-salt core in an oxygen plasma and subsequent reduction in a H_2 atmosphere [74]. (Reprinted with permission from Langmuir, 2007, 23, 5795, Figure 1. Copyright 2007 American Chemical Society.)

Reverse micelles or water-in-oil emulsions have also been used to make quasi 2-D films of Pt on glassy carbon substrates [74]. Homogeneously distributed Pt nanoparticles of defined size (25 ± 5 nm) and a defined average particle separation of 40 ± 10 nm were made. The steps involved in the process are illustrated in Figure 9.6. First, the micelles were formed by dispersing polystyrene (PS)-poly(2-vinylpyridine) (P2VP) in dry toluene for one week; subsequently the Pt-precursor salt was added. The emulsion was stirred for another week, prior to dip coating a glassy carbon substrate. The polymeric shell was decomposed in oxygen plasma, while reduction to Pt-metal was carried out by annealing in H_2. It was essential to anneal the self-assembled Pt-particles in H_2. Pt films studied after the oxygen-plasma treatment were not stable during electrochemical studies, namely the electrochemical oxidation of adsorbed CO. They appeared to have dissolved.

9.3.3.2 Preparation of Macroporous Catalyst Films

Other approaches for the electrodeposition of structured Pt based films involved polystyrene spheres that were pre-self-assembled on the substrate prior to deposition. The film thickness and pore volume can be varied by using different diameters of polystyrene spheres. 3D nano-network structures were made in this manner. Both the lyotropic liquid template and the self-assembled polystyrene template method have been employed to form Pt and "PtRu alloy" films [75, 76]. An example of a macroporous Pt-based film made using polystyrene spheres is shown in Figure 9.7.
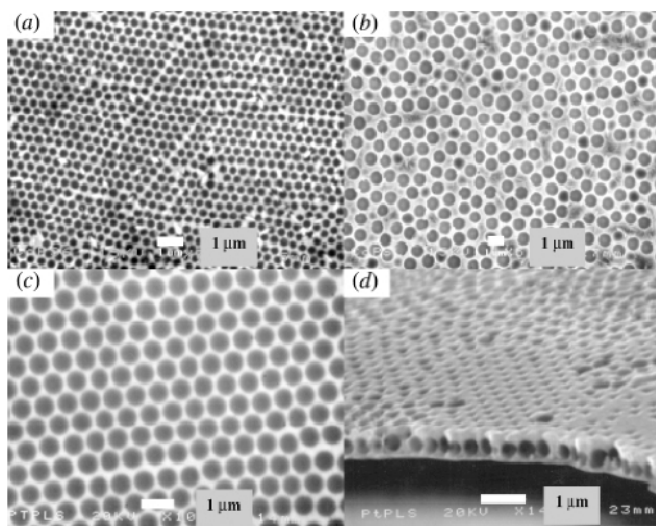
Figure 9.7. Scanning electron micrographs of macroporous platinum and cobalt films that were electrochemically deposited through polystyrene latex spheres preassembled on gold electrode surfaces. Figures 9.7 (a) and (b) show formed cobalt films, while Figures 9.7 (c) and (d) show formed Pt films [75]. (Bartlett PN, Birkin PR, Ghanem MA, Electrochemical deposition of macroporous platinum, palladium and cobalt films using polystyrene latex sphere templates, Chem Commun 2000;17:1671; Figure 1. Reproduced by permission of The Royal Society of Chemistry.)

9.3.3.3 Nano-structuring Substrates for Nanoparticle Deposition

Substrates themselves can also be nanostructured prior to the deposition of Pt-based nanocatalysts. Ordered nano-pits were introduced onto HOPG surfaces by oxidation with ozone at 300 °C [77, 78]. The nanostructured HOPG surfaces were subsequently used as substrates for the deposition of Pt nanoparticles by either electrochemical or thermal decomposition. Pt nanoparticles in the 2–3 nm size range were formed in this manner. For both deposition methods, electrochemical and thermal, the pits acted as nucleation sites for Pt deposition. The nucleation process was shown to be more reproducible as well as shifting to instantaneous rather than progressive nucleation in the case of Pt electrodeposition onto the nanostructured vs. the smooth, freshly cleaved HOPG substrates.
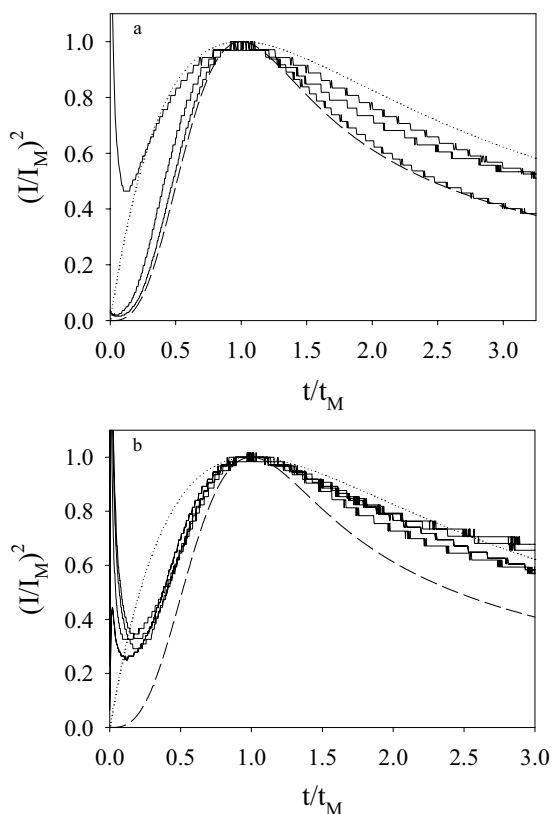
Figure 9.8. Reduced variable plots of electrochemical reduction of Pt metal onto (a) freshly cleaved, and (b) O_3 oxidized (0.15 ppm O_3, 300 °C) HOPG. The solid lines represent experimental data. The long and short dashed lines represent theoretical curves for instantaneous and progressive nucleation, respectively [78]. (Reproduced by permission of ECS—The Electrochemical Society, from Halvorsen H, Bock C, MacDougall B, Wang D, Potentiostatic deposition of platinum clusters onto freshly cleaved and ozone oxidized highly ordered pyrolytic graphite.)

This is shown in Figure 9.8(a) and (b) using non-dimensional plots for the Pt electrodeposition. The pits also stabilized the Pt nanoparticles prepared by thermal decomposition, and electrochemical measurements such as oxidative stripping of adsorbed CO could be carried out without measurably changing the Pt nanoparticles. Fundamentally different Pt particles were made, depending on the method, as indicated by large differences in the oxidation reaction of adsorbed CO, thus showing the importance of this method for fabricating "model" catalysts. The idea of forming Pt nanoparticles on HOPG surfaces was based on work reported by Savinova et al. [80]. In a series of papers, it was reported that Pt nanoparticles could be formed on glassy carbon substrates that were roughened by electrochemical pre-oxidation treatment. Pt nanoparticles of different average sizes were formed by first creating Pt nanoparticles on the substrates by thermal decomposition of a K_2PtCl_6 precursor salt. Subsequently, the Pt nanoparticles were enlarged by electrochemical growth in Pt-salt solutions. The smallest size of Pt particles formed in their work was 1.7 ± 0.5 nm and the largest was 3.1 ± 1.2 nm.

9.3.4 Shape Control

The synthesis of Pt and PtRu catalysts of particular shapes via the colloidal route has also attracted some attention. Colloidal methods have been tailored to allow for catalyst shape control. Minimal work has been done to determine the mechanism of shape control for platinum nanoparticles. However, a literature survey indicates that the reducing agent [8], the ratio of capping agent to platinum source [80], the identity of the capping agent [81], and the extent of particle growth [82] all contribute to the final shape of the nanoparticles. The reduction rate of the platinum salt greatly affects the shape of the Pt nuclei. Slow reduction by dihydrogen gas at room temperature is found to produce tetrahedral platinum nuclei which are enclosed with four {111} planes [80, 83–84]. The slow thermodynamically controlled process produces the shape that has the lowest surface energy. Equal growth rates for the {111} and {100} planes are caused by kinetic controlled growth of platinum particles. Fast reducing agents such as methanol tend to form truncated octahedral nuclei [8, 80].

Shape control is achieved if the capping agent encourages the growth of one crystal face over another to generate specific particle shapes. High capping agent to metal source ratios retain the shape of the nuclei with growth, while low capping agent to platinum source ratios selectively grow the {111} plane over the {100} plane. This is thought to be because at low ratios of capping agent to metal source the capping agent preferentially binds to the {100} plane, allowing preferential growth of the {111} plane, while at high capping agent to metal source ratios the capping agent binds to the {111} and {100} planes equally, therefore retaining the shape of the nuclei.

A recent publication describes combining seed-mediated synthesis, capping agent, and diffusion-controlled growth by slow reduction as the parameters for simultaneously controlling the shape and size of platinum nanoparticles [83]. The seed was prepared by reducing H_2PtCl_6 in the presence of REWOTERIC B14 (REWO), which acted as a stabilizer to prevent agglomeration. The resulting nanoparticles were 1 ± 0.2 nm. Tetrahedral Pt nanoparticles of different sizes were

prepared in a 10:1 polyvinylpyrolidene (PVP):K_2PtCl_4 solution by adding 0, 2, 5, and 10 % seed the seed percentage being with respect to the initial Pt^{4+} concentration. Particles of 8 ± 1, 5 ± 1, 2.5 ± 0.5, and 1.8 ± 0.3 nm size, respectively, were obtained after reduction overnight. Reduction of platinum salt occurs on the surfaces of the seeds, which act as nucleation centers. The high capping agent to platinum source ratio ensures the preservation of the particle's tetrahedral shape. The slow reducing agent, H_2, has a dual function in this experiment: it assists in the formation of tetrahedral nuclei and inhibits additional nucleation by promoting narrow size distribution.

The question remains whether these catalysts retain their shape and/or what shape they will adopt during exposure to electrocatalytic reactions.

9.4 Bi-metallic Catalysts

For efficient FC reactions bi-metallic catalysts are essential. Only in the case of PEMFC anodes that operate on neat H_2 is mono-metallic low-loading Pt used. In the case of neat H_2 the reaction is so fast that the amount of Pt catalyst, and hence the cost, are not of concern. However, in the case of FCs run on methanol or reformate gas (H_2 and CO), bi-metallic catalysts need to be used, the most common choices being bi-metallic catalysts consisting of Pt/Ru. Other combinations as well as ternary and quaternary catalyst formulations have also been tested. In the case of the cathode, where O_2 is reduced (ORR), Pt is the most commonly used catalyst. However, the ORR reduction kinetics are sluggish, so the amounts of Pt and hence the cathode catalyst costs are high. Other formulations, typically Pt catalysts in combination with metals from the iron group, are being considered with the goal of improving catalytic activities and replacing at least some of the Pt. The environment for both the anode and cathode reactions of PEMFCs is acidic, thus limiting the number of catalysts that can be used. Catalyst stability is of greater concern for the cathode than the anode, as in a FC the cathode operates at very positive potentials, enhancing corrosion of the catalyst and support. Catalyst sintering during operation is also a concern. To enhance the catalytic activity of the ORR catalysts, Pt has been alloyed with Fe, Cu, Ni, etc., and core-shell and skin-layer type catalysts consisting of Pt and iron group metal elements are being made and tested [85–90]. In the case of the core-shell catalyst, the core exists of one metal component that is surrounded by a skin of the active catalyst. A skin-layer catalyst typically starts with an alloy, from the surface of which the unstable component is leached.

In this section we will focus on the preparation of Pt/Ru catalysts and Pt catalysts made with the iron group. Ternary and quaternary catalysts are not discussed specifically. However, similar principles apply to their synthesis.

9.4.1 Synthesis of Alloy versus Two-phase Catalysts

A challenge for the preparation of FC catalysts is the formation of catalysts that consist of surfaces made, at the atomic level, of homogeneously distributed catalyst components. Pt forms bulk alloys of a wide range of concentrations with a number

of metals, thus ensuring distribution on the atomic level in bulk. However, the make-up of the surface and the bulk can be substantially different. Experiments as well as theoretical studies have shown that, particularly in the case of Pt, surface segregation takes place [92, 93]. Experimental work dating back to 1977 has shown that in H_2 atmospheres Pt preferably surface segregates while the surface is enriched with RuO_2 in an air/O_2 atmosphere of Pt/Ru catalysts, heat treated at 300 °C [91]. According to the theoretical work [92], when Pt is the host lattice it undergoes anti-segregation, meaning Pt prefers to be on the surface. Anti-segregation of Pt is the case with the majority of other metals. The exception is the combination of Pt and Pd, for which very little segregation is expected. Bulk alloys are traditionally formed by arc-melting the metals at high temperatures; hence, preferential segregation of one metal on the surface takes place. In order to limit surface segregation, catalyst synthesis needs to be carried out at low temperatures. The selection of the appropriate conditions allows for the synthesis of Pt-based catalysts at low temperatures. Alloy formation at low temperatures has also been shown to be possible [2]. For example, PtRu alloy powders of close to 45 at% Ru dissolved in the fcc Pt lattice were prepared. The key to the preparation of alloys in this manner is the very rapid and simultaneous reduction of the two noble metal precursor salts. This can be done using a large excess of strong reducing agent (e.g., $NaBH_4$). Synthesis of two-phase catalysts is in a sense simpler than the preparation of alloy catalysts, although the choice of the metal in the core vs. the shell will be dictated by the redox potentials of the two metal/metal-precursor salts and the respective reduction rates (discussed in Section 9.4.1.2).

9.4.1.1 Alloy Formation Energies, Phase Diagrams, and Quasi Vegard's Law

An important consideration for the preparation of multi-component catalysts is their nobility, i.e., the redox potentials, rate of reaction of the precursors, and miscibility of the metals (thermodynamic stability). One metal must be miscible in the lattice of the other in order to form an alloy. Phase diagrams are readily available and describe the existence of bulk alloys. The formation of an alloy is described by the alloy formation energy. Recently the alloy formation energy, ε, has been calculated for three cubic solution alloys (Pt,Ir), (Pt,Re), and (Pt,Ru) [93]. High-resolution plots of the lattice parameter vs. the atomic percentage of the metal dissolved in the host lattice, and cell energies as a function of the metal dissolved were calculated. Examples of such plots for (Pt,Ru) alloys are shown in Figure 9.9(a) and (b). ε was then calculated from the slope of the latter graph. Experimental data and theoretical calculations have shown that (Pt,Ru) and (Pt,Ir) alloys follow a quasi "Vegard's law" relationship over a wide range of concentrations. Fundamental differences in the bulk alloy formation of (Pt,Ru) and (Pt,Ir) alloys were suggested according to the calculated ε values. In the case of (Pt,Ru), the calculated bulk alloy formation energy is exothermic while the bulk alloy formation energy is calculated to be endothermic for (Pt,Ir) alloys. This suggests that (Pt,Ru) alloy formation is thermodynamically favored and achievable at low temperatures, while the endothermic formation energy calculated for (Pt,Ir) alloys suggests that (Pt,Ir) alloy formation requires external energy, i.e., higher temperatures.

(a)

(b)
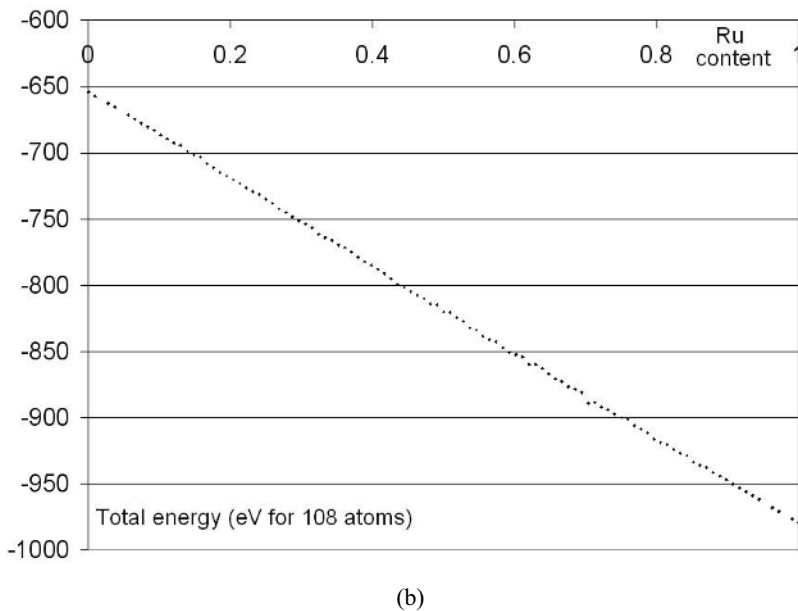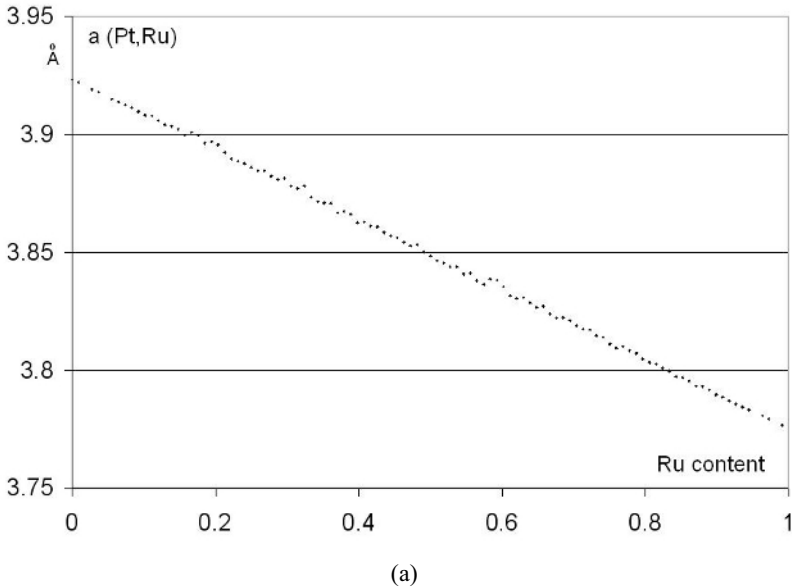
Figure 9.9. Figure 9.9(a) shows the calculated cell data vs. Ru content x for $(Pt_{1-x}Ru_x)$ system. The calculated data actually displays a very slight concavity. Figure 9.9(b) shows the total energy per simulation cell for $Pt_{1-x}Ru_x$ alloys. The data displays a slight concavity due to the fact that the energy of a Pt-Ru bond is very slightly lower than the average of a Pt-Pt and a Ru-Ru bond [93]. (Reprinted from Journal of Alloys and Compounds, 422, LePage Y, Bock C, Rodgers JR, Small step graphs of cell data versus composition for ccp solid-solution binary alloys: application to the (Pt,Ir), (Pt,Re) and (Pt,Ru) systems, 164, Figures 2a and b, respectively, ©2006 with permission from Elsevier.)

9.4.1.2 One-step and Two-step Synthesis: Alloy, Skeleton, and Skin-layer Catalysts
A one-step synthesis, i.e., the simultaneous reduction of the precursor salts, is more likely to result in alloy formation particularly at low temperatures. However, alloy formation in the bulk can be achieved by heat treating two-phase catalysts in a reducing environment. An example of the latter is the formation of PtCu alloys [90]. This reaction was carried out starting with commercially available Pt nanocatalysts supported on carbon black (Pt/C). The Pt/C catalysts were impregnated with $Cu(NO_3)_2 \bullet 6H_2O$ and subsequently reduced in H_2 at temperatures between 600 and 900 °C. Nanosized PtCu alloy catalysts were reportedly made in this manner. Copper was subsequently leached from the alloyed particles (either electrochemically or chemically in acidic solutions), thus resulting in a proposed skeletal-type catalyst. Some other catalysts that have been formed similarly, by leaching, consist of Pt and Fe [88]. Skin-type Pt/Ni and Pt/Fe bulk metal catalysts have also been formed by annealing, as will be discussed in Section 9.4.2.3. In some cases such catalysts are reported to have very high catalytic activity. Another possible advantage of these catalysts could be increased stability, namely increased resistance to sintering under FC operation. For example, it has been suggested that an increased resistance to sintering for e.g., Pt_3Ni_1/C over Pt/C catalysts is due to an anchoring effect of Ni upon Pt [94]. It should be noted that great care needs to be taken to eliminate even traces of O_2 in the synthesis of these catalysts at high temperatures and in the presence of transition metals such as Fe, to avoid severe corrosion of carbon.

The two-step synthesis (subsequent reduction of the precursor salts) is more likely to result in phase-separated catalysts, possibly core-shell catalysts. Typically a colloid of a particular metal is first formed then subsequently reacted with the salt of the second metal. Numerous examples of such reactions exist in the literature [95, 96]. The deposition of the second metal onto the preformed colloid can be driven by a redox reaction if the second metal is more noble than the metal of the preformed colloid, i.e., depending on the difference in the free energy (ΔG), which is determined by the difference in the equilibrium potentials, E_1 and E_2 of the redox reactions of the two metal/salts, as follows [97]:

$$\Delta G = -Z_1 Z_2 F(E_1 - E_2) \tag{9.11}$$

In Equation 9.13, Z_1, and Z_2 are the number of electrons involved for redox Reaction 9.1 and 9.2, respectively, and F is Faraday's constant. If ΔG is negative then the oxidized form, Ox_1, will be reduced by the reductant, Red_2. As an example, Pt can be readily deposited onto Cu surfaces and onto Au [97]. Deposition of Pt onto pre-reduced Ru surfaces has also been carried out using the same principles. Similarly, Ru has been deposited onto Cu surfaces, but to a smaller extent than Pt and Au. This is in fact seen experimentally, by preferential Ru deposition onto the rims of copper particles [97]. The equilibrium potentials, E_1 and E_2, are given by the metal and metal-salt involved, as defined by Nernst's law. It follows that the anion of the metal salt influences the E value and hence, ΔG. Through the selection of proper complexing ions it is possible to reverse the host and depositing metals. This has been shown for Pd deposition onto Rh surfaces

from Pd-nitrate solutions vs. Rh deposition onto Pd surfaces in chloride solutions [97].

It should be noted that deposition driven by differences in redox potentials results in the partial dissolution of the metal from the pre-formed colloid/particle. The re-dissolved metal salt can be rapidly reduced and re-deposited onto the existing colloid if the reaction is carried out in a reducing environment (as is the case in, e.g., colloidal 2-step synthesis). In such a case, the shell is likely to consist of a mixture of the two metals rather than a pure metal phase.

9.4.2 Sub-monolayer Deposition of Ad-metals

9.4.2.1 Copper Underpotential Deposition (UPD)
An interesting formation of bi-metallic catalysts involves the use of underpotential deposition (UPD) of Cu onto, e.g., Au [98]. Subsequently, the copper can be displaced by metals such as Pt, Pd, or Ag that are driven through favorable ΔG values. The replacement of Cu with metal, M, is an irreversible, spontaneous redox process, expressed through the respective equilibrium potentials (E), as follows:

$$\Delta G = E_{Cu^{2+}/Cu} - E_{M^{m+}/M}^{\theta \to 0} > 0 \tag{9.12}$$

Sub-monolayers of Pt, Pd, and a bilayer of Ag have been formed in this manner onto Au(111) surfaces.

9.4.2.2 Spontaneous Deposition
The formation of a sub-monolayer driven by a redox reaction, e.g., Pt deposition onto pre-reduced Ru surfaces, is discussed in Section 9.4.1.2. A large number of publications have also been devoted to the preparation of model catalyst systems consisting of Ru nanoparticles deposited onto single Pt crystals [39–41]. Figure 9.10 shows scanning tunnelling microscopy (STM) images of such catalysts. The most commonly used single crystal is Pt(111). The proposed reaction scheme can be summarized by the following steps: the Pt substrate is immersed in a two- to three-week-old solution of $RuCl_3$ in dilute $HClO_4$; aging of the solution is proposed to result in the formation of hydrated Ru(+IV)-species, e.g., $[RuO(H_2O)_4]^{2+}$; spontaneous deposition of the hydrated Ru(+IV)-species in contact with the Pt is proposed to take place according to Equation 9.13, the possible complementary reaction being the partial oxidation of the Pt surface, Equation 9.14.

$$\left[RuO(H_2O)_4 \right]^{2+} \to RuO_{2ads} + 3H_2O + 2H^+ \tag{9.13}$$

$$Pt + xH_2O \to PtO_xH_y + (2-y)H^+ + (2x-y)e^- \tag{9.14}$$
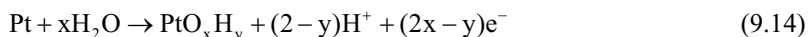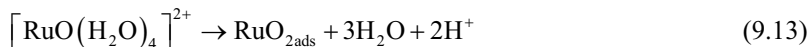
The adsorbed RuO_2 can then be electro-reduced according to Equations 9.17 and 9.18:

$$RuO_{2ads} + 2H^+ + 2e^- \rightarrow RuO_{ads} + H_2O \tag{9.15}$$

$$\left[RuO(H_2O)_4\right]^{2+} + A^- + e^- \rightarrow RuO_{ads} + A_{ads} + 4H_2O \tag{9.16}$$
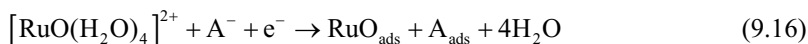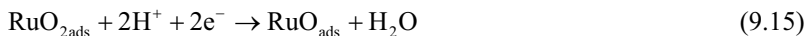
The coverage of the Ru nanoparticles depends on the Pt's crystallographic orientation.
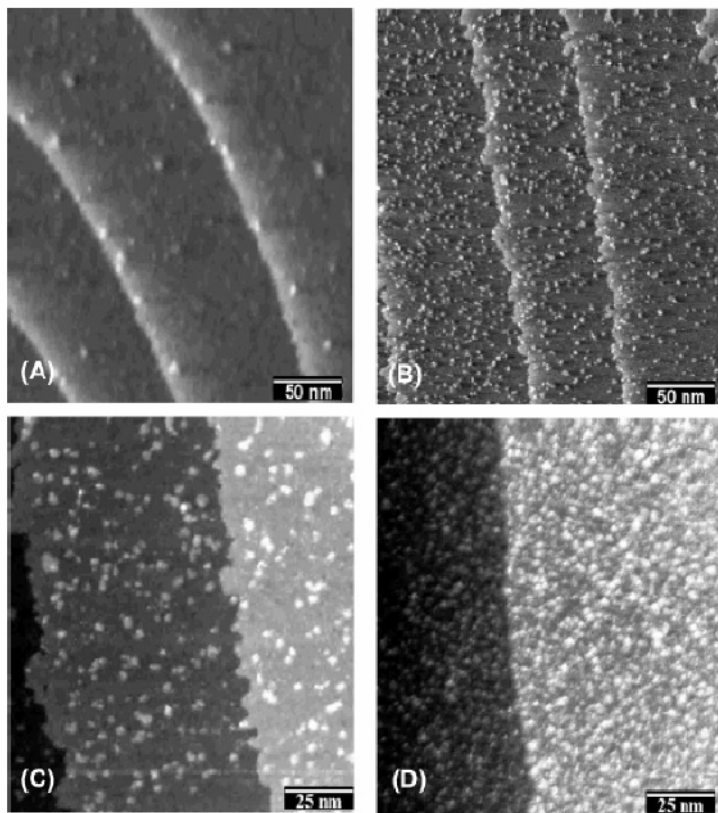
Figure 9.10. Scanning tunneling microscopy images of Ru nano-particles formed onto a Pt(111) single crystal. (A) Substrate without CO and prior to deposition, (B) deposited Ru particles for 5 min., (C) higher resolution image of (B), (D) deposited Ru particles for 30 min [40]. (Reprinted with permission from Maillard F, Lu C-Q, Wieckowski A, Stimming U, J. Phys. Chem. B, 2005, 109, 16230, Figure 1. Copyright 2005 American Chemical Society.)

9.4.2.3 Annealing/Heat Treatment of Catalysts

As discussed in Section 9.4.1.1, preferential layers of Pt can be formed by annealing alloy catalysts. Promising examples of carefully annealed Pt catalysts have been reported recently [99, 100]. The annealed samples show a high activity towards the ORR, which is attributed to a lower tendency to form surface oxides.

Bulk Pt_3Ni alloys were annealed in ultra-high vacuum to form a single atom Pt skin layer. The challenge remains to synthesize nanosized structures of these catalysts.

Another example of the influence of heat treatment on the make of the catalyst and catalyst surface has been shown by Nashner et al. [101]. They supported and subsequently decomposed a $PtRu_5C(CO)_{16}$ molecular cluster precursor at different temperatures in a H_2 atmosphere. Carbon supported Pt/Ru nanoparticles of 1.5 nm average diameter were prepared in this manner. At 100 °C the particles consisted of a disordered structure, with a Pt enriched core and Ru on the surface, while at 300 °C an inverted structure was formed, Pt being on the surface of the equilibrated nanoparticle. The schematic of the synthesis is shown in Figure 9.11.
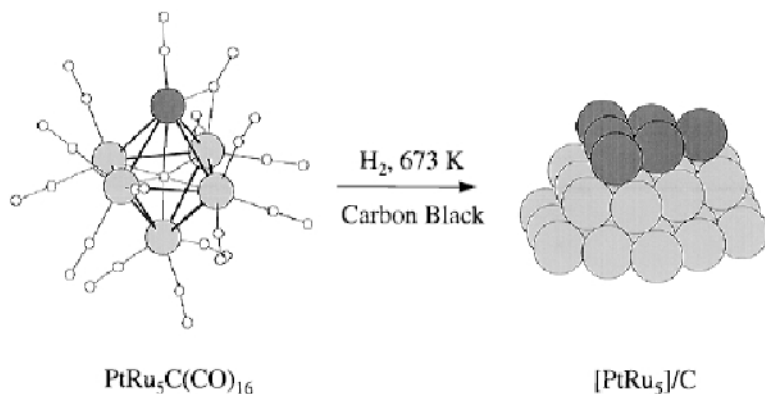
Figure 9.11. Schematic demonstrating the decomposition of a $PtRu_5C(CO)_{16}$ molecular precursor at 673 °C in H_2. The Pt (dark grey) is preferably deposited onto the Ru (light grey) [101]. (Reprinted with permission from J Am Chem Soc 1997;119:7760, Scheme 1. Copyright 1997 American Chemical Society.)

9.5 Non-noble Metal Catalyst Synthesis

9.5.1 Macrocyclic Complexes

There is considerable interest in the use of non-noble metals for fuel-cell catalysis, which is not surprising when one considers the cost of the noble metal Pt (at well over $900 US per troy ounce) and its noble metal alloying additions. In a PEM fuel cell using pure hydrogen at the anode, Pt loading requirements down to 0.05 mg Pt cm^{-2} are manageable. On the other hand, the cathode component of the MEA still requires a loading of ~1 mg Pt cm^{-2} in the best case scenario, due to the slow kinetics of the ORR.

This is a major reason why the majority of non-noble metal catalysis research has focused on the cathode part of the fuel cell system; this work began about 1964 with a paper in *Nature* by Jasinski indicating that N_4-metal chelates had electrochemical oxygen reduction capacity, and specifically with the discovery that CoN_4 phthalocyanine is an oxygen reduction catalyst in alkaline solution [102,

103]. Subsequently, it was shown that metallic N_4 phthalocyanine components were also active for the ORR in sulfuric acid solutions, with measured catalytic activity decreasing in the order Cu~Ni<Co<Fe [103].

Another important feature of the N_4-macrocyclics as oxygen cathode catalysts is the fact that they are quite tolerant to methanol oxidation, a definite advantage in a DMFC system where methanol cross-over through the membrane can occur. As well, the structure of the macrocyclic ligand can be changed (see [103], for example), with a potential modification of the complexes' catalytic ability towards oxygen. The nature of the "metal center" [Fe, Mn, Co, Ni, Cu, etc.], in conjunction with the chemical structure of the macrocycle, is found to dictate the degree of 4-electron vs. 2-electron oxygen reduction that occurs. Obviously, in operating fuel cell systems, 4-electron reduction to water is much preferred over 2-electron reduction to peroxide. It is believed that the redox potential for the metal couple in its two main oxidation states helps to dictate the catalytic activity of the macrocycles, with more positive redox potentials enhancing ORR activity [104]. Supporting the N_4-chelates on carbon or graphite is necessary for catalyst dispersion, and possible interactions with the conducting support need careful consideration. Subsequent heat treatment in inert atmospheres is necessary for both stability and catalytic activity, but the influence of "heat" is not simple, and compromises in conditioning are usually necessary (see below and, for example, [103]).

The interaction of the oxygen molecule with the metal or metal chelate surface has been studied in some detail (e.g., [105]), and linear single metal interactions (i), single metal oxygen interactions (ii), and bridged interactions (iii) have been suggested and investigated [105]:

[M—O—O]	[M⟨O〱O⟩]	[M—O—O—M]
(i)	(ii)	(iii)
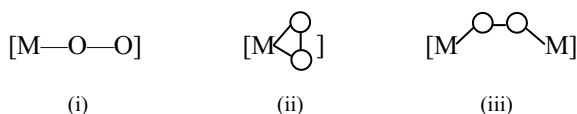
Obviously, the different types of interaction will lead to different kinetics and mechanisms, and different proportions of water to peroxide in the reaction product. Much has been written and speculated about these different interactions and the influence of metal d-orbital characteristics on the overall ORR. Reviews covering this aspect of the subject can be found in references such as [103] and [105]. On the whole, these conclusion can be drawn from the significant body of research on this topic: (a) Fe and Co macrocyclic complexes appear to constitute the best catalysts for oxygen reduction; (b) Ir complexes also appear to be quite active; (c) the redox potential for the metal ion couple plays a major role in dictating the activity of the ORR, with optimal redox potentials existing for maximum activity; (d) many of the non-noble metal catalysts lack the long-term stability needed for practical fuel cell applications; and (e) heat treatment of supported non-noble metal catalysts tends to increase both their activity towards oxygen reduction and their stability, but optimum heat treatments achieve the best "balance" of the two.

From the point-of-view of synthesizing these macrocyclic complexes, considerable research has been conducted and published over the past 40+ years. Going back to the early days of research on the phthalocyanine (Pc) complexes for

oxygen reduction, it was noted that the Pc components were insoluble in conventional solvents and water, so the catalysts were prepared by dissolving the chelates in concentrated H_2SO_4 then precipitating them onto a carbon substrate by the addition of water. Similar metal-organic chelates such as metal dibenzo-tetra-aza-annulene (MeTAA), metal tetraphenyl porphyrin (MeTPP), and its tetramethoxy derivative (MeTMPP), were discovered to have electrochemical activity [105], and were prepared on carbon supports by the impregnation method. Problems arose with the Me-N_4 chelates due to chemical attack by hydrogen peroxide generated during the ORR. The stability and activity could be improved by heating the chelates to 500–600 °C, and a number of theories have been advanced to explain these observations [103].

In 1989, the group of E. Yeager reported that the adsorption onto carbon of polyacrylonitrile (referred to as "pan") mixed with Co^{2+} or Fe^{2+} salts dissolved in dimethylformamide gave a catalyst for the ORR [106]. The material was pyrolyzed in argon at 800 °C and then used on a cathode catalyst in 85% phosphoric acid at 100 °C. A few years earlier, Yeager had published on the heat treatment of pyrrole-black polymer mixed with Co^{2+} or Fe^{2+} salts [107], and the catalytic activity for the ORR was believed to be due to the retention during pyrolysis of nitrogens of the pyrrole groups to bind the transition metal ions. Yeager and his group believed that the catalytic activity for the ORR in acid media was associated with the nitrogen precursor, the transition metal precursor, and the nature of the carbon support. The high-temperature heat treatment helps to generate nitrogen functionalities on the carbon support and reduce the metal ions to the metallic state. Upon contact with acid electrolyte, some of the metal atoms dissolve and catalytic sites develop. So, this approach was in contrast to the Me-N_4 chelate method discussed above whereby the metal and nitrogen components are part of the same precursor; instead, the metal and nitrogen belong to two different precursors. The Yeager method gave flexibility in catalyst preparation enabling the use of less expensive synthesis precursors.

In the ensuing 20+ years, much work has been done by many groups worldwide on these macrocycles as potential ORR electrocatalysts (see [103, 104]], and it has been confirmed and documented that the natures of the central metal atom (or ion) and the surrounding ligaments play crucial roles [108]. Much of that research has involved development of new synthesis methods and treatment procedures for these catalysts, which are prone to loss of catalytic activity with time and the generation of peroxide, given its associated chemical aggressiveness. While some of these novel catalysts have shown initial activities comparable to Pt, long-term performance is still the issue and until this is resolved (with, for example, optimum heat-treatment procedures), use of these novel materials in real operating fuel cell systems will not likely occur.

9.5.2 Methanol Tolerance and the Economics of these Catalysts

As stated at the beginning of this Section 9.5, a major driving force for the development of non-noble metal catalysts is the "lower-cost" factor (along with potential methanol tolerance in the case of the DMFC system). But even if the cost of large-scale synthesis of these non-Pt catalyst formulations in a fuel cell stable

form were extremely low (and this is certainly not guaranteed), there is still some question about just how "useful" they would be in an operating system. Gasteiger et al. raise this interesting question, namely that if the cathode catalyst were free, how much of it could one afford to use [109]? For example, if the catalytic activity was 1/100th that of Pt, one would need to use 100 times as much, which would be impractical from the point-of-view of fuel cell system volume, necessitating significant extra costs associated with additional membrane material, bipolar plates, and diffusion media (assuming that we cannot simply increase the catalyst layer thickness indefinitely because of diffusion limitations). Indeed, Gasteiger et al. suggest that the activity of a "cost-less" (i.e., free) cathode catalyst for automotive and light-duty applications would need to be no less than 1/10th of what could be achieved with current Pt catalyst technology. And of course, the non-noble metal chelate catalysts are not "free-of-charge" and have life-time expectancies "still-to-be-determined". Gasteiger et al. point out the vital need to obtain fuel cell performance data on "innovative catalyst systems" under conditions in which the data can be truly compared to an operating Pt catalyst system without the need for too many extrapolations and assumptions. They also stress that the performance of the Pt catalyst fuel cell system must be cited under true "state-of-the-art" catalytic activities, as opposed to those where detrimental conditions (such as Pt poisoning) influence results (and where such conditions can be handled by, e.g., electrode conditioning). By comparing the best results for non-noble metal ORR catalysts from the Dodelet [110–112] and Bron [113, 114] groups, to those for "standard" Pt catalysts, the conclusion is that the latter would still be superior to the former, even if the former catalysts were "free-of-charge". The non-noble metal ORR catalysts face serious durability issues, especially given that they are more prone to peroxide generation than their Pt counterparts (i.e., the 2-electron as opposed to the 4-electron reduction) [see 113, 114]. Indeed, the non-Pt ORR catalysts containing Fe are known to be catalytically attractive but the Fe can generate ferrous ions which are well known to convert hydrogen peroxide to peroxyl radicals [115]; these are highly aggressive to many materials, including Nafion. In light of the major activity and durability issues discussed above, further significant progress is needed before synthesized non-Pt-ORR catalysts can be usefully employed in real operating fuel cell systems, and this is not likely to occur for quite some time.

9.5.3 Transition Metal Chalcogenides

Another interesting class of ORR electrocatalysts that is attracting considerable attention are the non-Pt catalysts such as Ru-Mo chalcogenides (containing S, Te, or Se) or the simple Ru-Se compounds. While some noble metal is present, Pt itself is absent. Alonso-Vante was the first to show that Ru-based chalcogenides and chevrel-type phases (like Mo_4RuSe_8) show catalytic activity for the ORR in acid solutions and catalyze the 4-electron reduction to H_2O over the H_2O_2 route [116]. Indeed, the MoRuSe electrocatalysts generated only 3 to 4% H_2O_2 over the entire potential range for the ORR in acid electrolytes [117], thus demonstrating very high selectivity for the 4-electron ORR as opposed to the high degree of 2-electron reduction at pure Se electrodes. As well, these catalysts show high tolerance to

methanol oxidation, an important consideration for DMFC systems (see, e.g., [118]).

The RuMoSe compounds have chevrel phases [119] in which an octahedral cluster with six metal atoms is encased in a cube of chalcogens (see, e.g., [120]]. The molecular structures of these compounds, and their subsequent electronic properties, give the mixed metals (such as Ru/Mo) a high density of electronic d-states. This in turn gives rise to an abundant electron reservoir whereby the absorbed O_2 molecules can exchange electrons and be cathodically reduced to H_2O. These Ru-based chalcogenides are usually synthesized by solid-state reactions of the pure elements at temperatures ranging from 1200 to 1700 °C, and under high pressure [117, 121]. But this means that the synthesis procedures are complicated and therefore the compounds themselves are very expensive and probably not attractive for large-scale use. Low-temperature synthesis methods have been developed, the most prominent being either the thermolysis method or the colloidal method (see [122] and references therein for a related methodology, and also [123, 124]). In the thermolysis method, $Ru(CO)_{12}$ and elemental selenium, in either xylene or 1,2-dichlorobenzene as solvent, are refluxed at the boiling point in an inert atmosphere. Ru/Se catalysts can also be prepared through a thermochemical treatment, by the refluxing of colloidal Ru particles in Se-saturated xylene solvent. In this method, $RuCl_3$ dissolved in tetrahydrofuran is reduced via a reducing agent in ethanol and nanosized Ru particles are formed. These particles are further treated with aqueous selenious acid to give the Ru/Se catalyst. By modifying the colloidal synthesis procedure somewhat (impregnation/reduction method), the Ru/Se catalyst can be deposited on a porous carbon support for dispersion [125]. For the Ru/Se catalysts of the "carbonyl-tailored" types studied by Bron [126], the ORR activity increased with Se content, reaching a maximum at 15 mole%. As well, the amount of H_2O_2 generated at different reduction potentials decreased with addition of Se, this being especially true in the 0.6 to 0.7 V (NHE) potential range. Thus, the results are promising for such compounds, at least on the level of small-scale laboratory production and evaluation.

Based on the extensive research performed over the past 20 years, of which only a small fraction has been presented here, there is no doubt that real advances have been made in understanding the concept of electron reservoirs created in the chevrel-type cluster units for electrocatalysis of reactions like the ORR. The investigated catalytic materials are indeed novel, and seem to have the ability to provide coordination (through their catalytic centers) for oxygen reactivity and selectivity. They have certainly thrown light on the nature of the "complicated" ORR, and have provided researchers with a controlled system for the systematic investigation of this best known cathodic reaction.

9.5.4 Conclusions

Will such compounds (or even the macrocyclics discussed earlier) soon replace Pt as the FC catalytic material of choice? The answer is most probably "no", at least in the near future. Industry will go with what is tried and true, especially when long-term performance and reproducibly are paramount in such systems for "real-

world" applications. But this certainly does not mean that further research into these "novel" cathode formulations and their all-important synthesis procedures is not warranted. It may indeed be that some years down the road, such novel and specifically tailored electrocatalysts will replace Pt and its alloys. But until then, they will essentially remain very interesting materials for the fundamental investigations of students and researchers.

References

1. McKee DW, Norton JF. Catalytic exchange of methane and deuterium on platinum, ruthenium, and platinum-ruthenium alloys. J Phys Chem 1964;68(3):481.
2. Bock C, MacDougall B, LePage Y. Dependence of CH_3OH oxidation activity for a wide range of PtRu Alloys: detailed analysis and new views. J Electrochem Soc 2004;151(8):A1269.
3. Machida K, Fukuoka A, Ichikawa M, Enyio M. Preparation of platinum cluster-derived electrodes from metal carbonyl complexes and their electrocatalytic properties for anodic oxidation of methanol. J Electrochem Soc 1991;138:1958.
4. Dickinson AJ, Carrette LPL, Collins JA, Friedrich KA, Stimming U. Preparation of a Pt---Ru/C catalyst from carbonyl complexes for fuel cell applications. Electrochim Acta 2002;47:3733.
5. Longoni G, Chini P. Synthesis and chemical characterization of platinum carbonyl dianions $[Pt_3(CO)_6]_n^{2-}$ (n = ~10,6,5,4,3,2,1). A new series of inorganic oligomers. J Am Chem Soc 1976;98:7225.
6. Adams RD, Wu W. Adams RD, Wu W. Cluster synthesis. 41. New platinum-ruthenium cluster complexes from the reaction of diphenylacetylene $PhC{\equiv}CPh$ with $Pt_2Ru_4(CO)_{18}$. Synthesis and structural characterizations of $Pt_2Ru_3(CO)_8(\mu_3\text{-}\eta^2\text{-}PhC_2Ph)_2(\mu_4\text{-}\eta^2\text{-}PhC_2Ph)$, $Pt_3Ru_6(CO)14(\mu_3\text{-}\eta^2\text{-}PhC_2Ph)_3$, $Pt_2Ru_4(CO)14(\mu_3\text{-}\eta^2\text{-}PhC_2Ph)(\mu_4\text{-}\eta^2\text{-}PhC_2Ph)$, $Pt_3Ru_6(CO)_{18}(\mu_3\text{-}\eta^2\text{-}PhC_2Ph)_3$, and $PtRu_2(CO)_6(\mu_3\text{-}\eta^2\text{-}PhC_2Ph)(dppe)$. 1993, 12, 1248. Organometallics 1993;12:1248–56.
7. Alonso-Vante N. Carbonyl tailored electrocatalysts. Fuel Cells 2006;6:182.
8. Teranishi T, Hosoe M, Tanaka T, Miyake M. Size control of monodispersed Pt nanoparticles and their 2D organization by electrophoretic deposition. J Phys Chem B 1999;103:3818.
9. Watanabe M, Uchida M, Motoo S. Preparation of highly dispersed Pt + Ru alloy clusters and the activity for the electrooxidation of methanol. J Electroanal Chem 1987;229:395.
10. Petrow HG, Allen RJ, inventors; Protech Co, assignee. Finely particulated colloidal platinum compound and sol for producing the same, and method of preparation of fuel cell electrodes and the like employing the same. United States patent US4044193. 1977 Aug 23.
11. Ko IE. Sol-gel process. In: Ertl G, Knözinger H, Weitkamp J, editors. Preparation of solid catalysts. Weinheim: Wiley-VCH, 1999: 85–98.
12. Bronstein LM. Nanoparticles made in mesoporous solids. Top Curr Chem 2003;226:55.
13. McLeod EJ, Birss VI. Sol-gel derived WO_x and WO_x/Pt films for direct methanol fuel cell catalyst applications. Electrochim Acta 2005;51:684.
14. Marie J, Berthon-Gabry S, Achard P, Chatenet M, Pradourat A, Chainet E. Highly dispersed platinum on carbon aerogels as supported catalysts for PEM fuel cell-electrodes: comparison of two different synthesis paths. J Non-Cryst Solids 2004;350:88.

15. Cherstiouk OV, Simonov PA, Zaikovskii VI, Savinova ER. CO monolayer oxidation at Pt nanoparticles supported on glassy carbon electrodes. J Electroanal Chem 2003;554:241.

16. Maillard F, Eikerling M, Cherstiouk OV, Schreier S, Savinova E, Stimming U. Size effects on reactivity of Pt nanoparticles in CO monolayer oxidation: the role of surface mobility. Faraday Discuss 2004;125:357.

17. Liu H, Song C, Zhang L, Zhang J, Wang H, Wilkinson D, et al. A review of anode catalysis in the direct methanol fuel cell. J Power Sources 2006;155:95.

18. Gélin P, Primet M. Complete oxidation of methane at low temperature over noble metal based catalysts: a review. Appl Catal [2002];39:B1.

19. Rodriguez FJ, Sebastian PJ, Solorza O, Perez R. Mo–Ru–W chalcogenide electrodes prepared by chemical synthesis and screen printing for fuel cell applications. Int J Hydrogen Energy 1998;23:1031.

20. Spinacé EV, Neto AO, Linardi M. Electro-oxidation of ethanol on PtRu/C electrocatalysts prepared from $(\eta\text{-}C_2H_4)(Cl)Pt(\mu Cl)_2Ru(Cl)(\eta^3,\eta^3\text{-}C_{10}H_{16})$. J Power Sources 2003;124:426.

21. Zhang Y, Erkey C. Preparation of supported metallic nanoparticles using supercritical fluids: a review. J Supercrit Fluids 2006;38:252.

22. Pileni MP. Reverse micelles as microreactors. J Phys Chem 1993;97:6961.

23. Petit C, Pileni MP. Synthesis of cadmium sulfide in situ in reverse micelles and in hydrocarbon gels. J Phys Chem 1988;92:2282.

24. Courty A, Lisiecki I, Pileni MP. Vibration of self-organized silver nanocrystals. J Chem Phys 2002;116:8074.

25. Salzemann C, Lisiecki I, Urban J, Pileni MP. Anisotropic copper nanocrystals synthesized in a supersaturated medium: nanocrystal growth. Langmuir 2004;10:11772.

26. Salzemann C, Lisiecki I, Brioude A, Urban J, Pileni MP. Collections of copper nanocrystals characterized by different sizes and shapes: optical response of these nanoobjects. J Phys Chem B 2004;108:13242.

27. Xiong L, Manthiram A. Catalytic activity of Pt–Ru alloys synthesized by a microemulsion method in direct methanol fuel cells. Solid State Ionics 2005;176:385.

28. Godoi DRM, Perez J, Villullas HM. Influence of particle size on the properties of Pt–Ru/C catalysts prepared by a microemulsion method. J Electrochem Soc 2007;154:B474.

29. Eriksson S, Nylen U, Rojas S, Boutonnet M. Preparation of catalysts from microemulsions and their applications in heterogeneous catalysts. Appl Catal 2004;265:A207.

30. Uskoković V, Drofenik M. Reverse micelles: Inert nano-reactors or physioco-chemically active guides of the capped reactions. Adv Colloid Interface Sci 2007;133:23.

31. Lisieck I, Pileni MP. Synthesis of copper metallic clusters using reverse micelles as microreactors. J Am Chem Soc 1993;115:3887.

32. Kizling J. PhD dissertation. Stockholm: Royal Institute of Technology, 1991.

33. Shimazu K, Weisshaar D, Kuwana T. Electrochemical dispersion of Pt microparticles on glassy carbon electrodes. J Electroanal Chem 1987;223:223–34.

34. Zoval JV, Lee J, Gorer S, Penner RM. Electrochemical preparation of platinum nanocrystallites with size selectivity on basal plane oriented graphite surfaces. J Phys Chem B 1998;102:1166.

35. Lu G, Zangari G. Electrodeposition of platinum on highly oriented pyrolytic graphite. Part I: electrochemical characterization. J Phys Chem B 2005;109:7998.

36. Antoine O, Durand R. In situ electrochemical deposition of Pt nanoparticles on carbon and inside Nafion. Electrochem Solid-State Lett 2001;4:A55.

37. He Z, Chen J, Liu D, Tang H, Deng W, Kuang Y. Deposition and electrocatalytic properties of platinum nanoparticals on carbon nanotubes for methanol electrooxidation. Mater Chem Phys 2004;85:396.

38. Georgolios N, Jannakoudakis D, Karabinas P. Electrodeposition of pan-based carbon fibres. J Electroanal Chem 1989;264:235.

39. Hoster H, Iwasita T, Baumgartner H, Vielstich W. Pt–Ru model catalysts for anodic methanol oxidation: Influence of structure and composition on the reactivity. Phys Chem Chem Phys 2001;3(3):337.

40. Maillard F, Lu C-Q, Wieckowski A, Stimming U. Ru-decorated Pt surfaces as model fuel cell electrocatalysts for CO electrooxidation. J Phys Chem B 2005;109:16230.

41. Budevski E, Staikov G, Lorenz WJ. Fundamentals of electrocrystallization of metals. In: Electrochemical phase formation and growth. An introduction to the initial stages of metal deposition. New York: Wiley-VCH, 1996.

42. Greef R, Peat R, Peter LM, Pletcher D, Robinson J. Electrocrystallization. In: Kemp TJ, editor. Instrumental methods in electrochemistry. New York, Ellis Horwook Limited, 1985: 283–4.

43. Xue X, Liu C, Xing W, Lu T. Physical and electrochemical characterizations of PtRu/C catalysts by spray pyrolysis for electrocatalytic oxidation of methanol. J Electrochem Soc 2006;153:E79.

44. Patil PS. Versatility of chemical spray pyrolysis technique. Mater Chem Phys 1999;59:185.

45. Mueller R, Mädler L, Pratsinis SE. Nanoparticle synthesis at high production rates by flame spray pyrolysis. Chem Eng Sci 2003;58:1969.

46. Jairath R, Jain A, Tolles RD, Hampden-Smith MJ, Kodas TT. Introduction. In: Kodas T, Hampden-Smith M, editors. The chemistry of metal CVD. New York: Wiley-VCH, 1994: 28–30.

47. Huang SF, Chi Y, Bock C, MacDougall B, Carty A. Preparation of the Ru-Pt alloyed thin-films by chemical vapor deposition using single source precursor. Chem Vap Dep 2003;3:9.

48. Sivakumar P, Ishak R, Tricoli V. Novel Pt–Ru nanoparticles formed by vapour deposition as efficient electrocatalyst for methanol oxidation: Part I Preparation and physical characterization. Electrochim Acta 2005;50:3312.

49. Kodas TT, Hampden-Smith MJ. Overview of Metal CVD. In: Kodas T, Hampden-Smith M, editors. The chemistry of metal CVD. New York: Wiley-VCH, 1994: 432.

50. Antolini E, Salgado JRC, daSilva RM, Gonzalez ER. Preparation of carbon support binary Pt-M alloy catalysts (M=first row transition metals) by low/medium temperature methods. Mater Chem Phys 2007;101:395.

51. Harsha KSS. Thermal evaporation sources. In: Principles of physical vapor deposition of thin films. New York: Elsevier, 2006: 381–400.

52. Zhong D, Mishra B, Moore JJ, Madan A. Effect of pulsed plasma processing on controlling nanostructure and properties of thin film/coatings. Surf Eng 2004;20:19.

53. Denis MC, Lalande G, Guay D, Dodelet JP, Schulz R. High energy ball-milled Pt and Pt–Ru catalysts for polymer electrolyte fuel cells and their tolerance to CO. J Appl Electrochem 1999;29(8):951.

54. Lalande G, Denis MC, Guay D, Dodelet JP, Schulz R. Structural and surface characterizations of nanocrystalline Pt–Ru alloys prepared by high-energy ball-milling. J Alloys Compd 1999;292(1–2):301.

55. Denis MC, Gouerec P, Guay D, Dodelet JP, Lalande G, Schulz R. Improvement of the high energy ball-milling preparation procedure of CO tolerant Pt and Ru containing catalysts for polymer electrolyte fuel cells. J Appl Electrochem 2000;30(11):1243.

56. He C, Desai S, Brown G, Bollepalli S. PEM fuel cell catalysts: cost, performance, and durability. The Electrochemical Society Interface 2005; Fall:41–4.

57. Bregoli L. The influence of platinum crystallite size on the electrochemical reduction of oxygen in phosphoric acid. Electrochim Acta 1978;23:489.
58. Watanabe M, Sei H, Stonehardt P. The influence of platinum crystallite size on the electroreduction of oxygen. J Electroanal Chem 1989;261:375.
59. Kinoshita K. Particle size effects for oxygen reduction on highly dispersed platinum in acid electrolytes. J Electrochem Soc 1990;137(3):845.
60. Bock C, Birry L, MacDougall B. Manuscript in preparation.
61. Xue X, Bock C, MacDougall B. J Power Sources, to be submitted.
62. Turkevich J, Stevenson PC, Hillier J. A study of the nucleation and growth processes in the synthesis of colloidal gold. Disscuss Faraday Soc 1951;11:55.
63. Harriman A, Millward GR, Neta P, Richoux MC, Thomas JM. Interfacial electron-transfer reactions between platinum colloids and reducing radicals in aqueous solution. J Phys Chem 1988;92:1286.
64. Lide DR, editor. CRC handbook of chemistry and physics. 71st edition. Boston: CRC Press, 1990–1991.
65. Laine RM, Sellinger A, inventors; Canon KK, assignee. Preparation of supported nano-sized catalyst particles via a polyol process. United States Patent US6551960 B1, 2003 Apr 22.
66. Wang Y, Ren J, Deng K, Gui L, Tang Y. Preparation of tractable platinum, rhodium, and ruthenium nanoclusters with small particle size in organic media. Chem Mater 2000;12:1622.
67. Bock C, Paquet C, Couillard M, Button G, MacDougall B. Size selected synthesis of PtRu nano-catalysts and their application for organic electro-oxidation reactions. J Am Chem Soc 2004;126(25):8028.
68. Schmidt TJ, Noeske M, Gasteiger HA, Behm RJ, Britz P, Brijoux W, et al. Electrocatalytic activity of PtRu alloy colloids for CO and CO/H_2 electrooxidation: stripping voltammetry and rotating disk measurements. Langmuir 1997;13:2591.
69. Dubeau L, Coutanceau C, Garnier E, Leger JM, Lamy C. Electrooxidation of methanol at platinum–ruthenium catalysts prepared from colloidal precursors: atomic composition and temperature effects. J Appl Electrochem 2003;33:419.
70. Liu ZF, Ada ET, Shamsuzzoha M, Thompson GB, Nikles DE. Synthesis and activation of PtRu alloyed nanoparticles with controlled size and composition. Chem Mater 2006;18:4946.
71. Attard GS, Bartlett PN, Coleman NRB, Elliott JM, Owen JR, Wang JH. Mesoporous platinum films from lyotropic liquid crystalline phases. Science 1997;278:838.
72. Gollas B, Elliot JM, Bartlett PN. Electrodeposition and properties of nanostructured platinum films studied by quartz crystal impedance measurements at 10 MHz. Electrochim Acta 2000;45:3711.
73. Attard GS, Stephane A, Leclerc A, Maniquet S, Russell AE, Nandhakumar I, et al. Mesoporous Pt/Ru alloy from the hexagonal lyotropic liquid crystalline phase of a nonionic surfactant. Chem Mater 2001;13(5):1444.
74. Seidel YE, Lindstrom R, Jusyz Z, Cai J, Wiedwald U, Ziemann P, et al. Nanostructured Pt/GC model electrodes prepared by the deposition of metal-salt-loaded micelles. Langmuir 2007;23:5795.
75. Bartlett PN, Birkin PR, Ghanem MA. Electrochemical deposition of macroporous platinum, palladium and cobalt films using polystyrene latex sphere templates. Chem Commun 2000;17:1671.
76. C-Chien , Jeng CK-T. Noble metal fuel cell catalysts with nano-network structures. Mat Chem and Phys 2007;103:400.
77. Tracz A, Wegner G, Rabe JP. Scanning tunneling microscopy study of graphite oxidation in ozone-air mixtures. Langmuir 2003;19:6807.

78. Halvorsen H, Bock C, MacDougall B, Wang D. Potentiostatic deposition of platinum clusters onto freshly cleaved and ozone oxidized highly ordered pyrolytic graphite. J Electrochem Soc. Submitted 2008.

79. Cherstiouk OV, Simonov PA, Savinova ER. Model approach to evaluate particle size effects in electrocatalysis: preparation and properties of Pt nanoparticles supported on GC and HOPG. Electrochim Acta 2003;48:3851.

80. Teranishi T, Kurita R, Miyake M. Shape control of Pt nanoparticles. J Inorg Organomet Polym 2000;10:145.

81. Yoo JW, Lee S-M, Kim H-T, El-Sayed MA. Shape control of platinum nanoparticles by using different capping organic materials. Bull Korean Chem Soc 2004;25:395.

82. Petroski JM, Wang ZL, Green TC, El-Sayed MA. Kinetically controlled growth and shape formation mechanism of platinum nanoparticles. J Phys Chem B 1998;102:3316.

83. KingeS S, Bönnemann H. One-pot dual size- and shape selective synthesis of tetrahedral Pt nanoparticles. Appl Organomet Chem 2006;20:784.

84. Herricks T, Chen J, Xia Y. Polyol synthesis of platinum nanoparticles: control of morphology with sodium nitrate. Nano Lett 2004;4:2367.

85. Stonehardt P. Ber Bunsen-Ges Phys Chem 1990;94:913.

86. Luczak FJ, Landsman DA, inventors; Int Fuel Cells Corp, assignee. Ordered ternary fuel cell catalysts containing platinum and cobalt and method for making the catalysts. United States patent US4677092. 1987 Dec 23.

87. Mukerjee S, Srinivasan S. Enhanced electrocatalysis of oxygen reduction on platinum alloys in proton exchange membrane fuel cells. J Electroanal Chem 1993;357:201.

88. Toda T, Igarashi H, Watanabe M. Enhancement of the electrocatalytic O_2 reduction on Pt–Fe alloys. J Electroanal Chem 1999;460:258.

89. Chen G, Xia DG, Nie ZR, Wang ZY, Wang L, Zhang L, et al. Facile synthesis of Co-Pt hollow sphere electrocatalyst. Chem Mater 2007;19:1840.

90. Koh S, Strasser P. Electrocatalysis on bimetallic surfaces: modifying catalytic reactivity for oxygen reduction by voltammetric surface dealloying. J Am Chem Soc 2007;129:12624.

91. McNicol BD, Short RT. The influence of activation conditions on the performance of platinum/ruthenium methanol electro-oxidation catalysts surface enrichment phenomena. J Electroanal Chem 1977;81:249.

92. Ruban AV, Skriver HL, Norskov JK. Surface segregation energies in transition-metal alloys. Phys Rev B 1999;59(24):15990.

93. LePage Y, Bock C, Rodgers JR. Small step graphs of cell data versus composition for ccp solid-solution binary alloys: application to the (Pt,Ir), (Pt,Re) and (Pt,Ru) systems. J Alloys Compd 2006;422:164.

94. Colon-Mercado HR, Kim H, Popov BN. Durability study of Pt_3Ni_1 catalysts as cathode in PEM fuel cells. Electrochem Commun 2004;6:795.

95. Toshima N, Harada M, Yamazaki Y, Asakura K. Formation and growth of a ruthenium cluster in a Y zeolite supercage probed by xenon-129 NMR spectroscopy and xenon adsorption measurements. J Phys Chem 1992;96:9927.

96. Toshima N, Yonezawa T. Bimetallic nanoparticles—novel materials for chemical and physical applications. New J Chem 1998;22:1179.

97. Barbier J. Redox methods for preparation of bimetallic catalysts. In: Ertl G, Knözinger H, Weitkamp J, editors. Preparation of solid catalysts. Chichester: Wiley-VCH, 1999: 526.

98. Brankovic SR, Wang JX, Adzic RR. Metal monolayer deposition by replacement of metal adlayers on electrode surfaces. Surface Science Lett 2001;464:L173.

99. Stamenkovic VR, Mun BS, Arenz M, Mayhofer KJJ, Lucas CA, Wang G, et al. Trends in electrocatalysis on extended and nanoscale Pt-bimetallic alloy surfaces. Nat Mater 2007;6:241.

100. Stamenkovic VR, Fowler B, Mun BS, Wang G, Ross PN, Lucas CA, et al. Improved oxygen reduction activity on Pt$_3$Ni(111) via increased surface site availability. Science 2007;315:493.

101. Nashner MS, Frenkel AI, Adler DL, Shapley JR, Nuzzo RG. Structural characterization of carbon-supported platinum-ruthenium nanoparticles from the molecular cluster precursor PtRu$_5$C(CO)$_{16}$. J Am Chem Soc 1997;119:7760.

102. Jasinski R. A new fuel cell cathode catalyst. Nature 1964;201:1212.

103. Dodelet JP. Chapter 3. In: Zagal JH, Bedioni F, Dodelet JP, editors. N$_4$-macrocyclic metal complexes. New York: Springer, 2006:83–139.

104. Zagal JH, Paez MA, Silva SF. Chapter 2. In: Zagal JH, Bedioni F, Dodelet JP, editors. N$_4$-macrocyclic metal complexes. New York: Springer, 2006:41–82.

105. Jahnke H, Schonborn M, Zimmermann G. Organic dyestuffs as catalysts for fuel cells. Top Curr Chem 1976;61:133.

106. Gupta S, Tryk L, Bae D, Aldred I, Yeager WE. Heat-treated polyacrylonitrile-based catalysts for oxygen electroreduction. J Appl Electrochem 1989;19:19.

107. Gupta SL, Tryk D, Daroux M, Aldred W, Yeager E. In: Chin D, editor. Proceedings of the Symposium on Load Leveling and Energy Conservation in Industrial Processes. Pennington, NJ: The Electrochemical Society, 1986: 207.

108. Zagal JH. Chapter 37. In: Vielstich W, Lamm A, Gasteiger HA, editors. Handbook of fuel cells, Volume 2. London: Wiley, 2003: 544–54.

109. Gasteiger HA, Kocha SS, Sompalli B, Wagner FT. Activity benchmarks and requirements for Pt, Pt-alloy, and non-Pt oxygen reduction catalysts for PEMFCs. Appl Catal B 2005;56:9.

110. Jaoven F, Marcotte S, Dodelet JP, Lindbergh G. J Phys Chem B 2003;107:1376.

111. Faubert G, Cote R, Dodelet JP, Lefevre M, Bertrand P. Oxygen reduction catalysts for polymer electrolyte fuel cells from the pyrolysis of Fe^{II} acetate adsorbed on 3,4,9,10-perylenetetracarboxylic dianhydride. Electrochim Acta 1999;44:2589.

112. Lefevre M, Dodelet JP, Bertrand P. O$_2$ reduction in PEM fuel cells: activity and active site structural information for catalysts obtained by the pyrolysis at high temperature of Fe precursors. J Phys Chem B 2000;104:11238.

113. Bron M, Fiechter S, Bogdanoff P, Tributsch H. Fuel Cells: Fundam Syst 2002;2:137.

114. Bron M, Radnick J, Fieber M, Erdmann U, Bogdanoff P, Fiechter S. EXAFS, XPS and electrochemical studies on oxygen reduction catalysts obtained by heat treatment of iron phenanthroline complexes supported on high surface area carbon black. J Electroanal Chem 2002;535:113.

115. LaConti AB, Hamdan M, MacDonald RC. Chapter 49. In: Vielstich W, Lamm A, Gasteiger HA, editors. Handbook of fuel cells, Volume 3. London: Wiley, 2003: 647.

116. Alonso-Vante N, Tributsch A. Energy conversion catalysis using semiconducting transition metal cluster compounds. Nature (London) 1986;323:431.

117. Alonso-Vante N, Jaegermann W, Tributsch H, Houle W, Yvon K. Electrocatalysis of oxygen reduction by chalcogenides containing mixed transition metal clusters. J Amer Chem Soc 1987;109:3251.

118. Schmidt T, Paulus J, Gasteiger UA, Alonso-Vante HA, Behm NRJ. Oxygen reduction on Ru$_{1.92}$Mo$_{0.08}$SeO$_4$, Ru/carbon, and Pt/carbon in pure and methanol-containing electrolytes. J Electrochem Soc 2000;147:2620.

119. Chevrel R, Sergent M, Pringent J. Sur de nouvelles phases sulfurées ternaires du molybdène. J Solid State Chem 1971;3:515.

120. Alonso-Vante N. Chapter 36. In: Vielstich W, Lamm A, Gasteiger HA, editors. Handbook of fuel cells, Volume 2. London: Wiley, 2003: 534.

121. Zhang Y, Zhang L, Wilkinson J, Wang DPH. Progress in preparation of non-noble electrocatalysts for PEM fuel cell reactions. J Power Sources 2006;156:171.

122. Lee JW, Popov BN. Ruthenium-based electrocatalysts for oxygen reduction reaction – a review. J Solid State Electrochem 2007;11:1355.
123. Tributsch H, Bron M, Hilgendorff M, Schulenburg H, Dorbandt I, Eyert V, et al. Methanol-resistant cathodic oxygen reduction catalysts for methanol fuel cells. J Appl Electrochem 2001;31:739.
124. Liu L, Kim H, Lee J-W, Popov BN. Development of ruthenium-based catalysts for oxygen reduction reaction. J Electrochem Soc 2007;154:A123.
125. Zailovskii VI, Nagabhushana KS, Kriventsov VV, Cherepanova KN, Kvon RI, Bonnemann H, et al. Synthesis and structural characterization of Se-modified carbon-supported Ru nanoparticles for the oxygen reduction reaction. J Phys Chem B 2006: 110(13):6881–90; see also Zehl G, Dorbandt I, Schmithals G, Radnik J, Wippermann K, Richter B, et al. Preparation of carbon supported Ru-Se based catalysts and their electrochemical performance in DMFC cathodes. ECS Transactions 2006;3:1261.
126. Bron M, Bogdanoff P, Fiechter S, Dorbandt I, Hilgendorff M, Schulenburg H, et al. Influence of selenium on the catalytic properties of ruthenium-based cluster catalysts for oxygen reduction. J Electroanal Chem 2001;500:510.

10

Physical Characterization of Electrocatalysts

Shijun Liao, Baitao Li and Yingwei Li

10.1 Introduction

In recent years, fuel cells have attracted considerable attention due to their high energy efficiency with zero emissions [1]. Electrocatalysts are some of the key materials used in low-temperature fuel cells such as the polymer electrolyte membrane fuel cell (PEMFC) and the direct methanol fuel cell (DMFC). Creating high-performance catalysts is widely recognized as a key step for the further development and commercialization of low-temperature fuel cells.

The physical characterization of electrocatalysts is very important for several areas of research: (1) preparing new types of electrocatalysts with high activity and high selectivity, (2) recognizing electrocatalyst structures, and (3) investigating the mechanisms of catalysts and certain additives.

Electrocatalysts for application in low-temperature fuel cells (including PEMFCs and DMFCs) constitute a special type of heterogeneous catalyst. The most important difference between an electrocatalyst and a normal heterogeneous catalyst is that the former should have good conductivity, whereas most typical heterogeneous catalysts are insulators; therefore, most characterization techniques for electrocatalysts are the same as for regular heterogeneous catalysts, but some special techniques are required for electrocatalysts because of their conductivity .

For most PEM fuel cell catalysts, carbon black and other order carbon materials (such as carbon nanotubes) are usually used as support materials. These supports can give catalysts good electron conductivity, a very important feature in a fuel cell catalyst. Platinum and its alloys are popular active components, generally highly dispersed on the surface of support materials as micro- and nano-particles. Catalyst performance is related not only to the conductivity and supporting amounts of noble metals, but also, and more importantly, to the dispersion and composition of the active components. Because the hydrogen molecule is small and easily diffused in catalysts, in general the catalyst pore structure is not more important than the surface area.

Physical characterization of PEMFC catalysts includes measurement of the surface area, the electrochemical active surface area, the phase and composition of

active components, the particle size and size distribution of active components, the morphology and crystal planes, and other features.

10.2 Analysis of Composition and Phase of Catalyst

10.2.1 X-ray Diffraction (XRD) and Electron Diffraction (ED)

Principles
X-ray diffraction (XRD) is the most widely used technique to characterize materials. It is a non-destructive technique that reveals detailed information about the chemical composition and crystallographic structure of natural and manufactured materials.

X-rays were discovered by Wilhelm Conrad Röntgen in 1895. X-rays interact with electrons in matter and are scattered in various directions by these atomic electrons. If the scattering centers are separated by distances comparable to the wavelength of the X-rays, then interference between the X-rays scattered from particular electron centers can occur. For an ordered array of scattering centers this activity can give rise to interference maxima and minima.

Each crystalline substance has a characteristic arrangement of atoms which diffracts X-rays in a unique pattern. X-ray reflection takes place from lattice planes according to Bragg's Law:

$$n\lambda = 2d \sin \alpha \quad (n = 1,2,3,...)$$

where λ is the wavelength of the X-rays, d is the lattice spacing, α is the half-value of the diffraction angle, n is the order of the reflection and can be any whole number, and λ is determined by the type of X-ray tube; typical wavelengths used for X-ray experiments lie between 0.6 and 1.9 Å. Scanning a range of angles of reflection with a detector therefore gives a pattern of peaks with certain spacings and intensities. Planes going through areas with high electron density will reflect strongly whereas planes with low electron density will yield weak intensities.

Crystallography
About 95% of all solid materials can be described as crystalline. In crystallography, it is convenient to characterize a given crystal in terms of a set of planes. A real 3-dimensional crystal contains many sets of planes. The orientation and interplanar spacings of these planes are conventionally defined by the three integers *h*, *k*, and *l*, called Miller indices. These are determined by the points at which a given crystal plane intersects the three axes. Each plane can satisfy Bragg's Law and give a bright spot due to constructive interference. To account for all possible planes, Bragg's Law is usually rewritten (for a cubic system) as:

$$\frac{1}{d^2} = \frac{h^2 + k^2 + l^2}{a^2}$$

Therefore, by measuring the intensity and α angle, *d* can be calculated. If we can assign a set of (*h, k, l*) for a peak, then we can calculate the unit cell parameter according to Bragg's Law.

Mean Particle Size, Surface Area of Active Components
A perfect crystal would extend in all directions to infinity, so we can say that no crystal is perfect due to its limited size. Such a deviation from perfect crystallinity will lead to broadening of the diffraction peak. However, this type of peak broadening is negligible when the crystallite size is larger than 200 nm. Crystallite size is a measure of the size of a coherently diffracting domain. Due to the presence of polycrystalline diffracting domain aggregates, crystallite size may not be the same thing as particle size.

Scherrer first observed that small crystallite size could give rise to peak broadening. He derived a well-known equation for relating the crystallite size to the peak width, which is called the Scherrer formula:

$$t = K\lambda/(B \cos\alpha)$$

where t is the average dimension of crystallites; K is the Scherrer constant, a somewhat arbitrary value that falls in the range 0.87–1.0 (and is usually assumed to be 1); λ is the wavelength of the X-rays; and B is the integral breadth of a reflection (in radians 2α) located at 2α. B is often calculated relative to a reference solid (with crystallite size > 500 nm) added to the sample: $B^2 = B_s^2 - B_r^2$ (where B_s and B_r are peak widths of the sample and standard in radians).

Several factors could change XRD reflections, e.g., crystallite size, overlap of peaks, microstrain, lattice structure, and stacking faults.

Typical Example Analysis
XRD is a quick and essential method to determine catalyst stability by calculating the metal particle size. For example, alumina-supported Rh, Pt, and Pd catalysts exhibit good activity in the autothermal reforming of methane ($CH_4/H_2O/O_2/Ar$ = 40/30/20/10) [3]; however, Pd/Al_2O_3 easily loses its activity. This feature can be proven by XRD characterization. Figure 10.1 shows the XRD patterns for fresh and used catalysts, and Table 10.1 summarizes the average particle size. In Figure 10.1(a), the sharp peaks are assigned to gamma-alumina; no typical metal peak was observed due to the low metal loading (0.3 wt%) in the catalysts. In the case of Rh/Al_2O_3, Rh metal particles were highly dispersed on the used catalyst at the inlet as well as at the outlet. Very little aggregation of Pt was observed on the used catalyst at the outlet. However, the aggregation of Pd metal on the catalyst near the bed outlet was clearly observed; in fact, its initial methane conversion was 60%, which dropped to 55% after 4 hours of reaction. From thermogravimetric analysis (TGA) it is clear that almost no coke was deposited on the Rh/Al_2O_3 and Pt/Al_2O_3 catalysts; however, coke deposition was observed on Pd/Al_2O_3, as noted in Table 10.1.
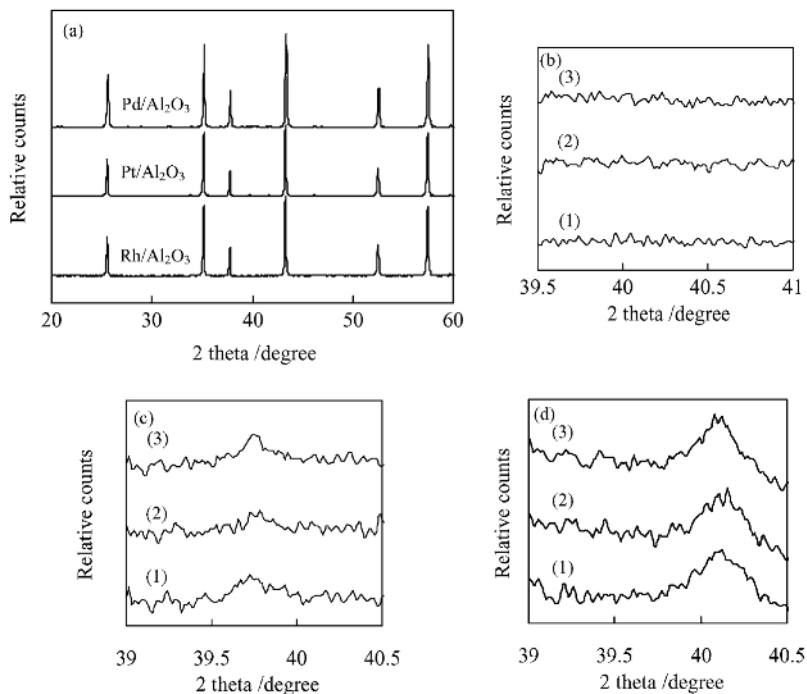
Figure 10.1. X-ray diffraction patterns of fresh and used catalysts: (a) fresh catalysts; (b) Rh/Al₂O₃; (c) Pt/Al₂O₃; (d) Pd/Al₂O₃. (1) fresh; (2) the used catalyst at the catalyst bed inlet; (3) the used catalyst at the catalyst bed outlet. Fresh: reduced in hydrogen flow at 1123 K. Used: reaction conditions of 1123 K, $CH_4/H_2O/O_2/Ar$ = 40/30/20/10, W/F = 0.40 gh mol^{-1}, 4 h [3]. (Reproduced from Applied Catalysis A – General, 275(1–2), Li BT, Maruyama K, Nurunnabi M, Kunimori K, Tomishige K, Temperature profiles of alumina-supported noble metal catalysts in autothermal reforming of methane, 157–72, 2004, with permission from Elsevier.)

It is well known that catalytic activity is strongly dependent on the shape, size, and distribution of the metal particles [6]. Furthermore, support also plays a vital role in the performance of a catalyst. Carbon is an excellent support in many ways: its high specific surface area is necessary for high metal loading; its pore structure is suitable for mass transfer; and its high conductivity of graphitization can reduce resistance in electron transportation. In research on catalyst structures, XRD has played an effective role in determining catalyst composition.

The rare noble metal Pt is the most commonly used metal in fuel cell catalysts. A Pt-based catalyst supported on carbon has both high intrinsic activity and great stability [7–10]. It is generally accepted that the catalytic activity of a Pt-based catalyst is highly dependent on the dispersion and the size distribution of the Pt crystallites [11, 12]. Therefore, much attention has been focused upon the preparation of highly dispersed Pt catalysts. Nanosized platinum particles dispersed on high-surface-area carbon substrates have been used as an electrocatalyst for both anode and cathode.

Table 10.1. Characterization of the catalysts [3, 74]. (From Applied Catalysis A – General, 275(1–2), Li BT, Maruyama K, Nurunnabi M, Kunimori K, Tomishige K, Temperature profiles of alumina-supported noble metal catalysts in autothermal reforming of methane, 157–72, 2004, with permission from Elsevier; and with permission from J Phys Chem B 2006;110:5343–50. Copyright 2006 American Chemical Society.)

Catalyst	Condition[a]	Position	Average particle size[b] (nm)	Amount of carbon deposition (mg/g-cat)
Rh/Al$_2$O$_3$	fresh		n.d.	—
	used	(inlet)	n.d.	0
	used	(outlet)	n.d.	0
Pt/Al$_2$O$_3$	fresh		10	—
	used	(inlet)	9	0
	used	(outlet)	14	0
Pd/Al$_2$O$_3$	fresh		30	—
	used	(inlet)	32	89
	used	(outlet)	42	171

[a]Sample weight: 0.1 g. Fresh: the catalyst was reduced in hydrogen flow at 1123 K. Used: reaction conditions of 1123 K, $CH_4/H_2O/O_2/Ar$ = 40/30/20/10, W/F = 0.40 gh mol^{-1}, 4 h.
[b]Calculated from Scherrer equation, using the half-width at half-height of the characteristic metal peak [4, 5].
[c]Carbon amount measured from TGA.
n.d. = not detected

A new microwave-assisted [13] polyol process was used to prepared platinum (Pt) and palladium (Pd) nanoparticles supported on Vulcan XC72 carbon. X-ray diffraction analysis showed (Figure 10.2) that the average particle sizes of Pt and Pd nanoparticles, which are uniformly dispersed on carbon, are 4 and 5 nm, respectively. The Pt/C and Pd/C catalysts exhibit four diffraction peaks that are indexed to the (1 1 1), (2 0 0), (2 2 0), and (3 1 1) planes of Pt and Pd, respectively. At 25 °C, the open circuit voltages for a single-stack test cell of a direct formic acid fuel cell using Pd/C and Pt/C catalysts are 0.74 and 0.685 V, respectively, while the corresponding peak power densities are 120 and 76.5 mWcm^{-2}. Preliminary data show that the Pd/C catalyst has a higher electrocatalytic activity for formic acid oxidation than the Pt/C catalyst.

On the other hand, carbon-supported Pt catalysts for the electrooxidation of formic acid are severely poisoned by the adsorbed CO intermediate of the reaction [14–16], although platinum is at present the best-known catalyst for the dissociative adsorption of small organic molecules. It has been demonstrated [17, 18] that PtRu and PtPd alloys can diminish this CO poisoning effect to some extent.
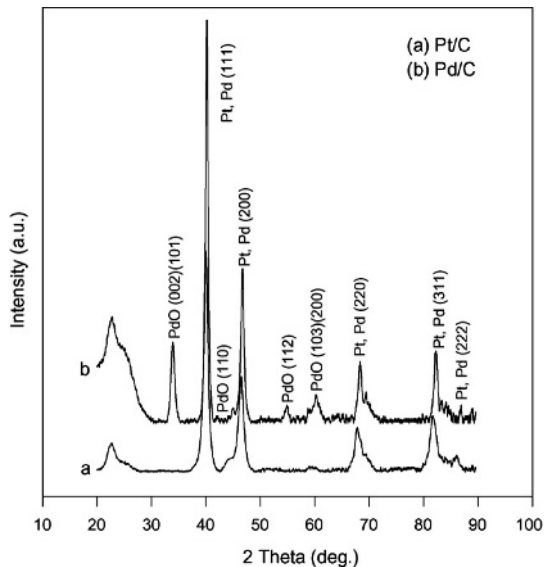
Figure 10.2. XRD patterns of microwave-synthesized Pt/C and Pd/C catalysts [13]. (Reproduced from Journal of Power Sources, 161(2), Liu ZL, Hong L, Tham MP, Lim TH, Jiang HX. Nanostructured Pt/C and Pd/C catalysts for direct formic acid fuel cells, 831–5, 2006, with permission from Elsevier.)

In PEMFCs, Pt-Co/C alloy catalysts show improved performance when used as cathode materials instead of Pt/C [19–22]. The enhancement of ORR activity observed for supported Pt-Co alloy electrocatalysts has been ascribed to both geometric factors (decrease of the Pt-Pt bond distance) and electronic factors (increase of Pt d-electron vacancy) [23, 24]. In direct ethanol fuel cells [25], a commercial carbon-supported Pt-Co (3:1) electrocatalyst has been investigated as a cathode material. The XRD patterns clearly show the five main characteristic peaks of the face-centered cubic (fcc) structure of crystalline Pt, namely, the planes (1 1 1), (2 0 0), (2 2 0), (3 1 1), and (2 2 2). The shift to higher angles of the Pt peaks in the Pt-Co electrocatalyst reveals alloy formation between Pt and Co, due to the incorporation of the base metal into the fcc structure of Pt. Furthermore, the lattice parameter of the Pt-Co/C (3:1) alloy electrocatalyst is in agreement with the lattice constant for the bulk Pt-Co (3:1) solid solution, indicating a high degree of alloying, which results in improved activity of the alloy for oxygen reduction.

Wang, Zhenbo et al. [26] studied the electrocatalytic activity of the Pt-Ru/C catalyst that was formed by thermal reduction with the acidic and alkaline $Pt(NH_3)_2(NO_2)_2$ solutions and the same acidic Ru compound as precursors. It was found that the XRD patterns (Figure 10.3) of the two catalysts showed Pt reflections for an fcc crystalline alloy structure. The catalyst prepared from the acidic $Pt(NH_3)_2(NO_2)_2$ as a precursor has a more homogeneous distribution of Pt-Ru metal particles on carbon. Its size is relatively small, about 3.7 nm. Its chemical composition is quite similar to the theoretical value of 1:1 (Pt:Ru). The catalyst prepared from the alkaline $Pt(NH_3)_2(NO_2)_2$ as a precursor has an uneven distribution of Pt-Ru particles on carbon, its size is relatively large, about 6.0 nm,

and the chemical composition of Pt and Ru was 6:4. The electrocatalytic activity of the two Pt-Ru/C catalysts was investigated in terms of the electrooxidation of methanol in H_2SO_4 solution. The peak current density from the cyclic voltammograms plot   showed that the Pt-Ru/C catalyst from   the acidic $Pt(NH_3)_2(NO_2)_2$ is 5.4 mA cm^{-2} higher than the catalyst from the alkaline solution. Therefore, the methanol electrooxidation performance of the Pt-Ru/C catalyst from the acidic $Pt(NH_3)_2(NO_2)_2$ solution is much better.
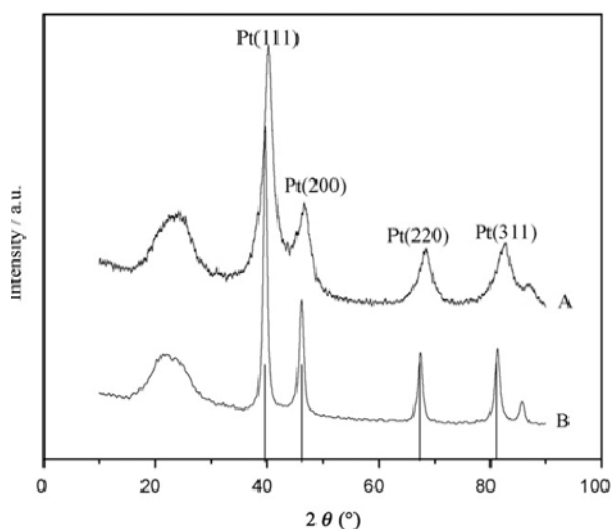
Figure 10.3. XRD patterns of Pt-Ru/C catalysts prepared from the acidic (A) and the alkaline (B) $Pt(NH_3)2(NO_2)_2$ as precursors [26]. (Reproduced from Journal of Power Sources, 163(2), Wang ZB, Yin GP, Shi PF. The influence of acidic and alkaline precursors on Pt Ru/C catalyst performance for a direct methanol fuel cell, 688–94, 2007, with permission from Elsevier.)

Recently,   several authors have explored ways to prepare mesoporous carbons that have a certain graphitic order, employing mesoporous silica materials as templates [27–32]. Pak et al. [33] investigated the effect of the graphitic character of ordered mesoporous carbons (OMCs) on the performances of OMC-supported catalysts for DMFCs. Two OMC samples with hexagonal mesostructure were prepared from phenanthrene and sucrose by the nanoreplication method, using mesoporous silica as a template (noted as POMC and SOMC, respectively). The average particle sizes of the catalysts estimated by the Debye-Scherrer equation were 2.7 and 2.5 nm for Pt/POMC and Pt/SOMC, respectively. The sizes of the Pt particles supported on OMCs were very small, considering that the metal content was as high as 60 wt%. Further structural characterizations revealed that both OMCs exhibited similar particle size, pore size, and high surface areas, whereas POMC exhibited a four-fold decrease in sheet resistance compared with SOMC, indicative of the higher electrical conductivity of POMC.

In addition, the pore diameter of the carbons could be controlled over a range of mesopore size by the use of an appropriate silica employed as a template [34].

It was found that the commercial colloidal silica TM-50 had the largest pore size. Thus, the catalyst Pt/TM-C has the finest particle size, and consequently it showed the best cell performance among the catalysts tested. In addition to the high surface area of the active metal, the large pore size of the Pt/TM-C appears to have a positive effect on the distribution of ionomer, resulting in easy formation of a triple-phase boundary.
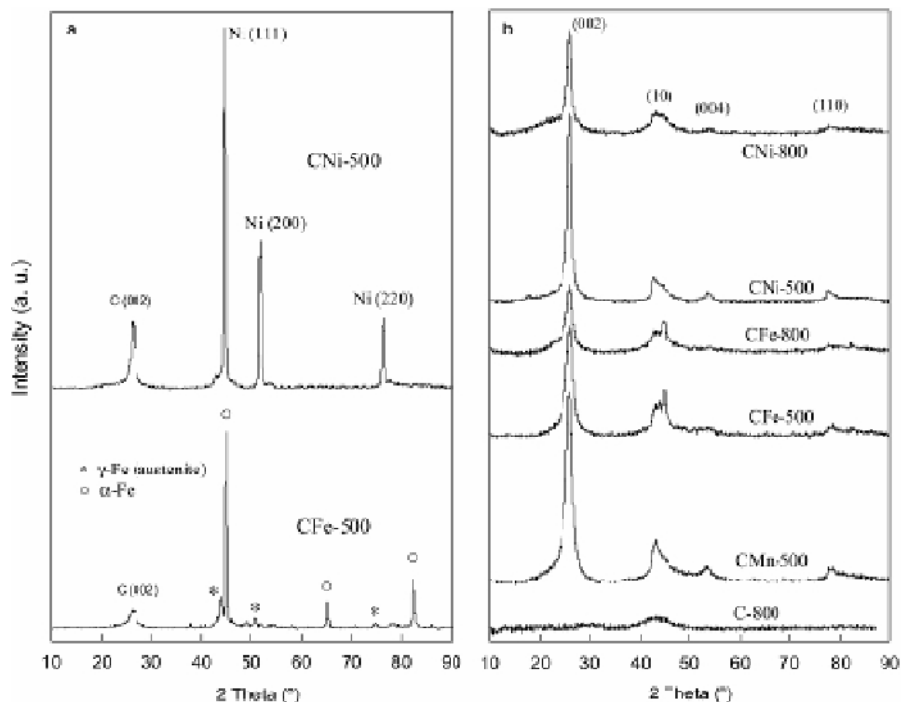
Figure 10.4. XRD patterns for the graphitized carbons (a) before and (b) after metal removal [35]. (Reproduced from Carbon, 44(3), Sevilla M, Fuertes AB. Catalytic graphitization of templated mesoporous carbons, 468–74, 2006, with permission from Elsevier.)

Fuertes et al. [35] reported a new synthetic strategy that is based on a combination of the template technique and the use of metal catalysts to create graphitic domains (catalytic graphitization). The XRD patterns in the wide-angle region were used to evaluate the graphitic nature of the synthesized carbon. The XRD spectra of the graphitized carbons are shown in Figure 10.4. As a reference, the XRD pattern of the non-graphitized C-800 (800 = temperature of carbonization) sample is also shown for reference. This sample does not exhibit any characteristic diffraction peak, which is consistent with an amorphous framework. In contrast, the graphitized materials exhibit intense XRD peaks at around 2 theta = 26°, 43°, 54°, and 78°, which can be assigned to the (0 0 2), (1 0 0), (0 0 4) and (1 1 0) diffractions of the graphitic framework, respectively. This shows that the graphitic structures were formed as a consequence of heat

treatment. The graphitization depends on the metal used as catalyst, and is greater for nickel than for iron and manganese. The porous characteristics of these materials change substantially with the temperature employed during the carbonization step. The graphitized carbons thus prepared exhibit electrical conductivities as high as 19.5 S cm^{-1}, up to two orders larger than those obtained with the non-graphitized samples.

Although carbon black-supported electrocatalysts have exhibited quite moderate performances on DMFCs so far [36], a new generation of electrocatalyst carbon supports, such as carbon spheres [37], graphite nanofibers [38], carbon nanohorns [39] and carbon nanotubes [40], are actively being sought and tested in the attempt to significantly improving membrane fuel cell performances. CNTs have been efficiently used as a support material for fuel cell catalysts (e.g., Pt and Pt-based alloys [41–47]). Compared to the typical carbon black electrocatalysts, the nanotube-supported platinum catalyst resulted in up to 140% improvement in efficiency for a proton exchange membrane (PEM) fuel cell [48]. A high catalytic performance for the oxygen reduction reaction and the methanol oxidation reaction has been reported. The possible reasons [49] are that the CNT-based catalysts could create special metal-support interactions, and have higher conductivity and lower organic impurities than the traditional carbon black-based ones. In particular, the experiments and theoretical calculations carried out by Britto et al. showed that a large number of defects in CNTs, such as pentagons at the nanotube tip and pentagon-heptagon defect pairs in the lattice and curvature, are beneficial to the oxygen reduction reaction [50].

Carbon nanotube-supported Pt-Ru (Pt-Ru/CNT) with a desired electrocatalyst composition has been successfully prepared [51]. It gave excellent single-cell DMFC performance with both anode and cathode electrocatalyst loadings at 4 mg cm^{-2}. At 60 °C, a power density of > 60 mW cm^{-2} at about 0.21 V was obtained. Figure 10.5(A) shows the XRD patterns of (a) acid-treated CNT and (b) Pt-Ru/CNT electrocatalysts. The acid-treated CNT exhibited characteristic diffraction peaks at $2\theta = 26.8°$, 43.1°, 53°, and 79°. The peaks attributed to the hexagonal graphite structures (0 0 2), (1 0 0), (0 0 4), and (1 1 0) of the multi-walled CNT have diminished or disappeared during the reductive deposition process, indicating the formation of Pt-Ru electrocatalyst on the CNT surfaces. The generated new diffraction peaks corresponded to Pt(1 1 1), Pt(2 0 0), Pt(2 2 0), and Pt(3 1 1) of the Pt-rich fcc phases. Further comparison with the XRD pattern of a Pt-Ru black standard, as shown in Figure 10.5(B), indicates that both do reveal similar characteristic peaks at the same positions, except for the remaining CNT signal at $2\theta = 26.8°$. This proves that the formation of electrocatalyst on the CNT surface by reductive deposition does indeed correspond to that of Pt-Ru. The absence of peaks for the Ru element in Pt-Ru/CNT can be attributed to the relatively small size of the Ru atom that is embedded in the Pt-Ru crystalline structure. The XRD pattern of the Pt-Ru/CNT matches perfectly well with that of the Pt-Ru black alloy reference, which directly proves the obtained Pt-Ru/CNT was an alloy catalyst. In addition, if the prepared catalyst was composed of independent Pt/Ru nanoparticles or a combination of the two, the distinctive peaks of the Ru element should appear in the XRD pattern. However, they did not. It was, therefore, concluded that the prepared Pt-Ru/CNT was indeed an alloy catalyst.
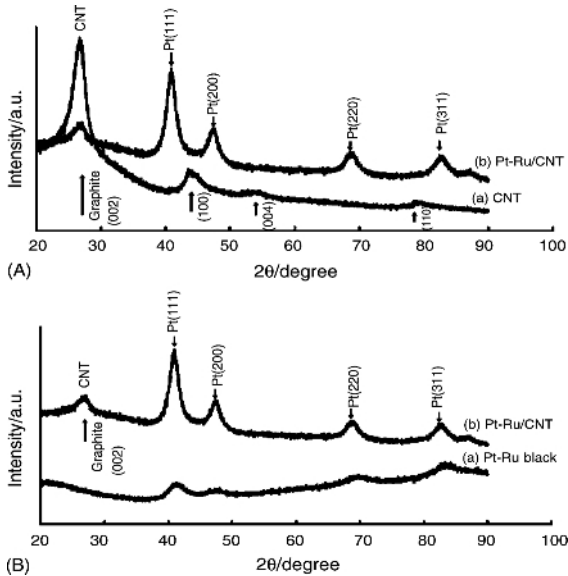
Figure 10.5. Comparison of XRD patterns: (A) shows that of (a) acid-treated CNT and (b) Pt-Ru/CNT; (B) shows that of (a) Pt-Ru black and (b) Pt-Ru/CNT [51]. (Reproduced from Journal of Power Sources, 160(1), Jeng KT, Chien CC, Hsu NY, Yen SC, Chiou SD, Lin SH, et al. Performance of direct methanol fuel cell using carbon nanotube-supported Pt-Ru anode catalyst with controlled composition, 97–104, 2006, with permission from Elsevier.)

Electron Diffraction (ED)
Electron diffraction is a collective elastic scattering phenomenon in which the electrons are scattered by atoms in a regular array or a crystal. Secondary waves are generated when an incoming plane electron wave interact with the atoms. Analogous to Huygens' principle for diffraction of light waves, the secondary waves interfere with each other, and diffraction patterns thus can be obtained.

Bragg's law can be employed to describe electron diffraction as it is used for XRD:

$$n\lambda = 2d\sin\Theta$$

Here d is the interplanar distance and can be calculated from ED patterns, because the wavelength λ of the electrons is known. Electron diffraction is a valuable tool in crystallography.

ED has three unique characteristics:

1. very strong reflection, because the wavelength of the electrons (e.g., 1.97 pm for 300 keV electrons) is much shorter than that of X-rays;
2. very small diffraction angles, generally in the range of 0–2°;
3. very strong interaction of electrons with samples, because the electrons are scattered by the positive potential inside the electron cloud, while X-rays interact with the electron cloud.
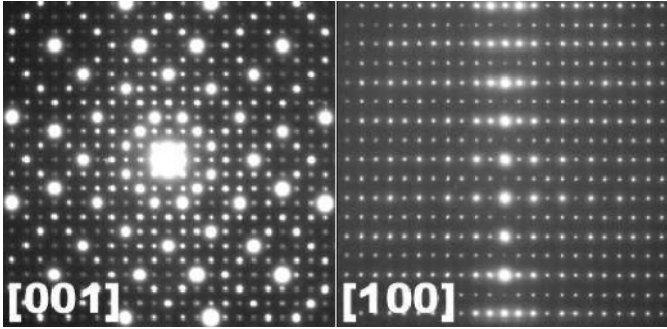
Figure 10.6. Electron diffraction patterns of Ta97Te60 along two perpendicular directions. The parameters of the tetragonal unit cell can be determined from these SAED patterns: a = 27.6, c = 20.6 Å [52]. (Reprinted with permission from Frank Krumeich, ETH Zurich.)

In recent years, electron diffraction has been used to characterize fuel cell catalysts, as information about the crystal symmetry of active components can be obtained from electron diffraction. Most of the electron diffraction for fuel cell catalysts is performed in a Transmission Electron Microscope (TEM), where the electrons pass through a thin film of the samples being studied. The resulting diffraction pattern is then observed on a fluorescent screen and recorded on photographic film or with a CCD camera.

10.2.2 X-ray Fluorescence (XRF), X-ray Emission (XRE), and Proton-induced X-ray Emission (PIXE)
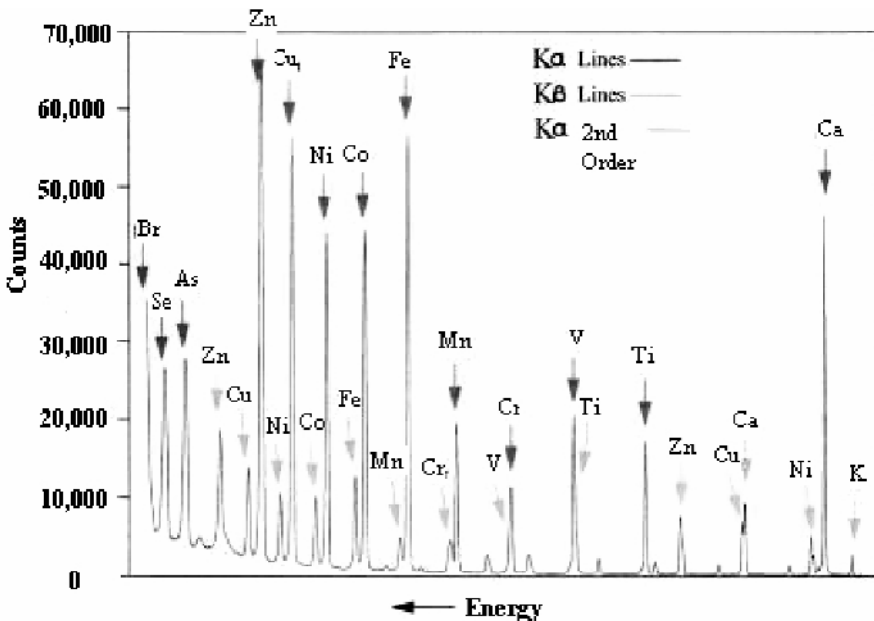
Figure 10.7. Typical wavelength dispersive XRF spectrum [53]

XRF, XRE, and PIXE are three related methods based upon similar principles. When a material is bombarded with high-energy X-rays or gamma rays, a secondary characteristic X-ray is then emitted. Currently, this characteristic X-ray is widely used for chemical analysis. For fuel cell catalysts, this is an ideal nondestructive method for analysing bulk composition, instead of traditional wet chemical methods and their automated successors like atomic absorption and atomic emission spectroscopy.

10.3 Measurement of Physical Surface Area and Electrochemical Active Surface Area

10.3.1 BET Method and Physical Surface Area

The surface area of solids has long been important in physical sciences, applied sciences, and environmental sciences, because this feature is capable of affecting the quality and utility of many materials. For this reason it is important to determine and control surface areas accurately. Likewise, knowledge of porosity and surface area are frequently important keys in understanding the structure, formation, and potential applications of different natural materials.

The most widely used and studied technique for estimating surface area is the so-called BET method, which stands for Brunauer, Emmett, and Teller, who published a paper in the Journal of the American Chemical Society in 1938 [54]. Their work allowed others to finally make sense of the adsorption of gases by a solid material with a complicated shape, and helped us interpret the relationship between surface area and adsorbed gas molecules. This method may seem complicated; however, its application is in fact quite straightforward and very easy to comprehend.

The BET method basically uses the surface of adsorbed gas molecules as a ruler. For example, take a nitrogen molecule. We know from other experiments that the area covered by a nitrogen molecule at liquid nitrogen temperature is 16.2 Å^2. Next, we need to figure out how many of these nitrogen molecules are required to completely cover the surface of the solid, so we expose the solid in a vacuum chamber to different amounts of a gas and measure the pressure in that chamber. We accept the important hypothesis that no more than one atom can occupy one site and the atoms do not interact with each other. The pressure will decrease as more and more gas molecules adsorb on the surface.

For different amounts of gas that have been added to the vacuum chamber, we find a certain amount of molecules that are in equilibrium and adsorbed on the surface. The result of the so-called adsorption and desorption isotherms is used to determine the amount of gas molecules adsorbed to a surface, according to the BET equation:

$$\frac{P}{V(P_0 - P)} = \frac{1}{V_m C} + \frac{(C-1)}{V_m C}\frac{P}{P_0}$$

where P is the equilibrium pressure, P_o the saturated vapor pressure, V the total volume of molecules added, and V_m the volume of gas molecules corresponding to the monolayer. From the experiment, a series of P and V can be obtained. Plotting $P/V(P_o-P)$ versus P/P_0 leads to a straight line. The slope and intercept of the line are $(C-1)/V_mC$ and $1/V_mC$, respectively, from which V_m can be obtained.

Nitrogen is used most often to measure BET surface, but if the surface area is very low, argon or krypton may be used, as both give a more sensitive measurement because of their lower saturation vapor pressures at liquid nitrogen temperature.

10.3.2 Electrochemical Hydrogen Adsorption/Desorption

The electrochemical active surface area (EASA) of fuel cell Pt-based catalysts could be measured by the electrochemical hydrogen adsorption/desorption method. For carbon supported Pt, Pt alloy, and other noble metals catalysts, the real surface area can be measured by the cyclic voltammetry method [55–59], which is based on the formation of a hydrogen monolayer electrochemically adsorbed on the catalyst's surface. Generally, the electrode for measurement is prepared by dropping catalyst ink on the surface of smooth platinum or glassy carbon substrate (e.g, a glassy carbon disk electrode or platinum disk electrode), followed by drying to form a catalyst film on the substrate. The catalyst ink is composed of catalyst powder, adhesive material (e.g., Nafion® solution), and solvent.

Figure 10.8 shows typical cyclic voltammograms of Pt/C and PtRu/C catalyst electrodes in 0.5 M H_2SO_4 solution. In the case of the Pt/C catalyst, two well-resolved peaks on the cathodic sweep at the low potentials area correspond to the hydrogen deposition on the electrode surface. The surface area can be calculated by the following equation [60–62]:

$$S_{ECSA} \ (m^2 \ g^{-1}) = \text{Charge area} \ (\mu C \ cm^{-2}) \ /[10 \times 210 \ (\mu C \ cm^{-2})$$
$$\times \text{Catalyst loading} \ (mg \ cm^{-2})] \qquad (10.1)$$

where S_{ECSA} is the active surface area of the catalyst and 210 is the ratio of electron amount to the active surface area, $\mu C.cm^{-2}$.

It should be noted that the hydrogen peaks are only observed for a very pure, clean Pt catalyst in acidic background solution. If the catalyst were modified with additives, the peaks would change or not even appear. Nonetheless, for most modified Pt/C catalysts the peaks are still suitable for estimating the active surface areas of catalysts. For PtRu/C and PtRuIr/C catalysts (as two examples), the estimated surface areas are very important in elucidating the catalysts' performance and properties.

Thus, the hydrogen peaks can be used not only to measure the active surface area of a catalyst but also to qualitatively estimate the "clearness" of a Pt/C catalyst.

The roughness factor is an important parameter in describing the dispersion and porous structure of the active components of a fuel cell catalyst. It is defined as:

$$fr = Ar/Ag \qquad (10.2)$$

where *A*r is the *real surface area* of the catalyst film measured by the electrochemical method, and *A*g is the *geometric surface area* of the substrate electrode (glassy carbon disk).
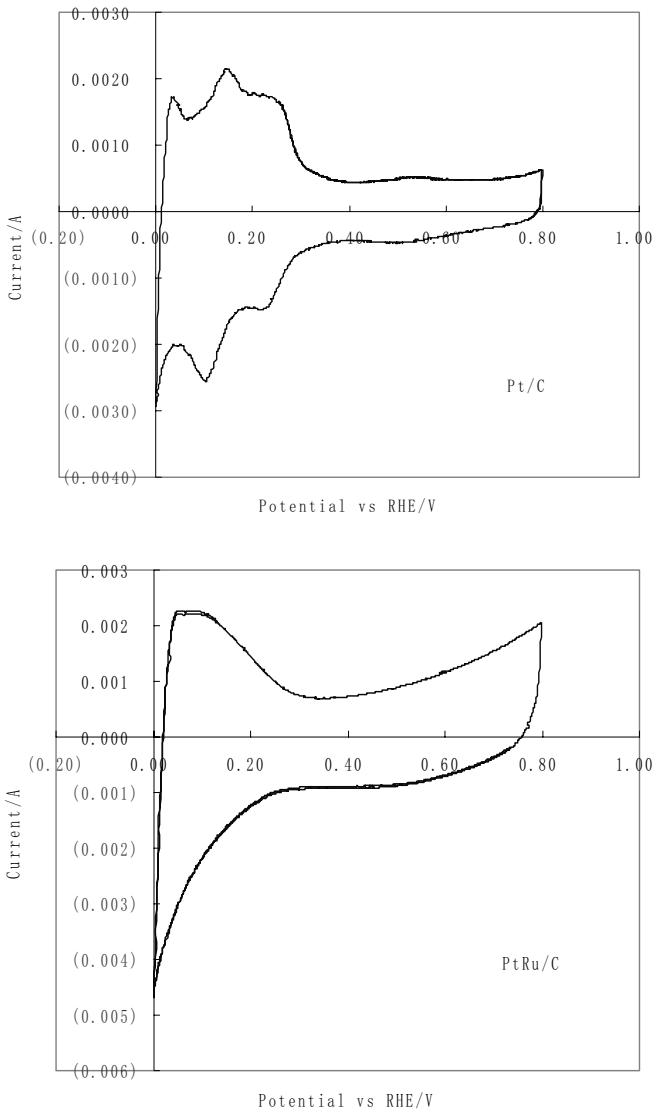
Figure 10.8. Cyclic voltammograms of Pt/C and PtRu/C catalyst electrodes in 0.5 M H_2SO_4 solution.

For a carbon black-supported platinum catalyst, the roughness factor can be very high (1 to 10^5), depending on the dispersion of the active components and their microstructure.

10.3.3 Typical Examples Analysis

Due to their excellent power density and good energy conversion efficiency, polymer electrolyte fuel cells (PEFCs) are promising candidates for transportation, as well as portable and stationary power systems [63]. In recent years, extensive research has been done on the oxygen reduction reaction on platinum at solid polymer electrolyte interfaces [64, 65]. Nafion is often used as the electrolyte in low-temperature fuel cell systems, as it enables the porous catalyzed carbon to be integrated into the electrolyte by extending the three-dimensional reaction zone [66, 67].

To make PEFCs a commercial reality, cost is a very important issue [68]. Many studies have dealt with the optimization of Nafion in the electrode structure [69]. Giorgi et al. [70] investigated the effect of Nafion loading in the catalyst layer of cathodes for PEFCs (Figure 10.9). The electrochemically active surface as a function of Nafion content in the electrode goes through a maximum at 0.67 mg cm^{-2}. A Nafion-less pore means a lack of protons on the catalytic sites and, as a consequence, a low oxygen concentration. An increase in Nafion concentration allows an increase in oxygen concentration and ionic portion, but if the polymer layer is too thick inside the pores it limits mass transport by retarding the access of gas to active sites. The optimal Nafion loading (0.67 mg cm^{-2}) minimizes charge transfer resistance, as well as ionic and gas transport limitations.
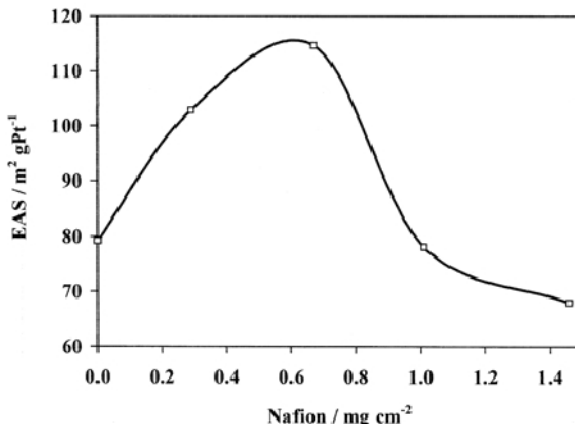
Figure 10.9. Electrochemically active surface (EAS) from cyclic voltammetry as a function of Nafion content in the catalytic layer (20 wt% PTFE/C in diffusion layer, 0.2 mg Pt cm^{-2} in catalyst layer) [70]. (Reproduced from Journal of Power Sources, 77(2), Antolini E, Giorgi L, Pozio A, Passalacqua E. Influence of Nafion loading in the catalyst layer of gas-diffusion electrodes for PEFC, 136–42, 1999, with permission from Elsevier.)

The preparation method [71, 72], such as what reducing agents are used, is another factor that affects the electrochemical active surface area. Liao et al. [73] prepared PtMoSi/C nanocatalysts by chemical reduction using formaldehyde, H_2, and hydrazine as reducing agents. They found that the EASA of a catalyst prepared using formaldehyde (28.4 m^2g^{-1}) is higher than the EASA of one prepared from

hydrogen (21.9 m^2g^{-1}) and hydrazine (21.6 m^2g^{-1}). It was also found that the catalyst with $n_{Pt}:n_{Mo}$ = 3:1 showed higher electrocatalytic activity and better tolerance to poisoning species in methanol oxidation than the commercial catalysts, which could be ascribed to the high dispersion of Pt nanoparticles on the carbon by the addition of silicomolybdic acid.

Table 10.2. Surface area (m^2g^{-1}) of MWCNTs with different tube diameters before and after oxidation treatment [74]. (Reprinted with permission from J Phys Chem B 2006;110:5343–50. Copyright 2006 American Chemical Society.)

MWCNTs	As-received	H_2SO_4/HNO_3	H_2SO_4/H_2O_2
⟨ 10 nm		310.5	
20–40 nm	88.6	86.4	92.4
40–60 nm		41.0	

Table 10.3. Average crystallite size of Pt nanoparticles, electrochemically active area (EAA), peak current density, and mass activity for the methanol oxidation reaction of various Pt/MWCNT nanocomposite catalysts. The average size of Pt nanoparticles was obtained by XRD analysis [84]. (Reproduced from Journal of Power Sources, 161(2), Travitsky N, Ripenbein T, Golodnitsky D, Rosenberg Y, Burshtein L, Peled E. Pt-, PtNi- and PtCo-supported catalysts for oxygen reduction in PEM fuel cells, 782–9, 2006, with permission from Elsevier.)

Pt/MWCNT catalysts	Pt particle size (nm)	Q_H (mC.cm^{-2})	EAA (m^2.g^{-1})	Peak current density at 0.68 V (mA.cm^{-2})	Mass activity at 0.68 V (A.g^{-1})
As-received MWCNTs	4.2	15.5	31.3	50.5	214.9
MWCNTs by H_2SO_4/H_2O_2	3.5	21.3	43.0	64.0	272.3
MWCNTs by H_2SO_4/HNO_3	2.9	27.5	51.4	90.3	384.3
Pt/MWCNTs-60s	4.0	18.8	38.1	61.6	262.1
Pt/MWCNTs-80s	3.8	21.6	43.7	71.7	305.2
Pt/MWCNTs-100s	2.9	27.5	51.4	90.3	384.3
Pt/MWCNTs-120s	13.7	12.5	25.4	40	170.2
Pt/MWCNTs-10 nm	2.9	31.7	64.3	101.0	429.8
Pt/MWCNTs-30 nm	2.9	27.5	51.4	90.3	384.3
Pt/MWCNTs-50 nm	4.4	24.1	48.8	74.5	317.0
E-TEK 40% Pt/C	n.a.	20.5	41.5	69.1	294.4

Jiang et al. [74] synthesized Pt electrocatalysts supported on multiwalled carbon nanotube (Pt/MWCNT) nanocomposites by a rapid intermittent microwave irradiation (IMI) technique for PEFCs and DMFCs. They found that Pt particle size and distribution on the MWCNT support are affected significantly by the oxidation treatment of MWCNTs, the IMI procedure, and the MWCNT tube diameter or surface area. The Pt/MWCNTs prepared with MWCNTs treated by H_2SO_4/H_2O_2 and H_2SO_4/HNO_3 oxidation treatment have a much better distribution and smaller sized Pt particles than those prepared without oxidation treatment (by TEM micrographs). As shown in Table 10.2, the specific surface area of the MWCNTs does not change significantly with the acid oxidation treatment. This indicates that the treatment would primarily enhance the functionality or defects of the MWCNTs. Table 10.3 shows that for Pt supported on as-received MWCNTs, the EAA is 31.3 m^2g^{-1}, and for Pt supported on H_2SO_4/H_2O_2- and H_2SO_4/HNO_3-treated MWCNTs, the EAAs are 43.0 and 51.4 m^2g^{-1}, respectively. Pt/MWCNTs synthesized with H_2SO_4/HNO_3-treated MWCNTs have the highest electrochemically active surface area, most likely due to the uniform distribution and small size of the Pt nanoparticles in comparison to those in a commercial Pt/C catalyst.

In addition, Shen et al. [75] prepared a novel three-dimensional electrode using polypyrrole (Ppy) and polystyrene spheres (PS) covered by a platinum catalyst instead of the conventional gas diffusion electrode, in order to reduce the sealing effect in liquid fuel cells. This new type of porous structured electrode allows liquid alcohol to penetrate the catalyst layer quite easily. The approach results in an increased active surface area for electrochemical reactions. The electrochemical active areas of platinum in Pt/Ppy/PS electrodes and E-TEK Pt/C electrodes, calculated by cyclic voltammograms [76, 77], are 4.5 and 23.6 cm^2g^{-1}, respectively, indicating a larger EAS for the three-dimensional electrode. Preliminary studies show an improved performance for methanol oxidation on a three-dimensional electrode as compared with a conventionally prepared electrode with the same platinum loading.

On the other hand, in recent years preparation on ordered mesoporous carbons has generated considerable research interest [78–81] because of their prominent characteristics, such as high surface area, relatively uniform pore size, and ordered pore structure. Zhao et al. [82] synthesized ordered graphitic mesoporous carbon, prepared by the chemical vapor deposition (CVD) of benzene in the pores of a mesoporous SBA-15 pure-silica template without loading any catalytic species. By controlling CVD time, one can avoid the formation of a dense carbon layer on the external surfaces of the template particles. The slightly lower BET surface area, pore volume, and pore size of carbon samples at CVD time of 2 h (C-2) as compared with a CVD time of 1h (C-1) may suggest that the longer CVD time brought more carbon into the pore channels or onto the external surface of the silica template. The electrochemical properties were also evaluated on the Pt/C-1, Pt/C-2, and Pt/C (E-TEK). Figure 10.10(a) shows the cyclic voltammograms of three catalysts in 0.5 M H_2SO_4. The electrochemical surface area for Pt/C-1 and Pt/C-2 is smaller than that for Pt/C (E-TEK). Because of the smaller Pt particle size and higher graphitic crystallinity of Pt/C (E-TEK), its mass activity (35 mA/cm^2) for room-temperature methanol oxidation is higher than that of Pt/C-1 (19

mA/cm^2) and Pt/C-2 (15 mA/cm^2). However, Pt/C-1 and Pt/C-2 displayed a higher specific activity than Pt/C (E-TEK), as can be seen in Figure 10.10(b). The presence of ordered mesopores of carbon supports C-1 and C-2 may also contribute to this higher specific activity because of the easy transport of methanol and oxidation products through these ordered pores.
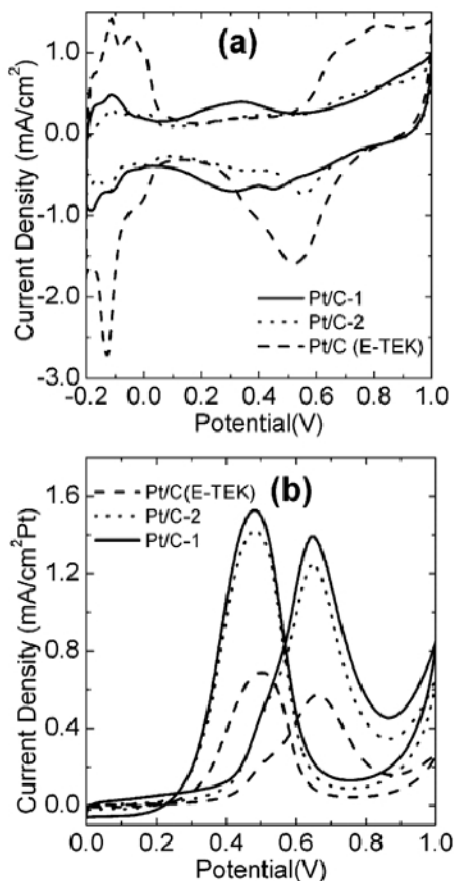
Figure 10.10. Cyclic voltammograms of Pt/C-1, Pt/C-2, and Pt/C (E-TEK) catalysts, measured at a scan rate of 20 mV s^{-1} at room temperature in electrolytes of (a) 0.5 M H$_2$SO$_4$ and (b) 1 M CH$_3$OH + 0.5 M H$_2$SO$_4$ [82]. (Reprinted with permission from Chem Mater 2005;17:3960–7. Copyright 2005 American Chemical Society.)

Although the most widely used supporting material for fuel cell catalysts is high-surface-area carbon (such as Vulcan® XC72), at elevated temperatures the carbon-to-catalyst contact burns. It has been found that the platinum particles are able to catalyze the combustion of the carbon support even at moderate temperatures (125–195 °C) [83]. In order to avoid these problems, some have tried to synthesize Pt catalysts supported on silica. Peled et al. have synthesized and characterized carbon- and silica-supported PtNi and PtCo catalysts via the same

electroless-deposition route [84]. Silica- and carbon-supported platinum and platinum-alloy catalysts were synthesized by a classic three-step electroless deposition method. As shown in Table 10.4, the PtNi- and the PtCo-supported catalysts have a smaller crystal size (as low as 2.2 nm) and larger electrochemical surface area (up to 57 m^2g^{-1}) than pure Pt-supported catalysts. SiO_2-supported powders have larger grains and lower ECSAs than the carbon-supported catalysts. This is due to the higher degree of agglomeration on their surface, which is attributed to the strong interaction of the metal particles with the silica support. The ECSAs of carbon-supported catalysts increased by 100% when alloyed with cobalt, and by more than 200% in the case of nickel. The enhancement of the ECSAs of the SiO_2-supported powders was comparable to the decrease in the grain size.

Table 10.4. Effect of alloying on Pt catalyst grain size and ECSA. [a] Weight percent of the metals is calculated from reagent concentrations. [b] Pure metal lattice parameters: $a_0(Pt) = 3.9231$ Å; $a_0(Ni) = 3.5238$ Å; $a_0(Co) = 3.5447$ Å [144]. (Reproduced from Journal of Electroanalytical Chemistry, 504(1), Shukla AK, Neergat M, Bera P, Jayaram V, Hegde MS. An XPS study on binary and ternary alloys of transition metals with platinized carbon and its bearing upon oxygen electroreduction in direct methanol fuel cells, 111–9, 2001, with permission from Elsevier.)

Catalyst code	Catalyst composition by EDS[a]	Grain size	Maximal ECSA [$m^2 g^{-1}$]	Lattice parameters[b] [Å]
BN5	Pt 65%/XC72	4.3	18	3.9151
BN13	$Pt_{51}Ni_{49}$ 65%/XC72	2.2	57	3.8486
BN15	$Pt_{48}Co_{52}$ 65%/XC72	2.7	32	3.8732
BT9	Pt 93%/SiO_2	5.8	3	3.9182
BT14	$Pt_{45}Ni_{55}$ 85%/SiO_2	3.2	6	3.8204
BT15	$Pt_{72}Co_{28}$ 85%/SiO_2	3.7	5	3.8767

10.4 Morphology of Catalysts and Their Active Components

Electron microscopes use a beam of highly energetic electrons to examine objects on a very fine scale. This examination can provide information on topography, morphology, and composition.

10.4.1 Scanning Electron Microscopy (SEM)

The Scanning Electron Microscope (SEM) is the premiere instrument in the generation of topographical images and elemental information, due to its superb resolution. The SEM uses light with a wavelength of 0.12 Angstroms, resulting in a resolution limit of 1 million diameters magnification of 10x to 10,000x with virtually unlimited depth of field.

The SEM uses a beam of electrons to scan the surface of a sample and build a three-dimensional image of the specimen. Electrons are generated in the electron gun. The most commonly used is a tungsten-hairpin gun in which a tungsten

filament serves as the source of electrons. By applying a current through the filament, the tungsten wire heats up and electrons are emitted. When the electron beam hits the sample, the interaction between the beam electrons from the filament and the sample atoms generates a variety of signals. Depending on the sample, these signals can include secondary electrons (electrons from the sample itself), backscattered electrons (beam electrons from the filament that bounce off the nuclei of atoms in the sample), X-rays, light, heat, and even transmitted electrons (beam electrons that pass through the sample). The secondary electron detector will detect low-energy electrons produced near the surface of the specimen, providing a predominantly topographical image. The back-scattered electron detector will detect high-energy electrons that have been scattered backward, and provide information about the differences in atomic number within a sample. The SEM's primary imaging method operates through the collection of those secondary electrons that are released by the sample.

Secondary Electron Imaging (SEI) works on the principle that this electron beam generates a "splash" of electrons with kinetic energies much lower than those of the primary incident electrons. Because of these "secondary" electrons' low energies and low penetration depth, their detection as a function of primary beam position makes it possible to attain high magnifications (as much as 100,000x in some cases) and high resolutions (up to ~40 Å resolution) without extensive sample preparation or damaging the sample. These secondary electrons are detected by a scintillation material, which is a radiation detector that produces flashes of light from the electrons. The light flashes are then detected and amplified by a photomultiplier tube.

Unlike the light microscope, in which light forms an instant "real image" of the specimen, the electrons in an SEM do not form a real image. Instead, the SEM scans its electron beam line by line over the sample. This is much like using a flashlight in a dark room to scan the room from side to side. A fast scan, which takes a couple of seconds, can generate a very grainy image. A slow scan produces a clear, sharp image but takes a minute or two to complete.

An SEM system with the various detectors can provide high-resolution imaging, quantitative elemental analysis of the "bulk" material, and fast elemental mapping, as well as other benefits.

10.4.2 Transmission Electron Microscopy

The Transmission Electron Microscope (TEM) was the first type of electron microscope to be developed and is patterned exactly on the Light Transmission Microscope, except that a focused beam of electrons is used instead of light to "see through" the specimen. It was developed by Max Knoll and Ernst Ruska in Germany in 1932, 35 years after J. J. Thompson's discovery of the electron. The technique quickly surpassed the resolution of optical microscopy, and in 1938 the first commercial instruments began to be produced by the Siemens-Halske Company in Berlin [85].

Using an electron microscope offers the advantages of increased magnification and resolution. The TEM passes an accelerated electron beam through a thin sample (50–300 Å). Some of the electrons are scattered by the atoms in the sample.

A phase distortion is created, resulting in a phase contrast that is used to create the image. The TEM enables the operator to see the "inside" of the sample rather than the surface.

The much lower wavelength of electrons makes it possible to achieve a resolution a thousand times better than that of a light microscope. However, in a TEM, in contrast to a light microscope, there is no change in the refractive index of the medium when the illumination beam is deflected; the vacuum in the lens is the same as the vacuum in the column. Deflection in a TEM is due to the electromagnetic properties of the lens, which are defined by electromagnetic plates that are only able to influence the path of the electrons, since all of the electrons carry a negative charge. The plates have a similar function to the glass lenses in a light microscope, in that they produce a deviation in the trajectory of the electrons from a point source, which causes them to converge at a single focal point. In this way, the electron beam is focused precisely. The TEM builds an image by way of differential contrast. Those electrons that pass through the sample go on to form the image, while those that are stopped or deflected by dense atoms in the specimen are subtracted from the image. In this way a black and white image is formed.

The main use of the Transmission Electron Microscope is to examine the structure, composition, or properties of a specimen in submicroscopic detail. One can see objects to the order of a few Angstroms (10^{-10} m). For example, it is possible to study small details in a cell or within inorganic materials down to near-atomic levels. The possibility for high magnifications has made the TEM a valuable tool in numerous fields such as biological, medical, and materials research.

10.4.3 Typical Examples

Catalytic activity is closely dependent on the method of preparation, so considerable attention has been focused upon new preparation methods to improve the performance of carbon-supported platinum alloy catalysts in DMFC applications. The simultaneous reduction of metal salts [86–88], microwave-assisted reactions [89, 90], micro-emulsion-based synthesis [91–93], and the reduction of single-source molecular precursors [94–99] have been used to various extents.

Platinum electrocatalysts are dispersed as small particles on high surface area conductive supports for effective use of costly Pt. The size of platinum particles, therefore, plays an important role in the oxygen reduction kinetics for fuel cell applications, in terms of both electrocatalytic activity and practical application of catalysts. Carbon-supported platinum shows a large surface area and increased catalytic activity. Alloy catalysts with various transition metals have been employed to increase the catalytic activity and reduce the cost. Various Pt-based alloy catalysts (binary, ternary, and quaternary alloy) have been tested over the last two decades. Many researchers have reported that Pt-based alloy catalysts show not only higher activity than Pt alone, but also exhibit good performance in the ORRs in PEFCs and DMFCs [100–108].

Supported PtRu alloys are so far considered the best anodic materials for DMFC [109, 110]. It is well known that the oxidation of methanol on platinum catalysts generates CO as an intermediate, which is a poison that adsorbs on the active sites of the catalyst. Ru forms oxygenated species at lower potentials than Pt and its presence in the catalyst promotes the oxidation of CO to CO_2, through the so-called bifunctional mechanism [111, 112].

Liu et al. [113] prepared PtRu nanoparticles supported on Vulcan XC72 carbon and carbon nanotubes by a microwave-assisted polyol process. Figure 10.11 presents typical TEM images of Vulcan-carbon-supported and CNT-supported catalysts, showing a remarkably uniform and high dispersion of metal particles on the carbon surface. The average diameters of 3.9±0.3 nm for PtRu/Vulcan carbon and 3.5±0.3 nm for PtRu/CNTs were accompanied by relatively narrow particle size distributions (2–6 nm). The electrooxidation of methanol was studied by cyclic voltammetry, linear sweep voltammetry, and chronoamperometry. It was found that both PtRu/C catalysts had high and more durable electrocatalytic activities for methanol oxidation than a comparative Pt/C catalyst. Preliminary data from a direct methanol fuel cell single stack test cell using the Vulcan-carbon supported PtRu alloy as the anode catalyst showed high power density.

(a)   (b)
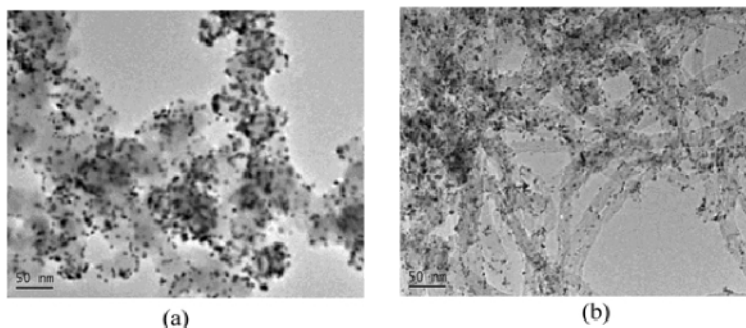
Figure 10.11. TEM images of microwave-synthesized PtRu nanoparticles supported on different carbon samples: (a) Vulcan XC72 carbon; (b) carbon nanotubes (nominal Pt loading, 20 wt%; Ru loading, 10 wt%) [113]. (Reprinted with permission from Langmuir 2004;20:181–7. Copyright 2004 American Chemical Society.)

The reduction procedure also affects the particle size in the catalyst. Lee et al. [114] compared carbon-supported PtRu nanoparticles prepared by different methods that involve the simultaneous chemical reduction of H_2PtCl_6 and $RuCl_3$ by $NaBH_4$ at room temperature (PtRu-1), by ethanol under reflux (PtRu-2), and by the thermal decomposition of a single-source molecular precursor [(bipy)$_3$Ru] (PtCl$_6$) (PtRu-3). Transmission electron microscopy (TEM) examinations show that the mean diameter of the PtRu nanoparticles is lowest for PtRu-1 (3.8 nm), followed by PtRu-2 (6.96 nm) and PtRu-3 (8.4 nm). Despite the fact that PtRu-3 from the single-source molecular precursor has the largest average particle diameter, it displays the lowest onset potential and the highest current density for methanol oxidation at room temperature. It is also the most CO tolerant among the three

differently prepared catalysts. This is attributed to the formation of a more homogeneous alloy nanoparticle.

In addition, Xin et al. [115] prepared multiwalled carbon nanotube-supported Pt (Pt/MWCNT) nanocomposites by both the aqueous solution reduction of a Pt salt (HCHO reduction) and the reduction of a Pt ion salt in ethylene glycol solution (EG). For comparison, a Pt/XC72 nanocomposite was also prepared by the EG method. The Pt/MWCNT catalyst prepared by the EG method has a high and homogeneous dispersion of spherical Pt metal particles with a narrow particle-size distribution.

Figure 10.12(a) is the micrograph of Pt/MWCNT (A) catalyst (prepared by the HCHO method). Pt clusters agglomerate to some extent and disperse on the surface of MWCNTs nonhomogeneously; Pt particles have a wide particle-size distribution ranging from 2 to 9 nm (Figure 10.13(a)) with a mean particle size of 3.4 nm. In contrast, in the Pt/MWCNT (B) sample (reduced by the EG method), as shown in Figure 10.12(b), a high and homogeneous dispersion of spherical Pt metal clusters is obtained.
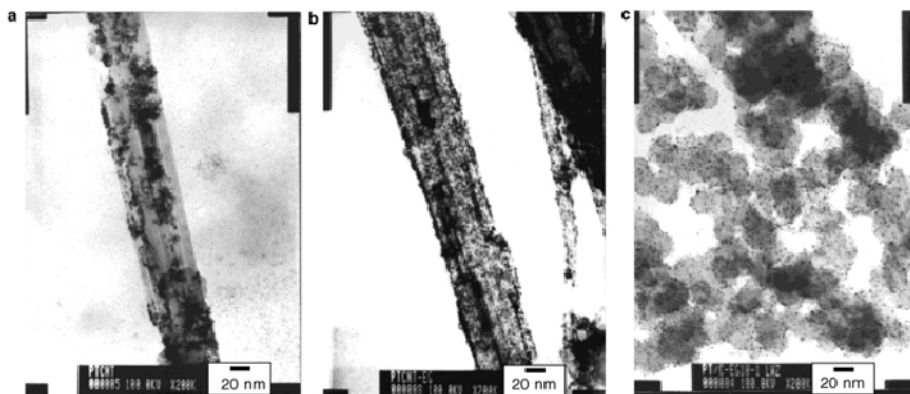
Figure 10.12. Bright-field TEM micrographs of (a) Pt/MWCNT (A) (prepared by the HCHO method), (b) Pt/MWCNT (B) (prepared by the EG method), and (c) Pt/XC72 (prepared by the EG method) nanocomposites [45]. (Reprinted with permission from J Phys Chem B 2003;107:6292–9. Copyright 2003 American Chemical Society.)

The histogram of Pt particle-size diameters for Pt/MWCNT (B) shows that the Pt particles have a narrow size dispersion ranging from 2 to 5 nm, with its peak centered at 2.6 nm. Pt particles are located on both the inner and outer surfaces of the MWCNTs. It appears that these MWCNTs have similar diameters (Figure 10.12(a) and (b)); however, the distribution of Pt particles is very different. The dispersion of Pt particles may be correlated with the oxidation of MWCNTs (i.e., more surface functional groups, caused by the oxidation of the MWCNT surface, appear to result in a higher density of Pt particles). The oxidized MWCNTs are more homogeneous in an EG solvent than in an aqueous solvent; perhaps this factor also determines the Pt distribution on MWCNTs because Pt precursors interact with MWCNTs better in EG solvents, which results in more Pt deposition on the support. In the case of XC72 carbon (Figure 10.12(c)), a similar experiment

results in the formation of a similar Pt particle distribution (2–4 nm) with particles having an average diameter of 2.2 nm. This implies that the EG synthesis method could lead to the formation of homogeneous small particles on different carbons (MWCNTs or XC72). In the case of the direct methanol fuel cell (DMFC) test, the Pt/MWCNT catalyst prepared by EG reduction is slightly superior to the catalyst prepared by aqueous reduction and displays significantly higher performance than the Pt/XC72 catalyst. These differences in catalytic performance between the MWCNT-supported or the carbon black XC72-supported catalysts are attributed to a greater dispersion of the supported Pt particles when the EG method is used, in contrast to aqueous HCHO reduction and to possible unique structural and higher electrical properties when contrasting MWCNTs with carbon black XC72 as a support.
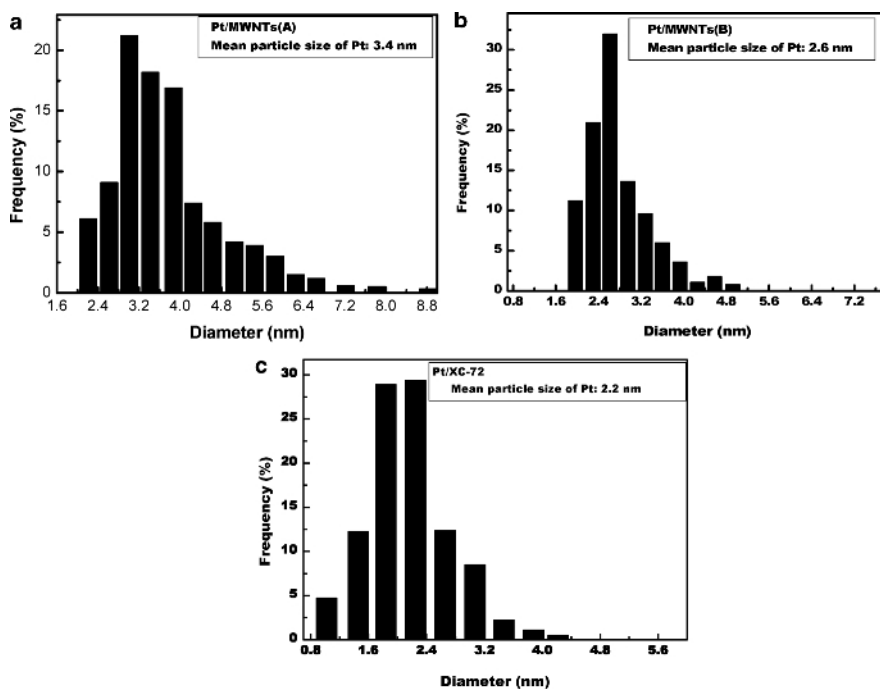
Figure 10.13. Histograms of Pt metal particle diameters for nanocomposites (a) Pt/MWCNTs (A), (b) Pt/MWCNTs (B), and (c) Pt/XC72. The size distribution and the mean size of the Pt particles of the catalysts were obtained by measuring more than 200 particles from bright-field micrographs [45]. (Reprinted with permission from J Phys Chem B 2003;107:6292–9. Copyright 2003 American Chemical Society.)

Hyeon et al. [116] successfully synthesized carbon nanocoils composed of nanometer-thick graphitic fibers by the catalytic graphitization of a resorcinol-formaldehyde gel. The carbon nanocoils were applied as electrode materials for direct methanol fuel cells. The SEM image reveals that the carbon materials consisted of particles approximately 100 nm in diameter (Figure 10.14(a)). The TEM image (Figure 10.14(b)) shows that each individual particle is composed of

5–10 nm thick coils. The HR-TEM image (Figure 10.14(c)) of a single nanocoil exhibits well-aligned graphitic layers. In order to evaluate the electrocatalytic activity of carbon-supported catalysts (Pt/Ru 1:1 alloy catalyst, 60 wt%), the methanol oxidative current of the catalysts was measured using a fundamental electrochemical system. It was found that the CNC-supported catalyst exhibited a substantially higher specific oxidation current of 80 A g^{-1} at 0.4 V (versus a normal hydrogen electrode (NHE)) near the kinetically controlled potential in the methanol reaction, compared to 20 A g^{-1} for the Vulcan XC72 supported catalyst and 14 A g^{-1} for the E-TEK supported catalyst.
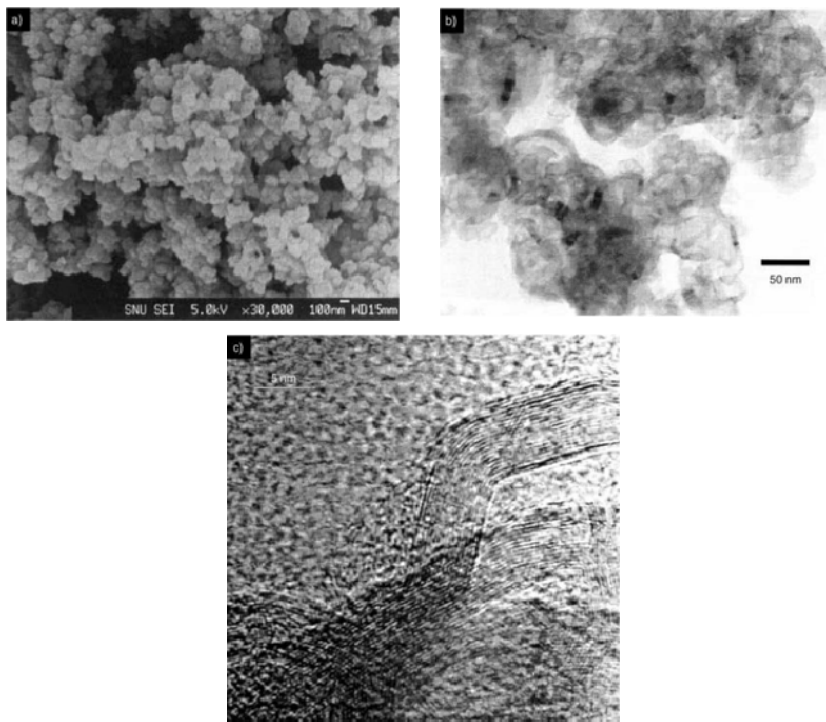
Figure 10.14. Electron microscope images of carbon nanocoils: a) field emission scanning electron microscope (FE-SEM) image, b) transmission electron microscope (TEM) image, and c) high-resolution transmission electron microscope (HR-TEM) image [116]. (Hyeon T, Han S, Sung YE, Park KW, Kim YW. High-performance direct methanol fuel cell electrodes using solid-phase-synthesized carbon nanocoils. Angew Chem Int Ed 2003;42:4352–6. Copyright Wiley-VCH Verlag GmbH & Co.KGaA. Reproduced with permission.)

Carbon nanotubes (CNTs) are a subject of great interest given their unique structure and excellent properties. They offer potential applications in electronic devices, catalysts, sensors, field-emission devices, and hydrogen-storage media [117–125]. The size and morphology of CNTs enable them to be a suitable catalyst support in which active metal particles may disperse on the external walls or be

encapsulated in the interior of the nanotubes. The metal particles on the external walls make contact with the reactant molecules more easily than do those encapsulated inside the internal channels of the CNTs [126–128]. The electrocatalytic mass activity of Pt clusters in a periodic array of ordered nanoporous carbon is higher than that of platinum in carbon black samples, and thus the former is suitable for oxygen reduction [129].

We conclude that carbon nanocoils (CNCs) are an excellent support for the electrodes of direct methanol fuel cells. Further, the CNC maintains stable catalytic activity by measuring power density versus time for up to 100 hr in a DMFC unit cell in the performance of fuel cells; since the durability of the electrode is significant for long-term applications, it is believed that the CNC is a highly promising electrode for long-term fuel cells. However, since the issue of durability and stability of the fuel cell electrode is very important, more in-depth study of these characteristics is still underway.

10.5 The Structure and Crystallography of Surface and Small Active Component Particles

10.5.1 Principles of Electron Spectroscopy for Chemical Analysis (ESCA)

Surface phenomena, a very common and yet extremely complicated subject, are with us in our daily lives as well as in our scientific research, such as studies in catalysis, adsorption, adhesion, corrosion, enzymatic reactions, and various solid state surfaces and interfaces. Surface analysis is the most direct and effective way to gain a fundamental knowledge of surface phenomena. Among the known surface-sensitive techniques and instruments, electron spectroscopy for chemical analysis (ESCA) is the most important and useful method for surface analysis. In addition to its surface sensitivity, ESCA is uniquely capable of providing surface chemical information such as oxidation state, chemical bonding, and precise sites of atoms in relation to crystal structure, as well as elemental compositions. In recent years ESCA has grown in popularity as a general analytical tool for every scientist dealing with surface properties of various materials. K. Siegbahn was awarded the Nobel Prize in 1981 partly for his pioneering work in ESCA.

ESCA involves energy analysis of electrons emitted from a surface after it has been bombarded with X-ray photons, ultraviolet photons, or electrons. If a material is irradiated with monochromatic photons (fixed energy) of frequency v, the photons may be absorbed, resulting in the emission of electrons. The energetics of the process can be defined by the Einstein relation:

$$h v = E_B + E_K$$

where E_B is the ionization energy or binding energy of the kth species of electron in the material, and E_K is the kinetic energy of the ejected electron [130]. The binding energy E_B can be deduced if the E_K can be measured using an electron energy analyzer. E_B is specific for a given electron in a given element. Thus, all the

methods of ESCA use the fact that some of the electrons ejected have energies characteristic of particular combinations of energy levels in the solid and so are characteristic of the types of atoms contained in the solid. In addition to elemental analysis and chemical state identification, ESCA allows the investigation of electronic structure, providing a picture of molecular orbitals for gas-phase species, valence band density of states, and core-level electron-binding energies for solids.

10.5.2 X-ray Photoelectron Spectroscopy (XPS)

In XPS the radiation is X-ray electrons. They are usually obtained from X-ray tubes with aluminum or magnesium anodes, which give lines at 1487 eV and 1254 eV, respectively. XPS, in common with other branches of electron spectroscopy, is essentially a surface analysis tool. It can be used to study electrons in both valence band and core states because the X-rays have sufficient energy for ionization of core levels in all elements of the periodic table except H and He (since these have no core levels), and the binding energies of these core levels are sufficiently unique to allow unambiguous assignment. XPS can be used to identify the atoms at surfaces by comparing the observed lines with either calculated core level binding energies or experimentally derived spectra from standards. Even though the electrons come from the inner core shells, their binding energies are affected by the state of chemical combination (e.g., the oxidation state), as this changes the effective force field of the nucleus. Hence, E_B exhibits a sensitivity to the chemical environment of the emitting atom (chemical bonding information), a chemical shift amounting to a spread of up to about 10 eV for many elements. On the other hand, XPS can be applied to bulk samples only if the surface is representative of the bulk composition. In many materials, the surface can be etched away gradually through bombardment by such projectiles as ions of argon. This makes it possible to examine the chemical elements present at successive depths within a sample by running an electron spectrum after each short treatment with ions. In addition to qualitative analysis, XPS can be applied for quantitative analysis because the number of emitted electrons is a function of the number of atoms on the surface.

Among all the methods of ESCA, XPS has been found to show the greatest applicability. It has been widely used for the surface characterization of materials, especially catalysts. As addressed above, XPS analysis can give sufficient information about the qualitative and quantitative elemental surface composition of a catalyst, the oxidation state of an atom, the chemical environment, and so forth. The following paragraphs give some typical analysis examples of XPS for fuel cell catalysts.

Polymer electrolyte and direct methanol fuel cells (PEFCs and DMFCs) are the most promising power sources for applications such as electric vehicles and electronic portable devices, due to their high power density, relatively quick startup, rapid response to varying loading, and low operating temperature [131]. Pt-based catalysts are the most important electrocatalysts in these fuel cells [132]. It has been widely reported that the catalytic activity of a Pt-based catalyst for the oxygen reduction reaction (ORR) and the methanol oxidation reaction in fuel cells is highly dependent on the oxidation states of the Pt crystallites on the surface of the catalyst [133, 134]. The oxidation states of Pt and the crystallites' contents can

be determined by XPS. Tian et al. [135] doped Pt on multiwalled carbon nanotubes (Pt/MWCNTs) by a rapid intermittent microwave irradiation (IMI) technique for PEFCs and DMFCs. The PtO_x ($x = 1, 2$) species was first deposited on the surface of MWCNTs by the IMI technique and subsequently reduced to Pt(0) with HCOOH. The reduction of PtO_x to Pt metal was confirmed by XPS analysis. XPS spectra of Pt/MWCNT nanocomposites before and after the reduction treatment are presented in Figure 10.15. Before the reduction treatment, the Pt 4f spectra were characterized by a doublet containing binding energies of 72.85 eV (Pt 4f7/2) and 76.2 eV (Pt 4f5/2) (Figure 10.15(a)). The two peaks had a binding energy difference of 3.35 eV and a peak area ratio of 4:3 that corresponds to the characteristic peaks of the Pt 4f(II). This indicates that most of the Pt species in Pt/MWCNT nanocomposites existed as Pt(II) before the reduction treatment. The Pt 4f spectrum can be deconvoluted into three species with binding energies of 71.1–74.4, 72.8–76.1, and 74.3–77.6 eV, which correspond to Pt(0), Pt(II), and Pt(IV), respectively. On the basis of the areas of Pt 4f7/2, the relative intensities of Pt(0), Pt(II), and Pt(IV) were calculated as 11.4%, 67.8%, and 20.8%, respectively. This indicates that the predominant Pt species in the Pt/MWCNTs before the reduction treatment were PtO and PtO_2.
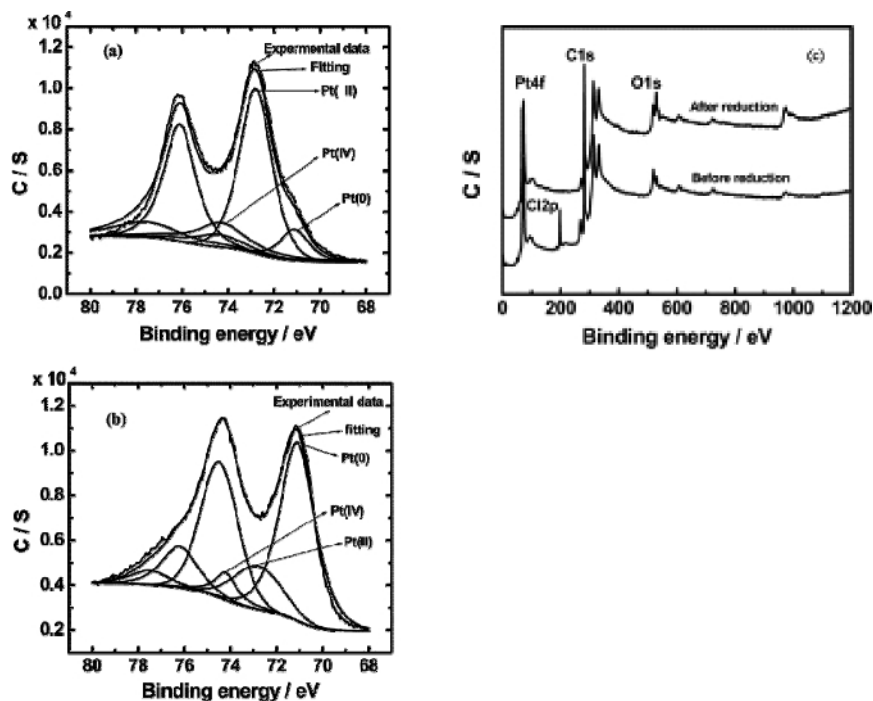
Figure 10.15. XPS spectra of the Pt/MWCNT nanocomposites. (a) Pt 4f spectra of the catalyst before reduction treatment; (b) Pt 4f spectra of the catalyst after reduction treatment; (c) XPS survey scan spectra of the nanocomposites before and after reduction treatment [135]. (Reprinted with permission from J Phys Chem B 2006;110:5343–50. Copyright 2006 American Chemical Society.)

The XPS spectra of the Pt/MWCNTs after reduction treatment were represented by the binding energies of Pt 4f7/2 and Pt 4f5/2 at 71.1 eV and 74.4 eV, respectively, characteristic binding energies of Pt(0) (Figure 10.15(b)). The relative intensities of Pt(0), Pt(II), and Pt(IV) were 70.5%, 20.5%, and 8.0%, respectively. The results indicate that most of the PtO_x in the Pt/MWCNTs after the reduction treatment is reduced to metallic Pt.

A survey XPS scan on a material can provide a qualitative analysis of the elemental composition on the surface. The XPS survey scan spectra of Pt/MWCNT nanocomposites before and after reduction treatment are shown in Figure 10.15(c). Elements of Pt, Cl, C, and O existed in the Pt/MWCNT nanocomposite before the reduction treatment. However, the Cl 2p peak vanished after the reduction, indicating removal of chloride ions in the reduced sample. The removal of halide ion impurities such as Cl$^-$ can improve the activities of the catalyst for CO oxidation and also direct methanol oxidation reactions in fuel cells [136, 137].

One of the most significant barriers to the widespread commercialization of PEFCs and DMFCs is the high cost of Pt. It is important to reduce the amount of noble metal in the catalyst while retaining a high electrocatalytic activity. One way to achieve this goal is to use bi- or tri-metallic catalysts combining platinum with other metals such as Ni, Co, Fe, Cu, Mo, Bi, and V in order to obtain PtM (M = metal) alloys. These alloys of transition metals with platinum have been found to exhibit significantly higher electrocatalytic activities towards the oxygen-reduction reaction than platinum in fuel cells [138–143]. XPS is a powerful technique for quantifying the surface oxidation states of the individual components of binary and/or ternary surface alloys. Shukla et al. [144] synthesized several binary and ternary alloys of transition metals with platinized carbon, and investigated their catalytic performances in the oxygen reduction reaction in solid polymerelectrolyte direct methanol fuel cells. The overall contents of metals in the catalysts were 20 wt%. The electrocatalysts were characterized by XPS to determine the valence states of the elements, compositions, and atomic ratios of the metal components. Figure 10.16 shows the Pt(4f) X-ray photoelectron spectra of the electrocatalysts. The spectra could be deconvoluted into three components labelled as 1, 2, and 3, which are ascribed to Pt metal, PtO, and PtO_2 signals, respectively. The relative intensities of the three components in each catalyst can be obtained from the areas for Pt 4f7/2. Among these electrocatalysts, Pt-Co/C was shown to possess a minimal amount of platinum oxides (Figure 10.16(b)).

The Cr(2p), Co(2p), and Ni(2p) X-ray photoelectron spectra for the samples were also studied, and the oxidation states of Cr, Co, and Ni as well as their relative intensities were obtained. From these data it was found that the Pt-Co/C sample had the lowest overall oxidizing components among the binary- and ternary-alloy electrocatalysts. Surface atomic ratios for Cr:Pt, Co:Pt, and Ni:Pt of the carbon supported electrocatalysts, obtained from their respective X-ray photoelectron spectra, are summarized in Table 10.5. The results indicate some surface enrichment of platinum metal in all the binary-alloy electrocatalysts, namely Pt–Cr/C, Pt–Co/C, and Pt–Ni/ C. However, a surface enrichment of base metals was found in the ternary-alloy electrocatalysts, as can be seen from Table 10.5. The results suggest a higher electrocatalytic activity towards the oxygen

reduction reaction on the Pt–Co/C electrocatalyst, due to the surface enrichment of Pt sites and the low metal oxide content in the electrocatalyst.
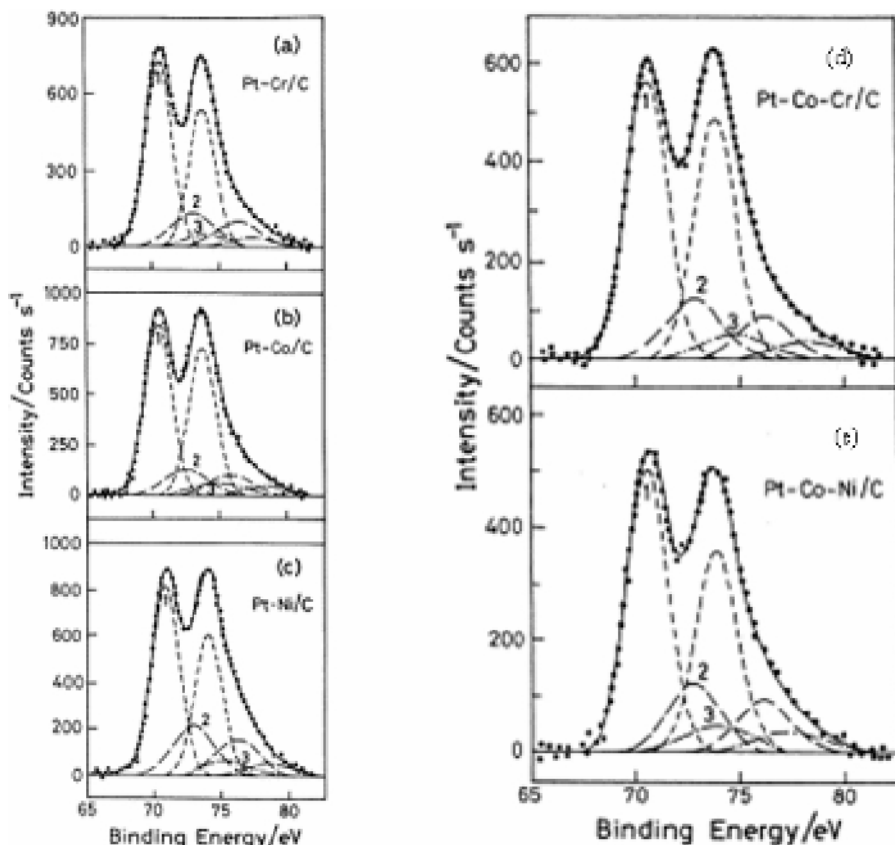
Figure 10.16. XPS of Pt(4f) core level region of (a) 20 wt% Pt–Cr/C, (b) 20 wt% Pt–Co/C, (c) 20 wt% Pt–Ni/C, (d) 20 wt% Pt–Co–Cr/C, and (e) 20 wt% Pt–Co–Ni/C electrocatalysts [144]. (Reproduced from Journal of Electroanalytical Chemistry, 504(1), Shukla AK, Neergat M, Bera P, Jayaram V, Hegde MS. An XPS study on binary and ternary alloys of transition metals with platinized carbon and its bearing upon oxygen electroreduction in direct methanol fuel cells, 111–9, 2001, with permission from Elsevier.)

Another obstacle for DMFC applications is the low catalytic activity of electrodes for both the oxygen reduction reaction and the methanol oxidation reaction. It is well known that the catalytic activity of an electrocatalyst is strongly dependent on the particle dispersion of the active components. Many doping techniques have been explored to widely distribute the active components on the catalyst supports [145–148]. In addition to the synthesis method, catalyst support also plays an important role in the dispersion of active components. Carbon materials with high surface areas (e.g., Vulcan XC72 carbon black) have been widely employed as electrocatalyst supports to enhance the dispersion of metal nanoparticles and thus to increase the utilization of the precious metal catalyst

[133]. However, the pristine surface of carbon materials is inert, making it a difficult substrate on which to attach metal deposits. Therefore, it is very important to develop effective techniques to improve adhesion through surface modification of carbon materials before metal deposition. Oxidation is a popular method, and many oxidants, such as HNO_3, $KMnO_4$, and HNO_3/H_2SO_4, have been used [149–151]. Li et al. [152] functionalized carbon nanotubes (CNTs) with high yields by treatment of CNTs in HNO_3 or H_2SO_4-$K_2Cr_2O_7$ and then doping Pt on the functionalized carbon nanotubes. It was found that platinum nanoparticles 1–5 nm in diameter were highly dispersed on the functionalized CNTs. Activity tests using a single stack PEM fuel cell showed that the Pt/CNT electrodes exhibited high electrocatalytic activity for oxygen reduction. XPS analyses were applied to examine the surface states of these carbon nanotube materials after modification. The O 1s spectra of the pristine and oxidized carbon nanotubes are compared in Figure 10.17, where it can be seen that a small amount of oxygen due to adsorbed oxygen species was detected on the pristine carbon nanotubes. A high density of oxygen-containing species was observed on the carbon nanotube surface after the HNO_3 or $K_2Cr_2O_7/H_2SO_4$ oxidative treatment (lines b and c of Figure 10.17). The shape of the functionalized carbon nanotubes at the high-energy side demonstrates the presence of highly oxidized components in double-bond-oxygen and acid configurations. The oxygen binding energies were shifted to higher values, indicating oxidation-induced acid-bonding characteristics. The higher binding energy in spectrum c suggests that the electrons in oxygen were more strongly bound to the surface carbon. This could be due to the use of different oxidation treatments (HNO_3 vs. $K_2Cr_2O_7$).

Table 10.5. Atomic ratios of the metal components in the electrocatalysts [144]. (Reprinted from Journal of Electroanalytical Chemistry, 504, Shukla AK, Neergat M, Bera P, Jayaram V, Hegde MS. An XPS study on binary and ternary alloys of transition metals with platinized carbon and its bearing upon oxygen electroreduction in direct methanol fuel cells, 111–9, 2001, with permission from Elsevier.)

Electrocatalyst	Cr:Pt	Co:Pt	Ni:Pt
20 wt% Pt/C			
20 wt% Pt–Cr/C	0.86 (0.67) [a]		
20 wt% Pt–Co/C		0.84 (0.72) [a]	
20 wt% Pt–Ni/C			0.86 (0.64) [a]
20 wt% Pt–Co–Cr/C	1.2 (0.53) [a]	0.54 (0.43) [a]	
20 wt% Pt–Co–Ni/C		0.60 (0.42) [a]	0.57 (0.33) [a]

[a] Values in parentheses indicate the bulk atomic ratios.
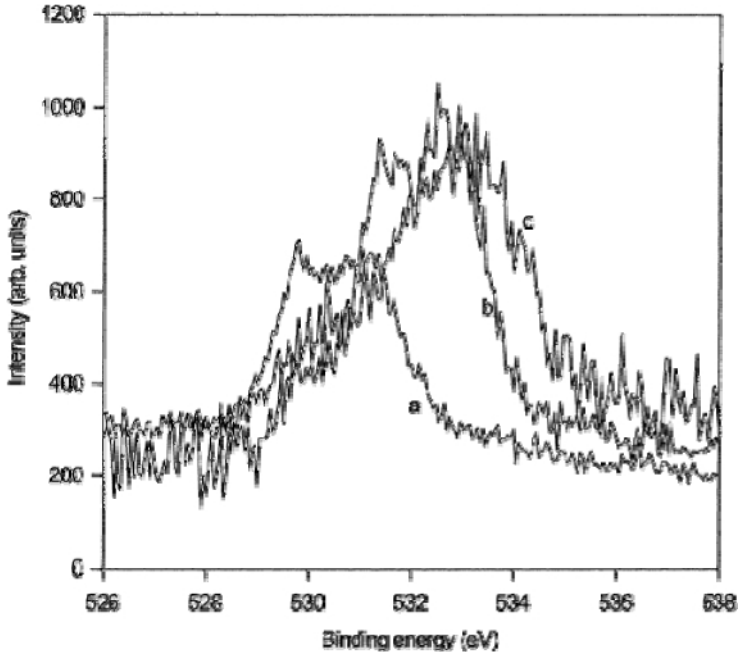
Figure 10.17. XPS measurements showing the effect of oxidation on the O 1s spectra of CNTs: (a) pristine; (b) HNO$_3$-treated CNTs; (c) K$_2$Cr$_2$O$_7$/H$_2$SO$_4$-treated CNTs [152]. (Reproduced with permission from Langmuir 2002;18:4054–60. Copyright 2002 American Chemical Society.)

Yttria-stabilized zirconia (YSZ) have been widely used as solid-state electrolytes for a range of applications such as solid oxide fuel cells, because of YSZ's high oxide ion conductivity and good stability. Atomic layer deposition (ALD) is an advanced chemical vapor deposition technique that can be a promising fabrication method to grow ultrathin doped oxide films, because the composition of ALD films can be altered at each atomic layer according to the desired ratios [153, 154]. Film composition of the YSZ membrane at various depths can be characterized by XPS analysis with the help of Ar ion surface etching. Shim et al. [155] synthesized YSZ films on Si$_3$N$_4$-buffered Si(100) wafers by using the ALD technique for solid oxide fuel cells. From the XPS compositional analysis, the measured yttria content was increased proportionally to the pulse ratio of Y/Zr. YSZ films with a target stoichiometry ((ZrO$_2$)$_{0.92}$(Y$_2$O$_3$)$_{0.08}$: 8% YSZ) were grown by employing a mix of pulse numbers, Zr/Y = 7:1 from XPS analysis. The film composition versus depth was also measured by XPS analysis with the help of Ar ion surface etching. The XPS depth profile of the YSZ films is shown in Figure 10.18. It can be seen that the composition of the films was 7–8% yttria, and remained similar through the entire film thickness. The XPS analysis results indicate that ultrathin YSZ films with uniform compositions were successfully synthesized using the ALD technique.
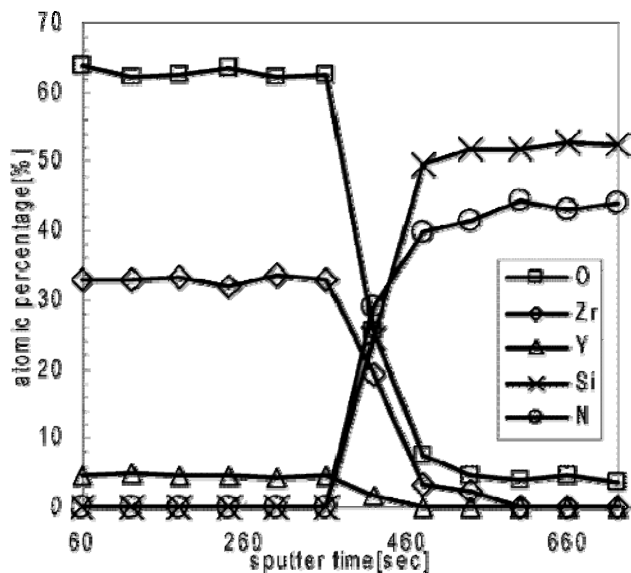
Figure 10.18. XPS depth profile of ALD YSZ films grown on Si_3N_4 substrates with pulse number ratio Zr/Y = 7:1 [155]. (Reproduced with permission from Chem Mater 2007;19:3850–4. Copyright 2007 American Chemical Society.)

10.5.3 UV-induced Photoelectron Spectroscopy (UVPS)

The threshold energy for ionization may be as little as 1.5 eV in the case of metals, but is usually far in excess of 5 eV for gaseous atoms or molecules. Thus, photoionization usually requires photons in the far ultra-violet (UV) region of the electromagnetic spectrum. In UVPS the source of radiation is usually a helium discharge lamp, which can be made so as to operate at 21.2 eV and 40.8 eV. Only valence electrons can be observed by UVPS because the helium radiation has insufficient energy to eject deep core electrons. Although the main characteristics of the valence band structure observed by UVPS do agree with those observed by XPS, considerably more structural information is available through the former, which provides an opportunity to obtain direct information about bonding, oxidation states, and molecular ionization potentials. However, it may not be possible to associate special peaks with individual atoms because of delocalization of electrons in molecular orbitals. Simple molecules can be identified using UVPS as a fingerprint technique. Therefore, UVPS does not appear to be an analytical tool comparable in versatility to XPS. UVPS is usually used in combination with other surface analysis techniques (e.g., XPS) to investigate the valence band structure of metals, alloys, semi-conductors, various adsorption phenomena, etc.

Ru-based catalysts have been identified as highly active catalysts for ammonia synthesis [156]. The catalytic activity of an Ru-based catalyst can be improved by the addition of alkali or earth-alkali promoters [157, 158]. Many kinetic and theoretic studies have been carried out in order to understand the role of these promoters in ammonia synthesis. Guraya et al. [159] investigated the alkali- and earth-alkali-promoted ruthenium catalysts supported on graphitized carbon by

means of XPS and UVPS, in order to study the effect of promoters on the electronic structure of this metal-support system. The XPS and UVPS spectra are shown in Figure 10.19. The C 1s XP spectra of reduced alkali-promoted catalysts showed a shift towards higher binding energies and an asymmetric broadening. However, neither nonpromoted nor Ba-promoted Ru/C samples exhibited such behavior after similar reduction treatments. Similarly, the UVP spectra of the Ru/C and Ba–Ru/C samples recorded after reduction did not show significant changes. The most important feature in the UVP spectra of the reduced alkali-promoted catalysts was the appearance of a well-defined Fermi edge, absent in the semimetal-like electronic structure of graphite (at essentially 0.0 eV). This implies an increase in the density of states at the Fermi level, indicating a shift of this level into the conduction band due to a charge transfer from the promoter to the graphite support. The Fermi level shift observed by UVPS can also be interpreted as a shift towards higher C 1s binding energy and asymmetric broadening in XP spectra, due to the offset introduced in the binding energy scale and the increasing probability of inelastic excitations near the Fermi level.
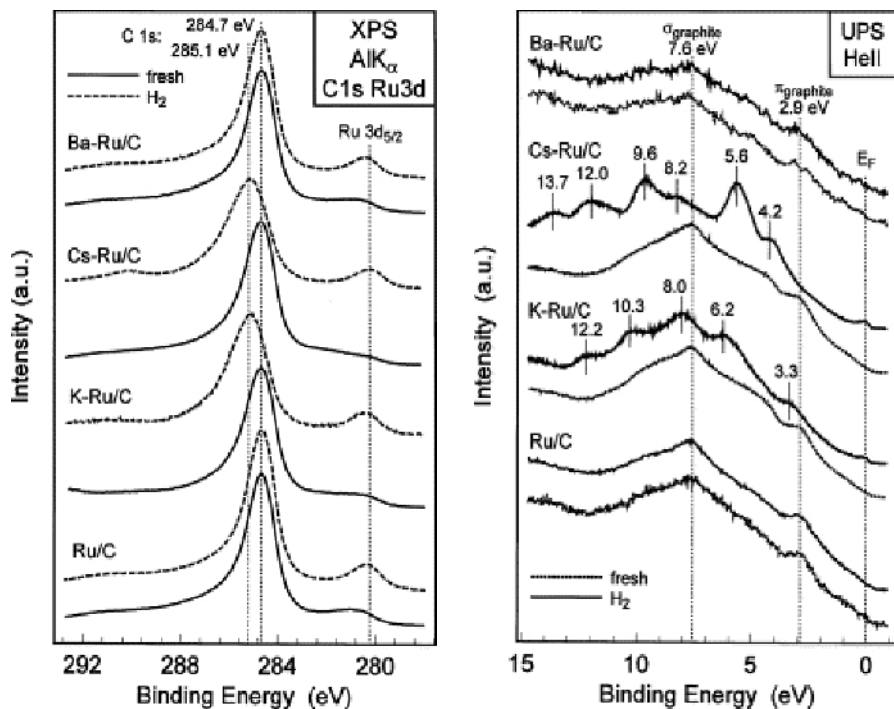
Figure 10.19. C 1s XP spectra (left panel), and UVP spectra (right panel) of all Ru-based samples, as prepared and after reduction [159]. (Reproduced from Applied Surface Science, 238(1–4), Guraya M, Sprenger S, Rarog-Pilecka W, Szmigiel D, Kowalczyk Z, Muhler M. The effect of promoters on the electronic structure of ruthenium catalysts supported on carbon, 77–81, 2004, with permission from Elsevier.)

Pt-based electrocatalysts in fuel cells are severely poisoned by the CO intermediate, which is strongly adsorbed on the Pt surface and considerably reduces its electroactivity. It has been widely accepted that the addition of Ru to Pt-based catalysts can promote CO removal by the so-called "bifunctional mechanism" [160, 161]. However, recent theoretical and experimental studies suggest that Mo-Pt combinations could be not only much cheaper but even more efficient catalysts for CO oxidation than Ru-Pt [162, 163]. To explore more effective metal promoters for CO removal, a fundamental understanding of the adsorption of CO on the metal promoter is very important. UVPS is a powerful surface analysis tool in adsorption studies. It can tell whether the adsorbate species on a solid surface is associative or dissociative, because the contributions of the two species to the valence electronic structure should be quite different.
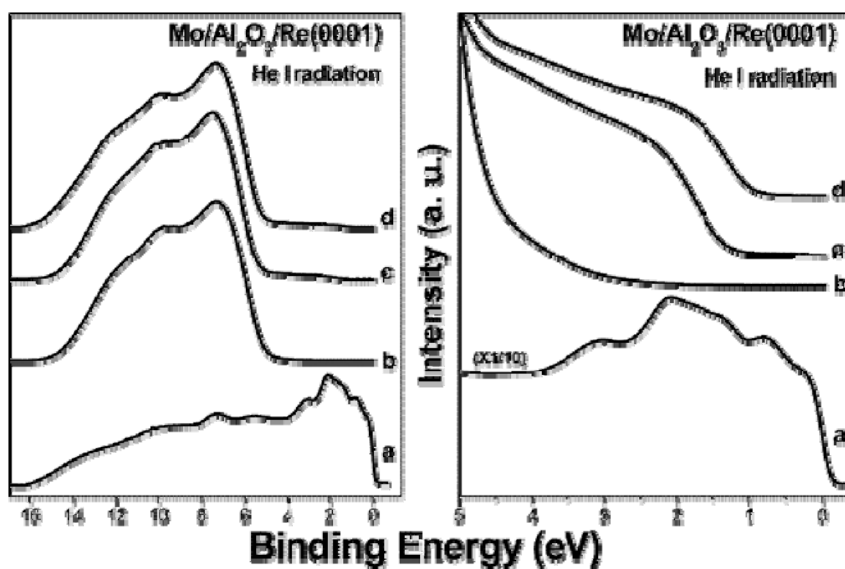
Figure 10.20. A series of UVPS of (a) a clean Re(0001) surface, (b) a clean Al_2O_3 film, (c) molybdenum deposition on the Al_2O_3 film at 300 K and then (d) annealed at 1000 K [164]. (Reprinted with permission from J Phys Chem B 2006;110:26105–13. Copyright 2006 American Chemical Society.)

Jiang et al. [164] used XPS and UVPS to investigate the adsorption of CO on the metallic molybdenum nanoparticles supported on a thin alumina film. Molybdenum deposition onto the thin Al_2O_3 film was achieved by physical vapor deposition at room temperature. UVPS was applied to monitor the valence band change of the Mo/Al_2O_3 model surface upon annealing, as shown in Figure 10.20. A new signal developed at 1.70 eV below the Fermi level, corresponding to the photoemission of the Mo 4d valence band on the surface. The lower valence band edge of the Mo nanoparticles on the film, below the Fermi level of the bulk molybdenum, could reduce the likelihood of electron back-donation and make the molecular adsorption of CO possible.

Figure 10.21 compares the difference in UP spectra for several model systems: CO exposure on thin Al_2O_3 film and the Mo/Al_2O_3 model surface, and $Mo(CO)_6$ exposure on thin Al_2O_3 film. When CO was dosed on the Mo/Al_2O_3 model surface at 100 K, the valence band emission was observed at 8.8 eV in binding energy, corresponding to the valence band emission of the $1\pi + 5\sigma$ orbitals in the adsorbed CO. The binding energy of this valence band emission is highly consistent with that of molybdenum subcarbonyls. In addition, the difference spectra of the Mo 4d valence band showed a weak but distinct emission at 3.5 eV when CO was dosed on the Mo/Al_2O_3 model surface, as can be seen in the right panel of Figure 10.21. This emission was absent in the case of CO exposure on the thin Al_2O_3 film, but was also present in the case of $Mo(CO)_6$ exposure on the film. These results indicate that an intermediate carbonyl-like species was formed on the Mo/Al_2O_3 model surface upon CO chemisorption.
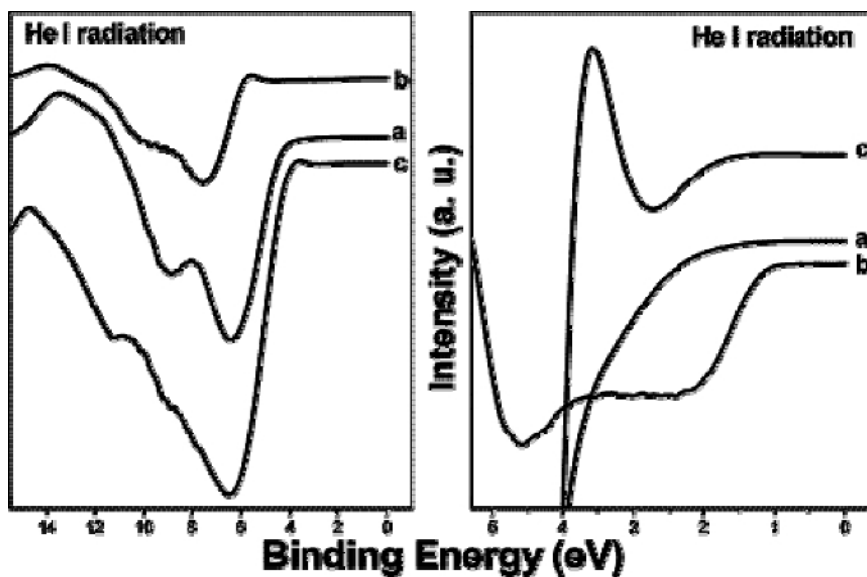
Figure 10.21. Comparison of differences in UVPS for (a) CO exposure on thin Al_2O_3 film, (b) CO exposure on a Mo/Al_2O_3 model surface, and (c) $Mo(CO)_6$ exposure on thin Al_2O_3 film. The difference spectrum was obtained by subtracting the spectrum on the surface, after exposure to the adsorbates, from the initial spectrum of the corresponding clean surface [164]. (Reprinted with permission from J Phys Chem B 2006;110:26105–13. Copyright 2006 American Chemical Society.)

10.5.4 Energy Dispersive Spectroscopy (EDS) and its Application

Electrons inelastically scattered within the excitation volume of a specimen deposit some energy in many atoms. In order to return to ground state, the atom releases a distinct quantum of energy. If the excited atom ejects an inner-shell electron, an outer-shell electron fills that vacancy and emits an X-ray having energy equal to the difference between the two electron shells. The detection of the X-rays emitted

by the specimen during electron-beam excitation is referred to as energy dispersive spectroscopy (EDS) or energy dispersive X-ray analysis (EDX).

K-shell electrons are more tightly bound than L-, M-, or N-shell electrons because the latter are progressively farther from the nucleus. For this reason, in a given atom K-shell electrons are more energetic than L-shell electrons, which in turn are more energetic than M-shell electrons. A given shell can be subdivided into α or β levels, i.e., Kα, Kβ, Lα, Lβ, etc., and may be further subdivided into $K\alpha_1$, $K\alpha_2$, $K\beta_1$, $K\beta_2$, etc. The intensity of the emission will be dependent on the probability that a given transition occurs, and that probability increases with a decrease in the distance between shells. However, the energy of the X-rays is determined by the energy difference between the two shells for a given transition.

The X-rays emitted carry a characteristic energy and wavelength, which when measured will reveal the elemental composition of the specimen. Even if it may not be possible to excite or detect all the characteristic X-rays of a given element, in general an element may be uniquely identified by the detectable lines. Energy dispersive spectrometers are capable of analyzing X-rays in the range of 0.7–20 keV emitted from elements with atomic numbers > 10. In addition to qualitative element analyses, quantitative analyses are possible because the intensity of the emitted radiation is proportional to the concentration of that element. But a precise quantitative analysis of elemental content cannot be expected, especially when a standard sample does not exist.

EDS is commonly associated with SEM or TEM analysis. A broad area of small particles on the SEM or TEM images can be selected for EDS analyses to obtain composition information for the selected region. Element mapping with EDS can be used to obtain the distribution of elements on the surface. The source of the X-rays is manifested as a grouping of extremely bright dots against a dark background, indicating where that element is absent.

Mixed-metal catalysts containing Pt (e.g., Pt-Ru) are currently favored for methanol oxidation in direct-methanol fuel cells (DMFCs). Pt-Ru/carbon nanocomposites have been prepared by a variety of chemical methods [165, 166]. A determination of the synthesized Pt-Ru alloy composition is very important to obtain the optimal composition for methanol electrooxidation. EDS analysis has been widely used to investigate the composition of the alloy particles [167, 168]. Moore et al. [167] prepared a Pt-Ru/Vulcan carbon powder nanocomposite with an alloy composition of $\sim Pt_{75}Ru_{25}$ using a single-source precursor for the methanol electrooxidation catalyst. Figure 10.22 shows a broad-area EDS spectrum of the synthesized $Pt_{75}Ru_{25}$/Vulcan carbon nanocomposite. The expected emission lines from Pt and Ru were apparent in the figure, indicating the presence of Pt and Ru in the nanocomposition. The Cu emissions are attributed to the copper grid of the sample holder and the Si emissions to trace amounts of clay present within the Vulcan carbon support. The relative integrated intensity of appropriate pairs of Pt and Ru emission lines gave a calculated Pt/Ru atomic ratio of 3:1 on the micron scale. The Pt/Ru stoichiometry determined by broad-area EDS is in good agreement with the chemical elemental analysis of the nanocomposite, which gave a Pt/Ru atomic ratio of $Pt_{2.95}Ru_1$.
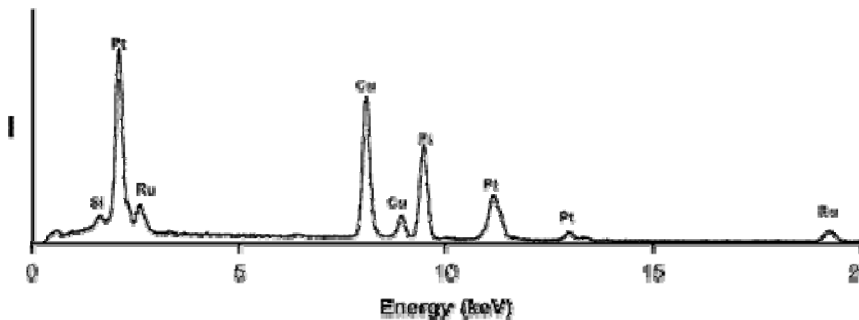
Figure 10.22. EDS spectrum of $Pt_{75}Ru_{25}$/Vulcan carbon nanocomposite [167]. (Reprinted with permission from Chem Mater 2003;15:3320–5. Copyright 2003 American Chemical Society.)

To investigate the compositional integrity of individual nanocrystals, the Pt/Ru atomic ratios of some randomly chosen nanocrystals (as shown in the TEM micrograph in Figure 10.23) within the nanocomposite have been examined by high-spatial-resolution energy dispersive spectroscopy (HR-EDS). The integrated intensities of the Pt $L\alpha_1$ and Ru $K\alpha_{1,2}$ emissions from individual alloy nanoclusters were collected. A plot of Pt/Ru atomic ratios versus nanoparticle size within the nanocomposite is shown in Figure 10.23. The average Pt/Ru ratio for nanoparticles was calculated to be 2.84 ± 0.75, which is within one standard deviation of Pt/Ru stoichiometry determined by bulk chemical elemental microanalysis. This indicates that gross phase separation of the two metals within the nanocomposite was not evident on the nanoscale among the particles examined.
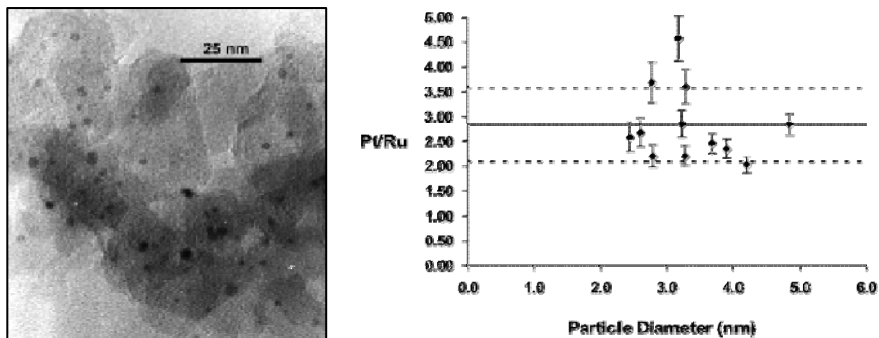
Figure 10.23. Bright-field TEM micrograph of the nanocomposite (left) and plot of Pt:Ru atomic ratios measured by HR-EDS for individual metal alloy nanoparticles (right) [167]. (Reprinted with permission from Chem Mater 2003;15:3320–5. Copyright 2003 American Chemical Society.)

Many efforts have been made to find the proper alternative to Nafion at elevated temperature operation for PEMFCs, as Nafion degrades at temperatures higher than 110–130 °C. It was found that the organic-inorganic composite membrane can improve its own mechanical strength and thermal stability at

elevated temperatures because the inorganic filler aids in increasing both qualities [169]. Zirconium phosphate hydrate is well known as an inorganic filler material. Thus, it is attractive to use it to modify the polymer electrolyte membrane. Woo et al. [170] prepared a zirconium phosphate composite membrane by soaking the sulfonated poly (fluorinated arylene ether)s (SDF-F) stepwise in zirconyl chloride and phosphoric acid solution. It was shown that the ZrP-modified membrane was much superior to the starting membrane at 100–140 °C. The distribution of Zr and P on the surface and through the cross-section of the SDF-F/ZrP membrane was investigated by EDS. The SEM photomicrographs and EDS mapping data are shown in Figure 10.24, where it can be seen that Zr and P were homogeneously distributed over the surface of the SDFF/ZrP membrane (b and c) and through the cross-section (e and f). These results demonstrated that the composite membranes had nano-sized ZrP within the pores and that the combination of organic polymers and inorganic materials was transformed into an interpenetrated network by the soaking method.
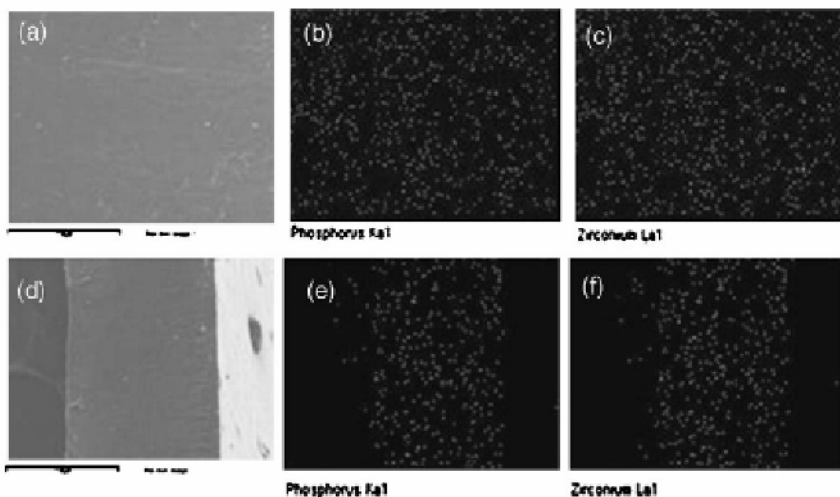
Figure 10.24. SEM images and EDS P-mapping and Zr-mapping of the surface (a–c) and cross-section (d–f) of the SDF-F/ZrP membrane [170]. (Reproduced from Electrochimica Acta, 51(27), Woo MH, Kwon O, Choi SH, Hong MZ, Ha HW, Kim K. Zirconium phosphate sulfonated poly (fluorinated arylene ether)s composite membranes for PEMFCs at 100 –140 °C, 6051–9, 2006, with permission from Elsevier.)

10.6 Analysis of the Stability of Catalysts by the Thermal Analysis Method

10.6.1 Principles

Thermal analysis refers to a group of techniques in which some physical property of the sample is monitored as a function of temperature while the temperature of

the sample, in a specified atmosphere, is programmed. The programme may involve heating or cooling at a fixed rate of temperature change, or holding the temperature constant, or any sequence of these.

In thermal analysis, changes in weight form the basis of thermogravimetry (TG), in which the weight of a sample is measured as a function of temperature. Derivative thermal gravimetry (DTG) is a method of expressing the results of TG by giving the first derivative curve as a function of temperature. Therefore, a DTG record plots dw/dt, i.e., the rate of weight loss against the temperature T. Differential thermal analysis (DTA) is a technique in which the difference in temperature (ΔT) between the sample and an inert reference material is measured as a function of temperature. The DTA curve is generally a plot of the difference in temperature (ΔT) as the ordinate against the temperature as the abscissa. Any physical or chemical change occurring to the test sample which involves the evolution of heat will cause its temperature to rise temporarily above that of the reference sample, thus producing an exothermic peak on the DTA plot. Differential scanning calorimetry (DSC) is a technique in which the difference in heat flow (power) needed to maintain the same temperature between a sample and a reference is monitored as a function of temperature. These techniques (TG, DTA, and DSC) are the most important in thermal analysis. TG tells us when a sample is losing or gaining weight (and how much), while DTA or DSC will tell us if that reaction or process is exothermic or endothermic (and often be capable of measuring the heat change of that event). Other properties can be measured, although the thermal analysis techniques to which they give rise have more limited ranges of applications. For example, thermomechanical analysis (TMA) measures the dimensional changes as a function of temperature, which is particularly useful in the study of metals, alloys, polymers, ceramics, and glasses. Electrothermal analysis measures the electrical conductivity as a function of temperature.

10.6.2 Application

Thermal analysis has been used to study a wide range of phenomena occurring on a large number of materials, e.g., catalysts, polymers, liquid crystals, metals and alloys, organic materials, inorganic compounds, ceramics and glasses, etc. There is such a variety of applications for thermal analysis that it is not possible to include every aspect here. This section presents a representative range of applications of the three most widely used techniques (i.e., TG, DTA, and DSC) in thermal analysis.

TG is chiefly used to determine content, as well as the temperature and course of decomposition. The selection of atmosphere (e.g., N_2 for pyrolysis, air for oxidation) often allows the various components to be distinguished (e.g., coal analysis, material analysis). The decomposition temperatures generally differ and allow determination of the type and quantity of the components, e.g., hydrates, binders, carbonates, copolymers, etc. Isothermal measurements can be used to determine adsorption/desorption isotherms of materials in order to reveal the geometry of the surface and pore structure, the sorption capacity and the sorption kinetics, etc.

DTA and DSC are frequently used to study the same phenomena. The DTA and DSC techniques can make accurate measurements of the temperatures of thermal events, and can detect the exothermic or endothermic nature of the events. The applications of DTA and DSC may be divided roughly into two categories:

1. Physical changes and measurements. These include melting, crystalline phase changes, changes in liquid and liquid crystalline states and in polymers, phase diagrams, heat capacity, glass transitions (Tg), thermal conductivity, diffusivity, emissivity, etc.
2. Chemical reactions, for example, dehydrations, decompositions, polymer curing, glass formation, oxidative stability, reaction kinetics, etc.

10.6.3 Typical Examples of Analysis

Catalyst stability is very important for the long-term operation of the catalyst in practical applications. Thermal analysis has been widely applied as a useful method to characterize the stability of catalysts. This section describes some representative examples of the application of thermal analysis to fuel cell electrocatalysts.

Platinum supported on high-surface-area carbon materials has been extensively investigated as the most active type of catalyst for proton exchange membrane (PEM) fuel cells. The advantages of such catalysts under fuel cell operation conditions include high surface area, sufficient electronic conductivity, and slow catalyst agglomeration. At present, one of the most significant drawbacks hindering the large-scale application of PEM fuel cell technology is the loss of performance of the Pt/C catalysts during extended operation. A number of mechanisms have been proposed for catalyst degradation in performance, including catalyst particle sintering, catalyst dissolution, membrane degradation, and possibly carbon support corrosion [171, 172].

Stevens et al. [173] investigated the thermal stability of the carbon-supported platinum electrocatalysts for PEM fuel cells at elevated temperatures under dry air conditions, and the thermal analysis results are shown in Figure 10.25. The DSC and TG data show that no significant weight loss or heat flow occurred on the BP2000 carbon before 400 °C, as can be seen from the left panel of Figure 10.25. This indicates that the carbon support on its own was thermally stable over the temperature range used for testing the platinum-loaded samples under dry air conditions. The isothermal weight data for the samples with different platinum loadings held at 195 °C are presented in the right panel of Figure 10.25 as a function of time. The fraction of carbon consumed on all samples increased with time, indicating the oxidation of the carbon support. The rate of carbon consumed increased as the platinum loading increased, especially for the higher platinum loadings, implying that there was an increase in overall reactivity with increasing platinum content on the catalysts. The results suggest that the presence of Pt facilitated the oxidation of carbon even at moderate temperatures (125–195 °C).
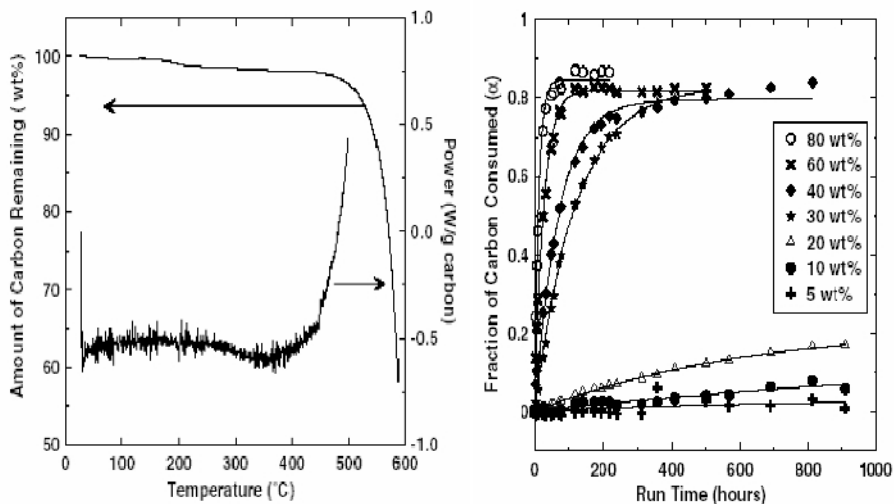
Figure 10.25. TG and DSC data for BP2000 carbon heated at 2.5 °C/min under flowing air (left panel) and the isothermal weight data for the samples with different platinum loadings held at 195 °C under flowing air (right panel) [173]. (Reproduced from Carbon, 43(1), Stevens DA, Dahn JR. Thermal degradation of the support in carbon-supported platinum electrocatalysts for PEM fuel cells, 179–88, 2005, with permission from Elsevier.)

Baturina et al. [174] studied the thermal stability of Vulcan XC72-supported Pt catalysts and PEM fuel cell catalyst layers in air by TG. Figure 10.26 shows the weight loss of carbon-supported Pt catalysts with different platinum loadings and pure Vulcan XC72 carbon in air as a function of temperature. There was no mass loss for pure Vulcan XC72 up to 550 °C. The weight change of the Pt/C catalysts followed a pattern different from that of Vulcan XC72, as shown in Figure 10.26(a). Between 40 and 200 °C little or no mass loss was observed for the Pt/C catalysts with 20–46% Pt loadings. Oxidation occurred gradually from 200 to 430 °C, with the exact range depending on composition (200–430 °C, 20%; 200–410 °C, 40%; 150–390 °C, 46%). An abrupt mass loss was observed at around 400 °C. These observations indicate that Pt accelerated carbon decomposition in all the carbon-supported Pt catalysts. Figure 10.26(b) shows weight loss and DTG for 46% Pt/C in air. The presence of a small shoulder with an onset at 150 °C (Figure 10.26(b), insert) is assigned to decomposition of carboxylic groups on the carbon surface. It seems that Pt also facilitated oxidation of these surface functional groups, which have been suggested as able to inhibit carbon combustion at lower temperatures [173]. These results indicate that the presence of Pt promotes the oxidation of carbon support in air.

The TG of the thermal decomposition of PEM fuel cell catalyst layer consisting of 46% Pt/Vulcan XC72/Nafion ionomer in air is shown in Figure 10.27. The TG data of 46% Pt/Vulcan XC72 and Nafion are included in Figure 10.27 for reference. The TG curve for the catalyst layer shows three distinct mass loss regions. The second mass loss region can be attributed to the decomposition of

Nafion. The decomposition temperature for Nafion in air was ~300 °C. The thermal decomposition temperature of Nafion in the catalyst layers was lowered by about 100 °C in the presence of Pt/C catalysts. This indicates that Pt also catalyzed the decomposition of Nafion in the PEM fuel cell catalyst layers. The third mass loss region is due to carbon oxidation.
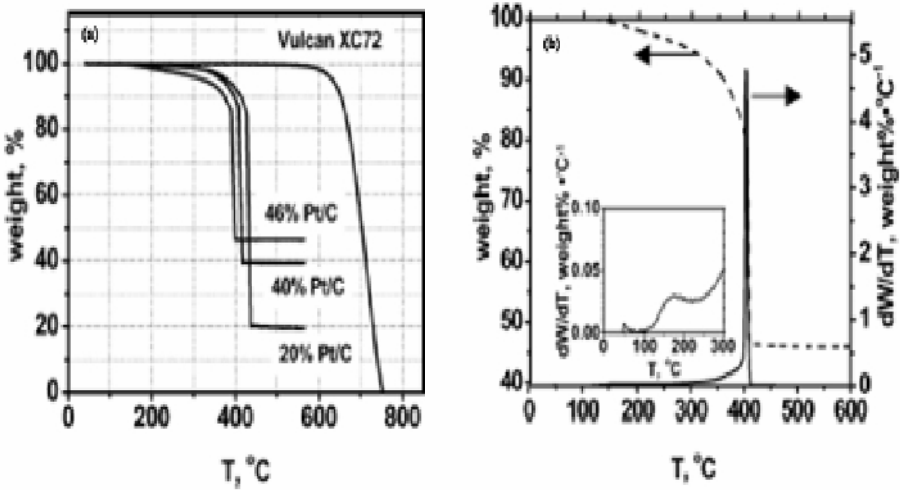
Figure 10.26. TG data of 20%, 40%, and 46% Pt/C in air (a) and DTG data for 46% Pt/C in air (b) [174]. (Reproduced with permission from Chem Mater 2006;18:1498–504. Copyright 2006 American Chemical Society.)
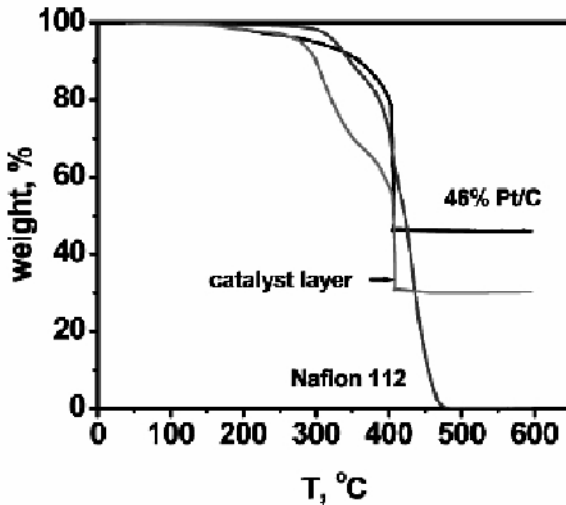
Figure 10.27. TG data for 46% Pt/C, Nafion 112, and Pt/C catalyst layer in air [174]. (Reproduced with permission from Chem Mater 2006;18:1498–504. Copyright 2006 American Chemical Society.)

The assignment of the mass losses and the volatile species of decomposition can be determined by TG coupled with mass spectrometry (TG-MS) [174–176]. Figure 10.28 shows the TG-MS data obtained as decomposition products of Nafion 112 and the Pt/C catalyst layer in air. As shown in Figure 10.28(a), the mass signal with m/e = 48 (SO_2) observed during Nafion decomposition at ~350 °C indicated desulfonation of Nafion. The curves with mass signals 44 (CO_2 and $C_2F_4O_2$) and 47 (COF_2 and $C_2F_4O_2$) closely followed each other. The much stronger ion current associated with the m/e = 44 peak indicated a major contribution from CO_2. The broad peaks at 450 °C can be related to the decomposition of the side chain and the polymer backbone. Figure 10.28(b) shows the mass signal data obtained on the Pt/C catalyst layer. The mass signals with m/e = 44 and 47 were no longer parallel, indicating there was a significant contribution from CO_2 to the total ion current. The peak at 450 °C, followed by the m/e = 45 mass signal, is ascribed mostly to CO_2. The small peak at ~200 °C (m/e = 44) is probably attributable to the thermal decomposition of carboxylic groups on the surface of carbon black.
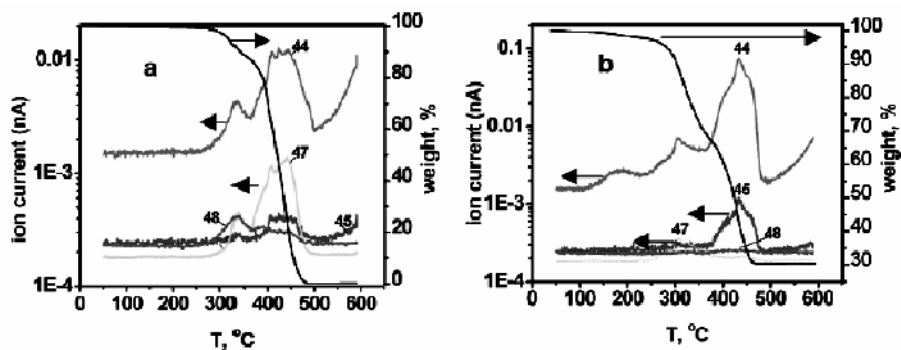
Figure 10.28. TG-MS data obtained as decomposition products of (a) Nafion 112 and (b) the Pt/C catalyst layer in air [174]. (Reproduced with permission from Chem Mater 2006;18:1498–504. Copyright 2006 American Chemical Society.)

PtRu catalyst is currently the most active anode catalyst for direct methanol fuel cells (DMFCs) [177–179]. Recently, it was found that the presence of RuO_xH_y species in PtRu catalyst greatly promoted the electrocatalysis of methanol oxidation [180–182]. The benefits of RuO_xH_y can be attributed to the electrons' and protons' conductibility and the surface OH group, which is suggested to be the key species in the methanol oxidation mechanism [177–183]. Therefore, a number of efforts have recently been made to obtain RuO_xH_y-rich catalyst instead of bimetallic PtRu alloy for DMFCs [184–186]. Yang et al. [186] prepared a PtRu/C catalyst by a low-cost impregnation method and characterized it by EDX, XRD, XPS, and TG. The presence of RuO_xH_y species on the PtRu/C catalyst and the thermal stability were investigated by TG/DTA. As shown in Figure 10.29, an initial endothermic loss between ambient temperature and 100 °C can be attributed to the removal of physisorbed water from the catalyst. The exothermic loss occurring between 300 and 600 °C is important evidence for the structural reconstruction accompanied by loss of structural water [181, 182]. This behavior

has been considered an unambiguous characteristic of hydrous oxides [182]. These data confirmed the presence of RuO_xH_y species in the synthesized PtRu/C catalyst. Methanol oxidation measurements at 60 °C showed that the prepared PtRu/C catalyst exhibited excellent performance for methanol oxidation. The obtained results support the suggested methanol oxidation mechanism whereby the surface OH group acts as the key species for methanol oxidation.
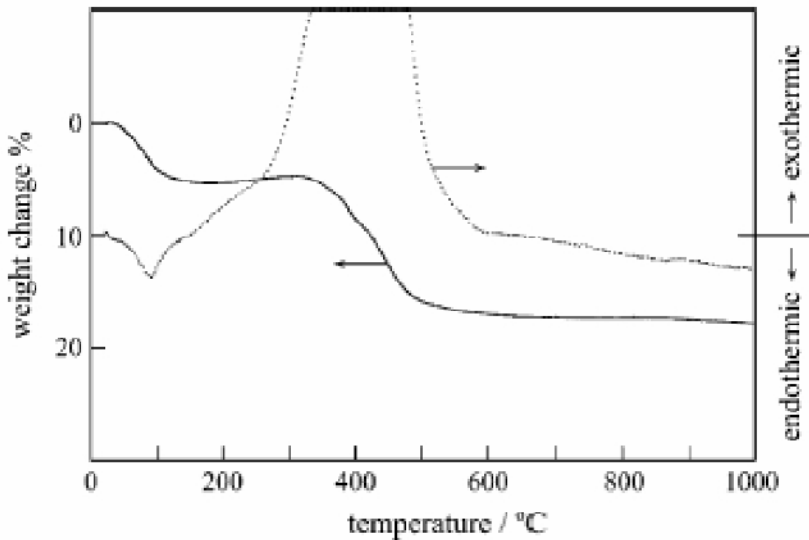
Figure 10.29. TG/DTA results for PtRu/C (40 wt% Pt + 20 wt% Ru) [186]. (Reproduced with permission from Chem Mater 2003;15:3552–7. Copyright 2003 American Chemical Society.)

A general problem with polymer membranes for fuel cells is that the instability of the materials shortens the lifetimes of fuel cells [187]. It has been demonstrated that the introduction of an inorganic filler can improve the polymer membrane structure with regard to water retention, thermal stability and the reduction of methanol crossover [188, 189]. Another important property for polymer membranes in fuel cells is proton conductivity. It has been found that the proton conductivity of the polymer membranes can be increased by sulfonation [190–194]. However, while the conductivities increase with the degree of sulfonation, the mechanical properties of the polymer membranes show a parallel progressive deterioration. To overcome these limits, hybrid membranes based on highly sulfonated poly(ether ether ketone) (SPEEK, DS = 0.9) and inorganic filler TiO_2 were synthesized via the *in situ* mixed sol-gel process [195]. The stabilities of the hybrid membranes were investigated by TG. Figure 10.30 shows the TG curves of SPEEK and composite SPEEK/TiO_2 membranes (R1, R2). R1 and R2 indicate the different routes to prepare the composite membranes. For all samples the first weight loss, up to 200 °C, can be due to the evaporation of residual solvent DMAC. The TG curves of the doped membranes clearly showed an increase in the

decomposition temperature of the sulfonic acid groups from 250 °C (SPEEK) to 270 °C (SPEEK/TiO$_2$ (R1)) and 330 °C (SPEEK/TiO$_2$ (R2)). This shift can be attributed to an interaction between the sulfonic group of SPEEK and the polar groups of TiO$_2$. The introduction of TiO$_2$ to the sulfonated PEEK membranes also led to reduced water uptake and good proton conductivity up to 120 °C, making the samples suitable for application as polymeric electrolytes at intermediate temperatures.
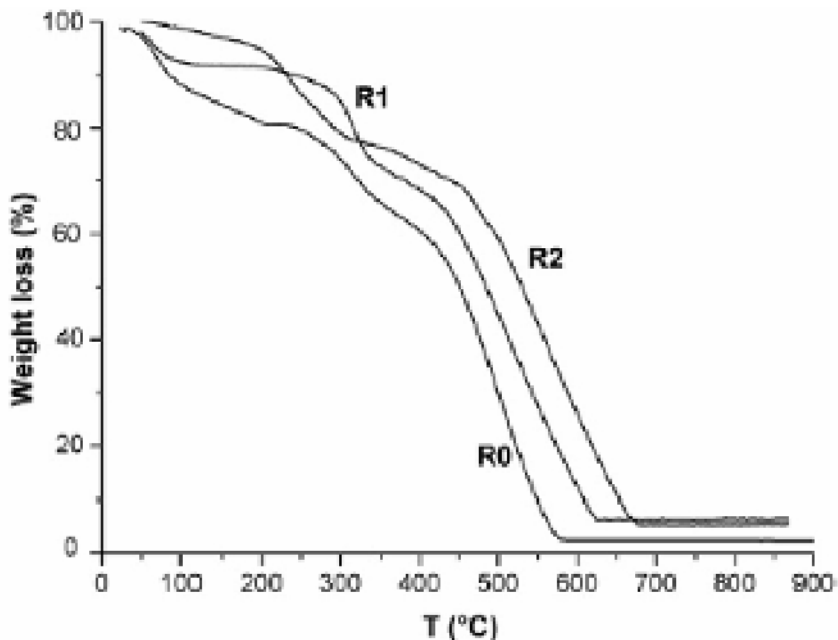
Figure 10.30. TG curves of SPEEK and composite SPEEK/TiO$_2$ membranes (R1, R2) [195]. (Reproduced from Journal of Membrane Science, 296(1–2), Luisa Di Vona M, Ahmed Z, Bellitto S, Lenci A, Traversa E, Licoccia S. SPEEK-TiO$_2$ nanocomposite hybrid proton conductive membranes via *in situ* mixed sol-gel process, 156–61, 2007, with permission from Elsevier.)

10.7 Other Structural Techniques for Characterizing the Bulk and Surface of Electrocatalysts

10.7.1 FTIR and UV-VIS

UV-VIS spectrophotometry is seldom used for characterization of the catalysts for low-temperature fuel cells, but Fourier transform infrared spectroscopy (FTIR) has been used by many researchers for characterization of low-temperature fuel cells through probing molecules adsorbed on catalysts. It has also been widely used to

investigate the mechanisms of adsorption and poisoning of catalysts, especially for DMFCs. FTIR is a very important tool to study the adsorption, migration, and poisoning mechanisms of carbon monoxide and other intermediates, and this research is of significant benefit in the exploration and development of CO-tolerant catalysts for PEMFCs fed by reformate gas and for DMFCs.
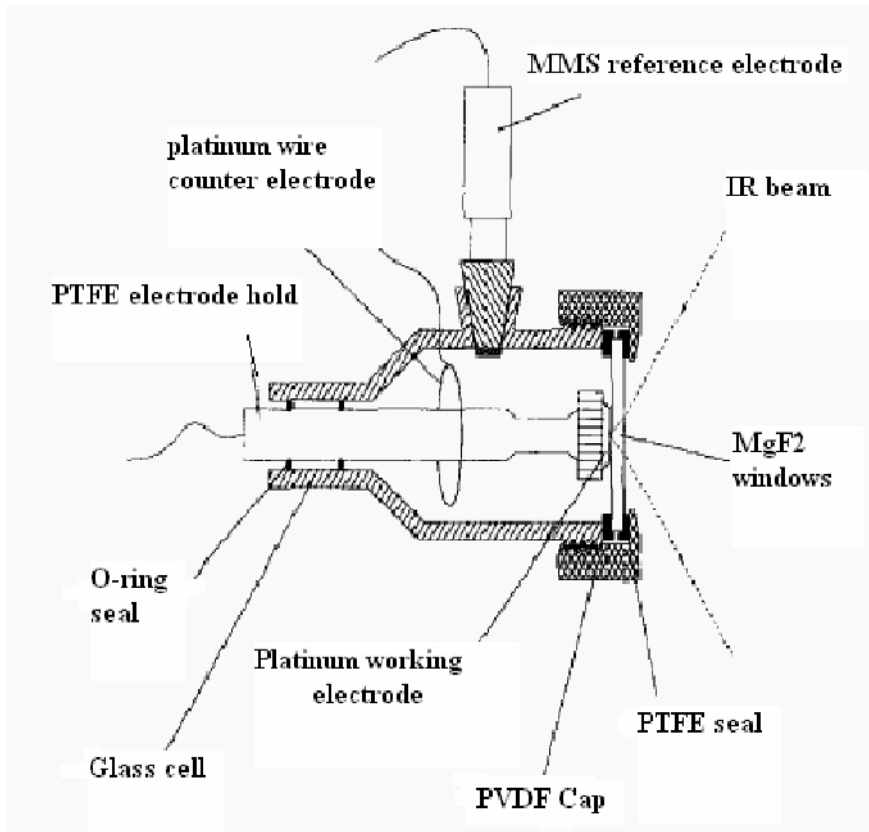
Figure 10.31. An apparatus for *in situ* electrochemical FTIR [196]. (Reproduced from Journal of Electroanalytical Chemistry, 401(1–2), Munk J, Christensen A. P, Hamnett A., Skou E. The electrochemical oxidation of methanol on platinum and platinum + ruthenium particulate electrodes studied by in-situ FTIR spectroscopy and electrochemical mass spectrometry, 215–22, 1996, with permission from Elsevier.)

Munke et al. [196] reported a technique (Figure 10.31) of *in situ* electrochemical FTIR and used it to study a real carbon-supported platinum + ruthenium catalyst. Different adsorptions were observed when methanol was electrooxidized at bulk Pt, Pt particles, and carbon-black-supported Pt + Ru electrodes, particularly with regard to the nature of the adsorbed CO species (Figure 10.32).
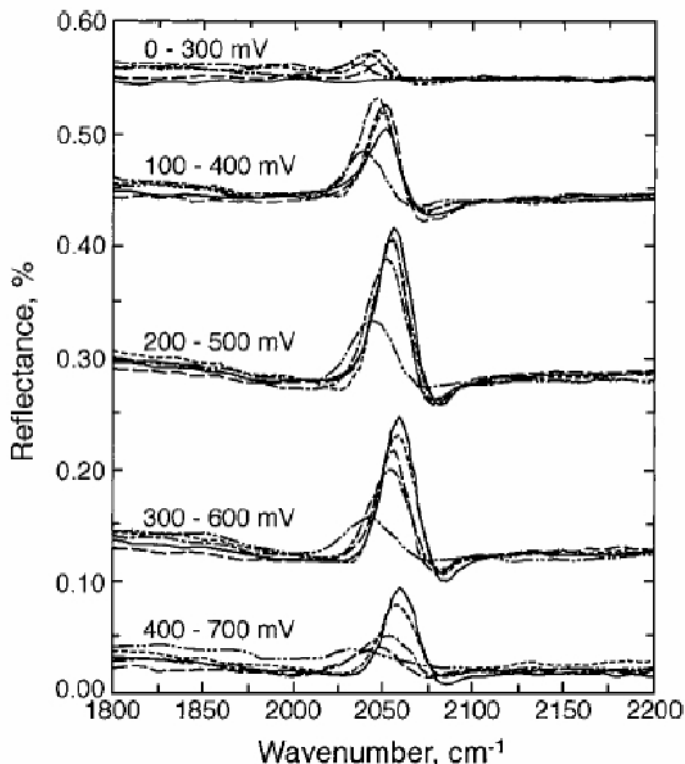
Figure 10.32. *In situ* electrochemical FTIR spectra of CO. (Reproduced with permission from J. Phys. Chem. B. 2000, 104(24), 5803–7. Copyright 2000 American Chemical Society.)

10.7.2 TPD/TPR

Temperature programmed desorption (TPD) and temperature programmed reduction (TPR) are popular for characterizing platinum-based catalysts for fuel cell applications, especially the TPR technique. Usually some thermodynamic and kinetic parameters of gas/solid desorption processes and decomposition reactions on surfaces involving gaseous products can be quantitatively measured by TPD, and promotion of additives can be investigated by TPR.

The basic principle for TPD can be described as follows. Usually the sample is introduced into a tubular chamber, and after vacuum treatment an adsorb gas is controllably introduced and adsorbed on the surface of sample. Then the sample containing the adsorbed gaseous species is heated at a programmed and linear rate, gases are released from the different type of adsorbed sites at different temperatures, and a TPD spectrum is obtained.

Some information about catalysts can be obtained by TPD techniques. The types of active sites on the surface can be determined by the number of desorption peaks; the adsorption strength (adsorbate-substrate binding energies) can be obtained by the maximum desorption temperature of the desorption peaks, and the

number of active sites can be estimated from the area of the desorption peak. It is important that the desorption activation energy can be measured by a series of experiments at various temperature rates.

Unfortunately, TPD has seldom been applied to the investigation of fuel cell catalysts, but TPR has been widely used for that purpose. TPR can be used to determine reduction sites present in the catalyst bulk and reveals the temperature at which the reduction at each type of site occurs.
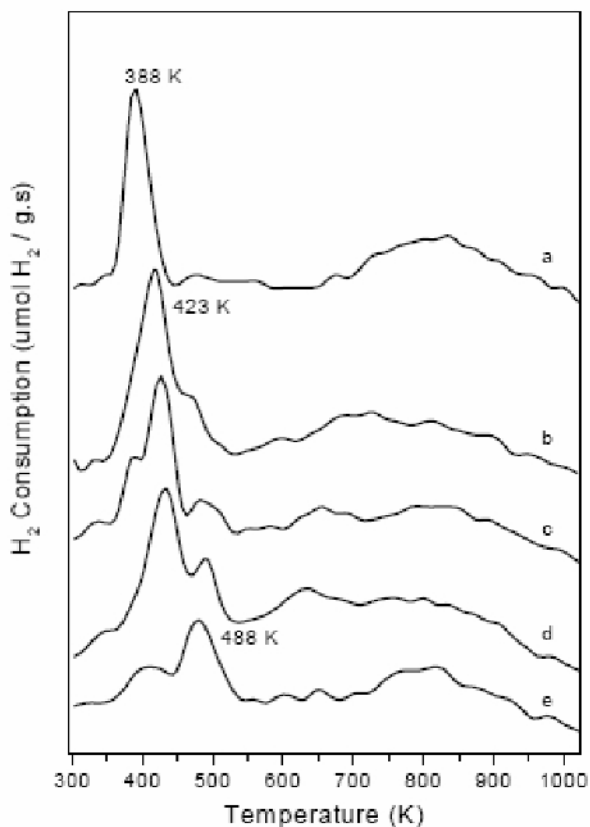
Figure 10.33. TPR profiles of the different carbon-supported Pt-Ru catalysts: (a) 2 wt% Pt/XC72R; (b) 2 wt% Pt–0.52 wt% Ru/XC72R; (c) 2 wt%Pt–1.03 wt% Ru/XC72R; (d) 2 wt% Pt–2.03 wt% Ru/XC72R; (e) 2 wt%Ru/XC72R [197]. (Reproduced from Catalysis Today, 93(5), Zhang YJ, Maroto-Valiente A, Rodriguez-Ramos I, Xin Q, Guerrero-Ruiz A. Synthesis and characterization of carbon black supported Pt-Ru alloy as a model catalyst for fuel cells, 619–26, 2004, with permission from Elsevier.)

TPR analysis is performed using the same system as TPD, but the flowing gas contains a proportion of hydrogen instead of the inert gas used in TPD analysis. While the gas is flowing, the temperature of the sample is increased linearly with time, when the temperature is high enough to make reduction occur, the consumption signal of hydrogen by the reduction reaction can be monitored. For

platinum-based fuel cell catalysts, the addition of second or third components, as well as the change of support, often changes the reduction temperature and improves the performance significantly. TPR analysis is usually a powerful tool to detect additive and support effects.

Zhang et al. [197] investigated a set of bimetallic Pt-Ru catalysts prepared by co-impregnation of carbon black with ruthenium (III) chloride hydrate and hydrogen hexachloroplatinate (IV) hydrate by temperature-programmed reduction (TPR). They found that the reduction temperature of Pt/XC72R catalyst was 388K; when ruthenium was added, the reduction temperature shifted to 428K, and for pure Ru/XC72R catalyst, the reduction temperature was 488K (Figure 10.33).

10.8 Conclusion

Physical characterization of low-temperature fuel cell catalysts is very important for the exploration and preparation of novel catalysts. The emergence of some new techniques, like electrochemical mass spectroscopy (EMS), and continuing progress in some traditional techniques, like SEM and TEM, will effectively improve the characterization of fuel cell catalysts.

References

1. Rastler D. Challenges for fuel cells as stationary power resource in the evolving energy enterprise. J Power Sources 2000;86:34–9.
2. Toda T, Igarashi H, Uchida H, Watanabe M. Enhancement of the electroreduction of oxygen on Pt alloys with Fe, Ni, and Co. J Electrochem Soc 1999;146:3750–6.
3. Li BT, Maruyama K, Nurunnabi M, Kunimori K, Tomishige K. Temperature profiles of alumina-supported noble metal catalysts in autothermal reforming of methane. Appl Catal A General 2004;275:157–72.
4. Hu Z, Wakasugi T, Maeda A, Kunimori K, Soma M, Uchijima T. A comparison of niobia- and vanadia-supported Rh catalysts: The behavior of $RhMO_4$ (M=Nb, V) on SiO_2 during calcinations and reduction treatments. J Catal 1991;127:276–86.
5. Ito S, Chibana C, Nagashima K, Kameoka S, Tomishige K, Kunimori K. CO hydrogenation over $RhVO_4/SiO_2$, Rh/V_2O_3 and Rh/SiO_2 catalysts: reduction and regeneration of $RhVO_4$. Appl Catal A General 2002;236:113–20.
6. Ahmadi TS, Wang ZL, Green TC, Henglein A, El-Sayed MA. Shape-controlled synthesis of colloidal platinum nanoparticles. Science 1996;272:1924–5.
7. Liu ZL, Gan LM, Hong L, Chen WX, Lee JY. Carbon-supported Pt nanoparticles as catalysts for proton exchange membrane fuel cells. J Power Sources 2005;139:73–8.
8. Colon-Mercado HR, Kim H, Popov BN. Durability study of Pt_3Ni1 catalysts as cathode in PEM fuel cells. Electrochem Comm 2004;6:795–9.
9. Salgado JRC, Antolini E, Gonzalez ER. Carbon supported Pt-Co alloys as methanol-resistant oxygen-reduction electrocatalysts for direct methanol fuel cells. Appl Catal B Environmental 2005;57(4):283–90.
10. Shukla AK, Raman RK, Choudhury NA, Prolkar KR, Sarode PR, Emura S, et al. Carbon-supported Pt–Fe alloy as a methanol-resistant oxygen-reduction catalyst for direct methanol fuel cells. J Electroanal Chem 2004;563:181–90.

11. Chai GS, Yoon SB, Yu JS, Choi JH, Sung YE. Ordered porous carbons with tunable pore sizes as catalyst supports in direct methanol fuel cell. J Phys Chem B 2004;108:7074–9.

12. Joo SH, Choi SJ, Oh I, Kwak J, Liu Z, Terasaki O, et al. Ordered nanoporous arrays of carbon supporting high dispersions of platinum nanoparticles. Nature 2001;412:169–72.

13. Liu ZL, Hong L, Tham MP, Lim TH, Jiang HX. Nanostructured Pt/C and Pd/C catalysts for direct formic acid fuel cells. J Power Sources 2006;161:831–5.

14. Jiang JH, Kucernak A. Nanostructured platinum as an electrocatalyst for the electrooxidation of formic acid. J Electroanal Chem 2002;520:64–70.

15. Park S, Xie Y, Weaver MJ. Electrocatalytic pathways on carbon-supported platinum nanoparticles: Comparison of particle-size-dependent rates of methanol, formic acid, and formaldehyde electrooxidation. Langmuir 2002;18:5792–8.

16. Lovic JD, Tripkovic AV, Gojkovic SLJ, Popovic KD, Tripkovic DV, Olszewski P, et al. Kinetic study of formic acid oxidation on carbon-supported platinum electrocatalyst. J Electroanal Chem 2005;581:294–302.

17. Schmidt TJ, Noeske M, Gasteiger HA, Behm RJ, Britz P, Brijoux W, et al. Electrocatalytic activity of PtRu alloy colloids for CO and CO/H_2 electrooxidation: stripping voltammetry and rotating disk measurements. Langmuir 1997;13:2591–5.

18. Arenz M, Stamenkovic V, Schmidt TJ, Wandelt K, Ross PN, Markovic NM. The electro-oxidation of formic acid on Pt-Pd single crystal bimetallic surfaces. Phys Chem Chem Phys 2003;5:4242–51.

19. Mukerjee S, Srinivasan S, Soriaga MP, McBreen J. Role of structural and electronic properties of Pt and Pt alloys on electrocatalysis of oxygen reduction. J Electrochem Soc 1995;142:1409–22.

20. Salgado JRC, Antolini E, Gonzalez ER. Pt-Co/C electrocatalysts for oxygen reduction in H_2/O_2 PEMFCs synthesized by borohydride J Electrochem Soc 2004;151:A2143–9.

21. Salgado JRC, Antolini E, Gonzalez ER. Structure and activity of carbon-supported Pt-Co electrocatalysts for oxygen reduction. J Phys Chem B 2004;108:17767–74.

22. Salgado JRC, Antolini E, Gonzalez RE. Preparation of Pt-Co/C electrocatalysts by reduction with borohydride in acid and alkaline media: the effect on the performance of the catalyst J. Power Sources 2004;138:56–60.

23. Jiang LH, Sun GQ, Sun SG, Liu JG, Tang SH, Li HQ, et al. Structure and chemical composition of supported Pt-Sn electrocatalysts for ethanol oxidation. Electrochim Acta 2005;50:5384–9.

24. Antolini E, Salgado JRC, Giz MJ, Gonzalez ER. Effects of geometric and electronic factors on ORR activity of carbon supported Pt-Co electrocatalysts in PEM fuel cells. Int J Hydrogen Energy 2005;30:1213–20.

25. Lopes T, Antolini E, Colmati F, Gonzalez ER. Carbon supported Pt-Co (3:1) alloy as improved cathode electrocatalyst for direct ethanol fuel cells. J Power Sources 2007;164:111–4.

26. Wang ZB, Yin GP, Shi PF. The influence of acidic and alkaline precursors on Pt Ru/C catalyst performance for a direct methanol fuel cell. J Power Sources 2007;163:688–94.

27. Lee J, Han S, Hyeon T. Synthesis of new nanoporous carbon materials using nanostructured silica materials as templates. J Mater Chem 2004;14:478–86.

28. Fuertes AB. A low-cost synthetic route to mesoporous carbons with narrow pore size distributions and tunable porosity through silica xerogel templates. Chem Mater 2004;16:449–55.

29. Kim T, Park S, Ryoo R. Synthetic route to ordered mesoporous carbon materials with graphitic pore walls. Angew Chem Int Ed 2003;42:4375–9.

30. Kim CH, Lee DK, Pinnavaia TJ. Graphitic mesostructured carbon prepared from aromatic precursors. Langmuir 2004;20:5157–9.

31. Fuertes AB, Alvarez S. Graphitic mesoporous carbons synthesized through mesostructured silica templates. Carbon 2004;42:3049–55.

32. Xia Y, Mokaya R. Synthesis of ordered mesoporous carbon and nitrogen-doped carbon materials with graphitic pore walls via a simple chemical vapor deposition method. Adv Mater 2004;16:1553–8.

33. Joo SH, Pak C, You DJ, Lee SA, Lee HI, Kim JM, et al. Ordered mesoporous carbons (OMC) as supports of electrocatalysts for direct methanol fuel cells (DMFC): effect of carbon precursors of OMC on DMFC performances. Electrochim Acta 2006;52:1618–26.

34. Joo JB, Kim P, Kim W, Yi J. Preparation of Pt supported on mesoporous carbons for the reduction of oxygen in polymer electrolyte membrane fuel cell (PEMFC). J Electroceram 2006;17:713–8.

35. Sevilla M, Fuertes AB. Catalytic graphitization of templated mesoporous carbons. Carbon 2006;44:468–74.

36. Kongkanand A, Vinodgopal K, Kuwabata S, Kamat PV. Highly dispersed Pt catalysts on single-walled carbon nanotubes and their role in methanol oxidation. J Phys Chem 2006;110:16185–8.

37. Yang RZ, Qiu XP, Zhang HR, Li JQ, Zhu WT, Wang ZX, et al. Monodispersed hard carbon spherules as a catalyst support for the electrooxidation of methanol. Carbon 2005;43:11–6.

38. Bessel CA, Laubernds K, Rodriguez NM, Baker RTK. Graphite nanofibers as an electrode for fuel cell applications. J Phys Chem B 2001;105:1115–8.

39. Yoshitake T, Shimakawa Y, Kuroshima S, Kimura H, Ichihashi T, Kubo Y, et al. Preparation of fine platinum catalyst supported on single-wall carbon nanohorns for fuel cell application. Physica B 2002;323:124–6.

40. Li WZ, Liang CH, Zhou WJ, Qiu JS, Li HQ, Sun GQ, et al. Homogeneous and controllable Pt particles deposited on multi-wall carbon nanotubes as cathode catalyst for direct methanol fuel cells. Carbon 2004;42:436–9.

41. Che GL, Lakshmi BB, Fisher ER, Martin CR. Carbon nanotubule membranes for electrochemical energy storage and production. Nature 1998;393:346–9.

42. Rajesh B, Thampi R, Bonard JM, Xanthopoulos N, Mathieu HJ, Viswanathan B. Carbon nanotubes generated from template carbonization of polyphenyl acetylene as the support for electrooxidation of methanol. J Phys Chem B 2003;107:2701–8.

43. Yen CH, Cui XL, Pan HB, Wang SF, Llin YH, Wan CM. Deposition of platinum nanoparticles on carbon nanotubes by supercritical fluid method. J Nanosci Nanotechno 2005;5:1852–7.

44. Chien CC, Jeng KT. Effective preparation of carbon nanotube-supported Pt-Ru electrocatalysts. Mater Chem Phys 2006;99:80–7.

45. Li WZ, Liang CH, Zhou WJ, Qiu JS, Zhou ZH, Sun GQ, et al. Preparation and characterization of multiwalled carbon nanotube-supported platinum for cathode catalysts of direct methanol fuel cells. J Phys Chem B 2003;107:6292–9.

46. Matsumoto T, Komatsu T, Arai K, Yamazaki T, Kijima M, Shimizu H, et al. Reduction of Pt usage in fuel cell electrocatalysts with carbon nanotube electrodes. Chem Commun 2004;7:840–1.

47. Girishkumar G, Vinodgopal K, Kamat PV. Carbon nanostructures in portable fuel cells: single-walled carbon nanotube electrodes for methanol oxidation and oxygen reduction. J Phys Chem B 2004;108:19960–6.

48. Gennett T, Landi BJ, Elich JM, Jones KM, Alleman JL, Lamarre P, et al. Fuel cell applications of nanotube-metal supported catalysts. Solid State Ionics 2002

Symposium; 2002 Dec 2–5; Boston. Mater Res Soc Symposium Proceedings 2003;756:379–84.

49. Li XG, Hsing IM. The effect of the Pt deposition method and the support on Pt dispersion on carbon nanotubes. Electrochim Acta 2006;51:5250–8.

50. Britto PJ, Santhanam KSV, Rubio A, Alonso JA, Ajayan PM. Improved charge transfer at carbon nanotube electrodes. Adv Mater 1999;11:154–7.

51. Jeng KT, Chien CC, Hsu NY, Yen SC, Chiou SD, Lin SH, et al. Performance of direct methanol fuel cell using carbon nanotube-supported Pt-Ru anode catalyst with controlled composition. J Power Sources 2006;160:97–104.

52. ETH Zurich [homepage on the Internet]. Zurich, Switzerland: ETH Zurich c2008 [updated 2007 Aug 29]. Electron diffraction – examples. Available from: http://www.microscopy.ethz.ch/ TEM_ED_examples.htm.

53. Wikipedia. [updated 2008 Feb 26]. X-ray fluorescence. Available from: http://en.wikipedia.org /wiki/X-ray_fluorescence.

54. Brunauer S, Emmett PH, Teller E. Adsorption of gases in multimolecular layers. J Am Chem Soc 1938;60:309–19.

55. Watanabe M, Makita K, Usami H, Motoo S. New preparation method of a high performance gas diffusion electrode working at 100% utilization of catalyst clusters and analysis of the reaction layer. J Electroanal Chem 1986;197:195–208.

56. Watanabe M, Tomikawa M, Motoo S. Experimental analysis of the reaction layer structure in a gas diffusion. J Electroanal Chem 1985;195:81–93.

57. Stevens DA, Dahn JR. Electrochemical characterization of the active surface in carbon-supported platinum electrocatalysts for PEM fuel cells. J Electrochem Soc 2003;150:A770–5.

58. Savinell RF, Zeller RL, Adams JA. Electrochemically active surface area. J Electrochem Soc 1990;137:489–94.

59. Yu JR, Yi BL, Han M, Cheng XL, Shao ZG, Zhang JX. High performance proton exchange membrane fuel cells. Electrochem 1999;5:448–54.

60. Hou JB, Yu HM, Zhang SS, Sun SC, Wang HW, Yi BL, et al. Analysis of PEMFC freeze degradation at –20 degrees °C after gas purging. J Power Sources 2006;162:513–20.

61. Xu HF, Liang YX, Du KQ, Han M, Yi BL. Electrode kinetics of oxygen reduction at Pt/Nafion interfaces. J Dalian Raiway Institute 1998;19:97–100.

62. Ticianelli EA, Derouin CR, Srinivasan S. Localization of platinum in low catalyst loading electrodes to attain high power densities in PEM fuel cell. J Electroanal Chem 1988;251:275–85.

63. Gottesfeld A, Zawodzinski TA. In: Alkire RC, Gerischer H, Kolb DM, Tobias CW, editors. Advances in electrochemical science and engineering, vol. 5 Weinheim:Wiley, 1997;195–301.

64. Prater KB. Polymer electrolyte fuel cells: a review of recent developments. J Power Sources 1994;51:129–44.

65. Kordesch K, Simander G. Fuel cells and their applications. Weinheim: Wiley-VCH, 1996;73.

66. Passalacqua E, Lufrano F, Squadrito G, Patti A, Giorgi L. Influence of the structure in low-Pt loading electrodes for polymer electrolyte cells. Electrochim Acta 1998;43:3665–73.

67. Oetjen HF, Schmidt VM, Stimming U, Trila F. Performance data of a proton exchange membrane fuel cell using H_2/CO as fuel gas. J Electrochem Soc 1996;143:3838–42.

68. Khan MR, Lin SD. Using Pt sols to prepare low Pt-loading electrodes for polymer electrolyte fuel cells. J Power Sources 2006;162:186–91.

69. Sasikumar G, Ihm JW, Ryu H. Dependence of optimum Nafion content in catalyst layer on platinum loading. J Power Sources 2004;132:11–7.

70. Antolini E, Giorgi L, Pozio A, Passalacqua E. Influence of Nafion loading in the catalyst layer of gas-diffusion electrodes for PEFC. J Power Sources 1999;77:136–42.

71. Loffler MS, Gross B, Natter H, Hempelmann R, Krajewski T, Divisek J. Synthesis and characterization of catalyst layers for direct methanol fuel cell applications Phys Chem Chem Phys 2001;3:333–6.

72. Pozio A, Silva RF, De Francesco M, Cardellini F, Giorgi L. A novel route to prepare stable Pt-Ru/C electrocatalysts for polymer electrolyte fuel cell. Electrochim Acta 2002;48:255–62.

73. Cai YF, Liu JM, Liao SJ. Preparation, characterization and electrocatalytic properties of promoted PtMoSi/C catalysts. Acta Phys-Chim Sin 2007;23:92–7.

74. Tian ZQ, Jiang SP, Liang YM, Shen PK. Synthesis and characterization of platinum catalysts on muldwalled carbon nanotubes by intermittent microwave irradiation for fuel cell applications. J Phys Chem B 2006;110:5343–50.

75. Xie FY, Tian ZQ, Meng H, Shen PK. Increasing the three-phase boundary by a novel three-dimensional electrode. J Power Sources 2005;141:211–5.

76. Perez J, Gonzalez ER, Ticianelli EA. Oxygen electrocatalysis on thin porous coating rotating platinum electrodes. Electrochim Acta 1998;44:1329–39.

77. Pozio A, De Francesco M , Cemmi A, Cardellini F, Giorgi L. Comparison of high surface Pt/C catalysts by cyclic voltammetry. J Power Sources 2002;105:13–9.

78. Schuth F. Endo- and exotemplating to create high-surface-area inorganic materials. Angwe Chem Int Ed 2003;42:3604–22.

79. Yang HF, Zhao DY. Synthesis of replica mesostructures by the nanocasting strategy. J Mater Chem 2005;15:1217–31.

80. Zhou HS, Zhu SM, Hibino M, Honma I, Ichihara M. Lithium storage in ordered mesoporous carbon (CMK-3) with high reversible specific energy capacity and good cycling performance. Adv Mater 2003;15:2107–11.

81. Hartmann M, Vinu A, Chandrasekar G. Adsorption of vitamin E on mesoporous carbon molecular sieves. Chem Mater 2005;17:829–33.

82. Su FB, Zeng JH, Bao XY, Yu YS, Lee JY, Zhao XS. Preparation and characterization of highly ordered graphitic mesoporous carbon as a Pt catalyst support for direct methanol fuel cells. Chem Mater 2005;17:3960–7.

83. Stevens DA, Dahn JR. Thermal degradation of the support in carbon-supported platinum electrocatalysts for PEM fuel cells. Carbon 2005;43:179–88.

84. Travitsky N, Ripenbein T, Golodnitsky D, Rosenberg Y, Burshtein L, Peled E. Pt-, PtNi- and PtCo-supported catalysts for oxygen reduction in PEM fuel cells. J Power Sources 2006;161:782–9.

85. Knoll M, Ruska E. Das Elektronenmikroskop. (The electron microscope.) Z Physik 1932;78:318–39.

86. Gurau B, Viswanathan R, Liu RX, Lafrenz TJ, Ley KL, Smotkin ES, et al. Structural and electrochemical characterization of binary, ternary and quaternary platinum alloy catalysts for methanol electro-oxidation. J Phys Chem B 1998;102:9997–10003.

87. Bonnemann H, Brinkmann R, Britz P, Endruschat U, Mortel R, Paulus UA. Nanoscopic Pt-bimetal colloids as precursors for PEM fuel cell catalysts. J New Mater Electr Sys 2000;3:199–206.

88. Paulus UA, Endruschat U, Feldmeyer GJ, Schmidt TJ, Bonnemann H, Behm RJ. New PtRu alloy colloids as precursors for fuel cell catalystc. J Catal 2000;195:383–93.

89. Boxall DL, Deluga GA, Kenik EA, King WD, Lukehart CM. Rapid synthesis of a Pt$_1$Ru$_1$/carbon nanocomposite using microwave irradiation: a DMFC anode catalyst of high relative performance. Chem Mater 2001;13:891–90.

90. Deivaraj TC, Chen WX, Lee JY. Preparation of PtNi nanoparticles for the electrocatalytic oxidation of methanol. J Mater Chem 2003;13:2555–60.

91. Zhang X, Chan KY. Microemulsion synthesis and electrocatalytic properties of platinum-cobalt nanoparticles. J Mater Chem 2002;12:1203–6.
92. Rojas S, Garcia-Garcia FJ, Jaras S, Martinez-Huerta MV, Fierro JLG, Boutonnet M. Preparation of carbon supported Pt and PtRu nanoparticles from microemulsion: electrocatalysts for fuel cell applications. Appl Catal A 2005;285:24–35.
93. Zhang X, Chan KY. Water-in-oil microemulsion synthesis of platinum ruthenium nanoparticles, their characterization and electrocatalytic properties. Chem Mater 2003;15:451–9.
94. Hills CW, Nashner MS, Frenkel AI, Shapley JR, Nuzzo RG. Carbon support effects on bimetallic Pt-Ru nanoparticles formed from molecular precursors. Langmuir 1999;15:690–70.
95. Steigerwalt ES, Deluga GA, Lukehart CM. Rapid preparation of Pt-Ru/graphitic carbon nanofiber nanocomposites as DMFC anode catalysts using microwave processing. J Nanosci Nanotechno 2003;3:247–51.
96. Steigerwalt ES, Deluga GA, Cliffel DE, Lukehart CM. A Pt-Ru/graphitic carbon nanofiber nanocomposite exhibiting high relative performance as a direct-methanol fuel cell anode catalyst. J Phys Chem B 2001;105:8097–101.
97. Steigerwalt ES, Deluga GA, Lukehart CM. Pt-Ru/carbon fiber nanocomposites: Synthesis, characterization, and performance as anode catalysts of direct methanol fuel cells. A search for exceptional performance. J Phys Chem B 2002;106:760–6.
98. Nashner MS, Frenkel AI, Somerville D, Hills CS, Shapley JR, Nuzzo RG. Core shell inversion during nucleation and growth of bimetallic Pt/Ru nanoparticles. J Am Chem Soc 1998;120:8093–101.
99. Nashner MS, Frenkel AI, Adler DL, Shapley JR, Nuzzo RG. Structural characterization of carbon-supported platinum-ruthenium nanoparticles from the molecular cluster precursor $PtRu_5C(CO)(16)$. J Am Chem Soc 1997;119:7760–71.
100. Toda T, Igarashi H, Watanabe M. Enhancement of the electrocatalytic O_2 reduction on Pt–Fe alloys. J Electroanal Chem 1999;460:258–62.
101. Li WZ, Zhou WJ, LI HQ, Zhou ZH, Zhou B, Sun GQ. Nano-structured Pt-Fe/C as cathode catalyst in direct methanol fuel cell. Electrochim Acta 2004;49:1045–55.
102. Mustain WE, Kepler K, Prakash J. CoPdx oxygen reduction electrocatalysts for polymer electrolyte membrane and direct methanol fuel cells. Electrochim Acta 2007;52:2102–8.
103. Stamenkovic VR, Fowler B, Mun BS, Wang GF, Ross PN, Lucas CA, et al. Improved oxygen reduction activity on $Pt_3Ni(111)$ via increased surface site availability. Science 2007;315:493–7.
104. Lima FHB, Lizcano-Valbuena WH, Teixeira-Neto E, Nart FC, Gonzalez ER, Ticianelli EA. Pt-Co/C nanoparticles as electrocatalysts for oxygen reduction in H_2SO_4 and H_2SO_4/CH_3OH electrolytes. Electrochim Acta 2006;52:385–93.
105. Ioroi T, Yasuda K. Platinum-iridium alloys as oxygen reduction electrocatalysts for polymer electrolyte fuel cells. J Electrochem Soc 2005;152:A1917–24.
106. Shukla AK, Neergat M, Bera P, Jayaram V, Hegde MS. An XPS study on binary and ternary alloys of transition metals with platinized carbon and its bearing upon oxygen electroreduction in direct methanol fuel cells. J Electroanal Chem 2001;504:111–9.
107. Arico AS, Shukla AK, Kim H, Park S, Min M, Antonucci V. An APS study on oxidation states of Pt and its alloys with Co and Cr and its relevance to electroreduction of oxygen. Appl Surf Sci 2001;172:33–40.
108. Neergat M, Shukla, AK, Gandhi KS. Platinum-based alloys as oxygen-reduction catalysts for solid-polymer-electrolyte direct methanol fuel cells. J Appl Electrochem 2001;31:373–8.
109. Wasmus S, Kuver A. Methanol oxidation and direct methanol fuel cells: a selective review. J Electroanal Chem 1999;461:14–31.

110. Kordesch K, Simader G. Fuel cells and their applications. Weinheim:VCH, 1996.

111. Gasteiger HA, Markovic NM, Ross PN Jr. H_2 and CO electrooxidation on well-characterized Pt, Ru, and Pt-Ru. 1. Rotating disk electrode studies of the pure gases including temperature effects J Phys Chem 1995;99:8290–301.

112. Yang H, Vogel W, Lamy C, Alonso-Vante N. Structure and electrocatalytic activity of carbon-supported Pt-Ni alloy nanoparticles toward the oxygen reduction reaction. J Phys Chem B 2004;108:11024–34.

113. Liu ZL, Lee JY, Chen WX, Han M, Gan LM. Physical and electrochemical characterizations of microwave-assisted polyol preparation of carbon-supported PtRu nanoparticles. Langmuir 2004;20:181–7.

114. Deivaraj TC, Lee JY. Preparation of carbon-supported PtRu nanoparticles for direct methanol fuel cell applications – a comparative study. J Power Sources 2005;142:43–9.

115. Li WZ, Liang CH, Zhou WJ, Qiu JS, Zhou ZH, Sun GQ. Preparation and characterization of multiwalled carbon nanotube-supported platinum for cathode catalysts of direct methanol fuel cells. J Phys Chem B 2003;107:6292–9.

116. Hyeon T, Han S, Sung YE, Park KW, Kim YW. High-performance direct methanol fuel cell electrodes using solid-phase-synthesized carbon nanocoils. Angew Chem Int Ed 2003;42:4352–6.

117. Liu ZL, Lin XH, Lee JY, Zhang W, Han M, Gan LM. Preparation and characterization of platinum-based electrocatalysts on multiwalled carbon nanotubes for proton exchange membrane fuel cells. Langmuir 2002;18:4054–60.

118. Snow ES, Perkins FK, Houser EJ, Badescu SC, Reinecke TL. Chemical detection with a single-walled carbon nanotube capacitor. Science 2005;307:1942–5.

119. Hertel T, Martel R, Avouris P. Manipulation of individual carbon nanotubes and their interaction with surfaces. J Phys Chem B 1998;102:910–5.

120. Wong SS, Harper JD, Lansbery PL, Lieber CM. Carbon nanotube tips: High-resolution probes for imaging biological systems. J Am Chem Soc 1998;120:603–4.

121. Dillon AC, Jones KM, Bekkedahl TA, Kiang CH, Bethune DS, Heben MJ. Storage of hydrogen in single-walled carbon nanotubes. Nature 1997;386:377–9.

122. Rajalakshmi N, Dhathathreyan KS, Govindaraj A, Satishkumar BC. Electrochemical investigation of single-walled carbon nanotubes for hydrogen storage. Electrochim Acta 2000;45:4511–5.

123. Rajalakshmi N, Ryu H, Shaijumon MM, Ramaprabhu S. Performance of polymer electrolyte membrane fuel cells with carbon nanotubes as oxygen reduction catalyst support material. J Power Sources 2005;140:250–7.

124. Koga K, Gao GT, Tanaka H, Zeng XC. Formation of ordered ice nanotubes inside carbon nanotubes. NATURE 2001;412:802–5.

125. Hynek S, Fuller W, Bentley J. Hydrogen storage by carbon sorption. Int J Hydrogen Energy 1997;22:601–10.

126. Ang LM, Hor TSA, Xu GQ, Tung CH, Zhao SP, Wang JLS. Decoration of activated carbon nanotubes with copper and nickel. Carbon 2000;38:363–72.

127. Che GL, Lakshmi BB, Martin CR, Fisher ER. Metal-nanocluster-filled carbon nanotubes: Catalytic properties and possible applications in electrochemical energy storage and production. Langmuir 1999;15:750–8.

128. Rajesh B, Thampi KR, Bonard JM, Viswanathan B. Preparation of a Pt-Ru bimetallic system supported on carbon nanotubes. J Mater Chem 2000;10:1757–9.

129. Joo SH, Choi SJ, Oh I, Kwak J, Liu Z, Terasaki O, et al. Ordered nanoporous arrays of carbon supporting high dispersions of platinum nanoparticles. Nature 2001;412:169–72.

130. Windawi H, Ho FFL. Applied electron spectroscopy for chemical analysis. New York: John Wiley & Sons, 1982.

131. Mehta V, Cooper JS. Review and analysis of PEM fuel cell design and manufacturing. J Power Sources 2003;114:32–53.
132. Ralph TR, Hogarth MP. Catalysis for low temperature fuel cells Part I: the cathode challenges. Platinum Metals Rev 2002;46:3–14.
133. Prabhuram J, Zhao TS, Wong CW, Guo JW. Synthesis and physical/electrochemical characterization of Pt/C nanocatalyst for polymer electrolyte fuel cells. J Power Sources 2004;134:1–6.
134. Yang B, Lu Q, Wang Y, Zhuang L, Lu J, Liu P. Simple and low-cost preparation method for highly dispersed PtRu/C catalysts. Chem Mater 2003;15:3552–7.
135. Tian Z, Jiang S, Liang Y, Shen P. Synthesis and characterization of platinum catalysts on multiwalled carbon nanotubes by intermittent microwave irradiation for fuel cell applications. J Phys Chem B 2006;110:5343–50.
136. Strmcnik D, Gaberscek M, Hocevar S, Jamnik J. The effect of halide ion impurities and Nafion on electrooxidation of CO on platinum. Solid State Ionics 2005;176:1759–63.
137. Zhao X, Sun G, Jiang L, Chen W, Tang S, Zhou B, Xin Q. Effects of chloride anion as a potential fuel impurity on DMFC performance. Electrochem Solid-State Lett 2005;8:A149–51.
138. Toda T, Igarashi H, Uccida H, Watanabe M. Enhancement of the electroreduction of oxygen on Pt alloys with Fe, Ni, and Co. J Electrochem Soc 1999;146:3750–6.
139. Jaksic MM, Hypo-hyper-d-electronic interactive nature of interionic synergism in catalysis and electrocatalysis for hydrogen reactions. Int J Hydrogen Energy 2001;26:559–78.
140. Antolini E, Formation of carbon-supported PtM alloys for low temperature fuel cells: a review. Mater Chem Phys 2003;78:563–73.
141. Slavcheva E, Nikolova V, Petkova T, Lefterova E, Dragieva I, Vitanov T, Budevski E. Electrocatalytic activity of Pt and PtCo deposited on Ebonex by BH reduction. Electrochim Acta 2005;50:5444–8.
142. Seo A, Lee J, Han K, Kim H. Performance and stability of Pt-based ternary alloy catalysts for PEMFC. Electrochim Acta 2006;52:1603–11.
143. Arico¡a, AS, Shuklab AK, Kimc H, Parkc S, Minc M, Antonucci V. An XPS study on oxidation states of Pt and its alloys with Co and Cr and its relevance to electroreduction of oxygen. Appl Surf Sci 2001;172:33–40.
144. Shukla AK, Neergat M, Bera P, Jayaram V, Hegde MS. An XPS study on binary and ternary alloys of transition metals with platinized carbon and its bearing upon oxygen electroreduction in direct methanol fuel cells. J Electroanal Chem 2001;504:111–9.
145. Schmidt TJ, Noeske M, Gasteiger AH, Behm RJ, Britz P, Brijoux W, Bonnemann H. PtRu alloy colloids as precursors for fuel cell catalysts: a combined XPS, AFM, HRTEM, and RDE study. J Electrochem Soc 1998;145:925–31.
146. Paulus UA, Endruschat U, Feldmeyer GJ, Schmidt TJ, Bonnemann H, Behm RJ. New PtRu alloy colloids as precursors for fuel cell catalysts. J Catal 2000;195:383–93.
147. Zhou Z, Wang S, Zhou W, Wang G, Jiang L, Li W, Song S, Liu J, Sun G, Xin Q. Novel synthesis of highly active Pt/C cathode electrocatalyst for direct methanol fuel cell. Chem Commun 2003;394–5.
148. Chen WX, Lee JY, Liu Z. Microwave-assisted synthesis of carbon supported Pt nanoparticles for fuel cell applications. Chem Commun 2002;2588–9.
149. Yu R, Chen L, Liu Q, Lin J, Tan KL, Ng SC, Chan HSO, Xu GQ, Hor TSA. Platinum deposition on carbon nanotubes via chemical modification. Chem Mater 1998;10:718–22.
150. Tsang SC, Chen YK, Harris PJF. Green MLH. A simple chemical method of opening and filling carbon nanotubes. Nature 1994;372:159–62.

151. Hwang KC. Efficient cleavage of carbon grathene layers by oxidants. J Chem Soc Chem Commun 1995;173–4.
152. Liu Z, Lin X, Lee J, Zhang W, Han M, Gan, L. Preparation and characterization of platinum-based electrocatalysts on multiwalled carbon nanotubes for proton exchange membrane fuel cells. Langmuir 2002;18:4054–60.
153. Nieminen M, Sajavaara T, Rauhala E, Putkonen M, Niinisto L. Surface-controlled growth of $LaAlO_3$ thin films by atomic layer epitaxy. J Mater Chem 2001;11:2340–5.
154. Hatanpaa T, Vehkamaki M, Mutikainen I, Kansikas J, Ritala M, Leskela M. Synthesis and characterisation of cyclopentadienyl complexes of barium: precursors for atomic layer deposition of $BaTiO_3$. Dalton Trans 2004;1181–8.
155. Shim JH, Chao C, Huang H, Prinz FB. Atomic layer deposition of yttria-stabilized zirconia for solid oxide fuel cells. Chem Mater 2007;19:3850–4.
156. Bielawa H, Hinrichsen O, Birkner A, Muhler M. The ammonia-synthesis catalyst of the next generation: barium-promoted oxide-supported ruthenium. Angew Chem Int Ed 2001;40:1061–2.
157. Forni L, Molinari D, Rossetti I, Pernicone N. Carbon-supported promoted Ru catalyst for ammonia synthesis. Appl Catal A 1999;185:269–75.
158. Hansen TW, Hansen PL, Dahl S, Jacobsen CJH. Support effect and active sites on promoted ruthenium catalysts for ammonia synthesis. Catal Lett 2002;84:7–12.
159. Guraya M, Sprenger S, Rarog-Pilecka W, Szmigiel D, Kowalczyk Z, Muhler M. The effect of promoters on the electronic structure of ruthenium catalysts supported on carbon. Appl Surf Sci 2004;238:77–81.
160. Arico AS, Srinivasan R, Antonucci V. DMFCs: from fundamental aspects to technology development. Fuel Cells 2001;1:133–61.
161. Watanabe M, Motoo S. Electroanalytical chemistry and interfacial electrochemistry. J Electroanal Chem 1975;60:267–77.
162. Grgur BN, Zhuang G, Markovic NM, Ross PN. Electrooxidation of H_2/CO mixtures on a well-characterized $Pt_{75}Mo_{25}$ alloy surface. J Phys Chem B 1997;101:3910–3.
163. Ishikawa Y, Liao MS, Cabrera CR. Energetics of H_2O dissociation and $CO_{ads} + OH_{ads}$ reaction on a series of Pt-M mixed metal clusters: a relativistic density-functional study. Surf Sci 2002;513:98–110.
164. Jiang Z, Huang W, Zhang Z, Zhao H, Tan D, Bao X. Multiple coordination of CO on molybdenum nanoparticles: evidence for intermediate $Mo_x(CO)_y$ species by XPS and UPS. J Phys Chem B 2006;110:26105–13.
165. Nashner MS, Frenkel AI, Somerville D, Hills CW, Shapley JR, Nuzzo RG. Core shell inversion during nucleation and growth of bimetallic Pt/Ru nanoparticles. J Am Chem Soc 1998;120:8093–101.
166. Pan C, Dassenoy F, Casanove MJ, Philippot K, Amiens C, Lecante P, Mosset A, Chaudret B. A new synthetic method toward bimetallic ruthenium platinum nanoparticles: composition induced structural changes. J Phys Chem B 1999;103:10098–101.
167. Moore JT, Corn JD, Chu D, Jiang R, Boxall DL, Kenik EA, Lukehart CM. Synthesis and characterization of a Pt_3Ru_1/Vulcan carbon powder nanocomposite and reactivity as a methanol electrooxidation catalyst. Chem Mater 2003;15:3320–5.
168. Boxall DL, Deluga GA, Kenik EA, King, WD, Lukehart CM. Rapid synthesis of a Pt_1Ru_1/carbon nanocomposite using microwave irradiation: a DMFC anode catalyst of high relative performance. Chem Mater 2001;13:891–900.
169. Kim YM, Choi SH, Lee HC, Hong MZ, Kim K, Lee HI. Organic-inorganic composite membranes as addition of SiO_2 for high temperature-operation in polymer electrolyte membrane fuel cells (PEMFCs). Electrochim Acta 2004;49:4787–96.

170. Woo MH, Kwon O, Choi SH, Hong MZ, Ha HW, Kim K. Zirconium phosphate sulfonated poly (fluorinated arylene ether)s composite membranes for PEMFCs at 100–140 °C. Electrochim Acta 2006;51:6051–9.

171. Wilson MS, Garzon HG, Sickafus KE, Gottesfeld S. Surface area loss of supported platinum in polymer electrolyte fuel cells. J Electrochem Soc 1993;140:2872–7.

172. St-Pierre J, Wilkinson DP, Knights S, Bos ML. Relationships between water management, contamination and lifetime degradation in PEFC. J New Mater Electrochem Syst 2000;3:99–106.

173. Stevens DA, Dahn JR. Thermal degradation of the support in carbon-supported platinum electrocatalysts for PEM fuel cells. Carbon 2005;43:179–88.

174. Baturina OA, Aubuchon SR, Wynne KJ. Thermal stability in air of Pt/C catalysts and PEM fuel cell catalyst layers. Chem Mater 2006;18:1498–504.

175. Roen LM, Paik CH, Jarvi TD. Electrocatalytic corrosion of carbon support in PEMFC cathodes. Electrochem Solid-State Lett 2004;7:A19–22.

176. Samms SR, Wasmus S, Savinell RF. Thermal stability of Nafion in simulated fuel cell environments. J Electrochem Soc 1996;143:1498–504.

177. Hogarth M, Ralph T. Catalysis for low temperature fuel cell, Part III: challenges for direct methanol fuel cell. Platinum Met Rev 2002;46:146–64.

178. Wasmus S, Kuver A. Methanol oxidation and direct methanol fuel cells: a selective review. J. Elctroanal Chem 1999;461:14–31.

179. McNicol BD, Rand D, Williams K. Direct methanol-air fuel cells for road transportation. J Power Sources 1999;83:15–31.

180. Rolison DR. Catalytic nanoarchitectures: the importance of nothing and the unimportance of periodicity. Science 2003;299:1698–701.

181. Long JW, Stroud RM, Swider-Lyons KE, Rolison DR. How to make electrocatalysts more active for direct methanol oxidation: avoid PtRu bimetallic alloys. J Phys Chem B 2000;104:9772–6.

182. Rolison DR, Hagans P, Swider-Lyons KE, Long JW. Role of hydrous ruthenium oxide in Pt-Ru direct methanol fuel cell anode electrocatalysts: the importance of mixed electron/proton conductivity. Langmuir 1999;15:774–9.

183. Iwasita T. Electrocatalysis of methanol oxidation. Electrochim Acta 2002;47:3663–74.

184. Thomas SC, Ren XM, Gettesfeld S. Influence of ionomer content in catalyst layers on direct methanol fuel cell performance. J Electrochem Soc 1999;146:4354–9.

185. Ren X, Wilson M, Gottesfeld S. High performance direct methanol polymer electrolyte fuel cell. J Electrochem Soc 1996;143:L12–15.

186. Yang B, Lu Q, Wang Y, Zhuang L, Lu J, Liu P. Simple and low-cost preparation method for highly dispersed PtRu/C catalysts. Chem Mater 2003;15:3552–7.

187. Gubler L, Gürsel S, Scherer G. Radiation grafted membranes for polymer electrolyte fuel cells. Fuel Cells 2005;5:317–35.

188. Savadogo O. Emerging membranes for electrochemical systems: Part II. High temperature composite membranes for polymer electrolyte fuel cell (PEFC) applications. J Power Sources 2004;127:135–61.

189. Alberti G, Casciola M. Composite membranes for medium-temperature PEM fuel cells. Annual review of materials science 2003;33:129–54.

190. Kerres, JA. Development of ionomer membranes for fuel cells. J Membr Sci 2001;185:3–27.

191. Hickner, MA, Ghassemi H, Kim YS, Einsla R, McGrath J. Alternative polymer systems for proton exchange membranes (PEMs). Chem Rev 2004;104:4587–611.

192. Kreuer, KD. On the development of proton conducting polymer membranes for hydrogen and methanol fuel cells. J Membr Sci 2001;185:29–39.

193. Kaliaguine S, Mikhailenko SD, Wang KP, Xing P, Robertson G, Guiver M. Properties of SPEEK-based PEMs for fuel cell application. Catal Today 2003;82:213–22.

194. Robertson GP, Mikhailenko SD, Wang K, Xing P, Guiver MD, Kaliaguine S. Casting solvent interactions with sulfonated poly(ether ether ketone) during proton exchange membrane fabrication. J Membr Sci 2003;219:113–21.
195. Luisa Di Vona M, Ahmed Z, Bellitto S, Lenci A, Traversa E, Licoccia S. SPEEK-TiO$_2$ nanocomposite hybrid proton conductive membranes via in situ mixed sol-gel process. J Membr Sci 2007;296:156–61.
196. Munk J, Christensen A. P, Hamnett A., Skou E. The electrochemical oxidation of methanol on platinum and platinum + ruthenium particulate electrodes studied by in-situ FTIR spectroscopy and electrochemical mass spectrometry. J Electroanal Chemistry 1996;401:215–22.
197. Zhang YJ, Maroto-Valiente A, Rodriguez-Ramos I, Xin Q, Guerrero-Ruiz A. Synthesis and characterization of carbon black supported Pt-Ru alloy as a model catalyst for fuel cells. Catalysis Today 2004;93:619–26.

11

Electrochemical Methods for Catalyst Activity Evaluation

Zhigang Qi

11.1 Electrochemical Cells

11.1.1 Introduction

Since a fuel cell is an electrochemical device, electrochemical methods are deemed to play important roles in characterizing and evaluating the cell and its components such as the electrode, the membrane, and the catalyst. The most popular electrochemical characterization methods include potential step, potential sweep, potential cycling, rotating disk electrode, rotating ring-disk electrode, and impedance spectroscopy. Some techniques derived from these methods are also used for fuel cell characterization.

An electrochemical reaction involves at least the following steps: transport of the reactants to the surface of the electrode, adsorption of the reactants onto the surface of the electrode, charge transfer through either oxidation or reduction on the surface of the electrode, and transport of the product(s) from the surface of the electrode. The purpose of the electrochemical characterizations is to determine the details of these steps.

The characterizations are carried out in various electrochemical cells. There are typically three types of cells: conventional 3-electrode cells, half-cells, and single cells. In those cells, the entity (e.g., catalyst, electrode) to be characterized forms the working electrode, the potential of which or the current passing through which is controlled or monitored. What happens on the working electrode is the sole interest of the investigation. The working electrode and another electrode, called the counter electrode, form a circuit, and the current flowing through this circuit will cause some reaction on the counter electrode as well. However, the investigation has no interest in what happens on the counter electrode, except that the reaction occurring on it should not interfere with the working electrode.

In order to minimize the impact of the solution (or electrolyte) resistance on the potential of the working electrode, a reference electrode is often used to form another circuit with the working electrode. Ideally, this electrode is non-polarizable and maintains a stable potential. There is high input impedance in the voltage

measurement equipment, which makes the current flowing in this circuit very small. Therefore, the impact of the uncompensated electrolyte resistance on the potential of the working electrode is minimized.

In this article, each section starts with a brief introduction to techniques, principles, and instrumentation, followed by examples for the purposes of illustration. The illustration is limited to low- to medium-temperature fuel cells such as the proton exchange membrane (PEM), direct liquid, and phosphoric acid fuel cells that involve protons as the ionic charge transport species.

11.1.2 Conventional 3-Electrode Cells

11.1.2.1 Structure of the Cell

Figure 11.1 depicts the basic structure of a conventional 3-electrode cell. The exposed surface of an electronically conducting disk such as glassy carbon, gold, or platinum sealed in an inert material such as glass is the working electrode. A piece of Pt coil or sheet with a surface area much larger than that of the working electrode is used as the counter electrode. The purpose of a larger counter electrode is to assure that the electrochemical reaction occurring on it is fast enough so that it does not impede the electrochemical reaction occurring on the working electrode. The reference electrode is typically hosted in a Luggin capillary whose fine tip can be placed very close to the surface of the working electrode to minimize the impact of the uncompensated electrolyte resistance without preventing the reactants from reaching the surface of the working electrode. The most popular reference electrodes are $Pt/H_2/H^+$ (standard/or normal/or dynamic hydrogen electrode), $Ag/AgCl/Cl^-$ (silver/silver chloride electrode), and $Hg/Hg_2Cl_2/Cl^-$ (calomel electrode). If the products from the counter electrode could potentially interfere with the reaction occurring on the working electrode, the counter electrode is often confined in a separate compartment from the working electrode by either a porous frit such as sintered porous glass or an electrolyte bridge.
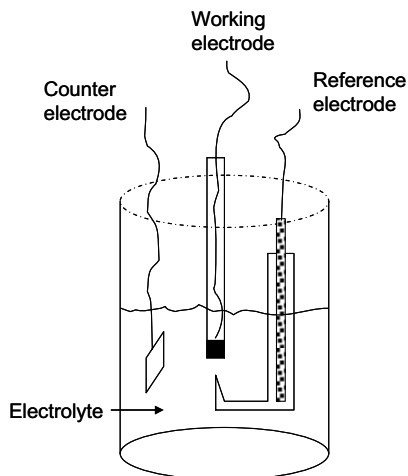
Figure 11.1. Illustration of the basic structure of a conventional 3-electrode cell

11.1.2.2 Preparation of the Electrode

For fuel cell applications, this kind of cell is typically used to screen new catalysts or to study reaction mechanisms and kinetics by coating the electrode with a layer of catalysts. A catalyst is first thoroughly mixed with other components in a solvent through agitation and/or sonication. Water is typically the major component of the solvent, along with some short chain alcohols such as ethanol and propanol. Other solvents may be added in order to create a formulation that can be dispersed onto the working electrode satisfactorily. Sonication and agitation can increase the temperature of the mixture, which may change its physical properties such as its viscosity. The catalyst formulation is then applied onto the surface of the working electrode and dried. It is important that the catalyst particles adhere to the surface of the working electrode. In order to enhance adhesion, additives may be used in the catalyst ink formulation. The most convenient additives are perfluorinated ionomers such as DuPont's Nafion. An additional thin ionomer layer can also be added on top of the catalyst layer to enhance adhesion. Drying the electrode at room temperature versus at a temperature above the glass transition temperature (T_g) of the ionomer can affect adhesion and the properties of the resulting catalyst layer. The surface of the electrode disk itself should be inactive to the electrochemical reaction. For example, if the catalyst particles under investigation are Pt-based, the disk material cannot be Pt. Instead, it could be glassy carbon, which does not catalyze the reactions.

If good adhesion is difficult to achieve, a cavity above the disk can be made to hold the catalyst. It is preferred that the height of the cavity be adjustable so that variable catalyst layer thicknesses can be studied.

11.1.2.3 Selection of the Electrolyte

A dilute aqueous acid solution (e.g., 0.1–1 M) is typically used as the electrolyte. The reason for using acid is that the fuel cell reactions involve protons (note: this article is limited to reactions having protons as the ionic charge transport species). Sulfuric acid (H_2SO_4) has been used in many studies. However, sulfate anions (SO_4^{2-}) can adsorb onto the surface of the Pt catalyst, which alters the reaction kinetics. Perchlorate anion (ClO_4^-) from perchloric acid ($HClO_4$) does not adsorb onto the surface of Pt catalysts, and, therefore, could be a better choice.

Since a perfluorosulfonic acid ionomer such as Nafion is normally used to make the catalyst layer, trifluoromethane sulfonic acid (CF_3SO_3H) is expected to behave more closely to the ionomer than the inorganic acids are. In addition, CF_3SO_3H and its anion ($CF_3SO_3^-$) do not adsorb onto the surface of the Pt catalyst and thus do not affect the reaction kinetics.

When an electrode is evaluated for a phosphoric acid (H_3PO_4) fuel cell (PAFC), H_3PO_4 becomes the preferred choice for the electrolyte. The test can be carried out in a dilute aqueous solution at a temperature below the boiling point of water. However, such a test does not represent the actual fuel cell environment, where the cell temperature can be as high as 200 °C and the H_3PO_4 is in a concentrated form containing only a small percentage of water. So, the test is better carried out near the actual fuel cell environment using a concentrated H_3PO_4.

At around 200 °C only a small percentage of H_3PO_4 dissociates into protons and $H_2PO_4^{2-}$ because of the lack of water. Meanwhile, some H_3PO_4 forms

oligomers due to dehydration. It is believed that it is mainly the H_3PO_4 rather than the $H_2PO_4^{2-}$ that adsorbs onto the surface of the Pt catalyst to slow down the reaction kinetics at such a temperature [13]. The adsorption of H_3PO_4 results in a thicker double layer than that resulting from the adsorption of H_2O, and thus increases the electron transfer barrier and reduces the oxygen reaction sites. The exchange current density for oxygen reduction in 98% H_3PO_4 is about 1 to 2 orders of magnitude lower than that in 85% H_3PO_4 [46]. Habib and Bockris found that the adsorption of H_3PO_4 onto Pt initially increases with the electrode potential, reaches a maximum at around 800 mV, and decreases at higher potentials [16].

At a temperature of around 200 °C the fuel cell reaction should proceed much more quickly than it does at the lower temperatures typical for PEM fuel cells (PEMFCs). However, since both H_3PO_4 and $H_2PO_4^{2-}$ can adsorb onto the surface of the Pt catalyst, they significantly lower the reaction kinetics, especially for the oxygen reduction reaction (ORR). Consequently, a PAFC operated at about 200 °C proceeds much more slowly than a PEMFC operated at less than 90 °C. As shown in Figure 11.2, the performance of the state-of-the-art PAFC operated at 160 °C is about 150 mV lower than that of a PEMFC operated at 70 °C.
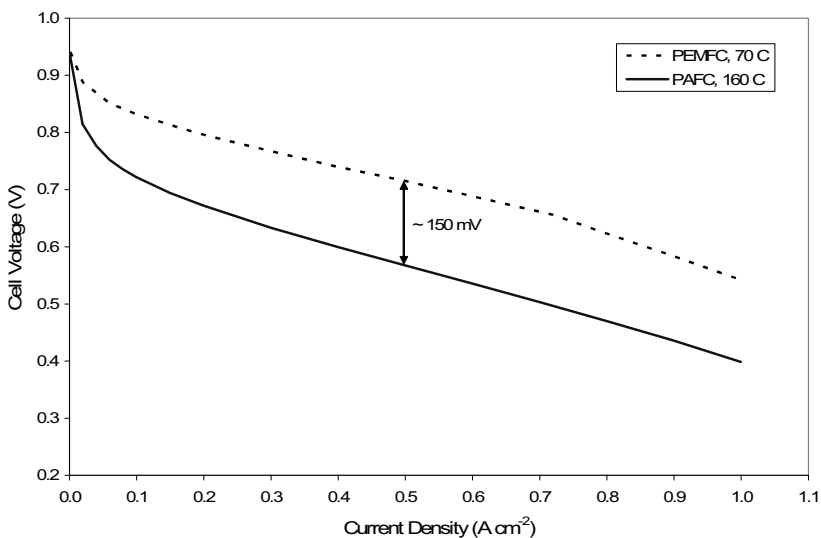
Figure 11.2. Performance comparison of the state-of-the-art PAFC operated at 160 °C with a PEMFC operated at 70 °C. Pt/C catalysts.

Another reason for the lower performance in H_3PO_4 is the low solubility and diffusivity of oxygen in it. They decrease with an increase in the concentration of the H_3PO_4. In 85 wt% acid, the solubility and diffusion coefficient of oxygen are about an order of magnitude and fivefold lower, respectively, than those in perfluorinated ionomers [42].

When a perfluorinated short chain acid such as CF_3SO_3H is added into H_3PO_4, the ORR performance is improved due to the higher oxygen solubility and diffusivity in CF_3SO_3H, and to the weakening of H_3PO_4 adsorption onto the

catalyst surface. However, since CF_3SO_3H has a high vapor pressure, it will evaporate quickly, and thus it has no practical usage. Other reported additives that vaporize at slower rates include potassium perfluorohexanesulfonate ($C_6F_{13}SO_3K$), potassium nonafluorobutanesulfonate ($C_4F_9SO_3K$), and perfluorotributylamine ($(C_4F_9)_3N$) [11].

The addition of 0.5 wt% perfluorosulfonimide (PFSI), $CF_3SO_2NHSO_2C_4F_9$, to 85% H_3PO_4 results in a 70 mV increase in the potential of the oxygen cathode at current densities up to 500 mA cm^{-2} at 70 °C [42]. Razaq et al. proposed that the PFSI physically adsorbs on the catalyst with the fluorocarbon tail towards the catalyst surface to create a "dry cave" environment, which favors the competitive adsorption of oxygen on the catalyst surface, and thus the ORR is enhanced. This adsorbed layer may be only a single molecule thick, and does not interfere with the transfer of water or protons at the interface.

Higher amount of additives or longer chained additives could wet the polytetrafluoroethylene (PTFE) in the electrodes and cause flooding. Flooding of the porous electrode has not been observed at 0.5 wt% of PFSI but has been observed at higher concentrations [42].

11.1.2.4 Control of Experimental Conditions

The primary condition that requires control is the cell temperature. Good control can be achieved by immersing the cell into a water or oil bath the temperature of which can be precisely controlled. If the design does not allow such a control strategy, an electrical heating element can be used. The latter method is, however, more likely to encounter frequent temperature oscillations because the heater may overshoot from time to time.

11.1.3 Half-cells

11.1.3.1 Design of the Cell

The performance of a fuel cell depends not only on the catalyst material but also on the structure of the electrode made from the catalyst material. Since catalyst particles such as Pt black or Pt/C do not stick to each other, a binding material is needed when an electrode is made. Polytetrafluoroethylene is widely used as the binding material for fuel cell electrodes, and it also functions as a water-repelling agent to minimize electrode flooding. When Nafion is used as the binding material, it significantly increases the catalyst-electrolyte-reactant triple phase boundaries, leading to higher catalyst utilization and a lower catalyst loading requirement.

A formulation consisting of catalyst particles and a binding agent is typically applied to a porous backing substrate such as carbon paper or carbon cloth. The backing provides not only a support to hold the catalyst mixture but also the electrical connection with other cell components.

A half-cell is often used to evaluate an electrode. Figure 11.3 illustrates the structure of a half-cell. An electrode is bonded onto one side of a piece of Nafion membrane and the resulting assembly is placed in a fixture in such a way that the Nafion membrane faces the electrolyte solution and the electrode backing side faces a gas chamber. Since the Nafion membrane is permselective, it allows only cations such as protons to pass through. Anions such as SO_4^{2-} should not be able to

pass through the membrane to reach the catalyst layer due to Donna exclusion. Meanwhile, the membrane is fully hydrated by the water in the electrolyte solution. Such a cell structure more or less mimics the situation in a real fuel cell. A ring made of corrosion-resistant metal such as Pt is placed in contact with the electrode backing for current collection. The tip of the Luggin capillary, which hosts a reference electrode, is placed near the surface of the Nafion membrane in order to reduce the voltage drop due to the uncompensated electrolyte resistance between the working and the reference electrodes.

Such a half-cell fixture enables quick screening of an electrode of interest without complications from what happens on the counter electrode. The electrode of interest can be either a cathode or an anode.
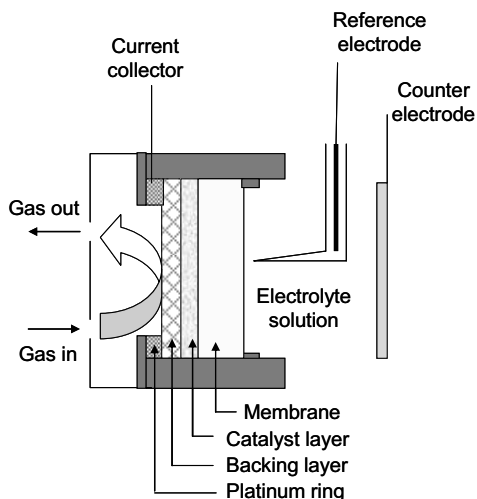
Figure 11.3. Illustration of the structure of a half-cell.

11.1.3.2 Selection of the Electrolyte
Electrolyte selection is very similar to what is described for the 3-electrode cell. Since the catalyst layer is separated from the aqueous electrolyte solution by a permselective ionomer membrane, only water and protons can transport through the membrane to reach the catalyst layer. This helps minimize or eliminate the adverse impact of anion adsorption (onto the catalyst surface) on the reaction kinetics.

The membrane is likely to swell in the aqueous solution and this could cause warping of the electrode/membrane assembly. This will then change the distance between the membrane and the tip of the Luggin capillary, which alters the uncompensated solution resistance slightly. So it is better to position the tip of the reference electrode after warping is complete. If the warping causes delamination of the electrode from the membrane, the testing result will be adversely affected.

One method to reduce the warping is to use a small membrane/electrode assembly. Another method is to add a stiff mesh on top of the membrane/electrode assembly. The mesh should be highly open and inert to the reaction environment.

11.1.3.3 Control of Experimental Conditions

In addition to the cell temperature, the flow rate, the inlet and outlet pressures, and the relative humidity (RH) of the gaseous reactant should be controlled. The temperature is controlled by the aqueous electrolyte into which the electrode/membrane assembly is immersed. The electrolyte temperature can itself be controlled by either a water or an oil bath. The flow rate of the gaseous reactant can be controlled by a flow meter or a mass flow controller. The inlet and back pressures of the reactant can be controlled by pressure regulators. The RH can be controlled by passing the reactant through a humidifier at a predetermined temperature. There are several types of humidifiers to choose from. The cheapest one is a sparging bottle that contains water.

11.1.4 Single Cells

11.1.4.1 Design of the Cell

A single cell can be conveniently used to test a membrane electrode assembly (MEA) consisting of an anode and a cathode bonded onto opposite sides of a membrane. The MEA is sandwiched between a pair of anode and cathode plates that have channels in which the reactants can flow. The edges of the MEA are sealed by a pair of gaskets to prevent leakage of the reactants. The plates are typically made of graphite materials with high corrosion resistance. If metallic materials are used for making the plates, they must be coated by a corrosion-resistant material such as gold or metal nitride. Current collectors in contact with the outer surface of the plates enable the measurement of the current and the voltage. Bolts and nuts are often used to tighten the cell to a predetermined compression or torque level via a pair of end plates. The end plates are insulated from the current collectors by the use of insulating materials.

The surface characteristics of the plates can have a significant impact on the fuel cell performance, stability, and durability. Both highly hydrophilic and hydrophobic surfaces help water removal from the flow-fields. Liquid water tends to form a thin layer on highly hydrophilic surfaces. This increases the contact area between the gaseous exhaust and the liquid water and thus aids the evaporation and removal of water. On the other hand, when the plate surface is highly hydrophobic, liquid water droplets have a low affinity to the surface, and they can be readily blown out by the gaseous exhaust.

The geometry of the flow-field also has a significant impact on the fuel cell. The geometry includes the width and the depth of the channel, the width of the land, and the shape and the length of the channel. A reasonable starting point for dimension optimization is 1 mm for the channel width, the channel depth, and the land width. The channels can be straight, without any twists and turns for the flow of the reactants. This kind of channel offers lower reactant pressure drop from the inlet to the outlet. The channels can also be serpentine with either single or multiple paths. Serpentine channels have twists and turns for the flow of the reactants and are normally longer than the straight channels, which cause a higher reactant pressure drop. Liquid water tends to accumulate at the turns. A higher pressure drop consumes more parasitic power, but it helps remove liquid water

from the cell to reduce the likelihood of flooding. Flow-through straight and serpentine channels are the most common flow-field designs.

An interdigited flow-field is a special type of flow-field in which there are separate reactant inlet and outlet channels. The reactants have to be pushed through the gas diffusion backing by a high enough pressure to get from the inlet channels to the outlet channels. Such a design encounters relatively high parasitic power losses when generating the required pressure. However, since the reactants get into the catalyst layers not only through diffusion but also through convection, higher fuel cell performance is achieved.

Another special type of flow-field is composed of many grids or islands, and the reactants flow among them. The flow pattern of the reactant can vary from moment to moment, and an extremely low reactant pressure drop is expected thanks to the many available paths. If there is an accumulation of water in some regions, the reactant is likely to bypass these regions and they become less active or even inactive until the accumulated water is removed.

When porous plates are used there can be no flow-fields at all. The reactants are pushed into the porous plates and are transported to the catalyst layers through both convection and diffusion. A high reactant pressure drop is expected. Action needs to be taken to prevent the mixing of the anode reactant and the cathode reactant through the porous plates.

In a single cell with an anode and a cathode, the measured cell voltage (V_{cell}) is the difference between the cathode potential (V_c) and the anode potential (V_a). If pure hydrogen is used as the fuel, the anode can be taken to be the reference electrode because its potential does not change much with current density, especially at current densities lower than about 0.5 A cm^{-2}. Then V_{cell} can be regarded as equivalent to the V_c.

If the hydrogen contains contaminates such as CO, or if a liquid such as methanol is used as the fuel in a direct methanol fuel cell (DMFC), the voltage loss at the anode becomes significant; thus it cannot be used as a reference electrode. There are two ways to figure out the individual potentials at the anode and the cathode. The first option is to replace the oxidant such as air with pure hydrogen at the cathode and use an external power supply to oxidize the fuel at the anode side. Protons produced from the oxidation transport through the membrane and combine with the electrons from the power supply to form hydrogen at the cathode side. Since the H$^+$ reduction reaction at the cathode has a negligible overpotential, it can be regarded as a reference electrode. Therefore, V_{cell} applied from the power supply represents the actual V_a. The V_c under the fuel cell mode is then the sum of V_a and V_{cell}.

The second option is to incorporate a reference electrode, as shown in Figure 11.4. A small electrode separate from the anode is bonded onto the membrane. Pure hydrogen is fed to this reference electrode so that it behaves like a dynamic hydrogen electrode (DHE) the potential of which is 0 V. The voltage measured between the anode or the cathode and this reference electrode is the V_a or the V_c. Such a cell design enables the measurement of the individual V_a and V_c in a single experiment, and thus it is very useful.
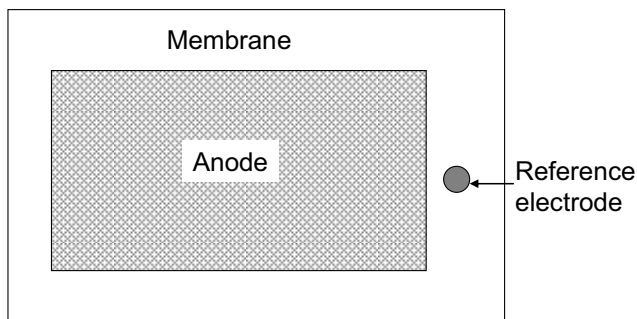
Figure 11.4. Illustration of an MEA with a reference electrode on the anode side.

11.1.4.2 Control of Experimental Conditions

The cell temperature and the RH, the flow rates, and the inlet and outlet pressures of both the anode and the cathode reactants should be controlled. In order to control the cell temperature, both heating and cooling means are typically used. One way to heat up the cell is to use rod-type heating cartridges, which are inserted into holes drilled into the flow-field plates. Although the flow-field plates have good thermal conductivity, it is likely that the temperature of the portion of the MEA or the plate nearest the heating rods is higher than areas that are farther away. Another way to heat up the cell is to use heating pads attached on the outer surfaces of the end plates, provided the end plates possess good thermal conductivity. Since the pads can be made large enough to cover the entire active area of the MEA, a more even temperature distribution over the MEA will be achieved. A third method to heat up the cell is to pump a preheated liquid through both the anode and the cathode plates. Such a method can achieve a very even temperature distribution, but takes more time.

Heating rods and pads can overheat from time to time, resulting in a cell temperature temporarily higher than the desired value. Also, when a high current density is drawn from the cell, it can cause the cell temperature to become higher than desired. Cooling a cell via natural or forced air convection is a simple but less effective process. A more effective way is to continuously circulate a liquid coolant such as water through the plates of the cell. The temperature of the coolant is controlled by a coolant tank. Coolant can also be used to warm up the cell. It is important that a high ionic resistance of the liquid coolant be maintained; otherwise, the electrodes will be shorted by the coolant and get damaged quickly. Liquid coolant can also cause corrosion of cell components and connection pipes.

Temperature-sensing devices such as thermal couples are used to monitor the temperature of the cell. The thermal couples should be placed as close as possible to the MEA in order to reflect the true MEA temperature. Thus they should be inserted into the flow-field plates rather than into the end plates. If the thermal couples are inserted into the end plates, the monitored temperature is likely to be lower than the actual MEA temperature because they are located farther away from the MEA, where the heat is generated. The thermal couples should also be inserted to a proper depth into the flow-field plates in order to capture the average temperature of the MEA. Without a liquid coolant, the center of the MEA is likely

to have a higher temperature than the edges due to the heat loss from the cell. If the thermal couples are inserted right to the center of the MEA, the monitored temperature is probably higher than the average MEA temperature. In contrast, if the thermal couples are inserted to the edge of the MEA, the monitored temperature is probably lower than the average MEA temperature. A best depth for the thermal couples could be the midpoint between the edge and the center of the MEA, and it should be determined experimentally.

It is very important to monitor and control the cell temperature as accurately as possible. For a PEMFC, water management is a tough challenge. If there is too much water in the fuel cell, the cell will be flooded. If there is not enough water, the cell will dry up. Both situations will lower the cell performance, stability, and durability. The RH of the reactants is typically controlled by controlling the temperature of the humidifier relative to the cell temperature. For example, if the cell temperature is 60 °C and the humidifier temperature is 55 °C, the RH of the reactant is 80%. However, if the actual cell temperature is 65 °C, the RH is only 63%. Running a cell at an RH lower than the desired value will cause the cell to decay more rapidly. The same is true if the cell is flooded.

11.2 Brief Principles of Electrochemical Instrumentation

All electrochemical techniques involve the use of electricity as either an input or an output signal. The function of an electrochemical instrument is to generate an input electrical signal and to measure the corresponding output electrical signal. The input signals can be a preprogrammed function of time, while the output signals often change with time. The signals are typically voltage, current, and charge. Charge is the integration of current with time. The input electrical signal causes the electrochemical reactions at the working and the counter electrodes. The rate of the reactions is controlled by the amplitude of the input signal and is represented by the amplitude of the output signal. More details will be given in the discussions of different types of electrochemical techniques.

11.3 Cyclic Voltammetry

11.3.1 Basic Principles

Cyclic voltammetry refers to cycling the potential between chosen low and high points and recording the current in the potential cycling region. The resulting potential versus current plot is called a voltammogram. The sweeping of the potential is carried out linearly, and the sweeping rate can be controlled in a wide range. Most studies are carried out with a potential scanning rate between 1 and 1000 mV s^{-1}.

Before the scanning starts, the working electrode is usually held at a potential that does not cause any electrochemical reactions. After the start of the scanning, the potential goes higher (or lower), and when it becomes high (or low) enough to

cause the oxidation (or reduction) of an electrochemically active species, an anodic (or cathodic) current appears. The anodic (or cathodic) current increases as the potential goes higher (or lower) because the reaction kinetics becomes faster. When the potential reaches the standard potential E°, the concentrations of the oxidized and the reduced forms of the electrochemically active species become equal on the surface of the electrode. The highest anodic (or cathodic) current is reached when the potential reaches a value at which all the reduced (or oxidized) form of the electrochemically active species at the electrode surface is consumed. The highest current is achieved at this moment because the mass transport rate of the electrochemically active species reaches a maximum rate, driven by the (largest) concentration gradient between the bulk concentration of the electrochemically active species and the surface concentration of this species. When the potential goes higher (or lower) beyond this point, the current starts to decline because the double-layer thickness increases, resulting in a less steep concentration gradient of the electrochemically active species. Therefore, an anodic (or a cathodic) peak develops. When the potential reaches the set high (or low) limit, it reverses direction and scans towards the set low (or high) limit. During this reversed potential scan the oxidized (or reduced) form of the electrochemically active species reacts, and develops a cathodic (or anodic) peak. The cathodic (anodic) peak is located at a slightly lower (higher) potential than the anodic (cathodic) peak. The cathodic and anodic peaks are of equal height (or, more accurately, equal area), unless there are complications caused by some side chemical or electrochemical processes.

If the electrochemical reactions are thermodynamically reversible, the positions of the cathodic or anodic peaks do not change with the potential scan rate (υ), and the peak height is proportional to the square root of the potential scan rate, $\upsilon^{1/2}$, according to the following equation (T = 25 °C):

$$i_p = (2.69 \times 10^5) n^{3/2} A D^{1/2} \upsilon^{1/2} C \qquad (11.1)$$

where i_p is the peak current (in amperes), n is the number of electrons per reactant molecule, A is the electrode area (in cm^2), υ is the potential scan rate (in $V\ s^{-1}$), D is the diffusion coefficient (in $cm^2\ s^{-1}$), and C is the bulk concentration of the reactant (in $mol\ cm^{-3}$) [2].

If the reactions are not completely reversible, the anodic peak potential becomes more positive and the cathodic peak potential becomes more negative. The separation of the two peaks becomes larger than in the reversible case.

Reversibility is often a relative term because it is related to the potential scan rate. A reaction that is reversible at low scan rates may become quasi-reversible (or even irreversible) at high scan rates. When the quasi-reversible starts, the peak current will become smaller than that expressed by Equation 11.1, and the curve of i_p versus $\upsilon^{1/2}$ starts to bend down.

A special case results when a monolayer or an ultra-thin layer of an electrochemically active species is confined to the electrode surface and the thickness of this layer is less than that of the diffusion layer within the experiment time scale. Mass transport resistance becomes negligible. Both the anodic and the cathodic peaks become symmetrical, and they look like mirror images of each

other. Integrating the current with time under the entire anodic (or cathodic) peak area gives the total charge of the oxidation (or reduction) process. From this charge the total amount of the electrochemically active species confined to the electrode surface can be calculated according to Faraday's law.

If the potential is swept in only one direction, it is called linear sweep voltammetry. In such an experiment, the investigator is not interested in what happens during the reversed potential scan.

11.3.2 Potential Step Experiment

Instead of cycling the potential, the potential can be changed in one step from one level (E_1) at which the overpotential (η_1) is too low to cause any reaction to another level (E_2) at which the overpotential (η_2) is so high that the reaction is controlled by the mass transport rate. The corresponding current versus time accompanying the potential step is recorded and analyzed; such an experiment is called chronoamperometry.

Prior to the potential step from E_1 to E_2, the concentration of the reactant at the surface of the electrode is the bulk concentration C. After the potential is stepped to E_2, the surface concentration of the reactant decreases to zero because it reacts immediately under the high overpotential η_2. As time proceeds, the reaction zone depletes, the diffusion distance from the bulk to the electrode surface increases, and thus the concentration gradient decreases. So, the current declines with time. On a planar electrode, the current i(t) at any time t is given by the Cottrell equation:

$$i(t) = (nFAD^{1/2}C)/(\pi^{1/2}t^{1/2}) \tag{11.2}$$

where n is the number of electrons involved in the electrochemical process per reactant species, F is the Faraday constant, A is the surface area of the electrode, and D and C are the diffusion coefficient and the concentration of the reacting species, respectively. The diffusion layer thickness (δ) changes with time according to $\delta = (\pi Dt)^{1/2}$. The plot of i(t) versus $t^{-1/2}$ is a straight line and the diffusion coefficient can be obtained from the slope provided C is known.

If a spherical electrode or a micro planar electrode is used in the experiment, the diffusion becomes spherical, and the Cottrell equation becomes

$$i(t) = (nFAD^{1/2}C)/(\pi^{1/2}t^{1/2}) + nFADC/r \tag{11.3}$$

where r is the diameter of the electrode. The plot of i(t) versus $t^{-1/2}$ is still a straight line. $D^{1/2}C$ and DC can be obtained from the slope and the intercept, respectively, and thus both D and C can be determined.

A potential step experiment is typically carried out for a duration of less than a few minutes for the following reasons. First, the reaction zone depletes quickly, so that a longer time is not needed to obtain a well-developed i–t curve. Second, over a longer time the results are likely to be complicated by convection due to the buildup of density gradients and the environmental vibration.

A charging current will exist during the short duration of the experiment. The charging current can be significant immediately following the potential step. Data obtained in the absence of the active species under the same condition are often used to correct for the charging current.

By integrating the current with time, the total charge (Q) due to the electrochemical reaction during the duration of the potential step experiment is obtained (for a planar electrode):

$$Q = (2nFAD^{1/2}C\, t^{1/2})/\pi^{1/2} \tag{11.4}$$

Q versus $t^{1/2}$ is a straight line, and $D^{1/2}C$ can be obtained from its slope.

11.3.3 Instrumentation: Potentiostat

The instrument used to perform cyclic voltammetry and potential step experiments is a potentiostat, which controls the voltage and measures the current. The potentiostat maintains the potential of the working electrode at a desired value with respect to the potential of the reference electrode. The current flows between the working and the counter electrodes in response to the potential of the working electrode.

A series of resistors in the electric circuit are used to adjust and maintain the potential of the working electrode. For example, in order to keep the potential of the working electrode constant during a potential step measurement that involves changing current, the resistance (R) of the resistors will be varied so that the voltage drop (iR) on the resistor is the same (Figure 11.5).
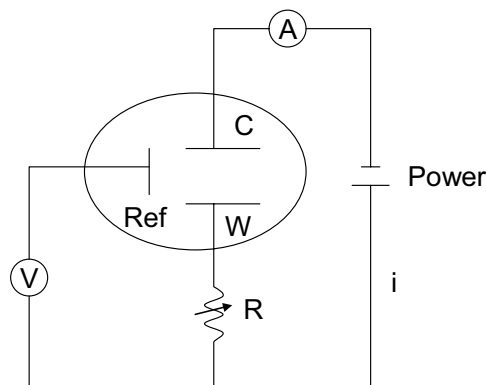
Ref: reference electrode
C: counter electrode
W: working electrode

Figure 11.5. Illustration of the basic circuitry of a potentiostat

An electrometer measures the voltage difference between the reference and the working electrodes. An electrometer has extremely high input impedance so that the input current is nearly zero, which enables the reference electrode to keep a

constant potential. The current passing through the working and the counter electrodes is determined by measuring the voltage drop through a known resistor according to Ohm's law.

When the electronic circuit is slightly modified so that the current is controlled and the corresponding potential of the working electrode is measured, it becomes a galvanostat.

11.3.4 Applications

11.3.4.1 Features of a Pt Electrode in Acidic Electrolyte

Pt is the most important catalyst material for PEMFCs, DMFCs, and PAFCs. Due to the relatively low operating temperatures of these fuel cells (from room temperature to about 200 °C), the reaction kinetics is slow, especially at the cathode for the ORR. Therefore, Pt and its alloys that have shown the highest catalytic activity in these fuel cells have to be used as the catalysts.

In an acidic electrolyte some interesting reactions occur at the surface of the Pt electrode. At potentials higher than about 0.8 V versus the standard hydrogen electrode (SHE), the Pt surface is oxidized to PtOH and PtO_x in the anodic potential scan direction, and these Pt oxides are reduced to the Pt form in the cathodic potential scan direction. At potentials lower than about 0.3 V, two pairs of peaks are observed due to the hydrogen adsorption and desorption. During the cathodic scan from 0.3 V down, underpotential deposition of hydrogen atoms occurs from the reduction of the protons:

$$Pt + H^+ + e^- \rightarrow Pt\text{-}H_{ad} \tag{11.5}$$
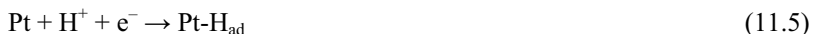
Hydrogen adsorption exhibits a few pairs of well-defined peaks due to the existence of different Pt crystallite facets.

Hydrogen evolution occurs when the potential moves to more negative values:

$$2Pt\text{-}H_{ad} \rightarrow 2Pt + H_2 \tag{11.6}$$

Usually, the potential sweeping direction is switched just before the H_2 evolution starts. Two anodic peaks are often observed from the desorption of the H atoms adsorbed on the different crystallite facets of Pt:

$$Pt\text{-}H_{ad} \rightarrow Pt + H^+ + e^- \tag{11.7}$$

For the pair of H adsorption/desorption peaks located at the relatively higher potential, the H adsorption proceeds more easily and the H desorption is more difficult. This means that the Pt-H bond is stronger for this pair of peaks than for the pair located at the lower potential.

11.3.4.2 Particle Size and Electrochemical Active Surface Area

Since Pt is a very expensive noble metal and only the atoms on the surface can participate in catalyzing electrochemical reactions, Pt is typically used with diameters between 2 and 4 nm for fuel cell applications. Smaller particles have

relatively more atoms on the surface, and the Pt dispersion, which is defined as the ratio of the number of the surface Pt atoms to the total number of Pt atoms, is higher.

Pt nanoparticles are normally deposited onto an electronic substrate such as carbon black. The support has several functions. It promotes the dispersion of Pt particles. It anchors Pt particles onto its surface through physicochemical interactions, which slows down the sintering rate of the Pt particles. It also provides electronic continuity for the Pt particles.

Several approaches can be used to make supported Pt catalysts. One method is to produce a Pt colloid through the use of a protection agent that adsorbs onto the surface of the Pt particles during their formation process. The protection agent can be a surfactant, a polymer, or a short chain organic molecule. The Pt nanoparticles will adsorb onto carbon black particles when the carbon black is added into the colloid. Subsequent washing of the resulting material will remove the protection agent.

Another method is to reduce a Pt precursor in the presence of carbon black. The carbon black support provides the nucleation and anchoring sites for the Pt particles during their formation. The size of the resulting Pt particles depends on the reaction conditions, such as the reaction rate (which is often affected by the temperature, the concentration of the reactants, and the strength of the reducing agent) and the number of nucleation sites on the support. Amorphous carbon black has a large number of nucleation sites, leading to the formation of smaller Pt particles. In contrast, graphitized carbon has a lower number of nucleation sites because only the surface defects can function as nucleation sites, and thus larger Pt particles are produced. For the same type of support, a higher Pt content tends to lead to larger particles because of the greater chance for subsequently formed Pt atoms to deposit onto existing Pt particles.

Pt particle size is typically determined by transmission electron microscopy (TEM). Very often a Gaussian-type distribution is observed. A narrower distribution means tighter control of the particle size.

X-ray diffraction (XRD) is often used to estimate the crystallite sizes of the Pt particles. The prominent Pt crystallite surfaces are (111), (200), and (220). The Pt crystallite sizes are calculated based on the broadening of the peaks using the Debye-Scherrer equation:

$$\text{Crystallite Size} = (0.9\lambda)/(\text{FWHM} \cdot \cos\theta) \tag{11.8}$$

where λ, FWHM, and θ are the wavelength of the X-ray, the full width at half maximum of the peak, and the incidence angle of the X-ray beam, respectively. It should be pointed out that XRD measures the crystallite size rather than the particle size. In addition, XRD determines the volume averaged crystallite size, and thus it may undercount the smaller crystallites.

If we assume that a Pt particle is spherical, its surface area will be given by the following equation:

$$S = 3/rd \tag{11.9}$$

where S is the surface area (cm^2g^{-1}), r is the radius of the Pt particle (cm), and d is the density of Pt ($g\ cm^{-3}$).

Since both the anode and the cathode reactions involve the transport of electrons, protons, and reactants/products, only the catalyst surfaces at the catalyst-ionomer-reactant three-phase regions are electrochemically active. This area is called the electrochemical active surface area (ECSA). The remaining catalyst surfaces that do not meet this three-phase boundary condition will not be able to participate in the electrochemical reaction. An ideal electrode should be able to use all the catalyst surfaces to achieve 100% surface utilization. Measuring the ECSA and comparing it with the total surface area of the catalyst particles based on the particle size and the catalyst loading reveals the actual utilization of the catalyst surface.

Typically, two electrochemical methods are used to estimate the ECSA. The first method uses the hydrogen adsorption/desorption peak areas. The adsorption peak area (current times time) should be integrated from the onset of H adsorption potential to just before the hydrogen gas evolution potential. The integration uses the capacitance charging current as a base line. The result is likely to be more accurate if the average of the cathodic and the anodic peak areas is used. The total ECSA of Pt is then calculated by dividing the integrated charge by 0.21 mC cm^{-2} Pt. This value is established based on the polycrystalline surface of Pt having a Pt atom surface density of 1.3×10^{15} per cm^2, and each Pt allows one hydrogen atom to adsorb [59]. If the Pt loading within the catalyst layer is known, then the mass-specific surface area of Pt can be calculated by dividing the ECSA by the loading.

A bare Pt disk electrode normally shows distinct hydrogen adsorption/desorption peaks, and the potential at which hydrogen gas evaluation starts is clearly discernible. In such cases, the peak areas caused by hydrogen adsorption/desorption can be obtained with good accuracy. However, a fuel cell electrode that has a low Pt loading and in which the Pt is dispersed on a support such as carbon often shows less distinctive hydrogen adsorption/desorption peaks, and the exact potential at which hydrogen gas evolution starts is difficult to determine (refer to Figure 11.27 and 11.31). In these cases, the ECSA is unlikely to be measured accurately.

Another method for electrochemically determining the ECSA is to use the oxidative stripping peak area of CO. CO can strongly adsorb onto the surface of Pt to form a monolayer. This monolayer will be removed quickly and completely by electrochemical oxidation at a high enough potential. The oxidation process converts CO to CO_2,

$$CO + H_2O \rightarrow CO_2 + 2H^+ + 2e^- \tag{11.10}$$

and results in a well-defined sharp peak during the anodic potential scan. No corresponding reduction current exists during the cathodic potential scan (Figure 11.6).

CO oxidation to CO_2 involves 2 electrons. If one CO molecule occupies one Pt atom in a linear adsorption configuration (Pt-CO_{ad}), the ECSA would be calculated by dividing the integrated CO oxidation charge area by 0.42 mC cm^{-2} Pt. If one CO molecules occupies two Pt atoms in a bridge adsorption configuration (2Pt-CO_{ad}),

the ECSA would be calculated by dividing the integrated CO oxidation charge area by 0.21 mC cm^{-2}. Studies have indicated that the manner in which CO adsorbs on the surface of Pt is affected by the potential. At a potential close to 0 V the CO adsorption is dominated by the linear adsorption [45].
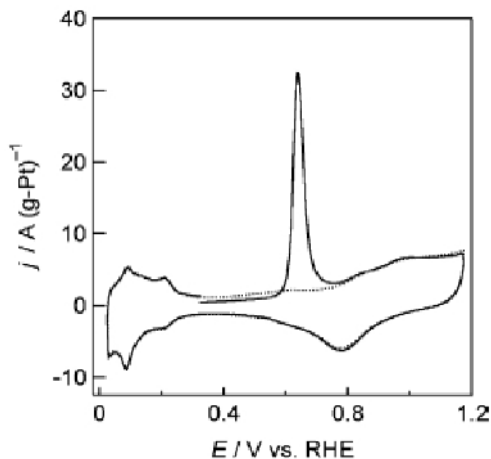
Figure 11.6. CO stripping voltammogram on Pt/C. T = 60 °C; 0.5 M H$_2$SO$_4$; scan rate = 10 mV s^{-1} [52]. (Reprinted from Journal of Electroanalytical Chemistry, 576(2), Sugimoto W, Aoyama K, Kawaguchi T, Murakami Y, Takasu Y, Kinetics of CH$_3$OH oxidation on PtRu/C studied by impedance and CO stripping voltammetry, 215–21, ©2005, with permission from Elsevier.)

When the surface of Pt is blocked by the adsorption of a CO monolayer, hydrogen adsorption becomes impossible. Then the cyclic voltammogram of Pt in the hydrogen adsorption and desorption potential region becomes featureless. Once the CO layer is removed through oxidation at higher potentials, the Pt surface becomes available again for hydrogen adsorption and desorption, and the corresponding peaks will appear (Figure 11.6) [52].

Since CO is poisonous to human beings, it is rarely used in a concentrated form for such experiments. Any gas mixture containing up to a small percentage of CO should be good enough for the experiments. CO adsorbs onto the surface of Pt quickly, and no more than 30 minutes is needed to have a full monolayer coverage of CO on Pt. The potential of the cell is maintained at a lower level than the CO oxidation potential during the CO adsorption process. Then an inert gas such as nitrogen or argon is used to purge out the CO-containing gas for a few minutes, leaving only the CO that adsorbs on the surface of Pt within the cell. A potential scanning can then be carried out to induce the oxidation of CO.

11.3.4.3 Catalyst Activity Analysis

Cyclic voltammetry can be used to qualitatively study catalyst activity towards a reaction. The study can evaluate either the relative activities of a series of catalysts towards the same reaction, or the activity of one catalyst towards a few different reactions. The activity of a catalyst can be gauged by both the onset potential and

the peak (or plateau) current. Higher activity will lead to an onset potential at a lower overpotential and a higher peak (or limiting) current.

H₂ Oxidation

Pt has an excellent catalytic ability for the H_2 oxidation reaction (HOR),

$$H_2 \rightarrow 2H^+ + 2e^- \qquad (11.11)$$

and very small overpotentials are encountered up to quite high current densities. However, H_2 is not a naturally available fuel, and it is often obtained through reforming hydrocarbon fuels such as methanol, methane, or propane. The resulting H_2-rich gas mixture, called reformate, often contains parts-per-million (ppm) levels of CO, even after a few cleaning steps such as the water-gas shift reaction,

$$CO + H_2O \rightarrow CO_2 + H_2 \qquad (11.12)$$

and the preferential oxidation,

$$CO + 1/2O_2 \rightarrow CO_2 \qquad (11.13)$$

Since CO can strongly adsorb onto the surface of a Pt catalyst, it blocks the reaction sites for H_2 oxidation, and thus a significant overpotential is encountered.
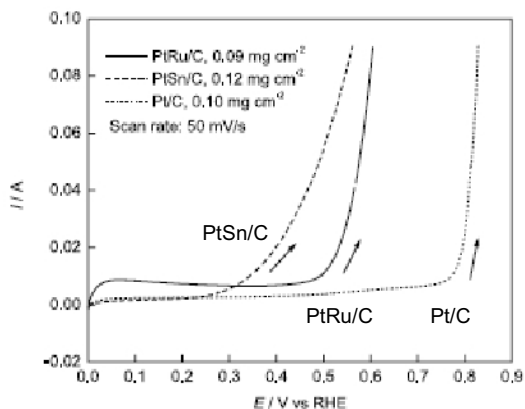
Figure 11.7. Cyclic voltammograms of H_2 oxidation in the presence of 2% CO on Pt/C (0.10 mg cm^{-2}), Pt$_{50}$Ru$_{50}$/C (0.09 mg cm^{-2}), and Pt$_3$Sn/C (0.12 mg cm^{-2}). T = 50 °C; scan rate = 50 mV s^{-1} [22]. (Reprinted from Journal of Electroanalytical Chemistry, 528(1–2), Leng Y-J, Wang X, Hsing I-M, Assessment of CO-tolerance for different Pt-alloy anode catalysts in a polymer electrolyte fuel cell using ac impedance spectroscopy, 145–52, ©2002, with permission from Elsevier.)

Some Pt alloys such as PtRu, PtMo, and PtSn have shown higher CO tolerance than Pt alone. Pt$_{50}$Ru$_{50}$ is the most popular commercial catalyst for CO-tolerance. Figure 11.7 shows the cyclic voltammograms during the oxidation of H_2 in the

presence of 2% CO [22]. The onset H_2 oxidation potentials were at about 0.3, 0.5, and 0.8 V for PtSn/C, PtRu/C, and Pt/C, respectively. Therefore, the CO tolerance increased in the order of Pt/C < PtRu/C < PtSn/C. The onset potentials were affected by the temperature; higher temperatures led to lower onset potentials. Leng et al. showed that the onset potential for H_2 oxidation on PtRu reduced from about 0.59 to 0.50 and to 0.42 V when the cell temperature was increased from 25 to 50 and to 70 °C in the presence of 2% CO.

It is generally believed that the higher CO tolerance of PtSn arises from the weaker adsorption of CO on the surface of PtSn [8], while the higher CO tolerance of PtRu is due to the fact that Ru can form an oxidized surface at lower potentials than Pt. The oxide group on the surface of Ru then helps the removal of CO from the Pt surface:

$$Pt\text{-}CO_{ad} + Ru\text{-}OH_{ad} \rightarrow Pt\text{-}Ru + CO_2 + H_2O \qquad (11.14)$$
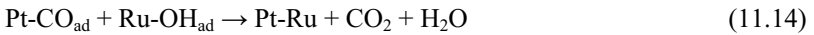
O₂ Reduction
Oxygen reduction is a sluggish process even with the most active catalysts known to date, such as Pt and some of its alloys:

$$1/2O_2 + 2H^+ + 2e^- \rightarrow H_2O \qquad (11.15)$$
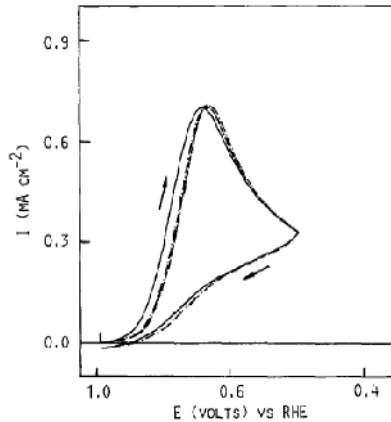
Figure 11.8. Cyclic voltammograms of ORR on Pt in 0.1 M PFSI (—), 0.1 M H_3PO_4 (---), or 0.1 M PFSI + 0.02 M H_3PO_4 (- · − ·). Solutions were saturated by O_2 at 1 atm.; T = 20 °C; scan rate = 10 mV s^{-1} [42]. (Reproduced by permission of ECS—The Electrochemical Society, from Razaq M, Razaq A, Yeager E. Perfluorosulfonimide as an additive in phosphoric acid fuel cell.)

The reaction is further slowed down if some electrolyte species adsorb onto the catalyst surface. Figure 11.8 shows the cyclic voltammograms for O_2 reduction on a Pt electrode in either 0.1 M perfluorosulfonimide ($CF_3SO_2NHSO_2C_4F_9$) (PFSI), 0.1 M H_3PO_4, or 0.1 M PFSI + 20 mM H_3PO_4 [42]. The oxygen reduction was an irreversible wave, and the peak currents in the three electrolyte solution were similar. However, the half-wave potential (the potential at 85% of the peak

current), $E_{1/2}$, was about 30 mV higher with perfluorosulfonimide than with the two electrolytes containing H_3PO_4. Since the presence of only 20 mM H_3PO_4 altered the half-wave potential so significantly, it indicated that H_3PO_4 could strongly adsorb onto Pt to affect the ORR adversely.

CH₃OH Oxidation

A direct liquid fuel cell offers several potential advantages over a hydrogen fuel cell because the liquid fuel has a higher specific volume energy density and is easier to transport and store. The challenges are the slow anode oxidation kinetics and the high fuel crossover rate from the anode to the cathode, which cause a direct liquid fuel cell to perform much more poorly than a hydrogen fuel cell.

Searching for a better catalyst for the oxidation of liquid fuels has been ongoing for decades. Since methanol does not contain any C-C bond and it can be almost completely converted to CO_2,

$$CH_3OH + H_2O \rightarrow CO_2 + 6H^+ + 6e^- \tag{11.16}$$

it has become the preferred liquid fuel. Alloyed catalysts such as PtRu with a 1:1 atomic ratio are the most active catalysts commercially available for methanol oxidation.

Sivakumar and Tricoli recently reported that a PtRuIr/Vulcan XC72R ternary catalyst is more active than a PtRu/Vulcan XC72R [49]. They prepared these catalysts through a vapor deposition route using $Pt(acac)_2$, $Ru(acac)_3$, and $Ir(acac)_3$ precursors (acac = acetylacetonate). The Ir content of the alloy was controlled by changing the sublimation temperature of $Ir(acac)_3$. PtRuIr/2 showed the highest methanol oxidation peak current, followed by PtRuIr/16 and then PtRu. The numbers of 2 and 16 refer to the atomic percentage of Ir within the alloys. CO-stripping voltammetry indicated that the onset CO oxidation potential was about 30 mV lower on PtRuIr/2 than on PtRu. Sivakumar and Tricoli attributed this lower onset potential to the higher catalytic activity of PtRuIr/2 over PtRu for the methanol oxidation.

Catalysts for the oxidation of other short chain alcohols and acids have also been actively investigated. Zhang et al. showed using linear sweep voltammetry that the ethanol onset oxidation potential was at approximately 0.58 V on Pt/C, while that on various Pt_x-WO_3/C was 0.15 to 0.28 V lower [65]. At the same time, the oxidation current on Pt_x-WO_3/C was much higher than that on Pt/C. So, Pt_x-WO_3/C had a higher catalytic activity than Pt/C towards the oxidation of ethanol. Chronoamperometry also showed a higher plateau current on Pt_x-WO_3/C.

Another attractive liquid fuel is formic acid (HCOOH), but its oxidation to CO_2 involves only 2 electrons, and thus its energy density is about 1/3 of that of methanol:

$$HCOOH \rightarrow CO_2 + 2H^+ + 2e^- \tag{11.17}$$

Liu et al. reported that at 25 °C Pd/C showed much higher catalytic activity over Pt/C with the open circuit voltage (OCV) of 0.74 versus 0.69 V and the peak power densities of 120 versus 77 mW cm^{-2} [24]. The higher catalytic activity of Pd

and Pd-based alloys was also reported by Larsen et al. [20]. It is believed that the higher activity of Pd towards the oxidation of formic acid is due to the acid being oxidized to CO_2 directly without going through a CO intermediate step. One indirect piece of evidence is that negligible CO buildup on Pd was observed by Larsen et al. when CO oxidative stripping was studied.

Choi et al. showed that PtAu was a better catalyst for formic oxidation than PtRu [6]. The onset oxidation potential on PtAu was as low as 0.1 V, which was 0.3 V lower than that on PtRu. At 30 °C with 6 M formic acid, the OCVs were 0.77 and 0.61 V, and the peak power densities were 94 and 74 mW cm^{-2} on PtAu and PtRu, respectively. They believed that the higher catalytic activity of PtAu for formic acid oxidation is due to the acid being oxidized to CO_2 directly.

Qi and Kaufman found that 2-propanol performed much better than methanol in the current density region lower than about 300 mA cm^{-2} [40, 39]. For example, at 61 °C and 80 mA cm^{-2}, a fuel cell gave out a voltage of 690 and 480 mV for 1M 2-propanol and methanol, respectively. The crossover rate of 2-propanol was only about 1/7 of that of methanol as measured by an electrochemical method [40]. They also found that a fuel cell could achieve an impressive performance using neat 2-propanol (e.g., 0.485 V at 200 mA cm^{-2}, 60 °C), while neat methanol showed negligible performance [41]. A potential problem with using 2-propanol is that the fuel cell performance decays quite fast, especially at high current densities. It was proposed that this decay was due to the poisoning of the anode by the intermediates formed from 2-propanol oxidation. In addition, 2-propanol may not be completely oxidized to CO_2.

11.4 Rotating Disk and Rotating Ring-disk Electrode Techniques

11.4.1 Theories and Principles

11.4.1.1 Rotating Disk Electrode Technique
The transport of reactants to or from an electrode usually proceeds through diffusion and convection (charged species can also transport through migration under an electrical field). Diffusion is the dominant process for the transport of the species around the surface of an electrode immersed in a stagnant electrolyte solution. There may be some natural convection going on due to the impact of environmental vibration and the uneven temperature distribution in the electrolyte, but its effect is minimal. In such cases, diffusion is exclusively used to account for the mass transport process.

The mass transport rate can be significantly increased when a forced convention is introduced. Convection can be achieved by creating a relative motion of the electrode with respect to the electrolyte. A popular method for creating such a relative movement is by rotating the electrode. Such a method is called a rotating disk electrode (RDE).

When an electrode spins, the reactant is dragged to the surface of the electrode, and the product is spun away from the surface of the electrode. There is still a stagnant reaction layer covering the surface of the electrode, and the reactant transports through this layer by diffusion. The thickness of this layer is controlled

by the angular velocity (s^{-1}) of the electrode, $\omega = 2\pi f$, where f is the number of revolutions per second. A higher angular velocity leads to a thinner diffusion layer. The electrode rotation rate is controlled in such a range that the flow of the reactant along the surface of the electrode follows a laminar pattern. A typical rotation rate ranges between 5 and 10,000 revolutions per minute (rpm).

Both diffusion and convection will determine the net mass transport rate of a reactant to the surface of the electrode. The convention controls the thickness of the diffusion layer and the diffusion controls the transport rate of the reactant through the diffusion layer. The flux normal to the electrode surface due to diffusion is given by $D(\partial^2 C/\partial x^2)$, and that due to convection is given by $\upsilon_x(\partial C/\partial x)$, where D is the diffusion coefficient of the species, C is the bulk concentration of the species, and υ_x is the solution velocity in the x direction, which is normal to the electrode surface.

In a linear potential sweep experiment performed on a RDE, the potential of the working electrode is scanned from a potential where no reaction occurs to a potential that causes a reaction to occur. A limiting current is achieved when the overpotential is high enough so that the reaction rate is determined by the mass transport rate of the reactant at a given electrode rotation rate. The surface concentration of the reactant drops to zero, and a steady mass transport profile is attained as C/L, where L is the diffusion layer thickness. At a fixed electrode rotation rate, L does not change, and thus C/L does not change. Therefore, a steady-state diffusion-controlled current is achieved, described by the Levich equation:

$$i_d = 0.620nFAD^{2/3}\omega^{1/2}v^{-1/6}C \qquad (11.18)$$

where v is the kinematic viscosity of the electrolyte solution: $v = \eta/d$, where η and d are the viscosity and density of the electrolyte solution, respectively. In the experiments, the potential scan rate should be slow enough with respect to the electrode rotation rate to achieve a steady-state reactant concentration profile. Otherwise, the i-E plot will show a peak (refer to the Cyclic Voltammetry section). A linear relationship exists between i_d and $\omega^{1/2}$ and this straight line goes through the (0, 0) origin.

Before the disk current reaches the limiting value, the current is affected by both the reaction kinetics and the mass transport rate. At the reaction onset potential, the current is controlled by the reaction kinetics and has little to do with the mass transport rate. The kinetic current is expressed as

$$i_k = nFAk_fC \qquad (11.19)$$

where k_f is the rate constant and is a function of the potential (or overpotential).

In the entire potential sweeping region, the overall current i is related to i_d and i_k according to the Koutecky-Levich equation:

$$1/i = 1/i_k + 1/i_d \qquad (11.20)$$

A plot of i^{-1} versus $\omega^{-1/2}$ is a straight line, the slope of which can be used to determine D (or $CD^{2/3}$), and the intercept of which on the y axis at $\omega^{-1/2} = 0$ enables the determination of k_f.

If the electrode is coated with a thin film such as Nafion, the reaction species has to diffuse through it to reach the electrode underneath. The Koutecky-Levich equation then becomes the following:

$$1/i = 1/i_k + 1/i_d + 1/i_f \tag{11.21}$$

$$i_f = nFAC_f D_f/\delta \tag{11.22}$$

where C_f and D_f are the concentration and diffusion coefficient of the reaction species within the film, respectively, and δ is the thickness of the film.

Since the reaction kinetics is very fast at the limiting current, i_k becomes much larger than either i_d or i_f, and the above equation is simplified to

$$1/i_{lim} = 1/i_d + 1/i_f = 1/i_d + \delta/nFAC_f D_f \tag{11.23}$$

From the intercept on the y axis of the plot of i_{lim}^{-1} versus $\omega^{-1/2}$, $C_f D_f$ can be obtained.

11.4.1.2 Rotating Ring-disk Electrode Technique

A rotating ring-disk electrode (RRDE) is obtained when a coaxial ring electrode is added outside the disk electrode. As the product that forms at the disk electrode is continuously swept away due to the rotation of the electrode, it will be detected by the ring electrode. Typically, the potential of the ring electrode (E_R) is set at a value high enough to cause the immediate reaction of the product coming from the disk electrode. E_R helps the identification of the product on the disk electrode, and the current observed at the ring electrode (i_R) shows how much product forms on the disk electrode. Typically, if reduction (or oxidation) occurs on the disk electrode, oxidation (or reduction) is arranged to occur on the ring electrode.

The ring current in relation to the disk current is controlled by the geometry of the disk (r_1, radius) and the ring electrodes (r_2, r_3, inner and outer radius, respectively) (Figure 11.9). The ratio of the ring current to the disk current is called the collection efficiency:

$$N = -i_R/i_D \tag{11.24}$$

where the negative sign means that the ring current and the disk current have opposite signs. N is solely determined by r_1, r_2, and r_3, and can be calculated using these numbers [2]. N can also be experimentally determined by using an electrochemically active species such as $Fe(CN)_6^{3-}$. The disk current from the reduction of $Fe(CN)_6^{3-}$ to $Fe(CN)_6^{4-}$ is generated, and the ring current from the oxidation of the resulting $Fe(CN)_6^{4-}$ is measured. Then N is calculated by the ratio of the two currents.
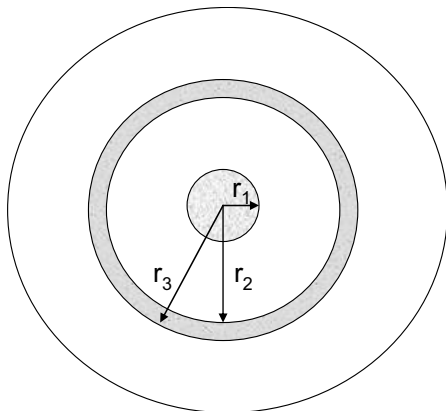
Figure 11.9. Illustration of a ring-disk electrode

RRDE is a very useful technique for estimating how much H_2O_2 is produced during the ORR process. H_2O_2 is a species that can cause damage to the fuel cell components.

11.4.2 Instrumentation

The potentiostat described earlier is used to control the potential of the working electrode and to measure the corresponding current for an RDE. A bipotentiostat is required for an RRDE because the potentials of both the disk electrode and the ring electrode need to be controlled. A bipotentiostat also allows the currents on both electrodes to be measured independently.

The disk and the ring-disk electrodes are normally sealed in a Teflon rod. The rotation of the rod is achieved by using a rotator through a brush-type contact. Basically, a motor drives the rotation of the rod mounted onto the rotator at controllable and adjustable rates ranging from about 5 to about 10,000 rpm. The rod is held in a vertical position with the electrode immersed in an electrolyte solution.

11.4.3 Fuel Cell-related Applications

11.4.3.1 H₂ Oxidation

Schmidt et al. used RDE to study the impact of the Nafion film thickness on the mass transport resistance for HOR (Figure 11.10) [48]. They first deposited a thin layer of Pt/C on the surface of a glassy carbon disk, and covered the Pt/C layer with a thin layer of Nafion. The purpose of the thin Nafion film was to improve the adhesion of the catalyst on the electrode surface. An additional mass transport resistance was encountered due to the presence of this thin Nafion film, and Equation 11.21 applies. Figures 11.10(a) and 11.10(b) show the limiting HOR current densities with 15 and 0.1 μm-thick Nafion films, respectively. Figure 11.10(c) shows the Koutecky-Levich plot for Nafion films of 0.1, 2.4, 3.6, and 15 μm thickness. Figure 11.10(d) shows the inverse of the Levich intercept ($\omega \rightarrow \infty$)

versus the inverse of the Nafion film thickness. The limiting current density changes little up to about $1/\delta = 2$ μm^{-1}, which means that a Nafion film with a thickness of less than 0.5 μm does not add additional resistance to the reactant diffusion. Schmidt et al. also used a 0.2 μm-thick Nafion film-coated electrode to measure the CO tolerance of Pt/Vulcan using RDE [47].
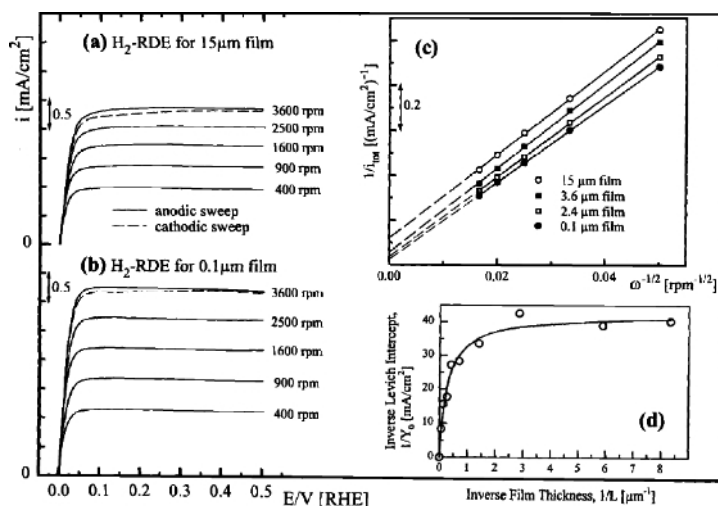
Figure 11.10. (a) Hydrogen oxidation on a 15 μm-thick Nafion film; (b) Hydrogen oxidation on a 0.1 μm-thick Nafion film; (c) Koutecky-Levich plots based on the hydrogen oxidation data with different Nafion film thicknesses; (d) Inverse Levich intercepts obtained from (c) vs. inverse film thickness. T = 25 °C; Pt loading = 7 μg cm^{-2}; 0.5 M H$_2$SO$_4$; scan rate = 10 mV s^{-1} [48]. (Reproduced by permission of ECS—The Electrochemical Society, from Schmidt TJ, Gasteiger HA, Stäb GD, Urban PM, Kolb DM, Behm RJ. Characterization of high-surface-area electrocatalysts using a rotating disk electrode configuration.)

11.4.3.2 O$_2$ Reduction

Lawson et al. used microelectrodes to determine the oxygen concentrations and diffusion coefficients within 0.7 M H$_3$PO$_4$ solution and Nafion thin films, respectively [21]. They determined D and C of oxygen in 0.7 M H$_3$PO$_4$ from the plots of i versus t$^{-1/2}$ (Equation 11.3) and i$_{lim}$$^{-1}$ versus ω$^{-1/2}$ (Equation 11.23), respectively, at a bare Pt microelectrode. Also, by plotting i^{-1} versus ω$^{-1/2}$ in the rising kinetic current region at various potentials, they determined i$_k$ through the intercepts (Equation 11.20). They determined D$_f$ and C$_f$ of oxygen in the Nation film from the plots of i$_{lim}$$^{-1}$ versus ω$^{-1/2}$ (Equation 11.23) and Q versus t$^{1/2}$ (Equation 11.4). They found that the oxygen diffusion coefficient in Nafion film was nearly one order of magnitude smaller than that in 0.7 M H$_3$PO$_4$ electrolyte, while the oxygen concentration within the Nafion film is about 3 times as large as that in 0.7 M H$_3$PO$_4$. The kinetic current at a Nafion-coated Pt was slightly higher than that at a bare Pt.

Using the same techniques, Parthasarathy et al. determined the impact of temperature on the oxygen diffusion coefficient and solubility in Nafion [32]. They

found that the diffusion coefficient increased with temperature while the solubility decreased with temperature, and both showed a steeper change at around 50 °C. They believed that this was related to the faster water uptake rate of the membrane up to 50 °C.

It has been well established that alloys of Pt with some base metals such as Co, Ni, and Cr have higher catalytic ability than Pt alone. Some alloys of Pt with other noble metals have also been shown to have higher catalyst ability. By analyzing the data from the Koutecky-Levich plots using Pt_xIr_y and Pt catalysts, Ioroi and Yasuda found that alloying Pt with 5 to 20% wt. Ir enhanced the kinetic current, i_k, for ORR by a factor of about 1.5 at 0.8 V [18].

RRDE is often used to study the extent of H_2O_2 formation during the ORR via the following side reaction:

$$O_2 + 2H^+ + 2e^- \rightarrow H_2O_2 \tag{11.25}$$

This is a 2-electron reaction process, and the H_2O_2 produced can form radicals such as ·OH and ·OOH. These radicals can attack the ionomer to cause it to decay. It is believed that radical attack is one of the major membrane failure mechanisms. Catalysts that lead to negligible formation of H_2O_2 or operating a fuel cell under conditions that lead to negligible formation of H_2O_2 are preferred in order to minimize such an attack.

In an RRDE configuration for evaluating the amount of H_2O_2 produced during ORR, the potential of the disk electrode scans from about 1.0 to 0.4 V or lower and the ring potential is kept constant at 1.2 to 1.4 V, which can quickly oxidize H_2O_2. The ratio of H_2O_2 formed from one O_2 molecule can be calculated by

$$X_{H_2O_2} = \left[\left(2I_R / N\right)\right] / \left(I_D + I_R / N\right) \tag{11.26}$$

where N, I_R, and I_D are the collection efficiency (refer to Equation 11.24), the current density at the ring, and the current density at the disk, respectively [25].

According to the a study by Paulus et al. [33], the ORR reached the diffusion-controlled current when the disk potential became lower than about 0.6 V, while a negligible amount of H_2O_2 was observed at the ring electrode when the disk potentials were higher than 0.6 V (Figure 11.11). A significant amount of H_2O_2 was detected at the ring electrode when the disk potential was in the hydrogen underpotential deposition region (e.g., < 0.3 V). Based on the disk and the ring currents, the amount of H_2O_2 was less than 1% when the disk potential was higher than 0.2 V, and it increased to higher than 5% at disk potentials lower than 0.1 V. The increase in the amount of H_2O_2 in the hydrogen adsorption region is believed to be due to the coverage of the disk electrode by the hydrogen atoms, which inhibits the 4-electron reduction of O_2.

What can be inferred from this experiment is that the amount of H_2O_2 produced at the cathode is low when a PEM fuel cell is under normal operation. If some oxygen gets into the anode (e.g., through diffusion or air bleed) a significant amount of H_2O_2 will form at the anode due to its low potential.
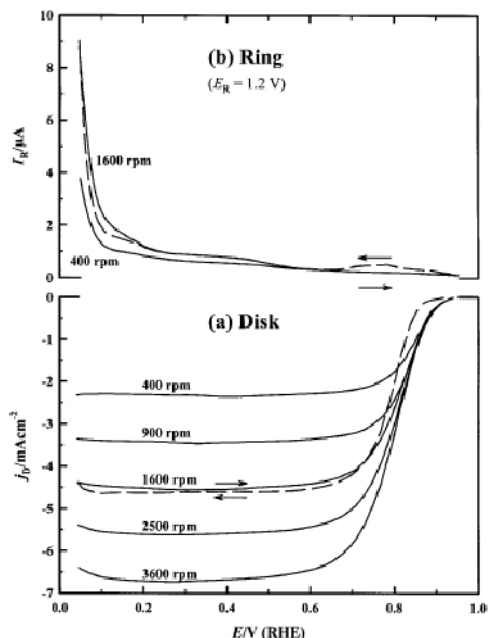
Figure 11.11. Potentiodynamic current densities on (a) glassy carbon disk for O_2 reduction and (b) Pt ring electrode for H_2O_2 oxidation obtained in an RRDE study. The disk electrode was coated by Pt/Vulcan with a Pt loading of 0.014 mg cm^{-2}. T = 60 °C; 0.5 M H_2SO_4 saturated with 1 bar O_2; scan rate = 5 mV s^{-1}; E_R = 1.2 V [33]. (Reprinted from Journal of Electroanalytical Chemistry, 495(2), Paulus UA, Schmidt T J, Gasteiger H A, Behm R J, Oxygen reduction on a high-surface area Pt/Vulcan carbon catalyst: a thin-film rotating ring-disk electrode study, 134–45, ©2001, with permission from Elsevier.)

11.5 Electrochemical Impedance Spectroscopy

11.5.1 Theories and Principles

An electrochemical reaction involves processes such as mass transport, charge separation, charge transfer, electronic and ionic resistances, and so on. These processes often have different time constants and they proceed on different time scales. The impact of these processes on the voltage and current measured in a direct current (DC) experiment is combined and convoluted.

Since alternating current (AC) can be generated at various frequencies, it offers a means to probe processes with different time constants. In a typical process, an AC input voltage is imposed onto a DC voltage that sets the system at a chosen steady state. The magnitude of the AC voltage is small enough (e.g., around 10 mV) that it does not disturb the steady state of the system, and a nearly linear AC current response to the AC voltage perturbation is achieved. The linear relationship between the voltage and current typically holds when the perturbation voltage is lower than the thermal voltage, V_T = RT/F. For example, at 25 °C, V_T is around 26

mV. In a linear relationship, the result is the same by perturbing the system using either a voltage (and thus measuring the corresponding current) or a current (and thus measuring the corresponding voltage). The frequency of the AC signal may vary from 1 MHz or higher to 1 mHz or lower. Fast processes can respond to AC perturbations at high frequencies, while slow processes can respond to only low-frequency perturbations. Therefore, processes with different time constants are deconvoluted.

When a sinusoidal AC voltage, $\dot{E} = E\sin\omega t$, is applied to a pure resistor (R) as $\dot{E}_R$, the corresponding current,

$$\dot{I} = \dot{E}_R/R = (E_R\sin\omega t)/R \tag{11.27}$$

is in phase with $\dot{E}_R$. Both $\dot{E}$ and $\dot{I}$ are vectors rotating at an angular frequency of ω. When $\dot{E}$ is applied to a capacitor (C) as $\dot{E}_C$, the corresponding current,

$$\dot{I} = C(d\dot{E}_C/dt) = \omega CE_C\cos\omega t = E_C\sin(\omega t + \pi/2)/X_C \tag{11.28}$$

is $\pi/2$ ahead of $\dot{E}_C$. Here $X_C = 1/(\omega C)$, and is called the capacitive resistance, which is a counterpart to the Ohmic resistance. Subscript $_R$ or $_C$ is used here to indicate that $\dot{E}$ is applied to either a resistor or a capacitor. If we plot vectors $\dot{E}$ and $\dot{I}$ in a complex plane, and assign the positive segment of the abscissa to $\dot{I}$, then $\dot{E}_R$ and $\dot{E}_C$ will have 0 and $\pi/2$ angles with $\dot{I}$, respectively. $\dot{E}_C$ falls on the ordinate and can be assigned as imaginary in a complex notation by using $j = (-1)^{1/2}$. Then $\dot{E}_C = -jX_C\dot{I}$, where j means $\dot{E}_C$ is $\pi/2$ degrees apart from $\dot{I}$, and the minus sign means that the voltage lags behind the current.

When $\dot{E}$ is applied to a resistor R and a capacitor C that are connected in series,

$$\dot{E} = \dot{E}_R + \dot{E}_C = \dot{I}(R - jX_C) = \dot{I}\dot{Z} \tag{11.29}$$

where $\dot{E}$ and $\dot{I}$ has a phase angle between 0 and $\pi/2$ with $\dot{I}$ being ahead of $\dot{E}$. Vector

$$\dot{Z} = R - jX_C \tag{11.30}$$

is called impedance. $\dot{E}$ has an angle (θ) with the x-axis given by $\tan\theta = X_c/R$. In a complex plane notation, R and X_C are plotted along the abscissa and the ordinate, and are typically called "real" and "imaginary" impedance, respectively (Figure 11.12). They are often expressed by Z_{Re} (or Z') and Z_{Im} (or Z"), respectively. Although the latter is called imaginary, it exists physically. The length of vector $\dot{Z}$ equals $(R^2 + X_C^2)^{1/2}$. The inverse of impedance is called admittance,

$$\dot{Y} = 1/\dot{Z} \tag{11.31}$$

and is equivalent to conductance.

The response of a reaction process to an AC perturbation is similar to that of a combination of resistors and capacitors, and this is not difficult to understand. Since electronic and ionic resistances will be encountered when electrons and ions move during an electrochemical process, it is obvious that resistors are involved in

the reaction process. At the same time, charge accumulation occurs at the electrode-electrolyte interface during the reaction process, so the process also involves capacitance. Therefore, we can use the combination of resistors and capacitors to simulate a reaction process via the so-called equivalent circuit approach.
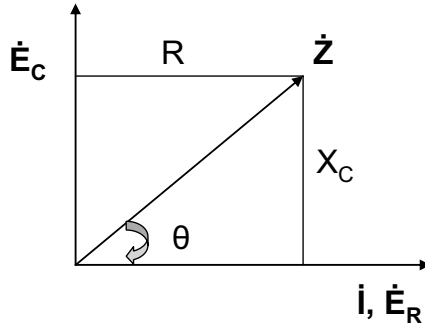
Figure 11.12. Illustration of impedance $\dot{Z}$ and its real and imaginary components

Figure 11.13 illustrates a basic equivalent circuit to represent a general electrochemical reaction. R_s represents the electric resistance, which consists of the ionic, electronic, and contact resistances. Since the electronic resistance is typically much lower than the ionic resistances for a typical fuel cell MEA, the contribution of the electronic resistance to R_s is often negligible. C_d is the double-layer capacitance associated with the electrode-electrolyte interfaces. Since a fuel cell electrode is three-dimensional, the interfaces include not only those between the surfaces of the electrodes and the membrane but also those between the catalysts and the ionomer within the electrodes. R_{ct} is the resistance associated with the charge transfer process and is called charge transfer resistance. Z_w is called the Warburg impedance; it describes the resistance arising from the mass transport processes.
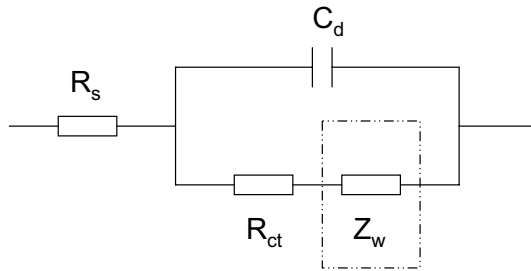
Figure 11.13. Illustration of a basic equivalent circuit for an electrochemical reaction. R_s – Ohmic resistance; R_{ct} – charge transfer resistance; C_d – double-layer capacitance; Z_w – Warburg impedance.

The major shortcoming of an equivalent circuit approach is that an impedance pattern obtained experimentally can be presented by more than one equivalent

circuit. So, an understanding of the physicochemical process is needed in order to build the right equivalent circuit model. The correctness of the equivalent circuit can also be validated if the experimental data are in agreement with those obtained by other techniques.

R_s, C_d, R_{ct}, and Z_w respond differently to AC sinusoidal excitations of various frequencies. A Nyquist plot showing the real impedance on the x-axis and the imaginary impedance on the y-axis in a complex plane is often used to illustrate the results of the equivalent circuit in response to excitations of a wide range of frequencies. Unless an extremely high frequency is used and wiring inductance cannot be eliminated, R_s often appears on the x-axis of the Nyquist plot as a single point at the high frequencies. A capacitor has negligible resistance at high frequencies and a huge resistance at low frequencies. When a resistor and a capacitor are connected in parallel, the combined impedance,

$$R_{total} = R_{ct}/(1 + \omega R_{ct} C_d) \tag{11.32}$$

is negligible at extremely high frequencies because the capacitor poses zero resistances (and thus all the AC current passes through it). The combined impedance at extremely low frequencies is the resistance of the resistor because the capacitor is just like an opened switch (and all the AC current passes through the resistor). The difference between the two intercepts on the x-axis is the resistance of the resistor, R_{ct}. At frequencies between the extreme high and the extreme low, the AC current passes through both the resistor and the capacitor, and the combined impedance forms a semicircle the radius r of which equals $R_{ct}/2$. The top point of the semicircle occurs at the frequency of $\omega = 1/R_{ct} C_d$.

At a lower frequency the double-layer is thicker than at a higher frequency, and the reaction rate can be affected by the mass transport rate of the reactant. The impact of the mass transport resistance can show up even at frequencies that are not very low if the reaction kinetics is very fast. Warburg impedance is generally used to represent the resistance due to the mass transport. Mathematically it can be shown that Z_{Im} and Z_{Re} of the Warburg impedance form a straight line with a slope of 45° with the abscissa (e.g., phase angle = 45°) [2]. For reactions with extremely fast kinetics, it is likely that the semicircle related to R_{ct} becomes too small to be observed and a 45° straight line due to the Warburg impedance shows up as the key feature.

Mass transport resistance is not limited only to the reactants or the products. Transport of other species such as electrons and protons can also pose mass transport resistance. For example, under dry conditions the transport of protons through the membrane and within the catalyst layers could dominate the mass transport process.

Hypothetically, if two kinetically slow reactions occur simultaneously (e.g., methanol oxidation on the anode and oxygen reduction on the cathode in a DMFC), and their time constants ($\tau = RC = 1/\omega_{peak}$) are different enough (e.g., over 2 orders of magnitude), the equivalent circuit will be like the one shown in Figure 11.14. The Nyquist plot shows two semicircles that represent the two reaction processes.
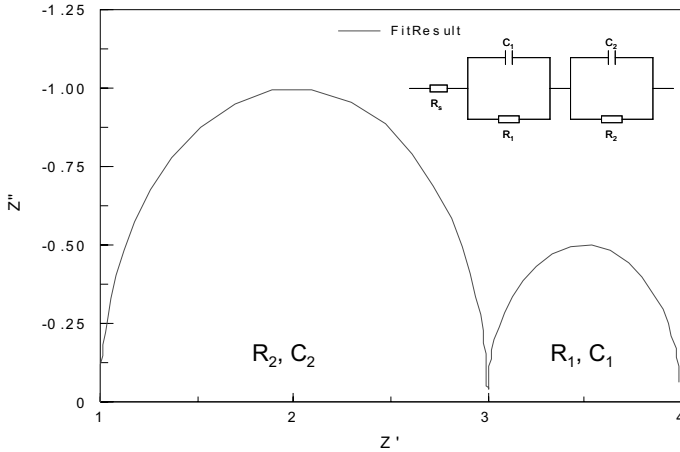
Figure 11.14. Illustration of equivalent circuit and the corresponding Nyquist plot for an electrochemical reaction involving two resolvable processes. $R_s = 1\ \Omega$; $R_1 = 1\ \Omega$; $C_1 = 10$ F; $R_2 = 2\ \Omega$; $C_2 = 0.001$ F; negligible Warburg impedance.

Induction is often observed at high frequencies in the 4th quadrant due to wiring. Short wires are helpful for minimizing the induction effects.

In reality, the double layer in an electrochemical reaction does not behave like a pure capacitor. The center of the semicircle does not fall on the real impedance axis. Instead, it falls below this axis. A constant phase element (CPE) is then used to describe the depressed semicircle (which is actually an arc):

$$X_{CPE} = 1/(\omega C)^{\alpha} \tag{11.33}$$

where α, called the phase parameter, is less than 1. For a pure capacitor, α equals 1. The phase angle for a pure capacitor is $-90°$, while for a CPE, the phase angle is $-90°$ multiplied by α. The center of the compressed semicircle will fall on a straight line that originates from the higher frequency intercept of the depressed semicircle and forms an angle with the real impedance axis in the 4th quadrant at

$$\Phi = (1-\alpha)90° \tag{11.34}$$

Thus $\alpha = 1 - \Phi/90$ (Figure 11.15)

A fuel cell electrode is porous and three-dimensional instead of flat. Its thickness varies at different locations. The reaction rates can be quite different from point to point due to the endless differences in the three-phase boundaries. The current distribution is not homogeneous at either micro- or macro-levels. For example, the inlet regions normally have higher current densities than the outlet regions. All these factors (three dimensions, uneven thickness, heterogeneous reaction rates, and uneven current distribution) could attribute to the double layers behaving differently from a pure capacitor.
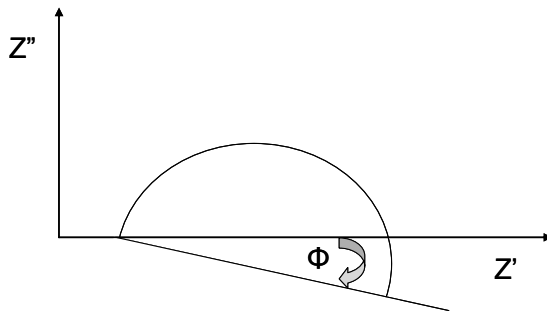
Figure 11.15. Illustration of a constant phase element on a Nyquist plot

11.5.2 Instrumentation

The equipment is required to perform three basic functions: generating a DC input signal, generating an AC input signal, and analyzing the results. A DC signal generator such as a potentiostat sets the cell at a steady state at a chosen voltage (or current). The AC signal generator adds a sinusoidal wave with varying frequencies on top of the DC signal. The cell response to the AC perturbation is analyzed by a frequency response analyzer (FRA).

11.5.3 Application in Fuel Cells

11.5.3.1 Measurement of Membrane Ionic Conductivity

Impedance can be used to measure the ionic resistance of an electrolyte membrane in either a two-probe or a four-probe configuration. In the two-probe configuration, two wires are placed near the ends of a rectangular piece of membrane for both the current generation and the voltage measurement. In the four-probe configuration, the current is generated through the outer two wires and the voltage is measured between the inner two wires. The advantage of the four-probe configuration is the minimization of the impact of contact resistance on the voltage measurement because the measuring device has high input impedance. If the distance between the voltage measuring wires is l, the thickness of the membrane is d, and the width of the membrane is w, then the in-plane bulk resistance of the membrane is

$$R = (\rho l)/(wd) \tag{11.35}$$

and thus $\rho = Rwd/l$.

Figure 11.16 shows the electrochemical impedance spectroscopy (EIS) of a Nafion 115 membrane measured using a two-probe configuration [61]. Pt strips 2 mm wide and 0.127 mm thick were used as the probes and were placed 0.4, 1.6, and 2.7 cm apart. Each Nyquist plot has a slightly depressed semicircle in the higher frequency region and a straight line in the lower frequency region. The resistance is the diameter of the semicircles. Xie et al. proposed that the charge build up at the membrane-probe interface accounted for the linear response in the lower frequency region. A good way to get the resistance value is to fit the

experimental points with an equivalent circuit. However, using the interpolation of either the semicircle or the straight line can serve as a reasonably good approximation.
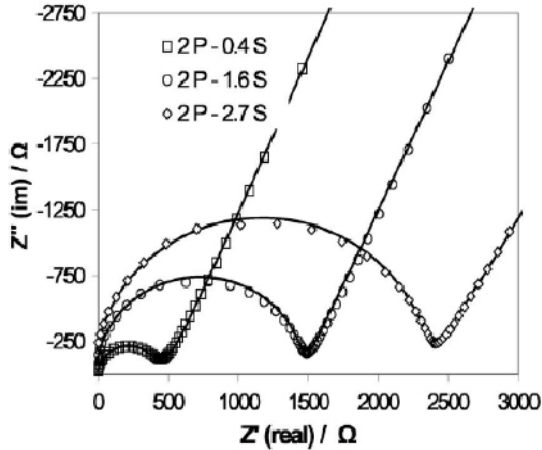
Figure 11.16. EIS of Nafion 115 membrane at 25 °C with two measuring probes 0.4, 1.6, and 2.7 cm apart [61]. (Reproduced by permission of ECS—The Electrochemical Society, from Xie Z, Song C, Andreaus B, Navessin T, Shi Z, Zhang J, et al. Discrepancies in the measurement of ionic conductivity of PEMs using two- and four-probe AC impedance spectroscopy.)

Sone et al. used a four-probe configuration to study the impact of temperature and RH on the ionic conductivity of a Nafion 117 membrane [50]. They quantified the conductivity change with RH and showed that the ionic conductivity of the membrane decreased with the heat-treatment temperature ranging from 80 to 120 °C. Heat treatment led to the microstructural change of the membrane and caused it to lose some of its ability to take up water.

The two-probe configuration can also be used to measure the through-plane resistance of a membrane by sandwiching the membrane between two Pt sheets or foils:

$$R = (\rho l)/s \tag{11.36}$$

where l and s are the thickness and the area of the membrane, respectively. Then $\rho = Rs/l$. Cahan and Wainright used such a configuration to characterize a Nafion 117 membrane [5]. Also, according to measurements taken by Zawodzinski et al. at 30 °C [64], the ionic conductivity of a Nafion 117 membrane is linearly related to the hydration level (λ) of the membrane. λ is defined as the number of water molecules held by each sulfonic acid group

$$\lambda = N_{H2O}/N_{SO3H} \tag{11.37}$$

EIS has also been used to measure the ionic resistance of catalyst layers. Poltarzewski et al. studied the ionic resistances of electrodes with varying Nafion loadings [36]. Guo et al. used porous electrode theory to derive a compact equation for the impedance response of a cathode at the OCV [14]. They found an increase in the ionic conductivity of catalyst layers with an increase in the Nafion loading from 0.33 to 1.13 mg cm^{-2}.
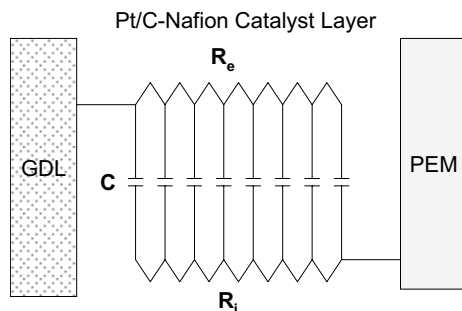
Figure 11.17. Illustration of the finite transmission-line equivalent circuit for a porous electrode

Li and Pickup used impedance to evaluate the impact of the Nafion loading on the ionic resistance of the cathode catalyst layer, and profiled the ionic resistance through the thickness of the catalyst layer [23]. They applied 1 V to the cathode, which was fed with nitrogen to mimic the OCV of a H_2/O_2 fuel cell. Under such conditions the Faradic current is negligible and the impedance spectrum is dominated by the double-layer capacitance of the catalyst/Nafion interface. The Nyquist plots consisted of a 45° region at higher frequencies and a nearly 90° region at lower frequencies. Since the process was basically charging a porous electrode, they used a finite transmission-line equivalent circuit to describe the impedance behavior (Figure 11.17). The electronic resistance rail, which represents the electron transport within a catalyst layer, and the ionic resistance rail, which represents the proton transport within a catalyst layer, are connected by capacitors that represent the catalyst/electrolyte interfaces within the catalyst layer. Simulation of the experimental data based on a transmission line consisting of 40 equal capacitors and 40 unequal ionic resistors allowed them to quantify the ionic conductance distribution through the thickness of the cathode at different Nafion loadings. They found that the ionic conductivity was fairly constant within about 3 μm from the membrane, and it then dropped steeply to nearly zero about 7 μm away from the membrane (Figure 11.18).

Zawodzinski et al. employed a hydrogen pumping technique to measure the number of water molecules dragged by a proton [64]. They assembled a membrane between two porous Pt electrodes and kept it in direct contact with liquid water at both sides. The amount of H_2O dragged by H^+ through the membrane from the anode to the cathode side at a given current was determined by measuring the change in the height of the water capillary columns. Their studies indicated that

one H^+ dragged about 1 and 3 H_2O molecules through Nafion 117 membrane at 30 °C at membrane hydration levels of 11 and 22 H_2O/SO_3H, respectively.
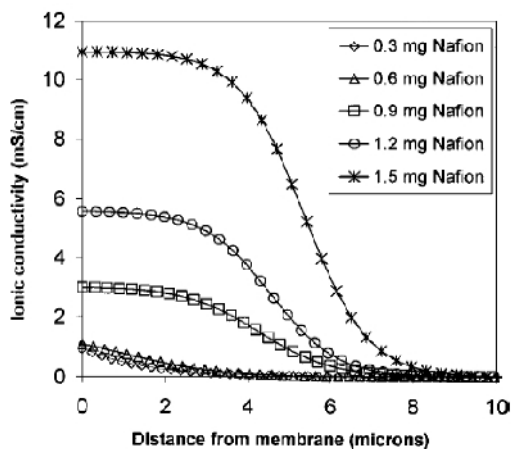
Figure 11.18. Proton conductivity profiles within catalyst layers with different Nafion loadings. T = 23 °C; cathode Pt loading = 0.4 mg cm^{-2} [23]. (Reproduced by permission of ECS—The Electrochemical Society, from Li G, Pickup PG. Ionic conductivity of PEMFC electrodes: effect of Nafion loading.)

Ren et al. reported that the electroosmotic drag numbers increased with temperature for a fully hydrated Nafion 117 membrane [44]. The drag numbers were reported to be 2 and 5 H_2O/H^+ at 15 and 130 °C, respectively. They obtained the drag numbers by balancing the water collected at the cathode in an operating DMFC, where water back-diffusion from the cathode to the anode is negligible.

11.5.3.2 H_2 Oxidation
The H_2 oxidation reaction is not difficult when Pt or some of its alloys are used as the catalyst in the fuel cell anode. Ciureanu and Wang studied the EIS of H_2 using a H_2/H_2 cell configuration at an OCV of 0 V. Two arcs in high- and low-frequency regions were observed (Figure 11.19) [7]). They attributed the high-frequency arc to the charge transfer process: $Pt\text{-}H_{ad} \rightarrow Pt + H^+ + e^-$ (Volmer reaction), and the low-frequency arc to the chemisorptions of H_2: $H_2 + 2Pt \rightarrow 2Pt\text{-}H_{ad}$.

Wiezell et al. developed a steady-state model to explain the EIS of the HOR on porous electrodes [57]. The model predicted that the EIS of the HOR would have three to four loops. The high-frequency loop is due to the Volmer reaction and the medium-frequency loop is due to the hydrogen adsorption. The low-frequency loops arise from the impact of the water content on both the reaction kinetics and the membrane ionic conductance. Experimentally Wiezell et al. observed two semicircles at 10^4 and 0.01–0.1 Hz, and they attributed them to hydrogen adsorption and the impact of water, respectively [58]. They believed that the loop for the Volmer reaction required extremely high frequencies in order to be measured experimentally.
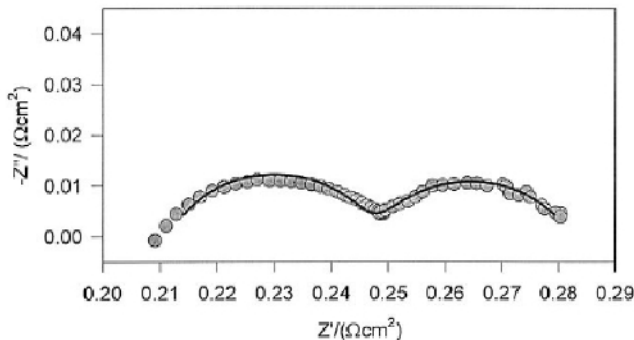
Figure 11.19. Impedance of H_2/H_2 cell at 0.0 V. Points—experimental data; line—curve fit using an equivalent circuit. T = 50 °C; anode or cathode Pt loading = 1.7 mg cm^{-2} [7]. (Reproduced by permission of ECS—The Electrochemical Society, from Ciureanu M, Wang H. Electrochemical impedance study of electrode-membrane assemblies in PEM fuel cells: I. electro-oxidation of H_2 and H_2/CO mixtures on Pt-based gas-diffusion electrodes.)

Since the HOR proceeds much faster than the ORR, its impedance normally becomes negligible in a H_2/O_2 fuel cell. In other words, the impedance in a H_2/O_2 fuel cell arises primarily from the ORR.

11.5.3.3 H_2 + CO Oxidation
Since CO can strongly poison the fuel cell catalyst, the HOR is seriously affected by the presence of CO. Figure 11.20 shows the EIS of HOR during poisoning by 100 ppm CO at a current density of 217 mA cm^{-2} [55]). Curve 1 was collected at the beginning of the experiment (t = 0 s) when negligible CO poisoning had occurred. It showed a depressed semicircle along with the onset of a second semicircle. Curve 2 was collected at t = 3601 s, and one and a half semicircles were observed. The real impedance is larger than that in curve 1 due to the poisoning of the electrode by CO. Curves 3 to 6 were collected at t = 5402, 7204, 9605, and 11404 s, respectively. The impedance increased with time, and the two semicircles were no longer resolvable visually. Also, pseudo-inductive behavior developed at the low frequencies and appeared below the x-axis. Inductive behavior means that the current is behind the voltage perturbation with a phase angle less than or equal to 90°.

The pseudo-inductive impedance pattern has also been observed by other researchers when H_2/CO was used as the fuel. The size of the impedance circle is related to the overpotential of the anode according to Wang et al [56]. A higher overpotential results in a smaller circle. Ciureanu and Wang [7] and Wang et al. [56] found that at potentials lower than the CO oxidation potential, the inductive behavior did not exist. Since the CO oxidation potential is lower on PtRu and PtSn than on Pt, the appearance of the inductive loop should appear at lower anode overpotentials on these alloys. This was indeed observed by Leng et al [22].

The pseudo-inductive behavior is known to happen in systems with adsorbed species the coverage of which changes with the potential [12]. Ciureanu and Wang postulated that the pseudo-inductive impedance in the presence of CO was due to

the oxidation of adsorbed CO coupled with the further oxidation of H_2 on the resulting CO-free Pt surface sites [7]. In other words, the current from H_2 oxidation is slightly delayed with respect to the voltage perturbation at a CO-poisoned electrode surface.
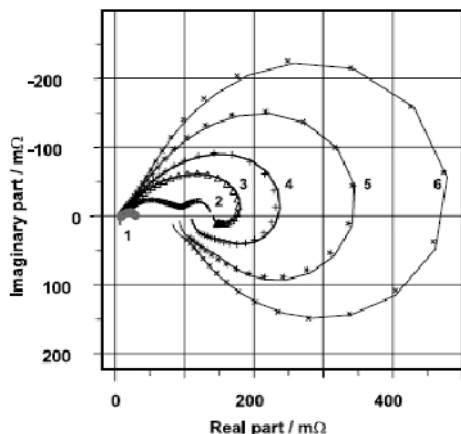
Figure 11.20. Nyquist plots measured at different times during poisoning of a Pt/C anode with 100 ppm CO in H_2. Cell T = 80 °C; current density = 0.217 A cm^{-2}; anode Pt loading = 0.4 mg cm^{-2}; Nafion 117 membrane [55]. (Reprinted from Electrochimica Acta, 48(25–26), Wagner N. and Schulze M., Change of electrochemical impedance spectra during CO poisoning of the Pt and Pt–Ru anodes in a membrane fuel cell (PEFC), 3899–907, ©2003, with permission from Elsevier.)

11.5.3.4 CH₃OH Oxidation

A pseudo-inductive pattern was also observed during the oxidation of methanol, implying that the oxidation process involves intermediates such as CO that adsorb onto the catalyst surface [28]. The impedance circle decreased with the increase of the anode overpotential. Müller et al. postulated that the decrease in the CO coverage with increasing potential had some time delay between the start of the potential perturbation and the establishment of a new steady-state coverage, and it was this phase delay that led to the inductive pattern.

Sugimoto et al. showed that only capacitive behavior was observed at an anode overpotential lower than the onset methanol oxidation potential [52]. The Nyquist plot was a slightly curved line with a slope in the vicinity of 90° at a potential lower than the onset oxidation potential. Only at a potential higher than the CO oxidation onset potential were (semi)circles with pseudo-inductive loops observed.

The impedance pattern from methanol oxidation was successfully modeled by assuming a porous electrode structure and a reaction mechanism that involves strongly adsorbed species such as CO [35].

11.5.3.5 O₂ Reduction

Impedance is often used to study the cathode reaction in a fuel cell configuration. Since the HOR proceeds much faster than the ORR, the H_2 anode is taken as a reference electrode the contribution of which to the impedance is negligible. In a

H$_2$/air fuel cell the Nyquist plot typically shows a high-frequency semicircle and a low-frequency semicircle, as shown in Figure 11.21. The high-frequency semicircle is related to the reaction kinetics. It becomes smaller as the cathode overpotential increases (or as the cell voltage decreases). The low-frequency impedance is believed to be due to mass transport resistance; evidence of this is that when the flow rate of air is increased, the impedance of this semicircle becomes smaller. Springer et al. demonstrated that when the air was replaced by oxygen, the semicircle at low frequencies disappeared completely [51]. A flooded electrode and a thicker gas diffusion layer (GDL) are expected to lead to a larger low-frequency impedance semicircle due to the increased mass transport resistance. The high-frequency intercept at the real axis is the ionic resistance plus the contact and the electronic resistances. The ionic resistance includes that of the membrane and that of the catalyst layers.
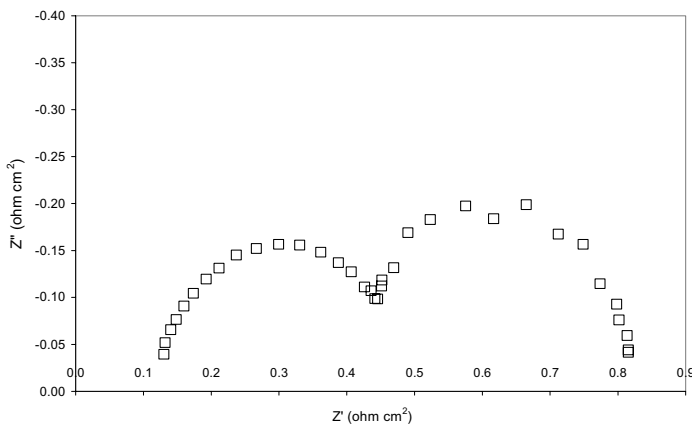
Figure 11.21. Nyquist plot of a H$_2$/air phosphoric acid fuel cell operated at 0.2 A cm^{-2}. T = 180 °C; air stoichiometry = 1.35; hydrogen stoichiometry = 10.

In addition to the equivalent circuit method, the impedance results can also be analyzed using mathematical models based on physicochemical theories. Guo and White developed a steady-state impedance model for the ORR at the PEM fuel cell cathode [15]. They assumed that the electrode consists of flooded ionomer-coated spherical agglomerates surrounded by gas pores. Stefan-Maxwell equations were used to describe the multiphase transport occurring in both the GDL and the catalyst layer. The model predicted a high-frequency loop due to the charge transfer process and a low-frequency loop due to the combined effect of the gas-phase transport resistance and the charge transfer resistance when the cathode is at high current densities.

In a DMFC, methanol can transport through the membrane to the cathode side, where it is oxidized. This results in a much lower mixed cathode potential. Piela et al. found that the cathode impedance spectrum in a DMFC also showed pseudo-inductive behavior. They modeled such a behavior by treating the cathode as a highly non-equipotential electrode consisting of the ORR and the methanol oxidation [35].

11.6 Current Interruption and Current Pulse Techniques

11.6.1 Principles and Instrumentation

The current interruption technique enables a quick evaluation of losses from a running fuel cell due to the Ohmic resistance and the charge transfer resistance. When a fuel cell runs at a current density with a negligible mass transport resistance, its voltage deviates away from the OCV because of the losses caused by the Ohmic resistance and the activation overpotential. If the load is removed suddenly, the loss due to the Ohmic resistance recovers instantly, while the loss due to the reaction kinetics disappears at a slower rate because of the capacitor-type behavior, giving a cell voltage versus time plot like the one schematically shown in Figure 11.22. Before time zero the cell is running at a current density of 0.7 A cm^{-2} with a voltage of 0.60 V. At time zero the cell is switched to the open circuit and the current drops to zero. The cell voltage immediately increases to 0.80 V from 0.60 V, and it then gradually approaches an OCV of 0.97 V. The instantaneous jump from 0.60 to 0.80 V represents the voltage loss due to the Ohmic resistance, V_{Ohm}, while the voltage difference between 0.80 and 0.97 V in the curved region arises from the charge transfer resistance, V_{ct}. Therefore, the resistances due to the Ohmic resistance, R_{ohm}, and that due to the reaction kinetics, R_{ct}, can be calculated according to the following:

$$R_{ct} = V_{ct}/I \tag{11.38}$$

$$R_{ohm} = V_{Ohm}/I \tag{11.39}$$
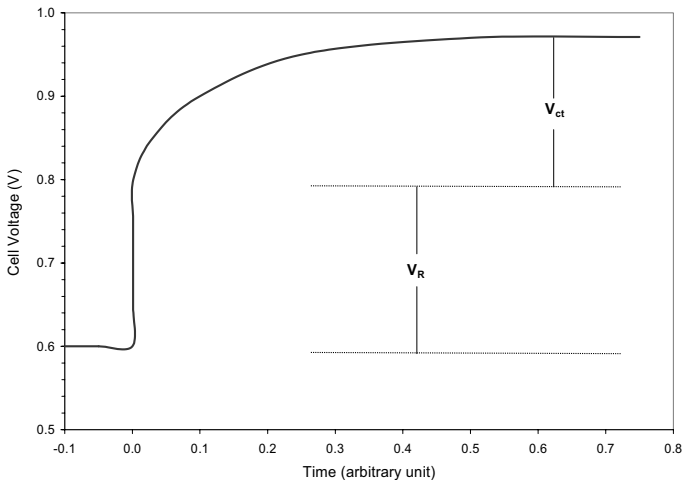
Figure 11.22. Schematic illustration of voltage vs. time plot during a current interruption experiment

Büchi et al. estimated that the Ohmic resistance responds to a current change in less than 0.5 ns, while the charge transfer resistance responds to a current change in

more than 10 ns [3]. So, the two processes can be well separated during a current interruption experiment.

The time constant during the discharge of an electrochemical process can be estimated by the following equation according to Newman [29]:

$$\tau_{ct} = (RTC)/Fi_o \qquad\qquad (11.40)$$

where C is the area specific capacitance and i_o is the exchange current density. A higher C and a lower i_o will result in a larger time constant. Since a fuel cell uses a porous electrode with large catalyst/electrolyte interfaces and the ORR is very sluggish, the time constant is expected to be much larger than that of the Ohmic resistance.

The current pulsing technique applies a very short current pulse to an electrochemical cell to disturb it temporarily. The cell is initially running at a steady state with current I_1 and voltage E_1. After a pulsing current I_2 is applied, the cell moves to another state with a current of $I_1 + I_2$ and voltage of E_2. When the pulsing current I_2 is stopped, the current returns to I_1, and the cell voltage will return to E_1. A voltage versus time pattern like the one shown in Figure 11.23 is the result [3]. The voltage difference between E_2 and E_3 in the vertical region corresponds to the Ohmic resistance, and it can be calculated by $(E_3-E_2)/I_2$. Since the pulsing duration is very short in such a measurement, it imposes little influence on the physical properties of the cell. For example, any additional heat generated by the pulsing current is negligible compared to that continuously generated by the fuel cell.

Because the time constants of the voltage decay in these measurements are so small, a fast digital oscilloscope is typically used for the measurement. It is connected to the anode and the cathode current collectors of the cell.
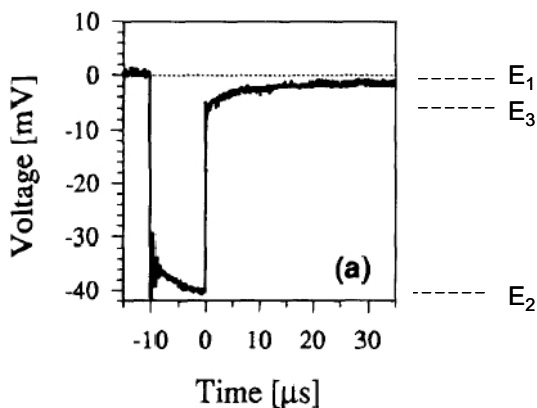
Figure 11.23. Cell voltage transients due to a 5 A, 10 µs pulse. Cell DC current density = 0.357 A cm^{-2}, T = 60 °C; electrode active area = 16.8 cm^2 [3]. (Reproduced by permission of ECS—The Electrochemical Society, from Büchi FN, Marek A, Scherer GG. *In situ* membrane resistance measurements in polymer electrolyte fuel cells by fast auxiliary current pulses.)

11.6.2 Application in Fuel Cells

As shown in Figure 11.23, Büchi et al. applied a 5 A pulse with a duration of 10 μs to a cell running at different current densities [3]. The 5 A pulse was applied to the cell at time –10 μs to cause its voltage to decline by about 40 mV. At time zero, the pulse was stopped and the cell voltage recovered quickly. The voltage change represented by the vertical line was due to the Ohmic resistance. The voltage difference from the tip of this vertical line to the dotted line, E_1-E_3, was the additional activation overpotential caused by the 5 A pulse.

It was pointed out by Büchi et al. that it is absolutely necessary to be able to produce the current decay within a few nanoseconds and to measure the voltage with at least a gigahertz of resolution in order to minimize the systemic error. The accuracy of the resistance measurement was independent of the pulse duration from 10 to 100 ns [3].
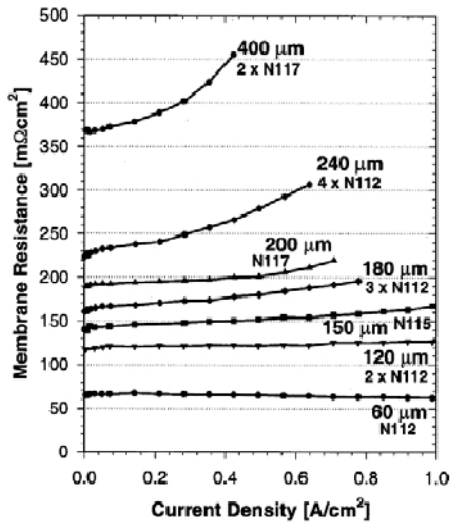
Figure 11.24. *In situ* resistances of Nafion membranes with different thicknesses as functions of current density. T = 60 °C; H_2/O_2 stoichiometry = 1.5/1.5; H_2 humidification dew point = 80 °C; dry O_2 [4]. (Reproduced by permission of ECS—The Electrochemical Society, from Büchi FN, Scherer GG. Investigation of the transversal water profile in Nafion membranes in polymer electrolyte fuel cells.)

By using fast 5 A pulses and measuring the voltage change in a 1 μs time window on running H_2/O_2 fuel cells operated at 60 °C with the hydrogen humidification dew point at 80 °C and no humidification to the oxygen, Büchi and Scherer determined the resistances of membranes with different thicknesses at different current densities (Figure 11.24) [4]. Except for the Nafion 112 membrane, all the membranes showed an increase in resistance with the increase in the current density, and thicker membranes caused larger increases in the resistance with the current density. By stacking multiple thinner membranes together for the membrane electrolyte, Büchi and Scherer found that the resistance increase with

current density was localized at the anode side of the membrane, and the center and the cathode side of the membranes changed little in resistance. Higher current density drags more water from the anode to the cathode, and thicker membranes reduce the amount of water back-diffusion from the cathode to the anode. Therefore, thicker membranes and higher current densities cause the drying up of the membrane at the anode side.

11.7 Steady-state I-V Polarization

11.7.1 Principles and Instrumentation

A fuel cell shows the highest voltage when it generates no current, and this voltage is called the OCV because it is the voltage when the electrical circuit is at the open state. When the circuit is closed and a current is drawn by a load, the cell voltage becomes lower than the OCV due to three major losses: activation, Ohmic resistance, and mass transport.

The activation loss dominates in the low current density region. For a low-temperature fuel cell, the loss is significant and a steep voltage decline exists (refer to Figure 11.2). As the overpotential increases enough, the reaction kinetics becomes high, and increasing the current density causes only a slight further increase in the overpotential due to activation. The dominating voltage loss is then caused by the Ohmic resistance of the cell, and thus a nearly linear I-V region is observed. When the current density is further increased, the rate of the reactant supply becomes a limiting factor, and a quick voltage decline occurs.

A test station is required for testing a fuel cell. A test station enables the control and measurement of the current and the voltage. The station also controls all the input parameters, such as the flow rate of the reactants, by using flow meters or mass flow controllers. A mass flow controller typically has an error of about ± 2% of the full scale. A 100-time difference in the flow rate is often encountered during the measurement when the current density is changed from 0.01 to 1.0 A cm^{-2}. So, a 2% flow rate error at the full scale can be many times higher at the lower flow rates. Very often, the flow rate is set at constant when the current densities are less than about 0.1 A cm^{-2}.

The station also provides means for humidifying the reactants. The temperature difference between the humidifiers and the cell determines the RH of the reactants. Accurate RH control is crucial for PEM fuel cells due to the significant impact of RH. The temperature is often monitored by thermal couples, and an error of ± 1 °C can be common. A 2 °C dew point error is equivalent to about 9% RH error at 60 °C, which could significantly affect the performance, stability, and durability of a fuel cell. The test station also has some built-in safety features that allow the station to be shut down either manually or automatically under dangerous or adverse situations.

A test station often has a power supply that can drive reactions to proceed in the direction opposite to the spontaneous direction. For example, a power supply can drive water electrolysis to occur, and can be used to measure methanol or hydrogen crossover rates.

11.7.2 Fuel Cell Hardware

11.7.2.1 Single Cells

Single cells with active areas of 5 to 50 cm^2 are often used to evaluate the performance and durability of MEAs. The result represents the average performance of the entire cell. For cells with active areas of around 5 cm^2, the flow rates of the reactants are very low at a given stoichiometry, and may not be easy to control accurately. Very often, a constant flow rate of a few times stoichiometry corresponding to the highest current density is used. In such cases, mass transport resistance is made artificially low and does not represent the situation in which a constant stoichiometry is used for the entire current density region.

11.7.2.2 Segmented Cells

Since the reactants will be consumed along the flow-fields, their concentrations at the inlets are always higher than those at the outlets. Therefore, the cell performs better in the inlet regions than in the outlet regions. Segmented cells offer an opportunity to estimate the actual performance and decay rates at different regions. There are basically three approaches to constructing a segmented cell. One approach is to segment an MEA into many sections that are insulated from each other while the flow-field plates are kept as a whole. In such a configuration, there are separate current leads for each segment of the MEA, but only two voltage leads for the entire anode and cathode plates. All the segments have the same voltage at any given moment of testing, but the current density varies from segment to segment (of the MEA). Another approach is to segment the flow-field plates into many sections that are insulated from each other while the MEA is kept as a whole. In this case, there are both current leads and voltage leads for each segment, and the voltage of each segment at any given moment of testing could be different. However, the voltage difference among different segments is not expected to be significant because they are electrically connected by the GDLs, which have quite good electronic conductivity. A third approach is to segment both the flow-field plates and the MEA. Such an approach minimizes the likelihood of cross-talk among segments with respect to both the current and the voltage.

In any design, the flow and distribution of the reactants should mimic those of non-segmented cells. The results can be used to guide the fine tuning of the flow-fields so that a more uniform performance among different regions is achieved. The results can also be used to validate or invalidate or to improve mathematical models.

11.7.2.3 Multi-cell Stacks

Since a single cell can generate only a voltage less than 1 V, many unit cells are typically electrically connected in series to form a stack. The number of cells in a stack will determine the output voltage and power from the stack.

The number of unit cells in a stack can range from 2 to hundreds. The stack has inlet and outlet manifolds for the anode reactant, the cathode reactant, and the coolant. The inlet manifolds allow the reactant (or coolant) equal opportunity to get to the inlet region of each unit cell. This helps minimize the uneven distribution of the reactant among different cells.

Uneven distribution of reactant among cells is often caused by the accumulation of water droplets within the flow-field channels. If water accumulates within the channels of a unit cell, it will pose a higher resistance to the flow of the reactant. This causes the cell to receive a smaller amount of the reactant, which in turn carries a smaller amount of water out of the channels. These two events reinforce each other, and eventually could result in the flow of the reactant into this cell being less than the stoichiometric amount, and reactant starvation occurs. Starvation of the fuel can quickly damage the cell. Once a single cell is damaged, the entire stack may have to be replaced.

Obviously, a stack with more cells has a higher likelihood of uneven reactant distribution. The surface characteristics of the plates often play an important role, as discussed earlier. It is believed that either highly hydrophobic or highly hydrophilic surfaces help the water removal. The operating conditions also play a key role in water removal. A higher temperature difference between the stack outlet and the inlet enables the exhaust to carry away more water as vapor. A higher reactant pressure drop from the inlet to the outlet helps push the liquid water out. The geometry of the flow-fields is also an important factor.

The performance of each cell in a stack is typically monitored individually. The I-V curves of all the cells are collected at the same time. Since the cells are connected in series, each cell is generating exactly the same amount of current at any given moment even if some cells are under reactant starvation. The difference in performance among cells is shown by the cell voltage. Uniform performance among cells is preferred.

11.7.3 Fuel Cell Performance

11.7.3.1 Empirical I-V Curve Expression

Since losses due to activation, Ohmic resistance, and mass transport are the three major losses a fuel cell suffers, the I-V performance curve can be empirically approximated by the following equation:

$$V = V_{ocv} - (RT/\alpha nF)\ln(i/i_o) - iR - (RT/nF)\ln(i/i_l) \tag{11.41}$$

where V_{ocv} is the open circuit voltage, α is the charge transfer coefficient, n is the number of electrons involved in the rate determining step of the reaction, i_o is the exchange current density, R is the total Ohmic resistance, and i_l is the limiting current. The second, third, and fourth terms on the right side of the equation represent the losses due to activation, Ohmic, and mass transport resistances, respectively.

Kim et al. showed that the loss due to the mass transport resistance was best fit by the following expression: $m\exp(ni)$, where m and n are constants having the units of potential and the reciprocal of current density, respectively [19]. They found that m was responsible for the increase in the slope of an I-V curve in the linear region, while n has a more predominant contribution to the rapid decline in the high current density region. However, the physicochemical meanings of m and n have not been established.

11.7.3.2 Tafel Equation

It was first formulated experimentally by Tafel in 1905 that the overpotential, η, is linearly related to $\log i$:

$$\eta = a + b\log i = a + (2.3RT/\alpha nF)\log i \tag{11.42}$$

The slope of the line is b, and is called the Tafel slope. When the Tafel line is extrapolated to the thermodynamic equilibrium potential, $E°$, where $\eta = 0$, the exchange current density, i_o, can be obtained.

The Tafel equation can be obtained through kinetic treatment of electrochemical processes provided the overpotential η is large enough. Bard and Faulkner indicated that whenever the current from the backward reaction contributes less than 1% of the total current, the Tafel equation will hold. Specifically, the Tafel equation holds when $|\eta| > 0.118/n$ V at 25 °C [2].

It becomes clear when Equations 11.41 and 11.42 are compared that the empirical Equation 11.41 is basically the Tafel Equation 11.42 plus terms to account for the mass transport resistance loss and the iR loss. It is then fair to say that the Tafel equation is valid only in the absence of mass transport resistance and when the Ohmic resistance is corrected.

Parthasarathy and Martin used a microelectrode covered by a Nafion 117 film as the electrolyte to study oxygen reduction kinetics in a three-electrode half-cell configuration [31]. Two Tafel slopes, –63 mV/decade and –118 mV/decade, were observed at the lower and the higher current density regions, respectively, at 25 °C. It is generally believed $n = 1$ for the ORR because the rate determining step is the first electron transfer:

$$Pt + O_2 + H^+ + e^- \rightarrow Pt\text{-}O_2H \tag{11.43}$$

Assuming the charge transfer coefficient, α, is 0.5, then the Tafel slope is calculated as –118 mV/decade at 25 °C. Parthasarathy et al. found that both the low and the high Tafel slopes were little affected by the temperature (30–80 °C), that α was nearly linearly related to the temperature, and that it increased from 0.5 at 27 °C to 0.6 at 87 °C [32]. Their studies indicated that the low Tafel slope corresponds to a potential region where the ORR occurs on a PtO_x surface, while the high Tafel slope corresponds to a potential region where the ORR occurs on oxide-free Pt surfaces. They seemed to agree with a hypothesis that the ORR process in the low Tafel slope region involves an initial fast charge transfer step followed by a rate-determining chemical step. In such a case the charge transfer coefficient is 1, and thus the Tafel slope calculated from $2.3RT/\alpha nF$ is around –60 mV/decade.

Extrapolation of the two Tafel slopes will result in two different exchange current densities. The smaller slope gives a lower exchange current density. Thus, it implies that the formation of Pt oxide hinders the oxygen reduction process. Parthasarathy et al. found that the activation energy for the oxygen reduction on oxide-covered Pt/Nafion was nearly three times as large as that on oxide-free Pt/Nafion surfaces [32].

11.7.3.3 Activity Comparison

An I-V curve is the best way to illustrate the performance of a cell because it shows not only the actual output from the cell but also the behaviors of the cell in different current density regions. When more than one I-V curve is plotted on the same chart, the higher ones mean a better performance. The composition and the structure of an MEA should be optimized in such a way that the best performance is achieved in the current density region where the fuel cell will be operated. For example, if the fuel cell is aiming at a low current density operation, the optimization should be focused on improving the low current density region. On the other hand, if the fuel cell will be used in a wide current density range from 0.05 to 1.5 A cm^{-2}, the MEA needs to be optimized for the entire current density region. The latter is often tougher to accomplish, and some compromises may have to be made between the lower and the higher current density regions.

The current density at about 900 mV cell voltage is often used to present the activity of an electrode. The current density divided by the total mass of the catalyst is called the mass specific activity, while the current density divided by the total surface area of the catalyst is called the area specific activity. A higher area specific activity indicates that the catalyst surface is more effectively used.

11.7.3.4 Determination of Exchange Current Density

When the overpotential, η, is negligibly small and the electrochemical reaction is at equilibrium,

$$R_{ct} = (RT)/(nFi_o) \qquad (11.44)$$

So,

$$i_o = (RT)/(nFR_{ct}) \qquad (11.45)$$

R_{ct} can be determined by EIS at OCV, as discussed earlier.

Another way to determine i_o is by extrapolating the Tafel plot to $\eta = 0$, as mentioned earlier.

11.8 Durability Evaluation

11.8.1 Introduction

Good durability is a key requirement for the commercialization of fuel cells. After many years of intensive research and development, conventional power generation technologies have achieved excellent durability. These technologies set up a benchmark for fuel cells to meet or, better, to exceed. At the time this article is being written, the reliability of a PEM fuel cell is much lower than that of an internal combustion engine, while the cost of the former is much higher than that of the latter.

A fuel cell decays with time, and the rate of decay determines its durability. The decay is related to the aging of the fuel cell components, especially the membrane electrolyte, the catalysts, and the catalyst support. The decay of the membrane will cause its thinning and mechanical property deterioration. The loss of its mechanical properties often causes a fuel cell to fail prematurely and catastrophically. The decay of the catalyst is normally due to the particle size increase and the particle dissolution and redistribution. Catalyst decay rarely causes a sudden failure of a cell. The decay of the catalyst-support is often related to its corrosion. Corrosion makes the electrode more prone to flooding and accelerates the growth and redistribution of the catalyst particles.

The following methods can help determine the root causes of the decay and gauge its extent.

11.8.2 Techniques

11.8.2.1 Open Circuit Voltage

The thermodynamic voltage of a H_2/O_2 fuel cell is at 1.21 V under standard conditions:

$$E = \Delta G/(nF) \tag{11.46}$$

where ΔG is the Gibbs free energy and $n = 2$ for $H_2 + 0.5\ O_2 \rightarrow H_2O$. However, a H_2/air fuel cell typically has an OCV of only around 1.0 V. This is due to the occurrence of hydrogen crossover through the membrane and the corrosion reactions of the cathode components such as the carbon catalyst-support,

$$C + 2H_2O \rightarrow CO_2 + 4H^+ + 4e^-,\ E^\circ = 0.21\ V \tag{11.47}$$

and the catalyst itself,

$$Pt + H_2O \rightarrow PtO + 2H^+ + 2e^-,\ E^\circ = 0.88\ V \tag{11.48}$$
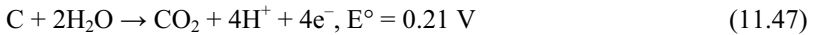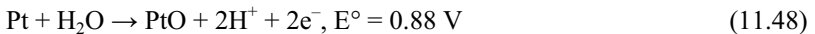
For example, if the H_2 crossover current density is 1 mA cm^{-2}, and assuming the number of electrons (n) involved in the rate determining step, the exchange current density (i_o), and the charge transfer coefficient (α) of the ORR are 1, 0.01 mA cm^{-2}, and 0.5, respectively, then the potential loss due to the hydrogen crossover is 0.12 V at T = 25 °C, calculated according to the following:

$$\Delta V = (RT/\alpha nF)\ln(i/i_o) \tag{11.49}$$

Please note that n, i_o, and α used in the calculation are for the ORR instead of the HOR. The reason is that H_2 splits into H^+ and e^- when it reaches the cathode, $H_2 \rightarrow 2H^+ + 2e^-$, and then the ORR forms water: $0.5O_2 + 2H^+ + 2e^- \rightarrow H_2O$. Since the overpotential due to the HOR is much smaller than that due to the ORR, the latter determines the cathode potential drop.

As the membrane decays with time, it can either become thinner or form more or larger pinholes, both of which lead to a higher H_2 crossover current. If the crossover current increases to 10 mA cm^{-2}, the voltage drop will be 0.18 V calculated according to Equation 11.49. Figure 11.25 illustrates the OCV drop versus H_2 crossover current density. So, based on the OCV drop, the severity of H_2 crossover can be estimated assuming that the mixed potential due to the carbon or Pt oxidation does not change significantly.
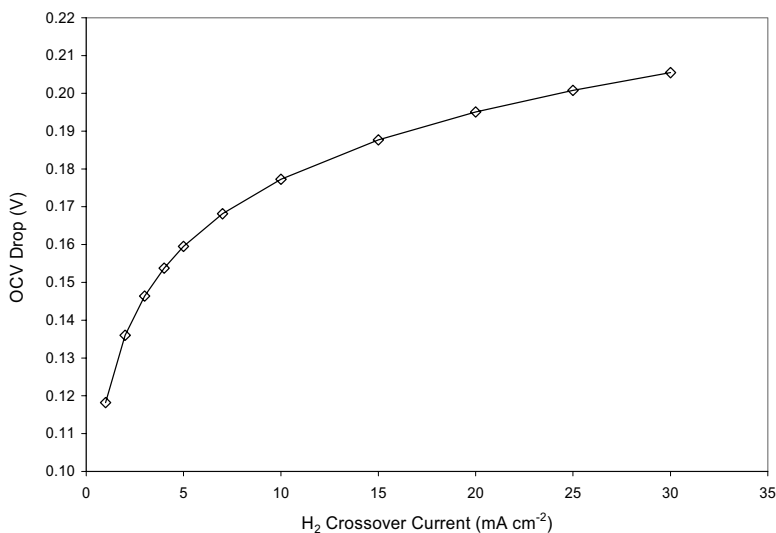
Figure 11.25. Illustration of calculated OCV drop vs. H_2 crossover current density. The calculation is based on $\Delta V = (RT/n\alpha F)\ln(i/i_o)$ by assuming $n = 1$, $i_o = 0.01$ mA cm^{-2}, and $\alpha = 0.5$.

Zhang et al. reported a more detailed analysis of OCV drop due to hydrogen crossover and the mixed potential at temperatures ranging from 23 to 120 °C [66]. Figure 11.26 illustrates the magnitudes of the hydrogen crossover current density through fresh Nafion 112 and 117 membranes and the increase of the hydrogen crossover current with temperature.

The OCV also declines if the anode and the cathode of an MEA are shorted. Shorting is normally caused by GDL fibers or catalyst clumps penetrating through the membrane. For membranes as thin as 20 μm, shorting is likely to occur. An effective way to distinguish the gas crossover from the electrode shorting is to study the OCV change versus the pressure difference between the anode and the cathode reactants. OCV does not change much with the pressure difference due to the electrode shorting, while it declines significantly with the pressure difference from the gas crossover.

Leaving a fuel cell at the OCV can accelerate the decay rate because a voltage around 1 V has strong oxidizing ability. Qi and Buelte studied the OCV impact on the performance of H_3PO_4 fuel cells, and found that the cathode Pt crystallite size measured by XRD increased by over 400% after 245 hours at OCV, while that of the anode changed little [38]. The EIS data showed significant increases in both the

kinetic resistance and the mass transport resistance. The mass transport resistance increase was presumably due to the oxidation of the carbon catalyst support at the OCV.
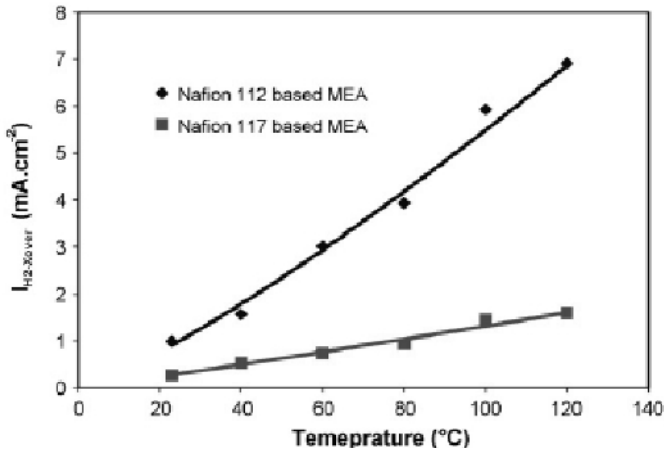
Figure 11.26. H_2 crossover current densities as a function of temperature at OCV with Nafion 112 and 117 membranes. H_2 backpressure = 3.0 atm.; RH = 100% [66]. (Reprinted from Journal of Power Sources, 163(1), Zhang J, Tang Y, Song C, Zhang J, Wang H, PEM fuel cell open circuit voltage (OCV) in the temperature range of 23 °C to 120 °C, 532–7, ©2006, with permission from Elsevier.)

Using cyclic voltammetry Xu et al. showed that significant Pt oxidation occurred at a potential of 0.85 V or higher, and the extent of oxidation increased with the potential [62]. Their studies indicated that both water and O_2 contribute to the formation of Pt oxide because a higher RH and a higher O_2 concentration result in a greater extent of Pt oxidation. They used the charge under the PtO_x reduction peak area to estimate the extent of Pt oxidation, as shown in Figure 11.27.

Ye et al. observed that gas bubbles formed at the anode in a DMFC at OCV when the oxygen flow rate at the cathode became slow enough [63]. The gases were identified as CO_2 and H_2. They proposed that the cell was composed of an upstream unflooded region and a downstream flooded region. The flooded region functioned as an internal load/connection for the unflooded region where regular reactions occurred, resulting in the formation of CO_2 at the anode. In the flooded region, methanol oxidation happened at the cathode side, and the resultant protons were transported through the membrane to the anode side where they were reduced to H_2. Therefore, both CO_2 and H_2 were produced at the anode side of the fuel cell.

A significant impact on the cathode has been found at OCV during either startup or shutdown if an air/fuel boundary forms at the anode [43, 53]. When a fuel cell is shut down, there is some fuel remaining in the anode and some air in the cathode, and the OCV is about 1 V. Their amounts become lower when they crossover through the membrane, and eventually some air from the environment seeps in. A fuel/air boundary forms when air gets into the anode side. The formation of such a boundary raises the potential of the cathode region that

overlaps with the air portion at the anode side to well over 1 V. Such a high potential causes severe oxidation of the carbon catalyst support at the cathode. Figure 11.28 shows that significant fuel cell performance loss occurred within 20 corrosion cycles [53].
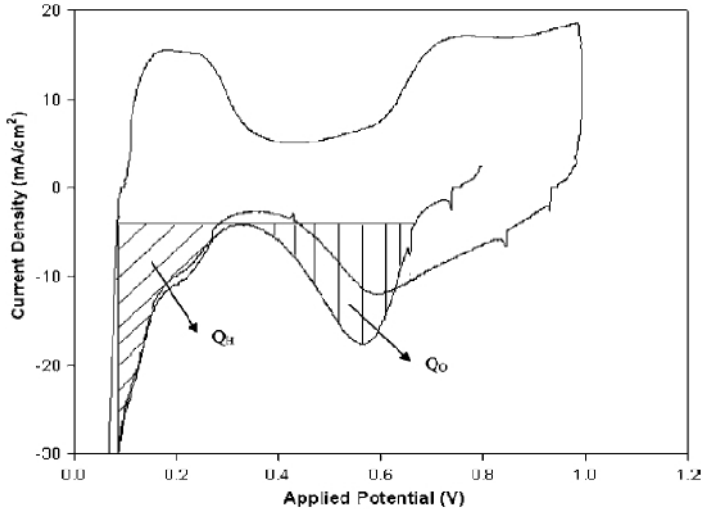
Figure 11.27. Cyclic voltammograms to illustrate the charge associated with hydrogen adsorption Q_H and that associated with platinum oxide reduction Q_O. Nafion 112 membrane; Pt/C cathode catalyst; T = 100 °C; scan rate = 30 mV s^{-1} [62]. (Reproduced by permission of ECS—The Electrochemical Society, from Xu H, Kunz R, Fenton JM. Investigation of platinum oxidation in PEM fuel cells at various relative humidities.)
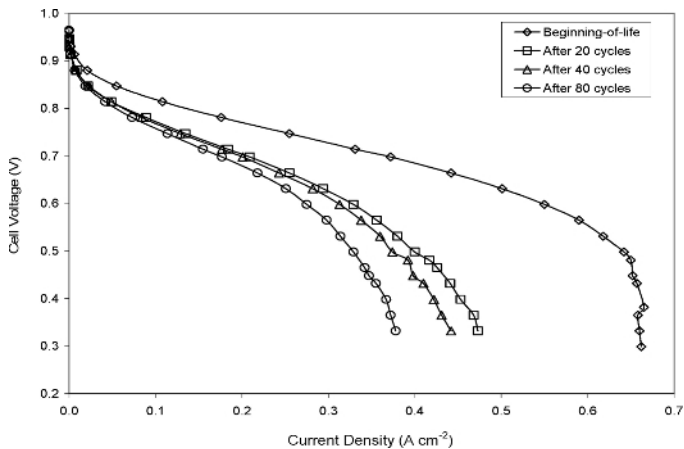
Figure 11.28. Effect of corrosion cycles on fuel cell performance. Cell T = 65 °C; cathode: air, RH = 100%; anode: reformate with 2% air bleed, RH = 100% [53]. (Reprinted from Journal of Power Sources, 158(2), Tang H, Qi Z, Ramani M, Elter JF, PEM fuel cell cathode carbon corrosion due to the formation of air/fuel boundary at the anode, 1306–12, ©2006, with permission from Elsevier.)

11.8.2.2 Measurement of Fuel Crossover Rate

The actual amount of fuel crossing over the membrane electrolyte at the open circuit can be measured electrochemically. During the measurement the fuel passes through the anode side and nothing or an inert gas such as nitrogen passes through the cathode side. Anode and cathode refer to the fuel cell mode throughout this article. An external power supply applies a positive voltage at the cathode. Once the fuel passes through the membrane to reach the cathode, it is quickly oxidized. The current is proportional to the amount of fuel crossing over according to Faraday's law.

Figure 11.29 shows the processes that occur during the measurement of methanol crossover. Methanol crossing over to the cathode is oxidized: $CH_3OH + H_2O \rightarrow CO_2 + 6H^+ + 6e^-$. The methanol crossover rate can be calculated by $n = i/6F$, where i is the crossover current (if the current is in a unit of amperes, n will be in a unit of mole s^{-1}). The protons produced from the methanol oxidation are transported through the membrane from the cathode to the anode, and form hydrogen at the anode side: $2H^+ + 2e^- \rightarrow H_2$. Since protons can drag methanol via electroosmosis, some methanol will be taken back to the anode before reaching the cathode. This results in an underestimation of the methanol crossover current by this electrochemical method.
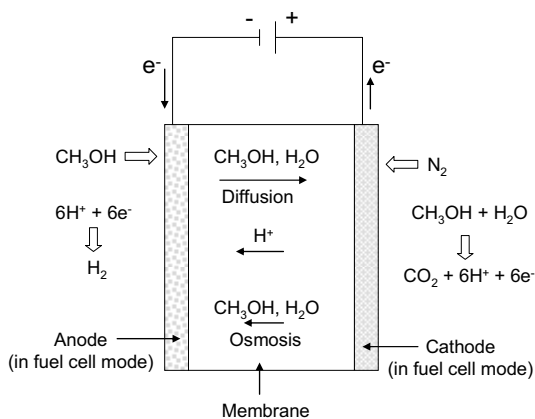
Figure 11.29. Illustration of the processes associated with the measurement of methanol crossover

The crossover current measured by this electrochemical method represents the situation only at the open circuit. When a fuel cell is under operation the fuel concentration at the anode/membrane interface is lower than its bulk concentration. Then, the crossover rate is lower than that at the open circuit.

When the H_2 crossover is measured by this type of electrochemical method, the reaction at the cathode side is $H_2 \rightarrow 2H^+ + 2e^-$. The H_2 crossover rate is calculated by $n = i/2F$. H_2 crossover current is an indication of the health of the membrane. It indirectly reflects the membrane decay rate, and is often used in accelerated testing. Figure 11.30 shows the H_2 crossover current through a Hyflon$^{\circledR}$ membrane under H_2/air, H_2/N_2, and N_2/air, respectively [26]. Under H_2/air the crossover

current started to increase exponentially after about 50 hours of testing, while under H_2/N_2 and N_2/air conditions the crossover current remained at about 1 mA cm^{-2} in the 300 hours of testing. This experiment indicated that the species that attack the membrane (e.g., radicals derived from H_2O_2) formed only in the presence of both H_2 and O_2. It has been widely accepted that the radical attack on perfluorinated ionomers occurs mainly through an unzipping process starting from the carboxylic acid groups (-COOH) located at the end of the polymer main chain [9]. Attack to the ether linkages also occurs but with much less severity.
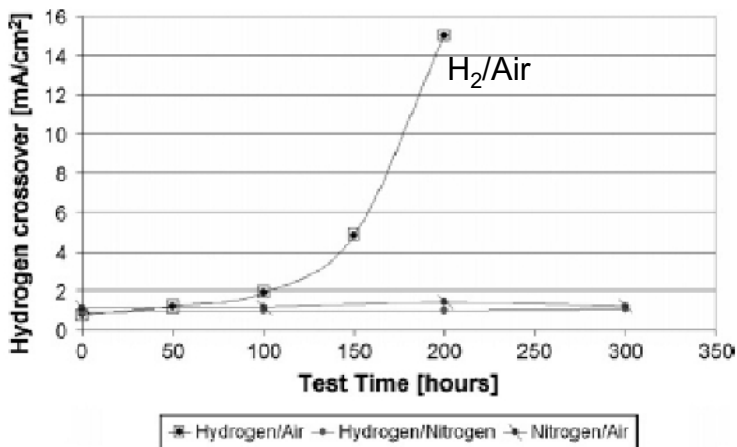
Figure 11.30. Hydrogen crossover rates through a Hyflon® extruded membrane under OCV tested with different reactants. Electrode area = 25 cm^2; Pt = 0.25 mg cm^{-2} at either anode or cathode; T = 70 °C; RH = 50% for both anode and cathode; membrane thickness = 50 μm; ionomer equivalent weight = 870 g $equiv^{-1}$ [26]. (Reprinted from Journal of Power Sources, 171(1), Merlo L, Ghielmi A, Cirillo L, Gebert M, Arcella V, Resistance to peroxide degradation of Hyflon® Ion membranes, 140–7, ©2007, with permission from Elsevier.)

11.8.2.3 Electrochemical Active Surface Area

The change in the ECSA shows how much of the electrode's active surface area is lost during a period of operation. A faster loss indicates that the durability of the electrode is lower. A major reason for the loss of the ECSA is the growth in the catalyst particle size. The initial particles sized around 2 to 4 nm have relatively high surface energy, and they tend to grow to form larger (e.g., ~15 nm), more stable particles with time. Other reasons include dissolution and redistribution of the catalyst particles [10]. Catalyst materials are sometimes observed within the Nafion membrane [60], and these catalysts will not be able to support the electrochemical reaction at the electrodes. Sometimes the anode catalyst materials are even found to migrate to the cathodes [34].

Figure 11.31 shows the beginning-of-life (BOL) and end-of-life (EOL) cyclic voltammograms of a PEMFC after 500 hours of stress test. The charge under the hydrogen desorption peak areas decreased from 1.37 C to 0.79 C, which implied that the ECSA was reduced by 43%.
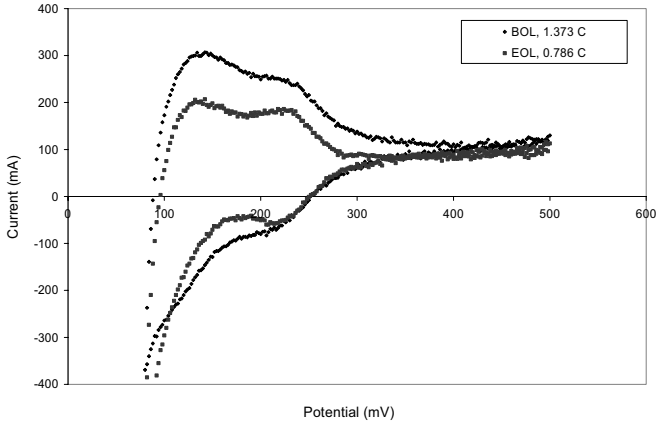
Figure 11.31. Cyclic voltammograms at BOL and EOL to illustrate the decline in the hydrogen adsorption and desorption areas

11.8.2.4 Oxygen Gain

Air is typically used as the oxidant at the cathode. It contains about 21% O_2 and 78% N_2. As the O_2 reacts at the cathode, a higher concentration of N_2 remains around the catalysts. This N_2 behaves like a blanket that slows down the new O_2 as it approaches the catalysts. Therefore, the cell encounters a higher mass transport resistance loss using air than using O_2.

During the operation of a fuel cell, the catalyst support at the cathode becomes more hydrophilic because of oxidation and corrosion. This favors the accumulation of water, and hence increases the mass transport resistance.
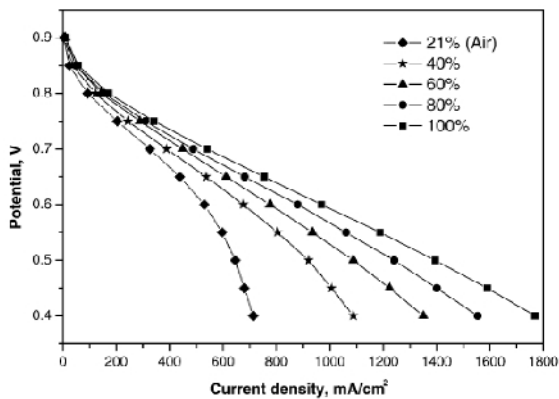
Figure 11.32. Effect of oxygen concentration in the cathode gas on fuel cell performance. Cell T = 80 °C; cathode dew point = 65 °C; anode dew point = 80 °C; Nafion 115 membrane; cathode Pt loading = 0.4 mg cm^{-2}; anode Pt loading = 0.3 mg cm^{-2} [37]. (Reprinted from Journal of Power Sources, 137(1), Prasanna M, Ha HY, Cho EA, Hong S-A, Oh I-H, Investigation of oxygen gain in polymer electrolyte membrane fuel cells, 1–8, ©2004, with permission from Elsevier.)

O_2 can be used to estimate the mass transport resistance loss associated with using air because the cathode suffers negligible mass transport loss when O_2 is used as the oxidant. Such a test is called the oxygen gain experiment. Figure 11.32 shows an example [37]. A larger oxygen gain indicates that the cathode suffers a higher mass transport resistance when air is used as the oxidant. The oxygen gain experiment is effective in gauging the mass transport properties of an electrode, and can shed some light on how to optimize the structure of the electrode.

Other contributions to the oxygen gain are the increase in the thermodynamic voltage and the reduction of the charge transfer resistance for the ORR because of the increase in the O_2 concentration (or partial pressure). So, the total gain consists of the gain due to the reduction of the mass transport resistance, the gain from the reduction of the oxygen reduction charge transfer resistance, and the increase in the thermodynamic voltage. Typically, the oxygen gain from the reduction of the mass transport resistance dominates, and it can be measured by performing EIS.

11.8.2.5 Hydrogen Gain

The hydrogen gain experiment is carried out at the anode to gauge the increase in the anode overpotential due to the presence of CO. Since CO can strongly adsorb onto the surface of Pt to block the reaction sites for H_2 oxidation, it seriously poisons the anode even at ppm levels. The poisoning leads to a higher overpotential for the oxidation of H_2.

CO poisoning is reversible. When an H_2 fuel containing CO is replaced by a pure H_2 fuel, the CO will gradually desorb from the Pt surface to rejuvenate fresh Pt sites for the HOR. Therefore, a lower anode overpotential is achieved. The potential difference between using an H_2 fuel containing CO and a pure H_2 fuel is called the hydrogen gain. It is a measurement of the CO tolerance of a fuel cell anode. A larger hydrogen gain indicates that the anode has lower CO tolerance.

Hydrogen gain can also be used to evaluate the impact of either fuel dilution or the presence of certain components such as CO_2. When an H_2 fuel mixture is produced by reforming hydrocarbon fuels, the content of H_2 ranges from about 40 to 70% on the dry basis. The other major components are CO_2 and N_2. If the fuel is humidified, it also contains water vapor. N_2 will have a dilution effect and the impact on the anode overpotential is on the level of a few mV. CO_2 is a little trickier because it not only can dilute the fuel but also has the potential to form some CO. The dilution effect is on the level of a few mV. The poisoning effect depends on how much CO forms from CO_2. CO could form from the reverse water-gas shift reaction:

$$CO_2 + H_2 \rightarrow CO + H_2O \tag{11.50}$$

Since the standard reduction potential of CO_2 to form HCOOH is at about –0.20 V [54],

$$CO_2 + 2H^+ + 2e^- = HCOOH \tag{11.51}$$

the formation of HCOOH or CO-type species from CO_2 via electrochemical reduction is less likely under normal fuel cell conditions.

Papageorgopoulos and de Bruijn showed that the CO-type species (e.g., CO, -COH, -COOH) formed from CO_2 did not form a complete monolayer on Pt catalysts, and its oxidation occurred at less positive potentials than that of a CO adlayer formed directly from CO [30]. They carried out the adsorption processes at 18 mV and believed that the adsorption of the former CO-type species from CO_2 included linear, bridge, and multiple bonds, while that of CO was exclusively linear. The CO oxidative stripping peaks became much smaller when the CO-type species was made on PtRu catalysts, indicating that less CO was formed on PtRu than on Pt. Such an experiment indicates that the reverse water-gas shift reaction occurs to a smaller extent when PtRu is used as the anode catalyst than when Pt is used.

Studies have shown that PtMo is a more CO-tolerant catalyst than PtRu in the absence of CO_2 [1]. However, in the presence of CO_2, PtMo showed inferior CO-tolerance to both PtRu and Pt [1]. Therefore, PtRu is a more universal anode catalyst for reformate-type fuels.

11.8.2.6 Hydrogen Pumping

When a positive voltage is applied to the anode, H_2 is oxidized to protons and electrons: $H_2 \rightarrow 2H^+ + 2e^-$. Protons transport through the membrane and combine with electrons to form H_2 at the cathode: $2H^+ + 2e^- \rightarrow H_2$. The net reaction is $H_{2\,(anode)} \rightarrow H_{2\,(cathode)}$. So, H_2 is electrochemically moved from the anode to the cathode in a pumping manner.

Since both H_2 oxidation and H^+ reduction encounter low overpotentials, the voltage required for the pumping process is low. The I-V curve is typically linear and the slope of the line is mainly the Ohmic resistance of the cell. However, in the presence of CO, the anode is poisoned and the pumping voltage can increase significantly with the pumping current density, (Figure 11.33)
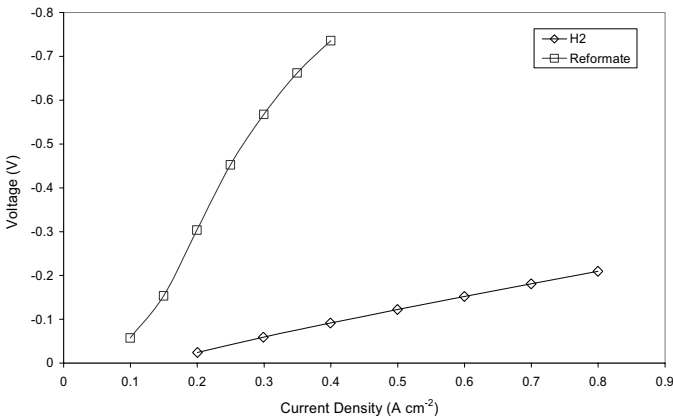
Figure 11.33. Hydrogen pumping I-V curves obtained from a H_3PO_4 fuel cell. T = 160 °C; Reformate contains 1% CO and 29% H_2, balanced by CO_2 and N_2.

He et al. discovered that hydrogen pumping can shorten the fuel cell incubation time and lead to higher performance [17]. During their experiment, hydrogen was

supplied to the anode and nothing or an inert gas such as nitrogen was supplied to the cathode. Then an external power supply drove the hydrogen pumping process for a period of a few minutes to 1 hour. After air was fed to the cathode, the fuel cell showed a much higher performance than it did before the hydrogen pumping.

Hydrogen pumping can also be used to separate H_2 from other components. For a fuel mixture containing H_2, CO_2, N_2, and CO, hydrogen pumping will transport H_2 to the other side of the electrolyte membrane and leave all the other components behind. Then high-purity H_2 is obtained.

Hydrogen pumping cells can constitute either a module on their own or a portion of a fuel cell stack. The power needed for hydrogen pumping can be supplied by the fuel cell stack.

11.9 Summary

A fuel cell and its components can be characterized by a variety of electrochemical methods. For the quick screening of new catalysts and for studying the reaction mechanisms and kinetics, controlled potential techniques (e.g., potential step, potential sweep, and potential cycling), rotating disk and rotating ring-disk electrodes, and impedance spectroscopy are popularly used. For the evaluation of fuel cell electrodes or MEAs, methods derived from these techniques are often used. These methods include cyclic voltammetry, impedance spectroscopy, current interruption and current pulsing techniques, I-V polarization, open circuit voltage, fuel crossover, oxygen gain, hydrogen gain, and hydrogen pumping.

List of Symbols

A	electrode geometric area
C	either bulk concentration of a reactant or capacitance
C_d	double-layer capacitance
d	density
D	diffusion coefficient
$E_{1/2}$	half-wave potential
$E°$	standard potential
E_R	potential of the ring electrode in RRDE
F	Faraday constant
i_d	diffusion-controlled current
i_D	current at the disk electrode in RDE or RRDE
I_D	current density at the disk electrode in RRDE
i_k	kinetic-controlled current
i_l	limiting current in the empirical I-V curve expression
i_{lim}	limiting current in RDE
i_o	exchange current density
i_p	peak current
i_R	current at the ring electrode in RRDE

I_R	current density at the ring electrode in RRDE
k_f	kinetic rate constant
n	either number of electrons per reactant molecule or number of electrons involved in the rate determining step
N	collection efficiency in RRDE
Pt/C	Pt supported on carbon
Q	charge
r	radius
R	resistance
R_{ct}	charge transfer resistance
R_s	electric resistance
S	surface area
T	temperature
T_g	glass transition temperature
V_a	anode potential
V_c	cathode potential
V_{cell}	cell voltage
V_{ct}	voltage loss due to charge transfer resistance
V_{ocv}	open circuit voltage
V_{Ohm}	voltage loss due to the Ohmic resistance
V_T	thermal voltage
X_C	capacitive resistance
X_{H2O2}	ratio of H_2O_2 to O_2 during ORR
$\dot{Y}$	admittance
$\dot{Z}$	impedance
Z_{Im}	imaginary impedance
Z_{Re}	real impedance
Z_w	Warburg impedance
α	phase parameter or charge transfer coefficient
δ	either thickness of a film or diffusion-layer thickness
ΔG	Gibbs free energy change of a reaction
η	either overpotential or viscosity
λ	either wavelength or the number of water molecules held by each sulfonic acid group
ν	kinematic viscosity
θ	either incidence angle in XRD or phase angle in EIS
ρ	resistivity
τ_{ct}	time constant during discharge of an electrochemical process
υ	potential scan rate
υ_x	solution velocity normal to electrode surface in RDE
Ω	angular velocity

References

1. Ball S, Hodgkinson A, Hoogers G, Maniguet S, Thompsett D, Wong B. The proton exchange membrane fuel cell performance of a carbon supported PtMo catalyst operating on reformate. Electrochem Solid-State Lett 2002;5:A31–4.
2. Bard AJ, Faulkner LR. Electrochemical methods: fundamentals and applications. New York: John Wiley & Sons, 1980.
3. Büchi FN, Marek A, Scherer GG. In situ membrane resistance measurements in polymer electrolyte fuel cells by fast auxiliary current pulses. J Electrochem Soc 1995;142:1895–901.
4. Büchi FN, Scherer GG. Investigation of the transversal water profile in Nafion membranes in polymer electrolyte fuel cells. J Electrochem Soc 2001;148:A183–8.
5. Cahan BD, Wainright JS. AC impedance investigations of proton conduction in Nafion™. J Electrochem Soc 1993;140:L185–6.
6. Choi JH, Jeong KJ, Dong Y, Han J, Lim TH, Lee JS, et al. Electro-oxidation of methanol and formic acid on PtRu and PtAu for direct liquid fuel cells. J Power Sources 2006;163:71–5.
7. Ciureanu M, Wang H. Electrochemical impedance study of electrode-membrane assemblies in PEM fuel cells: I. electro-oxidation of H_2 and H_2/CO mixtures on Pt-based gas-diffusion electrodes. J Electrochem Soc 1999;146:4031–40.
8. Crabb EM, Marshall R, Thompsett D. Carbon monoxide electro-oxidation properties of carbon-supported PtSn catalysts prepared using surface organometallic chemistry. J Electrochem Soc 2000;147:4440–7.
9. Curtin DE, Lousenberg RD, Henry TJ, Tangeman PC, Tisack ME. Advanced materials for improved PEMFC performance and life. J Power Sources 2004;131:41–8.
10. Ferreira PJ, la O' GJ, Shao-Horn Y, Morgan D, Makharia R, Kocha S, et al. Instability of Pt/C electrocatalysts in proton exchange membrane fuel cells: a mechanistic investigation. J Electrochem Soc 2005;152:A2256–71.
11. Gang X, Hjuler HA, Olsen C, Berg RW, Bjerrum NJ. Electrolyte additives for phosphoric acid fuel cells. J Electrochem Soc 1993;140:896–902.
12. Gao LJ, Conway BE. Poisoning effects of arsenic species on H adsorption and kinetic behaviour of the H_2 evolution reaction at Pt in KOH solution. J Electroanal Chem 1995;395:261–71.
13. Glass JT, Cahen GLJ, Stoner GE. The effect of phosphoric acid concentration on electrocatalysis. J Electrochem Soc 1989;136:656–60.
14. Guo Q, Cayetano M, Tsou YM, De Castro ES, White RE. Study of ionic conductivity profiles of the air cathode of a PEMFC by AC impedance spectroscopy. J Electrochem Soc 2003;150:A1440–9.
15. Guo Q, White RE. A steady-state impedance model for a PEMFC cathode. J Electrochem Soc 2004;151:E133–49.
16. Habib MA, Bockris JOM. In situ FT-IR spectroscopic study of electrochemical adsorption of phosphoric acid on platinum. J Electrochem Soc 1983;130:2510–2.
17. He C, Qi Z, Hollett M, Kaufman A. An electrochemical method to improve the performance of air cathodes and methanol anodes. Electrochem Solid-State Lett 2002;5:A181–3.
18. Ioroi T, Yasuda K. Platinum-iridium alloys as oxygen reduction electrocatalysts for polymer electrolyte fuel cells. J Electrochem Soc 2005;152:A1917–24.
19. Kim J, Lee SM, Srinivasan S. Modeling of proton exchange membrane fuel cell performance with an empirical equation. J Electrochem Soc 1995;142:2670–4.
20. Larsen R, Ha S, Zakzeski J, Masel RI. Unusually active palladium-based catalysts for the electrooxidation of formic acid. J Power Sources 2006;157:78–84.

21. Lawson DR, Whiteley LD, Martin CR, Szentirmay MN, Song JI. Oxygen reduction at Nafion film-coated platinum electrodes: transport and kinetics. J Electrochem Soc 1988;135:2247–53.
22. Leng YJ, Wang X, Hsing IM. Assessment of CO-tolerance for different Pt-alloy anode catalysts in a polymer electrolyte fuel cell using AC impedance spectroscopy. J Electroanal Chem 2002;528:145–52.
23. Li G, Pickup PG. Ionic conductivity of PEMFC electrodes: effect of Nafion loading. J Electrochem Soc 150 2003;C745–52.
24. Liu Z, Hong L, Tham MP, Lim TH, Jiang H. Nanostructured Pt/C and Pd/C catalysts for direct formic acid fuel cells. J Power Sources 2006;161:831–5.
25. Markovic NM, Gasteiger HA, Ross PN. Oxygen reduction on platinum low-index single-crystal surfaces in sulfuric acid solution: rotating ring-Pt(hkl) disk studies. J Phys Chem 1995;99:3411–5.
26. Merlo L, Ghielmi A, Cirillo L, Gebert M, Arcella V. Resistance to peroxide degradation of Hyflon® Ion membranes. J Power Sources 2007;171:140–7.
27. Mukerjee S, Urian RC, Lee SJ, Ticianelli EA, Mcbreen J. Electrocatalysis of CO tolerance by carbon-supported PtMo electrocatalysts in PEMFCs. J Electrochem Soc 2004;151:A1094–103.
28. Müller JT, Urban PM, Hölderich WF. Impedance studies on direct methanol fuel cell anodes. J Power Sources 1999;84:157–60.
29. Newman J. Ohmic potential measured by interrupter techniques. J Electrochem Soc 1970;117:507–8.
30. Papageorgopoulos DC, De Bruijn FA. Examining a potential fuel cell poison: a voltammetry study of the influence of carbon dioxide on the hydrogen oxidation capability of carbon-supported Pt and PtRu anodes J. Electrochem. Soc 149 2002;A140–5.
31. Parthasarathy A, Martin CR. Investigations of the O_2 reduction reaction at the platinum/Nafion® interface using a solid-state electrochemical cell. J Electrochem Soc 1991;138:916–21.
32. Parthasarathy A, Srinivasan S, Appleby AJ. Temperature dependence of the electrode kinetics of oxygen reduction at the platinum/Nafion® interface – a microelectrode investigation. J Electrochem Soc 1992;139:2530–7.
33. Paulus UA, Schmidt TJ, Gasteiger HA, Behm RJ. Oxygen reduction on a high-surface area Pt/Vulcan carbon catalyst: a thin-film rotating ring-disk electrode study. J Electroanal Chem 2001;495:134–45.
34. Piela P, Eickes C, Brosha E, Garzon F, Zelenaya P. Ruthenium crossover in direct methanol fuel cell with Pt-Ru black anode. J Electrochem Soc 2004;151:A2053–9.
35. Piela P, Fields R, Zelenay P. Electrochemical impedance spectroscopy for direct methanol fuel cell diagnostics. J Electrochem Soc 2006;153:A1902–13.
36. Poltarzewski Z, Staiti P, Alderucci V, Wieczorek W, Giordano N. Nafion distribution in gas diffusion electrodes for solid-polymer-electrolyte-fuel-cell applications. J Electrochem Soc 1992;139:761–5.
37. Prasanna M, Ha HY, Cho EA, Hong SA, Oh IH. Investigation of oxygen gain in polymer electrolyte membrane fuel cells. J Power Sources 2004;137:1–8.
38. Qi Z, Buelte S. Effect of open circuit voltage on performance and degradation of high temperature PBI–H_3PO_4 fuel cells. J Power Sources 2006;161:1126–32.
39. Qi Z, Hollett M, Attia A, Kaufman A. Low-temperature direct 2-propanol fuel cells. Electrochem Solid-State Lett 2002;5:A129–30.
40. Qi Z, Kaufman A. Performance of 2-propanol in direct-oxidation fuel cells. J Power Sources 2002;112:121–9.
41. Qi Z, Kaufman A. Liquid-feed direct oxidation fuel cells using neat 2-propanol as fuel. J Power Sources 2003;118:54–60.

42. Razaq M, Razaq A, Yeager E. Perfluorosulfonimide as an additive in phosphoric acid fuel cell. J Electrochem Soc 1989;136:385–90.

43. Reiser CA, Bregoli L, Patterson TW, Yi JS, Yang JD, Perry ML. et al. A reverse-current decay mechanism for fuel cells. Electrochem Solid-State Lett 2005;8:A273–6.

44. Ren X, Henderson W, Gottesfeld S. Electro-osmotic drag of water in ionomeric membranes: new measurements employing a direct methanol fuel cell. J Electrochem Soc 1997;144:L267–70.

45. Rush BM, Reimer JA, Cairns EJ. Nuclear magnetic resonance and voltammetry studies of carbon monoxide adsorption and oxidation on a carbon-supported platinum fuel cell electrocatalyst. J Electrochem Soc 2001;148:A137–48.

46. Scharifker BR, Zelenay P, Bockris JOM. The kinetics of oxygen reduction in molten phosphoric acid at high temperatures. J Electrochem Soc 1977;134:2714–25.

47. Schmidt TJ, Gasteiger HA, Behma RJ. Rotating disk electrode measurements on the CO tolerance of a high-surface area Pt/Vulcan carbon fuel cell catalyst. J Electrochem Soc 1999;146:1296–304.

48. Schmidt TJ, Gasteiger HA, Stäb GD, Urban PM, Kolb DM, Behm RJ. Characterization of high-surface-area electrocatalysts using a rotating disk electrode configuration. J Electrochem Soc 1998;145:2354–58.

49. Sivakumar P, Tricoli V. Pt-Ru-Ir nanoparticles prepared by vapor deposition as a very efficient anode catalyst for methanol fuel cells. Electrochem Solid-State Lett 2006;9:A167–70.

50. Sone Y, Ekdunge P, Simonsson D. Proton conductivity of Nafion 117 as measured by a four-electrode AC impedance method. J Electrochem Soc 1996;143:1254–9.

51. Springer TE, Zawodzinski TA, Wilson MS, Gottesfeld S. Characterization of polymer electrolyte fuel cells using AC impedance spectroscopy. J Electrochem Soc 1996;143:587–99.

52. Sugimoto W, Aoyama K, Kawaguchi T, Murakami Y, Takasu Y. Kinetics of CH_3OH oxidation on PtRu/C studied by impedance and CO stripping voltammetry. J Electroanal Chem 2005;576:215–21.

53. Tang H, Qi Z, Ramani M, Elter JF. PEM fuel cell cathode carbon corrosion due to the formation of air/fuel boundary at the anode. J Power Sources 2006;158:1306–12.

54. Vanýsek P. Electrochemical Series. In: Lide DR, Frederikse HPR, editors. CRC Handbook of Chemistry and Physics. 75th edn. FLCRC Press: Boca Raton, 1997.

55. Wagner N, Schulze M. Change of electrochemical impedance spectra during CO poisoning of the Pt and Pt–Ru anodes in a membrane fuel cell (PEFC). Electrochim Acta 2003;48:3899–907.

56. Wang X, Hsing IM, Leng YJ, Yue PL. Model interpretation of electrochemical impedance spectroscopy and polarization behavior of H_2/CO mixture oxidation in polymer electrolyte fuel cells. Electrochim Acta 2001;46:4397–405.

57. Wiezell K, Gode P, Lindbergh G. Steady-state and EIS investigations of hydrogen electrodes and membranes in polymer electrolyte fuel cells: I. modeling. J Electrochem Soc 2006;153:A749–58.

58. Wiezell K, Gode P, Lindbergh G. Steady-state and EIS investigations of hydrogen electrodes and membranes in polymer electrolyte fuel cells: II. Experimental. J Electrochem Soc 2006;153:A759–64.

59. Woods R. Hydrogen adsorption on platinum, iridium and rhodium electrodes at reduced temperatures and the determination of real surface area. J Electroanal Chem 1974;49217–26.

60. Xie J, Wood III DL, More KL, Atanassov P, Borup RL. Microstructural changes of membrane electrode assemblies during PEFC durability testing at high humidity conditions. J Electrochem Soc 2005;152:A1011–20.

61. Xie Z, Song C, Andreaus B, Navessin T, Shi Z, Zhang J, et al. Discrepancies in the measurement of ionic conductivity of PEMs using two- and four-probe AC impedance spectroscopy. J Electrochem Soc 2006;153:E173–8.
62. Xu H, Kunz R, Fenton JM. Investigation of platinum oxidation in PEM fuel cells at various relative humidities. Electrochem Solid-State Lett 2007;10:B1–5.
63. Ye Q, Zhao TS, Yang H, Prabhuram J. Electrochemical reactions in a DMFC under open-circuit conditions. Electrochem Solid-State Lett 2005;8:A52–4.
64. Zawodzinski, Jr. TA, Derouin C, Radzinski S, Sherman RJ, Smith VT, Springer TE. et al. Water uptake by and transport through Nafion® 117 membranes. J Electrochem Soc 1993;140:1041–7.
65. Zhang DY, Ma ZF, Wang G, Konstantinov K, Yuan X, Liu HK. Electro-oxidation of ethanol on Pt-WO$_3$/C electrocatalyst. Electrochem Solid-State Lett 2006;9:A423–6.
66. Zhang J, Tang Y, Song C, Zhang J, Wang H. PEM fuel cell open circuit voltage (OCV) in the temperature range of 23 °C to 120 °C. J Power Sources 2006;163:532–7.

12

Combinatorial Methods for PEM Fuel Cell Electrocatalysts

Hansan Liu and Jiujun Zhang

12.1 Introduction

12.1.1 Combinatorial Material Chemistry

Traditionally, chemists and material scientists rely on the slow and serendipitous trial-and-error process for discovering and developing new chemicals or materials. However, the conventional one-at-a-time, or one-by-one, methods are not capable of matching the pace of present-day material development. For example, in the area of drug discovery, it has been estimated theoretically that the number of possible drugs with molecular structures and weights attractive for pharmaceutical activity screening is 10^{18}. This number is $\sim10^3$ times larger than the number of chemical substances available from commercial sources or in-house collections. This number is also $\sim5\times10^{10}$ times larger than that listed in the Chemical Abstracts Service (CAS) database. It is impossible to screen the pharmaceutical activities of such a large number of potential drugs by using traditional one-by-one methods. For organic substances, if each substance contains more than 30 atoms of H, C, O, N, and S elements, the number of potential stable molecular structures is expected to be $\sim10^{63}$. For inorganic substances, possibilities include $\sim3\times10^3$ binaries, $\sim7\times10^4$ ternaries, $\sim1\times10^6$ quaternaries, and $\sim6\times10^{12}$ decanaries, which can be made from 75 useful and stable elements in the periodic table. These numbers exclude those with stoichiometric and structural diversity and different orders. Traditional one-by-one approaches will never be able to deal with the screening and optimization of these substances.

   Fortunately, the situation began to change when a new field of chemistry, called combinatorial chemistry, arose in the late 1980s. Combinatorial chemistry is an innovative approach to speed up the discovery and development of new molecules and materials. The early successes of combinatorial chemistry in the pharmaceutical industry have been followed by the discovery of a wide variety of important materials in chemistry and materials science. These materials range from catalysts, polymers, and zeolites to luminescent and magnetoresistive compounds,

agricultural materials, and high-temperature superconductors, dielectric, ferroelectric, and structural materials, as well as many others. Since Schultz and his group at the Lawrence Berkeley National Laboratory of UC Berkeley reported the usage of combinatorial methods for a search of superconductors in 1995, combinatorial chemistry has emerged as an exciting new paradigm for materials discovery. In the past two decades, this topic has attracted considerable scientific interest and research efforts in the fields of chemistry and material science.

In principle, the combinatorial method primarily includes two key steps: (1) combinatorial material libraries preparation and (2) high throughput chemical/physical screening. A combinatorial material library consists of many different samples with various compositions that are synthesized quickly, simultaneously, and in parallel. The combinatorial synthetic method contrasts with the time-consuming and labour-intensive traditional approaches, by which compounds are synthesized individually, one at a time. Through combinatorial methods, scientists can synthesize many hundreds or thousands of compounds at one time, instead of preparing only a few by a simple methodology. The combinatorial synthetic methods allow a very large number of substances to be synthesized much more rapidly and at lower cost than by traditional synthetic chemistry. High throughput screening is the process for rapid automated assessment of single or multiple properties of a large number of samples in the combinatorial libraries. Ideally, a useful high throughput screening method for combinatorial materials discovery should be capable of handling small-size samples with minimal sample preparation requirements, and should also have rapid turnaround in either serial or parallel analysis of library elements during or after the reaction and testing.

Basically, there are two different levels of combinatorial experiments: a discovery level and a focus level. A discovery level combinatorial screening is applied when totally new (alternative) materials are the targets of the search. The search motivation could be scientific curiosity and exploration of new materials. In some case, if the existing materials have no potential for further improvements, a discovery-level combinatorial screening may be used for alternative materials. This discovery screening can sample a broad and highly diverse range of parameter spaces. However, errors may occur because of the existing difference between combinatorial and conventional methods in synthesis and measurement conditions. Therefore, it is necessary to reproduce the materials resulting from the discovery screening by conventional synthesis, and confirm the expected function by conventional measurements. A focus-level combinatorial screening is used to accelerate the optimization process for material development. These materials could be either those revealed in the discovery screening stage or known materials. In these combinatorial experiments, relatively narrow and well-defined parameter spaces around known materials are sampled at high speed under conditions as close to the conventional experimentation conditions as possible. The goals of focus screening are to get reliable trends and optimized materials. Usually, systematic combinatorial work consists of both discovery and focus screening steps in order to achieve the goals of material development.

12.1.2 Electrocatalysis in PEM Fuel Cells

Proton exchange membrane (PEM) fuel cells are energy conversion devices, which operate by oxidizing a fuel (hydrogen or small organic molecules) at the anode and reducing oxygen at the cathode. In this process, a PEM is used as a separator between the anode and cathode, and also serves as an ionic conductor. The electrocatalysis in PEM fuel cells is mainly relevant to three kinds of fuel cell reactions: oxygen reduction reaction (ORR), hydrogen oxidation reaction (HOR), and methanol oxidation reaction (MOR), described as follows:

$$O_2(g) + 4H^+(aq) + 4e^- \rightarrow 2H_2O(l) \tag{12.1}$$

$$H_2(g) \rightarrow 2H^+(aq) + 2e^- \tag{12.2}$$

$$CH_3OH(aq) + H_2O(l) \rightarrow CO_2(g) + 6H^+(aq) + 6e^- \tag{12.3}$$

In a hydrogen-air/oxygen PEM fuel cell, electrocatalysts are necessary in order to catalyze the ORR (12.1) and HOR (12.2) at the cathode and anode, respectively. Normally, the ORR and HOR easily happen on the surface of noble metals such as platinum (Pt). However, in a hydrogen-fuelled PEM fuel cell, the reaction rate of the ORR is lower than that of the HOR by several orders. Therefore, the ORR at the cathode side dominates the overall performance of such a fuel cell. Thus, finding a good ORR electrocatalyst is one of the major subjects in PEM fuel cell electrocatalysis. To date, Pt is the most active and stable catalyst that can electrocatalyze the ORR at a practical rate in a PEM fuel cell. However, use of Pt is limited by its cost and rarity. In this sense, developing low or non-Pt ORR catalysts is highly desirable. There are two major strategies for cost-effective and high-performance catalysts: one is to lower Pt content in the catalysts through alloying other low-cost metals, without compromising performance; the other is to develop new non-Pt or even non-noble metal catalysts that are able to operate in a real fuel cell with acceptable activity and stability. For the HOR at the anode side, carbon monoxide (CO) as an impurity in the reforming hydrogen gas can poison the Pt surface, causing performance to drop. Even a very small amount of CO in the fuel can occupy and deactivate the Pt-active sites. Developing CO-tolerant catalysts for HOR is thus another R&D topic for hydrogen-fuelled PEM fuel cell electrocatalysis. Some platinum alloys such as PtRu have been found to be effective CO-tolerant catalysts for HOR.

In a direct methanol fuel cell (DMFC), the methanol oxidation reaction (MOR) is also a slow reaction in the whole electrochemical reaction process. Even using Pt as a catalyst, MOR is still much slower than HOR. The mechanism of MOR is much more complicated than those of ORR and HOR. The intermediates of MOR, including CO and CO-like species, can easily poison the Pt active site, causing large anode overpotential and then sluggish kinetics. Because liquid methanol is preferable to gaseous hydrogen, in terms of fuel storage and transportation, DMFC is thought to be the most promising fuel cell to be commercialized in the near future. A considerable global R&D effort in the DMFC community has been focused on cost-effective and high-performance catalysts for MOR. Lots of Pt-

based alloys have been explored as candidates for MOR catalysis. In addition, ORR at the cathode can also be depressed due to the methanol crossover that happens when methanol penetrates the membrane. The methanol in the cathode will lead to a direct MOR between the cathode oxygen and the methanol on the Pt catalyst, depressing the concentration of oxygen. In addition, the resulting intermediates can also poison the Pt active sites. Both effects can cause performance degradation. Therefore, finding methanol-tolerant ORR catalysts for the DMFC cathode is also an important aspect of fuel cell electrocatalysis [7].

In the past several decades, numerous studies [5–8] have been carried out to address challenges in the area of fuel cell electrocatalysis. Many alloys, compounds, and composites have been explored and validated as effective fuel cell electrocatalysts, through traditional one-at-a-time study strategies. However, there is much room for new exploration of electrocatalysts, such as composition-diverse binary, ternary, quaternary alloys, or non-noble metal oxides and composites. It seems that the traditional methods for new catalyst development are not fast enough for electrocatalyst breakthrough to align with the urgent demands of fuel cell technology. Combinatorial chemistry thus provides a possible solution to the current need for fuel cell electrocatalysis R&D. Since Reddington et al. first introduced combinatorial electrochemistry into the field of fuel cell electrocatalysis in 1998, combinatorial methods have been rapidly developed and successfully applied to the high throughput screening of fuel cell electrocatalysts. Although still in their maturing period, combinatorial methods have been effective and promise great advantages for the discovery of new catalysts for fuel cell technology.

12.2 Combinatorial Methods for Fuel Cell Electrocatalysis

Similar to the applications of combinatorial chemistry in other fields, combinatorial methods for fuel cell electrocatalysis include two key procedures: preparing catalyst libraries, and high throughput screening of the chemical/physical properties of catalysts. The technical challenges for this new application involve how to transplant the existing combinatorial library preparation methods into the area of fuel cell catalysis, including considerations of array design and how to modify existing screening methods or develop new screening methods to match the electrochemical requirements of fuel cell catalysts.

12.2.1 Catalyst Library Preparation

12.2.1.1 Gradient Arrays
Mapping strategy is often used to design multi-element combinatorial libraries with a form of composition gradients. For example, in the pioneering work of Reddington et al., a quaternary combinatorial library was designed by unfolding a three-dimensional phase diagram to a two-dimensional map, as shown in Figure 12.1.
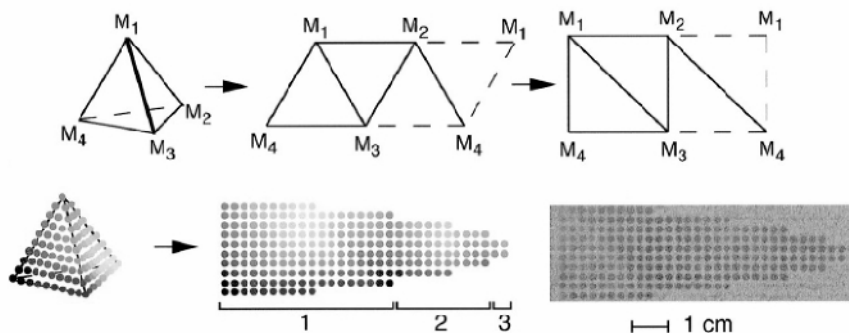
Figure 12.1. (Top) Unfolding of a quaternary phase diagram and mapping into two dimensions. (Lower left): at a resolution of 10 different compositions along each binary edge. This quaternary map contains 220 unique spots with composition varying smoothly across the array. Redundant binary lines (dashed lines in the top drawing) are eliminated in the map. The three nested shells in the phase diagram are marked by 1, 2, and 3 in the map. (Lower right): Inkjet-printed and subsequently borohydride-reduced array of electrocatalysts on Toray carbon paper [9]. (From Reddington E, Sapienza A, Gurau B, Viswanathan R, Sarangapani S, Smotkin ES, et al. Combinatorial electrochemistry: a highly parallel optical screening method for discovery of better electrocatalysts. Science 1998;280:1735–7. Reprinted with permission from AAAS.)

This mapping gives a smooth variation in composition across the array, as illustrated in the color map made from cyan, magenta, yellow, and black inks. According to the combinatorial theory, for a combinatorial map of n different components, the number of the total combinations N is given by Equation 12.4:

$$N(n,m) = \frac{(n+m-2)!}{(n-1)!(m-1)!}$$

(12.4)

where m is the number of compositions along a given binary edge in the map. In this case, $n = 4$, $m = 10$, so the total compositions $N = 12!/3!9!= 220$. It can be seen in Figure 12.1 that this quaternary array contains an outer shell of 4 elements (vertices), 48 binaries (edges), 112 ternaries (faces) and two inner shells containing 52 and 4 quaternaries. In total, there are 220 unique compositions. As shown in Figure 12.1, by customizing a commercially available inkjet printer with this quaternary pattern, the metal salt inks containing appropriate $H_2PtCl_6 \cdot 6H_2O$, $RuCl_3 \cdot xH_2O$, $OsCl_3$, K_2IrCl_6, $RhCl_3 \cdot 2.4H_2O$ and glycerol were printed onto Toray carbon paper. After borohydride reduction of these metal salt inks, a quaternary combinatorial catalyst library with 220 samples was prepared.

Another preparation method for gradient array is "gel-transfer" electrodeposition, which was developed by Hiller and coworkers. This method involves the controlled diffusion of precursor metal salts into a hydrated gel from spatially distinct locations, followed by an electrodeposition to create a surface composition gradient. As illustrated in Figure 12.2(a), a ternary catalyst gradient was created by diffusing precursor metal salts, from three different locations, into a

gel. A thin layer of 4% agarose gel was deposited onto a patterned ITO substrate. Glass capillaries were pierced through the gel at the three vertices of a triangle, through which the solutions of the metal salts were introduced. The metal salts were allowed to diffuse into the gel for several hours, a process which created a concentration gradient of the metal salts. The gel was then cut in the shape of a triangle and the metal ions were subsequently reduced onto the ITO surface by electrodeposition. The gel and photoresist were then removed, leaving a triangular-shaped three-component catalyst gradient on the ITO substrate. Figure 12.2(b) depicts a typical optical image of a concentration gradient of $Pt^{4+}/Ru^{3+}/Rh^{3+}$ ions within an agarose gel.
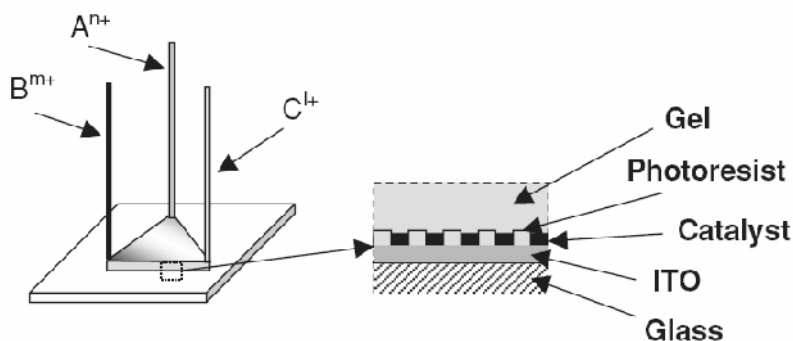
(a)
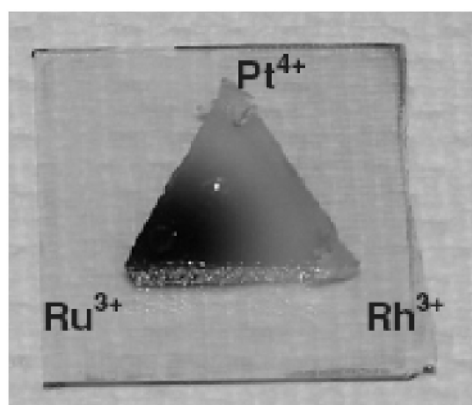
(b)

Figure 12.2. (a) Schematic of synthesis routine for a multi-component catalyst gradient by gel-transfer method. (b) Optical image of concentration gradient of $Pt^{4+}/Ru^{3+}/Rh^{3+}$ in agarose gel [12]. (Reproduced by permission of ECS—The Electrochemical Society, from Jayaraman S, Hillier AC. Electrochemical synthesis and reactivity screening of a ternary composition gradient for combinatorial discovery of fuel cell catalysts.)
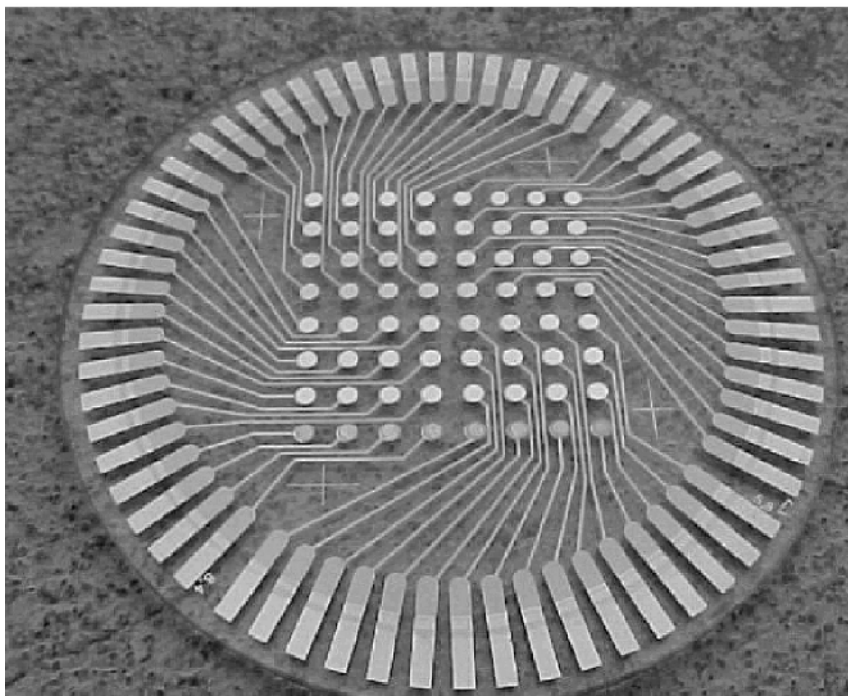
Figure 12.3. A 64-element addressable electrode array on a 3-inch quartz wafer which was used as a support for the synthesis of chemically diverse electrocatalyst libraries [13]. (Reprinted with permission from J Phys Chem B 2003;107:11013–21. Copyright 2003 American Chemical Society.)

12.2.1.2 Mask Arrays

Mask arrays are usually designed for the preparation of multi-metal alloys and oxides through the sputter deposition method. In a mask array, the catalyst compositions are controlled by designing the mask combinations. For instance, Strasser et al. invented a sputtering system for combinatorial studies of fuel cell electrocatalysis. A 64-element addressable electrode array was fabricated on an insulating 3-inch quartz wafer using lithographic techniques (Figure 12.3). Automated RF-magnetron vacuum sputtering was employed to rapidly synthesize the 64-element metal alloy electrocatalyst library (Figure 12.4[a]). The individual constituents of the synthesized catalyst composition were deposited onto the 64-element electrode array by controlling contact masks. A moving-shutter technique controlled the deposition process of thin-film gradients with ranges from a few Angstroms to several micrometers. Compositional variations in the thin films were achieved either by sputtering parallel and orthogonal thickness gradients or by sputtering multiple non-gradient metal slabs with varying thicknesses (Figure 12.4[b]). A ternary thin-film electrocatalyst library with the formulation of PtRuM (M=Co, Ni, W) was prepared using this technique.
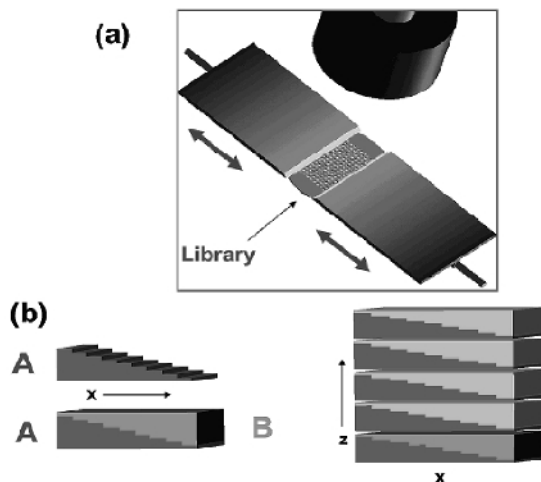
Figure 12.4. (a) An RF magnetron sputter technique with automated target selection, automated moving shutters, as well as physical shadow masking. (b) Sequential gradient sputtering of very thin material slabs which can lead to *in situ* formation of thin-film alloy on the contact spots. Superlattice deposition in z-direction can result in the build-up of thicker films of the desired stoichiometric gradient [13]. (Reprinted with permission from J Phys Chem B 2003;107:11013–21. Copyright 2003 American Chemical Society.)

12.2.1.3 Arrays of Conventional Electrodes

For some combinatorial experiments, in particular those focus-level combinatorial screening experiments, the number of experimental points is relatively low so that the high-resolution array designs can be fabricated by conventional catalyst preparation methods. For example, Guerin et al. adopted a traditional catalyst preparation method to fabricate a 64-element catalyst array for combinatorial electrochemical screening of fuel cell electrocatalysts, as shown in Figure 12.5. In this experiment, 8×8 glassy carbon rod electrodes were embedded in a glass-filled PTFE block. Volumetric suspensions of Pt/C powders containing Nafion in glacial acetic acid were manually deposited onto each electrode to form a 64-element catalyst array. The amount of Nafion in the deposits was controlled by adding 50 μL of 5 wt% Nafion suspension to the mixture of glacial acetic acid and Pt/C powder. In order to ensure the suspensions were homogeneous, the volumetric flasks containing these suspensions were vigorously shaken, using an ultrasound bath, for several hours prior to use. During the transfer of aliquots of the electrocatalyst suspensions, the volumetric flasks were immersed in the operating ultrasound bath throughout the process.

This preparation method of catalyst array has an advantage, which is that the high surface-area catalysts can be screened under similar circumstances as are used in the traditional half-cell electrochemical testing. An additional advantage is that through this approach, the effect of other chemical/physical variables besides composition can also be studied, for example, variables such as Pt loading and catalyst particle size, as has been done in Guerin's work.
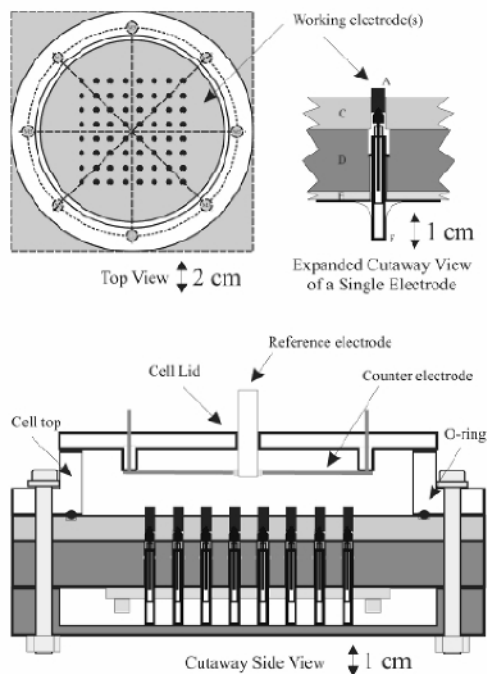
Figure 12.5. Schematic of the cell (viewed from the top, the side, and an expanded view of a single electrode) which was used for electrochemical screening of the 64-element array: (A) vitreous carbon electrode, (C) spring-loaded electrical contact, and glass filled PTFE array base plate, (D) polypropylene contact holder, and (E) a printed circuit board [14]. (Reprinted with permission from J Comb Chem 2004;6:149–58. Copyright 2004 American Chemical Society.)

12.2.2 Catalyst Activity Down-selection

12.2.2.1 Indirect Optical and Spectroscopic Screening

The optical detection method is widely used in combinatorial screening for biochemical affinity, organic host-guest interactions, and inorganic phosphorescence. The method is fast—regardless of the complexity of the array—simple to implement, and allows one to ignore the uninteresting majority of phase space. Reddington et al. [9] adopted this method for combinatorial screening of fuel cell electrocatalysts. They used a fluorescent indicator, quinine in a neutral solution, or NiPTP in a low pH solution to image the activity of the catalyst array. These chemicals are luminescent in their acid form. The fluorescent indicator could detect the presence of proton ions in the electrolyte, which resulted from the anodic methanol oxidation reaction. A typical example is illustrated in Figure 12.6, showing a Pt-Rh-Os ternary array screened in a 6 M methanol solution containing quinine indicator. The left shows an image in white light. The center shows a fluorescence image at low overpotential, displaying the most active region of composition space. To the right is a fluorescence image at high overpotential, with methanol oxidation occurring at every spot in the array. Based on optical

observation, the best anode composition in this ternary array was found to be $Pt_{62}Rh_{25}Os_{13}$, which was much better than Pt but slightly inferior to $Pt_{50}Ru_{50}$.
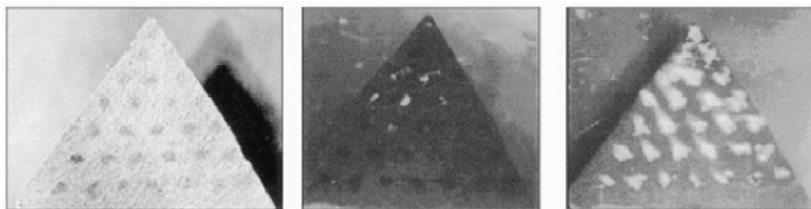
Figure 12.6. A Pt-Rh-Os ternary array in 6 M aqueous methanol solution containing a quinine indicator [9]. (From Reddington E, Sapienza A, Gurau B, Viswanathan R, Sarangapani S, Smotkin ES, et al. Combinatorial electrochemistry: a highly parallel optical screening method for discovery of better electrocatalysts. Science 1998;280:1735–7. Reprinted with permission from AAAS.)

The greatest advantage of the optical method is simplicity when screening large catalyst libraries, because this technique requires only aqueous indicator solutions and a hand-held UV lamp. However, this method has two major drawbacks: it is insensitive to minor differences in electrode activity and it does not provide direct electrochemical measurement, which is required for complete characterization.

Scanning electrochemical microscopy (SECM) can also be treated as a combinatorial screening method for fuel cell electrocatalysis. Through positioning a microelectrode probe near a substrate-electrolyte interface, SECM has an ability to create mass transfer between the tip and the sample (proportional to their separation). The resulting mass transfer rate is high enough to evaluate fast kinetic rate constants. Typically, it can evaluate a kinetic constant with two to three orders of magnitude higher value than that evaluated by the regular ring-disk electrode (RDE) technique. In addition, SECM also can perform interfacial measurements as a function of spatial position, a function which allows direct structure-function measurements on the catalytic surfaces, through imaging variations in reactivity that occur in conjunction with changes in surface composition or structure.

There are primarily two SECM modes developed for combinatorial screening of fuel cell electrocatalysts. The first is the tip collection-sample generation (TC-SG) mode [16]. The principle of this mode was presented in Figure 12.7(a), with methanol oxidation as a model reaction. Normally, SECM employs a fine electrode tip that is moved near a surface through an x–y–z positioning system. When the tip scans near the surface, the electrochemical current between the tip and the substrate can be measured. In Figure 12.7, proton reduction was used as the SECM tip reaction. The protons were produced by hydrogen oxidation or methanol oxidation, then electrocatalyzed by the catalysts on the substrate. These protons were then reduced at the tip. If the tip potential value were to be made sufficiently negative, the reduction of protons would be at a diffusion-controlled rate. The variations in the tip current with the position could be used to characterize the relative reactivity of the substrate at different conditions, such as electrolyte, bias voltage, temperature, etc. This technique, combined with its electrochemical reaction mechanism, enables visualization of the spatial distribution of reaction

rates across a catalyst library, thus aiding the search for new catalysts. One of the drawbacks of this method, however, is the pH limitation of the studied electrolyte. The other is the tip generation-sample collection (TG-SC) mode [17], which is targeted at the oxygen reduction reaction. The principle of this mode is shown in the Figure 12.7(b). In Figure 12.7, an ultramicroelectrode (UME) tip, controlled by the SECM, is placed close to the substrate and a constant oxidation current (i_T) is applied to the tip. Water is oxidized to oxygen on the UME, and a constant flow of oxygen is generated at the tip and diffused to the substrate. If the substrate potential is fixed at a value where oxygen should be reduced to water, the oxygen reached at the substrate surface will be reduced. The reduction rate of oxygen will be strongly dependent on the substrate potential and its electrocatalytic activity. The main advantage of this mode is that it can measure reactions inaccessible by the first mode, for example, the ORR in neutral or alkaline solutions. Figure 12.8 shows an example of SECM imaging of the ORR activities in a PtRu binary catalyst array.

(a)   (b)
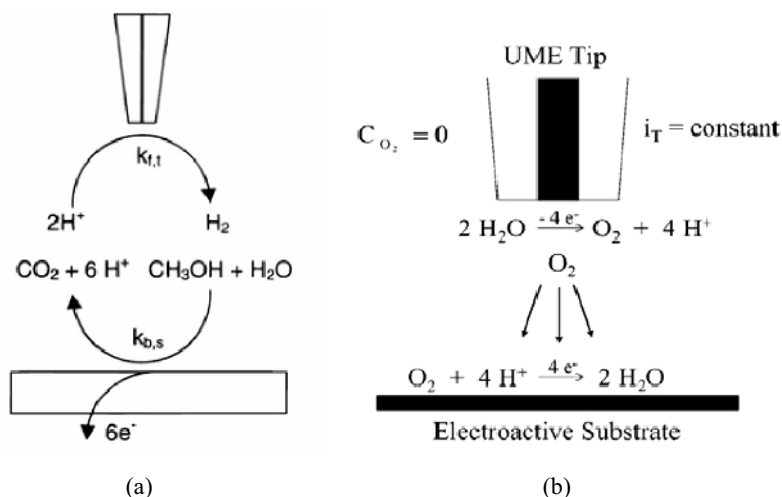
Figure 12.7. Scheme of (a) the tip collection-sample generation (TC-SG) mode [16], and (b) the tip generation-sample (TG-SC) collection mode [17] of SCEM combinatorial screening of fuel cell electrocatalysts. (Figure 12.7(a) reproduced by permission of ECS—The Electrochemical Society, from Shah BC, Hillier AC. Imaging the reactivity of electro-oxidation catalysts with the scanning electrochemical microscope. Figure 12.7(b) reprinted with permission from Anal Chem 2003;75:2967–74. Copyright 2003 American Chemical Society.)

Besides SECM, other spectroscopic methods, such as scanning differential electrochemical mass spectrometry (SDEMS) and IR thermography, were also used as combinatorial screening methods for fuel cell electrocatalysis. The principle of SDEMS is to use mass spectrometry to locally measure dissolved gases and volatile liquid species near the surfaces of catalyst arrays. IR thermography is based on reaction heat mapping. The heat results from the fuel cell electrochemical reactions on the catalyst arrays. Both methods can obtain reaction

information that has an indirect relationship with the electrochemical reactions; therefore, similar to optical methods, they have the drawbacks of insensitivity. Furthermore, some special instruments are also required.
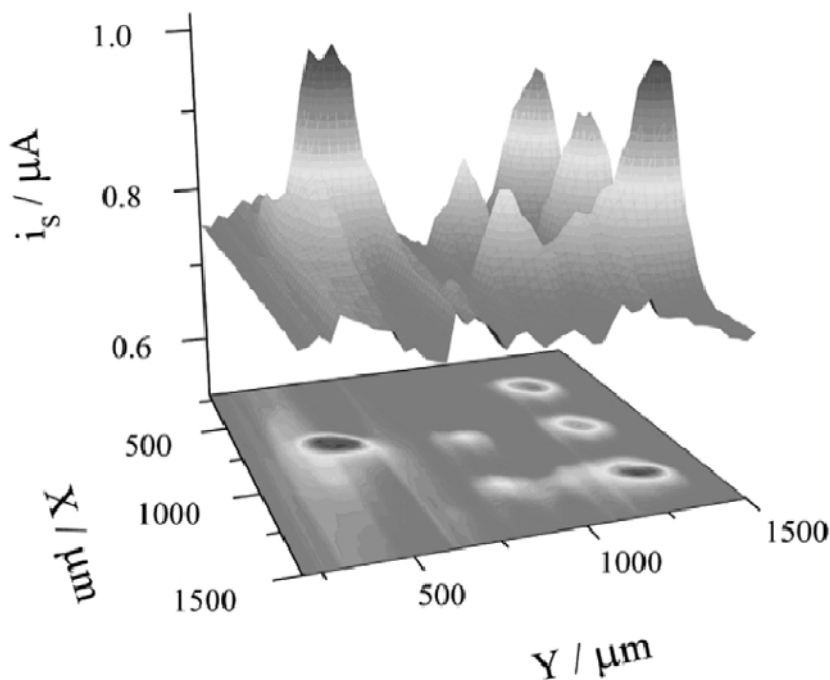
Figure 12.8. ORR images obtained by SECM (the TG-SC mode) screening of an array of Pt (left spot and right row) and Ru (middle row) spots supported on a glassy carbon [17]. (Reprinted with permission from Anal Chem 2003;75:2967–74. Copyright 2003 American Chemical Society.)

12.2.2.2 Direct Electrochemical Screening
The activity and performance of fuel cell electrocatalysts need to be evaluated in terms of electrochemical parameters, including current density and electrode potential. Electrochemical screening methods have been identified as ideal direct approaches for combinatorial studies of fuel cell catalysts. Two types of electrochemical measurement systems have been developed for combinatorial screening of fuel cell catalysts: the array half-cell system and the array single-cell system.

Figure 12.9 illustrates a typical array half-cell electrochemical screening system. In this system, the work electrode is a catalyst array that was prepared on a 2-inch silicon wafer with titanium nitride leads and pads, by the sputtering deposition technique. The catalyst array contains up to 100 combinatorial catalyst members. A glass cylinder and a silicone o-ring, both with a 38-mm diameter, are pressed on the wafer. In this way, the possible contact between the catalyst library pads and the electrolyte can be avoided. A plastic lid with a Teflon gasket is screwed on the assembly, fixing the entire cell in place. The whole array half-cell

system contains the studied electrode array, an Nb (coated by Pt) counter electrode, a calomel reference electrode, a thermocouple, and an air stone. A multi-potentiostat connected to the target electrode array (working electrodes) was used for electrode potential control. All individual target electrodes in the array share the same counter electrode and reference electrode. Cooper and McGinn [22] successfully applied this system to combinatorial screening of two ternary Pt-Ru-W and Pt-Ru-Co catalyst series for methanol oxidation reaction. In addition, the 64-element array electrochemical screening system developed by Guerin et al. [14] (shown in Figure 12.5) is also a good example of the array half-cell system for electrocatalyst combinatorial screening.
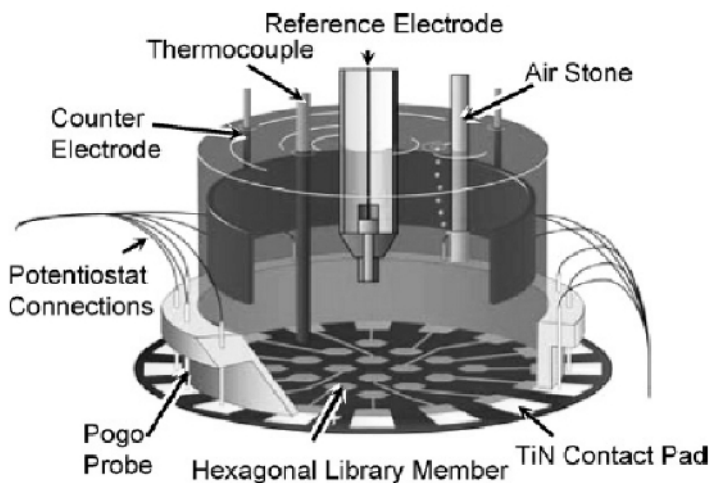
Figure 12.9. Schematic drawing of an assembled electrochemical cell for combinatorial screening catalyst libraries prepared by sputter deposition [22]. (Reprinted from Journal of Power Sources, 163(1), Cooper JS, McGinn PJ. Combinatorial screening of thin film electrocatalysts for a direct methanol fuel cell anode, 330–8, ©2006, with permission from Elsevier.)

Figure 12.10 shows an array single-cell electrochemical system, which was invented by Liu and Smotkin for electrocatalyst combinatorial screening in a real fuel cell circumstance. This array single-cell electrochemical system contains 25 individually controllable electrodes. Each electrode represents a miniaturized fuel cell: gaseous or liquid fuel can be introduced through fuel cell array flow fields. The catalyst layers were fabricated in exactly the same manner as for fuel cells. The fabrication methods used for the preparation of state-of-the-art membrane electrode assembly (MEA) were employed for the fabrication of the catalyst array, allowing catalyst testing with realistic reactant exposure histories (conditioning) and steady-state reaction conditions. The individual catalysts were prepared by traditional ink deposition technique and applied onto carbon paper. Array disks were punched and hot-pressed onto the Nafion membrane. For electrochemical measurements, a standard fuel cell counter electrode was used. In order to provide a large area and non-polarizable reference electrode, hydrogen gas was delivered to

the common cathode. The graphite sensor electrodes were pressed and inserted into the insulating ceramic flow field. Polarization curves for all array targets were recorded simultaneously using a multi-potentiostat. This array single-cell electrochemical system has a unique advantage over other combinatorial screening methods, in that its testing conditions are very close to the real fuel cell circumstances.
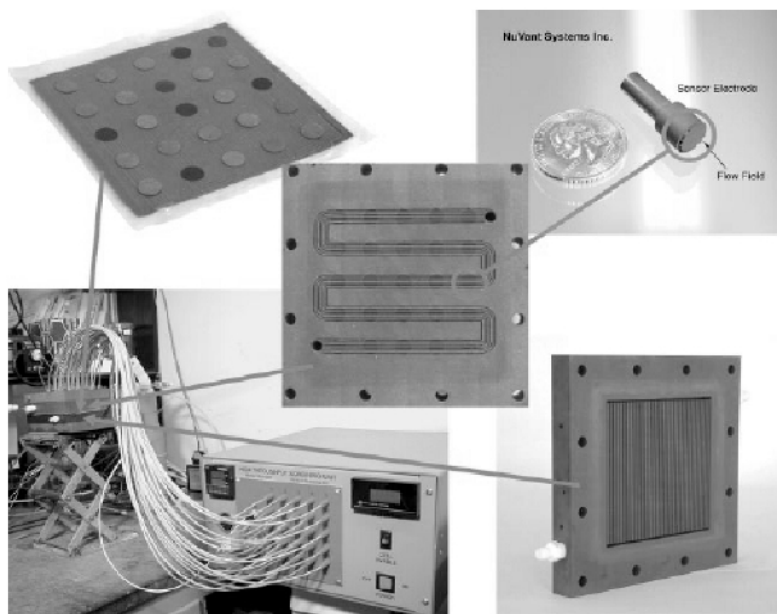
Figure 12.10. Component of array fuel cell: array flow field (center), clockwise from upper right: array MEA, graphite flow field sensor, counter electrode flow field, and assembled cell with multielectrode potentiostat [15]. (Reprinted, with permission, from the *Annual Review of Materials Research*, Volume 33 ©2003 by Annual Reviews www.annual reviews.org.)

12.3 Combinatorial Discoveries of Fuel Cell Electrocatalysts

Since Reddington et al. [9] first applied combinatorial electrochemistry to screen quaternary platinum alloys for DMFC anodes, many electrocatalysts, including noble metal alloys, non-noble metal alloys, metal oxides (perovskite), transition metal chalcogenides, as well as transition metal macrocycles, have been explored by these combinatorial methods for fuel cell electrocatalysts. Besides element screening and composition optimization, combinatorial methods were also useful in investigating the synthesis and reaction conditions, such as Nafion content in MEA inks, Pt loading in the catalyst layer, Pt particle size, sintering temperature, metal dissolution, and so on. Here, we describe several typical examples of using combinatorial methods to develop new electrocatalysts for PEM fuel cell reactions.

12.3.1 Low/Non-platinum Content Catalysts for PEM Fuel Cell Cathodes

Developing low or non-platinum content catalysts for ORR at the cathode is one of the major challenges in overcoming the cost barrier for PEM fuel cell commercialization. Two major approaches for this subject are: (1) alloying other noble or non-noble metals into Pt, and (2) exploring Pt-free metal compounds as effective and stable ORR electrocatalysts. There are a large number of new alloys and compounds that may be suitable for this purpose, although so far few new catalysts have been found to match the goal.
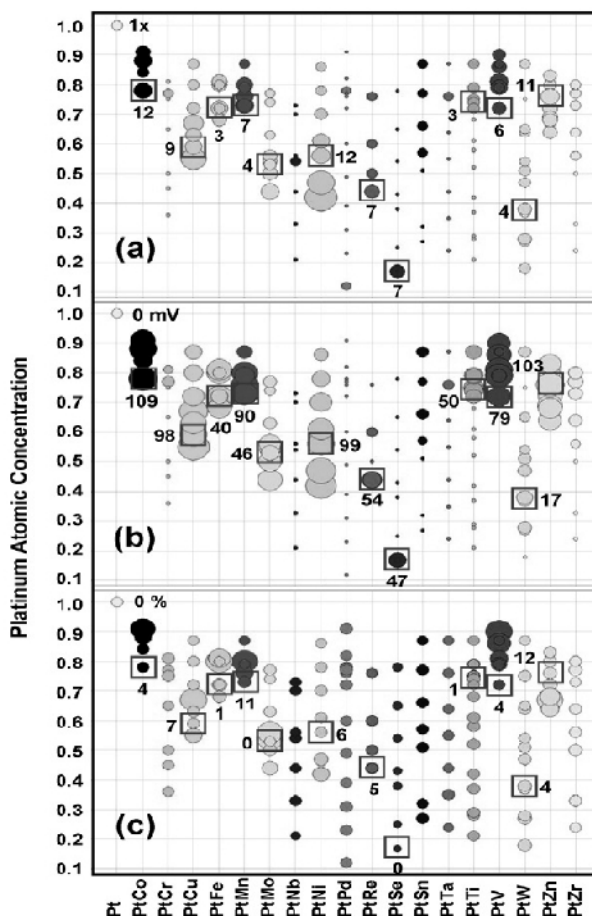
Figure 12.11. (a) Relative Pt mass-fraction specific activities at 0.8 V for Pt binary alloys; (b) half-wave potential (HWP) shifts of these alloys in comparison with pure Pt standard; (c) relative changes of Pt atomic concentration of these alloys after electrochemical corrosion testing [24]. (Reprinted from Journal of Power Sources, 165(1), He T, Kreidler E, Xiong L, Ding E. Combinatorial screening and nano-synthesis of platinum binary alloys for oxygen electroreduction, 87–91, ©2007, with permission from Elsevier.)

Compared to traditional methods, combinatorial methods show powerful capability for exploring such a huge number of catalyst candidates. For example, He et al. recently applied a multi-source physical vapor deposition technique to fabricate a series of binary Pt alloy thin film arrays, and employed a high throughput combinatorial screening for down-selection of a wide range of Pt-based binary alloy electrocatalysts for ORR. The candidates of these Pt-based binary alloy catalysts contained 18 base metals (Co, Cu, Fe, Mn, Mo, Ni, V, Zn, Cr, Nb, Pd, Re, Se, Sn, Ta, Ti, W, and Zr). Their catalyst array was electrochemically screened by a hydrodynamic multi-rotating disk electrode (M-RDE) system, which consists of 16 stations. Each station has a typical three-compartment electrochemical cell configuration, containing a conventional rotator (working electrode), a glass cell, a counter electrode, and a reference electrode. Using a multi-channel potentiostat, ORR reactions on all individual working electrodes in the array were measured simultaneously in oxygen-saturated 0.5 M H_2SO_4. The screening results were compared with a pure platinum baseline in terms of activity, stability and composition relationships. As shown in Figure 12.11, PtCo, PtNi, PtZn, and PtCu display higher catalytic activities towards oxygen electroreduction, but have poorer chemical stability in acid electrolytes. Alloys based on PtW, PtTi, and PtSe offer some modest catalytic activity improvements but have better chemical stabilities. These results are consistent with previous results obtained by the conventional one-at-a-time method, and also provide useful hints in exploring new ternary or quaternary alloy ORR catalysts with high activity and good stability.

12.3.2 CO-tolerant Catalysts for PEM Fuel Cell Anodes

Developing CO-tolerant Pt alloy catalysts for HOR at the fuel cell anode is also important in reducing the technical difficulties of purifying hydrogen fuel. At the current stage of technology, reforming hydrogen gas is more cost-effective than pure hydrogen. However, impurities (such as CO) in reforming gas can easily poison the catalysts. It has been identified that the poison effect could be minimized through alloying other metals with Pt catalysts. For example, PtRu shows much better CO-tolerance than pure Pt. Therefore, searching for more effective and cheaper CO-tolerant catalysts for HOR is necessary. Recently, Yang et al. demonstrated the effectiveness of combinatorial methods in studying the multi-element alloying effect of catalysts on the PEM fuel cell hydrogen oxidation reaction. $Pt_{1-x}M_x$ (M = Ru, Mo, Co, Ta, Au, Sn), randomly alloyed catalysts with a wide range of binary composition covering, were fabricated by DC magnetron sputtering technique. The catalyst activities were studied in a 64-electrode single-cell system using pure hydrogen or reformate that contained up to 50 ppm CO as fuel. When pure hydrogen was used, most of the binary compositions in the $Pt_{1-x}Ru_x$, $Pt_{1-x}Mo_x$, and $Pt_{1-x}Co_x$ samples were found to be better HOR catalysts. The HOR overpotentials when using $Pt_{1-x}Ta_x$, $Pt_{1-x}Au_x$, and $Pt_{1-x}Sn_x$ as catalysts were increased significantly if the compositions were at intermediate metal levels (Ta and Au > 50 atom. %, Sn > 40 atom. %). This implies that the alloying elements can significantly degrade Pt catalytic activity towards HOR. If the reformate was used as fuel (shown in Figure 12.12), Ru, Mo, and Sn were found to

improve the CO tolerance of Pt catalysts, although the intrinsic HOR catalytic activity of Pt decreased significantly with increasing Sn content. The addition of Co to Pt had no impact on CO tolerance, possibly due to the Co loss through dissolution during the fuel cell operation. The addition of Au to Pt led to an increase in HOR overpotential when CO was present. Small amounts of Ta gave a small reduction in HOR overpotential in the presence of CO, but the overpotentials were still too high for practical application in a reformate-fed fuel cell.
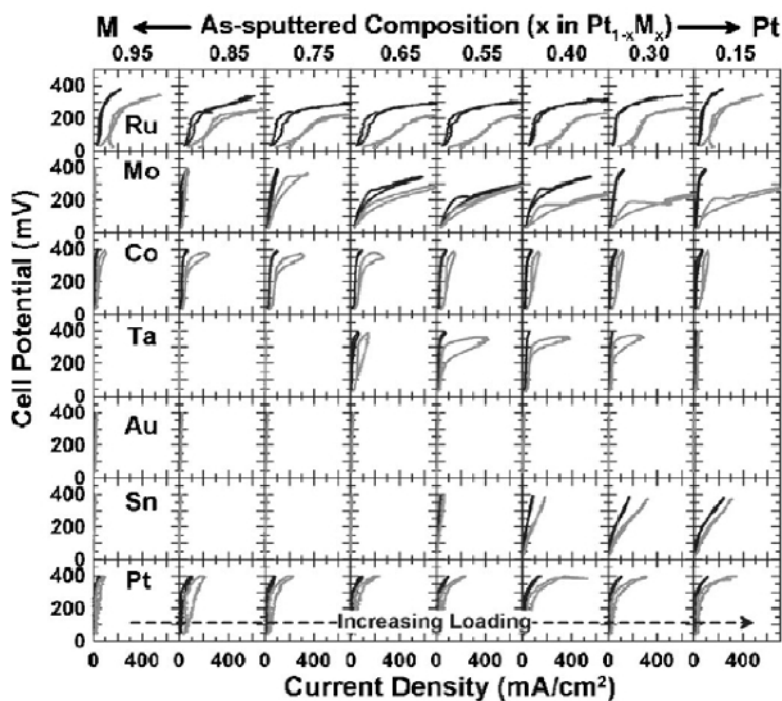
Figure 12.12. Representative CO-tolerance hydrogen oxidation polarization for the six binary systems studied. The measurements were made with (gray lines) 10 ppm and (black lines) 50 ppm CO in reformate fuel (40% H_2, 21% CO_2, 39% N_2) [25]. (Reproduced by permission of ECS—The Electrochemical Society, from Journal of the Electrochemical Society, Yang R, Bonakdarpour A, Bradley Eaton E, Stoffyn-Egli P, Dahn JR. Characterization and PEMFC testing of $Pt_{1-x}M_x$ (M=Ru,Mo,Co,Ta,Au,Sn) anode electrocatalyst composition spreads.)

12.3.3 Platinum Alloy Catalysts for Direct Methanol Fuel Cell Anodes

One large advantage of DMFC over the hydrogen fuel cell is the use of more manageable liquid methanol instead of hydrogen as fuel. However, the sluggish kinetics of the methanol oxidation reaction (MOR) leads to lower performance than in the H_2-fuelled PEMFC. Thus, developing high-efficiency MOR catalysts has attracted a great deal of attention in recent years. PtRu alloys have been identified as the best catalysts, so far, for MOR at DMFC anodes. In fact, the first application of combinatorial methods to fuel cell catalyst screening is the

exploration of new quaternary Pt alloy catalysts for DMFC anodes. A quaternary alloy, $Pt_{44}Ru_{41}Os_{10}Ir_5$, was found to be much more active than the state-of-the-art $Pt_{50}Ru_{50}$ catalyst if it was used as a DMFC anode catalyst, even though the latter catalyst had about twice the surface area of the former [9]. Following this pioneer work, many studies have been carried out using combinatorial methods to screen DMFC anode electrocatalysts. Cooper et al. [22] employed a sputtering technique to fabricate a series of ternary alloy catalyst libraries, and adopted an array half-cell electrochemical system to combinatorially investigate the Pt-Ru-W and Pt-Ru-Co ternary alloy systems as DMFC anode electrocatalysts. They found that the addition of W and Co into the Pt-Ru alloy had a positive effect on the DMFC performance. However, a change in optimum composition with the potential cycling of the electrode was observed. Initially, $Pt_{25}Ru_0W_{75}$ and $Pt_{17}Ru_{17}Co_{66}$ had 3 and 20 times better performances than the best binary Pt-Ru catalyst, respectively. However, after cycling the potential at 60 °C, the optimum ternary compositions were shifted from $Pt_{25}Ru_0W_{75}$ to $Pt_{44}Ru_{12}W_{44}$ and from $Pt_{17}Ru_{17}Co_{66}$ to $Pt_{12}Ru_{50}Co_{38}$, respectively, as shown in Figure 12.13. The optimum Pt-Ru-W and Pt-Ru-Co compositions show a peak MOR current density that was 1.5 and 2.5 times more than the best Pt-Ru binary composition, respectively. These results were different from those reported in other studies. The deviation was probably due to differences in the catalyst synthesis methods.
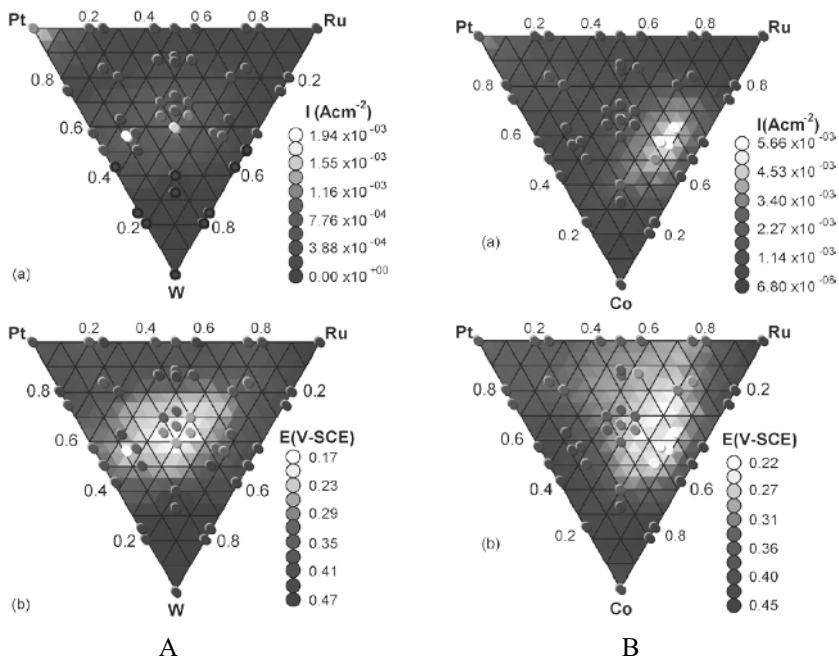
Figure 12.13. (a) Peak current densities and (b) onset potentials of methanol oxidation reaction electrocatalyzed by the combinatorial (A) Pt-Ru-W and (B) Pt-Ru-Co systems. [22]. (Reprinted from Journal of Power Sources, 163(1), Cooper JS, McGinn PJ. Combinatorial screening of thin film electrocatalysts for a direct methanol fuel cell anode, 330–8, ©2006, with permission from Elsevier.)
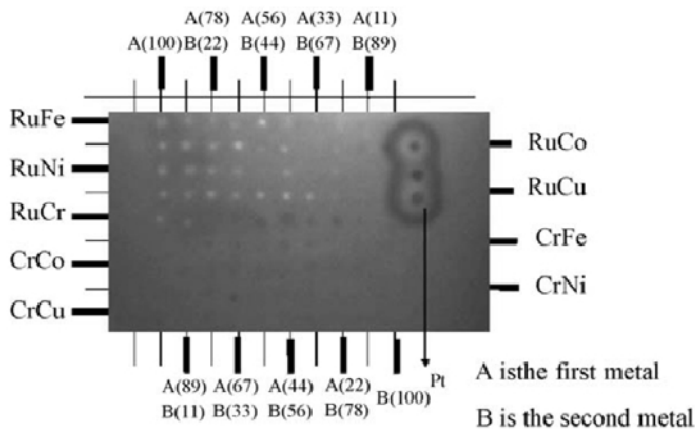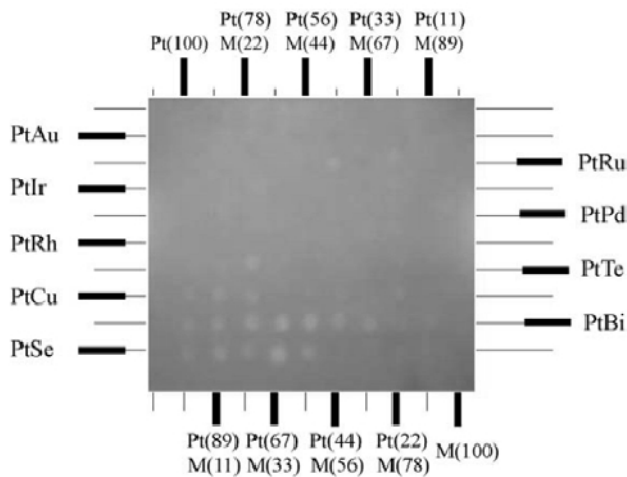
Figure 12.14. Fluorescence image of Pt and non-Pt binary array at 0.55 V vs. RHE in oxygen saturated electrolyte (pH = 4), which contained 100 mM fluorescein sodium salt, 0.2 M NaNO$_3$ and 0.5 M methanol [26]. (Reprinted from Applied Surface Science, 252(7), Liu JH, Jeon MK, Woo SI. High-throughput screening of binary catalysts for oxygen electroreduction, 2580–7, ©2006, with permission from Elsevier.)

12.3.4 Methanol-tolerant Catalysts for Direct Methanol Fuel Cell Cathodes

Combinatorial methods have also been applied to the area of exploring methanol-tolerant Pt and non-Pt alloy catalysts for DMFC cathodes. Liu et al. investigated a series of Pt-based and non-Pt binary alloys as ORR electrocatalysts by employing the high-throughput optical screening method. The catalyst arrays were prepared

by ink deposition technique, using an automatic dispenser followed by a thermal treatment. The ORR activities were evaluated in oxygen-saturated sulfuric acid containing 100 mM of fluorescein sodium salt as pH indicator. As illustrated in Figure 12.14, some of the Pt-based binary catalysts, including PtBi, PtCu, PtSe, PtTe, and PtIr, as well as the non-Pt catalysts, such as RuFe, show higher activities than pure Pt. All the active binary catalysts exhibit better methanol tolerance than Pt. In particular, the RuFe catalyst has a stronger methanol tolerance capability. Moreover, stability tests showed that after polarizing the binary arrays at 1.0 V in 1 M H_2SO_4, the obtained fluorescence images displayed the same brightness as those before polarization, suggesting that these binary catalysts were stable. This stability may suggest that the binary catalysts currently developed could be suitable candidates for PEM fuel cell or DMFC cathode catalysts, although further validation is necessary in real fuel cell operation.

12.4 Conclusions

Electrocatalysis is one of the important areas in PEM fuel cell development and commercialization. Although numerous researchers have been successful, over the past several decades, in searching for new fuel cell electrocatalysts, there are still large technical and cost gaps that need to be closed with respect to the commercialization of PEM fuel cells, including DMFCs. In order to speed up catalyst development, the combinatorial method has been identified as an effective way for new catalyst exploration and development. Since it was first introduced into fuel cell electrocatalysis ten years ago, the combinatorial method has developed rapidly and has shown significant advances in applications of fuel cell electrocatalysis. Many combinatorial catalyst library preparation methods (such as ink-jet printing, sputtering, electrodeposition, and traditional ink deposition) and high throughput screening methods (such as optical detection, electrochemical half-cell array, electrochemical single-cell array, SECM, SDEMS, and IR thermography) have been designed, invented, and improved. Various noble metal or non-noble metal alloys, compounds, and composites have been explored as candidates for electrocatalysts of major PEM fuel cell reactions, including ORR, HOR, and MOR.

However, the current combinatorial techniques still have some limitations for fuel cell catalyst synthesis and screening. The main drawback is that the current combinatorial catalyst libraries (gradient arrays and mask arrays) fabricated by high-speed and large-capacity preparation methods are not comparable to the traditional catalysts synthesized by state-of-the-art techniques. The differences between the synthetic methods may lead to different optimum compositions. In some rare cases, false information may lead to mistakes in interpreting results. Hence, for the further development of combinatorial methods in PEM fuel cell catalysis, improving the catalyst library preparation techniques is significant. It is also suggested that a complete combinatorial study of fuel cell electrocatalysis may include both discovery level and focus level experiments, where the catalyst libraries are fabricated by both high throughput methods and traditional methods,

respectively. And eventually, the optimal catalysts should be validated in real fuel cell testing.

It is worth noting that combinatorial chemistry has only been explored in the field of fuel cell electrocatalysis for a short time (around ten years). Therefore, it is still a developing and maturing technology. With improvement in both catalyst library preparation and screening techniques, combinatorial methods will become more important in new fuel cell electrocatalyst development. It is also believed that this combinatorial method will speed up new catalyst exploration, and thus accelerate developments toward PEM fuel cell breakthrough and commercialization.

References

1. Potyrailo RA. High throughput screening of materials. Technical Report 2001; GE Research & Development Centre 2001CRD137.
2. Xiang XD, Sun X, Briceno G, Lou Y, Wang KA, Chang H et al. A combinatorial approach to materials discovery. Science 1995;268:1738–40.
3. Koinuma H, Takeuchi I. Combinatorial solid-state chemistry of inorganic materials. Nature 2004;3:429–38.
4. Maier WF, Stowe K, Sieg S. Combinatorial and high-throughput materials science. Angew Chem Int Ed 2007;46:6016–67.
5. Hogarth MP, Ralph TR. Catalysis for low temperature fuel cells, Part I. The cathode challenges. Platinum Metals Review 2002;46:3–14.
6. Hogarth MP, Ralph TR. Catalysis for low temperature fuel cells, Part II. The anode challenges. Platinum Metals Review 2002;46:117–35.
7. Ralph TR, Hogarth MP. Catalysis for low temperature fuel cells, Part III. The challenges of DMFCs. Platinum Metals Review 2002;46:146–64.
8. Liu HS, Song CJ, Zhang L, Zhang JJ, Wang HJ, Wilkinson DP. A review of anode catalysis in the direct methanol fuel cell. J Power Sources 2006;155:95–110.
9. Reddington E, Sapienza A, Gurau B, Viswanathan R, Sarangapani S, Smotkin ES, et al. Combinatorial electrochemistry: a highly parallel optical screening method for discovery of better electrocatalysts. Science 1998;280:1735–7.
10. Gurau B, Viswanathan R, Liu R, Lafrenz TJ, Ley KL, Smotkin ES. Structural and Electrochemcial characterization of binary, ternary, and quaternary platinum alloy catalysts for methanol electro-oxidation. J Phys Chem B 1998;102:9997–10003.
11. Jayaraman S, Hillier AC. Construction and reactivity screening of a surface composition gradient for combinatorial discovery of electro-oxidation catalysts. J Comb Chem 2004;6:27–31.
12. Jayaraman S, Hillier AC. Electrochemical synthesis and reactivity screening of a ternary composition gradient for combinatorial discovery of fuel cell catalysts. Meas Sci Technol 2005;16:5–13.
13. Strasser P, Fan Q, Devenney M, Weinberg WH. High throughput experimental and theoretical predictive screening of materials – a comparative study of search strategies for new fuel cell anode catalysts. J Phys Chem B 2003;107:11013–21.
14. Guerin S, Hayden BE, Lee CE, Mormiche C, Owen JR, Russell AE, et al. Combinatorial electrochemical screening of fuel cell electrocatalysts. J Comb Chem 2004;6:149–58.
15. Smotkin ES, Diaz-Morales RR. New electrocatalysts by combinatorial methods. Annu Rev Mater Res 2003;33:557–79.

16. Shah BC, Hillier AC. Imaging the reactivity of electro-oxidation catalysts with the scanning electrochemical microscope. J Electrochem Soc 2000;147:3043–8.

17. Fernandez JL, Bard AJ. Scanning electrochemical microscopy 47: Imaging electrocatalytic activity for oxygen reduction in an acidic medium by the tip generation-substrate collection mode. Anal Chem 2003;75:2967–74.

18. Jambunathan K, Hillier AC. Measuring electrocatalytic activity on a local scale with scanning differential electrochemical mass spectrometry. J Electrochem Soc 2003;150 (6):E312–20.

19. Jambunathan K, Jayaraman S, Hillier AC. A multielectrode electrochemical and scanning differential electrochemical mass spectrometry study of methanol oxidation on electrodeposited Pt_xRu_y. Langmuir 2004;20:1856–63.

20. Shioyama H, Yamada Y, Ueda A, Kobayashi T. Screening of carbon supports for DMFC electrode catalysts by infrared thermography. Carbon 2003;41:579 –625.

21. Yamada Y, Ueda A, Shioyama H, Kobayashi T. High-throughput screening of PEMFC anode catalysts by IR thermography. Appl Surf Sci 2004;223:220–3.

22. Cooper JS, McGinn PJ. Combinatorial screening of thin film electrocatalysts for a direct methanol fuel cell anode. J Power Sources 2006;163:330–8.

23. Liu R, Smotkin ES. Array membrane electrode assemblies for high throughput screening of direct methanol fuel cell anode catalysts. J ElectroanalChem 2002;535:49–55.

24. He T, Kreidler E, Xiong L, Ding E. Combinatorial screening and nano-synthesis of platinum binary alloys for oxygen electroreduction. J Power Sources 2007;165:87–91.

25. Yang R, Bonakdarpour A, Bradley Eaton E, Stoffyn-Egli P, Dahn JR. Characterization and PEMFC testing of $Pt_{1-x}M_x$ (M=Ru,Mo,Co,Ta,Au,Sn) anode electrocatalyst composition spreads. J Electrochem Soc 2007;154 (4):A275–82.

26. Liu JH, Jeon MK, Woo SI. High-throughput screening of binary catalysts for oxygen electroreduction. Appl Surf Sci 2006;252:2580–7.

13

Platinum-based Alloy Catalysts for PEM Fuel Cells

Hansan Liu, Dingguo Xia and Jiujun Zhang

13.1 Introduction

Proton exchange membrane (or polymer electrolyte membrane) (PEM) fuel cells are one type of clean energy converting device that can contribute to sustainable world development. PEM fuel cells use hydrogen or hydrocarbons for fuel and air as the oxidant, reacting through a silent electrochemical process at low temperatures (60–90 °C) to convert chemical energy to electricity with zero or low emissions. This technology is attractive mainly due to its environmentally friendly nature and highly efficient energy conversion as compared to traditional energy technologies such as internal combustion engines (ICEs). At our current stage of development, two kinds of PEM fuel cells are the most promising for commercialization: the hydrogen (H_2)-fuelled PEM fuel cell, a major candidate for automobile applications to replace oil-dependant ICE technology; and the methanol-fuelled PEM fuel cell or direct methanol fuel cell (DMFC), which shows great potential for applications in portable electronic devices.

For the H_2-fuelled PEM fuel cell, the dominant challenges to commercialization are high cost and low reliability/durability. Both cost and reliability strongly depend on the electrocatalysts that drive the electrochemical reactions at the cathode and anode sides of a fuel cell. At this time, the most practical electrocatalysts in PEM fuel cells are platinum (Pt)-based catalysts. Due to the high cost and limited supply of Pt, reducing Pt loading in catalyst layers from the current level of 0.6–0.8 mg_{Pt} cm^{-2} to ~0.15 mg_{Pt} cm^{-2} is one of the key targets for automotive applications [1]. The most common strategy in Pt loading reduction to achieve this target is alloying other metal elements with Pt to form Pt alloying catalysts. This alloying practice not only reduces the noble metal content but also increases the catalytic activity. As is commonly recognized, the kinetics of the oxygen reduction reaction (ORR) at the cathode is the rate determining step in the whole fuel cell reaction, and requires much more catalyst than is needed for the anodic hydrogen oxidation reaction (HOR). Therefore, developing Pt-based alloys to increase the mass activity of the ORR by a factor of four is the activity benchmark and requirement for commercially feasible PEM fuel cells. Meanwhile, Pt-based alloys with carbon monoxide (CO) tolerance are also necessary for the

HOR at the anode, in order to overcome the problem of catalyst poisoning caused by CO impurity in the hydrogen gas.

In the case of the DMFC, which uses methanol as fuel, cell performance is normally lower than in H_2-fuelled cells, and Pt consumption in the catalysts/catalyst layers is also significantly higher due to the sluggish methanol oxidation reaction (MOR) at the anode. For early DMFC commercialization the target total catalyst loading for the entire membrane electrolyte assembly (MEA) (composed of both cathode and anode catalyst layers as well as membrane) must be reduced from the current 2.0–8.0 $mg_{Pt}\ cm^{-2}$ to a level < 1.0 $mg_{Pt}\ cm^{-2}$ without performance compromise [2]. Beside efforts to reduce cathode catalyst loading, developing Pt-based alloys with high activity towards the methanol oxidation reaction at the DMFC anode is equally important. In addition, in a DMFC, methanol crossover through the membrane from anode to cathode can also cause performance loss at the cathode. Therefore, methanol-tolerant Pt-based alloys at the cathode are also required for DMFCs.

It is generally recognized that the development of Pt-based alloys is one feasible strategy for Pt load reduction and activity enhancement in fuel cells, including both hydrogen-fuelled PEMFCs and DMFCs. In this chapter, we introduce the research and development of Pt-based alloy catalysts for both the ORR and the MOR. The alloying effect and corresponding mechanism as well as the stability of Pt-based alloy catalysts towards the ORR and MOR will be described in detail. The topics of CO- and methanol-tolerant Pt-based alloy catalysts will not be discussed in this chapter (please see instead Chapter 16, "CO-Tolerant Catalysts").

13.2 Pt-based Alloy Catalysts for PEM Fuel Cell Cathodes

13.2.1 The Alloying Effect on Cathode Catalyst Activity

The development of Pt-based alloys as electrocatalysts for the ORR can be traced back to the 1980s when United Technologies Corporation (UTC) disclosed the use of a series of Pt alloys (Pt-V, Pt-Co-Cr, Pt-Ir-Cr, Pt-Rh-Fe, etc.) as ORR catalysts for phosphoric acid fuel cells (PAFCs) [3]. After that, a large number of binary, ternary, and quaternary Pt-based alloys were studied and validated under PAFC conditions, showing better activity and/or stability when compared with pure Pt catalysts. There is no doubt that this development of Pt alloy catalysts in PAFC technology lays a solid knowledge foundation for the same use of Pt-based alloy catalysts in PEM fuel cells, although an automatic correlation with activity enhancement cannot be made due to the differences in fuel cell operating environments.

Early reports on the use of Pt alloys as ORR catalysts for PEM fuel cells were published by a group of scientists at Texas A&M University in the early 1990s [4–6]. They created a series of Pt alloys, including Pt-Ni, Pt-Co, Pt-Cr, Pt-Mn, and Pt-Fe, at high temperature (900 °C) under an inert atmosphere. These alloys can be expressed as Pt-M (where M is the non-noble metal alloying component). In the process of activity down-selection, a composition of 75(Pt):25(M) was found to be

optimal in achieving surface enrichment of M, based on crystallographic considerations. For fuel cell catalyst preparation, the alloy catalyst was loaded on high surface area carbon (Vulcan XC72) to form 20 wt% of supported catalyst. For the cathode catalyst layer, the catalyst loading was 0.3 $mg_{(Pt)}/cm^2$. A small unit of PEM fuel cell hardware was employed to validate catalyst activity. Testing was carried out using H_2 as fuel and O_2 as oxidant under a pressure range of 1–5 atm and a temperature range of 40–95 °C. Figure 13.1 shows IR-corrected Tafel plots for the catalyzed ORR, obtained at 5 atm and 95 °C with oxygen and hydrogen gases humidified at 100 and 105 °C, respectively. These results indicate that a performance gain of 20–30 mV compared to the performance with a Pt/C catalyst could be achieved, corresponding to a 2–5 times increase in specific activity. Among all Pt-M catalysts, Pt-Cr shows the highest activity.
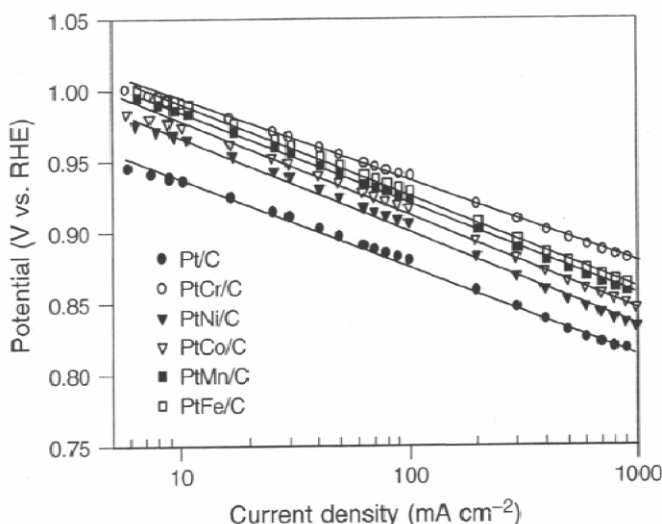
Figure 13.1. Steady-state IR-corrected Tafel plots for the cathodic ORR catalyzed by several binary Pt alloy electrocatalysts at 90 °C and 5 atm pressure. Performance of a Pt/C electrocatalyst is shown for comparison. The electrodes had a metal loading of 0.3 mg cm^{-2} and the loading of the metal on the carbon-supported catalyst was 20 wt%. The humidification temperature for the anode and cathode gas streams was kept at 10 and 5 °C above the cell temperature, respectively [6]. (From Mukerjee S, Srinivasan S. O$_2$ reduction and structure-related parameters for supported catalysts. In Vielstich W, Gasteiger HA, Lamm A, editors. Handbook of fuel cells – fundamentals, technology and applications. New York: John Wiley & Sons, 2003. Reproduced with permission.)

Johnson Matthey also carried out considerable work in the late 1990s on binary alloys such as Pt-Fe, Pt-Mn, Pt-Ni, Pt-Cr, Pt-Cu, and Pt-Ti [7]. For fuel cell catalysts, Pt alloys with a 50:50 Pt:M ratio were heat-treated at various temperatures to improve activity. The catalyst (20 wt% Pt alloy on Vulcan carbon) was integrated into an MEA with 25 cm^2 of active area for the fuel cell test. During fuel cell operation at 75 °C and 308/377 kPa pressure, H_2 and O_2 were used as the fuel and oxidant, respectively. It was found that a 20–40 mV performance

improvement could be obtained if Pt-Ti, Pt-Mn, and Pt-Fe were used as the catalysts. Similar apparent Tafel slopes of ~60 mV per decade were found for Pt and all Pt alloys, indicating that the ORR mechanisms catalyzed by Pt-M should be similar to the mechanism catalyzed by a pure Pt catalyst. Even using air as an oxidant, which is more practical in fuel cell applications, a performance enhancement of 25–30 mV was observed at some practical current densities.

Because the catalytic activity of a carbon-supported Pt alloy depends on the properties of both the metal particle and the carbon support, comparison between a supported alloy catalyst and pure Pt may not be accurate. Therefore, some comparisons were made using unsupported Pt-based alloys as ORR catalysts for PEM fuel cells. Toda et al. [8–10] investigated the electrocatalytic activity of Pt-Ni, Pt-Co, and Pt-Fe alloy thin films prepared by the sputtering technique. Hydrodynamic voltammetry with rotated electrodes was utilized to measure the ORR activity of the alloys in 0.1 M $HClO_4$ solution. A broad range of alloying compositions, with M varying from 10 to 80 at%, was explored. In comparison with a pure Pt catalyst, alloy catalysts showed a dramatic improvement in ORR activity. The most impressive performance (kinetic current density per real surface area at 0.76 V) was observed when using ~30 at% Ni, 40 at% Co, and 50 at% Fe. The kinetic current densities were over 10, 15, and 20 times higher than that of pure Pt. Paulus et al. [11, 12] also compared the alloying effect using carbon-supported Pt alloys and well-defined smooth bulk Pt alloys. Two kinds of bulk alloys, Pt-Ni and Pt-Co, were prepared using a series of sputtering and annealing cycles in an ultra-high vacuum (UHV) with a well-defined surface composition of Pt:M = 75:25. Several commercially available carbon-supported Pt alloy catalysts, i.e., 20 wt% Pt-Ni and Pt-Co on Vulcan XC72, were evaluated using 20 wt% Pt/C catalyst as a baseline. The rotating ring-disk electrode (RRDE) method was used to measure the electrochemical activity of these catalysts in 0.1 M $HClO_4$ solution at 20–60 °C. The results showed that only a small activity enhancement (the turnover frequency) of ~1.5 times could be observed for 25 at% Ni and Co catalysts, while for 50 at% Co catalyst supported on carbon, a significant enhancement of 2–3 times was observed. Meanwhile, the bulk Pt alloys showed a two-fold enhanced ORR activity versus the identically prepared polycrystalline Pt catalyst. Figure 13.2 shows the Tafel plots of the three unsupported catalysts in 0.1 M $HClO_4$ at 293 K with a rotating rate of 1600 rpm [13].

Most recently, Pt alloy catalysts that have the so-called structure of a Pt skin, i.e., with a pure Pt topmost atomic layer on the surface of the alloys, were reported to be the most active catalysts towards the ORR [14–17]. Stamenkovic et al. [14] studied the surface properties of Pt-M (M = Co, Ni, Fe) polycrystalline alloys prepared by sputtering, annealing, and leaching, respectively. They found two kinds of surface structure on the alloys, depending on the preparation procedure. The merely sputtered alloys could form Pt-skeleton outermost layers due to the dissolution of transition metal atoms in acid electrolyte, whereas the annealed alloys had a Pt-skin topmost layer containing only Pt. The catalytic activity towards the ORR on these two surfaces was much higher than that on a pure polycrystalline Pt surface, and the Pt-skin surface displayed the highest activity. In particular, the Pt_3Ni alloy with the (111) face was 10 times more active than the

Pt(111) surface, and 90 times more active than the current state-of-the-art Pt/C catalysts [17].
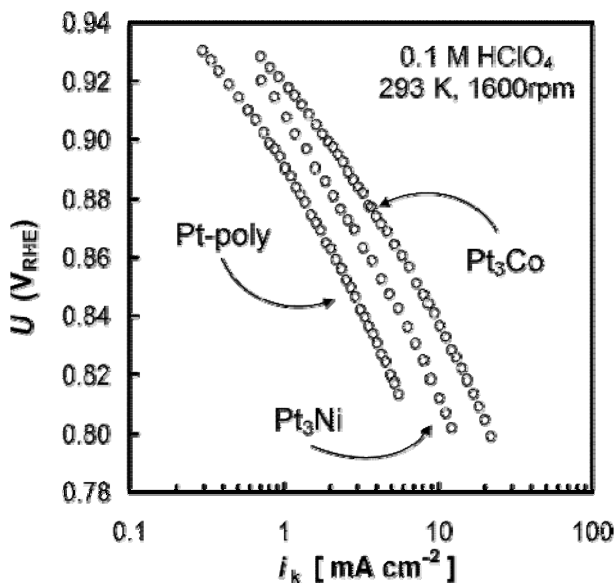
Figure 13.2. Tafel plots for sputtered surface (without Pt skin): Pt-polycrystalline, Pt₃Co, and Pt₃Ni in 0.1 M HClO₄ at 293 K [13]. (Reprinted with permission from J Phys Chem B 2002;106:11970–9. Copyright 2002 American Chemical Society.)

Based on the above review of the ORR activity of Pt alloys, it appears Pt-based alloys can improve specific activity and mass activity by several times relative to pure Pt catalyst in both an acid electrolyte and a real PEM fuel cell environment. In particular, the reported Pt₃Ni(111)-skin surface, which exhibits the most remarkable ORR catalytic activity that has ever been detected, looks very promising in terms of further activity improvement of Pt alloy catalysts for PEM fuel cell applications. The remaining challenge is how to create a fuel cell nanocatalyst with electronic and morphological properties that mimic the Pt₃Ni(111) surface.

13.2.2 Mechanism of the Alloying Effect on Cathode Catalysts

Enhancing catalyst activity towards the ORR through alloying Pt with other transition metal elements has attracted much attention in the past several decades. Although there is still some controversy over the mechanism of the alloying effect, several hypotheses have been proposed and broadly discussed in the literature. Some of the observations on the alloying effect in PAFCs were also seen in PEMFCs. For example, surface roughening of the Pt alloy was observed due to dissolution or leaching of the more easily oxidizable base metals in bulk alloys. This dissolution or leaching of M could lead to higher activity via an increase in surface area [18]. It has also been identified that the low-index crystal planes of Pt

show higher ORR reactivity than the high-index crystal planes. When Pt is alloyed with another metal, the proportion of low-index crystal plane increases as compared with the proportion in pure Pt, resulting in improved ORR activity [19]. However, the main alloying effects are generally classified as the structural effect, the OH_{ads} inhibition effect, and the electronic effect.

13.2.2.1 The Structural Effect

Jalan and Taylor [20] reported that the enhanced ORR activity of Pt alloys could be related to the decrease in Pt-Pt inter-atomic distance. They proposed that smaller Pt-Pt bond distances would provide more favorable sites for the dissociative adsorption of oxygen. Subsequently, many studies demonstrated that some base-metal elements with smaller atomic sizes than Pt will enter the crystal structure of Pt through substitution, resulting in lattice contraction and thereby a decrease in inter-atomic or nearest-neighbour distance between the Pt atoms. The alloys with lattice contraction are more active than Pt, while those with lattice expansion are less active. For example, Min et al. [21] investigated a series of Pt alloys and identified a relationship between the Pt-Pt nearest-neighbour distance and the specific ORR activity. As shown in Figure 13.3, a dozen Pt alloys display higher specific activities than does Pt alone, because these alloys have smaller Pt-Pt neighbour distances. They also found that the heat-treatment temperature and thereby the degree of alloying determined the Pt-Pt nearest-neighbour distance of the synthesized alloys.
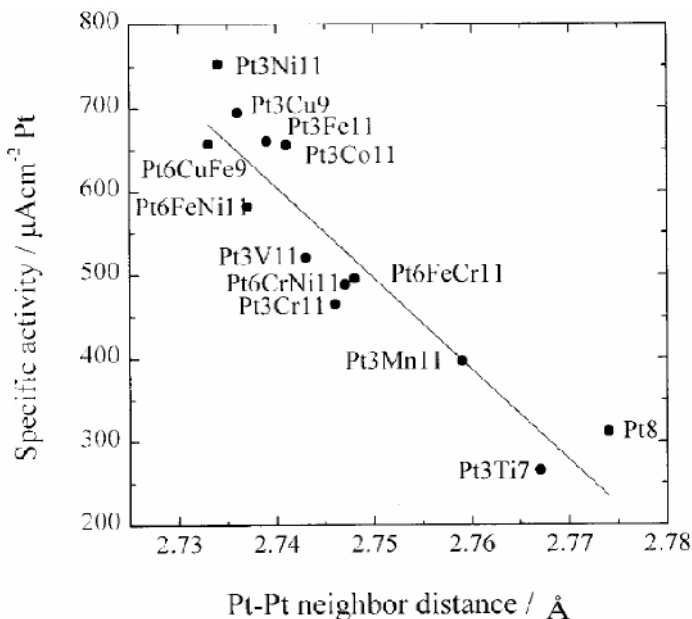
Figure 13.3. The relationship between the Pt-Pt nearest neighbour distance and specific activity [21]. (Reproduced from Electrochimica Acta, 45, Min M, Cho J, Cho K, Kim H. Particle size and alloying effects of Pt-based alloy catalysts for fuel cell applications. 4211–17, with permission from Elsevier.)

13.2.2.2 The OH$_{ads}$ Inhibition Effect

Generally, surface adsorbed oxygen species like OH or OOH are believed to be the reaction intermediates in the ORR. According to the classic catalytic volcano plot, the maximum reaction rate can be achieved when the surface adsorbed oxygen species are sufficiently and strongly bound to the surface to loosen the O-O bonds, but are sufficiently and weakly bound to the surface after electron transfer to allow desorption for product formation [22]. However, it was found that the ORR proceeded more slowly at a given potential on an oxidized Pt surface than on a bare Pt surface [23]. The majority of surface oxygen species (surface hydroxide or oxide) are considered to be poisoning species rather than intermediates, and the concentration of unpoisoned sites controls the reaction rate. Therefore, surface adsorbed OH on Pt could be an intermediate as well as a poisoning species in the ORR. Pt alloys were found to be able to inhibit the formation of OH$_{ads}$ on Pt and thereby enhance the catalytic activity of the ORR. Mukerjee et al. [5] found that the onset potential of OH$_{ads}$, which is known to typically occur above 0.8 V on Pt/C, shifted to more positive potentials for some Pt alloys. Depending on the alloying elements, the onset potential could be lowered by ~60 mV. In addition, for some surface-enriched Pt-skin or skeletal structure alloys, the higher ORR activity achieved was also attributed to weaker Pt-OH$_{ads}$ in the electronically modified Pt skin [14].

13.2.2.3 The Electronic Effect

The electronic effect associated with *d*-band vacancies also plays an important role in the enhancement of ORR activity on Pt alloys. Mukerjee et al. [5] investigated several Pt alloys (Pt-M: M = Fe, Co, Ni, Mn, Cr) with a focus on the fundamental aspects of electronic (*d*-band vacancy/atom) structure and short-range atomic order by both *in situ* XANES (X-ray absorption near edge structure) and EXAFS (extended X-ray absorption fine structure). It was found that alloying of Pt with some transition metal elements, which give rise to sharing of Pt d-electrons with the unfilled d-orbitals of the base metals, increased the Pt *d*-band vacancy. The extent of the increase was dependent on the electro-negativity of the transition element. Correlation of the ORR activity using a current density at 0.9 V with the *d*-band vacancy and the Pt-Pt bond distance showed a familiar volcano-type behavior for various binary Pt alloys, among which the Pt-Cr/C alloy was the most active catalyst. The change in electronic structure due to alloying was also thought to be the cause of the lattice contraction and the change in surface adsorption properties of the Pt alloys. Stamenkovic et al. [16] also studied the fundamental relationship between the experimentally determined surface electronic structure (the *d*-band center) and the ORR activity for Pt$_3$M (M = Ni, Co, Fe, Ti, V) surfaces. They found that the relationship exhibited a volcano-type behavior, with Pt$_3$Co having the highest activity, as shown in Figure 13.4. This behavior was attributed to the electronic structure-induced surface adsorption properties of Pt alloys. As they discussed, for a better ORR catalyst, the Pt alloy should counterbalance two opposing effects: the relatively strong adsorption energy of O$_2$ and the reaction intermediates (O$_2^-$, O$_2^{2-}$, H$_2$O$_2$, and so on), and the relatively low coverage by surface oxygen species, specifically adsorbed anions. For example, as in the case of Pt, if a metal surface binds oxygen, oxides, or anions too strongly,

the *d*-band center will be too close to the Fermi level and the ORR rate will be limited by the availability of OH_{ads}-free or anion-free Pt sites. On the other hand, when the *d*-band center is too far from the Fermi level, as in the case of Pt_3V and Pt_3Ti, the surface will be less covered by OH_{ads} or anions, but the adsorption energy of O_2 and the intermediates will be too low to enable a high turnover rate in the ORR. The resulting volcano-type trend, therefore, can be understood by the Sabatier principle: if the catalyst binds oxygen too strongly, the ORR rate will be limited by the rate of surface oxide and anion removal; if the catalyst binds oxygen too weakly, the ORR rate will be limited by the rate of electron and proton transfer to adsorbed O_2.
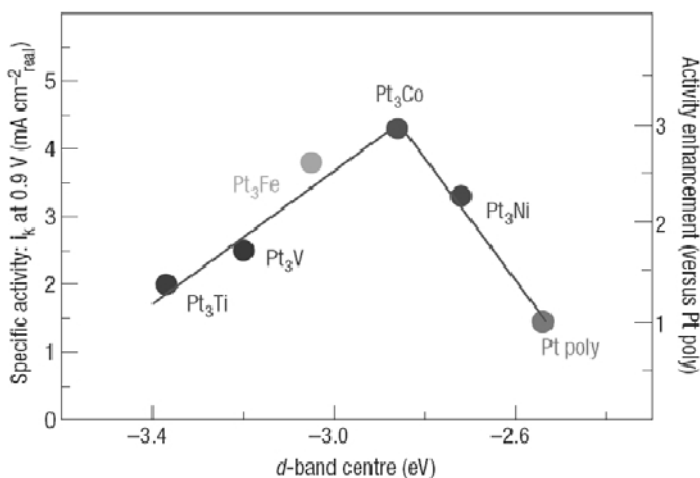
Figure 13.4. Relationships between the catalytic properties and electronic structure of Pt_3M alloys [16]. (Reprinted by permission from Macmillan Publishers Ltd: Nature Materials, Stamenkovic VR, Fowler B, Mun BS, Wang G, Ross PN, Lucas CA, et al. Trends in electrocatalysis on extended and nanoscale Pt-bimetallic alloy surfaces. Nat Mater 2007;6:241–7, copyright 2006.)

In practice, these effects do not exist alone in a Pt-based alloy system. They are often correlated to each other or synergize the alloying effect on the catalytic ORR activity. For example, the surprisingly high activity of the $Pt_3Ni(111)$ skin surface, which was recently reported to be 90 times more active than the current state-of-the-art Pt/C catalyst, was attributed to the synergy of the surface geometry, electronic structure, and surface adsorption [17]. In terms of surface structure, as shown in Figure 13.5(A), the first atomic layer was composed entirely of Pt in the near-surface region of $Pt_3Ni(111)$, whereas the second layer was Ni-rich (52% Ni as compared to 25% Ni in the bulk), and the third layer was Pt-enriched (87%). The surface electronic structure of $Pt_3Ni(111)$ was thus different from that of Pt(111), in that the *d*-band center was downshifted from –2.76 eV on Pt(111) to –3.10 eV on $Pt_3Ni(111)$. The Ni-induced modification of the Pt-skin electronic structure could result in contraction of the Pt surface atoms as well as a decrease in the surface coverage of the adsorbing species. As shown in Figure 13.5(B) and (C),

a dramatic negative shift (~150 mV) in H_{upd} formation and a positive shift (~100 mV) in OH_{ad} formation occurred on the $Pt_3Ni(111)$ skin, and the fractional coverage by H_{upd} and OH_{ad} were dramatically reduced by 50% relative to Pt(111). The less adsorbed species (OH_{ad}) on Pt could reduce the inhibitory (site-blocking) effect on O_2 adsorption. All of these effects eventually led to a 100 mV positive shift of the $Pt_3Ni(111)$ catalyzed half-potential in the ORR polarization curve as compared with the results for Pt(111).
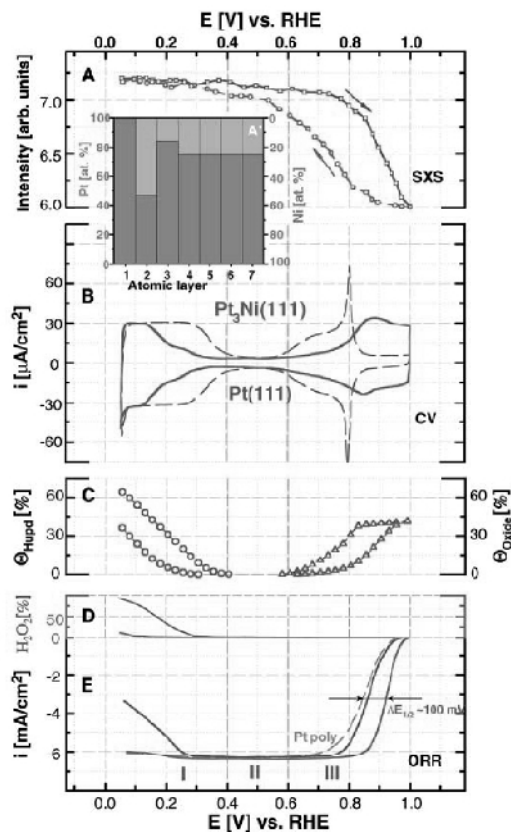
Figure 13.5. *In situ* characterization of $Pt_3Ni(111)$ surface in $HClO_4$ (0.1 M) at 333 K. (A) SXS data and (A') concentration profile revealed from SXS measurements. (B) Cyclic voltammogram in designated potential region as compared to that obtained from Pt(111) surface. (C) Surface coverage calculated from cyclic voltammograms of $Pt_3Ni(111)$ and Pt(111). (D) Green scale refers to hydrogen peroxide production in designated potential region and (E) ORR currents measured on $Pt_3Ni(111)$, Pt(111), and polycrystalline Pt surfaces. The arrows show the positive potential shift of 100 mV in electrode half-potential (DE112) between ORR polarization curves measured on Pt polycrystalline and $Pt_3Ni(111)$ surfaces. I, II, and III represent the potential region of H_{apd} adsorption/desorption processes, the double-layer region, and the region of OH_{ad} layer formation [17]. (From Stamenkovic VR, Fowler B, Mun BS, Wang G, Ross PN, Lucas CA, et al. Improved oxygen reduction activity on $Pt_3Ni(111)$ via increased surface site availability. Science 2007;315:493–7. Reprinted with permission from AAAS.)

13.2.3 Stability of Pt-based Alloy Cathode Catalysts

In a recent review on the durability and degradation of PEM fuel cells, electrocatalyst stability was primarily ascribed to Pt dissolution under non-equilibrium conditions as well as Pt particle growth (sintering) during fuel cell operation [24]. These issues also remain problematic for Pt-based alloy catalysts, whereas the stability of the alloying elements is an extra concern in alloy systems. The impact of alloying on the stability of cathode alloy catalysts in a PEM fuel cell environment can be considered from two perspectives: negative effects and positive effects.

In terms of the former, the chemical leaching of base metal elements from Pt alloys has a detrimental effect on fuel cell performance and results in decreased durability. In a PEM fuel cell, one necessary step is proton transfer within the membrane and the ionomer in the catalyst layer. The number of ion-exchange sites is limited in the membrane ($\sim$5 μmol cm-2) and the catalyst layer ($\sim$0.5 μmol cm-2) [1]. Metal cations from the dissolution of Pt alloys can easily occupy and poison these ion-exchange sites because metal cations have a stronger affinity with the sulfonic groups than do protons. The occupation of metal cations in the proton sites would: i) reduce membrane conductivity (or increase membrane resistance) due to dehydration, leading to higher membrane resistance; ii) increase the resistance of the catalyst layer due to higher ionomer resistance; iii) decrease oxygen diffusion in the ionomer film; and iv) degrade the membrane with some metal cations such as Fe, due to the well-known Fenton's effect. Besides these effects on the membrane and the catalyst layer, the chemical leaching of base metal elements from Pt alloys can also cause loss of the intrinsic alloying structure and thus a positive alloying effect on the catalytic ORR activity. All of these effects resulting from chemical leaching will essentially decrease the overall performance and accelerate fuel cell degradation.

As summarized by Gasteiger et al. [1], there are at least three possible causes for the leaching of base metals from Pt alloys in a PEM fuel cell environment: i) excess base-metal can deposit onto the carbon support during preparation; ii) incomplete alloying of the base element to the Pt can occur due to a low alloying temperature being applied during alloy synthesis; iii) even a well-alloyed base metal may leach out of the surface under PEM fuel cell operating conditions and leave a Pt-enriched surface or skin, since base metals are thermodynamically unstable under the electrode potentials in acidic electrolytes (even Pt alloys do not have high enough heats of mixing to confer stability). Therefore, the stability of Pt alloys is strongly related to preparation parameters such as precursors, composition, alloying temperature, post-treatment, and so on. This may be why various studies in the literature offer different conclusions on the stability of Pt alloys. For example, some researchers have emphasized that the stability of Pt alloys depends on the type of base metals. However, Antolini et al. [25] thought that the degree of alloying is the key factor in stability. They found that Cr and Co presented a higher degree of alloying with Pt than V, Ni, and Fe, resulting in Pt-Cr and Pt-Co catalysts having higher stability than Pt-V, Pt-Ni, and Pt-Fe.

Analysis of leaching causes has indicated that post-treatment of the alloy in acid media after preparation could mitigate the leaching effect on the stability of Pt

alloys. Gasteiger et al. [1] investigated the durability of Pt/C and pre-leaching Pt-Co/C-based MEAs in a short fuel cell stack. They observed that an enhancement or performance offset of 15–25 mV between the Pt/C and the pre-leaching Pt-Co/C could be maintained throughout 1000 hours of stack operation, within the limits of error. The degradation rates of the Pt/C and the pre-leaching Pt-Co/C MEAs were comparable, at about 50 and 60 µV h-1. The performance loss was attributed to the catalysts' stability because no membrane degradation was observed in their lifetime tests (Figure 13.6). With respect to the effect of pre-leaching on ORR activity, Watanabe et al. [26] found that the dissolution of base metals (Fe, Co, or Ni) from the surface of a Pt alloy at room temperature gave rise to a Pt skin within a few monolayers of the alloy surface, modifying the electronic structure and making it favorable to the ORR. However, when the temperature was raised above 60 °C, the ORR activity decreased due to excessive dissolution of base metals from the alloys.
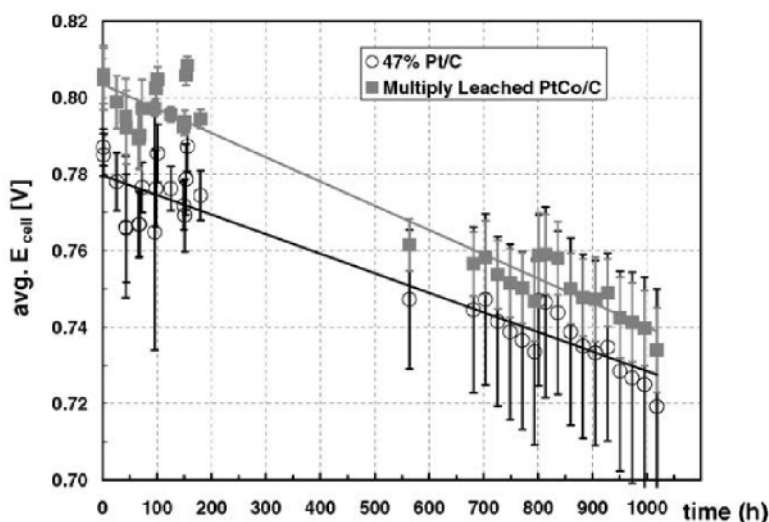
Figure 13.6. Durability of Pt/C and Pt_xCo_{1-x}/C-based MEAs tested in a short stack (active area = 465 cm^2) under H_2-air at a cell temperature of 80 °C and total reactant pressures of 150 kPa_{abs}, with both anode and cathode humidities at 100% and anode and cathode reactant stoichiometries of s = 2/2. Data are shown with the stack under a constant load of 0.20 A/cm^2 over 1000 h. Data were averaged over four cells of each type of MEA [1]. (Reprinted from Applied Catalysis B: Environmental, 56, Gasteiger HA, Kocha SS, Sompalli B, Wagner FT. Activity benchmarks and requirements for Pt, Pt-alloy, and non-Pt oxygen reduction catalysts for PEMFCs, 9–35, 2005, with permission from Elsevier.)

With respect to the positive effects of Pt alloying, some improvement in catalyst stability and fuel cell durability have also been observed. Several studies [1, 27–29] have demonstrated that alloy particles have better resistance to sintering than pure platinum particles. The sintering effect may be attributed to base metals hindering Pt mobility on carbon, as well as Pt alloy particles usually being larger than Pt alone. Yu et al. [30] found that some platinum alloy catalysts, particularly

those containing cobalt, showed remarkably improved stability in a dynamic fuel cell environment relative to unalloyed platinum. The Pt-Co/C catalyst displayed significant improvements in stability after a protocol of square-wave potential cycling between 0.87 and 1.2 V. The overall performance loss over 2400 cycles of the Pt-Co/C-based MEA was less than that of the Pt/C-based MEA. Although leaching of cobalt was observed through all the cycles, the loss of electrochemical area for the Pt-Co/C-based MEA was much less than that for the Pt/C-based MEA.
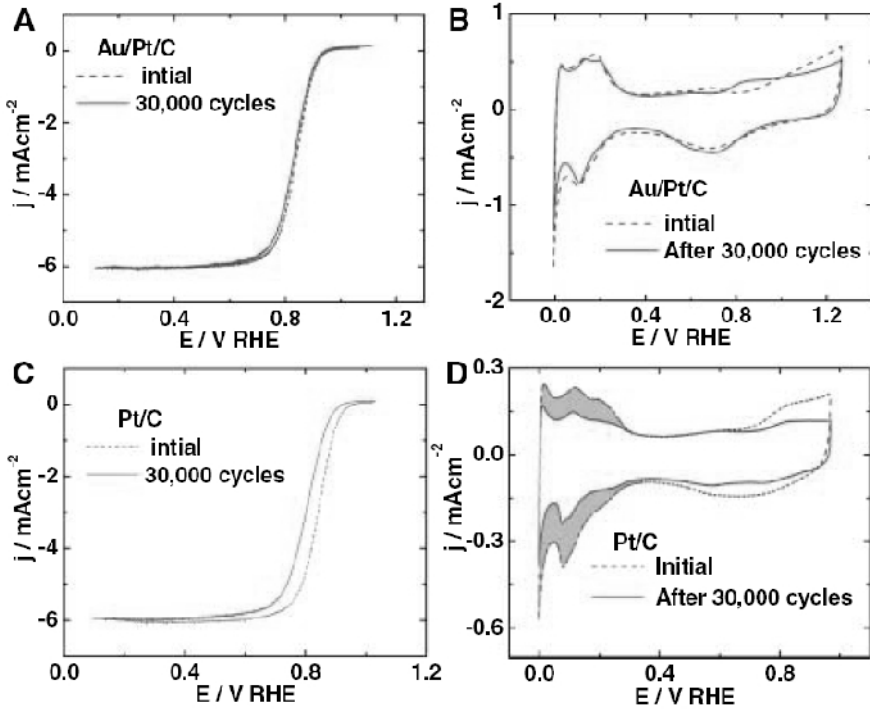
Figure 13.7. Polarization curves for O_2 reduction reaction on Au/Pt/C (A) and Pt/C (C) catalysts on a rotating disk electrode, before and after 30,000 potential cycles. Sweep rate: 10 mV/s; rotation rate: 1600 rpm. Voltammetric curves for Au/Pt/C (B) and Pt/C (D) catalysts before and after 30,000 cycles; sweep rates: 50 and 20 mV/s, respectively. The potential cycles were from 0.6 to 1.1 V in an O_2-saturated 0.1 M $HClO_4$ solution at room temperature. For all electrodes, the Pt loading was 1.95 mg (or 10 nmol) on a 0.164 cm^2 glassy carbon rotating disk electrode. The shaded area in (D) indicates the lost Pt surface area [31]. (From Zhang J, Sasaki K, Sutter E, Adzic RR. Stabilization of platinum oxygen-reduction electrocatalysts using gold clusters. Science 2007;315:220–2. Reprinted with permission from AAAS.)

Alloying also positively affects the stability of Pt catalysts because the base metals suppress Pt dissolution. It is known that Pt dissolution is one of the major causes in loss of fuel cell performance, especially under potential cycling regimes. Recently, Zhang et al. [31] reported that the modification of Pt nanoparticles using gold (Au) clusters could significantly impede Pt dissolution. This stabilizing effect

was validated in an accelerated stability test by continuously applying linear potential sweeps between 0.6–1.1 V. It is expected that in this potential range, Pt surface oxidation/reduction cycles occur that involve the formation of PtOH and PtO, causing the dissolution of Pt via the Pt^{2+} oxidation state. The results showed that after 30,000 cycles, the Au/Pt/C catalyst had only a 5 mV degradation in half-wave potential, with almost no loss of Pt surface area being observed. However, the Pt/C catalyst had a loss of 39 mV in half-wave potential and only ~55% of the original Pt surface area remained (Figure 13.7). Results from *in situ* X-ray absorption near edge spectroscopy (XANES) revealed that the oxidation of Pt nanoparticles modified by Au clusters required much higher potentials than that required for unmodified Pt nanoparticles. The higher Pt oxidation potential of the Au/Pt/C electrocatalyst was thus identified as the major mechanism for the stabilization effect of Au clusters. The shift of Pt oxidation potential was further correlated to the fact that the surface alloying of Au with Pt would modify the Pt electronic structure towards a lower Pt surface energy, or lower-lying Pt *d*-band states.

13.3 Pt-based Alloy Catalysts for DMFC Anodes

13.3.1 The Alloying Effect on Anode Catalyst Activity

Due to the facile poisoning effect of CO on Pt, many Pt-based binary alloys, such as Pt-Ru, Pt-Os, Pt-Sn, Pt-W, Pt-Mo, and so on, have been investigated as electrocatalysts for the methanol oxidation reaction (MOR) on the DMFC anode. Among them, the Pt-Ru alloy has been found to be the most active binary alloy catalyst, and is commonly used in state-of-the-art DMFCs [32].

Studies of the Pt-Ru alloy as an electrocatalyst for the MOR date from the 1960s when some Pt alloys, such as binary Pt-Ru and Pt-Mo, were found to have a better catalytic MOR activity than pure Pt black in 1 M H_2SO_4 [33]. The early studies mainly focused on bulk Pt alloys. In 1987, Watanabe et al. [34] reported the preparation of highly dispersed Pt-Ru alloy on carbon support in order to increase the metal catalyst surface area. Since then, in an effort to further maximize the activity of Pt-Ru catalyst, the optimization of carbon-supported Pt-Ru catalyst through preparation procedures became the subject of numerous studies, as reviewed in [2]. The catalytic activity of Pt-Ru/C catalyst, correlated to the properties of both alloy and support, strongly depends on the choice of the precursors, the deposition techniques, the supports, the electrode fabrication techniques, and so forth. The common criteria for a high-performance Pt-Ru/C catalyst are: i) a narrow nanoscale size distribution; ii) a uniform composition throughout the nanoparticles; iii) a fully alloyed degree; and iv) high dispersion on the carbon support. According to these criteria, some innovative and cost-effective preparation techniques, such as the glycol colloidal method and the spray pyrolysis method, have been developed and show promise for performance optimization through controlling synthetic procedures and conditions. Some new carbon materials, such as nano- and meso-structured carbons, have been demonstrated to be feasible as catalyst supports for enhancing the performance of Pt-Ru/C catalysts.

With a combination of advanced preparation methods and carbon supports, the currently used Pt-Ru/C catalysts could drive a state-of-the-art DMFC single cell with current densities of 200–600 mA cm^{-2} at a cell voltage of 400 mV, depending on the operating conditions. For example, Guo et al. [35] recently reported that a current density of 540 mA cm^{-2} at 400 mV was observed in a Pt-Ru/C catalyzed DMFC with a Pt loading of 1.33 mg cm^{-2}, operating at 90 °C, as shown in Figure 13.8.
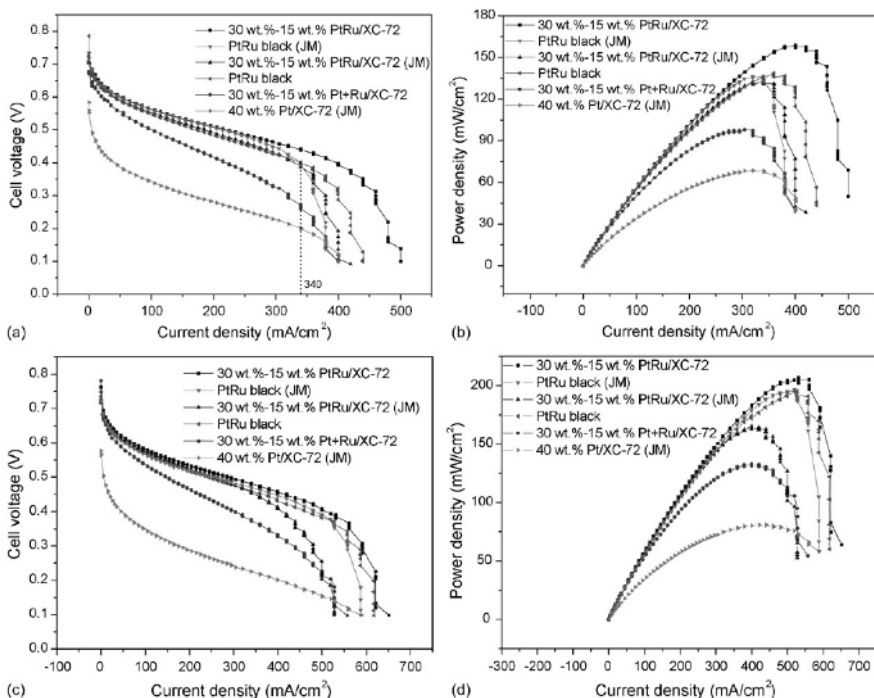
Figure 13.8. DMFC polarization (a and c) and power density (b and d) curves of various catalysts at 75 °C (a and b) and 90 °C (c and d), respectively. Methanol concentration at the anode: 1 mol L^{-1} with a flow rate of 1.0 mL min^{-1}; oxygen at cathode: non-humidified oxygen at a pressure of 0.2 MPa with a flow rate of 200 sccm. Except for Pt-Ru black and Pt-Ru black (JM) with a Pt loading of 2.66 mg cm^{-2}, the Pt loading of other anode catalysts is 1.33 mg cm^{-2}. 40 wt% Pt/XC72 (Johnson Matthey) used as the cathode catalyst with a Pt loading of 1.4 mg cm^{-2} [35]. (Reprinted from Journal of Power Sources, 168, Guo J, Sun G, Sun S, Yan S, Yang W, Qi J, et al. Polyol-synthesized PtRu/C and PtRu black for direct methanol fuel cells, 299–306, 2007, with permission from Elsevier.)

However, the power density of a DMFC using the state-of-the-art Pt-Ru/C anode catalyst is still a factor of ~10 lower than that of a hydrogen-fuelled PEM fuel cell if the same noble metal loading is used. The efficiency of DMFCs operating on Pt-Ru alloy catalysts may yet be insufficient for practical application. Thus, much investigation has been done to improve the performance of the Pt-Ru binary catalysts by the incorporation of a third metal, such as W, Mo, Co, Ni, V, Pd, Rh, Sn, Os, or Ir. Some of these ternary Pt-Ru-M alloy catalysts show

enhancement in their catalytic activity towards the MOR, as recently reviewed by Antolini [36, 37]. For example, Ley et al. [38] studied the effect of the element Os on the MOR activity catalyzed by the Pt-Ru-Os bulk alloy. Figure 13.9 shows the DMFC performance curves obtained with Pt, Pt-Ru (1:1), and Pt-Ru-Os (65:25:10) as anode catalysts. The open circuit voltages of the DMFC catalyzed by alloys were ~200 mV higher than that catalyzed by pure Pt, suggesting that the Pt catalyst was poisoned more extensively at open circuit voltage than were the alloy catalysts. Under load, the Pt-Ru-Os alloy-based DMFC also had superior performance to the Pt-Ru alloy-based cell. For example, at a cell voltage of 0.4 V, the Pt-Ru-Os catalyzed cell gave a current density of 340 mA cm^{-2}, while for the Pt-Ru catalyzed cell only 260 mA cm^{-2} could be observed. Gotz et al. [39, 40] investigated the catalytic activity of several carbon-supported ternary alloys towards methanol oxidation, and found the activity was in the order of Pt-Ru-W/C > Pt-Ru-Mo/C > Pt-Ru/C > Pt-Ru-Sn/C. In a single-cell test operated at 95 °C (1 M methanol and 0.4 mg cm^{-2} Pt), the Pt-Ru-W/C catalyst showed a 40% increase in current density at a cell voltage of 0.4 V as compared with the standard Pt-Ru/C catalyst.
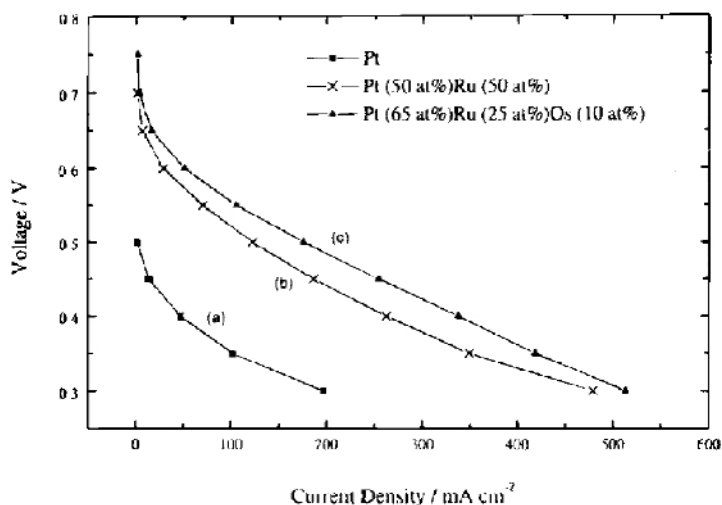
Figure 13.9. Liquid-feed DMFC polarization curves at 90 °C: (a) Pt, (b) Pt-Ru (1:1), and (c) Pt-Ru-Os (65:25:10). Methanol (0.5 M) was delivered to the anode at a flow rate of 25 ml/min with ambient backpressure. The oxidant was 10 psig dry O$_2$ with a flow rate of 400 ml/min [38]. (Reproduced by permission of ECS—The Electrochemical Society, from Ley KL, Liu R, Pu C, Fan Q, Leyarovska N, Segre C, et al. Methanol oxidation on single-phase Pt-Ru-Os ternary alloys.)

In addition, quaternary Pt-Ru-based alloys were also investigated as methanol oxidation catalysts for further improving the anode performance in DMFCs. Some of the quaternary alloys, such as Pt-Ru-W-Sn [41], Pt-Ru-Os-Ir [42], Pt-Ru-W-Mo [43], Pt-Ru-Ni-Zr [44], and Pt-Ru-Ir-Sn [45], have been demonstrated to be more active than the state-of-the-art Pt-Ru catalyst towards the MOR. Due to a huge

number of possible alloy compositions for ternary and quaternary alloys, combinatorial and high throughput screening methods have been adapted to discover and optimize the potential superior alloy catalysts (for more information, see Chapter 12, "Combinatorial Methods for PEM Fuel Cell Electrocatalysts").

13.3.2 Mechanism of the Alloying Effect on Anode Catalysts

It is known that the electrochemical oxidation of methanol on Pt involves several intermediate steps, such as dehydrogenation, CO-like species chemisorption, OH species adsorption, chemical interaction between adsorbed CO and OH compounds, as well as CO_2 evolution. The overall oxidation process of methanol to carbon dioxide proceeds through a six-electron transfer process [46]:

$$Pt + CH_3OH \rightarrow Pt(CO)_{ads} + 4H^+ + 4e^- \qquad (13.1)$$

$$Pt + H_2O \rightarrow Pt(OH)_{ads} + H^+ + e^- \qquad (13.2)$$

$$Pt(CO)_{ads} + Pt(OH)_{ads} \rightarrow CO_2 + 2Pt + H^+ + e^- \qquad (13.3)$$
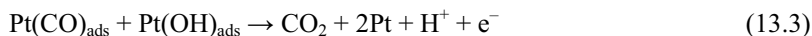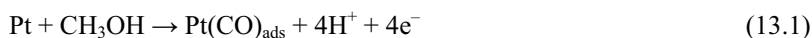
On a pure Pt surface, all Pt sites are involved in the steps of methanol dehydrogenation, chemisorption of methanol residues (such as CO), and the dissociative chemisorption of water. The strongly adsorbed CO can gradually occupy all the Pt active sites, resulting in Pt poisoning. In order to remove through Reaction 13.3 the Pt(CO)ads species produced in Reaction (13.1), the production of Pt(OH)ads in Reaction 13.2 becomes critical. Unfortunately, because the electrochemical potential of Reaction 13.2 is as high as 0.7 V vs. RHE, the formation of Pt(OH)ads becomes a problem. Developing a catalyst that can easily form M(OH)ads species at a low electrode potential for use in Reaction 13.3 is one of the key approaches. Therefore, a more active catalyst than Pt for methanol oxidation should result in water discharging to form M(OH)ads species at low potentials and then to weaken CO chemisorption or catalyze the oxidation of adsorbed CO. This is the basic principle of designing and developing Pt alloy catalysts for the methanol oxidation reaction.

Much work has been put into discovering the mechanism of the promoting effect of the alloying elements (such as Ru, Sn, W, etc.) on the activity of Pt catalysts towards the MOR. Although the nature of these binary alloys remains elusive, three major theories, i.e., the bi-functional effect, the electronic (ligand) effect, and the spillover effect, were established to explain the role of the second elements on the activity improvement of Pt binary alloys.

13.3.2.1 The Bi-functional Effect

Watanabe and Motoo [47] proposed a bi-functional mechanism to elucidate the MOR activity enhancement of Ru ad-atoms on Pt catalyst. The bi-functional mechanism says that the unique catalytic properties of each element in the alloy combine in a synergetic fashion to yield an alloy surface that is more active than each element alone. For the MOR on a Pt-Ru catalyst, the chemisorption of methanol on Ru sites is significantly less favored than on Pt sites, while the

chemisorption of oxygenated species happens much more easily on Ru sites rather than Pt sites. Water dissociation occurs on Ru sites with the formation of $Ru(OH)_{ads}$ species at a potential as low as 0.2 V vs. RHE, while methanol dehydrogenation occurs on Pt sites at a potential below 0.2 V vs. RHE. The adsorbed OH groups on Ru sites then combine with the adsorbed methanolic residues on the neighbouring Pt sites to produce carbon dioxide.

$$Ru + H_2O \rightarrow Ru(OH)_{ads} + H^+ + e^- \tag{13.4}$$

$$Pt(CO)_{ads} + Ru(OH)_{ads} \rightarrow CO_2 + Pt + Ru + H^+ + e^- \tag{13.5}$$
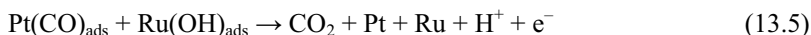
The bi-functional mechanism, although simple, can explain very well the promoted MOR activity of Pt-Ru alloy catalysts. This mechanism is also well adapted by other binary alloys such as Pt-Sn [48]. It has been identified that CO does not bind to the Sn sites, with the result that OH can more easily adsorb on the Sn sites without competition from CO. The synergetic effect on Pt and Sn sites gives rise to Pt-Sn, a very active CO electrooxidation catalyst. However, the strong adsorption of OH species on Sn sites, particularly at high potentials, makes the Pt-Sn catalyst inferior to the Pt-Ru catalyst for the methanol oxidation reaction.

Because the reaction steps, in particular the chemisorption of methanol on Pt sites, are temperature dependent, the bi-functional effect of Pt-Ru alloy shows an interesting correlation with the alloy composition. At low temperatures, adsorption of methanol on Pt requires an ensemble of three neighbouring Pt atoms, so the dehydrogenation of methanol on the Pt sites is the rate determining step. Thus, electrocatalysts with a good portion of arrangements of three neighbour Pt sites should have higher electrochemical activities. Gasteiger et al. [49] observed that methanol oxidation occurred more readily at room temperature on pure Pt-Ru alloys that had low Ru content (~10%), whereas at intermediate temperatures (60 °C) the reaction was faster on alloys with greater Ru content (~33%). However, at higher temperatures, the rate determining steps were the formation of OH groups through water dissociation on Ru sites, and the chemical interaction between adsorbed methanolic residues and these OH groups. The optimal Ru content can be determined by relevant synergism contributed from a favorable Pt-Ru surface with 50% atomic Ru, maximizing the production of OH coverage as well as improving the intrinsic rate constant.

13.3.2.2 The Electronic Effect

The second mechanism is the electronic (or ligand) effect. It says that the additional element can modify the Pt surface electronically [50]. Chemisorption of CO on Pt involves the donation of an electron pair from the σ* anti-bonding orbital of CO to the unfilled 5d-orbitals of Pt. A back donation of electrons from the Pt metal to the CO-orbitals further stabilizes their interaction. X-ray absorption spectroscopy studies [51] showed that alloying Sn with Pt caused partial filling of the Pt 5d-bands, resulting in a weaker chemisorption of CO. Combined with the easier adsorption of OH species on the Sn sites at low electrochemical potentials, the Pt-Sn alloy would enhance CO electrooxidation, and thus promote the

methanol oxidation reaction. However, due to the strong adsorption of OH species on Sn sites, Pt-Sn alloy shows less MOR activity at high potentials.

In contrast, Pt alloying with Ru can produce more Pt *d*-band vacancies, resulting in an increase in Pt-CO bond strength that would retard the methanol oxidation reaction [52]. However, this result has been challenged by other investigations. Iwasita et al. [53] observed a reduction in CO coverage on the electrode and an increase in the absorption frequency of the bound CO, in their FTIR experiments with Pt-Ru alloy. These results were attributed to the electronic effect of Ru on Pt, and consistent with the expectation that CO is less strongly adsorbed through a reduction in the back π bonding from Pt to the CO π* orbital. The reduction in π back-bonding will also lead to a higher positive charge on the carbon atom, rendering it more liable to nucleophilic attack by water, and permitting CO oxidation at lower potentials. Lu et al. [54] applied cyclic voltammetry (CV), temperature programmed desorption (TPD), electrochemical nuclear magnetic resonance (NMR), as well as radioactive labeling to probe the origin of the effect of ruthenium enhancement, through depositing Ru on a Pt electrode surface. They found that the changes in the bond energy of CO due to the ligand effect played only a minor role in enhancing CO tolerance. Instead, the main effect of ruthenium was to activate water to form OH. Quantitative estimation based on the TPD data indicated that the bi-functional effect was about 4 times larger than the ligand effect. More recently, Yang et al. [55] employed *in situ* surface-enhanced Raman spectroscopy (SERS) to investigate the electronic effect of Ru on the Pt-Ru MOR catalyst. They reported that the addition of Ru to Pt surfaces did not change the Pt-CO stretching frequency, suggesting that Ru has no significant electronic effect on Pt.

Apparently, controversy remains over the electronic effect of the Pt-Ru alloy. As Arico et al. [32] suggested, the electronic effect may be prominent for Pt-Sn catalysts and the bi-functional effect for Pt-Ru catalysts.

13.3.2.3 The Spillover Effect

The spillover effect was originally proposed for the improvement of hydrogen oxidation on Pt-WO_3 catalyst [56]. Shen et al. [57] adapted a similar mechanism to elucidate the enhancement of catalytic activity towards the MOR on Pt-WO_3. During methanol oxidation on Pt-WO_3 catalyst, the adsorbed hydrogen on Pt sites easily spills over to WO_3 to form a hydrogen tungsten bronze (H_xWO_3), thus freeing the Pt sites for methanol adsorption. Furthermore, water can be adsorbed on WO_3 at low overpotentials and may interact with CO adsorbed on Pt sites, thus facilitating methanol oxidation in a way similar to the bi-functional effect. A similar OH spillover effect was also suggested to explain MOR enhancement on Pt-Ru and Pt-Sn catalysts. Davies et al. [58] and Stamenkovic et al. [59] proposed that the OH species formed on Ru or Sn might spillover onto the neighboring Pt sites and react there with CO. Energetically, OH is adsorbed much more strongly on Sn or Ru than on Pt, but in the presence of water the situation may be different. According to Desai and Neurock's molecular dynamics calculations, an OH formed on Ru could easily pick up a hydrogen from a water molecule on a neighboring Pt atom, effectively transferring the OH from Ru to Pt [60].

The role of a second element in methanol oxidation on Pt alloy catalysts depends on how to lower the potential of water dissociation, to weaken the CO chemisorption, and to directly enhance the electrooxidation of CO on Pt. It is obvious that none of the binary alloy catalyst, even the most used Pt-Ru catalyst, contains all of the promoting effects simultaneously. The purpose of exploring ternary and quaternary Pt alloy catalysts is to combine all of the promoting effects into one alloy system to maximize the catalytic MOR activity. For example, Kim et al. [61] ascribed the enhancement of MOR activity on the Pt-Ru-Sn ternary alloy to the synergic effects of Ru as a water activator and Sn as an electronic modifier. Samjeske et al. [62] explained the synergic effect of Mo and Ru in the Pt-Ru-Mo ternary alloy by the way that Mo can shift the oxidation of weakly adsorbed CO on the Ru sites to lower potentials, facilitating the bi-functional effect.

13.3.3 The Stability of Pt-based Alloy Anode Catalysts

In general, the degradation of cathode electrocatalysts plays a major role in the performance loss of PEM fuel cells, including DMFCs. Pt or Pt-alloy electrocatalysts are though to be relatively stable in the fuel cell operation environment. However, the stability of Pt alloy anode catalysts, even the well-alloyed Pt-Ru catalyst, has a dominant effect on the entire fuel cell performance. Zelenay et al. [63, 64] recently discovered a phenomenon, the so-called "Ru crossover", in DMFCs, showing that Ru would dissolve from the anode Pt-Ru catalyst, migrate through the membrane, and re-deposit at the cathode. This Ru crossover would cause a performance loss through inhibiting or contaminating the oxygen reduction kinetics at the cathode, as well as degrading the membrane. The authors also found that Ru crossover could lead to significant Ru accumulation (up to 9 at%) in the cathode catalyst layer. As a result, a ~40 mV performance loss at normal DMFC operating conditions and over 200 mV loss under extreme conditions such as cell reversal operation were observed due to Ru crossover (Figure 13.10). Other work also observed a similar phenomenon of Ru crossover in studies of durability, degradation, and failure mechanisms in DMFCs [65–69]. The degree of ruthenium dissolution depends on the fuel cell operation conditions, such as anode potential and operating time. As seen in a Pourbaix diagram, metallic ruthenium is thermodynamically stable under normal DMFC operation conditions. The ruthenium dissolution was attributed to the presence of hydrous RuO_2 phase in the Pt-Ru catalyst, which can be leached out during operation. In some abnormal operations, such as over-discharging and cell reversal, ruthenium would dissolve from the alloy at high anode potentials (over 0.8 V vs. RHE) through reaction with water. The final chemical form was detected as ruthenium oxide. In order to eliminate the negative effect of Ru crossover, several approaches have been developed, including partial dissolution of ruthenium from the contaminated cathode via potential cycling, selective removal of mobile ruthenium from the anode, and pre-leaching of the loose ruthenium phase in acid.
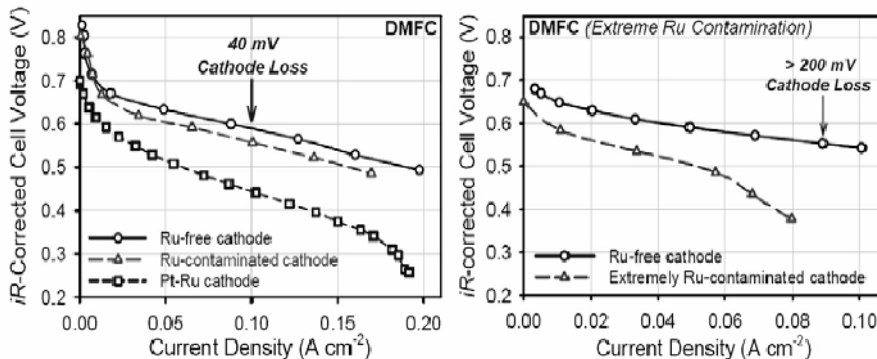
Figure 13.10. DMFC performance losses caused by average (left) and extreme (right) contamination of the cathode by ruthenium crossover. The polarization plot for a DMFC with a Pt-Ru cathode, instead of a Pt cathode, is shown for reference in the left-hand graph. Cell temperature: 75 °C [64]. (Reproduced by permission of ECS—The Electrochemical Society, from Zelenay P. Performance durability of direct methanol fuel cells.)

13.4 Concluding Remarks

Pt-based alloys have been developed for many years to improve the catalytic activity of the oxygen reduction reaction and the methanol oxidation reaction, and reduce Pt loading in the catalyst layers of the PEM fuel cell cathode and anode. Great progress has been made in recent years in terms of alloy activity screening, alloy mechanism discovery, and alloy stability investigation.

For Pt-based alloy catalysts of the ORR at the cathode, some Pt alloy formulations could display specific activity 2–4 times higher than pure Pt catalyst in both simulated and real PEMFC environments. The reported $Pt_3Ni(111)$ skin surface catalyst even showed 90-fold activity enhancement versus the state-of-the-art Pt/C catalyst, although the synthesis of such a nanoparticle catalyst is still challengeable and the activity enhancement needs to be validated in a real PEM fuel cell. Thanks to advanced characterization technologies, the mechanism of the alloying effect on the ORR has been investigated at molecular and atomic levels to reveal alloying element modification to the adsorption and dissociation of oxygen on the Pt surface. Understanding of the stability of Pt-based alloys has also been deepened and significantly improved. Even though some promising catalysts have been invented with respect to achieving the activity target for commercialization, further development of Pt-based alloy catalysts with high surface area and long stability is still necessary in the future.

With respect to Pt-based alloy catalysts for the MOR at the anode, Pt-Ru/C remains the best anode catalyst for DMFCs. Much work has been involved in optimizing the preparation, composition, and structure of the Pt-Ru alloy catalyst to maximize its activity. The alloying effects on the MOR have been explored in terms of the bi-functional, electronic, and spillover effects, although some controversy remains. With respect to catalyst stability, the ruthenium dissolution/crossover issue has been identified. Ternary and quaternary Pt alloy

catalysts need to be explored for further enhancement of the methanol oxidation reaction. Based on current work on ternary and quaternary alloy catalysts, more efforts should be put into understanding the alloying effects of the third and fourth elements, screening the appropriate composition of such complex systems, and addressing the effect of the extra elements on catalyst stability. It seems that the performance and cost of Pt-Ru/C-based DMFCs are still challenges for commercialization. Catalyst activity improvement remains the first task in developing future Pt-based alloy catalysts for the MOR.

References

1. Gasteiger HA, Kocha SS, Sompalli B, Wagner FT. Activity benchmarks and requirements for Pt, Pt-alloy, and non-Pt oxygen reduction catalysts for PEMFCs. Appl Catal B: Environmental 2005;56: 9–35.
2. Liu HS, Song CJ, Zhang L, Zhang JJ, Wang HJ, Wilkinson DP. A review of anode catalysis in the direct methanol fuel cell. J Power Sources 2006;155:95–110.
3. Thompsett D. Pt alloys as oxygen reduction catalysts. In Vielstich W, Gasteiger HA, Lamm A, editors. Handbook of fuel cells – fundamentals, technology and applications. New York: John Wiley & Sons, 2003.
4. Mukerjee S, Srinivasan S. Enhanced electrocatalysis of oxygen reduction on platinum alloys in proton exchange membrane fuel cells. J Electroanal Chem 1993;357:201–24.
5. Mukerjee S, Srinivasan S, Soriaga MP. Role of structural and electronic properties of Pt and Pt alloys on electrocatalysis of oxygen reduction. J Electrochem Soc 1995;142:1409–22.
6. Mukerjee S, Srinivasan S. O_2 reduction and structure-related parameters for supported catalysts. In Vielstich W, Gasteiger HA, Lamm A, editors. Handbook of fuel cells – fundamentals, technology and applications. New York: John Wiley & Sons, 2003.
7. Ralph TR, Hogarth MP. Catalysis for low temperature fuel cells: Part 1. The cathode challenges. Platinum Metals Rev 2002;46:3–14.
8. Toda T, Igarashi H, Watanabe M. Role of electronic property of Pt and Pt alloys on electrocatalytic reduction of oxygen. J Electrochem Soc 1998;145:4185–8.
9. Toda T, Igarashi H, Watanabe M. Enhancement of the electrocatalytic O_2 reduction on Pt-Fe alloys. J Electroanal Chem 1999;460:258–62.
10. Toda T, Igarashi H, Uchida H, Watanabe M. Enhancement of the electroreduction of oxygen on Pt alloys with Fe, Ni, and Co. J Electrochem Soc 1999;146:3750–6.
11. Paulus UA, Wokaun A, Scherer GG, Schmidt TJ, Stamenkovic V, Radmilovic V, et al. Oxygen reduction on carbon-supported Pt-Ni and Pt-Co alloy catalysts. J Phys Chem B 2002;106:4181–91.
12. Paulus UA, Wokaun A, Scherer GG, Schmidt TJ, Stamenkovic V, Markovic NM, et al. Oxygen reduction on high surface area Pt-based alloy catalysts in comparison to well defined smooth bulk alloy electrodes. Electrochim Acta 2002;47:3787–98.
13. Stamenkovic V, Schmidt TJ, Ross PN, Markovic NM. Surface Composition Effects in Electrocatalysis: Kinetics of Oxygen Reduction on Well-Defined Pt_3Ni and Pt_3Co Alloy Surfaces. J Phys Chem B 2002;106:11970–9.
14. Stamenkovic VR, Mun BS, Mayrhofer KJJ, Ross PN, Markovic NM. Effect of surface composition on electronic structure, stability, and electrocatalytic properties of Pt-transition metal alloys: Pt-skin versus Pt-skeleton surfaces. J Am Chem Soc 2006;128:8813–9.

15. Stamenkovic V, Mun BS, Mayrhofer KJJ, Ross PN, Markovic NM, Rossmeisl J, et al. Changing the activity of electrocatalysts for oxygen reduction by tuning the surface electronic structure. Angew Chem Int Ed 2006;45:2897–901.

16. Stamenkovic VR, Fowler B, Mun BS, Wang G, Ross PN, Lucas CA, et al. Trends in electrocatalysis on extended and nanoscale Pt-bimetallic alloy surfaces. Nat Mater 2007;6:241–7.

17. Stamenkovic VR, Fowler B, Mun BS, Wang G, Ross PN, Lucas CA, et al. Improved oxygen reduction activity on $Pt_3Ni(111)$ via increased surface site availability. Science 2007;315:493–7.

18. Paffett MT, Beery JG, Gottesfeld S. Oxygen reduction at $Pt_{0.65}Cr_{0.35}$, $Pt_{0.2}Cr_{0.8}$ and roughened platinum. J Electrochem Soc 1988;135;1431–6.

19. Kinoshita K. Particle size effects for oxygen reduction on highly dispersed platinum in acid electrolytes. J Electrochem Soc 1990;137:845–8.

20. Jalan V and Taylor EJ. Importance of interatomic spacing in catalytic reduction of oxygen in phosphoric acid. J Electrochem Soc 1983;130:2299–302.

21. Min M, Cho J, Cho K, Kim H. Particle size and alloying effects of Pt-based alloy catalysts for fuel cell applications. Electrochim Acta 2000;45:4211–17.

22. Norskov JK, Rossmeisl J, Logadottir A, Lindqvist L, Kitchin JR, Bligaard T, et al. Origin of the overpotential for oxygen reduction at a fuel-cell cathode. J Phys Chem B 2004;108:17886–92.

23. Wang JX, Markovic NM, Adzic RR. Kinetic analysis of oxygen reduction on Pt(111) in acid solutions: intrinsic kinetic parameters and anion adsorption effects. J Phys Chem B 2004;108:4127–33.

24. Borup R, Meyers J, Pivovar B, Kim YS, Mukundan R, Garland N, et al. Scientific aspects of polymer electrolyte fuel cell durability and degradation. Chem Rev 2007;107:3904–51.

25. Antolini E, Salgado JRC, Gonzalez ER. The stability of Pt-M (M = first row transition metal) alloy catalysts and its effect on the activity in low temperature fuel cells: a literature review and tests on a Pt-Co catalyst. J Power Sources 2006;160:957–68.

26. Wakabayashi N, Takeichi M, Uchida H, Watanabe M. Temperature dependence of oxygen reduction activity at Pt-Fe, Pt-Co, and Pt-Ni alloy electrodes. J Phys Chem B 2005;109:5836–41.

27. Colon-Mercado HR, Kim H, Popov BN. Durability study of Pt_3Ni_1 catalysts as cathode in PEM fuel cells. Electrochem Commun 2004;6:795–9.

28. Wei Z, Guo H, Tang Z. Methanol electro-oxidation on platinum and platinum-tin alloy catalysts dispersed on active carbon. J Power Sources 1996;62:233–42.

29. Salgado JRC, Antolini E, Gonzalez ER. Structure and activity of carbon-supported Pt-Co electrocatalysts for oxygen reduction. J Phys Chem B 2004;108:17767–74.

30. Yu P, Pemberton M, Plasse P. PtCo/C cathode catalyst for improved durability in PEMFCs. J Power Sources 2005;144:11–20.

31. Zhang J, Sasaki K, Sutter E, Adzic RR. Stabilization of platinum oxygen-reduction electrocatalysts using gold clusters. Science 2007;315:220–2.

32. Arico AS, Srinivasan, Antonucci V. DMFCs: from fundamental aspects to technology development. Fuel Cells 2001;1:133–61.

33. Bockris, JOM, Wroblowa H. Electrocatalysis. J Electroanal Chem 1964;7;428–51.

34. Watanabe M, Uchida M, Motoo S. Preparation of highly dispersed Pt plus Ru alloy clusters and the activity for the electrooxidation of methanol. J Electroanal Chem Interfacial Electrochem 1987;229;395–406.

35. Guo J, Sun G, Sun S, Yan S, Yang W, Qi J, et al. Polyol-synthesized PtRu/C and PtRu black for direct methanol fuel cells. J Power Sources 2007;168:299–306.

36. Antolini E. Platinum-based ternary catalysts for low temperature fuel cells. Part I. Preparation methods and structural characteristics. Appl Catal B: Environmental 2007;74:324–36.
37. Antolini E. Platinum-based ternary catalysts for low temperature fuel cells. Part II. Electrochemical properties. Appl Catal B: Environmental 2007;74:337–50.
38. Ley KL, Liu R, Pu C, Fan Q, Leyarovska N, Segre C, et al. Methanol oxidation on single-phase Pt-Ru-Os ternary alloys. J Electrochem Soc 1997;144:1543–8.
39. Gotz M, Wendt H. Binary and ternary anode catalyst formulations including the elements W, Sn and Mo for PEMFCs operated on methanol or reformate gas. Electrochim Acta 1998;43:3637–44.
40. Roth C, Gotz M, Fuess H. Synthesis and characterization of carbon-supported Pt-Ru-WO catalysts by spectroscopic and diffraction methods. J Appl Electrochem 2001;31:793–8.
41. Arico AS, Poltarzewski Z, Kim H, Morana A, Giordano N, Antonucci V. Investigation of a carbon-supported quaternary Pt-Ru-Sn-W catalyst for direct methanol fuel cells. J Power Sources 1995;55:159–66.
42. Reddington E, Sapienza A, Gurau B, Viswanathan R, Sarangapani S, Smotkin ES, et al. Combinatorial electrochemistry: a highly parallel, optical screening method for discovery of better electrocatalysts. Science 1998;280:1735–7.
43. Choi WC, Kim JD, Woo SI. Quaternary Pt-based electrocatalyst for methanol oxidation by combinatorial electrochemistry. Catal Today 2002;74:235–40.
44. Whitacre JF, Valdez T, Narayanan SR. Investigation of direct methanol fuel cell electrocatalysts using a robust combinatorial technique. J Electrochem Soc 2005;152:A1780–9.
45. Neburchilov V, Wang HJ, Zhang JJ. Low Pt content Pt-Ru-Ir-Sn quaternary catalysts for anodic methanol oxidation in DMFC. Electrochem Comm 2007;9:1788–92.
46. Hamnett A. Mechanism and electrocatalysis in the direct methanol fuel cell. Catal Today 1997;38:445–57.
47. Watanabe M, Motoo S. Electrocatalysis by ad-atoms: Part II. Enhancement of the oxidation of methanol on platinum by ruthenium ad-atoms. J Electroanal Chem 1975;60:267–73.
48. Frelink T, Visscher W, Van Veen JAR. On the role of Ru and Sn as promoters of methanol electro-oxidation over Pt. Surf Sci 1995;335:353–60.
49. Gasteiger HA, Markovic N, Ross PN, Cairns EJ. Temperature-dependent methanol electro-oxidation on well-characterized pt-ru alloys. J Electrochem Soc 1994;141:1795–803.
50. Parsons R, Vandemoot T. The oxidation of small organic molecules: a survey of recent fuel cell related research. J Electroanal Chem 1988;257:9–45.
51. Mukerjee S, McBreen J. The effect of Ru and Sn additions to Pt on the electrocatalysis of methanol oxidation: An in situ XAS investigation. Proceedings of the 2nd international symposium on new materials for fuel cells and modern battery systems. Savadogo O, Roberge PR, editors. Montreal, Canada: Ecole Polytechnique de Montreal;1997:548–59.
52. McBreen J, Mukerjee S. In situ X-ray absorption studies of a pt-ru electrocatalyst. J Electrochem Soc 1995;142:3399–404.
53. Iwasita T, Nart FC, Vielstich W. FTIR study of the catalytic activity of a 85:15 Pt. Ru alloy for methanol oxidation. Phys Chem Chem Phys 1990, 94:1030–4.
54. Lu C, Rice C, Masel RI, Babu PK, Waszczuk P, Kim HS, et al. UHV, electrochemical NMR, and electrochemical studies of platinum/ruthenium fuel cell catalysts. J Phys Chem B 2002;106:9581–9.

55. Yang H, Yang Y, Zou S. In situ surface-enhanced Raman spectroscopic studies of CO adsorption and methanol oxidation on Ru-modified Pt surfaces. J Phys Chem C 2007;111:19058–65.
56. Hobbs BS, Tseung ACC. High performance, platinum activated tungsten oxide fuel cell electrodes. Nature 1969;222:556–8.
57. Shen P, Chen K, Tseung ACC. Co-deposited Pt-WO$_3$ electrodes. Part 1. Methanol oxidation and in situ FTIR studies. J Chem Soc Faraday Trans 1994;90:3089–96.
58. Davies JC, Hayden BE, Pegg DJ, Rendall ME. The electro-oxidation of carbon monoxide on ruthenium modified Pt(1 1 1). Surf Sci 2002;496:110–20.
59. Stamenkovic VR, Arenz M, Lucas CA, Gallagher ME, Ross PN, Marković NM. Surface chemistry on bimetallic alloy surfaces: adsorption of anions and oxidation of CO on PtSn(111). J Am Chem Soc 2003;125:2736–45.
60. Desai S, Neurock M. A first principles analysis of CO oxidation over Pt and Pt Ru (111) surfaces. Electrochim Acta 2003;48:3759–73.
61. Kim T, Kobayashi K, Takahashi M, Nagai M. Effect of Sn in Pt-Ru-Sn ternary catalysts for CO/H and methanol electrooxidation. Chem Lett 2005;34:798–9.
62. Samjeské G, Wang H, Loffler T, Baltruschat H. CO and methanol oxidation at Pt-electrodes modified by Mo. Electrochim Acta 2002;47:3681–92.
63. Piela P, Eickes C, Brosha E, Garzon F, Zelenay P. Ruthenium crossover in direct methanol fuel cell with Pt-Ru black anode. J Electrochem Soc 2004;151:A2053–9.
64. Zelenay P. Performance durability of direct methanol fuel cells. ECS Transactions 2005;1:483–95.
65. Chen W, Sun G, Guo J, Zhao X, Yan S, Tian J, et al. Test on the degradation of direct methanol fuel cell. Electrochim Acta 2006;51:2391–9.
66. Gancs L, Hakim N, Hult BN, Mukerjee S. Dissolution of Ru from PtRu electrocatalysts and its consequences in DMFCs. ECS Trans 2006;3:607–18.
67. Sarma LS, Chen CH, Wang GR, Hsueh KL, Huang CP, Sheu HS, et al. Investigations of direct methanol fuel cell (DMFC) fading mechanisms. J Power Sources 2007;167:358–65.
68. Gancs L, Hult BN, Hakim N, Mukerjee S. The impact of Ru contamination of a PtC electrocatalyst on its oxygen-reducing activity. Electrochem Solid-State Lett 2007;10:150–4.
69. Chung Y, Pak C, Park GS, Jeon WS, Kim JR, Lee Y, et al. Understanding a degradation mechanism of direct methanol fuel cell using TOF-SIMS and XPS. J Phys Chem C 2008;112:313–8.

14

Nanotubes, Nanofibers and Nanowires as Supports for Catalysts

Xueliang Sun and Madhu Sudan Saha

14.1 Introduction

14.1.1 The Importance of Combining Nanotechnology and Clean Energy

The use of nanotechnology towards improving clean energy solutions is very important. There is a growing awareness that nanotechnology will have a profound impact on energy generation, storage, and utilization by understanding the significant differences of energy states and transport in nanostructures compared to macrostructures. Nanotechnology-based solutions are being developed for a wide range of energy solutions such as solar cells, hydrogen generation and storage, batteries, and fuel cells.

Energy shortages and environmental pollution are serious challenges that humanity is starting to face. The world demand for energy is expected to double from 14 terawatts (TW) in the year 2000 to 28 TW by the year 2050. Fuel cells are non-polluting and efficient energy conversion devices that are expected to play a dominant role in energy solutions of the future. However, fuel cells still face significant technological roadblocks that need to be overcome before they will become economically viable. One of the biggest challenges towards the commercialization of fuel cells is their low stability and the high cost of materials.

Many scientists see research in advanced nanotechnology and nanomaterials as an opportunity to address our significant energy and environmental challenges (e.g., see the article by R. Smalley, a winner of the Nobel Prize, in the June issue of *MRS Bulletin* in 2005). Nanomaterials have attracted great interest in recent years because of their unusual catalytic, mechanical, electrical and optical properties, all of which are obtained by confining their dimensions. For example, gold in bulk form is not chemically active, but at the nanoscale, a gold particle 3 nm in size is highly chemically active. Gold nanoparticles used as catalysts are therefore considered promising in chemical reactions such as the oxidation of CO. Further, gold nanowires are 100 times stronger than bulk gold because nanowires have fewer defects. Nanowires will be discussed in more detail later in the chapter. Among the advanced nanomaterials, nanotubes and nanowires are a class of novel

nanostructures that have attracted much attention as model systems for nanoscience and for various potential applications, including those related to composite materials, electrode materials, field emitters, nanoelectronics, and nanoscale sensors.

14.1.2 One-dimensional Nanomaterials Based New Catalyst Supports

Among the various types of fuel cells, proton exchange membrane (PEM) fuel cells offer several advantages including rapid start-up and shut-down, higher powder density, and all solid state components. However, a major challenge to the commercialization of PEM fuel cells is the high cost of the materials and the low stability of the electrodes, commonly referred to as the membrane electrode assembly (MEA). The PEM fuel cell MEA utilizes precious metal catalysts (such as Pt or Pt alloys) dispersed on carbon black substrate. These catalysts are estimated to contribute to as much as 50% of the total fuel cell cost. In a recent scientific review article by General Motors researchers [1], it was emphasized that the current state of the art platinum loading (~ 0.4 mg/cm^2) of PEM fuel cell electrodes must be reduced to levels lower than 0.1 mg/cm^2 to meet the target for commercialization.

It is well known that the activity of a catalyst depends significantly on the size of the Pt particles and their dispersion pattern over the support structures [2]. It has been found that the optimal dispersion pattern and Pt particle size can be obtained by using an appropriate preparation procedure on an ideal supporting material [3]. The ideal support should have the following structure and properties: (i) high surface area and good electrical properties, (ii) reactant gas access to the electrocatalysts, and (iii) high electrochemical stability under fuel cell operating conditions [4, 5]. Usually, carbon black supported Pt electrocatalysts are used as the electrode catalyst in PEM fuel cells [6]. Despite the high surface area of the carbon black particles, the carbon black-based electrocatalyst support have two main problems: (i) due to its dense structure, the carbon black-based support has significant mass transfer limitations, leading to a very low Pt utilization [4]; (ii) carbon black is known to undergo electrochemical oxidation into surface oxides as well as CO_2 at the cathode in the fuel cell. These oxides are subjected to low pH, high potential, high humidity, and high temperatures (~ 80 °C). As carbon black corrodes, noble metal nanoparticles (e.g., Pt) on carbon black will detach from the electrode and possibly aggregate to larger particles, resulting in Pt surface area loss, which subsequently lowers the performance of PEM fuel cells [7–9]. Therefore, many efforts have been made to search for new catalyst supports [10].

This chapter begins by briefly describing the processing techniques used to synthesize the nanostructures including carbon nanotubes, carbon nanofibers and nanowires. Next, the methods by which Pt nanoparticles can be deposited onto the nanostructures will be examined along with the surface functionalization of these nanostructures. This is followed by a review of fabrication processes of MEA fuel cells containing nanostructures. Finally, we give a summary of the stability of the nanostructure-based fuel cell electrodes.

14.2 Synthesis and Characterization of Carbon Nanotubes, Nanofibers and Nanowires

14.2.1 Structure and Synthesis Methods for Carbon Nanotubes

14.2.1.1 Introduction
Carbon nanotubes (CNTs), one of the key elements in the study of nanotechnology, are a new class of one-dimensional nanomaterials with unique structures and properties that have various potential applications including nanocomposite materials, nanoelectrode materials, field emitters, nanoelectronics, and nanoscale sensors. Since the discovery of carbon nanotubes by Dr. Iijima in 1991 [11], significant progress has been made towards CNTs synthesis, property investigation and potential applications. The extraordinary mechanical properties and unique electrical properties of CNTs have stimulated extensive research activities worldwide. The driving force in the nanotube science and technology field has been understanding these properties and exploring their potential applications. There have been many special issues of journals [12–14] in addition to several books [15–18] documenting nanotechnology.

CNTs can be classified into singlewalled carbon nanotubes (SWCNTs) and multiwalled carbon nanotubes (MWCNT), as shown in Figure 14.1. The structure with one cylinder is called a SWCNT. SWCNTs have a relatively smaller diameter, as low as 0.4 nm, and could be metallic or semiconducting in nature depending on their structure. The SWCNT structure is characterized by a chiral vector (*m,n*): armchair (n = m), zigzag (n = 0 or m = 0) or chiral (any other n and m), as shown in Figure 14.1(A). All armchair SWNTs are metals; those with *n–m* = 3*k*, where *k* is a nonzero integer, are semiconductors with a tiny band gap; and all others are semiconductors with a band gap that inversely depends on the nanotube diameter [19]. While semiconducting SWCNTs (S-SWCNTs) can be used to build high-performance field-effect transistors and sensors, metallic SWCNTs (M-SWCNTs) might be useful for interconnects. The structure that contains a concentric set of cylinders with a constant interlayer separation of 0.34 nm is called a MWCNT (Figure 14.1(B)). MWCNTs have relatively larger diameter, from a few nanometers to tens of nanometers and are conducting materials. The electronic properties of perfect MWCNTs are rather similar to those of perfect SWCNTs because the coupling between the cylinders is weak in MWCNTs.

As emphasized in *Nature* news (*Nature* 432, 2004, 791), CNT quality presents a serious problem for the use of nanotubes. The quality of the CNTs obtained from various suppliers, and even from the same supplier at different times, is highly unreliable. These CNTs can be significantly different in shape and structure, which limits the potential applied development of this new class of nanomaterials. Therefore, the prominent current challenges include two aspects relevant to CNTs: (i) the synthesis and control of their structure, alignment, and pattern and (ii) the development of a thorough understanding of their growth mechanisms.
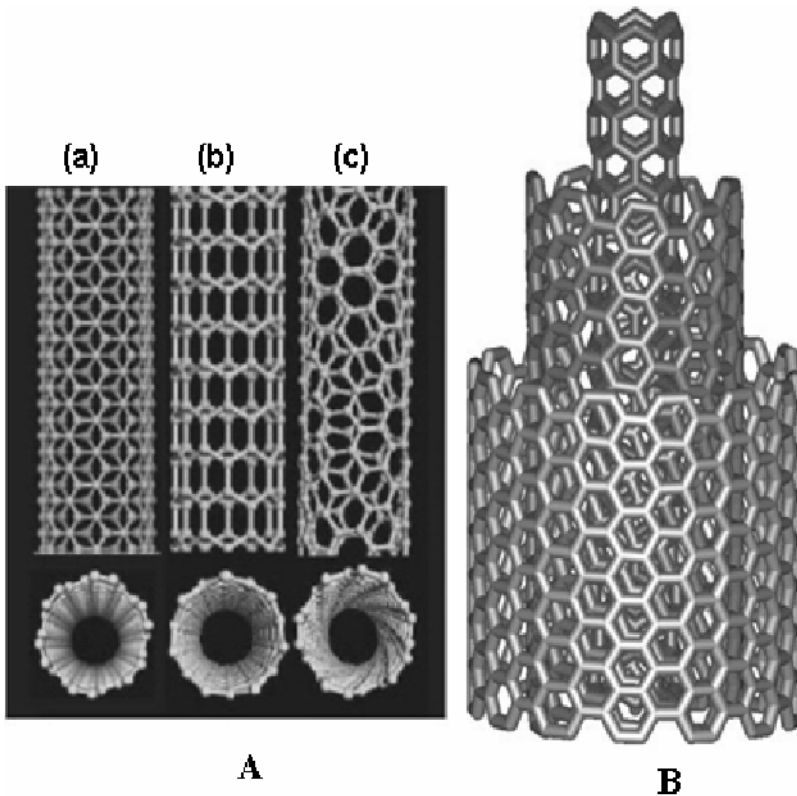
Figure 14.1. A. Schematic illustrations of the structures of (a) armchair, (b) zigzag, and (c) chiral SWNTs. B. Structure of a multi-walled carbon nanotube made up of three shells of differing chirality [160]. (From Balasubramanian K, Burghard M. Chemically functionalized carbon nanotubes. Small 2005;1:180–92. ©2005 Wiley-VCH Verlag GmbH & Co. KGaA. Reproduced with permission.)

14.2.1.2 Synthesis of Carbon Nanotubes

From the synthesis point of view, there were two significant findings in the early stages of nanotechnology after Iijima first discovered the MWCNTs in 1991. One great discovery was the SWCNTs made by Iijima and co-workers [20] in 1993 as well as Bethune and co-workers [21]. The other milestone, reached in 1996, was a relatively high yield synthesis of SWCNTs, which allowed investigations of physical properties to be carried out. Following these discoveries, efforts have been made toward high-quality and large scale synthesis of SWCNTs and MWCNTs with controlled structure and predictive fashion. Clearly, future development in nanotube-based science and technology will rely on the highly controlled synthesis of nanotube materials.

Generally, the synthesis methods of CNTs are arc discharge, laser ablation and chemical vapor deposition (CVD). While first two methods use high-energy input to release the carbon atoms from carbon-containing precursor molecules, CVD relies on carbon atomization via catalytic decomposition of carbon precursors on

the surface of transition metal particles. The advantage of the CVD method is such that it allows a scaled up production to the industrial level and to produce CNTs in a predictive fashion with controlled length, positions, and orientations on the substrates. Control over the CNT structure and growth is achieved through a series of experimental parameters such as process temperature, gas mixtures, pressure, flow rates and catalytic materials used. The CVD methods include various types such as general thermal CVD, a floating catalyst CVD, an aerosol-assisted CVD and plasma-enhanced CVD (PECVD).

For SWCNTs, many research groups [22–32] have made many significant findings using the thermal CVD method to grow high-quality and highly oriented SWCNTs. Recently, one significant advancement is the preferential growth of either semiconducting or metallic SWCNTs by PECVD. The challenge in synthesizing SWCNTs is the co-existence of semiconducting and metallic SWCNTs, which is determined by their diameter and chirality. However, SWCNTs can have different properties used for different applications. For example, semiconducting SWCNTs may be used for chemical and biological sensors while metallic SWCNTs may be used for fuel cell electrodes. Dai and his co-workers recently used PECVD to preferentially grow semiconducting SWCNTs [33].

Regarding MWCNTs, the floating catalyst CVD (FCCVD) and aerosol-assisted CVD (AACVD) are two significant methods to grow high-density and high-quality CNTs. The advantages of these two methods are that they are exceptionally cheap and well-suited for scaling up to mass production of CNTs with a defined nanotube diameter distribution. FCCVD has attracted considerable attention because it ensures continuous growth of highly-aligned and highly pure nanotubes, at a low reaction temperature, low cost and simple fabrication process. Compared with the traditional CVD method, the advantage of using the FCCVD method is to allow the catalyst and carbon source to be introduced into the reaction chamber simultaneously to produce well-aligned CNTs on the substrates [34]. Figure 14.2(a) shows a SEM image of high-density MWCNTs grown on a fuel cell backing (carbon paper) in Sun's group. The MWCNTs were synthesized by FCCVD using ferrocence as catalyst source and ethylene gas as carbon source at 800 °C. The MWCNTs totally cover the carbon substrate.

The AACVD involves pyrolysis of a mixed liquid aerosol, which consists of both a liquid hydrocarbon and the catalyst precursor [35]. Ferrocene, cobaltocene, cobalt nitrate, nickelocene and iron pentacarbonyl have been used as both catalysts and carbon sources. In addition, acetylene, benzene, toluene, xylene, mesitylene and tetrahydrofuran are used as solvents for additional carbon sources. Aligned MWCNTs products are typically produced by AACVD, but, SWCNTs can be obtained in certain instances [36]. Figure 14.2(b) shows SEM image of high-density MWCNTs grown on fuel cell backing (carbon paper) by AACVD in Sun's group. Ferrocene and xylene were used as the catalyst and carbon sources to grow MWCNTs. The MWCNTs completely covered the carbon paper substrate displaying the locally aligned features.
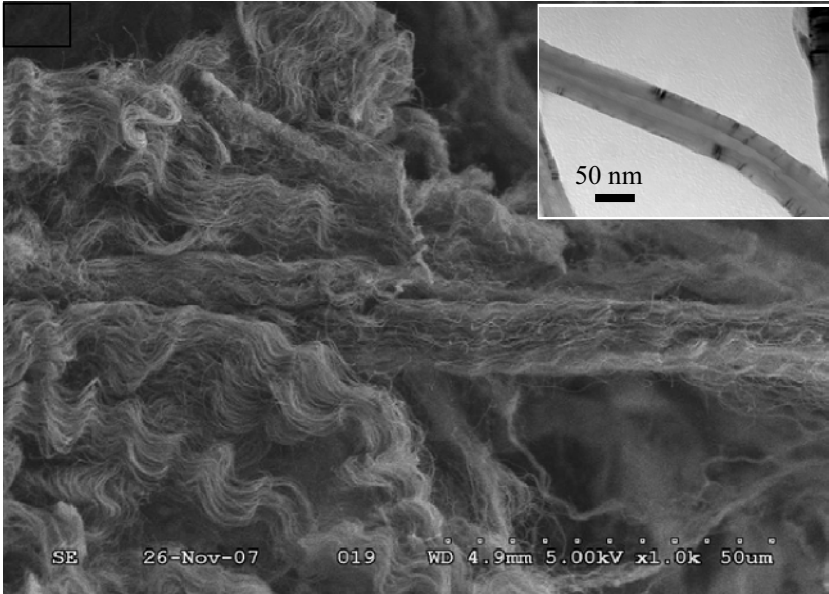
(a)
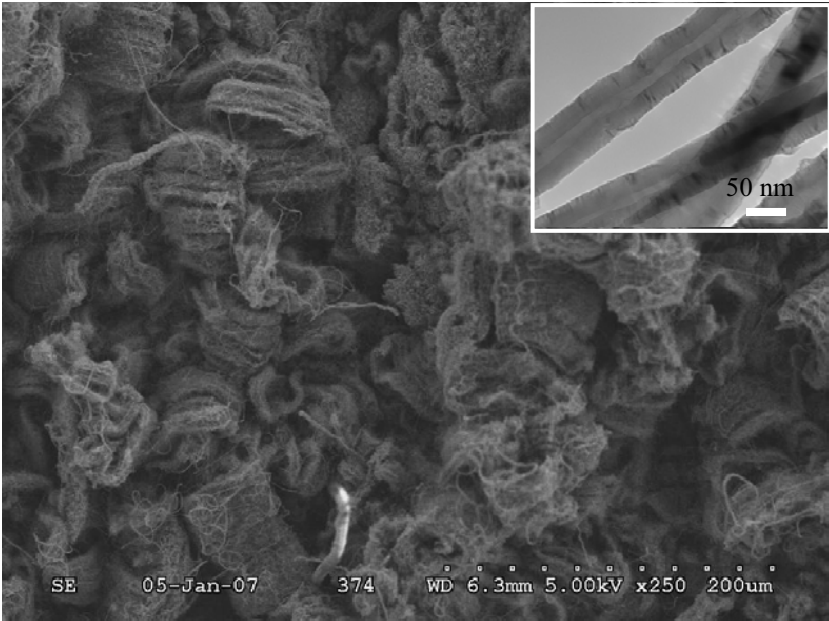
(b)

Figure 14.2. SEM images of MWCNTs grown on fuel cell backing by (a) floating catalyst CVD method and (b) aerosol-assisted CVD method. (Insets): TEM images.

14.2.2 Structure and Synthesis Methods for Carbon Nanofibers

The unique properties of carbon nanofibers (CNFs), sometimes called carbon filaments or filamentous carbon, have generated intense interest in the application of these new carbon materials toward a number of applications including selective absorption, energy storage, polymer reinforcement, and catalyst supports [37].

There are mainly three types of CNFs including "fishbone or herringbone", "platelet", and "ribbon" or "tubular" structures, as shown schematically in Figure 14.3 [38–40]. The CNF nanostructures consist of graphite sheets aligned in definite directions that are dictated by the catalytic entity selected for the growth process. The fishbone or herringbone CNFs (f-CNFs) reveal their graphene layers stacking obliquely with respect to the fiber axis. The platelet CNFs have their graphene layers being perpendicular to the axis. The ribbon CNFs display their graphene layers parallel to the growth axis. These nanofibers were grown via the catalytic decomposition of a carbon source over metal catalysts composed of copper, iron, nickel, or their bimetallic compounds [41, 42]. Unlike conventional graphite materials and nanotubes where the basal plane is exposed, the structure of carbon nanofibers is one where only edge regions are revealed. This feature allows CNFs to be used as a catalyst support for fuel cells discussed in detail later.
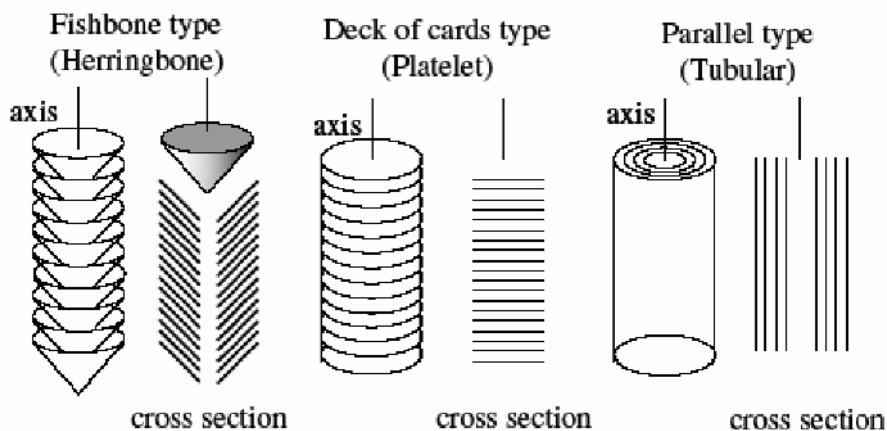
Figure 14.3. Schematic representation of three types of CNFs. (With kind permission from Springer Science+Business Media: Journal of Applied Electrochemistry, Progress in the synthesis of carbon nanotube- and nanofiber-supported Pt electrocatalysts for PEM fuel cell catalysis, 36, 2006, 507–22, Lee K, Zhang J, Wang H, Wilkinson DP, Figure 10, ©Springer.)

14.2.3 Structure and Synthesis Methods for Nanowires

14.2.3.1 Introduction
Nanowires (NWs), like CNTs, are also one-dimensional and well-defined crystalline structure with a high aspect ratio. NWs have demonstrated superior electrical, optical, mechanical and thermal properties. Unlike CNTs, NWs are non-carbon based materials that can consist of metals, semiconductors, or inorganic

compounds. The broad choice of various crystalline materials and doping methods make the electronic and optical properties of NWs adaptable with a high degree of freedom and precision. With the development of new synthesis methods, NWs have attracted more and more attention for sensor applications. Nature magazine recently predicted that "Nanowires, nanorods, nanowhiskers, it does not matter what you call them, they are the hottest properties in nanotechnology" (*Nature*, 419, 553, 2002). As an example, Figure 14.4 shows a collection of various nanostructures of ZnO synthesized by thermal evaporation of solid powders [43]. There are a few papers [44, 45] and books [46–49] dealing with the synthesis, characterization, properties and applications of NWs. A big challenge is to integrate NWs into multi-function assemblies in order to fabricate nanoscale electronic and photonic devices as well as biosensors. In this section, we will focus on their synthesis and growth process.
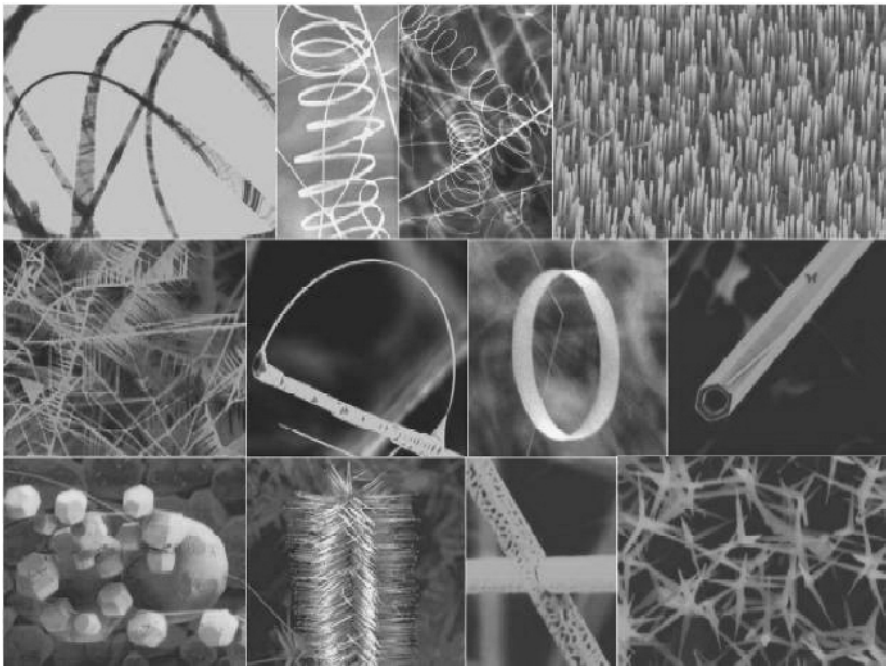
Figure 14.4. A collection of nanostructures of ZnO synthesized under controlled conditions by thermal evaporation of solid powders. Most of the structures presented can be produced with 100% purity [43]. (Reprinted from Materials Today, 7(6), Wang ZL, Nanostructures of zinc oxide, 26–33, ©2004, with permission from Elsevier.)

14.2.3.2 Synthesis of Nanowires
Synthesis methods of NWs basically include both vapor phase and solution techniques. Compared to physical methods such as nanolithography and other patterning techniques, chemical methods have been more versatile and effective in the synthesis of these nanowires. The chemical synthesis includes various methods: thermal evaporation, chemical vapor-phase deposition, metal-organic chemical

vapor-phase deposition, arc-discharge, laser ablation, sol-gel, template-based methods. The basic process of 1D nanostructure formation involves two fundamental steps: nucleation and growth. They can be simply categorized into (i) vapor-based growth; and (ii) solution-based growth. A major challenge in the synthesis of nanowires is to control their size, phase purity, crystallinity, and chemical composition. Therefore, a detailed understanding and control of the nucleation and growth processes at the nanometer scale is required.

Vapor Phase Growth of Nanowires

Vapor-liquid-solid Growth: The vapor-liquid-solid (VLS) growth mechanism was proposed by Wayner [50] in the 1960s when he studied the growth of mm-scale Si whiskers using Au as a catalyst. The advantage of the VLS growth mechanism is that it can control production of single-crystalline 1D nanostructure from a wide variety of inorganic materials including elemental semiconductors (Si, Ge, and B), III-V semiconductors (GaN, GaAs, GaP, InP, InAs), II-VI semiconductors (ZnS, ZnSe, CdS, CdSe), and oxides (ZnO, MgO, SiO_2) [45]. A typical VLS process involves the dissolution of gaseous reactants into nanosized liquid droplets of a catalyst metal, followed by nucleation and growth of the single-crystalline rods and then wires. Since the diameter of the nanowires is determined by the diameter of the catalyst particles, this method provides an efficient means to obtain uniform-sized nanowires. This mechanism has been widely accepted and applied for understanding the growth of various types of nanowires. The synthesis of NWs with controlled composition, size, purity and crystallinity required an increased understanding of the nucleation and growth processes at the nanoscale. An *in situ* high-temperature TEM revealed real-time observations of the growth of Ge nanowires, which confirms the VLS growth mechanism [51]. The experimental observations suggest that there are three growth stages: metal alloying, crystal nucleation and axial growth.

Vapor-solid Growth: The vapor-solid (VS) growth method, also called evaporation-condensation growth, is also a popular and simple method to grow oxide nanowires. In this process, the vapor species is first generated by evaporation, chemical reduction and gaseous reaction. The vapor is subsequently transported and condensed onto a substrate. Using this method, various oxide nanowires such as Zn, Sn, In, Cd, Mg, Ga and Si have been synthesized. For example, Zhu and co-workers have grown Si_3N_4, SiC, Ga_2O_3 and ZnO nanowires by heating the powders of these materials to elevated temperatures [52]. Wang and co-workers obtained nanobelts by this method [53]. Recently, Saha and co-workers [54] synthesized SnO_2 NWs directly on carbon paper via vapor solid growth from tin power at 850 °C. Figure 14.5 shows typical SEM and TEM images of the SnO_2 NWs grown on carbon fibers of carbon paper by thermal evaporation method. High-density SnO_2 NWs on carbon fibers of a carbon paper are an ideal support of Pt nanoparticles for fuel cell application [54].
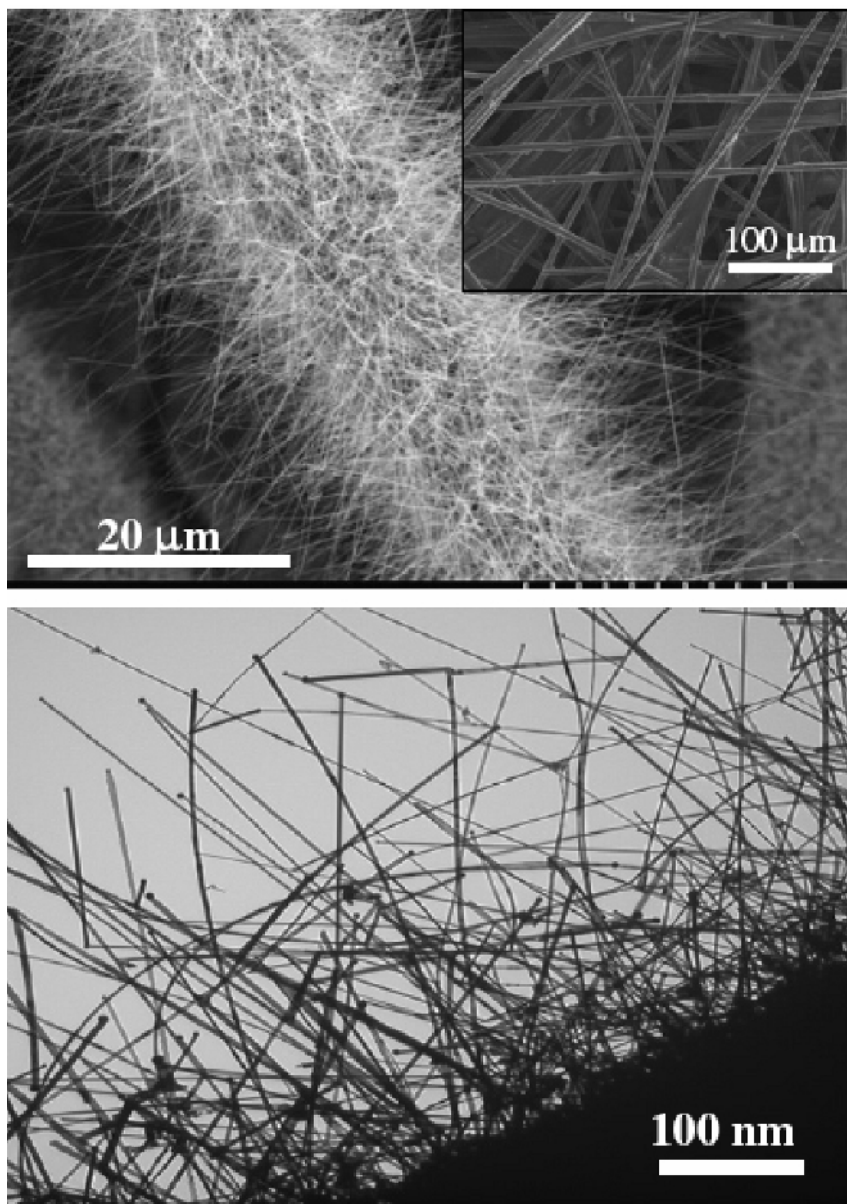
Figure 14.5. SnO$_2$ NWs grown on carbon fibers of carbon paper by thermal evaporation method: (top) SEM image showing high coverage of SnO$_2$ NWs on fibers of carbon paper (inset: fibers of bare carbon paper); (bottom) TEM image of SnO$_2$ NWs/carbon paper indicating morphologies of the nanowires [54]. (Reprinted from Electrochemistry Communications, 9(9), Saha MS, Li R, Sun X. Composite of Pt–Ru supported SnO$_2$ nanowires grown on carbon paper for electrocatalytic oxidation of methanol, 2229–34, ©2007, with permission from Elsevier.)

Solution-based Growth of Nanowires

Template-based Synthesis: Template-directed synthesis provides another convenient and versatile method for growing 1D nanostructures. In this approach, the template simply serves as a scaffold within which different material is synthesized and shaped into a nanostructure with its morphology complementary to that of the template. The templates could be nanoscale channels within mesoporous materials, porous alumina and polycarbonate membranes. The nanoscale channels are filled using, the solution, the sol-gel or the electrochemical method. The nanowires produced are released from the templates by removal of the host matrix [55]. Unlike the polymer membranes fabricated by track etching, anodic alumina membranes (AAMs) containing a hexagonally packed 2D array of cylindrical pores with a uniform size are prepared using anodization of aluminum foils in an acidic medium. Several materials have been fabricated into nanowires using AAMs in the templating process. The various inorganic materials include Au, Ag, Pt, TiO_2, MnO_2, ZnO, SnO_2, InO_3, CdS, CdSe, CdTe, electronically conducting polymers such as polypyrole, poly(3-methylthiophene), polyaniline and finally carbon nanotubules.

Although the nanowires synthesized using the template method are usually polycrystalline, recent studies have revealed that it is possible to synthesize single crystals of nanowires by carefully controlled conditions. For example, Neumann and co-workers have demonstrated that pulse electrodeposition could be used to selectively grow either single-crystalline copper nanowires [56]. In recent work, Cao and co-workers discovered that titanium nanowires, obtained from the electrophoretic deposition method, became single crystals once their diameters had been reduced below 15 nm [57].

In summary, the controlled synthesis of CNTs, CNFs, and NWs is critical in order for them to be used in practical applications. In particular, the nanostructures grown on carbon paper are ideal materials for fuel cell electrodes. In the next sections, we will focus on how to use them in fuel cells.

14.3 Synthesis and Characterization of Pt Catalysts Supported on Carbon Nanotubes, Carbon Nanofibers and Metal Oxide Nanowires

14.3.1 Introduction

Proton exchange membrane (PEM) fuel cells are efficient and nonpolluting electrical power generators based on two electrochemical reactions: the oxidation of hydrogen at the anode and the reduction of oxygen at the cathode. In recent years, the PEM fuel cells have been considered as an alternative to internal combustion engines, batteries, and thermal combustion power plants due to the high thermodynamic efficiency and the near-zero emission levels. However, there are many challenges that need to be addressed before the commercialization of the PEM fuel cells, such as hydrogen fuel infrastructure, durability, and cost issues [1].

Noble metals, such as Pt, Ru or Pt-Ru alloys, supported on high surface area carbon materials are important electrochemical catalysts for PEM fuel cells. It is well known that the catalytic activities highly depend on the size and dispersion of the metal nanoparticles on the support as well as the particle interactions with the support substrates [58, 59]. Carbon black support, the most common catalytic support, has good electronic conductivity, high surface area, good electrochemical performance and stability in acidic environments [60]. However, to reduce Pt loading through increasing the catalyst utilization and improving the catalyst activity, a new carbon support with a higher surface area is needed. The application of CNTs and CNFs as supports for the fuel cell catalysts have been a subject of great interest during the last few years due to the high surface area, excellent electronic conductivity, and high chemical stability [61, 62]. The main reason for using CNTs- and CNFs-supported Pt catalysts is to reduce Pt loading through increasing the catalyst utilization, and improving the catalyst activity. Electrocatalysts supported on CNTs or CNFs as electrodes in either PEMFCs [63–70] or direct methanol fuel cells (DMFCs) [71–74] have been examined extensively and the resulting supported catalysts gave better performance than those supported on commercial carbon black [67, 75].

A major challenge in the synthesis of CNTs and CNFs as supports for Pt electrocatalysts is to control the size and distribution of the Pt nanoparticles. Since the dispersion and particle size of Pt on the support material can strongly affect its utilization and catalytic activity [2], the synthesis of Pt nanoparticles supported by CNTs and CNFs are of fundamental and practical importance [63, 68, 76–79]. In a recent review, Lee et al. [80] described the various synthesis methods of the Pt electrocatalyst using CNTs and CNFs as the support of the Pt catalyst in the PEM fuel cell applications. The deposition, distribution, and crystalline size of Pt nanoparticles supported on CNTs and CNFs are significantly affected by factors including the synthesis method, oxidation treatment of CNTs and the Pt precursors. In this section, we will focus on the synthetic methods of depositing Pt nanoparticles onto CNTs and their morphology.

14.3.2 Methods for Depositing Pt Catalysts on Carbon Nanotubes (Pt/CNTs)

So far, many methods have been developed for the preparation of CNTs as a support for Pt catalysts. In principle, the preparation of CNTs as a support for Pt catalysts can be broadly divided into two categories: physical and chemical methods. The physical methods proceed with either the atomization of metals in a vacuum by thermal evaporation or sputtering while the Pt ions in a chemical synthesis method are reduced to neutral atoms. This is followed by particle growth. Compared with the physical methods, the chemical methods have the significant advantage of being able to easily control the primary structures of nanoparticles, such as size, shape, and composition, as well as to achieve mass production. A large variety of chemical methods have been reported for the preparation of CNTs as a support for Pt catalysts. Table 14.1 lists some selected examples of chemical methods used to prepare CNTs as a support for Pt catalysts that are relevant for fuel cell. Different growth control mechanisms and strategies are used in each of the different chemical deposition methods which are shown schematically in

Figure 14.6. For example, in the impregnation method, the size of the Pt nanoparticles is controlled by the structure of the support material which acts as the confining medium to restrict reaction, diffusion, and aggregation processes. In the colloidal method, the Pt size is controlled either by electrostatic hindrance or the addition of a protecting agent, which will adhere onto the surface of Pt nanoparticles. For the ion-exchange method, the surface groups of the support material provide the anchorage sites for the Pt particles and control the dispersion and distribution of the Pt nanoparticles. In this section, some examples of Pt deposition methods will be discussed.
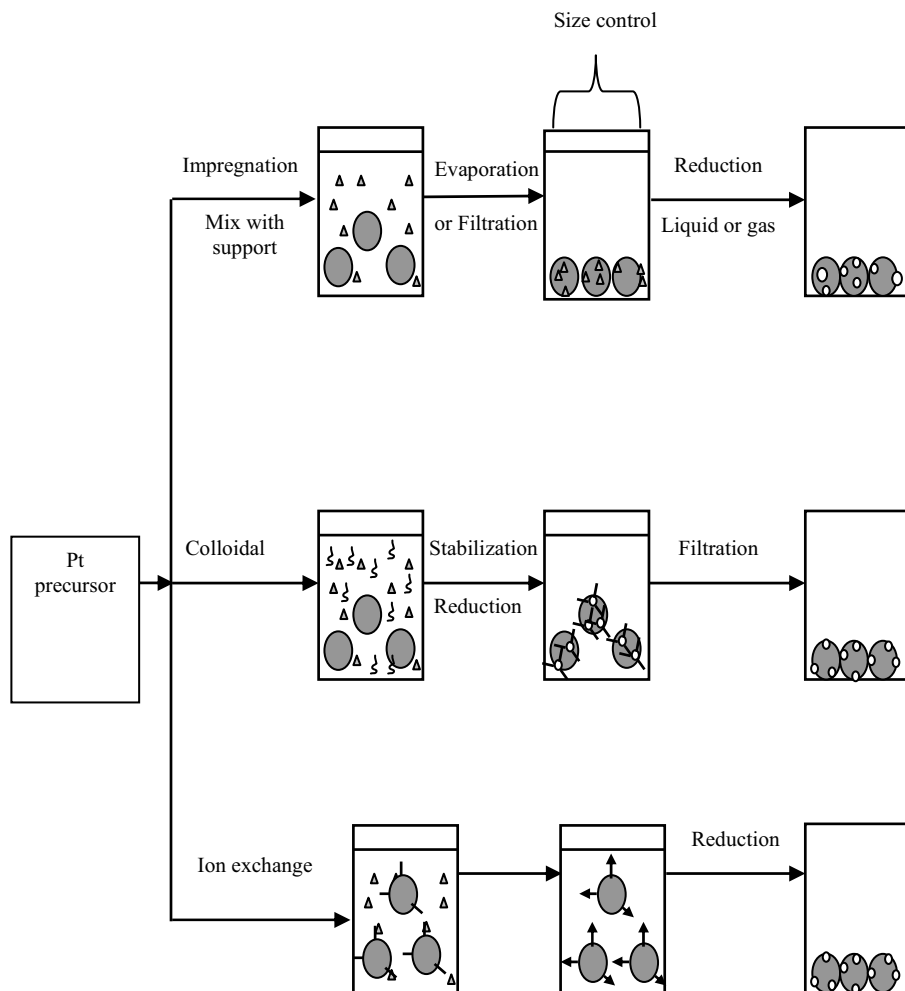
Figure 14.6. Schematic illustration of chemical methods to prepare Pt nanoparticles supported carbon nanotubes.

Preparation method	Support/Loading	Precursor	Size (nm)	Characterization	Electrode reaction	Ref.
Impregnation, ethylene glycol reduction	CNT/3.8–12% Pt	H_2PtCl_6, K_2PtCl_4	2–4	TEM, XPS	O_2 reduction in PEMFC	68
Impregnation, acetic acid reduction	CNT/0.42 mg/cm^2	Pt (II) acetylacetonate	2–3	TEM, XRD, XPS	O_2 reduction in PEMFC	70
Electrochemical deposition	SWNT	K_2PtCl_4	4–6	TEM, XRD, EDS	Methanol oxidation in H_2SO_4	90
Colloid	MWNT	H_2PtCl_6	2.2	TEM, XPS	O_2 reduction in H_2SO_4	100
Ion-exchange, H_2 reduction at 190 °C	MWNT/25 wt%	$Pt(NH_3)_2(NO_2)_2$	4.0	SEM, TEM, XPS	O_2 reduction in H_2SO_4	106
Microwave heated polyol	CNT/20 wt%	H_2PtCl_6	3.6	TEM, EDS, XPS	O_2 reduction in PEMFC	108
Sputtering	MWNT		2	SEM, TEM	–	116
	N-CNT	–	2	SEM, HRTEM, XPS	Methanol oxidation in H_2SO_4	118
Homogeneous deposition precipitation H_2 reduction at 200 °C	CNF/4.8 wt%	$Pt(NH_3)_4(NO_3)_2$	1–2	TEM, XPS	–	123
In situ polymerization	CNF	Pt (II) acetylacetonate	1–4	TEM, XPS	O_2 reduction in H_2SO_4	125
Electrochemical deposition	GCNF	H_2PtCl_6	40–50	SEM, EDS	Methanol oxidation in H_2SO_4	124
	NW/0.10 mg/cm^2	K_2PtCl_4	4–6	SEM, TEM	O_2 reduction, methanol oxidation in H_2SO_4	143

Table 14.1. Summary of synthesis methods for CNTs, CNF and NW-supported Pt nanoparticles with catalytic properties for fuel cell electrodes

14.3.2.1 Impregnation Method

The impregnation method is the most widely used wet-chemical method. This method is a simple and straightforward for depositing metal catalyst on the carbon support for the preparation of the PEM fuel cell catalysts and is thus an attractive choice for large-scale synthesis [66, 68, 81, 82]. This method involves the impregnation of the support material with a salt solution containing the metal to be deposited. This is followed by a reduction step. The procedure is shown schematically in the top flow line of Figure 14.6. During the impregnation step, a Pt precursor, e.g., $PtCl_6^{-2}$, is mixed with CNTs in aqueous solution to form a homogeneous mixture. The reduction step can be chemical or electrochemical. The chemical reduction step can either be carried out by liquid phase reduction using borohydride, formic acid or hydrazine as a reductive agent, or by a gas phase reduction using a flowing hydrogen gas as a reductive agent under elevated temperature. During the impregnation process, many factors can affect the size and size distribution of Pt nanoparticles. The chemical modifications of the surface of CNTs will play a major role in the deposition of Pt nanoparticles as the pristine surface of CNTs is relatively inert. An improved method is to functionalize the surface of CNTs first through a chemical reaction. The functionalization of CNTs will be discussed in Section 14.3.4.
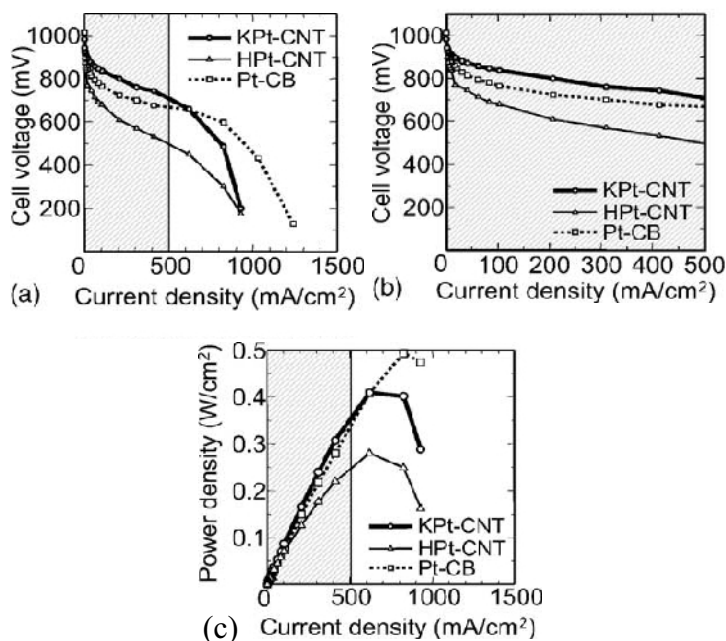
Figure 14.7. Current potential curves for the Pt-CB, the HPt-CNT, and the KPt-CNT electrodes. The curves below 500 mA/cm² were enlarged in (b). (c) Power current curves for the Pt-CB, the HPt-CNT, and the KPt-CNT electrodes [68]. (Reprinted from Catalysis Today, 90(3–4), Matsumoto T, Komatsu T, Nakano H, Arai K, Nagashima Y, Yoo E, et al. Efficient usage of highly dispersed Pt on carbon nanotubes for electrode catalysts of polymer electrolyte fuel cells, 277–81, ©2004, with permission from Elsevier.)

   Matsumoto and co-workers [68] synthesized Pt nanoparticles supported on CNTs using two Pt compounds; $H_2PtCl_6 \cdot 6(H_2O)$ or K_2PtCl_4. In their experiments, CNTs were heated and stirred with Pt compound in ethylene glycol at 40 °C for 2 h. Then this solution was added into 50 ml of 14 N HHO_3 and filtered. A commercial carbon black supported Pt (Pt-CB) electrocatalyst was used as a reference to compare the electrode's performance. Figure 14.7 shows the fuel cell performance for the KPt-CNT, HPt-CNT, and Pt-CB electrodes. They found that the Pt supported CNT electrodes showed comparable performance to the Pt-CB electrodes in Figure 14.7(a), and the KPt-CNT electrodes showed the highest voltages below 500 mA/cm^2 in Figure 14.7(b). The higher voltages of the KPt-CNT suggest either the formation of more effective triple-phase boundaries on the KPt-CNT electrodes than the other two electrodes or a higher conductivity compared to the Pt/CB electrodes. The electric power densities produced using the Pt/CNT electrodes are greater than that of the Pt/CB by a factor of two to four on the basis of the Pt load per power (see Figure 14.7(c)).
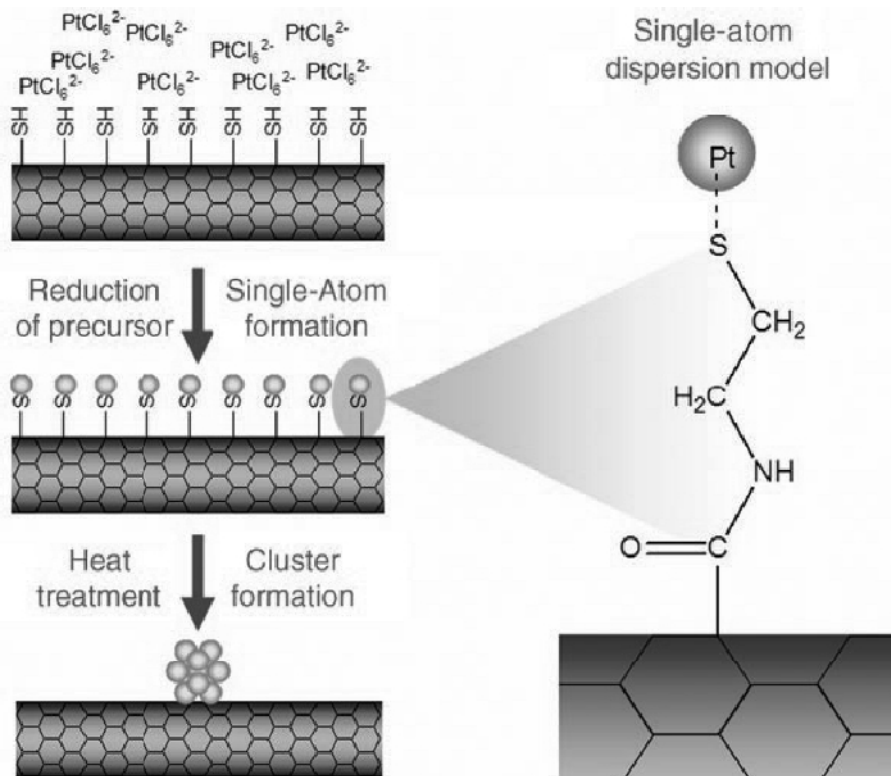
Figure 14.8. Single-atom-to-cluster approach for the formation of size-controlled Pt clusters on CNTs [83]. (Kim Y-T, Ohshima K, Higashimine K, Uruga T, Takata M, Suematsu H, et al. Fine size control of platinum on carbon nanotubes: from single atoms to clusters. Angew Chem Int Ed 2006;45:407–11. Copyright Wiley-VCH Verlag GmbH & Co. KGaA. Reproduced with permission.)
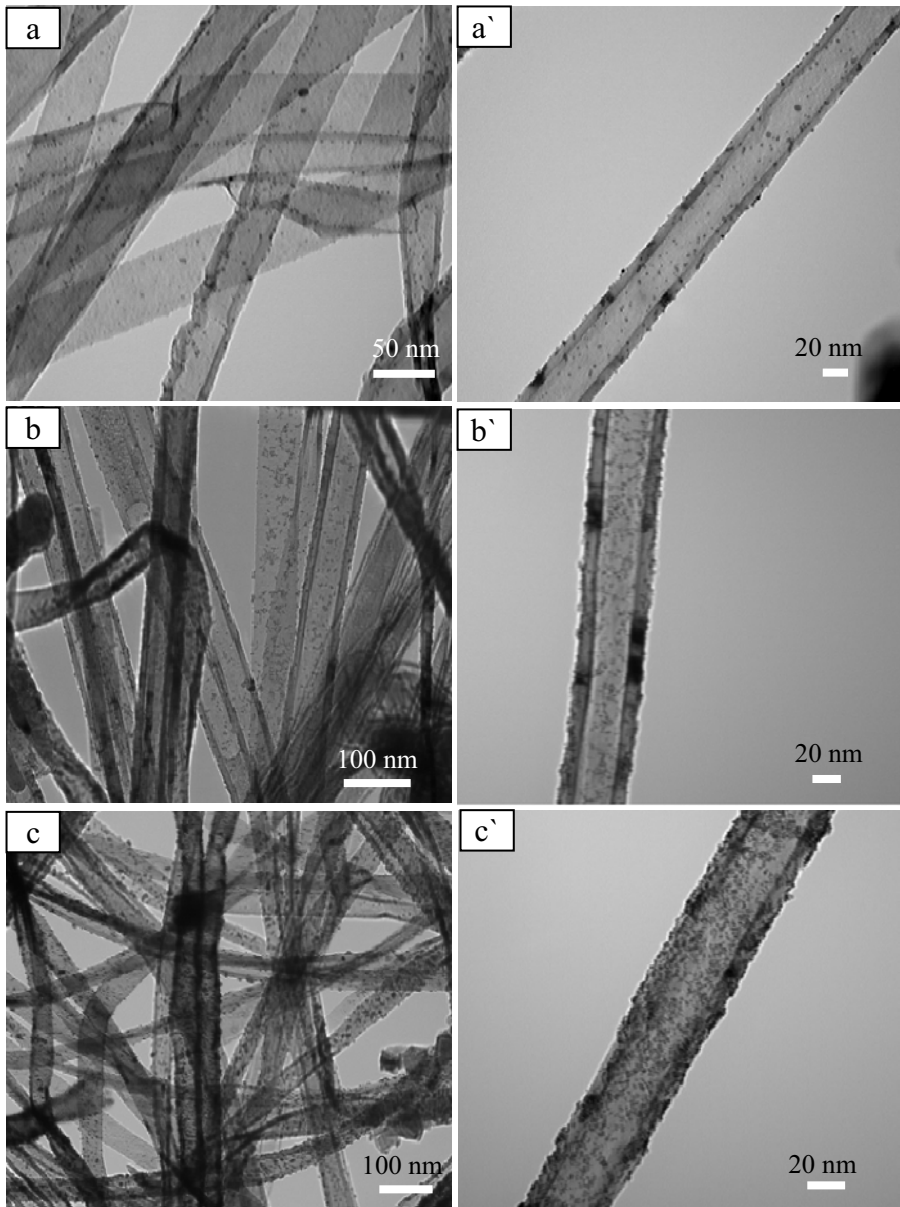
Figure 14.9. TEM images of Pt nanoparticles deposited on the CNTs/carbon paper from different concentrations of Pt precursor (a) 1 mM, (b) 2 mM and (c) 4 mM in glacial acetic acid. Right panel: Pt nanoparticles deposited on single CNT. The corresponding Pt loadings on the CNTs are 0.11, 0.24 and 0.42 mg_{Pt} cm^{-2} [70]. (Reprinted from Journal of Power Sources, 177(2), Saha MS, Li R, Sun X, High loading and monodispersed Pt nanoparticles on multiwalled carbon nanotubes for high performance proton exchange membrane fuel cells, 314–22, ©2008, with permission from Elsevier.)

Recently, Kim and co-workers [83] have proposed a new approach for the preparation of highly dispersed and size controlled Pt clusters on CNTs. They named this the single-atom-to-cluster approach and it is shown schematically in Figure 14.8. The key factor of this approach is the introduction of surface thiol groups on the CNTs. In their experiments, purified CNTs were stirred in concentrated H_2SO_4 and HNO_3 for 15 min in order to functionalize the CNTs; then they were chlorinated by refluxing for 12 h with $SOCl_2$ at 70 °C. The surface thiolated CNTs were carried out by a reaction with $NH_2(CH_2)_2SH$ in dehydrated toluene for 24 h at 70 °C. The Pt precursor was simultaneously reduced and supported on the thiolated CNTs by using $NaBH_4$ to form a monolayer of single Pt atoms. The heat treatment of the single Pt atoms that were supported on the CNTs was performed for 10 min at various temperatures followed by slow quenching to room temperature to form Pt clusters from single atoms. They found that the Pt clusters size can be controlled by heat treatment of Pt supported by CNTs. The high dispersion of Pt clusters i.e., small particle size and narrow size distribution was obtained by this method.

The synthesis of highly dispersed Pt nanoparticles with controlled loadings on CNTs remains a tough challenge because of the inertness of the CNT surface [80]. More recently, Saha et al. [70] developed a novel synthetic method for preparing uniformly dispersed high loading Pt nanoparticles on CNTs which were grown directly on carbon paper. The method consists of the treatment of the CNTs with glacial acetic acid which reduces the Pt ion on to the CNTs surface. Platinum acetylacetonate was added into glacial acetic acid and it was agitated in an ultrasonic bath for 10 min at room temperature. Then the CNTs grown on carbon paper were added to the solution and sonicated for 2 min. The beaker was placed on a hot plate and heated at a temperature of 110–120 °C for around 5 h under constant stirring. Afterward, the CNTs containing the Pt nanoparticles were washed with deionized water and dried at 90 °C over night in a vacuum oven. The monodispered Pt particles on the surface of the CNTs have a size between 2–4 nm depending on concentrations of the Pt precursor as shown in Figure 14.9. X-ray photoelectron spectroscopy analysis indicates that the glacial acetic acid, which acted as a reducing agent, had the capability to produce high density, oxygen-containing functional groups on the surface of CNTs which leads to high density and monodispersed Pt nanoparticles.

14.3.2.2 Electrochemical Method

Electrodeposition offers a novel way to deposit many metals, selectively, at desirable locations in the substrate through easily controlling the nucleation and growth of the metal nanoparticles. Pulse current, direct current and cyclic voltammetry are utilized to deposit Pt nanoparticles using the electrochemical methods. The electrochemical method has been used to deposit Pt onto carbon substrates at the anodes and cathodes of PEM fuel cells to improve the Pt utilization and reduce the Pt loading [84–86]. With the electrochemical method, the Pt loading can be reduced ten-fold without any significant loss of cell performance as compared to the conventional deposition technique [84]. Electrodeposition of Pt nanoparticles on CNTs has recently been reported by several groups [73, 87–90]. With the careful choice of substrate, deposition potential, and growth time, it is

possible to deposit nanoparticle with a high degree of monodispersity w.r.t. particle size [91–93].

Recently, an approach for the deposition of Pt particles with a narrow size distribution on CNTs was developed by Guo and Li [90, 94], involving three steps: (1) a gentler electrochemical activation of CNTs to introduce various oxide functional groups such as quinonyl, carboxyl, or hydroxyl groups without further damage of the CNTs, (2) formation of the octahedral complexes of Pt(IV) with functional groups on the surface of CNTs, (3) transformation of the CNTs surface complexes to Pt nanoparticles. The method for depositing Pt nanoparticles is shown schematically in Figure 14.10. Their TEM images revealed that the Pt nanoparticles are well dispersed in the CNTs that have a diameter of 4–6 nm [90].
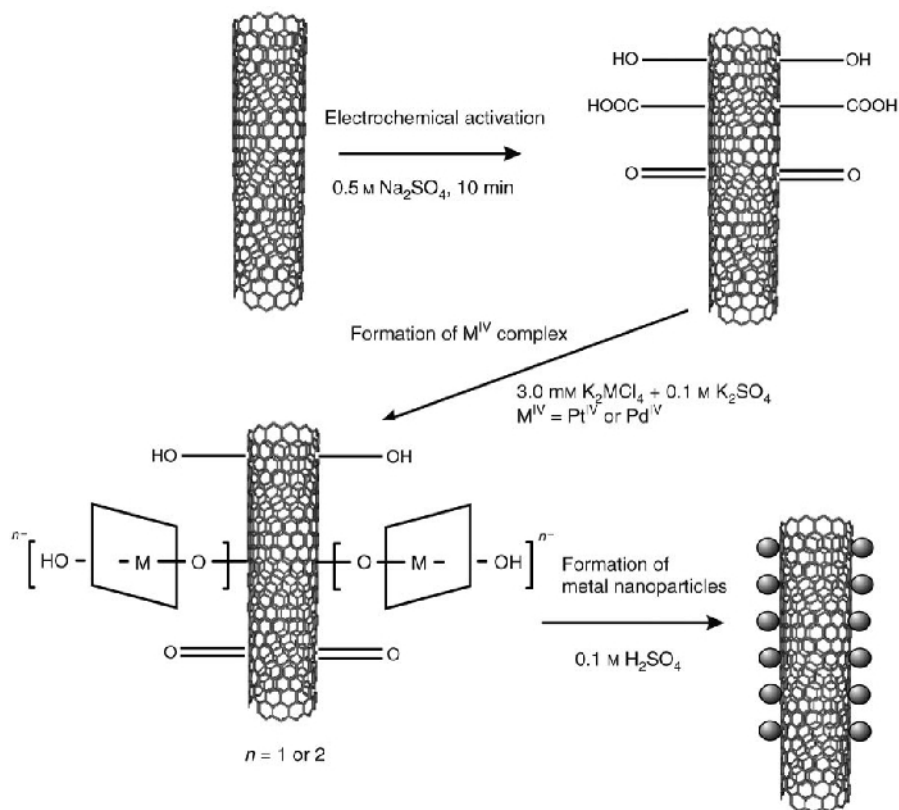
Figure 14.10. A schematic diagram illustrating three-step electrochemical deposition of Pt nanoparticles onto CNTs [90]. (Reprinted from Journal of Electroanalytical Chemistry, 573(1), Guo D-J, Li H-L, High dispersion and electrocatalytic properties of Pt nanoparticles on SWNT bundles, 197–202, ©2004, with permission from Elsevier.)

Direct potential control electrodeposition has been used for the formation of metal nanoparticles that are supported on CNTs [78, 95, 96]. For example, Day and co-workers [96] studied the nucleation and growth mechanisms of the electrodeposition of metals such as Ag and Pt onto nanostructures. In their study,

CNT networks were used as a template and the deposition of Pt was performed by stepping the potential from 0.0 V (where there was no electrode reaction) to –0.4 V (vs Ag/AgCl) for a period of 30 s and then back to an open circuit. This procedure allows the density and size of metal nanoparticles to be controlled by careful choice of the applied potential and deposition time. Figure 14.11 shows FE-SEM images taken after Pt deposition. A high density of nanoparticles was deposited close to the gold contact electrode within a distance of approximately 10 μm from the edge.
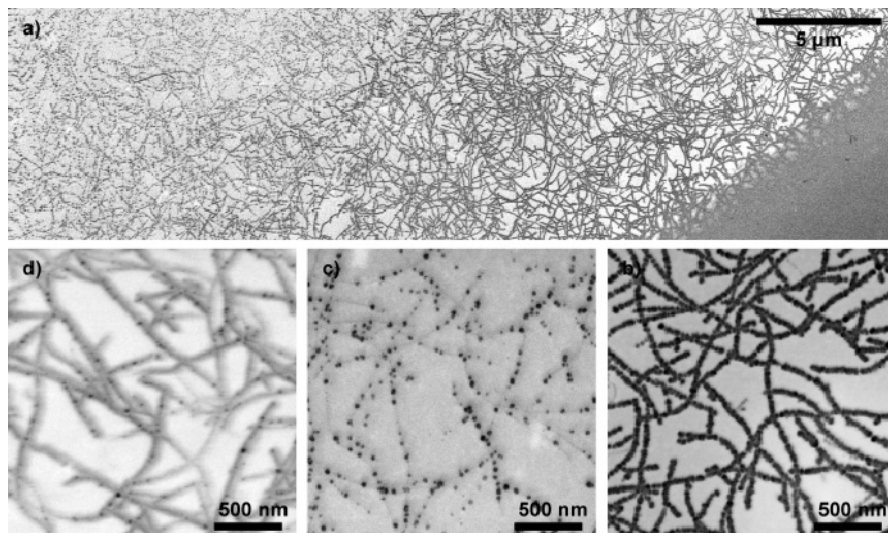
Figure 14.11. FE-SEM images showing (a) Pt deposited on CNTs from a solution containing 2 mM K_2PtCl_6 in 0.5 M perchloric acid by direct electrodeposition method. A deposition potential and time of –0.4 V (vs Ag/AgCl) and 30 s were used. The CNT network density was 6.8 μmSWNT μm^{-2}. In the bottom right of the image is the Au contact electrode which was also exposed to solution. (b)-(d) are higher resolution FE-SEM images: (b) close to, (c) ca. 15 μm from, and (d) further away (ca. 25 μm) from the contact electrode [96]. (Reprinted with permission from J Am Chem Soc 2005;127:10639–47. Copyright 2005 American Chemical Society.)

Another approach to controlling the electrodeposition of nanoparticles on pristine CNTs' surfaces was again reported by Day and co-workers [97]. The authors electrodeposited metal nanoparticles on pristine CNTs networks using a microcapillary electrochemical cell. Figure 14.12 illustrates a schematic of the microcapillary experimental setup. In their experiment, a microcapillary filled with the metal solution and a reference electrode is placed in contact with CNTs network, which is connected as a working electrode. Electrodeposition is promoted by applying a potential between the CNT network and the reference electrode. It was shown that by controlling the deposition potential and time, the number density, distribution, and nanoparticle size able to be controlled.
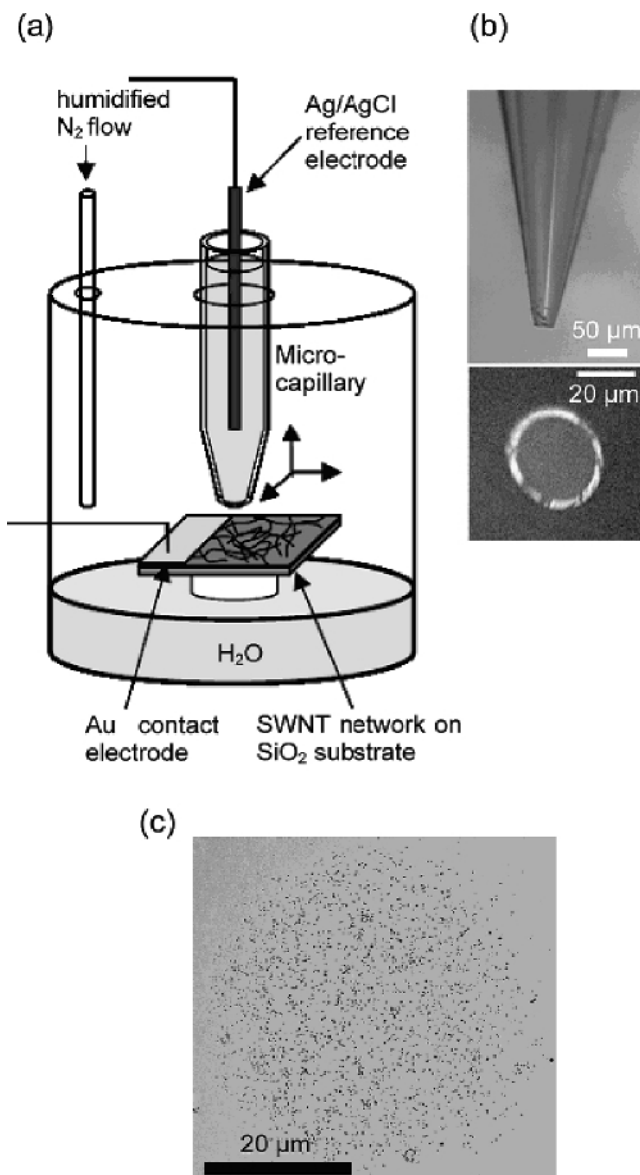
Figure 14.12. (a) Schematic of the microcapillary experimental setup. The substrate comprised a two-dimensional interconnected network of CNTs on a Si/SiO$_2$ surface. A gold band was evaporated onto the substrate to electrically connect the CNTs. A microcapillary, containing the electrodeposition solution, was positioned at different locations on the substrate using x,y,z micropositioners. (b) Optical images of the tip of a typical microcapillary side-on (top image) and end-on (bottom image). (c) FE-SEM image showing an area of electrolytically deposited Pt nanoparticles (deposition time and potential of 30 s and –0.3 V, respectively) on a CNT network over an area defined by the inner dimensions of the microcapillary [97]. (Reprinted with permission from Nano Lett 2007;7:51–7. Copyright 2007 American Chemical Society.)

Additionally, a hybrid thin-film electrode of CNTs containing Pt nanoparticles and [tetrakis(*N*-methylpyridyl)porphyrinato]cobalt (CoTMPyP) was fabricated by Qu et al. [88]. At first a $PtCl_6^{2-}$ layer was absorbed on the surface of the CoTMPyP-modified nanotube electrode through electrostatic interaction. This layer was then reduced electrochemically to yield Pt nanoparticles under constant potential at −0.7 V. They found that the hybrid film electrode exhibited high electrocatalytic activity for oxygen reduction to produce H_2O through a four electron pathway reduction with high stability.

14.3.2.3 Colloidal Method

In recent years, there has been considerable interest in the development of colloidal methods to prepare Pt catalysts supported on CNTs with a narrow particle size distribution [71, 98–102]. Usually, this method involves the preparation of a platinum metal colloid, followed by adsorption on the support, or in the formation of a Pt oxide colloid, followed by simultaneous reduction and adsorption, or adsorption followed by chemical reduction. The procedure is shown schematically in Figure 14.6. In the colloidal method, the size of the Pt nanoparticles is largely controlled or stabilized by the protecting agents, such as ligands, surfactants or polymers [103]. The colloidal metal nanoparticles are stabilized by either steric hindrance or by electrostatic charges. For example, Li and co-worker [100] used surfactant 3-(*N,N*-dimethyldodecylammonio) propanesulfonate (SB12) as a stabilizer to prepare Pt nanoparticles supported on CNTs by methanol reduction of H_2PtCl_6 [99, 100]. Before deposition of the Pt nanoparticles, an oxidative treatment of the CNTs was employed by an H_2SO_4-HNO_3 mixture to generate the carboxyl on the surface of the CNTs. The Pt nanoparticles were deposited on the functionalized CNTs by using the SB12-stabilized methanol reduction method. Well-dispersed Pt nanoparticles of an average size of 2.2 nm were produced on the external walls of the CNTs as shown in Figure 14.13 [100].

Though the colloidal method can provide a narrow size distribution of metal nanoparticles, the major drawback is the presence of a protecting agent, which may hinder the catalytic performance of the nanoparticles. Of course, the organic protecting shell can be removed by washing it in an appropriate solvent or by decomposition at an elevated temperature in an inert atmosphere. Therefore, it would be preferable to use the alternative route of preparing colloidal nanoparticles without the use of protecting agents. For example, Yoshitake and coworkers [101] reported that the use of $NaHSO_3$ and H_2O_2 appears to be suitable for the preparation of Pt oxide colloids without the use of a protecting agent. They used a single-walled carbon nanohorn (SWNH) as a support material. A SWNH is a new type of carbon nanotube with a horn-shaped sheath of single-walled graphene sheets. The fuel cell performance prepared with this method showed 20% higher performance than that of conventional Pt/C catalysts.

It was recently reported that the colloidal Pt nanoparticles may be protected by glycol, which serves as both a solvent and the protecting agent [71, 102]. For example, Kongkanand and co-workers [102] used ethylene glycol as a reducing agent to prepare well-dispersed Pt catalysts supported by polymer-wrapped CNTs. In their procedure, the CNTs were sonicated in *N,N*-dimethylformamide for 15 h to break up the nanotube bundles into individual CNTs. However, polymer such as

polystyrene sulfonate were added to the CNTs prior to 15 h sonication. Polystyrene sulfonate is expected to wrap around the individual CNTs by means of a thermodynamic driving force in order to reduce the hydrophobic interface between the tubes and polar solvent. The Pt nanoparticles were supported on these polymer-wrapped CNTs by the colloidal method. The Pt colloidal solution was synthesized using the reduction of $PtCl_4^{2-}$ by ethylene glycol at a pH of 12.5. These polymer-wrapped CNTs with Pt nanoparticles deposited on them have very high electrochemically active surface areas as shown in Figure 14.14. The increase in utilization efficiencies for Pt catalysts on these CNT supports can be attributed to the increased surface areas and also the well-dispersed nature of the carbon support and catalyst [102].
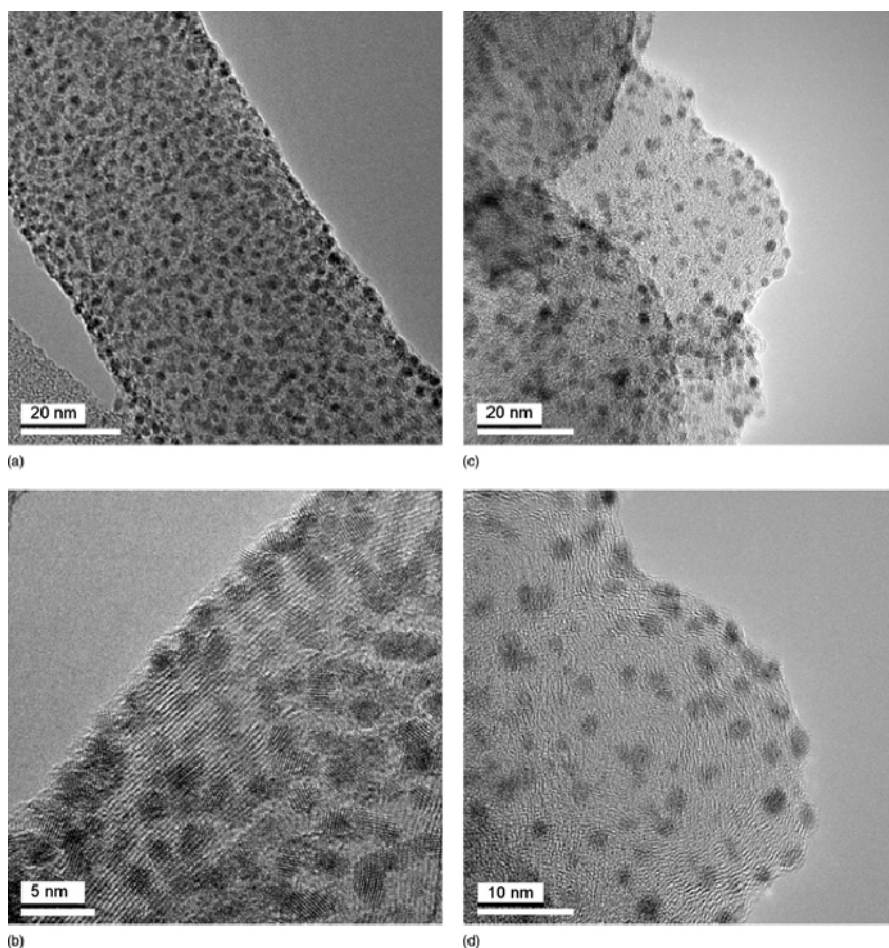
Figure 14.13. High-resolution TEM bright-field images of supported Pt catalysts prepared by SB12-stabilized method: (a) Pt/MWNTs-m, (b) Pt/MWNTs-m, (c) Pt/C, and (d) Pt/C [100]. (Reprinted by permission of ECS—The Electrochemical Society, from Li X, Ge S, Hui CL, Hsinga I-M. Well-dispersed multiwalled carbon nanotubes supported platinum nanocatalysts for oxygen reduction.)
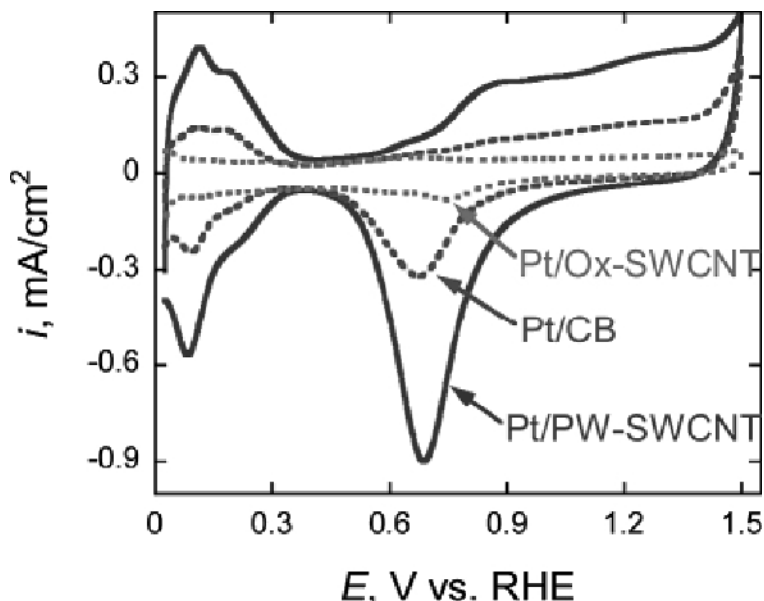
Figure 14.14. Cyclic voltammograms for Pt/PW-SWCNT, Pt/Ox-SWCNT, and Pt/CB recorded in 0.1 M HClO$_4$ at a scan rate of 0.02 V/s. The Pt loadings were 14 µg/cm^2 [102]. (Reprinted with permission from J Phys Chem B 2006;110:16185–89. Copyright 2006 American Chemical Society.)

14.3.2.4 Ion-exchange Method

An ion-exchange method is an effective technique for depositing Pt metal particles on the CNTs without using protective colloiding agents, reducing agents or precursor complexes which are not easy to decompose [104–106]. In this technique, a Pt cation complex such as $[Pt(NH_3)_4]^{2+}$ was ion-exchanged with hydrogen ions of the acid functional groups on the surface of the CNTs. The interaction between the acid functional groups and the Pt precursor affects the dispersion of the Pt particles. After the ion-exchange process, the Pt cation complex is reduced to Pt nanoparticles in an H$_2$ atmosphere. Yin and co-workers used an *in situ* ion-exchange method for preparing the electrode composed of Pt particles on the CNTs [104, 106]. In their experiments, the CNT electrode was electrochemically functionalized to generate the carboxyl functional groups on the surface of CNTs. Then the electrochemically functionalized CNT electrode was immersed in a solution of the platinum cation-complex salt for 48 h. As a result of this immersion, the hydrogen ions of the functional group on the surface of the CNT electrode undergo an ion-exchange process with the platinum cation complex. The immersed CNT electrode was then filtrated and washed with distilled water. Sufficient washing is important for obtaining a highly dispersed electrocatalyst. Reduction of the adsorbed platinum complex precursor to its metallic form was carried out by the treatment with hydrogen gas at 190 °C. They observed the Pt nanoparticles to be highly dispersed on the CNTs and their dispersion is much better than the catalyst prepared by the borohydride method [106].

14.3.2.5 Microwave Heated Polyol Method

Microwave irradiation through dielectric heating loss is fast, simple, uniform, energy efficient and has been widely used in preparative chemistry and materials synthesis [107]. Recently, there has been more reported successes in preparing high purity Pt or Pt-Ru nanoparticles supported on CNTs by a microwave-assisted polyol process [108–112]. The polyol process is normally used in preparing colloidal metal particles [113]. In the process, the polyol (most commonly ethylene glycol) solution containing the metal salt is refluxed at 120–170 °C to decompose the polyol to yield an *in situ* generated reducing species for the reduction of the metal ions to their elemental states [108, 110, 112]. The fine metal particles produced could additionally be captured by a support material suspended in the solution. Conductive heating is often used, but microwave dielectric loss heating may be a better synthesis option in view of its energy efficiency, speed, uniformity, and implementation simplicity [107]. In addition, the homogeneous microwave heating of the liquid samples could reduce the temperature and concentration gradients in the reaction medium, thus providing a more uniform environment for the nucleation and growth of metal particles. For example, Liu and coworkers [108] used a microwave-assisted polyol process for the synthesis of Pt nanoparticles supported on CNTs. Their synthesis procedure can be outlined as follows: an aqueous solution of H_2PtCl_6 is mixed with ethylene glycol and the pH of the solution is adjusted by the addition of KOH. Then, the purified CNTs are uniformly dispersed in the mixed solution by ultrasound. After a period of heating in a microwave oven, the resulting CNTs are then filtered and the residue is washed with acetone and dried at 100 °C over night in a vacuum oven.

The pH value of the Pt precursor solution is an important factor for the preparation of Pt/CNTs catalysts by the polyol process. The effect of the pH on the Pt particles' size and distribution were investigated by Li et al. [112]. In their experiments, the pH of the solution was adjusted to the desired value (3.4–9.2) by the addition of a KOH solution. Figure 14.15 shows TEM images of Pt/CNTs prepared by the microwave polyol process using different values of pH. At a lower pH range (pH 3.6–5.8), the Pt nanoparticles are agglomerated and not as well dispersed on the CNT surfaces. On the other hand, there was less agglomeration and a more uniform dispersion of Pt nanoparticles that are formed in the pH range of 7.4–9.2. Therefore, pH value in the solution plays an important role in controlling the Pt particle size and distribution. They also proposed the following mechanism to explain the pH effect during the formation of the Pt nanoparticle in ethylene glycol solution:

$$CH_2OHCH_2OH = CH_3CHO + H_2O \tag{14.1}$$

$$2CH_3CHO + (PtCl_6)^{2-} + 6OH^- = 2CH_3COO^- + Pt + Cl^- + 4H_2O \tag{14.2}$$

The acetate form in the second reaction will possibly form chelate-type complexes via its carboxyl groups and can also act as a stabilizer for the Pt metal collides,. At a low pH, the interactions between the Pt particles and acid form (acetic acid) are smaller. Therefore, Pt nanoparticles prepared at a low pH should be unstable and more agglomerated, thus have a larger size and a wider size distribution.
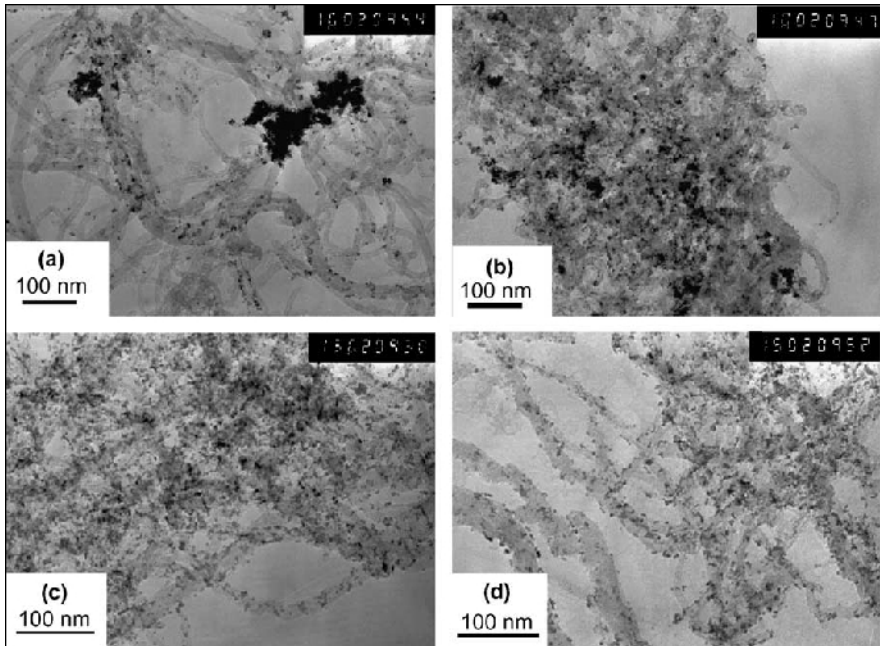
Figure 14.15. TEM images of microwave-synthesized Pt/CNTs from the ethylene glycol solutions of H_2PtCl_6 with different pH in the presence of CNTs: (a) pH = 3.6; (b) pH = 5.8; (c) pH = 7.4 and (d) pH = 9.2 [112]. (Reprinted from Carbon, 43(10), Li X, Chen W-X, Zhao J, Xing W, Xu Z-D, Microwave polyol synthesis of Pt/CNTs catalysts: Effects of pH on particle size and electrocatalytic activity for methanol electrooxidization, 2168–74, ©2005, with permission from Elsevier.)

14.3.2.6 Sputtering Method

Deposition of Pt metals on a carbon gas diffusion media by sputtering is an approach to reduce the Pt loading and enhance the catalyst utilization in fuel cells [114, 115]. Sputtering deposition techniques can produce a highly uniform particle distribution and the fabricating process is relatively simple. The particle size is determined by controlling the sputtering time and current. Recently, Hirano et al. [115] reported promising results using a thin layer of Pt that was deposited on wet proofed non-catalyzed gas diffusion electrode (equivalent to 0.01 mgPt/cm^2) by a sputtering technique. This demonstrated similar results as compared to a conventional Pt/C (0.4 mgPt/cm^2) electrode that can be obtained commercially. Later Cha and Lee [114], used an approach containing multiple sputtered layers (5 nm layers) of Pt interspersed with Nafion, carbon black and isopropanol ink (total loading equivalent of 0.043 mgPt/cm^2) which exhibited equivalent performance to conventional commercial electrodes with 0.4 mgPt/cm^2. Based on their results, sputtering is considered a new method of applying the Pt catalyst and necessitates a new methodology for creating the membrane electrode assembly (MEA) structure [114].

More recently, sputtering deposition techniques were used to produce thin platinum films on the surface of CNTs [116–118]. According to Chen et al. [116],

the sputtering deposition method could generate highly uniformed Pt nanoparticles on CNTs compared to those produced by the electroless deposition method. In their experiments, the CNTs were synthesized directly on the carbon cloth by a bias-assisted microwave plasma enhanced CVD method and the Pt nanoparticles were subsequently deposited on the CNTs.

A further adaptation of the sputtering deposition techniques found in the literature is to deposit Pt nanoparticles on nitrogen-containing CNTs (N-CNTs) for μDMFC applications [118]. A great deal of attention has been devoted to the N-CNTs [119, 120]. It has been reported that the N-CNTs have many advantages over general CNTs including the enhancement of interaction between the nanotube surface and the deposited Pt nanoparticles [121]. In the effort of Sun et al. [118], N-CNT arrays were grown on a Si substrate by microwave-plasma-enhanced CVD first and then used as a template for the Pt particles. The Pt nanoparticles were deposited on the sidewalls of N-CNTs over a large area using a DC sputtering method without any chemical pretreatment. TEM results showed that well-separated Pt nanoparticles would form with an average diameter of 2 nm on the bamboo-like structure of the N-CNTs as shown in Figure 14.16. Their results suggest that the nitrogen incorporation in the CNTs may play a critical role in the self-limited growth of the Pt nanoparticles. The cyclic voltammograms demonstrated that the Pt nanoparticles are indeed electrochemically active and thus promising for a future μDMFC device.
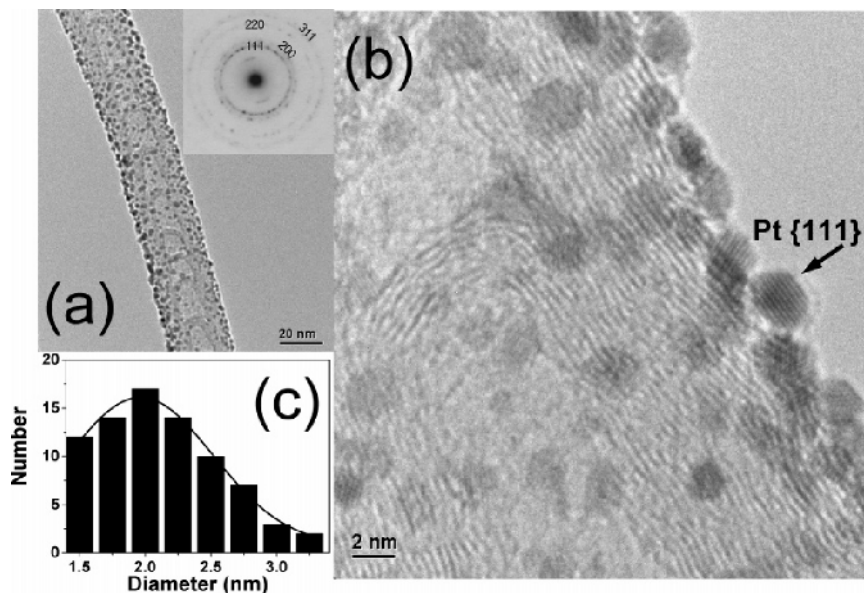
Figure 14.16. (a) TEM image of Pt nanoparticles on the sidewall of one single CNx NT with the corresponding SAED pattern in the inset. (b) HRTEM image of Pt nanoparticles on the sidewall of one single CNx NT. (c) A size histogram of Pt nanoparticles estimated from (b) [118]. (Reprinted with permission from Chem Mater 2005;17:3749–53. Copyright 2005 American Chemical Society.)

While the sputtering technique works well for the direct deposition method, the main drawback is the durability. In most cases the deposition has a relatively poor adherence to the substrate and under the variable conditions of load and temperature there is a greater probability that the deposits will sinter or dissolute.

14.3.3 Methods for Depositing Pt Catalysts on Carbon Nanofibers (Pt/CNFs)

In recent years, great interest has risen to adopt carbon nanofibers (CNFs) as a support of catalysts for PEM fuel cells due to their excellent mechanical, electrical and thermal properties [38, 67, 122–125]. A high dispersion of Pt nanoparticles supported on CNFs can be obtained due to their high surface area and unique structure mentioned previously [38, 67]. Additionally, the metal particles supported on the CNFs seem to be less susceptible to CO poisoning compared to the traditional catalyst systems [38]. In this section, the deposition of Pt nanoparticles on CNFs will be discussed.

Toebes and co-workers [123] prepared Pt catalysts supported by CNFs using $Pt(NH_3)_4(NO_3)_2$ as a precursor by homogeneous deposition precipitation (HDP) method. In the HDP method, the active phase or its precursor is deposited onto an existing support by slowly and homogeneously introducing the precipitating agent in such a way that the nucleation in the solution itself is avoided. In their experiments, a suspension of CNFs was introduced into demineralized water which was acidified to a pH of 3 with nitric acid and heated up to 90 °C under an inert atmosphere. Subsequently, urea and $Pt(NH_3)_4(NO_3)_2$ were added under vigorous stirring. The pH of the slurry was monitored to follow the process and to indicate its completeness. After 18 h the loaded CNFs were filtered and washed thoroughly with demineralized water, dried at 80° C in a nitrogen flow, and reduced in hydrogen at 200 °C for 1 h. Well-defined, CNFs-supported, Pt catalysts were prepared with a narrow size distribution, and a mean particle size of 1–2 nm.

Pt catalysts supported on graphite nanofibers for use as an electrode for fuel cell applications was investigated by Bessel et al. [38]. Three types of graphite nanofibers (ribbon, platelet and herringbone) were used as catalyst supports for platinum particle deposition by using the incipient wetness method. Catalysts consisting of 5 wt% platinum supported on "platelet" and "ribbon" type graphite nanofibers, which expose mainly edge sites to the reactants, were found to exhibit activities comparable to that displayed by about 25 wt% Pt on Vulcan carbon.

Zhang and co-workers [125] have developed a synthesis method for depositing Pt nanoparticles onto CNFs by an *in situ* polymerization of acrylonitrile in a porous anodic aluminum oxide (AAO) membrane template. Figure 14.17 shows a schematic diagram outlining the synthesis procedure. The author first fabricated a hexagonally packed porous AAO membrane by a two-step anodization using oxalic acid aqueous solution under a constant voltage of 40 V at 50 °C. Then, the pores are widened by a chemical etching in an aqueous 5% phosphorous acid solution at 30 °C. The AAO templates are immersed in a distilled acrylonitrile monomer (CH_3CH_2CN) containing 2, 2'-azo-bisisobutyronitrile and Pt(II) acetylacetonate. The polymerization and cyclization are carried out at 50°C and 220 °C, respectively, in the AAO templates for 10 h in air. The residual Al substrate is removed by dissolving it in a solution containing $CuCl_2$ and HCl. The

polyacrylonitrile (PAN) nanofibers in the AAO membrane were further pyrolyzed at 700 °C under a high vacuum for 6 h. Finally, the AAO template was dissolved in a NaOH aqueous solution. The Pt nanoparticles supported on the CNFs were then cleaned with distilled water, rinsed with ethanol and dried in liquid CO_2 to reduce the aggregation of nanofibers. They found that the Pt nanoparticles with an average size of 2.2 nm were produced using this method. It was observed that the Pt/CNFs catalyst exhibited higher onset potential for the oxygen reduction reaction and higher catalytic activity compared to that of Pt/C catalyst synthesized by a bulk polymer pyrolysis method without an AAO template.
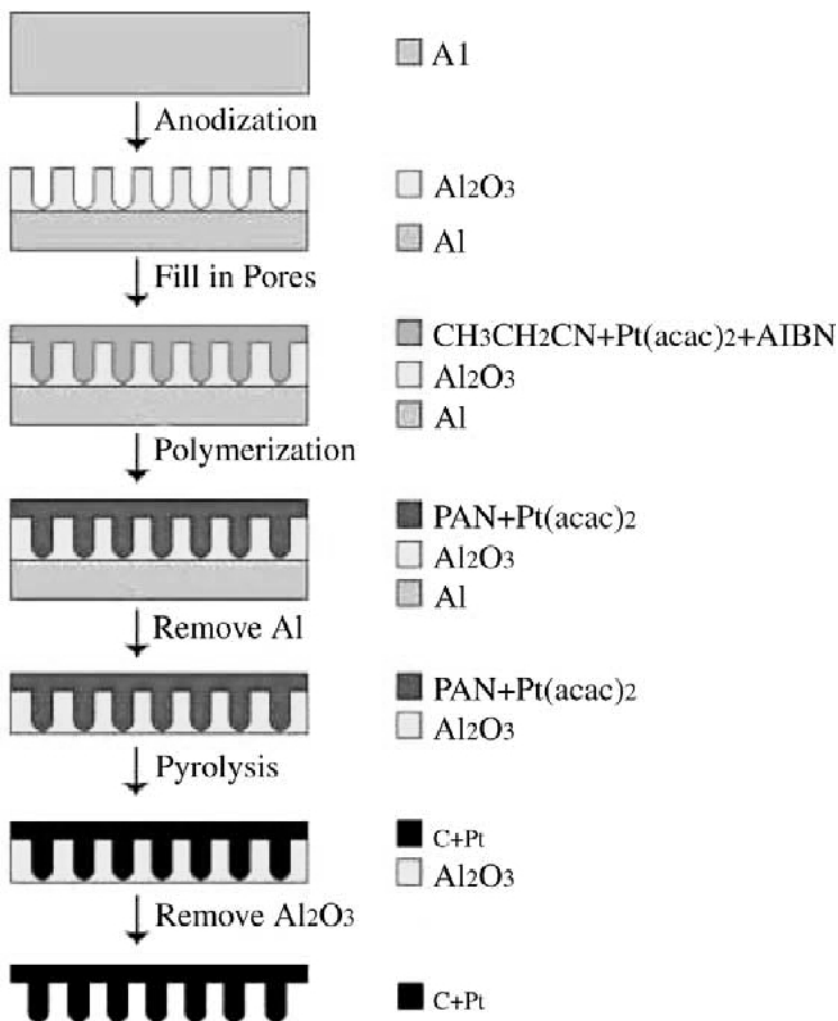
Figure 14.17. Schematic diagram of the fabrication of Pt-CNFs using an AAO membrane template [125]. (Reprinted from Chemical Physics Letters, 398(4–6), Zhang L, Cheng B, Samulski ET, *In situ* fabrication of dispersed, crystalline platinum nanoparticles embedded in carbon nanofibers, 505–10, ©2004, with permission from Elsevier.)

Tang and co-workers [124] employed an electrochemical method for the deposition of Pt nanoparticles on graphitic carbon nanofibers (GCNFs). In their efforts, Pt nanoparticles were electrodeposited on a GCNF/graphite working electrode from an acidic solution of H_2PtCl_6 by cyclic voltammetry under the condition of a deposition potential of $+0.1- -0.25$ V vs. SCE and a sweep rate of 15 mV/s. Before the Pt particle deposition, the GCNFs/graphite electrode was pretreated in 30 wt% HNO_3 aqueous solution for 40 min to remove the metallic nickel catalyst. To further increase the electrochemical activity of the surface of the GCNFs in the water solution, the GCNFs/graphite electrode was then cycled in the range of $-0.15 - +1.3$ V at a sweep rate of 50 mV/s in 0.5 M H_2SO_4 for 20 cycles. They observed that the Pt nanoparticles are uniformly dispersed on the whole surface of the GCNFs with a diameter of about 40–50 nm, which is smaller than that of the Pt/graphite electrode (100 nm).

14.3.4 Methods for Depositing Pt Catalysts on Metal Oxide Nanowires (Pt/NWs)

Apart from carbon nanotubes and carbon nanofibers, other one-dimensional (1D) nanostructured materials, such as nanowires, nanobelts and nanorods have received much interest due to their unique properties and extensive applications [45, 126–128]. Recently, a variety of 1D nanostructures with different compositions such as ZnO, SnO_2, WO_3, In_2O_3, CdO, MgO_2, MnO_2, TiO_2 and PbO_2 were successfully synthesized [129–131]. Unlike CNTs, nanowires (NWs) can be made of various compositions of materials with solid cores. For example, monometallic Pt, Au and Ag nanowires [132–134] and Pt nanowire networks [135] synthesized in highly ordered SBA-15 silica have been reported. The broader choice of various crystalline materials and easier doping methods provide highly tunable properties of NWs. For example, doping with indium (In) and antimony (Sb) can modulate the optical and electrical properties of SnO_2 NWs [136, 137]. Among various kinds of nanowires, certain metal oxide NWs have several unique advantages as supports for dispersing noble metal nanoparticles such as Pt for practical applications. First, unlike carbon black, metal oxide materials have catalytic properties. For example, SnO_2 nanoparticles combined with noble metal nanoparticles have enhanced the catalytic activities towards methanol oxidation [138, 139]. Second, there is a very strong interaction between Pt nanoparticles and the metal oxide surface. Third, gas permeability is expected to be high with the 3D electrode structure with nanowires that are grown on fuel cell backings like carbon paper. Finally, doping various elements into nanowires can be easily carried out to improve electronic conductivity, corrosion resistance, and thermal stability. Therefore, it is expected that integrated three-dimensional, nanowire-based, fuel cell electrodes will be ideal materials for providing a higher catalytic performance, higher catalyst utilization, a more efficient mass transport, and a longer fuel cell operational life. In collaboration with General Motors, Sun's group at the University of Western Ontario is exploring this direction in detail.

In 2007, Saha and co-workers [140] reported their studies on the metal catalysts supported on SnO_2 NWs prepared by the electrochemical deposition method. The uniqueness of the work compared to previous work reported in the literature is that

they were able to grow SnO_2 NWs directly on the carbon fibers of the carbon paper by a thermal evaporation method, followed by electrodeposition of the Pt nanoparticles onto the SnO_2 NWs [140]. Their novel process ensures that all the deposited Pt particles are in electrical contact with the external electrical circuit. The results from this study are the first demonstration of SnO_2 NWs-based composite electrodes consisting of Pt nanoparticles supported on SnO_2 NWs grown on carbon paper. Figure 14.18 shows the SEM and TEM images of the SnO_2 NWs grown on a commercially available carbon paper backing used in fuel cell applications. As shown in Figure 14.18(a), a thin layer of high-density SnO_2 NWs completely covers the surface of the carbon fibers in the carbon paper. The length of the SnO_2 NWs is in the range of 20 to 30 μm. Figure 14.18(c) presents the TEM image of the Pt nanoparticles electrochemically deposited on the SnO_2 NWs. Pt nanoparticles with a size of 4–6 nm can be observed clearly on the surface of NWs. Their results showed that higher electrocatalytic activities of the Pt/SnO_2 NWs/carbon paper composite electrode for both the oxygen reduction reaction and the methanol oxidation reaction have been achieved in comparison with standard Pt/C electrode. The higher electrocatalytic activities are attributed to the enhanced properties achieved by combining Pt nanoparticles with the SnO_2 NWs supports as well as the three-dimensional composite electrode structure. Such a hierarchical electrode with the combined properties will have potential applications for fuel cells.

At 3M Inc., a new class of support material, nanostructured thin film (NSTF), for PEM fuel cell applications has recently been developed [141, 142]. The NSTF support layer consists of a monolayer of oriented, crystalline, organic, whiskers structure that are obtained by thermal sublimation and the subsequent annealing of a red organic pigment. Catalysts are coated on top of the whiskers by chemical methods or by a vacuum deposition processes like sputtering, so as to encapsulate them with a polycrystalline thin film [141]. Figure 14.19 shows SEM images of the NSTF catalyst coated whiskers, roll-good fabricated by an all dry continuous process, prior to incorporation onto the surfaces of a PEM to form a catalyst coated membrane. The NSTF catalysts are comprised of high aspect ratio, elongated particles formed by vacuum coating catalyst thin films onto a monolayer of oriented, crystalline, organic whiskers [143]. The organic whiskers are highly inert thermally, chemically, and electrochemically. The thin film catalyst coating encapsulates the crystallized pigment whisker support particles, eliminating issues with oxidatively unstable supports. The thin film catalyst coatings consist of relatively large crystallite domains of nanoscopic particles, which give to the NSTF catalysts enhanced specific activity and resistance to loss of surface area by Pt dissolution [141, 142]. Most notable is the five-fold or greater gain in specific activity of the NSTF catalysts over high surface area dispersed Pt/carbon. However, one disadvantage with NSTF catalyst is its large Pt particle size (10–15 nm) and low electrochemical surface area (10 m^2/g_{Pt}).
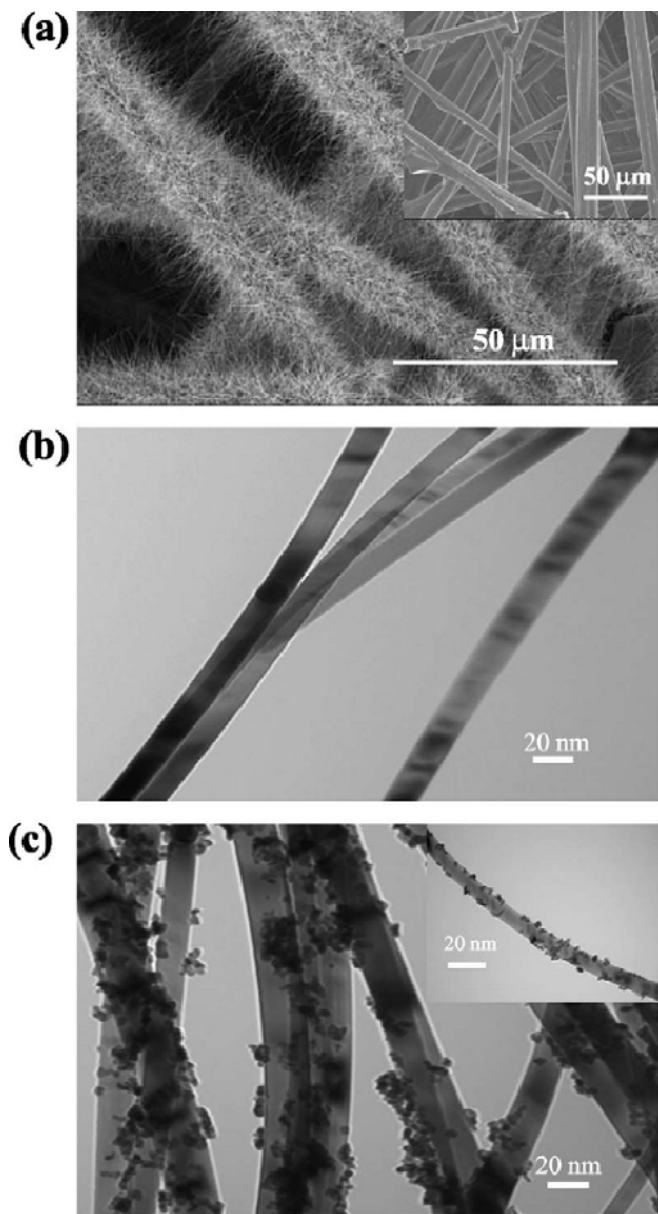
Figure 14.18. SEM and TEM micrographs of SnO_2 NWs grown on carbon fibers of carbon paper by thermal evaporation method. (a) SEM image showing full coverage of SnO_2 NWs on fibers of carbon paper. (Inset) Fibers of bare carbon paper. (b) TEM image showing individual SnO_2 NWs. (c) TEM images showing Pt nanoparticles electrochemically deposited onto SnO_2 NWs. (Inset) Pt nanoparticles deposited onto a single SnO_2 NW [70]. (Reprinted by permission of ECS—The Electrochemical Society, from Saha MS, Li R, Cai M, Sun X. High electrocatalytic activity of platinum nanoparticles on SnO_2 nanowire-based electrodes.)
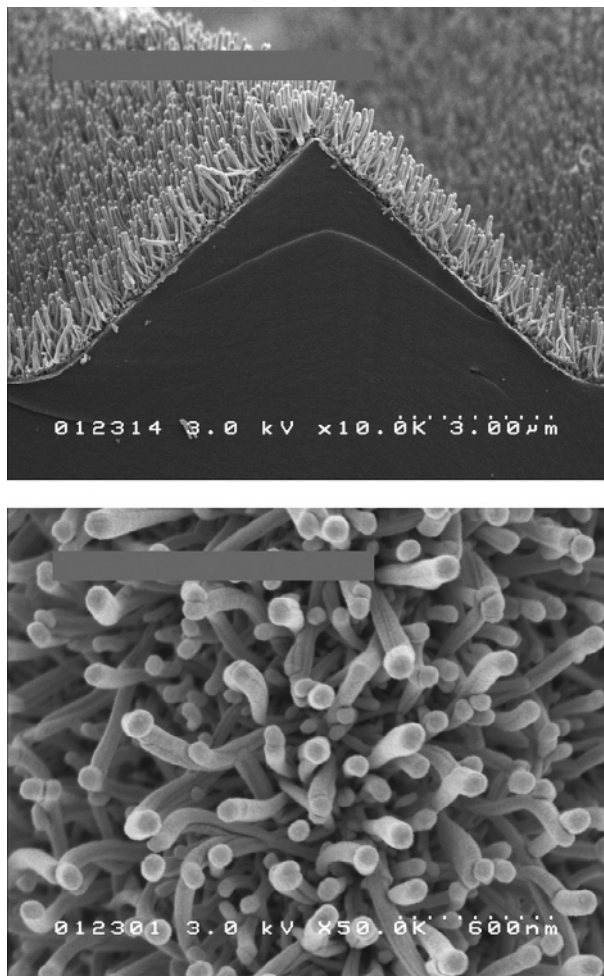
Figure 14.19. Scanning electron micrographs of typical NSTF catalysts as fabricated on a microstructured catalyst transfer substrate, seen (top) in cross-section with original magnification of ×10, 000, and (bottom) in planview with original magnification of ×50, 000. The dotted scale-bar is shown in each micrograph [141]. (Reprinted from Journal of Power Sources, 161(2), Debe MK, Schmoeckel AK, Vernstrom GD, Atanasoski R, High voltage stability of nanostructured thin film catalysts for PEM fuel cells, 1002–11, ©2006, with permission from Elsevier.)

14.3.5 Methods of Functionalizing of Carbon Nanotubes and Nanofibers-based Fuel Cell Electrodes

Much research has been conducted in the past decade in studying surface modification of carbon nanotubes. These efforts basically fall into two categories: covalent and non-covalent modification. Covalent surface modification of the reinforcing material involves a permanent change to the material surface such that it is functionalized with reactive groups which can later form a covalent bond with

another molecule [144, 145]. Non-covalent surface modification does not involve the formal chemical bond formation of a molecule and the surface of CNT. Examples of this type of interaction include Van der Waals forces, electrostatic forces, hydrogen bonding, and other attractive forces [146].

14.3.5.1 Covalent Functionalization

Surface Oxidation
Among various methods of functionalization, surface oxidation is probably the most widely used [147]. This treatment of CNTs can be performed by using different oxidants such as HNO_3, H_2SO_4, $KMnO_4$, $K_2Cr_2O_7$ and H_2O_2 [148–151]. The surface modification of CNTs could also be performed via an electrochemical method [94, 152]. As a result of this treatment, the aromatic conjugate ring system of the CNTs surface can be modified and the CNTs can be functionalized with functional groups such as hydroxyl (–OH), carboxyl (–COOH) and carbonyl (–C=O) [66, 153]. These surface functional groups have strong attraction forces toward metal ions than cling to the CNTs surface and some even have ion-exchange capabilities, such as the formation of carboxylic acid groups. Therefore, these surface functional groups serve as metal-anchoring sites to facilitate metal nuclei formation and electrocatalysts deposition. The chemical interaction between anchoring catalyst metal ions with a CNT functional surface could be proposed as following equation [147]:

$$CNT–COOH + M^+X^- \rightarrow CNT–COO^-M^+ + HX \quad (14.3)$$

where the carboxylic group on the CNT surface exchanges a proton with a metal ion (M^+).

The influence of the surface treatment on the deposition of Pt nanoparticles was investigated by Rajalakshmi et al. [66]. They functionalized the surface of CNTs by sonication and pre-treatment with 70% nitric acid. Compared with untreated CNTs, more uniform distribution of Pt nanoparticles of size about 3–5 nm was obtained for surface treated CNTs. The particle size of Pt may be correlated with the oxidation of CNTs, indicating that the efficient deposition of Pt nanoparticles is due to a strong interaction between the metal salt precursor and the functional surface group of oxidized CNTs. The Pt nanoparticles catalysts supported on CNTs were tested in a polymer electrolyte membrane fuel cell to test the oxygen reduction reaction. The electrode prepared with a catalyst pre-treated with HNO_3 gave a cell voltage of 680 mV at 500 mA/cm^2, whereas the other electrodes with catalysts treated by sonication gave a 40 mV lower performance.

Xu and co-workers [149] also investigated the effect of the treatment process on the deposition of Pt-nanoparticles onto CNTs. They found that the refluxing with the mixture solution of H_2SO_4 and HNO_3, and the immersion in the H_2O_2 solution are effective pretreatment methods for the depositing of Pt nanoparticles on the CNT's surface. The hybrid process, a treatment process with a H_2O_2 solution after the refluxing with the mixture solution of sulfuric and nitric acids, brought about the best effectiveness and obtained Pt-nanoparticles with a size of 3

nm on the CNT's surface, which exhibited the best catalytic properties in the PEM fuel cell.

Yu and co-workers [105] treated CNTs by using mixed acids (HNO_3-H_2SO_4). They proposed a mechanism of Pt deposition on the CNTs as shown in Figure 14.20. When CNTs are refluxed with a mixture of HNO_3-H_2SO_4, the surface graphitic layers of CNTs would react with the oxidants and produce a high density of various surface functional groups, such as carboxyl, carbonyl and phenolic groups. Upon the Pt ions introduction into the system, they would interact with and attach to these surface functional groups through an ion-exchange or coordination reaction and serve as nucleation precursors. Upon reduction of the surface Pt^{2+} ions by hydrogen, a well-dispersed deposition of the Pt metal nanoparticles on the surface of CNTs was obtained.
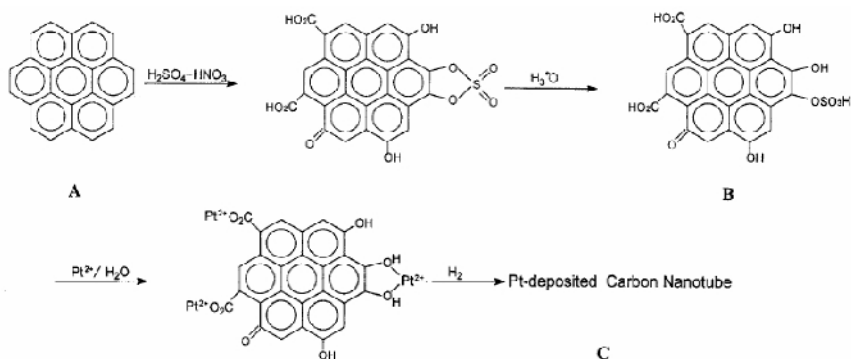
Figure 14.20. A schematic diagram for the preparation of dispersion of Pt on CNTs surface [105]. (Reprinted with permission from Chem Mater 1998;10:718–22. Copyright 1998 American Chemical Society.)

Sonochemical Treatment

Sonochemical treatment can be considered as an effective method to functionalize the CNT's surface [153, 154]. For example, Xing et al. [153] have shown that Pt nanoparticles deposited on sonochemically treated CNTs produce a much higher catalytic activity than those supported on carbon black when used in PEM fuel cells. In their experiment, the purified CNTs were added to a flask containing an acidic mixture of 8.0 M HNO_3 and 8.0 M H_2SO_4. The flask was then placed in an ultrasonic bath which was kept at 60 °C for 2 h. The surface treated CNTs are centrifugally separated from the acids and then thoroughly washed with deionized water. Pt nanoparticles were deposited on the sonochemically treated CNTs by reduction of the Pt salt precursor in an ethylene glycol-water solution.

Silane-assisted Treatment

Several groups reported the chemical functionalization of CNTs using silane coupling agents [69, 155–157]. For example, Dodelet and his co-workers [155] used a silane derivative to functionalize the CNTs surface with SO_3H functionalities for the deposition of Pt nanoparticles. The deposition of the Pt particles was carried out by immersing the CNTs in a solution containing $PtCl_2$,

silane derivative and water in ethanol [155] . Upon hydrolysis, the silane derivative formed a sulfonic acid-silicate, permitting the exchange of H^+ for the Pt_2^+ ions. After 2 h of immersion, the CNTs with the Pt precursor were removed from the solution and chemically reduced in a flow of H_2 and Ar. Figure 14.21 shows the TEM images of Pt nanoparticles deposited on CNTs in the absence and the presence of the silane precursor. It was observed in Figure 14.21(b) that the functionalization of CNTs with silane derivative facilitates the uniform deposition of Pt on the CNT's surface. Much smaller Pt particles (1.2±0.3 nm) are obtained when Pt ions are dispersed on CNTs using the silane derivative procedure to adsorb Pt ions onto the nanotubes.
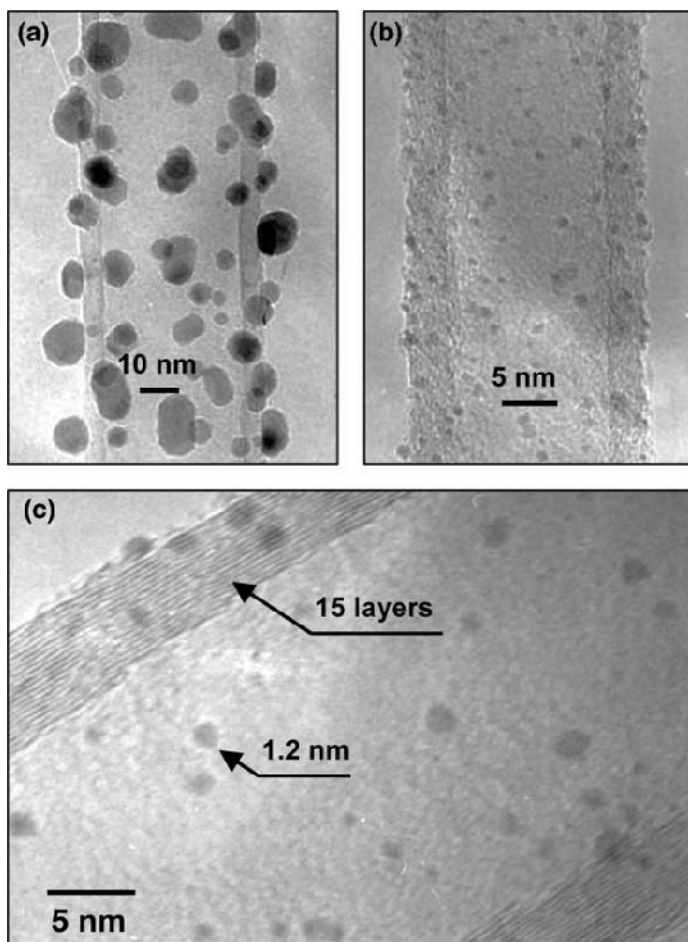
Figure 14.21. Transmission electron micrographs of Pt nanoparticles deposited on MWCNTs. (a) In the absence of the silane precursor; (b) in the presence of the silane precursor; (c) higher magnification TEM of (b) [155]. (Reprinted from Chemical Physics Letters, 379(1–2), Sun X., Li R., Villers D., Dodelet J P, Désilets S, Composite electrodes made of Pt nanoparticles deposited on carbon nanotubes grown on fuel cell backings, 99–104, ©2003, with permission from Elsevier.)

Ionic Liquids Treatment

Zhao et al. [158] described a method to functionalize the CNTs surface by using ionic liquids. The Pt nanoparticles catalysts supported on CNTs were prepared from a microwave heated, ethylene glycol solution with ionic liquids. They reported that the electrochemical surface area of Pt the nanoparticles supported on ionic liquids treated CNTs is 21% higher than the commercial Pt/C catalyst.

Electrochemical Modification

The surface of CNTs can be functionalized by covalent-bond formation via electrochemical coupling of aromatic diazonium salts and phenyl residues [159, 160]. For example, Guo and co-workers [94] developed a method for deposition of Pt nanoparticles through covalent modification of CNTs with 4-aminobenzene as shown in Figure 14.22. They first grafted an ordered 4-aminobenzene monolayer onto the CNT's surface by electro-reduction of 4-nitrobenzenediazonium tetrafluoroborate by cyclic voltammetry. Then $PtCl_6^{2-}$ was adsorbed onto the 4-aminobenzene monolayer-modified CNT's surface by electrostatic interaction. Finally, Pt nanoparticles could be obtained through pulsed potentiostatic reduction. They concluded that modifying a 4-aminobenzene monolayer on a CNT surface has several advantages: (1) The 4-aminobenzene group is modified on a CNTs surface via a C-C covalent bond which is strong and suitable as substrate for the deposition of nanoparticles, (2) Covalent bonding of two-dimensional 4-aminobenzene on a CNT's surface provides a uniform functional surface, which can effectively prevent the desired nucleation process on the CNTs surface and (3) The specific electrostatic interaction between the substrate and the adsorbed atom can cause particle size distributions to be considerably narrower than in the case of random nucleation.
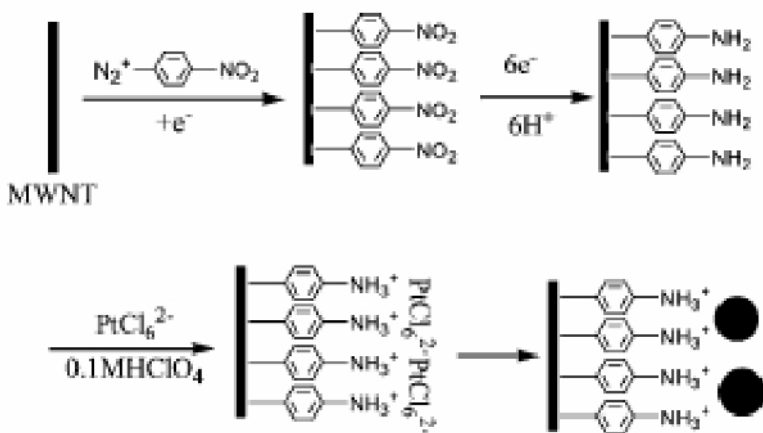
Figure 14.22. A schematic diagram for the preparation of dispersion of Pt on CNTs surface [94]. (Guo D-J, Li H-L. High dispersion and electrocatalytic properties of platinum on functional multi-walled carbon nanotubes. Electroanalysis 2005;17:869–72. ©Wiley-VCH Verlag GmbH & Co. KGaA. Reproduced with permission.)

14.3.5.2 Noncovalent Functionalization
Noncovalent functionalization of CNTs is particularly attractive because it offers the possibility of attaching chemical handles without affecting the electronic network of the tubes [161, 162]. A various species of polymers [163, 164], polynuclear aromatic compounds [165], surfactants [166, 167] and biomolecules [168] can nonspecifically bind with the external surface of CNTs without using their covalent coupling. The noncovalent interaction is based on van der Waals forces or π–π-stacking interactions [145, 169, 170]. Yang et al. [169] reported a method for the functionalization of CNTs with benzyl mercaptan as a interlinker for Pt nanoparticles. Figure 14.23 presents a schematic of benzyl mercaptan attached to CNTs. In their experiment [169], the CNTs were dispersed in deionized water and sonicated for 1 h to separate the nanotubes. Then the CNTs were mixed with benzyl mercaptan dissolved in ethanol, and then the solution was sonicated for 30 minutes to obtain a well-dispersed CNT mixture. The Pt nanoparticles were deposited either by evaporation in the preparation chamber with an electron-beam evaporator or by the addition of separately produced nanoparticles which were prepared by the wet chemical reduction of equal volumes of H_2PtCl_6 by HCOOH. The functionalized CNT surface interacts strongly with Pt nanoparticles through the formation of Pt-S bonds and results in a very high Pt nanoparticle loading both high dispersion and a narrow size distribution.
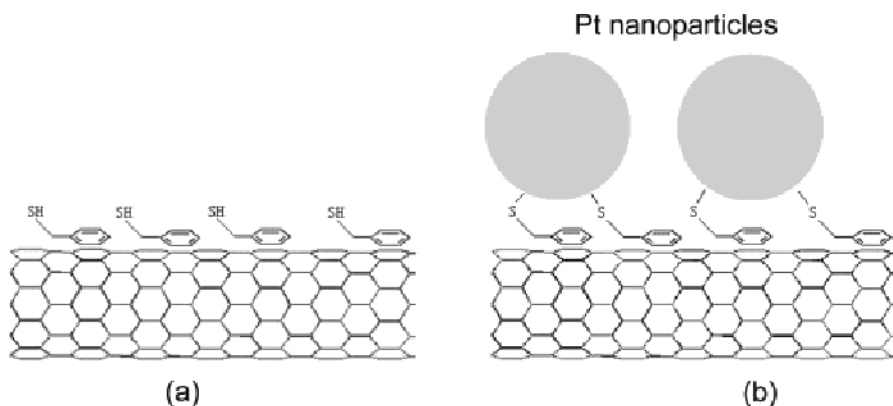
Figure 14.23. Schematics of (a) a CNT functionalized with benzyl mercaptan via π-π bonding and (b) the bonding of Pt nanoparticles to the functionalized CNT via covalent S-Pt bond formation [169]. (Reprinted with permission from Chem Mater 2006;18:5033–38. Copyright 2006 American Chemical Society.)

14.3.5.3 Nitrogen Doped Carbon Nanotubes as Surface Modification
The chemical modification of the surface of CNTs by acid treatment considerably reduces the mechanical and electronic performance of the tubes due to the introduction of large numbers of defects. The doping of CNTs with other elements (e.g., nitrogen) could be a particularly interesting way to modify their electrical and mechanical properties [120, 171, 172]. The additional electrons contributed by the nitrogen atoms provide electron carriers for the conduction band [173]. Nitrogen-doped nanotubes were found to be either metallic or narrow energy gap

semiconductors [174, 175], thus offering the possibility of greater electrical conductivity as compared to pure carbon nanotubes. Recently, nitrogen-doped CNTs (N-CNTs) were reported as being used as support materials in fuel cell catalysts, utilizing their enhanced dispersion of Pt nanoparticles [117, 118, 121, 176–179]. N-CNTs contain nitrogenated sites (substitutional and pyridinic nitrogen) that are chemically active. Therefore, it should be possible to avoid functionalization processes that use strong acid treatments, and it is relatively easy to deposit metal catalysts onto N-CNTs [117, 118, 121, 176, 177]. For example, Maiyalagan et al. [121] used N-CNTs as supports for Pt electrocatalysts and applied them for methanol oxidation reaction. They observed that the Pt particles were homogeneously dispersed on the nanotubes with particle sizes of 3 nm. An enhanced catalytic activity and stability toward methanol oxidation on Pt/N-CNTs as compared with commercial E-TEK Pt/C was observed. The enhanced electrocatalytic activity of Pt nanoparticles supported on N-CNTs was tentatively attributed the following factors which still require further investigation: (1) higher dispersion of Pt nanoparticles on the N-CNTs increases the availability of an enhanced electrochemically active surface area, (2) appearance of the specific active sites at the metal–support boundary and, (3) strong and specific metal–support interaction.

14.4 Activity Validation of the Synthesized Catalysts in a Fuel Cell Operation

Many studies have examined various aspects of PEM fuel cell performance as a function of operating conditions [180–182]. Gottesfeld wrote an excellent review of PEM fuel cells components and operation [183]. In addition to experimental characterization, much research has focused on first-principles-based modeling of the PEM fuel cells [184, 185]. Polarization occurs during operation of PEM fuel cells and it dramatically influences both the performance and the commercialization of the technology. In order to systematically improve the efficiency of the fuel cell, a better understanding of the reactions and mass transport in the cell is essential. In this section, the improvement of the MEA performance based on CNTs and CNFs catalysts will be discussed.

14.4.1 Fabrication of Membrane Electrode Assembly for Carbon Nanotubes and Nanofibers-based Catalysts

The membrane electrode assembly (MEA) is the core of the PEM fuel cell, where the chemical energy of the fuel (i.e., hydrogen) is converted into electricity through the electrochemical oxidation of fuel at the anode and the electrochemical reduction of oxygen at the cathode. The structure of the MEA in a single PEM fuel cell is shown schematically in Figure 14.24. The MEA consists of a proton exchange membrane, anode and cathode electrodes, and anode and cathode gas diffusion layers (GDL). Typically, these components are fabricated individually and then pressed together at high temperatures and pressures. Generally, two

different procedures are used to fabricate the MEA: the so-called gas diffusion layer (GDL)-based method and the membrane-based method [186]. The GDL-based method implies that the catalyst ink is directly painted or sprayed onto the pre-treated GDL and then hot pressed onto the membrane. Fabricating the MEA with the membrane-based method usually consists of spraying the catalyst ink directly onto a dry and fixed membrane, which is then sandwiched between two GDLs and followed by a hot pressing step.
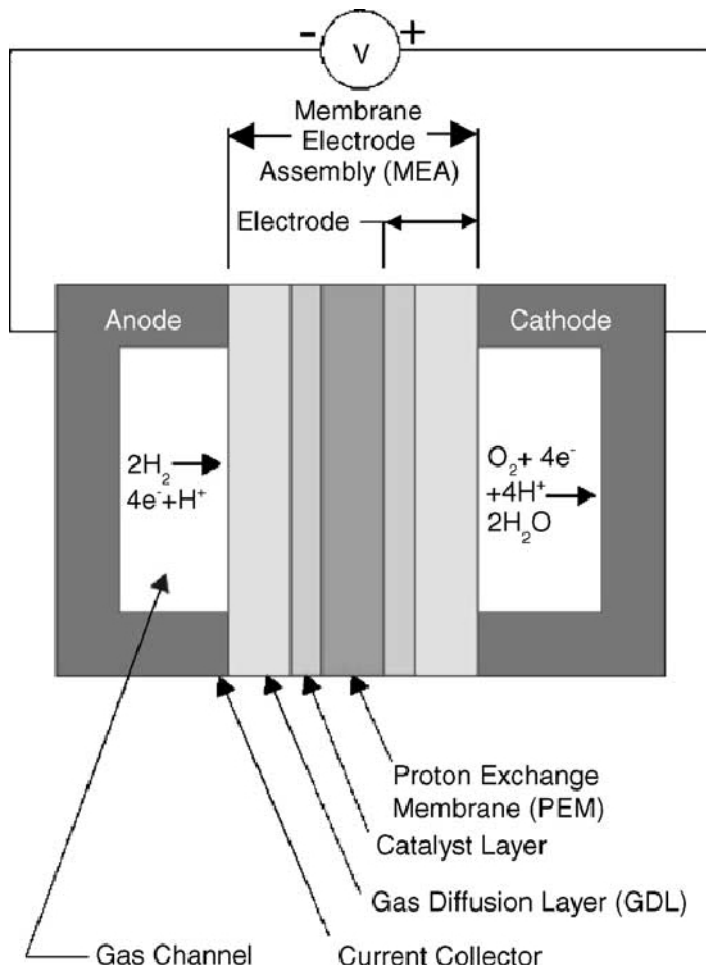
Figure 14.24. Schematic of a single typical proton exchange membrane fuel cell

The MEA with CNT-based electrocatalysts are usually prepared by using the conventional process of pasting mixed catalysts supported on CNTs and Nafion$^{®}$ solution onto a gas diffusion layer [63, 71, 81, 187, 188]. The method consists of, first, preparation of the catalyst ink by ultrasonicating appropriate amounts of Pt supported on CNTs, Nafion solution and isopropyl alcohol [188]. The slurry was then coated on the gas diffusion layer by the brush method and dried at 80 °C. The

gas diffusion layer of the electrodes consisted of carbon powder with polytetrafluoroethylene, deposited onto a carbon cloth or paper substrate. Finally, a thin layer of Nafion solution was spread onto the surface of the electrode. The MEA was prepared by placing the above electrodes on the both sides of the pre-treated Nafion membrane, followed by hot pressing. For example, Li and co-workers [189] have prepared electrodes from a mixture containing Pt catalysts supported on CNTs, Nafion solution and distilled H_2O, which was then ultrasonically blended for 1 h. The mixture was spread uniformly across the surface of a carbon paper substrate which was previously hydrophobically treated. The MEA was prepared by sandwiching a Nafion membrane between the anode and cathode. They found a higher activity in the oxygen reduction reaction and better performance of the direct methanol fuel cell when compared to the catalyst supported on commercial carbon [189].
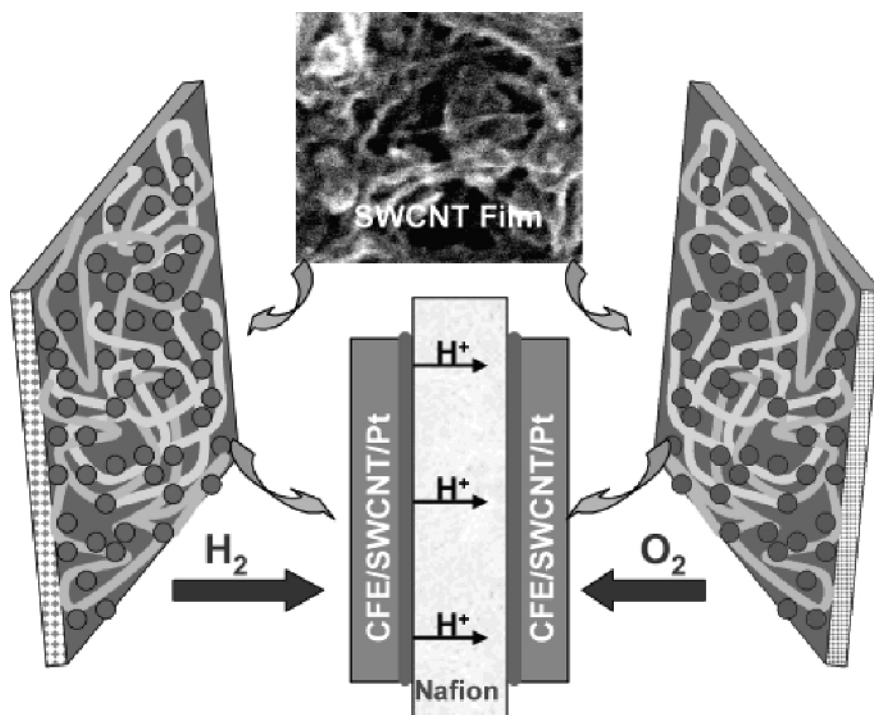
Figure 14.25. CNT-based membrane electrode assembly for a PEM fuel cell [190]. (Reprinted with permission from Langmuir 2005;21:8487–94. Copyright 2005 American Chemical Society.)

Girishkumar and co-workers [190] reported a preparation procedure for the MEA using CNTs as a support for PEM fuel cells. A schematic representation of their CNT-based proton exchange membrane assembly for a H_2/O_2 based fuel cell is shown in Figure 14.25. In their experiment, an electrophoretic deposition technique was employed to cast films of CNTs on carbon fiber paper. Two carbon paper electrodes are kept ~5 mm apart in a cell containing a CNT suspension in

tetrahydrofuran. When a DC voltage of ~40 V was applied, a slow movement of CNTs from the suspension toward the positive electrode and the assembly of CNTs, as a film on the carbon fiber electrode, was observed. The thickness of the films was controlled by varying the time of electrophoretic deposition. A second electrophoresis step was used to deposit the Pt catalysts on the CNT film. The MEA was fabricated by hot pressing the cathode and anode electrodes on either side of the pretreated Nafion membrane. For an eventual fuel cell application, this method has the additional advantage that they can control the loading of carbon support and catalysts by simply varying the time and DC voltage used in the electrophoretic procedure. They observed that the loading of CNTs on the anodes has an effect on the power densities. The CNT-based MEA exhibits higher power density than carbon black at a higher anodic back pressure.

Li and co-workers [191] have developed a simple filtration method for the preparation of an oriented array of Pt supported on a CNT film for PEM fuel cells. They deposited the Pt nanoparticles on the CNTs before the film formation and then used filtration as a means to form an oriented film of Pt/CNTs on the Nafion membrane, which is then used as the catalyst layer in the fabrication of the MEA for PEM fuel cell. Figure 14.26 shows a schematic diagram of the fabrication process for the oriented Pt/CNT-film-based MEA. Pt particles were deposited on the CNT's surface through a chemical reduction of H_2PtCl_6 by ethylene glycol. The Pt/CNT combination was then filtered through 0.2-µm-pore hydrophilic nylon filter paper. The deposited film was then transferred onto a Nafion membrane by pressing the CNT-coated side of the filter onto the Nafion membrane. Finally, the oriented Pt/CNT-film-coated Nafion membrane, and a gas diffusion layer were hot pressed to obtain an MEA. A higher performance was achieved with oriented Pt/CNT-based MEA than Pt/C and non-oriented Pt/CNT-based MEAs.
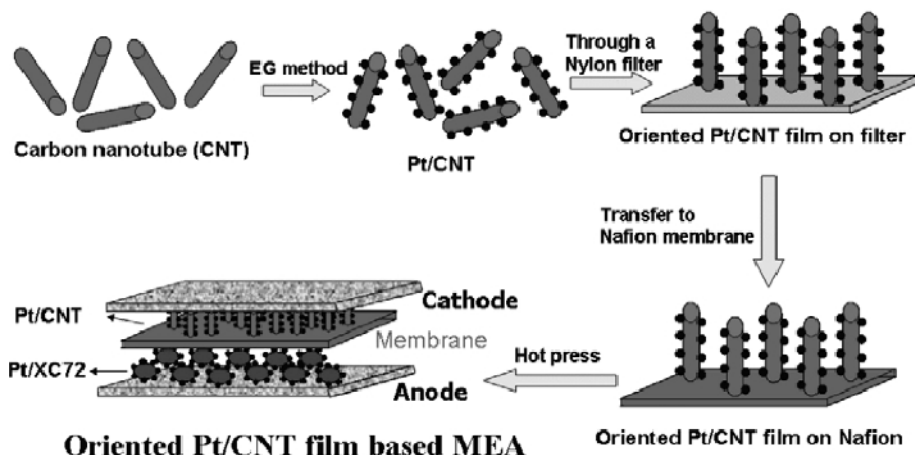
Figure 14.26. Schematic of the fabrication process for the oriented Pt/CNT-film-based MEA [191]. (Reprinted with permission from Langmuir 2005;21:9386–89. Copyright 2005 American Chemical Society.)

Recently, a new approach for composite electrode fabrication involving the growth of CNTs directly on the carbon fibers of a fuel cell baking with subsequent deposition of Pt nanoparticles was developed [65, 69, 70, 87, 155, 192]. Yan and co-workers [65, 87] described how CNTs that are grown directly on carbon paper could be used to fabricate an MEA. They first synthesized CNTs directly on carbon paper by chemical vapor deposition and then attached the Pt to the CNTs by electrodeposition. Then they applied a hydrophobic gas diffusion layer to the face of the CNT on the opposite side of the carbon paper. The gas diffusion ink was prepared by ultrasonicating the mixture of carbon black, polytetrafluoroethylene solution and isopropanol for 30 min. The carbon loading was approximately 2.5 mg/cm^2 and was sintered at 350 °C in Ar for about 1 h. For fabricating the MEA, the cathode electrode was a CNTs-carbon paper composite while the conventional Pt/C electrode was used as the anode electrode. The CNT electrode backings were hydrophobically treated by spraying them with a 1 mg/cm^2 PTFE/Vulcan XC72 mixture (1:3 weight ratio in 2-propanol). The MEA was heat-pressed at 140 °C, first at 500 lb for 1 min, then at 950 lb for 40 s.

14.4.2 Performance of Carbon Nanotubes and Nanofibers Membrane Electrode Assembly

Many research groups have reported the fuel cell performance of Pt nanoparticles supported on CNTs at the cathode of H$_2$/O$_2$ fuel cells or direct methanol fuel cells [63, 65, 66, 68, 69, 71, 81, 87, 188, 189, 191–193]. It has been shown that the performance of a CNT-based MEA is better than that of conventional Pt/C MEA [65, 71, 81, 189, 191–193]. For example, Matsumoto and coworkers [193] conducted the fuel cell tests of the MEA with CNTs used as a support for Pt catalysts at the cathode. The authors concluded that enhancements in PEM fuel cell performance are observed by using the CNT cathode in comparison to a conventional carbon cathode in a low current density region (Figure 14.27). The voltage drop above 400 mA/cm^2 was ascribed to the proton diffusion.

Saha and co-workers [70] developed a synthetic method to deposit Pt nanoparticles on CNTs that were grown on commercially-used carbon paper by the reduction of the Pt precursor with glacial acetic acid. Figure 14.28 shows the single cell performance for the MEA made with a CNT-based electrode as the cathode and standard E-TEK electrode as the anode for H$_2$/O$_2$ fuel cells. Compared with the standard Pt/C electrode, the CNT-based electrode exhibited higher single-cell performance in a H$_2$/O$_2$ fuel cell. At a fixed cell voltage of 0.6 V, the current density of the Pt/CNT/carbon paper composite is 1.58 A/cm^2 which is 27 % higher than the standard E-TEK electrode (1.16 A/cm^2). The corresponding power densities normalized on the basis of Pt loading were 2.19 W mg^{-1}$_{Pt}$ (Pt/CNT/carbon paper composite) and 1.42 W/mg$_{Pt}$ (standard E-TEK electrode) at 0.6 V, showing a significant increase in the power density of about 0.77 W/mg$_{Pt}$ for the Pt/CNT/carbon paper composite. It is clearly evident that the current density at 900 mV ($i_{900\ mv}$) for the Pt/CNT/carbon paper composite is significantly higher than the E-TEK electrode (approximately 66%), which can be attributed to the improved dispersion of Pt nanoparticles on the CNT's surface and to the 3D structure of CNT-based electrodes.
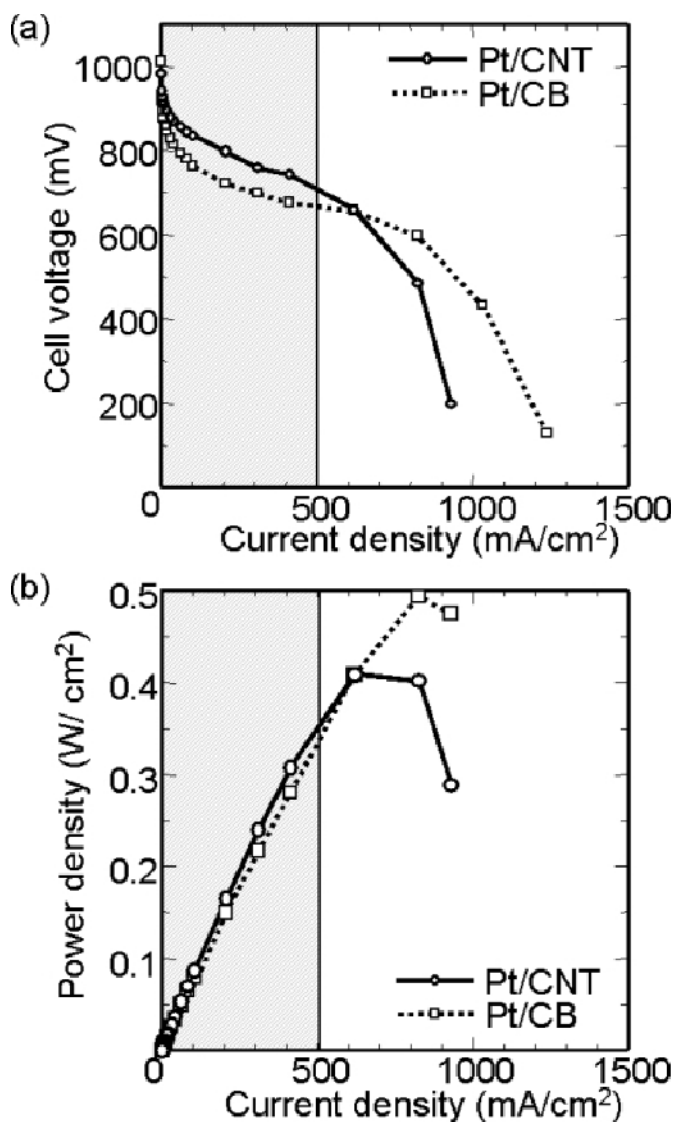
Figure 14.27. Performance of the Pt/CNT and the Pt/CB electrodes. (a) Current density–cell voltage curves. (b) Power density–current density curves [193]. (From Matsumoto T, Komatsu T, Arai K, Yamazaki T, Kijima M, Shimizu H, et al. Reduction of Pt usage in fuel cell electrocatalysts with carbon nanotube electrodes. Chem Commun 2004:840–1. Reproduced by permission of The Royal Society of Chemistry.)
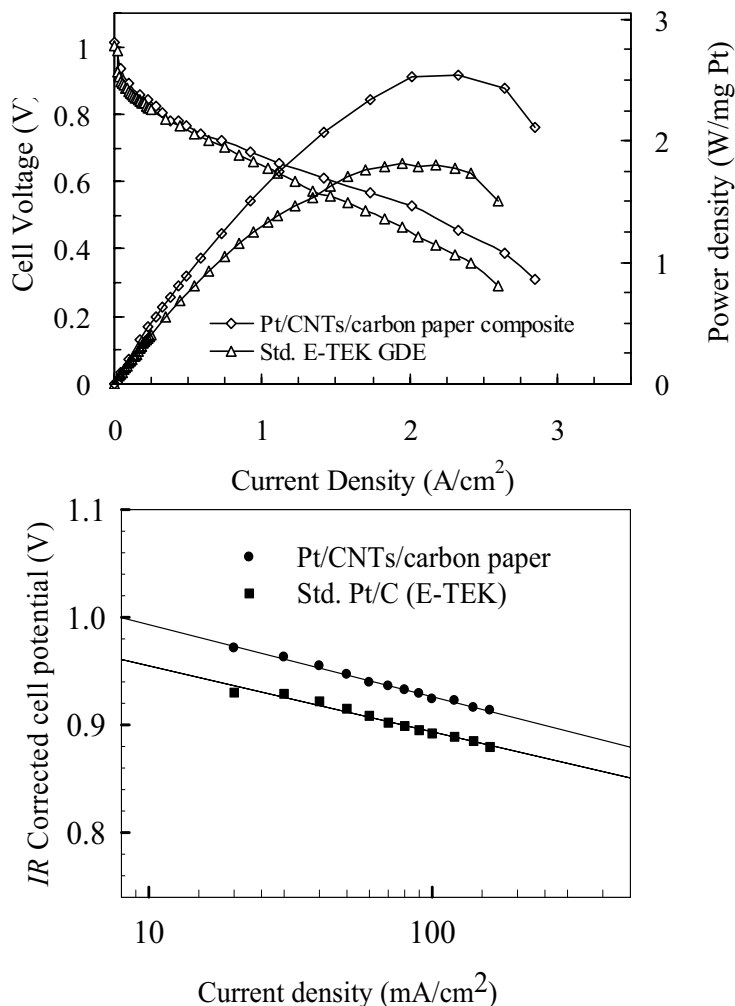
Figure 14.28. (a) Polarization characteristics of the MEAs fabricated with of CNTs electrode (0. 42 mg$_{Pt}$/cm^2) and standard E-TEK electrode (LT140E-W; 0.5 mg$_{Pt}$/cm^2) as cathode electrodes for H$_2$/O$_2$ at 80 °C, Nafion$^®$ 112 membrane, 25/30 psig anode and cathode back pressure. Anode electrodes were E-TEK electrode with 0.5 mg$_{Pt}$/cm^2. (b) *IR* corrected Tafel plots for comparison of kinetic parameters [70]. (Reprinted from Journal of Power Sources, 177(2), Saha MS, Li R, Sun X, High loading and monodispersed Pt nanoparticles on multiwalled carbon nanotubes for high performance proton exchange membrane fuel cells, 314–22, ©2008, with permission from Elsevier.)

Yan and co-workers [65] conducted polarization curve measurement in a PEM fuel cell with CNT-based electrodes. They found an improved polarization behavior for the CNT-based MEA throughout the whole potential range compared to the conventional Pt/C MEA. In activation controlled regions, the measured current density for the CNT-based electrode is higher than that of the conventional electrode (e.g., 153 mA/cm^2 vs. 98 mA/cm^2 at potential of 0.8 V), indicating that

the CNT-based electrode showed a higher activity toward oxygen reduction. The authors attributed the enhanced activity of the oxygen reduction to the unique structure of CNTs. According to Britto et al. [194], the CNT has improved charge transfer and better electrical conductivity than carbon black. They also observed that the improvement in cell potential and power density is more significant at higher current density regions, indicating a better mass transport for the CNT-based electrode.

14.5 Stability of Carbon Nanotubes and Nanofibers-based Fuel Cell Electrodes

Understanding the long-term stability of the PEM fuel cell is of crucial importance as this technology approaches its commercialization stage. In order to meet the requirements for commercial applications, a long life over 40, 000 hours (= 10 years in the daily start and stop (DSS) mode) is required for PEM fuel cell stacks in the stationary cogeneration systems and at least 5, 000 h (equivalent to 150, 000 driven miles) for automotive conditions [195]. Therefore, performance degradation of PEM fuel cells and the degradation of the component materials has attracted extensive attention in recent years [196, 197]. However, the failure modes for PEM fuel cells are not well documented and the degradation causes and mechanisms are not fully understood [198]. Recently, Borup et al. [10] reviewed the current understanding of PEM fuel cell degradation. Another review by Shao et al. [199] described the state-of-art understanding of the durability issues of Pt based catalysts under real or simulated PEMFC conditions. The approaches to improve catalyst durability and the methods for studying these issues are also discussed. It has been found that the degradation of the fuel cell performance is primarily due to the decay of the membrane-electrode-assembly (MEA) [200–202]. Variation of parameters such as overpotential (under conditions of variable load, and fuel starvation), start-up and shutdown, working temperature and relative humidity, etc. can severely effect the catalyst durability. Platinum particle sintering in carbon black used as a support for platinum catalysts can be seen during cell operation [203]. Impurity ions affect the membrane proton conductivity and oxygen reduction kinetics [204, 205]. Hydrogen peroxide formation, which is formed electrochemically and chemically during operation, is one of the potential deteriorating factors of PEMFC [206]. Electrochemical oxidation of the carbon support to CO_2 and, to a lesser extent, CO, has been reported to occur at the cathode of a fuel cell [207]. In this section, the stability enhancement of the catalysts support and investigation methodologies will be discussed.

In the state of the art PEM fuel cell, carbon black is normally used as the support materials for catalysts. But carbon support is subject to degradation under chemically and electrochemically oxidizing conditions [207–210]. Roen et al. [209] observed catalyzed oxidation of carbon black in PEM fuel cells. It was proposed that CO would adsorb on Pt particles below 0.6 V and it was subsequently oxidized. In an another study, Kangasniemi et al. [208] observed progressive oxidations of carbon black in H_2SO_4, which may indicate that inside oxidations of carbon black support may have occurred. Therefore, considerable

efforts have been made to the development of new carbon support materials to improve electrode stability [10]. Carbons with a high graphitization degree as support materials and alloying Pt with some other metals are proved to be effective ways to improve the catalyst durability. Compared with carbon black, a higher durability of carbon nanostructure materials [211], e.g., CNTs and CNFs-based electrodes, has been revealed recently [212, 213]. Several research groups have reported that CNTs are more resistant to electrochemical oxidation than carbon black with and without Pt on them [8, 212, 214, 215]. As discussed in a review of CNTs for catalysis applications [216], the orientation of the graphene sheets and pretreatments can influence the nature of the surface and, consequently, the interaction with the catalysts. The nitrogen atom incorporated in CNTs is expected to improve the durability of the resultant catalysts because of the enhanced π-bonding [217, 218] and the basic property [219], which are due to the strong electron donor behavior of nitrogen [220, 221].

In the carbon-supported, Pt catalyst, the interaction is attributed to the presence of a Pt–support electronic effect. The specific metal–support interaction is through the electron transfer from the Pt clusters to the oxygen atoms of the surface of the support [222]. In many cases, chemical bonds are formed or charge transfer takes place between the contacting phases. The Pt–carbon support interaction is considered to be beneficial to the enhancement of the catalytic properties and to improve the stability of the electrocatalyst [223, 224].

The long-term operation data obtained from a fuel cell under real operating conditions is very useful for the performance evaluation of a fuel cell in terms of the durability. In industry, three methodologies are always used for the PEM fuel cell durability studies. One major method involved in long-term durability studies in PEM fuel cells has been the so-called post-mortem examination of individually boiled components. Another common approach within the industry is to operate a cell or stack for a given period of time, and then disassemble the components for post-mortem examination. Durability data is often accumulated in bulk to determine the expected power loss over time and sources of catastrophic failure for prototypes or nearly commercial ready sets of components. However, testing of fuel cells for lengthy periods of time is time-consuming and also costly [225]. Thus, the so called accelerated degradation test (ADT) is commonly used to study the degradation behaviors [226, 227]. To date, four different accelerated parameters or a combination of these parameters have been employed in accelerated life testing: (1) thermal degradation under hot air conditions, (2) reduced humidity, (3) open-circuit cell operation and (4) electrochemically forced aging under simulated cell conditions. Most of the methods relied on the traditional carbon support. Only a few publications are available regarding durability investigation of CNTs as a catalyst support for PEM fuel cells [8, 212, 213]. For example, Shao et al. [212] investigated the durability of CNTs used as a support for Pt catalysts using an ADT test in a three-electrode cell setup. They first prepared a gas diffusion electrode (GDE) by spraying the catalytic ink on the hydrophobized carbon paper. Then the GDE as the working electrode was held vertically in a chamber filled with 0.5 mol/L H_2SO_4, with the catalyst layer exposed to the electrolyte solution. This mimics the environment of the electrode membrane interface in PEM fuel cells. A fixed potential of 1.2 V vs. a reversible hydrogen

electrode was applied to the working electrode for 192 h. Cyclic voltammetry was used to characterize the electrochemical surface area, which can be determined by the charge of the hydrogen adsorption/desorption region. The electrochemical surface area of Pt/C degrades by 49.8% during the 192 h test time, compared with 26.1% for Pt/CNTs, which is due to Pt particle growth and Pt loss from the support in the form of Pt ions and Pt particles.

The durability of CNTs under conditions simulating the cathode environment of the PEMFC was examined by Wang and coworkers [213]. In their experiment, Pt nanoparticles supported on CNTs were immersed in an N_2 purged H_2SO_4 solution and applied a potential of 0.9 V for different durations at 60 °C. The Pt surface area was then determined by integrating the hydrogen desorption peak of the cyclic voltammogram, after correcting for double layer charging current. They found that almost 80% of Pt surface area was lost for carbon black after 168 h of oxidation treatment, while only 37% loss was observed for CNTs. Furthermore, most of the surface area loss for the case of the MWNT occurs within 72 h, and after 72 h the rate for the Pt area loss is very small indicating that CNTs could potentially provide much higher durability than carbon black.

14.6 Conclusions and Future Perspective

This chapter reviewed various one-dimensional catalyst supports including carbon nanotubes, carbon nanofibers and metal oxide nanowires as replacement of carbon black support to increase the utilization of platinum and enhance the durability of electrodes in fuel cells.

In recent years, interest in the development of PEM fuel cells have considerably increased and the commercial potentials to become the power plant for the next generation and nonpolluting automobile engine have been viewed. Although PEM fuel cells have begun to move from the demonstration phase to commercialization due to the impressive research effort in recent years, significant challenges including high materials cost and the low stability of the electrodes remain to be solved [228]. The platinum used as an electrocatalyst is one of the most expensive materials for the fuel cell electrode. Therefore, a lot of work has been devoted to lowering the amount of platinum used in electrodes. However, it is necessary to obtain a more effective catalyst, both in catalytic performance and electric conductivity. To achieve a higher efficiency of the electrocatalyst, platinum has to be well dispersed on the support. For this reason, it is desirable that the support material provides a suitable specific area and surface chemistry as well as a good electrical conductivity. In the state of the art PEM fuel cells, the microporous carbon blacks, such as Vulcan XC72 have been most frequently used as supports of the electrocatalysts. Despite its widespread use, high surface-area carbon support in PEM fuel cell electrodes is susceptible to corrosive conditions, which include low pH, high potential, high humidity, and high temperatures.

Recently, novel carbon nanostructure materials such as single-wall carbon nanohorns, carbon nanofibers (CNFs) and carbon nanotubes (CNTs) have been proposed as promising support materials for PEM fuel cell catalysts [80]. The main reason for using CNTs as a support for Pt catalysts is to improve the

electrocatalytic activity and reduce the usage of the platinum catalyst. In this chapter, we presented an overview of the processing techniques used to synthesize the nanostructures including CNTs, CNFs and nanowires (NWs). We then discussed the methods by which Pt nanoparticles can be deposited onto the nanostructures and the major challenges in the synthesis of CNTs and CNFs-supported Pt electrocatalysts.

The effective attachment of Pt nanoparticles uniformly dispersed onto CNTs or CNFs remains a difficult challenge because of the inertness of their surface. Therefore, CNTs' surfaces need to be functionalized in order to obtain reactive sites for the adhesion of Pt metal particles. We presented some of the recent advances in the development of reliable methods for the chemical functionalization of the CNTs. The doping of CNTs with other elements (e.g., nitrogen) could be a particularly interesting way to modify their electronic and mechanical properties. Particularly, nitrogen-doped CNTs contain nitrogenated sites (substitutional and pyridinic nitrogen) that are chemically active. Therefore, it should be possible to avoid functionalization processes that use strong acid treatments, and attach Pt nanoparticles onto the nitrogen-doped CNTs.

We presented the use of metal oxide NWs as a catalyst support for PEM fuel cells. It was reported that the nanowire-based electrode exhibited higher electrocatalytic activity both for the oxygen reduction reaction and the methanol oxidation reaction as well as enhanced the CO tolerance in comparison to a standard Pt/C electrode [140]. Therefore, it is expected that integrated three-dimensional nanowire-based fuel cell electrodes will be ideal materials for providing a higher catalytic performance, higher catalyst utilization, efficient mass transport, and a longer fuel cell operational life. However, many challenges for nanowire-based support still remain such as improved electrical conductivity and corrosion resistance.

We also discussed the durability issues of PEM fuel cell catalysts which have been recently recognized as one of the major barriers to the commercialization of fuel cells [10]. To use carbon with a higher graphitization degree as support materials and to alloy Pt with other metals can improve the catalyst durability. Compared with carbon black, several research groups have reported that the use of CNTs can be promising in effectively reducing the carbon corrosion problem [213].

The Pt–support interaction has been paid more and more attention to in the carbon support catalyst studies. This interaction has been considered to have an effect on the growth, the structure, and the dispersion of platinum particles on the carbon supports, thus providing potential benefits to the improvement of catalytic properties and the stability of the electrocatalyst [224].

Acknowledgements

References

1. Gasteiger HA, Kocha SS, Sompalli B, Wagner FT. Activity benchmarks and requirements for Pt, Pt-alloy, and non-Pt oxygen reduction catalysts for PEMFCs. Appl Catal B: Environ 2005;56:9–35.
2. Kinoshita K. Particle size effects for oxygen reduction on highly dispersed platinum in acid electrolytes. J Electrochem Soc 1990;137:845–48.
3. Chen WX, Lee JY, Liu Z. Microwave-assisted synthesis of carbon supported Pt nanoparticles for fuel cell applications. Chem Commun 2002:2588–89.
4. Ralph TR, Hogarth MP. Catalysis for low temperature fuel cells. Platinum Met Rev 2002;46:3–14.
5. Stevens DA, Hicks MT, Haugen GM, Dahn JR. Ex situ and in situ stability studies of PEMFC catalysts. J Electrochem Soc 2005;152:A2309–15.
6. Wieckowski A, Savinova ER, Vayenas CG. Catalysis and electrocatalysis at nanoparticle surfaces. New York: Marcel Dekker, 2003.
7. Liu JG, Zhou ZH, Zhao XX, Xin Q, Sun GQ, Yi BL. Studies on performance degradation of a direct methanol fuel cell (DMFC) in life test. Phys Chem Chem Phys 2004;6:134.
8. Shao Y, Yin G, Zhang J, Gao Y. Comparative investigation of the resistance to electrochemical oxidation of carbon black and carbon nanotubes in aqueous sulfuric acid solution. Electrochim Acta 2006;51:5853–7.
9. Shao Y, Yin G, Wang Z, Gao Y. Proton exchange membrane fuel cell from low temperature to high temperature: material challenges. J Power Sources 2007;167:235–42.
10. Borup R, Meyers J, Pivovar B, Kim YS, Mukundan R, Garland N, et al. Scientific aspects of polymer electrolyte fuel cell durability and degradation. Chem Rev 2007;107:3904–51.
11. Iijima S. Helical microtubules of graphitic carbon. Nature 1991;354:56.
12. Beguin F, Ehrburger P. Special issue on carbon nanotubes. Carbon 2002;40:1619–842.
13. Haddon RC. Special issue on carbon nanotubes. Acc Chem Res 2002;35:997–1113.
14. Dresselhaus MS, Dai H. Special issue on carbon nanotubes. MRS Bull 2004;29:237–81.
15. Harris PJF. Carbon nanotubes and related structures: new materials for the 21st century. Cambridge: Cambridge University Press, 1999.
16. Dresselhaus MS, Dresselhaus G, Avouris P. Carbon nanotubes: synthesis, structure, properties, and applications. In: Topics in applied physics, volume 80. New York: Springer-Verlag, 2001.
17. Saito R, Dresselhaus G, Dresselhaus MS. Physical properties of carbon nanotubes. London: Imperial College Press, 1998.
18. Meyyappan M. Carbon nanotubes: science and applications. Boca Raton, FL: CRC Press, 2005.
19. Baughman RH, Zakhidov AA, Heer WA. Carbon nanotubes – the route toward applications. Science 2002;297:787–92.
20. Iijima S, Ichibashi T. Single-shell carbon nanotubes of 1-nm diameter. Nature 1993;363:603–5.
21. Bethune DS, Kiang CH, Devries MS, Gorman G, Savoy R, Vazquez J, et al. Cobalt-catalysed growth of carbon nanotubes with single-atomic-layer walls. Nature 1993;363:605–7.
22. Franklin N, Dai H. An enhanced CVD approach to extensive nanotube networks with directionality. Adv Mater 2000;12:890–4.
23. Su M, Zhang B, Liu J. A scalable CVD method for the synthesis of single-walled carbon nanotubes with high catalyst productivity. Chem Phys Lett 2000;322:321–6.

24. Nikolaev P, Bronikowski MJ, Bradley RK, Rohmund F, Colbert DT, Smith KA, et al. Gas-phase catalytic growth of single-walled carbon nanotubes from carbon monoxide. Chem Phys Lett 1999;313:91–7.
25. Flahaut E, Govindaraj A, Peigney A, Laurent C, Rao CN. Synthesis of single-walled carbon nanotubes using binary Fe, Co, Ni alloy nanoparticles prepared in situ by the reduction of oxide solid solutions. Chem Phys Lett 1999;300:236–42.
26. Colomer JF, Stephan C, Lefrant S, Tendeloo GV, Willems I, Kanya Z, et al. Large-scale synthesis of single-wall carbon nanotubes by catalytic chemical vapor deposition CCVD method. Chem Phys Lett 2000;317:83–9.
27. Ren ZF, Huang ZP, Xu JW, Wang JH, Bush P, Siegal MP, et al. Synthesis of large arrays of well-aligned carbon nanotubes on glass. Science 1998;282:1105–7.
28. Li WZ, Xie SS, Qian LX, Chang BH, Zou BS, Zhou WY, et al. Large-scale synthesis of aligned carbon nanotubes. Science 1996;274:1701–3.
29. Pan ZW, Xie SS, Chang BH, Wang CY, Lu L, Liu W, et al. Very long carbon nanotubes. Nature 1998;394:631–2.
30. Fan S, Chapline M, Franklin N, Tombler T, Cassell A, Dai H. Self-oriented regular arrays of carbon nanotubes and their field emission properties. Science 1999;283:512–14.
31. Maruyama S, Kojima R, Miyauchia Y, Chiashia S, Kohno M. Low-temperature synthesis of high-purity single-walled carbon nanotubes from alcohol. Chem Phys Lett 2002;360:229–34.
32. Hata K, Futaba DN, Mizuno K, Namai T, Yumura M, Iijima S. Water-assisted highly efficient synthesis of impurity-free single-walled carbon nanotubes. Science 2005;306:1362–64.
33. Li Y, Mann D, Rolandi M, Kim W, Ural A, Hung S, et al. Preferential growth of semiconducting single-walled Carbon nanotubes by a plasma enhanced CVD method. Nano Lett 2004;4:317–21.
34. Ci L, Wei B, Liang J, Xu C, D. Wu D. Preparation of carbon nanotubules by the floating catalyst method. J Mater Sci Lett 1999;18:797–9.
35. Hou X, Choy KL. Crystal growth of ZnS films by a charged aerosol-assisted vapor deposition process. Chem Vap Deposition 2006;12:583–5.
36. Vivekchand SRC, Cele LM, Deepark FL, Raju AR, Govindaraj A. Carbon nanotubes by nebulized spray pyrolysis. Chem Phys Lett 2004;386:313–18.
37. Rodriguez NM. A review of catalytically grown carbon nanofibers. J Mater Res 1993;8:3233–50.
38. Bessel CA, Laubernds K, Rodriguez NM, Baker RTK. Graphite nanofibers as an electrode for fuel cell applications. J Phys Chem B 2001;105:1115–8.
39. Ismagilov ZR, Kerzhentsev MA, Shikina NV, Lisitsyn AS, Okhlopkova LB, Barnakov CN, et al. Development of active catalysts for low Pt loading cathodes of PEMFC by surface tailoring of nanocarbon materials. Catal Today 2005;102(103):58–66.
40. Zhu YA, Sui ZJ, Zhao TJ, Dai YC, Cheng ZM, Yuan WK. Modeling of fishbone-type carbon nanofibers: a theoretical study. Carbon 2005;43:1694–9.
41. Rodriguez NM, Kim MS, Baker RTK. Promotional effect of carbon monoxide on the decomposition of ethylene over an iron catalyst. J Catal 1993;144:93–108.
42. Krishnankutty N, Rodriguez NM, Baker RTK. The effect of copper on the structural characteristics of carbon filaments produced from iron catalyzed decomposition of ethylene. Catal Today 1997;37:295–307.
43. Wang ZL. Nanostructures of zinc oxide. Mater Today 2004;7:26–33.
44. Hu JT, Odom TW, Libier CM. Chemistry and physics in one dimension: Synthesis and properties of nanowires and nanotubes. Acc Chem Res 1999;32:435–45.

45. Xia Y, Yang P, Sun Y, Wu Y, Mayers B, Gates B, et al. One-dimensional nanostructures: synthesis, characterization, and applications. Adv Mater 2003;15:353–89.
46. Yang P. Chemistry of nanostructured materials. Hackensack, NJ: World Scientific Publishing, 2003.
47. Rao CNR, Muller A, Cheetham AK. The chemistry of nanomaterials: synthesis, properties and application. Weinheim: Wiley-VCH Verlag GmbH & Co., 2004.
48. Cao GZ. Nanostructures & nanomaterials: synthesis, properties & applications. Singapore: World Scientific Publishing, 2004.
49. Wang ZL. Nanowires and nanobelts: materials, properties and devices. Norwell, MA: Kluwer Academic Publishers, 2003.
50. Wagner RS, Ellis WC. Vapor-liquid-solid mechanism of single crystal growth. Appl Phys Lett 1964;4:89–90.
51. Wu Y, Yang P. Direct observation of vapor–liquid–solid nanowire growth. J Am Chem Soc 2001;123:3165–6.
52. Zhang Y, Wang N, Gao S, He R, Miao S, Liu J, et al. A simple method to synthesize nanowires. Chem Mater 2002;14:3564–8.
53. Pan ZW, Dai ZR, Wang ZL. Nanobelts of semiconducting oxides. Science 2001;291:1947–9.
54. Saha MS, Li R, Sun X. Composite of Pt-Ru supported SnO_2 nanowires grown on carbon paper for electrocatalytic oxidation of methanol. Electrochem Commun 2007;9:2229–34.
55. Jin C, Xiang X, Jia C, Liu W, Cai W, Yao L, et al. Electrochemical fabrication of large-area, ordered Bi_2Te_3 nanowire arrays. J Phys Chem B 2004;108:1844–7.
56. Takahashi K, Limmer SJ, Wang Y, Cao GZ. Synthesis and electrochemical properties of single-crystal V_2O_5 nanorod arrays by template-based electrodeposition. J Phys Chem B 2004;108:9795–800.
57. Cao GZ. Growth of oxide nanorod arrays through sol electrophoretic deposition. J Phys Chem B 2004;108:19921–31.
58. Gamez A, Richard D, Gallezot P, Gloaguen F, Faure R, Durand R. Oxygen reduction on well-defined platinum nanoparticles inside recast ionomer. Electrochim Acta 1996;41:307–14.
59. Tauster SJ, Fung SC, Baker RTK, Horsley JA. Strong interactions in supported-metal catalysts. Science 1981;211:1121–5.
60. Lu Q, Yang B, Zhuang L, Lu J. Anodic activation of PtRu/C catalysts for methanol oxidation. J Phys Chem B 2005;109:1715–22.
61. Ajayan PM, Zhou OZ. Applications of carbon nanotubes. Topics in Applied Physics 2001;80:391–425.
62. Pham-Huu C, Keller N, Roddatis VV, Mestl G, Schloegl R, Ledoux MJ. Large scale synthesis of carbon nanofibers by catalytic decomposition of ethane on nickel nanoclusters decorating carbon nanotubes. Phys Chem Chem Phys 2002;4:514–21.
63. Liu Z, Lin X, Lee JY, Zhang W, Han M, Gan LM. Preparation and characterization of platinum-based electrocatalysts on multi-walled carbon nanotubes for proton exchange membrane fuel cells. Langmuir 2002;18:4054–60.
64. Carmo M, Paganin VA, Rosolen JM, Gonzalez ER. Alternative supports for the preparation of catalysts for low-temperature fuel cells: the use of carbon nanotubes. J Power Sources 2005;142:169–76.
65. Wang X, Waje M, Yan Y. CNT-based electrodes with high efficiency for PEMFCs. Electrochem Solid-State Lett 2005;8:A42–4.
66. Rajalakshmi N, Ryu H, Shaijumon MM, Ramaprabhu S. Performance of polymer electrolyte membrane fuel cells with carbon nanotubes as oxygen reduction catalyst support material. J Power Sources 2005;140:250–7.

67. Steigerwalt ES, Deluga GA, Lukehart CM. Pt-Ru/Carbon fiber nanocomposites: synthesis, characterization, and performance as anode catalysts of direct methanol fuel cells. A search for exceptional performance. J Phys Chem B 2002;106:760–6.

68. Matsumoto T, Komatsu T, Nakanoa H, Arai K, Nagashima Y, Yooa E, et al. Efficient usage of highly dispersed Pt on carbon nanotubes for electrode catalysts of polymer electrolyte fuel cells. Catal Today 2004;90:277–81.

69. Villers D, Sun SH, Serventi AM, Dodelet JP. Characterization of Pt nanoparticles deposited onto carbon nanotubes grown on carbon paper and evaluation of this electrode for the reduction of oxygen. J Phys Chem B 2006;110:25916–25.

70. Saha MS, Li R, Sun X. High loading and monodispersed Pt nanoparticles on multiwalled carbon nanotubes for high performance proton exchange membrane fuel cells. J Power Sources 2008;177:314–22.

71. Li WZ, C. H. Liang, W. J. Zhou, J. S. Qiu, Z. H. Zhou, G. Q. Sun, et al. Preparation and characterization of multi-walled carbon nanotube-supported platinum for cathode catalysts of direct ethanol fuel cells. J Phys Chem B 2003;107:6292–9.

72. Che G, Lakshmi BB, Martin CR, Fisher ER. Metal-nanocluster-filled carbon nanotubes: catalytic properties and possible applications in electrochemical energy storage and production. Langmuir 1999;15:750–8.

73. He Z, J. Chen, D. Liu, Zhou H, Kuang Y. Electrodeposition of Pt–Ru nanoparticles on carbon nanotubes and their electrocatalytic properties for methanol electrooxidation. Diamond Relat Mater 2004;13:1764–70.

74. Wu G, Chen YS, Xu BQ. Remarkable support effect of SWNTs in Pt catalyst for methanol electrooxidation. Electrochem Commun 2005;7:1237–43.

75. Li W, Liang C, Qiu J, Zhou W, Han H, Wei Z, et al. Carbon nanotubes as support for cathode catalyst of a direct methanol fuel cell. Carbon 2002;40:791–4.

76. Lordi V, Yao N, Wei J. Method for supporting platinum on single-walled carbon nanotubes for a selective hydrogenation catalyst. Chem Mater 2001;13:733–7.

77. Che GL, Lakshmi BB, Fisher ER, Martin CR. Carbon nanotubule membranes for electrochemical energy storage and production. Nature (London, UK) 1998;393:346–9.

78. Girishkumar G, K. Vinodgopal, P.V. Kamat. J Phys Chem B 2004;108:19960.

79. Rajesh B, Thampi KR, Bonard JM, Xanthopoulos N, Mathieu HJ, Viswanathan B. Carbon nanotubes generated from template carbonization of polyphenyl acetylene as the support for electrooxidation of methanol. J Phys Chem B 2003;107:2701–8.

80. Lee K, Zhang J, Wang H, Wilkinson DP. Progress in the synthesis of carbon nanotube- and nanofiber-supported Pt electrocatalysts for PEM fuel cell catalysis. J Appl Electrochem 2006;36:507–22.

81. Li W, Liang C, Zhou W, Qiu J, Li H, Sun G, et al. Homogeneous and controllable Pt particles deposited on multi-wall carbon nanotubes as cathode catalyst for direct methanol fuel cells. Carbon 2004;42:436–9.

82. Xue B, Chen P, Hong Q, Lin J, Tan KS. Growth of Pd, Pt, Ag and Au nanoparticles on carbon nanotubes. J Mater Chem 2001;11:2378–81.

83. Kim Y-T, Ohshima K, Higashimine K, Uruga T, Takata M, Suematsu H, et al. Fine size control of platinum on carbon nanotubes: from single atoms to clusters. Angew Chem Int Ed 2006;45:407–11.

84. Taylor EJ, Anerson EB, Vilambi NRK. Preparation of high-platinum-utilization gas diffusion electrodes for proton-exchange-membrane fuel cells. J Electrochem Soc 1992;139:L45–6.

85. Choi KH, Kim HS, Lee TH. Electrode fabrication for proton exchange membrane fuel cells by pulse electrodeposition. J Power Sources 1998;75:230–5.

86. Thompson SD, Jordan LR, Forsyth M. Platinum electrodeposition for polymer electrolyte membrane fuel cells. Electrochim Acta 2001;46:1657–63.

87. Wang C, Waje M, Wang X, Tang JM, Haddon RC, Yan Y. Proton exchange membrane fuel cells with carbon nanotube based electrodes. Nano Lett 2004;4:345–8.
88. Qu J, Shen Y, Qu X, Dong S. Preparation of hybrid thin film modified carbon nanotubes on glassy carbon electrode and its electrocatalysis for oxygen reduction. Chem Commun 2004:34–5.
89. Cui HF, J. S. Ye, W. D. Zhang, J. Wang, F. S. Sheu. Electrocatalytic reduction of oxygen by a platinum nanoparticle/carbon nanotube composite electrode. J Electroanal Chem 2005;577:295–302.
90. Guo D-J, Li H-L. High dispersion and electrocatalytic properties of Pt nanoparticles on SWNT bundles. J Electroanal Chem 2004;573:197–202.
91. Penner RM. Mesoscopic metal particles and wires by electrodeposition. J Phys Chem B 2002;106:3335–8.
92. Walter EC, Zach MP, Favier F, Murray BJ, Inazu K, Hemminger JC, et al. Metal nanowire arrays by electrodeposition. Chem Phys Chem 2003; 4:131–8.
93. Favier F, Walter EC, Zach MP, Benter T, Penner RM. Hydrogen sensors and switches from electrodeposited palladium mesowire arrays. Science 2001;293:2227–31.
94. Guo D-J, Li H-L. High dispersion and electrocatalytic properties of platinum on functional multi-walled carbon nanotubes. Electroanalysis 2005;17:869–72.
95. Quinn BM, Dekker C, Lemay SG. Electrodeposition of noble metal nanoparticles on carbon nanotubes. J Am Chem Soc 2005;127:6146–7.
96. Day TM, Unwin PR, Wilson NR, Macpherson JV. Electrochemical templating of metal nanoparticles and nanowires on single-walled carbon nanotube networks. J Am Chem Soc 2005;127:10639–47.
97. Day TM, Unwin PR, Macpherson JV. Factors controlling the electrodeposition of metal nanoparticles on pristine single walled carbon nanotubes. Nano Lett 2007;7:51–7.
98. Lee C-L, Ju Y-C, Chou P-T, Huang Y-C, Kuo L-C, Oung J-C. Preparation of Pt nanoparticles on carbon nanotubes and graphite nanofibers via self-regulated reduction of surfactants and their application as electrochemical catalyst. Electrochem Commun 2005;7:453–8.
99. Li X, Hsing IM. The effect of the Pt deposition method and the support on Pt dispersion on carbon nanotubes. Electrochim Acta 2006;51:5250–8.
100. Li X, Ge S, Hui CL, Hsinga I-M. Well-dispersed multiwalled carbon nanotubes supported platinum nanocatalysts for oxygen reduction. Electrochem Solid-State Lett 2004;7:A286–9.
101. Yoshitake T, Shimakawa Y, Kuroshima S, Kimura H, Ichihashi T, Kudo Y, et al. Preparation of fine platinum catalyst supported on single-wall carbon nanohorns for fuel cell application. Physica B 2002;323:124–6.
102. Kongkanand A, Vinodgopal K, Kuwabata S, Kamat PV. Highly dispersed Pt catalysts on single-walled carbon nanotubes and their role in methanol oxidation. J Phys Chem B 2006;110:16185–9.
103. Kuo PL, Chen CC, Jao MW. Effects of polymer micelles of alkylated polyethylenimines on generation of gold nanoparticles. J Phys Chem B 2005;109:9445–50.
104. Shao Y, Yin G, Wang J, Gao Y, Shi P. Multi-walled carbon nanotubes based Pt electrodes prepared with in situ ion exchange method for oxygen reduction. J Power Sources 2006;161:47–53.
105. Yu R, Chen L, Liu Q, Lin J, Tan K-L, Ng SC, et al. Platinum deposition on carbon nanotubes via chemical modification. Chem Mater 1998;10:718–22.
106. Wang J, Yin G, Shao Y, Wang Z, Gao Y. Platinum deposition on multiwalled carbon nanotubes by ion-exchange method as electrocatalysts for oxygen reduction. J Electrochem Soc 2007;154:B687–93.

107. Galema SA. Microwave chemistry. Chem Soc Rev 1997;26:233–8.
108. Liu Z, Gan LM, Hong L, Chen W, Lee JY. Carbon-supported Pt nanoparticles as catalysts for proton exchange membrane fuel cells. J Power Sources 2005;139:73–8.
109. Chen W-X, Lee JY, Liu Z. Preparation of Pt and PtRu nanoparticles supported on carbon nanotubes by microwave-assisted heating polyol process. Mater Lett 2004;58:3166–9.
110. Chen W, Zhao J, Lee JY, Liu Z. Microwave heated polyol synthesis of carbon nanotubes supported Pt nanoparticles for methanol electrooxidation. Mater Chem Phys 2005;91:124–9.
111. Liu Z, Lee JY, Chen W, Han M, Gan LM. Physical and electrochemical characterizations of microwave-assisted polyol preparation of carbon-supported PtRu nanoparticles. Langmuir 2004;20:181–7.
112. Li X, Chen W-X, Zhao J, Xing W, Xu Z-D. Microwave polyol synthesis of Pt/CNTs catalysts: Effects of pH on particle size and electrocatalytic activity for methanol electrooxidization. Carbon 2005;43:2168–74.
113. Ahmadi TS, Wang ZL, Green TC, Henglein A, El-Sayed MA. Shape-controlled synthesis of colloidal platinum nanoparticles. Science 1996;272–3:1924.
114. Cha SY, Lee WM. Performance of proton exchange membrane fuel cell electrodes prepared by direct deposition of ultrathin platinum on the membrane surface. J Electrochem Soc 1999;146:4055–60.
115. Hirano S, Kim J, Srinivasan S. High performance proton exchange membrane fuel cells with sputter-deposited Pt layer electrodes. Electrochim Acta 1997;42:1587–93.
116. Chen CC, Chen CF, Hsu CH, Li IH. Growth and characteristics of carbon nanotubes on carbon cloth as electrodes. Diamond Relat Mater 2005;14:770–3.
117. Wang C-H, Shih H-C, Tsai Y-T, Du H-Y, Chen L-C, Chen K-H. High methanol oxidation activity of electrocatalysts supported by directly grown nitrogen-containing carbon nanotubes on carbon cloth. Electrochim Acta 2006;52:1612–17.
118. Sun C-L, Chen L-C, Su M-C, Hong L-S, Chyan O, Hsu C-Y, et al. Ultrafine platinum nanoparticles uniformly dispersed on arrayed CNx nanotubes with high electrochemical activity. Chem Mater 2005;17:3749–53.
119. He M, Zhou S, Zhang J, Liu Z, Robinson C. CVD growth of N-doped carbon nanotubes on silicon substrates and its mechanism. J Phys Chem B 2005;109:9275–9.
120. Glerup M, Castignolles M, Holzinger M, Hug G, Loiseau A, Bernier P. Synthesis of highly nitrogen-doped multi-walled carbon nanotubes. Chem Commun 2003:2542–3.
121. Maiyalagan T, Viswanathan B, Varadaraju UV. Nitrogen containing carbon nanotubes as supports for Pt–alternate anodes for fuel cell applications. Electrochem Comm 2005;7:905–12.
122. Guo J, Sun G, Wang Q, Wang G, Zhou Z, Tang S, et al. Carbon nanofibers supported Pt–Ru electrocatalysts for direct methanol fuel cells. Carbon 2006:152–7.
123. Toebes ML, van der Lee MK, Tang LM, Huis in't Veld MH, Bitter JH, van Dillen AJ, et al. Preparation of carbon nanofiber supported platinum and ruthenium catalysts: comparison of ion adsorption and homogeneous deposition precipitation. J Phys Chem B 2004;108:11611–19.
124. Tang H, Chen J, Nie L, Liu D, Deng W, Kuang Y, et al. High dispersion and electrocatalytic properties of platinum nanoparticles on graphitic carbon nanofibers (GCNFs). J Coll Interface Sci 2004;269:26–31.
125. Zhang L, Cheng B, Samulski ET. In situ fabrication of dispersed, crystalline platinum nanoparticles embedded in carbon nanofibers. Chem Phys Lett 2004;398:505–10.
126. Edelstein AS, Cammarata RC, editors. Nanomaterials: synthesis, properties and applications. Boca Raton, FL: CRC Press, 1996.
127. Wu B, Heidelberg A, Boland JJ. Mechanical properties of ultrahigh-strength gold nanowires. Nat Mater 2005;4:525–9.

128. Nalwa HS. Handbook of nanostructured materials and nanotechnology, volume 1: synthesis and processing. Amsterdam: Elsevier, 2000.

129. Dai ZR, Gole JL, Stout JD, Wang ZL. Tin oxide nanowires, nanoribbons, and nanotubes. J Phys Chem B 2002;106:1274–9.

130. Lu H-Y, Chu S-Y, Cheng S-H. The vibration and photoluminescence properties of one-dimensional ZnO nanowires. J Crys Growth 2005;274:506–11.

131. Dang HY, Wang J, Fan SS. The synthesis of metal oxide nanowires by directly heating metal samples in appropriate oxygen atmospheres. Nanotechnology 2003;14:738–41.

132. Ryoo R, Ko CH, Kruk M, Antochshuk V, Jaroniec M. Block-copolymer-templated ordered mesoporous silica: array of uniform mesopores or mesopore-micropore network? J Phys Chem B 2000;104:11465–71.

133. Han Y, Kim JM, Stucky GD. Preparation of noble metal nanowires using hexagonal mesoporous silica SBA-15. Chem Mater 2000;12:2068–9.

134. Huang MH, Choudrey A, Yang P. Ag nanowire formation within mesoporous silica. Chem Commun 2000:1063–4.

135. Shin HJ, Ko CH, Ryoo R. Synthesis of platinum networks with nanoscopic periodicity using mesoporous silica as template. J Mater Chem 2001;11:260–1.

136. Chan IM, Cheng W-C, Hong FC. Enhanced performance of organic light-emitting devices by atmospheric plasma treatment of indium tin oxide surfaces. Appl Phys Lett 2002;80:13–15.

137. Wan Q, Wang TH. Single-crystalline Sb-doped SnO_2 nanowires: synthesis and gas sensor application. Chem Commun 2005:3841–3.

138. Jiang L, Sun G, Zhou Z, Sun S, Wang Q, Yan S, et al. Size-controllable synthesis of monodispersed SnO_2 nanoparticles and application in electrocatalysts. J Phys Chem B 2005;109:8774–8.

139. Santos AL, Profeti D, Olivi P. Electrooxidation of methanol on Pt microparticles dispersed on SnO_2 thin films. Electrochim Acta 2005;50:2615–21.

140. Saha MS, Li R, Cai M, Sun X. High electrocatalytic activity of platinum nanoparticles on SnO_2 nanowire-based electrodes. Electrochem Solid-State Lett 2007;10:B130–3.

141. Debe MK, Schmoeckel AK, Vernstrom GD, Atanasoski R. High voltage stability of nanostructured thin film catalysts for PEM fuel cells. J Power Sources 2006;161:1002–11.

142. Bonakdarpour A, Wenzel J, Stevens DA, Sheng S, Monchesky TL, Löbel R, et al. Studies of transition metal dissolution from combinatorially sputtered, nanostructured $Pt^{i-x}M^x$ (M = Fe, Ni; 0<x<1) electrocatalysts for PEM fuel cells. J Electrochem Soc 2005;152:A61–72.

143. Debe MK. Chapter 45. In: Handbook of fuel cells – fundamentals technology and applications. Vielstich W, Lamm A, Gasteiger HA, eds. New York: John Wiley & Sons, 2003.

144. Hirsch A. Functionalization of single-walled carbon nanotubes. Angew Chem Int Ed 2002;41:1853–959.

145. Tasis D, Tagmatarchis N, Bianco A, Prato M. Chemistry of carbon nanotubes. Chem Rev 2006;106:1105–36.

146. Lin Y, Taylor S, Li HP. Advances toward bioapplications of carbon nanotubes. J Mater Chem 2004;14:527–41.

147. Ebbesen TW, Hirua H, Bisher ME, Treacy MMJ, Shreeve-Keyer JL, Haushalter RC. Decoration of carbon nanotubes. Adv Mater 1996;8:155–7.

148. Hwang K. Efficient cleavage of carbon graphene layers by oxidants. J Chem Soc, Chem Commun 1995:173–4.

149. Xu C, Chen J, Cui Y, Han Q, Choo H, Liaw PK, et al. Influence of the surface treatment on the deposition of platinum nanoparticles on the carbon nanotubes. Adv Eng Mater 2006;8:73–6.

150. Tsang SC, Chen YK, Harris PJF, Green MLH. Nature 1994;372:159.
151. Lago RM, Tsang SC, Lu KL, Chen YK, Green MLH. Filling carbon nanotubes with small palladium metal crystallites: the effect of surface acid groups. J Chem Soc, Chem Commun 1995:1355–6.
152. He Z, Chen J, Liu D, Tang H, Deng W, Kuang Y. Deposition and electrocatalytic properties of platinum nanoparticles on carbon nanotubes for methanol electrooxidation. Mater Chem Phys 2004;85:396–401.
153. Xing YC. Synthesis and electrochemical characterization of uniformly-dispersed high loading Pt nanoparticles on sonochemically-treated carbon nanotubes. J Phys Chem B 2004;108:19255–9.
154. Yang C, HU X, Wang D, Dai C, Zhang L, Jin H, et al. Ultrasonically treated multi-walled carbon nanotubes (MWCNTs) as PtRu catalyst supports for methanol electrooxidation. J Power Sources 2006;160:187–93.
155. Sun X, Li R, Villers D, Dodelet JP, Desilets S. Composite electrodes made of Pt nanoparticles deposited on carbon nanotubes grown on fuel cell backings. Chem Phys Lett 2003;379:99–104.
156. Ma PC, Kim J-K, Thang BZ. Functionalization of carbon nanotubes using a silane coupling agent. Carbon 2006;44:3232–8.
157. Velasco-Santos C, Martýnez-Hernández AL, Lozada-Cassou M, Alvarez-Castillo A, Castaño V, M.;. Chemical functionalization of carbon nanotubes through an organosilane. Nanotechnology 2002;13:495–8.
158. Zhao ZW, Guo ZP, Ding J, Wexler D, Ma ZF, Zhang DY, et al. Novel ionic liquid supported synthesis of platinum-based electrocatalysts on multiwalled carbon nanotubes. Electrochem Comm 2006;8:245–50.
159. Bahr JL, Yang J, Kosynkin DV, Bronikowski MJ, Smalley RE, Tour JM. Functionalization of carbon nanotubes by electrochemical reduction of aryl diazonium salts: a bucky paper electrode. J Am Chem Soc 2001;123:6536–42.
160. Balasubramanian K, Burghard M. Chemically functionalized carbon nanotubes. Small 2005;1:180–92. Copyright Wiley-VCH Verlag GmbH & Co. KGaA.
161. Dyke CA, Tour JM. Overcoming the insolubility of carbon nanotubes through high degrees of sidewall functionalization. Chem Eur J 2004;10:812–17.
162. Moghaddam MJ, Taylor S, Gao M, Huang SM, Dai LM, McCall MJ. Highly efficient binding of DNA on the sidewalls and tips of carbon nanotubes using photochemistry. Nano Lett 2004; 4:89–93.
163. Andrews R, Jacques D, Qian D, Rantell T. Multiwall carbon nanotubes: Synthesis and application. Acc Chem Res 2002;35:1008–17.
164. Wu G, Li L, Li J-H, Xu B-Q. Methanol electrooxidation on Pt particles dispersed into PANI/SWNT composite films. J Power Sources 2006;155:118–27.
165. Nakashima N, Tomonari Y, Murakami H. Water-soluble single-walled carbon nanotubes via noncovalent sidewall-functionalization with a pyrene carrying ammonium ion. Chem Lett 2002;31:638–9.
166. Moore VC, Strano MS, Haroz EH, Hauge RH, Smalley RH. Individually suspended single-walled carbon nanotubes in various surfactants. Nano Lett 2003; 3:1379–82.
167. Matarredona O, Rhoads H, Li Z, Harwell JH, Balzano L, Resasco DE. Dispersion of single-walled carbon nanotubes in aqueous solutions of the anionic surfactant NaDDBS. J Phys Chem B 2003;107:13357–67.
168. Katz E, Wilner I. Biomolecule-functionalized carbon nanotubes: Applications in nanobioelectronics. Chem Phys Chem 2004;5:1084–104.
169. Yang D-Q, Hennequin B, Sacher E. XPS demonstration of π-π interaction between benzyl mercaptan and multiwalled carbon nanotubes and their use in the adhesion of Pt nanoparticles. Chem Mater 2006;18:5033–8.

170. Liu L, Wang T, Li J, Guo ZP, Dai L, Zhang D, et al. Self-assembly of gold nanoparticles to carbon nanotubes using a thiol-terminated pyrene as interlinker. Chem Phys Lett 2003;367:747–52.

171. Wang EG. Nitrogen-induced carbon nanobells and their properties. J Mater Res 2006;21:2767–73.

172. Ewels CP, Glerup M. Nitrogen doping in carbon nanotubes. J Nanosci Nanotech 2005;5:1345–63.

173. Terrones M, Ajayan PM, Banhart F, Blase X, Carroll DL, Charlier JC, et al. N-doping and coalescence of carbon nanotubes: Synthesis and electronic properties. Appl Phys A 2002;74:355–61.

174. Miyamoto Y, Cohen ML, Louie SG. Theoretical investigation of graphitic carbon nitride and possible tubule forms. Solid State Commun 1997;102:605–8.

175. Huang Y, Gao J, Liu R. Structure and electronic properties of nitrogen-containing carbon nanotubes. Synth Me. 2000;113:251–5.

176. Zamudio A, Elias AL, Rodriguez-Manzo JA, Lopez-Urias F, Rodriguez-Gattorno G, Lupo F, et al. Efficient anchoring of silver nanoparticles on N-doped carbon nanotubes. Small 2006;2:346–50.

177. Wang C-H, Du H-Y, Tsai Y-T, Chen C-P, Huang C-J, Chen LC, et al. High performance of low electrocatalysts loading on CNT directly grown on carbon cloth for DMFC. J Power Sources 2007;171:55–62.

178. Kuiyang J, Ami E, Linda SS, Pulickel MA, Richard WS, Nicole G, et al. Selective attachment of gold nanoparticles to nitrogen doped carbon nanotubes. Nano Lett 2003;3:275–7.

179. Ozaki JI, Anahara T, Kimura N, Oya A. Simultaneous doping of boron and nitrogen into a carbon to enhance its oxygen reduction activity in proton exchange membrane fuel cells. Carbon 2006;44:3358–61.

180. Bernardi DM. Water-Balance Calculations for Solid-Polymer-Electrolyte Fuel Cells. J Electrochem Soc 1990;137:3344–50.

181. Parthasarathy A, S. Srinivasan, A.J. Appleby, C.R. Martin. Electrode kinetics of oxygen reduction at carbon-supported and unsupported platinum microcrystallite/Nafion® interfaces. J Electroanal Chem 1992;339:101–21.

182. Ticianelli EA, Derouin CR, Srinivasan S. Localization of platinum in low catalyst loading electrodes to attain high power densities in SPE fuel cells. J Electroanal Chem 1988;251:275–95.

183. Gottesfeld S. In: Tobias C, ed. Advances in electrochemical science and engineering. New York: Wiley and Sons, 1997.

184. Springer TE, Zawodzinski TA, Gottesfeld S. Polymer electrolyte fuel cell model. J Electrochem Soc 1991;138:2334–42.

185. Bernardi DM, Verbrugge MW. A mathematical model of the solid-polymer-electrolyte fuel cell. J Electrochem Soc 1992;139:2477–91.

186. Kocha SS. Principles of MEA preparation. In: Vielstich W, Lamm A, Gasteiger H, editors. Handbook of fuel cells – fundamentals, technology and applications. Chichester, UK: Wiley, 2003;538.

187. Jeng K-T, Chien C-C, Hsub N-Y, Yen S-C, Chiou S-D, Lin S-H, et al. Performance of direct methanol fuel cell using carbon nanotube-supported Pt–Ru anode catalyst with controlled composition. J Power Sources 2006;160:97–104.

188. Yuan F, Ryu H. The synthesis, characterization, and performance of carbon nanotubes and carbon nanofibres with controlled size and morphology as a catalyst support material for a polymer electrolyte membrane fuel cell. Nanotechnology 2004;15:S596–602.

189. Li W, Liang C, Qiu J, Zhou W, Han H, Wei Z, et al. Carbon nanotubes as support for cathode catalyst of a direct methanol fuel cell. Carbon 2002;40:791–4.

190. Girishkumar G, Rettker M, Underhile R, Binz D, Vinodgopal K, McGinn P, et al. Single-wall carbon nanotube-based proton exchange membrane assembly for hydrogen fuel cells. Langmuir 2005;21:8487–94.
191. Li W, Wang X, Chen Z, Waje M, Yan Y. Carbon nanotube film by filtration as cathode catalyst support for proton-exchange membrane fuel cell. Langmuir 2005;21:9386–9.
192. Waje MM, Wang X, Li W, Yan Y. Deposition of platinum nanoparticles on organic functionalized carbon nanotubes grown in situ on carbon paper for fuel cells. Nanotechnology 2005;16:395–400.
193. Matsumoto T, Komatsu T, Arai K, Yamazaki T, Kijima M, Shimizu H, et al. Reduction of Pt usage in fuel cell electrocatalysts with carbon nanotube electrodes. Chem Commun 2004:840–1.
194. Britto PJ, Santhanam KSV, Rubio A, Alonso JA, Ajayan PM. Improved charge transfer at carbon nanotube electrodes. Adv Mater 1999;11:154–7.
195. Wilkinson DP, St-Pierre J. In: Vielstich W, Gasteiger HA, Lamm A, editors. Handbook of fuel cells – fundamentals, technology and applications. Wiley, 2003;611–26.
196. Collier A, Wang H, Yuan XZ, Zhang J, Wilkinson DP. Degradation of polymer electrolyte membranes. Int J Hydrogen Energy 2006;31:1838–54.
197. Hoffman EN, Yushin G, Barsoum MW, Gogotsi Y. Synthesis of carbide-derived carbon by chlorination of Ti2AlC. Chem Mater 2005;17:2317–22.
198. Fowler M, Mann RF, Amphlett JC, Peppley BA, Roberge PR. In: Vielstich W, Gasteiger HA, Lamm A, editors. Handbook of fuel cells – fundamentals, technology and applications. New York: Wiley, 2003;663.
199. Shao Y, Yin G, Gao Y. Understanding and approaches for the durability issues of Pt-based catalysts for PEM fuel cell. J Power Sources 2007;171:558–66.
200. Cleghorn S, Mayfield D, Moore D, Moore J, Rusch G, Sherman T, et al. A polymer electrolyte fuel cell life test: 3 years of continuous operation. J Power Sources 2006;158:446–54.
201. Luo Z, Li D, Tang H, Pan M, Yuan R. Degradation behavior of membrane–electrode-assembly materials in 10-cell PEMFC stack. Int J Hydrogen Energy 2006;31:1831–7.
202. Cheng X, Chen L, Peng C, Chen Z, Zhang Y, Fan Q. Catalyst microstructure examination of PEMFC membrane electrode assemblies vs. time. J Electrochem Soc 2004;151:A48–52.
203. Wilson MS, Garzon HG, Sickafus KE, Gottesfeld S. Surface area loss of supported platinum in polymer electrolyte fuel cells. J Electrochem Soc 1993;140:2872–7.
204. Ralph TR, Hogarth MP. Catalysis for low temperature fuel cells. Part II. The anode challenges. Plat Met Rev 2002;46(3):117–35.
205. Okada T, Ayato Y, Satou H, Yuasa M, Sekine I. The effect of impurity cations on the oxygen reduction kinetics at platinum electrodes covered with perfluorinated ionomer. J Phys Chem B 2001;105:6980–6.
206. LaConti AB, Hamdan M, McDonald RC. Mechanisms of membrane degradation. In: Vielstich W, Gasteiger HA, Lamm A, editors. Handbook of fuel cells – fundamentals, technology and applications. New York: Wiley, 2003;647.
207. Willsau J, Heitbaum J. The influence of Pt-activation on the corrosion of carbon in gas diffusion electrodes – a DEMS study. J Electroanal Chem 1984;161:93–101.
208. Kangasniemi KH, Condit DA, Jarvi TD. Characterization of Vulcan electrochemically oxidized under simulated PEM fuel cell conditions. J Electrochem Soc 2004;151:E125–32.
209. Roen LM, Paik CH, Jarvi TD. Electrocatalytic corrosion of carbon support in PEMFC cathodes. Electrochem Solid-State Lett 2004;7:A19–22.

210. Mathias MF, Makharia R, Gasteiger HA, Conley JJ, Fuller TJ, Gittleman CJ, et al. Two fuel cell cars in every garage? Interface 2005;14:24–35.
211. Ganesan R, Lee JS. An electrocatalyst for methanol oxidation based on tungsten trioxide microspheres and platinum. J Power Sources 2006;157:217–21.
212. Shao Y, Yin G, Gao Y, Shi P. Durability study of Pt/C and Pt/CNTs catalysts under simulated PEM fuel cell conditions. J Electrochem Soc 2006;153:A1093–7.
213. Wang X, Li W, Chena Z, Waje M, Yan Y. Durability investigation of carbon nanotube as catalyst support for proton exchange membrane fuel cell. J Power Sources 2006;158:154–9.
214. Zheng HJ, Ma CN, Wang W, Huang JG. Nanorod tungsten carbide thin film and its electrocatalytic activity for nitromethane electroreduction. Electrochem Comm 2006;8:977–81.
215. Guo CL, Liu Y, Ma XJ, Qian YT, Xu LQ. Synthesis of tungsten carbide nanocrystal via a simple reductive reaction. Chem Lett 2006;35:1210–11.
216. Serp P, Corrias M, P. Kalck. Carbon nanotubes and nanofibers in catalysis. Appl Catal A: Gen. 2003;253:337–58.
217. Maldonado S, Stevenson KJ. Influence of nitrogen doping on oxygen reduction electrocatalysis at carbon nanofiber electrodes. J Phys Chem B 2005;109:4707–16.
218. Coloma F, Sepulvedaescribano A, Rodriguezreinoso F. Heat-treated carbon-blacks as supports for platinum catalysts. J Catal 1995;154:299–305.
219. Dommele SV, De Jong KP, Bitter JH. Nitrogen-containing carbon nanotubes as solid base catalysts. Chem Commun 2006:4859–61.
220. Czerw R, Terrones M, Charlier JC, Blase X, Foley B, Kamalakaran R, et al. Identification of electron donor states in N-doped carbon nanotubes. Nano Lett 2001;1:457–60.
221. Strelko VV, Kuts VS, Thrower PA. On the mechanism of possible influence of heteroatoms of nitrogen, boron and phosphorus in a carbon matrix on the catalytic activity of carbons in electron transfer reactions. Carbon 2000;38:1499–503.
222. Escard JJ, Leclerc C, Contour JP. Catalysis 1973;29:31.
223. Biloul A, Coowar F, Contamin O, Scarbeck G, Savy M, Ham Dvd, et al. Oxygen reduction in acid media on supported iron naphthalocyanine: effect of isomer configuration and pyrolysis. J Electroanal Chem 1990;289:189–201.
224. Yu X, Ye S. Recent advances in activity and durability enhancement of Pt/C catalytic cathode in PEMFC: Part I. Physico-chemical and electronic interaction between Pt and carbon support, and activity enhancement of Pt/C catalyst. J Power Sources 2007;172:133–44.
225. Xie J, Wood DL, Wayne DM, Zawodzinski TA, Atanassov P, Borup RL. Durability of PEFCs at high humidity conditions. J Electrochem Soc 2005;152:A104–13.
226. Ferreira PJ, la O GJ, Shao-Horn Y, Morgan D, Makharia R, Kocha S, et al. Instability of Pt/C electrocatalysts in proton exchange membrane fuel cells. J Electrochem Soc 2005;152:A2256–71.
227. Stevens DA, Dahn JR. Thermal degradation of the support in carbon-supported platinum electrocatalysts for PEM fuel cells. Carbon 2005;43:179–88.
228. Costamagna P, Srinivasan S. Quantum jumps in the PEMFC science and technology from the 1960s to the year 2000: Part II. Engineering, technology development and application aspects. J Power Sources 2001;102:253–69.

15

Non-noble Electrocatalysts for the PEM Fuel Cell Oxygen Reduction Reaction

Kunchan Lee, Lei Zhang and Jiujun Zhang

15.1 Introduction

Proton exchange membrane (PEM) fuel cells, including direct liquid (methanol, ethanol, and formic acid) fuel cells (DLFCs), have drawn a great deal of attention in recent years as energy conversion devices, due to their high efficiency and low/zero emissions. It is generally recognized that one of the key advantages of the PEM fuel cell stack is its fitness for the automobile industry as a zero-emission power supply. But while great progress has been made in the last several decades in the research and development of PEM fuel cells [1–3], the major challenges hindering fuel cell commercialization, i.e., high cost and low durability, are still unsolved. One of the major contributors to cost is fuel cell catalysis (platinum (Pt)-based catalysts). Therefore, new alternative catalysts to reduce or replace expensive Pt are necessary.

In this effort to reduce the cost of fuel cell catalysts, two major approaches are currently very active: Pt loading reduction and non-noble electrocatalyst exploration. In the case of Pt loading reduction [4], two principle avenues have been explored: 1) increase Pt catalytic activity and reduce Pt content through alloying with other transition metals such as Cr, Ni, Fe, Co, etc., and 2) improve Pt utilization by increasing the surface area and dispersion of Pt nanoparticles using high-surface carbon supports. The first approach can effectively create active alloy catalysts with strong activity towards the oxygen reduction reaction (ORR). However, there are many concerns about the long-term stability of these Pt-alloy catalysts due to the leaching of the non-noble metals in the fuel cell operating environment. This leaching causes the following problems: (a) catalytic activity degradation or loss, (b) degradation of membrane proton conductivity by metal ionic contamination, and (c) increase of catalyst layer resistance at the cathode. The second approach, to improve Pt utilization by evenly dispersing Pt nanoparticles on a high-surface carbon support, effectively reduces Pt loading. However, Pt particle size reduction is limited (> 2–3 nm), and further increasing the active surface area seems to be impossible [5]. For such supported Pt catalysts, the agglomeration of Pt nanoparticles is the major problem during fuel cell lifetime

testing. This agglomeration reduces the active Pt area, resulting in performance degradation in long-term operation.

Most importantly, due to the limited global supply of Pt, which is in high demand for jewelry and other industries in addition to fuel cells, the price of Pt has dramatically increased in the last several decades. This suggests that all gains in reducing Pt loading for fuel cells will be offset by this price increase. It is thus debatable whether or not Pt load reduction is a solution for reducing fuel cell cost. Other precious metals such as Pd, Ir, and Ru, which also show catalytic activity towards the ORR and can be used as fuel cell catalysts, have also seen dramatic price rises in the last several decades. Clearly they are not suitable solutions either.

In order to reduce fuel cell catalyst cost, alternative electrocatalysts that are both cost-effective and highly active must be developed. Non-noble catalyst development has become more and more intensive in recent years [6]. For example, perovskite-type and spinel-type oxides and tungsten carbides have been explored as alternative electrocatalysts to platinum. They show promising catalytic activities towards the oxygen reduction and hydrogen oxidation reactions. However, most of these catalysts demonstrate activity and stability in alkaline solutions. In a PEM fuel cell, which uses strong acidic electrolytes, these catalysts are not favorable. Currently, heat-treated transition metal macrocycles seem to be one of most promising non-noble electrocatalysts in strong acid electrolytes [7]. Although they show activity levels close to those of Pt-based catalysts for the ORR in acidic media, their level of stability is the major drawback when they are employed as PEM fuel cell catalysts.

Non-noble catalysts should be the future catalysts for sustainable fuel cell commercialization. Despite several challenges, such as low catalytic activity, poor stability, and our present lack of fundamental understanding of the catalytic mechanism, non-noble catalysts are still very attractive because of their globe abundance and low cost. It is believed that in the face of urgent pressures to reduce environmental pollution and yet maintain or increase energy sources – in particular, the strong drive for fuel cell commercialization – non-noble catalyst exploration and development will intensify. Breakthroughs in the development of non-noble catalysts that exhibit strong performance and stability in fuel cell operation will come in the near future. In this chapter, we present the history of non-noble catalyst development, current progress and challenges, and future R&D directions.

15.2. Transition Metal Macrocycles for the Oxygen Reduction Reaction

In 1964, Jasinski reported his pioneering work on using cobalt phthalocyanine, adsorbed on carbon and nickel electrodes, as a promising catalyst for the reduction of oxygen [8]. Following Jasinski's work, many other transition metal macrocyclic N_4-complexes, including porphyrins, phthalocyanines, and tetraazannulenes, were also explored. The transition metals evaluated include Mn, Ru, Pd, Pt, Ir, Cr, Ni, Cu, Zn, Mo, Al, Sn, Sb, Ga, Na, Ag, vanadyl ion, as well as uranyl ion. All of these compounds show a certain level of electrocatalytic activity towards the ORR [6, 9].

Among these catalysts, Fe- and Co-macrocyclic complexes have exhibited the highest electrocatalytic activity. These catalysts also have shown remarkable selectivity: they have no catalytic activity towards methanol oxidation. Since then, Fe- and Co-macrocyclic complexes have been extensively studied as the most promising ORR selective materials in the effort to replace expensive noble metal Pt catalysts for PEM fuel cell applications, including DMFC applications.

With respect to the catalytic ORR mechanism, Beck et al. and Zagal et al. [10, 11] proposed that the ORR catalyzed by transition metal N_4-chelates mainly involves a modified "redox catalysis". The first step in the mechanism is the adsorption of oxygen on the catalyst metal center to form an oxygen-catalyst adduct, followed by electron transfer from the metal center to bound O_2. This adduct undergoes further reduction to give intermediate species like water or peroxide (which can be reduced further to generate water). The reduced N_4-chelates will be regenerated to complete the catalytic cycling:

$$XMe^{II} + O_2 \Leftrightarrow (XMe^{\delta+}...O_2^{\delta-}) \tag{15.1}$$

$$(XMe^{\delta+}...O_2^{\delta-}) + H^+ \rightarrow (XMe^{III}...O_2H)^+ \tag{15.2}$$

$$(XMe^{III}...O_2H)^+ + H^+ + e^- \rightarrow XMe + \text{intermediates } (H_2O_2) \tag{15.3}$$

$$H_2O_2 + XMe \rightarrow H_2O + 1/2\ O_2 \tag{15.4}$$
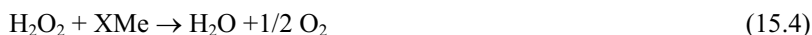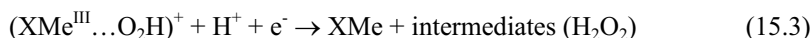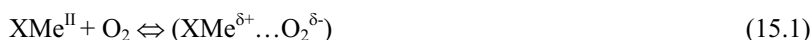
Further studies discovered that the activity and stability of such transition metal macrocyclic complexes could be significantly improved by heat treatment. For the last several decades, heat treatment has been employed to convert macrocyclic complexes to more active and stable catalysts for the ORR. However, long-term stability still remains the problem. One hypothesis is that the hydrogen peroxide produced during the ORR process can attack the catalysts and damage their active sites, resulting in performance degradation. Heat treatment can destroy the structure of the ligand and form surface $Fe-N_x$ or $Co-N_x$ species which are active towards the ORR [7]. However, the structures of such active sites are still not well understood, although tremendous analysis has been done using sophisticated instruments.

It has been recognized that the electrocatalytic activity and stability of Fe- and Co- macrocyclic complexes can be strongly affected by other factors such as the type of central transition metal ion, the ligand structure, the type of support, the method of synthesis, etc. In what follows, these factors will be discussed in more detail.

15.2.1. The Central Transition Metal Effect

Depending on the nature of the central metal, the oxygen reduction reaction takes place either via a 2-electron transfer pathway to peroxide, or a 4-electron transfer pathway to water, or a mixed pathway of 2- and 4-electron transfers. The central metal ion of a macrocycle seems to play a decisive role in the ORR mechanism. Most Fe complexes can reduce oxygen directly to water through a 4-electron

transfer pathway, while most Co complexes give peroxide as the main product through a 2-electron transfer pathway. For N_4 chelates (phthalocyanines) as catalysts, the activity order of the catalyzed ORR follows the pattern of Fe > Co > Ni > Cu ≈ Mn [12]. Alt et al. [13] explained this activity sequence by molecular orbital (MO) theory. According to their model, the back bonding of filled d_{xz} and d_{yz} orbitals and empty d_z^2 orbitals favors the partial electron transition from the metal to the empty or partially filled π^* orbitals of oxygen. In general, Co complexes have higher electrochemical stability than Fe complexes, whether or not they are heat-treated. The stability sequence of metal macrocyclic complexes was summarized by Jiang et al. [14] as Co > Fe > Mn.

The formation of dimetal face-to-face macrocycles can effectively promote a 4-electron transfer pathway from oxygen to water. For example, such catalysts include dicobalt face-to-face porphyrins [15], and pillared dicobalt cofacial porphyrins [16], as well as other binuclear and polynuclear Co phthalocyanines [17]. In this catalyst, two Co centers can provide two adsorption sites for O_2 to form a bridge adsorption, facilitating a 4-electron transfer process, as suggested by Anson et al. [18, 19].

It has also been reported that O_2 reduction efficiency could also be improved by using two different metal centers, as proposed by Chu et al. [20]. In order to combine the advantages of an Fe complex (4-electron ORR pathway to water) with the high electrochemical stability of Co complexes, they heat-treated a mixture of two transition metalloporphyrins (V/Fe, Co/Fe, Ni/Fe, or Cu/Fe) to form a bimetal catalyst, and tested its ORR activity. The ORR activity was then compared to that catalyzed by heat-treated single transition metalloporphyrin. They found that the heat-treated mixture of Fe- and Co-tetraphenylporphyrins gave a much higher catalytic ORR activity than the heat-treated single Fe-tetraphenylporphyrin or Co-tetraphenylporphyrin. This was also attributed to the formation of a face-to-face structure with two kinds of metal active sites. The interaction between two different transition metals and oxygen molecules promotes O-O bond breakage, resulting in an easier 4-electron transfer to form H_2O. High loading of heat-treated Co-naphthalocyanine (CoNPc) on carbon black was suggested as an alternative way to prompt a 4-electron reaction pathway to water, whereby two mono-layers of CoNPc were found to generate optimum activity [21].

Although Fe and Co macrocyclic complexes exhibit high electrocatalytic activity towards the ORR, a growing number of studies have indicated that transition metals may not be required for the reduction of oxygen on carbonaceous materials, as long as such materials can be properly activated by incorporating active nitrogen sites. The studies suggest that, rather than being directly part of the active sites, metal particles may act as the catalysts for active site formation during high-temperature heat treatment [22].

15.2.2. The Ligand Effect

Ligands also play an important role in the catalyzed ORR. They not only serve as part of the active site, but also keep the metal in a stable form on the electrode surface. The substituents of the macrocycle ligand seem to have less effect in comparison with the type of macrocycle [23]. Phthalocyanine (Pc), tetrasulfophthalocyanine (TSP), tetracarboxyphthalocyanine (TcPc), polymeric phthalocyanine, tetraphenylporphyrin (TPP), tetramethoxyphenylporphyrin (TMPP), and dibenzotetraazaannulene (TAA) all can form complexes with Fe and Co. The majority of thus formed complexes have ORR catalytic activity.

Cobalt-phthalocyanine   Cobalt-tetrasulfophthalocyanine

Tetramethoxyphenylporphyrin   Dihydrodibenzotetraazaannulene
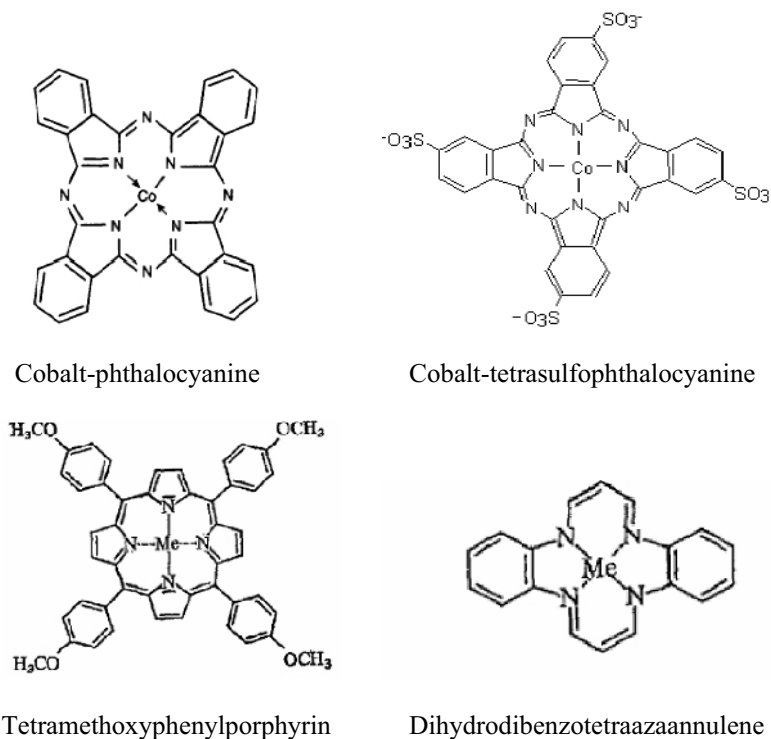
Figure 15.1. Structures of typical metal N_4 chelates and ligands [24–26]. (Co-tetrasulfophthalocyanine image reproduced from Castellani AM, Gonclaves JE, Gushiken Y. The use of carbon paste electrodes modified with cobalt tetrasulfonated phthalocyanine adsorbed in silica/titania for the reduction of oxygen. J New Mater Electrochem Syst 2002;5:169–72, Figure 1, reprinted with permission from JNMES. Cobalt-phthalocyanine image reproduced from Li J, Wu X, Yuan R, Lin H, Yu R. Cobalt phthalocyanine derivatives as neutral carriers for nitrite-sensitive poly(vinyl chloride) membrane electrodes. The Analyst 1994;119:1363–6, Figure 1, reproduced by permission of The Royal Society of Chemistry. Bottom images reprinted from Jahnke H, Schonbron M, Zimmerman G. Organic dyestuffs as catalysts for fuel cells. Top Curr Chem 1976;61:133–81, Figure 1, with kind permission of Springer Science+Business Media.)

Figure 15.1 shows the molecular structure of several typical metal N_4 chelates and ligands [24–26]. The ORR catalytic activity of these complexes can be partially attributed to the inductive and mesomeric effects of the ligand on the central metal ion. However, when these as-prepared complexes were tested in a PEM fuel cell environment, they could not show enough chemical/electrochemical stability. For example, even at a temperature of 50 °C, Fe-phthalocyanine could be disintegrated in an acid electrolyte [27]. Biloul et al. [28] tested and compared the stability of 800 °C heat-treated Co-tetramethoxyphenylporphyrin (TpOCH$_3$PPCo) and its derivatives (Co-trifluoromethylphenylporphyrin (CF$_3$PPCo) and Co-tetraazaannulene (CoTAA) as ORR catalysts at a current density of 100 mAcm^{-2} with 300 hrs of lifetime under fuel cell conditions. The stability order was observed as: CoTAA >> TpOCH$_3$PPCo > TpOCF$_3$PPCo. To improve the stability of these complexes, an attempt was made to enlarge the organic part of the molecule and create a stronger attachment of the catalyst onto the support base. Unfortunately, the results did not seem promising [29].

15.2.3. The Heat-treatment Effect

Since the 1970s, it has been reported that the heat treatment of metal N_4 chelates at high temperature could significantly increase their catalytic activity and stability towards the electroreduction reaction of oxygen [13, 26]. Since then, this pioneering work has led to worldwide research interest. Figure 15.2 shows the effect of heat treatment on CoTAA catalytic activity. Maximum ORR catalytic activity can be achieved at a heat-treatment temperature of 600 °C, and optimal stability at 800–900 °C.
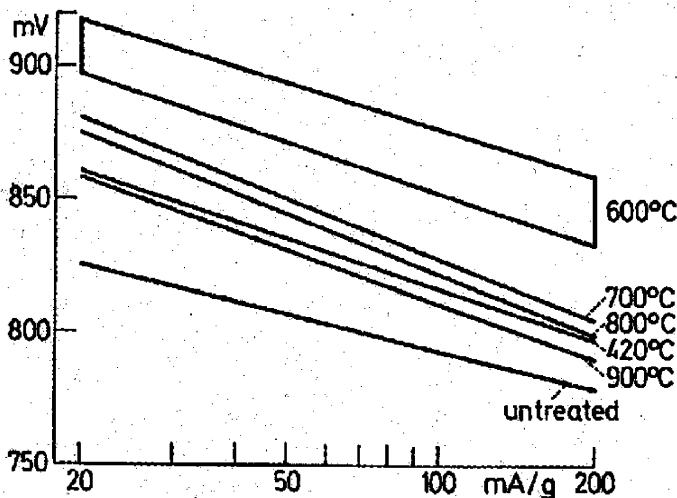
Figure 15.2. Dependence of thermal activation on heat-treatment temperature of CoTAA (Electrolyte: 4.5 N H$_2$SO$_4$) [26]. (Reprinted from Jahnke H, Schonbron M, Zimmerman G. Organic dyestuffs as catalysts for fuel cells. Top Curr Chem 1976;61:133–181, Figure 22, with kind permission of Springer Science+Business Media.)

Some recent results have revealed that the optimal activity for N_4-chelate catalysts is normally obtained at a heat-treatment temperature range of 500–700 °C [30–32]. However, it has also been discovered that a higher pyrolysis temperature (> 800 °C) is necessary in order to achieve stable performance in a PEM fuel cell environment. A deleterious effect on electrode performance was observed at temperatures higher than 1100 °C [33]. Even for some carbon-supported Fe- and Co-phthalocyanines, stability can also be considerably improved. For example, an almost 50 times greater enhancement in electrocatalytic activity was achieved at an electrode potential of 700 mV (vs. NHE) when carbon-supported Co-phthalocyanine was heat-treated in an environment of N_2 or Ar at 700–800 °C [34]. Furthermore, in experiments with carbon-supported Ru-phthalocyanine, heat treatment at 650 °C could increase the catalytic activity by 20 times at 800 mV (vs. NHE). Unfortunately, there was no insignificant improvement in catalyst stability. Not all heat-treated carbon-supported metal phthalocyanines gave positive results. For example, the activities and stabilities of Zn- and Mn-phthalocyanines were not affected by heat treatment [34]. The duration of heat treatment for these complexes is usually around 0.3~5 hrs.

When heat treatment is performed at a lower temperature range such as 500–700 °C, the active catalytic site can be identified as a Me-N_4 moiety. However, at a higher temperature range (i.e., > 800 °C), the structure of the catalytic active site is still unclear. According to some work [35–37], the Me-N_4 super-sites would disappear when the temperature was too high, suggesting that the nature of such active sites is changed due to higher temperature. In identifying the catalytic sites produced at high-temperature pyrolysis, Dodelet et al. [38] investigated the activity and active sites of Fe precursors. They pyrolyzed perylene tetracarboxylic dianhydride (PTCDA) together with Fe and N precursors, then employed an instrumental method called Time-of-Flight Secondary Ion Mass Spectrometry (ToFSIMS) for active site identification. The only species detected in their work was FeN_2C_4+.

Heat treatment can facilitate bonding of the metal ions to the surface nitrogen of a graphite particle surface. The graphite particle surface serves as the catalyst support. It is believed that the inner core structure of the N_4 macrocycle remains after pyrolysis and then acts as a catalytic center towards the ORR. The better electrochemical stability of the centers has been assumed to be the result of electronic integration into a stable carbon particle [39].

15.2.4. The Effect of the Synthesis Method

Since the structure of these N_4-chelate catalysts will be largely destroyed at high pyrolysis temperatures, it might not be necessary to use expensive metal macrocyclic complexes as precursors for active catalyst preparation [40]. It is expected that if a mixture of basic components, i.e., transition metal sources such as Fe or Co, nitrogen donors, and carbon supports, could be treated at a high temperature, catalytically active sites such as metal-N_4 or $FeN_2C_4^+$ might be formed [41]. Several research groups have reported their work on this alternative preparation route with various transition metal, nitrogen, and carbon containing species as precursors. This approach creates a very attractive strategy for

electrocatalyst preparation using more popular and cheaper starting materials. The most popular transition metal precursors that have been employed are Fe or Co inorganic salts such as sulfates, acetates, hydroxides, chlorides, and cyanides, and Fe complexes such as ferrocene [42–45]. Inorganic precursors might be more cost-effective for commercialization.

Nitrogen sources are critical to catalytic activity. Nitrogen-containing chemicals such as polyacrylonitrile, tetracyanoquinodimethane, ethylenediamine, 1,2-phenylenediamine, hydrogen phthalocyanine, as well as pyrroles, have been found to be effective precursors for catalyst preparation [46, 47]. N-containing gases such as NH_3 [48] or acetonitrile [49], and N-containing groups on a modified carbon support (e.g., HNO_3/NH_3 treated carbon support) [50] have also been employed as nitrogen sources for the preparation process. It is clear that the most important factor is the nitrogen content of the materials. It was found that higher nitrogen content yielded higher catalytic surface site density and then better electrocatalysts [51].

Carbon support could be another factor affecting catalytic activity. Jaouen et al. [51] studied the effect of carbon support on catalytic activity and found that the activity varied with the specific surface area, pore size distribution, and N or O content of the carbon support.

Metal loading on the carbon support may also affect catalytic activity. Lalande et al. [52] studied the effect of transition metal Co loading (0 to 8 weight percent) on the activity and stability of heat-treated carbon-supported Co-phthalocyanine at a temperature range of 500–1100 °C. They found an optimum value for Co loading on the carbon support (~3.5 weight percent). This optimum Co loading was not dependent on the heat-treatment temperature. They also found that the optimum Co loading value corresponded to full monolayer coverage of the Co-phthalocyanine on the carbon support. Faubert et al. [53] reported the effect of Fe loading on catalytic activity by heating Fe-adsorbed PTCDA in an environment of $Ar+H_2+NH_3$. It was found that the catalytic activity at first was increased by increasing Fe content, but levelled off when the Fe content was greater than 0.5 weight percent. It is believed that excess Fe favors the formation of aggregates which contain catalytic inert metallic and/or carbidic iron.

Lalande et al. [45] proposed a multi-step pyrolysis method for O_2 reduction catalyst preparation. Wei et al. [49] carried out some comparisons between one-step and multi-step pyrolysis. In their experiments, catalysts containing carbon, nitrogen, and cobalt were prepared. In the multi-step pyrolysis method, the first pyrolysis step was to pyrolyze the carbon support (Vulcan XC72R) with a nitrogen precursor (acetonitrile) in a flowing argon atmosphere, and then to introduce the cobalt precursor (cobalt sulfate) into the reactor for the second step. The second step was to pyrolyze the mixture of the product and the introduced cobalt precursor in a flowing argon atmosphere. It was also found that the pyrolysis sequence has a strong impact on catalyst activity. For example, the onset electrode potential for the ORR (E_{onset}) catalyzed by catalysts produced in different pyrolyzation sequences was about 790~800 mV (vs. RHE), similar to that obtained with a cobalt-centered macrocycle catalyst synthesized by one-step pyrolysis at 1000 °C [54, 55].

More recently, Ye et al. [56] proposed a new sol-gel method combined with a supercritical drying technique for the preparation of nanocomposite electrocatalysts

for oxygen reduction. They claimed that their method has a structure-preserving ability and favors a nanoscale mixing of the constituents, and then can produce a remarkably homogeneous solution. The chemical, physical, and morphological properties of catalysts produced using this sol-gel method were claimed to be significantly isotropic. Compared to other preparation methods, this new sol-gel method has some unique and competitive features. The first step of this synthesis method was the mixing of an inorganic salt (e.g., $Fe(NO_3)_3$ or $CoCl_2$) or an organometallic compound (e.g., Co(III) acetylacetonate) with polyacrylonitrile (PAN) in N,N-dimethylformamide (DMF)/water to form a well-mixed solution. The mixed solution was degassed when heated to approximately 120 °C. When the solution was cooled, a polymer gel containing the metallic compound was obtained by thermally induced phase separation. The polymer gel was then pre-treated at 220 °C, followed by a pyrolysis step at 900 °C under an argon atmosphere. In this way, a non-noble catalyst showed strong catalytic activity and relatively high stability for the ORR in acid conditions.

Bogdanoff et al. [39] found that the activity of pyrolyzed carbon-supported CoTMPP could be limited by the morphology of the products. Thus, they introduced a new preparation strategy, which led to an *in situ* formed graphite-like carbon matrix with uniform catalytic centers. In their method, metal oxalates were added into the reaction as foaming agents during the heat treatment. The purpose of adding metal oxalate foaming agents was to suppress the particle aggregation and increase the surface area of the macrocycle catalysts (up to 800 m^2g^{-1}). In this way, the catalytic activity could be improved by an increase in the catalyst.

In addition, some new heat-treatment techniques for synthesizing highly active macrocyclic complexes have been reported. These methods can effectively create favorable morphology and increase the catalyst surface area. For example, Liu et al. [57] recently developed an ultrasonic spray pyrolysis (USP) technique to synthesize CoTMPP/C catalysts. The USP method is a continuous, one-step, scalable method to prepare unaggregated spherical and uniform particles with controllable particle size. The carbon-supported CoTMPP particles synthesized by this method have a high surface area of 834 m^2g^{-1}. In a rotating ring-disk electrode (RRDE) measurement, the ORR catalyzed by this CoTMPP displayed double the activity of a catalyst prepared by the conventional heat-treated method. A fuel cell performance of 0.4 V at 110 $mAcm^{-2}$ using such a USP-derived CoTMPP/C as the cathode catalyst was achieved, compared to a performance of 0.4 V at 40 $mAcm^{-2}$ obtained using the same cell with a conventional heat-treated CoTMPP/C catalyst. At a higher cell voltage such as 0.7 V, the USP-derived catalyst generated a current density of 55 $mAcm^{-2}$, which is two times greater than that obtained using a conventional catalyst. These results demonstrated that the favorable morphology of a CoTMPP/C catalyst created by ultrasonic spray pyrolysis has a significant effect on catalyst activity, even under fuel cell operating conditions.

Zelenay et al. [58] explored Co-polypyrrole (CoPPy) material as a PEM fuel cell cathode catalyst. The composite CoPPy catalyst, even without heat treatment, could generate a power density of ~0.15 Wcm^{-2} in a H_2-O_2 fuel cell and displayed no signs of performance degradation for more than 100 hrs. Their results show that hetero-atomic polymers can be used not only to stabilize the non-noble metals in a PEM fuel cell environment but also to generate active sites for the ORR. Study of

the interaction between the catalyst and oxygen also demonstrates that CoPPy forms stable end-on, side-on, and bridged oxygen adducts. Furthermore, the side-on and bridged oxygen adducts are more stable than the end-on adducts. Since side-on and bridged oxygen adducts greatly elongate O-O bond lengths, they generally lead to 4-electron reduction products. They thus differ significantly from Co macrocyclic catalysts, which cannot form these types of oxygen adducts and generally yield 2-electron reduction products.

For the purposes of comparison, Table 15.1 lists the typical methods employed for the preparation of Fe and Co heat-treated electrocatalysts and their corresponding electro-catalytic activities towards oxygen reduction reaction.

Table 15.1. Preparation methods for Fe- and Co-based catalysts for the ORR

Methods	Starting Chemicals	Operating Environment	Possible Catalysts Produced	Catalytic Activity Towards ORR	Ref.
Pyrolyzed metal-N_4 macrocycles	Fe- or Co-N_4 macrocycles	Pyrolyzed at ~1000 °C, with carbon support in argon	CoPc/C	Onset potential: ~800 mV (vs. RHE)	[46, 47]
Single-step Method	Independent Fe or Co precursors, N and C sources	Pyrolyzed at ~1000 °C in argon	CNCo	Onset potential: 790~800 mV (vs. RHE)	[41]
Multi-step Method	Independent Fe or Co precursors, N and C sources	Pyrolyzed at ~1000 °C in argon	CNCo	Onset potential: 790~800 mv (vs. RHE)	[41]
Sol-gel Method	Independent Fe or Co precursors, N and C sources	DMF/water solvent, pyrolyzed at 900 °C in argon	PAN-Co or PAN-Fe	600 mV for PAN-Fe, 550 mV for PAN-Co and 710 mV (vs. NHE) for Pt at maximum current	[48]
Plasma method	Fe-oxalate/ CoTMPP		CoTMPP	> 100~500 mA/mg at 700 mV	[31]
Ultrasonic spray pyrolysis (USP) method	Co salts, H_2TMPP	Pyrolyzed at ~800 °C in nitrogen	CoTMPP	~850 mV (vs. RHE) (open circuit potential)	[49]
Impregnation method	Co salts, polypyrrole	Reflux at 80 °C	CoPPy	~200 mAcm^{-2} at 500 mV	[50]

15.3. Non-noble Transition Metal Carbides and Nitrides for the ORR

Transition metal carbides and nitrides are two major kinds of electrode materials. This is due to their good electrical conductivity, corrosion resistance, and electrocatalytic activity. In the past several decades, some studies have been done on these materials as electrocatalysts for hydrogen and methanol oxidation and oxygen reduction reactions in alkaline and acid solutions [59–63]. This section will briefly review transition metal carbides and nitrides and then introduce current state-of-the-art catalysts explored in acidic media.

15.3.1 Carbides

Transition metal carbide is one of the most widely studied catalyst materials because of its superior electrical conductivity. In 1963, Mazza and Trassatti [59] first found that several transition metal carbides such as tungsten, titanium, and tantalum are active towards the oxygen reduction reaction in sulfuric acid. Among them, tungsten carbide in particular is superior to the other carbides. However, their ORR catalytic activities were not high enough for them to be employed in fuel cells. For the kinetic parameter of tungsten-carbide-catalyzed ORR, Voinov et al. [64] reported that the ORR exchange current density catalyzed by tungsten carbide (containing 0.1% cobalt) was 1×10^{-9} Acm^{-2} in 1 M perchloric acid. This value is almost the same order of magnitude as that of a platinum electrode in an acidic medium [5].

Recently, there have also been several approaches to using the transition metal carbides as non-noble electrocatalysts in the PEM fuel cell. In particular, since tungsten carbide (WC) shows platinum-like characteristics in terms of electronic structure and chemisorption of hydrogen and oxygen [61–63], it has attracted much interest for its new application as an electrode material for fuel cells. Levy and Boudart [65] postulated that the Pt-like behavior of tungsten carbide is due to the change of electron distribution in tungsten by the addition of carbon, resulting in tungsten carbide having a similar valence band structure to that of platinum. This was proven by an X-ray photoelectron spectroscopy (XPS) analysis: the states of electronic density of tungsten carbide at Fermi level are very similar to those of platinum. Figure 15.3 compares the XPS valence bands for tungsten carbide, Pt, and tungsten. The density of states at the Fermi level, $N(E_F)$, of tungsten carbide has an intermediate character between that of tungsten and of Pt, The Fermi level of tungsten falls in a region of low density of d-like states. The Fermi level of Pt falls in a region of high density of d-like states. Unfortunately, the observation of a more platinum-like $N(E_F)$ in tungsten carbide cannot provide a complete explanation for its observed catalytic behavior. However, it is believed that a high $N(E_F)$ is a necessary but not sufficient condition for high catalytic activity. As electrocatalysts for fuel cells, tungsten carbides have attracted a lot of interest in hydrogen and methanol oxidation in acid solution [60, 66–73]. On the other hand, due to the low stability of tungsten carbides in a corrosive environment, there have

been relatively very few studies on the oxygen reduction reaction in both alkaline and acid solutions.
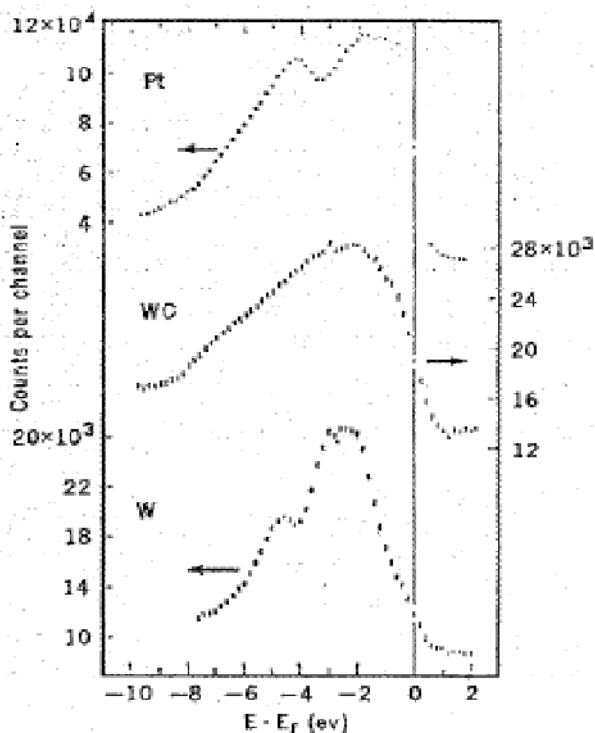
Figure 15.3. Valence band XPS spectra of WC, Pt, and W [61]. (From Bennett LH, Cuthill JR, McAlister AJ, Erickson NE. Electronic structure and catalytic behavior of tungsten carbide. Science 1974;184:56365. Reprinted with permission from AAAS.)

It is generally known that tungsten carbide is not stable in alkaline solution because it dissolves. However, Vijh et al. [74] observed that cobalt-cemented tungsten carbide (Co-WC) presented considerable stability in alkaline solution. This tungsten carbide dissolved over 0.7 V vs. RHE under a nitrogen atmosphere. However, such dissolution was not observed under an oxygen atmosphere at the same electrode potential. Although some ORR catalytic activity was also observed on this carbide, this catalyst was more favorable for the reduction reaction of hydrogen peroxide rather than the oxygen reduction reaction.

In an effort to stabilize tungsten carbides, adding tantalum to tungsten carbide was found to be effective in improving stability at high electrode potentials and in a strong acidic atmosphere [75]. This carbide was fabricated by the reactive sputtering method using tungsten carbide and tantalum metal. Figure 15.4 demonstrates that a Ta-added WC (WC+Ta, $W_{42}Ta_{24}C_{34}$) electrode is electrochemically stable on Nafion® electrolyte at the employed potential range and at 30 °C and 60 °C, while a pure WC electrode will be oxidized at potentials above 0.5 V vs. DHE. Through the reactive sputtering reaction between tungsten

carbide and tantalum metal, the following components were formed in a WC+Ta electrode:

$$WC + Ta \rightarrow WC + W\text{-}Ta + TaC_x + Ta + C \tag{15.5}$$
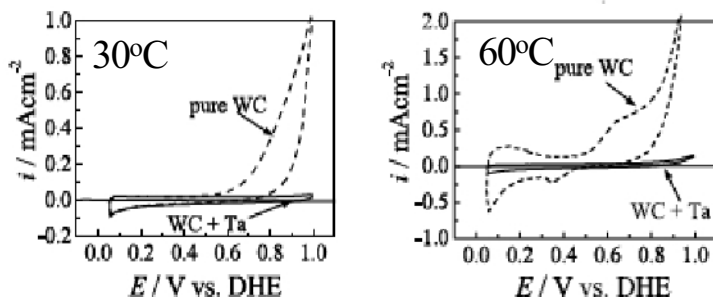
Figure 15.4. Comparison of cyclic voltammograms on Nafion® electrolyte under N_2 atmosphere. Scan rate = 100 mV/s [75]. (Reprinted from Electrochimica Acta, 49(21), Lee K, Ishihara A, Mitsushima S, Kamiya N, Ota K-I, Stability and electrocatalytic activity for oxygen reduction in WC + Ta catalyst, 3479–85, ©2004, with permission from Elsevier.)

Among them, the W-Ta alloy has the highest stability in a corrosive atmosphere. The formation of this alloy might protect against the surface oxidation of the WC+Ta electrode. The WC+Ta electrode also exhibited a considerably high onset potential for the ORR compared to pure WC, i.e., 350 mV higher than pure WC. This is the highest value for carbide materials so far reported. Such high activity was explained by the fact that the W-Ta alloy might restrain the oxidation of the surface active site, i.e., tungsten carbide. Similar stability and activity were also observed in chromium-added tungsten carbide (WC+Cr) [76].

For other metal-based carbides, $Ni_{33}Ta_{41}C_{26}$ was reported as a possible electrocatalyst for the oxygen reduction and hydrogen oxidation reactions [77]. This carbide deposited on carbon paper by DC magnetron sputtering is quite passive against corrosion in 1.5 M sulfuric acid up to 70 °C in a wide range of electrode potential (–0.65 V to 0.25 V vs. mercury/mercurous sulfate reference electrode). This anti-corrosion property resulted from the effect of tantalum addition. Ta was able to form a thin Ta_2O_5 film on the particle, protecting the catalyst from corrosion. The effect of tantalum on $Ni_{33}Ta_{41}C_{26}$ is similar to that of WC+Ta discussed above. Unfortunately, however, Ta_2O_5 oxide is an electron insulator.

In a continuous study of the Ni-Ta-C system, Dhan et al. [78] examined the structure, corrosion resistance, and electrocatalytic activity of thin film libraries of carbides such as $Ta_xNi_yC_{1-x-y}$ $(0.1 < x < 0.5, 0 < y < 0.9)$ and $Ta_{1-x-y}Ni_xC_y$ $(0 < x < 0.18$ and $0.82 < y < 0.86)$. These materials were combinatorially prepared by a DC magnetron sputtering method. It was found that the corrosion stability of these materials in 1.0 M H_2SO_4 at 80 °C could be increased by increasing the Ta content. With respect to the catalyzed ORR, their activity could be increased by increasing the Ni content. The highest catalytic activity was observed when $Ta_{0.01}Ni_{0.16}C_{0.83}$ was used. The composition ratio in $Ta_{0.01}Ni_{0.16}C_{0.83}$ is different from that in a

previous report by Burstein et al. [77] in terms of optimal ORR catalytic activity. The conclusions obtained by this work [78] with respect to the benefits of Ta and Ni for stability and catalytic activity are consistent with those of previous reports: Ta can improve the corrosion resistance and Ni promotes catalytic activity. Additionally, the catalytic activity of these ternary carbides also strongly depends on heat treatment. As the heat-treatment temperature was increased up to 800 °C, the ORR catalytic activity was also enhanced accordingly. However, no further improvement could be seen after the heat-treatment temperature was further increased beyond 800 °C.

15.3.2 Nitrides

Nitrides as electrocatalysts in PEM fuel cell applications have not been intensively investigated as compared with other non-noble metal catalysts. However, their unique electrochemical properties and stability in electrolytes with a wide pH range might provide promising opportunities to be used as electrocatalysts for PEM fuel cells. In the 1960s, Giner and Swette [79] reported titanium nitride to be a novel non-noble catalyst for fuel cells. This nitride was then investigated as an ORR catalyst in 2 M potassium hydroxide solution at 75 °C. Titanium nitride exhibited less corrosion than metal titanium. Moreover, it has quite high ORR activity, as shown in Figure 15.5. It can be seen that titanium metal shows an ORR onset potential at 300 mV vs. RHE, while its nitride can give a value of ~800 mV. This nitride can catalyze a nearly 4-electron reaction from oxygen to water in alkaline solution. Such catalytic behavior is much different from that of titanium metal, which can only catalyze a 2-electron reaction from O_2 to peroxide. It was suggested that the nitridation of metals, such as titanium, iron, nickel, and cobalt, could help to increase their ORR activity.

The nitridation of cobalt was also examined in a neutral electrolyte solution by Azuma et al. [80]. They used a cobalt plate as the target and prepared cobalt-nitride (Co_xN) on a smooth titanium metal plate by the reactive sputtering technique. Co_xN is not stable in acidic solution due to dissolution. In alkaline solution, the material particle is covered by an insulating oxide layer. Although it is stable in a neutral solution such as Na_2SO_4 (pH 6.0), electrochemical oxidation and dissolution at potentials more positive than 0.3 V vs. SCE also make it unstable. The Co_xN catalyst showed an ORR catalytic activity at potentials less than 0.1 V vs. SCE. This potential value is much higher than that catalyzed by pure metal cobalt, which showed a potential less than –0.5 V vs. SCE. It is interesting to note that this Co nitride could promote a 4-electron reduction from O_2 to H_2O, which is more prevalent than a Pt catalyst. The measured overall electron transfer number for catalyzed ORR by this Co nitride was around 3.4 to 3.7 compared to the value of 3.3 obtained using a Pt catalyst. The improved ORR by Co_xN was interpreted according to a modification mechanism, i.e., the electronic structure of the Co atoms in Co_xN could be modified by the surrounding nitrogen atoms to form a similar structure as the CoN_4 chelate catalyst. Since both the top-on type and bridge-type adsorptions of oxygen are possible stereochemically on the Co_xN surface, the ORR on this nitride surface may be favorable for a 4-electron pathway.
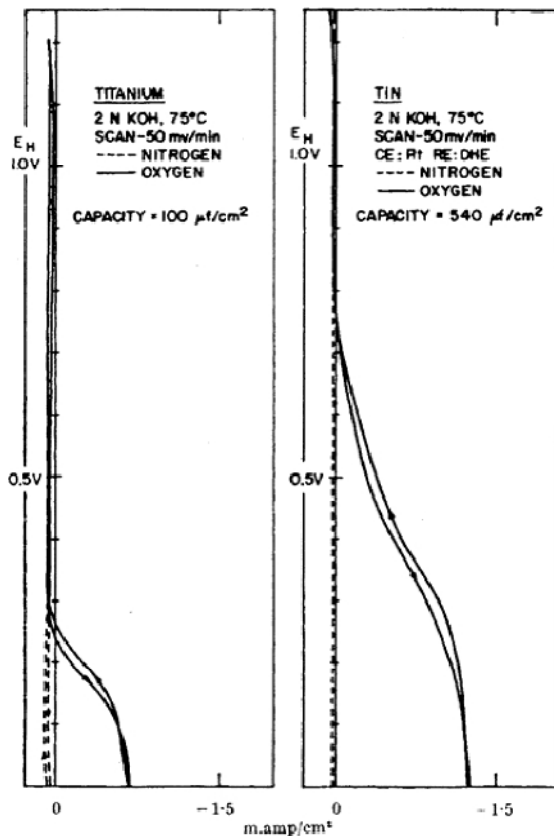
Figure 15.5. I-V curves for titanium and titanium nitride in N_2 and O_2 atmosphere [79]. (Reprinted by permission from Macmillan Publishers Ltd. Nature. Giner J, Swette L. Oxygen reduction on titanium nitride in alkaline electrolyte. 1996;211(5055):1291–2, ©1966.)

Molybdenum nitrides are another type of nitride being explored as PEM fuel cell catalysts. Recently, Zhang et al. [81, 82] investigated tungsten and molybdenum nitrides in sulfuric acid and single cell tests in an effort to improve catalyst activity and stability. In their study, W_2N/C and Mo_2N/C catalysts were synthesized by temperature-programmed reaction under flowing NH_3 gas. The obtained Mo_2N/C and W_2N/C catalysts presented considerably high activity towards the ORR in acidic media with onset potentials of 0.7 V and 0.6 V vs. SHE, respectively. In particular, Mo_2N/C displayed an ORR electron transfer number of 3.8, indicating that most of the oxygen was reduced to water through a 4-electron pathway. It was also found that molybdenum could be partially oxidized to $Mo^{\delta+}N^{\delta-}$ in Mo_2N. As a result, the surface of Mo_2N could have unsaturated Mo and N atoms, resulting in some four-fold-type vacancies. These vacancies are highly active towards molecular O_2 dissociation. This association is similar to that on dicobalt cofacial porphyrin lined by four-atom bridges [83]. This type of O_2 adsorption and dissociation model was adapted to explain their Mo_2N/C catalyst, as

described in Figure 15.6. The change of electron distribution in Mo, induced by addition of nitrogen, probably promotes the dissociation and adsorption of oxygen, resulting in an improved ORR catalysis.
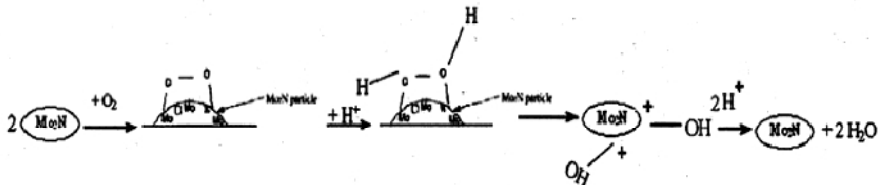
Figure 15.6. Proposed ORR mechanism for Mo_2N/C catalyst [81]. (Reprinted from Electrochemistry Communications, 8(5), Zhong Hexiang, Zhang Huamin, Liu Gang, Liang Yongmin, Hu Jingwei and Yi Baolian, A novel non-noble electrocatalyst for PEM fuel cell based on molybdenum nitride, 707–12, ©2006, with permission from Elsevier.)

15.3.3 Oxynitrides

Normally, metal nitrides show high stability and activity towards the ORR in alkaline solution. However, very few reports have dealt with acidic media. Most recently, a new type of semi-conductive materials, metal-oxygen-nitrogen compounds, has been explored for ORR catalysis. For the first time in the world, Ota et al. [84–88] discovered that metal-oxygen-nitrogen compounds are stable and active towards the ORR in acidic media. In their first study, they prepared Ta oxynitride (TaO_xN_y) and nitrides with different nitrogen contents through a chemical reaction of Ta_2O_5 with NH_3 gas at 850 °C. As shown in Figure 15.7, the prepared Ta oxynitride and nitride have different structures. TaO_xN_y has the same structure as monoclinic ZrO_2 (baddeleyite), while the structure of Ta_3N_5 contains TaN_6 octahedra, similar to Ti_3O_5 (anosovite). The non-stoichiometric Ta oxynitrides have many defects in their crystals, resulting in the increased electrical conductivity of semi-conductive Ta nitrides. Through chemical and electrochemical measurements, it was proven that these oxynitrides are very stable in sulfuric acid at electrode potentials below 1.2 V vs. RHE. The high stability of Ta oxynitride was attributed to the highest oxidation state (+5) of Ta. This suggests that any further oxidation of Ta^{5+} to degrade the catalyst structure is impossible. It was also observed that the catalytic ORR activity was strongly dependent on the chemical composition ratio of oxygen and nitrogen. The highest activity was observed at Ta:O:N = 1:0.92:1.05, i.e., $TaO_{0.92}N_{1.05}$. It is interesting to note that the oxidized Ta oxynitride surface was more active than the bare surface. This behavior is different from that of a Pt catalyst. When a Pt surface is covered with Pt oxide, the ORR activity will be dramatically reduced. Considering the PEM fuel cell cathode atmosphere, in which oxygen is present, a metal oxide layer on the catalyst (for example, Pt) will easily form in particular in a low current density range. This metal oxide layer will compromise the fuel cell performance. For a Ta oxynitride cathode catalyst, such a Ta oxide layer will benefit rather than compromise fuel cell performance.
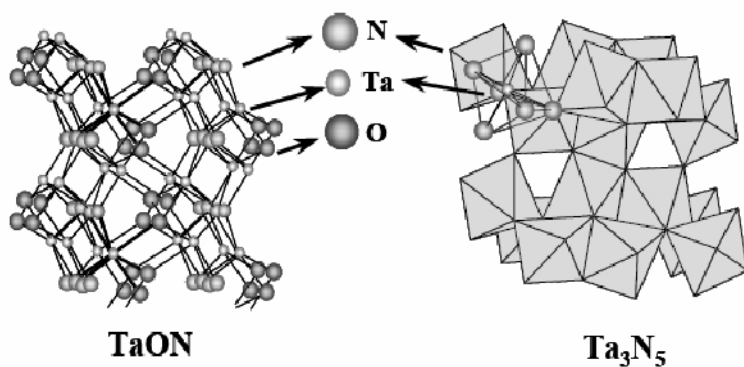
Figure 15.7. Schematic structure of TaON and Ta_3N_5 [89]

In their continuing studies, Ota's group also found that the heat treatment of metal oxynitrides played an important role in the improvement of catalytic activity and stability. They prepared TiO_xN_y and ZrO_xN_y thin films deposited on glassy carbon by the reactive sputtering method. Then these oxynitrides were heat-treated at various temperatures from 50 °C to 800 °C. The TiO_xN_y and ZrO_xN_y thus obtained exhibited superior chemical stability to Pt in 0.1 M H_2SO_4. For example, the solubility of TiO_xN_y and ZrO_xN_y is 2.5×10^{-7} and 5×10^{-8} mol cm^{-3}, respectively, while Pt has a solubility of 5.6×10^{-7} mol cm^{-3}. Both of these oxynitrides showed strong dependency on heat-treatment temperature for their catalytic ORR activity. The catalytic ORR activity increased with increasing heat-treatment temperature, showing maximum activity at 800 °C. Higher heat-treating temperature results in higher crystallinity and more defects in the crystals. Figure 15.8 shows the electron beam diffraction patterns of the crystal lattice, obtained using a Fourier transform mapping of the TEM images. Two kinds of crystalline structure are observed at 50 °C and 500 °C, respectively. These patterns are not consistent with the Zr oxynitrides and oxides. In Zr oxynitride, the crystal lattice might mainly consist of Zr oxides and can be strained because some of the nitrogen is dissolved in the lattice; the oxide phase could be also strained due to film deposition during a non-equilibrium state at the lower temperature. In addition, the pattern at 700 °C can be identified with monoclinic ZrO_2. At heat treatment below 500 °C, ZrO_xN_y has very low crystallinity or is almost amorphous. However, when temperature is increased beyond 500 °C, a dramatic increase in crystallinity can be observed. More interestingly, a linear relationship between the crystallinity and activity can be obtained, as shown in Figure 15.9. This result suggests that the increased crystallinity and defects may contribute to the improvement in catalytic activity. In the case of TiO_xN_y, as the heat-treatment temperature increases, the structure of Ti oxynitride can be transferred from a TiON structure to a TiO_2 (rutile) structure, accompanied by an increase in crystallinity. It is believed that the TiO_2 (rutile) structure is more active than the TiON structure in terms of the ORR. This result was also confirmed in a study on TiO_2 oxide catalyst [90].
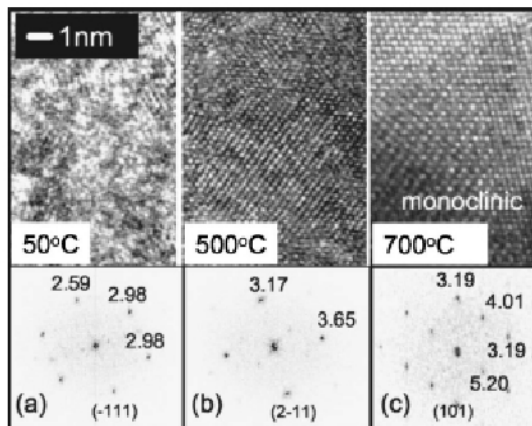
Figure 15.8. Cross-sectional surface of TEM images and the electron beam diffraction patterns of crystal lattice in ZrO_xN_y prepared at 50, 500 and 700 °C [86]. (Reproduced by permission of ECS—The Electrochemical Society, from Doi S, Ishihara A, Mitsushima S, Kamiya N, Ota KI. Zirconium-based compounds for cathode of polymer electrolyte fuel cell.)
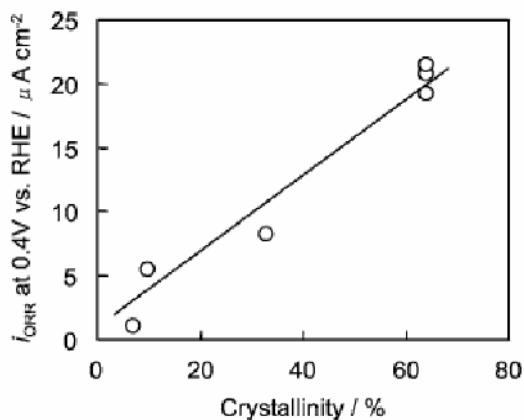
Figure 15.9. Relationship between crystallinity and ORR current density [86]. (Reproduced by permission of ECS—The Electrochemical Society, from Doi S, Ishihara A, Mitsushima S, Kamiya N, Ota KI. Zirconium-based compounds for cathode of polymer electrolyte fuel cell.)

More recently, other research groups also investigated the ORR mechanism catalyzed by a carbon-supported ZrO_xN_y catalyst prepared by chemical reaction with NH_3 at 950 °C. It is worthwhile noting that the ZrO_xN_y/C can catalyze the ORR through a 4-electron transfer pathway. The measured electron transfer number is 3.8, which is very close to the value catalyzed by Pt/C and/or Mo_2N/C. This is a very promising result, demonstrating that non-noble metal nitrides can have the same catalytic behavior as noble metal catalysts. In a single fuel cell test

at 80 °C, it was confirmed that this oxynitride catalyst could have stability for up to 50 hours. The activity and stability achieved on this oxynitride is promising.

Mixed transition-metal oxynitrides with perovskite structure have also been investigated in acidic media. Domen et al. [91] explored perovskite-type compounds such as $LaTiO_2N$, $ANbO_2N$, and $ATaO_2N$ (A = Ca, Sr, Ba, etc.), as shown in Figure 15.10. These oxynitrides were originally explored as photocatalysts. Later, it was found that the band gap could be narrowed by the addition of alkali earth metals such as Ca, Sr, and Ba. It was expected that increasing the electron carrier density and changing the band cap by doping typical elements could contribute positively to the conductivity and activity of metal oxynitrides. All these oxynitrides were found to be stable electrochemically and chemically in acid solution. Their catalytic ORR activities were remarkably high, showing onset potentials of 0.8 V, 0.85 V and 0.8 V vs. NHE in 0.1 M H_2SO_4 for $LaTiO_2N$, $BaNbO_2N$, and $SrNbO_2N$, respectively. In the case of $LaTiO_2N$, it was suggested that mixed coordination of Ti^{3+} and Ti^{4+} in the $LaTiO_2N$ structure could be more active towards the ORR compared with Ti^{3+} coordinated in TiN and Ti^{4+} in TiO_2.
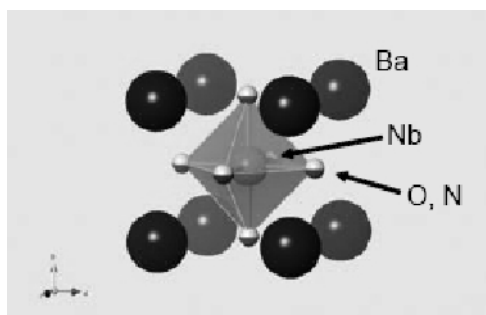
Figure 15.10. Schematic structure of perovskite oxynitride ($BaNbO_2N$) [91]. (Reproduced with permission from New Energy and Industrial Technology Development Organization (NEDO).)

15.3.4 Carbonitrides

Metal carbonitrides (metal-carbon-nitrogen compounds) are another kind of potential non-noble metal catalyst for the ORR. However, compared to carbides and nitrides, carbonitrides seem less popular. Recently, these compounds have attracted some attention due to their electrochemical properties and stabilities. In pioneer studies, Ota's and Dahn's groups [92–96] investigated electrocatalytic ORR activity and the corresponding stability of carbonitrides as catalysts, with a focus on Ta, Cr, Fe, and Co metals in strong acidic media. Using nitrogen and carbon or metal carbides as starting materials, they synthesized several metal carbonitrides by the reactive sputtering method. Ta-C-N and Cr-C-N carbonitrides prepared by Ota's group were reported to have comparable stability to metal oxynitrides [92, 93]. Both these carbonitrides showed improved catalytic ORR with increasing heat-treatment temperature. The highest catalytic activities were obtained at 800 °C.

Dahn's group also investigated the effect of heat-treatment temperature on catalytic activity in the range from 700 °C to 1000 °C. Their heat-treatment process was different from that of Ota's group, which heated the substrates in an ultra-high vacuum chamber during the sputtering process, while Dahn's group annealed the samples after the sputtering process. It is expected that a thin oxide film could have been formed on the surface of as-prepared carbonitride in the latter process because the sample might have had a chance to be exposed to air during transfer of the sample to the furnace. If this happened, the oxide formed on the surface might have affected the chemical composition of the carbonitride surface and its catalytic ORR activity during the heat treatment. However, Fe carbonitride annealed at 800 °C showed the best catalytic ORR activity, indicating that the optimum temperature is well consistent with Ota's result.

Both groups also found a consistent fact that nitrogen content can be decreased by increasing heat-treatment temperature. The catalytic ORR activity was strongly affected by the ratio of metal, oxygen, and nitrogen. This ratio could be optimized by heat-treatment temperature in order to achieve optimal ORR activity. In addition, increased crystallinity by heat treatment was found to be one of the most important factors affecting catalytic activity. This observation was also confirmed using a Co-C-N compound as an ORR catalyst [95, 96]. Unfortunately, most of these carbonitride compounds produced considerable hydrogen peroxides (20–80%) during the oxygen reduction reaction in acid media. If these materials are used as fuel cell cathode catalysts, such high H_2O_2 production would cause performance degradation.

Recently, 3M Corporation [97] successfully conducted fuel cell durability tests using Fe-C-N/TiC as the cathode catalyst. This TiC-supported Fe-C-N catalyst showed a stable performance over 1000 hours at a cell voltage of 0.6 V, which is the longest durability of non-noble metal catalysts yet reported in a real fuel cell environment. Beside TiC, some conductive and electrochemically stable materials, including carbides, silicides, nitrides, and their combinations, could also be used as catalyst supports for the ORR.

15.4 Transition Metal Chalcogenides for the ORR

Since Alonso-Vante and Tributsch [98] first reported Ru-Mo-Se chalcogenides as ORR catalysts in 1986, transition metal chalcogenides have been researched for last two decades as one type of promising material among non-noble transition metal catalysts [6, 98, 99]. These compounds have a cluster structure with a repeating crystal lattice containing a metal ion cluster in the center, surrounded by several non-metal ions. For example, in a binary compound of $M^1_6X_8$ (M^1 = high-valent transition metal, e.g., Mo; X = chalcogen, e.g., S, Se, or Te), each lattice contains a central octahedral metal cluster with six metal ions surrounded nearly cubically by eight chalcogen ions [6]. There are also ternary compounds such as $Mo_6M^2_xX_8$ (M^2 = intercalated metal guest ion) and pseudobinary compounds such as $Mo_6M^3_xX_8$ (M^3 = foreign metal ions which replace the Mo in the octahedral M cluster). Cluster compounds of this type have been investigated as electrocatalysts for oxygen reduction and all of them appeared to have some level of activity. The

$Mo_6M^2_xX_8$ compound was found to be electrochemically unstable due to deintercalation at positive electrode potentials. Extensive studies have focused on the mixed transition metal cluster compounds ($Mo_6M^3_xX_8$, called pseudobinaries). When M^3 is ruthenium, this compound displays the best activity among the other metals investigated. It is known that this remarkable activity is attributable to the presence of the octahedral mixed metal clusters. These clusters act as reservoirs for electron transfer from the electrode to coordinated O_2 on the clusters. Figure 15.11 shows the catalytic mechanism on a cluster based on the ternary Mo-Ru-Se compound. Recently, various metal-based chalcogenides such as Ir-, Pt-, Os-, and Rh-based as well as Ru-based have been reported for their high catalytic activities and stabilities [100–103]. However, all these chalcogenides are actually based on precious metals. In terms of price and limited supplies, the chalcogenides using noble metals are not feasible alternative catalysts. Although there have not been intensive efforts to study non-noble metal chalcogenides, recently new challenges in this area have been reported for PEM fuel cells. In the remainder of this section, novel non-noble metal chalcogenide catalysts are briefly introduced.
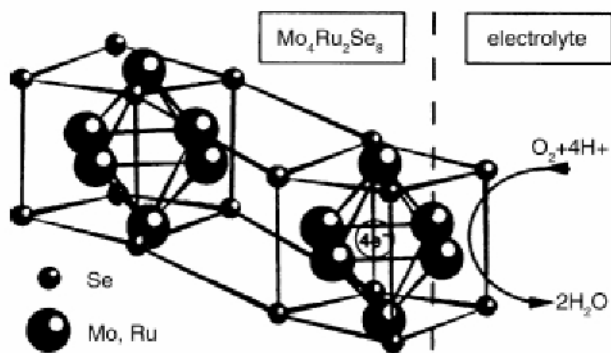
Figure 15.11. Interaction of molecular oxygen in acid medium at the Chevrel phase cluster-electrolyte interface [6]. (Reprinted from Journal de Physique, vol. 7, C2, The Catalytic Centre of Transition Metal Chalcogenides vis-à-vis the Oxygen Reduction Reaction: An *In situ* Electrochemical EXAFS Study, Alonso-Vante, N. et al. ©1997, with permission from EDP Sciences.)

Since the 1970s, cobalt-based chalcogenides have been studied as ORR catalysts in acidic media. Baresel et al. [104] reported the ORR electrocatalytic activity of chalcogenides based on different transition metals between the IV group and VIII group. Various binary and ternary transition metal chalcogenides that have been explored are listed in Table 15.2. Among them, Co sulfide (Co_3S_4) was proven to have the highest catalytic activity in acid solution. The substitution of sulfur by selenium or tellurium can affect the ORR activity significantly. The catalytic activity is in the order of S > Se > Te. Moreover, it was found that a ternary Co-Ni-S system with spinel structure was more active than a binary Co-S system. The authors explained that the activity can be increased by decreasing the difference between the O 2p orbital and the highest occupied d orbital energies of

the transition metal sulfide. The orbital energy difference, ΔE, in various metal sulfides decreases in the order Ta > Mo > Ti > Cr > W > V > Ni > Co. Therefore, Co sulfide, having the smallest $\Delta E = 1$ eV, has the highest ORR activity.

Table 15.2. Catalytic activity of various transition metal chalcogenides for ORR in 4N H_2SO_4 at 70 °C [104]. (Reprinted from Baresel VD, Sarholz W, Scharner P, Schmitz. Transition metal chalcogenides as oxygen catalysts for fuel cells. Berichte Der Bunsen-Gesellschaft 1974;78:608–11, with kind permission of Deutsche Bunsen-Gesellschaft für Physikalische Chemie.)

Chalcogenide catalysts	mA/m^2 at 600 mV vs. RHE
95% $CoS_{0.96}$, 5% Co_3S_4	1300
99% CoS_2	958
90% Co_9S_8, 10% β-$CoS_{1.035}$	217
83% $CoSe_2$, 17% $CoSe_{0.5}$	76
45% $CoTe_2$, 45% Te, 10% Co_3Te_4	39
48% NiS_2, 48% $Ni_{1.03}$, 4% Ni_3S_4	120
48% $NiSe_2$, 48% Ni_3Se_4, 4% Se	92
48% NiTe, 48% Te, 4% NiO	1
45% NiS_2, 45% $NiS_{1.03}$, 10% NiS	34
80% MoS_2, 20% γ-Co_6S_5	9
VS_4, V_3S_4, S = 1:1:1	3
50% Cr_2S_3, 50% Cr_7S_8	0.7
99% TiS_2	0.2
99% WS_2	0.08
98% TaS	< 0.02
99% MoS_2	< 0.02
47% $CoCr_2S_4$, 47% Cr_2S_3, 6% $CrS_{1.035}$	6.8
CoV_2Se_4	5
$FeNb_2S_4$	4.4
$NiCr_2S_4$	4.5
$CoTi_2S_4$	4.1
$CoTi_2Se_4$	1.7
92% $FeCr_2S_4$, 8% Cr_2S_3	1.6
33% CoS_2, 33% Co_3S_4 (spinel), 33% $NiCo_2S_4$	2150

(a) binary

(b) ternary
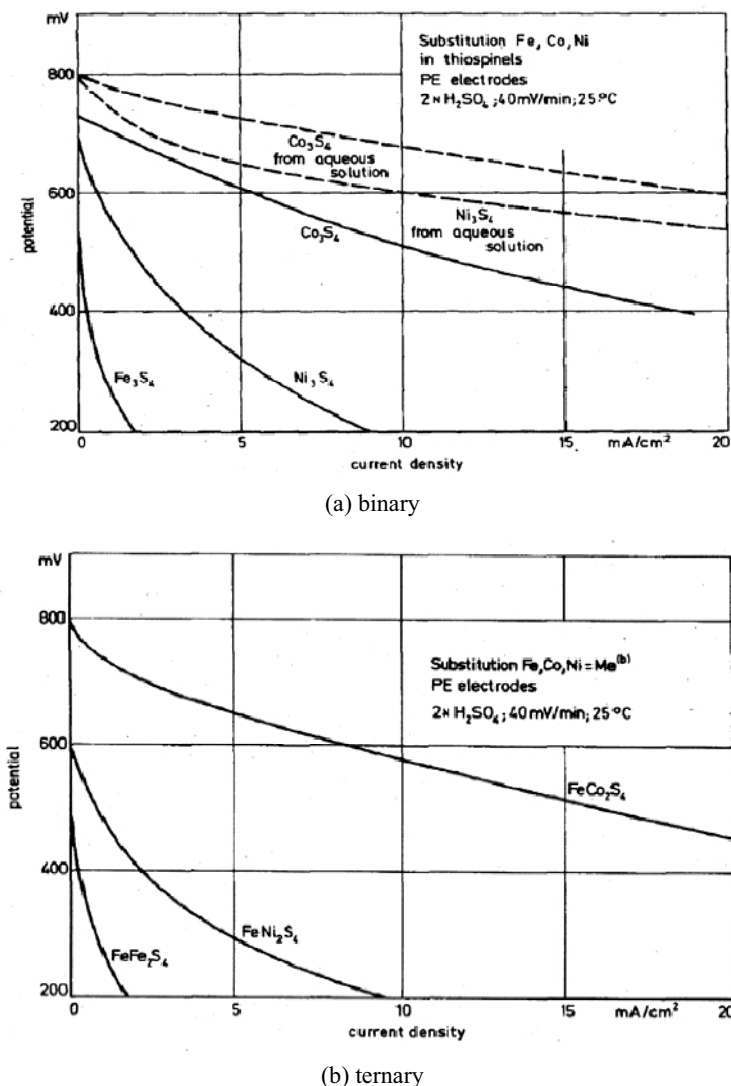
Figure 15.12. Current-potential curves of various chalcogenide-catalyzed oxygen reduction reactions in sulfuric acid [105]. (Reprinted from Electrochimica Acta, 20(2), Behret H, Binder H, Sandstede G, Electrocatalytic oxygen reduction with thiospinels and other sulphides of transition metals, 111–17, ©1975, with permission from Elsevier.)

Behret et al. [105, 106] also investigated the catalytic ORR activity and mechanism catalyzed by thiospinel-type sulfides with a focus on metals such as Co, Ni, and Fe. The thiospinel sulfides have a $Me^{(a)}Me^{(b)}_2S_4$ formulation, where $Me^{(a)}$ represents an ion on the tetrahedral sites and $Me^{(b)}$ an ion on the octahedral sites. They prepared these thiospinel sulfides by two different methods, one at high temperature and the other at low temperature. For the high-temperature method, the sulfur and metal components were ball-milled in a degassed atmosphere and

then the temperature was elevated for the reaction between the chalcogen and metals. For the low-temperature method, the thiospinel chalcogenides were precipitated in an aqueous solution of metal thiosulfates by bubbling air. They could replace one metal atom ($Me^{(a)}$) while keeping the other ($Me^{(b)}$) constant, or replace $Me^{(b)}$ with an $Me^{(a)}$ constant. The metals they used were Fe, Ni, and Co. Within this series of chalcogenides, the best results were obtained for cobalt. Figure 15.12 compares the ORR currents catalyzed by various binary and ternary thiospinels. It can be seen that binary Co_3S_4 sulfide and ternary sulfide containing cobalt show the highest catalytic activity. The effect of metals on the catalytic activity is in a favorable order of Co > Ni > Fe. This result is consistent with Baresel's suggested relationship between catalytic ORR activity and the metal orbital energy difference.

The synthesis method can also affect the catalytic ORR activity and stability. Cobalt sulfide prepared in aqueous solution at low temperature has a much higher activity than that prepared at high temperature. However, the former is not as stable against corrosive attack in acid solution. It was found that replacement of the chalcogen could effectively change the catalytic activity. When a chalcogen element such as sulfur is replaced with selenium or tellurium to form Me_3Se_4 or Me_3Te_4, or partly replaced to form Me_2SeS_2 or Me_2TeS_2, the catalytic ORR activity can be dramatically decreased. Co_3S_4 was identified as the most active ORR catalyst among the synthesized $Me^{(a)}Me^{(b)}_2S_4$ chalcogenides. For the ORR mechanism, it was found that the Co_3S_4 catalyst mainly catalyzed a 2-electron reduction process to produce hydrogen peroxide at potentials above 0.5 V vs. RHE in sulfuric acid solution. By shifting the electrode potential in a negative direction, a 4-electron reduction from oxygen to water could be observed. Unfortunately, the portion of this 4-electron pathway in the whole ORR process catalyzed by Co_3S_4 catalyst was small (< 10%).
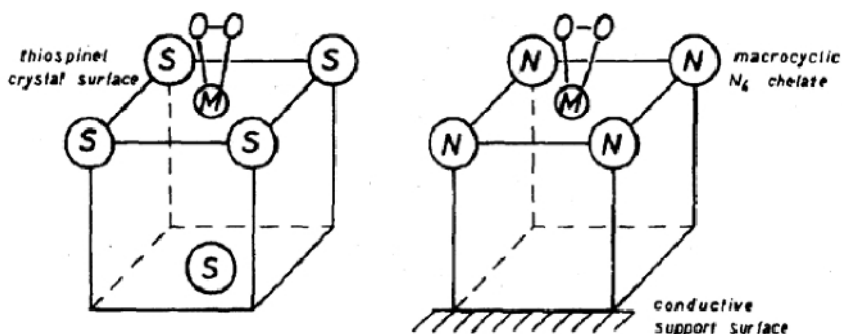
Figure 15.13. Metal coordination in chalcogenide and macrocyclic chelate [105]. (Reprinted from Electrochimica Acta, 20(2), Behret H, Binder H, Sandstede G, Electrocatalytic oxygen reduction with thiospinels and other sulphides of transition metals, 111–17, ©1975, with permission from Elsevier.)

In the structure of thiospinel sulfide, each metal atom is surrounded by four sulfur atoms in a square planar pattern, and the fifth coordination position is occupied by an anion, as seen in Figure 15.13. This square planar system is similar

to the structure of macrocyclic N_4 chelates, which are active towards the ORR. In this macrocyclic N_4 chelate, the metal ion inside the chelate is surrounded by four nitrogen atoms and the fifth coordination position is occupied by an active carbon. For both of these S_4 and N_4 structures, the adsorption, dissociation, and reduction processes of oxygen molecules might be similar.

Extensive studies have been carried out to further improve the activity of the cobalt sulfide catalyst [107]. A considerable improvement in the catalytic activity of cobalt disulfide has been reported, although this was found to have less ORR catalytic activity than that of cobalt thiospinel in previous studies. In a recent study by Campbell et al. [107], cobalt disulfide (CoS_2) was prepared in the form of a thin film by reactive sputtering and the form of supported powders by the precipitation method. These cobalt sulfides have a pyrite structure, in which the sulfur atoms are paired in the lattice as complex S_2^{2-} anions. The CoS_2 with this structure was considerably active and stable towards the ORR. An ORR open circuit potential (OCP) at 0.83 V vs. RHE was observed. Although iron sulfide, FeS_2, has the same pyrite structure, its activity was found to be much lower than that of cobalt (Figure 15.14). Measurements using X-ray photoelectron spectroscopy (XPS) and auger electron spectroscopy (AES) revealed that the surface of this catalyst was sulfur-rich. This surface condition may be necessary to protect the underlying material from metal dissolution. Adding a third element to this CoS_2 could change its catalytic ORR activity. For example, the addition of tungsten could decrease the activity while Ni could improve it. In particular, $CoNiS_2$ could raise the OCP up to 0.89 V vs. RHE. This value is 80 mV higher than that of CoS_2 and very close to that of Pt. The $CoNiS_2$ catalyst is more active than catalysts of thiospinel cobalt sulfides. The $CoNiS_2$ system also has a S_2^{2-} pyrite structure like CoS_2. It is believed that this S_2^{2-} pyrite structure may play an important role in the ORR catalyzed by cobalt sulfide.
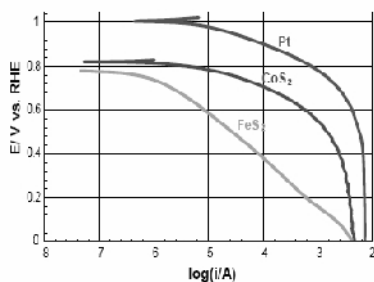
Figure 15.14. E-log (i) plots for oxygen reduction on Pt, CoS_2, and FeS_2 in O_2-saturated 0.1 M $HClO_4$. Potential scan rate: 5 mV/s. Electrode rotating rate: 2000 rpm [107]. (Reprinted from Campbell S. Development of transition metal/chalcogen based cathode catalysts for PEM fuel cells. DOE hydrogen program, FY 2004 annual progress report 2004:389–91. With permission of DOE.)

The ORR mechanism catalyzed by cobalt sulfide was also elucidated by a theoretical approach based on quantum chemistry as well as experimental validation. Reyimjan et al. [108] carried out a theoretical analysis of the catalytic

ORR process on the catalyst surface of Co_9S_8 using the slab band quantum computational approach. They suggested that the partially OH-covered surface (202) of Co_9S_8 with pentlandite structure should be active towards the ORR. The predicted steps of the oxygen reduction cycle on a partially OH-covered 202 surface can be seen in Figure 15.15. Following the first step of the reduction at 0.83 V, the O on sulfur is reduced spontaneously to OH_{ads} because its reversible potential is higher (1.03 V). After the reduction of two O atoms, the sequential reductions of the adsorbed OH groups to water will occur at the relatively favorable potentials of 0.89 and 0.74 V, respectively. These final two steps complete the reduction cycle by regenerating the initial hydroxylated surface. The 0.74 V step may determine the overpotential for the overall 4-electron ORR, which is similar to the case for a platinum catalyst. It also can be seen that on the catalyst surface, water molecules do not block the active sites because their bonding strength is much weaker. The heat loss (1.13 eV) from O_2 dissociative chemisorption may be necessary for a 4-electron reduction process. It is predicted that a better catalyst should have less heat release when O_2 is bound to or dissociated on it.
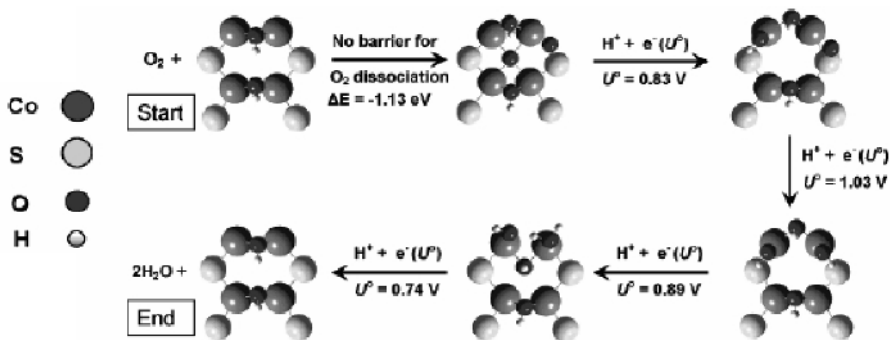
Figure 15.15. Top view of the reduction cycle for O_2 on the partially OH_{ads}-covered (202) surface of Co_9S_8 [108]. (Reprinted with permission from J Phys Chem B 2006;110:936–41. Copyright 2006 American Chemical Society.)

Cobalt selenides have also been explored as ORR catalysts over the last several years. Previous studies showed that cobalt selenides were not as active and stable as cobalt sulfides. However, recent studies have achieved excellent improvement in the performance of cobalt selenides in acidic media. Campbell et al. [109] prepared $Co_{1-x}Se$, including carbon-supported $Co_{1-x}Se$, by both the reactive sputtering and the precipitation methods in aqueous solution. It was also observed that the Se-rich surface could improve the stability of Co selenides. In the case of a thin film Co-Se catalyst, the Se content increase could effectively improve the catalytic ORR activity. After electrochemical tests of the catalyzed ORR, it was found that the Se/Co ratio increased remarkably, indicating that some of the cobalt might be dissolved into the electrolyte. Nonetheless, the catalytic activity was still very high, suggesting that extra selenium around the cobalt has an insignificant effect on the catalytic activity. Figure 15.16 shows the polarization curves for supported Co-Se

powder in O_2-saturated H_2SO_4. The supported Co-Se powder exhibits considerably ORR current compared to carbon, Co, and Se. In addition, its OCP in saturated O_2 is also relatively high, i.e., 0.78 V vs. RHE. However, as can be seen in Figure 15.16(b), the ORR current from the Co-Se powder is approximately doubled when the amount of catalyst is doubled, strongly suggesting that the catalytic activity is mainly limited by the ORR kinetics rather than by mass transport. The Tafel slopes for catalyzed ORR on Co-Se thin film and powder were –133 mV/dec and –167 mV/dec, respectively. It is still not clear why these two forms of Co-Se selenides have significantly different ORR Tafel slopes.
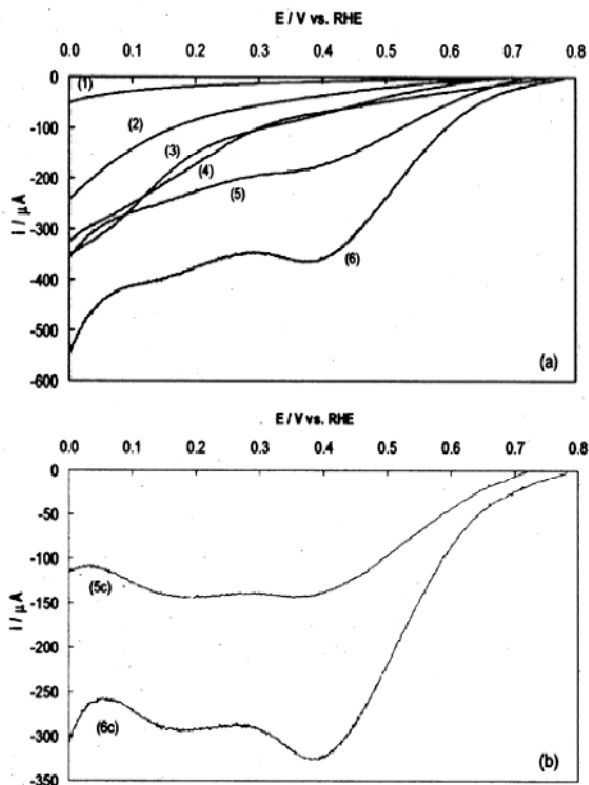
Figure 15.16. (a) ORR cathodic curves measured from: (1) glassy carbon, (2) XC72R carbon, (3) Co on XC72R, (4) Se on XC72R, (5) Co-Se on XC72R single loading, and (6) Co-Se on XC72R double loading; (b) curves (5) and (6) after background correction (subscript c) in O_2-saturated 0.5 M H_2SO_4 at 30 °C, electrode rotation rate: 2000 rpm [109]. (Reprinted with permission from J Phys Chem B 2006;110:10762–70. Copyright 2006 American Chemical Society.)

According to previous studies by Behret and Campbell [105, 107], the doping of tungsten into cobalt sulfide had a negative effect on the ORR activity. However, Lee et al. [110] recently proved that tungsten could promote the catalytic activity of Co-Se. They synthesized unsupported W-Co-Se powder by chemical reaction in

organic solvent at 140 °C. The resultant W-Co-Se powder was amorphous, which differs from the binary Co-Se powder (containing a crystalline phase) in Campbell's study. Figure 15.17 shows the ORR polarization curves in H_2SO_4 solution. The diffusion-limited ORR currents on the W-Co-Se catalyst show strong dependency on the electrode-rotating rate, while that catalyzed by binary Co-Se was controlled by ORR kinetics. This suggests that the doping of tungsten to a cobalt selenide catalyst can dramatically enhance the catalytic ORR activity. The effect of metal doping on the ORR activity seems to differ depending on the nature of the chalcogen used.
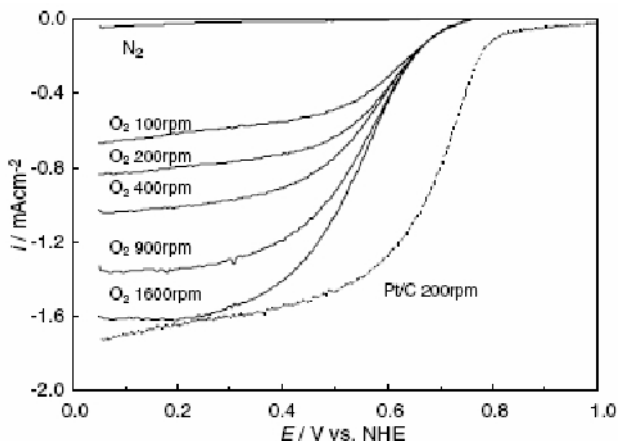
Figure 15.17. ORR polarization curves for W-Co-Se and Pt/C in 0.5 M H_2SO_4 at 25 °C. Potential scan rate: 5 mV/s. Pt/C loading is 122 μg/cm^2 [110]. (Reprinted from Electrochemistry Communications, 9(7), Lee Kunchan, Zhang Lei and Zhang Jiujun, Ternary non-noble metal chalcogenide (W–Co–Se) as electrocatalyst for oxygen reduction reaction, 1704–8, ©2007, with permission from Elsevier.)

It was confirmed by XPS analysis that the oxidation states of cobalt and tungsten in the W-Co-Se catalyst are much higher than those in their oxides WO_3 and CoO. The stability of W-Co-Se is related to the effect of selenium; that is, selenium plays a role in protecting the electrochemical oxidation of cobalt and tungsten in a selenide compound. In terms of the activity, a charge transfer from metals to selenium changes the density of state (DOS) at Fermi level for these metals, which might be active sites. Such a change in DOS could play an important role in catalysis. For the ORR mechanism, it was proven that W-Co-Se catalyst mainly has a 2-electron reduction process.

15.5 Metal Oxides for the ORR

Metal oxide catalysts have been extensively studied over the last several decades for their ORR catalytic activities and electrochemical behaviors. Two types of metal oxide, the perovskite-type and spinel-type oxides, are the most attractive

electrode materials due to their high electrical conductivity and outstanding catalytic behavior [111–119].
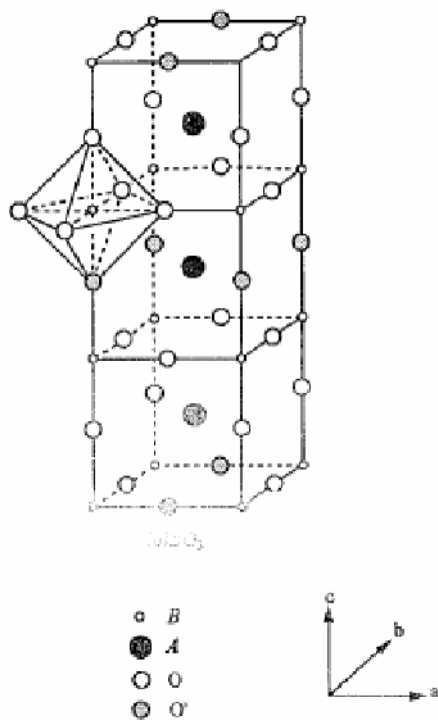
Figure 15.18. ABO_3 ideal perovskite structure showing oxygen octahedron containing the B ion lined through corners to form a tridimensional cubic lattice [119]. (Reprinted with permission from Chem Rev 2001;101:1981–2017. Copyright 2001 American Chemical Society.)

Among perovskite-type oxides, lanthanoid element-transition metal complex oxides have been recognized as promising electrocatalysts for the oxygen reduction reaction in alkaline electrolyte. This type of oxide has high electrical conductivity at room temperature (in the order of $1–10^4/\Omega cm$) and significant stability against anodic oxidation in alkaline solution [120–122]. The general chemical formula of perovskite-type oxide is ABO_3, as represented in Figure 15.18. A and B are cations with different sizes, A being the larger cation and B the smaller. In this structure, B is 6-fold coordinated and A is 12-fold coordinated with the oxygen anions. As can be seen in Figure 15.18, the corner-sharing octahedral forms the skeleton of the structure, in which the center position is occupied by the A cation. Alternatively, this structure can also be viewed with the B cation placed in the center of the octahedron and the A cation in the center of the cube. The catalytic activity and electrochemical behavior of perovskite-type oxides could be affected by the sort of A and B cations. As summarized in what follows, certain effects of A and B cations on catalytic activity and stability have been identified [123, 124]:

1. Activity and stability are strongly dependent on the nature of the B cation.
2. In the case that the B cation is cobalt, $ACoO_3$ perovskite oxides will be very active ORR catalysts but they are not stable chemically in concentrated alkaline solution. In contrast, $AFeO_3$ perovskite oxides whose B cation is iron are very stable but not active catalysts.
3. In the case that the B cation is manganese, $AMnO_3$ perovskite oxides show very high activity and stability. The catalytic ORR activity strongly depends on the nature of the A cation, in the order of La > Pr > Nd > Sm > Gd > Y > Dy > Yb.

When lanthanoid ions, which are trivalent, are replaced by less valent ions, the ion valences of the B site will be changed, and at the same time the oxygen defect will be increased for charge compensation. It is believed that such a partial substitution by divalent or monovalent ions may result in improved conductivity and catalytic activity [123, 125]. For example, $La_{1-x}A_xMnO_3$ (A=Na, K, or Rb) perovskite oxides in which the La^{3+} is partially substituted by alkali ions exhibited promising catalytic behaviors in alkaline solution. Figure 15.19 compares the oxygen reduction catalysis of $La_{1-x}A_xMnO_3$ catalyst in 8 M KOH solution. Partially substituted $La_{1-x}A_xMnO_3$ electrodes show prominent oxygen reduction activity compared to $LaMnO_3$ electrodes. Among them, Rb substitution to form $La_{0.8}Rb_{0.2}MnO_3$ with x = 0.2 gives the highest ORR activity. The activity order is Rb > K > Na. These alkali ions can also affect the ORR mechanism. For example, the order favoring 4-electron transfer from O_2 to H_2O was found to be: Rb > K > Na > La. In these perovskite oxides, Mn^{3+} and Mn^{4+} were considered the active sites; in particular, Mn^{4+} could be stabilized by the partial substitution of alkali ions. This stabilized Mn^{4+} site is believed to be responsible for the favored 4-electron reduction pathway.
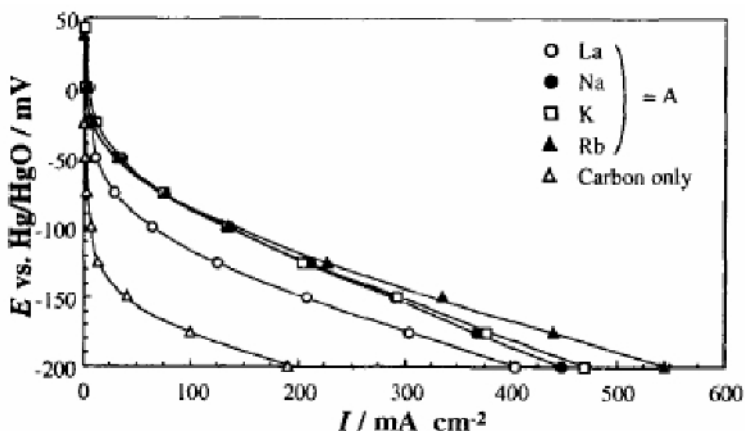
Figure 15.19. Polarization curves of gas diffusion-type oxygen electrode loaded with $La_{0.8}A_{0.2}MnO_3$ (A=Na, K, or Rb) in 8 M KOH at 60 °C [123]. (Reprinted from Hayashi M, Hyodo T, Miura N, Yamazoe N. Electrochemical oxygen reduction properties of perovskite-type oxides $La_{1-x}A_xMnO_3$ (A=Na, K. Rb) in concentrated alkaline solution. Electrochemistry 2000;68:112–18. With kind permission of the Electrochemical Society of Japan.)

For spinel-type oxides, the general chemical formula can be represented as AB_2O_4, in which A is the cation in a tetrahedral site and B is another cation in an octahedral site. All oxygen anions are arranged as a close cubic array with cations filling 1/2 of the octahedral and 1/8 of the tetrahedral positions, as shown in Figure 15.20. The unit cell of $A_8B_{16}O_{32}$ contains 32 anions, arranged in the densest cubic packing and forming 64 tetrahedral and 32 octahedral sites, in which 8 tetrahedrals (A site) and 16 octahedrals (B site) are occupied by cations [126]. A non-ideal spinel structure is formed as a result of the anion shifts from sites on the face-centered cubic lattice toward the nearest tetrahedral ion. In general, normal, inverse, and mixed spinels can be distinguished depending on the cationic distribution among the available positions. In the case of a normal distribution in a binary $A[B]_2O_4$ spinel, two B cations occupy the octahedral, while the A cations are located on the tetrahedral sites in the lattice. In the inverse $B[AB]O_4$ spinel, both A and B cations are distributed statistically in the octahedral sites, whereas only B cations are located in tetrahedral positions. There are also intermediate distributions, which can be characterized by specifying the fraction of B ions on tetrahedral sites, $A_{1-x}B_x[A_xB_{2-x}]O_4$. The thermodynamic stability of the cation distribution in binary spinels depends on the stabilization energy values of octahedral and tetrahedral oxygen coordination with different cations. These oxides were considered to have highly defective structures since the oxygen anions are in excess [127]. The excess of oxygen anions is believed to be the major factor determining the electrochemical properties of the defects. In these defects, some of the M^{3+} and M^{2+} can be converted to M^{4+} and M^{3+}, respectively, forming an "electroconductivity chain". This chain can serve as a bridge for electron or hole transfer between the bulk and the surface of the spine oxides, resulting in the electrochemical reaction of bi- and tri-valent cations at the surface active center. It has been discussed that several factors such as ionic defects, electronic defects, crystallinity, lattice distortion, and surface electronic structure could have strong effects on the electrocatalytic activity of spinel-type oxides [138].
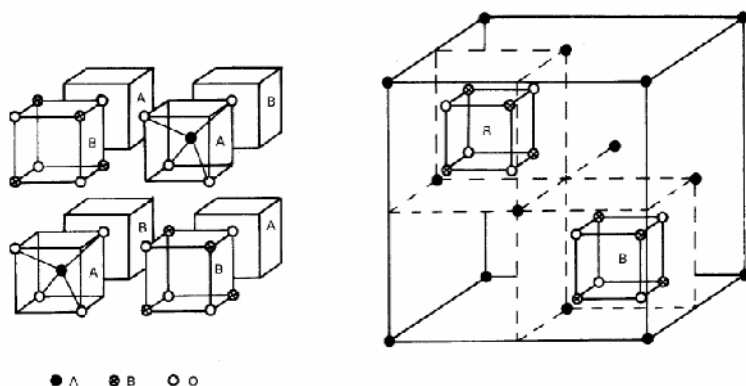
Figure 15.20. Idealized spinel structure. The lattice is built by alternating AO_4 and B_4O_4 units [126]. (With kind permission from Springer Science+Business Media: Journal of Materials Science (full set), Synthesis and features of binary cobaltite spinels, 29, 285–93, D. Klissurski, Figure 3, ©2005 Springer.)

Most of the spinel-type oxides as well as the perovskite-type oxides present high catalytic activity and stability towards the ORR in an alkaline solution. However, there are very few studies of these oxides in acidic media due to their low catalytic activity and stability, in particular for practical applications in PEM fuel cells in which the electrolyte has a strongly acidic environment. In pioneer studies, binary copper manganite ($Cu_xMn_{3-x}O_4$, $0 < x < 1.8$) was reported to be active towards ORR in a slightly acidic medium (pH 6.6) [129–131]. These spinel-type oxides have low electrical resistivity, in the range of 2.7 to 300 Ωcm at 25 °C. It was reported that the catalytic ORR activity of $Cu_{1.4}Mn_{1.6}O_4$ was much higher than that of platinum [129]. Outstanding activity was attributed to the Mn^{4+} and Mn^{3+} cations. The Mn^{4+} can accept an electron from the solid substrate to form Mn^{3+} and then Mn^{3+} donates the electron to adsorbed oxygen molecules or atoms:

$$Mn^{4+} + e^- \rightarrow Mn^{3+} \tag{15.6}$$

$$Mn^{3+} + O_2 \rightarrow Mn^{4+} + O_2^- \tag{15.7}$$

Recently, rutile-type TiO_2 oxides and other single-metal oxides have been also actively studied in the effort to improve ORR catalytic activity and stability in strong acidic media [90, 132–134]. It was found that TiO_2 could catalyze the ORR with small amounts of hydrogen peroxide in alkaline solution, displaying a nearly 4-electron O_2 reduction reaction from oxygen to water [132]. Mentus [133] clarified that this ORR 4-electron transfer pathway could be transferred to a 2-electron transfer pathway when the solution was changed from basic to acidic. Unfortunately, this TiO_2 catalyst has a very limited catalytic activity towards the ORR in both alkaline and acid solutions as compared with other metal oxides such as perovskite and spinel.

It was also recently found that the ORR activity catalyzed by TiO_2 is strongly dependent on the synthesis temperature [90]. Different preparation temperatures could result in various crystalline structures of TiO_2, such as TiO_2 (rutile), TiO, and Ti_nO_{2n-1} (magneli phase). For example, a significant improvement in catalytic ORR activity was observed on TiO_2 prepared at 900 °C, at which temperature the catalyst obtained had a higher TiO_2 (rutile) ratio compared with those catalysts prepared at other temperatures. Figure 15.21 shows the relationship between catalytic ORR activity and the ratio of rutile (110) plane to total TiO_2 crystalline phase, prepared at various temperatures. It can be seen that the catalytic ORR activity increases by increasing the ratio of $I_{(110)}/I_{total}$, where I is XRD peak intensity. Maximum activity was obtained at 900 °C. This indicates that the specific crystalline structure, such as TiO_2 rutile, might play an important role in improved catalytic ORR activity.

Additionally, other single metal oxides, such as ZrO_{2-x}, TiO_{2-x}, SnO_{2-x}, NbO_{2-x}, and Co_3O_{4-x} have also been investigated as ORR catalysts in strongly acidic media [135, 136]. These oxides were prepared by the reactive sputtering method in an ultra-high vacuum system. The thin film oxides of ZrO_{2-x} and Co_3O_{4-x} were found to have catalytic activity towards the ORR and better chemical and electrochemical stability in sulfuric acid than platinum. However, the mechanism for the observed

catalytic activity is still not clear. Table 15.3 summarizes typical non-noble metal oxide catalysts reported for the ORR in both alkaline and acid solutions.
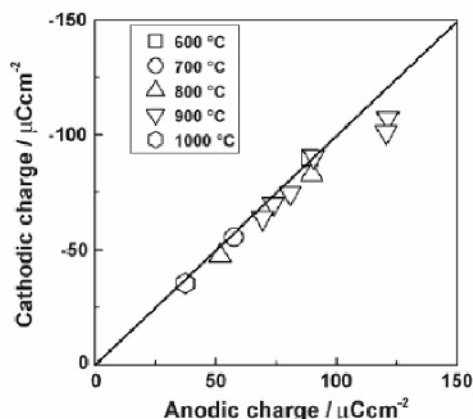
Figure 15.21. Relationship between the potential at -0.1 μAcm^{-2} and the XRD peak intensity of TiO_2 (rutile) (110) plane ($I_{(110)}/I_{total}$) [90]. (Reprinted from Electrochimica Acta, 52(7), Kim Jin-Hwan, Ishihara Akimitsu, Mitsushima Shigenori, Kamiya Nobuyuki and Ota Ken-Ichiro, Catalytic activity of titanium oxide for oxygen reduction reaction as a non-platinum catalyst for PEFC, 2492–7, ©2007, with permission from Elsevier.)

Table 15.3. Summary of non-noble metal oxides as electrocatalyts for the ORR

Oxide type	Components	References
Perovskite-type oxides	$LnMnO_3$, $Ln_{1-x}Me'_xMnO_3$, $Me'MnO_3$ (Ln=La, Pr, Nd, Sn, Gd, Y, Dy,Yb… Me'=Ca, Sr, Ba)	[124, 137–139]
	$Ln_{1-x}Me'_xMe''O_3$, $Ln_{1-x}Me'_xMe''_{1-y}Me''_yO_3$, $LnMe''O_3$ (Me''=Co, Fe, Ni, Cu)	[116, 121, 140–148]
	$La_{1-x}Me''_xO_3$ (Me''=Na, K, Rb)	[123]
Spinel-type oxides	Co_3O_4	[149–151]
	$Me''Co_2O_4$ (Me''=Mn, Ni)	[152–157]
	$LiMn_{2-x}Me''_xO_4$ (Me''=Co, Fe)	[158]
	$Cu_xMn_{3-x}O_4$, $Me''_{1-x}Cu_xMn_2O_4$ (Me''=Ni, Cr)	[129, 130, 159]
	$A_xB_yMn_{3-(x+y)}O_4$	[131]
	$Ni_xAl_{1-x}Mn_2O_4$	[160]
Other oxides	TiO_2	[90, 132–134]
	MnO_2 or Mn_xO_y	[161–164]
	CrO_2	[165]
	ZrO_{2-x}, Co_3O_{4-x}	[135, 136]

15.6 Conclusions

For PEM fuel cell commercialization, Pt-based catalysts do not seem to be the solution in terms of both cost and performance. It is strongly believed that non-noble metal electrocatalysts should be the most important way to replace current state-of-the-art Pt-based catalysts. Although there are still many barriers to the practical use of non-noble electrocatalysts, significant progress has been made over the last several decades in both fundamental understanding and technical development.

Since the 1960s, non-noble materials have been extensively explored as potential ORR electrocatalysts, and great progress has been achieved in catalytic activity and stability. Great effort has also been made to establish a fundamental understanding of the reaction mechanisms in order to develop new catalysts and improve catalyst performance. So far, most studies have been concentrated on transition metal oxides and macrocycles. In general, metal oxides with perovskite and spinel structures can only survive in alkaline media, where significant catalytic ORR activity and stability occur. In acidic media, the most promising non-noble ORR catalysts are transition metal macrocycles, in particular the heat-treated $Fe-N_4$ and $Co-N_4$ catalysts. In studies of these catalysts, significant progress has been made in understanding catalysis mechanisms and the factors affecting ORR activity and stability.

Other materials, including carbides, nitrides, oxynitrides, carbonitrides, and chalcogenides, have also been explored as new non-noble metal catalysts. Some of them demonstrate promising catalytic ORR activity and superior stability in acidic media.

Although significant improvement has been achieved in the catalytic activity and stability of fuel cell non-noble catalysts, nothing so far is actually better than Pt-based catalysts. More intensive research and development are necessary, with a focus on the exploration of new catalyst materials and activity/stability improvement. It is believed that a breakthrough in non-noble catalysts will be made in the near future, under the strong driving forces of clean energy demands and fuel cell commercialization, as well as globalized R&D efforts.

References

1. Larminie J, Dick A. Fuel cell systems explained. New York: John Wiley & Sons Ltd; 2000.
2. Arita M. Technical issues of fuel cells systems for automotive application. Fuel Cells 2002;2:10–14.
3. Sato N. Environmental science and energy technologies of automotive engineering in the 21st century. Oyo Butsuri 2003;72:857–64.
4. Gasteiger HA, Kocha SS, Sompalli B, Wagner FT. Activity benchmarks and requirements for Pt, Pt-alloy, and non-Pt oxygen reduction catalysts for PEMFCs. Appl Catal B 2005;56:9–35.
5. Kinoshita K. Electrochemical oxygen technology. New York: John Wiley & Sons Ltd, 1992:1–112.

6.   Zhang L, Zhang J, Wilkinson DP, Wang H. Progress in preparation of non-noble electrocatalysts for PEM fuel cell reactions. J Power Sources 2006;156:171–82.

7.   Bezerra CWB, Zhang L, Liu H, Lee K, Marques ALB, Marques EP, et al. A review of heat-treatment effects on activity and stability of PEM fuel cell catalysts for oxygen reduction reaction. J Power Sources 2007;173:891–908.

8.   Jasinski R. A new fuel cell cathode catalyst. Nature 1964;201:1212–13.

9.   Zagal JH. Macrocycles. In: Vielstich W, Gasteiger HA, editors. Handbook of fuel cells – fundamental, technology and applications, volume 2. New York: John Wiley & Sons Ltd, 2003;37:544–54.

10. Beck F. The redox mechanism of the chelate-catalysed oxygen cathode. J Appl Electrochem 1977;7:239–45.

11. Zagal JH. Metallophthalocyanines as catalysts in electrochemical reactions. Coord Chem Rev 1992;119:89–136.

12. Wiesener K, Ohms D, Neumann V, Franke R. N_4 macrocycles as electrocatalysts for the cathodic reduction of oxygen. Mater Chem Phys 1989;22:457–75.

13. Alt H, Binder M, Sandstede G. Mechanism of the electrocatalytic reduction of oxygen on metal chelates. J Catal 1973;28:8–19.

14. Jiang R, Xu L, Jin R, Dong S. Chemically modified electrode XI: Preparation and stability of metallotetraphenylporphyrin adsorbed on glassy carbon electrode. Fenxi Huaxue 1985;13:270–75.

15. Durand RR, Bencosme CS, Collman JP, Anson FC. Mechanistic aspects of the catalytic reduction of dioxygen by cofacial metalloporphyrins. J Am Chem Soc 1983;105:2710–18.

16. Chang CK, Liu HY, Abdalmuhdai I. Mechanistic aspects of the catalytic reduction of dioxygen by cofacial diporphyrin catalysts. J Am Chem Soc 1984;106:2725–6.

17. van der Putten A, Elzing A, Visscher W, Barendrecht E, Harcourt RD. Increased valence theory and the four electron reduction of molecular oxygen to water. J Mol Struct (Thermochem) 1988;180:309–18.

18. Oyama N, Anson FC. Catalysis of electrode processes by multiply-charged metal complexes electrostatically bound to polyelectrolyte coatings on graphite electrodes, and the use of polymer-coated rotating disk electrodes in diagnosing kinetic and conduction mechanisms. Anal Chem 1980;52:1192–8.

19. Collman JP, Denisevich P, Konai Y, Marrocco M, Koval C, Anson FC. Electrode catalysis of the four-electron reduction of oxygen to water by dicobalt face-to-face porphyrins. J Am Chem Soc 1980;102:6027–36.

20. Chu D, Jiang R. Novel electrocatalysts for direct methanol fuel cells. Solid State Ionics 2002;148:591–9.

21. Biloul A, Contamin O, Scarbeck G, Savy M, Palys B, Riga J, et al. Oxygen reduction in acid media: influence of the activity of CoNPc(1,2) bilayer deposits in relation to their attachment to the carbon black support and role of surface groups as a function of heat treatment. J Electroanal Chem 1994;365:239–46.

22. Matter PH, Ozkan US. Non-metal catalysts for dioxygen reduction in an acidic electrolyte. Catal Lett 2006;109:115–23.

23. Drazic DM, Ledinski ZV, Zecevic SK. Transition metal catalysts for porous carbon air-electrodes in neutral chloride electrolytes. J Appl Electrochem 1983;13:337–40.

24. Li J, Wu X, Yuan R, Lin H, Yu R. Cobalt phthalocyanine derivatives as neutral carriers for nitrite-sensitive poly(vinyl chloride) membrane electrodes. The Analyst 1994;119:1363–6.

25. Castellani AM, Gonclaves JE, Gushiken Y. The use of carbon paste electrodes modified with cobalt tetrasulfonated phthalocyanine adsorbed in silica/titania for the reduction of oxygen. J New Mater Electrochem Syst 2002;5:169–72.

26. Jahnke H, Schonbron M, Zimmerman G. Organic Dyestuffs as catalysts for fuel cells. Top Curr Chem 1976;61:133–81.

27. Kretzschmar C, Wiesiner K. Study of the operation of tungsten carbide anode and iron phthalocyanine cathodes in fuel cells with a sulphuric acid electrolyte. Elektrokhimiya 1978;14:1330–4.

28. Biloul A, Gouerec P, Savy M, Scarbeck G, Besse S, Riga J. Oxygen electrocatalysis under fuel cell conditions: behaviour of cobalt porphyrins and tetraazaannulene analogues. J Appl Electrochem 1996;26:1139–46.

29. Zhong W, Dong X, Chen S, Lin W. A new non-noble metal electro-catalyst for the reduction of oxygen. Battery Bimonthly 2003;33:245–8.

30. Faubert G, Lalande G, Cote R, Guay D, Dodelet JP, Weng LT, et al. Heat-treated iron and cobalt tetraphenylporphyrins adsorbed on carbon black: Physical characterization and catalytic properties of these materials for the reduction of oxygen in polymer electrolyte fuel cells. Electrochim Acta 1996;41:1689–701.

31. Lalande G, Cote R, Tamizhmani G, Guay D, Dodelet JP, Dignard-Bailey L, et al. Physical, chemical and electrochemical characterization of heat-treated characterization of heat-treated tetracarboxylic cobalt phthalocyanine adsorbed on carbon black as electrocatalyst for oxygen reduction in polymer electrolyte fuel cells. Electrochim Acta 1995;40:2635–46.

32. Bron M, Fiechter S, Hilgendorff M, Bogdanoff P. Catalysts for oxygen reduction from heat-treated carbon-supported iron phenantroline complexes. J Appl Electrochem 2002;32:211–16.

33. Iliev I, Gamburtsev S, Kaisheva A. Optimization of the pyrolysis temperature of carbon-CoTMPP catalysts for air electrodes in alkaline media. J Power Sources 1986;17:345–52.

34. Vasudevan P, Santosh, Mann N, Tyagi S. Transition metal complexes of porphyrins and phthalocyanines as electrocatalysts for dioxygen reduction. Transition Met Chem 1990;15:81–90.

35. van Veen JAR, Colijin HA, van Baar JF. On the effect of a heat treatment on the structure of carbon-supported metalloporphyrins and phthalocyanines. Electrochim Acta 1988;33:801–4.

36. Weng LT, Bertrand P, Lalande G. Surface characterization by time-of-flight SIMS of a catalyst for oxygen electroreduction: pyrolyzed cobalt phtholcyanine-on-carbon black. Appl Surf Sci 1995;84:9–21.

37. Bae IT, Tryk DA, Scherson DA. Effect of heat treatment on the redox properties of iron porphyrins adsorbed on high area carbon in acid electrolytes: An in Situ Fe K-Edge X-ray Absorption Near-Edge Structure Study. J Phys Chem B 1998;102:4114–17.

38. Lefevre M, Dodelet JP, Bertrand P. O_2 reduction in PEM fuel cells: Activity and active site structural information for catalysts obtained by the pyrolysis at high temperature of Fe precursors. J Phys Chem B 2000;104:11238–47.

39. Bogdanoff P, Herrmann I, Hilgendorff M Dorbandt I, Fiechter S, Tributsch H. Probing structural effects of pyrolysed CoTMPP-based electrocatalysts for oxygen reduction via new preparation strategies. J New Mater Electrochem Syst 2004;7:85–92.

40. Bouwkamp AL, Visscher W, Veen JA. Electrochemical reduction of oxygen: an alternative method to prepare active CoN_4 catalysts. Electrochim Acta 1999;45:379–86.

41. Faubert G, Cote R, Guay D, Dodelet JP, Denes G, Poleunis C, et al. Activation and characterization of Fe-based catalysts for the reduction of oxygen in polymer electrolyte fuel cells. Electrochim Acta 1998;43:1969–84.

42. Gupta S, Tryk D, Bae I, Aldred W, Yeager E. Heat-treated polyacrylonitrile-based catalysts for oxygen electroreduction. J Appl Electrochem 1989;19:19–27.

43. Fournier J, Lalande G, Cote R, Guay D, Dodelet JP. Activation of various Fe-based precursors on carbon black and graphite supports to obtain catalysts for the reduction of oxygen in fuel cells. J Electrochem Soc 1997;144:218–226.

44. Ohms D, Herzog S, Franke R, Neumann V, Wiesener K. Influence of metal ions on the electrocatalytic oxygen reduction of carbon materials prepared from pyrolyzed polyacrylonitrile. J Power Sources 1992;38:327–34.

45. Lalande G, Cotre R, Duay D, Dodelet JP, Weng LT, Bertrand P. Is nitrogen important in the formulation of Fe-based catalysts for oxygen reduction in solid polymer fuel cells? Electrochim Acta 1997;42:1379–88.

46. Martin Alves MC, Tourillon G. Influence of complexation processes on the catalytic properties of some polymer-based cobalt compounds for oxygen electroreduction. J Phys Chem 1996;100:7566–72.

47. Sirk AHC, Campbell SA, Birss VI. Oxygen reduction by sol derived Co, N, C, O-based catalysts for use in proton exchange membrane fuel cells. Electrochemical and Solid-State Letters 2005;8:A104–7.

48. He P, Lefevre M, Faubert G, Dodelet JP. Oxygen reduction catalysts for polymer electrolyte fuel cells from the pyrolysis of various transition metal acetates adsorbed on 3,4,9,10-perylenetetracarboxylic dianhydride. J New Mater Electrochem Syst 1999;2:243–51.

49. Wei G, Wainright JS, Savinell RF. Catalytic activity for oxygen reduction reaction of catalysts consisting of carbon, nitrogen and cobalt. J New Mater Electrochem Syst 2000;3:121–29.

50. Wang H, Cote R, Faubert G, Guay D, Dodelet JP. Effect of the pre-treatment of carbon black supports on the activity of Fe-based electrocatalysts for the reduction of oxygen. J Phys Chem B 1999;103:2042–9.

51. Jaouen F, Marcotte S, Dodelet JP, Lindbergh G. Oxygen reduction catalysts for polymer electrolyte fuel cells from the pyrolysis of iron acetate adsorbed on various carbon supports. J Phys Chem B 2003;107:1376–86.

52. Lalande G, Tamizhmani G, Cote R, Dignard-Bailey L, Trudeau ML, Schulz R, et al. Influence of loading on the activity and stability of heat-treated carbon-supported cobalt phthalocyanine electrocatalysts in solid polymer electrolyte fuel cells. J Electrochem Soc 1995;142:1162–8.

53. Faubert G, Cote R, Dodelet JP, Lefevre M, Bertrand P. Oxygen reduction catalysts for polymer electrolyte cells from the pyrolysis of Fe^{2+} acetate adsorbed 3,4,9, lo-perylenetetracarboxylic dianhydride. Electrochim Acta 1999;44:2589–603.

54. Tamizhmani G, Dodelet JP, Guay D, Lalande G, Capuano GA. Electrocatalytic activity of nafion-lmpregnated pyrolyzed cobalt phthalocyanine. J Electrochem Soc 1994;141:41–5.

55. van der Putten A, Elzing A, Visscher W, Barendrecht E. Oxygen reduction on pyrolysed carbon-supported transition metal chelates. J Electroanal Chem 1986;205:233–44.

56. Ye S, Vijh AK. Non-noble metal-carbonized aerogel composites as electrocatalysts for the oxygen reduction reaction. Electrochem Commun 2004;5:272–5.

57. Liu H, Song C, Tang Y, Zhang J. High-surface-area CoTMPP/C synthesized by ultrasonic spray pyrolysis for PEM fuel cell electrocatalysts. Electrochim Acta 2007;52:4532–8.

58. Bashyam R, Zelenay P. A class of non-precious metal composite catalysts for fuel cells. 2006;443:63–6.

59. Mazza F, Trassatti S. Tungsten, titanium, and tantalum carbides and titanium nitrides as electrodes in redox systems. J Electrochem Soc 1963;110:847–9.

60. Binder H, Kohling A, Kuhn W, Lindner W, Sandstede G. Tungsten carbide electrodes for fuel cells with acid electrolyte. Nature 1969;224:1299–300.

61. Bennett LH, Cuthill JR, McAlister AJ, Erickson NE. Electronic structure and catalytic behavior of tungsten carbide. Science 1974;184:56365.
62. Ross PN Jr, Stonehart P. Surface characterization of catalytically active tungsten carbide (WC). J Catal 1975;39:298–301.
63. Colton RJ, Huang JTJ, Rabalais JW. Electronic structure of tungsten carbide and its catalytic behavior. Chem Phys Lett 1975;34:337–9.
64. Voinov M, Buhler D, Tannenberger H. Oxygen reduction on tungsten carbide. J Electrochem Soc 1971;118:1137–8.
65. Levy RB, Boudart M. Platinum-like behavior of tungsten carbide in surface catalysis. Science 1973;181:547–9.
66. Bohm H. Adsorption und anodische oxydation von wasserstoff an wolframcarbid. Electrochim Acta 1970;15:1273–80.
67. Ross PN Jr, Stonehart P. The relation of surface structure to the electrocatalytic activity of tungsten carbide. J Catal 1977;48:42–59.
68. Sokolsky DV, Palanker VS, Baybatyrov EN. Electrochemical hydrogen reactions on tungsten carbide. Electrochim Acta 1975;20:71–7.
69. Zoltowski P. The mechanism of the activation process of the tungsten carbide electrode. Electrochim Acta 1986;31:103–11.
70. Okamoto H, Kawamura G, Ishikawa A, Kudo T. Activation of (W, Mo)C methanol anodic oxidation catalysts using alkaline solution. J Electrochem Soc 1987;134:1649–53.
71. Machida KI, Enyo M. Preparation of WC_x thin films by RF sputtering and their electrocatalytic property for anodic methanol oxidation. J Electrochem Soc 1990;137:871–6.
72. Bonoel G, Musuex E, Lelercq L, Tassin N. Study of hydrogen oxidation on carbides. Electrochim Acta 1991;36:1543–7.
73. McIntyre DR, Burstein GT, Vossen A. Effect of carbon monoxide on the electrooxidation of hydrogen by tungsten carbide. J Power Sources 2002;107:67–73.
74. Vijh AK, Jacques R, Belanger G. The electrochemical reduction of oxygen on cobalt-cemented tungsten carbide. J Power Sources 1983;9:1–10.
75. Lee K, Ishihara A, Mitsushima S, Kamiya N, Ota KI. Stability and electrocatalytic activity for oxygen reduction in WC+Ta catalyst. Electrochim Acta 2004;49:3479–85.
76. Lee K, Ishihara A, Mitsushima S, Kamiya N, Ota KI. Transition metal carbides for new cathode material of polymer electrolyte fuel cell. Electrochemical Society Proceeding Volume 2004–21, Proton Conducting Membrane Fuel Cells IV, 2004;213–20.
77. McIntyre DR, Vossen A, Wilde JR, Burstein GT. Electrocatalytic properties of a nickel-tantalum-carbon alloy in an acidic electrolyte. J Power Sources 2002;108:1–7.
78. Yang R, Bonakdarpour A, Dhan JR. Investigation of sputtered Ta-Ni-C as an electrocatalyst for the oxygen reduction reaction. J Electrochem Soc 2007;154:B1–7.
79. Giner J, Swette L. Oxygen reduction on titanium nitride in alkaline electrolyte. Nature 1966;211:1291–2.
80. Azuma M, Kashihara M, Nakato Y, Tsubomura H. Reduction of oxygen to water on cobalt-nitride thin film electrodes prepared by the reactive RF sputtering technique. J Electroanal Chem 1988;250:73–82.
81. Zhong H, Zhang H, Liu G, Liang Y, Hu J, Yi B. A novel non-noble electrocatalyst for PEM fuel cell based on molybdenum nitride. Electrochem Commun 2006;8:707–12.
82. Zhong H, Zhang H, Liang Y, Zhang J, Wang M, Wang X. A novel non-noble electrocatalyst for oxygen reduction in proton exchange membrane fuel cells. J Power Sources 2007;164:572–7.

83. Frapper G, Pelissier M, Hafner J. CO adsorption on molybdenum nitride's γ-$Mo_2N(100)$ surface: Formation of NdCdO species? A density functional study. J Phys Chem B 2000;104:11972–11976.

84. Ishihara A, Lee K, Doi S, Mitsushima S, Kamiya N, Hara M, et al. Tantalum oxynitride for a novel cathode of PEFC. Electrochemical and Solid-State Letters 2005;8:A201–3.

85. Yato K, Doi S, Ishihara A, Mitsushima S, Kamiya N, Ota KI. Effect of heat treatment of titanium oxynitride as platinum-free electrocatalyst on oxygen reduction reaction. Suiso Enerugi Shisutemu 2006;31:58–65.

86. Doi S, Ishihara A, Mitsushima S, Kamiya N, Ota KI. Zirconium-based compounds for cathode of polymer electrolyte fuel cell. J Electrochem Soc 2007;154:B362–9.

87. Doi S, Liu Y, Ishihara A, Mitsushima S, Kamiya N, Ota K. Zirconium nitride and oxynitride for new cathode of polymer electrolyte fuel cell. ECS Transactions 2006;1:17–25.

88. Ishihara A, Doi S, Liu Y, Mitsushima S, Kamiya N, Ota K. Tantalum nitride and oxynitride for new cathode of polymer electrolyte fuel cell. ECS Transactions 2006;1:51–60.

89. Lee K. Ph.D dissertation, Yokohama National University, 2004.

90. Kim JH, Ishihara A, Mitsushima S, Kamiya N, Ota KI. Catalytic activity of titanium oxide for oxygen reduction reaction as a non-platinum catalyst for PEFC. Electrochim Acta 2007;52:2492–7.

91. Domen K. Report code number 100010143. New Energy and Industrial Technology Development Organization (NEDO), Strategic development of PEFC technologies for practical application, development of technology for next-generation fuel cells, development of alternative(low-cost) precious metal catalyst, FY 2005–2006 progress reports;2007. Available from: http://www.tech.nedo.go.jp/servlet/TopPageServlet?KENSAKU=HOKOKUSYO&kensakuHoho=Barcode_Kensaku&db=n&SERCHBAR CODE=100010143.

92. Kim JH, Ishihara A, Mitsushima S, Kamiya N, Ota KI. Oxygen reduction reaction of Ta-C-N prepared by reactive sputtering with heat treatment. Electrochemistry 2007;75:166–8.

93. Kim JH, Ishihara A, Mitsushima S, Kamiya N, Ota KI. New non-platinum cathode based on chromium for PEFC. Chem Lett 2007;36:514–15.

94. Easton EB, Bonakdarpour A, Dahn JR. Fe-C-N oxygen reduction catalysts prepared by combinatorial sputter deposition. Electrochemical and Solid-State Letters 2006;9:A463–7.

95. Yang R, Bonakdarpour A, Easton EB, Stoffyn-Egli P, Dahn JR. Co–C–N oxygen reduction catalysts prepared by combinatorial magnetron sputter deposition. J Electrochem Soc 2007;154:A275–82.

96. Yang R, Stevens K, Bonakdarpour A, Dahn JR. Dependence of the activity of sputtered Co–C–N oxygen reduction electrocatalysts on heat-treatment temperature. J Electrochem Soc 2007;154:B893–901.

97. Atanasoski R. Novel approach to non-precious metal cataysts. DOE hydrogen program, FY 2007 Annual progress report;2007;820–24. Available from: http://www.hydrogen.energy.gov/pdfs/progress07/v_e_1_atanasoski.pdf

98. Alonso-Vante N, Tributsch H. Energy conversion catalysis using semiconducting transition metal cluster compounds. Nature 1986;323:431–2.

99. Alonso-Vante N. Chevrel phases and chalcogenides. In: Vielstich W, Gasteiger HA, editors. Handbook of fuel cells – fundamental, technology and applications, volume 2. New York: John Wiley & Sons Ltd; 2003;36:534–43.

100. Lee K, Zhang L, Zhang J. A novel methanol-tolerant Ir-Se chalcogenide electrocatalyst for oxygen reduction. J Power Sources 2007;165:108–13.

101. Gochi-Ponce Y, Alonso-Nunez G, Alonso-Vante N. Synthesis and electrochemical characterization of a novel platinum chalcogenide electrocatalyst with an enhanced tolerance to methanol in the oxygen reduction reaction. Electrochem Commun 2006;8:1487–91.

102. Reeve RW, Christensen PA, Hamnett A, Haydock SA, Roy SC. Methanol tolerant oxygen reduction catalysts based on transition metal sulfides. J Electrochem Soc 1998;145:3463–3471.

103. Fischer C, Alonso-Vante N, Fiechter S, Tributsch H. Electrocatalytic properties of mixed transition metal tellurides (Chevrel-phases) for oxygen reduction. J Appl Electrochem 1995;25:1004–8.

104. Baresel VD, Sarholz W, Scharner P, Schmitz. Transition metal chalcogenides as oxygen catalysts for fuel cells. Ber Bunsen-Ges Phys Chem 1974;78:608–11.

105. Behret H, Binder H, Sandstede G. Electrocatalytic oxygen reduction with thiospinels and other sulphides of transition metals. Electrochim Acta 1973;20:111–17.

106. Behret H, Binder H, Clauberg W, Sandstede G. Comparison of the reaction mechanisms of electrocatalytic oxygen reduction using transition metal thiospinels and chelates. Electrochim Acta 1978;23:1023–9.

107. Campbell S. Development of transition metal/chalcogen based cathode catalysts for PEM fuel cells. DOE hydrogen program, FY 2004 annual progress report 2004:389–91; FY 2005 annual progress report 2005:850–53; FY 2006 annual progress report 2006:799–803; FY 2007 annual merit review proceedings 2007:FC6. Available from: http://www.hydrogen.energy.gov/annual_progress.html.

108. Reyimjan A, Sidik RA, Anderson AB. Co_9S_8 as a catalyst for electroreduction of O_2: Quantum chemistry predictions. J Phys Chem B 2006;110:936–41.

109. Susac D, Sode A, Zhu L, Wong PC, Teo M, Bizzotto D, et al. A methodology for investigating new nonprecious metal catalysts for PEM fuel cells. J Phys Chem B 2006;110:10762–70.

110. Lee K, Zhang L, Zhang J. Ternary non-noble metal chalcogenide (W-Co-Se) as electrocatalyst for oxygen reduction reaction. Electrochem Commun 2007;9:1704–8.

111. Brenet JP. Electrochemical behaviour of metallic oxides. J Power Sources 1979;4:183–90.

112. Seiyama T, Yamazoe N. Perovskite-type oxides and their applicability to catalysis: properties in relation to the defect structure. Kagaku 1982;37:314–16.

113. Arai H. Current status and future prospect for catalyst technology. Shokubai 1988;30:598–602.

114. Yamazoe N, Teraoka Y. Oxide catalysts. Kikan Kagaku Sosetsu 1988;3:36–43.

115. Yamazoe N, Teraoka Y. Oxidation Catalysis of perovskites – relationships to bulk structure and composition (valency, defect, etc.). Catal Today 1990;8:175–99.

116. Klissurski D, Uzunova E. Review synthesis and features of binary cobalite spinels. J Mater Sci 1994;29:285–93.

117. Yasuda H, Misono M. Catalysis of perovskite. Kikan Kagaku Sosetsu 1997;32:149–58.

118. Roberts GL. A review of mixed-transition metal oxides as potential bifunctional electrode. Reviews in Process Chemistry and Engineering 2000;3:151–74.

119. Pena MA, Fierro JLG. Chemical structures and performance of perovskite oxides. Chem Rev 2001;101:1981–2017.

120. Kudo T, Obayashi H, Gejo T. Electrochemical behavior of the perovskite-type $Nd_{1-x}Sr_xCoO_3$ in an aqueous alkaline solution. J Electrochem Soc 1975;122:159–63.

121. Obayashi H, Kudo T. Some electric and electrochemical properties of the perovskite-type $Ln_{1-x}M_xCoO_3$ (Ln=lanthanoid, M=calcium, strontium, and barium). Electrochemistry 1976;44:503–7.

122. Kudo T, Obayashi H, Yoshida M. Rare earth cobaltites as oxygen electrode materials for alkaline solution. J Electrochem Soc 1977;124:321–5.

123. Hayashi M, Hyodo T, Miura N, Yamazoe N. Electrochemical oxygen reduction properties of perovskite-type oxides $La_{1-x}A_xMnO_3$ (A=Na, K. Rb) in concentrated alkaline solution. Electrochemistry 2000;68:112–18.

124. Hyodo T, Hayashi M, Miura N, Yamazoe N. Catalytic activities of rare-earth manganites for cathodic reduction of oxygen in alkaline solution. J Electrochem Soc 1996;143:L266–7.

125. Voorhoeve RJH, Remeika JP, Trimble LE, Cooper AS, Disalvo FJ, Gallagher PK. Perovskite-like $La_{1-x}K_xMnO_3$ and related compounds: Solid state chemistry and the catalysis of the reduction of NO by CO and H_2. J Solid State Chem 1975;14:395–406.

126. Klissurski D, Uzunova E. Review synthesis and features of binary cobalite spinels. J Mater Sci 1994;29:285–93.

127. Wen TC, Kang HM. Co-Ni-Cu ternary spinel oxide-coated electrodes for oxygen evolution in alkaline solution. Electrochim Acta 1998;43:1729–45.

128. Trasatti S. Electrocatalysis in the anodic evolution of oxygen and chlorine. Electrochim Acta 1984;29:1503–12.

129. Nguyen Cong H, Chartier P, Brenet J. Reduction electrocatalytique de l'oxygene sur electrodes solides d'oxydes mixtes contenant des ions maganese. I. Cas des manganites de cuivre $Cu_xMn_{3-x}O_4$ (0 < x < 1.8) en milieu légèrement acide. J Appl Electrochem 1977;7:383–93.

130. Nguyen Cong H, Chartier P, Brenet J. Reduction electrocatalytique de l'oxygene sur electrodes solides d'oxydes mixtes contenant des ions maganese. II. Rôle due couple Mn^{3+}-Mn^{4+} en sites ocatédriques. J Appl Electrochem 1977;7:395–406.

131. Nguyen Cong H, Brenet J. Comportement électrocatalytique vis à vis de la réduction d'oxygène des oxydes mixtes $A_xB_yMn_{3-(x+y)}O_4$. J Appl Electrochem 1980;10:433–9.

132. Parkinson B, Decker F, Juliao JF, Abramovich M, Chagas HC. The reduction of molecular oxygen at single crystal rutile electrodes. Electrochim Acta 1980;25:521–5.

133. Mentus SV. Oxygen reduction on anodically formed titanium dioxide. Electrochim Acta 2004;50:27–32.

134. Baez VB, Graves JE, Pletcher D. The reduction of oxygen on titanium oxide electrodes. J Electroanal Chem 1992;340:273–86.

135. Liu Y, Ishihara A, Mitsushima S, Kamiya N, Ota KI. Zirconium oxide for PEFC cathodes. Electrochemical and Solid-State Letters 2005;8:A400–2.

136. Liu Y, Ishihara A, Mitsushima S, Kamiya N, Ota KI. Transition metal oxides as DMFC cathodes without platinum. J Electrochem Soc 2007;154:B664–9.

137. Matsuki K, Mori K, Kamada H. Electrocatalysis by $CaMnO_{3-x}$ of oxygen reduction in alkaline solution. Electrochemistry 1984;52:174–9.

138. Hyodo T, Hayashi M, Mitsutake S, Miura N, Yamazoe N. Oxygen reduction activities of praseodymium manganites in alkaline solution. J Ceramic Soc Japan 1997;105:412–17.

139. Imaizumi S, Shimanoe K, Teraoka Y, Yamazoe N. Oxygen reduction property of ultrafine $LaMnO_3$ dispersed on carbon support. Electrochemical and Solid-State Letters 2005;8:A270–2.

140. Meadowcroft DB. Low-cost oxygen electrode material. Nature 1970;226:847–8.

141. Tseung ACC, Bevan HL. A reversible oxygen electrode. J Electroanal Chem 1973;45:429–38.

142. Van Buren FR, Broers GHJ, Bouman AJ, Boesveld C. The electrochemical determination of oxygen ion diffusion coefficients in $La_{0.50}Sr_{0.50}CoO_{3-y}$ experimental results and related properties. J Electroanal Chem 1978;88:353–61.

143. Obayashi H, Kudo T. Perovskite-type compounds as electrode catalysts for cathodic reduction of oxygen. Mater Res Bull 1978;133:1409–13.

144. Karlsson G. Reduction of oxygen on LaNiO$_3$ in alkaline solution. J Power Sources 1983;10:319–31.
145. Moon HD, Lee HI. A study on the catalytic characteristics of oxygen reduction in an alkaline fuel cell I: Synthesis of La$_{0.6}$Sr$_{0.4}$Co$_{1-x}$Fe$_x$O$_3$ and reduction of oxygen, a study on the catalytic characteristics of oxygen reduction in an alkaline fuel cell II: characterization of La$_{0.6}$Sr$_{0.4}$Co$_{1-x}$Fe$_x$O$_3$ by using XRD, TG and TPR. Kongop Hwahak 1996;7:543–64.
146. Gu J, Sheng S, Li GQ, Sui ZT. Catalytic activities of La$_{1-x}$Ca$_x$Fe$_{1-y}$Co$_y$O$_3$ for oxygen reduction. Wuji Cailiao Xuebao 1999;14:618–22.
147. Song SD, Tang ZY, Pan LZ, Nan JM. Study on the electrochemical properties of La$_{1-x}$Sr$_x$Ni$_{1-y}$Fe$_y$O$_3$ bifunctional oxygen electrode. Huaxue Xuebao 2005;63:363–71.
148. Tian G, Chi Y, Fu H, Li L, Zhang G, Li R. Electrocatalytic performances of perovskite-like complex oxides La$_{2-x}$Sr$_x$CuO$_{4+\lambda}$ air electrode catalyst for oxygen reduction. Heilongjian Daxue Ziran Kexue Xuebao 2005;22:481–4.
149. Savy M. Oxygen reduction in alkaline solution on semiconducting cobalt oxide electrodes. Electrochim Acta 1968;13:1359–76.
150. Efremov BN, Tarasevich MR, Zakharkin GI, Zhukov SR. Stability and electrochemical activity of cobalt (Co$_3$O$_4$) spinel in an alkaline solution. Elektrokhimiya 1978;14:1504–9.
151. Bagotzky VS, Shumilova NA, Khrushcheva EI. Electrochemical oxygen reduction on oxide catalysts. Electrochim Acta 1976;21:919–24.
152. King WJ, Tseung ACC. The reduction of oxygen on nickel-cobalt oxides II correlation between crystal structure and activity of Co$_2$NiO and related oxides. Electrochim Acta 1974;19:493–8.
153. Tarasevich MR, Vilinskaya VS, Khutornoi AM, Burshtein RKh, Makordei FV, Tkach YuA. Adsorption and electroreduction of molecular oxygen on oxide catalysts II: mechanism of cathodic reduction of oxygen on nickel cobaltate (NiCo$_2$O$_4$). Elektrokhimiya 1976;12:504–7.
154. Singh RN, Koenig JF, Poillerat G, Chartier P. Thin films of Co, O, and NiCo$_2$O$_4$ prepared by the method of chemical spray pyrolysis for electrocatalysis Part IV. The electrocatalysis of oxygen reduction. J Electroanal Chem 1991;314:241–57.
155. Sugawara M, Ohno M, Matsuki K. Oxygen reduction catalysis of Mn–Co spinel oxides on a graphite electrode in alkaline solution. J Mater Chem 1997;7:833–6.
156. Rios E, Gautier JL, Poillerat G, Chartier P. Mixed valency spinel oxides of transition metals and electrocatalysis: case of the Mn$_x$Co$_{3-x}$O$_4$ system. Electrochim Acta 1998;44:1491–7.
157. Nissinen T, Valo T, Gasik M, Rantanen J, Lampinen M. Microwave synthesis of catalyst spinel MnCo$_2$O$_4$ for alkaline fuel cell. J Power Sources 2002;106:109–15.
158. Li N, Yan X, Jin Y, Li S, Lin B. Spinel-type oxides LiMn$_{2-x}$M$_x$O$_4$ [M=Co, Fe, (CoFe)] as electrocatalyst for oxygen evolution/reduction in alkaline solution. J Appl Electrochem 1999;29:1351–4.
159. Ortiz J, Gautier JL. Oxygen reduction on copper chromium manganites. Effect of oxide composition on the reaction mechanism in alkaline solution. J Electroanal Chem 1995;391:111–18.
160. Ponce J, Rehspringer JL, Pillerat G, Gautier JL. Electrochemical study of nickel–aluminium–manganese spinel Ni$_x$Al$_{1-x}$Mn$_2$O$_4$. Electrocatalytical properties for the oxygen evolution reaction and oxygen reduction reaction in alkaline media. Electrochim Acta 2001;46:3373–80.
161. Matsuda Y, Yamashita K, Takasu Y. Characteristics of manganese dioxide-active carbon as an oxygen electrode in alkaline-type fuel cells. Electrochemistry 1983;51:925–30.

162. Yang J, Xu JJ. Nanoporous amorphous manganese oxide as electrocatalyst for oxygen reduction in alkaline solutions. Electrochem Commun 2003;5:306–11.

163. Calegaro ML, Lima FHB, Ticianelli EA. Oxygen reduction reaction on nanosized manganese oxide particles dispersed on carbon in alkaline solutions. J Power Sources 2006;158:735–9.

164. Yang CC, Hsu ST, Chien WC, Shih MC, Chiu SJ, Lee KT, et al. Electrochemical properties of air electrodes based on MnO_2 catalysts supported on binary carbons. Int J Hydrogen Energy 2006;31:2076–87.

165. Manoharan R, Goodenough JB. Oxygen reduction on CrO_2 bonded to a proton-exchange membrane. Electrochim Acta 1995;40:303–7.

16

CO-tolerant Catalysts

Siyu Ye

16.1 Introduction

Fuel cell systems offer the promise of economically delivering power with environmental and other benefits. Recently, polymer electrolyte membrane fuel cells (PEMFCs) have passed the demonstration phase and have partly reached the commercialization stage due to impressive research efforts. Nevertheless, there are still some technological challenges to be solved. Among those challenges, (i) choice of fuel (gasoline, methanol, or hydrogen), (ii) efficient fuel processing, with reduction of weight, volume, and carbon monoxide (CO) residuals, and (iii) development of anode electrocatalysts tolerant to CO at levels of 50 ppm (with a noble metal loading of 0.1 mg cm^{-2} or less) are deemed to be the most significant barriers that PEMFCs must overcome to achieve complete commercialization. The first and second challenges are closely related to the source and purity of hydrogen as the fuel.

 The simplest and highest performing PEMFC systems employ pure hydrogen as the fuel. Since H_2 storage and supply devices are an issue, feeding the anode with the reformate of liquid alcohols, gasoline, or natural gas is the most popular choice, as they are readily available. The alcohols, gasoline, or natural gas are reformed using steam, partial oxidation, or autothermal reforming to produce the reformate – a hydrogen-rich gas stream (H_2, 40–70%) containing carbon dioxide (CO_2, 15–25%), carbon monoxide (CO, 1–2%), and small quantities of inert gases, such as nitrogen and water vapor. However, at current PEMFC stack operating temperatures of around 80 °C, the membrane electrode assemblies (MEAs) within the stack cannot tolerate such high CO levels. Therefore, the reformate must be passed from the reformer to a shift reactor and then to a catalytic preferential oxidation (PROX) reactor to reduce the CO content to less than 100 ppm, and in some cases down to a few ppm. The reformate can then enter the stack and react in the anode electrocatalyst layer of the MEA. The additional reformer, shift and PROX reactors significantly complicate and add extra cost to the PEMFC system [1]. For instance, Cu-based catalysts [2] were ordinarily used as the shift-converter catalysts in plants; however, it is difficult to use a Cu-based catalyst in the domestic-use PEMFC system. The PEMFC system would be frequently turned on

and off, and when it was turned off, the Cu catalyst would be easily oxidized by steam and air, and eventually deactivated. Therefore, precious metal catalysts such as Pt catalysts supported on CeO_2-containing oxides were used in the PEMFC system. On the other hand, Pd [3], Au [3], Pt, or Ru [5] is used as the catalyst for preferential oxidation of CO at low temperature. Among these, the Ru catalyst exhibited high performance for preferential oxidation of CO and long-term stability under a low O_2/CO molar ratio [5]. In any case, considerable amounts of precious metals were used in both a shift converter unit and a CO preferential oxidation unit, resulting in high cost. Moreover, this complicated system containing a CO-removal unit led to low efficiency and reliability. Therefore, developing CO-tolerant anode catalysts is a key priority. The US DOE 2011 targets for fuel cell stack CO tolerance are 500 ppm on steady state (with 2% max air bleed) and 1000 ppm on transient [6].

In a PEMFC, when operating with pure hydrogen at practical current densities, the anode potential is typically less than +0.1 V (vs. RHE (reversible hydrogen electrode)). Under such operating conditions the cell potential is only slightly lower than the cathode potential and the MEA performance essentially reflects the cathode operation. However, when using reformate as a fuel, the CO in the reformate stream binds very strongly to the Pt electrocatalyst sites in the anode catalyst layer, at the typical MEA operating temperature of 80 °C. Even at ppm levels of CO, the CO coverage is above 0.98 [7]. The adsorbed CO prevents the dissociative electrosorption of hydrogen and dramatically lowers the cell potential produced by the MEA, since a much higher anode potential is required to sustain the rate of hydrogen electrooxidation [8]. Poisoning of Pt anode electrocatalysts by CO is deemed to be one of the most significant barriers to be overcome in the development of PEMFC systems.

In addition, CO was found to be a poisoning adsorbate during the oxidation of methanol and other small organic molecules [9]. An important although not unique aspect of the catalysis of methanol oxidation in direct methanol fuel cells (DMFC) is related to the catalysis of CO oxidation. Therefore, methanol and CO oxidation reactions are both discussed in several reviews [10–12].

There are a number of ways to overcome the CO poisoning of electrocatalysts [13–15], namely: (i) advanced reformer design; (ii) use of CO-tolerant catalysts; (iii) oxidant bleeding into the fuel feed stream; (iv) employment of a bilayer (composite) anode structure; (v) higher cell operating temperature; (vi) use of membranes for CO separation; and (vii) pulsing the cell voltage to low values during cell operation, forcing the anode potential to operate for a short time at a potential positive enough to electrochemically oxidize CO to CO_2.

(i) *Advanced reformer design.* Most of the reformers, including the auxiliary processors that are currently available, are capable of producing a CO content of 50 ppm or less after a warm-up period of up to 2 h. To acquire the bleeding oxidant effect by modifying the reformer, many researchers have considered the possibility of designing a new reformer to which auxiliary processors are fitted for clean-up steps, e.g., as shift converters and a selective oxidizer [16–18]. These methods would, however, increase the complexity and cost of the fuel cell system. Even when these additional stages are used, it is difficult to maintain low CO levels

during start-up and transient operations without the addition of an air bleed into the fuel stream [13, 19–24].

(ii) *Use of CO-tolerant catalysts.* Because the use of CO-tolerant electrocatalysts would be more efficient and cause fewer associated problems, this is generally considered the most promising way for solving the CO poisoning problem in PEMFCs. A common approach consists of utilizing a second metal in the Pt-based anode catalyst, able to form oxygenated species (metal-OH) at potentials lower than for pure Pt [18, 25]. Following a bifunctional mechanism, these metal-OH species act as a source of oxygen, required for the oxidation of adsorbed CO to CO_2, liberating active Pt sites on the surface of the catalyst material where the adsorption and oxidation of the gaseous hydrogen takes place [26]. It has been also proposed that CO tolerance can be achieved by an electronic effect [27, 28], which is associated with an energy shift of the Pt 5d electronic states caused by the second element and resulting in a weakening of the Pt–CO interactions.

It has been found that the use of a second element with Pt, such as Ru, Sn, Co, Cr, Fe, Ni, Pd, Os, Mo, Mn, etc., in the form of an alloy or a co-deposit yields significant improvement in the CO-tolerance relative to pure Pt [29–38]. Among these various Pt-based binary systems, the most commonly used catalyst is carbon-supported PtRu alloy (PtRu/C). This material is known to enhance CO tolerance, which can be ascribed to the electronic modification of Pt-Ru in PtRu alloys that decreases the CO binding energy on Pt and also binds OH strongly on the Ru active sites in the PtRu alloys [39]. Within this system, the performance of PEMFCs has been improved for fuel streams containing CO [40–42].

(iii) *Oxidant bleeding into the fuel feed.* Even with PtRu in a well-designed anode layer with the reformate operation there are losses in cell potential that are not recovered. The air bleed technique [8, 43] must be employed to introduce ≤ 2% air into the fuel stream to catalyze the oxidation of CO to CO_2. This recovers the cell potential losses at 100 ppm CO and most of the small loss due to 25% CO_2. Low levels of oxygen or oxygen-evolving compounds [8, 43–46] are bled into the fuel feed to decrease CO poisoning. With this procedure, the levels of CO produced in the reforming reaction can be reduced by reactions such as the water-gas shift (WGS) reaction and the selective oxidation of CO. (Note: CO can also be diminished by the methanation reaction with hydrogen but this is not efficient because it consumes the hydrogen.) Many working groups have reported that oxidant bleeding can be effective. In addition, hydrogen peroxide (H_2O_2) in an anode humidifier has been successfully used to mitigate the level of CO in H_2-rich feed [45, 46]. In this case, however, fuel utilization will certainly be decreased and safety issues must also be considered [47]. During the bleeding of oxidant process, roughly one out of every 400 O_2 molecules participates in the oxidation of CO [48], and the remaining oxygen chemically combusts with hydrogen. This combustion reaction not only lowers the fuel efficiency, but might also accelerate the sintering of catalyst particles, leading over time to a performance decline. In addition, the chemical combustion might also create pinholes in the electrolyte membrane, which could result in cell failure. The increased temperature on the catalyst surface and accelerated membrane failure are drawbacks to this method if moderation is not observed. For this reason, a bilayer anode structure using a

platinum group metal-based gas-phase catalytic oxidation layer between the gas diffusion substrate and the PtRu electrocatalyst layer was adopted to extend the anode lifetime [43]. This moves the heat generation away from the PtRu electrocatalyst layer and the membrane.

(iv) *Employment of a bilayer (composite) anode structure.* In accordance with the fuel selection, a more effective tolerance of CO in a PEMFC can be achieved by modifying the structure of the catalyst, i.e., with a composite or a double-layer. For example, the structure is designed to make the CO react with the CO-active electrocatalyst in advance at a separate layer and have the main hydrogen react at another layer with the traditional Pt electrocatalyst. There is still scope to optimize this type of structure and thus make the method even more effective for the suppression of CO poisoning. Although many attempts have been made in the last few decades to develop Pt-based binary or ternary electrocatalysts for replacing or reducing the platinum in the catalysts of PEMFCs, there has been less effort towards developing CO-tolerant electrodes by modifying their structure. The electrode structure relates to the diffusion process and reaction dynamics. In other words, because the diffusion coefficients of H_2 and CO are different, it is possible to design a special composite electrode structure according to the fuel components. In doing so, the anodes can be made with different electrocatalyst components, contents, and pore distributions. Therefore, this is considered to be a promising alternative approach to decreasing the poisoning of PEMFC anodes [43, 49–51].

Ralph et al. [43] discussed improvements in the reformate (CO and CO_2) tolerance at the anode and in extending the MEA durability. Improvements have been achieved by advances in platinum/ruthenium electrode design, in the application of bilayer anodes for durable air bleed operation. Johnson Matthey and Ballard Power Systems have significantly extended anode lifetimes by introducing a bilayer anode structure, in which a carbon-supported Pt-based catalyst layer is inserted between the PtRu electrocatalyst layer and the anode substrate [52]. It has been shown that the bilayer anode structure achieved a comparable MEA performance to the standard anode when operating both on reformate and on pure hydrogen. More importantly, the bilayer anode did not require an increase in the level of the air bleed beyond 3% to sustain the MEA performance, even after 2000 hours of continuous operation. This minimizes the degree of electrocatalyst sintering and significantly reduces the possibility of membrane pin-holing. Using the bilayer anode has resulted in stable MEA performances over many thousands of hours of continuous operation. For example, for an MEA with a bilayer anode containing 0.35 mg Pt cm^{-2} the reformate performance with a 2% air bleed was stable after in excess of 8000 hours of continuous operation. This bilayer approach may produce the required MEA lifetimes for PEMFC applications that need an air bleed to sustain reformate operation.

Wan and Zhuang [51] proposed a novel layer-wise anode structure to improve the CO-tolerance ability and utilization efficiency of the catalyst. The layer-wise structure consists of an outer and an inner catalyst layer. The outer catalyst layer, acting as a CO barrier, is composed of two nano-Ru layers (0.06 mg cm^{-2}) by the magnetron sputtering deposition method and a $Pt_{50}Ru_{50}$ layer (0.10 mg cm^{-2}) by the screen-printing method on the GDL. The inner catalyst layer providing the hydrogen oxidation reaction is a pure Pt layer (0.07 mg cm^{-2}) prepared by the

direct-printing method on the PEM. The roles of the outer and inner catalyst layers in the improvement of CO-tolerance ability and utilization efficiency of catalyst for the proposed catalyst layer structure were investigated. SEM, X-ray, EDS, and EPMA analysis were used to characterize microstructures, phases, chemical composition, and distributions for the obtained electrocatalyst layers. The hydrogen fuel containing 50 ppm $CO + 2\%$ O_2 is continuously fed to the anode side to investigate the dependence of CO-tolerance ability over time for the MEAs, respectively. A combination of two deposited nano-Ru layers with a printed $Pt_{50}Ru_{50}$ layer to form the outer catalyst layer for the anode electrode provides superior CO-tolerance capability to that of conventional and Haug's structures [53] in the presence of 2% O_2 and oxygen-free hydrogen containing 50 ppm CO fuels. In the oxygen-free hydrogen fuel containing 50 ppm CO, the deposited nano-Ru layer functions as a separator and/or for the physical/chemical adsorption of CO from hydrogen. The excess CO completely transforms to CO_2 by the third $Pt_{50}Ru_{50}$ layer at the outer catalyst layer. While in the presence of 2% O_2 hydrogen fuel containing 50 ppm CO, the deposited nano-Ru layer functions as a filter of CO from hydrogen, which reacts with the produced hydroxyl group from oxygen to form CO_2. The excess CO reacts with the hydroxyl group formed from oxygen and water on the surface of the third $Pt_{50}Ru_{50}$ layer of the outer catalyst layer, producing CO_2. The fuel entering the inner catalyst layer is thus free of CO. The inner direct-printed Pt catalyst layer can thus maintain high activity in the hydrogen oxidation reaction. In other words, it is possible by combining two structures to achieve a low noble metal loading MEA with high CO-tolerance capability in both oxygen-free and oxygen-present hydrogen fuels containing 50 ppm CO.

(v) *Higher cell operating temperature.* There is a considerable drive to raise the operating temperatures of the PEMFC to above 100 °C. This would raise the system efficiency and dramatically improve the CO tolerance of Pt-based electrocatalysts. For example, the CO coverage on Pt drops from in excess of 0.98 at 80 °C to ~0.5 at 160 °C [54]. At this temperature a Pt-based anode can function in the presence of 1 to 2% CO rather than with ppm levels of CO, eliminating the need for the PROX reactor. If the temperature can be raised to 160 °C, studies in the phosphoric acid fuel cell (PAFC) with 1 to 2% CO indicate that PtRh and PtNi may offer superior CO tolerance [55, 56]. Indeed, at 200 °C pure Pt is the favored electrocatalyst in the PAFC. At higher temperatures PtRu may not be the electrocatalyst of choice in the PEMFC. There is currently much research [57] aimed at developing membranes capable of proton conduction at 120 to 200 °C.

(vi) *Use of membranes for CO separation.* There is also considerable interest at the present time in the development of membranes designed for purification and separation. One approach has been the development of high-temperature (140 °C) membranes [58]. The CO tolerance of PEMFCs increases with increasing temperature [59]. Therefore, to decrease CO poisoning, it is desirable to develop high-temperature membranes. On the other hand, increasing temperature decreases the life of the membrane and renders maintenance of membrane hydration more difficult. Work on phosphoric acid-doped polybenzimidazole revealed long-term chemical and mechanical stability at high temperature [60]. Nevertheless, there were still problems with membrane cycle-life and hydration. Other membrane

approaches can be used for separating hydrogen from gas mixtures. For example, the palladium membrane has been studied extensively but is still very expensive for use in fuel cells [61].

(vii) *Pulsing cell voltage or current.* It is possible to pulse periodically the load current [62], which reduces the potential on the cell to a value low enough to promote electrooxidation of CO on the surface. In fact, if the cell is kept at constant current in certain conditions it will start oscillations by itself [63]. The problem arises in accommodating both of those techniques into a fuel cell stack. It is most likely that some blend of using a catalyst with high resistance to poisoning and a dynamic cleaning technique could be used in future cells.

The poisonous influence of carbon monoxide on platinum catalyst layers is well researched (e.g., [64–67]). Some reported work and critical reviews on CO tolerance and CO-tolerant catalysts have been published recently by Ralph et al. [43, 68, 69], Urian et al. [70], Ruth et al. [71], and Wee and Lee [15]. Other reviews of PEMFC CO poisoning can be found in the literature [11–13, 72–75].

This review discusses the mechanism of CO tolerance and the development of CO-tolerant catalysts. The development of Pt-based binary/ternary metallic electrocatalysts and Pt-free electrocatalysts is discussed. Useful information is also provided on characterization methods for the understanding of the mechanism of CO tolerance and the evaluation of anode electrocatalysts.

16.2 Mechanisms of CO Tolerance

PEMFC performance degrades when CO is present in the fuel gas; this is referred to as CO "poisoning", a term that may have to be revised, as discussed later in this chapter. Several studies have investigated the deleterious effect of carbon monoxide on platinum catalyst layers (e.g., [64–67]). This results from the attachment of a CO molecule onto the catalyst surface, thereby reducing the surface available for hydrogen reactions. Linear or bridge-bonded CO species are formed on the catalyst surface [64, 67, 76]. Such strong binding has been explained by electron donation from the 5σ carbon monoxide orbital to metal, and subsequent transfer of two electrons from the d metal atomic orbital to the antibinding $2\pi^*$ CO orbital, as shown in Figure 16.1. This electron transfer is known as back-donation.

Despite its importance for low-temperature fuel cells, the exact mechanism of CO oxidation on Pt and the role of co-catalysts are still far from being understood. On Pt(1 1 1), the saturation coverage of CO corresponds to a (2×2)–3CO adlayer with a coverage of $\nu = 0.75$ at low potentials according to STM and FTIR results [77]. Here, the coverage ν is the ratio of CO molecules to Pt-surface atoms. At a potential around 0.4 V, a part of the adsorbate is oxidized, and the adlayer transforms into a lower coverage adlayer with $\nu = 0.68$; Villegas et al. have suggested a $(\sqrt{19} \times \sqrt{19})$R 23.4° structure based on STM results [77]. It is generally accepted that the oxidation of the adlayer proceeds according to a Langmuir-Hinshelwood mechanism. The exact identity of the oxygen species, however, is not really clear. Also, the literature describes contradictory results concerning the

surface diffusion of CO. Whereas fast diffusion should lead to the classical rate equation for a Langmuir–Hinshelwood mechanism as usually treated in textbooks (the rate is proportional to $\Theta(1 - \Theta)$, where Θ is the ratio between coverage and maximum coverage), slow diffusion leads to an oxidation behavior determined by a nucleation and growth mechanism [78–82].
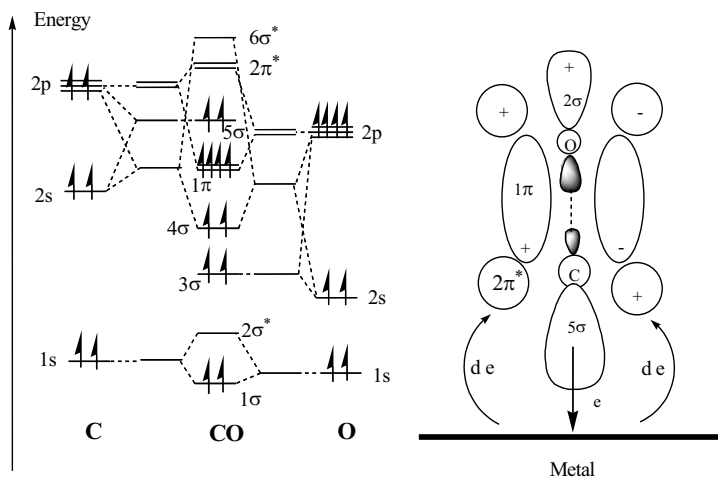
Figure 16.1. The energy level of carbon monoxide molecules, and the formation of metal-carbon monoxide bonding [449]. (Reprinted from Grgur BN, Marković NM, Lucas CA, Ross PN. Electrochemical oxidation of carbon monoxide: from platinum single crystals to low temperature fuel cells catalysis. Part I: carbon monoxide oxidation onto low index platinum single crystals. J Serb Chem Soc 2001;66:785–97. With permission from the Serbian Chemical Society.)

The transition between the high coverage phase and low coverage phase leads to the so-called pre-peak in cyclic voltammetry, which was also observed on polycrystalline Pt and other surfaces (like vicinally stepped Pt(1 1 1) [24, 83–85]), and which is often referred to as a weakly adsorbed state. By recording potential transients during oxidation of the adsorbed CO under galvanostatic conditions, it has been shown that the oxidation of that amount of CO that desorbs during the transition between the two adsorbate states does not follow any of the Langmuir-Hinshelwood-type rate equations [86]. The transients rather suggest an Eley Rideal mechanism. Probably, CO is oxidized at defect sites on the surface, the number of which is constant and to which CO diffuses quickly at high coverage. In contrast, the galvanostatic potential transients during further complete oxidation showed the potential maximum typical for both types of Langmuir-Hinshelwood mechanisms (i.e., fast or slow diffusion) only after oxidation of approximately one tenth of the adsorbate at nearly constant potential.

The promotional effect of ruthenium in improving the CO tolerance of Pt anode catalysts for proton exchange membrane fuel cells (PEMFCs) has long been recognized [87] and carbon-supported PtRu catalysts are currently seen as the best anode catalysts when reformate is the anode feed in such fuel cells [43, 88].

However, there is also an ongoing debate concerning the action of co-catalysts. The mechanism by which the promotion occurs was described by Watanabe and Motoo [89] as bifunctional, with Ru supplying oxygen species at lower potentials that facilitate the removal of adsorbed CO from the active Pt sites (by the activation of water to form OH) as well as decreasing the strength of the Pt–CO bond via a perturbation of electronic properties of the Pt atoms (a ligand effect). It has also been shown that neither of these two effects alone is able to explain the co-catalytic effect of Ru in fuel cell anodes [90]. Considerable effort has gone into further understanding the details of this mechanism and several excellent reviews are available that summarize the findings [12, 91, 92].

In the case of less noble co-catalysts, it is also often assumed that they act according to the bifunctional mechanism. In the case of Mo, this effect seems to be limited to the oxidation of the weakly adsorbed CO [93]. The $Pt_3Sn(hkl)$ alloys have shown a high activity for bulk CO oxidation that is correlated to a weakly adsorbed state of CO, with an onset potential that is lower by approximately 300 mV [34]. Moreover, it was also demonstrated with Sn modifications of Pt single crystal surfaces that a major promoting effect is the shift in the onset potential of the oxidation of the weakly adsorbed state of CO to much lower values and, in addition, that the population of the weakly adsorbed state is drastically increased [24, 83, 94]. A prerequisite for the high CO oxidation activity of Sn/Pt surfaces is a uniform distribution of co-adsorbed Sn, e.g., by step decoration of the Pt(3 3 2) electrode. The oxidation potential of the "strongly adsorbed state", on the other hand, is hardly shifted. It is therefore assumed that contrary to what is generally believed, Sn mainly has an electronic influence on neighboring Pt atoms, changing the binding energy of CO to Pt. On a Pt(1 1 1) electrode, Sn is much less active, and this is due to the formation of 2D islands, which, however, are very mobile in the absence of co-adsorbed CO, as shown in a recent STM study [39]. For the maximum coverage ν (ratio of Sn atoms to surface Pt atoms) of Sn on Pt(1 1 1), a value of 0.33 was postulated. This was only based on a correlation of the oxidation peak charge (presumably OH adsorption on or within the Sn adlayer on Pt(1 1 1)) to the suppression of hydrogen adsorption.

16.2.1 Electrochemistry of Carbon Monoxide and Hydrogen

In order to understand the behavior of a PEMFC in the presence of CO, the electrochemistry of CO and hydrogen on the surface of platinum must be understood. This is because platinum or its alloys are invariably used and needed in low-temperature acid electrolyte fuel cells to facilitate the electrochemical reaction for the production of electric power. The electrochemistry of CO in an acidic environment has been studied extensively [95] and reviewed by Baschuk and Li [96]. CO oxidation and adsorption occurs on the (1 0 0) and (1 1 0) sites of platinum in an acid electrolyte. The adsorption of CO involves CO linearly bonded to platinum, and the adsorption isotherm is that of a Tempkin isotherm, which can be written as [97]:

$$\theta_{CO} = -\frac{\Delta G_o^0}{r} - \frac{RT}{r}\ln H + \frac{RT}{r}\ln\left(\frac{[CO]}{[H_2]}\right) \tag{16.1}$$

The interaction parameter and the free energy of adsorption were found to be functions of temperature, and in addition, the interaction parameter was found to be highly dependent on catalyst structure. Also, this relation was only valid for relatively high temperatures of greater than 130 °C; for low temperatures, such as those encountered in a PEMFC, the coverage appeared to be a function of the anode potential as well as the concentration, in addition to the temperature and catalyst structure.

The oxidation of CO occurs from a voltage range of 0.6–0.9 V, depending on the voltage sweep rate used in the voltammetry experiment [95]. The rate of oxidation of CO at low coverage is rapid while the rate is poisoned by a high coverage of CO. This dependence on coverage could be explained if the electrochemical oxidation of CO involved adjacent surface sites [98].

$$CO_{dissolved} + M + H_2O \rightarrow \underbrace{CO \qquad H_2O}_{\text{adjacent sites}} \tag{16.2}$$

where the structure is:

adjacent sites

$CO_{dissolved} + M + H_2O \rightarrow$ CO   H$_2$O
(each bonded to M)

linear adsorbed CO + Adsorbed H$_2$O

$$\underset{\underset{M}{|}\quad\underset{M}{|}}{CO \text{-----} OH} \longrightarrow CO_2 + e^- + H^+ + 2M \tag{16.3}$$

adjacent sites   activated complex

CO   H$_2$O $\longrightarrow$ CO ----- H$_2$O ------ e$^-$ $\longrightarrow$ CO ------- OH +
(each bonded to M)   (16.4)
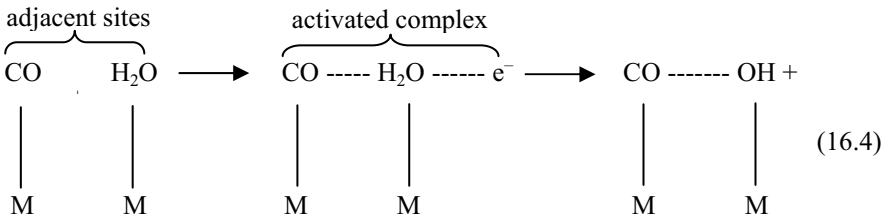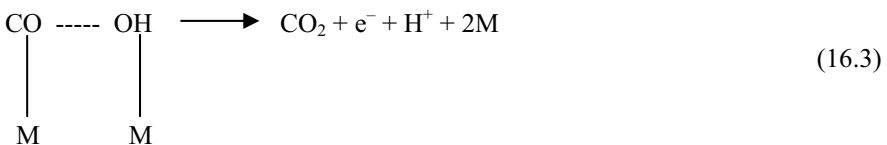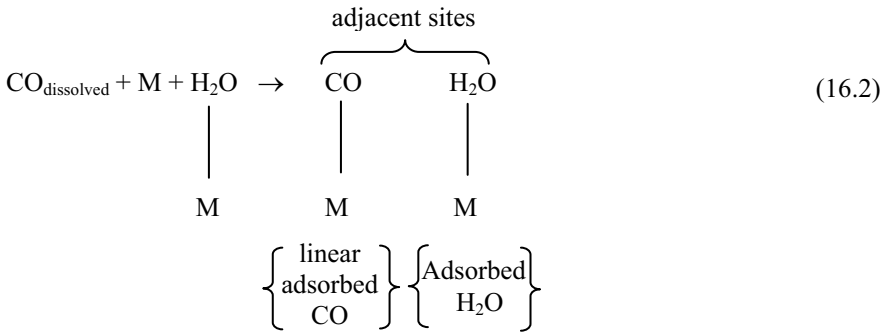
where M is a metal adsorption site. Equation 16.2 is a very rapid adsorption step; in most experimental situations, the rate of CO adsorption is controlled by the diffusion of CO to the metal catalyst surface. This step determines the initial

surface concentration of the reactant pairs. Equation 16.3 is the electron-transfer step, which is rate determining for any fixed concentration of reactant pairs. Equation 16.4 is the final electron transfer reaction and is assumed to be rapid compared to Equation 16.3. This mechanism of CO oxidation can be thought of as CO lowering the energy of activation for the dissociation of water, and is similar to the catalyzed gas-phase oxidation of CO by oxygen.

The oxidation of hydrogen and the effect of CO in an acid environment have also been extensively studied. The mechanism for electrochemical hydrogen oxidation over smooth platinum in an acid electrolyte is the slow dissociation of adsorbed hydrogen molecules to hydrogen atoms, known as the Tafel reaction, followed by the fast electrochemical oxidation of the adsorbed hydrogen atoms, known as the Volmer reaction [99]. This is illustrated below:

$$H_2 + 2M \leftrightarrow 2MH \qquad\qquad \text{Tafel} \qquad\qquad (16.5)$$

$$2MH \leftrightarrow 2M + 2H^+ + 2e^- \qquad \text{Volmer} \qquad\qquad (16.6)$$
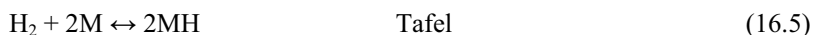
It was also discovered that the dissociative chemisorption of hydrogen on platinum was independent of both surface geometry and crystallite size, leading to the result that the exchange current density for the hydrogen reaction was independent of catalyst structure [100].

The mechanism of CO poisoning of the hydrogen oxidation reaction was found to be as follows [100]. CO chemisorbs on the platinum sites to the exclusion of hydrogen. This is possible because CO is more strongly bonded to platinum than is hydrogen, as indicated by a greater potential required for the oxidation of CO than of hydrogen, and a sticking probability of CO on platinum 15 times higher than that of hydrogen on platinum. Also, if the Gibbs free energy of adsorption of hydrogen and CO are compared and it is assumed that the Gibbs free energy of adsorption for CO continues to become more negative as temperature decreases, CO will preferentially adsorb to platinum due to the more negative Gibbs free energy of adsorption. The result is that even a relatively small concentration of CO can result in the complete coverage of the platinum surface, to the exclusion of the hydrogen. In spite of CO preferentially adsorbing on the platinum surface, the rate of hydrogen oxidation on even the few remaining platinum sites is so rapid that it controls the surface potential or free energy of the catalyst. Unfortunately, because this potential is less than the potential needed to oxidize CO, the coverage of CO remains at that dictated by the CO adsorption isotherm. Thus, the mechanism of CO poisoning of hydrogen oxidation is that linearly-bonded CO blocks sites for the dissociative chemisorption of hydrogen, and the current density, or reaction rate, of hydrogen in the presence of CO is reduced and can be written as:

$$i_{H_2/CO} = i_{H_2}(1 - \theta_{CO})^2 \qquad\qquad (16.7)$$

Thus, the coverage of CO on the platinum electrode surface becomes a significant parameter in the performance of an electrode. In the experimental studies cited earlier, it was concluded that the coverage of CO was a function of potential as

well as CO partial pressure. Also of interest, CO and hydrogen do not interact during their co-adsorption at temperatures of less than 200 °C. However, it has been noted that the apparent activation energy for hydrogen oxidation increases with increasing CO concentration, indicating an increased difficulty for the hydrogen to oxidize in the presence of CO [97]. This was speculated to be because either CO preferentially adsorbed to the "best" sites for hydrogen oxidation or hydrogen was involved in the CO oxidation process.

Another aspect of CO poisoning that has been studied is termed carbon dioxide (CO_2) poisoning. At CO_2 concentrations in excess of 25%, the voltage losses in the anode are greater than what can be accounted for through the reactant dilution, or the so-called Nernst losses [101]. It was theorized that this was due to CO_2 converting to CO through either the reverse water gas shift reaction:

$$CO_2 + H_2 \rightarrow CO + H_2O \qquad (16.8)$$
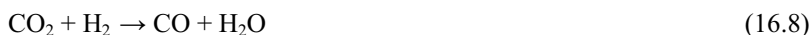
or by the electroreduction of CO_2:

$$CO_2 + 2H^+ + 2e^- \rightarrow CO + H_2O \qquad (16.9)$$

Wilson et al. [101] discovered that the severity of CO_2 poisoning decreased if all of the anode catalyst was tied up within an electroactive structure. Since Equation 16.8 requires only a catalyst site in contact with the gas phase, this indicates that Equation 16.8 is more prevalent than Equation 16.9, which requires a site with good gas, ionic, and electronic access.

Table 16.1. The equilibrium concentration, in ppm, of CO with varying temperature, relative humidity and total pressure. CO concentration for a total pressure of 3 atm is given in parentheses while the values not in parentheses are the result of a total pressure of 1 atm. The initial concentration of dry gas is 25% CO_2 and 75% H_2 [96]. (From Baschuk J, Li X, Carbon monoxide poisoning of proton exchange membrane fuel cells, International Journal of Energy Research, ©2001 John Wiley & Sons Limited. Reproduced with permission.)

Temperature (°C)	Initial relative humidity of H_2O			
	0	50	80	100
25	1310 (1310)	106 (308)	65.2 (198)	51.5 (159)
50	2590 (2590)	98.0 (315)	56.6 (194)	42.9 (153)
80	4920 (4920)	62.2 (269)	26.0 (152)	15.0 (113)
95	6500 (6500)	35.7 (233)	7.25 (119)	1.44 (82.0)

An increase in temperature will increase the equilibrium concentration of CO, if the initial relative humidity is zero. However, with the initial presence of water vapor in the fuel stream, an increase in temperature will decrease the equilibrium concentration of CO. This is because the partial pressure of water increases at higher temperatures, which drives Equation 16.8 to the left and results in a

decreased CO concentration. An increase in total pressure results in an increased equilibrium concentration of CO due to the larger partial pressures of CO_2 and H_2, which drives Equation 16.8 to the right. The majority of equilibrium concentrations of CO calculated in Table 16.1 are well in excess of the 2–10 ppm CO that a PEMFC can tolerate and thus operation with 25% CO_2 should be impossible. However, the fact that cell operation is possible under these conditions may be explained by the fact that the water gas shift reaction does not proceed rapidly at temperatures experienced by a PEMFC. As a result, the actual concentration of CO may be much less in an operating PEMFC than the equilibrium value shown in Table 16.1. This may also explain why the effect of this CO_2 poisoning is minimal if CO is already present, as the effect of CO is much greater than that of the CO_2 poisoning [74]. Thus, the production of CO from CO_2 was found to be kinetically limited and the effect was negligible unless no CO was initially present in the fuel gas and the concentration of CO_2 was high (say, 25% or higher).

16.2.2 Characteristics of PEMFC CO Poisoning

The polarization of a PEMFC in the presence of CO yields interesting results. Oetjen et al. [102] examined the effect of CO on a PEMFC performance. The cell operating temperature was 80 °C and CO concentrations of 25, 50, 100, and 250 ppm were used in the fuel gas. It was found that for hydrogen and 25 ppm CO, the cell polarization curve looked similar to the curve without CO, only with a more negative slope. However, for CO concentrations greater than 100 ppm, the polarization curve had two distinct slopes. The lower slope was explained by the adsorption and oxidation kinetics of hydrogen and CO at the anode. At increasing current densities, the potential of the anode increased to values at which adsorbed CO could be oxidized to CO_2, thus leading to higher reaction rates for hydrogen adsorption and oxidation. The poisoning of a PEMFC is illustrated in Figure 16.2. It was also found that the poisoning effect takes a significant amount of time to reach steady state, as illustrated in Figure 16.3. The CO poisoning could be reversed by operation at open circuit voltage with pure hydrogen for 2–3 h. Therefore, the CO poisoning effect must be taken as a transient phenomenon in the operation of PEMFCs used in transportation applications. Similar PEMFC performance data with CO in the fuel gas can be found in the literature [101, 103, 104].

Zawodzinski et al. [105] compared their PEMFC poisoning data with others' and found discrepancies in the amount of CO that could be tolerated. It was surmised that these discrepancies may have been due to different flow rates. Lower flow rates allow better CO tolerance via the oxidation of CO by oxygen crossover from the cathode to the anode, thus freeing up sites for the hydrogen oxidation reaction. This conjecture may be confirmed by an estimate of the amount of oxygen crossover from the cathode.
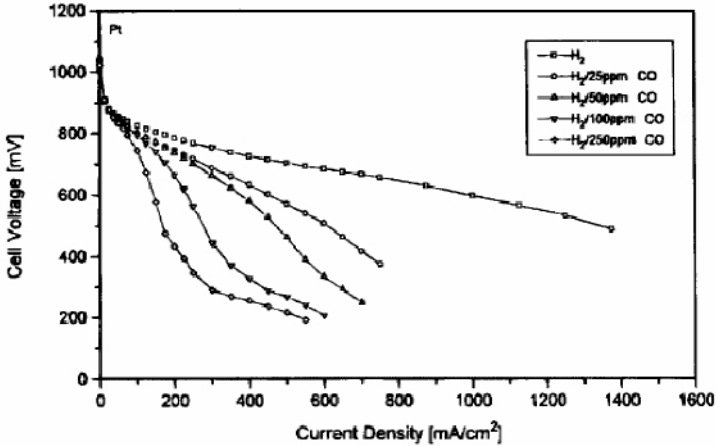
Figure 16.2. Illustration of the effect of CO on a PEMFC [102]. (Reproduced by permission of ECS—The Electrochemical Society, from Oetjen H-F, Schmidt VM, Stimming U, Trila F. Performance data of a proton exchange membrane fuel cell using H_2/CO as fuel gas.)
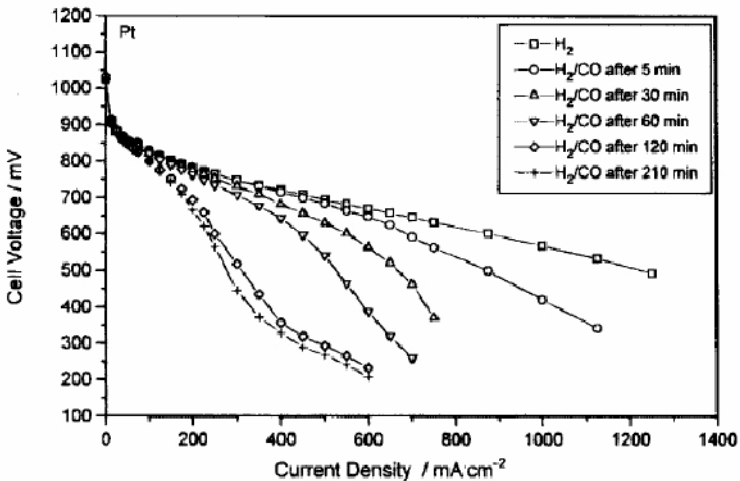
Figure 16.3. Illustration of the transient nature of the CO poisoning of a PEMFC. CO concentration is 100 ppm [102]. (Reproduced by permission of ECS—The Electrochemical Society, from Oetjen H-F, Schmidt VM, Stimming U, Trila F. Performance data of a proton exchange membrane fuel cell using H_2/CO as fuel gas.)

16.2.3 Bifunctional Mechanism of CO Tolerance

Despite the wealth of research in this area, the reasons for the effectiveness of Pt-Ru over other alloys are still hotly debated. Two widely accepted mechanisms for the oxidation of CO from the Pt-Ru surface exist [31, 106–109]: (1) the

"bifunctional" mechanism and (2) the direct mechanism, enabled by the ligand or electronic effect.

To remove CO_{ads} from the surface it is necessary to generate some oxygenated species that can react with CO_{ads} to produce CO_2 and release some free sites on Pt surfaces for the hydrogen oxidation reaction. The mechanism for the oxidative removal of the CO_{ads} from platinum anodes has been a topic of intense investigation for the past 40 years. The overall reaction for removing CO_{ads} is

$$CO_{ads} + H_2O = CO_2 + 2H^+ + 2e \qquad E_{o\ 25\ °C} = -0.10\ V\ (vs.\ NHE) \qquad (16.10)$$
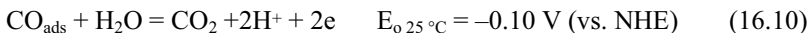
The mechanism of hydrogen oxidation in the H_2/CO mixtures on platinum has been given by Equations 16.2–16.6.

Hydrogen oxidation reaction occurs on the free sites liberated during the time between CO_{ads} oxidative removal, Equation 16.4, and CO re-adsorption from solution, Equation 16.2. At the low potential ($E < \sim0.6\ V$) the rate constant of CO_b re-adsorption is much higher than the rate constant for CO_{ads} oxidation, and in practical terms only an infinitely small number of platinum sites could be liberated for H_2 oxidation.

The hydrogen oxidation reaction reaches maximum at the same potential where CO_{ads} is oxidized by Pt-OH (coverage with CO_{ads} in that potential region tends to zero). According to this, it is necessary to provide a supply of OH species to adjunct platinum atoms covered by CO_{ads} using some other metal that does not adsorb CO. This is known as a bifunctional catalyst. Schematic representation of such a catalyst is given in Figure 16.4.
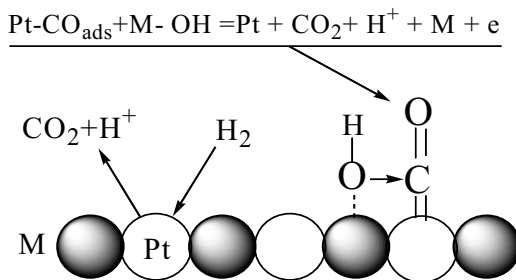
Figure 16.4. Bifunctional catalyst (schematic representation)

Based on early work by Watanabe and Motoo [89] (originally on the enhanced oxidation of CO and methanol at Pt electrodes with various oxygen-adsorbing adatoms [34, 39, 81–83, 90, 93, 94]), a bifunctional mechanism involving water activation by Ru (Equation 16.11) and subsequent CO electrooxidation on a neighboring Pt atom (Equation 16.12) has been postulated by a number of groups [20, 102, 103, 110–112].

$$Ru + H_2O = Ru–OH + H^+ + e^- \qquad (16.11)$$

$$Pt–CO + Ru–OH = CO_2 + H^+ + e^- + Pt + Ru \qquad (16.12)$$

It should be noted that Ru-OH means simply oxygen-containing surface species at the Ru surface; the exact nature of this species is still unknown.

To investigate the mechanism of CO tolerance by PtRu, half-cell studies in H_2SO_4 at 80 °C with PEMFC anode structures containing Nafion were performed using pure CO as the reactant. The half-cell outlet gas was analyzed using in-line mass spectrometry for evidence of CO_2 – to examine PtRu for CO electrooxidation activity (Equation 16.12). The results indicated that CO electrooxidation was occurring on PtRu at above +0.25 V (vs. RHE). This is some 0.2 V less anodic than required for pure Pt electrocatalysts and reflects the greater ability of the Ru to adsorb water (Equation 16.11), as compared with Pt. In the cyclic voltammograms measured in H_2SO_4 at 25 °C, the promotional effect from PtRu is also reflected in a lower peak potential for CO electrooxidation at the electrodes: PtRu (+0.5 V (vs. RHE)) compared with Pt (+0.8 V (vs. RHE)). Both the half-cell and the cyclic voltammetry studies confirmed that at anode potentials above +0.25 V (vs. RHE) the improved CO tolerance of PtRu is due to the enhanced electrocatalysis of CO electrooxidation to CO_2 (Equations 16.11 and 16.12).

This mechanism has been adopted as the explanation of CO-tolerant H_2 oxidation on other Pt-M alloy catalysts. Although practically all transition metals are oxidized in acid solutions, the fact is that only a few metals alloyed with platinum show certain activity for oxidation of H_2/CO mixtures, as such metals have to be able to provide OH at low potential (e.g., near the hydrogen reversible potential). Research has been conducted on both Pt–M bimetallic nanocrystals such as Pt-Ru, Pt-Sn, and Pt-Mo [20, 21, 35, 113] and M-decorated Pt single crystals involving Ru [16–20, 26, 44–47, 70, 81, 106–108, 114–122, 123–128], Mo [24, 70, 126–128, 129–131], Sn [26 , 29–31, 125] and other transition metals [42, 114, 129, 130]. The bifunctional mechanism is generally acknowledged as the dominant effect for single-crystal Pt decorated by other metals, particularly for Ru on Pt(111) [46, 106–108, 124].

16.2.4 Direct Mechanism of CO Tolerance (Ligand or Electronic Effect)

The bifunctional mechanism does not take into account a possible change in the CO binding energy on Pt induced by Ru (often referred to as an electronic effect), nor does it directly describe the effect of CO and OH competitive adsorption on the Ru. The origin of such an effect has not yet been completely understood. On the one hand, according to the *d*-band shift model of Hammer and Norskov [131], it was proposed that the addition of a second element, by donating electron density, provides modification of the electronic interactions between Pt and the CO adsorbate. Such a "ligand effect" [118, 132–136] results in a decrease of the Pt–CO bond strength and yields facile CO_{ads} electrooxidation, either directly by OH deposited on the Pt surface, or by enhancing Pt–H_2O activation and thereby allowing the reaction of OH and CO directly on the Pt. The ligand model proposes that ruthenium modifies the electronic properties of platinum, weakening the Pt–CO bond and thereby lowering the CO electrooxidation potential.

The electronic effect has been suggested to provide increased tolerance to CO in reformate systems, presumably by weakening the Pt–CO bond and decreasing the CO coverage, thereby increasing the anode efficiency by leaving more surface sites free for H adsorption at low potential [31]. Additionally, the ligand effect has been shown to have a large effect on Pt atoms near Ru islands for Ru/Pt(111), but Pt atoms far from these islands are minimally affected [116]. The externally exposed Ru islands are known to be in some stage of oxidation in an aqueous electrode (i.e., RuO_nH_m) at nearly all potentials [127]. Recent experiments using well-defined PtSn and PtMo electrodes [119, 120, 127, 128] have shown that both surfaces are better CO oxidation catalysts than PtRu, even though both may not be particularly useful as practical CO-tolerant hydrogen or methanol oxidation catalysts. This enhanced performance compared with PtRu was ascribed to a lack of adsorption of CO on either Sn or Mo, leaving more adsorption sites for oxygen-containing species.

The consequences of the ligand effect and the bifunctional mechanism for CO oxidation on Pt/Ru have been debated extensively in the literature. The emerging consensus seems to be that the ligand effect is less important than the bifunctional mechanism [106, 107, 138–142]. Some authors have attempted to quantitatively determine the relevance of the ligand effect as compared to the bifunctional mechanism, with Masel, Wieckowski, and coworkers concluding that about 20% of the enhancement in CO oxidation afforded by Ru deposition can be attributed to the ligand effect, while the remaining 80% of the enhancement is due to the bifunctional mechanism [106, 107].

16.2.5 Surface Science Study and Modeling of CO-tolerance Mechanism

CO adsorption and oxidation have been studied for many years, but a greater understanding was achieved by the development of *ex situ* and *in situ* spectroscopic and microscopic methods for application in electrochemistry [9, 143–146], together with the use of well-defined nanocrystalline electrode surfaces [147]. The opportunity to study *in situ* electrooxidation of carbon monoxide [148–157] under fuel cell reaction conditions has brought significant progress in understanding interfacial electrochemistry on metallic surfaces. In combination with conventional electrochemical methods these techniques have been used to find connections between the microscopic surface structures and the macroscopic kinetic rates of the reactions.

Pt-Ru alloy [158–160] or Ru modified Pt surfaces [161] are known to be prominently effective catalysts for methanol oxidation. Watanabe and Motoo [87] introduced a "bifunctional mechanism" into electrochemical interfaces in that Ru in Pt-Ru alloy surfaces supplies OH moieties to promote CO oxidation on neighboring Pt surfaces. In this context, it is crucial to elucidate water or hydroxide that are anticipated to adsorb on Ru in the alloy or modified Pt electrode surfaces. Nevertheless, there have been substantial uncertainties on this point because of experimental constraints in vibrational spectroscopy relevant for this purpose, e.g., poor sensitivity or uncompensated interruption by bulk solution species in IRAS (infrared reflection absorption spectroscopy). Watanabe and co-workers recently reported that water molecules were detected on the Pt-Ru alloy surfaces, a finding

dissimilar to those for Pt surfaces, using ATR-IR spectroscopy [108]. It seems, however, that the surface morphology of their Pt [160] and Pt-Ru alloy films [108] prepared with a sputtering method was not optimized to obtain fairly large enhancement for the IR absorption from adsorbates. Possibly, the enhancement factor of such Pt films was not sufficiently large to detect rather weak water bands, as absorbance of the O–H stretch is about 1/18 compared to on-top CO. In contrast, Pt films prepared by electroless plating give much larger IR absorption for adsorbates by a factor of > 10 [161–163]. Concerning the bifunctional mechanism, Friedrich et al. reported on the Ru-modified Pt(1 1 1) surface that (1) an Ru island with 2–5 nm size and monoatomic height is formed by electrochemical deposition, of which coverage is feasibly controlled by the deposition potentials, and (2) the CO oxidation peak is shifted to more negative potentials by ~120–130 mV due to a cooperative mechanism between Pt and Ru involving CO surface mobility [112, 164, 165]. At this stage, it appeared necessary to characterize water and CO adsorbed on various alloy or modified Pt surfaces, using ATR-SEIRA spectroscopy to provide information on the role of Ru in their catalytic activity. Consequently, it was found using ATR-SEIRA spectroscopy that (1) preferentially adsorbed CO on the Ru surface was oxidized up to ~+0.3 V, (2) it induced marked adsorption of water on the empty Ru surface, which could accelerate the following CO oxidation on the adjacent Pt surface, compatible with the bifunctional mechanism, and (3) diffusion of surface species from Ru to Pt was indicated in a dilute CH_3OH solution. Highly sensitive ATR-SEIRA spectroscopy was used by Futamata and Luo [166] to elucidate water, CO, and electrolyte anions adsorbed on the Ru-modified Pt film electrode. CO on Ru domains was oxidized below ~+0.3 V, followed by pronounced water adsorption. Since the oxidation potential of CO on the Pt domain was significantly reduced compared to that on bare Pt, these water molecules on Ru obviously prompted CO oxidation on the adjacent Pt surface, consistent with the bifunctional mechanism. Diffusion of adsorbate from Ru to Pt surfaces was indicated in dilute CH_3OH solution by spectral changes with potential.

In order to understand the mechanism of CO and methanol electrooxidation on binary platinum alloys catalysts, much work is needed on the surface structure (including its electronic aspects) and its relationship with the reactivity. Adsorbed carbon monoxide exhibits a surface-sensitive behavior, which influences the vibrational frequencies of the C–O band. Consequently, *in situ* Fourier transform infrared (FTIR) spectroscopy appears to be a useful technique for studying CO interaction with the surface. CO tolerance of carbon-supported $Pt_{80}Ru_{20}$, $Pt_{80}Os_{20}$, and $Pt_{85}Co_{15}$ electrocatalysts has been studied by García et al. [167] in 0.1 M perchloric acid solution, applying cyclic voltammetry and *in situ* FTIR spectroscopy. It was shown that FTIR spectra can be acquired during CO oxidation at these technical materials in an electrochemical cell, yielding valuable information on the reactivity and allowing predictions on their behavior in a polymer electrolyte membrane fuel cell (PEMFC). Linear adsorbed CO is the main adsorbate, but small amounts of bridge-bonded CO are also formed. Moreover, COH species seem also to be present for $Pt_{80}Os_{20}$ and $Pt_{85}Co_{15}$. All bimetallic alloys are able to oxidize adsorbed CO at lower potentials than platinum, and a shift of about 0.20 V has been determined. From the FTIR spectra, fundamental

information can be obtained on the CO adsorption energies and metal properties of these systems.

The electronic effect may be inferred from XPS measurements of the Pt(111)/Ru system [168] and X-ray absorption spectroscopy (XAS) measurements of Pt/Ru alloy nanoparticles [29], which have indicated a transfer of electron density from Pt to Ru. The electrocatalytic activity for oxidation in the presence of 100 ppm CO has been investigated by Watanabe et al. [169] using XPS and FTIR, on a series of binary Pt alloy electrocatalysts with non-precious metals of various compositions. At these CO-tolerant electrodes, the equilibrium coverage of CO was suppressed to values less than ~0.6. Based on X-ray photoelectron spectroscopy (XPS) data, it was found that the surfaces of all non-precious metal alloys are composed of a thin Pt layer with an electronic structure different from that of pure Pt, indicating an increased 5d vacancy of Pt in the layers of the CO-tolerant alloys. The CO coverage, particularly with multi-bonding, was lowered due to decreased electron donation from the Pt band to the $2\pi^*$ orbital of CO. A weakening of bond strength between the Pt skin layer and CO was also indicated by *in situ* FTIR, suggesting that the H_2 oxidation sites are not blocked by CO due to its enhanced mobility. Thus, the mechanism of CO tolerance described above at the Pt skin on alloy surfaces was proposed as a "detoxification mechanism".

XPS and FTIR spectroscopy have also been used by Tillman et al. [170] to study the co-adsorption of CO with Sn on Pt(1 1 1). It was concluded that Sn exerts an electronic influence on CO molecules adsorbed in its neighborhood. This influence leads to the disappearance of the band at 1780 cm^{-1} indicative of the (2×2)–3CO adlayer at low potentials and to a shift of CO from the strongly adsorbed state to the weakly adsorbed state. Alternatively, the disappearance of the 1780 cm^{-1} band might also be explained by a disturbed order in the neighborhood of the Sn islands. Such an effect is observed for CO adsorbed at unmodified stepped surfaces, but it does not lead to a shift to the weakly adsorbed state. In addition, there also seems to be an effect according to the bifunctional mechanism, which is active only for the weakly adsorbed state but extends over all the surface, including that part of the adsorbate that is not electronically influenced by Sn. Similar to the case of Mo, this effect does not work for the strongly adsorbed CO.

In situ XAS measurements, including both X-ray absorption near edge spectroscopy (XANES) and extended X-ray absorption fine structure (EXAFS) at the PtL_3 and RuK edges, have been used by Scott et al. [171] on three different carbon-supported PtRu electrocatalysts in an electrochemical cell in 1 M $HClO_4$ with 0.3 M methanol. The CO and OH adsorbate coverage on Pt and Ru were determined as a function of the applied potential via the novel delta XANES technique, and the particle morphology was determined from EXAFS and a modeling technique. Both the bifunctional and direct CO oxidation mechanisms, the latter enhanced by electronic ligand effects, were evident for all three electrocatalysts; however, the dominant mechanism depended critically on the particle size and morphology. Both the Ru island size and overall cluster size had a very large effect on the CO oxidation mechanism and activation of water, with the bifunctional mechanism dominating for more monodispersed Ru islands, and the direct surface ligand effect dominating in the presence of larger Ru islands.

Stamenković et al. [172] reviewed the research of *in situ* CO oxidation on well characterized Pt$_3$Sn(hkl) surfaces. Bimetallic single crystals Pt$_3$Sn(110) and Pt$_3$Sn(111) have been characterized for *in situ* CO oxidation. Following UHV characterization, crystals were transferred into the electrochemical environment where surface electrochemistry of adsorbed CO was studied *in situ* by infrared spectroscopy. Changes in band morphology and vibrational properties − splitting of the band and increase in the frequency mode − were found on Pt$_3$Sn(hkl) and correlated to Pt(hkl) surfaces. Continuous oxidative removal of adsorbed CO starts as low as E < 0.1 V, which is an important property for CO-tolerant catalysts. In addition to electronic effects, other factors, such as surface structure and intermolecular repulsion between adsorbed species, are responsible for the high catalytic activity of Pt$_3$Sn(hkl) alloys.

Electrochemical nuclear magnetic resonance (EC-NMR) spectroscopy has emerged as one useful probe with which to investigate the surface electronic properties of catalyst nanoparticles [173, 174]. ^{13}C EC-NMR of adsorbed CO is particularly informative since it can be used to deduce both the electronic properties of the nanoparticle surfaces as well as the nature of CO bonding with the transition metal [116, 175–177]. This provides a powerful method to correlate the surface electronic alterations with catalytic activity variations and yields a firm basis for rational synthesis of bimetallic nanoparticle catalysts with improved activities in fuel cells. NMR studies on Pt nanoparticles modified by spontaneous deposition of Ru have demonstrated changes in the metal–CO bonding that result from Ru modification. On CO-covered Pt/Ru nanoparticles, ^{13}C NMR spectra (Figure 16.5) show the presence of two broad peaks. Each of these spectra can be deconvoluted into two Gaussians, whose peak areas have the same ratio as Pt and Ru on the Pt/Ru surface, in excellent agreement with the CO-stripping data. Thus, EC-NMR discriminates between the two populations: Pt/Ru–CO and Pt–CO, as has previously been shown by using infrared methods [109, 119, 178]. On the other hand, the NMR spectrum of ^{13}CO adsorbed on Ru-black also shows only one peak, centered at a much lower chemical shift compared to the Pt/Ru samples.

Unlike CO adsorbed onto supported Ru nanoparticles, CO adsorbed on Ru-black showed a large isotropic shift and a symmetric broadening of the NMR spectrum. In all these catalysts, the spin-lattice relaxation time (T1) has followed the Korringa behavior characteristic of metallic systems [179]. Thus, CO adsorbed on Pt/Ru catalysts attains metallic properties due to the mixing of CO molecular orbitals with the conduction electron states of the transition metal. This observation strongly suggests that the electronic influence of Ru on surface Pt atoms is only a local effect, and Pt atoms situated away from Ru sites retain their original electronic band structure properties.

Results of CO temperature programmed desorption (TPD) measurements on Ru-modified Pt single crystals have demonstrated a weaker Pt–CO bond than on pure Pt surfaces [107, 117, 180], again pointing toward a decreased availability of Pt d electrons for forming the Pt–CO bond [181]. The decreased availability of d electrons may be understood as a consequence of the lowering of the d band center, as described in the Norskov model [182]. Similar CO TPD results were obtained on the inverted Ru(0001)/Pt surface, on which the ligand effect and the strain effect were deconvoluted through elegant experiments with varied Pt deposit thicknesses

[183]. The deconvolution of the two effects has also been accomplished through computational work [184, 185]. The effect of PtRu surface alloy formation on hydrogen adsorption/desorption and of CO co-adsorption on hydrogen adsorption on a bimetallic PtRu surface was investigated by TPD, using a PtRu surface alloy (40% Pt surface atoms) as an example [186].
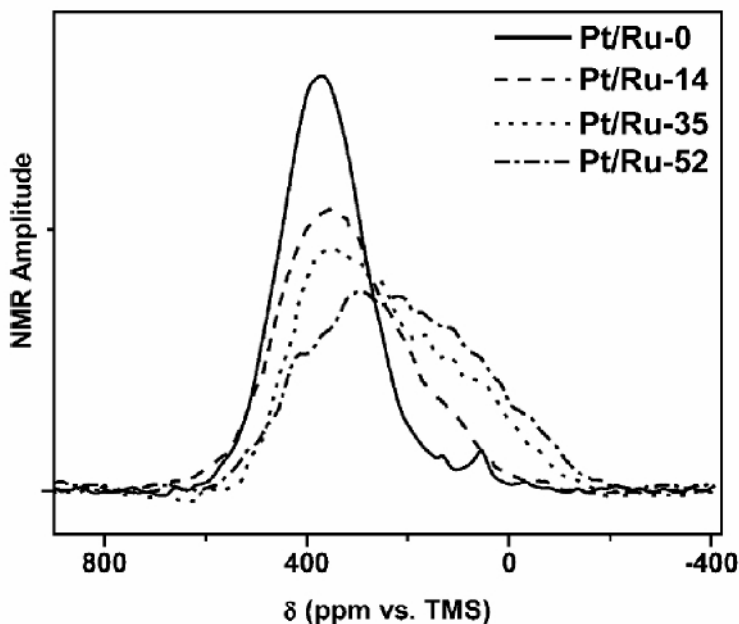
Figure 16.5. 13C NMR spectra of adsorbed CO on Pt and Pt/Ru catalysts [116]. (Reprinted with permission from J Am Chem Soc 2002;124:468–73. Copyright 2002 American Chemical Society.)

The concentration and distribution of the Pt surface atoms were determined by high-resolution scanning tunneling microscopy (STM), which provides further information for the mechanistic interpretation of the results and the underlying physical effects.

Electrochemical impedance spectroscopy (EIS) technique has been used for the experimental assessment of CO tolerance on different Pt-alloy catalysts and at different temperatures [187]. Hsing et al. [187] proposed that the critical potential at which pseudo-inductive behavior occurs could be used as a criterion for the evaluation of CO tolerance. A mathematical impedance model based on two state-variables (Pt-H and Pt-CO) was also developed to elucidate the reaction kinetics and mechanism of the H_2/CO oxidation on a Pt/C catalyst [188]. In fact, this study has given better insight into explicitly understanding the impedance patterns and the quantitative assessment of the effect of applied potentials upon the oxidation reaction kinetics in a broad range of applied potentials. Nevertheless, with the consideration of only two adsorbed species, Pt-H and Pt-CO, the impedance model based on two state-variables was not able to explain the experimental observation

of reversing impedance patterns in the II and III quadrants at high potentials. The model with two state-variables assumes that the water molecules are responsible for the electrooxidation of CO species. However, this is not the case in the high potential region, where the possibility of the dissociation of water molecules is more pronounced and consequently, OH species can be generated. The neglect of this aspect in the two state-variables model is the probable reason for its inability to explain the reversed impedance pattern. An impedance model based on three state-variables (Pt-CO, Pt-H, and Pt-OH) has been proposed by Wang and Hsing [189] for the kinetics investigation of H_2/CO electrooxidation on Pt/C and its alloys (PtRu/C and PtSn/C). The simulation results of Pt/C in a high potential range exhibit unusual reversal behavior of the impedance pattern in the II and III quadrants. This behavior reveals the change of the rate determining step from CO oxidation to CO adsorption. The experimental impedance results of the alloy PtRu/C are in agreement with the simulation studies, and suggest that the enhanced CO oxidation observed on the alloy can be well explained by the promoted OH_{ads} generation on the Ru surface at low potential. Meanwhile, a different reaction mechanism has been elucidated for the PtSn/C. It has been concluded that the promoted OH generation is the primary reason for enhanced activity towards CO oxidation on the PtRu/C. The high activity of the PtSn/C system towards H_2/CO oxidation is due to the combination of the promoted OH generation, exclusion of CO on Sn sites, and minimization of CO adsorption caused by the intermetallic bonding.

Based on CO thermal desorption data obtained on PtRu surface alloy model surfaces, Buatier de Mongeot et al. [135] also suggested that the improved CO tolerance is at least partly caused by a significant reduction in CO adsorption energy on these PtRu catalysts compared to CO adsorption on platinum. Similar results and conclusions were reached in recent density functional theory calculations [27], which showed a significant reduction in the CO adsorption energy on both Ru(0 0 0 1) surfaces covered by a pseudomorphic Pt monolayer and substitutional Pt surface atoms in a Ru(0 0 0 1) substrate, as compared to CO adsorption on Pt(1 1 1) [27, 135, 189, 190] or comparable cluster geometries [191]. CO adsorption and CO removal, however, are only part of the reactions going on in a reformate-operated PEMFC. The current determining step is the electrooxidation of hydrogen (hydrogen oxidation reaction – HOR), which for most platinum metal and platinum alloy electrodes is largely determined by the respective steady-state hydrogen coverage. Two important questions to be answered are therefore (i) how much are hydrogen adsorption and the H_{ad} steady state coverage under reaction conditions affected by the presence of co-adsorbed CO, and (ii) what is the influence of PtRu alloy formation on hydrogen adsorption and H/CO co-adsorption? Quantitative data on the influence of the CO coverage on the HOR rate are scarce [99, 192–194]. Recently, Jusys et al. reported a nonlinear relation between CO coverage and HOR rate, with smaller effects in the low CO coverage regime for the HOR on carbon-supported Pt catalysts [195]. For PtRu no such data exist. Electrocatalytic measurements showed no measurable effect of PtRu alloy formation on the HOR activity; this was tentatively attributed to the very high activity of the remaining, accessible Pt surface atoms, which are sufficiently active that possible differences in the activity are masked by transport limitations [111].

Likewise, little is known about the energetics and kinetics of hydrogen adsorption on bimetallic PtRu surfaces at the solid-vacuum interface, or about the influence of co-adsorbed CO on these properties. Diemant et al. [185] have shown that hydrogen (deuterium) adsorption on a bimetallic PtRu layer, which is pseudomorphic on a Ru(0 0 0 1) substrate, is considerably weaker than on an unmodified Pt(1 1 1) or Ru(0 0 0 1) surface. Following the d band model introduced by Nørskov and coworkers, this reduction in metal–H bond strength is attributed to a strain-induced modification of the electronic properties of Pt-rich adsorption ensembles. Co-adsorption of CO leads to a further weakening of hydrogen adsorption. This is explained by a CO-induced displacement of the adsorbed hydrogen from strongly binding Ru-rich ensembles to less strongly binding Pt-rich ensembles. Even a 100 K adsorption temperature post exposure to CO causes a partial displacement of adsorbed hydrogen. At elevated temperatures and pressures, as are present in a fuel cell, these effects will result in a severe reduction of the steady-state hydrogen coverage. Further improvement of the CO tolerance of PEMFC anode catalysts by the use of platinum alloys will be limited by the reduction in hydrogen electrooxidation activity due to a reduction in the steady-state hydrogen coverage, which is caused by the same electronic effects responsible for the reduction of the steady state CO_{ad} coverage.

Quantum chemical calculations offer the opportunity to probe details of catalytic chemistry that are difficult to obtain from experiments, and they should be employed not only for understanding the mechanism in detail, but also at the screening level of catalyst design. Shubina and Koper [184] described the results of quantum chemical calculations of CO and OH interacting with a variety of bimetallic surfaces, in order to assess from the computational viewpoint the molecular nature of the bifunctional mechanism and the electronic effects involved. They considered in some detail the results of density-functional calculations of CO and OH adsorption on PtRu, PtMo, PtSn, and a number of Pt-modified transition metals such as Rh and Ir. The advantage of using quantum-chemical calculations is that they give direct information on the binding energetics of the different species, which are relatively difficult to extract from electrochemical measurements. Moreover, calculations permit one to establish the quantum chemical nature of the surface bond and the different factors involved, and how these might be related to measurable properties of chemisorbates such as their vibrational characteristics. In this way, quantum-chemical calculations provide invaluable information to complement and correctly interpret experimental data, even if the calculated systems considered may appear rather idealized compared with the experimental catalysts. Concerning the PtRu alloy, they found that mixing of Pt with Ru weakens the binding of both CO and OH to the Pt surface sites. By contrast, the CO and OH binding gets stronger as Pt is mixed in. The surface with the weakest CO binding energy in their calculation is Pt_{ML}-Ru(0001). Interestingly, a similar surface was recently found to have good CO tolerant properties [109]. Also, there is no apparent correlation between the binding energy of CO and the internal C-O and Me-C stretching frequency on the different PtRu surfaces. According to the calculations, the PtMo and PtSn systems seem to be better CO oxidation catalysts than PtRu. On PtMo, CO does not have a strong preference for either site, whereas OH has a clear preference for Mo. On PtSn, CO

interacts only with Pt, and OH (or oxygen) interacts preferentially with Sn. If CO tolerance is related to good hydrogen oxidation properties, a low CO coverage may be sufficient. For such systems, Pt overlayer systems seem quite promising The CO binding energy of these systems is primarily determined by Pt-Pt distance in the overlayer. Contracted overlayers lead to low CO bonding energies, expanded overlayers to high CO bonding energies.

The adsorption properties of CO on Pt_3Sn were investigated by Gűlmen et al. [196] using quantum mechanical calculations. The (111), (110), and (001) surfaces of Pt_3Sn were generated with all possible bulk terminations, and on these terminations all types of active sites were determined. The adsorption energies and the geometries of the CO molecule at those sites were found. Those results were compared with the results obtained from the adsorption of CO on similar sites of Pt(111), Pt(110) and Pt(001) surfaces. The comparison reveals that adsorption of CO is stronger on Pt surfaces; this may be the reason why catalysts with Pt_3Sn phase do not suffer from CO poisoning in experimental works. With the aim of understanding in detail the interactions between CO and the metal adsorption sites, the local density of states (LDOS) profiles were produced for atop-Pt adsorption, for both the carbon end of CO for its adsorbed and free states, and the Pt atom of the binding site. The study showed that: (i) inclusion of a Sn atom at the adsorption site structure causes a dramatic decrease in stability, which limits the number of possible CO adsorption sites on the Pt surface, (ii) the presence of Sn causes angles different from 180° for M–C–O orientation, (iii) the presence of Sn in the neighborhood of Pt on which CO is adsorbed causes superposition of the $5\sigma/1\pi$ derived-state peaks at the carbon end of CO and changes in the adsorption energy of CO, (iv) Sn present beneath the adsorption site strengthens the CO adsorption, whereas neighboring Sn on the surface weakens it for all Pt_3Sn surfaces tested, and (v) the most stable site for CO adsorption is the atop-Pt site of the mixed atom termination of Pt_3Sn(110).

16.3 Development of CO-tolerant Catalysts

Because the use of CO-tolerant electrocatalysts would be more efficient and cause fewer associated problems, it is generally considered the most promising way for solving the CO poisoning problem in PEMFCs. It is well established that binary systems of CO-tolerant electrocatalysts, with Pt as one of the components, can exhibit a substantial resistance to the presence of CO in the fuel stream. It has been found that the use of a second element with Pt, such as Ru, Sn, Ge, Co, Cr, Fe, Ni, Pd, Os, Mo, Mn, etc., in the form of an alloy or a co-deposit yields significant improvement in the CO-tolerance relative to pure Pt [20, 21, 34, 35, 67, 89, 110, 111, 197–208]. Among these various Pt-based binary systems, PtRu/C is still regarded as the most efficient anode electrocatalyst for both reformate and methanol fuel, due to its electronic or bifunctional effects in reducing CO poisoning [209–211]. Superior CO-tolerance has been evidenced for alloyed PtRu materials [13, 14, 102, 212, 213] or Ru-decorated Pt electrocatalysts [112, 164, 165, 214–222]. Therefore, the development of CO-tolerant electrocatalysts is still concentrated on Pt or PtRu-based bimetallic catalyst systems. Some reported work

and critical reviews on this topic have been published recently by Ralph [43, 68, 69] and Urian et al. [70].

Ternary catalyst systems, typically based on a PtRu alloy, have also been investigated and their performance has been compared with that of pure Pt/C or PtRu/C [129, 223–227]. Specifically, PtRu alloys with Ni, Pd, Co, Rh, Ir, Mn, Cr, W, Zr, and Nb have been investigated. Nevertheless, there remain associated problems with the preparation method and the enhancement of electrochemical performance.

Many papers in recent years have presented details of new preparation methods and the performance of Pt-based electrocatalysts such as PtSn/C, PtMo/C, PtRuMo/C, PtRu-HxMoO$_3$/C, and PtRu/(carbon nanotubes). In addition, efforts to develop Pt-free electrocatalysts such as PdAu/C have been undertaken.

Watanabe et al. [226] recently classified the Pt alloys studied into 3 groups with respect to their CO tolerance. The first group of alloys exhibits excellent stability for H$_2$ oxidation in the presence of 100 ppm CO, the second exhibits stability for 1 h and the third exhibits no CO tolerance, i.e., they are comparable to pure Pt. The first contains PtFe alloys such as Pt$_{95}$Fe$_5$, Pt$_{85}$Fe$_{15}$, Pt$_{56}$Fe$_{44}$, and Pt$_{40}$Fe$_{60}$, PtNi alloys such as Pt$_{76}$Ni$_{24}$ and Pt$_{56}$Ni$_{44}$, PtCo alloys such as Pt$_{82}$Co$_{18}$ and Pt$_{57}$Co$_{43}$, PtMo alloys such as Pt$_{67}$Mo$_{33}$ and Pt$_{55}$Mo$_{45}$, and the conventional PtRu alloys such as Pt$_{93}$Ru$_7$, Pt$_{57}$Ru$_{43}$, Pt$_{50}$Ru$_{50}$, and Pt$_{35}$Ru$_{65}$, where the numbers after an element symbol are the concentration of the element expressed in atom%. The second group includes PtMn alloys such as Pt$_{80}$Mn$_{20}$ and Pt$_{48}$Mn$_{52}$, PtSn alloys such as Pt$_{78}$Sn$_{22}$ and Pt$_{79}$Sn$_{51}$, PtAg alloys such as Pt$_{87}$Ag$_{13}$ and Pt$_{54}$Ag$_{46}$, and PtZn alloys such as Pt$_{70}$Zn$_{30}$ and Pt$_{52}$Zn$_{416.}$ The third group contains Pt$_{80}$Cr$_{20}$, Pt$_{52}$Cr$_{48}$, Pt$_{85}$Cu$_{15}$, Pt$_{70}$Ge$_{30}$, Pt$_{40}$Ge$_{60}$, Pt$_{90}$Nb$_{10,}$ Pt$_{55}$Nb$_{45}$, Pt$_{65}$Pd$_{35}$, Pt$_{66}$In$_{34}$, Pt$_{76}$Sb$_{24}$, Pt$_{48}$Sb$_{52}$, Pt$_{80}$W$_{20}$, Pt$_{50}$W$_{50}$, Pt$_{81}$Au$_{19}$, Pt$_{57}$Au$_{43}$, Pt$_{64}$Pb$_{33}$, and Pt$_{65}$Bi$_{35}$.

Figure 16.6 shows examples of saturated CO coverage on Pt and the alloys after H$_2$ oxidation for a prolonged period in the presence of 100 ppm CO. The CO coverage (θ_{CO}) on all of the CO-tolerant alloys is suppressed to values less than 0.6, while the other groups of alloys and pure Pt are almost completely covered with CO [228]. In the case of PtFe alloys, for example, the addition of only 5% Fe to Pt reduces the saturated θ_{CO} to less than 0.3, resulting in the same activity level as those of other compositions or combinations.

It should be noted that the non-noble alloying metal has to be stable in the severe environment of the catalyst layer, where a major component is a strong perfluorosulfonic acidic. Fuel cell operation may produce changes in the catalyst crystallinity, particle surface composition, and the oxidation state of M, which consequently may decrease the CO tolerance [229]. Ishikawa et al. [230], by using relativistic density-functional calculations, found that the alloying metals should be those that possess low-activation energies for H$_2$O dissociation and for the CO$_{ads}$ + OH$_{ads}$ → COOH$_{ads}$ reaction. Once COOH$_{ads}$ is formed, it rapidly forms CO$_{2,ads}$ (+H$_{ads}$) because of its decomposition. Based on energetic predictions emphasizing water activation, it was predicted that the most suitable alloying metals for the CO electrooxidation are Mo, W, and Os, with Ru close behind. Among the several possibilities of binary alloys, PtRu has shown the most promising performance for the hydrogen oxidation reaction in the presence of CO [67, 111]. However, the low natural abundance of Ru is a drawback of this catalyst for practical uses, and for

this reason alternative approaches have been sought, some of them with recent promising results [43, 169], that will be reviewed here.
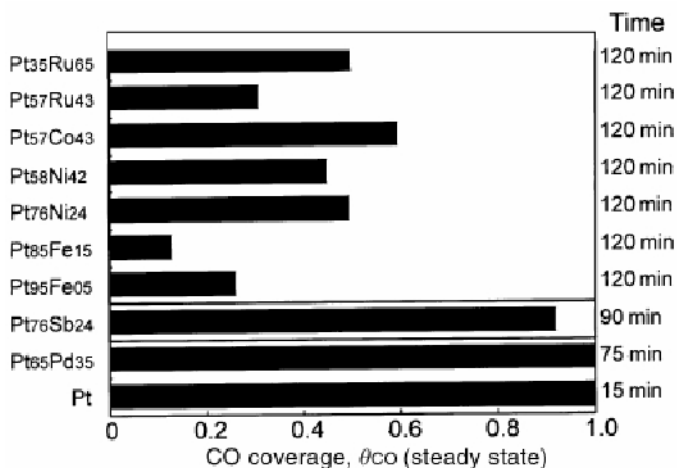
Figure 16.6. Equilibrium coverage of CO on the alloy electrodes in 0.1 M HClO₄ saturated with 100 ppm balance gas. Alloy compositions are shown on the left-hand side. Potential for CO adsorption: 50 mV vs. RHE, rotation rate of electrodes during the CO adsorption: 1500 rpm [169]. (Igarashi H, Fujino T, Zhu Y, Uchida H, Watanabe M. CO tolerance of Pt alloy electrocatalysts for polymer electrolyte fuel cells and the detoxification mechanism. Phys Chem Chem Phys. 2001;3:306–14. Reproduced by permission of The Royal Society of Chemistry.)

16.3.1 PtRu Binary System

16.3.1.1 PtRu Catalysts
The most commonly used anode electrocatalyst in PEMFCs is the platinum-ruthenium binary catalyst (PtRu). Based on early work by Watanabe and Motoo [89] (on methanol electrooxidation), a bifunctional mechanism involving water activation by Ru (Equation 16.11) and subsequent CO electrooxidation on a neighboring Pt atom (Equation 16.12) has been postulated by a number of groups [20, 102, 103, 110–112]. In fact, this system evidently enhances CO tolerance and decreases the CO binding energy on platinum due to its electronic or bimetallic effects. It has been proposed that the addition of ruthenium to platinum can improve CO tolerance through either a ligand effect [157] or through a bifunctional mechanism [133], and possibly a combination of the two.

It is well documented [102, 103, 118, 231–233] that in the PEMFC at 80 °C PtRu alloys are much more tolerant to CO poisoning than pure Pt electrocatalysts. This has made them the electrocatalysts of choice for reformate operation. For example, Figure 16.7 shows the large improvement in CO tolerance for an MEA with an anode based on a $Pt_{50}Ru_{50}$ alloy electrocatalyst prepared as 20 wt% Pt, 10 wt% Ru supported on Vulcan XC72R. The cell potentials are significantly higher at all current densities compared with the MEA based on pure Pt, for operation with hydrogen containing 10, 40, and 100 ppm CO. This improved CO tolerance

has resulted in much effort to optimize the PtRu electrocatalyst for reformate operation.
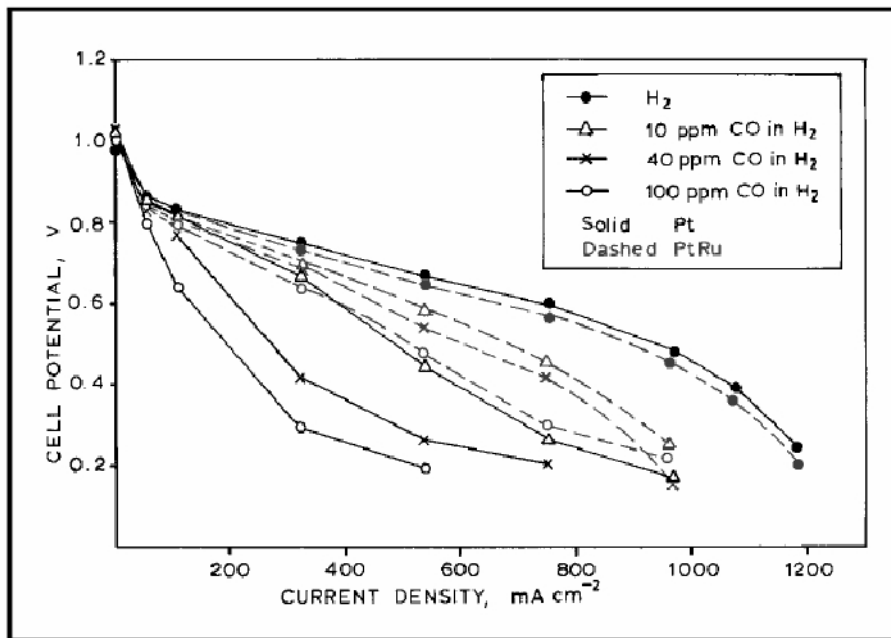
Figure 16.7. Progressive poisoning from 10, 40, and 100 ppm CO on pure Pt and $Pt_{50}Ru_{50}$ alloy anodes. Increased CO tolerance is shown by the $Pt_{50}Ru_{50}$ alloy anodes. The anodes are prepared from 20 wt% Pt on Vulcan XC72R or 20 wt% Pt, 10 wt% Ru on Vulcan XC72R at a loading of 0.25 mg Pt cm^{-2}. The cathode uses 40 wt% Pt/Vulcan XC72R at a loading of 0.6 mg Pt cm^{-2}. The MEAs are based on catalyzed substrates bonded to Nafion NE-115 membrane. The Ballard Mark 5E single cell is operated at 80 °C, 308/308 kPa, 1.3/2 stoichiometry with full internal membrane humidification [43]. (Reprinted from Ralph TR, Hogarth MP. Catalysis for low temperature fuel cells, part II: the anode challenges, Plat Met Rev 2002;46(3):117–35. With permission from Platinum Metals Review.)

16.3.1.2 Effect of PtRu Composition

The HOR performance of PtRu alloys in the presence of CO has been studied extensively [20, 209] and it has been shown that the HOR overpotential for CO-containing hydrogen decreases as the ruthenium content increases, reaching a minimum around the 1:1 (atomic ratio) composition.

Using a 20 wt% Pt, 10 wt% Ru/Vulcan XC72R electrocatalyst, the effect of alloy formulation on CO tolerance was examined by Johnson Matthey [43], both as fully alloyed and as completely unalloyed materials, with a nominal composition of $Pt_{50}Ru_{50}$. The unalloyed $Pt_{50}Ru_{50}$ was prepared by depositing Ru onto a pre-reduced Pt electrocatalyst. XRD confirmed that there was no alloying from the Pt lattice spacing of 0.392 nm, which is equivalent to pure Pt. In addition, there was no significant crystalline Ru, suggesting the Ru was present as amorphous Ru oxide. The peak potential for CO electrooxidation (Equation 16.10) at the unalloyed $Pt_{50}Ru_{50}$ occurred at +0.44 V (vs. RHE), close to the +0.37 (vs. RHE) for

the $Pt_{50}Ru_{50}$ alloy and much lower than the +0.58 V (vs. RHE) for the pure Pt electrocatalyst. With hydrogen containing 100 ppm CO as reactant the specific activity for hydrogen electrooxidation was measured. At +0.010 V (vs. RHE) the specific activity increased from 8 mA cm^{-2} Pt for pure Pt to 25 mA cm^{-2} PtRu for the unalloyed $Pt_{50}Ru_{50}$ and to 60 mA cm^{-2} PtRu for the $Pt_{50}Ru_{50}$ alloy. This suggests that the alloying process, which incorporates the Ru into the Pt lattice (and reduces the Pt lattice spacing), is important for improving the CO tolerance. Besides enhancing the intimate contact between the Pt and the Ru, extended X-ray absorption fine structure (EXAFS) analysis has shown that alloying removes electron density from the Pt [29]. Both these effects are capable of promoting a lower CO coverage on Pt and increasing the hydrogen electrooxidation activity of the anode.

A possible consequence of these findings is that low Ru contents might not show such high CO tolerance in the PEMFC. The Ru content in a fully alloyed 20 wt% Pt, Ru/Vulcan XC72R electrocatalyst was lowered from $Pt_{50}Ru_{50}$ to the mined ratio of $Pt_{70}Ru_{30}$, and then examined in the PEMFC. The XRD lattice spacing of 0.390 nm confirmed a $Pt_{70}Ru_{30}$ alloy was formed. For hydrogen containing 10, 40, and 100 ppm CO, MEAs prepared with $Pt_{70}Ru_{30}$ matched the performances in Figure 16.7 for the $Pt_{50}Ru_{50}$ electrocatalyst at an identical anode loading of 0.25 mg Pt cm^{-2}. This confirmed that at an atomic ratio of $Pt_{70}Ru_{30}$ there is sufficient Ru incorporated into the Pt lattice to adequately modify the CO tolerance of Pt. These findings were in agreement with the fundamental kinetic work of Gasteiger et al. [110], who used 1000 ppm CO in hydrogen and bulk, planar $Pt_{50}Ru_{50}$ and $Pt_{90}Ru_{10}$ alloys. The findings also agree with the more applied results in the PEMFC of Iwase and Kawatsu [103] for alloys of composition $Pt_{85}Ru_{15}$ to $Pt_{15}Ru_{85}$, all based on 20 wt% Pt, 10 wt% Ru/Vulcan XC72R electrocatalysts. They found that the CO tolerance was significantly lower only at Ru contents below $Pt_{80}Ru_{20}$ or above $Pt_{20}Ru_{80}$. However, there have also been a few reports of lower CO tolerance at lower Ru levels, including $Pt_{70}Ru_{30}$ [102]. This highlights the importance of the manufacturing route for the degree of PtRu alloying and for the nature of the electrocatalyst surface. This variability probably accounts for the significant spread in CO tolerances reported for PtRu anode electrocatalysts [234].

Stevens et al. [235] prepared $Pt_{1-x}Ru_x$ random alloy samples via dc magnetron sputtering. The alloys were deposited through shadow masks onto 3M nanostructured thin-film catalyst support for testing in a 64-electrode PEMFC. Electron microprobe data confirmed that linear composition gradients covering almost the whole binary range were prepared. The phases present were examined with XRD. All samples were found to have the Pt fcc structure at high Pt content. At high Ru content, only hexagonal close-packed (HCP) Ru was seen. Electron microprobe measurements on catalyst electrodes after fuel cell testing showed that the Ru-based alloys were stable to corrosion. Alloying Pt with intermediate levels of Ru led to lower CO-stripping onset potentials, implying improved CO tolerance. Hydrogen oxidation polarization curves were measured for the alloy gradients to determine overpotentials as a function of composition, with a reformate fuel containing up to 50 ppm CO. The $Pt_{1-x}Ru_x$ composition spreads all showed lower overpotentials at intermediate M content with 50 ppm CO (approximate as-sputtered ranges: Ru: 0.2 < x < 0.9), implying that these binary catalysts would be

more CO-tolerant than Pt alone. An overpotential of approximately 200 mV was required for the Ru-containing samples before the surface became clean enough to support high current densities, consistent with the CO-stripping voltammetry results.

16.3.1.3 Effect of PtRu Particle Size

The optimum particle size for methanol oxidation has been the subject of several investigations and the values vary with the preparation procedure, the conditions of the reaction, and the metals present in the catalyst. It has been found that the optimum specific activity for Pt was achieved with particle sizes of 3 nm [236]. Other reports [239, 240] conclude that the specific activity declines below 4.5 nm. Particles below 5.0 nm have enough coordination sites to produce strong Pt–OH bonds, leading to high coverage with this species. Mukerjee and McBreen have studied the role of the geometric parameters and the changes in the electronic structure due to specific adsorbates, such as hydrogen and oxygenated species (OH and CO), on methanol oxidation [239]. They found by X-ray absorption spectroscopy that, for particle sizes of carbon-supported Pt clusters below 5.0 nm, there is a strong adsorption of H, OH, and C1-compounds such as CO. On these small particles, H adsorption is strong enough to induce restructuring and morphological changes in Pt clusters at negative potentials. Moreover, the strong adsorption of OH for potentials more positive than 0.8 V inhibits the reduction of oxygen, and the combined effect of strongly adsorbed CO and OH impedes the oxidation of methanol.

16.3.1.4 Stability of PtRu Catalysts and the Impact on Oxygen Reduction Reaction Activity

Fuel cell operation may produce changes in the catalyst crystallinity, particle surface composition, and the oxidation state of M, which consequently may decrease the CO tolerance [229]. Knights et al. [240] investigated several of the key mechanisms attributed to fuel cell power loss over extended periods of time and provided an overview of those operating conditions that influence durability. The authors claimed that by enhancing the water retention at the anode side in combination with advanced electrocatalyst designs, the degradation of PtRu via the dissolution of noble metals could be avoided. However, most PtRu materials were found to be prone to preferential leaching of Ru, especially in the presence of methanol [241–243], thereby entailing undesired changes in the composition and, consequently, in the activity of the electrocatalyst [243]. Earlier reports have proposed that the onset potential of Ru oxidation can be somewhere between 0.2 and 0.4 V vs. RHE [12, 289, 217, 243]. It was observed [244] that a large amount of Ru leaves by the dissolution of the thermodynamically instable (oxide) phases, which can largely be removed by washing. At the same time, the PtRu alloy matrix seems less prone to leach Ru. Focusing on the mechanism behind Pt and Ru corrosion, Chen et al. [242] demonstrated through potential cycling of the anode in a DMFC that dissolution of the anode electrocatalyst contributes to a lower catalytic activity for methanol electrooxidation. A study by Piela et al. [245] showed that the impact of Ru dissolution on fuel cell performance is complicated by Ru crossover from the anode to the cathode side. Because the mobility and

transport of metal ions in PEMs are well documented [246–248], it is reasonable to evaluate the indirect effects of Ru corrosion and mobility in terms of overall PEMFC performance, especially because the concentration of the leached Ru is expected to exceed trace levels [243, 245]. Ruthenium crossover in DMFCs was recently discovered by the Los Alamos Group [245]. In their pioneering work, X-ray fluorescence and CO-stripping data evidenced the transport of Ru across the PEM and its deposition on the Pt cathode, respectively, under various DMFC operating conditions. Such a series of events with Ru was also confirmed in single-cell experiments [243], in which the DMFC was operated in the mass transport-limited region under massive methanol crossover. Interestingly, no accumulation of Ru in the Nafion membrane could be detected by energy dispersive X-ray spectroscopy (EDX). Rather, dissolved Ru species were assumed to travel across the PEM and fill the drained voids in the cathode electrocatalyst layer. In those pores, Ru^{n+} concentration is predicted to reach the several moles per liter level [249]. Ru contamination can impair oxygen reduction activity more severely, as was evidenced by the corresponding rotating disk electrode study. Unlike the observed progressive decrease in surface oxide coverage on Pt with increasing Ru^{n+} contamination, oxygen reduction seems to occur at a minimum activity level beyond a certain Ru coverage on Pt. Such a lower limit of ORR activity beyond a threshold Ru^{n+} concentration was attributed to the ability of Ru adatoms to reduce molecular oxygen at sufficiently high overpotential [250, 251].

Ru leaching from PtRu fuel cell anode electrocatalysts can have a dramatic impact on the activity of a Pt/C oxygen-reducing cathode. Even from highly diluted Ru-containing electrolytes (micromolar concentration range), Ru deposits instantly onto Pt and remains stable on its surface in the electrode potential window of the ORR. Rotating disk electrode data [244] showed that the rate of oxygen reduction can decrease by a factor of eight, which can translate to a ~160 mV overpotential penalization in galvanostatic conditions. Polarization curves recorded for fuel cells with clean and Ru-contaminated Pt cathodes suggest that Ru contamination plays a crucial role in the unrecoverable performance degradation of PEMFCs. Because a typically ten-times larger Pt loading in fuel cell cathodes is not expected to compensate for the suspected several orders of magnitude higher Ru^{n+} concentration in the voids of the cathode electrode layer [245], those data stress that Ru contamination can indeed play a major role in the performance degradation of PEMFCs and especially of DMFCs. Unless highly stable PtRu anode electrocatalysts are developed, the problem of Ru crossover and contamination at the cathode should be addressed by either novel fuel cell designs such as laminar-flow fuel cells [252, 253], in which crossover is reduced using less Ru-permeable membranes, or by more Ru-tolerant ORR electrocatalysts in PEMFCs.

16.3.2 PtMo Binary System

Under reformate-feed conditions, carbon-supported PtRu alloys are widely used as reasonably reformate-tolerant anode catalysts [254–257]. However, the CO tolerance of PtRu is still unsatisfactory for the higher CO concentrations expected at system start-up or during changes in load. Moreover, the limited availability of

Ru may become a significant problem before stationary PEMFC systems can be placed on the market. Many Pt-based catalysts have thus been proposed as alternatives to PtRu. Based on the ''bifunctional mechanism'' in CO removal, along with anodic hydrogen oxidation, the search for oxophilic components [198] has been the main trend in the development of alternative CO-tolerant electrocatalysts for the PEMFC. Those with the most successful and cost-effective combinations so far have been Pt_3Mo and Pt_4Mo [21–23, 258]. Recent theoretical and experimental studies suggest that Pt-Mo combinations could be not only much cheaper, but even more efficient catalysts for CO oxidation than PtRu [21–23, 230, 258]. Bimetallic PtMo alloy catalysts have thus attracted considerable attention for their high catalytic activity in H_2 oxidation with CO/H_2 feed [22, 23, 70, 126, 127, 204, 225, 259–263]. Such enhanced performance in contrast with PtRu was ascribed to (1) the lack of adsorption of CO on Mo, leaving more adsorption sites for oxygen-containing species that are acting as CO oxidation reagents within the frame of such a bifunctional mechanism, or (2) changes in Pt–Pt atomic distance, which modifies the Pt–CO adsorption energy [230].

Grgur et al. [22, 23] reported the electrochemical oxidation of H_2, CO, and CO/H_2 on well-characterized $Pt_{70}Mo_{30}$ bulk alloy or carbon-supported PtMo (3:1 or 4:1) catalysts in sulfuric acid solution. Their work suggested a similar bifunctional mechanism with Ru in the role of Mo in PtMo alloy: an increase in free Pt sites by the oxidative removal of adsorbed CO. Mukerjee et al. [70, 127, 204] showed two- to three-fold enhancement of the CO tolerance of PtMo in a PEM fuel cell compared to that of PtRu, which was ascribed to the onset of CO oxidation at very low potentials (~100 mV). The PtMo (atomic ratio = 5:1) electrocatalyst also displays a lower variation in overpotential losses than the PtRu counterpart [126, 204, 263]. Recently, the high CO tolerance of PtMo catalysts has also been reported by Santiago et al. [262, 263]. The catalytic activity of Mo/C for the water-gas shift (WGS) reaction was observed using a fixed-bed catalytic reactor, and they concluded that the CO tolerance of PtMo is due to lowering of the CO concentration in the gas channel inside the electrode through the chemical reaction catalyzed by Mo-species. With regard to the PtMo alloy, Mo atoms have been reported to have oxygen-containing ligands even at H_2 potentials, which were responsible for the excellent CO tolerance [23, 260]. This notion was supported by the results for Mo K-edge XANES spectra, which showed that Mo was present as hydrated oxides with a valence state of +IV at 0 V [260].

A $Pt_{75}Mo_{25}$ alloy was prepared [43] as 20 wt% Pt, 3 wt% Mo by sequentially depositing Pt oxide and Mo oxide followed by thermal reduction at high temperature. Half-cell measurements in H_2SO_4 at 80 °C using Nafion-containing electrodes were performed to determine the specific activity for hydrogen electrooxidation in the presence of 100 ppm CO. It was shown that for the Pt_3Mo alloy electrode with pure CO, there is considerable specific activity for CO electrooxidation starting from anode potentials of +0.05 V (vs. RHE). Mass spectrometry of the exhaust gas confirmed that the electrooxidation current was due to product CO_2 formation. This indicated that at anode potentials below +0.2 V (vs. RHE) (needed for efficient PEMFC operation), the CO tolerance of the PtMo electrocatalyst comes from promoting CO electrooxidation (Equation 16.10). The low electrode potentials required for CO electrooxidation were also evident in the

cyclic voltammograms. For the Pt_3Mo alloy electrode a broad oxidation current starting at +0.15 V (vs. RHE) is complicated by Mo surface redox reactions [264]. These results are in direct contrast to those from both the pure Pt and the PtRu alloy electrodes. There is no detectable specific activity for CO electrooxidation below +0.2 V (vs. RHE) and no product CO_2 was detected in the half-cell exhaust gas. There was no electrooxidation activity measured at these low electrode potentials for either the PtRu alloy or the pure Pt electrodes in the cyclic voltammograms. Greatly improved CO tolerance for hydrogen containing from 40 to 100 ppm CO has been confirmed using MEAs containing $Pt_{50}Mo_{50}$ catalysts [43]. $Pt_{67}Mo_{33}$ alloy showed almost the same polarization properties for H_2 oxidation in the presence and absence of 100 ppm CO, while H_2 was hardly observed on pure Pt after 2 h CO adsorption [169]. CO poisoning of H_2 oxidation was not observed on this PtMo alloy at all. However, as the CO concentration is reduced, the benefit due to the $Pt_{75}Mo_{25}$ alloy electrocatalyst is also reduced, until at 10 ppm CO the PtRu alloy electrocatalyst is the more CO-tolerant. The difference in reaction order for the $Pt_{75}Mo_{25}$ and the PtRu alloys is perhaps indicative of the distinct mechanisms of CO-tolerance operating at the electrocatalysts.

A much larger issue than the MEA performance at low ppm levels of CO was found for the $Pt_{75}Mo_{25}$ alloy. When operating on hydrogen with 25% CO_2, the $Pt_{75}Mo_{25}$ alloy showed poor CO_2 tolerance [43]. Poor CO_2 tolerance of the PtMo system reflects an increased ability of the electrocatalyst to promote the electroreduction of CO_2 (Equation 16.9). This produces much higher coverage of the "Pt–CO" poison. The source of the CO tolerance shown by the PtMo electrocatalyst, namely its ability to electrooxidize CO (Equation 16.10) also results in an ability to catalyze the reverse electroreduction reaction (Equation 16.9). PtMo alloy catalysts have been reported to be more susceptible to poisoning by CO_2 compared to PtRu [70, 127, 260, 265]. A performance evaluation on CO(100 ppm)/H_2 and CO_2(25%)/H_2 showed that the voltage loss with PtMo (7:1) catalyst caused by 25% CO_2 is much greater than that with PtRu, while PtMo shows better performance than PtRu on CO(100 ppm)/H_2 [260]. Systematic evaluation of the CO_2 tolerance of PtMo with various atomic ratios showed that variation of the PtMo atomic composition affects the tolerance to CO_2, and a similar voltage loss on CO_2/H_2 was observed for PtMo(1:1)/C and PtRu(1:1)/C [70]. Recently, Mukerjee et al. [127] reported no significant additional voltage loss for a PtMo(1:1) anode upon the addition of 21% CO_2 compared to the cell voltage on CO(100 ppm)/H_2. These reports suggest that the CO_2 tolerance of PtMo alloy catalysts is highly influenced by the catalyst composition and/or the method of catalyst preparation.

In 2007, $Pt_{1-x}Mo_x$ binary composition spreads were deposited via dc magnetron sputtering through shadow masks onto 3M nanostructured thin-film catalyst support by Stevens et al. [235]. Electron microprobe data confirmed that linear composition gradients covering almost the whole binary range were prepared. The phases present were examined with XRD. All samples were found to have the Pt fcc structure at high Pt content. The body-centered cubic (bcc) Mo phase was also formed for compositions containing greater than 35 atom% Mo, dominating at high Mo content. Electron microprobe measurements on catalyst electrodes after fuel

cell testing showed some loss of Mo in $Pt_{1-x}Mo_x$ alloys containing > 40 atom% Mo. Hydrogen oxidation measurement results obtained from testing with CO-free reformate suggest that $Pt_{1-x}Mo_x$ at high Mo levels may be binary alloys that are able to catalyze the RWGS reaction. RWGS CO poisons the platinum surface, requiring larger overpotentials for a given current density. CO-stripping voltammetry measurements indicated that alloying Pt with intermediate levels of Mo led to lower CO-stripping onset potentials, implying improved CO tolerance. The $Pt_{1-x}Mo_x$ composition spreads all showed lower overpotentials at intermediate M content with 50 ppm CO (approximate as-sputtered ranges: Mo: 0.4 < x < 0.7), implying that the binary catalysts would be more CO-tolerant than Pt alone. Mo gave lower overpotentials (for x in $Pt_{1-x}Mo_x$ ~0.5 as-sputtered) than Ru and Sn, especially at low current densities.

The relative magnitude of the electrooxidation of CO and the electroreduction of CO_2 will depend strongly on the concentrations of each reactant and on the PEMFC operating conditions. At present, for operation below 100 °C, the reformate streams usually contain much more CO_2 than CO. As a consequence, for full reformate operation with hydrogen containing both 25% CO_2 and 40 ppm CO, the PtRu alloy is much more tolerant than the $Pt_{75}Mo_{25}$ alloy [43]. Thus, today, with typical reformate feeds that contain CO_2, PtRu remains the electrocatalyst of choice for PEMFC operation below 100 °C. Based on those results, Ralph et al. [43] pointed out that the search for alternative electrocatalysts to provide improved CO tolerance by electrooxidizing CO at low anode potentials may be fundamentally flawed for current PEMFC stack operating conditions. They suggested that membrane purification [266] could be adopted to reduce CO_2 to ppm levels. Using membrane purification would allow PtMo to show a clear benefit over PtRu electrocatalysts at CO concentrations greater than 10 ppm.

16.3.3 PtSn Binary System

Evaluation of CO oxidation on PtSn electrocatalyst systems has been investigated in earlier work [26, 34, 267–274]. It was demonstrated that bimetallic PtSn catalysts with an oxide support display superior catalytic activity for CO oxidation [35, 275–278]. In 2000, Crabb et al. [267] applied a PtSn/C anode electrocatalyst, prepared by a surface organometallic chemistry method, in a PEMFC. Their preparation method involved a selective means of adding a second metal to the surface of another. This produced a controlled surface reaction between an organometallic species of the second metal (tetrabutyl- or tetraethyl-tin) with a pre-reduced monometallic platinum metal catalyst. The PtSn/C prepared by this method gave enhanced activity that resulted in a large decrease in the onset potential of CO oxidation compared with that for Pt/C. It was claimed that this enhancement was caused by the addition of Sn to the Pt/C-suppressed chemisorption of both the hydrogen and the carbon monoxide. Furthermore, in using this method, only a small amount of Sn was required to decrease the onset potential of CO oxidation. Analysis with TEM, EDX, and XPS provided evidence of a bimetallic effect, as the Pt and Sn appeared together on the support and the catalysts consisted mainly of metallic platinum in close association with tin oxide after exposure to air.

The Pt_3Sn alloy has been found to be a more effective CO electrooxidation catalyst than pure Pt and thus more active for hydrogen oxidation in the presence of CO than pure Pt, with the activity strongly dependent on the surface orientation. The (111) face, in particular, is very active for CO electrooxidation [279]. In addition to electronic effects, other factors, such as surface structure and intermolecular repulsion between adsorbed species are responsible for the high catalytic activity of Pt_3Sn(hkl) alloys. This enhanced CO tolerance has also been used to improve DMFC performance [280]. A Pt_3Sn/C catalyst was synthesized by Lim et al. [281] via borohydride reduction and hydrothermal treatment for the anode electrode of a low-temperature fuel cell. In the TEM image, the PtSn nanoparticles were uniformly well-dispersed on the carbon support with an average particle size of around 2.4 nm. Good distribution of the Pt_3Sn/C nanoparticles is known to be an important factor in catalytic activity. The oxidation of CO on the Pt_3Sn/C catalyst occurred at a lower potential than that on the commercial catalysts. It appeared that Sn has the ability to promote the oxidation of adsorbed CO at low potentials. The removal of the CO adsorbed onto Pt proceeded via its reaction with OH adsorbed onto the Sn or Sn oxide sites formed by the dissociative adsorption of water.

It has been shown that at low Sn contents, the Pt_3Sn phase is easier to form, and an increase in the Sn content will prompt the main alloy structure to change to the PtSn phase. As for CO-stripping over the PtSn/C catalyst, it had already been indicated that oxidation of the CO adsorbed on Pt sites is promoted by the adjacent Sn atoms in the Pt_3Sn alloy [282]. Despite reports that Sn can supply the OH to improve the oxidation of CO_{ad}, it has been proposed that the electroactivity of PtSn/C catalyst is proportional to the amount of Pt_3Sn phase present, without any contribution for CO oxidation derived from the PtSn phase, Pt/SnO_2 clusters, or other structures [271]. Stevens et al. [235] prepared $Pt_{1-x}Sn_x$ binary composition spreads via dc magnetron sputtering through shadow masks onto 3M nanostructured thin-film catalyst support. All samples were found to have the Pt fcc structure at high Pt content. At high Sn content, only tetragonal Sn was seen. Electron microprobe measurements on catalyst electrodes after fuel cell testing showed some loss of Sn in $Pt_{1-x}Sn_x$ alloys containing > 80 atom% Sn. The HOR overpotentials for the $Pt_{1-x}Sn_x$ samples increased significantly for compositions at intermediate metal levels (Sn > 40 atom%), implying that the alloying elements significantly degraded the HOR capability of Pt. CO-stripping voltammetry measurements indicated that alloying Pt with intermediate levels of Sn led to lower CO-stripping onset potentials, implying improved CO tolerance. The $Pt_{1-x}Sn_x$ composition spreads all showed lower overpotentials at intermediate M content with 50 ppm CO (approximate as-sputtered ranges: Sn: $0.1 < x < 0.4$), implying that binary catalysts would be more CO-tolerant than Pt alone.

16.3.4 PtM (M = Fe, Co, Ni, Ta, Rh, Pd) Binary Systems

PtFe alloys such as $Pt_{95}Fe_5$, $Pt_{85}Fe_{15}$, $Pt_{56}Fe_{44}$, and $Pt_{40}Fe_{60}$, PtCo alloys such as $Pt_{82}Co_{18}$, and $Pt_{57}Co_{43}$, and PtNi alloys such as $Pt_{76}Ni_{24}$, and $Pt_{56}Ni_{44}$ are within the same group as PtRu and PtMo that exhibits excellent stability for the activity of H_2 oxidation in the presence of 100 ppm CO, in comparison with pure Pt, as classified

by Watanabe et al. [169]. They studied the cyclic voltammograms on Pt and Pt-Fe alloy surfaces. From the cyclic voltammograms in the solution saturated with and without CO, it is clear that the blank anodic current on the Pt skin of the Pt-Fe alloy electrode commences to increase at about 0.6 V, which is ~0.2 V less positive than that of the pure Pt and shows a larger current at more positive potentials in comparison with the blank cyclic voltammograms on the pure Pt. This result infers that the Pt skin surface on the alloy has a larger affinity, or oxidizing property, to water molecules than the bulk pure Pt. On the alloy electrode with the saturated CO adlayer, the anodic current for CO oxidation begins to increase at about 0.6 V, corresponding to the onset of the water molecule oxidation or the adsorption of OH species, and shows only one anodic peak at 0.73 V without any shoulder peak. On the other hand, the oxidation of the adsorbed CO on pure Pt starts at a potential less positive than 0.55 V and shows a peak at ~0.7 V via a small pre-shoulder. The shoulder current and the less positive onset potential can be ascribed to carboxyl radicals formed on the pure Pt surface [160, 283]. Despite almost the same total CO adlayer coverage on the Pt skin and the pure Pt, the electric charge (per real Pt surface area) for the CO adlayer oxidation on the Pt skin layer is larger than that of the pure Pt; this indicates that the former adlayer involves CO species with a larger number of electrons per Pt site, associated with the oxidation reaction not as a carboxyl radical or bridge-bonded CO but as linear CO.

Cobalt is used to promote CO oxidation in reformers [284, 285], suggesting PtCo alloys may be useful catalysts for H_2 oxidation in the presence of CO. PtCo alloys have been proposed as improved methanol oxidation catalysts [286] because cobalt may assist with CO removal (CO is an intermediate in methanol electrooxidation) through a mechanism analogous to the PtRu bifunctional mechanism. PtCo alloys have also been studied as improved ORR catalysts [200, 287, 288]. In addition to their improved ORR kinetics, these alloys have been shown to be more tolerant to methanol crossover in direct methanol fuel cells (DMFCs), again possibly through improved CO removal kinetics [289]. However, Stevens et al. [235] observed no impact on CO-stripping with the addition of cobalt to Pt, and explained this as due to surface cobalt dissolving away.

Tantalum is resistant to corrosion because it forms a passivation layer under all practical conditions. In a study of $Pt_{1-x}Ta_x$ alloys, it was shown that all of the tantalum was retained across the whole $Pt_{1-x}Ta_x$ binary range after exposure to 0.5 M H_2SO_4 at 80 °C for 1 week [290]. This means that if a PtTa catalyst composition with improved performance is developed, it is likely that the composition will give stable performance over time. There are few reports in the literature on the use of PtTa alloys in PEMFC applications. The most relevant work, completed by Papageorgopoulos et al. [210], involved a study of alloys of platinum with molybdenum, niobium, and tantalum. In this study it was shown that Pt_6Ta was more active than pure platinum for hydrogen oxidation in the presence of CO. Stevens et al. [235] prepared $Pt_{1-x}Ta_x$ binary composition spreads via dc magnetron sputtering through shadow masks onto 3M nanostructured thin-film catalyst supports. A nanocrystalline/amorphous PtTa phase formed for compositions containing at least 30 atom% Ta and the fcc phase was no longer observed. Electron microprobe measurements on catalyst electrodes after fuel cell testing showed that the Ta-based alloys were stable to corrosion. The HOR overpotentials

for the $Pt_{1-x}Ta_x$ samples increased significantly for compositions at intermediate metal levels (> 50 atom%), implying that the alloying elements significantly degraded the HOR capability of Pt. CO-stripping voltammetry measurements indicated that alloying Pt with intermediate levels of Ta may lead to lower CO-stripping onset potentials, implying improved CO tolerance.

Gómez et al. [291] studied rhodium adlayers on Pt(1 1 1) substrates prepared by electrodeposition from dilute Rh^{3+} acidic solutions. For the electrooxidation of CO, the experimental behavior cannot be described as a linear combination of the behavior of Pt and Rh regions: there is a sizable shift of the voltammetric CO oxidation curve toward less positive values. In addition, two different voltammetric contributions are distinguishable, reaching to split voltammetric peaks. A bifunctional mechanism as proposed by Watanabe and Motoo [89] would be applicable in this case. Rhodium adatoms would adsorb OH, which would react with CO molecules adsorbed both at the center of the islands and at the platinum sites in the vicinity of the Rh islands. This would correspond to the first peak in the CO voltammetric stripping wave. The second (at more positive potentials) would correspond to the oxidation of CO adsorbed on Pt sites and needing to diffuse to the island edges in order to combine with adsorbed OH. The periphery of the islands would contain the bifunctional catalytic centers. The reaction in the center of the islands is especially slow probably because of a high adsorption energy for both CO and OH, which leads to a much higher real energy of activation. In any case, the adsorptive and catalytic activity of the adlayers differ from those of the bulk Pt(1 1 1) and Rh(1 1 1) electrodes. The existence of strain in the film, together with a diminution in the coordination number for adatoms at the edges of the islands, are considered to be at the origin of the observed behavior.

The PtPd bimetallic system also exhibits a high resistance against CO poisoning from the oxidation of formic acid [292–294]. Stonehart [295, 296] proposed PtPd alloys as suitable electrocatalysts in phosphoric acid fuel cells for hydrogen oxidation. According to his study, the alloys were more tolerant than platinum alone, were resistant to sintering, and could be prepared with a very high surface area. An extensive examination of the PtPd alloy system showed that a minimum in hydrogen polarization, for constant current density, was obtained at 50–50 atom% levels [296]. However, PtPd alloys have given an inferior performance of Pt in a PEMFC [103]. The potential use of carbon-supported $PtPd_y$ electrocatalysts (where y = 1–6) as CO-tolerant anodes for PEMFC applications has been investigated by Papageorgopoulos et al. [297]. Since exploratory experiments conducted in their lab in the past revealed extremely poor performance for PtPd catalysts with up to 50 atom% Pd, only Pd-rich electrocatalysts, supported on high surface area carbon and doped with Nafion, have been prepared. Cyclic voltammetry experiments at 80 °C, the operating temperature of the PEMFC, reveal that upon CO saturation, a lower fraction of surface sites is poisoned in the case of $PtPd_y$ as compared to Pt, resulting in higher amounts of adsorbed hydrogen. By increasing the Pd content, this effect becomes more pronounced. Fuel cell tests demonstrated that the need for reasonable hydrogen oxidation currents, with and without CO, necessitates the presence of Pt in the catalyst. As a type of CO-tolerant PEMFC anode catalyst, $PtPd_y$ catalysts exhibit enhanced CO tolerance compared to Pt under operating conditions, with

PtPd$_4$ providing the best results. More importantly, improved performance compared to PtRu is demonstrated with 100 ppm or more of CO in the fuel stream.

16.3.5 PtRuM (M = Mo, Sn, W, Cr, Zr, Nb, Ag, Au, Rh, Os, and Ta) Ternary Systems

Of all the platinum alloys tested, platinum-ruthenium alloys, typically around the 1:1 composition, are the only ones to have been introduced commercially. However, even the PtRu catalyst still suffers a loss of 25 and 40% in the maximum power density obtained when the H$_2$ feed contains 25 and 100 ppm CO, respectively [102], although injection of 4.5% O$_2$ in the fuel stream was found to restore the performance with 100 ppm CO to that of pure hydrogen [8]. Other elements such as Mo [126, 204, 263] and Sn [35] when alloyed with platinum have also shown some promise in terms of improving CO tolerance, possibly performing better than the platinum-ruthenium alloys. They have not as yet been introduced into commercial applications, probably because PEMFC catalysts need to perform well under a variety of operating conditions for long periods of time with minimal degradation in performance. Non-noble elements such as Mo and Sn have the potential to corrode during operation, which may impact long-term stability. In addition, although these alloys are more CO-tolerant than pure Pt, the HOR overpotentials in the presence of CO are still very high relative to the overpotentials of the HOR in a CO-free gas feed.

It is likely that further improvements in CO tolerance will only be found in more complex (e.g., ternary, quaternary, etc.) alloy systems. The range of compositions that can be studied in such systems is enormous and realistically can only be mapped well through the use of high throughput materials science methods. Several CO-tolerant Pt-containing anodes exist, such as Pt/Ru/Sn [225], Pt/Ru/W [225], Pt/Ru/Mo [225], Pt/Ru/Os [233], and Pt/Ru/Pd [298, 299]. There is interest in determining whether there would be any synergistic effects if both elements were incorporated into Pt, with Mo increasing the rate of CO removal at low current densities, leading to low overpotentials at low to moderate current densities with Ru providing high current capability at higher overpotentials. Pt-based ternary electrocatalysts, such as PtRuMo (Mo 10 wt%), do give better performance than those of PtRu/C in the presence of CO.

In 2002, Papageorgopoulos et al. [210] investigated the effect on CO tolerance of including a metal M (M = Mo, Nb, and Ta) in Pt/C and PtRu/C. This was undertaken by comparing the cyclic voltammetry data and cell performance of the modified catalysts with those of traditional Pt/C and PtRu/C catalysts [210]. The new catalysts were binary PtM/C and ternary PtRuM/C (Vulcan XC72) systems, with a 20 wt% metal loading. The results showed that the inclusion of 10 at% Mo in PtRu – Pt$_9$Ru$_9$Mo$_2$ – produced an electrocatalyst with higher activity in the presence of CO than PtRu/C. Two earlier sets of studies prompted these experiments. One was work demonstrating that PtMo/C gave an up to three-fold enhancement in performance with H$_2$ (100 ppm CO)/O$_2$ compared with PtRu/C in the absence of CO$_2$ in the fuel [23, 204, 300]. The other research [224, 225] had reported the improved behavior of PtRu binary catalysts with the incorporation of a third metal, such as Cr, Zr, or Nb.

In another report, Pinheiro and co-workers [301] studied a number of PtRuMo catalysts and found that $Pt_{70}Ru_{20}Mo_{10}$ was a more effective fuel oxidation catalyst than PtRu for DMFCs. At low Mo content, $Pt_xRu_yMo_z$ (e.g., $Pt_{70}Ru_{26}Mo_4$) dispersed as nanoparticles in a conducting polymer matrix was found to give higher methanol oxidation current densities at 400 mV and in full DMFC fuel cell testing than PtRu alone [224]. These reports were all consistent with the finding that relatively low Mo levels can improve either CO tolerance or methanol oxidation performance relative to PtRu alone. In order to study this composition space in more detail, Stevens et al. [302] prepared a $(Pt_{1-x}Ru_x)_{1-y}Mo_y$ ($0 < x < 1$, $0 < y < 0.3$) ternary composition spread catalyst array and tested the HOR capabilities of 64 discrete catalyst compositions across this phase space in a 64-electrode proton exchange membrane fuel cell. The film was found to be reasonably stable when exposed to acid at 80 °C. The ratio of Ru to Pt across the composition spread was unchanged after a sample film was exposed to acid at 80 °C for one week, implying minimal Ru dissolution. There was evidence for some loss of Mo at the high Mo end of the composition spread during acid testing, most likely indicative of loss of Mo from the surface. CO-stripping voltammetry results showed that the addition of Ru to Pt led to a reduction in the onset potential for CO-stripping, coupled with an increase in CO-stripping area. The results also showed that the addition of Mo to Pt led to a reduction in both CO-stripping onset potential and CO-stripping area. These results were consistent with those obtained on equivalent binary composition spreads reported in an earlier paper. The addition of both Ru and Mo to Pt led to a combination of these trends. All compositions, with the exception of those containing high Ru content, showed good hydrogen oxidation catalytic activities. At low Ru content, the overpotential for hydrogen oxidation in the presence of 10 and 50 ppm CO at moderate current densities was very large (400 mV), highlighting the impact of poor CO tolerance on catalytic activity for Pt. As either the Mo or Ru content increased, the HOR overpotential measured under simulated reformate decreased. Optimum performance at 500 mA/cm^2 was recorded on channels containing both Ru and Mo, e.g., $Pt_{0.40}Ru_{0.35}Mo_{0.25}$, in addition to Pt. Air bleed was beneficial for electrodes with low Mo content, where it helped slow down the rate of CO poisoning as the potential was swept to lower values. Air bleed was found to have very little impact on hydrogen oxidation in the presence of CO for electrodes containing moderate to high (within the range prepared) Mo content. Electrodes in the optimum performance region performed at least as well with no air bleed as electrodes with minimal Mo content performed with air bleeds. These results all suggest that compositions around $Pt_{0.40}Ru_{0.35}Mo_{0.25}$ are worth examining further as candidates for the anode in improved CO-tolerant fuel cells.

Well-dispersed ternary PtRuSn catalysts of various atomic ratios (60:30:10, 60:20:20, and 60:10:30) were deposited onto carbon using a modified alcohol-reduction process by Wu et al. [303]. The alloy phase structure and surface morphology for each variation of the PtRuSn/C catalysts were determined by XRD and HR-TEM. In order to evaluate the contributions of Ru and Sn in the different stages of ethanol oxidation, electrochemical oxidations of adsorbed CO, ethanol, acetaldehyde, and acetic acid were performed on each PtRuSn/C catalyst. The results indicated that the Ru-rich PtRuSn/C catalyst (60:30:10) exhibited the lowest

onset potential for the electrooxidations of adsorbed CO, which may be partially attributed to it having the highest Ru content and also to the abundant Pt$_3$Sn structures in the catalyst, which was confirm by XRD analysis. On the other hand, the amount of Ru or Sn alloyed with Pt usually is smaller than nominally predicted, because some of these atoms are present as amorphous species on the catalyst surface, most likely as oxides [283]. So, as expected, Sn will exist in part as SnO$_2$ surrounding Pt alloy, which was confirmed by the XRD pattern at the 2θ value of 33.1 and 52.1 in the Sn-rich PtRuSn/C catalyst (60:10:30).

Venkataraman et al. [304] investigated four ternary catalysts, Pt-Ru-Ag, Pt-Ru-Au, Pt-Ru-Rh, and Pt-Ru-W$_2$C, as anode electrocatalysts for the oxidation of hydrogen containing carbon monoxide. These third components were selected as co-catalysts that help in CO oxidation and/or which reduce CO adsorption on Pt. The catalysts were either alloys or intimate admixtures of the components. Alloying non-adsorbing or weakly adsorbing components can modify the nature of the adsorbed CO by modifying the electronic structure (filling of d orbitals) as observed with PtSn alloys [305], and by introducing a steric or ensemble effect as observed with PdAg alloys [306]. The nature of CO adsorption on Pt and Pd was modified from bridged to linearly-bonded CO by the addition of Sn and Ag, respectively. Tungsten carbide has good stability in acid solutions and has electronic properties similar to platinum. Tungsten carbide has also been found to be a good CO-tolerant catalyst in a phosphoric acid fuel running on unprocessed methanol reformate gas [307]. Gold has been found to lend CO tolerance to Pd. Rhodium is a very good catalyst for hydrogen electrooxidation and has been found to enhance the activity of Pt in a PtRh [56] alloy catalyst. The Pt-Ru-W$_2$C (1:1:0.4 molar ratio) oxidizes CO at a lower potential (~200 mV), and the polarization for oxidation of hydrogen-containing CO was lower than the widely used PtRu (1:1 molar ratio) catalyst. At low polarization, the Pt-Ru-W$_2$C catalyst showed twice the activity of the PtRu catalyst when the oxidation currents were normalized to the Pt area. W$_2$C appears to aid in the oxidation of CO. X-ray diffraction and CO-stripping voltammetric studies indicate that the presence of a third component reduces the amount of Ru alloyed with Pt in the catalyst and increases the potential at which CO oxidation occurs. The anode polarization was found to be higher than that of PtRu for all ternary catalysts other than Pt-Ru-W$_2$C.

Though these ternary catalysts still suffer anode polarization losses in the presence of CO, optimization of the composition and structure of the catalyst and use of new components could lead to further improvements in CO tolerance.

16.3.6 The Pt, PtRu-MO$_x$ (M = Mo, W, and V) System

It has been mentioned previously that bimetallic PtMo alloy catalysts have attracted considerable attention as alternatives to PtRu for their high catalytic activity in H$_2$ oxidation with CO/H$_2$ feed [22, 23, 70, 127, 204, 225, 259–263]. With regard to the PtMo alloy, Mo atoms have been reported to have oxygen-containing ligands even at H$_2$ potentials, which were responsible for the excellent CO tolerance [23, 204]. This notion was supported by the results for Mo K-edge XANES spectra, which showed that Mo was present as hydrated oxides with a valence state of +IV at 0 V [204]. It has been reported that carbon-supported nano-

sized Pt/Mo-oxide heterogeneous catalyst has improved CO tolerance [308, 309]. In Pt/MoO$_x$ catalyst, both Pt and MoO$_x$ nanoparticles were dispersed on the support surface, and therefore Mo would be present as a stable oxide form under PEMFC conditions. A performance evaluation of CO(100 ppm)/H$_2$ showed that the CO tolerance of Pt/MoO$_x$ was nearly comparable to that of alloy catalysts [127, 225], and the role played in CO tolerance by O$_2$ that has crossed over from the cathode was discussed [309]. While the oxygen that permeates from the cathode mitigates CO poisoning to some extent, the CO tolerance of Pt/MoO$_x$ is most likely to be dominated by intrinsic mechanisms such as bifunctional CO removal and/or the WGS reaction. CO tolerance of these non alloy-type anode catalysts is due to the interaction between Pt and metal oxides affected by the nature of the Pt catalyst [310]. Therefore, it is important to examine the nature of the intrinsic CO tolerance of Pt/MoO$_x$ catalysts for the further development of catalysts. Ioroi et al. [311] prepared carbon-supported Pt/Mo-oxide catalysts, and the reformate tolerances of Pt/MoO$_x$/C and conventional PtRu/C anodes were examined to clarify the features and differences between these catalysts. Fuel cell performance was evaluated under various reformate compositions and operating conditions, and the CO concentrations at the anode outlet were analyzed simultaneously using on-line gas chromatography. Pt/MoO$_x$ showed better CO tolerance than PtRu with CO(80 ppm)/H$_2$ mixtures, especially at higher fuel utilization conditions, which was mainly due to the higher catalytic activity of Pt/MoO$_x$ for the water-gas shift (WGS) reaction and electrooxidation of CO. In contrast, the CO$_2$ tolerance of Pt/MoO$_x$ was much worse than that of PtRu with a CO$_2$(20%)/H$_2$ mixture. The results of voltammetry indicated that the coverage of adsorbates generated by CO$_2$ reduction on Pt/MoO$_x$ was higher than that on PtRu, and therefore, the electrooxidation of H$_2$ is partly inhibited on Pt/MoO$_x$ in the presence of 20% CO$_2$. With CO(80 ppm)/CO$_2$(20%)/H$_2$, the voltage losses of Pt/MoO$_x$ and PtRu were almost equal to the sum of the losses with each contaminant component. The behavior of the CO concentration at the anode outlet is essentially the same as in the case of CO(80 ppm)/H$_2$. Although the adsorbate coverage on Pt/MoO$_x$ increases in the presence of 20% CO$_2$, CO molecules in the gas phase could still adsorb on Pt through an adsorbate "hole" to promote WGS or electrooxidation reactions, which leads to a reduction in the CO concentration under CO/CO$_2$/H$_2$ feeding conditions.

The Pt-WO$_x$ system has been the subject of several research studies and in sulfuric acid a co-catalytic activity for oxidation of H$_2$/CO is shown by tungsten, although the effect is not as strong as that for ruthenium [199, 225, 312, 313]. At the potential of a PEMFC anode, tungsten is supposed to be active as a redox catalyst which is present in an oxidized state and written as WO$_{3-x}$. The co-catalytic activity is supposed to be due to a rapid change of the oxidation state of W, involving the postulated redox couples W(VI)/W(IV) [314] or W(VI)/W(V) [312]. These redox activities render the tungsten sites active for either the dissociative adsorption of water or the oxidation of adsorbed hydrogen. In 2003, based on the results of previous papers [199, 315–318] that showed the addition of Mo or W (especially for PtRu/WO$_3$/C [317]) could enhance the CO tolerance of catalysts, Hou et al. [319] prepared new composite catalysts of PtRu–H$_x$MO$_3$/C (M = Mo and W) by dispersing PtRu particles in a composite support composed of

colloidal H_xMO_3 (M = W or Mo) and Vulcan XC72. These authors investigated the performance of the catalyst by comparing its electrochemical behavior with that of PtRu/C. The contents of the noble metals in all the catalysts were 20 wt% Pt and 10 wt% Ru, and the content of H_xMO_3 in PtRu–H_xMO_3/C was 20 wt%. It was found that the noble metals in both PtRu/C and PtRu–H_xMO_3/C were uniformly and highly dispersed on the supports, and there were no obvious differences when a composite support was used instead of the carbon support. Both H_xWO_3 and H_xMoO_3 existed in an amorphous form, and provided sufficient interfaces between the noble metals and the transition metal oxides in the catalysts. Such a structure promises a better CO tolerance than PtRu/C by lowering the starting potential for CO oxidation and by improving the H_2 oxidation when active sites on the noble metals are blocked by CO. In single-cell performance tests of all the catalysts, operated with H_2/50 ppm CO and H_2/100 ppm CO, those with PtRu–H_xMoO_3/C electrodes were better than those with PtRu/C. These results were attributed to the presence of sufficient interfaces between the noble metals and transition metal oxides in the catalysts and to the bifunctional effects of CO electrooxidation reactions strengthened by the existence of active water that is bonded on the transition metal oxides.

CO_{ads} cannot spillover the carbon substrate, which implies that contact between the co-elements is necessary to improve the CO_{ads} tolerance. Maillard et al. [320] thus adopted another tactic in which the interface between the electrocatalyst and the substrate provides new electrocatalytic sites. This is the case of tungsten bronzes H_xWO_y-supported Pt electrocatalysts in which the (electro)catalytic activity is provided by metallic platinum and the Brönsted acid function by WO_x. Pt-WO_x/C composite materials elaborated via a two-step impregnation-electrochemical reduction method have been characterized and tested by Maillard et al. [320] for the electrooxidation of CO/H_2 mixtures. TEM and EDS measurements revealed that WO_x imperfectly covered the C particles. Nanometer-sized or agglomerated Pt particles were found on the WO_x/C surface. XRD measurements revealed the absence of diffraction peaks characteristic of crystalline WO_x and could indicate that this material is amorphous. No evidence of alloying between the Pt and W was observed. WO_x/C evidenced stability in acidic medium (1M H_2SO_4) within the time scale of their experiments (1 day) and survived extensive potential sweeping up to 1.4 V vs. RHE. The H de-intercalation from WO_x is clearly visible in cyclic voltammograms at 0.1 V vs. RHE, H intercalation into WO_x being hidden by the electrochemical features associated with Vulcan XC72R. Pt nanoparticles have been electrodeposited onto this material. The results suggested that WO_x very slightly modifies the electronic density of the Pt nanoparticles. A significant improvement toward the electrooxidation of a CO_{ads} monolayer was observed for the composite material compared to pure Pt/C electrocatalyst, which is evidenced by a new electrooxidation peak at 0.55 V vs. RHE (v = 0.02 Vs^{-1}). As the electrical charge below this electrooxidation peak is sweep-rate-dependent, it is probably associated with the electrooxidation of CO_{ads} on Pt sites at the interface with the WO_x/C support. Potentiostatic measurements revealed that Pt-WO_x/C materials presented comparable CO tolerance to 20 wt% PtRu/C at short times ($t < 3000$ s). Significant degradation of the electrocatalytic performances is evidenced at longer times. A likely reason for this is the lower

equilibrium CO_{ads} coverage observed with perfect PtRu alloys. Comparison of these data with the literature suggests that the best CO_{ads} tolerance with Pt-WO_x materials is achieved when the interaction between Pt and WO_x materials is maximized.

Pereira et al. [321] investigated the anodes with Pt-WO_x/C and phosphotungstic acid (PTA)-impregnated Pt/C electrocatalysts. The choice of phosphotungstic acid is based upon its high protonic activity, suitable oxygen affinity properties [322, 323], and previously demonstrated positive action on CO oxidation with Pt-Ru/C catalysts [324]. Heteropolyacids (like PWA, PMoA, SiWA, etc.) containing these oxides were selected by Gatto et al. [325] for the development of CO-tolerant electrodes. Different electrodes were prepared by using a spray technique for both diffusive and catalytic layers. The catalytic layer was obtained using a 30 wt% Pt/Vulcan as an electrocatalyst mixed with a Nafion solution for the standard electrode (SE). CO-tolerant electrodes were prepared by adding different weight percentages (6–15%) of phosphomolybdic acid (PMoA) to SE, and for all the prepared electrodes, the Pt loading was maintained as a constant at 0.5 mg cm^{-2}. By feeding the fuel cell with H_2–CO/air, an improvement in the cell performance proportional to the increase of the percentage of PMoA was observed. The best value was reached by using a percentage of inorganic compounds in the range of 12–15 wt%. A short time test (160 h) was carried out at 80 °C in H_2–CO/air with an average power density of 220 mWcm^{-2}, confirming the stability of the system. The right compromise between the Pt catalyst and the heteropolyacid ratio could be a helpful tool in limiting Pt poisoning. Quite a high performance was achieved for the PEMFC fed with H_2 + 100 ppm CO and with anodes containing 0.4 mg PtWO_x cm^{-2}, and also for those with 0.4 mg Pt cm^{-2} impregnated with ~1 mg PTA cm^{-2}. However, a decay of the single cell performance with time was observed, and this was attributed to an increase of the membrane resistance due to the polymer degradation promoted by the crossover of the tungsten species throughout the membrane.

16.3.7 Ru-modified Pt Catalysts and Pt-modified Ru Catalysts

In recent years, investigation of the mechanism of promotion as well as the search for more active or less expensive PtRu catalysts has turned to the study of Ru modified Pt and/or Pt modified Ru catalysts. Spendelow et al. have recently reviewed the results of such studies [12]. Although not all of the catalysts produced by the modification of carbon-supported Pt particles by Ru exhibit performances in a fuel cell environment that are any better than that of the best conventionally prepared PtRu/C catalysts, they and Ru-modified single crystal Pt surfaces have proved useful in providing a more detailed understanding of the bifunctional mechanism. In particular, Herrero et al. [326] showed that OH adsorption on Ru sites on a Pt(1 1 0) surface could be identified as active in the bifunctional mechanism (their study was of methanol oxidation, enhancement of which is thought also to occur via the bifunctional mechanism). Evidence of a local electronic modification of Pt atoms near Ru atoms on a modified surface has also been provided by such studies [107, 112, 168, 180]. The relative contributions of water activation and the electronic perturbation of Pt have been debated in the

literature, with the consensus being that most of the enhancement may be attributed to water activation at the Ru sites [106, 107, 132].

Modification of Pt nanoparticles by Ru has been accomplished using a variety of Ru pre-cursors [217, 220, 327–329]. The spontaneous deposition from acidic aqueous solutions of $RuCl_3$ [217, 220, 327] has been shown to result in the formation of ruthenium oxides on the surface of the Pt, which after subsequent reduction form metallic Ru islands [217]. Fachini et al. showed that $Ru_3(CO)_9(CH_3CN)_3$ in dichloromethane could be used [328]. The adsorbed Ru species was reduced by treatment with H_2. Most recently it has been shown that $Ru(C_5H_5)_2$ in heptane can be reacted with the reduced Pt/C surface and subsequently treated with H_2 to selectively deposit Ru on the Pt and not the C support [329]. The resulting catalyst was shown, using XRD and EXAFS, to consist of a ruthenium oxide decorated surface, which upon electrochemical reduction formed a metallic PtRu surface alloy. The results obtained in this study further inform the understanding of the role of Ru in promoting the oxidation of CO at PtRu alloy surfaces, by providing direct evidence of the presence of both Ru^{3+} and Ru^{4+} species at the surface of PtRu catalyst particles in the potential region in which CO oxidation occurs.

Ru-modified Pt surfaces can be prepared in a variety of ways, all starting with a pure Pt surface that is subsequently modified by Ru deposition from a gas phase, an aqueous phase, or a non-aqueous liquid phase. A variety of methods have been used to deposit Ru submonolayers on Pt surfaces, including wet electroless deposition (either spontaneous deposition [215, 330] or forced deposition [178, 232]), electrodeposition [326, 331–333], vacuum deposition by evaporation [334, 335] or chemical vapor deposition [107, 117], and deposition from a variety of organic and inorganic Ru precursors dissolved in non-aqueous solvents [328, 329, 336]. Studies on Pt single crystals have verified that the deposition results in the growth of three-dimensional Ru islands (Volmer-Weber growth) [116, 335, 338], as would be expected based on the higher surface energy of Ru compared with Pt (reference [338] and references therein). The method of Ru deposition influences the resulting surface structure, with consequences for electrocatalysis.

In agreement with previous observations on PtRu alloy surfaces [18, 20, 67, 339], ruthenium-modified Pt surfaces exhibit a substantial electrocatalytic enhancement toward the oxidation of adsorbed CO, demonstrated by the shift of the CO oxidation peak to more negative values [112, 116, 180]. FTIR spectra on the CO-covered electrodes indicate that the electrocatalytic activity of the Ru-modified Pt(111) for CO oxidation is slightly higher than that of a 50:50 Pt/Ru alloy [116].

A new method based on spontaneous deposition of Pt on Ru has recently been demonstrated for Pt [340] and Pd [341] deposition on a Ru(0001) single crystal surface, which involves a reduction of H_2PtCl_6 coupled with the oxide formation on Ru [340]. A selective Pt deposition on Ru (no deposition on carbon) is attainable without the application of an external potential [342]. Spontaneous deposition of Pt on Ru nanoparticles can be used to control the Pt cluster size and to tune the electronic and catalytic properties of PtRu catalysts. In addition, this approach facilitates a considerable reduction of Pt loadings by depositing Pt at the surface of Ru nanoparticles rather than having Pt throughout the PtRu

nanoparticles. Brankovic et al. [109] used this new method for the preparation of PtRu and similar bimetallic electrocatalysts. It involves a spontaneous deposition of Pt submonolayers on metallic Ru nanoparticles, which yields electrocatalysts with a considerably lower Pt loading and higher CO tolerance than the commercial PtRu alloy electrocatalysts. The method offers a unique possibility to place the Pt atoms onto the surface of Ru nanoparticles, which very likely makes almost all of them available for hydrogen oxidation, in contrast to the PtRu alloy catalysts that have Pt throughout the nanoparticles. Thus, an ultimate reduction of Pt loading can be achieved. It also facilitates a fine-tuning of the electrocatalyst's activity and selectivity by changing the coverage (the cluster size) of Pt for optimal performance under required CO tolerance levels.
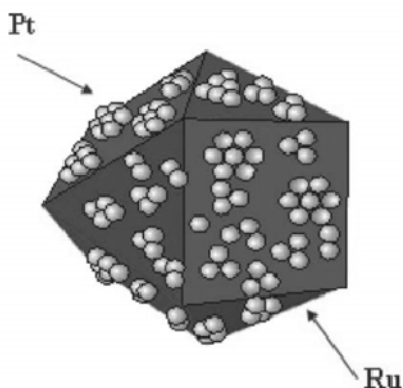
Figure 16.8. A cubo-octahedral particle model for the electrocatalyst, consisting of the Ru particle with two-dimensional Pt islands on its surface [343]. (Reprinted from Electrochimica Acta, 49(22–23), Sasaki K, Wang J.X, Balasubramanian M, McBreen J, Uribe F and Adzic R.R, Ultra-low platinum content fuel cell anode electrocatalyst with a long-term performance stability, 3873–7, ©2004, with permission from Elsevier.)

An active anode electrocatalyst, consisting of 1/8 of a monolayer of Pt on a surface of carbon-supported Ru nanoparticles, has been shown to exhibit excellent long-term performance stability in an operating fuel cell [343]. Figure 16.8 depicts a proposed structural model for the active electrocatalyst; it shows a cubo-octahedral model of the Ru particle with two-dimensional islands of Pt on its surface. The electrocatalyst has reduced susceptibility to poisoning by CO, in addition to the strong segregation of the Pt atoms on the Ru substrate that determines this characteristic. Kinetic parameters were determined by electrochemical techniques using thin-film rotating disk electrodes. X-ray absorption spectroscopy near edge structure was used to determine the d-band vacancies of a Pt submonolayer on a surface of carbon-supported Ru nanoparticles, and to relate it to the bonding strength of CO. XANES, electrochemical and gas-phase experimental data, and DFT calculations suggest there is a favorable electronic effect that reduces CO adsorption energy in a Pt submonolayer on a Ru catalyst, compared to pure Pt and PtRu alloys. In addition to the high activity for H_2 oxidation and CO tolerance, the strong segregation of Pt from the Ru substrate

is a key factor that ensures this catalyst's stability. Such segregation can be predicted using simple thermodynamic considerations of surface tensions, the enthalpy of mixing and the atomic radii of the two metals [344], and recent DFT calculations [345]. The latter show that a Pt overlayer on a Ru substrate represents a very strongly segregated system, in agreement with the observed stability of the catalytic activity of the PtRu [345] over 1000 h at 80 °C.

16.3.8 PtRu on Functionalized Carbon and Carbon Nanotube Systems

Because the size and structure of nanoparticles have a significant effect on catalytic reactions, well-controlled nanostructures are essential for creating efficient catalysts. In general, this is achieved by supporting the noble metal on a high-surface-area carbon support, such as Vulcan XC72, which maximizes the specific surface area of the noble metal and therefore its activity per unit weight. With respect to the electrocatalyst, an alternative approach to enhance the catalyst performance could be the search for suitable active supporting materials for Pt or Pt-M alloy [346]. In order to improve metallic dispersion it would be advantageous to utilize large surface carriers displaying a high number of anchoring sites. Thus, increasing the amount of surface functional groups of the support without decreasing its surface area would increase the dispersion of the metallic function. In a similar vein, small particles would be more active than large ones, since their surface area would be maximized. However, it must be taken into account that for small particles, strong interaction with the support may play a key role in their catalytic behavior. As well, it must be considered that the high Miller index crystal faces expose surface irregularities such as kinks and steps. Such defects may increase the intrinsic activity of a metal [347]. In spite of the large body of information concerning the CO oxidation reaction on Pt and carbon-supported Pt catalysts, there is a lack of studies dealing with the effect of the support nature in such processes.

Acid treatment can improve the performance of the carbon-supported activated catalysts [348]. Usually, additional treatments of the support are essential to remove (partially) any surface contaminant. Such contaminants are known to decrease the surface area of the deposited Pt [301]. There is no clear relationship between the amount of oxide surface groups in the carbon and the amount of anchored metal. Recently, a series of PtRu electrocatalysts supported over modified carbon displayed better performances than the commercial ones that have been reported [349]. Chemical modification of carbon Vulcan XC72R for fuel cell applications has been undertaken by de la Fuente et al. [350], with the aim of optimizing the anchoring of metallic particles. Treated carbons were used as carriers for the deposition of Pt nanoparticles and used as electrocatalysts. The influence of the carbon treatment as well as that of the Pt nanoparticles generation and their deposition route have been studied. Carbon modification by chemical treatment leads to an enhancement of the amount of surface oxygen groups. However, neither larger amount of Pt nor better Pt dispersion was observed during the preparation of Pt/C samples. Final particle size depended on the strength of the reducing agent, although the actual nature of the reducing agent has to be taken carefully into account. The ability of Pt/C samples towards CO oxidation depended

to a larger extent on the nature of the support than on the nature of the Pt particles, although both aspects should be taken into account. A single CO-stripping peak was observed over samples prepared on treated carbons, due to the homogenization of the sample surface after the treatment. CO mobility over actual electrocatalysts formulations, i.e., carbon-supported Pt, is low, resulting in broad or double CO-stripping peaks, depending on the support treatment.

Being a new form of carbon materials [351], carbon nanotubes (CNTs) have been a main focus of many current research efforts since recent development in large-scale syntheses of the material has significantly increased their availability [352, 353]. Due to their unique structure, high surface area, low resistance, and high stability, CNTs are considered promising supporting materials for electrocatalysts in PEMFC technology [279, 354–360]. A number of earlier investigations have shown that Pt deposited on CNTs can exhibit high activity for methanol electrooxidation as well as oxygen electro-reduction [279, 355–534]. But a pretreatment of the CNT support in oxidative mineral acid was always found to be beneficial for a homogeneous metal deposition and thus better for catalytic performance [279, 355, 356, 361–363]. Oxidative pretreatment can affect the density of surface functional groups, which could be necessary for better metal deposition and metal-support interaction [279]. The characteristics of nanosized Pt electrocatalyst deposited on carbon nanotubes (CNTs) were studied by Li et al. [364] with CO-stripping voltammogram and chronoamperometry measurements. The CNTs were pretreated by oxidation in HNO_3, mixed $HNO_3+H_2SO_4$, and $H_2SO_4+K_2Cr_2O_7$ solutions, respectively, to enable surface modification. Well-homogenized Pt particles (average size: ~3 nm) were loaded onto the pretreated CNT samples by a modified colloidal method. The morphology, crystallinity, and surface properties of CNTs were modified by pretreatments with oxidative mineral acids. In particular, pretreatment of the as-received CNTs with mixed $HNO_3+H_2SO_4$ acids produced material CNTs-II having fairly large mesoporosity at pore sizes larger than 10 nm, higher concentration of surface functional groups, and good graphitic crystallinity. The CO-stripping cyclic voltammetric measurements showed that the Pt/CNT catalysts are more tolerant to CO poisoning, since the CO electrooxidation peak potentials over these Pt/CNT catalysts are 40–160 mV lower than that over the conventional Pt/XC72 catalyst. Moreover, they found that the pretreatment of CNTs in mixed $HNO_3+H_2SO_4$ solution was very beneficial for the performance enhancement of Pt/CNT electrocatalyst; the catalyst obtained as such gave the lowest peak potential and the highest catalytic activity for the electrooxidation of CO. Larger amounts of oxygen-containing functional groups, a higher percentage of mesopores, and higher graphitic crystallinity of the pretreated CNTs were considered crucial for performance enhancement, e.g., by strengthening the interaction between Pt nanoparticles and the CNT support and enhancing the mass diffusion in the electrochemical reaction.

In 2005, Gonzalez and co-workers [365] reported the performance of PtRu catalysts supported on carbon nanotubes [366, 367] for H_2 + 100 ppm CO. Their results were similar to those of PtRu on Vulcan XC72, with an overpotential of 100 mV at 1 Acm^{-2} in a PEMFC. By contrast, a direct methanol fuel cell gave power densities and activity levels that exceeded those obtained with PtRu/Vulcan XC.

16.3.9 PtAu Binary System

Typically, gold is considered to be a poor choice as a fuel cell electrocatalyst. However, gold would be a stable alloying element, although still expensive. PtAu alloys have been studied as potential DMFC catalysts and have shown methanol oxidation activity [368] for specific structures. Gold catalysts are also effective for removing CO from H_2 gas streams in reformers [369].

$Pt_{1-x}Au_x$ binary catalysts prepared by Stevens et al. [235] were found to have the Pt fcc structure across the whole composition range. Electron microprobe measurements on catalyst electrodes after fuel cell testing showed that the Au-based alloys were stable to corrosion. The HOR overpotentials for the $Pt_{1-x}Au_x$ samples increased significantly for compositions at intermediate metal levels (Au > 50 atom%), implying that the alloying elements significantly degraded the HOR capability of Pt. The results obtained from testing with CO-free reformate suggest that $Pt_{1-x}Au_x$ may be binary alloys that are able to catalyze the RWGS reaction. RWGS CO poisons the platinum surface, requiring larger overpotentials for a given current density. CO-stripping voltammetry measurements indicated that the addition of Au to platinum led to an increase in the CO-stripping onset potential. With ~75 atom% Au, a CO-stripping peak could no longer be seen. The peak may have shifted to higher potentials, meaning that the CO binds even more strongly to the Pt and results in a catalyst that is even less CO-tolerant than Pt. The lack of a CO-stripping peak may also mean that little or no CO binds to gold and/or that the presence of gold minimizes the amount of CO that binds to Pt. It is unclear from these data, therefore, whether the addition of gold is beneficial to Pt in terms of improving CO tolerance. The results of hydrogen oxidation polarization curves with a reformate fuel containing up to 50 ppm CO showed that $Pt_{1-x}Au_x$ binary does not improve CO tolerance. There was no HOR activity up to 400 mV vs. H_2, regardless of composition prepared. This implies that the addition of Au to Pt does not improve CO tolerance in any way; in fact, it is quite possible that $Pt_{1-x}Au_x$ alloys require even higher potentials to remove adsorbed CO.

16.3.10 Pt-free Systems

Although not to the same extent as Pt, palladium is another noble metal of high catalytic activity, which is used in some industrially relevant reactions [370]. Pd is a very good electrocatalyst for organic fuel electrooxidation [371] and has the remarkable ability to store and release substantial amounts of hydrogen [372]. While voltammetry studies have indicated stronger CO bonding on Pd [373] as predicted [27], another study [374] showed that the release of hydrogen occluded in palladium may provide a viable route for lowering the surface concentration of adsorbed CO.

In Pt-free electrocatalysts, the surfaces of PdAu/C electrocatalysts are less strongly poisoned by CO than those of PtRu at temperatures of 60 °C. In 2001, Schmidt et al. [65] reported the CO tolerance of PdAu/C (Vulcan XC72) that was prepared via bimetallic colloidal precursors. This work was based on an earlier study by Fishman [375] in which PdAu-black alloys provided a highly active medium for the hydrogen oxidation reaction and a second metal (Au) produced

surfaces that did not adsorb CO under the operating conditions of a phosphoric acid fuel cell (PAFC). In addition, much lower CO adsorption energies on different poly- and single-crystalline PdAu surfaces, compared with pure Pd or pure Pt surfaces, were found from ultrahigh vacuum (UHV) studies [376]. At low overpotentials, these were more free active surface sites for hydrogen oxidation on PdAu than on PtRu at room temperature. Furthermore, at an elevated temperature of 60 °C, the surface of the PdAu/C appears to be less strongly poisoned by CO than that of PtRu/C, which gives rise to a larger concentration of free active Pd sites for H_2 oxidation. The superior activity of PdAu compared with PtRu/C was shown by CO/H_2 oxidation measurements at fuel-cell-relevant anode potentials (0.50–0.10 V). However, these results were obtained at temperatures below 60 ° C and further improvements, such as optimizing the PdAu/C with respect to particle size, alloy homogeneity, and stoichiometry are required.

A Pt/SnO_2 anode catalyst has been developed for PEMFC using CO-contaminated H_2 [310, 377]. The Pd/C and Pt/C anodes modified with SnO_2 nanoparticles for the PEMFC were investigated by Takeguchi et al. [379] using pure and 500 ppm CO-contaminated H_2 as fuel gas. Modification of the Pd/C anode with SnO_2 nanoparticles enhanced the cell performance in pure H_2, while modification of the Pt/C anode somewhat lowered the performance. Since Pd/SnO_2 and Pt/SnO_2 were known to be active for the low-temperature oxidation of CO, avoidance of CO poisoning of Pt-group metals was expected [379]. The effect of SnO_2 addition on the performances of the cell with the Pd anode in CO-contaminated H_2 was examined. The SnO_2 addition to the anode somewhat decreases the electrochemical activity in pure H_2, but clearly increases the CO tolerance of the anode catalysts. It was revealed by CO pulse titration that the SnO_2-containing catalysts adsorbed CO more weakly than the other catalysts without SnO_2 nanoparticles. This phenomenon was derived from the interaction between Pt or Pd atoms and SnO_2 nanoparticles, since these catalysts mixed with carbon did not exhibit intermetallic compounds. The cell voltage with the $Pd/SnO_2/C$ anode in 500 ppm CO-contaminated H_2 was 0.41 V at a current density of 0.2 A/cm^2, while that in pure H_2 was 0.59 V. The $Pd/SnO_2/C$ anode exhibited good tolerance to CO poisoning, since the anode adsorbed CO more weakly. Neither electrochemical oxidation of CO nor a shift reaction contributed to the CO tolerance of the $Pd/SnO_2/C$ anode.

16.4 Preparation of CO-tolerant Catalysts

The first step in the development of an anode catalyst is preparation. Several approaches have been used for the production of catalysts, both supported and unsupported. It is generally agreed that preparation has an important influence on catalyst performance [380]. Several techniques have been used to prepare the catalysts, such as colloidal chemistry methods [381–385], the impregnation method [386–390], and the reverse micelles method [391, 392]. Although the colloidal chemistry methods and the reverse micelles method produce very promising results, they are very complex compared to the impregnation method. The

application of these methods is still hindered by the complex colloid synthesis or catalyst preparation, which leads to non-competitive catalyst prices.

Reduction of the metallic ions from their salts with sulfite [209], borohydride [383], formaldehyde [393], hydrazine [394], or formic acid [395] has been proposed, resulting in catalysts with such diverse physical characteristics that direct comparison of their electrochemical performances is a rather difficult task. In the case of bimetallic catalysts, the reduction of both metals can be done simultaneously or one after the other, as was described for Pt-Ru/C [396] and Pt–Co/C [397].

Catalysts can also be prepared by melting, arc-melting in an argon atmosphere, ion-beam implantation, etc., followed by heat treatment for homogenization. In some cases due to strong segregations during the heat treatment, surface composition can differ from bulk composition. An example of this is PtMo alloy. The bulk composition of the alloy was 66 mol% Pt and 33 mol% Mo (Pt_2Mo). But after UHV annealing treatment at 970 K for 30 min, the resulting surface concentration of Mo was 23 mol%, and after Ar ion (0.5 keV) spattering, 30 mol%,

It is known that the use of well-defined substrates (single-crystal electrodes) allows a more detailed understanding of the action mechanism of the two types of surface atoms. There are two main potential ways of preparing these surfaces. First, one could think of preparing single crystals of alloys with different compositions and cut them to obtain alloy surfaces with different orientations. Second, one of the components would be deposited (either reversibly or irreversibly) onto a single crystal of the other component. The first approach, only partially explored in electrochemical environments [37, 40, 202, 398–400], suffers from several drawbacks. Only some binary systems have solubility in the whole range of composition (total miscibility) and segregation can easily occur during the experiment, especially in the course of electrode pretreatment (i.e., during the flame-annealing procedure). On the other hand, the second procedure allows separation of the pretreatment of the electrode from the preparation of the bimetallic surface. Also, a whole range of coverage is attainable in most cases. However, adatoms of elements with high cohesive energy show a strong tendency to form islands, or even three-dimensional clusters or nanoparticles, at the surface, it not being possible to obtain bimetallic surfaces with a random distribution of both types of atoms (two-dimensional substitutional alloys). Goméz et al. [291] explored the deposition and electrocatalytic activity of a number of adatoms on platinum single-crystal electrodes, focusing especially on irreversibly adsorbed adatoms. Two main types of adatoms have been investigated: those of elements of the p-block in the periodic table (see, for example, Refs. [401–405]) and those of platinum-group metals (see, for example, Refs. [406–411]). The first are characterized by low cohesive energy and electronegativities that are rather different from that of platinum, which leads to the formation of ordered open structures composed of isolated adatoms at a relatively low coverage. High cohesive energies and electronegativities similar to that of the platinum substrate characterize the second group of adatoms (platinum-group metals). Many of the corresponding bimetallic surfaces possess intrinsic adsorption and electrocatalytic properties, in some instances distinct from those of the corresponding bulk substrate electrodes. Effects from the underlying substrate on the surface states as

well as the generation of new bimetallic sites at the edges of the islands are two of the factors explaining this particular behavior. Among the noble well-ordered bimetallic surfaces formed by Pt and another element, great attention has been devoted to Pd/Pt(1 1 1) [400, 406, 407, 410–415] and Ru/Pt(1 1 1) [46, 122, 215], and to a lesser extent to Pd/Pt(1 0 0) [292, 407, 416], Rh/Pt(1 1 1) [408, 412, 417], and Ru/Pt(1 0 0) [215, 337]. Some work has been devoted to Os/Pt(1 1 1) [330], Rh/Pt(1 0 0) [409, 418], Pt/Rh(1 0 0) [418], Pt/Au(1 1 1) [419, 420], and Pt/Ru(0 0 0 1) [340]. One of the systems only partially explored is that of Rh adlayers on Pt(1 1 1). The preparation and characterization of these adlayers was presented a number of years ago [408, 412, 417].

Table 16.2. Physical characterization of PtRu alloy electrocatalysts [43]. (Reprinted from Ralph TR, Hogarth MP. Catalysis for low temperature fuel cells, part II: the anode challenges, Plat Met Rev 2002;46(3):117–35, 2002. With permission from Platinum Metals Review.)

Electrocatalyst	XRD crystallite size, nm	Calculated metal area m^2g^{-1} PtRu	CO chemisorption, metal area, m^2g^{-1} PtRu	XRD lattice parameter, nm
67 wt% Pt, 33 wt% Ru (unsupported)	2.9	114	77	0.388
40 wt% Pt, 20 wt% Ru supported on XC72R	2.5	131	104	0.388
20 wt% Pt, 10 wt% Ru supported on XC72R	1.9	150	139	0.388

For industrial-scale manufacture of PtRu alloy electrocatalysts, Johnson Matthey use an aqueous slurry route with chemical reduction to form the metal alloy particles [421]. Table 16.2 shows physical characterization data of an unsupported $Pt_{0.5}Ru_{0.5}$ alloy black electrocatalyst and two high metal loaded $Pt_{0.5}Ru_{0.5}$ alloys supported on Vulcan XC72R carbon black at 40 wt% Pt, 20 wt% Ru, and at 20 wt% Pt, 10 wt% Ru. Particularly interesting is the high metal dispersion of all of the electrocatalysts, especially at high metal loadings. The X-ray diffraction (XRD) crystallite sizes are 2.9 nm (PtRu black), 2.5 nm (40 wt% Pt, 20 wt% Ru), and 1.9 nm (20 wt% Pt, 10 wt% Ru). These are much lower than the corresponding values of 5.8 nm (Pt black), 4.5 nm (60 wt% Pt), and 2.8 nm (30 wt% Pt) for the corresponding pure Pt electrocatalysts. The high degree of PtRu dispersion is most probably a reflection of the surface characteristics of the materials. Although the $Pt_{0.5}Ru_{0.5}$ electrocatalysts were well alloyed, the contraction in the lattice parameter shown in Table 16.2 suggests all were slightly

Pt-rich (that is, $Pt_{0.59}Ru_{0.41}$). The lack of any crystalline Ru-rich phases in the XRDs suggests that the unalloyed Ru is present as an amorphous phase. Cyclic voltammetry and X-ray photoelectron spectroscopy (XPS) studies indicated that the surface of the electrocatalysts were rich in amorphous Ru oxide. This amorphous Ru oxide may play an important role in the co-deposition of the PtRu particles and in reducing the degree of sintering during the electrocatalyst manufacturing process. Many research efforts have been devoted to improving the catalytic performance of PtRu/C by increasing the catalyst dispersion [360, 422–430], and optimizing the atomic ratio [431–436] and surface state of PtRu [118, 218, 321, 437–439]. Although there have been many debates over the optimal composition ratio in the PtRu/C alloy catalyst, the 1:1 atomic ratio of Pt and Ru was widely employed.

Previously, it was known that a simple way to produce the alloy catalyst of the desired composition, in a wet-chemistry based method, is to match the ratio of metallic precursor concentrations to the target value. However, Kim et al. [424] recently showed that the synthesis parameters can significantly affect the yield of Pt and Ru loadings, and consequently the composition of Pt and Ru. In recent years, there has been considerable interest in the development of colloidal methods to prepare Pt-based fuel cell catalysts with narrow particle size distribution and homogeneous catalyst dispersion [422, 360, 426–428, 440, 441]. The investigation of Li et al. [442] focused on the effect of the synthesis conditions of a surfactant-stabilized colloidal method [441] upon the loss of Pt and Ru loadings and thus upon the Pt:Ru ratio in the resultant catalysts. Well-dispersed PtRu/C catalysts were prepared by supporting surfactant-stabilized PtRu hydrosol on carbon, followed by heat treatment at elevated temperature. The effect of the synthesis conditions and the heat treatment on the composition and electrocatalytic properties of PtRu/C towards methanol oxidation was systematically investigated. It was found that the pH environment and the reaction temperature could greatly affect the yields of Pt and/or Ru loadings, resulting in a final PtRu composition far from the expected nominal value. Moreover, after a post-heat-treatment process, the electrocatalytic activity of PtRu colloidal catalysts can be much improved, the enhancement of which can largely be explained by the improved alloy formation and removal of surfactant from the catalyst as demonstrated by the XRD and XPS analyses, respectively.

Early studies revealed that rare earth oxides could interact with the noble metals to prepare catalysts of an unusual and unexpectedly high degree of dispersion and stabilization [443]. An efficient impregnation-reduction method, which is easy to control and does not need protective reagents and thermal treatments, was applied to synthesize uniform PtRu spherical nanoparticles with small size [448]. At the same time, Nd_2O_3 was introduced as a dispersing reagent during the preparation step to control the crystallite growth of noble metals and enhance the degree of dispersion of the catalysts. TEM, XRD, and the CO-stripping voltammetry experiment results showed that noble metal particles of the PtRu/C catalysts are highly dispersed uniformly on the support and have similar morphology, and that the PtRu/C catalysts prepared adding Nd_2O_3 have smaller particle size and higher degree of dispersion of the PtRu particles than the PtRu/C catalyst prepared without adding Nd_2O_3. Well-dispersed catalysts with an average

particle size of about 2 nm were achieved. The electrochemically active surface area of the different PtRu/C catalysts was determined by the CO_{ad} stripping voltammetry experiment. The effect of Nd_2O_3 on the degree of dispersion of the noble metal and the reasons for the higher catalytic activity of the best in-house prepared PtRu/C catalyst were discussed. This preparation method also has other advantages, such as no need for protective reagents or thermal treatments, simple preparation procedure, and good reproducibility.

A carbon-supported PtRu/C catalyst (PtRu-2/C) was prepared by a simple reversal of the order of mixing in catalyst preparation [445]: adding the metal precursor salts to a carbon slurry of $NaBH_4$ instead of adding $NaBH_4$ to a carbon slurry of the metal precursor salts (PtRu-1/C), as is more commonly done. These modifications in the preparation method resulted in catalysts of different attributes. The improved performance did not come from smaller particle size and/or a higher state of metal dispersion, since PtRu-2/C had neither. It has been reported that homogeneous PtRu alloys are far less reactive than bulk mixtures of Pt metal, Pt hydrous oxides, hydrous and dehydrated RuO_2 [446, 447]. The enhanced activity was attributed to the presence of the mixed (electronic and ionic) conductor, hydrous ruthenium oxide [448]. The presence of mixed phases in PtRu-2/C and a single phase in PtRu-1/C was evident from CO-stripping voltammetry. In addition to PtRu, the mixed phases in PtRu-2/C have been identified as Pt(0) (based on a typical CO-stripping peak at 0.54 V and the well-defined hydrogen adsorption/desorption region), and platinum and ruthenium oxides (from XPS analyses). The lower cell resistance for PtRu-2/C relative to PtRu-1/C also suggests the existence of more electronically conducting components, presumably the mixed conductor hydrous ruthenium oxide.

Although as described above these alloy systems have been studied by a number of research groups, it is difficult to directly compare one system to another because of differences between sample preparation methods and experimental techniques. Such multielement comparisons do not appear routinely in the literature because the amount of work involved in sample preparation and testing using traditional "one at a time" methods is prohibitive. Thus, a paper published by Stevens et al. [235] demonstrated the usefulness of composition spread preparation and analysis techniques for fuel cell catalyst research. Furthermore, performance measurements of $Pt_{1-x}M_x$ composition were used to identify more complex ternary or quaternary composition for future studies.

16.5 Conclusions

An overview of the mechanism of CO tolerance and the development of CO-tolerant catalysts, including Pt-based binary/ternary metallic electrocatalysts and Pt-free electrocatalysts, was presented. For many PEMFC applications, fuel containing CO other than pure H_2 is the most practical choice. The use of CO-tolerant electrocatalysts is generally considered the most promising way for solving the CO poisoning problem in PEMFCs. CO-tolerant catalysts are thus still being investigated by numerous research groups and will be for many years. CO-tolerant anodes usually contain a PtRu alloy as the state-of-the-art catalyst. The mechanism

of CO oxidation and the CO tolerance of PtRu catalysts with well-defined surfaces has been investigated and clarified.

Although an electrocatalytic enhancement afforded by the addition of Ru to Pt catalysts is universally recognized, the exact mechanism of enhancement is still the subject of some debate. It is widely agreed that the bifunctional mechanism of Ru enhancement is a significant factor, and most authors agree that this is more important than any electronic (ligand) effects. Still, it seems that the ligand effect plays at least a small role. The relative effect of the two mechanisms depends on both the surface structure and the reaction being studied.

Based on the bifunctional mechanism of CO tolerance, it is necessary to find a metal that can provide OH at as low a potential as possible (e.g., near the hydrogen reversible potential). Although PtRu is widely used as a reasonably reformate-tolerant anode catalyst, its CO tolerance is still unsatisfactory for the higher CO concentrations expected at system start-up or during changes in load. Moreover, the limited availability of Ru may become a significant problem before stationary PEMFC systems can be placed on the market. A wide range of Pt alloys has been examined in an attempt to modify the CO and hydrogen electrosorption properties of Pt – to reduce the CO coverage and increase the rate of hydrogen electrooxidation. It was shown that below 100 °C none of the Pt alloys was superior to PtRu but that the CO tolerance of PtRh approached that of PtRu. There are many bimetallic catalysts. Among them, PtRu, PtSn, and PtMo are the best CO-tolerant catalysts. Pt-Fe, Pt-Ni, and Pt-Co alloys have been found to exhibit excellent CO tolerance in H_2 oxidation, similar to that of the PtRu alloy. PtRuW and PtRuMo showed an improved CO tolerance over Pt and PtRu catalysts in the presence of 50–100 ppm of CO. It should be noted that practically all transition metals are oxidized in acid solutions. Non-precious metals such as Fe or Mo will be leached out, at least from the surface, and a Pt skin layer is formed, in contrast to the precious metal Ru in the PtRu alloy.

Although attempts to find a more active catalyst than Pt/Ru have been ongoing for decades, the Pt/Ru systems still shows the best activity and stability for oxidation reactions relevant to anodes in direct methanol and reformate-fed fuel cells. Despite extensive study of Pt/Ru surfaces, many unanswered questions remain. The ideal distribution of Ru in or on Pt-based electrocatalysts is also a subject of debate. Another area of debate focuses on the question of the ideal oxidation state of Ru in Pt/Ru catalysts. Thus, there is reason to hope that further study and optimization of the Pt/Ru system may yield even more active electrocatalysts. Ru leaching from PtRu fuel cell anode electrocatalysts has a dramatic impact on the activity of a Pt/C oxygen-reducing cathode, and thus has a major role in the performance degradation of PEMFCs, particularly of DMFCs. Unless highly stable PtRu anode electrocatalysts are developed, the problem of Ru crossover and contamination at the cathode should be addressed by novel fuel cell designs where crossover is omitted, by less Ru-permeable membranes, or by more Ru-tolerant ORR electrocatalysts in PEMFCs.

There is a considerable drive to raise the operating temperatures of the PEMFC to above 100 °C. This would raise the system efficiency and dramatically improve the CO tolerance of Pt-based electrocatalysts. If the temperature can be raised to 160 °C, studies in the phosphoric acid fuel cell (PAFC) with 1 to 2% CO indicate

that PtRh and PtNi may offer superior CO tolerance. Indeed, at 200 °C pure Pt is the favored electrocatalyst in the PAFC. At higher temperatures PtRu may not be the electrocatalyst of choice in the PEMFC. There is currently much research aimed at developing membranes capable of proton conduction at 120 to 200 °C.

PEMFC research directed towards the development of CO-tolerant anode electrocatalysts will furthermore be well suited to direct alcohol fuel cells, particularly direct methanol fuel cells. Success in the arenas of cost and complexity reduction rely on continued advances in materials development and fabrication routes, and are essential for realizing the market and environmental potential of fuel cells. In the next couple of years it is likely that much research and development will still focus on reducing the costs of existing fuel cell stack materials and increasing the durability of available components. This means that innovative materials scientists and engineers can still have a major impact on the commercialization of fuel cell technology. The challenge is to design, and process economically, materials that would allow PEMFC stacks and associated reformers to operate at elevated temperatures (over 120 °C). Material scientists and engineers have the opportunity to overcome these challenges and to ensure that fuel cells become a commercial success.

Acknowledgements

References

1. Trimm DL, Önsan ZI. Onboard fuel conversion for hydrogen-fuel-cell-driven vehicles. Catal Rev 2001;43:31–84.
2. Herman RG, Klier K, Simmons GW, Finn BP, Bulko JB, Kobylinski TP. Catalytic synthesis of methanol from CO/H_2: I. Phase composition, electronic properties, and activities of the $Cu/ZnO/M_2O_3$ catalysts. J Catal 1979;56:407–29.
3. Gadgil MM, Sasikala R, Kulshreshtha SK. CO oxidation over Pd/SnO_2 catalyst. J Mol Catal 1994;87:297–309.
4. Haruta M, Tsubota S, Kobayashi T, Kageyama H, Genet KJ, Delmon B. Low-temperature oxidation of CO over gold supported on TiO_2, α-Fe_2O_3, and Co_3O_4. J Catal 1993;144:175–92.
5. Echigo M, Shinke N, Takami S, Higashiguchi S, Hirai K, Tabata T. Development of residential PEFC cogeneration systems: Ru catalyst for CO preferential oxidation in reformed gas. Catal Today 2003;84:209–15.
6. US Department of Energy. Fuel cell. In: DOE multi-year research, development and demonstration plan: planned program activities for 2005–2015. Available on: http://www1.eere.energy.gov/hydrogenandfuelcells/mypp/pdfs/fuel_cells.pdf.
7. Ralph TR, Hards GA, Thompsett D, Gascoyne JM. Fuel cell seminar extended abstracts; 1994 Nov 28–Dec. 1; San Diego, CA: p. 199.
8. Gottesfeld S, Pafford J. A new approach to the problem of carbon monoxide poisoning in fuel cells operating at low temperatures. J Electrochem Soc 1988;135:2651–2.

9. Beden B, Lamy C, Bewick A, Kumimatsu K. Electrosorption of methanol on a platinum electrode. IR spectroscopic evidence for adsorbed CO species. J Electroanal Chem 1981;121:343–7.

10. Crown A, Kim H, Lu GQ, de Moraes IR, Rice C, Wieckowski A. Research toward designing high activity catalysts for fuel cells: structure and reactivity. J New Mat Electrochem Systems 2000;3:275–84.

11. Iwasita T. Methanol and CO electrooxidation. In: Vielstich W, Gasteiger HA, Lamm A, editors. Handbook of fuel cells – fundamentals, technology and applications, Vol 2. New York: John Wiley & Sons, 2003: 603–24.

12. Spendelow JS, Babu PK, Wieckowski A. Electrocatalytic oxidation of carbon monoxide and methanol on platinum surfaces decorated with ruthenium. Curr Opin Solid State Mater Sci 2005;9:37–416.

13. Adams WA, Blair J, Bullock KR, Gardner CL. Enhancement of the performance and reliability of CO poisoned PEM fuel cells. J Power Sources 2005;145:55–61.

14. Iorio T, Yasuda K, Siroma Z, Fujiwara N, Miyazaki Y. Enhanced CO-tolerance of carbon-supported platinum and molybdenum oxide anode catalyst. J Electrochem Soc A 2003;150:A1225–30.

15. Wee JH, Lee KY. Overview of the development of CO-tolerant anode electrocatalysts for proton-exchange membrane fuel cells. J Power Sources 2005;157:128–35.

16. Kuk ST, Wieckowski A. Methanol electrooxidation on platinum spontaneously deposited on unsupported and carbon-supported ruthenium nanoparticles. J Power Sources 2005;141:1–7.

17. Spendelow JS, Lu GQ, Kenis PJA, Wieckowski A. Electrooxidation of adsorbed CO on Pt(1 1 1) and Pt(1 1 1)/Ru in alkaline media and comparison with results from acidic media. J Electroanal Chem 2004;568:215–24.

18. Lin WF, Iwasita T, Vielstich W. Catalysis of CO electrooxidation at Pt, Ru, and PtRu alloy. An in situ FTIR study. J Phys Chem B 1999;103:3250–3257.

19. McGovern MS, Waszczuk P, Wieckowski A. Stability of carbon monoxide adsorbed on nanoparticle Pt and Pt/Ru electrodes in sulfuric acid media. Electrochim Acta 2006;51:1194–8.

20. Gasteiger HA, Markovic N, Ross PN Jr, Cairns EJ. Co electrooxidation on well-characterized Pt-Ru Alloys. J Phys Chem 1994;98:617–625.

21. Grgur BN, Zhuang G, Marković NM, Ross PN Jr. Electrooxidation of H_2/CO mixtures on a well-characterized $Pt_{75}Mo_{25}$ alloy surface. J Phys Chem B 1997;101:3910–3.

22. Grgur BN, Marković NM, Ross PN Jr. Electrooxidation of H_2, CO, and H_2/CO mixtures on a well-characterized $Pt_{70}Mo_{30}$ bulk alloy electrode. J Phys Chem B 1998;102:2494–501.

23. Grgur BN, Marković NM, Ross PN. The electro-oxidation of H_2 and H_2/CO mixtures on carbon-supported Pt_xMo_y alloy catalysts. J Electrochem Soc 1999;146:1613–9.

24. Massong H, Wang H, Samjeske G, Baltruschat, H. The co-catalytic effect of Sn, Ru and Mo decorating steps of Pt(111) vicinal electrode surfaces on the oxidation of CO. Electrochim Acta 2000;46:701–7.

25. Pozio A, Giorgi L, Antolini E, Passalacqua E. Electroxidation of H_2 on Pt/C Pt–Ru/C and Pt–Mo/C anodes for polymer electrolyte fuel cell. Electrochim Acta 2000;46:555–61.

26. Lee SJ, Mukerjee S, Ticianelli EA, McBreen L. Electrocatalysis of CO tolerance in hydrogen oxidation reaction in PEM fuel cells. Electrochim Acta 1999;44:3283–93.

27. Christoffersen E, Liu P, Ruban A, Skriver HL, Norskov JK. Anode materials for low-temperature fuel cells: a density functional theory study. J Catal 2001;199:123–31.

28. Giorgi L, Pozio A, Bracchini C, Giorgi R, Turtu S. H_2 and H_2/CO oxidation mechanism on Pt/C, Ru/C and Pt–Ru/C electrocatalysts. J Appl Electrochem 2001;31:325–34.

29. McBreen J, Mukerjee S. In-situ X-ray-absorption studies of a Pt-Ru electrocatalyst. J Electrochem Soc 1995;142:3399–404.

30. Mukerjee S, McBreen J. An in situ X-ray absorption spectroscopy investigation of the effect of Sn additions to carbon-supported Pt electrocatalysts: Part I. J Electrochem Soc 1999;146:600–6.

31. Koper MTM. Electrocatalysis on bimetallic and alloy surfaces. Surf Sci 2004;548:1–3.

32. Gallagher ME, Lucas CA, Stamenkovic V, Marković NM, Ross PN. Surface structure and relaxation at the $Pt_3Sn(1\ 1\ 1)$/electrolyte interface. Surf Sci 2003;544:L729–34.

33. Morimoto Y, Yeager EB. Comparison of methanol oxidations on Pt, PtRu and PtSn electrodes. J Electroanal Chem 1998;444:95–100.

34. Wang K, Gasteiger HA, Marković NM, Ross PN Jr. On the reaction pathway for methanol and carbon monoxide electrooxidation on Pt-Sn alloy versus Pt-Ru alloy surfaces. Electrochim Acta 1996;41:2587–93.

35. Gasteiger HA, Marković NM, Ross PN Jr. Electrooxidation of CO and H_2/CO mixtures on a well-characterized Pt_3Sn electrode surface. J Phys Chem 1995;99:8945–9.

36. Paffett MT, Gebhard SC, Windham RG, Koel BE. Chemisorption of carbon monoxide, hydrogen, and oxygen on ordered tin/platinum(111) surface alloys. J Phys Chem 1990;94:6831–9.

37. Haner AN, Ross PN. Electrochemical oxidation of methanol on tin-modified platinum single-crystal surfaces. J Phys Chem 1991;95:3740–6.

38. Marković NM, Widelov A, Ross PN, Monteiro OR, Brown IG. Electrooxidation of CO and CO/H_2 mixtures on a Pt-Sn catalyst prepared by an implantation method. Catal Lett 1997;43:161–6.

39. Xiao X-Y, Tillmann S, Baltruschat H. Scanning tunneling microscopy of Sn coadsorbed with Cu and CO on Pt(111) electrodes. Phys Chem Chem Phys 2002;4:4044–50.

40. Stamenkovic VR, Arenz M, Lucas CA, Gallagher ME, Ross PN, Marković NM. Surface chemistry on bimetallic alloy surfaces: adsorption of anions and oxidation of CO on $Pt_3Sn(111)$. J Am Chem Soc 2003;125:2736–45.

41. Hayden BE, Rendall ME, South O. Electro-oxidation of carbon monoxide on well-ordered Pt(111)/Sn surface alloys. J Am Chem Soc 2003;125:7738–42.

42. Arenz M, Stamenkovic V, Ross PN, Marković NM. Preferential oxidation of carbon monoxide adsorbed on Pd submonolayer films deposited on Pt(1 0 0). Electrochem Commun 2003;5:809–13.

43. Ralph TR, Hogarth MP. Catalysis for low temperature fuel cells, part II: the anode challenges. Platinum Metals Rev Vol No pp 2002;46(3):117–135.

44. Waszczuk P, Wieckowski A, Zelenay P, Gottesfeld S, Coutanceau C, Leger JM, et al. Adsorption of CO poison on fuel cell nanoparticle electrodes from methanol solutions: a radioactive labeling study. J Electroanal Chem 2001;511:55–64.

45. Lu GQ, White JO, Wieckowski A. Vibrational analysis of chemisorbed CO on the Pt(1 1 1)/Ru bimetallic electrode. Surf Sci 2004;564:131–40.

46. Lu GQ, Waszczuk P, Wieckowski A. Oxidation of CO adsorbed from CO saturated solutions on the Pt(111)/Ru electrode. J Electroanal Chem 2002;532:49–55.

47. Brankovic SR, Marinkovic NS, Wang JX, Adzic RR. Carbon monoxide oxidation on bare and Pt-modified Ru(1010) and Ru(0001) single crystal electrodes. J Electroanal Chem 2002;532:57–60.

48. Bellows RJ, Marucchi-Soos E, Reynolds RP. The mechanism of CO mitigation in proton exchange membrane fuel cells using dilute H_2O_2 in the anode humidifier. Electrochem Solid State Lett 1998;1:69–70.

49. Lindstrom RW, inventor; Protech Co., assignee. Electrocatalytic gas diffusion electrode employing thin carbon cloth layer. US Patent US4647359. 1987 Mar 3.

50. Yu H, Hou Z, Yi B, Lin Z. Composite anode for CO tolerance proton exchange membrane fuel cells. J Power Sources 2002;105:52–57.

51. Wan C-H, Zhuang Q-H. Novel layer wise anode structure with improved CO-tolerance capability for PEM fuel cell. Electrochim Acta 2007;52:4111–23.

52. Wilkinson DP, Voss HH, Prater KB, Hards GA, Ralph TR, Thompsett D, inventors; Johnson Matthey PLC, Ballard Power Systems, assignees. Electrode. US Patent US5795669. 1998 Aug 18.

53. Haug A, White RE, Weidner JW, Huang W, Shi S, Rana N, et al. Using sputter deposition to increase CO tolerance in a proton-exchange membrane fuel cell. J Electrochem Soc 2002;149:A868–72.

54. Wilkinson DP, Thompsett D. In: Proceedings of the second international symposium on new materials for fuel cell and modern battery systems. Savadogo O, Roberge PR, editors. Montreal, Canada: Les edition de l'Ecole Polytechnique de Montreal, 1997: 266.

55. McKee DW, Pak MS. Electrocatalysts for hydrogen/carbon monoxide fuel cell anodes. J Electrochem Soc 1969;116:516–20.

56. Ross PN, Kinoshita K, Scarpellino AJ, Stonehart P. Electrocatalysis on binary alloys: I. Oxidation of molecular hydrogen on supported Pt−Rh alloys. J Electroanal Chem 1975;59:177–89.

57. Hogarth M, Glipa X. High temperature membranes for solid polymer fuel cells. Report issued by Johnson Matthey Technology Centre to the ETSU on behalf of the Department of Trade and Industry as ETSU F/02/00189/REP; DTI/Pub URN 01/893; 2001.

58. Hogarth WHJ, Diniz da Costa JC, Lu GQ. Solid acid membranes for high temperature (at 140 °C) proton exchange membrane fuel cells. J Power Sources 2005;142:223–37.

59. Springer TE, Rockward T, Zawodzinski TA, Gottesfeld S. Model for polymer electrolyte fuel cell operation on reformate feed: effects of CO, H_2 dilution, and high fuel utilization. J Electrochem Soc 2001;148:A11–23.

60. Benicewicz BC. In: Advances in materials for PEM fuel cell systems. Polymer Division, American Chemical Society; Asilomar, California; 2003 February 23–27.

61. Kikuchi E. Membrane reactor application to hydrogen production. Catal Today 2000;56:97–101.

62. Thomason AH, Lalk TR, Appleby AJ. Effect of current pulsing and "self-oxidation" on the CO tolerance of a PEM fuel cell. J Power Sources 2004;135:204–11.

63. Zhang J, Datta R. Sustained potential oscillations in proton exchange membrane fuel cells with PtRu as anode catalyst. J Electrochem Soc 2002;149:1423–31.

64. Beden B, Bewick A, Kunimatsu K, Lamy C. Infrared study of adsorbed species on electrodes: adsorption of carbon monoxide on Pt, Rh and Au. J Electroanal Chem 1982;142:345–56.

65. Schmidt TJ, Jusys Z, Gasteiger HA, Behm RJ, Endruschat H, Boennemann U. On the CO tolerance of novel colloidal PdAu/carbon electrocatalysts. J Electroanal Chem 2001;501:132–40.

66. Bhatia KK, Wang C-Y. Transient carbon monoxide poisoning of a polymer electrolyte fuel cell operating on diluted hydrogen feed. Electrochim Acta 2004;49:2333–41.

67. Kabbabi A, Faure R, Durand R, Beden B, Hahn F, Leger JM, et al. In situ FTIRS study of the electrocatalytic oxidation of carbon monoxide and methanol at platinum–ruthenium bulk alloy electrodes. J Electroanal Chem 1998;444:41–53.

68. Ralph TR, Hogarth MP. Catalysis for low temperature fuel cells part I the cathode challenges. Platinum Met Rev 2002;46:3–14.

69. Ralph TR, Hogarth MP. Catalysis for low temperature fuel cells part III the challenges for the direct methanol fuel cell. Platinum Met Rev 2002;46:146.

70. Urian RC, Gulla AF, Mukerjee S. Electrocatalysis of reformate tolerance in proton exchange membranes fuel cells: Part I. J Electroanal Chem 2003;554–555:307–24.

71. Ruth K, Vogt M, Zuber R. Development of CO-tolerant catalysts. In: Vielstich W, Gasteiger HA, Lamm A, editors. Handbook of fuel cells – fundamentals, technology and applications, Vol 3. New York: John Wiley & Sons, 2003: 489–96.

72. Watkins DS. Research, development and demonstration of solid polymer fuel cell systems. In: Fuel cell systems. Blomen L, Mugerwa M, editors. New York: Plenum Press, 1993: 493–530.

73. Hirschenhofer JH, Stauffer DB, Engleman RR. Fuel cells: a handbook. 3rd rev. Reading: Gilbert/Commonwealth, Inc., 1994.

74. Bellows RJ, Marucchi-Soos EP, Buckley DT. Analysis of reaction kinetics for carbon monoxide and carbon dioxide on polycrystalline platinum relative to fuel cell operation. Ind Eng Chem Res 1996;35:1235–42.

75. Divisek J, Oetjen H-F, Peinecke V, Schmidt VM, Stimming U. Components for PEM fuel cell systems using hydrogen and CO containing fuels. Electrochim Acta 1998;43:3811–5.

76. Beden B, Bewick A, Lamy C. A study by electrochemically modulated infrared reflectance spectroscopy of the electrosorption of formic acid at a platinum electrode. J Electroanal Chem 1983;148:147–60.

77. Villegas I, Weaver MJ. Carbon monoxide adlayer structures on platinum (111) electrodes: A synergy between in-situ scanning tunneling microscopy and infrared spectroscopy. J Chem Phys 1994;101:1648–60.

78. Petukhov AV. Effect of molecular mobility on kinetics of an electrochemical Langmuir-Hinshelwood reaction. Chem Phys Lett 1997;277:539–44.

79. Petukhov AV, Akemann W, Friedrich KA, Stimming U. Kinetics of electrooxidation of a CO monolayer at the platinum/electrolyte interface. Surf Sci 1998;402–404:182–6.

80. Koper MTM, Jansen APJ, Santen RAv, Lukien JJ, Hilbers PAJ. Monte Carlo simulations of a simple model for the electrocatalytic CO oxidation on platinum. J Chem Phys 1998;109:6051–62.

81. Koper MTM, Jansen APJ, Lukkien J. Lattice–gas modeling of electrochemical Langmuir–Hinshelwood surface reactions. Electrochim Acta 1999;45:645–51.

82. Koper MTM, Lukien JJ, Jansen APJ, van Santen RA. Lattice gas model for CO electrooxidation on Pt-Ru bimetallic surfaces. J Phys Chem B 1999;103:5522–9.

83. Massong H, Tillmann S, Langkau T, Abd El Meguid EA, Baltruschat H. On the influence of tin and bismuth UPD on Pt(111) and Pt(332) on the oxidation of CO. Electrochim Acta 1998;44:1379–88.

84. Lebedeva NP, Koper MTM, Feliu JM, van Santen RA. Role of crystalline defects in electrocatalysis: mechanism and kinetics of CO adlayer oxidation on stepped platinum electrodes. J Phys Chem B 2002;106:12938–47.

85. Lebedeva NP, Koper MTM, Herrero E, Feliu JM, van Santen RA. Cooxidation on stepped Pt[n(111)×(111)] electrodes. J Electroanal Chem 2000;487:37–44.

86. Samjeské G, Xiao X-Y, Baltruschat H. Ru decoration of stepped Pt single crystals and the role of the terrace width on the electrocatalytic CO oxidation. Langmuir 2002;18:4659–66.

87. Watanabe M, Motoo S. Electrocatalysis by ad-atoms part II. Enhancement of the oxidation of methanol on platinum by ruthenium ad-atoms. J Electroanal Chem 1975;60:267–73.

88. Ralph TR, Hards GA. Powering the cars and homes for tomorrow. Chem Ind (London) 1998;9:337–42.

89. Watanabe M, Motoo S. Electrocatalysis by ad-atoms: part III. Enhancement of the oxidation of carbon monoxide on platinum by ruthenium ad-atoms. J Electroanal Chem 1975;60:275–83.
90. Liu P, Norskov JK. Kinetics of the anode processes in PEM fuel cells - the promoting effect of Ru in PtRu anodes. Fuel Cells 2001;1:192–201.
91. Parsons R, Vandernoot T. The oxidation of small organic molecules: A survey of recent fuel cell related research. J Electroanal Chem 1988;257:9–45.
92. Hamnett A. Mechanism of methanol electro-oxidation. In: A.Wieckowski, editor. Interfacial electrochemistry: theory, experiment, and applications. New York: Marcel Dekker, 1999: 843–83.
93. Samjeské G, Wang H, Löffler T, Baltruschat H. CO and methanol oxidation at Pt-electrodes modified by Mo. Electrochim Acta 2002;47:3681–92.
94. Berenz P, Tillmann S, Massong H, Baltruschat H. Decoration of steps at Pt single crystal electrodes and its electrocatalytic effect. Electrochim Acta 1998;43:3035–43.
95. de Becdelievre AM, de Becdelievre J, Clavilier J. Electrochemical oxidation of adsorbed carbon monoxide on platinum spherical single crystals. Effect of anion adsorption. J Electroanal Chem 1990;294:97–110.
96. Baschuk J, Li X. Carbon monoxide poisoning of proton exchange membrane fuel cells. Int J Energy Res 2001;25:695–713.
97. Dhar HP, Christner LG, Kush AK. Nature of CO adsorption during H_2 oxidation in relation to modeling for CO poisoning of a fuel cell anode. J Electrochem Soc 1987;134:3021–6.
98. Gilman S. The mechanism of electrochemical oxidation of carbon monoxide and methanol on platinum II: the "reactant pair" mechanism for electrochemical oxidation of carbon monoxide and methanol. J Phys Chem 1964;68:70–80.
99. Stonehart P, Ross P. The commonality of surface processes in electrocatalysis and gas-phase heterogeneous catalysis. Cat Rev – Sci Eng 1975;12:1–35.
100. Vogel W, Lundquist J, Ross P, Stonehart P. Reaction pathways and poisons-II. The rate controlling step for electrochemical oxidation of hydrogen on Pt in acid and poisoning of the reaction by CO. Electrochim Acta 1975;20:79–93.
101. Wilson M, Derouin C, Valerio J, Gottesfeld S. Electrocatalysis issues in polymer electrolyte fuel cells. Proceedings of the Intersociety Energy Conversion Engineering Conference 1993;1:1203–8.
102. Oetjen H-F, Schmidt VM, Stimming U, Trila F. Performance data of a proton exchange membrane fuel cell using H_2/CO as fuel gas. J Electrochem Soc 1996;143:3838–42.
103. Iwase M, Kawatsu S. Optimized CO tolerant electrocatalysts for polymer electrolyte fuel cells. In: Proton conducting membrane fuel cells I. Gottesfeld S, Halpert G, Landgrebe A, editors. Electrochemical Society Proceedings 1995;95–23:12–23.
104. Schmidt VM, Ianneillo R, Oetjen H-F, Reger H, Stimming U, Trila F. 1995. Oxidation of H_2/CO in a proton exchange membrane fuel cell. In: Proton conducting membrane fuel cells I. Gottesfeld S, Halpert G, Landgrebe A, editors. Electrochemical Society Proceedings 1995;95–23:1–11.
105. Zawodzinski TA, Karuppaiah C, Uribe F, Gottesfeld S. Aspects of CO tolerance in polymer electrolyte fuel cells: some experimental findings. In: Electrode materials and processes for energy conversion and storage I. Srinivasan S, McBreen J, Khandkar AC, Tilak VC, editors. Proceedings of the Electrochemical Society 1997;97(13):139–146.
106. Lu C, Rice C, Masel RI, Babu PK, Waszczuk P, Kim HS, et al. UHV, electrochemical NMR, and electrochemical studies of platinum/ruthenium fuel cell catalysts. J Phys Chem B 2002;106:9581–9.

107. Lu C, Masel RI. The effect of ruthenium on the binding of CO, H_2, and H_2O on Pt(110). J Phys Chem B 2001;105:9793–7.

108. Yajima T, Uchida H, Watanabe M. In-situ ATR-FTIR spectroscopic study of electro-oxidation of methanol and adsorbed CO at Pt-Ru alloy. J Phys Chem B 2004;108:2654–9.

109. Brankovic SR, Wang JX, Adžić RR. Pt submonolayers on Ru nanoparticles: a novel low Pt loading, high CO tolerance fuel cell electrocatalyst. Electrochem Solid-State Lett 2001;4:A217–20.

110. Gasteiger HA, Markovic NM, Ross PN. H_2 and CO electrooxidation on well-characterized Pt, Ru, and Pt-Ru. 2. Rotating disk electrode studies of CO/H_2 mixtures at 62 degree C. J Phys Chem 1995;99:16757–67.

111. Gasteiger HA, Markovic NM, Ross PN. H_2 and CO electrooxidation on well-characterized Pt, Ru, and Pt-Ru. 1. Rotating disk electrode studies of the pure gases including temperature effects. J Phys Chem 1995;99:8290–301.

112. Friedrich KA, Geyzers KP, Linke U, Stimming U, Stumper J. CO adsorption and oxidation on a Pt(111) electrode modified by ruthenium deposition: an IR spectroscopic study. J Electroanal Chem 1996;402:123–8.

113. Zawodzinski TA, Springer TE, Gottesfeld S. The 1997 joint international meeting of ECS and ISE. ECS Meeting Abstracts 1997;97–2:1228.

114. Kua J, Goddard WA III. Oxidation of methanol on 2nd and 3rd row group VIII transition metals (Pt, Ir, Os, Pd, Rh, and Ru): application to direct methanol fuel cells. J Am Chem Soc 1999;121:10928–41.

115. Denis MC, Gouerec P, Guay D, Dodelet JP, Lalande G, Schulz R. Improvement of the high energy Ball-Milling preparation procedure of CO tolerant Pt and Ru containing catalysts for polymer electrolyte fuel cells. J Appl Electrochem 2000;30:1243–53.

116. Tong YY, Kim HS, Babu PK, Waszczuk P, Wieckowski A, Oldfield E. An NMR investigation of CO tolerance in a Pt/Ru fuel cell catalyst. J Am Chem Soc 2002;124:468–473.

117. Lamouri A, Gofer Y, Luo Y, Chottiner GS, Scherson DA. Low energy electron diffraction, X-ray photoelectron spectroscopy, and CO-temperature-programmed desorption characterization of bimetallic ruthenium–platinum surfaces prepared by chemical vapor deposition. J Phys Chem B 2001;105:6172–7.

118. Camara GA, Giz MJ, Paganin VA, Ticianelli EA. Correlation of electrochemical and physical properties of PtRu alloy electrocatalysts for PEM fuel cells. J Electroanal Chem 2002;537:21–9.

119. Lin WF, Zei MS, Eiswirth M, Ertl G, Iwasita T, Vielstich W. Electrocatalytic activity of Ru-modified Pt(111) electrodes toward CO oxidation. J Phys Chem B 1999;103:6968–77.

120. Qi Z, Kaufman A. CO-tolerance of low-loaded Pt/Ru anodes for PEM fuel cells. J Power Sources 2003;113:115–23.

121. Viswanathan R, Hou G, Liu R, Bare SR, Modica F, Mickelson G, et al. In-situ XANES of carbon-supported Pt-Ru anode electrocatalyst for reformate-air polymer electrolyte fuel cells. J Phys Chem B 2002;106:3458–65.

122. Koper MTM, Lebedeva NP, Hermse CGM. Dynamics of CO at the solid/liquid interface studied by modeling and simulation of CO electro-oxidation on Pt and PtRu electrodes. Faraday Discuss 2002;121:301–11.

123. Koper MTM, Shubina TE, van Santen RA. Periodic density functional study of CO and OH adsorption on Pt-Ru alloy surfaces: Implications for CO tolerant fuel cell catalysts. J Phys Chem B 2002;106:686–92.

124. Lebedeva NP, Koper MTM, Feliu JM, van Santen RA. Mechanism and kinetics of the electrochemical CO adlayer oxidation on Pt(111). J Electroanal Chem 2002;524–525:242–51.

125. Camara GA, Ticianelli EA, Mukerjee S, Lee SJ, McBreen J. The CO poisoning mechanism of the hydrogen oxidation reaction in proton exchange membrane fuel cells. J Electrochem Soc 2002;149:A748–53.

126. Mukerjee S, Urian RC. Bifunctionality in Pt alloy nanocluster electrocatalysts for enhanced methanol oxidation and CO tolerance in PEM fuel cells: electrochemical and in situ synchrotron spectroscopy. Electrochim Acta 2002;47:3219–31.

127. Mukerjee S, Urian RC, Lee SJ, Ticianelli EA, McBreen J. Electrocatalusis of CO tolerance by carbon-supported PtMo electrocatalysts in PEMFCs. J Electrochem Soc 2004;151:A1094–103.

128. Russell AE, Maniguet S, Mathew RJ, Yao J, Roberts MA, Thompsett D. In situ X-ray absorption spectroscopy and X-ray diffraction of fuel cell electrocatalysts. J Power Sources 2001;96:226–32.

129. Goetz M, Wendt H. Composite electrocatalysts for anodic methanol and methanol-reformate oxidation. J Appl Electrochem 2001;31:811–7.

130. Skelton DC, Tobin RG, Lambert DK, DiMaggio CL, Fisher GB. Oxidation of CO on gold-covered Pt(335). J Phys Chem B 1999;103:964–71.

131. Hammer B, Norskov JK. Electronic factors determining the reactivity of metal surfaces. Surf Sci 1995;343:211–20.

132. Liu P, Logadottir A, Norskov JK. Modeling the electro-oxidation of CO and H_2/CO on Pt, Ru, PtRu and Pt_3Sn. Electrochim Acta 2003;48:3731–42.

133. Krausa M, Vielstich W. Study of the electrocatalytic influence of Pt/Ru and Ru on the oxidation of residues of small organic molecules. J Electroanal Chem 1994;379:307–14.

134. Frelink T, Visscher W, Vanveen JAR. On the role of Ru and Sn as promotors of methanol electro-oxidation over Pt. Surf Sci 1995;335:353–60.

135. Buatier de Mongeot F, Scherer M, Gleich B, Kopatzki E, Behm RJ. CO adsorption and oxidation on bimetallic Pt/Ru(0001) surfaces – a combined STM and TPD/TPR study. Surf Sci 1998;411:249–62.

136. Watanabe M, Zhu YM, Igarashi H, Uchida H. Mechanism of CO tolerance at Pt-Alloy anode catalysts for polymer electrolyte fuel cells. Electrochemistry 2000;68:244–51.

137. Roth C, Benker N, Buhrmester T, Mazurek M, Loster M, Fuess H, et al. Determination of O[H] and CO coverage and adsorption sites on PtRu electrodes in an operating PEM fuel cell. J Am Chem Soc 2005;127:14607–15.

138. El-Shafei AA, Hoyer R, Kibler LA, Kolb DM. Methanol oxidation on Ru-modified preferentially oriented Pt electrodes in acidic medium. J Electrochem Soc 2004;151:F141–5.

139. Davies JC, Hayden BE, Pegg DJ. The modification of Pt(110) by ruthenium: CO adsorption and electro-oxidation. Surf Sci 2000;467:118–30.

140. Frelink T, Visscher W, Cox AP, Vanveen JAR. Ellipsometry and dems study of the electrooxidation of methanol at Pt and Rupromoted and Sn-promoted Pt. Electrochim Acta 1995;40:1537–43.

141. Roth C, Benker N, Buhrmester T, Mazurek M, Loster M, Fuess H, et al. Determination of O[H] and CO coverage and adsorption sites on PtRu electrodes in an operating PEM fuel cell. J Am Chem Soc 2005;127:14607–15.

142. Waszczuk P, Lu GQ, Wieckowski A, Lu C, Rice C, Masel RI. UHV and electrochemical studies of CO and methanol adsorbed at platinum/ruthenium surfaces, and reference to fuel cell catalysis. Electrochim Acta 2002;47:3637–52.

143. Iwasita T. Progress in the study of methanol oxidation by in situ, ex situ and on-line methods. In: Advances in electrochemical science and engineering. Gerischer H, Tobias Ch, editors. Verlag Chemie 1990;1:127–70.

144. Wolter O, Giordano C, Heitbaum J, Vielstich W. Proceedings of the symposium on electrocatalysis. Pennington, NJ: The Electrochemical Society, 1982: 235.

145. Bittins-Cattaneo B, Cattaneo E, Königshoven P, Vielstich W. New developments in electrochemical mass spectroscopy. In: Electroanalytical chemistry: a series of advances. Bard AJ, editor. New York: Marcel Dekker, New York: vol 17, ch 3, 181–220.

146. Iwasita T, Nart FC. In situ infrared spectroscopy at electrochemical interfaces. Prog Surf Sci 1997;55:271–340.

147. Clavilier J, Armand D, Sun SG, Petit M. Electrochemical adsorption behaviour of platinum stepped surfaces in sulphuric acid solutions. J Electroanal Chem 1986;205:267–77.

148. Ocko BM, Wang J, Davenport A, Isaacs H. In situ x-ray reflectivity and diffraction studies of the Au(001) reconstruction in an electrochemical cell. Phys Rev Lett 1990;65:1466–9.

149. Faguy PW, Markovic N, Adzic RR, Fierro CA, Yeager EB. A study of bisulfate adsorption on Pt(111) single crystal electrodes using in situ Fourier transform infrared spectroscopy. J Electroanal Chem 1990;289:245–62.

150. Tidswell IM, Markovic NM, Ross PN. Potential dependent surface relaxation of the Pt(001)/electrolyte interface. Phys Rev Lett 1993;71:1601–4.

151. Sawatari Y, Inukai J, Ito M. The structure of bisulfate and perchlorate on a Pt(111) electrode surface studied by infrared spectroscopy and ab-initio molecular orbital calculation. J Electron Spec 1993;64/65:515–22.

152. Nart FC, Iwasita T, Weber M. Vibrational spectroscopy of adsorbed sulfate on Pt(111). Electrochim Acta 1994;39:961–8.

153. Lucas C, Markovic NM, Ross PN. Observation of an ordered bromide monolayer at the Pt(111)-solution interface by in-situ surface X-ray scattering. Surf Sci 1995;340:L949–54.

154. Kolb DM. Reconstruction phenomena at metal-electrolyte interfaces. Prog Surf Sci 1996;51:109–73.

155. Itaya K. In situ scanning tunneling microscopy in electrolyte solutions. Prog Surf Sci 1998;58:121–247.

156. Hughes VB, Miles R. cyclic voltammetric investigation of adsorbed residues derived from methanol on platinum-based electrocatalysts. J Electroanal Chem 1983;145:87–107.

157. Ticanelli E, Beery JG, Paffett MT, Gottesfeld S. An electrochemical, ellipsometric, and surface science investigation of the PtRu bulk alloy surface. J Electroanal Chem 1989;258:61–77.

158. Richardz E, Wohlmann B, Vogel U, Hoffschulz H, Wandelt K. Surface and electrochemical characterization of electrodeposited PtRu alloys. Surf Sci 1995;335:361–71.

159. Markovic NM, Ross PN Jr. Surface science studies of model fuel cell electrocatalysts. Surf Sci Rep 2002;45:117–229.

160. Watanabe M, Zhu Y, Uchida H. Oxidation of CO on a Pt-Fe alloy electrode studied by surface enhanced infrared reflection-absorption spectroscopy. J Phys Chem B 2000;104:1762–8.

161. Miki A, Ye S, Osawa M. Surface-enhanced IR absorption on platinum nanoparticles: an application to real-time monitoring of electrocatalytic reactions. Chem Commun 2002;1500–1.

162. Futamata M, Luo L, Nishihara C. ATR–SEIR study of anions and water adsorbed on platinum electrode. Surf Sci 2005;590:196–211.

163. Chen YX, Miki A, Ye S, Sakai H, Osawa M. Formate, an active intermediate for direct oxidation of methanol on Pt electrode. J Am Chem Soc 2003;125:3680–1.

164. Friedrich KA, Geyzers KP, Dickson AJ, Stimming U. Fundamental aspects in electrocatalysis: from the reactivity of single-crystals to fuel cell electrocatalysts. J Electroanal Chem 2002;524–525:261–72.

165. Cramm S, Friedrich KA, Geyzers K-P, Stimming U, Vogel R. Surface structural and chemical characterization of Pt/Ru composite electrodes: a combined study by XPS, STM and IR spectroscopy. Fres J Anal Chem 1997;358:189–92.

166. Futamata M, Luo L. Adsorbed water and CO on Pt electrode modified with Ru. J Power Sources 2007;164:532–7.

167. García G, Silva-Chong JA, Guillén-Villafuerte O, Rodríguez JL, González ER, Pastor E. CO tolerant catalysts for PEM fuel cells: spectroelectrochemical studies. Catal Today 2006;116:415–21.

168. Vericat C, Wakisaka M, Haasch R, Bagus PS, Wieckowski A. Binding energy of ruthenium submonolayers deposited on a Pt(111) electrode. J Solid State Electrochem 2004;8:794–803.

169. Igarashi H, Fujino T, Zhu Y, Uchida H, Watanabe M. CO tolerance of Pt alloy electrocatalysts for polymer electrolyte fuel cells and the detoxification mechanism. Phys Chem Chem Phys 2001;3:306–14.

170. Tillmann S, Samjeské G, Friedrich KA, Baltruschat H. The adsorption of Sn on Pt(1 1 1) and its influence on CO adsorption as studied by XPS and FTIR. Electrochim Acta 2003;49:73–83.

171. Frances J, Scott E, Mukerjee S, Ramaker DE. CO coverage/oxidation correlated with PtRu electrocatalyst particle morphology in 0.3 M Methanol by in situ XAS. J Electrochem Soc 2007;154:A396–406.

172. Stamenković V, Arenz M, Blizanac BB, Mayrhofer KJJ, Ross PN, Marković NM. In situ CO oxidation on well characterized $Pt_3Sn(hkl)$ surfaces: A selective review. Surf Sci 2005;576:145–57.

173. Tong YY, Wieckowski A, Oldfield E. NMR of electrocatalysts. J Phys Chem B 2002;106:2434–46.

174. Babu PK, Oldfield E, Wieckowski A. Nanoparticle surfaces studied by electrochemical NMR. In: Modern aspects of electrochemistry, vol. 36. Vayenas C, Conway BE, White RE, editors. New York: Kluwer Academic/Plenum Publishers, 2003: 1–50.

175. Rudaz SL, Ansermet J-P, Wang P-K, Slichter CP. NMR study of chemosorption bond of carbon monoxide on platinum. Phys Rev Lett 1985;54:71.

176. Yahnke MS, Rush BM, Reimer JA, Cairns EJ. Quantitative solidstate NMR spectra of CO adsorbed from aqueous solution onto a commercial electrode. J Am Chem Soc 1996;118:12250–1.

177. Babu PK, Kim HS, Chung J-H, Oldfield E, Wieckowski A. Bonding and motional aspects of CO adsorbed on the surface of Pt nanoparticles decorated with Pd. J Phys Chem B 2004;108:20228–32.

178. Iwasita T, Hoster H, John-Anacker A, Lin WF, Vielstich W. Methanol oxidation on PtRu electrodes. Influence of surface structure and Pt-Ru atom distribution. Langmuir 2000;16:522–9.

179. Slichter CP. Principles of magnetic resonance. 3rd ed. Berlin: Springer-Verlag, 1992.

180. Davies JC, Hayden BE, Pegg DJ. The electrooxidation of carbon monoxide on ruthenium modified Pt(110). Electrochim Acta 1998;44:1181–90.

181. Blyholder G. Molecular orbital view of chemisorbed carbon monoxide. J Phys Chem 1964;68:2772–7.

182. Hammer B, Morikawa Y, Norskov JK. CO chemisorption at metal surfaces and overlayers. Phys Rev Lett 1996;76:2141–4.

183. Schlapka A, Lischka M, Gross A, Kasberger U, Jakob P. Surface strain versus substrate interaction in heteroepitaxial metal layers: Pt on Ru(0001). Phys Rev Lett 2003;91:016101.

184. Shubina TE, Koper MTM. Quantum-chemical calculations of CO and OH interacting with bimetallic surfaces. Electrochim Acta 2002;47:3621–36216.

185. Diemant T, Hager T, Hoster HE, Rauscher H, Behm RJ. Hydrogen adsorption and coadsorption with CO on well-defined bimetallic PtRu surfaces—a model study on the CO tolerance of bimetallic PtRu anode catalysts in low temperature polymer electrolyte fuel cells. Surf Sci 2003;541:137–46.

186. Leng YJ, Wang X, Hsing IM. Assessment of CO-tolerance for different Pt-alloy anode catalysts in a polymer electrolyte fuel cell using ac impedance spectroscopy. J Electroanal Chem 2002;528:145–52.

187. Wang X, Hsing IM, Leng Y-J, Yue PL. Model interpretation of electrochemical impedance spectroscopy and polarization behavior of H_2/CO mixture oxidation in polymer electrolyte fuel cells. Electrochim Acta 2001;46:4397–405.

188. Wang X, Hsing IM. Kinetics investigation of H_2/CO electro-oxidation on carbon supported Pt and its alloys using impedance based models. J Electroanal Chem 2003;556:117–26.

189. Koper MTM, Lukkien JJ. Modeling the butterfly: influence of lateral interactions and adsorption geometry on the voltammetry at (1 1 1) and (1 0 0) electrodes. Surf Sci 2002;498:105–15.

190. Ge Q, Desai S, Neurock M, Kourtakis K. CO adsorption on Pt-Ru surface alloys and on the surface of Pt-Ru bulk alloy. J Phys Chem B 2001;105:9533–6.

191. Liao M-S, Cabrera CR, Ishikawa Y. A theoretical study of CO adsorption on Pt, Ru and Pt–M (M=Ru, Sn, Ge) clusters. Surf Sci 2000;445:267–82.

192. Ishikawa Y, Cabrera CR, Liao M-S. Oxidation of methanol on platinum, ruthenium and mixed Pt–M metals (M=Ru, Sn): a theoretical study. Surf Sci 2000;463:66–80.

193. Igarashi H, Fujino T, Watanabe M. Hydrogen electro-oxidation on platinum catalysts in the presence of trace carbon monoxide. J Electroanal Chem 1995;391:119–23.

194. Markovic NM, Lucas CA, Grgur BN, Ross PN. Surface electrochemistry of CO and H_2/CO mixtures at Pt(100) interface: Electrode kinetics and interfacial structures. J Phys Chem B 1999;103:9616–23.

195. Jusys Z, Kaiser J, Behm RJ. Electrooxidation of CO and H_2/CO mixtures on a carbon-supported Pt catalyst—a kinetic and mechanistic study by differential electrochemical mass spectrometry. Phys Chem Chem Phys 2001;3:4650–60.

196. Gűlmen MA, Sűmer A, Aksoylu AE. Adsorption properties of CO on low-index Pt_3Sn surfaces. Surf Sci 2006;600:4909–21.

197. Napporn WT, Leger J-M, Lamy C. Electrocatalytic oxidation of carbon monoxide at lower potentials on platinum-based alloys incorporated in polyaniline. J Electroanal Chem 1996;408:141–7.

198. Ley KL, Liu R, Pu C, Fan Q, Leyarovska N, Segree C, et al. Methanol oxidation on single-phase Pt-Ru-Os ternary alloys. J Electrochem Soc 1997;144:1543–8.

199. Chen KY, Shen PK, Tseung ACC. Anodic oxidation of impure H_2 on Teflon-bonded Pt-Ru/WO_3/C electrodes. J Electrochem Soc 1995;142:L185–6.

200. Mukerjee S, Srinivasan S. Enhanced electrocatalysis of oxygen reduction on platinum alloys in proton exchange membrane fuel cells. J Electroanal Chem 1993;357:201–24.

201. Mukerjee S, Srinivasan S, Soriaga MP, McBreen J. Role of structural and electronic properties of Pt and Pt alloys on electrocatalysis of oxygen reduction. J Electrochem Soc 1995;142:1409–22.

202. Gasteiger HA, Markovic NM, Ross PN. Structural effects in electrocatalysis: electrooxidation of carbon monoxide on Pt_3Sn single-crystal alloy surfaces. Catal Lett 1996;36:1–8.

203. Stalnionis G, Tamasauskaite-Tamasiunaite L, Pautieniene A, Sudavicius VA, Jusys Z. Modification of a Pt surface by spontaneous Sn deposition for electrocatalytic applications. J Solid State Electrochem 2004;8:892.

204. Mukerjee S, Lee SJ, Ticianelli EA, McBreen J, Grgur BN, Markovic NM, et al. Investigation of enhanced CO tolerance in proton exchange membrane fuel cells by carbon supported PtMo alloy catalyst. Electrochem Solid State Lett 1999;2:12–5.

205. Crabb EM, Ravikumar MK. Synthesis and characterisation of carbon-supported PtGe electrocatalysts for CO oxidation. Electrochim Acta 2001;46:1033–41.

206. Aberdam D, Durand R, Faure R, Gloaguen F, Hazemann JL, Herrero E, et al. X-ray absorption near edge structure study of the electro-oxidation reaction of CO on $Pt_{50}Ru_{50}$ nanoparticles. J Electroanal Chem 1995;398:43–7.

207. Gasteiger HA, Markovic N, Ross PN, Cairns EJ. Methanol electrooxidation on well-characterized platinum-ruthenium bulk alloys. J Phys Chem 1993;97:12020–9.

208. Gasteiger HA, Markovic N, Ross PN, Cairns EJ. Electro-oxidation of small organic molecules on well-characterized Pt-Ru alloys. Electrochim Acta 1994;39:1825–32.

209. Watanabe M, Uchida M, Motoo S. Preparation of highly dispersed Pt + Ru alloy clusters and the activity for the electrooxidation of methanol. J Electroanal Chem 1987;229:395–406.

210. Papageorgopoulos DC, Keijzer M, de Bruijn FA. The inclusion of Mo, Nb and Ta in Pt and PtRu carbon supported electrocatalysts in the quest for improved CO tolerant PEMFC anodes. Electrochim Acta 2002;48:197–204.

211. Gasteiger HA, Kocha SS, Sompalli B, Wagner FT. Activity benchmarks and requirements for Pt, Pt-alloy, and non-Pt oxygen reduction catalysts for PEMFCs. Appl Catal B Environ 2005;56:9–35.

212. Wiese W, Emonts B, Peters R. Methanol steam reforming in a fuel cell drive system. J Power Sources 1999;84:187–93.

213. Vielstich W, Lamm A, Gasteiger H, editors. Handbook of fuel cells, vol. 3, part 3. West Sussex, UK: Wiley, 2003: 349–464.

214. Tremiliosi G, Kim H, Chrzanowski W, Wieckowski A, Grzybowska B, Kulesza P. Reactivity and activation parameters in methanol oxidation on platinum single crystal electrodes 'decorated' by ruthenium adlayers. J Electroanal Chem 1999;467:143–56.

215. Chrzanowski W, Wieckowski A. Ultrathin films of ruthenium on low index platinum single crystal surfaces: an electrochemical study. Langmuir 1997;13:5974–59716.

216. Chrzanowski W, Wieckowski A. Surface structure effects in platinum/ruthenium methanol oxidation electrocatalysis. Langmuir 1998;14:1967–70.

217. Waszczuk P, Solla-Gullon J, Kim HS, Tong YY, Montiel V, Aldaz A, et al. Methanol electrooxidation on platinum/ruthenium nanoparticle catalysts. J Catal 2001;203:1–6.

218. Maillard F, Lu G-Q, Wieckowski A, Stimming U. Ru-decorated Pt surfaces as model fuel cell electrocatalysts for CO electrooxidation. J Phys Chem B 2005;109:16230–43.

219. Maillard F, Gloaguen F, Hahn F, Léger J-M. Electrooxidation of carbon monoxide at ruthenium-modified platinum nano-particles: evidence for CO surface mobility. Fuel Cells 2002;2:143–52.

220. Maillard F, Gloaguen F, Léger JM. Preparation of methanol oxidation electrocatalysts: ruthenium deposition on carbon-supported platinum nanoparticles. J Appl Electrochem 2003;33:1–8.

221. Dubau L, Hahn F, Coutanceau C, Léger JM, Lamy C. On the structure effects of bimetallic PtRu electrocatalysts towards methanol oxidation. J Electroanal Chem 2003;554:407–15.

222. Dubau L, Coutanceau C, Garnier E, Léger JM, Lamy C. Electrooxidation of methanol at platinum–ruthenium catalysts prepared from colloidal precursors: atomic composition and temperature effects. J Appl Electrochem 2003;33:419–29.

223. Holleck GL, Pasquariello DM, Clauson SL. Carbon monoxide tolerant anodes for proton exchange membrane (PEM) fuel cells. II. Alloy catalyst development In: proceedings of the 2nd international symposium on proton conducting membrane fuel cells 1998;2:150.

224. Lima A, Coutanceau C, Léger JM, Lamy C. Investigation of ternary catalysts for methanol electrooxidation. J Appl Electrochem 2001;31:379–86.

225. Götz M, Wendt H. Binary and ternary anode catalyst formulations including the elements W, Sn and Mo for PEMFCs operated on methanol or reformate gas. Electrochim Acta 1998;43:3637–44.

226. Aricò AS, Cretì P, Giordano N, Antonucci V. Chemical and morphological characterization of a direct methanol fuel cell based on a quaternary Pt-Ru-Sn-W/C anode. J Appl Electrochem 1996;26:959–67.

227. Liu R, Iddir H, Fan Q, Hou G, Bo A, Ley KL, et al. Potential-dependent infrared absorption spectroscopy of adsorbed CO and X-ray photoelectron spectroscopy of arc-melted single-phase Pt, PtRu, PtOs, PtRuOs, and Ru electrodes. J Phys Chem B 2000;104:3518–31.

228. Watanabe M, Igarashi H, Fujino T. Design of CO tolerant anode catalysts for polymer electrolyte fuel cell. Electrochemistry 1999;67:1194–6.

229. Uribe FA, Valerio JA, Garzon FH, Zawodzinski TA. PEMFC reconfigured anodes for enhancing CO tolerance with air bleed. Electrochem Solid-State Lett 2004;-7:A376–9.

230. Ishikawa Y, Liao MS, Cabrera CR. Energetics of H_2O dissociation and $CO_{ads}+OH_{ads}$ reaction on a series of Pt–M mixed metal clusters: a relativistic density-functional study. Surf Sci 2002;513:98–110.

231. Dinh HN, Ren X, Garzon FH, Zelenay P, Gottesfeld S. Electrocatalysis in direct methanol fuel cells: in-situ probing of PtRu anode catalyst surfaces. J Electroanal Chem 2000;491:222–33.

232. Janssen MMP, Moolhuysen J. Binary systems of platinum and a second metal as oxidation catalysts for methanol fuel cells. Electrochim Acta 1976;21:869–716.

233. Liu R, Ley KL, Pu C, Fan Q, Leyarovska N, Segre C, et al. In: Electrode processes, VI. Wieckowski A, Itaya K, editors. Electrochemical Society Proceedings Series 1996;96–8:341–55.

234. Gottesfeld S, Zawodzinski TA. Polymer electrolyte fuel cells. In: Advances in electrochemical science and engineering. Alkire RC, Gerischer H, Kolb DM, Tobias CW, editors. New York: Wiley-VCH, 1997: vol 5, ch 4, 195–301.

235. Stevens DA, Rouleau JM, Mar RE, Bonakdarpour A, Atanasoski RT, Schmoeckel AK, et al. Characterization and PEMFC testing of $Pt_{1-x}M_x$ (M = Ru,Mo,Co,Ta,Au,Sn) anode electrocatalyst composition spreads. J Electrochem Soc 2007;154:B566–76.

236. Attwood PA, McNicol BD, Short RT. The electrocatalytic oxidation of methanol in acid electrolyte: preparation and characterization of noble metal electrocatalysts supported on pre-treated carbon-fibre papers. J Appl Electrochem 1980;10:213–22.

237. Frelink T, Visscher W, van Veen JAR. Particle size effect of carbon-supported platinum catalysts for the electrooxidation of methanol. J Electroanal Chem 1995;382:65–72.

238. Kabbabi A, Gloagen F, Andolfatto F, Durand R. Particle size effect for oxygen reduction and methanol oxidation on Pt/C inside a proton exchange membrane. J Electroanal Chem 1994;373:251–4.

239. Mukerjee S, McBreen J. Effect of particle size on the electrocatalysis by carbon-supported Pt electrocatalysts: an in situ XAS investigation. J Electroanal Chem 1998;448:163–71.

240. Knights SD, Colbow KM, St-Pierre J, Wilkinson DP. Aging mechanisms and lifetime of PEFC and DMFC. J Power Sources 2002;127:127–34.

241. Pozio A, Silva RF, De Francesco M, Cardellini F, Giorgi L. Erratum to "A novel route to prepare stable Pt–Ru/C electrocatalysts for polymer electrolyte fuel cell": [Electrochim Acta 48 (3): 255–262]. Electrochim Acta 2003;48:1625.

242. Chen W, Sun G, Liang Z, Mao Q, Li H, Wang G, et al. The stability of a PtRu/C electrocatalyst at anode potentials in a direct methanol fuel cell. J Power Sources 2006;160:933–9.

243. Gancs L, Hakim N, Hult B, Mukerjee S. Dissolution of Ru from PtRu electrocatalysts and its consequences in DMFCs. ECS Trans 2006;3(1):607–18.

244. Gancs L, Hult BN, Hakim N, Mukerjee S. The impact of Ru contamination of a Pt/C electrocatalyst on its oxygen-reducing activity. Electrochem Solid-State Lett 2007;10:B150–4.

245. Piela P, Eickes C, Brosha E, Garzon F, Zelenay P. Ruthenium crossover in direct methanol fuel cell with Pt-Ru black anode. J Electrochem Soc 2004;151:A2053–9.

246. Shi M, Anson FC. Mobilities and concentration profiles of counterion catalysts incorporated in Nafion coatings on electrodes. Electrochim Acta 1998;44:1301–5.

247. Okada T. Effect of ionic contaminants. In: Handbook of fuel cells: fundamentals, technology, applications. Vol 3. Vielstich W, Gasteiger HA, Lamm A, editors. New York: John Wiley & Sons, 2003: 627.

248. LaConti AB, Hamdan M, McDonald RC. Mechanism of membrane degradation. In: Handbook of fuel cells: fundamentals, technology, applications. Vol 3. Vielstich W, Gasteiger HA, Lamm A, editors. New York: John Wiley & Sons, 2003: 647.

249. Zelenay P. In: Fuel cells durability: stationary, automotive, portable. 1st ed. Brookline, MA: Knowledge Press, 2006: 61.

250. Stamenkovic V, Grgur BN, Ross PN, Markovic NM. Oxygen reduction reaction on Pt and Pt-bimetallic electrodes covered by CO. J Electrochem Soc 2005;152:A277–82.

251. Cao D, Wieckowski A, Inukai J, Alonso-Vante N. Oxygen reduction reaction on ruthenium and rhodium nanoparticles modified with selenium and sulfur. J Electrochem Soc 2006;153:A869–74.

252. Choban ER, Spendelow JS, Gancs L, Wieckowski A, Kenis PJA. Membraneless laminar flow-based micro fuel cells operating in alkaline, acidic, and acidic/alkaline media. Electrochim Acta 2005;50:5390–8.

253. Ranga JS, Gancs L, Choban ER, Primak A, Natarajan D, Markoski LJ, et al. Air-breathing laminar flow-based microfluidic fuel cell. J Am Chem Soc 2005;127:16758–9.

254. Ghenciu AF. Review of fuel processing catalysts for hydrogen production in PEM fuel cell systems. Curr Opin Solid State Mater Sci 2002;6:389–99.

255. Mehta V, Cooper JS. Review and analysis of PEM fuel cell design and manufacturing. J Power Sources 2003;114:32–53.

256. Costamagna P, Srinivasan S. Quantum jumps in the PEMFC science and technology from the 1960s to the year 2000; Part II. Engineering, technology development and application aspects. J Power Sources 2001;102:253–69.

257. Schaller KV, Gruber C. Fuel cell drive and high dynamic energy storage systems–opportunities for the future city bus. Fuel Cells Bull 2000;3:9–13.

258. Grgur BN, Markovic NM, Ross PN. Electrochemical oxidation of carbon monoxide: from platinum single crystals to low temperature fuel cells catalysts. Part II. Electrooxidation of H_2, CO and H_2/CO mixtures on well characterized PtMo alloy. J Serb Chem Soc 2003;68:191–206.

259. Gouérec P, Denis MC, Guay D, Dodelet JP, Schulz R. High energy ballmilled Pt-Mo catalysts for polymer electrolyte fuel cells and their tolerance to CO. J Electrochem Soc 2000;147:3989–96.

260. Ball S, Hodgkinson A, Hoogers G, Maniguet S, Thompsett D, Wong B. The proton exchange membrane fuel cell performance of a carbon supported PtMo catalyst operating on reformate. Electrochem Solid-State Lett 2002;-5:A31–4.

261. Crabb EM, Ravikumar MK, Qian Y, Russell AE, Maniguet S, Yao J, et al. Controlled modification of carbon supported platinum electrocatalysts by Mo. Electrochem Solid-State Lett 2002;-5:A5–9.

262. Santiago EI, Giuseppe GA, Camara A, Ticianelli EA. CO tolerance on PtMo/C electrocatalysts prepared by the formic acid method. Electrochim Acta 2003;48:3527–34.

263. Santiago EI, Batista MS, Assaf EM, Ticianelli EA. Mechanism of CO tolerance on molybdenum-based electrocatalysts for PEMFC. J Electrochem Soc 2004;151:A944–9.

264. Grgur BN, Markovic NM, Ross PN. In: Second international symposium on proton conducting membrane fuel cells II. Gottesfeld S, Fuller TF, Halpert G, editors. Pennington, NJ: The Electrochemical Society, 1998: PV 98–27, p. 176.

265. Janssen GJM. Modelling study of CO_2 poisoning on PEMFC anodes. J Power Sources 2004;136:45–54.

266. Moss TS, Peachey NM, Snow RC, Dye RC. Multilayer metal membranes for hydrogen separation. Int J Hydrogen Energy 1998;23:99–106.

267. Crabb EM, Marshall R, Thompsett D. Carbon monoxide electr-oxidation properties of carbon-supported PtSn catalysts prepared using surface organometallic chemistry. J Electrochem Soc 2000;147:4440–7.

268. Honma I, Toda T. Temperature dependance of kinetics of methanol electro-oxidation on PtSn alloys. J Electrochem Soc 2003;150:A1689–92.

269. Zhou WJ, Zhou B, Li WZ, Zhou ZH, Song SQ, Sun GQ, et al. Performance comparison of low-temperature direct alcohol fuel cells with different anode catalysts. J Power Sources 2004;126:16–22.

270. Lamy C, Rousseau S, Belgasir EM, Coutanceau C, Leger J-M. Recent progress in the direct ethanol fuel cell: development of new platinum–tin electrocatalysts. Electrochim Acta 2004;49:3901–8.

271. Arenz M, Stamenkovic V, Blizanac BB, Mayrhofer KJ, Markkovic NM, Ross PN. Carbon-supported Pt–Sn electrocatalysts for the anodic oxidation of H_2, CO, and H_2/CO mixtures.: Part II: the structure–activity relationship. J Catal 2005;232:402–10.

272. Colmati F, Antolini E, Gonzalez ER. Pt–Sn/C electrocatalysts for methanol oxidation synthesized by reduction with formic acid. Electrochim Acta 2005;50:5496–503.

273. Lee D-Y, Hwang S-W, Lee I-S. A study on composite PtRu(1:1)-PtSn(3:1) anode catalyst for PEMFC. J Power Sources 2005;145:147–53.

274. Jiang L, Sun G, Sun S, Liu J, Tang S, Li H, et al. Structure and chemical composition of supported Pt–Sn electrocatalysts for ethanol oxidation. Electrochim Acta 2005;50:5384–9.

275. Srinivasan R, De Angeles RJ, Davis BH. Alloy formation in Pt-Sn-alumina catalysts: In situ X-ray diffraction study. J Catal 1987;106:449–57.

276. Srinivasan R, De Angeles RJ, Davis BH. Structural studies of Pt-Sn catalysts on high and low surface area alumina supports. Catal Lett 1990;4:303–8.

277. Srinivasan R, Rice LA, Davis BH. Electron microdiffraction study of Pt-Sn-alumina reforming catalysts. J Catal 1991;129:257–68.

278. Srinivasan R, Davis BH. X-ray diffraction and electron microscopy studies of platinum-tin-silica catalysts. Appl Catal A Gen 1992;87:45–67.

279. Liu ZL, Lin XH, Lee JY, Zhang W, Han M, Gan LM. Preparation and characterization of platinum-based electrocatalsyts on multiwalled carbon nanotubes for proton exchange membrane fuel cells. Langmuir 2002;18(10):4054–60.

280. Yu RQ, Chen LW, Liu QP, Lin JY, Tan KL, Ng SC, et al. Platinum deposition on carbon nanotubes via chemical modification. Chem Mater 1998;10(3):718–22.

281. Lim D-H, Choi D-H, Lee W-D, Park D-R, Lee H-I. The effect of Sn addition on a Pt/C electrocatalyst synthesized by borohydrode reduction and hydrothermal treatment for a low-temperature fuel cell. Electrochem Solid-State Lett 2007;10:B87–90.

282. Neto AO, Vasconcelos TRR, Da Silva RWRV, Linardi M, Spinace EV. Electro-oxidation of ethylene glycol on PtRu/C and PtSn/C electrocatalysts prepared by alcohol-reduction process. J Appl Electrochem 2005;35:193–8.

283. Zhu Y, Uchida H, Watanabe M. Oxidation of carbon monoxide at a platinum film electrode studied by Fourier transform infrared spectroscopy with attenuated total reflection technique. Langmuir 1999;15:8757–64.

284. Kwak C, Park TJ, Suh DJ. Preferential oxidation of carbon monoxide in hydrogen-rich gas over platinum–cobalt–alumina aerogel catalysts. Chem Eng Sci 2005;60:1211–7.

285. Yan J, Ma JX, Cao P, Li P. Preferential oxidation of CO in H_2-rich gases over Co-promoted Pt-γ-Al_2O_3 catalyst. Catal Lett 2004;93:55–60.

286. Page T, Johnson R, Hormes J, Noding S, Rambabu B. A study of methanol electro-oxidation reactions in carbon membrane electrodes and structural properties of Pt alloy electro-catalysts by EXAFS. J Electroanal Chem 2000;485:34–41.

287. Mukerjee S, Srinivasan S. Enhanced electrocatalysis of oxygen reduction on platinum alloys in proton exchange membrane fuel cells. J Electroanal Chem 1993;357:201–24.

288. Antolini E, Salgado JRC, Giz MJ, Gonzalez ER. Effects of geometric and electronic factors on ORR activity of carbon supported Pt–Co electrocatalysts in PEM fuel cells. Int J Hydrogen Energy 2005;30:1213–20.

289. Antolini E, Salgado JRC, Gonzalez ER. The methanol oxidation reaction on platinum alloys with the first row transition metals: The case of Pt–Co and –Ni alloy electrocatalysts for DMFCs: A short review. Appl Catal B 2006;63:137–49.

290. Bonakdarpour A, Lobel R, Sheng S, Monchesky TL, Dahn JR. Acid stability and oxygen reduction activity of magnetron-sputtered $Pt_{1-x}Ta_x$ ($0 \leq x \leq 1$) films. J Electrochem Soc 2006;153:A2304–13.

291. Gómez R, Gutiérrez de Dios FJ, Feliu JM. Carbon monoxide oxidation and nitrous oxide reduction on Rh/Pt(1 1 1) electrodes. Electrochim Acta 2004;49:1195–1208.

292. Llorca MJ, Feliu JM, Aldaz A, Chavilier J. Formic acid oxidation on Pd_{ad} + Pt(100) and Pd_{ad} + Pt(111) electrodes. J Electroanal Chem 1994;376:151–60.

293. Baldauf M, Kolb DM. Formic acid oxidation on ultrathin Pd films on Au(hkl) and Pt(hkl) electrodes. J Phys Chem 1996;100:11375–81.

294. Lu GQ, Crown A, Wieckowski A. Formic acid decomposition on polycrystalline platinum and palladized platinum electrodes. J Phys Chem B 1999;103:9700–11.

295. Stonehart P. Fuel cell with Pt/Pd electrocatalyst electrode. United States Patent US4407906. 1983 Oct 4.

296. Stonehart P. Electrocatalyst advances for hydrogen oxidation in phosphoric acid fuel cells. J Hydrogen Energy 1984;9:921–8.

297. Papageorgopoulos DC, Keijzer M, Veldhuis JBJ, de Bruijn FA. CO tolerance of Pd-rich platinum palladium carbon-supported electrocatalysts. J Electrochem Soc 2002;149:A1400–4.

298. He C, Kunz HR, Fenton JM. Evaluation of platinum-based catalysts for methanol electro-oxidation in phosphoric acid electrolyte. J Electrochem Soc 1997;144:970–9.

299. Stonehart P, Watanabe M, Yamamoto N, Nakamura T, Hara N, Tsurumi K, inventors. Tanaka, Precious Metal Ind., Stonehart Ass. Inc., assignees. Electrocatalyst. United States Patent US5208207. 1993 May 4.

300. Zhang H, Wang Y, Fachini ER, Cabrera CR. Electrochemically codeposited platinum/molybdenum oxide electrode for catalytic oxidation of methanol in acid solution. Electrochem Solid State 1999;2:437–9.

301. Pinheiro ALN, Oliveira-Neto A, de Souza EC, Perez J, Paganin VA, Ticianelli E, et al. Electrocatalysis on noble metal and noble metal alloys dispersed on high surface area carbon. J New Mater Electrochem Syst 2003;6(1):1–16.

302. Stevens DA, Rouleau JM, Mar RE, Atanasoski RT, Schmoeckel AK, Debe MK, et al. Enhanced CO-tolerance of Pt–Ru–Mo hydrogen oxidation catalysts. J Electrochem Soc 2007;154:B1211–9.

303. Wu G, Swaidan R, Cui G. Electrooxidations of ethanol, acetaldehyde and acetic acid using PtRuSn/C catalysts prepared by modified alcohol-reduction process. J Power Sources 2007;172:180–8.

304. Venkataraman R, Kun HR, Fenton JM. Development of new CO tolerant ternary anode catalysts for proton exchange membrane fuel cells. J Electrochem Soc 2003;150:A278–84.

305. Verbeek H, Sachtler WHM. The study of the alloys of platinum and tin by chemisorption. J Catal 1976;42:257–67.

306. Wise H. Role of surface composition in co adsorption on Pd-Ag catalysts. J Catal 1976;43:373–5.

307. Fleischmann R, Boehm H. Dechema Monographs 1982;92:309.

308. Ioroi T, Fujiwara N, Siroma Z, Yasuda K, Miyazaki Y. Platinum and molybdenum oxide deposited carbon electrocatalyst for oxidation of hydrogen containing carbon monoxide. Electrochem Commun 2002;4:442–6.

309. Ioroi T, Yasuda K, Siroma Z, Fujiwara N, Miyazaki Y. Enhanced CO-tolerance of carbon-supported platinum and molybdenum oxide anode catalyst. J Electrochem Soc 2003;150:A1225–30.

310. Matsui T, Fujiwara K, Okanishi T, Kikuchi R, Takeguchi T, Eguchi K. Electrochemical oxidation of CO over tin oxide supported platinum catalysts. J Power Sources 2006;155:152–6.

311. Ioroi T, Akita T, Yamazaki S, Siroma Z, Fujiwara N, Yasuda K. Comparative study of carbon-supported Pt/Mo-oxide and PtRu for use as CO-tolerant anode catalysts. Electrochim Acta 2006;52:491–8.

312. Machida K, Enyo M, Adachi G, Shiokawa J. Methanol oxidation characteristics of rare earth tungsten bronze electrodes doped with platinum. J Electrochem Soc 1988;135:1955–61.

313. Shen PK, Tseung ACC. Anodic oxidation of methanol on Pt/WO_3 in acidic media. J Electrochem Soc 1994;141:3082–90.

314. Shukla AK, Ravikumar MK, Aricò AS, Candiano G, Antonucci V, Giordano N, et al . Methanol electrooxidation on carbon-supported $Pt-WO_{3-x}$ electrodes in sulphuric acid electrolyte. J Appl Electrochem 1995;25:528–32.

315. Tseung ACC, Chen KY. Hydrogen spill-over effect on Pt/WO_3 anode catalysts. Catal Today 1997;38:439–43.

316. Shen PK, Chen KY, Tseung ACC. CO oxidation on $Pt-Ru/WO_3$ electrodes. J Electrochem Soc 1995;142:L85–6.

317. Chen KY, Sun Z, Tseung ACC. Preparation and characterization of high-performance $Pt-Ru/WO_3$-C anode catalysts for the oxidation of impure hydrogen. Electrochem Solid State Lett 2000;3:10–2.

318. Roth C, Goetz M, Fuess H. Synthesis and characterization of carbon-supported Pt–Ru–WO_x catalysts by spectroscopic and diffraction methods. J Appl Electrochem 2001;31:793–8.

319. Hou Z, Yi B, Yu H, Lin Z, Zhang H. CO tolerance electrocatalyst of PtRu-H_xMeO_3/C (Me = W, Mo) made by composite support method. J Power Sources 2003;123:116–25.

320. Maillard F, Peyrelade E, Soldo-Olivier Y, Chatenet M, Chaînet E, Faure R. Is carbon-supported $Pt-WO_x$ composite a CO-tolerant material? Electrochim Acta 2007;52:1958–67.

321. Gustavo L, Pereira S, dos Santos FR, Pereira ME, Paganin VA, Ticianelli EA. CO tolerance effects of tungsten-based PEMFC anodes. Electrochim Acta 2006;4061–6.

322. Giordano N, Aricò AS, Hocevar S, Staiti P, Antonucci PL, Antonucci V. Oxygen reduction kinetics in phosphotungstic acid at low temperature. Electrochim Acta 1993;38:1733–41.

323. Giordano N, Staiti P, Aricò AS, Passalacqua E, Abate L, Hocevar S. Analysis of the chemical cross-over in a phosphotungstic acid electrolyte based fuel cell. Electrochim Acta 1997;42:1645–52.

324. Aricò AS, Modeca E, Ferrara I, Antonucci V. CO and CO/H_2 electrooxidation on carbon supported Pt–Ru catalyst in phosphotungstic acid ($H_3PW_{12}O_{40}$) electrolyte. J Appl Electrochem 1998;28:881–7.

325. Gatto I, Saccà A, Carbone A, Pedicini R, Urbani F, Passalacqua E. CO-tolerant electrodes developed with phosphomolybdic acid for polymer electrolyte fuel cell (PEFCs) application. J Power Sources 2007;171:540–5.

326. Herrero E, Franaszczuk K, Wieckowski A. A voltammetric identification of the surface redox couple effective in methanol oxidation on a ruthenium-covered platinum (110) electrode. J Electroanal Chem 1993;361:269–73.

327. Franszczuk K, Sobkowski J. The influence of ruthenium adatoms on the oxidation of chemisorbed species of methanol on a platinum electrode by a radiochemical method. J Electroanal Chem 1992;327:235–45.

328. Fachini ER, Diaz-Ayala R, Casado-Rivera E, File S, Cabrera CR. Surface coordination of ruthenium clusters on platinum nanoparticles for methanol oxidation catalysts. Langmuir 2003;19:8986–93.

329. Crabb EM, Ravikumar MK, Thompsett D, Hurford M, Rose A, Russell AE. Effect of Ru surface composition on the CO tolerance of Ru modified carbon supported Pt catalysts. Phys Chem Chem Phys 2004;6:1792–8.

330. Crown A, Moraes IR, Wieckowski A. Examination of Pt(111)/Ru and Pt(111)/Os surfaces: STM imaging and methanol oxidation activity. J Electroanal Chem 2001;500:333–43.

331. Szabo S, Bakos I. Investigation of ruthenium deposition onto a platinized platinum-electrode in sulfuric-acid media. J Electroanal Chem 1987;230:233–40.

332. Friedrich KA, Geyzers KP, Marmann A, Stimming U, Vogel R. Bulk metal electrodeposition in the sub-monolayer regime: Ru on Pt(111). Z Phys Chem 1999;208:137–50.

333. Morimoto Y, Yeager EB. CO oxidation on smooth and high area Pt, Pt-Ru and Pt-Sn electrodes. J Electroanal Chem 1998;441:77–81.

334. Jarvi TD, Madden TH, Stuve EM. Vacuum and electrochemical behavior of vapor deposited ruthenium on platinum (111). Electrochem Solid-State Lett 1999;2:224–7.

335. Davies JC, Hayden BE, Pegg DJ, Rendall ME. The electrooxidation of carbon monoxide on ruthenium modified Pt(111). Surf Sci 2002;496:110–20.

336. Cao DX, Bergens SH. An organometallic deposition of ruthenium adatoms on platinum that self poisons at a specific surface composition. A direct methanol fuel cell using a platinum–ruthenium adatom anode catalyst. J Electroanal Chem 2002;533:91–100.

337. Crown A, Johnston C, Wieckowski A. Growth of ruthenium islands on Pt(hkl) electrodes obtained via repetitive spontaneous deposition. Surf Sci 2002;506:L268–74.

338. Jiang Q, Lu HM, Zhao M. Modelling of surface energies of elemental crystals. J Phys Condens Matter 2004;16:521–30.

339. Ianniello R, Schmidt VM, Stimming U, Stumper J, Wallau A. Co adsorption and oxidation on Pt and Pt-Ru alloys – dependence on substrate composition. Electrochim Acta 1994;39:1863–9.

340. Brankovic SR, McBreen J, Adzic RR. Spontaneous deposition of Pt on the Ru(0001) surface. J Electroanal Chem 2001;503:99–104.

341. Brankovic SR, McBreen J, Adzic RR. Spontaneous deposition of Pd on a Ru(0 0 0 1) surface. Surf Sci 2001;479:L363–8.

342. Adzic RR, Brankovic SR, Wang JX. Carbon monoxide tolerant electrocatalyst with low platinum loading and a proces for its preparation United State patent pending, 2001.

343. Sasaki K, Wang JX, Balasubramanian M, McBreen J, Uribe F, Adzic RR. Ultra-low platinum content fuel cell anode electrocatalyst with a long-term performance stability. Electrochim Acta 2004;49:3873–7.

344. Campbell CT. Bimetallic surface chemistry. Annu Rev Phys Chem 1990;41:775–837.

345. Rubin AV, Skriver HL, Nørskov JK. Surface segregation energies in transition-metal alloys. Phys Rev B 1999;59:15990–6000.

346. Lasch K, Hayn G, Jörissen L, Garche J, Besenhardt O. Mixed conducting catalyst support materials for the direct methanol fuel cell. J Power Sources 2002;105(2):305–10.

347. Somorjai G. Introduction to surface chemistry and catalysis. New York: Wiley, 1994: 442–595.

348. Nakamura T, Yamada M, Yamaguchi T. Catalytic properties of $Mo(CO)_6$ supported on activated carbon for ethene homologation. Appl Catal A Gen 1992;87(1):69–79.

349. de la Fuente JLG, Martinez-Huerta MV, Rojas S, Peňa MA, Terreros P, Fierro JLG. Enhanced methanol electrooxidation activity of PtRu nanoparticles supported on H_2O_2-functionalized carbon black. Carbon 2005;43(14):3002–5.

350. de la Fuente JLG, Rojas S, Martínez-Huerta MV, Terreros P, Peňa MA, Fierro JLG. Functionalization of carbon support and its influence on the electrocatalytic behaviour of Pt/C in H_2 and CO electrooxidation. Carbon 2006;44:1919–29.

351. Iijima S. Helical microtubules of graphitic carbon. Nature 1991;354(6348):56–7.

352. Ebbesen TW, Ajayan PM. Large-scale synthesis of carbon nanotubes. Nature 1992;358(6383):220–2.

353. Li WZ, Xie SS, Qian LX, Chang BH, Zou BS, Zhou WY, et al. Large-scale synthesis of aligned carbon nanotubes. Science 1996;274(5293):1701–3.

354. Ebbesen TW, Lezec HJ, Hiura H, Bennett JW, Ghaemi HF, Thio T. Electrical conductivity of individual carbon nanotubes. Nature 1996;382(6586):54–6.

355. Che GL, Lakshmi BB, Martin CR, Fisher ER. Metal-nanocluster filled carbon nanotubes: catalytic properties and possible applications in electrochemical energy storage and production. Langmuir 1999;15(3):750–16.

356. Joo SH, Choi SJ, Oh I, Kwak J, Liu Z, Terasaki O, et al. Ordered nanoporous arrays of carbon supporting high dispersions of platinum nanoparticles. Nature 2001;412(6848):169–72.

357. Sun X, Li R, Villers D, Dodelet JP, Desilets S. Composite electrodes made of Pt nanoparticles deposited on carbon nanotubes grown on fuel cell backings. Chem Phys Lett 2003;379(1–2):99–104.

358. Pyun SI, Rhee CK. An investigation of fractal characteristics of mesoporous carbon electrodes with various pore structures. Electrochim Acta 2004;49(24):4171–80.

359. He ZB, Chen JH, Liu DY, Zhou HH, Kuang YF. Electrodeposition of PtRu nanoparticles on carbon nanotubes and their electrocatalystic properties for methanol electrooxidation. Diam Relat Mater 2004;13:1764–79.

360. Liu ZL, Lee JY, Chen WX, Han M, Gan LM. Physical and electrochemical characterizations of microwave-assisted polyol preparation of carbon-supported PtRu nanoparticles. Langmuir 2004;20(1):181–7.

361. Yu JS, Kang S, Yoon SB, Chai G. Fabrication of ordered uniform porous carbon networks and their application to a catalyst supporter. J Am Chem Soc 2002;124(32):9382–3.

362. Li WZ, Liang CH, Qiu JS, Xin Q. Carbon nanotubes as support for cathode catalyst of a direct methanol fuel. Carbon 2002;40(5):791–4.

363. Li WZ, Liang CH, Zhou WJ, Xin Q. Preparation and characterization of multiwalled carbon nanotube-supported platinum for cathode catalysts of direct methanol fuel cells. J Phys Chem B 2003;107(26):6292–9.

364. Li L, Wu G, Xu B-Q. Electro-catalytic oxidation of CO on Pt catalyst supported on carbon nanotubes pretreated with oxidative acids. Carbon 2006;44:2973–2983.

365. Carmo M, Paganin VA, Rosolenand JM, Gonzalez ER. Alternative supports for the preparation of catalysts for low-temperature fuel cells: the use of carbon nanotubes. J Power Sources 2005;142:169–76.

366. Rodrigues NM, Chambers A, Baker RTK. Catalytic engineering of carbon nanostructures. Langmuir 1995;11:3862–6.

367. Gadd GE, Blackford M, Moricca S, Weebb N, Evans PJ, Smith AM, et al. The world's smallest gas cylinders. Science 1997;277:933–6.

368. Luo J, Maye MM, Kariuki NN, Wang LY, Njoki P, Lin Y, et al. Electrocatalytic oxidation of methanol: carbon-supported gold–platinum nanoparticle catalysts prepared by two-phase protocol. Catal Today 2005;99:291–7.

369. Cameron D, Holliday R, Thompson D. Gold's future role in fuel cell systems. J Power Sources 2003;118:298–303.

370. Ullmann's encyclopedia of industrial chemistry, Vol. A21. Gerhartz W, Elvers B, editors, Weinheim, Germany: VCH, 1992: 113.

371. Machida K, Enyo M. In situ X-ray diffraction study of hydrogen entry into Pd and Pd-Au alloy electrodes during anodic HCHO oxidation. J Electrochem Soc 1987;134:1472–4.

372. Lewis FA. The palladium hydrogen system. London: Academic Press, 1967.

373. Thompsett D, Cooper SJ, Hards GA. Report ETSU F/02/00014/REP/1, 1998.

374. Yepez O, Scharifker BR. Oxidation of CO on hydrogen-loaded palladium. J Appl Electrochem 1999;29:1185–90.

375. Fishman JH, inventor; Leesona Corp., assignee. Method of generating electricity comprising contacting a Pd/Au alloy black anode with a fuel containing carbon monoxide. United State Patente US3510355. 1970 May 5.

376. Eley DD, Moore PB. The adsorption and reaction of CO and O_2 on Pd---Au alloy wires. Surf Sci 1981;111:325–43.

377. Okanishi T, Matsui T, Takeguchi T, Kikuchi R, Eguchi K. Chemical interaction between Pt and SnO_2 and influence on adsorptive properties of carbon monoxide. Appl Catal A 2006;298:181–7.

378. Takeguchi T, Anzai Y, Kikuchi R, Eguchi K, Ueda W. Preparation and characterization of CO-tolerant Pt and Pd anodes modified with SnO_2 nanoparticles for PEFC. J Electrochem Soc 2007;154:B1132–7.

379. Okumura M, Masuyama N, Konishi E, Ichikawa S, Akita T. CO oxidation below room temperature over Ir/TiO_2 catalyst prepared by deposition precipitation method. J Catal 2002;208:485–9.

380. Wasmus S, Küver A. Methanol oxidation and direct methanol fuel cells: a selective review. J Electroanal Chem 1999;461:14–31.

381. Bonnemann H, Brinkmann R, Britz P, Endruschat U, Mortel R, Feldmeyer G, et al. J New Mater Electrochem Syst 2000;3:199.

382. Paulus U, Endruschat U, Feldmeyer G, Schmidt T, Behm R. New PtRu alloy colloids as precursors for fuel cell catalysts. J Catal 2000;195:383–93.

383. Luna A, Camara G, Paganin V, Ticianelli E, Gonzalez E. Effect of thermal treatment on the performance of CO-tolerant anodes for polymer electrolyte fuel cells. Electrochem Commun 2000;2:222–5.

384. Antolini E, Giorgi L, Cardellini F, Passalacqua E. Physical and morphological characteristics and electrochemical behaviour in PEM fuel cells of PtRu/C catalysts. J Solid State Electrochem 2001;5:131–40.
385. Pozio A, Silva R, De Francesco M, Cardellini F, Giorgi L. A novel route to prepare stable Pt–Ru/C electrocatalysts for polymer electrolyte fuel cell. Electrochim Acta 2002;48:255–62.
386. Che G, Lakeshmi B, Fisher E, Martin C. Carbon nanotubule membranes for electrochemical energy storage and production. Nature 1998;393:346–9.
387. Antolini E, Cardellini F. Formation of carbon supported PtRu alloys: an XRD analysis. J Alloys Compd 2001;315:118–22.
388. Steigerwalt E, Deluga G, Cliffel D, Lukehart C. A Pt-Ru/graphitic carbon nanofiber nanocomposite exhibiting high relative performance as a direct-methanol fuel cell anode catalyst. J Phys Chem B 2001;105:8097–101.
389. Fujiwara N, Shiozaki Y, Tanimitsu T, Yasuda K, Miyazaki Y. Precursor effects in PtRu electrocatalysts as a direct methanol fuel cell anode. Electrochemistry 2002;70:988–90.
390. Hills C, Mack N, Nuzzo R. The size-dependent structural phase behaviors of supported bimetallic (Pt-Ru) nanoparticles. J Phys Chem B 2003;107:2626–36.
391. Liu Y, Qiu X, Chen Z, Zhu W. A new supported catalyst for methanol oxidation prepared by a reverse micelles method. Electrochem Commun 2002;4:550–3.
392. Zhang X, Chan KY. Water-in-oil microemulsion synthesis of platinum-ruthenium nanoparticles, their characterization and electrocatalytic properties. Chem Mater 2003;15:451–9.
393. Roth C, Martz N, Fuess H. Characterization of different Pt–Ru catalysts by X-ray diffraction and transmission electron microscopy. Phys Chem Chem Phys 2001;3:315–9.
394. Goodenough JB, Hamnett A, Kennedy BJ, Manoharam R, Weeks SA. Porous carbon anodes for the direct methanol fuel cell—I. The role of the reduction method for carbon supported platinum electrodes. Electrochim Acta 1990;35:199–207.
395. Lizcano-Valbuena WH, Paganin VA, Leite CA, Galembeck F, Gonzalez ER. Catalysts for DMFC: relation between morphology and electrochemical performance. Electrochim Acta 2003;48:3869–78.
396. Colmati F Jr, Lizcano-Valbuena WH, Camara GA, Ticianelli EA, Gonzalez ER. Carbon monoxide oxidation on Pt-Ru electrocatalysts supported on high surface area carbon. J Braz Chem Soc 2002;13:474–82.
397. Shukla AK, Neegat M, Bera P, Jayaram V, Hegde MS. An XPS study on binary and ternary alloys of transition metals with platinized carbon and its bearing upon oxygen electroreduction in direct methanol fuel cells. J Electroanal Chem 2001;504:111–9.
398. Watson DJ, Attard GA. The electro-oxidation of glucose using platinum–palladium bulk alloy single crystals. Electrochim Acta 2001;46:3157–61.
399. Watson DJ, Attard GA. Surface segregation and reconstructive behaviour of the (1 0 0) and (1 1 0) surfaces of platinum–palladium bulk alloy single crystals: a voltammetric and LEED/AES study. Surf Sci 2002;515:87–93.
400. Schmidt TJ, Markovic NM, Stamenkovic V, Ross PN, Attard GA, Watson DJ. Surface characterization and electrochemical behavior of well-defined Pt-Pd{111} single-crystal surfaces: a comparative study using Pt{111} and palladium-modified Pt{111} electrodes. Langmuir 2002;18:6969–75.
401. Clavilier J, Feliu JM, Aldaz A. An irreversible structure sensitive adsorption step in bismuth underpotential deposition at platinum electrodes. J Electroanal Chem 1988;243:419–33.
402. Feliu JM, Fernández-Vega A, Aldaz A, Clavilier J. New observations of a structure sensitive electrochemical behaviour of irreversibly adsorbed arsenic and antimony

from acidic solutions on Pt (111) and Pt (100) orientations. J Electroanal Chem 1988;256:149–63.

403. Gómez R, Llorca MJ, Feliu JM, Aldaz A. The behaviour of germanium adatoms irreversibly adsorbed on platinum single crystals. J Electroanal Chem 1992;340:349–55.

404. Feliu JM, Gómez R, Llorca MJ, Aldaz A. Electrochemical behavior of irreversibly adsorbed selenium dosed from solution on Pt(h,k,l) single crystal electrodes in sulphuric and perchloric acid media. Surf Sci 1993;289:152–62.

405. Feliu JM, Llorca MJ, Gómez R, Aldaz A. Electrochemical behaviour of irreversibly adsorbed tellurium dosed from solution on Pt(h, k, l) single crystal electrodes in sulphuric and perchloric acid media. Surf Sci 1993;297:209–22.

406. Clavilier J, Llorca MJ, Feliu JM, Aldaz A. Preliminary study of the electrochemical adsorption behaviour of a palladium modified Pt(111) electrode in the whole range of coverage. J Electroanal Chem 1991;310:429–35.

407. Clavilier J, Llorca MJ, Feliu JM, Aldaz A. Electrochemical structure-sensitive behaviour of irreversibly adsorbed palladium on Pt(100), Pt(111) and Pt(110) in an acidic medium. J Electroanal Chem 1993;351:299–319.

408. Gómez R, Feliu JM. Rhodium adlayers on Pt(111) monocrystalline surfaces. Electrochemical behavior and electrocatalysis. Electrochim Acta 1998;44:1191–205.

409. Gutiérrez de Dios FJ, Gómez R, Feliu JM. Preparation and electrocatalytic activity of Rh adlayers on Pt(1 0 0) electrodes: reduction of nitrous oxide. Electrochem Commun 2001;3:659–64.

410. Álvarez B, Climent V, Rodes A, Feliu JM. Potential of zero total charge of palladium modified Pt(111) electrodes in perchloric acid solutions. Phys Chem Chem Phys 2001;3:3269–76.

411. Álvarez B, Rodes A, Pérez JM, Feliu JM. Two-dimensional effects on the in situ infrared spectra of CO adsorbed at palladium-covered Pt(111) electrode surfaces. J Phys Chem 2003;107:2018–28.

412. Inukai J, Ito M. Electrodeposition processes of palladium and rhodium monolayers on Pt(111) and Pt(100) electrodes studied by IR reflection absorption spectroscopy. J Electroanal Chem 1993;358:307–15.

413. Attard GA, Al-Akl A. Palladium adsorption on Pt(111): a combined electrochemical and ultra-high vacuum study. Electrochim Acta 1994;39:1525–30.

414. Climent V, Markovic NM, Ross PN. Kinetics of oxygen reduction on an epitaxial film of palladium on Pt(111). J Phys Chem B 2000;104:3116–20.

415. Arenz M, Stamenkovic V, Schmidt TJ, Wandelt K, Ross PN, Markovic MN. The effect of specific chloride adsorption on the electrochemical behavior of ultrathin Pd films deposited on Pt(1 1 1) in acid solution. Surf Sci 2003;523:199–209.

416. Attard GA, Price R. Electrochemical investigation of a structure sensitive growth mode: palladium deposition on Pt(100)-hex-R0.7° and Pt(100)-(1×1). Surf Sci 1995;335:63–74.

417. Attard GA, Price R, Al-Akl A. Electrochemical and ultra-high vacuum characterisation of rhodium on Pt(111): a temperature dependent growth mode. Surf Sci 1995;335:52–62.

418. Tanaka K, Okawa Y, Sasahara A, Matsumoto Y. Chapter 18. In: Solid–liquid electrochemical interfaces. ACS symposium series. Washington DC: American Chemical Society, 1997.

419. Uosaki K, Ye S, Oda Y, Haba T, Kondo T. Electrochemical epitaxial growth of a Pt(111) phase on an Au(111) electrode. J Phys Chem B 1997;101:7566–72.

420. Brankovic SR, Wang JX, Adzic RR. Metal monolayer deposition by replacement of metal adlayers on electrode surfaces. Surf Sci L 2001;474:L173–9.

421. Keck L, Buchanan JS, Hards GA, inventors; Johnson Matthey PLC, assignee. Catalyst material. United States Patent US5068161. 1991 Nov 26.

422. Schmidt TJ, Noeske M, Gasteiger HA, Behm RJ, Britz P, Bönnemann H. PtRu alloy colloids as precursors for fuel cell catalysts. J Electrochem Soc 1998;145:925–31.

423. Boxall DL, Deluga GA, Kenik EA, King WD, Lukehart CM. Rapid synthesis of a Pt₁Ru₁/carbon nanocomposite using microwave irradiation: a DMFC anode catalyst of high relative performance. Chem Mater 2001;13:891–900.

424. Kim JY, Yang ZG, Chang C-C, Valdez TI, Narayanan SR, Kumta PN. A sol-gel-based approach to synthesize high-surface-area Pt-Ru catalysts as anodes for DMFCs. J Electrochem Soc 2003;150:A1421–31.

425. Kim T, Takahashi M, Nagai M, Kobayashi K. Preparation and characterization of carbon supported Pt and PtRu alloy catalysts reduced by alcohol for polymer electrolyte fuel cell. Electrochim Acta 2004;50:817–21.

426. Liu Z, Ling XY, Su X, Lee JY. Carbon-supported Pt and PtRu nanoparticles as catalysts for a direct methanol fuel cell. J Phys Chem B 2004;108:8234–40.

427. Bock C, Paquet C, Couillard M, Botton GA, MacDougall BR. Size-selected synthesis of PtRu nano-catalysts: reaction and size control mechanism. J Am Chem Soc 2004;126:8028–37.

428. Chan K-Y, Ding J, Ren J, Cheng S, Tsang KY. Supported mixed metal nanoparticles as electrocatalysts in low temperature fuel cells. J Mater Chem 2004;14:505–16.

429. Lizcano-Valbuena WH, de Azevedo DC, Gonzalez ER. Supported metal nanoparticles as electrocatalysts for low-temperature fuel cells. Electrochim Acta 2004;49:1289–95.

430. Sarma LS, Lin TD, Tsai Y-W, Chen JM, Hwang BJ. Carbon-supported Pt–Ru catalysts prepared by the Nafion stabilized alcohol-reduction method for application in direct methanol fuel cells. J Power Sources 2005;139:44–54.

431. Chu D, Gilman S. Methanol electro-oxidation on unsupported Pt-Ru alloys at different temperatures. J Electrochem Soc 1996;143:1685–90.

432. Jusys Z, Kaiser J, Behm RJ. Composition and activity of high surface area PtRu catalysts towards adsorbed CO and methanol electrooxidation—: A DEMS study. Electrochim Acta 2002;47:3693–706.

433. Lee SA, Park K-W, Choi J-H, Kwon B-K, Sung Y-E. Nanoparticle synthesis and electrocatalytic activity of Pt alloys for direct methanol fuel cells. J Electrochem Soc 2002;149:A1299–304.

434. Antolini E. Formation of carbon-supported PtM alloys for low temperature fuel cells: a review. Mater Chem Phys 2003;78:563–73.

435. Solla-Gullon J, Vidal-Iglesias FJ, Montiel V, Aldaz A. Electrochemical characterization of platinum–ruthenium nanoparticles prepared by water-in-oil microemulsion. Electrochim Acta 2004;49:5079–88.

436. Bock C, Blakely M-A, MacDougall B. Characteristics of adsorbed CO and CH₃OH oxidation reactions for complex Pt/Ru catalyst systems. Electrochim Acta 2005;50:2401–14.

437. Aricò AS, Antonucci PL, Modica E, Baglio V, Kim H, Antonucci V. Effect of Pt---Ru alloy composition on high-temperature methanol electro-oxidation. Electrochim Acta 2002;47:3723–32.

438. Sirk AHC, Hill JM, Kung SKY, Birss VI. Effect of redox state of PtRu electrocatalysts on methanol oxidation activity. J Phys Chem B 2004;108:689–95.

439. Park K-W, Sung Y-E. Catalytic activity of platinum on ruthenium electrodes with modified (electro)chemical states. J Phys Chem B 2005;109:13585–9.

440. Bönnemann H, Nagabhushana KS. Advantageous fuel cell catalysts from colloidal nanometals. J New Mater Electrochem Syst 2004;7:93–108.

441. Hui CL, Li XG, Hsing IM. Well-dispersed surfactant-stabilized Pt/C nanocatalysts for fuel cell application: dispersion control and surfactant removal. Electrochim Acta 2005;51:711–9.
442. Li X, Hsing I-M. Surfactant-stabilized PtRu colloidal catalysts with good control of composition and size for methanol oxidation. Electrochim Acta 2006;52:1358–65.
443. Sanchez MG, Park S, Maselli JM, City E, Graham JR. United States Patent 3830756, 1974.
444. Chen L, Guo M, Zhang H-F, Wang X-D. Characterization and electrocatalytic properties of PtRu/C catalysts prepared by impregnation-reduction method using Nd_2O_3 as dispersing reagent. Electrochim Acta 2006;52:1191–8.
445. Zeng J, Lee JY. More active PtRu/C catalyst for methanol electrooxidation by reversal of mixing sequence in catalyst preparation. Mater Chem Phys 2007;104:336–41.
446. Rolison DR. Catalytic nanoarchitectures--the importance of nothing and the unimportance of periodicity. Science 2003;299:1698–1701.
447. Rolison DR, Hagans PL, Swider KE, Long JW. Role of hydrous ruthenium oxide in Pt-Ru direct methanol fuel cell anode electrocatalysts: the importance of mixed electron/proton conductivity. Langmuir 1999;15:774–9.
448. Long JW, Stroud RM, Swider-Lyons KE, Rolison DR. How to make electrocatalysts more active for direct methanol oxidation-avoid PtRu bimetallic alloys. J Phys Chem B 2000;104:9772–6.
449. Grgur BN, Marković NM, Lucas CA, Ross PN. Electrochemical oxidation of carbon monoxide: from platinum single crystals to low temperature fuel cells catalysis. Part I: carbon monoxide oxidation onto low index platinum single crystals. J Serb Chem Soc 2001;66:785–97.

17

Reversal-tolerant Catalyst Layers

Siyu Ye

17.1 Introduction

Fuel cells present a promising technology for providing clean, efficient electric power in a variety of applications. They are the most environmentally friendly alternative to internal combustion engine technology in vehicles. They also have applications in portable electronics, as well as distributed and back-up power. The last few years have witnessed a tremendous increase in the research and development of fuel cells, including the development of new materials, new system designs, and new operating methods. While many breakthroughs have been made, technical and economic barriers for commercialization still exist. For a polymer electrolyte membrane fuel cell (PEMFC) – the most promising fuel cell technology – to be used commercially in stationary or transportation applications, cost and durability are the major challenges. In transportation applications, fuel cell technologies face more stringent cost and durability requirements: a fuel cell system needs to cost less than \$50/kW with a 5,000 hour lifespan (150,000 miles equivalent) and have the ability to function over the full range of vehicle operating conditions (–40 to +90 °C). For stationary applications, a fuel cell system operating on natural gas needs to achieve 40% electrical efficiency and 40,000 hours durability at \$750/kW [1]. To be commercially viable, however, fuel cell systems must also exhibit adequate reliability in operation, even when the fuel cells are subjected to conditions outside the preferred operating range. As PEMFCs approach commercialization, significant progress is being made towards producing systems that achieve the optimum balance of cost, efficiency, reliability, and durability.

The ability of the fuel cell to operate under a wide range of conditions with different system characteristics is described by the term "fuel cell operational flexibility". Optimum fuel cell operational flexibility must take into account both specified conditions and an estimated amount of unexpected, or "out-of-specification", conditions over the fuel cell target lifetime. Some of the conditions to consider include: reactant composition and flow rates, operating and environmental temperature and pressure, humidification levels, peak load

requirements and turn-down ratios, duty-cycle characteristics (including percentage of time at different load points), and required rate of transient responses.

Some factors are known to affect the life of PEM fuel cells. While platinum is an exceptionally active catalyst, its performance can quickly degrade. For PEMFC durability, deterioration in fuel cell performance is mostly due to degradation of the electrocatalyst, in addition to membrane degradation [2]. A number of mechanisms can contribute to catalyst degradation, including: catalyst agglomeration and catalyst dissolution/migration [3, 4]. It was found that Pt particle size increase is accelerated by potential cycling [3, 4]. It has also been observed that the size and morphologies of the Pt nanoparticles varied greatly from the cathode surface to the cathode-membrane interface after potential cycling [5, 6]. Carbon oxidation and corrosion has been observed during PEM fuel cell start-up and shutdown operations [5, 7–9]. Mass transport properties degrade as a result of the accumulation of excess water in the gas diffusion pores [10, 11]. Impurity ions affect the membrane proton conductivity and oxygen reduction kinetics [12, 13]. In addition to membrane degradation, catalyst oxidation/dissolution, catalyst sintering, and cathode carbon corrosion, anode voltage reversal also severely affects fuel cell durability and reliability [14–18]. The development of a reversal-tolerant catalyst layer will be reviewed here.

During normal operation of a PEM fuel cell, fuel is electrochemically oxidized at the anode catalyst, typically resulting in the generation of protons, electrons, and possibly other species, depending on the fuel employed. The protons are conducted from the reaction sites at which they are generated, through the electrolyte, to electrochemically react with the oxidant at the cathode catalyst. The electrons travel through an external circuit, providing useable power, and then react with the protons and oxidant at the cathode catalyst to generate water as the reaction product.

In operation, the output voltage of an individual fuel cell under load is generally below one volt. Therefore, in order to provide greater output voltage, multiple cells are usually stacked together and connected in series to create a higher voltage fuel cell stack. End plate assemblies are placed at each end of the stack to hold the stack together and to compress the stack components together, thereby sealing and providing adequate electrical contact between various stack components. Fuel cell stacks can be further connected in series and/or parallel combinations to form larger arrays for delivering higher voltages and/or currents. However, fuel cells in series are potentially subject to voltage reversal, a situation in which a cell is forced to the opposite polarity by the other cells in the series. This can occur when a cell is unable to produce the current forced through it by the rest of the cells. It is possible that one or more membrane-electrode assemblies (MEAs) or groups of cells within a stack, or even a complete stack in a multi-stack system, can be driven into voltage reversal by other stacks in an array. Several conditions can lead to voltage reversal in a PEM fuel cell, including insufficient oxidant, fuel, or water, low or high cell temperatures, and certain problems with cell components or construction. High reactant utilization is generally required for most applications in order to maximize fuel efficiency and reduce system parasitic load, size, and weight that may be associated with the oxidant and fuel delivery and/or storage systems. Transient operation, particularly under the demanding

conditions of automotive applications, introduces greater challenges due to rapid load changes and the resulting wide range of conditions.

During high overall stack utilization, uneven flow sharing between cells can result in partial fuel and/or air starvation conditions in individual cells. A lack of system response during a sudden change in reactant demand will lead to fuel and oxidant starvation. This situation can be exacerbated by the presence of liquid water in channels or by other blockages, resulting in further flow sharing difficulties that in extreme cases can lead to complete starvation conditions. One example of such a condition is sub-zero start-up or operation. As long as the stack temperature remains below zero Celsius, the cells are prone to ice formation and subsequent flow channel blockage. Figure 17.1 [15] presents the change in cell voltage and the equivalent module power with time during freeze start-up from −15 °C. Negative values in the cell voltage for some cells can be clearly observed in the early stage of the freeze start-up. Although stack and system operation can be designed to reduce these occurrences, it is generally accepted that rapid heating of the stack to minimize ice formation is desirable. Alternatively, a flow field channel may be blocked due to deformation or inert gas blanketing the MEA. Reversal generally occurs when one or more cells experience a more extreme level of one of these conditions compared to other cells in the stack. While each of these conditions can result in negative fuel cell voltages, the mechanisms and consequences of such a reversal may differ, depending on which condition caused the reversal.
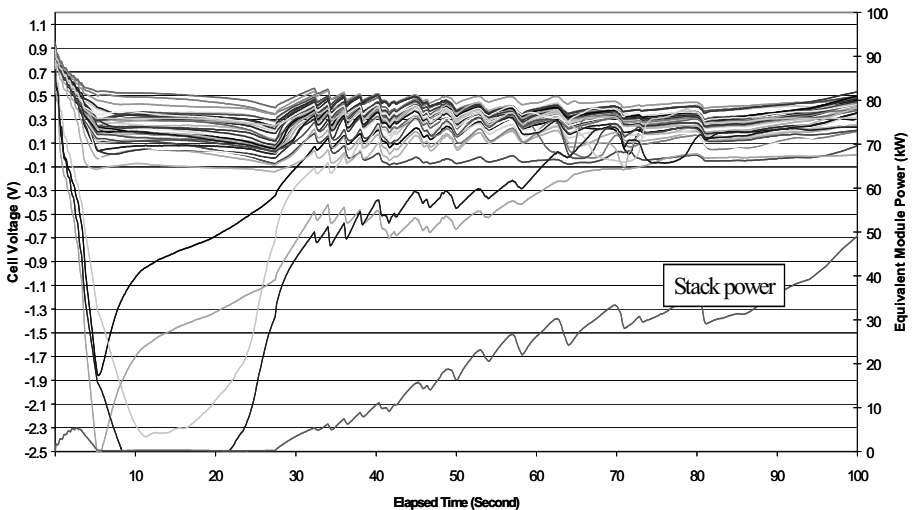
Figure 17.1. Cell voltage and equivalent module power vs. time during freeze start-up from −15 °C

Aside from the loss of power associated with one or more cells going into voltage reversal, this situation poses durability and reliability concerns as well. Undesirable electrochemical reactions may occur, which can detrimentally affect, or degrade, fuel cell components. For example, when there is an inadequate supply

of fuel (e.g., fuel starvation due to ice formation, water flooding at the anode, fuel supply problems, and the like) to a PEM fuel cell, there can be a rise in the absolute potential of the fuel cell anode, leading to electrolysis of the water present at the anode and to oxidation (e.g., corrosion) of the anode components. Such component degradation reduces the reliability and performance of the affected fuel cell and, in turn, its associated stack and array. Fuel starvation, an inadequate supply of fuel to the MEA at the anode, is the most damaging source of cell voltage reversal [17].

In this review, both cathode and anode voltage reversals, and the damage caused by voltage reversal will be presented. The development of a reversal-tolerant catalyst layer using different strategies, including enhancing water retention, using more corrosion-resistant catalyst support, and adding a water electrolysis catalyst into the anode structure will be reviewed.

17.2 Cell Voltage Reversal

17.2.1 Air Starvation

During normal operation of a PEM fuel cell on hydrogen fuel, the following electrochemical reactions take place:

$$\text{at the anode:} \qquad H_2 = 2H^+ + 2e^- \qquad\qquad (17.1)$$

$$\text{at the cathode:} \qquad \tfrac{1}{2}O_2 + 2H^+ + 2\,e^- = H_2O \qquad\qquad (17.2)$$

$$\text{overall:} \qquad H_2 + \tfrac{1}{2}O_2 = H_2O \qquad\qquad (17.3)$$
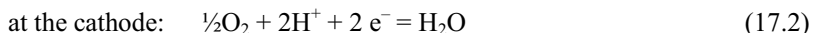
However, with insufficient oxidant (oxygen) present, the protons produced at the anode cross the electrolyte and combine with electrons directly at the cathode to produce hydrogen gas.

$$2H^+ + 2e^- = H_2 \quad E_{0,\,25\,°C} = 0.00 \text{ V (vs. NHE)} \qquad\qquad (17.4)$$
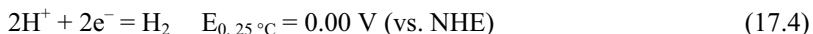
The anode reaction and the anode potential remain unchanged and the PEM fuel cell acts as a hydrogen pump. The cathode potential drops due to the lack of oxygen and the presence of hydrogen, and the cell voltage generally drops to very low levels or may even become negative. Since the oxidation of hydrogen gas and the reduction of protons are both very facile on Pt-based electrocatalysts (that is, small overpotential), the voltage across the fuel cell during this type of reversal is quite small. Hydrogen production actually begins at small positive cell voltages (for example, 0.03 V) because of the large hydrogen concentration difference present in the cell. The cell voltage observed during this type of reversal depends on several factors (including the current and cell construction) but, at current densities of about 0.5 A cm^{-2}, the fuel cell voltage may typically be more than or about –0.1 V.

An insufficient oxidant condition can arise when there is water flooding in the cathode, oxidant supply problems, and the like. Such conditions then lead to low magnitude voltage reversals with hydrogen being produced at the cathode. Significant heat may also be generated in the affected cell(s). These effects raise potential reliability concerns. However, the low potential experienced at the cathode does not typically pose a significant corrosion problem for the cathode components. Nonetheless, some degradation of the membrane may occur from the lack of water production and from the heat generated during reversal. Also, the continued production of hydrogen may result in some damage to the cathode catalyst.

17.2.2 Fuel Starvation

In a PEM fuel cell system, there can be several sources of cell voltage reversal but most damaging is fuel starvation of the cell at the anode. A different situation occurs when there is insufficient fuel present. In this case, the cathode reaction and thus the cathode potential remain unchanged. However, the anode potential rises to the potential for water electrolysis. Then, as long as water is available, electrolysis takes place at the anode. However, the potential of the anode is then generally high enough to slowly start oxidizing typical components used in the anode, for example, the carbons employed as supports for the catalyst, or the electrode substrates. Thus, some anode component oxidation typically occurs along with electrolysis. (Thermodynamically, oxidation of the carbon components actually starts to occur before electrolysis. However, it has been found that electrolysis appears to be kinetically preferred and thus proceeds at a greater rate.) The reactions in the presence of oxidizable carbon-based components are typically: at the anode in the absence of fuel:

$$H_2O = \frac{1}{2}O_2 + 2H^+ + 2\ e \qquad\qquad {}^-E_{0,25\ °C} = 1.23\ V \qquad\qquad (17.5)$$

and

$$\frac{1}{2}C + H_2O = 2CO_2 + 2H^+ + 2e^- \qquad E_{0,25\ °C} = -0.21\ V \qquad\qquad (17.6)$$
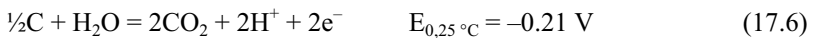
More current can be sustained by the electrolysis reaction if more water is available at the anode. However, if not consumed in the electrolysis of water, current is instead used in the corrosion of the anode components. If the supply of water at the anode runs out, the anode potential rises further and the corrosion rate of the anode components increases. Thus, there is preferably an ample supply of water at the anode in order to prevent degradation of the anode components during reversal.

Studies at Ballard Power Systems [12] have shown that the electrochemical processes in this case can be monitored by following the cell voltage with time and by gas chromatographic analysis of the anode outlet gas for oxygen and CO_2 production. Figure 17.2 shows the typical response from an MEA with a carbon-supported PtRu anode. In this case, the cathode reaction and the cathode potential remain unchanged and the change in cell voltage reflects the anode potential. As

the anode is starved of fuel the anode potential increases until water electrolysis occurs (assuming water is available) (Equation 17.5). Figure 17.2 shows that at 40 mA cm^{-2}, this corresponds to a cell voltage of –0.6 V. After falling quickly to –0.6 V, the cell voltage gradually decays to –0.9 V, corresponding to an anode potential of +1.4 to +1.7 V (vs. RHE). That the resulting water electrolysis plateau in Figure 17.2 is due to Equation 17.5 was confirmed by the high current efficiency for oxygen evolution. At such a high anode potential, a small degree of carbon corrosion (Equation 17.6) accompanies water electrolysis, as shown in Figure 17.2 by the small quantity of CO_2 detected in the anode outlet gas.
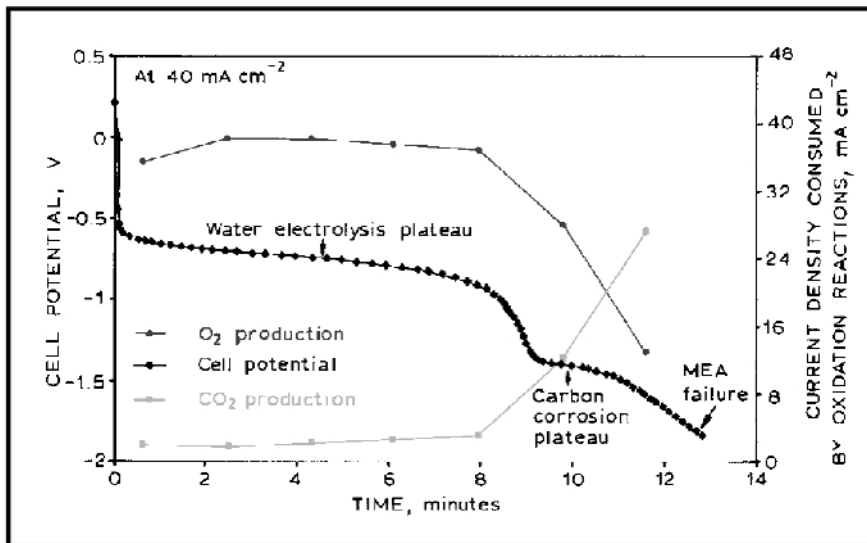
Figure 17.2. The change in the cell voltage at 40 mA cm^{-2} and the rate of oxygen and CO_2 produced at an MEA during voltage reversal due to fuel starvation. The anode is prepared from 20 wt% Pt, 10 wt% Ru/Shawinigan at a loading of 0.25 mg Pt cm^{-2}. The cathode uses Pt black at a loading of 4.0 mgPt cm^{-2}. The MEAs are based on catalyzed substrates bonded to Nafion NE-1135 membrane. Operating conditions: nitrogen (at the anode, replicating fuel starvation)/air, 200/200 kPa, 1.5/2 stoichiometry. The oxygen and CO_2 were detected in the anode outlet gas using gas chromatography [17]. (Reprinted from Ralph TR, Hogarth MP. Catalysis for low temperature fuel cells, part II: the anode challenges, Plat Met Rev 2002;46(3):117–35. With permission from Platinum Metals Review.)

If the supply of water to the anode electrocatalyst runs out or if the Pt-based anode electrocatalyst is deactivated for water electrolysis, the cell voltage moves to more negative potentials. Figure 17.2 shows a carbon corrosion plateau as the cell voltage reaches –1.4 V, corresponding to an anode potential of +2.1 V (vs. RHE). At this stage the current is sustained increasingly by carbon corrosion rather than by water electrolysis, as shown in Figure 17.2 by the increase in the rate of CO_2 production and the decrease in the rate of oxygen production in the anode chamber. Significant irreversible damage to the MEA occurs since the anode electrocatalyst carbon support, the anode gas diffusion substrate and the anode flow field plate (if

carbon-based) all corrode. After a few minutes in this condition the MEA is normally electrically shorted due to the significant amount of heat generated in the membrane.

It can be seen that the voltage of a fuel cell experiencing fuel starvation is generally much lower than that of a fuel cell receiving insufficient oxidant. During reversal from fuel starvation, the cell voltage ranges around –1 V when most of the current is carried by water electrolysis. However, when electrolysis cannot sustain the current (for example, if the supply of water runs out or is inaccessible), the cell voltage can drop substantially (to much less than –1 V) and is theoretically limited only by the voltage of the remaining cells in the series stack. Current is then carried by corrosion reactions of the anode components or through electrical shorts, including dielectric breakdown of the membrane electrolyte, which may develop as a result. Additionally, the cell may dry out, leading to very high ionic resistance and further heating. The impedance of the reversed cell may increase such that the cell is unable to carry the current provided by the other cells in the stack, thereby further reducing the output power provided by the stack.

Fuel starvation can arise when there is severe water flooding at the anode, fuel supply problems, and the like. Such conditions then lead to high-magnitude voltage reversals (i.e., the cell voltage can drop to less than –1 V) with oxygen being produced at the anode. Significant heat may again be generated in the reversed cell. These effects raise more serious reliability concerns than in an oxidant starvation condition. Very high potentials may be experienced at the anode, thereby posing a serious concern about anode corrosion and hence, reliability.
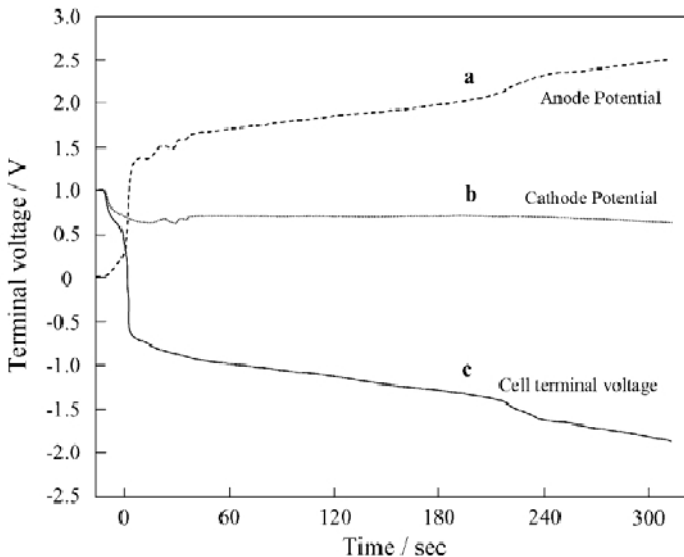
Figure 17.3. The time-dependent changes of the anode and cathode potential during the cell voltage reversal experiment [19]. (Reprinted from Journal of Power Sources, 130(1–2), Taniguchi A, Akita T, Yasuda K, Miyazaki Y, Analysis of electrocatalyst degradation in PEMFC caused by cell reversal during fuel starvation, 42–9, ©2004, with permission from Elsevier.)

   The potential change of the cell terminal voltage and individual electrodes during the cell voltage reversal experiment can be measured using a reference electrode [19]. The typical time-dependent change of the cell terminal voltage during an experiment is shown in Figure 17.3. In addition, this figure shows the time-dependent change of the anode and cathode potentials versus RHE. It was observed that the cell terminal voltage rapidly dropped to a negative voltage and the MEA changed polarity due to cell voltage reversal as soon as the experiment started. After this initial rapid drop, the cell voltage showed a steady decrease with time. Cell voltage reversal occurred when the anode potential increased and became more positive than the cathode potential. As soon as the experiment began, the anode potential quickly increased to nearly 1.5 V and water electrolysis occurred because the anode was starved of fuel [17], consistent with what has been described previously [12].

17.2.3 Electrocatalyst Degradation in PEM Fuel Cells Caused by Cell Voltage Reversal During Fuel Starvation

Various circumstances can result in a fuel cell being driven into voltage reversal by other cells in the series stack. Irreversible damage to the MEAs may be caused by such cell voltage reversal incidents. The most damaging source of cell voltage reversal is reactant starvation, an inadequate supply of fuel to the MEA at the anode [17]. There are some reports about a reactant starvation problem in the phosphoric acid fuel cell (PAFC) [20–22]. In the early 1990s, Mitsuda and Murahashi studied the changes in the electrode potential in the plane of the PAFC under reactant starvation conditions, for the Moonlight Project in Japan. This work made it clear that there is a polarization distribution in the horizontal plane of PAFC electrodes, by experiment using a single cell equipped with multi-reference electrodes [21, 22]. As for the PEMFC, Sanyo Electric reported performance degradation caused by reactant starvation in a national R&D project on PEM fuel cells [23].
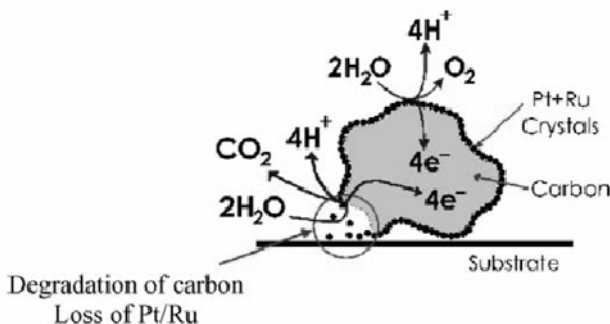
Figure 17.4. Schematic representation of degradation of carbon catalyst support during operation in the absence of fuel [18]. (Reprinted from Journal of Power Sources, 127(1–2), Knights SD, Colbow KM, St-Pierre J, Wilkinson DP, Aging mechanisms and lifetime of PEFC and DMFC, 127–34, ©2004, with permission from Elsevier.)

Most current technology development is focused on the use of platinum (or platinum and ruthenium) supported on carbon particles, in order to reduce the amount of platinum required on the anode down to 0.05–0.45 mg cm^{-2}, as described in [10]. These types of anodes are prone to degradation during fuel starvation due to the reaction in Equation 17.6, the oxidation of carbon, which is catalyzed by the presence of platinum [11]. This reaction proceeds at an appreciable rate at the electrode potentials required to electrolyze water in the presence of platinum (greater than approximately 1.4 V [24]). This is shown schematically in Figure 17.4. The catalyst support is converted to CO_2, and Pt and/or Ru particles may be lost from the electrode, resulting in loss of performance.
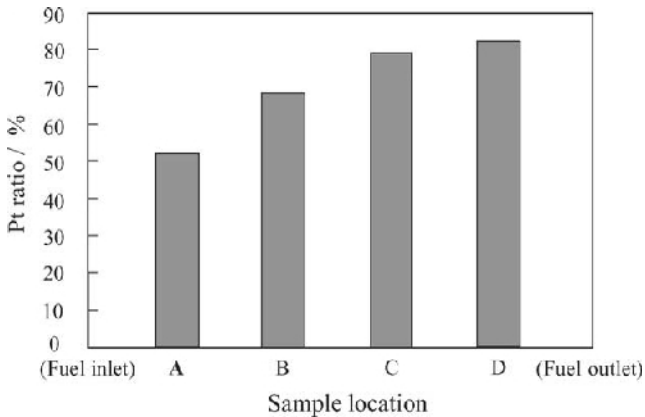
Figure 17.5. The dependence of the Pt ratio to Ru, Pt/(Ru + Pt), of the anode catalyst layer after the cell voltage reversal experiment for 2 min, determined by EDX on the sample location [19]. (Reprinted from Journal of Power Sources, 130(1–2), Taniguchi A, Akita T, Yasuda K, Miyazaki Y, Analysis of electrocatalyst degradation in PEMFC caused by cell reversal during fuel starvation, 42–9, ©2004, with permission from Elsevier.)

The damage to the electrocatalyst caused by cell voltage reversal during PEM fuel cell operation with fuel starvation was investigated by Taniguchi et al. [19]. The samples from degraded MEAs were characterized. Chemical analysis of the anode catalyst layer of MEA samples by energy dispersive X-ray analysis (EDX) was used to demonstrate ruthenium dissolution from the anode catalyst particles. The relative changes in the Pt:Ru ratio before and after the cell voltage reversal experiment provided information to assess the anode catalyst degradation. The change in the Pt:Ru ratio, Pt/(Ru + Pt), of the PEMFC anode plane under cell voltage reversal for 2 min is shown in Figure 17.5. A significant decrease in the Ru content was detected in the region located near the fuel outlet area. The platinum ratio increased from the fuel inlet region to the fuel outlet region, as shown in this figure. In the anode of PEM fuel cells operated on reformed gas for practical use, the hydrogen concentration downstream is significantly reduced compared with that upstream. This change indicates that the region where fuel starvation occurs suffers severely from degradation in the anode plane. Figure 17.6 shows the relative changes in the Pt:Ru ratio, Pt/(Ru+Pt), near the fuel outlet region before

and after the cell voltage reversal experiment, at different times. It was observed that the platinum ratio of the anode catalyst layer clearly increased after cell voltage reversal. The Pt:Ru ratio of the anode catalyst layer was also measured using X-ray photoelectron spectroscopy (XPS), as shown in this figure. Strictly speaking, the XPS measurement might not reflect the status of the interface between the catalyst layer and membrane, which is the most important electrochemical reaction zone [25], because the measurement was taken on the back surface of the catalyst layer. However, the results were similar to those measured by EDX. The values for degraded samples measured by XPS were slightly higher than those measured by EDX. Although nearly bulk information about the catalytic active particles can be obtained by XPS, since the particle size is very small, the higher Pt ratio measured by XPS possibly suggests a Pt surface-rich composition of catalyst particles.
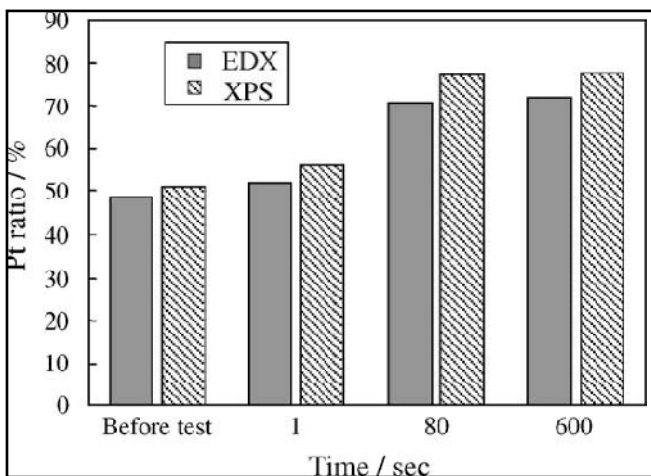
Figure 17.6. The relative changes in the Pt ratio to Ru, Pt/(Ru + Pt), near the fuel outlet region before and after the cell voltage reversal experiment at different times, determined by EDX and XPS [19]. (Reprinted from Journal of Power Sources, 130(1–2), Taniguchi A, Akita T, Yasuda K, Miyazaki Y, Analysis of electrocatalyst degradation in PEMFC caused by cell reversal during fuel starvation, 42–9, ©2004, with permission from Elsevier.)

A reduced carbon monoxide (CO) tolerance was found by CO-stripping voltammetry and measurement of deteriorated fuel cell performance. Figure 17.7 shows I–V curves of the cell after different experimental periods during the cell voltage reversal test. These curves were measured under the condition of enough hydrogen fuel containing 50 ppm CO being supplied. The original performance of the cell was lowered by increasing the experimental time. Notably, the performance of the cell after cell voltage reversal for 7 min showed the typical form of anode CO poisoning [26]. This kind of degradation behavior suggests deterioration of CO tolerance by the anode catalyst. The effect on the cathode was also evaluated via the I–V curves, under the condition of enough pure hydrogen fuel being supplied, before and after the cell voltage reversal experiment, for 10 min. A performance loss due to the cell voltage reversal was also observed, which

was attributed to the degradation of the cathode catalyst, as in the case of pure hydrogen fuel, the anode overpotential is negligible when Pt or PtRu is the anode catalyst [27].
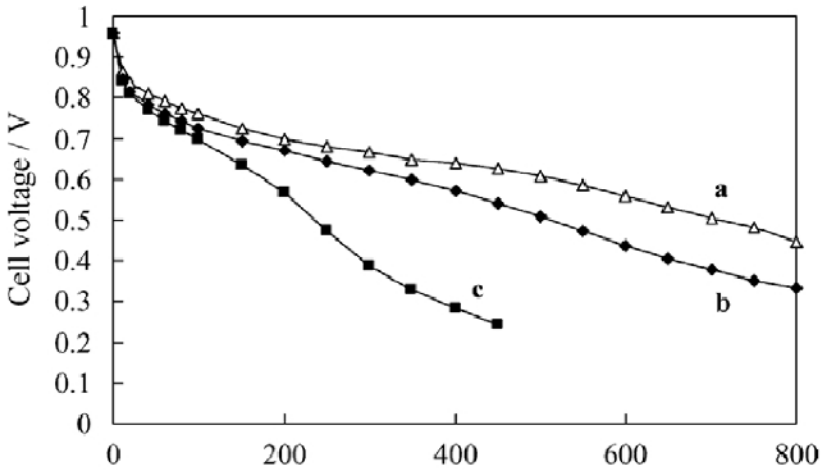
Figure 17.7. The change in current-voltage performance of a PEMFC by the cell voltage reversal experiment: (a) before experiment; (b) after experiment for 3 min; and (c) after experiment for 7 min [19]. (Reprinted from Journal of Power Sources, 130(1–2), Taniguchi A, Akita T, Yasuda K, Miyazaki Y, Analysis of electrocatalyst degradation in PEMFC caused by cell reversal during fuel starvation, 42–9, ©2004, with permission from Elsevier.)

Surface area loss of cathode platinum due to catalyst agglomeration was also detected by transmission electron microscopy (TEM) analysis and cyclic voltammetry. The behaviors of both electrodes were measured and anode degradation could be attributed to the high anode potential. Fuel starvation caused severe and permanent damage to the electrocatalysts of the PEMFC.

17.3 Development of Reversal-tolerant Catalyst Layers

The adverse effects of voltage reversal can be prevented, for instance by employing diodes [28] capable of carrying the current across each individual fuel cell or by monitoring the voltage of each individual fuel cell and shutting down an affected cell if a low voltage situation is detected. However, given the total number of individual cells in a fuel cell stack, such approaches can be quite complex and expensive to implement. Alternatively, other conditions associated with voltage reversal may be monitored instead and appropriate corrective action taken if reversal conditions are detected. For instance, a specially constructed sensor cell [29] may be employed that is more sensitive than other cells in the stack to certain conditions leading to voltage reversal (for example, fuel starvation of the stack). Thus, instead of monitoring every cell in a stack, only the sensor cell need be monitored and used to prevent widespread cell voltage reversal under such

conditions. However, other conditions leading to voltage reversal may exist that a sensor cell cannot detect (for example, a defective individual cell in the stack). Another approach is to employ exhaust gas monitors that detect voltage reversal by detecting the presence of, or abnormal amounts of, species in an exhaust gas of a fuel cell stack that originate from reactions that occur during reversal [30]. While exhaust gas monitors can detect a reversal condition occurring within cells in a stack and they may suggest the cause of the reversal, such monitors do not identify specific problem cells and they do not generally provide any warning of an impending voltage reversal.

Instead of or in combination with the preceding, a catalyst layer design approach may be preferred such that, in the event that reversal does occur, the fuel cells are either more tolerant to the reversal or are controlled in such a way that degradation of any critical component is reduced. Such an approach may be particularly preferred if the conditions leading to reversal are temporary. If the cells can be made more tolerant to voltage reversal, it may not be necessary to detect for reversal and/or shutdown the fuel cell system during a temporary reversal period. The results that demonstrated significantly improved cell voltage reversal tolerance, without compromising performance, are reported here.

17.3.1 Reversal Tolerance Cathode Catalyst Layer

Water management is one of the critical issues to be solved in the design and operation of PEM fuel cells. Water is produced at the cathode of PEMFCs. If water is not removed effectively, it accumulates at the cathode of the fuel cell, causing electrode flooding. The consequence is oxygen starvation, thus increasing the concentration overpotential of the cathode. In the worst scenarios, a proton (H^+) reduction reaction, instead of the oxygen reduction reaction (ORR), might occur at the cathode. Not only will this cause a cathode potential drop, but also the output voltage of a single cell would likely be reversed due to oxygen starvation. Particularly in the case of small fuel cells operated at room temperature, water flooding may appear [31]. If active control of water management cannot be guaranteed due to the size and power demands of the auxiliary equipment, passive possibilities of intervention are required. One alternative is to manipulate the characteristics of the used diffusion or backing layers [31, 32].

To study and resolve the voltage reversal problem, a MnO_2–Pt/C composite electrode was used by Wei et al. [33] to replace the conventional Pt/C electrode. This choice was based upon the fact that the electrochemical reduction of MnO_2 has almost the same Nernstian potential as the ORR, as shown below:

$$MnO_2 + 4H^+ + 2e^- = Mn_2^+ + 2H_2O \ (E_0 = 1.23 \ V) \tag{17.7}$$
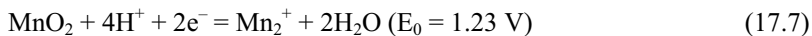
The reaction in Equation 17.7 can replace the ORR in the case of oxygen starvation. Thus, the voltage reversal effect (VRE) resulting from the proton reduction reaction (PRR) could be avoided without the use of a fan to scavenge the excess water. Two environments, N_2- and O_2-saturated H_2SO_4, were adopted to simulate two cases, i.e., O_2 starvation and O_2 richness. It was found that MnO_2–Pt/C can prevent the voltage reversal effect to a certain extent. In a N_2-saturated

1M H_2SO_4 solution, the current density of the Pt/C electrode, made of 0.6 mg Pt cm^{-2}, was close to 0, while for the MnO_2–Pt/C composite electrode, made of 0.4 mg Pt cm^{-2} and 0.8 mg MnO_2 cm^{-2}, it was as high as 10 mA cm^{-2}. Though the current generated on the MnO_2–Pt/C composite electrode in the case of oxygen starvation is not as great as that in the case when it is oxygen rich, the current might be high enough for some applications, such as powering a radio, hearing-aid, and such-like miniature devices. This illustrates that the introduction of MnO_2 into the Pt/C catalyst not only can alleviate, to a certain extent, the voltage reversal problem in the case of oxygen starvation, but also can play a synergistic role with Pt/C in the catalysis of the ORR, in oxygen-rich conditions. In an O_2-saturated 1 M H_2SO_4 solution, the MnO_2 in a MnO_2–Pt/C composite electrode primarily plays a catalytic role in the ORR by enhancing the catalytic behavior of Pt for the ORR. The impedance spectra of MnO_2–Pt/C and Pt/C electrodes were carried out for the two gases in bubbled electrolyte, which further confirmed that MnO_2 in the composite electrode does substitute for oxygen as an electron-acceptor in the case of oxygen starvation. The discharged MnO_2 can then be restored to its initial state, regardless of whether it is in oxygen-rich or starved conditions.

17.3.2 Reversal Tolerance Anode Catalyst Layer

During voltage reversal, electrochemical reactions may occur that result in the degradation of certain components in the affected fuel cell. Depending on the reason for the voltage reversal, there can be a rise in the absolute potential of a fuel cell anode. This can occur, for instance, when the cause is an inadequate supply of fuel (that is, fuel starvation). During such a reversal in a solid polymer fuel cell, water present at the anode may be electrolyzed. When significant water electrolysis occurs, the fuel cell voltage typically remains above about –1 V, but this voltage depends on several variables, including the amount of water present, the amount of fuel present, the current drawn, and the temperature. It is preferable to have electrolysis occur rather than component oxidation. When water electrolysis reactions at the anode cannot keep up with the current forced through the cell, the absolute potential of the anode can rise to a point where oxidation (corrosion) of anode components takes place, typically irreversibly degrading the components. Therefore, a solid polymer fuel cell can be made more tolerant to voltage reversal by increasing the amount of water available for electrolysis during reversal, thereby channeling the current forced through the cell into the more innocuous electrolysis of water rather than the detrimental oxidation of anode components. By increasing the amount of water in the vicinity of the anode catalyst during normal operation, more water is available at the anode catalyst in the event of a reversal. Thus, modifications to the anode structure that result in more water being present at the anode catalyst during normal operation lead to improved tolerance to voltage reversal. In addition to enhancing the presence of water at the anode through modifications to the anode structure, a PEM fuel cell can be made more tolerant to voltage reversal by incorporating an additional catalyst, a water electrolysis catalyst, at the anode to promote the electrolysis of water. In these ways, more of the current being forced through the cell is consumed by the electrolysis of water than by the oxidation of the anode components.

17.3.2.1 Enhancing the Presence of Water at the Anode

In a typical PEM fuel cell, water generated at the cathode diffuses through the polymer membrane to the anode. Restricting the passage of this water through the anode structure and into the exhaust fuel stream means more water remains in the vicinity of the catalyst. This can be accomplished, for example, by making the anode catalyst layer or an anode sublayer impede the flow of water (in either vapor or liquid phase) [17, 18, 30]. For instance, adding a hydrophobic material such as polytetrafluoroethylene (PTFE) to either of these layers makes them more hydrophobic, thereby hindering the flow of water through the anode. Figure 17.8 shows the benefit of adding PTFE to the anode catalyst layer to enhance the voltage reversal tolerance. The cell voltage response over time of different four-cell stacks with different anode designs is also shown. Each stack was subjected to fuel starvation conditions through an equivalent number of cycles, then finally starved of hydrogen and allowed to go into voltage reversal until an average cell voltage of –2 V was reached. The length of time the cells operated prior to reaching –2 V is a measure of robustness to fuel starvation. Addition of PTFE into the anode catalyst layer extended the reversal time to more than 20 minutes from less than 5 minutes. The reversal tolerance was improved more than 4 times simply by the addition of PTFE into the anode catalyst layer.
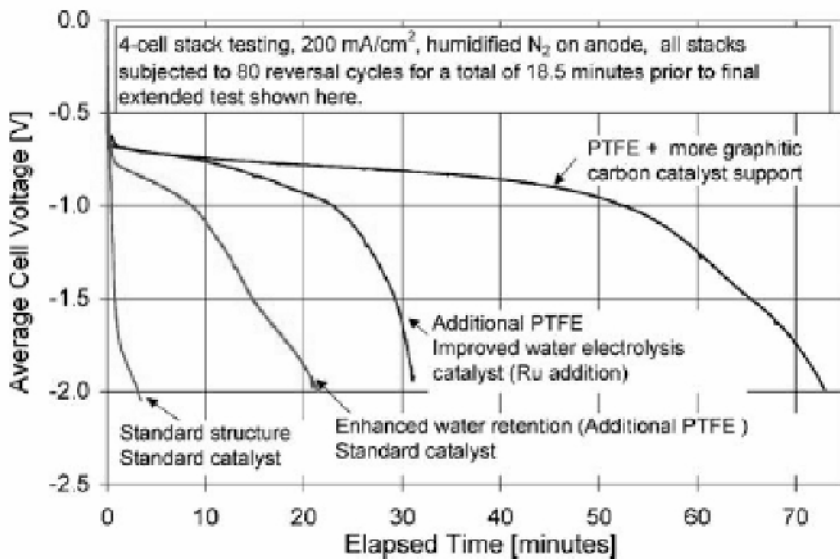
Figure 17.8. Comparison of different anode structures in severe failure testing. Each cell has an equivalent cathode (~0.7 mg cm^{-2} Pt, supported on carbon). Testing was conducted at 200 mA cm^{-2} with fully humidified nitrogen on the anode. Anode loading was ~0.3 mg cm^{-2} Pt supported on carbon (varied materials and compositions). Each curve represents the results from a 4-cell stack, each cell of identical composition. Four separate stack tests were run to generate the curves [18]. (Reprinted from Journal of Power Sources, 127(1–2), Knights SD, Colbow KM, St-Pierre J, Wilkinson DP, Aging mechanisms and lifetime of PEFC and DMFC, 127–34, ©2004, with permission from Elsevier.)

Alternatively, other additives (for example, graphite, other carbons, or titanium oxide powders) may be employed to reduce the porosity of either layer, thereby impeding the flow of water through the anode. It may be advantageous to employ a porosity-reducing additive mixture of polytetrafluoroethylene and acetylene carbon black, in which the anode catalyst layer comprises between about 12% and 32% by weight of polytetrafluoroethylene and between about 0.03 and 0.2 mg cm^{-2} of acetylene carbon black.

Another approach for increasing the amount of water in the anode catalyst layer is to boost the water content in the catalyst layer components. A conventional catalyst layer, for instance, may contain up to 30% by weight amount of fully hydrated perfluorosulfonic ionomer. Thus, an increase in water content can be accomplished by increasing the amount of the water-containing ionomer used in the catalyst layer or by employing a different ionomer with higher water content. Alternatively, more hygroscopic materials may be incorporated into the anode catalyst layer to retain more water therein.

The present approach makes fuel cells more tolerant to voltage reversal by facilitating water electrolysis at the anode during reversal, through providing sufficient water at the anode. It is thus an advantageous method *in situ*ations where electrolyzing more water is beneficial (for example, during a fuel starvation condition not caused by water flooding at the anode). Further, it is primarily advantageous for fuel cells operating directly on gaseous fuels. This is because liquid feed fuel cells typically employ an aqueous fuel mixture containing an abundance of water and thus an ample supply is generally already available to the anode during normal operation.

17.3.2.2 Using a More Corrosion-resistant Catalyst Support

As shown in Reaction 17.6, carbon corrosion is one of key causes of failure during voltage reversal. Using a more robust catalyst support (e.g., more graphitic carbon or non-carbon support materials) is beneficial for impeding or eliminating component degradation [14, 15, 18]. Figure 17.8 shows that using more graphitic carbon support increases the extended reversal time from ~20 minutes to 75 minutes. A more than three-fold improvement of voltage reversal tolerance was thus achieved.

It was also found that increasing catalyst coverage on the support to reduce the contact of carbon with reactants (e.g., using a higher weight percentage Pt on the carbon) [12, 13, 30, 34] is also an effective way to retard carbon corrosion. Figure 17.9 shows the cell voltage of 10-cell stacks with 2 different anode structures as a function of time during pulse reversal testing. The cells were subjected to current pulses (200 mA cm^{-2}) while operating on nitrogen and air. The pulse testing consisted of three sets of 30× on/off pulses. With the anode catalyst layer comprised of 40% Pt/20% Ru on more graphitic carbon support, the cell voltage was the same across all the 30× on/off reversal pulses (~0.8 V, at which voltage nearly all the current was consumed by water electrolysis – see Figures 17.2 and 17.3). In contrast, the anode structure consisting of 20% Pt/10% Ru on Vulcan carbon support reached –2 V at the last pulse. As has been pointed out (Figure 17.2), MEA failure occurs when the cell voltage reaches –2 V.
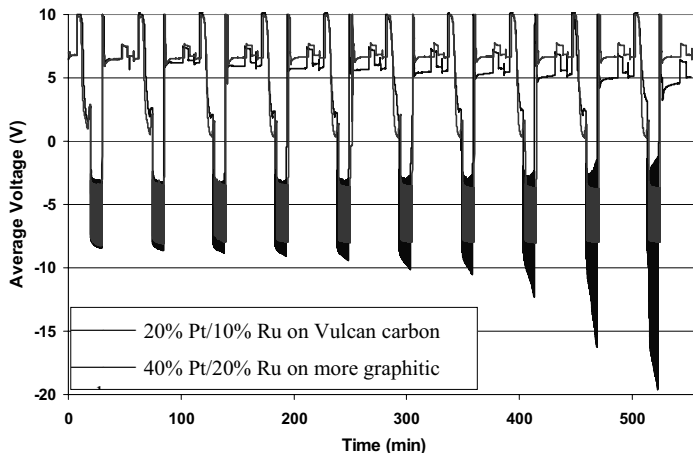
Figure 17.9. Cell voltage as a function of time during pulse reversal testing at 200 mA cm^{-2}

17.3.2.3 Addition of Water Electrolysis Catalyst

In addition to enhancing the presence of water at the anode through modifications to the anode structure, a PEM fuel cell can be made more tolerant to voltage reversal by incorporating an additional catalyst, a water electrolysis (oxygen evolution reaction, OER) catalyst, at the anode to promote the electrolysis of water [14–16, 18]. In this way, more of the current forced through the cell may be consumed by the electrolysis of water than by the oxidation of the anode components. In a reversal-tolerant fuel cell, the anode comprises a first catalyst composition for evolving protons from the fuel and a second catalyst composition for water electrolysis.

Noble metal oxides as electrocatalysts (particularly IrO_2 and RuO_2 or their mixtures – numerous investigations are concerned with oxides of rutile structure [35–40]) are well established in many industrial electrochemical processes in the form of dimensionally stable anodes (DSA), as developed by Beer [41]. RuO_2 has exhibited excellent activity in both Cl_2 and O_2 evolutions. The Tafel slope for O_2 evolution is only 0.031–0.041 V dec^{-1} in the low-potential region and 0.042–0.066 V dec^{-1} in the high-potential region [42, 43]. Unfortunately, RuO_2 and RuO_2–TiO_2, the latter widely used in the chlorine-alkali industry, are not stable for O_2 evolution in acidic environments, as their service lives are under 4 h at a current density of 0.5 A cm^{-2} in 0.25–0.5 M H_2SO_4 solutions [44, 45]. The electrochemical stability of these electrodes is significantly improved by selecting proper dispersing agents. Burke and McCarthy [46] increased the service life of the electrode by a factor of 5.3 through adding 20 molar percent of ZrO_2 to the RuO_2 layer. Iwakura and Sakamoto [45] studied the effect of adding SnO_2 to RuO_2 and found that the electrode with a molar ratio of Ru:Sn = 30:70 had a service life of about 12 h, four times longer than that of the pure RuO_2-coated electrode, under accelerated life test conditions (0.5 A cm^{-2}, 0.5 M H_2SO_4, 30 °C). Investigation of RuO_2-based DSA for oxygen evolution has continued in recent years. Oxide mixtures of interest include RuO_2–Nb_2O_5 [47], RuO_2–PbO_2 [48, 49], and RuO_2–Co_3O_4 [50]. Despite

their good activity for oxygen evolution, none of them has a service life over 20 h in accelerated life tests. Obviously, these electrocatalysts lack sufficient stability for industrial applications. The poor electrochemical stability of RuO_2-based DSA for O_2 evolution is principally due to the easy conversion of ruthenium from stable dioxide into unstable tetraoxide at a high electrical potential [51].

Recently, IrO_2-based materials have been examined for the anode or oxygen evolution electrode by Tunold et al. [52–55]. Most DSA electrodes are prepared by the thermal decomposition of metal precursors onto titanium substrates. This method is thought to be unsuitable for PEM water electrolyzers due to the difficulty of achieving good contact between the electrocatalytic layer and the membrane electrolyte. Therefore, to obtain an electrocatalytic layer on the membrane, either pre-prepared powders may be applied as an ink to the membrane [56, 57] or electrocatalytic particles can be synthesized directly on the surface or within the membrane [58, 59]. Many methods are available for the synthesis of noble metal-based oxides. The Adams fusion method [60] has been widely used to produce fine noble metal oxide powders [52–54, 61], and is based on the oxidation of metal precursors in a molten nitrate melt. Sol-gel methods have also proven useful in producing noble metal-based oxides [62–66], however, the precursor type can affect the properties of the material [66], as can the solvent removal stage [67]. Preparation of metal oxides by thermal or chemical oxidation of metallic colloids is an interesting concept as there exists a wide range of methods to synthesize such colloids [68, 69]. The polyol method is a relatively simple way to synthesize nanosized noble metal colloids such as iridium or ruthenium by the reduction of metal precursors in ethylene glycol [70, 71]. Additional steps include the separation of the metallic colloids from the ethylene glycol by centrifugation, followed by thermal oxidation in air at elevated temperatures.

Previously it has been shown that SnO_2 improves the stability of IrO_2–RuO_2 anodes in PEM water electrolyzers [61]. It has also been suggested that SnO_2 does not reduce the activity of RuO_2 as much as TiO_2 does [72]. For these reasons, the addition of SnO_2 to IrO_2 has been investigated by Tunold et al. [73]. In their previous work [74, 75], Chen et al. developed a stable ternary IrO_2–Sb_2O_5–SnO_2 electrocatalyst for O_2 evolution. In this oxide mixture, IrO_2 serves as the catalyst for O_2 evolution, SnO_2 as the dispersing agent, and Sb_2O_5 as the dopant for conductivity improvement. The service life of a Ti/IrO_2–SnO_2–Sb_2O_5 electrode containing only 10 molar percent of IrO_2 in the oxide coating is as high as 1600 h at a current density of 1 A cm^{-2} in a 3 M H_2SO_4 solution. Recently, they extended their investigation to RuO_2–Sb_2O_5–SnO_2 [76] because Ru is much cheaper and more active than Ir in oxygen evolution. In this ternary oxide coating, RuO_2 serves as the catalyst, SnO_2 as the dispersing agent, and Sb_2O_5 as the dopant. The accelerated life test showed that the Ti/RuO_2–Sb_2O_5–SnO_2 electrode containing 12.2 molar percent of RuO_2 nominally in the coating had a service life of 307 h in 3 M H_2SO_4 solution under a current density of 0.5A cm^{-2} at 25 °C, which is more than 15 times longer than other types of RuO_2-based electrodes. Instrumental analysis indicated that RuO_2–Sb_2O_5–SnO_2 was a solid solution with a compact structure, which contributed to the stable nature of the electrode. Since both SnO_2 and Sb_2O_5 are very stable chemically, the homogeneous mixing of RuO_2 with SnO_2 and Sb_2O_5 by forming a solid solution decreases the rate of RuO_2 dissolution. This

leads to a significant increase in the electrode service life. In addition, the RuO_2–SnO_2–Sb_2O_5 film has a compact structure, which further enhances the electrode stability. Their experimental results showed that RuO_2–Sb_2O_5–SnO_2 can be a very active and stable electrode for O_2 evolution. Using mixed oxides to improve the electrocatalytic properties and the stability/selectivity of the electrode has been the target of many studies [37, 38, 77–80]. De Faria et al. [81] demonstrated that partial substitution of TiO_2 by CeO_2 in a RuO_2-based electrode material improves the electrocatalytic activity for OER, but decreases the mechanical stability of the mixture. In a recent paper [82], Santana et al. reported the surface properties of the RuO_2 + TiO_2 + CeO_2 + Nb_2O_5 system and showed the instability caused by CeO_2 can be reduced introducing a small Nb_2O_5 content. They also systematically investigated the electrocatalytic properties of $[Ru_{0.3}Ti_{0.6}Ce]_{(0.1-x)}O_2[Nb_2O_5]_{(x)}$ with $(0 \leq x \leq 0.1)$ for OER (and the chlorine evolution reaction) and the stability of these oxide electrodes throughout the experiments [83]. For oxygen evolution a 30 mV Tafel slope was obtained in the presence of CeO_2, while in its absence a 40 mV coefficient was observed. The intrinsic electrocatalytic activity is mainly due to electronic factors that result from synergism between the Ru and Ce oxides. The highest global electrocatalytic activity observed for higher CeO_2 contents is attributed to electronic and geometric factors, while the true electrocatalytic activity depends on the electronic factor. The electrode stability is closely related to the composition. Comparison of the anodic voltammetric charges obtained before and after each set of experiments does not support significant electrode wear during the OER. The higher the CeO_2 content, the less stable the coating, which is probably related to the coating fragility of the porous structure formed by the CeO_2-containing oxide mixture. On the other hand, introduction of Nb_2O_5 causes a stabilization of the oxide mixture by forming a more compact layer.

Nanocrystalline oxide powders of the type $Ir_xSn_{1-x}O_2$ ($0.2 \leq x \leq 1$) have been produced and characterized, primarily for use as oxygen evolution electrocatalysts in proton exchange membrane (PEM) water electrolyzers [73]. Two methods were used: the modified polyol method and the Adams fusion method. X-ray diffraction analysis suggests that an iridium-tin oxide solid solution with a rutile structure can be produced using the modified polyol method, with a linear relationship between lattice parameters and composition. The crystal size of the solid solution phase is below 15 nm for all compositions, indicating that the addition of tin also causes the average crystal size to increase from around 3.5 to 15 nm. The Adams fusion method resulted in at least two separate oxide phases, namely a tin-rich oxide and an iridium-rich oxide. X-ray photoelectron spectroscopy (XPS) analysis revealed no significant difference between the bulk and surface compositions, and showed that the iridium was present in at least two valent states. The electrical resistivity of the powders was compared, and an exponential increase in resistivity with tin addition was found. Overall, the resistivity measurements suggest that the limit for tin addition is around 50–60 mol% due to the high ohmic losses expected at higher tin contents in a PEM water electrolyzer.

Many studies pertaining to water electrolysis electrocatalysis in regenerative fuel cells have been published. The catalytic materials used are in general metal alloys and oxides. More recent studies have shown that Pt_1Ir_1 (numbers in subscripts indicate atomic ratios) or 50% Pt/50% IrO_2 (wt%) can be used in

regenerative fuel cells. Reasonable efficiencies and lifetimes were achieved [84–86]. Other studies have shown that Rh/Ru (1:1)-oxide and Ir/Rh (1:2)-oxide are also promising oxygen electrode catalysts in regenerative fuel cells. Chen et al. [87] showed that combinatorial discovery can be used to identify better dual-use catalysts, by superimposing activity maps to create a consensus map. Because the combinatorial method provides activity data for the entire composition space, it is more straightforwardly adapted to this task than other systematic optimization methods. Electrode arrays containing 715 unique combinations of five elements (Pt, Ru, Os, Ir, and Rh) were prepared by them via borohydride reaction of aqueous metal salts, and were screened for activity as oxygen reduction and water oxidation catalysts. Using a consensus map, catalysts that showed high activity for both reactions and good resistance to anodic corrosion were identified in the Pt–Ru-rich region of the Pt–Ru–Ir ternary. The ternary catalyst $Pt_{4.5}Ru_4Ir_{0.5}$ is significantly more active than the Pt_1Ir_1 bifunctional catalyst for both the water oxidation and oxygen reduction reactions. While the best ternary catalyst is close to Pt_1Ir_1 in composition, the latter is unstable with respect to anodic corrosion. A detailed kinetic comparison of the anodically stable catalysts $Pt_{4.5}Ru_4Ir_{0.5}$ and Pt_1Ir_1 showed that the addition of the oxophilic element Ru increases the reaction rate by stabilizing S–O bonds $(S \equiv$ surface atom$)$ and accelerating the oxidative deprotonation of S–OH groups. The pH dependence of the electrode kinetics was particularly useful in determining that the difference arises from stabilization of surface oxide species, which accelerates the oxidative deprotonation of surface OH groups.

To improve voltage reversal tolerance of PEM fuel cells, water electrolysis catalysts have been incorporated into anode structures by Johnson Matthey and Ballard Power Systems [12–17]. In such a reversal-tolerant fuel cell, the anode comprises a first catalyst composition for evolving protons from the fuel and a second catalyst composition for water electrolysis.

The second catalyst composition is incorporated for the purposes of electrolyzing water at the anode during voltage reversal situations. Preferred compositions thus include precious metal oxides, particularly those in the group consisting of ruthenium oxide and iridium oxide. Such oxides are characterized by the chemical formulae RuO_x and IrO_x, where x is greater than 1 and particularly about 2. Preferred compositions may also comprise mixtures and solid solutions of precious metal oxides, or mixtures and solid solutions of precious metal oxides and valve metal oxides, such as TiO_y (where y is less than or about equal to 2), for example.

Figure 17.10 shows the performance in Ballard stack hardware of three different cell-reversal-tolerant electrocatalysts prepared by Johnson Matthey. In this case the MEAs have received significant prior cell-reversal periods to drive the anodes to the limit of their tolerance. The impact that inclusion of a water electrolysis electrocatalyst has on the ability of the anode to sustain water electrolysis is evident. At the standard 40 wt% Pt, 20 wt% Ru/Shawinigan carbon black-based anode, the water electrolysis plateau is so short that it is difficult to detect. Only by using a cell reversal-tolerant electrocatalyst in the anode water electrolysis are plateaus evident in Figure 17.10. As a result, the degree of carbon corrosion is significantly reduced by the cell-reversal-tolerant electrocatalysts. The

typical PtRu anode electrocatalyst layer shows carbon corrosion after only 15 seconds of operation under the final cell-reversal conditions of Figure 17.10. This is extended to 4.5 minutes by adding RuO_2 to the electrocatalyst layer, to 24 minutes using RuO_2/TiO_2, and to 48 minutes with RuO_2/IrO_2 in the anode layer. While the carbon corrosion plateaus are not clear in Figure 17.10, the relative rate of production of CO_2 and oxygen confirmed the time scale required for significant levels of carbon corrosion. The improvement in reversal tolerance by adding a water electrolysis catalyst to the anode structure has also been demonstrated in Figure 17.8. After this extended cell-reversal testing, returning the more cell-reversal-tolerant anodes (optimized for PEMFC operation) to normal fuel cell operation indicated that there was negligible loss in the MEA power output. This contrasts with MEA failure in the absence of the water electrolysis electrocatalyst. In addition, incorporation of the water electrolysis electrocatalyst in the favored anode structures adds very little extra pgm to the MEA (< 0.1 mg cm^{-2}). Thus, this safeguard to the stack durability comes at little additional MEA cost.
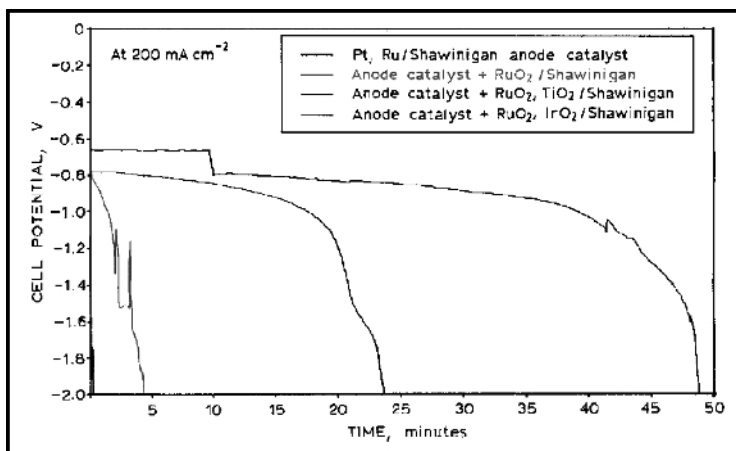
Figure 17.10. The change in cell voltage at 200 mA cm^{-2} during cell voltage reversal due to fuel starvation at a $Pt_{0.5}Ru_{0.5}$ alloy anode containing different water electrolysis electrocatalysts. The MEAs were first subjected to cell voltage reversal at 200 mA cm^{-2} for 5 minutes, then for 3 sets of 30 pulses (10 seconds on, 10 seconds off) with 15-minute recovery periods on hydrogen/air, completed by a final overnight recovery period. The anode loading is 0.1 mg Pt cm^{-2}. The water electrolysis electrocatalysts were prepared from 20 wt% RuO_2/Shawinigan, 20 wt% RuO_2, TiO_2/Shawinigan or 20 wt% RuO_2, IrO_2/Shawinigan and added at an anode loading of 0.1 mg Ru cm^{-2} [17]. (Reprinted from Ralph TR, Hogarth MP. Catalysis for low temperature fuel cells, part II: the anode challenges, Plat Met Rev 2002;46(3):117–35. With permission from Platinum Metals Review.)

Further voltage-reversal tolerance can be obtained by 1) employing a catalyst support that is more resistant to oxidative corrosion than conventional catalyst supports, 2) using certain anodes with a higher catalyst loading or coverage on a corrosion-resistant support, and 3) incorporating an additional or second catalyst

composition that promotes the electrolysis of water. A significant improvement in reversal tolerance (over 100 times greater than for a conventional anode) has been obtained by employing 2) and 3) [14–16]. Figure 17.11 shows the cell voltage during reversal testing (at 200 mA cm^{-2}) for different anode designs, where the time when the cell voltage reached –2 V was used as the criterion for reversal tolerance (see Figure 17.2). It can be seen from Figure 17.11 that improvement in reversal tolerance appeared with the incorporation of a second catalyst composition for the electrolysis of water (RuO_2 was used here) to a conventional (e.g., Vulcan) carbon-supported Pt/Ru, used as a baseline design here (15 and 28 minutes, respectively, were spent when the cell voltage reached –2 V). When using a more corrosion-resistant catalyst support (e.g., Shawinigan) for Pt/Ru plus a second catalyst composition for the electrolysis of water ($RuIrO_2$ was used here), further improvement in reversal tolerance was demonstrated. With the increase of metal content on the Shawinigan support (40% Pt/20% Ru over 20% Pt/10% Ru, supported on Shawinigan, with the same platinum loading of the anode, even with no additional catalyst to promote water electrolysis), the improvement over the previous anode design was evident (it took 167 minutes to reach –2 V). The most significant improvement in reversal tolerance among all of the other anode designs was manifested when incorporating both a more corrosion-resistant catalyst (40% Pt/20% Ru supported on Shawinigan) and a second catalyst composition for the electrolysis of water (e.g., $RuIrO_2$). This design was operated under extended reversal conditions for 2515 minutes before the cell voltage reached –2 V (167 times longer than the baseline design). Furthermore, this design demonstrated lower performance loss (less than 30 mV on air/H_2) than the other designs even though it was operated in reversal for a much longer time.
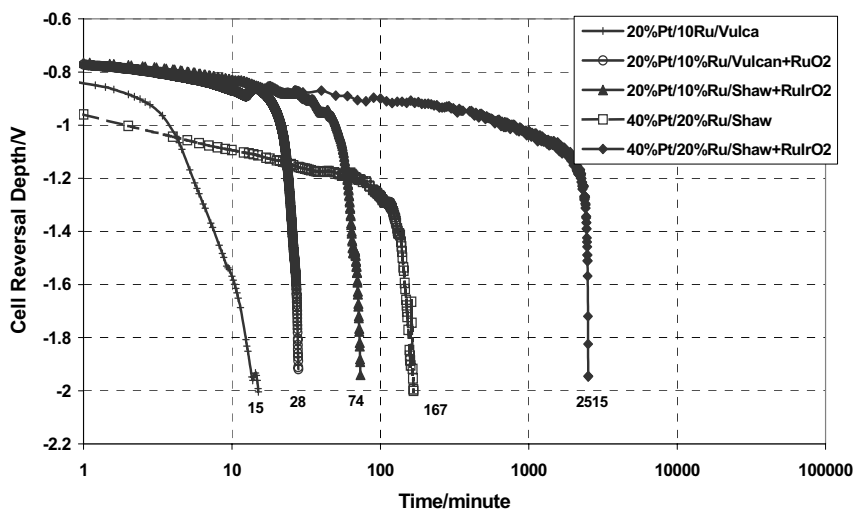
Figure 17.11. The change in cell voltage at 200 mA cm^{-2} during cell voltage reversal due to fuel starvation at different anode catalyst layer structures. The MEAs were first subjected to cell voltage reversal at 200 mA cm^{-2} for 5 minutes, then for 3 sets of 30 pulses (10 seconds on, 10 seconds off), with 15-minute recovery periods on hydrogen/air and a final overnight recovery period.

17.4 Conclusions

An overview of cell voltage reversal due to reactant starvation has been presented. A major durability issue arises at the anode if the MEA is starved of fuel. Cell voltage reversal tolerance can be improved by 1) enhancing the water retention in the anode structure, 2) employing a catalyst support that is more resistant to oxidative corrosion than conventional catalyst supports, 3) using certain anodes with a higher catalyst loading or coverage on a corrosion-resistant support, and 4) incorporating a second or additional catalyst composition that promotes the electrolysis of water. A significant improvement in reversal tolerance (over 100 times greater than that of a conventional anode) has been obtained by a combination of those strategies.

It has been demonstrated that increased durability/reliability are possible without sacrificing performance, through the careful selection of appropriate materials.

The use of reversal-tolerant cells has significant benefits for PEM fuel cell technology development:

- significantly increases the reliability
- much longer lifetime due to increased durability
- excellent operational flexibility under a wide range of operating conditions.

Acknowledgements

References

1. US Department of Energy [homepage on the Internet]. Washington, DC. c2007 [updated 2007 Oct]. DOE Multi-year research, development and demonstration plan: planned program activities for 2005–2015. Available from: http://www1.eere.energy.gov/hydrogenandfuelcells/mypp/pdfs/fuel_cells.pdf
2. Cleghorn SJC, Mayfield DK, Moore DA, Moore JC, Rusch G, Sherman TW, et al. A polymer electrolyte fuel cell life test: 3 years of continuous operation. J Power Sources 2006;158:446–54.
3. Borup RL, Davey JR, Garzon FH, Wood DL, Inbody MA. PEM fuel cell electrocatalyst durability measurements. J Power Sources 2006;163:76–81.
4. Li J, He P, K Wang, Davis M, Ye S. Characterization of catalyst layer structural changes in PEMFC as a function of durability testing. ECS Transactions 2006;3.1:743–51.
5. Ye S, Hall M, Cao H, He P. Degradation resistant cathodes in polymer electrolyte membrane fuel cells. ECS Transactions 2006;3.1:657–66.
6. Borup R, Meyers J, Pivovar B, Kim YS, Mukundan R, Nancy G. et al. Scientific aspects of polymer electrolyte fuel cell durability and degradation. Chem Rev 2007;107:3904–51.

7. Hao T, Zhigang Q, Manikandan R, Elter JF. PEM fuel cell cathode carbon corrosion due to the formation of air/fuel boundary at the anode. J Power Sources 2006;158:1306–12.
8. Yu X, Ye S. Recent advances in activity and durability enhancement of Pt/C catalytic cathode in PEMFC Part I. Physico-chemical and electronic interaction between Pt and carbon support, and activity enhancement of Pt/C catalyst. J Power Sources 2007;172:133–44.
9. Yu X, Ye S. Recent advances in activity and durability enhancement of Pt/C catalytic cathode in PEMFC Part II: Degradation mechanism and durability enhancement of carbon supported platinum catalyst. J Power Sources 2007;172:145–54.
10. Costamagna P, Srinivasan S. Quantum jumps in the PEMFC science and technology from the 1960s to the year 2000: part i. fundamental scientific aspects. J Power Sources 2001;102:242–52.
11. Passalacqua E, Vivaldi M, Giordano N, Anotonucci PL, Kinoshita K. In: Proceedings of the 27th intersociety energy conversion engineering conference. 1992;929294:3.425–31.
12. Knights SD, Wilkinson DP, Campbell SA, Taylor JL, Gascoyne JM, Ralph TR. PCT WO 01/15247 A2, 1 March 2001.
13. Taylor JL, Wilkinson DP, Wainwright DS, Ralph TR, Knights SD. PCT WO 01/15249 A2, 1 March 2001.
14. Ye S, Beattie P, Campbell SA, Wilkinson DP. Anode catalyst compositions for a voltage reversal tolerant fuel cell. US Patent Appl 2004/0013935.
15. Ye S, Beattie P, Bai K. 2005 Fuel Cell Seminar. November 14–18, 2005. Palm Springs, CA, USA.
16. Ye S, Stability of anode catalysts and their effect on PEMFC performance degradation. Presentation to Gordon Research Conference, July 22–27, 2007. Bryant University, Rhode Island, USA.
17. Ralph TR, Hogarth MP. Catalysis for low-temperature fuel cells, Part II: the anode challenges. Platinum Metals Rev 2002;46:117–35.
18. Knights SD, Colbow KM, St-Pierre J, Wilkinson DP. Aging mechanisms and lifetime of PEFC and DMFC. J Power Sources 2002;127:127–34.
19. Taniguchi A, Akita T, Yasuda K, Miyazaki Y. Analysis of electrocatalyst degradation in PEMFC caused by cell reversal during fuel starvation. J Power Sources 2004;130:42–9.
20. Tsutsumi Y, Sone I, Nanba Y. In: Abstract of the 1986 fuel cell seminar. 1986 Oct 26–29; Tucson, AZ; 110.
21. Mitsuda K, Murahashi T. Air and fuel starvation of phosphoric acid fuel cells: a study using a single cell with multi-reference electrodes. J Appl Electrochem 1991;21:524–30.
22. Mitsuda K, Murahashi T. Polarization study of a fuel cell with four reference electrodes. J Electrochem Soc 1990;137:3079–85.
23. Sakamoto S, Karakane M, Maeda H, Miyake Y, Susai T, Isono T. In: Abstract of the 2000 fuel cell seminar. 2000 Oct 30–Nov 2; Portland, OR;141.
24. Billings RE. The hydrogen world view. Independence, MO: American Academy of Science, 1991.
25. Bevers D, Wohr M, Yasuda K, Oguro K. Simulation of a polymer electrolyte fuel cell electrode. J Appl Electrochem 1997;27:1254–64.
26. Lemons RA. Fuel cells for transportation. J Power Sources 1990;29:251–64.
27. Bernadi D, Verbrugge M. A mathematical model of the solid-polymer-electrolyte fuel cell. J Electrochem Soc 1992;139:2477–91.

28. Knights SD, De Vaal JW, Lauritzen MV, Wilkinson DP. Electrochemical fuel cell stack having a plurality of integrated voltage reversal protection diodes. US Patent 7235315. 2007.

29. Barton RH. Cell voltage monitor for a fuel cell stack. US Patent 6724194. 2004.

30. Knights SD, Taylor JL, Wilkinson DP, Wainwright DS. Fuel cell anode structures for voltage reversal tolerance. US Patent 6517962. 2003.

31. Tüber K, Pócza D, Hebling C. Visualization of water buildup in the cathode of a transparent pem fuel cell. J Power Sources 2003;124:403–14.

32. Park GG, Sohn YJ, Yang TH, Yoon YG, Lee WY, Kim CS. Effect of PTFE contents in the gas diffusion media on the performance of PEMFC. J Power Sources 2004;131:182–7.

33. Wei ZD, Ji MB, Hong Y, Sun CS, Chan SH, Shen PK. MnO_2–Pt/C composite electrodes for preventing voltage reversal effects with polymer electrolyte membrane fuel cells.J Power Sources 2006;160:246–51.

34. Knights SD, Taylor JL, Wilkinson DP, Campbell SA. PCT WO 01/15254 A2, 1 March 2001.

35. Tomcsányi L, De Battisti A, Hirschberg G, Varga K, Liszi J. The study of the electrooxidation of chloride at RuO_2/TiO_2 electrode using CV and radiotracer techniques and evaluating by electrochemical kinetic simulation methods. Electrochim Acta 1999;44:2463–72.

36. Consonni V, Trasatti S, Pollak F, O'Grady WE. Mechanism of chlorine evolution on oxide anodes study of pH effects. J Electroanal Chem 1987;228:393–406.

37. De Faria LA, Boodts JFC, Trasatti S. Electrocatalytic properties of Ru + Ti + Ce mixed oxide electrodes for the Cl_2 evolution reaction. Electrochim Acta 1997;42:3525–50.

38. Arikado T, Iwakura C, Tamura H. Some oxide catalysts for the anodic evolution of chlorine: reaction mechanism and catalytic activity. Electrochim Acta 1978;23:9–15.

39. Alves VA, Da Silva LA, Boodts JFC, Trasatti S. Kinetics and mechanism of oxygen evolution on IrO_2-based electrodes containing Ti and Ce acidic solutions. Electrochim Acta 1994;39:1585–9.

40. Mráz R, Srb V, Tich´y S. Experimental activation energies for evolution of oxygen and chlorine on oxide electrodes. Electrochim Acta 1973;18:551–4.

41. Beer H. British Patent 1,147,442. 1969.

42. Yeo RS, Orehotsky J, Visscher W, Srinivasan S. Ruthenium-based mixed oxides as electrocatalysts for oxygen evolution in acid electrolytes. J Electrochem Soc 1981;9:1900–4.

43. Melsheimer J, Ziegler D. The oxygen electrode reaction in acid solution on RuO_2 electrode prepared by the thermal decomposition method. Thin Solid Films 1988;163:301–8.

44. Loucka T. The reason for the loss of activity of titanium anodes coated with a layer of RuO_2 and TiO_2. J Appl Electrochem 1977;7:211–4.

45. Iwakura C, Sakamoto K. Effect of active layer composition on the service life of (SnO_2 and RuO_2)-coated Ti electrodes in sulfuric acid solution. J Electrochem Soc 1985;132:2420–3.

46. Burke LD, McCarthy M. Oxygen gas evolution at, and deterioration of, RuO_2/ZrO_2-coated titanium anodes at elevated temperature in strong base. Eletrochim Acta 1984;29:211–6.

47. Terezo AJ, Pereira EC. Preparation and characterization of Ti/RuO_2–Nb_2O_5 electrodes obtained by polymeric precursor method. Electrochim Acta 1999;44:4507–13.

48. Musiani M, Furlanetto F, Bertoncello R. Electrodeposited PbO_2+RuO_2: a composite anode for oxygen evolution from sulphuric acid solution. J Electroanal Chem 1999;465:160–7.

49. Bertoncello R, Cattarin S, Frateur I, Musiani M. Preparation of anodes for oxygen evolution by electrodeposition of composite oxides of Pb and Ru on Ti. J Electroanal Chem 2000;492:145–9.

50. Da Silva LM, De Faria LA, Boodts JFC. Electrochemical impedance spectroscopic (EIS) investigation of the deactivation mechanism, surface and electrocatalytic properties of $Ti/RuO_2(x)+Co_3O_4(1-x)$ electrodes. J Electroanal Chem 2002;532:141–50.

51. Hine F, Yasuda M, Noda T, Yoshida T, Okuda J. Electrochemical Behavior of the oxide-coated metal anodes. J Electrochem Soc 1979;126:1439–45.

52. Rasten E, Hagen G, Tunold R. Proc. energy and electro chemical processes for a cleaner environment. Pennington, NJ: The Electrochemical Society, 1991;151.

53. Rasten E, Hagen G, Tunold R. Electrocatalysis in water electrolysis with solid polymer electrolyte. Electrochim Acta 2003;48:3945–52.

54. Marshall A, Børresen B, Hagen G, Tsypkin M, Tunold R. First European hydrogen energy conference. 2003 Sep 2–5; Grenoble, France; CO1/71.

55. Marshall A, Børresen B, Hagen G, Tsypkin M, Tunold R. Nanocrystalline $Ir_xSn_{(1-x)}O_2$ electrocatalysts for oxygen evolution in water electrolysis with polymer electrolyte – effect of heat treatment. J New Mat Electrochem Syst 2004;7:197–204.

56. Gottesfeld S, Zawodzinski T. Polymer electrolyte fuel cells. In: Advances in electrochemical science and engineering. Alkire RC, Gerischer H, Kolb DM, Tobias CW, editors. Vol. 5. New York: Wiley, 1997;195–301.

57. Wilson M, Gottesfeld S. Thin-film catalyst layers for polymer electrolyte fuel cell electrodes. J Appl Electrochem 1992;22:1–7.

58. Millet P, Pineri M, Durand R. New solid polymer electrolyte composites for water electrolysis. J Appl Electrochem 1989;19:162–6.

59. Takenaka H, Torikai E, Kawami Y, Wakabayashi N. Solid polymer electrolyte water electrolysis. Int J Hydrogen Energy 1982;7:397–403.

60. Adams R, Shriner R. Platinum oxide as a catalyst in the reduction of organic compounds. III. Preparation and properties of the oxide of platinum obtained by the fusion of chloroplatinic acid with sodium nitrate. J Am Chem Soc 1923;45:2171–9.

61. Hutchings R, Müller L, Stucki S. A structural investigation of stabilized oxygen evolution catalysts.J Mater Sci 1984;19:3987–94.

62. Murakami Y, Ohkawauchi H, Ito M, Yahikozawa K, Takasu Y. Preparations of ultrafine IrO_2-SnO_2 binary oxide particles by a sol-gel process. Electrochim Acta 1994;39:2551–4.

63. Murakami Y, Tsuchiya S, Yahikozawa K, Takasu Y. Preparation of ultrafine IrO_2-Ta_2O_5 binary oxide particles by a sol-gel process. Electrochim Acta 1994;39:651–4.

64. Ito M, Murakami Y, Kaji H, Ohawauchi H, Yahikozawa K, Takasu Y. Preparation of ultrafine RuO_2-SnO_2 binary oxide particles by a sol-gel process. J Electrochem Soc 1994;141:1243–5.

65. Kameyama K, Shohji S, Onoue S, Nishimura K, Yahikozawa K, Takasu Y. Preparation of ultrafine RuO_2-TiO_2 binary oxide particles by a sol-gel process. J Electrochem Soc 1993;140:1034–7.

66. Lassali T, Boodts J, Bulhoes L. Effect of Sn-precursor on the morphology and composition of $Ir_{0.3}Sn_{0.7}O_2$ oxide films prepared by sol–gel process. J Non-Cryst Solids 2000;273:129–34.

67. Boiadjieva T, Cappelletti G, Ardizzone S, Rondinini S, Vertova A. Nanocrystalline titanium oxide by sol–gel method. The role of the solvent removal step. Phys Chem Chem Phys 2003;5:1689–94.

68. Bönnemann H, Richards R. Nanoscopic Metal Particles – Synthetic Methods and Potential Applications**. Euro J Inorg Chem 2001;2001:2455–80.

69. Toshima N, Yonezawa T. Bimetallic nanoparticles—novel materials for chemical and physical applications. New J Chem 1998;22:1179–201.
70. Bonet F, Delmas V, Grugeon S, Herrera-Urbina R, Silvert P, Tekaia-Elhsissen K. Synthesis of monodisperse Au, Pt, Pd, Ru and Ir nanoparticles in ethylene glycol. Nanostruct Mater 1999;11:1277–84.
71. Kurihara L, Chow G, Schoen P. Nanocrystalline metallic powders and films produced by the polyol method. Nanostruct Mater 1995;5:607–13.
72. Trasatti S. Physical electrochemistry of ceramic oxides. Electrochim Acta 1991;36:225–41.
73. Marshall A, Børresen B, Hagen G, Tsypkin M, Tunold R. Preparation and characterisation of nanocrystalline $Ir_xSn_{1-x}O_2$ electrocatalytic powders. Mater Chem Phys 2005;94:226–32
74. Chen XM, Chen GH, Yue PL. Stable Ti/IrO_x-Sb_2O_5-SnO_2 Anode for O_2 Evolution with Low Ir Content. J Phys Chem B 2001;105:4623–8.
75. Chen GH, Chen XM, Yue PL. Electrochemical Behavior of Novel Ti/IrO_x-Sb_2O_5-SnO_2 Anodes. J Phys Chem B 2002;106:4364–9.
76. Chen X, Chen G. Stable Ti/RuO_2–Sb_2O_5–SnO_2 electrodes for O_2 evolution. Electrochim Acta 2005;50:4155–9.
77. De Faria LA, Boodts JFC, Trasatti S. Physico-chemical and electrochemical characterization of Ru-based ternary oxides containing Ti and Ce. Electrochim Acta 1992;37:2511–8.
78. Da Silva LM, Boodts JFC, De Faria LA. Oxygen evolution at $RuO_2(x)$+$Co_3O_4(1−x)$ electrodes from acid solution. Electrochim Acta 2001;46:1369–75.
79. De Pauli CP, Trasatti S. Composite materials for electrocatalysis of O_2 evolution: IrO_2+SnO_2 in acid solution. J Electroanal Chem 2002;538:145–51.
80. Da Silva LM, Boodts JFC, De Faria LA. Chlorine evolution reaction at $Ti/(RuO_2$ +$Co_3O_4)$ electrodes. J Braz Chem Soc 2003;14:388–95.
81. De Faria LA, Boodts JFC, Trasatti S. Electrocatalytic properties of ternary oxide mixtures of composition $Ru_{0.3}Ti_{(0.7−x)}Ce_xO_2$: oxygen evolution from acidic solution. J Appl Electrochem 1996;26:1195–9.
82. Santana MHP, Da Silva LM, De Faria LA. Investigation of surface properties of Ru-based oxide electrodes containing Ti, Ce and Nb. Electrochim Acta 2003;48:1885–91.
83. Santana MHP, De Faria LA. Oxygen and chlorine evolution on RuO_2+ TiO_2 + CeO_2 + Nb_2O_5 mixed oxide electrodes. Electrochim Acta 2006;51:3578–85.
84. Dhar HP. A unitized approach to regenerative solid polymer electrolyte fuel cells. J Appl Electrochem 1992;23:32–7.
85. Shao Z, Yi B, Han M. Bifunctional electrodes with a thin catalyst layer for 'unitized' proton exchange membrane regenerative fuel cell. J Power Sources 1999;79:82–5.
86. Swette LL, Laconti AB, McCatty SA. Proton-exchange membrane regenerative fuel cells. J Power Sources 1994;47:343–51.
87. Chen G, Delafuente DA, Sarangapani S, Mallouk TE. Combinatorial discovery of bifunctional oxygen reduction – water oxidation electrocatalysts for regenerative fuel cells. Catalysis Today 2001;67:341–55.

18

High-temperature PEM Fuel Cell Catalysts and Catalyst Layers

Chaojie Song, Rob Hui and Jiujun Zhang

18.1 Opportunities and Challenges for High-temperature PEM Fuel Cells

Proton exchange membrane fuel cells (PEMFCs), including direct methanol fuel cells (DMFCs), are considered one of the most promising types of energy converting devices due to their low/zero pollution emission, high power density, and high energy conversion efficiency. However, commercialization faces several major technical challenges, the top three being high cost, unsatisfactory durability, and operational flexibility. The last several decades have witnessed great efforts to overcome these challenges. Operating a PEMFC at temperatures greater than 90 °C is one approach [1].

High-temperature PEM fuel cells (HT-PEMFCs) operated at > 90 °C are considered the next generation of fuel cell technology for cost reduction and reliability in terms of improved reaction kinetics, catalyst tolerance, heat rejection, and water management. However, one of the main challenges hindering their success is material degradation, in particular degradation of the catalyst and membrane.

In this chapter we will focus on catalysts and catalyst layers of HT-PEMFCs. To facilitate the discussion, the advantages and challenges of HT-PEMFCs are also discussed at the beginning of this chapter. We also present the current understanding of the degradation mechanism of catalysts at high temperatures. Finally, we review progress in HT-PEMFC catalysis and suggest future research directions.

18.1.1 Advantages of High-temperature PEM Fuel Cells

18.1.1.1 Improved Reaction Kinetics with Increasing Temperature [1, 2]
In a H_2/O_2 (or air) PEMFC, the cathode reaction is the oxygen reduction reaction (ORR):

$$O_2 + 4H^+ + 4e^- \leftrightarrow 2H_2O \tag{i}$$

The relationship between the current density and the overpotential is given by the following Equation 18.1:

$$I_c = i_{O_2}^o (e^{\frac{n_{aO}\alpha_O F\eta_c}{RT}} - e^{-\frac{n_{aO}(1-\alpha_O)F\eta_c}{RT}}) \tag{18.1}$$

where I_c is the cathode current density, $i_{O_2}^o$ is the exchange current density for cathodic O_2 reduction, $n_{\alpha O}$ is the number of electrons transferred in the rate determining step, α_o is the electron transfer coefficient, F is the Faraday constant, R is the gas constant (8.314 J.mol^{-1}.K^{-1}), and T is the temperature (K).

η_c in Equation 18.1 is the cathodic overpotentials, and is expressed as $E_c^r - E_c$, where E_c^r is the thermodynamic electrode potentials (or reversible electrode potentials) for the cathodic O_2 reduction reaction.

For the anode hydrogen oxidation reaction (HOR),

$$H_2 \leftrightarrow 2H^+ + 2e^- . \tag{ii}$$

The relationship between current density and overpotential is given by Equation 18.2

$$I_a = i_{H_2}^o (e^{\frac{n_{aH}\alpha_H F\eta_a}{RT}} - e^{-\frac{n_{aH}(1-\alpha_H)F\eta_a}{RT}}) \tag{18.2}$$

where I_a is the anode current density while $i_{H_2}^o$ is the exchange current density for anodic H_2 oxidation. η_a can be expressed as $E_a - E_a^r$, where E_a^r is the thermodynamic electrode potentials (or reversible electrode potentials) for anodic H_2 oxidation. $n_{\alpha H}$ is the number of electrons transferred in the rate determining step, α_H is the electron transfer coefficient.

The parameters of $i_{H_2}^o$, $n_{\alpha H}$, and α_H for H_2 oxidation, and $i_{O_2}^o$ $n_{\alpha O}$, and α_o for O_2 reduction can be obtained from experimental measurements based on Equations 18.1 and 18.2.

In a fuel cell, the current density for both anode and cathode are equal. Thus I_c in Equation 18.1 equals I_a in Equation 18.2. Since the exchange current density of H_2 oxidation (10^{-4} A/cm^2) is significantly larger than that of O_2 reduction ($\sim 10^{-9}$ A/cm^2), the fuel cell reaction kinetics is mainly dominated by the O_2 reduction reaction.

Temperature Effect on the Exchange Current Density
Increase in temperature leads to an increase in exchange current density. For both the H_2 oxidation and O_2 reduction reactions, the exchange current density change

with temperature follows the Arrhenius Equations 18.3 and 18.4 for cathode and anode, respectively:

$$i_{O_2}^o = I_{O_2}^o e^{-(E_c^o / RT)} \tag{18.3}$$

$$i_{H_2}^o = I_{H_2}^o e^{-(E_a^o / RT)} \tag{18.4}$$

where $I_{O_2}^o$ and $I_{H_2}^o$ are the cathode and anode exchange current densities at infinite temperature, respectively, E_c^o and E_a^o are the reaction activation energies for cathode and anode, respectively, while R and T have their usual significance. According to these equations, the linear plots of log($I_{O_2}^o$) ~1/T and log($I_{H_2}^o$) ~1/T can give the slopes, from which the reaction activation energies can be obtained. For the O_2 reduction reaction on Pt catalysts, the reaction activation energy is reported to be in the range of 21–83 kJ/mol. The values obtained are strongly dependent on the catalysts used. For the H_2 oxidation reaction, reaction activation energies of 10–35 kJ/mol were reported on Pt catalysts, also depending on the catalysts used [2].

Temperature Effect on Other Kinetic Parameters
Increasing temperature can also affect the kinetic parameters ($n_{\alpha H}$, α_H, $n_{\alpha O}$, and α_o). Although, the temperature effect on $n_{\alpha H}$, α_H, and $n_{\alpha O}$ is insignificant, the effect of temperature on α_o is not. The electron transfer coefficient for ORR (α_o) on a Pt electrode is dependent on temperature, given by Equation 18.5

$$\alpha_O = \alpha_O^o T \tag{18.5}$$

where α_O^o equals 0.001678 and T is temperature in Kelvin [2, 3].

In summary, the increase in reaction kinetics for both the ORR and the HOR is mainly due to the increase in the exchange current density. For the ORR, the change in the electron transfer co-efficiency (α_o) with temperature can also affect the ORR kinetics. Therefore, it is beneficial to operate a fuel cell at higher temperatures for kinetic improvement of the fuel cell reactions.

18.1.1.2 Improved Contaminant Tolerance with Increasing Temperature

CO Poisoning of Pt Surface
Typical low-temperature proton exchange membrane fuel cells (LT-PEMFCs), operated at temperatures lower than 90 °C, use H_2 as fuel. H_2 is not a naturally occurring resource, and is mainly produced by reforming organic fuels such as natural gas and methanol or by coal gasification. The reforming process produces H_2 with traces of impurities, mainly CO, H_2S, and SO_2, among which CO is the

most challenging because it can strongly adsorb on the Pt catalyst surface and thereby block H_2 absorption. Normally, CO has two adsorption modes with a Pt catalyst: linear-bond CO and bridge-bond CO. It was found that CO absorption occurred mainly through a linearly bonding mode [4], which can create a higher CO surface coverage and lead to severe catalyst poisoning. Based on the linear adsorption model, at a fixed overpotential the H_2 oxidation current was related to the CO surface coverage by Equation 18.6 [5, 6]:

$$\frac{i_{CO+H_2}}{i_{H_2}} = (1-\theta_{CO})^2 \tag{18.6}$$

where i_{CO+H_2} is the H_2 oxidation current density in the presence of CO with a surface coverage of θ_{CO} and i_{H_2} is the current density without CO present. Equation 18.6 holds for both planar electrodes and gas diffusion electrodes in phosphoric acid electrolytes as well as in phosphoric acid fuel cells. However, in PEMFCs, Igarashi et al. [7] suggested that the current ratio should be directly proportional to $(1-\theta_{CO})$ rather than $(1-\theta_{CO})^2$. Nonetheless, increasing CO coverage leads to a decrease in the hydrogen oxidation current.

The exchange current density for H_2 oxidation on a clean surface ($i_{H_2}^o$) and on a poisoned Pt surface ($i_{H_2+CO}^o$) can be given by the following equations:

$$i_{H_2}^o = 2Fk_{at}C_{H_2}(1-\theta_0)^2 \tag{18.7}$$

$$i_{H_2+CO}^o = 2Fk_{at}C_{H_2}(1-\theta_0)^2(1-\theta_{CO})^2 \tag{18.8}$$

where k_{at} is the chemical rate constant for H_2 dissociation, C_{H_2} is the concentration of H_2 in the bulk electrolyte, and θ_0 is the equilibrium coverage of the surface by H_2 at a current density of zero. The exchange current density of the HOR on a CO-poisoned surface is smaller than that on a non-poisoned surface. Higher θ_{CO} results in a low exchange current density for the HOR.

CO poisoning of the Pt surface could also increase the activation energy of the H_2 oxidation reaction. Dahr et al. [4] reported that the reaction activation energy could be increased from 1.8 kCal/mol for pure H_2 to 10.6 kcal/mol for H_2 containing 8.7% CO.

Temperature Effect on CO Adsorption
The adsorption of CO on the Pt electrode has a negative entropy of –39 cal/mol/K [4], leading to a decrease in standard free energy as temperature increases. The coverage of CO follows Equation 18.9 [4]:

$$\theta_{CO} = \frac{-\Delta G^0}{r} - \frac{RT}{r}\ln H + \frac{RT}{r}\ln[CO]/[H_2] \qquad (18.9)$$

where ΔG^0 is the standard free energy of adsorption, r is the interaction parameter, and H is the Henry's law constant for CO solubility. As the temperature increases, the ΔG^0 value decreases, resulting in a decrease in θ_{CO} at a fixed ratio of [CO]/[H$_2$]. According to Equation 18.6, the decrease in θ_{CO} can effectively improve the H$_2$ oxidation current density. In other words, at high temperature, if θ_{CO} is kept constant, (unchanged), a high [CO]/[H$_2$] ratio will be allowed according to Equation 18.9, suggesting that the catalyst is more tolerant to CO at high temperature. Experimental results reported by a number of studies using half cells and fuel cells showed that CO tolerance could be increased by 25 times, from several tens of ppm to 1000–1300 ppm, when temperature was increased from 70 to 120 °C [8–11]. At 200 °C, CO tolerance is even up to 30,000 ppm [8].

18.1.1.3 Improving Water Management by Increasing Temperature

One of the key components in PEMFCs is the proton exchange membrane (also called the polymer electrolyte membrane). The membrane conducts protons from anode to cathode and separates anode from cathode. In addition, a small amount of polymer electrolyte (ionomer) is also needed in the catalyst layer to provide a three-phase boundary where proton, electron, and gas can meet for the reaction. Currently the commonly used polymer electrolyte is Nafion, a sulfonated perfluorinate polymer. Its proton conductivity is strongly dependent on water content. In general, higher water content results in higher conductivity. To provide enough water for the membrane, a humidifier is normally required in a PEMFC system.

Water transport involved in a PEMFC includes five parts [12]: water brought in by humidified gas, water removed at the outlet, electroosmosis from anode to cathode, back-diffusion from the cathode to the anode side, and water produced from the fuel cell reaction at the cathode side. During fuel cell operation, protons produced at the anode catalyst layer must travel through the polyelectrolyte to the cathode, where they react with O$_2$ and electrons to form product water. The protons produced at the anode will react with water to form hydronium ions such as H(H$_2$O)$_n^+$, which then travel to the cathode. The amount of water transferred with each proton is called the electroosmotic drag coefficient, which is in the range of 0 to 5 depending on the anode humidification [13–15]. Back-diffusion refers to water transport due to the water concentration gradient. The water accumulated at the cathode will back-diffuse from the cathode to the anode through the polyelectrolyte. The water mass balance inside an MEA can be described as follows: at the anode, water gain is caused by humidified hydrogen and water back-diffusion, while water loss is caused by electroosmotic drag and the evaporated water brought out by outlet gases.

There exists an optimum water balance during fuel cell operation. Therefore, maintaining the water balance for both anode and cathode sides is important. Unbalanced water transport at the anode side may cause anode dehydration and

unbalanced water transport at the cathode side may cause water flooding. For example, if the fuel cell is operated at high current densities, extra liquid water will be produced by the cathode reaction. If this extra water is not removed effectively, water flooding occurs, resulting in low performance. At high temperatures, the extra liquid water in the fuel cell membrane electrode assembly (MEA) may be evaporated, facilitating rapid water removal. Figure 18.1 shows the fuel cell polarization curves obtained at 80 °C and 120 °C. At 120 °C the cell performance in the high current density range is much better than that at 80 °C. This is due to improved water management.
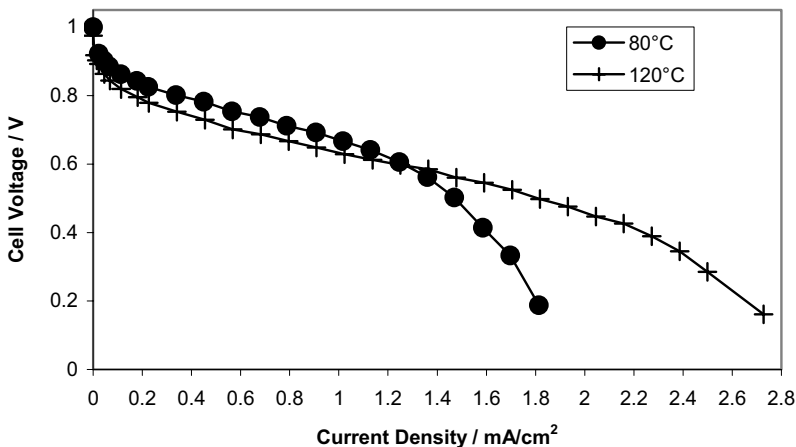
Figure 18.1. Polarization curves obtained at 80 °C and 120 °C with a backpressure of 30 psig. MEA active area: 4.4 cm^{-2}. H$_2$/air gases with 100% RH [2]. (Reprinted from Electrochimica Acta, 52(7), Song C, Tang Y, Zhang J, Zhang J, Wang H, Shen J, et al., PEM fuel cell reaction kinetics in the temperature range of 23–120 °C, 2552–61, ©2007, with permission from Elsevier.)

18.1.1.4 Improved Heat Rejection with Increased Temperature [1, 16]
A considerable amount of the energy (about 40–50%) produced by an operating PEMFC is in the form of heat. In order to keep the fuel cell at low temperature operation, this heat must be removed quickly. However, if the fuel cell operates at low temperature (< 90°C), the heat rejection rate by natural air convection is not sufficient. A cooling sub-system is needed in a fuel cell system for heat removal. This cooling sub-system increases not only the system parasitic loss but also the volume and weight of the fuel cell system. The heat transfer rate is proportional to the temperature difference between the fuel cell stack and the environment. A larger temperature difference results in a faster heat transfer rate. Thus, increasing the fuel cell operating temperature could increase the heat transfer rate, reducing the load for the cooling system. On the other hand, if the fuel cell can be operated at temperatures above 100 °C, the heat can be recovered as steam, which is then usable for heating purposes. The reduced load and the recovered heat could increase the mass-specific and volume-specific power density and increase the overall system efficiency.

18.1.2 Routes to Increase the Operating Temperature

Currently the materials in PEMFCs are designed for low-temperature operation. Two key materials, catalyst and membrane, must be considered if the fuel cell is operated at high temperatures. For example, the Nafion membrane has shown high ionic conductivity at temperatures lower than 80 °C at fully hydrated conditions. In the presence of liquid water, Nafion could absorb 21–22 H_2O per sulfonic acid group. At temperatures higher than 100 °C, each sulfonic acid group can only absorb 14 H_2O, which shows a lower conductivity. In addition, operating Nafion membranes at temperatures greater than 100 °C could lead to internal structure change, resulting in a permanent loss of conductivity [17]. With respect to catalysts, the currently used carbon-supported catalysts can easily loss their catalytic activity if the fuel cell is operated at high temperatures, mainly due to carbon support oxidation. The oxidation of carbon support results in: (1) the delaminating of metal catalyst particles from the carbon supports; these delaminated metals (for example, Pt) could become electronically isolated and thereby useless; (2) the sintering or agglomeration of the Pt catalyst. At higher temperatures, the Pt particles tend to form larger particles through a dissolving-redepositing mechanism. This catalyst degradation causes loss in catalyst electroactive surface area, reduction in catalytic activity, as well as water flooding. The effect is more pronounced when PEMFCs are operated at high temperatures of 120–300 °C [18].

Two major paths exist to increase operating temperature: to develop high-temperature proton exchange membranes or high-temperature catalysts. So far most of the work on HT-PEMFCs has been focused on the development of membranes. For example, new membranes such as polybenzoimidazole (polymer electrolyte PBI) membrane, and inorganic materials doped with Nafion composite membranes such as zirconium phosphate-Nafion composite membrane have been developed [1, 19]. Solid acids such as $CsHSO_4$ and CsH_2PO_4 have also been used as electrolyte materials in fuel cells that can be operated at temperatures up to ~250°C [20–22]. Only a few studies have focused on high-temperature catalyst development, and these will be introduced in Sections 18.2.1 and 18.2.3.

18.1.3 Challenges of Catalysts/Catalyst Layers

Currently the most commonly used catalysts in PEMFCs are composed of carbon-supported Pt. In long-term fuel cell operation, the stability and durability of the catalyst is always problematic. Carbon oxidation and Pt sintering or agglomeration can result in loss of electroactive surface on the catalysts, degrading fuel cell performance. These problems are more pronounced when the PEMFC is operated at high temperatures. Our recent experiments showed that when a PEMFC was operated at 300 °C for 4 hours, significant performance loss was observed (see Figure 18.2). The imminent challenge is to develop new catalysts that can have long-term stability under fuel cell operating conditions and survive high-temperature operation.
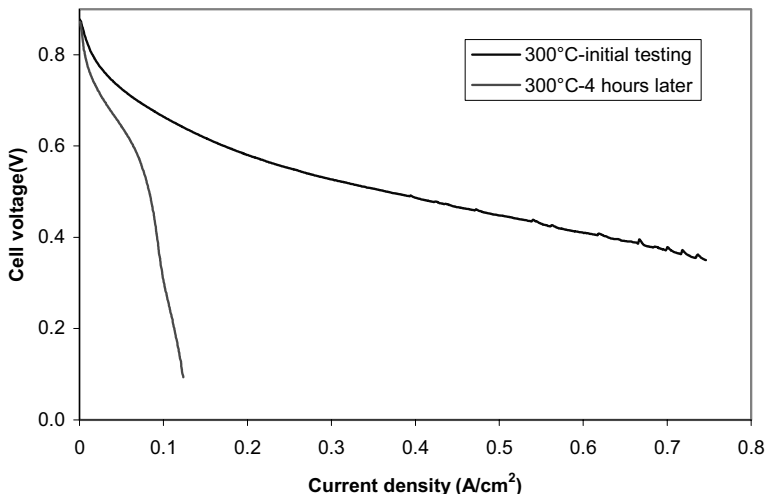
Figure 18.2. Polarization curves of a PBI-based MEA, obtained at 300 °C initially and after 4 hours [23]. Ambient backpressure, H_2 flow rate: 0.1 L/min; air flow rate: 0.4 L/min.

Catalyst layers in state-of-the-art PEMFCs are prepared using catalyst ink, which consists of catalyst, ionomers (Nafion), and other solvents. The structure and the components of the catalyst layer have been optimized for low-temperature operation. However, at high-temperature operation, due to the absence of liquid water, the mass transport in the catalyst layer should be different. Thus, catalyst layers with different structures and different components should be designed for high-temperature operation. Another challenge is the ionomer used in the catalyst layer. Currently Nafion is primarily used as the ionomer in the catalyst layer to conduct protons for most PEMFCs. As we mentioned before, at high temperatures, the conductivity of Nafion can decrease, resulting in poor fuel cell performance. Thus, selecting suitable ionomers for high-temperature catalyst layers is also critical in HT-PEMFC research.

18.2 Catalysts for High-temperature PEM Fuel Cells

18.2.1 Current Research Activities

For a low-temperature PEMFC, the most common problems for reliability and durability are degradation of catalysts and catalyst support oxidation. A number of papers have been published in this area, the details of which will be given in Section 18.2.2. It is expected that at high temperatures, these problems will be more pronounced. Recently, however, high-temperature PEMFC catalysts have begun to attract researchers' attention, and several papers have been published. Liu et al. [24, 25] developed a Pt_4ZrO_2/C catalyst and found that it was more durable than Pt/C in PEMFCs operated at 150 °C. Other research activities have mainly focused on the development of oxidation-resistant supports (Section 18.2.3).

18.2.2 Degradation of Catalysts at High Temperatures

Research on the degradation of catalysts has mainly focused on low-temperature PEMFCs (< 90 °C) [28–42]. For high-temperature operation, studies on catalyst degradation have been in the areas of phosphoric acid fuel cells (PAFCs) and PBI-based MEAs [41–43]. Since the catalysts used in PAFCs are the same as those in PEMFCs, the degradation mechanisms should be applicable to high-temperature PEMFCs. Normally, catalyst degradation includes two parts: Pt catalyst degradation and carbon support oxidation.

18.2.2.1 Pt Degradation

Pt degradation is manifested by Pt particle agglomeration, Pt particle isolation, and Pt dissolution. The observable phenomena are an increase in Pt particle size and a loss of electroactive surface area. For example, Pt particle size is ~3 nm at the beginning of lifetime (BOL) testing, while after the durability testing or accelerated aging testing the particle size could increase to 10 or even 20 nm [26–39].
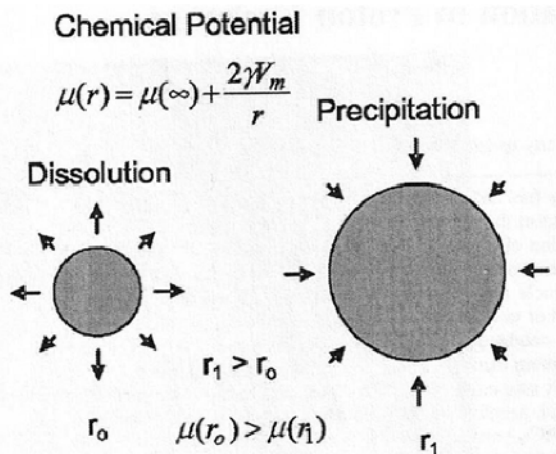
Figure 18.3. A schematic showing the mechanism of particle growth by dissolution/precipitation. The chemical potential of smaller particles is higher than that of larger particles [32]. (Reproduced by permission of ECS—The Electrochemical Society, from Virkar AV, Zhou Y. Mechanism of catalyst degradation in proton exchange membrane fuel cells.)

Although other degradation mechanisms such as crystalline migration have been proposed [27–31], it seems that experimental results support an Ostwald ripening process, where the growth of catalyst particle size during PEMFC operation is ascribed to Pt dissolution and re-deposition [32]. On the other hand, the oxidation of catalyst carbon support can also lead to loss of Pt nanoparticles and particle size growth (see Section 18.2.2.2). In the Ostwald ripening process, smaller platinum particles dissolve in the ionomer phase and re-deposit on larger particles, resulting in the disappearance of small particles and the growth of larger particles. Dissolution of the smaller Pt particles occurs in either neutral (Pt^0) or

ionic form (Pt^{2+}) or both, due to the chemical potential difference of differently sized particles as well as the high operating potential on the catalysts (cathode side). Figure 18.3 shows the Ostwald ripening process and the chemical potential of the particles. The transport of these species is through the liquid and/or the ionomer, and the transport of electrons is through the carbon support, as shown in Figure 18.4.
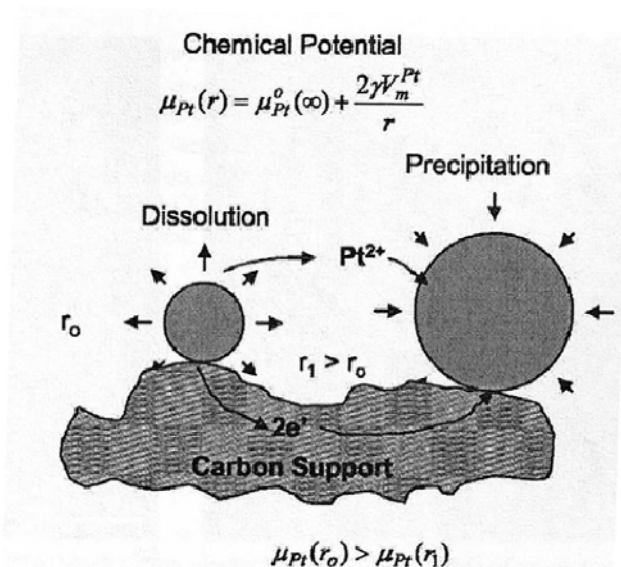
Figure 18.4. Transport of Pt from a smaller particle to a larger particle by coupled transport of Pt^{2+} through the liquid and/or ionomer and the transport of electrons through the carbon support when the Pt particles are in contact with electronically conducting carbon [32]. (Reproduced by permission of ECS—The Electrochemical Society, from Virkar AV, Zhou Y. Mechanism of catalyst degradation in proton exchange membrane fuel cells.)

In a PEMFC, the potential is usually high at the cathode side under operating conditions, especially under open circuit conditions, where the following reaction occurs [32]:

$$Pt \rightarrow Pt^{2+} + 2e^- \tag{iii}$$

$$Pt + H_2O \rightarrow PtO + 2H^+ + 2e^- \tag{iv}$$

$$PtO + 2H^+ \rightarrow Pt^{2+} + H_2O \tag{v}$$

The Pt^{2+} can also transport in the catalyst layer to the membrane. Soluble Pt^{2+} was detected in the effluent of the cathode [33]. Pt particles were observed in the membrane [31, 33–35], and redistributed Pt was also found in the catalyst layer [31]. Figure 18.5 shows the Pt species transport re-distribution in the catalyst layer.
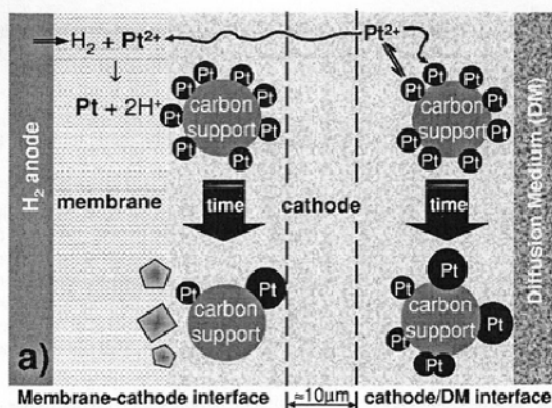
Figure 18.5. Schematic representing platinum surface area loss on the nanometer scale, where platinum particles grow on carbon support via Ostwald ripening, and on the micrometer scale, where dissolved platinum species diffuse toward the membrane [31]. (Reproduced by permission of ECS—The Electrochemical Society, from Ferreira PJ, la O' GJ, Shao-Horn Y, Morgan D, Makharia R, Kocha S, et al. Instability of Pt/C electrocatalysts in proton exchange membrane fuel cells.)

The Pt particle growth is `understandable due to the high cathode potential. However, at the anode side, Pt particle growth was also observed, although the situation was less severe than at the cathode side. For example, after 10,000 cycles of scanning the cathode potential from 0.6 V to 1.0 V (anode as both reference and counter electrode), Pt particle size at the anode side was found to increase from 2.3 nm to 4.0 nm, and at the cathode side from 2.3 to 10.5 nm [31]. In fuel cell lifetime testing, particle growth of the anode catalyst was also reported [34]. Since most studies have focused on the cathode side, no satisfactory explanation for anode catalyst growth is given in the literature. Based on results for other nanoparticles such as Ag, Xie et al. explained that the standard potential of nanoparticles is different from that of the bulk materials, and that the standard redox potential can be shifted to a more negative value [34]. The negative shift in redox potential could lead to the oxidation of Pt nanoparticles at the anode side, resulting in dissolution and re-deposition [34].

It is also observed that the Pt degradation rate in PEMFCs is dependent on operating conditions, cell voltage, and temperature. Unfortunately, the literature results are not comparable because different conditions and methods were used. A surface area loss rate of 7.14×10^{-3} m^2/g-Pt/hr over a 1000-hour period of operation was reported at a current density of 1.07 A/cm^2, a backpressure of 30 psig, and 100% RH [34]. A 63% surface area loss was reported for an MEA after 10,000 potential cycles in the voltage range of 0.6–1.0 V at 80 °C [31].

High cell voltage (or high cathode potential) can lead to a high Pt degradation rate. This is because Pt oxidation is favored at high electrode potential. Wang et al. [30] studied the effect of cell voltage on Pt dissolution rate and found that an increase in potential from 0.65 to 1.1 V could lead to an increase in the Pt dissolution rate. However, further increase in potential led to a decrease in

dissolution rate. Aragane et al. found that in phosphoric acid fuel cells, the Pt dissolution rate consistently increased as cell voltage was changed from 0.6 to 1.0 V [41].

An increase in temperature can result in an increase in Pt degradation. Bi et al. studied catalyst degradation by cycling the MEA potential between 0.87–1.2 V at 40, 60, and 80 °C, respectively [26]. They found that the reduction in surface area with the potential cycling could be described by Equation 18.10:

$$\ln[\frac{S(N) - S_{min}}{S_0 - S_{min}}] = -kN \tag{18.10}$$

where N is the potential cycle number, k is the first rate order constant for Pt degradation, S_{min} is the minimum surface area subjected to potential cycling, and S_0 is the initial surface area of the MEA. The first rate order for Pt degradation, k, is related to the temperature according to Equation 18.11 [37]:

$$\ln[k] = \ln(G) - \frac{E_a}{RT} \tag{18.11}$$

where E_a is the activation energy for the Pt degradation reaction, G is the degradation rate constant at infinite temperature, while R and T have their usual significance. For Pt/C catalysts in the temperature range of 65–90 °C, an activation energy of 25 kJ/mol was obtained by Bi et al. [26] and 23 kJ/mol by Debe et al. [36]. In a high-temperature range of 150–230 °C, Aragane et al. also found that the Pt dissolution rate increased with increasing temperature [41]. Using the data of Aragane et al., we calculated that the activation energy of Pt dissolution was around 25 kJ/mol (as shown in Figure 18.6, where the unit of k is mg/cm^2/hr).
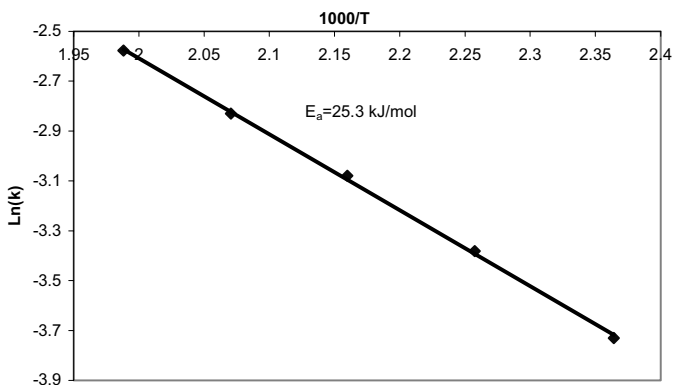
Figure 18.6. Plot of Ln(k) vs. 1000/T, calculated based on the data from [41]

18.2.2.2 Carbon Support Degradation

Due to its unique properties, such as high electric conductivity, carbon is the most commonly used catalyst support for PEMFCs. An ideal carbon support should have

good electrical conductivity, high surface area, and a porous structure that allows for filling with polymer electrolyte, maximising the three-phase interface (catalyst – proton conductor – electron conductor) [44]. Although other kinds of carbon have been studied, the most commonly used carbon support is Vulcan XC72.

In PEMFCs, carbon support particles together with catalyst particles are exposed to corrosive environments, including high water content, low pH, high potential (cathode side), high oxygen concentration, and high temperature (> 90°C). Carbon corrosion or oxidation can be expressed as reaction (vi):

$$C + H_2O \rightarrow CO_2 + 4H^+ + 4e^- \qquad E^o = 0.207 \text{ V vs. SHE} \qquad (vi)$$

where E^o is the Nernst electrode potential at standard conditions and SHE is the standard hydrogen potential. Although the operating potential at the cathode side (0.5–0.9 V) is much more positive than 0.207 V, carbon corrosion is very slow at a typical PEMFC operating temperature due to its sluggish reaction kinetics. This slow oxidation rate makes carbon support an ideal material in low-temperature PEMFCs. However, for high-temperature operation, carbon corrosion will become more pronounced, especially at an operating temperature of ~200 °C [45, 46]. On the other hand, even in low-temperature operation, carbon corrosion can be problematic over prolonged lifetime testing [46–48]. In addition, most of the studies on carbon corrosion have shown that the presence of Pt on the carbon support can accelerate the corrosion of carbon [49–54]. Stevens and Dahn [49] found that carbon corrosion increased as Pt loading increased (Figure 18.7).
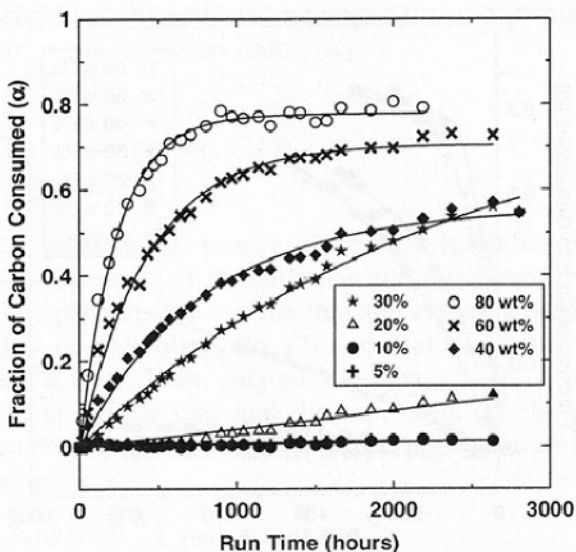
Figure 18.7. Isothermal weight data for samples with different platinum loadings held at 150 °C [49]. (Reprinted from Carbon, 43(1), Stevens DA. and Dahn JR, Thermal degradation of the support in carbon-supported platinum electrocatalysts for PEM fuel cells, 179–88, ©2005, with permission from Elsevier.)

Kinetically, carbon is oxidized through the following mechanism, expressed by reactions (vii-ix) [57, 58], where the carbon in the lattice structure is oxidized to generate surface oxide, followed by hydrolysis and gasification of oxidized carbon to CO_2. The subscript "s" in reactions (vii–ix) denotes the surface species.

$$C_s \rightarrow C_s^+ + e^- \qquad\qquad \text{(vii)}$$

$$C_s^+ + 1/2H_2O \rightarrow C_sO + H^+ \qquad\qquad \text{(viii)}$$

$$C_sO + H_2O \rightarrow CO_2 + 2H^+ + 2e^- \qquad\qquad \text{(ix)}$$

Temperature has a significant effect on carbon oxidation. An increase in temperature leads to a significant increase in the carbon oxidation rate. Roen et al. [50] find that for both Vulcan carbon and Pt/C, increasing temperature from 30 °C to 70 °C could result in an increase in CO_2 production due to carbon oxidation, as shown in Figure 18.8. Stevens and Dahn found a similar trend in the temperature range of 125–195 °C, and reported a CO oxidation activation energy of 106 kJ/mol on Pt/C catalyst [49].
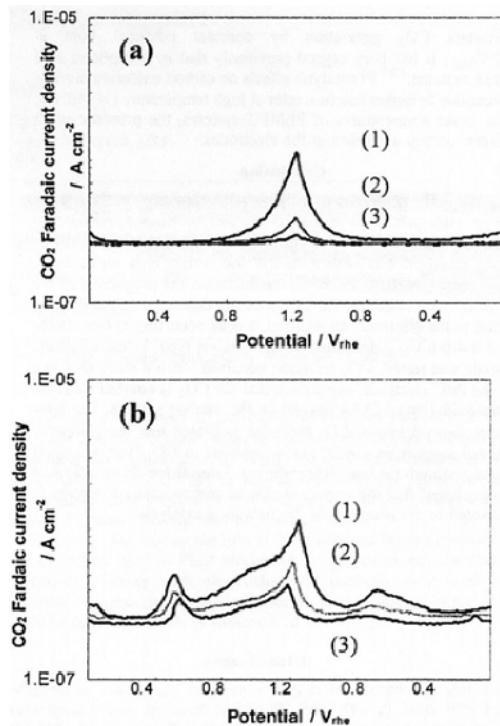
Figure 18.8. CO_2 mass spectrum profiles on (a) Vulcan carbon and (b) commercially available Primea Gore MEA cathode (Pt/C) at (1) 70 °C, (2) 50 °C, and (3) 30 °C [50]. (Reproduced by permission of ECS—The Electrochemical Society, from Roen LM, Paik CH, Jarvi TD. Electrocatalytic corrosion of carbon support in PEMFC cathodes.)

Mathias et al. found that the carbon oxidation rate (represented by CO_2-producing current) for 50% Pt/C could be expressed as Equation 18.12 [47]:

$$i_{CO_2} \propto 10^{\frac{E}{TS}} e^{-E_a/(RT)} t^{-m} \qquad (18.12)$$

where E is the electrode potential, S is the entropy, E_a is the activation energy (67 kJ/mol), and m is the time decay parameter, which equals 0.3; R and T have their usual significance. According to this equation, the carbon losses at 0.9 V and 1.2 V at 80 °C for two catalysts (50% Pt/C and a 30% Pt-alloy/C$_{corr-resistant}$) were calculated, as shown in Figure 18.9. It can be seen that the corrosion-resistant carbon gives a low carbon corrosion rate at both voltages.
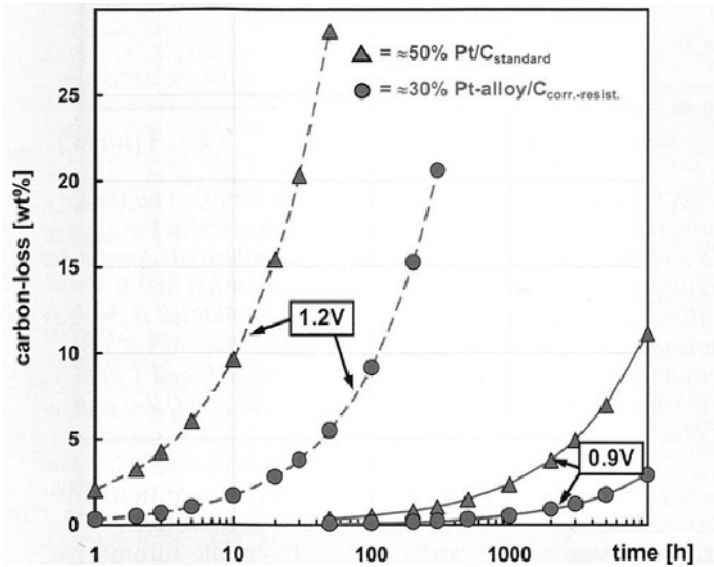
Figure 18.9. Carbon weight loss vs. time for two different catalysts at both 0.9 V and 1.2 V and 80 °C (100% RH, 120 kPa$_{abs}$) [47]. (Reproduced by permission of ECS—The Electrochemical Society, from Mathias MF, Makharia R, Gasteiger HA, Conley JJ, Fuller TJ, Gittelman CJ, et al. Two fuel cell cars in every garage?)

The increase in the carbon oxidation rate with increasing temperature compromises the suitability of carbon application in HT-PEMFCs. Although the carbon-supported catalysts used in phosphoric acid fuel cells have achieved 40,000 hours in lifetime tests, carbon corrosion is still one of the problems [57]. For HT-PEMFCs, since the operating temperature is close to that in a PAFC, carbon corrosion is expected to be a problem as well, one that needs attention. Carbon oxidation not only results in the loss of carbon, destroying the attachment of Pt nanoparticles to carbon particles, but also changes the hydrophobicity of the carbon surface. Formation of surface carbon–oxygen groups makes the surface more hydrophilic, resulting in water management problem [58].

18.2.3 Catalyst Support Strategy to Improve High-temperature Catalysts/Catalyst Layers

In order to overcome the carbon corrosion problem, several strategies have been developed. Carbon materials with more graphite component showed improved corrosion resistance capability [59–61]. Carbon nanotubes (CNT) have been found to be more corrosion-resistant than Vulcan carbon [62–66]. In 168 hours of measurement under a simulated PEMFC cathode environment, multiwalled carbon nanotube (MWCNT) showed a 30% lower corrosion current than Vulcan carbon [63]. In this period of oxidation, 80% of the Pt surface area was lost for Pt/Vulcan carbon while only a 37% loss was observed for the MWCNT-supported Pt catalyst [64]. Shao et al. [65] reported that Pt/C degraded 49%, while Pt/CNT degraded 26% in 192 hours of testing under simulated PEM fuel cell conditions.

Boron-doped diamond was used as a support for Pt catalysts and showed some improved oxidation resistance [67, 68]. 2000 cycles of potential dynamic test between the potentials of oxygen and hydrogen evolutions in 0.1 M $HClO_4$ (1–6 mA/cm^2) showed that the dispersed Pt particles on the Boron-doped diamond support were extremely stable, as no loss in the activity was observed [67]. During 2 hours of polarization in 85% H_3PO_4 at 170 °C and 0.1 A/cm^2, the Pt/boron-doped composite electrode was also extremely stable [68]. These results might make the boron-doped diamond a good candidate for high-temperature PEMFC applications.

Wang et al. proposed some strategies to develop durable catalyst supports, using graphitized carbons as scaffolds and protecting the carbon surface with tungsten carbide, oxycarbides, or conductive metal oxides [69]. Unfortunately, no durability results were reported.

Another strategy is to manipulate the interaction between the support and the catalyst. Enhanced interaction between the catalyst and the carbon support may improve the catalytic activity and enhance the stability of the electrocatalyst [70–72]. Jacques et al. [70] investigated the interaction between Pt nanoparticles and zeolite support, and suggested that this interaction may modify the catalytic properties of the Pt nanoparticles. Bagotzky et al. [71] studied several different supports for Pt catalysts and observed that the interaction between the Pt and the supports could affect the catalytic activity. Halla et al. [72] studied the interaction between the Pt nanoparticles and the carbon support, and proposed that this interaction controlled the growth of Pt particles. These studies suggested that the catalytic properties and the stability of Pt nanoparticles could be manipulated by changing the metal-support interaction.

Introducing a transition metal oxide to the Pt/C catalyst could also lead to improved corrosion resistance [24, 25, 73–75]. It was reported that introducing TiO_2 to the Pt/C catalyst, forming Pt/TiO_2/C, could avert Pt agglomeration, improve the catalytic activity, and enhance the catalyst's CO tolerance [73–75]. Introducing ZrO_2 also led to improved corrosion resistance [24, 25]. This may be due to the interaction between the Pt and the transition metal oxide. Pt and Ti/Zr/W are metals with d-band electrons. The interaction between metals is expected to be stronger than that between metal and non-metal, such as Pt and carbon.

Heat-treatment could also stabilize the carbon support against electrochemical corrosion and improve catalyst stability [61, 76–78]. Stonehart [77] showed that

heat-treatment could stabilize the carbon against corrosive degradation and increase the lifetime of the carbon support-based Pt catalysts. It was realized that the Pt catalysts with heat-treated carbon support were more stable than those without heat-treated supports, due to the strong interaction between the Pt particles and the basic anchoring sites on the carbon surface. In addition, heat treatment of the carbon support at 370 °C in air improved catalyst stability to the extent that it even remained stable in a 60 °C sulphuric acid solution [78]. Proper heat treatment of carbon supports could also impart to the catalyst the graphitic character of the carbon, resulting in improved corrosion resistance [61, 79].

18.2.4 High-temperature Catalyst Layers – Components and Structure

The catalyst layer structures and components in HT-PEMFCs should be different from those used in low-temperature PEMFCs. For example, water management in an HT-PEMFC is not a problem and thus the required hydrophobicity of the catalyst layer might not be a factor for HT-MEAs. Obviously, Nafion, the commonly used ionomer for low-temperature MEAs, is not suitable for HT applications. Unfortunately, the design and evaluation of HT catalyst layers have not yet attracted attention. This is most likely due to the lack of suitable materials for HT-MEA fabrication. For example, although a significant number of publications look at high-temperature membrane and ionomer development, these ionomers have seldom been used in a catalyst layer to replace Nafion, possibly due to the technical difficulties of doing so.

Phosphoric acid-doped polybenzimidazole (PA-PBI) membrane is the most common type for HT-PEMFCs. It was also introduced in the catalyst layer as an ionomer to improve proton conductivity [8, 80–83]. Similar to the application of Nafion ionomer in the catalyst layer, polybenzimidazole (PBI) solution was incorporated into the catalyst layer by an impregnation method (the electrode was soaked in a PBI solution), by a gluing method (the PBI membrane was coated by PBI solution), or by a brushing method (the PBI solution was brushed onto the electrode) [80].

Unfortunately, while catalyst components and structures in low-temperature MEAs have attracted considerable attention, optimization of high-temperature catalyst layer structures and components seems little studied. Lobato et al. [83] investigated the effect of the catalytic ink preparation method on the performance of HT-PEMFCs. They employed two methods for catalyst layer preparation: the solution method and the colloid method. In the solution method, catalyst ink was prepared by mixing the catalyst (20% Pt/C) and PBI solution (5% PBI in dimethylacetamide). In the colloid method, acetone was added to the mixture of catalyst and PBI solution, which made the PBI form a colloid suspended in the solvent. They found that electrodes prepared by the solution method showed better performances at 150 °C and 175 °C, and that the electrodes prepared by the colloid method gave a better performance at 125 °C. This is probably due to differences in catalyst layer structure (see Section 18.2.7).

18.2.5 Strategies for HT Catalyst/Catalyst Layer Performance Improvement and Mitigation

In the literature, few studies have focused on performance improvement and mitigation of high-temperature catalyst layers. For LT-PEMFCs, materials used in the catalyst layer preparation are commercially available. For HT-PEMFCs, materials are not only different from those in LT-PEMFCs but also differ from study to study. For example, in PBI membrane-based MEAs, Pt/C catalyst and PBI ionomer were used in the catalyst layer [80–83]. However, in a CsH_2PO_4 membrane-based catalyst layer, no ionomer was used [22]. It is expected that improvement and mitigation of a high-temperature catalyst layer should depend on the materials used, and the catalyst layer structures should be optimized according to the materials employed.

18.2.6 Suggestions for Future Work

Development of high-temperature proton exchange membranes and catalysts for HT-PEMFCs are equally important in terms of the long-term sustainability of fuel cell technology and commercialization. Based on a review of the literature as well as our understanding, we would like to suggest several future research topics for high-temperature catalyst development:

(1) Development of highly durable catalyst supports, such as carbon with more graphitic components, ceramic, and carbon-ceramic composite materials, which could survive in a high-temperature environment.

(2) Enhancement of the interaction between the supports and the catalysts to stabilize Pt nanoparticles and improve catalytic activity.

(3) Development of new catalysts such as highly durable non-noble catalysts. For long-term sustainable PEMFC commercialization, non-noble catalysts are the solution because of the limited supply and high cost of Pt.

(4) Optimization of HT-PEMFC catalyst and catalyst layer composition and structure through innovative design, evaluation, as well as fundamental understanding.

18.2.7 Typical Example Analysis

Transition metal oxide has high thermal stability and has been used in the development of high-temperature membranes. Recently, Liu et al. [24] developed a $PtZrO_2/C$ (atomic ratio Pt:Zr = 4:1) catalyst with high thermal stability and corrosion resistance [24]. The catalyst was prepared by deposition of ZrO_2 on carbon, followed by deposition of Pt on the ZrO_2/C composite material. The developed catalyst was evaluated by an accelerated aging test, where the potential of the MEA was cycled between 0.6 and 1.2 V. Figure 18.10 shows the catalyst particle size change after 3000 cycles. For comparison, an MEA made from commercially available catalyst (Pt/C) was also tested using the same conditions and the results are shown in Figure 18.11. The particle size of the $PtZrO_2/C$ catalyst was increased from ~4 nm to ~6nm, while the particle size of commercially available Pt/C catalyst was increased from ~3 nm to ~12 nm,

indicating that Pt nanoparticles on ZrO_2/C are more resistant to agglomeration or sintering.
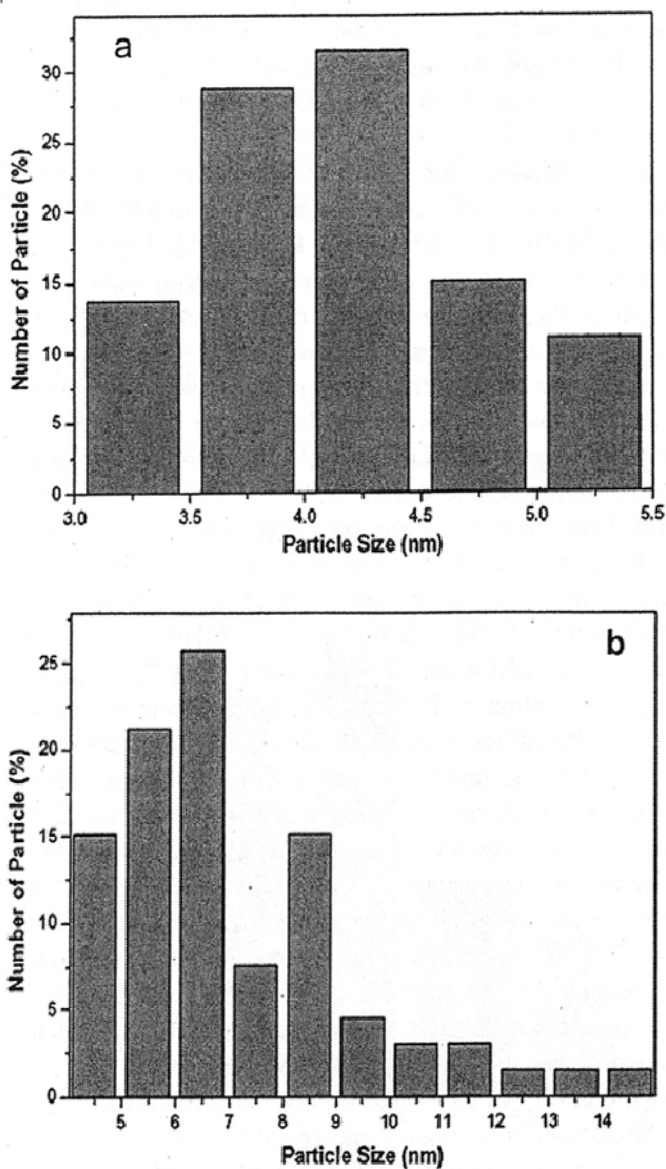
Figure 18.10. Histograms of the particle size distribution of the $PtZrO_2/C$ catalyst before (a) and after (b) the potential cycling test [24]. (Reprinted from Electrochemistry Communications, 9(1), Liu G, Zhang H, Zhai Y, Zhang Y, Xu D, Shao Z, Pt_4ZrO_2/C cathode catalyst for improved durability in high temperature PEMFC based on H_3PO_4 doped PBI, 135–41, ©2007, with permission from Elsevier.)
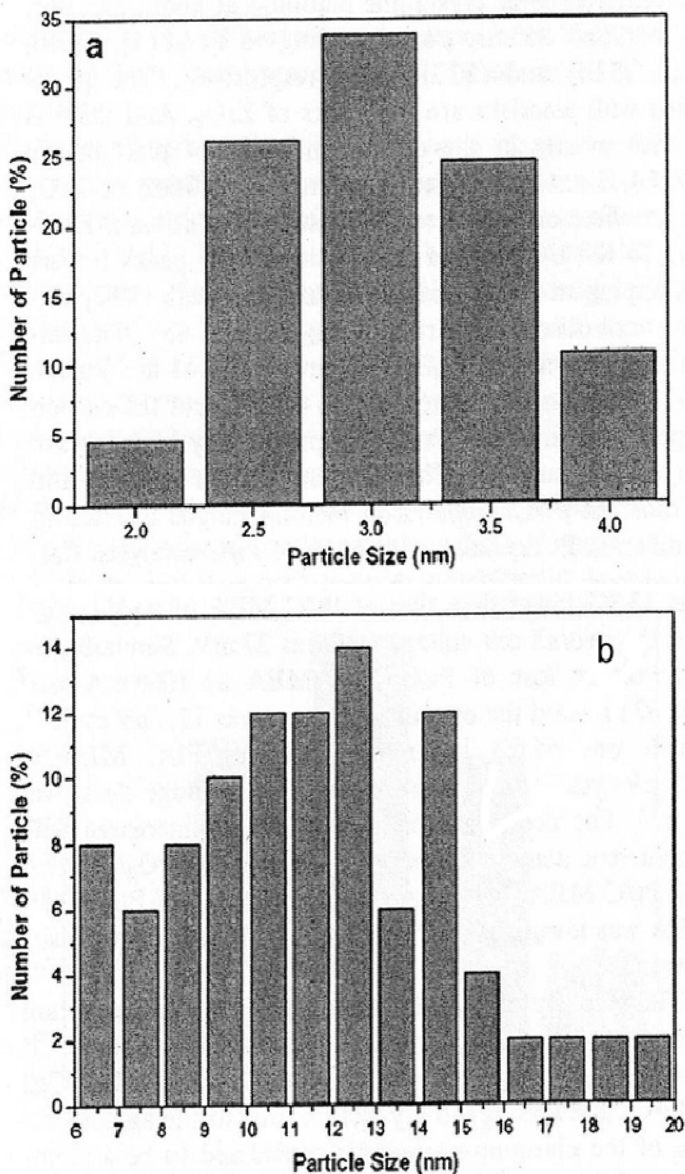
Figure 18.11. Histograms of the particle size distribution of the commercially available Pt/C catalyst before (a) and after (b) the potential cycling test [24]. (Reprinted from Electrochemistry Communications, 9(1), Liu G, Zhang H, Zhai Y, Zhang Y, Xu D, Shao Z, Pt_4ZrO_2/C cathode catalyst for improved durability in high temperature PEMFC based on H_3PO_4 doped PBI, 135–41, ©2007, with permission from Elsevier.)

For fuel cell testing at 150 °C, the performance degradation of the MEA made from the $PtZrO_2$/C catalyst, after 3000 cycles of aging, is less significant than that

of the commercially available Pt/C catalyst, as shown in Figure 18.12. It is believed that the improved durability and sintering resistance are mainly due to the improved support strategy. Pt particles adjacent to the ZrO_2 support could prevent the Pt from sintering. However, a fundamental understanding of the mechanism is still needed for further improvements.
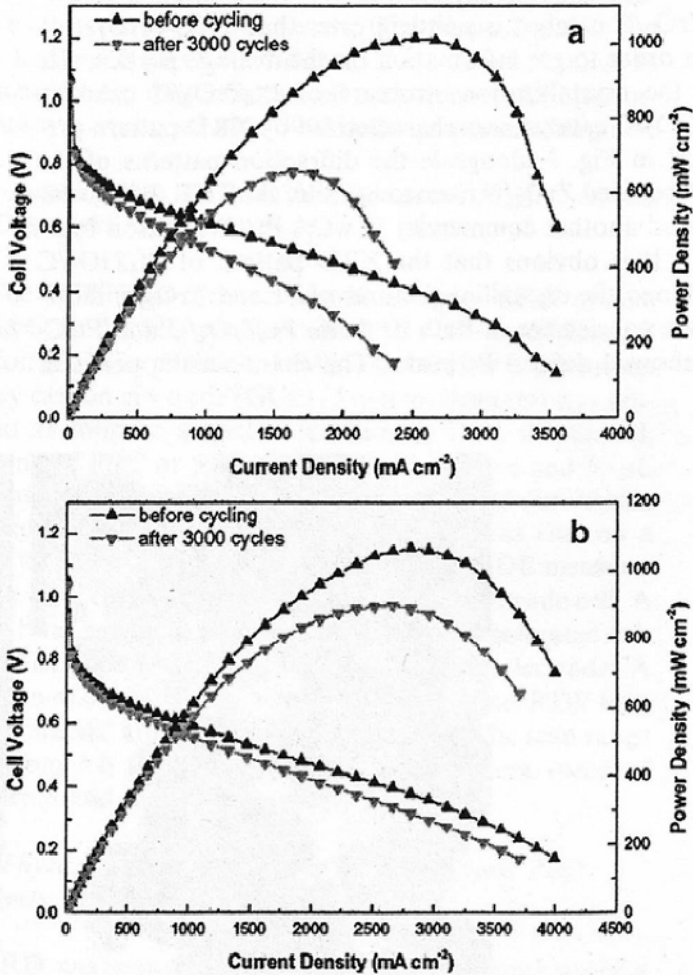
Figure 18.12. Polarization curves of (a) commercially available Pt/C-based MEA and (b) $PtZrO_2$/C-based MEA before and after the potential sweep test for 3000 cycles between 0.6 and 1.2 V vs. SHE. Cell temperature: 150 °C, H_2/O_2, ambient pressure, no pre-humidification [24]. (Reprinted from Electrochemistry Communications, 9(1), Liu G, Zhang H, Zhai Y, Zhang Y, Xu D, Shao Z, Pt_4ZrO_2/C cathode catalyst for improved durability in high temperature PEMFC based on H_3PO_4 doped PBI, 135–41, ©2007, with permission from Elsevier.)

The work of Lobato et al. is a typical example of high-temperature MEA preparation, as shown in Figure 18.13 [83]. The catalyst layer structure is illustrated in Figure 18.14. The solution method gave a more uniform and denser structure with lower secondary pore volume than the colloid method, due to the uniform distribution of PBI in the solution. In the colloid method, PBI forms agglomerates, resulting in the enlargement of secondary pores.
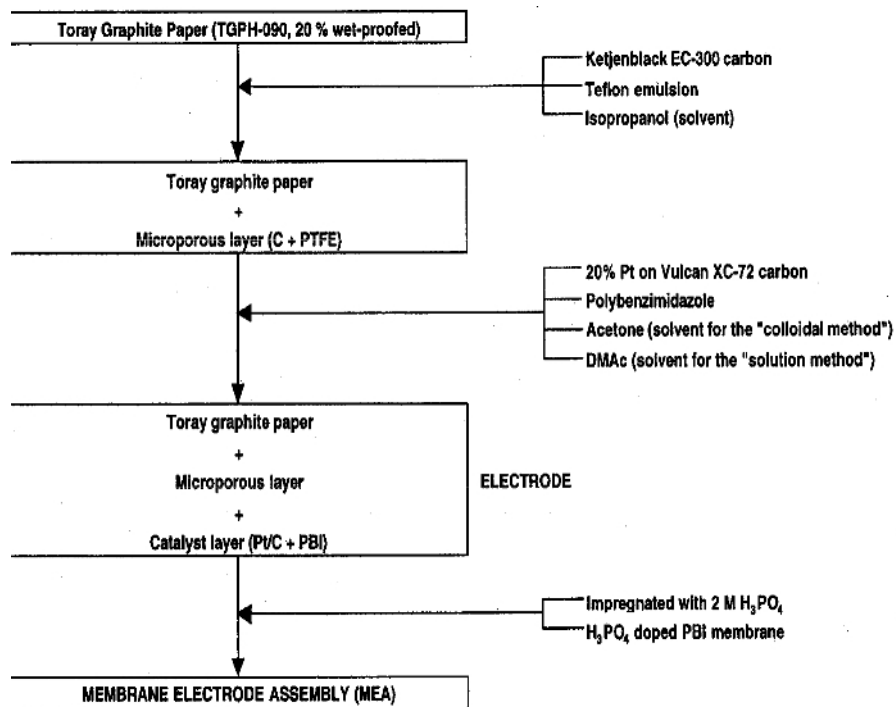
Figure 18.13. Schematic of the procedure for MEA fabrication [83]. (Reprinted from Journal of Power Sources, 157(1), Lobato J, Rodrigo MA, Linares JJ, Scott K, Effect of the catalytic ink preparation method on the performance of high temperature polymer electrolyte membrane fuel cells, 284–92, ©2006, with permission from Elsevier.)

Structural differences can significantly affect MEA properties. For example, the MEA prepared by the colloid method showed a high Pt utilization (21%), low Tafel slope (221 mV/dec), and low charge transfer resistance (10.7 Ω), while the solution method gave a Pt utilization of 12%, a Tafel slope of 390 mV/dec, and a charge transfer resistance of 20.9 Ω. The cell performances of the two MEAs are shown in Figure 18.14. These performance differences are possibly due to structural differences in the catalyst layer. Electrodes prepared by the colloid method have an open structure with enlarged secondary pores that facilitate mass transfer. Therefore, that catalyst layer structure can affect HT-PEMFC performance. With respect to optimization of the catalyst layer structure, more work is needed on design, fabrication, and fundamental understanding.
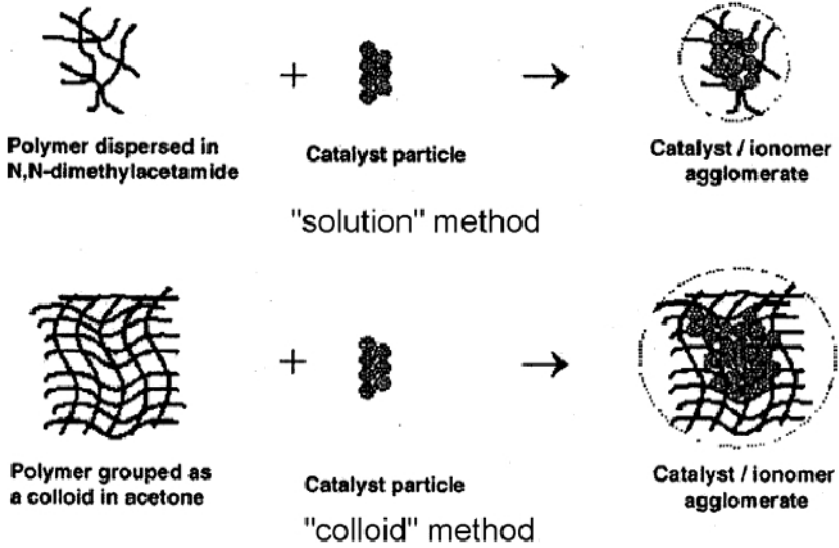
Figure 18.14. Electrode structures prepared by the solution method and the colloid method, respectively [83]. (Based on Figure 5 in Journal of Power Sources, 157(1), Lobato J, Rodrigo MA, Linares JJ, Scott K, Effect of the catalytic ink preparation method on the performance of high temperature polymer electrolyte membrane fuel cells, 284–92, ©2006, with permission from Elsevier.)
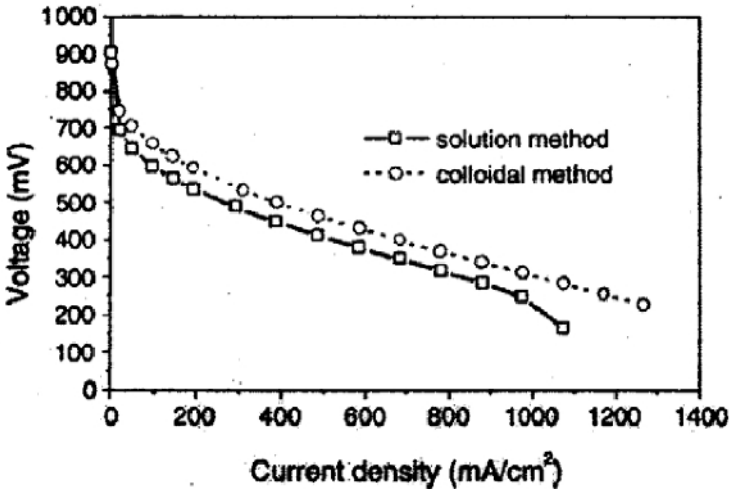
Figure 18.15. Polarization curves obtained with MEAs prepared by the two methods. Cell temperature 125 °C, ambient pressure (H_2/O_2), no prehumidification [83]. (Reprinted from Journal of Power Sources, 157(1), Lobato J, Rodrigo MA, Linares JJ, Scott K, Effect of the catalytic ink preparation method on the performance of high temperature polymer electrolyte membrane fuel cells, 284–92, ©2006, with permission from Elsevier.)

18.3 Summary

High-temperature PEMFCs (i.e., > 90 °C) have several advantages over low-temperature PEMFCs (i.e., < 90 °C) in terms of reaction kinetics, contaminant tolerance, water management, and heat rejection. However, at high-temperature operation, material degradation is the main challenge. Therefore, development of materials, including catalysts, that are suitable for high-temperature operation is the main task for those working on HT-PEMFCs.

To date, the major focus has been upon the degradation of materials in low-temperature PEMFCs. Research has identified that catalyst degradation occurs primarily in two ways: catalyst sintering/agglomeration and catalyst support oxidation. Catalyst sintering/agglomeration is caused by Pt dissolution/re-deposition, resulting in the growth of Pt particles, and by Pt migration, leading to Pt deposition in membranes and redistribution in the catalyst layer. Carbon support oxidation can result in the detachment of the catalyst particles from the support, reducing Pt utilization. Both catalyst sintering/agglomeration and carbon support oxidation are temperature dependent, and therefore high-temperature operation would lead to more severe catalyst degradation.

Little attention has been paid to high-temperature catalyst layer development. Due to the unique characteristics of HT-PEMFCs and the different properties of HT materials, the HT-PEMFC catalyst layer is expected to be more variable in composition than its low-temperature counterpart.

The development of high-temperature catalysts/catalyst layers is still in its early stages. This area requires more attention and effort in order to achieve a breakthrough in PEMFC technology and commercialization.

References

1. Zhang J, Xie Z, Zhang J, Tang Y, Song C, Navessin T, et al. High temperature PEM fuel cells. J Power Sources 2006;160:872–91.
2. Song C, Tang Y, Zhang J, Zhang J, Wang H, Shen J, et al. PEM fuel cell reaction kinetics in the temperature range of 23–120 °C. Electrochim Acta 2007;52:2552–61.
3. Damjanovic A. Temperature dependence of symmetry factors and the significance of the experimental activation energies. J Electroanal Chem 1993;355:57–77.
4. Dahr HP, Christner LG, Kush AK. Nature of CO adsorption during oxidation in relation to modeling for CO poisoning of a fuel cell anode. J Electrochem Soc 1987; and references therein 134:3021–6.
5. Dhar HP, Christner LG, Kush AK, Maru HC. Performance study of a fuel cell Pt/C anode in presence of CO and CO_2, and calculation of adsorption parameters for CO poisoning. J Electrochem Soc 1986;133:1574–82.
6. Vogel W, Lundquest J, Ross P, Stonehart P. Reaction pathways and poisons-II the rate controlling step for electrochemical oxidation of hydrogen on Pt in acid and poisoning of the reaction by CO. Electrochim Acta 1975;20:79–93.
7. Igarashi H, Fujino T, Watanabe M. Hydrogen electro-oxidation on platinum catalysts in the presence of trace carbon monoxide. J Electroanal Chem 391 1995;119–23.
8. Li Q, He R, Gao J, Jensen JO, Bjerrum NJ. The CO poisoning effect in PEMFCs operational at temperatures up to 200°C. J Electrochem Soc 2003;150:A1599–605.

9. Mahorta S, Datta R. Membrane supported non-volatile acidic electrolytes allow higher temperature operation of polymer electrolyte membrane fuel cells. J Electrochem Soc 1997;144:L23–6.

10. Wang J, Wavinell RF, Wainright J, Litt M, Yu H. A H_2/O_2 fuel cell using acid doped polybenzimidazole as polymer electrolyte. Electrochim Acta 1996;41:193–7.

11. Lakshmanan B, Huang W, Olmeijer D, Weidner JW. Polyetheretherketone membranes for elevated temperature PEMFCs. Electrochem Solid-State Lett 2003;6:A282–5.

12. Zhang J, Tang Y, Li H, Song C, Xia Z, Wang H, et al. Effect of relative humidity on PEM fuel cell performance at elevated temperatures, available online. Electrochim Acta 2008.

13. Song C, Chua CJ, Tang Y, Zhang J, Zhang J, Li J, et al. Voltage jump during polarization of a PEM fuel cell operated at low relative humidities. Int J Hydrogen Energy 2008. Accepted.

14. Ise M, Kreuver KD, Maier J. Electroosmotic drag in polymer electrolyte membranes: an electrophoretic NMR study. Solid-State Ionics 1999;125:213–23.

15. Ma Y, Hu J, Ma H, Yi B, Zhang H. Effect of water transport properties on a PEM fuel cell operating with dry hydrogen. Electrochim Acta 2006;51:6361–6.

16. Shao Y, Yin G, Wang Z, Gao Y. Proton exchange membrane fuel cell from low temperature to high temperature: material challenges. J Power Sources 2007;167:235–42.

17. Hinatsu JT, Mizuhata M, Takenaka H. Water uptake of perfluorosulfonic acid membranes from liquid water and water vapour. J Electrochem Soc 1994;141:1493–8.

18. Tang Y, Zhang J, Song C, Zhang J. Single PEMFC design and validation for high-temperature MEA testing and diagnosis up to 300 °C. Electrochem Solid-State Lett 2007;10:B142–6.

19. Savadogo O. Emerging membranes for electrochemical systems Part II: high temperature composite membranes for polymer electrolyte fuel cell applications. J Power Sources 2004;127:135–61.

20. Haile SM, Boysen DA, Chisholm CRI, Merle RB. Solid acids as fuel cell electrolytes. Nature 2001;410:910–13.

21. Boysen DA, Uda T, Chisholm CRI, Haile SM. High-performance solid acid fuel cells through humidity stabilization. Science 2003;303:68–70.

22. Uda T, Haile SM. Thin membrane solid acid fuel cell. Electrochem Solid-State Lett 2005;8:A245–6.

23. Zhang J, Tang Y, Song C, Zhang J. Unpublished results.

24. Liu G, Zhang H, Zhai Y, Zhang Y, Xu D, Shao Z. Pt_4ZrO_2/C cathode catalyst for improved durability in high temperature PEMFC based on H_3PO_4 doped PBI. Electrochem Commun 2007;9:135–41.

25. Liu G, Zhang H, Zhong H, Hu J, Xu D, Shao Z. A novel sintering resistant and corrosion resistant Pt_4ZrO_2/C catalyst for high temperature PEMFCs. Electrochim Acta 2006;51:5710–14.

26. Bi W, Fuller TF. Temperature effects on PEM fuel cells Pt/C catalyst degradation. J Electrochem Soc 2008;155:B215–21.

27. Wilson MS, Garzon FH, Sickafus KE, Gottesfeld S. Surface area loss of supported platinum in polymer electrolyte fuel cells. 1993;140:2872–7.

28. Darling RM, Meyer JP. Kinetic model of platinum dissolution in PEMFCs. J Electrochem Soc 2003;150:A1523–7.

29. Omelas R, Stassi A, Modica E, Arico AS, Antonucci V. Accelerated degradation tests for Pt/C catalysts in sulphuric acid. ECS Transactions 2006;3:633–41.

30. Wang X, Kumar R, Meyers D. Effect of voltage on platinum dissolution. Electrochem Solid-State Lett 2006;9:A225–7.

31. Ferreira PJ, la O' GJ, Shao-Horn Y, Morgan D, Makharia R, Kocha S, et al. Instability of Pt/C electrocatalysts in proton exchange membrane fuel cells. J Electrochem Soc 2005;152:A2256–71.

32. Virkar AV, Zhou Y. Mechanism of catalyst degradation in proton exchange membrane fuel cells. J Electrochem Soc 2007;154:B540–7.

33. Xie J, Wood DL III, Wayne DM, Zawodzinski TA, Atanassov P, Borup RL. Durability of PEFCs at high relative humidity conditions. J Electrochem Soc 2005;152:A104–13.

34. Xie J, Wood DL III, More KL, Atanassov P, Borup RL. Microstructural changes of membrane electrode assemblies during PEFC durability testing at high humidity conditions. J Electrochem Soc 2005;152:A1011–20.

35. Bi W, Gray GE, Fuller TF. PEM fuel cell Pt/C dissolution and deposition in Nafion electrolyte. Electrochem Solid-State Lett 2007;10:B101–4.

36. Debe MK, Schmoeckel AK, Verstrom GD, Atanasoski R. High voltage stability of nanostructured thin film catalysts for PEM fuel cells. J Power Sources 2006;161:1002–11.

37. Paik CH, Saloka GS, Graham GW. Influence of cyclic operation on PEM fuel cell catalyst stability. Electrochem Solid-State Lett 2007;10:B39–42.

38. Guilminot E, Corcella A, Chatenet M, Maillard F, Charlot F, Berthome G, et al. Membrane and active layer degradation upon PEMFC steady-state operation. J Electrochem Soc 2007;154:B1106–14.

39. Merzougui B, Swathirajan S. Rotating disk electrode investigation of fuel cell catalyst degradation due to potential cycling in acid electrolyte. J Electrochem Soc 2006;153:A2220–6.

40. Stevens DA, Hicks MT, Haugen GM, Dahn JR. Ex situ and in situ stability studies of PEMFC catalysts. J Electrochem Soc 2005;152:A2309–15.

41. Aragane J, Urushibata H, Murahashi T. Effect of operational potential on performance decay rate in phosphoric acid fuel cell. J Appl Electrochem 1996;26:147–52.

42. Aragane J, Murahashi T, Odaka T. Change of Pt distribution in the active components of phosphoric acid fuel cell. J Electrochem Soc 1988;135:844–50.

43. Zhai Y, Zhang H, Xing D, Shao Z. The stability of Pt/C catalyst in H$_3$PO$_4$/PBI PEMFC during high temperature life test. J Power Sources 2007;164:126–33.

44. Dicks AL. The role of carbon in fuel cells. J Power Sources 2006;156:128–41.

45. Pyun SI, Ryu YG, Choi SH. Corrosion behaviour of platinum-catalyzed carbon in phosphoric acid solution. Carbon 1994;32:161–4.

46. Yu X, Ye S. Recent advances in activity and durability enhancement of Pt/C catalytic cathode in PEMFC, Part II: Degradation mechanism and durability enhancement of carbon supported platinum catalyst. J Power Sources 2007;172:145–54.

47. Mathias MF, Makharia R, Gasteiger HA, Conley JJ, Fuller TJ, Gittelman CJ, et al. Two fuel cell cars in every garage? Interface 2005;14(3):24–35.

48. Kinoshita K, Bett J. Determination of carbon surface oxides on platinum-catalyzed carbon. Carbon 1974;12:525–33.

49. Stevens DA, Dahn JR. Thermal degradation of the support in carbon supported platinum electrocatalysts for PEM fuel cells. Carbon 2005;43:179–88.

50. Roen LM, Paik CH, Jarvi TD. Electrocatalytic corrosion of carbon support in PEMFC cathodes. Electrochem Solid-State Lett 2004;7:A19–22.

51. Alderucci V, Pino L, Antonucci PL, Roh W, Cho J, Kim H, et al. XPS study of surface oxidation of carbon supported Pt catalysts. Mater Chem Phys 1995;41:9–14.

52. Passalacqua E, Antotnucci PL, Vivaldi M, Patti A, Antonucci V, Giordano N, et al. The influence of Pt on the electrooxidation behaviour of carbon in phosphoric acid. Electrochim Acta 1992;37:2725–30.

53. Willsau J, Heitbbaum J. The influence of Pt-activation on the corrosion of carbon in gas diffusion electrodes—A DEMS study. J Electroanal Chem 1984;161:93–101.

54. Rewick RT, Wetrcek PR, Wiase H. Carbon gasification in the presence of metal catalysts. Fuel 1974;53:274–9.

55. Kinoshita K, Bett J. Electrochemical oxidation of carbon black in concentrated phosphoric acid at 135°C. Carbon 1973;11:237–47.

56. Kangasniemi KH, Condit DA, Jarvi TD. Characterization of Vulcan electrochemically oxidized under simulated PEM fuel cell conditions. J Electrochem Soc 2004; 151:E125–32.

57. King JM, McDonald B. Experience with 200 kW PC25 fuel cell power plant. In: Handbook of fuel cells – fundamentals, technology, and applications, volume 4. Vielstich W, Gasteiger H, editors. Chicester, UK: John Wiley & Sons, 2003: 832–43.

58. Kinoshita K, Bett J. Influence of electrochemical treatment in phosphoric acid on the wettability of carbon. Carbon 1975;13:405–9.

59. Rodriguez-Reinoso F. The role of carbon materials in heterogeneous catalysis. Carbon 1998;36:159–75.

60. Kinoshita K. Carbon: Electrochemical and physicochemical properties. New York: John Wiley & Sons, 1988.

61. Landsman DA, Luczak FJ. Catalyst studies and coating technologies. In: Handbook of fuel cells – fundamentals, technology, and applications, volume 4. Vielstich W, Gasteiger H, editors. Chicester, UK: John Wiley & Sons, 2003: 811–31.

62. Wang C, Waje M, Wang X, Tang JM, Haddon RC, Yan Y. Proton exchange membrane fuel cells with carbon nanotube based electrodes. Nano Lett 2004;4:345–8.

63. Wang X, Waje M, Yan Y. CNT based electrodes with high efficiency for PEMFCs. Electrochem Solid-State Lett 2005;8:A42–4.

64. Wang X, Li W, Chen Z, Waje M, Yan Y. Durability investigation of carbon nanotube as catalyst support for proton exchange membrane fuel cell. J Power Sources 2006;158:154–9.

65. Shao Y, Yin G, Gao Y, Shi P. Durability study of Pt/C and Pt/CNTs catalysts under simulated PEMFC conditions. J Electrochem Soc 2006;153:A1093–7.

66. Carmo M, Pagain VA, Rosolen JM, Gonzalez ER. Alternative supports for the preparation of catalysts for low-temperature fuel cells: the use of carbon nanotubes. J Power Sources 2005;142:169–76.

67. Wang J, Swain GM. Fabrication and evaluation of platinum/diamond composite electrodes for electrocatalysis. J Electrochem Soc 2003;150 E24–32.

68. Wang J, Swain GM, Tachibana T, Kobashi K. Incorporation of Pt particles in boron doped diamond thin films applications in electrocatalysis. Electrochem Solid-State Lett 2000;3:286–9.

69. Wang Y, Lin Y, Viswanathan V, Liu J, Zhang C, Campbell S, et al. Development of alternative and durable high performance cathode supports for PEM fuel cells. 2007 DOE presentations, Washington DC, 2007.

70. Vedrine C, Dufaux M, Naccache C, Imelik B. X-ray photoelectron spectroscopy study of Pd and Pt ions in type Y-zeolite. Electron transfer between metal aggregates and the support as evidenced by X-ray photoelectron spectroscopy and electron spin resonance. J Chem Soc Faraday Trans 1978;74:440–50.

71. Bagotzky VS, Skundin AM. Electrocatalysts on supports—I. Electrochemical and adsorptive properties of platinum microdeposits on inert supports. Electrochim Acta 1984;29:757–65.

72. Halla SC, Subramaniana V, Teeterb G, Rambabu B. Influence of metal–support interaction in Pt/C on CO and methanol oxidation reactions. Solid-State Ionics 2004;175:809–13.

73. Shim J, -Lee CR, -Lee HK, -Lee JS, Cairns EJ. Electrochemical characteristics of Pt–WO$_3$/C and Pt–TiO$_2$/C electrocatalysts in a polymer electrolyte fuel cell. J Power Sources 2001;102:172–7.

74. Xiong L, Manthiram A. Synthesis and characterization of methanol tolerant Pt/TiOx/C nanocomposites for oxygen reduction in direct methanol fuel cells. Electrochim Acta 2004;49:4163–70.

75. Chen J, Sarma LS, Chen C, Cheng M, Shih S, Wang G, et al. Multi-scale dispersion in fuel cell anode catalysts: Role of TiO_2 towards achieving nanostructured materials. J Power Sources 2006;159:29–33.

76. Bezerraa CWB, Zhang L, Liu H, Lee K, Marques ALB, Marques EP, et al. A review of heat-treatment effects on activity and stability of PEM fuel cell catalysts for oxygen reduction reaction. J Power Sources 2007;173:891–908.

77. Stonehart P. Carbon substrates for phosphoric acid fuel cell cathodes. Carbon 1984;22:423–31.

78. Uchida M, Aoyama Y, Tanabe M, Yanagihara N, Eda N, Ohta A. Influences of both carbon supports and heat-treatment of supported catalysts on electrochemical oxidation of methanol. J Electrochem Soc 1995;142:2572–6.

79. Coloma F, Sepblveda-Escribano A, Rodriguez-Reinoso F. Heat-treated carbon-blacks as supports for platinum catalysts. J Catal 1995;154:299–305.

80. Wang J, Savinell RF, Wainright J, Litt M, Yu H. A H_2/O_2 fuel cell using acid doped polybenzimidazole as polymer electrolyte. Electrochim Acta 1996;41:193–7.

81. Li Q, Hjuler HA, Bjerrum NJ. Oxygen reduction on carbon supported platinum catalysts in high temperature polymer electrolytes. Electrochim Acta 2000;45:4219–26.

82. Li Q, Hjuler HA, Bjerrum NJ. Phosphoric acid doped polybenzimidazole membranes: Physicochemical characterization and fuel cell applications. J Appl Electrochem 2001;31:773–9.

83. Lobato J, Rodrigo MA, Linares JJ, Scott K. Effect of the catalyst ink preparation method on the performance of high temperature polymer electrolyte membrane fuel cells. J Power Sources 2006;157:284–92.

19

Conventional Catalyst Ink, Catalyst Layer and MEA Preparation

Huamin Zhang, Xiaoli Wang, Jianlu Zhang and Jiujun Zhang

19.1 Introduction

The membrane electrode assembly (MEA) is the heart of proton exchange membrane fuel cells (PEMFCs), including direct methanol fuel cells (DMFCs), and determines both fuel cell performance and durability. The MEA component materials, structure, and fabrication technologies play important roles in performance improvement and optimization. For example, the catalyst layers, where the electrochemical reactions take place, are the most important of the several components in PEMFCs. An MEA contains an anode gas diffusion layer (GDL), an anode catalyst layer (CL), a proton exchange membrane (PEM), a cathode catalyst layer, and a cathode gas diffusion layer. An ideal MEA would allow all active catalyst sites in the catalyst layer to be accessible to the reactant (H_2 or O_2), protons and electrons, and would facilitate the effective removal of produced water from the CL and GDL. Over the past several decades, great efforts have been made to optimize the catalyst layer and MEA, and many catalyst layer/MEA structures and fabrication methods have been developed. As a result, MEA performance with advanced catalyst layers has been significantly improved by employing different fabrication methods [1–4], changing the catalyst layer structures [5–11], and using different components [5–8].

This chapter will address the preparation methods for catalyst inks, catalyst layers, and MEAs, with a focus on the fabrication processes.

19.2 Principles of Gas Diffusion Electrodes and MEA Structures

The electrodes in PEMFCs, including both cathode and anode, are multi-component and gas porous matrices, also called gas diffusion electrodes (GDEs). A GDE is generally composed of a reaction layer (the CL) and an accessorial layer (the GDL). The GDL, adjacent to the catalyst layer and the flow field, plays an important role in PEMFC performance and has several functions: (1) transportation

of reactants: the GDL should be able to provide reactant pathways from the flow field channels to the catalyst layer and uniformly distribute the reactants onto the whole reaction surface; (2) transportation of liquid water: the GDL offers pathways for liquid water removal from the catalyst layer to the flow field channels; (3) conduction of electrons: the GDL allows electron transfer from the bipolar plate to the catalyst layer or vice versa; (4) mechanical support: the GDL should be able to support the catalyst layers and the proton exchange membrane against pressure from the gases and the assembly force; and (5) heat conduction: the GDL should be able to effectively remove the produced heat from the catalyst layer. The GDL has a typical dual-layer structure with a macro-porous substrate layer (SL) and a coated thinner microporous layer (MPL), as illustrated in Figure 19.1.
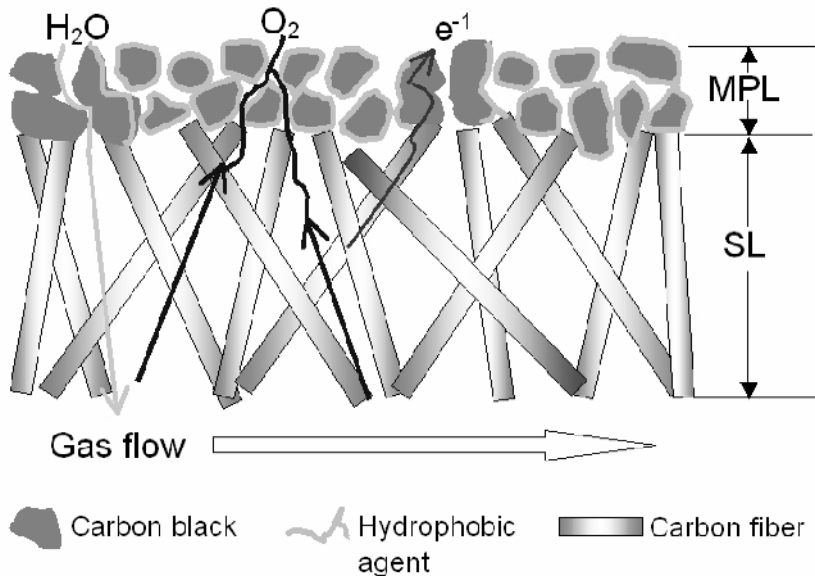
Figure 19.1. Schematic diagram of a dual-layer cathode gas diffusion layer

A well-qualified substrate layer should have excellent gas permeability, high electron conductivity, smooth surface, good mechanical strength, proper wettability, stable chemical and heat properties, as well as low cost. The most common SL materials used in PEMFCs are carbon-fiber-based products, such as non-woven carbon papers and woven carbon cloths. This is mainly due to their high porosity ($\geq 70\%$) and good electrical conductivity. Besides these carbon materials, some metal substrates such as sintered porous titanium and stainless steel fiber felt have also been explored as SLs [12–14] because of their high mechanical strength, ductility, and low cost.

Adding a surface layer onto the SL has proven to be an effective way of improving the water/gas management of the whole GDL [15–18]. The microporous layer (MPL, also called a carbon base, in industry) consists of carbon or graphite particles mixed with a hydrophobic agent, usually polytetrafluoroethylene (PTFE),

which serves as a binder. Typically, the MPL has a pore size in the order of the carbon agglomerates, between 100 and 500 nm, with a thickness of 5–50 μm, while the SL has a 10–30 μm pore size and 100–300 μm thickness. The primary purpose of the MPL is water management and reactant redistribution. It can provide effective wicking of liquid water from the cathode CL into the SL, and then effective transportation of gases in the opposite direction. It also contributes significantly to the reduction of electrical contact resistance between the SL and CL.

The catalyst layer (CL) is a key component in the GDE, as the location where electrochemical reactions take place. For example, in order to carry out the oxygen reduction reaction (ORR) ($\frac{1}{2}O_2 + 2H^+ + 2e^- \rightarrow H_2O$), the catalyst particles must be in contact with both electronic and protonic conducting materials, and there must be some passages for the transportation of the reactants to the catalytic reaction sites as well as paths for the reaction product (H_2O) to exit. In a catalyst layer, protons travel through an electrolyte (ionomer) and electrons travel through electrically conductive solids, including the catalyst itself. Therefore, the catalyst particles must be in close contact with each other, the electrolyte, and the adjacent GDL. Moreover, the reactant gas (O_2) and the produced water travel mainly through the voids, so the electrode must be porous enough to allow gas to diffuse to the reaction sites and liquid water to wick out. Figure 19.2 schematically shows a three-phase boundary where catalyst, reactants, and electrolyte meet for electrochemical reactions. In the diagram this reaction boundary essentially is a line, not an area, which would result in a limited current. However, the actual reaction zone is larger than a single three-phase boundary line because some reactant gases can diffuse through the electrolyte polymer to the catalyst surface.
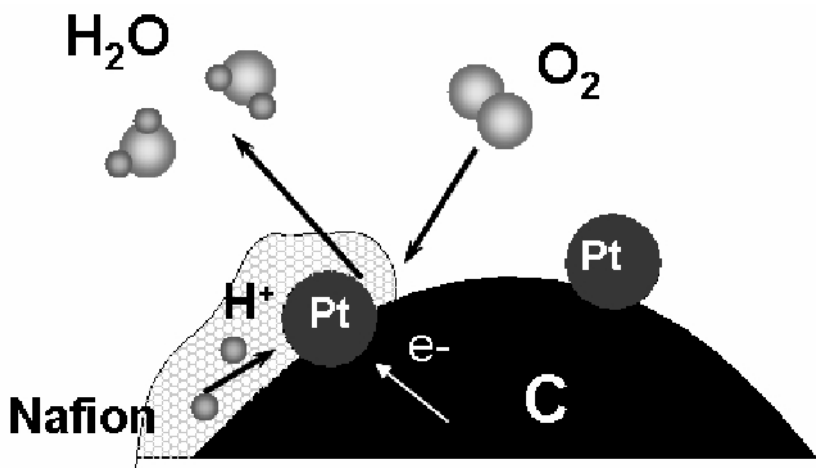
Figure 19.2. Schematic diagram of a three-phase reaction boundary

In a PEMFC, the combination of anode/membrane/cathode is referred to as a membrane electrode assembly (MEA). Normally, the MEA is a five-layer composite structure that includes anode GDL, anode CL, membrane, cathode GDL,

and cathode CL. Two different typical MEA structures have been developed according to the CL location, as illustrated in Figure 19.3. Applying catalyst ink onto the GDL leads to a basic two-layer structure called a catalyst coated GDL (CGDL), while directly applying catalyst ink onto both sides of the proton exchange membrane results in a three-layer structure called a catalyst coated membrane (CCM). Then a final five-layer MEA is formed by sandwiching a membrane between two CGDLs or a CCM between two GDLs.

CGDL   PEM CGDL   GDL   CCM GDL

Anode GDL
Anode CL
PEM
Cathode CL
Cathode GDL

5-layer MEA
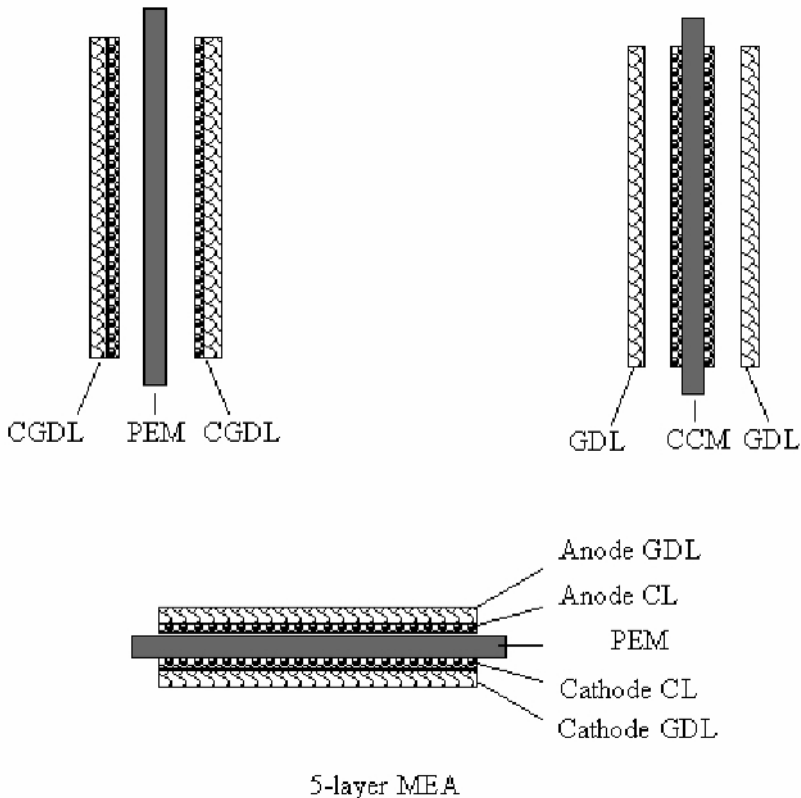
Figure 19.3. Schematic diagram of an MEA

The catalyst layers need to be designed to generate high rates of the desired reactions and minimize the amount of catalyst necessary for reaching the required levels of power output. An ideal catalyst layer should maximize the active surface area per unit mass of the electrocatalyst, and minimize the obstacles for reactant transport to the catalyst, for proton transport to exact positions, and for product removal from the cell; these requirements entail an extension of the three-phase boundary. In general, individual property specifications should be a compromise between conflicting requirements. The catalyst layer structure should be optimized with respect to the interactions between components, with trade-offs between several effects.

This chapter focuses on the preparation of catalyst inks, catalyst layers, and MEAs.

19.3 Catalyst Layer

The catalyst layer is the region where electrochemical reactions occur. The large challenges in PEMFC research arise from catalyst layers because their structures are quite complicated and heterogeneous. The first-generation CLs using PTFE-bonded Pt black electrocatalysts displayed high performance but at a prohibitively high cost [19]. These conventional electrodes generally have a high platinum loading, up to 4 mg/cm^2. One of the most significant improvements has been made by Raistrick [20], who fabricated a CL with dispersed Pt/C and by painting solubilized ionomer. These electrodes with 0.4 mg Pt/cm^2 loading demonstrated the same performance as the first-generation electrodes with 4 mg Pt/cm^2 [20]. With thin-film methods, the Pt loading was further lowered down to a level of 0.1–0.3 mg/cm^2 [8, 21–23], and even to 0.01–0.02 mg/cm^2 with the sputtering-deposition method [24]. The 2010 target of the United States Department of Energy, to have PEMFCs for transportation applications, needs to achieve a total Pt catalyst loading of 0.3 mg Pt /cm^2 (total Pt loading of cathode and anode) with a performance of 0.8 V @ 0.4 A/cm^2 or 0.85 V @ 0.1 A/cm^2 under 80 °C, 250 kPa, and H$_2$/air operation.

The important properties of a catalyst layer, such as electronic/protonic conductivity, porosity, active reaction area, as well as catalytic activity, are mainly determined by the fabrication method and the properties of the components. To date, several manufacturing techniques have been developed, such as blading, painting, printing, spraying, rolling, and screening. It is difficult to judge which method is the best because each has unique qualities.

19.3.1 Preparation of Catalyst Ink

Catalyst ink, containing the catalyst, an electrolyte (ionomer) and/or hydrophobic agent, and certain solvents, is a liquid precursor of the catalyst layer. When preparing the ink, the contents of each component are the first consideration, followed by its uniformity and viscosity. In general, catalyst ink should be stirred or ultrasonically dispersed thoroughly to ensure all the nano-scaled catalyst particles come into contact with the other components uniformly. If lower viscosity catalyst ink is being applied on a porous GDL substrate, the ink could penetrate the inside of the substrate, leading to wasted catalyst as well as a water "flooding" problem. However, if the viscosity is too high, the resultant catalyst layer will have problems with non-uniform dispersion or hard drying. According to the bonders used, there are three kinds of catalyst inks, as shown in Figure 19.4; the corresponding catalyst layers made from these inks are also shown.
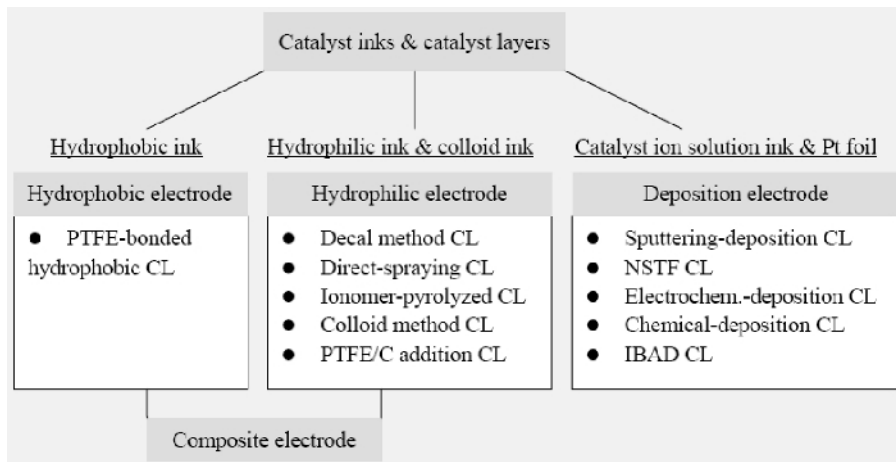
Figure 19.4. Classification of catalyst ink and catalyst layers

19.3.1.1 Hydrophobic Ink

Hydrophobic ink, containing a catalyst and a hydrophobic agent (such as Polytetrafluoroethylene (PTFE), polyvinylidene fluoride (PVDF)), is used to prepare a hydrophobic type of catalyst layer. The typical process for the preparation can be summarized as follows:

1. Stir a mixture of Pt/C catalyst and solvent (e.g., ethanol) highly and disperse it in an ultrasonic machine;
2. Add a diluted PTFE emulsion to the above mixture, followed by thorough ultrasonic stirring to form a catalyst ink;
3. Heat the mixture in a temperature water bath to form a paste that is suitable for transferring onto a GDL.

PTFE induced in a CL not only acts as a binder to stabilize the catalyst particles but also imparts hydrophobicity to the CL and provides passways for gas transportation. However, if the PTFE content is too high the catalyst particles could become wrapped, resulting in decreased electron conductivity and catalyst utilization. Normally, a content of 10–40% is considered optimal.

19.3.1.2 Hydrophilic Solution and Colloid Ink

In a hydrophilic ink, the CL binder is replaced with a hydrophilic perfluorosulfonate ionomer (PFSI, e.g., Nafion). It is well known that Nafion ionomer exists in different states according to the dielectric constants of solvents, ε. For example, Nafion forms a solution in solvents with $\varepsilon > 10$, a colloid in those with ε between 3 and 10, and a precipitate in those with $\varepsilon < 3$. Typically, a solution state with ethanol or isopropyl alcohol and a colloidal state with butyl acetate have been widely used in prior studies.

One of the key parameters in such a hydrophilic ink is the PFSI content. The optimum amount and distribution of the ionomer in the CL is a trade-off between the requirements of maximum contact between ionomer and Pt particles, and

minimum electron/gas transport resistances. This maximum ionomer-Pt contact is required to guarantee maximum protonic conductivity. Gas transport inside the catalyst layer could be affected by both decreased porosity and liquid water trapping. Decreased porosity is caused mainly by occupation of the solid ionomer, while liquid water trapping is caused primarily by the hydrophilic property of the ionomer. For a supported catalyst like Pt/C, the carbon has a much larger surface area than that of the Pt particles. Therefore, only if the carbon surface is covered by the ionomer can contact between the ionomer and Pt particles be guaranteed. Normally, the ratio of ionomer to carbon (*I/C*) is about 0.8~1.

19.3.1.3 Pt Ion Solution Ink and Pt Foil

The third method is to use Pt ion solution ink, such as Pt^{2+} or Pt^{4+} salt solution, rather than using a well-prepared Pt/C or Pt-alloy/C catalyst. In this way, catalyst sites at desired positions in the catalyst layer can be formed through a reduction process. Alternatively, a Pt foil can also be used as the Pt resource in most of the sputtering-deposition method for CL preparation.

19.3.2 Preparation of the Catalyst Layer

In accordance with the component distribution in a catalyst layer, two categories of catalyst layer have been employed during the development of PEM fuel cells. The first is the uniform catalyst layer, in which all components distribute uniformly; this kind of CL is widely used in the fuel cell industry. The second is the non-uniform catalyst layer, in which one or more components have gradients across the whole catalyst layer, from the GDL side to the membrane side or from fuel cell inlet to outlet. The following sections will discuss these two categories in detail.

19.3.2.1 Uniform Catalyst Layer

PTFE-bonded Hydrophobic Catalyst Layer
PTFE-bonded hydrophobic electrodes are the modified versions of gas diffusion electrodes developed for PAFCs. In preparation, the catalyst particles are mixed with PTFE emulsion to form a catalyst ink, which is then cast onto the GDL. In order to provide ionic transport to the catalyst sites, the PTFE-bonded catalyst layers are generally impregnated with an ionomer, commonly Nafion, by brushing or spraying. A typical preparation process is detailed as follows:

1. Coat a PTFE-bonded hydrophobic ink onto the GDL and then dry to remove the solvent;
2. Bake the electrode subsequently at 240–340 °C for 40 minutes to remove surfactants in the PTFE emulsion and hydrophobilize the electrodes;
3. Spray a certain amount of Nafion solution onto the surface of the catalyst layer to form the ionic paths;
4. Dry the as-prepared electrode at room temperature to remove the solvents.

Such a PTFE-bonded hydrophobic catalyst layer is a breakthrough in catalyst layer preparation technology for PEMFCs. First, this technique uses a carbon-

supported platinum catalyst to replace a platinum black catalyst. This replacement can reduce platinum usage more than ten-fold without compromising catalyst layer performance. More importantly, proton transport is enhanced significantly by impregnating the CL with a proton conducting material (Nafion) between the electrode and the membrane. For fuel cell performance optimization, a PTFE content of 20~40 wt% and an ionomer to carbon (in a Pt/C catalyst-based catalyst layer) ratio of 0.8~1 have proven to be optimal parameters for forming an efficient electrode. To date, the performance of such an electrode has been improved significantly and corresponding mass production has been achieved.

Figure 19.5 schematically shows the structure of PTFE-bonded electrodes. The advantages and disadvantages of such electrodes depend on the preparation processes and materials used. The unique use of such a PTFE in the catalyst layer can improve the gas transport limitation considerably. However, if too much PTFE is used, negative effects can be observed. For example, the catalyst layer wrapping effect will cause a decrease in both electron conductivity and catalyst utilization. In addition, the process of impregnating the top of the catalyst layer surface with Nafion ionomer could lead to an asymmetric distribution within the whole CL. If the sprayed Nafion ionomer does not penetrate the electrode to a sufficient depth, the deeper layer catalyst particles will not come in contact with the ionomer, leading to a higher resistance in proton transport and leaving the uncontacted Pt inactive. These inactive Pt particles are denoted by blank circles in Figure 19.5. The platinum utilization in such an electrode is only 10–20% [7]. Note that assembled MEAs with such electrodes are prone to delamination due to the different swelling degrees of the electrode and membrane, resulting in a discontinuity in the ion path and decreased cell longevity.
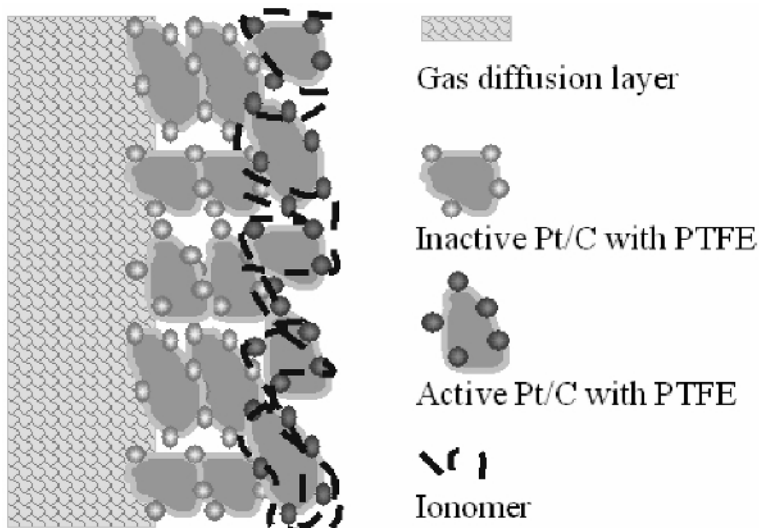
Figure 19.5. Schematic of a PTFE-bonded hydrophobic electrode

Ionomer-bonded Hydrophilic Catalyst Layer

As discussed above, it is vital to extend the contact area between the catalyst and the protonic ionomer in order to improve catalyst utilization. To meet this requirement, ionomer-bonded hydrophilic catalyst layers have been developed. The hydrophilic ink, prepared by mixing the catalyst and ionomer directly, ensures sufficient contact between the catalyst particles and the ionomer. It was found that an ionomer-bonded hydrophilic catalyst layer could improve Pt utilization by up to 45.4% [25].

Ionomer-bonded hydrophilic catalyst layers can be classified into two categories, according to differences in preparation processes and structures: the membrane-based hydrophilic catalyst layer and the GDL-based hydrophilic catalyst layer. In addition, some modified versions of such hydrophilic catalyst layers have also been explored. These will be discussed in detail in the following sub-sections.

Membrane-based Hydrophilic Catalyst Layer. Wilson and Gottesfeld [8, 21–23] suggested an ionomer-bonded hydrophilic catalyst layer prepared with the decal transfer method. The so-called decal transfer process includes two key steps: (1) coating catalyst ink onto a blank substrate (e.g., PTFE film) then (2) transferring the coat onto the membrane (as shown in Figure 19.6). A typical preparation procedure is as follows:

1. Prepare a uniformly distributed hydrophilic ink (Pt/C catalyst, Nafion solution and water/glycerol as a solvent). The weight ratio of carbon/water/glycerol is about 1:5:20.
2. Paint the PTFE film with a layer of ink and then bake this catalyzed film in an oven until dry. If the desired catalyst loading is not achieved, more painting will help.
3. Decal the coated layer onto a polymer electrolyte membrane by a hot-pressing process (i.e., press at 70~90 atm for 90 seconds under 140 °C).
4. Cool down and then release the blank substrate from the coating film, leaving the film adhered to the membrane surface.
5. Place gas diffusion layers against the catalyzed film to form an MEA.

Normally, glycerol is used in the ink preparation, which prevents the decal film from spontaneously combusting during the drying process in an oven; this prevention is mainly due to the low evaporation rate of glycerol. A cation exchanged ionomer and membrane (such as tetrabutylammonium ion (TBA^+) or Na^+ form) are also used more frequently in ink preparation. With these agents, the transferring temperature can be increased to as high as 200 °C without any damage to the film structure, facilitating effective contact between the ionomer and the catalyst particles, as well as strong bonding to the membrane. In addition, a robust pseudo-crystalline structure of ionomer can also be formed in the catalyst layer. The catalyzed membrane assembly is thereafter converted to the H^+ form by light boiling in a 0.1 M H_2SO_4 solution and rinsing in deionized water prior to assembly into the MEA.
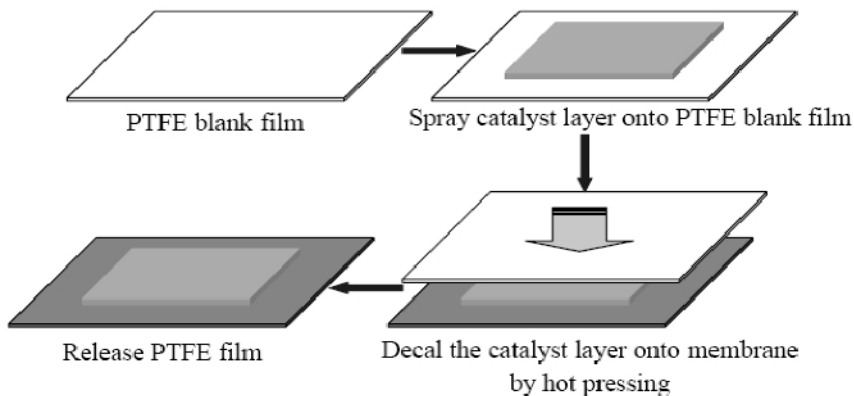
Figure 19.6. Process flow diagram of thin film decal transfer technology

In order to further improve the ionic connection between the membrane and the catalyst layer [8, 26–30], a technology called catalyst coated-membrane (CCM) has recently been developed. In a CCM, the catalyst ink composed of catalyst, proton exchange ionomer, and solvent is sprayed directly onto both sides of the proton exchange membrane (e.g., Nafion membrane) to form anode and cathode catalyst layers. In this way, a three-layer (anode catalyst, membrane, and cathode catalyst layer) CCM is formed. The CCM is then sandwiched with two GDLs to make an MEA. A hot-press bonding step for this MEA may not be necessary when it is assembled into a single cell. Of course, a hot-press step may help if the heating and pressing conditions are optimized. Commercially available CCMs can give a performance of 0.65 V at a current density of 1.0 A/cm^2 under operating conditions of 80 °C, 50% relative humidity (RH), and 7 psig.

Besides a wet-spraying method for CCMs, a dry-spraying method was also developed by Gulzow et al. [31, 32] without using solvents. In this process, composite catalyst powders, ionomer, and PTFE are mixed in a knife mill. The mixture is then atomized and sprayed with a nitrogen stream through a slit nozzle directly on both sides of the membrane, followed by a hot rolling procedure to improve both electric and ionic contacts. The advantages of the dry layer technique are its simplicity without solvent evaporation steps, as well as its unique ability to create graded layers with multiple mixture streams.

GDL-based Hydrophilic Catalyst Layer. Catalyst layers can also be formed by spraying hydrophilic catalyst ink onto a GDL [33–36]. Qi and Kaufman [36] presented a low-Pt-loading high-performance electrode for PEM fuel cells by this method. They simply mixed together the catalyst with cold Nafion solution and water, without any additional organic solvent, and then pasted the mixture onto the GDL to form the electrode. Using E-TEK 20 wt% Pt/C, the catalyst layer with 30 wt% Nafion content and 0.12 mg/cm^2 Pt loading yielded the best performance, 0.72 W/cm^2 under ambient pressure. This performance could be further improved using several effective activation methods. One was to boil or steam the electrodes or MEAs before fuel cell testing [37]. The second method was H_2 evolution on electrodes using an external power source [38]; H_2 evolution could change the

porosity and tortuosity of the catalyst layer and improve catalyst utilization and fuel cell performance. The third method was to operate the MEAs at elevated temperature and pressure before operation at normal conditions [39, 40].

Figure 19.7 shows a schematic structure of an ionomer-bonded electrode. The notable advantages of such an electrode can be summarized as follows: (1) improved bonding between the membrane and the catalyst layer, (2) a uniform continuity of the electronic and ionic paths for all catalyst sites due to the uniform dispersion of catalyst in the ionomer, (3) high Pt utilization, attributed to good contact between the catalyst and the protonic conductor, and (4) relatively low catalyst loading without performance losses. However, there are still some inevitable disadvantages for this kind of catalyst layer. First, due to the lack of hydrophobic passages, gas transportation from the GDL to the reaction sites is difficult, and the produced water tends to accumulate in the electrode and block the gas transport paths, leading to a decrease in fuel cell performance. Second, because the ionomer degrades, its ability to bind with the catalyst particles will decrease, causing lowered reliability as well as durability problems.
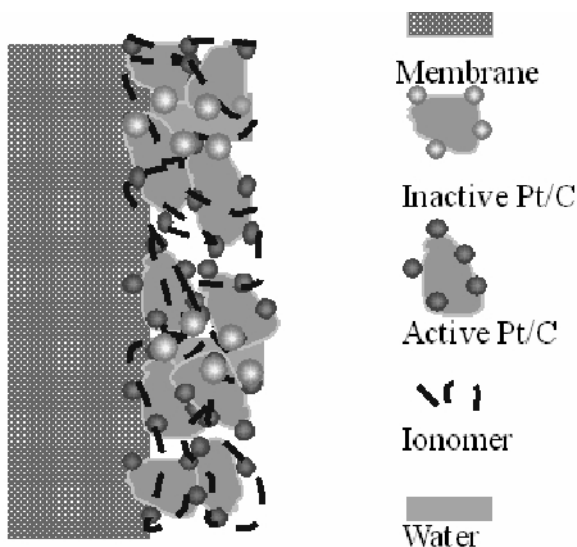
Figure 19.7. Schematic of an ionomer-bonded hydrophilic electrode

Modified Hydrophilic Catalyst Layer

Colloid Method: In order to improve gas transport through the ionomer-bonded hydrophilic catalyst layer, some modified hydrophilic electrodes have also been developed. One technique is called the colloid method, which changes Nafion into a colloid state. The colloid ionomer (such as Nafion) can adsorb catalyst particles to form larger catalyst/Nafion agglomerates. It is believed that the colloid method benefits the construction of the CL microstructure and enhances gas transportation [41–45]. Uchida et al. [41, 42] first proved that butyl acetate with a ε of 5.01 was the best solvent to form PFSI colloids for the preparation of a catalyst layer. The detailed steps are as follows:

1.   Add butyl acetate into the PFSI solution to form an ionomer colloid.
2.   Add the Pt/C particles into the above colloid solution; in this step, the mixture is transformed into a paste by ultrasonically coagulating the Pt/C catalyst adsorbed PFSI chains.
3.   Spread the paste over the GDL to form an electrode.

A colloid method such as this should be more suitable for applying catalyst ink onto a porous GDL because the larger catalyst agglomerates do not easily penetrate deeply into the GDL. Improved cell performance was observed with the catalyst layer prepared using this colloid method, which could be attributed to the increased reaction area, the reduced internal resistance, and the enhanced reactant mass transport.

Ionomer-pyrolyzed Method: To improve gas transfer through the hydrophilic catalyst layer, another technique called the ionomer-pyrolyzed method has also been developed [46]. This method can effectively introduce hydrophobic gas paths into the catalyst layer through pyrolyzing a part of the ionomer, making it hydrophobic.

The preparation steps are as follows:

1.   Prepare a hydrophilic catalyst ink consisting of catalyst, Nafion, and alcohol.
2.   Spread this catalyst ink onto a gas diffusion layer, then dry it to form a pre-electrode.
3.   Heat-treat this pre-electrode in a temperature range from 280 to 340 °C for 1 hour under inert gas.
4.   Spray a small amount of Nafion ionomer solution onto the surface of the electrode with a Nafion loading of 0.05–0.2 mg/cm^2 then dry the electrode at room temperature.

It is known that Nafion has a hydrophobic Teflon-like backbone and hydrophilic sulfonic groups ($-SO_3H$) at the end of the side chains, which make it proton conductive. Thermogravimetric/mass spectrometric (TG-MS) measurement during heat-treatment in the temperature range of 275 to about 380 °C showed a sharp mass loss peak corresponding to the release of sulfur dioxide. This result indicated that the sulfonic group in the ionomer was decomposed in this temperature range to form sulfur dioxide gas. Similar results were also reported in [47].

In the ionomer-pyrolyzed method, after heat-treatment of the pre-electrode in the temperature range of 280–340 °C, part of the Nafion ionomer in the catalytic layer can be pyrolyzed, losing its sulfonic acid group. This part of the ionomer can act as hydrophobic material in the electrode, performing the same function as PTFE in a PTFE-bonded electrode. The rest of the unpyrolyzed ionomer can still serve as the proton conductive material. In the final step, a small amount of Nafion ionomer solution is sprayed onto the surface of the electrode to increase the adherence between the catalyst layer and the membrane. Therefore, the ionomer-pyrolyzed electrode not only guarantees ionic and electronic contact but also provides passage for the gases and avoids flooding, thereby improving Pt

utilization. Compared to a PTFE-bonded electrode, much better fuel cell performance can be achieved with an ionomer-pyrolyzed electrode, as shown in Figure 19.8.
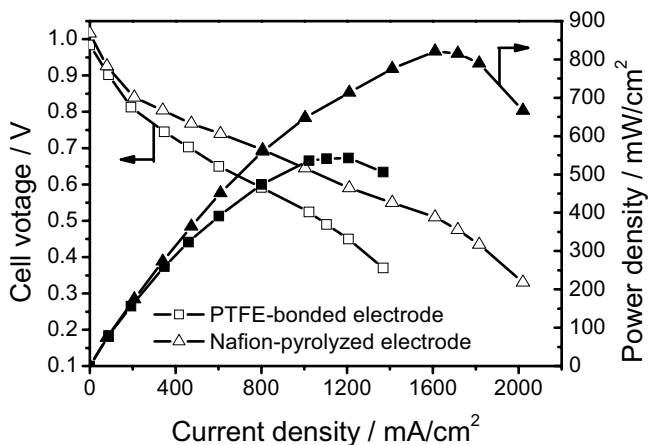
Figure 19.8. Performance of MEAs with different electrodes [46]. (Reproduced from Zhang J, Wang X, Hu J, Yi B, Zhang H. A novel method for preparing PEMFC catalytic layers. Bulletin of the Chemical Society of Japan 2004;77:2289–90, with kind permission from the Chemical Society of Japan.)

Adding PTFE/C in a Hydrophilic Electrode: Another method for modifying the hydrophilic ionomer-bonded electrode is to introduce hydrophobic materials into the electrode to form gas passages. PTFE-supported carbon (PTFE/C) composite powder is the first choice because of its excellent compatibility with the electrode. However, due to the high tenacity and low fluidity of PTFE, it is difficult to break PTFE/C into very small particles. Two ways have been proposed: (1) the mechanical milling method in liquid nitrogen [48] and (2) the intermittent microwave irradiation (IMI) method [49]. Mechanical milling is a complicated and time-consuming process, and the resultant PTFE/C powder is not uniform. The IMI method is more convenient and can achieve a uniformly distributed PTFE/C composite. Unfortunately, the drawback of IMI is that it is not easy to control the PTFE content precisely. Taking a PTFE/C with PTFE loading of 30 wt% as an example, the IMI synthesis steps are as follows [49]:

1. Mix 4.0 g carbon black and 150 ml deionized water together thoroughly under stirring.
2. Add 120 g PTFE emulsion (with a concentration of 5 wt% diluted by deionized water) to the above carbon suspension under stirring.
3. After the evaporation of water, a nominal 60 wt% PTFE/C mixture can be obtained and is treated by intermittent microwave irradiation (IMI); the IMI is cycled with "30 s on, 90 s off" to decompose the surfactant in the PTFE emulsion and recover the hydrophobicity of the PTFE until the final PTFE loading of 30 wt% is achieved.

The fabrication procedure for a catalyst layer modified by adding the as-prepared PTFE/C composite powder is as follows:

1. Prepare Nafion ionomer-impregnated Pt/C catalyst ink by dispersing Pt/C catalyst and Nafion solution in isopropanol, followed by a thorough ultrasonic treatment; the weight ratio of Nafion to the carbon support of Pt/C is controlled at ~4:5.
2. Add the butyl acetate to the dispersion to promote *in situ* deposition of Nafion on the Pt/C catalyst, forming a Pt/C/Nafion dispersion.
3. Mix the Pt/C/Nafion dispersion and PTFE/C composite powder together under stirring, forming Pt/C/Nafion-PTFE/C composite catalyst ink; the percentage of PTFE/C nanocomposite in the Pt/C/Nafion-PTFE/C catalyst layer is about 30%.
4. Spray the as-prepared composite catalyst ink directly on one side of the membrane to form a catalyst layer.
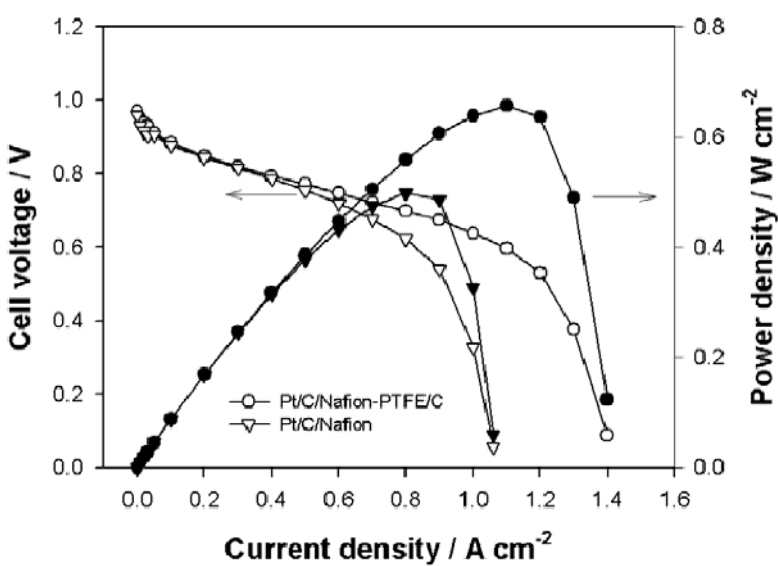
Figure 19.9. Polarization curves and the corresponding power density curves of fuel cells with a Pt/C/Nafion-PTFE/C catalyst cathode and a Pt/C/Nafion membrane-based cathode, respectively. Measured at 80 °C. The hydrogen and air reactant gases were externally humidified at 90 °C and 85 °C, respectively. The flow rates were 50 mL min^{-1} for hydrogen and 200 mL min^{-1} for air [49]. (Reprinted from Electrochemistry Communications, 8(7), Tian ZQ, Wang XL, Zhang HM, Yi BL, Jiang SP, Microwave-assisted synthesis of PTFE/C nanocomposite for polymer electrolyte fuel cells, 1158–62, ©2006, with permission from Elsevier.)

The polarization curves in Figure 19.9 show that incorporation of PTFE/C nanocomposite into the Pt/C/Nafion catalyst can significantly improve the mass transport property of the catalyst layer without any negative effect on the electrocatalytic activity of the Pt catalysts.

Dual-bonded Composite Catalyst Layer

Regarding the inherent problems with proton/gas transport for the hydrophobic or hydrophilic types of catalyst layers, a dual-bonded composite CL was suggested first by Zhang et al. [50, 51] in order to alleviate the drawbacks and promote the merits of the individual CL. Zhang and Shi [52, 53] also investigated such dual-bonded composite CLs by optimizing various components used. This dual-bonded CL cathode has two layers. The first is the hydrophobic layer with PTFE as a binder material, which is fabricated directly on the surface of the GDL. The second is a hydrophilic layer with Nafion as a binder material, which is fabricated on top of the hydrophobic layer surface. The typical preparation process can be summarized as follows:

1. Apply a PTFE-bonded hydrophobic ink on the surface of the GDL as the hydrophobic layer;
2. Bake this hydrophobic layer in an oven at a temperature of 200–350 °C for 30–60 minutes to hydrophobilize the layer;
3. Then apply a Nafion-bonded hydrophilic ink onto the top surface of the above hydrophobic layer as a hydrophilic layer, and at the same time can also ionize the hydrophobic layer.
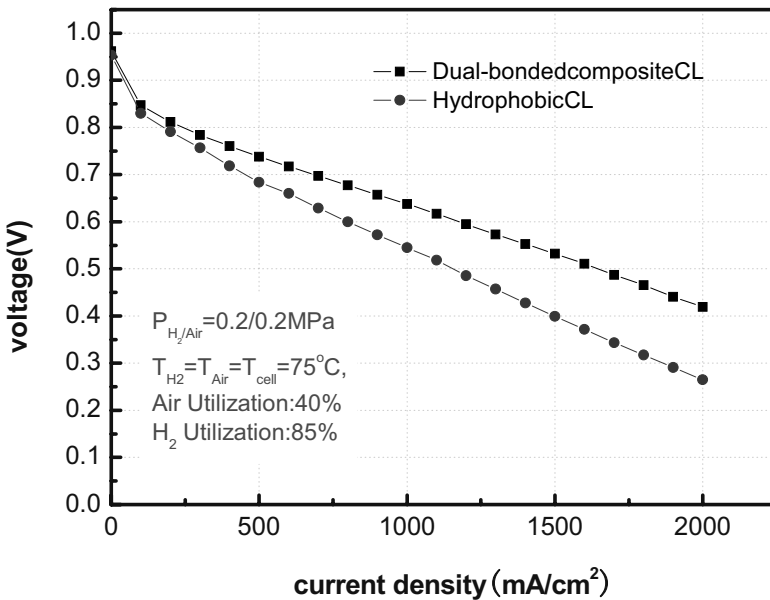
Figure 19.10. Cell performances with different catalyst layers

The dual-bonded CL has both hydrophobic and hydrophilic properties, ensuring enough protonic conductivity as well as smooth gas transfer pathways. As expected, the cell performance of such a dual-bonded composite CL is obviously higher than that of a conventional PTFE-bonded hydrophobic CL (as seen in Figure 19.10). Moreover, the catalyst dosage in such an electrode can be increased

in order to achieve the desired higher output power. Though the preparation process of such a dual-bond electrode is a little fussy, it is a promising and practical method to achieve relatively higher performance and better durability.

Super-thin Deposition Catalyst Layer
A trend in electrode preparation is to reduce the catalyst layer thickness to improve the mass transfer efficiency at the interface, such as the efficient movement of protons, electrons, and dissolved reactants in the reaction zone. In addition, a thinner electrode will be beneficial to reduce catalyst loading and increase mass power density. The deposition technique is an effective way to achieve a thinner electrode through depositing a nano-scale catalyst film on the substrate. Deposition methods include chemical vapor deposition, physical or thermal vapor deposition, sputtering deposition, electrochemical deposition, chemical deposition, as well as ion beam deposition. The following sections will focus on electrodes fabricated with these various deposition methods.

Sputtering-deposition Electrode. Sputtering is widely used in the preparation of thin catalyst layers. The resultant CLs have demonstrated high performance even at an ultra-low level of Pt loading [24, 54, 55]. In general, the sputtering process is carried out in an evacuated chamber. The typical sputtering steps are as follows:

1.   Mount the substrate (either the GDL or the membrane) in the sputtering chamber, with one side facing up or down towards the catalyst target.
2.   Evacuate the chamber and then fill argon to a pressure between 1.3 and 6.7 Pa.
3.   Initiate the sputtering process by applying a high voltage between the target and the chamber wall. Depending on the desired catalyst loading, the process is continued until the targeted loading is achieved.
4.   Upon completion of the sputtering, readmit air to the chamber and remove the substrate.

The performance of a sputtering catalyst layer is sensitive to the amount of sputtered catalyst, the substrate material, and the morphology of the substrate. The sputtering layer generally has a thickness of 2–15 nm (corresponding to an ultra-low level of platinum loading of 0.005–0.03 mg/cm^2). The surface roughness of the substrate has a significant effect on the Pt layer adhesion and morphology. Applying an additional thin layer on the substrate before catalyst layer deposition, such as a chromium, palladium, or gold thin film layer, can modify the substrate's seeding, improving the growth of the platinum catalyst film and enhancing electrical conductivity. In addition, to extend the three-phase reaction zone a two-dimensional active layer was developed by sputter-depositing alternating layers of Pt and Nafion-carbon ink onto the membrane or the gas diffusion layer [56–58]. The results demonstrated that such multiple sputtering could also effectively improve performance.

Nanostructured Thin Film (NSTF) Electrode. Debe et al. [59, 60] employed sputter technology and deposited catalyst on a nanostructured thin film (NSTF). This NSTF is an oriented crystalline organic whisker. Perylene red (PR) is a highly useful organic material for growing the NSTF. To form an electrode, the

catalyst/PR nanostructured film is decaled to the surface of the proton exchange membrane to form a catalyst layer. Scanning electron microscope (SEM) cross-sectional views of a nanostructured whisker support and a catalyst coated NSTF are shown in Figure 19.11. There are two primary differences between the NSTF catalyst layer and the conventional catalyst layer (using Pt/C): (1) the former is at least ten times thinner than the latter, which has significant implications for the electrochemically active area as well as for the water and heat generation rates per unit volume of the electrode, and (2) the former contains no additional ionomer, such as Nafion, for ion transport. But no increasing ionic resistance is observed because of the short distance between the proton exchange membrane and the active catalyst surface sites. The second difference becomes more significant when a fuel cell is operated at higher current densities. For conventional electrodes, only a fraction of the catalyst layer is utilized, whereas the NSTF layer appears to be 100% utilized at all current densities.
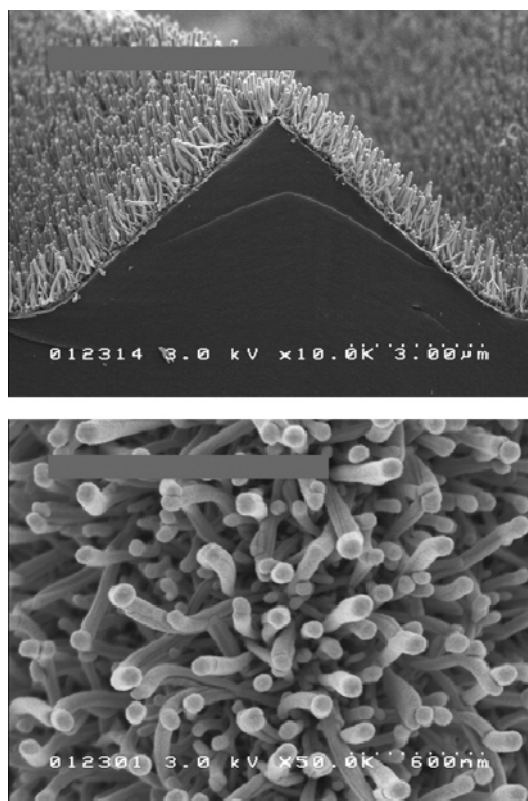
Figure 19.11. Scanning electron micrographs of typical NSTF catalysts as fabricated on a microstructured catalyst transfer substrate, seen (top) in cross-section with original magnification of ×10,000 and (bottom) in plane view with original magnification of ×50,000. The dotted scale-bar is shown in each micrograph [59]. (Reprinted from Journal of Power Sources, 161(2), Debe MK, Schmoeckel AK, Vernstrom GD, Atanasoski R, High voltage stability of nanostructured thin film catalysts for PEM fuel cells, 1002–11, ©2006, with permission from Elsevier.)

Besides Debe's electrode, Tang et al. [61] produced a carbon nanotube thin film with ultra-low Pt loading (Pt on multi-walled carbon nanotubes (MWNTs)) through a polycarbonate filtration membrane. Compared to the results presented by both Los Alamos National Lab (LANL) and 3M Corporation, as shown in Figure 19.12, this thin-film cathode catalyst layer with a loading of 6 μg Pt/cm^2 could give a mass activity of 250 A/mg Pt, which is the highest activity reported so far.
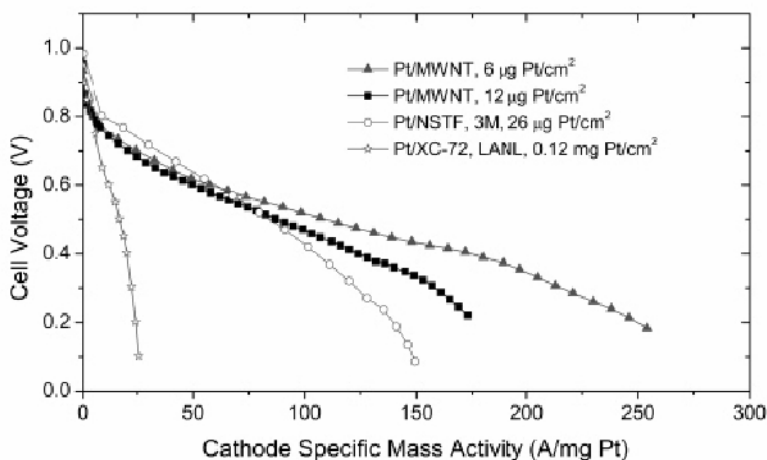
Figure 19.12. Comparison of mass activity of Pt/MWNTs thin film with Pt loading of 6 μg Pt/cm^2 (▲); Pt/MWNTs thin film with Pt loading of 12 μg Pt/cm^2 (■); 3M Corporation, Pt/NSTF with Pt loading of 26 μg Pt/cm^2 (□); Los Alamos National Lab, Pt/C with Pt loading of 120 μg Pt/cm^2 (☆) [61]. (Reprinted with permission from J Phys Chem C 2007;111:17901–4. Copyright 2000 American Chemical Society.)

As discussed, the sputtering technique is a very useful method to achieve an ultra-low Pt loading in the catalyst layer. A unique advantage of the sputtering technique is that the catalyst utilization is extremely high. In addition, the sputtering method facilitates the preparation of a nano-scale Pt catalyst layer with a precise thickness, which could simplify fuel cell water/thermal management and eliminate mass transfer loss. Furthermore, the sputtering process allows the deposition of Pt on various substrates, such as the GDL, membrane, and other supports. However, although the sputtering CLs showed remarkably higher mass activity than the conventional layer, the validated output power density still falls short.

Electrochemical-deposition Electrode. Vilambi-Reddy et al. [62] presented the early research on the electrochemical deposition electrode. They developed an electrochemical catalyzation (ECC) technique to deposit platinum catalyst particles selectively in the regions accessible to both ions and electrons. In the ECC technique, a hydrophobic porous carbon paper was first coated with dispersed carbon particles and PTFE to form a substrate. Then the Nafion ionomer was impregnated onto this carbon substrate. This substrate was then placed into a platinum acid-plating bath, along with a platinum counter electrode. One side of this substrate, without Nafion, was masked with a non-conducting film, which

could guarantee that the platinum would only be deposited on the regions impregnated with Nafion. When an interrupted DC current was applied to the electrodes in the plating bath, catalyst ions would pass through the Nafion to the carbon particles and be deposited on those areas where protonic and electronic conduction coexisted. The resulting platinum particle sizes ranged from 20 to 35 Å, with a Pt loading of 0.05 mg/cm^2. In terms of mass activity, i.e., mA/mg Pt, a tenfold increase was observed for the ECC prepared electrode, contributing to higher platinum utilization. In addition, the electrodeposited method was also used to deposit catalyst particles through the membrane and into the membrane-electrode interfacial region, or directly onto the carbon substrate [63, 64].

   Chemical-deposition Electrode. Chemical techniques can also be employed in the fabrication of catalyst layers by platinizing the surface of a Nafion membrane. One approach [65, 66] is to expose one side of the Nafion membrane to a reductant solution (e.g., hydrazine solution) and the other side to a platinic acid solution. The reductant diffuses across the membrane to react with platinic acid and form a Pt catalyst layer. In another impregnation-reduction method [3, 67, 68] a cationic salt, such as Pt(NH$_3$)$_4$Cl$_2$, is first impregnated into the Nafion membrane, followed by exposing this membrane to a reductant, such as NaBH$_4$. As shown in Figure 19.13, a dense and porous platinum film can be formed using this chemical deposition technique.
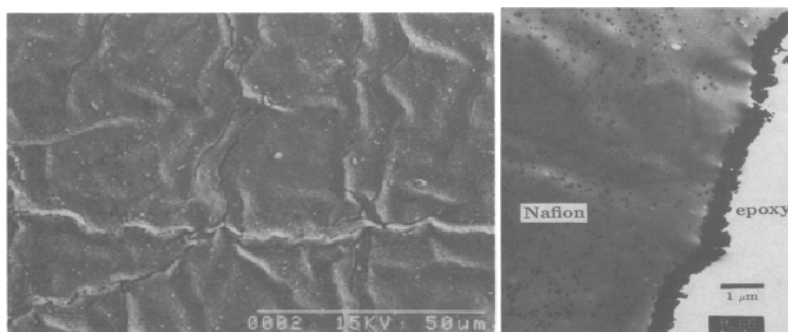
Figure 19.13. SEM top view and TEM side view of a non-equilibrium impregnation-reduction electrode. Deposition conditions: 0.6 mM Pt(NH$_3$)$_4$Cl$_2$, 1 mM NaBH$_4$, 40 minutes impregnation time, 2 hours reduction time, 50 °C [3]. (Reprinted by permission of ECS—The Electrochemical Society, from Liu R, Her W-H, Fedkiw PS. *In situ* electrode formation on a Nafion membrane by chemical platinization.)

   A unique advantage of electrodes fabricated by chemical techniques is improved proton conductivity due to sufficient contact between the Nafion membrane and the catalyst layer. The disadvantages are poor mass transportation through the catalyst layer and lower platinum activity, caused by large particle size.

   Ion-beam Assisted Deposition (IBAD) Electrode. The ion-beam assisted deposition (IBAD) technique has been previously used for a wide range of applications [69], and the detailed methodology can be found in [70]. Dual IBAD is a vacuum-deposition process that combines physical vapor deposition (PVD) with ion-beam bombardment. A vapor of coating atoms is generated with an

electron-beam evaporator and deposited on the substrate. Ions are simultaneously extracted from the plasma and accelerated into the growing PVD film at energy levels of several hundred to several thousand electron volts (500–2000 eV). Two ion beams are used in the dual IBAD approach: one is to roughen the substrate and the other is to embed the target atoms (such as Pt). Saha et al. [71, 72] prepared a series of ultra-low pure Pt-based electrodes (with Pt loading of 0.04–0.12 mg Pt/cm^2, the corresponding film thicknesses ranged between 250 and 750 Å) by the dual IBAD method on the surface of a commercially available GDL (LT1400, E-TEK). These electrodes were compared with a conventional E-TEK electrode having a total MEA Pt loading of 1 mg Pt/cm^2. The results showed that a mass specific power density of 0.297 g Pt/kW may be possible at 0.65 V if using a dual IBAD electrode containing a 250 Å deposit with a total catalyst loading of 0.08 mg Pt/cm^2. This activity is superior to that of the conventional MEA with a total loading of 1 mg Pt/cm^2. Furthermore, the dual IBAD method also has an advantage in terms of mass manufacturability of the PEMFC electrodes. However, in comparison with the performance target of 0.8–0.9 W/cm^2 at 0.65 V, this technique could give a performance of only 0.27–0.43 W/cm^2, mainly due to high mass transport losses.

19.3.2.2 Gradient Configuration Catalyst Layer

Most of the catalyst layers described above have uniform structures and compositions over the whole catalyst layer. However, current distribution measurements (or current mapping) and the corresponding mathematical models indicate that current density is strongly dependent on the relative position on the MEA; in other words, different locations across the MEA can give different current densities or reaction rates. This is mainly due to the non-uniform distribution of the reactant concentrations along the flowfield channels. It is understandable that the electrochemical reaction consumption of the reactant, as well as product water accumulation along the MEA in-plane direction, lead to a gradual decrease in reactant concentration from fuel cell inlet to outlet. In this non-uniform reactant distribution, the configuration of flowfield channels plays an important role. Along the MEA through-plane direction, the electrochemical reaction prefers to occur at zones close to the membrane in the catalyst layer. Therefore, in order to ensure an efficient electrochemical reaction and sufficient utilization of the catalyst, a decreasing gradient distribution of the catalyst from the membrane side to the GDL side would be favorable. With respect to this, some "fine gradient" electrodes with non-uniform structure and composition in the in-plane direction or through-plane direction have been explored.

In-plane Catalyst Gradient Electrode

A non-uniform electrode was introduced in 1989 [73]. In this electrode, the electrocatalyst concentration increased along the direction parallel to the electrode substrate. It is expected that the effect of increased catalyst loading in the direction of gas flow could balance the effect of diminishing reactants in the gas stream. In this way, the reaction rate could be substantially uniform across the electrode surface. Prasanna et al. [74] employed the catalyst-gradient method for single fuel cell fabrication, and found that it was an effective way to reduce Pt loading without

any loss in fuel cell performance. Various gradient electrodes have been designed, as shown in Figure 19.14 (a). The corresponding cell performance is also given in Figure 19.14 (b). It can be seen that with the same catalyst loading (0.3 mg/cm^2), the gradient electrode displays much better performance than does the non-gradient electrode, particularly in the high current density range. The disadvantage is that the fabrication of a non-uniform electrode is much more complicated than that of a uniform electrode.
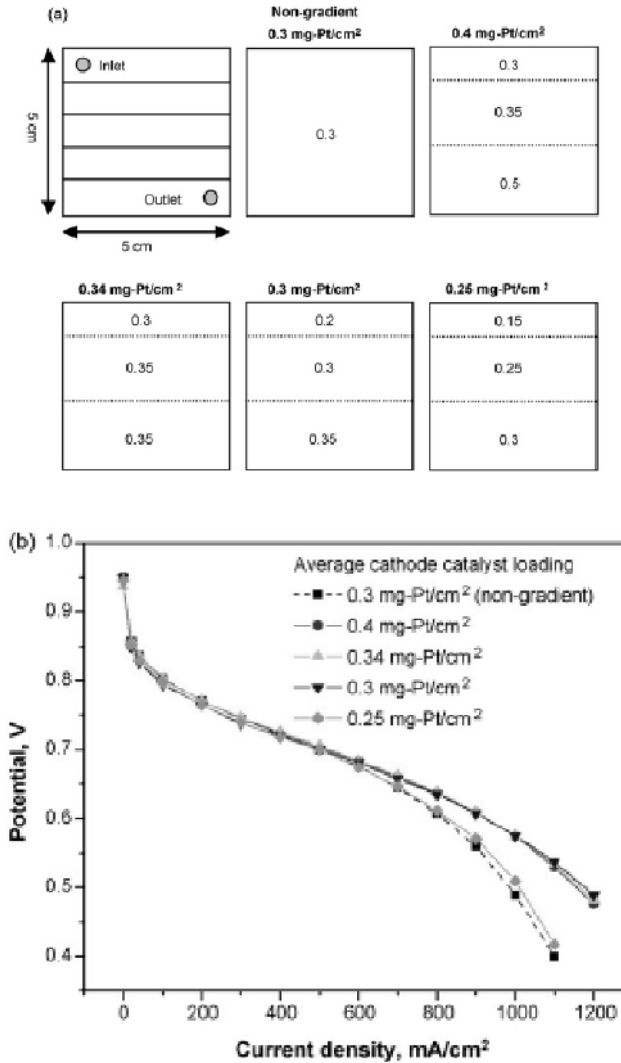
Figure 19.14. (a) Distribution of the cathode catalyst loading in a gradient electrode, (b) cell performance of non-gradient and gradient electrodes [74]. (Reprinted from Journal of Power Sources, 166(1), Prasanna M, Cho EA, Kim H-J, Oh I-H, Lim T-H, Hong S-A, Performance of proton-exchange membrane fuel cells using the catalyst-gradient electrode technique, 53–8, ©2007, with permission from Elsevier.)

Through-plane Catalyst Gradient Electrode

An electrode with the catalyst gradient along the through-plane direction contains a series of catalyst layers from the GDL side to the membrane. Each catalyst layer has its own catalyst loading that differs from the others'. A typical example is a PTFE-bonded or ionomer-bonded catalyst layer with an additional sputtered Pt layer on the top surface of the CL or membrane. The objectives of this method are to reduce the thickness of the supporting catalyst layer and increase the catalyst concentration in the layer adjacent to the membrane. The catalyst through-plane gradient configuration is also beneficial in terms of catalyst utilization improvement. For example, Ticianelli et al. [5, 75, 76] made this kind of electrode by sputtering a 50 nm Pt layer on a PTFE-bonded layer and testing its performance. They found that with a highly concentrated Pt localized in the layer near the membrane, the activation as well as the ohmic losses within the catalyst layer were diminished and the power density was improved significantly. Similar conclusions were also obtained by Mukerjee et al. [77].

Other Composition Gradient Electrodes

Besides the catalyst gradient in the catalyst layer, other components such as the hydrophobic agent (PTFE) and proton conductive polymer (Nafion) may also need to be adjusted in order to optimize gas/water transportation and electron/proton transfer. It can be expected that the catalyst layer adjacent to the gas diffusion layer side should be more hydrophobic to ensure much more of the reactants penetrates the inside of the electrode. While near the membrane side, more proton conductive polymer is needed to ensure a continuous network for proton conduction. Therefore, a non-uniform catalyst layer with a decreasing PTFE loading and an increasing Nafion content along the through-plane direction from GDL to membrane should be more efficient.

Song et al. [78] presented a multi-layer agglomerate model for the performance analysis of a non-uniform catalyst layer. The catalyst layer is assumed to be composed of several sub-layers with different material properties, such as agglomerate size, agglomerate porosity or sub-layer porosity, and so on. The effects of different material property combinations in these sub-layers on the whole catalyst layer performance were studied numerically. The results showed that the performance of the catalyst layer was strongly dependent on the properties of the sub-layer adjacent to the membrane. Furthermore, decreasing agglomerate sizes, increasing agglomerate porosities, or decreasing sub-layer porosities along the direction from the side of the gas diffusion layer to the side of the membrane will also improve the performance of the whole catalyst layer.

Non-uniformity in an electrode is also developed according to the configuration of the flowfield channels [79]. The MEA area that is in contact with the landing areas of the flowfield plate has no catalyst, and only the channel area is coated with catalyst. In this way, it is possible to reduce the quantity of expensive electrocatalyst material while maintaining the same cell performance.

Although a non-uniform catalyst layer can improve fuel cell performance to some extent, the preparation process is complicated and difficult to control. Therefore, this kind of catalyst layer is not suitable for mass production.

19.4 Preparation of the MEA

The MEA, which is composed of anode, membrane, and cathode, is a key unit in PEM fuel cells. The MEA is normally prepared by sandwiching a membrane between an anode and cathode under hot pressing. Before hot pressing, the membrane usually needs to be pre-treated in order to remove impurities and completely protonate the membrane. In practice, the membrane is treated in 3% H_2O_2(aq) and then in 1 M H_2SO_4(aq) for 1 hour each at 60–80 °C, followed by careful washing with double-distilled water.

The hot-pressing process (also called MEA bonding) is a simple way to assemble the anode, cathode, and proton exchange membrane together, and ensures interfacial contact between the electrode and the membrane. The bonding conditions of the hot-pressing process, such as the bonding temperature, pressure, and time, play an important role in obtaining high-performance MEAs. For example, the glass transition temperature of Nafion is about 125 °C, which restricts the hot-pressing temperature. However, at temperatures much lower than the glass transition temperature of the membrane, the Nafion resin in both the catalyst layer and the membrane will not melt, so ionomeric contact with the catalyst and between the catalyst layer and the membrane will become a problem, resulting in poor catalyst utilization and higher ionic resistance. On the other hand, if a much higher bonding temperature is used, the membrane may lose its water retention properties, the ionomer acidic group may degrade, and the catalyst layer may be partially delaminated from the membrane. Therefore, an optimal temperature value exists for hot pressing. As for the hot-pressing pressure, the choice is strongly dependent on the electrode's mechanical strength, porosity, and thickness. The porosity of the electrode decreases with increasing bonding pressure, which limits mass transport. Moreover, the carbon fibers are prone to being crushed under a very high pressure. However, high pressure can result in a thinner catalyst layer, favoring mass transport. Therefore, the choice of bonding pressure should also be optimized. Hot-pressing time is another important parameter affecting the contact between the membrane and the electrode, as well as the porosity of the electrode. It seems that as the hot-pressing time increases, the ionic conductivity and three-phase reaction area in the catalyst layer first increase and then decrease, resulting in a reduction in the porosity and mass transport rates [80]. Normally, hot pressing is conducted in a temperature range of 120–160 °C, and a time period of 30–300 seconds.

It is worth noting that the hot-pressing process is not necessary for some kinds of MEAs. For example, when a CCM is used in a fuel cell, the CCM can be put directly between two pieces of GDL and assembled into the fuel cell hardware.

19.5 Summary and Outlook

This chapter has addressed the fabrication technologies for catalyst inks, catalyst layers, and MEAs. Due to the electrochemical reactions taking place in the three-phase areas of fuel cell catalyst layers, the proton conductor, electron conductor, and reactants must meet together at all active catalyst sites. Passages for proton,

electron, gas, and water transport must co-exist at the same time in a catalyst layer. The preparation procedures for catalyst inks, catalyst layers, as well as MEAs have a strong effect upon the formation of such passages. There is no doubt that high fuel cell performance is primarily determined by how the catalyst ink, catalyst layer, and MEA are prepared.

During the development of PEMFCs, many kinds of catalyst layers have been designed and accordingly, many techniques have also been developed to fabricate these catalyst layers. It is still difficult to make fair comparisons among the techniques developed. Besides the fabrication method, electrode performance also strongly depends on its components and the materials used in the catalyst ink, catalyst layer, and MEA. Therefore, the greatest challenge in achieving efficient and cost-effective electrodes for fuel cell commercialization remains to achieve a breakthrough in materials exploration, such as catalyst and membrane materials.

References

1. Hirano S, Kim J, Srinivasan S. High performance proton exchange membrane fuel cells with sputter-deposited Pt layer electrodes. Electrochim Acta 1997;42:1587–93.
2. Dearnaley G, Arps JH. Method of depositing a catalyst on a fuel cell electrode. United States patent US 6159533. 2000 Dec 12.
3. Liu R, Her W-H, Fedkiw PS. In situ electrode formation on a Nafion membrane by chemical platinization. J Electrochem Soc 1992;139:15–23.
4. Hogarth MP, Munk J, Shukla AK, Hamnett A. Performance of carbon-cloth bound porous-carbon electrodes containing an electrodeposited platinum catalyst towards the electrooxidation of methanol in sulphuric acid electrolyte. J Appl Electrochem 1994;24:85–8.
5. Ticianelli EA, Derouin CR, Srinivasan S. Localization of platinum in low catalyst loading electrodes to to attain high power densities in SPE fuel cells. J Electroanal Chem 1988;251:275–95.
6. Kumar GS, Raja M, Parthasarathy S. High performance electrodes with very low platinum loading for polymer electrolyte fuel cells. Electrochim Acta 1995;40:285–90.
7. Srinivasan S, Velev OA, Parthasarathy A, Manko DJ, Appleby AJ. High energy efficiency and high power density proton exchange membrane fuel cells – electrode kinetics and mass transport. J Power Sources 1991;36:299–320.
8. Wilson MS, Gottesfeld S. High performance catalyzed membranes of ultra-low Pt loadings for polymer electrolyte fuel cells. J Electrochem Soc 1992;139:L28–30.
9. Antoine O, Bultel Y, Ozil P, Durand R. Catalyst gradient for cathode active layer of proton exchange membrane fuel cell. Electrochim Acta 2000;45:4493–500.
10. Prasanna M, Ha HY, Cho EA, Hong SA, Oh IH. Investigation of oxygen gain in polymer electrolyte membrane fuel cells. J Power Sources 2004;137:1–8.
11. Gasteiger HA, Panels JE, Yan SG. Dependence of PEM fuel cell performance on catalyst loading. J Power Sources 2004;127:162–71.
12. Hottinen T, Mikkola M, Mennola T, Lund P. Titanium sinter as gas diffusion backing in PEMFC. J Power Sources 2003;118:183–8.
13. Wan N, Wang C, Mao Z. Titanium substrate based micro-PEMFC operating under ambient conditions. Electrochem Commun 2007;9:511–16.
14. Liu J, Sun G, Zhao F, Wang G, Zhao G, Chen L, et al. Study of sintered stainless steel fiber felt as gas diffusion backing in air-breathing DMFC. J Power Sources 2004;133:175–80.

15. Lin G, Van Nguyen T. Effect of thickness and hydrophobic polymer content of the gas diffusion layer on electrode flooding level in a PEMFC. J Electrochem Soc 2005;152:A1942–8.
16. Qi Z, Kaufman A. Improvement of water management by a microporous sublayer for PEM fuel cells. J Power Sources 2002;109:38–46.
17. Pasaogullari U, Wang C-Y. Two-phase transport and the role of micro-porous layer in polymer electrolyte fuel cells. Electrochim Acta 2004;49:4359–69.
18. Park G-G, Sohn Y-J, Yang T-H, Yoon Y-G, Lee W-Y, Kim C-S. Effect of PTFE contents in the gas diffusion media on the performance of PEMFC. J Power Sources 2004;131:182–7.
19. Wilson MS, Valerio JA, Gottesfeld S. Low platinum loading electrodes for polymer electrolyte fuel cells fabricated using thermoplastic ionomers. Electrochim Acta 1995;40:355–63.
20. Raistrick ID. Electrode assembly for use in a solid polymer electrolyte fuel cell. United States patent US 4876115. 1989 Oct 24.
21. Wilson MS, Gottesfeld S. Thin-film catalyst layers for polymer electrolyte fuel cell electrodes. J Appl Electrochem 1992;22:1–7.
22. Springer TE, Wilson MS, Gottesfeld S. Modeling and Experimental Diagnostics in Polymer Electrolyte Fuel Cells. J Electrochem Soc 1993;140:3513–26.
23. Wilson MS. Membrane catalyst layer for fuel cells. United States patent US 5234777. 1993 Aug 10.
24. O'Hayre R, Lee S-J, Cha S-W, Prinz FB. A sharp peak in the performance of sputtered platinum fuel cells at ultra-low platinum loading. J Power Sources 2002;109:483–93.
25. Cheng X, Yi B, Han M, Zhang J, Qiao Y, Yu J. Investigation of platinum utilization and morphology in catalyst layer of polymer electrolyte fuel cells. J Power Sources 1999;79:75–81.
26. Mussel RD, Rehg TJ. Active layer for membrane assembly. United States patent US 5882810. 1999 Mar 16.
27. Hulett JS. Method of making MEA for PEM/SPE fuel cell. United States patent US 6074692. 2000 Jun 13.
28. Hunt AT. Materials and processes for providing fuel cells and active membranes. United States patent US 6403245. 2002 Jun 12.
29. Escribano S, Aldebert P. Electrodes for hydrogen/oxygen polymer electrolyte membrane fuel cells. Solid State Ionics 1995;77:318–23.
30. Hsu CH, Wan CC. An innovative process for PEMFC electrodes using the expansion of Nafion film. J Power Sources 2003;115:268–73.
31. Gulzow E, Kaz T. New results of PEFC electrodes produced by the DLR dry preparation technique. J Power Sources 2002;106:122–5.
32. Gulzow E, Schulze M, Wagner N, Kaz T, Reissner R, Steinhilber G, et al. Dry layer preparation and characterisation of polymer electrolyte fuel cell components. J Power Sources 2000;86:352–62.
33. Dhar HP. Method for catalyzing a gas diffusion electrode. United States patent US 5521020. 1996 May 28.
34. Shin SJ, Lee JK, Ha HY, Hong SA, Chun HS, Oh IH. Effect of the catalytic ink preparation method on the performance of polymer electrolyte membrane fuel cells. J Power Sources 2002;106:146–52.
35. Paganin VA, Ticianelli EA, Gonzalez ER. Development and electrochemical studies of gas diffusion electrodes for polymer electrolyte fuel cells. J Appl Electrochem 1996;26:297–304.
36. Qi Z, Kaufman A. Low Pt loading high performance cathodes for PEM fuel cells. J Power Sources 2003;113:37–43.

37. Qi Z, Kaufman A. Enhancement of PEM fuel cell performance by steaming or boiling the electrode. J Power Sources 2002;109:227–9.

38. He C, Qi Z, Hollett M, Kaufman A. An electrochemical method to improve the performance of air cathodes and methanol anodes. Electrochem Solid-State Lett 2002;5:A181–3.

39. Qi Z, Kaufman A. Activation of low temperature PEM fuel cells. J Power Sources 2002;111:181–4.

40. Qi Z, Kaufman A. Quick and effective activation of proton-exchange membrane fuel cells. J Power Sources 2003;114:21–31.

41. Uchida M, Aoyama Y, Eda N, Ohta A. New preparation method for polymer-electrolyte fuel cells. J Electrochem Soc 1995;142:463–8.

42. Uchida M, Fukuoka Y, Sugawara Y, Ohara H, Ohta A. Improved preparation process of very-low-platinum-loading electrodes for polymer electrolyte fuel cells. J Electrochem Soc 1998;145:3708–13.

43. Yang T-H, Yoon Y-G, Park G-G, Lee W-Y, Kim C-S. Fabrication of a thin catalyst layer using organic solvents. J Power Sources 2004;127:230–3.

44. Yoon YG, Park GG, Yang TH, Han JN, Lee WY, Kim CS. Effect of pore structure of catalyst layer in a PEMFC on its performance. Int J Hydrogen Energy 2003;28:657–62.

45. Fernandez R, Ferreira-Aparicio P, Daza L. PEMFC electrode preparation: influence of the solvent composition and evaporation rate on the catalytic layer microstructure. J Power Sources 2005;151:18–24.

46. Zhang J, Wang X, Hu J, Yi B, Zhang H. A novel method for preparing pemfc catalytic layers. Bull Chem Soc Japan 2004;77:2289–90.

47. Samms SR, Wasmus S, Savinell RF. Thermal stability of Nafion® in simulated fuel cell environments. J Electrochem Soc 1996;143:1498–504.

48. Uchida M, Aoyama Y, Eda N, Ohta A. Investigation of the microstructure in the catalyst layer and effects of both perfluorosulfonate ionomer and PTFE-loaded carbon on the catalyst layer of polymer electrolyte fuel cells. J Electrochem Soc 1995;142:4143–9.

49. Tian ZQ, Wang XL, Zhang HM, Yi BL, Jiang SP. Microwave-assisted synthesis of PTFE/C nanocomposite for polymer electrolyte fuel cells. Electrochem Commun 2006;8:1158–62.

50. Zhang H, Dong M, Qiu Y, Yi B, Wang X, Wang X. A multilayer catalyst layer for PEMFCs and its preparation. Republic of China patent CN 1744360. 2006 Mar 8.

51. Zhang H, Dong M, Qiu Y, Tang Q, Yi B, Liu B, et al. A gas diffusion electrode for PEMFC and its preparation method. Republic of China patent CN 1553534. 2006 Sep 6.

52. Zhang X, Shi P. Dual-bonded catalyst layer structure cathode for PEMFC. Electrochem Commun 2006;8:1229–34.

53. Zhang X, Shi P. Nafion effect on dual-bonded structure cathode of PEMFC. Electrochem Commun 2006;8:1615–20.

54. Gruber D, Ponath N, Muller J, Lindstaedt F. Sputter-deposited ultra-low catalyst loadings for PEM fuel cells. J Power Sources 2005;150:67–72.

55. Nakakubo T, Shibata M, Yasuda K. Membrane electrode assembly for proton exchange membrane fuel cells prepared by sputter deposition in air and transfer method. J Electrochem Soc 2005;152:A2316–22.

56. Cha SY, Lee WM. Performance of proton exchange membrane fuel cell electrodes prepared by direct deposition of ultrathin platinum on the membrane surface. J Electrochem Soc 1999;146:4055–60.

57. Haug AT, White RE, Weidner JW, Huang W, Shi S, Stoner T, et al. Increasing proton exchange membrane fuel cell catalyst effectiveness through sputter deposition. J Electrochem Soc 2002;149:A280–7.

58. Wan C-H, Lin M-T, Zhuang Q-H, Lin C-H. Preparation and performance of novel MEA with multi catalyst layer structure for PEFC by magnetron sputter deposition technique. Surf Coat Technol 2006;201:214–22.

59. Debe MK, Schmoeckel AK, Vernstrom GD, Atanasoski R. High voltage stability of nanostructured thin film catalysts for PEM fuel cells. J Power Sources 2006;161:1002–11.

60. Debe MK. Novel catalysts, catalysts support and catalysts coated membrane methods. In: Vielstich W, Gasteiger HA, Lamm A, editors. Handbook of fuel cells – fundamentals, technology and applications, volume 3. Chichester, UK: Wiley, 2003;576–89.

61. Tang JM, Jensen K, Waje M, Li W, Larsen P, Pauley K, et al. High performance hydrogen fuel cells with ultralow Pt loading carbon nanotube thin film catalysts. J Phys Chem C 2007;111:17901–4.

62. Vilambi-Reddy NRK, Anderson EB, Taylor EJ. High utilization supported catalytic metal-containing gas-diffusion electrode, process for making it, and cells utilizing it. United States patent US 5084144. 1992 Jan 28.

63. Verbrugge MW. Selective electrodeposition of catalyst within membrane-electrode structures. J Electrochem Soc 1994;141:46–53.

64. Hogarth M, Munk J, Shukla A, Hamnett A. Performance of carbon-cloth bound porous-carbon electrodes containing an electrodeposited platinum catalyst towards the electrooxidation of methanol in sulphuric acid electrolyte. J Appl Electrochem 1994;24:85–8.

65. Takenaka H, Torikai E, Kawami Y, Wakabayashi N. Solid polymer electrolyte water electrolysis. Int J Hydrogen Energy 1982;7:397–403.

66. Takenaka H, Torikai E. Membrane electrode assembly for proton exchange membrane fuel cell and its preparation. Japan patent JP5538934. 1980 Mar 18.

67. Fedkiw PS, Her W-H. An impregnation-reduction method to prepare electrodes on Nafion SPE. J Electrochem Soc 1989;136:899–900.

68. Fedkiw Jr PS. Preparing in situ electrocatalytic films in solid polymer electrolyte membranes, composite microelectrode structures produced thereby and chloralkali process utilizing the same. United States patent US 4959132. 1990 Sep 25.

69. Hoshino T, Watanabe K, Kometani R, Morita T, Kanda K, Haruyama Y, et al. Development of three-dimensional pattern-generating system for focused-ion-beam chemical-vapor deposition. J Vac Sci Technol B 2003;21:2732–6.

70. Kotov DA. Broad beam low-energy ion source for ion-beam assisted deposition and material processing. Rev Sci Instrum 2004;75:1934–6.

71. Gulla AF, Saha MS, Allen RJ, Mukerjee S. Dual ion-beam-assisted deposition as a method to obtain low loading-high performance electrodes for PEMFCs. Electrochem Solid-State Lett 2005;8:A504–8.

72. Saha MS, Gulla AF, Allen RJ, Mukerjee S. High performance polymer electrolyte fuel cells with ultra-low Pt loading electrodes prepared by dual ion-beam assisted deposition. Electrochim Acta 2006;51:4680–92.

73. Breault RD. Fuel cell, a fuel cell electrode, and a method for making a fuel cell electrode. United States patent US 4851377. 1989 Feb 28.

74. Prasanna M, Cho EA, Kim HJ, Oh IH, Lim TH, Hong SA. Performance of proton-exchange membrane fuel cells using the catalyst-gradient electrode technique. J Power Sources 2007;166:53–8.

75. Ticianelli EA, Derouin CR, Redondo A, Srinivasan S. Methods to advance technology of proton exchange membrane fuel cells. J Electrochem Soc 1988;135:2209–14.

76. Ticianelli EA, Beery JG, Srinivasan S. Dependence of performance of solid polymer electrolyte fuel cells with low platinum loading on morphologic characteristics of the electrodes. J Appl Electrochem 1991;21:597–605.
77. Mukerjee S, Srinivasan S, Appleby AJ. Effect of sputtered film of platinum on low platinum loading electrodes on electrode kinetics of oxygen reduction in proton exchange membrane fuel cells. Electrochim Acta 1993;38:1661–9.
78. Song D, Wang Q, Liu Z, Navessin T, Holdcroft S. Numerical study of PEM fuel cell cathode with non-uniform catalyst layer. Electrochim Acta 2004;50:731–7.
79. Frost JC, Gascoyne JM, Hards GA, Wilkinson DP, Prater KB. Manufacture of electrodes. United States patent US 5871860. 1999 Feb 16.
80. Zhang J, Yin G-P, Wang Z-B, Lai Q-Z, Cai K-D. Effects of hot pressing conditions on the performances of MEAs for direct methanol fuel cells. J Power Sources 2007;165:73–81.

Spray-based and CVD Processes for Synthesis of Fuel Cell Catalysts and Thin Catalyst Layers

Radenka Maric

20.1 Introduction

In spite of many efforts and improvements by thousands of scientists worldwide, PEMFCs and DMFCs have not been commercially used. State-of-the-art electrocatalysts for PEMFCs rely on large quantities of platinum to achieve acceptable performance levels. This presents a significant hurdle to market acceptance of FC-powered vehicles; a commercially viable electrocatalyst will require nearly an order-of-magnitude reduction in Pt usage to meet both cost and Pt availability constraints. Pt fine particles are dispersed on carbon blacks with a large surface area to reduce the total Pt used and to enhance catalytic activity. This activity depends not only on the primary structure of the catalyst Pt/carbon composites (i.e., carbon surface area, Pt particle size, Pt surface area, etc.), but also on the secondary structure (i.e., aggregation and agglomeration of carbon grains).

Catalyst production methods must meet commercial standards for mass manufacturing such as scalability, reproducibility, and quality. Conventional MEA manufacturing practices involve screen printing, flexographic printing, gravure printing, spraying or rolling, and calendering [1]. Electrocatalyst processing falls into two distinct manufacturing methods: electrocatalyst powder formation and *in situ* electrocatalyst formation. Powder formation is achieved either by more conventional solution precipitation/impregnation techniques or by newer spray-based methods such as spray pyrolysis and combustion chemical vapor deposition (CCVD). *In situ* electrocatalyst formation involves forming the composite platinum/carbon (Pt/C) catalyst directly on the proton exchange membrane (PEM) or gas diffusion layer (GDL) and includes techniques such as physical vapor deposition (PVD), chemical vapor deposition (CVD), combustion chemical vapor deposition, reactive spray deposition technology (RSDT) and electrochemical deposition. The drivers for each process are cost, performance, and reliability, which cannot be separated from the MEA because the electrode structure (porosity, thickness, catalyst type, ionomer content, kinetic losses, ohmic losses, and transport losses) is not only a function of the electrocatalyst itself but also of the way in which it is formed or deposited. Raw material cost reduction takes the form

of improved catalyst utilization and alternative formulations, while manufacturing costs are driven down by reducing the number of processing steps, using continuous processing, and avoiding energy- or time-intensive steps such as vacuum environments.

The electrocatalytic activity of Pt/C catalysts is influenced by many factors, such as average particle size, relative crystallinity, surface groups, surface morphology, and the Pt–C interface [2–6]. Therefore, when Pt/C catalysts are prepared using different methods or different carbon supports, many factors can influence their electrocatalytic activity, leading to different conclusions. Using Pt/C catalysts prepared by different methods, Attwood et al. [7] found that the best average size of Pt particles in a Pt/C catalyst for methanol oxidation is about 3 nm. Frelink et al. [8] indicated that the electrocatalytic activity of Pt/C catalysts for methanol oxidation decreases as the Pt particle size decreases in the range 4.5–1.2 nm. Takasu et al. [9] came to a similar conclusion using a Pt catalyst supported on glassy carbon electrodes with Pt particle sizes from 7 to 2 nm. Watanabe et al. [10] reported that no Pt particle size effect was observed when Pt/C catalysts with different sizes of Pt particles on different carbon supports were prepared by the same method.

Direct deposition techniques can have many advantages over bulk ink processing techniques. For instance, a thin catalyst layer applied between the electrode and electrolyte is in the immediate neighborhood with respect to both the proton-conducting membrane and the electrode, and since at high cell current densities and gas permeability limitations thick catalyst layers are only active closest to the gas supply a thin layer eliminates platinum underutilization [11]. Multi-objective optimization techniques are necessary that can uncover Pareto optimal fronts and generate several acceptable choices in catalyst layer design or processing conditions. In terms of MEA cost reduction, novel electrocatalyst production technologies might enable minimization of the production steps typically followed in conventional "ink-based" deposition techniques. *In situ* electrocatalyst formation (e.g., by PVD, CVD, RSDT) offers the opportunity to reduce the number of steps and therefore the potential to reduce cost (provided the new processing costs are not higher) by avoiding ink-based deposition processes altogether [12–14]. In most CVD processes the CVD material is formed on the surface of a substrate, but in some cases the substrate can react with a deposit to form a compound. In cases where powder is desirable, high reaction concentrations and temperatures are deliberately used so that homogeneous nucleation will take place in the gas phase. The reaction gases in a CVD process are introduced separately, or premixed and passed into the reaction area, depending on whether the gases will react before they reach the substrate, which is to be avoided unless powder formation is desired [15, 16].

In this chapter, we review the spray-based powder production method, flame-based process, and CVD process for electrocatalyst powder production or direct film deposition, and describe the attributes of this process in terms of the nature of the catalyst produced, the particle size, and the influences on MEA layer structure, performance, and cost.

20.2 Spray Pyrolysis Approach

20.2.1 Current Research Activities

One of the approaches to producing catalyst material is synthesizing Pt particles on a carbon support and then applying a catalyst layer by screen-printing. Ultrasonic spray pyrolysis (USP) is an important approach for synthesizing solid-state material, is widely applied in the ceramic industry and the field of heterogeneous catalysis, and is used to synthesize Pt particles on carbon supports [17]. The powders based on spray production are expected to be advantageous in their intrinsic catalytic properties and thus to allow higher overall utilization of the noble metals.

In the other approach involving *in situ* electrocatalyst formation the electrocatalyst is not produced as a discrete powder but is formed directly on the substrate, such as the PEM, the GSL, or a release layer [18]. Benitzel et al. [19] used an electrospray technique to spray catalyst by applying a voltage between capillary tubes, in which the ink is forced to flow to the carbon cloth substrate.

20.2.2 Spray Conversion and Aerosol Routes for Powder Manufacturing

Spray-based powder production methods fall into one of several classes, depending upon the temperature range in which the gas/liquid-to-particle conversion takes place. Spray drying (< 150 °C), spray conversion (100–500 °C), and spray pyrolysis (> 500 °C) each occur at increasingly higher temperature ranges, and the effects on the reagents increase on a continuum from relatively unchanged to total chemical conversion. A schematic for the conversion process is given below:

The spray process begins with a liquid precursor (dissolved or suspended reactants) together with a gas, which are then atomized into droplets that exist in a controlled droplet distribution range. The atomized spray is injected into a gas phase processing unit and heated. The heating step effects the chemical and physical transformations of the droplets to the final powder product. Compositions and microstructures of the particles are a function of:

- residence time
- reactive nature of the droplet
- temperature
- gas composition

A key asset to this process is the ability to stop the reaction/densification/sintering of the particles by the use of a quenching agent to rapidly cool the process stream. This can be effected by water, cool surfaces, or gas. The value in the process is the ability to hold a high temperature for a short period of time while maintaining a certain particle size and distribution necessary for the complex composition and structuring of an effective catalyst. An added processing bonus is the absence of need for any surfactants to disperse carbon during formation, which can introduce surface contamination.

The electrocatalyst powder is formed by co-deposition of an aqueous precursor of platinum (e.g., Pt, PtRu, PtCoNi, etc.) along with a colloidal suspension of the carbon support. As the solvent evaporates in the process chamber the precursors are chemically and thermally converted into their final form on the surface of the carbon support. Simultaneous control over composition and microstructure offers important performance optimizations not available with other techniques.

A schematic representation of the spray pyrolysis processes is provided in Figure 20.1(b) and typically involves solvent evaporation, thermally or chemically induced reactions, crystal nucleation, and crystal growth. Therefore, this process can be used to produce a wide variety of materials compositions, combined with uncommon microstructures and morphologies. A key feature of the process is that the physical and/or chemical evolution of the particles can be arrested at any stage by quenching of the reaction media.
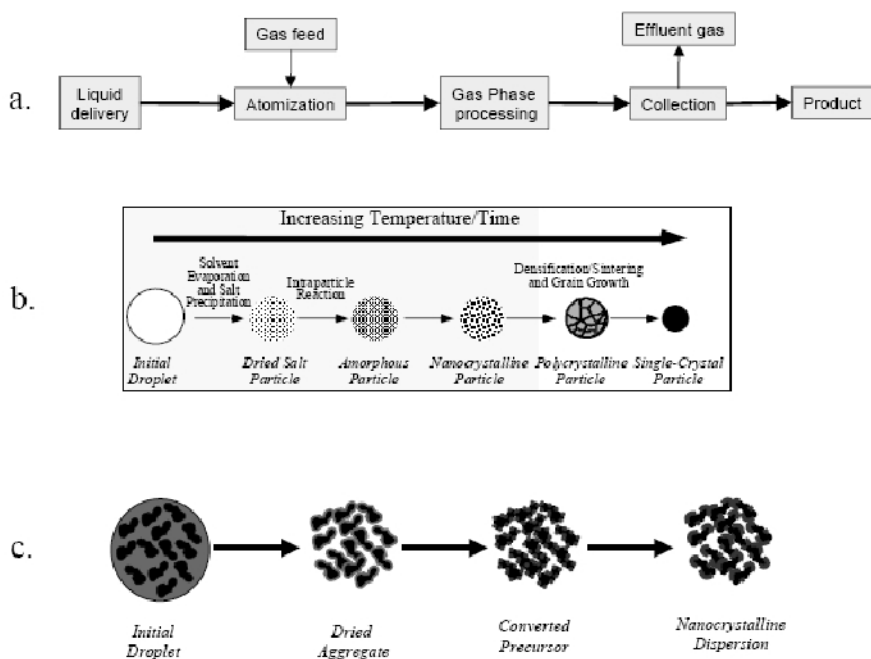
Figure 20.1. a) Schematic representation of spray-pyrolysis process flow; b) schematic representation of processes occurring during a spray-based production of unsupported materials; c) schematic representation of processes during the spray-based production of supported electrocatalysts. (Reprinted with permission of Cabot Corporation.)

Using these methods, both the composition and the microstructure can be varied. It is the combination of these attributes – control over microstructure at a number of different length scales and over composition, simultaneously – that is extremely important to the performance of the electrocatalyst powder in an MEA. The spray-based manufacturing approach can relatively independently vary three main characteristics of the powder batch: a) particle size (from an average size

below 1 micron to tens of microns – in the case of electrocatalyst powders this is the aggregate size (see later this chapter) with mono-, bi-, or tri-modal distributions), b) particle microstructure (porous hollow, dense, composite, with various compositional distributions), and c) nanosized active phases can be deposited within the structure of each particle and the composition of this nanodispersed phase can be varied from a single element to a multi-component composition.

From a manufacturing point of view spray-based processes are naturally continuous and can be operated in either continuous mode or semi-continuous mode.

In the context of electrocatalyst powder production, this spray-based process is better described in Figure 20.1(c). The process involves the formation of an aqueous liquid containing chemicals that act as precursors to the desired final dispersed phases (e.g., Pt, PtRu, PtCoNi, MnO_x) together with a colloidal suspension of the carbon support. This aqueous liquid is converted into an aerosol (droplets containing the dissolved or suspended ingredients), the aerosol is entrained in a gas stream, the gas is heated, the solvent evaporates, and the precursors are thermally or chemically converted into their final form on the surface of the carbon support [20].

In the case of the electrospray technique, a catalyst is sprayed by applying a voltage between a capillary tube, and the high electric field when the solution emerges generates a mist of highly charged droplets. During the process, the droplets are reduced in size by evaporation of the solvent and/or by "Coulomb explosion" (droplet subdivision resulting from the high charge density). In order to force the catalytic ink to pass through the capillary tube, a nitrogen pressurized tank is used [19].

20.2.3 Pt Nanoparticle Preparation via Spray Route

Spray-based methods can produce carbon-supported electrocatalyst powders with a controlled aggregate size and aggregate size distribution. The hierarchical structure of an electrocatalyst powder batch is illustrated in Figure 20.2.

Cabot's *Dynalyst*® family of electrocatalysts is designed for use in applications ranging from cost-sensitive to performance-driven PEM fuel cell applications. Dynalyst® electrocatalyst powders are manufactured to meet specific performance requirements based on their structure, composition and precious metal loading in the electrode layers. Dynalyst® 20SR1 – 20% Pt/C electrocatalyst has excellent electrochemical performance at low precious metal loadings in the MEA. A loading of 0.1–0.3 mg Pt/cm^2 in the electrode layer is recommended to achieve optimum performance and Pt utilization.

Dynalyst® 20SR1 – 20% Pt/C electrocatalyst particles are micron-sized aggregates with controlled average particle size. Depending on the electrode printing method, various powder dispersion methods can be employed such as milling and/or sonication. However, extensive milling or sonication may be detrimental to the catalyst's performance. The optimal Nafion®-to-carbon ratio in the electrode ink needs to be adjusted depending on the targeted fuel cell operating conditions, such as pressure and reactant humidification levels.
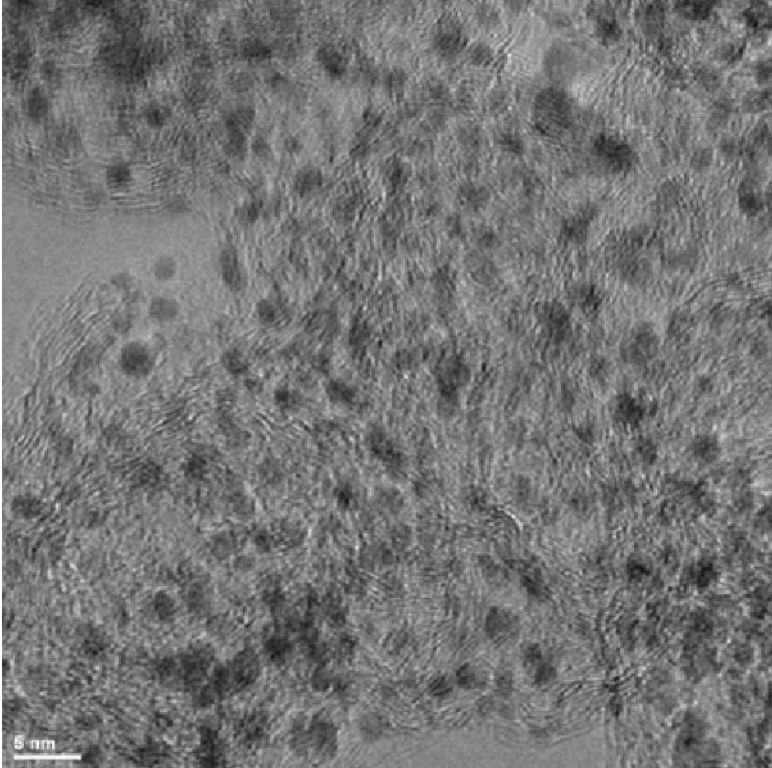
Figure 20.2. High-resolution TEM image of Dynalyst® electrocatalyst. (Reprinted with permission of Cabot Corporation.)

20.2.4 Morphology of Catalyst Deposited by Spray Pyrolysis

In spray-based processing routes the processing of electrocatalyst powders can be achieved under conditions such that each aggregate has a spherical morphology with a size and size distribution that is derived from the size and size distribution of the droplets. In the case of the aggregates shown in Figure 20.3, this corresponds to an average aggregate size in the range of 1–10 μm. The aggregate size distribution can be varied to give a modality that varies from a tight monomodal distribution to a broad tri-modal distribution.

Such control over the average aggregate size at this length scale (1–10 μm) is important for at least two reasons. Firstly, the size distribution of the aggregates affects the packing characteristics of the particles in the electrode layers. The packing characteristics in turn have a strong influence on the pore structure of the layer. The pore sizes and pore size distribution in this microporous (sub-micron to several micron) size range (dictated by the aggregate size and size distribution) have a strong influence on, and offer flexibility in, control over the transport characteristics of the electrode layer. This is important to the performance of the MEA, especially under high current density operation, as shown in the next section.

Secondly, the formation of controlled size and size distribution aggregates directly from the powder production process is in a range that is suitable for a variety of deposition methods.
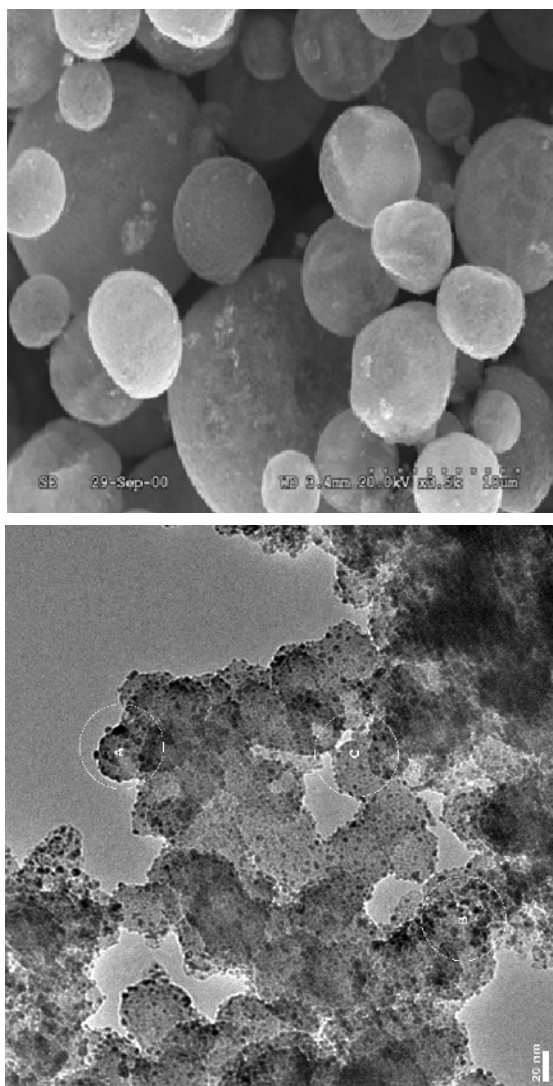
Figure 20.3. Structure of electrocatalysts produced by spray-based manufacturing. This example shows 20 wt% Pt on Vulcan XC72. (Reprinted with permission of Cabot Corporation.)

Thus, spray-based synthesis avoids the additional processing steps to control the size of the aggregates that are often required for electrocatalysts prepared by solution precipitation/impregnation techniques. For example, inks or pastes containing electrocatalyst powders produced by solution precipitation routes are

often ball milled to convert the wide distribution of aggregate sizes (from 10 μm to several mm) to the necessary agglomerate size and thereby form a stable suspension for the specific deposition process. This aspect is illustrated in Figure 20.4, which compares SEM microphotographs and particle (aggregate) size distribution data for a conventional (precipitated/impregnated) catalyst and a spray-processed one. The milling processing step not only introduces cost, but can also lead to materials loss and contamination. Finally, macroporous gas diffusion electrodes and MEAs are often achieved by using pore-forming agents, which are removed in a subsequent processing step. Through control of the aggregate size and size distribution, this step may also be avoided.
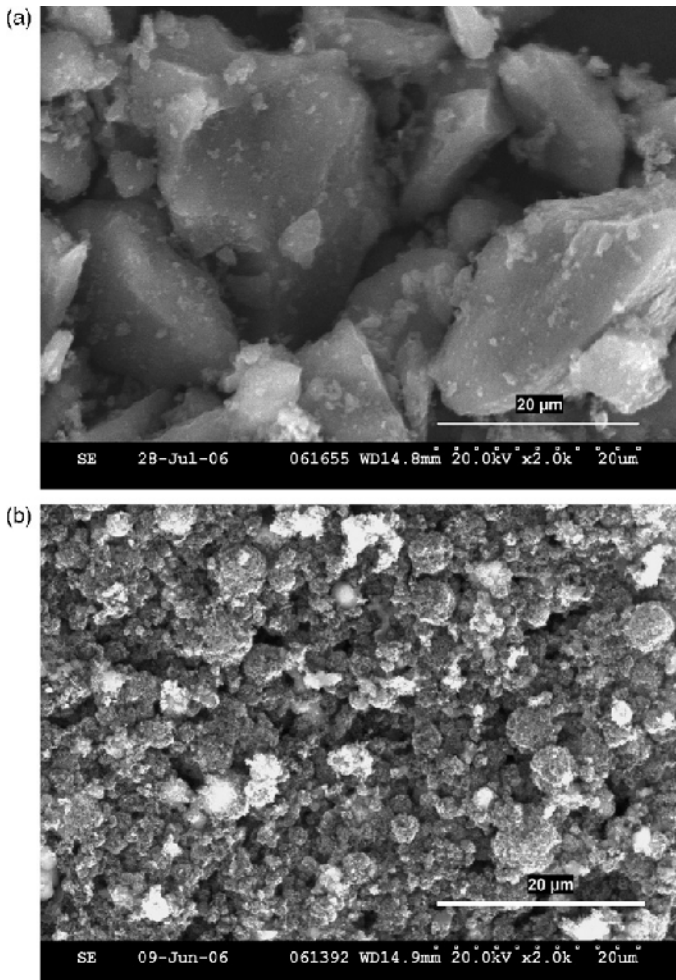
Figure 20.4. Scanning electron micrographs of a) aggregates obtained in a conventional electrocatalyst synthesis and b) aggregate size distribution of the electrocatalyst powders obtained by spray conversion. (Images courtesy of NRC-IFCI.)

20.2.5 Electrochemical Performance

Electrocatalyst powders produced by spray-based routes exhibit excellent performance characteristics under relatively mild operating conditions and low platinum loadings, due to the combination of good dispersion of the PGM over the support surface and control over the agglomerate size and distribution. There is also an emerging hypothesis that non-traditional electrocatalyst manufacturing methods can lead to higher specific activity of the active material. To date this has been mainly claimed for methods that involve *in situ* catalyst formation (i.e., direct deposition of the catalyst onto the PEM) [21, 22]. There is also evidence for this improved specific and mass activity in electrocatalyst powders prepared by spray-based manufacturing methods, as described below. We speculate that the common feature of these electrocatalyst production processes that leads to higher specific and mass activity compared to solution precipitation/impregnation is that they are all based on processes that produce kinetic products rather than thermodynamic products. As a result, the increased activity can be explained by a non-equilibrium distribution of crystal faces in the active catalyst nanoparticles or by the presence of surface defects that have higher activity. It is also possible that the apparent mass activity can be explained by higher accessibility of the active catalyst sites in the MEAs derived from the newer production methods compared to the traditional methods. It is noteworthy that of the processes that lead to higher specific and mass activity electrocatalysts, the spray-based process described here is the only electrocatalyst powder production process. Support for the increased specific activity of supported Pt/carbon catalysts in the oxygen reduction reaction can be found when the performance of the electrocatalysts made by the spray method is compared to that of conventional electrocatalysts with the same Pt loading under otherwise identical conditions (Pt and ionomer loadings in the MEA, anode catalyst, printing technique, and test conditions).

As shown in Figure 20.5, the spray-based electrocatalyst made by Cabot Corporation demonstrates a three-fold increase in mass activity (expressed in current per mass of Pt) compared to conventionally compared electrocatalysts. However, if the activity is compared on a specific activity basis (expressed as current per surface area of Pt) the specific activity for the spray-based catalyst is up to five times higher (estimate based on the measured surface areas for the spray-based catalyst of Pt, 50 m^2/g and conventional catalysts of 65 m^2/g Pt by cyclic voltammetry).

A large number of factors are involved in measuring the performance of electrocatalyst powders in an MEA. These include both the external operating conditions (gas humidity, gas stoichiometries and compositions, temperature, gas flow field, gasketing measurement procedure) and the internal composition and structural optimization of the MEA (ionomer content, ionomer distribution, electrode layer thickness, nature of the gas diffusion layer, assembly conditions etc.) [23].
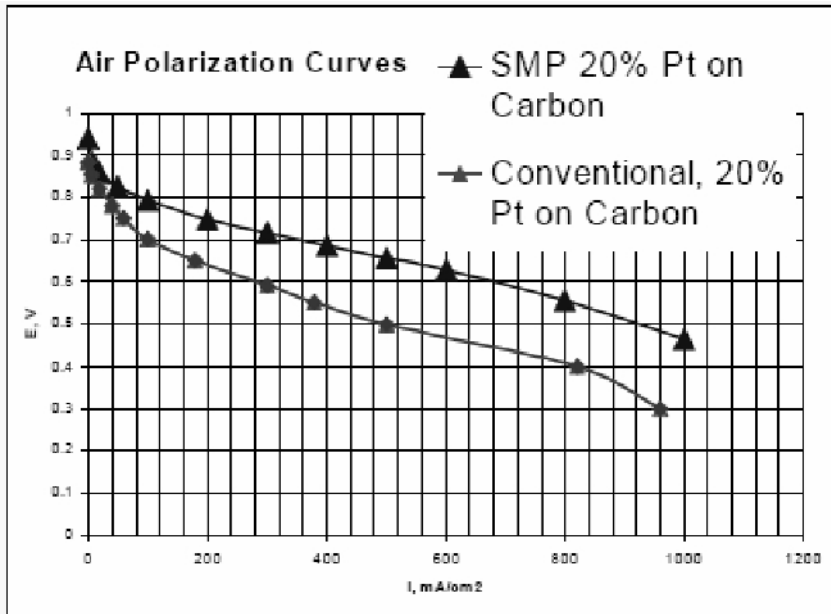
Figure 20.5. Comparison of hydrogen/air polarization curves for spray-based and conventional electrocatalysts at 0. 2 mgPt/cm^2 cathode loadings; anode catalyst is identical at 0.05 mgPt/cm^2. Single 50 cm^2 cell PEM MEA performance measured at 50 °C and atmospheric pressure at constant flow, corresponding to stoichiometry of 1.2 for hydrogen and 2.2 for air at 1 A/cm^2, and with 100% humidification of the gases, Nafion 112 membrane. (Reproduced with permission of Cabot Corporation.)

20.2.6 Electrocatalytic Activity and Stability of Pt-based Catalysts

A typical electrochemical performance of 20 wt% Pt/C spray pyrolysis prepares the electrocatalyst in oxygen and air, as shown in Figure 20.6 under the conditions indicated. A comparison of the performance in oxygen versus air shows that good kinetic performance is maintained over the ohmic- and transport-loss regions. The close proximity of the polarization curves in oxygen and air is an indication of minimal losses due to transport limitations, especially at high current densities. We speculate that the good performance at high current density is based on control over the aggregate structure of the electrocatalyst powder. Experimental verification of this hypothesis comes from the results shown in Figure 20.7, where the only difference between the two measurements is in the change in aggregate structure of the electrocatalyst powder. Clearly there is no change in performance in the kinetically limited regime, but there is a strong drop in performance in the ohmic and transport-limited regions.
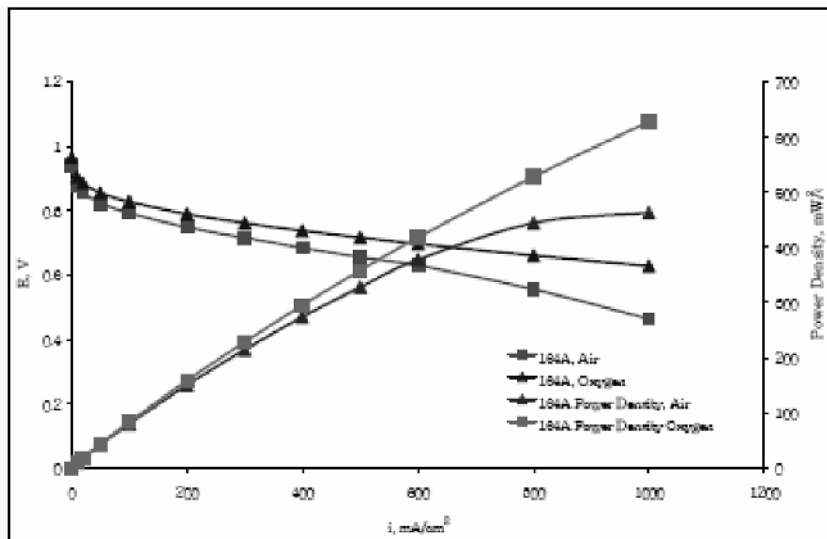
Figure 20.6. Performance of a spray-manufactured electrocatalyst: polarization and power density curves for a single MEA PEM fuel cell with a 20 wt% Pt/Shawinigan black electrocatalyst employed as cathode catalyst at 0.2 mg Pt/cm^2 loading. Performance measured at 50 °C at atmospheric pressure in a 50 cm^2 cell at constant flow corresponding to stoichiometry of 1.2 for hydrogen and 2.2 for air at 1 A/cm^2, and with 100% humidification of the gases, Nafion 112 membrane. (Reproduced with permission of Cabot Corporation.)
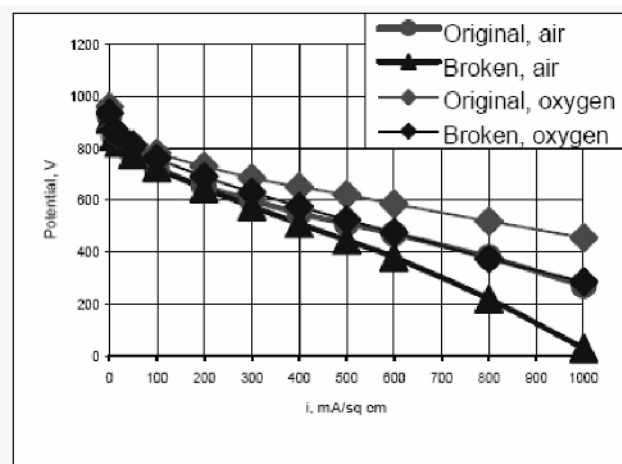
Figure 20.7. Effect of the aggregate structure on the performance of a spray-manufactured electrocatalyst: polarization density curves for a single MEA fuel cell with a 20 wt% Pt/Shawinigan electrocatalyst employed as cathode catalyst at 0.2 mg Pt/cm^2 loading for the original powder and the powder in which the aggregate structure was crushed intentionally. Performance measured at 50 °C in a 50 cm^2 cell at atmospheric pressure and constant flow corresponding to stoichiometry of 1.2 for hydrogen and 2.2 for air at 1 A/cm^2, and with 100% humidification of the gases, Nafion 112 membrane. (Reproduced with permission of Cabot Corporation.)

Long-term durability under cycling protocols is shown in Figure 20.8. The following test conditions have been applied: 50 cm^2 MEA, cycling under H$_2$/air at 80 °C and 100 RH between 0.7 and 0.9 V IR-free voltage (30 s hold under each potential), combined with periodical evaluation of the Pt surface area using cycling voltammetry and performance. Pt alloy catalyst prepared by spray pyrolysis shows a 30% loss of surface area after 20,000 cycles, and no further loss is observed until 30,000 cycles, while the Pt-supported catalyst shows loss even after 30 cycles.
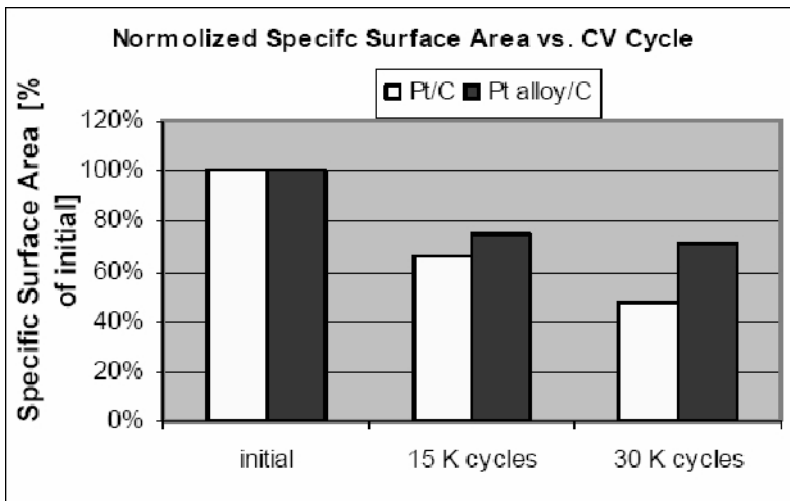
Figure 20.8. Long-term durability under cycling protocols. (Reproduced with permission of Cabot Corporation.)

20.2.7 Typical Examples Analysis

Cabot is developing electrocatalyst materials through design, development, and production to create a highly reproducible, low-cost, high-volume electrocatalyst powder manufacturing process based on spray conversion technology, a unique manufacturing and development platform.

Using this platform, Cabot can achieve unparalleled control over dispersion, composition and microstructure, leading to unrivaled electrochemical performance. In the spray conversion process, feedstock, comprising a liquid containing dissolved non-volatile precursors and suspended solids, is atomized to form droplets and the droplets are heated to form powders. Through control over the temperature and time history during the processing of the droplets, the characteristics of the final particles, such as microstructure, morphology, crystallinity, catalyst dispersion, and porosity, can be precisely controlled. From a manufacturing point of view spray-based processes are naturally continuous and can be operated in either continuous or semi-continuous mode with specified batch volumes to optimize raw material traceability. The key parameters, such as residence times and temperature distributions, are well understood and modeled. This ensures the scalability of this manufacturing approach and reproducibility of the materials characteristics. Many unique compositions and microstructures

unattainable by conventional techniques can be synthesized by Cabot's spray conversion technology, with few limitations on types of supports and metal precursors.

Most of the typical electrocatalyst compositions derived by conventional precipitation/impregnation routes can also be produced. Figure 20.9 shows a Cabot-based production method.
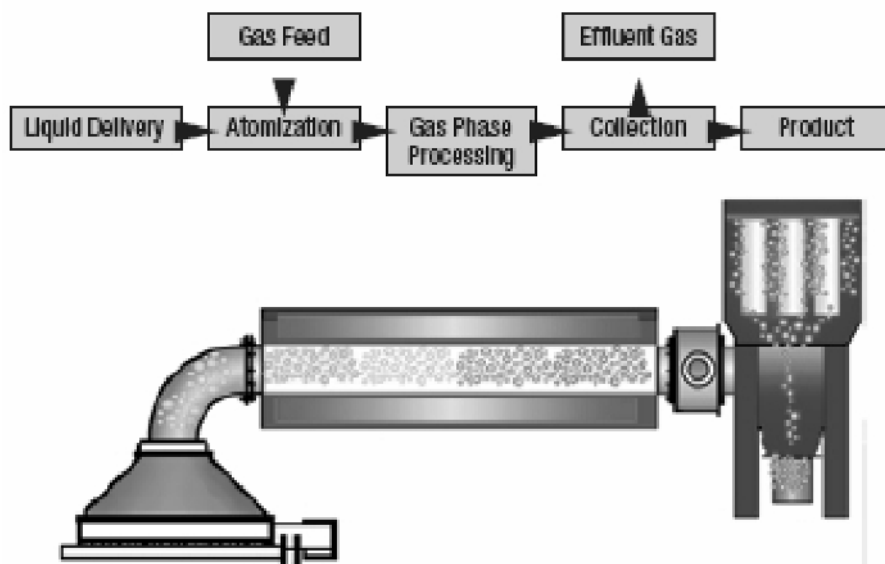
Figure 20.9. Cabot's spray-based powder production platform. (Reproduced with permission of Cabot Corporation.)

20.3 Deposition of Catalyst Layer by CVD

In 1890, high-purity nickel was deposited by Mond in the first reported metal-organic chemical vapor deposition process. With regard to the platinum group metals, Marboe et al. [24] first described (1947) the deposition of platinum, but it was the work of Rand et al. [25, 26] that marked the actual starting point of detailed noble-metal CVD studies. The first attempts at noble-metal deposition in the absence of a carrier gas gave films containing important amounts of impurities. Girolami and co-workers later reported the synthesis of high-quality palladium and platinum films, still without using a carrier gas, and showed the great importance of choosing the right precursor complexes [27]. At the same time, the groups of Kaesz and Puddephatt described noble-metal deposition using a reactive gas such as dihydrogen or dioxygen [28, 29]. As a result, high-purity depositions were obtained along with dramatic decreases in the temperature of deposition. However, despite the excellent results reported concerning thin-film deposits on planar substrates (mainly for electronics applications), relatively few studies on CVD of catalytic materials have been reported. Dossi and co-workers have prepared

palladium and platinum/zeolite catalysts by adsorption of organometallic complexes from a gaseous phase, the supported materials then being heated in an H_2/He flow at high temperature [30–32].

20.3.1 Current Research Activities

In order to improve catalyst activity, it is important to reduce the size of metal particles. As mentioned in recent literature [33], chemical vapor deposition (CVD) is a promising process for the preparation of nano-sized catalyst particles. The use of multiwalled carbon nanotubes as a platinum support for proton exchange membrane fuel cells has been investigated as a way to reduce the cost of fuel cells through an increased utilization of platinum. Decreasing the amount of Pt used in a PEMFC via increasing the utilization efficiency of Pt has been one of the major concerns during the past decade [34]. Growing carbon nanotube arrays directly on the carbon paper and then subsequently electrodepositing the Pt selectively on the carbon nanotubes promises to improve Pt utilization by securing an electronic route from Pt to the supporting electrode in a PEMFC.

Carbon nanotubes (CNTs) are key materials in nanotechnology, and many researchers have reported CNT growth methods such as arc discharge [35], thermal CVD [36], hot-filament assisted CVD [37], plasma CVD [38], and laser assisted production [39]. Considering the thermal CVD method alone, many different carbon sources could be used, such as hydrocarbons (acetylene, ethane, methane) [36], carbon monoxide (CO) [40], and alcohol [37]. Catalytic metals such as iron, molybdenum, cobalt, and nickel, and their mixtures, are popular means of CNT-CVD growth. Furthermore, how the catalytic metal is coated onto the substrate is an important consideration, for which the choices include the use of sputtered pure metal films, metal-complex solutions, and zeolite for the supported materials [41]. It is also important to control the diameter of CNTs; the diameter strongly depends on the size of the catalytic metal particle and therefore on the thickness of the metallic thin films formed with sputtered metal atoms. It has been reported that the quality of CNTs mainly depends on the initial stage of nucleation [42, 43]. Generally, there are two categories of carbon nanotubes: single-walled nanotubes (SWNTs) and multiwalled nanotubes (MWNTs). MWNTs should have a relatively high electrical conductivity.

For catalysts used at the anode of a DMFC, Pt–Ru nanoparticles deposited on CNTs have attracted a great deal of attention due to the renowned Pt–Ru bi-functional mechanism for methanol oxidation and CO oxidation, and the unique characteristics of CNTs [44–47].

At Argonne National Laboratory, they are exploring a novel approach of preparing Pt-free electrocatalysts based on recent efforts at synthesizing aligned carbon nanotubes (ACNT) through a CVD process [48]. The nanotube diameter can be varied from 10 to 100 nm with the orientation perpendicular to the substrate. The geometry and shape of the nanotube depends on the CVD conditions and the precursor. The CVD mixture is composed of an inexpensive, volatile TM organometallic compound such as Fe or Co metallocene, a hydrocarbon, and a carrier gas of H_2/Ar. At elevated temperatures, the organometallic decomposes to

form a catalytic center on the substrate that catalyzes the hydrocarbon into a graphene sheet, which subsequently folds into a nanotube.

20.3.2 Film Formation from Vapor Phase by CVD

In most CVD processes the CVD material is formed on the surface of the substrate, but in some cases the substrate can react with a deposit to form a compound. Conventionally, the CVD method is performed in the presence of transition metal catalyst particles supported on a substrate. The CVD method enables the selective production of MWCNTs or SWCNTs, depending on the reaction chemistry and process parameters, such as temperature. Furthermore, pre-determined CNT structures can be formed via catalyst patterning on the substrate [see, e.g., 49–51]. Alternatively, the catalytic CNT synthesis can be performed in the gas phase without support material [52, 53].

The CVD synthesis is carried out in multiple steps. The first step involves the introduction of the catalyst or catalyst precursor on the support. This can be realised, for example, by impregnating the substrate with metal-containing precursor solution, by sputtering a thin metal layer, or by dispersing metal-containing organic carriers on the substrate. The second step is a heat treatment, which results in either the thermal decomposition of the metal-containing precursor compounds, fracturing the sputtered metal film, or the removal of the organic carrier by combustion, yielding metal or metal oxide particles at the substrate surface. Subsequently, the CNT growth proceeds in the presence of the carbon source or, in the case of metal oxide particles, is preceded by reduction in a hydrogen (H_2) atmosphere.

Carbon-containing molecules, ranging from carbon monoxide (CO), alcohols, and fullerenes to aliphatic and aromatic hydrocarbons, can be used as sources of carbon [49, 54]. At low partial pressures of the carbon source, SWCNTs are formed, whereas higher vapor pressures lead to MWCNTs. The use of oxygen-containing species such as water or alcohol has been shown to enable the synthesis of high-purity SWCNTs. This was proposed to improve the efficiency of SWCNT production, as it prolongs the catalyst lifetime by removing amorphous carbon from the particle surface [51]. The method is a batch process, where the CNT growth continues for a set reaction time and the product is collected from a substrate or the reactor walls after cooling. The reaction times vary from minutes to hours and the reactor temperatures are commonly 600–1200 °C.

The supported CVD method enables the formation of ordered free-standing SWCNT mats with thicknesses up to 2.5 mm, and individual SWCNTs as long as 4 cm, at growth rates of 250 and 66 µm/min, respectively [51]. The formation of SWCNTs generally takes place when the catalyst particle diameter is less than 5 nm [49]. Nanoparticles of iron, nickel, cobalt, or molybdenum, either alone or as mixtures, are most commonly used as catalysts in CNT production [49]. The suitability of transition metals as catalysts for CNT synthesis is due to their various physical and chemical properties, including melting temperature, equilibrium vapor pressure and carbon diffusion rate in the metal, and on their ability to catalyze the carbon source decomposition reaction. The high solubility of carbon in transition metals is regarded as one of the most important factors enabling their use as

catalysts in the production of CNTs. The higher yield of CNTs with bi-metallic catalysts has been attributed to particle melting point reduction, increase in the carbon solubility, and the formation of well-dispersed metal clusters upon segregation during CNT formation.

In gas-phase CVD synthesis, formation of both the catalyst particles and the SWCNT takes place in the gas phase and the product is ideally collected from the gas phase by aerosol particle collection methods, such as filters and cold collectors [53]. The catalyst particles are most commonly formed by thermal decomposition of gaseous organometallic precursor compounds, such as ferrocene, cobaltocene, and iron pentacarbonyl [52, 53]. Solid precursors are vaporized prior to transport into the reactor. Liquid precursors can be introduced either as vapor by way of saturating the carrier gas or as droplets [52]. The catalyst precursor vapor thermally decomposes in the heated reactor and subsequently forms the catalyst nanoparticles via nucleation, condensation, and coagulation processes. Additionally, colloidal solutions of metal particles have been used as catalysts by injecting them into the reactor [55]. Similar to the supported CVD method, the gas-phase method uses nanometer-sized transition metal particles as catalysts, and the distribution of the SWCNT diameters correlates with the size distribution of the catalyst particles [56, 57]. The selection of appropriate carbon sources is similar for both the gas-phase and supported CVD methods, i.e., acetylene, CO, ethanol, benzene, toluene, etc. have been used [e.g., 10, 53, 54]. The addition of a sulfur-containing additive, thiophene, has been claimed to promote CNT growth due to a reduction in the melting temperature of the metal-sulfur particles, or modification of the catalyst particle surface [55]. One of the main differences between the supported and gas-phase CVD methods is the residence time, which in the gas-phase method is in the order of seconds. Laminar flow reactors are generally used. However, turbulent jets and water-cooling injectors have been used to enhance catalyst and carbon precursor mixing in an attempt to control catalyst particle size [53].

The gas-phase synthesis of SWCNTs has been coupled on a few occasions with product collection directly from the gas phase, e.g., with filters and cold collectors [52]. More commonly, the product is collected from the reactor surfaces after cooling. This, however, allows catalyst nanoparticle and SWCNT nucleation and growth at the reactor surfaces in a manner similar to the supported CVD method.

In conventional gas-phase CVD, catalyst particle formation takes place simultaneously with carbon source decomposition and SWCNT formation in the reactor. Ferrocene decomposition (465 °C) and CO disproportionation (preferably 400–900 °C) take place at similar temperatures, which prevents excessive catalyst particle growth before disproportionation takes place. The most efficient SWCNT formation from CO in the gas-phase CVD method was obtained with ferrocene as the catalyst precursor at 700–900 °C, i.e., at conditions corresponding to the smallest mean catalyst particle size (as described in more detail later), and most efficient CO disproportionation reaction. The morphology of the catalyst nanoparticles depended on the gas atmosphere in the reactor. The presence of H_2 during ferrocene decomposition resulted in the formation of catalyst particles with larger primary sizes. Figure 20.10 shows the schematic of a chemical vapor process in which a thin-film metal catalyst is used.
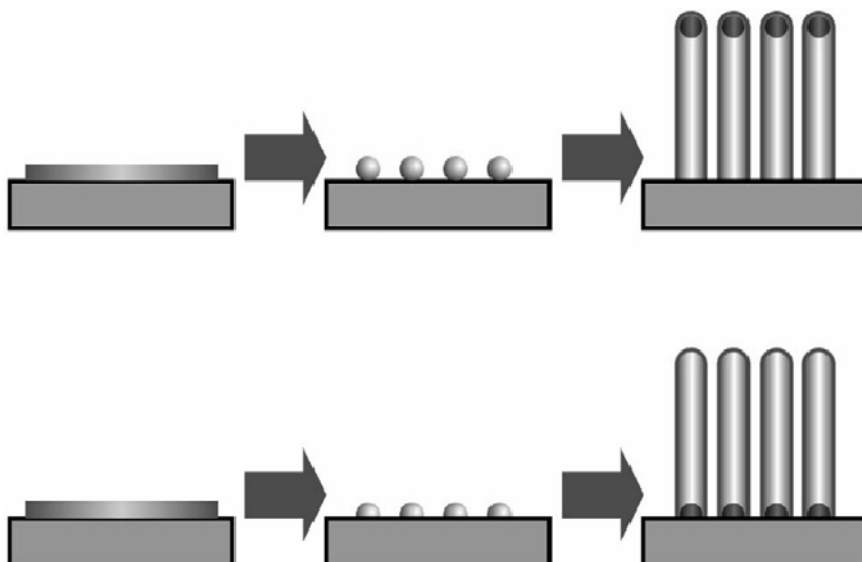
Figure 20.10. Two growth modes commonly observed in CVD: a) tip growth and b) base growth [62]. (Reproduced with permission from Teo KBK, Lacerda RG, Yang MH, Teh AS, Robinson LAW, Dalal SH, et al. Carbon nanotube technology for solid state and vacuum electronics. IEE Proc-Circuits Devices Syst 2004;151(4):443–51.)

At the growth temperature, the metal sinters to form nanoclusters due to the cohesive forces of the metal atoms. Two types of growth are possible, based on the metal interacting with the substrate (cf. wetting or non-wetting of the metal with the surface): base growth or tip growth [58, 59] as shown in Figure 20.10. As the catalyst decomposes the hydrocarbon gas, the carbon dissolves in the catalyst and precipitates out from its circumference as the CNT [58]. Carbon tubes, in contrast to a solid carbon filament, tend to form when the catalyst particle is 50 nm or less because if a filament of graphitic sheets were to form, it would contain an enormous percentage of "edge" atoms in the structure. These edge atoms have dangling bonds, which make the structure energetically unfavorable. The closed structure of tubular graphene shells is free of dangling bonds and provides a stable solution to this problem, and hence the CNT is the energetically favorable and stable structural form of carbon at these tiny dimensions [60]. Thus, the catalyst acts as a "template" from which the CNT is formed, and by controlling the catalyst size and reaction time, one can easily tailor the CNT diameter and length, respectively, to suit [61].

20.3.3 Morphological and Microstructural Stability

Since CVD-based techniques are free of carbonaceous particles they allow the direct growth of CNTs on substrates. In the work of K.B.K. Teo et al., carbon nanotube growth was performed by adding acetylene to the NH_3 gas flow (at a ratio of typically 20%) for 15 min [62]. If exactly the same catalyst and growth conditions are used in the presence of a plasma discharge (i.e., PECVD), vertically

aligned carbon nanotubes are grown on the substrate as shown in Figure 20.11(b). The nanotubes align vertically during growth because of the presence of a perpendicular electric field from the plasma sheath on the substrate surface [63].

(a)   (b)
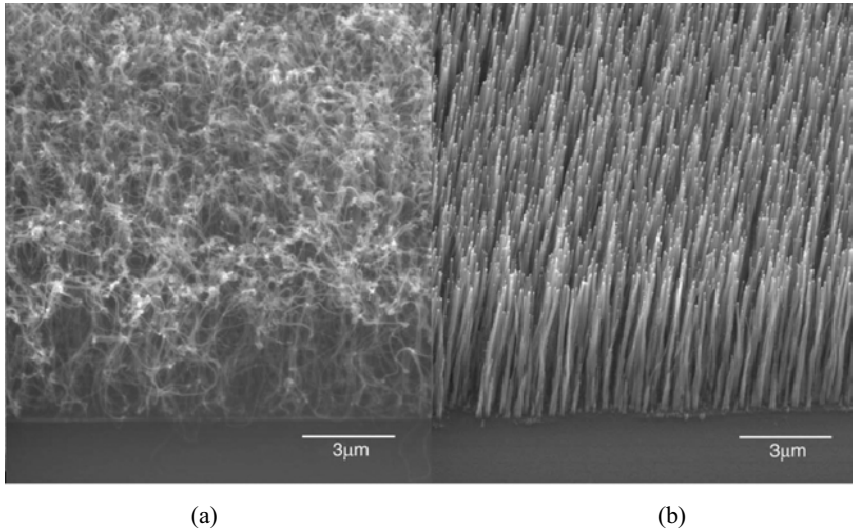
Figure 20.11. (a) Thermal CVD process, which produces a curly carpet of CNTs as seen here. Some areas on the substrate in (a) did not have catalyst, resulting in a "crop-circle" effect at the micrometer scale. (b) When plasma-enhanced CVD is used, the CNTs align vertically during growth to give straight structures as seen in (b). This is believed to be due to the electric field inherent in the plasma sheath, which guides the CNTs upwards during growth [62]. (Reproduced with permission from Teo KBK, Lacerda RG, Yang MH, Teh AS, Robinson LAW, Dalal SH, et al. Carbon nanotube technology for solid state and vacuum electronics. IEE Proc-Circuits Devices Syst 2004;151(4):443–51.)

In the work of Ming-Chi Tsai et al. CNTs were grown directly on polytetrafluoroethylene (PTFE)-treated carbon cloths (10×20 mm^2, Electrochem, Inc.) via a thermal CVD process [64]. Prior to the process, a thin layer of 30 nm Ti followed by 10 nm Ni were deposited on carbon cloths by electron gun evaporation. The Ni layer acted as a catalyst for growing CNTs, and the Ti thin film was a buffer for enhancing the adhesion of Ni and the subsequently grown CNTs onto the fibers of the carbon cloths. The prepared specimens were then placed into a tube furnace and thermally treated at 800 °C for 10 min under a mixed-gas atmosphere of 200 standard cubic centimetres per minute (sccm) Ar and 200 sccm NH$_3$. A 30 sccm ethylene gas stream as a carbon source, along with a gas mixture of 280 sccm Ar and 90 sccm NH$_3$, were then introduced into the furnace at 800 °C for 10 min. The furnace was then cooled down to ambient temperature under Ar atmosphere. Prior to the electrodeposition of Pt or Pt–Ru nanoparticles, all the specimens with CNTs directly grown on carbon cloths (CNT/CC) underwent a hydrophilic treatment at 50 mV s^{-1} for 100 cycles with potential ranging from −0.25 to +1.25 V$_{SCE}$ in an O$_2$-saturated 2 M H$_2$SO$_4$ aqueous solution at ambient conditions. With a three-electrode electrochemical system, Pt or Pt–Ru

nanoparticles were electrodeposited onto the foregoing specimens via a potentiostatic approach at two different applied potentials. The surface morphologies of the Pt and Pt–Ru particles deposited on CNTs is show in Figure 20.12. In general, cubic, hexagonal, and some triangular-shaped nanoparticles of ~4.48 to ~9.49 nm in diameter were observed in the case of pure Pt deposition, according to histogram analyses (Figures 20.12 (a) and (c)). This suggested that these nanoparticles bear the structures of cubes, truncated octahedrons, and tetrahedrons. In the cases of samples with Pt–Ru, particles of sizes ranging from 4.80 to 5.22 nm with few agglomerations are seen in Figures 20.12 (b) and (d). It was speculated that the agglomerations of Pt–Ru nanoparticles were due to the co-deposition of Ru, which enhanced the agglomeration of Pt in the EG-containing electrolytes.
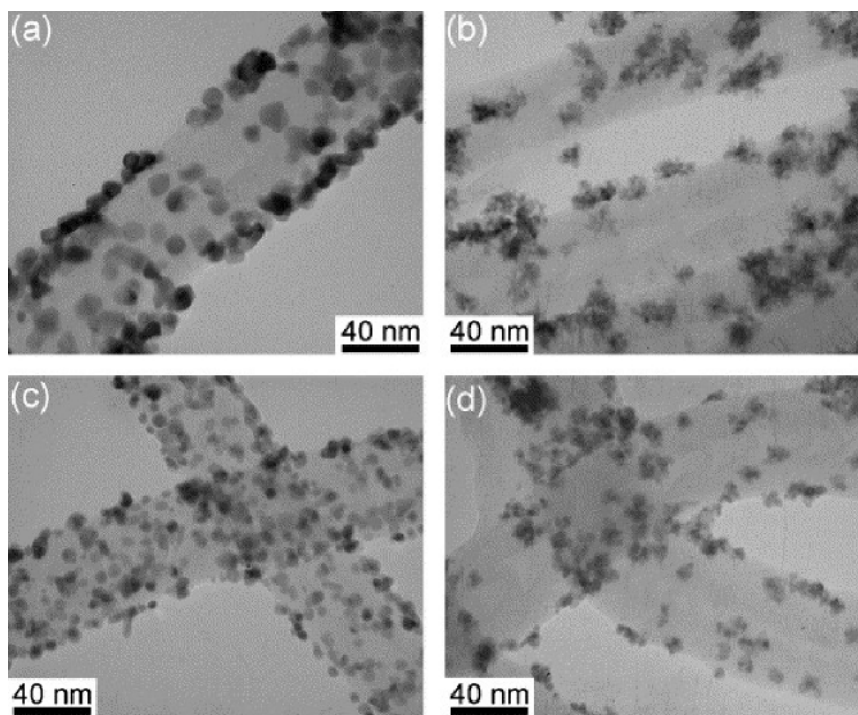
Figure 20.12. TEM micrographs of working specimens with Pt (a) and (c), and working specimens with Pt–Ru (b) and (d) [64]. (Reproduced from Electrochemistry Communications, 8(9), Tsai MC, Yeh TK, and Tsai CH, An improved electrodeposition technique for preparing platinum and platinum-ruthenium nanoparticles on carbon nanotubes directly grown on carbon cloth for methanol oxidation, 1445–52, ©2006, with permission from Elsevier.)

20.3.4 Electrochemical Performance and Catalytic Activity

From the work of Ming-Chi Tsai et al. it was found that nanosized catalysts in the form of pure Pt (~4.5 to ~9.5 nm) or Pt–Ru (~4.8 to 5.2 nm) particles were

successfully electrodeposited on the surfaces of CNTs by potentiostatic electrodeposition in mixed ethylene glycol and H_2SO_4 aqueous solutions [64]. The measured loadings of Pt and Pt–Ru catalysts on the CNT/CC specimens (referred to hereafter as the "working specimens") are shown in Table 20.1. Loadings of Pt and Ru on these specimens ranged from 61.4 to 307.8 μg cm^{-2} and from 17.1 to 95.0 μg cm^{-2}, respectively. Furthermore, it was found that the loadings of both Pt and Ru deposited at -0.45 V_{SCE} were actually larger than those deposited at -0.30 V_{SCE} (A02 versus B02, and A01 versus B01), in spite of possible interference from hydrogen evolution. In comparison, the loading of Pt on A02 was less than that on A01, which was probably due to the simultaneous presence of the Ru precursor salt during the electrodeposition process. However, this effect did not occur in the case of electrodeposition at -0.45 V_{SCE}, and might be attributed to a much better reduction efficiency of the Pt and Ru precursor salts at this potential [65].

Table 20.1. Estimated loadings and atomic ratios of Pt and Pt–Ru on A01, A02, B01, and B02 specimens [64]. (Reproduced from Electrochemistry Communications, 8(9), Tsai MC, Yeh TK, and Tsai CH, An improved electrodeposition technique for preparing platinum and platinum-ruthenium nanoparticles on carbon nanotubes directly grown on carbon cloth for methanol oxidation, 1445–52, 2006, with permission from Elsevier.)

Specimen	Catalyst loadings (μg cm−2)		Pt:Ru (at%)
	Pt	**Ru**	
A01	76.3	–	–
A02	61.4	17.1	1:0.54
B01	115.1	–	–
B02	307.8	95.0	1:0.59
J–M	582	195	1:0.65

On the other hand, the loadings of Ru deposits were lower than those of Pt deposits at both deposition potentials. In addition, the Pt–Ru catalysts electrodeposited on CNT/CC formed solid solutions, as confirmed by XRD analyses [65]. Through the electrochemical tests of methanol oxidation on the working specimens, it was found that the specimens with Pt–Ru catalysts exhibited better electroactivity (current density of methanol oxidation per unit Pt loading mass) than the specimens with only Pt (Figure 20.13). Direct electrooxidation is a very complex reaction because many intermediate species are involved. In an acidic medium this reaction requires platinum-based catalysts, even though Pt exhibits rather low activity [66].

Furthermore, the working specimen with Pt–Ru catalysts electrodeposited at -0.45 V_{SCE} revealed better electrochemical characteristics than the others in terms of mass activity and suppression of CO poisoning, and it proved to be a better electrode for methanol oxidation [64]. The electrochemical characteristics of methanol oxidation on the prepared specimens were analyzed by cyclic voltammetry in mixed methanol and sulfuric acid solutions. The physical

chemistry performance of the Pt–Ru/CNTs electrode in the aspects of mass activity (normalized current density of methanol oxidation vs. Pt loading), 542.6 A/g cm^2, and $i\,f\,/i\,b$ value (the ratio of forward peak current density to reverse peak current density), 13.36, was superior to that of the commercial Pt–Ru/C electrode with a mass activity of 168.3 A/g:cm^2 and an $i\,f\,/i\,b$ value of 10.66.
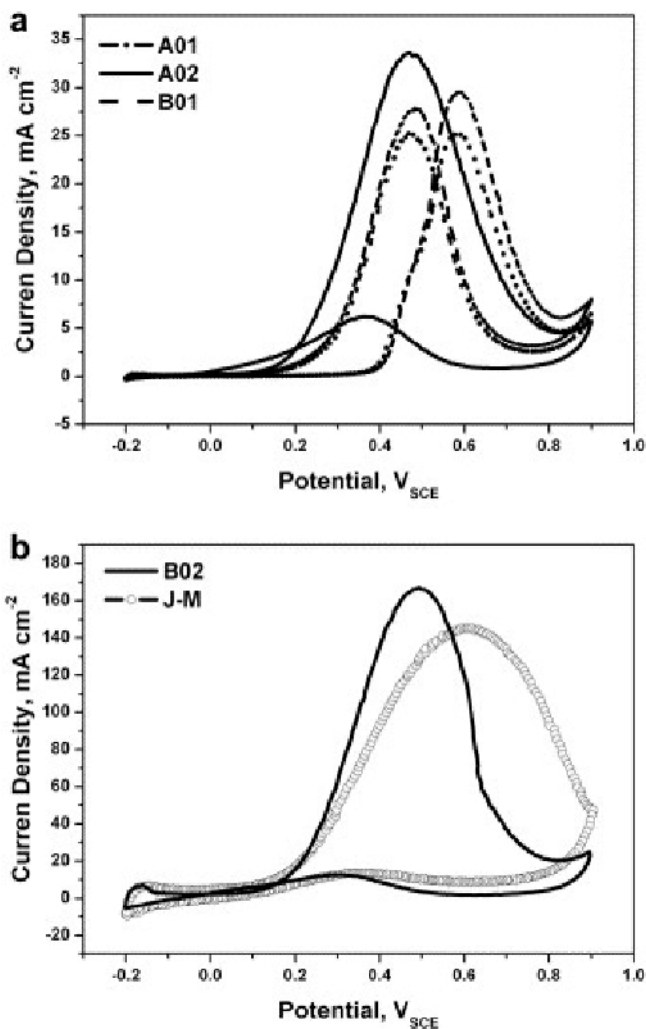
Figure 20.13. Cyclic voltammograms of the (a) A01, A02, B01, and (b) B02 and J–M specimens at 20 mV s−1 in N$_2$-saturated 0.5 M H$_2$SO$_4$ + 1 M CH$_3$OH aqueous solutions. The electrochemical tests were conducted under ambient pressure and a controlled temperature of 30 °C and the CV curves were taken from the fifth cycle [64]. (Reproduced from Electrochemistry Communications, 8(9), Tsai MC, Yeh TK, and Tsai CH, An improved electrodeposition technique for preparing platinum and platinum-ruthenium nanoparticles on carbon nanotubes directly grown on carbon cloth for methanol oxidation, 1445–52, ©2006, with permission from Elsevier.)

The electrochemical properties of the Pt/MWCNT composites and the PtRu/MWCNT composites prepared with the initial weight ratio of $RuCl_3 \cdot 3H_2O:H_2PtCl_6 \cdot 6H_2O:MWCNTs$ of 1:2:2 under the initial CO_2 pressure of 6.5 MPa were presented by An et al. [67]. The cyclic voltammograms (CVs) of the Pt/MWCNT and the PtRu/MWCNT electrodes in 0.5 M N_2-saturated H_2SO_4 solution are displayed in Figure 20.14. The Pt/MWCNT electrode exhibits several redox peaks at negative potentials for the hydrogen adsorption-desorption and one pair of voltammetric peaks at positive potential for the redox process of platinum (solid line), which is characteristic of a typical platinum electrode. These redox peaks were not clearly recorded at the PtRu/MWCNT electrode (dotted line) because of the co-existence of ruthenium, which is consistent with the peaks of the PtRu electrode.
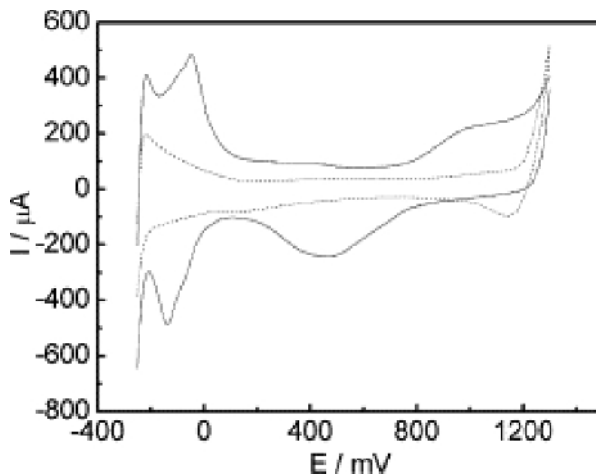
Figure 20.14. Cyclic voltammograms (CVs) at Pt/MWCNT (solid line) and PtRu/MWCNT (dotted line) electrodes in 0.5 M N_2-saturated H_2SO_4 solution. Scan rate: 100 mV/s.

Figure 20.15 compares the CVs for methanol oxidation at the PtRu/MWCNT (dotted line) and Pt/MWCNT (solid line) electrodes in 0.5 M H_2SO_4. CVs at the PtRu/MWCNT electrode are relatively different from those obtained at the Pt/CNT electrode; at the former electrode, CH_3OH oxidation occurs at a potential more negative (~190 mV) than that at the Pt/MWCNT electrode (solid line), indicating that the co-existence of Ru accelerates the electron-transfer kinetics for CH_3OH oxidation.

Moreover, at the PtRu/MWCNT electrode only one peak was recorded for CH_3OH oxidation, demonstrating that there is almost no electrode fouling from the carbon monoxide (CO) produced during the oxidation process. The observed low overpotential and the diminished electrode fouling at the PtRu/MWCNT electrode could be elucidated in terms of the bifunctional mechanism described by Watanabe et al., in which Ru was proposed to be able to promote the oxidation of strongly adsorbed CO on Pt by supplying an oxygen source (Ru-OH$_{ad}$) [68]. In Watanabe's work the alloy anode exhibits a lower saturated coverage with CO than does pure Pt. Linear CO is observed predominantly on the alloy electrode, differing from

both linear and bridged CO beside COOH on pure Pt [68]. The negative shift of the wave number for the linear CO stretching and the broadening of the half-wave width at the alloy also indicate the weakening of metal-CO bonding and the increased mobility of the adsorbed CO, respectively. As a presumable effect of the electronic structure change at the Pt skin, the dissociation/oxidation of adsorbed water as well as the formation of adsorbed HOOH species are clearly observed beyond 0.6 V in an electrolyte solution without CO [68]. The mechanism of CO tolerance at the Pt skin on top of the alloy surface with an increased *d*-band vacancy is supported by the present SEIRAS data, as the "detoxification mechanism" is featured by an increased mobility of the adsorbed CO with suppressed coverage.
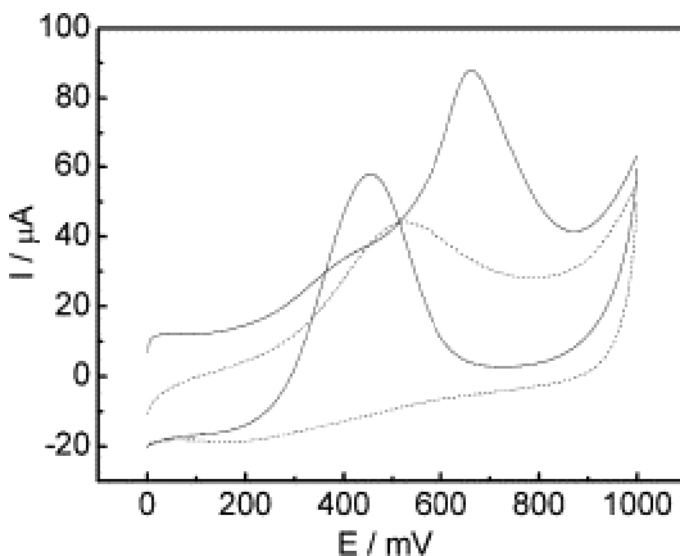
Figure 20.15. CVs for the oxidation of methanol on Pt/MWCNT (solid line) and PtRu/MWCNT (dashed line) electrodes in 0.5 M H_2SO_4 solution containing 1 M methanol. Scan rate: 20 mV/s.

20.3.5 Typical Examples Analysis

Current carbon-supported, fine-particle dispersed catalysts have fundamentally limiting issues due to carbon corrosion and the instability of nanometer particles. More recently some new catalyst structures were used to increase the catalytic efficiency. For example, 3M Corporation used a nanostructure electrode [69, 70]. In this structure, an acicular nanopolymer whisker supports deposited acicular nanoscopic catalytic particles. At first, an organic material is deposited on a substrate. Then the deposited layer is annealed in a vacuum and forms a dense array of acicular nanopolymer whiskers. The preferred length of the whiskers is equal to or less than 1 micrometer. Then, catalyst thin film is deposited on the supporting whiskers. The diameter of the catalyst particles is less than 10 nm and the length is less than 50 nm. In a Pt and Ru loading range of 0.09–0.425 mg/cm^2,

the fuel cell obtained satisfactory catalytic efficiency. However the process is complicated by non-electrical conducting nanopolymer whiskers and transferring the catalyst coated polymer whisker layers onto carbon electrodes. The 3M typical whisker structure is shown in Figure 20.16.

Figure 20.16. As-grown 3M, PR149 whiskers. (Image reproduced courtesy of 3M Corporation.)

The crystal growth occurs via an emergent screw dislocation on the whisker tip. The surface morphology of the thin-film catalyst coating is process- and material-dependent. The volume of the catalyst coating depends on the material density and mass loading. The mass specific area or m^2/g of the catalyst depends on the geometric surface area (diameter and length) of the PR149 whiskers. The intrinsic roughness of the catalyst coating contributes to the surface area as well. In the 3M structure the catalyst coated whiskers are transferred to the PEM from the microstructured substrate. This forms a catalyst coated membrane (CCM).

The catalyst support contains no carbon black and the organic pigment is EC-stable. The catalyst support is a high aspect ratio crystalline whisker.

A current baseline performance standard or 3M catalyst with 0.15 mg Pt/cm^2 total per MEA is shown in Figure 20.17. The combined effect of the reduced microstructured feature size of the NSTF substrate and the reduced anode loading allows over 500 mV at 2 A/cm^2 and 150 kPa inlet pressure for the first time. The 3M catalyst demonstrates a ten-fold gain in catalyst specific activity: < 0.3 g Pt/kW, equivalent or higher mass activity combined with durability.
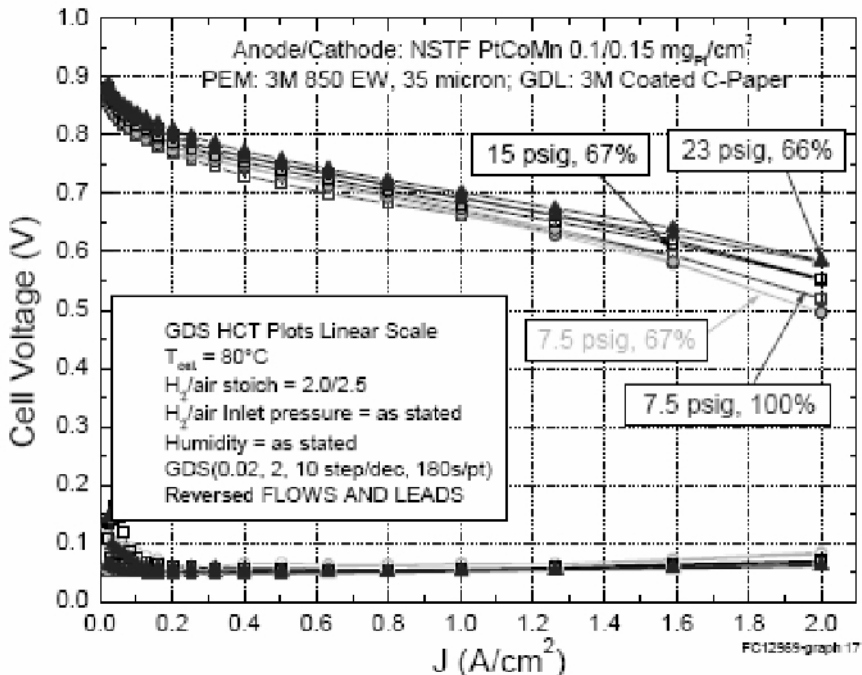
Figure 20.17. Electrochemical performance of 3M structure. (Image reproduced courtesy of 3M Corporation.)

20.4 Flame-based Processing

Recent advances in aerosol and combustion science and engineering now allow scalable flame synthesis of mixed oxides, metal salts, and even pure metals in the form of nanoparticles and films with closely controlled characteristics [71–76]. Flame processes are classified into vapor-fed and liquid-fed, depending on the employed state of the metal precursor [77]. Liquid-fed flame processes are distinguished for their flexibility in producing materials of various compositions and morphologies that result in unique product functionalities.

The general principle behind flame synthesis of materials is the decomposition and oxidation of evaporated metal precursors in a flame, thereby forming stable metal-oxide monomers followed by nucleation, aggregation/agglomeration and, to some extent, coalescence of aggregated nanoparticles. These flame-produced materials are in many cases attractive since they are formed directly in one step. In contrast to wet-chemistry synthesis routes, there is no need for a calcination step in order to obtain the desired crystal phases, because these phases are formed directly at the high temperature conditions in the flame. Thus, flame synthesis is a flexible synthesis method where the product properties can be tuned by changing the composition of the precursor gas and the flame operating conditions. The specific surface area of particles can to some extent be controlled by quench-cooling the

product gas after a short residence time in the flame [78]. Thus, there are mainly the following process variables: flame peak-temperature, residence time at elevated temperature, and precursor loading/composition. Standard chemical engineering tools such as flame reactor design and computational fluid dynamics (CFD) are important tools in terms of optimizing the process properties and product properties. For the conventional industrial application of flame synthesis, that is the production of, e.g., titania and carbon black, the product particles are collected on filters and packed for shipping [79]. However, flame processes can be applied directly in additional product or process engineering concepts: flame synthesis of composite metal oxides and catalysts; formation of membrane layers by deposition of nanoparticles from the gas phase; coating of substrate surfaces; and preparation of catalyzed hardware, e.g., applying the catalyst directly on the process equipment and surfaces of otherwise standard unit operations [80].

20.4.1 Current Research Activities

Depending on the final application and on the available metal precursors, several flame synthesis methods are available. In each case, except for spray flames where the solvent is the main fuel, the fuel is either methane or hydrogen and the oxidant is air or oxygen-enriched air:

- *diffusion flames*: fuel, oxidant, and evaporated metal precursor in a carrier gas are fed through separate tubes/annuli of concentric tubes [76, 77];
- *premixed flames*: fuel, oxidant, and evaporated metal precursor are mixed and fed to a flat flame [80, 81];
- *premixed flames with precursor jet*: a jet of evaporated metal precursor in a flow of carrier gas is injected into a flat, premixed fuel/oxidant flame [82, 79].
- *spray flames*: an organic solution of one or more metal compounds is fed to an air-assisted spray nozzle where the generated aerosol-jet is combusted using supporting hydrogen flames [71].

Other flame types such as the counter-diffusion flame can be used [73]. In all cases, particles are formed once the volatile metal compounds are converted to stable metal oxide or metal nanoparticles in the high-temperature environment of the flame.

nGimat developed a flame process called chemical combustion vapor deposition (CCVD) to deposit catalyst particles for FC application [83]. The CCVD process can in one step directly make both the electrocatalyst and the electrode on a gas-diffusion layer or membrane substrate. Reducing process steps to form the electrocatalyst layer can greatly reduce processing costs and increase production throughput with the simple, low-cost CCVD process. nGimat demonstrated the ability to make Pt- and Ru-containing electrocatalyst layers that demonstrate similar performance to commercially available E-TEK PtRu materials. The CCVD process is based on nGimat's NanoSpray[SM] Combustion Processing technology. In the process, precursors (metal-bearing chemicals used to coat an object) are first dissolved in a solution, which typically is a combustible fuel. This solution is then atomized to form microscopic droplets by means of nGimat's

proprietary Nanomiser® device. These droplets are next carried by an oxygen stream to the flame where they are combusted. A substrate (the material being coated) is coated by simply drawing it in front of the flame. The heat from the flame provides the energy required to vaporize the droplets and for the precursors to react and deposit on the substrate. One of the strengths of the CCVD process is the variety of deposited materials and substrates that can be utilized.

The National Research Council of Canada's Institute for Fuel Cell Innovation (NRC-IFCI) is developing a new concept in fuel cell spray deposition technology, for a thin-film catalyst layer directly deposited on the ionomer membrane with a flame spraying process called reactive spray deposition technique (RSDT) [84]. One of the ways RSDT differs from CCVD, which is an open atmosphere flame-based deposition technique, is in the method used to produce the heat necessary for atomization as well as solution storage and delivery. RSDT allows the possibility of actually passing a supercritical solution into an atomizer rather that having the atomizer take a solution to the supercritical point in the nozzle prior to exiting as a spray.

In flame synthesis of metal oxide particles, the residence time and temperature of the flame zone must be sufficient to transform the volatile precursors into oxide molecules and to reach the desired crystalline structure of particles formed by the collision/coalescence process. Further exposure to high temperature results in loss of valuable surface area by sintering, but this can be avoided using quench-cooling.

20.4.2 Atomization Process

In the flame process after dissolving Pt and Pt precursors in appropriate solvents, the solution is sprayed through a nozzle to produce micron-sized droplets that burn out in a flame, resulting in metal atoms and/or metal oxide molecules in the gas phase. nGimat's novel device is referred to as the Nanomiser® device because of its ability to produce an aerosol of controlled size down to the sub-micron range, from 0.002 to 4 L/min flow rates, without any atomizing gas. The ability to produce small-size droplets with narrow size distribution is of critical importance in the NanoSpray^{SM} Combustion Processing technology, where precursor solutions are converted to an ultrafine mist that is efficiently combusted and creates vapor for use in nanopowder and thin film deposition applications. In addition, it can be used, without combustion of the aerosol, to spray polymers for film or nanopowder formation. During the initial steps, chemical precursors such as metal nitrates or metal organics (i.e., 2-ethylhexanoate, acetylacetonate), among others, are dissolved in suitable solvents, which also act as a fuel for combustion. Water-soluble precursors may also be dissolved in water and then mixed with a suitable liquid or gas fuel.

In the work of Chakraborty et al. the solution was usually pumped by using a syringe pump through a gas-assisted nozzle to spray the precursor solution to the flame zone as small droplets [85]. The nozzle consisted of a capillary tube of outer diameter 0.9 mm (inner diameter 0.6 mm), situated in an opening of 1.4 mm diameter, creating an annular space of 0.9 mm^2. The design of the nozzle was similar to the one used by Mädler et al. [71]. The precursor solution was passed through the capillary tube at 0.5 mL min^{-1} and oxygen was introduced as both

dispersion and oxidation gas through the annulus at 2.2 L min^{-1}. The spray aerosol was ignited by eight hydrogen-fed supporting flames made by horizontal injection through eight equidistant holes drilled in a hollow metal ring that was placed around the aerosol jet. Droplet size distributions were measured by laser diffraction, while droplet lifetimes were calculated using a spray combustion model to explain for the first time the difference in flame structure and, especially, product powder characteristics when air or oxygen was used as the oxidant/dispersion gas [71].

Figure 20.18 shows droplet size distribution for the NanoSpraySM process of a typical nGimat solution (measured using Malvern Sizer 2600). Note that the detector limit is 1.2 micrometers. To obtain insight into the process of droplet burning, a simplified model of single-droplet combustion is used that has been successful in describing spray flames and liquid fuel rocket engines [71]. This model is based on liquid-vapor phase equilibrium at the interface with fuel species and oxidizer species conservation in the inner and outer region, respectively, and energy balances at the droplet liquid-vapor interface and its flame sheet. Additionally assumed are: no droplet interactions, single-component liquid fuel with zero solubility for gases, uniform and constant pressure, and a gas phase consisting of three "species" – fuel, oxidizer, and combustion products.
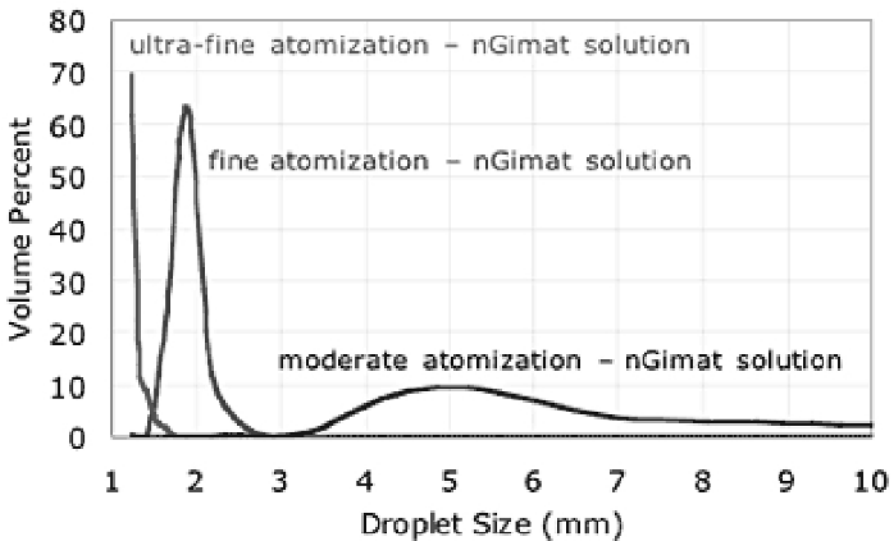
Figure 20.18. Droplet size distribution for the NanoSpray^{SM} Combustion Processing of a typical nGimat solution (measured using Malvern Sizer 2600). (Reproduced courtesy of nGimat.)

20.4.3 Particle Formation in the Flame

The flame flash vaporizes the meta-stable droplets of solvent with precursors, which then decompose to yield reactive vapor intermediates that ultimately condense, forming the nanoparticles (see Figure 20.19). The number and size of

nuclei formed in the flame are a function of the solution, density, viscosity, surface tension, and concentration. In the case of fuel cell catalyst deposition, synthesized nanoparticles are then captured or deposited directly on the GDL or Nafion® membrane. It has been shown how the specific surface area can be closely controlled through oxidant or fuel composition and flow rate [71]. The formed nanoparticles can be quench-cooled after a short residence time in the flame. In flame synthesis of metal oxide particles, the residence time and temperature of the flame zone must be sufficient to transform the volatile precursors into oxide molecules and to reach the desired crystalline structure of particles formed by the collision/coalescence process. Further exposure to high temperature results in loss of valuable surface area by sintering, but this can be avoided using quench-cooling. As presented by Maric et al. [84], in the case of the direct deposition of the catalyst layer on Nafion®, it is important that the temperature of the flame is kept below 100 °C in order not to destroy the Nafion® membrane.
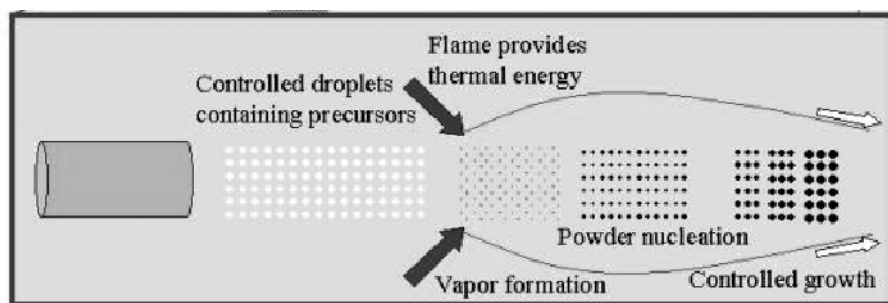
Figure 20.19. Schematic of nanoparticles production via nanospray combustion synthesis process. (Reproduced courtesy of nGimat.)

The optimal situation would be to minimize unnecessary loss of surface area by "freezing" the sintering of aggregated Pt primary particles after a short residence time in the flame, before they become mixed up with carbon and ionomer particles.

nGimat has made Pt-carbon-ionomer electrocatalyst composite layers on gas diffusion carbon paper using the NanoSpray[SM] Combustion process. The Pt nanoparticles are formed directly onto the carbon particle and mix with ionomer before all are deposited onto the GDL substrate.

Figure 20.20 shows comparative transmission electron microscopy data for Johnson Matthey HISPEC 4000 and NanoSpray[SM] Combustion-prepared catalyst material. NanoSpray[SM] Combustion-produced catalyst exhibits Pt domains on the order of 2–10 nm attached to a carbon support, which is desirable for maximized surface area and minimized Ostwald ripening of the active catalyst material. This is comparable to the supported structure observed in the Johnson Matthey HISPEC 4000 catalyst shown on the right side of Figure 20.20.

The ability to make thinner electrodes is usually advantageous for enhancing mass transport characteristics. In the case of NanoSpray[SM] Combustion-prepared materials, electrode layer thickness (20–25 μm) is not necessarily a determining factor of performance because the enhanced porosity allows for thicker electrodes without compromising mass transport behavior.

<div align="center">(a)   (b)</div>
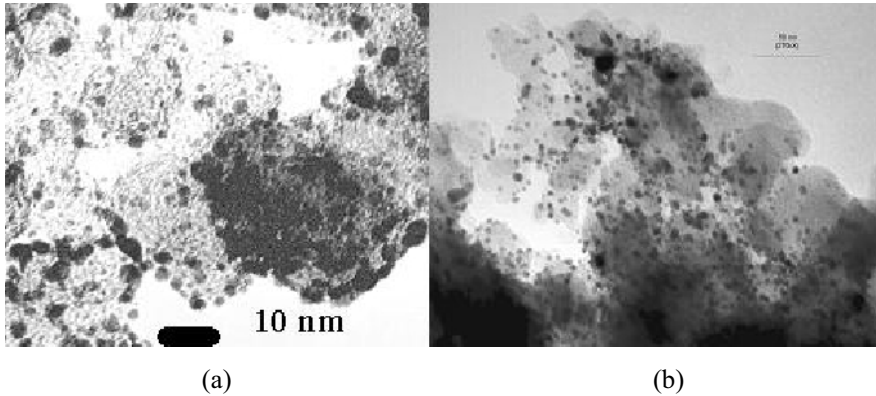
Figure 20.20. High resolution TEM of (a) NanoSpray^{SM} Combustion-prepared electrocatalyst and(b) Johnson Matthey HiSPEC 4000 carbon supported (40%) material; the scalebar in (b) reads 50 nm. (Reproduced courtesy of nGimat.)

In the RSDT process configuration, a polymer electrolyte membrane is used as the substrate and coated with a compositional grading of platinum and carbon support. Additionally, Nafion® ionomer is added and deposited separately for further processing. The platinum layer is deposited directly on a Nafion® 211 membrane as a column structure, and the platinum loading is reduced in the layer closest to the GDL. An entire low loading (< 0.05 mg/cm^2 Pt) thin film (1–3 μm) catalyst layer is deposited directly from precursors with this approach. Figure 20.21 shows a cross-section of the catalyst layer, with Figure 20.21(a) the Pt sub layer and Figure 20.21(b) the gradient layer of Pt, carbon, and Nafion®.
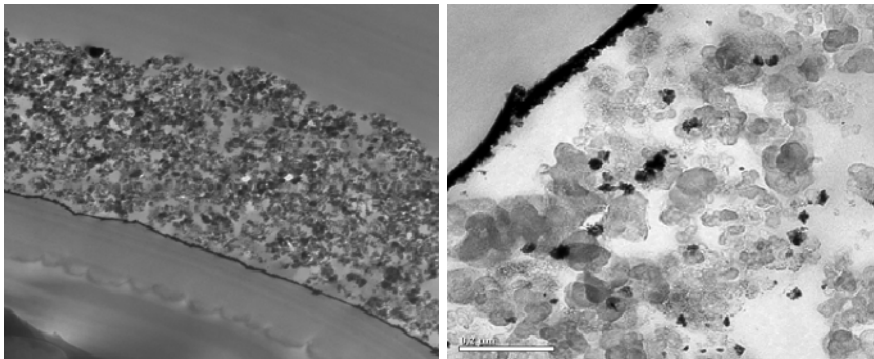
Figure 20.21. TEM cross-section examination of the catalyst layer (unpublished NRC-IFCI data)

20.4.4 Particle Size Control

In order to control particle size it is possible to use water or air to cool the flame. Cold air, provided from a water-cooled quenching ring, has been used to quench the aerosol coming out of the flame [78]. The quenching helps decrease the

average particle size by suddenly lowering the temperature and thus decreasing the rate of sintering. The product particles were collected directly on the GDL (Toray TGPH090) by withdrawing the nanoparticle aerosol from the flame through it by using a gas-ejector vacuum pump (PIAB Classic). Here, the Vulcun carbon-painted GDL was, in principle, applied as a catalyst nanoparticle filter. The thin carbon layer improves filtration efficiency as well as anode performance in methanol electrooxidation [86].

In the case of direct deposition on Nafion® substrate, since that is only stable at lower temperatures the flame must be cooled before it reaches the substrate surface. The NRC-IFCI was doing such cooling using an air knife system that cut the flame at a set distance from the nozzle body. The distance, angle, and position of the air knife system control the substrate temperature. In general, in the flame process there are several parameters that can be modified in order to optimize the platinum deposition process. These are:

Liquid Flow

- Flow Rate
- Composition

    - Solvent type and concentration
    - Propellant concentration
    - Precursor concentration

- Nozzle Temperature
- Pump Pressure
- Tip Oxygen

Pilot Flame

- Oxygen Flow Rate
- Fuel Flow Rate

Geometry

- Air Knife Angle
- Air Knife
- Air Knife Flow Rate
- Deposition Distance
- Substrate Temperature/Holding Mechanism
- Deposition Path and Speed

All of these parameters need to be optimized in order to obtain the desired particle size and improve the deposition rate and consistency.

The size of platinum particles made during RSDT deposition was measured using mapping with TEM images. The TEM images of particles formed by RSDT are shown in Figure 22. It can be seen that the maximum particle size is below 5 nm and the deposition size is uniform. Note that Figure 20.22 shows a TEM grid after only a few seconds of deposition, and therefore does not show the density of the final coating.
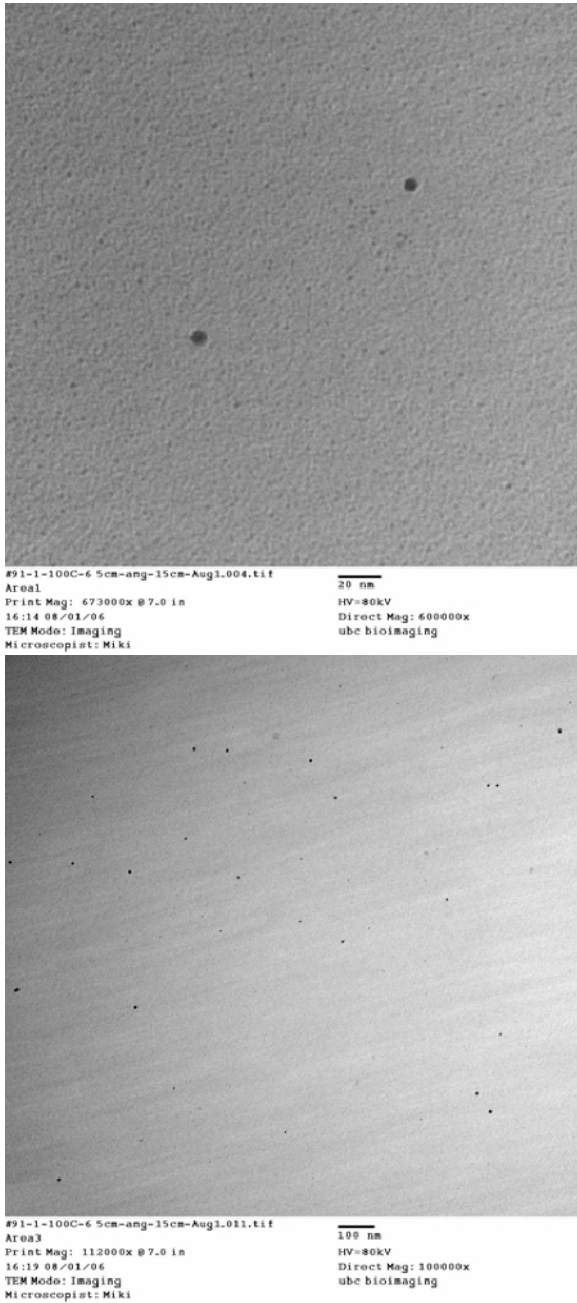
Figure 20.22. Typical TEM picture of Pt loading on TEM grid deposited by RSDT (unpublished NRC-IFCI data)
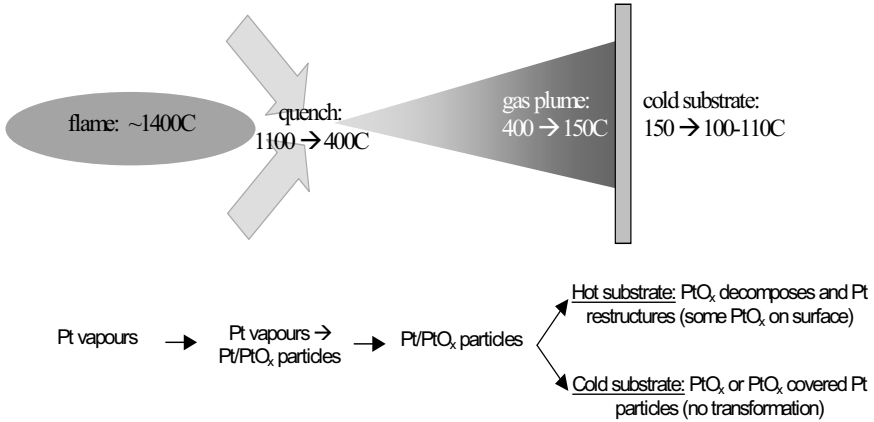
Figure 20.23. Description of Pt-O formation in the RSDT process (unpublished NRC-IFCI data)

The Pt formation during the RSDT process is schematically shown in Figure 20.23, while Figure 20.24 shows the temperature profile during catalyst deposition on Nafion® membrane. Note that the non-oscillating sections of the graph are due to communication loss with the measuring instrument and should be discounted. Conductivity measurements were done on the supplied Nafion® samples before and after heating the samples to ensure that the degradation of the substrate was not significant at these temperatures and deposition times.
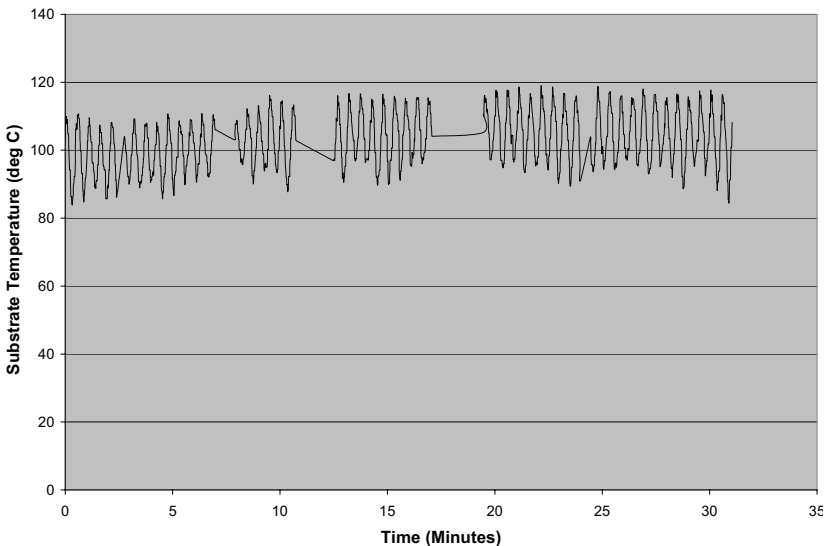
Figure 20.24. Substrate temperature profile during RSDT deposition (unpublished NRC-IFCI data)

20.4.5 Electrochemical Performance and Catalytic Activity of the Flame Deposited Catalyst

Using their flame-based technique, nGimat has prepared carbon-supported Pt and PtRu alloy-based composites on gas diffusion electrodes, with significantly improved oxygen reduction behavior and CO tolerance over commercially available materials. This CCVD processing technology has superior production rates of electrocatalyst layers and material cost advantages over conventional screen-printing techniques [87, 88]. nGimat low-loaded (< 0.2 mg/cm^2 Pt) cathode materials have exhibited 30–50 mV improvements in air performance over screen-printed Johnson Matthey catalyst-based materials at 0.3 A/cm^2. This is attributed to a more porous electrocatalyst layer structure [87]. Effective platinum surface areas are routinely 2–3 times lower than those obtained using Johnson Matthey HISPEC 4000 catalyst making. Long-term degradation remains high at 700–1500 µV/hr over the first twenty-four hours of operation, with increases in ohmic loss being the most significant loss observed, attributed to unoptimized Pt-C connection in the catalyst.
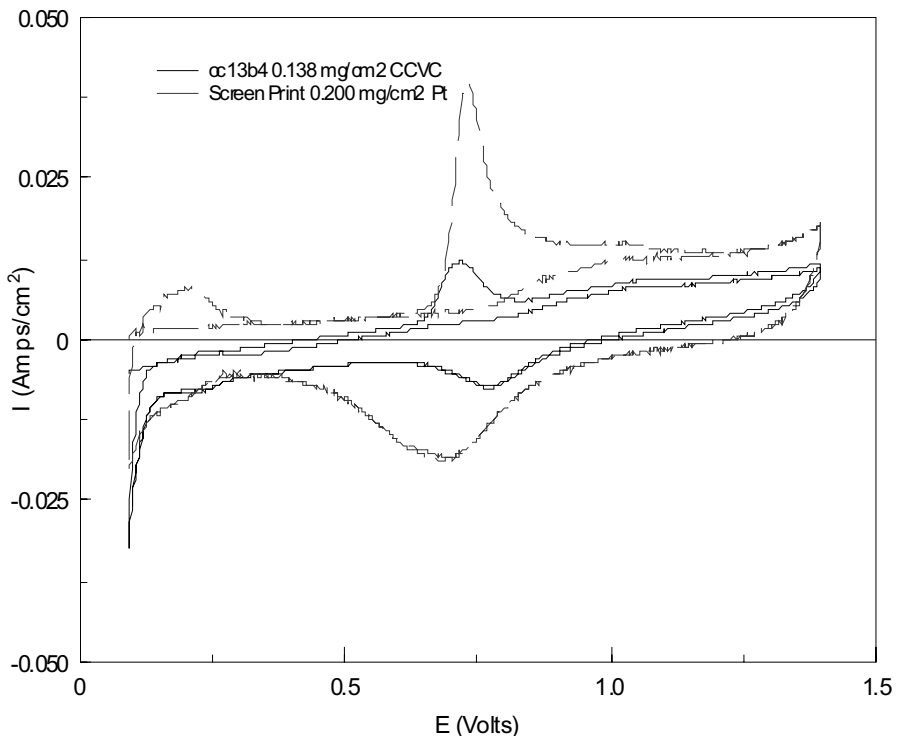
Figure 20.25. Comparative CO stripping cyclic voltammograms (unpublished NRC-IFCI data)

Half-cell CO tolerance results show 100–200 mV decreases in ignition potential over Johnson Matthey HISPEC-based materials. Figure 20.25 shows comparative CO stripping cyclic voltammograms for screen-printed Johnson Matthey HISPEC 5000 and NanoSpray^{SM} Combustion-prepared electrocatalyst layers on a GDL from nGimat.

Here it is shown that HISPEC 5000 has a dimensionless effective Pt surface area (EPSA) of 120.7 while this number is 38 for the nanospray combustion-prepared sample. The voltammetric comparison also shows the onset of surface oxide/hydroxide reduction at higher potentials for the NanoSpray^{SM} Combustion-prepared sample, suggesting easier surface oxygen reduction kinetics than is seen for the screen printed material.

Slow Sweep Voltammetric Polarization Curves
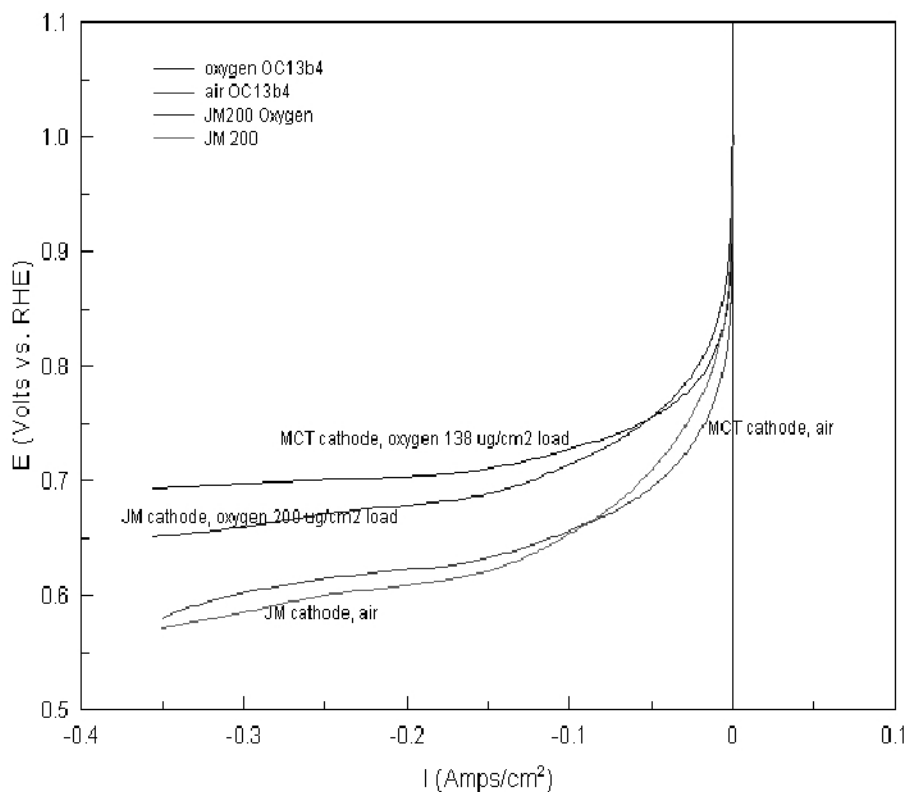
Figure 20.26. Slow-sweep voltammetric "polarization" curves comparing conventional screen-printed Johnson-Matthey HISPEC catalysts with CCVD-grown materials. Conditions: 0.5 M H_2SO_4 electrolyte, Pt counter electrode, RHE at 40 °C. (Reproduced courtesy of nGimat.)

It is apparent from Figure 20.26 that NanoSpray^{SM} Combustion-prepared cathodes, with a lower platinum loading of 0.138 mg/cm^2 as compared to the

Johnson Matthey loading of 0.200 mg/cm^2, perform with similar power outputs in basic electrochemical tests. Fuel cell load tests on nGimat client test stands verify that there is comparable performance between nGimat representative samples (0.25 mg/cm^2 loading) and commercially available electrocatalyst layers with approximately 0.3 mg/cm^2 Pt loadings. This result is attributed to microstructural differences in the electrocatalyst layer.
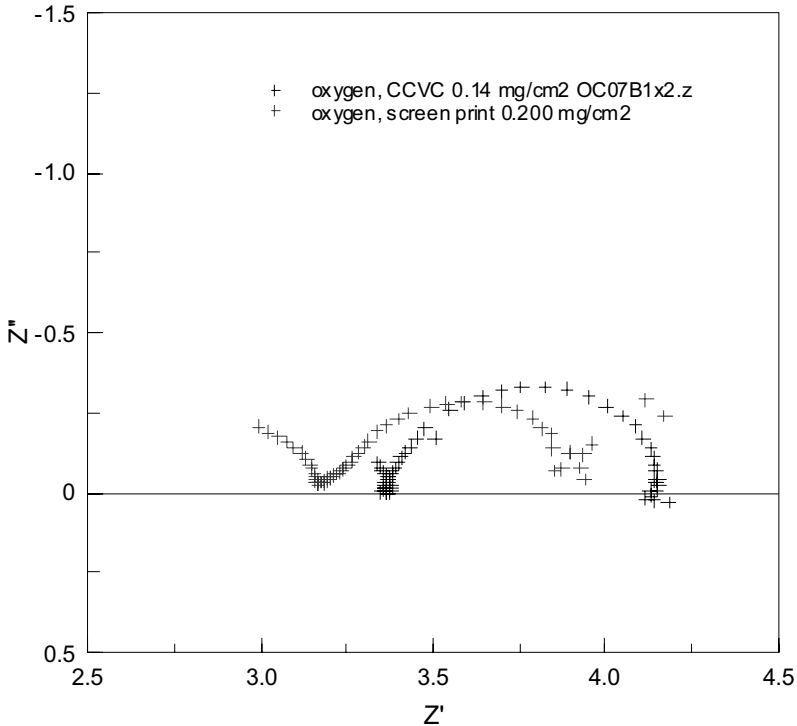
Figure 20.27. Comparative Nyquist plot impedance spectra of screen-printed Johnson Matthey based material and (CCVC) NanoSpray^{SM} Combustion-based electrocatalyst layer in oxygen, 40 °C, H$_2$SO$_4$ electrolyte Pt counter electrode, H$_2$ reference, 0.6 V vs. reference potentiostatic conditions. (Reproduced courtesy of nGimat.)

Figure 20.27 shows comparative Nyquist plot impedance spectra of screen-printed Johnson Matthey based material shown above and (CCVC) NanoSpray^{SM} Combustion-based electrocatalyst layer. The resistances, Rp, associated with each spectrum show that the screen-printed sample has a polarization resistance of 0.78 ohms, while that of the NanoSpray^{SM} Combustion sample is 0.812 ohms. A constant phase element fit factor (CPE-P) comparison shows that the NanoSpray^{SM} Combustion-prepared sample exhibits a behavior closer to a capacitor than does the screen-printed counterpart (0.86 vs. 0.77), which is related to its more open pore structure. Deviation from capacitive behavior has been modeled [89, 90] as a measure of the pore sizes in electrode structures, whereby lower pore diameters and longer lengths represent greater deviation (and thus lower CPE fit values)

because of the relative difficulty of charge penetration through a longer, thinner tube than across a wider, shorter channel. In the spectrum, smaller, longer pores are manifested as a collapsing of the semicircle.

H$_2$-O$_2$ polarization curve comparison
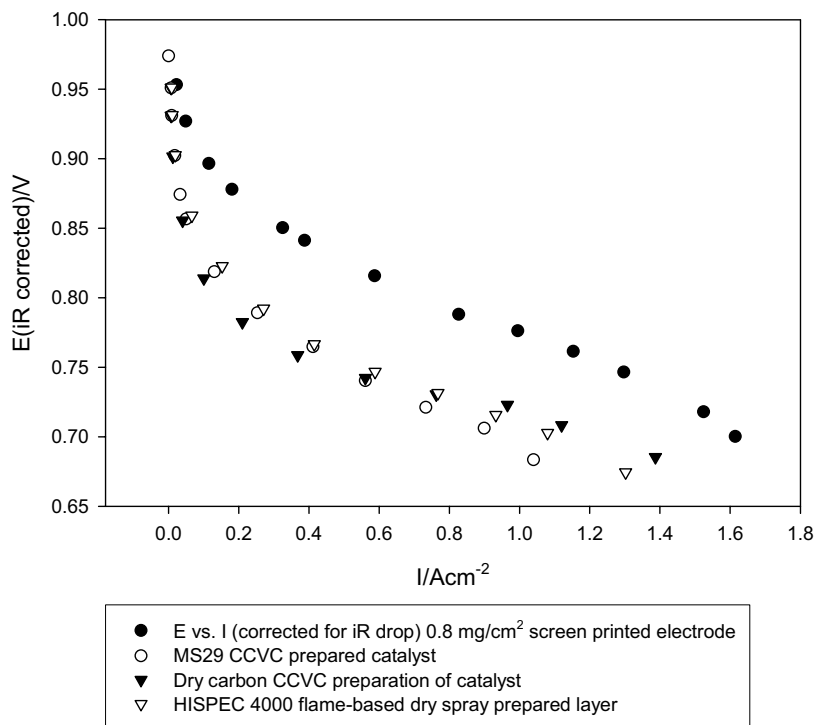
Figure 20.28. Comparative H$_2$-O$_2$ polarization curves for electrodes prepared with different coating techniques on gas diffusion electrode substrate. (Reproduced courtesy of nGimat.)

NanoSpray[SM] Combustion-prepared samples undergo significant performance degradation on the order of 1000 uV/hr over the first 24 hours. Figure 20.28 shows comparative hydrogen-oxygen polarization performance for screen-printed Johnson Matthey based samples, NanoSpray[SM] Combustion-prepared catalyst, and dry-spray Johnson Matthey electrocatalyst layers deposited on gas diffusion electrodes. With the exception of the 100–150 mV advantage at 1 A/cm^2 that is observed when the 0.8 mg/cm^2 screen-printed sample is compared to lower loading NanoSpray[SM] Combustion-prepared samples, electrocatalyst layers prepared using the different NanoSpray[SM] Combustion methods and Johnson Matthey flame sprayed samples all have comparable performance at this current density. After twenty-four hours of continuous operation at 0.5 A/cm^2, the oxygen performance degrades in all but the screen-print prepared samples, as outlined in Table 20.2. Since these data are taken in oxygen and not air on the cathode side, the

degradation rates likely reflect a loss in active catalytic surface area, either through mechanisms such as Ostwald ripening or loss of ohmic contact between the active Pt and carbon support. It is shown that the degradation rate drops by nearly a factor of four when dry carbon introduction is used over wet carbon, suggesting improved bonding by a hotter condensation of the two materials in the plume downstream of the flame.

Table 20.2. Degradation data for samples prepared using screen-printing and combustion methods. Conditions: 0.5 A/cm^2, 80 °C, hydrogen-oxygen, 30 psi backpressure each side. (Reproduced courtesy of nGimat.)

Cathode sample	24 hr Degradation rate/μVhr-1	Preparation method	Catalyst
OCO7B	769	NanoSpray^{SM} Combustion, dry carbon introduction	*In situ* NanoSpray^{SM} Combustion
QL04A	250	Flame spraying	HISPEC 4000
MS29	2800	NanoSpray^{SM} Combustion, wet C introduction	*In situ* NanoSpray^{SM} Combustion
NB78D	0	Screen printing	HISPEC 4000

20.4.6 Typical Examples Analysis

The next presented example is not a typical one but rather a future way to go as a one-step process, with reduced Pt loading on the cathode side, 0.05 mg/cm^2, and thin catalyst film, 5 μm.

The NRC-IFCI worked on direct catalyst layer formation with RSDT, focusing on the composition and thickness of the catalyst layer. The deposition time for a 5 μm-thick catalyst is approximately 15 minutes. The bulk material of the RSDT coating was Pt, and Pt-O bonds could be seen on the surface by XPS [91]. From the literature it can be seen that during these depositions, a highly disordered, non-stoichiometric mixture of Pt and O forms when Pt vapors are quenched. Pt oxides are meta-stable at low temperatures and decompose upon heating [02]. We hypothesize that the residence time of our particles in the hot gas plume is too short to decompose this oxide layer, so they reach the cold substrate, cool, and remain there as oxides. These oxides can then been reduced to Pt by submersion in NaBH$_4$ or during CV cycling, as completed at the NRC-IFCI and described in previous reports [93]. However, for samples deposited at higher temperatures or without quenching, very little Pt-O can be seen. This is likely due to the Pt-O bonds breaking (a chemical process, not desorption) in the high-temperature environment. Data reported in the literature [94, 95] show decomposition starting at ~400K (~130 °C) and completing at ~670K (~400 °C). The decomposition is a function of both residence time and temperature, and is complete for the high-temperature RSDT coatings. At intermediate temperatures a mixture of Pt and Pt-O exists. In order to investigate the contribution of Pt-O bonds to the performance of the

catalyst layer, and have a sample comparable to the XPS results, further cyclic voltammetry was completed. These samples were prepared as follows: 1) platinum was deposited by RSDT on a graphite electrode substrate (diameter 3 mm) using the same low-temperature deposition conditions as for previous catalyst layers; 2) a CV electrode with a plain platinum surface was also measured for reference; the RSDT electrode was cycled in a 0.5 M solution of sulfuric acid for 10 cycles in each voltage range; 3) the voltage was increased by 100 mV, and step 3) was repeated up to the oxygen desorption limit. The results are presented in Figure 20.29.
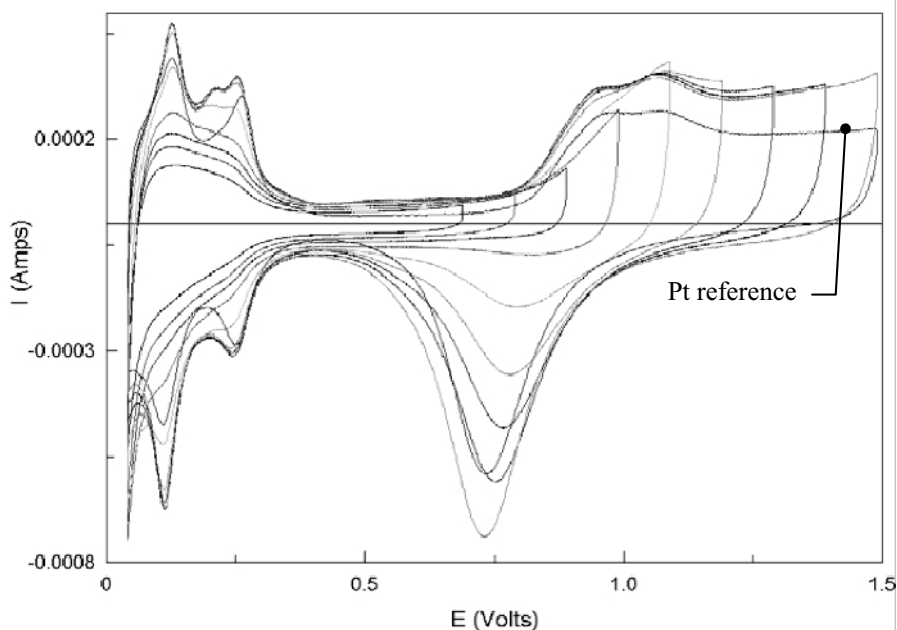
Figure 20.29. Cyclic voltammetry of a RSDT-prepared Pt/graphite electrode (unpublished NRC-IFCI data)

In Figure 20.29, each CV curve is the result of 10 cycles. The voltage was changed in 0.1 V increments in order to determine whether the change in CV curve was simply due to increased wetting of the surface or whether restructuring of the surface was necessary to obtain a fully active layer. From these results we see that a very active Pt layer can be formed, with a much higher preferred 111 orientation than that of our flat platinum reference. Both the RSDT prepared layer and the reference show a Pt peak at ~0.27 V. A significant number of papers published on the topic reference a platinum peak at this same location (see [95, 96]).

The location of the Nafion® in the catalyst layer prepared by RSDT is believed to be different from that in a catalyst layer produced by a more standard ink process. It is hypothesized that the Nafion® and ink form a matrix, upon which the platinum particles deposit in the vapor plume. In order to verify the location of the Nafion® within the network, a representative catalyst layer was stained with lead.

Figure 20.30 shows the location of platinum in a normal RSDT-prepared catalyst layer.
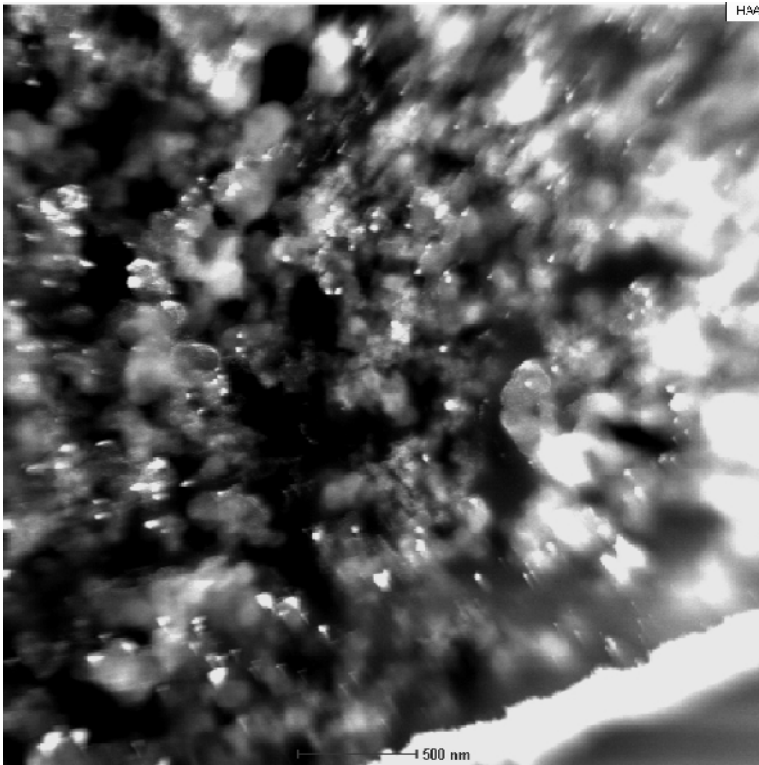
Figure 20.30. Darkfield image of unstained catalyst later (Pt shown in white) (unpublished NRC-IFCI data)

The resulting TEM images of this stained catalyst layer without platinum are shown in Figure 20.31. These can be compared to the unstained images in Figure 20.30.

The performance of the MEA with different Pt cathode catalyst loading is shown in Figure 20.32. The anode loading is 0.05 mg/cm^2. The manufactured catalyst layer has a performance of 0.65 V at 1 A/cm^2 with 0.05 mg/cm^2 Pt loading using pure oxygen.

The data presented show that under H$_2$ and O$_2$, even at a very low loading such as 0.03 mg/cm^2 on the cathode side and 0.05 mg/cm^2 on the anode side, significant performance was measured. The data show that by controlling the morphology of the catalyst layer a significant reduction in Pt loading, without compromising performance, can be obtained for specific testing conditions.
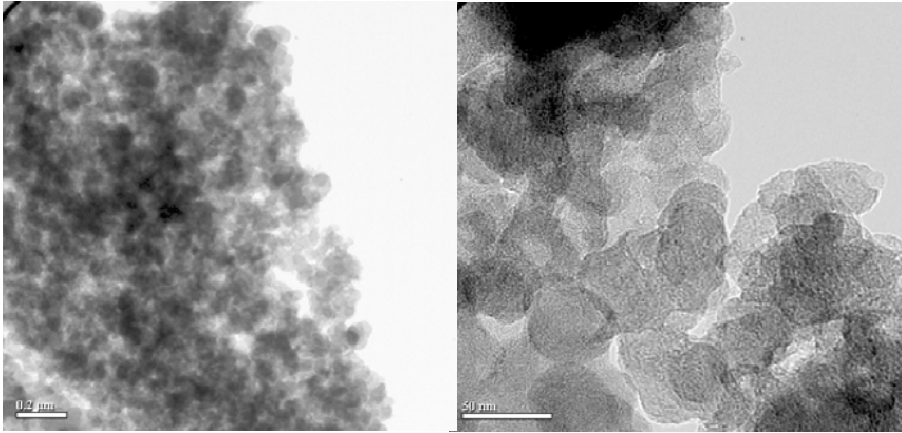
Figure 20.31. Lead-stained Nafion® TEM images without platinum present (unpublished NRC-IFCI data)
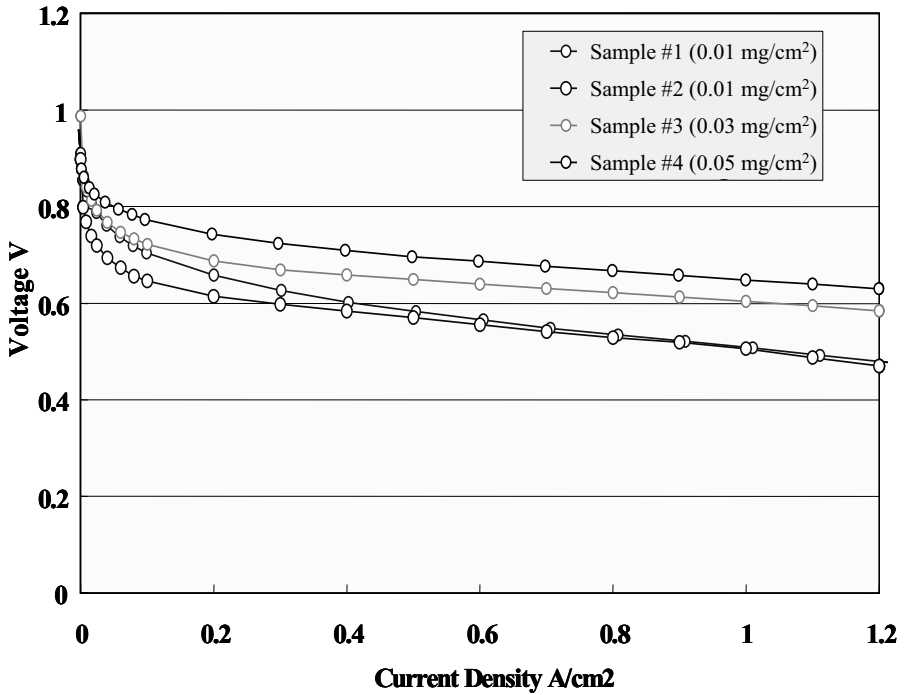
Figure 20.32. Polarization curves of 0.01 to 0.05 mg/cm^2. 80 °C, 100%RH, 0.261 NL/min H$_2$/ 0.625 NL/min O$_2$ (anode/cathode) (unpublished NRC-IFCI data)

20.5 Summary

Production methods must meet commercial standards for mass manufacturing, such as scalability, reproducibility, and quality. *In situ* electrocatalyst formation involves forming the composite platinum/carbon (Pt/C) catalyst directly on the PEM or GDL and involves techniques such as physical vapor deposition (PVD), chemical vapor deposition (CVD), combustion chemical vapor deposition (CCVD), reactive spray deposition technology (RSDT), and electrochemical deposition. The drivers for each process are cost, performance, and reliability, which cannot be separated from the MEA because the electrode structure (porosity, thickness, catalyst type, ionomer content, kinetic losses, ohmic losses, and transport losses) is not only a function of the electrocatalyst itself but also the way in which it is formed or deposited. Raw-material cost reduction takes the form of improved catalyst utilization and alternative formulations, while manufacturing costs are driven down by reducing the number of processing steps, using continuous processing, and avoiding energy- or time-intensive steps such as vacuum environments. Multi-objective optimization techniques are necessary that can uncover Pareto optimal fronts and generate several acceptable choices in catalyst layer design or processing conditions. The cost-effective use of PEMFCs is possible if the content of Pt in PEMFCs, primarily in the cathode, is substantially reduced. The target is to achieve Pt loading in the cathode at 0.02 mg/cm^2.

In reality, the reconciliation of high-performance materials (i.e., low Pt loading, Pt alloys, non-noble catalyst) with low degradation and low-cost targets is an extremely challenging issue. Incentives and technological improvements are needed to overcome socio-economic hurdles in the first phase of transition, where there will otherwise be short-term losses when engaging in new technologies. Among the critical factors that determine the long-term profits of the transition towards a future hydrogen-based society are cost reduction and efficiency improvement.

Acknowledgements

References

1. Ralph TR, Hogarth MP. Catalysis for low temperature fuel cells. Plat Met Rev 2002;46(1):3–14.

2. Hamnett A. Mechanism and electrocatalysis in the direct methanol fuel cell. Catal Today 1997;38:445–57.
3. Prado-Burguete C, Linares-Solano A, Rodríguez-Reinoso F, Salinas-Martínez de Lecea C. The effect of oxygen surface groups of the support on platinum dispersion in Pt/carbon catalysts. J Catal 1989;115:98–106.
4. Roy SC, Harding AW, Russell AE, Thomas KM. Spectroelectrochemical study of the role played by carbon functionality in fuel cell electrodes. J Electrochem Soc 1997;144:2323–8.
5. Shukla AK, Ravikumar MK, Roy A, Barman SR, Sarma DD, Aricò AS, et al. Electro-oxidation of methanol in sulfuric acid electrolyte on platinized-carbon electrodes with several functional-group characteristics. J Electrochem Soc 1994;141:1517–22.
6. Mukerjee S. Particle size and structural effects in platinum electrocatalysis. J Appl Electrochem 1990;20:537–48.
7. Attwood PA, McNicol BD, Short RA. The electrocatalytic oxidation of methanol in acid electrolyte: preparation and characterization of noble metal electrocatalysts supported on pre-treated carbon-fibre papers. J Appl Electrochem 1980;10:213–22.
8. Frelink T, Visscher W, Van Veen JAR. Particle size effect of carbon supported platinum catalysts for the electrooxidation of methanol. J Electroanal Chem 1995;382:65–72.
9. Takasu Y, Iwazaki T, Sugimoto W, Murakami Y. Size effects of platinum particles on the electro-oxidation of methanol in an aqueous solution of $HClO_4$. Electrochem Commun 2000;2:671–4.
10. Watanabe M, Saegusa S, Stonehart P. High platinum electrocatalyst utilizations for direct methanol oxidation. J Electroanal Chem 1989;271:213–20.
11. Hampden-Smith M, Atanassova P, Atanassov P, Kodas T. Manufacture of electrocatalyst powders by a spray-based production platform. In: Vielstich W, Lamm A, Gasteiger H, editors. Handbook of fuel cells: fundamentals, technology, applications, volume 3. New York: Wiley, 2003.
12. Hunt AT, Cochran JK, Carter WB, inventors; Georgia Tech Research Corp, assignee. Combustion chemical vapor deposition of films and coatings. United States patent US 5652021, 1997 Jul 29.
13. Kodas TT, Hampden-Smith MJ. The chemistry of metal CVD. New York: VCH, 1994.
14. Maric R, Roller J, Neagu R, Fatih K. Low Pt thin cathode layer catalyst layer by reactive spray deposition technology. In: 2007 Fuel cell seminar & exposition. ECS Transactions 2008;12. In press.
15. Shaijumon MM, et al. Synthesis of multi-walled carbon nanotubes in high yield using Mm based AB_2 alloy hydride catalysts and the effect of purification on their hydrogen adsorption properties. Nanotechnology 2005;16(4):518–24.
16. Shaijumon MM, Ramaprabhu S, Rajalakshmi N. Platinum/multiwalled carbon nanotubes-platinum/carbon composites as electrocatalysts for oxygen reduction reaction in proton exchange membrane fuel cell. Appl Phys Lett 2006;88(25):3105–11.
17. Kodas T, Hampden-Smith MJ. Aerosol processing of materials. New York: John Wiley & Sons, 1999: 440.
18. Hampden-Smith M, Atanassova P, Atanassov P, Kodas T. Hampden-Smith M, Atanassova P, Atanassov P, Kodas T. Manufacture of electrocatalyst powders by a spray-based production platform. In: Vielstich W, Lamm A, Gasteiger H, editors. Handbook of fuel cells: fundamentals, technology, applications. New edition, in press.
19. Benitez R, Soler J, Daza L. Novel method for preparation of PEMFC electrodes by the electrospray technique. J Power Sources 2005;151:108–13.
20. Hampden-Smith M, Atanassova P, Atanassov P, Kunze K, Napolitano P, Bhatia R, et al. Electrocatalyst powders, methods for producing powders and devices fabricated from same. United States patent US 6967183, 2005 Nov 22.

21. Debe MK. Novel catalysts, catalysts support and catalyst coated membrane methods. Chapter 45 in: Vielstich W, Lamm A, Gasteiger H, editors. Handbook of fuel cells: fundamentals, technology, applications, volume 3. New York: Wiley, 2003.

22. Debe MK. High performance matching PEM fuel cell components and pilot manufacturing processes. In: Annual progress report, fuel cells for transportation. Department of Energy, Office of Energy Efficiency and Renewable Energy, Office of Transportation Technology, 2001: 113.

23. Starz KA, Koehler, Ruth J, Vogt KM. Advanced MEA technology for mobile PEMFC applications. SAE Transactions 2002;111(3):812–17.

24. Marboe EC, inventor; Glass Science Inc, assignee. Deposition of metal on glass from metal formats. United States patent 2430520. 1947 Nov 11.

25. Rand MJ. Chemical vapor deposition of thin-film platinum. J Electrochem Soc 1973;120:686–92.

26. Rand MJ. I-V characteristics of PtSi-Si contacts made from CVD platinum. J Electrochem Soc 1975;122:811–17.

27. Gozum JE, Pollina DM, Jensen JA, Girolami GS. "Tailored" organometallics as precursors for the chemical vapor deposition of high-purity palladium and platinum thin films. J Am Chem Soc 1988;110:2688–93.

28. Chen YJ, Kaesz HD, Thridandam H, Hicks RF. Low-temperature organometallic chemical vapor deposition of platinum. Appl Phys Lett 1988;53:1591–9.

29. Kumar R, Rashidi M, Puddephatt RJ. New precursors for chemical vapour deposition of platinum and the hydrogen effect on CVD. Polyhedron 1989;8:551–9.

30. Dossi C, Bartsch A, Losi P. Chemical vapor deposition methods for the controlled preparation of supported catalytic materials. In: Proceedings of the Congress Adv Synth Methodol Inorg Chem 1991:83–91.

31. Dossi C, Psaro R, Ugo R, Zhang CZ, Sachtler WMH. Non-acidic Pd/Y zeolite catalysts from organopalladium precursors: preparation and catalytic activity in MCP reforming. J Catal 1994;149:92–9.

32. Sordelli L, Martra G, Psaro R, Dossi C, Coluccia S. Intrazeolite large palladium clusters prepared by organometallic chemical vapour deposition. J Chem Soc Dalton Trans 1996;5:720–8.

33. Tsai M, Yeh T, Tsai C. An improved electrodeposition technique for preparing platinum and platinum-ruthenium nanoparticles on carbon nanotubes directly grown on carbon cloth for methanol oxidation. Electrochem Comm 2006;8(9):1445–52.

34. Srinivasan S, Velev OA, Parthasarathy A, Manko DJ, Appleby AJ. High energy efficiency and high power density proton exchange membrane fuel cells. Electrode kinetics and mass transport. J Power Sources 1991;36:299–305.

35. Zhao X, Ohkohchi M, Wang M, Iijima S, Ichihashi T, Ando Y. Preparation of high-grade carbon nanotubes by hydrogen arc discharge. Carbon 1997;35:775–81.

36. Mukhopadhyay K, Koshio A, Sugai T, Tanaka N, Shinohara H, Konya Z, et al. Bulk production of quasi-aligned carbon nanotube bundles by the catalytic chemical vapour deposition (CCVD) method. Chem Phys Lett 1999;303:117–24.

37. Okazaki T, Shinohara H. Synthesis and characterization of single-wall carbon nanotubes by hot-filament assisted chemical vapor deposition. Chem Phys Lett 2003;376:606–11.

38. Choi YC, Shin YM, Lee YH, Lee BS, Park GS, Lee NS, et al. Controlling the diameter, growth rate, and density of vertically aligned carbon nanotubes synthesized by microwave plasma-enhanced chemical vapor deposition. Appl Phys Lett 2000;76:2367–9.

39. Kanzow H, Schmalz A, Ding A. Laser-assisted production of multi-walled carbon nanotubes from acetylene. Chem Phys Lett 1998;295:525–30.

40. Nikolaev P, Bronikowski MJ, Kelley Bradley R, Rohmund F, Colbert DT, Smith KA, et al. Gas-phase catalytic growth of single-walled carbon nanotubes from carbon monoxide. Chem Phys Lett 1999;313:91–7.
41. Sugai T, Okazaki T, Yoshida H, Shinohara H. Syntheses of single- and double-wall carbon nanotubes by the HTPAD and HFCVD methods. New J Phys 2004;6:21–32.
42. Suekane O, Nagasaka T, Kiyotaki K, Nosaka T, Nakayama Y. Rapid growth of vertically aligned carbon nanotubes. Jpn J Appl Phys 2004;43:L1214–16.
43. Wang C, Waje M, Wang X, Tang JM, Haddon RC, Yan Y. Proton exchange membrane fuel cells with carbon nanotube based electrodes. Nanoletters 2004;4(2):345–8.
44. Lin Y, Cui X, Yen CH, Wai CM. PtRu/carbon nanotube nanocomposite synthesized in supercritical fluid: a novel electrocatalyst for direct methanol fuel cells. Langmuir 2005;21(24):11474–9.
45. Liu Z, Lee JY, Chen W, Han M, Gan LM. Physical and electrochemical characterizations of microwave-assisted polyol preparation of carbon-supported PtRu nanoparticles. Langmuir 2004;20(1):181–7.
46. Liang Y, Zhang H, Yi B, Zhang Z, Tan Z. Preparation and characterization of multi-walled carbon nanotubes supported PtRu catalysts for proton exchange membrane fuel cells. Carbon 2005;43(15):3144–52.
47. Han KI, Lee JS, Park SO, Lee SW, Park YW, Kim H. Studies on the anode catalysts of carbon nanotube for DMFC. Electrochim Acta 2004;50(2–3):791–4.
48. Yang J, Liu D-J, Gosztola DJ. Functionalized aligned carbon nanotubes as a novel catalytic electrode for PEM fuel cells. 2006 Fuel Cell Seminar; 2006 Nov 13–17; Honolulu, HI.
49. Dai H, Rinzler AG, Nikolaev P, Thess A, Colbert DT, Smalley RE. Single-wall nanotubes produced by metal-catalyzed disproportionation of carbon monoxide. Chem Phys Lett 1996;260:471–5.
50. Franklin NR, Li Y, Chen RJ, Javey A, Dai H. Patterned growth of single-walled carbon nanotubes on full 4-inch wafers. Appl Phys Lett 2001;79:4571–3.
51. Hata K, Futaba DN, Mizuno K, Namai T, Yumura M, Iijima S. Water-assisted highly efficient synthesis of impurity-free single-walled carbon nanotubes. Science 2004;306:1362–4.
52. Bladh K, Falk LKL, Rohmund F. On the iron-catalysed growth of single-walled carbon nanotubes and encapsulated metal particles in the gas phase. Appl Phys A 2000;70:317–22.
53. Nikolaev P, Bronikowski M, Bradley R, Rohmund F, Colbert D, Smith K, et al. Gas-phase catalytic growth of single-walled carbon nanotubes from carbon monoxide. Chem Phys Lett 1999;313:91–7.
54. Okada S, Saito S, Oshiyama A. New metallic crystalline carbon: three dimensionally polymerized C_{60} fullerite. Phys Rev Lett 2000;85:5672.
55. Kim Y-N, inventor; KH Chemicals Co Ltd, assignee. Preparation of carbon nanotubes. United States patent US 7329398. 2008 Feb 12.
56. Teixeira da Silva V, Passos FB, editors. Selected contributions of the XX Ibero-American symposium of catalysis. Catal Today 2008;133–135:1–930.
57. Nasibulin AG, Pikhitsa PV, Jiang H, Kauppinen EI. Correlation between catalyst particle and single-walled carbon nanotube diameters. Carbon 2005;43:2251–7.
58. Baker RTK. Catalytic growth of carbon filaments. Carbon 1989;27:315–19.
59. Rodriguez NM. Review of catalytically grown carbon nanofibers. J Mater Res 1993;8:3233–5.
60. Tibbetts GG. Growth of carbon fibres in stainless steel tubes by natural gas pyrolysis. J Cryst Growth 1984;66:632–8.

61. Chhowalla M, Teo KBK, Ducati C, Rupesinghe NL, Amaratunga GAJ, Ferrari AC, et al. Growth process conditions of vertically aligned carbon nanotubes using plasma enhanced chemical vapor deposition. J Appl Phys 2001;90:5308–13.

62. Teo KBK, Lacerda RG, Yang MH, Teh AS, Robinson LAW, Dalal SH, et al. Carbon nanotube technology for solid state and vacuum electronics. IEE Proc Circuits Devices Syst 2004;151(4):443–51.

63. Cheung CL, Kurtz A, Park BH, Lieber CM. Diameter-controlled synthesis of carbon nanotubes. J Phys Chem B 2002;106:2429–38.

64. Tsai MC, Yeh TK, Tsai CH. An improved electrodeposition technique for preparing platinum and platinum-ruthenium nanoparticles on carbon nanotubes directly grown on carbon cloth for methanol oxidation. Electrochem Comm 2006;8(9):1445–52.

65. Gloaguen F, Léger JM, Lamy C. Electrocatalytic oxidation of methanol on platinum nanoparticles electrodeposited onto porous carbon substrates. J Appl Electrochem 1997;27:1052–60.

66. Beden B, LeÂger JM, Lamy C. Electrocatalytic oxidation of oxygenated aliphatic organic compounds at noble metal electrodes. In: Modern aspects of electrochemistry, volume 22. Bockris, JO'M, Conway BE, White RE, editors. New York: Plenum Press, 1992: 97–264.

67. An G, Yu P, Mao L, Sun Z, Liu Z, Miao S, et al. Synthesis of PtRu/carbon nanotube composites in supercritical fluid and their application as an electrocatalyst for direct methanol fuel cells. Carbon 2007;45(3):536–42.

68. Watanabe M, Zhu YM, Igarashi H, Uchida H. Mechanism of CO tolerance at Pt-alloy anode catalysts for polymer electrolyte fuel cells. Electrochem 2000;68(4):244–51.

69. Debe MK, Haugen GM, Steinbach AJ, Thomas JH III, Ziegler RJ, inventors; Minnesota Mining and Manufacturing Company, assignee. Catalyst for membrane electrode assembly and method of making. United States patent US 5879827. 1999 Mar 9.

70. Debe MK, Haugen GM, Steinbach AJ, Thomas JH III, Ziegler RJ, inventors; 3M Innovative Properties Company, assignee. Catalyst for membrane electrode assembly and method of making. United States patent 6040077. 2000 Mar 21.

71. Madler L, Kammler HK, Mueller R, Pratsinis SE. Controlled synthesis of nanostructured particles by flame spray pyrolysis. J Aerosol Sci 2002;33(2):369–89.

72. Johannessen T, Pratsinis SE, Livbjerg H. Computational fluid-particle dynamics for the flame synthesis of alumina particles. Chem Eng Sci 2000;55:177–88.

73. Miquel FP, Katz JFJF. Formation and characterization of nanostructured V-P-O particles in flames: a new route for the formation of catalysts. J Mater Res 1994;9:746–75.

74. Mosleh M. Preparation of micro porous ceramic membranes by flame generated aerosol nano-particles [dissertation]. Lyngby: Technical University of Denmark, 2004.

75. Mueller R, Mädler L, Pratsinis SE. Nanoparticle synthesis at high production rates by flame spray pyrolysis. Chem Eng Sci 2003;58(10):1969–76.

76. Schulz H, Mädler L, Strobel R, Jossen R, Pratsinis SE, Johannessen T. Independent control of metal cluster and ceramic particle characteristics during one-step synthesis of Pt/TiO_2. J Mater Res 2005;20(10):2568–77.

77. Strobel R, Pratsinis SE. Flame aerosol synthesis of smart nanostructured materials. J Mater Chem 2007;174743–56.

78. Hansen JP, Jensen JR, Livbjerg H, Johannessen T. Synthesis of ZnO particles in a quench-cooled flame reactor. AIChE J 2001;47:2413–18.

79. Johannessen T, Koutsopoulos S. One-step flame synthesis of an active Pt/TiO_2 catalyst for SO_2 oxidation—a possible alternative to traditional methods for parallel screening. J Catal 2002;205(2):404–8.

80. Johannessen T, Jensen JR, Mosleh M, Johansen J, Quaade U, Livbjerg H. Flame synthesis of nanoparticles applications in catalysis and product/process engineering. Chem Eng Res Des 2004;82(A11):1444–52.
81. Garijo EG, Jensen AD, Glarborg P. Reactivity of coal char in reducing NO. Combust Flame 2004;136(1):2249–53.
82. Windeler RS, Friedlander SK, Lehtinen KEJ. Production of nanometer-sized metal oxide particles by gas phase reaction in a free jet. I: Experimental system and results. Aerosol Sci Technol 1997;27:174–9.
83. Breitkopf R, Hwang J, Maniei F, Hunt A, Faguy P. Carbon supported Pt nanomaterials for fuel cell applications using combustion chemical vapor condensation. NSTI Nanotechnology Conference & Trade Show; 2003 Feb 23–27; San Francisco, CA.
84. Maric R, Roller J, Fatih K, Neagu R, Tuck A. Low Pt thin cathode layer catalyst layer by reactive spray deposition technology. 2007 Fuel Cell Seminar & Exposition; 2007 Oct 15–19; San Antonio, TX.
85. Chakraborty D, Chorkendorff I, Johannessen T. Metamorphosis of the mixed phase PtRu anode catalyst for direct methanol fuel cells after exposure of methanol: In situ and ex situ characterizations. J Power Sources 2007;173(1):110–20.
86. Jensen MB. Anode optimization for polymer electrolyte fuel cells—with flame spray pyrolysis deposited catalytic particles [dissertation]. Lyngby: Technical University of Denmark, 2005.
87. Hunt AT, Carter WB, Cochran JK Jr. Combustion chemical vapor deposition: a novel thin film deposition techniques. Appl Phys Lett 1993;63(2):266–8.
88. Hunt AT, Cochran JK, Carter WB, inventors; Georgia Tech Research Corporation, assignee. Combustion chemical vapor deposition of films and coatings. United States patent US 5652021. 1997 Jul 29; Hunt AT, Hwang TJ, Shao H, inventors; Georgia Tech Research Corporation, assignee. Combustion chemical vapor deposition of phosphate films and coatings. United States patent US 5858465. 1999 Jan 12; Hunt AT, Cochran JK, Carter WB, inventors; Georgia Tech Research Corporation, assignee. Method for the combustion chemical vapor deposition of films and coatings, United States patent US 5863604. 1999 Jan 26; Hunt AT, Cochran JK, Carter WB, inventors; Georgia Tech Research Corporation, assignee. Method for the combustion chemical vapor deposition of films and coatings, United States patent US 6013318. 2001 Jan 11.
89. De Levie R. The influence of surface roughness of solid electrodes on electrochemical measurements. Electrochim Acta 1965;10:113–130.
90. De Levie R. On porous electrodes in electrolyte solutions—IV. Electrochim Acta 1964;9:1231–45.
91. NRC-IFCI internal report II, RSDT technology for a thin, low Pt loading catalyst, March 2007.
92. Kolobov AV, Wilhelm F, Rogalev Shima AT, Tominaga J. Thermal decomposition of sputtered thin PtO_x layers used in super-resolution optical disks. Appl Phys Lett 2005;86(12):1909–18.
93. NRC-IFCI internal report I, RSDT technology for a thin, low Pt loading catalyst, January 2007.
94. Peuckert M. XPS investigation of surface oxidation layers on a platinum electrode in alkaline solution. Electrochim Acta 1984;29(10):1315–20.
95. Lamy-Pitra E, Barbier J. Platinum modified by electrochemical deposition of adatoms. Appl Catal A 1997;149:49–87.
96. Lin R, Shih S. Kinetic analysis of the hydrogen oxidation reaction on Pt-black/Nafion electrode. J SolidState Electrochem 2006;10(4):243–9.

21

Catalyst Layer/MEA Performance Evaluation

Jianlu Zhang and Jiujun Zhang

21.1 Introduction

The membrane electrode assembly (MEA) is a key unit of proton exchange membrane (PEM) fuel cells, including direct methanol fuel cells (DMFCs). In general, the MEA is composed of an anode gas diffusion layer (GDL), an anode catalyst layer, a membrane (the PEM), a cathode catalyst layer, and a cathode gas diffusion layer. The MEA materials, structures, components and fabrication technologies have strong effects on the corresponding fuel cell performance. In particular, the catalyst layers, where the electrochemical reactions take place, are the most important components. Theoretically, in an ideal catalyst layer all catalyst particle sites would be accessible to the reactant gas (H_2 or O_2), protons, and electrons. In order to achieve this, the distributions of the electron conductor, proton conductor, catalyst sites, and gas pores should be uniform in a catalyst layer.

Over the past several decades, many efforts have been made to develop high-performance PEM fuel cells. MEA performance with advanced catalyst layers has been significantly improved by employing different fabrication methods [1–4], changing the catalyst layer structures [5–11], and using different components [5–8]. During PEM fuel cell (PEMFC) performance optimization, how to evaluate catalyst layers and their corresponding MEAs becomes critical. The major purpose of such an evaluation is to understand the relationship between fuel cell performance and MEA component structures/compositions. Based on this understanding, catalyst layer/MEA optimization with respect to performance can be carried out in terms of materials used, component compositions, and fabrication parameters. One example is identifying various cell voltage losses in order to determine whether improvements can be achieved via optimization of the electrode/membrane structures and the diffusion medium properties. Through optimizing the catalyst layers and MEAs, catalyst utilization can be improved, gas diffusion overpotential reduced, and membrane ohmic losses decreased, while water management inside the catalyst layers/MEAs can also be improved. Therefore, catalyst layer/MEA evaluation is a necessary step in fuel cell development. Accordingly, many physical-chemical and electrochemical methods

have been developed to evaluate the performance of the catalyst layer/MEA. In this chapter, the principles and methods of catalyst layer/MEA evaluation will be introduced, with some detailed analysis.

21.2 Theoretical Analysis

21.2.1 Open Circuit Voltage (OCV) of the PEMFC

For an electrochemical cell, the electrical work, W_e, is equal to the change in the Gibbs free energy, ΔG between products and reactants:

$$W_e = -\Delta G \tag{21.1}$$

In general, the electrical work (W_e) produced by the electrochemical reaction is the product of the charge (Q) and the cell voltage (E):

$$W_e = QE \tag{21.2}$$

The total charge transferred in this electrochemical reaction can be calculated according to Equation 21.3:

$$Q = nNq \tag{21.3}$$

where n is the number of electrons transferred per reactant molecule during the electrochemical reaction, N is Avogadro's number (6.022×10^{23}), and q is the charge of one electron (1.602×10^{-19} C/e). It is known that the product of N and q is Faraday's constant, and the value is 96487 C/mol·e. Therefore, the electrical work can be expressed as Equation 21.4:

$$W_e = nFE \tag{21.4}$$

Combining (21.4) and (21.1), an alternative expression is obtained in Equation 21.5:

$$\Delta G = -nFE \tag{21.5}$$

Fuel cells are electrochemical devices that convert chemical energy directly to electrical energy and heat energy. Equation 21.5 only represents the electrical energy portion; the heat energy portion will not be pursued in this discussion. Based on thermodynamic considerations, an electrochemical reaction normally produces about 70–80% electrical energy and 20–30% heat energy. For a typical PEM fuel cell running on hydrogen and air, the electrode reactions occurring at the anode and the cathode, respectively, are as follows:

$$H_2 \leftrightarrow 2H^+ + 2e^- \tag{21.6}$$

$$O_2 + 4H^+ + 4e^- \leftrightarrow 2H_2O \tag{21.7}$$

At standard conditions (25 °C, 1 atm), the anode electrode potential (E_a^0) is 0.0 V (vs. standard hydrogen electrode (SHE)) and the cathode electrode potential (E_c^0) is 1.229 V (vs. SHE). The protons generated at the anode transport across the membrane to the cathode. The electrons generated during hydrogen oxidation pass through the external circuit to the cathode, where they complete the electrochemical reduction of oxygen and produce water. The overall fuel cell reaction is:

$$2H_2 + O_2 \rightarrow 2H_2O \tag{21.8}$$

The fuel cell voltage at an open circuit condition is called the open circuit voltage (OCV). This OCV is defined as the difference between the standard potentials of the cathode (E_c^0) and the anode (E_a^0), and its value is 1.229 V at standard conditions. Note that this OCV is strongly dependent on the temperature and pressure. If the fuel cell is loaded with an electrical current, the cell voltage will be lower than the OCV due to the electrode polarizations (or electrode overpotentials).

In general, a fuel cell OCV, E^{OCV}, can be expressed as Equation 21.9:

$$E^{OCV} = E_c^r - E_a^r \tag{21.9}$$

where E_c^r and E_a^r are the Nernst electrode potentials for the cathode and anode, respectively. They can be expressed in the Nernst forms shown in Equations 21.10 and 21.11:

(for the cathode reaction: $O_2 + 4H^+ + 4e^- \rightarrow 2H_2O$)

$$E_c^r = E_c^0 + \frac{RT}{4F}\ln(P_{O_2}[H^+]^4) \tag{21.10}$$

(for the anode reaction: $H_2 \rightarrow 2H^+ + 2e^-$)

$$E_a^r = E_a^0 + \frac{RT}{2F}\ln(\frac{[H^+]^2}{P_{H_2}}) \tag{21.11}$$

In Equations 21.10 and 21.11, as defined before, E_c^0 and E_a^0 are the standard cathode and anode potentials, respectively. E_c^0 is a temperature-dependent constant

(= $1.229 - 0.000846 \times (T - 298.15)$ [12]), E_a^0 is zero at any temperature, P_{O_2} and P_{H_2} are the partial pressures (atm) of O_2 and H_2, respectively, and $[H^+]$ is the molar concentration of protons (mol.L^{-1}). A theoretical OCV can be calculated by deriving Equations 21.10 and 21.11 to yield Equation 21.12 [13]:

$$E_{\text{theor}}^{\text{OCV}} = 1.229 - 0.000846(T - 298.15) + \frac{RT}{4F} \ln[P_{O_2}(P_{H_2})^2] \qquad (21.12)$$

21.2.2 Exchange Current Density, i_0

The exchange current density can be understood as a reaction rate at either the forward or the backward reaction of an equilibrium reaction at the reversible potential (when overpotential is zero by definition). At the reversible potential the reaction is in equilibrium, meaning that the forward and backward reactions progress at the same rates.

For a redox reaction:

$$O + ne^- \Leftrightarrow R \qquad (21.13)$$

at equilibrium, there is no net current flow. However, at the interface of electrode/solution, a dynamic equilibrium exists and the electron transfer processes are still going on in both directions. Because both processes occur at equal rates, the cathodic current is balanced by the anodic current. This ongoing current in both directions is called the exchange current density (i_0). The net current density is the difference between the cathodic and anodic current densities. A system with a large exchange current density has fast kinetics and can respond rapidly to a change in potential. Otherwise, the system has a sluggish electron transfer rate.

In PEM fuel cells, the exchange current density for the electrochemical oxygen reduction reaction (ORR, $\sim 10^{-8} - 10^{-9}$ A cm^{-2}) is much smaller than that of the hydrogen oxidation reaction (HOR, $\sim 10^{-3} - 10^{-4}$ A cm^{-2}). Due to the larger HOR exchange current density, the HOR at the anode Pt nanoparticle/PEM interface is much faster than the ORR at the cathode interface [14]. In other words, the overpotential for the HOR is negligibly small compared with that of the ORR when the anode is adequately hydrated. The overall electrochemical kinetics of PEMFCs is therefore dominated by the relatively slow oxygen reduction reaction.

21.2.3 Tafel Slope, b

The relationship between the net current density, the exchange current density, the overpotential, and the electron transfer coefficient is given by the Butler-Volmer equation for either cathode or anode reaction:

$$i = i_f - i_b = i_0 (e^{\frac{\alpha n_\alpha F \eta}{RT}} - e^{-\frac{(1-\alpha) n_\alpha F \eta}{RT}}) \qquad (21.14)$$

where, i is the net current density, i_f is the current density in the forward direction of Reaction 21.13, i_b is the current density in the backward direction, i_o is the exchange current density, α is the electron transfer coefficient, n_a is the electron transfer number in the rate determining step, and η is the overpotential. The overpotential is defined as the potential difference between the electrode potential at a certain current density and the electrode potential at zero current density (reversible potential). If the forward reaction is dominant the overpotential can be expressed as η_f, and if the backward reaction is dominant, as η_b.

At low overpotential (< 30 mV), Equation 21.14 can be written as Equation 21.15:

$$i = i_o \frac{nF\eta_f}{RT} \qquad \text{(forward direction)} \qquad (21.15)$$

$$i = i_o \frac{nF\eta_b}{RT} \qquad \text{(backward direction)} \qquad (21.16)$$

Equations 21.15 and 21.16 indicate that net current density varies linearly with overpotential. At high overpotential, if the forward reaction rate is much higher than that of the backward reaction, i.e., $i_f \gg i_b$, Equation 21.14 can be simplified as Equation 21.17:

$$i = -i_f - i_o \exp(-\alpha n_a F \eta_f / RT) \qquad (21.17)$$

Taking ln on both sides of Equation 21.17, 21.18 can then be obtained:

$$\ln i = \ln i_f = \ln i_o + (-\frac{\alpha n_\alpha F}{RT} n_f) \qquad (21.18)$$

Equation 21.18 applies to the forward reaction; a similar expression for the backward reaction is expressed in Equation 21.19:

$$\ln i = \ln i_f = \ln i_o + \frac{\alpha n_\alpha F}{RT} n_f \qquad (21.19)$$

According to Equations 21.18 and 21.19, overpotentials can be expressed as Equations 21.20 and 21.21 for forward and backward reactions, respectively:

$$\eta_f = \frac{2.303 RT}{\alpha n F} \log i_o - \frac{2.303 RT}{\alpha n F} \log i \qquad \text{(forward direction)} \qquad (21.20)$$

$$\eta_b = \frac{2.303RT}{\alpha nF}\log i_o - \frac{2.303RT}{\alpha nF}\log i \quad \text{(backward direction)} \qquad (21.21)$$

These equations have been expressed as an empirical equation by Tafel:

$$\eta = a + b\log i \qquad (21.22)$$

In Equation 21.22, b is the Tafel slope. In electrochemistry, the graph of the logarithm of the current density i against the overpotential η in the high overpotential limit is called the Tafel plot [15], as shown in Figure 21.1. The slope b is 2.303 RT/αn_αF. The intercept at $\eta = 0$ gives the exchange current density, i_0.
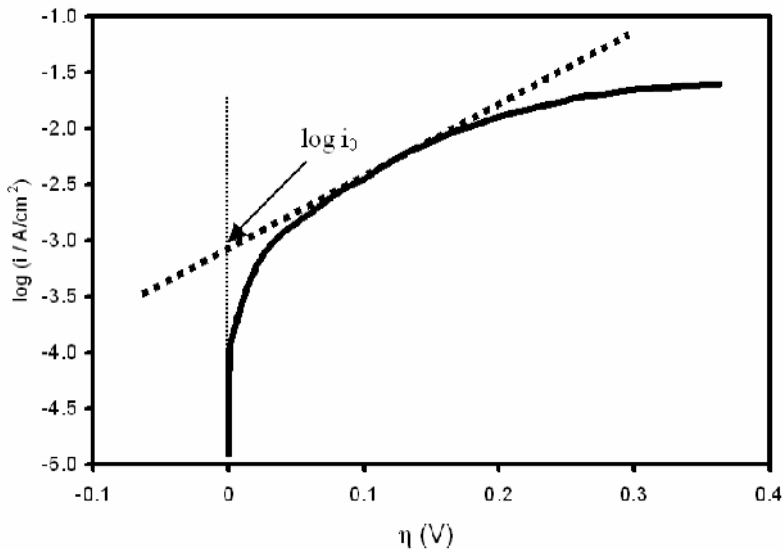
Figure 21.1. Plot of η vs. log of anodic current with $\alpha = 0.5$

For both the HOR and the ORR, the dependence of b on temperature can be derived by differentiating Equation 21.23:

$$\frac{\partial b}{\partial T} = -\frac{2.3R}{\alpha n_\alpha F} \qquad (21.23)$$

Assuming that the reaction mechanism and α are independent of temperature, b varies linearly with temperature. For $\alpha n_\alpha = 1$, $\frac{\partial b}{\partial T} \approx 0.2mV\,K^{-1}$. However, several groups [16–19] reported two sets of Tafel slopes that are differentiated by the current density regime on a Pt electrode. One Tafel parameter corresponds to the ORR at a Pt oxide-covered surface (Temkin adsorption conditions, low current

density, b = 60 mV/decade) and the other to the ORR at a Pt oxide-free surface (Langmuirian conditions, high current density, b = 120 mV/decade). Experimentally, the Tafel slope of the ORR process was found to increase with increasing temperature in the low current density region, while it was independent of temperature in the high current density region [19].

21.2.4 Polarization Curve Analysis

Figure 21.2 shows a typical polarization curve (or current-voltage curve) of PEMFCs. This curve results from both the anodic HOR and the cathodic ORR reactions. The actual cell voltage is much lower than the ideal cell voltage and the theoretical cell voltage. When the current is drawn from a fuel cell, the actual cell voltage will drop from its ideal due to several types of irreversible losses, as shown in Figure 21.2. The drop is mainly caused by mixed potential and fuel crossover, activation overpotential, ohmic overpotential, as well as mass transfer (concentration) overpotential.
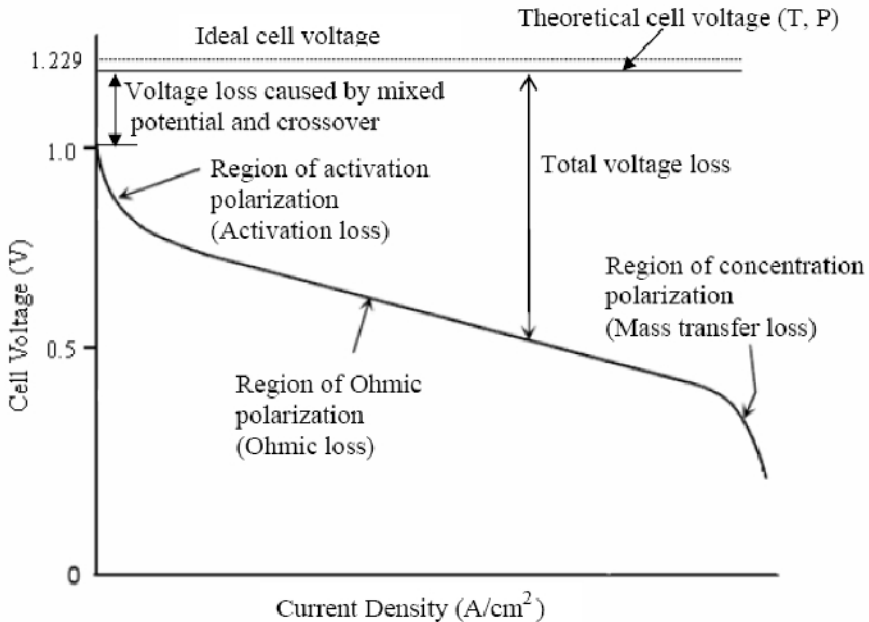
Figure 21.2. Typical polarization curve of a PEM fuel cell

1) *Voltage drop caused by mixed potential and fuel crossover.* The mixed potential at electrodes is due to unavoidable parasitic reactions that tend to lower the equilibrium electrode potential. For a mixed cathode potential, a local-cell mechanism has been put forward to explain the Pt-O_2 reaction mechanism at the electrode in an O_2-saturated acidic solution [20, 21]. The mixed potential is composed of both the cathodic O_2/H_2O reaction potential ($O_2 + 4H^+ + 4e^- \leftrightarrow 2H_2O$,

E_c^o = 1.229 V (vs. NHE)), and the Pt/PtO anode reaction potential (Pt + H_2O ↔ PtO + $2H^+$ + $2e^-$, $E_{Pt/PtO}^o$ = 0.88 V (vs. NHE)). The local electrochemical reaction on the Pt surface could create a PtO surface coverage of 30%, with 70% of the surface remaining as pure Pt. At steady-state mixed potential, a complete layer of Pt-O can never be achieved in order to keep the reaction of Pt to PtO continuous, due to the diffusion of Pt-O into the bulk metal. The reported mixed cathode potential is around 1.06 V (vs. NHE) at standard conditions [20, 21] with an O_2 partial pressure dependence of 15 mV·atm^{-1}. Furthermore, the H_2 that has crossed over through the membrane from anode to cathode can form a local half-cell electrochemical reaction on the cathode, such as H_2 ↔ $2H^+$ + $2e^-$, resulting in a mixed cathode potential similar to that of the half-cell reaction (Pt + H_2O ↔ PtO + $2H^+$ + $2e^-$). The mixed potentials are the dominant sources of voltage losses at open circuits [13].

2) *Activation loss (overpotential).* Activation overpotential (η_{act}) is caused by the kinetics of the electrode reactions. It is associated with both sluggish reaction kinetics and low catalyst activity. The effects of these losses are most pronounced at low current densities (< 0.1 A/cm^2). Minimization of the activation overpotential thus requires maximization of the catalyst area available for reactions and improvement of catalyst activity.

3) *Ohmic loss (overpotential).* Ohmic overpotential (η_{ohm}) is caused by ionic and electronic resistances. It consists of the ionic resistance of the membrane plus the bulk and contact electronic resistances of the construction materials. Because both the electrolyte and the fuel cell electrodes obey Ohm's law, the ohmic losses can be expressed by the equation

$$\eta_{ohm} = IR_{ohm} \qquad (21.24)$$

where I is the fuel cell current density flowing through the cell and R_{ohm} is the total cell ohmic resistance, which includes electronic ($R_{electronic}$), ionic (R_{ionic}), and contact ($R_{contact}$) resistances:

$$R_{ohm} = R_{electronic} + R_{ionic} + R_{contact} \qquad (21.25)$$

In relative terms, the largest single source of ohmic losses is from the membrane. A simple way to determine the ohmic resistance is employ the impedance spectroscopic method. In a fuel cell impedance spectrum, the ohmic resistance is the real value of the impedance of the point for which the imaginary impedance is zero at the maximum frequency. The effects of these losses are most pronounced at intermediate current densities. Minimizing the ohmic losses requires effective water management in the membrane, excellent electron conductive materials, and minimal contact resistance.

4) *Mass transfer loss (overpotential).* Mass transfer (or concentration) overpotential (η_{conc}) is caused by the concentration gradients of the reactants. As shown in Figure 21.2, at high current densities the current-voltage curve begins to

bend down sharply. This is due to mass diffusion limitations on the electrodes (especially on the cathode), resulting in a lack of reactant reaching the catalyst sites. The effects of these losses are most pronounced at high current densities (> 0.5 A/cm^2). To minimize the concentration overpotential requires good electrode structure as well as effective water management in the catalyst layer and the gas diffusion layer.

The total overpotential (η_{total}) of a PEM fuel cell is the sum of the anode overpotential (η_a), cathode overpotential (η_c), and ohmic overpotential (η_{ohm}), as expressed as Equation 21.26:

$$\eta_{total} = \eta_a + \eta_c + \eta_{ohm} \tag{21.26}$$

Both η_a and η_c are mainly composed of activation overpotential (η_{act}) and concentration overpotential (η_{conc}). Thus, η_{total} can also be expressed as Equation 21.27. The actual cell potential is equal to the reversible cell voltage (E_r, open circuit voltage) reduced by the voltage losses, as shown in Equation 21.28.

$$\eta_{total} = (\eta_{act} + \eta_{conc})_a + (\eta_{act} + \eta_{conc})_c + \eta_{ohm} \tag{21.27}$$

$$E_{cell} = E_r - \eta_{total} \tag{21.28}$$

Generally, the exchange current density of the anode reaction ($H_2 \rightarrow 2H^+ + 2e^-$) is approximately 5–6 orders of magnitude larger than that of the cathode reaction ($\frac{1}{2}O_2 + 2H^+ + 2e^- \rightarrow H_2O$). Therefore, apart from the ohmic resistance, the majority of the fuel cell voltage losses occur on the cathode due to the sluggish kinetics of the oxygen reduction reaction. In most cases, the anode overpotential is negligible compared to that of the cathode. Therefore, the polarization curve over the entire current density range can be semi-empirically expressed in a general form as Equation 21.29 [22]:

$$E = E^r + b\log(i_o) - b\log(i) - Ri - m\exp(ni) \tag{21.29}$$

where E represents the cell voltage, E^r the reversible potential, b the Tafel slope, i the current density, i_0 the exchange current density of the cathodic ORR, R the cell resistance, and m and n are parameters characterizing mass transport effects.

21.3 Physical Chemistry Evaluation of Catalyst Layer

21.3.1 Pore Structure Analysis of Catalyst Layer

Due to the fuel cell reactions occurring inside the matrix catalyst layers, the reactant (gas or liquid) must pass through a gas diffusion layer (GDL) into the

catalyst layer. Therefore, a porous structure for both the catalyst layers and the GDL is necessary. A parameter, called porosity, is normally used to describe the porous structure. This parameter is also closely related to fuel cell performance. The well-known methods used to comprehensively characterize the porosity of electrodes are mercury porosimetry, capillary flow porometry, and standard porosimetry [23].

The effective diffusivity of the gas phase in porous media, D_{eff}, is related to porosity (ε) and tortuosity (τ) according to the Bruggeman correlation [24], as shown in Equation 21.30:

$$D_{eff} = D^0 [\varepsilon(1-S)]^\tau \tag{21.30}$$

where D^0 is the diffusion coefficient and S is the liquid saturation. As for the liquid phase, the driving force, capillary pressure (P_c), can be expressed as Equation 21.31 [25]:

$$P_c = \sigma \cos(\theta)(\varepsilon/K)^{1/2} J(S) \tag{21.31}$$

where σ presents the surface tension, θ is the contact angle, K is the absolute permeability, and $J(S)$ is the Leverett function.

The porosity of a gas diffusion layer (GDL) or a catalyst layer (CL) may be easily calculated from its real weight, the density of the solid phase, and the compressed thickness, as expressed in Equation 21.32 [26]:

$$\varepsilon = 1 - \frac{W_A}{\rho_{real} d} \tag{21.32}$$

where W_A is the real weight (g/cm^{-2}), ρ_{real} is the solid-phase density (for carbon-based materials, ρ_{real} varies between 1.6 and 1.9 g/cm^3), and d is the thickness (either compressed or uncompressed).

For a GDL or CL in PEM fuel cells, a high porosity is desirable in order to minimize the gas-phase diffusion losses, but extremely high porosities could also lead to an increase in electrode electronic resistance.

21.3.2 Protonic and Electronic Conductivity in the Catalyst Layer

High protonic and electronic conductivity are highly desirable to optimize the CL structure with respect to high fuel cell performance. The measured fuel cell voltage (V_{cell}) can be alternatively expressed as Equation 21.33:

$$V_{cell} = E^{OCV} - \eta_c - \eta_a - I_{cell} R_{cell} \tag{21.33}$$

where η_c and η_a are the cathode and anode overpotentials, respectively, I_{cell} is the fuel cell current density, and R_{cell} is the fuel cell internal resistance – which includes membrane resistance, proton transfer resistance in the catalyst layer, and all kinds of contact resistance between the fuel cell components. It can be seen from Equation 21.33 that high fuel cell internal resistance (R_{cell}) can result in low cell performance. R_{cell}, can be measured by AC impedance spectroscopy at the high end of the AC frequency. Because R_{cell} is dominated by the membrane resistance (R_m), the resistance measured by AC impedance spectroscopy at the high end of the AC frequency is usually considered to be the membrane resistance, R_m. The membrane resistance here represents the proton transfer resistance within the fuel cell membrane and indirectly reflects the membrane conductivity. Aside from their transport in the membrane, protons also need to transfer to active catalytic sites in the catalyst layer. Proton transfer within the catalyst layer can also cause proton transfer resistance in the catalyst layer ($R_{CL}^{H^+}$). This proton transfer resistance reflects the proton conductivity in the catalyst layer. Experimental studies [27–30] have already indicated that the performance of catalyst layers strongly depends on the proton conductivity. The electrolyte materials, electrolyte loading, components and structure, as well as the ratio of electrolyte (e.g., Nafion) to carbon, the temperature, and the water activity affect the proton conductivity in a catalyst layer. Moreover, the fuel cell operating conditions can also affect the proton conductivity in a catalyst layer. Zhang et al. [31] found that the proton transfer resistance was very large in a catalyst layer when the fuel cell was operated at 0% relative humidity (RH). Although a few papers [32–34] have been published on catalyst layer proton conductivity, to the best of our knowledge there is still no reliable experimental method to measure the proton conductivity of a catalyst layer separately and accurately. The electronic conductivity of the catalyst layer also depends on the used materials, the carbon loading, the components, and the structure. The electronic conductivity can be determined by the method described by Pantea et al. [35]. Using this method, Du et al. [34] measured the electronic conductivity of a catalyst layer by impedance spectroscopy measurements over the frequency range of 10–200 Hz using a SI 1260 Impedance/Gain-Phase Analyzer and found that the effective electronic conductivity decreased with an increasing Nafion volume fraction in the catalyst layers.

21.3.3 Wettability of the Catalyst Layer

Hydrophobicity and hydrophilicity play complex and critical roles in both the gas diffusion layer and the catalyst layer of a PEM fuel cell. A suitable hydrophobicity is necessary for better PEM fuel cell performance. If an electrode is too hydrophilic, the electrode is easily flooded by condensed water, resulting in a dramatic decrease in fuel cell performance. The hydrophobicity and hydrophilicity can be controlled by the choice of carbon, the ionomer/carbon ratios, the content of

the hydrophobic agent (usually PTFE), and the pre-treatment and fabrication procedures.

To date, there are two major types of catalyst layer fabrication techniques. One is to cast or spray the catalyst ink onto the gas diffusion layer to form a catalyzed GDL (CGDL), which is hydrophobic and has a thickness of about 20–50 μm; the other is to deposit or spray catalyst ink onto the proton exchange membrane to form a catalyst coated membrane (CCM), a hydrophilic layer with a thickness of 5–10 μm.
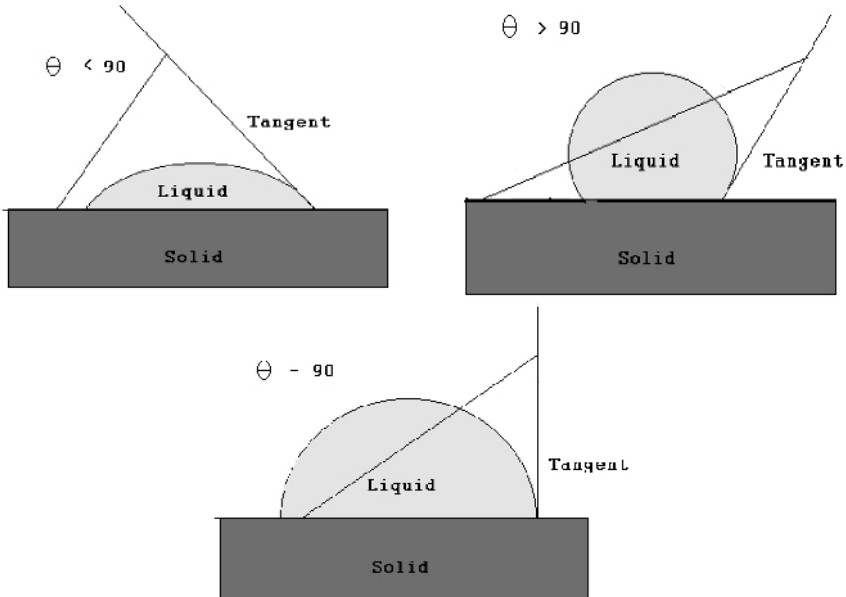
Figure 21.3. Principle of contact angle measurement [36]. (Image courtesy of KSV Instruments.)

One of the most popular experimental methods for characterizing the hydrophobicity and hydrophilicity of catalyst layers is contact angle (θ) measurement. A contact angle, θ, describes the shape of a liquid droplet resting on a solid surface. When a tangent line is drawn from the droplet to touch the solid surface, the angle between this tangent line and the solid surface is called the contact angle (θ), as can be seen in Figure 21.3 [36]. A low θ value indicates that the liquid spreads, or wets well, while high values indicate poor wetting. If the angle θ is less than 90° the liquid is said to wet the solid; if it is greater than 90° it is said to be non-wetting. A zero contact angle represents a complete wetting. The sessile drop method is the most common to measure the contact angle of a water droplet on the sample surface. The drop size should be small enough to eliminate the influence of the drop's weight (Figure 21.4).
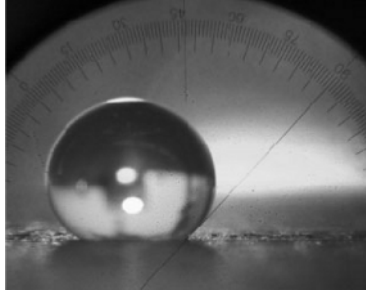
Figure 21.4. Drop of water in sessile drop measurement of contact angle [37]. (Reproduced from Wang CY. Two-phase flow and transport. In: Vielstich W, Lamm A, Gasteiger HA, editors. Handbook of fuel cells – fundamentals, technology and applications, volume 3. Chichester, England: Wiley, 2003;337–47. Copyright John Wiley & Sons Limited.)

Contact angle measurement has been broadly accepted for material surface analysis related to wetting, adhesion, and absorption. Zawodzinski and Gottesfeld [38] investigated the contact angle of water on the surface of a prehydrated Nafion membrane and found that the ionomer surface exhibited a wide range of values for the contact angle with water. Furthermore, the contact is also time-dependent: it relaxes slowly from one value to another over tens of minutes as the ionic groups re-orient to the changing environment. Brack [39] also studied the membrane properties by means of contact angle measurement and found that the contact angle increased with dehydration of the membrane. Yu and Ziegler [40] characterized the catalyst layers using CCM. They found that the first attachment of a water droplet at the catalyst layer surface showed a relatively high contact angle, and then the contact angle decreased with time, as shown in Figure 21.5 [40]. This could be due to water absorption into the polymer materials in the porous catalyst layer. They also found that a CCM with a higher contact angle showed better fuel cell performance at 0.8 A/cm^2 due to a lower mass transport resistance. Furthermore, they found that the contact angles differed slightly with water droplet location due to the non-uniform distribution of pore size in the catalyst layer.
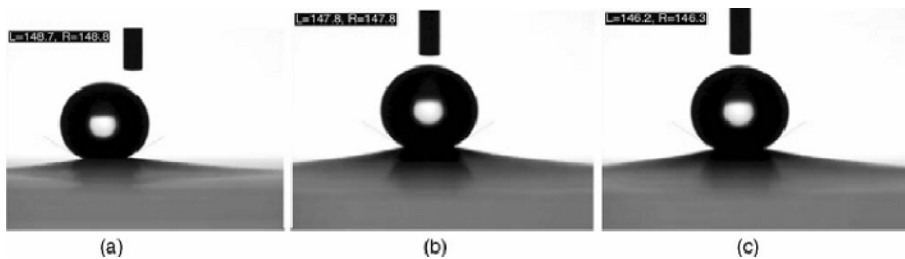
Figure 21.5. The time-dependent contact angle of a catalyst layer with wetting process: (a) 0 s, for the first attachment of the water droplet at the catalyst layer surface, the contact angle is 148.7°; (b) 60 s, the measured contact angle is 147.8°; (c) 100 s, the measured contact angle is 146.2° [40]. (Reprinted from Electrochimica Acta, 51(7), Yu HM, Ziegler C, Oszcipok M, Zobel M, Hebling C, Hydrophilicity and hydrophobicity study of catalyst layers in proton exchange membrane fuel cells, 1199–207, ©2006, with permission from Elsevier.)

Yu and Ziegler [40] also employed an environmental scanning electron microscope (ESEM method) as a contact angle analysis tool to investigate hydrophobicity and hydrophilicity on inhomogeneous materials. They measured the contact angles of the catalyst layer before and after MEA evaluation, and found that the catalyst layer became more hydrophilic after MEA evaluation; thus, this hydrophilic increase could be the cause of lower fuel cell performance.

21.4 Catalyst Layer Evaluation in a Half-cell

21.4.1 Rotating Disk Electrode (RDE) Test

The rotating disk electrode method (RDE) has been widely used for electrochemical analysis and evaluation, as it can ensure an electrode reaction under well-described hydrodynamic conditions. Recently, with the development of PEM fuel cells, it has been widely used to screen the activity of some electrocatalysts (e.g., Pt-based, non-noble catalysts) towards fuel cell reactions, such as oxygen reduction [41–44], hydrogen oxidation [45, 46], methanol oxidation [47, 48], and CO tolerance [49] in simulated fuel cell environments. Thin-film RDE [50, 51] and porous RDE [43] are the types commonly used in the study of PEM fuel cells. A porous RDE can usually be prepared by spreading a certain amount of catalyst ink onto a glass carbon disk, after which the catalyst-ink-covered disk is dried at room temperature to evaporate the solvents. The thickness of the catalyst layer formed is calculated approximately according to the loading and density of the catalyst, and the area of the glass carbon disk. The catalyst ink is usually prepared by mixing the electrocatalyst, the electrolyte (e.g., Nafion), and the solvent in a certain ratio. In this method, the glass carbon disk can be covered by a single layer, in which the catalyst and the electrolyte are homogeneously distributed. This situation is comparable to the simulated "agglomerate" model of a fuel cell electrode. For a thin-film RDE, the glass carbon disk is usually covered by two layers. One is the inner layer of the catalyst and the other is the Nafion outer layer. In this case, the reactant (O_2 or H_2) first diffuses through a Nafion film and then reacts at the catalyst surface. This situation is comparable to the simulated "thin-film" model of fuel cell electrodes.

Typical examples discussed below can help us gain a better understanding of the application of RDEs. Jiang et al. [44] studied the ORR at a rotating disk electrode with multiple small potential steps. Figure 21.6 shows a serial of current-potential curves for the ORR at a HT-FeTPP/CoTPP/PG rotating disk electrode in an O_2-saturated 0.5 M sulfuric acid electrolyte. With increasing rotation rate, the catalytic current increases. The kinetic analysis of the ORR at the catalyst coated RDE can be carried out by the Koutecky-Levich equation:

$$\frac{1}{i} = \frac{1}{i_k} + \frac{B}{\omega^{1/2}}$$

(21.34)

where i and i_k are the catalytic current density and the kinetic current density, respectively, B is the Koutecky-Levich slope, and ω is the rotating rate. As shown in Figure 21.7, all plots are straight lines. When the electrode potential is moved in the cathodic direction, the intercept becomes smaller, suggesting that the kinetic process for the catalytic oxygen reduction reaction at the catalyst coated electrode speeds up.
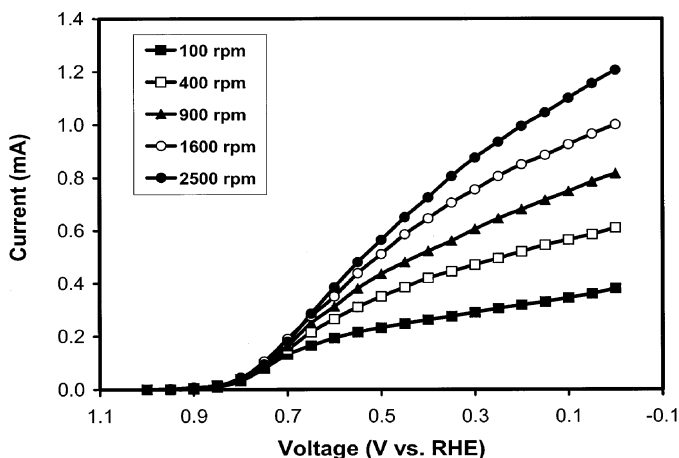
Figure 21.6. Polarization curves at various rotation rates for oxygen reduction at a HT-FeTPP/CoTPP-coated rotating disk electrode in O_2-saturated 0.5 M H_2SO_4 solution [44]. (Reprinted from Electrochimica Acta, 45(24), Jiang R, Chu D, Multiple small potential steps at a rotating disk electrode and applications, 4025–30, ©2000, with permission from Elsevier.)
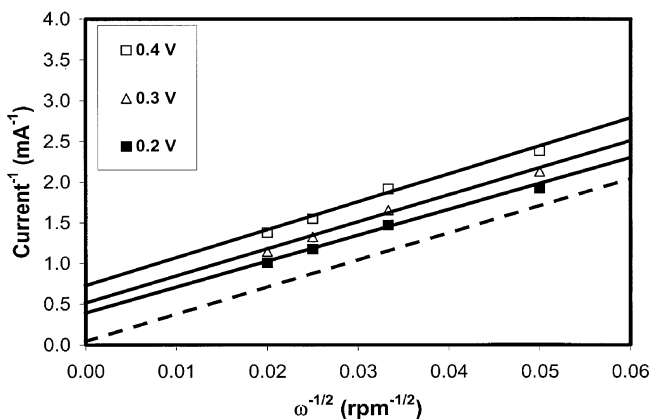
Figure 21.7. Koutecky-Levich plot for oxygen reduction at a HT-FeTPP/CoTPP-coated rotating disk electrode in O_2-saturated 0.5 M H_2SO_4 solution. Catalyst loading: 2.0 mg. The dashed line shows calculated results for the O_2 4-electron reduction by diffusion process [44]. (Reprinted from Electrochimica Acta, 45(24), Jiang R, Chu D, Multiple small potential steps at a rotating disk electrode and applications, 4025–30, ©2000, with permission from Elsevier.)

Gasteiger et al. [45] studied H_2 oxidation on a rotating disk electrode with Pt, Ru, and Pt-Ru catalysts. As shown in Figure 21.8 (a), with an increase in rotation rate, the catalytic current density also increases. The inverse of the intercept of the Levich line (as shown in the insert of Figure 21.8 (a)), 8.08×10^{-3} mA/cm^2, is equivalent to the kinetic current density, i_k. Figure 21.8 (b) shows H_2 electrooxidation on pure Ru in 0.5 M H_2SO_4. It can be seen that even at the maximum current density, the catalytic activity of Ru towards H_2 is at least 2–3 orders of magnitude lower than that of Pt. The potential dependence of H_2 oxidation on pure Ru (as shown in the insert of Figure 21.8 (b)) shows that when the potential is more positive than the value at the maximum current density (~0.2 V), Ru becomes inactive towards H_2. The electrooxidation of H_2 on Pt-Ru (50 atomic% Ru surface composition) was indistinguishable from the data on pure Pt, within experimental error. This indicated that even if the activity of pure Ru towards H_2 oxidation were to be zero, the rate of H_2 electrooxidation on the remaining Pt active sites would have exceeded the rate of the diffusion transport of H_2 to the electrode surface. From the results of these experiments, it can be concluded that at low temperature (25 °C), Pt and the Pt-Ru catalyst have similar activity towards H_2 electrooxidation, while the activity of pure Ru is much lower than that of Pt.

(a)   (b)
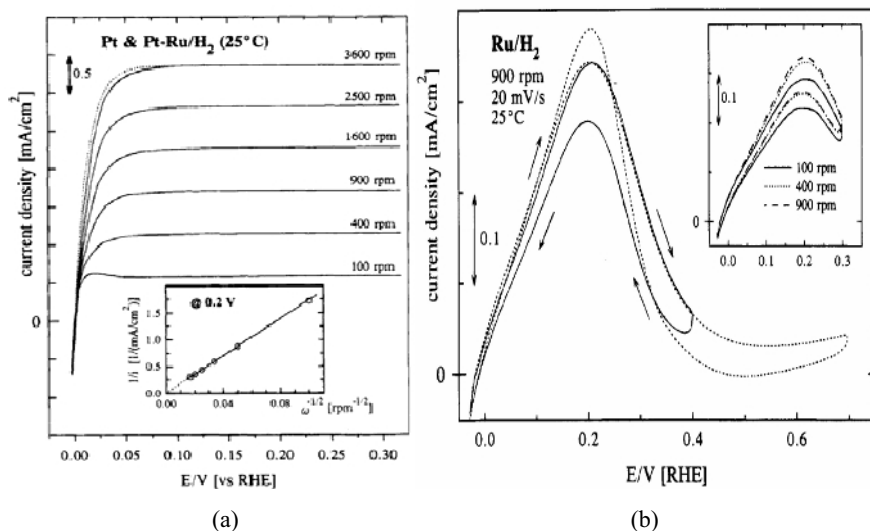
Figure 21.8. (a) Hydrogen reduction and oxidation current densities during positive-going sweeps (20 mV/s) on a Pt RDE in 0.5 M H_2SO_4 saturated with H_2 at 25 °C (rotation rates are indicated in the figure). A Levich plot at 0.2 V with a least-squares regression line is shown in the inset. (b) Potentiodynamic (20 mV/s) hydrogen oxidation current densities on a sputter-cleaned Ru RDE in 0.5 M H_2SO_4 saturated with H_2 at 25 °C and 900 rpm for different positive potential limits. The insert shows the rotation rate dependence [45]. (Reprinted with permission from J Phys Chem 1995;99:8290–301. Copyright 1995 American Chemical Society.)

21.4.2 Cyclic Voltammetry (CV) Test

Cyclic voltammetry (CV) is one of the most widely used electrochemical techniques for acquiring qualitative information about electrochemical reactions. Measurement using cyclic voltammetry can rapidly provide considerable information about the thermodynamics of redox processes and the kinetics of heterogeneous electron-transfer reactions, as well as coupled chemical adsorption and reactions. Cyclic voltammetry is often the first experiment performed in an electroanalytical study. In particular, it can rapidly reveal the locations of the redox potentials of the electroactive species. CV is also used to measure the electrochemical surface area (ECSA, m^2/g catalyst) of electrocatalysts (e.g., Pt/C catalyst) in a three-electrode system with a catalyst coated glass carbon disk electrode as a working electrode [52]. Figure 21.9 shows a typical CV curve on Pt/C. Peaks 1 and 2 correspond to hydrogen electroadsorption on Pt(100) and Pt(111) crystal surfaces, respectively. The H_2 electroadsorption can be expressed as Equation 21.35:

$$Pt + H^+ + e^- \rightarrow Pt - H_{ads} \tag{21.35}$$

Peaks 3 and 4 correspond to H_2 electrodesorption on Pt(111) and Pt(100) crystal surfaces, respectively, and can be expressed as:

$$Pt - H_{ads} \rightarrow Pt + H^+ + e^- \tag{21.36}$$
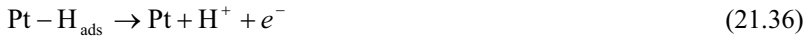
Peak 5 represents the oxidation of the Pt surface; this process can be expressed as follows:

$$Pt + H - O - H \rightarrow Pt - O - H + H^+ + e^- \tag{21.37}$$

$$Pt - O - H + H - O - H \rightarrow Pt - (O - H)_2 + H^+ + e^- \tag{21.38}$$

$$Pt - (O - H)_2 \rightarrow Pt - O + H - O - H \tag{21.39}$$
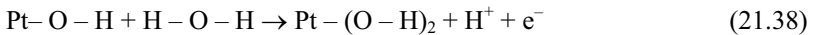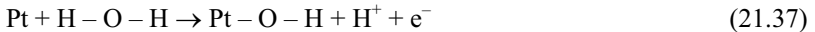
Peak 6 represents the reduction of Pt oxide, which can be expressed as Equation 21.40:

$$Pt - O + 2H+ + 2e^- \rightarrow Pt + H - O - H \tag{21.40}$$

The ECSA (m^2/g Pt) can be calculated according to Equation 21.41:

$$ECSA = \frac{Q_H}{L_{Pt}Q_f} \times 10^{-4} \tag{21.41}$$

where Q_H is the Coulombic charge with a unit of mC, and the value is usually calculated as the average value between the amounts of charge exchanged during the electroadsorption (Q') and electrodesorption (Q'') of H_2 on Pt sites; L_{Pt} is the Pt loading on the studied electrode, with a unit of g; Q_f is the required Coulombic charge to desorb the hydrogen when a clean Pt surface is covered by a monolayer of hydrogen, and its value is 0.21 mC/cm^2.
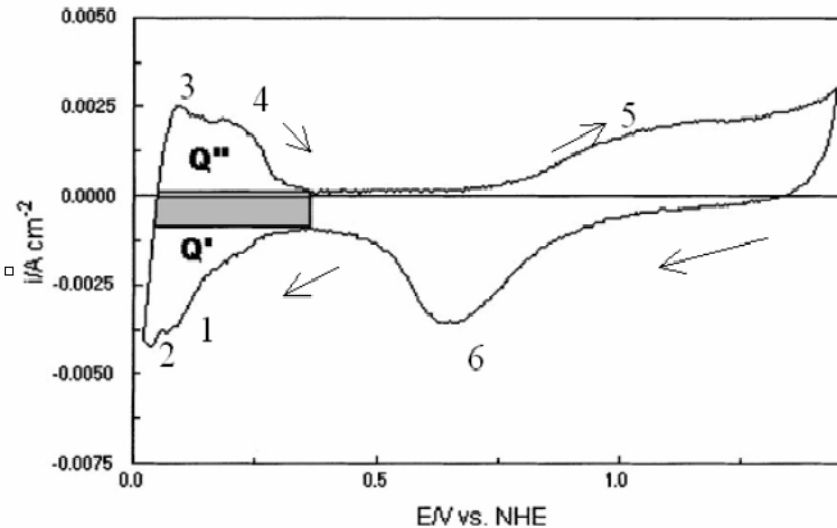
Figure 21.9. Typical CV curve on Pt/C catalyst. Q' and Q'' represent the amount of charge exchanged during the electroadsorption and desorption of H_2 on Pt sites, and the filled area is the contribution of the double-layer charge [52]. (Reprinted from Journal of Power Sources, 105, Pozio A, De Francesco M, Cemmi A, Cardellini F, Giorgi L. Comparison of high surface Pt/C catalysts by cyclic voltammetry, 13–19, ©2002, with permission from Elsevier.)

CV can also be widely used for the *in situ* diagnosis of the catalyst layer. Because the catalyst layer is a matrix structure, rather than a smooth electrode surface, not all of the catalyst surface can be accessible to the reaction. However, CV is also a useful tool for catalyst active area measurement, for example, the determination of electrode Pt surface area (EPSA, the active Pt surface area in a unit electrode, cm^2/cm^2) [53, 54]. To determine the EPSA of the cathode/anode in a single fuel cell, the cathode/anode compartment is purged with humidified N_2 and serves as the working electrode, while the anode/cathode compartment is flushed with humidified H_2, serving as both counter and reference electrodes. Then the CV curve can be recorded on the single cell. The EPSA can be calculated using Equation 21.42:

$$EPSA = \frac{Q_H}{AQ_f} \tag{21.42}$$

where Q_H is the Coulombic charge with a unit of mC; A is the active area of the electrode, with a unit of cm^2; and the value Q_f is 0.21 mC/cm^2.

In situ cyclic voltammograms are useful in assessing the EPSA and electroactive surface areas of a catalyst layer. In order to obtain comparable results, the process has to be performed identically in terms of the measurement method, operating conditions, and catalyst layer state. Otherwise, large variability in the results is to be expected.

During the electrode fabrication process, it is not guaranteed that all of the ECSA will be available for electrochemical reaction, due to either insufficient contact with the solid electrolyte or electrical isolation of the catalyst particles. Therefore, Pt utilization is one of the most important parameters for evaluating a catalyst layer and an electrode. Using the CV technique, Pt utilization can be determined by measuring the electrochemical surface area of the Pt catalyst and the active Pt surface area (SA, m^2) in a catalyst layer. Pt utilization can de defined as the ratio of the active Pt surface area in a catalyst layer to the electrochemical surface area of the Pt catalyst.
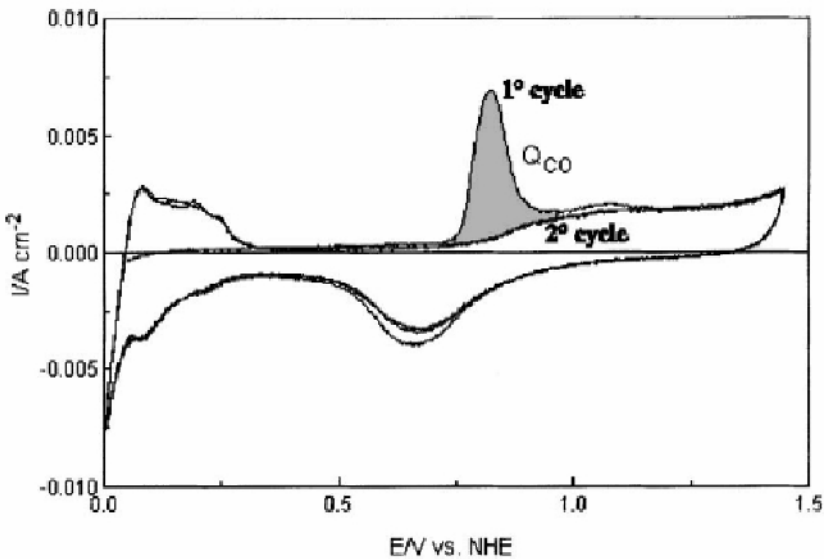
Figure 21.10. Cyclic voltammograms (10 mV s^{-1}) at 25 °C in the potential range 0–1400 mV vs. NHE on Pt/C (E-TEK) with (first cycle) and without (second cycle) a CO-adsorbed ad-layer. The filled area represents the charge related to the CO oxidation reaction [52]. (Reprinted from Journal of Power Sources, 105, Pozio A, De Francesco M, Cemmi A, Cardellini F, Giorgi L. Comparison of high surface Pt/C catalysts by cyclic voltammetry, 13–19, ©2002, with permission from Elsevier.)

Besides the hydrogen desorption method, the CO (carbon monoxide) stripping method has also been used in CV measurement to characterize the catalyst [52] and diagnose the fuel cell catalyst layer [55, 56]. Figure 21.10 shows two cyclic voltammograms obtained on Pt/C with a CO-adsorbed ad-layer. The peak at about

0.87 V versus NHE, in the first cycle, represents the electrooxidation of the irreversibly adsorbed CO. The calculated peak charge, Q_{CO}, is related to the following reaction:

$$Pt - CO + H_2O \rightarrow Pt + CO_2 + 2e^- + 2H^+ \qquad (21.43)$$

The ECSA can be calculated according to Equation 21.44:

$$ECSA = \frac{Q_{CO}}{L_{Pt} \times 0.484} \qquad (21.44)$$

where Q_{CO} is the charge under the CO peak; L_{Pt} is the Pt loading on the electrode; and the value of 0.484 represents the charge density required to oxidize a monolayer of CO on smooth Pt [57, 58]. Similar to the H_2 desorption method, the CO stripping method can also be used to determine the EPSA and Pt utilization.

21.4.3 Polarization Curves in a Half-cell

The half-cell method is also useful to get the polarization curve for the investigation of electrochemical half-reactions, including the ORR, the HOR, and the methanol oxidation reaction (MOR). Du et al. [59] investigated the effect of methanol on the cathode behavior of a DMFC in a half-cell. The half-cell consisted of a normal DMFC cathode and a membrane that made contact with an electrolyte solution (H_2SO_4 or H_2SO_4 and methanol), in which a reference electrode (RE) and a counter electrode (CE) were installed. Figure 21.11 compares the steady-state polarization curves at different working conditions. Curve A corresponds to the pure ORR in the absence of methanol; curve B corresponds to the pure MOR in the absence of oxygen; curve C corresponds to the net behavior of the simultaneous ORR and MOR; and curve D is the algebraic sum of curves A and B by assuming that the MOR and ORR proceed independently of each other. As shown in Figure 21.11, at high potentials, curves C and D were very close, indicating that the MOR and ORR were not noticeably affected by each other. At lower potentials, however, curve C deviated significantly from curve D, reflecting a strong interaction between the ORR and MOR. In addition, the difference between curve C and curve D was larger at a higher methanol concentration (Figure 21.11 (a)) than at a lower one (Figure 21.11 (b)), indicating a stronger interaction with a higher methanol concentration. This interaction may be due to the increased MOR partial current or poisoning of the ORR by the methanol adsorbates [59, 60].

   Figure 21.12 [61] shows the polarization curves for an oxygen cathode and methanol anode obtained at 75 °C in half-cells with 3 M and 1.5 M H_2SO_4 as electrolytes, respectively. At low current densities, the system appears to be governed by a high degree of polarization. The activation losses are about 100 mV and 200 mV for the ORR and MOR, respectively. At high overpotentials, the polarization curve is linear in current, indicating that the ohmic resistance may be

dominant. If the cell voltage is the potential difference between cathode and anode, the open circuit voltage (OCV) of the fuel cell should be around 0.9 V.
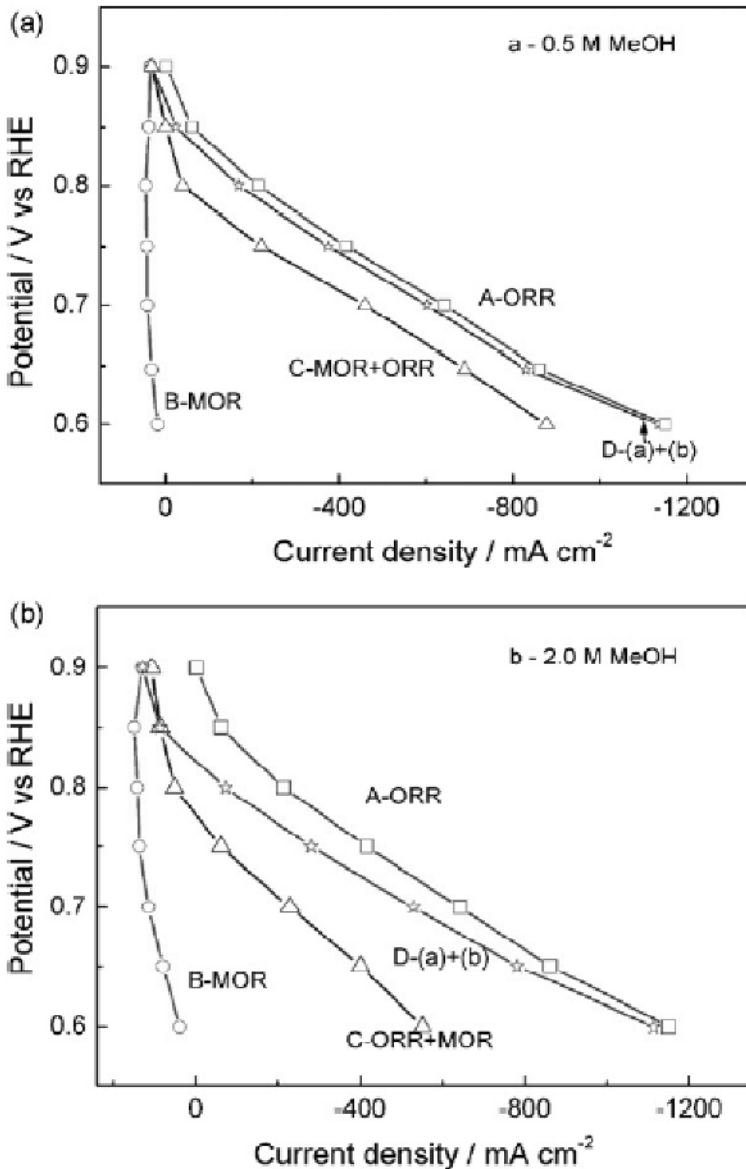
Figure 21.11. (a) and (b) Polarization behaviors of the cathode: (A) O_2 electrode without methanol; (B) N_2 electrode with methanol; (C) O_2 electrode with methanol; (D) algebraic sum of curves A and B (gas flow rate: 20 mL min^{-1}) [59]. (Reprinted from Electrochimica Acta, 52, Du CY, Zhao TS, Yang WW. Effect of methanol crossover on the cathode behavior of a DMFC: a half-cell investigation. 5266–71, ©2007, with permission from Elsevier.
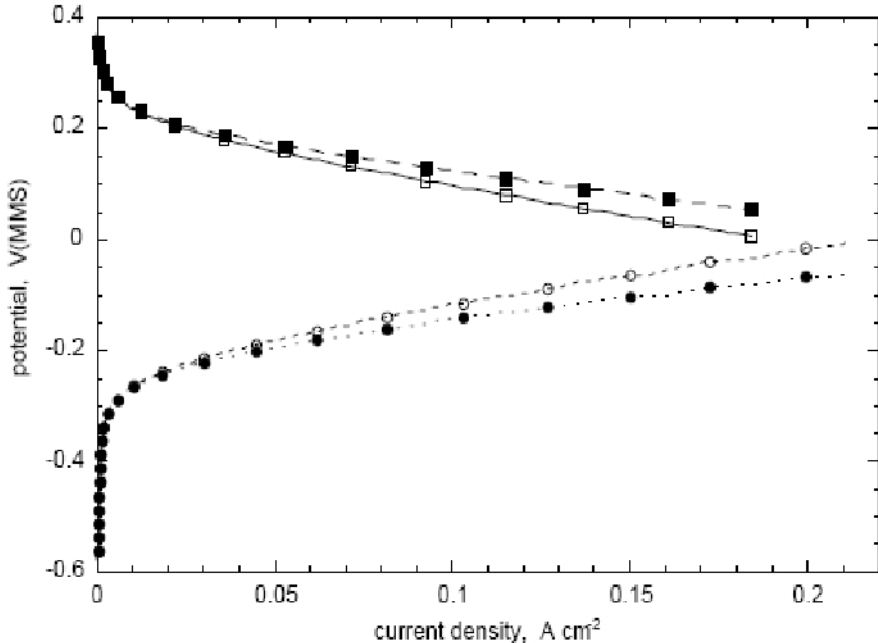
Figure 21.12. Polarization curves for oxygen cathode ($\square$, $\blacksquare$) and methanol anode ($\bigcirc$, $\bullet$) at 75 °C in half-cells with 3 M and 1.5 M H_2SO_4 as electrolytes, respectively. The data corrected for the ohmic potential drop ($\blacksquare$, $\bullet$) are also shown. Cathode: 1.16 mg Pt/cm^2, anode: 1.4 mg PtRu/cm^2 [61]. (Reprinted from Journal of Power Sources, 128, Reeve RW, Burstein GT, Williams KR. Characteristics of a direct methanol fuel cell based on a novel electrode assembly using microporous polymer membranes, 1–12, ©2004, with permission from Elsevier.)

21.5 MEA Evaluation by the Single-cell Test

The single fuel cell test is one of the most direct and effective methods for the evaluation of catalyst layers and MEAs. Even if the results obtained by a half-cell test are very promising, the single-cell test is still a necessary step for performance validation of the developed catalyst layer and MEA.

21.5.1 Test Station

A test station is required for the single-cell test. Test stations are designed to measure and control the following parameters during the tests: (1) temperature, pressure, humidity, and flow rates of reactants, (2) temperature, pressure, and flow rate of coolant, and (3) current and voltage of the fuel cell. Usually, a test station system consists of gas control station, fuel cell, load bank, data acquisition/control unit, as well as control software, as shown in Figure 21.13 [62]. Sometimes, a coolant sub-system is needed, especially for fuel cell stack testing. The gas control station (including gas meter unit and humidifier) is used to regulate the gas

velocity, backpressure, temperature, and relative humidity. A safety unit is required as well to detect and remove any explosive gases leaking from the test station. There are basically two methods – external and internal – for humidifying the fuel cell reactants and the fuel cell membrane. The simplest and most widely used is the external method, which forces the dry reactant gas to bubble through water to produce the feed gas with the desired humidity level. The fuel cell loads are supplied by a load bank that can provide several load modes: constant current, voltage, and power. A data acquisition/control unit can monitor and collect all data from the test station and fuel cell system. Control software is provided for monitoring, controlling, and organizing the testing processes.
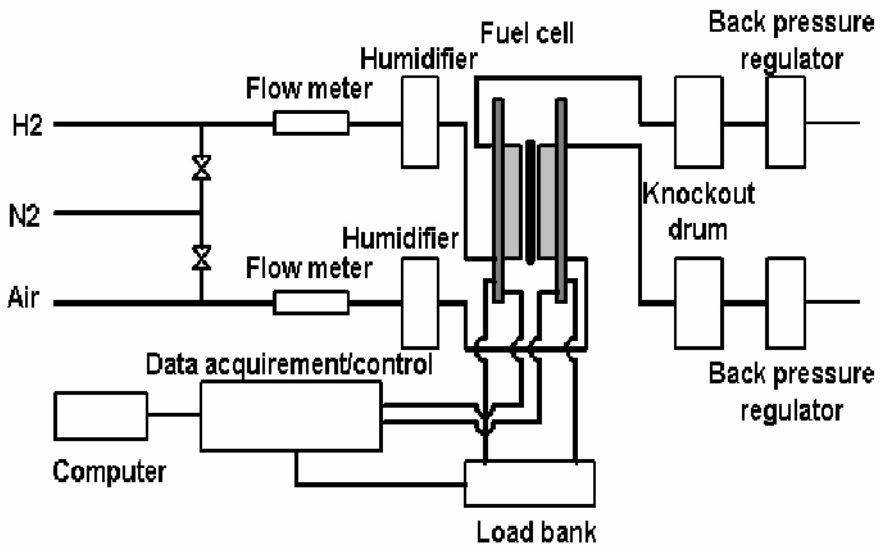
Figure 21.13. Schematic of a test station [62]. (Reprinted from Journal of Power Sources, 160, Zhang J, Xie Z, Zhang J, Tang Y, Song C, Navessin T, et al. High temperature PEM fuel cells, 872–91, ©2006, with permission from Elsevier.)

In the whole test system, the fuel cell is one of the most important components. A fuel cell hardware design includes the flow field design, material selection, sealing design, manifold design, and assembly strategy design. Figure 21.14 shows a schematic illustration of a single cell [63]. The carbon plate/current collector is isolated from the end plate (aluminum) with a plastic plate that also serves as a gas manifold. Gaskets are used to seal the MEA. A variable pressure bladder, controlled with nitrogen gas, is used to compress and seal the cell assembly. The cell heating is accomplished with a pair of heat tapes. The inner 60 W heat tapes, which are glued onto the copper current collector plates, allow the cell to operate at the desired temperature.
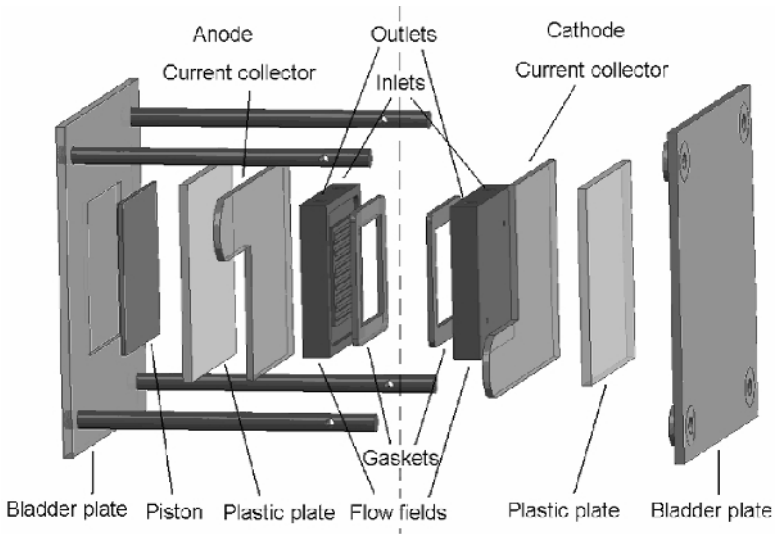
Figure 21.14. Assembly of a single cell [63]. (Reproduced by permission of ECS—The Electrochemical Society, from Tang Y, Zhang J, Song C, Liu H, Zhang J, Wang H, et al. Temperature dependent performance and *in situ* AC impedance of high-temperature PEM fuel cells using the Nafion-112 membrane.)

21.5.2 Polarization Curve

The most common indicator for fuel cell performance is the polarization (or current-voltage) curve. There are basically two data collection modes in obtaining the polarization curve. One is to adjust the current density then record the cell voltage, the other is to adjust the cell voltage then record the current density. The former is the most popular mode in fuel cell performance data collection. After a series of current and voltage values are collected, the cell voltage will be plotted as a function of current density. Figure 21.2 shows the typical polarization curve of a PEM fuel cell. After the polarization curve is obtained, the MEA power density (cell voltage × current density) can be plotted as a function of current density, accordingly. From the power density curve, the maximum power density of the fuel cell MEA can be known. For a fuel cell stack, the maximum volume power density and the mass power density can be obtained as well.

The cell performance (polarization curve) strongly depends on the operating conditions, such as temperature, pressure, relative humidity (RH), gas flow rates, etc. Normally, the performance increases with increasing temperature, pressure, RH, and gas flow rate.

21.5.3 Resistance Test – AC Impedance Test

In addition to performance tests, diagnosis is also important in single-cell testing. The AC impedance method (called electrochemical impedance spectroscopy (EIS)) is a powerful technique for fuel cell performance diagnosis that can provide detailed information on individual losses such as kinetics, mass transfer, and

membrane resistance. EIS was traditionally employed to determine the double-layer capacitance of an electrode/electrolyte interface [64], as well as to characterize the electrical properties of materials and interfaces. This method has also been demonstrated to be successful in fuel cell performance diagnosis and optimization. The major application areas of EIS in PEM fuel cell development include the optimization of MEA fabrication, the operation condition effect, membrane-related conductivity measurements, fuel cell contamination diagnosis, water "flooding" improvement, as well as catalyst layer structure optimization.

There are two major methods used to measure impedance: time domain and frequency domain techniques. The typical frequency domain technique uses a potentiostat and a frequency response analyzer. During measurement, the working electrode potential is modulated sinusoidally with respect to the reference electrode. The AC impedance obtained is a frequency-dependent complex number at each frequency that can be plotted in various ways. One of the popular methods is to plot imaginary impedance against real impedance (called the complex plane). This is also called the Nyquist plot. By fitting this impedance plot to a model, an equivalent circuit (EC) for the system can be obtained. In the literature, many kinds of equivalent circuits have been developed to fit the AC impedance spectra. Results using different ECs might be quite different from each other. However, if the results are self-contained, they should be useful in explaining the observed experimental phenomena. The following section illustrates several typical examples of EIS application in fuel cell research and development.
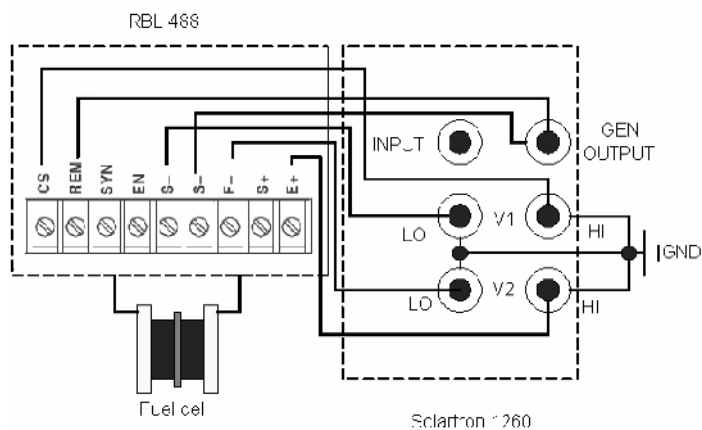
Figure 21.15. Connections between the Solartron 1260 FRA, RBL 488 load bank, and fuel cell [63]. (Reproduced by permission of ECS—The Electrochemical Society, from Tang Y, Zhang J, Song C, Liu H, Zhang J, Wang H, et al. Temperature dependent performance and *in situ* AC impedance of high-temperature PEM fuel cells using the Nafion-112 membrane.)

Zhang et al. [13, 31, 54] and Tang et al. [63] applied EIS to the *in situ* diagnosis of fuel cell performance in a temperature range of 23 °C to 200 °C. Figure 21.15 shows the schematic of an AC impedance measurement system for fuel cell *in situ* diagnosis [63]. In their studies, a Solartron 1260 frequency response analyzer (FRA) was used for methodological development and AC impedance diagnosis.

This instrument can generate DC, AC, and their combined control signals, and the AC sinusoid signal range can be from 10 μHz to 32 MHz. Their study used a single channel load bank (RBL 488 series 100–60–400, TDI), which can be controlled with signals via an external program. The magnitude of the voltage signal inputting to the load bank, which is DC, AC, or a combination thereof, can be in the range of 0–10 volts. This load bank has three current control ranges of 6 A, 30 A, and 60 A. For the AC mode of the load bank, the frequency range of the controlling AC sinusoid signal is 0.06 Hz to 20 kHz. The control signal generated by the FRA is connected to the REM and S-ports located on the rear panel of the load bank. This signal contains two components, the DC and the AC. For example, if the control mode is a constant current load, then this signal should command the load bank to deliver a combined current. The load bank will transfer this control signal into the fuel cell load level. The values of all signals are referred to S-ports. Before running the experiments, the voltage and current density ranges in the load bank should be chosen according to the expected fuel cell performance. The cell voltage response goes to FRA "V_1" and "V_2" for analysis. The obtained impedance information is sent to a computer for data display and analysis, performed by a powerful software package called ZPlot.

Electric noise is always an issue for AC impedance measurement. In the fuel cell impedance experiments shown in Figure 21.15, differential input with a floating ground was chosen to reduce the noise and harmonic signals from externally wired circuits. To decrease the noise, an oscilloscope was connected to the fuel cell current collectors to monitor the noise level. Experiments showed that the electronic connection depicted in Figure 21.15 could effectively reduce noise.

Figure 21.16 (a) and (b) show the AC impedance spectra of a single PEM fuel cell operated at 80 °C, 3.0 atm, and 100% relative humidity (RH) and 0% RH, respectively. Two semi-circles appear clearly on each spectrum. One is in the high-frequency domain and represents the charge transfer resistance predominated by the charger transfer resistance of the ORR process. The other is in the low-frequency domain and represents the mass transfer resistance, which includes the proton transfer resistance and mass (O_2 and H_2) transfer resistances in the catalyst layer. The intercept of the plot on the Z' axis at the high-frequency end represents the fuel cell internal resistance predominated by membrane resistance, from which the through-plane membrane resistance in a real operating fuel cell can be measured *in situ*. As shown in Figure 21.16, at 100% RH, the first semicircle shrinks and the second one expands with increasing current density, indicating that the fuel cell electrochemical reactions are dominated by the kinetics at low current density range and limited by the mass transfer within the catalyst layer at high current density range (> 1.2 A/cm^2). However, in the case of 0% RH, the situation becomes more complicated. In order to gain a better understanding of the EIS difference between 100% and 0% RH, an equivalent circuit was constructed to describe the process, as shown in the Figure 21.16 (a) insert [31]. R_m is the high-frequency resistance (intercept on the Z' axis at the high-frequency end), which represents the fuel cell internal resistances, predominated by membrane resistance. R_t is the charge transfer resistance for the ORR and HOR (predominated by the ORR charge resistance), and CPE_1 (the constant phase element) represents the R_t associated catalyst layer capacitance properties. R_{mt} is the resistance related to the

mass transfer of reactant gases in catalyst layers. CPE_2 represents the R_{mt}-associated capacitance. The circuit is a simplified approach according to the flooded-agglomerate model (FAM) for porous gas-diffusion electrodes, where the electrochemical and mass transfer processes within the catalyst layer are described by a transient network circuit including several elements such as electrolyte resistance, double-layer capacitance, Faradaic impedance, etc. [65, 66].
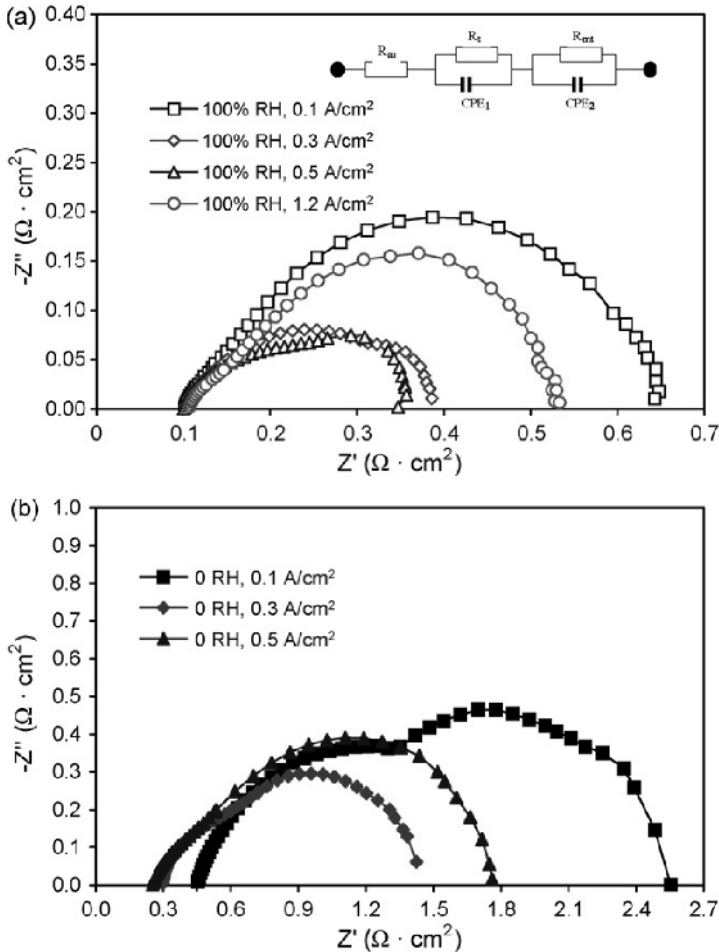
Figure 21.16. *In situ* AC impedance spectra in the frequency range of 10,000–0.01 Hz. Single fuel cell with an active MEA area of 4.4 cm^2 operated at 80 °C, 3.0 atm absolute backpressure: (a) 100% RH, (b) 0% RH. The stoichiometries of H$_2$ and air are 1.5 and 2.0, respectively. Standard MEA with Nafion 112 membrane and a total Pt loading of 1.0 mg/cm^2. The insert is the equivalent circuit for data fitting [31]. (Reprinted from Electrochimica Acta, 52, Zhang J, Tang Y, Song C, Cheng X, Zhang J, Wang H. PEM fuel cells operated at 0% relative humidity in the temperature range of 23–120 °C, 5095–101, ©2007, with permission from Elsevier.)

The data simulated using the equivalent circuit is plotted as a function of current density, as shown in Figure 21.17 [31]. Compared to the resistance values at 100% RH, the membrane resistance, charge transfer resistance, and mass transfer resistance all jump dramatically. This would lead to a dramatic decrease in fuel cell performance. When a PEM fuel cell is operated at 0% RH, the membrane and the catalyst layer are dry and proton transfer is difficult in both the membrane and the catalyst layer ionomer. The large mass transfer resistance at 0% RH in the whole current range (even at 0.1 A/cm^2) mainly comes from the proton transfer resistance in the catalyst layer. The dry environment could also slow down the charger transfer process and result in a high charge transfer resistance.
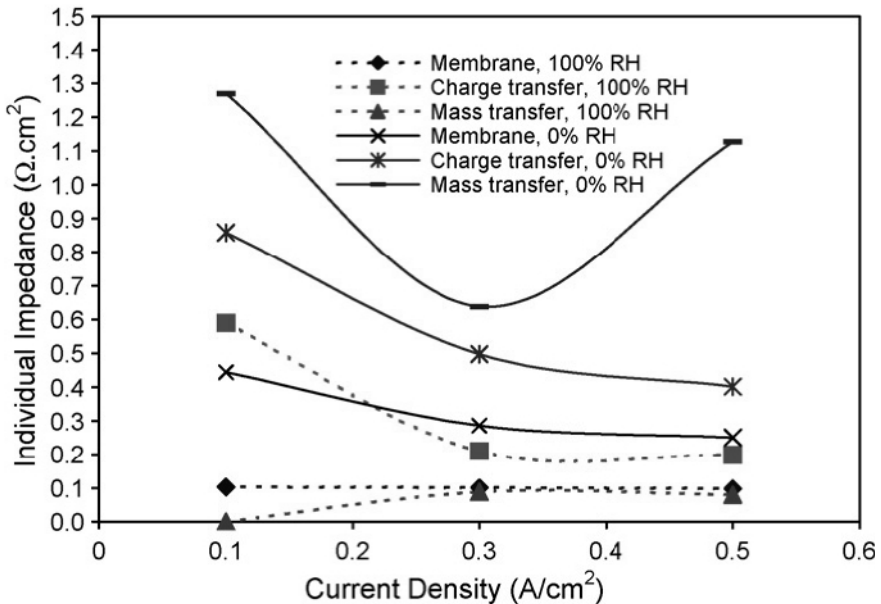
Figure 21.17. Simulated individual AC impedances as a function of current density. The simulation was based on the data in Figure 21.17 according to the equivalent circuit in Figure 21.16 (a) [31]. (Reprinted from Electrochimica Acta, 52, Zhang J, Tang Y, Song C, Cheng X, Zhang J, Wang H. PEM fuel cells operated at 0% relative humidity in the temperature range of 23–120 °C, 5095–101, ©2007, with permission from Elsevier.)

21.5.4 Permeability/Crossover Test

The proton exchange membrane used in PEM fuel cells (e.g., Nafion membrane) is a porous material, with some undesirable permeability for gases and liquids. When the fuel cell is running, the fuel, such as H$_2$ or methanol, will diffuse from anode to cathode through the membrane, and at the same time the oxidant (e.g., O$_2$) will diffuse from cathode to anode. This phenomenon is called crossover and is undesirable in practical fuel cell operation. Hydrogen crossover can have at least three effects, including fuel efficiency reduction, cathode potential depression, and aggressive peroxide radical formation. The hydrogen that crosses over can directly

react with oxygen at the cathode surface, resulting in a lower cathode potential and a lower PEM fuel cell open circuit voltage (OCV) [13]. More severely, this direct reaction between H_2 and O_2 at the cathode can produce peroxide radicals, which attack not only the catalyst layer but also the membrane, causing significant catalyst layer and membrane degradation [67]. In addition, it has been confirmed that the formation of hot points [68] or hydrogen peroxide [69, 70] by the highly exothermal chemical reaction between H_2 and O_2 can also lead to pin holes in membranes, accelerating membrane degradation and even destroying the MEA, and causing safety problems. The highly exothermal chemical reaction between H_2 and O_2, catalyzed by a Pt catalyst, can also accelerate the sintering of the catalyst.

The gas permeability of a membrane can be measured using both physical and electrochemical methods. The physical method is first to assemble a piece of membrane into a single cell; then the probe gas (such as H_2, or O_2) is flowed into one side of the cell and an inert gas (such as Ar or He) is flowed into the other side at the same time. The pressures on both sides are kept at the same level. The probe gas crosses over through the membrane to the other side and flows out by the inert gas. The outlet of the inert gas is connected to a gas chromatograph (GC) to determine the concentration of the probe gas in the inert gas stream, and the permeability of the membrane is then calculated according to the gas concentration. This method is simple and convenient, but not an *in situ* approach.

The gas crossover can also be measured *in situ* by electrochemical methods. Song et al. [71] described a method to measure H_2 crossover using lineal sweep voltammetry (LSV). In their experiment, the anode served as both reference and counter electrodes with H_2 flowing, and the cathode served as a working electrode with N_2 flowing. The hydrogen supplied to the MEA reference electrode permeated the membrane and reached the opposite electrode, where hydrogen was electrochemically oxidized at the cathode by the applied voltage from the potentiostat. The cell potential was scanned from 0.01–0.50 V. The hydrogen that passed through the membrane was measured as a mass transport ''limiting current'' in the voltage range of 0.35–0.50 V.

Our study [72] measured the H_2 crossover *in situ* at high temperatures using an electrochemical method. The processes for the H_2 crossover measurement were as follows. A MEA was assembled into a fuel cell and then the humidified hydrogen and nitrogen stream were introduced into the anode and cathode, separately. After 30 minutes of N_2 flushing through the cathode to remove residual air, a Solartron 1287 potentiostat was connected to the fuel cell for H_2 crossover measurements, with the working electrode probe connected to the cathode and the counter/reference electrode probes connected together to the anode. A steady-state electrochemical method was used to record the current produced from the oxidation of crossed H_2 from the anode at an applied cathode potential of 0.5 V relative to the potential of the H_2-flushed anode. At this cathode potential, all H_2 that has crossed over from the anode to the cathode should be completely oxidized, giving a current indicative of the amount of hydrogen that has crossed over. The obtained current was defined as $I_{H_2}^{cross}$ (unit: A) for the calculation of the H_2 crossover rate ($J_{H_2}^{cross}$, mol cm^{-2} s^{-1}). The following Faraday's equation was used to obtain the H_2 crossover rate:

$$J_{H_2}^{cross} = \frac{I_{H_2}^{cross}}{nFA} \tag{21.45}$$

where n is the electron number of H_2 oxidation (= 2), A is the MEA active area (cm^2), and F is the Faraday constant (A·s·mol^{-1}).

The study indicated that the H_2 crossover rate depends on the fuel cell operating temperature and backpressure, and the gas RH.

21.6 Lifetime/Durability Testing of the MEA

MEAs in PEM fuel cells require sufficient lifetimes for applications in transportation and/or stationary power generation. During lifetime testing, the PEMFC performance should be stable and the operation behavior reliable. However, PEM fuel cells at present cannot guarantee lifetimes of 5,000 hours for mobile or transportation applications and 40,000 hours for stationary applications. The durability of the fuel cell, strictly related to the lifetime, is defined as the ability of a cell to resist permanent change in performance over time. Normally, lifetime degradation is not a catastrophic failure. However, it does indicate that the MEA degradation is not recoverable or reversible.

21.6.1 Mechanisms of MEA Degradation

In the past several decades much effort has been put into the testing, diagnosis, and mitigation of MEA durability. Many mechanisms of MEA degradation have been proposed, such as membrane degradation, contamination, catalyst degradation, structural change of the catalyst layer, sealing material failure, and so on. Borup et al. [73] have provided a detailed review of PEM fuel cell degradation mechanisms. In this section we will give a brief introduction to these mechanisms.

Membrane degradation is one of important factors that cause fuel cell performance degradation. It includes loss of proton conductivity and increased gas permeability. When the membrane is contaminated by impurities from the fuel or oxidant and those released from the components of the MEA, the proton conductivity of the membrane will decrease. After the fuel cell is run for a long time, the membrane polymer will be chemically degraded. For example, loss of the SO_3H group could result in proton conductivity loss. For a H_3PO_4-doped polybenzimidazole (PBI) membrane, H_3PO_4 will be lost with the water produced during fuel cell operation and lead to loss of proton conductivity. These proton conductivity losses make the fuel cell performance degrade during long-time operation. H_2 crossover from anode to cathode is also inevitable during fuel cell operation. H_2 directly reacts with oxygen at the cathode catalyst surface and produces H_2O_2, which attacks not only the catalyst layer but also the membrane, causing significant catalyst-layer and membrane degradation [67]. In addition, the highly exothermal chemical reaction between H_2 and O_2 can lead to the formation of hot points [68] and pin holes in membranes, accelerating membrane degradation

and even destroying the MEA. Mechanical failure of the membrane is also a mode of membrane degradation [74].

Contamination of fuel and/or oxidant is another important factor causing fuel cell performance degradation [75]. For example, air pollutants such as NO_x and SO_x can cause the degradation of a fuel cell cathode. This problem is unavoidable when the fuel cell uses air as the oxidant. Some urban areas have air contaminants such as CO, NO_x, sulfur compounds, volatile organic compounds, etc. Even a low level of contaminants can lead to fuel cell performance degradation through poisoning of the Pt catalyst. The contaminants in hydrogen usually come from fuel manufacturing processes such as the reforming of hydrocarbons or the oxidation of natural gas. These processes can yield a hydrogen-rich gas that contains some amount of carbon monoxide or other (sulfur-based) impurities. The CO and sulfur-based impurities can strongly adsorb on the Pt catalyst surface and lead to severe degradation in fuel cell performance. Both anode and cathode contamination are important degradation modes, causing fuel cell kinetic, ohmic, and mass transfer losses.

Catalyst degradation is another important MEA failure mode, and includes Pt catalyst sintering/ripening, Pt or Pt alloy dissolution/migration, as well as carbon support corrosion. It is well known that Pt particle size can increase with fuel cell lifetime. This increase can lead to a decrease in the electrochemical Pt surface area, resulting in degraded fuel cell performance as well as decreased durability. During fuel cell operation, Pt can also be dissolved in the catalyst layer through electrochemical or chemical reactions [76, 77]. The soluble platinum species can migrate within the catalyst layer and into the membrane [78, 79], then react with crossed hydrogen and precipitate in the ionomer and membrane, resulting in undesired Pt particle distribution. The deposited Pt particles in the membrane will become hot pots for pinhole development. The surface oxidation of Pt by water or oxygen-containing gas at high cathodic potential has been reported [80, 81]. Pt oxide formation will decrease the Pt active surface area in the catalyst layer and also decrease the fuel cell OCV, due to the mixed potential between the Pt oxidation and oxygen reduction reactions.

Carbon support corrosion in a fuel cell is another cause of catalyst degradation. Noble metals are usually supported on a high surface area carbon support to increase utilization of the metals. Carbon corrosion can take place according to Equation 21.46:

$$C + 2H_2O = CO_2 + 4H^+ + 4e^- \tag{21.46}$$

with a standard potential of 0.207 V [82]. Although carbon is thermodynamically unstable, its slow reaction kinetics allow the use of carbon in low-temperature fuel cell applications. Corrosion of the carbon support can occur in three situations: normal operation of a fuel cell, fuel starvation, and partial coverage of hydrogen [82]. The rate of carbon corrosion depends on operating temperature and cell potential. For high-temperature PEM fuel cells, more attention should be paid to carbon corrosion because of the rapid rate of corrosion that occurs, particularly at high cell voltage (e.g., OCV).

Besides the above degradation modes, loss of hydrophobicity in the catalyst layer also contributes to performance degradation during lifetime testing. During the operation of a fuel cell, the hydrophobic material (typically polytetrafluoroethylene (PTFE)) in the catalyst layer can gradually lose its surface hydrophobicity, resulting in a water management issue [83], in particular a water "flooding" problem.

The durability of a fuel cell also depends on operating conditions such as temperature, start and stop cycle, relative humidity, operating current, or voltage. Tang et al. [84] operated a PBI membrane-based fuel cell in the temperature range of 160^-300 °C and found that the cell voltage could drop 120 mV at 0.32 A/cm^2 after 6 hours of operation at 240 °C. Operating a fuel cell in a frozen environment could cause a change in membrane mechanical strength due to brittleness or other reasons, resulting in a decrease in fuel cell performance.

21.6.2 Durability Testing

Durability testing takes a long time in an operation environment, which is difficult as normally several thousand hours are necessary to obtain a meaningful conclusion. In the development of durability testing, some *in situ* and *ex situ* methods and techniques for material evaluation have been used, such as scanning electron microscopy (SEM), transmission electron microscopy (TEM), X-ray diffraction (XRD), inductively coupled plasma mass spectrometry (ICP-MS), CV, EIS and so on. However, new electrochemical and/or physical techniques are desirable to gain a better understanding of durability failure modes and then improve fuel cell durability and reliability.
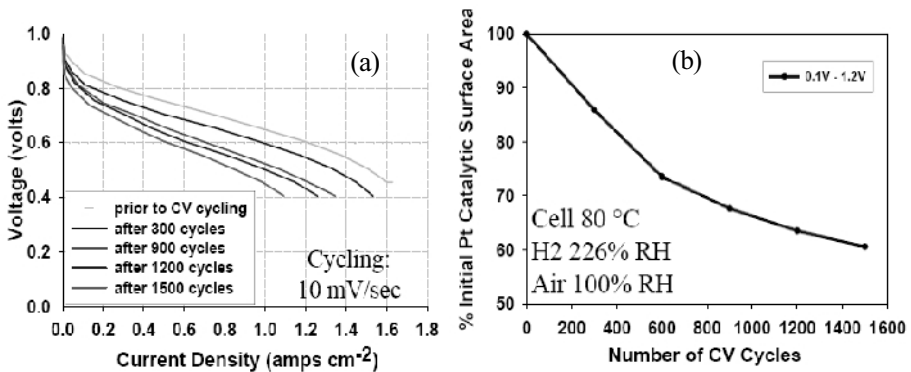
Figure 21.18. Polarization curves (a) and the active Pt surface area, (b) after CV cycling between 0.1 and 1.2 V [86]. (Reprinted from Borup R, Davey J, Wood D, Garzon F, Inbody M, Guidry D. PEM fuel cell durability. In: 2005 DOE hydrogen program review. US DOE Hydrogen Program 2005 Annual Merit Review and Peer Evaluation Meeting; 2005 May 23–26; Arlington, VA. With permission from DOE.)

The best and simplest reliable method to test the durability of a fuel cell is to run the fuel cell directly, hour by hour, at the desired conditions. However, this

method is costly in time and materials so accelerated durability test (ADT) methods are needed. Normally, ADTs can be carried out under more "stressful" conditions compared to actual use conditions in order to accelerate fuel cell failure. In recent years, some ADT methods have been developed, such as CV cycling, load and temperature cycling [85], high-temperature operation [84], and low/no humidity operation [31, 68]. Figure 21.18 shows the polarization curves and active Pt surface areas after CV cycling [86]. Apparently, as the CV cycle increases the fuel cell performance decreases greatly due to the loss of active Pt surface area.

The lifetime of a fuel cell is greatly shortened under accelerated testing. Therefore, a correlation between the accelerated and the actual tests must be established in order to confidently predict fuel cell durability. The failure modes in both accelerated and actual tests should be the same, otherwise the correlation and the accelerated test are meaningless. Unfortunately, very few such correlations have been achieved so far.

21.7 Conclusions

This chapter has discussed the evaluation of the catalyst layer/MEA of PEM fuel cells. Catalyst layers and MEAs are the most important components in a PEM fuel cell. Therefore, their evaluation plays a critical role in the development and commercialization of PEM fuel cells. This evaluation can be carried out through physical characterization, half-cell tests, single-cell test, as well as lifetime/durability tests. Lifetime/durability is the final and decisive validating step. In order to diagnose and optimize catalyst layer/MEA performance, many physical and electrochemical methods have been developed over the past decades. *In situ* AC impedance (EIS) and cyclic voltammetry (CV) are very useful techniques for diagnosing PEM fuel cells. However, rapid and effective testing methods are still needed to achieve a fundamental understanding of fuel cell performance degradation mechanisms.

References

1. Hirano S, Kim J, Srinivasan S. High performance proton exchange membrane fuel cells with sputter-deposited Pt layer electrodes. Electrochim Acta 1997;42:1587–93.
2. Dearnaley G, Arps JH. Method of depositing a catalyst on a fuel cell electrode. United States patent US 6159533. 2000 Dec 12.
3. Liu R, Her W-H, Fedkiw PS. In situ electrode formation on a Nafion membrane by chemical platinization. J Electrochem Soc 1992;139:15–23.
4. Hogarth MP, Munk J, Shukla AK, Hamnett A. Performance of carbon-cloth bound porous-carbon electrodes containing an electrodeposited platinum catalyst towards the electrooxidation of methanol in sulphuric acid electrolyte. J Appl Electrochem 1994;24:85–8.
5. Ticianelli EA, Derouin CR, Srinivasan S. Localization of platinum in low catalyst loading electrodes to to attain high power densities in SPE fuel cells. J Electroanal Chem 1988;251:275–95.

6. Kumar GS, Raja M, Parthasarathy S. High performance electrodes with very low platinum loading for polymer electrolyte fuel cells. Electrochim Acta 1995;40:285–90.
7. Srinivasan S, Velev OA, Parthasarathy A, Manko DJ, Appleby AJ. High energy efficiency and high power density proton exchange membrane fuel cells – electrode kinetics and mass transport. J Power Sources 1991;36:299–320.
8. Wilson MS, Gottesfeld S. High performance catalyzed membranes of ultra-low Pt loadings for polymer electrolyte fuel cells. J Electrochem Soc 1992;139:L28–30.
9. Antoine O, Bultel Y, Ozil P, Durand R. Catalyst gradient for cathode active layer of proton exchange membrane fuel cell. Electrochim Acta 2000;45:4493–500.
10. Prasanna M, Ha HY, Cho EA, Hong SA, Oh IH. Investigation of oxygen gain in polymer electrolyte membrane fuel cells. J Power Sources 2004;137:1–8.
11. Gasteiger HA, Panels JE, Yan SG. Dependence of PEM fuel cell performance on catalyst loading. J Power Sources 2004;127:162–71.
12. Amphlett JC, Baumert RM, Mann RF, Peppley BA, Roberge PR, Harris TJ. Performance modeling of the Ballard Mark IV solid polymer electrolyte fuel cell. J Electrochem Soc 1995;142:9–15.
13. Zhang J, Tang Y, Song C, Zhang J, Wang H. PEM fuel cell open circuit voltage (OCV) in the temperature range of 23 °C to 120 °C. J Power Sources 2006;163:532–7.
14. Jiang J, Kucernak A. Investigations of fuel cell reactions at the composite microelectrodesolid polymer electrolyte interface. I. Hydrogen oxidation at the nanostructured Pt Nafion membrane interface. J Electroanal Chem 2004;567:123–37.
15. Faculty of Chemical Technology, University of Split [homepage on the Internet]. Split, Croatia: Eni Geralic; ©2004–2005. Chemistry dictionary and glossary. Available from: http://www.ktf-split.hr/glossary/en_index.html.
16. Damjanovic A, Brusic V. Electrode kinetics of oxygen reduction on oxide-free platinum electrodes. Electrochim Acta 1967;12:615–28.
17. Damjanovic A, Genshaw MA. Dependence of the kinetics of O_2 dissolution at Pt on the conditions for adsorption of reaction intermediates. Electrochim Acta 1970;15:1281–3.
18. Parthasarathy A, Martin CR, Srinivasan S. Investigations of the O_2 reduction reaction at the platinum/nafion interface using a solid-state electrochemical cell. J Electrochem Soc 1991;138:916–21.
19. Parthasarathy A, Srinivasan S, Appleby AJ, Martin CR. Temperature dependence of the electrode kinetics of oxygen reduction at the platinum/Nafion interface – a microelectrode investigation. J Electrochem Soc 1992;139:2530–7.
20. Hoare JP. Rest potentials in the platinum-oxygen-acid system. J Electrochem Soc 1962;109:858–65.
21. Thacker R, Hoare JP. Sorption of oxygen from solution by noble metals I. Bright platinum. J Electroanal Chem 1971;30:1–14.
22. Kim J, Lee S-M, Srinivasan S, Chamberlin CE. Modeling of proton exchange membrane fuel cell performance with an empirical equation. J Electrochem Soc 1995;142:2670–4.
23. Volfkovich YM, Bagotzky VS. The method of standard porosimetry 1. Principles and possibilities. J Power Sources 1994;48:327–38.
24. Meredith RE, Tobias CW. Conduction in heterogeneous systems. In: Tobias CW, editor. Advances in electrochemical science and engineering, Vol. 2. New York: Interscience, 1962; 15–47.
25. Wang CY, Cheng P. Multiphase flow and heat transfer in porous media. Adv Heat Trans 1997;30:93–196.
26. Barbir F. Main cell components, materials properties and processes. In: Barbir F, editor. PEM fuel cells: theory and practice. Amsterdam Boston: Elsevier Academic press, 2005;73–113.

27. Li G, Pickup PG. Ionic conductivity of PEMFC electrodes. J Electrochem Soc 2003;150:C745–52.

28. Lee SJ, Mukerjee S, McBreen J, Rho YW, Kho YT, Lee TH. Effects of Nafion impregnation on performances of PEMFC electrodes. Electrochim Acta 1998;43:3693–701.

29. Cheng X, Yi B, Han M, Zhang J, Qiao Y, Yu J. Investigation of platinum utilization and morphology in catalyst layer of polymer electrolyte fuel cells. J Power Sources 1999;79:75–81.

30. Shin SJ, Lee JK, Ha HY, Hong SA, Chun HS, Oh IH. Effect of the catalytic ink preparation method on the performance of polymer electrolyte membrane fuel cells. J Power Sources 2002;106:146–52.

31. Zhang J, Tang Y, Song C, Cheng X, Zhang J, Wang H. PEM fuel cells operated at 0% relative humidity in the temperature range of 23–120 °C. Electrochim Acta 2007;52:5095–101.

32. Saab AP, Garzon FH, Zawodzinski TA. Determination of ionic and electronic resistivities in carbon/polyelectrolyte fuel-cell composite electrodes. J Electrochem Soc 2002;149:A1541–6.

33. Saab AP, Garzon FH, Zawodzinski TA. The effects of processing conditions and chemical composition on electronic and ionic resistivities of fuel cell electrode composites. J Electrochem Soc 2003;150:A214–8.

34. Du CY, Shi PF, Cheng XQ, Yin GP. Effective protonic and electronic conductivity of the catalyst layers in proton exchange membrane fuel cells. Electrochem Commun 2004;6:435–40.

35. Pantea D, Darmstadt H, Kaliaguine S, Summchen L, Roy C. Electrical conductivity of thermal carbon blacks: Influence of surface chemistry. Carbon 2001;39:1147–58.

36. KSV Instruments USA [homepage on the Internet]. Helsinki, Finland: KSV Instruments Ltd.; ©2008 [updated 2005 Jan 28]. Contact angles. Available from: http://www.ksvinc.com/contact_angle.htm.

37. Wang CY. Two-phase flow and transport. In: Vielstich W, Gasteiger HA, Lamm A, editors. Handbook of fuel cells – fundamentals, technology and applications, Vol 3. Chichester, England: Wiley, 2003;337–47.

38. Zawodzinski TA, Gottesfeld S, Shoichet S, McCarthy TJ. The contact angle between water and the surface of perfluorosulphonic acid membranes. J Appl Electrochem 1993;23:86–8.

39. Brack H-P, Slaski M, Gubler L, Scherer GG, Alkan S, Wokaun A. Characterisation of fuel cell membranes as a function of drying by means of contact angle measurements. Fuel Cells 2004;4:141–6.

40. Yu HM, Ziegler C, Oszcipok M, Zobel M, Hebling C. Hydrophilicity and hydrophobicity study of catalyst layers in proton exchange membrane fuel cells. Electrochim Acta 2006;51:1199–207.

41. Kabbabi A, Gloaguen F, Andolfatto F, Durand R. Particle size effect for oxygen reduction and methanol oxidation on Pt/C inside a proton exchange membrane. J Electroanal Chem 1994;373:251–4.

42. Gamez A, Richard D, Gallezot P, Gloaguen F, Faure R, Durand R. Oxygen reduction on well-defined platinum nanoparticles inside recast ionomer. Electrochim Acta 1996;41:307–14.

43. Maillard F, Martin M, Gloaguen F, Leger JM. Oxygen electroreduction on carbon-supported platinum catalysts. Particle-size effect on the tolerance to methanol competition. Electrochim Acta 2002;47:3431–40.

44. Jiang R, Chu D. Multiple small potential steps at a rotating disk electrode and applications. Electrochim Acta 2000;45:4025–30.

45. Gasteiger HA, Markovic NM, Ross PN Jr. H_2 and CO electrooxidation on well-characterized Pt, Ru, and Pt-Ru. 1. Rotating disk electrode studies of the pure gases including temperature effects. J Phys Chem 1995;99:8290–301.

46. Innocente AF, Angelo ACD. Electrocatalysis of oxidation of hydrogen on platinum ordered intermetallic phases: kinetic and mechanistic studies. J Power Sources 2006;162:151–9.

47. Tripkovic AV, Popovic KD, Grgur BN, Blizanac B, Ross PN, Markovic NM. Methanol electrooxidation on supported Pt and PtRu catalysts in acid and alkaline solutions. Electrochim. Acta 2002;47:3707–14.

48. Honma I, Toda T. Temperature dependence of kinetics of methanol electro-oxidation on PtSn alloys. J Electrochem Soc 2003;150:A1689–92.

49. Schmidt TJ, Gasteiger HA, Behm RJ. Rotating disk electrode measurements on the co tolerance of a high-surface area Pt/Vulcan carbon fuel cell catalyst. J Electrochem Soc 1999;146:1296–304.

50. Paulus UA, Schmidt TJ, Gasteiger HA, Behm RJ. Oxygen reduction on a high-surface area Pt/Vulcan carbon catalyst: a thin-film rotating ring-disk electrode study. J Electroanal Chem 2001;495:134–45.

51. Schmidt TJ, Gasteiger HA, Stab GD, Urban PM, Kolb DM, Behm RJ. Characterization of high-surface-area electrocatalysts using a rotating disk electrode configuration. J Electrochem Soc 1998;145:2354–8.

52. Pozio A, De Francesco M, Cemmi A, Cardellini F, Giorgi L. Comparison of high surface Pt/C catalysts by cyclic voltammetry. J Power Sources 2002;105:13–19.

53. Song C, Tang Y, Zhang JL, Zhang J, Wang H, Shen J, et al. PEM fuel cell reaction kinetics in the temperature range of 23–120 °C. Electrochim Acta 2007;52:2552–61.

54. Zhang J, Tang Y, Song C, Zhang J. Polybenzimidazole-membrane-based PEM fuel cell in the temperature range of 120–200 °C. J Power Sources 2007;172:163–71.

55. Shinozaki K, Hatanaka T, Morimoto Y. Pt utilization analysis using CO adsorption. ECS Transactions 2007;11:497–507.

56. Vidakovic T, Christov M, Sundmacher K. The use of CO stripping for in situ fuel cell catalyst characterization. Electrochim Acta 2007;52:5606–13.

57. Ciureanu M, Wang H. Electrochemical impedance study of electrode-membrane assemblies in pem fuel cells: I. Electro-oxidation of H_2 and H_2/CO mixtures on pt-based gas-diffusion electrodes. J Electrochem Soc 1999;146:4031–40.

58. Weaver MJ, Chang SC, Leung LWH, Jiang X, Rubel M, Szklarczyk M, et al. Evaluation of absolute saturation coverages of carbon monoxide on ordered low-index platinum and rhodium electrodes. J Electroanal Chem 1992;327:247–60.

59. Du CY, Zhao TS, Yang WW. Effect of methanol crossover on the cathode behavior of a DMFC: a half-cell investigation. Electrochim Acta 2007;52:5266–71.

60. Chu D, Gilman S. The influence of methanol on O_2 electroreduction at a rotating Pt disk electrode in acid electrolyte. J Electrochem Soc 1994;141:1770–3.

61. Reeve RW, Burstein GT, Williams KR. Characteristics of a direct methanol fuel cell based on a novel electrode assembly using microporous polymer membranes. J Power Sources 2004;128:1–12.

62. Zhang J, Xie Z, Zhang J, Tang Y, Song C, Navessin T, et al. High temperature PEM fuel cells. J Power Sources 2006;160:872–91.

63. Tang Y, Zhang J, Song C, Liu H, Zhang J, Wang H, et al. Temperature dependent performance and in situ AC impedance of high-temperature PEM fuel cells using the Nafion-112 membrane. J Electrochem Soc 2006;153:A2036–43.

64. Sluyters-Rehbach M. Impedances of electrochemical systems: terminology, nomenclature and representation, part I: cells with metal electrodes and liquid solutions. Pure Appl Chem 1994;66:1831–91.

65. Paik W-K, Springer TE, Srinivasan S. Kinetics of fuel cell reactions at the platinum/solid polymer electrolyte interface. J Electrochem Soc 1989;136:644–9.
66. Bisquert J, Garcia-Belmonte G, Fabregat-Santiago F, Compte A. Anomalous transport effects in the impedance of porous film electrodes. Electrochem Commun 1999;1:429–35.
67. Collier A, Wang H, Zi Yuan X, Zhang J, Wilkinson DP. Degradation of polymer electrolyte membranes. Int J Hydrogen Energy 2006;31:1838–54.
68. Yu J, Matsuura T, Yoshikawa Y, Islam MN, Hori M. In situ analysis of performance degradation of a PEMFC under nonsaturated humidification. Electrochem Solid-State Lett. 2005;8:A156–8.
69. Teranishi K, Kawata K, Tsushima S, Hirai S. Degradation mechanism of PEMFC under open circuit operation. Electrochem Solid-State Lett 2006;9:A475–7.
70. Inaba M, Kinumoto T, Kiriake M, Umebayashi R, Tasaka A, Ogumi Z. Gas crossover and membrane degradation in polymer electrolyte fuel cells. Electrochim Acta 2006;51:5746–53.
71. Song Y, Fenton JM, Kunz HR, Bonville LJ, Williams MV. High-performance PEMFCs at elevated temperatures using Nafion 112 membranes. J Electrochem Soc 2005;152:A539–44.
72. Cheng X, Zhang J, Tang Y, Song C, Shen J, Song D, et al. Hydrogen crossover in high-temperature PEM fuel cells. J Power Sources 2007;167:25–31.
73. Borup R, Meyers J, Pivovar B, Kim YS, Mukundan R, Garland N, et al. Scientific aspects of polymer electrolyte fuel cell durability and degradation. Chem Rev 2007;107:3904–51.
74. Huang X, Solasi R, Zou Y, Feshler M, Reifsnider K, Condit D, et al. Mechanical endurance of polymer electrolyte membrane and PEM fuel cell durability. J Poly Sci Part B: Poly Phys 2006;44:2346–57.
75. Cheng X, Shi Z, Glass N, Zhang L, Zhang J, Song D, et al. A review of PEM hydrogen fuel cell contamination: Impacts, mechanisms, and mitigation. J Power Sources 2007;165:739–56.
76. Kinoshita K, Lundquist JT, Stonehart P. Potential cycling effects on platinum electrocatalyst surfaces. J Electroanal Chem 1973;48:157–66.
77. Darling RM, Meyers JP. Kinetic model of platinum dissolution in PEMFCs. J Electrochem Soc 2003;150:A1523–7.
78. Ferreira PJ, la O GJ, Shao-Horn Y, Morgan D, Makharia R, Kocha S, et al. Instability of Pt/C electrocatalysts in proton exchange membrane fuel cells. J Electrochem Soc 2005;152:A2256–71.
79. Schulze M, Schneider A, Gulzow E. Alteration of the distribution of the platinum catalyst in membrane-electrode assemblies during PEFC operation. J Power Sources 2004;127:213–21.
80. Paik CH, Jarvi TD, O'Grady WE. Extent of PEMFC cathode surface oxidation by oxygen and water measured by CV. Electrochem Solid-State Lett 2004;7:A82–4.
81. Peuckert M, Yoneda T, Betta R A D, Boudart M. Oxygen reduction on small supported platinum particles. J Electrochem Soc 1986;133:944–7.
82. Fuller T, Gray G. Carbon corrosion induced by partial hydrogen coverage. ECS Trans 2006;1:345–53.
83. Schulze M, Christenn C. XPS investigation of the PTFE induced hydrophobic properties of electrodes for low temperature fuel cells. Appl Surf Sci 2005;252:148–53.
84. Tang Y, Zhang J, Song C, Zhang J. Single PEMFC design and validation for high-temperature MEA testing and diagnosis up to 300 °C. Electrochem Solid-State Lett 2007;10:B142–6.

85. Hicks M, Pierpont D, Turner P, Watschke T. Accelerated testing and lifetime modeling for the development of durable fuel cell meas. ECS Trans 2006;1:229–37.
86. Borup R, Davey J, Wood D, Garzon F, Inbody M, Guidry D. PEM fuel cell durability. In: 2005 DOE hydrogen program review. US DOE Hydrogen Program 2005 Annual Merit Review and Peer Evaluation Meeting; 2005 May 23–26; Arlington, VA.

22

Catalyst Layer Composition Optimization

Wei Xing

As an alternative clean energy technology, the proton exchange membrane fuel cell (PEMFC) could be widely used in residential, transportation, and military applications. However, several factors currently limit fuel cell system commercialization: low stack performance, short lifetime, and high cost. Catalyst layer composition is a key component in determining both stack performance and lifetime. Therefore, catalyst layer composition optimization is highly significant for improving MEA stability and continuity, enhancing stack lifetime, and reducing the overall system cost. This chapter discusses the main factors in catalyst layer composition that determine MEA performance.

22.1 Catalyst Layer Materials Selection and Evaluation

22.1.1 Catalyst Selection

The catalyst layer plays a significant role in defining the performance of the MEA. Furthermore, according to the United States Department of Energy fiscal year 2005 annual progress report, the catalyst layer accounts for 77% of the whole cost of a fuel cell stack [1]. To achieve high performance and reduce the cost of the MEA, catalyst selection should be the foremost task. Since the electrochemical reaction of the PEMFC is heterogeneous, taking place in a unique triple-phase interface, many catalyst features such as composition, morphology, particle size, and dispersion dramatically influence the activity and stability of the MEA. To ensure good performance, an electrocatalyst has to fulfill several requirements:

(1) *High electrochemical activity and contamination tolerance.* An electrocatalyst should be of high intrinsic activity, to diminish electrochemical reaction polarization and enhance energy conversion efficiency. More specifically, the anode catalyst should have the ability to resist detrimental by-products such as CO and other intermediates that poison the active reaction surface; the cathode catalyst should have the ability to restrain crossover methanol oxidation when liquid methanol is selected as the fuel.

(2) *High electrochemical area (ECA)*. To improve utilization and further reduce catalyst loading, the noble metal catalyst should be highly dispersed and have a high ECA.

(3) *Stability and durability*. The electrocatalyst in a PEMFC always works in a highly acidic environment in which a solid polymer membrane is employed. The catalyst therefore should have high corrosion resistance to maintain its chemical stability. At the same time, the catalyst has to keep its activity and specific surface stable during its whole working potential. Moreover, high durability is also a key requirement, as a PEMFC is expected to operate for tens of thousands of hours.

(4) *Good electrical conductivity*. The electrocatalyst not only provides a location for the electrochemical reaction but also acts as the main conductor for electron transfer. It thus should have good electrical conductivity to minimize resistive losses in the catalyst layer.

(5) *Appropriate catalyst support*. It is generally recognized that support greatly influences the activity of the electrocatalyst and the performance of the MEA in a PEMFC. On the one hand, the inert support fixes the active phase on its surface, preventing the active phase from agglomerating; on the other hand, it also interacts with the active phase, improving its activity and selectivity. Therefore, a catalyst support should have a large surface area, high electrical conductivity, acceptable chemical stability, as well as low cost.

In addition, the catalyst should be inexpensive to fabricate and manufacturable in high volumes with good reproducibility.

Table 22.1. Commercial Pt/C catalysts for PEMFCs

Supplier	Product	XRD Pt crystalline size, nm	CO chemisorption metal area, m^2g^{-1} Pt
Johnson Matthey	37 wt% Pt/AC 01	2.3	130
Johnson Matthey	47 wt% Pt/AC 01	2.4	100
Johnson Matthey	57 wt% Pt/AC 01	2.8	85
Johnson Matthey	67 wt% Pt/AC 01	3.5	60
E-TEK	10 wt% Pt/Vulcan XC72R	2.0	140
E-TEK	20 wt% Pt/Vulcan XC72R	2.5	112
E-TEK	30 wt% Pt/Vulcan XC72R	3.2	88
E-TEK	40 wt% Pt/Vulcan XC72R	3.9	72
E-TEK	60 wt% Pt/Vulcan XC72R	8.8	32
E-TEK	80 wt% Pt/Vulcan XC72R	25	11
E-TEK	Pt black	100	28

Platinum-based particle catalysts including Pt black powder, carbon-supported Pt, and carbon-supported Pt alloy are the most active, efficient, applicable, and

successful catalysts for fuel cell reactions in state-of-the-art MEAs. They are widely employed both as anode catalysts to oxidize fuel and as cathode catalysts to reduce oxygen. A number of suppliers, e.g., Johnson Matthey, E-TEK, Tanaka KK, and OMG, presently offer fuel cell catalysts. Some commercially available Pt/C catalysts are listed in Table 22.1.

Originally, Pt black was used as the PEMFC electrocatalyst, and as an auxiliary power source in the Gemini space flights it exhibited excellent long-term performance but at a prohibitively high cost. As is shown in Table 22.1, the Pt black powders are always poorly dispersed and thus have low utilization. Subsequently, carbon-supported Pt was used in place of Pt black and the catalyst loading was dramatically reduced [2]. Ongoing research has mainly focused on developing supported Pt alloys, to further increase catalyst activity and reduce loading.
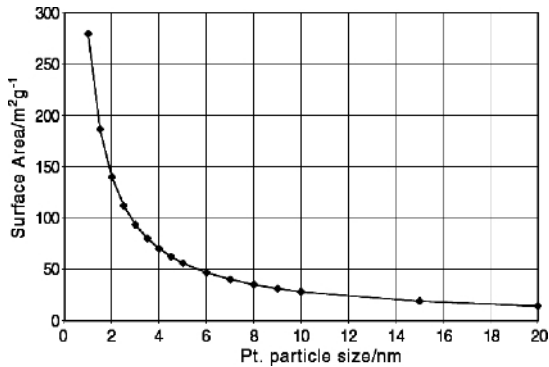
Figure 22.1. Relationship of Pt surface area to particle size, based on spherical geometry [3]. (Reproduced from Thompsett D. Catalysts for the proton exchange membrane fuel cell. In: Hoogers G, editor. Fuel cell technology handbook. Boca Raton: CRC Press, 2003. With permission from CRC.)

Currently, hydrogen and methanol are the main fuels used in PEMFCs. The electrochemical oxidation of hydrogen on a wide range of metal surfaces is very facile, but in the acidic environment in which the catalyst must work only Pt and Pd show reasonable activity and stability. Many factors influence the activity and stability of a Pt/C catalyst, of which the dispersion of Pt particles seems to be particularly important. In general, to achieve the maximum number of active sites, Pt particles are finely dispersed on an inert support. The relationship between Pt particle size and surface area can be calculated by the following simple relationship (assuming spherical particles) [3]:

$$S = 6 / (\rho_{Pt} \times d)$$

where S is the Pt surface area, ρ_{Pt} is the Pt density, and d is the particle diameter. The relationship is shown in Figure 22.1, where it can be seen that an increase in Pt particle size from 2 to 4 nm causes the Pt surface area to drop by half. Therefore, to achieve the maximum number of sites, the Pt particles need to be dispersed as finely as possible. Figure 22.2 shows the cyclic voltammetry (CV) of different

proprietary catalysts prepared by our laboratory in N_2-saturated 0.5 mol/L H_2SO_4. The effect of particle size on the ECA is clear.
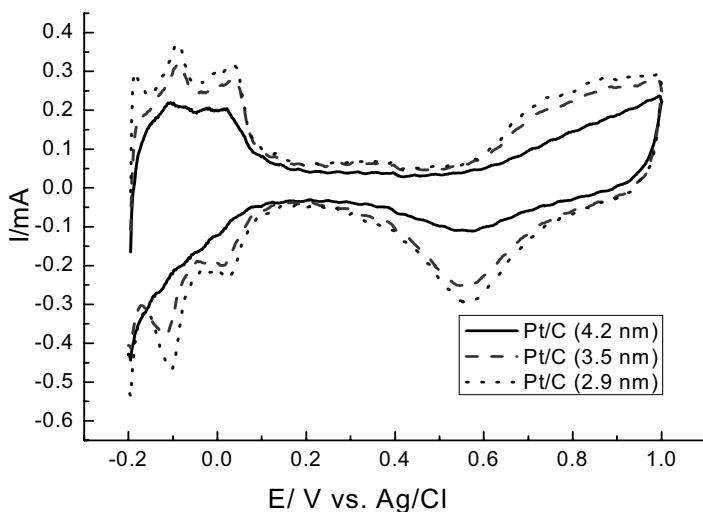
Figure 22.2. CV for different particle sizes of Pt/C in N_2-saturated 0.5 mol/L H_2SO_4; room temperature; scan rate: 50 mV/s

Although the Pt/C catalyst shows practical activity towards hydrogen oxidation, when a reformate stream is employed as fuel the catalyst may become unusable in the PEMFC because of catalyst poisoning. It is well known that the CO in the reformate stream binds very strongly to Pt sites. The adsorbed CO prevents the dissociative electrosorption of H_2 and dramatically lowers the cell potential produced by the MEA, since a much higher anode potential is required to sustain the rate of hydrogen electrooxidation. Furthermore, it has been discovered that CO_2 also poisons the catalyst by generating CO through the reverse water gas shift reaction (RWGSR) and CO_2 electroreduction [4]. One of the methods to counter the problem of catalyst poisoning is catalyst alloying.

Significant efforts have been made over several decades to develop CO-tolerant Pt alloy electrocatalysts. These electrocatalysts generally fall into two categories [4]. The first includes a wide range of Pt alloys that have been examined in an attempt to modify the CO and hydrogen electrosorption properties of Pt, in order to reduce the CO coverage and increase the rate of hydrogen electrooxidation. Iwase and Kawatsu [5] investigated 10 of these catalysts: PtRu/C, PtIr/C, PtV/C, PtRh/C, PtCr/C, PtCo/C, PtNi/C, PtFe/C, PtMn/C, and PtPd/C. They found that only the PtRu/C catalyst, when exposed to reformate gas with 100 ppm of CO, showed cell performance equivalent to that of a pure hydrogen cell with a single metal Pt/C catalyst. The second category of electrocatalysts involves modifying Pt with metal oxides to catalyze the electrooxidation of CO to CO_2 at operating anode potentials. This reduces the CO coverage and increases the number of Pt electrocatalyst sites available for hydrogen electrooxidation. These electrocatalysts comprise a variety of carbon-supported PtMo, PtW, PtCoMo, and $PtWO_3$ catalysts [6–9]. It was

reported that a carbon-supported PtMo catalyst with a Pt:Mo ratio of 4:1 showed only a ~50 mV loss in performance with 100 ppm CO in H_2, as compared to its performance in pure H_2. In contrast, a carbon-supported PtRu catalyst (Pt:Ru = 1:1) showed a ~160 mV loss. However, when the CO_2 in the reformate was under consideration, the PtMo/C showed inferior performance. As CO_2 is a significant component of reformed hydrocarbon fuel, such CO_2 intolerance limits the use of PtMo catalysts in practical PEMFC systems [10].

In addition to the two categories of catalyst described above, Ross et al. [11] developed a non-platinum based alloy, Au-Pd/C, which showed promising CO tolerance. They reported a three-fold improvement in electrooxidation of CO/H_2 with their catalyst as compared to a PtRu catalyst. Schmidt et al. [12] also prepared a PdAu/C electrocatalyst, and the CO/H_2 oxidation measurements made by the thin-film rotating disk method showed the superior activity of PdAu as compared with a PtRu catalyst. However, further no further reports on that catalyst-based MEA are available.

To date, the carbon-supported PtRu alloy catalyst is still the main choice for reformate operating PEMFCs. It is generally accepted that the enhanced CO tolerance of PtRu/C is attributable to both a bi-functional mechanism [13–14] and an electronic effect [15–16]. The bi-functional mechanism involves water activation by Ru and subsequent CO electrooxidation on a neighbouring Pt atom. In the electronic effect, the Ru alloying reduces the Pt electron density, which should weaken the Pt-CO bond strength and decrease CO coverage on the PtRu, thus increasing the number of electrocatalyst sites available for hydrogen electrosorption and electrooxidation. However, which mechanism plays a more important role in enhancing CO tolerance is still not clear. Some work has been devoted to optimizing the PtRu composition. Iwase and Kawatsu [5] reported that equivalent performance was found for 20 wt% PtRu/C catalysts with Pt:Ru ratios from 85:15 to 15:85, when operated on a fuel of 100 ppm CO in H_2. They also showed that alloying the Pt and Ru was necessary to give optimum CO-tolerant performance. Oetjen et al. [17] found that carbon-supported $Pt_{0.5}Ru_{0.5}$ showed better CO tolerance than other PtRu compositions. Antolini et al. [18] investigated PEMFC performance using PtRu/C electrocatalysts by E-TEK with different Ru contents. The best value was obtained for a Pt:Ru catalyst with an atomic ratio of 1:1. However, Qi and Kaufman [19] found that PtRu/C catalysts with the same Pt:Ru 1:1 atomic ratio and the same Pt-Ru crystallite size but made by different manufacturers have different CO tolerances under the same operating conditions. It is therefore suggested that optimal catalyst composition can be related to both surface composition (depending on the catalyst preparation method) and unalloyed Ru [20].

As the carbon-supported PtRu alloy catalyst seems the most practical for use in PEMFCs, many studies have investigated PtRu alloying with a third element, e.g., W, Mo, Sn, Nb, Au, Ag, Ir, Ni, in an attempt to further improve catalytic activity [21–25]. Some of the elements, such as W, Mo, Sn, Ir, and Ni clearly show further improvement in activity due to the co-catalytic effect, while other elements, such as Nb, Au, and Ag show no improvement but rather a negative effect CO/H_2 electrooxidation activity. Furthermore, catalysts with different metal atomic ratios show unparallel activity toward CO/H_2 electrooxidation. In summary, the

electrochemical activity of carbon-supported Pt–Ru–M catalysts depends on their intrinsic parameters such as the type of third metal, the metal atomic ratio, the degree of alloying of Ru and M, the particle size, and the current density. In addition, composite catalysts PtRu-H_xMO_3/C (M = Mo and W), prepared by dispersing PtRu particles in a composite support composed of colloidal H_xMO_3 (M = W or Mo) and Vulcan XC72, were also developed [26]. The catalysts showed a better CO tolerance than PtRu/C, by lowering the starting potential for CO oxidation and improving the H_2 oxidation when active sites on the noble metals were blocked by CO.
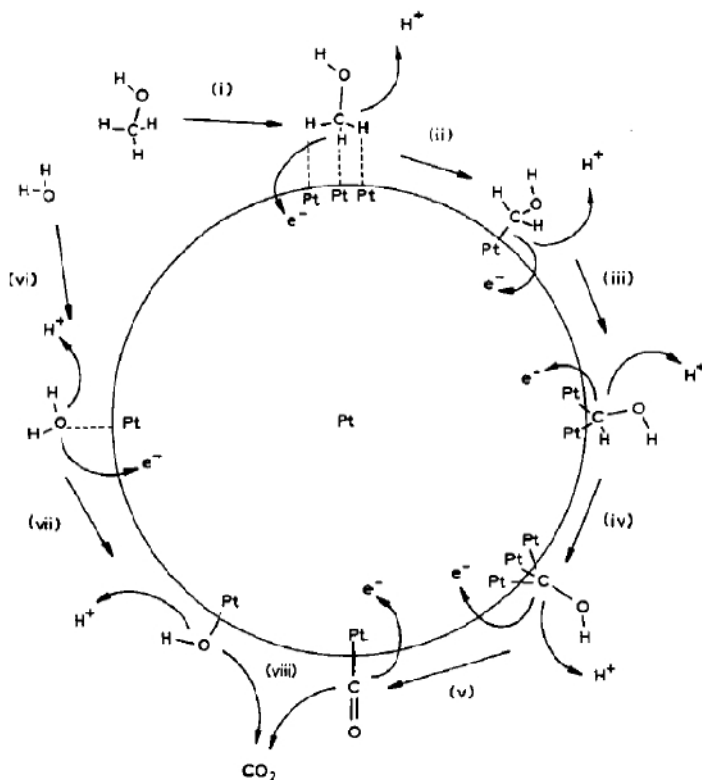
Figure 22.3. A reaction scheme of methanol oxidation on the Pt catalyst surface [27]. (Reproduced from Hogarth MP, Ralph TR. Catalysis for low temperature fuel cells Part III: challenges for the direct methanol fuel cell, Plat Met Rev 2002;46(4):146–64, ©2002, with permission from Johnson Matthey PLC.)

When liquid methanol is employed as the fuel, the sluggish methanol oxidation kinetics on the anode catalyst may be the main hindrance, dramatically reducing the overall MEA performance. Much work has focused on exploring anode catalysts that can effectively enhance the methanol electrooxidation kinetics. Currently, only Pt-based electrocatalysts display the necessary activity and stability in the acidic environment of the DMFC. Figure 22.3 shows the generally accepted

mechanism of methanol oxidation on a Pt catalyst [27]. The methanol oxidation activity of pure Pt rapidly decays in the low-potential region due to the strongly bound intermediates, mainly the -CO$_{ads}$. Therefore, the development of Pt-based electrocatalysts has mainly been directed at the addition of a secondary component (e.g., Ru, Sn, W, Re) that can provide an adsorption site capable of forming OH$_{ads}$ species at low potentials adjacent to poisoned Pt sites [28]. In addition, other factors besides good CO tolerance, such as methanol adsorption and dehydrogenation, play an important role in the methanol oxidation reaction. Thus, the carbon-supported PtRu catalyst is again considered to be the most promising anode material. In addition, some ternary catalysts based on carbon-supported PtRu catalysts show enhanced activity and have also been developed for methanol oxidation [29].
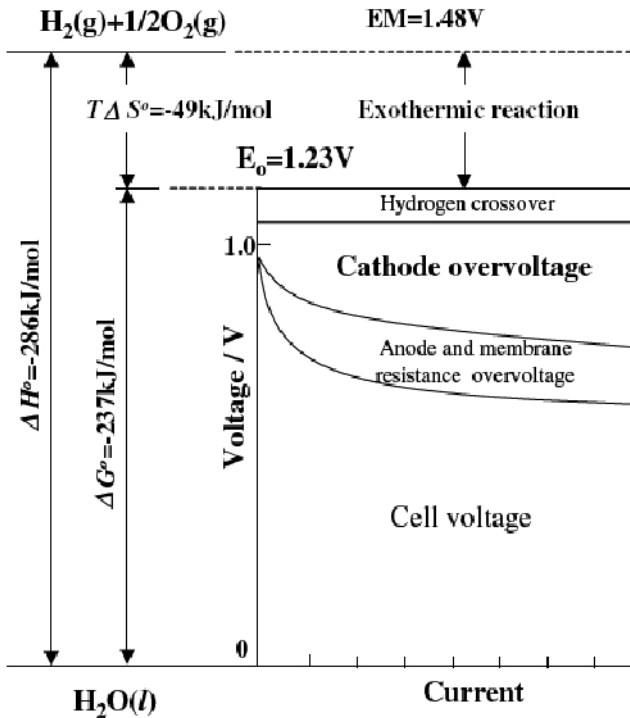
Figure 22.4. Overpotential components in a PEMFC [30]. (With kind permission from Springer Science+Business Media: Journal of Applied Electrochemistry, Progress in the synthesis of carbon nanotube- and nanofiber-supported Pt electrocatalysts for PEM fuel cell catalysis, 36(5), 2006, 507–22, Lee K, Zhang J, Wang H, Wilkinson DP, Figure 1, ©Springer.)

MEA performance is also seriously limited by the sluggish electroreduction of oxygen on the state-of-the-art Pt/C cathode catalyst in both PEMFCs and DMFCs. As is shown in Figure 22.4, the overpotential for the oxygen reduction reaction (ORR) in a PEMFC contributes about 80% of the total cell voltage loss [30]. In

order to reduce the overpotential of the ORR and further improve cathode efficiency, high-activity ORR catalysts need to be developed. Based on early work with PAFC cathodes, many studies have focused on alloying the Pt/C catalyst with a base-metal to improve the catalytic activity. Mukerjee and Srinivasan [31] reported that the carbon-supported PtCr, PtCo, and PtNi alloy catalysts showed a 20–30 mV activity gain over Pt/C at a low current density range. Johnson Matthey [32] investigated carbon-supported PtFe, PtMn, PtNi, PtTi, and PtCr for PEMFCs, demonstrating that PtTi, PtMn, and PtFe catalysts could enhance fuel cell performance by 20–40 mV in a practical current density range. Xiong et al. [33] investigated carbon-supported Pt-M (M = Fe, Co, Ni, and Cu) in PEMFCs and found that the Pt-M alloy catalysts showed improved catalytic activity for the ORR in comparison with Pt, and the Pt-Co catalyst presented the best performance among the various alloy catalysts investigated. It appears that the use of Pt-alloy catalysts to enhance activity and lower costs is a feasible approach for implementation in practical PEMFCs.

However, the stability of the carbon-supported Pt-M catalysts may also limit their application in PEMFCs. In the acidic environment the base-metal may leach out of the catalysts. The base-metal cations can easily exchange with protons in the membrane or ionomer, giving rise to decreased membrane/ionomer conductivity, dehydration of the membrane, and a decreased oxygen diffusion coefficient in the ionomer [34]. Some authors reported high catalyst stability after more than 1000 hours of duration tests in PEMFCs [31, 34]. On the other hand, the materials had poor stability following short-duration (a few hours) measurements in half cells [35–36]. There are also conflicting views on the main factor influencing catalyst stability. Some authors [32, 36] consider that the stability of non-noble metals in an acid environment depends on the type of metal, while Antolini et al. [37] have suggested that the stability of these catalysts depends on the degree of alloying and, to a lesser extent, on the metal particle size, and not on the kind of M. Despite contradictory outcomes for Pt-M catalysts in PEMFCs, it is still generally accepted that the use of carbon-supported Pt-M catalysts as cathode materials in low-temperature fuel cells is preferable, provided that their activity and stability can be further improved.

The carbon support also plays an important role in MEA performance. Catalyst utilization is greatly increased and the loading greatly reduced as a result of the chosen carbon support. On the one hand, the carbon material has a strong influence on the properties of supported noble metal catalysts, such as metal particle size, morphology, size distribution, alloy degree, stability, and dispersion. On the other hand, carbon supports can also affect the performance of supported catalysts in various ways, such as mass transport and catalyst layer electronic conductivity, electrochemical active area, and metal nanoparticle stability during operation. Carbon blacks are generally used as supports for catalysts, and there are two main types: oil-furnace blacks and acetylene blacks; some commonly used carbon black supports are listed in Table 22.2 [3]. Recently, there has also been report of carbon nanomaterials being used as supports; however, when applied to fuel cells these materials still face some challenges, such as carbon nanomaterial synthesis, metal loading, and electrode preparation [38].

Table 22.2. Carbon blacks that have been used as support for Pt catalysts in PEMFCs [3]. (Reproduced from Thompsett D. Catalysts for the proton exchange membrane fuel cell. In: Hoogers G, editor. Fuel cell technology handbook. Boca Raton: CRC Press, 2003. With permission from CRC.)

Carbon	Supplier	Type of carbon	BET surface area (m^{2}g^{-1})[a]	DBP adsorption (units)[b]
Vulcan XC72	Cabot Corp.	Furnace black	250	900
Black Pearls 2000	Cabot Corp.	Furnace black	1500	330
Ketjen EC300J	Ketjen Black International	Furnace black	800	360
Ketjen EC600JD	Ketjen Black International	Furnace black	1270	495
Shawinigan	Chevron	Acetylene black	80	–
Denka black	Denka	Acetylene black	65	165

[a] BET: Braunauer-Emmett-Teller method
[b] DBP: dibutyl phthalate number (measure of carbon void volume)

22.1.2 Gas Diffusion Layer (GDL) and Microporous Layer (MPL) Materials Selection

As an important component in PEMFCs, the gas diffusion layer (GDL) provides mechanical support for the catalyst layer, an electronic pathway for electrons, and a flow channel for the reacting gas and product water. To fulfill these functions, it has to meet several requirements. Firstly, as a base substrate for the catalyst layer, the GDL should have a surface that reduces contact resistance while having sufficient mechanical strength and flexibility. Secondly, as an electronic conductor between the bipolar plate and the catalyst layer, the GDL should have high conductivity. To improve gas distribution and water management, the GDL should be porous and hydrophobic. In addition, it should have good heat conductivity for heat management, and high corrosion resistance to keep the MEA stable. Typically, wet-proofed carbon paper and carbon cloth with a thickness of 100–300 μm are used as the GDL in PEMFCs. Both of them are carbon-fiber-based porous materials: carbon paper is non-woven while carbon cloth is a woven fabric. Figure 22.5 shows SEM images of these two GDL substrates. A number of suppliers, e.g., Toray, SGL, and Ballard presently offer carbon GDLs. Table 22.3 lists some commercial carbon papers provided by Toray.

It can be observed that PEMFC performance employing carbon cloth GDLs is different from that when using carbon paper GDLs. Ralph et al. [39] showed that at high current density with internal humidification in Ballard Mark V cells the carbon cloth offered a distinct advantage compare to carbon paper. They deemed the surface porosity and hydrophobicity of the carbon cloth substrate to be more favorable for the movement of liquid water, and thus both water management and

mass transport were enhanced. Frey et al. [40] investigated different prefabricated MEAs with different carbon GDLs. They found that the best performance for a MEA with carbon paper as the GDL was obtained when the membrane electrode unit was hot-pressed. When using carbon cloth as the GDL, better performance was obtained when the GDL was hot-pressed together with the MEA. Wang et al. [41] set up a numerical model to explore the fundamentals behind experimentally observed performance differences between the two carbon GDLs. The results indicated that carbon cloth is the better choice as a GDL material at high-humidity operation due to the low tortuosity of the pore structure and the rough textural surface that facilitates droplet detachment. However, under dry conditions, carbon paper shows better performance due to its more tortuous structure, which prevents the loss of product water to dry gas streams, thus increasing the membrane hydration level and reducing the ohmic loss.
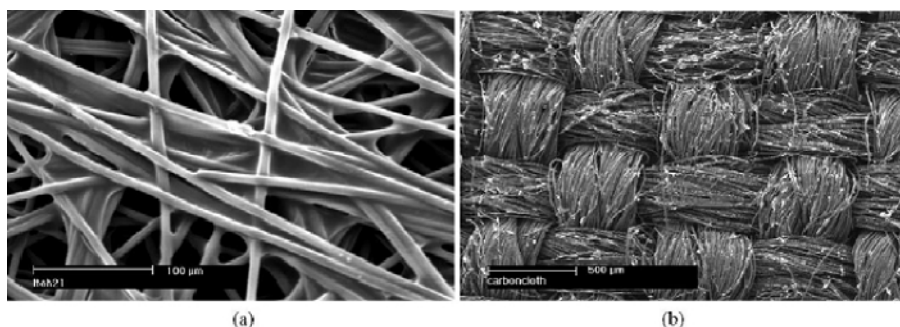
Figure 22.5. SEM of: (a) carbon paper and (b) carbon cloth [125]. (Reprinted from Journal of Power Sources 134(1), Lu GQ, Wang CY. Electrochemical and flow characterization of a direct methanol fuel cell, 33–40, ©2004, with permission from Elsevier.)

Table 22.3. Physical properties of TGP-H carbon paper

Unit	Thickness (mm)	Electrical resistivity (mΩcm)		Porosity (%)	Bulk density (g/cm^3)
		through plane	in plane		
TGP-H-030	0.09	70	5	75	0.42
TGP-H-060	0.17	70	5	73	0.49
TGP-H-090	0.26	70	5	73	0.49
TGP-H-120	0.35	70	5	73	0.49

The thickness of the GDL substrate is important in determining the performance of PEMFCs. Lin and Nguyen [42] investigated the effect of carbon paper GDL substrate thickness on electrode flooding and cell performance. They found that the pore volume and through-plane permeability of GDLs are two main factors influencing performance. Gas transport and liquid water removal were enhanced with a thinner GDL due to the higher superficial velocity at a given air

volumetric flow rate. However, the thinner GDL was more sensitive to water accumulation because of the smaller pore volume. In the SGL carbon paper group, the thinnest paper – which is more sensitive to water and has the lowest permeability – showed the worst performance. In the Toray carbon paper group, the 275 μm and 370 μm carbon papers have the same permeability, and neither are sensitive to water, so the thicker demonstrated poorer performance. The 190 μm carbon paper has the highest permeability but is more sensitive to water, so the competing effects put its performance in between those of the 275 μm and 370 μm carbon papers. Xu et al. [43] also investigated the effect of carbon paper GDL substrate thickness on the cell performance of DMFCs. Their results showed that the thinnest carbon paper yielded the lowest cell voltage of nearly the entire current region. As carbon paper thickness increased so did cell voltage, and the medium-thickness carbon paper gave the highest voltage. However, with a further increase in carbon paper thickness, the cell voltage remained in the low current density region, dropping rapidly with increasing current density. They suggested that the change in cell performance is caused solely by changes in the mass transfer resistance.

Some alternative GDL substrates have also been developed for PEMFCs. Campbell et al. [44] developed a new type of GDL consisting of a poorly conducting carbon web filled with an electrically conducting filler, such as carbon black. Glora et al. [45] investigated the use of resorcinol-formaldehyde aerogel film reinforced with carbon fibers. They implemented the GDL in a test cell and found a power density only 1/6 that of a typical PEMFC, but this was attributed to poor catalyst layer preparation rather than the GDL. Shao et al. [46] developed a porous structure based on Ti mesh, pre-coated with carbon as the GDL of a DMFC. Wan et al. [47, 48] also described an integrated composite MEA (ICMEA) using a porous metal sheet as the GDL. Both of their MEAs showed acceptable performance. Yazici [49] also proposed a new type of GDL using perforated GRAFCELL® natural graphite in a DMFC. The cell performance showed advantages over a cell with a commercial GDL. The author suggested that large open areas with intrinsic permeability and proper polytetrafluoroethylene (PTFE) application helped in the effective transport of gas and liquid within the perforated GRAFCELL® natural graphite GDL for better DMFC performance over conventional diffusion media at room temperature.

To ensure good water management, the GDL is typically wet-proofed. The wet-proofed GDL can drain out product water to keep its pores from becoming clogged, which prevents diffusion of the reacting gas and further affects the PEMFC's overall power output performance. Wet-proofed GDLs are usually prepared by immersing the GDL substrate in a hydrophobic agent dispersion, such as PTFE and FEP. However, the hydrophobic agent is not an electric conductor and reduces the porosity. Therefore, the amount of hydrophobic agent applied should be carefully controlled. Lim and Wang [50] showed that an MEA with a 10 wt% FEP-impregnated cathode GDL provided a higher power density than one with 30 wt% FEP-impregnated carbon paper. They suggested that the excessive FEP impregnation results in significant blockage of surface pores and hence a highly restricted surface for reactant transport and product removal. Recently, a new surface plasma treatment method has also been developed to improve the

GDL's hydrophobic properties. Pai et al. [51] investigated MEA performance with a CF_4 plasma-treated carbon cloth GDL. Polarization measurement showed that the CF_4 plasma-treated module indeed enhanced cell performance, as compared to MEAs with a non-wet-proofed GDL, a 10 wt% PTFE dip-coated GDL, and a commercially available GDL. The CF_4 plasma treatment does not leave excessive hydrophobic material residuals to block or seal the gas diffusion pores, thus the surface-plasma-treated GDL shows a promising future with PEMFCs.

To enhance intimate electronic contact with the catalyst layer and further improve both gas and water transport, a microporous layer (MPL) composed of carbon black powder and a hydrophobic agent such as PTFE is applied to the GDL substrate. The resulting pores in the MPL are primarily between 0.1–0.5 μm in diameter, much smaller than the pore size of the carbon paper (10–50 μm), so the MPL also prevents the catalyst ink from penetrating the GDL substrate, which decreases catalyst utilization. Thus, in that configuration, the GDL is divided into two layers: a macro-porous carbon substrate and a microporous composite layer. Figure 22.6 shows the schematic of a double-layer GDL.
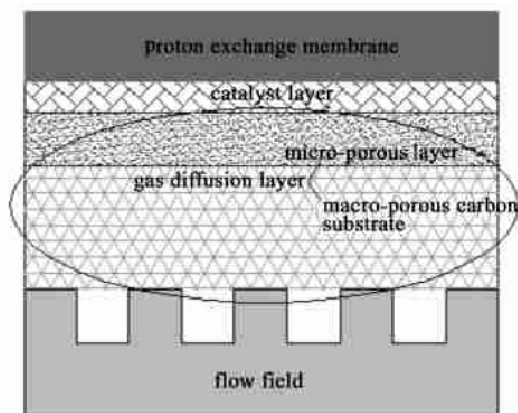
Figure 22.6. Schematic of a double-layer gas diffusion layer

The thickness of the MPL is critical to fuel cell performance. Paganin et al. [52] showed that the performance of their thin-film electrodes increased considerably when the MPL thickness was increased from 15 to 50 μm, but when the thickness was further increased the performance dropped. According to these researchers, if the MPL is too thin, the cell total resistance increases for want of a sufficient carbon/PTFE layer to establish good electronic contact between the rough macroporous substrate and the catalyst layer; conversely, if the MPL is too thick, the diffusion distance and electrical resistance increase.

The hydrophobic agent content in the MPL can also influence cell performance. PTFE is the most commonly used hydrophobic agent. As PTFE content increases, the pore size decreases, resulting in higher mass transport resistance, while if the PTFE content gets too low, the water removal capability drops, resulting in electrode flooding. Paganin et al. [52] showed that the PTFE content in an MPL was optimal at a value of 15 wt%. Lufrano et al. [53] found that the optimal PTFE

content was 20 wt%, though no significant change in performance was found when varying the content from 10 to 60 wt%. However, when the oxidant stream consisted of air, performance was more influenced by PTFE content at elevated current densities. Williams et al. [54] suggested that the optimal PTFE content in an MPL for near-saturated operation is between 15 and 20 wt%.

Besides the typically used Vulcan XC72, various types of carbon black powder with different morphologies and pore structures have been employed to prepare MPLs. Jordan et al. [55] showed that acetylene black carbon with a low micropore volume and an optimized thickness delivered a better performance in PEMFCs than Vulcan XC72. Passalacqua et al. [56] investigated several carbon blacks and graphite as MPL carbon materials. Their results showed that Shawinigan with high pore volume and small average pore size gave the best performance. Antolini et al. [57] compared the performance of cathodes with Shawinigan and Vulcan XC72 in MPLs and showed that the PEMFC using Shawinigan in the cathode MPL outperformed the one using Vulcan XC72, particularly at high current densities and high oxygen pressure. Recently, Wang et al. [58] developed a novel bi-functional MPL which consists of composite carbon powders of acetylene black carbon and Black Pearls 2000 carbon. Enhanced cell performance was obtained by using the MPL with composite carbon black. Park et al. [59] also fabricated a composite MPL comprising 25 wt% carbon nano-fiber and 75 wt% Vulcan XC72 that showed the best cell performance. They deemed that the thinner MPL, achieved by adapting the carbon nano-fibers, affected the performance by enhancing gas permeability and electric conductivity while simultaneously maintaining water management ability.

Some pore formers have also been employed to modify the microstructure of the MPL. Kong et al. [60] studied the effect of MPL pore size distribution on cell performance by adding various amounts of pore former. They found that a combination of heat treating and pore former addition produced the highest porosity and power density. Tang et al. [61] prepared an MPL with graded porosity (GMPL) by printing with different contents of pore former and studied the effect of this GMPL on the performance of a PEMFC. The results showed enhanced cell performance due to the graded pore structure, especially at high current densities.

In addition, when the anode GDL in a DMFC is under consideration, Nafion ionomer is also employed as a binder in the MPL to make the GDL hydrophilic. Neergat et al. [62] investigated cell performance in different PEMFCs with hydrophobic anodic MPLs and hydrophilic anodic MPLs. Their results showed that the cell with a hydrophilic anodic MPL containing 10 wt% Nafion yielded better performance. Zhang et al. [63] investigated the influence of anode GDLs on the performance of low-temperature DMFCs, and the properties of mass transport and CO_2 removal at these anode GDLs. Again, the MEAs with the hydrophilic anode MPLs comprised of carbon blacks and 10 wt% Nafion showed superior performance to the MEAs with hydrophobic MPLs. In addition, the hydrophilic anode GDLs improved CO_2 removal.

22.2 Fabrication Optimization Processes for the Catalyst Layer of MEAs

22.2.1 GDL Substrate Preparation

Typically, to avoid MEA flooding, carbon paper or carbon cloth GDL substrates are wet-proofed using PTFE dispersion, the most common of which is commercially available. The detailed preparation process of PTFE dispersion is as follows. Tetrafluoroethylene (TFE) was polymerized through stirring it under pressure in an aqueous solution of polymerization emulsifier such as ammonium polyfluorocarboxylate, in the presence of ammonium persulfate or succinic acid peroxide as a polymerization initiator. An aqueous dispersion containing a certain weight ratio of PTFE particles was obtained, with an average particle diameter of about 0.20 μm. A nonionic surfactant such as polyoxyethylene alkyl phenyl ether or polyoxyethylene alkyl ether was then added to the PTFE particles, the pH was adjusted to 9–10 with aqueous ammonia, and the suspension was heated while stirring then left at a moderate temperature. After a brief standing period, the dispersion was divided into a transparent aqueous solution upper layer and an aqueous lower layer having a high concentration of PTFE particles. The upper layer was then removed to obtain a concentrated PTFE dispersion. This dispersion was added to the dilute nonionic surfactant solution to adjust the PTFE content to a desired weight ratio. The nonionic surfactant is the most important agent in defining the properties of PTFE dispersion. Originally, polyoxyethylene alkyl phenyl ether was used in PTFE dispersion. However, a surfactant containing a benzene ring in its structure can convert into a harmful organic aromatic compound on thermal decomposition, giving rise to air pollution. Also, such a surfactant is insufficiently volatile and degrades upon heating, which can lead to deposits on the electrode that impair MEA performance. Therefore, polyoxyethylene alkyl ether is now developed for its relatively lower decomposition temperature, as a substitute for polyoxyethylene alkyl phenyl ether [64, 65].

In wet-proofing treatment, carbon paper or carbon cloth GDL substrates are usually cleaned by rinsing in acetone to remove contaminants. The GDL substrate is then dipped in a PTFE dispersion and dried. This step is repeated until the desired PTFE content is coated on the substrate. After that, the impregnated GDL substrate is baked at a relative low temperature (e.g., 280 °C) to remove the surfactant, then sintered at a relative high temperature (e.g., 350 °C) to melt the PTFE. A wide range of PTFE loadings have been used in the GDL substrate, typically from 5 wt% to 30 wt%. The PTFE loading controls the hydrophobic/hydrophilic properties of the GDL substrate, which are vital to water management. The hydrophobic pores allow reactant gas transport and prevent water vapor from condensing and gathering, averting electrode flooding. The higher the PTFE loading, the more hydrophobic is the GDL. However, the entire GDL substrate surface cannot be made hydrophobic because a hydrophilic surface is also needed for liquid water transport. Consequently, an optimal distribution of hydrophobic and hydrophilic surface is needed [42].

To ensure more uniform PTFE covering, the GDL substrate is always sintered after the above-described coating with PTFE; the sinter temperature is higher than

the PTFE melting point. Bevers et al. [66] investigated the effect of sintering temperature on GDL substrate characteristics and showed that sintering improved gas permeability: the higher the sintering temperature, the better the gas diffusion in the GDL substrate. However, the through-plane electrical conductivity was negatively affected by higher sintering temperature. Therefore, sintering temperature selection should be a tradeoff between gas permeability and conductivity.

22.2.2 Microporous Layer (MPL) Preparation and Optimization

As described above, the microporous layer (MPL) composed of carbon black and a hydrophobic agent is applied to the GDL substrate to improve electrical conductivity and mass transport. The MPL is generally prepared as follows. A homogeneous suspension of carbon black and PTFE emulsion is made by mixing and stirring these in an ultrasonic bath. The suspension is then sprayed or spread on the GDL substrate. After drying, the sample is baked and sintered as described above for GDL substrate hydrophobic treatment. A homogeneous distribution of carbon and PTFE is desirable to guarantee a uniform porous structure in the diffusion layer for efficient mass transport as well as in-plane and through-plane electronic conductance. The choice of preparation strategy is decisive for obtaining a homogeneous suspension. Lindermeir et al. [67] suggested that the commonly used preparation method of stirring is difficult to control and leads to problems during the subsequent processing steps, because of the short duration of suspension stability and the wide range of particle sizes. They used a computer controlled wet-ball-mill to prepare the suspension and showed that ball-milling improved stability, reduced sedimentation, and hence extended processability. The resulting narrow particle size distribution simplified further processing.

Besides the most widely used wet methods such as filtering, spreading, and spraying, the dry deposition technique has also been developed to prepare MPLs. The detailed preparation process is as follows. A mixture of carbon and PTFE powder driven by a gas pump through mesh is deposited on the surface of a wet-proofed GDL substrate. After that, the mixture together with the wet-proofed GDL substrate is sintered at 350 °C to melt the PTFE. Finally, the GDL is rolled to flatten its surface. The distance between the roller and stainless steel plate is kept constant by adjusting a gauge. Figure 22.7 shows a schematic diagram for preparing a GDL by the dry deposition technique. Yu et al. [68] suggested that the dry deposition technique allows simple mass production of GDLs and better repeatability compared with the wet method, and is easily scaled up for industrial requirements. In addition, during the process no solvents are required, so the dry technique is environmentally benign and avoids dry time, which is promising for commercial applications.

Generally, the hydrophobic property of an MPL is adjusted by adopting different binders and controlling their content. In most cases, PTFE is employed as the binder for a hydrophobic MPL, while in the anodic GDL of a DMFC Nafion is also used in the MPL to make the GDL hydrophilic. A hydrophilic MPL may facilitate methanol transport and improve CO_2 removal, resulting in better cell performance [63, 67]. But in most cases, the more important factor influencing

GDL hydrophobicity is PTFE content in the MPL. The greater the PTFE content, the more hydrophobic the GDL [43]. However, a hydrophilic liquid transport path is also needed, so there is an optimum PTFE content for the MPL, as described above. The hydrophobic property of the MPL is generally characterized by contact angle measurement, the most common method being sessile drop. The measurement procedure is as follows [69]. A 15 µL droplet of water is made by placing the tip of a syringe close to the sample surface. The water droplet is then attached to the sample surface but prior to this, the wetting process is recorded until no significant change at the surface is observed. Then the contact angle is measured.
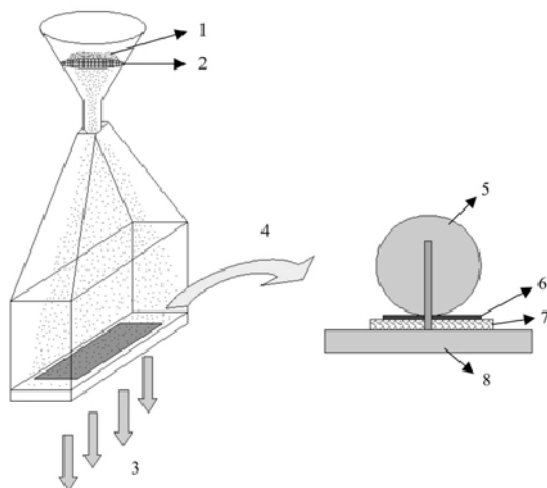
Figure 22.7. Schematic diagram of dry deposition technique: (1) mixture of carbon and PTFE powders, (2) mesh, (3) gas pump, (4) high-temperature sinter, (5) roller, (6) microporous layer, (7) macroporous substrate, (8) stainless steel plate [68]. (Reproduced by permission of ECS—The Electrochemical Society, from Yu J, Yoshikawa Y, Matsuura T, Islam MN, Hori M. Preparing gas-diffusion layers of PEMFCs with a dry deposition technique.)

MPL thickness is primarily controlled by the applied carbon loading. It is generally accepted that a thin MPL improves gas transport and facilitates the removal of water, but it has high electronic resistance and does not give a non-permeable support for coating with the catalyst layer, while a thick MPL hampers gas accessibility because of the lengthened path through the MPL and also has poor gas diffusivity. Hence, an intermediate carbon loading may be beneficial [52, 55, 70, 71]. Also, Song et al. [72] showed that optimal carbon loading of the MPL yielded the maximum active area for the catalyst in the catalyst layer.

The pore structure of the MPL is always tailored by the carbon type and pore former. According to current literature [58, 68], the pores in a GDL are mainly in three size ranges: macropores (10–100 µm), mesopores (0.1–10 µm), and micropores (< 0.1 µm). The macropores formed by PTFE are hydrophobic and mainly act as gas passages. The micropores, which are derived from the original

carbon powder, function as liquid water passages because water vapor is easily condensed into liquid water in a smaller pore. For mesopores, those with PTFE are hydrophobic while those without are hydrophilic. It seems that the acetylene-black-based GDL outperforms the Vulcan XC72-based GDL in terms of higher pore volume and lower microporosity [55–57, 68, 70]. In addition, some pore formers are also used to tailor the pore structure of the GDL [60, 61]. Generally, the pore forming treatment is carried out as follows. Pore former is mixed with a carbon suspension; after the suspension has been applied to the GDL substrate and dried, the MPL is treated in acid solution, or sintered in an oven, or subjected to a combined treatment, according to what pore former is used.

Bulk porosity, hydrophobic/hydrophilic porosity, and pore size distribution are the most important parameters of the GDL microstructure. Bulk porosity and hydrophobic/hydrophilic porosity are always determined as follows [54, 58]. The sample is immersed in water and then in decane. The water fills only the hydrophilic pores while the decane can fill both hydrophilic and hydrophobic pores. By weighing the sample before and after measurement, total pore volume and hydrophilic pore volume can be calculated. The solid volume of the GDL is calculated using the principle of buoyancy. The bulk or hydrophilic porosity of the GDL is defined as its total pore volume or hydrophilic pore volume divided by the sum of its total pore volume and its solid volume. Hydrophobic porosity is determined by subtracting the hydrophilic porosity from the bulk porosity. Pore distribution is determined by mercury-intrusion porosimetry [54]. Measurement is made of the amount of mercury that penetrates the pores of the sample as a function of the applied pressure. The pressure required for mercury to penetrate a certain size of pore is a function of the pore diameter. The pore size distribution of the GDL is then collected and analysis yields the cumulative pore size distribution.

22.2.3 Catalyst Ink Composition and Preparation

Generally, catalyst ink is prepared by dispersing appropriate amounts of catalyst and ionomer solution in a mixture of solvent. All mixtures are stirred vigorously and ultrasonicated to achieve a uniform suspension. Originally, PTFE was used as the catalyst layer binder, as it was in phosphoric acid fuel cells (PAFCs). However, the Nafion membrane in a PEMFC does not penetrate into the catalyst layer in the way that a liquid electrocatalyst does, so the reaction area is limited to the membrane/catalyst layer interface, resulting in low Pt utilization. Subsequently, Nafion has been used as a binder and proton conductor to increase the reaction area, boosting Pt utilization dramatically [2]. When Nafion solution is mixed with solvent, the mixture may become a solution, a colloid, or a precipitate. If the mixture is a solution (i.e., the "solution method"), excessive ionomer may cover the carbon surface, resulting in decreased Pt utilization. When the mixture is a colloid (the "colloidal method"), ionomer colloids adsorb the catalyst powder and the size of the catalyst powder agglomerates increases; as a result, the porosity of the catalyst layer increases and accordingly, the mass transfer resistance diminishes. The continuous network of ionomers throughout the catalyst layer also increases, improving proton movement from the catalyst to the membrane [73].
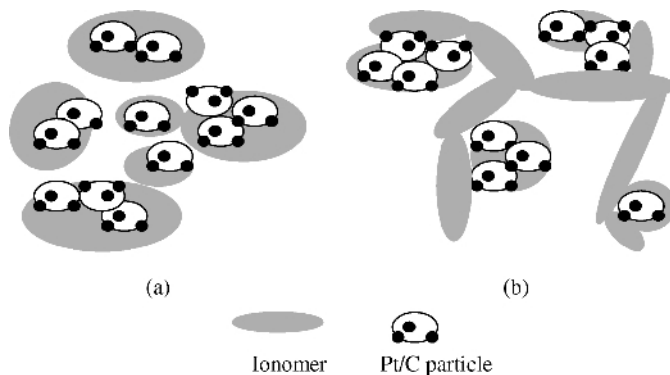
Figure 22.8. Schematic diagram of the microstructures in the catalytic layer according to the catalyst ink preparation method [73]: (a) solution method, (b) colloidal method. (Reprinted from Journal of Power Sources, 106(1–2), Shin SJ, Lee JK, Ha HY, Hong SA, Chun HS, Oh IH. Effect of the catalytic ink preparation method on the performance of polymer electrolyte membrane fuel cells, 146–52, ©2002, with permission from Elsevier.)

The properties of the solvent in catalyst ink play an important role in determining catalyst layer microstructure and cell performance. It is known that the dielectric constant (ε) of the solvent influences the degree of aggregation of the Nafion ionomers. In solvents with $\varepsilon > 10$, a solution is formed; in solvents with ε between 3 and 10, a colloidal solution is formed; and in solvents with $\varepsilon < 3$, precipitation occurs [74]. A less polar solvent forms a relatively larger agglomerate and thus bigger pores, which facilitate mass transfer. Also, a less polar solvent can result in higher proton conductivity in the catalyst layer [75]. Both enhanced mass transfer rate and higher proton conductivity improve cell performance. However, the catalyst ink deposition process requires a compromise between the dielectric constant and other properties such as the viscosity, boiling point, and carbon wet capacity of the solvent [76]. High viscosity is needed to maintain a stable catalyst ink suspension. For higher catalyst metal loading, higher viscosity is required. For example, glycerol has high viscosity and is generally added to catalyst ink to increase the latter's paintability and stability. But this solvent has a high boiling point and may remain in the catalyst layer, blocking the pores and thus decreasing gas transport [77]. Chisaka et al. [78] showed that for MEAs not subjected to the steaming process, when the mass ratio of glycerol to carbon (r_{gc}) is more than 5, the remaining glycerol is proportional to r_{gc}. Cell performance decreases with increasing r_{gc} because the remaining glycerol blocks the pores and reduces the number of reaction sites. In addition, the carbon wet capacity of the solvent may also be an important factor. Lim et al. [79] suggested that the high hydrophobicity of the MPL toward the deionized water solvent might not allow the ink to penetrate the layer's surface and hence decreases the integrity between the catalyst layer and the MPL, resulting in a high interfacial ohmic resistance at the interface.

The Nafion content in catalyst ink should be controlled appropriately. Too little Nafion and the ionic conductivity of the catalyst layer is insufficient, leading to low Pt utilization and high ohmic resistance; too much Nafion and the gas accessibility and electronic conductivity of the catalyst layer are insufficient [52,

72, 80, 81]. Figure 22.9 shows the effect of Nafion content in catalyst ink on catalyst layer structure. Passalacqua et al. [81] suggested that the optimum Nafion content in catalyst ink is located at about NFP (Nafion percentage) 30–35% and is independent of the Pt loading on the carbon in the catalyst, the Pt content in the electrode, and the kind of perfluorosulfonic ionomer used. The NFP they used was defined as the percentage of the Nafion per total catalyst and Nafion weight. However, Sasikumar et al. [82] showed that optimum Nafion content depends on Pt loading. It seems that the optimal Nafion content in catalyst ink is related to the eventual thickness of the Nafion film in the catalyst layer.
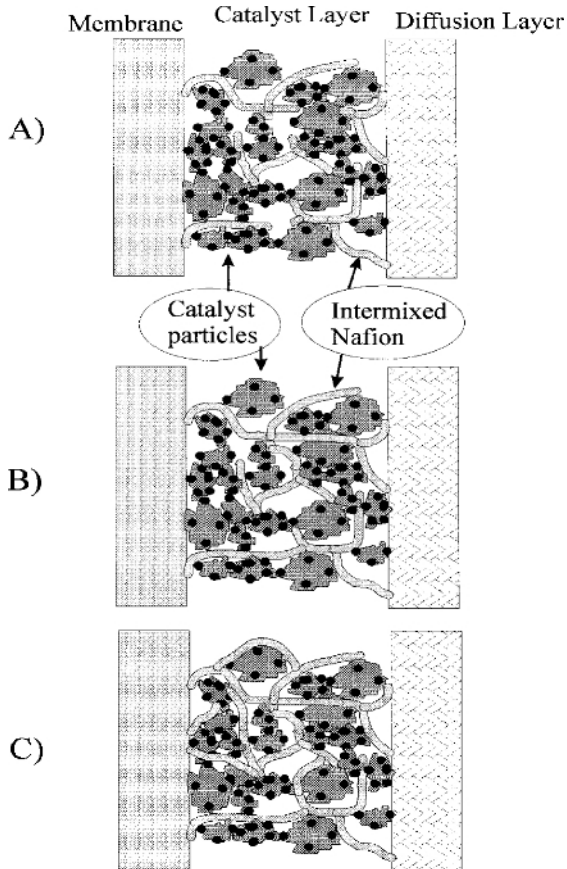
Figure 22.9. Schematic planar representation of the catalytic layer [81]: (A) at low Nafion content, not all the catalyst particles are connected to the membrane by a Nafion bridge; (C) when there is too much Nafion not all the catalyst particles are electronically connected to the diffusion layer; (B) at the optimal Nafion content all the catalyst particles have good connections for ionic and electronic conduction. (Reprinted from Electrochimica Acta, 46(6), Passalacqua E, Lufrano F, Squadrito G, Patti A, Giorgi L. Nafion content in the catalyst layer of polymer electrolyte fuel cells: effects on structure and performance, 799–805, ©2001, with permission from Elsevier.)
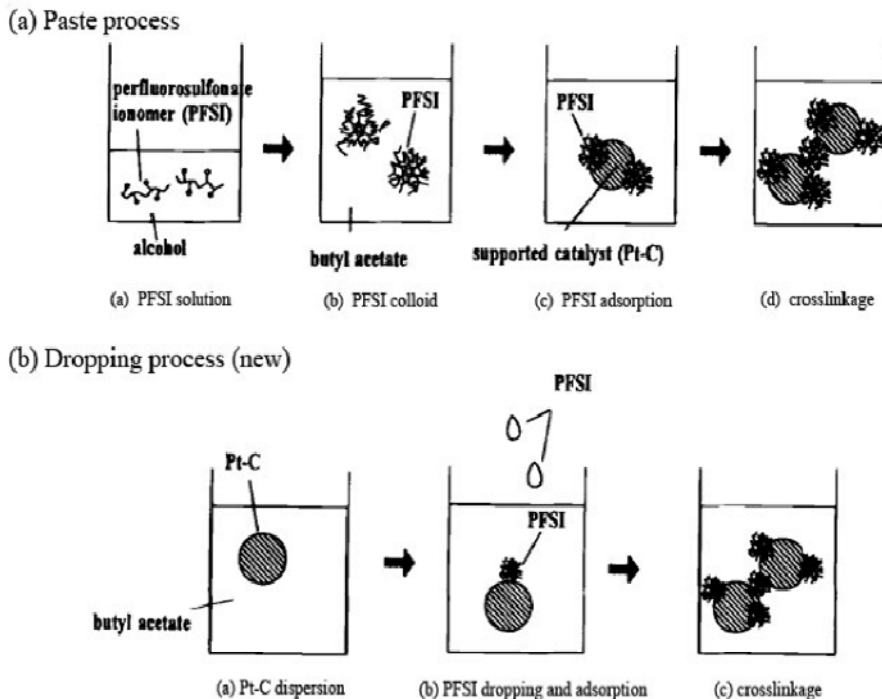
Figure 22.10. Schematic of the catalyst ink preparation process [83]. (Reproduced by permission of ECS—The Electrochemical Society, from Uchida M, Fukaoka Y, Sugawara Y, Ohara H, Ohta A. Improved preparation process of very-low-platinum-loading electrodes for polymer electrolyte fuel cells.)

The catalyst ink mixing process is also vital for determining catalyst layer microstructure and cell performance. The mixing procedure may affect ionomer distribution and thus catalyst utilization. Uchida et al. [83] showed that the dropping process was better than the paste process in decreasing catalyst loading. As shown in Figure 22.10, in the dropping process the PFSI colloid was adsorbed immediately after formation on the Pt/C catalyst before coagulation took place, so the PFSI was finely dispersed on the Pt/C at a reduced thickness. Mass transport of gas to the reaction sites was also accelerated through the dropping process. Consequently, reaction area was increased, and internal resistance as well as the supply of the reaction gas was improved. Wang et al. [84] showed that a NaOH pretreatment of the Nafion solution before addition to the catalyst mixture was beneficial for achieving uniform distribution of the catalyst and ionomer, resulting in higher electrochemical active area (ECA) and better performance for a DMFC. It was reported that converting Nafion to a thermoplastic form by ion-exchanging the Nafion with tetrabutylammonium ion (TBA$^+$) endowed the catalyst layer with stability and durability, and enhanced the cell performance [85, 86]. It has also been reported that the dispersion method can affect the morphology and porosity of the catalyst layer and thus the cell performance. Lim et al. [79] demonstrated that ball-milling processed catalyst ink showed a higher current density in the kinetic

controlled region than ink processed by ultrasonication. This was attributed to the larger catalyst agglomerates of the ball-milling processed catalyst ink, which led to a lower electronic ohmic drop and a lower ionic ohmic drop. Song et al. [87] showed that heat treatment of catalyst ink in an autoclave at 200 °C under pressurized conditions enhanced the penetration of the ionomer into the primary pores of the catalyst agglomerates, thus increasing catalyst utilization and improving cell performance.

22.2.4 Carbon-supported Catalyst Layer Fabrication

Originally, carbon-supported catalyst layers were prepared by the PTFE-bound method [88]. In these catalyst layers, the carbon-supported catalyst particles bounded by a hydrophobic PTFE were cast to the GDL. Then the PTFE-bound catalyst layers were impregnated with Nafion to provide ionic transport to the catalyst sites [89]. However, due to poor ion conductivity, the catalyst utilization in these catalyst layers is relatively low. Recently, the PTFE-bound method has been replaced by the thin-film method to fabricate carbon-supported catalyst layers. Through the thin-film method, catalyst utilization is greatly improved and therefore catalyst loading is reduced. In this method, the PTFE is replaced by Nafion to form a catalyst ink, and the ink is then applied to the GDL or the membrane. Applying the ink to the GDL has the advantage of preserving the membrane from chemical attacks by the solvents in the catalyst ink. However, it seems that the catalyst layer does not come into close contact with the membrane and therefore the electrode is prone to delamination [90]. Generally, there are two ways of applying the catalyst ink to the membrane, namely the decal transferring process and the direct coating process. In the former, the catalyst layer is cast onto a PTFE blank and then decaled to the membrane. In the latter, the membrane is coated directly with the catalyst layer. Frey et al. [40] suggested that the decal transfer process includes the risk of uneven or incomplete catalyst transfer from the PTFE blank to the membrane. It has been reported that the direct coating process provides better ionic connection between the membrane and the ionomer in the catalyst layer [91].

Typically, the catalyst ink is applied to the GDL or the membrane by hand painting or spraying. The catalyst layer uniformity is not easily controlled by hand painting. In addition, the process is time-consuming and has poor reproducibility. Spraying is faster than hand painting and allows a more uniform catalyst distribution. It also has the potential for mass production with good reproducibility; however, a considerable amount of catalyst is often wasted in the feed lines, which could increase the cost of production. Recently, new technology has been developed to apply catalyst ink onto the GDL or the membrane, such as doctor-blade spreading [92, 93], electrophoretic deposition (EPD) [94], electrospraying [95, 96], inkjet printing [97], and rolling [98, 99].

Saab et al. [92, 93] developed a doctor-blade spreading technique for preparing the catalyst layers in a faster and highly reproducible fashion. The ink was coated onto laser jet transparency material with a doctor blade device driven by an X-Y chart recorder time base. The chart recorder time base is a highly accurate mechanical drive with a broad range of selectable speeds (20–0.05 cm/s), which is useful when compensating for liquids of varying viscosity. Machined aluminum

slabs are used as the substrate support, and sit on the table of the X-Y chart recorder. The coating procedure entails positioning the doctor blade apparatus above the hot press transfer substrate (usually fiberglass-reinforced Teflon), micropipetting an appropriate amount of material onto the substrate in front of the blade, and activating the time base to drive the spreader through the liquid until the coat has covered a sufficient area. They showed that with appropriate catalyst ink and transfer decal, doctor-blade spreading was not only significantly more precise and faster than hand painting, but also produced cells with nearly 25% higher current density in the critical voltage operating region.

   Morikawa et al. [94] proposed an electrophoretic deposition (EPD) technique for preparing the catalyst layer without further mechanical pressing, which is suitable for a very thin or a very rigid membrane. Figure 22.11 shows a schematic of the EPD cell. In this technique, the Nafion membrane was set in the middle of the cell. The left compartment contained $HClO_4$ aqueous solution and the right contained the catalyst ink. Two Pt electrodes were used as cathode and anode to apply a high voltage to the cell. After construction, the EPD cell was immersed in an ice bath to maintain the temperature in the course of the EPD process. The thickness of the catalyst layer was controlled by EPD duration or catalyst ink concentration. Using EPD they successfully prepared a catalyst layer with high Pt utilization that consisted of only fine carbon particles, and was smaller and more uniform than that prepared by the conventional painting method.
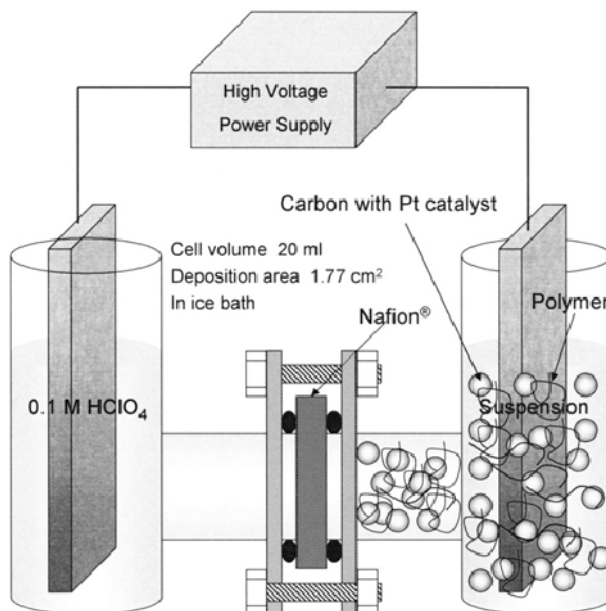
Figure 22.11. Schematic of an EPD cell [94]. (Reproduced by permission of ECS—The Electrochemical Society, from Morikawa H, Tsuihiji N, Mitsui T, Kanamura K. Preparation of membrane electrode assembly for fuel cell by using electrophoretic deposition process.)

An electrospraying technique was also developed for preparing the catalyst layer [95, 96]. Figure 22.12 shows a schematic of the set-up for electrospray and a detail of the electrospray process. The electrospraying technique consists of applying a voltage (3300–4000 V) between a capillary tube, in which the ink is forced to flow, and the carbon cloth substrate. The effect of the high electric field, when the solution emerges, is to generate a mist of highly charged droplets. During this process, the droplets are reduced in size by evaporation of the solvent and/or by "Coulomb explosion" (droplet subdivision resulting from the high charge density). In order to force the catalyst ink to pass through the capillary tube, a nitrogen-pressurized tank was used. The catalyst ink was put in an ultrasonic bath to keep it in a homogeneous mixture. The carbon support was moved by means of an X-Y axes coordinated system, which was controlled by a software application. By this technique, the electrospray-prepared catalyst layer showed enhanced cell performance compared to that prepared by a conventional technique.
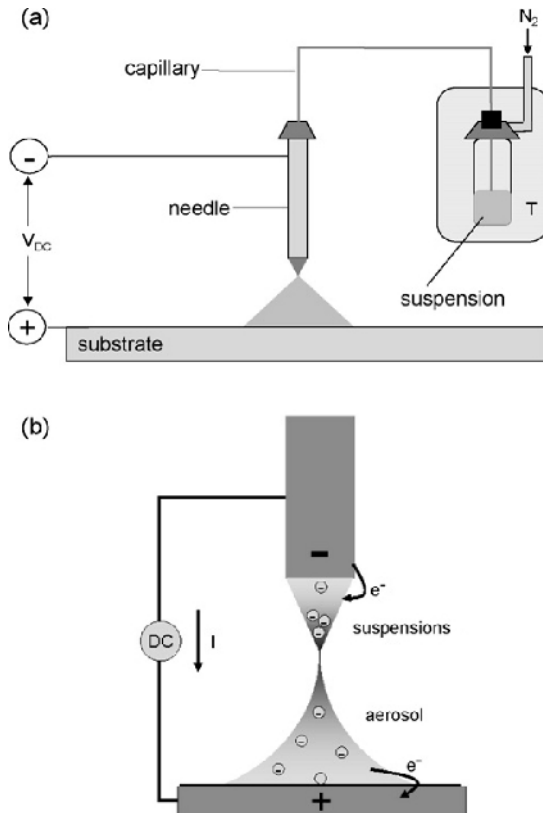
Figure 22.12. (a) Schematic of the set-up for electrospray deposition of Pt/C suspensions, (b) detail of the electrospray process in the needle-to-substrate space [96]. (Reprinted from Journal of Power Sources, 169(1), Chaparro AM, Benitez R, Gubler L, Scherer GG, Daza L. Study of membrane electrode assemblies for PEMFC, with cathodes prepared by the electrospray method, 77–84, ©2007, with permission from Elsevier.)

Recently, Taylor et al. [97] presented an inkjet printing technique to deposit catalyst ink onto GDLs. With a fixed nozzle volume, each printing delivers precise picolitre control of deposition, which is useful for creating an MEA with ultra-low (< 0.05 mg Pt cm^{-2}) loadings. According to their description, a commercially available thermal inkjet printer was used. The specifications report a maximum resolution of 1200 dpi×1200 dpi and a drop size of 28 pl. Standard black ink cartridges were used to print the catalyst inks. After emptying, the cartridges were cleaned in a sonication bath for 30 min. The catalyst inks were then placed inside the ink well and the cartridge was loaded into the printer. Carbon cloth was cut into squares and the squares were attached to standard white paper using double-sided tape. A black square of catalyst ink was printed onto the GDL using the "best print quality" feature in the printer settings to achieve the printer's best resolution. The paper containing the GDL was then reloaded into the paper tray and the printing was repeated until the desired loading was achieved. By inkjet printing, they prepared catalyst layers with ultra-low Pt loading, which is not easily attained using conventional methods, giving some of the highest Pt utilization reported in the literature.

Besides the techniques described above, which use wet catalyst ink, a dry production technique based on rolling was also developed [98, 99]. In the latter form [99] of this technique, a carbon-supported catalyst with the desired amount of binder powder is mixed in a mill, and the mixed powder is then atomized and sprayed in a nitrogen stream through a slit nozzle directly onto a membrane, resulting in a uniformly distributed layer. The reactive layer is then fixed and thoroughly connected to the membrane by passing both through a calender. Figure 22.13 shows a schematic of the dry production technique. The technique is simple and has a high degree of automation. Also, during all production steps no solvents are used, which avoids drying steps. In addition, the catalyst loading can be controlled to a low level. Therefore, this technique can be scaled up and has the potential to meet industrial requirements.
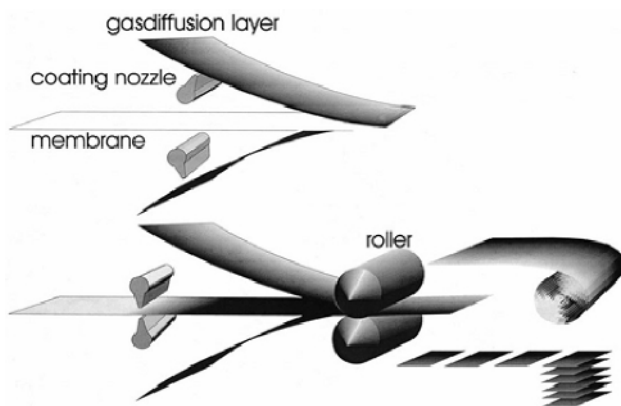
Figure 22.13. Schematic of the dry production technique for PEMFC MEAs [99]. (Reprinted from Journal of Power Sources, 86(1–2), Gulzow E, Schulze M, Wagner N, Kaz T, Reissner R, Steinhilber G, et al. Dry layer preparation and characterisation of polymer electrolyte fuel cell components, 352–62, ©2000, with permission from Elsevier.)

To maximize the triple-phase reaction zone and increase catalyst utilization, the microstructure of the carbon-supported catalyst layer should be optimized. This can be done by carefully selecting the solvent, appropriately controlling the Nafion content, and employing the proper fabrication process as described above. Besides that, the Pt/C ratio in the catalyst and the carbon support should also be carefully selected. Under a definite loading, if the Pt/C ratio is too low the thickness of the catalyst layer increases, resulting in high mass transport hindrance, whereas if the Pt/C ratio is too high the catalyst particle size increases, resulting in low catalyst activity [52, 100]. The carbon support also plays a significant role in determining the catalyst layer pore structure. Generally, there are two distinctive pore size distributions in the catalyst layer, namely the primary and secondary pores [80, 101, 102]. The primary pore is the space in and between the primary particles in the carbon agglomerates, and the secondary pore is the space between the carbon agglomerates. Considering that the Pt catalyst locates in the primary pores, it is necessary to increase the primary pore size for more Nafion to penetrate into the primary pore and enhance the gas transport. Uchida et al. [103] showed that improved PEMFC performance was achieved by an optimal carbon support with a large pore volume able to distribute the Nafion over the Pt inside the agglomerate. Bang et al. [104] showed that including a carbon microsphere in the catalyst layer facilitated mass transport and thus improved cell performance.

22.2.5 Pt Catalyst Layer Fabrication

In a carbon-supported catalyst layer, Pt nanoparticles are supported on high-surface carbon black and uniformly mixed with ionomers to maximum the reaction sites, thus improving the Pt utilization and lowering the Pt loading. However, owing to the agglomeration of Pt/C powders, not all Pt particles come into contact with the ionomer so there are still some Pt particles not being utilized effectively, leading to a low mass activity. Also, owing to the low density of carbon, the carbon support may lead to a thick catalyst layer, which decreases mass transport and increases ohmic resistance. In addition, under a definite catalyst loading, attempts to increase the Pt ratio in a carbon-supported catalyst would lead to larger particle size, which decreases catalyst activity. Therefore, a Pt catalyst layer strategy has also been developed to lower Pt loading, focusing on localizing Pt where the electrocatalytic reaction takes place.

The Pt catalyst layer is generally fabricated by electrodeposition and sputtering. Electrodeposition can selectively deposit platinum onto the active reaction regions where protons and electrons are accessible, because only in those regions are there electron transport channels and metal ion transport channels resulting from the hydrophilicity of Nafion particles [105]. Taylor et al. [106, 107] first reported this method to improve the utilization of Pt catalyst. According to their description, a Nafion solution was impregnated into the uncatalyzed carbon electrode and platinum was electrodeposited from a commercial plating bath. Platinum ions diffused through a thin layer of Nafion formed on the surface of the uncatalyzed carbon electrode and were electrodeposited only in regions with ionic and electronic conductivity. Antonine et al. [108] first impregnated carbon with H_2PtCl_6 and then applied electrochemical pulses to deposit Pt in a Nafion active

layer. The method allows a smaller active layer thickness and high Pt mass ratio (40%) with a narrow size distribution in the range of 2–4 nm. However, in terms of Pt concentration distribution it has a profile like that of a carbon-supported catalyst layer, and Cl^- ions produced from the electrodeposition of Pt from H_2PtCl_6 remain in the active layer, which poisons the Pt and reduces its catalytic activity, according to Kim et al. [109, 110]. Therefore, they directly electrodeposited Pt on the surface of the carbon blank electrode. Using a pulse electrodeposition technique, it is possible simultaneously to create Pt particles smaller than 5 nm and to increase the Pt ratio up to 75 wt% near the surface of the electrode, resulting in a 5 μm-thick catalyst layer with most of the Pt in close contact with the membrane. Their results indicated that pulse electrodeposition may be an attractive technique to achieve industry goals of reducing catalyst cost and increasing efficiency in PEMFCs.
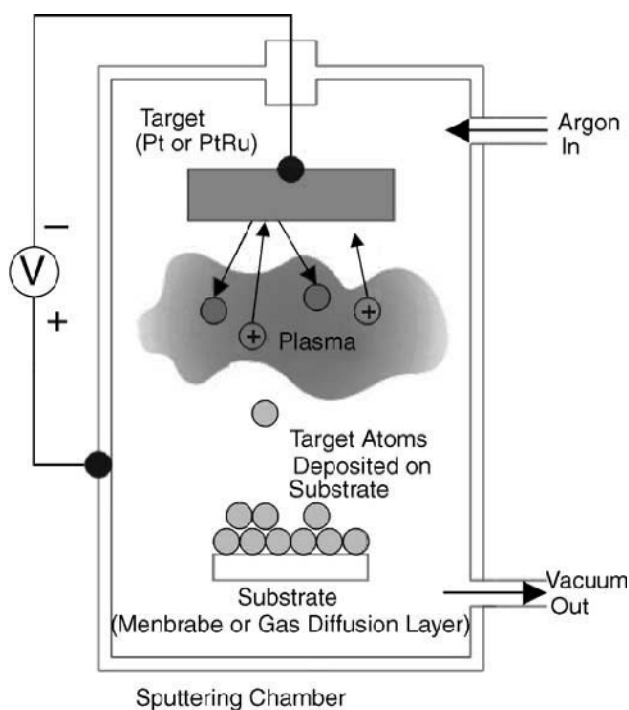
Figure 22.14. Schematic of sputtering in argon plasma for fabricating PEMFC electrodes [88]. (Reproduced from Journal of Power Sources, 130(1–2), Litster S, McLean G. PEM fuel cell electrodes, 61–76, ©2004, with permission from Elsevier.)

Sputtering is another fabrication method widely used for its potential to provide lower catalyst loading as well as thinner layers. The sputtering of catalyst layers consists of a vacuum evaporation process that removes portions of a coating material (the target) and deposits a thin and resilient film of the target material onto an adjacent substrate, which can be either the GDL or the membrane [88]. Figure 22.14 shows a schematic of the sputtering process. To attain good performance, the

sputtering process should fulfill the following requirements [111, 112]. First, it should maximize the available amount of triple-phase zone and readily drain the product water, making it mandatory that the catalyst layer be very thin and placed close to the hydrophobic diffusion layer. Second, the catalyst layer should adhere strongly to the membrane in order to reduce ohmic losses and support the high mechanical stress produced during operation. In addition, it should provide Pt particles of a size smaller than 10 nm, the average size of the carbon-supported catalyst particles, to further reduce loading. Cha et al. [111] obtained ultra-high utilization of Pt catalyst by alternating layers of sputtered Pt (5 nm thick) and a painted mixed electron- and proton-conducting layer of carbon black particles in an ink of the Nafion ionomer. Repeating successive application of these layers up to five times improved Pt utilization and enhanced cell performance. O'Hayre et al. [112] directly sputtered Pt on the surface of a Nafion membrane and showed that the performance of the sputtered Pt fuel cells depends strongly on the thickness of the sputtered catalyst layer. When the layer is very thin, there are only islands of Pt. Once a nominal thickness of 4 nm is reached, the islands coalesce into a single film. At this thickness, a fine crack structure can be found in the film, which provides gas access to the reaction sites closest to the membrane and increases catalyst utilization. When the thickness is increased further, the crack structure becomes coarser and gas transport to the reaction sites is thus limited. Therefore, films only 5–10 nm thick yield the best fuel cell performance.

22.2.6 MEA Fabrication and Optimization

The MEA consists of a proton exchange membrane, two catalyst layers, and two GDLs. Typically, there are two types of MEA configuration. A and B. The type A MEA is made by applying the catalyst layer to the GDL first, then hot pressing the two catalyst coated substrates (CCSs) onto a pretreated membrane. For the type B MEA, the catalyst layer is applied to the pretreated membrane first, and the catalyst coated membrane (CCM) is then combined with two GDLs by hot pressing. Figure 22.15 shows the two types of configuration. The type B configuration seems to be preferable, as it provides intimate contact between the membrane and the catalyst layer, so better ion conductivity and higher catalyst utilization is expected [67].

Before being used in the MEA, the Nafion membrane is usually cleaned and pretreated as follows. After fully swelling in deionized water, the Nafion membrane is boiled in 5% H_2O_2 for 1 h to remove organic impurities, then it is cleaned in boiling deionized water for 1 h. After that, the Nafion membrane is boiled again in 0.5 M H_2SO_4 for 1 h to remove the metal compound and convert the membrane into H^+ form; this is followed by cleaning in the boiling deionized water for another 1 h. Then the membrane is stored in deionized water at room temperature prior to use. In some cases, the membrane is boiled in NaOH aqueous solution instead of H_2SO_4 solution to convert the membrane into Na^+ form, cleaned in the boiling deionized water for 1 h, then fixed with a frame and dried in a vacuum oven at 80 °C. After the catalyst ink is applied to the membrane, the whole MEA is reprotonated by immersion in lightly boiling H_2SO_4 solution [90, 91, 113].
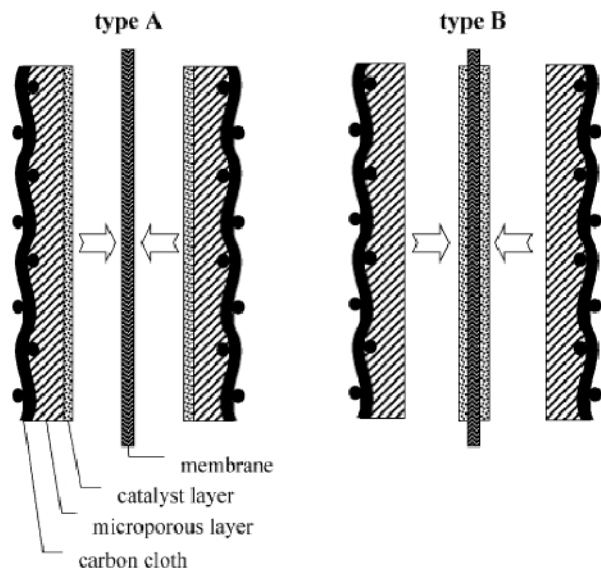
Figure 22.15. Configuration of catalyst/diffusion substrate and membrane for types A and B MEAs [67]. (Reprinted from Journal of Power Sources, 129(2), Lindermeir A, Rosenthal G, Kunz U, Hoffmann U. On the question of MEA preparation for DMFCs, 180–7, ©2004, with permission from Elsevier.)

Generally speaking, the thicker the membrane the less significant is the H_2 crossover. However, using a thick membrane carries the risk of increasing the membrane resistance. Due to the low solubility and diffusivity of H_2 in the ionomer, the H_2 crossover in a PEMFC is not as significant as the methanol crossover in a DMFC. Therefore, using the thinner membrane in a PEMFC is preferable [114]. For H_2 crossover measurement, H_2 was fed to the anode compartment while N_2 was fed to the cathode compartment. The cathode compartment was used as the working electrode; the anode compartment was used as the counter electrode as well as the dynamic hydrogen reference electrode. By applying a dynamic potential from 0.05 to 0.6 V at a scan rate of 2 mV s^{-1}, the limiting H_2 oxidation current was used as an indication of the H_2 crossover [114, 115].

To provide better contact between the catalyst layer and the membrane, the MEA components are usually hot pressed together. The temperature for hot pressing is usually about 130 °C, slightly above the glass transition temperature of Nafion, with the pressure ranging from 2 to 350 kg cm^{-2} and the hot pressing time ranging from 30 to 300 s. The structure, porosity, and performance of the MEA can be influenced by hot pressing, especially for DMFCs. Kuver et al. [116] reported that carbon cloth can be mechanically damaged by pressures exceeding 100 kg cm^{-2}. Zawodzinshi et al. [117] found that hot pressing can cause Nafion dehydration, which leads to irreversible performance loss in the MEA. Song et al. [118] showed that the pressing pressure is the main parameter influencing cell performance. The performance of the MEA that was hot pressed at 155 kg cm^{-2}

was much worse than that of the MEAs not hot pressed or pressed at a lower pressure of 43 kg cm^{-2}. Chen et al. [119] also showed that the MEA hot pressed at a low pressure showed better performance, which is attributed to the higher porosity of the cathode electrode. Zhang et al. [120] investigated in detail the effect of hot pressing conditions on the performances of MEAs. They showed that the cell resistance of MEAs that were hot pressed at higher temperature (135 °C) and pressure (120 kg cm^{-2}) and for a longer time (90 s) decreased because of the good contact between membrane and electrodes. But too high pressure increased the cell resistance of the MEA due to the difficulty of electron transport across the broken carbon paper. The porosity of the electrode decreased after hot pressing, which restricted mass transport, but its thickness also decreased, which shortened mass transport. Also, by increasing the hot pressing temperature, pressure, and time, the activating time required for the MEA to reach optimum performance was increased.

To further increase Pt utilization and improve performance, several treatments can be applied to the MEA after it is made. Qi et al. [121] showed that treatment of the MEA with steam or boiling water for a short time dramatically increased performance. According to them, steaming or boiling the MEA may fully hydrate the Nafion and open some "dead" regions that were blocked by the Nafion. Also, He et al. [122] described a H_2 evolution method to activate the MEA. After running the cell in H_2/air flow for about 3 h, H_2 evolution was carried out on the cathode using the following procedure. First, the cathode was purged with N_2, the cathode inlet was turned off, and the outlet was kept open. After that, a current of 200 mA/cm^2 was applied to the cell for 20 min using a power supply with the positive and negative terminals connected to the cell anode and cathode, respectively. By this method, it was found that the oxygen reduction overpotential was reduced. He et al. suggested that the better performance is caused by a change in the MEA's porosity and tortuosity, which increases the number of reactant-catalyst-electrolyte sites.

22.3 MEA Performance Verification with its Catalyst Layer Fabrication Optimization Process

22.3.1 MEA Performance Characterization

MEA performance is generally characterized by measuring the polarization curve and the electrochemical impedance spectroscopy. For these measurements, the MEA is sandwiched between two bipolar plates. An electrical heater and thermocouple are embedded in the plates to maintain the desired operating temperature. Insulation rubber gaskets are used to prevent the cell from leaking. Hydrogen and oxygen or air reactant are fed to the anode and cathode compartments, respectively, with or without prehumidifying. Usually, the cell is conditioned by operating at low loading to activate the MEA. After that, the polarization curve is recorded galvanostatically by stepping the current from zero to the maximum test current density. The voltage at each current density is allowed to stabilize before measurement. The polarization curve is effective and intuitional

to characterize the performance. However, separation of the electrochemical and ohmic contributions to polarization requires additional experimental techniques. This can be done by measuring the electrochemical impedance spectroscopy. Generally, electrochemical impedance spectroscopy is conducted in a galvanostatic or potentiostatic model in the frequency range of 100 kHz to 0.01 Hz. The amplitude of the AC voltage is 5–10 mV. Wagner [123] showed that by varying the operating conditions, such as cell potential or current density and gas supply, the cell impedance can be split into electrode impedances and electrolyte resistance. Furthermore, the electrode impedances can be separated into different impedances representing different reaction steps. Integration over the current densities of the individual impedance elements enables calculation of the individual polarization curves and voltage losses in the fuel cell, and determination of the rate determining reaction steps, depending on current density and humidification.

22.3.2 MEA Water Management Characterization

Good water management in the MEA is critical to achieve high performance. If there is not enough water, the membrane dries out and its resistance increases dramatically, while if too much water is generated and not immediately removed, MEA flooding occurs and transport of reactants is hindered. Both membrane drying and MEA flooding result in performance loss. To better understand water management and further provide guidance for MEA design, it is of significant importance to measure the water distribution *in situ*. A transparent fuel cell has been widely used for *in situ* water measurement [124, 125]. In this method, replacement of the bipolar plate by a transparent material and electrically conductive flow-field plate to create a window allows the direct observation of water droplets moving in the flow-field channel and emerging from the MEA. For more *in situ* water measurement methods, we refer the reader to a recent review given by Jean St-Pierre [126].

22.3.3 MEA CO and Other Contamination Tolerance

It is known that some contaminants in either fuel or air streams can severely poison the anode, membrane, and cathode, resulting in dramatic performance drops [127]. The most extensively investigated contaminant is CO. The CO tolerance property of the MEA can be improved by carefully selecting the catalyst and designing the MEA structure. The selection of catalysts has been described above. The modification of MEA structure to enhance CO tolerance is also under development. Huag et al. [128] showed that by placing a layer of carbon-supported Ru as a filter between the Pt catalyst and the GDL, the CO tolerance was enhanced as compared with the tolerance of a PtRu catalyst layer. Yu et al. [129] also proposed a composite anode MEA for a CO-tolerant PEMFC. The composite anode contained a CO-active PtRu catalyst layer and a traditional Pt catalyst layer. The modified MEA showed excellent cell performance and CO tolerance with reduced noble metal loading.

22.3.4 MEA Lifetime Enhancement via MEA Fabrication Process Improvement

The MEAs fabricated by the hot pressing method are usually inclined to delamination at both anode and cathode interfaces after long-term operation, leading to degradation in cell performance and reduction of cell lifetime, especially in DMFCs [130–131]. Therefore, it is necessary to improve the interfacial contact in the MEA. Wang et al. [132] introduced a Nafion layer between the membrane and the catalyst layer to improve the interfacial contact in the MEA. The ruinous test by soaking the MEA in 1:1 (v/v) ethanol solution showed that the MEA prepared by this process indeed enhanced durability. Liang et al. [131] developed a glue method for fabricating MEAs. Instead of hot pressing, they introduced a Nafion solution as a binding agent between a membrane and a catalyst layer. The MEA fabricated by the glue method showed a significant improvement in operational stability compared with the conventional hot pressed MEA.

References

1. Carlson EJ, Kopf P, Sinha J, Sriramulu S, Yang Y. Cost analyses of fuel cell stack/systems. DOE 2005 Annual Progress Report, 2005.
2. Wilson MS, Gottesfeld S. Thin-film catalyst layers for polymer electrolyte fuel cell electrodes. J Appl Electrochem 1992;22 (1):1–7.
3. Thompsett D. Catalysts for the proton exchange membrane fuel cell. In: Hoogers G, editor. Fuel cell technology handbook. Boca Raton: CRC Press, 2003.
4. Ralph TR, Hogarth MP. Catalysis for low temperature fuel cells Part II: the anode challenges. Plat Met Rev 2002;46(3):117–35.
5. Iwase M, Kawatsu S. Optimized CO tolerant electrocatalysts for polymer electrolyte fuel cells. In: Gottesfeld S, Halpert G, Landgrebe AR, editors. Proceedings of the first international symposium on proton conducting membrane fuel cells I; 1995 October 8–13; Chicago, Illinois. Pennington, NJ: The Electrochemical Society, 1995:12–18.
6. Cooper SJ, Gunner AG, Hoogers G, Thompsett D. Reformate tolerance in proton exchange membrane fuel cells: electrocatalyst solutions. In: Savadogo O, Roberge PR, editors. Proceedings of the second international symposium on new materials for fuel cell and modern battery systems; 1997 July 6–10; Montreal: École Polytechnique de Montréal, 1997: 286–96.
7. Mukerjee S, Lee SJ, Ticianelli EA, McBreen J, Grgur BN, Markovic NM, et al. Investigation of enhanced CO tolerance in proton exchange membrane fuel cells by carbon supported PtMo alloy catalyst. Electrochem Solid State Lett l999;2(1):12–5.
8. Grgur BN, Markovic NM, Ross PN. The electro-oxidation of H_2 and H_2/CO mixtures on carbon-supported Pt_xMo_y alloy catalysts. J Electrochem Soc 1999;146(5):1613–9.
9. Gunner AG, Hyde TL, Potter RJ, Thompsett D, inventors; Johnson Matthey PLC, assignee. Catalyst. United States patent US 5939220. 1999 Aug 17.
10. Ball S, Hodgkinson A, Hoogers G, Maniguet S, Thompsett D, Wong B. The proton exchange membrane fuel cell performance of a carbon supported PtMo catalyst operating on reformate. Electrochem Solid State Lett 2002;5(2):A31–4.
11. Ross PN, Markovic, Schmidt TJ, Stamenkovic. New electrocatalysts for fuel cells. DOE 2000 Annual Progress Report, 2000.

12. Schmidt TJ, Jusys Z, Gasteiger HA, Behm RJ, Endruschat U, Boennemann H. On the CO tolerance of novel colloidal PdAu/carbon electrocatalysts. J Electroanal Chem 2001;501(1–2):132–40.

13. Watanabe M, Motoo S. Electrocatalysis by ad-atoms: Part III. Enhancement of the oxidation of carbon monoxide on platinum by ruthenium ad-atoms. J Electroanal Chem 1975;60(3):275–83.

14. Zhuang L, Jin J, Abruna HD. Direct observation of electrocatalytic synergy. J Am Chem Soc 2007;129(36):11033–5.

15. Iwasita T, Nart FC, Vielstich W. An FTIR study of the catalytic activity of a 85:15 Pt-Ru alloy for methanol oxidation. Ber Bunsenges Phys Chem 1990;94:1030–4.

16. McBreen J, Mukerjee S. In situ X-Ray absorption studies of a Pt-Ru electrocatalyst. J Electrochem Soc 1995;142(10):3399–404.

17. Oetjen HF, Schmidt VM, Stimming U, Trila F. Performance data of a proton exchange membrane fuel cell using H_2/CO as fuel gas. J Electrochem Soc 1996;143 (12):3838–42.

18. Antolini E, Giorgi L, Cardellini F, Passalacqua E. Physical and morphological characteristics and electrochemical behaviour in PEM fuel cells of PtRu/C catalysts. J Solid State Electrochem 2001;5(2):131–40.

19. Qi Z, Kaufman A. CO-tolerance of low-loaded Pt/Ru anodes for PEM fuel cells. J Power Sources 2003;113(1):115–23.

20. Antolini E. Formation of carbon-supported PtM alloys for low temperature fuel cells: a review. Mater Chem Phys 2003;78(3):563–73.

21. Gotz M, Wendt H. Binary and ternary anode catalyst formulations including the elements W, Sn and Mo for PEMFCs operated on methanol or reformate gas. Electrochim Acta 1998;43(24):3637–44.

22. Papageorgopoulos DC, Keijzer M, de Bruijn FA. The inclusion of Mo, Nb and Ta in Pt and PtRu carbon supported electrocatalysts in the quest for improved CO tolerant PEMFC anodes. Electrochim Acta 2002;48(2):197–204.

23. Venkataraman R, Kunz HR, Fenton JM. Development of new CO tolerant ternary anode catalysts for proton exchange membrane fuel cells. J Electrochem Soc 2003;150(3):A278–84.

24. Liang Y, Zhang H, Zhong H, Zhou X, Tian Z, Xu D, et al. Preparation and characterization of carbon-supported PtRuIr catalyst with excellent CO-tolerant performance for proton-exchange membrane fuel cells. J Catal 2006;238(2):468–76.

25. Liang Y, Zhang H, Tian Z, Zhu X, Wang X, Yi B. Synthesis and structure-activity relationship exploration of carbon-supported PtRuNi nanocomposite as a CO-tolerant electrocatalyst for proton exchange membrane fuel cells. J Phys Chem B 2006;110(15):7828–34.

26. Hou Z, Yi B, Yu H, Lin Z, Zhang H. CO tolerance electrocatalyst of PtRu-H_xMeO_3/C (Me = W, Mo) made by composite support method. J Power Sources 2003;123(2):116–25.

27. Hogarth MP, Ralph TR. Catalysis for low temperature fuel cells Part III: challenges for the direct methanol fuel cell. Plat Met Rev 2002;46(4):146–64.

28. Wasmus S, Kuver A. Methanol oxidation and direct methanol fuel cells: a selective review. J Electroanal Chem 1999;461(1–2):14–31.

29. Antolini E. Platinum-based ternary catalysts for low temperature fuel cells: Part II. electrochemical properties. Appl Catal B Environ 2007;74(3–4):337–50.

30. Lee K, Zhang J, Wang H, Wilkinson DP. Progress in the synthesis of carbon nanotube- and nanofiber-supported Pt electrocatalysts for PEM fuel cell catalysis. J Appl Electrochem 2006;36(5):507–22.

31. Mukerjee S, Srinivasan S. Enhanced electrocatalysis of oxygen reduction on platinum alloys in proton exchange membrane fuel cells. J Electroanal Chem 1993;357(1–2):201–24.

32. Ralph TR, Keating JE, Collis NJ, Hyde TI. Oxygen reduction electrocatalysts in solid polymer fuel cell membrane electrode assemblies. ETSU Contract Report F/02/00038/REP, 1997.

33. Xiong L, Kannan AM, Manthiram A. Pt-M (M=Fe, Co, Ni and Cu) electrocatalysts synthesized by an aqueous route for proton exchange membrane fuel cells. Electrochem Commun 2002;4(11):898–903.

34. Gasteiger HA, Kocha SS, Sompalli B, Wagner FT. Activity benchmarks and requirements for Pt, Pt-alloy, and non-Pt oxygen reduction catalysts for PEMFCs. Appl Cata B Environ 2005;56(1–2):9–35.

35. Wakabayashi N, Takeichi M, Uchida H, Watanabe M. Temperature dependence of oxygen reduction activity at Pt-Fe, Pt-Co, and Pt-Ni alloy electrodes. J Phys Chem B 2005;109(12):5836–41.

36. Paulus UA, Wokaun A, Scherer GG, Schmidt TJ, Stamenkovic V, Markovic NM, et al. Oxygen reduction on carbon-supported Pt-Ni and Pt-Co alloy catalysts. J Phys Chem B 2002;106 (16):4181–91.

37. Antonlini E, Salgado JRC, Gonzalez ER. The stability of Pt-M (M = first row transition metal) alloy catalysts and its effect on the activity in low temperature fuel cells: a literature review and tests on a Pt-Co catalyst. J Power Sources 2006;160 (2):957–68.

38. Liu H, Song C, Zhang L, Zhuang J, Wang H, Wilkinson DP. A review of anode catalysis in the direct methanol fuel cell. J Power Sources 2006;155(2):95–110.

39. Ralph TR, Hards GA, Keating JE, Campbell SA, Wilkinson DP, Davis M, et al. Low cost electrodes for proton exchange membrane fuel cells. J Electrochem Soc 1997;144(11):3845–57.

40. Frey T, Linardi M. Effects of membrane electrode assembly preparation on the polymer electrolyte membrane fuel cell performance. Electrochim Acta 2004;50(1):99–105.

41. Wang Y, Wang CY, Chen KS. Elucidating differences between carbon paper and carbon cloth in polymer electrolyte fuel cells. Electrochim Acta 2007;52(12):3965–75.

42. Lin G, Nguyen TV. Effect of thickness and hydrophobic polymer content of the gas diffusion layer on electrode flooding level in a PEMFC. J Electrochem Soc 2005;152(10):A1942–8.

43. Xu C, Zhao TS, Ye Q. Effect of anode backing layer on the cell performance of a direct methanol fuel cell. Electrochim Acta 2006;51(25):5524–31.

44. Campbell SA, Stumper J, Wilkinson DP, Davis MT, inventors; Ballard Power Systems Inc, assignee. Porous electrode substrate for an electrochemical fuel cell. United States patent US 5863673. 1999 Jan 26.

45. Glora M, Wiener M, Petricevic R, Probstle H, Fricke J. Integration of carbon aerogels in PEM fuel cells. J Non-Cryst Solids 2001;285(1–3):283–7.

46. Shao ZG, Lin WF, Zhu F, Christensen PA, Li MQ, Zhang H. Novel electrode structure for DMFC operated with liquid methanol. Electrochem Commun 2006;8(1):5–8.

47. Wan N, Wang G. An integrated composite membrane electrode assembly (ICMEA) and its application in small H_2/air fuel cells. J Power Sources 2006;159(2):951–5.

48. Wan N, Mao Z, Wang C, Wang G. Performance of an integrated composite membrane electrode assembly in DMFC. J Power Sources 2007;163(2):725–30.

49. Yazici MS. Mass transfer layer for liquid fuel cells. J Power Sources 2007;166(2):424–9.

50. Lim C, Wang CY. Effects of hydrophobic polymer content in GDL on power performance of a PEM fuel cell. Electrochim Acta 2004;49(24):4149–56.

51. Pai YH, Ke JH, Huang HF, Lee CM, Zen JM, Shieu FS. CF_4 plasma treatment for preparing gas diffusion layers in membrane electrode assemblies. J Power Sources 2006;161(1):275–81.

52. Paganin VA, Ticianelli EA, Gonzalez ER. Development and electrochemical studies of gas diffusion electrodes for polymer electrolyte fuel cells. J Appl Electrochem 1996;26(3):297–304.

53. Lufrano F, Passalacqua E, Squadrito G, Patti A, Giorgi L. Improvement in the diffusion characteristics of low Pt-loaded electrodes for PEFCs. J Appl Electrochem 1999;29(4):445–8.

54. Williams MV, Begg E, Bonville L, Kunz HR, Fenton JM. Characterization of gas diffusion layers for PEMFC. J Electrochem Soc 2004;151(8):A1173–80.

55. Jordan LR, Shukla AK, Behrsing T, Avery NR, Muddle BC, Forsyth M. Diffusion layer parameters influencing optimal fuel cell performance. J Power Sources 2000;86(1–2):250–4.

56. Passalacqua E, Squadrito G, Lufrano F, Patti A, Giorgi L. Effects of the diffusion layer characteristics on the performance of polymer electrolyte fuel cell electrodes. J Appl Electrochem 2001;31(4):449–54.

57. Antolini E, Passos RR, Ticianelli EA. Effects of the carbon powder characteristics in the cathode gas diffusion layer on the performance of polymer electrolyte fuel cells. J Power Sources 2002;109(2):477–82.

58. Wang XL, Zhang HM, Zhang JL, Xu HF, Tian ZQ, Chen J, et al. Micro-porous layer with composite carbon black for PEM fuel cells. Electrochim Acta 2006;51(23):4909–15.

59. Park GG, Sohn YJ, Yim SD, Yang TH, Yoon YG, Lee WY, et al. Adoption of nano-materials for the micro-layer in gas diffusion layers of PEMFCs. J Power Sources 2006;163(1):113–8.

60. Kong CS, Kim DY, Lee HK, Shul YG, Lee TH. Influence of pore-size distribution of diffusion layer on mass-transport problems of proton exchange membrane fuel cells. J Power Sources 2002;108(1–2):185–91.

61. Tang H, Wang S, Pan M, Yuan R. Porosity-graded micro-porous layers for polymer electrolyte membrane fuel cells. J Power Sources 2007;166(1):41–6.

62. Neergat M, Shukla AK. Effect of diffusion-layer morphology on the performance of solid-polymer-electrolyte direct methanol fuel cells. J Power Sources 2002;104(2):289–94.

63. Zhang J, Yin GP, Lai QZ, Wang ZB, Cai KD, Liu P. The influence of anode gas diffusion layer on the performance of low-temperature DMFC. J Power Sources 2007;168(2):453–8.

64. Miura T, Hayashi T, inventors; Daikin Industries Ltd, assignee. Aqueous polytetrafluoroethylene dispersion composition and use thereof. United States patent US 6153688. 2000 Nov 28.

65. Konabe K. Fluoropolymer dispersion and electrode composition containing same. US Patent 20060078800. 2006 Apr 13.

66. Bevers D, Rogers R, Von Bradke M. Examination of the influence of PTFE coating on the properties of carbon paper in polymer electrolyte fuel cells. J Power Sources 1996;63(2):193–201.

67. Lindermeir A, Rosenthal G, Kunz U, Hoffmann U. On the question of MEA preparation for DMFCs. J Power Sources 2004;129(2):180–7.

68. Yu J, Yoshikawa Y, Matsuura T, Islam MN, Hori M. Preparing gas-diffusion layers of PEMFCs with a dry deposition technique. Electrochem Solid State Lett 2005;8(3):A152–5.

69. Yu HM, Ziegler C, Oszcipok M, Zobel M, Hebling C. Hydrophilicity and hydrophobicity study of catalyst layers in proton exchange membrane fuel cells. Electrochim Acta 2006;51(7):1199–207.
70. Jordan LR, Shukla AK, Behrsing T, Avery NR, Muddle BC, Forsyth M. Effect of diffusion-layer morphology on the performance of polymer electrolyte fuel cells operating at atmospheric pressure. J Appl Electrochem 2000;30(6):641–6.
71. Lee HK, Park JH, Kim DY, Lee TH. A study on the characteristics of the diffusion layer thickness and porosity of the PEMFC. J Power Sources 2004;131(1–2):200–6.
72. Song JM, Cha SY, Lee WM. Optimal composition of polymer electrolyte fuel cell electrodes determined by the AC impedance method. J Power Sources 2001;94(1):78–84.
73. Shin SJ, Lee JK, Ha HY, Hong SA, Chun HS, Oh IH. Effect of the catalytic ink preparation method on the performance of polymer electrolyte membrane fuel cells. J Power Sources 2002;106(1–2):146–52.
74. Uchida M, Aoyama Y, Eda N, Ohta A. New preparation method for polymer-electrolyte fuel cells. J Electrochem Soc 1995;142(2):463–8.
75. Kim JH, Ha HY, Oh IH, Hong SA, Lee HI. Influence of the solvent in anode catalyst ink on the performance of a direct methanol fuel cell. J Power Sources 2004;135(1–2):29–35.
76. Fernandez R, Ferreira-Aparicio P, Daza L. PEMFC electrode preparation: influence of the solvent composition and evaporation rate on the catalytic layer microstructure. J Power Sources 2005;151:18–24.
77. Yang TH, Yoon YG, Park GG, Lee WY, Kim CS. Fabrication of a thin catalyst layer using organic solvents. J Power Sources 2004;127(1–2):230–3.
78. Chisaka M, Daiguji H. Effect of glycerol on micro/nano structures of catalyst layers in polymer electrolyte membrane fuel cells. Electrochim Acta 2006;51(23):4828–33.
79. Lim C, Allen RG, Scott K. Effect of dispersion methods of an unsupported Pt-Ru black anode catalyst on the power performance of a direct methanol fuel cell. J Power Sources 2006;161(1):11–8.
80. Uchida M, Aoyama Y, Eda N, Ohta A. Investigation of the microstructure in the catalyst layer and effects of both perfluorosulfonate ionomer and PTFE-loaded carbon on the catalyst layer of polymer electrolyte fuel cells. J Electrochem Soc 1995;142(12):4143–9.
81. Passalacqua E, Lufrano F, Squadrito G, Patti A, Giorgi L. Nafion content in the catalyst layer of polymer electrolyte fuel cells: effects on structure and performance. Electrochim Acta 2001;46(6):799–805.
82. Sasikumar G, Ihm JW, Ryu H. Dependence of optimum Nafion content in catalyst layer on platinum loading. J Power Sources 2004;132(1–2):11–17.
83. Uchida M, Fukaoka Y, Sugawara Y, Ohara H, Ohta A. Improved preparation process of very-low-platinum-loading electrodes for polymer electrolyte fuel cells. J Electrochem Soc 1998;145(11):3708–13.
84. Wang S, Sun G, Wu Z, Xin Q. Effect of Nafion ionomer aggregation on the structure of the cathode catalyst layer of a DMFC. J Power Sources 2007;165(1):128–33.
85. Wilson MS, Valerio JA, Gottesfeld S. Low platinum loading electrodes for polymer electrolyte fuel cells fabricated using thermoplastic ionomers. Electrochim Acta 1995;40(3):355–63.
86. Yoon YG, Park GG, Yang TH, Han JN, Lee WY, Kim CS. Effect of pore structure of catalyst layer in a PEMFC on its performance. Int J Hydrogen Energy 2003;28(6):657–62.
87. Song JM, Suzaki S, Uchida H, Watanabe M. Preparation of high catalyst utilization electrodes for polymer electrolyte fuel cells. Langmuir 2006;22(14):6422–8.
88. Litster S, McLean G. PEM fuel cell electrodes. J Power Sources 2004;130(1–2):61–76.

89. Ticianelli EA, Derouin CR, Redondo A, Srinivasan S. Methods to advance technology of proton exchange membrane fuel cells. J Electrochem Soc 1988;135(9):2209–14.

90. Xiong L, Manthiram A. High performance membrane-electrode assemblies with ultra-low Pt loading for proton exchange membrane fuel cells. Electrochim Acta 2005;50(16–17):3200–4.

91. Chun YG, Kim CS, Peck DH, Shin DR. Performance of a polymer electrolyte membrane fuel cell with thin film catalyst electrodes. J Power Sources 1998;71(1–2):174–8.

92. Saab AP, Garzon FH, Zawodzinski TA. Determination of ionic and electronic resistivities in carbon/polyelectrolyte fuel-cell composite electrodes. J Electrochem Soc 2002;149(12):A1541–6.

93. Bender G, Zawodzinski TA, Saab AP. Fabrication of high precision PEFC membrane electrode assemblies. J Power Sources 2003;124(1):114–7.

94. Morikawa H, Tsuihiji N, Mitsui T, Kanamura K. Preparation of membrane electrode assembly for fuel cell by using electrophoretic deposition process. J Electrochem Soc 2004;151(10):A1733–7.

95. Benitez R, Soler J, Daza L. Novel method for preparation of PEMFC electrodes by the electrospray technique. J Power Sources 2005;151:108–13.

96. Chaparro AM, Benitez R, Gubler L, Scherer GG, Daza L. Study of membrane electrode assemblies for PEMFC, with cathodes prepared by the electrospray method. J Power Sources 2007;169(1):77–84.

97. Taylor AD, Kim EY, Humes VP, Kizuka J, Thompson LT. Inkjet printing of carbon supported platinum 3-D catalyst layers for use in fuel cells. J Power Sources 2007;171(1):101–6.

98. Bevers D, Wagner N, Von Bradke M. Innovative production procedure for low cost PEFC electrodes and electrode/membrane structures. Int J Hydrogen Energy 1998;23(1):57–63.

99. Gulzow E, Schulze M, Wagner N, Kaz T, Reissner R, Steinhilber G, et al. Dry layer preparation and characterisation of polymer electrolyte fuel cell components. J Power Sources 2000;86(1–2):352–62.

100. Prasanna M, Ha HY, Cho EA, Hong SA, Oh IH. Investigation of oxygen gain in polymer electrolyte membrane fuel cells. J Power Sources 2004;137(1):1–8.

101. Watanabe M, Tomikawa M, Motoo S. Experimental analysis of the reaction layer structure in a gas diffusion electrode. J Electroanal Chem 1985;195(1):81–93.

102. Xie J, More KL, Zawodzinski TA, Smith WH. Porosimetry of MEAs made by "thin film decal" method and its effect on performance of PEFCs. J Electrochem Soc 2004;151(11):A1841–6.

103. Uchida M, Fukuoka Y, Sugawara Y, Eda N, Ohta A. Effects of microstructure of carbon support in the catalyst layer on the performance of polymer-electrolyte fuel cells. J Electrochem Soc 1996;143(7):2245–52.

104. Bang JH, Han K, Skrabalak SE, Kim H, Suslick KS. Porous carbon supports prepared by ultrasonic spray pyrolysis for direct methanol fuel cell electrodes. J Phys Chem C 2007;111(29):10959–64.

105. Wei ZD, Chan SH, Li LL, Cai HF, Xia ZT, Sun CX. Electrodepositing Pt on a Nafion-bonded carbon electrode as a catalyzed electrode for oxygen reduction reaction. Electrochim Acta 2005;50(11):2279–87.

106. Taylor EJ, Anderson EB, Vilambi NRK. Preparation of high-platinum-utilization gas diffusion electrodes for proton-exchange-membrane fuel cells. J Electrochem Soc 1992;139(5): L45–6.

107. Vilambi Reddy NRK, Anderson EB, Taylor EJ, inventors; Physical Sciences Inc, assignee. High utilization supported catalytic metal-containing gas-diffusion electrode,

process for making it, and cells utilizing it. United States patent US 5084144. 1992 Jan 28.

108. Antoine O, Durand R. In situ electrochemical deposition of Pt nanoparticles on carbon and inside Nafion. Electrochem Solid State Lett 2001;4(5):A55–8.

109. Kim H, Popov BN. Development of novel method for preparation of PEMFC electrodes. Electrochem Solid State Lett 2004;7(4):A71–4.

110. Kim H, Subramanian NP, Popov BN. Preparation of PEM fuel cell electrodes using pulse electrodeposition. J Power Sources 2004;138(1–2):14–24.

111. Cha SY, Lee WM. Performance of proton exchange membrane fuel cell electrodes prepared by direct deposition of ultrathin platinum on the membrane surface. J Electrochem Soc 1999;146(11):4055–60.

112. O'Hayre R, Lee SJ, Cha SW, Prinz FB. A sharp peak in the performance of sputtered platinum fuel cells at ultra-low platinum loading. J Power Sources 2002;109(2):483–93.

113. Song SQ, Liang ZX, Zhou WJ, Sun GQ, Xin Q, Stergiopoulos V, et al. Direct methanol fuel cells: the effect of electrode fabrication procedure on MEAs structural properties and cell performance. J Power Sources 2005;145(2):495–501.

114. Gasteiger HA, Panels JE, Yan SG. Dependence of PEM fuel cell performance on catalyst loading. J Power Sources 2004;127(1–2):162–71.

115. Jiang J, Hall TD, Tsagalas L, Hill DA, Miller AE. Photographic production of metal nano-particles for fuel cell electrodes. J Power Sources 2006;162(2):977–84.

116. Kuver A, Vogel I, Vielstich W. Distinct performance evaluation of a direct methanol SPE fuel cell. A new method using a dynamic hydrogen reference electrode. J Power Sources 1994;52(1):77–80.

117. Zawodzinski TA, Springer TE, Uribe F, Gottesfeld S. Characterization of polymer electrolytes for fuel cell applications. Solid State Ionics 1993;60(1–3):199–211.

118. Song C, Pickup PG. Effect of hot pressing on the performance of direct methanol fuel cells. J Appl Electrochem 2004;34(10):1065–70.

119. Chen CY, Tao CS. Characterization of electrode structures and the related performance of direct methanol fuel cells. Int J Hydrogen Energy 2006;31(3):391–8.

120. Zhang J, Yin GP, Wang ZB, Lai QZ, Cai KD. Effects of hot pressing conditions on the performances of MEAs for direct methanol fuel cells. J Power Sources 2007;165(1):73–81.

121. Qi Z, Kaufman A. Enhancement of PEM fuel cell performance by steaming or boiling the electrode. J Power Sources 2002;109(1):227–9.

122. He C, Qi Z, Hollett M, Kaufman A. An electrochemical method to improve the performance of air cathodes and methanol anodes. Electrochem Solid State Lett 2002;5(8):A181–3.

123. Wagner N. Characterization of membrane electrode assemblies in polymer electrolyte fuel cells using a.c. impedance spectroscopy. J Appl Electrochem 2002;32(8):859–63.

124. Tuber K, Pocza D, Hebling C. Visualization of water buildup in the cathode of a transparent PEM fuel cell. J Power Sources 2003;124(2):403–14.

125. Lu GQ, Wang CY. Electrochemical and flow characterization of a direct methanol fuel cell. J Power Sources 2004;134(1):33–40.

126. St-Pierre J. PEMFC in situ liquid-water-content monitoring status. J Electrochem Soc 2007;154(7): B724–31.

127. Cheng X, Shi Z, Glass N, Zhang L, Zhang J, Song D, et al. A review of PEM hydrogen fuel cell contamination: impacts, mechanisms, and mitigation. J Power Sources 2007;165(2):739–56.

128. Haug AT, White RE, Weidner JW, Huang W. Development of a novel CO tolerant proton exchange membrane fuel cell anode. J Electrochem Soc 2002;149(7):A862–7.

129. Yu H, Hou Z, Yi B, Lin Z. Composite anode for CO tolerance proton exchange membrane fuel cells. J Power Sources 2002;105(1):52–7.

130. Liu J, Zhou Z, Zhao X, Xin Q, Sun G, Yi B. Studies on performance degradation of a direct methanol fuel cell (DMFC) in life test. Phys Chem Chem Phys 2004;6(1):134–7.

131. Liang ZX, Zhao TS, Prabhuram J. A glue method for fabricating membrane electrode assemblies for direct methanol fuel cells. Electrochim Acta 2006;51(28):6412–8.

132. Wang S, Sun G, Wang G, Zhou Z, Zhao X, Sun H, et al. Improvement of direct methanol fuel cell performance by modifying catalyst coated membrane structure. Electrochem Commun 2005;7(10):1007–12.

23

Catalyst Layer Degradation, Diagnosis and Failure Mitigation

Jing Li

23.1 Introduction

Faced with rapidly rising air pollution-related health risks, sky-rocketing oil prices, and diminishing natural resources, scientists and engineers are now seeking clean and efficient alternatives to petroleum as energy sources. The hydrogen fuel cell, using hydrogen and oxygen from air as fuel, could achieve efficiencies of electric power generation in the 50–65% range. As a "clean" electric power source, fuel cells can be used to power vehicles, back-up the power supply for electric devices, and store electricity in power stations by converting water into hydrogen and oxygen during off-peak hours. The only by-products are water and heat. The proton exchange membrane fuel cell (also called polymer electrolyte membrane fuel cell, PEMFC) is a highly promising power source candidate for zero emission vehicles, stationary applications, backup power units, materials handling, and small electronics. Fuel cells are currently the only technology that can effectively provide pollution-free energy for both transportation and electric utilities. The use of fuel cell vehicles (FCVs) will partially reduce the global dependency on petroleum as a fuel.

In the past several decades, a variety of fuel cells have been developed. These can be classified by the type of electrolyte used in the cells, and include: 1) polymer electrolyte membrane fuel cell, 2) alkaline fuel cell (AFC), 3) phosphoric acid fuel cell (PAFC), 4) molten carbonate fuel cell (MCFC), and 5) solid oxide fuel cell (SOFC). Hydrogen has many merits as a fuel for fuel cells in most applications. It is highly reactivity when suitable catalysts are used. It can be produced from hydrocarbons, obtained as a by-product of chemical plans, or generated by water electrolysis using solar or nuclear power. It also has high energy density. Therefore, hydrogen has been chosen as a PEMFC fuel for many applications. The most common and economical oxidant is gaseous oxygen, which is readily available from air. A typical single PEMFC consists of an anode, a cathode, a proton conductive membrane, and two bipolar plates (Figure 23.1).
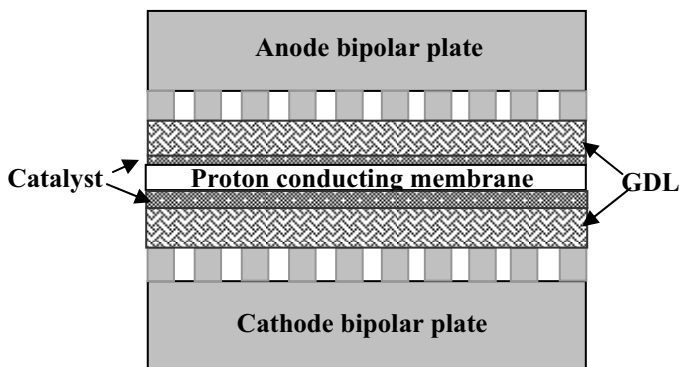
Figure 23.1. Schematic diagram of PEMFC structure

In a PEMFC, hydrogen is fed continuously to the anode (negative electrode) and oxygen or air is fed continuously to the cathode (positive electrode) through a flow field on the bipolar plates. At the anode, hydrogen is oxidized and a proton is transferred to the cathode through the proton conductive membrane. Meanwhile, electrons are produced and flow through an external circuit to the cathode. Oxygen (often obtained from air) is electro-catalyzed on the cathode catalyst surface and reduced to oxygen anions after receive four electrons per molecule, called the oxygen reduction reaction (ORR). The electrochemical reactions take place at the cathode to produce water. The functions of the proton conductive membrane are to provide a proton pathway, to separate the hydrogen and oxygen gases, and to electrically isolate the anode and cathode. Both anode and cathode in a PEMFC have gas distribution layers (GDLs) that are usually made of carbon fiber and/or sub-micron carbon particles with a bonding agent. The GDL functions as a gas distribution medium to allow gas flow from the gas channels in a bipolar plate to the catalyst layer. The GDL also conducts electrons from the anode catalyst layer to the cathode catalyst layer for electrochemical reaction.

The functions of porous electrodes in fuel cells are: 1) to provide a surface site for gas ionization or de-ionization reactions, 2) to provide a pathway for gases and ions to reach the catalyst surface, 3) to conduct water away from the interface once these are formed, and 4) to allow current flow. A membrane electrode assembly (MEA) forms the core of a fuel cell and the key electrochemical reactions take place in the MEA. MEA performance is severely affected by electrode composition, structure, and geometry, and especially by cathode structure and composition, due to poor oxygen reduction kinetics and transport limitations of the reactants in the cathode catalyst layer.

Catalytic layers in the anode and cathode are also critical components in a PEMFC. Platinum (Pt) or a Pt-Ru alloy supported by nano-carbon particles is often used as the catalyst in the anode [1–6]. Favorable electronic properties have been suggested by density-functional theory studies, which have shown that the CO adsorption energy is the lowest on the Pt monolayer located above Ru compared with the adsorption energies on pure Pt, pure Ru, and a Pt-Ru mixed surface layer over Pt [7, 8]. The bifunctional mechanism [4] suggests that Ru provides an active surface for oxidative removal of adsorbed CO at the neighboring Pt sites. Thus, a

Pt-Ru alloy catalyst with high CO tolerance is used in the anode, especially when a reformate H_2-rich gas (in which CO content is high) is used for fuel.

An ideal cathode should have: 1) a large interface between gas phases and/or polymer electrode and catalyst, 2) highly efficient proton transport, 3) high transportation capacity for oxygen and easy by-product removal (i.e., condensed or gaseous water), 4) high electronic conductivity, 5) excellent chemical resistance and good mechanical properties to maintain an effective porous structure during fuel cell operation, and 6) high tolerance to contamination. Pt nano-particles supported on carbon particle surfaces are commonly used in cathode catalyst layers [9–11]. Using platinum supported on high-surface-area carbon (e.g., Vulcan XC72R) as the electrocatalyst rather than pure Pt black yields a ten-fold reduction in platinum loading. To conduct protons to reactive spots, a proton conducting polymer (e.g., Nafion) is impregnated into the catalyst layer [12]. This breakthrough technology creates a Pt catalyst with a particle size as low as ~3 nm and a very high active surface area, as well as proton transport networks . The structured cathode creates a three-dimensional network that makes mass transport and electrochemical reactions at the heterogeneous interface more efficient [13]. Recently, platinum binary or ternary alloys such as Pt-Co, Pt-Cr, or Pt-Co-Cu are being tested in PEMFCs to decrease the precious metal content in the catalyst layer and increase the ORR efficiency.

Reliability and durability are the most important considerations in PEMFCs. The durability of fuel cell systems operating under automotive conditions has not been clearly established. Fuel cell power systems need to be as durable and reliable as current automotive engines, i.e., 5,000-hour lifespan (150,000 miles equivalent) and be able to function over the full range of external environmental conditions (–40 °C to +40 °C). Analysis of various standardized US vehicle drive cycles reveals that a vehicle experiences roughly 300,000 load (voltage) cycles between peak power (0.7 V) and idle (0.9 V) through its life of 5,500 h. The long-term vehicle performance degradation target of $\leq$ 3 µV/h over 5,500 h requires an absolute voltage loss of $\leq$ 17 mV over the projected 300,000 large voltage cycles (0.7↔0.9 V) [14]. The durability of catalysts has become a major concern in fuel cell development. Under fuel cell operating conditions, the cathode catalyst layer can degrade through platinum sintering and dissolution, especially in conditions of load-cycling and high electrode potentials. Carbon support corrosion is another challenge at high electrode potentials and can worsen under load cycling and high-temperature operation. Stationary power requires that PEMFC systems operate on natural gas or LPG that achieves 40% electrical efficiency and 40,000 hours of durability at low cost. CO tolerance, long-term stability of the anode catalyst layer, and low loading of noble metals for cost reduction are also some of the challenges that need to be overcome for stationary power applications. Although significant attention has been focused upon fundamentally understanding catalyst degradation and the development of novel catalysts and structures, we are not yet close to making durable electrodes at low cost for the commercializing of fuel cells. In this chapter, we will focus on degradation of anode and cathode catalysts, and diagnostic methods for electrode failure after fuel cell operations. Failure mechanisms will also be discussed.

23.2 Diagnosis of Catalyst Layer Degradation: Fuel Cell Failure Analysis

Learning from failures is essential to develop new products and improve product quality. A learning cycle of fuel cell product development learning cycle is shown Figure 23.2. Failure analysis for fuel cells is relatively young compared with existing failure analysis in mature industries such as the semiconductor manufacturing. Despite a significant effort in recent years to determine failures and understand failure mechanisms [9, 15–19], failure modes for PEMFCs are not well documented and the causes and mechanisms of degradation are not fully understood. Development of diagnostic tools and characteristic methods for fuel cells, especially for porous electrodes, is an active area of research for scientists and engineers.
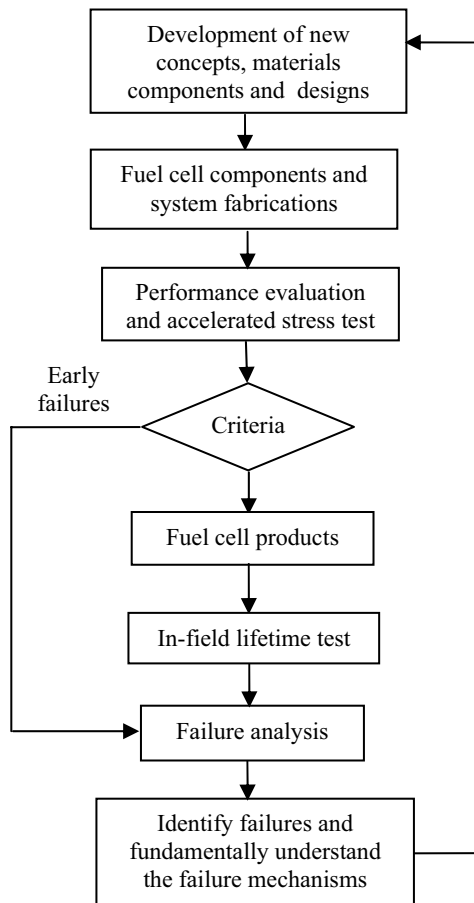
Figure 23.2. Learning from failures – a fuel cell product development cycle

23.2.1 Diagnostic Tools to Identify Catalyst Degradation During Fuel Cell Operation: Electrochemical Methods

A fuel cell is a typical electrochemical device. Thus, the electrochemical analysis methods developed for other electrochemical devices can be directly used or modified for diagnosis of fuel cell degradation, including catalyst layer degradation. Cyclic voltammetry and polarization curve analysis are very frequently used in failure analysis and degradation diagnosis.

23.2.1.1 Cyclic Voltammetry for Fuel Cell Electrode Analysis

Cyclic voltammetry (CV) is perhaps the most versatile electroanalytical technique for the study of electroactive species. CV is usually used to characterize electrochemical reactions and electrode surface absorption, and has become increasingly popular in all fields of chemistry as a means of studying redox reaction rates in a wide potential range. CV is also a typical method for the study of reaction mechanisms, as its mathematical description has been developed sufficiently to enable kinetic parameters to be determined.

One of applications of CV is to measure catalyst surface area and determine catalyst utilization [10, 15, 20–22]. The Pt surface area is measured either from the cyclic voltammogram of a gas diffusion electrode (GDE) in 1 mol/dm^3 sulfuric acid or from a MEA in a single cell stack. The potential is cycled, typically at 20 or 30 mV/s, between 0 and +1.2 V (vs. RHE) until a stable voltammogram is obtained. The hydrogen adsorption charge is measured (Equation 23.1) from the voltammogram. The intrinsic Pt catalyst surface area, A_{Pt}, or the electrochemical area (ECA) can be determined using a rotating disk electrode (RDE) configuration by integrating the hydrogen adsorption/desorption area of the voltammogram. The number of Pt surface atoms is estimated from the Coulombic charge for hydrogen adsorption/desorption, Q_H, assuming 210 $\mu C/cm^2_{Pt}$ after double layer correction [22]. The ECA can be calculated using Equation 23.2:

$$Pt + H^+ + e^- = Pt\text{-}H \tag{23.1}$$

$$ECA\ (cm^2_{Pt}/g_{Pt}) = Q_H\ (\mu C/cm^2)/[210\ (\mu C/cm^2_{Pt}) \times L_{Pt}\ (g_{Pt}/cm^2)] \tag{23.2}$$

where L_{Pt} represents Pt loading in the electrode. By dispersing catalyst powder onto a glassy carbon RDE, the Pt surface area obtained from ECA measurement is close to that measured from high-resolution transmission electron spectroscopy (HRTEM) [15]. However, Pt particles in the MEA are always partially covered with polymer electrolyte or disconnected from the carbon support by being completely trapped in the polymer electrolyte during MEA processing. Not all of the Pt surfaces are available for the reaction. The electrode platinum surface area (EPSA), on the other hand, is a measure of the platinum surface area potentially available for reaction in the GDE. The Pt surface area measured from the cyclic voltammogram of a MEA in a single fuel cell stack or a GDE in an *ex situ* CV test is smaller than the ECA. Pt utilization can be defined as:

$$\text{Pt utilization (\%)} = \text{EPSA}(\text{cm}^2_{Pt}/\text{cm}^2)/[\text{ECA }(\text{cm}^2_{Pt}/\text{g}_{Pt}) \times \text{L}_{Pt}\ (\text{g}_{Pt}/\text{cm}^2)]$$
$$\times 100\% \tag{23.3}$$

An *ex situ* cyclic voltammetry procedure was developed to measure the EPSA of electrodes, which employed the test setup used to measure the catalyst ECAs [20]. A method similar to using the Coulombic charge for hydrogen adsorption/desorption to estimate Pt surface area is another simple and frequently used method called a CO-stripping voltammogram. CO oxidation in the presence of Pt as the electrocatalyst occurs in the range of 0.7 V to 0.87 V, depending on the Pt crystalline surfaces. The CO stripping potential is 0.87 V on Pt(111), 0.79 V on Pt(100), and 0.70 V on Pt(110) [15]. The electrocatalysis reactions of CO on a Pt surface are assumed to be a two-electron process:

$$Pt\!-\!\!-\!CO + H_2O \leftrightharpoons Pt + CO_2 + 2H+ + 2e\text{-} \tag{23.4}$$

$$[Pt]_2\!-\!\!-\!CO + H_2O \leftrightharpoons 2Pt + CO_2 + 2H+ + 2e\text{-} \tag{23.5}$$
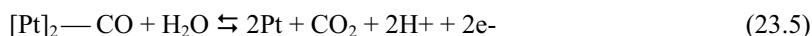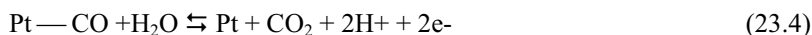
The ECA can be calculated from the Coulombic charge of CO stripping using Equation 23.6. Readers are referred to [20] and [15] for more details about the experimental setup.

$$\text{ECA }(\text{cm}^2_{Pt}/\text{g}_{Pt}) = Q_{CO}\ (\mu C/\text{cm}^2)/[420\ (\mu C/\text{cm}^2_{\ Pt})\times \text{L}_{Pt}\ (\text{g}_{Pt}/\text{cm}^2)] \tag{23.6}$$

CV is frequently used to determine EPSA changes during fuel cell operation, in order to monitor catalyst surface area decrease due to Pt particle agglomeration or to Pt dissolution or migration into the membrane, and to analyze electrode contamination and anode degradation. These uses of CV will be discussed in later sections.

23.2.1.2 Polarization Curve and Fuel Cell Performance

A polarization curve, i.e., an I-V curve of a fuel cell stack under certain operating conditions, is frequently used to describe fuel cell performance and determine performance decay with time. Polarization curve analysis can provide the most important kinetic parameters, such as the Tafel slope, exchange current density, cell resistance, limiting current density, and specific activity of Pt. A single fuel cell potential can be described by:

$$E_c = E^0 - \eta_{act} - \eta_{ohm} - \eta_{mass}$$

where E^0 is the thermodynamic open circuit potential, η_{act} is the active overpotential arising from the kinetics of charge transfer reactions, η_{ohm} is the ohmic overpotential arising from component resistances, and η_{mass} is the mass transfer overpotential arising from the limited rate of mass transfer. The I-V curve, as shown in the Figure 23.3 [10], is divided into three regimes in which one of the overpotentials is dominant.
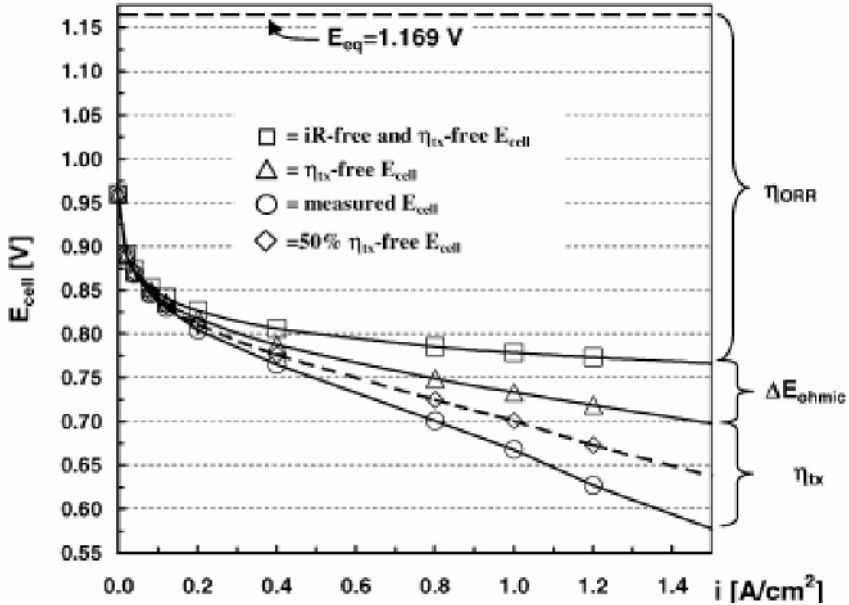
Figure 23.3. (a) Circular symbols: 50 cm^2 single-cell H$_2$/air performance at T$_{cell}$ = 80 °C (80 °C dew point, i.e., 100% RH) at a total pressure of 150 kPa$_{abs}$ and stoichiometric flow of s = 2.0/2.0 (controlled stoichiometric flow for $i \geq 0.2$ A/cm^2; 0.2 A/cm^2 flow at $i < 0.2$ A/cm^2); catalyst coated membrane (CCM) based on a ~25 μm low-EW membrane (~900 EW) coated with electrodes consisting of ca. 50 wt% Pt/carbon (0.4/0.4 mgPt/cm^2 (anode/cathode)) and a low-EW ionomer (~900 EW; ionomer/carbon ratio = 0.8/1). (b) Square symbols: E$_{cell}$ vs. i for the mass-transport-free and ohmically corrected (i.e., iR-free) E$_{cell}$/i-curve shown in (a). *In situ* measurements of high-frequency resistance vs. current density were obtained at 1 kHz (ranging from 45 to 55 mV cm^2) and used for the ohmic correction. (c) Triangular symbols: addition of the ohmic losses, ΔE$_{ohmic}$, to the polarization curve shown in (b). (d) Diamond symbols: E$_{cell}$/i-curve shown in (a) corrected for 50% of the mass transport losses [10]. (Reprinted from Applied Catalysis B, 56(1–2), Gasteiger HA, Kocha SS, Sompalli B, Wagner FT, Activity benchmarks and requirements for Pt, Pt-alloy, and non-Pt oxygen reduction catalysts for PEMFCs, 9–35, ©2005, with permission from Elsevier.)

The thermodynamic open circuit potential is usually expressed by Equation 23.7:

$$E^0 = \frac{-\Delta G(T)}{2 \cdot F} + \frac{RT}{2 \cdot F} \ln \frac{pH_2 \cdot pO_2^{0.5}}{pH_2O} \tag{23.7}$$

When a load is applied to the fuel cell and the current flows through the circuit, the active overpotential from the kinetics of charge transfer reactions, the ohmic overpotential from component resistances, and the mass transfer overpotential from the limited rate of mass transfer will rise. The Butler-Volmer Equation (Equation 23.8) describes a relation between the overpotential and the current density on an

electrode surface; the Tafel expression is more often used in the analysis of the I-V plot:

$$E_c = E^0 - b \log i - i\text{R} \tag{23.8}$$

where i is the current density, which is equal to current per unit area, i_0 is the exchange current density, b is the Tafel slope, and R is the cell resistance. By fitting experiment data to the Tafel equation, the various voltage loss terms can be quantified [10, 23]. The ohmic voltage loss, $\eta_{ohm} = i\text{R}$, can be measured directly via either current-interrupt or high-frequency resistance measurements. An iR-free cell potential can be expressed as follows:

$$E_{c(,iR\text{-}free)} = E^0 - \eta_{act} - \eta_{mass} = E^0 + b \log I \tag{23.9}$$

Compared with oxygen reduction overpotential, both kinetic and mass-transport losses of the hydrogen electrode can be neglected. Therefore, the iR-free cell voltage, $E_{c(iR\text{-}free)}$, of a fuel cell operating on H_2/O_2 at low current densities (0.1 A/cm^2) is controlled by voltage loss due to the O_2 reduction kinetics, i.e., by the η_{act} term in Equation 23.6. The cathode overpotential term, $\eta_{act,}$ for Pt catalysts at low current density (< 0.1 A/cm^2) follows the Tafel equation:

$$\eta_{act} = a + b \log I \tag{23.10}$$

A conceptual polarization curve that would be obtained in the absence of mass transport and ohmic resistances can be constructed by extrapolating the iR-free cell voltage obtained at low current densities (< 0.1 A/cm^2) by means of Equation 23.10, indicated by the square symbols in Figure 23.3 [10]. In the Tafel equation, the Tafel slope b is

$$b = \frac{RT}{\alpha nF} \tag{23.11}$$

where α is the transfer coefficient, n is the number of electrons, and F is the Faraday constant.

The performance of a PEMFC can be expressed through the analytical formulation of the polarization curve. Simultaneous estimation of the parameters through analysis of the polarization curve can be helpful in diagnosis of PEMFC degradation and identification of degradation mechanism. Some models and testing methods have been developed to characterize PEMFC performance through polarization curve analysis [25, 26].

23.2.1.3 Electrochemical Impedance Spectroscopy (EIS)

Electrochemical impedance spectroscopy (EIS) has been used to characterize the ionic conductivity of conducting polymers in the electrode, separating this ionic resistance from the membrane and ohmic contact resistances at the interfaces [24–31]. Such measurements are helpful in quantifying degradation of the ionomer in

the electrodes with time, and understanding the effect of operating conditions on MEA performance. EIS has been used in PEMFC-related research to study ORR kinetics [27] and to characterize transport losses [28–31]. There are two different ways to describe the physics and electrochemistry of a fuel cell: *i*) using a system of differential equations, or *ii*) using a finite transmission line of resistors and capacitors [24, 29], as shown in Figure 23.4. The transmission line model can be thought of as a finite difference approximating to the corresponding differential equations [24]. The corresponding EIS for porous electrodes in a fuel cell is often modeled by a finite transmission-line equivalent circuit [24, 29]. The circuit for the catalyst layer (Figure 23.4) contains two parallel resistive rails, one representing electron transport through the conducting carbon support and the other ion transport through the interparticle regions. These two rails are connected by capacitors representing the electrolyte-catalyst (C+Pt) differential capacitance, which is assumed to be uniformly distributed through the catalyst layer [29].
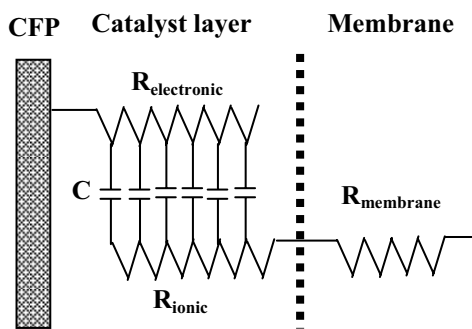
Figure 23.4. Finite transmission-line equivalent circuit describing the impedance behavior of a PEMFC electrode [29]. (Reproduced by permission of ECS—The Electrochemical Society, from Lefebvre M, Martin RB, Pickup PG. Characterization of ionic conductivity profiles within proton exchange membrane fuel cell gas diffusion electrodes by impedance spectroscopy.)

Two experimental methods to characterize the catalyst layer are described in the literature [24]: the "H_2/O_2 method" in which pure hydrogen and oxygen and nonzero DC current are used, and the "H_2/N_2 method" in which pure nitrogen is used on the cathode and zero DC current. These two methods have been chosen because the catalyst layer physics simplify to cases in which parameters such as ohmic resistance, CL electrolyte resistance, and double-layer capacitance can be readily extracted from impedance data [24].

23.2.2 *Ex situ* Tools for Characterization of Catalyst Degradation During Fuel Cell Operation

Electrochemical methods used in the diagnosis of fuel cell degradation provide directly macro-phenomena about fuel cell degradation. Hypothesis and degradation mechanisms can be deduced from electric measurement results, e.g., from analysis of polarization curves. To fundamentally understand catalyst layer degradation in

fuel cell operation, many methods developed for material characterization are frequently used in the diagnosis of catalyst layer degradation.

23.2.2.1 Electron Microscopy

Electron microscopy, such as scanning electron microscopy (SEM) and transmission electron microscopy (TEM), is a powerful tool for catalyst structure and phase analysis. TEM with energy dispersive X-ray spectroscope (EDX) has high resolution up to the atomic level and the capability for both imaging and element analysis. Catalyst particles used in fuel cell electrodes usually have a dimension range of 2–5 nm. Morphology is difficult to identify with other tools, even field emission scanning electron microscopy (FESEM). Although STM (scanning tunneling microscopy) and AFM (atomic force microscopy) can reach similar resolutions, both methods require a smooth sample surface, ideally a single crystal surface. Therefore, they are rarely used in porous electrode analysis.

Figure 23.5 is a typical TEM image of a Pt catalyst on a carbon support with polymer electrolyte. The Pt particles, polymer electrolyte, carbon support for the Pt, and voids can be identified clearly. Using EDX and electron diffraction, the elements of the phases and crystal structure can also be determined. TEM has been widely used to measure the catalyst particle size and surface area, to determine Pt dissolution and migration into the membrane, to analyze the catalyst layer structures and catalyst alloy phases, and to identify MEA failures [32–39].
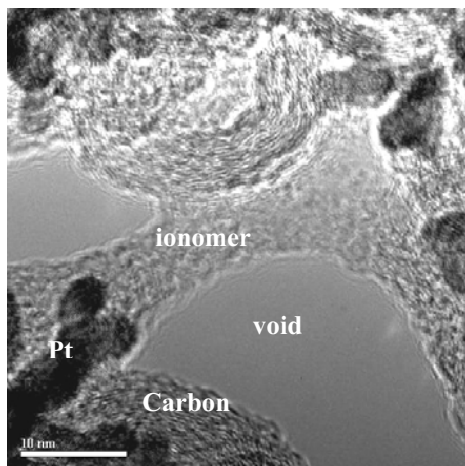
Figure 23.5. A typical TEM image of a catalyst layer. Magnification: 400,000X.

Sample preparation of the porous electrode for TEM investigation is critical in order to obtain clear images of all phases in the catalyst layer. Ultra-microtome, solvent dispersion and FIB (fast ion beam bombardment) sample preparation methods have been investigated. The ultra-microtome technique, introduced first by Blom et al. in Oak Ridge National Laboratory [32], is often used to make thin slides of a catalyst layer sample impregnated with epoxy for TEM investigation.

SEM is another common tool in catalyst structure and morphology analysis Unlike TEM, in which the image is obtained from transmission electrons, the image in SEM is obtained from second or back scattering electrons reflected from the sample surface. With a field emission gun, SEM can achieve 3 nm resolution. Although FESEM's resolution is lower than TEM's, sample preparation for SEM is much simpler than for TEM. In addition, a larger area of sample can be viewed using SEM, and an SEM image provides more information on the sample's surface morphology. SEM with FIB (dual beams) is also used to slice samples for TEM or to generate 3D images for the investigated samples. Thus, SEM has been widely used to characterize catalyst structure and analyze fuel cell failure.

A field emission scanning electron microscope with a cryogenic stage and sample preparation unit (CRYO-FESEM) was introduced by Li et al. at Ballard Power Systems to characterize ice distribution in the catalyst layer and gas distribution layer (GDL) of PEMFCs under isothermal constant voltage (ICV) operation at subzero temperature [40]. The analysis method was designed to ensure that the entire experiment, from sample preparation to CRYO-FESEM characterization, was carried out under subzero (°C) conditions so that the water was always kept in a frozen state without thawing. Figure 23.6 shows examples of CRYO-FESEM images and the image analysis method [40].
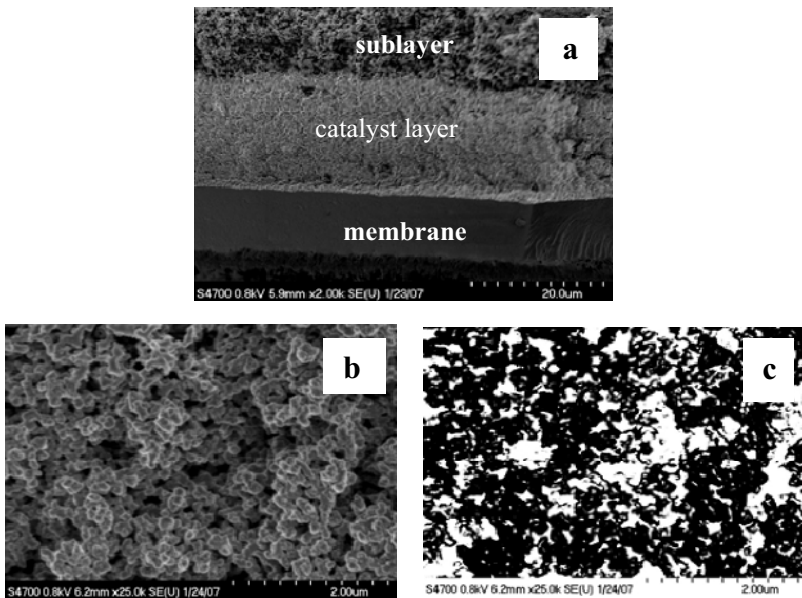
Figure 23.6. CRYO-SEM image analysis. a) SEM image of a cross-section of the MEA2 under frozen state, b) a close-up of a sublayer in a), and c) the same image of a) converted into a binary image with histogram analysis using Image-Pro Plus software.

X-ray diffraction is a very useful tool for analysis of crystal structure and crystalline size. Phase identification using X-ray diffraction relies mainly on the positions of the peaks in a diffraction profile and to some extent on the relative intensities of these peaks. The shapes of the peaks, however, contain additional and

often valuable information. The shape, particularly the width, of the peak is a measure of the amplitude of thermal oscillations of the atoms at their regular lattice sites. Crystallite size can also cause peak broadening. The well-known Scherrer Equation (Equation 23.12) [42] explains peak broadening in terms of incident beam divergence, which makes it possible to satisfy the Bragg condition for non-adjacent diffraction planes. Once instrument effects have been excluded, the crystallite size is easily calculated as a function of peak width (specified as the full width at half maximum peak intensity (FWHM)), peak position, and wavelength.

$$L_{vol} = K \lambda / \beta \cos \theta_{(radians)} \qquad (23.12)$$

where K is a constant approximately equal to 0.89–0.94, λ is the X ray wavelength, and β is the integral breadth of the diffraction peak.

The first detailed X-ray diffraction (XRD) studies on PEMFC electrodes were performed by Wilson et al. [43] using a Warren-Averbach Fourier transformation method for determining the weighted crystallite sizes. Warren and Averbach's method takes into account not only the peak width but also the shape of the peak. This method is based on a Fourier deconvolution of the measured peaks and the instrument broadening to obtain the true diffraction profile. This method is capable of yielding both crystallite size distribution and lattice microstrain. The particle-size distributions can be determined from the actual shape of the diffraction peaks, with the use of Warren-Averbach analysis.

The specific Pt surface area for a sample, S_{Pt} (m^2/g_{Pt}), can be approximated using the following summation:

$$S_{Pt} = \sum_{n=1}^{\infty} W_n S(n) \qquad (23.13)$$

where n is the characteristic diameter (in nanometers) of the particles within the nth domain, W is the mass fraction of platinum within the nth domain, and $S(n)$ is the specific surface area (in units of m^2/g_{Pt}) of spherical platinum crystallites with a diameter of n nm.

For particle size analysis, XRD operation and sample preparation is simple. It represents an average particle size in a larger sample size, as compared with TEM. However, TEM imaging analysis can provide particle size distributions for different locations in the catalyst layer, particle aggregation information, and element composition, which cannot be obtained from XRD analysis. Many TEM analyses result in particle size profiles that are not as heavily biased toward the smaller particles as these XRD results are [33, 43]. Ferreira et al. [33] observe that the volume averaged diameter (2.3 nm) determined from X-ray powder diffraction is slightly different from the volume/area averaged diameter (3.0 nm) from TEM measurement. The imaging effects as well as the low contrast between the smaller particles and the carbon background limit the ability of the TEM to resolve many of the smaller particles (< 1nm). In one case, the particles in a supported catalyst of subnanometer Pt clusters that could not be observed with TEM were readily

detected by XRD. Therefore, the volume/area average diameter from TEM would be slightly larger than that from X-ray diffraction.

Figure 23.7 shows a typical example of the X-ray powder diffraction pattern of a pristine Pt/Vulcan powder sample collected at normal incidence, in comparison with patterns of the anode and cathode in a cycled Pt/Vulcan MEA sample collected at 1° incidence [33]. The average platinum crystal sizes (volume averaged) of pristine and cycled Pt/Vulcan samples were estimated using the Scherrer equation, by measuring the full width half maximum of the $\{111\}_{Pt}$, $\{200\}_{Pt}$, and $\{220\}_{Pt}$ X-ray powder diffraction peaks. Upon cycling between 0.6 and 1.0 V, the volume averaged platinum crystal size in the cycled MEA cathode increased significantly to 10.5 nm, from 2.3 nm in the pristine Pt/Vulcan sample. The Pt agglomeration will be discussed in later sections.
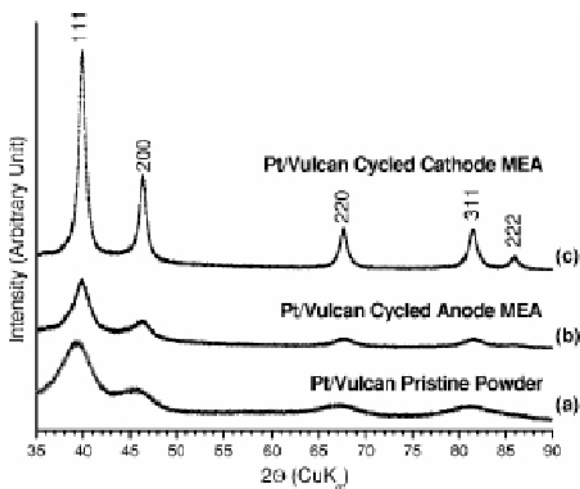
Figure 23.7. (a) X-ray powder diffraction pattern of the pristine Pt/Vulcan powder sample collected at normal incidence was compared to those of anode (b) and cathode (c) in the cycled Pt/Vulcan MEA sample collected at 1° incidence [33]. (Reprinted by permission of ECS—The Electrochemical Society, from Ferreira PJ, la O' GJ, Shao-Horn Y, Morgan D, Makharia R, Kocha S, Gasteiger HA. Instability of Pt/C electrocatalysts in proton exchange membrane fuel cells.)

Chemical bond information for materials can be determined with inferred and/or Raman spectroscopy, SIMS (second ion mass spectroscopy) and TOF-SIMS (time-of-flight secondary ion mass spectroscopy). Chemical bond information, especially on the materials surfaces, can be obtained with TOF-SIMS. Micro-IR and micro-Raman spectroscopes have been developed to map the chemical compositions of samples on a micrometer scale. The chemical species presented in MEAs after different lifetime tests were studied by a Raman spectrometer [36]. Cheng and co-workers observed a significant shift in the Raman bands of ruthenium oxide (RuO_2) from 528, 646, and 716 cm^{-1} in a single crystal to 506, 616, and 675–680 cm^{-1} of amorphous ruthenium oxide at the anode side of MEAs. Although the RuO_2 was initially present in the powder sample of the anode

catalyst, the intensity of Raman peaks increased considerably after lifetime tests and sharper peaks were observed for the 1000 h MEA [36].

Electrocatalytic reactions occur on catalyst surfaces. The catalyst surface structure and chemically bonded or physically absorbed substances on the catalyst surface exert strong influences on catalyst activity and efficiency. X-ray photoelectron spectroscopy (XPS) (also known as electron spectroscopy for chemical analysis (ESCA), auger emission spectroscopy (AES), or auger analysis) is a failure analysis technique used to identify elements present on the surface of the sample. For instance, this can be used to identify Pt and carbon surface chemical species that may present histories of chemical reactions or contamination in the catalyst layer. AES and XPS can also provide depth profiles of element analysis. Wang et al. [41] studied XPS spectra of carbon and Pt before and after fuel cell operation. They observed a significant increase in O 1s peak value for each oxidized carbon support, the result of a higher surface oxide content in the support surface due to electrochemical oxidation. However, sample preparation in AES and XPS analysis is critical because these methods are very sensitive to a trace amount of contaminants on sample surfaces, and detect as little as 2–10 atoms on the sample surface.

23.2.3 Durability and Accelerated Stress Testing

Fuel cells, especially for automotive applications, must operate over a wide range of operating and cyclic conditions. A desirable operating temperature range is from below the freezing point to well above the boiling point of water. The humidity can range from dry to saturated (100% relative humidity, RH). The anode side of the cell may be exposed to hydrogen and air during different parts of the driving and start/stop cycles. The half-cell potentials can vary from 0 to > 1.5 volts due to the start/stop cycles. The lifetime of the fuel cell is significantly impacted by the operating conditions. Many factors, for instance, Pt sintering, particle growth, Pt dissolution, and carbon support corrosion, can affect catalyst layer durability. All of these factors are accelerated under load-cycling. Because so many interrelated issues are involved in durability analysis of a PEMFC, many broad studies addressing all of these factors and operating conditions are needed. A conventional durability test requires progressively longer hours per test as the cell/stack design nears completion. A final configuration of PEMFC components could be tested for a total of up to 10,000 h or more before a prototype design is frozen. The prototype stack must then be validated for another ~5,000 h before being integrated with the system [9]. An accelerated stress test (AST) is demanded by developers for screening new components and new designs. In order to assess the lifetime of fuel cell products, questions of how to evaluate durability under various operating conditions and how to compare data taken under different conditions must be solved.

In the past few years, many AST methods used for individual components have been developed, but they tend not to conform to standardized protocols; different developers test products using their own protocols, and the operating conditions used to study the degradation mechanisms and durability of various components

thus tend to vary. Therefore, it is difficult to compare the data obtained from various developers.

The United States Department of Energy (DOE) and the Freedom CAR Fuel Cell Technical Team have recently released a set of durability-test protocols that includes tests of electrocatalysts (see Table 23.1) and of electrocatalyst supports (see Table 23.2) as well as other components [44]. The documents describe testing protocols to assess the performance and durability of fuel cell components for automotive and stationary applications. These protocols are intended to establish a common approach for determining and projecting the durability of PEMFC components under simulated automotive drive cycle conditions.

Table 23.1. Electrocatalyst cycle and metrics [44]. (Reproduced from United States Department of Energy. DOE cell component accelerated stress test protocols for PEM fuel cells: electrocatalysts, supports, membranes, and membrane electrode assemblies. 2007. With permission from DOE.)

Cycle	Step change: 30 s at 0.7 V and 30 s at 0.9 V. Single cell 25–50 cm^2	
Number	30,000 cycles	
Cycle time	60 s	
Temperature	80 °C	
Relative Humidity	Anode/cathode 100/100%	
Fuel/Oxidant	Hydrogen/Nitrogen	
Pressure	150 kPa absolute	
Metric	**Frequency**	**Target**
Catalytic activity*	Beginning and End of Life	≤ 60% mass loss of initial catalytic activity
Polarization curve from 0 to ≥1.5 A/cm^2 **	After 0, 1k, 5k, 10k and 30k cycles	≤ 30 mV loss at 0.8 A/cm^2
ECSA/Cyclic Voltammetry	After 1, 10, 30, 100, 1000, 3000 cycles and every 5000 cycles thereafter	≤ 40% loss of initial area

* Activity in A/mg @150 kPa abs backpressure at 900 mV iR-corrected on H_2/O_2, 100% RH, 80 °C
** Polarization curve per USFCC "Single Cell Test Protocol" Section A6

The actual lifetime of a fuel cell in a vehicle undergoing driving and start/stop cycles may or may not be accurately predicted by these protocols. More studies are needed to link the AST results to the actual lifetime, including identifying failures, understanding failure mechanisms, and modeling data to predict the lifetime of products.

Table 23.2. Support cycle and metrics [44]. (Reproduced from United States Department of Energy. DOE cell component accelerated stress test protocols for PEM fuel cells: electrocatalysts, supports, membranes, and membrane electrode assemblies. 2007. With permission from DOE.)

Cycle	Hold at 1.2 v for 24 h; run polarization curve and ECSA; repeat for total 200 h. Single cell 25–50 cm^2
Total time	Continuous operation for 200 h
Diagnostic frequency	24 h
Temperature	95 °C
Relative Humidity	Anode/cathode 80/80%
Fuel/Oxidant	Hydrogen/Nitrogen
Pressure	150 kPa absolute

Metric	**Frequency**	**Target**
CO_2 release	On-line	< 10% mass loss
Catalytic Activity*	Every 24 h	≤60% loss of initial catalytic activity
Polarization curve from 0 to ≥1.5 A/cm^2 **	Every 24 h	≤ 30 mV loss at 1.5 A/cm^2 or rated power
ECSA/Cyclic Voltammetry	Every 24 h	≤40% loss of initial area

*   Activity in A/mg @150 kPa abs backpressure at 900 mV iR-corrected on H_2/O_2, 100% RH, 80 °C

** Polarization curve per USFCC "Single Cell Test Protocol" Section A6

23.3 Anode Catalyst Layer Degradation

23.3.1 Anode Catalyst Layer Degradation Caused by Contamination

PEM fuel cells use air as a source of oxygen and hydrogen as fuel. Pollutants in the air and impurities in the hydrogen gas can harm the anode and cathode catalyst layers and, in severe cases, can permanently damage the MEA. The impurities in hydrogen, CO, H_2S, NH_3, organic sulfur-carbon, and carbon-hydrogen compounds, come mainly from fuel processing. Air pollutants such as NO_x, SO_x, and hydrocarbons arise mainly from vehicle exhaust and industrial emissions. Table 23.3 lists U.S. National Ambient Air Quality Standards (NAAQS). In high air pollution regions, especially in developing countries and industrial areas, the pollutant concentration can exceed the amounts in Table 23.3. Traces of metal ions, especially Fenton agent such as Fe^{2+} and Cu^+, coming from the humidifier or other components are also harmful to the ionomers in the catalyst layer. The effect

of contaminants on the performance and durability of fuel cells is one of the most important issues in fuel cell operation and applications [45, 46]. Understanding contamination mechanisms and developing mitigation strategies has drawn a great deal of attention to fuel cells and their applications in the automobile industry. For the impacts, mechanisms, and mitigation of contamination in PEM hydrogen fuel cells, readers are referred to the reviews of Cheng [46], Baschuk [47], and their co-workers.

Table 23.3. National Ambient Air Quality Standards (NAAQS)

Pollutant	Primary Stds.	Averaging Times
Carbon Monoxide	9 ppm ($10 \ mg/m^3$)	8-hour [1]
	35 ppm ($40 \ mg/m^3$)	1-hour [1]
Nitrogen Dioxide	0.053 ppm ($100 \ \mu g/m^3$)	Annual (Arithmetic Mean)
Ozone	0.08 ppm	8-hour
	0.12 ppm	1-hour (Applies only in limited areas)
Sulfur Oxides	0.03 ppm	Annual (Arithmetic Mean)
	0.14 ppm	24-hour [1]
	0.5 ppm [2] ($1300 \ \mu g/m^3$)	3-hour [1]

(1) not to be exceeded more than once per year
(2) secondary standards

23.3.1.1 Anode Contamination by Carbon Oxide

Carbon monoxide in the fuel gas, especially in reformate H_2-rich gas, has become a major concern in PEM fuel cells, particularly at operating temperatures < 80 °C. Stream reforming of natural gas (stream methane reforming (SMR)) or of gasoline or diesel is the most common method of producing commercial bulk hydrogen. In gasoline reforming, relatively simple water gas shift reactors typically achieve a CO level of 5000–10000 ppm. In methanol reforming, the amount of CO produced is lower, but the reformate still contains about 1000 ppm CO. In reforming hydrogen, even using a selective oxidation process, the CO concentration could be in the range of 2–100 ppm, which could poison the anode catalyst layer, resulting in lower fuel cell performance and reduced energy conversion efficiency.

Theoretical analysis indicates that CO poisons the anode reaction through preferentially adsorbing to the platinum surface and blocking active sites. CO absorbs on the platinum sites to the exclusion of hydrogen because CO is more strongly bonded to platinum than is hydrogen, which is indicated by a greater potential required for CO oxidation than for hydrogen oxidation, and a sticking probability of CO on platinum 15 times higher than that of hydrogen on platinum

[47, 48]. CO molecules adsorbed on a Pt surface could be either one CO molecule on one adsorption site (so-called linear adsorption) or one CO molecule on two adjacent Pt surface adsorption sites (bridge-adsorption) [49, 50]. Linear adsorption, therefore, should yield higher CO coverage on the Pt surface. The adsorption equilibrium is strongly in favor of adsorption, and desorption takes place most easily via oxidation of CO to CO_2. The oxygen atoms necessary for the reaction are then obtained from dissociation of the humidification water or the water present in the proton exchange membranes. In Camara's model [49], the linear- and bridge-bonded adsorbed CO, and the linear-bonded CHO and COOH derivatives are considered poisoning species. For all catalysts, CO oxidation starts mainly at the bridge-bonded sites. Only at high overpotentials does the linearly adsorbed CO start to be oxidized, and in this new situation the number of holes on the CO monolayer is sufficient to permit more significant hydrogen oxidation currents.

$$CO + Pt \rightarrow Pt \overset{\overset{\displaystyle O}{\vdots}}{\underset{}{}} CO \quad \text{(linear-bonded)} \tag{23.14a}$$

$$CO + Pt \cdots Pt \rightarrow Pt \cdots Pt \overset{\overset{\displaystyle O}{\vdots}}{} CO \quad \text{(bridge-bonded)} \tag{23.14b}$$
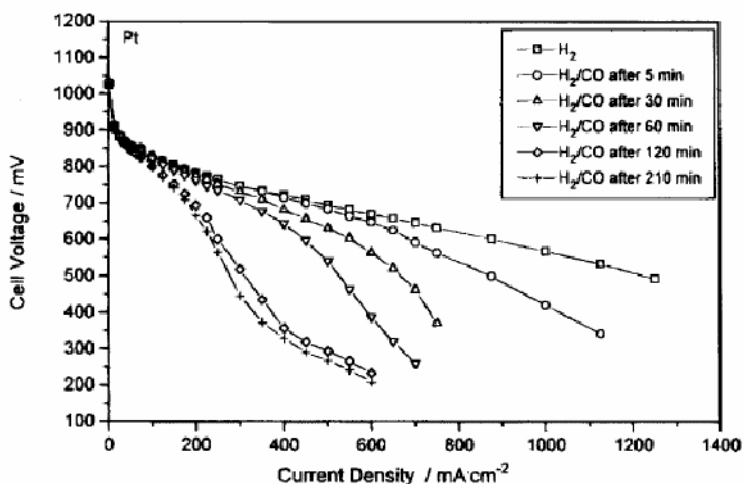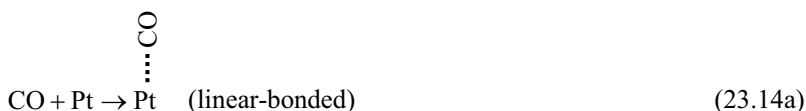
Figure 23.8. Effect of CO contamination time on fuel cell performance in H_2/100 ppm CO during the poisoning period; anode and cathode: Pt on Vulcan XC72; T = 80 °C; $P_{(H2)}$ = 0.22 MPa, $P_{(O2)}$ = 0.24 MPa [51]. (Reprinted by permission of ECS—The Electrochemical Society, from Oetjen H-F, Schmidt VM, Stimming U, Trila F. Performance data of a proton exchange membrane fuel cell using H_2/CO as fuel gas.)

CO poisoning of the Pt electrocatalyst in the anode causes fuel cell performance loss. The effect of CO poisoning on fuel cell performance is strongly

related to the CO concentration, the exposure time, and the cell operation temperature and pressure. Higher concentration and longer exposure time lead to a bigger loss in voltage, as shown in Figures 23.8 and 23.9 [51]. Increasing the cell temperature could effectively reduce CO adsorption on the catalyst surface by promoting CO oxidation. Using a current density at the cell voltage loss of 10 mV to define CO tolerance, Li et al. [50] found that the CO tolerance of the Pt catalyst at 200 °C is 1.3 A/cm² for 1% CO in hydrogen. It drops to 1.2 and 0.3 A/cm² at 175 and 150 °C, respectively. At 125 °C, however, 0.1% CO in hydrogen can only be tolerated at current densities lower than 0.3 A/cm². The tolerance at 80 °C is only 0.2 A/cm² for 0.0025% CO (~25 ppm) in hydrogen [50].
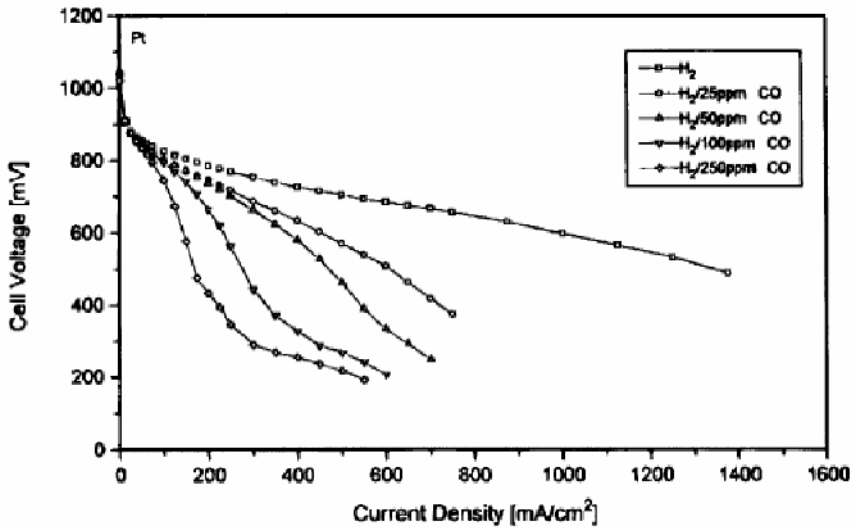
Figure 23.9. Effect of CO concentration on fuel cell performance; anode and cathode: Pt on Vulcan XC72; T = 80 °C; $P_{(H2)}$ = 0.22 MPa, $P_{(O2)}$ = 0.24 MPa [51]. (Reproduced by permission of ECS—The Electrochemical Society, from Oetjen H-F, Schmidt VM, Stimming U, Trila F. Performance data of a proton exchange membrane fuel cell using H₂/CO as fuel gas.)

To achieve a high level of CO tolerance, another method is to use an alloyed platinum catalyst having increased intrinsic tolerance to CO, such as Pt-Ru or Pt-Mo [52–54]. The Pt-Ru alloy has been widely used as an anode catalyst in fuel cells. The oxidation of CO on a Pt-Ru alloy electrode occurs at potentials of 170–200 mV lower than that of a pure Pt electrode [47], as illustrated in Figure 23.10. The lower oxidation potential of Ru compared with Pt leads to the preferential adsorption of water on the Ru atoms, creating Ru-OH and allowing the CO adsorbed on the Pt atoms to oxidize with the adjacent Ru-OH through the reactant pair mechanism [47]:

$$Ru\text{-}OH + Pt\text{-}CO \rightarrow Ru + Pt + CO_2 + H^+ + e^- \tag{23.15}$$

Thus, it would be expected that the best performance would occur on an electrode where Ru and Pt atoms are adjacent to one another. However, oxidation of Ru causes Ru to dissolve and cross over to the cathode, resulting in cell performance decline. This will be discussed in the following section.
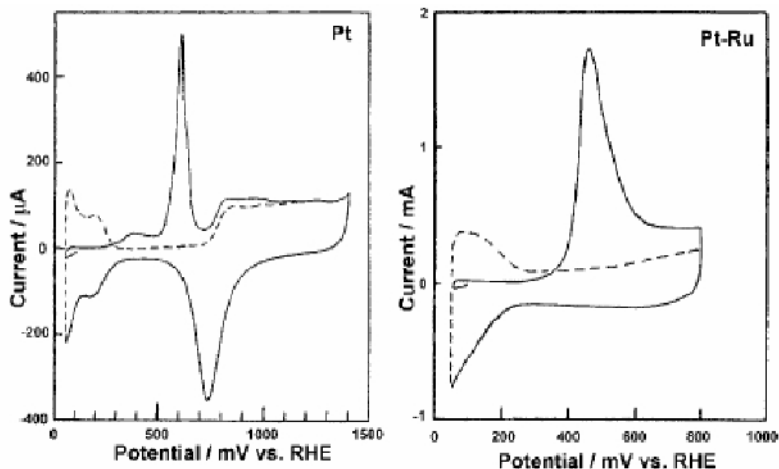
Figure 23.10. Comparison of the oxidation of CO on Pt and Pt-Ru [55]. (Reprinted from Electrochimica Acta, 39(11–12), Ianniello R, Schmidt VM, Stimming U, Stumper J, Wallau A, CO adsorption and oxidation on Pt and Pt-Ru alloys: dependence on substrate composition, 1863–9, ©1994, with permission from Elsevier.)

Air bleeding at the cell operational stage is another approach to mitigate CO poisoning [56–57]. Injection of 1–6% air, for instance, into the fuel stream can catalyze chemical oxidation of CO, originally by the platinum anode catalyst itself. Introduction of oxygen into the anode gas stream could also occur through the use of hydrogen peroxide (H_2O_2) in the anode humidifier. The hydrogen peroxide decomposes to hydrogen and oxygen in the anode, and the oxygen oxidizes the CO. The main advantage of using H_2O_2 as opposed to O_2 bleeding is to avoid the safety problem associated with mixing hydrogen and oxygen gases.

23.3.1.2 Anode Contamination by Sulfur-containing Species
Sulfur-containing species, such as sulfur dioxide (SO_2) and sulfur hydrogen (H_2S), in the fuel or air stream of a fuel cell are also strongly adsorbed on the Pt catalyst surface. H_2S can be catalyzed by Pt to form Pt–S_{ads} and H_2 on the Pt surface [58]:

$$Pt + H_2S \rightarrow Pt–S_{ads} + H_2 \tag{23.16}$$

or to form platinum hydrogen sulfide and platinum hydrogen through the following paths [46]:

$$Pt + H_2S \rightarrow Pt–H_2S_{ads} \tag{23.17a}$$

$$Pt + HS^- + H^+ \rightarrow Pt\text{–}HS_{ads}^- + H^+ \tag{23.17b}$$

$$Pt\text{–}HS_{ads}^- + H^+ \rightarrow Pt + H_2S \tag{23.18}$$

$$Pt + H^+ \rightarrow Pt^+\text{–}H_{ads} \tag{23.19}$$

where Pt^+ represents an equivalent positive charge on the Pt surface. Further oxidation of the adsorbed SH and H_2S form platinum sulfide:

$$Pt\text{–}SHn \rightarrow Pt\text{–}S_{ads} + nH^+ + ne^- \quad (n = 1 \text{ or } 2) \tag{23.20}$$
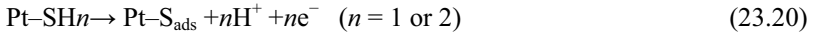
A trace amount of H_2S in the fuel or air stream could degrade the cell performance significantly, mainly through the poisoning effect of the Pt catalysts. A 0.1 ppm level of H_2S in the fuel stream could cause a 250 mV cell voltage drop within 300 hours at $0.5A/cm^2$ load [59]. Unlike in the case of CO poisoning, the presence of Ru in the Pt catalyst cannot provide sufficient tolerance to H_2S poisoning. Cathode exposure to 200 ppm H_2S for 10.5 hours caused complete deterioration in cell performance [58], which was only partially recoverable when neat air was introduced to the cathode side for 70.5 hours.

SO_2 adsorption on a Pt electrode would occur by linearly and bridged adsorbed S species. These two forms of chemisorbed S species on Pt at 80 °C were reported to be responsible for catalyst poisoning [46]. Electrochemical reduction from SO_2 to S on a Pt electrode, producing SO intermediates, was also suggested [46]:

$$Pt + SO_2 + 2H^+ + 2e^- \rightarrow Pt\text{–}SO_{ads} + H_2O \tag{23.21}$$

$$Pt\text{–}SO_{ads} + 2H^+ + 2e^- \rightarrow Pt\text{–}S_{ads} + H_2O \tag{23.22}$$
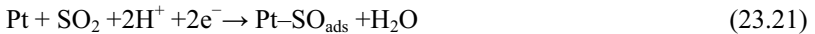
The performance of a fuel cell with 1 ppm of SO_2 in the air stream dropped 35% after 100 hours [60]. Absorbed SO_2 on the catalyst layer decreased the active surface area of the electrocatalyst. Cell performance could be only partially recovered by oxidation of SO_2 [59].

An electrocatalyst with high tolerance to sulfur-containing species has not yet been reported. Pre-purifying of gas streams to remove the sulfur-containing species is needed to avoid catalyst contamination by these materials.

23.3.2 Anode Catalyst Layer Degradation–Voltage Reversal

Cell voltage reversal could occur in a stack with serial cells or even a complete stack in a multi-stack system during fuel cell operation. When a weaker cell in a stack is not capable of producing the required current, voltage produced in other cells in the stack will apply to this cell and then drive the cell to become an "electrolysis cell" rather than a "battery", resulting in a negative voltage. Cell reversal is more likely to occur under conditions that expose weaker cells, e.g., low stoichiometries, electrode flooding at high current density, fuel cell start-up and shutdown operations, etc. The cell reversal can also occur in stack arrays when an entire stack is driven into voltage reversal by the other stacks.

Oxygen starvation caused by air stoichiometry or electrode flooding can lead to cell reversal. When there is insufficient oxygen at the cathode to combine with the protons coming across the membrane, the oxygen reduction reaction (ORR)

$$O_2 + 4H^+ + 4e^- = 2H_2O \ (E^0 = 1.23 \text{ V}) \tag{23.23}$$
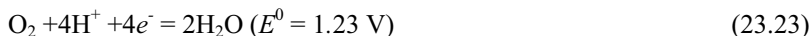
will be replaced by the proton reduction reaction (PRR)

$$2H_3O^+ + 2e^- = H_2 + 2H_2O \ (E^0 = 0.00 \text{ V}) \tag{23.24}$$
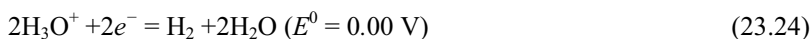
Therefore, the protons will be reduced with the electrons directly to produce hydrogen gas. Essentially, the cell turns into a hydrogen pump, with the hydrogen being oxidized at the anode and reduced at the cathode. Since the oxidation of the H_2 and the reduction of the H^+ are both very facile, the voltage drop across the cell at zero air stoichiometry will be quite small. In the absence of oxygen, the hydrogen production actually begins at small positive cell voltages (e.g., 0.03 V) because the cell has a strong H_2 concentration difference. Although heat will be generated in this case, there are not many reports of electrode or cell damage caused by oxygen starvation.
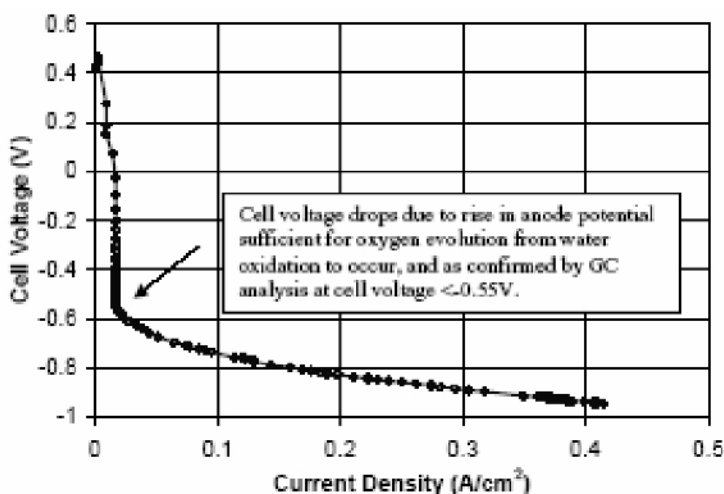
Figure 23.11. Fuel starvation polarization. Humidified anode/cathode feed streams: nitrogen/air. 3 bar, 75 °C, 4 mg/cm² Pt on each of the cathode and anode [61]. (Reprinted by permission of ECS—The Electrochemical Society, from Knights SD, Colbow KM, St-Pierre J, Wilkinson DP. Aging mechanisms and lifetime of PEFC and DMFC.)

Voltage reversal caused by fuel starvation has been observed both in stack applications and in controlled laboratory experiments [61]. Many factors, such as severe water flooding, stack manifold problems, and flow field blockage, particularly at a low pressure drop across the cells, can cause localized fuel starvation. If hydrogen is no longer available to be oxidized, the voltage at the anode will rise to that required to oxidize water (electrolysis). The electrolysis of

the water will result in the evolution of oxygen and protons at the anode, a reversal reaction of Equation 23.23. Figure 23.11 [61] presents a complete fuel starvation polarization with nitrogen flowing on the anode (no hydrogen). The cell voltage drops sharply due to a rise in anode potential to the level of water oxidation. Taniguchi et al. determined a time-dependent change of cell terminal voltage in a cell reversal degradation experiment with reference electrodes in both anode and cathode [62]. Cell reversal occurs when the fuel cell stack is loaded and not enough fuel is supplied to the anode. The anode potential quickly increased from 0 V to 1.5 V, as shown in Figure 23.12 [62]. It is also observed that the anode potential increases with fuel utilization. At 95% fuel utilization the anode potential rises to between about 0.4 V and 0.5 V, and the cathode potential at the fuel outlet approaches the open circuit voltage [63]. High anode potential could also occur when oxygen crosses over to the anode side and at the same time the fuel supply is insufficient. High anode potential will lead to carbon corrosion and Ru dissolution, resulting in anode catalyst layer degradation. Ru crossover from anode to cathode can also contaminate the cathode and decrease the catalytic activity of the cathode catalyst, which will be discussed in Section 23.3.3.
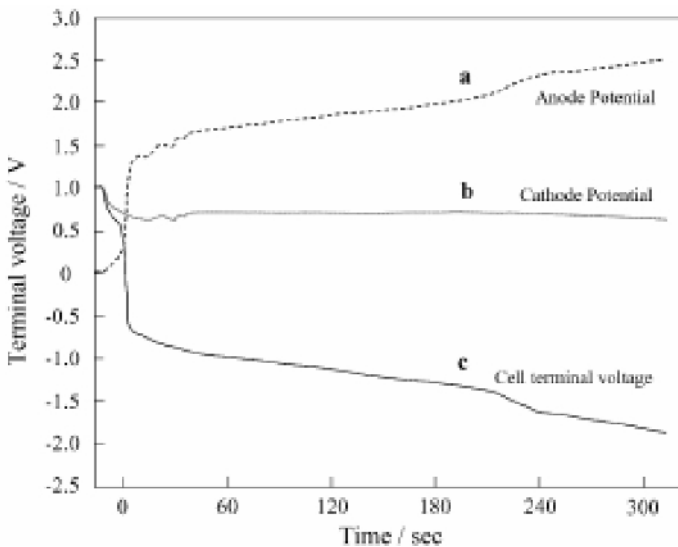
Figure 23.12. Time-dependent changes in the anode and cathode potential during a cell reversal experiment [62]. (Reprinted from Journal of Power Sources, 130(1–2), Taniguchi Akira, Akita Tomoki, Yasuda Kazuaki and Miyazaki Yoshinori, Analysis of electrocatalyst degradation in PEMFC caused by cell reversal during fuel starvation, 42–9, ©2004, with permission from Elsevier.)

Mitigation of the anode degradation caused by voltage reversal can be achieved through modification of the anode structure to favor oxidation of water over carbon. Knights et al. [61] suggest some strategies to accomplish this, including enhanced water retention on the anode (e.g., through modifications to the PTFE and/or ionomer, and addition of water-blocking components such as graphite); use

of improved catalysts to reduce the required anode potential for water electrolysis and thus the associated carbon oxidation (e.g., additional Ru or Ir on the anode); use of a more robust catalyst support (e.g., more graphitic carbon or alternative support materials); and increased catalyst coverage on the support to reduce contact between carbon and reactants (e.g., higher weight percentage Pt on the carbon). They also demonstrate that an anode structure with PTFE and more graphitic carbon catalyst support is superior to other anode structures in the cell voltage response over time of four different stacks with different anode designs [61], as shown in Figure 23.13.
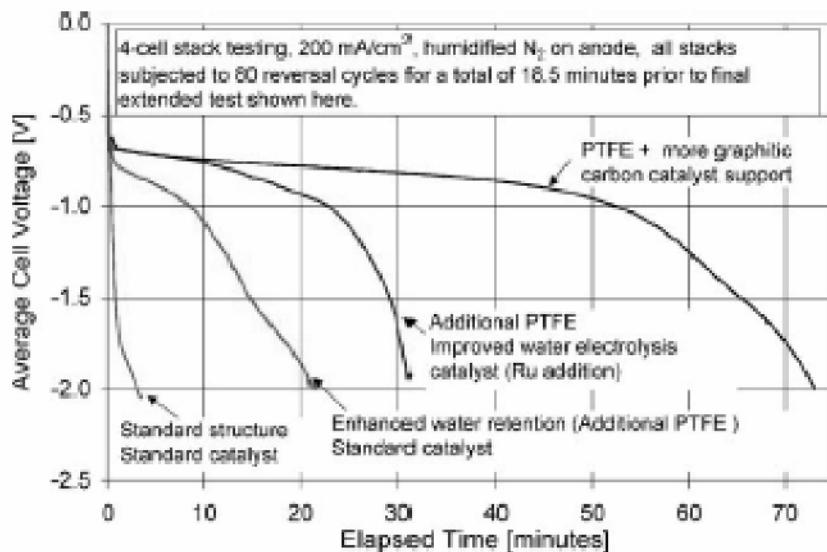
Figure 23.13. Comparison of different anode structures in severe failure testing. Each cell has an equivalent cathode (~0.7 mg/cm^2 Pt, supported on carbon). Testing conducted at 200 mA/cm^2, fully humidified nitrogen on the anode. Anode loading at ~0.3 mg/cm^2 Pt supported on carbon (varied materials and compositions). Each curve represents the results from a four-cell stack with each cell in the stack having identical composition. Four separate stack tests were run to generate the curves [61]. (Reprinted by permission of ECS—The Electrochemical Society, from Knights SD, Colbow KM, St-Pierre J, Wilkinson DP. Aging mechanisms and lifetime of PEFC and DMFC.)

23.3.3 Ru Leaching and Crossover

Pt-Ru alloy is widely used as an anode catalyst in PMEFCs and DMFCs. Although anode catalyst degradation has been much less studies than cathode catalyst degradation, which has a significant effect on cell performance, Ru leaching and re-deposition on the Pt surface of the cathode has recently attracted attention, especially with respect to DMFCs [64, 65]. Ru leaching from Pt-Ru anode electrocatalysts and crossing over to the cathode can have a dramatic impact on the activity of a Pt/C oxygen-reduction cathode [64, 65]. Ru metal is thermodynamically unstable under some fuel cell operating conditions. Under normal conditions, the anode potential is lower than 0.2 V. However, when voltage

reversal occurs during fuel starvation as discussed above, the anode potential can rise to a higher level, especially in start/stop operations, resulting in the dissolution of Ru metal. Piela [65] at Los Alamos National Laboratory reported that Ru crossover occurs both under abnormal conditions, such as cell reversal resulting in very high anode potentials, and under normal DMFC operating conditions such as life testing. The presence of Ru in the cathode is detected by X-ray fluorescence analysis [65]. Ru metal is expected to be thermodynamically stable up to about 0.8 V vs. RHE. Under normal fuel cell operating conditions (0.2–0.4 V vs. RHE), the most likely underlying cause of the Ru crossover is dissolution of intrinsic thermodynamically unstable oxide phases. Gances et al. [64] found that the Ru/Pt atomic ratio was decreased from the nominal 50 atom% Ru and 50 atom% Pt in pristine PtRu black to 30.3 atom% Ru and 69.7 atom% Pt after washing in 0.5 M H_2SO_4 acid solution. The ratio of Ru to Pt in the acid-treated catalyst is only slightly changed to 28.3 atom% Ru and 71.7 atom% Pt under further hydrogen electro-oxidation in the potential cycling experiment (from 0.2 to 0.4 V vs. RHE for 6 hours). This observation indicates that the thermodynamically unstable Ru oxide phases can largely be removed by washing with acid. At the same time, the PtRu alloy matrix seems less prone to leach Ru, except in the case of anode voltage reversal.
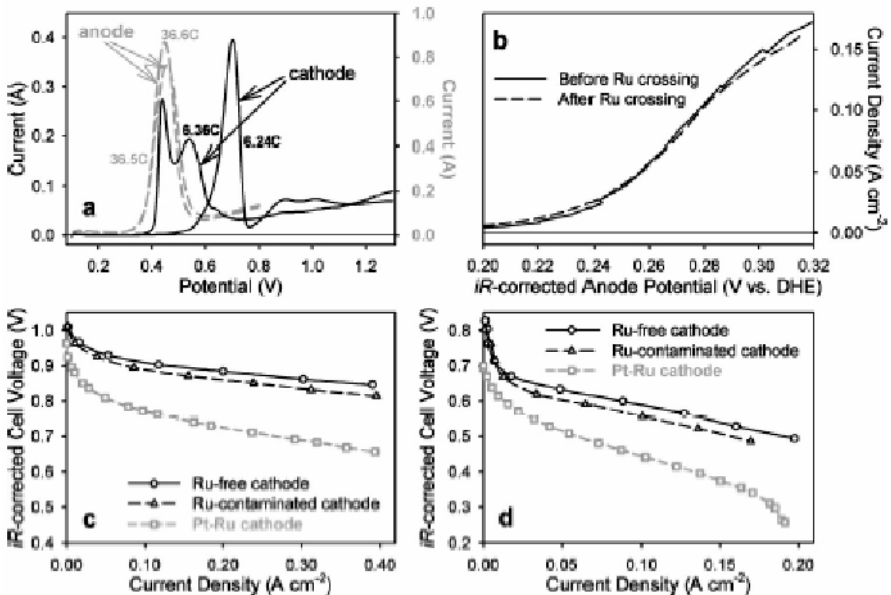
Figure 23.14. Impact of ruthenium on oxygen reduction performance: (a) CO stripping scans for the cathode and anode, (b) steady-state anode polarization plots before and after contamination of the cathode, (c) H_2-air steady-state polarization curves, and (d) DMFC steady-state polarization curves. Methanol concentration 0.3 M, anode potential during contamination 1.3 V vs. hydrogen counter/quasi-reference electrode, cell temperature 75 °C [65]. (Reprinted by permission of ECS—The Electrochemical Society, from Piela P, Eickes C, Brosha E, Garzon F, Zelenaya P. Ruthenium crossover in direct methanol fuel cell with Pt-Ru black anode.)

The presence of Ru at the cathode has a negative impact on the oxygen reduction kinetics. The Ru could deposit on the Pt surface in the cathode. Rotating disk electrode data show that the rate of oxygen reduction can decrease by a factor of eight, which can translate to an overpotential of approximately 160 mV in galvanostatic conditions [64]. Piela et al. compare the polarization curves of Ru-free, Ru-contaminated, and Pt-Ru cathodes. In the H_2-air fuel cell operating mode, the cell voltage drops by ~25 mV across the current density range used, as shown in Figure 23.14(c), and by ~40 mV in DMFC operating mode (Figure 23.14(d)). Ru crossover and contamination at the cathode can be a major issue in the performance degradation of a fuel cell. Mitigation of Ru contamination could be possible through developing stable PtRu anode catalysts, novel fuel cell designs, or more Ru-tolerant cathode catalysts.

23.4 Cathode Catalyst Layer Degradation

The performance and durability of a membrane electrode assembly (MEA) is affected significantly by the cathode electrode composition and structure, due to the poor kinetics of oxygen reduction and reactant transport limitations. Utilization and stability of platinum or its alloys in the PEMFC play important roles in fuel cell efficiency, durability, and the drive for cost reduction through reduced Pt loadings. Cathode catalyst layer degradation is a critical issue for fuel cell durability to meet the requirement of > 5000 hours for automotive applications and > 40,000 for stationary applications.

Cathode catalyst layer degradation is mainly caused by loss in the electrochemical active surface area (ECSA) of Pt or its alloys. Loss of surface area (for Pt or its alloys) in the fuel cell is believed to occur by some combination of the following four processes [10, 33–36, 66, 67]: 1) formation of larger particles via Pt dissolution from smaller particles (Ostwald ripening); 2) coalescence of Pt nanoparticles by thermal motion (sintering) or loss of the carbon support due to carbon corrosion; 3) Pt migration into the catalyst electrolyte or membranes, and 4) Pt trapped in the catalyst layer ionomer during electrode fabrication. Carbon corrosion could lead to damage of the porous structure of the catalyst layer, resulting in increased mass transport loss. Each of these processes will be discussed in the following sections.

23.4.1 Platinum Dissolution During Fuel Cell Operation

23.4.1.1 Thermodynamic Stability of Platinum Under Fuel Cell Operating Conditions
Although platinum is regarded as a very stable metal in acidic environments, its long-term stability under fuel cell operating conditions has attracted much attention recently due to loss of platinum surface area during fuel cell operation. Thermodynamically stable phases of platinum metal and its oxides have been discussed in the literature, and the main electrochemical reactions are summarized in the following equations [9, 33, 68, 69]:

$$Pt + H_2O = PtO + 2H^+ + 2e^- \qquad E^0 = 0.980 - 0.591pH$$

<div align="right">(23.25 and 23.25') [68, 69]</div>

$$PtO + H_2O = PtO_2 + 2H^+ + 2e^- \qquad E^0 = 1.045 - 0.0591pH$$

<div align="right">(23.26 and 23.26') [68, 69]</div>

$$PtO_2 + H_2O = PtO^{3+} + 2H^+ + 2e^- \qquad E^0 = 2.000 - 0.0591pH \qquad (23.27) [68]$$

$$Pt^{2+} + H_2O = PtO + 2H^+ \qquad \log(Pt^{2+}) = -7.06 - 2pH \qquad (23.28) [68]$$

$$Pt = Pt^{2+} + 2e^- \qquad E^0 = 1.188 + 0.0295 \log(Pt^{2+}) \quad (23.29) [68]$$

$$Pt = Pt^{2+} + 2e^- \qquad E^0 = 0.963 + 0.0295 \log(Pt^{2+}) \ (23.29') [69]$$

$$Pt^{2+} + 2H_2O = PtO_2 + 4H^+ + 2e^- \qquad E^0 = 0.837 - 0.1182pH - 0.0295 \log(Pt^{2+})$$

<div align="right">(23.30) [68]</div>

$$Pt^{2+} + 2H_2O = PtO_2 + 4H^+ + 2e^- \qquad E^0 = 1.062 - 0.1182pH - 0.0295 \log(Pt^{2+})$$

<div align="right">(23.30') [69]</div>
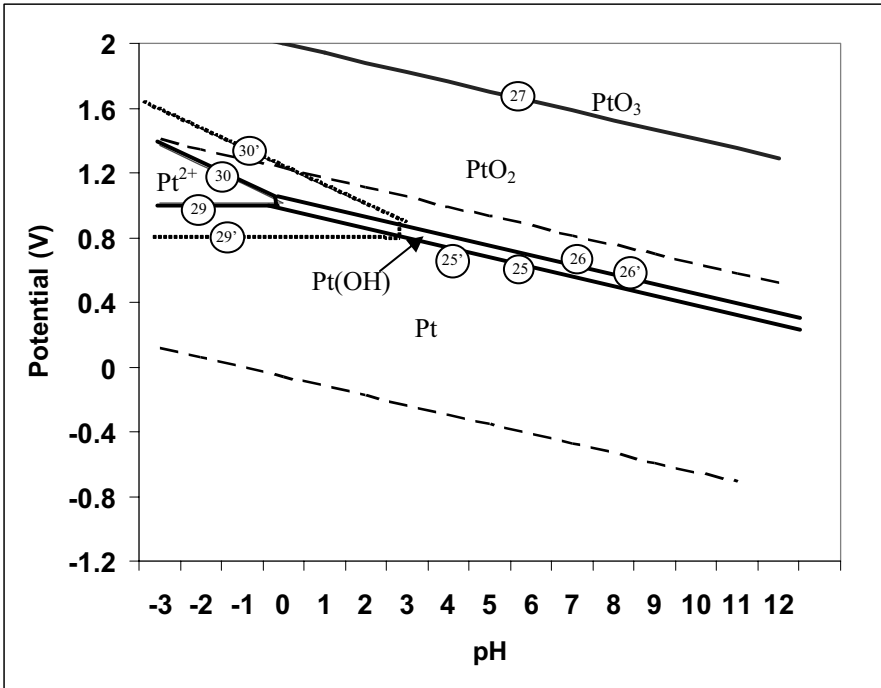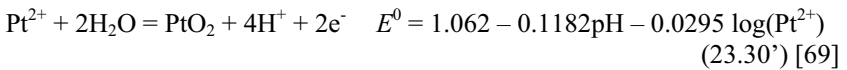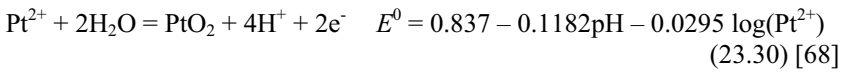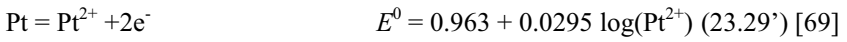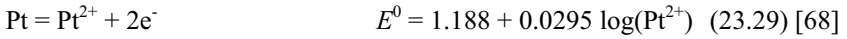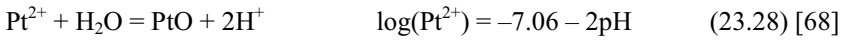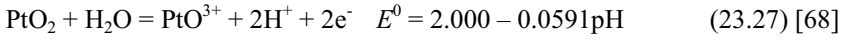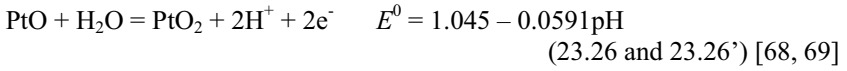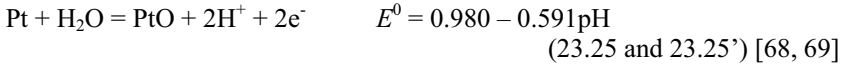
Figure 23.15. Potential-pH diagram for the platinum-water system at 25 °C

Lack of thermodynamic data limits analysis of Pt stability at fuel cell operation temperatures. Potential and pH diagrams, also termed a Pourbaix diagram, of Pt-H_2O can be derived from thermodynamic data provided by Pourbaix [9, 68], as shown by the solid lines in Figure 23.15, in which Pt^{2+} equilibrium concentration is assumed to be approximately 1.0×10^{-6} M. For comparison, data obtained from Lee et al. [69] is represented by the dashed lines in Figure 23.15. The standard equilibrium potential for Pt/Pt^{2+} at Pt^{2+} activity equal to 1 is 1.188 V from Pourbaix's data (Equation 23.29), but only 0.963 V from Lee's data (Equation 23.29'). There is also a discrepancy in the Pt^{2+} equilibrium with PtO_2 between Equations 23.30 and 23.30'. Therefore, Lee's data represents a larger Pt^{2+} stable region in the E-pH diagram than does Pourbaix's data. The Pt equilibrium concentration will reach $\sim 1.0 \times 10^{-6}$ M at 0. 8 V based on Lee's data, but it does not reach that concentration until 1 V, from Pourbaix's data.
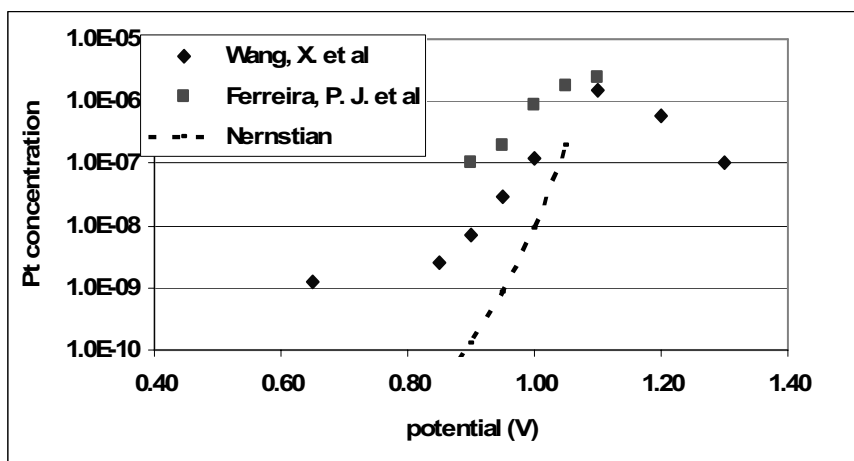
Figure 23.16. Equilibrium soluble platinum as a function of potential. Solid circles, 80 °C, 2–3 nm platinum particles of a 46 wt% Pt/C powder (Tanaka) in 0.5 M H_2SO_4[33]; triangles, 23 °C Pt wire in 0.57 M perchloric acid [70]. (Reprinted by permission of ECS—The Electrochemical Society, from Wang X, Kumar R, Myersz DJ. Effect of voltage on platinum dissolution relevance to polymer electrolyte fuel cells.)

Equilibrium soluble concentrations of Pt as a function of potential in perchloric acid electrolyte and H_2SO_4 are presented in Figure 23.16 [33, 70]. Wang et al. [70] found that the actual Pt^{2+} equilibrium concentration with Pt wire and 10 wt% of Pt/C in 0.57 M perchloric acid electrolyte was approximately 1×10^{-8} M at 0.9 V and 23 °C. Ferreira et al. [33] reported a Pt^{2+} equilibrium concentration of approximately 1×10^{-7} M with 46 wt% of Pt/C in H_2SO_4 at 80 °C and 0.9 V. However, both experimental potential dependences of Pt^{2+} equilibrium concentrations are much weaker than the Nernstian behavior for Pt/Pt^{2+} dissolution equilibrium, as shown in Figure 23.16. The potential dependence observed by Wang [70] and Ferreira [33] in the 0.8 to 1.1 V region is approximately 90 to 100 mV for a ten-fold increase in the dissolved Pt concentration at 25 °C. This is much

higher than the 29.5 mV per decade predicted for a two-electron Nernstian dissolution reaction (Equation 23.29). It is not fully understood at present whether the species in solution that are in equilibrium with platinum are Pt^{2+} only or Pt^{2+} plus other Pt oxide species, nor how fluorine and chlorine ions affect the equilibrium of platinum/platinum complexes. More thermodynamic data is needed to clarify the Pt/Pt^{2+} equilibrium and the effect of potential on equilibrium phases and concentration. Despite this discrepancy in understanding, there are clear tendencies toward increasing platinum dissolution while the potential and temperature increase.

23.4.1.2 Kinetics of Platinum Dissolution

The platinum electrochemical dissolution rate in fuel cell operation is a critical durability issue due to loss of catalyst surface area vs. time. The dissolution behavior and solubility of platinum are governed by the chemical state of the platinum surface and the equilibrium platinum species in the solution. Temperature, pH, electrolyte composition, potential, and particle size are all major factors influencing the solubility and the dissolution rate. Potential cycling of Pt electrodes has been extensively investigated, and the platinum electrode dissolution rates from the literature are summarized in Table 23.5 [9, 33, 70–74]. Both Pt(II) and Pt(IV) species were detected in sulfuric solution after potential cycling from 0.41–1.46 V [73]. Pt dissolution was confirmed by a positive charge difference, i.e., anodic charge larger than cathodic charge ($Q^a > Q^c$) in cyclic voltammogram [73]. Mitsushima et al. [74] studied the consumption rate of Pt in sulfuric acid under potential cycling with different scanning waves in 1 M H_2SO_4 at 40 °C. They found that among the triangular waves between 0.5 to 1.8 V vs. RHE, the consumption rate of symmetric waves and fast cathodic asymmetric triangular waves is a few ng/cm^2 per cycle. However, the consumption rate is about 24 ng/cm^2 per cycle using a slow cathodic triangular wave, which is 20 V s^{-1} anodic and 0.5 V s^{-1} cathodic. They suggested that the electron transfer number was about 2 for the slow cathodic triangular wave and about 4 for the symmetric waves. For the Pt dissolution mechanism, a dissolution reaction with 4-electron oxidation is suggested [74]:

$$Pt \rightarrow Pt^{4+} + 4e^- \tag{23.31}$$

As a dissolution reaction with 2-electron oxidation, the platinum is suggested to be oxidized by water first:

$$Pt + 2H_2O \rightarrow PtO_2 + 4H^+ + 4e^- \tag{23.32}$$

and then to follow the reduction process of potential cycling:

$$PtO_2 + 4H^+ + 2e^- \rightarrow Pt^{2+} + 2H_2O \tag{23.33}$$

The sum reaction of Equations 23.32 and 23.33 is a 2-electron oxidation reaction. Whether Pt dissolution follows a 4-electron or 2-electron reaction would be dependent on the properties of the surface oxide layer. The less stable oxide layer

might form by the "slow cathodic" wave and the dissolution of Pt may follow the 2-electron reaction [74].

Table 23.4. Pt dissolution rate [9, 33, 70–74]

Dissolution Rate (g/cm^2s)	Dissolution Rate (g/cm^2 per cycle)	Pt form	Conditions
7.5×10^{-11}	4.5×10^{-9}	Pt sheet	Potential cycling, 0.05 to 1.4 V, 45 mV/s, 23 °C, 1M H_2SO_4
1.0×10^{-10}	5.5×10^{-9}	Pt wire	Potential cycling, 0.41 to 1.46 V 40 mV/s, 25 °C, 1M H_2SO_4
2.8×10^{-11}	3.3×10^{-9}	Pt disk	Potential cycling, 0.4 to 1.4 V, 8.3 mV/s, 25 °C, 0.1M $HClO_4$
3.8×10^{-11}	4.8×10^{-9}	Pt disk	Potential cycling, 0.41 to 1.46 V, 8.3 mV/s, 25 °C, 1M H_2SO_4
1.5×10^{-7}	3×10^{-9}	Pt wire	0.5 to 1.5 V, 100 V/s, 40 °C, 1M H_2SO_4
1.4×10^{-14}	N/A	10% wt% Pt/C	0.9 V static potential, 23 °C, 0.57 M $HClO_4$
1.7×10^{-14}	N/A	Pt wire	0.9 V static potential, 23 °C, 0.57 M $HClO_4$

The dissolution rate of Pt during potential cycling increases with the maximum potential E_H below 1.8 V vs. RHE, as shown in Figure 23.17 [74]. From 1.8 to 2.4 V, the Pt dissolution rate is independent of E_H due to the formation of a Pt oxide corrosion resistance layer. The Pt dissolution rate is strongly related to the number of oxidation-reduction cycles rather than the duration time of cycles or the oxidation state. The Pt dissolution rate at the high frequency of potential cycling (100 V/s) is approximately 1.5×10^{-7} $g/cm^2 \cdot s$, which is 4 orders higher than the rate at ~40 mV/s cycling [74].

Darling and Meyers developed mathematical models to simulate Pt dissolution. They assumed that the Pt dissolution rate is determined by potential, particle diameter, and the Pt oxide coverage ratio on the particle surface [76, 77]. The results of these simulations indicate that platinum oxidation has a marked effect on the stability of platinum in PEM fuel cell operation. In their model, the oxide layer on the particle surface protects Pt metal from sustained dissolution when the cathode is exposed to high potentials. They also found that platinum is quite soluble when the gas phase is switched from hydrogen to oxygen. Although it is unlikely that a fuel cell will be continuously operated in this region, hydrogen crossover might accelerate local Pt dissolution.
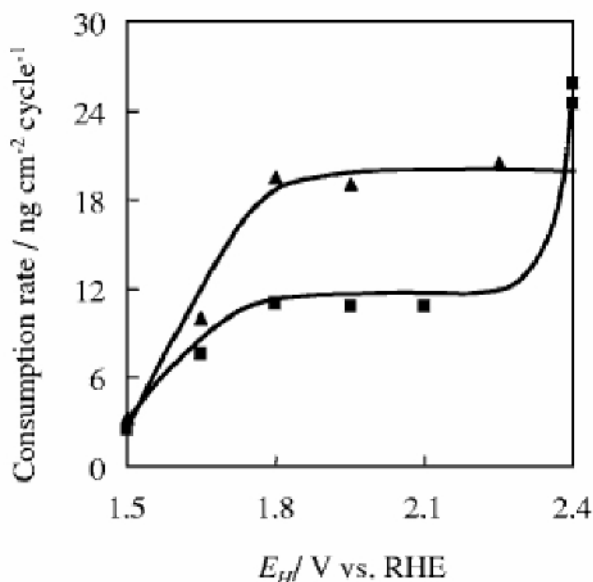
Figure 23.17. Pt consumption rate as a function of maximum potential E_H in potential cycling with a minimum potential $E_L = 0.5$ V vs. RHE at 40 °C in 1 M H_2SO_4 for 50 Hz of the symmetric rectangular waves (square) and 100 V s^{-1} (25–50 Hz) of the symmetric triangular waves (triangle) [74]. (Reprinted by permission of ECS—The Electrochemical Society, from Mitsushima S, Kawahara S, Ota K, Kamiya N. Consumption rate of Pt under potential cycling.)

23.4.1.3 Stability of Pt-M Alloys Used as Catalysts in Fuel Cells

Pt-M binary or ternary alloys (M = Co Cr, Mo, V, Ti, W, Al, Ag, Fe, Ni, Au) are being investigated for fuel cell applications as replacements for pure platinum, to lower cost and improve performance [78–83]. The stability of the alloys under fuel cell operating conditions is a major concern because the non-noble metals are less stable than noble metals in acidic conditions. The cobalt metal phase, for instance, is unstable thermodynamically and tends toward being Co^{2+} in acidic conditions under fuel cell operation potential. Co^{2+} and Co^{3+} stable regions in the Co-H_2O Pourbaix diagram [84] cover the whole range of PEMFC operating potential and pH (Figure 23.18). Antolini et al. [79] summarized the stability of Pt-M alloy catalysts in low-temperature fuel cells. The stability of non-noble metals in an acidic environment depends on the type of metal: Pt–Cr and Pt–Co are usually considered more stable than Pt–V, Pt–Ni, and Pt–Fe. The stability of these catalysts depends on the degree of alloying. The non-noble metals as "true" alloy solutions, not as mixtures of heterogeneous phases, in the Pt-M catalyst can lower its thermodynamic activity; consequently, it is less soluble. Generally, Cr and Co presents a higher degree of alloying with Pt than V, Ni, and Fe. This could explain their higher stability in acidic media.
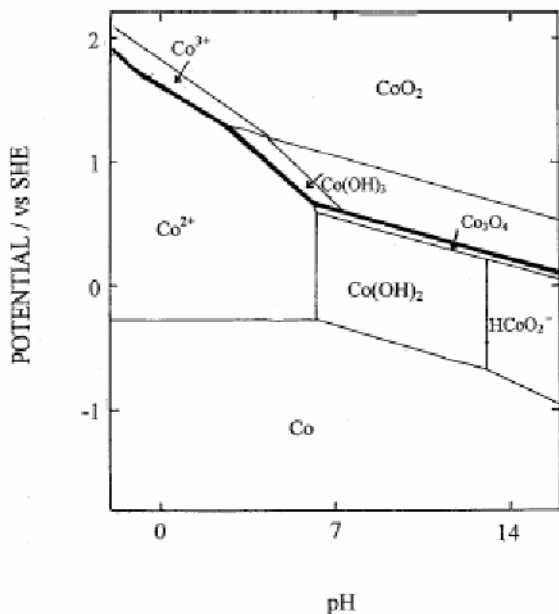
Figure 23.18. Pourbaix diagram of Co-water system [84]. (Reprinted by permission of ECS—The Electrochemical Society, from Bahrololoom ME, Gabe DR, Wilcox GD. Development of a bath for electrodeposition of zinc-cobalt compositionally modulated alloy multilayered coatings.)

Gasteiger et al. indicated at least three possible causes for the leaching of base-metal from a Pt-alloy/C catalyst in PEMFCs: 1) excess base-metal deposited onto the carbon support during preparation, 2) incomplete alloying of the base element to Pt due to a low alloying temperature being applied during formation of the alloy, and 3) even a well-alloyed base-metal may leach out of the surface under PEMFC operating conditions and leave a Pt-enriched surface or skin, since base-metals are thermodynamically unstable under PEMFC potentials in acidic electrolytes.

In the case of PEM fuel cells, the contamination of the membrane by cationic impurities has detrimental effects on membrane properties with regard to conductivity, water management, and durability. Metal cations from the dissolution of the catalyst can easily exchange with a proton of the membrane/ionomer because metal cations have a stronger affinity with the sulfonic group than protons do. Therefore, Mukerjee [85] and Gasteiger [78] have proposed pre-leaching of the alloy to minimize the contamination of the MEA during operation. In an *ex situ* leaching experiment, the unleached pristine Pt_xCo_{1-x}/C catalyst exhibited the greatest dissolution of the cobalt, close to 37 wt% as measured by ICP analysis, after immersing in 0.5 M H_2SO_4 at 90 °C under air for a period of 24 h, whereas the pre-leached Pt_xCo_{1-x}/C catalyst had less than 4 wt% of Co dissolved. Gasteiger also demonstrated that the MEA with pre-leached Pt_xCo_{1-x}/C cathode had similar durability as the MEA with Pt/C, as shown in Figure 23.19 [78].
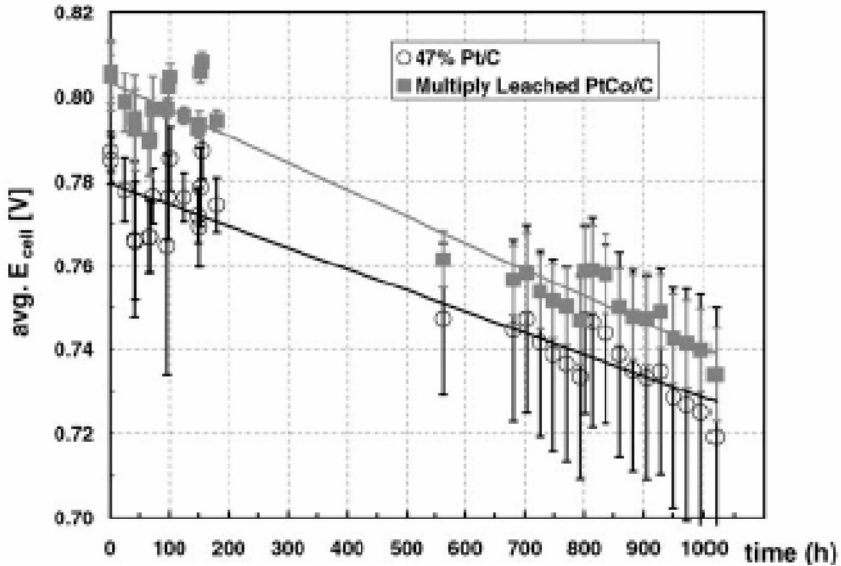
Figure 23.19. Durability of Pt/C and Pt_xCo_{1-x}/C MEAs tested in a short stack (active area = 465 cm^2) under H$_2$-air at a cell temperature of 80 °C and total reactant pressures of 150 kPa$_{abs}$ with anode and cathode humidities at 100%, anode and cathode reactant stoichiometries of s = 2/2. Data are shown with stack under a constant current density load of 0.20 A/cm^2 over 1000 h. Data are averaged over four cells of each type of MEA [78]. (Reprinted from Applied Catalysis B: Environmental, 56(1–2), Gasteiger HA, Kocha SS, Sompalli B, Wagner FT, Activity benchmarks and requirements for Pt, Pt-alloy, and non-Pt oxygen reduction catalysts for PEMFCs, 9–35, ©2005, with permission from Elsevier.)

23.4.2 Pt Accumulation and Distribution in the Membrane after Fuel Cell Operation

Pt^{z+} (either Pt^{2+} or Pt^{4+}) dissolved from the catalyst surface in the cathode can migrate into the membrane and redeposit there, growing into large particles [33–35, 37, 86]. Those Pt particles accumulate in the membrane close to the cathode catalyst layer to form a "band", which can be observed using SEM or TEM, as shown in Figure 23.20. Larger particles with an average size of 140 nm were observed in the membrane around 5–6 μm away from the membrane/catalyst interface in the voltage cycling test (0.6–1.2 V) with air flowing in the cathode (Figure 23.21) [37]. Most of the small particles have a size range from 5–30 nm and disperse in the membrane from the cathode/membrane interface to halfway across the membrane. The Pt distribution in the membrane during the voltage cycling test is dependent on the cathode atmosphere. With flowing nitrogen in the cathode, larger particles (averaging ~130 nm) accumulate closer to the cathode catalyst layer (~1 μm away from the catalyst layer as compared with ~5 μm in O$_2$ flowing through the cathode), as shown in Figure 23.21 (left).
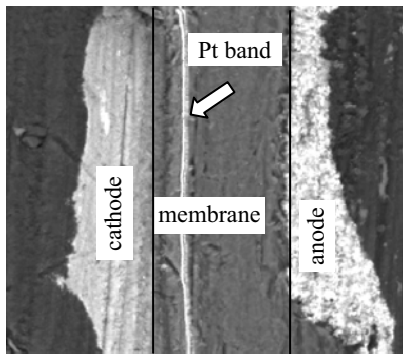
Figure 23.20. Platinum band in the membrane after voltage cycling (0.6–1.2 V) with air flowing in the cathode; SEM image, 1600x. Unpublished data.
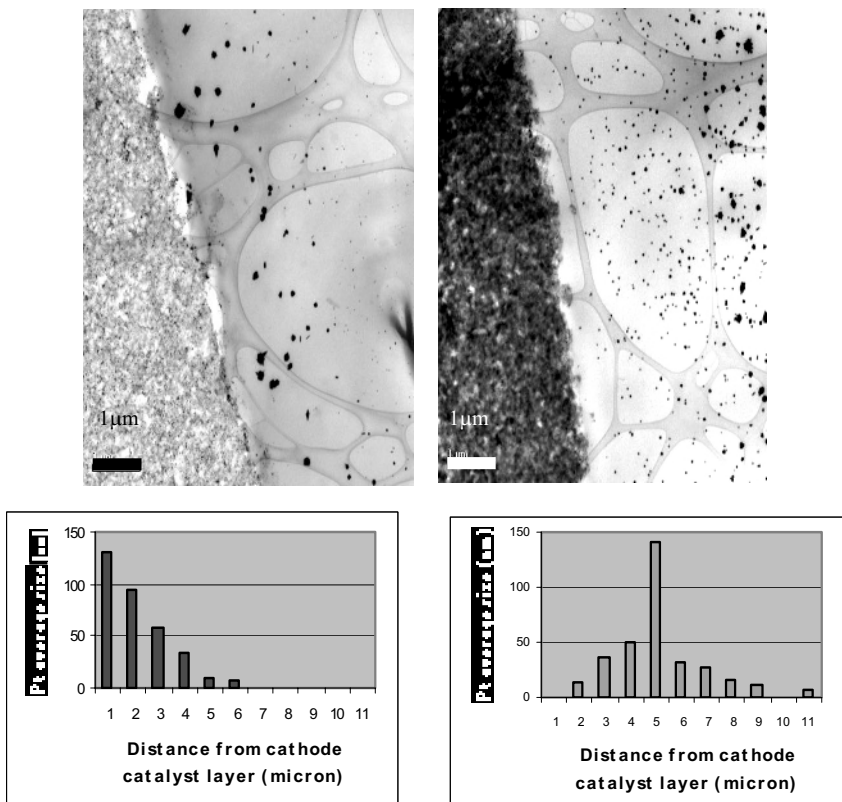
Figure 23.21. TEM image of membrane close to membrane/cathode interface (top) and Pt particle size distribution (bottom) from a MEA cross-section after AST voltage cycling under air flowing in cathode (bottom right) and N_2 flowing in cathode (bottom left) [37]. (Reprinted by permission of ECS—The Electrochemical Society, from Li J, He P, Wang K, Davis M, Ye S. Characterization of catalyst layer structural changes in PEMFC as a function of durability testing.)

Pt deposition in the membrane could follow this reaction [33]:

$$Pt^{z+} + H_2 \rightarrow Pt + 2H^+ \tag{23.34}$$

Hydrogen from the anode crosses over through the membrane toward the cathode. It chemically reduces oxidized platinum species (such as Pt^{2+} or Pt^{4+}) in the membrane into platinum metal. The platinum nucleates and grows in the membrane close to the cathode. Meanwhile, hydrogen and oxygen could be catalyzed by the platinum particles to form water:

$$H_2 + O_2 \xrightarrow{Pt} H_2O \tag{23.35}$$

High oxygen potential in the voltage cycling test with air flowing in the cathode could decrease the concentration of H_2 in the membrane crossed over from the anode. Therefore, the reaction interface of the reduction of Pt by H_2 (Equation 23.34) moves toward the anode in air. In the case of N_2 flowing in the cathode during voltage cycling, the H_2 concentration near the membrane/cathode interface is much higher than in the cathode flowing with oxygen, with the result that Pt deposition occurs almost near the interface. Often, it is not identifiable under low resolution SEM but can be seen under TEM.

Similarly, Pt particles were observed in the ionomer in the catalyst layer. It is not clear yet whether Pt accumulated in the membrane would affect the membrane properties and fuel cell performance. In any case, those catalyst particles, whether they are in the membrane or the ionomer, are isolated from the carbon support that is the electron path network. They cannot act as catalysts for oxygen reduction catalysis at all.

23.4.3 Loss of Platinum Surface Area Due to Agglomeration

Loss of catalyst electrochemical surface area (ECSA), as discussed above, could be caused by Pt dissolution and migration into the membrane. In addition, increase in Pt particle size during fuel cell operation is another cause of ECSA loss in the catalyst layer. Loss of Pt surface area vs. time during fuel cell operation has been observed in both the phosphoric acid fuel cell [87–89] and PEMFC operations [9, 33, 90]. An increase in Pt particle size from 2–3 nm up to more than 10 nm during durability testing in the catalyst layer has been reported, determined by X-ray diffraction [46] or TEM image analysis [9, 33–38, 90].

23.4.3.1 Pt Agglomeration in Fuel Cell Performance

Causes of the increase in Pt particle size have been discussed in the literature [9, 33–38]. Pt particle size increase could occur through an Ostwald ripening process, i.e., platinum dissolution and redeposition under fuel cell operating conditions, especially under high potential in the start-up and shut-down processes. It could also be caused by coalescence growth of platinum nanoparticles via platinum nanocrystallite migration on the carbon support or platinum particle agglomeration triggered by corrosion of the carbon support. Figure 23.22 shows particle size

distributions of pristine Pt/C powder, cathode catalyst layers for a fresh MEA, and an MEA in a 10-cell stack operated for 2500 hours using an advanced automotive duty cycle (AADC) [37]. With respect to the irregular shape of the particles, Feret-min (F_{min}) and Feret-max (F_{max}) were used to describe the particles' geometrical dimensions. Pre-aggregated Pt particles can be seen in the pristine Pt/C powder (Figure 23.22(a)). Two or more small Pt particles seem to have been deposited or to have grown together at the carbon grain boundaries. The joined part of the aggregated particles may not be electrochemically active. The difference between F_{min} and F_{max} describes a deviation of the particle from a sphere, which is significant in the pristine Pt/C powders. Agglomeration could start from those already touched particles, forming a spherical shape with low surface energy through the Ostwald ripening or coalescence processes. The Pt nanoparticles have very high surface activity. They agglomerate rapidly at first in fuel cell operation, resulting in a quick catalyst surface area loss. This was observed in phosphoric acid fuel cell operation under static conditions at 191 °C. The surface area of Pt declines rapidly from ~60 m^2/g at the beginning to ~30 m^2/g during the first 2000 hours and then tends to level off to an area of about 20 m^2/g after 5000 hours until 20,000 hours [87].

Potential cycling significantly accelerates the Pt particle agglomeration process. The electrochemical surface area of the cathode catalyst layer decreased from 64.5 m^2/g$_{Pt}$ in Pt/C powder to 25.7 m^2/g$_{Pt}$ in the MEA of 10-cell stacks based on Ballard's Mark9 technology after operation for 2500 hours using an advanced automotive duty cycle (AADC) [37]. The Pt particle's shape is nearly spherical (see image in Figure 23.22(c)) after agglomeration. Distributions of the F_{min} and F_{max} have almost the same peak value of ~10 nm. Under a highly accelerated stress test, the agglomeration of Pt particles is more rapid. For instance, a potential cycling between 0.6 and 1.0 V under H$_2$–N$_2$ at 80 °C and 100% RH leads to a reduction of the ECSA of platinum from 63 m^2/g$_{Pt}$ in the pristine cathode to 40 m^2/g$_{Pt}$ after 2000 cycles (~37% of the initial area) in 20 hours and to 23 m^2/g$_{Pt}$ after 10,000 cycles in 100 hours (63% of the initial area), as show in Figure 23.23 [33]. This reduction in platinum specific area would amount to a minimum cathode kinetic voltage loss of 31 mV, approximately 300 µV/h. In another highly accelerated stress test, 1000 cycles from 0.6 V to 1.5 V led to a reduction of ECSA in the cathode catalyst layer to 13.6 m^2/g$_{Pt}$, approximately 80% of the initial area (Table 23.5), which is far below that of the MEA at the end of life in the 2500 h AADC durability test. Obviously, the higher the cycling potential, the faster will be the reduction in electrochemical surface area.

Table 23.5 also lists the Pt surface area calculated from TEM and from EPSA measurement [37]. The Pt surface area of the fresh MEA catalyst layer is also smaller than that of the pristine Pt/C powder. The geometric surface areas of Pt particles calculated from TEM images are larger than the electrochemical active area (ECA). This discrepancy may in part be due to electrochemical inactivity for those Pt particles covered by the ionomer (see Figure 23.22(b)) or embedded in the carbon support.
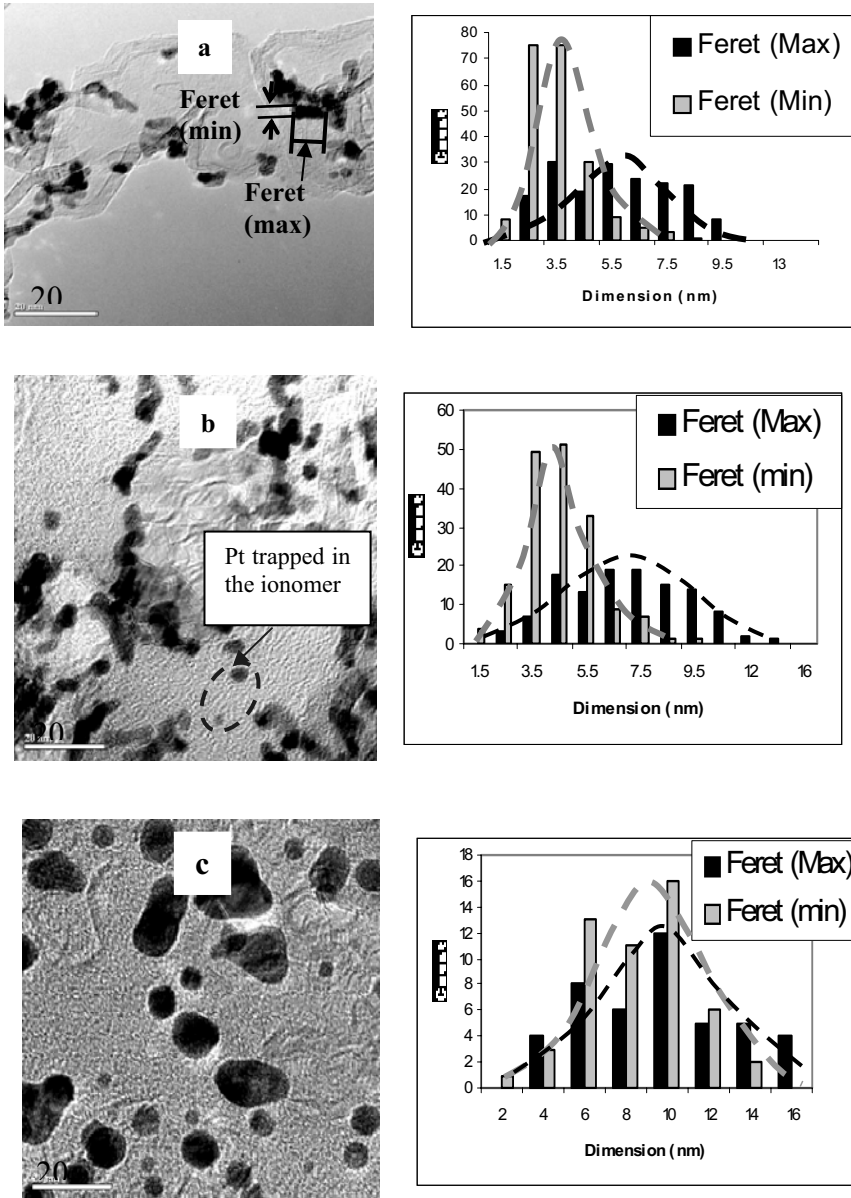
Figure 23.22. F_{min} and F_{max} distributions of (a) the Pt/C fresh powder, (b) cathode catalyst layers for a fresh MEA, and (c) an MEA after durability testing (10-cell stacks based on Ballard's Mark9 technology operated for 2500 hours using an advanced automotive duty cycle (AADC), 2,500 hours) [37]. (Reprinted by permission of ECS—The Electrochemical Society, from Li J, He P, Wang K, Davis M, Ye S. Characterization of catalyst layer structural changes in PEMFC as a function of durability testing.)

Table 23.5. Geometric and electrochemical active surface area of Pt in the catalyst layer [37]. (Reprinted by permission of ECS—The Electrochemical Society, from Li J, He P, Wang K, Davis M, Ye S. Characterization of catalyst layer structural changes in PEMFC as a function of durability testing.)

Samples	Surface area (m²/g Pt) from TEM	Surface area (m²/g Pt) from EPSA measurement
Pt/C #1 30% Pt	82.48	78.4
Pt/C #2 50% Pt	68.55	64.5
MEA fresh	54.17	37.2
MEA HAST in air	32.34	18.2
MEA HAST in N_2	28.34	17.5
MEA AADC (2500 h)	31.17	25.7
MEA AST 0.6-OCV cycling	21.13	13.6
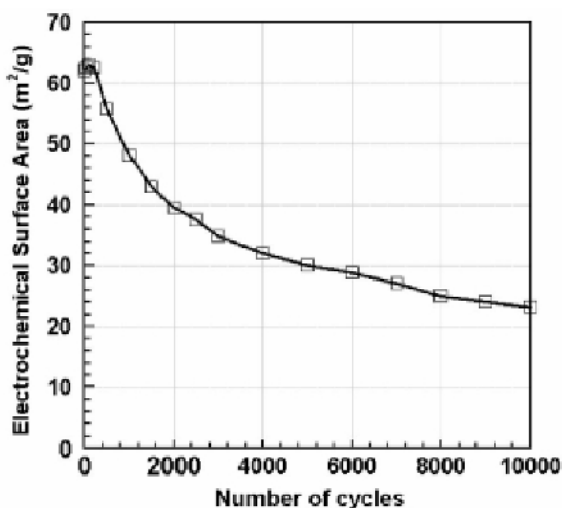
Figure 23.23. Platinum surface area of the cathode with TKK 46 wt% Pt/Vulcan catalyst over 10,000 potential cycles at 20 mV/s in the voltage range 0.6–1.0 V at 80 °C under humidified H_2–N_2 (anode-cathode) [33]. (Reprinted by permission of ECS—The Electrochemical Society, from Ferreira PJ, la O' GJ, Shao-Horn Y, Morgan D, Makharia R, Kocha S, Gasteiger HA. Instability of Pt/C electrocatalysts in proton exchange membrane fuel cells.)

23.4.3.2 Pt Distribution Changes in Catalyst Layer in Fuel Cell Performance

Pt dissolution, redeposition, and agglomeration cause Pt to be redistributed in the catalyst layer. The redistribution of Pt concentration and particle size in the cathode catalyst layer has been observed using TEM after both the durability test and the highly accelerated stress test. Figures 23.24 and 23.25 show the redistribution of particle size and concentration of Pt in the cathode catalyst layer.

The concentration of Pt in the catalyst layer is lower in the area near the catalyst/membrane interface. This may be caused by Pt dissolution and migration into the membrane (see discussion in 23.4.2). After 52,000 cycles (0.6 V–OCV) of voltage cycling, a Pt depletion layer approximately 3 μm in width formed in the cathode catalyst layer near the catalyst/membrane interface (Figure 23.25). Most of the Pt in this layer migrated into the membrane or was washed out due to Pt dissolving at high potential. This phenomenon was observed in the sample from HAST voltage cycling test with cathode air flowing. There was no depletion layer in the sample with N_2 flowing in the cathode. High oxygen potential and current flow may accelerate the dissolution and transportation of the Pt from the catalyst layer into the membrane.
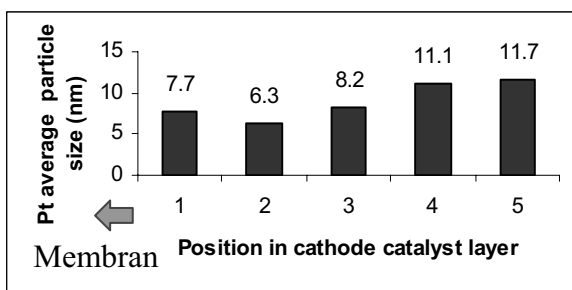
Figure 23.24. Pt particle size distribution in the cathode catalyst layer after HAST [37]. (Reprinted by permission of ECS—The Electrochemical Society, from Li J, He P, Wang K, Davis M, Ye S. Characterization of catalyst layer structural changes in PEMFC as a function of durability testing.)

Another interesting fact is that the mean value of the particle size decreases from the sublayer/catalyst interface to the catalyst/membrane interface in the HAST voltage cycling test with air flowing in the cathode, as shown in Figure 23.24. In considering the mechanisms of Pt agglomeration and migration, Pt migration into the membrane is possible by dissolution at high potential and formation of a Pt^{++} species, followed by chemical reduction by H_2 and redeposition in the membrane. If the transport rate of Pt near the catalyst/membrane interface is faster than the rate of Pt redeposition in that area under high oxygen potential, Pt could have small particles and low concentration in the catalyst layer/membrane interface. The worst case observed was formation of a depletion layer (Figure 23.25). When per-fluorosulfonated ionomer was in the catalyst layer and membrane, fluoride ion (F^-) was also detected in the outlet due to ionomer degradation [90]. In the presence of halide ions in the electrolyte, the Pt dissolution potential becomes more negative. A water-soluble complex ion $(PtF_x)^{z-}$ may form in the presence of fluorine, accelerating Pt dissolution. In this case, high ionomer concentration near the membrane/catalyst interface may cause the formation of a Pt depletion layer. However, the opposite result was observed in a phosphoric acid fuel cell durability test [89]. The Pt particles in a cathode near an electrolyte matrix are larger than the others. The average Pt particle size was 11.7 nm at the GDL (Baking paper) side, 8.2 nm at the center and 7.7 nm near the membrane/cathode

interface in a PEMFC accelerated cycling test. It is not clear whether this difference is due to a difference in the fuel cell system or a difference in operating conditions. Similarly, large Pt particles accumulating at the cathode catalyst layer and membrane interface are observed in the potential cycling test with H_2-N_2 rather than H_2-O_2 flowing through the anode and cathode. Therefore, different accelerate stress test conditions could lead to different failure mechanisms. We require more fundamental studies to understand the failure mechanisms. Proper selection of AST modes to predict fuel cell lifetime should not be overlooked.
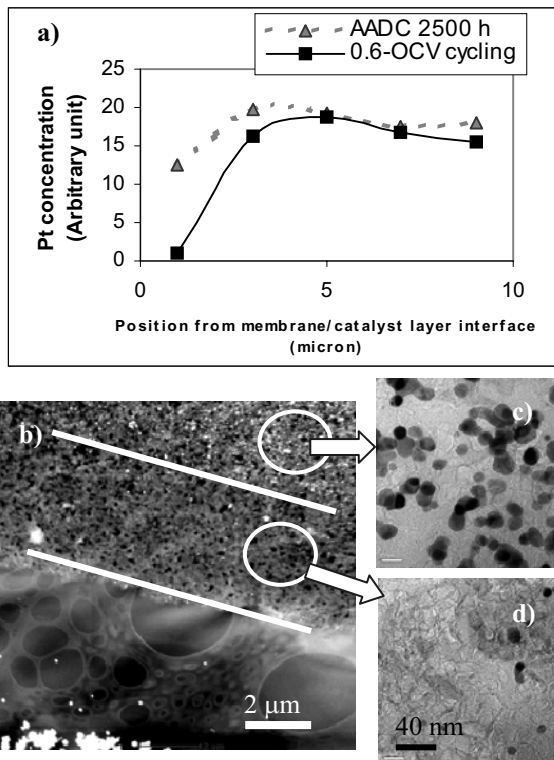
Figure 23.25. (a) Pt concentration distribution after HAST and AADC durability test, (b) STEM images of the cathode catalyst layer after 52,000 voltage cycles 90.6–OCV). Note the region between the two green lines is the Pt depletion layer. Close-up TEM images in (c) and (d) represent the area of the catalyst layer outside the Pt depletion layer and in the depletion layer, respectively [37]. (Reprinted by permission of ECS—The Electrochemical Society, from Li J, He P, Wang K, Davis M, Ye S. Characterization of catalyst layer structural changes in PEMFC as a function of durability testing.)

23.4.4 Carbon Corrosion of Catalyst Layer

Catalyst carbon support is thermodynamically unstable at PEMFC operating conditions. Carbon corrosion can result in degradation of the catalyst layer.

Electrochemical corrosion of carbon material in aqueous acid electrolytes could follow the reaction:

$$C + 2\,H_2O = CO_2 + 4H^+ + 4e^- \qquad E^0 = 0.207\ V \qquad (23.36)$$

This reaction is thermodynamically allowable at the potentials at which the fuel cell cathode operates, but it is believed to be almost negligibly slow in that potential range at PEMFC operation temperatures ($< 100\ °C$). However, PEFCs in automotive applications undergo an estimated 30,000 startup-shutdown cycles over the life of a vehicle. After an unprotected fuel cell shutdown, there will be unreacted air and hydrogen at the cathode and anode, respectively. If the anode exhaust port is not closed after shutdown, air will diffuse into the anode side, creating an air/H_2 boundary. If the stack has been shut down and the anode is filled with air, the H_2/air boundary will be created when hydrogen flows into the anode in the startup process. In such startup-shutdown cycles, H_2/air fronts in the anode compartment could cause local fuel starvation. In this situation, a high potential of up to ~1.2 to 1.5 V is established in the fuel starvation regions and a reverse current flows internally in the electrodes through the fuel-rich and fuel-starvation regions [91–93], as shown in Figure 23.26; the red line is the anode polarization curve. When fuel starvation occurs, the hydrogen potential shifts positively. Since fuel starvation happens locally, that part of the cell not experiencing starvation still runs normally. The normal and abnormal cell parts are electronically connected through the conductive plates. Thus, the cell voltages of these two parts should be very close to one another. From Figure 23.26 we can see that in order to keep the cell voltage (the potential difference) the same as in the normal cell part, the potentials of the abnormal part shift to the high positions at both anode and cathode. In this position, the cathode reaction is actually an oxidation reaction rather than an oxygen reduction reaction. In a very severe fuel starvation case, carbon corrosion and water hydrolysis reactions can concurrently occur. The abnormal part of the cell is no longer a spontaneous electrochemical cell, but an electrolysis cell driven by the normal part of the cell.

Carbon corrosion of the catalyst layer in the PEMFC can be monitored through determining the CO_2 gas emitted from the stack [14, 94–96]. Figure 23.27 shows a typical trend of cell voltage and carbon dioxide concentration in cathode exhaust under cycling of OCV, loading, and cathode nitrogen purge processes. CO_2 gas generates immediately when the stack is switched from cathode nitrogen purge to OCV operation [94]. Carbon corrosion of the catalyst layer can also be observed directly using SEM [37, 93]. After the carbon corrodes, the catalyst layer becomes thinner. Cathode catalyst layer thinning of 50% at a highly corroded region was observed in 220 cycles of potential cycling from 0.6 to 1.0 V, as shown in Figure 23.28 [37].
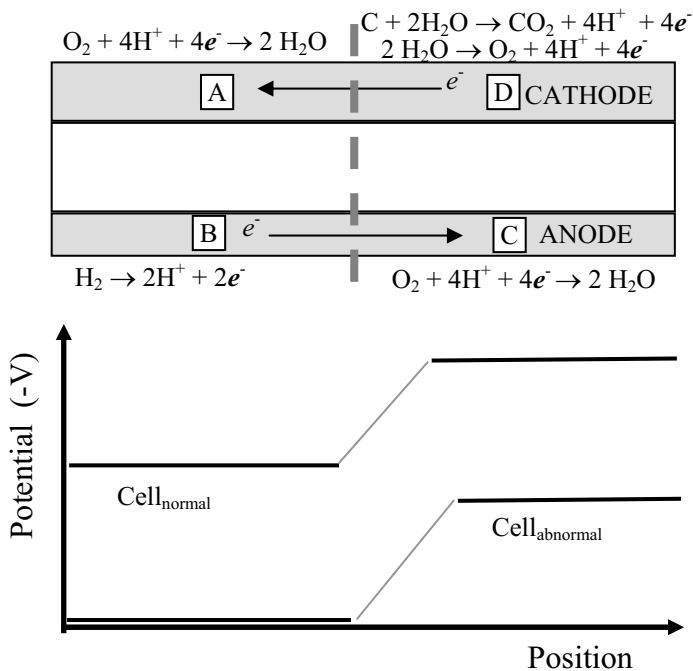
Figure 23.26. A schematic illustration of reactions in four distinct regions when an air/fuel boundary is formed at the anode. Region D experiences a potential about twice that of the OCV, and thus carbon in that region would be corroded quickly.
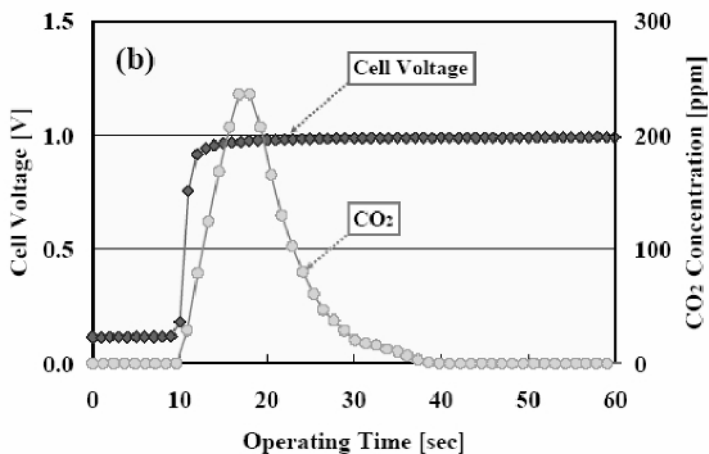
Figure 23.27. Typical trend of cell voltage and carbon dioxide concentration in cathode exhaust at the beginning of the OCV step [94]. (Reprinted by permission of ECS—The Electrochemical Society, from Chizawa H, Ogami Y, Naka H, Matsunaga A, Aoki N, Aoki T. Study of accelerated test protocol for PEFC focusing on carbon corrosion.)
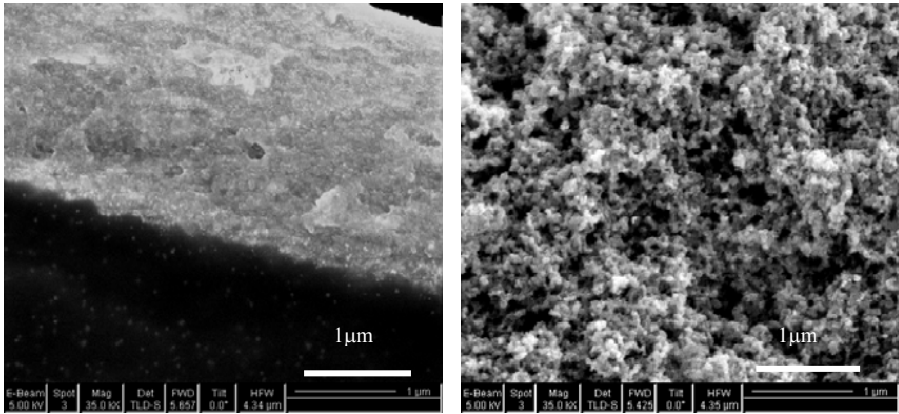
Figure 23.28. SEM image of cross-sections of the cathode catalyst layer with high surface area carbon support: left, after 220 cycles of voltage cycling from 0.6 V–OCV, and right, a fresh MEA [37]. (Reprinted by permission of ECS—The Electrochemical Society, from Li J, He P, Wang K, Davis M, Ye S. Characterization of catalyst layer structural changes in PEMFC as a function of durability testing.)

The corrosion rate of carbon can be accelerated in the presence of Pt on the carbon surface. Oxidation of carbon in the presence of Pt could be accelerated by the following radical reactions [96]:

$$Pt—H_2O + O_2 \prod PtOH + HOO^\bullet \qquad (23.37)$$

$$PtOH + O_2 \prod PtO + HOO^\bullet \qquad (23.38)$$

$$PtOH + HOO^\bullet \prod PtO + HOOH \qquad (23.39)$$

$$HOO^\bullet + HOO^\bullet \prod O_2 + HO^\bullet \qquad (23.40)$$

and

$$(23.41)$$
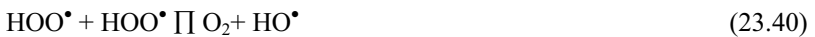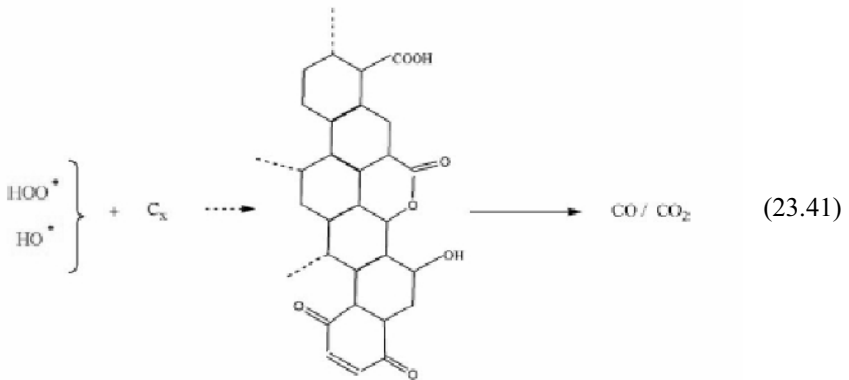
Jarvi et al. [97] demonstrated that the rate of CO_2 emission from a Pt/C electrode was higher than from a carbon-only electrode at high potentials, measured by on-line mass spectrometry in a CV experiment, as shown in Figure 23.29. The magnitude of the CO_2 peaks with respect to the cell potential depended on the Pt mass fraction in the electrode. The CO_2 generation rate increased in the order of 0% Pt < 10% Pt < 39% Pt in the electrodes. However, Ball et al. argue that the presence of Pt in the support carbon does not significantly change the amount of carbon corroded during a 24-h steady state hold at 80 °C, 1.2 V_{RHE} in 1 M H_2SO_4. The carbon corrosion rate is dominated by the type of carbon rather than the presence of Pt. Although different opinions are held on the role of Pt in carbon corrosion, a consistent view is that high surface area carbon is less stable than heat-treated or graphitized carbon that generally has a low surface area [95, 96].
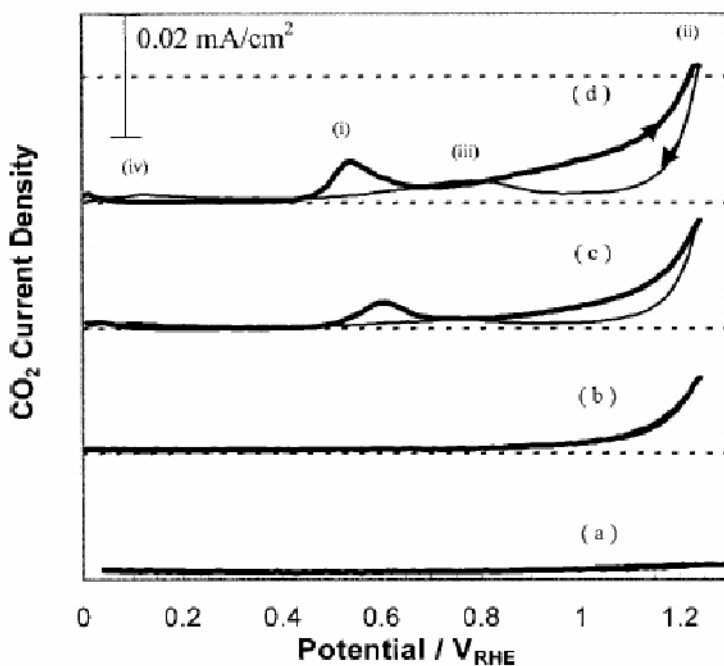
Figure 23.29. Comparison of CO_2 mass spectra profiles for MEAs with (a) Vulcan-coated gas-diffusion layer pressed against the Nafion 117 membrane, (b) 0% Pt (Vulcan only) on Nafion 112, (c) 10 % Pt/C on Nafion 112, and (d) 39% Pt/C on Nafion 112. The electrochemical cycles were performed at 2 mV/s, 50 °C, with research-grade He on the cathode (50 cm^3/min) and dilute $H_2 \sim 4\%$ H_2/N_2) on the anode (500 cm^3/min), passed through the saturators at 50 °C. The mass spectra were converted by a known 1% CO_2 calibration gas and then converted into a Faradaic current of CO_2 [97]. (Reprinted by permission of ECS—The Electrochemical Society, from Roen, LM, Paik CH, Jarvi TD. Electrocatalytic corrosion of carbon support in PEMFC cathodes.)

In acid electrolytes, the mechanism of electrochemical carbon corrosion is generally thought to proceed via a three-step process involving a 4-electron

oxidation reaction [95, 97]. The redox couples on carbons are associated with quinone and hydroquinone structures [95, 96, 98–100]. The carbon is oxidized in Step 1 (Equation 23.42) to allow the formation of oxidized carbon intermediates by 2-electron partial oxidation in Step 2 (Equation 23.43), or through the radical reaction in Equation 23.41:

$$C_s \rightarrow C_s^+ + e^- \qquad (23.42)$$

$$C_s + 1/2\ H_2O \rightarrow C_sO + H^+ \qquad (23.43)$$

The final step of the corrosion process (Step 3) is the formation of carbon dioxide.

$$2C_sO + H_2O \rightarrow C_sO + CO_2 + 2H^+ + 2e^- \qquad (23.44)$$
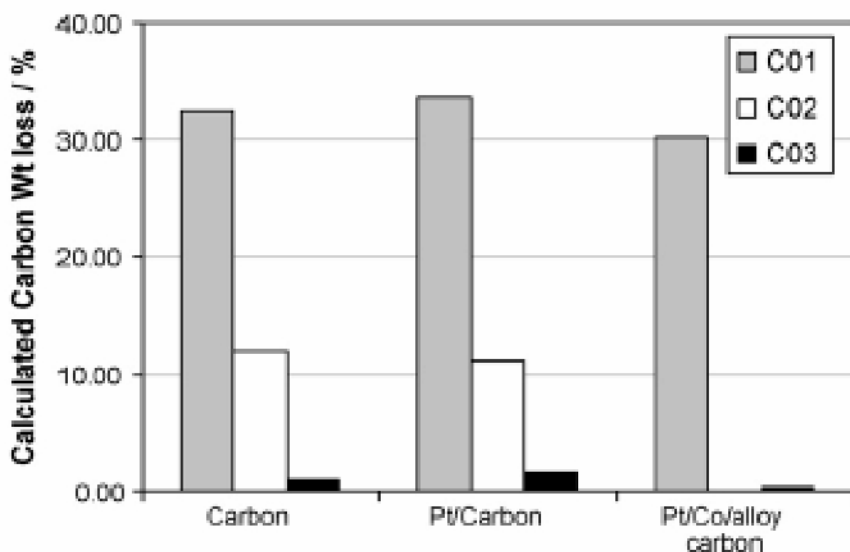
Figure 23.30. Comparison of the cumulative carbon corrosion following a 24-h 1.2 V potentiostatic hold at 80 °C in 1 M H_2SO_4 for two commercial carbons C01, C02 and one heat-treated carbon C03, and platinum and Pt/Co alloy catalysts on these carbons [95]. (Reprinted from Journal of Power Sources, 166(1), Prasanna M, Cho EA, Kim H-J, Oh I-H, Lim T-H, Hong S-A, Performance of proton-exchange membrane fuel cells using the catalyst-gradient electrode technique, 18–25, ©2007, with permission from Elsevier.)

The presence of electroactive species on a wide variety of carbons can be determined using cyclic voltammetry. A summary of some of these results is given in Table 23.6 [98]. However, quantitative determination of surface functional groups seems to be difficult [99], although a classification of those surface groups has been attempted by XPS and FTIR.

Table 23.6. Electrochemically active species on carbon and aromatic compounds [98]. (Reprinted from Carbon, 11(4), Kinoshita K, Bett JAS, Potentiodynamic analysis of surface oxides on carbon blacks, 403–11, ©1973, with permission from Elsevier.)

System	Redox potential (mv)	Surface group
Chloranil/graphite in 3N H_2SO_4	668 (NHE)	quinone/hydroquinone
Anthraquinoid dyes in cont. H_2SO_4	450–650 (Fe^{2+}/Fe^{3+})	quinone reduction
ISAF furnace black in 0.1 M $NaNO_3$, dimethylformamide	966 (S.C.E.)	hydroquinone oxidation
Pyrolytic carbon in 1 M H_2SO_4	1300–1700 (S.C.E.)	hydroquinone oxidation
	0–400 (S.C.E.)	quinone/hydroquinone
Carbon fibers in tetra-N-butyl ammonium; Chlorate in DMF	–2100 (S.C.E.)	reduction of carbonyl or aromatic heterocycles
Pyrographite in 1 N H_2SO_4	600 (NHE?)	oxygen adsorption and desorption

Corrosion of the cathode catalyst support carbon deprives the catalyst of its support. The small catalyst particles collapse and agglomerate into large ones, consequently losing surface area. The catalyst particles, after losing their support, are disconnected from the electric network originally available through the carbon support, resulting in deactivation of the oxygen reduction reaction due to loss of the electron pathway. In addition, the porous structure of the catalyst layer can be destroyed if the support carbon is severely corroded, as shown in Figure 23.28 [37]. This will raise the mass transport loss significantly due to blockage of gas access paths and ohmic loss arising from an increase in electric resistance after the conductive carbon corrodes. Figure 23.31 [14] shows the impact of accelerated carbon support corrosion on the polarization curves of 50 cm^2 MEAs with both a 50% Pt/C$_{standard}$ and a 30 wt% Pt alloy/C$_{corr.-resist.}$ cathode catalyst. With a standard carbon support in the cathode catalyst layer, the MEA performance declines rapidly over time; significant ohmic and mass transfer losses can be seen from those I-V curves. However, with corrosion resistance of the carbon support in the cathode catalyst layer, the MEA performance (I-V curve) after 100 hours of an accelerated corrosion test is almost the same as the performance at the beginning of the test.

Developing novel catalyst support materials is essential to mitigate catalyst degradation. Carbon has many advantages over other materials. The physical and chemical properties can be tailored by changing the types of carbon. Highly graphitized carbon is more chemically stable than high surface area amorphous carbon and has high electric conductivity as well. However, the surface area of highly graphitized carbon is lower and yields a low catalyst layer ECA. Selecting the type of carbon support may require balancing durability and performance. Carbon nanotubes (CNTs) and nanofibers (CNFs) are nanoscale carbon cylinders of rolled up graphene sheets (in CNTs) or aligned graphene slices (in CNFs). CNTs and CNFs [101–106] deposited with Pt or Pt-Ru alloys as electrocatalysis

electrodes for fuel cell applications have been investigated. Although CNTs are shown to be more oxidation resistant than carbon black, the improvement may not be sufficient to provide the necessary benefits for commercialization, in light of the high cost of this material. Using metal oxides or carbides as catalyst supports for fuel cell applications is still in the early research stages. Ebonex, a mixed valence TiO_x material, is a commercial conductive substance, but fuel cell performance using Pt/TiO_x as a catalyst is lower than that with a Pt/C catalyst. Although other efforts are being made to find alternatives to carbon supports, no successful materials have yet been reported.
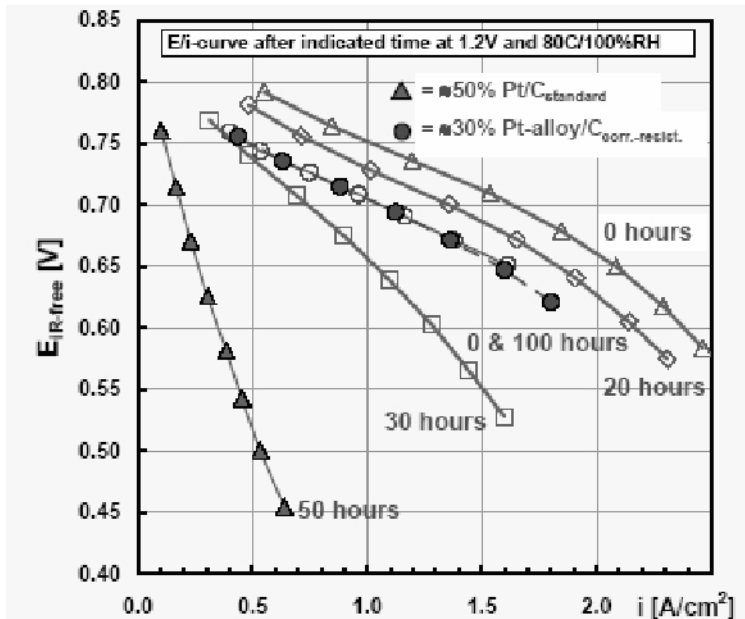
Figure 23.31. Impact of accelerated carbon support corrosion on the E/I performance curves of 50 cm² MEAs with both a ≈50% Pt/C$_{standard}$ and a ≈30 wt% Pt alloy/C$_{corr.-resist.}$ cathode catalyst. MEA cathodes were subjected to accelerated carbon support corrosion at 1.2 V and 80 °C for the indicated times, using fully humidified H_2/N_2 gas streams (anode/cathode). H_2/air (stoichiometric flows of s = 3/3) performance curves were recorded at 80 °C, 50% RH, and 150 kPa$_{abs}$ (MEAs with ≈25 μm membranes, catalyst loadings of 0.2–0.4 mgPt/cm²) [14]. (Reprinted by permission of ECS—The Electrochemical Society, from Mathias MF, Makharia R, Gasteiger HT, Conley JJ, Fuller TJ, Gittleman CJ, et al. Two fuel cell cars in every garage?)

23.5 Summary

Durability is one of the major remaining barriers to commercialization of fuel cells. In order to achieve good long-term performance, it is necessary for all of the components to maintain their integrity. Therefore, materials selection, MEA and stack fabrication, and system configuration are critical when designing fuel cells.

The electrical, chemical, physical, and mechanical properties of the components need to be tailored to reach an optimum state in terms of performance, cost, and durability. Developing electrocatalysts to achieve the US Department of Energy (DOE) technical targets (see Table 23.7) for transportation applications requires a breakthrough in novel material development and structure design. Catalyst layer degradation impacts significantly on the durability of the fuel cell. With respect to cost reduction, researchers are seeking electrocatalyst electrodes with as low noble metal loading as possible; for instance, the DOE suggests a total loading (anode loading + cathode loading) of 0.2 mg/cm^2 by 2015. Achieving the durability target at such low loading is much more challenging. More emphasis should be put on fundamental understanding of the catalyst degradation mechanism and on developing strategies and solutions to mitigate degradation.

Table 23.7. Technical targets: electrocatalysts for transportation applications [106]. (Reproduced from United States Department of Energy. Technical Plan – Fuel Cells. 2007. With permission from DOE.)

Characteristic	Units	2005 Status		Stack Targets	
		Cell	Stack	2010	2015
Platinum group metal total content (both electrodes)	g/kW (rated)	0.6	1.1	0.3	0.2
Platinum group metal (PGM) total loading	mg PGM/cm^2 electrode area	0.45	0.8	0.3	0.2
Cost	$/kW	9	55	5	3
Durability with cycling	hours	> 2000	~2000	5000	5000
Operating temp < 80 °C	hours	N/A	N/A	2000	5000
Operating temp > 80 °C					
Electrochemical area loss	%	90	90	< 40	< 40
Electrocatalyst support loss	mV after 100 hours @ 1.2 V	> 30	N/A	< 30	< 30
Mass activity	A/mg Pt @ 900 mViR-free	0.28	0.11	0.44	0.44
Specific activity	μA/cm^2 @ 900 mViR-free	550	180	720	720
Non-Pt catalyst activity per volume of supported catalyst	A/cm^3 @ 800 mViR-free	8	N/A	> 130	300

References

1. Ralph TR, Hogarth MP. Catalysis for low temperature fuel cells-part II: the anode challenges. Platinum Metal Rev 2002;46:117–35.
2. Brankovic SR, Wang JX, Adzic RR. Pt submonolayers on Ru nanoparticles - a novel low Pt loading, high CO tolerance fuel cell electrocatalyst. Electrochem Solid-State Lett 2001;4:A217–20.
3. Brankovic SR, Wang JX, Zhu Y, Sabatini R, McBreen J, Adzic RR. Electrosorption and catalytic properties of bare and Pt modified single crystal and nanostructured Ru surfaces. J Electroanal Chem 2002;524:231–41.
4. Watanabe M, Motoo S. Electrocatalysis by ad-atoms. J Electroanal Chem 1975;60:275–83.
5. Wang JX, Brankovic SR, Zhu Y, Hanson JC, Adzic RR. Kinetic characterization of PtRu fuel cell anode catalysts made by spontaneous Pt deposition on Ru nanoparticles. J Electrochem Soc 2003;150:A1108–17.
6. Gastaiger HA, Markovic NMPN, Ross EJ, Cairns. CO electrooxidation on well-characterized Pt-Ru alloys. J Phys Chem 1994;98:617–25.
7. Liao MS, Cabrera CR, Ishikawa Y. A theoretical study of CO adsorption on Pt, Ru and Pt–M (M=Ru, Sn, Ge) clusters. Surf Sci 2000;445:267–82.
8. Koper MTM, Shunina TE, Santen RA. Periodic density functional study of CO and OH adsorption on Pt-Ru Alloy surfaces: implications for CO tolerant fuel cell catalysts. J Phys Chem B 2002;106:686–92.
9. Borup R, Meyers J, Pivovar B, Kim YS, Mukundan R, Garland N, et al. Scientific aspects of polymer electrolyte fuel cell durability and degradation. Chem Rev 2007;107(10):3904–51.
10. Gasteiger HA, Kocha SS, Sompalli B, Wagner FT. Activity benchmarks and requirements for Pt, Pt-alloy, and non-Pt oxygen reduction catalysts for PEMFCs. Appl Catal B 2005;56:9–35.
11. Antolini E, Salgado JRC, Gonzalez ER. The stability of Pt–M (M = first row transition metal) alloy catalysts and its effect on the activity in low temperature fuel cells. J Power Sources 2006;160:957–68.
12. Raistrick ID, inventor; United States Department of Energy, assignee. Electrode assembly for use in a solid polymer electrolyte fuel cell. United States patent US 4876115. 1989 Oct 24.
13. Costamagna P, Srinivasan S. Quantum jumps in the PEMFC science and technology from the 1960s to the year 2000. J Power Sources 2001;102242–52.
14. Mathias MF, Makharia R, Gasteiger HT, Conley JJ, Fuller TJ, Gittleman CJ, et al. Two fuel cell cars in every garage? ECS Interface 2005;3:24–35.
15. Smith TJ, Gasteiger HA, Stab GD, Urban PM, Kolb DM, Behm RJ. Characterization of high-surface-area electrocatalysts using a rotating disk electrode configuration. J Electrochem Soc 1998;145:2354–58.
16. Perry ML, Fuller TF. A historical perspective of fuel cell technology in the 20th Century. J Electrochem Soc 2002;149:S59–67.
17. Fowler M, Mann RF, Amphlett JC, Peppley BA, Roberge PR. Reliability issues and voltage degradation. In: Handbook of fuel cells: fundamentals, technology and applications, volume 3. Vielstich W, Lamm A, Gasteiger HA, editors. New York: Wiley, 2003: 663–77.
18. Wilkinson DP, St-Pierre J. Durability. In: Handbook of fuel cells: fundamentals, technology and applications, volume 3. Vielstich W, Lamm A, Gasteiger HA, editors. New York: Wiley, 2003:611–26.
19. Chalk SG, Miller JF. Key challenges and recent progress in batteries, fuel cells, and hydrogen storage for clean energy systems. J Power Sources 2006;159:73–80.

20. Ralph TR, Hards GA, Keating JE, Campbell SA, Wilkinson DP, Davis M, et al. Low cost electrodes for proton exchange membrane fuel cells, performance in single cells and Ballard stacks. J Electrochem Soc 1997;144:3845–57.

21. Gancs L, Hult BN, Hakim N, Mukerjee S. The impact of Ru contamination of a Pt/C electrocatalyst on its oxygen-reduction activity. Electrochem Solid-State Lett 2007;10:B150–4.

22. Kinoshita K, Stonehart P. Chapter 4. In: Modern aspects of electrochemistry, volume 12. Bockris J O'M, Conway, BE, editors. New York: Plenum Press, 1997: 227–35.

23. Gasteiger HA, Gu W, Makharia R, Mathias MF, Sompalli B. Beginning-of-life MEA performance: efficiency loss contributions. In: Handbook of fuel cells: fundamentals, technology and applications, volume 3. Vielstich W, Lamm A, Gasteiger HA, editors. New York: Wiley, 2003: 593–610.

24. Makharia R, Mathias MF, Daniel R, Baker DR. Measurement of catalyst layer electrolyte resistance in PEFCs using electrochemical impedance spectroscopy. J of Electrochem Soc 2005;152:A970–7.

25. Lee JH, Lalk TR, Appleby AJ. Modeling electrochemical performance in large scale proton exchange membrane fuel cell stacks. J Power Sources 1998;70:258–68.

26. Santarelli MG, Torchio MF, Cochis P. Parameters estimation of a PEM fuel cell polarization curve and analysis of their behavior with temperature. J Power Sources 2006;159:824–35.

27. Parthasarathy A, Dave B, Srinivasan S, Appleby AJ, Martin CR. The platinum microelectrode/Nafion interface: an electrochemical impedance spectroscopic analysis of oxygen reduction kinetics and Nafion characteristics. J Electrochem Soc 1992;139:1634–41.

28. Springer TE, Zawodzinski TA, Wilson MS, Gottesfeld S. Characterization of polymer electrolyte fuel cells using AC impedance spectroscopy. J Electrochem Soc 1996;143:587–99.

29. Lefebvre M, Martin RB, Pickup PG. Characterization of ionic conductivity profiles within proton exchange membrane fuel cell gas diffusion electrodes by impedance spectroscopy. Electrochem Solid-State Lett 1999;2:259–61.

30. Saab P, Garzon FH, Zawodzinski TA. Determination of ionic and electronic resistivities in carbon/polyelectrolyte fuel-cell composite electrodes. J Electrochem Soc 2002;149:A1541–6.

31. Saab P, Garzon FH, Zawodzinski TA. The effects of processing conditions and chemical composition on electronic and ionic resistivities of fuel cell electrode composites. J Electrochem Soc 2003;150:A214–18.

32. Blom DA, Dunlap JR, Nolan TA, Allarda LF. Preparation of cross-sectional samples of proton exchange membrane fuel cells by ultramicrotomy for TEM. J Electrochem Soc 2003;150:A414–18.

33. Ferreira PJ, La O GJ, Shao-Horn Y, Morgan D, Makharia R, Kocha S, et al. Instability of Pt/C electrocatalysts in proton exchange membrane fuel cells. J Electrochem Soc 2005;152:A2256–71.

34. Yasuda K, Taniguchi A, Akita T, Toroi T, Siroma Z. Characteristics of a platinum black catalyst layer with regard to platinum dissolution phenomena in a membrane electrode assembly. J Electrochem Soc 2006;153:1599–603.

35. Xie J, Wood III DL, More KL, Atanassov P, Borup RL. Microstructural changes of membrane electrode assemblies during PEFC durability testing at high humidity conditions. J Electrochem Soc 2005;152:A1011–1020.

36. Cheng X, Peng CC, Chen Z, Zhang Y, Fan Q. Catalyst microstructure examination of PEMFC membrane electrode assemblies vs. time. J Electrochem Soc 2004;151:A48–52.

37. Li J, He P, Wang K, Davis M, Ye S. Characterization of catalyst layer structural changes in PEMFC as a function of durability testing. ECS Transactions 2006;31743–51.
38. Roth C, Martz N, Fuess H. An X-ray diffraction and transmission electron microscopy study of Pt–Ru fuel cell catalysts before and after operation. J Appl Electrochem 2004;34:345–8.
39. Cheng X, Yi B, Han M, Zhang J, Qiao Y, Yu J. Investigation of platinum utilization and morphology in catalyst layer of polymer electrolyte fuel cells. J Power Sources 1999;79:75–81.
40. Li J, Lee S, Roberts J. Ice formation and distribution in the catalyst layer during freeze-start process — CRYO-SEM investigation. ECS Trans 2007;11(1):595.
41. Wang J, Yin J, Shao Y, Zhang S, Wang Z, Gao Y. Effect of carbon black support corrosion on the durability of Pt/C catalyst. J Power Sources 2007;171:331–9.
42. Jones FW. The measurement of particle size by the X-Ray method. Proc R Soc London Ser A 1938;166(924):16–43.
43. Wilson MS, Garzon FH, Sickafus KE, Gottesfeld S. Surface area loss of supported platinum in polymer electrolyte fuel cells. J Electrochem Soc 1993;140:2872–7.
44. United States Department of Energy. DOE cell component accelerated stress test protocols for PEM fuel cells: electrocatalysts, supports, membranes, and membrane electrode assemblies. 2007 Mar. Available from: http://www1.eere.energy.gov/hydrogenandfuelcells/fuelcells/pdfs/component_durability_profile.pdf.
45. Zhang J, Wang H, Wilkinson DP, Song D, Shen J, Liu ZS. Model for the contamination of fuel cell anode catalyst in the presence of fuel stream impurities. J Power Sources 2005;147:58–71.
46. Cheng X, Shi Z, Glass N, Zhang L, Zhang JJ, Songa D, et al. A review of PEM hydrogen fuel cell contamination: Impacts, mechanisms, and mitigation. J Power Sources 2007;165:739–56.
47. Baschuk JJ, Li X. Carbon monoxide poisoning of proton exchange membrane fuel cells. Int J Energy Res 2001;25:695–713.
48. Vogel W, Lundquist J, Ross P, Stonehart P. Reaction pathways and poisons-II. The rate controlling step for electrochemical oxidation of hydrogen on Pt in acid and poisoning of the reaction by CO. Electrochim Acta 1975;20:79–93.
49. Camara GA, Ticianelli EA, Mukerjee S, Lee SJ, McBreen J. The CO poisoning mechanism of the hydrogen oxidation reaction in proton exchange membrane fuel cells. J Electrochem Soc 2002;149:A748–53.
50. Li Q, He R, Gao J, Jensen JO, Bjerrum NJ. The CO poisoning effect in PEMFCs operational at temperatures up to 200 °C. J Electrochem Soc 2003;150:A1599–605.
51. Oetjen H-F, Schmidt VM, Stimming U, Trila F. Performance data of a proton exchange membrane fuel cell using H_2/CO as fuel gas. J Electrochem Soc 1996;143:3838–42.
52. Mukerjee S, Lee SJ, Ticianelli EA, McBreen J, Grgur BN, Markovic NM, et al. Investigation of enhanced CO tolerance in proton exchange membrane fuel cells by carbon supported PtMo alloy catalyst. Electrochem Solid-State Lett 1999;2:12–15.
53. Adcock PA, Pacheco SV, Norman KM, Uribe FA. Transition metal oxides as reconfigured fuel cell anode catalysts for improved CO tolerance: polarization data. J Electrochem Soc 2005;152:A459–66.
54. He C, Kunz HR, Fenton JM. Electro-oxidation of hydrogen with carbon monoxide on Pt/Ru-based ternary catalysts. J Electrochem Soc 2003;150:A1017–24.
55. Ianniello R, Schmidt VM, Stimming U, Stumper J, Wallau A. CO adsorption and oxidation on Pt and Pt-Ru alloys: dependence on substrate composition. Electrochim Acta 1994;39:1863–9.

56. Gottesfeld S, Pafford J. A new approach to the problem of carbon monoxide poisoning in fuel cells operating at low temperatures. J Electrochem Soc 1988;135:2651–2.

57. Divisek J, Oetjen H-F, Peinecke V, Schmidt VM, Stimming U. Components for PEM fuel cell systems using hydrogen and CO containing fuels. Electrochim Acta 1998;43:3811–15.

58. Mohtadi R, Lee W-K, Van Zee JW. Assessing durability of cathodes exposed to common air impurities. J Power Sources 2004;138:216–25.

59. Knights S, Jia N, Chuy C, Zhang J. Fuel Cell Seminar 2005: Fuel Cell Progress, Challenges and Markets; 2005 Nov 14–18; Palm Springs, CA.

60. Jing F, Hou M, Shi W, Fu J, Yu H, Ming P, et al. The effect of ambient contamination on PEMFC performance. J Power Sources 2007;166:172–6.

61. Knights SD, Colbow KM, St-Pierre J, Wilkinson DP. Aging mechanisms and lifetime of PEFC and DMFC. J Power Sources 2004;127:127–34.

62. Taniguchi A, Akita T, Yasud K, Miyazaki Y. Analysis of electrocatalyst degradation in PEMFC caused by cell reversal during fuel starvation. J Power Sources 2004;130:42–9.

63. Mitsuda K, Murahashi T. Polarization study of a fuel cell with four reference electrodes. J Electrochem Soc 1990;137:3079–85.

64. Gances L, Hult BN, Hakim N, Mukerjee S. The impact of Ru contamination of a Pt/C electrocatalyst on its oxygen-reducing activity. Electrochem Solid-State Lett 2007;10:B150–4.

65. Piela P, Eickes C, Brosha E, Garzon F, Zelenaya P. Ruthenium crossover in direct methanol fuel cell with Pt-Ru black anode. J Electrochem Soc 2004;151:A2053–9.

66. Yasuda K, Taniguchi A, Akita T, Toroi T, Siroma Z. Characteristics of a platinum black catalyst layer with regard to platinum dissolution phenomena in a membrane electrode assembly. J Electrochem Soc 2006;153:A1599–603.

67. Watanabe M, Tsurumi K, Mizukami T, Nakamura T, Stonehart P. Activity and stability of ordered and disordered Co-Pt alloys for phosphoric acid fuel cells. J Electrochem Soc 1994;141:2659–68.

68. Pourbaix M, Muylder J, Zoubov N. Electrochemical properties of the platinum metals. Platinum Metals Rev 1959;3:47–53.

69. Lee JB. Elevated temperature potential-pH diagrams for the Cr-H_2O, Ti-H_2O, Mo-H_2O and Pt-H_2O systems. Corrosion 1981;37:467–81.

70. Wang X, Kumar R, Myersz DJ. Effect of voltage on platinum dissolution relevance to polymer electrolyte fuel cells. Electrochem Solid-State Lett 2006;9:A225–7.

71. Kinoshita K, Lundquist JT, Stonehart P. Potential cycling effects on platinum electrocatalyst surfaces. J Electroanal Chem 1973;48(2):157–66.

72. Yasuda K, Taniguchi A, Akita T, Ioroi T, Siroma Z. Platinum dissolution and deposition in the polymer electrolyte membrane of a PEM fuel cell as studied by potential cycling. Phys Chem Chem Phys 2006;8:746–52.

73. Rand DAJ, Woods R. A study of the dissolution of platinum, palladium, rhodium and gold electrodes in 1 M sulphuric acid by cyclic voltammetry. J Electroanal Chem 1972;35:209–18.

74. Mitsushima S, Kawahara S, Ota K, Kamiya N. Consumption rate of Pt under potential cycling. J Electrochem Soc 2007;154:B153–8.

75. Darling RM, Meyers JP. Mathematical model of platinum movement in PEM fuel cells. J Electrochem Soc 2005;152:A242–7.

76. Darling RM, Meyers JP. Kinetic model of platinum dissolution in PEMFCs. J Electrochem Soc 2003;150:A1523–7.

77. Raghuveer V, Manthiram A, Bard A. Pd-Co-Mo electrocatalyst for the oxygen reduction reaction in proton exchange membrane fuel cells. J Phys Chem B 2005;109:22909–12.

78. Gasteiger H, Kocha S, Sompalli B, Wagner F. Activity benchmarks and requirements for Pt, Pt-alloy, and non-Pt oxygen reduction catalysts for PEMFCs. Appl Catal B 2005;56:9–35.
79. Antolini E, Salgado J, Gonzalez E. The stability of Pt–M (M = first row transition metal) alloy catalysts and its effect on the activity in low temperature fuel cells. A literature review and tests on a Pt–Co catalyst. J Power Sources 2006;160:957–68.
80. Toda T, Igarashi H, Uchida H, Watanabe M. Enhancement of the electroreduction of oxygen on Pt alloys with Fe, Ni, and Co. J Electrochem Soc 1999;146:3750–6.
81. Paulus UA, Wokaun A, Scherer GG. Oxygen reduction on carbon-supported Pt-Ni and Pt-Co alloy catalysts. J Phys Chem B 2002;106:4181–91.
82. Wakabayashi N, Takeichi M, Uchida H, Watanabe M. Temperature dependence of oxygen reduction activity at Pt-Fe, Pt-Co, and Pt-Ni alloy electrodes. J Phys Chem B 2005;109:5836–41.
83. Thompsett D. Pt alloys as oxygen reduction catalysts. In: Handbook of fuel cells: fundamentals, technology and applications, volume 2. Vielstich W, Lamm A, Gasteiger HA, editors. Chicester, UK: Wiley, 2003: 467–80.
84. Bahrololoom ME, Gabe DR, Wilcox GD. Development of a bath for electrodeposition of zinc-cobalt compositionally modulated alloy multilayered coatings. J Electrochem Soc 2003;150:C144–51.
85. Mukerjee S, Srinivasan S. O_2 reduction structure-related parameters for supported catalysts. In: Handbook of fuel cells: fundamentals, technology and applications, volume 2. Vielstich W, Lamm A, Gasteiger HA, editors. Chicester, UK: Wiley, 2003: 502–43.
86. Bi W, Gray GE, Fuller TF. PEM fuel cell Pt/C dissolution and deposition in Nafion electrolyte. Electrochem Solid-State Lett 2007;10:B101–4.
87. Gruver GA, Pascoe RF, Kunz HR. Surface area loss of platinum supported on carbon in phosphoric acid electrolyte. J Electrochem Soc 1980;127:1219–24.
88. Honji A, Mori T, Tamura K, Hishinuma Y. Agglomeration of platinum particles supported on carbon in phosphoric acid. J Electrochem Soc 1988;135:355–9.
89. Aragane J, Murahashi T, Odaka T. Change of Pt distribution in the active components of phosphoric acid fuel cell. J Electrochem Soc 1988;135:844–50.
90. Xie J, Wood DL III, Wayne DM, Zawodzinski TA, Atanassov P, Borup RL. Durability of PEFCs at high humidity conditions. J Electrochem Soc 2005;152:A104–13.
91. Reiser CA, Bregoli L, Patterson TW, Yi JS, Yang D, Perry ML, et al. A reverse-current decay mechanism for fuel cells. Electrochem Solid-State Letters 2005;8:A273–6.
92. Tang H, Qi Z, Ramani M, Elter JF. PEM fuel cell cathode carbon corrosion due to the formation of air/fuel boundary at the anode. J Power Sources 2006;158:1306–12.
93. Meyers JP, Darling RM. Model of carbon corrosion in PEM fuel cells. J Electrochem Soc 2006;153:A1432–42.
94. Chizawa H, Ogami Y, Naka H, Matsunaga A, Aoki N, Aoki T. Study of accelerated test protocol for PEFC focusing on carbon corrosion. ECS Trans 2006;3:645–55.
95. Ball SC, Hudson SL, Thompsett D, Theobald B. An investigation into factors affecting the stability of carbons and carbon supported platinum and platinum/cobalt alloy catalysts during 1.2V potentiostatic hold regimes at a range of temperatures. J Power Sources 2007;171:18–25.
96. Cai M, Ruthkosky MS, Merzougui B, Swathirajan S, Balogh MP, Oh SH. Investigation of thermal and electrochemical degradation of fuel cell catalysts. J Power Sources 2006;160:977–86.
97. Roen LM, Paik CH, Jarvi TD. Electrocatalytic corrosion of carbon support in PEMFC cathodes. Electrochem Solid-State Lett 2004;7:A19–22.

98. Kinoshita K, Beti JAS. Potentiodynamic analysis of surface oxides on carbon blacks. Carbon 1975;11:403–7.
99. Boehm HP. Surface oxides on carbon and their analysis: a critical assessment. Carbon 2002;40:145–9.
100. Kinoshita K, Beti JAS. Electrochemical oxidation of carbon black in concentrated phosphoric acid at 135 °C. Carbon 1972;11:237–41.
101. Lee K, Zhang J, Wang H, Wilkinson D. Progress in the synthesis of carbon nanotube- and nanofiber supported Pt electrocatalysts for PEM fuel cell catalysis. J Appl Electrochem 2006;36:507–22.
102. Wang X, Waje M, Yan YS. CNT-based electrodes with high efficiency for PEMFCs. Electrochem Solid-State Lett 2005;8:A42–4.
103. Li W, Liang CW, Zhou W, et al. Preparation and characterization of multiwalled carbon nanotube-supported platinum for cathode catalysts of direct methanol fuel cells. J Phys Chem B 2003;107:6292–9.
104. Zaragoza-Martin F, Sopena-Escario D, Morallon EC, Salinas-Martinez de Lecea C. Pt/carbon nanofibers electrocatalysts for fuel cells Effect of the support oxidizing treatment. J Power Sources 2007;171:302–9.
105. Zheng J, Wang M, Zhang X, Wu Y, Li P, Zhou X, et al. Platinum/carbon nanofiber nanocomposite synthesized by electrophoretic deposition as electrocatalyst for oxygen reduction. J Power Sources 2008;175(1):211–16.
106. US Department of Energy. Technical Plan – Fuel Cells. 2007. Available from http://www1.eere.energy.gov/hydrogenandfuelcells/mypp/pdfs/fuel_cells.pdf.

Acronyms and Abbreviations

AACVD	aerosol-assisted CVD
AADC	advanced automotive duty cycle
AAM	anodic alumina membrane
AAO	anodic aluminum oxide
AC	alternating current
acac	acetylacetonate
ACF	activated carbon fiber
ACL	anode catalyst layer
ADF	Amsterdam Density Functional
ADT	accelerated degradation test *or* accelerated durability test
AEMFC	anion exchange membrane fuel cell
AES	auger electron spectroscopy
AFC	alkaline fuel cell
AFM	atomic force microscopy
AIMD	*ab initio* molecular dynamics method
AO process	anthraquinone process
AST	accelerated stress test
BET	Brunnauer, Emmett, and Teller
BOL	beginning-of-life
CAS	Chemical Abstracts Service
CCDL	catalyst coated diffusion layer
CCL	cathode catalyst layer
CCM	catalyst coated membrane
CCS	catalyst coated substrate
CCVD	combustion chemical vapor deposition
CDM	catalyzed diffusion media
CE	counter electrode
CF$_3$PPCo	Co-trifluoromethylphenylporphyrin
CFD	computational fluid dynamics
CGMD	coarse-grained molecular dynamics
CG-MS	coarse-grained molecular simulation
CL	catalyst layer

CMPsf	chloromethylated polysulfone
CNF	carbon nanofiber
CNT	carbon nanotube
CNWS	carbon-Nafion-water-solvent
CoNPc	Co-naphthalocyanine
CoPPy	Co-polypyrrole
CoTAA	Co-tetraazaannulene
CoTMPyP	[tetrakis(N-methylpyridyl)porphyrinato]cobalt
CoTSP	Co(II) tetrasulfonatephthalocyanine
Co-WC	cobalt-cemented tungsten carbide
CPE	constant phase element
CRYO-FESEM	field emission scanning electron microscope with cryogenic stage and sample preparation unit
CV	cyclic voltammetry
CVD	chemical vapour deposition
DAFC	direct alcohol fuel cell
DC	direct current
DEFC	direct ethanol fuel cell
DEMS	differential electrochemical mass spectroscopy
DFAFC	direct formic acid fuel cell
DFT	density functional theory
DHDBTAA	dihydrodibenzotetraazaannulene
DHE	dynamic hydrogen electrode
DHP	dihexadecyl hydrogen phosphate
DLFC	direct liquid fuel cell
DMAc	dimethylacetic acid
DMF	N,N-dimethylformamide
DMFC	direct methanol fuel cell
DOE	United States Department of Energy
DOS	density of state
DSA	dimensionally stable anode
DSC	differential scanning calorimetry
DSS	daily start and stop
DTA	differential thermal analysis
DTG	derivative thermal gravimetry
EA	electron affinity
EAA	electrochemically active area
EAM	embedded atom method
EAS	electrochemically active surface
EASA *or* ECSA	electrochemical active surface area
EC	equivalent circuit
ECA	electrochemical area
ECC	electrochemical catalyzation
EC-NMR	electrochemical nuclear magnetic resonance
ED	electron diffraction
EDS	energy dispersive spectroscopy
EDX	energy dispersive X-ray analysis

EELS	electron energy loss spectroscopy
EG	ethylene glycol solution
EIS	electrochemical impedance spectroscopy
EMIS	electrochemically modulated infrared spectroscopy
EMS	electrochemical mass spectroscopy
EOL	end-of-life
EPD	electrophoretic deposition
EPMA	electron probe micro-analysis
EPSA	electrode Pt surface area
ESCA	electron spectroscopy for chemical analysis
EXAFS	extended X-ray absorption fine structure
FAM	flooded-agglomerate model
FC	fuel cell
FCCVD	floating catalyst CVD
f-CNF	fishbone or herringbone CNF
FCV	fuel cell vehicle
$Fe^{III}TPFPP$	5,10,15,20-Tetrakis (pentafluorophenyl)-21H,23H-porphine iron (III)
FEP	fluorinated ethylene propylene
FePPIX	Fe protoporphyrin IX
FESEM *or* FE-SEM	field emission scanning electron microscopy
FeTPP	Fe meso-tetraphenylporphine
FeTPyP	Fe meso-tetra(3-pyridyl)porphine
FF	flow field
FRA	frequency response analyzer
FTIR	Fourier transform infrared spectroscopy
FWHM	full width at half maximum
GC	glassy carbon
GCNF	graphitic carbon nanofibers
GDE	gas diffusion electrode
GDL	gas diffusion layer
GGA	generalized gradient approximation
GMPL	graded porosity micro-porous layer
HER	hydrogen evolution reaction
HEV	hydrogen evolution reaction
HHV	higher heating value
HOPG	highly ordered pyrolytic graphite
HOR	hydrogen oxidation reaction
HR-EDS	high-spatial-resolution energy dispersive spectroscopy
HR-TEM	high-resolution transmission electron microscope
HT-PEMFC	high-temperature PEM fuel cell
HWP	half-wave potential
IBAD	ion-beam assisted deposition
ICE	internal combustion engine
ICMEA	integrated composite membrane electrode assembly
ICP-MS	inductively coupled plasma mass spectrometry

ICV	isothermal constant voltage
IMI	intermittent microwave irradiation
IP	ionization potential
IRRAS	infrared reflection-absorption spectroscopy
LANL	Los Alamos National Laboratory
LDA	local density approximation
LDOS	local density of states
LHV	lower heating value
LJ	Lennard-Jones potential
LSV	lineal sweep voltammetry
LT-PEMFC	low-temperature PEM fuel cell
MBE	molecular beam epitaxial
MCFC	molten carbonate fuel cell
MD	molecular dynamic
MEA	membrane electrode assembly
MeTAA	metal dibenzo-tetra-aza-annulene
MeTMPP	metal tetramethoxy porphyrin
MeTPP	metal tetraphenyl porphyrin
MOR	methanol oxidation reaction
MPL	micro-porous layer
MPS	molecular precursor state
M-RDE	multi-rotating disk electrode
MS-CG	multi-scale coarse graining
MSE	mercury/mercurous sulfate reference electrode
M-SWCNT	metallic SWCNT
MWCNT	multiwalled carbon nanotube
MWNT	multi-wall nanotubes
Na(AOT)	sodium 2 bis (2-ethylhexyl)sulfosuccinate
NAAQS	US National Ambient Air Quality Standards
Nafion	a perfluorinated sulfonic acid ionomer manufactured by DuPont
N-CNT	nitrogen-containing CNT *or* nitrogen-doped CNT
NEXAFS	near-edge X-ray absorption fine structure spectroscopy
NHE	normal hydrogen electrode
NMR	nuclear magnetic resonance
NRC-IFCI	National Research Council of Canada Institute for Fuel Cell Innovation
NS	nanostructure
NSTF	nanostructured thin film
NW	nanowire
OCV	open circuit voltage
OMC	ordered mesoporous carbon
OPD	overpotential deposition
ORR	oxygen reduction reaction
PAFC	phosphoric acid fuel cell
PAN *or* pan	polyacrylonitrile
PAni	polyaniline
PA-PBI	phosphoric acid-doped polybenzimidazole

PBI	polybenzoimidazole
PCA	process control agent
PCFC	protonic ceramic fuel cell
PECVD	plasma-enhanced CVD
PEFC	polymer electrolyte fuel cell
PEG	polyethylene glycol
PEM	proton exchange membrane *or* polymer electrolyte membrane
PEMFC	polymer electrolyte membrane fuel cell *or* proton exchange membrane fuel cell
PFSA	perfluorosulfonate (*or* perfluorosulfonic) acid
PFSI	perfluorosulfonated ionomer *or* perfluorosulfonimide
PGM	platinum group metal
PIXE	proton-induced X-ray emission
PMoA	phosphomolybdic acid
PNP	Poisson-Nernst-Planck
POMC	phenanthrene ordered mesoporous carbon
ppm	parts per million
Ppy	polypyrrole
PR	perylene red
PROX	catalytic preferential oxidation
PRR	proton reduction reaction
PS	polystyrene spheres
PSD	pore size distribution
PTCDA	perylene tetracarboxylic dianhydride
PTFE	polytetrafluoroethylene
PVD	physical vapour deposition
PVDF	polyvinylidene fluoride
PZC	point of zero charge
RDE	rotating disk electrode
RDF	radial distribution function
rds	rate determining step
RE	reference electrode
REV	representative elementary volume element
REWO	REWOTERIC B14
RH	relative humidity
RHE	reversible hydrogen electrode
RRDE	rotating ring disk electrode
RSDT	reactive spray deposition technology/technique
RVC	reticulated vitreous carbon
RWGS	reverse water gas shift
RWGSR	reverse water gas shift reaction
SAED	selected area electron diffraction
SB12	surfactant 3-(*N,N*-dimethyldodecylammonio) propanesulfonate
SC	Sutton-Chen potential
SCE	saturated calomel reference electrode
SDEMS	scanning differential electrochemical mass spectrometry
SDF-F	sulfonated poly (fluorinated arylene ether)s

SECM	scanning electrochemical microscopy
SEI	secondary electron imaging
SEM	scanning electron microscope
SERS	surface-enhanced Raman spectroscopy
SHE	standard hydrogen reference electrode
SL	substrate layer
slpm	standard liter per minute
SMR	stream methane reforming
SOFC	solid oxide fuel cell
SOMC	sucrose ordered mesoporous carbon
SPC	single point charge
SPE	solid polymer electrolyte
SPEEK	sulfonated poly(ether ether ketone)
SSCE	saturated silver/silver chloride reference electrode
S-SWCNT	semiconducting SWCNT
STM	scanning tunnelling microscopy
SWCNT	singlewalled carbon nanotube
SWNH	singlewalled carbon nanohorn
SWNT	singlewall nanotubes
TAA	dibenzotetraazaannulene
TBA	tetrabutylammonium
TcPc	tetracarboxyphthalocyanine
TC-SG	tip collection-sample generation
TEM	transmission electron microscope
TFE	Tetrafluoroethylene
TF-RDE	thin-film rotating disk electrode
TG	thermogravimetry
TGA	thermogravimetric analysis
TG-MS	thermogravimetry-mass spectrometry
TG-SC	tip generation-sample collection
THF	tetrahydrofuran
TMA	trimethylamine
TMA	thermomechanical analysis
TMAOH	tetramethylammoniumhydroxide
TMEDA	tetramethylethylenediamine
TMMDA	tetramethylmethanediamine
TMPP	tetramethoxyphenylporphyrin
TOF-SIMS	time-of-flight secondary ion mass spectroscopy
TPD	temperature programmed desorption
TpOCH$_3$PPCo	Co-tetramethoxyphenylporphyrin
TPP	tetraphenylporphyrin
TPR	temperature programmed reduction
TS	transition state
TSP	tetrasulphophthalocyanine
TW	terawatt
UGF	uncompressed graphite felt
UHV	ultra-high vacuum

UME	ultramicroelectrode
UPD	underpotential deposition
UPS	uninterruptible power supply
UVPS	UV-induced photoelectron spectroscopy
USP	ultrasonic spray pyrolysis
UV-VIS	ultraviolet-visible
VLS	vapor-liquid-solid
VOC	volatile organic species
VRE	voltage reversal effect
VS	vapor-solid
WC	tungsten carbide
WGS	water-gas shift
XANES	X-ray absorption near edge structure
XAS	X-ray absorption spectroscopy
XPS	X-ray photoelectron spectroscopy
XRD	x-ray diffraction
XRE	X-ray emission
XRF	X-ray fluorescence
YSZ	yttria-stabilized zirconia
ZrP	zirconyl chloride and phosphoric acid

Contributor Biographies

Dr. Jiujun Zhang (General Editor) is a Senior Research Officer and PEM Catalysis Core Competency Leader at the National Research Council of Canada Institute for Fuel Cell Innovation (NRC-IFCI). Dr. Zhang received his B.S. and M.Sc. in Electrochemistry from Peking University in 1982 and 1985, respectively, under the supervision of Professors Wenzhi Yang and Shengmin Cai, and his Ph.D. in Electrochemistry from Wuhan University in 1988, under the supervision of Professors Quanxing Cha, Juntao Lu, and Zigang Feng. After completing his Ph.D., he took a position as an associate professor at the Huazhong Normal University for two years. Starting in 1990, he carried out three terms of postdoctoral research at the California Institute of Technology with Professor Fred C. Anson, York University with Professors A.B.P. Lever and William J. Pietro, and the University of British Columbia with Professor Colin Oloman. Dr. Zhang has over twenty-six years of R&D experience in theoretical and applied electrochemistry, including over twelve years of fuel cell R&D (among these six years at Ballard Power Systems and four years at NRC-IFCI), and three years of electrochemical sensor experience. Dr. Zhang holds seven adjunct professorships, including one at the University of Waterloo and one at the University of British Columbia, and supervises several M.Sc. and Ph.D. students. He also currently supervises over ten researchers. His research is based on: low/non-Pt cathode catalyst development with long-term stability for catalyst cost reduction; preparation of novel material-supported Pt catalysts through ultrasonic spray pyrolysis; catalyst layer/cathode structure; fundamental understanding through first principles theoretical modeling; catalyst layer characterization and electrochemical evaluation; and preparation of cost-effective MEAs for fuel cell testing and evaluation. Dr. Zhang has co-authored more than 140 research papers published in refereed journals and holds over ten U.S. patents. He has also produced in excess of seventy industrial technical reports. Dr. Zhang is an active member of The Electrochemical Society, the International Society of Electrochemistry, and the American Chemical Society.

Dr. Christina Bock is a Senior Research Officer at the National Research Council of Canada (NRC). She has more than fifteen years of experience in

electrochemistry for water remediation, energy storage, and energy production. Dr. Bock is currently leading the project "Catalysts for Energy Conversion and Energy Storage" at the NRC Institute for Chemical Processes and Environmental Technologies (ICPET). The project consists of several sub-projects that are a mixture of developmental research on the laboratory scale and work with fuel cell test units. Over the past years the project has largely focused on direct methanol and proton exchange membrane fuel cells, with an emphasis on catalysts and catalyst layer development. Over the years, she has collaborated with several Canadian companies and other national laboratories. She has expertise in controlled catalyst synthesis on the nanoscale (U.S. patent application pending). In 2005, Dr. Bock received the Lash Miller Award of the Canadian section of the Electrochemical Society for her work in catalyst synthesis and novel characterization approaches. She is also actively involved with The Electrochemical Society, currently as chair of the New Technology Sub-committee.

Dr. Michael Eikerling (NRC-IFCI/SFU) has been an Assistant Professor in the Department of Chemistry at Simon Fraser University since May 2003. He received his Diploma in Theoretical Condensed Matter Physics from RWTH Aachen University, Germany, in 1995 and his Ph.D. in Theoretical Chemical Physics from the Technische Universität (TU) München in Germany in 1999. Thereafter, he spent periods as a research associate at the Research Centre Jülich in Germany, the Los Alamos National Laboratory, and TU München. He is an expert in physical theory and modelling of materials for fuel cells, with more than ten years of experience in this field. His position involves a 50% secondment to the National Research Council of Canada Institute for Fuel Cell Innovation. This shared appointment provides excellent conditions for combining fundamental research on the structure and properties of proton conducting media and complex electrodes, with applied research on the operation and optimization of fuel cells. Major themes of Dr. Eikerling's research explore: (i) structural and dynamic properties of proton-conducting materials for fuel cells – using molecular-scale computer simulations and analytical theory to establish relations between chemical structure, mesoscopic morphology, transport of protons and water, and fuel cell performance; (ii) kinetic processes in nanoparticle electrocatalysis – developing simulation tools (Monte-Carlo and molecular dynamics) and analytical theories to understand the effects of catalyst particle size and surface structures on electrocatalytic activity, and the role of the substrate material; and (iii) catalyst layer modelling – understanding relations between random heterogeneous structures, water balance, and fuel cell performance. This research contributes to the fundamental understanding of structure-property relationships, the diagnostics of materials properties and fuel cell operation, and the identification of routes towards advanced structural design of proton conductors and electrodes.

Dr. Előd Gyenge is an Associate Professor in the Department of Chemical and Biological Engineering at the University of British Columbia, Vancouver, Canada. In 2007 he was awarded the inaugural Elisabeth and Leslie Gould Professorship. Dr. Gyenge received his M.Eng. in Chemical Engineering/Industrial Organic

Chemistry from University Babes-Bolyai, Cluj-Napoca, Romania in 1990, with a thesis in the area of organic electrosynthesis, under the supervision of Professor Liviu Oniciu. In 1995 and 2001, respectively, Dr. Gyenge received his M.A.Sc. and Ph.D. degrees in Chemical Engineering (specializing in Electrochemical Engineering) from the University of British Columbia. His Ph.D. thesis dealt with novel interfacial methods of oxygen electroreduction enhancement for hydrogen peroxide electrosynthesis, and was conducted under the supervision of Professor Colin Oloman. After completing his Ph.D., he worked in industrial R&D as a Senior Consultant for Electrochemical Processes at BC Research Inc. (presently incorporated in Cantest Ltd.). In this capacity Dr. Gyenge was instrumental in developing patented technologies in the area of lead-acid batteries, metal-air fuel cells, and zinc electrowinning. As a professor at the University of British Columbia, he conducts a dynamic group of graduate students and postdoctoral fellows, carrying out research in the area of electrocatalysis, interfacial phenomena, and electrochemical engineering, with emphases on electrochemical power sources (direct methanol, ethanol, formic acid, and borohydride fuel cells) and electrosynthesis. These activities have been reported in many refereed journal publications, conference proceedings, and invention disclosures. In addition to research, Dr. Gyenge teaches both senior undergraduate and graduate-level courses on fuel cells and electrochemical engineering. He is a member of the Electrochemical Society, the International Society of Electrochemistry, the American Chemical Society, and the Canadian Society of Chemical Engineering, a joint member of the American Institute of Chemical Engineering, and a foreign member-at-large of the General Assembly of the Hungarian Academy of Sciences. Dr. Gyenge dedicates the Chapter "Electrocatalytic Oxidation of Methanol, Ethanol, and Formic Acid" to the memory of Prof. Dr. Doc. Liviu Oniciu (University Babes-Bolyai, Cluj-Napoca, Romania), who introduced him to electrochemistry and encouraged him from early on to pursue research in this field.

Helga Halvorsen is a Ph.D. candidate at the University of Ottawa, Canada. Under the supervision of Dr. Barry MacDougall, her thesis work focuses on the development of Pt nanocatalyst systems. Helga received her M.Sc. from the University of Western Ontario while studying coupled diffusion in surfactant solutions. She is the recipient of an Ontario Graduate Student Scholarship, in addition to several local awards for academic and research excellence.

Dr. Shiqiang (Rob) Hui is a Senior Research Officer and Acting Group Leader for High-Temperature Fuel Cells at the National Research Council of Canada Institute for Fuel Cell Innovation. He is an adjunct professor at the University of British Columbia, Canada and at three other major universities in China. Dr. Hui received his Ph.D. in Materials Science and Engineering at McMaster University in 2000. He has conducted research and development for materials, processing, and characterization for more than twenty years. Dr. Hui has worked on various projects, including chemical sensors, solid oxide fuel cells, magnetic materials, gas separation membranes, nanostructured materials, thin film fabrication, and protective coatings for metals. He has led or been involved in over thirty national and international projects funded by government or industry in China, the USA,

and Canada. Dr. Hui is an active member of The Electrochemical Society and has more than eighty research publications.

Dr. Kunchan Lee is a Research Associate at the National Research Council of Canada Institute for Fuel Cell Innovation (NRC-IFCI). Dr. Lee received his B.S. and M.Sc. from Pukyung National University in 1997 and 1999, respectively, and his Ph.D. in Materials Science and Engineering from Yokohama National University in 2004 under the supervision of Professor Ken-ichiro Ota. After completing his Ph.D., he carried out postdoctoral research at Yokohama National University as a researcher for Japan Science and Technology Agency (JST) with Professor Ken-ichiro Ota, and then at NRC-IFCI as a postdoctoral fellow of the Natural Sciences and Engineering Research Council of Canada (NSERC) with Dr. Jiujun Zhang. He has over seven years of research and development experience in material science and electrochemistry, including electrocatalysts and polymer membranes for PEM fuel cells. Currently, he has been conducting research on the development and evaluation of new non-noble electrocatalysts such as carbides, nitrides, chalcogenides, and macrocycles for PEM fuel cells. Dr. Lee has co-authored more than twenty refereed research papers and holds one Japan patent.

Dr. Baitao Li received her Ph.D. in Applied Chemistry from the University of Tokyo, Japan in 2003, under the supervision of Professor Fujimoto Kaoru; her dissertation focused on the synthesis of oxygenates from middle olefin in heterogeneous systems. In the same year, she commenced post-doctoral work in the laboratory of Dr. Tomishige Keiichi at the University of Tsukuba, Japan, where she worked on syngas production from methane reformation. She currently is at the Department of Chemistry and Chemical Engineering, South China University of Technology, in Guangzhou, China. She has published many papers in the Journal of Catalysis, Catalysis Today, Applied Catalysis, etc. Her research interests lie in synthesis and applications of catalytic materials, and the evaluation of catalytic reaction mechanisms by computational chemistry.

Dr. Hui Li is a Research Associate and PEMFC Contamination Consortium project leader at the National Research Council of Canada Institute for Fuel Cell Innovation (NRC-IFCI). Dr. Li received her B.S. and M.Sc. in Chemical Engineering from Tsinghu University in 1987 and 1990, respectively, under the supervision of Professor Jingshan Tong. After completing her M.Sc., she joined Kunming Metallurgical Institute as a research engineer for four years and then took a position as an associate professor at Sunwen University (then a branch of Zhongshan University) for eight years. In 2002, she started her Ph.D. program in Electrochemical Engineering at the University of British Columbia under the supervision of Professor Colin Oloman. After obtaining her Ph.D. in 2006, she carried out one term of postdoctoral research at the Clean Energy Research Centre (CERC) at the University of British Columbia with Professor Colin Oloman and Professor David Wilkinson. In 2007, she joined the Low-temperature PEMFC Group at NRC-IFCI, under the supervision of Dr. Jiujun Zhang. Dr. Li has years of research and development experience in theoretical and applied electrochemistry and in electrochemical engineering. Her research is based on PEMFC

contamination testing and contamination mitigation; preparation and development of electrochemical catalysts with long-term stability; catalyst layer/cathode structure; and catalyst layer characterization and electrochemical evaluation. Dr. Li has co-authored more than fifteen research papers published in refereed journals and has one technology licensed to the Mantra Energy Group. She has also produced many industrial technical reports.

Dr. Jing Li is a senior R&D materials scientist in Automotive Fuel Cell Cooperation (AFCC). Dr. Jing Li received his Ph.D. in Physical Chemistry of Metallurgy and Materials at the Central South University of Technology, China. He held the positions of assistant professor and professor at the Institute of Physical Chemistry of Metallurgy and Materials (IPMM), Central South University of Technology, China from 1988 to 1994. In 1991–1992 and 1995–1996 Dr. Li worked as a visiting scientist in the Department of Applied Chemistry, University of Tokyo, Japan, and from 1996–1999, he worked as a Senior Research Associate in the Department of Electrical and Computer Engineering, and the Department of Chemistry, University of Toronto. He moved from academy to industry in 1999 when he joined JDS Uniphase as a senior material scientist, and then worked at Ballard Power Systems as as a senior material scientist from 2003 to 2008. As a material scientist for over 20 years, Dr. Li has been working on nanostructured materials, polymer physics and chemistry, fuel cell catalyst and carbon materials, metals, and fiber optical materials. He has published more than fifty research papers in refereed journals and holds over seven patents in China, Japan, and the USA. He is an active member of The Electrochemical Society.

Dr. Yingwei Li is Professor of Physical Chemistry at the South China University of Technology, China. He received his B.S. (1998) and Ph.D. (2003) in Physical Chemistry from Tsinghua University, China. His Ph.D. work, on catalytic synthesis of iso-C_4 hydrocarbons from CO hydrogenation, was carried out under the supervision of Professors Shaoyi Peng, Qiming Zhu, and Dehua He. From 2003 to 2004 he was a postdoctoral fellow at the University of Calgary, Canada, working with Professor Peter D. Clark on oxidative dehydrogenation of C_2-C_5 alkanes. He returned to China in 2004 as a Research Fellow at Tsinghua University, where he worked with Professor Dehua He on hydrogen production from steam reforming of methanol. From 2005 to 2007 he was a postdoctoral fellow at the University of Michigan, USA, working with Professor Ralph T. Yang on hydrogen storage by spillover and the desulfurization of liquid fuels by adsorption. His research interests focus on hydrogen energy and catalysis chemistry, with particular recent interests being the production of hydrogen from alcohols and biomass, hydrogen storage on nanostructures, and fuel cell catalysts. He is the first author of over twenty peer-reviewed publications, and holds four patents, including two US patents.

Dr. Shijun Liao is a Professor at South China University of Technology. He received his B.S. and M.Sc. in Physical Chemistry from Huazhong Normal University in 1982 and from Jilin University in 1988, respectively, and his Ph.D. in Industrial Catalysis from South China University of Technology in 1999, under the

supervision of Professor Wang Lefu. After completing his Ph.D., Dr. Liao worked as a postdoctoral fellow from 2000 to 2001 in Professor Linkov's group at the University of the Western Cape in South Africa, and in 2005, he worked in Professor Viola Birss's group at the University of Calgary, Canada as a visiting scientist. He has worked in universities for twenty-six years, and has been engaged in fuel cell and fuel cell catalysis research since 2000. Dr. Liao supervises more than twenty M.Sc. and Ph.D. students, as well as six researchers. His research is focused on preparation of novel anode and cathode catalysts, novel preparation methods for high-performance Pt-based and Pd-based catalysts, preparation of membrane electrode assemblies, and development of large power stacks for power station and vehicle applications. His main research achievements include a high-pressure colloidal method for preparation of high-performance catalysts, and a novel catalyst-coated membrane technique for preparation of high-performance MEAs. Dr. Liao has co-authored more than 130 research papers published in refereed journals and holds over ten China patents. One of his research achievements has received an award from the China Education Ministry for its successful application in industry. Dr. Liao is an active member of the Catalysis Society of China, the Associate Editor of the Journal of Nanomaterials, and a board member of several Chinese journals.

Dr. Hansan Liu is a Research Associate at the National Research Council of Canada Institute for Fuel Cell Innovation. He obtained his Ph.D. in the electrochemistry research group at Xiamen University, China, and has over ten years of research experience in the field of electrochemical energy conversion and storage devices, including Ni-MH batteries, lithium ion batteries, solar energy devices, supercapacitors, DMFCs, and PEMFCs. His research interests include fuel cell electrocatalysis, electrode materials of rechargeable batteries and capacitors, photoelectrocatalysis, and aerosol techniques for nanomaterial synthesis. Dr. Liu has authored or co-authored three book chapters, three patents (two pending), over thirty peer-reviewed journal papers, and eight industrial technical reports. Dr. Liu is a member of The Electrochemical Society as well as the International Society of Electrochemistry.

Dr. Kourosh Malek received his M.Sc. in Physical (Electro)Chemistry in 1997 from Sharif University of Technology, Iran. After commencing his Ph.D. in 1997, he moved to the Netherlands to continue his doctoral research work in the Department of Chemical Engineering at Delft University of Technology (TU Delft). He received his Ph.D. with honours in 2001, in physical chemistry emphasizing electrochemistry and catalysis. From 2001–2004 he was a postdoctoral research fellow in the Department of Chemical Engineering, TU Delft, working on the modelling of transport in heterogeneous porous media, and carried out several projects in the field of computational molecular catalysis and transport in porous media. This was followed by a research (*onderzoeker*) appointment at Schuit Institute of Catalysis, Eindhoven, Netherlands, working on molecular heterogeneous catalysis and the computational study of catalytic reactions, prior to joining the National Research Council of Canada Institute for Fuel Cell Innovation (NRC-IFCI) as a Research Officer in May 2006. Dr. Malek is

proficient in using multi-scale computer simulations for applications in heterogeneous catalysis and fuel cells. He also has a solid background in electrochemistry and molecular heterogeneous catalysis. Most of his research interests relate to the central theme of modeling and simulation of diffusion and reaction phenomena from the micro-scale (atomic) up to the macro-scale. His current research area includes self-organization phenomena in PEM fuel cells, modeling of diffusion and reaction in nanoporous (electro)catalysts and membranes, dynamic properties of heterogeneous nanoporous materials, and meso-scale simulations of diffusion and reaction processes in nanoporous catalysts with rough internal surfaces.

Dr. Zhigang Qi, currently a corporate Fellow at MTI Micro Fuel Cells Inc., is an electro/analytical chemist and materials scientist. Dr. Qi has diverse technical and managerial training. He received his B.Sc. and M.Sc. from the University of Science and Technology Beijing in 1985 and 1988, respectively. After teaching there for about two and a half years, he went to Canada and received a second M.Sc. from Memorial University of Newfoundland in 1993, and a Ph.D. from McGill University in 1996. He then worked with Professor Peter Pickup at Memorial University as a postdoctoral fellow for one and a half years. In 1997, Dr. Qi joined H Power Corp. as a Senior Staff Scientist and the Supervisor of the Electrochemistry Lab. In 2003, he moved to Plug Power Inc. as the Manager of the Analytical and Fundamentals group and was promoted to Corporate Fellow in late 2004. Dr. Qi joined MTI Micro Fuel Cells in November 2007. In the last twelve years, Dr. Qi has focused on improving the performance and durability of proton exchange membrane fuel cells, direct methanol fuel cells, and phosphoric acid fuel cells at both component and system levels. He has made a number of significant contributions to advancing these technologies, and some of his work has created new research directions. He has fifty-seven articles in peer-reviewed journals, six invited book chapters, twelve publications in proceedings volumes, and holds eight US patents, eight pending US patent applications, and numerous invention disclosures. Dr. Qi has been elected as an Editorial Board Member of the Journal of Power Sources since 2006. He also teaches "Fuel Cell Technology" as an adjunct professor at the Graduate College of Union University. He is a member of The Electrochemistry Society and the American Chemical Society.

Dr. Madhu Sudan Saha is a Research Associate with Professor Brant A. Peppley at Queen's-RMC Fuel Cell Research Centre, Canada. Dr. Saha received his B.Sc. and M.Sc. in Chemistry from Dhaka University in 1993 and 1995, respectively, under the supervision of Professor Rowshan J. Mannan, and his D.Sc. in Electrochemistry from Tokyo Institute of Technology in 2001 under the supervision of Professor Takeo Ohsaka. The same year he took a position as a Research Scientist at Permelec Electrode Ltd., Japan, where he was responsible for developing high-performance MEAs for PEM fuel cells and for the electrochemical synthesis of biologically important organics. In 2004, he came to Northeastern University, USA, as a Research Scientist to work with Professor Sanjeev Mukerjee, investigating methanol crossover and cell performance in DMFCs, and developing ultra-low Pt-loading electrodes for PEMFC applications.

Dr. Saha also worked as a Research Associate with Professor Xueliang Sun at the University of Western Ontario, Canada. Dr. Saha has over seven years of R&D experience in theoretical and applied electrochemistry, including over two years of fuel cell R&D. He has co-authored more than twenty-five research papers published in refereed journals and holds over ten patents. He has also produced in excess of twenty industrial technical reports. Dr. Saha is an active member of The Electrochemical Society and the American Chemical Society. He was awarded the Monbukagakusho Fellowship from the Ministry of Education, Culture, Sports, Science and Technology, Japan (1998–2001). His research focuses on nanostructured materials, including nanotubes and nanowires synthesis, and electrochemical characterization and applications as alternative electrode supports for PEM fuel cells.

Dr. Pei Kang Shen is a Professor and Director of the Advanced Energy Materials Research Laboratory (AEMRL) at the Sun Yat-Sen University in China. Dr. Shen received his B.S. in Electrochemistry from Xiamen University in 1982. He spent seven years in Xiamen University as Assistant Lecturer before going to Essex University as a Senior Visiting Scientist in 1989. Dr. Shen received his Ph.D. in Chemistry from Essex University in 1992 under the supervision of Professor Alfred C. C. Tseung. He has continued to carry out research on fuel cells and functional materials since 1992 at Essex University, Hong Kong University, and the City University of Hong Kong. Dr. Shen moved to Sun Yat-Sen University in 2001. He is currently leading a highly interdisciplinary team of over twenty research members, including postdoctoral, doctoral, and masters students. For more than twenty years, Dr. Shen has been involved in research areas covering fuel cells and batteries, the electrochemistry of nanomaterials, nanocomposite functional materials, and high-performance polymer materials. Dr. Shen has co-authored more than 150 journal papers and holds over ten patents. He is an active member of The Electrochemical Society, the International Society of Electrochemistry, and the American Chemical Society.

Dr. Zheng Shi obtained her Ph.D. in Physical Chemistry from Dalhousie University in 1990. Dr. Shi has over fifteen years of theoretical modeling experience in the fields of electronic structure, reaction mechanisms, drug development, catalysis development, and structure activity relationships. She has worked at several pharmaceutical companies as well as universities, including Simon Fraser University and the University of British Columbia, prior to joining the National Research Council of Canada Institute for Fuel Cell Innovation. Currently, Dr. Shi is working in the area of fuel cell catalysis development and catalyst contamination studies. Dr. Shi's research focuses on the fundamental understanding of electrocatalysis reaction mechanisms, and the development of structure activity relationships and fuel cell contamination kinetic models.

Dr. Chaojie Song is a Research Officer at the National Research Council of Canada Institute for Fuel Cell Innovation (NRC-IFCI). He received his B.Sc. in Chemistry from Lanzhou University (1984), and his M.Sc. in Electrochemistry from Hebei Normal University (1989) under the supervision of Professors Wenzhi

Zhang and Xizun Wu. He received his Ph.D. in Inorganic/Analytical Chemistry from the University of New Brunswick (1997–2001) under the supervision of Professor Gilles Villemure, working on layered silicate clays, mesoporous molecular sieve silicas, and the use of these nanostructured materials in modified electrodes. He then conducted postdoctoral work under the supervision of Professor Kurt R. Hebert and Professor Surya K. Mallapragada at Iowa State University (April–December 2001). In 2002, he joined Professor Peter G. Pickup's group at Memorial University of Newfoundland as a postdoctoral fellow, and then as a research associate in December 2003, working on fuel cell catalyst development. He joined the NRC-IFCI in 2004 as a NSERC (Natural Sciences and Engineering Research Council) postdoctoral fellow, a research associate, and then a research officer under the supervision of Dr. Jiujun Zhang, working on high-temperature PEM fuel cells and fuel cell catalyst development. Dr. Song has over seventy research publications, including journal papers, conference presentations, and industrial technical reports. Dr. Song is an active member of The Electrochemical Society.

Professor Xueliang (Andy) Sun is a Canada Research Chair in the development of nanomaterials for fuel cells, and Associate Professor at the University of Western Ontario, Canada. Dr. Sun received his Ph.D. in Materials Chemistry in 1999 at the University of Manchester, UK, followed by work as a postdoctoral fellow at the University of British Columbia, Canada and as Research Associate at l'Institut national de la recherche scientifique (INRS), Canada. He has extensive experience in materials and in surface science more generally. In recent years, Dr. Sun has established a remarkable track record in nanoscience and nanotechnology for clean energy, mainly in the areas of synthesis and structure control of one-dimensional nanomaterials such as carbon nanotubes and nanowires, as well as their applications for fuel cells. He has published over thirty papers in peer-reviewed journals and one book chapter. He has also authored or co-authored seven patents for the synthesis of carbon nanotubes and nanowires as well as their application as fuel cell electrodes. At the University of Western Ontario, Dr. Sun is currently supervising over ten researchers, including research associates, postdoctoral fellows, and graduate students. Dr. Sun and his group have been developing various methods such as chemical vapor deposition, solution-based, and template methods to fabricate carbon nanotubes, nanowires, and nanoparticles as fuel cell electrodes. Dr. Sun has established extensive collaborations with General Motors (GM), Ballard Power Systems, the Canadian Department of National Defence (DND), INCO Ltd., and the Canadian Space Agency (CSA) to work on nanomaterials and fuel cells. Dr. Sun is an active member of The Electrochemical Society and the Materials Research Society.

Dr. Haijiang Wang is a senior research officer, project manager of multi-projects, and core competency leader of the Unit Fuel Cell Team at the National Research Council of Canada Institute for Fuel Cell Innovation (NRC-IFCI). He is leading a team of over ten researchers to carry out research and development on novel fuel cell design, novel fuel cell materials, fuel cell diagnosis, and durability. Dr. Wang received his Ph.D. in Electrochemistry from the University of Copenhagen,

Denmark in 1993. He then joined Dr. Vernon Parker's research group at Utah State University as a postdoctoral researcher to study electrochemically generated anion and cation radicals. In 1997 he began working with Natural Resources Canada as a research scientist to conduct research on fuel cell technology. In 1999 he joined Ballard Power Systems as a senior research scientist to continue his research on fuel cell technology. After spending five years with Ballard Power Systems, he joined NRC-IFCI in 2004. He is currently adjunct professor at five universities, including the University of British Columbia and the University of Waterloo. To date, Dr. Wang has accumulated twenty-five years of professional research experience in electrochemistry and fuel cell technology. He has published over fifty journal papers, forty industrial reports, given more than thirty conference papers or presentations, and holds three patents.

Dr. Qianpu Wang received his Diploma in Metallurgy Engineering from the Central South University, China in 1986 and his Ph.D. in Multiphase Flow from the Norwegian University of Science and Technology, Norway in 2001. He then joined the National Research Council of Canada Institute for Fuel Cell Innovation (NRC-IFCI) as a post-doctoral fellow until 2004. Thereafter he has been a research officer at NRC-IFCI. His research interests include fundamental understanding of mass transport limitations, catalyst utilization in catalyst layers, and fuel cell/stack modeling and optimization.

Dr. Xiaoli Wang is an engineer in the Fuel Cell Vehicle Division of the Shanghai Automotive Industry Corporation of China (SAIC). She received her B.S. in Chemical Engineering from Dalian University of Technology in 2001. Dr. Wang then went on to study at the Dalian Institute of Chemical Physics, Chinese Academy of Sciences (CAS-DICP), where she received her Ph.D. in Chemical Engineering in 2006 under the supervision of Professor Huamin Zhang. Dr. Wang has over five years of experience in the research and development of proton exchange membrane fuel cells. Her research involves electrode design, catalyst layer/MEA characterization, and catalyst synthesis and electrochemical evaluation. She currently focuses on research for fuel cell engine systems, and is participating in a development project on fuel cell cars that will feature in the 2010 World Exposition in Shanghai. Dr. Wang has co-authored eleven research papers published in refereed journals, and holds five China patents.

Dr. Wei Xing is professor and leader of the Chemical Power Research Section at the Changchun Institute of Applied Chemistry (CIAC), Chinese Academy of Sciences. Dr. Xing received his B.S. in Chemical Engineering from Zhejiang University in 1987 under the supervision of Professor Qingyang Shen, and his Ph.D. in Physical Chemistry from CIAC in 1995 under the supervision of Professors Shiquan Xi and Tianhong Lu. After completing his Ph.D., he worked as a researcher at the Hong Kong Productivity Council for three years. From 1999 to 2001, he worked as an associate professor at CIAC, and from 2001 to the present, he has worked as a professor and section leader at CIAC. His research interests are focused on fundamental understanding of the electrochemical system of PEM fuel cells (PEMFCs), including direct methanol fuel cells (DMFCs), as well as

materials (catalysts and membranes) and integrated technologies of PEMFCs and DMFCs. Dr. Xing has over twenty years of R&D experience in theoretical and applied electrochemistry, including over ten years of fuel cell R&D. He has co-authored more than 100 research papers published in refereed journals and holds over twenty China and US patents. He has completed and directed many national scientific projects, such as the National High Techniques Program "Direct Alcohol Fuel Cell", and the Key Nature Science Foundation "Fundamental Research on Direct Alcohol Fuel Cell", amongst others. Dr. Xing is a syndic of the Chinese Chemical Society, a fellow of the Chinese Society of Electrochemistry, and a member of the Academic Committee of the CIAC. He is also a member of the International Society of Electrochemistry and of the American Chemical Society.

Dr. Siyu Ye received his B.Sc. in 1982 and his Ph.D. (under the supervision of Professors Zhaowu Tian and Renyuan Qian) in 1988, both from Xiamen University. He was a Volkswagen Foundation Postdoctoral Fellow (award accompanied by research funding) at the University Duisburg-Essen, Germany (1988–1991) and Postdoctoral Fellow at the University of Québec at Montréal, Canada (1991–1993). From 1994 to 2000, he was a senior research scientist at the Hydro-Québec Research Institute, Canada. In 2000, Dr. Ye joined Ballard Power Systems as a senior research scientist. He was promoted to principal research scientist in 2002. He is also an Adjunct Professor at the University of British Columbia, Canada. Dr. Ye is recognized as a leading world expert in electrocatalysis and electrocatalyst development for fuel cells. He has been instrumental in developing Ballard's high-performance, durable anode and cathode catalyst technology. Presently, Dr. Ye is leading Ballard's next-generation catalyst technology development, including catalyst layer design and processing. He has more than ten years of fuel cell experience, with expertise in catalyst materials, electrodes, and MEA design. He also has over sixty peer-reviewed papers, as well as many patents and patent applications. Dr Ye is co-author of the book *Optical Methods in Electrochemistry*, published by Science Press (Beijing) in 1990, and has been an invited speaker at many professional conferences.

Dr. Xiao-Zi Yuan is a Research Officer in the Unit Cell Team at the National Research Council of Canada Institute for Fuel Cell Innovation (NRC-IFCI). Dr. Yuan received her B.S. and M.Sc. in Electrochemical Engineering from Nanjing University of Technology in 1991 and 1994, respectively, under the supervision of Professor Baoming Wei, and her Ph.D. in Material Science from Shanghai Jiaotong University in 2003, under the supervision of Professor Zifeng Ma. After completing her M.Sc., she held a lecturer position at Nantong University for six years, and after completing her Ph.D. was an associate professor there for one year. Beginning in 2005, she held a three-year postdoctoral research position at NRC-IFCI with Dr. Haijiang Wang. Dr. Yuan has over fourteen years of R&D experience in applied electrochemistry, including over eight years of fuel cell R&D (among these three years at Shanghai Jiaotong University, one year at Fachhochschule Mannheim, and four years at NRC-IFCI). Currently her research focuses on the areas of PEMFC design, testing, and diagnosis, and the study of PEMFC durability. Dr. Yuan has published more than twenty research papers in

refereed journals and holds five China patents. She has also produced over ten technical reports.

Professor Huamin Zhang is the PEMFC key materials and technology group leader as well as the director of the DICP-SAMSUNG Fuel Cell Joint Lab and of the DICP-BORONG Redox Flow Storage Battery Joint Lab at Dalian Institute of Chemical Physics, Chinese Academy of Sciences (CAS-DICP). Professor Zhang received his B.S. from Shandong University in 1982, and his M.Sc. and Ph.D. from Kyushu University in Japan in 1985 and 1988, respectively, under the supervision of Professor Noboru Yamazoe. After completing his Ph.D., Professor Zhang worked in Japan on projects in function materials, catalytic materials, solid oxide materials, and fuel cells. As a professor and the director of the Fuel Cell Center at DICP since 2000, he has been in charge of: the "Fuel Cell Engine" project of the national "863" high-technology project "Fuel Cell Vehicle", supported by the National Ministry of Science and Technology; the Knowledge Innovation Program "Large Power Proton Exchange Membrane Fuel Cell Engine and Hydrogen Source", supported by the Chinese Academy of Sciences; the international cooperation project "Key Technology of Fuel Cells", supported by the National Ministry of Science and Technology; and the Orientated Project of the Knowledge Innovation Program "Fluoride Ionomer for PEMFC", supported by the Chinese Academy of Sciences. Presently, he is the scientist responsible for the national "863" high-technology project "Research on Testing the Key Materials, Components, and Environmental Adaptability of Fuel Cells". Under his leadership Professor Zhang's team successfully developed a 30 kW fuel cell engine and a 100 kW fuel cell engine for China's first fuel cell mini-bus and first fuel cell bus, respectively. Professor Zhang's current research interests are in low-Pt and non-noble metal electrocatalysts, self-humidified membranes, advanced MEA fabrication and process technologies for PEMFCs, and vanadium redox flow batteries. Professor Zhang has co-authored more than 150 research papers published in refereed journals.

Dr. Jianlu Zhang is a Research Associate at the National Research Council of Canada Institute for Fuel Cell Innovation (NRC-IFCI). Dr. Zhang received his B.S. in Chemistry from Liaocheng University in 1998, his M.Sc. in Applied Chemistry from Dalian University of Technology in 2001 under the supervision of Professors Xianyun Su and Tianxi Cai, and his Ph.D. in Physical Chemistry from Dalian Institute of Chemical Physics, Chinese Academy of Sciences (CAS-DICP) in 2005, under the supervision of Professor Huamin Zhang. He carried out his postdoctoral research at NRC-IFCI as an NSERC (Natural Sciences and Engineering Research Council) postdoctoral fellow for two years under the supervision of Dr. Jiujun Zhang. Dr. Zhang has over seven years of experience in the research and development of proton exchange membrane fuel cells (PEMFCs) as well as two years of experience in industrial catalyst research and development. Currently, his research focuses on PEMFCs, including fuel cell design, testing and diagnosis, catalyst layer/MEA characterization and electrochemical evaluation, contamination study, and fundamental understanding of high-temperature ($> 90^{o}$C) PEM fuel cells

(HT-PEMFCs). Dr. Zhang has co-authored twenty-six research papers published in refereed journals and holds five China and Korea patents.

Ms. Lei Zhang received her BE in Materials Science and Engineering from Wuhan University of Technology in 1990, her first M.Sc. majoring in Inorganic Chemistry from Wuhan University in 1993, and her second M.Sc. in Materials Chemistry from Simon Fraser University in 2000. After completing her first M.Sc., she took a position as a materials engineer at Lorrex Health Product Co. for five years, where she led various projects managing the R&D and manufacturing of health-related electronic products. From 2002 to 2004, Ms. Zhang worked as a research scientist and a key technical resource for Molecular Membrane Technologies on molecular sieve membrane development. Ms. Zhang has over ten years of R&D experience in nanomaterials, ceramics, membranes, and catalysts, including over three years of fuel cell R&D. At present, Ms. Zhang is a Research Council Officer and PEM Catalysis Core Competency Project Technical Leader working at the National Research Council of Canada Institute for Fuel Cell Innovation (NRC-IFCI). Her research is based on low/non-Pt cathode catalyst development with long-term stability for catalyst cost reduction; preparation of low/non-Pt catalysts; catalyst layer/cathode structure; catalyst layer characterization and electrochemical evaluation; and preparation of cost-effective MEAs for fuel cell testing and evaluation. Ms. Zhang has co-authored more than twenty research papers published in refereed journals and holds three US patents. She has also produced in excess of twenty industrial technical reports.

Author Index

Subject Index